Progress on Safety of

Structures in Fire

结构火灾安全进展

Proceedings of the 8th International Conference on Structures in Fire

第八届结构火灾安全国际会议论文集

June 11-13, 2014, Shanghai, China

Volume I

Edited by
Guo-Qiang LI Venkatesh K. R. KODUR
Shou-Chao JIANG Jian JIANG
Su-Wen CHEN Guo-Biao LOU

同济大学出版社
TONGJI UNIVERSITY PRESS

图书在版编目(CIP)数据

结构火灾安全进展: 第八届结构火灾安全国际会议论文集 = Structures in fire:proceedings of the eighth international conference: 英文 / 李国强等主编. -- 上海: 同济大学出版社, 2014.6
ISBN 978-7-5608-5494-6

Ⅰ. ①结… Ⅱ. ①李… Ⅲ. ①防火－建筑结构－结构设计－国际学术会议－文集－英文 Ⅳ. ①TU352.5-53

中国版本图书馆 CIP 数据核字(2014)第 088466 号

结构火灾安全进展——第八届结构火灾安全国际会议论文集

Structures in Fire—Proceedings of the 8th International Conference on Structures in Fire

李国强　Venkatesh K. R. KODUR　**蒋首超**　**等**　**主编**

责任编辑　季　慧　　特约编辑　何亚楣　　责任校对　徐春莲　　封面设计　陈益平

出版发行　同济大学出版社　　www.tongjipress.com.cn
(地址：上海市四平路 1239 号　邮编: 200092　电话:021-65985622)
经　　销　全国各地新华书店
印　　刷　同济大学印刷厂
开　　本　787mm×1 092mm　1/16
印　　张　84.5　　(上、下册)
字　　数　1 690 000　　(上、下册)
版　　次　2014 年 6 月第 1 版　　2014 年 6 月第 1 次印刷
书　　号　ISBN-978-7-5608-5494-6

定　　价　1 000.00 元　(上、下册)

ACKNOWLEDGEMENT

The conference organizers would like to thank the following sponsors for their much appreciated support to the Conference.

State Key Laboratory of Disaster Reduction in Civil Engineering

Department of Building Engineering, Tongji University

AkzoNobel Protective Coatings China

Tongji Architectural Design (TJAD) (Group) Co., Ltd

SCIENTIFIC COMMITTEE

Chairman

Venkatesh Kodur, Michigan State University, USA

Track 1: Applications of Structural Fire Safety Engineering

Bin Zhao (Leader)	**CTICM, France**
Daniel Joyeux	Efectis France, France
Florian Block	Buro Happold, UK
Olivier Vassart	Arcelor Mittal, Luxembourg
Susan Lamont	Arup, UAE
Ralph Hamerlinck	BOUWEN MET STAAL, Netherlands
Zhaopeng Ni	Tianjin Fire Research Institute, China
Jiann Yang	NIST, USA

Track 2: Concrete structures and any other topics

Kang Hai Tan (Leader)	**Nanyang Technological University, Singapore**
Pietro Gambarova	Politech. Milan , Italy
Faris Ali	University of Ulster , UK
Bo Wu	South China University of Technology, China
Mark Green	Queen's University, Canada
Luke Bisby	University of Edinburgh, UK
Pradeep Bhargava	IIT Roorkee, India
Tony Abu	UC Canterbury, New Zealand
Zhaohui Huang	Brunel University, UK
Luc Taerwe	University of Gent, Belgium
Colin Bailey	University of Manchester, UK

Track 3: Timber structures and fire protection materials

Mario Fontana (Leader)	**ETHZ, Switzerland**
Massimo Fragiacomo	University of Sassari, Italy
Joachim Schmid	SP, Sweden
Steve Craft	Forintek, Canada
Marc Janssens	SW Research Inst, USA

Andrea Frangi	ETHZ, Switzerland
Andy Buchanan	University of Canterbury, New Zealand

Track 4: Numerical Modeling

Asif Usmani (Leader)	**University of Edinburgh, UK**
Martin Gillie	University of Edinburgh, UK
Basam Izzuddin	Imperial College, UK
Zhaohui Huang	University of Sheffield, UK
Jean-Marc Franssen	University de Liège, Belgium
Angus Law	Arup, UK
Suwen Chen	Tongji University, China
Ann Jeffers	University of Michigan, USA

Track 5: Composite structures

Guo Qiang Li (Leader)	**Tongji University, China**
Markus Knobloch	ETHZ, Switzerland
Peter Schaumann	University of Hannover, Germany
Linhai Han	Tsinghua University, China
Ali Nadjai	University of Ulster, UK
Dhionis Dhima	CSTB, France
João Paulo Rodrigues	Universidade de Coimbra, Portugal

Track 6: Steel Structures

Paulo Vila Real (Leader)	**University of Aveiro, Portugal**
Yong C. Wang	University of Manchester, UK
Frantisek Wald	Czech Technical University in Prague, Czech Republic
Didier Talamona	University of Newcastle, Australia
Jyri Outinen	Ruukki Construction Oy, Finland
Ian Burgess	University of Sheffield, UK
Maria Garlok	Princeton University, USA
Michael D. Engelhardt	University of Texas at Austin, USA
Raul Zaharia	University of Timisoara, Romania
Leroy Gardner	Imperial College, UK

ORGANISING COMMITTEE

G.Q. Li, Chair	(李国强)	Tongji University, China
H.H. Zhu	(朱合华)	Tongji University, China
Y. Yuan	(袁　勇)	Tongji University, China
J.Z. Xiao	(肖建庄)	Tongji University, China
K.X. Hu	(胡克旭)	Tongji University, China
S.W. Chen	(陈素文)	Tongji University, China
S.C. Jiang	(蒋首超)	Tongji University, China
J.T. Yu	(余江滔)	Tongji University, China
G.B. Lou	(楼国彪)	Tongji University, China
J. Jiang	(姜　健)	Tongji University, China
L.H. Han	(韩林海)	Tsinghua University, China
B. Wu	(吴　波)	South China University of Technology, China
Y.L. Dong	(董毓利)	HuaQiao Universigy, China
J.C. Zhao	(赵金城)	ShangHai Jiao Tong University, China
W.Z. Zheng	(郑文忠)	Harbin Institute of Technology, Harbin, China
X.H. Qiang	(强旭红)	Harbin Institute of Technology, Harbin, China
G.P. Shu	(舒赣平)	Southeast University, China
L.J. Qu	(屈立军)	Chinese People's Institute Of Armed Police Force, Langfang, China
C.G. Fu	(傅传国)	Shandong Jianzhu University, Jinan, China
Y. Du	(杜　咏)	Nanjing University of Technology, Nanjing, China
P.J. Wang	(王培军)	Shandong University, Jinan, China
W.Y. Wang	(王卫永)	Chongqing University, Chongqing, China
J.F. Wang	(王静峰)	Hefei University of Technology, Hefei, China
H.T. Zhou	(周焕廷)	Wuhan University of Technology, Wuhan, China
J. Zeng	(曾　杰)	Shanghai Fire Bureau, Shanghai, China
Z.P. Ni	(倪照鹏)	Tianjin Fire Research Institute, Tianjin, China

STEERING COMMITTEE

Jean-Marc Franssen	University of Liege, Belgium
Andy Buchanan	University of Canterbury, New Zealand
Venkatesh Kodur	Michigan State University, USA
Paulo Vila Real	University of Aveiro, Portugal

PREFACE

Structural fire safety has raised growing concerns in the design of infrastructures. The "Structures in Fire" (SiF) specialized workshop series was conceived in the late 1990's and the "First International SiF workshop" was held in Denmark in 2000. The workshop was then held every two years until 2008 with the title changed from workshop to conference. Under this new framework the 5th-7th International Conference on SiF were held in Singapore (2008), USA (2010) and Switzerland (2012), respectively. The main mission of SiF conferences is to provide an opportunity for researchers and engineers to share their research, technology and expertise with their peers at an international forum.

Following the great success of previous workshops and conferences, Tongji University was selected to host the 8th International Conference on Structures in Fire SiF'14 in Shanghai on June 11-13, 2014.

The response to call for papers for SiF’14 was overwhelming and the Organizing Committee received more than 280 abstracts for this year’s conference. As a first attempt for parallel sessions, a total of 155 papers from 29 countries were selected for publication in the conference proceedings. The papers are subdivided into 8 chapters with themes including *Applications of Structural Fire Safety Engineering, Steel Structures, Concrete Structures, Composite Structures, Timber Structures, Fire Protection Materials, Numerical Modeling, and any other topics*. It is hoped that the high quality of the technical papers presented in this proceedings will enable researchers and practioners to develop greater insight of structural fire engineering, so that safer structures will be designed for fire-resistance.

We would like to thank all the members of the Scientific Committee for reviewing the abstracts within an incredibly short period of time, in particular the support of Professors Bin Zhao, Kang Hai Tan, Mario Fontana, Asif Usmani, Guo Qiang Li and Paulo Vila Real, taking the burden of the track leaders for the Scientific Committee. Our sincere appreciation must be presented to the SiF Steering Committee for guiding the review process and for providing direction to the successful organization of this conference. Our sincere thanks also go to all authors—the quality of the book is just the corollary of the high standard of their contributions and research activity. Finally, we would like to appreciate the effort and extraordinary support provided by all the members of the Organizing Committee, especially the staff at Tongji University.

Guo-Qiang LI
Chairman of Organizing Committee
Venkatesh K.R. KODUR
Chairman of Scientific Committee

Shanghai, June 2014

CONTENTS

Volume Ⅰ

Steel Structures

Concrete Structures

Timber Structures

Volume Ⅱ

Composite Structures

Connections

Numerical Modeling

Applications of Structural Fire Safety Engineering

Materials Behavior

STEEL STRUCTURES

EFFECT OF FIRE EXPOSURE ON THE PLASTIC MOMENT-SHEAR DIAGRAMS FOR HOT-ROLLED WIDE-FLANGED STEEL SECTIONS

Mahmud M.S. Dwaikat*

* Assistant Prof., Civil Engineering Dept., An-Najah National University, Nablus, Palestine
e-mails: m.m.dwaikat@najah.edu

Keywords: Moment-shear interaction, Elevated temperature, Fire, Structural steel, Finite element analysis, Plastic capacity, Codes and standards, Simplified approach

Abstract. *There is a lack of experimental and theoretical studies that address the plastic moment-shear (M-V) interaction capacity curves under fire conditions. The current paper presents a numerical study investigating the effect of fire exposure on the plastic M-V capacity curves of doubly-symmetric, wide-flanged (WF), hot-rolled steel sections. Validated finite element (FE) models to test this effect were constructed using ANSYS. Also, a simplified plastic sectional analysis, intended to be used by engineering practitioners, is proposed for generating the plastic M-V interaction curves. The comparative study shows that the fire-induced non-uniform heating of the section plates affects the shape of the plastic M-V interaction capacity curves. The study also shows that the approach for M-V interaction adopted in the Eurocode is very conservative at room-temperature, but turns out to be barely sufficiently conservative under fire conditions.*

1 INTRODUCTION

There are different approaches in the current codes and practices on how to consider the interaction between bending moment and shear force on the plastic carrying capacity of steel sections. For example, in the AISC 2005 specifications [1], the plastic moment-shear (M-V) interaction is neglected for hot rolled wide-flanged (WF) steel sections altogether. The explicit interaction between moment and shear is however considered in the presence of torsional moment, but for hollow-square steel (HSS) sections only. Also, in deep sections prone to shear buckling (such as plate girders and other built-up sections), the M-V interaction is acknowledged only implicitly through a series of modifications to the moment or shear capacities. The Eurocode [2] considers the M-V interaction on the plastic moment capacity of steel I-more explicitly.

There are many reasons that call for a more explicit consideration of the plastic M-V interaction in the design process. For instance, in some beams the location of maximum shear force and bending moment coincide, and thus the formation of a plastic hinge at such location is likely to be governed by the combined action of both bending moment and shear force. Further, when the beam is exposed to fire, the effect of shear on the moment capacity (or vice versa) may not be similar to how it is at room-temperature. Under fire conditions, the strength and stiffness of steel deteriorates in a dramatic fashion [3]. Also, for a beam that is exposed to a fire from 3 sides, a thermal gradient across the depth of the cross-section develops. Such thermal gradient often leads to a significant variation in the mechanical properties of steel along the depth of the cross-section due to the varied weakening and deterioration of the material properties that are caused by differential heating [4, 5]. This fire-induced inhomogeneity in the cross section can have many implications, such as a shift of the center of flexural rigidity (*EI*) of the cross-section and distinct strength reductions for the individual plates of the cross section [5-7]. Therefore, the M-V interaction at room temperature may not be valid under fire conditions.

There have been quite an abundance of experimental, numerical and analytical studies on the interaction of M-V capacity of hot-rolled WF and built-up sections at ambient temperature. However, the scarcity of studies on the same topic under fire conditions is remarkable. Such scarcity could be attributed to the dominant perception that beams under fire generally fail by forming flexural plastic hinges at the locations of maximum bending moments, and that the influence of shear is negligible. Also, most of the studies that were concerned with "near-support" behavior under fire, were focused mostly on the behavior of the connection rather than the member itself.

The many experimental and numerical studies on the M-V interaction were mainly focused on room-temperature behaviour [8-12]. In the early 1960's, Basler [13] proposed a model for the shear strength of WF sections which was then used, in conjunction with a lower bound plastic analysis, to devise an interaction formula for the M-V action on such sections. The model proposed by Basler [13] was both simple and accurate enough for predicting the failure points in the previous experiments. The simplicity and accuracy of the model helped get it adopted in the AISC (1999) [14] and AASHTO (1998) [15] specifications.

It should be stressed that the studies mentioned above were conducted on the M-V capacity under room-temperature conditions only. The effect of fire and fire-related degradation of strength and stiffness on such interaction has rarely been studied, if at all. Given the premise presented above, this paper addresses the effect of fire exposure on the M-V plastic capacity of WF steel.

2 EXISTING INTERACTION FORMULAE

Some common plastic M-V interaction curves are plotted in Figure 1 for comparison. The Eurocode EN1993 [2] explicitly acknowledges the M-V interaction on the plastic capacity of steel sections in a form of a reduction factor for the plastic moment capacity. The effect of shear on the plastic moment capacity is thus computed as:

$$M_n = \left[(1-\rho^2)F_y\right]Z_p \tag{1}$$

with $\rho = 2V_u/V_p - 1 \geqslant 0$. Z_p is the plastic section modulus and F_y is the yield strength of steel. The plastic shear capacity is computed as $V_p = 0.6F_yA_v$ and is valid for $A_f/A_w \geqslant 0.6$ as long as the average shear stress in the section does not cause yielding, i.e.: $V_u / A_w \leqslant 0.6F_y$.

In the Eurocode 3 [2], the interaction between shear and moment under fire is not explicitly considered, but it can be inferred from the given regulations that the room-temperature equations can also be used under fire conditions but with the material properties reduced due to fire induced degradation. Equation 1 above can be directly re-written as an explicit M-V interaction equation in the form:

$$\frac{M_n}{M_p} + \left(\frac{2V_u}{V_p} - 1\right)^2 = 1.0 \tag{2}$$

with the term $2V_u/V_p - 1$ maintained as nonnegative, and $M_p = F_yZ_p$.

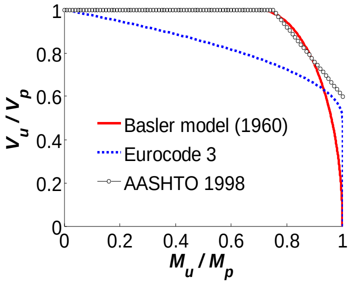

Figure 1. Comparing the existing M-V interaction formulae.

On the other hand, and in the AISC (2005) [1] specifications, the interaction M-V interaction on the plastic capacity of WF sections is explicitly ignored. An implicit M-V interaction is somehow considered through the reduction of the moment capacity only when the shear force tends to cause buckling of the web plate. An explicit interaction formula is present for other types of steel sections (such as HSS) when the shear force is combined with torsional and flexural moments. AISC (2005) [1] permits the use of post-buckling strength (via tension field action) for evaluating the shear strength, with the M-V interaction considered implicitly on the buckling capacity and in the restrictions on the use of tension field action. The original explicit M-V interaction equation as proposed by Basler (1961) has the form:

$$\left(\frac{M_u - M_{yf}}{M_p - M_{yf}}\right)^2 + \left(\frac{V_u}{V_p}\right)^2 = 1 \tag{3}$$

In which $M_{yf} = F_y h B_{FtF}$ is the yield moment considering the flanges only. The equation above is adopted into the earlier AISC and AAHSTO specifications [14, 15] by simple linearization as:

$$\frac{M_u}{M_p} + 0.625\frac{V_u}{V_p} = 1.375 \tag{4}$$

3 SIMPLIFIED PLASTIC SECTIONAL ANALYSIS

If we assume the strain distribution due to bending to be linear, the normal stress (σ) due to bending can be calculated using material stress-strain relationships. Imposing a Von Mises yield criterion, the relation between the moment-induced normal stress and the shear stress needed until plastic failure at any given point in the cross-section, is maintained and used to back-calculate the shear force required for full plastic failure. In hypothesizing such failure, an implicit assumption is made that the failure mode of the segment is due to full plasticity. Web and/or flange buckling is thus excluded in this study.

Based on the discussion above, a plastic sectional analysis can be conducted for calculating the "reserved" shear capacity under a given applied bending moment using the following algorithm:

- The cross section domain Ω is discretized into n fibres each with a width of b_i.
- At a given exposure time, the steel temperature distribution $T(y_i)$ is obtained from heat transfer analysis for each location y_i in the section Ω.
- For a given curvature κ (thus, a given bending moment M_κ) the mechanical flexural strain ε_i^m at location y_i is obtained by subtracting the thermal strain $\alpha\Delta T_i$ from the total strain as follows:

$$\varepsilon_i^m = (y_i - Y_{NA})\kappa - \alpha(T_i - 20) \tag{5}$$

- The parameter Y_{NA} represents the location of the neutral axis of the cross section for the value of the curvature and instant of fire exposure. The neutral axis will shift its location because of the non-uniform thermal gradient. Y_{NA} is obtained through iterations by setting the total axial resultant force P on the cross section equal to zero (for pure bending), which will be explained in the next step.
- Based on the strain and temperature, the stress $\sigma_i(\varepsilon_i^m, T_i)$ is obtained from the temperature dependent constitutive material relationships for steel. The bending moment is computed by integrating the normal stress profile across the cross-section Ω as follows:

$$M_\kappa = \int_\Omega y\sigma_i dA = \sum_{i=1}^n \mathrm{sign}(y_i - Y_{NA})(y_i - Y_{NA})\ \sigma_i(\varepsilon_i^m, T_i) b_i \Delta y \tag{6}$$

that is subjected to the condition of zero axial force for pure bending; i.e.:

$$P = 0 = \int_\Omega \sigma_i dA = \sum_{i=1}^n \mathrm{sign}(y_i - Y_{NA})\sigma_i(\varepsilon_i^m, T_i) b_i \Delta y \tag{7}$$

The required shear stress profile for full plastic failure is then computed through imposing Von Mises criterion, namely:

$$\tau_{xy}^{*}(T_i) = \frac{1}{\sqrt{3}}\sqrt{\left(F_y(T_i)\right)^2 - \left(\sigma_i(\varepsilon_i^m, T_i)\right)^2} \tag{8}$$

The shear force V is computed by direct integration of these shear stresses calculated above:

$$V = \int_{\Omega} \tau_{xy}^{*} dA = \sum_{i=1}^{n} \tau_{xy}^{*}(T_i)\, t_w \Delta y \tag{9}$$

Note that in Equation (9) the shear stress in the flange is assumed to occur over a thickness of the web t_w because of the shear-lag phenomenon. If we take the entire width of the flange to carry the same shear stress, under a small bending moment, the shear capacity would be unrealistically magnified. The jostle for determining the “effective” width of the flange is deliberately avoided for sake of simplicity and lack of reliable methods.

4 COMPARISON WITH FINITE ELEMENT RESULTS

While many tests were conducted on the effect of combined moment and shear loading on the carrying capacity of hot-rolled WF steel sections, there is a notable lack of experiments that address this particular issue under fire conditions. It would be desirable to have experimental data on this issue, but considering the substantial costs of these experiments, it seems prudent, if not necessary, to provide a preliminary numerical model. In this study, a high-fidelity finite element model is constructed using ANSYS commercial package [16]. The model is used to generate results on the behavior of WF steel sections under combined shear and moment loading as it will be explained hereafter.

4.1 High-fidelity finite element modelling

A two-phase three-dimensional finite element model is created using ANSYS [16]. In the first phase the model generates the thermal response of the steel section upon exposure to a fire scenario. The second phase takes as input the spatial distribution of the temperature in the steel section and then carries out a nonlinear structural analysis of the steel section. The two phases are thus coupled in one direction: i.e. thermal-then-structural analysis. The details of these two types of analyses are outlined below.

4.1.1 Thermal analysis

In this phase of analysis, transient heat transfer analysis is conducted using a 2D finite element model constructed using ANSYS, a well-known commercial software package [16]. Figure 2 (a) shows a finite element mesh for a steel section with contour fire protection. The steel cross-section is modelled using solid 2D plane elements (PLANE55) while the fire-exposed boundaries of the cross-section are modelled using 1D special elements (SURF151). Both convection and radiation heat fluxes were imposed on the exposed boundaries. The ambient (bulk) temperature (T_∞) surrounding the faces of the SURF151 elements was assumed to be equal to the fire temperature (T_f) that follows the standard ISO 834 fire curve [17]. More details about the thermal analysis model and the properties of the materials (either structural steel or spray-applied fire resisting materials) can be found in [3, 18-19].

4.1.2 Structural analysis

In this phase, the fire-induced temperature variation within the cross-section is applied on the 3D structural model of a beam segment, which in turn is subjected to the structural loads (moment and shear). The 3D model, shown in Figure 2(b), is created using 8-noded shell elements. The element (SHELL281) is a serendipity element that has eight nodes with six degrees of freedom at each node: 3 translations and 3 rotations, and it accounts for geometric and material nonlinearities. The temperature-dependent constitutive material model, as specified in the Eurocode 3, is used in the analysis. The boundary conditions imposed on the structural model are shown in Figure 2(c) and were meant to simulate a structural continuity of the segment as it belongs to a beam.

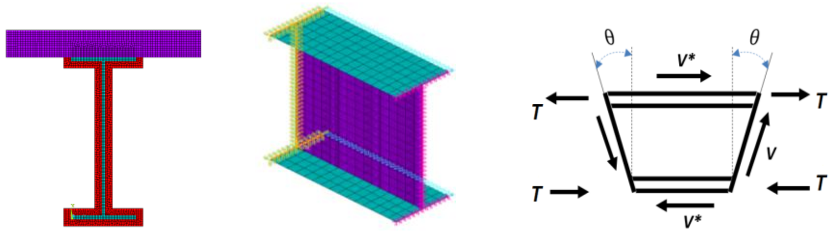

(a) Mesh for thermal analysis (b) Mesh for structural analysis (c) Side view schematic

Figure 2. FE discretization for thermal and structural analyses with the applied constraints.

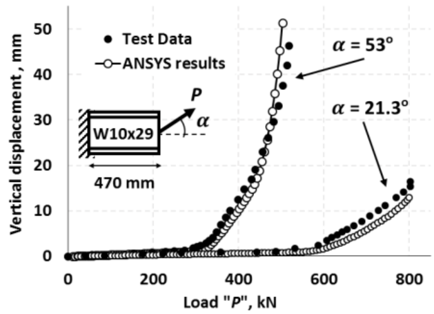

Figure 3. Comparing results from ANSYS FE model to results from experiments in Ref. [8].

4.2 Analysis procedure and controls

For a given time step (t) during fire exposure, the failure envelope ($M_u(t)$,$V_u(t)$) is established as follows. The temperature distribution at that given exposure time is obtained from thermal analysis and then applied to the nodes of the structural model as body heat. The beam is allowed to expand without restraint. Then a bending moment (M) is applied followed by applying a shear force (V). The shear force is increased until runaway failure of the beam. This will give us a failure point for that time step (M_u, V_u). This is repeated for different values of M between 0 and $M_u(t)$, until the entire failure curve is generated.

4.3 Validation of the finite element models

The FE model for thermal analysis and its validation can be found in earlier works [18-19]. The experiments conducted by Kusuda and Thrulliman [8] are used for the validation of the structural FE model. The results of the validation process are shown in Figure 3, which compares results from the FE model to the test data. In the experiments, segments of beam W10×29 were subjected to different levels of combined loading as shown in the little schematic within Figure 3. Overall, the comparison with the test data shows that the FE model can capture realistic behaviour of the beam segments under combined moment-shear-tension loading.

5. RESULTS AND DISCUSSION

Typical results of thermal analysis in the form of temperature profile across the cross section were generated for protected and unprotected steel sections (W24×76 and W27×194) under 3-sided fire exposure to the ISO834 standard fire [17]. When compared to protected steel sections, the unprotected sections develop a highly nonlinear thermal gradient. For the unprotected steel sections, the temperature of the web is often higher than the temperatures of the flanges. Therefore, it is expected that the weakening of the web due to fire occurs at a faster rate than the weakening of the flanges. It is therefore also expected that this will have an effect on the shape of the M-V interaction diagram. The temperature profiles were applied to the steel section and then structural analysis was conducted until failure as explained in Section 4.2.

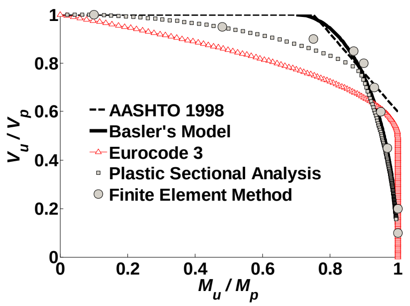

(a) At room-temperature

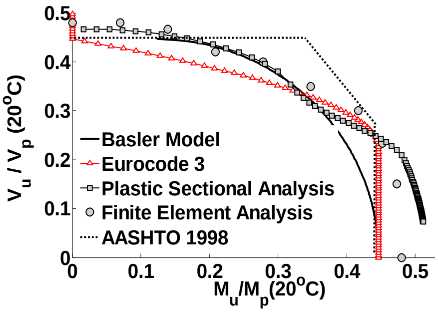

(b) After 10 min. of fire exposure (unprotected)

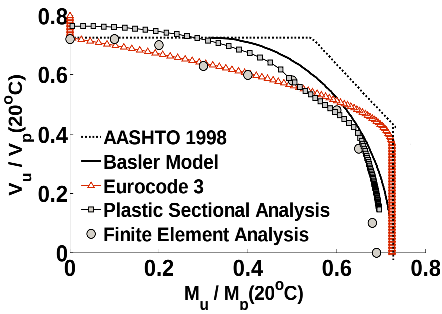

(c) After 100 min. of fire exposure (protected)

Figure 4. Plastic M-V Interaction curves for section W24x76 at a) room temp., b) 10 min. to fire exposure without fire insulation, and c) 100 min. to fire exposure with fire insulation.

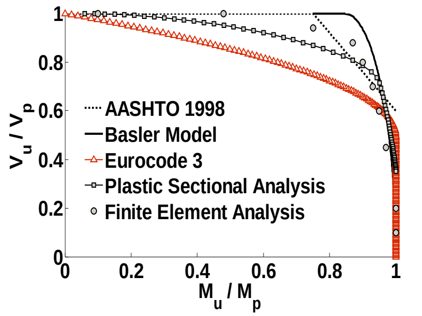

(a) At room-temperature

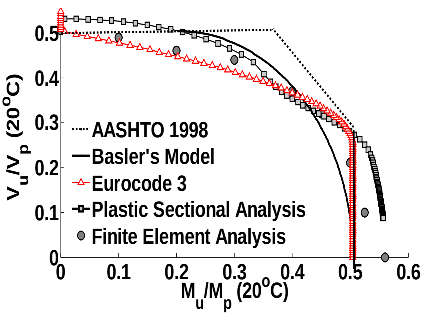

(b) After 10 min. of fire exposure (unprotected)

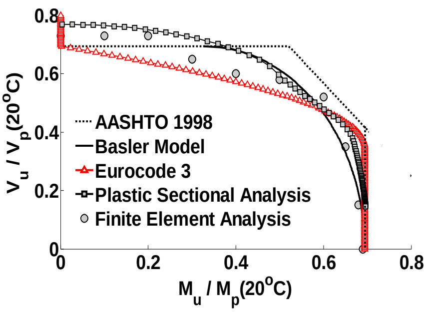

(c) After 100 min. of fire exposure (protected)

Figure 5. Plastic M-V Interaction curves for section W27x194 at a) room temp., b) 10 min. to fire exposure without fire insulation, and c) 100 min. to fire exposure with fire insulation.

Figures 4 and 5 show the results of plastic M-V interaction curves for two different sections under different cases of fire exposure. The results in Figure 4 are for section W24×76, while in Figure 5 the results are for section W27×194. These two sections were chosen so as to represent different ratios of web-to-flange areas (A_w/A_f). For section W24×76; A_w/A_f = 1.67, while for section W27×194; A_w/A_f = 1.02. The latter section thus has somewhat “thicker” flanges as compared to the first section.

As shown in Figures 4 and 5, M-V interaction curves were generated considering three cases for each section; namely, at room-temperature, after 10 minutes of fire exposure considering no insulation against fire, and after 100 minutes of fire exposure considering fire-proof insulation. Both sections were exposed to ISO 834 standard fire. The M-V diagrams in Figures. 6 and 7 are generated as per Eurocode 3 (Equation (2)), Basler’s model (Equation (3)), AASHTO linearized formula (Equation (4)), in addition to the plastic sectional analysis and finite element methods. While in the finite element and plastic sectional analysis methods the full temperature profile is utilized, the Eurocode and ASSHTO equations use only the average temperature. For the Basler model, the average temperature of the flanges is used since Basler’s interaction equation (Equation (3)) makes a distinction between the bending moment carried by the flanges and the bending moment carried by the entire section.

From Figures 4(a) and 5(a), it can be seen that the Eurocode provides the most conservative M-V capacity compared to other methods. Plastic sectional analysis seems to be on the safe side when compared to results from finite element analysis. The predictions using Basler model match fairly well with the results from finite element, except when the applied shear is high. In Figures 4(b) and 5(b), the Eurocode still provides conservative M-V interaction curves for unprotected steel sections. Methods based on Basler’s model tend to provide less conservative predictions for section W27×194 when compared to those for section W24×76.

In Figure 4(c) and 5(c), predictions based on the Eurocode method remain conservative when the shear loading is more than 50% of the room-temperature plastic shear capacity. Basler’s model produces non-conservative predictions for the M-V diagrams for the insulated fire exposed steel section.

Since the temperature distribution is non-uniform, the average temperature gives only a good indication for the temperature of the web for the case of unprotected steel. In the case of protected steel, the average temperature gives an indication of the temperature of the bottom flange. In the case where no fire protection is used (Figures 4(b) and 5(b)), strength deterioration in the web of the section might have a direct effect on the overall capacity reduction, since it has a higher temperature than the rest of the section. Thus the predictions by the Eurocode and Basler methods are generally conservative for unprotected steel sections, since these methods utilize the average temperatures of the sections.

For the cases where fire protection is used (Figures 4(c) and 5(c), the capacity reduction is mainly affected by the strength deterioration of the bottom flange, because it has a higher temperature than the rest of the section. This might provide an explanation for the non-conservative predictions by the different methods at higher values of applied bending moment. The non-conservatism is more evident for section W24×76 than for section W27×194, probably due to the fact that the first section has “thinner” flanges, and thus suffers more dramatic reduction in its bending capacity due to heat.

6. CONCLUSIONS

There is a lack of analytical, numerical, and above all experimental studies on the effect of moment-shear loading on the capacity of steel beams under fire conditions. This paper has presented a finite element study accompanied with simplified plastic sectional analysis for generating the plastic M-V interaction diagrams for WF steel sections. The study shows that the fire-induced non-uniform heating of the steel section has an effect on the M-V interaction diagrams. When different methods were compared with finite element results, it was found that the implicit interaction equation presented in the Eurocode appears to perform better in capturing the variation of the M-V diagrams under fire conditions. Further theoretical and experimental research is required to incorporate the effect of plate instabilities on the M-V diagrams.

REFERENCES

[1] AISC. Steel Construction Manual, 13th edition, *American Institute of Steel Construction,* Inc., Chicago, IL., 2005.

[2] EN1993. Eurocode 3: Design of steel structures. Part 1-2: General rules - Structural fire design, EN1993-1-2, *European Committee for Standardization*, Brussels, Belgium, 2005.

[3] Kodur, V.K.R., Dwaikat, M.M.S, and Fike R., "High-Temperature Properties of Steel for Fire Resistance Modelling of Structures", *Journal of Materials in Civil Engineering*, ASCE, 22(5), 423-434, 2010.

[4] Dwaikat, M.M.S., Kodur, V.K.R., Quiel, S.E., Garlock, M.E.M., "Experimental Behaviour of Steel Beam-Columns Subjected to Fire-Induced Thermal Gradients", *Journal of Constructional Steel Research*, 67(1), pp. 30-38, 2011.

[5] Dwaikat, M.M.S and Kodur, V.K.R. "A Simplified Approach for Evaluating Plastic Axial and Moment Capacity Curves for Beam-Columns with Non-uniform Thermal Gradients", *Engineering Structures*, 32(5), pp.1423-1436, 2010.

[6] Kodur, V.R, Garlock, M.E, Dwaikat, M.S, Quiel, S., "Collaborative Research: Fire Engineering Guidelines for the Design of Steel Beam-Columns", *Proceedings of 2009 NSF Engineering Research and Innovation Conference*, Honolulu, Hawaii, 2009.

[7] Garlock, M.E.M. and Quiel, S.E. "Mechanics of Wide-Flanged Steel Sections with Thermal Gradients Due to Fire Exposure," *International Journal of Steel Structures*, Korean Society of Steel Construction, 7(3), 153-162, 2007.

[8] Kusuda, T. and Thurlimann, B., "Strength of wide-flange beams under combined influence of moment, shear and axial force," Fritz Laboratory Reports. Paper 1658., 1958.

[9] Zentz, A. "Experimental moment-shear interaction and TFA behavior in hybrid plate girders." MS thesis, University of Missouri– Columbia, Columbia, Mo., 2002.

[10] Azizinamini, A., Hash, J. B., Yakel, A. J., and Farimani, R. "Shear capacity of hybrid plate girders." *J. Bridge Eng.*, 12(5), 535–543, 2007.

[11] White D. W., Barke M. G. and Azizinamini A. "Shear Strength and Moment-Shear Interaction in Transversely Stiffened Steel I-Girders", *Journal of Structural Engineering*, Vol. 134, No. 9, pp. 1437 – 1449, 2008.

[12] Aydemir, M., White, D. W., and Jung, S. K. "Shear strength and moment shear interaction in HPS hybrid I-girders." Structural Engineering, Mechanics and Materials Rep. No. 25, School of Civil and Environmental Engineering, Georgia Institute of Technology, Atlanta, 2004.

[13] Basler, K., "Strength of plate girders under combined bending and shear", *Proc. ASCE*, 87, (ST7), Reprint No. 187 (210) (61-14)". Fritz Laboratory Reports. Paper 71, 1961.

[14] Rush, C. B. "Experimental tension field action behavior in HPS plate girders." MS thesis, University of Missouri–Columbia, Columbia, Mo., 2001.

[15] American Institute of Steel Construction (AISC). Load and resistance factor design specification for structural steel buildings, Chicago. 1999

[16] American Association of State and Highway Transportation Officials (AASHTO) AASHTO LRFD bridge design specifications, 2nd Ed., with 1999, 2000, 2001 and 2002 Interims, Washington, D.C. (1998).

[17] ANSYS Multiphysics. Version 14.0 UP20111024, ANSYS Inc., Canonsburg, (2011).

[18] ISO 834, "Fire resistance tests – elements of building construction. International Organization for Standardization", (1975).

[19] Dwaikat M.M.S and Kodur V.K.R., "A simplified approach for predicting temperatures in fire exposed steel members", *Fire Safety Journal*, Vol. 55(1), pp. 87-96, 2013.

[20] Dwaikat, M.M.S and Kodur, V.K.R. "A simplified approach for predicting temperature profile in steel members with locally damaged fire protection", *Journal of Fire Technology*. v. 48 (2) p. 493-512, 2012.

ANALYSIS OF THE RESPONSE OF A STEEL GIRDER BRIDGE TO DIFFERENT TANKER FIRES DEPENDING ON ITS STRUCTURAL BOUNDARY CONDITIONS

Guillem Peris-Sayol*, Ignacio Payá-Zaforteza* and Jose Alós-Moya*

* ICITECH, Departamento de Ingeniería de la Construcción. Universitat Politècnica de Valencia
e-mails: guipesa2@upv.es, igpaza@upv.es, joalmo11@upv.es

Keywords: Fire, Bridge, Steel girder bridge, Tanker fire, CFD

Abstract. *The response of a bridge under a fire scenario is an under researched topic not covered in the codes. This paper presents an approach to evaluate the fire response of the most exposed girder of a simply supported steel girder bridge designed by the Federal Highway Administration (FHWA) of the USA spanning 12.2* m *under three different fire scenarios. The analyses use computational fluid dynamics (CFD) to create the fire model, and finite element (FE) software for obtaining the thermo-mechanical response of the girder. Results show that:(1) scenarios with the fire load close to the abutments are the most unfavorable, (2) it is necessary to use horizontal springs at the pinned support to appropriate model the restrain to the longitudinal movement of the bridge deck, (3) two values of the spring constant are enough to capture the response of the bridge, and (4) the value of the spring constant influences the failure time, the failure mode and the final deflections.*

1 INTRODUCTION

Bridges are a critical component of the transportation system which have suffered severe damage due to fires as proved e.g. by Garlock at al [1] and by a bridge failure survey carried out in 2011 and cited in [1] which collected data related to 1746 bridge failures from the departments of transportation of 18 US states. This survey showed that fire had caused more bridge collapses than earthquakes and that fire had been the fifth cause of bridge collapses.

Despite its importance, bridge fires have got very little attention in the past, especially considering that bridge fires are different to building or tunnel fires and deserve a particular approach (see [2] for more details). Within this context, this paper uses a three step approach to analyze the effects of fires on bridges. The approach consists of: (1) a fire model of the fire event using CFD techniques, (2) a thermal model using FE and (3) a study of the mechanical response using FE and considering the non-linear response of the structure with temperature dependent material properties. More specifically, the paper focuses on the fire response of a simply supported steel girder bridge under real fire conditions corresponding to the accident of a tanker truck carrying 35 m^3 of gasoline. Additionally, the paper discusses the influence of the structural boundary conditions in the response of the bridge.

2 CASE STUDY

The prototype bridge used in our study is a simply supported bridge designed by the Federal Highway Administration (FHWA) of the United States of America whose fire response was first studied by Payá-Zaforteza and Garlock [3]. The bridge spans 12.2 m and its cross section and plan view are shown in Figure 1. The bridge consists of five hot rolled steel girders of type W33x141. The beams support a reinforced concrete slab 0.2 m deep but the slab is not connected to the girders and, therefore, there is no composite action. Transverse diaphragms are placed at mid span and at the supports to laterally stiffen the bridge deck. The bridge has two expansion joints at its extremities with a width of 3.6 cm. At ambient temperature, material properties correspond to the nominal values for A36 steel and therefore its minimum yield stress is 250 Mpa. The response of this bridge to the hydrocarbon fire and considering several constitutive models and construction materials was previously analysed by Payá-Zaforteza and Garlock in References [2] and [3].

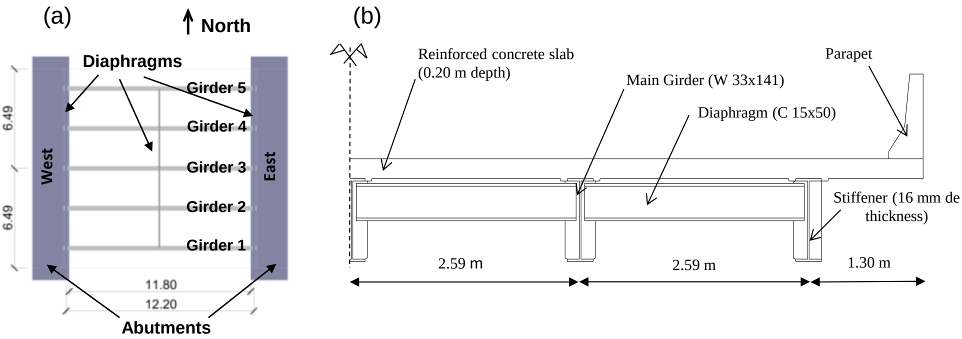

Figure 1. (a) Plan view (without the concrete slab) and (b) half section of the bridge.

3 COMPUTATIONAL FLUID DYNAMIC MODEL (CFD)

Several fire models of hypothetical fire events have been developed with the software Fire Dynamics Simulator (FDS) [4]. A FDS model predicts numerically in a control volume fire engineering variables such as temperatures, heat fluxes or gas pressures involved in a fire event. It is based on CFDs techniques and contains large eddy simulation (LES) turbulence models. In this study, a LES turbulence model with a coefficient of Smagorinsky equal to 0.2 has been used.

Building a FDS model requires defining: (1) a control volume with its boundary conditions which represents the volume where all the analysis takes place, (2) a geometry included in the control volume which represents the geometry of the case study, (3) a mesh or discretization of the control volume, (4) material properties (conductivity, density, specific heat and emissivity), (5) fire sources, (6) a combustion model and (7) sensors or elements of the model where the outputs (e.g. temperatures) are recorded.

From the analysis of previous studies (see Garlock et al. [1], Alós-Moya et al. [5], and Peris-Sayol et al. [6]), it can be inferred that a tanker truck carrying gasoline is the worst scenario possible. More specifically, three fire scenarios related to the position of the tanker fire have been considered. The scenarios are defined in Figure 2 and correspond to a tanker truck centered under the central girder of the bridge (Girder 3) and located close to the west abutment (scenario “fire1”), under the bridge mid-span (scenario “fire2”) or close to the east abutment (scenario “fire3”). Note that the difference between fire1 and fire3 is the different kind of support near the abutment (the deck is supported by a roller in the west abutment and is fixed in the east abutment). The tanker truck was modelled as a horizontal surface of 25 m^2 (12 × 2.5m) at one meter above the road level and with a heat release rate (HRR) of 2400 kW/m^2, which is the HRR corresponding to a gasoline pool fire with a diameter exceeding 3 m [7]. As an example, Figure 3 shows the FDS results (temperatures) corresponding to the scenario “fire2”.

4 FINITE ELEMENT MODEL

The thermo-mechanical response of the bridge is obtained with a model of the most exposed girder (Girder 3) built in the finite element software Abaqus. The Abaqus analysis consists of 2 steps. In the first step (a) the thermal analysis is carried out by using the adiabatic surface temperature [8] given by FDS as an input and, (b) the heat transfer method provides the transient nodal temperatures with respect to time using the thermal properties of the material. In the second step (the structural analysis), the nodal temperatures are read from the thermal analysis and corresponding temperature dependent mechanical material properties are used to find the equilibrium of the structure. Note that in the step 1 the concrete slab is included in the model and the analysis, whereas in the step 2 the slab influence is neglected because the bridge is not a composite bridge although appropriate boundary conditions that take into account the influence of the slab are considered.

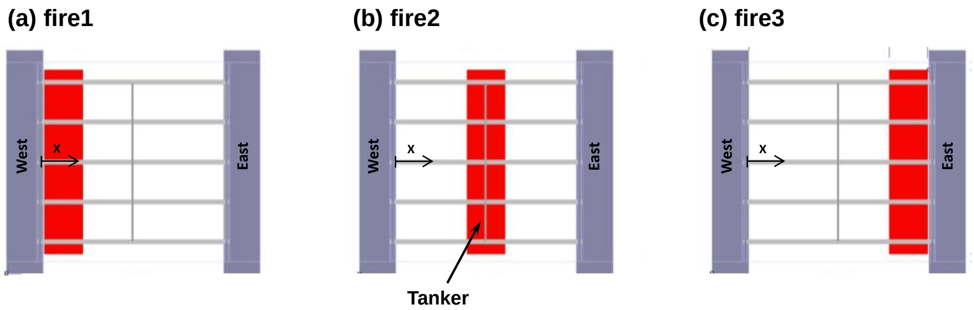

Figure 2. Fire scenarios considered.

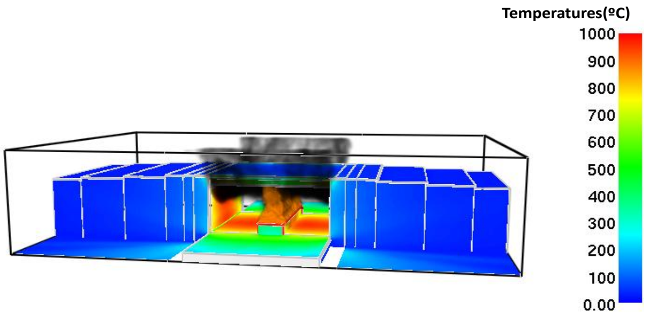

Figure 3. View of the FDS results (temperatures) corresponding to the fire load “fire2”.

4.1 Mesh

Figure 4 shows the mesh used for the thermal and mechanical analyses. Abaqus DC3D8 elements were used for the thermal models whereas Abaqus C3D8 elements were used for the mechanical analysis. The first element has 8 nodes with one degree of freedom in each node, whereas the second element has 8 nodes and 3 degrees of freedom in each node. FE mechanical analysis includes geometric and material non-linearity, and the use of 3D elements is motivated by the need to capture local phenomena such as web buckling. As Figure 4 shows, the mesh is finer in mid-span and supports because those are areas of high stress. The FE model has 20693 nodes and 14164 finite elements in thermal analysis and 18183 nodes and 12624 elements in the mechanical analysis. The difference between both models is the consideration of the slab.

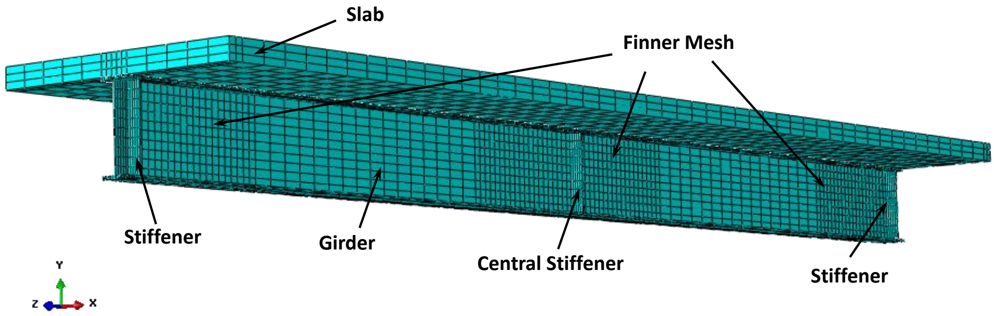

Figure 4. Mesh used in the FE model.

4.2 Material Properties

The thermal and mechanical properties of the materials of the bridge, steel and concrete, have been taken from Eurocodes 2 and 3. The steel used is A36, with a yielding limit of 250 MPa and the strain hardening proposed in Eurocode 3. Engineering values of stresses (σ) and strains (ε) were converted into true stress strain laws (σ_n-ε_n) and introduced in Abaqus. Concerning concrete, only thermal properties have been characterized in the heat transfer model (density, specific heat and conductivity). Regarding the thermal conductivity of concrete, the upper limit proposed in Eurocode 2 was used.

4.3 Boundary Conditions

The studied bridge is a single span simply supported bridge. The east support is fixed and the west support is a roller. The restrictions of both supports in the model are applied on a surface that represents the support. This surface is in the bottom face of the bottom web, in the area of contact between the stiffener and beam. The length of the surface is 46 mm and the width is 293 mm (beam width).

As suggested by previous studies [2, 5, 6] a limitation to the roller support displacement has been considered in the analysis. The beam cannot expand indefinitely due to the existence of the abutment. Therefore, the maximum longitudinal displacement of the girder equals the expansion joint width (3.6 cm).

In this paper, only the most exposed girder (named Girder 3 in Figure 2) is analysed. The influence of the diaphragms is considered by preventing the transverse displacement of the beam in the area of contact diaphragm-stiffener. The influence of the concrete slab in the mechanical model is considered by preventing the transverse displacement of the upper face of the top flange.

4.4 Thermal Loads

FDS obtains the adiabatic surface temperatures in selected nodes of the CFD model. The adiabatic surface temperature (T_a) is a fictitious temperature obtained assuming that the structural element is a perfect insulator and is an equivalent fire temperature when calculating the heat flux to an exposed temperature. This resource serves to transfer the results from the fire models to the thermo-mechanical models. The way it works is explained in detail in Alós-Moya et al. [5]. Adiabatic temperatures vary along the axis of the bridge and also within the girder cross section. However, and given a certain a cross section of the girder, all the points located in the same face of the girder (north, south or bottom face) have a very similar adiabatic temperature. To transform FDS results to Abaqus inputs, the curves describing the adiabatic temperatures have been transformed in steeped curves stepped as shown in Fig. 5. Each stepped curve has 16 steps, being the temperature at each step the average of all the temperatures measured by FDS in the step and zone. In Abaqus heat transfer model, a heat transfer coefficient (h_c) of 35 W/m^{2}K and an emissivity coefficient (ε) of 0.7 corresponding to a petrol fire were used according to EC-1 and EC-3.

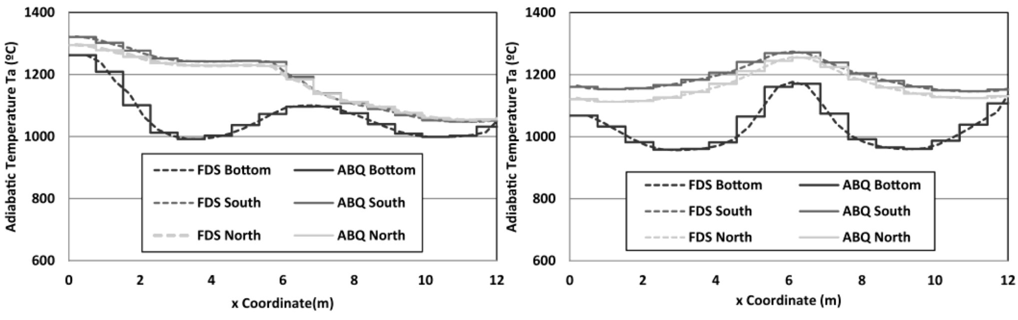

Figure 5. Girder 3. Example of a 16 step discretization of the adiabatic temperature curves for merging CFD with Abaqus: (a) load case *fire1*; (b) load case *fire2*.

4.5 Gravity Loads

Gravity loads considered in this paper are: (a) 2067 N per meter corresponding to the self-weight of the steel girder and 12704 N per meter corresponding to the self-weight of the concrete slab and (b) 9838 N per meter corresponding to the pavement and the self-weight of the parapet distributed between the five beams. Note that, according to the results of previous studies [2, 5, 6] live loads do not have an appreciable influence in the fire response of the bridge and have not been included in the study.

4.6 Failure Assessment

The failure criteria proposed by Payá-Zaforteza and Garlock [2] have been used. According to them, the structure fails when ultimate strain ε_u, is reached or becomes unstable. This fact can be identified as a rapid increment of the maximum vertical deflection, as a movement of roller (west end support) towards the center of span or as instability due to either lateral or web buckling.

5 RESULTS AND DISCUSSION

The paper aims to study the influence on the fire response of the bridge of (a) the structural boundary conditions at the fixed support, and (b) the position of the fire load. These topics are discussed next.

5.1 Influence of the structural boundary conditions at the fixed support

As explained in Section 4.3, the longitudinal expansion of the girder towards the west abutment is limited to the expansion joint width. Therefore, once the west end of Girder 3 contacts the abutment, thermal expansion is restrained and a horizontal reaction appears in the pinned support located at the east end of the girder. This reaction increases with the time and reaches a peak value until the yielding of the support makes the horizontal reaction decrease. Figure 6 shows this evolution for the three fire loads considered in this study.

According to Figure 6, horizontal reactions reach a maximum 90 seconds after the beginning of the fire and their peak value is close to 2200 kN, which is almost seventeen times the vertical reaction at the pinned support (130 kN). In these conditions, the pinned support might fail to restrain the longitudinal movement of the girder and would become a horizontal spring. As it is very difficult to provide a value of the spring constant at the pinned support (k_p), the authors have analyzed six different values ranging from k_p=0 to infinite. In the first case, the pinned support becomes a roller whereas in the second case the pinned support does not suffer any modification with compared to its initial state. Table 1 details the values of k_p considered and the analyses names. Note that the cases with k_p=0 and k_p=1000 N/m gave the same results and have been merged to a single case with $k_p \leqslant 1000$ N/m. These analyses were carried out for the three fire loads, but for the sake of brevity only the load case “fire2” results are shown.

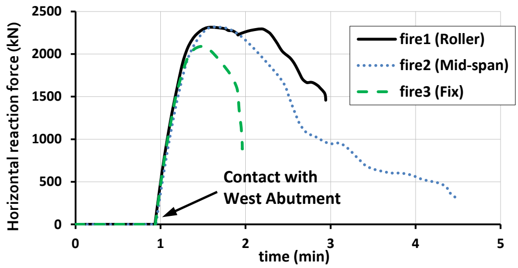

Figure 6. Evolution of the horizontal reaction force at the pinned support for the fire scenarios considered in the study.

Table 1. Study of the conditions of the pinned support conditions. Cases analysed.

Analysis name	Spring constant, k_p (N/m)
fire2-k⩽10000	⩽ 10000
*fire2-k*1000000	1000000
*fire2-k*10000000	10000000
*fire2-k*100000000	100000000
fire2-fix	∞

Figure 7 plots the evolution of the maximum vertical deflection of Girder 3 for the different cases reported in Table 1. It can be seen that the analyses *fire2-k*⩽10000 and *fire2-fix* contain all the analyses and, therefore, should be retained as envelope cases. Times to failure are very similar in both of them but the fix case has smaller deflections (12 cm versus the 35 cm of the case *fire2-k*⩽10000). As expected, the higher the value of k_p, the closer to the fix case becomes the behavior of the girder .

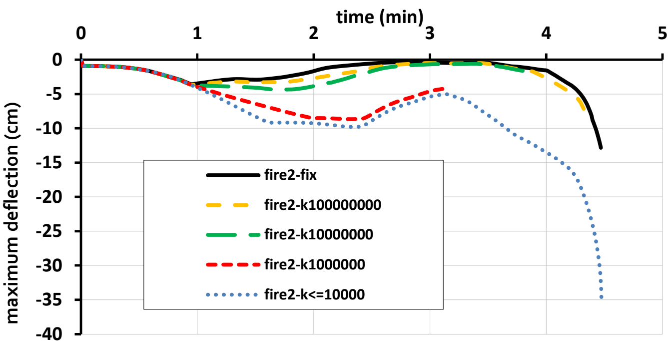

Figure 7. Vertical displacement of the girder for different spring constants values for the *fire2* case (tanker truck in mid-span).

Figure 8 shows the plastic strains at the moment of failure for the cases *fire2-fix* and *fire2-k*⩽10000. The model *fire2-fix* fails due to the yielding of the pinned support region and with much smaller yielding in mid span. This model also experiences lateral buckling with transverse displacements close to 0.16 m and with buckling length equal to half the span length (distance between transverse diaphragms). The model *fire2-k*⩽10000 fails by web buckling, and lateral buckling has a much smaller importance (maximum transverse displacements in the order of 6 cm).

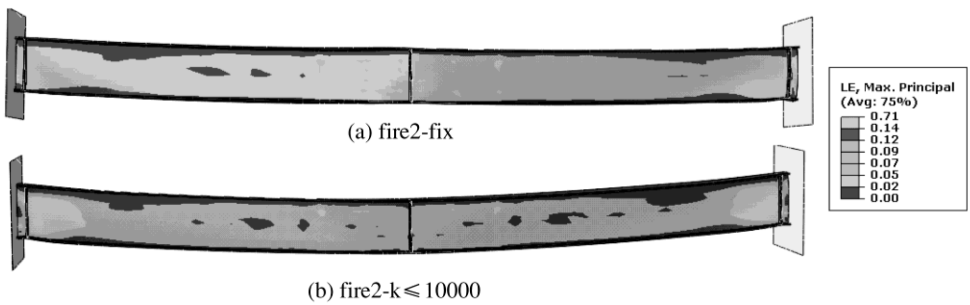

Figure 8. Plastic Strain at the moment of failure: (a) model *fire2-fix* and (b) model *fire2-k*⩽10000.

5.2 Influence of the fire scenario

Table 2 details the response of the bridge to the three fire scenarios detailed in Figure 2. Following the findings of Section 5.1, only results corresponding to two values of k_p (0 and ∞) are shown.

Table 2. Results of the analyses.

Name Analysis	Tanker Location	Failure Time (min)	Maximum Deflection (m)	Maximum Transversal Displacement (m)	Mode
fire1-fix	West Ab.	2.9	- 0.17	0.15 (lateral buckling)	LB, S
fire1-k_0	West Ab.	3.0	- 0.24	0.07 (web buckling)	WB, S
fire2-fix	Mid-span	4.5	- 0.12	0.16 (lateral buckling)	LB, S
fire2-k_0	Mid-span	4.5	- 0.35	0.06 (lateral buckling)	LB, S
fire3-fix	East Ab.	2.0	- 0.07	0.07 (lateral buckling)	LB, S
fire3-k_0	East Ab.	3.0	- 0.24	0.07 (web buckling)	WB, S

LB: Instability due to lateral buckling, R: Instability noticed by the movement of west support (roller) towards the center of span, S: Ultimate strain reached, WB: Instability due to web buckling in the contact with the abutment.

Table 2 shows that the case *fire3-fix* corresponding to the tanker close to the pinned support represents the worst scenario, as it has the lowest time to failure: 2 min. (44% and 66% of the times to failure of the cases *fire2-fix* and *fire1-fix* respectively). Failure is the result of the yielding of the steel as a consequence of the decrease of the steel strength caused by the high temperatures in combination with the compressive stresses existing in the area of the girder close to the fixed support (see Figure 9(a)).

When the slmodt null stiffness spring is used to model the pinned support, both the *fire3-k0* and *fire1-k0* have the same time to failure, 3 min., and failure mode: web buckling in the region of the girder over the support which is the closest to the fire load (see Figure 9(b)). In these cases, web buckling happens because the high temperatures and the corresponding loss of steel strength make the girder unable to withstand the high shear forces that appear in the support region.

6 CONCLUSIONS

This paper analyzes the fire response of a simply supported steel girder bridge submitted to three different fire scenarios. The following conclusions can be drawn: (a) the values of the horizontal reactions and stresses in the pinned support make it necessary to consider that the longitudinal movement of the girder is restrained by a horizontal spring, (b) two values of the spring constant (k_p=0 and k_p=∞) are enough to capture the response of the girder, (c) the value of the spring constant influences the failure time, the failure mode and final deflections and (d) fire scenarios with the fire load close to the bridge abutments are the most unfavorable.

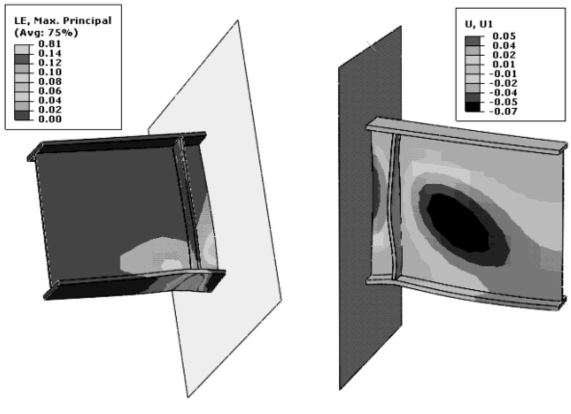

(a) fire3-fix (b) fire3-k0

Figure 9. Failure modes for the scenario *fire3*: (a) strains in the model *fire3-fix*; (b) transverse deformations in the model *fire3-*k_0.

ACKNOWLEDGEMENTS

Funding for this research has been provided by the Spanish Ministry of Science and Innovation (research project BIA 2011–27104) and the Universitat Politècnica de València (Research and Development Support Program PAID-06-11).

REFERENCES

[1] Garlock M.E.M., Paya-Zaforteza I., Kodur V. and Gu L., "Fire hazard in bridges: review, assessment and repair strategies". *Engineering Structures* 35:89–98, 2012.

[2] Payá-Zaforteza I. and Garlock M.E.M., "A numerical investigation on the fire response of a steel girder bridge". *Journal of Constructional Steel Research* 75:93–103, 2012.

[3] Payá-Zaforteza I and Garlock, MEM., "A 3D numerical analysis of a typical steel highway overpass bridge under a hydrocarbon fire". In: *Proceedings of the fifth international conference for structures in fire*. East Lansing, USA, 2010. p. 11–8.

[4] Mc Grattan K., McDermott R., Hostikka S. and Floyd J., *Fire dynamics simulator (version 5). User's guide*. NIST Special Publication 1019–5, Gaithersburg, MD, USA; 2010.

[5] Alos-Moya J, Paya-Zaforteza I., Garlock M.E.M., Loma-Ossorio E., Schiffner D. and Hospitaler A., "Analysis of a bridge failure due to fire using computational fluid dynamics and finite element models". *Engineering Structures*, 2014. http://dx.doi.org/10.1016/j.engstruct.2014.02.022. In press.

[6] Peris-Sayol G., Alós-Moya J., Payá-Zaforteza I., Hospitaler-Pérez A., "Estudio paramétrico de la respuesta termo-estructural de un puente metálico multijácena sometido a incendios reales". Informes de la Costrucción 2014; 66 (N ºExtra-1), doi: http://dx.doi.org/10.3989/ic.13.077

[7] Society of Fire Protection Engineers. *SFPE Handbook of Fire Protection Engineering*. 3th Edition. NFPA, USA; 2002. ISBN 087765-451-4

[8] Wickström U., Duthinh D. and McGrattan K. "Adiabatic surface temperature for calculating heat transfer to fire exposed structures". *Interflam 2007*; 2:943–53, September 2007.

8th International Conference on Structures in Fire
Guo-Qiang LI, Venkatesh K. R. KODUR, Shou-Chao JIANG, Jian JIANG, Su-Wen CHEN, Guo-Biao LOU (Eds.)
Shanghai, China, June 11-13, 2014

EXPERIMENTAL TESTS AND NUMERICAL MODELLING ON EIGHT SLENDER STEEL COLUMNS UNDER INCREASING TEMPERATURES

Jean-Marc Franssen*, Bin Zhao and Thomas Gernay***

* University of Liege, Belgium
e-mails: jm.franssen@ulg.ac.be, thomas.gernay@ulg.ac.be

** C.T.I.C.M., France
e-mail: bzhao@cticm.com

Keywords: Steel, Column, Class 4, Slender section, Fire resistance, Test, Modelling

Abstract. *This paper is about a series of experimental fire tests on eight full scale steel columns made of slender I shaped class 4 sections. Six columns were made of welded sections (some prismatic and some tapered members) and two columns were with hot rolled sections. The nominal length of the columns was 2.7 meters with the whole length being heated. The load was applied at ambient temperature after which the temperature was increased under constant load. The load was applied concentrically on some tests and with an eccentricity in other tests. Heating was applied by electrical resistances enclosed in ceramic pads. Numerical simulations were performed using shell elements of the software. The paper presents the results obtained in terms of failure mode and ultimate temperature, in the experimental tests and in the numerical simulations.*

1 INTRODUCTION

When stocky steel members are submitted to compression or bending, they deform globally, which means that their longitudinal axis is bent but their sections does not change in shape. Members made of slender plates, on the contrary, distort on the whole length and may also exhibit short waves distortions. Such behaviour is much more complex than the behaviour of stocky sections and this is the reason why design methods for slender members are lagging behind design methods developed for other members. Eurocode 3 [1], for example, recommends that the temperature in Class 4 sections should be designed according to a method that is a direct extrapolation of a method developed for room temperature, the extrapolation being based on reasonable but unverified hypotheses. Alternatively, the steel temperature should not exceed 350 °C.

In order to fill the lack of knowledge about slender elements behaviour at elevated temperatures, a European research project called FIDESC4 has been funded by the RFCS. This project involves experimental testing, parametric numerical analyses and development of simple design rules. The present paper reports the characteristics and the results of the FIDESC4 experimental test campaign performed at the University of Liege on slender steel columns at elevated temperatures.

2 TEST SET-UP

2.1 Heating of the specimens

The specimens were not tested in a gas furnace used for standard fire resistance tests. It was preferred to heat the specimens with electric resistance inserted in ceramic pads, for the reasons detailed below.

In order to allow for a better comparison of the structural behaviour between all specimens, it was desired to follow the same temperature increase rate in all specimens, independent of the thermal massivity of the specimen. If the standard fire curve is applied in the furnace, different specimens with different massivity will heat up at different rates. On the other hand, it is difficult to control the rate of temperature increase in the steel specimen with a gas furnace. Such furnaces are normally designed to follow the standard fire curve, which means that a significant amount of power is released in the furnace as soon as the burners are turned on in order to cope with the rapid temperature increase shown by the standard ISO834 fire curve during the first instants of the test. The electric heating system is designed to follow a prescribed temperature heating rate directly measured on the steel specimen.

Another reason for using electric heating is that this allows a more uniform temperature distribution in the specimens. A gas furnace is indeed heated by a discrete number of burners, the location of which can induce a non-uniform temperature distribution in the specimen because of the radiation of the flame of each burner. In addition to that, the gas burners may not be evenly distributed around the specimen. The ceramic pads, on the contrary, are easily distributed symmetrically around the specimens.

A series of blank tests was nevertheless performed on an unloaded specimen. The first reason was to verify that the thermal insulating blankets that had been installed surrounding the specimen and the ceramic pads would be sufficient to generate the desired heating rate until the desired maximum temperature. The second reason was to verify the uniform character of the temperature distribution in the steel specimen. In the first tests, a significant temperature difference was observed in the web of the section between the zones that were directly covered by a ceramic heating pad and the zone that were not covered (it is not possible to cover all the surface of the specimen with ceramic pads; some zones are covered while some zones are not covered). With a heating rate of 100 ℃/hour, temperature differences in the order of 50 to 80 degrees Celsius were observed for two locations in the web separated by only 130 mm. Decreasing the heating rate or allowing for some minutes of constant temperature at, say, every 100 ℃ step, did not prove to solve the problem. The problem was solved when a practical arrangement was found that allowed the ceramic pads not to be in direct contact with the steel specimen. A gap of around 10 mm was provided between the pads and the steel section and it appeared as if convection in this gap surrounding the column reduced very significantly the temperature differences. With a heating rate of 100 ℃/h up to 300 ℃ and 200 ℃/h up to 600 ℃, the maximum temperature difference was, at the end of the test, only 27 ℃. The tests of the loaded specimen were thus performed at a heating rate of 200 ℃/h, with the heating pads separated in 6 different zones, each zone being controlled independently.

Finally, it is much easier to measure lateral displacements of the column with the electric system than in a gas furnace. Two rods were inserted through the insulating blankets at mid-level of the column, in perpendicular directions. The horizontal displacements in two directions could thus be measured and even the global buckling mode could be visually observed in the last instants before failure, which helped in the decision process leading to the unloading of the specimen before excessive damage is induced in the equipment.

2.2 Loading of the specimens

Each specimen was fabricated with a stiff steel end plate welded at each end of the column; the thickness of the plate varied from 20 to 35 mm. In these plates were drilled 4 holes which allowed bolted connection with another steel plate that was part of a hinge support. The distance between the axis of the hinge and the end plate of the hinge was 132.5 mm. Between the two steel plates were inserted two plates of high density insulting material (15mm + 20 mm, Promatect-H) in order to limit the heat losses from the specimen to the support, see the clearer plates on Figure 1. Such heat loss would indeed generate a non-uniform temperature distribution along the column length and, potentially, damage the hinge. The insulating product has an average compressive strength in the order of 4 N/mm ^{2}up to 600 ℃.

Figure 1. Hinged support.

The hinges were assumed to provide no restrain to rotation around one axis while preventing the rotation around the perpendicular axis. Preliminary numerical simulations performed with shell finite elements of the code SAFIR [2] showed that such support conditions were sufficient to induce failure in the direction of the strong axis of the section; no torsional compression buckling or buckling in the direction of the weak axis would occur (except when this is desired and the section is turned by 90 degrees). It was thus not necessary to provide mechanical means of lateral restraint that would have divided in two the buckling length in the direction of the weak axis.

2.3 Test procedure

The specimen was first loaded at room temperature and the load was thereafter kept constant for 15 minutes. The temperature in the steel column was then increased at a constant rate while the load was maintained (longitudinal thermal expansion was not restrained).

Applied load, temperature in the steel member art different point, as well as axial displacement and two transverse displacements at mid-level were recorded continuously.

The temperature was increased until the hydraulic system could not maintain the load constant in the hydraulic jack. At this time, axial and lateral displacements exhibit a rapid increase and the development of global buckling was clearly visible.

3 TESTED MEMBERS

Eight columns were tested, some with the load applied eccentrically, at one end or at both ends, and some with nominally axial loading. In fact, a small eccentricity of 5 mm was systematically applied in order to induce buckling in the direction of the weak axis and, also, in order to decrease the relative value of the uncertainty that nevertheless exists on the positioning of the load. This uncertainty is estimated to be in the order of 1 mm. The test arrangements were as described in Table 1.

Two tests were performed on hot rolled sections, 4 tests on prismatic welded sections and 2 tests on tapered welded sections. The nominal length of all specimens was 2, 700 mm measured from end plate to end plate (that is, not counting the thickness of the plates). The hinge supports were always turned in such a way to favour buckling in the direction of the applied eccentricity (rotation allowing displacements in the direction of the eccentricity and preventing displacements in the other direction).

Table 1. Test arrangements.

Test	Section	Class of the web	Class of the flange	Eccentricity And direction (mm)	Applied load (kN)
1	IPE240AA 237/120/5,2/8,3	4	1	5 – 5, weak	144.5
2	450/150/4/5	4	4	5 – 5, weak	122.4
3	450/150/4/5	4	4	5 – 5, weak	204.0
4	500-300/300/4,5/5	4	4	6 – 6, strong	348.0
5	360/150/4/5	4	4	71 – 71, strong	231.3
6	360/150/4/5	4	4	177.5 – 177.5, strong	166.4
7	HE340AA 320/300/8,5/11,5	3	3	100 – 0, strong	760.8
8	450-300/150/4/5	4	4	150 – 0, strong	219.0

Initial geometrical imperfections were measured for each specimen in the web and in each flange. Table 2 gives the amplitude of the global imperfections in mm measured in the direction of the weak axis and of the local imperfections in the web and in the flange, the value of the thickness and of the measured yield strength for the web and for the flange and the length of the column (including the end plates). No coupon tests were available for tests 4 and 5.

Table 2. Geometrical imperfections.

Test	Length (mm)	Global imperfection (mm)	Local imperf. in the web (mm)	Yield strength in the web (N/mm^2)	Local imperf. in the flange (mm)	Yield strength in the flange (N/mm^2)
1	2 740	1,5	0,2	445.5	0,3	397.8
2	2 760	2,7	3,2	464.7	2,4	404.0
3	2 760	5,4	2,7	464.7	4,7	404.0
4	2 750	1,8	4,5	-	1,5	-
5	2 760	2,2	3,4	-	1,6	-
6	2 760	1,0	2,2	464.5	1,2	404.0
7	2 755	1,5	0,5	579.5	0,6	530.5
8	2 760	1,0	2,8	579.5	1,5	530.5

4 TEST RESULTS

Table 3 gives the temperature reached at time of failure and the mean features of the failure mode.

In the philosophy of *open data*, more data such as temperature –displacement curves or pictures of the columns after failure can be found on http://hdl.handle.net/2268/163773.

Table 3. Critical temperatures.

Test	Temperature from the tests (℃)	Temperature by SAFIR (℃)	Failure mode in the tests
1	610	572	Global in the weak axis direction, no local buckling
2	608	594	Global in the weak axis direction, local buckling in the flanges
3	452	459	
4	520	535	Global in the strong axis direction, local buckling in the flanges, lateral torsional buckling at mid-level
5	510	526	Global in the strong axis direction, local buckling in the flanges
6	530	531	Essentially local buckling
7	623	630	Global in the strong axis direction, local buckling in the flanges and in the web at mid-level
8	505	537	Local buckling in the flange, some lateral torsional buckling at mid-level

5 NUMERICAL SIMULATIONS

The tests were modelled first before the tests, based on the nominal characteristics of the material properties. These simulations served first to indicate the type of failure mode to be expected and they showed that it was not necessary to provide lateral restrain at mid-level of the column to force the global buckling in the desired direction: the applied eccentricity and the difference in restrain with respect to rotation in both axes provided by the hinges would be sufficient to induce failure in the desired direction. The simulations also served to choose the load to be applied during the test in order to obtain failure in the desired temperature range (from 500 to 600 degrees Celsius).

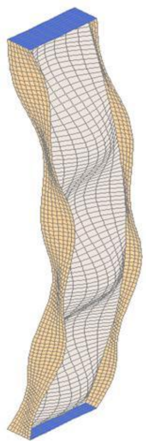
Figure 2. Geometrical imperfections.

After the tests, simulations were performed again based on the measured values of the yield strength, of the steel temperature, of the applied load and of the applied eccentricity. The geometrical imperfections were simplified and represented by half a sinusoidal in the direction of the weak axis for the global imperfection and sinusoidal waves for the flanges and for the web. Figure 2 illustrates the initial geometry of a specimen, with the imperfections being amplified to be more visible.

In order to get the correct buckling length of the column, the nominal length presented in table 2 was increased by 167.5 mm at each end of the column in order to take into account the extra length provided by the insulating plates (35 mm) and by the hinge (132.5 mm). These extra lengths were modelled by rigid extensions in order to take into account the fact that no local buckling can develop in these regions.

The critical temperatures are presented in Table 3. Figure 3 presents the comparison between experimental results and numerical results. The average value of the ratio SAFIR/Test is 1.01 with a standard deviation of 0.04. The numerical model validated by this comparison is presently being used in a series of parametric analyses performed in order to generate a data base of results. This data base will be used to develop and validate a design method for the fire resistance of slender columns.

6 CONCLUSIONS

A series of eight full scale experimental tests has been performed on slender steel columns under increasing temperature. The test set-up, tested specimens, testing procedure and test results are documented, for the essential features in this paper and for all details in an *open data* philosophy. These tests increase our knowledge about the failure modes of slender columns. They can also serve as a validation base of numerical models or design models.

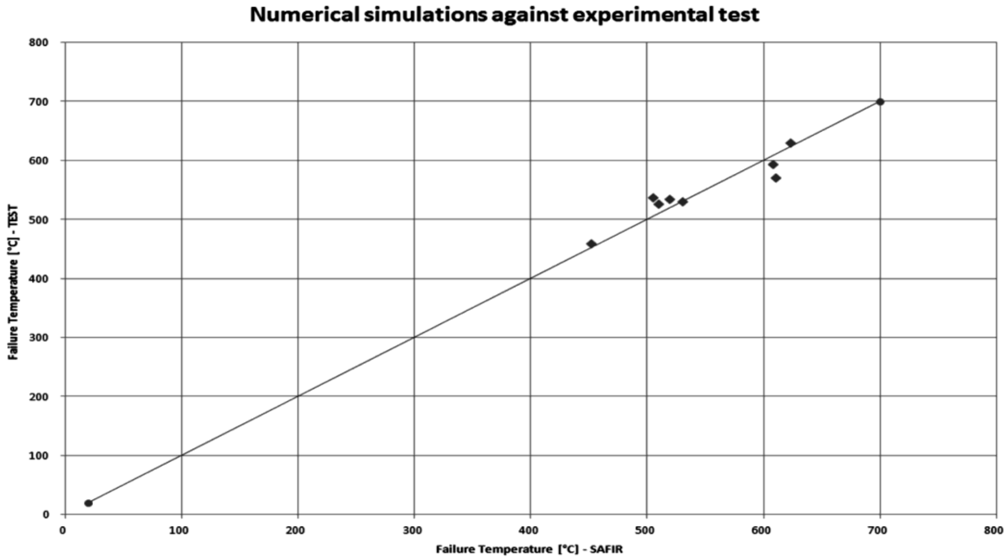

Figure 3. Comparison between experimental tests and numerical simulations.

ACKNOWLEDGEMENTS

The experimental test campaign has been conducted at University of Liege in the framework of the RFCS research project FIDESC4.

REFERENCES

[1] European Committee for Standardization**,** *Eurocode 3 - Design of steel structures - Part 1-2: General rules – Structural fire design*, Brussels. 2005.

[2] Franssen, J.-M. "SAFIR: A thermal/structural program for modeling structures under fire. *Engineering Journal*, American Institute of Steel Construction Inc, 42(3), 143-158. http://hdl.handle.net/2268/, 2005.

EXPERIMENTAL STUDY ON AXIALLY AND ROTATIONALLY RESTRAINED HIGH STRENGTH STEEL COLUMNS IN FIRE

Wei-Yong Wang*, Yong Ge*, Tian-Zi Liu* and Guo-Qiang Li**

*College of Civil Engineering, Chongqing University, Chongqing, 400045, P. R. China，
wywang@cqu.edu.cn
**State Key Laboratory for Disaster Reduction in Civil Engineering, School of Civil Engineering, Tongji University, Shanghai, 200092, P. R. China, gqli@tongji.edu.cn

Keywords: High strength Q460 steel, Column, Experiment, Restraint

Abstract. *Fire tests were performed to investigate the behavior of the restrained high strength Q460 steel columns when exposed to fire. Four full-scale columns were loaded axially and tested horizontal in a furnace dimension of 3.6m×4.6m×3.3m (width×length×height). Specimens were tested with several combinations of load level and degree of axial and rotational restraint under ISO-834 standard temperature curves. Temperature distribution and structural response of column in the furnace were recorded. The axial force in the column was generated by the strange gauge on the short column which supports bottom end of the column. The test results showed that the different combinations of tested parameters had a significant influence on the fire response of high strength steel columns. For the lower load ratio, the columns failed by global flexure buckling and for higher load ratio, the torsional buckling become significant.*

1 INTRODUCTION

The beauty of high strength stele is large elastic strength and high strength steel is most efficient when it is allowed to develop the full yield stress. Using the high strength steel in buildings, the overall weight of structures can be significantly reduced, resulting in savings in fabrication, erection, transportation to the site and smaller foundations. Lightweight and thin elements are also desirable for architecture and creative design of aesthetic members and structures [1]. Because of the advantages of high strength steel, in the past few years, steel contractors have placed an emphasis on the use of high strength steel members in construction. High strength Q460 steel is a new kind of high strength steel and widely used in Far East counties, especially in China.

The fire resistance provisions for steel structures in current design standards are based on conventional structural steel properties and does not account for high temperature properties of high strength steel. For mild steel, the behavior of restrained steel columns at elevated temperatures has been widely studied[2-7]. But there are only few literatures for high strength steel columns at elevated temperatures. High strength steel columns with nominal yield strength of 690 N/mm^2 has been studied by Rasmussen and Hancock [8,9] at room temperature. Material properties of high strength BISPLKATE80 steel at elevated temperature and the behavior and design of high strength BISPLKATE80 steel columns at elevated temperatures have been carried out by Chen et al [10,11]. Wang et al [12] performed tests on mechanical properties of high strength Q460 steel. Up to date, there is still lack of information for the fire resistance of high strength steel columns, especially for the test data on the fire behavior of high strength steel columns. To better understand the behavior of high strength steel columns in fire, an experimental program was undertaken at Tongji University. The restrained high strength steel column specimen were deliberately fabricated and designed. The usefulness of this research is in providing authentic and original test data for fire response and failure of restrained high strength steel columns in steel structures.

Our investigation is composed of two parts. This paper, Part 1 of the experimental study, presents the experimental results of 4 full-scale high strength steel columns conducted recently at Tongji University. These columns are of practical sizes and subjected to a standard ISO-834 temperature curves. Different load ratio and restraint stiffness were investigated. A companion paper, part 2 of finite element study, will present the FEM simulation and parametric study on the behavior of high strength Q460 steel columns in fire.

2. FIRE RESISTANCE TEST

2.1 Test apparatus

This paper outlines an experimental program of restrained high strength Q460 steel column tests under elevated temperature. The test set-up is comprised of four parts, furnace, reaction frame, load system, and specimen. The dimension of furnace is 3.6m wide, 4.6m long and 3.3m high. The maximum heat power the furnace can produce is 5MW. Eight natural gas burners located within the furnace provide thermal energy, while ten thermocouples, distributed throughout the test chamber, monitor the furnace temperature during a fire test.

During the fire test, these furnace temperatures are used to automatically adjust fuel supply, and maintain a temperature course consistent with the pre-determined standard or realistic fire scenarios. In this way, the furnace temperature can be maintained along a desired curve.

A horizontal self-reaction test frame of ultra high stiffness was designed to minimize frame movement and was laid on the top of furnace. Axial load was applied horizontally by a pressure actuator with capacities of 1000 kN. Any one of specimen includes a steel column and two steel beams which provide the axial and rotation restraint to the test column. The column was connected to the two beams with extend end-plate joints and the beams connected to reaction frame by four steel corbels. There is a short column connected the right beam with frame and transfer the applied load from the column to the frame. The furnace and layout of specimen in the furnace is shown in Figure 1. Columns were orientated such that they bent about the weak axis.

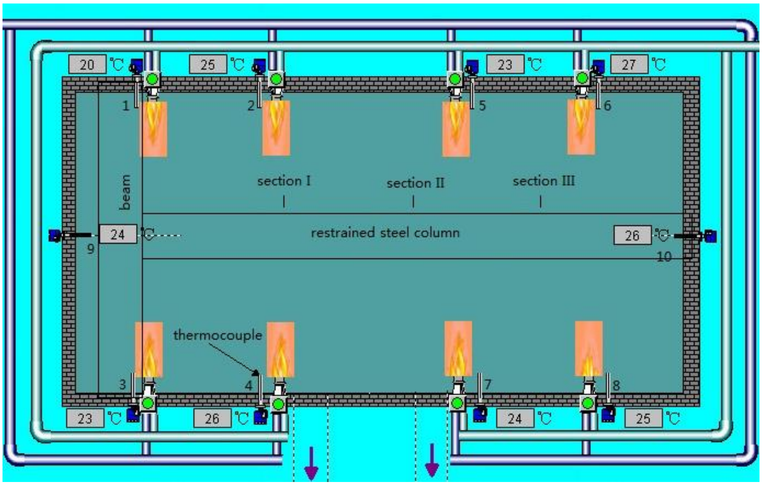

Figure 1. Plan of furnace and layout of specimen.

2.2 Test instrumentation

The test specimens were instrumented with thermocouples, strain gauges, and displacement transducers to monitor their thermal and mechanical response during the fire tests.

Steel temperatures were measured using Type-K Chrome-alumel thermo-couples, 2.0 mm thick, installed at three cross-sections (0.25, 0.5 and 0.75 times of length) along the length of each column. The furnace temperature was measured using ten thermocouples distributed spatially inside the furnace in accordance with the ISO-834 test procedures.

Three strain gages were attached to the short column connected with right beam to generate the axial force developed in the restrained steel column. Horizontal oriented linear variable differential transformers (LVDT) were attached at two distinct locations at the top of column and mid-span in order to calculate axial displacement and deflection. The pressure in the horizontal actuators was also recorded as a measure of applied axial load. All the instrumentations in the test were shown in Figure 2.

2.3 Test specimen

Four bared steel columns specimens connected with eight beams were tested to failure in this study, namely S-1, S-2, S-3 and S-4. Two load levels and two restraint stiffness were considered in the test. The slenderness ratio and ultimate load bearing capacity at room temperature for the column is 48 and 1730kN respectively.

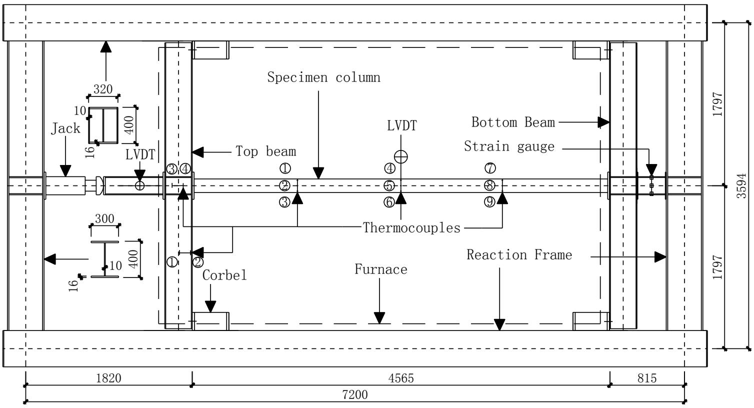

Figure 2. Test set-up and instrumentation.

All test columns used an H200x195x8x8 cross-section with Q460 steel (Fy=585 MPa) and were fabricated to a length of 4.48 m. All the beams used an H200×150×6×9 or H300×150×6.5×9 cross-section with Q235 steel (Fy=280 MPa) and were fabricated to a length of 3.2 m. To obtain the mechanical properties of steel at room temperature, standard coupon tests were conducted and the ASTM A370 test protocol was followed [13].

The load level defines as the ratio of load applied on the column to the ultimate load bearing capacity at ambient temperature as expressed

$$R = \frac{N}{N_{\mathrm{cr}}} \tag{1}$$

where N is the load applied on the top of the column and N_{cr} is the ultimate load bearing capacity at ambient temperature.

The degree of axial restraint represents as the axial restrain ratio, which means the ratio of restraint stiffness provided by the beam to the compression stiffness of column at the ambient temperature as expressed

$$\beta_a = \frac{K_b}{K_c} = \frac{48EI_b}{l_b^3} \Bigg/ \frac{EA_c}{l_c} \tag{2}$$

Where K_b is the defection stiffness of beam; K_c is the compression stiffness of column; I_b is the moment of inertia of beam; l_b is the length of beam; A_c is the cross sectional area of column; l_c is the length of column.

The degree of rotational restraint represents as the rotational restraint ratio, which is the ratio of rotational stiffness at the mid-span of beam to the rotation stiffness of column. Taking the axial load applied on the column into consideration, the ratio can be expressed as [14]

$$\beta_a = \frac{K_{rb}}{K_{rc}} = \frac{6EI_b}{l_b} \Bigg/ \left(\frac{\varphi \sin\varphi - \varphi^2 \cos\varphi}{2 - 2\cos\varphi - \varphi \sin\varphi} \right) \cdot \frac{EI_c}{l_c} \cdot \frac{6EI_b / l_b + \varphi^2 tg\varphi / \left(tg\varphi - \varphi\right) \cdot EI_c / l_c}{6EI_b / l_b + \left(\varphi \sin\varphi - \varphi^2 \cos\varphi\right) / \left(2 - 2\cos\varphi - \varphi\sin\varphi\right) \cdot EI_c / l_c} \tag{3}$$

Where K_{rb} is the rotational stiffness at the mid-span of beam; K_{rc} is rotation stiffness of column; $\varphi = l_c \sqrt{N / \left(EI_c\right)}$.

The detail information about the specimen is tabulated in Table 1.

Table 1. Parameters of specimen.

Specimen No.	Beam section	Load	Axial restraint ratio	Rotation restraint ratio
S-1	H200×150×6×9	390kN	0.065	17.8
S-3	H300×150×6.5×9	390kN	0.099	27.4
S-3	H300×150×6.5×9	710kN	0.099	47.5
S-4	H200×150×6×9	725kN	0.065	32.5

2.4 Test procedure

The test procedure comprises of the following steps.

(1) Install the specimen into the reaction frame and instrumentation on the specimen, including the thermocouple, strain gauge and LVDT.

(2) Apply the load. This loading was applied in two phases: a preloading phase and formal loading phase. Before any load was applied, all the measurement channels were scanned to record the initial readings. Then, the loading from hydraulic jack was increased to 10% of target load level, kept for few minutes and then released until it was reduced to zero. This preloading process was repeated twice to confirm that the displacement and strain gauges exhibit linear variation with the load and all the readings returned to their initial values after the load was completely released. Following preloading, the load was increased slowly until to the target load level. Then the load was maintained constant during the fire test.

(3) Start the furnace and observe the test phenomenon during the test.

(4) Stop the furnace if the axial displacement or deflection of the test column increases up to the maximum range.

(5) Save all the data generated in the test, including temperature, displacement and strain.

3. TEST RESULTS

Data generated from the fire tests is used to study the overall performance of axial-rotational restraint high strength Q460 steel exposed to fire. Thermal response, structural response, and failure patterns are compared to evaluate the effect of load level and degree of axial and rotational restraint on the behavior of high strength steel columns.

3.1 Thermal response

Specimen S-1, exposed to the ISO-834 standard fire as shown in Figure 3, experienced increasing temperature until the test ended at about 24 min. The average rate of temperature increase for the column was approximately 29°C/min.

As can be seen from Figure 3, at the first several minutes, the furnace temperature can not follow standard curve due to the air in the furnace need to be heated. After 3-5 minutes, the furnace temperature follows the standard temperature closely. The column was directly exposed to fire and the temperature increase very quickly, which is attributed to the thin flange and web of the column. Thermocouples across the column section recorded nearly uniform temperatures that did not exceed 50°C, and therefore temperature gradient effects on the column were relatively negligible and the cross-sectional mean temperature at column was used to represent the specimen temperature in the section of structure response.

During the test, the left beam was wrapped with fire insulation blanket and the temperature increase is very slow (the maximum temperature is about 260°C). After about 24 minutes, the furnace was turn off because the specimen experience failure and great deformation was observed. After the burnings in the furnace distinguished, the temperature of air in the furnace and column experienced rapid decrease due to the heat energy supply was cut off and the heat in the furnace was continuously taken away by the chimney of the furnace. But the temperature of beam decreased slowly (as show in Figure 5). There are two reasons result in these phenomenon, one is the temperature is low and the other one is the protection of fire insulation lead to the slow heat lose.

The temperature recorded for specimen S-2, S-3 and S-4 had a similar trend with specimen S-1 as show in Figures 3-5.

3.2 Structural response

The structural performance of the column specimens was measured using the displacements and strains recorded during the fire tests, and the data is reflected in Figure 6. The A and M denote the axial displacement and deflection at mid-span respectively. The axial displacement and deflection curves were calculated using horizontal displacement data recorded by the horizontal LVDT attached to the top and mid-point of each specimen. Positive axial force denotes compression. Positive axial displacement denotes elongation of column due to thermal expand.

During the fire tests, each column experienced thermal expansion upward against the restraint of the loading frame due to their increased temperature, which generated a corresponding increase in axial load. Figure 6 show that reductions in strength and stiffness eventually lead to a rapid decrease in both axial displacement and axial load as the column approached failure.

It should be pointed out that in reality, a heated axially restrained column normally will experience post-buckling behavior during contraction stages. This has been investigated theoretically by Franssen [15] and Wang [16]. However, due to the limitation of the test set-up, the post-buckling responses were not examined in this study.

3.3 Fire resistance

The failure times and critical temperature for the four tested columns are shown in Table 2. Failure is defined as the time when the columns can not maintain the applied load (i.e. when the sudden decrease in axial load and displacement shown in Figure 7). Critical temperature is defined as the temperature at the time of failure. The time to reach failure from the start of fire exposure is defined as fire resistance. This definition of failure contrasts with the traditional prescriptive-based approach in which failure is often assumed to occur when steel attains its critical temperature regardless of loading behaviour.

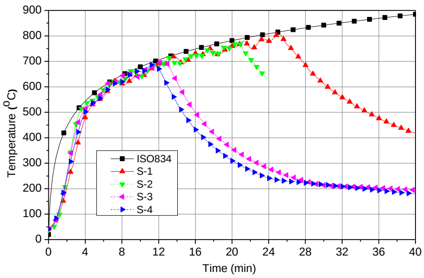

Figure 3. Temperature distribution of furnace.

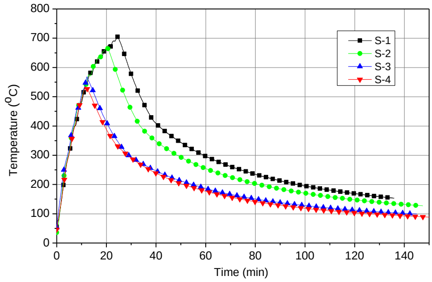

Figure 4. Temperature distribution of columns.

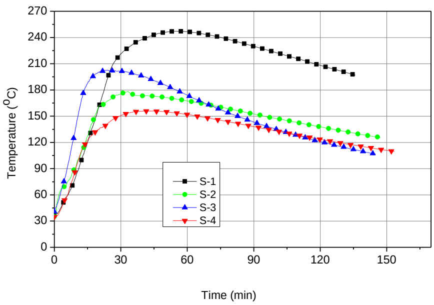

Figure 5. Temperature distribution of beams.

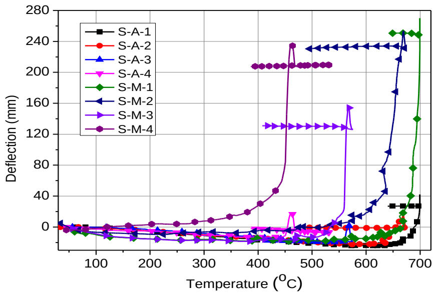

Figure 6. Test result as a function of temperature.

Table. 2 Critical temperature and failure time for specimens.

Specimen No.	Load Ratio	Critical temperature	Failure time
S-1	0.22	688°C	24min
S-3	0.22	637°C	18min
S-3	0.4	560°C	12min
S-4	0.4	452°C	9min

Figure 7 shows the failed shape of each column. It is clearly shown that for specimen S-1 and S-2, the global flexural buckling around weak axis happens during the test and for Specimen S-3 and S-4, flexural and torsion buckling can be observed significantly. This is probably attributed to the influence of load level on the structural behavior during the test. The load eccentricity for the specimen result in the additional moment around the axis of column and lead to torsion buckling at elevated temperatures. The further analysis and discussion on the damage pattern of specimen will be conducted in the companion paper.

4. CONCLUSIONS

A detailed experimental study has been carried out to investigate the restrained high strength Q460 steel columns subjected to rising temperature. During the test, axial loads were maintained constant throughout the heating. Totally, two different load levels were studied; for one load ratio, two different restraints were considered. In brief, the experimental results show that

(1) Bared restrained high strength Q460 steel columns exposed to fire can not last a long time even with a very low load level.

(2) The rotation restraint and axial restraint has great influence on the fire resistance of high strength steel columns.

(3) For high load levels, the failure of specimens often experience both flexural and torsion buckling and for low load levels, only flexural buckling was observed in the test columns.

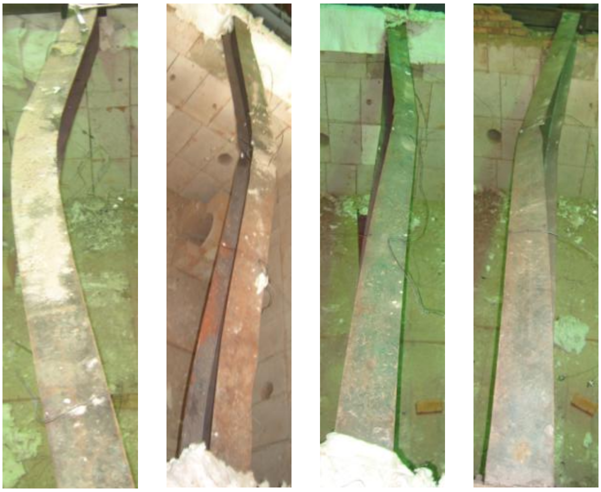

(a) S-1 (b) S-2 (c) S-3 (d) S-4

Figure 7. Failure of specimens.

ACKNOWLEDGEMENTS

The authors wish to acknowledge the support of Natural Science Foundation of China (51008320) and Special foundation of Chongqing postdoctoral research project (201103007). Any opinions, findings, and conclusions or recommendations expressed in this paper are those of the author s and do not necessarily reflect the views of the sponsors.

REFERENCES

[1] Girao Coelho AM, Bijlaard FSK. Experimental behaviour of HSS end-plate connections, *Journal of Constructional Steel Research* 2007, 63 (9): 1228-1240.

[2] Simms WI, O'Connor DJ, Ali F, Randall M. An experimental investigation on the structural performance of steel columns subjected to elevated temperatures. *Journal of Applied Fire Science* 1996; 5(4):269-84.

[3] Ali F, Nadjai A, Talamona D. Effect of rotational restraint on performance of steel columns in fire. *Journal of Applied Fire Science* 2004; 13(1):21-34.

[4] Tan KH, Toh WS, Huang ZF, Phng GH. Structural responses of restrained steel columns at elevated temperatures. part 1: Experiments. *Engineering Structures* 2007; 29(8):1641-52.

[5] Rodrigues JP, Neves IC, Valente JC. Experimental research on the critical temperature of compressed steel elements with restrained thermal elongation. *Fire Safety Journal* 2000; 35(2):77-98.

[6] Wang YC, Davies JM. An experimental study of non-sway loaded and rotationally restrained steel column assemblies under fire conditions: Analysis of test results and design calculations. *Journal of Constructional Steel Research*, 2003; 59(3):291-313.

[7] Ali F, O'Connor D. Structural performance of rotationally restrained steel columns in fire. *Fire Safety Journal* 2001; 36(7):679-91.

[8] Rasmussen KJR, Hancock GJ. Plate slenderness limits for HSS sections. *Journal of Constructional Steel Research* 1992; 23(1):73-96.

[9] Rasmussen KJR, Hancock GJ. Tests of HSS columns. *Journal of Constructional Steel Research* 1995; 34(1):27–52.

[10] Chen J, Young B, Uy B. Behaviour of high strength structural steel at elevated temperatures. *Journal of Structural Engineering*, ASCE 2006; 132(12):1948-54.

[11] Chen J, Young B. Design of HSS columns at elevated temperatures [J]. *Journal of Constructional Steel Research*, 2008, 64(6): 689-703.

[12] Wang WY, Liu B, Venkatesh Kodur. Effect of Temperature on Strength and Elastic Modulus of High Strength Steel [J], ASCE-*Journal of Material in Civil Engineering.* Under review.

[13] American Society for Testing and Materials International (ASTM). *Designation: A370-09 Standard test methods and definitions for mechanical testing of steel products.* West Conshohocken, PA; 2009.

[14] Chen SF. Guide to stability design of steel structures [M], 2nd edition. Beijing, China *Architecture and Building Press*, 2004. (In Chinese)

[15] Franssen JM. Failure temperature of a system comprising a restrained column submitted to fire. *Fire Safety Journal*, 2000, 34:191-207.

[16] Wang YC. Post buckling behaviour of axially restrained and axially loaded steel columns under fire conditions. *Journal of Structural Engineering*, ASCE 2004, 130(3):371-80.

8th International Conference on Structures in Fire
Guo-Qiang LI, Venkatesh K. R. KODUR, Shou-Chao JIANG, Jian JIANG, Su-Wen CHEN, Guo-Biao LOU (Eds.)
Shanghai, China, June 11-13, 2014

TEMPERATURE DISTRIBUTION IN PROTECTED STEEL SECTION SUPPORTING A CONCRETE SLAB ON TOP

Dmitrij Podolski*,, Ji-Feng Yuan* and Yong-Chang Wang****

* Exova Warringtonfire, UK
e-mails: dmitrij.podolski@exova.com, jifeng.yuan@exova.com

** School of Mechanical, Aerospace and Civil Engineering, The University of Manchester, UK
e-mail: yong.wang@manchester.ac.uk

Keywords: Deep web beam, Elemental section factor, Temperature difference, EN 1994-1-2

Abstract. *This paper presents the results of an analysis of 64 fire test results to assess accuracy of EN 1994-1-2 [1] for calculating temperature distribution within protected steel section supporting concrete slab on top. Temperature differences between the web and the lower flange of a number of Universal Beam (UB) sections were obtained from commercial fire resistance tests under the standard cellulosic fire temperature-time curve. The results of this analysis indicate that regardless of the depth of the steel section, the difference between average steel web and lower flange temperatures of the 64 tested sections is small. In the region of interest where the overall mean steel temperature was from 500 °C to 650 °C, the maximum difference between elemental (lower flange, web) temperatures and the overall mean steel temperature was less than 33 °C (Figure 5). In fact, the maximum difference between web/flange temperatures for the deep sections (>500mm) was comparable with that for the shallow sections (<500mm). Uniform temperature in the protected steel section can be assumed. Using the EN 1994-1-2 method to calculate different elemental temperatures for a selection of 7 deep beams, the maximum difference between the web and lower flange temperatures was 136°C (Table 2). However, in the fire tests, the maximum temperature difference between the web and lower flange was 38°C.*

1 INTRODUCTION

Because the strength of steel significantly decreases at high temperatures, fire protection is often necessary to protect steel so as to reduce its temperature rise under fire exposure. In EN 1994-1-2 [1], the temperature distribution in protected steel section supporting a concrete slab on the top flange is assumed to be uniform if the steel section depth does not exceed 500mm. However, if the depth of the steel section exceeds 500mm, the temperature distribution is assumed to be non-uniform and the temperatures of the upper flange, the web and the lower flange should be calculated separately using their individual section factors. Because the web of an 'I' beam section is usually thinner than the flange, the EN 1994-1-2 method gives a higher web temperature. This assumption has little influence on calculating bending moment capacity of the beam. However, since the web of a steel section resists shear force, if shear resistance governs, a high web temperature means that the beam has a very low limiting temperature for the lower flange. Since it is the lower flange temperature that determines the required fire resistance thickness, a high fire protection thickness would be required, which makes the construction costly.

This paper examines accuracy of the assumption in EN 1994-1-2. This study was carried out using temperatures measured in commercial fire tests carried out at Exova on 64 protected steel sections supporting composite slab on the top flange.

2 EXPERIMENTAL STUDY

2.1 Test specimens

A total of 64 one metre long Universal Beam (UB) sections protected with different thicknesses of intumescent coatings were fire tested over a number of years at Exova. 31 steel sections were classified as deep (>500mm) with overall depth of the section ranging from 610mm to 1016mm. The other 33 sections were shallow (<500mm) with the overall depth ranging from 102mm to 406mm.

2.2 Instrumentation for measurement of steel temperatures

Each of the steel sections was provided with a number of stainless steel sheathed K-type 1.5mm in diameter thermocouples which were fixed to the steelwork prior to application of the protective coatings. The thermocouples were spaced over the length of the steel section on the upper surface of the lower flange and at mid-height of the web. All thermocouple tips were inserted into pre-drilled holes. Figure 1 shows locations of the thermocouples fixed in accordance with two fire resistance test standards.

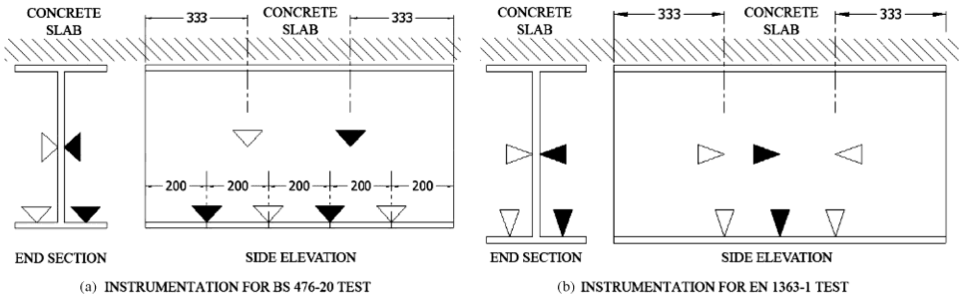

Figure 1. Locations of thermocouples, (a) for BS 476-20 fire exposure [2], (b) for EN 1363-1 fire exposure [3].

2.3 Test procedure

A gas fired 4m long by 3m wide by 3m deep furnace was used to conduct the fire tests and the fire exposure was according to BS 476-20 [2] or EN 1363-1 [3]. To minimize heat transfer at the ends, the test specimens were insulated at these positions. In all cases the beam sections were fixed to the soffit of the concrete slabs which also formed the roof of the furnace, to achieve three sided exposure. Temperatures of the steelwork and within the furnace were monitored continuously and recorded for the duration of each fire test. The fire tests were terminated after the required steel temperatures for the tests had been achieved.

2.4 Test results

Mistakes in the preparation stage may result in failure of the intumescent coating char during a fire test. Therefore, where possible, test specimen behaviour was observed. As a result of complete or partial failure of the protective coating, the steelwork temperatures recorded by some of the thermocouples significantly differed from the corresponding temperatures read by the remaining thermocouples fixed to the same element (the lower flange or the web) of the steel section. Under this circumstance, the inappropriate thermocouple readings were omitted to minimise errors in analysis.

Figure 2 shows differences in average temperatures between the web and the lower flange for the 31 sections deeper than 500mm. The average temperature of the whole section ranges from 500 ℃ to 650 ℃, which is the main region of interest in fire protection, for dry intumescent coating thickness ranging from 0.165mm to 6.053mm. Dots represent sections with higher temperature in the web than in the lower flange and squares are for specimens which experienced lower temperatures in the web than in the bottom flange. It is not surprising to see that as the coating thickness increases, the temperature difference decreases. This is because increase in coating thickness slows down the heating rate to the steel elements, hence allowing heat conduction between the steel elements to reach thermal equilibrium.

The highest temperature difference of 88 ℃ is for intumescent coating thickness of 0.247mm. After performing a detailed investigation of the original test report, it was found that the protection material unexpectedly detached (as a result of incorrect preparation) from the specimen and led to 230 ℃ difference between temperatures measured at the same locations (mid-height of web, top surface of lower flange, Figure 1, instrumentation method (b)) of the section. The thermal data generated from this specimen was omitted from further calculations and drawing the trendline. Among the other results, the maximum temperature difference was 60 ℃.

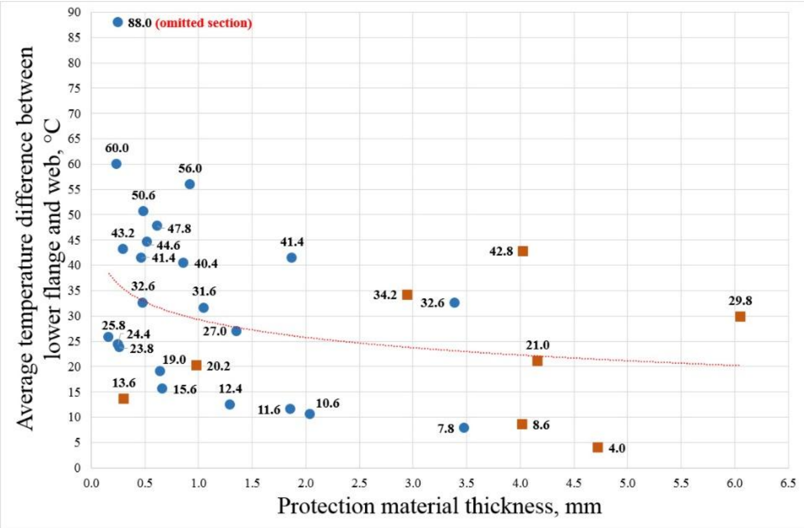

Figure 2. Intumescent coating thickness - temperature difference relationship for steel sections deeper than 500mm.

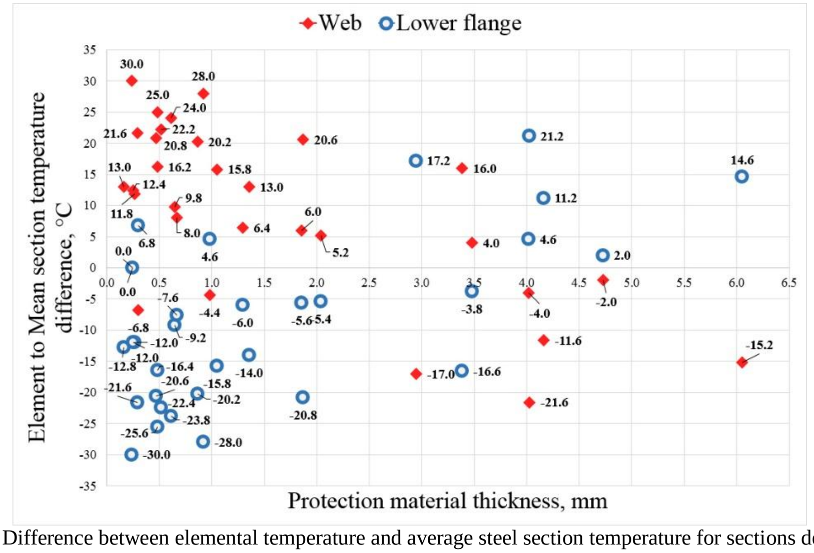

Figure 3. Difference between elemental temperature and average steel section temperature for sections deeper than 500mm, square for the web, dot for the lower flange.

Figure 3 presents differences in temperatures between the elements and the mean steel section temperature. A positive value means higher elemental temperature than the average section temperature. In most cases, the web was hotter than the average steel section and the flange cooler, because the web was thinner than the flange. The maximum difference between the elemental temperature and the average steel section temperature is 30°C. With this margin of difference in temperatures, it is acceptable to use the average steel section temperature for both the lower flange and the web.

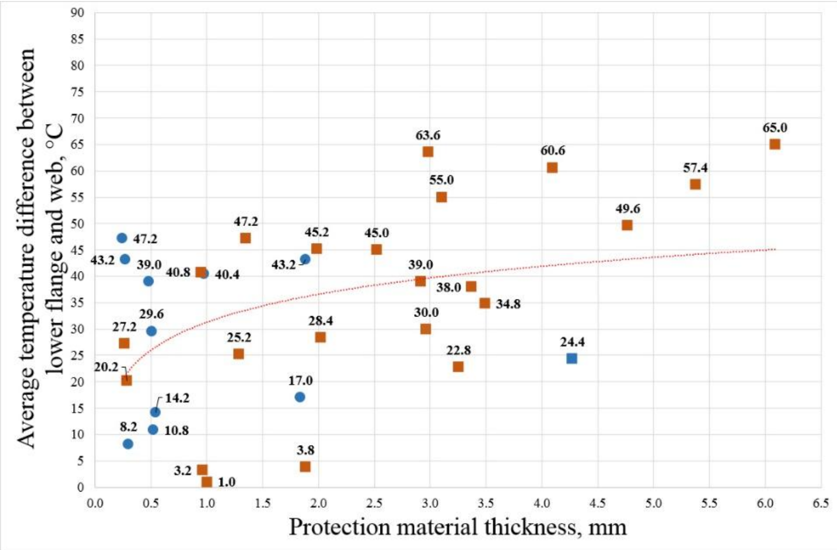

Figure 4. Intumescent coating thickness - temperature difference relationship for steel sections not exceeding 500mm depth.

Figure 4 shows temperature differences for steel sections shallower than 500mm. The intumescent coating dry film thickness ranged from 0.244mm to 6.087mm. The dot markers are for sections with higher temperature in the web than in the lower flange and square markers are for sections with lower temperatures in the web than in the bottom flange. Overall, the temperature difference increased slightly as the protection thickness increased, which is opposite to the trend shown in Figure 2 for the deep sections. The maximum temperature difference was 65°C.

The trend in Figure 4 may be explained by the two competing factors that cause the steel section temperature distribution to be slightly non-uniform. When the intumescent coating thickness is low and therefore the heating rate to the steel section is relatively high, the temperature difference between the web and the flange is mainly dependent on the steel thickness. Therefore, the web tends to have a higher temperature than the lower flange because of its smaller thickness. As the coating thickness increases, the heating rate is slow so the effect of differential web and flange thickness diminishes, as shown in Figure 2 for the trend of temperature distribution in deep sections. However, for shallow sections, heat loss from the web to the cooler concrete slab becomes dominant, resulting in increasing difference between the lower flange and web temperatures with the web temperature being lower.

If the web temperature is lower than the lower flange temperature, assuming uniform temperature in the steel section is on the safe side. Therefore, for shallow sections, the EN 1994-1-2 assumption of uniform steel section temperature is acceptable. However, when the web temperature is higher than the lower flange temperature, a comparison of the results in Figure 4 with those in Figure 2, indicates the temperature differences in both shallow and deep beams are very similar. The EN 1994-1-2 division of steel sections into shallow (not exceeding 500mm) and deep (greater than 500mm) sections is not logical.

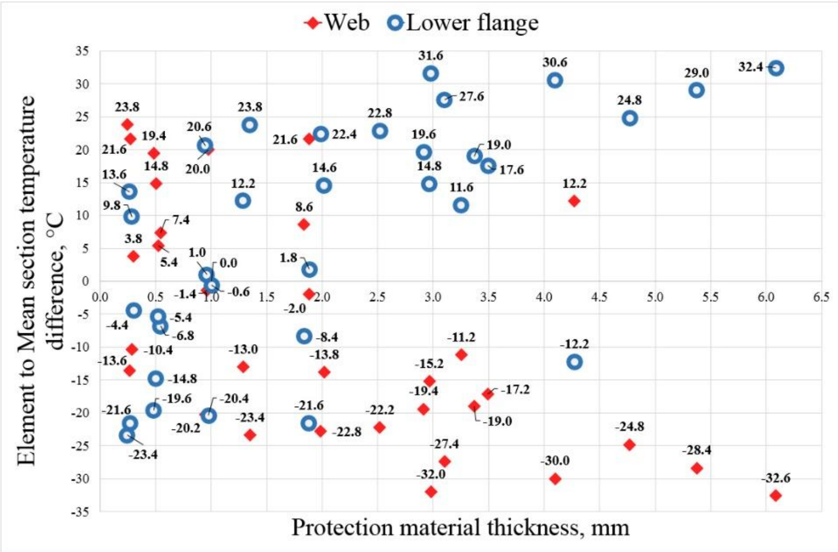

Figure 5. Difference between elemental temperature and average steel section temperature for sections not exceeding 500mm depth, square for the web, dot for the lower flange.

Similarly, Figure 5 presents temperature differences between the elements and the mean steel section temperature for shallow beams. As in Figure 3, a positive value means higher elemental temperature than the average section temperature. As concluded for Figure 3, using the average steel section temperature is acceptable both the lower flange and the web.

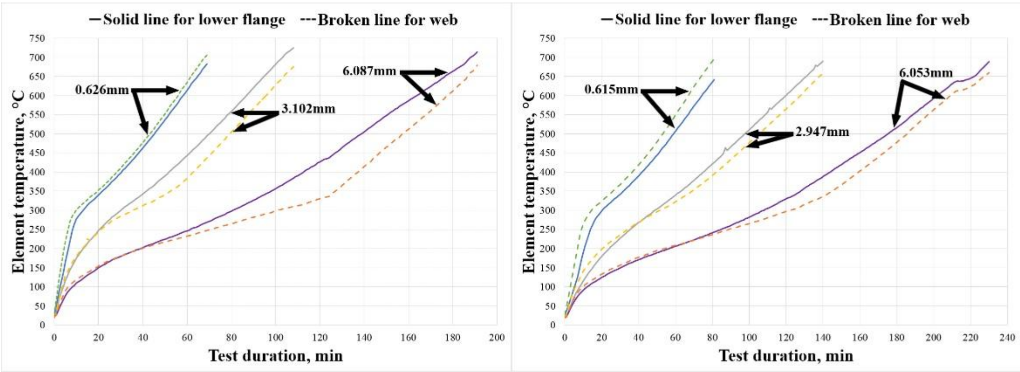

(a) Shallow sections (<500mm) (b) Deep sections (>500mm)

Figure 6. Temperature – time curves for web and lower flange of a selection of shallow and deep sections, (a) for shallow sections, (b) for deep sections.

Figure 6 further presents lower flange and web temperature-time relationships for a selection of shallow (<500mm) and deep sections (>500mm). The pair of curves for the web and lower flange of each beam are close and also the results for the deep and shallow sections are very similar.

3 IMPLICATION OF EUROCODE RECOMMENDATION

This section compares web and lower flange temperatures calculated using EN 1994-1-2 recommendation with the test results for steel sections deeper than 500mm. To do so, the average steel section temperatures are used to obtain the effective thermal conductivity of intumescent coatings.

The temperature increase $\Delta\theta_{a,t}$ for a lightly insulated steel section may be calculated using the following equation, taken from EN 1994-1-2.

$$\Delta\theta_{a,t} = \frac{\lambda_{p,t} A_p}{d_p V c_a \rho_a}\left(\theta_t - \theta_{a,t}\right)\Delta t \tag{1}$$

where $\lambda_{p,t}$ is the effective thermal conductivity of the coating at time t, A_p/V is the section factor of the protected steel section, d_p is fire protection thickness, c_a and ρ_a are the specific heat and the density of steel, respectively, θ_t is the average gas temperature at time t, $\theta_{a,t}$ is steel temperature at time t and Δt is the time interval.

The inverse solution of Equation (1) gives the effective thermal conductivity of the fire protection material at elevated temperatures, using Equation (2) below.

$$\lambda_{p,t} = \frac{\Delta\theta_{a,t}}{\frac{(\theta_t - \theta_{a,t}) A_p/V}{\frac{1}{d_p} c_a \rho_a}\Delta t} \tag{2}$$

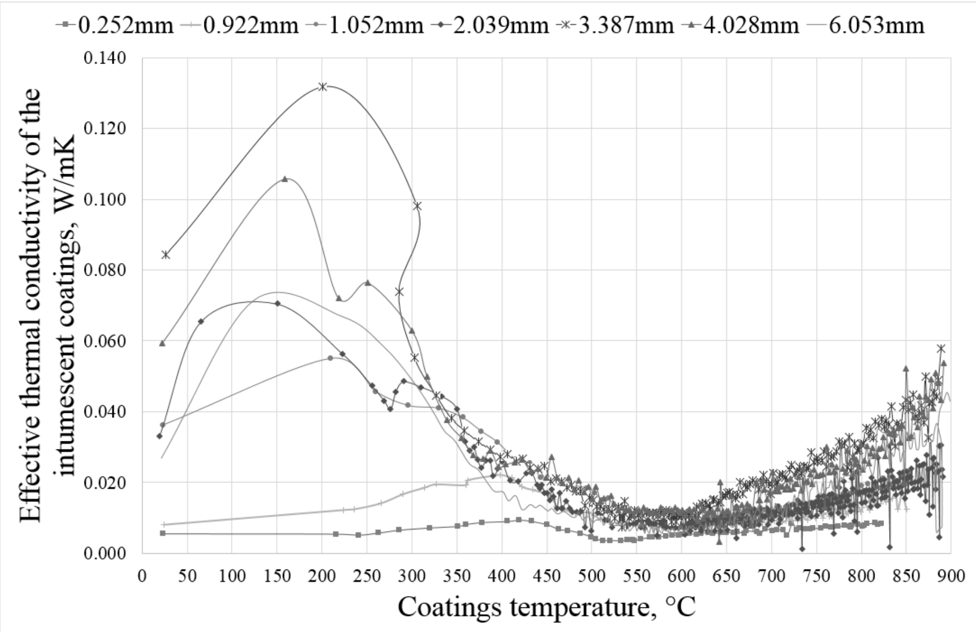

Figure 7. Calculated effective thermal conductivity of intumescent coatings for steel sections deeper than 500mm.

Using the average steel section temperature in Equation (2), the effective thermal conductivity of intumescent coatings for seven sections (details shown in Table 1) were calculated and the results are shown in Figure 7.

Table 1. Details of specimens used to calculate elemental temperatures according to EN 1994-1-2.

Serial Size	Intumescent coating thickness (mm)
610mm × 305mm × 238kg/m	0.252
1016mm × 305mm × 487kg/m	0.922
610mm × 305mm × 238kg/m	1.052
610mm × 305mm × 238kg/m	2.039
610mm × 305mm × 238kg/m	3.387
610mm × 305mm × 179kg/m	4.028
610mm × 305mm × 179kg/m	6.053

Using the thermal conductivity values in Figure 7 and the overall, individual lower flange and web section factors, different temperatures were calculated for the seven steel sections in Table 1. Table 2 compares the calculated temperature differences (web temperature – lower flange temperature) with the test results where the overall mean steel temperature ranges from 500 ℃ to 650 ℃. The EN 1994-1-2 calculations give temperature differences in excess of 100^{o}C in most cases whilst the test results show temperature differences of less than 50^{o}C in most cases.

Table 2. Comparison of web-lower flange temperature difference between calculations using EN 1994-1-2 and fire tests for deep sections.

Fire protection thickness, mm	Source	Temperature differences between web and lower flange where the overall mean steel temperature is				
		500°C	550°C	600°C	620°C	650°C
0.252	Fire test	28	27	24	23	20
	EN 1994-1-2	124	123	118	113	103
0.922	Fire test	57	58	57	55	53
	EN 1994-1-2	127	128	128	125	117
1.052	Fire test	26	29	32	35	36
	EN 1994-1-2	124	125	122	117	101
2.039	Fire test	8	10	11	12	13
	EN 1994-1-2	118	118	115	109	92
3.387	Fire test	24	29	35	37	38
	EN 1994-1-2	135	136	132	126	106
4.028	Fire test	50	51	44	40	29
	EN 1994-1-2	133	135	131	125	109
6.053	Fire test	39	33	28	27	22
	EN 1994-1-2	111	111	109	106	93

4 CONCLUSIONS

Using commercial fire test results for 64 intumescent coating protected steel sections, this paper assesses the temperature distribution recommendation in EN 1994-1-2 for steel sections with concrete slab on top. EN 1994-1-2 recommends that if the steel section depth exceeds 500mm, individual section factors for the lower flange and the web should be used when calculating their temperatures. From the results of an analysis of the test results and comparison between calculated and fire test results, this paper concludes that this EN 1994-1-2 recommendation is not justified. Regardless of depth of the steel section, the temperature differences between the web and the lower flange are similar. In fact, the average elemental temperature difference from the mean section temperature is reasonably small with the maximum being 33^{o}C (Figure 5). This means that the steel section temperature can be assumed to be uniform. In contrast, if the EN 1994-1-2 recommendation is followed, the temperature difference between the web and the lower flange would be much greater, often more than 100^{o}C.

The web of an I-section is much thinner than the flange. Therefore, the EN 1994-1-2 assumption for deep beams leads to much higher temperatures in the web than in the lower flange. This has important consequences on limiting temperatures of steel sections and hence specification of their fire protection thicknesses. In the majority of fire protection designs, only one limiting temperature for the entire steel section is specified. This temperature is that of the lower flange. If the temperature distribution is uniform, the lower flange usually governs under the maximum bending moment in the beam. However, if the temperature distribution in non-uniform and the web has a much higher temperature than the lower flange, then the web under the maximum shear force may govern design. This could give a much lower limiting temperature for the beam which is that of the lower flange. Using the lower limiting temperature of the steel section would then lead to a much higher fire protection thickness.

The results of this paper suggest that this EN 1994-1-2 recommendation should be changed and that temperature in fire protected steel sections should be assumed uniform.

REFERENCES

[1] European Committee for Standardization (CEN). *EN 1994-1-2: 2005 Eurocode 4 – Design of composite steel and concrete structures. Part 1-2: General rules - Structural fire design.* CEN, Brussels, Belgium, 53-61, 2005.

[2] The British Standard Institution (BSI). *BS 476 Part 20: Method for determination of the fire resistance of elements of construction (general principles).* BSI, London, UK, 1987.

[3] European Committee for Standardization (CEN). *EN 1363-1: 2012 Fire resistance tests. Part 1: General requirements.* CEN, Brussels, Belgium, 2012.

A NUMERICAL INVESTIGATION OF STEEL FRAME ROBUSTNESS IN FIRE

L. Chen*

*China Building Technique Group CO., Ltd
email: chenlu@hotmail.co.uk

Keywords: Fire, Robustness, Catenary action, Steel frame, Joint, Component based method

Abstract. *This paper reports the results of a series of numerical parametric studies on robustness of steel frame in fire. Specifically, it investigates effectiveness of providing alternative load paths as outlined in the UK Building Regulations [1]. The scenario is removal of an internal column and the alternative load path is catenary action in the connected beams. In this situation, joint behaviour is the key to control progressive collapse whether at ambient temperature or in fire. This research incorporates realistic joints. It will investigate how joint details may be changed to improve structural robustness in fire. The results of this research indicate that it is not possible for a frame to survive fire attack without progressive collapse if one corner column is removed. Survival of removal of an internal column is possible, but only by hanging the beams on the upper floors. Moreover, the vertical fire spread should be prevented to avoid structural progressive collapse.*

1. INTRODUCTION

Progressive structural collapse is the failure of one or several structural members leading to failure of adjacent structural members and further spreading to the entire structure. To prevent progressive structural collapse, it is important that the initially damaged structure has the ability to redistribute the out-of-balance loads [2]. The ability of a structure to prevent progressive collapse is termed robustness. One of the means of achieving robustness is to tie all the principal structural members together so that if one of these members fails, the entire structure can hold together to prevent whole structure collapse. The principal load carrying mechanism in this system is catenary action. In order to satisfy this requirement, the connections should be strong enough to transfer the 'tying force' between the connected beams and columns. Because catenary action is activated when the connected beams undergo very large deflections, it is also important that the joints should have high rotation capacity. Some research studies [3-6] have investigated implications of using catenary action on joints and on columns. These studies have led to recommendations on the required performance of joints and columns to enable catenary action to be developed in the attached beams.

This paper concentrates on steel frames. Although the tying force method has been extensively adopted in design codes and standards at ambient temperature, there has been relatively little research to investigate its applicability in fire. Wang and Wald [7] made some preliminary recommendations for achieving structural robustness in fire and commented on the effectiveness of catenary action in fire. Wang et al. [8] further explained how structural robustness may be provided in a number of scenarios. The main objectives of this paper are to perform some detailed investigations to assess the conditions for using catenary action in steel framed structures to control progressive collapse and also to assess the influence of fire spread. Realistic joints modelled using the component based method [6, 9] will be used in this research. However, to simplify the investigation, 2D frames will be used so this investigation does not consider out-of-plane behaviour. Moreover, no consideration of the effects of composite action is taken because this research is mainly aimed at developing an understanding of the alternative load transfer mechanisms in steel framed structures after experiencing some fire damages.

2. METHODOLOGY OF INVESTIGATION

2.1 Basic frame arrangement and structural members

The two dimensional frame arrangement is shown in Figure 1(a). It is a three-bay, three-floor steel framed structure. The storey height is 4m and the bay span is 9m. All the columns have the same size (305×305×198UC) and so are all the beams (457×191×82UB). The beams are all connected to the major axes of the columns. The cross-bracing system is in the middle bay of the frame and all bracing members use circular hollow sections (CHS 114×5). The bracing members are pinned to the connected columns and beams. The columns are simply supported at their bases. Following the research from Chen and Wang [3], the extended endplate connection using Fire Resistant (FR) bolts and a 15mm thickness endplate was found to allow the connected beam to develop a high level of catenary action. Since the purpose of this investigation is to find out how the frame structure redistributes loads on the assumption that catenary action in the beams can develop, this type of connection is adopted in this research. The columns and beams are subjected to concentrated loads as shown in Figure 1(a). In the basic case, the maximum load ratio for the columns is 0.5 (ratio of the applied load to the maximum load capacity of the simply supported column with one storey effective length) and the beam load ratio is also 0.5 (ratio of the applied load to the plastic bending moment capacity of the simply supported beam). Figure 1(a) also describes the notation system for all of the structural members. Figure 1(b) shows detailed dimensions of the beam-column joint. The mechanical properties of each structural member are identical to [3] and the reductions factors and elongation coefficients for the FR bolts are from Sakumoto et al. [10].

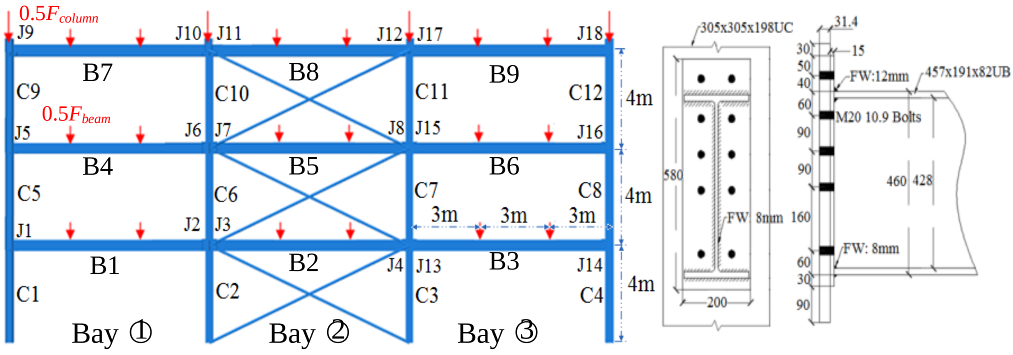

(a) Frame (b) Typical extended endplate connection

Figure 1. Simulation frame and typical connection details (C: column, B: beam, J: connection) .

2.2 Temperature distributions in different structural members

The columns were assumed to be uniformly heated along the cross-section, but the beams were non-uniformly heated to simulate the thermal shielding effects of a concrete slab on top. The temperatures of the beam bottom flange and the beam web were assumed to be the same, but the temperatures of the beam top flange were defined as being 0.8 times the temperatures of the beam bottom flange. The temperature of the connection was taken to be 0.75 times the temperature of the beam bottom flange. The temperature profiles for the columns and the beam bottom flange and web were calculated using the simple method in Eurocode EN-1993-1-2 [11] for unprotected steel sections subjected to the standard fire condition [12], but without considering the shadow effect. Since the results will be presented based on steel temperature, this is considered acceptable.

2.3 Simulation method

Based on Chen and Wang [9], using the component based model for joints and line elements for beams/columns, is able to faithfully and effectively simulate realistic frame structural behaviour when the beam developed a very high level of catenary action. This model was used in this study.

2.4 Fire scenarios

Fire spread to adjacent fire compartments is considered to be one of the main causes of fire-induced progressive collapse. Therefore, in this research, three fire scenarios were considered which are shown Figure 2. In real fire situations, the temperature–time relationship of the fire in the fire compartment into which the fire is spread will have a delay phase following the fire in the originating fire compartment. Due to the difficulty of modelling this realistic fire spread, this research assumed that in fire scenarios 2 and 3, the fire attacked both compartments at the same time, i.e. the fire temperature-time curve in both compartments was the same. It should be pointed out if fire scenario 3 occurs, the inner bottom column (C2) and crossing bracing system may be damaged. To investigate the steel frame robustness in fire, some modifications are necessary as shown in Figure 2(c): (1) Column (C2) at the ground floor was removed; (2) The cross bracing system in the basic frame was removed but the structure was provided with lateral supports at beam levels; (3) The applied load on the failure column was removed; (4) Columns C1 and C3 were fully fire protected.

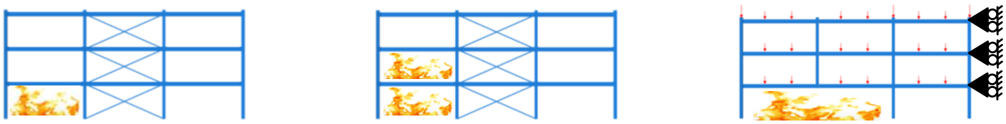

(a) Fire scenario 1 (b) Fire scenario 2 (vertical spread) (c) Fire scenario 3 (horizontal spread)

Figure 2. Different fire scenarios.

3. FIRE SCENARIO 1: FIRE IN THE CORNER COMPARTMENT IN BAY

In this fire scenario (Figure 2(a)), because the columns were heated without fire protection, the highlighted edge column (C1) in Figure 3(a) failed. At the column failure, connection J1 tried to prevent column C1 from buckling. With increasing temperature on connection J1, the capacity of connection J1 degraded and then connection failure started from the fracture of the bottom bolts as shown in Figure 3 (a). In this situation, the bending moments at the ends of beams B4 and B7 on the right hand side suddenly increased and these beams become cantilevers (Figure 3(b)). This drastically increased the bending moments in joints J6 and J10, resulting in their bolt fracture as shown in Figure 3(a).

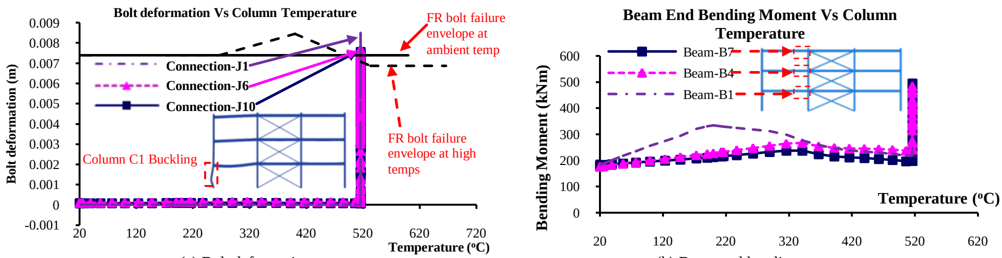

(a) Bolt deformation (b) Beam end bending moment

Figure 3. Bolt fracture after column buckling at the left hand side of Bay.

Two more simulations using different connections (flush endplate and rigid connections) were carried out. The connection details and simulation results are represented in Table 1. The failure mode was effectively the same as that using the flush endplate connection, due to column C1 failure accompanied by connection fracture. For using the idealised rigid/full strength connection, the failure mode was column failure accompanied by plastic hinges forming at the ends of the right side beams (B1, B4 and B7). Since the flush endplate connection provided the lowest rotational restraint to the column, the edge column C1 failure temperature was the lowest, however, the difference between the different connections is very small.

Table 1. Connection effects on the frame failure with edge column failure.

Connection	Bolt	Endplate Thickness	Endplate Steel Grade	Bending Moment Resistance	Failure Type	Column Failure Temp (^{o}C)
Extended endplate	FR/M20	15mm	S275	Limited	Column C1 failure/Bolt Fracture	516
Flush endplate	G10.9/ M20	15mm	S275	Limited	Column C1 failure/Bolt Fracture	512
Rigid/Full strength	--	--	--	Infinite	Column C1 failure/Plastic hinges at the beam ends	522

Development of catenary action in the beams requires the surrounding structure to be able to support the additional catenary action force and that the column boundary condition should be modified to reflect the loss of lateral restraint due to the beam in catenary action. This has been demonstrated in the sub-assembly study from [6]. In this exercise of fire scenario 1, the above requirements were ensured by controlling the column temperature to be below its limiting temperature corresponding to the condition when its effective length is two storeys high and its limiting temperature is calculated including the additional catenary action force. A new numerical analysis using these conditions gave the column limiting temperature as 182^{o}C.

Figure 4 demonstrates the effects of different column heating regimes. When the column temperature (the maximum being capped at 160^{o}C) was controlled to be lower than the new limiting temperature of 182^{o}C and the extended endplate connections with FR bolts were used for fire scenario 1, the frame survival temperature was increased to 856^{o}C due to beam failure. Using the flush endplate connections with G10.9/M20 bolts, the beam failed at 732^{o}C due to connection failure.

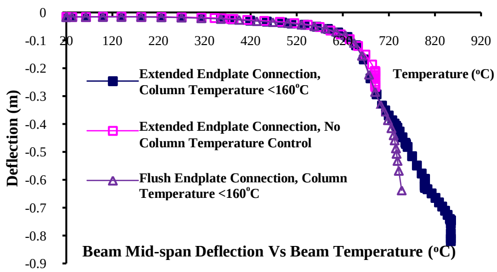

(a) Beam mid-span deflection

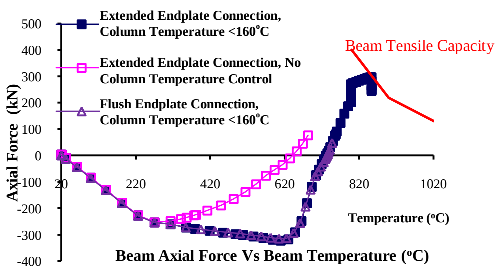

(b) Beam axial force

Figure 4. Comparison of beam mid-span deflections and axial forces.

To summarize, corner column failure should be prevented because of the lack of alternative load carrying mechanisms for the beams. Under fire conditions, the columns should be designed based on modified boundary condition (increased effective length) and additional force (beam catenary action force).

4. FIRE SCENARIO 2: THE EFFECTS OF VERTICAL FIRE SPREAD

Two cases were carried out for fire scenario 2 (Figure 2 (b)): one with no control over the column temperature and one with cool columns (artificial). The results show without controlling the column temperature, the failure mode (column C1 buckling) and failure temperature (507°C) were the same as in the previous simulation of fire in one compartment only (fire scenario 1).

When the columns were cool, failure still occurred, but this time structural failure involved the entire three storey columns being pulled in by the beams in catenary action as shown in Figure 5(a). This is similar to the failure mechanism demonstrated by Usmani et al. [13] for the World Trade Centre towers. Prevention of this failure mode would necessitate the columns being designed for an effective length of three storeys and with consideration of additional forces from the beams in catenary action. The columns used in this exercise were not sufficiently large to enable a substantial development of catenary action. Therefore, the edge column size was increased to 356×406×634UC to give the same load ratio (0.5) as the basic case and the maximum column temperature (440°C) was controlled just below the column limiting temperature (464°C). The load ratio (0.5) and column limiting temperature both were calculated considering the beam maximum catenary force developed from Beams B1 and B4 and the column effective length being three storeys high. The frame survival temperature (beam temperature) was increased from 757°C to 856°C. Figure 5(b) and (c) show that beams B1 and B4 developed large beam deflections and very high beam catenary action. Again, the final failure was beam fracture when the beam tensile capacity was reached.

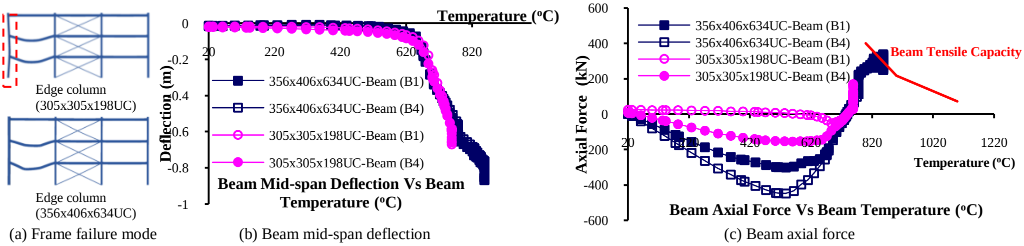

Figure 5. Comparison of frame failure modes, beam mid-span deflections and beam axial forces using different size columns (Fire Scenario 2).

The above examples demonstrate that vertical fire spread has severe implications for structural robustness in fire and should be prevented. In conclusion, the column effective length should be increased to reflect the number of floors under fire attack, and the additional catenary forces from the connected beams should be included.

5. FIRE SCENARIO 3: THE EFFECTS OF HORIZONTAL FIRE SPREAD

This fire scenario simulates the situation of failure of a fire exposed column, leading to fire compartment failure and fire spread as shown in Figure 2(c). Three cases were analyzed to investigate the effects of different applied beam loads on the frame robustness. The details are listed in Table 2.

Table 2. Details of case studies for frame involving inner column failure.

Case ID	Connection Type	Beam Load Ratio	Location of Beam Load
1	Extended endplate connection /FR bolt	0.5	All beams
2	Extended endplate connection /FR bolt	0.5	Beams at the first floor
3	Extended endplate connection /FR bolt	0.3	All beams

In Case 1, all the beams were subjected to 0.5 load ratio. This resulted in fracture of connections J1, J4, J5, J8 simultaneously at ambient temperature because the applied bending moments in the beams were increased by a factor of four after doubling their span. Figure 6 shows developments of bolt deformation in these joints, which exceeded their ambient temperature deformation capacities before the beam loads reached the maximum target value of 106.75kN and the axial force of column C6 suddenly changed from compression to tension and then dropped to indicate frame failure (Figure 6).

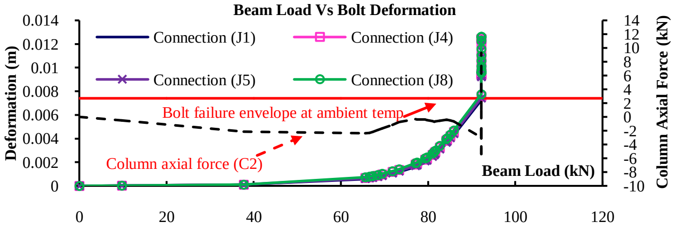

Figure 6. Load- Bolt deformation relationships (Case 1).

Since the objective of this research is to investigate alternative load transfer paths after some structural damage, it was considered useful to simulate a case in which the connections did not fail at ambient temperature. Therefore, in Case 2, loads were removed from the top two floors. Owing to the spare capacities of the two top beams, the fire exposed beams were able to hang from columns C6 and C10. This allowed the fire exposed beams to act as 9m span beams. Because the columns at C1 and C3 were fully protected, they were able to sustain the catenary action in the beams. No bolt failure was detected (Figure 7(a)). Eventually, failure was due to the beam reaching its tensile capacity at a very high temperature (852°C) as shown in Figure 7(d). Figure 7(b) shows that the axial force in the column C6 was tensile, indicating pulling the fire exposed beams. Figure 7(c) and (d) show that beams B1 and B2 experienced large beam deflections and very high catenary action forces which means beam catenary action was utilized to increase the frame survival temperature.

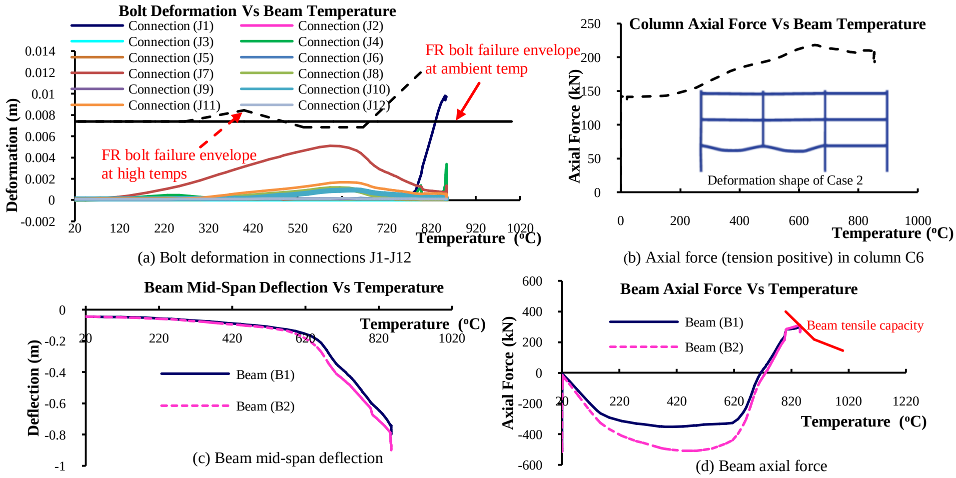

Figure 7. Key structural behaviour for Case 2 of fire scenario 3.

In Case 3, the applied beam loads were at the lower bound of accidental loading. The beams managed to survive the applied loads at ambient temperature with 18m spans. As the temperature increased in the fire exposed beams, their bending moment capacities reduced and it was not possible for them to survive as 18m span beams. Therefore, the columns above the fire exposed beams at C2 position started to pull them. The first failure happened when the bottom bolt of connection J7 started fracturing at a beam temperature of 538°C as indicated in Figure 8(a), but there was no total structural failure. The frame suddenly lost stability and then found equilibrium as shown in Figure 8(b) which shows the axial force evolution in the column (C6) above the fire exposed beams. At 596°C, the frame again temporarily became unstable due to bolts in connection J8 starting to fracture, but it also recovered soon. When the beam temperature reached 606°C (Figure 8(a)), fracture of connections J6, J10 and J11 led to progressive failure of the structure because there was no alternative load carrying mechanism when the loads in the other connections became progressively higher. The axial tensile force in column C6 instantaneously jumped (Figure 8(b)) indicating failure of the frame. The reason for the connections (J7) in the middle span (18m long beam) on the second floor to fracture first can be explained using Figure 8(c), (d) and (e). Although the beam middle sagging bending moment acting on connection J7 was smaller than the bending moment on connection J11 on the top floor, in order to be in equilibrium with the compressive force in the heated beam, connection J7 was also subjected to a very high tensile force whilst connection J11 was in compression. As a result of the combined effect of the a bending moment and axial tensile force, the bottom bolt experienced higher tension force in J7 than in J11 as shown in Figure 8(f), which led to earlier failure of connection J7 than J11.

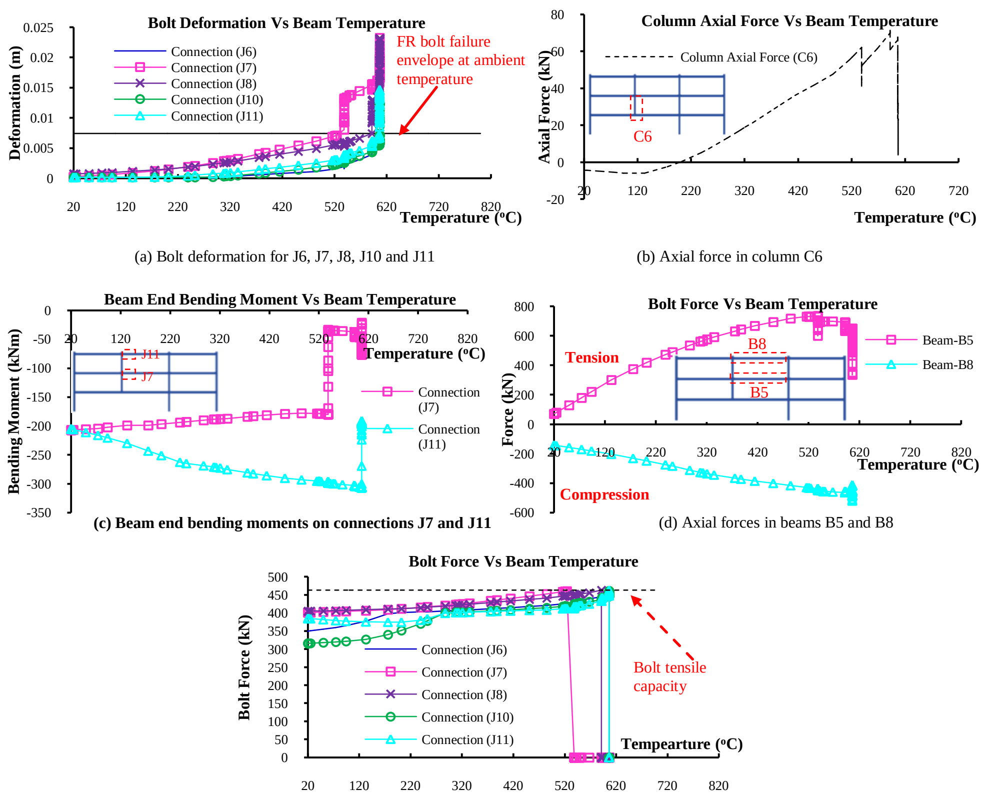

(a) Bolt deformation for J6, J7, J8, J10 and J11

(b) Axial force in column C6

(c) Beam end bending moments on connections J7 and J11

(d) Axial forces in beams B5 and B8

(e) Bolt forces in connections J6, J7, J8, J10 and J11

Figure 8. Key structural behaviour for Case 3 of fire scenario 3.

The above simulation results suggest that it is very difficult for a frame to survive the loss of a column in fire due to doubling of the beam spans. To provide the damaged structure with sufficient robustness, a possible load carrying mechanism is to activate the upper structure as a hanging system for the fire exposed structure like Case 2. This may be provided by a deep truss structure across the entire span of the building.

6. CONCLUSIONS

This paper has reported the results of a number of numerical simulations to investigate how to improve steel frame robustness in fire. Three fire scenarios were considered. The following conclusions can be drawn:

(1) If the fire occurs in the corner compartment, the bottom edge column may buckle, and using stronger joints would not be an effective method of controlling progressive collapse. Other methods, such as increasing the bending moment capacity of the floor slab, will be necessary. If failure of the bottom edge column can be prevented, then beam catenary action can be utilized with strong and ductile joints to increase the frame survival temperature.

(2) Vertical fire spread should be prevented, otherwise there is a high risk of building progressive collapse.

(3) If an inner column is damaged in fire attack, it is very difficult for the frame to survive since the beam span is doubled and the beam bending moment quadrupled. To prevent total structural failure, an upper structure with sufficient spanning capacity should be provided to hold the fire exposed structure.

REFERENCES

[1] Office of the Deputy Prime Minister (ODPM), The building regulations 2000-Approved Document A, London, 2010.

[2] Davison, B., G.W. Owens, and S.C. Institute, Steel Designers' Manual: Blackwell Science, 2003.

[3] Chen, L. and Y.C. Wang, "Methods of improving survivability of steel beam/column connections in fire", Journal of Constructional Steel Research. 79(0): p. 127-139, 2012.

[4] Elsawaf, S., ROBUSTNESS OF CONNECTIONS TO CONCRETE-FILLED STEEL TUBULAR COLUMNS UNDER FIRE DURING HEATING AND COOLING, University of Manchester, 2012.

[5] Elsawaf, S. and Y.C. Wang, "Methods of improving the survival temperature in fire of steel beam connected to CFT column using reverse channel connection", Engineering Structures. 34: p. 132-146, 2012.

[6] Chen, L., ROBUSTNESS IN FIRE OF STEEL FRAMED STRUCTURES WITH REALISTIC CONNECTIONS, University of Manchester, 2012.

[7] Wang, Y.C. and F. Wald. Robustness under fire, COST Action C26, in Malta, 2008.

[8] Wang, Y.C., I.W. Burgess, F. Wald, and M. Gillie, Performance based fire engineering of structures London: Taylor & Francis, 2012.

[9] Chen, L. and Y.C. Wang, "Efficient modelling of large deflection behaviour of restrained steel structures with realistic endplate beam/column connections in fire", Engineering Structures. 43(0): p. 194-209, 2012.

[10] Sakumoto, Y., K. Keira, F. Furumura, and T. Ave, "Tests of Fire-Resistant Bolts and Joints", Journal of Structural Engineering-Asce. 119(11): p. 3131-3150, 1993.

[11] European Committee for Standardisation (CEN), Eurocode 3: Design of Steel Structure, Part 1.2: General rules-Structural fire Design, Brussels, British Standards Institution, 2005.

[12] International Standard Organization (ISO), Fire Resistance Tests, Element of Building Construction, Geneva, International organization for Standardization, 1975.

[13] Usmani, A.S., Y.C. Chung, and J.L. Torero, "How did the WTC towers collapse: a new theory", Fire Safety Journal. 38(6): p. 501-533, 2003.

A NEW DESIGN METHOD TO TAKE INTO ACCOUNT THE LOCAL BUCKLING OF STEEL CROSS-SECTIONS AT ELEVATED TEMPERATURES

Carlos Couto*, Paulo Vila Real*, Nuno Lopes* and Bin Zhao**

* LABEST University of Aveiro, Portugal
e-mails: ccouto@ua.pt, pvreal@ua.pt, nuno.lopes@ua.pt
** CTICM – Centre Technique Industriel de la Construction Métallique, Paris, France
e-mail: bzhao@cticm.com

Keywords: Local buckling, Fire, Steel, Cross-section, Plate, Eurocode

Abstract. *In this work, the mechanical resistance of slender cross-sections exposed to fire where local buckling has a predominant role in the ultimate strength is investigated. A numerical study is performed by using a finite element analysis software for evaluating the existing design methods preconized in Part 1.2 of the Eurocode 3 cross-sectional resistance calculation. This comparison shows the need of more realistic formulae when using simple calculation methods for the design in case of fire. A new methodology to take into account the local buckling of steel cross-sections is presented based on expressions previously developed by the authors to calculate the effective width of thin plates at elevated temperatures. A comparison of the resistance calculated with this methodology against numerical results is made, showing the validity and accuracy of this proposal.*

1 INTRODUCTION

Slender cross-sections when submitted to compression may buckle due to instability phenomena known as local buckling. Local buckling prevents the attainment of the yield stress in one or more parts of the cross-section and strongly affects the ultimate cross-section resistance and consequently the load bearing capacity of the members and, therefore, it has to be taken into account in the design. Thus, the Eurocode 3 (EC3) [1], defines four classes (Class 1 to 4) of cross-sections regarding how local buckling affects the load bearing capacity as a function of the limits of the width-to-thickness ratio (slenderness) of the internal and/or outstand elements (plates) of the cross-sections, the higher the ratio the higher the classification of the elements and the higher the influence of local buckling on the cross-sectional resistance. For Class 4 sections, the EC3 provides in its Part 1.5 [2] two methods to account for the effects of local buckling, namely the effective width method and the reduced stress method, that is considering a reduced cross-section (or stress) instead of the gross cross-section (or the yield stress).

At elevated temperatures, the Part 1.2 of the EC3 [3] suggests for Class 4 cross-sections a default critical temperature of 350 ºC if no fire design is made. Alternatively, the same concepts as for normal temperature can be used according to the recommendations of informative Annex E of the Part 1.2 of the Eurocode 3. Where it is suggested that i) the effective cross-section be determined with the effective width method as for normal temperature, i.e. using the material properties at normal temperature and (ii) to use the simple calculation methods with the design value for the steel yield strength as the 0.2% proof strength instead of the stress at 2% total strain, as normally used in the fire design of other cross-sectional classes. Some previous investigation [4–6] demonstrated however that this methodology is conservative.

A numerical study based on the finite element analysis using the software SAFIR [7] is made to assess the resistance of several slender cross-sections submitted to axial compression and bending about the major-axis. It is demonstrated through a parametric investigation that the existing rules from Part 1.2 of Eurocode 3 [3] are not safe because local buckling occurs at elevated temperatures prior to the development of the elastic bending resistance or the gross cross-section compression resistance and for Class 4 cross-sections, it is shown that the cross-sectional resistance is underestimated if the cross-section is built up simultaneous of plates prone to local buckling and not.

To overcome these inconsistencies, a new method to take into account the local buckling of steel cross-sections at elevated temperatures is presented based on the expressions previously developed by the authors to calculate the effective width of thin plates at elevated temperatures and is validated against experimental and numerical results, thus proving to be safe and accurate.

2 DESIGN PROVISIONS TO TAKE INTO ACCOUNT LOCAL BUCKLING

2.1 Eurocode 3

For Class 4 cross-sections, in order to consider local buckling in the design a reduced cross-section can be determined, being this method referred in the literature as the effective width method. The reduced (or effective) cross-section is determined by calculating the effective widths of the compressed parts through a reduction factor for the plate buckling resistance. According to the EC3, for internal elements under compression this reduction factor is calculated as shown in Reference 8.

$$\begin{aligned} \rho &= 1 && \text{for } \bar{\lambda}_p \leq 0.5+\sqrt{0.085-0.055\psi} \\ \rho &= \frac{\bar{\lambda}_p - 0.055(3+\psi)}{\bar{\lambda}_p^{\,2}} && \text{for } \bar{\lambda}_p > 0.5+\sqrt{0.085-0.055\psi} \end{aligned} \tag{1}$$

and for outstand elements under compression by

$$\begin{aligned} \rho &= 1 && \text{for } \bar{\lambda}_p \leq 0.748 \\ \rho &= \frac{\bar{\lambda}_p - 0.188}{\bar{\lambda}_p^{\,2}} && \text{for } \bar{\lambda}_p > 0.748 \end{aligned} \tag{2}$$

where $\bar{\lambda}_p$ is the non-dimensional slenderness of a plate as defined in the EC3,

$$\bar{\lambda}_p = \sqrt{\frac{f_y}{\sigma_{cr}}} = \sqrt{\frac{f_y}{k_\sigma \dfrac{\pi^2 E t^2}{12(1-\nu^2)b^2}}} = \frac{b/t}{\sqrt{k_\sigma}\sqrt{\dfrac{\pi^2}{12(1-\nu^2)}}}\frac{1}{\sqrt{\dfrac{E}{f_y}}} = \frac{b/t}{28.4\varepsilon\sqrt{k_\sigma}} \; . \tag{3}$$

with, σ_{cr}, k_σ and ε given in EC3.

At elevated temperatures, Part 1.2 of the EC3, suggests for Class 4 cross-sections a default critical temperature of 350ºC if no other calculation is made. Additionally, some further guidance is given in the Annex E for the fire design of this type of cross-sections being recommended that an effective cross-section be determined using the material properties at normal temperature, and when using the simple calculation methods the design value for the steel yield strength to consider corresponds to the 0.2% proof strength instead of the stress at 2% total strain as for the other classes.

In fact, at elevated temperatures, the reduction factor for plate buckling would be, according to Equations (1) and (2), $\rho_\theta = \rho_\theta(\bar{\lambda}_{p,\theta})$ with the corresponding non-dimensional slenderness at elevated temperatures, given by

$$\bar{\lambda}_{p,\theta} = \sqrt{\frac{f_{y,\theta}}{\sigma_{cr,\theta}}} = \sqrt{\frac{k_{0.2p,\theta}}{k_{E,\theta}}}\sqrt{\frac{f_y}{\sigma_{cr}}} \cong 1.0\sqrt{\frac{f_y}{\sigma_{cr}}} = \bar{\lambda}_p \tag{4}$$

The ratio $\sqrt{k_{0.2p,\theta}/k_{E,\theta}}$ is almost equal to 1.0, and since $\bar{\lambda}_{p,\theta} \cong \bar{\lambda}_p$, Eq. (1) and Equations (2) show that it can be considered $\rho_\theta = \rho$.

This methodology however, has the disadvantage of underestimating the cross-sectional resistance if only some of the plates of the cross-section are susceptible to local buckling. Thus, in this case, using the 0.2% proof strength for the whole cross-section is very limiting. Take, for example, an element submitted to pure bending with a regular I-shaped cross-section with Class 1 flanges and Class 4 web. In this case using the 0.2% proof strength due to the web classification is very restrictive because in this type of cross-sections it is usual that around 80% of the bending resistance is provided by the flanges that will have no local buckling problems.

2.2 New proposal

Due to the limitations mentioned previously, the authors have developed new expressions for the plate reduction factor (ρ) [9] in order to replace the use of the design yield stress corresponding to 0.2% proof strength ($f_{0.2\mathrm{p},\theta}$) with the stress for 2% total strain ($f_{\mathrm{y},\theta}$). The proposed design curves have been calibrated as closer as possible to the existing design curve of the Eurocode 3 by introducing the factors α_θ and β_θ on the expressions of Part 1.5 of Eurocode 3 (see Equations (1) and (2)).

According to this proposal, for internal compression elements the following expressions is given:

$$\rho_\theta = \frac{\left(\bar{\lambda}_p + \alpha_\theta\right)^{\beta_\theta} - 0.055\left(3+\psi\right)}{\left(\bar{\lambda}_p + \alpha_\theta\right)^{2\beta_\theta}} \leq 1.0 \tag{5}$$

and for outstand compression elements:

$$\rho_\theta = \frac{\left(\bar{\lambda}_p + \alpha_\theta\right)^{\beta_\theta} - 0.188}{\left(\bar{\lambda}_p + \alpha_\theta\right)^{2\beta_\theta}} \leq 1.0 \tag{6}$$

The coefficients to be used in equations (5) and (6) are given in Table 1.

Table 1. Coefficients to be used in equations (5) and (6).

Internal compression elements	Outstand compression elements
$\alpha_\theta = 0.9 - 0.315\dfrac{k_{0.2p,\theta}}{\varepsilon_\theta k_{y,\theta}}$	$\alpha_\theta = 1.1 - 0.630\dfrac{k_{0.2p,\theta}}{\varepsilon_\theta k_{y,\theta}}$
$\beta_\theta = 2.3 - 1.1\dfrac{k_{0.2p,\theta}}{k_{y,\theta}}$	$\beta_\theta = 2 - 1.1\dfrac{k_{0.2p,\theta}}{k_{y,\theta}}$
$\varepsilon_\theta = 0.85\varepsilon = 0.85\sqrt{235/f_y}$	

Based on the assumption that the influence of the temperature on the range of the critical temperatures usually expectable for steel members (from 350ºC to 750ºC) are negligible, a simpler approach is also considered, based on a reference temperature of 450ºC, leading to a simpler yet accurate design. Accordingly, for internal compression elements the following expressions is suggested:

$$\rho = \frac{\left(\bar{\lambda}_p + 0.9 - \dfrac{0.26}{\varepsilon}\right)^{1.5} - 0.055\left(3+\psi\right)}{\left(\bar{\lambda}_p + 0.9 - \dfrac{0.26}{\varepsilon}\right)^{3}} \leq 1.0 \tag{7}$$

and for outstand compression elements:

$$\rho = \frac{\left(\overline{\lambda}_p + 1.1 - \dfrac{0.52}{\varepsilon}\right)^{1.2} - 0.188}{\left(\overline{\lambda}_p + 1.1 - \dfrac{0.52}{\varepsilon}\right)^{2.4}} \leq 1.0 \tag{8}$$

with $\varepsilon = \sqrt{235 / f_y}$. In this study, Equations (5) and (6) when used are referred as “Full Proposal” and Equations (7) and (8) when used are referred as “Simple Proposal”. In Figure 1 a comparison is made between the Full Proposal for different temperatures and the Simple Proposal.

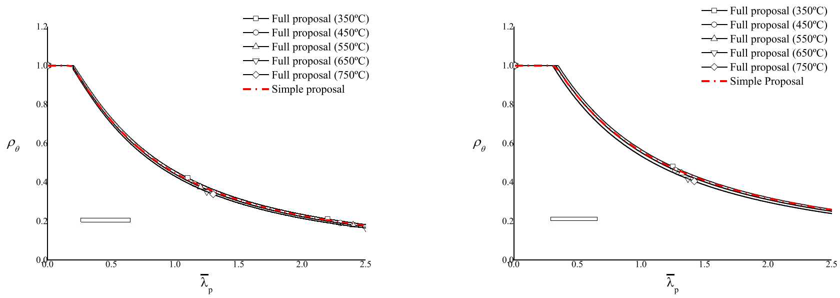

Figure 1. Comparison between the Full proposal and Simple proposal for internal and outstand elements in compression (steel grade S355).

2.3 Simple design methods to calculate the cross-sectional resistance at elevated temperatures

For members in compression, the cross-sectional resistance at elevated temperatures, $N_{\mathrm{c,fi,t,Rd}}$ can be calculated according to Table 2 assuming that no flexural buckling will occur and for members in bending, the design moment resistance $M_{fi,t,Rd}$ of a laterally restrained member with a uniform temperature θ_a can be determined according to Table 3.

Table 2. Determination of the compression resistance at elevated temperatures.

Methodology	Section Classification	Cross-sectional resistance in compression	Effective cross-section area A_{eff}
EC3	Class 1, 2 and 3	$N_{\mathrm{c.fi.t.Rd}} = A k_{y,\theta} f_y / \gamma_{\mathrm{M.fi}}$	Not applicable
	Class 4	$N_{\mathrm{c.fi.t.Rd}} = A_{eff} k_{0.2p,\theta} f_y / \gamma_{\mathrm{M.fi}}$	See Section 2.1
New proposal	Class 1 and 2	$N_{\mathrm{c.fi.t.Rd}} = A k_{y,\theta} f_y / \gamma_{\mathrm{M.fi}}$	Not applicable
	Class 3 and 4	$N_{\mathrm{c.fi.t.Rd}} = A_{eff} k_{y,\theta} f_y / \gamma_{\mathrm{M.fi}}$	See Section 2.2

Table 3. Determination of the member bending about the major axis resistance at elevated temperatures.

Methodology	Section Classification	Cross-sectional resistance in bending	Minimum effective section modulus $W_{eff,min,y}$
EC3	Class 1 and 2	$M_{fi,t,Rd} = W_{pl,y} k_{y,\theta} f_y / \gamma_{M,fi}$	Not applicable
	Class 3	$M_{fi,t,Rd} = W_{el,y} k_{y,\theta} f_y / \gamma_{M,fi}$	Not applicable
	Class 4	$M_{fi,t,Rd} = W_{eff,min,y} k_{0.2p,\theta} f_y / \gamma_{\mathrm{M,fi}}$	See Section 2.1
New proposal	Class 1 and 2	$M_{fi,t,Rd} = W_{pl,y} k_{y,\theta} f_y / \gamma_{M,fi}$	Not applicable
	Class 3 and 4	$M_{fi,t,Rd} = W_{eff,min,y} k_{y,\theta} f_y / \gamma_{\mathrm{M,fi}}$	See Section 2.2

3 NUMERICAL MODEL

Geometric and material non-linear analysis of shell element models representing members in bending and axial compression was conducted with the software SAFIR [7]. The ability of SAFIR to model local buckling with shell elements was validated by Talamona and Franssen [10]. The members were discretized into several quadrangular shell elements with four nodes and six degrees of freedom (3 translations and 3 rotations) using a mesh with 20 divisions on the flange, 20 divisions on the web and 100 divisions along the length. To avoid numerical problems, an additional layer of shell elements with higher thickness was used in the extremities of the structural elements to apply the loads that correspond to the applied end moments or the axial compression force. The cross-sectional resistance at elevated temperatures was determined in SAFIR using a transient dynamic analysis, i.e. by first increasing the temperature to the desired value and then apply an increasing load until the collapse occurs. The temperature has been considered uniform along the cross-section so that a comparison between the numerical results and the simple design equations is possible. Numerical model user for compression and bending about major-axis are depicted in in Figure 2.

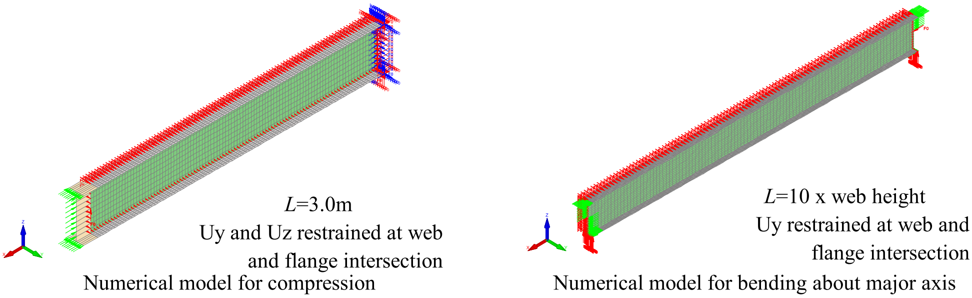

Figure 2. Numerical model for the determination of cross-sectional resistance of the elements.

Geometrical imperfections were introduced in the models by changing the node coordinates in function of the first eigenmode which has been scaled as the geometric fabrication tolerances defined in EN 1090-2 [11]: 80% of $B/100$ or 80% of $H_w/100$, being B the flange width and H_w the web height in accordance to the recommendations of Part 1.5 of Eurocode 3 [2]. Residual stresses were not considered.

4 PARAMETRIC STUDY

A parametric study was performed considering several cross-sections submitted to axial compression and bending in the major axis. The number of cross-sections and classification is shown in Figure 3. Four different temperatures were chosen, namely 350, 450, 550 and 700ºC and the steel grades S235, S355 and S460 have been used. The model used in this numeric investigation is the one described in section 3.

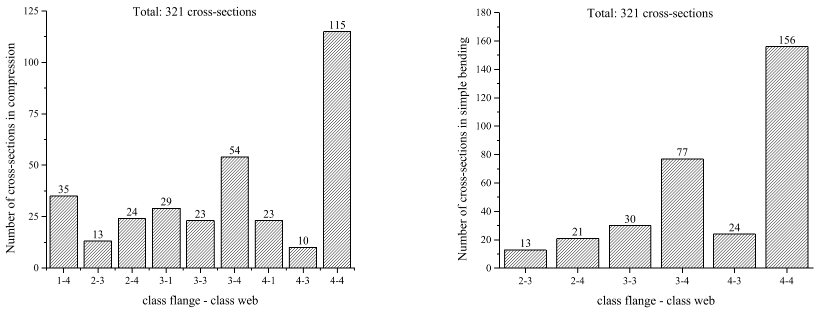

Figure 3. Number and classification of cross-sections used in the numerical study at elevated temperatures.

5 RESULTS AND COMPARISON TO SIMPLE DESIGN METHODS

Herein, the results obtained for the cross-section resistance of members in compression and bending about major-axis with Finite Element Analysis are shown. A comparison with the simple design methods prescribed in the Part 1.2 of EC3 is made and discussed, and the improvements and accuracy of using the new approach developed in this study is highlighted. In Figure 4, the results obtained with SAFIR are compared with the simplified design methods of Part 1.2 of EC3.

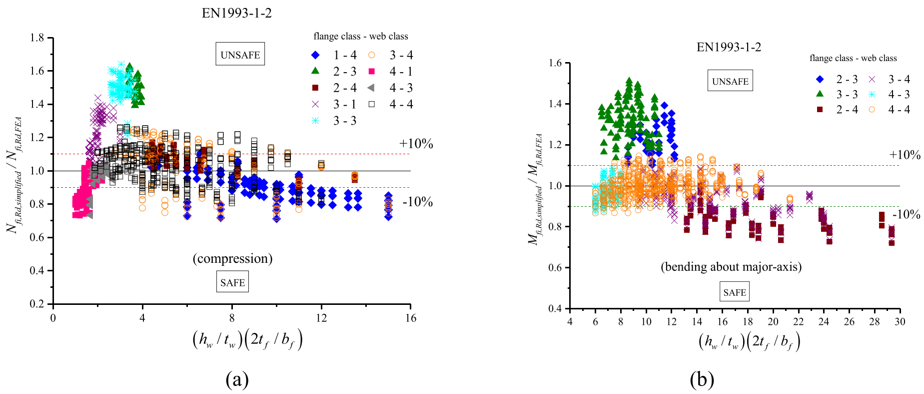

Figure 4. Comparison between the cross-sectional resistance obtained with FEA and Part 1.2 of EC3.

For Class 3 profiles the current simple design methods of Part 1.2 of the EC3 are unsafe and the observation of the failure mode shows that local buckling occurs reducing the cross-sectional resistance and preventing the cross-section from reaching its overall compression or flexural load (see Figure 5(a)).

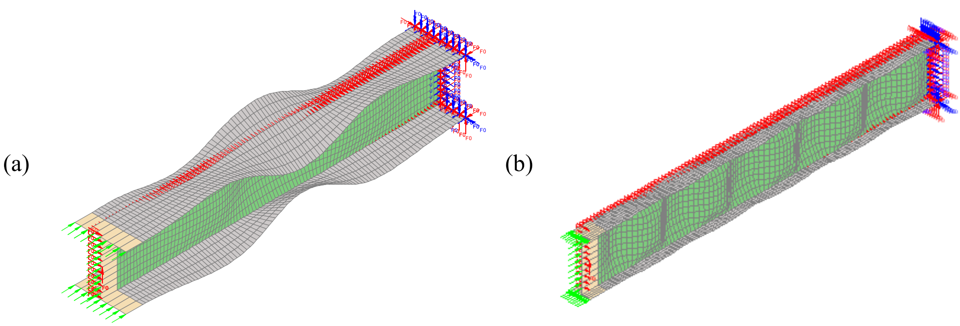

Figure 5. Deformed shape (x5) at collapse for (a) Class 3 profile and (b) Class 4 profile with Class 1 Flanges.

For Class 4 cross-sections, results are mainly conservative especially if the cross-section is composed also by Class 1 or 2 plates because there is an additional load-carrying capacity provided by those plates that is not accounted for by considering that the whole cross-section may be affected by local instabilities (see Figure 5 (b)).

In Figure 6 and Figure 7, a comparison between the results of FEA and those predicted by the Full Proposal and Simple Proposal respectively are shown.

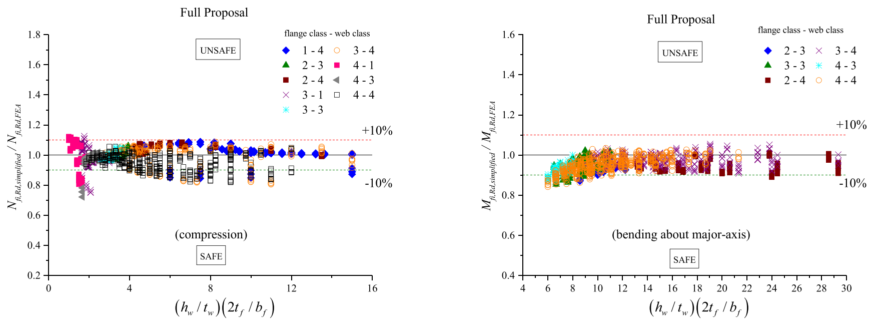

(a) (b)

Figure 6. Comparison between the cross-sectional resistance obtained with FEA and Full Proposal.

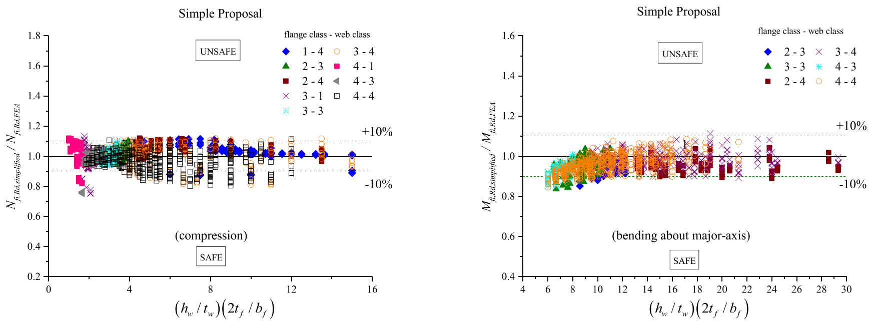

(a) (b)

Figure 7. Comparison between the cross-sectional resistance obtained with FEA and with the Simple Proposal.

Both methods, the Full Proposal and the Simple Proposal, show better agreement with the results from FEA demonstrating they are an accurate methodology to estimate the cross-sectional resistance since a better agreement to the FEA numerical investigation is obtained. Although the Simple Proposal leads to results slightly on the safer side than the Full Proposal as it is easily understandable, it provides a methodology that is easier to use and yet accurate.

6 CONCLUSIONS

In this study, the resistance of several cross-sections where local buckling can occur under axial compression and bending was investigated at elevated temperatures. A numerical study with the FEA software SAFIR was conducted for a significant number of cross-sections, and a comparison to the actual design methodology of Part 1.2 of the EC3 was made showing that the current existing methodology to calculate the cross-sectional resistance is inaccurate leading to both very conservative and unsafe results. This is justified by three reasons, (i) the effect of the temperature is not correctly taken into account and (ii) local buckling occurs prior to what is currently assumed and (iii) considering the 0.2 % proof strength as the design yield stress, for the whole cross-section is conservative if a Class 4 cross-section is composed also of plates with minor classification, i.e. which are not prone to local buckling.

A new design method to take into account the local buckling of steel cross-sections at elevated temperatures was proposed. This method is based on the expressions previously developed by the authors to calculate the effective width of thin plates exposed to fire and considering the steel yield strength as the stress corresponding to 2% total strain irrespective of the class of the cross-section. Two options are given to the designer: a Full Proposal where the effective cross-section is temperature dependent, meaning that the designer needs to calculate an effective cross-section for each temperature, although it is the most rigorous approach to the issue of dealing with local buckling at elevated temperatures it is also more complex; and a Simple Proposal, for which the effective cross-section is not temperature dependent, leading to a much simpler calculation yet safe-sided. The accuracy and validity of both the Full proposal and the simplified version for calculating the effective cross-sections was confirmed on the basis of the numerical investigation performed in this study and by comparison with experimental results.

ACKNOWLEDGEMENTS

The work in this paper was supported by the European Commission, Research Fund for Coal and Steel in the frame of the research project "FIDESC4 - Fire Design of Steel Members with Welded or Hot-rolled Class 4 Cross-sections", Grant Agreement Number RFSR-CT-2011-00030.

REFERENCES

[1] CEN, "EN 1993-1-1, Eurocode 3: Design of steel structures - Part 1-1: General rules and rules for buildings." European Committee for Standardisation, Brussels, 2005.

[2] CEN, "EN 1993-1-5, Eurocode 3 - Design of steel structures - Part 1-5: Plated structural elements." European Committee for Standardisation, Brussels, pp. 1–53, 2006.

[3] CEN, "EN 1993-1-2, Eurocode 3: Design of steel structures - Part 1-2: General rules - Structural fire design." European Committee for Standardisation, Brussels, 2005.

[4] Knobloch M., M. Fontana, "Strain-based approach to local buckling of steel sections subjected to fire," *J. Constr. Steel Res.*, vol. 62, no. 1–2, pp. 44–67, Jan. 2006.

[5] Renaud C., B. Zhao, "Investigation of simple calculation method in EN 1993-1-2 for buckling of hot rolled class 4 steel members exposed to fire," in *Fourth International Workshop "Structures in Fire,"* 2006, pp. 199–211.

[6] Quiel S. E., M. E. M. Garlock, "Calculating the buckling strength of steel plates exposed to fire," *Thin-Walled Struct.*, vol. 48, no. 9, pp. 684–695, Sep. 2010.

[7] Franssen J.-M., "SAFIR, A Thermal/Structural Program Modelling Structures under Fire," *Eng. Journal, A.I.S.C.*, vol. 42, no. 3, pp. 143–158, 2005.

[8] Cen, "Publication N1664E - Corrigendum to EN 1993-1-5 Eurocode 3 : Design of steel structures - Part 1-5 : Plated structural elements," 2009.

[9] Couto C., P. Vila Real, N. Lopes, B. Zhao, "Effective Width Method to Account for the Local Buckling of Steel Thin Plates at Elevated Temperatures," *Submitted to Thin Walled Struct.*

[10] Talamona D., J.-M. Franssen, "A Quadrangular Shell Finite Element for Concrete and Steel Structures Subjected to Fire," *J. Fire Prot. Eng.*, vol. 15, no. 4, pp. 237–264, Nov. 2005.

[11] CEN, "EN 1090-2: Execution of steel structures and aluminium structures - Part 2 : Technical requirements for steel structures." European Committee for Standardisation, Brussels, 2008.

EXPERIMENTAL INVESTIGATION ON COLD-FORMED STEEL BEAMS WITH WEB STIFFENERS SUBJECTED TO FIRE

João Paulo C. Rodrigues*, Luís Laím* and Hélder D. Craveiro*

* ISISE – Institute Sustainability and Innovation on Structural Engineering, University of Coimbra, Portugal.
e-mails: jpaulocr@dec.uc.pt, luislaim@uc.pt, heldercraveiro.eng@gmail.com

Keywords: Cold-formed, Steel, Sigma, Beams, Fire, Experimental

Abstract. *This paper presents the results of a study on the behaviour of cold-formed galvanized steel beams under fire conditions, basing on the results of a large programme of experimental tests. It was investigated the influence of web stiffeners in the sections and of the axial restraining to the thermal elongation of the beams. In other words, it was studied the flexural behaviour of 2 types of beams ($\sum$ and 2$\sum$ beams) in case of fire and, in order to obtain a better correlation of the results. In addition, their structural response was compared with other similar beams (C and lipped-I beams). Temperatures in the furnace and at several points of the beams, as well as, deformations and restraining forces and moments were measured to achieve those goals and consequently to assess the critical time and temperature of these beams. Finally, the results showed above all that CFS beams with web stiffeners may have different structural responses under fire conditions depending on the section shape and the loading conditions.*

1 INTRODUCTION

The use of cold-formed steel (CFS) profiles in buildings is a solution that is under continuous development, and so it will remain a challenge for the next few years. Studies in this area are still few, and mostly of a numerical nature. However, there are some that address the most important phenomena related to these elements at room temperature, including post-buckling resistance (local and distortional buckling) [1], global flexural, torsional and flexural-torsional buckling, shear resistance of stud walls [2], bending resistance [3] and resistance of some type of screwed connections.

Cold-formed steel behave quite differently from hot-rolled steel members, since the latter are mostly found in class 1 or 2 cross-sections, while the former are class 3 or 4, according to EN1993-1.1 [4]. This is due to the high slenderness of the cross-section's walls (high ratio width/thickness of the wall) and the low torsional stiffness (much lower than the flexural stiffness), and to the fact that in many of these cross-sections, the shear centre does not coincide with the centre of gravity and the great majority of the cross-sections are open and either mono symmetric or completely asymmetric. Consequently, these members may buckle at a stress level lower than the yield point of steel. It is therefore clear that cold-formed steel members are more susceptible to instability (local and global) than hot-rolled ones, and there are still many open questions to investigate. However, cold-formed steel sections can be strengthened by forming edge and web stiffeners in the sections. As it is an emerging technology and since a great variety of profiles with different geometric shapes can be easily produced, it is of the utmost importance that studies in this field should be undertaken.

Another interesting point is that when it comes to fire, the fire resistance of this kind of members is quite compromised due to the combination of the high thermal conductivity of steel and the high section factor of these structural members (small wall thickness) both of which lead to a rapid rise in steel temperature in a fire. Another important issue is that the deterioration of steel mechanical properties with increasing the temperature can induce serious deformation of structural members or even the premature failure of a building. As well as that it is expected that the rigidity of these stiffeners and the strengthening of steel in these regions decrease when the CFS members are exposed to high temperatures [5].

It is still worth mentioning that the structural behaviour of CFS members with stiffeners was rarely studied before by other authors at ambient temperature [6,7] and that there has been a lack of studies in this field at high temperatures, especially in CFS beams. The major part of the research works published until now is on simple CFS members (composed of just one CFS profile with U and C-shaped sections) subject to elevated temperatures [8,9]. Some of them concluded that the limit temperature of 350 °C, recommended by EN1993-1.2 [10], is overly conservative [11,12].

This paper intends therefore to study experimentally the structural behaviour of sigma CFS beams (∑ and 2∑) under fire conditions. The experimental tests on CFS beams under fire conditions were conducted at the Laboratory of Testing Materials and Structures (LEME) of the University of Coimbra (UC), in Portugal. The main objectives of these tests were to assess the critical temperature and time of the studied beams as well as to observe the effect of the stiffeners on beams as the rigidity of these stiffeners and the strengthening of steel in these regions decrease with increasing temperature, comparing their behaviour with similar beams (C and lipped-I beams). Other important goal of this research work was also to investigate the influence of the axial restraint to the thermal elongation of the beam on the parameters mentioned before. Finally, other objectives of this research were to observe their failure modes and post-buckling response as well as to compare the structural performance of the different beams.

2 EXPERIMENTAL TESTS

2.1 Test Specimens

The specimens consisted of CFS beams made of one or two sigma-shaped (Σ) profiles (Figure 1). The cross-sections of these sigma profiles were 255 mm tall, 70 mm wide and 2.5 mm thick. The insides bend radius and the length of the edge stiffeners were 2 and 25 mm, respectively. In addition, bent angles of 90º and 120º were respectively employed in the outer and inner corners of the profiles' web. The beam span was 3.0 m for all specimens, in such a way that the beams and their supports could be accommodated by the furnace available in the laboratory. The two sigma-shaped profiles were connected back-to-back by means of Hilti S-MD03Z 6.3x19 carbon steel self-drilling screws in S235 structural steel to form an I-shaped beam with edge and web stiffeners (2-Σ beam). Hence, these screws were placed along the longitudinal direction of the specimens in the upper and lower parts of the web, as illustrated in Figure 1, and their spacing was about 650 mm (L/4.5). All the profiles were still made of S320GD+Z structural steel.

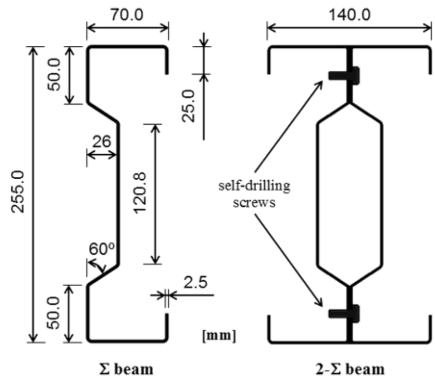

Figure 1. Scheme of the cross-sections of the tested beams.

2.2 Test Set-up

A general view of the experimental system used in the fire tests of the beams is shown in Figures 2, which essentially consisted of a reaction frame (no. 1 in Figure 2), a hydraulic jack (no. 2 in Figure 2) to apply loading, a modular electric furnace (no. 3 in Figure 2) to simulate fire conditions, and roller and pinned supports (no. 4 in Figure 2) to provide a simply supported beam. As it can be seen in the figure, the test specimens (no. 5 in Figure 2) were loaded at two points 1.0 m each (one-third of the beam span) from the supports of the beam in such a way that between the two loading points the beam was under pure bending state (four point bending test). The loading was applied by an ENERPAC hydraulic jack, model RR 3014 (no. 2 in Figure 2), which was hung on a two-dimensional reaction frame (no. 1 in Figure. 2) that consisted of two HEB300 columns and a HEB300 beam of S355 steel class. This hydraulic jack had a maximum loading capacity in compression of 295 kN and a maximum stroke length of 360 mm and was controlled by a servo hydraulic central unit W+B NSPA700/DIG2000. Additionally, beneath the hydraulic jack a Novatech F204 load cell of 250 kN capacity (no. 6 in Figure 2) was mounted in order to monitor the applied load during the fire tests. This loading was transferred from the hydraulic jack to the specimen by a HEA160 column (no. 7 in Figure 2) and applied at two points on the specimen by means of a HEB140 beam (no. 8 in Figure 2), both filled up with fire-protection mortar between the profile flanges to prevent their destruction by the high temperatures developed during fire resistance tests.

The specimens were heated with a horizontal modular electric furnace (no. 3). This furnace was 4500 mm × 1000 mm × 1000 mm in internal dimensions and capable to heat up to 1200 °C and to follow fire curves with different heating rates. A spherical plain bearing (no. 9 in Figure 2) and a spherical hinge (no. 10 in Figure 2) were also assembled in the loading system in such a way that the load applied on the beams could easily follow the local, distortional and global deformations of the beams during the tests, especially, the lateral buckling. The tested beams were statically determinate over a roller and pinned support. These ones were made of refractory stainless steel, typically used for elevated temperature applications, and prevented the vertical displacement, the lateral displacement and the lateral rotation of the beams. In addition, the roller support allowed the horizontal displacement of the beams in contrast to the pinned support.

Furthermore, the experimental system still comprised two axial restraining steel beams (Figure 3), in order to simulate the axial restraint to the thermal elongation of the beams. Thus, the axial restraining system was composed of two simply supported beams, one with high bending stiffness (near the pinned support) (no. 1 in Figure 3) and the other with low bending stiffness (near the roller support) (no. 2 in Figure 3). Note that the specimen was connected to the axial restraining beams by means of a HEB220 profile (near the pinned support) (no. 3 in Figure 3) and a threaded rod system (near the roller support) (no. 4 in Figure 3) which allowed to eliminate the clearances between the specimen and those beams. At the end of this HEB220 profile and this threaded rod system, a steel semi-sphere was placed (no. 5 in Figure 3), covered with a thin layer of Teflon, so that the displacements were possible without friction. It is worth mentioning that this way allowed studying only the effect of axial restraining on the fire resistance of CFS beams (without any interference of rotational restraint). Also, a Novatech F204 load cell of 500 kN capacity was mounted in order to monitor the axial restraining forces generated in the test specimen (no. 6 in Figure 3) during the fire resistance tests. The actual axial stiffness, ka, was about 15 kN/mm which was taken indirectly from the experimental results and numerical simulations, trying to use and reproduce as faithful as possible the actual boundary conditions of a beam when is inserted in a real CFS building structure.

Finally, the instrumentation of the beams still included linear variable displacement transducers (LVDTs) for vertical displacement measurements (at mid-span for instance) and type K thermocouples for thermal measurements in the furnace and at different points of the specimen’s cross-section. It is noticed that the LVDTs were placed in the basement floor of the Laboratory, below the testing floor, to protect them from the high temperatures. The data acquisition was done by a TML data logger, model TDS-530.

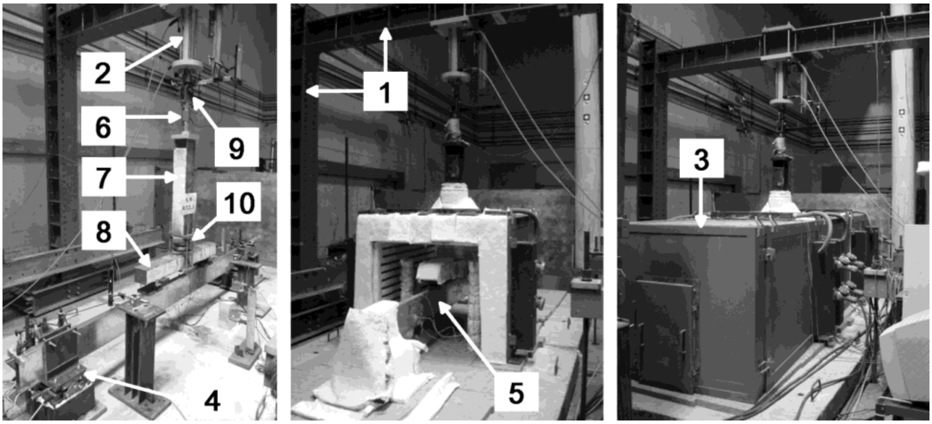

Figure 2. Test set-up for structural fire tests of CFS beams.

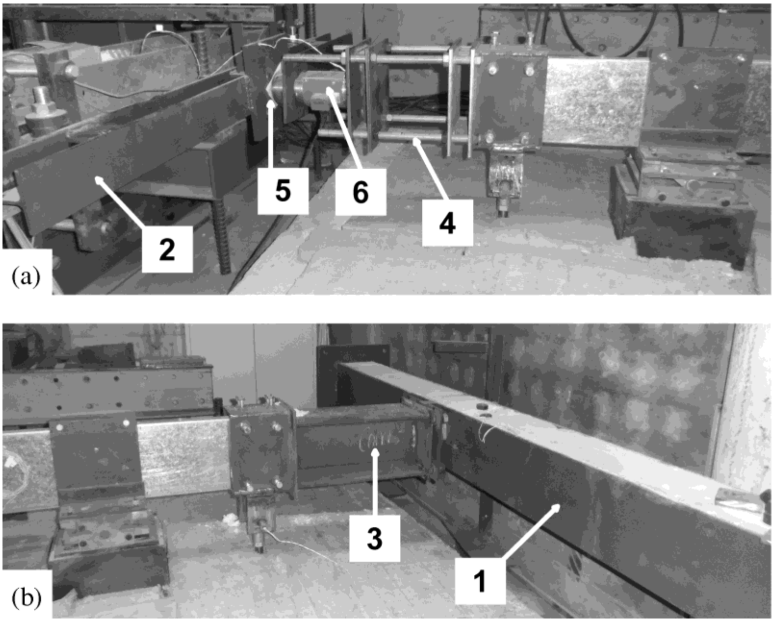

Figure 3. Detail of the axial restraining beams with low (a) and high (b) bending stiffness.

2.3 Test Plan

The experimental programme consisted of 12 structural fire resistance tests on CFS beams, 6 of which were just simply supported beams and 6 others were the same beams but with restrained thermal elongation. So, for each series of 6 fire tests, 3 tests for each type of beam were carried out (2 types of beams were studied, ∑ and 2∑ beams), in order to obtain a better correlation of the results. This experimental programme is summarized in Table 1. For example, the reference B_ka-Σ_3 indicates the third test (3) of the sigma (Σ) beam (B) with axial restraint (ka) to thermal elongation of the beam. On the other hand, $k_{a,b}$ and P_0 means respectively the axial stiffness of the beam and the initial applied load on the beam.

Table 1. Test plan.

Test reference	Non-dimensional Slenderness	$k_{a,b}$ (kN/mm)	P_0 (kN)	*ka* (kN/mm)
B-Σ_1 **B-Σ_2** **B-Σ_3**	1.08	80	11.24	0
B-2Σ_1 **B-2Σ_2** **B-2Σ_3**	0.70	160	34.15	0
B_ka-Σ_1 **B_ka-Σ_2** **B_ka-Σ_3**	1.08	80	11.24	15
B_ka-2Σ_1 **B_ka-2Σ_2** **B_ka-2Σ_3**	0.70	160	34.15	15

2.4 Test Procedure

To achieve the goals of this investigation, these experimental tests were performed in two stages: loading and heating stage. First, the specimens were loaded up to the target force under load control at a rate of 0.1 kN/s. The load level applied on the beams, P_0, was 50 % of the design value of the load-bearing capacity of the beams at ambient temperature (Table 1), and calculated in accordance with the methods proposed in Eurocode 3 part 1.3 [13]. The loading intended to simulate the serviceability load of a beam inserted in a real building structure. Finally, the heating stage was started after the desired load was reached. Thus, the specimens were uniformly heated up according to a fire curve as near as possible to the standard fire curve ISO 834 [14]. During the heating period, the load was kept constant until the specimen buckled, where the beam deformation was too large or the maximum stroke of hydraulic jack was reached.

2.5 Results and Discussion

Figure 4 shows, as an example, the evolution of the temperatures in the cross-section of the test beam B_ka-Σ_3 at mid-span as well as the furnace temperature and the standard fire curve ISO 834 [14] as a function of time. As expected the temperature in the cross-section (θ_{S-1}, θ_{S-2} and θ_{S-3}) remained practically uniform during all test. It can also be observed that the furnace temperature exhibited a delay in the relation to the ISO 834 fire curve [14] because the initial minutes of the curve is very difficult for an electric furnace to reproduce and this becomes worse for larger furnaces (high initial thermal inertia). However, the furnace temperature tends to be closer to the programmed ISO 834 fire curve [14] when the time increases and, above all, the evolution of temperatures inside the furnace over time was very uniform in all fire tests, meaning that the tests are comparable. It is also important to say that the evaluation of the behaviour of this kind of structures as a function of temperature is much more important than as a function of time.

On the other hand, Figure 5 presents the evolution of the vertical displacements of the test beams B-Σ_2, B-2Σ_2, B_ka-Σ_3 and B_ka-2Σ_2, for instance, as a function of the respective beam temperature. From this figure, it can be seen that the axial restraint had a bad effect on the structural behaviour of beams under fire conditions, as expected. When about 15 kN/mm of axial restraint was imposed on beams, their critical temperature dropped significantly, for instance, from 680 ℃ to 564 ℃ for the Σ beams and from 601 ℃ to 524 ℃ for the 2Σ beams (Figure 5), corresponding to a decrease of 17 and 13%, respectively. Other interesting point to note is that the web stiffeners may have a better role to play in beams under combined axial compression force and bending moment than in beams under just bending moment. For instance, the reduction in the critical temperature between the simply supported beams B-

Σ_2 and B-2Σ_2 was of 80 ºC, whereas between the axially restrained beams B_ka-Σ_3 and B_ka-2Σ_2 was of 40 ºC. Last but not least, comparing this kind of beams with beams without web stiffeners (Figure 6), it is also important to emphasize that lipped-I beams without web stiffeners under bending moment may present an enhanced fire behaviour (higher critical temperature) than lipped-I beams with web stiffeners (Figure 6(a)), but when these beams are under combined axial compression force and bending moment the opposite happens (Figure 6(b)).

Figure 7 provides a general idea of how the Σ and 2-Σ beams behave as a function of its temperature in terms both of deformation and of axial restraining forces. This graph represents the typical behaviour of a real beam under high uniform temperatures and inserted in a building structure, in which it is submitted to restraint to thermal elongation. Due to the effect of the thermal action, the axial compression force on the beam begins to increase until it reaches a maximum value. After this maximum it begins to decrease due to deterioration of mechanical properties of steel with temperature and to the instability phenomenon, including local, distortional and global buckling. The critical temperature was defined in these tests as that at the time when the restraining forces on it returned to the value of the initial applied axial load (failure criteria in terms of strength), which was very similar to that at the time when beam deflection was about equal to $L^2/(400h)$, where L is the beam length and h the height of the cross-section (failure criteria in terms of deformation [14]), as it can be seen in Figure 7. The difference between the axial restraining forces generated in these beams during the fire tests may have resulted from the fact that the lateral deformations of the 2-Σ beams could be higher than the ones of the Σ beam and thus presenting lower axial restraining forces.

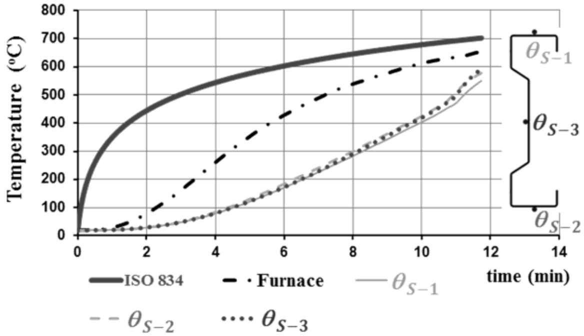

Figure 4. Evolution of temperatures of the test beam B_ka-Σ_3 at mid-span as a function of time.

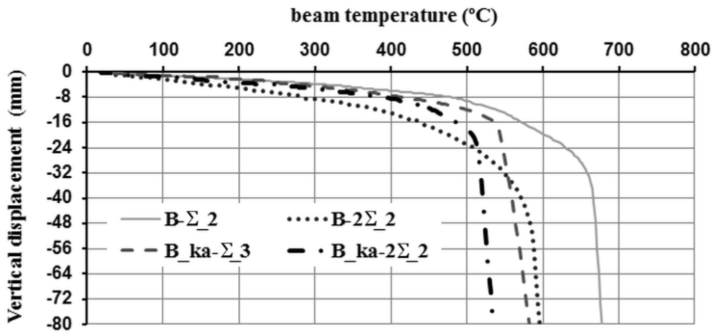

Figure 5. Evolution of vertical displacements of the beams at mid-span as a function of temperature.

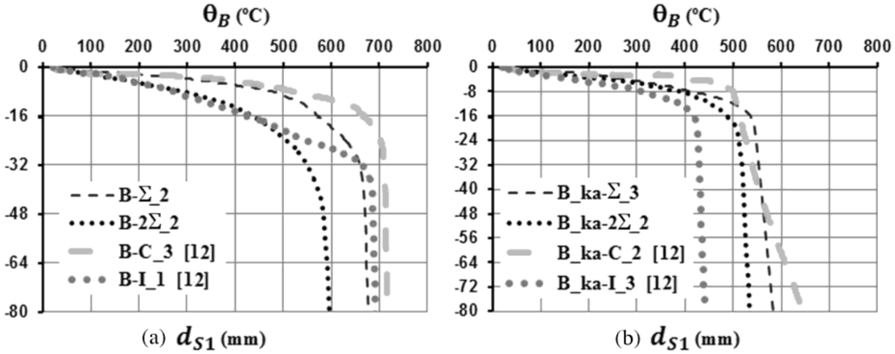

Figure 6. Comparison of vertical displacement at mid-span of simply supported (a) and axially restrained (b) beams with and without web stiffeners.

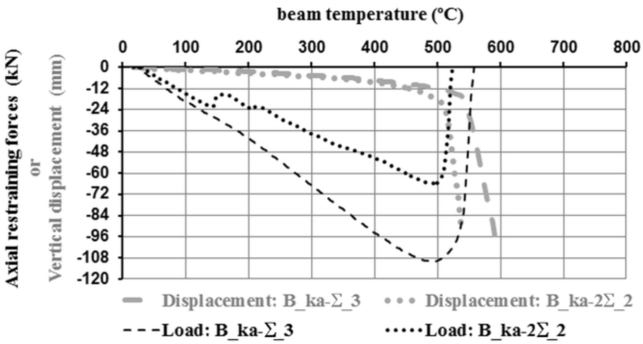

Figure 7. Evolution of axial restraining forces in the beams as a function of temperature.

2.6 Failure Modes of the Beams

Figure 8 illustrates, as example, the failure modes of the Σ (a) and 2-Σ (b) beams under fire conditions and with restrained thermal elongation. Since all fire tests were performed inside the horizontal modular electric furnace, only the final shape of the beams could be observed. Hence, it was only observed that the failure modes of the beams involved distortional and lateral-torsional buckling and still, but less visible, local buckling. However, the authors believe that the lateral-torsional buckling was the main failure mode responsible for the collapse of these beams and that the distortional buckling appeared on the compression flange of the beams during the lateral-distortional buckling of the respective beam, since the loading conditions avoided the free rotation of the flange during the lateral rotation of the beam.

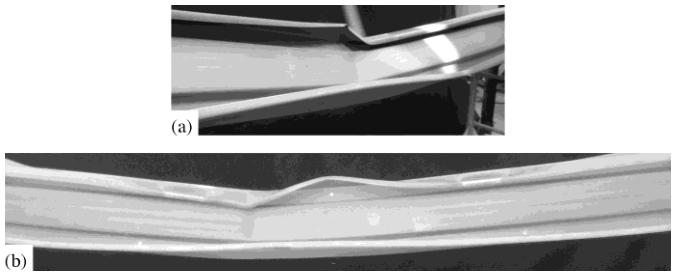

Figure 8. Failure modes of the test beams (a) B_ka-Σ_1 and (b) B_ka-2Σ_2.

3 CONCLUSIONS

The main conclusion of this research study was that CFS beams with web stiffeners may have different structural responses under fire conditions depending on the section shape. In other words, whereas the Σ beams presented similar critical temperatures to the C beams independently of boundary conditions, the 2-Σ beams behaved differently from the lipped-I beams. When the beams are not axially restrained, the beams without web stiffeners may present a better structural behaviour under fire conditions, in contrast to beams which are axially restrained to the thermal elongation. Therefore, it is worth mentioning that the use of CFS beams with web stiffeners might not be always a good solution. In addition, it was also clearly seen that the lateral-torsional buckling was not the only relevant failure mode of the Σ beams in contrast to the C beams [12]. Finally, in general the axial restraint had a negative effect on the fire resistance of the beams, as expected, but once again, it was demonstrated that its effect depended on the relation between the axial stiffness of the surrounding structure and the elastic axial stiffness of the beam. In this particular case of study, the axial restraint decreased the critical temperature by 17% for the Σ beam and 13% for the 2-Σ beam.

REFERENCES

[1] Dinis P.B. and Camotim D., "Local/distortional mode interaction in cold-formed steel lipped channel beams", *Thin-Walled Structures*, 48, 771-785, 2010.

[2] Pan C.-L. and Shan M.-Y., "Monotonic shear tests of cold-formed steel wall frames with sheathing", *Thin-Walled Structures*, 49, 363-370, 2011.

[3] Wang H. and Zhang Y., "Experimental and numerical investigation on cold-formed steel C-section flexural members", *Journal of Constructional Steel Research*, 65, 1225-1235, 2009.

[4] EN1993-1.1: Design of steel structures. General rules and rules for buildings. European Committee for Standardization. Brussels, Belgium, June 2004.

[5] Ranawaka T. and Mahendran M., "Numerical modeling of light gauge cold-formed steel compression members subjected to distortional buckling at elevated temperatures", *Thin-Walled Structures*, 48, 334-344, 2010.

[6] Zhang J.-H. and Young B., "Compression tests of cold-formed steel I-shaped open sections with edge and web stiffeners". *Thin-Walled Structures*, 52, 1-11, 2013.

[7] Li L.-Y., "Analyses of distortional buckling of cold-formed sigma purlins using EN1993-1-3", *Journal of Constructional Steel Research*, 65 (12), 2099-2102, 2009.

[8] Kaitila O., "Imperfection sensitivity analysis of lipped channel columns at high temperatures", *Journal of Constructional Steel research*, 58, 333-351, 2002.

[9] Kankanamge N.D., "Structural behaviour and design of cold-formed steel beams at elevated temperatures", Ph.D. thesis, Queensland University of Technology, Brisbane, Australia, 2010.

[10] EN1993-1.2: Design of steel structures. General rules. Structural fire design. European Committee for Standardization, Brussels, Belgium, June 2004.

[11] Lu W., Mäkeläinen P. and Outinen J. "Numerical simulation of catenary action in cold-formed steel sheeting in fire", *Journal of Structural Mechanics*, 40 (3), 28-37, 2007.

[12] Laim L., Rodrigues J.P.C. and Silva L.S., "Experimental Analysis on Cold-Formed Steel Beams Subjected to Fire", *Thin-Walled Structures*, 74, 104-117, 2014.

[13] EN1993-1.3: Design of steel structures. General rules. Supplementary rules for cold-formed members and sheeting. European Committee for Standardization. Brussels, Belgium, March 2004.

[14] ISO 834-1: Fire resistance tests – elements of building construction, Part 1: general requirements, International Organization for Standardization ISO 834, Geneva, Switzerland, 1999.

8th International Conference on Structures in Fire
Guo-Qiang LI, Venkatesh K. R. KODUR, Shou-Chao JIANG, Jian JIANG, Su-Wen CHEN, Guo-Biao LOU (Eds.)
Shanghai, China, June 11-13, 2014

THE EFFECT OF AXIAL AND ROTATIONAL RESTRAINTS ON THE PERFORMANCE OF COLD-FORMED STEEL BEAMS SUBJECTED TO FIRE

Luís Laím* and João Paulo C. Rodrigues*

* ISISE – Institute Sustainability and Innovation on Structural Engineering, University of Coimbra, Portugal.
e-mails: luislaim@uc.pt, jpaulocr@dec.uc.pt

Keywords: Cold-formed, Steel, Beams, Fire, Axial restraint, Rotational restraint

Abstract. *This paper is mainly aimed at the structural performance of compound cold-formed galvanized steel beams under fire conditions, based on the results of a large programme of experimental tests and numerical simulations, using the advanced finite element program ABAQUS. The main objective of this research was to assess the failure modes, the critical temperature and the critical time of the studied beams. Other important goals of this research work were also to investigate the influence of the cross-sections (C, lipped-I, R and 2R beams) and, above all, of the axial restraint (0, 0.45, 1, 7.5, 15, 30, ∞ kN/mm) to the thermal elongation of the beam and the rotational restraint at beam supports (0, 15, 150, 300, 1200 and ∞ kN.m/rad) on the fire resistance of this kind of beams.*

1 INTRODUCTION

There are still fewer studies related to the behaviour of cold formed steel (CFS) members subject to high temperatures. It is well-known that fire is a phenomenon which deteriorates its structural behaviour. The high thermal conductivity of steel and the high section factor of these structural members (very thin wall thickness) can lead to a rapid rise in steel temperature in a fire and together with the deterioration of its mechanical properties as a function of temperature may cause serious deformation of structural members and the premature failure of the building, like it happens with the hot-rolled steel structural members [1]. Since the structural behaviour of usual bare steel members under fire conditions may constitute a limiting ultimate limit state condition, investigations into CFS members under fire are required, especially because there are an absence of simplified calculations methods for fire design of CFS structures, unlike for hot-rolled steel members, see EN1993-1.2 [2].

There are also only a few numerical studies on the behaviour of CFS members subject to elevated temperatures. Some studies concluded that the increase of the magnitude of the local imperfections may lead to a relatively straightforward decrease of the initial stiffness of the member while the magnitude of the global imperfections may have more influence on the ultimate load of the member [3]. For example, Kaitila [3] observed that the ultimate compressive load of a C column may be reduced by 5.1% when the global imperfection magnitude increases from L/1000 to L/500 and may also be reduced by 3.9% when the local imperfection magnitude increases from h/200 to h/100 at 600 ºC. However, failure by distortional buckling may be further affected by the initial geometric imperfections. Ranawaka and Mahendran [4] noted that the maximum load capacity of a C column may be reduced by 20% and 30% when the distortional imperfection magnitude increases from zero to 2tn at 20 ºC and 500 ºC, respectively. In addition, it seems that the design method given in EN1993-1.2 [2] is over-conservative for all temperatures except for CFS beams with very high slenderness values [5]. Kankanamge and Mahendran

[5] also concluded from a parametric study that the EN1993-1.3 design methods [6] with buckling curve b are unsafe or over-conservative for some temperatures, especially in the intermediate slenderness region. Therefore, they proposed the use of other buckling curves for different temperature ranges for the fire design of CFS lipped channel beams. It is noticed that the methods established in Eurocode 3 were investigated by these authors in fire design by using the CFS mechanical properties at elevated temperatures [7]. With regard to the maximum temperature in CFS members, EN1993-1.2 [2] has enforced a limit of 350 ℃, which seems to be overly conservative [8], especially, on the fire behaviour of beams.

Another important thing to point out is that most scientific investigations in this area are based on the structural behaviour of simple members (composed of just one CFS profile) as well as they do not take generally into account the effect of the surrounding structure on the member subjected to fire, in opposition to this study. This paper therefore intends to fill the knowledge gap in this almost unexplored field and bring a better understanding about these issues. So, this paper is mainly aimed at the structural performance of cold-formed galvanized steel beams under fire conditions, based on the results of a large programme of experimental tests and numerical simulations, using the advanced finite element program ABAQUS [9]. The influence of the cross-sections, the axial restraint to the thermal elongation of the beam and the rotational stiffness of the beam supports was investigated. Several fire tests were thereby carried out in order to assess mainly the fire resistance and the critical temperature of the respective beams. These ones make it possible to validate the developed finite element model and consequently to obtain reliable numerical results.

2 EXPERIMENTAL INVESTIGATION

2.1 Tested Beams

The specimens consisted of beams made of one or more CFS profiles, namely, C (lipped channel) and U (channel) profiles (Figure 1). All these profiles had the same nominal thickness (2.5 mm), nominal flange width (43 mm) and inside bend radius (2 mm). The edge stiffeners of the C profiles were 15 mm long and, finally, the nominal web width was 250 mm for the C profiles and 255 mm for the U profiles. As it can also be seen in Figure 1, the lipped I beams consisted of two C connected by the respective profiles' web, whereas the R beams consisted of one C profile and one U profile connected by the respective profiles' flange. The 2R beams, like its own name say, were made of two R beams connected each other by the respective C profiles' web. These connections were materialized by means of 6.3 mm diameter steel self-drilling screws. The beam span, *L*, was 3.0 m for all specimens and the distance between the screws along beam was about 1 m (*L*/3). All profiles were still made of S280GD+Z structural steel and the screws of S235 steel.

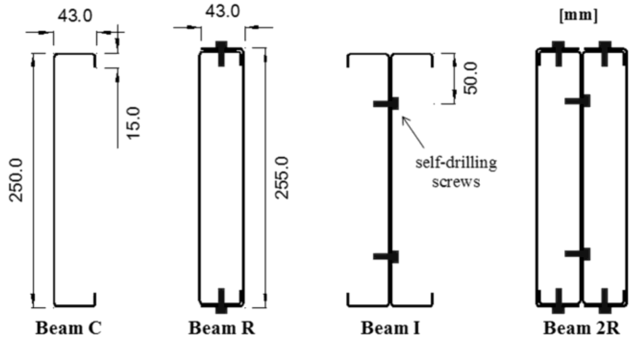

Figure 1. Scheme of the cross-sections of the tested beams.

2.2 Test Method

A schematic view of the experimental system used in the fire tests is illustrated in Figure 2. The test set-up essentially consisted of a reaction frame, a hydraulic jack to apply loading, a modular electric fire resistance furnace to simulate fire conditions, and roller and pinned supports (ns. 2 and 3) to provide a simply supported beam. The test specimens (no. 1) were loaded at two points equally spaced from each beam support (1.0m, which was one-third of the beam span) in such a way that between the two loading points the beam was under pure bending state (four point bending test).

Furthermore, the experimental system still comprised four restraining steel beams in the fire tests, two of them (perpendicular to the testing beam) to simulate the axial restraint to the thermal elongation of the beam (ns. 4 and 5) and the other two with the purpose of simulating the rotational stiffness of the beam supports (ns. 6 and 7). It is noticed that these last two beams were placed in the basement floor of the Laboratory, below the testing floor. Also note that the specimen was connected to the rotational restraining beams by means of pin-ended steel threaded rods (they passed through the holes of the slab of the Laboratory – no. 11). In addition, there was still a threaded rod system (near the roller support) (no. 10) with the purpose of eliminating the clearances between the specimen and the axial restraining beams. A steel semi-sphere was also placed between the ends of the specimen and those beams (no. 10) so that this kind of test set-up allowed studying separately the effects of axial and rotational restraining on the fire resistance of CFS beams. At last, load cells were mounted in order to monitor the axial restraining forces generated in the test specimen (no. 10) and the restraining forces (ns. 8 and 9) due to the rotational restraint imposed by cantilever beams (ns. 6 and 7) during the fire tests. The actual axial, *ka*, and rotational, *kr*, stiffness were about 15 kN/mm and 150 kN.m/rad, respectively, which were taken indirectly from the experimental results and from numerical simulations. These restraining systems intended to reproduce as faithful as possible the actual boundary conditions of a beam when is inserted in a real CFS building structure, making it possible to understand how the surrounding structure effects a CFS beam when is subjected to fire. Stiffness values as realistic as possible were considered on these tests.

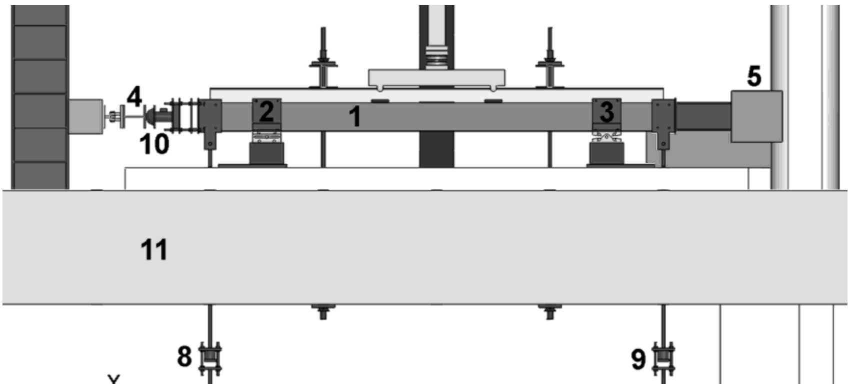

Figure 2. Overview of the test set-up for CFS beams.

2.3 Test Plan and Procedure

The experimental tests on CFS beams under fire conditions were conducted at the Laboratory of Testing Materials and Structures (LEME) of the University of Coimbra (UC), in Portugal. The experimental programme consisted of 36 structural fire tests of CFS beams, 12 of which were just simply supported beams, 12 others were the same beams but with restrained thermal elongation, and the others were beams with axial and rotational restraint. So, for each series of 12 fire tests, 3 tests for each type of beam were carried out (4 types of beams were studied), in order to obtain a better correlation of the results. For example, the reference B_ka+kr-C_3 indicates the third test (3) of the C (C) beam (B) with axial (ka) and rotational (kr) restraint.

To achieve the goals of this scientific investigation, these fire resistance tests were performed in two stages: loading and heating stage. First, the specimens were loaded up to the target force under load control at a rate of 0.1 kN/s. The load level applied on the beams was 50 % of the design value of the load-bearing capacity of the beams at ambient temperature, calculated in accordance with the methods proposed in EN1993-1-3 [6]. The loading intended to simulate the serviceability load of a beam inserted in a real building structure. Finally, the heating stage was started after the desired load was reached. Thus, the specimens were heated according to the standard fire curve ISO 834 [10]. During the heating period, the load was kept constant until the specimen buckled, where the beam deformation was too large or the maximum stroke of hydraulic jack was reached.

3 NUMERICAL INVESTIGATION

3.1 Finite Element Type and Mesh

All CFS beams were modeled by using shell elements (S4R) for the profiles and solid elements (C3D8R) for the screws, as well as many researchers in this area recommend these types of elements [11 and 12]. The influence of the finite element size on the behaviour of CFS beams was first studied. It was found that good simulation results could be obtained by using finite element meshes of 5 mm× 5 mm, 10 mm× 10 mm or 20 mm× 20 mm. To save computational time, finite element meshes of 10 mm × 10 mm for C, lipped I and R beams and of 15 mm × 15 mm for 2R beams were generated automatically by the ABAQUS program and used in all simulations. In relation to the screws, an approximately 2 mm mesh size was used.

3.2 Material Modeling

Material non-linearity in the specimens was modelled with Von Mises criteria and isotropic hardening. Stress-strain relationship of CFS profiles was described by a gradual yielding behaviour followed by a considerable period of strain hardening [13], whereas an elastic-perfectly plastic behaviour was assumed for the steel screws. A yield strength of 295 MPa and a tensile strength of 412 MPa were used and obtained from tensile coupon tests at ambient temperature. All other components were modeled as elastic, i.e. the elastic modulus was equal to 210 GPa and the Poisson’s ratio to 0.3. Residual stresses and cold-work of forming (where the apparent yield stress in the corners is increased) were ignored in these analyses. The thermal properties of the CFS at elevated temperatures considered in the model (mass density, expansion, thermal conductivity and specific heat) were those given in EN1993-1-2 [2]. The reduction factors for the yield strength of steel at elevated temperatures were still obtained from the EN1993-1-2, annex E [2], whereas the reduction factors for the Young modulus were taken from Kankanamge (2010) [8]. Lastly, the resultant emissivity was taken as 0.2 (considering the emissivity of the furnace’s electric resistance and the profiles equal to 0.7 and 0.3, respectively), due to the mirror surface of the zinc coating on the profiles used.

3.3 Analysis Method

A three-dimensional numerical model was used to describe all buckling modes observed in the experimental tests (Figure 3). As it can be seen in this figure, the axis system of the model is such that Z axis lies in the longitudinal direction of the beam while *X* and *Y* axes lie in the major and minor axes of the beam’s cross-section, respectively. The beam supports and the loading were applied on rigid plates attached to beams so as to distribute possible concentrated forces on them. On other hand, all simulated beams were still modeled using the centre line dimensions. Therefore, two assumptions were introduced in these analyses for modeling the contact behaviour between the profiles and also between these ones and the screws. Firstly a tangential friction coefficient of 0.2 and a hard contact between the profile surfaces was assumed and secondly a rough and hard contact between the profiles and the screws was considered. At last, for the modelling of the axial and rotational restraining system, a linear spring model was used as it is illustrated in Figure 3.

Three types of analysis were employed by using the developed finite element model: elastic buckling, heat transfer and nonlinear static analyses. Elastic buckling analysis was performed to establish the buckling modes which were observed in the experimental tests, thus using them to input the geometric imperfections in the nonlinear analysis. After knowing their effects on structural response of this kind of beams and comparing with the results of the experimental tests, it was observed that a suitable maximum value for global imperfections was found to be approximately $L/1000$, for distortional imperfections t and for local imperfections $h/200$, where L, t and h stand for the length of the beam, the thickness and the height of the beam cross-section, respectively. In the heat transfer analysis, a 4-node linear heat transfer quadrilateral (DC2D4) was chosen to estimate the temperature distribution in the cross-sections of the beams. The fire action was defined by two types of surface, namely, “film condition” and “radiation to ambient” which correspond respectively to heat transfer by convection and radiation. As it is recommended by the EN1991-1.2 [14], a coefficient of heat transfer by convection equal to 25 W/(m^{2}K) was used for the parametric study. Finally, a structural analysis was undertaken with the purpose of simulating the performance of CFS beams under fire conditions until failure. The nonlinear geometric parameter (*NLGEOM=ON) was set to deal with the geometric nonlinear analysis, namely, with the large displacement analysis.

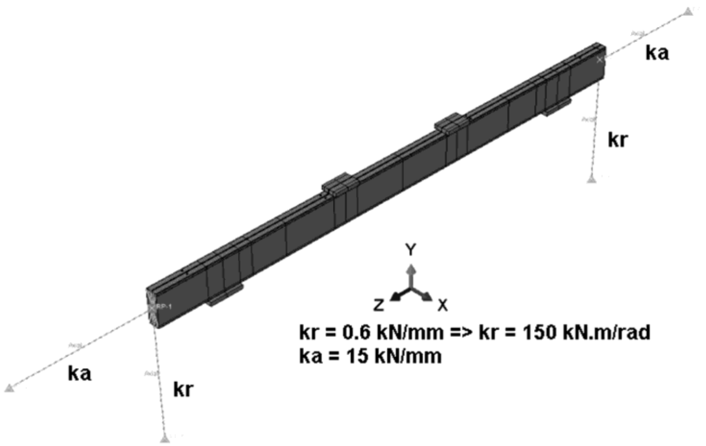

Figure 3. Numerical model used in the finite element analysis.

4 VALIDATION OF THE FINITE ELEMENT MODEL

4.1 Axial Restraining Forces in the Beams

Figure 4 shows, as an example, the comparison of the axial restraining force-temperature (N_A - θ_B) curves of the axially restrained beams. As expected, due to the effect of the thermal action, the axial force on the beam begins to increase until it reaches a maximum value. After this maximum it begins to decrease due to deterioration of mechanical properties of steel with temperature and instability phenomenon. The critical temperature is defined in these tests as that at the time when the restraining forces on it returned to the value of the initial applied axial load (failure criteria in terms of compressive strength). It is also important to emphasize that the effect of axial restraint depends on the relation between the axial stiffness of the surrounding structure and the elastic axial stiffness of the beam as well as on the relation between the bending stiffness about the weak and the strong axis, since when 15 kN/mm of axial restraint was imposed on beams, their critical temperature dropped significantly in some cases, for instance, from 718 °C to 529 °C for the C beams, from 691 °C to 443 °C for the lipped I beams, from 735 °C to 504 °C for the R beams and from 731 °C to 664 °C for the 2R beams. Lastly, all curves from finite element analysis (FEA) fit closely with the experimental curves, especially in what concerns to the critical temperature of the respective beams, as it can be seen in Figure 4. In the most cases, the critical temperatures predicted by the numerical model (continuous line) were 10% lower than the experimentally measured results, indicating that the estimated data were on the safe side but not too conservative either.

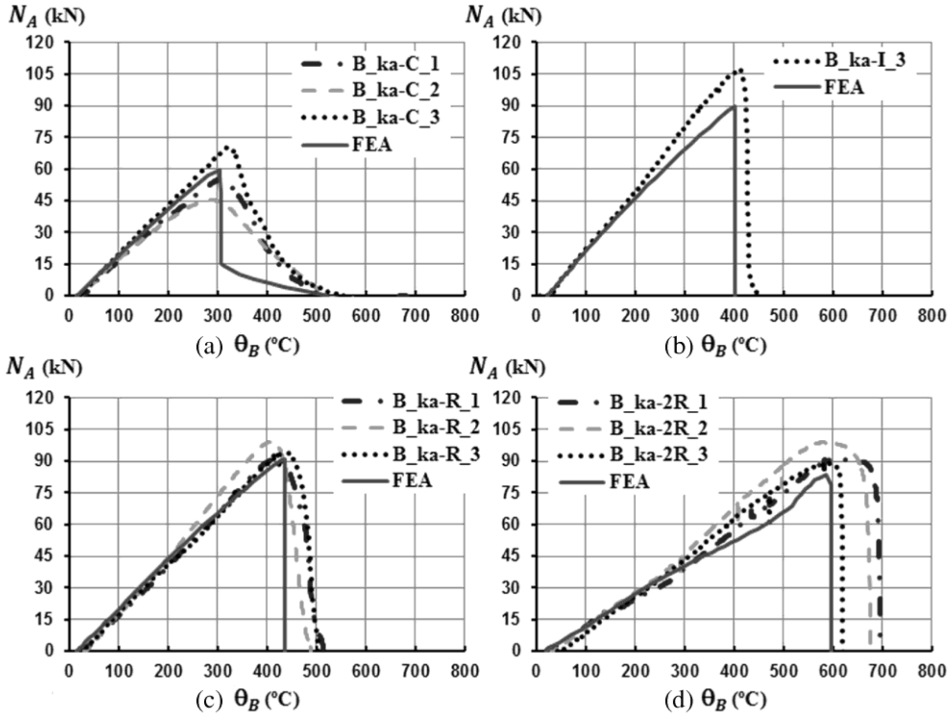

Figure 4. Comparison of the FEA and experimental axial restraining forces in the axially restrained C (a), lipped I (b), R (c) and 2R (d) beams.

4.2 Failure Modes of the Beams

For instance, Figures 5(b) and 6(b) illustrate the FEA failure modes of the simply supported C and R beams under fire conditions and each one can be respectively contrasted to the experimental failure modes as shown in Figures 5(a) and 6(a). Once again, it can be seen clearly by both kinds of figures that the finite element model predicted the behaviour of CFS beams with an acceptable precision. It was possible to observe that the lateral-torsional buckling was the main failure mode responsible for the collapse of the C beams (Figure 5) and the distortional buckling for the collapse of the R beams (Figure 6). In addition, it was still noticed that the web collapse of the R beams only occurred after the distortional buckling of the U profile.

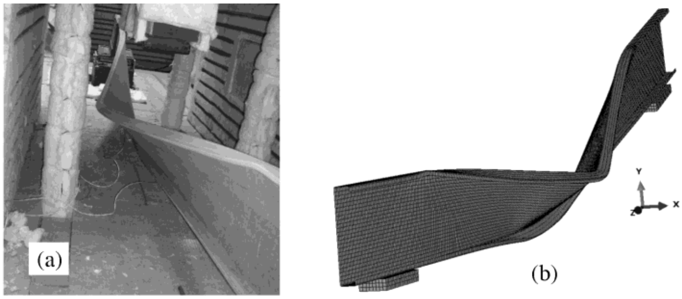

Figure 5. Experimental (a) and numerical (b) configuration of the deformed C beam after test.

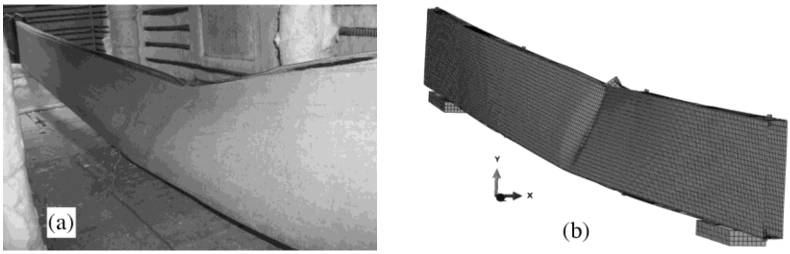

Figure 6. Experimental (a) and numerical (b) configuration of the deformed R beam after test.

5 EFFECT OF AXIAL AND ROTATIONAL RESTRAINT

Figure 7 provides a general idea of how the axial and rotational restraint affects the critical temperature of a CFS beam. In other words, it is shown the critical temperature, θ_{cr}, of a C beam with the same cross-section as the one tested in Laboratory as a function of its slenderness, λ_{LT}, for 50% of load level (LL) and for different axial restraints, *ka*, (Figure 7(a)) and rotational restraints, *kr*, (Figure 7(b)). Note that both parameters were study separately. When it was investigated the influence of the axial restraint the rotational restraint was kept constant and equal to 0, while the rotational restraint was also investigated for an axial restraint constant, but equal to 15 kN/mm, because when there is rotational restraint in real situations it is quite probably that there is axial restraint as well. Thus, from this figure it is quite interesting to observe that effect of the surrounding structure decreases with increasing slenderness of the beams and beyond 7.5 kN/mm of axial restraint or beyond 150 kN.m/rad of rotational restraint there is no more any change in the critical temperature of the C beam.

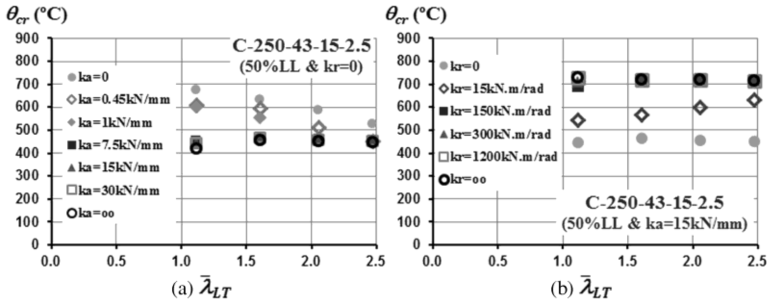

Figure 7. Effect of axial (a) and rotational (b) restraint on the critical temperature of a C beam.

6 CONCLUSIONS

The main conclusions of this investigation were that the critical temperature of this kind of beams with restrained thermal elongation may drop significantly (about 30% in some cases, comparing with the simply supported beams) and, beyond a certain value of axial or rotational stiffness of the surrounding structure (about 12% of the axial stiffness and 8% of the rotational stiffness of the beam for C-shaped cross-sections) it may be no longer possible to change the fire resistance of the beam. On the other hand, it also seems that when the slenderness of the beams increases the effect of the axial or rotational restraint tends to be less significant. In addition, it was observed that in general the axial restraint has a negative effect on the fire resistance of beams (tends to reduce it) in contrast to the rotational restraint, as it was expected. Other important conclusion of this research was that the failure modes of the axially and rotationally restrained CFS beams were much more complex and non-linear than the ones observed in the simply supported beams or even in the axially restrained beams (there were more interactions between and among the pure buckling modes usually presented in these members).

REFERENCES

[1] Correia A.J.P.M. and Rodrigues J.P.C., “Fire resistance of steel columns with restrained thermal elongation”, *Fire Safety Journal*, 50, 1-11, 2012.

[2] EN1993-1.2: Design of steel structures. General rules. Structural fire design. European Committee for Standardization, Brussels, Belgium, June 2004.

[3] Kaitila O., “Imperfection sensitivity analysis of lipped channel columns at high temperatures”, *Journal of Constructional Steel research*, 58, 333-351, 2002.

[4] Ranawaka T. and Mahendran M., “Numerical modeling of light gauge cold-formed steel compression members subjected to distortional buckling at elevated temperatures”, *Thin-Walled Structures*, 48, 334-344, 2010.

[5] Kankanamge N.D. and Mahendran M., “Behaviour and design of cold-formed steel beams subject to lateral-torsional buckling at elevated temperatures”, *Thin-Walled Structures*, 61, 213-228, 2012.

[6] EN1993-1.3: Design of steel structures. General rules. Supplementary rules for cold-formed members and sheeting. European Committee for Standardization. Brussels, Belgium, March 2004.

[7] Kankanamge N.D. and Mahendran M., “Mechanical properties of cold-formed steels at elevated temperatures”, *Thin-Walled Structures*, 49, 26-44, 2011.

[8] Kankanamge N.D., “Structural behaviour and design of cold-formed steel beams at elevated temperatures”, Ph.D. thesis, Queensland University of Technology, Brisbane, Australia, 2010.

[9] ABAQUS/CAE Standard User’s Manual, version 6.10-1, Simulia Corp., USA, 2010.

[10] ISO 834-1: Fire resistance tests – elements of building construction, Part 1: general requirements, International Organization for Standardization ISO 834, Geneva, Switzerland, 1999.

[11] Dinis P.B. and Camotim D., “Local/distortional mode interaction in cold-formed steel lipped channel beams”, *Thin-Walled Structures*, 48, 771-785, 2010.

[12] Chung K.F. and Ip K.H., “Finite element modeling of bolted connections between cold-formed steel strips and hot rolled steel plates under static shear loading”, *Engineering Structures*, 22 (10), 1271-1284, 2000.

[13] Feng M., Wang Y.C. and Davies J.M., “Structural behaviour of cold-formed thin-walled short steel channel columns at elevated temperatures. Part 2: Design calculations and numerical analysis”, *Thin-Walled Structures*, 41, 571-594, 2003.

[14] EN1991-1.2, Eurocode 1- Actions on structures - Part 1-2: General actions - Actions on structures exposed to fire, CEN, Brussels, 2002.

8th International Conference on Structures in Fire
Guo-Qiang LI, Venkatesh K. R. KODUR, Shou-Chao JIANG, Jian JIANG, Su-Wen CHEN, Guo-Biao LOU (Eds.)
Shanghai, China, June 11-13, 2014

BEHAVIOUR AND RESISTANCE OF COLD-FORMED STEEL BEAMS WITH LIPPED CHANNEL SECTIONS UNDER FIRE CONDITIONS

Flávio Arrais*, Nuno Lopes* and Paulo Vila Real*

* LABEST — Civil Engineering Department, University of Aveiro, Portugal
e-mails: arrais.f@ua.pt, nuno.lopes@ua.pt, pvreal@ua.pt

Keywords: Steel beams, Cold-formed, Buckling, Fire, Eurocode 3, New proposal

Abstract. *Steel structural elements composed of cold-formed thin walled sections, are common in buildings due to their lightness and ability to support large spans. These cold-formed profiles are more susceptible to the occurrence of local and distortional buckling phenomena. Additionally, in these members the lateral-torsional buckling is also a common failure mode. This work presents a numerical analysis of the behaviour of simply supported beams with cold-formed channel sections in case of fire. An extensive parametric study, considering different steel grades, cross-section slenderness and loading types, is presented. Comparisons between the numerical results and analytical methodologies rules, such as the Eurocode 3 Part 1-2, using its Annex E or its French National Annex where a different constitutive law is recommended for cold-formed profiles, are also made.*

1 INTRODUCTION

The cold-formed steel profiles can be applied to almost all existing buildings typologies. The use of these profiles in construction began around 1850 in the United States and United Kingdom. However, they were not widely used in buildings until 1940 [1]. The cold-formed profiles are commonly used in buildings due to its lightness and ability to support large spans, being quite common as roof or walls support elements [2].

The structural steel elements with thin walled cold-formed sections, subjected to simple bending, are characterized by being able to have the possibility of failure modes occurrence such as local, distortional and global (lateral buckling on elements under bending). These instability phenomena and its influence on the ultimate strength at normal temperature have been widely studied in recent years [3,4]. However, its behaviour in fire has not received the same attention. In fact, the fire resistance evaluation of cold-formed profiles has a major role in the design of these elements. The thin walls of these profiles, together with the steel high thermal conductivity, provide a great loss of strength and stiffness on these structural elements [5].

The fire resistance analysis of beams can be performed using calculation programs with various complexity levels, ranging from those based on simplified methods defined in the Eurocodes, to more complex ones with nonlinear analysis, based on the finite element method and included in the designated advanced calculation methods, as referred in the Eurocodes. The fire resistance of buildings structures with thin walled profiles has been calculated using advanced methods with finite element programs that consider the local buckling (e.g. with shell elements). These methods are not easily accessible to designers who regular design cold-formed steel profiles based on prescriptions of Eurocode 3 (EC3).

This work presents a numerical analysis of the behaviour of simply supported members with cold-formed lipped channel sections (C) in case of fire when subjected to simple bending. For this purpose, an extensive parametric study, considering different steel grades, different cross-section slenderness and different loading types, is here presented. These numerical results are compared with the design prescriptions of Part 1-2 of EC3 [6]. Moreover, the French National Annex (FN Annex) of this Part [7] proposes the use of different design formulae and different steel constitutive law for cold-formed profiles at elevated temperatures, which will also be analyzed and applied in this work. Finally and following the obtained results, new proposals for the safety evaluation of cold-formed lipped channel profiles at elevated temperatures are here presented.

The fire resistance of cold-formed steel lipped channel beams analysis is obtained using geometrically and materially nonlinear analyses including imperfections (GMNIA) by applying the software SAFIR (developed at the University of Liège in Belgium) [8] for different temperatures. This software uses the finite element method (FEM) for geometric and material non-linear analysis, and was especially developed for the study of structures in fire.

2 CASE STUDY AND MODEL DESCRIPTION

2.1 Case study

In this section, the main parameters that define the different models applied to perform the parametric study are presented. Simply supported beams subjected to different loadings (Figure 1), different steel grades with different channel cross-sections slenderness (Table 1) were analyzed.

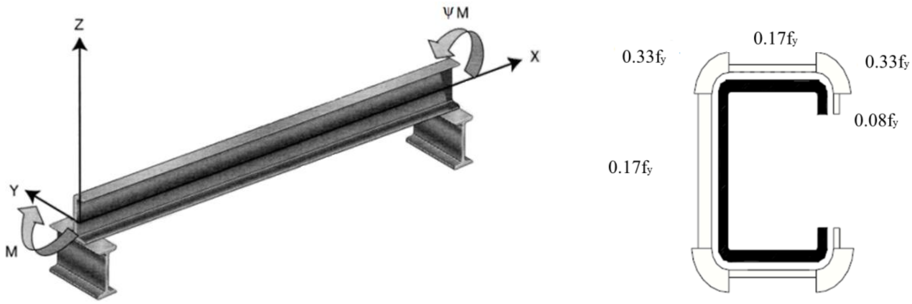

Figure 1. Simply supported beam with the loading type studied and residual stresses adopted [9].

Table 1. Cross-sections analyzed and respective dimensions * [10], **[11].

Designation	Web (mm)	Flange (mm)	Lip (mm)	Thickness (mm)
C_229×64×20×(1.5)*	229	64	20	1.5
C_170×64×20×(1.5)	170	64	20	1.5
C_229×48×20×(1.5)	229	48	20	1.5
C_229×64×15×(1.5)	229	64	15	1.5
C_100×50×10×(1.6)**	100	50	10	1.6

Beams subjected to uniform bending (ψ=1) and non-uniform bending moments (ψ=0 e ψ= –1), for different high temperatures, were studied. The influence of the yield strength (280, 320, 360, 460 MPa) on ultimate strength of these elements was also analyzed.

For this study, the temperatures 350 °C, 500 °C and 600 °C were adopted, which represent the range of common critical temperatures in these types of thin walled cold-formed steel elements.

2.2 Numerical Model

In the finite element model, shell finite elements were used due to the walls high slenderness. Loads were applied, in the parallel directions to the beam axis, according to the linear stresses distribution resulting from simple bending around the strong axis imposing uniform bending in the beams. The restrictions were imposed in order to reproduce one end pinned support and one roller support. In Figure 2, the numerical model with constraints and loads is presented.

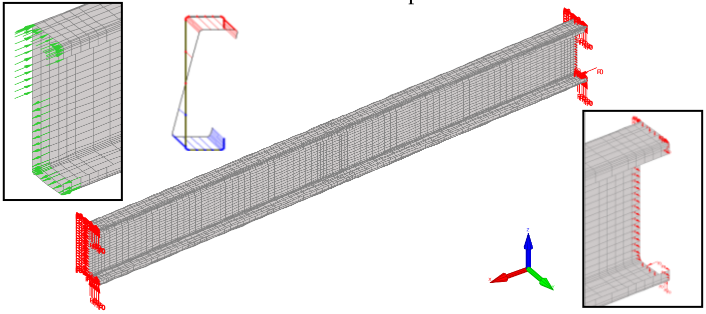

Figure 2. Adopted numerical model for lipped channel sections.

The used constitutive law for the ultimate load bearing capacity determination with the FEM simulations was the one prescribed in Part 1–2 of EC3 using its Annex E. The FN Annex of this same Part of EC3 proposes the application of different stress-strain relationships. These new material laws are obtained from different reduction factors for the yield strength and young modulus at high temperatures. The FN Annex proposes lower values for these reduction factors. Figure 3 illustrates the differences obtained for 500 ℃. The constitutive law of the FN Annex was also used applied on the numerical results.

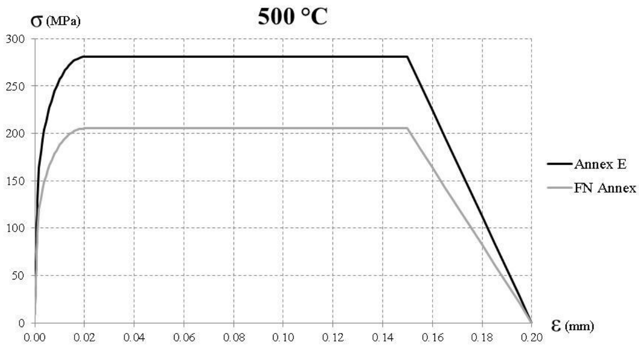

Figure 3. Constitutive law for 500 ℃ according to the Annex used.

Residual stresses were considered, due to press-braking manufacturing process (Figure 1) for being the most common manufacturing process [12]. Also, geometric imperfections such as the local, distortional and global were taken into account in these models analysis. The characterization of the influence of initial geometric imperfections on the fire resistance has been studied in previous works [13].

To generate the different shapes for all geometric imperfections, CAST3M [14] with RUBY [15] programs were used. To consider the local, distortional and global imperfections on numerical models the Table 2 shows the maximum magnitude for the three buckling modes applied, were b is the height of the web or width of the flange, whichever presents the larger deflection, and L the respective beam length. The values given in Table 2 correspond to 80% of geometric fabrication tolerances, according to Annex C of Part 1–5 from EC3 [16], described on section D.1 from Annex D of EN 1090–2+A1 [17].

Table 2. Geometric imperfections magnitude.

Local	Distortional	Global
$0.8\times\frac{b}{100}$	$0.8\times\frac{b}{100}$	$0.8\times\frac{L}{750}$

Following the recommendations of Part 1–5 from EC3, the combined geometric imperfections were introduced. According the EC3, in combining imperfections a leading imperfection should be chosen and the accompanying imperfections may have their values reduced to 70%. The leading imperfection was chosen in function of the achieved lower resistances. Due to the manufacturing process, cold-formed steel sections have flat walls and rounded corners, corresponding to folding plate zones. The geometry of these sections is covered by the Annex C of Part 1–3 from EC3 [18], to obtain the cross sectional resistance moment. Under these prescriptions, the methodology to obtain the effective cross-sections for local instability mode is different from the methodology for distortional instability mode. The first is based on the effective width method and the latter is based on the reduced thickness method, respectively. It was not considered the increased yield strength in the corners due to the cold-formed process.

In the comparisons made in these paper it was used the numerically obtained resistance of the cross-section and critical moment for the slenderness calculation.

3 PROVISIONS OF PART 1-2 OF EUROCODE 3

Table 3 shows the conditions and expressions presented on the Part 1-2 of EC3, considering the Annex E and the FN Annex, used in the present study for lateral-torsional buckling under fire conditions for Class 4 cross-sections.

Table 3. Equations for lateral-torsional buckling under fire conditions for cold-formed profiles.

General condition	
$\frac{\mathrm{M_{fi,Ed}}}{\mathrm{M_{b,fi,t,Rd}}} \le 1{,}0$	
Design lateral-torsional buckling resistance moment at time t for a laterally unrestrained beam Class 4	
$\mathrm{M_{b,fi,t,Rd}} = \chi_{LT;fi} W_{eff,y} k_{0.2,p,\theta} \frac{f_y}{\gamma_{M,fi}}$	
Reduction factor for lateral-torsional buckling in the fire design situation	
$\chi_{LT,fi} = \frac{1}{\phi_{LT,\theta} + \sqrt{(\phi_{LT,\theta})^2 - (\bar{\lambda}_{LT,\theta})^2}}$	
Non-dimensional slenderness for lateral-torsional buckling in the fire design situation	
$\bar{\lambda}_{LT,\theta} = \bar{\lambda}_{LT} \sqrt{\frac{k_{0,2,p,\theta}}{k_{E,\theta}}}$	
Non-dimensional slenderness for lateral-torsional buckling	
$\bar{\lambda}_{LT} = \sqrt{\frac{W_{eff,y} f_y}{M_{cr}}}$	
Part 1-2 of EC3 + Annex E	**Part 1-2 of EC3 + FN Annex**
$\phi_{LT,\theta} = \frac{1}{2}\left[1 + \alpha\bar{\lambda}_{LT,\theta} + (\bar{\lambda}_{LT,\theta})^2\right]$	$\phi_{LT,\theta} = \frac{1}{2}\left[1 + \alpha_{LT}(\bar{\lambda}_{LT,\theta} - 0.2) + (\bar{\lambda}_{LT,\theta})^2\right]$
$\alpha = 0.65\sqrt{\frac{235}{f_y}}$	$\alpha_{LT} = 0.34$ (value from Table 6.1, section 6.3.2.2 of Part 1-1 of EC3, lateral buckling curve b)
$k_{y,\theta}, k_{p,\theta}, k_{0,2,p,\theta}, k_{E,\theta}$ (values from Table 3.1 Part 1-2 of EC3, and Table E.1 of Annex E)	$k_{y,\theta}, k_{p,\theta}, k_{0,2,p,\theta}, k_{E,\theta}$ (values from Table AN6.1 of FN Annex, and Table 2-12 of reference [19])
$W_{eff,y}$ is the effective section modulus and M_{cr} the elastic critical moment for lateral/torsional buckling.	

4 DISCUSSION OF THE RESULTS

In this section, the influence of the cross-section slenderness, of the steel grade and loading type on the ultimate load bearing capacity, of the cold-formed steel beams with lipped channel sections obtained numerically in fire conditions, is analyzed and compared with the simple calculation rules prescribed in Part 1–2 of EC3, considering the Annex E and the FN Annex parameters. With the purpose of analysing only the member buckling curve and not the cross-section resistance, in the numerical results the cross-section resistant moment and the critical moment were made equal to the numerically obtained results.

4.1 Influence of the cross-section slenderness

To study the influence of the different cross-section slenderness, five cross-sections with different dimension values were chosen. Each one was analyzed for the yield strength equal to 360 MPa and considering the uniform bending case (ψ=1). Under these conditions, all cross-sections were Class 4.

Comparing the numerical results with the EC3 it is possible to conclude that the obtained values are on the safe side and sometimes too conservative. Due to the space limitation only few examples are presented. Observing the Figure 4, Annex E is more conservative than FN Annex, providing this last a more precise approximation to the numerical resistances. The differences observed between the different cross-sections results were small.

4.2 Influence of the steel grade

Using one of the cross-sections studied, it was possible to analyse the influence of the steel grade varying the yield strength, using the 280, 320, 360 and 460 MPa values, under the uniform bending type (ψ=1). Considering these assumptions, all cross-sections were Class 4 at high temperatures.

In Figure 5 are presented the results for 320 and 460 MPa and it is possible to observe, comparing the numerical results with EC3 rules, that the results are again on the safe side and the influence of the steel grade can be neglected. Differences between the different steel grades are minimal.

4.3 Influence of the loading type

To evaluate the different loading types it was analyzed the same cross-section used to study the influence of the steel grade, C_229×64×20×(1.5) (Class 4 cross-section), and applying the different non-uniform bending moments (ψ ratio 0 and –1). For this case it was used the yield strength of 360 MPa.

In non-uniform bending cases, it was observed a failure mode of shear buckling for the small lengths. For this reason, the correspondent values were not taken into account in this paper. From the Figure 6, it is possible to conclude that the numerical values are over conservative when compared with the EC3. With the decrease of the ψ ratio the values will be diverging from the EC3 curve. It is important to considerer the *f* reduction factor according to the loading type.

5 NEW DESIGN PROPOSAL

The previous analysis showed the necessity of a new design method for the fire design of cold-formed steel beams subjected to lateral-torsional buckling. The actual calculation rules are too conservative. Thus, new formulations were developed, based on simple changes on the actual expressions from EC3 and a modified reduction factor. Two proposals are made. First only a plateau at slenderness of 0.3 was tested and afterwards, as some improvements could still be introduced, the consideration of a new imperfection factor is also analyzed.

5.1 Proposal with a plateau (New proposal 1 - α from EN1993-1-2)

For the new proposal all the main formulation of Part 1-2 of EC3 remains, modifying the following parameter:

$$\phi_{LT,\theta} = \frac{1}{2}\left[1 + \alpha(\overline{\lambda}_{LT,\theta} - 0.3) + (\overline{\lambda}_{LT,\theta})^2\right] \tag{1}$$

To consider the different loading types, a modified reduction factor is proposed [20] given by:

$$\chi_{LT,fi,\mathrm{mod}} = \frac{\chi_{LT,fi}}{f} \leq 1 \quad \text{where} \quad f = 1 - 0.5(1 - k_c) \tag{2}$$

k_c is a correction factor taken into account the ψ ratio given by:

$$k_c = 0.125\psi^2 + 0.225\psi + 0.65 \leq 1 \tag{3}$$

The results were better adjusted to this new proposal curve rendering them not as conservative as the current rules (see Figures 4 to 6).

5.2 Proposal with a plateau and a new imperfection factor (New Proposal 2 - α=0.34)

For this new proposal all the main considerations of the previous presented Proposal 1 remains but an imperfection factor for lateral-torsional buckling $\alpha_{LT} = 0.34$, value from Table 6.1, section 6.3.2.2 of Part 1-1 of EC3, lateral buckling curve b is used, instead of the α from Part 1-2 of EC3. The results showed a good adjustment to this new proposal curve, as presented on Figures 4 to 6.

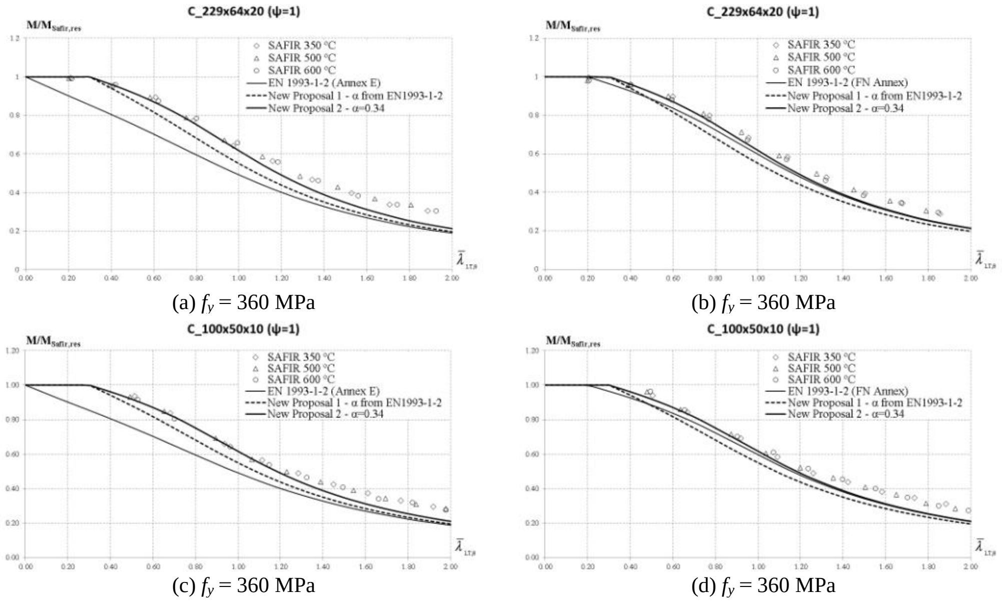

(a) f_y = 360 MPa (b) f_y = 360 MPa

(c) f_y = 360 MPa (d) f_y = 360 MPa

Figure 4. Comparison of the results for different cross-sections applying EN1993-1-2 Annex E and FN Annex.

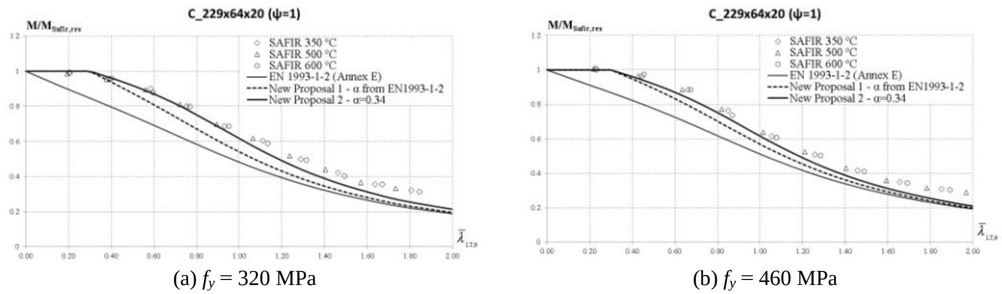

(a) f_y = 320 MPa (b) f_y = 460 MPa

Figure 5. Comparison of the results for different steel grades applying EN1993-1-2 Annex E.

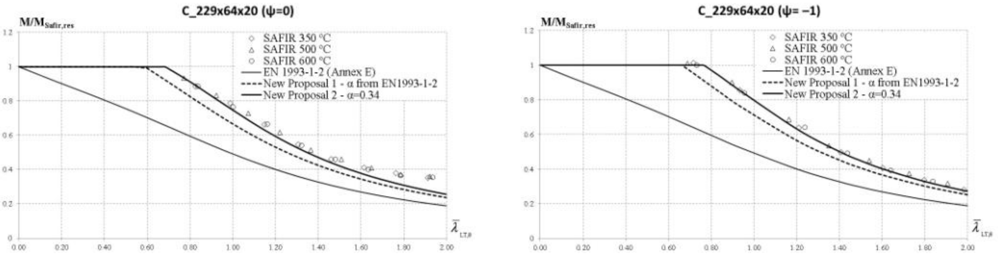

(a) f_y = 360 MPa (b) f_y = 360 MPa

Figure 6. Comparison of the results for different loading types applying EN1993-1-2 Annex E.

Figure 7 shows the accuracy of the design prescriptions of EC3-Annex E, EC3-FN Annex, and the New Proposal 2 - α=0.34. It can be observed that the New Proposal 2 presents the most precise approximations to the numerical results.

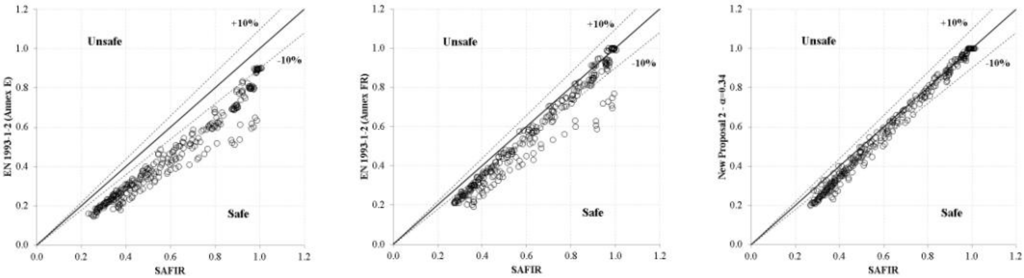

(a) (b) (c)

Figure 7. Comparison between the numerical results and the different rules from EC3 and the New Proposal 2.

6 CONCLUSIONS

In this work it was presented an extensive parametric study of the lateral-torsional buckling behaviour of simply supported members with cold-formed lipped channel sections (C), in case of fire, when subjected to simple bending. The influence of the different steel grades, cross-section slenderness and loading types was evaluated.

A comparison between the ultimate loads and the formulae prescribed in EC3 was performed, concluding that the calculation rules are on the safe side and sometimes too conservative. It was possible to observe that the Annex E is more conservative than the FN Annex, having the latter showed a good agreement with the numerical results.

New proposals for the design of cold-formed steel beams subjected to simple bending were presented in this work. These proposals were developed in order to introduce the minimum changes in the existing formulae providing at the same time safety and accuracy when compared to the numerical results.

7 ACKNOWLEDGMENTS

The author acknowledges the financial support of the FCT – Portuguese Foundation for Science and Technology in the framework of the research grant SFRH/BD/90455/2012.

REFERENCES

[1] ASRO (Asociatia standardizare din România), *Introduction to cold-formed steel design*, Technical document ICS 91.010.30;91.080.10, 2008

[2] Silvestre N., Camotim D., “Construção em aço leve”, *Journal of CMM – Associação Portuguesa de Construção Metálica e Mista*, Year 11, nº 20, March de 2010

[3] Silvestre N., Camotim D., “On the mechanics of distortion in thin-walled open sections”. *Thin-Walled Structures*, Vol. 48. n. º7. p. 469-481, 2010.

[4] Camotim D., Gonçalves R., “Thin-walled member plastic bifurcation analysis using generalised beam theory”, *Advances in Engineering Software*, Vol. 38. p. 637-646, 2007.

[5] Laim L., Rodrigues J. P. C., “Modelação numérica de vigas em aço enformadas a frio submetidas ao fogo”, *Congress on Numerical Methods in Engineering – CMNE*, Coimbra, Portugal, 2011.

[6] CEN, *EN 1993-1-2, Eurocode 3: Design of Steel Structures - Part 1-2: General rules - Structural fire design*, Belgium, 2005.

[7] CEN, *NF EN 1993-1-2, Eurocode 3: Calcul des structures en acier – Annexe Nationale à la NF EN 1993-1-2: Calcul du comportment au feu*, Belgium, 2004.

[8] Franssen J.-M., “SAFIR. A Thermal/Structural Program Modelling Structures under Fire”; *Engineering Journal, A.I.S.C.*, Vol. 42, No. 3, pp. 143-158, 2005.

[9] Schafer B. W., Peköz T, "Computational modeling of cold-formed steel: characterizing geometric imperfections and residual stresses", *J. of Constr. Steel Res., Elsevier*. Vol. 47, n 3, 193-210, 1998.

[10] Schafer B. W., “Designing Cold-Formed Steel Using the Direct Strength Method”, *18th International Specialty Conference on Cold-Formed Steel Structures*, Orlando, Florida, 2006.

[11] Wang X. P., Lam S. S. E., Chung K. F., "Cross section distortion due to cutting of cold-formed steel lipped C-section", *Thin-Walled Structures*. Vol. 44, n. º3, p. 271-280, 2006.

[12] Dubina D., Ungureanu V., Landolfo R., *Design of Cold-formed Steel Structures. Eurocode 3: Design of Steel Structures. Part 1-3: Design of Cold-formed Steel Structures*, ECCS, 2012.

[13] Lopes N., Arrais F., Vila Real P., “Resistência ao fogo de vigas metálicas com secções enformadas a frio”, *2nd CILASCI, Ibero-Latin-American Congress on Fire Safety*, Portugal, pp. 127-136, 2013.

[14] CAST3M., *development sponsored by French Atomic Energy Commission*; 2012. <http://www-cast3m.cea.fr/>

[15] Couto C., Vila Real P., Lopes N., *RUBY: An interface software for running a buckling analysis of SAFIR models using Cast3M*, University of Aveiro, 2013.

[16] CEN, *EN 1993-1-5, Eurocode 3: Design of Steel Structures - Part 1-5: Plated structural elements.* Brussels, Belgium, 2006.

[17] CEN, *EN 1090-2+A1, Execution of steel structures and aluminium structures - Part 2: Technical requirements for steel structures*. Brussels, Belgium, 2008.

[18] CEN, *EN 1993-1-3, Eurocode 3: Design of Steel Structures - Part 1-3: Supplementary rules for cold-formed members and sheeting*, Belgium, 2006.

[19] Zhao B., Kruppa J., Renaud C., O'Connor M., Mecozzi E., Apiazu W., Demarco T., Karlstrom P., Jumppanen U., Kaitila O., Oksanen T., Salmi P., *Calculation rules of lightweight steel sections in fire situations*, European Commission, Luxembourg, 2005.

[20] Lopes N., Vila Real P., Simões da Silva L., Franssen J.-M., “Lateral-torsional buckling on carbon steel and stainless steel beams with lateral loads plus end moments in case of fire”, *6th Int. Conf. on Structures in Fire SiF’10*, East Lansing, USA, 2010.

8th International Conference on Structures in Fire
Guo-Qiang LI, Venkatesh K. R. KODUR, Shou-Chao JIANG, Jian JIANG, Su-Wen CHEN, Guo-Biao LOU (Eds.)
Shanghai, China, June 11-13, 2014

A STUDY ON A THEORETICAL RELATIONSHIP BETWEEN STRAIN HARDENING OF STEEL AND PLASTIC REGION LENGTH IN A STEEL BEAM SUBJECTED TO FIRE

Fuminobu OZAKI*

*Associate Professor, Dr. Eng., Graduate School of Environmental Studies, Nagoya University
e-mails: ozaki@dali.nuac.nagoya-u.ac.jp

Keywords: Attenuation of thermal stress, Plastic deformation, Strain hardening, Steel beam

Abstract. *This paper presents a relationship between strain hardening of steel and plastic region length in a steel beam subjected to fire. A theoretical simple fire response analysis is proposed to investigate elasto-plastic behavior of the statically indeterminate heated beam. From observation of parametric calculations, it is clarified that large plastic region length in the beam, which is induced by the large strain hardening, is effective to avoiding strain concentration. This contributes to the robust attenuation of the thermal stress at the fire.*

1 INTRODUCTION

It is well known that strain hardening of steel has a significant influence upon plastic deformation capacity of steel members at seismic performance based designs. In some countries (for instance, Japan and the Unite States), mechanical property of steel closely related to the plastic deformation capacity is standardized. A yield ratio of the steel, which is given by a ratio of a yield point to a tensile strength at ambient temperature, is one of the most important mechanical property to estimate the plastic deformation capacity. When applying the low yield ratio steel for the steel member, plastic region in the member is widely extended (Kato, 1990). This contributes to avoiding strain concentration in the member and delaying local buckling or ductile cracks at severe earthquake events. For the reason, a relationship between the strain hardening or the yield ratio of the steel and the seismic performance (for example, plastic deformation capacity and energy dissipating capacity) of the steel members have been studied by many past researches, experimentally, numerically and theoretically.

In a field of fire safety engineering, fire resistant performance based designs for the steel buildings have been proposed (European Committee Standardization, 2005; Architectural Institute of Japan, 1999). They offer verification methods on structural fire resistance of the heated members such as columns, beams and connections. Most of them are relating to "load bearing capacity" at the fire, while their "plastic deformation capacity" has not been described in detail.

In accordance with the past study (Suzuki, 1995), theoretical ultimate strength of the steel member at the fire, which is based on the simple plastic theory, is unrelated to the thermal stress. This fact is based on an assumption that the members possess the full plastic deformation capacity. The thermal stress generated in the heated members is attenuated (damped) by plastic deformation of themselves, with increasing temperature (Suzuki, 1995). Many simple calculation methods proposed by the Architectural Institute of Japan (1999) are based on the above assumptions. It is, that is, suggested that proposed verification methods cannot be applied for the members that possess the poor plastic deformation capacity. It is, therefore, considered that the strain hardening or the yield ratio of the steel must be investigated as one of influence factors for the structural fire resistance.

This paper presents theoretical relationships between the strain hardening of steel and the plastic region length of the heated steel beam at the fire. To investigate elasto-plastic behavior of the statically indeterminate heated beam, a theoretical simple fire response analysis is proposed.

2 A THEORETICAL FIRE RESPONSE ANALYSIS FOR A HEATED BEAM AT THE FIRE

Figure 1 shows a calculation model (a left-half partial beam model). The temperature is gradually and uniformly rising. A thermal elongation of the heated beam is restricted by peripheral members at room (ambient) temperature *RT*. They are modeled as an elastic spring (stiffness $\overline{K}$) in the calculation model. A vertically concentrated constant load P is applied at the center of the beam. It is assumed that a sectional shape of the beam is given by ideal double flange models (Figure 1). An equilibrium condition of force is based on the small deformation theory.

In the heated beam, an axial compressive force is generated. This is the thermal stress. The temperature T when the beam yields is given by solving an Equation (1).

$$\frac{1}{1+K_b(T)/\overline{K}}\frac{\alpha E(T)AT}{N_y(T)}+\frac{0.5Pl}{M_p(T)}-1=0 \qquad (1)$$

Where, α is a liner coefficient of expansion of the steel (=12×10^{-6} 1/°C), $E(T)$ is Young's modulus at the temperature T, $M_p(T)$ is full plastic moment of the beam, $N_y(T)$ is yield axial force of the beam, A is sectional area of the beam and $\overline{K}$ is elastic spring stiffness.

$K(T)$ is given by $E(T)A/l$, $E(T)$ is given by $\overline{E}\kappa_e(T)$. $M_p(T)$ and $N_y(T)$ are respectively given by $\overline{M}_p\kappa(T)$ and $\overline{N}_y\kappa(T)$. A symbol with a over line (for instance, $\overline{M}_p$ or $\overline{N}_y$) means a value at the ambient temperature. $\kappa(T)$ is a reduction factor for the yield stress and $\kappa_e(T)$ is it for the Young's modulus(Figure 2). They are respectively given by the Architectural Institute of Japan (1999).

When the beam behaves plastically at the elevated temperature, the equilibrium condition of the force for a minute temperature increment dT at beam end section are respectively given by the following equations.

$$dN = A\left(\frac{\partial\sigma(\varepsilon_c,T)}{\partial T}dT+\frac{\partial\sigma(\varepsilon_c,T)}{\partial\varepsilon_c}d\varepsilon_c\right) \qquad (2)$$

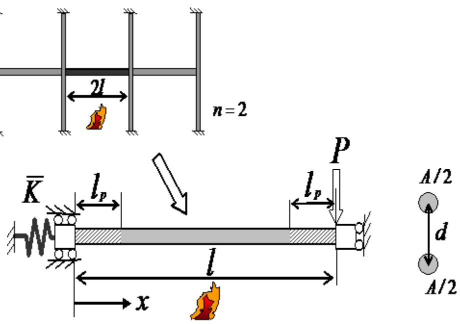

Figure 1. A theoretical calculation model.

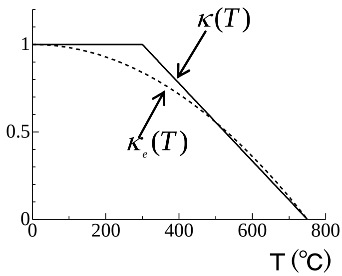

Figure 2. Reduction factors of steel.

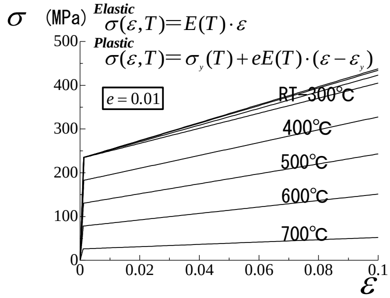

Figure 3. σ -ε Relationships.

$$\frac{\partial\sigma(\varepsilon_c,T)}{\partial T}dT+\frac{\partial\sigma(\varepsilon_c,T)}{\partial\varepsilon_c}d\varepsilon_c=\frac{\partial\sigma(\varepsilon_t,T)}{\partial T}dT+\frac{\partial\sigma(\varepsilon_t,T)}{\partial\varepsilon_t}d\varepsilon_t \tag{3}$$

Where, $\sigma(\varepsilon,T)$ is stress depending on both strain and temperature, ε_c and ε_t are compressive and tensile strain for flanges at the beam end section, respectively. N is axial compressive force.

It is supposed that stress and strain relationships at the elevated temperature is given by bi-linear models (Figure 3). The strain hardening coefficient $E_t(T)$ in the bi-liner models is given by $E_t(T)=e\cdot E(T)$ (e: the ratio of $E_t(T)$ to $E(T)$, Figure 3).

A compatibility condition of the axial displacement of the heated beam model for the minute temperature increment dT is given by the following equation.

$$\frac{d\varepsilon_c+d\varepsilon_t}{2}l_p+\frac{\varepsilon_c+\varepsilon_t}{2}dl_p=\alpha\cdot l\cdot dT-dN\left(\frac{l-2l_p}{E(T)A}+\frac{1}{\overline{K}}\right) \tag{4}$$

Where, l_p is plastic region length of the beam (Figure 1).

It is supposed that both $d\varepsilon_c$ and $d\varepsilon_t$ in the plastic region are constantly positive values. This means that elastic unloading at the beam end section is not generated in this theoretical model. This assumption is verified by numerical approaches (FE analyses) in the next section.

On the other hand, a yield condition of the beam section for the minute temperature increment dT is given by the following equation.

$$\frac{N+dN}{N_y(T+dT)}+\frac{P\cdot(0.5l-(l_p+dl_p))}{M_p(T+dT)}-1=0 \tag{5}$$

$d\varepsilon_c$, $d\varepsilon_t$, dl_p and dN in the Equation(2)-(5) are unknown incremental quantities. They can be explicitly determined by solving four simultaneous liner equations (2)-(5). The response calculation results (ε_c, ε_t, l_p or N) are given by adding the incremental values($d\varepsilon_c$, $d\varepsilon_t$, dl_p or dN), respectively.

3 FIRE RESPONSE CALCULATION RESULTS

Figures 4 show theoretical calculation results. Their calculation parameters are given by l = 3500 mm, A = 6 000mm^2, sectional depth d = 500mm, P = $0.3\overline{M}_p/l$, respectively. Numerical results obtained by a finite element analysis (FE analysis) using a beam element are shown in Figures 2. In the FE analysis, material and geometric non-linearity and hysteretic rule of the steel at the elevated temperature are

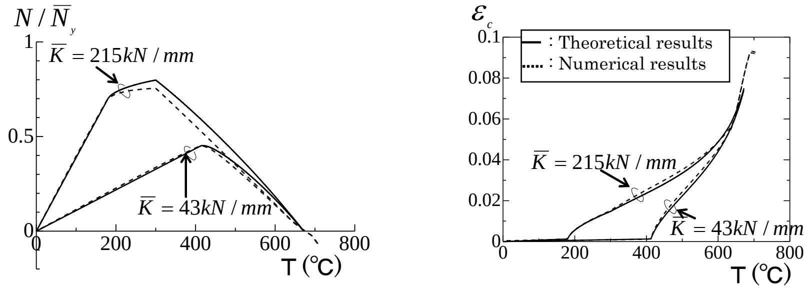

Figures 4. Calculation results.

respectively considered (AIJ, 1999). The elastic spring stiffness $\overline{K}$ of the peripheral members at the ambient temperature are determined by the following equation.

$$\overline{K}=n\cdot\frac{24\overline{E}I_C}{h^3} \tag{6}$$

Where, n is a total number of the peripheral columns at the ambient temperature (for instance, n=2 for the frames shown in the figure 1), I_C is a geometrical moment of inertia of the columns and h is column height. It is supposed that the column height h and its geometrical moment of inertia I_C are given by the same values of beam length l and geometrical moment of inertia of the beam $I_b\,(=Ad^2/4)$, respectively. Supposing that n is given by 5 and 2 respectively, the values of $\overline{K}$ are equal to 215 and 43 kN/mm, respectively.

As shown in the Figure 4, theoretical and numerical results are approximately corresponding. In the case of the FE analysis, which is taken steel load-unload hysteretic rule at the elevated temperature into account, the plastic strain at the beam end is monotonously increasing. That is, the section at the beam end has behaved in the plastic loading at the elevated temperature, as with the assumption used in theoretical calculation. Additionally, in this process, it is well known that both plastic deflection and plastic axial shortening of the heated beam are monotonously increasing while the axial force (thermal stress) is gradually reducing (Suzuki, 1995; AIJ, 1999). This is the attenuation of the thermal stress, which is induced by the plastic deformation of the heated beam. This also means that the heated members dissipate energy corresponding to the thermal stress, by plastic deformations of itself. The axial force $N/\overline{N}_y$ of the numerical result at around 630 °C becomes tensile force, because the beam exhibits the geometric non-linear effects, which is represented by the hammock behavior (Suzuki, 1995).

Figures 5-8 show the theoretical parametric calculation results. The plastic axial shortening component δ_p is given by integrating the increment $d\delta_p\,(=0.5(d\varepsilon_c+d\varepsilon_t)l_p+0.5(\varepsilon_c+\varepsilon_t)dl_p)$. On the other hand, the plastic rotational angle component θ_p is given by $\theta_p=0.5(\phi_e-\phi_p)l_p$, where, ϕ_e is a curvature of the ideal double section at the beam end and ϕ_p is given by $\phi_p=M_p(T)/(E(T)I_b)$.

It is obvious that there is a strong correlation among the plastic region length l_p, the strain ε_c and the strain hardening of the steel (parameter *e*). To avoid the large strain concentration, the plastic region length l_p must be widely extended. When the steel possesses the large strain hardening, the strain concentration is relieved (Figures 7 and 8). On the other hand, l_p is hardly extended at the small strain hardening (e=0.0001 or 0.005). Their calculation results show the large strain concentration (Figure 7 and 8) when the thermal stress $N/\overline{N}_y$ is completely attenuated (damped).

At the fire resistant design for the steel structures, a design limit temperature is given by the theoretical collapse temperature based on the simple plastic theory using the small deformation theory (AIJ, 1999). The theoretical collapse temperature, when the heated beam behaves in collapse mechanism by the plastic hinges, is given by the temperature when the thermal stress is equal to zero (Suzuki, 1995; AIJ, 1999). From observation of theoretical and numerical calculation results(Figures 4-8), it is clarified that two lines of them using the different spring stiffness ($\overline{K}$ =215 and 43 kN/mm) approach closely at the collapse temperature(at N=0). This means that strain state and member displacements at the collapse temperature based on the small deformation theory are independent of the thermal stress induced by the thermal elongation. This also means that the theoretical loads, temperature and displacements are independent of self-strain of the heated member and force application order (Suzuki, 1995; AIJ, 1999).

It is expected that the large plastic region length l_p contributes to raising the collapse temperature, because occurrence of the local buckling or the ductile cracks might be delayed by avoiding the strain concentration and strength degradation of the beam is controlled by it.

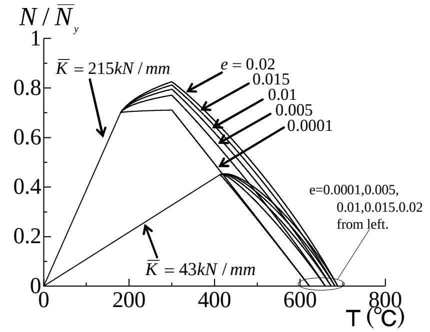

Figure 5. Theoretical parametric calculation results N.

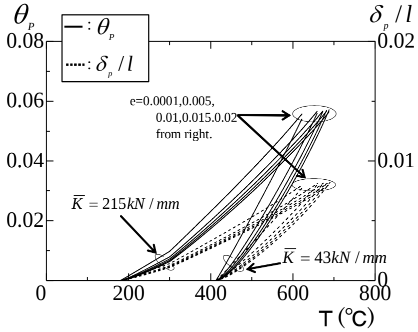

Figure 6. Theoretical parametric calculation results θ_p, δ_p.

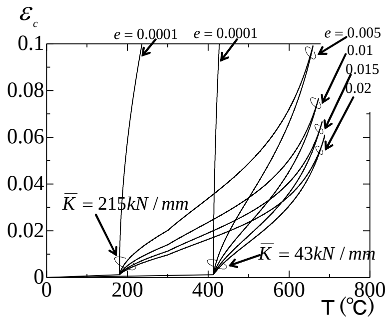

Figure 7. Theoretical parametric calculation results ε_c.

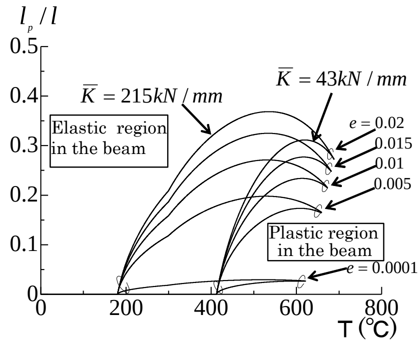

Figure 8. Theoretical parametric calculation results l_p.

4 PARAMETRIC CALCULATION RESULTS USING DESIGN STRESS - STRAIN RELATIONSHIPS

In this section, the fire response calculation results using the design stress - strain relationships for the heated beam model(Figure 1) are explained. Figures 9 show the stress - strain relationships proposed by AIJ and Eurocode3, respectively (AIJ, 1999; European Committee Standardization, 2005).

The Equation (4), which is given by the compatibility condition of the axial displacement, is completed in the case when the stress - strain relationship is only the bi-liner model. For the design stress - strain relationship curves, the compatibility condition is approximately given by using the following equation.

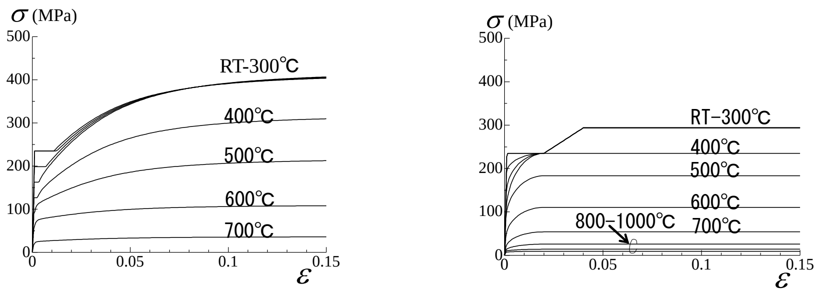

Figures 9. Stress - strain relationships.
(Left: AIJ curves, Right: Eurocode curves)

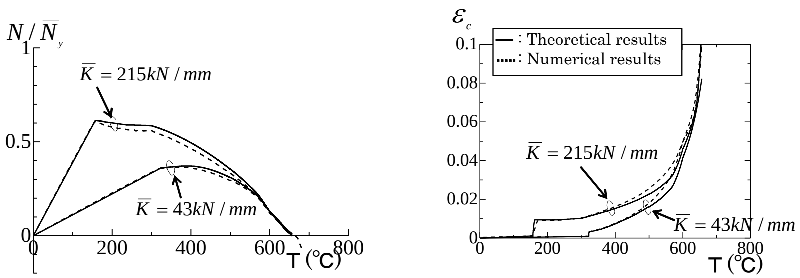

Figures 10. Calculation results (AIJ curves).

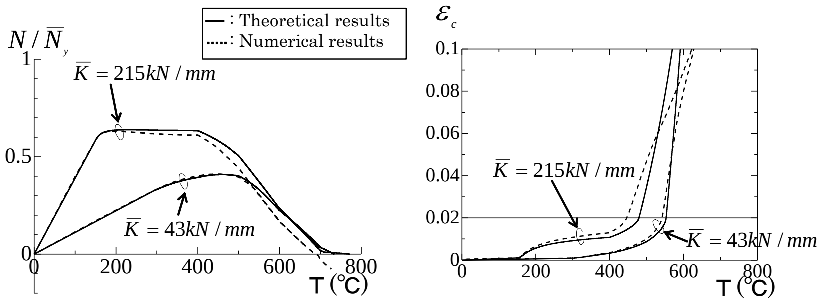

Figures 11. Calculation results (Eurocode curves).

$$\frac{1}{\gamma}\left(\frac{d\varepsilon_c+d\varepsilon_t}{2}l_p+\frac{\varepsilon_c+\varepsilon_t}{2}dl_p\right)=\alpha\cdot l\cdot dT-dN\left(\frac{l-2l_p}{E(T)A}+\frac{1}{\overline{K}}\right) \tag{7}$$

Where, γ is an average strain hardening ratio, which is given by $\gamma = E_o / E_t(\varepsilon_c, T)$. $E_t(\varepsilon_c, T)$ is a tangent modulus of the stress-strain curve corresponding to the strain ε_c and the temperature T. E_o is given by $E_o = E_t(0.5(\varepsilon_c+\varepsilon_s), T)$ and ε_s is the strain at a starting point of the strain hardening in the stress and strain curve.

Figures 10 and 11 show the calculation results for both theoretical and numerical analyses. For the analytical calculations, both AIJ and Eurocode curves have been respectively converted into the true stress - true strain relationships.

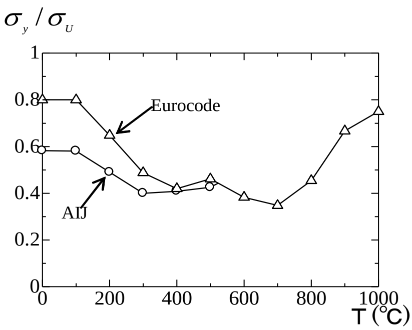

Figure 12. Yield ratio of stress -strain curves.

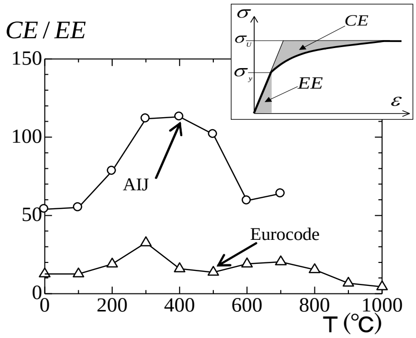

Figure 13. Complementary energy CE of stress -strain curves.

As shown in Figure 11, the strain ε_c in the case of the Eurocode curves is rapidly increasing after ε_c is over 0.02, because the stress - strain relationships of the Eurocode curves (Figure 9) do not possess the strain hardening in this region. For the fire response analyses using the Eurocode curves, the large strain concentrations might be induced in the middle of attenuating (damping) the thermal stress.

The yield ratios (= σ_y / σ_U, σ_y : yield point, σ_U : tensile strength) and the energy ratio CE / EE of a complementary energy CE to an elastic strain energy EE for the above design stress - strain relationships are respectively shown in Figures 12 and 13. It is well known that the complementary energy CE in the stress - strain relationship is strongly related to the plastic deformation capacity of the steel members (beam, beam-columns and beam-column welted connections, etc.) for the seismic performance (Sato et. al, 2006). It is obvious that the Eurocode curves has the smaller complementary energy CE than the AIJ curves. For the actual stress - strain relationships, it is considered that the small complementary energy CE might become one of the factors to reduce the fire resistant performance of the steel members, from viewpoints of the strain concentration or the robust thermal stress attenuation capacity.

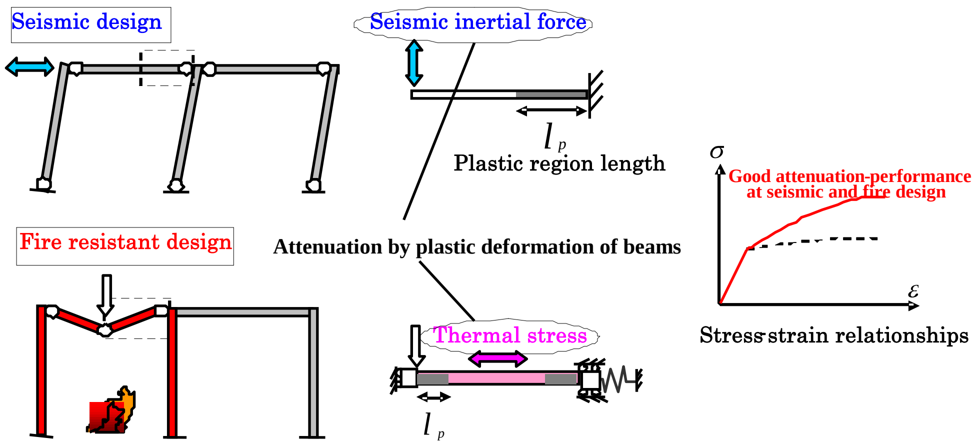

Figures 14. Outline of required seismic and fire resistant performance of steel beams from viewpoints of plastic deformaton.

5 CONCLUSIONS

To attenuate the thermal stress at the fire, the heated member must be plastically deformed. It is expected that the large strain hardening of the steel contributes to increasing the plastic deformation at the fire, because of avoiding the strain concentration in the heated member. The existing simple calculation methods based on the simple plastic theory can be applied for the members that possess the full plastic deformation capacity. It is, that is, considered that the strain hardening, the yield ratio and the complementary energy for the steel stress - strain relationships at the elevated temperature become significant influence factors for the fire resistant design, from the viewpoint of the attenuation of the thermal stress. It means that the steel members must possess the large plastic deformation capacity to attenuate (damp) both seismic inertial force and thermal stress at the seismic and fire resistant design (Figure 14).

REFERENCES

[1] European Committee Standardization(2005): EN1993-1-2 Eurocode3: Design of steel structures Part 1-2: General rules - Structural fire design

[2] Kato, B.(1990):"Deformation Capacity of Steel Structure", *J. Steel Construction Research, Volume 17, 33-94*

[3] Architectural Institute of Japan(1999), Recommendation for Fire Resistant Design of Steel Structures*(in Japanese)*

[4] Suzuki, H.(1995): "Ultimate Temperatures of Steel Frames subjected to Fire" , *J. Structural and Construction Eng., AIJ, 477, 147-156,(in Japanese)*

[5] Sato, A. and Ono, T. (2006): "ROTATION CAPACITY OF THE BEAM-TO-COLUMN CONNECTIONS" , *J. Structural and Construction Eng., AIJ, 600, 171-178,(in Japanese)*

EXPERIMENTAL STUDY OF POST FIRE PERFORMANCE OF HIGH-STRENGTH BOLTS UNDER COMBINED TENSION AND SHEAR

A. Kawohl*, A. Renner* and J. Lange*

* Institute for Steel Structures and Materials Mechanics, TU Darmstadt
e-mails: kawohl@stahlbau.tu-darmstadt.de, renner@stahlbau.tu-darmstadt.de, kollar@stahlbau.tu-darmstadt.de

Keywords: Connection, High-strength bolts, Fire test, Post fire performance, EC 3, Tension and shear

Abstract. *The post fire performance of high-strength bolts is of special interest when a building structure is evaluated after an event of fire. In contrast to conventional structural steel, high-strength bolts do not recover their original strength and material properties. For the evaluation of complete building structures the behaviour of the joints and the used bolts is therefore essential.*

Previous tests on grade 10.9 bolts under pure tension have been conducted at the TU Darmstadt. Based on these tests reduction factors to calculate the remaining load bearing capacity were stated. Further tests on grade 10.9 bolt sets under combined tension and shear were carried out to verify if the stated reduction factors are also valid for shear and combined tension and shear. For these tests grade 10.9 bolts were heated to temperatures up to 900 °C and tested under different tension-shear-relations after cooling.

1 INTRODUCTION

To calculate the resistance of bolts in fire EN 1993-1-2, Annex D [1] gives global reduction factors depending only on the members temperature. These global reduction factors are valid for all bolt grades even though tests have shown that different alloying materials and varying treatment methods can lead to a relevant change of strength under high temperatures. However the Eurocodes give no possibility to evaluate the post-fire performance of structures. So far there are few publications to be found on the post-fire performance of high-strength bolts.

A number of tests on grade 10.9 bolts under pure tension, both during and after an event of fire have been carried out at the Institute for Steel Structures and Materials Mechanics (TU Darmstadt) [2], [3]. The test results show that the tensile strength of the bolts decreases at temperatures larger than 450 °C, but post fire performance is still relevant up to a final tested temperature of 800 °C.

Renner et al. [3] give two reduction factors for the evaluation of post fire performance of grade 10.9 bolts. The minimum reduction factor $k_{Red,\ min}$ was determined on basis of tests on specimens without additional mechanical loading. The maximum reduction factor $k_{Red,max}$ results from tests on specimens that were mechanically and thermally loaded.

$$k_{\mathrm{Re}d,\min} = \begin{cases} 1.0 & 20°C \le T \le 500°C \\ -1.434 \cdot 10^{-3} \cdot T + 1.717 & 500°C \le T \le 800°C \end{cases} \tag{1}$$

$$k_{\mathrm{Re}d,\max} = \begin{cases} 1.0 & 20°C \le T \le 450°C \\ -2 \cdot 10^{-3} \cdot T + 1.9 & 450°C \le T \le 800°C \end{cases} \tag{2}$$

The post fire performance of a bolt set grade 10.9 should generally lie between the equations (1) and (2) depending on the load during the fire.

The equations (1) and (2) are based on the results from different pure tension tests. The post fire performance under shear and combined tension and shear was not part of this research. In order to get a better understanding how applied loads may affect the post fire performance of high-strength bolts a new test series was carried out where the bolts were tested under pure and combined tension and shear.

2 EXPERIMENTAL STUDY

To get a first oversight a test series on M20 shank bolts of the grade 10.9 was carried out. These bolts are commonly used in steel structures. The tests were executed on whole bolt sets with a clamping length of 88 mm. The bolts were loaded until failure. The load application was displacement controlled at a testing rate of 2 mm/min.

2.1 Test setup

To be able to compare the results of the post fire performance with results of bolts at room temperature the same test setup was used as for tests series from Renner/Lange [5]. The test setup enables the application of both load components tension and shear simultaneously under realistic fitting conditions. At this, the bolt fastens two slabs together which are then drawn apart under a certain angle. By splitting the applied load into the vectors tangential and orthogonal to the bolt axis one receives the tension and shear components of the load. Altogether there are three load application fixtures with which each two angles respectively two V/N-relations can be tested. Figure 1 shows the load application fixture for 0° (pure tension) and 45° (V/N-relation = 1.0). The other tested angles are 15°, 30°, 67.5° and 90° (pure shear). Further a shear test with two shear planes was conducted.

Next to the failure load and the total displacement, the gap and the shift were measured between the two bolted slabs. For the evaluation of the load bearing capacity mainly the failure load is of interest. The gap and shift were measured to control if the load application fixtures twisted or tilted unplanned.

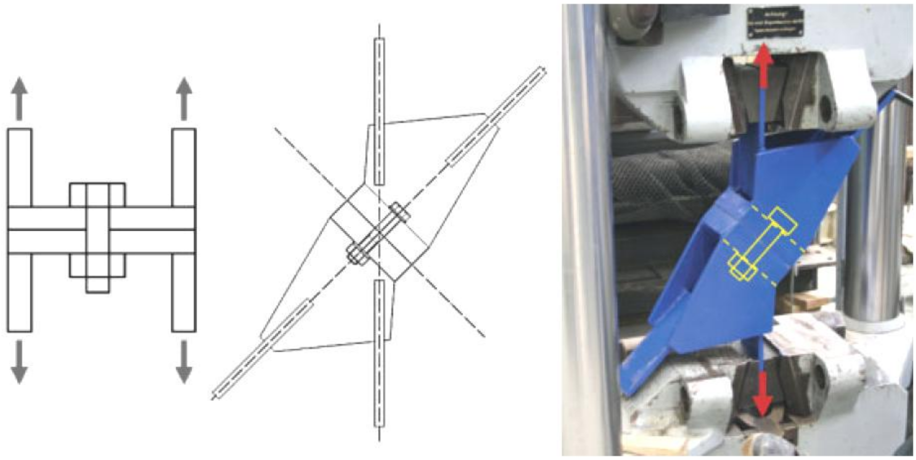

Figure 1. Test setup: principle of load application (left), sketch of one of the load application fixture, used for two different loading angles (centre), test specimen in testing machine (right) [4].

2.2 Tests conducted

The aim was to assess whether the kind of loading has a noticeable influence on the post fire performance of high-strength bolts. Therefore a first small test programme was put together. The bolts chosen are grade 10.9 M20 bolts due to their common use in steel structures in Europe. For each angle and applied temperature only one bolt was tested. Due to the unexpected results at the temperatures 700 °C, 800 °C and 900 °C the pure tension tests (angle 0°) were repeated with a second specimen. Also at a loading angle of 45 ° a second bolt preheated to 900 °C was tested because the failure load of the first test was significantly higher than expected.

The tests described in [3] have shown that only at temperatures higher than the tempering temperature (~480 °C) considerable differences become noticeable. Therefore temperatures beneath this temperature were not tested. As temperatures 500 °C, 700 °C, 800 °C and 900 °C were defined. The bolts were heated to these temperatures and then cooled slowly to room temperature. The process of cooling – slowly or instant – has an influence on the post fire performance of the bolt beginning at temperatures of 800 °C [3].

The specimens were heated to the desired temperature which was then kept for one hour. Kirby has shown in [6] that the duration of how long a bolt is exposed to high temperatures has no influence on the post fire performance.

3 RESULTS AND INTERPRETATION

3.1 Failure loads

The results of the tests are summarized in table 1. The total force is the failure load measured. The tension and shear loads were calculated by splitting the failure load into the tangential and orthogonal vectors. Next to the results of the post-performance tests you can find the results from Renner [5] for the same bolts at room temperature. Equal to the tests conducted by González [2] there is only a marginal difference between the load bearing capacity of the non-heated bolts and the bolts heated to 500 °C.

Table 1. Results of post fire performance tests – failure loads.

20 °C [3] (room temperature, average values)			
angle	total force in kN	tension in kN	shear in kN
0 °	274.3	274.3	0
15 °	293.6	283.6	76.0
30 °	264.5	229.1	132.3
45 °	237.2	167.7	167.7
67,5 °	218.1	83.5	201.5
90 °	230.4	0.0	230.4
90 °-2s	215.4	0.0	215.4
500 °C			
angle	total force in kN	tension in kN	shear in kN
0 °	275.2	275.2	0.0
15 °	299.4	289.2	77.5
30 °	278.6	241.3	139.3
45 °	241.9	171.0	171.0
67,5 °	222.3	85.1	205.4
90 °	230.1	0.0	230.1
90 °-2s	214.4	0.0	214.4
700 °C			
angle	total force in kN	tension in kN	shear in kN
0 °	175.1	157.1	0.0
	178.1	178.1	0.0
15 °	200.3	193.5	51.8
30 °	191.3	165.7	95.7
45 °	177.6	125.6	125.6
67,5 °	157.5	60.3	145.5
90 °	167.9	0.0	167.9
90 °-2s	158.2	0.0	158.2
800 °C			

angle	total force in kN	tension in kN	shear in kN
0 °	169.4	169.4	0.0
	171.7	171.7	0.0
15 °	198.0	191.2	51.2
30 °	180.0	155.9	90.0
45 °	163.4	115.6	115.6
67,5 °	148.2	56.7	136.9
90 °	152.1	0.0	152.1
90 °-2s	145.6	0.0	145.6
	900 °C		
angle	total force in kN	tension in kN	shear in kN
0 °	204.7	204.7	0.0
	231.9	231.9	0.0
15 °	214.2	206.9	55.4
30 °	207.5	179.7	103.8
45 °	221.4	156.5	156.5
	199.0	140.7	140.7
67,5 °	178.6	68.4	165.0
90 °	181.1	0.0	181.1
90 °-2s	189.2	0.0	189.2

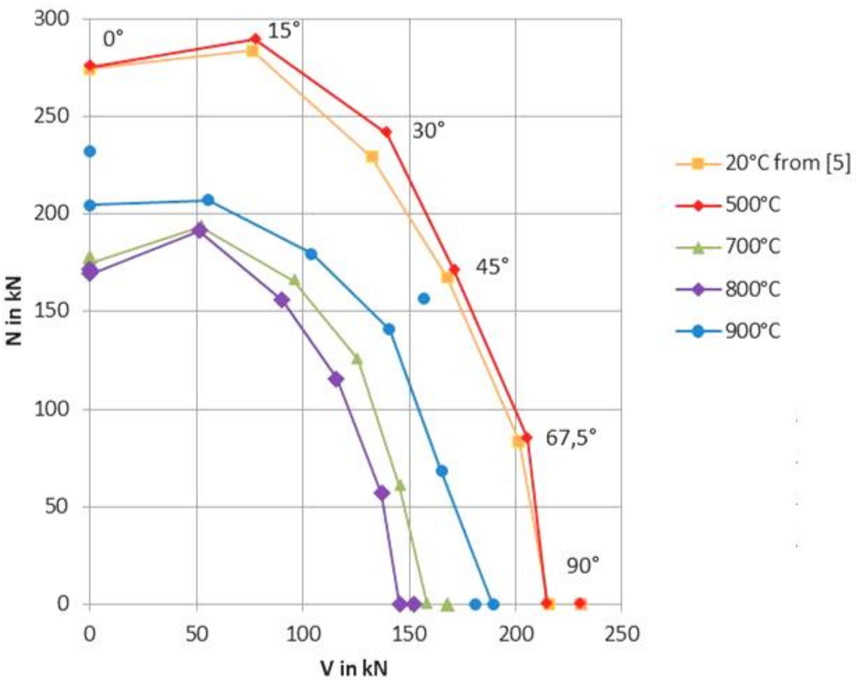

Figure 2. Failure loads of bolts with shank in shear plane.

In Figure 2 the failure loads are shown as a diagram. For a better comparison of the different temperatures, lines were drawn between the measured values. For pure shear the values of the tests with two shear planes were used. When tested only with one shear plane the bolts will be slightly inclined, which results in higher load capacities Also for the pure tension tests at 700 °C, 800 °C and 900 °C the smaller values of failure loads were used to be on the safe side. This is also true for the tests at a loading angle of 45 ° and bolts heated up to 900 °C. At an angle of 45 – a tension-shear-relation of 1.0 – the difference between the original load bearing capacity and the post fire performance is the smallest.

Table 2 shows the calculated shear-to-tension-coefficient α_v for the different temperatures. The pure tension failure happens in the threaded part and the pure shear failure in the shank part. The difference of the two section areas – the thread section is 78% of the shank section- has to be included in the calculation of α_v. The values for α_v for the pre-heated bolts are higher than the original α_v value.

The different values for $\alpha_{v,}$ as well as the varying difference between the original load bearing capacity and the post-fire performance depending on the tension-shear-relations show, that the load applied does have an influence on the load bearing capacity of high strength bolts.

Table 2. Calculated strength coefficient α_v.

Temperature	20 °C	500 °C	700 °C	800 °C	900 °C
α_v (calculated)	0.61	0.61	0.70	0.67	0.72

Figure 3 shows the shank bolts after testing. By means of the fracture appearances the rising ductility can be seen by the necking of the thread.

Figure 3. Shank bolts after failure, preheated to 500 °C (top, left), 700 °C (top, right), 800 °C (bottom, left) and 900 °C (bottom, right).

3.1 Comparison with pure tension tests [3]

As stated in the introduction it is of interest if the reduction factors based on the pure tension tests given in [3] can be applied when bolts are stressed under shear or combined tension and shear. Because the bolts in the here presented test series were not mechanically loaded during the heating process it was to be expected that the test results correlate with the reduction factor $k_{Red,min}$ according to equation (1). As shown in Figure 4 this is mainly true.

The results for the tests under pure tension (angle 0 °) and at an angle of 15 ° for the bolts preheated to 700 °C lie under the load capacity of 20 °C with the reduction factor $k_{Red,min}$ but still above the load with the reduction factor $k_{Red,max}$. It can be presumed that this may be due to uncertainties in the testing process.

The failure loads of the bolts heated to 900 ℃ are not shown in Figure 5 as the above stated reduction factors do not cover this temperature.

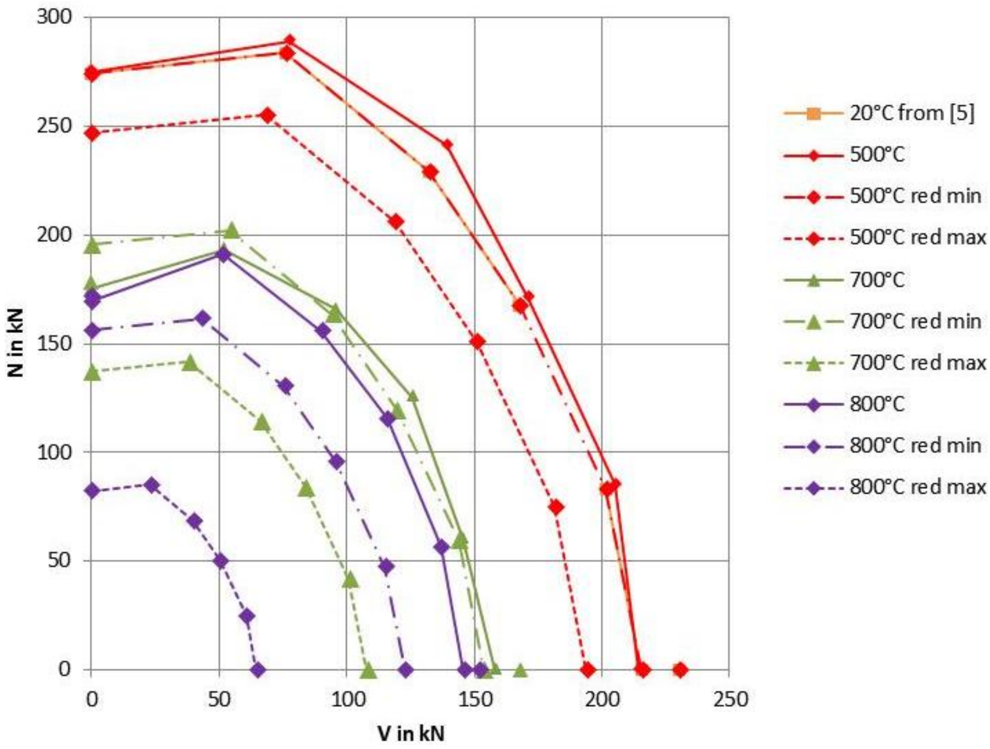

Figure 4. Failure loads of bolts with shank in shear plane compared to failure loads calculated with $k_{Red,min}$ and $k_{Red,max}$ from [3].

Figure 4 shows clearly that the reduction factors for 800 ℃ are on the safe side. For the evaluation of post fire performance it is therefore possible to apply the reduction factors also on bolts under shear or combined tension and shear.

3.2 Comparison with the normative interaction rules

The load-bearing behaviour of high-strength bolts under combined tension and shear loading at room temperature is currently analyzed at the Institute for Steel Structures and Materials Mechanics (TU Darmstadt) by Renner [5]. Motivation are the regulations in Eurocode 3 part 1-8 [7] which differ greatly from the former regulations in the German DIN [8]. Whereas in the DIN the rules are based on a quadratic interaction of tension (N) and shear (V) in the form of:

$$\left(\frac{N}{N_{Rd}}\right)^2 + \left(\frac{V}{V_{Rd}}\right)^2 \leq 1.0 \tag{3}$$

the Eurocode gives a more conservative bi-linear interaction:

$$\frac{\mathrm{N}}{1.4 \cdot \mathrm{N}_{\mathrm{Rd}}} + \frac{\mathrm{V}}{\mathrm{V}_{\mathrm{Rd}}} \leq 1.0 \tag{4}$$

If the shank is in the shear plane the difference is even lager. The DIN allowed an interaction verification with the tension load bearing capacity of the shank – where the interaction actually takes place. The Eurocode on the other hand only allows to use the tension load bearing capacity of the thread. As stated in the beginning it was of interest if for bolts exposed to high temperature the same load carrying interaction appears as for bolts at room temperature. Equally it is to be checked in which way the results coincide with the interaction rules given by the Eurocode respectively the German DIN. For bolts at room temperature Renner has shown in [5] that the quadratic interaction rule in the DIN is quite appropriate for thread bolts. On the other hand it is also stated, that the quadratic interaction rule is not on the safe side for bolts with the shank in the shear plane. The new bi-linear interaction rule given by the Eurocode 3 [8] is nonetheless far on the safe side.

In Figure 5 it is visible that this finding can be transferred to the here tested bolts. The failure loads of the bolts preheated to 900 ℃ slightly break ranks. Because this temperature is higher than the quenching temperature further material tests are necessary to finally evaluate these results.

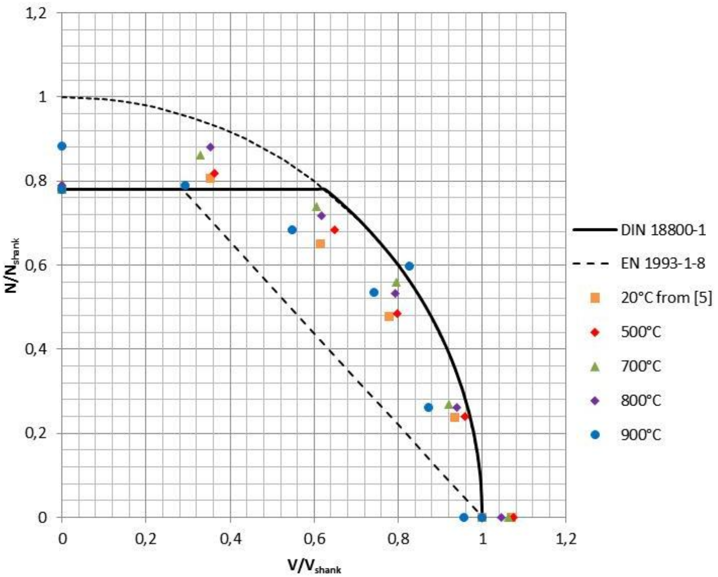

Figure 5. Results related to the measured load bearing capacities for pure tension and shear, compared to interaction rules in EN 1993-1-8 [8] and DIN 18800-1 [7].

4 CONCLUSIONS

The here illustrated tests are a first step to evaluate the post fire performance of high-strength bolts under combined tension and shear. The results indicate that it does have an influence if the bolts are loaded under combined tension and shear. To be able to reach significant conclusions further test series are necessary. As the failure loads show a large scatter it is necessary to conduct further tests with a larger number of bolts.

In addition only bolts that have been loaded by thermal load have been tested. Further tests are planned where bolts are simultaneously thermally and mechanically loaded to be able to evaluate the influence. Furthermore examinations of other kinds of bolts such as thread bolts and bolts with the grade 8.8 are planned.

Another aspect that needs further investigation is the behaviour of the bolts pre-heated to 900 ℃. Here the material properties need to be looked at closer at a microscopic perspective. Not until further tests were carried out it will be shown whether the here emerging perceptions are really appropriate.

REFERENCES

[1] DIN EN 1993-1-2: Eurocode 3: Design of steel structures, Part 1-2: General rules – Structural Fire design. German Version; EN 1993-1-2:2005 + AC:2009

[2] González Orta, F., *Untersuchungen zum Material- und Tragverhalten von Schrauben der Festigkeitsklasse 10.9 während und nach einem Brand*, Veröffentlichungen des Instituts für Stahlbau und Werkstoffmechanik der Technischen Universität Darmstadt, Heft 91, Darmstadt, 2011.

[3] Renner, A., González F., Lange, J., "Experimental study of post fire performance of high-strength bolts under pure tension", *Structures in Fire - 8th International Conference on Structures in Fire,* June 11-13, 2014.

[4] Renner, A., Lange, J., "Load –bearing behavior of high-strength bolts in combined tension and shear", *Steel Construction*, 5 (3), 151-157, 2012.

[5] Renner, A., Lange, J., "Versuche zur Zug-Abscherinteraktionstragwirkung von Schrauben", *Stahlbau*, 83 (4), 2014.

[6] Kirby, B. R., "The Behaviour of High-Strength Grade 8.8 Bolts in Fire", J. Constr. Steel Research, 33, 3-38, 1995.

[7] DIN EN 1993-1-8: Eurocode 3: Design of steel structures, Part 1-8: Design of joints. German version; EN 1993-1-8:2010-12.

[8] DIN EN 18800-1: Steel structures, Part 1: design and construction. DIN 18800-1:2008-11.

8th International Conference on Structures in Fire
Guo-Qiang LI, Venkatesh K. R. KODUR, Shou-Chao JIANG, Jian JIANG, Su-Wen CHEN, Guo-Biao LOU (Eds.)
Shanghai, China, June 11-13, 2014

EXPERIMENTAL STUDY OF POST FIRE PERFORMANCE OF HIGH-STRENGTH BOLTS UNDER PURE TENSION

A. Renner*, F. González and J. Lange***

* Institute for Steel Structures and Materials Mechanics, TU Darmstadt
e-mails: renner@stahlbau.tu-darmstadt.de, kollar@stahlbau.tu-darmstadt.de

** Goldbeck GmbH, formerly Institute for Steel Structures and Materials Mechanics, TU Darmstadt
e-mail: Fernando.Gonzalez@goldbeck.de

Keywords: Connection, High-strength bolts, Fire test, Post fire performance

Abstract. *The assessment of the remaining load bearing capacity of a building after an event of fire is fundamental to the development of a restoration or demolition concept. Normally conventional construction steel (steel grade S235 or S355) gets its origin material properties back after cooling, thus a main focus should be set on the evaluation of the connections. Due to their manufacturing process the material properties of high-strength bolts can be totally different after being exposed to fire [5]. Their post fire load bearing capacity and performance depend utterly on the thermal and mechanical exposure during the fire and likewise the hardening process during their manufacturing.*
To get a better knowledge of the residual strength of high-strength bolts grade 10.9 after exposure to a fire a series of tests was conducted both on specimen and complete bolt sets. These were heated to temperatures up to 800 °C both with and without additional mechanical load and tested after cooling.

1 INTRODUCTION

High strength bolts receive their strength due to a tempering and quenching process, where they get heated up to a high temperature, at which the steel changes its crystalline structure. Cooling the bolts down quite fast afterwards hinders the structure to change back to its original pattern and enables it to carry much higher loads.

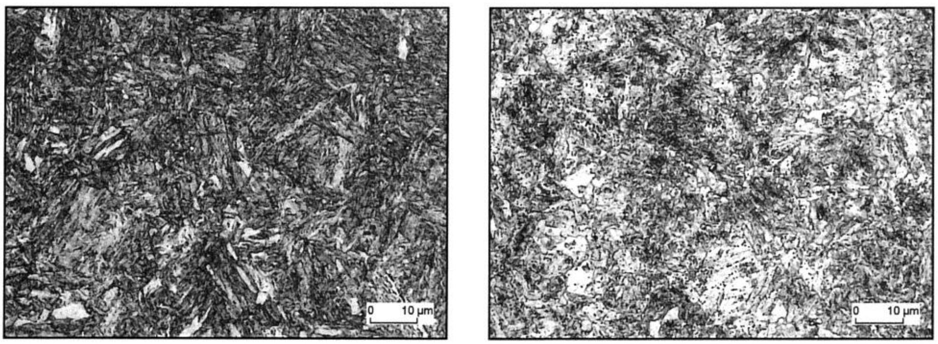

Figure 1. Polished micrograph section of bolts grate 10.9; left: as delivered, right: after heating to 700 °C [1].

If a high-strength bolt is heated up again to a level higher than the quenching temperature - as it might happen in an event of fire - and cools down again in an uncontrolled way, the material properties will change totally. Standards give no information on the load capacity which can be assumed in that case.

High-strength bolts of a grade 10.9 possess a martensitic structure due to the hardening. The acicular structure is preserved when the material is heated up again, but carbide precipitations occur in the structure that get bigger the higher the temperature gets. This can be observed in Figure 1. Simultaneously tetragonal martensite is chanced into less tensed up cubistic martensite, which reduces the hardness of the material. Not until the austenising temperature (approx. 800 °C) is reached, the material rigidity, which was achieved by the martensite formation, gets totally lost.

2 EXPERIMENTAL STUDY

The residual material properties of a bolt after an event of fire do not only depend on the temperature they have suffered during the fire. The cooling rate has a major influence; a slow cooling process will give the material time to restructure, which softens the former high strength material, whereas an instant cooling, which might be caused by firefighting water, will cause a quenching effect and re-harden the bolt.

Another factor that might influence the material properties of the bolt is the load the bolt was subjected to during the fire and the cooling process. This can not only cause a plastic deformation in a bolt (which was in a cold stage clearly only loaded in its elastic load range) but might also influence the material structure when the bolt cools down.

Considering all these possibilities a test program on the post fire performance of bolts of a grade 10.9 was developed. Bolts and specimens were tested considering the following terms of influence:

- **Slow cooling process:**
  Specimens and sets of bolts were heated and left to cool down really slow (as it might happen after a fire situation).
- **Instant cooling process:**
  Specimens and sets of bolts were heated and quenched straight away using cold water (as it might happen if a connection is hit by firefighting water).
- **Heating with mechanical load:**
  Specimens were heated to a certain temperature, put to a constant load and tested after a slow cooling process. Bolts that were pulled until failure under elevated temperatures were cut into slices and their Vickers hardness was determined.

Table 1. Overview conducted tests.

Tension test on thermally loaded specimen after slow cooling										
Temperature in °C	20 °	300 °	400 °	450 °	500 °	550 °	600 °	650 °	700 °	800 °
Number of Tests	3	-	-	-	3	-	3	-	3	3
Tension test on thermally loaded specimen after instant cooling										
Temperature in °C	20 °	300 °	400 °	450 °	500 °	550 °	600 °	650 °	700 °	800 °
Number of Tests	-	-	-	-	3	-	3	-	3	3
Tension test on thermally and mechanically loaded specimen										
Temperature in °C	20 °	300 °	400 °	450 °	500 °	550 °	600 °	650 °	700 °	800 °
Stress in N/mm²	-	900	750	600	400	200	120	-	-	-
Number of Tests	-	1	2	2	2	2	2	-	-	-
Tension test on thermally loaded bolt sets after slow cooling										
Temperature in °C	20 °	300 °	400 °	450 °	500 °	550 °	600 °	650 °	700 °	800 °
Number of Tests	-	-	-	-	3	-	3	-	3	3

Tension test on thermally loaded bolt sets after instant cooling										
Temperature in °C	20 °	300 °	400 °	450 °	500 °	550 °	600 °	650 °	700 °	800 °
Number of Tests	-	-	-	-	3	-	3	-	3	3
Vickers hardness test on thermally and mechanically loaded bolt sets										
Temperature in °C	20 °	300 °	400 °	450 °	500 °	550 °	600 °	650 °	700 °	800 °
Number of Tests	1	1	1	1	1	1	1	1	1	-

Table 1 summarizes all conducted tests in detail. The temperatures for tests without mechanical load were chosen above the tempering temperature of the bolts (~480 °C), which has to be exceeded to get a change in the material strength. The tested temperatures for tests on specimen with thermal and mechanical load start at 300 °C. The applied stress was chosen slightly beyond the $R_{p0.2}$-point, which was determined by a previous test series (see [3]).

Other than the speed of the cooling process the duration a bolt is exposed to the high temperature does not have much influence on the post fire behaviour of the bolt, as Kirby has shown in [2]. Specimen and bolt sets were heated up to the required temperature, which was than kept for 30 minutes.

2.1 Shape of Specimen and test conduction

Tension test specimens were cut from hot-dip galvanised bolts size M16 grade 10.9. The bolt diameter was chosen rather small on purpose to avoid variations of the material hardness over the bolt thickness. The tension test specimen were cut as proportional specimen following the DIN EN 10002-5, see Figure 2. The specimens that were exposed only to a thermal load had a cross-section of 8 mm at an initial gauge length of 40 mm; for space reasons the specimens that were loaded both thermally and mechanically had to be slightly smaller, they had a diameter of 6 mm and a gauge length of 30 mm. For the tests on bolt sets shank bolts M20 grade 10.9 with a length of 170 mm were tested.

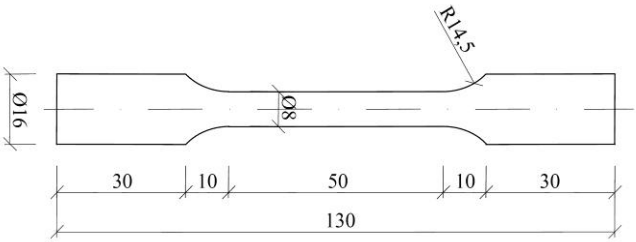

Figure 2. Tension test specimen dimensions, specimen with thermal load, cut from bolts M16 grade 10.9.

Both specimen and bolts were tested with tension machines. The elongation in the specimen gauge length was measured by an extensometer until yielding started. After that point machine displacement was used. For the bolt set tests the elongation was recorded only by the machine displacement.

A tension test on bolts that were both thermally and mechanically loaded was not conducted. Instead, bolts that were tested to failure under elevated temperatures were cut into slices afterwards and the Vickers hardness was measured.

3 RESULTS AND INTERPRETATION

3.1 Results of tests on specimen

The fracture faces of the specimen are shown in Figure 3. They illustrate the change of the material structure and the different types of material failure, after it has been exposed to high temperatures.

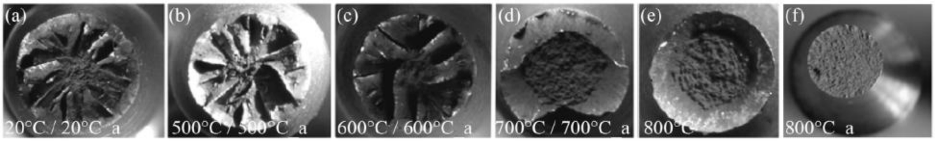

Figure 3. Fracture faces of thermal loaded specimen [1].

The results of the tension tests of the specimens that were only thermally loaded are given in Figure 4. The expected reduction of strength is clearly visible. For a temperature around the tempering temperature during the fire the stress-strain-curve still equals the curve of the not-heated specimen. With increasing temperature the change becomes more and more distinctive; beside the decrease of the tensile strength the breaking strain increases. The nearer the fire temperature gets to the austenising temperature (approx. 800 °C) the more the material curves adapt to the one of the origin steel, above 600 °C a yield point and the characteristic Lüders bands occur.

The speed of cooling barely influences the material properties up to a temperature of 700 °C. But if the austenising temperature is exceeded the speed of cooling has a magnificent influence, the quenched material will develop a new martensitic structure, which causes a significant rise in strength and a strong reduction of the breaking strain.

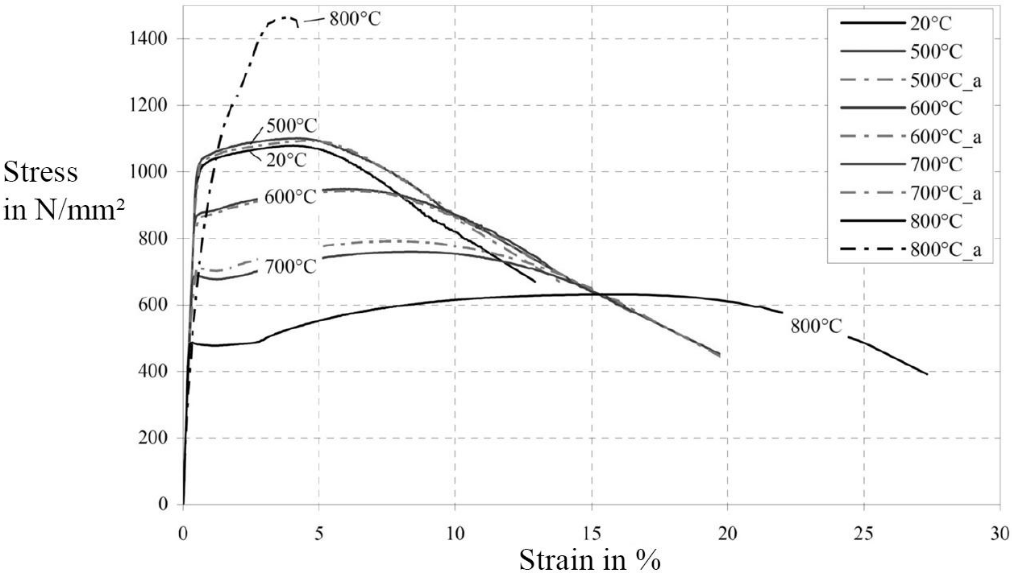

Figure 4. Stress-strain-curves of thermally loaded specimen tension tests (a: instant cooling) [1].

The strength reduction for thermally loaded specimens can be calculated using the following function:

$$k_{\mathrm{Re}d,\min} = \begin{cases} 1.0 & 20°C \le T \le 500°C \\ -1.434 \times 10^{-3} \cdot T + 1.717 & 500°C \le T \le 800°C \end{cases} \quad (1)$$

The results of the thermally and mechanically loaded specimen are shown in Figure 5. The influence of the stress during the heating is clearly visible. For temperatures below the tempering temperature the maximum strength is even higher than for the origin material. Simultaneously the maximum is reached earlier and the braking strain is much smaller.

For higher temperatures the material is clearly weakened by the additional stress during the heating period. The curves show a Lüders band, which does not occur in only thermally loaded specimen until a temperature above 600 °C. A similar behaviour was observed by Wohlfeil [4], who worked with thermally an mechanically loaded specimens of fine-grained steel grade S460M and S460N.

Figure 6 shows a direct comparison of the test results for the two temperature levels that were conducted with and without mechanical load. The significant difference can be easily observed. A reason for this behaviour could be that the creeping process during the loading leads to an alignment in the dislocation lines of the material, which causes a loss in strength.

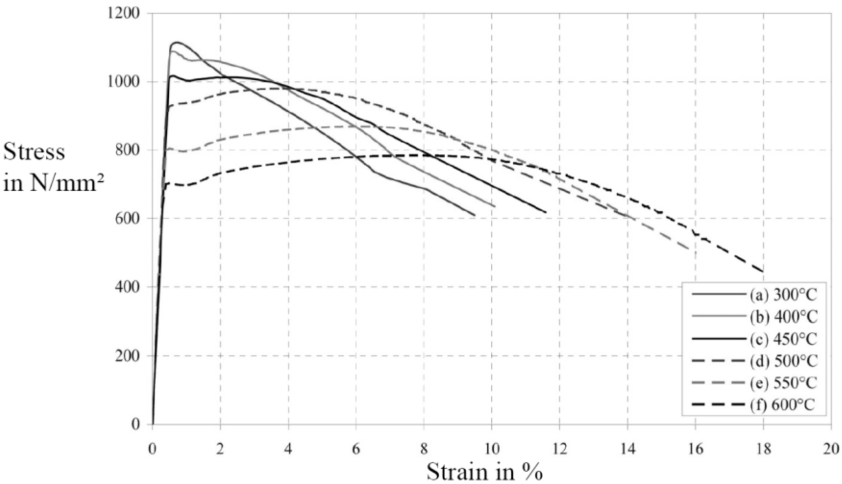

Figure 5. Stress-strain-curves of thermally and mechanically loaded specimen tension tests [1].

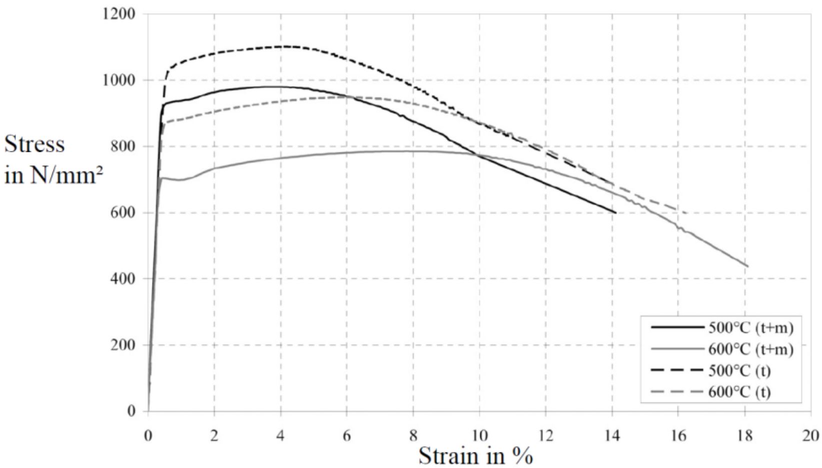

Figure 6. Comparison of specimen with and without additional mechanical load during heating [1].

The results show that the reduction factor given in Equation (1) is no longer valid, if a specimen is loaded additionally with a mechanical load.

3.1 Results of tests on bolt sets

The results of the tests on bolt sets are summarised in Table 2. Equal to the results of the specimen tests the failure load stays constant up to a temperature of 500 °C. Above this point a continuous reduction can be observed. Equation (1) can also be used to describe this decrease.

Table 2. Results of tests on bolt sets.

Temperature in °C	20 °	500 °	600 °	700 °	800 °
	Breaking load in kN (average values)				
Slow cool down	268,3	270,0	228,7	197,7	163,7
Instant cool down	-	273,3	241,3	201,3	172,7
	Elongation in mm (average values)				
Slow cool down	4,1	5,2	9,3	15,9	16,5
Instant cool down	3,8	4,9	8,4	14,4	9,1

Bolts tested at room temperature are supposed to fail by thread stripping. As shown in Figure 6 this is not the case for bolt sets that have been exposed to high temperatures. The greasing of threat and nut evaporates at high temperatures, causing a raise of friction between nut and bolt. This hinders the widening of the nut, which is essential for the thread stripping. All heated bolts break in the threat, the weakest section of the bolt.

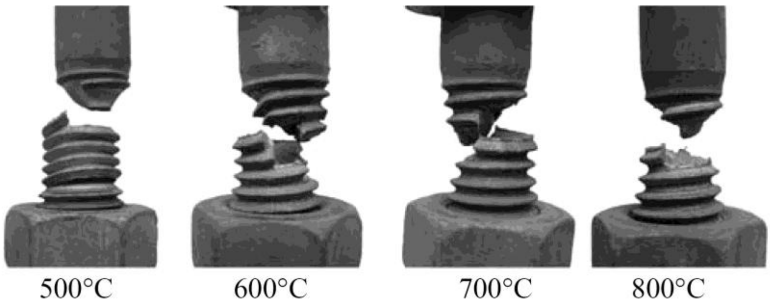

Figure 6. Bolt sets after break [1].

Other than with the specimen an instant cooling does not have a major effect on bolt sets even at a heating temperature of 800 °C. This shows that the diameter of a quenched piece does have an influence on how big the quenching effect is. The bolt sets that were heated up to 800 °C do only show a slightly higher failure load when quenched, still, an influence can be observed by looking at the elongation, the quenched bolt is not as ductile as the one that could cool down slowly.

The bolt sets that were tested in tension tests were only exposed to the thermal loading during the heating, not with an additional constant stress, which is hard to realise with whole bolt sets. Because the specimen tests showed that mechanical loading does have a major influence it was searched for a way to determine the loss of strength.

According to Kirby [2] the remaining strength can be appraised by the Vickers hardness. Bolts from another test series, which had been pulled apart under high temperatures to determine their failure load, were reused for this reason. Because the tests (see [3]) were run until failure, this can be considered as the worst case of mechanical load for the bolt. Bolt specimens were sliced up and the Vickers hardness was tested on seven slices per bolt. The results are shown in Figure 7.

As expected the hardness starts dropping above 500 ° degree. The results match quite well with the ones of the thermally and mechanically loaded specimen and the reduction factor from Equation (1) is here as well not valid any more.

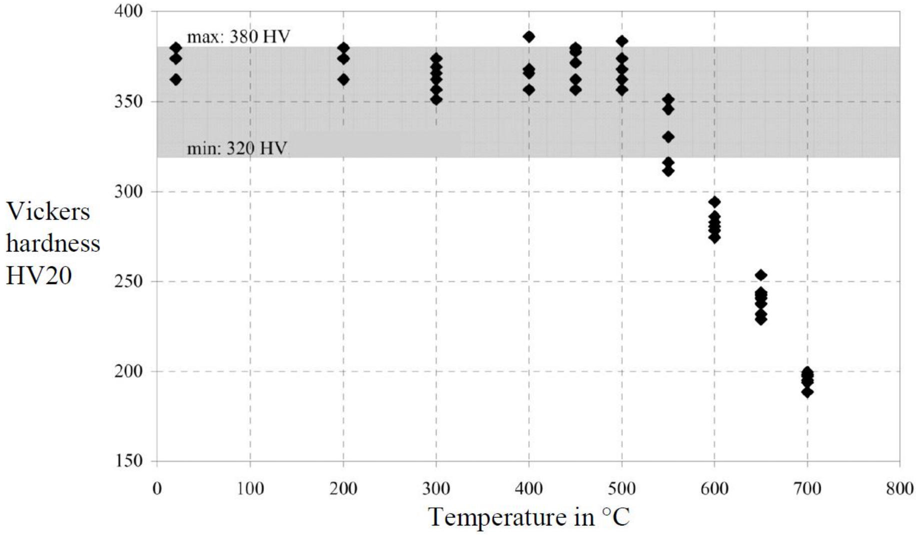

Figure 7. Vickers hardness of thermally and mechanically loaded bolt sets [1].

4 CONCLUSIONS

To assess the post fire performance of high-strength bolts of grade 10.9 an extensive test program on specimen as well as on bolt sets was conducted.

It can be assumed that the bolt will still be able to carry its load after cooling, if it suffers no more than 450 °C during a fire. At higher temperatures the maximum bearable strength drops constantly.

Here the load during the fire period plays a major rule. For not mechanically loaded specimen and bolts a minimum reduction factor $k_{Red,min}$ was deduced in Equation (1), which gives the maximal left bolt strength after an event of fire. A maximum reduction factor $k_{Red,max}$ can be developed from the tests on specimen and bolts, which were exposed both to thermal and mechanical load. The applied loads in these tests were near the maximum left bearable load (specimen) or the actual failure load (bolt sets), hence the reduction factor estimated with these results can be treated as the worst case reduction factor and gives the minimal left bearable load:

$$k_{Red,\max} = \begin{cases} 1.0 & 20°C \le T \le 450°C \\ -2 \times 10^{-3} \cdot T + 1.9 & 450°C \le T \le 800°C \end{cases} \tag{2}$$

The results of all tests are summarised in Figure 8. The reduction factors $k_{Red,min}$ and $k_{Red,max}$ are also given there. These two factors give the engineer a good estimation of the residual load bearing capacity.

For the restoration of a building other factors have to be taken into account. The bolt might be less ductile, even when it was only exposed to temperatures below 450 °C (especially if it was loaded near its maximum load during the fire). Further factors like a possible plastic elongation and the loss of pre-tension should also be thought of and investigated thoroughly.

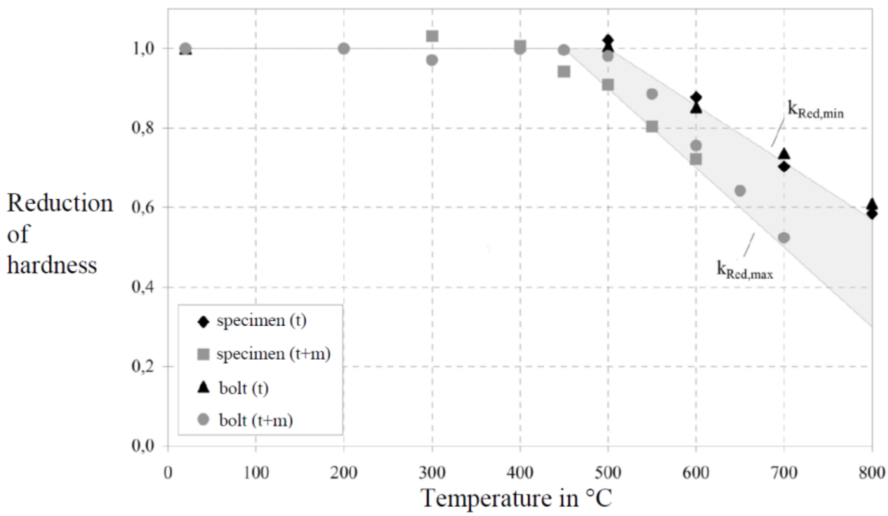

Figure 8. Reduction of hardness for thermal (t) and thermal and mechanical (t+m) loaded specimen and bolt sets [1].

REFERENCES

[1] González Orta, F., *Untersuchungen zum Material- und Tragverhalten von Schrauben der Festigkeitsklasse 10.9 während und nach einem Brand*, Veröffentlichung des Instituts für Stahlbau und Werkstoffmechanik der Technischen Universität Darmstadt, Heft 91, Darmstadt, 2011

[2] Kirby, B.R., “The Behaviour of High-Strength Grade 8.8 Bolts in Fire”, *J. Construct. Steel Research*, 33, S. 3-38, 1995.

[3] Lange, J., González, F. “Behavior of High-Strength Grade 10.9 Bolts under Fire Conditions”, *Structural Engineering International*, International Association for Bridge and Structural Engineering (IABSE), SEI Volume 22, No. 4, 470-475, November 2012

[4] Wohlfeil, N., *Werkstoffgesetze von S460 unter Brandeinwirkung und nach der Abkühlung*, Veröffentlichung des Instituts für Stahlbau und Werkstoffmechanik der Technischen Universität Darmstadt, Heft 77, Darmstadt, 2006

[5] Hass, Rüdiger, Meyer-Ottens, Claus, Richter, Ekkehard, *Stahlbau Brandschutz Handbuch*, Ernst & Sohn Verlag, Berlin, 1993

[6] DIN EN 1991-1-2: Eurocode 1: General actions, Part 1-2: Actions on structures exposed to fire. German version EN 1991-1-2:2002 + AC:2009

[7] DIN EN 1993-1-2: Eurocode 3: Design of steel structures, Part 1-2: General rules - Structural fire design. German version EN 1993-1-2:2005 + AC:2009

[8] DIN EN ISO 6892-1: Metallic materials - Tensile testing - Part 1: Method of test at room temperature (ISO 6892-1:2009); German version EN ISO 6892-1:2009

[9] DIN EN ISO 6892-2: Metallic materials - Tensile testing - Part 2: Method of test at elevated temperature (ISO 6892-2:2011); German version EN ISO 6892-2:2011

[10] DIN EN 10002-5:1992-02, “Tensile testing of metallic materials; method of testing at elevated temperature” German version EN 10002-5:1991

8th International Conference on Structures in Fire
Guo-Qiang LI, Venkatesh K. R. KODUR, Shou-Chao JIANG, Jian JIANG, Su-Wen CHEN, Guo-Biao LOU (Eds.)
Shanghai, China, June 11-13, 2014

NUMERICAL ANALYSIS ON THE FIRE BEHAVIOUR OF STEEL PLATE GIRDERS

Claudio Scandella, Markus Knobloch and Mario Fontana

ETH Zurich, Institute of Structural Engineering, 8093 Zurich, Switzerland
e-mails: scandella@ibk.baug.ethz.ch, knobloch@ibk.baug.ethz.ch, fontana@ibk.baug.ethz.ch

Keywords: Fire behaviour, Fire resistance, Steel plate girders, Elevated temperatures, Shear buckling

Abstract. *This paper presents a numerical analysis on the fire behaviour of steel plate girders. The numerical model, used to perform a parametric study, was validated with results of an experimental study. The parametric study shows that steel plate girders, which develop local flange buckling due to bending moments at ambient temperature, may fail due to shear web buckling under fire conditions. A comparative study reveals that common simplified analytical models adopted from ambient temperature design using hot material properties only are not suitable and can even lead to unconservative design results for standard fire situations.*

1 INTRODUCTION

Stability effects strongly influence the structural behaviour and the resistance of steel structures subjected to fire. Recent studies on the cross-sectional capacity considering local buckling as well as global member buckling are described in [1]. Shear buckling is crucial for steel plate girders and is an important factor for the safe and economical design of buildings and bridges. Therefore, analytical fire design models that pay attention to this kind of instability effect are important.

Due to elevated temperatures in fire, the strength and stiffness of steel decreases rapidly, and the stress-strain-relationship becomes distinctly nonlinear. Furthermore, compatibility stresses caused by constrained thermal expansion can have a strong influence on the stability behaviour of steel members. During a fire, thin webs heat up faster than flanges of common I-shaped steel cross-sections, which lead to compressive stresses in the web. These compressive stresses can aggregate or even cause shear buckling. Additionally, steel plate girders, which develop local flange buckling due to bending moments at ambient temperature may fail due to shear web buckling under fire conditions [2,3].

Three basic analytical models, namely the Cardiff model [4], the Basler model [5] and the rotated stress field theory [6] adopted in EN 1993-1-5 [7] are commonly used for the ambient temperature design of steel plate girders subjected to shear. It is not yet finally investigated whether these analytical models for ambient temperature design can directly be adapted to fire design. Based on an experimental investigation of steel plate girders loaded mainly in shear at elevated temperatures, Vimonsatit et al. [8] conclude that shear buckling becomes less apparent for higher temperatures and nonlinear stress-strain response. In a recent study, Salminen and Heinisuo [9] found that for the shear resistance of steel plate girders at elevated temperatures there is a strong influence if whether the temperature distribution across the web plate is uniform or non-uniform. A comparative study by Glassman and Garlock [10] shows that the analytical model of Basler [5] using hot material properties for the yield strength and Elastic modulus according to [11] leads to conservative design results for isolated steel plates. Kodur and Naser [12] show that shear limiting state can be a dominant failure mode in steel plate girders subjected to fire. A recent study [13] confirms that the stress-strain relationship strongly influences the load-carrying behaviour of steel members in shear. A distinct nonlinear behaviour decreases the shear strength. Furthermore, a simplified model for the shear load-displacement behaviour of steel plate girders with slender webs in fire is proposed.

2 NUMERICAL ANALYSIS OF STEEL PLATE GIRDERS IN FIRE

2.1 Numerical Model

A three-dimensional FEM-model for transversely stiffened steel plate girders loaded in a four-point bending configuration was developed using the implicit Finite-Element-Code ABAQUS/Standard. The web and the flanges forming the double-symmetric I-shaped cross-sections of the girders were modelled as plates using four-node shell-elements with a reduced integration scheme (S4R elements in the ABAQUS element-library). The longitudinal axis of the girders coincided with the global X-axis and the vertical deflection direction with the global Z-axis as illustrated in Figure 3a. A shape according to the first eigenmode was implemented as an initial geometric imperfection with an amplitude of $h/200$, with h being the clear depth of the web plates between the flanges. The boundary conditions of the simply supported beam were applied in the reference nodes of analytical rigid surfaces modelling stiff plates of rocker-bearing type supports. Lateral buckling was prevented by constraining the corresponding displacement of points of the upper flange equidistantly at $s/15$, with s being the span of the girders. The concentrated loads were applied in the reference nodes of analytical rigid surfaces representing stiff loading plates. The welded joints between the different plates forming the girders (flanges, webs and transverse stiffeners) were modelled with multi-point constraints enforcing full coupling of all global displacements and rotations at the contacting nodes. The classical von Mises-plasticity model was used for the material behaviour of the steel, considering temperature-dependence of the stress-strain-relationship and the thermal expansion according to EN 1993-1-2 [11].

2.2 Validation of the Numerical Model

The numerical model was validated with results of an extensive experimental study on steel plate girders at ambient temperature performed by Basler et al. [14]. Basler et al. conducted collectively 33 tests on steel plate girders with different cross-sections and different test setups. For the validation of the numerical model of the present study, 12 tests on I-shaped cross-sections were considered, namely the tests G2T1, G4T1, G6T1, G6T2, G7T1, G8T1, G8T2, G8T3, G8T4, G9T1, G9T2 and G9T3 according to the labelling of [14].

Figure 1 (left) shows a comparison between the numerical and the experimental results of the ultimate load F_u. An agreement of the calculated ultimate load with the experimental data within a range of 8% could be established. Figure 1 (right, bottom) compares the load-deflection behaviour of the numerical simulation (continuous line) to the experiment (dotted line) of test G6T1 as an example. The test setup is also shown in Figure 1 (right, top). In this specific test, two concentrated loads, F, were applied at girders' end, where the pictured deflection, w, is also measured.

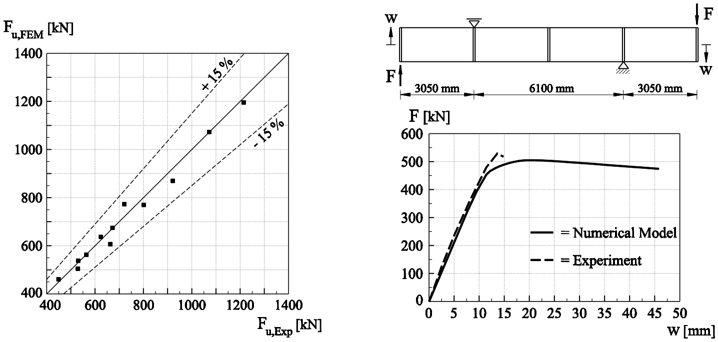

Figure 1. Validation of the numerical model (left) and results of girder G6T1 (right).

2.3 Simulation procedure

The simulation procedure evaluating numerically the fire resistance of preloaded steel plate girders was divided into four different calculation steps containing: (1) An eigenmode analysis to determine the shape of the initial geometric imperfection, (2) an ultimate load analysis at ambient temperature, (3) a heat transfer analysis in order to determine the varying temperature field in time of the girders when subjected to ISO 834 standard fire and (4) a fire resistance analysis of the preloaded girder by implementing the varying temperature field in time in a static analysis until failure.

2.4 Fire behaviour of steel plate girders

The fundamental structural fire behaviour of preloaded steel plate girders was analyzed using the numerical results. The behaviour of girders, which fail due to shear buckling in fire, can be divided into two phases: (1) A pre-critical range starting with the beginning of the fire exposure and ending when web buckling has fully developed. The latter occurring due to an increase of compressive stresses in the web because of constrained thermal strains. (2) A post-critical range characterised at the beginning by constant rates of the girders' deformations (midspan deflection, out-of-plane deflection of the web) until a runaway failure sets in at the end.

The structural behaviour of steel plate girders subjected to fire is analysed in detail using the results of girder G48 as an example. This girder featured a change in failure mode from bending failure at ambient temperature (Figure 2, top) to shear failure in fire (Figure 2, bottom). The geometry of this girder is listed in Table 1 together with the prevailing load ratio (with respect to ultimate load at ambient temperature) of, μ_R = 0.6, and the fire resistance reached at, t_R = 856 s, under ISO 834 standard fire exposure.

Figure 2. Failure of girder G48 at ambient temperature (top, scale factor = 2.0) and in fire (bottom, scale factor = 5.0).

Figure 3 shows the setup of the numerical simulation and the deformations calculated during the standard fire exposure starting at, $t = 0\ s$. The midspan deflection, w, and its rate, $\dot{w}$, (Figure 3(d)), were selected as quantities detecting global failure when increasing unboundedly. Additionally an unbounded increase of: (1) the out-of-plane deflection, v, of the web in cross-section A-A and its rate, $\dot{v}$, (Figure 3(e)), would indicate shear buckling failure, whereas (2) the rotation, φ, of the upper flange in cross-section B-B and its rate, $\dot{\varphi}$, (Figure 3(f)), would indicate bending failure. At the beginning of the fire exposure the girder shows a midspan deflection of, w = 36.5 mm, due to the preloading of, F_R = 176.4 kN. Figure 3g depicts the temperature-time-curves at different points in the girder's cross-section A-A (Figure 3(b)) and indicates that the thin web (t_w = 7 mm) heats up faster than the flanges (t_f = 20 mm). However, due to the compatibility condition of the cross-section, the web is partially constrained in its thermal expansion by the flanges. Therefore, a self-equilibrating stress state arises within the cross-section leading to additional compressive stresses in the web (σ_3 and σ_4, Figure 3(h)) and tension stresses in the flanges (σ_1 and σ_2, Figure 3(h)).

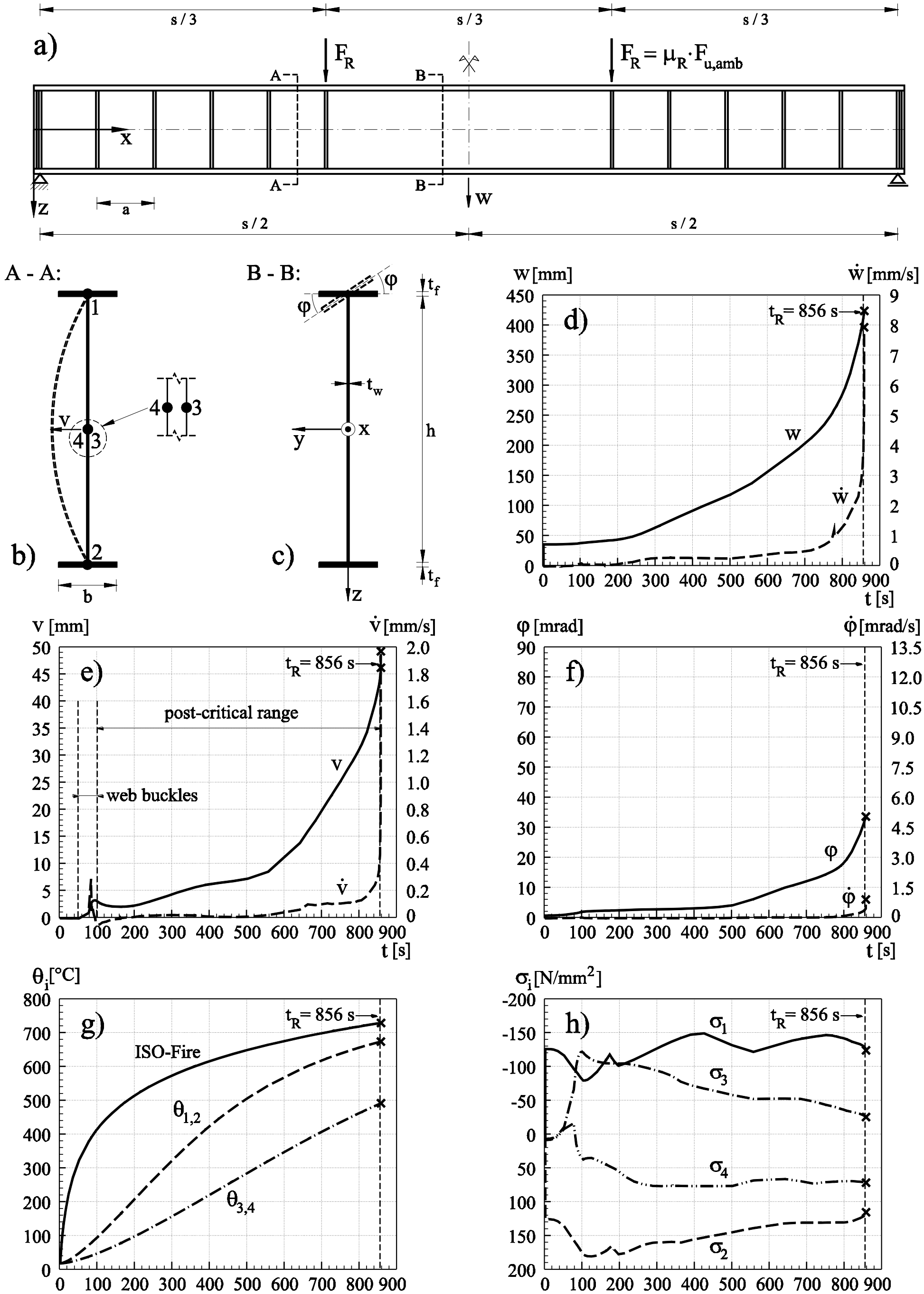

Figure 3. Setup of the numerical simulation and results of girder G48 in fire.

The increase in compressive stresses in the web is limited by the beginning of local web buckling starting at, t_1 = 51 s, of fire exposure (Figure 3(e)). Simultaneously, bending stresses develop in the web lowering the compressive stresses on the convex side of the buckle, σ_4, and increasing them on the concave side, σ_3 (Figure 3(h)). Buckling of the web is accomplished at the point in time, t_2 = 100 s, when the out-of-plane deflection, v, ceases to increase (Figure 3(e)). From this moment onwards the girder is in the post-critical range and its midspan deflection increases with an almost constant rate, $\dot{w}$, until the onset of a runaway failure at, t_3 = 700 s. Failure of the girder finally occurs at, t_R = 856 s, when both the rate of the midspan deflection, $\dot{w}$, and the rate of the out-of-plane deflection, $\dot{v}$, approach a vertical asymptote. Simultaneously, the rotation of the upper flange, φ, however, remains bounded indicating thus shear failure.

Additional numerical studies were conducted in order to check whether the thermally induced compressive stresses in the web caused the change in failure mode from a bending failure at ambient temperature to a shear failure in fire. Therefore, the entire girders' cross-section was heated up uniformly with a moderate constant rate of 7.3 ℃/min. Figure 4 shows girder G48 in its ultimate state when heated up uniformly. In this case, there is no temperature difference between the flanges and the web. Hence, the lack of additional compressive stresses in the web prevents the latter from buckling, as can be seen in Figure 4 (in opposition to Figure 2, bottom).

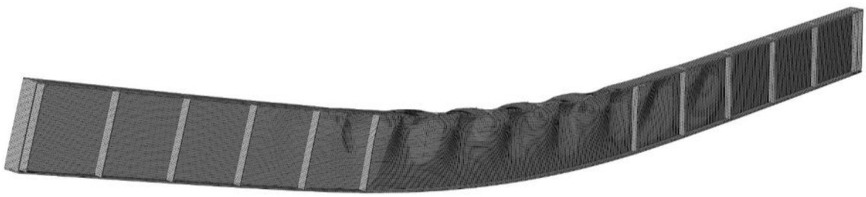

Figure 4. Failure of girder G48 when heated up uniformly (scale factor = 5.0).

Figure 5 illustrates the numerical results of girder G48 when heated up uniformly. After a fire exposure with a constant heating rate of 7.3 ℃/min at, t = 4162 s, the fire resistance, t_R, is reached when the curves of, w, and, $\dot{w}$, approach a vertical asymptote. At this point in time, the curves of the rotation of the upper flange, φ, and its rate, $\dot{\varphi}$, approach a vertical asymptote too, indicating failure due to bending. This is in opposition to the change in failure mode of girder G48 when subjected to ISO 834 standard fire. This indicates that the change in failure mode – from a bending failure at ambient temperature to a shear failure in fire – is induced by compatibility stresses due to a temperature difference between the flanges and the web.

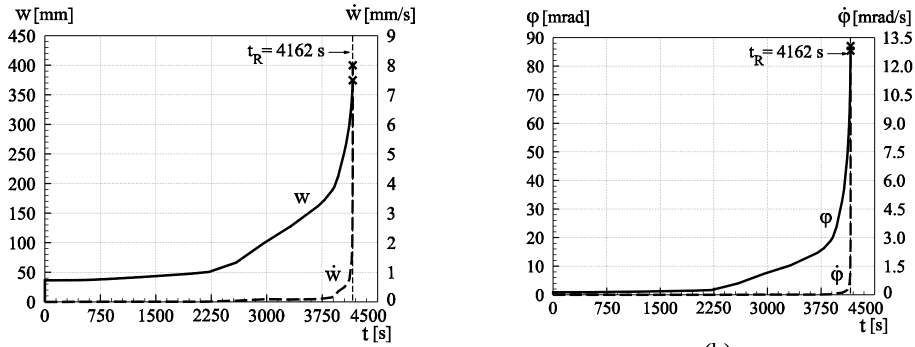

(a) (b)

Figure 5. Results of girder G48 when heated up uniformly.

2.5 Parametric study

The influence of different parameters on the fire resistance and the failure mode was comprehensively analysed in a numerical parametric study containing 105 numerical fire simulations. The parameters varied included: (1) The depth-to-thickness ratio β of the web plate, (2) the load ratio μ_R (with respect to ultimate load at ambient temperature $F_{u,amb}$) and (3) the aspect ratio α of the web plate.

Table 1 shows the geometry, input parameters, fire resistance and failure mode of three different types of girders: (1) Type I with transverse stiffeners over the whole girders' length, (2) Type II with transverse stiffeners only between the supports and the loads and (3) Type III, analogous to Type II but with higher aspect ratios α of the web plate. The results of the numerical study show that some steel plate girders which fail due to bending at ambient temperature, develop shear failure in fire (e.g. girder G49). Increasing the load ratio led to a bending failure even under fire conditions (e.g. girder G50). Steel girders with smaller depth-to-thickness ratios of the web also failed due to bending in fire (e.g. girder G54). Steel plate girders with a high aspect ratio of the web plate, however, failed due to the development of shear buckling even for small depth-to-thickness ratios of the webs (e.g. girder G89).

3 COMPARATIVE STUDY

Common analytical models according to Eurocode 3 [7], Basler [5] and Cardiff [4] – originally developed to determine the shear capacity of steel plate girders at ambient temperature – were adapted for fire design using temperature-dependent material properties for the Elastic modulus and the yield strength according to EN 1993-1-2 [11]. The temperatures of the web and the flanges, needed to calculate the reduction-factors k_E (Elastic modulus) and k_y (yield strength), were taken with their maximal value from the numerical simulation at failure time t_R.

For ambient temperature design, all three analytical models lead to suitable results. For fire design, however, the simplified analytical models neglecting thermal strains lead to inappropriate results for some cases. Figure 6 compares the shear resistance in fire according to Basler (left) and Eurocode 3 (right) to the numerical results. A simplified analytical model according to Eurocode 3 adapted only for temperature related reduction of the Elastic modulus and the yield strength leads to higher shear capacities than the numerical results for girders with high aspect ratios (α = 2.5). For girders with small aspect ratios (α = 1.0), the simplified analytical model leads to lower shear capacities than the numerical results (Figure 6, right). On the other hand, a simplified analytical model according to Basler (without considering an M-V-interaction) adapted only for temperature dependent reduction of the Elastic modulus and the yield strength overestimates the shear capacities for almost all girders (Figure 6, left), regardless of whether the aspect ratio is small (α = 1.0) or high (α = 2.5).

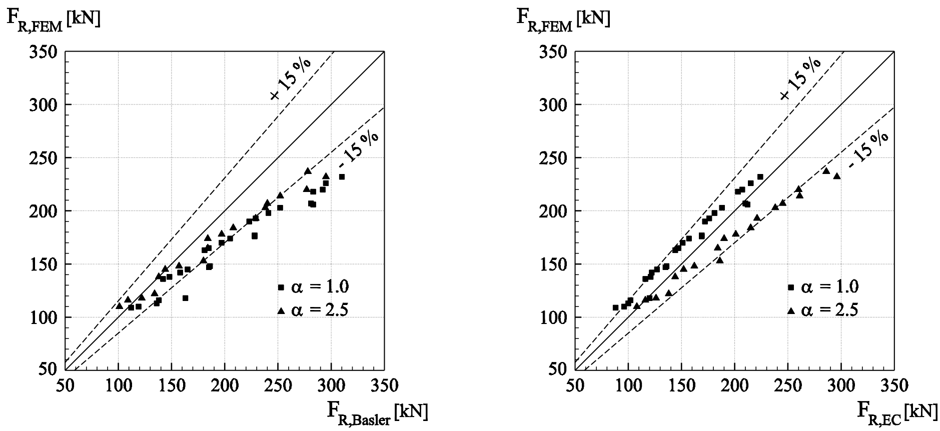

Figure 6. Comparative study: Fire-adapted model Basler (left); Fire-adapted model Eurocode 3 (right).

Table 1. Geometry, input parameters and numerical results.

CONSTANT PARAMETERS FOR ALL TYPES I - III								TYPE I							TYPE II							TYPE III						
Span of girder	Clear depth of web plate	Width of flanges	Thickness of flanges	Thickness of web plate	Yield stress at ambient temperature	Depth-to-thickness ratio of web plate	Load ratio in fire	**Girder**	Width of web plate	Aspect ratio of web plate	Ultimate load at ambient temperature	Fire resistance	**Failure mode at ambient temperature**	**Failure mode in fire**	**Girder**	Width of web plate	Aspect ratio of web plate	Ultimate load at ambient temperature	Fire resistance	**Failure mode at ambient temperature**	**Failure mode in fire**	**Girder**	Width of web plate	Aspect ratio of web plate	Ultimate load at ambient temperature	Fire resistance	**Failure mode at ambient temperature**	**Failure mode in fire**
s [mm]	**h** [mm]	**b** [mm]	t_f [mm]	t_w [mm]	f_y [N/mm^2]	$\beta = \frac{h}{t_w}$ [-]	μ_R [-]	**G** [-]	**a** [mm]	$\alpha = \frac{a}{h}$ [-]	$F_{u,amb}$ [kN]	t_R [s]	**Failure ambient** [-]	**Failure fire** [-]	**G** [-]	**a** [mm]	$\alpha = \frac{a}{h}$ [-]	$F_{u,amb}$ [kN]	t_R [s]	**Failure ambient** [-]	**Failure fire** [-]	**G** [-]	**a** [mm]	$\alpha = \frac{a}{h}$ [-]	$F_{u,amb}$ [kN]	t_R [s]	**Failure ambient** [-]	**Failure fire** [-]
17'500	1'150	250	20	5	235	230	0.4	**1**	1'150	1	275	875	**Bending**	**Shear**	**36**	1'150	1	272	930	**Bending**	**Shear**	**71**	2'875	2.5	275	705	**Bending**	**Shear**
							0.5	**2**				773			**37**				793			**72**				580		
							0.6	**3**				681			**38**				688			**73**				493		
							0.7	**4**				596			**39**				605			**74**				431		
							0.8	**5**				516			**40**				524			**75**				356		
17'500	1'150	250	20	6	235	192	0.4	**6**	1'150	1	290	984	**Bending**	**Shear**	**41**	1'150	1	283	997	**Bending**	**Shear**	**76**	2'875	2.5	290	821	**Bending**	**Shear**
							0.5	**7**				865			**42**				879			**77**				709		
							0.6	**8**				775			**43**				791			**78**				615		
							0.7	**9**				691			**44**				709			**79**				540		
							0.8	**10**				610			**45**				628			**80**				476		
17'500	1'150	250	20	7	235	164	0.4	**11**	1'150	1	295	1'056	**Bending**	**Shear**	**46**	1'150	1	294	1'057	**Bending**	**Shear**	**81**	2'875	2.5	296	910	**Bending**	**Shear**
							0.5	**12**				937			**47**				940			**82**				811		
							0.6	**13**				855			**48**				856			**83**				724		
							0.7	**14**				771			**49**				769			**84**				650		
							0.8	**15**				686		**Bending**	**50**				680		**Bending**	**85**				607		
17'500	1'150	250	20	8	235	144	0.4	**16**	1'150	1	308	1'060	**Bending**	**Bending**	**51**	1'150	1	306	1'061	**Bending**	**Bending**	**86**	2'875	2.5	306	1'015	**Bending**	**Shear**
							0.5	**17**				958			**52**				960			**87**				891		
							0.6	**18**				868			**53**				870			**88**				832		
							0.7	**19**				768			**54**				766			**89**				758		
							0.8	**20**				667			**55**				658			**90**				650		**Bending**
17'500	1'150	250	20	9	235	128	0.4	**21**	1'150	1	321	1'052	**Bending**	**Bending**	**56**	1'150	1	319	1'049	**Bending**	**Bending**	**91**	2'875	2.5	319	1'052	**Bending**	**Bending**
							0.5	**22**				949			**57**				949			**92**				949		
							0.6	**23**				859			**58**				856			**93**				855		
							0.7	**24**				755			**59**				751			**94**				747		
							0.8	**25**				649			**60**				614			**95**				616		
17'500	1'150	250	20	10	235	115	0.4	**26**	1'150	1	334	1'043	**Bending**	**Bending**	**61**	1'150	1	333	1'043	**Bending**	**Bending**	**96**	2'875	2.5	333	1'041	**Bending**	**Bending**
							0.5	**27**				939			**62**				941			**97**				940		
							0.6	**28**				853			**63**				845			**98**				846		
							0.7	**29**				749			**64**				741			**99**				740		
							0.8	**30**				633			**65**				604			**100**				592		
17'500	1'150	250	20	15	235	77	0.4	**31**	1'150	1	403	1'054	**Bending**	**Bending**	**66**	1'150	1	408	1'049	**Bending**	**Bending**	**101**	2'875	2.5	408	1'049	**Bending**	**Bending**
							0.5	**32**				944			**67**				947			**102**				947		
							0.6	**33**				862			**68**				855			**103**				854		
							0.7	**34**				760			**69**				754			**104**				752		
							0.8	**35**				593			**70**				545			**105**				545		

4 CONCLUSIONS

The paper presented a detailed numerical study on the ambient temperature and fire behaviour of steel plate girders. It shows that constrained thermal strains have a marked influence on the shear capacity of steel members under fire conditions and can aggregate or even cause shear web buckling. Steel plate girders, which fail due to bending at ambient temperature, may develop shear web buckling in fire. A comparative study reveals that commonly simplified analytical models adopted from ambient temperature design using only hot material properties for the Elastic modulus and the yield strength are not suitable and can lead to unconservative design results for standard fire situations.

An experimental study on the fire behaviour of steel plate girders is desirable and could confirm the findings of the presented numerical study.

REFERENCES

[1] Knobloch M., Fontana M. (2014). Stability of steel structures in fire. State-of-the-art, recent studies in Switzerland and future trends. In: Stahlbau 83 (4), p. 257-264

[2] Scandella C. (2013). Numerische Untersuchungen zum Schubbeulverhalten im Brandfall. Master Thesis. Institute of Structural Engineering, ETH Zurich (unpublished)

[3] Knobloch M. (2001). Theoretische Untersuchungen zum Tragverhalten von dünnwandigen I-Profilen bei erhöhten Temperaturen. Diploma Thesis. Institute of Structural Engineering, ETH Zurich (unpublished)

[4] Porter D.M., Rockey K.C., Evans H.R. (1975). The collapse behaviour of plate girders loaded in shear. In: The Structural Engineer, 53 (8), p. 313-325

[5] Basler K. (1961). Strength of plate girders in shear. In: Journal of the Structural Division ASCE, 87 (ST7), p. 151-180

[6] Höglund T. (1973). Design of thin plate I girders in shear and bending with special reference to web buckling. In: Division of Building Statics and Structural Engineering, Royal Institute of Technology, Stockholm, Sweden, Bulletin No. 94

[7] CEN (2010). EN 1993-1-5: Eurocode 3: Design of steel structures – Part 1.5: Plated structural elements. Brussels

[8] Vimonsatit V., Tan K., Qian Z. (2007). Testing of Plate Girder Web Panel Loaded in Shear at Elevated Temperature. In: Journal of Structural Engineering, 133 (6), p. 815-824

[9] Salminen M., Heinisuo M. (2014). Numerical analysis of thin steel plates loaded in shear at non-uniform elevated temperatures. In: Journal of Constructional Steel Research, 97 (2014), p. 105-113

[10] Glassman J., Garlock M. (2013). Shear Buckling Behavior of Steel Plate Girders at Elevated Temperatures. In: Structures Congress 2013, p. 2872-2883

[11] CEN (2010). EN 1993-1-2: Eurocode 3: Design of steel structures – Part 1.2: General rules – Structural fire design. Brussels

[12] Kodur V.K.R., Naser M.Z. (2014). Effect of shear on fire response of steel beams. In: Journal of Constructional Steel Research, 97 (2014), p. 48-58

[13] Ohtsuka T., Knobloch M., Fontana M. (2013) Shear capacity of steel plate girders with slender webs in fire. In: Research and Applications in Structural Engineering, Mechanics and Computation. Proceedings of the fifth International Conference on Structural Engineering, Mechanics and Computation, Cape Town, South Africa

[14] Basler K., Yen B.T., Mueller J.A., Thürlimann B. (1960). Web buckling tests on welded plate girders. Fritz Engineering Laboratory, Lehigh University, Bethlehem, Pennsylvania. Lehigh University Institute of Research, Report No. 251-11

8th International Conference on Structures in Fire
Guo-Qiang LI, Venkatesh K. R. KODUR, Shou-Chao JIANG, Jian JIANG, Su-Wen CHEN, Guo-Biao LOU (Eds.)
Shanghai, China, June 11-13, 2014

LATERAL-TORSIONAL BUCKLING OF CLASS 4 STEEL WELDED BEAMS AT ELEVATED TEMPERATURE

Martin Prachar*, Michal Jandera*, Frantisek Wald* and Bin Zhao**

* Czech Technical University in Prague, Faculty of Civil Engineering, Czech Republic
e-mails: martin.prachar@fsv.cvut.cz, michal.jandera@fsv.cvut.cz, wald@fsv.cvut.cz

** CTICM, Centre Technique Industriel de la Construction Métallique, Saint-Aubin, France
e-mail: BZHAO@CTICM.com

Keywords: steel structure, fire resistance, Class 4 section, lateral-torsional buckling, numerical modelling

Abstract. *This paper presents research in behaviour of laterally unrestrained beams (I or H section) of Class 4 cross-sections at elevated temperatures, which is based on an undergoing research program focused on fire design of slender sections. Three Class 4 section beams were tested at temperatures 450 and 650 °C. One of the beams was tapered. The design of the test set-up and description of the experiment is given. The tests were subsequently used for FE model validation. Later, a parametric study was performed in general FE software ABAQUS. Finally, all the numerical data are shown and compared to existing design codes. A recommendation for the further refinement of the design formulas is also given.*

1 INTRODUCTION

The area of research in slender cross-sections in case of fire is very important as only little investigation was made and only few experimental data have been collected until now. In the framework of the RFCS project FIDESC4 - Fire Design of Steel Members with Welded or Hot-rolled Class 4 Cross-sections, several simply supported beams were tested at four point bending at different temperatures. The tests were carried out at the Czech Technical University in Prague and the beams were also subjected to lateral torsional buckling.

Despite the current EC3 contains a number of simple rules for design of Class 4 cross-sections at elevated temperature, based on recent numerical simulations they were found to be over-conservative. Through refining these rules, a significant material savings could be achieved which would leave to higher competitiveness of the steel structures. Therefore, new well representing design models, which simulate the actual behaviour of the structures exposed to fire, are crucial. These design rules should be based on extensive numerical simulation validated on experimental data. This is also in the scope of the current research, however not published in the paper. The paper is limited to lateral-torsional buckling behaviour only.

Determination of the bending resistance for members subjected to lateral torsional buckling of Class 1 to 3 cross sections at elevated temperature (EC3 Part 1.2 [1]) is based on the same principles as the design at room temperature according to the EC3 Part 1.1 [2]. However it differs in using one imperfection factor only for all types of cross-sections. Informative Annex E of the standard [1] recommends using the design formulas for slender (Class 4) sections as well. But there is a restriction of critical temperature value and different reduction of yield strength is used (0.2% proof strength for Class 4 instead of 2.0% proof strength for stockier Class 1 to 3 sections). The presented research covers also tapered members (non-uniform height along the length). For them a limited design procedure is given in the informative Annex BB of the standard EC3 Part 1.1 [2] applicable for the room temperature only. The additional possibility is used clause 6.3.4 (General Method) given in EC3 Part 1.1. The suitability of this approach for Class 1 to 3 cross-section and ambient temperature was verified in [3]. The resistance of the non-uniform members according to the General Method was analyzed and compared with numerical results and the procedures of clauses 6.3.1 to 6.3.3 of EC3 1.1. Another possible approach is given by EC3 Part 1-5 [4]. This approach allows taking into account interaction of plate buckling and lateral torsional buckling. Annex B gives rules for defining the reduction factor for the member resistance in case of non-uniform members. In case of lateral torsional buckling, the reduction factor used should be the minimum of the reduction factor ρ given by EC3 1.5 in clause B1 and χ_{LT} - value for lateral torsional buckling according to EC3 1.1. 6.3.2. However, the lateral torsional buckling curves are always lower. This in fact leads to the method in clause 6.3.2., but with neglecting the local buckling effect by considering the elastic section modulus for slender beams. The possibility of using these above described rules for fire design as well has not been confirmed yet.

2 EXPERIMENTS

In the described research, three beams were tested. They were based and calibrated on preliminary numerical GMNIA models in FE software ABAQUS. In order to achieve global buckling failure mode as the main failure, different boundary condition and load distributions were modelled.

Simply supported beams with two equal concentrated loads applied symmetrically were chosen for the test scheme. The area of the constant moment (space between the two forces) was the only heated part and also free to lateral and torsional buckling. The rest of the beam was at the room temperature. The tests induced constant bending moment without shear in the central part of the span. To prevent possible web failure by concentrated load, web stiffeners were considered at the load points and supports.

The bending tests were performed on steady state, meaning the beams were heated first and the load was applied later. Steel grade S355 was used for all beams. The experimental test set-up is shown in Figure 1. The two load-application points were laterally restrained and point pinned supports were applied at the beam ends as shown in Figure 2.

The three tests vary in the cross-sections and considered temperatures were made. Table 1 presents the used cross-sections, which were fabricated by welding. Two tests were performed on beam with constant cross-section. One test was performed on the tapered beam. The tests were controlled by displacement (vertical deflection at mid-span) which was set for 3.5 mm per minute. Final deformation at the end of experiments was 50 mm at mid-span and failure was reached.

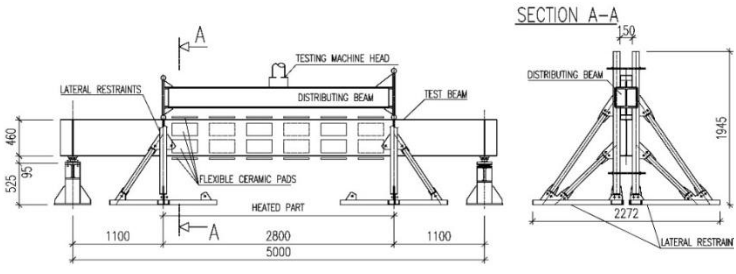

Figure 1. Detailed experimental test set-up.

(a) (b)

Figure. 2. Pinned point supports: (a) fixed; (b) free.

Table 1. Tested sections.

Test number	Dimensions [mm]		Classification	Non-dimensional slenderness
Test 1 450 ℃	h = 460 b = 150 t_f = 5 t_w = 4	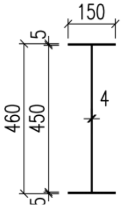	Web – Class 4 $\bar{\lambda}_p = 1.07$ Flange – Class 4 $\bar{\lambda}_p = 0.96$	$\bar{\lambda}_{LT} = 0.91$ $\bar{\lambda}_{LT,\theta} = 0.86$
Test 2 450 ℃	h = 460 b = 150 t_f = 5 t_w = 4	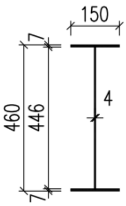	Web – Class 4 $\bar{\lambda}_p = 1.1$ Flange – Class 4 $\bar{\lambda}_p = 0.69$	$\bar{\lambda}_{LT} = 0.92$ $\bar{\lambda}_{LT,\theta} = 0.88$
Test 3 Tapered Beam 650 ℃	h_A = 460 h_B = 620 b = 150 t_f = 7 t_w = 4	End-section A-B 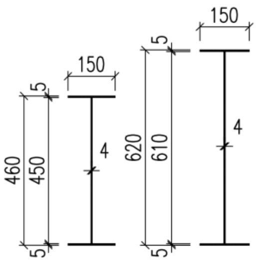	Web – Class 4 $\bar{\lambda}_{p(A)} = 1.07$ $\bar{\lambda}_{p(B)} = 1.52$ Flange – Class 4 $\bar{\lambda}_{p(A;B)} = 0.96$	
NOTE	Classification - according to EN 1993-1-2 Plate slenderness - according to EN 1993-1-2 Annex E			

3 NUMERICAL ANALYSES AND ITS COMPARATION WITH EXPERIMENTS

3.1 Model description

The experimental tests were replicated by means of the finite element method program ABAQUS [5]. The beam was meshed using quadrilateral conventional shell elements S4. The element has four integration points. The material law was defined by elastic-plastic nonlinear stress-strain diagram. The true material stress-strain relationship was calculated from the static engineering stress-strain curves obtained from the coupon tests. The reductions of material properties as well as the material nonlinearity were taken as recommended by the EC3 1.2. The measured values of the steel mechanical properties (yield strength and young modulus at room temperature) and the measured temperatures were adopted in the models. All experimental data have been used for verification of the numerical model. The mesh and boundary conditions are shown in Figure 3. The eigenmodes obtained from elastic buckling analysis were used as the initial geometric imperfection shape for the post buckling analysis. Two imperfection shapes were considered: the beam 1st local buckling mode and 1st global buckling mode (LTB) shapes. The imperfection amplitudes were evaluated from the initial geometry measurement.

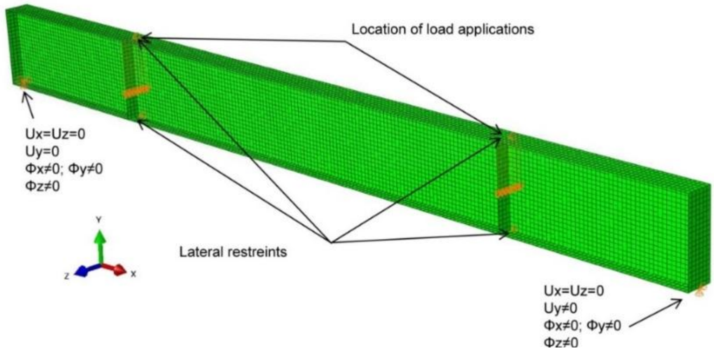

Figure 3. Boundary conditions.

3.2 Experimental and numerical results

The tests included all necessary data needed for the FE model validation. Namely initial imperfections, temperature of beams, material properties (tested at room temperature only), horizontal and vertical deflection at midspan and angle of section torsion at midspan were measured. The experimental results were compared with the numerical results in terms of load-deflection curves.

In the comparison below, the results of the test are shown together with the numerical results. Figure 4 shows the failure deformed shape of the test 2 obtained on the experimental tests and on the numerical analyses. Comparison of the load-deflection curve is shown in Figure 5. The load corresponds to the total force imposed on the two load application points. The shown displacement corresponds to the vertical displacement at the bottom flange at mid span.

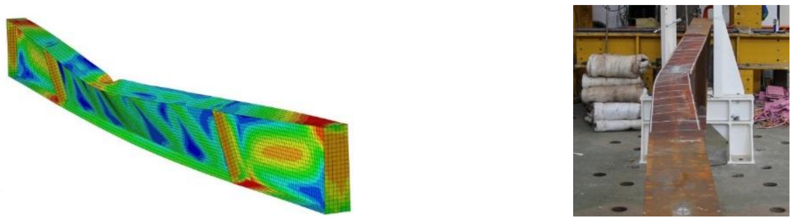

Figure 4. Failure mode in ABAQUS analysis and after the test.

The obtained results demonstrate the difficulties of lateral torsional buckling tests, moreover, which are highlighted by the elevated temperature. The problem of friction at the lateral restraints significantly affected the test 1. The experimental curve of load displacement relationship is not smooth and the force is a suddenly increasing in some regions. The obtained experimental initial stiffness is different from the numerical curves mainly in test 1 and 3. The temperatures were varied during the test slightly and were not uniform for the whole section. The temperatures that were employed in the numerical model were considered by the average temperature for each part of the beam (web, upper flange, bottom flange). The maximum loads in the tests 1 and 2 are higher than the values form the numerical models. Overall, the approximations are reasonable considering the nature of the different parameters involved in the presented tests, as for instance the heating process. The numerical model was able to predict the behaviour of beams observed in the tests, however mostly just for the mode of failure (Figure 4). The model was subsequently used for a parametric study.

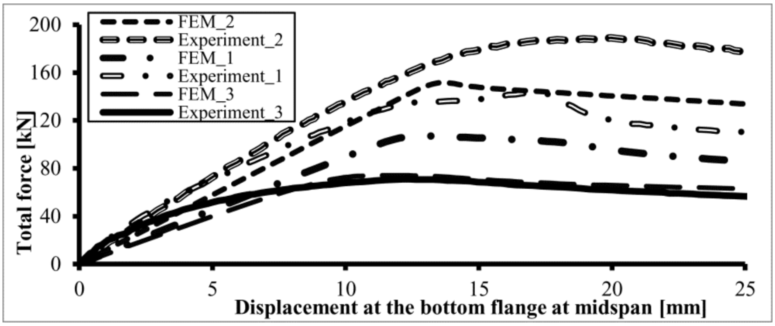

Figure 5. Load-displacement relation for the three beams: experimental and numerical.

4 PARAMETRIC STUDY

The parametric study is believed to cover the whole practical range of laterally unrestrained slender beams with Class 4 cross-sections in case of fire. Different steel grade, temperature, and non-dimensional slenderness were taken into account. The variable parameters of the study are listed in Table 2. They were applied for all investigated cross-sections – eight constant and six tapered. It covered 1260 cases. One of the cross-sections, namely 1000x7 / 300x12, was simulated with several other parameters. It was a different moment distribution, boundary conditions in terms of preventing warping and location of the load in respect to the shear centre. It brought extra 810 cases.

Table 2. Variable parameters of the parametric study.

Steel grade	S355; S460
Temperature	20; 350; 450; 550; 700 °C
Non dimensional slenderness	0.2; 0.4; 0.6; 0.8; 1.0; 1.2; 1.5; 1.8
Boundary condition	Simply supported beam ($k_{\mathrm{z}} = 1;\ k_{\mathrm{w}} = 1$)
Residual stress	Welded profile
Moment distribution	Uniform bending diagram

The geometrical imperfections (local and global) have been introduced in the model by the elastic buckling eigenmodes. According to the Annex C of the EC3 1.5, the amplitude of imperfections was chosen as 80% of the fabrication tolerances given in the EN 1090-2 [6]. Combination of the local and global imperfection was again assumed by the same Annex C. The leading imperfection corresponding to the lowest critical stress was chosen and included with the whole magnitude of the amplitude. The accompanying imperfection had the value of the amplitude reduced to 70%. Small part of the results for several selected cross-sections (see, Table 3) is presented in the text below.

4.2 Constant cross-section

In Figure 6, the comparison between beam resistance given by EC3 ($M_{b,Rd}$) and resistance obtained numerically (M_{FEM}) for different temperature is shown for steel grade S355. The charts on the right hand side show comparison between the current lateral torsional buckling curve given by the EC3 1.2 and the numerical results obtained with ABAQUS for laterally unrestrained beams.

Based on the recent numerical simulation, contemporary design rules for determination of moment resistance of Class 4 cross-section at elevated temperature are in discussion. For the correctness of the comparison it was aimed to eliminate all possible variables in the calculation except the lateral torsional buckling. Therefore the resistance of cross-section was determined in ABAQUS and used in both cases, FEM and EC3 calculation. The section resistance was calculated as resistance of the longest beam in the study, but laterally restrained (simple bending resistance). The used critical moment was also estimated numerically.

Table 3. Investigated sections.

CONSTANT I – SECTION				
$\mathbf{H_{web} x\ t_{web}}$ $\mathbf{/B_{flange} x\ t_{flange}}$	**Classification**			
	Normal / elevated temperature S355		**Normal / elevated temperature S460**	
450x4 / 150x5	Class 4/4 web	Class 4/4 flange	Class 4/4 web	Class 4/4 flange
450x5 / 250x16	Class 3/4 web	Class 2/3 flange	Class 4/4 web	Class 3/3 flange
1000x5 / 300x10	Class 4/4 web	Class 4/4 flange	Class 4/4 web	Class 4/4 flange
1000x8 / 300x20	Class 4/4 web	Class 1/3 flange	Class 4/4 web	Class 3/3 flange

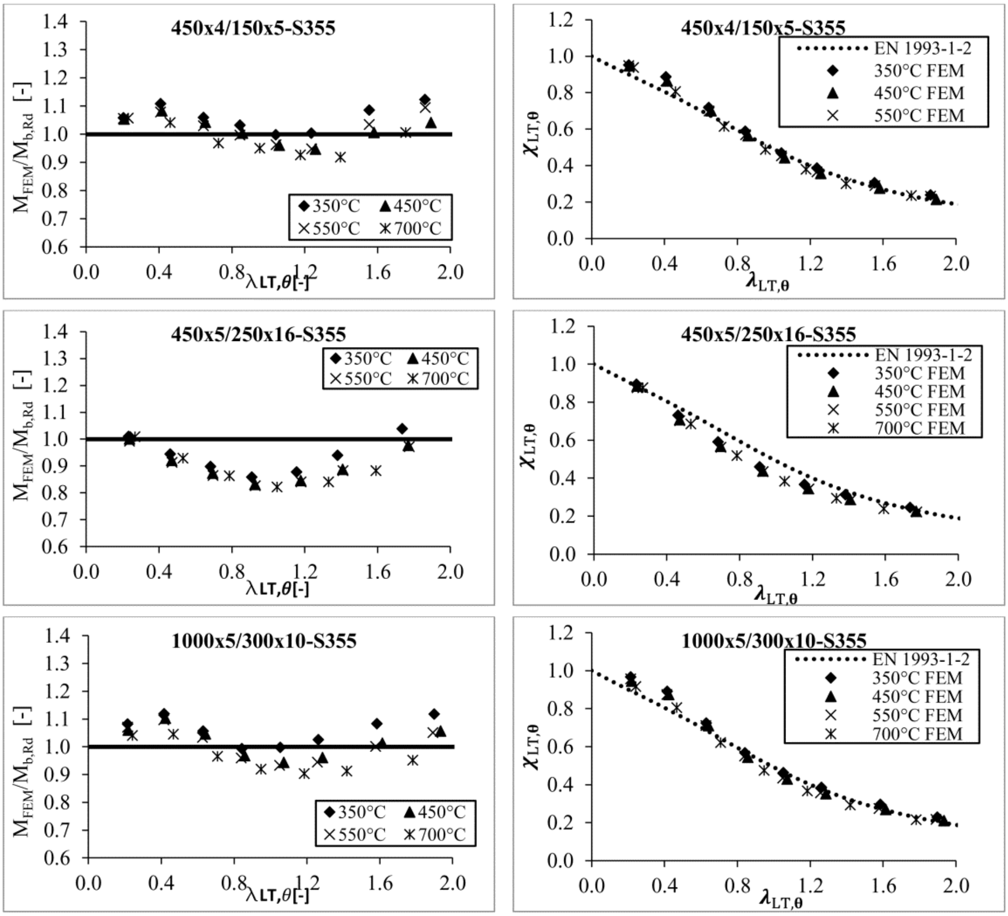

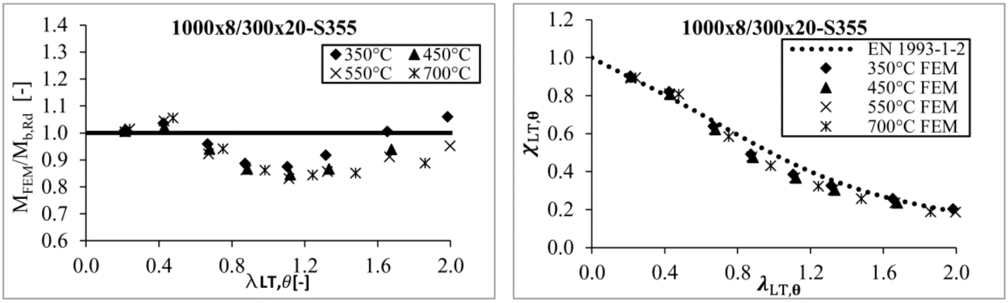

Figure 6. Comparison between the beam resistance resp. buckling reduction χ_{LT} given by the numerical simulations and according to EC3 1.2.

4.2 Tapered beams

The Table 4 present the tapered beams, which were numerically modelled. The same principles as for constant cross-section models were used. For the correctness of the comparison, it was aimed to eliminate all possible variables in the calculation except the lateral torsional buckling. The resistance of cross-section for each temperature and each length of beams were therefore determined in ABAQUS.

Most difficult part of the resistance calculation is determination of the critical section and its resistance. In the comparison shown below (Figure 7), the following procedure was chosen. The non-dimensional slenderness was calculated as:

$$\bar{\lambda}_{\mathrm{LT},\theta} = \sqrt{\frac{M_{\mathrm{Rk}}}{M_{\mathrm{cr}}}} \cdot \sqrt{\frac{1}{k_{\mathrm{E},\theta}}} \tag{1}$$

where:

M_{Rk} is the resistance of cross-section determined in ABAQUS for the desired temperature;

M_{cr} is the critical moment at room temperature obtained from LTBeam, multiplied by a reduction factor for the elasticity modulus $k_{\mathrm{E},\theta}$ depending on the temperature.

M_{FEM} is the tapered beam resistance obtained from ABAQUS. $M_{\mathrm{b,Rd}}$ is the resistance calculates according to EC3 1.1 clause 6.3.2 using the non-dimensional slenderness as (1).

Table 4. Investigated tapered sections.

TAPERED BEAM		
$(\mathbf{H_{web1}} - \mathbf{H_{web2}})\mathbf{x}\, \mathbf{t_{web}}/\mathbf{B_{flange}}\mathbf{x}\, \mathbf{t_{flange}}$	**Classification**	
	Normal / elevated temperature S355	
(450-250)x5 / 250x16	Class (1 to 3) / (2 to 4) web	Class 2/3 flange
(1000-500)x5 / 300x10	Class 4/4 web	Class 4/4 flange
(1000-500)x8 / 300x20	Class (2 to 4) / (3 to 4) web	Class 1/3 flange
(1000-750)x5 / 300x10	Class 4/4 web	Class 4/4 flange
(1000-750)x8 / 300x20	Class (3 to 4) /4 web	Class 1/3 flange
(1800-350)x9 / 250x24	Class (1 to 4) / (1 to 4) web	Class 1/1 flange

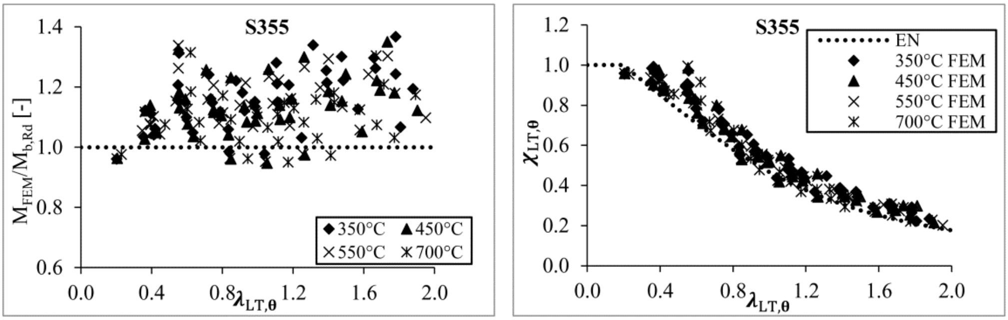

Figure 7. Comparison between the tapered beam resistance resp. buckling reduction χ_{LT} given by the numerical simulations and according to EC3 1.1. 6.3.2.

5 CONCLUSIONS

According to the obtained results, it appears that the discussion on Class 4 beams design at elevated temperature is necessary. The comparison shows some consistent differences between the FEM results and the EC3 approaches for beams at elevated temperature and highlight difficulty which Class 4 brings to lateral torsional buckling design. Authors are not aware that lateral torsional buckling curves were verified for beams with Class 4. In the case of non-uniform member, it seems that it is possible to use a simplified calculation model that is consistent with a constant cross-section member. Assuming an accurate determination of the critical section and its resistance of cross-section. Future investigation will be made and the results and will be presented on the conference.

6 ACKNOWLEDGEMENTS

The presented research was supported by the RFCS research project FIDESC4. The presentation of the work was supported by the Student`s Grant of the Czech Technical University in Prague, SGS13/124/OHK1/2T/11.

REFERENCES

[1] CEN European Committee for Standardisation, 2005. *EN 1993–1–2, Eurocode 3, Design of Steel Structures – Part 1–2: General rules - Structural fire design,* Brussels, Belgium.

[2] CEN European Committee for Standardisation, 2005. *EN 1993–1–1, Eurocode 3, Design of Steel Structures – Part 1–1: General rules and rules for buildings,* Brussels, Belgium.

[3] Marques L, Simões da Silva L, Rebelo C. "Application of the general method for the evaluation of the stability resistance of non-uniform members", *Proceedings of ICASS,* Hong Kong, 16–18 December; 2009.

[4] CEN European Committee for Standardisation, 2005. *EN 1993–1–5, Eurocode 3, Design of Steel Structures – Part 1–5: Plated structural elements,* Brussels, Belgium.

[5] Hibbitt, Karlsson & Sorensen, 2010. *ABAQUS: Analysis user's manual, Volumes I-IV, version 6.10,* Inc., Providence, R.I, USA.

[6] EN European Committee for Standardisation, 2008. *EN 1090-2, Execution of steel structures and aluminium structures – Part 2: Technical requirements for steel structures,* Brussels, Belgium.

8th International Conference on Structures in Fire
Guo-Qiang LI, Venkatesh K. R. KODUR, Shou-Chao JIANG, Jian JIANG, Su-Wen CHEN, Guo-Biao LOU (Eds.)
Shanghai, China, June 11-13, 2014

THERMAL SIMULATION OF STEEL PROFILES WITH INTUMESCENT COATING ADJACENT TO SPACE-ENCLOSING ELEMENTS

Peter Schaumann*, Florian Tabeling* and Waldemar Weisheim*

* Institute for Steel Construction, Leibniz University Hannover
e-mails: schaumann@stahl.uni-hannover.de, tabeling@stahl.uni-hannover.de, weisheim@stahl.uni-hannover.de

Keywords: intumescent coating, numerical simulation, restrained foaming

Abstract *In this paper advanced numerical investigations regarding the heating behaviour of steel elements protected by an intumescent coating with an adjacent trapezoidal steel sheet are presented. The main objective is to evaluate the influence of an unprotected trapezoidal steel sheet on the temperature of coated I-section profiles. For this purpose, a three-dimensional finite element model of a coated I-section profile is developed in Abaqus taking into account the restrained foaming process of the intumescent coating due to the adjacent member explicitly. After the validation of the finite element model against own fire tests, the steel temperatures of a coated I-section profile with and without an adjacent trapezoidal steel sheet, resulting from fire exposure according to ISO-834, are compared to demonstrate the influence of the steel sheet in detail.*

1 INTRODUCTION

Structural steel elements protected by intumescent coatings (IC) are often applied to space-enclosing elements in practical usage. In case of fire the IC is restrained in its thermal expansion in those regions and the intumescent foam cannot rise. In consequence, the thermal protection effect of the IC as well as the temperature in the coated steel element is influenced due to adjacent space-enclosing elements. Especially an adjacent trapezoidal steel sheet (TSS) leads to a complex temperature distribution in a coated I-section profile due to its specific geometry. Regarding the covered flange, in case of fire there are areas with fully developed foam and areas in which the expansion of IC is restrained (Figure 1). The main objective of the presented investigations is to quantify the influence of a trapezoidal steel sheet on the heating behaviour of an I-section profile fire protected by an IC.

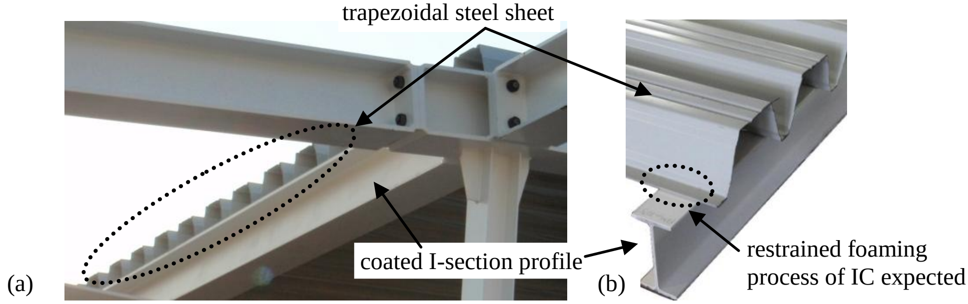

Figure 1. Coated I-section profile with an adjacent trapezoidal steel sheet: (a) within a steel construction and (b) in a detailed illustration.

To date the fire design of structural steel elements with IC is based on technical approvals. The influence of space-enclosing elements on the temperature distribution cannot be considered in detail. In German design codes an additional protection of the adjacent space-enclosing elements by IC is required to ensure the load bearing capacity of coated steel elements in the fire situation.

In order to evaluate the influence of an adjacent trapezoidal steel sheet on the heating behaviour of an I-section profile, fire tests were performed first. Therefore a coated I-section profile (IPE 200) as well as an additional equivalent coated I-section profile with an adjacent trapezoidal steel sheet was investigated. The influence of the trapezoidal steel sheet on the heating behaviour is pointed out by comparing the steel temperatures of both I-section profiles resulting from a fire exposure according to ISO-834 for 60 minutes. Afterwards advanced numerical methods and material properties of IC are described to predict the heating behaviour of coated I-section profiles in a three-dimensional model by taking into account the foaming process as well as a restrained expansion behaviour of the IC. This model permits to regard the development of the temperature field of the I-section profile in detail. Furthermore, the model is validated against the above mentioned fire tests by comparing the measured and calculated steel temperatures. Based on the validated model, the development of the steel temperatures of coated I-section profiles with and without an adjacent trapezoidal steel sheet are compared to each other. Finally, the influence of adjacent trapezoidal steel sheets on the heating behaviour of I-section profiles is quantified.

2 EXPERIMENTAL INVESTIGATIONS

In order to evaluate the influence of a restrained foaming process of IC due to adjacent trapezoidal steel sheets on the heating behaviour of steel profiles, a fire test was conducted at the material testing laboratory MPA Braunschweig in 2012 within the scope of a national research project [1]. Besides a simply coated IPE 200 profile, an additional equivalent I-section profile with an adjacent trapezoidal steel sheet (Fischer T135) was chosen as test specimen (Figure 2). In both cases the I-profiles were 1,100 mm long and coated with a solvent-borne intumescent coating. The averaged dry film thickness of test specimen 1 was 700 μm and of test specimen 2 750 μm. As illustrated in Figure 2a the test specimens were arranged within the furnace near by the gas burner to ensure a thermal exposure according to ISO-834. Since the test specimens were arranged at the bottom of the furnace, whereas the position of the gas burner was about 900 mm above the ground, a direct exposure to the flames could be excluded for the test specimens. The whole fire test was recorded using a water cooled video camera, which was positioned in front of the test specimens.

To ensure a continuous measurement of the steel temperatures, several thermocouples were arranged in multiple rows on the upper (covered) and bottom flange as well as on the web of the test specimen 1 and 2. Two thermocouples of each test specimen are chosen to point out the temperature development within the test bodies in this paper. In Figures 2(b) and 2(c) the position and the labels of the thermocouples are shown in detail.

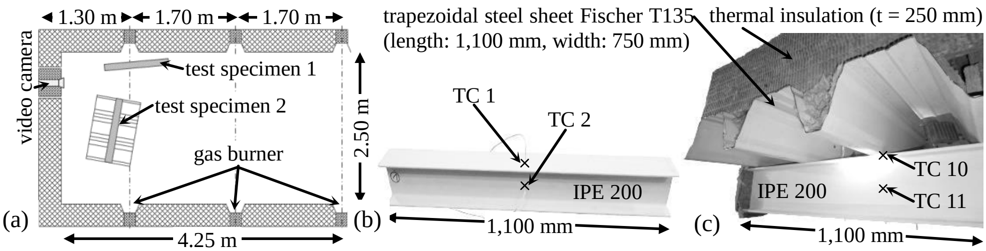

Figure 2. Experimental setup: (a) schematic illustration of the furnace and the test specimens (b) test specimen 1: coated I-section profile IPE 200 (t_{IC} = 750 μm) (c) test specimen 2: coated I-section profile IPE 200 (t_{IC} = 700 μm) with an adjacent trapezoidal steel sheet.

The measured steel temperatures of both test specimens are illustrated in Figure 6. In case of the unaffected test specimen 1, the measured temperatures in the upper flange and in the web are nearly identical (Figure 6a). While the upper flange exhibits a temperature of 593 °C after a fire exposure time of 30 minutes, the measured temperature in the web is only 20 K higher (613 °C). Nevertheless, the steel temperatures of test specimen 1 exceed the critical temperature of 500 °C, which is defined within the technical approval of intumescent coatings. The exceeded steel temperatures can be ascribed to both, a significantly high gas temperature in the first 15 minutes of the fire test and an insufficient scaled dry film thickness of the intumescent coating.

In the case of test specimen 2 the temperatures in the covered flange and the web of the I-profile underneath the low beading of the TSS deviates significantly from the measured temperatures of test specimen 1 (Figure 2b). Unlike in the previous case the upper flange exhibits a temperature of 742 °C after a fire exposure time of 30 minutes, while the web temperature is 671 °C, thus resulting in a significant temperature gradient within the steel profile. Nevertheless, the temperature of the covered flange underneath the high beading of the TSS is still similar to test specimen 1 (c.f. Tabeling [2]). Therefore the temperature gradient as well as the significant temperature rise within test specimen 2 clearly points out the influence of the trapezoidal steel sheet and in consequence the influence of the restrained foaming process of the IC on the heating behaviour of the steel profile.

3 ADVANCED NUMERICAL METHODS AND MATERIAL PROPERTIES OF INTUMESCENT COATINGS

The advanced numerical simulations are performed using the finite element software Abaqus [3] in a fully coupled thermal-stress analysis. A fully coupled thermal-stress analysis is strictly necessary due to the fact, that heating of the IC results in a foaming process as well as the foaming process affects the temperature development of the IC. Moreover a large-displacement formulation is used whereas the elements are formulated in the current configuration using the current nodal positions. In this manner, the volumetric change of the IC during the foaming process is considered within the numerical simulation. Besides the expansion behaviour of IC, shrinkage processes are taken into account explicitly as well to consider the high temperature behaviour of IC close to reality. To take the foaming process of the IC into account, a thermal expansion coefficient α_T is formulated in Abaqus [3] considering logarithmic strains:

$$\alpha_T = \frac{\ln\left(d_{cur}/d_{ini}\right)}{\theta_{cur}-\theta_{ini}} = \frac{\ln\left(d_{ini}\cdot\alpha/d_{ini}\right)}{\theta_{cur}-\theta_{ini}} = \frac{\ln\left(\alpha\right)}{\theta_{cur}-\theta_{ini}} \tag{1}$$

with
α_T = thermal expansion coefficient (1/K)
d_{cur} = current thickness of IC ($d_{cur} = \alpha \cdot d_{ini}$) (mm)
d_{ini} = initial thickness of IC (mm)
θ_{cur} = current IC-temperature (°C)
θ_{ini} = initial IC-temperature (°C)
α = thermal expansion factor (-)

As can be seen from Equation (1), the thermal expansion factor α of the IC is of major importance for the implementation of the foaming process in Abaqus [3]. In order to determine the expansion factor of IC, additional own small scale fire tests were performed. In this context, different IC were applied on thin steel plates and exposed to ISO-834. The foaming process was recorded during these fire tests and evaluated afterwards in a video analysis. Detailed information concerning these fire tests will be presented in Tabeling [2] very soon. The measured expansion factor of IC as a function of temperature is shown in Figure 3a.

Furthermore the expansion factor, containing the volumetric change of IC, is a fundamental basis with regard to the development of the additional material properties needed in thermomechanical analyses. Concerning the thermal conductivity of IC, the porosity ψ of IC can be described as a function of the IC-temperature using the following equation:

$$\psi(\theta) = \frac{\alpha - 1}{\alpha} \tag{2}$$

The mathematical evaluation of Equation (2) is depicted in Figure 3a. Based on the porosity, the thermal conductivity can be calculated according to an equation based on di Blasi [4] including an approach of Staggs [5] concerning the thermal radiation within the pores:

$$\lambda_{eq}(\theta) = \psi \cdot (\lambda_P + 4 \cdot \sigma \cdot \theta_M^3 \cdot d_P) + (1-\psi) \cdot \lambda_{IC} \tag{3}$$

with λ_{eq} = equivalent thermal conductivity (W/(m K))
λ_P = thermal conductivity of the gas within the pores (W/(m K))
λ_{IC} = thermal conductivity of the IC for room temperature conditions (W/(m K))
ψ = porosity (-)
σ = Stefan-Boltzmann-Constant (W/(m²K⁴))
θ_M = Temperature of the IC (K)
d_P = diameter of pores (m)

As can be indicated in Equation (3), several parameters are strictly necessary to determine the thermal conductivity of IC in detail. Here, the diameter of the pores is assumed as 1.2 mm and the thermal conductivity of IC for room temperature conditions is assumed to λ_{IC} = 0.45 W/(m K) based on investigations of Tabeling [2]. The equivalent thermal conductivity of IC is shown in Figure 3b as a function of temperature.

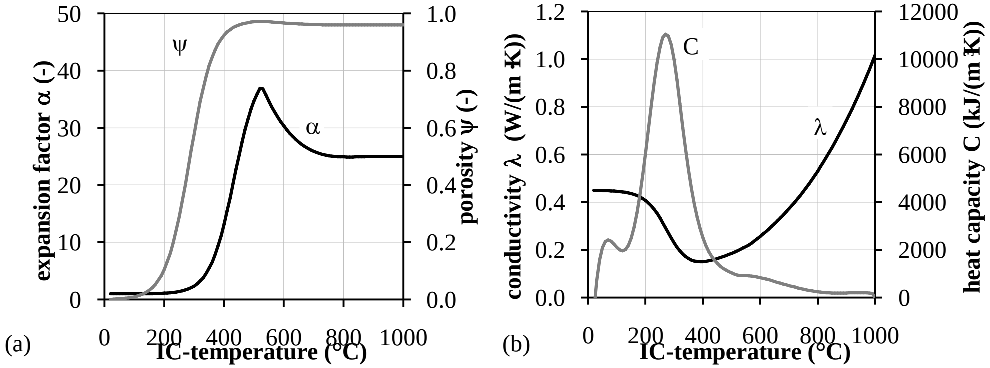

Figure 3. Material properties of IC: (a) expansion factor and porosity (b) thermal conductivity and heat capacity.

In order to formulate a detailed material model for the simulation of the heating behaviour of IC, the heat capacity of IC is derived. Therefore differential scanning calorimetry (dsc) analyses were performed including thermogravimetrical investigations, which are presented in Tabeling [2] as well. The measured heat capacity of IC is shown in Figure 3b. Additionally, a young's modulus of the IC of 1,0 N/mm² is assumed for the reason, that it is strictly required for a thermomechanical analysis.

Based on the presented advanced numerical methods and material properties of IC, the simulation of the high temperature behaviour of IC, including the foaming process of IC explicitly, is enabled. Based on this, a finite element model of an I-section (IPE 200) is developed according to test specimen 1, which is presented in [6]. Furthermore a three-dimensional model of an equivalent I-section with an adjacent trapezoidal steel sheet according to test specimen 2 is developed. The model is discretized by using C3D8T elements which allows a three dimensional thermomechanical simulation (see Figure 4).

As can be seen in Figure 4, symmetrical conditions are used to reduce the calculation time whereas adiabatic boundary conditions are considered in the symmetrical plain. Furthermore, adiabatic conditions are set on top of the trapezoidal steel sheet to take into account a thermal insulation in this area. Moreover the IC is discretized very detailed within the area of the lower beading of the trapezoidal steel sheet to ensure a foaming process close to reality. Finally, the model is exposed to ISO-834 including thermal coefficients for the emissivity $\varepsilon_{IC} = 0.8$ and $\varepsilon_{Steel} = 0.7$ whereas the convection coefficient is assumed as $\alpha_c = 25$ W/(m²K). The material properties of steel are set according to DIN EN 1993-1-2 [7].

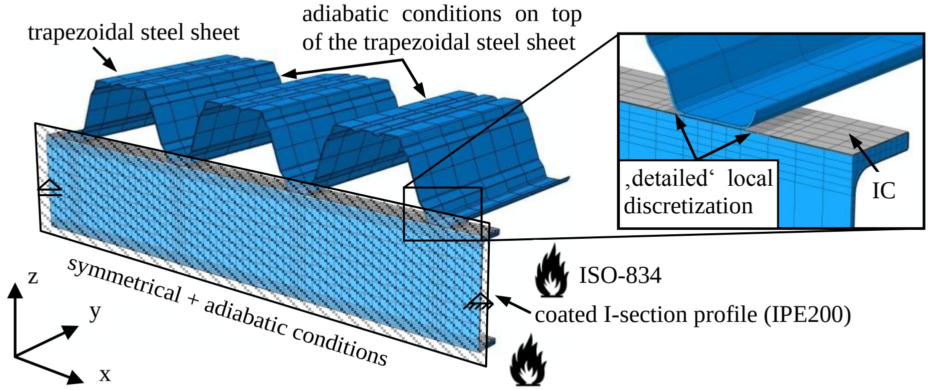

Figure 4. Finite element model of a coated I-section profile with an adjacent trapezoidal steel sheet.

To take a restrained thermal expansion of the IC into account, the User Subroutine *UExpan* is implemented in Abaqus [3]. Besides a temperature-dependent thermal expansion behaviour of the IC, formulated in UExpan, an additional dependency of the thermal expansion on the arising pressure in the finite element is implemented in this way. Hence, when the IC gets in contact with the trapezoidal steel sheet during the expansion and the stress in the elements increases, the thermal expansion is switched off. As a consequence, the IC does not expand anymore and the intumescent foam remains in its current configuration. In this manner, the restrained foaming process of the IC at the upper flange is considered in detail. While the IC-foam is fully developed in the area of the upper beading, the foaming process of the IC in the area of the lower beading of the trapezoidal steel sheet is considered as restrained (see Figure 5).

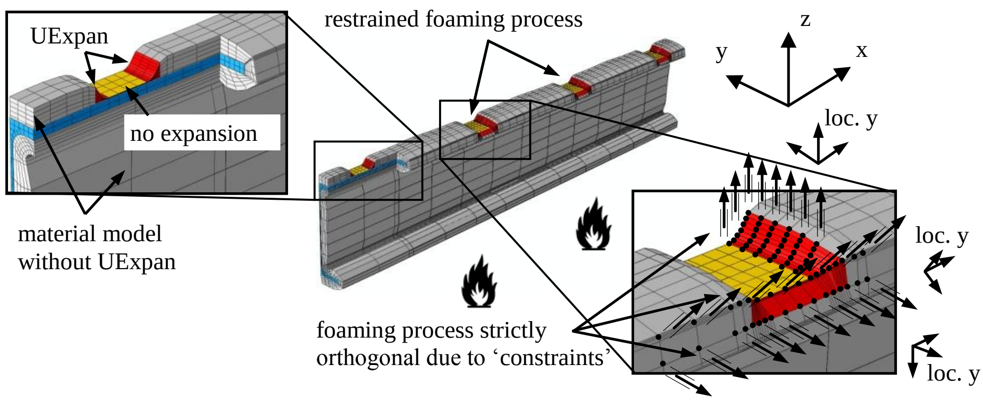

Figure 5. Finite element model of a coated I-section profile with an adjacent trapezoidal steel sheet under the consideration of a restrained foaming process of the IC.

As can be seen in this figure, the User Subroutine *UExpan* is only used in those areas, where a restrained thermal expansion of the IC is expected. In contrast to that, the thermal expansion behaviour of the IC in the area of the lower beading of the trapezoidal steel sheet is neglected due to the fact, that the IC is not able to build the foam here. In the remaining areas a material model is assigned, which neglects the restriction of the restrained thermal expansion behaviour of the IC. Furthermore, it can be seen in Figure 5, that in the areas in which the User Subroutine UExpan is applied, ‘constraints’ are implemented in order to ensure a strictly orthogonal foaming process (local y-direction). Due to the specification of a strictly orthogonal expansion behaviour, excessive distortions of the elements are prevented when the IC gets in contact with the trapezoidal steel sheet within the foaming process.

In this manner, the effect of the trapezoidal steel sheet on the thermal protection effect of the IC is considered explicitly. In this context, the heat flux due to thermal conductivity of the heated trapezoidal steel sheet into the coated upper flange of the I-section is considered as well.

4 VALIDATION OF THE ADVANCED NUMERICAL MODEL

In order to verify the predicted temperatures of the finite element model, the results obtained by the advanced numerical methods are validated against the test data of section 2. Therefore the comparison between the predicted and the measured steel temperatures of the test specimens are discussed in the following. In Figure 6a both, the measured and the calculated temperatures of test specimen 1 are illustrated. It is apparent, that the web temperature as well as the upper flange temperature is slightly overestimated by the finite element model in the first ten minutes, when the measured gas temperature is underlying as fire exposure curve. Nevertheless, the difference between the predicted and the measured temperature decreases with increasing duration of fire exposure. After a fire exposure time of 30 minutes the predicted upper flange temperature (576 °C) deviates from the measured flange temperature (593 °C) only by 17 K. Also the deviation of 39 K (experiment: 613 °C, simulation: 574 °C) between the web temperatures lies within tolerable limits.

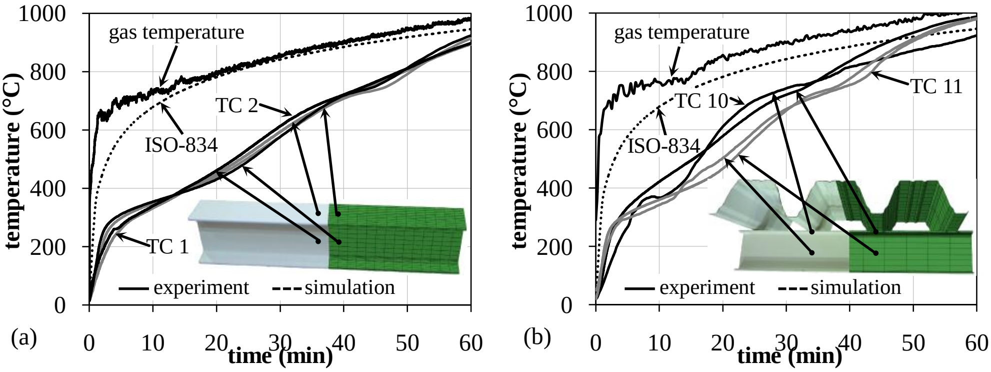

Figure 6. Comparison between the experimentally derived and by finite element method calculated steel temperatures for: (a) test specimen 1 (IPE 200, t_{IC} = 750 µm) (b) test specimen 2 (IPE 200, t_{IC} = 700 µm, trapezoidal steel sheet).

To verify the predicted temperatures of the modelled I-section profile with the adjacent trapezoidal steel sheet, a comparison between the measured and the calculated steel temperatures of the covered flange and the web underneath the low beading of the trapezoidal steel sheet are illustrated in Figure 6b. Taking the measured gas temperature of test specimen 2 as basis for the fire exposure curve of the finite element model leads analogous to test specimen 1 to higher predicted temperatures in the first ten to fifteen minutes. But the difference between the predicted and the measured temperatures decrease as well with increasing duration of fire exposure. After 30 minutes the calculated web temperature (665 °C) differs from the measured web temperature (670 °C) only by 5 K. Also the difference between the covered flange temperatures of 21 K (experiment: 741 °C, simulation: 720 °C) lies within tolerable limits.

Hence, the results of the conducted validation underline distinctively, that the new developed material model for IC, which takes the foaming process and the restrained build-up of the IC foam structure due to adjacent space-enclosing elements into account, leads to reliable and very promising results close to reality for the prediction of three-dimensional temperature distributions of I-section profiles.

5 QUANTIFICATION OF THE INFLUENCE OF AN ADJACENT TRAPEZOIDAL STEEL SHEET ON THE TEMPERATURE FIELD

The fire test results of Chapter 2 point out, that the restrained foaming process of IC due to adjacent space-enclosing elements results in a temperature rise within the steel profile. To quantify the influence of a trapezoidal steel sheet and in consequence the influence of the restrained foaming process of IC on the temperature progress of the steel profile in detail, advanced numerical calculations were conducted, using the nominal standard fire curve (ISO-834) as fire exposure.

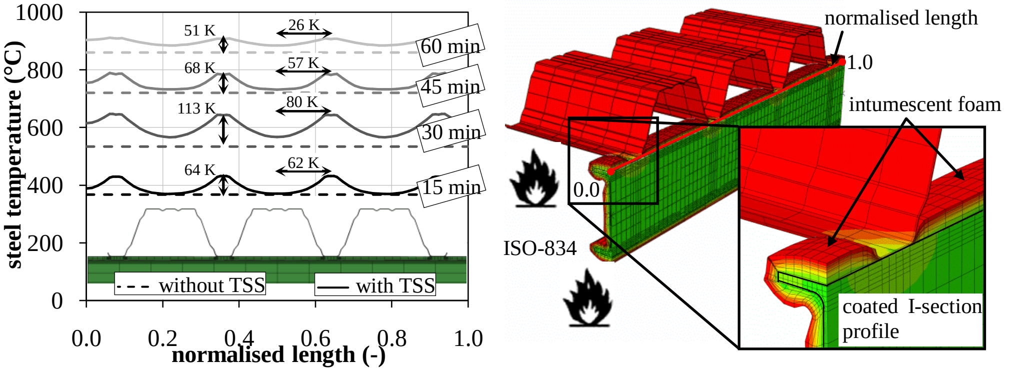

Figure 7. Results of the advanced numerical calculation: depiction of the steel temperature of a coated I-section profile with and without the influence of an adjacent trapezoidal steel sheet (TSS) and illustration of the finite element model of the coated IPE 200 profile in case of fire with an IC in the foamed and restrained configuration.

In order to quantify the influence of the adjacent trapezoidal steel sheet on the temperature field of the steel profile, the upper flange temperatures along the normalised length of an IPE 200 profile with and without a trapezoidal steel sheet are compared to each other. Based on the additional heat input resulting from the trapezoidal steel sheet, a local temperature rise within the upper flange of the steel profile is ascertainable (see Figure 7a). As a consequence a temperature gradient ($\Delta\theta = 62$ K) along the profile between the lower and upper beading of the trapezoidal steel sheet ensues already after 15 minutes of fire exposure. Compared to the unaffected steel profile, the upper flange of the profile with the trapezoidal steel sheet exhibits a 64 K higher temperature underneath the lower beading during this time.
With increasing fire exposure time a temperature rise within the area of the restrained IC can be recognised, resulting in a 113 K higher upper flange temperature after 30 minutes compared to the unaffected profile. Although the upper flange temperature underneath the upper beading rises as well, a temperature gradient ($\Delta\theta = 80$ K) along the steel profile is still present. Only at the end of fire exposure time (60 minutes) a homogenisation according to the upper flange temperatures arises, resulting in a reduction of the temperature gradient along the steel profile to merely 26 K.

Hence, the results of the advanced numerical investigations point out that the restrained foaming process of IC due to adjacent space-enclosing elements results in a significant temperature rise within the steel profile. However, this rise in temperature occurs only locally in the area of the low beading of the trapezoidal steel sheet, resulting from additional heat input. Consequently, these results lead to the recommendation that steel profiles have generally to be coated four-sided, even if space-enclosing elements adjoin to the upper flange, thus ensuring a lower temperature rise within the profile.

6 CONCLUSIONS

In this paper, experimental and advanced numerical investigations on coated I-section profiles with and without adjacent trapezoidal steel sheets in case of fire are presented. The main objective of these investigations is to evaluate the influence of a trapezoidal steel sheet on the heating behaviour of I-section profiles with intumescent coatings (IC).

Therefore experimental investigations are performed first, whereas coated I-section profiles with and without an adjacent trapezoidal steel sheet are examined. Besides the investigation of a restrained foaming process of IC, these fire tests serve as a basis for the validation of the advanced numerical model.

In order to simulate the heating behaviour of coated I-section profiles with and without adjacent trapezoidal steel sheets, advanced numerical methods and models as well as material properties concerning the high temperature behaviour of IC are developed. Within this simulation a restrained foaming process of IC due to an adjacent trapezoidal steel sheet is enabled for the first time. To validate, the calculated and measured steel temperatures are compared to each other, showing a very good agreement. Based on the validated finite element model both, a coated I-section profile with and without an adjacent trapezoidal steel sheet are exposed to ISO-834 and compared to each other. The results point out, that an adjacent trapezoidal steel sheet and consequently a restrained foaming process of IC results in partially significant higher steel temperatures in the covered flange. In this context, the flange within the area of the lower beading is affected by higher temperatures particularly.

The newly developed advanced numerical methods and material parameters of IC enable the prediction of the high temperature behaviour of coated I-section profiles taking into account the foaming process as well as a restrained thermal expansion of IC for the first time. With respect to a performance-based fire design of coated steel elements in special configurations, an innovative and individual evaluation is enabled.

ACKNOWLEDGEMENTS

The results have been produced during the German research project ‘Optimierter Einsatz intumeszierender Anstriche im Stahlbau’ (IGF 17200 N). The project IGF 17200 N from DASt was funded by the ‘Federal Ministry for Economic Affairs and Energy’ via AiF. The authors express their deep gratitude.

REFERENCES

[1] Mensinger, M.; Schaumann, P.; Kraus, P.; Tabeling, F.: Optimised applications of intumescent coatings on steel elements (in German: Optimierter Einsatz intumeszierender Anstriche im Stahlbau); IGF-Vorhaben 17200N / Deutscher Ausschuß für Stahlbau e.V. (DASt). 2014. – research report (to be published).

[2] Tabeling, F.: High temperature behaviour of intumescent coating on steel constructions (in German: Zum Hochtemperaturverhalten dämmschichtbildender Brandschutzsysteme im Stahlbau). *Hannover, Leibniz Universitaet Hannover, Institute for steel construction,* Phd-Thesis, 2014 (will be published in the end of 2014).

[3] ABAQUS: *Abaqus/Standard Version 6.10. Pawtucket: Hibbit, Karlsson & Sorensen, Inc.* 2011.

[4] Di Blasi, C.; Branca, C.: Mathematical Model for the Nonsteady Decomposition of Intumescent Coatings. *American Institute of Chemical Engineers Journal Bd. 47.* Wiley, 2001, P.2359–2370.

[5] Staggs, J. E. J.: Thermal conductivity estimates of intumescent chars by direct numerical simulation. *Fire Safety Journal Bd. 45.* Wiley, 2010, P. 228–237.

[6] Kraus, P.; Mensinger, M.; Schaumann, P.; Tabeling, F.: Investigations of Steel Elements with Intumescent Coating connected to Space-Enclosing elements in Fire. In: *Application of Structural Fire Engineering (ASFE)*. Prag, 2013, S. 447–453.

[7] EN 1993-1-2: Eurocode 3: Design of steel structures – part 1-2: General rules – Structural fire design. Brussels, Belgium: Comité Européen de Normalisation, 2010.

THE TEMPERATURE OF ZINC COATED STEEL MEMBERS IN FIRE

Jiří Jirků* and František Wald*

* Czech Technical University in Prague, Faculty of Civil Engineering, Thákurova 7, 166 29 Prague
e-mails: jiri.jirku@fsv.cvut.cz, wald@fsv.cvut.cz

Keywords: Surface emissivity, Zinc coating, Fire test

Abstract. *This paper is focused on the description of three fire tests for specification of surface emissivity of galvanized steel members in fire. Two experiments were performed in the horizontal furnace and one was the part of full scale fire test. Two fire tests verified preliminary results, which were obtained in the first fire test in the horizontal furnace. The paper sums up experiments, used specimens and also shows results.*

1 INTRODUCTION

Influence of surfacing to the fire resistance is not currently described. Eurocode EN 1993-1-2 [1] does not specify a value of surface emissivity for galvanized components for calculations of fire resistance of steel structures. In fire engineering, it is necessary to assume all surfaces as graybody with defined emissivity, which is temperature and wavelength independent.

The theory of heat transfer in civil engineering is described, analytical and numerical models for heat transfer analysis, are well known. The three mechanisms of heat transfer – conduction, convection and radiation – are considered. Convection and radiation creates boundary conditions for heat conduction inside the heated members. Thanks to changing of surface emissivity by zinc coating of steel members, the value of radiative heat flux can be influenced.

The heat flux, which is by radiation caused, is described as

$$q_r = \varepsilon_{res} \cdot \sigma \cdot \left[(\theta_g + 273)^4 - (\theta_s + 273)^4 \right] \tag{1}$$

where θ_g and θ_s are temperatures of gas and steel in °C, σ is Stefan – Boltzmann constant, ε_{res} is resultant emissivity and is calculated as follows:

$$\varepsilon_{res} = \frac{1}{1/\varepsilon_f + 1/\varepsilon_s - 1} \tag{2}$$

where ε_f is the emissivity of the fire (for the ambient temperature air, $\varepsilon_f = 1$) and ε_s is emissivity of the surface of a structural element.

The final value of ε_{res} had been under research by scientists, but they reached no satisfactory consensus for one value. In the full version of Eurocode EN 1993-1-2 [1] is recommended to use $\varepsilon_{res} = 0{,}7$. Gjoel in [5] proposed heat transfer model, which taking into account the effect of the composition of gasses in the fire compartment and its influence on heat transfer by radiation. Gjoel described equation for calculation of radiative heat flux with considering of this effect of gaseous composition as:

$$q_r = \sigma \cdot \left[\varepsilon_g \cdot \left(\theta_g + 273\right)^4 - \alpha_g \cdot \left(\theta_s + 273\right)^4\right] \tag{3}$$

where ε_s is the total gas emissivity and α_g is total gas absorptivity. These values are temperature dependent and are calculated as follows:

$$\alpha_g = h_c + \sigma \cdot \varepsilon_g \cdot \left[4 \cdot \left(\theta_g + 273\right)^3\right] \tag{4}$$

and

$$\varepsilon_g = 0.458 - 1.29 \times 10^{-4} \cdot \theta_g \tag{5}$$

for most common composition of gases 10% carbon dioxine, 10% water vapour and 80% nitrogen mixture.

1.1 Cone calorimeter tests

The first tests were prepared by Heinisuo and Jutila, see [6], in calorimeter. These tests confirmed positive influence of zinc coating to the structures´temperature during fire. The specimens were by heat flow from cone calorimeter heated. Calculated value of emissivity for zinc coated steel members below 420 ℃ was determined as 0.2. In [6] was also positive influence of the ratio A_m/V for temperature of zinc coated members in fire described. If the ratio is smaller, than the positive influence of zinc coating for fire resistance is getting larger.

Next sets of fire tests for verification and description of positive influence of zinc coating for structures´temperature during fire were by Czech Technical University in Prague performed and are described below.

2 FIRE TESTS

For determination of the surface emissivity of galvanized steel structures in fire were several tests that confirm this positive trend carried out. The first fire test was performed in 2010. This one was followed by two experiments in 2011.

The identical specimens were for fire tests used. This had enabled, that the results from all fire test could be compared.

2.1 Fire test in the horizontal furnace 2010

2.1.1 Test specimens

For experiment purposes eight specimens were prepared. They were divided into two general groups, for open and closed cross sections. For open cross section were chosen IPE 200 and for hollow sections hollow tubes TR 114,3 × 4. Each specimen was 1 m long. Specimens ready for the test can be seen in Figure 1.

At the furnace were specimens as a small columns in couples with and without zinc coated surface placed. Each couple was between burners located, not to be influenced by the fire from the heat source and also for elimination of irregular temperature redistribution inside the furnace during the fire test. To ensure that heat transfer will be only by the members´surface provided, both ends were covered by the mineral and heat resistant wool.

(a) (b)

Figure. 1. (a) Test specimens hollow cross section; (b) Test specimens of the open cross section.

Temperature of specimens during fire was measured by coated thermocouples. Each specimen was by one 2 mm diameter thermocouple equipped, this was at half height placed. The gas temperature in the fire compartment was by six 3 mm thermocouples measured. They were near the measured specimens located.

2.1.2 Properties of zinc surface

Half of specimens was zinc coated and second part was left without any surfacing.. Temperature of zinc coating bath was 457 ℃ and average thickness of the zinc surface layer from 16 measurements for each specimen was 119 μm, max. 142.8 μm, min. 95.9 μm. Composition of the zinc bath was for specimens IPE 3, IPE 4 and TR7 identical – Zn min. 98,5%, Pb max. 1.5%. For specimen TR8 was different composition of zinc bath with added Al chosen. This ensured higher shininess of the surface. In the zinc bath for TR8 was about 0,03% Al added. The temperature of zinc bath was for the first set of specimens 460 ℃ and for TR8 456 ℃.

2.1.3 Properties of zinc surface

Specimens were to simulated fire at the horizontal furnace at the fire laboratory in Veseli nad Luznici exposed. The dimension of the furnace is 4.5 m × 3.0 m. The gas temperature was simulated in accordance to nominal temperature curve. The curve of gas temperature and measured steel members temperature for open cross sections are shown in Figure 2.

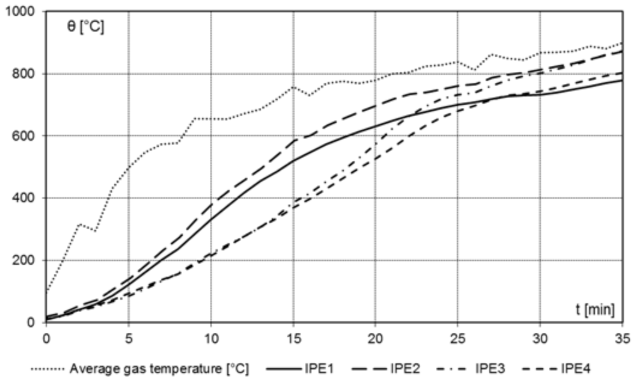

Figure 2. Measured temperatures on open cross sections.

2.1.4 The analytical evaluation of the test results

The step by step method was for analytical evaluation modified. Endless members were assumed - only two dimensional heat transfer (no conduction) were taken into account. Increase of temperature of steel member is by net heat flux, which consists of two mechanisms caused.

$$q_{net,r} = q_{net} - q_{net,c} \tag{6}$$

where q_{net} is net heat flux, $q_{net,c}$ is heat flux by convection, $q_{net,\mathrm{r}}$ is heat flux by radiation

The final value of $\varepsilon_{\mathrm{res}}$=0,7 for steel profiles without surfacing was in accordance to EN 1993-1-2 [1] assumed. This value was assumed as known. From this assumption was regression analysis made. On the basis of this analysis was heat transfer coefficient α_{c} determined. In the first 30 minutes of fire test was an average value of heat transfer coefficient calculated on members without any surfacing α_{c} = 4 W/m^{2}K. When this value was known, it was possible to calculate emissivity for zinc coated members for each time step. Average emissivity value was from these values calculated. Values of calculated emissivity are assumed as follows in Table 1.

Table 1. Surface emissivity for different test specimens.

Specimen	Surfacing	Emissivity
IPE 3	Zn	0,318
IPE 4	Zn	0,234
TR 7	Zn	0,444
TR 8	Zn-Al	0,293

The final value of emissivity for zinc coated members in fire was an average value from all calculated. Uncertainty of the results is in determined value α_{c} for steel members without coating included, i.e. ε_{m} = 0,7. An average value of resultant emissivity of galvanized elements was calculated as $\varepsilon_{\mathrm{res}}$ = 0,32.

2.2 Natural fire test in Veseli nad Luznici

For verification of the effect of surface emissivity of galvanized steel structure to a temperature of steel members in the real fire conditions were specimens into compartment in full scale fire test placed, see Figure 3. Zinc coated specimens were during the second fire test at the first floor of experimental building monitored. The surface emissivity of galvanized elements, which was calculated from the results of fire experiments in a horizontal furnace in 2010, was verified. Zinc specimens were hung under the ceiling structure on logs with a diameter of 10 mm, see Figure 3, in the compartment area with expected highest gas temperature. The arrangement of specimens at the compartment eliminated an uneven temperature distribution. Profiles were arranged in pairs, always galvanized and without zinc coated surface. Specimens were isolated at both ends by mineral fibre wool so that the sample simulated the endless element and the heat transfer occur only its outer surface.

(a) 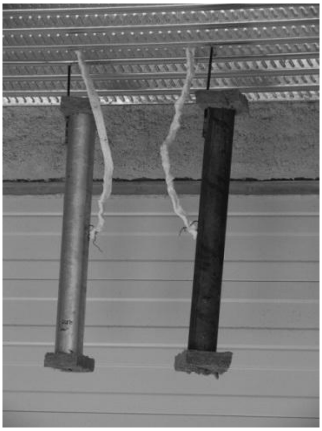 (b) 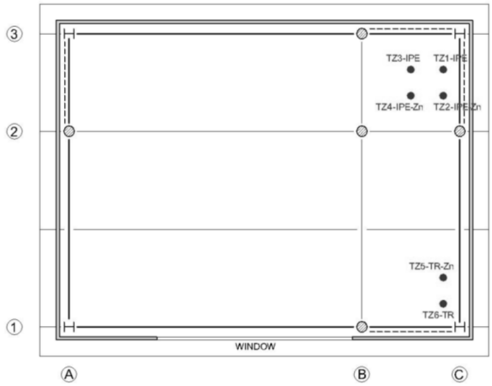

Figure 3. Specimens a) under the ceiling of the compartment b) location of specimens in the compartment.

For specimens were used open and closed cross-sections, length 1 m. First half of specimens was done without surfacing - samples TZ1 - IPE, TZ3 - IPE, TZ6 - TR and second half was galvanized - specimens TZ2 - IPE, TZ4 - IPE, TZ5 - TR. Technology of galvanizing for both IPE specimens was chosen identical. Galvanizing temperature reached 447 °C, average coating thickness 157.8 μm, max. 171.4 μm, min. 138,4 μm. It was used a conventional galvanizing bath without additional chemical elements such as Al, Pb, Bi, Sn, etc. A conventional bath was also for galvanizing of circular closed cross sections profile TR 114.3 × 4 used, temperature of galvanizing was 458 ℃, average thickness of the coating 110 μm.

2.2.1 Specimens' temperatures

Temperature of each specimen was measured by one 2 mm diameter thermocouple, which was placed at the half height of each specimen. The gas temperature at the fire compartment was measured by twenty 3 mm thermocouples and seven plate thermocouples.

Figure 4. Detail of surface of zinc coated member after fire.

2.2.2 Evaluation of the full scale fire test in Veseli nad Luznici

For evaluation was the same value of the resultant surface emissivity ε_{res} = 0.32 assumed. This was from results of the horizontal furnace fire test calculated.

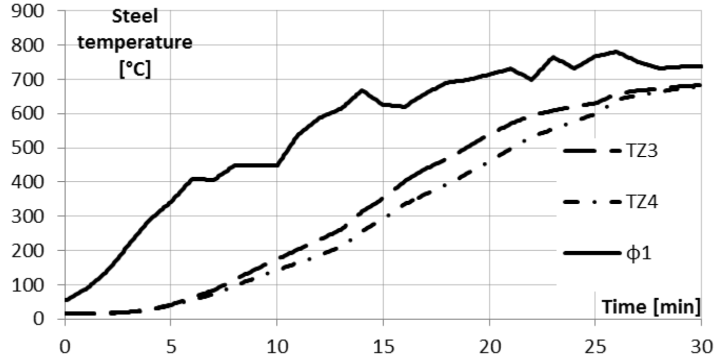

Figure 5. Comparison of gas temperature (ϕ1), measured temperature of zinc coated member (TZ4) and measured temperatures of the element without surfacing (TZ3) .

Table 2. Calculated surface emissivity of galvanized members.

Specimen	Surfacing	Surface emissivity
TZ2 - IPE	Zn	0,290
TZ4 - IPE	Zn	0,280
TZ5 - TR	Zn	0,400

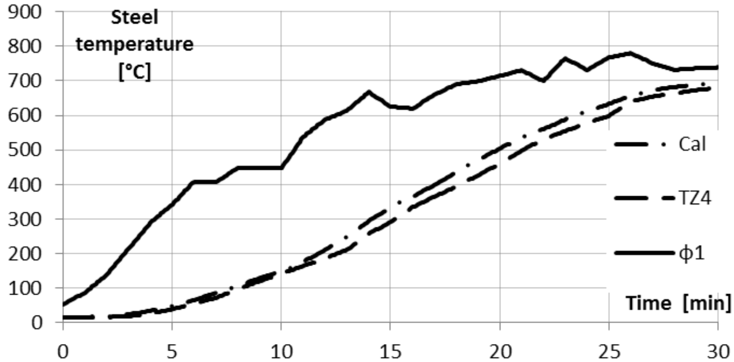

Figure 6. Comparison of gas temperature (ϕ1), measured and calculated (Cal) temperatures for zinc coated member (TZ4), for emissivity 0,32.

2.3 Fire test in the horizontal furnace 2011

The third fire test was at the horizontal furnace in 2011 performed. This fire test was exactly the same as the fire test in horizontal furnace in 2010 and was prepared for the purpose of verification of data, obtained in the previous fire tests.

For verification of the value of surface emissivity was already calculated value for emissivity of zinc coated members ε_{res} = 0.32 used. In the Figure 7 is good correlation between measured and calculated results especially in the first 20 mins of fire shown.

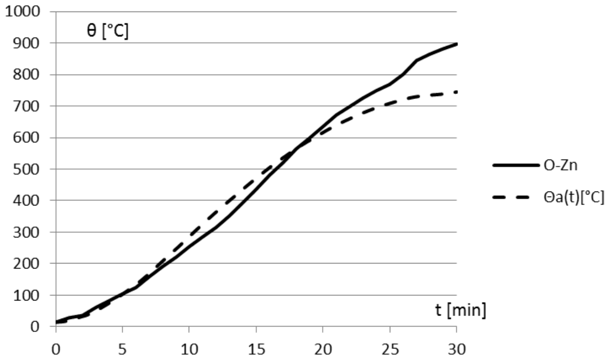

Figure 7. Comparison of measured (Θ_a) and calculated (O-Zn) temperatures for emissivity 0,32.

3 SIGNIFICANCE TO DESIGN

In this example was the beam, which is the part of ceiling in a shopping centre evaluated. The temperature and fire resistance, which was prescribed to R15, were compared.

3.1 Calculated beam description

The beam was by permanent g_k and live load q_k loaded. The span of the beam was 7.4 m. The class of used steel was S 235. Calculated beam is shown in Figure 8.

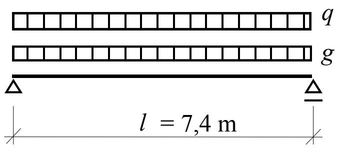

Figure 8. Calculated beam.

3.2 Design process

The design in normal temperature got cross section of this beam. It was used beam IPE 300 with concrete desk on the upper flange. The fire design was by the method of critical temperature calculated. The critical temperature $\theta_{a,cr}$ for this beam was calculated as follows:

$$\mu_0 = \frac{E_{fi,d}}{R_{fi,d}} = \frac{M_{fi,d}}{M_{fi,Rd,d}} = \frac{83{,}3}{147{,}7} = 0{,}563 \tag{7}$$

$$\theta_{a,cr} = 39{,}19 \ln\left[\frac{1}{0{,}9674\,\mu_0^{3{,}833}} - 1\right] + 482 = 39{,}19 \ln\left[\frac{1}{0{,}96740{,}563^{3{,}833}} - 1\right] + 482 \tag{8}$$

$$\theta_{a,cr} = 565{,}2°C$$

For calculation of temperature of the steel members was step by step method used. The resultant emissivity of steel member ε_{res} = 0.7 for beam without any surfacing was used. Calculated temperature in 15th min was 618 °C. In the case of reduced emissivity for zinc coated member ε_{res} = 0.32, the temperature of steel member in 15th min only 500 °C was obtained. Member without any surfacing would collapse and beam with zinc coated surface would resist until 17th min of fire. In Figure 9 are differences in temperatures of zinc coated member and member without any surface finishing compared.

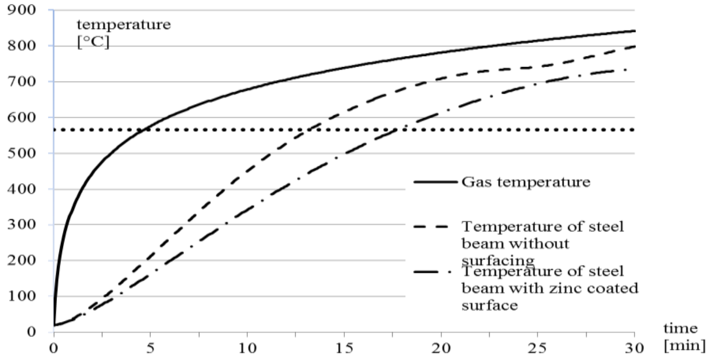

Figure 9. Calculation of temperatures of steel members with and without surfacing.

4 CONCLUSIONS

The fire tests were performed for specification of the value of surface emissivity. This value was in the first fire test specified, in next two tests were than verified obtained results.

Calculated value for resultant emissivity of zinc coated members in fire is 0.32. In the figures above good correlation between measured and calculated results especially in the first 20 mins of fire is shown.

Solved example shows improving of fire resistance of steel structure thanks to reduction of the steel members ´surface emissivity.

ACKNOWLEDGEMENT

This contribution was thanks to support of grant SGS14/037/OHK1/1T/11, *Energy efficient design of hybrid structures ´fire resistance* prepared.

REFERENCES

[1] EN 1993-1-2, *Eurocode 3: Design of Steel Structure, part 1.2: General Rules – Structural Fire Design,* British Standards Institution, London, 2005.

[2] EN 1991-1-2, *Eurocode 1: Actions on Structures, Part 1.2: General Actions - Actions on Structures Exposed to Fire,* British Standards Institution, London 2002.

[3] Jirků J., Wald F., Jandera M., *Increase of the fire resistance by galvanizing, Proceedings: 17th Hot Dip Galvanizing Conference*. Ostrava, 2011, 99-107.

[4] Wang, Y.C. *An introduction to heat transfer, Steel and Composite structures*. London : Spon Press, 2002.

[5] Gjoel, J. I.: *A New Approach to Modeling Heat Transfer in Compartment Fires. Fire Safety Journal*, vol.31, 1998, 227-237.

[6] Heinisuo, M. *Effect of zinc coating to the resistance of WQ-beam bottom flange in fire*. Tampere, 2011.

EXPERIMENTAL INVESTIGATION OF TIME- AND TEMPERATURE-DEPENDENT STABILITY OF STEEL COLUMNS IN FIRE

Mohammed A. Morovat*, Michael D. Engelhardt*, Todd A. Helwig* and Eric M. Taleff**

* Ferguson Structural Engineering Laboratory, Department of Civil, Architectural and Environmental Engineering, The University of Texas at Austin
e-mails: morovatma@mail.utexas.edu, mde@mail.utexas.edu, thelwig@mail.utexas.edu

** Department of Mechanical Engineering, The University of Texas at Austin
e-mail: taleff@mail.utexas.edu

Keywords: Column stability, ASTM A992 Steel, Thermal creep, Fire, Elevated temperatures

Abstract. *This paper describes the problem of creep buckling that arises when structural steel columns are exposed to fire temperatures. Experimental evidence is presented to show the effect of thermal creep of structural steel on the buckling capacity of steel columns at 600 °C. Analytical and computational predictions of the time-dependent buckling of steel columns subjected to fire are also presented and evaluated against expremintal results. Both analytical and computational methods utilize material creep models for ASTM A992 steel developed by the authors. Predictions from this study are also compared with those from Eurocode 3 and the AISC Specification. Results from presented work clearly show that buckling of steel columns at elevated temperatures is highly time-dependent.*

1 INTRODUCTION

The ability of steel columns to carry their design loads is greatly affected by time- and temperature-dependent mechanical properties of steel at high temperatures due to fire. It is well known that structural steel loses strength and stiffness with temperature, especially at temperatures above 400 °C. Further, the reductions in strength of steel are also dependent on the duration of exposure to elevated temperatures. The time-dependent response or creep of steel plays a particularly important role in predicting the collapse load of steel columns subjected to fire temperatures. Specifically, creep of steel leads to the creep buckling phenomenon, where the critical buckling load for a steel column depends not only on slenderness and temperature, but also on duration of applied load.

This paper presents highlights of an extensive testing program underway by the authors to investigate the effects of time-dependent material behavior or creep on buckling of steel columns subjected to fire. Material characterization tests have been conducted at temperatures up to 1000 °C to evaluate tensile and creep properties of ASTM A992 steel at elevated temperatures. In addition, buckling tests on W4×13 wide flange columns under pin-end conditions are conducted to characterize short-time and creep buckling loads at elevated temperatures. The column test results are further used to verify analytical and computational tools developed by the authors to model the time-dependent buckling of steel columns at elevated temperatures. Test results are also compared against code-based predictions from Eurocode 3 and the AISC Specification.

2 STRUCTURAL STEEL AT ELEVATED TEMPERATURES

As already mentioned, mechanical properties and stress-strain behavior of structural steel undergo significant changes under elevated-temperature conditions. Since the stress-strain curve used for analysis of column buckling is expected to have a significant impact on the column strength predictions, the temperature- and time-dependent behavior of structural steel at elevated temperatures is briefly discussed in this section. The emphasis will be on ASTM A992 steel since this is the steel used in the reported column buckling tests.

2.1 Fundamental time-and temperature-dependent behavior of structural steel

The general terms creep and time-dependent behavior of steel refer to progressive deformation of steel in response to stress and temperature. To characterize the creep of steel at elevated temperatures, creep tests are usually conducted by subjecting a steel specimen to constant load in tension, hence constant engineering stress at a specific temperature, and then measuring engineering strain as a function of time. A typical creep curve for structural steel is often divided into the three stages of primary, secondary and tertiary creep. In the primary stage, the curve is nonlinear and typically exhibits a decreasing creep strain rate with increase in time. In the secondary stage, the creep strain rate is almost constant, and this stage is often referred to as steady-state creep. In the tertiary stage, the creep strain rate increases with time in an unstable manner. It is important to note that, for structural steel, the shape of the creep curve, the magnitude of the creep strains and the time scale are greatly affected by both the temperature and the stress level.

As will be shown later, thermal creep of structural steel becomes significant within the time, temperature, and stress regimes expected in a building fire. In addition, creep tests provide data that can be used directly to account for the time-dependent behavior of structural steel at high temperatures. More specifically, as a result of conducting creep tests, creep can be considered explicitly in analysis of steel structures for fire effects.

2.2 Background research

Understanding and characterizing the behavior of structural steel at elevated temperatures have been the subjects of significant research efforts [1-5]. A careful examination of literature on structural steel at high temperatures reveals that there has been some recognition of the effect of creep on the stress-strain behavior of structural steel at elevated temperatures for fire applications [1-3]. In fact, research efforts focused on evaluating the effects of loading-rate and heating-rate on the behavior of structural steel at elevated temperatures should be viewed as attempts to implicitly consider the time-dependent or creep response of structural steel. Along with these efforts, some researchers tried to explicitly model and characterize the time-dependent behavior of constructional steel by conducting the conventional high-temperature creep tests [3-5]. Creep tests and their significance in predicting the time-dependent behavior of structural steel for fire design applications are discussed in the following sections and emphasized throughout the paper.

2.3 Time-and temperature-dependent behavior of ASTM A992 steel

In this section, representative results of a comprehensive set of tensile and creep experiments on ASTM A992 steel at elevated temperatures are presented and discussed to further emphasize the significance of creep and application of creep tests in predicting the stress-strain behavior of structural steel for fire design applications.

2.3.1 Implicit thermal creep: loading-rates in tension tests

As mentioned earlier, time-dependent effects on stress-strain behavior of structural steel can be investigated in a tension test run at different displacement or strain rates. Sample results of such tests on ASTM A992 steel (web materials from W30×99 section, F_y = 62 ksi) are presented in figure 1, where stress-strain curves are compared at cross-head displacement rates of 0.01 and 0.1 in./min and at 600 and 700 ℃. It should be pointed out that tests reported in figure 1 were conducted in steady-state temperature conditions, in which the specimens were heated up to a specified temperature and then loaded to failure while maintaining the same temperature. During the initial heating process, the load was maintained at zero to allow free expansion of the specimen. More details on tension tests on ASTM A992 steel at elevated temperatures can be found in previous publications by the authors [1, 4].

As can be seen in figure 1, for the considered temperatures, a displacement rate of 0.1 in./min results in yield and tensile strengths, which are 30 to 40% higher than those obtained at 0.01 in./min. The significant change in mechanical properties as a result of change in loading rates, as observed in figure 1, is an indication of creep of structural steel at elevated temperatures. However, quantifying the amount of creep represented in stress-strain curves shown in figure 1 is a formidable task. As a result, curves plotted in figure 1 are implicit indications of the effect of creep on stress-strain behavior of structural steel at high temperatures. Therefore, rate-dependent stress-strain curves may not be suitable for direct use in design applications where accurate predictions of the response at any specific time and temperature point in a fire environment is required. As will be shown in the following sections, conventional creep tests provide data that can potentially be utilized in such design applications.

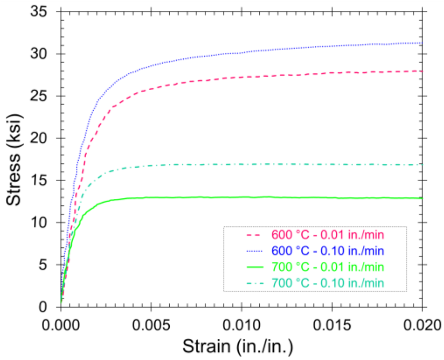

Figure 1. Stress-strain curves compared at two different cross-head displacement rates.

2.3.2 Explicit thermal creep: conventional creep tests

As explained previously and shown in other publications [1,3-5], conducting a conventional creep test is a more robust approach for characterization of the time-dependent behavior of structural steel at elevated temperatures with potential application to structural-fire engineering problems. An extensive series of high-temperature creep tests were performed on tension specimens of ASTM A992 steel. For these tests, the specimens were heated to the target temperature under no load. Load was then applied to the specimen, and held at a constant level, usually for a period of two hours. The initial application of the load, from zero to the target value was done rapidly, typically in less than 5 seconds, to minimize the influence of creep in the initial loading process. More details on tensile creep tests on ASTM A992 steel at elevated temperatures can be found in different publications by the authors [4, 6].

Representative results of creep tests on ASTM A992 steel are shown in figure 2 for materials from the flanges of the W4×13 section (F_y = 50 ksi). This figure simply shows the measured creep strain versus time response of ASTM A992 steel after being exposed to specified constant stresses at 600 ℃ and 700 ℃. As can be observed from Figure 2, it is clear that creep effects are highly significant at temperatures on the order of 600 ℃ to 700 ℃; temperatures that can be expected in steel members during a fire. It should be specifically noted that some of the curves in Figures 2(a) and 2(b) show very large creep strains in the time frame of one-hour, which may be considered a representative time frame for a compartment fire. Interestingly, the curve corresponding to the stress of 8.7 ksi at 700 ℃ enters the tertiary stage of creep in less than 10 minutes, with a rapid increase in creep strain over a short time interval.

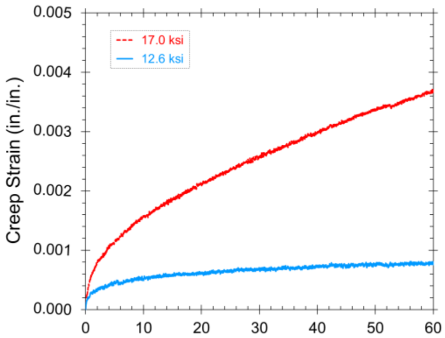

(a) 600 ℃.

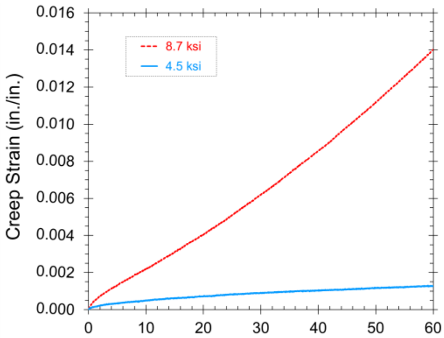

(b) 700 ℃.

Figure 2. Representative creep test results for the flange materials of W4×13 [4].

As part of the comprehensive material creep investigation of structural steel at elevated temperatures, constitutive equations have been developed to describe creep of ASTM A992 steel at elevated temperatures. One of these models is in the form of a normalized power-law, which is capable of modeling both primary and secondary creep. Equation 1 represents the general form of this creep model. Note that a strain hardening formulation has been utilized to better represent the creep behavior of structural steel under variable stress conditions (stress redistribution in structural members).

$$\frac{d\varepsilon_c}{dt} = \frac{1}{\tau}\left(\frac{\sigma}{\sigma_u}\right)^m (\varepsilon_c)^{-\mu} \tag{1}$$

In this equation, ε_c is creep strain and σ is stress. The parameters m, μ, τ and σ_u are temperature-dependent material properties. The quantity σ_u is the ultimate stress of steel at the temperature in consideration, and μ is strain-hardening exponent. The quantity τ has a unit of time and introduced in equation 1 as a result of stress normalization. The term $(1/\tau)$ in equation 1 is therefore an average constant creep rate corresponding to the ultimate stress, σ_u.

It should be emphasized that despite its simple form, the Norton-Bailey power-law creep has been shown to accurately represent the primary creep behavior of most steels for high-temperature industrial applications [4, 6]. By normalizing the stress term with respect to the ultimate stress at the temperature of interest, Equation 1 provides an improved accuracy of creep predictions in cases of high stresses and temperatures, cases that commonly occur in structural-fire applications. Moreover, since many structural-fire problems involve relatively rapid heating to very high temperatures, the early stages of creep can play a significant role in predicting the behavior of steel members and structures subjected to fire. Application of the model in equation 1 to predict creep buckling of steel columns will be presented and discussed in the following sections of this paper.

2.3.3 Implicit thermal creep: isochronous stress-strain representation

Constitutive equations for thermal creep of steel, like the one shown in Equation (1), are powerful tools for modeling the effect of creep explicitly in advanced analysis of steel structures subjected to fire. However, these constitutive models, expressing strain as a function of time at constant stress, are not suitable for simple calculations and routine design purposes. Representation of creep curves in the form of isochronous stress-strain curves provides a practical mean to implicitly consider time-dependent effects in analysis of steel members for fire conditions without the need for explicit creep calculations. Generally speaking, isochronous stress-strain curves are constant-time stress-strain curves derived from creep curves. In other words, isochronous stress-strain curves represent the effect of time on the stress-strain behavior of structural steel at elevated temperatures. The development of isochronous stress-strain curves from creep test data are explained in different publications by the authors [6-8]. Representative isochronous stress-strain curves based on equation 1 at 600 ℃ are shown here in figure 3. The application of isochronous stress-strain curves in creep buckling predictions will be discussed later in this paper.

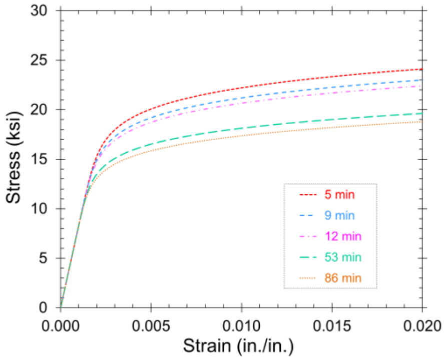

Figure 3. Representative isochronous stress-strain curves for ASTM A992 steel at 600 ℃.

3 STEEL COLUMNS AT ELEVATED TEMPERATURES

In this part of the paper, the concept of creep buckling is introduced and the influence of thermal creep of structural steel on the stability of steel columns exposed to fire temperatures is presented and discussed. The focus is on presenting some results of elevated-temperature buckling tests conducted on steel columns made of ASTM A992 steel, the most common grade of structural steel used in U.S. building construction practice.

3.1 Fundamental time-and temperature-dependent behavior of steel columns

The terms *creep buckling* and *time-dependent buckling*, as used herein, refer to the phenomenon in which the critical buckling load for a column depends not only on slenderness and temperature of the column, but also on the duration of applied load. Since creep effects are not significant at room temperature, the buckling load for a steel column of given effective slenderness KL/r at room temperature is independent of the duration of applied load. As temperature increases, the initial buckling load (at time zero) decreases, due to the decrease in material strength, modulus and proportional limit. Consequently, the buckling capacity at initial application of load depends only on temperature. But, as temperature increases and material creep becomes significant, the buckling load depends not only on temperature, but also on the duration of load application.

3.2 Background research

Several past analytical, computational and experimental studies have examined various aspects of column strength at elevated temperatures [6-10]. A comprehensive review of the literature on steel columns at high temperatures reveals that there has been some recognition of the effect of creep on the buckling behavior of steel columns at elevated temperatures [6-8, 10]. In fact, research focused on evaluating the effects of loading-rate and heating-rate on the strength of steel columns at elevated temperatures should be viewed as attempts to implicitly consider the effect of thermal creep on the buckling capacity of steel columns. It is important to note that there seems to be a lack of recognition that the fundamental behavior of steel columns at elevated temperatures is conceptually different from that at room temperature. More specifically, for a steel column exposed to fire, buckling may take place in a few minutes under loads considerably smaller than the critical load of the column at a particular temperature. Developing this fundamental understanding led some researchers in the past to conduct creep buckling tests on steel columns at elevated temperatures [10].

3.3 Buckling tests on ASTM A992 steel columns

This section provides some details of the experimental column buckling studies conducted at the University of Texas at Austin - Ferguson Structural Engineering Laboratory. The aim of the testing program was to evaluate the effect of creep and loading rate on the overall load-carrying capacity of ASTM A992 steel columns at elevated temperatures. A complete account of the column buckling test program will be reported in an upcoming publication by Morovat [6].

3.3.1 Equipment, specimens and the test set-up

An extensive series of buckling tests were conducted on W4×13 pin-ended columns that were 51-inches in length and made of ASTM A992 steel. Since buckling capacity of steel columns at high temperatures is very sensitive to the end restraints, as was shown, for example, by Furumura and Ave [10], a fixture consisting of knife-edges is designed to obtain pin-end conditions and to minimize the effect of friction in column tests. The knife-edges are made out of Viscount 44, a hardened tool steel with high yield strength, so that they can be used for several tests with negligible wear. In addition, care has been taken to eliminate load eccentricity in column buckling tests by careful alignment of the columns. Initial geometric imperfection of the column specimens and residual stresses are also measured [6].

A 550 kip (2500 kN) capacity MTS 311.41 test frame with water cooled wedges was used to conduct the tests. The heating system consisted of an electric furnace, the furnace temperature controller, and the data acquisition system for recording and monitoring column temperatures. An ATS split box furnace with 54 in. × 26.5 in. × 16.5 in. heated enclosure was used as the heating device. The furnace generates heat using electrical coils embedded in its walls, and is separated into upper, middle and lower heating zones that can be individually controlled using an ATS temperature controller. Three thermocouples are located inside the furnace to measure the furnace air temperature.

Figure 4. A column specimen after a buckling test at 600 ℃ along with the testing frame and furnace.

The testing frame and the split-box electrical furnace used in this research are illustrated in Figure 4. A representative column specimen following a buckling test at 600 ℃ also appears in Figure 4.

3.3.2 Testing procedure and results

All the column tests reported herein are steady-state temperature tests, in which columns are first heated to the target temperature under no load and then tested under uniform temperature conditions.

At each temperature, two types of tests were conducted as part of this research. The first series of elevated-temperature column buckling experiments conducted in this research are displacement-controlled tests. For these tests, the columns were first heated to the target temperature under no load. Once the column reached the target temperature, the load was increased until buckling. The peak load resisted by the column is referred to as the short-time buckling capacity. These tests are referred to herein as “Short-Time Buckling” tests. These tests were conducted using two different displacement-controlled loading rates: 0.01 in./min and 0.05 in./min. For example, at 600 ℃, the buckling capacity was 68-kips when loaded at 0.05 in./min, and was 63-kips when loaded at 0.01 in./min. Figure 5 shows the load-deflection curves corresponding to short-time buckling tests performed under two different displacement rates at 600 ℃. As can be seen clearly, the buckling capacity of the steel columns at high temperatures is quite sensitive to the loading rate, reflecting the creep behavior of steel at elevated temperatures.

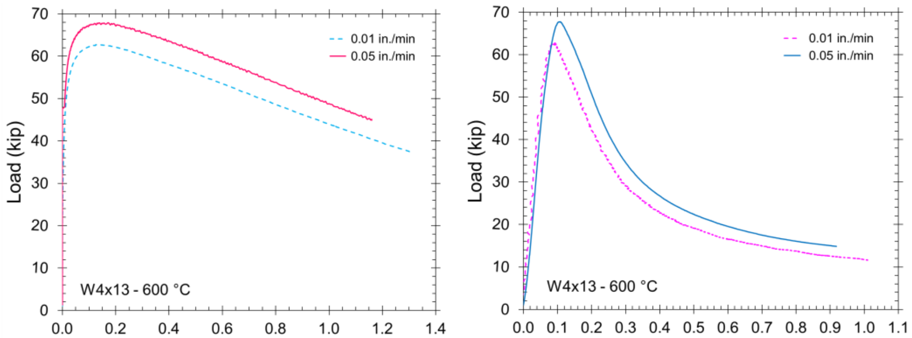

(a) Load vs. mid-height lateral deflection (b) Load vs. axial deflection

Figure 5. Rate effects on the buckling behavior of steel columns at elevated temperatures (W4×13, 51 in. long).

The second series of elevated-temperature column buckling experiments conducted in this research are force-controlled creep buckling tests. For these tests, the column was first heated to the target temperature under no load. A load was then applied to the column that was less than the "Short-Time Buckling" capacity. The load was held constant on the column, and the time to buckling was measured. In this paper, these tests are referred to as "Creep Buckling" tests. For example, at 600 ℃, when a load of 61 kips was applied to the column, the column buckled after 5 minutes. When a load of 54 kips was applied to the column, the column buckled after 85 minutes.

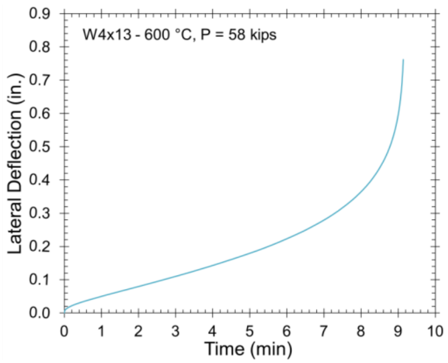

Figure 6. Mid-height lateral deflection as a function of time representing the creep buckling phenomenon at high temperatures (W4×13, 51 in. long).

The creep buckling phenomenon can be best visualized by plotting mid-height lateral deflection versus time curves, a sample of which is presented in Figure 6 for a creep buckling test under the applied load of 58 kips at 600 ℃. As can be seen, the rate of change of deflection with time increases very slowly at the beginning and then increases more rapidly until the column no longer can support its load. The time at which the displacement-time curve becomes nearly vertical represents the failure time. Figure 6 further depicts the highly time-dependent buckling behavior of steel columns at elevated temperatures.

3.4 Analytical and computational buckling predictions

In this section, analytical and computational procedures, developed previously by the authors [7, 8] to predict buckling capacity of steel columns at elevated temperatures are compared against experimental results to further evaluate the accuracy of their predictions.

3.4.1 Analytical and computational creep buckling procedures

As explained in previous publications [7, 8], for the analytical creep buckling studies, the concept of time-dependent tangent modulus proposed by Shanley [7, 8] is utilized, along with the creep material models developed in this study for ASTM A992 steel and shown in equation 1. This analytical method basically uses the Euler buckling equation and replaces Young's Modulus, E, with the tangent modulus, E_T, which is a function of time, stress and temperature. In order to calculate the time-dependent tangent modulus, the isochronous stress-strain curves need to be constructed.

Computational predictions of creep buckling are developed using Abaqus [7, 8]. In order to simulate creep buckling on Abaqus, first, temperature is increased to the desired level, and then a fraction of the zero-time buckling load is applied to the column. No material creep is considered in these two steps. Next, the column is allowed to creep over the time period of 50 hours under the sustained load. Finally, the time-to-buckle due to creep is estimated. It should be pointed out here that to get the zero-time buckling load, an inelastic load-deflection analysis has to be performed. This has been done in Abaqus by using a nonlinear analysis scheme called Riks Analysis. Moreover, to model initial geometric imperfections, an Eigen-value buckling analysis is performed. The initial shape of the column is taken as the shape of the first buckling mode, and the magnitude of the imperfection is chosen as a fraction of the column length. As far as material modeling is concerned, the inelastic material model at elevated temperatures is defined using the fast tension tests conducted in this research study, and the creep material model is that presented in equation 1 and explained in the previous section. 3D hexahedral eight-node linear brick elements, C3D8R, have been utilized to model the columns on Abaqus.

3.4.2 Comparison with experiments

Column buckling predictions from analytical and computational procedures are compared with test results at 600 ℃ and presented in figure 7. The analytical predictions are for a perfect column, while the computational one is for a column with initial crookedness of Δ_o = 0.005 in. Before making any observations on Figure 7, one should be aware of inherent uncertainties with regards to the predictions in this figure. Uncertainties in material creep behavior and model are major issues to be noted. Further, the fact that the presented experimental data are obtained from different column specimens from the same heat of steel but with different initial imperfections is another source of uncertainty in the results. Regardless of these uncertainties, several important observations can still be made on figure 7. First, for higher values of buckling load, the column does not actually deform very much before buckling takes place (the growth of initial bow due to creep is not that significant). Therefore, analytical solutions representing perfect columns are in better agreement with test results. On the other hand, under the application of lower buckling loads, columns deform significantly at the onset of buckling making predictions from the analytical approach to be conservative. Second, reasonable agreement can be observed between computational predictions and test results. This agreement implies that with a simple power-law creep (shown in equation 1 and mainly suitable for modeling primary creep), column buckling behavior can be captured reasonably accurately.

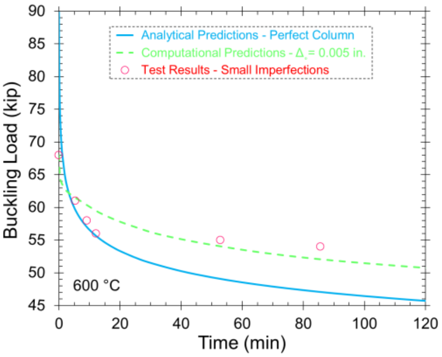

Figure 7. Evaluation of analytical and computational predictions against test results at 600 ℃.

The results of experimental buckling program shown in Figure 7 are also listed in Table 1. The experimental data shown in Table 1 further demonstrate that buckling of steel columns at elevated temperatures is *highly time-dependent*. For example, at 600 ℃, measured column capacities for the same W4×13 ASTM A992 section varied from 54 kips to 68 kips, depending on the rate and duration of load application. Also listed in Table 1 are column capacities predicted with Abaqus, using the stress-strain curves developed in this study, for various amounts of initial geometric imperfections. Three levels of imperfection were considered. Δ_o = 0.051 in. corresponds to L/1000, Δ_o = 0.005 and 0.010 in. reflect the actual estimated imperfections of the test columns. The Abaqus simulations did not explicitly model time-dependent material response. Note that all of the Abaqus predictions of short-time buckling strengths are in good agreement with corresponding experimental values. Similar tests and analyses were also conducted for this column at temperatures of 650 °C and 700 °C, and will be reported in an upcoming publication by Morovat [6].

Table 1. Predictions of Buckling Strengths of 51 in. W4×13 Columns at 600 ℃.

P_{cr} (kip)									
Abaqus Predictions			Buckling Test Results						
Δ_o (in.)			Short-Time Buckling		Creep Buckling				
0.005	0.010	0.051	Rate (in./min)		Time-to-Buckling (min)				
68.0	65.0	62.0	0.01	0.05	5	9	12	53	85
			63.0	67.8	61.0	58.0	56.0	55.0	54.0

4 TREATMENT OF HIGH-TEMPERATURE BUCKLING IN DESIGN CODES

In this section results obtained from creep buckling tests will be compared with the corresponding elevated-temperature column strength predictions of AISC [12] and Eurocode 3 [11].

Measured buckling capacities corresponding to buckling times in the range of 5 to 85 minutes at 600 ℃ (table 1) are plotted in figure 8(a). Creep buckling predictions from buckling tests at 700 ℃ are also shown in figure 8(b). Buckling capacities from buckling tests at 700 ℃ correspond to buckling times in the range of 10 to 133 minutes. For comparison, buckling predictions for the W4×13 section are also presented using both Eurocode 3 [11] and using AISC [12].

As can be observed in figure 8, although both the Eurocode 3 [11] and AISC [12] predict column strength as a function of temperature, and do not consider duration of load and temperature exposure (i.e., they do not explicitly consider creep buckling effects), their predictions for the buckling capacity of the column in consideration, with KL/r of 51-inches and temperatures of 600 and 700 ℃, are conservative (in case of Eurocode 3 for buckling times less than 60 minutes at 700 ℃). This observation, however, should not be construed to suggest that the code-based predictions of column buckling will generally be conservative. It should be specifically noted that the column specimens in this study had very small geometric imperfections (in the order of *L*/5000), while the initial crookedness of typical steel columns are in the order of *L*/1000. Since creep buckling of steel columns is sensitive to the magnitude of initial imperfections, predictions from design codes might not be conservative for some temperatures and slenderness ratios [6-8].

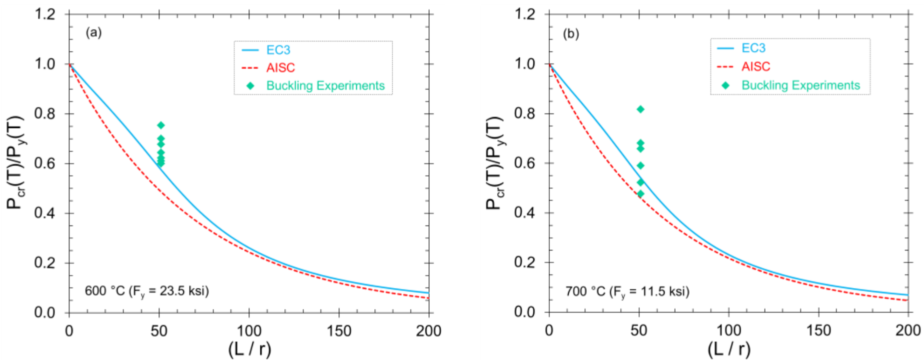

Figure 8. Comparison of experimental creep buckling predictions with code-based buckling estimates.

5 CONCLUSIONS

The analyses and experiments presented in this paper are still preliminary and limited in scope, and therefore do not yet support any broad conclusions. However, a key point is that the experiments clearly indicate that time-dependent material response (creep) has a very large effect on column strength at elevated temperatures. As a result, any predictions of column capacity using finite-element analyses that do not explicitly include time-dependent material response should be viewed with considerable caution.

Results of this work clearly indicate that thermal creep of steel has a very large effect on strength of steel columns at high temperatures due to fire. Therefore, any predictions of column capacity using code-based equations that do not explicitly include time-dependent response of structural steel should be viewed with caution.

ACKNOWLEGEMENTS

The research reported herein was conducted as part of a research project on *Creep Buckling of Steel Columns Subjected to Fire* supported by the National Science Foundation (NSF Award 0927819). The support of the National Science Foundation and of the former NSF Program Director M.P. Singh is gratefully acknowledged. The authors also gratefully acknowledge Gerdau-Ameristeel for donating materials for this research. The authors thank Matthew Gomez of Gerdau-Ameristeel for his support of this research.

REFERENCES

[1] Lee J., Morovat M.A., Hu G., Engelhardt M.D. and Taleff E.M., "Experimental Investigation of Mechanical Properties of ASTM A992 Steel at Elevated Temperatures", AISC *Engineering Journal*, 50(4), 249-272, 2013.

[2] Cooke G.M.E., "An Introduction to Mechanical Properties of Structural Steel at Elevated Temperatures", *Fire Safety Journal*, 13(1), 45-54, 1988.

[3] Harmathy T.Z. and Stanzak, W.W., "Elevated-Temperature Tensile and Creep Properties of Some Structural and Prestressing Steels", *Fire Test Performance, ASTM STP 464*, American Society for Testing and Materials, 186-208, 1970.

[4] Morovat M.A., Lee J., Engelhardt M.D., Taleff E.M., Helwig T.A. and Segrest V.A., "Creep Properties of ASTM A992 Steel at Elevated Temperatures", *Advanced Materials Research*, 446-449, 786-792, 2012.

[5] Fujimoto M., Furumura F. and Ave T., "Primary Creep of Structural Steel (SM50A) at High Temperatures", *Trans. of Architectural Institute of Japan*, 306, 148-156, 1981.

[6] Morovat M.A., *Creep Buckling of Steel Columns Subjected to Fire*, Ph.D. Dissertation, Department of Civil, Architectural and Environmental Engineering, The University of Texas at Austin, 2014.

[7] Morovat M.A., Engelhardt M.D., Taleff E.M. and Helwig T.A., "Importance of Time-Dependent Material Behavior in Predicting Strength of Steel Columns Exposed to Fire", *Applied Mechanics and Materials*, 82, 350-355, 2011.

[8] Morovat M.A., Engelhardt M.D., Helwig T.A. and Taleff E.M., "Influence of Creep on the Stability of Steel Columns Subjected to Fire", *Proceedings of the Annual Stability Conference*, St. Louis, Missouri, April 16-20, 2013.

[9] Ali F., Mcdonagh J., Nadjai A. and Talamona D., "Effect of Severe Fire on Performance of Steel Columns", *Journal of Applied Fire Science*, 12(1), 55-64, 2004.

[10] Furumura F., Ave T. and Kim W.J., "Creep Buckling of Steel Columns at High Temperatures", *Trans. of Architectural Institute of Japan*, 361, 142-151, 1986.

[11] Eurocode 3, *Design of Steel Structures. Part 1-2: General rules. Structural Fire Design*, EN 1993-1-2 European Committee for Standardization, CEN, 2006.

[12] American Institute of Steel Construction (AISC), *Specification for Structural Steel Buildings*, Standard ANSI/AISC 360-11, Chicago, 2011.

8th International Conference on Structures in Fire
Guo-Qiang LI, Venkatesh K. R. KODUR, Shou-Chao JIANG, Jian JIANG, Su-Wen CHEN, Guo-Biao LOU (Eds.)
Shanghai, China, June 11-13, 2014

ANALYSING BRAZILIAN AND EUROPEAN EXISTING METHODOLOGIES FOR FIRE DESIGN OF COMPRESSED COLD FORMED STEEL MEMBERS

Saulo J. C. Almeida*, João Paulo C. Rodrigues, Jorge M. Neto* and Luis M. Laim****

*Engineering School of São Carlos, University of São Paulo, Brazil, saulojca@sc.usp.br, jmunaiar@sc.usp.br

**University of Coimbra, Portugal; jpaulocr@dec.uc.pt, luislaim@hotmail.com

Keywords: Cold formed steel, Column, Fire, Restraining, Design

Abstract. *This paper presents the results from the comparative analysis between design and experimental ultimate loads at high temperatures obtained for compressed cold-formed steel members. In this study were evaluated the design methods of the Eurocode 3 Part 1.2 (2005) and NBR 14323:2013 as well as the Eurocode 3 Part 1.3 (2006) changing the steel mechanical properties in function of the temperature. The test results were provided from an experimental investigation on cold formed steel columns subjected to fire with restraining to the thermal elongation. From the results it has been observed that the design methods requires adjusts in order to prescribe with good accuracy the ultimate load capacity for cold formed steel columns at high temperatures. Furthermore, only considering the degradation of the steel properties with the temperature is not sufficient for an accurate design methodology.*

1 INTRODUCTION

The strength calculations of cold formed steel (CFS) members are carried out at several levels of complexity depending on the purpose of its use. For the standard design of compression members at ambient temperature the Effective Width Method (EWM) and the recently developed Direct Strength Method (DSM) [1] may be applied. The EWM is formally available in the Eurocode 3, Parts 1.3 and 1.5 [2 and 3] and in the North American Specification [4], whereas the DSM is available in the Appendix 1 of the North American Specification [5] and the Australia/ New Zealand Standard [6].

When it comes to fire, the design rules are commonly based on past research on hot-rolled steel members. These design guidelines are usually used for CFS members at elevated temperatures by using the same design guidelines for CFS members at ambient temperature and replacing the mechanical properties of steel at ambient temperature with the respective reduced mechanical properties at elevated temperatures, as it is established in the Brazilian Standards [7]. To make matters worse, EN1993-1.2 [8] recommends a limit of 350 ºC for the maximum temperature of members with class 4 cross-sections, which seems to be overly conservative [9, 10 and 11]. However, the Annex E of the EN1993-1.2 [8] allows using the design guidelines developed based on hot-rolled steel members for CFS members at elevated temperatures, but the area of the member cross-section must be replaced by the effective area and the section modulus by the effective section modulus, determined in accordance with EN1993-1-3 [2] and EN 1993-1-5 [3], i.e. based on the material properties at ambient temperature. Besides, the mechanical characteristics (0.2% yield strength) of hot-rolled steel and CSF members must be different.

Therefore, it is the objective of this work to investigate the accuracy of the current design guidelines for CFS compression members under uniform fire conditions. Finally, to accomplish this goal, a series of experimental tests was performed on CFS columns with different boundary conditions and with restrained thermal elongation. These results were thereby compared with the predictions from different currently available design rules (NBR 14323 [7] and EN1993-1.2 [8]) and modified design methods (EN1993-1.2 [8] and EN1993-1.3 [2]), in order to observe if there are safe and consistent regulations for fire design of these members.

2 EXPERIMENTAL STUDY

Figure 1 shows the test set up of the experimental tests performed at the Laboratory Testing of Materials and Structures of University of Coimbra (UC), in Portugal, on CFS columns [12]. As shown in figure 1, in the high temperature tests were taken into account the influence of the axial and rotational restraints on the columns behaviour. The columns had 3000 mm tall with C, I and 2R sections and were tested with fixed and pin-ended supports. The columns steel grade was the S280GD. The load applied in the tests was equal to 30% of the design value of the buckling load of the columns at room temperature determined according to EN1993 – 1.3 [2].

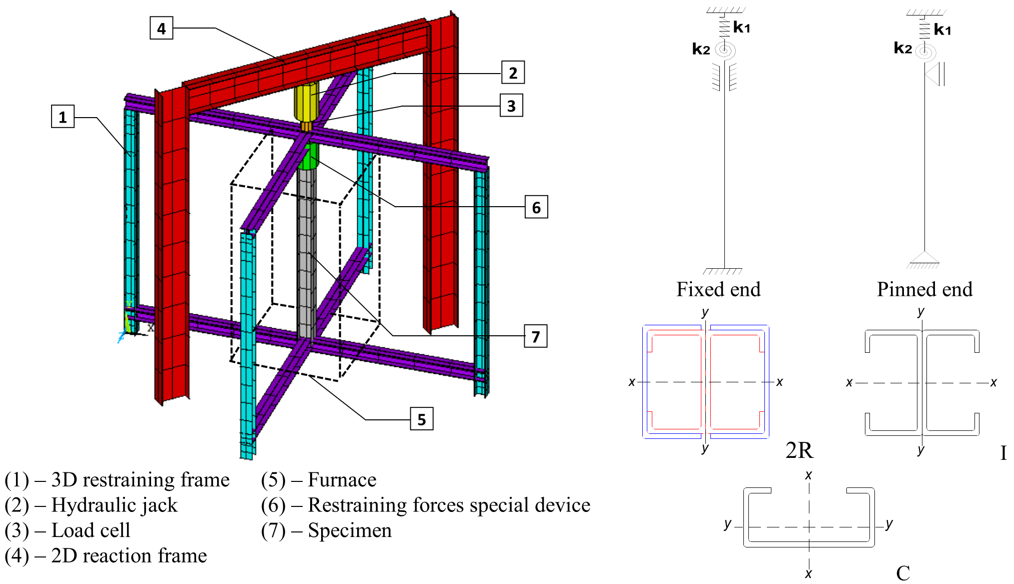

Figure 1. Test Set-up.

3 DESIGN METHODS

Table 1 show the resume for EN1993-1.2 and NBR 14323 design methods and table 2 the resume for EN1993-1.3 with the modification done in order to assess the use of this design code for fire design. In accordance with EN 1993-1.2 the resistance of members with class 4 cross section should be verified for axial compression ($N_{b,fi,t,Rd}$) and for bending and axial compression (equations 1 and 2). The effective area (A_{eff}) and effective section modulus (W_{eff}) should be obtained from EN 1993-1.3.

In accordance with NBR 14323 design code the fire resistance of compressed CFS members susceptible to local buckling is the smaller value between the fire resistance for global buckling and distortional buckling. The effective cross section area (A_{ef}) and the reduction factor for distortional buckling (χ_{dist}) in the fire design situation should be determined in accordance with Brazilian code NBR 14762 (2010) [13], i.e. based on the material properties at ambient temperature. Furthermore, the effective area should be determined for the cross section yielding limit state ($\sigma = f_y$) and global buckling limit state ($\sigma = \chi_{fi} f_y$), where σ is the maximum allowable compression stress.

The main difference between the EN1993-1.2 and NBR 14323 design methods are the effective area calculations and the non-dimensional slenderness for temperature θ, as shown in Table 1. The EN1993-1.2 takes into account the shift of the effective centroid which induces additional combined bending and compression verification in accordance with equations 1 and 2. Additionally, for sections susceptible to distortional buckling the EN1993-1.2 prescribes the distortional buckling resistance reducing the stiffeners effective area. On the other hand, NBR 14323 does not take into account the shift of the effective centroid and prescribes the distortional resistance applying a reduction factor for distortional buckling in fire design situation. Both design codes prescribe the fire resistance reducing the yield strength and young's modulus with the same reduction factors for temperature θ.

Table 1. Design methods for class 4 compressed members: *EN1993-1.2 and NBR 14323*.

Parameter	EN1993 – 1.2	NBR 14323
Design buckling resistance	$N_{b,fi,t,Rd} = \chi_{fi} A_{eff} k_{p0.2,\theta} f_y$	$N_{fi,Rd} = \chi_{fi} k_{\sigma,\theta} A_{ef} f_y$ *(Global Buckling)*
		$N_{fi,Rd} = \chi_{dist} k_{\sigma,\theta} A_g f_y$ *(Distortional Buckling)*
Reduction factor for flexural buckling in the fire design situation	$\chi_{fi} = \dfrac{1}{\varphi_\theta + \sqrt{\varphi_\theta^2 - \bar{\lambda}_\theta^2}}$	$\chi_{fi} = \dfrac{1}{\varphi_{0,fi} + \sqrt{\varphi_{0,fi}^2 - \lambda_{0,fi}^2}}$
	$\varphi_\theta = \dfrac{1}{2}(1 + \alpha\bar{\lambda}_\theta + \bar{\lambda}_\theta^2)$	$\varphi_{0,fi} = 0.5(1 + \alpha\lambda_{0,fi} + \lambda^2{}_{0,fi})$
Imperfection factor	$\alpha = 0.65\sqrt{235/f_y}$	$\alpha = 0.022\sqrt{\dfrac{E}{f_y}}$
Non-dimensional slenderness for temperature θ	$\bar{\lambda}_\theta = \bar{\lambda}[k_{p0.2,\theta}/k_{E,\theta}]^{0,5}$	$\lambda_{0,fi} = \dfrac{\lambda_0}{0.85}$
Non-dimensional slenderness for room temperature	$\bar{\lambda} = \dfrac{l_{fi}/i}{\pi\sqrt{\dfrac{E}{f_y}}}$	$\lambda_0 = \sqrt{\dfrac{A_g f_y}{N_e}} = \dfrac{l_{e,fi}/r}{\pi\sqrt{\dfrac{E}{f_y}}}$
Bending and axial compression	Equations (1) and (2)	Does not consider the shift of effective centroid

EN1993 – 1.2:
A_{eff}: effective area for room temperature
$K_{p0.2,\theta}$: reduction factor for yield strength
f_y: yield strength for room temperature
$K_{E\theta}$: reduction factor young modulus
L_{fi}: effective length for high temperature
i: gyration radius

NBR 14323:
A_{ef}: Effective area for room temperature
$k_{\sigma\theta}$: Reduction factor for yield strength
f_y: Yield strength for room temperature
A_g: Gross section area
χ_{dist}: Reduction factor for distortional buckling in the fire design situation
N_e: Buckling load
r: gyration radius

$$\frac{N_{fi,Ed}}{\chi_{\min,fi} A_{eff} k_{p0.2,\theta} \frac{f_y}{\gamma_{M,fi}}} + \frac{k_y M_{y,fi,Ed}}{W_{eff,y} k_{p0.2,\theta} \frac{f_y}{\gamma_{M,fi}}} + \frac{k_z M_{z,fi,Ed}}{W_{eff,z} k_{p0.2,\theta} \frac{f_y}{\gamma_{M,fi}}} \leq 1 \tag{1}$$

$$\frac{N_{fi,Ed}}{\chi_{z,fi} A_{eff} k_{p0.2,\theta} \frac{f_y}{\gamma_{M,fi}}} + \frac{k_{LT} M_{y,fi,Ed}}{\chi_{LT,fi} W_{eff,y} k_{p0.2,\theta} \frac{f_y}{\gamma_{M,fi}}} + \frac{k_z M_{z,fi,Ed}}{W_{eff,z} k_{p0.2,\theta} \frac{f_y}{\gamma_{M,fi}}} \leq 1 \tag{2}$$

In accordance with EN 1993-1.3 design method, a compressed cold formed steel member should verify the following limit states: (i) resistance of cross section (N_{CRd}), (ii) buckling resistance (N_{bRd}) (flexural buckling, torsional buckling and torsional-flexural buckling), combined compression and bending (cross section) and combined bending and axial compression (member), as shown in Table 2. In order to assess the EN1993-1.3 for fire design, it was used its design method reducing the material properties with the reduction factor for the young's modulus and yield strength and using the reduction factor for flexural buckling in fire design situation in accordance with EN1993-1.2, as shown in Table 2.

Table 2. Design methods resumes: *EN1993-1.3 and EN1993-1.3 modified.*

Parameter	EN1993 – 1.3 (room temperature)	EN1993 – 1.3 (modified)
$N_{C,Rd}$ and $N_{C,Rd,fi}$: design resistance of cross section for room temperature and fire design respectively.	$N_{C,Rd} = \frac{A_{eff} f_y}{\gamma_{M0}}$	$N_{C,Rd,fi} = \frac{A_{eff,fi} f_{y,fi}}{\gamma_{M0}}$
$N_{b,Rd}$ and $N_{b,Rd,fi}$: design buckling resistance for room temperature and fire design respectively.	$N_{b,Rd} = \frac{\chi A_{eff} f_y}{\gamma_{M0}}$	$N_{b,Rd,fi} = \frac{\chi_{fi} A_{eff,fi} f_{y,fi}}{\gamma_{M0}}$
χ and χ_{fi}: reduction factor for flexural buckling for room temperature and fire design respectively.	$\chi = \frac{1}{\Phi + \sqrt{\Phi^2 - \overline{\lambda}^2}}$	$\chi_{fi} = \frac{1}{\Phi_{fi} + \sqrt{\Phi_{fi}^2 - \overline{\lambda}_{fi}^2}}$
	$\Phi = \frac{1}{2}(1+\alpha(\overline{\lambda}-0,2)+\overline{\lambda}^2)$	$\Phi_{fi} = \frac{1}{2}(1+\alpha(\overline{\lambda}_{fi})+\overline{\lambda}_{fi}^2)$
α: imperfection factor	$a_0 \rightarrow \alpha = 0.13$ $a \rightarrow \alpha = 0.21$ $b \rightarrow \alpha = 0.34$ $c \rightarrow \alpha = 0.49$ $d \rightarrow \alpha = 0.76$	$\alpha = 0.65\sqrt{235/f_y}$
$\overline{\lambda}$ and $\overline{\lambda}_{fi}$: non-dimensional slenderness for room temperature and fire design respectively.	$\overline{\lambda} = \sqrt{\frac{A_{eff} f_y}{N_{cr}}}$	$\overline{\lambda}_{fi} = \sqrt{\frac{A_{eff,fi} f_{y,fi}}{N_{cr,fi}}}$

Table 2. Design methods resumes: *EN1993-1.3 and EN1993-1.3 modified (cont.).*

(combined compression and bending) (cross section)	$\left(\frac{N_{Ed,fi}}{N_{C,Rd,fi}}\right)^{0.8}+\left(\frac{M_{Ed,fi}}{M_{b,Rd,fi}}\right)^{0.8}\leq 1$	$\left(\frac{N_{Ed,fi}}{N_{C,Rd,fi}}\right)^{0.8}+\left(\frac{M_{Ed,fi}}{M_{b,Rd,fi}}\right)^{0.8}\leq 1$
(combined bending and axial compression) (member)	$\left(\frac{N_{Ed,fi}}{N_{b,Rd,fi}}\right)^{0.8}+\left(\frac{M_{Ed,fi}}{M_{b,Rd,fi}}\right)^{0.8}\leq 1$	$\left(\frac{N_{Ed,fi}}{N_{b,Rd,fi}}\right)^{0.8}+\left(\frac{M_{Ed,fi}}{M_{b,Rd,fi}}\right)^{0.8}\leq 1$

A_{eff} and $A_{eff,fi}$: Effective area for room temperature and fire design respectively
N_{ed} and $N_{ed,fi}$: Axial force for room temperature and fire design respectively
M_{Ed} and $M_{Ed,fi}$: Bending moment for room temperature and fire design respectively

Table 3 shows the critical temperature and the respective reduction factors for each column, which were obtained by linear interpolation. C-F, I-F and 2R-F are the columns with fixed ends and the C-P, I-P and 2R-P are the columns with pinned ends. In [14] were measured the yield strength and young's modulus at high temperature for tensile coupon tests with G250 steel grade and thickness of 1.55 mm. These steel properties are similar to the columns steel grade from the experimental tests carried out in [12]. Then, the reduction factors from [14] were used to assess the EN1993 – 1.2 design method.

Table 3. Reduction factors for yield strength and Young's modulus.

Section	Member	θ_{cr} (°C)	EN1993 – 1.2*		Kankanamge e Mahendran [14]	
			$K_{p0.2,\theta}$	$K_{E,\theta}$	$k_{\sigma,\theta}$	$K_{E,\theta}$
C-F	P01-F	435.05	0.608	0.665	0.433	0.546
	P02-F	383.48	0.671	0.717	0.516	0.627
I-F	P03-F	362.23	0.699	0.738	0.548	0.653
	P04-F	338.9	0.729	0.761	0.582	0.670
2R-F	P05-F	408.33	0.640	0.692	0.478	0.608
	P06-F	458.23	0.580	0.642	0.394	0.493
C-P	P07-P	251.95	0.833	0.848	0.782	0.740
	P08-P	261.2	0.823	0.839	0.754	0.732
I-P	P09-P	408.3	0.640	0.692	0.478	0.608
	P10-P	369.97	0.689	0.730	0.536	0.648
2R-P	P11-P	504.03	0.521	0.588	0.319	0.393
	P12-P	432.22	0.611	0.668	0.438	0.553

θ_{cr} – Critical temperature; * $K_{p0.2,\theta}$ and $k_{E,\theta}$: Equal for NBR 14323.
$k_{\sigma,\theta}$ and $k_{E,\theta}$ – Reduction factor for yield strength and young modulus respectively

4 RESULTS

Tables 4, 5, 6 and 7 present the experimental test, EN1993 – 1.2, NBR 14323 and EN1993 – 1.3 ultimate loads. The ultimate loads determined with the EN 1993-1.2 presented grate dispersion in relation to the experimental test results. Furthermore the results presented dependence of the boundary conditions. For instance, for I section with pinned ends the design ultimate loads were from the safe side. On the other hand, for I section with fixed ends the results were from the unsafe side. The best agreement between EN 1993-1.2 and tests ultimate loads was for members with C section, as shown in the Table 4.

Two additional analyses were carried out to assess the EN 1993-1.2 design method. In the first one the ultimate loads were obtained using the EN 1993-1.2 design method with the reduction factors determined in [14], as shown in Table 5. In accordance with Tables 4 and 5 (Exp/EC3* and Exp/N_{ER}^{a} results), the ultimate load determined with EN 1993-1.2 and the reduction factors from [14] keep better agreement with experimental test results. The second analysis was carried out using the reduction factors from [14] and changing the EN 1993-1.2 imperfection factor α, as shown in Table 5 (Exp/N_{ER}^{b} column). According to the results from these new analyses, using different imperfection factors for each cross section type improves the agreement between EN 1993-1.2 design method and experimental test results.

Table 4. Comparison between experimental and design ultimate loads: EN 1993-1.2.

Section (Member)		Time (min)	θ_{cr} (°C)	N_R(Exp) (kN)	$N_{c,R}$ (kN)	$N_{b,R}$ (kN)	N_{ER1} (kN)	N_{ER2} (kN)	Exp/ EC3*
C-F	P01	5.38	435.05	32.7	43.5	23.1	30.1	**14.7**	**2.22**
	P02	5.94	383.48	33.7	48.0	25.3	33.2	**16.0**	**2.11**
C-P	P07	5.06	251.95	15.3*	59.6	12.7	41.2	**9.0**	**1.70**
	P08	5.70	261.20	14.3*	58.9	12.6	40.7	**8.9**	**1.61**
I-F	P03	7.18	362.23	61.5	100.0	**61.9**	**---**	**---**	**0.99**
	P04	6.48	338.90	58.8	104.3	**64.3**	**---**	**---**	**0.91**
I-P	P09	8.45	408.30	38.5	91.6	**28.7**	**---**	**---**	**1.34**
	P10	7.27	369.97	40.7	98.6	**30.4**	**---**	**---**	**1.34**
2R-F	P05	7.67	408.33	75.0	155.1	**119.4**	**---**	**---**	**0.63**
	P06	8.10	458.23	75.8	140.5	**108.6**	**---**	**---**	**0.70**
2R-P	P11	11.93	504.03	70.8	126.2	**69.3**	**---**	**---**	**1.02**
	P12	13.40	432.22	77.0	148.0	**80.2**	**---**	**---**	**0.96**

N_{ER1}: Axial resistant force for combined compression and bending (cross section)
N_{ER2}: Axial resistant force for combined bending and axial compression (member)
*EC3 – Equal to N_{ER2} for members with C cross section
* For these tests the initial load was 60 % of the loadbearing capacity determined with EN1993 – 1.3

Table 5. Comparison: Experimental vs. design ultimate loads - *EN 1993-1.2* with $K_{\sigma,\theta}$ *e* $K_{E\theta}$ from [14].

Section (Member)		θ_{cr} (°C)	N_R(Exp) (kN)	N_{ER}^{a} (kN)	Exp/ N_{ER}^{a}	N_{ER}^{b} (kN)	Exp/ N_{ER}^{b}	Imperfection factor (α)
C-F	P01	435.05	32.7	12.0	2.72	16.4	1.99	$0.10\sqrt{235/f_y}$
	P02	383.48	33.7	14.2	2.37	19.4	1.74	
C-P	P07	251.95	15.3*	9.5	1.62	10.4	1.47	$0.40\sqrt{235/f_y}$
	P08	261.20	14.3*	9.3	1.54	10.0	1.42	
I-F	P03	362.23	61.5	50.3	1.22	40.1	1.53	$1.20\sqrt{235/f_y}$
	P04	338.90	58.8	52.9	1.11	42.1	1.40	
I-P	P09	408.30	38.5	23.9	1.61	26.8	1.44	$0.45\sqrt{235/f_y}$
	P10	369.97	40.7	25.9	1.57	29.0	1.40	
2R-F	P05	408.33	75.0	91.2	0.82	53.2	1.41	$3.00\sqrt{235/f_y}$
	P06	458.23	75.8	75.0	1.01	43.7	1.73	
2R-P	P11	504.03	70.8	43.9	1.61	38.9	1.82	$0.90\sqrt{235/f_y}$
	P12	432.22	77.0	60.8	1.27	53.9	1.43	

N_{ER}^{a}: Axial resistant force for EN 1993-1.2 with $K_{\sigma,\theta}$ e $K_{E\theta}$ from [14]
N_{ER}^{b}: Axial resistant force for EN 1993-1.2 with $K_{\sigma,\theta}$ e $K_{E\theta}$ from [14] and imperfection factor (α)

From Table 6, in general the NBR 14323 (2013) design method keeps agreement with the experimental test results. The NBR 14323 design method prescribed the ultimate load on the safe side for the C and I cross-sections, which are the more used in Brazil. Only for 2R section with fixed ends the NBR 14323 was not able to prescribe with accuracy the ultimate load. However it is possible that the NBR 14323 would not be able to prescribe the ultimate load for 2R section with pinned ends too. The test ultimate loads for 2R section with pinned and fixed ends were so similar which induce to conclude that the pinned columns did not develop any rotation in the boundaries during the tests and the ultimate load prescribed for NBR 14323 not corresponds to the real boundary condition for these members.

Table 6. Comparison between experimental and design ultimate loads: NBR 14323.

Section	Member	Time (min)	θ_{cr} (°C)	NR (Exp) (kN)	NR_L (kN)	NR_{Dist} (kN)	NR_G (kN)	Exp/ NR_G
C-F	P01	5.38	435.05	32.7	46.2	45.5	**19.0**	**1.72**
	P02	5.94	383.48	33.7	51.1	50.3	**20.9**	**1.61**
C-P	P07	5.06	251.95	15.3*	63.6	62.4	**10.2**	**1.50**
	P08	5.70	261.20	14.3*	62.6	61.6	**10.1**	**1.42**
I-F	P03	7.18	362.23	61.5	106.3	104.7	**54.4**	**1.13**
	P04	6.48	338.90	58.8	110.8	109.2	**56.7**	**1.04**
I-P	P09	8.45	408.30	38.5	97.3	95.9	**22.3**	**1.73**
	P10	7.27	369.97	40.7	104.7	103.2	**24.0**	**1.70**
2R-F	P05	7.67	408.33	75.0	162.5	183.6	**115.6**	**0.65**
	P06	8.10	458.23	75.8	147.3	166.4	**104.7**	**0.72**
2R-P	P11	11.93	504.03	70.8	132.3	149.5	**57.3**	**1.24**
	P12	13.40	432.22	77.0	155.2	175.3	**67.2**	**1.15**

NR_{Exp} – Experimental test ultimate load
NR_L, NR_{Dist} and NR_G: Ultimate load for local, distortional and global buckling respectively

Table 7. Comparison between experimental and design ultimate loads - *EN 1993-1.3* modified: EN 1993-1.3 design method changing the material properties with $K_{p0.2,\theta}$ *e* $K_{E\theta}$ and using the reduction factor for flexural buckling in accordance with EN1993-1.2.

Section (Member)		Time (min)	θ_{cr} (°C)	NR(Exp) (kN)	$N_{c,R}$ (kN)	$N_{b,R}$ (kN)	N_{ER1} (kN)	N_{ER2} (kN)	Exp/ EC3*
C-F	P01	5.38	435.05	32.7	48.0	24.5	35.4	**18.2**	**1.80**
	P02	5.94	383.48	33.7	51.9	26.4	37.8	**19.4**	**1.74**
C-P	P07	5.06	251.95	15.3*	61.7	12.8	43.7	**10.8**	**1.42**
	P08	5.70	261.20	14.3*	61.1	12.7	43.3	**10.7**	**1.34**
I-F	P03	7.18	362.23	61.5	107.3	**64.9**	**---**	**---**	**0.95**
	P04	6.48	338.90	58.8	110.9	**67.0**	**---**	**---**	**0.88**
I-P	P09	8.45	408.30	38.5	110.1	**29.4**	**---**	**---**	**1.31**
	P10	7.27	369.97	40.7	106.1	**31.1**	**---**	**---**	**1.31**
2R-F	P05	7.67	408.33	75.0	176.4	**133.1**	**---**	**---**	**0.56**
	P06	8.10	458.23	75.8	164.5	**124.1**	**---**	**---**	**0.61**
2R-P	P11	11.93	504.03	70.8	152.4	**77.2**	**---**	**---**	**0.92**
	P12	13.40	432.22	77.0	170.7	**87.0**	**---**	**---**	**0.89**

*EC3 – Equal to N_{ER2} for members with C cross section

Table 7 shows the results from the analysis carried out with the EN 1993-1.3 design method. According to Table 7 results, only members with C cross section keep good agreement between design and test results. The ultimate loads for members with I and 2R sections were totally on the unsafe side.

5 CONCLUSIONS

EN1993 – 1.2 design method requires adjusts for satisfactorily determine the ultimate load carrying capacity of the CFS columns in fire. In order to obtain accurate results with the actual EN 1993-1.2

design format it is important using different reduction factors for different classes of steel grades and different imperfection factors (α) for different cross sections. This work also showed that NBR 14323 design method is able to prescribe the ultimate of CFS members with I and C cross sections with good accuracy but needs improvements to compound the 2R sections. Finally, it was shown that EN1993-1.3 design method with modification was not able to prescribe the load carrying capacity of members with 2R section and I section with fixed ends for fire design. Nevertheless changes such as those aforementioned and suggested for EN 1993-1.2 make the NBR 14323 and EN 1993-1.3 suitable to prescribe the load carrying capacity in fire situation for all sections investigated.

ACKNOWLEDGEMENTS

The authors gratefully acknowledge to the Portuguese cold-formed steel profile maker PERFISA S.A. (www.perfisa.net), the Portuguese Foundation for Science and Technology – FCT (www.fct.mctes.pt), the São Paulo Research Foundation (FAPESP) and the Brazilian National Council for the Improvement of Higher Education (CAPES) for their supports.

REFERENCES

[1] Schafer B.W., “Review: The Direct Strength Method of cold-formed steel member design”, *Journal of Constructional Steel Research*, 64, 766-778, 2008.

[2] EN1993-1.3: Design of steel structures. General rules. Supplementary rules for cold-formed members and sheeting. European Committee for Standardization. Brussels, Belgium, 2004.

[3] EN1993-1-5: Eurocode 3: Design of steel structures, Part 1-5: Plated structural elements, European Committee for Standardisation, Brussels, Belgium, October 2006.

[4] AISI S100-1996: AISI specification for the design of cold-formed steel structures members. American Iron and Steel Institute, Washington (DC), USA; 1996.

[5] AISI S100-2004 - Appendix 1: Design of cold-formed steel structural members using the Direct Strength Method. In: 2004 supplement to the North American Specification for the design of cold-formed steel structures. American Iron and Steel Institute, Washington (DC), USA; 2004.

[6] Standards Australia, SA, AS/NZS 4600 Cold formed steel structures, Sydney, Australia, 1996.

[7] NBR 14323 - Structural fire design of steel and composite steel and concrete structures for buildings, Brazilian Association of Technical Standards (ABNT), Rio de Janeiro, 2013.

[8] EN1993-1.2: Design of steel structures. General rules. Structural fire design. European Committee for Standardization, Brussels, Belgium, April 2005.

[9] Kankanamge N.D., “Structural behaviour and design of cold-formed steel beams at elevated temperatures”, Ph.D. thesis, Queensland University of Technology, Brisbane, Australia, 2010.

[10] Lu W., Mäkeläinen P. and Outinen J. “Numerical simulation of catenary action in cold-formed steel sheeting in fire”, Journal of Structural Mechanics, 40 (3), 28-37, 2007.

[11] Laim L., Rodrigues J.P.C. and Silva L.S., “Experimental Analysis on Cold-Formed Steel Beams Subjected to Fire”, Thin-Walled Structures, 74, 104-117, 2014.

[12] Almeida S.J.C., Analysis on the behaviour of cold formed steel columns under fire conditions with restrained thermal elongation. PhD Thesis in Civil (University of Sao Paulo) and Fire Safety Engineering (University of Coimbra), 2012.

[13] NBR 14762 - Design of cold-formed steel structures, Brazilian Association of Technical Standards (ABNT), Rio de Janeiro, 2010.

[14] Kankanamge N.D., Mahendran M. “Mechanical properties of cold formed steels at elevated temperatures”, Thin-Walled Structures. 49: 26 – 44, 2011.

8th International Conference on Structures in Fire
Guo-Qiang LI, Venkatesh K. R. KODUR, Shou-Chao JIANG, Jian JIANG, Su-Wen CHEN, Guo-Biao LOU (Eds.)
Shanghai, China, June 11-13, 2014

MODELS FOR ANALYZING WEB SHEAR BUCKLING RESPONSE OF BRIDGE STEEL PLATE GIRDERS UNDER FIRE

Jonathan D. Glassman* and Maria E. M. Garlock*

* Department of Civil & Environmental Engineering, Princeton University
e-mails: jdglassm@princeton.edu, mgarlock@princeton.edu

Keywords: Web shear buckling, Strut-and-tie, Fire, Bridge, Postbuckling

Abstract. *Web shear buckling has been of interest to engineers since the late 1880s. Tension field theory was developed to compute the postbuckling shear strength of steel girder web plates. This paper proposes a strut-and-tie approach to calculate postbuckling shear strength that relies on the simultaneous development of tension and compression stresses in the web plate after elastic shear buckling has occurred. The proposed model has the potential to offer improved accuracy for computing the ultimate shear buckling strength at both ambient and elevated temperatures.*

1 INTRODUCTION

Joseph M. Wilson first documented postbuckling shear strength in stiffened plate girder webs when he noted in 1886 that the vertical stiffeners act like the posts of a Pratt truss, while the web carries the duty of handling the tensile stresses[1-3] [1, 2, 3]. In 1931, Herbert Wagner proposed what authors have referred to as the fundamental assumption: compressive stresses cease to increase in a web panel once elastic shear buckling has occurred, therefore any postbuckling shear strength is attributed to the formation of a diagonal tension field [2, 4].

Work carried out at Lehigh University over 50 years later is credited with developing the first tension field theory for practical design purposes by building upon Wilson's observations and Wagner's fundamental assumption. The postbuckling shear strength was presented as the summation of the elastic shear buckling strength plus strength contributions from diagonal tensile stresses that develop within a defined tension field. This tension field theory makes two key assumptions: (1) that the vertical stiffeners carry large axial forces from the tension field (as suggested by Wilson), and (2) that compressive stresses don't contribute to the postbuckling shear strength (as suggested by Wagner).

Numerical investigations carried out in the late 1980s and as recently as 2006 have found that both of the key assumptions of tension field theory are incorrect. The vertical stiffeners do not carry large axial loads that result from the development of diagonal tensile stresses within the tension field, and compressive stresses actually continue to increase into the postbuckling range[5-7] [2, 5, 6, 7].

The motivation for the work presented in this paper is to present a new approach to web shear buckling that accounts for the compressive load path. Previous work from the authors has found that the existing tension field theory does not always match with finite element results at elevated temperatures [8]. The new model proposed in this paper aims to address these observed discrepancies.

2 BACKGROUND

Konrad Basler proposed a tension field theory for steel plate girders that forms the basis of our current understanding of web shear buckling [9]. The American Association of State Highway

Transportation Officials (AASHTO) uses Basler's model as the basis for their design equations [10, 11]. The ultimate shear buckling stress, τ_u, is calculated as [3]:

$$\tau_u = \tau_{cr} + \sigma_{yw}\left(1 - \frac{\tau_{cr}}{\tau_{yw}}\right)\left(\frac{\sin\theta_d}{2 + \cos\theta_d}\right) \tag{1}$$

In Equation. (1), σ_{yw} is the yield stress of the web, τ_{yw} is the shear yield stress (calculated as $0.6\sigma_{yw}$), θ_d is the angle of the panel diagonal with respect to the flanges, and τ_{cr} is the elastic shear buckling stress, which can be calculated from the following equation [3, 12]:

$$\tau_{cr} = \frac{k\pi^2 E}{12\left(1 - \nu^2\right)\left(D/t_w\right)^2} \tag{2}$$

In Equation. (2), E is Young's modulus, v is Poisson's ratio, D/t_w is the slenderness ratio, and k is the shear buckling coefficient, which depends on the span-to-depth ratio, a/D, as well as the assumed boundary conditions. For a web plate that is simply supported on all four edges,

$$k = k_{ss} = 4.00 + \frac{5.34}{\left(a/D\right)^2} \text{ for } a/D < 1 \qquad k = k_{ss} = 5.34 + \frac{4.00}{\left(a/D\right)^2} \text{ for } a/D \geqslant 1 \tag{3}$$

The k values can also be calculated if a flange is explicitly considered [13], but since this paper focuses only on simply supported plates Equation. (3) is sufficient. Other shear buckling equations have been proposed [e.g. 13] but Equation. (1) represents that most widely used in current practice [11].

3 STRUT-AND-TIE MODEL

The proposed strut-and-tie model maps the complicated behavior of web shear buckling onto a simpler structural system of a compression strut that has increased strength due to the tension "tie" [14]. The components, kinematics, and equations that represent the model are discussed next.

3.1 The equivalent column

Figure 1(a) is a schematic for a web plate with a span between transverse stiffeners, a, depth, D, and diagonal length, L, in a state of pure shear stress, τ. The solid diagonal arrows represent the tensile stresses, while the dashed diagonal arrows represent the compressive stresses. In this schematic, both are idealized to be concentrated within diagonal bands labeled as either tension tie or compression strut.

Figure 1(b) is a rotated image of Figure 1(a) such that the compression strut is vertical and τ is replaced with the corresponding axial loads, P (in compression) and T (in tension). The equivalent column model is shown in the middle of the compression strut with a rigid bar where the tension tie crosses the column. This rigid bar is only assumed to fully form when $P=P_u$, the ultimate buckling load of the equivalent column.

Figures 1(c) and (d) show the equivalent column model for $P=P_{cr}$ and $P=P_u$, respectively, where P_{cr} is the elastic flexural buckling strength. In Figure 1(c), the equivalent column buckles as a pinned-pinned column. Once $P>P_{cr}$, however, the rigid bar begins to form, which represents additional stability provided by the formation of a tension field in the web. At $P=P_u$, the equivalent column has three distinct segments: a rigid bar segment of length w^{ST}, and two segments outside of w^{ST} with equal lengths of $L_r/2$.

3.2 Derivation of V_u

Figure 2 shows the relationship between P_{cr} and the critical shear bucking load, V_{cr}, for a simply supported plate, where $P_{cr} = V_{cr}$ (L/D). Allowing V_{cr} to equal Eqn. (2) multiplied by $D \cdot t_w$ and letting $k=k_{ss}$ (for a simply supported web plate) results in:

$$P_{cr} = \frac{k_{ss}\pi^2 E D t_w}{12\left(1-\nu^2\right)\left(D/t_w\right)^2}\frac{L}{D} \tag{4}$$

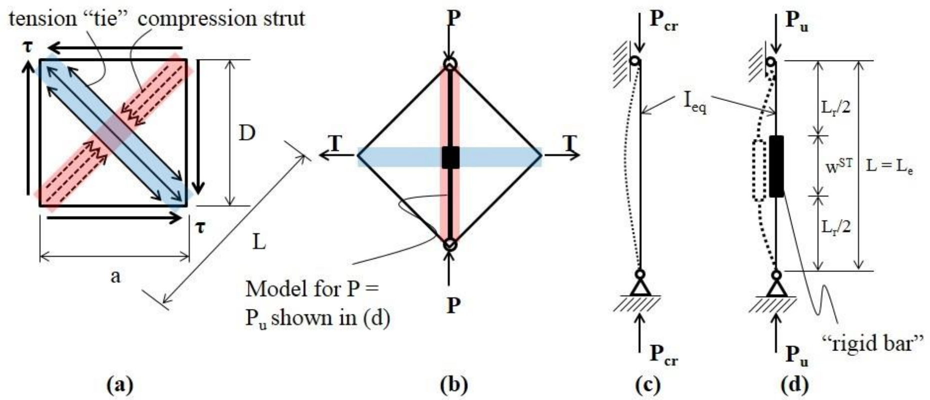

Figure 1. Schematic of (a) pure shear for a web plate, (b) rotation of Figure 1(a) such that the compression strut is vertical, (c) equivalent column model when P=P_{cr}, and (d) when P=P_u.

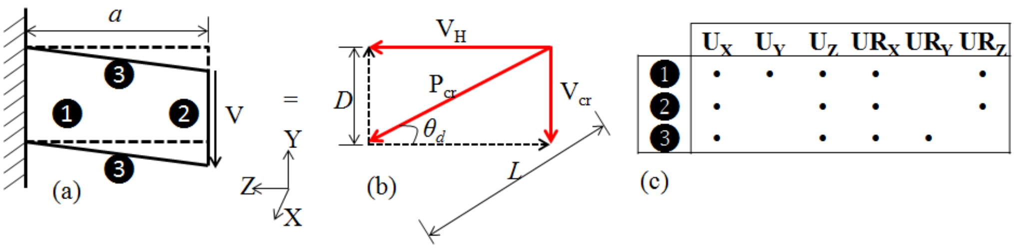

Figure 2. Plate with simply supported, pure shear boundary conditions (“•” indicates a locked degree of freedom) [8].

The elastic flexural buckling strength of a column is determined from the well-known equation:

$$P_{cr} = \frac{\pi^2 E I_{eq}}{\left(k_{e1}L\right)^2} \tag{5}$$

Setting Eqn. (4) equal to Eqn. (5) and solving for I_{eq} (using k_{e1}=1.0 for a pinned-pinned column):

$$I_{eq} = \frac{k_{ss} D t_w L^2}{12\left(1-\nu^2\right)\left(D/t_w\right)^2}\frac{L}{D} \tag{6}$$

It is assumed that Figure 1(d) represents the buckling of a column of length $L_r/2$ that is pinned on one end and fixed but free to translate on the other. Setting Equation. (5) equal to P_u, I_{eq} equal to Equation. (6), $L = L_r/2$, and k_{e1}=k_{e2} = 2.0, results in:

$$P_u = \frac{k_{ss}\pi^2 E D t_w}{12\left(1-\nu^2\right)\left(D/t_w\right)^2}\left(\frac{L}{L_r}\right)^2 \frac{L}{D} \tag{7}$$

Equation. (7) equals the ultimate flexural buckling strength of the equivalent column from Figure 1(d). To obtain V_u, we use Figure 2 by replacing P_{cr} with P_u and V_{cr} with V_u, obtaining $V_u = P_u\,(D/L)$. Inserting Equation. (7) into this expression for V_u results in the strut-and-tie value of V_u:

$$V_u^{ST} = V_{cr}\left(\frac{L}{L_r}\right)^2 \tag{8}$$

What remains is to develop a formulation for L_r, but to do this we need to solve for w^{ST} since from Figure 1(d) it is seen that $L_r = L - w^{ST}$. In the next section a formulation for w^{ST} is proposed.

4 DETERMINING W^{ST}

4.1 FE models

Six FE models were used to develop equations for w^{ST} as shown in Figure 4. The FE models and nonlinear solver were previously validated with published experimental results [8, 15]. S4 (doubly curved, general-purpose, finite membrane strains) shell elements were used to mesh the models in Abaqus [16]. Mesh convergence was studied using eigenvalue extraction analyses. All FE models have D=1.47 m, t_w=0.011 m, and D/t_w=134. The material properties at 20°C are Young's modulus, E=2e11 N/m^2, and Poisson's ratio, ν=0.3. Two values of yield strength were studied: σ_y=250 MPa and 345 MPa. Six span-to-depth ratio values (a/D) were selected: 1.0, 1.4, 1.5, 2.0, 2.5, and 3.0. The model with a/D=1.4 was based on the standard design for a 27.43 m (90 foot) long steel plate girder highway bridge based on the Standard Plans for Highway Bridges [17] and should be representative of many steel girder bridges in use across the United States.

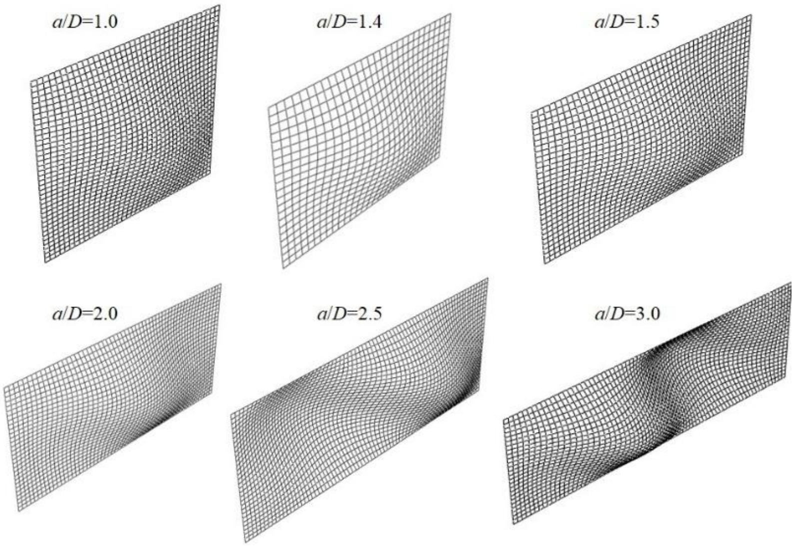

Figure 4. FE models used for the study; the elastic buckling shape at 20°C is shown for all cases.

4.2 Proposed formulation for w^{ST}

The proposed formulation for w^{ST} will be based on the finite element models described previously. Setting V_u^{ST} from Equation. (8) equal to the finite element solution for V_u (notated as V_u^{FE}), one can solve for L_r, from which $w^{ST*} = L - L_r$. We label this w^{ST} with a * to differentiate it from the proposed w^{ST} equation that we will give later. w^{ST*} is the width that the rigid bar in Figure 1(d) needs to be for the finite element solution to match exactly with the V_u^{ST} formulation of Equation (8).

Figure 5 plots w^{ST*} values versus a/D for σ_y values of 250 MPa and 345 MPa. Also shown in Figure 5 is the linear regression of the data points belonging to each σ_y set. It is seen that the relationship between w^{ST*} and a/D is nearly linear. The proposed equations for w^{ST} are based on the linear regression as follows:

For σ_y = 250 MPa: $$w^{ST} = 0.356\left(a/D\right) - 0.064 \quad (9a)$$

For σ_y = 345 MPa: $$w^{ST} = 0.423\left(a/D\right) + 0.092 \quad (9b)$$

Since Equation. (8) does not consider σ_y, the effect of σ_y on V_u is accounted for with w^{ST}. Equation. (1) assumes that σ_y is always reached in the tension field at V_u; however, previous research conducted by the authors has found that this assumption is not always true for temperatures exceeding 100°C [8]. Making V_u a function of w^{ST} instead of σ_y moves away from this assumption.

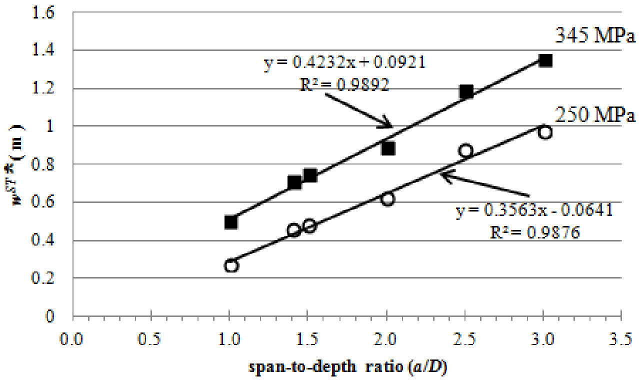

Figure 5. Plot of w^{ST*} versus a/D for σ_y values of 250 MPa and 345 MPa.

5 VALIDATION OF STRUT-AND-TIE MODEL WITH FE MODELS

5.1 Ambient Temperature Results

Table 1 compares V_u^{FE} with V_u^{ST} from Equation. (8) that uses Equation. (9) to calculate L_r. V_u^{FE} values were also compared with V_u^{BT} values calculated with Equation. (1) multiplied by $D{\cdot}t_w$. Table 1 shows that the V_u^{ST}/V_u^{FE} ratios are close to a value of 1.0, which is due to the close fit of the data to the line drawn in Figure 5. The V_u^{BT}/V_u^{FE} ratios vary depending on a/D and are sometimes 18% different from the FE solution. Table 1 also compares the w^{ST} values calculated from Equation. (9) with w^{FE}, which is the measured width of the tension field (crossed by the compression strut) in the FE models as shown in Figure 6. The tension field can be readily identified as a concentrated band of tensile stresses in the FE model. The w^{ST}/w^{FE} values have good agreement, suggesting that the w^{ST} values are physically reasonable.

Table 1. Comparison of V_u (kN) and w^{ST} (m) values with FE analysis (ambient temperature).

σ_y (MPa)	a/D	V_u^{ST} (kN)	V_u^{BT} (kN)	V_u^{FE} (kN)	V_u^{ST}/V_u^{FE}	V_u^{BT}/V_u^{FE}	w^{ST} (m)	w^{FE} (m)	w^{ST}/w^{FE}
250	1.0	2069	1895	2014	1.03	0.94	0.29	0.33	0.88
	1.4	1760	1611	1800	0.98	0.89	0.43	0.46	0.95
	1.5	1717	1693	1730	0.99	0.98	0.47	0.47	1.00
	2.0	1610	1380	1600	1.01	0.86	0.65	0.69	0.94
	2.5	1558	1589	1587	0.98	1.00	0.83	0.81	1.02
	3.0	1515	1313	1515	1.00	0.87	1.00	1.10	0.91
345	1.0	2701	2292	2642	1.02	0.87	0.52	0.49	1.05
	1.4	2269	1924	2310	0.98	0.83	0.68	0.6	1.14
	1.5	2204	2090	2226	0.99	0.94	0.73	0.69	1.05
	2.0	2032	1615	1966	1.03	0.82	0.94	0.82	1.14
	2.5	1937	1986	1971	0.98	1.01	1.15	1.2	0.96
	3.0	1891	1548	1883	1.00	0.82	1.36	1.31	1.04

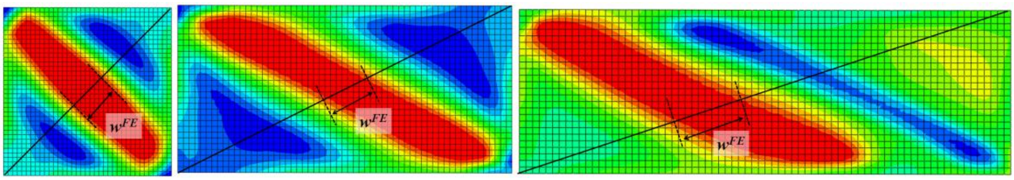

(a) (b) (c)

Figure 6. Representative cases for determining w^{FE} for a/D of (a) 1.0; (b) 2.0 and (c) 3.0 at 20°C.

5.2 Elevated Temperature Results

The strut-and-tie model was tested for accuracy at elevated temperatures. Figure 7 plots w^{ST}/w^{FE} for various temperatures representing fire conditions, where a value of 1.0 implies that the proposed strut-and-tie model is in good agreement with the finite element results. This study is currently only performed for σ_y=250 MPa and the authors are currently developing the results for σ_y=345 MPa. Results show that w^{ST}/w^{FE} values fluctuate with temperature for all 6 a/D values. As the temperature increases, w^{ST} as predicted from the strut-and-tie model may vary significantly with w^{FE}.

Based on Figure 5, it was originally hypothesized that w^{ST} would decrease with increasing temperature due to the decrease in σ_y. Figure 7 shows, however, that the w^{FE} may be 50% larger or smaller than the predicted w^{ST} value for temperatures of 800°C and less; above 800°C, w^{FE} may be up to 4 times larger than w^{ST}.

Figure 7 indicates that the strut-and-tie model, while accurate at ambient temperatures, needs to be adjusted for elevated temperature conditions, in particular for temperatures larger than 800°C. Current research by the authors is investigating this adjustment.

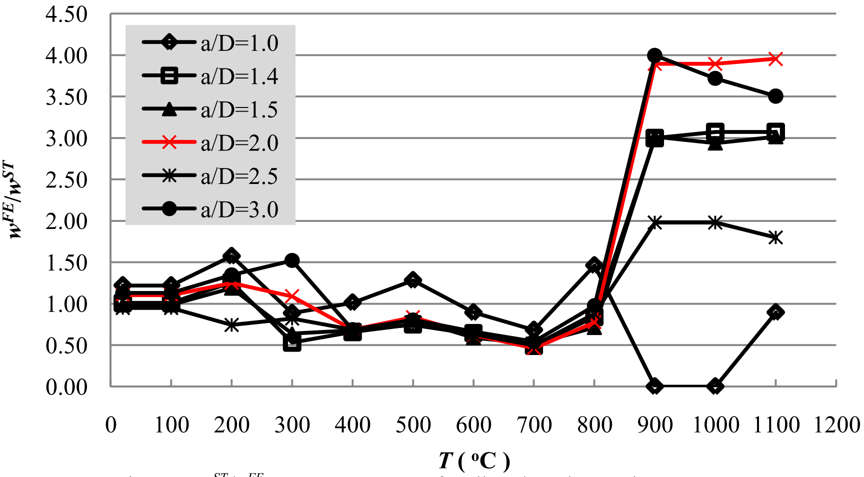

Figure 7. w^{ST}/w^{FE} versus temperature for all 6 a/D values and σ_y=250 MPa.

6 CONCLUSIONS

This paper presented a new model for web shear buckling that incorporates the contribution of compressive stresses to the postbuckling shear strength. The significance of this work is that it moves away from traditional tension field theory that assumes compressive stresses cease to increase once elastic shear buckling has occurred. Additionally, the proposed strut-and-tie approach has the potential to offer an alternative and accurate way of calculating V_u for web plates with various a/D and σ_y values.

At ambient temperature, the model works well for the D/t_w ratio studied (=134). Additional work is needed to fully investigate the accuracy of the model for other D/t_w ratios. Additionally, the model needs to be adjusted for elevated temperatures representing fire conditions. These additional investigations are part of the current work being developed by the authors.

ACKNOWLEDGMENTS

The authors would like to acknowledge Dr. Jean H. Prévost from Princeton University and Theodore Zoli from HNTB Corporation. This research was made with Government support under and awarded by DoD, Air Force Office of Scientific Research, National Defense Science and Engineering Graduate (NDSEG) Fellowship, 32 CFR 168a, provided to Mr. Glassman. This research was also sponsored by the National Science Foundation (NSF) under grant CMMI-1068252. All opinions, findings, and conclusions expressed are of the authors and do not necessarily reflect the policies and views of the sponsors.

REFERENCES

[1] J. M. Wilson, "On Specifications for Strength of Iron Bridges," *Trans. ASCE,* vol. 15, no. Part I, pp. 401-403, 489-490, 1886.

[2] C. H. Yoo and S. C. Lee, "Mechanics of Web Panel Postbuckling Behavior in Shear," *Journal of Structural Engineering,* vol. 132, no. 1, pp. 1580-1589, 2006.

[3] R. D. Ziemian, Guide to Stability Design Criteria for Metal Structures, 6th ed., Hoboken: John Wiley & Sons, 2010.

[4] H. Wagner, ""Flat Sheet Metal Girder with Very Thin Metal Web", Tech. Notes. 604, 605, 606,"

National Advisory Committee on Aeronautics, Washington, DC, 1931.

[5] C. Marsh, W. Ajam and H.-K. Ha, "Finite Element Analysis of Postbuckled Shear Webs," *Journal of Structural Engineering,* vol. 114, no. 7, pp. 1571-1587, 1988.

[6] K. N. Rahal and J. E. Harding, "Transversely stiffened girder webs subjected to shear loading - part 1: behaviour," *Proceedings of the Institution of Civil Engineers,* vol. 89, no. 2, pp. 47-65, 1990.

[7] K. N. Rahal and J. E. Harding, "Transversely stiffened girder webs subjected to shear loading - part 2: stiffener design," *Proceedings of the Institution of Civil Engineers,* vol. 89, no. 2, pp. 67-87, 1990.

[8] J. D. Glassman and M. Garlock, "Web shear buckling equations for steel plate girder bridges at elevated temperatures," *submitted for publication in the Journal of Constructional Steel Research,* 2013.

[9] K. Basler, "Strength of Plate Girders in Shear," *Trans. ASCE,* vol. 128, no. 2, 1961.

[10] American Association of State Highway and Transportation Officials, "AASHTO LRFD Bridge Design Specifications (6th Edition)," 2012. [Online]. Available: http://www.knovel.com/knovel2/Toc.jsp?BookID=4852. [Accessed 13 February 2013].

[11] D. W. White and M. G. Barker, "Shear Resistance of Transversely Stiffened Steel I-Girders," *Journal of Structural Engineering,* vol. 134, no. 9, pp. 1425-1436, 2008.

[12] S. P. Timoshenko and J. M. Gere, Theory of Elastic Stability, Second Edition, New York: McGraw-Hill Book Company, Inc., 1961.

[13] S. C. Lee and C. H. Yoo, "Strength of Plate Girder Web Panels Under Pure Shear," *Journal of Structural Engineering,* vol. 124, no. 2, pp. 184-194, 1998.

[14] J. D. Glassman and M. E. M. Garlock, "Strut-and-Tie Models for Web Shear Buckling of Steel Plate Girders," submitted to ASCE Journal of Structural Engineering, 2014.

[15] V. Vimonsatit, K.-H. Tan and Z.-H. Qian, "Testing of Plate Girder Web Panel Loaded in Shear at Elevated Temperature," *Journal of Structural Engineering,* vol. 133, no. 6, pp. 815-824, 2007.

[16] Dassault Systemes, "Abaqus 6.11ef Online Documentation," [Online]. [Accessed 2014].

[17] FHWA, Federal Highway Administration, "Standard Plans for Highway Bridges, Volume II, Structural Steel Superstructures," 1982.

[18] D. M. Porter, K. C. Rockey and H. R. Evans, "The Collapse Behavior of Plate Girders Loaded in Shear," *Struct. Eng.,* vol. 53, no. 8, pp. 313-325, 1975.

[19] European Committee for Standardization (CEN), "Eurocode 1: Actions on Structures - Part 1-2: General Actions - Actions on Structures Exposed to Fire," CEN, Brussels, 2002.

8th International Conference on Structures in Fire
Guo-Qiang LI, Venkatesh K. R. KODUR, Shou-Chao JIANG, Jian JIANG, Su-Wen CHEN, Guo-Biao LOU (Eds.)
Shanghai, China, June 11-13, 2014

DESIGN STRATEGIES OF FIRE SAFETY FOR STEEL ROOF TRUSSES EXPOSED TO LOCALIZED FIRE

Su-Min Lin*, Yong Du* and Jian-Xin Fu**
College of Civil Engineering, Nanjing Tech University, China
e-mails: linsumin@njut.edu.cn, yongdu_mail@njut.edu.cn

** Zhongtian Construction Group, Zhejiang Steel Structure LTD
e-mail: fubeibei1006@163.com

Keywords: Steel roof truss, Localized fire, Fire safety design, Critical temperature, Fire buckling resistance

Abstract. *Steel trusses are usually employed to cover the large span buildings, and fire-resistance capacity is very important to ensure the fire safety for this type of roof structure within fire ultimate limit state. A series of steel roof truss models has been established by using ANSYS software and the behaviors of truss exposed to localized fire were under study. Then, the fire-resistance capacity of steel roof trusses under key factors has been developed by parametric method and proved by structural mechanical theory. The theoretical and numerical studies have indicated that the loading ratio, fire location, size of fire bed, fire temperature distribution and lateral bracing system for upper chords are key influencing parameters, for the fire load-bearing capacity of steel roof trusses. Finally, several strategies have been presented for the roof truss fire safety design.*

1 INTRODUCTION

Steel trusses are always with large span and covered large volume space e.g. airport boarding halls, warehouses, storages etc. The steel truss structure should have sufficient load-bearing capacity under the localized fire duration. See Figure 1 and Figure 2, the buildings with steel truss roof have been exposed to seriously fire. Tongji University has carried out the fire-resistance bearing capacity of steel truss in large space fires [1], but taken no account of the lateral bracing system for upper chords and non-uniform temperature distribution exposed to localized fires. Central South University has researched the fire-resistance performance of staggered steel truss system for steel frame floor [2], The fire behaviour of a single steel truss with tubular chords exposed to standard fire has been carried out by Shanghai Jiao Tong University [3]. Based on the achievements mentioned above, further research of roof truss exposed to localized fires has been developed by numerical method and mechanical analysis as below.

Figure 1. An airport facility with steel truss in fire in Canada.

Figure 2. An aircraft warehouse with steel truss in fire in USA.

2 CONDITIONS OF STRUCTURAL ANALYSIS FOR TRUSSES IN FIRE

It is essential to give the material properties of steel at elevated temperature for structural fire analysis. The yield strength, elasticity modulus and thermal expansion coefficient are given by CECS200:2006[4]. Stress-strain relation of steel at elevated temperature is determined by the nominal stress due to 0.15% strain.

2.1 Temperature distribution and load ratio

The non-uniform temperature distribution without flame radiation is given by[5]

$$T_z = T_g^{\max}\left[\eta + (1-\eta)e^{(D/2-x)/7}\right], \text{ if } x < D/2 \text{, then } x = D/2 \tag{1}$$

$$D = 2\sqrt{A_q/\pi}$$

where, T_z is the temperature distribution equation of the distance, x, from the plume centerline to a point in horizontal plane above fire bed; T_g^{max} is the maximum temperature in the non-uniform temperature distribution; η is non-uniform factor of temperature distribution and the degree of non-uniform increasing with the smaller value, listed in table 1; D is the effective diameter of fire bed.

In most case, the shape coefficient of chords for steel roof truss exceeds 250 m^{-1}, then, smoke temperature distribution can instead of temperature in global steel truss approximately [6]. Right above the fire bed, there is an extremely thermal zone subjected to the most strong flame radiation and hot smoking, shown in Figure 3, the size of the extremely heat zone is taken as the circle with radius from 1.5m to 3.5m dependent on the size of fire bed, and the larger fire bed is possible. H is the distance from fire bed to the lower chords of truss. The degree of non-uniform temperature can be described by 'η' range from 0.85 to 0.25. The degree of non-uniform temperature distribution is more heavily with the value of 'η' decreasing.

Table 1. Factor η with dimension of buildings.

A_{sp}/ m^2	H/m				
	6	9	12	15	20
500	0.60	0.65	0.70	0.80	0.85
1000	0.50	0.55	0.60	0.70	0.75
3000	0.40	0.45	0.50	0.55	0.60
6000	0.25	0.30	0.40	0.45	0.50

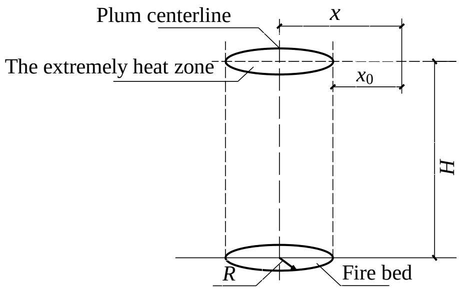

Figure 3. The extremely heat zone location.

2.2 Lateral restraints

The outline of a single-span roof truss is simple support at each end, and symmetrical about the centre line shown in Figure 4(a). The geometric scheme and number of chords are shown as Figure 4(a), and the section type of upper and lower chords is double angles with short leg closely spaced built-up, shown as Figure 4(b), the web chords is double angles with equal legs shown in Figure 4(c). The lateral bracing system or roof rigid link bar provides lateral restraints for upper chords, shown as Figure 5. It is specified that the buckling length about the *y-y* axies for upper chords is dependent on the distance between two adjacent points at which the upper chord is braced against lateral displacement in horizontal plane.[7] If upper lateral bracing system is destroyed partly, the upper chords will be with longer buckling lengths in horizontal plane. Figure 6 shows different lateral braced points location.

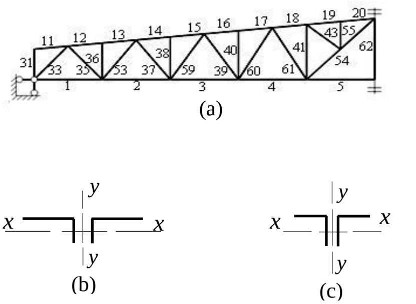

Figure 4. (a) The system scheme and number of chords; (b) Double angles with short leg loosely spaced built-up; (c) Double angles with equal legs.

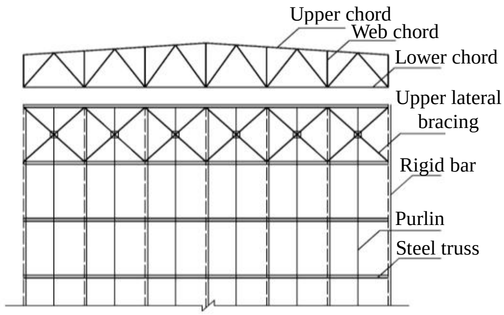

Figure 5. Steel trusses with upper lateral brace system.

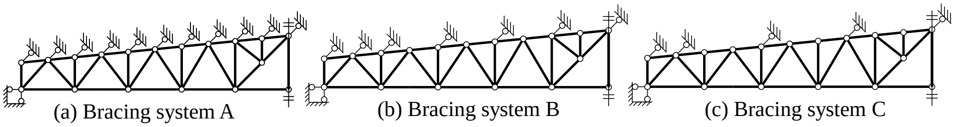

Figure 6. Lateral bracing system.

2.3 Fire bed location

It is assumed that the fire location is right below the truss and would locate at three points, shown as Figure 7.

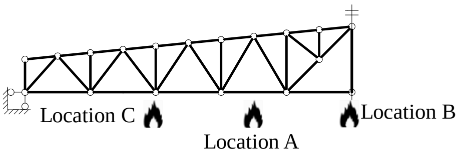

Figure 7. Fire location.

3 PARAMETRIC ANALYSIS

The degree of non-uniform temperature distribution, fire location, braced point for upper chords, fire bed size and load ratio are taken as key parameters for roof truss fire analysis.

3.1 Finite element analysis

The finite element analysis model for the steel roof truss shown in Figure 4 was established by ANSYS software. Element LINK8 is employed to simulate chords, and hinges at each node.

Load ratios for compression chords and tension chords are given by

$$(N/\varphi A)/f_y = \text{Initial load ratio for compression chords} \tag{2}$$

$$(N/A)/f_y = \text{Initial load ratio for tension chords} \tag{3}$$

where, N is the axial internal force of chords at ambient temperature, φ is the reduction coefficient, A is the size of the cross-section, f_y is the nominal value of yield strength.

Load ratio ranges from 0.9 to 0.1, and changes with the size of section chords. The maximum load ratio can be taken as 1.0 based on fully stress criterion. As we known, each chord can be with the similar load ratio but unequal. For example, the upper chords are always with the integrated section along the span, but the internal force between adjacent nodes varies along the span. Then, each upper chord is with different load ratio.

The temperature distribution is determined by Equation (1). The mechanical state of each chord under each temperature step should been checked by the fire limit state.

The axial tension chords at elevated temperature should be checked by

$$\frac{N}{A_n} \le \eta_T f_y \tag{4}$$

where, N is the axial tension force in chords under design combined loadings at elevated temperature; A_n is the net section size of chords; f_y is the yield strength of steel at ambient temperature; η_T is the strength reduction factor at elevated temperature.

The axial compression chords at elevated temperature should be checked by

$$\frac{N}{\varphi_T A} \le \eta_T f_y \tag{5-1}$$

$$\text{and} \quad \varphi_T = \alpha_c \varphi \tag{5-2}$$

where, φ , φ_T is the reduction coefficient for axial compression chords at ambient temperature and elevated temperature respectively; α_c is the reduction coefficient for buckling factor at elevated temperature, given by reference [4].

The numerical analysis for roof truss with lateral bracing location A, shown in Figure 6(a), was carried out under fire location A, load ratio R=0.7, and η= 0.7. The global truss fell to failure with $18^{\#}$ chord buckling. The stress history of chord $18^{\#}$ keeps in constant almost, shown as Figure 8. Numerical analysis indicates that there is no thermal stress subjected to localized fire. Checked by Equation (5-1), the chord $18^{\#}$ failed at 520℃ with the yield strength decreasing at elevated temperature. In the view of mechanical theory, for simple support truss without redundancy there is no thermal stress in each chord and the fire-resistance capacity of global roof truss is dependent on a single chord. The mechanical analysis meets to numerical simulation well, then, the collapse history can be derived by Equation (5-1) directly.

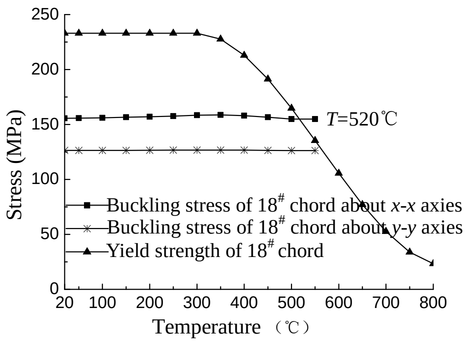

Figure 8. Failure history for chord 18#.

3.2 The effects of non-uniform temperature distribution

Chords of the global truss will be at different elevated temperature due to localized fire with non-uniform temperature distribution. However, the yield strength of a chord near fire bed decreases more heavily than those far away. T_{max} represents of the maximum temperature right above the fire bed. Shown as Figure 9, the yield strength histories decay more heavily with the point moving to fire bed. Shown as Figure 10, the yield strength histories decay more heavily with the more non-uniform temperature at the same point, x_0 =1.5m. Then, the fire ultimate limit state, right term of the equation (5-1), is dependent on the location of chords and the degree of the non-uniform temperature distribution. According to the equation (5-1), Figure 9 and Figure 10, the stress history of a chord which will primarily meet to the yield strength at elevated temperature is dependent on its load ratio, location and the degree of the non-uniform temperature distribution. In general, the chord with the highest load ratio right above the fire bed or adjacent to the fire bed should be checked by Equation (4) or Equation (5).

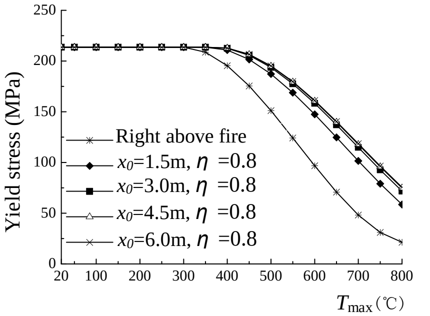

Figure 9. Yield strength decaying at different points in ceiling exposed to a localized fire.

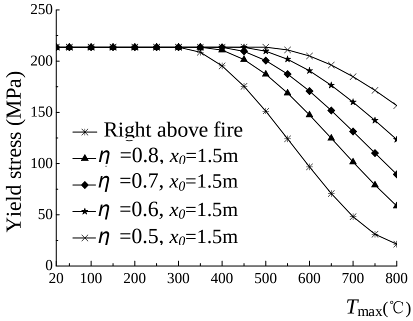

Figure 10. Yield strength decaying at, x_0=1.5m, point in ceiling exposed to localized fires.

3.3 The effects of loading ratio

Initial loading ratio of chords represents of the residual space before buckling. It is obvious that the chords with lower initial loading ratio would get higher loading capacity complying with fire ultimate limit state. Shown as Figure 11, the critical temperature increased with the decreasing of the loading ratio, *R*. With the different location of braced points for upper chords, the critical temperature of a truss decreased while load ratios increasing, shown as Figure 12.

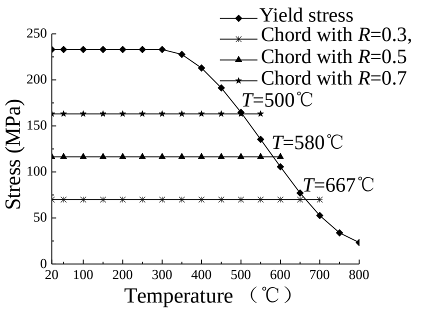

Figure 11. Critical temperature of a chord decreasing with the increasing of load ratio.

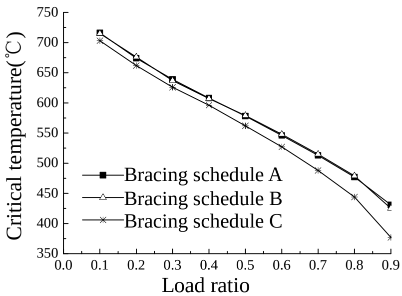

Figure 12. Critical temperature of truss varied with load ratio in different braced point location.

3.4 The effects of braced points for upper chords in horizontal plane

Shown as Figure 6, the buckling length of upper chords about *y*-*y* axies becomes longer with the larger distance between two adjacent lateral braced points. The geometric feature about *x*-*x* axies is different from that about *y*-*y* axies significantly for double angle section. As we know, the longer buckling length of the upper chord will induce larger slenderness ratio and lower reduction coefficient. Then, the fire load-bearing capacity should be checked by Equation (5-1) about two axies for upper chords.

In Table 2, there are different values of buckling stress for each upper chord due to different lateral bracing location. Where, L_x is the buckling length about *x*-*x* axies, σ_x is the buckling stress about *x*-*x* axies, L_y is the buckling length about *y-y* axies, σ_y is the buckling stress about *y-y* axies. The axies is shown in Figure 4(b).

If lateral bracing location as Figure 6(a), the upper chords are with the same buckling length about two axies. Then, the buckling stress about *x-x* axies is larger than *y-y* axies, listed in Table 2. Shown as Figure 6(b), the distance between two adjacent braced points about *y-y* axies is twice as the Figure 6(a). The buckling stress about *y-y* axies became greater, but still lower than the buckling stress about *x-x* axies, listed in Table 2. However, shown as Figure 6(c), the distance between two adjacent lateral bracing points is three times as the Figure 6(a). Then, the buckling stress about *y-y* axies greater than *x-x* axies, and determined the fire buckling resistance for upper chords. With the greater buckling stress due to large buckling length, the critical temperature of global truss would decrease, shown as Figure 12. It is proposed that the buckling length of upper chords in the horizontal plane is varied with the distance between two adjacent bracing points about *y-y* axies, and the larger buckling length of upper chords would reduce the critical temperature of global truss.

Table 2. The buckling length and buckling stress for upper chords.

Chord number	Inside truss plane		Bracing system A		Bracing system B		Bracing system C	
	L_x (cm)	σ_x (MPa)	L_y (cm)	σ_y (MPa)	L_y (cm)	σ_y (MPa)	L_y (cm)	σ_y (MPa)
20#	150.8	176.8	150.8	145.1	301.6	167.5	452.4	296.2
19#	150.8	176.8	150.8	145.1	301.6	167.5	452.4	296.2
18#	150.8	173.5	150.8	142.4	301.6	164.4	452.4	290.7
17#	150.8	170.2	150.8	139.7	301.6	161.3	452.4	285.2
16#	150.8	170.2	150.8	139.7	301.6	161.3	452.4	204.3
15#	150.8	147.1	150.8	120.7	301.6	139.4	452.4	176.6
14#	150.8	147.1	150.8	120.7	301.6	139.4	452.4	176.6
13#	150.8	94.2	150.8	77.3	301.6	89.3	452.4	113.1
12#	150.8	94.2	150.8	77.3	301.6	89.3	452.4	113.1
11#	150.8	0.0	150.8	0.0	150.8	0.0	150.8	0.0

3.5 The effects of fire bed location and size

The temperature histories of each chord are different exposed to localized fire and can be described by Equation (1). Shown in Figure 13, the temperature history of chord $18^{\#}$ is greater than chord $19^{\#}$ and chord $20^{\#}$ under fire location A. Although the buckling stress of chord $18^{\#}$ is less than chord $19^{\#}$ and chord $20^{\#}$ listed in table 2, the yield strength of chord $18^{\#}$at elevated temperature decays more greatly than chord $19^{\#}$ and chord $20^{\#}$ specially after 300℃, shown as figure 14. The buckling stress of chord $18^{\#}$ met the yield strength at 500℃ and failed primarily.

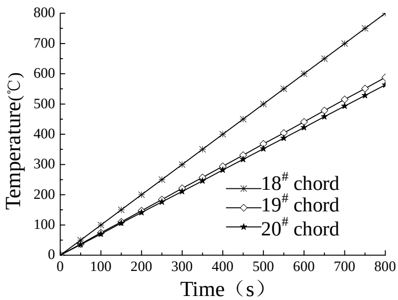

Figure 13. Temperature history for chords under fire location A.

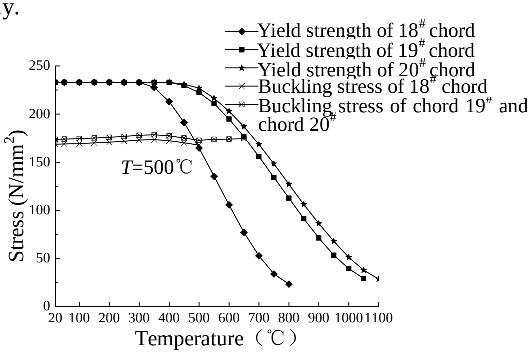

Figure 14. Stress history and recession of bearing capacity for chords under fire location A.

Under the fire location C shown in figure 7, chord 59# is right above the fire and with the higher temperature and lower buckling stress than chord 19#, shown in Figure 15 and Figure 16 respectively. The yield strength of 59#at elevated temperature decays more greatly than chord 19# specially after 300℃, shown as Figure 16. The buckling stress of chord 59# met the yield strength at 540℃ and failed primarily.

It is proposed that the chords right covered by the extremely heat zone would survive the most seriously fire damage because the yield strength of these chords decays most sharply than others. Among these members, the one with the maximum load ratio would become the key chord, which determines the global truss fire-resistance capacity.

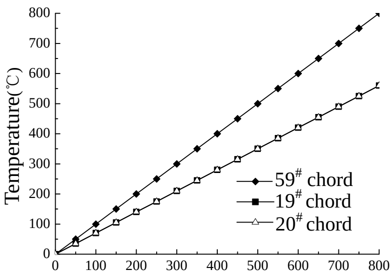

Figure 15. Temperature history chords for fire location C.

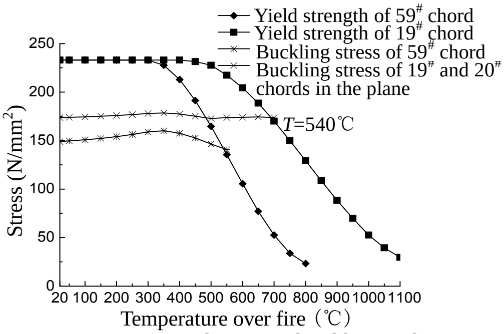

Figure 16. Stress history and yield strength decaying of chords for fire location C.

Under the larger size of the fire bed, more chords will be covered by the extremely heat zone, and the value of the maximum load ratio would vary. With the variation of the load ratio, the critical temperature of the roof truss will change.

4 FIRE SAFETY DESIGN STRATEGIES FOR ROOF TRUSSES

Based on the studies illustrated above, there are some fire safety strategies for roof trusses as followings. A chord with the maximum load ratio and covered by extremely heat zone should be checked by Equation (4) and Equation (5). If there is a chord adjacent the extremely heat zone with the higher load ratio than the chord with the highest load ratio in extremely heat zone, this chord also should be checked. For section type with single symmetry axies, the fire resistance should be checked about the lower radius of gyration. In order to operate the compression chords fire resistance sufficiently, the maximum load ratio of lower chords should be lower than that of web chords. For upper chords, the lateral restraint should be taken into account as follows.

Fire bed location is with random in a way. According to the fire bed position on the floor, the failure model of a upper chord is divided into three types.

(1) The fire position is right below the roof truss with lateral bracing system, and the chord of truss falls to failure before lateral brace system. The point of lateral restraint is shown in Figure 6(a), and the upper chord is with the same buckling length. Only buckling resistance about the weaker radius of gyration should be checked.

(2) The fire position is right below the roof truss with rigid bar or purlines only, and the chord of truss falls to failure before rigid connected bar. The point of rigid bar is shown in Figure 6(b), and the buckling length about the vertical axies (y-y) is longer than the horizontal axies (x-x) for upper chords. Then, buckling resistance of upper chords about two directions should be checked, and the others should be checked about the weaker radius of gyration only.

(3) The fire position is between two trusses and part of the bracing system or rigid bars damaged primarily. The lateral restraints are shown in Figure 6(c), and the buckling length about the vertical axies (*y*-*y*) is much longer than the horizontal axies (*x*-*x*) for upper chords. Then, only buckling resistance of upper chords about vertical axies (*y*-*y*) should be checked.

5 CONCLUSIONS

Compared the results from numerical analysis using ANSYS software to mechanical analysis for steel roof trusses, it is proposed that the fire-resistance of a single chord is dependent on the loading ratio, non-uniform temperature distribution, lateral bracing system, the size of fire bed and location. The fire response of roof trusses is elaborated as followings.

(1) There is no redistribution rout for the simple support roof truss, and the critical temperature of truss is determined by the fire-resistant bearing capacity of a single chord.

(2) Right above the fire bed, there is the extremely heat zone and the size of the zone is dependent on the fire bed. The chord covered by the extremely heat zone with the maximum load ratio shall be focus, which would be the key member.

(3) The critical temperature of roof truss will increase with the decreasing of load ratio.

(4) The lateral bracing system is important for the buckling resistance of the upper chord exposed to localized fire. With the distance between the adjacent point of lateral bracing system increasing, the fire-resistant capacity of upper chords is decreasing.

Finally, several fire safety design strategies have been presented for roof trusses exposed to localized fire, which can help civil engineers to improve the fire-resistance capacity of steel roof trusses efficiently and conveniently.

REFERENCES

[1] Huang J Q, “Study on the approach for fire resistance design of large planar space building steel structure” [D], *Tongji University*, 2006, Shanghai.

[2] Chen C K, Zhang D, “Finite element analysis of high temperature response to 3D model of steel staggered truss system”, *The academic conference proceedings of the steel structure*, 462-465, 2010, Beijing.

[3] Liu M L, Zhao J C, “Anti-fire experiment and element analysis of steel planar circular tubular truss”, *Low temperature architecture technology*, 164(2), 27-29, 2012.

[4] CECS 200:2006, Technical code for Fire safety of steel structures in Buildings, *National Institute of Standards for Engineering, China*, 2006.

[5] Du Yong, Li Guo-qiang, “A New Temperature Curve for Analysis of Structural Fire-resistance”, *Fire Safety Journal*, 54(11), 113-120, 2012.

[6] Du Y, Li G Q, “Simplified algorithm of steel member at elevated temperature in large space fire based on field model”, *Fire Science and Technology*, 25(3), 299-303, 2006.

[7] GB50017, “Code for design of steel structures”, *Ministry of Construction of the People’s Republic of China*, 2003 [s].

BEHAVIOR OF STEEL COMPONENTS SUBJECTED TO LOCALIZED FIRE

Chao Zhang*, John L. Gross* and Lisa Choe*

* National Institute of Standards and Technology, National Fire Research Laboratory, Fire Research Division, Gaithersburg, MD 20899-1070, USA
e-mails: chao.zhang@nist.gov, john.gross@nist.gov, lisa.choe@nist.gov

Keywords: Localized fire, Numerical simulation, Steel beam, Steel Column, Temperature gradient, Buckling

Abstract. *Recent numerical studies on the behavior of steel components subjected to a localized fire are presented. Sequentially coupled thermo-mechanical simulations were conducted to predict the steel temperature distribution, the deformation mode and failure temperature of restrained beams, the lateral torsional buckling resistance of simply supported beams, and the buckling behavior of unrestrained and restrained steel columns. Heat fluxes from a localized fire to the exposed surfaces of the beams were calculated according to correlations derived from localized fire tests. Simple approaches were provided to calculate the temperature of steel columns surrounded by and adjacent to a localized fire. The main findings of these studies were: the behaviour of a steel component in a localized fire may be totally different from that of the component in a standard fire, and the failure temperature of a steel component in a localized fire may be much lower than that of the component in a standard fire.*

This study illustrates the importance of (1) using realistic, worst-case fires in conducting structural design for fire, and (2) accounting for the behavior of the structural system as a whole. The technical basis underpinning such calculations is currently lacking and is the motivation for the development of the National Fire Research Laboratory (NFRL) at the National Institute of Standards and Technology (NIST). This facility is capable of conducting full scale structure tests under real fires such as localized and compartment fires.

1 INTRODUCTION

A building structure should be designed to maintain its stability for a specified period of time in the fires happened during its service life. To achieve this goal, in prescriptive codes, the building components are required to have sufficient fire resistance ratings determined by the standard fire tests. Although the standard fire bears little resemblance to a real fire, it is used because it is considered to represent a worst-case fire such that, if a component can survive the standard fire exposure, it can survive a real fire. This assumption is valid when the failure of a building component is presumed to be dependent only on its mean temperature achieved. However, when the failure of a component is caused by the thermal gradient, design based on the standard fire may be not conservative.

Real fires start from localized burning, and will not develop to flashover in an open space or in large open-plan compartments. Temperatures of gas and exposed steel components are not uniform. To date, the heating mechanism of steel components subjected to localized burning or localized fire has been investigated both experimentally and numerically. Hasemi et al. [1] experimentally studied the heating mechanism of a ceiling/beam system exposed to a localized fire. Heat fluxes to a flat ceiling with and without a steel I beam were measured. Surface temperatures of the beam were also measured. Kamikawa et al. [2] experimentally studied the heating mechanism of steel columns exposed to a localized fire. Heat flux and temperature measurements were conducted on a square steel tube column adjacent to and surrounded by fire sources. Sokol et al. [3] measured the temperature of a steel column located in the center of a compartment adjacent to a localized fire. Byström et al. [4] measured the temperature of a steel tubular column located at the center of a pool fire source. Zhang and Li [5, 6] numerically investigated the heating mechanism of steel components exposed to a localized fire by using the CFD software Fire Dynamic Simulator (FDS) [7]. Jeffers and Sotelino [8] simulated the thermal-mechanical behavior of a simply supported steel beam exposed to a localized fire by a fiber element approach. However, there is a lack of investigation on the structural behavior of steel components subjected to localized fire.

This paper reports some recent numerical studies on the behavior of steel components subjected to a localized fire. Thermal calculation approaches in localized fire were presented. Structural performance of steel components in a localized fire was investigated and compared with that in uniform heating conditions.

2 THERMAL CALCULATION IN LOCALIZED FIRE

2.1 Heat release rate

The heat release rate (HRR) of a real fire can be measured by cone calorimetry. In design work, the natural fire safety concept (NFSC) is widely used to represent the fire conditions [9]. As shown in Figure 1, the NFSC fire is assumed to be t-square in the growth stage and decay stage begins at the time when 70% of design fire load is consumed.

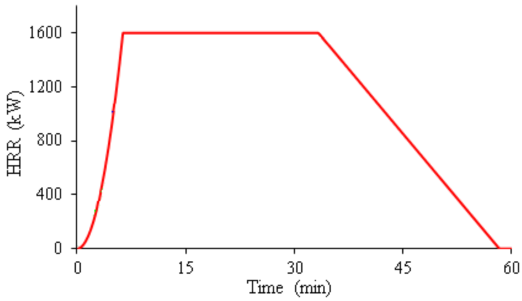

Figure 1. Heat release rate curve for a NFSC fire.

2.2 Heat flux to a steel I beam beneath a ceiling

The heat fluxes incident onto different parts of an I-beam beneath a ceiling can be calculated by the following correlations given in SFPE handbook [10]: the incident heat flux to the downward face of the lower flange is

$$\dot{q}_{in} = 518.8e^{-3.7y_B} \tag{1}$$

the incident heat flux to the upward face of the lower flange and the web is

$$\dot{q}_{in} = 148.1e^{-2.75y_C} \tag{2}$$

and the incident heat flux to the downward face of the upper flange is

$$\dot{q}_{in} = 100.5e^{-2.85y_C} \tag{3}$$

where y_i (i= B, C) is a parameter, given by

$$y_i = \frac{r + H_i + z_0}{L_i + H_i + z_0} \tag{4}$$

where r is the horizontal distance between the fire centreline and the calculated point along the beam; H_c and H_b are the distances between the fire and the ceiling, and the fire and the lower flange of the beam, respectively; L_b and L_c are the horizontal flame length along the lower and upper flanges of the I beam.

The net heat flux transferred to a exposed surface is calculated by [11,12]

$$\dot{q}_{net} = \dot{q}_{in} - h_c (T_{surf} - 20) - \varepsilon_{res}\sigma[(T_{surf} + 273)^4 - (20 + 273)^4] \tag{5}$$

Where h_c is the convective heat transfer coefficient, taken as 9 W/(m^{2}K) for localized fires [9]; T_{surf} is the temperature of the exposed surface; ε_{res} is the resultant emissivity at the exposed surface; and σ is the Stefan-Boltzmann constant, taken as 5.67 $\times 10^{-8}$ W/(m^{2}K^4).

2.3 Heat flux to a steel column surrounded by a localized fire

Where a steel column is surrounded by a localized fire, the column is fully engulfed in either flame or the plume, similar to heating during post-flashover fires. Therefore, the simplifications and assumptions used for post-flashover fires are adopted in this paper in calculating the temperature of steel columns surrounded by a localized fire, and the radiative heat flux transferred to a steel column surrounded by a localized fire is calculated by [13]

$$\dot{q}_r = \varepsilon_{res}\sigma[(T_g + 273)^4 - (T_{surf} + 273)^4] \tag{6}$$

where T_g is the centreline temperature of the fire plume for the localized fire without obstructions (e.g., a steel column), calculated according to [14].

2.4 Heat flux to a steel column adjacent to a localized fire

Thermal radiation from a localized fire to an adjacent column is calculated based on a solid cylinder model, which represents the localized fire as a solid cylinder and assumes thermal radiation is emitted from the side surfaces [13]. The net heat flux transferred from a localized fire to an adjacent surface is calculated by Eq.5 with replacing $\dot{q}_{in}$ by the incident heat flux from the fire, $\dot{q}_f$, calculated by

$$\dot{q}_f = F\varepsilon_{res}E_f \tag{7}$$

where F is the view factor; and E_f is the emissive power to the surface.

2.5 Temperature of exposed steel column

The temperature of exposed steel columns is calculated by the numerical models by solving the three-dimensional (3D) heat conduction equation under the heat flux boundary conditions for various situations in localized fire. The numerical models are described below.

3 STEEL BEAMS SUBJECTED TO LOCALIZED FIRE

3.1 Investigated cases

Figure 2 illustrates the investigated cases for steel I beams subjected to flame impingement from a localized fire. The failure behavior of restrained steel I beams, and the lateral torsional buckling (LTB) behaviour of simply supported steel I beams were investigated.

Table 1 gives the characteristics of the investigated cased for restrained steel I beams. Two steel beams of various load ratios (LR) and dimensions under different restraint conditions were considered. The ceiling height was 2 m. The fire source was located at the floor and just below the center of the beams. A NFSC localized fire and the standard ISO834 fire were considered. The HRR-time curve for the NFSC fire is shown in Figure 1. Detailed description can be found in [11].

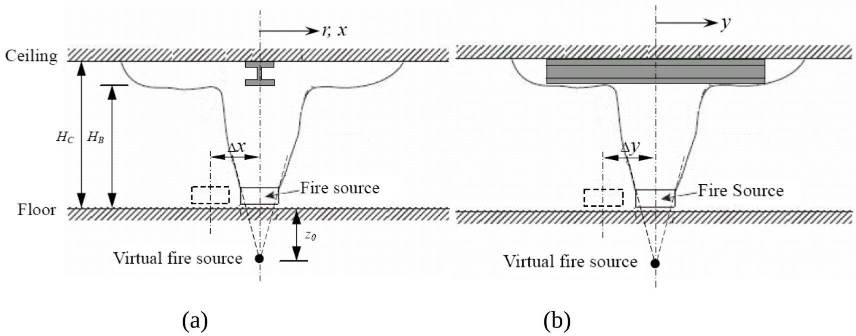

Figure 2. Illustration of a steel I beam exposed to a localized fire.

Table 1. Investigated cases for restrained steel beam.

Case	Beam	Restraints	LR	Failure mode	T_{fail} (^oC)
1-a/b	#1	R[c]&A[d]	0.5	Buckling/Buckling	720[a]/676[b]
2-a/b	#1	A	0.5	Buckling/Deflection	687/649
3-a/b	#2	R&A	0.7	Buckling/Deflection	798/703
4-a/b	#2	A	0.7	Buckling/Deflection	454/514

Note: [a]NFSC fire case; [b]ISO834 fire case; [c] rotational restraint; [d]axial restraint

Table 2. Investigated cases for lateral torsional buckling of steel beams.

Beam	Load type	LR	Δx (m)	Δy (m)	Fire type	T_{LTB} ($_oC$)
#1	Uniform	0.3	0 to 6.5 bs	0	NFSC, ISO834	794 to 686, 695
#1	Uniform	0.3	0	L/4	NFSC	802
#1	Uniform	0.5	0 to 10.5 bs	0	NFSC, ISO834	727 to 586, 611
#1	Uniform	0.5	0	L/4	NFSC	758
#1	Uniform	0.7	0 to 18.5 bs	0	NFSC, ISO834	603 to 429, 503
#1	Uniform	0.7	0	L/4, L/8	NFSC	675, 625
#1	Uniform	0.8	0 to 24.4 bs	0	NFSC, ISO834	502 to 312, 424
#1	Uniform	0.9	0 to 32.2 bs	0	NFSC, ISO834	354 to 180, 302
#1	P at L/2	0.7	0 to 22.1 bs	0	NFSC, ISO834	571 to 330, 491
#1	P at L/2	0.7	0	L/4, L/8	NFSC	705, 632
#1	P at L/4	0.7	0 to 19.6 bs	0	NFSC, ISO834	708 to 398, 490
#1	P at L/4	0.7	0	L/4, L/8	NFSC	556, 630
#2	Uniform	0.7	0 to 9.3 bs	0	NFSC, ISO834	548 to 329, 426

Table 2 gives the investigated cases for lateral torsional buckling behavior of simply supported unrestrained steel I beams. Uniform load, mid-span point load and point load at quarter length were considered, which were marked as “uniform”, “P at L/2”, and “P at L/4”, respectively. A NFSC localized fire and the standard ISO834 were considered. The location of the NFSC fire was varied in different cases. As shown in Fig.2, Δx denotes the distance between the flame axis and geometric center of the cross section, and Δy denotes the distance between the flame axis and the section having the maximum external moment. The term b_s denotes the beam width. Detailed description can be found in [12].

3.2 Temperature of steel I beams

When a steel I beam is subjected to a NFSC fire which is located just below the beam center, the temperature distributions within the beam are highly non-uniform both across and along the beam, and the location of the maximum temperature changes with time. At the very beginning of the developing phase, the maximum temperature is located at the lower flange; then, the maximum temperature moves to the web and stays within the web during the later developing and steady burning phases, respectively; during the decay phase, the maximum temperature moves from the web to the upper flange.

3.3 Structural performance of restrained steel I beams

The failure modes and failure temperatures (marked as T_{fail}) are summarized in Table 1. The failure temperature for restrained beams is defined as the maximum steel temperature when a restrained beam either reaches a deflection limit (L/20, L is the beam length) or buckles. Restrained Beams buckled in all localized fire cases, while restrained beams in the standard ISO834 fire buckled in some cases. For cases 1 to 3, the failure temperatures in the standard ISO834 fire are lower than those in the NFSC localized fire; but for case 4, the failure temperature in the standard ISO834 fire is higher than that in the NFSC localized fire (T_{fail} in the standard ISO834 fire is 514 ℃ and 13% higher than that in the NFSC localized fire).

3.4 Structural performance of simply supported I beams

The lateral torsional buckling temperature (T_{LTB}), defined as the maximum temperature in a steel beam at which lateral torsional buckling (LTB) occurs, were also provided in Table 2. When the fire source is near the geometric center of the section, or when Δx is small, T_{LTB} for the NFSC localized fire is higher than that for the standard ISO834 fire. However, when Δx is large, the T_{LTB} for the NFSC localized fire will be lower than that for the standard fire, and the maximum difference can reach 161 ℃. When Δx is large enough (i.e. far from the beam centerline), LTB will not occur.

4 STEEL COLUMNS SUBJECTED TO LOCALIZED FIRE

4.1 Investigated cases

Figure 3 illustrates the investigated cases for steel columns subjected to a localized fire. Unrestrained, axially restrained, and rotationally restrained steel columns surrounded by and adjacent to a localized fire were investigated. Table 3 gives the characteristics of the investigated cases, see Reference [13] for detail.

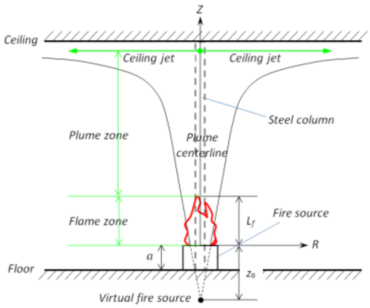

(a)

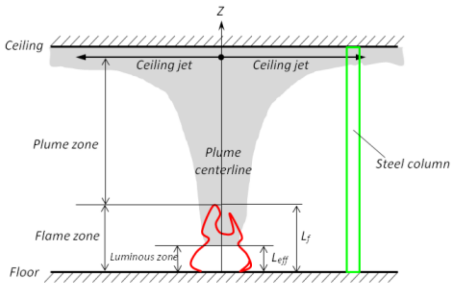

(b)

Figure 3. Illustration of a steel column subjected a localized fire. (a) column is surrounded by the localized fire; (b) colume is adjacent to the localized fire.

Table 3. Investigated cases for lateral torsional buckling of steel beams.

Sec	*L* (m)	λ	*a/L*	$(D_x\text{-}D_f/2)/b_s$	D_y/h_s	*LR*	R_a	R_r
C1	3 to 6.6	47.4 to 104.3	0 to 0.9	-	-	0.3 to 0.8	0 to 0.1	0 to 100
C2	3	119.1	0	-	-	0.5	0 to 0.1	0 to 100
C3	6.0	58.7	0	-	-	0.5	0 to 0.1	0 to 100
C1	4.5	71.1	-	1 to 3	0.5 to 10	0.5	0 to 0.1	0 to 100
C2	3.0	119.1	-	1 to 6.3	0.5 to 15	0.5	0 to 0.1	0 to 100
C3	6.0	58.7	-	1	0.5	0.5	0 to 0.1	0 to 100

4.2 Temperature of steel columns

When a steel column is surrounded by a localized fire, the temperature distributions in the column are non-uniform, both transversally and longitudinally, and are generally symmetric about both the strong and weak axes of the cross section. The steel temperatures decrease with height. When a steel columns is adjacent to a localized fire, the temperature distributions in the column are non-uniform, both transversally and longitudinally, and may be generally asymmetric about either the strong or the weak axes of the cross section, depending on the location of the localized fire relative to the column.

4.3 Buckling of steel columns surrounded by a localized fire

When a bare steel column is surrounded by a localized fire, steel temperatures near the burning surface are close to the flame temperature, while steel temperatures far from the burning surface remain close to room temperature. Due to the large temperature gradient, thermal expansion of the "hot" portions of the column is restrained by the "cool" portions, which results in compressive thermal stresses in the "hot" portions. The compressive thermal stresses, combining with the compressive stresses resulting from the column load may lead to local buckling of the "hot" portions which have been weakened by high temperature (i.e., loss of strength and stiffness), as shown in Figure 4 in which the web and flanges of the column near the burning surface undergo local buckling. The column load at elevated temperature is a combination of the initial load at room temperature, and a restraining force if there is an axial restraint. Therefore, failure of a steel column surrounded by a localized fire is caused by local buckling of the "hot" portions (the "cool" portions are at low temperatures such that global buckling does not occur). At ambient temperature, and in the standard ISO834 fire, the investigated steel columns were failed by global buckling. Since the critical temperature at which local buckling occurs is higher than the temperature at which global buckling occurs, the buckling temperatures for steel columns surrounded by a localized fire are higher than those for the columns subjected to the standard ISO834 fire.

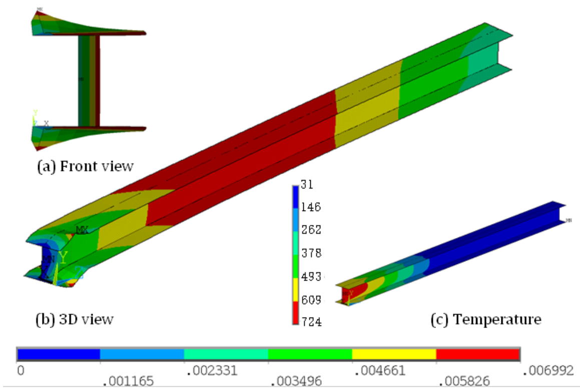

Figure 4. Failure mode of steel columns surrounded by a localized fire.

4.4 Buckling of steel columns adjacent to a localized fire

The location of a localized fire relative to the column has a significant effect on the column buckling temperature, as shown in Tables 4 and 5. When a localized fire is located near a column, changing the location of the fire source may result in significant changes in both the column heating and buckling temperature. When a localized fire is located far away from a column (e.g. cases with D_y/h_s>10.5 in Table 4), the column will not be buckled by fire.

For unrestrained columns, the buckling temperatures in some localized fire cases are much lower than those for both the standard ISO834. For axially restrained columns, buckling temperatures for some localized fire cases are lower than those for the standard ISO834 fire. For rotationally restrained columns, buckling temperatures for the localized fire are higher than for the standard ISO834 fire.

Steel columns failed by global buckling in the investigated adjacent fire cases. Depending on the location of the localized fire relative to the column, steel column may buckling with or without a lateral displacement, as shown in Figure 5 When a steel column is adjacent to a localized fire,

Table 4. Buckling temperature of Column 2 (section 2, L=3 m) for various D_x.

$(D_x$-$D_f/2)/b_s$	1	2	5	6	6.2	6.25	6.3	ISO834
R_a=0, R_r=0	433	463	531	537	536	537	-	544
R_a=0.1, R_r=0	353	344	330	323	322	322	322	201
R_a=0, R_r=100	727	-	-	-	-	-	-	671

Table 5. Buckling temperature of Column 1 (section 1, L=4.5 m) for various D_y.

D_y/h$_s$	0.5	1.0	2.0	3.0	7.0	8.0	10.0	10.5	ISO834
R_a=0, R_r=0	577	582	565	506	417	-	-	-	578
R_a=0.1, R_r=0	499	501	482	414	333	321	306	-	363
R_a=0, R_r=100	674	678	657	-	-	-	-	-	597

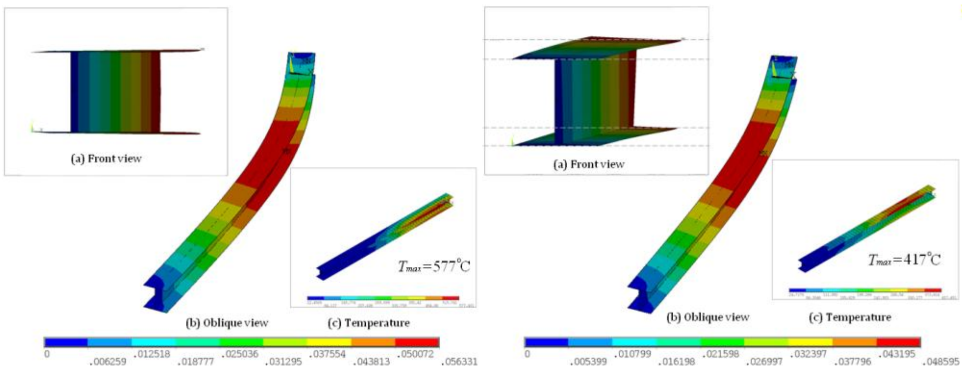

(a) $D_x = D_f + b_s$, $D_y = 0.5h_s$ (b) $D_x = D_f + b_s$, $D_y = 7h_s$

Figure 5. Failure modes of steel columns adjacent to a localized fire.

CONCLUSIONS

Recent numerical studies on the behavior of steel components subjected to a localized fire are presented. The main findings and conclusion of those studies include:

- The temperature distributions within the steel components subjected to localized fire are highly non-uniform both across and along the components.
- The deformation mode of restrained steel beam subjected to localized fire may be significantly different from that of a beam subjected to the standard fire. The failure temperatures for restrained steel beams subjected to localized fire may be, in some cases, lower than those for restrained beams subjected to the standard fire.
- The lateral torsional buckling temperature of simply supported steel I beams in localized fire may be hundreds of degrees lower than that in the standard fire.

- Steel columns surrounded by localized fire fail by local buckling, while the columns subjected to uniform heating conditions fail by global bending buckling.
- Buckling temperature for steel columns adjacent to localized fire may be much lower than those for steel columns subjected to either the standard fire or uniform heating condition
- Reliance on the standard fire test may lead to a not conservative design if there is a potential for a real fire to be localized.

REFERENCES

[1] Hasemi Y., Yokobayashi Y., Wakamatsu T., Ptchelintsev A., "Modeling of heating mechanism and thermal response of structural components exposed to localized fires: A new application of diffusion flame modeling to fire safety engineering", *NIST Internal Report 6030*, National Institute of Standards and Technology, Gaithersburg, Maryland, 1997.

[2] Kamikawa D., Hasemi Y., Wakamatsu T., Kagiya K., "Experimental flame heat transfer correlations for a steel column adjacent to and surrounded by a pool fire", *Fire Safety Science*, 2003;7:989-1000.

[3] Sokol Z., Wald F., Kallerova P., Bonnet N., "Column behaviour during localized fire test", *Proceedings of the Sixth International Conference on Structures in Fire*, V. Kodur, J.-M. Franssen (eds.), East Lansing, 24-31, 2010.

[4] Bystrom A., Sjostrom J., Wickstrom U., Veljkovic M., "Large scale test on thermal exposure to steel column exposed to localized fire", *Proceedings of the Seventh International Conference on Structures in Fire*, M. Fontana, A. Frangi, M. Knobloch (eds.), Switzerland, 185-194, 2012.

[5] Zhang C., Li G.Q., "Thermal behaviour of a steel beam exposed to a localized fire – numerical simulation and comparison with experimental results", *Proceedings of the Fourth International Conference on Protection of Structures against Hazards*, Beijing, China, 2009.

[6] Zhang C., Li G.Q., "Thermal response of steel columns exposed to localized fires – numerical simulation and comparison with experimental results", *Journal of Structural Fire Engineering*, 2011;2:311-317.

[7] McGrattan K., McDermott R., Hostikka S., Floyd J. "Fire dynamics simulator (version 5) user's guide", *NIST special publication 1019-5*, National Institute of Standards and Technology, Gaithersburg, Maryland, 2010.

[8] Jeffers A.E., Sotelino E.D., "An efficient fiber element approach for the thermo-structural simulation of non-uniformly heated frames", *Fire Safety Journal*, 2012;51:18-26.

[9] BSI, "Eurocode 1: actions on structures – part 1.2: general actions – actions on structures exposed to fire", *British Standard*, 2002.

[10] Lattimer B.Y., "Heat fluxes from fires to surfaces", *SFPE handbbok of fire protection engineering*. 3rd ed. Maryland: Society of Fire Protection Engineers, 2002 [Section 2-4].

[11] Zhang C., Li G.Q., Usmani A., "Simulating the behaviour of restrained steel beams to flame impingement from localized fires", *Journal of Constructional Steel Research*, 2013;83:156-65.

[12] Zhang C., Gross J.L., McAllister T.P., "Lateral torsional buckling of steel W-beams subjected to localized fires", *Journal of Constructional Steel Research*, 2013;88:330-8.

[13] Zhang C., Gross J.L., McAllister T.P., Li G.Q., "Behavior of unrestrained and restrained bare steel columns subjected to localized fire", *Journal of Structural Engineering*, 2014.

[14] Zhang C., Li G.Q., "Fire dynamic simulation on thermal actions in localized fires in large enclosure", *Advanced Steel Construction*, 2012;8:124-36.

CONCRETE STRUCTURES

8th International Conference on Structures in Fire
Guo-Qiang LI, Venkatesh K. R. KODUR, Shou-Chao JIANG, Jian JIANG, Su-Wen CHEN, Guo-Biao LOU (Eds.)
Shanghai, China, June 11-13, 2014

BEHAVIOR OF FULL-SCALE TWO-WAY CONCRETE SLABS WITH SIMPLY SUPPORTED EDGES

Yu-Li Dong*

*College of Civil Engineering, Huaqiao University, China
Email: DongYL@hqu.edu.cn

KeyWords: Concrete two-way slab, Large deflection, Fire, Von Karman equations, Tensile membrane action

Abstract. *Two tests of full-scale simply supported two-way concrete slabs under furnace environment are described in this paper. The details of support condition, arrangement of reinforcement, position of displacement transducers and thermocouple trees are introduced. The experimental results, including temperature distribution, central vertical deflection and edge horizontal deflection of the concrete slabs are given. Based on the results, the Von Karman governing differential equations for thin plates are introduced to describe the slabs at large deflections. Considering that Young's modulus decreases as the average temperature of the slab increases, the variation of deflection caused by thermal gradient and by constant loads is calculated respectively. Comparison between calculated total deflection variation and the test results shows good correlation.*

1 INTRODUCTION

In a building fire, membrane action at large displacements can be beneficial to the survival of reinforced or composite floor slabs used in different building structures. By utilizing membrane action significant cost savings can be achieved. During the 1960s, significant experimental and theoretical research work [1-8] was conducted to investigate the behavior of concrete floor slabs subjected to large vertical displacements. This work showed that concrete slabs at large vertical displacements could support loads considerably greater than those calculated using the well-established yield-line approach. The mechanism to support this greater load was known to be tensile membrane action, which could form within the slab regardless whether the slab was restrained or unrestrained horizontally at its boundaries. Recently, several real fires in composite steel framed buildings in the U.K. have shown that tensile membrane action in composite slabs plays a very significant role in maintaining structural stability. The composite slabs, supported by non fire-protected beams, suffered very large mid-span deflections but did not collapse. Full scale fire tests at the Cardington Large Building Test Facility [9] have also confirmed this behavior. This phenomenon has initiated a great deal of interest in the steel industry around the world because it has the potential to reduce the amount of passive fire protection in steel framed structures.

The determination of the membrane action of concrete slabs at large deflection has become the focus for investigators [10-14]. Usmani and Cameron [15] introduce a three-step method that analyses the capacity limit of laterally restrained RC slabs in fire: first, the temperature distribution over the depth of the slab is estimated for a given fire scenario; after then, the deflected shape of the RC slab and its membrane stress state is determined by solving the governing differential equations at large deflection for thin plates; finally, an energy based method is used to determine the maximum load that the slab could carry based on the geometric form and stress state determined in the previous steps. Anthony et al. [16] incorporate both thermal and mechanical effects into the prediction of slab behavior in fire conditions and use the various Rayleigh-Ritz approaches to classical large-deflection plate theory. The method is found to produce accurate predictions of deflections and membrane actions.

In this paper, the experimental results of two full-scale two-way concrete slabs subjected to fire, including the furnace temperatures, the temperature distribution over the depth of the slabs, deflections and horizontal displacements in the plane of the slabs, will be described. Based on these results, by solving the Von Karm differential equations at large deflection for thin plates, the deflections of the slabs, caused by the temperature gradient and induced by the load at different temperatures, are determined respectively.

2 EXPERIMENTAL RESULTS

Two flat slabs are tested. Each slab measures 5.0m × 6.66 m, with a thickness of 120 mm. The clear span of the slabs is 4.5 m×6 m, which gives an aspect ratio of 1.33. The arrangement of reinforcement in the slabs is shown in Figure 1. The clear span is assumed to be the actual span of the slab, as shown in Figure 2. The slabs are simply supported on all the four sides above the furnace which has an opening of 3.8m×5.4 m. The slabs are horizontally unrestrained and are loaded with a constant uniformly distributed load of 2KN/m2. The slabs are all heated from underneath with the ISO 834 standard fire curve for three hours.

Grade 3 hot-rolled reinforcing bars of 8 mm diameter are placed with 200 mm spacing along the long direction and 180 mm spacing along the short direction. The reinforcement clear cover is 15 mm. The mesh in the slabs is arranged so that the bars along the short direction are placed below those along the long direction. The yield strength and ultimate strength are 435 MPa and 580 MPa, respectively.

Commercial normal weight concrete with crushed lime-stone acting as coarse aggregate (maximum size 30 mm) is used for the slabs and the specified compressive strength is 30MPa. The cubic compressive strength of the concrete is 31.5 MPa.

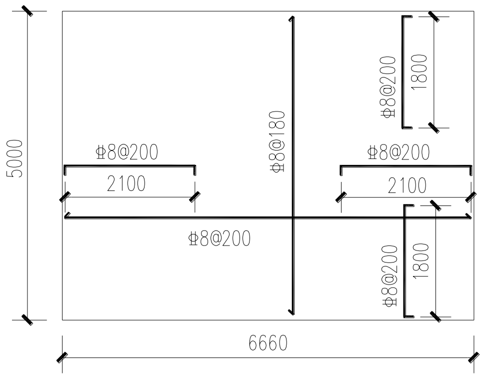

Figure 1. Arrangement of reinforcement in slabs (dimension in mm).

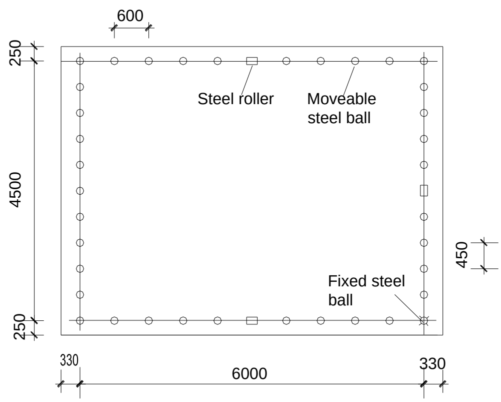

Figure 2. Configuration of ee-support (dimension in mm).

All specimens have type-K thermocouples on the reinforcing steel to measure the steel temperatures. The thermocouples on the reinforcing steel are placed at mid-height of the steel bars. Type-N thermocouples on the thermocouple trees are used to measure the temperatures across the thickness of the slabs. The arrangement of thermocouple trees and its details are shown in Figure 3. Each thermocouple tree consists of seven thermocouples distributing vertically with a spacing of 20 mm.

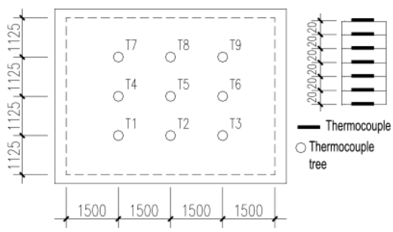

Figure 3. The position of thermocouple trees and its details (dimension in mm).

The vertical and horizontal deflections of the slabs are measured during the fire test. Figure 4 shows the position of the vertical and horizontal displacement transducers. The limit ranges of the transducers are from 50-300 mm. The vertical deflections are measured across the centre of the slab in both the long and short directions. The horizontal displacements are also measured in both directions at the edges of the slab, with a purpose-designed set-up.

For slab 1, at 10 minutes the first crack, marked as ① on top of the slab appears at about 1/4 longitudinal span of the slab (Fig.5), running in the transverse direction. At 13 minutes, crack ② occurs in the middle of the slab, running in the parallel direction with crack ①. At 18 minutes, crack ③ appears at about 3/4 longitudinal span of the slab, running in the transverse direction also. At 37 minutes, crack ④ appears in the vicinity of 1/4 longitudinal span, running in the longitudinal direction. At 43 minutes crack ⑤ appears, which is symmetric to crack ④. The maximum width of crack ①, ② and ③ reaches 5mm without flames passing through during test.

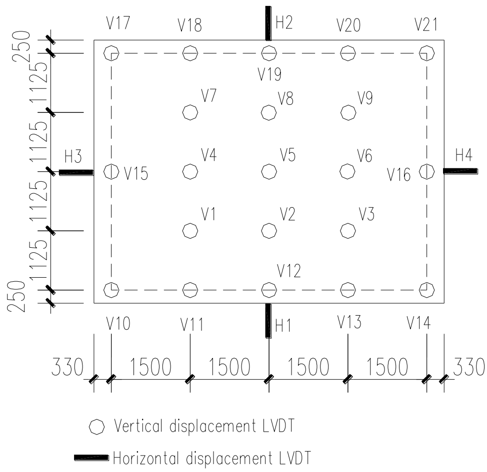

Figure 4. Position of vertical and horizontal displacement transducers (dimension in mm).

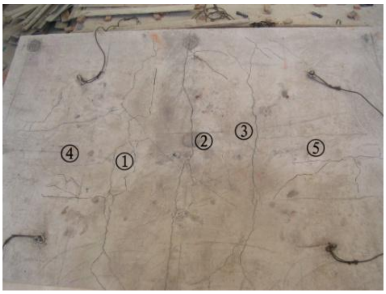

Figure 5. Top view of slab after the test.

Figure 6. Bottom view of slab after test.

The slab's bottom surface, which is exposed to fire (Figure 6), shows many cracks with a regular spacing of 200 mm at the edges which are not exposed to fire. The spacing of the cracks is in accordance with the bar spacing in the long direction, yet running in both longitudinal and transverse directions. Diagonal cracks with a regular spacing of 100-150 mm are also observed at the corners.

Figure 7 shows the variation of the central vertical deflections of the slab during the fire. The deflections measured by the nine LVDTs are plotted. It can be seen that the slab deflects downwards more rapidly in 100 minutes after ignition and reaches 162 mm at mid-span by 97 minutes, which is equal to 1.67 mm per minute. After the first 100 minutes, the deflection rate of the slab decreases. The slab deflects at a steady rate of approximately 0.84 mm per minute for the remaining duration of the test. When the test is stopped at 210 minutes, the mid-span deflection reaches 272 mm. The deflections recorded by V8, V9 and V6 are not given, because they are almost identical to that by V2, V3 and V4 for symmetry.

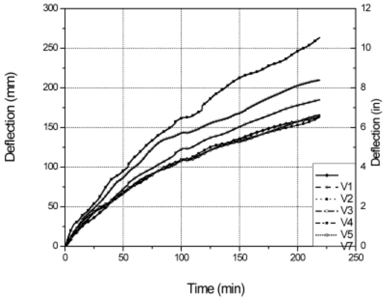

Figure 7. Central vertical deflections of the slab 1.

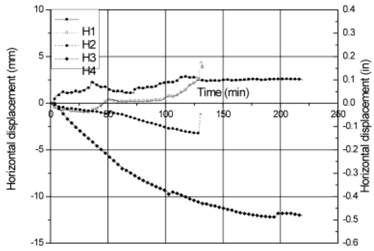

Figure 8. Edge horizontal deflections of the slab 1.

Figure 8 shows the measured horizontal deflections of the slab. The horizontal deflections are due to the expansion and downward deflections in the centre region of the slab. H1 and H2 measure the horizontal deflections in the transverse direction of the slab while H3 and H4 measure the deflections in the longitudinal direction. The edge connected to LVDT H1 always deflects inward; the edge connected to H2 moves outwards very slightly during the initial stage, which reaches a maximum value of -0.97 mm at 32 minutes. After then, the latter edge deflects inwards until it reaches a minimum of 4.7 mm. H2 does not function properly after 130 minutes. Along the long direction, the slab expands at a linear rate until 60 minutes and continues in a slower non-linear manner. The outward deflection of H4 reaches a maximum of -12 mm at the end of the test. The three edges move outward initially, due mainly to the thermal expansion. According to elasticity, the short direction of slab bears much more loading than the long direction. If the deformation caused by the short direction loading is larger than the thermal expansion, the short direction will commence to move inward. The deformation caused by the long direction loading is smaller than the thermal expansion and therefore the long direction always moves outward.

Figure 9 shows the temperature rise of the thermocouple tree embedded in the slab. The thermocouples are attached along a circular concrete specimen with a small diameter every 20 mm distance across the slab depth. The maximum temperature at the bottom of the slab reaches 829℃ and the top one reaches 133℃ by the end of the test. The graph shows a plateau in the temperature rise at 100℃ level. This is attributed to the increase of the moisture from the heated side to the unheated side of the slab.

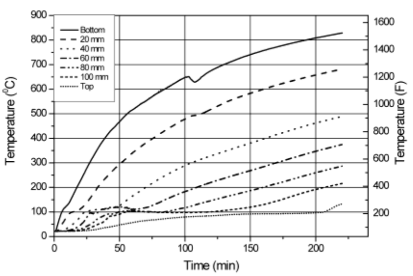

Figure 9. Temperatures of the thermocouple tree of slab 1.

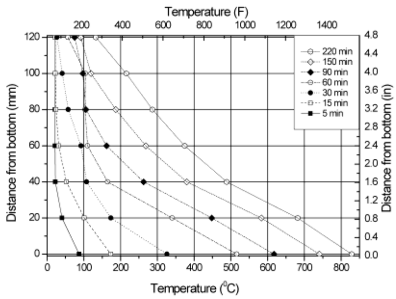

Figure 10. Temperature distribution over the slab depth.

Figure 10 shows the temperature distribution across the slab depth at different time. It can be found that the temperature gradient increases quickly with time. The temperature gradients are 300℃ at 30 minutes and 696 ℃ at 220 minutes, respectively. The maximum temperature rise of the unheated side of the slab does not exceed the failure criterion of 140℃.

The experimental phenomenon and the experimental results of slab 2 are similar to that of slab 1 and are therefore not described here.

3 DETERMINATION OF THE DEFLECTION

As mentioned above, the concrete slabs used in the fire experiments should be categorized as thin plates. By considering equilibrium conditions and strain compatibility, the governing equation of small-deflection behavior of thin elastic plates is:

$$D\left(\frac{\partial^4 w}{\partial x^4}+2\frac{\partial^4 w}{\partial x^2\partial y^2}+\frac{\partial^4 w}{\partial y^4}\right)=q \tag{1}$$

However, in fire, the combination of thermal deflection and degradation of the material properties of the slab requires the consideration of large deflections. When the deflection of the mid-surface exceeds the thickness of the slab, significant strains are generated in the mid-plane. Therefore, von Karman[17] defined the governing equations for large deflections of elastic plates as follows:

$$D\left(\frac{\partial^4 w}{\partial x^4}+2\frac{\partial^4 w}{\partial x^2\partial y^2}+\frac{\partial^4 w}{\partial y^4}\right)=q+h\left(\frac{\partial^2 F}{\partial y^2}\frac{\partial^2 w}{\partial x^2}+\frac{\partial^2 F}{\partial x^2}\frac{\partial^2 w}{\partial y^2}-2\frac{\partial^2 F}{\partial x\partial y}\frac{\partial^2 w}{\partial x\partial y}\right) \tag{2}$$

$$\left(\frac{\partial^4 F}{\partial x^4}+2\frac{\partial^4 F}{\partial x^2\partial y^2}+\frac{\partial^4 F}{\partial y^4}\right)=E\left[\left(\frac{\partial^2 w}{\partial x\partial y}\right)^2-\frac{\partial^2 w}{\partial x^2}\frac{\partial^2 w}{\partial y^2}\right] \tag{3}$$

where w is the deflection function for the slab, F is the Airy stress function, E is the Young's modulus, ν is the Poisson's ratio, D is the flexural rigidity of the slab.

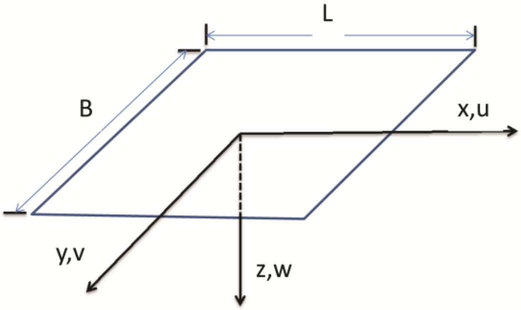

Figure 11. Geometry of rectangular plate.

3.1 Deflection caused by the thermal gradient

To calculate the deflection of a slab subjected to thermal gradient, two governing differential equations must be solved: the equilibrium equation and the compatibility equation [20] which, for an isotropic flat slab subject to thermal gradient, can be written as

$$D_T\left(\frac{\partial^4 w}{\partial x^4}+2\frac{\partial^4 w}{\partial x^2\partial y^2}+\frac{\partial^4 w}{\partial y^4}\right)-h\left(\frac{\partial^2 F}{\partial y^2}\frac{\partial^2 w}{\partial x^2}+\frac{\partial^2 F}{\partial x^2}\frac{\partial^2 w}{\partial y^2}-2\frac{\partial^2 F}{\partial x\partial y}\frac{\partial^2 w}{\partial x\partial y}\right)+\frac{1}{1-\nu}\left(\frac{\partial^2 M^T}{\partial x^2}+\frac{\partial^2 M^T}{\partial y^2}\right)=0 \tag{4}$$

$$\left(\frac{\partial^4 F}{\partial x^4}+2\frac{\partial^4 F}{\partial x^2\partial y^2}+\frac{\partial^4 F}{\partial y^4}\right)-E_T\left[\left(\frac{\partial^2 w}{\partial x\partial y}\right)^2-\frac{\partial^2 w}{\partial x^2}\frac{\partial^2 w}{\partial y^2}\right]+\frac{1}{h}\left(\frac{\partial^2 N^T}{\partial x^2}+\frac{\partial^2 N^T}{\partial y^2}\right)=0 \tag{5}$$

where E^T is the Young's modulus at temperature T, D^T is the flexural rigidity of the slab at temperature T, and M^T is the thermal moment and N^T is the thermal force.

$$M^T = E_T\alpha\int_{-h/2}^{h/2} T(z)zdz = E_T\alpha T_{,Z}\frac{h^3}{12} \tag{6}$$

$$N^T = E_T\alpha\int_{-h/2}^{h/2} T(z)dz = E_T h\alpha\Delta T \tag{7}$$

Where T,z represents the thermal gradient and △T represents the temperature rise.
The E^T decreases with time according to:

$$E^T = (-0.0011\times T+0.83)E \tag{8}$$

Figure 11 shows the slab to be analyzed. The slab is assumed to be simply supported along all four boundaries such that at x=±L/2:

$$w=0, M_x=0; \tag{9}$$

and at y=±B/2:

$$w=0, M_y=0; \tag{10}$$

To obtain a solution of the governing differential equations it is necessary to represent the deflection of the slab and the thermal moment as double Fourier series.

$$w(x,y)=\sum_{m=1}^{\infty}\sum_{n=1}^{\infty} w_{mn}\cos\frac{m\pi x}{L}\cos\frac{n\pi y}{B} \tag{11}$$

$$M^T(x,y)=\sum_{m=1}^{\infty}\sum_{n=1}^{\infty} M_{mn}^T\cos\frac{m\pi x}{L}\cos\frac{n\pi y}{B} \tag{12}$$

Considering only the first term in the series, The Airy stress function F may be chosen as[15]:

$$F=-\frac{w_{11}^2\pi^2 E}{8(1-\nu^2)}\left(\frac{1}{B^2}+\nu\frac{1}{L^2}\right)\frac{x^2}{2}-\frac{E\alpha\Delta T}{1-\nu}\frac{x^2}{2}-\frac{w_{11}^2\pi^2 E}{8(1-\nu^2)}\left(\frac{1}{L^2}+\nu\frac{1}{B^2}\right)\frac{y^2}{2}-\frac{E\alpha\Delta T}{1-\nu}\frac{y^2}{2}$$
$$+\frac{w_{11}^2\pi}{32}\left(\frac{L^2}{B^2}\cos\frac{2\pi x}{L}+\frac{B^2}{L^2}\cos\frac{2\pi y}{B}\right) \tag{13}$$

By using Maple 17, given the recorded temperature distributions during the test, the solution has been obtained, as shown in Figure 12.

3.2 Deflection caused by the constant loading

During the test of the two simply-supported slabs subjected to fire, the load applied to the slabs remains constant. When the deflection reaches over the depth of the slab, the governing equations should be written as:

$$D_T\left(\frac{\partial^4 w}{\partial x^4}+2\frac{\partial^4 w}{\partial x^2\partial y^2}+\frac{\partial^4 w}{\partial y^4}\right)=q+h\left(\frac{\partial^2 F}{\partial y^2}\frac{\partial^2 w}{\partial x^2}+\frac{\partial^2 F}{\partial x^2}\frac{\partial^2 w}{\partial y^2}-2\frac{\partial^2 F}{\partial x\partial y}\frac{\partial^2 w}{\partial x\partial y}\right) \quad (14)$$

$$\left(\frac{\partial^4 F}{\partial x^4}+2\frac{\partial^4 F}{\partial x^2\partial y^2}+\frac{\partial^4 F}{\partial y^4}\right)=E_T\left[\left(\frac{\partial^2 w}{\partial x\partial y}\right)^2-\frac{\partial^2 w}{\partial x^2}\frac{\partial^2 w}{\partial y^2}\right] \quad (15)$$

in which the loading q keeps constant, but the Young's modulus varies with average temperature increase.

Similar to the above process, the deflection of the slab and the load are chosen as double Fourier series:

$$w(x,y)=\sum_{m=1}^{\infty}\sum_{n=1}^{\infty}w_{mn}\cos\frac{m\pi x}{L}\cos\frac{n\pi y}{B} \quad (16)$$

$$q(x,y)=\sum_{m=1}^{\infty}\sum_{n=1}^{\infty}q_{mn}\cos\frac{m\pi x}{L}\cos\frac{n\pi y}{B} \quad (17)$$

and the Airy stress function F may be chosen as[15]:

$$F=\frac{w_{11}^2\pi}{32}\left(\frac{L^2}{B^2}\cos\frac{2\pi x}{L}+\frac{B^2}{L^2}\cos\frac{2\pi y}{B}\right) \quad (18)$$

By using Maple 17, input the recorded temperature distributions, consider the deterioration of the Young's modulus as the average temperature increase, the solution has been obtained, as shown in Figure 12. It is shown that a large part of the slab deflection subjected to fire are mainly caused by the thermal gradient, and the deflection caused by the constant load or due to the deteriorated material properties is less.

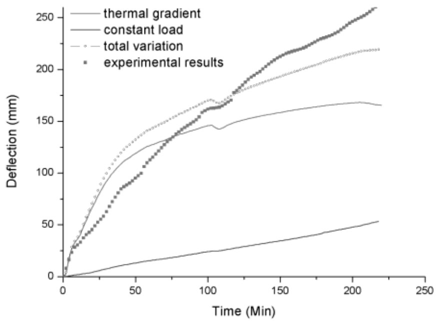

Figure 12. Comparison of deflections with time.

4 CONCLUSIONS

The experimental results of two-way concrete slabs subjected to fire are described. The details of the test slabs, the temperature distributions , deflections and horizontal displacements are all given. It is noted that the maximum deflection reached over two times of the depth of the slabs, so the Von Karman differential equations for thin plates are introduced. Using the recorded temperature distributions as the input data and the Maple 17, the Von Karman equations are solved. It is found that:

(1) Tensile membrane action exists within the slab when the slab reaches a large deflection;

(2) The deflection caused by thermal gradient is larger than that caused by constant loading;

(3) The deviation of the deflection due to the thermal gradient and the constant loading attributes only to the first term of the double Fourier series.

REFERENCES

[1] Mossa PJ, Dhakal RP, Wangb G, A. H. B. The fire behaviour of multi-bay, two-way reinforced concrete slabs.
[2] Park R. Ultimate strength of rectangular concrete slabs under short-term uniform loading with edges restrained against lateral movement. Proceedings of the Institution of Civil Engineers 1964;28:125-150.
[3] Sawczuk A, Winnick L. Plastic behavior of simply supported reinforced concrete plates at moderately large deflections. Int J. Solids Struct 1965;1(1):97-110.
[4] Kemp KO. Yield of a square reinforced concrete slab on simple supports,allowing for membrane forces. The Structural Engineer 1967;45(7):235-240.
[5] Taylor R, DRH M, B. H. Effect of the arrangement of reinforcement on the behavior of reinforced concrete slabs. Mag Concrete Res 1966;18(55):85-94.
[6] Morley CT. Yield Line Theory for Reinforced Concrete Slabs at Moderately Large Deflections. Mag Concrete Res 1967;19(66):211-221.
[7] Taylor RA. A note on a possible basis for a new method of ultimate load design of reinforced concrete slabs. Mag Concrete Res 1965;17(53):183-186.
[8] Janas M. Large plastic Deformations of reinforced concrete slabs. Int. J.Solids Structures 1968;4(1):61-74.
[9] Foster S, Chladna M, Hsieh C, Burgess I, Plank R. Thermal and structural behaviour of a full-scale composite building subject to a severe compartment fire. Fire Safety J 2007;42(3):183-199.
[10] Bailey CG. Membrane action of unrestrained lightly reinforced concrete slabs at large displacements. Eng Struct 2001;23(5):470-483.
[11] Bailey CG. Membrane action of slab/beam composite floor systems in fire. Eng Struct 2004;26(12):1691-1703.
[12] Bailey CG, White DS, Moore DB. The tensile membrane action of unrestrained composite slabs simulated under fire conditions. Eng Struct 2000;22(12):1583-1595.
[13] Dong YL, Fang YY. Tensile Membrane Effects of Concrete Slabs in Fire. Mag Concrete Res 2010;62(1):17-23.
[14] Dong YL. Tensile membrane effects of concrete slabs in fire. Mag Concrete Res 2010;V.62(No.7):497-505.
[15] Usmani AS, N. J. K. C. Limit capacity of laterally restrained reinforced concrete floor slabs in fire. Cement Concrete Comp 2004;26(2):127-140.
[16] Anthony KA, Ian WB, Roger JP. Tensile Membrane Action of Thin Slabs Exposed to Thermal Gradients. J Eng Mech-Asce 2013;V.139(No.11):1497-1507.
[17] Chia C. Nonlinear Analysis of Plates. New York: McGraw-Hill International Book Company; 1980. p 422.

RESEARCHES ON THE FIRE RESISTANCE DESIGN METHOD FOR RC BEAMS STRENGTHENED WITH CFRP LAMINATES

Ke-Xu Hu and Wei Gong

Research Institute of Structural Engineering and Disaster Reduction, Tongji University,
1239 Siping Road, Shanghai 200092, China
e-mails: kexuhu@tongji.edu.cn, weigong890413@qq.com

Keywords: CFRP-strengthened RC beam, Fire protection, Parametric analysis, Construction measure, Fire test

Abstract. *Externally coating of fireproof materials for reinforced concrete (RC) structures strengthened with carbon fiber reinforced polymer (CFRP) is widely used in actual engineering. In order to research the design method against fireproof coating's peeling off in fire, finite elements analysis and construction measures experiments were carried out in this paper. The finite elements analysis taking the different fireproof materials, thickness of coating, loading ratio, CFRP strengthening ratio and depth-span ratio as the parameters, the specimen's mid-span deflection under fire as the output target were carried out using finite elements software ANSYS. The results showed that the thickness of coating, loading ratio and depth-span ratio were the main factors influencing the fire resistance performance of RC beams. A simplified formula to calculate the thickness of fireproof coating was also proposed based on the analysis data. Tests on actual structural members were carried out in this project to optimize the design of fireproof RC beams strengthened by means of CFRP laminates. We tested different fireproof materials including thick fireproof coating, ultra-thin fireproof coating, fireproof panel and normal cement mortar with different construction measures respectively. Based on the experimental results, the different construction measures for thick fireproof coating, ultra-thin fireproof coating and cement mortar were presented and recommended in actual engineering applications*.

1 INTRODUCTION

In recent years, CFRP has been widely used in civil engineering applications due to its high strength, lightness, corrosion resistance performance and ease of application. Currently, most applications of CFRP are in bridges and infrastructures where fire safety is not the first consideration and different countries also formulated technical specifications for the design and construction of structure strengthened with CFRP under ordinary temperature [1-3]. However, when CFRP is used in buildings, CFRP-strengthened RC structures must satisfy fire resistance requirements specified in building codes and standards. Although CFRP systems present great potential, widespread application is being hindered due to concerns regarding their performance at high temperature.

When CFRP is exposed to high temperature typically 300℃－500℃, the organic matrix begin to decompose with the release of heat, smoke, soot and toxic volatiles. Furthermore, the adhesives used to stick CFRP are mostly epoxy organics which glass transition temperature T_g are generally between 65℃ and 80℃ [2], the strength, stiffness and bond properties of CFRP are severely deteriorated when temperature approaching T_g. In particular, the bond between CFRP and concrete, which is critical to maintain effectiveness of the strengthening systems, is also severely reduced at temperature above T_g. In some cases, deterioration of bond properties actually begins at temperatures below T_g. Related studies have found that structures strengthened with CFRP without fire protection measures hardly satisfy the fire resistance requirements whereas proper protection measures can improve its fire resistance performance significantly [4].

The experimental and theoretical researches on fire resistance design method for CFRP-strengthened RC structures are just beginning and there is no related standard to guide the actual application. Aiming to study the fire resistance design method for RC beams strengthened with CFRP laminates, this paper analyzed the main parameters which influence the RC beams' fire resistance performance using finite elements analysis software ANSYS, a simplified formula to calculate the thickness of different fireproof coating was also proposed based on the analysis data; At last, tests on actual structural members were carried out in this project to optimize the design of fireproof RC beams strengthened by means of CFRP laminates.

2 FINITE ELEMENTS ANALYSIS

Related researches on the main factors influencing the fire resistance performance of CFRP-strengthened RC beams have obtained some positive results. Bo Wu at South China University of Technology summarized that the fire endurance of RC beams strengthened with CFRP was affected by the coating thickness, loading ratio, CFRP strengthening ratio, concrete cover thickness, reinforcement ratio and depth-span ratio [5]. Dr. Williams at Queen's University found that the arrangement, thickness and thermal conductivity of the coating, glass transition temperature and ignition temperature of the colloid materials were main factors influencing the FRP-strengthened RC flexural members' fire resistance performance [6]. Dr. Ahmed found that the FRP strengthening ratio, bonding deterioration, axial restraint and loading ratio were the main factors concerning the fire resistance performance whereas concrete strength, aggregate types and bonding layer thickness didn't have the evident influences [7]. Wanyang Gao at Tongji University found that the thickness, thermal conductivity and glass transition temperature of the fireproof coating were the main factors influencing the fire endurance of RC beams [8].

2.1 Parameter analysis

Extended numerical analysis using finite elements analysis software ANSYS was carried out in this paper based on the previous researches [9], we took the loading ratio, CFRP strengthening ratio, depth-span ratio, coating thickness and reinforcement ratio as the parameters and analyzed three different fireproof materials which were thick fireproof coating, ultra-thin fireproof coating and normal cement mortar. The values of parameters are shown in table 1. The modelling process of the RC beams strengthened with CFRP laminates were specified in [10]. Considering the requirements of A level fire endurance (⩾2 hours), the firing time in this analysis was 7200 seconds according to the ISO-834 standard fire curve.

Table 1. Values of parameters.

Loading ratio	0.4、0.6、0.8、1.0	Depth-span ratio	1/15、1/12、1/8
CFRP strengthening ratio	0.1、0.2、0.3、0.4	Reinforcement ratio	0.6%、1.2%
Coating thickness* (mm)	10、20、30、40 / 1.0、2.0、3.0 / 25、35、45		

*The values of coating thickness are thick fireproof coating, ultra-thin fireproof coating and normal cement mortar respectively.

The change trends of mid-span deflection under high temperature can reflect the RC beams' fire resistance performance indirectly [10]. Figures 1-3 are the different influences of loading ratio, CFRP strengthening ratio, coating thickness and depth-span ratio on mid-span deflection of CFRP-strengthened RC beams protected by different fireproof materials.

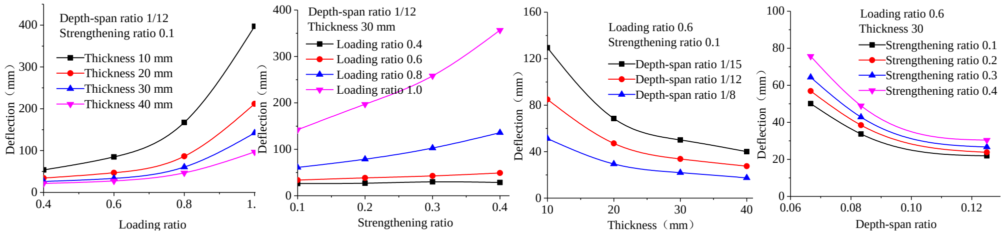

(a) Influence of loading ratio (b) Influences of CFRP strengthening ratio (c) Influence of coating thickness (b) Influences of CFRP depth-span ratio

Figure 1. The effects of parameters on mid-span deflection under thick fire coating.

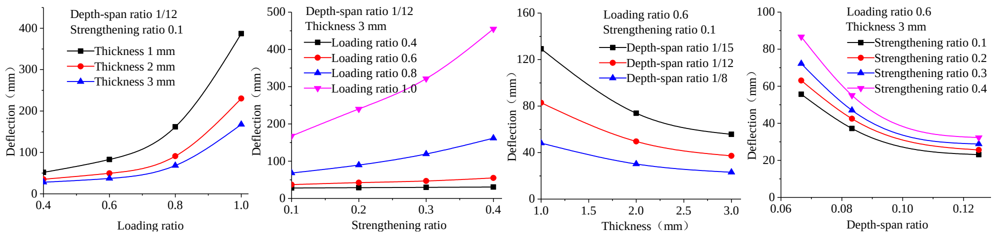

(a) Influence of loading ratio (b) Influences of CFRP strengthening ratio (c) Influence of coating thickness (b) Influences of CFRP depth-span ratio

Figure 2. The effects of parameters on mid-span deflection under ultra-thin fire coating.

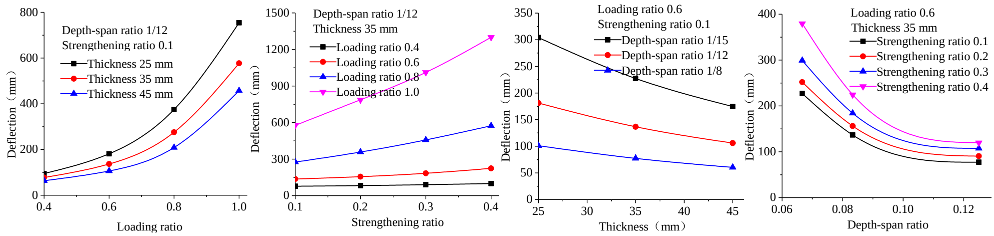

(a) Influence of loading ratio (b) Influences of CFRP strengthening ratio (c) Influence of coating thickness (b) Influences of CFRP depth-span ratio

Figure 3. The effects of parameters on mid-span deflection under cement mortar fire coating.

From Figures 1-3 we could find: (1) The beam's mid-span deflection increased with the increasing loading ratio, and the change velocity of deflection decreased with the increase of coating thickness; (2) The deflection increased with the increasing loading ratio, and this phenomenon was more obviously with the larger loading ratio. Because after the failure of the CFRP laminates, the previous bearing capacity provided by CFRP laminates will transfer to RC beams; (3) The deflection decreased with the increasing coating thickness, and the change velocity of deflection decreased with the increasing depth-span ratio; (4) The deflection decreased with the increasing depth-span ratio, and the deflection with different CFRP strengthened ratio kept the same change trends.

It could be obtained from the above analysis that the loading ratio, coating thickness and depth-span ratio affected the beam's fire resistance performance significantly whereas the CFRP strengthening ratio has little influence.

2.2 Equation to calculate the thickness of fireproof coating

Different fireproof materials have different fire resistance performance and mechanism, the coating thickness also need to be determined according to the actual demands. Finite analysis is very complex and takes much time in calculating the coating thickness in practical engineering. To simplify the calculating process, we proposed a simplified formula by means of fitting analysis to calculate the different coating thickness [10].

We chose the usual domain of the parameters for the convenience of actual applications, the loading ratio H=0.4-1.0, CFRP strengthening ratio J_{cfrp}=0.1-0.4, depth-span ratio K=12-8, the reinforcement ratio was between 0.6% and 1.2%. Based on the previous finite analysis data by means of fitting analysis, we obtained Equation (1) and (2) to calculate the coating thickness (The equations were only used to calculate the CFRP-strengthened RC beams' fireproof coating thickness for 2 hours fire endurance requirements).

$$T = \frac{p_0}{D} \times (J_{cfrp}^2 + p_1 \times J_{cfrp} + p_2) \times (H^2 + p_3 \times H + p_4) \times (K^2 + p_5 \times K + p_6) - p_7 \tag{1}$$

$$D = L^2 / 400d \tag{2}$$

Where T is the coating thickness (mm), D is the mid-span deflection (mm), L is the span of the beam (mm), d is the height of the beam (mm), p_0-p_7 can be obtained from Table 2, the reinforcement ratio between 0.6% and 1.2% can use liner interpolation method.

Table 2. The values of parameters in the equation.

Coating type	Reinforcement Ratio	Parameters							
		P_0	P_1	P_2	P_3	P_4	P_5	P_6	P_7
Thick coating	0.60%	157.504	0.414	0.240	-0.837	0.217	10.246	2.708	1.837
	1.20%	11.460	17.364	2.494	-0.851	0.218	7.693	52.439	3.603
Ultra-thin coating	0.60%	62.756	0.785	0.271	-0.873	0.225	-12.420	82.117	0.697
	1.20%	74.015	0.351	0.104	-0.873	0.220	-2.386	76.201	1.168
Cement mortar	0.60%	987.943	0.672	0.483	-0.631	0.158	-12.651	78.283	5.252
	1.20%	12.396	113.098	22.385	-0.698	0.170	-9.236	74.438	11.752

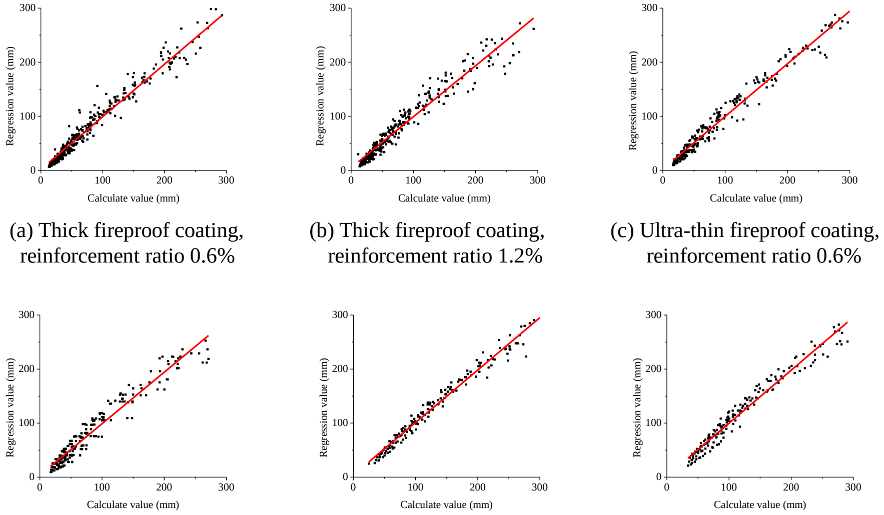

(a) Thick fireproof coating, reinforcement ratio 0.6%
(b) Thick fireproof coating, reinforcement ratio 1.2%
(c) Ultra-thin fireproof coating, reinforcement ratio 0.6%
(d) Ultra-thin fireproof coating, reinforcement ratio 1.2%
(e) Cement mortar, reinforcement ratio 0.6%
(f) Cement mortar, reinforcement ratio 1.2%

Figure 4. Comparison between the regression value and the calculate value.

Figure 4 is the fireproof coating thickness comparison of RC beam strengthened with CFRP laminates between the calculate value obtained through ANSYS analysis and the regression value obtained using Equation (1) and (2) [10]. From the comparison we can find the average value of regression value/ calculate value ratio is 0.975-0.997, the mean square error is 0.085-0.214 and the coefficient variation is 0.086-0.217. The regression value is in good agreement with the calculating value.

3 CONSTRUCTION MEASURES EXPERIMENTS

Tests on actual structural members were carried out in this project to optimize the design of fireproof RC beams strengthened by means of CFRP laminates. The fireproof materials used in the tests were thick fireproof coating, ultra-thin fireproof coating, fireproof panel and normal cement mortar.

In order to simulate the actual engineering applications, the bottom of the specimens were stuck with CFRP laminates which width was equal to the beam bottom. The end of the beams was stuck with two U-shaped CFRP stirrups to fix the CFRP laminates. Two thermocouples were installed at the beam's bottom and side to measure the temperature of glue layer. The details of the specimens are shown in figure 5.

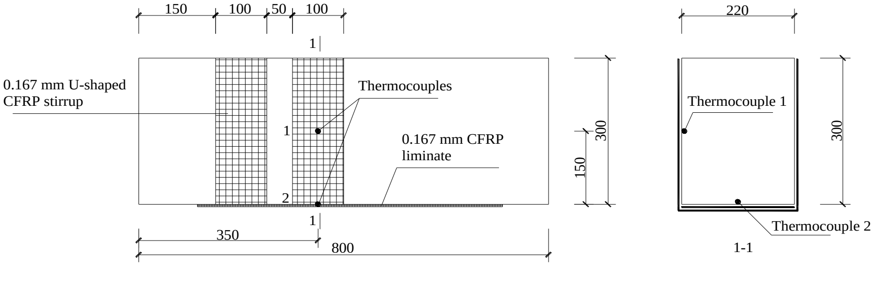

Figure 5. Test specimen.

3.1 Construction measures

3.1.1 Thick fireproof coating

Thick fireproof coating will form an enamel-like protective layer when heated, the layer can shield the base material and prevent the heat radiation. In addition, some materials of thick fireproof coating will absorb heat and release non-flammable vapours to consume heat, decrease flame temperature and dilute oxygen concentration. Except the good fire resistance performance, thick fireproof coating also has the hydration, low cost and weather resistance characteristics.

The thick fireproof coating used in tests was produced in Shanghai and its design thickness was 20 mm, a U-shaped steel wire mesh was set in the coating layer [11]. The coating was divided into two layers by the steel wire mesh and the thickness of each layer was 10 mm. The steel wire mesh was fixed with M6 expansion bolt and its specification was 10 mm × 10 mm. The details of the specimen are shown in Figure 6. (Due to the thick fireproof coating has a poor bonding property with CFRP, we put some quartz sand on the CFRP laminates to improve its bonding property.)

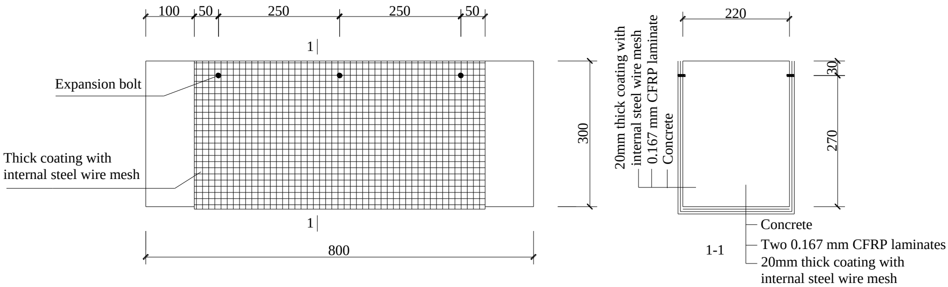

Figure 6. Details of the test specimen with thick fireproof coating.

3.1.2 Ultra-thin fireproof coating

Ultra-thin fireproof coating will decomposed and release large amounts of inert gases when heated, the inert gases will dilute the combustible gases and oxygen concentration to slow down the combustion. In addition, the ultra-thin fireproof coating will expand and foaming when exposed in fire, forming a porous lightweight carbonized foam layer to prevent heat transfer.

The construction measure of ultra-thin fireproof coating was coated a 10 mm cement mortar layer with internal steel wire mesh firstly and then coated a 1.5 mm ultra-thin fireproof coating. The details of the specimen are shown in Figure 7.

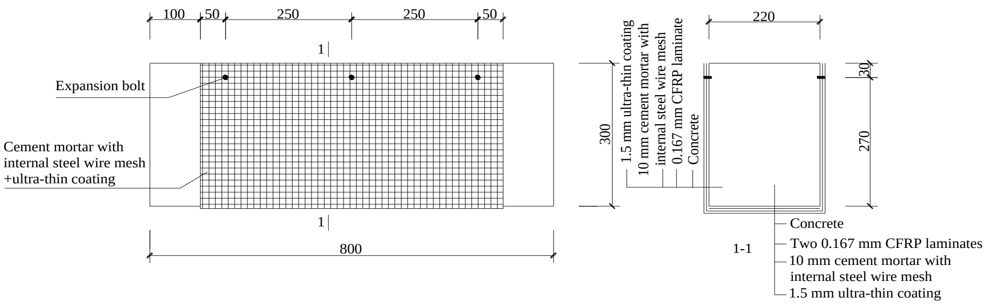

Figure 7. Details of the test specimen with ultra-thin fireproof coating.

3.1.3 Fireproof panel

Fireproof panel is a kind of plate materials generally consisted of inorganic materials and modified substances. Fireproof panel can maintain certain strength under high temperature and has the dimensional stability and fire insulation capacity.

The fireproof panel used in this test was inorganic non-combustible composite board (glass magnesium board). Two layers of 5mm thick fireproof panels were stuck on the specimen's side and bottom using staggered joint connection and fixed with expansion bolts, refractory steel and flat steel. The details are shown in Figure 8.

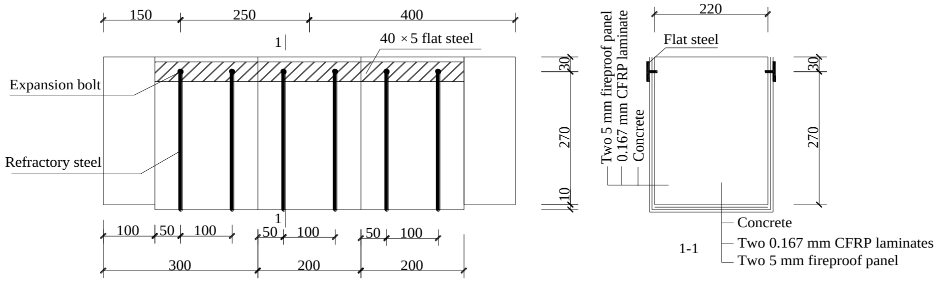

Figure 8. Details of the test specimen with fireproof panel.

3.1.4 Cement mortar

Cement mortar can spray or paint on the surface of the RC structures. In the case of low fire resistance requirements, cement mortar can be used as the fireproof coating due to its low coat, and ease to application.

In order to study and compare the fire resistance performance between cement mortar and fireproof materials, we took the same construction measures as the thick fireproof coating. The details are shown in Figure 9.

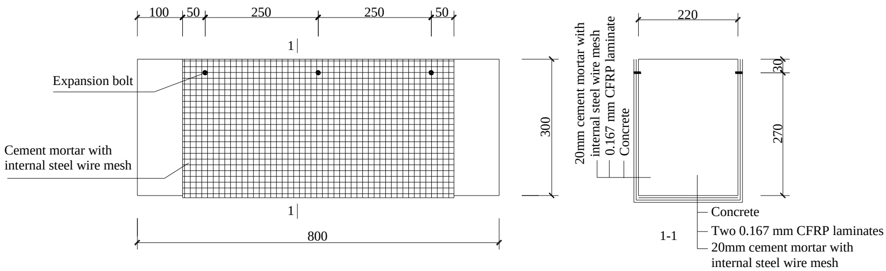

Figure 9. Details of the test specimen with cement mortar.

3.2 Phenomena of tests

The fire tests were carried out in Tongji University. The specimens were exposed to fire on three sides for 2 hours according to the ISO-834 standard fire curve. The main purpose of the tests was to study the effectiveness of the construction measures on protecting the CFRP laminates, we only cared about the fireproof coating's cracking and peeling off process and the glue layer's temperature.

3.2.1 Thick fireproof coating

There were only some small cracks on the bottom and side of the beam and no obvious peeling off after test, the construction measure in the test was effective and feasible. The specimen after fire test is shown in Figure 10 (a).

3.2.2 Ultra-thin fireproof coating

In the ultra-thin fireproof coating test, the coating later began to foaming after 2 minutes exposed in fire. Due to the foaming process was uneven, the cracks were emerged and then filled up with the foam. The fireproof coating wasn't peeled off after the test and the construction measure was effective and feasible. The details are shown in Figure 10 (b).

(a) Thick coating (b) Ultra-thin coating (c) Fireproof panel (d) Cement mortar

Figure 10. Specimens after fire tests.

3.2.3 Fireproof panel

The fireproof panel test was stopped after 1 hour exposed in fire due to volumes of black smoke was belched out from the furnace with slight peculiar smell. After the test we found the refractory steels used to fix the panels were fractured and some panels at the bottom of the beam were peeled off. The panels were become warped and friable. The details are shown in Figure 10 (c).

3.2.4 Cement mortar

The outer layer cement mortar at beam side was peeled off partially but the steel wire mesh was not exposed, the inner layer cement mortar was still intact. The details after test are shown in Figure 10 (d).

3.3 Fire resistance performance of the different fireproof materials

In order to compare the fire resistance performance of the different fireproof materials, we removed the coatings after the test. The surface of the specimens with thick fireproof coating, ultra-thin fireproof coating and fireproof panels were intact, the CFRP laminates were not totally oxidated and still had the bonding capacity with the concrete. The details are shown in Figure 11 (a)~(c).The CFRP laminates were peeled off protected by the cement mortar and the details are shown in Figure 11 (d).

(a) Thick coating (b) Ultra-thin coating (c) Fireproof panel (d) Cement mortar

Figure 11. The surface of specimens after fire tests.

3.4 Recommended construction measures

Based on the tests results, the following construction measures are recommended for thick fireproof coating, ultra-thin fireproof coating and cement mortar respectively.

3.4.1 Thick fireproof coating

The thick fireproof coating is prone to crack and peel off due to its thickness, so we recommend use wire mesh and expansion bolts to fix it. The coating should be layered coated and the wire mesh should be put in the outer layer, the details are shown in Figure12 (a).

3.4.2 Ultra-thin fireproof coating

Before coating the ultra-thin fireproof coating, we recommend to coat a cement mortar layer with wire mesh firstly and use quartz sand to improve the bonding properties between the coating and CFRP laminates. The details are shown in Figure12 (b).

3.4.3 Cement mortar

We can put U-shaped wire mesh in the cement mortar and use expansion bolts to fix it, the cement mortar also need to be layered coated and the construction quality need to be guaranteed. The details are shown in Figure 12 (c).

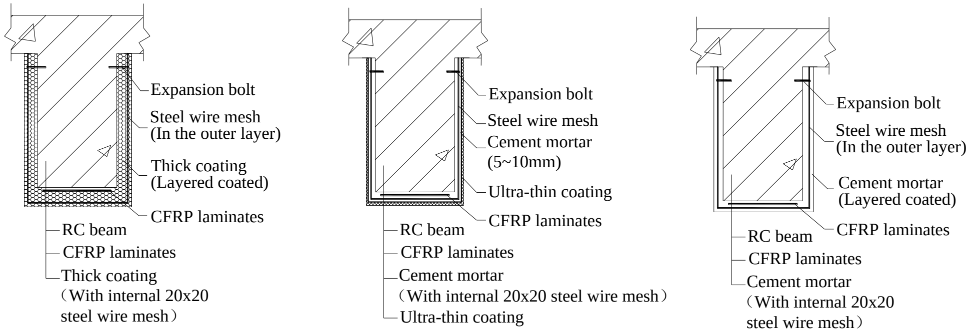

(a) Thick coating (b) Ultra-thin coating (c) Cement mortar

Figure 12. Recommended construction measures.

4 CONCLUSIONS

According to the finite analysis and the construction measure experiments we obtained the following conclusions:

(1) The loading ratio, coating thickness and depth-span ratio affect the beam's fire resistance performance significantly whereas the CFRP strengthening ratio has a smaller influence.

(2) A simplified formula to calculate the different fireproof coating thickness of beams strengthened with CFRP laminates was proposed and verified.

(3) Based on the fire tests the thick fireproof coating is recommended in actual applications, and then was the ultra-thin fireproof coating. The cement mortar also can be used under the low fire resistance requirements.

REFERENCES

[1] CECS146-2003, *Technical specification for strengthening concrete structure with carbon fiber reinforced polymer laminate*, (in Chinese)

[2] ACI44012R-021 *Guide for the design and construction of externally bonded FRP systems for strengthening concrete structures*, Farmington Hills, Michigan: American Concrete Institute, 2002.

[3] CANPCSAS806-02: *Design and construction of building components with fiber-reinforced polymers*, Mississauga, Canada: Canadian Standards Association, 2002.

[4] Williams B., Kodur V., Green M.F., et al, "Fire endurance of fiber-reinforced polymer strengthened concrete T-beams", *ACI Structural Journal*, 105(1), 2008.

[5] Wu B., Wan Z.J., and Wang F., "Analysis of fire endurance of reinforced concrete beams strengthened in flexure with carbon fiber sheets", *Earthquake Resistant Engineering and Retrofitting*, 30(2):101-108, 2008. (in Chinese)

[6] Williams B., *Fire performance of FRP-strengthened reinforced concrete flexural members*, Queen's University, 2004.

[7] Ahmed A., *Behavior of FRP-strengthened reinforced concrete beams under fire conditions*. Michigan State University, 2010.

[8] GAO W.Y., HU K.X., LU Z.D., “Nonlinear analysis of insulated carbon fiber reinforced polymer strengthened reinforced concrete beams in fire”, *Journal of Tongji University (Natural Science)*, 37(5):575-582, 2009. (in Chinese)

[9] Peng D.P., *Researches on the method of fire-resisting design of RC beams strengthened with CFRP*, Shanghai: Tongji University, 2012. (in Chinese)

[10] Wang W.H., *Further researches on the method of fire protection of CFRP-strengthened reinforced concrete beams*, Shanghai: Tongji University, 2013. (in Chinese)

[11] Guangdong Provincial Department of housing and Urban-Rural construction, *DJB/T 15-81-2011 Code for Fire Resistance Design of Concrete Building Structures*, Beijing: China Architecture & Buildings Press, 2011. (in Chinese)

8th International Conference on Structures in Fire
Guo-Qiang LI, Venkatesh K. R. KODUR, Shou-Chao JIANG, Jian JIANG, Su-Wen CHEN, Guo-Biao LOU (Eds.)
Shanghai, China, June 11-13, 2014

BEHAVIOUR OF PRESTRESSED CONCRETE HOLLOW-CORE SLABS UNDER STANDARD AND DESIGN FIRE EXPOSURE

Anuj M. Shakya* and Venkatesh K. R. Kodur*

* Michigan State University, Department of Civil and Environmental Engineering, USA
e-mails: shakyaan@msu.edu, kodur@egr.msu.edu

Keywords: Precast concrete slabs, Fire performance, Hollowcore slabs, Fire tests, Numerical model

Abstract. *The behaviour of precast prestressed concrete (PC) hollow-core slabs under standard and design fire conditions is presented in this paper. A numerical model was developed in ANSYS to trace the response of PC hollow-core slabs under fire scenarios. This model accounts for geometric and material nonlinearities, presence of core, and temperature dependent thermal and mechanical properties of concrete, reinforcing steel and prestressing steel. The model was validated against test data obtained from fire tests on four PC hollow-core slabs. Predicted temperature and deflection from the numerical model compare well with measured data from fire tests indicating that the proposed model is capable of tracing the behavior of PC hollow-core slabs under standard and design fire conditions. Also, results from numerical studies and fire tests clearly show that typical hollow-core slabs can sustain service loads for at least two hours under standard and design fire conditions.*

1 INTRODUCTION

In recent years prestressed concrete (PC) hollow-core concrete slabs are finding increasing applications in buildings due to numerous advantages, such as cost effectiveness, architectural aesthetics, speedy construction, space utilization and low maintenance costs, they offer over other floor systems. Structural fire safety is one of the key considerations in buildings and hence, building codes generally specify fire resistance requirements for floors/slabs. Currently, fire resistance rating of hollow-core slabs is evaluated through prescriptive methods wherein, fire resistance is determined based on slab thickness and concrete cover thickness to reinforcement. These prescriptive rules, developed based on data from standard fire tests, consider only limited parameters and often, do not yield realistic fire resistance.

PC hollow-core slabs generally comprise of concrete and prestressing strands as reinforcement. Flexural capacity of such hollow-core slabs is mainly governed by the stress levels attained in strands. Under fire conditions, both concrete and prestressing steel experience strength degradation, leading to degradation in moment capacity with fire exposure time. When the moment capacity drops below the moment due to applied loading, failure of the slab can occur through strength limit state. The moment capacity at which failure occurs is linked to temperature in prestressing strands defined as critical temperature. Other limit states that govern failure in these slabs are insulation criteria, wherein failure in said to occur when temperature on the unexposed surface exceeds limiting temperature, or integrity criteria when flame breaches through the unexposed side of the slab. The time to reach any of these limiting criteria is referred to as fire resistance of the slab. The rate, at which moment capacity degrades, is a function of number of parameters including cover thickness, core size, fire scenario, load level and support restraints.

In the last four decades, several experimental and few numerical studies have been carried out to evaluate fire resistance of PC hollow-core slabs [1-14]. Most of these studies were limited to standard fire exposure and were focused on developing fire resistance ratings for hollow-core slabs. In most cases, critical temperature in strand was applied as limiting criteria to evaluate failure of these slabs. In these studies spalling, bond and shear crushing were identified as possible factors contributing to failure in PC hollow-core slabs. However, the reasoning for different failure patterns in hollow-core slabs is not discussed. Further, these fire tests did not consider the effect of some of the critical parameters, such as fire scenario and restraint conditions on the behaviour of hollow-core slabs. Thus, the behaviour of PC hollow-core slabs, under realistic fire, loading and restraint conditions, is not well established.

To overcome some of these limitations, a numerical model was developed for tracing the fire response of hollow-core slabs. For validating the numerical model, two sets of fire tests were carried out on four PC hollowcore slabs, wherein critical parameters affecting fire response of these hollow-core slabs were varied. This paper presents the development and validation of the numerical model for tracing fire response of hollow-core slabs.

2 NUMERICAL MODEL

A three-dimensional non-linear finite element model is developed using ANSYS finite element package for tracing the fire response of hollowcore slabs [15]. This model accounts for geometric and material nonlinearities, size of hollowcore, temperature induced property degradation in concrete, reinforcing steel and prestressing steel as well as loading and restraint support conditions. Fire resistance analysis of a hollowcore slab is carried out at various time steps through a sequentially coupled thermal and structural analysis by incrementing time from the start of fire exposure (ignition) till failure of the slab. The time at which failure occurs is taken to be the fire resistance of the slab. The main steps associated with fire resistance analysis at each time step comprise of,

（1）establishing temperatures due to fire exposure,

（2）generating cross-sectional temperature profile through thermal analysis,

（3）evaluating flexural capacity and deflections.

（4）applying various limiting failure criteria to determine failure of slab.

2.1 Discretization of slabs

For the fire resistance analysis, the given PC hollow-core slab is discretized into elements. Two sets of elements are used for undertaking thermal and structural analysis in ANSYS [15]. For thermal analysis, SOLID70, LINK33 and SURF152 are used, and for structural analysis SOLID65, LINK180 and SURF154 are utilized.

SURF152 is a surface effect element and is capable of simulating heat transfer from fire source to the surface of the slab through radiation and convection. This element was overlaid onto fire exposed surface of slab and onto open surfaces of hollow-core cores to simulate radiation and convection of heat from fire source onto the bottom surface of the slab and from lower surface of hollow-cores to upper surfaces of cores respectively. SOLID70 element, capable of simulating 3-D thermal conduction, is used to simulate heat transmission into inner concrete layers from the fire exposed surface of slab. This SOLID70 element has eight nodes with a single degree of freedom at each node namely, temperature, and is applicable to a 3-D steady-state or transient thermal analysis. LINK33 is an uniaxial element with capability to conduct heat between nodes under steady-state or transient state heating conditions. LINK33 element also has a single degree of freedom, temperature, at each nodal point. The three thermal elements are switched into structural elements after completion of thermal analysis as:

（1）SOLID70 3-D solid thermal elements are transformed into SOLID65 3-D concrete solid elements.

（2）LINK33 thermal line elements are transformed into LINK180 prestressing strands line elements.

（3）SURF152 thermal surface effect elements are transformed into SURF154 elements.

In structural analysis, SOLID65 3-D element is used to model concrete. The SOLID65 element is capable of simulating cracking in tension in three orthogonal directions, crushing in compression, plastic deformations, and creep. This element is defined by eight nodes having three degrees of freedom at each node: translation in nodal x, y, and z directions. LINK180 3-D spar element is used to model prestressing strands in the slab. This element can capture uniaxial tension or compression and has three degrees of freedom at each node: translation in the nodal x, y, and z directions. Plasticity, creep, rotation, and large strain deformations in prestressing steel can also be simulated using this element. SURF154 element does not have any role (contribution) in structural analysis. A typical PC hollow-core slab, discretized into various elements, is shown in Figure 1.

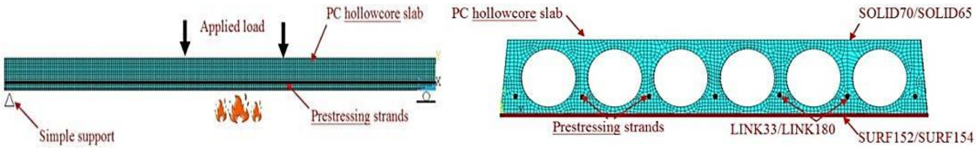

（a）Elevation （b）Cross-section

Figure 1. Layout of a typical PC hollow-core slab and its discretization for finite element analysis.

2.2 Material properties

For fire resistance analysis, temperature dependent thermal and mechanical properties of constituent material are to be provided as input data. The thermal properties include thermal conductivity, specific heat and emissivity factors, while mechanical properties include density, elastic modulus, poison's ratio, stress-strain relations and thermal expansion. These properties of concrete and prestressing strands are defined as varying with temperature using the relations specified in Eurocode 2 [16].

In slabs, top fibers of the slab are subjected to compression, while bottom fibers are subject to tension. Thus, prestressing strands remain in tension throughout loading (and fire) phase and thus, only tensile behavior is to be simulated in strands. However, concrete can be subjected to both tension and compression and hence, concrete behavior in both compression and tension regimes is to be captured. Thus, in ANSYS, plastic behavior of concrete is defined using Willam and Warnke's constitutive model [17], which is capable of accounting for concrete behavior in both tension and compression. The compressive plastic behavior is defined as isotropic multi-linear stress-strain curve varying with temperature, while tensile behavior is defined using damage parameters. In ANSYS, the damage in concrete is defined in terms of crack opening and crack closing parameters. These parameters are defined as open and close crack shear transfer coefficients, (βt and βc respectively) and are taken to be 0.2 and 0.7 respectively [17].

2.3 Fire, loading and boundary conditions

A PC hollow-core slab when exposed to fire is subjected to both thermal and mechanical loading. To simulate realistic conditions, analysis starts with the application of structural (mechanical) loading on the slab, which is generally a percentage of total flexural capacity of the slab. After initial deflection stabilizes, the slab is exposed to fire (thermal) loading. Both mechanical and thermal loading are continued until failure occurs in the slab. The slab can be subjected to any specified fire exposure conditions, which is to be input as a time-temperature curve (points). This can be a standard fire (ASTM E119 [18], ISO834 [19]) or a typical design fire comprising of heating and cooling phase. Also, the slab can be provided with any type of support condition and is to be specified by fixing the nodal degrees of freedom at support nodes. The support condition can be either simply-supported or restrained. Figure 2(a) shows a layout of a typical hollow-core slab with applied loading and boundary conditions.

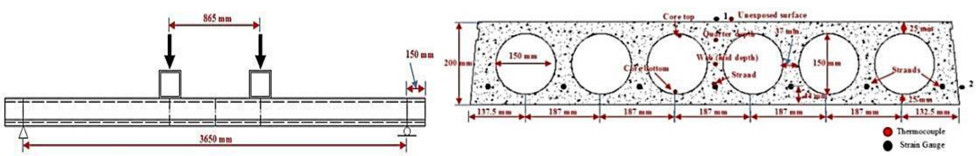

(a) Four point loading scheme for fire tests (b) Cross-sectional details with location of thermocouples and strain gauges

Figure 2. Details of a typical prestressed concrete hollow-core slab.

2.4 Failure limit states

Failure in horizontal members such as floors and slabs, under fire exposure, is typically assessed based on insulation, integrity and stability criteria as specified in ASTM E119 [18] or ISO834 [19]. Based on insulation criteria, failure of slab is said to occur when the average temperature on the unexposed surface of the slab exceeds 139 ℃ (measured at 9 points) or a maximum of 181 ℃, above initial temperature, at any single point of the unexposed surface of the slab. As per integrity criteria, failure of slab is said to occur when flame breaches through the unexposed side (surface) of the slab through any fire induced cracks or holes. Under stability criteria, failure occurs when the moment capacity of the slab, at the critical section, drops below the moment caused due to applied loading. In most previous studies, the strength failure in hollow-core slabs is linked to critical temperature reached in prestressing strands, which is taken as 427 ℃. Although convenient this simplistic correlation applicable when the slab is subjected to a load equivalent to 50 percent of its capacity, does not yield realistic fire resistance for other levels of loading.

In addition to above limit states, deflection or rate of deflection can indicate imminent failure of horizontal members (beams or slabs) under fire conditions [20]. This deflection limit state is given in British Standard (BS 476) [21] and was also applied to evaluate failure in hollow-core slabs. Based on BS 476 [21] criteria, failure of a slab occurs when the maximum deflection in the slab exceeds L/20 at any fire exposure time, or the rate of deflection exceeds $L^2/9000d$ (mm/min) after attaining a maximum deflection of L/30, where, L = span length of the slab (mm), and d = effective depth of the slab (mm).

3 FIRE RESISTANCE EXPERIMENTS

For the purpose of validating above discussed numerical model, fire resistance tests were carried out on four PC hollow-core slabs, designated as Slab 3, Slab 4, Slab 5 and Slab 6. The parameters that were varied in these tests included aggregate type, fire scenario, and support restraints.

3.1 Fabrication of slabs

All four PC hollow-core slabs were 4 m in length, 1.2 m in width, and 200 mm in depth, and had six cores and seven prestressing strands as reinforcement. The cores in the slabs were of 150 mm diameter, with 25 mm concrete thickness at the bottom of the core. The prestressing strands were of 12.7 mm diameter and were of low relaxation strand type, with tensile strength of 1860 MPa. The concrete cover thickness over the strands was 44 mm. Geometric and material characteristics of these slabs are presented in Table 1 and a detailed cross sectional configuration of a typical PC hollow-core slab is shown in Figure 2(b).

Table 1. Geometric and material characteristics of tested slabs.

Parameter	Slab 2 to 6
Dimension (length × width × thickness)	$4 \times 1.2 \times 0.2\ m^3$
Cores	Six 150 mm Ø
Concrete design compressive strength	75 MPa
Prestressing strand	Seven – 12.7 mm 1860 MPa low relaxation

Hollow-core slabs were cast at a local fabrication plant through extrusion process, wherein concrete mix is injected through an extrusion die to take predesigned shape. The slab was extruded over prestressed strands on 150 m long bed. The hollow-core slabs were designed as per PCI design manual provisions [22] to meet industry specifications. Two batch mixes of concrete were used to fabricate the slabs, namely carbonate aggregate, batch mix for Slab 3, Slab 5 and Slab 6, and siliceous aggregate batch mix for Slab 4. The mix proportions used in two batch mixes of concrete remained same, but coarse aggregate type was different. Batch 1 mix had carbonate based coarse aggregate, while Batch 2 mix had siliceous based coarse aggregate. All six slabs were cured for 2 months in plant yard and then shipped to Michigan State University (MSU) Civil Infrastructural Laboratory, where they were stored at 25 ℃ and 40% relative humidity till fire tests were undertaken. The compressive strength of concrete and relative humidity of slabs were measured periodically during curing stage, and the measured values on day of the test, prior to fire testing, are listed in Table 2.

Table 2. Summary of test parameters and results.

Test slab	Aggregate type	Test day Compressive strength (f'_c), MPa	Applied Loading (% of capacity)	Support condition	Test day RH %	Fire scenario	Failure modes	Spalling
Slab 3	Carbonate	75	60	SS	55	DF2	-	-
Slab 4	Siliceous	91	60	SS	55	DF2	-	Minor
Slab 5	Carbonate	75	60	AR	55	ASTM -E119	Crushing of Concrete	-
Slab 6	Carbonate	75	60	SS	55	ASTM -E119	Flexural cracks	-

Note: SS = simply supported, AR = axially restrained, RH = relative humidity, '-' = not failed or no spalling observed

The slabs were instrumented with thermocouples, strain gauges, LVDTs (linear variable displacement transducer) and load cells. Thermocouples were placed to monitor temperatures on strand, mid depth, quarter depth, core bottom, core top and on unexposed (top) surface. Strain gauges were installed to measure progression of thermal and mechanical strains in strand and top surface of slab of slab. LVDTs were installed on slabs to record progression of mid-span deflections during fire exposure and load cells were placed at supports of restrained slab to measure fire induced axial force. Location of thermocouples, strain gauges and deflection gauges on the slab is illustrated in Figure 2(b).

3.4 Test conditions and procedure

Fire resistance tests on PC hollow-core slabs were carried out using the structural fire test furnace commissioned at MSU Civil Infrastructure Laboratory. This test furnace is designed to simulate simultaneous application of thermal and structural loading, as well as restraint conditions, to which a slab might be subjected during a fire event. The furnace details together with test set-up are illustrated in Figure 3. Two PC hollow-core slabs were tested in each fire test by subjecting them to predetermined fire, structural loading, and boundary conditions. Slabs 3, 4 and 6 were tested under simply-supported end conditions, while Slab 5 was restrained at supports for longitudinal/axial expansion. Superimposed loading was applied using hydraulic actuators through extension columns, and were distributed along the slab width using hollow steel sections (HSS 8×8×½ [23]). Four point loading scheme was adopted to apply loading on these slabs, as shown in Figure 2(a).

To study the realistic response of hollow-core slabs under different fire scenarios, the slabs were tested under two different fire scenarios. In Test 1, Slab 3 and Slab 4 were tested under design fire exposure (DF2) to simulate typical ventilation controlled office fire, comprising of 120 minutes of growth phase followed by a decay phase. In Test 2, Slab 5 and 6 were tested under standard ASTM E119 fire [20], representing growth phase of fire only. During fire tests, all four slabs were subjected to a load level equivalent to 60% of the flexural capacity of slabs.

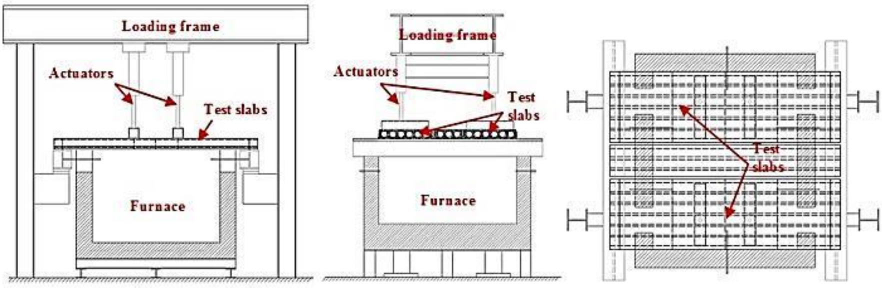

(a) E-W elevation (b) N-S elevation (c) Plan

Figure 3. Test setup for undertaking fire resistance tests on PC hollow-core slabs.

4 MODEL VALIDATION

The above discussed numerical model is validated by comparing predicted response parameters with those measured in fire resistance tests for four hollow-core slabs. A comparison of predicted and measured thermal and structural response parameters is presented in Figure 4, Figure 5 and Table 3. Identical test conditions were simulated in the model with regards to aggregate type, fire time-temperature curve, load level and support condition. The fire behavior of these slabs is presented in terms of temperature progression, mid-span deflection, axial restraint force, and crack propagation and spalling pattern. The failure time of slabs is evaluated based on four different failure criteria discussed in Section 2.4 and compared with that obtained from fire tests in Table 3.

4.1 Thermal response

First stage of model validation is achieved by comparing predicted cross-sectional temperatures in the slabs with those measured in fire tests, as illustrated in Figure 4. All four Slab 3 to Slab 6, exhibit similar temperature progression, and a good agreement between the measured and predicted sectional temperatures can be seen in Figure 4.

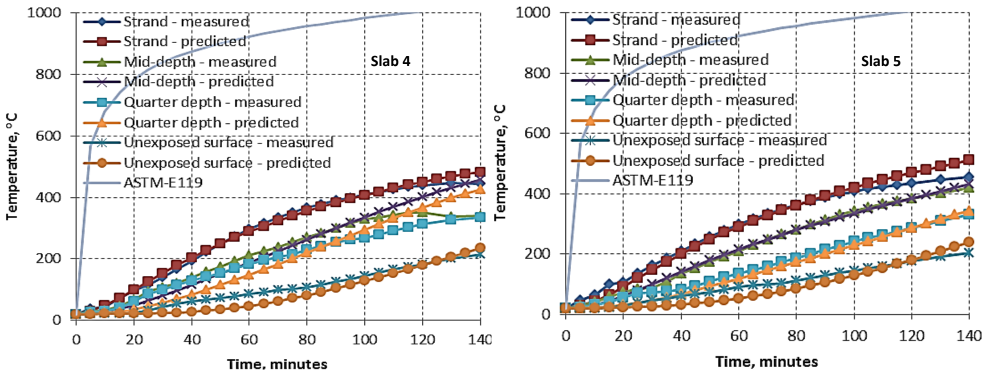

Figure 4. Comparison of measured and predicted sectional temperatures in Slab 4 and Slab 5.

In the first 20 minutes of fire exposure, the temperatures at the level of strand, mid-depth, quarter depth and unexposed surface gradually increase with time. As expected, the temperature in concrete layers farther from the fire exposure surface are lower than those layers closer to the exposure surface. This temperature progression trend is also predicted by the numerical model, as shown in Figure 4. Beyond 20 minutes of fire exposure, temperatures at all locations increase at a gradual pace with time. The temperature on the unexposed surface of Slab 4, 5 and 6 reach the limiting temperature of 181 ℃ at 120 minutes into fire exposure, whereas unexposed temperature in Slab 3 does not exceed this temperature limit throughout the fire exposure duration. This infers that as per ASTM-E119 limiting criterion, Slabs 4, 5 and 6 attain failure based on insulation (unexposed surface temperature) criterion. However, all slabs continue to carry load without any signs of failure from strength degradation. At this time (120 minutes) the strand temperature is 500 ℃, which clearly infers that the evaluation of fire resistance based on attaining certain strand temperature might not yield realistic fire resistance in hollow-core slabs.

4.2 Structural response

The structural validation of the model is carried out by comparing predicted and measured mid-span deflections and fire induced restraint force in Slab 3 to Slab 6, as illustrated in Figure 5. The overall trends in Figure 5(a) and (b) show a good agreement between predicted and measured mid-span deflections for all four slabs and axial restraint force in Slab 5.

The structural response plotted in Figure 5(a) and (b) can be grouped into three stages as marked in these figures. In Stage 1, in first 20 minutes of fire exposure, the deflections in all slabs increase at a slow pace and these deflections result mainly from thermal strains generated due to high thermal gradients that occur in early stage of fire exposure. In Slab 5 with restrained supports, these thermal gradients produce rapid increase in axial force in Stage 1, as can be seen in Figure 5(b). Concrete and strands undergo very little strength degradation in this stage due to low temperatures in concrete and strands.

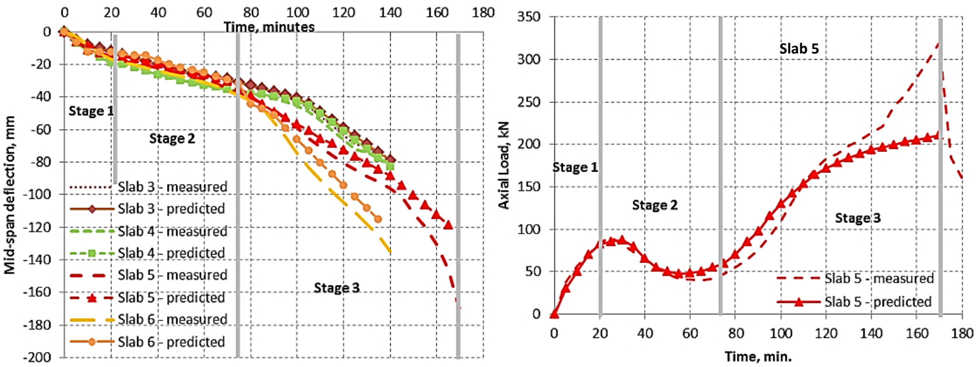

(a) Mid-span deflections (b) Axial restraint force

Figure 5. Comparison of measured and predicted structural response.

In Stage 2, after 20 minutes into fire exposure, deflections increase at a slightly slower pace due to reduction in thermal gradients, as temperatures increase in inner layers of concrete. The deflection in this stage is mainly attributed to degradation of strength and modulus in concrete and strand due to increase in sectional temperatures. The axial restraint force in Slab 5, plotted in Figure 5(b), decreases in this stage, and this is also attributed to degradation in strength and modulus properties. Finally, in Stage 3, beyond 75 minutes, deflections in all four slabs and axial restraint force in Slab 5 increase at a rapid pace, and this is mainly attributed to high creep strains resulting from very high temperatures in concrete and strands, which reach above 500 ℃.

Overall, there is a good agreement in predicted and measured deflections and restraint force in Stage 1 and Stage 2. However, in the Stage 3 of fire exposure, the model predicts slightly lower deflections in all slabs and slightly lower restraint force in Slab 5, and this can be mainly attributed to the fact that the high temperature properties of concrete and prestressing strand used in the model do not explicitly account for high temperature creep strains. The material constitutive relations for concrete and strand used in the numerical model is taken from Eurocode 2 [16]. These relations account for partial creep and do not take into account full effects of temperature induced creep.

Table 3. Comparison of measured and predicted fire resistance.

Test slab	Failure limit criteria	Fire resistance (min.)	
		Measured	Predicted
Slab 3	-	-	-
Slab 4	Unexposed T	120	120
Slab 5	Unexposed T	120	120
Slab 6	Unexposed T	120	120

Note: T = Temperature, '-' = not failed or not available

Visual observations made during and after fire tests show that all slabs developed flexural cracks in early stages of fire, originating from the bottom fire exposed surface. In addition, Slab 3 and Slab 6 also developed some level of shear cracking during early stages of fire exposure. However, these shear cracks did not affect the flexural capacity of the slabs, as these cracks were restricted to lower parts of the slab and did not propagate through the top portion of the slab. The flexural and shear cracks widened in all four slabs with fire exposure time, but failure due to widening of flexural cracks occurred only in Slab 6. Axially restrained Slab 5 failed though severe flexural cracking and crushing of concrete on the top surface at the mid-span section. Slab 5 sustained fire exposure for a longer period than the other three slabs, but showed severe concrete damage on the fire exposed surface. In addition, fire induced spalling did not occur in Slabs 3, 5 and 6, which were made of carbonate aggregate concrete, while Slab 4, fabricated with siliceous aggregate concrete, showed minor pitting (spalling) on the fire exposed surface. This minor spalling in siliceous aggregate concrete Slab 4 is attributed to stronger interlocking and bond between cement paste and aggregate surface, which increases the risk of pore pressure induced spalling [24, 25].

The validity of the model is also established by comparing predicted fire resistance from the model against measured fire resistance from tests, as tabulated in Table 3. The failure time of different slabs under fire exposure was evaluated by applying different failure limit states as per ASTM-E119, as discussed in Section 2.4. As discussed earlier, unexposed surface temperature in Slabs 4, 5 and 6 reached a limiting temperature of 181 ℃ at 120 minutes into fire exposure, and that in Slab 3 did not exceed this limiting temperature in both test and model. Thus, based on insulation criteria, these slabs exhibit a minimum of 120 minutes of fire resistance. However, all slabs continued to carry load, and based on structural response parameters obtained from tests and model, it can be inferred that strength failures did not occur in Slab 3 and Slab 4, but failure due to strength degradation occurred in Slab 5 and Slab 6 at 170 and 140 minutes respectively. Numerical model gives similar predictions and show that failure occurs at 165 minutes (time step) in Slab 5 and at 135 minutes in Slab 6. In the model, convergence issues experienced at these time steps can be associated with onset of instability in Slabs 5 and 6 due to significant degradation of stiffness in both concrete and prestressing steel from high sectional temperatures, and this indicates imminent failure of these slabs. The fire resistance in Slab 5 is about 30 minutes higher than that in Slab 6, and this is due to the effect of axial restraints which enhanced the stiffness of the slab.

5 CONCLUSIONS

Based on the results presented in this paper, the following conclusions can be drawn on the fire behavior of PC hollow-core slabs:

（1）Hollowcore slabs, similar to the ones discussed in this paper, can sustain standard or typical design fire exposure up to two hours, under typical service level loading.

（2）Axial restraint has significant influence on the fire response of hollowcore slabs, and can enhance fire resistance by 30 minutes.

（3）Fire resistance of PC hollowcore slabs, evaluated based on strands temperature although convenient, does not represent realistic fire resistance.

（4）Proposed finite element based numerical model is capable of tracing the fire behavior of PC hollowcore slabs under standard and design fire conditions.

REFERENCES

[1] Abrams M. S., “Fire tests of hollow-core specimens with and without roof insulation,” *PCI J.*, Feb. 1976.

[2] Borgogno W., “Structural behavior of slim floor covering with concrete hollow slabs at room temperature and elevated temperature,” Eidgenossische Technische Hochschule, Zurich, Germany, 1997.

[3] Andersen N. E. and Lauridsen D. H., “Danish Institute of Fire Technology Technical Report X 52650 Part 2 – Hollowcore concrete slabs,” DIFT, Denmark, 1999.

[4] Schepper L. and Anderson N. E., “Danish Institute of Fire Technology and COWI Technical Report PG 10724 – Fire test of deck elements,” COWI and DEFT, Denmark, 2000.

[5] Acker A. V., “Shear resistance of prestressed hollowcore floors exposed to fire,” *Struct. Concr. J. Fib Thoman Telford Fib*, vol. 4, no. 2, pp. 65–74, 1464–4177, 2003.

[6] Lennon T., “Precast concrete hollowcore slabs in fire,” *Struct. Eng.*, vol. 81, no. 8, pp. 30–47, 2003.

[7] Fellinger J. H. H., “Shear and anchorage behavior of fire exposed hollow core slabs,” DUP Science, Delft, Netherland, 2004.

[8] Jensen J. F., “Hollowcore slabs and fire - Documentation on shear capacity,” Danish Prefab Concrete Association, Danish Institute of Fire Technology, Denmark, 2005.

[9] Breccolotti M., Materazzi A. L., and Venanzi I., “Full scale investigations on the fire performance of HPLWC hollowcore slabs,” in *Structures in Fire SiF’06*, Naples, Italy, 2006.

[10] Bailey C. G. and Lennon T., “Full-scale fire tests on hollowcore floors,” *Struct. Eng.*, vol. 86, no. 6, pp. 33–39, 2008.

[11] Aguado J. V., Espinos A., Hospitaler A., Javier O., and Romero M. L., “Fire resistance of hollowcore slabs. Influence of reinforcement arrangement,” presented at the Structures in Fire SiF’12, Zurich, Switzerland, 2012.

[12] Dotreppe J. and Franssen J., “Precast hollow core slabs in fire: Numerical simulation and experimental tests,” presented at the Structures in Fire Sif ’04, Ottawa, Canada, 2004.

[13] Chang J. J., Buchanan A. H., Dhakal R. P., and Moss P. J., “Hollowcore concrete slab exposed to fire,” *Fire Mater.*, vol. 32, no. 6, pp. 321–331, 2008.

[14] Min J. K., Moss P. J., Dhakal R. P., and Buchanan A. H., “Modelling the fire resistance of prestressed concrete floors using multi-spring connection elements,” presented at the Structures in Fire Sif ’10, Michigan State University, Lansing.

[15] ANSYS, *Finite element computer code*. ANSYS, Inc., 2011.

[16] Eurocode2, “Design of concrete structures, Part1-2: general rules-structural fire design. ENV 1992-1-2,” CEN: European Committee for Standardization, UK, 2004.

[17] Willam K. and Warnke E., “Constitutive model for the triaxial behavior of concrete,” *Int. Assoc. Bridge Struct. Eng.*, 1975.

[18] ASTM, “Standard test methods for fire tests of building construction and materials. Test Method E119-12,” American Society for Testing and Materials, West Conshohocken, PA, 2011.

[19] International Standard (E), “Fire resistance tests: Elements of building construction. Part 1: General Requirements. ISO834-1-1999,” International Organization for Standardization, Switzerland, 1999.

[20] Kodur V. K. R. and Dwaikat M., “Performance-based fire safety design of reinforced concrete beams,” *J. Fire Prot. Eng.*, vol. 17, no. 4, pp. 293–320, 2007.

[21] BS 476–20, “Fire tests on building materials and structure—part 20: method for determination of the fire resistance of elements of construction,” CEN: European Committee for Standardization, Brussels, Belgium, 1987.

[22] PCI, *Design for Fire Resistance of Precast/Prestressed Concrete*, 3rd ed., vol. MNL-124–11. 2011.

[23] AISC, *Steel Construction Manual*, 14th ed. Chicago, IL: American Institute of Steel Construction,

2010.

[24] Kodur V. K. R. and Harmathy T. Z., “Properties of building materials. Section 1, Chapter 10,” in *SFPE handbook of fire protection engineering*, 4th ed., Bethesda, MD: Society of Fire Protection Engineers, 2012.

[25] Ichikawa Y. and England G. L., “Prediction of moisture migration and pore pressure build-up in concrete at high temperatures,” *Nucl. Eng. Des.*, vol. 228, no. 1–3, pp. 245–259, Mar. 2004.

A RE-EXAMINATION OF THE MECHANICS OF TENSILE MEMBRANE ACTION IN COMPOSITE FLOOR SLABS IN FIRE

Ian Burgess*, Shan-Shan Huang* and Savina Staikova**

* University of Sheffield, United Kingdom
e-mails: ian.burgess@sheffield.ac.uk, s.huang@sheffield.ac.uk

** TU Darmstadt, Germany
e-mail: sa_vi05@hotmail.com

Keywords: Steel Frames, Fire, Composite Slab, Tensile Membrane Action, BRE Method

Abstract. *This paper presents a re-examination from first principles of the mechanics of tensile membrane action (TMA) of thin rectangular concrete floor slabs, transversely supported around their edges. An existing simplified method of assessing the contribution of TMA to the fire resistance of a composite slab, including unprotected steel down-stand beams in its interior area, appears to have some serious mechanical shortcomings in its fundamental assumptions. This paper describes, and presents results from, a re-examination of the mechanics of TMA of thin concrete floor slabs in fire conditions, starting from the same initial state of an optimal small-deflection yield-line hinge pattern. The basic formulation considers plain flat slabs, but is in no way limited to these, or to isotropic reinforcement. It is based on a large-deflection plastic analysis. The resulting formulation accounts for the plasticity and fracture of the reinforcing mesh, which is usually weaker in tension than the slab in which it is embedded, and the compressive strength of the concrete. It allows the changes in stress patterns around the yield lines to be monitored, from negligible deflection to complete failure of the slab, and provides a rational way of predicting when a through-depth tensile crack will occur; in fire conditions this is usually taken as an integrity failure of the separating function of the floor slab. If necessary the method can then follow the further development of this cracked mechanism up to full loss of structural load capacity. Like-against-like comparisons are made against the enhancements predicted by the existing method, and it can be seen that these are by no means identical; nor are the predictions by one method consistently conservative relative to the other.*

1 INTRODUCTION

The Cardington fire tests [1] conducted in 1995-1996 on a purpose-built full-scale composite-framed building were instrumental in inspiring the upsurge in research interest, which continues to the present, in the real performance of framed buildings in fires. In the specific context of composite steel-concrete framing systems the outstanding observation from the six tests in the initial series was that, despite the fact that steel down-stand beams experienced temperatures considerably in excess of their codified critical temperatures [2], and would have collapsed if tested individually under the same loadings in normal furnace-test conditions, no composite beam experienced runaway collapse. In the aftermath of the tests it became apparent that the reason for this apparent enhancement of the strength of the arrays of identical composite beams which make up floor slabs was the two-way continuity of the concrete slab panels themselves. The high biaxial curvatures which are engendered by large deflections of heated parts, effectively vertically supported by cool structure around their edges, cause the appearance of a zone of 'hydrostatic' tensile membrane stress in the central area of a panel; this is a two-dimensional analogy to catenary tension in a cable. However, while a catenary cable requires supports which resist horizontal pull-in force as well as the vertical load supported, this horizontal reaction in highly-deflected slabs is provided by a peripheral ring of compressive membrane stress. This combination of membrane stresses is known as Tensile Membrane Action (TMA), and its existence depends on a panel having good vertical support around its edges, and on the extent of the deflection of its central region; the panel's load-carrying capacity increases with its deflection, subject to the strength of the material of which it is made. In fire conditions, TMA of the highly deformed concrete slab effectively carries the loading when the strength of the unprotected down-stand steel beam sections has reduced dramatically at high temperatures.

A simplified design method to calculate the strength of a composite slab panel within its allowable range of deflection, when the strengths of steel down-stands have been degraded considerably by high temperatures, was published by Bailey and Moore [3, 4] of BRE in 2000. This method is based to a very large extent on a calculation of the enhanced load capacity of concrete slabs at high deflections due to their membrane strength, which had been published by Hayes [5] in 1968. The method has since then become widely used in practical fire engineering design in the UK, both in its original form and as a development published as the software TSLAB [6]. In New Zealand Clifton [7] devised a further variant of the same rationalization, which is also available as public-domain design software. The European project FRACOF has recently published reports [8, 9, 10] recommending a design process which is almost indistinguishable from that given by the generic BRE/Bailey documents. This seems likely to be adopted in the next round of developments to Eurocode 4 Part 1-2.

The BRE/Bailey method depends directly on the original calculation of enhancement of strength as a result of increasing deflection, in the form in which it was published by Hayes. It is not possible to follow the complete sequence of the derivation, since major steps are not reported, but it is clear that some ad hoc assumptions are made. The method culminates in a deflection-dependent enhancement factor which multiplies the small-deflection plastic capacity of the slab, as determined by the yield-line method. Enhancement factors in each of the two principal directions are aggregated from individual enhancement factors due to the membrane effect and the bending resistance, and then these are combined in a weighted-mean process, which is hard to explain or to justify, into a single enhancement factor. The model is based on a slab which has initially formed the optimal yield-line pattern and, on further deflection, has experienced a through-depth tensile crack across its shorter width at the middle of its longer length. This is a mechanism which has been observed in tests on loaded thin slabs, and the fact that the system of forces shown in Figure 1(a) is used in the calculation indicates that it is the equilibrium of this cracked system that is being considered. This same assumption was made by Burgess et al. [11] using different kinematic assumptions. In both cases the enhancement is clearly to the structural load-carrying capacity after the mid-span tensile crack is in existence, rather than the occurrence of that crack, which constitutes a compartment integrity failure in the fire case.

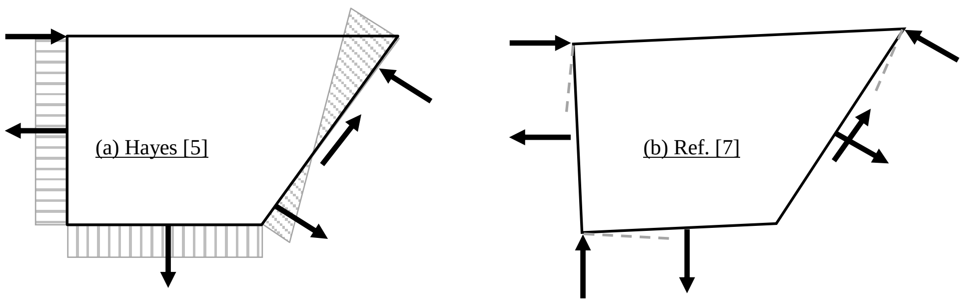

Figure 1. Kinematics of (a) Hayes [5] enhancement model and Burgess *et al.* [7] model.

Since the Hayes calculation was intended only to model structural capacity at ambient temperature it does not attempt to predict the occurrence of the central through-depth crack, and since the rebar's assumed stress-strain curves include no definition of fracture increased deflection will continuously provide increased enhancement to capacity. The BRE/Bailey method was thus faced with the need to define a safe limiting deflection at which the through-depth crack still has unbroken rebar crossing it. This deflection was rationalised as consisting of two parts; the first due simply to differential thermal expansion across the depth of the concrete slab, leading to 'thermal bowing' under an arbitrary linear temperature gradient, and the second due to stress-induced mechanical extension of the rebar up to a safe limiting strain. The safety margin on the latter was originally given by dividing the ambient-temperature proportional limit strain by 2.4; in the FRACOF recommendations this is reduced to 2.0. However, these two components are superposed in a totally irrational way; the thermal bowing deflection is based on a simple beam model which allows horizontal movement of one support, whereas the mechanical strain is based on a beam which has both ends fixed. These cases simply cannot be superposed.

The work reported in this paper attempts a re-examination of the large-deflection response of a thin concrete slab, using a yield-line approach to the small-deflection plastic limit as a datum for the behaviour as deflections increase. This seems quite rational for lightly reinforced slabs, which do not exhibit tension stiffening and therefore create discrete localised crack patterns which form the yield lines; there is little incentive for a yield-line pattern to change once it has formed. It is clear that, once a yield-line pattern has formed at the small-deflection plastic capacity, increased deflection initially simply amplifies this mode, progressively stretching the rebar (usually mesh) across the widening cracks and changing the shapes of the concrete compression zones along these yield lines. During this process the bars in either the *x*- or *y*-directions may fracture, the crack-width at which this happens depending on their own ductility, their positive anchorage points in the concrete, and their bond characteristics. In structural terms failure may occur when the enhanced load capacity reduces consistently below the applied load; a temporary reduction which is re-stabilized on further deflection does not constitute structural failure. Since the method is to be used in the fire context, integrity of the slab as a compartment-separating element must also be considered. The most severe approach to this limiting condition would be to assume that integrity is lost when there is no contact between the faces of a crack at any point on the yield-line pattern. This may be too restrictive, especially for composite slabs cast on profiled steel decking, and an alternative may be either to specify a minimum acceptable crack width or to identify the occurrence of the through-depth tensile crack which changes the mechanism, at a specified concrete tensile strength.

2 EQUILIBRIUM AND KINEMATICS OF YIELD-LINE MECHANISM

A two-way spanning rectangular slab panel of aspect ratio r, which is transversely supported along all its four edges, is considered. In the present case the slab is considered as isolated (having no continuity with adjacent panels across its edges). The slab is lightly reinforced with a welded mesh, which for the purposes of this paper is considered to be isotropic, and the two layers of bars are assumed to lie effectively at a single mean level within the slab. The transverse loading on the slab is increased until a plastic yield-line crack pattern forms, in the characteristic arrangement shown in Figure 2.

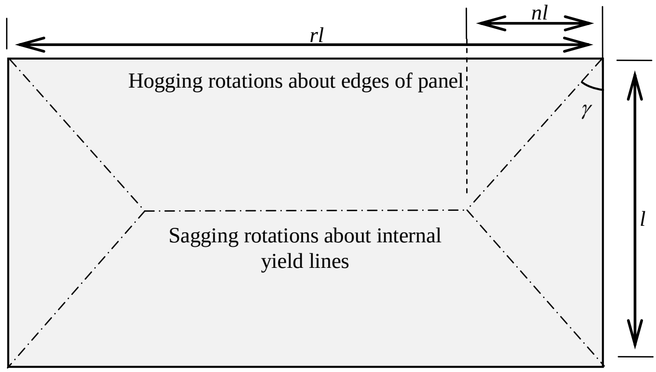

Figure 2. Small-deflection yield-line mechanism.

All plastic energy analysis methods are inherently upper-bound, but the optimum yield-line mechanism, giving the lowest possible failure load intensity, is exact, and is given by:

$$n = \frac{1}{2r}\left(-1 + \sqrt{1+3r^2}\right) \tag{1}$$

The general assumptions for the materials involved are that steel rebar across a yield-line only acts plastically in tension where it is stretched, and that concrete is only active in compression where the yield-line surfaces overlap, and that in these zones it is at the ultimate stress of the concrete. It is assumed that the slab facets remain flat but rotate compatibly (creating the same intersection displacement δ_A) about their respective edge supports. The geometry of the crack opening at certain depths from the top surface and certain distances from supports, given compatible overlap movements Δx and Δy (Figure 3) at the top surfaces at the slab corners, gives crack opening components at coordinates *(x, y)* from the slab corner, and depth *z* from the top surface, of

$$u = \Delta x - \theta z - \frac{\theta^2 x}{2} \tag{2}$$

$$v = \Delta y - \emptyset z - \frac{\emptyset^2 y}{2} \tag{3}$$

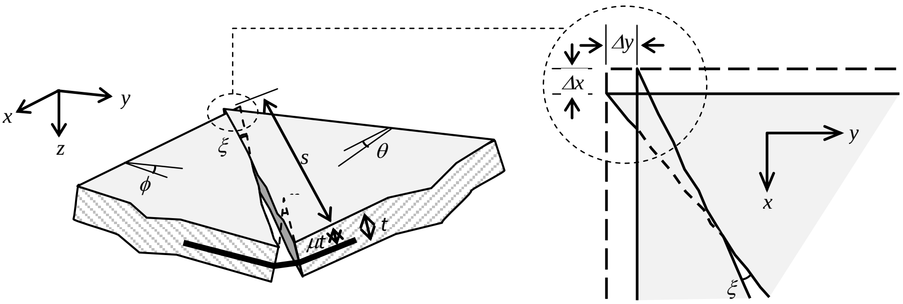

Figure 3. Crack opening at a certain depth and distance from supports, and corner top surface overlaps.

Since the concrete compression zones must be compatible in the *x*- and *y*-projections, and since both θ and $\emptyset$ cause the same lateral deflection δ_A at the yield-line intersection, the relationships $\Delta y = 2n\Delta x$ and $\emptyset = 2n\theta$ exist.

At any section through the yield lines there can be a combination of concrete in compression, from the top surface of the slab downwards, and rebar in plastic tension. However the extent of the concrete compression zone depends on the position and the geometric relationships shown in Figure 3; if the separation extends from the bottom to the top of the slab at this point there is no compressive block. In addition, if the reinforcement is located within the compression block at this location, then it is considered as having no stress; alternatively, if the crack separation at the rebar level exceeds that at which the bars fracture, then there it clearly has no tensile stress. The key options for concrete compression and steel tensile yield are shown in Figure 4, which contains two views of the yield-line crack surface, projected onto the *x-z* plane.

Figure 4(a) shows the situation shortly beyond initial yield-line failure, when the concrete stress block in the central yield line reduces in depth and compressive stress increases at the slab corners. In Figure 4(b) the central compression block has disappeared, which is indicated by a negative value of z_2 . Figure 4(c) shows the length $x_{lim,1y}$ beyond which the crack width has become greater than that at which the *y*-direction rebar fractures, and $x_{t,1}$, marking the point at which the rebar passes into the compression block. These cases do not cover the entire field of possibilities; under some circumstances the depth z_1 of the compression block may go below the reinforcement depth before any rebar fracture takes place, or before compression has ceased in the central yield line. Equally, reinforcement fracture may begin at any stage, depending on its ductility. A final case of the concrete stress block, not shown in the figure, may occur when z_1 exceeds the depth of the slab, when the stress block becomes trapezoidal.

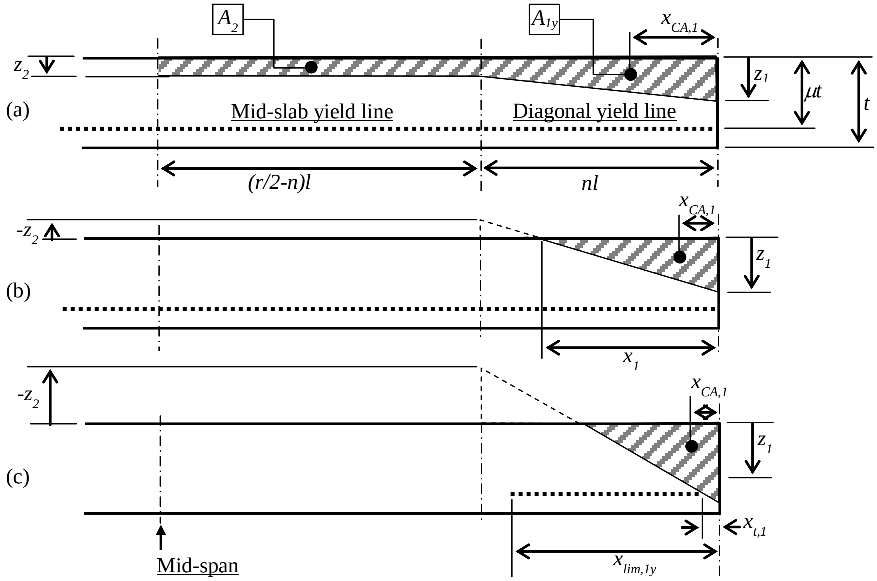

Figure 4. Key dimensions of concrete compression block and active rebar lengths.

The steel and concrete force components acting on the yield lines are summarised in Figure 5. Since the reinforcing mesh is aligned with bars in the x and y directions there are two tensile resultants T_{x1} and T_{y1} , which are essentially independent of one another, on each diagonal yield line. On the other hand, the concrete compression block simply presents resolved parts in the x and y directions. On the central yield line the tensile component T_{y2} vanishes instantaneously when the y-rebar fractures; the compression component C_{y2} vanishes when z_2 passes from positive to negative.

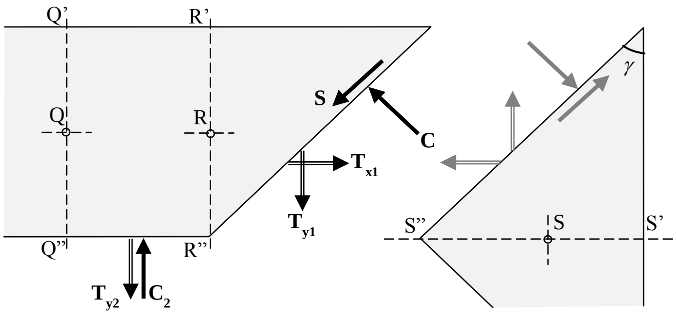

Figure 5. Force components acting on slab facets.

Equilibrium of the forces and eliminating the concrete shear resultant S gives:

$$T_{x1}\cos\gamma + (T_{y1} + T_{y2})\sin\gamma = C + C_{y2}\sin\gamma \tag{4}$$

If the plastic strength of the concrete is denoted f_c and the strengths of rebar per unit width of mesh perpendicular to bars in the x and y directions respectively are f_{px} and f_{py} , the forces are:

$$C = A_1 f_c \tag{5}$$

$$C_{y2} = A_{2y} f_c \tag{6}$$

$$T_{y1} = (x_{lim,1y} - x_{t,1}) f_{py} \tag{7}$$

$$T_{x1} = (y_{lim,1x} - y_{t,1}) f_{px} \tag{8}$$

$$T_{y2} = (r/2 - n) l f_{py} \tag{9}$$

3 SOLUTION FOR DEFLECTIONS AND FORCES

Solution for the amplified yield-line mechanism as the deflection of the central yield line is incremented from zero has been implemented in a spreadsheet. The force definitions shown in Equations (5) to (9) are substituted into Equation (4) and expressed as functions of Δx. The slab width and aspect ratio, the reinforcement mesh areas in the x and y directions, depth and ductility (fracture strain), and the strengths of steel and concrete can be changed. The rebar fracture crack widths are based on the defined fracture strain and a 'free length' of bar, which in the simplest case is assumed to be the whole length of bar in the appropriate direction between adjacent transverse bars. This is logical, since welds at these points will act as anchors either side of a crack, but is not conservative. If bond is maintained between the concrete and steel between the anchor points and the crack faces, then the limiting crack-width will decrease. Some investigation of the effects of using various debonding theories has been done, but will not be reported in this paper.

In the spreadsheet values of Δx are calculated as the deflection increases. It is necessary to test these values for compatibility in a series of 30 scenarios, assuming different concrete stress block shapes and different reinforcement fracture conditions. This is typical of limit-state analysis; only one scenario produces exact results, while all others are inherently upper-bound. The cases which are tested are listed in Table 1.

Table 1. Cases of compression block and rebar assumptions to be tested.

Compression block		Reinforcement mesh fractured					
		None	Central y	Diag. x	Diag. y	Central + diag. x	Diag. x and y
Full	above mesh	a1	a1'	a1*	a1**	a1*'	a1***
	below mesh	a2	a2'	a2*	a2**	a2*'	a2***
Triangular	above mesh	b1	b1'	b1*	b1**	b1*'	b1***
	below mesh	b2	b2'	b2*	b2**	b2*'	b2***
Trapezoidal		c1	c1'	c1*	c1**	c1*'	c1***

When Δx has been evaluated for the correct case it is then possible to use Equations (5) to (9) to calculate the magnitudes and positions of each of the internal force components at any displacement. The in-plane bending moments about axes through the points indicated by Q, R and S in Figure 5 can then be calculated. There is no net force across any of the three lines (Q'Q", R'R" or S'S") marked through these points, and so there are elastic in-plane linearly-varying stress distributions across each of these lines. As the deflection of the slab increases the maximum value of the concrete tensile stress also increases, and at some point this will initiate the through-depth tensile crack which constitutes an integrity failure in the fire limit state.

With respect to the basic enhancement of capacity of the slab with deflection, a simple plastic work balance method, previously used in [11], is applied. The forces calculated in Equations (5) to (9) all correspond to plastic action in either rebar or concrete. The corresponding movement distances can be calculated at the positions of the components; for reinforcement these are the centres of the appropriate lengths in x or y over which rebar orthogonal to these lengths acts; for concrete they are the centroids of the appropriate compression stress blocks.

The external work (or loss of potential energy) of the uniformly distributed transverse loading, of intensity p, is expressed in the same way as for small deflections:

$$W_{ext} = pl^2\delta_A\left(\frac{r}{2}-\frac{n}{3}\right) \tag{10}$$

Since rigid-perfectly plastic behaviour is being assumed for the reinforcing mesh,

$$W_{ext} = W_{int} \tag{11}$$

Thus the load capacity of the slab, at any deflection δ_A, is therefore:

$$p = W_{int}/\left[l^2\delta_A\left(\frac{r}{2}-\frac{n}{3}\right)\right] \tag{12}$$

4 APPLICATION OF THE PROCEDURE

In order to demonstrate the application of the procedure outlined above, the results for an example slab will now be considered. The essential data for the slab is given in Table 2 below.

Table 2. Data for the slab example.

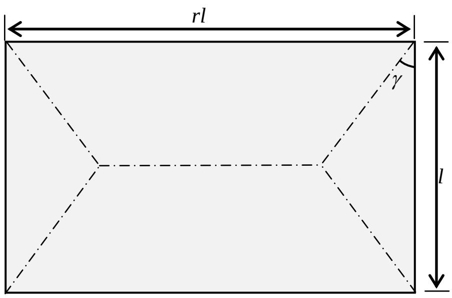

Concrete	
Minor length l = 6m	f_c = 30Mpa
Major length rl = 9m	
Thickness t = 130mm	
Steel	
Mesh depth μt = 50mm	f_y = 500Mpa
Mesh area x-dir. = 142mm^2/m	Ductility = 10%
Mesh area y-dir. = 142mm^2/m	
Mesh bar spacing = 200mm	

The variation of the internal force components on the yield lines is shown in Figure 6(a). The main phases of behaviour can be seen from the changes in the forces depicted here. At $\delta A/t$=0.087 the concrete stress block (C_2) on the central yield line vanishes, while the reinforcement across this yield line (Ty2) remains intact until $\delta A/t$=1.698, when all the bars across this yield line fracture abruptly. At $\delta A/t$=2.497 the y-direction reinforcement across the diagonal yield lines begins to fracture progressively from the intersections towards the slab corners, followed by the x-direction reinforcement at $\delta A/t$=2.737. As deflection increases further it can be seen that all non-zero forces reduce as the remaining reinforcement is reduced.

Figure 6(b) shows the maximum in-plane tensile bending stresses in the slab at the 3 sections Q'Q", R'R" and S'S" as the deflection increases. It can be seen that all three increase until the simultaneous fracture of the central yield-line reinforcement, with the stress at Q'Q" slightly higher than that at R'R". However, there is clearly a value of the maximum tensile stress at which tensile fracture happens and a through-depth tension crack is initiated. In Eurocode 2 [12] the tensile strength of concrete is related to its compressive strength largely in terms of tabulated data, which in general terms give values between 6% and 11% of the cylinder strength. For the present example, this range would give a surprisingly low permissible deflection if used as a limit to the permissible range.

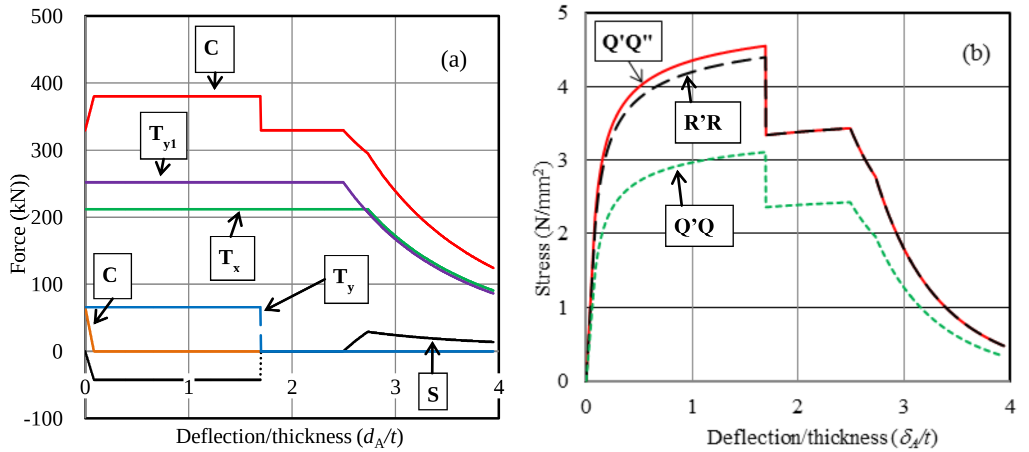

Figure 6. (a) Force component values on slab facets; (b) Maximum concrete tensile stresses on sections Q'Q" and R'R" in trapezoidal facet, S'S" in triangular facet.

In Figure 7(a) the load capacity enhancement factor for the example slab is plotted against the relative deflection. It can be seen that, for the parameter values defined in Table 2, the enhancement is extremely close to that given by the generic Hayes or BRE method at the stage before the rebar across the central yield line has fractured. Beyond this point some strength is gradually regained until the mesh across the diagonal yield lines begins to fracture, beyond which the load capacity is progressively lost with further deflection. The limiting deflection prescribed by the generic BRE method, assuming a temperature difference of 770°C between the top and bottom slab surfaces, is marked at δ_A/t=3.0005. Since no thermal effects have been considered in the enhancement calculation, the BRE limiting deflection bvased only on the rebar strain limit, without the thermal deflection component, has also been marked.

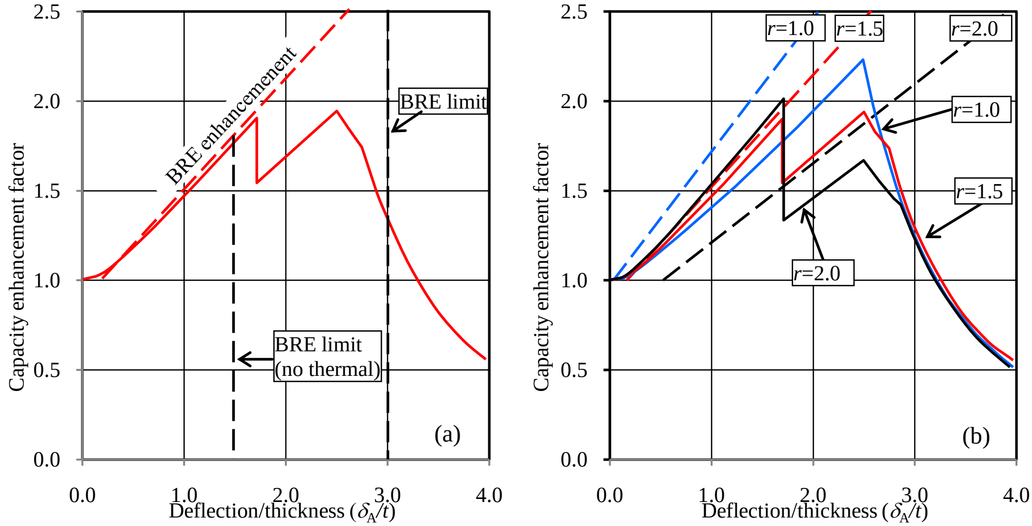

Figure 7. (a) Load capacity enhancement factor for the example slab (Table 2); (b) Comparison of enhancement factors for slabs of aspect ratio 1.0, 1.5 and 2.0 with their BRE method enhancement factors.

In Figure 7(b) the enhancement characteristics for slabs of aspect ratio 1, 1.5 and 2 are compared, with the Hayes/BRE enhancement curves for the same aspect ratios. It is notable that, although the initial enhancement curves for r=1.5 are very close, those for r=1.0 and r=2.0 differ considerably. For a square slab (r=1.0) the BRE method's enhancement is greater than that of the present approach, whereas for r=2.0 it is lower. Hence, the BRE method cannot be characterised either as consistently conservative or unconservative in terms of the enhancement of yield-line capacity that it predicts with deflection.

5 CONCLUSIONS

This paper has shown the principles of a simplified method of representation of the load-capacity enhancement in thin slabs due to tensile membrane action at high deflections. Although the major current use of this phenomenon in structural engineering is to increase the capacity of composite slabs in fire conditions, the work presented is not directly temperature-related. Heat transfer may affect the results if the reinforcing mesh heats by conduction to a temperature at which its strength is reduced significantly, before initial yield-line failure occurs. Once the yield-line cracks have formed, the exposed bars crossing the cracks will increasingly be affected by convection and radiation; the extent of this heating will depend on the time of exposure, the width of the crack and the vertical position of the mesh in the concrete. There is clearly more work to be done before the effect of this heating of reinforcement can be included logically. Before this is done it may be necessary to represent the bonding of bars either side of a crack in a more realistic way. Since TMA is of interest when attached steel down-stand beams are used across the interior areas of the slab without fire protection, the effect of rapid heating of these beams, both on the form of the yield-line mechanism and on the TMA itself, is currently being investigated.

However, the like-against-like comparisons made here have shown that the existing simplified method, based on Hayes's work in the 1960s and Bailey's extensions in the early 2000s, which includes seemingly illogical assumptions in its treatment of enhancement of load capacity and in its assessment of the limiting deflection, is inconsistent with the treatment of TMA presented in this paper, which is based on well-established principles of solid mechanics.

REFERENCES

[1] Newman, G. M., Robinson, J. T. and Bailey, C. G. (2006), *Fire Safe Design: A New Approach to Multi-Storey Steel-Framed Buildings*, Second Edition, SCI Publication P288, The Steel Construction Institute, UK

[2] CEN, *EN 1994-1-2:2005: Eurocode 4. Design of composite steel and concrete structures. Part 1-2: General Rules - Structural fire design*. European Committee for Standardization (CEN), Brussels, 2005.

[3] Bailey, C.G. and Moore, D.B., "The structural behaviour of steel frames with composite floor slabs subject to fire - Part 1 Theory", *The Structural Engineer* , **78** (11), (2000) pp 19-27.

[4] Bailey, C.G. and Moore, D.B., "The structural behaviour of steel frames with composite floor slabs subject to fire - Part2: Design", *The Structural Engineer*, **78** (11), (2000) pp28-33.

[5] Hayes, B., "Allowing for membrane action in the plastic analysis of rectangular reinforced concrete slabs", *Magazine of Concrete Research*, **20** (65), (1968) pp205-212.

[6] Simms, W.I. and Bake, S., *TSLAB V3.0 User Guidance and Engineering Update*, SCI publication P390, 2010.

[7] Clifton, C., *Design of composite steel floor systems for severe fires*, HERA publication, Manaukau City, New Zealand (2006).

[8] Vassart, O. and Zhao, B., *FRACOF: Fire resistance assessment of partially protected composite floors: Engineering Background*, Arcelor/Mittal & CTICM, 2011.

[9] Vassart, O. and Zhao, B., *FRACOF : Fire resistance assessment of partially protected composite floors: Design guide*, Arcelor/Mittal & CTICM, 2011.

[10] Vassart, O. and Zhao, B. (2013), *Membrane action of composite structures in case of fire*, ECCS TC3 Report no. 132, 2013.

[11] Burgess, I.W., Dai, X. and Huang, S.-S., 'An Alternative Simplified Model of Tensile Membrane Action of Slabs in Fire', *Proc. Applications of Structural Fire Engineering*, Prague, Czech Republic, (2013) pp361-368.

[12] CEN, *EN 1992-1-1:2004: Eurocode 4. Design of composite steel and concrete structures. Part 1-1: General Rules and rules for buildings*. European Committee for Standardization (CEN), Brussels, 2004.

8th International Conference on Structures in Fire
Guo-Qiang LI, Venkatesh K. R. KODUR, Shou-Chao JIANG, Jian JIANG, Su-Wen CHEN, Guo-Biao LOU (Eds.)
Shanghai, China, June 11-13, 2014

EXPERIMENTAL STUDY ON FIRE BEHAVIOR OF INSULATED FULL-SCALE CFRP-STRENGTHENED RC BEAMS UNDER SERVICE LOAD

Kun Dong* and Ke-Xu Hu

*Research Institute of Structural Engineering and Disaster Reduction, Tongji University
1239 Siping Road, Shanghai 200092, China
e-mails: doku121314@163.com, kexuhu@tongji.edu.cn

Keywords: RC beams, CFRP-Strengthened, Fire protection, Fire test, Behaviour of fire resistance

Abstract. *In this paper, a series of experimental study conducted to investigate the fire behaviour of insulated full-scale CFRP-strengthened reinforced concrete (RC) beams is presented. Four rectangular CFRP-strengthened RC beams, respectively insulated with thick fireproof coating system, ultra-thin fireproof coating system and calcium silicate board system, were tested under ISO-834 standard fire and service load. The thermal and structural response of these beams in fire were recorded and analyzed. The results show that satisfactory fire endurances for CFRP-strengthened concrete beams can be obtained with the protection of these three systems above. The major role of fire insulation materials was delaying the failure of adhesive in the early stage, and reducing the performance degradation of concrete and internal reinforced bars after the bond failure of CFRP-concrete interface. Also, it is indicated that effective anchorages of CFRP and reasonable anchoring constructions of insulation system play important roles in assuring the fire-resistant capability of CFRP-strengthened concrete beams.*

1 INTRODUCTION

In recent years, Carbon Fiber Reinforced Polymers (CFRP) are gaining increasing confidence in strengthening projects of concrete structures due to their vast advantages, such as high strength, low weight, endurance and convenience. However, the strength and stiffness of CFRP are severely reduced at elevated temperature. In particular, the bond property of the interface between CFRP and concrete is also severely deteriorated at temperature above T_g, the glass transition temperature of adhesive. Once such deteriorations have occurred, the effectiveness of the strengthening systems begins to fail, which puts the strengthened structures in danger [1]. In addition, the properties of concrete and steel material will also be deteriorated at elevated temperature, which makes the structures more dangerous. The available research shows that it is difficult to reach a certain fire resistant rating for un-insulated CFRP-strengthened beams, whereas the same beam with fire protection can obtain significantly better fire resistance [2]. Therefore, it is necessary and meaningful to do fireproof protection on CFRP-strengthened concrete members, and the fire behaviour of these insulated members needs more in-depth investigation.

2 LITERATURE REVIEW

In the last two decades, several fire tests have been conducted due to concerns regarding the performance of CFRP-strengthened RC beams exposed to fire.

Deuring [3] conducted fire tests on six RC beams strengthened with external CFRP strips and steel plates under ISO 834 standard fire exposure. These tests showed that without fire protection, interaction between CFRP and concrete was lost in the first 10 minutes of fire exposure, whereas the insulated

CFRP-concrete interfaces were able to withstand the exposure of fire for close to 60 minutes. It was suggested that thermal insulation was quite important to maintain effective bond under fire conditions.

Blontrock et al. [4] tested ten CFRP-strengthened RC beams insulated with various fire insulation schemes. Based on the results from fire tests, the authors concluded that mechanically anchored insulation provided more effective protection for bond interaction, compared with adhesive anchored insulation; U-shaped insulation also improved fire endurance of CFRP-strengthened RC beams.

Williams et al. [5-7] conducted a series of mid-scale fire tests on CFRP-strengthened RC members protected with VG-EI-R insulation under standard fire exposure. Barnes et al. [8] tested 24 CFRP-strengthened RC beams under standard fire conditions to study the effectiveness of insulation. These test results indicated that interaction between CFRP and concrete was almost completely lost once the temperature of adhesive exceeded glass transition temperature (T_g).

Chowdhury et al. [9] tested four insulated CFRP-strengthened beam-slab assemblies (T-beams) in fire and studied the post-fire behaviour of these T-beams. The tests indicated that, with sufficient fire protection, CFRP-strengthened T-beams after fire tests were capable of retaining most of their original un-strengthened flexural capacity.

Ahmed et al. [10] conducted fire resistance experiments on four RC beams strengthened with CFRP. The test variables included type of fire exposure, anchorage zone, insulation type, and restraint conditions. Ahmed demonstrated that fire-induced axial restraint helps in increasing load-carrying capacity of CFRP-strengthened RC beams in fire.

Previous researches have indicated that fire protection plays a critical role in maintaining a certain fire resistant rating of CFRP-strengthened RC beams. However, most of these tests available in literatures express concerns about whether the fire resistant rating is reached. There are few tests conducted to investigate fire resistant mechanism and reasonable insulation configuration of insulated CFRP-strengthened RC beams.

3 EXPERIMENTAL PROGRAM

To research the fire resistant mechanism of different fire insulation systems, four rectangular CFRP-strengthened RC beams were tested by exposing them to standard fire condition and service load. The test variables included insulation material, insulation configuration, and location of anchorage zone.

3.1 Materials

3.1.1 Concrete and Steel Reinforcement

The measured cubic compressive strength of concrete at 28 days was 30.7MPa. The maximum aggregate size was 20 mm, and the specimens were cured in a laboratory. The longitudinal steel bars used in these specimens had three different diameters of 12 mm, 16 mm, and 20 mm, respectively with yield strength of 368MPa, 375MPa, and 372MPa. The coefficient of thermal expansion in the longitudinal direction was 2×10^{-4}m/(m·℃) for concrete and 1.208×10^{-5}m/(m·℃) for steel bars. The elastic modulus of concrete and steel bars was 3.0×10^{4} MPa and 2.0×10^{5} MPa, respectively.

3.1.2 CFRP Sheets and Adhesive

CFRP sheets (12K-T700SC) of 200 mm width and 0.167 mm thickness were used in these tests. The properties were given by *Toray Industries*: elastic modulus, E=2.6×10^{5}MPa, density, ρ=300g/m^2, the longitudinal coefficient of thermal expansion, α=-1×10^{-6} m/(m·℃). The measured ultimate tensile strength of CFRP sheets was 4030MPa. The epoxy adhesive and primer (TH-PR/MER) used in tests were both two-part systems. They had a elastic modulus of 2.98GPa and a T_g of 73°C after fully cured.

3.1.3 Thermal Insulation Materials

Type 1 Thick Fireproof Coating. The thick fireproof coating, used in the test, was produced by the second factory of the Hili Group Ltd in Shanghai. The properties for the coating at room temperature quoted by the manufacturer were as follows: density of 500 $kg\ m^{-3}$, specific heat capacity of 1000 $J\ kg^{-1}\ K^{-1}$, and thermal conductivity of 0.12 $W\ K^{-1}\ m^{-1}$.

Type 2 Calcium Silicate Board. The calcium silicate board, used in the test, was produced by the Huida insulation materials Group Ltd in Shanghai. The properties for the board at room temperature provided by the manufacturer were as follows: density of 250$kg\ m^{-3}$, specific heat capacity of 740 $J\ kg^{-1}\ K^{-1}$, and thermal conductivity of 0.061$W\ K^{-1}\ m^{-1}$.

Type 3 Ultra-thin Fireproof Intumescent Coating. The ultra-thin fireproof coating, used in the test, was produced by Shanghai Xinhua Fire Inhibitor Factory. The properties for the coating at room temperature quoted by the manufacturer were as follows: density of 600$kg\ m^{-3}$, specific heat capacity of 800 $J\ kg^{-1}\ K^{-1}$, and thermal conductivity of 0.06$W\ K^{-1}\ m^{-1}$.

3.2 Test Specimens

The four specimens for fire tests, simply named L1, L2, L3 and L4, consisted of rectangular RC beam, CFRP strengthening system and insulation system. The RC beams of specimen L1 and L2 were of 200 mm width, 450 mm depth and 4.7 m span length, while the RC beams of specimen L3 and L4 were of 200 mm width, 500 mm depth and 5.2 m span length. There were two 12 mm steel bars for L1 and L2, two 16 mm steel bars for L3 and three 20 mm steel bars for L4 as flexural reinforcement, and two 8 mm steel bars for L1 and L2, two 12 mm steel bars for L3 and L4 as hanger bars. The stirrups used as shear reinforcement for all the specimens were of 6 mm diameter and 200 mm spacing.

After cured for 40d, the RC beams were strengthened with two layers of CFRP sheets. The concrete surface was roughened by sand blasting to partially expose the aggregate. Then, two layers of CFRP sheets were roller-applied at the beam soffit. Thus the bearing capacity was enhanced by 73% for L1 and L2, 57% for L3, and 40% for L4. In addition, U-wrap anchorages at the end of beams were applied to provide additional anchorage. The design details of un-insulated specimens are shown in Figure 1.

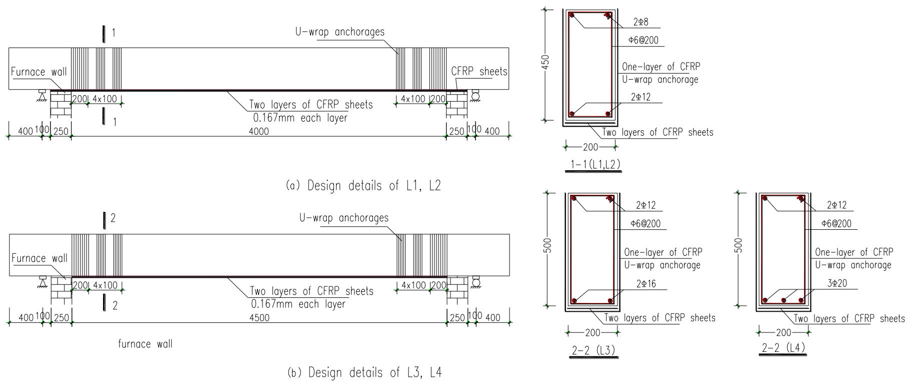

Figure 1. Design details of the un-insulated specimens (unit: mm).

3.3 Insulation of Beams

The strengthened beams were cured for 7 days and then applied with U-shaped insulation system. Figure 2 shows the insulation detail for specimen L1 and L2, insulated with thick fireproof coating. Specimen L1 was protected along the entire span with 50 mm thick coating (Completely-Protected), while thick fireproof coating was applied in the anchorage zone of specimen L2 (1100 mm from the end of support) with a thickness of 50 mm and in the intermediate region with a thickness of 20 mm (Partly-Protected). Layered construction of thick fireproof coating was adopted to ensure greater uniformity. Each layer was about 10 mm thick, and the construction interval was 24 hours at least.

On the entitle length of specimen L3, calcium silicate board was glued by applying a layer of average 2 mm thickness of high-temperature adhesive (refer to Figure 3). On the outside of insulation, refractory steel wire was used for further fixation. Specimen L4 was insulated with ultra-thin fireproof coating of an average thickness of 1.52 mm, which was layered roller-applied on the strengthened beam. In total, the roller construction was divided into 10 times, and the interval was 12 hours.

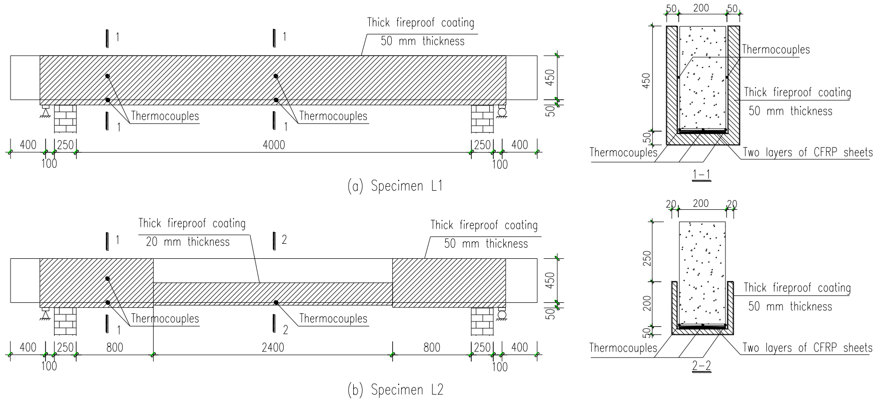

Figure 2. Insulation and thermocouples details for specimen L1 and L2.

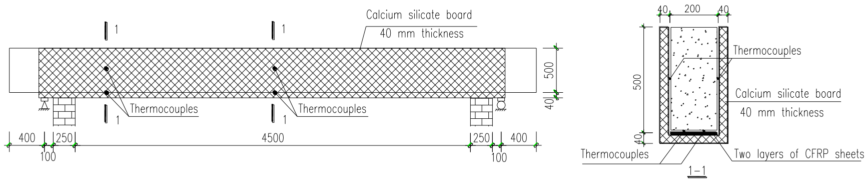

Figure 3. Insulation and thermocouples details for specimen L3.

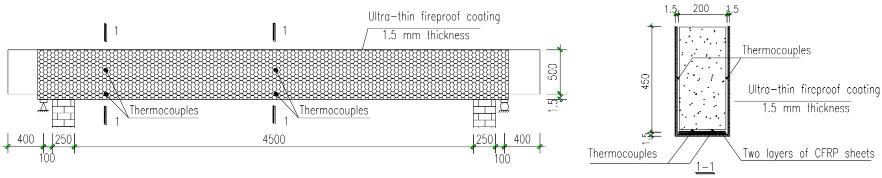

Figure 4. Insulation and thermocouples details for specimen L4.

3.4 Test Set-Up and Measuring Devices

The first series tests on specimen L1 and L2 were conducted in the China Classification Society Shanghai Far East Fire Test Center, while the rest tests on specimen L3 and L4 were conducted at Fire Resistance Horizontal Test Furnace in Tongji University. The test furnace, shown in Figure 5, consists of fire chamber, loading device, temperature control system, data acquisition and processing system. Located within the furnace in two rows, eight gas burners provide thermal energy following the standard fire curve, while ten internal thermocouples monitor the furnace temperature during a fire test. Such an excellent integration makes the tests simple and convenient.

Figure 5. Test furnace.

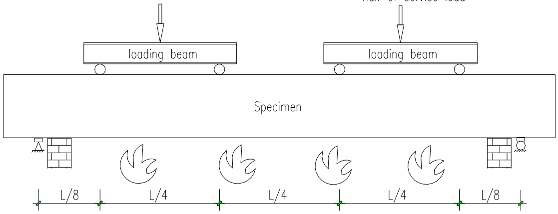

Figure 6. Loading arrangement.

Table 1 shows the relevant details of the specimens in fire tests. The specimens were simply supported at the ends with an unsupported length of 4.0 m for L1, L2 and 4.5 m for L3, L4. For specimen L1 and L2, the location of CFRP anchorage zone was designed 250 mm length out of the fire zone, while the whole CFRP sheets used on specimen L3 and L4 were all in fire (refer to Figure 1). Service loads were applied to specimens before the fire test started. Figure 6 shows the loading arrangement of these tests. The service loads included four equivalent concentrate loads, locating respectively in 1/8, 3/8, 5/8 and 7/8 of net span. The load was applied approximately 30minutes before the start of the test until steady condition was reached.

Table 1. Details of the specimens in tests.

Specimen	Length in fire (m)	Insulation Material	Insulation Configuration	Thickness (mm)	Anchorage zone	Load ratio
L1	4.0	thick coating	Completely-Protected	50	out of fire	0.435
L2	4.0	thick coating	Partly-Protected	50（20）	out of fire	0.435
L3	4.5	calcium silicate board	Completely-Protected	40	in fire	0.630
L4	4.5	ultra-thin coating	Completely-Protected	1.5	in fire	0.630

After about 30 minutes under service loads, the specimens were exposed to fire from three sides and heated according to the standard curves of ISO834–1975,

$$T - T_0 = 345\lg(8t + 1)$$

where t is the temperature rising time, also the time duration of fire test, min; T is the temperature in furnace at t moment, ℃; T_0 is the initial temperature, ℃.

During the tests, Type-K thermocouples were used at two different sections of the specimens to measure the CFRP-concrete interface temperatures. As shown in Fig. 2 to Fig. 4, these thermocouples were located on bottom and side surface of the specimens. In addition, mid-span deflections were also measured by displacement transducers.

4 TEST RESULTS

4.1 Observation of Test Process

4.1.1 Specimen L1

The interface temperature went up slowly in the first 10 min, and the vapor came out from the surfaces of specimen continuously. While heating to 28 min, two-layer thick fireproof coating fell off from the bottom of the mid-span, and vertical cracks appeared on the side coating. Continuing to 150 min, the mid-span deflection no longer increased. Then the test was terminated. After test, it was observed that several vertical cracks on the side coating were evenly distributed along the longitudinal direction. Figure 7a shows that two layers of coating fell off from the bottom of the specimen. The surface coating was removed to detect the internal condition and it was found that the vertical cracks only generated on the surface coating, and the internal coating was basically intact (refer to Figure 7(b)).

4.1.2 Specimen L2

The test of specimen L2 had the same phenomenon as specimen L1 in 20 min after started. After 27 min, horizontal cracks between the coating and CFRP sheets appeared on the coating where the thickness changed, as shown in Figure 8(a). From 34 minutes on, the cracks widened gradually, then flames came out from the cracks, and CFRP sheets started to burn. After 44 min, the coating in mid-span completely dropped on the ground, CFRP began to burn very-rapidly (refer to Figure 8(b)). The carbon fiber burnt down completely at 90 minutes of fire exposure. While heating to 117 min, the deflection of reinforced concrete beam reached 130 mm, and then suddenly collapsed.

(a) The falling of coating (b) Internal condition

Figure 7. Observation of specimen L1 after fire test.

(a) Horizontal cracks (b) Burning CFRP

Figure 8. Observation of specimen L2 in fire test.

4.1.3 Specimen L3

In the earlier stage of the test, the vapor came out from the surfaces of calcium silicate board continuously. After 52 minutes of fire exposure, the deflection began to increase rapidly from 11.03 mm to 143.6mm in 122 min, when the concrete begin to blow out under fire and service load. Considering the specimen L3 was close to failure, the test was terminated. After cooled, it was observed that some cracks appeared on the surface of the board and the board was apart from the beam, but did not drop down due to the fixation of steel wire, shown in Figure 9(a). Figure 9(b) shows that the CFRP sheets in mid-span were completely detached after the test, and no strength benefit was obtained.

4.1.4 Specimen L4

The vapor came out from the surfaces of the specimen in 15 min after test started. With continuing to heat, tiny drops of moisture were constantly seeping out of the end of specimen. When heating to 124 min, the mid-span deflection was up to 269.2mm, which was beyond the upper limit value, one twentieth of the span length. Then, test was terminated. Figure 10(b) shows that the ultra-thin fireproof coating was foamed to a layer of 10 mm thickness with some cracks on the surface. Furthermore, the fireproof coating of the bottom surface of specimen L4 was fully dropped due to premature burning of CFRP sheets, as shown in Figure 10(b).

(a) Cracks on the board (b) Internal condition

Figure 9. Observation of specimen L3 after fire test.

(a) The foaming of coating (b) The bottom surface

Figure 10. Observation of specimen L4 after fire test.

4.2 Thermal Response

Figure 11 shows time-temperature progression for all the specimens at CFRP-concrete interface.

It is evidently shown in Fig.11a, Fig.11c and Fig.11e that temperatures at CFRP-concrete interfaces of specimen L1, L2 and L3, protected by thick fireproof coatings and calcium silicate board, increased slowly followed by a temperature plateau around 100℃. The interface temperature at bottom surface of specimen L1 reached the temperature plateau after 40 minutes of fire exposure, and held on this plateau for about 60 minutes. For specimen L2 and L3, the time when the temperature plateau was reached was 40 min and 60 min after test started, and the lasting time on this plateau was 65 min and 20 min. This temperature plateau can be attributed to evaporation of free and chemically bonded water in the insulation materials that consumed large amounts of energy. When the external environment was in fire, the waters in the insulation materials moved and gathered to the low temperature zone (the surface of CFRP), then evaporated by absorbing heat, which reduced the increase of the temperature at CFRP-concrete interface.

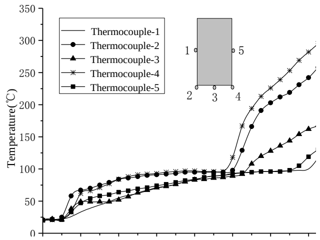

(a) Temperature at end section of specimen L1

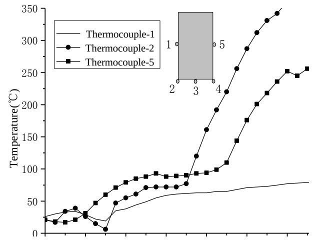

(b) Temperature at mid-span section of specimen L1

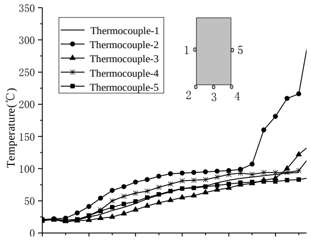

(c) Temperature at end section of specimen L2

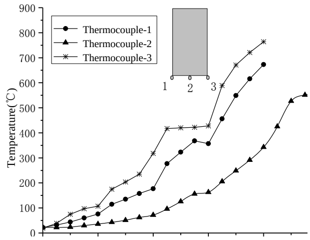

(d) Temperature at mid-span section of specimen L2

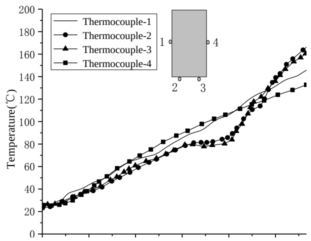

(e) Temperature at end section of specimen L3

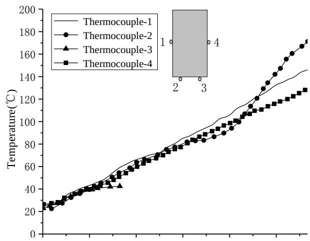

(f) Temperature at mid-span section of specimen L3

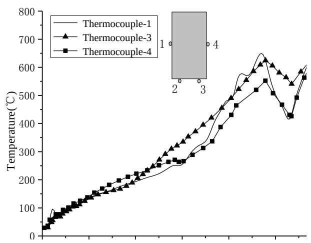

(g) Temperature at end section of specimen L4

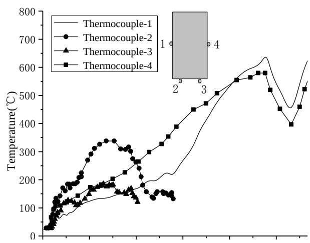

(h) Temperature at mid-span section of specimen L4

Figure 11. Temperature recorded at various locations of beams during fire test.

Referring to specimen L4, which was insulated with ultra-thin fireproof intumescent coating, the temperature increase at CFRP-concrete interface was very rapid, and temperature plateau did not appear during the test. This is due to the premature failure of insulation system at bottom surface, which made the bottom surface in the condition without fire protection. Since the foaming temperature (100℃~150℃)

of ultra-thin coating was higher than glass transition temperature (73℃) of the adhesives, the bond of interface was lost before the insulation material worked. After bond failure, debonding of CFRP sheets resulted in the ultra-thin coating falling off from bottom surface (refer to Figure 10(b)). In the test on specimen L4, an interruption of ten minutes was used for obstacle checking, so a backdrop came out at about 95 min on the time-temperature curve.

As can be seen from Figure 11, the first two types of insulation materials, thick fireproof coatings and calcium silicate board, play a good insulating role in the testing process. The temperature of interface at the side surface of specimen L1, L2 and L3 was always lower than 250 ℃ within 120 minutes. The maximum temperature of CFRP at the center of bottom surface was 179 ℃ and 198 ℃, respectively for specimen L1 and L3, while the maximum temperature was 574 ℃ for specimen L2 because of the early failure of insulation on the bottom surface.

It is mentioned above that glass transition temperature T_g of the adhesives used in the test is about 73℃. Figure 11 shows that, the moment that temperature T_g was reached respectively was 35 min of fire exposure for specimen L1, 40 min for specimen L2, 55 min for specimen L3, and 10 min for specimen L4. These test data show that in fire test process, although the specimens were protected with insulation materials, adhesives still was failure in the early stage due to the premature reach to the temperature T_g. Therefore, after the bond failure of the interface, the major role of fire insulation materials was reducing the performance degradation of concrete and internal reinforced bars, by slowing down the temperature increase of these two materials.

4.3 Structural Response

Time-deflection curve of the specimens are shown in Figure 12.

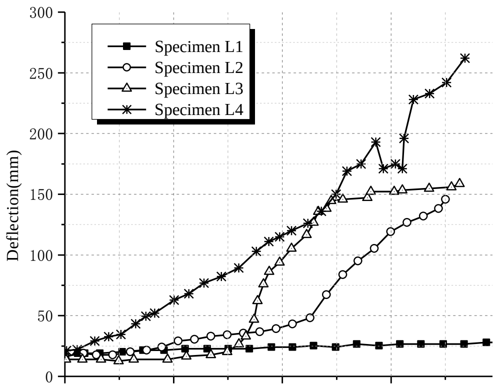

Figure 12. Time-deflection curves of specimen L1，L2，L3 and L4.

The deflection progression of specimen L1 is not much different than that of specimen L2 in the early stage, which shows that partly-protected configurations worked just as well as completely-protected configurations before the falling of insulation. However, after 75min when the insulation of middle span fell off and the CFRP sheets nearly burn out, the CFRP-strengthened RC beam degenerated into original RC beam, so that mid-span deflection of specimen L2 increased rapidly. Throughout the entitle process, the deflection of specimen L1 increased slowly with a smaller value, which illustrates that the strengthening system of CFRP always worked well, due to protection of the insulation material.

Within 40min after the test started, deflection of specimen L3 is basically the same as specimen L1 and L2. After 50min, the deflection of specimen L3 has a greater increase than that of specimen L1. This is due to the difference in position of CFRP anchorage zone in fire tests. The anchorage zone of CFRP sheets on specimen L1 extends 250 mm outside of fire chamber, thus reducing the heat-related deteriorates during the entire test. Although the bond of interface in the middle span was lost at high temperature, CFRP sheets can still be able to work as tension reinforcement, as a result of the existence of bonding in the anchorage zone. By contrast, the CFRP anchorage zone of specimen L3 was all in fire, so that the bond failure of the interface resulted in large slippage between concrete and carbon fibers after the temperature of adhesive exceeded T_g. Since then, the CFRP strengthening system gradually lost effectiveness. This is the reason that the deflection of specimen L3 increased rapidly.

Shown in Figure 12, the time-deflection curve of specimen L4 is approximates parabolic, and always increases fastest. This is mainly contributed to that the strength benefit was lost after 10 min of exposure to fire. Due to the premature failure of CFRP strengthening system, both the service load and fire load were applied on the original RC beam. Another reason is that the load ratio for specimen L4 is higher than that for L1 and L2. Therefore, the mid-span deflection increased rapidly all the time.

5 FIRE BEHAVIOUR

To summarize and analysis these results mentioned above, the following discussions are presented.

(1) U-shaped insulated CFRP-strengthened RC beams, protected respectively with 50mm thick fireproof coating, 40 mm calcium silicate board and 1.5 mm ultra-thin fireproof coating on whole span, are all capable of achieving fire endurance rating of 2 hours. On the contrary, the CFRP-strengthened RC beam without insulation system, corresponding to specimen L3, just has a fire endurance rating of less than 30 min [11]. It is indicated that using U-shaped fire insulation for CFRP-strengthened RC beams is a kind of effective methods

(2) Though reached the temperature T_g within 60 minutes, specimen L1, L3 and L4 can continue to bear the load until the end of the test. Further, the maximum deflections of the three specimens at 2 hours are all less than one twentieth of the span length. These results show that the insulation systems have contributed not only to delay the failure of adhesive, but also to prevent the properties of RC beam from being deteriorated acutely.

(3) The temperature plateau around 100℃ has a time span of 60 minutes for specimen L1 and L2, and for specimen L3, the time span is 20 minutes. Although the temperature plateau has already exceeded glass transition temperature T_g of the adhesives, the plateau is helpful to slow down the heat-related degradation of specimens, especially for the beams insulated with thick fireproof coating. Furthermore, the adhesives usually has a T_g value of 65℃—80℃. If the properties of adhesive can be further improved, with T_g beyond 100℃, better fire performance of insulated CFRP-strengthened beams will be obtained.

(4) According to time-deflection curve of the tests, it can be seen that the deflection of the specimens with anchorage zone out of fire are obviously smaller than that of the specimens with anchorage zone in fire. Further, even though the temperature of adhesive exceeded T_g, the deflection increase is still not large. This is contributed to the effectiveness of the anchorage zone of CFRP sheets. As to specimen L1 and L2, the bond between CFRP and concrete did not failure at lower temperature, which ensured the effectiveness of the strengthening systems. On the contrary, the specimens L3 and L4 have greater deflection due to the large interface slippage at the anchorage zone. It can be concluded that additional anchorage measures are needed to ensure the effectiveness of the anchorage for the specimens with anchorage zone in fire.

(5) Visual observations in fire tests indicated that specimen L2 has a good fire resistance performance in the early with only several fine cracks, but the performance started to suffer after the falling of insulation material, and at last specimen L2 collapsed. On the contrary, Specimen L3, as a result of the fixation with steel wire, performed well all the time. It is obviously demonstrated that anchoring measures and construction quality of insulation system are also importance factors to assure the fire-resistant capability of insulated CFRP-strengthened RC beams.

According to above-mentioned analysis results, fire resistance of CFRP-strengthened RC beams could be improved by the following measures: (1) Choose the particular adhesive with its T_g beyond 100℃ as the adhesive and matrix, (2) Strengthen the end anchorage of CFRP, (3) Fix the insulation material with reasonable constructions.

6 CONCLUSIONS

Based on experimental studies, the following conclusions can be drawn:

(1) Satisfactory fire endurances of 2 hours for CFRP-strengthened concrete beams, respectively insulated with thick fireproof coating, calcium silicate board and ultra-thin fireproof coating on whole span, can be obtained under the fire and service load.

(2) The major role of fire insulation materials was delaying the failure of adhesive in the early stage, and reducing the performance degradation of concrete and internal reinforced bars of the beam during the later stage.

(3) According to the test results of specimens, especially the specimens insulated with thick fireproof coating, a significant temperature plateau around 100℃ appears in time-temperature curve at CFRP-concrete interfaces. If the adhesives with T_g beyond the temperature plateau can be used, combined with the effect of temperature plateau, better fire performance of insulated CFRP-strengthened RC beams will be obtained.

(4) Bond effectiveness of anchorage zone plays an important role in assuring the fire-resistant capability. If the anchorage zone of CFRP sheets are all in fire, additional anchorage measures could be applied to obtain better fire performance.

(5) Reasonable anchoring constructions of insulation materials provide a crucial support for CFRP-strengthened concrete beams to reach a certain fire resistant rating. Further studies on anchoring constructions of insulation materials will be needed.

REFERENCES

[1] Hu Kexu, He Guisheng, Lu Fan, “Experimental study on fire protection methods of reinforced concrete beams strengthened with carbon fiber reinforced polymer”, *Frontiers of Architecture and Civil Engineering in China*, 1(4), 399-404, 2007.

[2] Williams B., Kodur V.K.R., Green M F., et al. “Fire endurance of fiber-reinforced polymer strengthened concrete T-beams”, *ACI Structural Journal*, 105(1), 2008.

[3] Deuring M., “Brandversuche an nachtraglich verstarkten tragern aus beton”, in Research Report EMPA No.148,795. 1994, Swiss Federal Laboratories for Materials Testing and Research: Dubendorf, Switzerland.

[4] Blontrock H., Taerwe L., Vandevelde P., “Fire tests on concrete beams strengthened with fibre composite laminates”, *Proceedings of the International PhD Symposium in Civil Engineering, Vienna* , Konrad Bergmeister(ed.), *Austria* (5-7/10), Volume 2, 151-161, 2000.

[5] Williams B., “Fire Performance of FRP-Strengthened Reinforced Concreet Flexural Members”, [Doctorate thesis], Canada, Queen’s University, 2004.

[6] Kodur V.K.R., Bisby L.A., Green M.F., “Fire endurance of FRP-strengthened reinforced concrete columns”, NRCC-46633，872-881, 2004.

[7] Williams B., Kodur V.K.R., Bisby L.A., et al. “Fire insulation schemes for FRP-strengthened concrete slabs”, *Composites, Part A: applied science and manufacturing*, 37, 1151-1160, 2006.

[8] Barnes R. and Fidell J., “Performance in fire of small-scale CFRP strengthened concrete beams”, *Journal of Composites for Construction*, DOI: 10.1061/ (ASCE) 1090–0268(2006) 10:6(503).

[9] Chowdhury E.U., Bisby L.A., Green M.F., et al., “Residual behavior of fire-exposed reinforced concrete beams prestrengthened in flexure with fiber-reinforced polymer sheets”, *Journal of Composites for Construction*, 12(1), 61-68, 2008.

[10] Ahmed A., Kodur V.K.R., “The experimental behavior of FRP-strengthened RC beams subjected to design fire exposure”, *Engineering Structures*, 33(7), 2201-2211, 2011.

[11] Gao Wanyang, Hu Kexu, Lu Zhoudao, “Nonlinear analysis of insulated carbon fiber reinforced polymer strengthened reinforced concrete beams in fire”, *Journal of Tongji University: (Natural Science)*, 37(5), 575-582, 2009 .(in Chinese)

8th International Conference on Structures in Fire
Guo-Qiang LI, Venkatesh K. R. KODUR, Shou-Chao JIANG, Jian JIANG, Su-Wen CHEN, Guo-Biao LOU (Eds.)
Shanghai, China, June 11-13, 2014

EXPERIMENTAL AND NUMERICAL INVESTIGATION OF POST-TENSIONED CONCRETE FLAT SLABS IN FIRE

Ya Wei*, F. T. K. Au*, Jing Li and N. C. M. Tsang*****

* Department of Civil Engineering, the University of Hong Kong, Hong Kong, China
e-mails: weiya@hku.hk, francis.au@hku.hk

** Department of Civil Engineering, South China University of Technology, Guangzhou, China
e-mail: scutlijing@126.com

*** Department of Civil Engineering, Architecture and Building, Coventry University, UK
e-mail: aa8607@coventry.ac.uk

Keywords: Concrete spalling, Fire, High-strength self-compacting concrete, Post-tensioned flat slab

Abstract. *Tests of four post-tensioned high-strength self-compacting concrete flat slab specimens have been conducted under fire condition. Tendon distributions including distributed-distributed and banded-distributed patterns as well as various loading ratios were considered. Two of the specimens with lower moisture contents demonstrated excellent fire resistance performance, while the others with relatively high moisture contents experienced severe concrete spalling. The test results obtained from the tests are presented and discussed with respect to temperature distributions, deflections, crack patterns and concrete spalling. Moreover, numerical modelling employing the package ABAQUS has been conducted to help interpret the test results in order to get better understanding of slabs in fire.*

1 INTRODUCTION

Post-tensioned (PT) concrete flat slabs with unbonded tendons have been increasingly adopted in both commercial and residential buildings for floor systems all over the world with the remarkable merits of reduced span-to-depth ratio and enhanced load-carrying capacity. Nevertheless, the fire resistance design requirements for flat slabs presented in the codes ACI 318-08 [1] and BS EN 1994-1-2 [2] and the professional manual [3] based on limited research results obtained decades ago are mainly prescriptive. Improved understanding of the true behaviour of flat slabs under fire conditions will therefore be helpful to better fire resistance design in consideration of structural safety and cost.

The pioneering research on PT concrete flat slabs exposed to ASTM E119 standard fire has been reported by Gustaferro [4], where no concrete spalling occurred and the fire resistance periods exceeded 3 hours. From the studies, recommendations of minimum concrete cover and critical temperature of prestressing steel tendons were proposed for required fire resistance periods. However, as pointed out by Gales *et al.* [5], these tests could be out of date with respect to construction material and technique employed, and quite insufficient for performance-based fire resistance design. Nevertheless, few fire tests of PT concrete flat slabs have been carried out since then, except for the fire tests of one-way PT concrete slabs conducted in the recent decade mainly in Mainland China and the UK. Yuan *et al.* [6] have investigated the effects of sequential fire exposure on continuous unbonded PT concrete slabs, namely exposing the middle span to fire for 90 minutes and then the end span to fire for 90 minutes in succession, or in reverse. It was concluded from the investigation that the damage modes of the slabs was related to the sequence of fire exposure. Zheng *et al.* [7] have tested simply supported PT concrete slabs and two-span PT concrete slabs with the two spans exposed to fire simultaneously, where specimens were cast with normal strength concrete with calcareous coarse aggregate. The strength ranged from 40 MPa to 60 MPa and the moisture content from 2.36% to 3.98% by mass. In the experiments, concrete spalling was observed, and an envelope diagram was proposed with respect to normal stress, concrete strength and moisture content for preliminary judgment of possibility of concrete spalling. In the UK, Bailey and Ellobody [8] conducted fire tests of simply supported PT concrete slabs with unbonded tendons at the same time, taking into consideration the aggregate types and longitudinal restraints, and found that the behaviour of the slab was dominated by the thermal expansion of aggregate and longitudinal restraints could reduce the deflection of the slab because of arching action formed in the slab due to the restraining force.

Previous tests have provided us better understanding of the performance of one-way PT normal-strength concrete slabs under fire condition. Further investigation is therefore necessary to understand the structural fire performance of two-way PT flat slabs, particularly their deformation and load-carrying mechanisms. Moreover, high-strength self-compacting concrete (HSSCC) is becoming increasingly popular in modern building construction, but it is sensitive to concrete spalling when exposed to fire due to its relatively low permeability and lower porosity [9,10]. Therefore, the present investigation is to explore the behaviour of PT HSSCC flat slabs with unbonded tendons under fire based on experimental and numerical approaches.

2 TESTS AND NUMERICAL MODELS

2.1 General

The test specimens, denoted as Test-1, Test-2, Test-3 and Test-4, respectively, are identical in geometry but different in tendon arrangement and loading ratio, as shown in Table 1. The tendon arrangement in each direction may be banded or distributed. The designed prestressing level is specified by the ratio of the final average PT tendon stress to the ultimate strength. The design loading ratio is that of the applied loads including the self-weight of slab to the ultimate loading capacity of the slab.

Table 1. Parameters investigated in the tests.

Test Case	Tendon distribution	Design prestressing level	Design loading ratio
Test-1	Distributed-Distributed	0.37	0.50
Test-2	Banded-Distributed	0.50	0.35
Test-3	Distributed-Distributed	0.50	0.50
Test-4	Banded-Distributed	0.50	0.35

Figure 1 shows one of the test specimens, which comprises a flat slab supported on four columns seated on a base grid of beams. Only the central panel of the slab enclosed by the columns was exposed to fire, while the rest of slab and columns were protected from fire with ceramic wool. The numerical model of one quarter of the specimen shown in Figure 2 was established employing the ABAQUS package. The concrete and prestressing tendons were modelled by 3D solid elements while the steel reinforcing bars were modelled by 3D truss elements. Frictionless contact between the prestressing tendons and the surrounding concrete was assumed in the model. The thermal and mechanical properties of the materials at elevated temperature and the thermal parameters for convection and radiation were taken from BS EN 1991-1-2 [11] and BS EN 1992-1-2 [2], respectively. The concrete used for the slab and columns in the tests was grade C60 HSSCC with granite aggregate and ground granulated blast-furnace slag (GGBS), with composition given in Table 2. Grade C40 normal concrete was used for the support beams.

Figure 1. Overview of one test specimen.

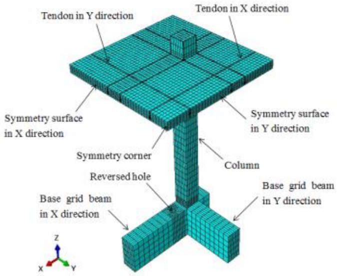

Figure 2. Numerical model of a quarter of specimen.

Table 2. High-strength self-compacting concrete mixture (kg/m^3).

Cement	GGBS	Fine aggregate	Coarse aggregate	Water	Additives
394	106	650	1060	142	11.65

2.2 Specimens

The specimens were designed according to BS EN 1992-1-1 [12] and ACI 318 [1] to reduced scale due to the dimensional limitation of the furnace. Figure 3 shows the details of dimensions and reinforcement of the specimens. The slab is square in plan with sides of 3.1 m and depth of 95 mm. The columns have square cross sections of 200 mm by 200 mm with a clear height from the top of base to the soffit of slab of 1850 mm. The base beams have a breadth of 200 mm and depth of 400 mm, and have lengths of 2600 mm and 1800 mm in X and Y directions respectively. Besides, top and bottom steel reinforcing bars of the slab were mild steel round bars of grade 235 and 6 mm diameter provided with concrete cover of 15 mm. High yield steel deformed bars of grade 335 and 12 mm diameter were provided to the columns and base beams as longitudinal reinforcement, while mild steel round bars of grade 235 and 6 mm diameter were used as stirrups. The concrete cover to the reinforcement in columns and base beams was 25 mm.

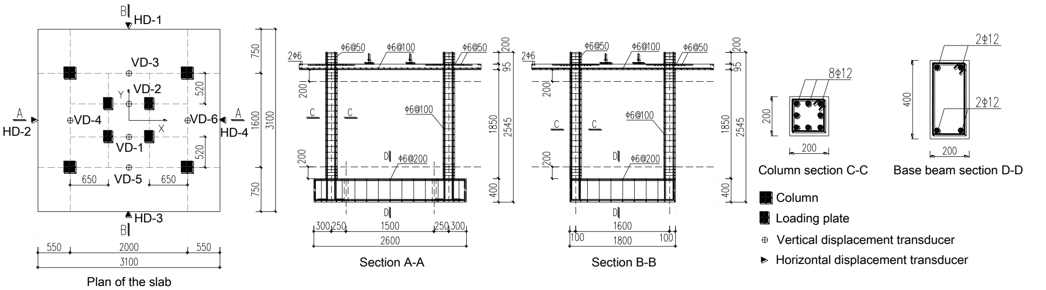

Figure 3. Configuration of test specimens and arrangement of loading and displacement transducers (dimensions in mm).

Figure 4 shows the tendon arrangement for two specimens. Figure 4(a) shows the Distributed-Distributed tendon arrangement, where tendons in the X direction denoted as X1 to X6 adopt the profile “Tendon-profile-a1” while tendons in the Y direction denoted as Y1, Y2, Y5 and Y6 adopt the profile “Tendon-profile-a2” and those denoted as Y3 and Y4 adopt the profile “Tendon-profile-a3”. Figure 4(b) shows the Banded-Distributed tendon arrangement, where tendons in the X direction denoted as X1 to X6 adopt the profile “Tendon profile-b1” while tendons in the Y direction denoted as Y1 and Y6 adopt profile “Tendon profile-b2” and those denoted as Y2 to Y5 adopt profile “Tendon profile-b3”.

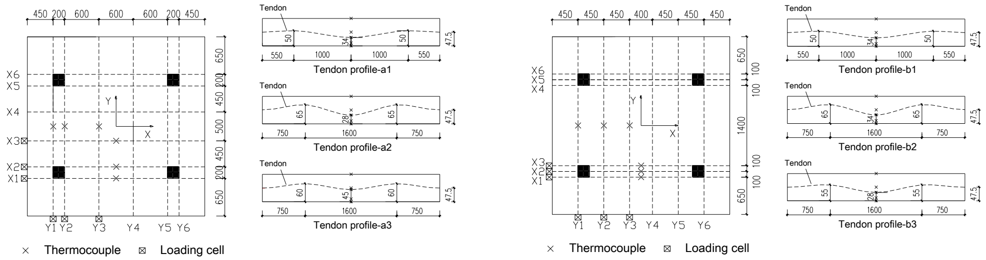

(a) Distributed-Distributed (b) Banded-Distributed

Figure 4. Arrangement of tendons and thermocouples (dimensions in mm).

The mild steel round bars of grade 235 had measured properties of elastic modulus of 190 GPa, yield strength of 248 MPa and ultimate strength of 410 MPa, while the corresponding measured properties of high yield steel deformed bars of grade 335 were 196 GPa, 458 MPa and 582 MPa, respectively. The strand has a nominal diameter of 12.7 mm and cross sectional area of 98.7 mm^2, which is greased and housed in a polypropylene sleeve with thickness of 1 mm. In view of the reduced scale, the minimum concrete cover to the tendons was 21.5 mm. The measured mechanical properties of strand at ambient temperature included elastic modulus of 211GPa, 0.2% proof stress of 1805 MPa and ultimate strength of 2008 MPa.

2.3 Instrumentation

The deflections of slabs were measured by Linear Variable Displacement Transducers (LVDTs) denoted as VD-1 to VD-6 in Figure 3. LVDTs VD-1 and VD-2 were used to monitor the deflections of the central panel at the loading points; VD-3 and VD-5 were used to monitor the deflections at the middle of column strips in the X direction; and VD-4 and VD-6 were used to monitor the defections at the middle of column strips in the Y direction. Self-made and calibrated load cells were used to measure the tendon forces during tensioning. Thermocouples were placed in the specimen to measure the temperature distributions of the slab as shown in Figure 4. Taking the middle of X3 as an example, X3-B, X3-S, X3-P, X3-M and X3-T denote the bottom, bottom reinforcement, tendons, middle and top of the slab respectively where the temperatures were measured by thermocouples.

2.4 Test procedure

The furnace used as shown in Figure 5(a) has a clear height of 1.8 m, clear width of 3.0 m and clear length of 4.0 m. The loading system is comprised of a hydraulic jack with a loading capacity of 500kN and simply supported steel beams in contact with four steel load spreaders, as shown in Figure 5(b). Firstly, loads were applied on the slab through the loading system and were kept constant for 15 mins for stability. Afterwards, fire was started in the furnace for testing with the applied loads maintained. The fire curves monitored in the four tests are compared with the ISO 834 standard fire curve in Figure 5(c), which shows reasonable agreement.

(a) (b) (c)

Figure 5. Test furnace and loading system: (a) furnace; (b) loading system; and (c) furnace fire curve.

Besides, the HSSCC strengths at 28 days and on the test day, average initial forces of tendons and those after loss, loads not including self-weight of the slabs, and moisture contents were recorded as shown in Table 3.

Table 3. Concrete strength, tendon forces, applied loads and moisture content for the tests.

Test Case	Concrete strength (MPa)		Forces of tendons (kN)		Loads (kN)	Moisture content
	28 Days	Day of test	Initial	After loss		
Test-1	78.9	76.6	98.4	72.4	85.7	2.27%
Test-2		75.6	119.7	95.4	85.7	2.36%
Test-3		79.5	127.3	94.8	125.7	2.62%
Test-4		81.4	123	91.5	85.7	2.52%

3 RESULTS AND DISCUSSIONS

Results obtained from the tests are presented covering the temperature distributions, deflections, crack patterns and concrete spalling. These results are also discussed based on numerical modelling for better understanding the PT flat slabs in fire.

3.1 Temperature distributions

Figure 6 shows the variations of temperature distribution in the slabs with time. While Figures 6(a) and 6(b) show relatively smooth temperature curves, Figures 6(c) and 6(d) appear irregular as a result of severe concrete spalling. As shown in Figures 6(a) and 6(b), the temperature of the slab soffit rose quickly after starting of fire due to heat transfer through radiation and convection. Obviously, with the increase of distance from the soffit, the temperature had a slower heating rate due to the relatively high thermal resistance of concrete. There are only slight differences between the temperatures measured at X3 and Y3 in Test-1, and Y3 and Y2 in Test-2 at the same level. However, in Test-1 the temperature of tendon X3 was much higher than that of Y3 as the concrete covers to them were 27.5 mm and 38.5 mm respectively. Therefore it can be concluded that the measured temperature distributions are reliable and reasonably accurate. Besides, Figures 6(a) and 6(b) show excellent agreement between the numerical results and test results, verifying that the thermal properties of materials and thermal parameters in the numerical model are reliable.

Interestingly, there are plateaus observed in the tendon temperatures in Figures 6(a), 6(b) and 6(c) in the range from about 130 C to 160 C. This may be caused by the melting of polypropylene sleeves in conjunction with moisture evaporation, but it cannot be simulated by the present numerical models. In addition, the temperature distributions were severely affected by the continuous concrete spalling since 5 minutes after the test began. For example, the temperatures of the soffit and reinforcement increased dramatically at the temperature of 200 C. Besides, comparing the temperatures of X3-P in Test-1 and X3-P in Test-3, the former is much lower than the latter, indicating that concrete spalling can accelerate the increase of tendon temperature.

The temperatures at the top surface of the central panel in the first two tests without concrete spalling are further examined. In Test-1, it reached 160 C after 75 minutes of fire exposure, and the fire was conservatively discontinued as the tendon temperature already exceeded the critical temperature of 350 C prescribed in BS EN 1992-1-2 [2]. In Test-2, it reached 240 C at 120 minutes after commencement. In accordance with the failure criteria in BS 476-20 [13] with respect to insulation, Test-1 did not violate the criteria but Test-2 did. Generally, Test-2 only had a fire resistance of 90 minutes according to the criteria, but it survived 120 minutes still with structural integrity and stability.

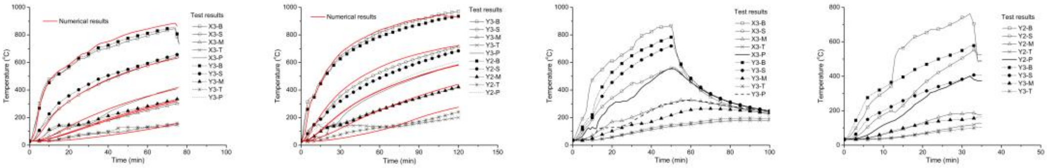

(a) Test-1 (b) Test-2 (c) Test-3 (d) Test-4

Figure 6. Temperature variations of central panel of slab.

3.2 Deflections

Figure 7 shows the deflections of the slabs in Test-1 and Test-2, where VD-C is the average value of VD-1 and VD-2 denoting the deflection of central panel, VD-X is the average of VD-3 and VD-5 denoting the deflection of column strip in the X direction, and VD-Y is the average of VD-2 and VD-6 denoting the deflection of column strip in the Y direction. The deflections are mainly governed by the thermal gradients across the depth of the slabs and the consequent thermal expansions [14], as well as restrained thermal thrust forces. Moreover, the mechanical properties of concrete, reinforcement and prestressing tendons degraded and stress relaxation of tendons with the increase of temperature all resulted in the reduced stiffness of the slab and further contributed to the increase of deflections.

Figures 7(a) and 7(b) show that deflections of the central panel increased rapidly in the initial 15 minutes. Afterwards, the increases of deflections gradually slowed down with time due to the reduced temperature gradient and increased thermal restraint thrust forces provided by the columns and the surrounding cold parts of slab. The deflections of the column strips in the X direction and the Y direction also increased a lot in the first 15 minutes but they slowed down afterwards or even remained constant. The deflections are mainly caused by the flexural deformation of the central panel in the two orthogonal directions leading to the flexural deformation of the column strips. Moreover, VD-X is larger than VD-Y because the column strip span in the X direction is larger than that in the Y direction and hence the former has smaller flexural stiffness. Besides, as observed in Figure 7(b), after the initial 90 minutes, VD-C changed slightly faster, while VD-X and VD-Y had no obvious changes. This can be explained by the cracks that appeared in and parallel with the column strips. The cracks weakened the integrity of the slab releasing the rotation restraints from the cold parts of slab, further leading to the increase of deflection in the central panel.

The predicted deflections obtained from numerical modelling show reasonable agreement with those obtained from Test-1 and Test-2, but obvious discrepancies still exist as shown in Figure 7. The discrepancies may be attributed to two aspects. One is that the thermal expansion of concrete considered in numerical modelling, which is taken to be that of siliceous normal concrete from BS EN 1992-1-2 [2], while the concrete in the tests is HSSCC. The other aspect is that transient thermal creep strain of concrete was not explicitly considered. Further refinement is necessary.

(a) Test-1 (b) Test-2

Figure 7. Deflections of the slabs.

3.3 Crack distribution

From Figure 8(a) showing the crack distribution at the top surface of slab in Test-1 after fire, the cracks mainly appeared in the column strips adjacent to the cold parts of slab approximately in an elliptic pattern. As observed during the test, cracks first appeared in and parallel with column strips in the Y direction after the initial 25 minutes. Figure 8(b) shows the maximum principal stress distribution obtained from numerical modelling at that time. The maximum tensile stresses are mainly distributed in the column strips adjacent to the cold parts of slab, which is consistent with the crack distribution. Moreover, the tensile stresses are mainly caused by negative moments induced by the restraints of the adjacent cold parts of slab on the doubly curved deformation of the central panel. Interestingly, neither cracking nor spalling was observed at the soffit of the central panel as shown in Figure 8(c), because the in-plane concrete stresses at the soffit of slab were either slightly tensile or even compressive in two directions due to restrained thermal expansion.

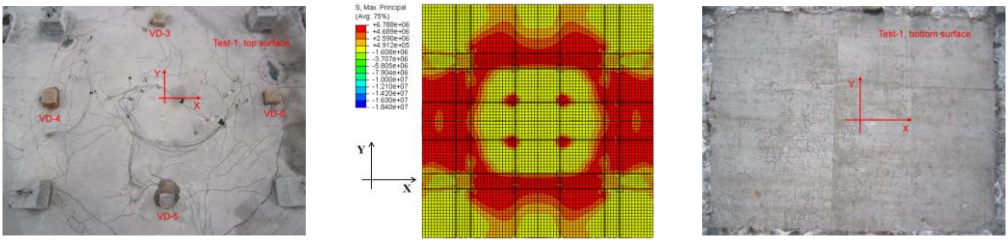

(a) Cracks at top surface after fire | (b) Stress distribution at top surface after 25 minutes in fire | (c) Cracks at soffit after fire

Figure 8. Cracking and stress distribution of the slab in Test-1.

Figure 9 shows that the cracking and tensile stress distributions of the slab in Test-2 are similar to those in Test-1, and the soffit shows neither cracking nor spalling. However, Test-2 survived more than 120 minutes of fire exposure which resulted in more cracks at the top surface, as shown in Figure 9(a). Besides, the tensile stress distribution of the slab is slightly different as stress concentration is slightly more significant in column strips in the X direction than that in the Y direction as shown in Figure 9(b) because of the additional tensile stress perpendicular to the banded prestressing tendons. The tensile stress distribution is consistent with the crack distribution, which further validates the numerical model.

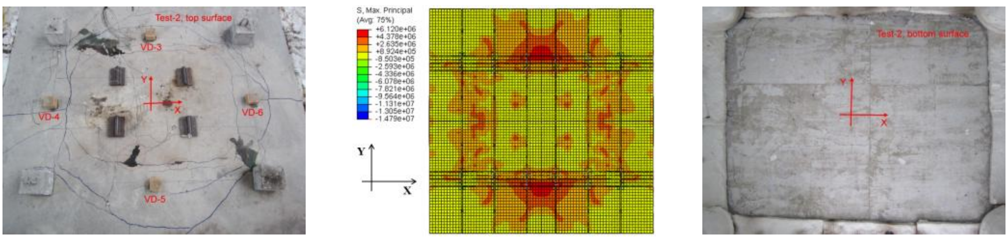

(a) Cracks at top surface after fire | (b) Stress distribution at top surface after 25 minutes in fire | (c) Cracks at soffit after fire

Figure 9. Cracking and stress distributions of the slab in Test-2.

The cracks mainly appeared around the boundary between the central panel and the surrounding cold parts of slab resulting in the release of restraints to the central panel. It suggests that the load-carrying capacity of the slab should be greatly reduced but it was not the case, as the deflection still developed steadily without collapse. Besides, the fact that the soffit of slab remained smooth implied that the expected flexural deformation based on yield line theory might not work. So one may deduce that tensile membrane action has been significant, affecting the load-carrying mechanism of the slab. Moreover, it can be seen that tendon distribution has minor effects on the crack patterns. However the impact on the tensile stress distribution is obvious, where Distributed-Distributed tendon distribution is relatively beneficial to the uniform distribution of tensile stress.

3.4 Concrete spalling

In Test-3, a series of popping sounds were heard intermittently heard since 5 minutes after fire exposure and they continued for 25 minutes. Then several big “bangs” were heard as well. Afterwards, it remained more or less quiet, but after 35 minutes of fire exposure, a strong cracking sound was heard. After 40 minutes of fire exposure, a small area of concrete exploded at the top surface of slab near the load spreader, which is denoted as TS-1 (where TS stands for top spalling) in Figure 10(a). After 50 minutes of fire exposure, another relatively large area of concrete exploded also near the load spreader, which is denoted as TS-2, and the test was terminated. Finally no through hole was formed in the slab. At the end of 40 minutes of fire exposure, the water that appeared earlier on the top surface was evaporated completely, leaving behind the slab dry in appearance. It suggests that the explosive spalling is mainly caused by the thermal and compressive stresses in accordance with Hertz [15].

Detailed examination of the slab after fire revealed a large area of concrete at the soffit of slab having spalled as shown in Figure 10(b). Different degrees of spalling are observed, which are denoted as BS-1, BS-2 and BS-3 (where BS stands for bottom spalling). BS-1 is less severe with only concrete cover having spalled, while BS-2 and BS-3 are quite severe as the concrete above the bottom layer of reinforcement has spalled, where compressive stresses have been relatively large at commencement of fire as shown in Figure 10(c). Besides, one strand fractured due to direct exposure to fire. The overall spalling is more than half of the soffit area, but it is not uniform possibly due to non-uniform moisture distribution.

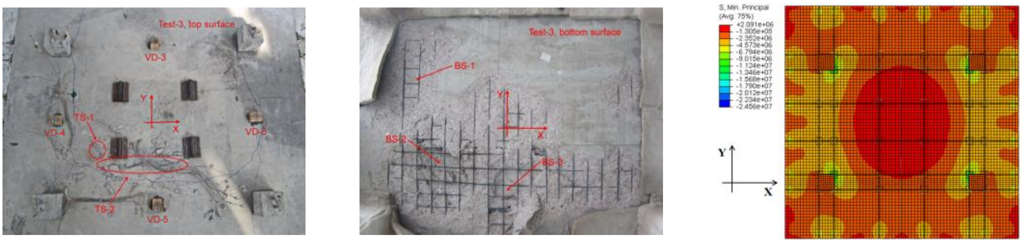

(a) Top surface spalling (b) Soffit spalling (c) Compressive stress distribution at soffit at commencement of fire

Figure 10. Concrete spalling and stress distribution in Test-3.

In Test-4, similar sounds were heard as well. The differences are that the popping sounds were more intensive from the time after 10 minutes of fire exposure to the end, unlike those intermittent sounds in Test-3. In particular, near the end of test, significant explosive spalling happened forming a through hole in the slab with crushed concrete pieces flying upward violently, and the spalled area and position are denoted as TS-1 in Figure 11(a). Just a few seconds later, similar explosive spalling happened again, which was much stronger and much larger in area, and this is denoted as TS-2. Nevertheless, the slab did not collapse. The spalling still can be mainly attributed to the thermal and compressive stresses for the slab has been dried by heat already.

By examining the soffit of slab as shown in Figure 11(b), it can be found that nearly the whole area of soffit concrete has spalled except for a small part in the central panel. The violent spalling mainly occurred approximately at the quarter positions of the panel in the two directions, as the compressive stresses were distributed as shown in Figure 11(c). As the column supported corners were protected from fire, the most violent spalling therefore occurred at the quarter position that was reasonably close to the corner, under large compressive stresses and pore pressure in concrete, and just outside the perimeter of the top reinforcement layer. It indicates that the top reinforcement also plays an important role in preventing through spalling. Moreover, there was neither fracture of tendons nor reinforcing bars.

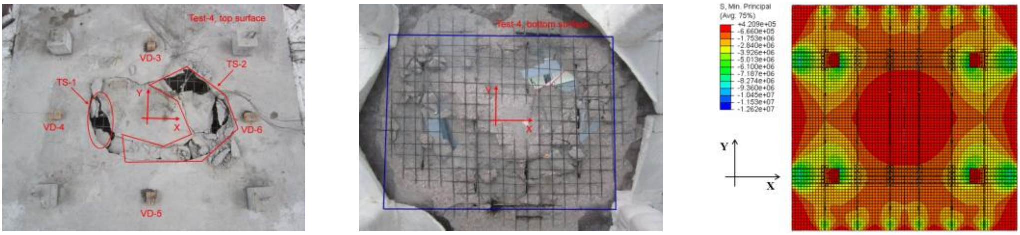

(a) Top surface spalling (b) Soffit spalling (c) Compressive stress distribution at soffit at commencement of fire

Figure 11. Concrete spalling and stress distribution in Test-4.

Test-1 and Test-3 have the same loading ratio, and their moisture contents are 2.27% and 2.62%, respectively. Test-2 and Test-4 have identical parameters, except that their moisture contents are 2.36% and 2.52%, respectively, but they have completely different results. Obviously, the moisture content is significant in accounting for the differences, and is the main factor regarding possible concrete spalling. More importantly, one may assume that there is a threshold moisture content between 2.36% and 2.53% that triggers concrete spalling under certain compressive stresses.

Besides, the degree of spalling in Test-3 is less severe compared with that in Test-4 because the compressive stresses at the soffit of the central panel as induced by the applied loads and post-tensioning in Test-3 were smaller than those of Test-4, even though the moisture content in Test-3 is slightly higher, which indicates that a high loading ratio has caused less severe concrete spalling. When the concrete was completely dried by heating, explosive concrete spalling still happened, suggesting that spalling was caused by compressive stresses as a result of restrained thermal expansion and flexural compression at the top surface of slab.

4 CONCLUSIONS

Among the four tests, two of the specimens with lower moisture contents demonstrated excellent fire resistance performance without concrete spalling. The other two specimens with higher moisture contents experienced severe concrete spalling leading to shorter fire resistance periods. The following conclusions can be drawn:

(1) The tendon distribution has minor effect on the structural responses of the slabs. The deflections of slabs are mainly governed by temperature distribution and thermal expansion, and restrained thermal thrust forces. The crack distribution is mainly governed by the doubly curved deformation of slabs and the negative moments induced.

(2) The cracks did not lead to the collapse of slab. Instead they released some of the restraints to the doubly curved deformation of the central panel, which further contributed to the formation of tensile membrane action that enhanced the fire resistance of the slabs.

(3) There may be a threshold moisture content that triggers concrete spalling under certain compressive stresses. In the tests, the threshold is between 2.36% and 2.53%.

(4) The loading ratio has obvious effect on the degree of concrete spalling. A higher loading ratio gives less severe concrete spalling.

(5) Concrete spalling is mainly governed by moisture content and compressive stresses. After the concrete spalling is triggered, it develops in a progressive manner. However, with the progress of fire, the effect of moisture content gradually reduces while the effect of ensuing compressive stresses becomes

more important.

ACKNOWLEDGEMENTS

The work described here has been supported by the Research Grants Council (RGC) of Hong Kong Special Administrative Region, China (RGC Project No.: HKU 710012E) and the State Key Laboratory of Subtropical Building Science of South China University of Technology, China (Project No.: 2011KA02).

REFERENCES

[1] ACI 318-08, *Building code requirements for structural concrete (ACI 318-08) and commentary*, ACI Standard, American Concrete Institute, Farmington Hills, Mich, USA, 2008.

[2] BS EN 1992-1-2, *Eurocode 2: design of concrete structures—part 1-2: general rules-structural fire design*, British Standards Institution, London, UK, 2004.

[3] PTI, *Post-Tensioning Manual*, sixth edition, Post-Tensioning Institute, Phoenix, AZ, 2006.

[4] Gustaferro A., Fire resistance of post-tensioned structures, *Journal of the Prestressed Concrete Institute*, 18(2), 38-63, 1973.

[5] Gales J., Bisby L. and Gillie M., Unbonded post tensioned concrete in fire: A review of data from furnace tests and real fires, *Fire Safety Journal*, 46(4), 151-163, 2011.

[6] Yuan A., Dong Y. and Gao L., Behavior of unbonded prestressed continuous concrete slabs with the middle and edge span subjected to fire in sequence, *Fire Safety Journal*, 56, 20-29, 2013.

[7] Zheng W, Hou M., Shi D. and Xu M, Experimental study on concrete spalling in prestressed slabs subjected to fire, *Fire Safety Journal*, 45(5), 283-297, 2010.

[8] Bailey C. and Ellobody E, Fire tests on unbonded post-tensioned one-way concrete slabs, *Magazine of Concrete Research*, 61(1), 67-76, 2009.

[9] Noumowe A.,Carre H.,Daoud A.,Toutanji H., High-strength self-compacting concrete exposed to fire test, *Journal of Materials in Civil Engineering*, 18(6), 754-758, 2006.

[10] Anagnostopoulos N., Sideris K. and Georgiadis A., Mechanical characteristics of self-compacting concretes with different filler materials, exposed to elevated temperatures, *Materials and Structures*, 42(10), 1393-1405, 2009.

[11] BS EN 1991-1-2, *Eurocode 1: Actions on structures – Part 1-2: General actions – Actions on structures exposed to fire*, British Standards Institution, London, UK, 2002.

[12] BS EN 1992-1-1. *Eurocode 2: Design of concrete structures – Part 1-1: General rules and rules for buildings*, British Standards Institution, London, UK, 2004.

[13] BS 476-20, *Fire tests on building materials and structures – Part 20: Method for determination of fire resistance of elements of construction (general principles),* British Standards Institution, London, UK, 1998.

[14] Usmani A., Rotter J., Lamont S., Sanad A. and Gillie M., Fundamental principles of structural behaviour under thermal effects, *Fire Safety Journal*, 36(8), 721-744, 2001.

[15] Hertz K., Limits of spalling of fire-exposed concrete, *Fire Safety Journal*, 38(2), 103-116, 2003.

8th International Conference on Structures in Fire
Guo-Qiang LI, Venkatesh K. R. KODUR, Shou-Chao JIANG, Jian JIANG, Su-Wen CHEN, Guo-Biao LOU (Eds.)
Shanghai, China, June 11-13, 2014

FIRE RESISTANCE OF PRESTRESSED CONCRETE HOLLOWCORE FLOORS - A META-ANALYSIS ON 162 FIRE TEST RESULTS

Wim Jansze[*], Ronald Klein-Holte[*], Arnold van Acker[*], Bruno Della Bella[*], Gösta Lindström[*], Jean-Paul Py[*], Matthieu Scalliet[*], Andreas Nitsch[*] and Hermann Benhöfer*

[*] BIBM, the European Federation for Precast Concrete, Rue d'Arlon 55, B-1040, Brussels, Belgium
e-mails: wim.jansze@consolis.com, info@bibm.org

Keywords: Prestressed hollow core slabs, Fire, Failure mechanism, Statistical analysis, Design rules

Abstract. *Since decades many fire tests on prestressed concrete hollow-core floors have been executed in fire testing laboratories throughout Europe. In 2010, these unexplored fire tests were collected in a database in order to analyze systematically the behaviour of hollow-core slabs under fire conditions. The Holcofire database [1] on prestressed hollow-core fire tests covers the period 1966 - 2010 and contains a collection 162 independent analysable fire test results. This study addresses the meta-analysis that compares the database with the models and design rules given in the European design standard EN1992-1-2:2004, the European product standard EN1168:2005+A3:2011, and the requirements given in the European fire testing standards EN1363-1:1999 (+ EN1363-2:1999) and EN1365-2:1999. The meta-analysis on the database concludes that 100% of the fire test results can be explained by the European standards relevant for testing the structural behaviour of hollow-cores under fire. The bending capacity and the shear and anchorage capacity of hollow cores under fire are statistically assessed to be safe.*

1 INTRODUCTION

The precast concrete hollow core slab is a widely applied and successful floor construction product. The product has been in high demand for the last decades due to its highly efficient design, structural efficiency, lean production method, and sustainability. Every year, around 25 million square metres of precast concrete hollow core floors are erected in Europe. The estimated total stock of hollow core floors currently installed in Europe is 1,000 million square meters. The product has been tested intensively on many aspects in order to get approval by authorities. Accordingly, also its fire resistance. The fire resistance of a product is determined using a standard fire test. Then, the load bearing resistance of a product is indicated in minutes of exposed fire. Since the 1960s a large number of fire tests have been executed throughout Europe in various fire laboratories.

In 2010, these independent but unexplored fire tests were collected under the European project Holcofire [1] as it was believed that these fire tests contain a wealth of information on the behaviour of hollow-core slabs under fire conditions. The Holcofire database on prestressed hollow core fire tests covers a period of 45 years from 1966 until 2010 and contains 162 individual analysable fire test results. The objective is to get both factual and statistical insight on the failure mechanisms of hollow-cores during fire, and to check the capacities against the standards. Therefore, in a meta-analysis the database is mirrored against the models and design rules given in the European design standard EN1992-1-2:2004 and the European product standard EN1168:2005+A3:2011, and against the requirements given in the European fire testing standards EN1363-1:1999 (+ EN1363-2:1999) and EN1365-2:1999. A meta-analysis is a systematic method of evaluating data statistically, is based on results on the same problem of independent studies, and produces stronger conclusions than can be provided by any individual study.

2 HOLCOFIRE DATABASE WITH 162 INDEPENDENT ANALYSABLE RESULTS

In the Holcofire database, a total of 162 independent analysable fire test results on prestressed hollow core floor units and floor structures covering the period 1966-2010 have been collected. An extract of the database is tabulated in [1]. Every fire test result has been given a unique Holcofire number between H1 and H162. To summarize these fire tests in this paper, an overview is presented hereunder. The collected fire tests have been concentrated around certain fire test laboratories and test themes, namely:

- First market acceptance tests in Germany at TUB (Braunschweig) in 1966.
- Belgium studies by CBR (Lier) and RUG (Gent) starting in 1971 up to 1999 as pioneering studies addressing bending and shear phenomena.
- Finnish studies performed by VTT-PAL (Helsinki) between 1971 and 1991 as pioneering studies to understand the bending phenomena of hollow core slabs in structures under fire.
- French CTICM (Mezieres-les-Metz) and Swiss ETH EMPA (Dubendorf) studies on slim floor structures between 1992 and 1996, and tests conducted at SPTRI (Borås) by Peikko in 2009.
- Studies between 1983 and 1996 for market acceptance tests in Austria at IBS (Linz), in Germany at TUB (Braunschweig), in Italy at CSI (Milan) and IG (Bellaria).
- Danish shear studies executed by DIFT (Hvidovre) and SPTRI (Borås) between 1998 and 2005;
- Dutch TNO (Delft) studies addressing shear on double web elements between 1999 and 2001.
- Study of a complete building structure with hollow core floors under natural fire conditions in UK at BRE (Middlesbrough) in 2007 addressing connections between slabs and supports.
- Studies in Eastern part of Europe between 2001 and 2010 for acceptance tests in new markets in Poland at ITB (Katowice), in Slovenia at ZAG (Ljublana), and in Belarus at RIFS (Minsk).
- Small scale tests on slab slices in The Netherlands by Efectis (Delft) conducted in 2010 focusing on horizontal cracking observed in the so-called Rotterdam fire case [1].

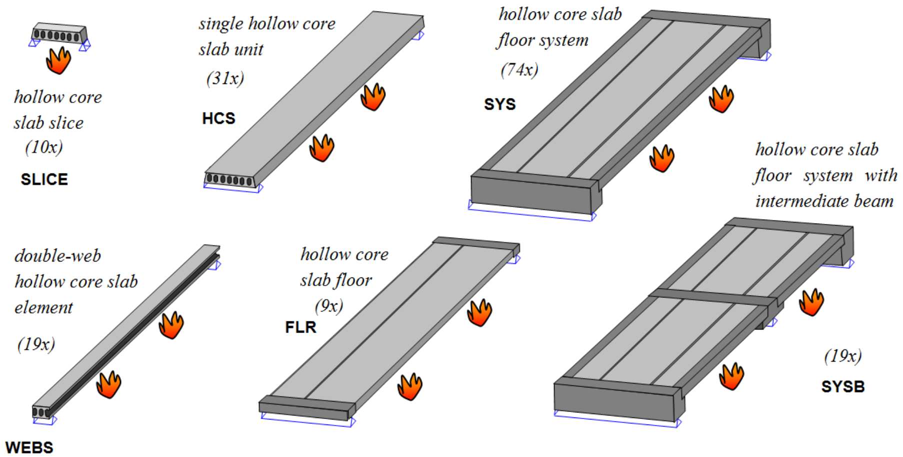

Figure 1. Principle of test set-up lay-outs in database (N = 162).

Figure 1 sketches the fire test set-up lay-outs that are present in the Holcofire Database. In 10 fire tests [SLICE] slices supported in transversal direction were used. In 19 fire tests [WEBS] double-web elements were used. In 31 fire tests [HCS] only a single hollow core element was tested on the furnace, mostly without connections. In 9 fire tests [FLR] a floor was constructed consisting of 1.5 slabs with one filled joint. 93 test results on floors [SYS] and [SYSB] were constructed as a system with 2 slabs or more, and were erected with connection reinforcement with the supporting beams and some peripheral tie beam around the floor. Of that, 19 individual analysable fire test results consisted of a test set up with an intermediate beam in order to study slim floors or only shear phenomena and exclude bending.

3 IDENTIFICATION OF FAILURE MECHANISMS IN HOLCOFIRE DATABASE

As defined in the Eurocode "Basis of structural design" EN 1990 3.2(2)P and 6.4.3.3(4), fire is to be considered as an accidental action. In principle only the ultimate limit state has to be verified. This means that large deformations and important local damage are acceptable on condition that the basic requirements REI are satisfied. R is the load bearing resistance of the construction or parts of it, that can be assured for a specific period of time. This study focuses particularly on R.

The Holcofire database provides independent but registered information on controlled tests on hollow core slabs and floors under fire conditions in order to verify design models. In most of the cases the objective of the fire tests was to reach a certain fire resistance time. In some cases premature failure took place, but in other cases tests were intended to fail in order to study a certain failure mechanism. In the Holcofire Database the following groups of failure mechanisms can be distinguished (Figure 2):

- In 102 fire test results the fire resistance R(EI) was obtained and granted as failure did not take place. Of these, in 80 fire test results the fire test was completely stopped and reported on. In 22 fire tests, the test continued. Of that 22, in 8 fire tests the test was finally stopped without any failure and in 14 fire test a failure occurred. These tests were executed either with continuing fire under same loading, or without fire and increasing the load. This "additional testing" was also documented in the test reports.
- In 60 fire test results the fire resistance time was not granted. In 3 fire tests the test was stopped without a failure. In 57 test results the researchers observed a failure before a targeted R(EI) was reached, either unexpectedly or intended. The fire resistance time varied between a range from 10 minutes up to 135 minutes.
- In total in 91 test results (*note: 80+8+3*) a failure did not occur, in 71 test results failure took place. The observed failure mechanisms in the 71 fire test results were;
    - 11 fire test results resulted in a bending failure of the cross section;
    - 42 fire test results exhibited a clear shear and anchorage failure;
    - 6 fire test results exhibited a combined shear-bending interaction failure;
    - 5 fire test results showed extensive explosive spalling;
    - 4 fire test results showed clearly horizontal cracking through the webs;
    - 3 fire tests another failure type occurred (punching, bond, and unknown).

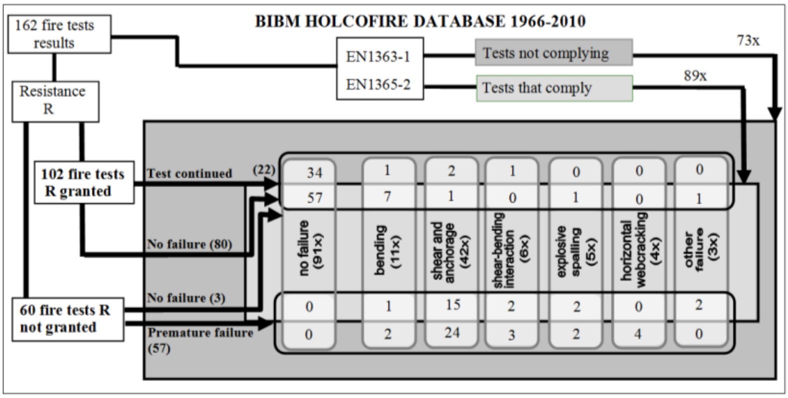

Figure 2. Holcofire fire test database and identification of failure mechanisms.

4 BENDING RESISTANCE UNDER FIRE

To determine the bending resistance under fire, the ultimate load bearing capacity of a heated cross section is calculated using a simplified cross-section method and taking into account the reduction of the characteristic strength of prestressing steel conform EN1992-1-2. Because the bending resistance of a hollow core floor is governed by the degradation of the strength of the prestressing reinforcement in function of the temperature, strand temperatures were compared with theoretical predictions in 25 fire tests. The analysis on 25 fire tests shows that the ratio of mean-measured temperature over calculated temperature is 99.8% while the coefficient of variation is 14.9%. These 25 fire tests cover fires from 45 minutes to more than 2 hours and contain hollow core slabs with axis distances between 30 mm to 60 mm and with mean strand temperatures ranging from 250 ℃ to 500 ℃. It is concluded that the calculated strand temperature with EN1992-1-2 Figure A.2, although based on solid slab, gives an accurate prediction of the mean temperature in the strands. But it is also evident from the analysis that in a fire test the scatter in temperature could easily be more than 30% higher than the mean temperature of the strands.

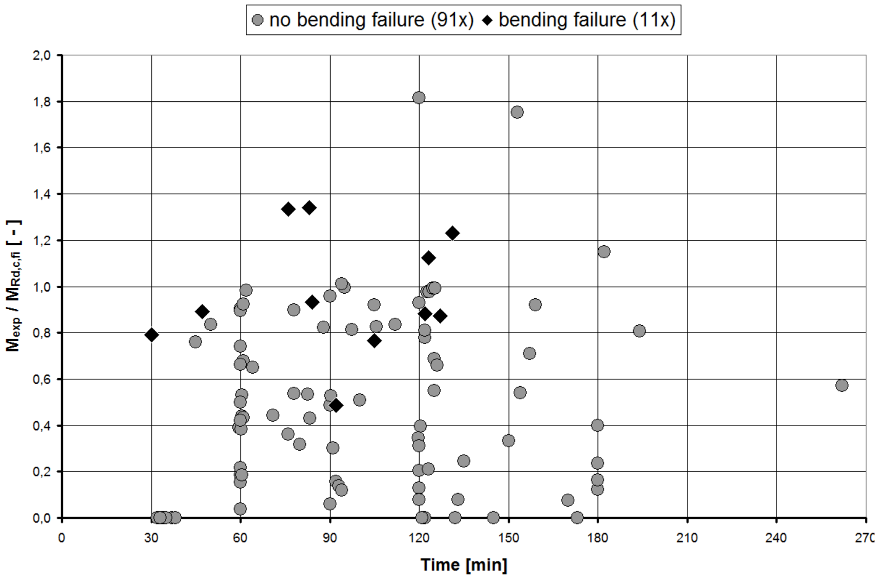

Figure 3. Ratio of experimental bending moment over bending capacity under fire in relation to time.

From Figure 2 emerges that 102 (91+11) fire test results can be analyzed for bending resistance. In 11 fire tests from the database the bending capacity was exceeded. These tests were stopped as according to EN1363-1 the rate of deflection was exceeded. Recalculation of these 11 fire tests shows that the increasing rate of deflection can be attributed to material degradation of the prestressing strands leading to a bending failure. See in Figure 3 the recalculated tests represented by the black data points which range between 80% and 140% except for test H19 (at 50%). In the test some cracks occurred in the underflange and the temperature in the strands most probably were much higher than calculated with EN1992-1-2 Figure A.2. To conclude, it is calculated that the average of the 11 fire tests results in which the bending capacity was governing is 96.9% (M_{exp} / $M_{Rd,c,fi}$) with a 24.0% coefficient of variation.

Regarding the 91 fire test results that did not fail in bending, all tests have been recalculated for bending capacity according to EN1992-1-2. See the grey data points in Figure 3. In the recalculation of the bending capacity at the time the fire test was stopped, in 87 fire tests the experimental bending moment was indeed lower than 100% of the calculated bending capacity, in only 4 fire tests the ratio was above 100%. However, as in some original test reports data was lacking, and accounting for some scatter in the strand temperatures, 87 out of 91 test (95.6%) under 100% is a very good prediction.

With the "Maximum Likelihood Method" (see note at end of paper) the 91 fire test results where the bending capacity was not exceeded can be taken into account. The principle behind this is that, under a certain load, also tests not leading to failure indicate that bending is then not governing and thus can be statistically included; the likelihood is high when the ratio M_{exp} / $M_{Rd,c,fi}$ is around 100% or above. It is then calculated that the average of ratio (M_{exp} / $M_{Rd,c,fi}$) increases from 96.9% to 106.1% with a 22.8% coefficient of variation with the maximum likelihood if also the 91 non-failed tests are included. Accordingly, it is concluded from the statistical analysis over the recalculation of the 11 plus 91 fire tests that the simplified expression given by EN1992-1-2 calculates safely whether a bending failure should take place or not. This confirms that the EN1192-1-2 gives a safe prediction for the ultimate load bearing bending capacity of a heated cross section using the simplified cross-section method.

5 SHEAR AND ANCHORAGE RESISTANCE UNDER FIRE

From Figure 2 emerges that for the recalculation of the shear and anchorage capacity, 42 fire tests that exhibited a shear and anchorage failure can be analyzed as well as the 102 fire tests that reached the required fire resistance time R and did not fail in shear. In Figure 4 the black data points are the 42 fire tests that failed by shear and anchorage, while the grey data points are the 102 fire tests that did not fail. By recalculating the shear and anchorage capacity according to EN1168 Annex G of 102 fire tests, it was demonstrated that in 80 of the fire test results the actual shear load was lower (<100%) than the calculated shear and anchorage capacity according to EN1168 Annex G, while in 22 fire tests the shear load was higher (>100%) than the calculated capacity. But 18 out of these 22 fire tests showed a higher capacity by means of the system effect since the fire tests were conducted on floor systems. As became evident from the study, the system effect is not accounted for in the EN1168 Annex G formula. The "system effect" is an increase in shear capacity mainly caused by the introduction of a longitudinal blocking effect that closes the vertical cracks and acts positively on the shear and anchorage capacity.

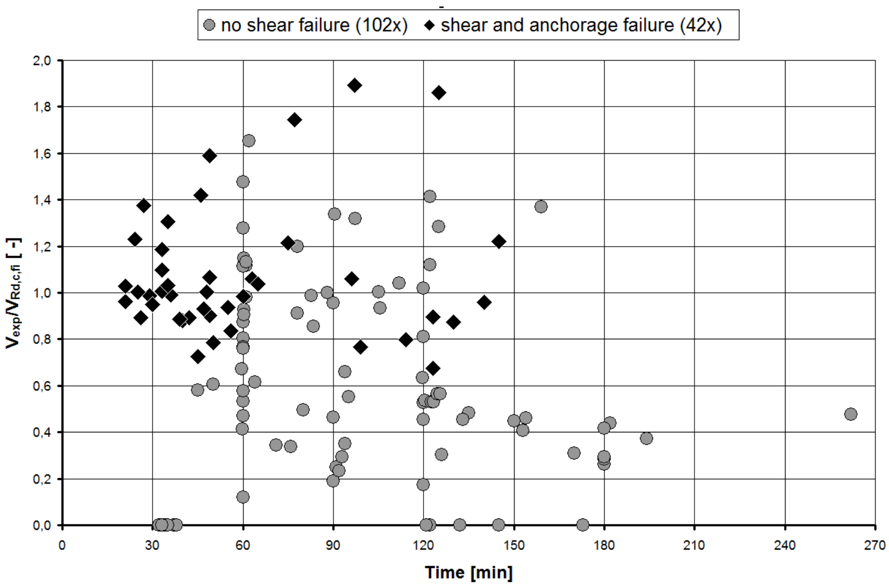

Figure 4. Ratio of experimental shear load over shear and anchorage capacity under fire in relation to time.

A statistical analysis was made by means of the "Maximum Likelihood Method" (*see note end of paper*) using the results of the 42 recalculated fire tests that failed by shear and anchorage, and including the results of 92 of the 102 fire tests in which R was granted (but not double counting 3 shear tests and taking into account the 7 fire tests on slices). The principle behind this maximum likelihood method is that, under a certain load, also tests not leading to failure indicates at a certain probability that shear is then not governing and thus can be statistically included. The conclusions from the statistical analysis are:

- EN1168 Annex G does not account for the "system effect" (safe approach). From the analysis it became evident that the system effect has a positive influence on the shear and anchorage capacity. Therefore, the conclusion is splitted in two parts: for single slab units without system effect (used mainly in laboratory fire testing), and floors with system effects (more relevant for practical applications). Both the 42 fire tests that failed as well as the 92 fire tests that did not fail are included (Note: *the conclusions are valid for the 28 day mean strength of the concrete that is used to calculate the design capacity for shear and anchorage under fire conditions according to EN1168 Annex G. Note that normally a fire tests is conducted after a longer period of hardening*):
    - Single slab without system effect. When taking into account 28 of the 42 fire tests that failed in shear and anchorage, and by the maximum likelihood method 27 of the 92 fire tests that reached the required fire resistance time, the ratio ($V_{exp}/V_{Rd,c,fi}$) of the fire tests results are 98.8% of the calculated shear capacity, and coefficient of variation is 22.3%. Hence, EN1168 Annex G basically calculates well the capacity of one single slab unit. A single slab has no interaction with a surrounding structure: the slab is simply supported; the slab is either without or with connection reinforcement placed in the joint or core anchored to the support structure (connection reinforcement at mid height or lower); and a structural topping is or is not present on the single slab.
    - Floor with a "system effect". When taking into account 14 of the 42 fire tests that failed in shear and anchorage, and by the maximum likelihood method 65 of the 92 fire tests that reached the required fire resistance time, the ratio ($V_{exp}/V_{Rd,c,fi}$) of the fire tests results are 129,0% of the calculated shear capacity, and coefficient of variation is 24.3%. Hence, EN1168 Annex G neglects the excess capacity by virtue of the "system effects" that can be considered as additional safety. A floor system has interaction with the surrounding floor field: the joints are filled between the slab to form a floor field; the slabs are cast against the support (either a beam or a wall); the slabs are either with or without connection reinforcement placed in the joint or in the core and anchored into the support structure (connection reinforcement at mid height or lower); a peripheral tie beam, or equivalent, is cast around the floor; and a structural topping could be present but is not needed for systems effect.
- The scatter in time with a coefficient of variation of 75,9% for all 42 fire tests is however very high. But when taking into account only floor systems and neglecting outliers, it is 37.0%.
- It can be concluded from the fire tests and shear capacity calculations at ambient temperature (shear flexure according to EN1992) that the shear capacity calculated for fire at 0 minutes is on average higher than 100% of the flexural shear capacity at ambient temperature, and 70% at 120 minutes. In between, a linear interpolation can be applied.
- Further, the outcome of Annex *G* shear capacity is mainly sensible to parameters as amount of connection reinforcement, amount of prestressing reinforcement, mean concrete (cylinder) strength, and geometry of the slab.
- It is recommended that EN1168 Annex *G* states that for fire calculation $\eta 1$ = 0.7 (bad bond conditions) should be used for normal strands, and for protruding parts $\eta 1$ = 1.0 can be used.

From this meta analyses, that evaluates the empirical formula of EN1168 Annex G formula against 42 fire tests carried out in numerous laboratories where shear and anchorage was governing failure, and 102 fire tests that did not fail in shear when R was granted, it is strongly concluded that the EN1168 Annex *G* shear formula for hollow core slabs is safe for the application of hollow core slabs in floor systems.

6 SHEAR-BENDING INTERACTION RESISTANCE UNDER FIRE

From Figure 2 emerges that in 6 fire test the shear-bending interaction led to failure. In the Holcofire analysis it emerged that shear-bending interaction was the governing failure type, as in a fire test it is not so easy to simulate a live load. In practice, mostly, the maximum shear load is acting at the support where the bending moment is low, while the maximum bending moment is acting at midspan where the shear load is low. But in laboratory tests it is typically seen that using point loads causes a high shear force where the bending moment is also at its maximum; the so called *V-M* interaction..

However, in the standards shear-bending interaction is not defined. Therefore, for shear-bending interaction in the relevant cross section the unity check formula (V_{exp} / $V_{\mathrm{Rd,c,fi}}$ + M_{exp} / $M_{\mathrm{Rd,c,fi}}$) is used. The analysis on the 6 fire test results showed that with this interaction formula the average of the ratio (V_{exp} / $V_{\mathrm{Rd,c,fi}}$ + M_{exp} / $M_{\mathrm{Rd,c,fi}}$) is 125%, and coefficient of variation is 17%. Hence, also the interaction formula gives a safe prediction of the combined failure mechanism.

7 SPALLING AND HORIZONTAL WEB CRACKING UNDER FIRE

From the database in Figure 2 emerges that in a total of 9 fire test results explosive spalling and horizontal web cracking took place. These phenomena mostly took place at about 15-25 minutes after start of ISO fire. In 5 fire tests the extensive explosive spalling led to local damage of the underflange of the slab. The standards prescribe a moisture content of maximum 3% w/w that can be obtained by 3 months storage under indoor conditions (≈20 °C, ≈50% RH). In 2 tests the moisture content was between 2,5-3,0%, but in 3 tests the moisture content was unknown. In [1] also another 4 tests were identified were spalling took place although moisture content was below 3%. But these tests did not lead to failure. It is however remarkable that all fire tests with spalling at the soffit were conducted on floor systems. It is therefore concluded that this spalling is not spalling due to moisture, but spalling due to transversal blocking of the underflange of the hollow core slab, or so-called buckling spalling.

It is also evident from the database in Figure 2 that in case of 4 fire tests horizontal cracks in the webs occurred which led to local failure. The tested specimen were parts of a hollow core, namely SLICE and WEBS of Figure 1. It is evident that these test configurations did not comply with the standard EN1365-2 that states that the exposed length of a floor should be at least 4 m and exposed width 2 m. The design standard EN1992-1-2 does not include rules for horizontal web cracking, but by a sophisticated 2D mechanical computer model based on material models from EN1992-1-2 it was demonstrated that due to restrained conditions in transversal direction horizontal cracks can occur in the webs, or buckling spalling at the soffit. This restrained condition in transversal direction can be caused by either a thick structural topping or by blocking of a cold surrounding structure in case of local fires. Despite, in practical application blocking of the surrounding structure is diminished by shrinkage cracks, particularly in XC1 conditions, and less in XC3 applications. As in fire tests the slabs are dried our on beforehand, and then assembled, the absence of shrinkage possibilities in the system could also explain why spalling phenomena are observed more frequently in fire tests than in practical applications. Moreover, [1] also demonstrated that when buckling spalling or horizontal web cracking occur in real structures, it cannot lead to a failure mechanism regarding R as concrete hollowcore floor structures are very redundant.

Hence, both the spalling phenomena and horizontal cracking can be fully explained with the developed mechanical model in [1] in conjunction with the models from the standards EN1992-1-2 and EN1365-2. It is therefore concluded that also the 9 fire test results can be fully explained. A lesson learned here is that, more generally spoken, the 9 fire tests from the database indicate that restrained conditions can lead to spalling phenomena and horizontal web cracking phenomena in certain cases. Both phenomena were indeed observed in the Rotterdam fire case on October 2007 [1]. But similar damages can be observed also in other types of (precast) concrete floors, like filligran and cast in-situ. Similarly, as for hollow core floors, these floors also show redundancy after a fire.

8 OTHER FAILURE TYPES

From Figure 2 emerges that in 3 fire test results another failure type occurred. One fire test showed bond problems with 15.2 mm diameter strands in a 2.4 m wide slab. Another fire test showed punching failure at an edge. And the failure mode of a third test could not be retrieved from the authentic test report, although the fire resistance time was already granted. Anyway, the results of these tests do not say much about the overall behaviour of hollow core slabs under fire conditions.

9 CONCLUSIONS

The meta-analysis on the independent 162 fire test results confirm that floors consisting of hollow core slabs have outstanding load bearing capacity and excellent resistance to fire. The extensive testing of hollow core slabs in fire laboratories and analysis of the fire tests confirm once again that hollow core floor systems meet all regulatory, quality and safety requirements. The results justify the conclusion that society can continue to rely fully on the solid structural performance of floors consisting of hollow core slabs when the models and design rules from the European design standards EN1992-1-2:2004, product standard EN1168:2005+A3:2011, and the requirements given in the European fire testing standards EN1363-1:1999 (+ EN1363-2:1999) and EN1365-2:1999 are used. With these standards, 100% of the fire test results of the database can be explained. In 102 fire tests R was granted. The observed failure mechanisms in the 162 fire test results are bending, shear and anchorage, shear-bending interaction, and spalling and horizontal web cracking. It is however argued that spalling and horizontal web cracking is not likely to occur in practical applications as a result of unblocking due to shrinkage in transverdal direction, and cannot lead to failure as a result of the redundancy of the floor in longitudinal direction.

It is concluded from the database that the mean experimental bending moment under fire is 106.1% of the bending capacity calculated with the standard EN1992. For single tested slabs and slabs in floor systems, the mean experimental shear capacity is 98.8% and 129.0% respectively of the shear and anchorage capacity calculated with EN1168 Annex G. In fire test where the combined shear-bending interaction was governing, the mean experimental capacity was 125.0% of the theoretical interaction.

REFERENCES

[1] Jansze, W., van Acker, A. Della Bella, B., Klein-Holte, R., Lindström, G. Py, J-P., Scalliet, M., Nitsch†, A., Benhöfer, H., *Structural behaviour of prestressed concrete hollowcore floors exposed to fire,* BOXpress Education (info@boxpress.nl), ‘s Hertogenbosch, The Netherlands, ISBN 978-90-8891-812-4, 226 pages, Book published 24 January 2014.

NOTE ON MAXIMUM LIKELIHOOD METHOD

In the background study [1] the “Maximum Likelihood Method” is used to include the approximately 100 results that did not fail during a fire tests. When taking the maximum likelihood into account, a better mean and scatter of the ratio (capacity experiment over capacity calculated) can be determined. The principle is that a test leading not to failure contains information on the failure behaviour assessed. Namely, it indicates that the assessed failure type is not governing under a certain load. In the method of “Maximum Likelihood” the values of the average and the scatter that maximize the function L are the maximum likelihood estimators.

Hence, $L = f(x_1)\, f(x_2)\, f(x_3) \cdots f(x_n) \cdot F(x_1)\, F(x_2)\, F(x_3) \cdots F(x_m)$. In the function L, $f(x_n)$ remains the probability density function, and $F(x_m)$ is the probability distribution function. In this function $F(x_m)$, the variable $\Phi(.)$ is the distribution function of the standard normal distribution variable (with average 0 and standard deviation 1): $F(x_m) = \Phi\{x_m\text{-}\mu / \sigma\}$.

EXPERIMENTAL STUDY ON FIRE BEHAVIORS OF SEISMIC DAMAGED RC COLUMNS

Bo Wu* and Wei Xiong*

* State Key Laboratory of Subtropical Building Science, Department of Civil Engineering, South China University of Technology, Guangzhou 510640, P. R. of China
e-mails: bowu@scut.edu.cn, xiongweiscut@sina.com

Keywords: RC columns, Cyclic loading test, Fire test, Fire behaviours

Abstract. *Cyclic loading test was conducted first to produce seismic damage in eight concrete specimens, and then the eight damaged specimens and one undamaged control specimen were subjected to fire. The test variables include intended drift ratio, axial load ratio, transverse reinforcement ratio, and shear span ratio of the columns in the specimens. From the experimental investigations, it is found that: (a) when both the drift ratio and axial load ratio are large enough to produce severe seismic damage in reinforced concrete columns, the fire resistance of the damaged columns are obviously weakened; (b) lower axial load ratio leads to longer fire endurance and larger thermal elongation for the seismic damaged columns; (c) the influence of transverse reinforcement ratio on the fire behaviors of seismic damaged columns is very limited; and (d) lower shear span ratio results in marginally better fire performances of the seismic damaged columns.*

1 INTRODUCTION

Fire disasters often occur following earthquakes due to the failure of gas/electric/fuel services in seismic regions. Fire performances of undamaged reinforced concrete (RC) structures are usually satisfactory because the reinforcements are effectively protected by the concrete cover. However, the loss of concrete cover in seismic damaged structural members gives rise to faster heat penetration and severer degradation of material properties. As a result, fire performances of severely damaged structures may be weakened to a great extent. Some past earthquakes were followed by fires bringing about great loss (e.g., the fires following the 1906 San Francisco, 1923 Tokyo, 1971 San Fernando, 1994 Northridge and 1995 Kobe earthquakes [1]).

Recently, some researchers have paid their attentions to fire performances of seismic damaged whole structures [1-4]. However, in the authors' opinion, fire behaviors of the whole structures are difficult to handle at present because the fire performances of seismic damaged structural members haven't been fully investigated. So it is important to make a better understanding about the fire behaviors of seismic damaged RC columns through experimental studies.

2 EXPERIMENTAL PROGRAMME

2.1 Test specimens

Nine RC specimens (including eight seismic damaged specimens and one undamaged control specimen) were fabricated. Each specimen consisted of two identical columns, and the two columns were restrained by strong beams on both ends as shown in Figure1. The strength and stiffness of the strong beams were designed to be much higher than those of the columns.

Four parameters were considered in the cyclic loading tests, including the column's intended drift ratio α, axial load ratio n, shear span ratio λ, and volumetric transverse reinforcement ratio ρ_{yh}. Details of

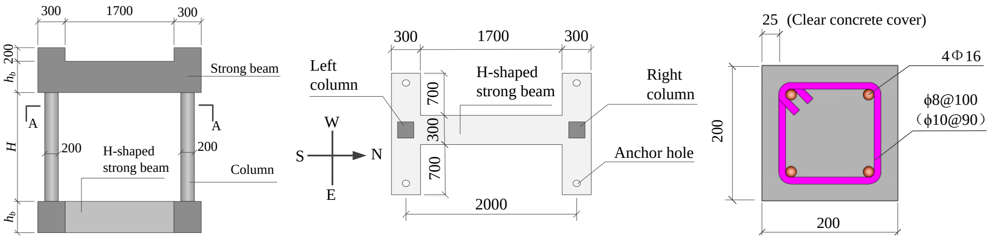

(a) Elevated view (b) A-A section view (c) Reinforcement details

Figure 1. Schematic diagram of specimens (unit: mm).

the specimens are listed in Table 1, and the specimens are identified by the notation — D#N#V#S#, where "D" stands for the drift ratio (D100: α=1/100, D65: α=1/65, D40: α=1/40, and D26: α=1/26), "N" indicates the axial load ratio (N25: n=0.25, and N50: n=0.50), "S" gives the shear span ratio (S3: λ=3, and S4: λ=4), and "V" refers to the volumetric transverse reinforcement ratio (V126: ρ_{yh}=1.26%, and V218: ρ_{yh}=2.18%). The reinforcement details of the columns are given in Fig.1(c). The measured yield strengths of the steel bars with diameters of 8 mm, 10 mm and 16 mm are, respectively, 389 MPa, 356 MPa and 433MPa. The 28-day and test-day 150 mm cubic compressive strengths of the concrete are 24.2 MPa and 25.3 MPa, respectively.

Table 1. Details and measured fire resistance of specimens.

Notation	H (mm)	h_b (mm)	α	n	λ	Transverse reinforcement (ρ_{yh})	FR (min)
D0N50V126S4			0	0.50	4	Φ8@100mm (1.26%)	122
D100N50V126S4			1/100	0.50	4	Φ8@100mm (1.26%)	119
D65N50V126S4			1/65	0.50	4	Φ8@100mm (1.26%)	115
D40N50V126S4	1600	450	1/40	0.50	4	Φ8@100mm (1.26%)	51
D26N25V126S4			1/26	0.25	4	Φ8@100mm (1.26%)	136
D65N50V218S4			1/65	0.50	4	Φ10@90mm (2.18%)	120
D65N25V218S4			1/65	0.25	4	Φ10@90mm (2.18%)	157
D65N50V126S3	1200	400	1/65	0.50	3	Φ8@100mm (1.26%)	134
D65N50V218S3			1/65	0.50	3	Φ10@90mm (2.18%)	129

2.2 Test setups and procedures

Both the setup for cyclic loading test and that for fire test are shown in Fig.2. During the cyclic loading test, a MTS actuator with a loading capacity of 1000 kN was employed to produce horizontal load reversals at the top of the specimens. Vertical compressive load was applied first and then kept constant throughout the cyclic loading test. The lateral loading program is illustrated in Fig.3. In the load-controlled phase, a single cycle was imposed on the specimen at each load level. After the yielding of the specimen, the displacement-controlled phase commenced, and two cycles were carried out at each displacement level equalling to 1, 2, 3, …, times of the yield displacement. Once a certain displacement level was first larger than αH (here α is the intended drift ratio in Table 1, and H is shown in Figure 1), this displacement level was changed to αH and two cycles were conducted at this new level, and after that the test terminated.

After the completion of the cyclic loading test, the eight damaged specimens and the one undamaged control specimen were tested in fire in a furnace chamber at South China University of Technology. For

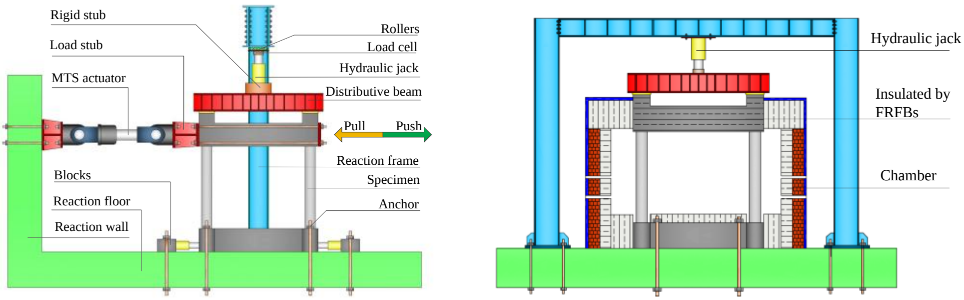

(a) Setup for cyclic loading test (b) Setup for fire test

Figure 2. Schematic diagrams of test setups.

each damaged specimen, the vertical load in the fire test was the same as that in the cyclic loading test and maintained constant during the heating process. The average temperature in the furnace chamber was automatically controlled to follow the ISO834 standard curve. Figue 4 depicts a comparison between the ISO834 standard curve and the measured average temperature-time curve in the furnace for Specimen D65N25V218S4.

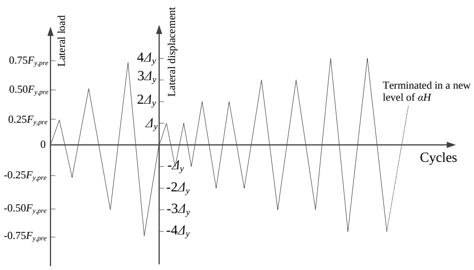

Figure 3. Lateral loading sequence.

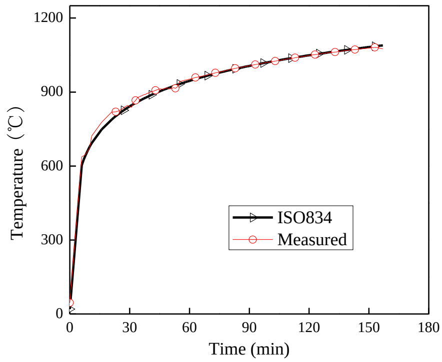

Figure 4. Measured average temperature-time curve in furnace for Specimen D65N25V218S4.

All sides of the columns were exposed to fire, while both the top and bottom strong beams were insulated by using the fire-retardant fiber blankets (FRFBs). The heating time related to the fail of the specimen (i.e., the vertical load provided by the hydraulic jack couldn't be maintained any longer) is defined as fire resistance of the specimen.

2.3 Instrumentations

In the cyclic loading test, the horizontal load and the specimen's lateral displacement were automatically collected by the data loggers. In the fire test, both the thermal and structural responses were measured. For a damaged specimen, type-K thermocouples with a diameter of 3 mm were installed in Sections 1-1, 2-2 and 3-3 (Figure 5) to measure the internal temperatures related to different regions, and three thermocouples were placed at each section. For the undamaged control specimen, only three thermocouples were placed at Section 3-3. In addition, two linear variable differential transducers (LVDTs) were instrumented on the top of the two columns for each specimen to monitor the axial deformations of the columns in fire (Figure 5).

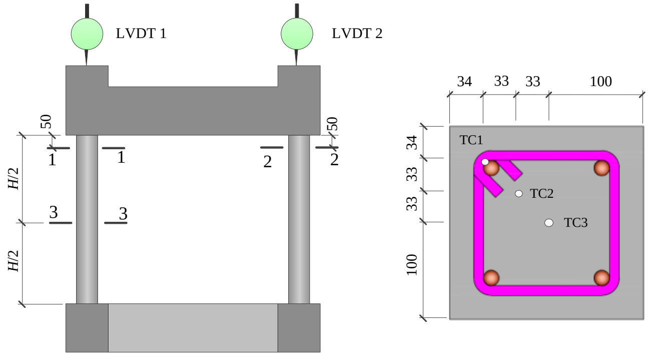

Figure 5. Locations of thermocouples and LVDTs (unit: mm).

3 TEST RESULTS AND DISCUSSIONS

With the increasing of the drift ratio and axial load ratio, the damage of the specimens' columns became severer. Specimen D40N50V126S4 experienced the severest damage in the cyclic loading test, while the seismic damage of Specimen D100N50V126S4 was negligible. Views of D40N50V126S4 in different test stages are shown in Fig.6. It can be seen that severe concrete spalling occurred at the plastic hinge of the left column during the cyclic loading test, and this specimen collapsed at this position in the following fire test. Because the main objective of this study is to investigate the fire performances of the seismic damaged columns, the detailed results related to the cyclic loading test are omitted here.

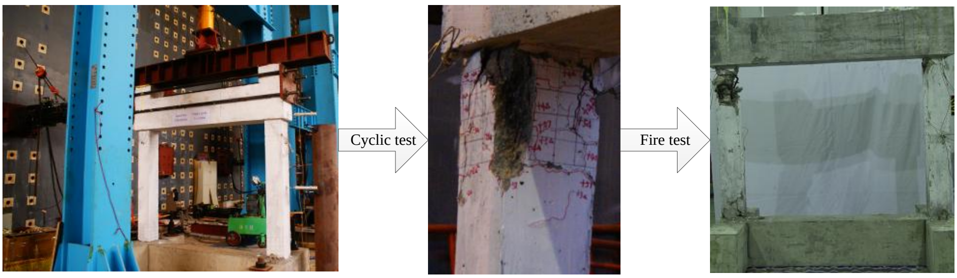

(a) Before cyclic loading test (b) Plastic hinge of left column (c) After fire

Figure 6. Views of D40N50V126S4 related to different stages.

3.1 Thermal responses

The measured temperature-time curves for Specimens D40N50V126S4 and D65N50V218S3 are plotted in Figure 7. The thermocouples located at TC1 and TC2 on Section 1-1 of D40N50V126S4 may be damaged during the cyclic loading test, so the temperatures related to these two points are unavailable. It can be seen from this figure that:

(a) The measured temperatures on Sections 1-1 and 2-2 in the damaged plastic hinge regions are generally lower than those on the undamaged Section 3-3. Similar trends are observed for other specimens. Maybe it is attributed to the fact that the unheated strong beam absorbed a great deal of heat from the column’s plastic hinge region.

(b) At the heating time of 51 min, the measured temperatures at TC1 and TC2 on Section 2-2 in the damaged plastic hinge region of D40N50V126S4 are higher than those at TC1 and TC2 on Sections 1-1 and 2-2 in the damaged plastic hinge regions of D65N50V218S3. This may be attributed to the severer spalling of concrete cover of D40N50V126S4 (see Figure 6 (b)) during the cyclic loading test.

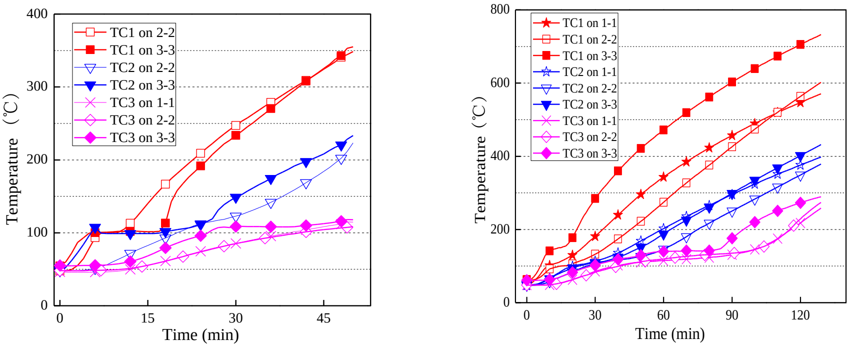

(a) D40N50V126S4 (b) D65N50V218S3

Figure 7. Measured temperatures-time curves for Specimens D40N50V126S4 and D65N50V218S3.

3.2 Fire resistance

A comparison of the fire endurances of nine specimens is given in Table 1. By comparing the data of Specimens D0N50V126S4, D100N50V126S4, D65N50V126S4 and D40N50V126S4, it is found that the fire endurance drops slightly at first with the increasing of the intended drift ratio α from 0 to 1/65, but when the intended drift ratio attains 1/40, the fire endurance decreases dramatically. However, the fire endurance of Specimen D26N25V126S4 with an especially large intended drift ratio of 1/26 is satisfactory due to the lower axial load ratio. In other words, when both the drift ratio and the axial load ratio are large enough to produce severe seismic damage in RC columns, the fire resistance of the columns are obviously weakened.

The effect of axial load ratio on fire resistance of seismic damaged columns can be examined by comparing Specimens D40N50V126S4 and D65N50V218S4 with Specimens D26N25V126S4 and D65N25V218S4. The fire endurance of D65N50V218S4 is 37 min lower than that of D65N25V218S4. Similarly, the fire endurance of D40N50V126S4 is significantly lower than that of D26N25V126S4 although the drift ratio of D26N25V126S4 is larger than that of D40N50V126S4. It can be concluded that the axial load ratio has a profoundly effect on fire resistance of seismic damaged columns.

With regard to the effect of transverse reinforcement on fire resistance of seismic damaged columns, it can be seen that the fire endurance of D65N50V218S4 with larger volumetric transverse reinforcement ratio is slightly longer than that of D65N50V126S4. But on the other hand, the fire endurance of D65N50V218S3 is slightly shorter than that of D65N50V126S3. This implies that the influence of transverse reinforcement on fire resistance of seismic damaged columns is inconspicuous.

Test results also show that the shear span ratio influences the fire resistance of seismic damaged columns to some extent. The fire endurances of D65N50V126S3 and D65N50V218S3 are, respectively, 15 min and 9 min longer than those of D65N50V126S4 and D65N50V218S4, implying that with the decreasing of the shear span ratio, the fire endurance of seismic damaged column generally increases.

3.3 Structural responses

The measured axial deformation-time curves are given in Figure 8. It can be seen that: (a) similar to the test results of undamaged columns under fire [5, 6], all the seismic damaged columns in this paper expand in the early heating stage, due to thermal expansion of the concrete and steel bars; and (b) in the late heating stage, the damaged columns contract because of the deterioration of the materials' mechanical properties. In addition, the axial deformation-time curves of the two columns in a specimen are close to each other in the early heating stage, but are quite different from each other in the late heating stage due to some randomness involved in the test.

The effect of drift ratio on structural responses of seismic damaged columns can be obtained by

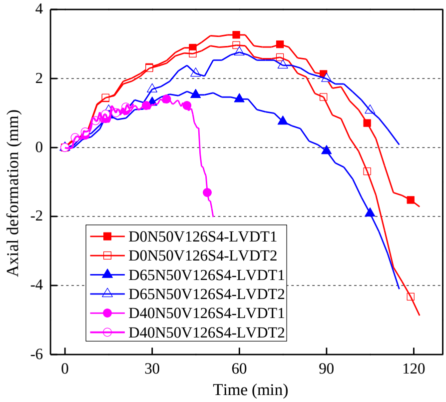

(a) D0N50V126S4, D65N50V126S4 and D40N50V126S4

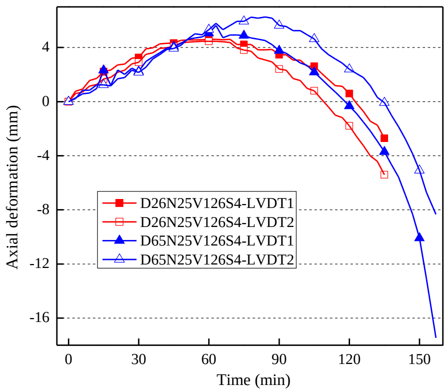

(b) D26N25V126S4 and D65N25V126S4

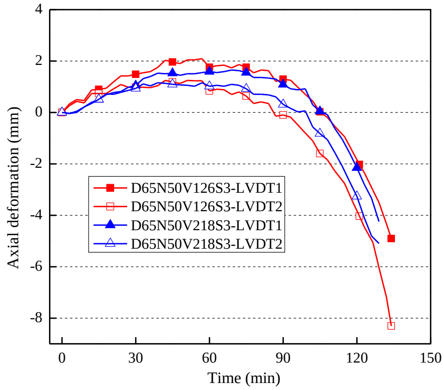

(c) D65N50V126S3 and D65N50V218S3

Figure 8. Measured axial deformation-time curves of specimens.

comparing the curves in Figures 8(a) and (b). It is found that with the increasing of the intended drift ratio, the maximum elongation of the column decreases gradually. This is because the larger the drift ratio is, the severer the concrete damage during the cyclic loading test is, leading the actual axial load ratio (i.e., a ratio of the applied load to the reduced load bearing capacity of the damaged column) increases, and finally resulting in less thermal elongation. Specimen D40N50V126S4 experienced significant concrete spalling during the cyclic loading test, so the reduction of its load carrying capacity is remarkable, this leading to extremely early failure of this specimen in fire and quite small thermal elongation.

By comparing the curves in Figure 8(a) with those in Figure 8(b), it is clearly seen that the maximum elongations of the specimens with an axial load ratio of 0.5 are less than those of the specimens with an axial load ratio of 0.25. Again the influence of volumetric transverse reinforcement ratio on structural performances of seismic damaged columns can be neglected according to the measured results shown in Figure 8(c). In addition, the maximum elongations of the two specimens with a shear span ratio of 3 given in Figure 8(c) are somewhat smaller than that of specimen D65N50V126S4 illustrated in Figure 8(a), due to the length of the columns in the former two specimens being only 1200 mm.

4 CONCLUSIONS

Based on the results of this study, the following conclusions can be drawn:

(1) The measured temperatures on Sections 1-1 and 2-2 in the damaged plastic hinge regions are generally lower than those on the undamaged Section 3-3.

(2) When both the drift ratio and axial load ratio are large enough to produce severe seismic damage in RC columns, the fire resistance of the columns are obviously weakened.

(3) The axial load ratio has a profoundly effect on the fire behaviors of seismic damaged columns, and lower axial load ratio leads to longer fire endurance and larger thermal elongation.

(4) The influence of transverse reinforcement ratio on the fire behaviors of seismic damaged columns is very limited.

(5) Lower shear span ratio results in marginally better fire performances of the seismic damaged columns.

ACKNOWLEDGEMENTS

The research reported was financially supported by the National Natural Science Foundation of China (51025829, 51378225), the Funds of State Key Laboratory of Subtropical Building Science of China (2011ZB07, 2013ZB24), and the Fundamental Research Funds for the Central Universities (2012 ZP0011). The financial supports are highly appreciated.

REFERENCES

[1] Sharma U. K., Bhargava P., Singh B., Singh Y., Kumar V., Kamath P., Usmani A., Torero J., Gillie M., Pankaj P., May I., and Zhang J., "Full-scale testing of a damaged reinforced concrete frame in fire", *Proceedings of the Institution of Civil Engineers-Structures and Buildings*, 165(7), 335-346, 2012.

[2] Mostafaei H., and Kabeyasawa T., "Performance of a six-story reinforced concrete structures in post-earthquake fire', *9th US National and 10th Canadian Conference on Earthquake Engineering ,* Including Papers from the 4th International Tsunami Symposium, 1-10, 2010.

[3] Ervine A., Gillie M., and Panka., "Behaviour of earthquake damaged reinforced concrete structures in fire". *Structures on Fire – Proceedings of the Sixth International Conference*, V. Kodur, J.-M. Franssen (eds.), DEStech Publications, Lancaster, 224-230, 2010.

[4] Ronagh H. R., and Behnam B., "Investigating the Effect of Prior Damage on the Post-earthquake Fire Resistance of Reinforced Concrete Portal Frames", *International Journal of Concrete Structures Material,* 6(4), 209-220, 2012.

[5] Lie T. T., and Irwin R. J., "Evaluation of the fire resistance of reinforced concrete columns with rectangular cross-section". *Internal Report No.601, Institute for Research in Construction*, Canada, 79pp, 1990.

[6] Raut N., K., and Kodur V., K., R., "Response of High-Strength Concrete Columns under Design Fire Exposure", *Journal of Structural Engineering*, 137(1), 69-79, 2011.

8th International Conference on Structures in Fire
Guo-Qiang LI, Venkatesh K. R. KODUR, Shou-Chao JIANG, Jian JIANG, Su-Wen CHEN, Guo-Biao LOU (Eds.)
Shanghai, China, June 11-13, 2014

STRENGTH AND STABILITY OF SLAB PANEL SUPPORT BEAMS

B. Zhang*, M. Su*, G.C. Clifton, A.K. Abu** and T. Gu****

* SPIIRE, Christchurch, New Zealand; * COSL, New Plymouth, New Zealand
e-mails: bing.zhang@spiire.co.nz, miao19163@gmail.com

** Department of Civil and Environmental Engineering, University of Auckland, New Zealand

** Department of University of Canterbury, Christchurch, New Zealand;

** Holmesfire, Auckland, New Zealand
e-mail: c.clifton@auckland.ac.nz; tony.abu@canterbury.ac.nz; ted.gu@holmesfire.com

Keywords: SPM, Fire, Membrane, Model, Vulcan

Abstract. *The Slab Panel Method (SPM) is a structural fire safety design method for steel-framed buildings with composite floor systems. A 3D model of an 18 m × 12 m slab panel, representative of a typical composite floor, was developed in the Finite Element Analyses (FEA) software Vulcan. The results of FEA runs show that, in this case, the secondary edge beams are more sensitive to the level of design loading than the primary edge beams in generating dependable two-way action within the slab panel. The current (2006) recommendations on loading from the SPM are potentially un-conservative for isolated panels with edge beams with simple supports. The results also show that the SPM gives accurate deflection predictions for an isolated slab panel. The effects of the initial state of the deflections on the final collapse mechanism cannot be analyzed due to the numerical models being unable to develop the full collapse mechanism before the analyses stopped running due to numerical instability.*

1 INTRODUCTION

The Slab Panel Method (SPM) is a structural fire safety design method for determining the fire resistance of steel-framed buildings with composite floor systems exposed to severe fire attack. SPM applies to floor systems comprising a mix of unprotected and protected floor support beams and accounts for the increase in fire resistance from two-way floor system deformation in severe fires [1].

The traditional method of fire safety design for steel-framed buildings, which is based on the behaviour of individual steel members in Standard Fire Resistance Tests, is to prescribe passive fire protection on all exposed steel columns and support beams. Actual fires in multi-storey buildings and full-scale fire tests [2-4] have demonstrated that it is not necessary to apply passive fire protection to all the exposed steel beams in buildings with composite floor systems in order for the floor system to remain stable in severe fires. These case studies have shown that the improved performance of steel-framed buildings in severe fires is principally due to the enhanced load carrying capacity of the composite floor as a result of tensile membrane action [5, 6].

Tensile membrane action is a mechanism that develops during severe fire action in a floor panel in which the panel edges are effectively supported in the vertical plane but the mid-span region of the panel is allowed to deform vertically downwards. This deformation develops two-way tension action across the interior of the panel, with this tension being resisted by a ring shaped compression zone in the concrete and support beams around the perimeter of the panel. The applied load on the panel is transferred out to the supporting edges, then into the columns. The application to fire of the tension membrane model was first formulated by Bailey and Moore in 2000 [5, 7]. The SPM is a generalised application of the Bailey procedure, with additional strength checks and detailing requirements to ensure that the deformations can be dependably developed [8]. It has been under ongoing development [9] since the release of the current (2006) edition [1].

SPM divides a concrete composite floor into a number of rectangular slab panels [1]. The support edge beams and columns of the slab panels are protected by fire protection materials, while the internal beams (within the slab panel) are left unprotected. The edge beams are either secondary beams or primary beams in the composite floor system. Under severe fire conditions, tensile membrane action develops within the slab panel, and applied loads are supported by the protected support edge beams. The current version of the SPM [1] assigns the loading to the slab panel support beams based on the tributary areas from the yield line pattern of a vertically supported slab panel onto the supporting beams, and designs the support beams for fire in accordance with individual member based provisions of the New Zealand Steel Standard, NZS 3404:1997[10].

For the tensile membrane model to work as intended, the edge supports must be effectively stiff. If the edge beams develop plasticity, the slab panel will form a plastic collapse mechanism involving both the interior and edge beams [11]. Research by Abu et. al. [12, 13] has shown that the load carrying capacity of the potential plastic collapse mechanism is less than that of the tensile membrane mechanism, therefore making it essential that the edge supports perform as intended. SPM sets criteria for the expected deflection of these edge beams to ensure the two-way action can be developed.

A research project has been conducted to investigate the strength and stability requirements of the edge beams of an 18 m × 12 m slab panel which was designed to the SPM for 60 minutes of exposure to the Standard fire (ISO 834). A 3D computer model of the slab panel was developed in FEA software VULCAN which had been developed principally to simulate the behaviour of composite floor systems in fire [14]. The aims of the project were to determine the required design loading for the 18 m × 12 m slab panel to retain its dependable two-way behaviour through the full Fire Resistance Rating (FRR) specified, to compare the predicted performance using SPM with the results of Finite Element Analyses (FEA), and to determine whether the final collapse mechanism would be affected by the initial state of deflections when the slab first deformed through flexural mechanism and developed into large deformation state.

2 METHODOLOGY

2.1. Defining the slab panel

The investigations were based on the 18 m × 12 m slab panel in a steel-framed building. The layout, dimensions and the steel member sizes of the slab panel are shown in Figure 1.

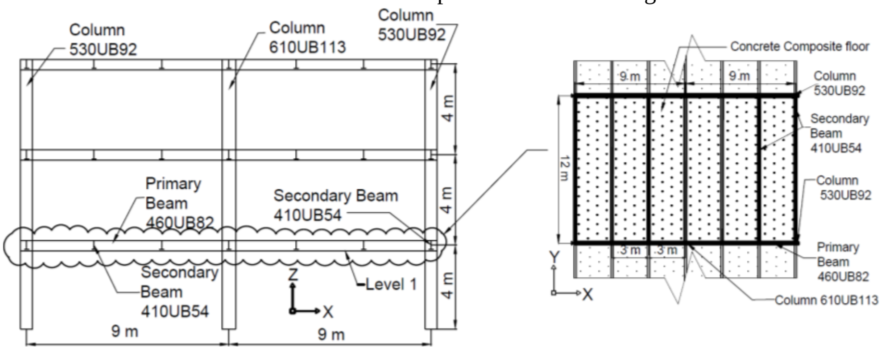

Figure 1. An elevation view of the steel-framed building and a plan view of the 18 m × 12 m slab panel.

2.2. Defining fire protection, material properties and slab profile

The supporting edge beams and all the columns were protected by sprayed mineral fibre while the interior secondary beams were unprotected. There was one slab per floor. The concrete material was normal weight concrete with a compression strength of 25 MPa, a cracked shear factor of 0.25, a Poisson's ratio of 0.2, a density of 2350 kg/m^3, and a moisture content of 3%. The steel material had a yield stress of 300 MPa, a Young's modulus of 205000 MPa and a Poisson's ratio of 0.3. The reinforcement bars in the slab were hot rolled with a yield stress of 500 MPa and a Young's modulus of 205 GPa.

ComFlor 60 [15] ,with a total slab depth of 130 mm, was adopted as the steel decking. The anti-cracking mesh size was SE82 with a cross sectional area of 251 mm^2 per metre width i.e. 8 mm diameter of hot rolled steel wire with 500 MPa yield strength at 200 mm spacing.

2.3 Defining loadings

The structure was assumed to be designed for 'office' occupancy and the design load (w*) for the ultimate limit state for fire was 5.2 KPa ,in accordance with New Zealand Structural Design Actions Standard, NZS 1170:2002[16] The design load-carrying capacity (w_u) from SPM software (version 3.1.1 revision 182) for the 18 m × 12 m slab panel was 5.68 kPa. The slab panel was loaded with w* or w_u.

Two loading conditions, normal loading (NL) and enhanced loading (EL), were applied to the design of the thickness of the sprayed mineral fibre. Under severe fire conditions in a uniformly loaded slab panel with all edges vertically simply supported, the SPM considers the supporting edge beams resist the loads within the tributary areas from the yield line pattern as shown in Figure 2. For the NL, the tributary area for a secondary beam (Side 2 and 4) is a triangle with a height equalling L1 (Area B or D); while the tributary area for a primary beam (Side 1 and 3) is a trapezoid (Area A or C). For the EL, the tributary area for the secondary beam is also a triangle but with a height equalling half of L_x, i.e. tributary area equals $L_x^2/4$; the load on the primary beam is uniform ($L_x/2$ the full length), i.e. tributary area of loading equals $L_x/2 \times L_y$ on each side of the supporting beam.

The edge beams were treated as either exterior or interior. No line load was applied to the exterior edge beams and a line clad was applied to the interior edge beams to account for the extra load from the adjacent slab panel.

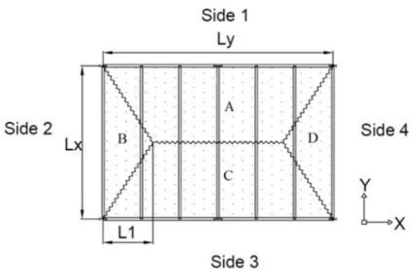

Figure 2. SPM yield line pattern.

2.4 Modelling the slab panel in Vulcan

The slab panel was modelled in Vulcan as an assembly of beams, columns, springs, shear connectors and slab. Finite element geometries of a slab panel were generated by the Wizard function in Vulcan. Springs were utilized to model the beam-to-column and beam-to-beam connections. The shear studs between the beams and the concrete slab were modelled as discrete shear connectors. The composite action between the secondary beams and the slab was assigned to be full while that between the primary and the slab was assigned to be partial. The ultimate shear strength of the shear connectors was taken as 332 MPa. The diameter of the shear connectors was 19 mm. and the spacing between the shear connectors was made 300 mm. The slab was divided into thirteen horizontal layers and the reinforcement was modelled as two smeared layers in the slab at the appropriate heights within the slab. An element density of 1 m × 1m was chosen for the slab panel. An element density of 0.5 m × 0.5 m was also adopted in three FEA runs to perform mesh size sensitivity analyses.

2.5. Defining temperature profiles

The bottom of the slab panel and supporting members were assumed to be subjected to an ISO 834 fire. Two aspects of the temperature were defined, i.e. the temperature growth with time and the temperature distributions across sections of the members.

The temperature growth with time in different steel members, slab, and springs were defined as temperature curves (variation with time) which were attached to appropriate parts of the slab panel 3D model in Vulcan. The temperature distributions across sections of the members were defined as temperature patterns (variation across member cross-sections) which were assigned to appropriate cross-sections of the components.

FaST [17], a FEA program based on the finite difference method capable of calculating temperature growth with time in steel sections under a range of common exposure condition with different passive fire protections and insulation thicknesses, was used to generate the temperature growth with time for the unprotected beams, protected beams and protected columns in the ISO fire.

A one-dimensional thermal analysis of the concrete slab under the ISO fire was performed in ABAQUS to obtain the temperature distribution which represented the temperature distribution across the cross-section of the concrete slab. The resulted data were imported into Vulcan and attached to the slab section.

The temperatures of springs between protected beams and columns were assumed to be the average temperatures of the beams and columns that the springs were connected to. The temperatures of springs between unprotected beams and protected beams or columns were taken to be the temperatures of the unprotected beam multiplied by 0.88, in accordance with EN1993-1-2:2005[18].

Three temperature patterns were assigned to different parts of the slab panel model. A uniform temperature pattern was assigned to the protected beams and columns; a bilinear temperature pattern was assigned to the concrete slab; and a Flange-Web-Flange temperature pattern was assigned to the unprotected beams.

2.6 Specifying outputs

The displacements of the nodes (Figure 3) in X, Y and Z directions of were output into spreadsheets for analyses.

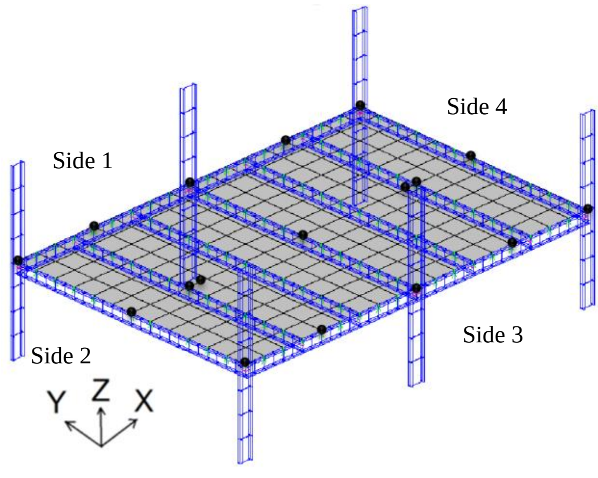

Figure 3. A 3D slab panel model showing the nodes.

2.7 Defining boundary conditions

By fixing DOFs of the nodes i.e. translation and rotation in global X, Y and Z directions (TX, TY, TZ, RX, RY and RZ), various boundary conditions were applied to the model to simulate different support conditions of the slab panel. Five support conditions were applied to the generic slab panel model: (1) isolated panel; (2) panel with one interior edge; (3) panel with two interior edges; (4) panel with three interior edges; and (5) internal panel.

3. RESULTS

3.1 A summary of the FEA runs

A total of seventeen FEA runs were carried out on the 18 m × 12 m slab panel 3D model with different applied loads, support conditions and insulation thicknesses. The element density of the slab panel was 1 m^2 in all the Runs except for Run 12 to 14 in which the slab had an element density of 0.5 m^2. The slab panel was loaded with 5.2 kPa (w^*) in Runs 9 to 11 and 5.68 kPa (w_u) in all other runs. Three runs, i.e. Run 1, 5 and 15, were used in the analyses of the results. Table 1 gives a summary of the three runs.

Table 1. Summary of Run 1, 5 and 15.

Run	Side	Edge Support Conditions	Side Fixities	Passive Fire Protection, mm	Line Load	Failed to Converge at (minutes)
1	1	exterior	no	8		60.06
	2	exterior	no	27		
	3	exterior	no	8		
	4	exterior	no	27		
5	1	interior	RX,TY	14	Yes	66
	2	interior	RX,TY	13		
	3	interior	RX,TY	14	Yes	
	4	interior	RX,TY	13		
15	1	exterior	no	8		62.76
	2	exterior	no	13		
	3	exterior	no	8		
	4	exterior	no	13		

3.2 Deflection predictions given by the SPM

The SPM Program generates two limiting deflection predictions: (1) D_{limit} - the maximum allowed vertical deflection of the slab panel relative to the pre-fire position of the adjacent supports; (2) D_{max} - the maximum slab panel central vertical deflection [1]. The SPM gave a D_{limit} of 1090 mm and a D_{max} of 1180 mm for the 18 m × 12 m slab panel at 60 minutes FRR.

The fire protected supporting beams deflect during the fire. Based on previous real fire tests and advanced FEA, the protected support beam deflection was taken as equal to L/75 at the 60 minutes FRR [1]. In this case, the deflection was assumed to be 160 mm (indicated as D_{SB} in Figure 4) at the 60 minutes FRR for the secondary beam, 120 mm (indicated as D_{PB} in Figure 4) for the primary beam. These parameters were used in the comparisons of the outputs of the FEA runs.

3.3 Data analyses

The analyses of the performance of the slab panel under the normal loading and the enhanced loading were based on three FEA runs: (1) Run 1, which was an isolated slab panel under the enhanced loading;
(2) Run 5, which was an internal slab panel under the normal loading;
(3) Run 15, which was an isolated slab panel under normal loading.

3.3.1 Deflection predictions of the SPM and displacements of the FEA runs

Figure 4 shows the central displacements in Z-direction of these three runs and the deflection predictions at 60 minutes FRR from the SPM Program.

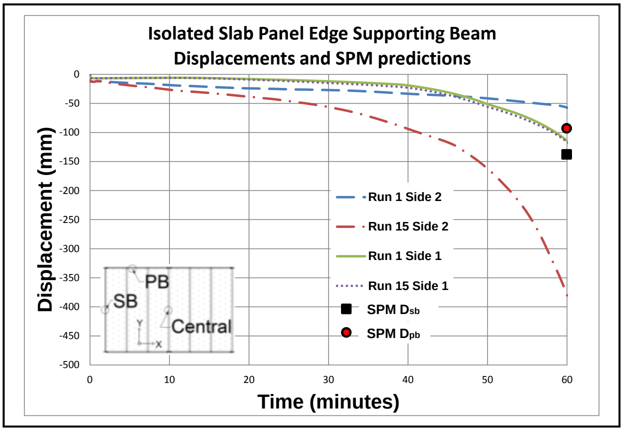

Figure 4. Central slab displacements and SPM deflection predictions at 60 minutes FRR.

3.3.2 Deflection predictions of the SPM and the edge supporting beam displacements of the FEA runs

Figure 5 shows the edge beam displacements in Z-direction of the Run 1 and 15 and the edge supporting beam deflections predictions from the SPM at 60 minutes FRR. Side 1 represents the primary beam and side 2 the secondary beam.

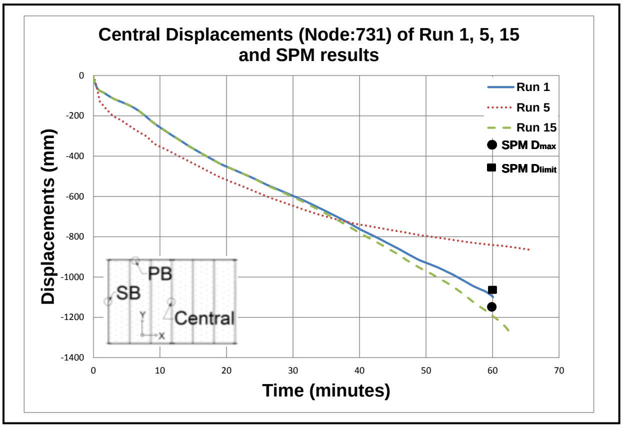

Figure 5. Edge beam supporting displacements and SPM deflection predictions at 60 minutes FRR.

6 DISCUSSION

It can be seen from Figure 4 that at 60 minutes, the central displacement of the panel with the enhanced loading equals 1097 mm, which is slightly more than D_{limit} (1090 mm); that of the panel with the normal loading equals 1193 mm, which is also slightly more than D_{max} (1180 mm). It shows that, in this case, the SPM generates accurate deflection predictions for isolated slab panels and conservative predictions for internal slab panels.

It appears that the deflections of the isolated slab panel under the enhanced loading and the internal slab panel under the normal loading did not undergo sudden increase before the FEA runs failed to converge, which indicates the two-way action is still in the stable state of constant increase in deformation with increasing time. The isolated slab panel under the normal loading shows sign of sudden increase of deflection just before the FEA run failed to converge, which indicates that the two way action started to change into one way action involving plastic collapse of the secondary edge beams and the slab panel. The reasons for the failure of the FEA run to converge could be the physical failure of the slab panel or the numerical failure of the 3D model, therefore the final collapse mechanism cannot be determined beyond its initial stages of development.

Figure 5 shows that the displacements of the secondary beam with normal loading are clearly more than those of the secondary beam with enhanced loading on an isolated slab panel. The deflection at 60 minutes reaches 380 mm under the normal loading, which is more than double of the specified deflection limit of 160 mm; while the deflection under the enhanced loading is only 57 mm, which is within the deflection limit. The displacements of the primary edge beams under the normal loading are very close to those under the enhanced loading. The deflection at 60 minute equals 114 mm under the normal loading and 116 mm under the enhanced loading. Both are less than the deflection limit of 120 mm. The results show that, for an isolated slab panel, the secondary edge beams are more sensitive to the level of design loading than the primary edge beams in generating dependable two-way action within the slab panel. They also indicate that the normal loading, which is recommended by the current (2006) version of the SPM [1], is potentially un-conservative for a simply supported isolated slab panel.

7 CONCLUSIONS

The results of the FEA runs show that, for an 18 m × 12 m slab panel that is representative of a typical composite floor, the secondary edge beams are more sensitive to the level of design loading than the primary edge beams in generating dependable two-way action within the slab panel. On an isolated panel, which is what the SPM model assumes, the secondary edge beams exceed the specified deflection limit under normal loading and are within the limit under enhanced loading. However, the primary edge beams are within the deflection limit under both normal and enhanced loading. Therefore, current recommendations on loading from the SPM of design are potentially un-conservative for isolated panels with edge beams with simple supports and need increasing as recommended herein. The results also show that the SPM gives accurate deflection predictions for an isolated slab panel. The effects of the initial state of the deflections on the final collapse mechanism cannot be analysed due to the numerical model being unable to develop the full collapse mechanism before the analyses stopped running, due to numerical instability.

REFERENCES

[1] Clifton, G.C., *Design of Composite Steel Floor Systems for Severe Fires, HERA Report R4-131*, New Zealand HERA, Manukau City, 2006.

[2] Wang, Y.C., *Steel and Composite Structures-Behaviour and design for fire safety*, Taylor and Francis Group, London and New York , 2002.

[3] Kirby, B., *The Behaviour of a Multi-Storey Steel Framed Building Subject to Fire Attack-Experimental Data*, British Steel Swinden Technology Centre, United Kingdom, 1998.

[4] Thomas et al, I., *Fire Tests of the 140 William Street Office Building*, BHP Co Ltd, Melbourne, Australia, 1993.

[5] Bailey, C.G. and D.B. Moore, *The structural behaviour of steel frames with composite floorslabs subject to fire: Part 1: Theory.* The Structural Engineer. **78**(11): p. 19-27, 2000.

[6] Clifton, G.C., M. Hinderhofer, and R. Schmid, *Design of Multi-Storey Steel Framed Buildings with Unprotected Secondary Beams or Joists for Dependable Inelastic Response in Severe Fires.* Steel Design and Construction Bulletin. **60(February)**: p. 1-58, 2001.

[7] Bailey, C.G. and D.B. Moore, *The structural behaviour of steel frames with composite floorslabs subject to fire: Part 2: Design.* The Structural Engineer. **78**(11): p. 28-33, 2000.

[8] Clifton, G.C. *Design Of Multi-Storey Steel Framed Buildings With Unprotected Secondary Beams Or Joists For Dependable Inelastic Response In Severe Fires*. in *Second International Workshop Structures in Fire*. University of Canterbury, Christchurch, New Zealand, 2002.

[9] Lim, Z.Y., *Testing of Slab Panel Method Program in Severe Fire*, G.C. Clifton, Editor, The University of Auckland, Auckland, 2012.

[10] Standards New Zealand, *NZS 3404:1997 Steel Structures Standard*, SNZ: Wellington, NZ, 1997.

[11] Bailey, C.G., *Membrane action of slab/beam composite floor systems in fire.* Engineering Structures. **26**(12): p. 1691-1703, 2004.

[12] Abu, A.K., I.W. Burgess, and R.J. Plank, *Slab panel vertical support and tensile membrane action in fire.* Steel and Composite Structures. **8**(3): p. 217-230, 2008.

[13] Abu, A., V. Ramanitrarivo, and I. Burgess, *Collapse Mechanisms of Composite Slab Panels in Fire.* Journal of Structural Fire Engineering. **2**(3): p. 205-216, 2011.

[14] Huang, Z., I.W. Burgess, and R. J. Plank, *Effective stiffness modelling of composite concrete slabs in fire.* Engineering Structures. **22**(9): p. 1133-1144, 2000.

[15] Corus New Zealand, *ComFlor 60-Composite Floor Decking*, Auckland, New Zealand, 2008.

[16] Standards New Zealand, *AS/NZS 1170:2002 Structural Design Actions Part 1- Permanent,imposed and other actions*, SNZ, Wellington, NZ, 2002.

[17] HERA, *FaST Ver1.0 User Manual and Commentary*, New Zealand Heavy Engineering Research Association, 2004.

[18] British Standards Institution, *BS EN 1993-1-2:2005 Eurocode 3: Design of steel structures*, in *Part 1-2: General rules — Structural fire design*, London, UK, 2005.

8th International Conference on Structures in Fire
Guo-Qiang LI, Venkatesh K. R. KODUR, Shou-Chao JIANG, Jian JIANG, Su-Wen CHEN, Guo-Biao LOU (Eds.)
Shanghai, China, June 11-13, 2014

REINFORCED CONCRETE SLABS IN FIRE: EXPERIMENTAL INVESTIGATIONS ON REINFORCEMENT MESH ORIENTATION

Duc Toan Pham*, Patrick de Buhan, Céline Florence*, Jean Vivien Heck*, Stéphane Charuel* and Romuald Avenel***

* Université Paris-Est, Centre Scientifique et Technique du Bâtiment (CSTB), 84 avenue Jean Jaurès, Champs-sur-Marne, 77447 Marne-la-Vallée Cedex 2, France
e-mail: ductoan.pham@cstb.fr

** Université Paris-Est, Laboratoire Navier (Ecole des Ponts ParisTech, IFSTTAR, CNRS UMR 8205), 6-8 avenue Blaise Pascal, Cité Descartes, Champs-sur-Marne, 77455 Marne-la-Vallée Cedex 2, France
e-mail: patrick.debuhan@enpc.fr

Keywords: Four-point bending test, Mesh orientation, Fire resistance, Reinforced concrete slab

Abstract. *This paper describes two series of tests carried out on slab elements with variable reinforcement mesh orientation under both ambient and elevated temperature conditions. A four-point bending was imposed up to failure of the 16 such specimens. The test results will provide useful experimental data for validating future models that are usually based on some specific assumptions. Among the tests, failure bending moment of slabs reinforced by steel bars arranged along the longitudinal and orthogonal axes of the specimen is compared with value predicted by an approach based on the yield-design theory.*

1 INTRODUCTION

A great amount of research has been devoted over the last twenty years to the study of fire resistance of concrete structures, mainly as regards the degradation of mechanical material properties and thermal-induced deformations. When subjecting a structural element such as slab to fire, additional efforts such as membrane, bending and torsional forces, may be generated. The failure modes further depend on thermal gradient, solicitations direction, material strength properties and degree of reinforcement. In most cases the volume proportion of steel can be considered small: steel may often occupy from 0.5% to 4% of concrete volume. Neglecting their shear and bending resistance, the concrete being regarded as a matrix material, the state of stress is almost uniaxial in the reinforcement.

This contribution deals with the mechanical behaviour up to failure of reinforced concrete slab elements in bending. The paper aims first at assessing the influence of two parameters, the mesh orientation and the thermal loading. Moreover, it aims at constitute a useful data base to validate models to predict failure.

An experimental campaign of 16 reinforced concrete slabs has been conducted at the CSTB. The test conditions included different mesh orientations and thermal loading. Firstly, the paper describes the reinforced concrete slab specimens, the test setup related to its loading and the instrumentation. Then the results of both ambient and fire condition tests are reported. In the case of slabs made up of steel bars arranged along the longitudinal and orthogonal axes of the specimen, results are used to validate an approach based on the yield design theory.

2 EXPERIMENTAL PROGRAM

2.1 Test slabs

The test programme comprised two series of slabs as follows:

- A-series: 8 slabs at ambient temperature.
- H-series: 8 slabs at high temperatures.

All slabs were 120cm-long, 45cm-wide and 10cm-thick. Fiber concrete B40F [1] was used to construct test slabs in order to prevent spalling of concrete due to fire. The slabs were reinforced by steel bars of 6mm of diameter, approximately spaced 7.5cm. The steel bars were arranged in two orthogonal arrays placed near the bottom face with 2cm of concrete cover, and positioned at various angles α, namely 0°, 20° and 45°, with respect to the axis of the slabs.

The characteristics of the 16 slabs are summarized in Tab. 1. The slabs were identified by reinforcement mesh orientation. Concrete cylinders (16×32cm) were cast with the test specimens to measure tensile and compressive strengths, f_t and f_c, of concrete material at ambient condition. They were tested at 28 days and 90 days for standard reference. The results showed in Table 1 were obtained at 90 days. Likewise, tensile tests were performed on representative samples of steel bars to measure their uniaxial strength f_y.

Table 1. Characteristics of test slabs.

Specimen	Weight (kg)	f_t (MPa)	f_c (MPa)	f_y (MPa)	α	Specimen age (day)
A1_0°	122	2	24	595	0°	94
A2_20°	120	2	24	595	20°	94
A3_45°	121	2	24	595	45°	97
A4_0°	127	2.5	27.8	621.3	0°	90
A5_20°	129	2.5	27.8	621.3	20°	91
A6_45°	126	2.5	27.8	621.3	45°	90
A7_0°	128	2.5	27.8	621.3	0°	238
A8_20°	127	2.5	27.8	621.3	20°	238
H1_0°	119	2	24	595	0°	94
H2_0°	120	2	24	595	0°	93
H3_20°	118	2	24	595	20°	97
H4_20°	120	2	24	595	20°	101
H5_45°	120	2	24	595	45°	96
H6_0°	125	2.5	27.8	621.3	0°	96
H7_20°	125	2.5	27.8	621.3	20°	94
H8_45°	125	2.5	27.8	621.3	45°	91

2.2 Test setup

Tests were conducted on a rigid frame designed at the CSTB (Figure 1). Slabs were placed in a horizontal position on two rollers (span of 110cm) allowing free thermal expansion. The lateral sides of the slabs were stress free. During the fire tests, they are protected by glass wool thermal insulation.

The load was applied to the slabs through an upper support with two 33.6cm-spaced rollers. This configuration allows defining a central area in which the bending moment is constant at its maximum, thus making it possible to evaluate the ultimate bending moment in the absence of any shear force.

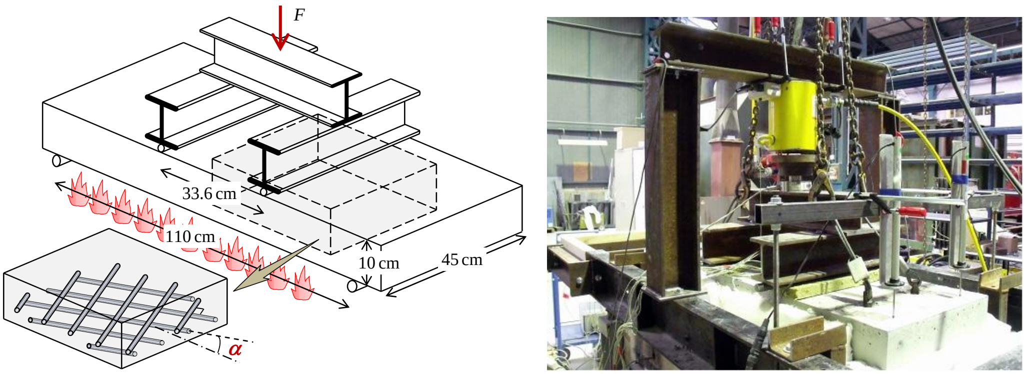

Figure 1. Test configuration and implementation of a fire test.

In performing the fire tests, lower surface of the slabs was exposed to ISO 834 fire [2] and the mechanical loading was applied after 120 minutes of fire exposure. Note that the ISO 834-curve is purely conventional and is generally used for laboratory tests to facilitate the reproductibility and comparison of results.

2.3 Instrumentation

Temperatures were recorded with an electronic data acquisition system. The standardized thermal program was monitored via thermocouples placed inside the furnace. Burners were manually controlled, so as to make sure that the prescribed temperature evolution actually follows the ISO 834 curve.

Temperatures of concrete material were measured with thermocouples positioned at different locations across the slab thickness. The thermocouples were placed in central area of each slab with a minimum distance of 15cm from vertical sides, in order to avoid edge effects.

During the tests, the applied load and the resulting deflection evolution were continuously recorded up to collapse by another electronic data acquisition system. The force was measured by a load cell. The load was controlled by the displacement of a hydraulic jack. The measurement of the deflection was performed by means of two wire sensors fixed on the rigid frame and connected with the non-exposed face of the slabs.

3 RESULTS OF TESTS AND DISCUSSIONS

In this section, the experimental results are presented and discussed with reference to the failure load and the stiffness of the slab specimens in relation with their reinforcement mesh orientations and associated thermal loading. Experimental data were exported and force versus deflection curves were plotted to investigate their thermal-mechanical behaviour.

3.1 Results of tests at ambient temperature

Figure 3 shows the force-deflection curves of 6 ambient tests. For the three tests A1 to A3, the increase of applied force was stopped as soon as instability of the slab was observed. The maximum deflection was slightly limited. In order to approach failure, the loading had to be further increased to reach higher deflections such as in the case of three tests A4 to A6.

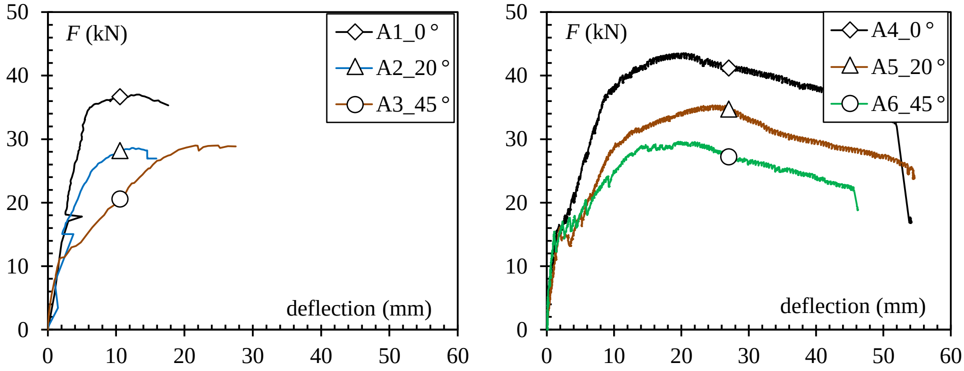

Figure 3. Force-deflection curves of ambient tests A1 to A6.

As can be seen from Figure 3, the behaviour becomes strongly non-linear after a first linear elastic phase. Then the force-deflection curves tend to the horizontal, which is characteristic of a ductile behaviour. The maximum force significantly decreases when the steel bars are no longer parallel to the orthogonal axis of the slabs.

For the two slabs A7 and A8, the procedure was slightly modified by applying a first preliminary loading-unloading cycle in order to wipe off any tensile strength of concrete. In comparison with results of tests A4 and A5, a quite significant decrease of the maximum force was observed (Figure 4). In addition, both the maximum force and initial stiffness decreased with the increase of reinforcing angle.

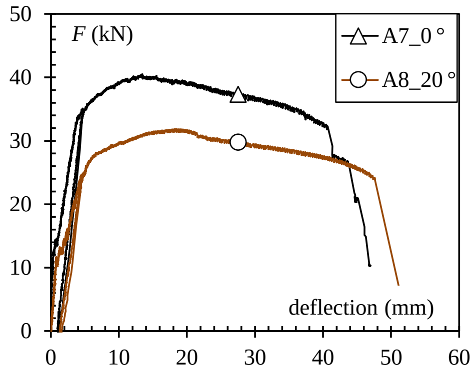

Figure 4. Force-displacement curves of ambient tests A5 and A7.

The test curve A8 displays a slightly smaller slope at the origin than that of A7, that is a smaller elastic stiffness. When comparing elastic linear and unloading-loading phases, a decrease of slope can also be observed. This loss of stiffness is an indicator of damage.

3.2 Results of tests at high temperatures

3.2.1 Recorded temperatures

The ambient temperature at the beginning of each test was recorded (value around 18^{o}C). For each measuring point at a given time, average values of temperatures were calculated. Table 2 provides temperatures at various locations across the thickness of the fire test specimens at 120 minutes of fire exposure. Since the diameter of steel bars is small, their temperature could be considered as corresponding to that of the concrete located at the same position.

Table 2. Temperatures at different thickness within the slabs at 120 minutes.

Distance/ exposed-face	Temperature (℃)							
	H1	H2	H3	H4	H5	H6	H7	H8
0 cm	1041	1044	1053	1050	1060	1053	1078	1049
1 cm	814	797	778	754	783	768	739	751
2 cm	688	665	655	674	665	658	636	641
3 cm	588	570	548	578	579	562	548	544
4 cm	497	466	463	*X**	497	477	453	458
5 cm	419	407	395	408	411	404	394	386
6 cm	357	338	334	*X**	343	345	333	327
8 cm	276	261	277	274	270	257	254	240
10 cm	*X**	*X**	*X**	179	178	204	197	190

*X**: data not available

During heating, the deformation of slabs under the combined action of thermal loading (thermal curvature and thermal expansion) and the slab self-weight was clearly visible. Figure 5 displays the deflection recorded as function of fire exposure times for 8 fire tests H1 to H8.

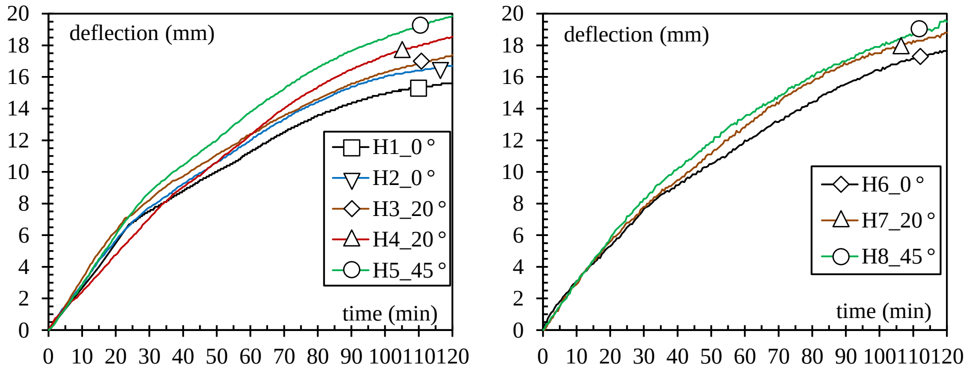

Figure 5. Deflection-time curves of tests H1 to H8.

3.2.2 Applied load versus deflection

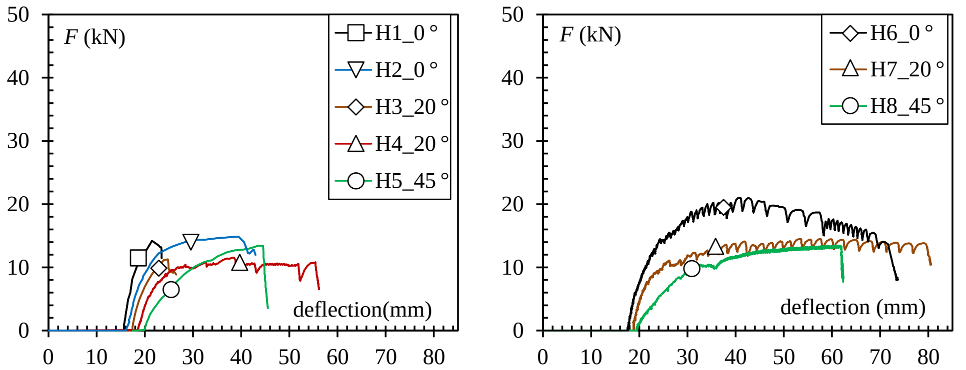

Figure 6. Force-deflection curves of tests H1 to H8.

At the target time of 120 minutes, the loading was applied leading to higher deflections of the slabs. The force-deflection curves could be displayed in Figure 6. The initial deflection was due to thermal loading and slab self-weight as explained in the above section.

In comparing with results of ambient tests (Figures 3 and 4), Figure 6 shows a significant decrease of the load bearing capacity when the slabs were subjected to fire. A decrease of at least 50% of the maximum applied load could be observed. The behaviour remains non-linear and ductile. This figure also shows a decrease of the maximum applied load in relation with the reinforcement schemes. For more details of all tests, Table 3 below summarises the recorded maximum applied loads.

Table 3. Results of maximum applied load.

Ambient tests		Fire tests	
Specimen	Pick of applied load (kN)	Specimen	Pick of applied load (kN)
A1_0°	37.00	H1_0°	14.19
A2_20°	28.59	H2_0°	14.88
A3_45°	29.00	H3_20°	11.28
A4_0°	43.56	H4_20°	10.43
A5_20°	35.32	H5_45°	13.41
A6_45°	29.60	H6_0°	20.96
A7_0°	40.51	H7_20°	14.51
A8_20°	31.85	H8_45°	13.47

4 VALIDATION OF THE YIELD DESIGN APPROACH

In this section, only results of slabs 0° are used to validate an approach based on the yield design theory (see [3] for more details).

4.1 A yield design approach

The failure bending moment load could be predicted from solving the following yield design problem on a reinforced concrete slab.

According to the yield design reasoning [4-6], the potentially safe bending moment M of a reinforced concrete section is defined as the moment which can be equilibrated by a stress distribution in the slab (stress tensor fields in the concrete, tensile force distributions along the reinforcements), verifying the respective strength conditions of concrete and steel at any point of the slab.

Considering a thermal gradient over the slab thickness, the following uniaxial stress distribution in the concrete material, along with axial force in the reinforcement, shown in Figure 7 are considered. It simply means that both concrete and reinforcing bars reach their positive tensile (resp. negative compressive) strengths corresponding to their temperatures.

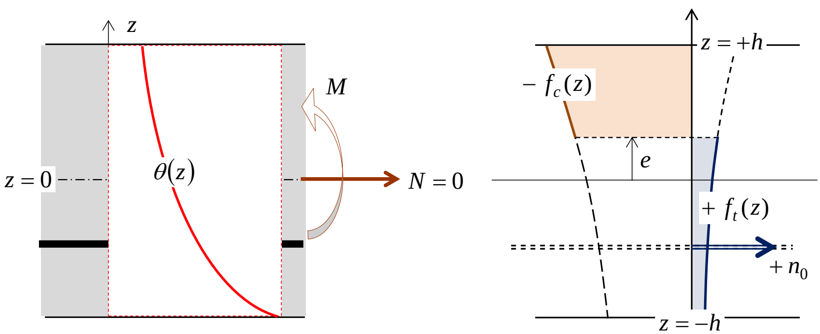

Figure 7. Stress profiles in the slabs used in the lower bound static approach of yield design.

The corresponding value of the loading parameter in equilibrium with such stress distributions may be easily calculated, leading to the determination of the failure bending moment. This solution could be also confirmed from implementing the upper bound kinematic approach of yield design, thus determining the exact failure load.

4.2 Comparison of experimental failure loads with those predicted by the yield design approach

The theoretical results are now compared with the test experimental results obtained in the campaign presented above. Performing such comparisons first requires clarifying the question of the concrete material tensile strength: can it be still considered as non-zero after the occurrence of cracking, notably due to fire-induced temperature increase? In fact, the brittleness of concrete failure suggests that it drops to zero as soon as its tensile strength is reached. Such a complete loss of tensile strength will therefore be assumed in the yield design approach.

The thermal gradients over the slab thickness are obtained from the temperatures recorded in Table 2. However, since the evolution of material strength properties with temperatures were not directly measured in this work, temperature dependence allowing for the decrease of characteristic strength of concrete and steel materials are referred to Eurocode 2- Part 1-2 [7].

Considering the test configuration which is symmetric, the bending moment is maximal at mid-span. The corresponding value may be approximately estimated as the sum of two components relating to the applied load and the slab self-weight. The applied load is obtained from the direct measurement. Note that the load is applied to the specimen by means of two rollers of the upper support, which itself weighs 50kg. So the real applied force on the slabs will be the sum of the measured force and the weight of this upper support.

Having measured the weight of all slabs and of the maximum force, results of both experimental and theoretical predictions are reported in Table 4. A fairly good agreement between them can be observed, expressed through the ratio of the maximum bending moments, which remains close to 1.

Table 4. Comparison of predicted maximum bending moments with results of tests.

Specimen	Self-weight (kg)	Self-weight of upper support (kg)	F (kN)	Pick of M_{test} (kN.m/m)	Pick of M_{pred} (kN.m/m)	M_{pred} / M_{test}
A1_0°	122	50	37.00	7.015	7.300	1.04
A4_0°	127	50	43.56	8.223	7.672	0.93
A7_0°	128	50	40.51	7.665	7.672	1.00
H1_0°	120	50	14.19	2.831	2.516	0.89
H2_0°	119	50	14.88	2.956	2.899	0.98
H6_0°	125	50	20.96	4.078	3.170	0.78

The agreement seems to be better for the tests performed at ambient temperature than for to those at high temperatures. For the test A4, the yield design approach underestimates the bearing capacity. This may be due to the fact that no tensile strength of the concrete was taken into account in the theoretical analysis. This influence has been seen in testing the slab A7 where a unloading-loading cycle was performed. In this case, a better correlation was obtained. Similarly, the calculations also underestimate the load bearing capacity of the specimens in fire. This is, perhaps, due to the fact that the tensile strength of concrete has not been taken into account and the coefficients adopted for reducing the strength resistances of concrete and steel are those from Eurocode 2 Part 1-2 [7] which provides recommended conservative design values.

5 CONCLUSIONS

The purpose of this experimental study was to investigate the influence of temperature increase on the reinforced concrete strength properties associated with different loading conditions and reinforcement schemes. The paper has provided the detailed description of the experimental program and results in both ambient and elevated temperature conditions. The results show a decrease of the load bearing capacity and stiffness in fire conditions, as a function of the reinforcement orientation. For the slabs reinforced by steel bars arranged along the longitudinal and orthogonal axes of the specimen, comparisons have also been made on the failure load predicted by a yield design approach in which particular importance is attributed to the degradation of material properties under fire-induced thermal loading. Other data presented here can be used to further validate numerical models as well as simple design methods.

REFERENCES

[1] Mindeguia J. C., *Contribution expérimentale à la compréhension des risques d'instabilité thermique des bétons*, Ecole doctorale des sciences exactes et de leurs applications, Université de Pau et des Pays de l'Adour, 2009.

[2] EN1991-1-2. Eurocode 1: Actions on structures-Part 1-2: General actions-Actions on structures exposed to fire, 2002.

[3] Pham D. T., de Buhan P., Florence C., and Nguyen H. H., "Analytical interaction diagrams for reinforced concrete sections in fire conditions", *Conference and Exhibition on Fire Science and Engineering - Proceedings of the Thirteenth International Conference*, Interscience Communications Ltd, London, 1095-1105, 2013.

[4] Salençon J., *Calcul à la rupture et analyse limite*, Presses de l'Ecole Nationale des Ponts et Chaussées, Paris, 1983.

[5] Salençon J., *Yield design*, ISTE Ltd and John Wiley and Sons, Inc, Great Britain and the United States, 2013.

[6] de Buhan P., *Plasticité et calcul à la rupture*, Presses de l'Ecole Nationale des Ponts et Chaussées, Paris, 2007.

[7] EN1992-1-2. Eurocode 2: Design of concrete structures-Part 1-2: General rules-Structural fire design, 2004.

8th International Conference on Structures in Fire
Guo-Qiang LI, Venkatesh K. R. KODUR, Shou-Chao JIANG, Jian JIANG, Su-Wen CHEN, Guo-Biao LOU (Eds.)
Shanghai, China, June 11-13, 2014

YIELD DESIGN-BASED ANALYSIS OF HIGH RISE CONCRETE WALLS SUBJECTED TO FIRE LOADING CONDITIONS

Duc Toan Pham*, Patrick de Buhan, Céline Florence*, Jean Vivien Heck* and Hong Hai Nguyen***

* Université Paris-Est, Centre Scientifique et Technique du Bâtiment (CSTB), 84 avenue Jean Jaurès, Champs-sur-Marne, 77447 Marne-la-Vallée Cedex 2, France
e-mail: ductoan.pham@cstb.fr

** Université Paris-Est, Laboratoire Navier (Ecole des Ponts ParisTech, IFSTTAR, CNRS UMR 8205), 6-8 avenue Blaise Pascal, Cité Descartes, Champs-sur-Marne, 77455 Marne-la-Vallée Cedex 2, France
e-mail: patrick.debuhan@enpc.fr

Keywords: High rise wall, Reinforced concrete, Fire loading, Yield design approach

Abstract. *Relying on a simplified illustrative model, a yield design-based approach is developed for analysing the stability of high rise walls (that are larger than the dimensions of experimental test furnaces) under fire conditions. The implementation of the method combines two original features: first, the preliminary determination of interaction diagrams reflecting the local decrease in strength of the wall due to thermal loading; second, the thermal-induced geometry changes which are explicitly accounted for in the overall failure design of the wall. Application of the approach is illustrated in either evaluating the fire resistance of a wall with a given height or predicting the maximum height that the wall could reach for a fire exposure time.*

1 INTRODUCTION

With a potential increasing use in industrial buildings, high rise concrete walls are reinforced concrete structures for which the analysis of fire behaviour requires a more sophisticated approach than for conventional structures. Due to the thermal-induced deformations, such structures exhibit important out-of-plane (horizontal) displacements, which in turn induce eccentricity of the gravity forces (self-weight) with respect to the initial plane. As a consequence, bending moments are generated in the wall in addition to the axial force, which is usually known as a second order (or P-delta) effect. As the eccentricity increases, the moment due to self-weight eccentricity also increases, thus subjecting the wall to higher bending moments. At the same time, elevated temperature leads to a degradation of constitutive materials. Consequently, material degradation combined with increased bending can cause the collapse of the structure.

The purpose of the present contribution is to extend the yield design approach [1-2] in order to analyse the global stability of high rise walls. This contribution will demonstrate how it is possible to combine the global deformed configuration analysis with that of the local cross-sectional degradation. Unlike most of the classical approaches which are based on conventional limitations concerning the strains experienced by the concrete material and reinforcing steel, the yield design approach, as applicable to various problems in the field of civil engineering [2], only requires that stress (and not strain) limitations be prescribed to the constituent materials in the form of a strength or failure criterion, with no reference to other mechanical characteristics, such as the deformability properties. To put it simply, this theory is fundamentally based on verifying the compatibility between static equilibrium of a structure subjected to given loading conditions and strength requirements expressed through the materials failure criteria, without it being necessary to resort to tedious and sophisticated incremental computations. This approach is also selected for several reasons, among which its ability to provide closed form expressions, allowing to perform parametric studies involving various geometries and loading configurations, and thus avoiding numerical problems.

2 FIRE RESISTANCE EVALUATION PROCESS

The problem under consideration amounts to investigate the stability in fire conditions of a reinforced concrete wall whose height is larger than width and vertical boundary conditions are sufficiently flexible so that the analysis of the wall could be simplified to that of a simple beam. The wall is uniformly subjected to fire on one side as well as to its self-weight. Following the standard temperature versus time histories advocated by design codes [3] for modelling the action of a fire on a structure, a heat transfer analysis may be firstly carried out on the wall. In the case of simple wall member such as that considered here, one-dimensional heat propagation across the wall thickness suggests that the field of temperature increase resulting from such a thermal loading will depend on the thickness-coordinate only.

Given any such profile of temperature increase, the approach consists of three main steps:

- Step n°1: *determination of local solicitations*. This phase consists in evaluating the deformed shape of the wall under the combined actions of a thermal gradient and the wall self-weight, then to calculate the resulting local solicitations in each section.
- Step n°2: *determination of temperature dependent interaction diagrams*. The objective of this phase is to determine the normal force and bending moment failure loads of a heated wall cross-section.
- Step n°3: *stability analysis of the wall in its deformed configuration*.

2.1 Step n°1: determination of local solicitations

Adopting a simplified model, the reinforced concrete wall is illustratively and schematically described as a vertical beam of height *H*, initially straight and articulated at both ends as sketched in Figure 1. The wall is subjected to its self-weight characterized by a constant linear density *w* and a uniform temperature gradient $\theta(y)$ along its height, resulting in a constant curvature and then to a preliminary deformed shape of equation:

$$u_\theta(x) = x(x-H)/2\rho_\theta \tag{1}$$

where ρ_θ is the radius of curvature, rotations being assumed to be small enough at any point of the wall. This thermal-induced change of geometry induces an out-of-plane eccentricity of the self-weight and then additional elastic bending deformations, so that the new deformed shape, characterized by the distribution of horizontal displacement $u(x)$, satisfies the differential equation:

$$\left(u(x) - u_\theta(x)\right)'' = M(x)/(EI)_\theta \tag{2}$$

with boundary conditions corresponding to simple supports at both ends:

$$u(x=0) = u''(x=0) = u(x=H) = u''(x=H) = 0 \tag{3}$$

where $(EI)_\theta$ is the flexural rigidity corresponding to a profile of temperature, considered as constant along the entire height of the wall.

On account of the new deformed shape, the distribution of compression forces and bending moments along the wall height can be written as:

$$\begin{aligned} N(x) &= w(x-H) \\ M(x) &= -wHu(x) + \left[\frac{w}{H}\int_0^H u(x)dx\right]x - w\int_0^x [u(s)-u(x)]\,\mathrm{d}s \end{aligned} \tag{4}$$

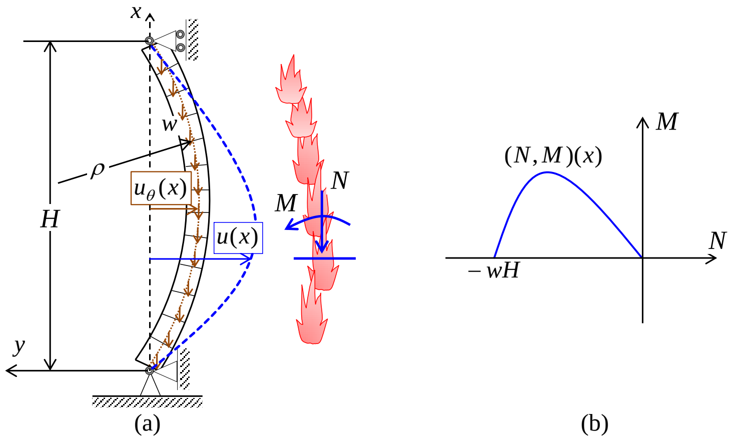

Figure 1. (a) Schematic of deformed shapes of the wall and (b) Distribution solicitations curve.

As seen from Equation (4), the expression of the bending moment involves complex integrals. Combining and deriving with respect to x both Equation (2) and Equation (4), a third order differential equation could be obtained:

$$u'''(x)+\frac{w}{(EI)_\theta}(H-x)u'(x)=c \tag{5}$$

where c is a constant to be determined. Following [4] a linear change of variable:

$$x=\left(\frac{(EI)_\theta}{w}\right)^{1/3}X+H \tag{6}$$

could be made in order to simplify the coefficient of the term containing $u'(x)$ in Eqation (4), so that Equation (4) can be converted into a more convenient form:

$$u'''(X)-Xu'(X)=\left(\frac{(EI)_\theta}{w}\right)c \tag{7}$$

Taking advantage of special functions represented by generalized hypergeometric series, one may write:

$$_pF_q(a_1,\cdots,a_p;b_1,\cdots,b_q;X)=\sum_{k=0}^{\infty}d_kX^k \tag{8}$$

where $d_0=1$ and $\frac{d_{k+1}}{d_k}=\frac{(k+a_1)(k+a_2)\cdots(k+a_p)}{(k+b_1)(k+b_2)\cdots(k+b_q)}\frac{1}{k+1}$, so that the following general closed-form solution for Equation (7) may be found:

$$u(X)=c_1X\left[{}_1F_2\left(\frac{1}{3};\frac{2}{3},\frac{4}{3};\frac{X^3}{9}\right)\right]+c_2\frac{X^2}{2}\left[{}_1F_2\left(\frac{2}{3};\frac{4}{3},\frac{5}{3};\frac{X^3}{9}\right)\right]+c_3\frac{X^3}{3}\left[{}_2F_3\left(1,1;\frac{4}{3},\frac{5}{3},2;\frac{X^3}{9}\right)\right]+c_4 \tag{9}$$

where c_i, i=1 to 4 are four constants that could be determined from the boundary conditions (3) modified for the new variable. As a result, it is possible to calculate the final deformed shape and in turn, derive the normal force and bending moment in each section. The corresponding solicitations curve can be drawn in the (N,M)-plane, as shown in Figure 1(b).

2.2 Step n°2: determination of temperature dependent interaction diagrams

Referring to an orthonormal frame $Oxyz$ (Figure 2), the interaction diagrams are determined from the solution of a yield design problem defined on a reinforced concrete beam modelled as a square parallelepiped of thickness $2h$ along the Oy-axis, and sides conventionally taken equal to unity along the Ox and Oz-axes (see [5] for more details). It is made of a homogeneous concrete material obeying the Mohr-Coulomb strength condition and reinforced by longitudinal steel bars placed along the Ox-direction. Such a reinforced concrete beam is subjected to mechanical loading conditions defined as follows.

- Body forces (weight) are neglected.
- The left hand section (x=0) is in smooth contact with a fixed vertical punch, while the right hand section (x=1) is in smooth contact with a rigid punch in horizontal translation of velocity $\dot{\delta}$ at mid height (y=0) and rotation of angular velocity $\dot{\alpha}$ about the z-axis.
- The remaining horizontal (y=±h) and vertical sides are stress free.

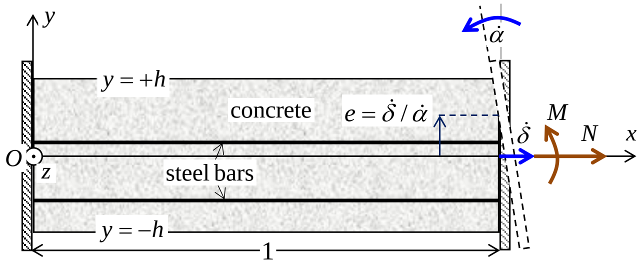

Figure 2. Reinforced concrete beam subjected to axial force and bending moment.

Considering any kinematically admissible (K.A.) velocity field $\underline{U}$, defined as complying with the velocity boundary conditions depending on $\dot{\delta}$ and $\dot{\alpha}$, the work of the external forces in any such field, may be put in the following form:

$$W_e(\underline{U}) = N\dot{\delta} + M\dot{\alpha} \tag{10}$$

where N and M may be interpreted as the axial force along Ox and bending moment about Oz exerted on the right hand side of the beam, which is thus subjected to a two-parameter loading mode.

According to the yield design reasoning [1-2], the so-called domain K of potentially safe loads (N,M), is defined as the set of loads which can be equilibrated by a stress distribution in the beam (stress tensor fields in the concrete, tensile force distributions along the reinforcements), verifying the respective strength conditions of concrete and steel at any point of the beam. The boundary of this domain, locus of the extreme or failure loads, is called the *interaction diagram* of the reinforced concrete beam subjected to combined axial and bending loadings.

What about thermal loading? Apart from deteriorating the material properties of the reinforced concrete components, fire loading conditions induce important modifications of the initial state of the structure from generating for instance thermo-mechanical stresses. It should be pointed out however, that such stress fields are self-equilibrated, and have therefore no influence on the values of the limit loads, which is in the present case, the interaction diagram. Indeed, it is a well-known result of associated elasto-plasticity theorems and related limit analysis (see for instance [2]), that limit loads are insensitive to the elastic characteristics, loading path followed to reach them or initial state of stress of the structure, due for instance to previous thermal loading. As a consequence, the sole influence to be expected from fire loading on the interaction diagram of the reinforced concrete beam section should be attributed to the degradation of the concrete and steel strength.

Thus, introducing the experimentally-based relationships linking the degradation of local material strength properties to the fire-induced temperature increase, the strength of concrete and reinforcement will be reduced through the introduction of non-dimensional multiplicative factors:

$$f_t(y) = k_t(\theta(y))\, f_t \quad ; \quad f_c(y) = k_c(\theta(y))\, f_c \quad \text{and} \quad n_0(y) = k_s(\theta(y))\, f_y A_s \tag{11}$$

where k_t, k_c and k_s are decreasing functions of the temperature increase θ, equal to one for θ=20 °C (ambient temperature), while n_0 represents the tensile-compressive resistance of the reinforcing bar, equal to the product of the constituent material (steel) uniaxial strength f_y by its cross sectional area A_s.

Given any value e, comprised between $-h$ and $+h$, the two following uniaxial stress fields in the concrete material, along with axial forces in the reinforcements are considered (see Fig. 3). It simply means that in configuration (*a*) both concrete and reinforcing bars reach their positive tensile (resp. negative compressive) strengths when located below (resp. above) the plane of equation $y=e$. The opposite applies in configuration (*b*).

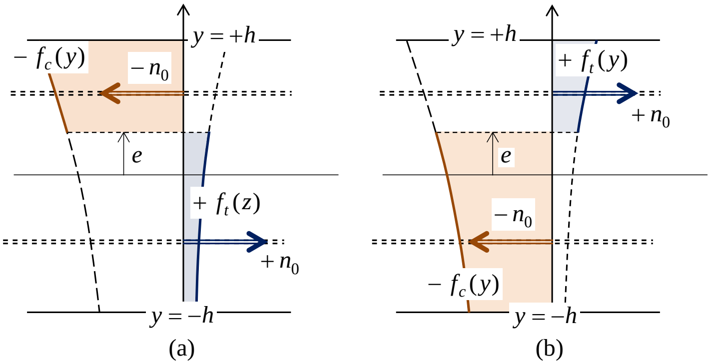

Figure 3. Stress profiles in the cross-section used in the lower bound static approach of yield design.

It can be immediately seen that those stress distributions obviously comply with the respective strength conditions of the concrete material and steel reinforcing bars. Besides, they satisfy the equilibrium equations in the absence of body forces, while the discontinuity of stress when crossing the $y=e$ plane remains admissible. The corresponding values of the loading parameters in equilibrium with such stress distributions may be easily calculated, leading to the determination of a failure surface in the (N,M)-plane, that is the interaction diagram.

This solution could be confirmed from implementing the upper bound kinematic approach of yield design. It thus describes the exact failure curve (interaction diagram) in the (N,M)-plane. It should be emphasized that the solution thus obtained has also been favourably compared with Eurocode-based predictions in the case of ambient temperature, as well as with available experimental results [5].

2.3 Step n°3: stability analysis of the wall in its deformed configuration

On account of the previously determined local solicitations along the wall determined from step n°1 and strength capacities (interaction diagram) of the heated cross-section calculated in step n°2, the process could be now completed. For evaluating the stability of the structure, the combined bending moments-axial forces distributions resulting from the equilibrium of the wall in its deformed shape, should be compared with the (N,M) interaction diagram modified by the applied thermal loading. More precisely, for a given height and a given fire exposure time, the stability of a wall is ensured as far as the curve representing the solicitation distribution along the wall height remains entirely inside the strength domain delimited by the interaction diagram in the (N,M)-plane. Collapse occurs at a section where the curve of solicitation distribution becomes tangent to the interaction diagram as shown in Figure 4.

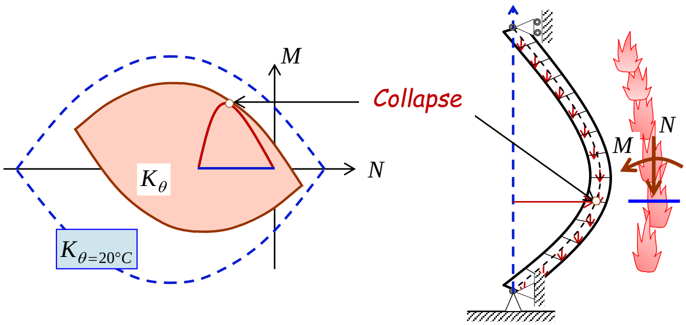

Figure 4. Stability analysis of the wall in its deformed configuration.

It should be noted that the failure of one section, as considered in this approach, implies the complete failure of the entire wall. This is due to the fact that the considered beam structure is statically determinate, the first yield point and ultimate limit load being coincident.

For illustrative purpose, the approach will be now implemented on the problem stated above. The following example may help clarify the effect of high temperature increase on the stability of such slender structures in two different ways: the degradation of the wall strength capacities expressed through the reduced interaction diagram on the one hand, the thermal-induced out-of-plane change of geometry of the wall which will generate bending moments in addition to compressive loads on the other hand.

2.4 Implementing the method on an illustrative example

Assuming that the wall is exposed to an ISO 834 fire [3] on its right hand side with different time durations (60, 90 and 120min), the following set of data has been selected:

- Rectangular cross-section $0.15\times 1\,\mathrm{m}^2$.
- Normal weight concrete with siliceous aggregates, f_c=32MPa, f_t=2.5MPa.
- Two layers of hot rolled reinforcing steel of 10 bars of diameter 6mm with 3cm of concrete cover at top and bottom, f_y=500MPa.
- The characteristic strengths of materials are considered to be temperature dependent referring to Eurocode 2-Part 1-2 [6].
- Self-weight of constant density w=3.5kN/m.
- Thermal radii of ρ_{60}=31m, ρ_{90}=24m and ρ_{120}=20m corresponding to 60, 90 and 120min of fire exposure, and corresponding flexural rigidities of $(EI)_{60}$=2.69MNm^2, $(EI)_{90}$=2.21MNm^2 and $(EI)_{120}$=1.92MNm^2.

A preliminary heat transfer analysis aimed at evaluating the temperature increase distribution across the wall thickness should be first conducted. Figure 5(a) shows the temperature profiles across the thickness obtained for instance by the SAFIR computer program [7]. Introducing these thermal gradients into the above described calculation procedure, the corresponding interaction diagrams could be determined as shown in Figure 5(b).

It thus clearly appears that temperature increase affects the strength properties of the reinforced concrete section, in the form of a quite significant reduction of the strength domain. The fire loading leads to an increase of temperature (Figure 5(a)), resulting in a decrease of material strength parameters and finally to a shrinkage of the interaction diagram (Figure 5(b)), and thus to a much smaller global resistance of the reinforced concrete wall.

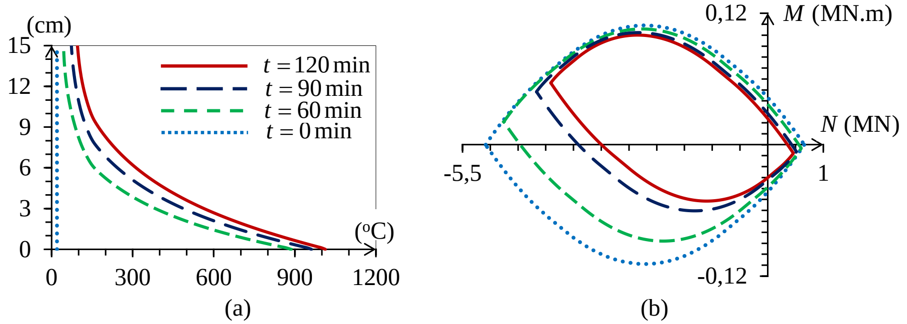

Figure 5. Temperature distributions across the wall thickness and interaction diagrams for different fire exposures.

Focussing on a given fire exposure, for example 120min, the interaction diagram remains constant, while the solicitation curves proportionally increase with the heights examined.

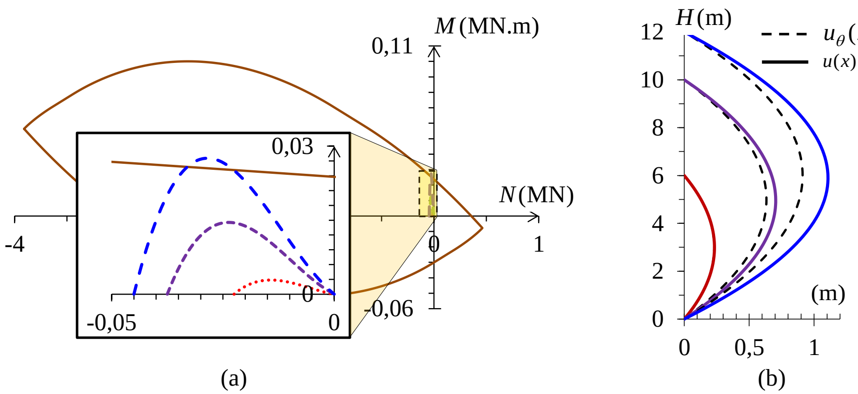

Figure 6. Stability condition of various walls exposed to fire for 120min.

The change in deformed shape of various walls (6m, 10m and 12m) is shown in Figure 6(b). It appears that the horizontal out-of-plane displacement due to thermal loading is strongly increasing with the height of the wall. For the 6m-high wall, the additional horizontal displacement due to self-weight is negligible, while for the 10m and 12m-high walls, the response is quite different since the additional displacements due to self-weight are much more pronounced. The higher the wall, the larger is the relative difference between the thermal deformed shape and the total deformed shape. Such a second order effect does not influence the fire behaviour for normal height walls, but becomes quite significant for high rise walls. This point is further illustrated in Figure 6(a), where the region of the (N,M)-plane close to the origin has been magnified. It may be observed from this figure that the solicitation curve intersects the interaction diagram as soon as the wall becomes higher than 12m. More precisely, it may be shown that collapse occurs for a wall of about 11.4m-high.

For a wall higher than 12m, say 13m, the minimum fire duration for which its collapse is triggered can also be estimated from the above described procedure.

As mentioned earlier, fire loading of the wall leads to shrinkage of the interaction diagram on the one hand, increase of solicitation in each section, due to the change of geometry, on the other hand, so that failure occurs when the two corresponding curves come into contact. The present results, shown in Figure 7, indicate that the wall of height 13m will not resist more than 90min in fire, the critical section being located at a height of about 5m.

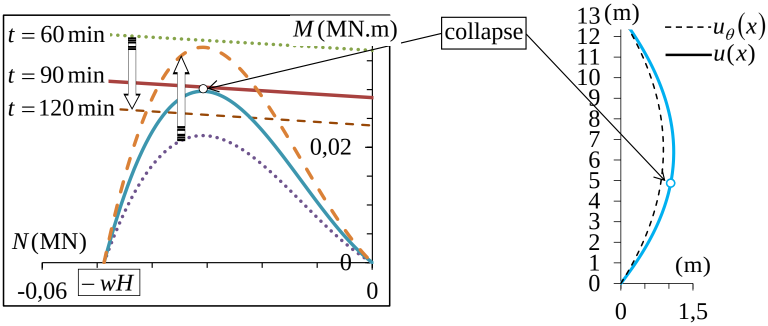

Figure 7. Yield design-based analysis of the 13m-high wall.

3 CONCLUSIONS

Relying on some simplified assumptions, this paper proposes a comprehensive and consistent approach for evaluating the fire resistance of high rise concrete walls. The method is based on the yield design theory at two stages. First as regards the determination of the strength criterion expressed in the form of an interaction diagram parameterized by the thermal loading, then as concerns the analysis of the load-bearing capacity of the wall in its fire-induced deformed configuration. This contribution features important advantages which favour simplicity for the user. It allows performing parametric studies without it being necessary to resort to complex numerical simulations.

The procedure has been implemented on examples illustrating each step of the evaluation process, making it possible to highlight both fire effects on the individual members' strength properties and second order effects due to thermal-induced geometry changes. With regard to the thermal aspect, the calculation could be generalized to non-uniform temperature distributions due to the fact that the wall is not fully exposed to fire. Moreover, the application of this method should be extended to high rise walls modelled as two dimensional plates and not just one dimensional beams as in the present simplified analysis.

REFERENCES

[1] Salençon J., *Calcul à la rupture et analyse limite*, Presses de l'Ecole Nationale des Ponts et Chaussées, Paris, 1983.

[2] de Buhan P., *Plasticité et calcul à la rupture*, Presses de l'Ecole Nationale des Ponts et Chaussées, Paris, 2007.

[3] EN1991-1-2. Eurocode 1: Actions on structures-Part 1-2: General actions-Actions on structures exposed to fire, 2002.

[4] Sampaio Jr. J. H. B., and Hundhausen J.R., "A mathematical model and analytical solution for buckling of inclined beam-columns", *Applied Mathematical Modelling*, 22, 405-421, 1998.

[5] Pham D. T., de Buhan P., Florence C., and Nguyen H. H., "Analytical interaction diagrams for reinforced concrete sections in fire conditions", *Conference and Exhibition on Fire Science and Engineering-Proceedings of the Thirteenth International Conference*, Interscience Communications Ltd, London, 1095-1105, 2013.

[6] EN1992-1-2. Eurocode 2: Design of concrete structures-Part 1-2: General rules-Structural fire design, 2004.

[7] Franssen J. M., "SAFIR: A thermal/structural program for modeling structures under fire", *Engineering Journal*, 42, 143-158, 2005.

INFLUENCE OF DUCTILITY ON THE BEHAVIOUR OF RC FRAMES IN POST EARTHQUAKE FIRE

Asif H. Shah*, Praveen Kamath*, Umesh K. Sharma*, Pradeep Bhargava*, Asif Usmani, GR Reddy***, Tarvinder Singh*** and Hitesh Lakhani*****

* Dept. of Civil Engineering, Indian Institute of Technology, Roorkee, Roorkee- 247667, India
e-mails: shahaasifhussain@gmail.com, praveen.kamath@hotmail.com, umuksh@rediffmail.com, bhpdpfce@iitr.ernet.in

**Institute for Infrastructure and Environment, The University of Edinburgh, Edinburgh EH9 3JL, UK
e-mail: asif.usmani@ed.ac.uk

***Reactor Safety Division, Bhabha Atomic Research Centre, Trombay, Mumbai – 400094, INDIA
emails: hiteshrssred@barc.gov.in, tarvindersinghs@gmail.com, hitesh.mbm2009@gmail.com

Keywords: RC frame, Post-earthquake fire, Ductile detailing, Non-ductile detailing

Abstract. *Two full scale Reinforced Concrete frames with different reinforcement confinement levels were constructed and subjected to a simulated earthquake followed by a compartment fire. The simulated earthquake caused wider cracks and concrete spalling in the frame with non-ductile detailing. The fire damage was more pronounced also with extensive spalling due to the attainment of higher temperatures in the structural elements of RC frame with non-ductile detailing. Post fire residual strength of the non-ductile detailed frame was 65% while it was 95% in the RC frame with ductile detailing.*

1 INTRODUCTION

Structural fire testing is undergoing rejuvenation with full scale tests being performed on various structural systems. The conventional, and widely used, method for fire testing, where in single structural elements are subjected to a standard fire test[1] and the thereby obtaining a fire resistance rating which is mainly in the form of a time to failure, has of late been noticed to have a number of drawbacks[2] though the method is still widely used. The perception that the concrete structures behave well in fire has led to overly simplified design guidelines, in the form of concrete cover, even though the behaviour of structural systems in fire is proved to be quite complex due to interaction effects between different structural elements of the structural system. This simplification in design procedure was a result of standard fire tests of simple building elements or isolated structural assemblies in testing furnaces which subject the loaded elements to a standard temperature-time curve. The issues of the inherent problems, which are associated with using simplified single element based laboratory tests subjected to standard temperature-time curves, are being solved by performing large scale non standard fire tests using real fires. This shift in testing philosophy from prescriptive standard fire testing to large scale non standard fire testing using real fires has been aimed at understanding the global behaviour of structures in fire which has received relatively little attention in the past. The significance of performing the large scale tests is reflected by the lack of experimental data on the performance of complete concrete structures in fire.

Fire tests on full scale concrete structures are very uncommon and very few tests have been carried on complete structural systems. In their experimental testing, Vecchio and Sato [3] subjected three large-scale reinforced concrete portal frame models to combinations of thermal and mechanical loads under different test conditions and the results indicated that the thermal loads can result in significant stressing of a structure and can lead to concentrated damage in local regions. Full scale test on a reinforced concrete frame conducted at Cardington, UK [4] provided an insight into the structural behaviour of a heated concrete structure. Although this test suffered from instrumentation failure prior to its end rendering the dataset incomplete, a number of observations were derived from these tests. This test showed that the spalling of the floor slab was extensive and exposed the bottom steel reinforcement. Although concrete spalling considerably reduced the flexural strength of the slab, collapse did not occur which could be attributed to slab behaving in compressive membrane action. In the first of its kind, Sharma et al [5] tested a damaged reinforced concrete frame in fire. An Reinforced Concrete (RC) frame assemblage was first subjected to simulated earthquake loading which was followed by subjecting the damaged frame to a compartment fire. Massive spalling in different elements of the assemblage was observed. Even though the strength of the frame was reduced after the fire, the frame assemblage escaped the complete structural failure. The test provided a massive data in terms of temperatures, strains, displacements as recorded for the beams, columns and the roof slab.

Various parameters related to the structural performance of concrete structures subjected to elevated temperatures are being studied by the researchers' world over. In developing countries like India, most of the concrete structures have been built without ductile detailing of the reinforcement. The old buildings have been designed without confining reinforcement. The study of behaviour in fire and earthquakes of these structures with non-ductile detailing is thus very important. Thus the main aim of the present investigation is to study the influence of ductility on the behaviour of RC Frames in Post earthquake fire. In this paper, a comparison, vis- à-vis ductility, will be drawn between the behaviours of two full-scale RC Framed structures subjected to Post Earthquake fire. It is hoped that the results presented here provide the means to reduce the uncertainties associated with the behaviour of concrete structures in fire.

2 THE TEST ARRANGEMENT AND THE TEST PROCEDURE

2.1 The RC frame structures

Two RC frames were constructed and tested first against simulated seismic loading followed by subjecting the frame to one hour compartment fire. The first frame *(tested in September 2012)* was designed as a ductile frame with the ductile detailing as per the recommendations of IS: 13920-1993 [6], whereas, the second frame *(tested in November 2013)* was designed without any ductile detailing. However, minimum shear reinforcement recommendations of IS 456:2000 [7] were used in the design of the second frame. While the structural elements in both the RC frames had same dimensions, the reinforcement levels were different in the two frames. The stirrup spacing in columns of RC frame with non-ductile detailing was 200 mm throughout the height of the column and that in the columns of RC frame with ductile detailing it was 150 mm in middle half portion and 75 mm in end regions to give extra confinement. The stirrups spacing in beams was 100 mm and 200 mm in the RC frames with ductile detailing and with non ductile detailing respectively. It was also maintained that the hooks of the stirrups in the ductile detailed frame were bent at 135^o while in the non-ductile detailed frame the hooks were bent at 90^o. Both the Frames had the plan and elevation of symmetrical G+3-storeyed RC framed building from which, a sub-assemblage of a single frame was constructed for testing as shown in figure 1. The test frames consisted of four columns (300 mm × 300 mm), four plinth beams (230 mm × 230 mm), four roof beams (230 mm × 230 mm) and a roof slab (120 mm thick). All the elements of the test frame were cast monolithically with the column fixedity at the base being provided by the termination of all the four columns into a 900 mm thick RC raft foundation of plan size 6900 mm × 8700 mm. Equivalent gravity load, the wall load and the live load on the roof slab were imposed as per the recommendations of the Indian seismic design code, IS 1893 (Part-1):2002 [8]. An M30 concrete was designed, and utilized for the construction of the RC frames. The aggregates used were locally available crushed stone aggregates of nominal size of 20 mm and 12.5 mm.

2.2 Instrumentation

Data recorded for the structural aspects consisted of temperatures within the roof slab, columns, beams, and the compartment ; strains on the rebars embedded in all the structural elements of the RC frames; deflections of the roof slab at different points both vertical as well as horizontal. Extensive instrumentation was planned for both the test frames and a number of sensors were installed in these frames to record the data. The temperature measurement was taken by means of thermocouples embedded in concrete at a number of points and at different levels. A total of 314 thermocouples were utilized for the measurement of the temperatures. The stains were recorded by pasting strain gauges on the steel rebars at different locations in the RC frames. For the measurement of strains during the different phases of the experimental testing 80 strain gauges were pasted at different locations of the frame on the steel rebars. An array of displacement transducers were used to record the deflection of roof slab during the earthquake and the fire loading. The horizontal displacement of the beams and the roof slab was also recorded using the displacement transducers mounted on a secondary steel frame which was independent of the RC test frames. All the sensors were connected to a data logger in a specially designed control room where from the data was stored in a number of personal computers.

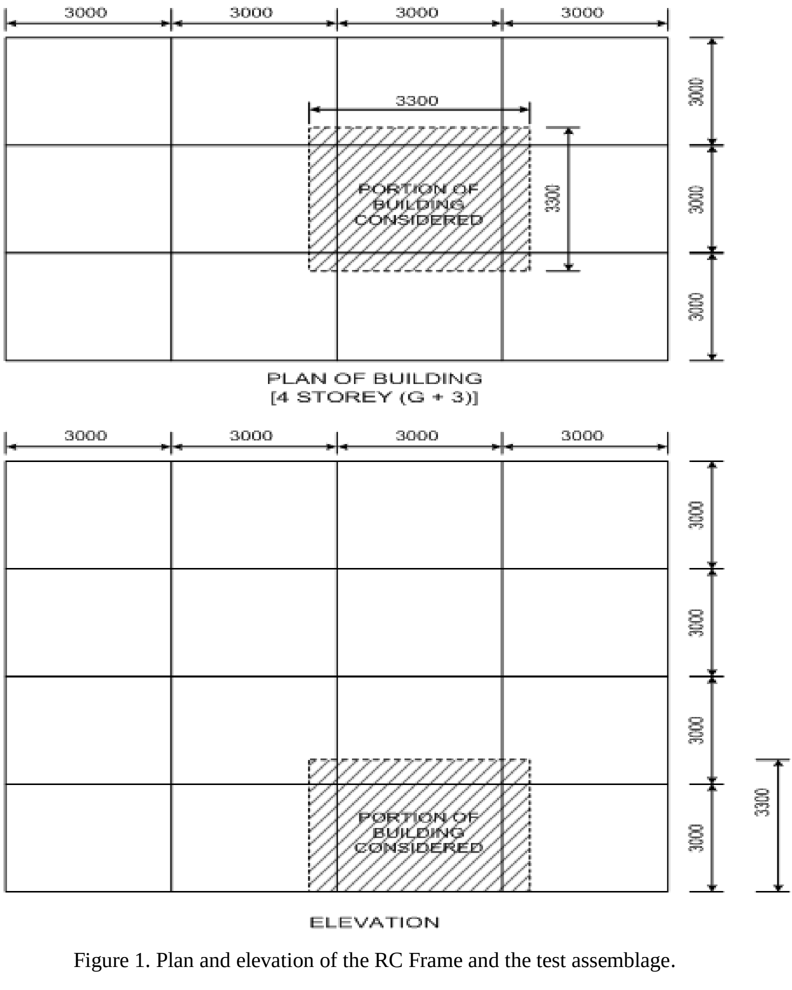

Figure 1. Plan and elevation of the RC Frame and the test assemblage.

2.3 Test procedure

A three phase test procedure was adopted and followed in testing both the RC frames which consisted of subjecting the frames to a simulated cyclic lateral load in a quasi-static fashion followed by a one hour compartment fire and then each frame was subjected to a residual load test. The simulated cyclic lateral load was applied onto the RC frames using two double acting hydraulic actuators acting in tandem with each other against a strong reaction wall. The main aim of the mechanical loading was to induce a damage corresponding to the collapse prevention (S5) performance level as prescribed by FEMA 356:2000 [9]. The damage level was ensured by subjecting the RC frames to a maximum roof level lateral displacement of 150 mm corresponding to a roof drift ratio of 4 % as given in [9]. At the outset of the tests both the frames were subjected to a number of push pull cycles during which the displacements and the strains were recorded into the computer.

Following the simulated lateral seismic load test, the RC frames were subjected to a full scale fire test wherein a designed compartment fire was developed using kerosene as the fire load. The fire load was kept same in both the frames with the peak burning rate of 0.117 $kg/m^2/s$ corresponding to a peak fuel flow rate of 1.43×10^{-4} m^3/s which was maintained using a fixed head. This was done in order to attain a gas temperature of about 1000 ℃ within 5 minutes after ignition to simulate a realistic compartment fire [5]. The compartmentalization to the RC test frames was provided by assembling together four fire proof panels around the frames. These panels were provided with a thick layer of ceramic wool inside to as to ensure that the heat loss doesn't take place across the panels. Ventilation to the fire compartment was ensured by providing a window of 1 m × 3 m along one of the faces of the RC frames. Both the frames were put to fire and the data in terms of temperatures, strains; displacements were recorded in a computer via a data logger, besides other important observations were noted down during the course of fire. The fire test continued for one hour duration and thereafter the oil supply to the tray was cut off and the data was taken for 36 hours to take all the temperatures in heating and the cooling regimes.

After exposing the RC frames to compartment fire, the fire panels were removed and the RC frames were again tested under simulated lateral seismic load for measuring the residual lateral load capacities of the frames. After each testing phase of the experimental programme Non destructive tests (NDT) were also performed on the frame at the various stages of test program. The aim of these in-situ tests was to detect and quantify the damage in various structural elements of frame after each stage of loading.

3 RESULTS

3.1 The mechanical behaviour

Figures 2 (a) and (b) show the load-displacement hysteresis as obtained from the loading cycles of ductile frame and non-ductile frame respectively. The load corresponding to the maximum displacement of 150 mm in ductile frame was 400 kN while as in non-ductile frame the load corresponding to the maximum deflection of 150 mm was measured to be 319 kN.

In the frame with ductile detailing, the nucleation and propagation of cracks did not initiate up to 20 mm displacement cycles. Cracks on columns and beams initiated during 20 mm and 30 mm push cycles respectively. Mostly the cracks were initiated on the planes perpendicular to the loading direction and these cracks further propagated in the subsequent cycles. Numerous numbers of fine cracks were observed in the RC frame with the crack widths in different members varying from 0.1 mm to 2.4 mm with no spalling at the joints as in Figure 3 (a). At the end of the mechanical loading the residual plastic displacement of 19 mm was recorded upon unloading in the RC frame with ductile detailing.

The RC frame with non-ductile detailing showed the signs of cracking from the initial 10 mm cycle with the cracks getting wider with each successive loading cycle. Cracks were mostly localized with wider cracks at the ends of beam column joints. At the end of 50 mm cycle, cracks as wider as .4 mm were observed on the columns. After 80 mm cycle a number of diagonal shear cracks started forming at the ends of plinth and top beams, with these shear cracks running into the slab offsets. With the start of 100 mm cycles the cracking noise was quite audible and the spalling of cover concrete started at the beam

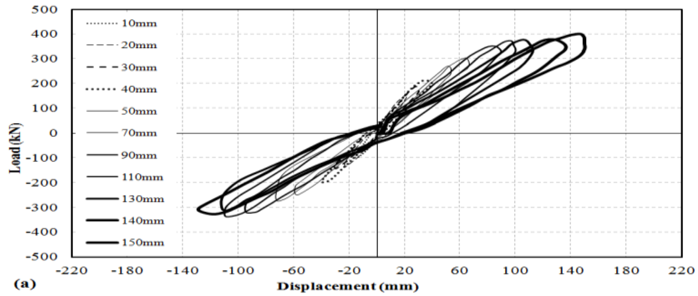

Figure 2. (a) Load-Displacement hysteresis for RC frame with Ductile detailing.

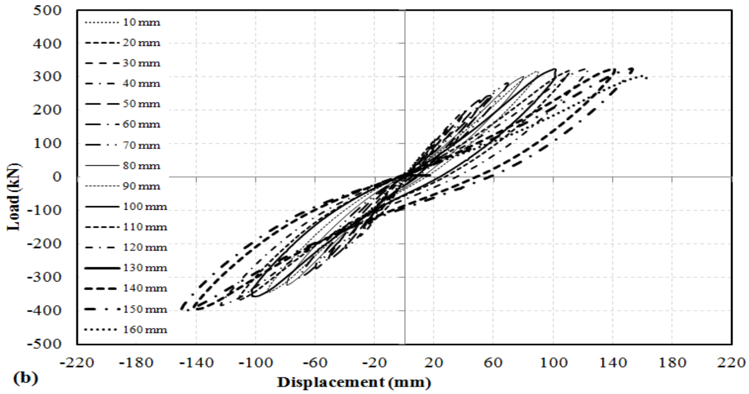

Figure 2. (b) Load-Displacement hysteresis for RC frame with Non-ductile detailing.

olumn joints. The cracks in the beams started running into slabs near top beams, symptomatic of composite action between the RC slab of the test frame and the roof beams. Cracks with a width of 4 mm started appearing in beams near joints. Extensive spalling was observed in the top beams in the direction of loading. A spall volume of 230 mm × 60 mm × 16 mm was registered at one of the beam column joints with the resulting exposure of underlying rebars. In one of the top beams all the three bars at the beam column joint buckled between the shear stirrups as in Figure 3 (b). At the end of mechanical loading it was seen that the number of fine cracks the as less in the RC frame with non-ductile detailing with more number of wider cracks than in the frame with ductile detailing. A plastic residual displacement of 41 mm was recorded after unloading in the RC frame with non-ductile detailing.

3.2 The fire behaviour

Figures 4 (a) and (b) depict the compartment time-temperature history at one of the key locations of the RC frames with ductile detailing and non-ductile detailing respectively. The temperature history shows a 18 hour log with a complete heating and cooling cycle. The maximum temperature recorded during the course of fire was 1370 °C in RC frame with ductile detailing and 1369 °C in RC frame with non-ductile detailing. Though the uniformity of maximum compartment temperature should not be mistakenly taken as uniformity in the exposure levels for different structural elements as the fire dynamics is dependent on a number of factors which cannot be controlled during fire at such a large scale e.g. the direction of wind blowing at the time of test, the exposure levels in the different elements of the RC frames was different. It was seen that owing to the extensive cracking in the RC frame with non-ductile detailing, the temperature rise in its structural elements was rapid as compared to the ductile frame.

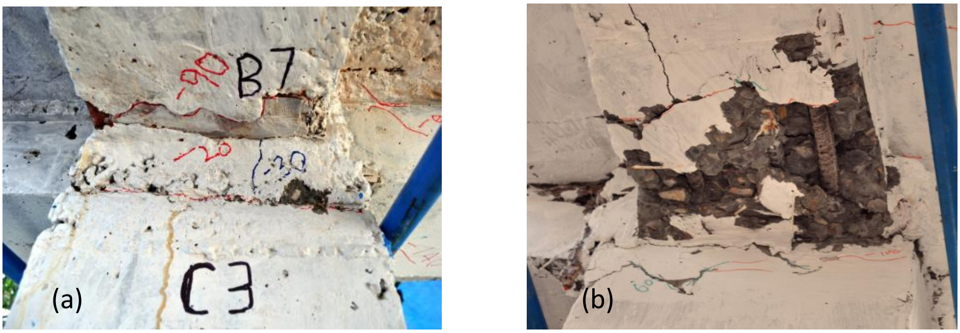

Figure 3. Beam column joint after seismic loading in RC frame with (a) Ductile detailing and (b) Non-ductile detailing..

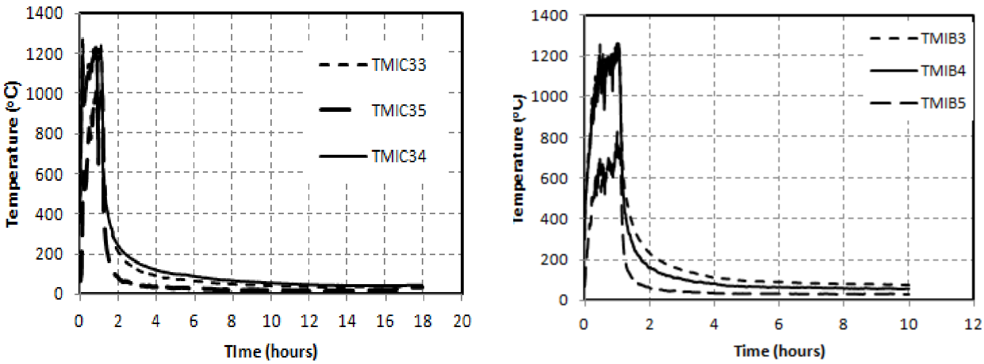

Figure 4. Temperature profile in (a) Non Ductile Frame (b) Ductile frame.

In the RC frame with non-ductile detailing spalling was observed in all the structural elements with massive spalling in the slab. During the course of fire it was seen that the slab started to spall within 4 minutes of the fire with intense bullet shot sound like noise heard at 5 minutes. The spalling was intense at 6 minutes which corresponded to a slab temperature of 300°C. Post fire inspection of the structure revealed the damage in various structural elements. As seen in Figure 5 (a), slab spalled extensively, attributed to high temperature gradients across the slab cross section, with most of the cover concrete lost exposing the reinforcement. At some sections the reinforcement cross section was reduced by melting of the steel. Sintering of aggregate was also seen in most of the slab area. A maximum temperature of 845 °C was recorded in the slab section near column 1 of the RC frame with Non-ductile detailing while a temperature of about 450 °C was recorded at the point in RC frame with ductile detailing. Figure 5(b) shows the post fire picture of the roof slab of RC frame with ductile detailing. This high temperature build up in the non-ductile detailed RC frame can be attributed to extensive wide cracks developed during the seismic load test. Figure 6 (a) shows the variation of temperature with time in a slab cross section near column 1 of both the RC frames. It can be seen that the temperatures at a given time at a given depth at a slab section is higher in RC frame with non ductile detailing (NDTSC1D1-D3) than those in RC frame with ductile detailing (DTSC1D1-D3). This can attributed to higher amount of damage in the RC frame with Non-ductile detailing. A number of LVDT's were instrumented to measure the deflection of the slab during both the tests, however the slab LVDT's in the first test malfunctioned during the fire tests and the displacements could not be measured. Figure 6 (b) shows the vertical slab deflections. The peak deflection at the centre of the slab was around 21 mm, which recovered to 10 mm on cooling. Since the fire duration was long and high temperatures penetrated into the concrete slab, the majority of the deflections recorded will have resulted from both thermal curvatures as well as from the loss of material stiffness or strength.

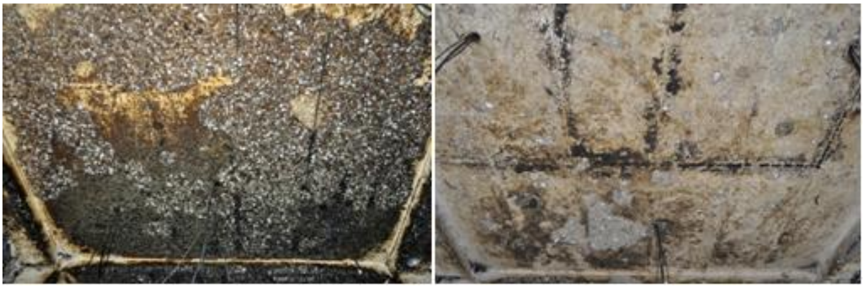

Figure 5. Post fire picture of slab for RC frame with (a) Non-ductile detailing and (b) ductile detailing.

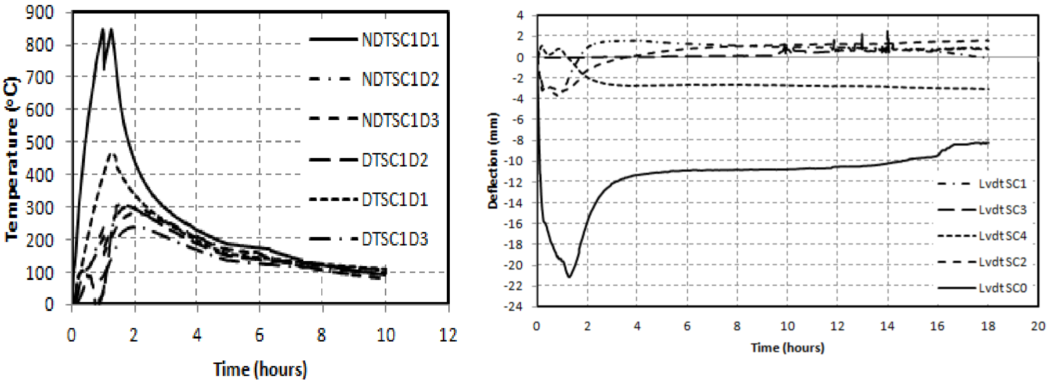

Figure 6. (a) Temperature profiles in the slab cross sections; (b) Slab deflections during fire in RC frame with non-ductile detailing.

Similar kind of behaviour was displaced by other structural elements of the RC with higher damage and deterioration of the concrete in non-ductile detailed frame.

3.3 Residual behaviour

Residual capacity tests provided a better picture of the influence of ductility on the Post earthquake fire behaviour of the RC frames. While reduction in load carrying capacity was only 5% at the displacement of 150 mm in RC frame with ductile detailing, the reduction in load carrying capacity was about 35 % at the displacement of 150 mm in RC frame with non ductile detailing. Figure 7 gives the comparison of the loading envelops of the residual tests of the two frames.

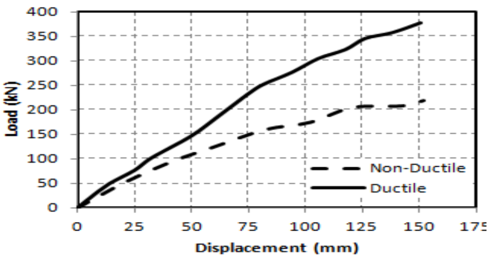

Figure 7. Load displacement plots from residual capacity tests.

4 CONCLUSIONS

Observations from the above tests show that the ductile detailing has a marked influence on the behaviour of RC frame in post earthquake fire. The data show that there will be considerable differences in temperature within a heated concrete structure due to the localised nature of compartment fires. This is in marked contrast to the assumptions made in most design procedures. In about 80 % of the structural members the temperatures in the RC frame with ductile detailing were much higher than those in the ductile detailed frame. This could be attributed to the higher number of wider cracks caused due to the simulated seismic loads. Higher damage in terms of concrete deterioration, spalling, cracking, deflections etc was observed in the RC frame with non-ductile detailing. The slab of the non-ductile detailed RC frame underwent extensive spalling with most of the cover concrete lost rendering the reinforcement exposed to fire to cause the damage to the reinforcement which was manifested by the loss in the reinforcement cross sections at a number of points in the slab. The post fire residual capacity of the non-ductile detailed frame was reduced to 65% of the original capacity while in the ductile detailed frame it was reduced to 95%.

The results from the tests will allow benchmarking of both computer and analytical models of structural behaviour, heat transfer and material behaviour.

ACKNOWLEDGEMENTS

The authors thankfully acknowledge the financial support received from Board of Research in Nuclear Sciences (BRNS)-Mumbai and the U.K.- India Educational and Research Initiative (UKIERI) for conducting this study.

REFERENCES

[1] ISO (International Organisation for Standardization) (1975), *ISO 834: Fire resistance tests. Elements of building construction*. ISO, Geneva, Switzerland.

[2] Drysdale D, An Introduction to Fire Dynamics, 2nd edn. Wiley, Chichester, UK, 1998

[3] Vecchio, F. J. and Sato, J. A. , "*Thermal gradient effects in reinforced concrete frame structures*", ACI, Structural Journal, V. 87, No. 3, , pp. 262-275, 1990.

[4] Bailey, C., "*Holistic behaviour of concrete buildings in fire*", Proceedings, Institute of Civil Engineers: Structures & Buildings, V.152, Issue 3, pp. 199-212, 2002

[5] Sharma U.K, et al, "*Full-scale testing of a damaged reinforced concrete frame in fire*", Proceedings, Institute of Civil Engineers: Structures & Buildings, V.165, Issue SB7, pp. 335-346, 2012

[6] Bureau of Indian Standards," *Ductile detailing of reinforced concrete structures subjected to seismic forces-Code of practice, IS 13920:1993, (Reaffirmed 2008)*", BIS New Delhi.

[7] Bureau of Indian Standards, "*Indian Standard Plain and Reinforced Concrete, Code of Practice, IS 456:2000, (Fourth Revision)*", BIS New Delhi

[8] Bureau of Indian Standards , "*Criteria for earthquake resistant design of structures: Part 1 General provisions and buildings, IS 1893:2002, (Reaffirmed 2007)*", BIS New Delhi

[9] FEMA, "*Pre-standard and commentary for the Seismic rehabilitation of buildings*", FEMA 356, 2000

ULTIMATE LOAD OF SLABS IN FIRE ENHANCED BY TENSILE MEMBRANE ACTION WITH FLEXIBLE SUPPORTING EDGE BEAMS

Kang-Hai Tan* and Tuan-Trung Nguyen*

* Nanyang Technological Univ., School of Civil and Environmental Engineering, Singapore
e-mails: CKHTAN@ntu.edu.sg, nguyentt@ntu.edu.sg

Keywords: Tensile membrane action, Beam-slab systems, Slabs, Flexible support, Fire, Analytical

Abstract. *A number of previous analytical studies have been conducted to predict the enhanced load-bearing capacity of slabs due to tensile membrane action. These analytical approaches are based on an implicit assumption that vertical supports along the slab panel boundaries at all times during a fire do not deform. In reality the edge beams do deform even though they are fire-protected, and thus this assumption may be nullified. This renders their predictions to be unconservative when there is significant deflection of protected edge beams. This work looks at the actual condition where the protected supporting edge beams do deflect, and the slab still bends in synclastic curvature. The authors propose a semi-analytical model which can predict the load-bearing capacity of the composite beam-slab floor systems under fire conditions enhanced by tensile membrane action, but reduced by deflection of the protected edge beams. Its feature is that the deflection of the protected edge beams can be taken into account of calculation of the slab enhancement factor.*

1 INTRODUCTION

At ambient temperature, the applied load on the slab in a composite floor system is distributed from the slab to the secondary beams in one-way action. The load path involved in resisting the permanent and variable loads under ambient condition is: slab → secondary beams → main beams → columns.

Under severe fire conditions, if the secondary interior beams are unprotected, due to degradation of strength in fire they lose most of their strength. As a result, the beams form plastic hinges and the load path at ambient temperature cannot be maintained. The load-carrying mechanism changes to a two-way bending system. The region involving the slab and the unprotected interior beams is known as *a slab panel*. Under severe fire conditions, the load applied to a slab panel is distributed in a load path as follows: slab → supporting edge beams → columns.

The slab panel develops its load-bearing capacity in the deformed state through a combination of yield-line mechanism and tensile membrane action. A number of analytical studies [1-4] have attempted to predict the enhanced load-bearing capacity of slab due to TMA. Among these approaches, a well-known approach, namely, the Bailey-BRE method [1], has been adopted in the SCI Publication P288 [5] and applied in the UK practice. These analytical approaches are based on an implicit assumption that vertical supports along the slab panel boundaries at all times during a fire do not deform. The task of providing the necessary vertical support requires the edge beams to be sufficiently protected so that deflections are small. This is so that the slab can bend in synclastic curvature.

However, in reality the edge beams do deform even though they are fire-protected, and thus this assumption may be nullified. This renders their predictions to be unconservative when there is significant deflection of protected edge beams. On the other hand, tensile membrane action can still be mobilized although the protected edge beams deform, provided that the plastic hinges do not form on the edge beams. Once the plastic hinges form on the protected edge beams, tensile membrane action will disappear.

The authors' work presented in this paper looks at the actual condition where the protected supporting edge beams do deflect, and the slab still bends in synclastic curvature. The authors propose a semi-analytical model to predict the load-bearing capacity of the slab enhanced by tensile membrane action, but reduced by deflection of the protected edge beams. The proposed model was developed based on the BRE-Bailey method. The innovative feature is that the proposed model can take account of vertical deflection of the protected edge beams.

2 PROPOSED SEMI-ANALYTICAL METHOD

2.1 Assumptions

The following assumptions are adopted in the model: (1) the slab panel is assumed to be unrestrained against horizontal movement, and supported along four edges by the protected beams; (2) the load supported by the flexural behaviour of the composite slab is calculated based on the lower-bound yield-line mechanism, assuming that the interior beams have zero resistance; (3) the protected edge beams are assumed to be simply supported without any lateral restraint; (4) the load distribution on the edge beams at collapse follows the shape of the segments of the yield line mechanism, i.e. triangular loading distribution for the short-span beams and trapezoidal loading distribution for the long-span beams; (5) torsional rigidity of the edge beams is assumed to be negligible; (6) the load-carrying capacity of the steel interior beams and the slab (enhanced due to membrane action) are added together.

Based on the author's test results [6], the second assumption is accurate and conservative. Therefore, the slab panel is considered unrestrained against horizontal movement in the proposed model.

When calculating the load capacity of the slab, the proposed model uses the second assumption, in which the lower-bound yield-line mechanism in the slab is adopted. This is a short coming of the proposed model since it cannot take into account the interaction between the slab and the unprotected interior beams. The contribution of the unprotected interior beams on the load capacity of the composite beam-slab system in fire is considered by the sixth assumption.

In the sixth assumption, when calculating the additional load supported by unprotected interior beams in fire, the beams should be considered as steel beams. To validate this assumption, comparisons between the proposed model and the test results are conducted with two cases, i.e. the interior beams are treated as composite beams and as steel beams. They are not presented in this paper.

2.2 Failure modes

A composite floor system may fail due to failure mechanism of the slab panel or due to the composite beam-slab collapse mechanisms which involve failure of both the panel and the beams. These two failure mechanisms, i.e. single slab panel (Figure 1) and beam-slab collapse mechanisms (Figure 2), are the two failure mode mechanisms.

In terms of the failure mode of the slab panel alone, Bailey and Toh [7] proposed two failure modes as shown in Figure 1, based on their fire tests conducted on isolated slabs. The first failure mode is due to fracture of the mesh reinforcement across the short span at the centre of the slab. A second failure mode occurs due to crushing of the concrete in the corners of the slab where high compressive in-plane forces develop.

As observed in the authors' tests [6], the authors adopt these two failure modes of the slab panel (Figure 1) in estimating the enhancement factor of the slab due to TMA.

The composite beam-slab collapse mechanisms may appear if plastic hinges form in the perimeter beams and the yield lines occur across the centre of the slab as shown in Figure 2. These collapse mechanisms were proposed by Abu *et al.* [8] and have been included in SCI Publication P390 [9].

The most important condition for the mobilization of TMA is that the slab must bend in synclastic curvature. Once the 'folding' mechanism has formed, TMA will vanish, leading to failure of the system. Therefore, the edge beams must be checked to ensure a minimum required moment resistance in order that the composite collapse mechanisms do not occur. Verification of the resistance of the edge beams [9] must be conducted in order to ensure that the failure mechanisms of single slab panel (Figure 1) will occur.

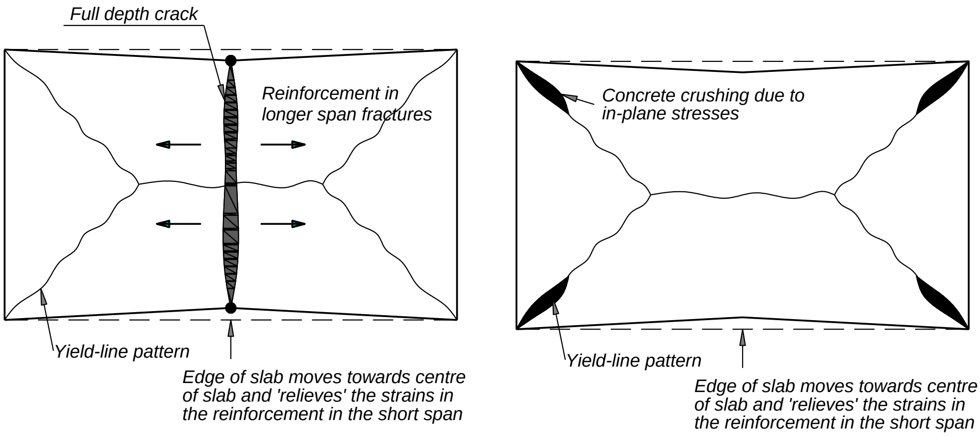

(a) Tensile failure of mesh reinforcement (b) Compressive failure of concrete

Figure 1. Assumed failure modes for isolated slab panels [7].

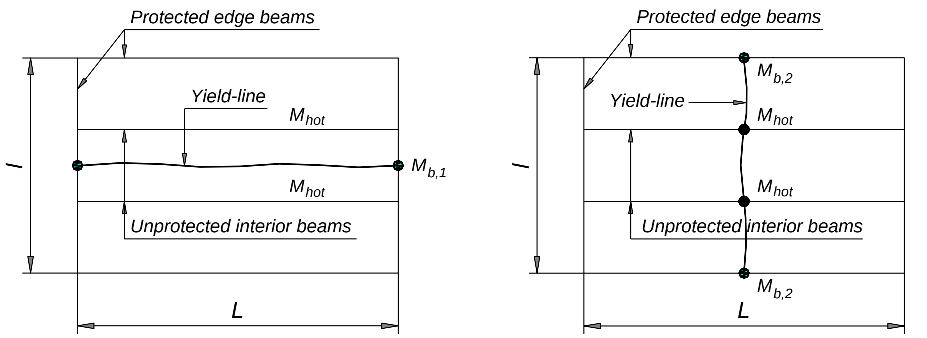

(a) Yield line parallel to the unprotected beam (b) Yield line perpendicular to the unprotected beam

Figure 2. Composite collapse mechanisms [8].

2.3 Proposed enhancement factor

The authors propose a semi-analytical model which can predict the load-bearing capacity of the slab enhanced by tensile membrane action by taking account of vertical deflections of the protected edge beams. The proposed model was developed based on the BRE-Bailey method [7], in which the load supported by the flexural behaviour of the composite slab is calculated based on the lower-bound yield-line mechanism, assuming that the interior beams have zero resistance. The overall enhancement factor can be calculated by Equation (1). The deformed shape of a slab-beam floor system is shown in Figure 3.

$$\begin{aligned} e_1^* &= e_{1m}^* + e_{1b} \\ e_2^* &= e_{2m}^* + e_{2b} \end{aligned} \tag{1}$$

and the overall enhancement is given by:

$$e^* = e_1^* - \frac{e_1^* - e_2^*}{1 + 2\mu a^2} \tag{2}$$

where e_{1m}^* and e_{2m}^* are the contribution of membrane forces to load bearing capacity of elements 1 and 2, respectively; e_{1b} and e_{2b} are the factors which take into account of the effect of membrane forces on the bending resistance due to the presence of axial force of elements 1 and 2, respectively.

The predicted load bearing capacity of the slab enhanced by TMA is calculated by Equation (3):

$$q_{s,\theta} = e^* \times p_{y,\theta} \tag{3}$$

where $p_{y,\theta}$ is the yield-load of the slab at temperature θ.

In the Bailey-BRE method, the values e_1 and e_2 are calculated based on the equilibrium of elements 1 and 2 with *the vertical rigid supports*. Therefore, the method has to assume that the supports along the edges of the slab panel remain rigid, and it cannot consider vertical deflections of the edge beams.

In the proposed approach, the values e_1^* and e_2^* are calculated based on the equilibrium of elements 1 and 2 with *the vertical deformed supports*. Deflection of the edge beams is determined based on the deflected shape.

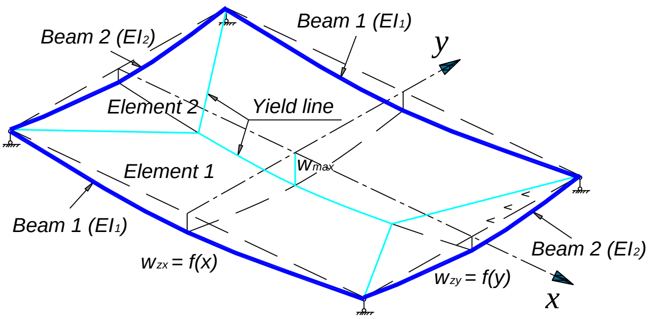

Figure 3. Deformed shape of a slab-beam floor system.

2.4 In-plane stress distribution

The in-plane stress distribution is assumed to be similar to the Bailey-BRE method as shown in Figure 4. It is assumed that the in-plane forces comprise compressive membrane forces around the perimeter of the slab and tensile membrane forces in the central area of the slab. The magnitude of the forces is defined by the constants k and b which depend on the dimensions of the slab. The derivations of the in-plane stress distribution are conducted by Hayes [10] and Bailey and Moore [1]. Only the results are given below.

The parameters k and b are determined from equilibrium of the in-plane stress distribution. The intersection point of the yield lines is defined by the parameter n calculated using the yield-line theory.

$$k = \frac{4na^2(1-2n)}{4n^2a^2+1} + 1 \quad ; \quad n = \frac{1}{2\sqrt{\mu a^2}}\left[\sqrt{3\mu a^2+1} - 1\right] \le 0.5 \tag{4}$$

where a is the aspect ratio of the slab (L/l) and μ is the ratio of the yield moment capacity of the slab in orthogonal directions (should always be less than or equal to 1.0).

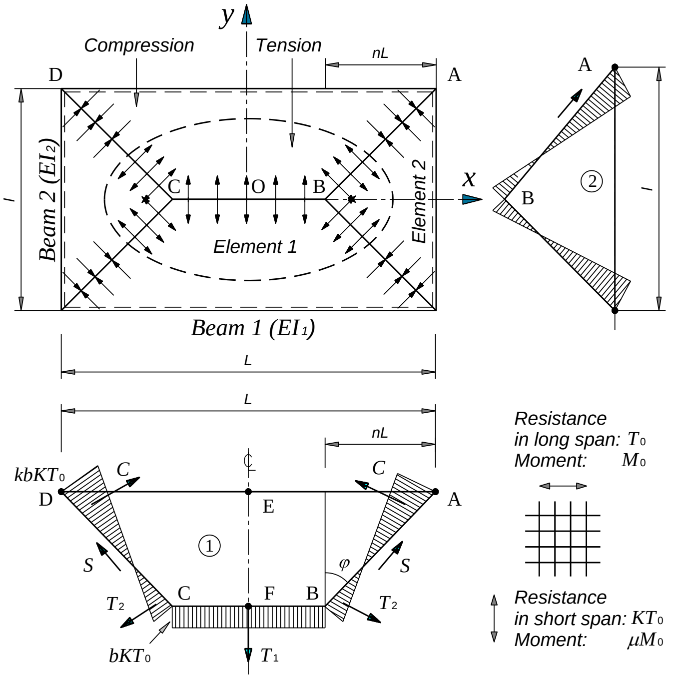

Figure 4. In-plane stress distribution for membrane action.

The yield-line resistance of the slab panel at temperature θ can be calculated by Equation (5).

$$p_y = \frac{24\mu M_0}{l^2}\left[\sqrt{3+\frac{1}{\left(\sqrt{\mu}a\right)^2}}-\frac{1}{\sqrt{\mu}a}\right]^{-2} \tag{5}$$

The constant b is chosen as the minimum value in the following two expressions, which are associated with two failure modes of the slab as shown in Figure 1(a) and (b):

$$b=\frac{1.1l^2}{8K(A+B+C-D)} \quad ; \quad b=\frac{1}{kKT_0}\left[0.85 f_{ck}0.45\left(\frac{d_1+d_2}{2}\right)-T_0\left(\frac{K+1}{2}\right)\right] \tag{6}$$

where d_1 and d_2 are the effective depths in both orthogonal directions; A,B,C,D are the geometric parameters [7].

T_0 and KT_0 are the resistance of the reinforcing mesh per unit width in long and short spans, respectively. The bending moments M_0 and μM_0 per unit width of the slab in long and short spans respectively can be calculated by:

$$\mu M_0 = KT_0 d_1\left(\frac{3+(g_0)_1}{4}\right) \quad ; \quad M_0 = T_0 d_2\left(\frac{3+(g_0)_2}{4}\right) \tag{7}$$

where $(g_0)_1$ and $(g_0)_2$ are parameters which define the flexural stress block in short and long spans, respectively;

For element 1, the membrane force along the yield line BC (Figure 4) is constant and is equal to:

$$N_x\big|_{BC} = -bKT_0 \tag{8}$$

The membrane force along the yield line AB (element 1), at a distance of x from the centre point of the slab O is given by:

$$N_x\big|_{AB} = -bKT_0 + \frac{x-(L/2-nL)}{nL}\left(k+1\right)bKT_0 \tag{9}$$

The membrane force along the yield line for element 2, at a distance y from B can be expressed as:

$$N_y = -bKT_0 + \frac{y}{l/2}\left(k+1\right)bKT_0 \tag{10}$$

2.5 Out-plane stress distribution

Based on the fourth assumption, beam 1 (long-span beam) is subjected to a trapezoidal load with the maximum value $q_1 = ql/2$. Beam 2 (short-span beam) is subjected to a triangular load with the maximum value $q_2 = q(nL)$. The deformed shapes of beam 1 and beam 2 are $w_{zx}(x)$ and $w_{zy}(y)$, respectively. The deflection of the slab is w_m. The out-of-plane stress distribution is shown in Figure 5.

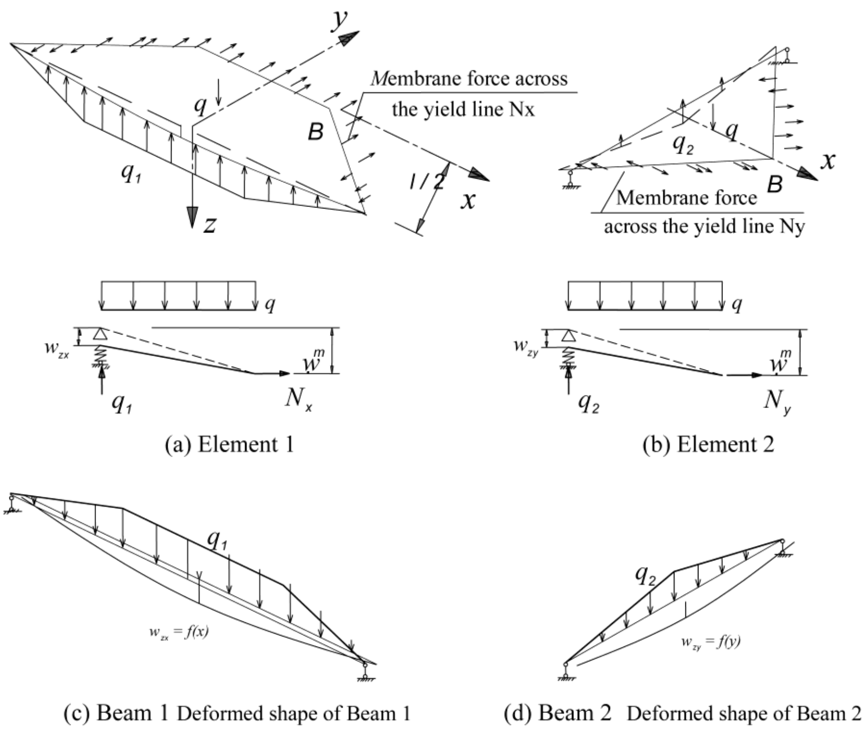

Figure 5. Out-of-plane stress distribution for membrane action.

Deformed shape of the edge beams

Deflection of the edge beams (beams 1 and 2) at elevated temperatures consists of two components: one from the trapezoidal load (beam 1) or from the triangular load (beam 2) transferred from the slab (Figures 6 and 7), and another from thermal gradient over the composite section of the edge beams.

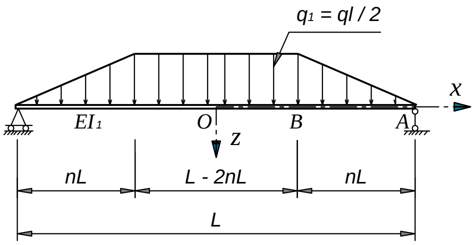

Figure 6. Load transferred to Beam 1.

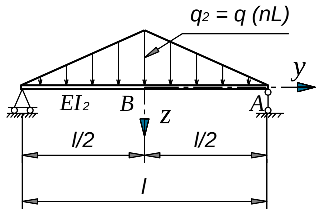

Figure 7. Load transferred to Beam 2.

The deformed shape of beam 1 can be calculated by Equations. (11) and (12).
Segment OB: $0 \le x \le L/2 - nL$:

$$w_{zx}^{(1)} = w_{zx\max} - \frac{1}{EI_1}\left[M_{xO} \times \frac{x^2}{2} - q_1\frac{x^4}{24}\right] + \alpha T_{,zb1}\left(\frac{L^2}{8} - \frac{x^2}{2}\right) \tag{11}$$

Segment BA: $L/2 - nL \le x \le L/2$:

$$w_{zx}^{(2)} = w_{zx\max} - \frac{1}{EI_1}\left[M_{xO} \times \frac{x^2}{2} - q_1\frac{x^4}{24}\right] - \frac{1}{EI_1}\frac{q_1}{nL}\frac{\left(x-(L/2-nL)\right)^5}{120} + \alpha T_{,zb1}\left(\frac{L^2}{8} - \frac{x^2}{2}\right) \tag{12}$$

where $T_{,zb1}$ is the thermal gradient over the total depth of beam 1, α is the thermal expansion.

The maximum deflection $w_{zx\max}$ due to the load can be found from the boundary condition: $w_{zx}^{[2]} = 0$ at $x = L/2$.

$$w_{zx\max} = \frac{q_1}{EI_1}\left[\frac{1}{24}\left[8(nL)^2 + 12(nL)(L-2nL) + 3(L-2nL)^2\right] \times \frac{1}{8}L^2 - \frac{1}{24}\left(\frac{L}{2}\right)^4 + \frac{(nL)^4}{120}\right] \tag{13}$$

The maximum bending moment of the beam due to the load M_{xO} is:

$$M_{xO} = \frac{q_1}{24}\left[8(nL)^2 + 12(nL)(L-2nL) + 3(L-2nL)^2\right] \tag{14}$$

Substituting Equations. (13) and (14) to (11) and (12), one can obtain the deformed shape of beam 1.

Similarly, the deflection Eq. for beam 2 due to both the load and the elevated temperatures is given in Eq. (15) with $0 \le y \le l/2$.

$$w_{zy}(y) = w_{zy\max} - \frac{1}{EI_2}\left[M_{yB} \times \frac{y^2}{2} - q_2\frac{y^4}{24} + \frac{2}{l}q_2 \times \frac{y^5}{120}\right] + \alpha T_{,zb2}\left(\frac{l^2}{8} - \frac{y^2}{2}\right) \tag{15}$$

where $w_{zy\max}$ is the maximum deflection due to the load, and M_{yB} is the maximum bending moment of the beam due to the load:

$$w_{zy\max} = \frac{1}{120}\frac{q_2 l^4}{EI_2} \quad \text{and} \quad M_{yB} = \frac{1}{12}q_2 l^2 \tag{16}$$

Substituting Equations (16) to (15), one can obtain the deformed shape of beam 2.

Contribution of membrane forces to load bearing capacity (e_{1m}^*, e_{2m}^*)

Taking moment about the support for element 1 (Figure 5), we have:

$$\int_{BC} N_x\left(w_m - w_{zx}^{(1)}\right)dx + 2\int_{AB} N_x\left(\frac{L/2-x}{nL}w_m - w_{zx}^{(2)}\right)dx - \text{Moment due to } \sum q = 0 \tag{17}$$

Substituting Equations. (8), (9), (11) and (12) to (17):

$$\begin{aligned}&2\int_0^{L/2-nL} bKT_0\left(w_m - w_{zx}^{(1)}\right)dx + 2\int_{L/2-nL}^{L/2}\left[bKT_0 - \frac{x-(L/2-nL)}{nL}(k+1)bKT_0\right]\times\left[\frac{L/2-x}{nL}w_m - w_{zx}^{(2)}\right]dx\\&-q(L-2nL)\frac{l}{2}\frac{l}{4} - q\times nL\times\frac{l}{2}\times\frac{l}{6} = 0\end{aligned} \tag{18}$$

It should be noted that $q_1 = ql/2$. After integrating and regrouping, with a slab deflection w_m, one can find a value of q according to Element 1 denoted as q_{1m}^*. The contribution of membrane forces to load bearing capacity according to Element 1 is given by:

$$e_{1m}^* = q_{1m}^* / p_{y,\theta} \tag{19}$$

where $p_{y,\theta}$ is the yield-line load of the slab at temperature θ.

Taking moment about the support for element 2 (Figure 5), we have:

$$2\int_{AB} N_y\left(\left(1-\frac{y}{l/2}\right)w_m - w_{zy}\right)dy - \text{Moment due to } \sum q = 0 \tag{20}$$

Substituting Equations (10) and (15) to (20):

$$2\int_0^{l/2}\left[bKT_0 - \frac{y}{l/2}(k+1)bKT_0\right]\times\left[\left(1-\frac{y}{l/2}\right)w_m - w_{zy}\right]dy - \frac{1}{6}ql\times(nL)^2 = 0 \tag{21}$$

It should be noted that $q_2 = q(nL)$. After integrating and regrouping, with a slab deflection w_m, one can find a value of q according to Element 2 denoted as q_{2m}^*. The contribution of membrane forces to load bearing capacity according to Element 2 is given by:

$$e_{2m}^* = q_{2m}^* / p_{y,\theta} \tag{22}$$

Effect of membrane forces on bending resistance capacity (e_{1b}, e_{2b})

The effect of the membrane forces on the bending resistance along the yield lines is evaluated by considering the yield condition when axial load is present. This effect does not depend on deflection of the edge beams. Therefore, the factors e_{1b} and e_{2b} are similar to the Bailey-BRE method [7].

After finding the factors e_{1m}^* and e_{2m}^*, the overall enhancement factor can be estimated by Eq. (2), and the load-bearing capacity of the slab enhanced by tensile membrane action can be found by Eq. (3).

3 MODEL VALIDATION

Verification of the resistance of the edge beams [9] must be conducted first in order to ensure that the failure mechanisms of single slab panel (Figure 1) will occur.

For each specimen, the test result was compared with the prediction from the Bailey-BRE method and the proposed model. For the specimens without unprotected interior beams, the comparisons were quite straightforward. For the specimens with unprotected interior beams, the bending resistance of interior beams was calculated in order to check if these beams have failed. If the interior beams had failed, the total test load of 15.8 kN/m^2 was totally resisted by the slab. The enhancement factor determined from the test was compared with those calculated from the two models, i.e. the Bailey-BRE and the proposed approaches.

Since the Bailey-BRE method cannot consider deflection of the edge beams, the enhancement factor predicted by the Bailey-BRE method is calculated with the two deflections as shown in Eqs. (23) & (24).

$$\text{Absolute slab deflection: } w_m \tag{23}$$

$$\text{Relative slab deflection: } w_r = w_m - \frac{1}{2}\left(w_{MB} + w_{PSB}\right) \tag{24}$$

3.1 Specimens without unprotected interior beams

Among the authors' test series there were two specimens without interior beams, i.e. S1 and S3-FR. At the loading phase, the two specimens were loaded to a value of 15.8 kN/m^2, corresponding to a load ratio of about 2.0 for S1 and S3-FR, respectively. The tests were terminated when reinforcement fractured above the edge beams (S1) or compression ring crushed near the corners of the slab (S3-FR). More details of these specimens can be found in [6].

Table 1. Comparison of the proposed model and the Bailey-BRE model for the specimens without interior beams.

					Total capacity			Prediction / Test		
Test	p_{test}	MB defl.	PSB defl.	Slab defl.	Bailey (Eq. 23)	Bailey (Eq. 24)	Model	Bailey (Eq. 23)	Bailey (Eq. 24)	Model
	kN/m^2	mm	mm	mm	kN/m^2	kN/m^2	kN/m^2			
S1	15.6	28	58	131	15.8	12.91	13.5	1.01	0.83	0.86
S3-FR	16.0	33	28	115	17.1	14.6	14.7	1.07	0.91	0.92
							M =	1.04	0.87	0.89

The comparisons for the specimens without unprotected interior beams are shown in Table 1. It can be seen that based on the absolute slab deflection (Equation (23)), the Bailey-BRE method over-predicts the test results by 4%, whereas the method is conservative if the relative slab deflection is used instead (Equation (24)). The proposed method predicts the test results more accurately than the Bailey-BRE method. It is because the authors' model can take into account the deflected shape of the edge beams. The discrepancy between the proposed model and the test results for these specimens is 11%.

3.2 Specimens with unprotected interior beams

Among the authors' test series there were six specimens with interior beams. Two specimens presented in the authors' companion paper, i.e. P215-M1099 and P486-M1099, are used here for the comparison.

Table 2. Comparison of the proposed model and the Bailey-BRE model for the specimens with interior beams.

					Total capacity			Prediction / Test		
Test	p_{test}	MB defl.	PSB defl.	Slab defl.	Bailey (Eq. 23)	Bailey (Eq. 24)	Model	Bailey (Eq. 23)	Bailey (Eq. 24)	Model
	kN/m^2	mm	mm	mm	kN/m^2	kN/m^2	kN/m^2			
P215-M1099	15.6	38	57	124	18.0	14.2	15.0	1.15	0.91	0.96
P486-M1099	15.5	55	94	139	18.7	12.9	15.7	1.20	0.83	1.01
							M =	1.175	0.87	0.985

The comparisons for the specimens with unprotected interior beams are shown in Table 2. It can be seen that based on the absolute slab deflection, i.e. the deflection of the edge beams is not taken into account, the enhancement factors predicted by the Bailey-BRE method are greater than the test results by 17.5%. If the relative deflection is used instead, the Bailey-BRE method is conservative. The proposed model predicts the load-bearing capacity of composite beam-slab systems very well. The discrepancy between the proposed model and the test results for these specimens is only 1.5%.

4 CONCLUSIONS

This paper presents a semi-analytical model which can predict the load-bearing capacity of composite beam-slab floor systems under fire conditions enhanced by tensile membrane action, but reduced by deflection of the protected edge beams.

The proposed model was validated with the authors’ test results conducted in Nanyang Technological University. The validations showed that the proposed model give conservative and more accurate predictions compared to the Bailey-BRE method. The model can take account of the beam-slab interactions under fire conditions and gives guidance on the required stiffness of edge beams which the Bailey-BRE method does not provide.

ACKNOWLEDGMENTS

The research presented in this paper was funded by Agency for Science, Technology and Research (A*Star Singapore) under Grant No. M4070013. The financial support of A*Star is gratefully acknowledged.

REFERENCES

[1] Bailey C.G. and Moore D.B., "Structural behaviour of steel frames with composite floorslabs subject to fire: Part 1: Theory", *Structural engineer London*, 78(Compendex), 19-27, 2000a.

[2] Usmani A.S. and Cameron N.J.K., "Limit capacity of laterally restrained reinforced concrete floor slabs in fire", *Cement and Concrete Composites*, 26(2), 127-140, 2004.

[3] Zhang N.-S. and Li G.-Q., "A new method to analyze the membrane action of composite floor slabs in fire condition", *Fire Technology*, 46(Compendex), 3-18, 2010.

[4] Burgess I.W., Xu D., and Shan-Shan H. "An Alternative Simplified Model of Tensile Membrane Action of Slabs in Fire", *Application of Structural Fire Engineering (ASFE)*. 19-20 April 2013 Prague, Czech Republic361-367, 2013.

[5] Newman G.M., Robinson J.T., and Bailey C.G., *Fire Safe Design: A new Approach to Multi-Story Steel-Framed Buildings*, in *SCI Publication P288* 2006, The Steel Construction Institute.

[6] Nguyen T.T. and Tan K.H. "Testing of Composite Slab-beam Systems at Elevated Temperatures", *7th International Conference on Structures in Fire (SiF)*. 6-8 June 2012 Zurich, Switzerland, Swiss Federal Institute of Technology Zurich, 247-256, 2012.

[7] Bailey C.G. and Toh W.S., "Behaviour of concrete floor slabs at ambient and elevated temperatures", *Fire Safety Journal*, 42(6-7), 425-436, 2007.

[8] Abu A., Ramanitrarivo V., and Burgess I. "Collapse mechanisms of composite slab panels in fire", *6th International Conference on Structures in Fire, SiF'10, June 2, 2010 - June 4, 2010*. East Lansing, MI, United states, DEStech Publications Inc., 382-389, 2010.

[9] Simms W.I. and Bake S., *TSLAB V3.0 User Guidance and Engineering Update*, in *SCI Publication P390* 2010, The Steel Construction Institute.

[10] Hayes B., "Allowing for membrane action in plastic analysis of rectangular reinforced concrete slabs", *Magazine of Concrete Research*, 20(65), 205-212, 1968a.`

8th International Conference on Structures in Fire
Guo-Qiang LI, Venkatesh K. R. KODUR, Shou-Chao JIANG, Jian JIANG, Su-Wen CHEN, Guo-Biao LOU (Eds.)
Shanghai, China, June 11-13, 2014

FIRE SPALLING OF CONRETE – A RE-ASSESSMENT OF TEST DATA

Robert Jansson* and Lars Boström*

*SP Technical Research Institute of Sweden, Fire Research
e-mails: robert.jansson@sp.se, lars.bostrom@sp.se

Keywords: Concrete, Spalling, Experimental study, Statistical analysis

Abstract. *In a state-of-the-art report on the fire design of concrete structures by fib (2007), the randomness of fire spalling testing is described as substantial. No more reference was given to the test method that was used or the spalling depths that were measured during the experiments. As the variation in results during fire resistance testing can have a crucial influence on the fire rating this question deserves more attention. A medium scale test method previously used at SP Technical Research Institute of Sweden is analysed in an effort to shed some more light on this issue. The random factor from analysing 110 fire tests with this method are shown to not be substantial.*

1 INTRODUCTION

The subject of this paper is fire spalling of concrete and more precise the apparent randomness of the phenomenon. The following citations and variations of these can be found in many places in the literature.

“..in some tests 10 specimens were tested with 5 spalling and 5 non-spalling.” [1]

”For specimens from the same batch, and under identical conditions, some could spall while others do not.” [2]

Typically, as in the case of the two references above, no further reference to relevant empirical studies supporting this statement are given or to what extent of spalling they are referring to. The reason for this is probably that this is by many authors assessed as common knowledge. The motivation for this introduction is not to say that their statements are per definition wrong, as there are some results looking random out there, but it is to point out that this is an important aspect to examine as if the statement is generally true a large amount of effort and research are worthless.

2 FIRE SPALLING OF CONRETE - BACKGROUND

One of the earliest printed descriptions of fire spalling of concrete was done by Barret 1854 [3] where concrete containing flint aggregate was described to “split, and yield under the action of fire”. In the 18th hundreds it was also believed that one of the causes for fire spalling of concrete was the application of water during firefighting [4]. I the case of pre-stressed concrete this water application factor was later put in doubt by the grand old man regarding fire and concrete in Germany, Karl Kordina [5]. But water, or moisture, has always been regarded as being an important influencing factor on fire spalling of concrete although in different contexts. It was shown already 1905 that liquid water often pours out on the non-fire exposed side of large slabs during fire testing [6] and this is identified as one of the large challenges for a successful thermo hydro mechanical model of behaviour of concrete at high temperature [7] as this flow, through the colder areas of the slabs, is concentrated to cracks, i.e. typical models found in the literature with averaged properties will fail as all moisture will be absorbed by the porosity before reaching the other side with that approach. A key idea of the influence from presence of water on fire spalling, also postulated in 1905 [8], is that it contributes to a build-up of a steam pressure which breaks off pieces of the concrete. This theory was then presented in slightly different forms during the 19^{th} hundreds, as an example Shorter and Harmathy [9] added the phenomenological description of an accumulated moisture clog in front of the high pressure zone that now also have been shown experimentally [7,10], see Figure 1.

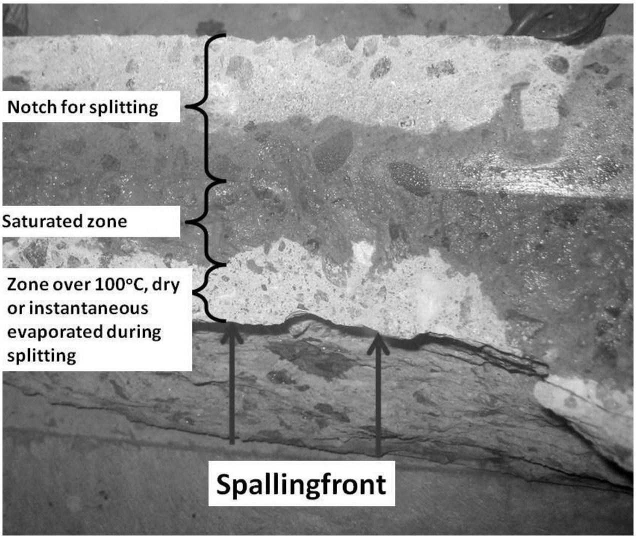

Figure 1. The moisture clog in front of the spalling front. Visualised by splitting a 600 × 500 × 200 mm^3 concrete slab during a fire test [7].

Two other theories related to moisture as an important part of the spalling phenomena are the frictional forces from vapour flow theory [11,12] and the reduction on mechanical properties from presence of water in the saturated zone [7,13,14]. Yet another moisture related theory is that the Boiling Liquid Expanding Vapour Explosion (BELVE) [15,16] where super-heated liquid water in the pore system is rapidly expanding during crack initiation contributes to the violent behaviour.

In contrast to the moisture based theories Bažant [17], on the other hand, claims that when a crack is opened the space available for expansion is immediately increased by several orders of magnitude making the pressure from water only a secondary factor in the fire spalling phenomenon. His theory on the main factor is that thermal stresses can lead to *''brittle fracture and delamination buckling caused by compressive biaxial stresses parallel to the heated surface''*. Other theories based on thermal expansion and restrain was postulated by Saito [18] and Dougill [19]. According to the later the violent energy released during the fire spalling event is similar to the violent behaviour that can occur during a compression test in a slightly flexible testing machine. i.e. accumulated energy in colder areas of the cross section, equivalent with the machine, leads to the violent mode of failure. A more detailed overview of the history of fire spalling of concrete and different theories can be found in References [7] and [20].

Empirical observations of fire spalling include both a type of flaking from the surface and/or an instantaneous explosion of whole cross sections. In Figure 2 the result of the former type is shown in a perspective from the cold side where a continuous flaking process of the 200 mm thick cross section led to holes through the whole thickness after 40 minutes of fire exposure. The other type, the instantaneous explosion of whole cross sections is usually associated with two sided exposure as an example during exposure of the web of beams [21] or during material testing of small cylinders of high strength concrete [22]. In Figure 3 this explosive type is illustrated.

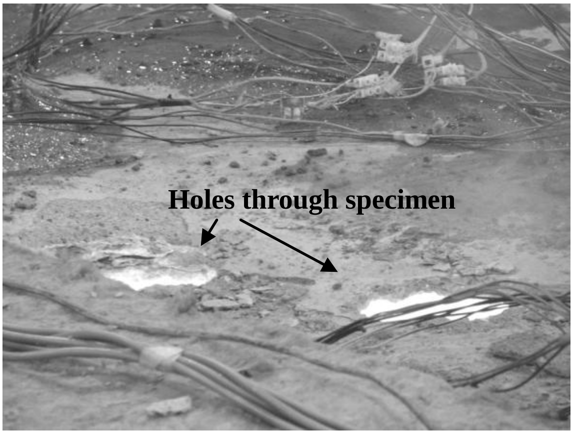

Figure 2. Severe spalling breaking through the 200 mm thick concrete specimen after 40 minutes of exposure to the hydrocarbon fire curve. [7].

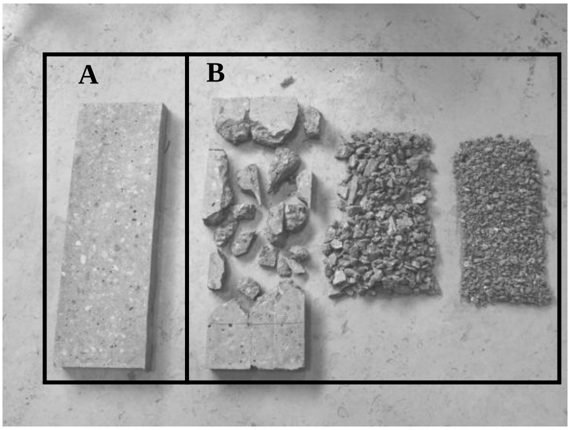

Figure 3. Specimens with thickness 40 mm made of 4.5 years old SCC, w/c ratio 0.4 with 140 kg/m^3 limestone powder. (A) A specimen before test. (B) Fractions of a specimen exploded after 11 minutes of standard fire exposure from two sides and loaded with a small load from the top. [7].

The study described more in detail in this paper is on the flaking type of spalling, i.e. during exposure from one side. An empirical observation done by the authors during this type of spalling tests is that higher strength concrete often gives smaller flakes and slower heating rate leads to thicker flakes or regions that are instantaneous shot away.

2 A RE-ASSESSMENT OF TEST DATA

In a test program on Self Compacting Concrete (SCC) described by Boström and Jansson [23] 110 fire tests on slabs with the size 600mm × 500mm × 200 mm equipped with an internal post stressing tensioning system was performed. Out of this 110 fire tests 100 were performed in pairs with identical test specimens. Previous analyses of data from these tests have only been conducted with one parameter at a time, see for example Figure 4 presented at the SiF 2008 conference [24]. However, as several parameters were varied at the same time, it is a difficult task to isolate the impact of a single parameter. So predictions of spalling based on only a single parameter was not possible. The only influence that was clear from the original study was the impact of the presence or absence of load on the specimens [23]. If a compressive load was applied with post-tensioned bars the spalling depth was greater than if it was absent, but no significant difference was observed between different load levels in the tested interval.

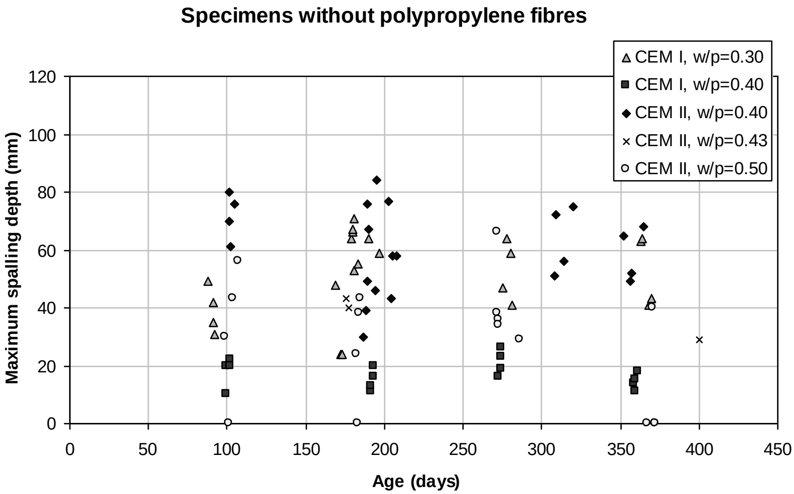

Figure 4. Effect of age on the maximum spalling depth [24].

To investigate the test data more in depth and especially the randomness indicated in figure 4 and in the introduction of this paper, a more in depth statistical study has been performed. The major question to answer is whether it is even possible to develop such a model or if an unknown randomization effect exists prohibiting this. Obviously some of the parameters are interdependent which complicates the interpretation of the results. As a consequence only limited focus will be placed on any conclusions drawn concerning the importance of single parameters as these are tentative at best. The goal of the analysis is then to make a multiple least squares fit of all available material and test method dependent parameters, see Table 1, to predict the measured average spalling depth results as well as possible.

In this re-assessment of the results only tests conducted without the inclusion of PP fibres in the mix are analysed. The analysis is based on the mean depth of spalling measured on the fire exposed area of the slabs. Spalling depths for the different specimens were between 0 and 53 mm with an average spalling depth of 20 mm. Out of the 110 tests analysed, 100 were performed in pairs with identical test specimens. By analysing these 50 pairs we see that the average deviation in spalling depth between two identical tests was 6 mm (which is ±3 mm from the mean value) and the greatest deviation in spalling depth between two identical tests was 21 mm (which is ±11 mm from the mean value). This analysis shows that there is no large deviation between identical tests.

Table 1. Span of values in the 110 fire tests on SCC analysed. Tests from Boström and Jansson [7][24].

Factor in experiments and model	Span of values in experiments min	max	Unit	Comment
Water/powder ratio	0.25	0.55	[-]	
Water/cement ratio	0.3	0.71	[-]	
Cement type	1*	2 *	[-]	CEM I or CEM II
Water in mix	168	230	kg/m3	
Cement in mix	300	560	kg/m3	
Limestone filler in mix	0	252	kg/m3	
Air content during moulding	2	12	%	Some mixes were designed to include much air
T 50 during moulding	1	7.5	sec	
Strength at 28 days	35	82	MPa	
Fire curve	1*	4*	[-]	10 °C/min, slow heating curve, standard fire curve and hydrocarbon fire curve
Applied stress during fire test	0	10.6	MPa	
Moisture content at test day	4.1	6.6	%	
Age at test day	88	400	days	
Strength at test day	39	105	MPa	

* *This is numerical values given to be able to investigate with a least squares fit whether an influence is detectable.*

To investigate the predictability a multiple least squares fit of the 14 parameters listed in Table 1 was performed in the spread sheet program EXCEL. To optimize the model to the test data, nonlinear functions of the different test parameters were used. Each nonlinear function was optimized to obtain as high r^2 value as possible for the prediction. Using this approach, there is an obvious risk that the model will not work well outside the parameters studied but this has not been the aim of the application and it has only been tested within the range of input parameters. The best model, based on fitting all the 110 tests to spalling depth data, is shown in Table 2.

Table 2. Indices defining the best fit of 14 parameters to spalling test data of all 110 tests (reported to 4 significant figures). The table (equation) should be read row after row [7]. The span of values for each parameter represented in the test series inside which the fit is valid can be seen in Table 1.

	Fire curve ^	1	X	-4.074	+
+	Stress^	0.001	X	14.38	+
+	Cement type^	1	X	21.86	+
+	Moisture^	0.04	X	490.7	+
+	Age/100^	2	X	-1.132	+
+	Air^	-3	X	-57.74	+
+	T50^	0.5	X	7.699	+
+	w/p^	10	X	3727	+
+	w/c^	-5	X	-0.039	+
+	(Limestone filler/100)^	0.4	X	10.58	+
+	(Strength/100)^	1	X	86.81	+
+	(water/100)^	-10	X	-1983	+
+	(cement/100)^	1.5	X	2.563	+
+	(28d strength/100)^	1	X	-26.74	+
+	-605.1	=	Average spalling depth [mm]		

The prediction made by this multiple least squares model is shown in Figure 5. This model's fit of the test data is good, especially when considering the deviation of test data between two tests described above.

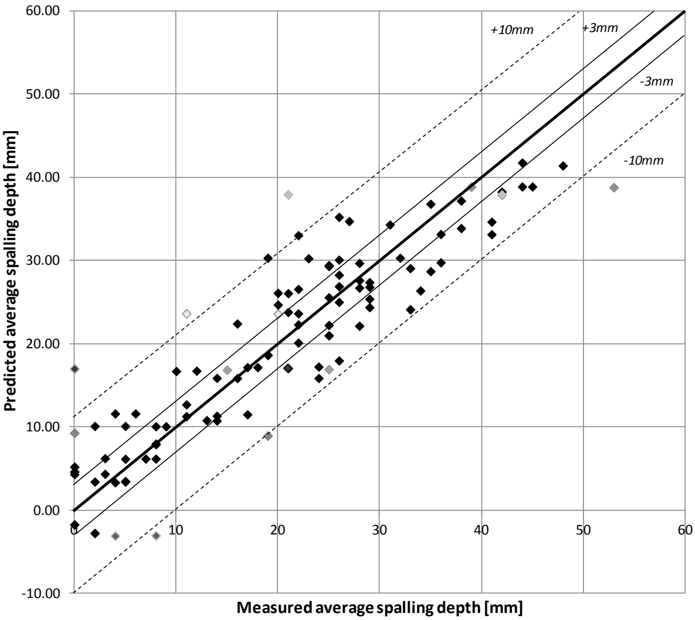

Figure 5. Measured vs. predicted values using a least square model for best fit (r^2 =0.81). Coloured dots in same grey scale show pairs of two identical tests.

The robustness of this approach is important to examine more in detail. If 15 of the 110 tests are randomly removed from the multiple least squares fit and a new best fit is constructed based on the remaining 95 tests, this new best fit can be used to predict the 15 removed tests. The accuracy of these predictions gives an indication of how sensitive the modelling approach is to the data set. This approach was used ten times and the full results can be seen in reference 7. No large deviation in the precision of the prediction, as represented by the r2 values ranging from 0.81 to 0.85, could be identified with this randomization method which indicates that the approach is sound.

The function found for stress that gave the best fit for all test data, r2= 0.81 instead of 0.76, was the function shown in Table 2 i.e. the conclusion already drawn from the initial study that the application of an external load was important but the size of this load (given compressive stresses up to 10 MPa) was not as important. A similar conclusion was drawn by Copier [25]. As concrete used in practice often is in compression or restrained by its surroundings, a medium scale spalling test method is best designed by including this factor in some way, i.e. if tests without any load or restraint are conducted the spalling depths are much lower.

3 CONCLUSIONS

In summary, this re-assessment of test data leads to three conclusions valid for the test series analyzed and the chosen analysis method, i.e.:

(1) the spalling behaviour is dependent on many factors but it is possible to predict the spalling inside a dataset with a fairly high accuracy,

(2) the random scatter in results is not alarmingly large as indicated by the citation from fib (2007) [1] in the beginning of this paper, and

(3) the application of a compressive load during testing of concrete in the medium scale tests influences the results substantially.

REFERENCES

[1] fib (2007) "Fire Design of Concrete Structures – Materials, structures and modelling", State-of-the-art Report, fib Working Party 4.3-1, Bulletin 38, 2007

[2] Majorana C. E., Salomoni V. A., Mazzucco G. and Khoury G. "An approach for modelling concrete spalling in finite strains" *Mathematics and Computers in Simulation*, published online, 2009

[3] Barret "On the French and other methods of constructing iron floors", *Civil Engineering and Architect's Journal,* Vol XVII, pp 94, 1854

[4] Ingle J. "Recent improvements in the application of concrete to fire-proof constructions", *London Civil Engineering and Architects' Journal*, 1866

[5] Kordina K. "Fire resistance of prestressed concrete" *Proceedings of a symposium on the fire resistance of prestressed concrete, held under the auspices of the F.I.P. Commission on Fire resistance of prestressed concrete at Braunschweig*, Germany, 1965

[6] Woolson I. "Investigation of the Effect of Heat Upon the Crushing Strength and Elastic Properties of Concrete", *Proceedings of the American Society for Testing Materials*, Philadelphia, USA, 1905

[7] Jansson R. "Fire spalling of concrete- Theoretical and Experimental studies" PhD Thesis at the Royal University of Technology, Stockholm, Sweden , 2013

[8] Miller R. P. Contribution to the discussion at the end of the report "Investigation of the Effect of Heat Upon the Crushing Strength and Elastic Properties of Concrete" by Ira Woolson, *Proceedings of the American Society for Testing Materials,* Philadelphia, USA, 1905

[9] Shorter G. W. & Harmathy T. Z. Discussion on the article “The fire resistance of concrete beams” by Ashton and Bate, *Proceedings, Institute of Civil Engineers*, Vol. 20, p. 313, 1961

[10] Jansson R. and Boström L. “Fire spalling – the moisture effect” *Proceedings of the 1st International Workshop on Concrete Spalling due to Fire Exposure - From Real Life Experiences and Practical Applications to Lab-scale Investigations and Numerical Modelling*, MFPA Institute Leipzig, Germany, September 3-5, 2009

[11] Meyer-Ottens C., “Zur Frage der Abplatzungen an Betonbauteilen aus Normalbeton bei Brandbeanspruchung“, PhD-thesis, Braunshweig, Germany, 1972

[12] Waubke N. V. and Schneider U., ”Tensile stress in concrete due to fast vapour flow“, *Proceedings of the international RILEM symposium “Pore Structure and Properties of Materials”,* Prauge, September, 1973.

[13] Jansson R. and Boström L. “The influence of pressure in the pore system on fire spalling of concrete”, *Proceedings of 5th Conference on Structure in Fire*, Singapore, May 28-30, 2008.

[14] Jansson R. and Boström L. (2010). “The influence of pressure in the pore system on fire spalling of concrete” *Fire Technology*, Vol 43, No 1, 2010, pp 217-230.

[15] Petrov-Denisov V.G., Maslennikov L.A. and Pitckob A.M. “Heat- and moisture transport during drying and first heating of heat resistant concrete. *Concrete and Reinforced Concrete* 1972;2: 17–8 (In Russian). as cited by Hertz K. “Limits of Spalling of Fire-Exposed Concrete” *Fire Safety Journal 38*, pp.103-11, 2003

[16] Ichikawa Y. “Predictions of pressures, heat and moisture transfer leading to spalling of concrete in fire”, PhD Thesis, Imperial Collage, London, Great Britain, 2000.

[17] Bažant , Z. P. “Concrete Creep at High Temperature and its Interaction with Fracture: Recent Progress”, *Concreep-7 Conference: Creep, Shrinkage and Durability of Concrete and Concrete Structures*, Nantes, France, pp 449–460, 2005

[18] Saito H. “Explosive spalling of prestressed concrete in fire” *Fire resistance on prestressed concrete; proceedings of a symposium on the fire resistance of prestressed concrete, held under the auspices of the F.I.P. Commission on Fire resistance of prestressed concrete at Braunschweig*, Germany, June, 1965

[19] Dougill J. W. “Modes of failure of concrete panels exposed to high temperatures” *Magazine of Concrete Research*, Vol 24, No 79, 1972

[20] Jansson R. “Fire spalling of concrete - A historical overview”, Key note in the *Proceedings of the 3rd International RILEM Workshop on Concrete Spalling due to Fire Exposure*, Paris, France, Sept. 2013

[21] Jansson R. and Boström L. “Fire test of loaded beams” *Proceedings of the 2nd International RILEM Workshop on Concrete Spalling due to Fire Exposure*, Delft, The Netherlands, Oct. 2011

[22] Hertz K. “Explosion og reststyrke af varmepåvirket silikabeton” (in Danish), Report 162, Danmarks tekniske Höjskole, Lyngby, 1982.

[23] Boström L., Jansson R. Self-Compacting Concrete Exposed to Fire SP Report 2008:53, SP Technical Research Institute of Sweden, Borås, 2008

[24] Boström L. and Jansson R. “Results from two research programs on spalling of concrete” *Proceedings of 5th Conference on Structure in Fire*, Singapore, May 28-30, 2008.

[25] Copier, W.J. “Spalling of normalweight and lightweight concrete on exposure to fire”, Report 24 (2), *Heron*, The Nederlands, 1979

8th International Conference on Structures in Fire
Guo-Qiang LI, Venkatesh K. R. KODUR, Shou-Chao JIANG, Jian JIANG, Su-Wen CHEN, Guo-Biao LOU (Eds.)
Shanghai, China, June 11-13, 2014

DEFORMATION AND RESPONSE OF CONTINUOUS AND RESTRAINED POST-TENSIONED CONCRETE SLABS AT HIGH TEMPERATURES

John Gales* and Luke Bisby**

*Carleton University
e-mail: john.gales@carleton.ca

**University of Edinburgh
e-mail: luke.bisby@ed.ac.uk

Keywords: High temperature creep, Post-tensioned concrete, Non-standard fire tests, Continuity, restraint

Abstract. *The improvement of modelling capabilities that could enable defensible performance based structural fire design of post-tensioned (PT) concrete buildings requires detailed validation data from densely instrumented experiments that incorporate as many of the relevant structural properties of as-built construction as possible. Experiments are presented on three 3-span continuous, restrained PT concrete slab strips under sustained service loading and exposed to severe localized heating under constant incident heat flux. A similar yet highly complex deflection response to high temperature is presented for all three slabs. The possible physical mechanisms responsible for the observed complex high temperature deformation response are presented and discussed. The overarching objective is to help steer future research for the development of rational fire safety strategies for PT concrete (and reinforced concrete) buildings by interrogating these systems' real behaviour in realistic fire scenarios.*

1 INTRODUCTION AND MOTIVATION

Performance-based design is the growing paradigm in contemporary structural engineering, and structural fire safety engineering is no exception to this. Advocates of performance-based methodologies seek to adopt sophisticated fire strategies tailored to individual buildings and needs. In particular, these strategies are being applied to optimized reinforced concrete buildings, including those that apply steel prestressing tendons as post-tensioned (PT) reinforcement. However, the current understanding of prestressing steel behaviour at high temperature is based largely on outdated research that fails to properly account for material property changes at elevated temperatures. Furthermore, real fires in real PT concrete buildings have the potential to induce – indeed have induced in real fires – unique failure mechanisms that cannot be observed or accounted for using standard fire furnace tests [1]. Current modelling tools used to establish structural fire safety engineering strategies may thus lack realistic experimental validation and verification, leading to the development of potentially unconservative performance-based strategies for PT concrete buildings (indeed for all concrete buildings). To support the improvement of modelling capabilities that would enable credible performance based design of PT concrete buildings, there is a need for densely instrumented experiments that incorporate as many of the relevant structural properties (post-tensioning, continuity, restraint, realistic scale, unbonded reinforcement, etc. of as-built PT construction as possible; this need is partly addressed in the current paper by presenting experiments on three 3-span continuous, restrained PT concrete slabs (slab strips) under sustained service loading and exposed to severe localized heating using radiant heaters. While initial outcomes of these slab tests have been presented by Gales et al. 2013 [2], the unique deflection response that was observed has not previously been presented in detail. This paper addresses this shortcoming by providing an expanded discussion of the observed deformation response in an attempt to steer future research towards improving capabilities in engineering rational performance based fire design of PT concrete buildings.

2 EXPERIMENTAL METHODOLOGY

The test program was designed to be the most simplistic slab that could still account for as many of the relevant structural properties of as-built PT concrete construction as possible. The resulting tests are the first to consider continuous, PT configurations at high temperature including axial, vertical and rotational restraint across multiple spans, whilst also accounting for bonded and unbonded PT construction. The testing configuration is illustrated in Figure 1. The slabs (denoted A, B, and C) were cast from concrete of grade C40/50 with 10 mm maximum size mixed gravel aggregate. Each slab was cast with a single embedded parabolic profile seven-wire steel prestressing tendon (Grade 1860, with a minimum prescribed concrete axis distance cover of 35 mm) and non-prestressed mild steel reinforcement (Grade 500, with an axis distance of 25 mm). Slabs A and C had unbonded PT tendons, whereas Slab B had a bonded PT tendon. It is important to note that the draped parabolic prestressing tendon profile resulted in an eccentric prestressing force at midspan.

2.1 Test procedure

The slabs were tested individually after curing for at least six months. The testing procedure for each slab is reviewed in this section; specific details being provided where the individual tests differed.

The testing procedure began by connecting the slabs to fixed steel supports connected to a structural strong floor, thus creating a frame of representative restraining stiffness of a real PT building. This supporting system resulted in the slabs being continuous over three spans with two small end cantilevers. The restraining frame was instrumented with strain gauges to allow indirect measurement of forces exerted on the supports during high temperature exposure. After the slabs were connected to the restraining frame their prestressing tendons were post-tensioned while monitoring structural response. The tendon in Slab B was grouted after post-tensioning to create a bonded PT condition, as already noted. To simulate a longer total unbonded tendon length, Slab C incorporated a disc spring anchorage at the dead end anchorage; this was specifically tuned to a specific stiffness so as to simulate an additional length of unbounded prestressing tendon.

After waiting for short-term prestressing losses and time for the grout hardening in Slab B, the slabs were loaded with lead bricks to give a sustained loading of approximately 2 KN/m of span length. These bricks were used since with small deflections they remain stationary and they can be directly exposed to temperatures below 300 ℃. Sustained loading during high temperature testing was approximately 40% of the calculated design ultimate capacity (with reduction factors taken as unity). After loading, the short-term behaviour of the slabs was monitored.

The slabs were then heated by locally exposing the central span only to heat from an array of propane-fired radiant heaters placed beneath the slabs. The thermal exposure was highly repeatable between tests [2]. Localized heating was chosen since it has been shown by the authors to be the most critical for stressed unbonded prestressing tendons, for which localized heating can rapidly lead to tendon rupture. This is due to complex interactions between stress relaxation (due to creep elongation and thermal expansion), strength and stiffness reductions at elevated temperatures (see [3] for discussion). Since Slab C incorporated a disc spring anchorage to simulate a longer total tendon length, this resulted in a smaller effective heated length ratio for this slab. Once the code-prescribed critical temperatures of the prestressing tendon were achieved, as indicated by monitoring temperatures in the concrete at the tendon axis distance depth, the radiant heaters were turned off and the cooling phase response was also monitored. The critical tendon temperature for slabs A and B was taken as 350 ℃ (based on guidance from Eurocode [4]), whereas the critical temperature was assumed to be 427 ℃ for Slab C (based on guidance from IBC guidance [5]).

2.2 Instrumentation

Deformations and temperatures were recorded at various locations during all stages of testing (including the post-tensioning and loading stages). All three slabs were densely instrumented to record temperatures, with 24 K-type thermocouples within the central span. Temperatures were also monitored outside the heated region. In the central span both unexposed and exposed surface temperatures were recorded, as well as temperatures at the prestressing and non-prestressed reinforcement axis distances. Three ‘spring-pot’ (SP) transducers were used to measure slab deflections at mid-span (one SP) and quarter-span (two SPs) for all tests. The unheated spans were also monitored for deflection at their mid spans. Two load cells were used to measure prestressing tendon stress levels at both end anchorages for all tests (including Slab B with a bonded tendon). A thermal camera was used to accurately characterize the exposed surface temperatures of the slab within the heated region. A high-resolution digital image correlation system was used to monitor deformations throughout the heating phases of the tests.

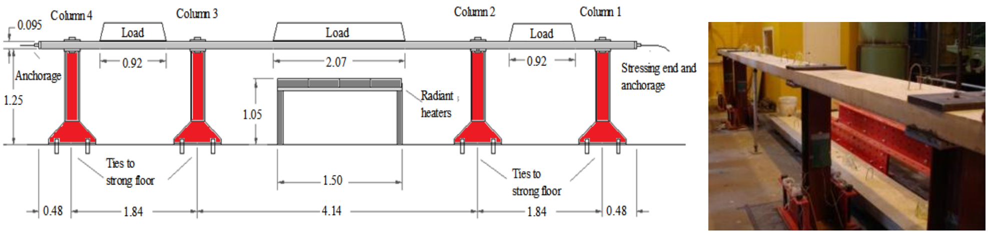

(a) (b)

Figure 1. (a) Schematic showing the test set up and selected geometry (dimensions in m) and (b) a photo of Slab A after being attached to the restraining frame.

3 DEFLECTION RESPONSE DURING HEATING AND COOLING

All three tests showed a highly complex, similar, and in several respects, unexpected deflection response during high temperature exposure, despite the structural system’s relatively simple construction. For all stages of high temperature testing, a generalised summary of the measured deflections for the Slab A is noted numerically in Figure 2 (with the deflection profile artificially amplified for clarity and shown relative to deflections at the onset of heating). The figure shows several phases of slab deformation that occurred during testing (phases denoted 1-3 in heating and 4-5 in cooling). All slabs exhibited a similar response to heating and cooling. Figure 2, shows that deflection values were generally small (peaking at approximately 10 mm or span/400). In addition, testing also revealed that with localized heating, the slabs did not follow a typical gravity deflection profile for the central span. Rather deflection was primarily influenced by thermal bowing brought on from differential thermal gradients in the through-thickness.

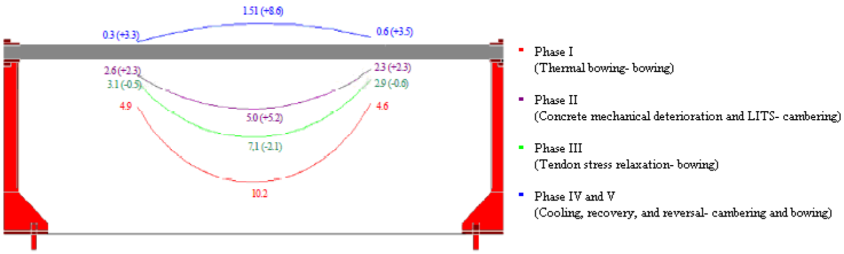

Figure 2. Slab A deflections at various phases of the test (values in mm, refer to Figure 3).

Figures 3-5 summarise the slabs' thermal and structural responses with time during both heating and cooling (measurements taken at mid-span). For rapid comparison, these figures present the mid-span vertical deflection relative to start time of heating, maximum thermal gradient (i.e. difference in temperature between the heated face and the cool face), exposed soffit surface temperature, and prestressing tendon (axis distance) temperature with time from the onset of heating. The average lateral restraining force developed on the 4 columns (measured by instrumenting and calibrating the vertical cantilever column supports with electrical resistance strain gauges) as well as the prestressing tendon stress level measured at the end anchorages for all tests are also shown. While such a complex and interesting deflection response has not been previously observed in traditional 'pass-fail' testing of simply supported elements tested in furnaces, they have considerable importance for demonstrating a credible ability to model real PT concrete structures when exposed to fire; a discussion of, and possible explanations for, the observed physical mechanisms that might be responsible are therefore given in this section.

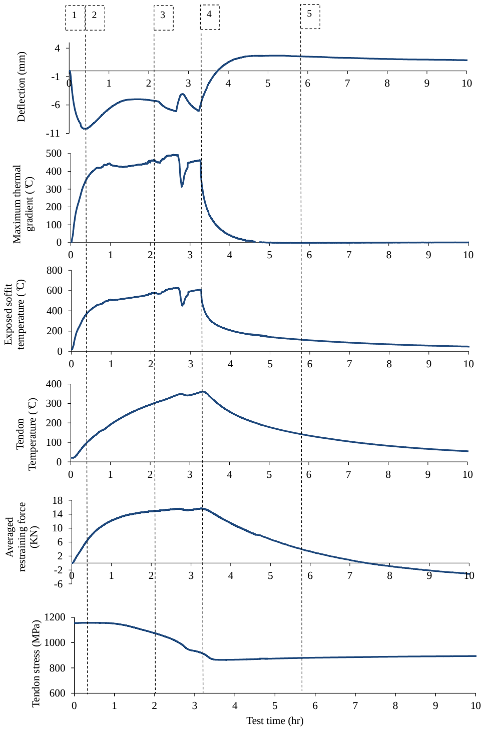

Figure 3. Slab A behavioural response (unbonded).

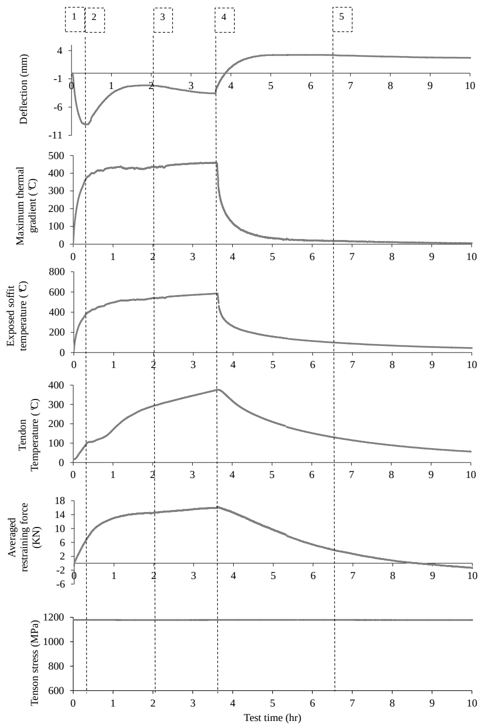

Figure 4. Slab B behavioural response (bonded).

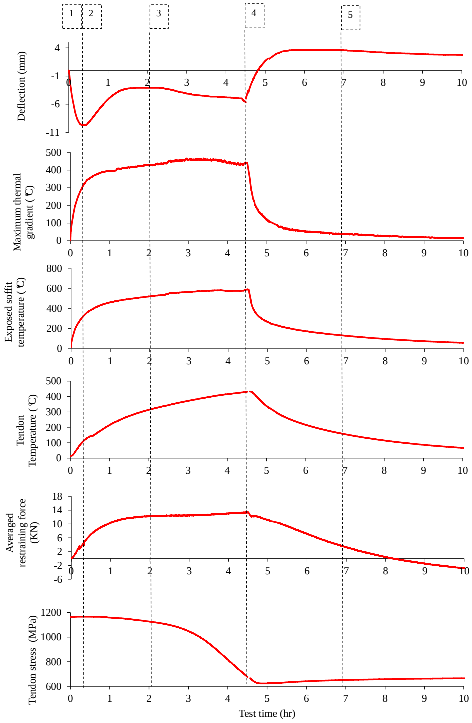

Figure 5. Slab C behavioural response (unbonded).

3.1 Phase I – Thermal Bowing

The similarities in response are striking, despite the differences in prestress characteristics for the three slabs. In all tests, rapid downward deflection was observed initially. Nearly 10 mm of initial downward deflection was observed in the first 30 minutes of heating in all tests.

This behaviour is easily explained. Figures 3 - 5 show that this phase of deflection is likely dependent on thermal bowing of the concrete. This is influenced by increasing thermal gradients with time (>350 ℃) and the resulting differential thermal expansion of the concrete through its thickness. The resulting restraining forces measured during this phase also increase with the development of the thermal gradient. Since prestressing tendon temperatures were observed to peak around 100 ℃ during this phase in all slab tests, little stress relaxation is expected. Indeed, a small *increase* in tendon stress (approximately 10 MPa in both unbounded slabs A and C) due to mechanical re-stressing of the prestressing tendons in Slabs A and C from bowing and slab elongation would be expected and is observed.

This phase ends when deflection reverses and the slabs begin to deflect upwards.

3.2 Phase II – Concrete Mechanical Deterioration and LITS

The second phase, showing upward deflection of the slab (i.e. a cambering of 5 - 7 mm in all tests), is less easily explained. Figures 3-5 indicate that cambering is observed despite an increasing thermal gradient for the full duration this phase. The gradient reaches 420-435 ℃ by the end of the phase and would lead to an expectation of additional thermal bowing and downward deflection in the absence of any prestressing force. An increase in restraining force also continues to closely follow the trends of an observed temperature gradient increase; however the slabs do not continue to deflect downward. It is clear that multiple, interrelated thermal and physical mechanisms must be occurring to cause this response.

This cambering response may be influenced by loss of stiffness of the heated concrete near the heated face. The exposed surface of the concrete in all cases in this phase ranges from 400 to 550 ℃. Concrete is known to suffer substantial stiffness losses at these temperatures. This stiffness loss supports an upward movement of the effective neutral axis of bending due to the eccentric prestress changes within the heated region. With the loss of stiffness and the maintenance of high prestressing levels in the tendon (measured prestress relaxation was at most 10% by the end of this phase for slabs A and C) it would be expected that the slabs would camber during this phase in testing. Under high initial compressive forces induced on the slab from post-tensioning, the upward movement of the slab can also be influenced by the occurrence of load-induced thermal straining (LITS) of the concrete within the heated region (see [6] for further discussion of LITS). The deflection response is further complicated by a possible (however minor in this case) shift in tendon eccentricity due to the melting of the polypropylene extrusion sheath (slabs A and C) or plastic corrugated duct (Slab B). This may occur for tendon axis distance temperatures exceeding 100 ℃ and would decrease the tendon eccentricity by at most 2 mm. This eccentricity change would have had a very small contribution to actually increase downward deflection (rather than cause camber). Phase II was considered to have ended when slab cambering transitioned once again into a downward deflection trend.

3.3 Phase III – Tendon Stress Relaxation

Cambering ceased in Phase II, followed once again by downward deflections when the prestressing tendon temperatures neared 300 °C, as is indicated in Figures 3-5. This deflection was small at approximately 2 mm for all slabs.

In Phase III, the deflection trend resembles the beginnings of a traditional creep curve for a steel prestressing tendon [3]; this appears as the result of the known tendon stress relaxation at higher tendon temperatures, due to thermal relaxation and creep elongation and causing an effective loss of pre-compression of the slab. Gales et al. 2012 [3] have previously identified that most modern prestressing tendons show rapidly accelerating creep at temperatures above 300 °C. The resulting reductions in tendon stress can cause global increases in deflection for the PT slabs, thus cancelling out the cambering effects of the locally heated region that occurred in Phase II. During Phase III, the thermal gradient is still observed however it is almost stationary and the rate of this increase is diminished significantly; subsequently additional deflection anticipated from thermal bowing is considered to be small. In Slab B there is a possibility that the bond between the tendon and grout had deteriorated effectively making a section of the PT reinforcement unbonded. This effect would create localized tendon stress relaxation zones within the slab. A post-test slab evaluation of the Slab B identified a region of slough off cover spalling, within this region significant cracking in the post tensioning grout was confirmed. This indicates that the bond may be compromised and localized relaxation of the tendon permitted.

Interestingly, in the test on Slab A, the radiant heaters failed briefly due to ‘blowback’ during Phase III. Figure 3 shows the sudden deflection response of the slab in cooling, immediately and profoundly effecting nearly all measurements and clearly demonstrating the importance of differential thermal gradients on concrete structures (i.e. as for steel structures, thermal deflections are far more significant than mechanical ‘load induced’ deflections). When the heaters failed, cooling of the slab began and cambering the slab resulted due to a decrease of the thermal gradient. The heaters were then re-ignited, and the slab, again under increasing thermal gradient, began to deflect again and resumed its similar response.

None of the slabs were taken to ‘failure’ (i.e. structural collapse). Heating was terminated once the prestressing steel tendons reached temperatures considered to be ‘critical’ (350 °C as in Europe [4] for slabs A and B, and 427 °C as in USA [5] for Slab C).

3.4 Phases IV and V – Cooling, Recovery, and Reversal

Upon halting the heat exposure the cooling phase was monitored for several hours (during phases IV and V). During these stages all slabs reversed their deflections by cambering approximately 7 – 9 mm after cooling.

Phase IV appears to be controlled by thermal contraction due to reductions of thermal gradient. This behaviour was briefly observed for Slab A in Phase III during ‘accidental’ cooling as noted above. During the initial portions of Phase IV, the prestressing steel tendon continued to relax in prestress, despite the overall cooling of the slab. This may be influenced by accelerating creep damage of the prestressing tendon as its temperatures still exceeded 300 °C, and to the ‘thermal wave’ which will continue in the concrete even after the heating is removed. Once the prestressing tendon temperature dropped below 300 °C this prestress loss stopped and subsequently the tendon began to regain (recover) prestress as a result of thermal contraction of the steel on cooling. This would have also influenced the slabs’ deflections. However, rather than arch the slab up in camber due to tendon stress increase, the slab once again begins to show a new deflection phase. Phase V could be considered to occur when the exposed soffit of the slabs began to near 100 °C in cooling. The slabs all began to deflect down slightly at this stage of testing. This deflection behaviour could be explained by the slabs’ absorbing moisture from the atmosphere and thereby rehydrating the lime in the Portland cement. This action (however minor) could cause an expansive effect on the slab and act to deflect the slab downward.

Interestingly all slabs exhibited a relative camber after cooling (i.e. after cooling the residual deflection of all slabs was *up* relative their pre-heating condition). All slabs indicated a gradual decrease in the relative restraining force exerted on the columns, settling on a relative residual ‘pull-in’ restraining force on all supporting columns. All slabs also had less recovery of deflection when compared to the thermal bowing observed in Phase I. These behaviours are indicative of permanent plastic deformation of the structural system (both concrete and steel prestressing) and could potentially have significant consequences on a post-fire assessment of structural stability in real buildings (i.e. assessment of UPT buildings cannot necessarily rely on vertical slab deflection to provide an indication of structural damage due to heating). Slabs A and C exhibited more deflection as compared with Slab B, this likely due to prestress relaxation in the unbounded tendons for these two slabs. The bonded slab (Slab B) presumably maintained a greater proportion of its initial prestress and thus experienced the least overall deflection throughout testing.

3.5 Summary

For every fire and every PT structural configuration that might exist in a real UPT building the aforementioned five phase deflection response clearly cannot be assumed to be observed in all cases. As suggested by the discussion above, the deformation response of the slabs is controlled by a number of test variables and thermal/physical mechanisms. For instance, the severity and uniformity of heating induced on the slabs will play a highly significant role on the degradation of concrete properties and the in-service stress level of the post- tensioning steel. Different structural dimensions, PT tendon drape, loading level, restraining frame stiffness, and two-way reinforcement and prestressing (membrane actions) would all influence the observed response in a real building; in ways which are not yet understood. A different deflection response should be expected if experimental procedures are even slightly varied. The purpose of the current paper is simply to demonstrate the complexity of response, as a warning to those who claim that the response of UPT structures in fire is credibly understood; <u>they are not</u>. In the absence of additional testing, modelling may shed light on the response of these structures in different structural configurations. This assumes that modelling can demonstrate an ability to account for the complexities observed in the tests presented herein.

4 STEERING FUTURE RESEARCH

The tests presented herein provide real data for the development and validation of computational tools to enable analysis of full structural response of PT buildings in real fires. The slabs were not designed to provide ‘pass-fail’ fire test criteria for prescriptive design; such tests cannot account for the complexities of as-built construction. The tests represent the most simplistic experimental design possible which account for as many relevant as-built construction features as possible. The validation of modelling capability based on these (and other) tests will hopefully eventually enable designers to develop rational fire safety strategies for PT concrete buildings (or other optimized concrete building types). However, several areas require additional research attention to correctly account for the complexities in deformation observed in these tests; these are:

- **Mechanical re-stressing of unbonded tendons** – When exposed to heating, many inter-related structural mechanisms may influence the stress level of unbonded prestressing tendons. Additional research should attempt to consider the roles of thermal bowing, loss of pre-compression, and restraint on the stress level of unbonded tendons.
- **High temperature relaxation of prestressing tendons** – Deformation was shown to be heavily dependent on tendon stress relaxation due to thermal relaxation and creep elongation (particularly in Phase III). Although efforts have been made by the authors in the past to describe this behaviour with simplified modelling [3], an increasing error with the rate of heating can be identified in that work.

Future work must be done to define a tendon stress relaxation model that can correctly account for variable heating rates.

- **Consequences of tendon rupture** – None of the tests were able to examine the effect of prestressing steel rupture on load carrying capacity of UPT slabs. Research is needed to understand the effects of immediate load shedding to bonded (non-prestressed) steel reinforcement and whether the structure can maintain the applied load after tendon rupture.
- **Concrete behaviour in fire** – A detailed study into the thermal and mechanical behaviour of concrete and concrete structures may aid modelling efforts in the future to evaluate the responses observed during these tests. In addition, spalling; cracking; LITS; stiffness loss; material parameters in cooling etc. all need research to give confidence in modelling concrete behaviour. This is crucial to fully evaluate the behaviours observed; particularly the deformation shown in Phase II in all tests.
- **Accurate model inputs** – Any high temperature model must adequately account for the initial conditions of the structural system. For example the degree of pre-compression, forces exerted on the columns from post-tensioning etc. will aid in determining the degree of flexural/compressive prestress in the concrete at the start of heating, thereby allowing appropriate consideration of load-induced temperature effects.

5 CONCLUSIONS

The continuous, restrained, one-way spanning PT slabs tested herein exhibited five distinct phases of deflection under severe, localized heating and cooling. These trends appear to be influenced by a complex interplay between stiffness degradation of concrete, prestressing steel tendon plastic deformation, and differential thermal expansion/contraction. Attempts to numerically model these simplistic structural systems in fire must defensibly account for these (and other) complexities to be considered entirely credible; research needs have been identified to progress towards this objective. This will lead eventually to the development of rational fire safety strategies for optimised PT concrete buildings in real fires.

ACKNOWLEDGEMENTS

The authors acknowledge the financial support of NSERC Canada, The Ove Arup foundation, Ove Arup and Partners Limited, the Royal Academy of Engineering, and the School of Engineering at the University of Edinburgh. Dr Tim Stratford and Michal Krajcovic are also acknowledged for their considerable assistance.

REFERENCES

[1] Gales, J., Bisby, L., and Gillie, M, “Unbonded Post Tensioned Concrete in Fire: A Review of Data from Furnace Tests and Real Fires”, *Fire Safety Journal*, 46, 151-163, 2011.

[2] Gales, J., Bisby, L., Stratford, T., and Krajcovic, M. “Tests of continuous post-tensioned concrete slabs under localised fires”, *Interflam 2013: 13th International Conference and Exhibition on Fire Science and Engineering.* Royal Holloway College, Windsor, UK. 1131-1142, 2013.

[3] Gales, J., Bisby, L., and Stratford, T. “New Parameters to Describe High Temperature Deformation of Prestressing Steel determined using Digital Image Correlation” *Structural Engineering International*. 22(4), 476-486, 2012.

[4] IBC. “International Building Code.” International Code Council, USA, 2012.

[5] CEN. “Eurocode 2: Design of Concrete Structures, Parts 1-2: General rules- Structural fire design, EN 1992-1-2.” European Committee for standardization, 2004.

[6] Khoury, GA. “Strain of Heated Concrete during Two Thermal Cycles. Part 2: Strain during First Cooling and Subsequent Thermal Cycle” *Magazine of Concrete Research*, 58, 387-400, 2006.

8th International Conference on Structures in Fire
Guo-Qiang LI, Venkatesh K. R. KODUR, Shou-Chao JIANG, Jian JIANG, Su-Wen CHEN, Guo-Biao LOU (Eds.)
Shanghai, China, June 11-13, 2014

FIRE RESISTANCE BEHAVIOR OF REINFORCED CONCRETE BEAMS STRENGTHENED WITH NEAR SURFACE MOUNTED CFRP STRIPS

Jiang-Tao Yu*, Jing Chen*, Yu-An Liu* and Zhou-Dao Lu*

*Research Institute of Engineering & Disaster Reduction, Tongji University, Shanghai, China
e-mails: jyjuly@163.com

Keywords: Fire resistance, CFRP, Near surface mounted, Fire insulation

Abstract: *Near-surface-mounted (NSM) technique is becoming increasingly popular in the strengthening of reinforced concrete (RC) structures. The existing of concrete cover protects CFRP from environmental and mechanical impact, and may potentially enhance the fire resistance of NSM strengthened beam. To figure out the performance of NSM beam exposed to fire, totally 12 RC simply supported beams were constructed for test. 11 CFRP strengthened beams and 1 normal beam was constantly loaded under ISO 834 standard fire. 4 main factors, namely strengthening method (near surface mounted technique (NSM) / externally bonded technique (EB)), type of adhesive (epoxy / magnesium oxychloride cement), fire protection materials (thin intumescent coating / thick coating) and fire insulation pattern (rabbet / single-sided / three-sided), were highlighted in this paper. In general, on three-sided, MOC, thick coating protected NSM beam showed the best fire resistance in test.*

1 INTRODUCTION

Externally bonded (EB) CFRP strengthened method is one of the most popular methods used in the rehabilitation of reinforced concrete (RC) structure. Because CFRP is flammable and the adhesive (mostly epoxy) is prone to softening under high temperature, its bearing capacity is really hard to be guaranteed under fire exposure [1,2-5]. Studies [1,2,6,7] have shown that CFRP materials with no fire protection has little resistive capacity in fire. Additionally, in the service life, structures will be inevitably exposed to a variety of loads, for example, thermal impact, wind load or earthquake, which would incur damages to fire insulation's or even total falling off. When structure strengthened with external CFRP is subjected to fire, the flaw of fire protection will no longer prevent CFRP from burning, and lead to a further dropping off of fire insulation, which at last cause a totally loss of fire protection.

In recent years, near surface mounted (NSM) strengthened method is widely used at home and abroad. CFRP rebar or strips are embedded into the concrete cover, which can not only avoid abnormal loading, like fraction and impact force, but also reduce surface treatment work of concrete and improve the working efficiency. Compared with EB, NSM has better fire resistance behaviour [8], whose advantages are as follows: firstly, CFRP is wrapped up by adhesive, which can isolate the oxygen and reduce strength reduction due to oxidation. Secondly, both CFRP and adhesive are coated by concrete cover, so their temperature should be lower than those strengthened by EB, which will significantly delay the time of softening. Last but not least, the exposed area of NSM is less than EB, so the damage of fire insulation protection has less effect on NSM.

To sum up, fire resistant behaviour of NSM strengthened method is supposed to be better than that of EB strengthened method theoretically. In this paper, fire tests were carried out on 11 CFRP flexural strengthened concrete beams and 1 normal beam. The influence of strengthening methods (embedded / stick method), type of adhesive (epoxy / magnesium oxychloride cement), fire protection materials (thin intumescent coating / thick coating) as well as fire protection pattern (rabbet protection / single beam bottom protection / on three sides) were studied. The reason of CFRP strengthened beams deterioration in fire were analysed at the end of paper.

2 TEST BEAMS

12 concrete beams were cast for the test [9]. The details of specimens are showed in Table 1 and Figure 1. The test beams had a design span of 2600 mm and the loading span was 2400mm as well as a cross section of 200mm×300mm uniformly. Both the longitudinal reinforcements were 4 φ 12, with stirrup of φ 10@100. The axial compressive strength of concrete was 43MPa. The adhesive for CFRP was epoxy (EP) and magnesium oxychloride cement (MOC) respectively. Two kinds of fire-retardant coating were adopted for test. The thick one was tunnel fire-retardant coating SH-1, and the thin one was ultra-thin intumescent fire-retardant coating. The two CFRP strips with cross section of 2mm×10mm were embedded in to the bottom of each beam. The corresponding width of CFRP sheet was 146mm (0.167 mm in thickness). Both CFRP sheet and strip have a uniform length of 2600mm in longitudinal direction.

Table 1. Specimen program.

No	Specimen	Temperature	Strengthening technique	Adhesive	Insulation material	Coating pattern	Coating thickness
1	T0	ISO 834	\	\	\	\	\
2	TA-0		NSM	MOC	\	\	\
3	TA1		NSM	EP	Thick coating	Rabbet	10mm
4	TA2					3-sided	25mm
5	TA3			MOC		Rabbet	10mm
6	TA4					3-sided	25mm
7	TA5			EP	Thin Intumescent coating	1-sided	2mm
8	TA6					3-sided	2mm
9	TA7			MOC		1-sided	2mm
10	TA8					3-sided	2mm
11	TB1		EB	EP	Thick coating	3-sided	25mm
12	TB2			MOC			

Beams were tested in two batches. Each batch included 6 beam specimens. The layout of heating and loading is shown in Figure 2. The first batch consisted of no fire protection beams (T0 and TA0) and weakly protected beams (TA1, TA3, TA5 and TA7), and the concentrated load applied by hydraulic jacks was constant 55kN. The beams in the second batch were strongly fire-protected beams, which consisted of TA2、TA4、TA6、TA8、TB1 and TB2, and the concentrated load was constant 75kN. The batch temperature rose according to ISO834 temperature curve. When the deformation value at middle span reached 50mm, the specimen were believed reaching its ultimate state in fire, and test were terminated.

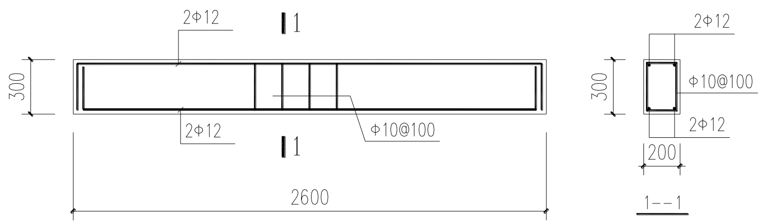

Figure 1. Specimen size and reinforcement situation.

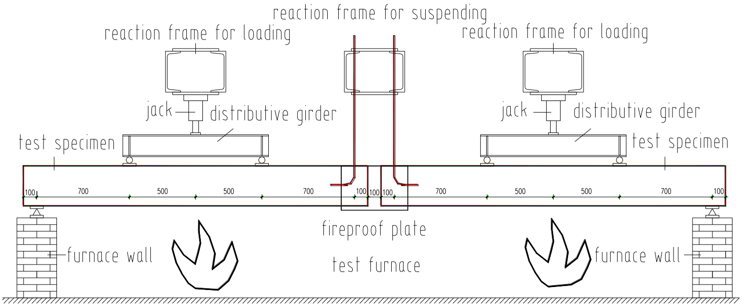

Figure 2. Schematic diagram of specimen under fire and loads.

3 TEST ANALYSIS

3.1 Failure mode

After fire exposure, specimens were taken out of batch and cooled in air. Specimens TA0, TA1 and TA3 were no or weakly fire-protected NSM beams. It was found after test that insulation material and adhesive in the rabbet cracked longitudinally in bending region of beam, and the thick coating filled in the rabbet cracked and fell off partially. EP adhesive turned black as well as MOC turned dark grey. Both EP and MOC adhesives were seriously damaged and could be crushed by fingers easily; CFRP strips apparently were oxidized and changed to flocculent particles. TA5 and TA7 were thin coating, single-sided protected NSM beams. The fire-retardant coating expanded in the process of heating. At the end of test, most of coating was found falling off due to the air disturbance in combustion.

In the second fire test, specimen TA2 and TA4 were thick coating, three-sided protected NSM beams. After test, we could see a main crack in the thick fire-retardant coating with much tiny crack around, and the colure turned from grey to white, which is showed in Figure 3. Specimen TA6 and TA8 were thin coating, three-sides protected NSM beams. The ultra-thin coating was seen nearly disappearing because of the air disturbance, as showed in Figure 4. The adhesive for CFRP strip showed similar observations as that in in the first test.

TB1 and TB2 were thick-coating protected beams strengthened with externally bonded CFRP sheets. Delaminate the thick fire-retardant coating of TB1 and TB2 when beams after fire, we saw that EP adhesive of TB1 had completely disappeared and black carbide trace left on the surface of beam, while MOC in TB2 basically remained intact, and insulated CFRP from exposing directly to fire.


Figure 3. Crack in thick fire-retardant coating .


Figure 4. thin fire-retardant coating fell off.

3.2 Deflection development and fire endurance of specimen

The mid-span deflection vs. fire duration curves of all specimens in the first and second tests are listed in Figure 5 and Figure 6 respectively. Table 2 shows the quantitative fire duration. TA3 was rabbet protected beam and its deflection-time curve was close to the unprotected beam TA0, which indicates that rabbet protection pattern had little effect on enhancing the fire resistance of specimen. TA5 and TA7 were both single-side protected beams with EP and MOC adhesives respectively. Compared with TA3 and TA0, TA5 and TA7 show smaller deflection increasing rate in heating, indicating that single-sided protection was more effective than rabbet protection. Additionally, TA7 with MOC adhesive performed even better than EP beam, showing the advantage of MOC adhesive under elevated temperature. Single-sided protection on the bottom of beam retarded heat transferring from the bottom side, but had little effect on the lateral sides that was exposed to fire simultaneously, and the temperature of steel in the corner of beam didn't be influenced significantly.

Both TA7 and TA8 were thin coating protected and NSM strengthened beams. TA8 has a three-sided protection and the corresponding fire exposure time was 126 minutes, while that of TA7 (single-sided) was 110 minutes. What's more, TA2, TA4 and TA8 resisted fire exposure of more than 2 hours, showed better fire resistance performance among all the 12 specimens. It should be noted, all these 3 specimens were protected by 3 sides.

Both TA7 and TA5 were thin fire-retardant, single-sided protected, NSM strengthened beams. TA7 was strengthened with MOC, as TA5 was strengthened with EP. The increasing rate curve of TA7's deflection was slower than that of TA5, and fire endurance of TA7 was longer than that of TA5, which indicated that under same protection, fire resistance of NSM beams with MOC adhesive was better than it with EP.

In figure 6 and Table 2, TA2 and TA4 were both thick coating, three-sided protected and NSM beams, and performed much better than TB1 and TB2 protected in the same say but EB strengthened. Which showed that under same protection measure, NSM strengthened method exhibited better performance than EB strengthened method.

TA4 and TA8 were strengthened with NSM strips and MOC adhesive. TA4 was three-sided thick coating protected beam as TA8 was three-sided, thin coating beam. It could be found from figure 6 and Table 2 that the remarkable difference between TA4 and TA8. Both thick fire-retardant coating and thin intumescent fire-retardant coating could restrain the temperature rising, but thin intumescent fire-retardant coating was sensitive to the environment in fire, and severe air turbulence did reduce the adhesion of coatings, which at last leaded to the failure of fire protection. In comparison, thick coating shows overwhelming advantage on fire insulation over thin fire-retardant coating.

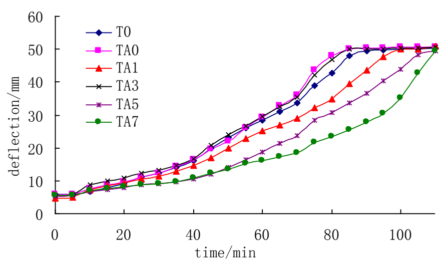

Figure 5. The deflection - time curves at mid-span. (1st batch)

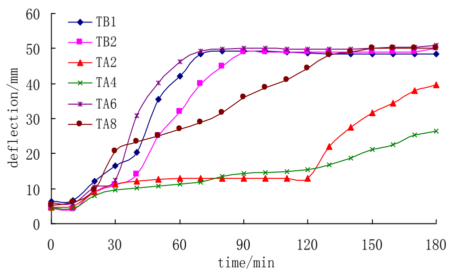

Figure 6. The deflection - time curves at mid-span (2nd batch).

Table 2. Fire endurance of specimen.

1st batch test (55kN)				2nd batch test (75kN)			
Specimen	Elapsed time (min)	Specimen	Elapsed time (min)	Specimen	Elapsed time (min)	Specimen	Elapsed time (min)
T0	86	TA3	83	TA4	>180	TA2	>180
TA0	82	TA5	106	TA8	126	TA6	72
TA1	101	TA7	110	TB2	86	TB1	72

3.3 Relationship between deformation and temperature of steel and bonder

Figure 7 and Figure 8 illustrate respectively the deflection vs. steel temperature curve and deflection vs. adhesive temperature curve of beams in the first batch test. It was showed in Figure 7 that due to the contribution of CFRP strips, all the deflection of strengthened beams TA0, TA1, TA3, TA5 and TA7 was smaller than that of T0 at the same steel temperature. Figure 5 illustrates that TA0, TA1, and TA3 perform similarly in deflection-time curves. From Figure 7 and Figure.8, we see their adhesive and steel temperatures were fairly close. Whereas, at the same deflection, the temperatures, either at adhesive or near steel, of single-sided protected beams, saying TA5 and TA7, were less than the rabbet protected beams, TA1and TA3. It further verifies that thin coating but single-side protection was more effective than thick coating but rabbet protection. Rabbet protection is again proved inefficient in protecting CFRP.

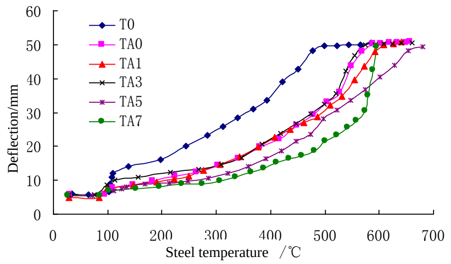

Figure 7. deflection-steel temperature curve of beams in the first batch.

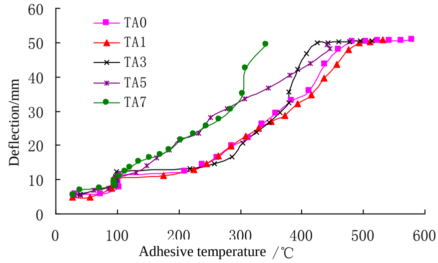

Figure 8. deflection-adhesive temperature curve of beams in the first batch.

Figure 9 and Figure 10 plot the deflection-steel temperature curve and deflection-adhesive temperature curve of specimens in the second test, respectively. It was showed in Figure 9 that EB strengthened beams, TB1and TB2, finished most of the deflection and reached their limits when steel temperature was about 90℃, and in this period, their adhesive temperatures rose from 90℃ to 148℃ and from 86℃ to 145℃, respectively. Because of the different bonding position, adhesive temperature of NSM beams, TA2 and TA4, was always lower than that of TB1 and TB2. It further demonstrates the remarkable superiority of NSM in fire resistance. Comparison is also made between TA2 and TA4. Figure 9 and Figure 10 shows the steel and adhesive temperature of TA2 and TA4 was fairly close at early stage, but separated as time elapsed. Specifically, when steel temperature exceeds 200℃, the deflection of TA2 increased quickly and exceeds it of TA4. This can be partially attributed to the difference of bonding property of MOC and EP under high temperature. Figure 9 demonstrates that the deflections magnitude of three-sided, thin coating protected, NSM beams (TA6 and TA8) was between three-sided, thick coating protected, EB beams (TB1 and TB2) and three-sided, thick coating protected, NSM beams (TA2 and TA4). The CFRP of TA6, TA8 contributed less than that of TB1and TB2, but more than that of TA2 and TA4. The effect of NSM over EB seems more significant than that of fire protection.

Figure 10 demonstrates the influences of strengthening pattern and fire protection on adhesive temperature, which is quite similar with that of steel reinforcement in Figure 9 and will not be further discussed in this paper.

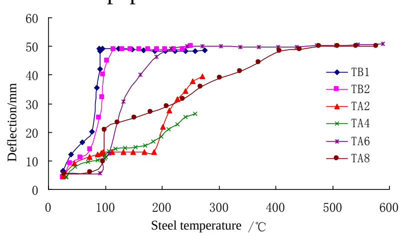

Figure 9. Deflection-steel temperature curve of beams in the second batch.

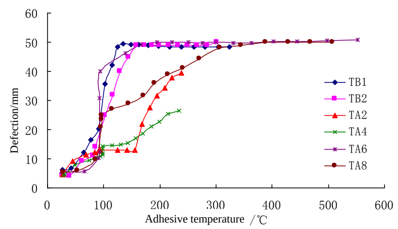

Figure 10. Deflection-adhesive temperature curve of beams in the second batch.

4. CONCLUSIONS

In this paper, fire tests according to ISO834 were carried out on 11 CFRP flexural and one non-strengthened RC beam. The tests mainly focused on the influence of strengthening technologies (NSM /EP method), the type of adhesive (epoxy organic adhesive / magnesium oxychloride cement), fire protection materials (ultra-thin intumescent fire-retardant coating / thick cementitious coating) as well as fire protection position (rabbet protection, single-sided bottom protection or three-sided protection) on the fire endurance of bending structural members under elevated temperatures. The experimental results show as follows:

(1) Both thick fire-retardant coating and ultra-thin intumescent fire-retardant coating can effectively restrain the thermal transfer in beams cross-section, but ultra-thin intumescent coating was sensitive to the air turbulence. The shedding of coating degraded fire protection effect and at last leaded to failure of bending specimens. Compared with thin fire-retardant coating, thick fire-retardant was more effective.

(2) Different protection pattern made great difference in fire. Simply protecting the strip rabbet cannot effectively restrain CFRP's temperature from increasing, while single-sided protection of CFRP strip shows enhancement. The three-sided protected beams resisted fire much longer than the beams under rabbet and single-sided protection. Therefore, three-sided protection is really commended for FRP strengthened structural member.

(3) Under same protection pattern, NSM strengthened beams had longer fire endurance than EB strengthened beams, which suggested the superiority of NSM strengthened method in fire resistance.

(4) Under same protection measure, NSM strengthened beams with MOC adhesive had stronger fire endurance than those with EP, which showed the advantage of MOC material under elevated temperatures.

REFERENCES

[1] HU Kexu and HE Guisheng, "Experimental Study on Fire Protection Methods of Carbon Fiber Reinforced Polymer Strengthened Reinforced Concrete Beams", *Journal of Tongji University*, 34(11):1451-1456, 2006.

[2] GAO Wanyang, HU Kexu and LU Zhoudao, "Research Trends and Progress of CFRP strengthened structure exposed to fire"， *2nd International Conference on Advances in Concrete & Structures* ,2008

[3] GAO Wanyang, LU Zhoudao and HU Kexu, "Modeling the behavior of insulated CFRP-strengthened reinforced concrete beams exposed to fire"，*2nd International Conference on Advances in Concrete & Structures*, 2008.

[4] Hu kexu and Gao Wanyang, "Fuzzy Synthetic Evaluation of Fire Hazard for NO.1 Department Store of Shanghai", *Progress in Safety Science and Technology Series*, 2006

[5] ZHENG Wenzhong, WAN Fuxiong and LI Shiguang, "Expermiental research of fire performance on reinforced concrete slabs strengthened w ith CFRP sheets bonded with inorganic adhesive", *5th International Conference on Advances in Concrete & Structures* , 31(10):89-97 2009

[6] Gao Wanyang, "Experimental Study and Theoretical Analysis of Carbon Fiber Strengthened Concrete Beams Exposed to Fire", *Master thesis, college of civil engineering, Tongji University*, 2007

[7] Xu Zhisheng, KAI Feng and Zhang Zhenwei, "Experimental analysis of CFRP used to strengthen RC beam after fire", *Journal of Harbin institute of technology*, 37（1）：98-100, 2005

[8] Rein G., Abecassis Empis C. and Carvel R., "The dalmamock fire tests: experiments and modelling, Published by school of engineering and electronics", University of Edinburgh, 2007.

[9] YUAN Liu, "Study on Fire Resistance Behavior of Reinforced Concrete Flexural Members Strengthed with Near Surface Mounted CFRP Strips", *PhD thesis, college of civil engineering, Tongji University*, 2013

FIRE-INDUCED RESTRAINT TO COLUMNS IN CONCRETE FRAMED STRUCTURES

Nguyen T. Thang* and K.H. TAN**

* National University of Civil Engineering, Hanoi, Vietnam
e-mail: thangcee@gmail.com

** Nanyang Technological University, Singapore
e-mail: ckhtan@ntu.edu.sg

Keywords: Fire-induced, Restraint, Column, Concrete, Frame, Structures

Abstract. *This paper investigates the axial restraint exerted onto reinforced concrete (RC) columns when a fire occurs locally in a framed building. Analytical and numerical analyses are conducted on prototype reinforced concrete framed structures, in which the column can be located at different positions on the layout such as interior, exterior, and corner positions. Simplified and practical design equations are derived to determine parameters that have significant effect on axial restraint. Four worked examples are carried out to provide numerical values of restraint ratios to the investigated column. These values are practical and useful for studying the behaviour of reinforced concrete columns subjected to fire.*

1 INTRODUCTION

Due to their different thermal responses, beams and columns framing together in structures are constrained from free elongation when a localized fire occurs. It has been indicated from a numerical approach proposed by Dwaikat et al. [1] and validated by a number of experimental studies [2] that fire resistance of reinforced concrete (RC) beams increases when they are restrained. However, for RC columns the issue may be different since additional thermal-induced compression forces, coupled with deteriorations of material strength and stiffness at elevated temperatures, may cause premature failure in either squashing or instability mode. Thus, a proper evaluation of thermal-induced restraint forces on a heated column in a concrete structure is critical for the analysis of its fire resistance.

In column fire resistance analysis, thermal-induced axial restraint can be represented by a normalized ratio of axial restraint stiffness K_r with respect to column axial stiffness K_c, so that $\alpha_r=K_r/K_c$, so-called axial restraint ratio. It was specified in a number of research works [3,4] that for steel columns, this restraint ratio α_r is in a practical range of 0.01 to 0.35. However, there has not been any reported practical range for α_r of reinforced concrete columns.

In this paper, axial restraint to reinforced concrete columns when a fire occurs locally in a framed building is investigated analytically. Theoretical analyses are conducted on columns located at different positions on a typical regular building layout, namely, interior, exterior, and corner positions. Simplified and practical equations are derived to determine the critical parameters. A number of worked examples are conducted to provide practical values of restraint ratio when evaluating the fire resistance of RC columns at different locations in a building layout.

2 ANALYTICAL DERIVATIONS

The layout of one storey (j) of a prototype concrete framed building is shown in Figure 1(a). There are four and three beam spans, namely, $Bx(j)$ and $By(j)$, with equal beam lengths of L_x and L_y along x- and *y*-directions, respectively. Basically, there are three types of columns in this layout. Columns supporting storey (*j*) that are located at interior, exterior, and corner positions are denoted as $C^i(j)$, $C^e(j)$, and $C^c(j)$, respectively. Typical frame elevations in A- and 3-axes are respectively depicted in Figures 1(b) and 1(c), in which it is assumed that the building has a number of *n* storeys with an identical storey height = *H*.

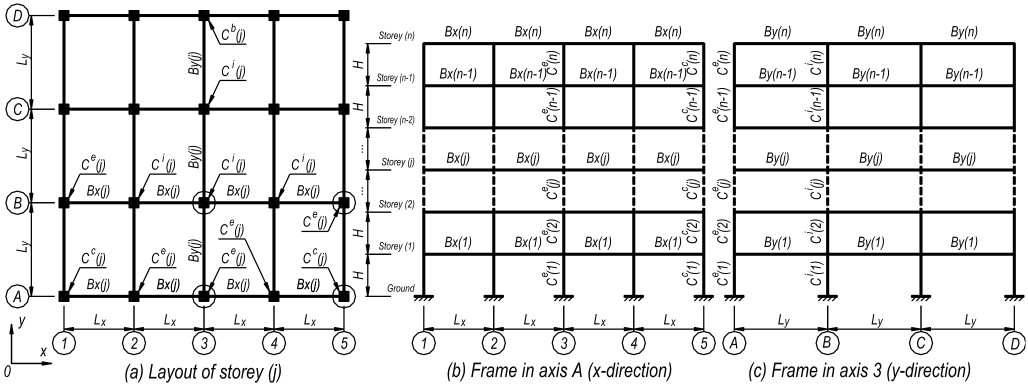

Figure 1. Prototype concrete building.

When a localized fire occurs near to a column supporting storey (*j*), the heated column tends to thermally expand in the vertical direction. As a result, this column exerts vertical forces onto the ends of all the beams framing into its lower and upper ends. For the heated columns at corner and exterior positions, this phenomenon is shown in Figures 2(a) and 2(b), respectively.

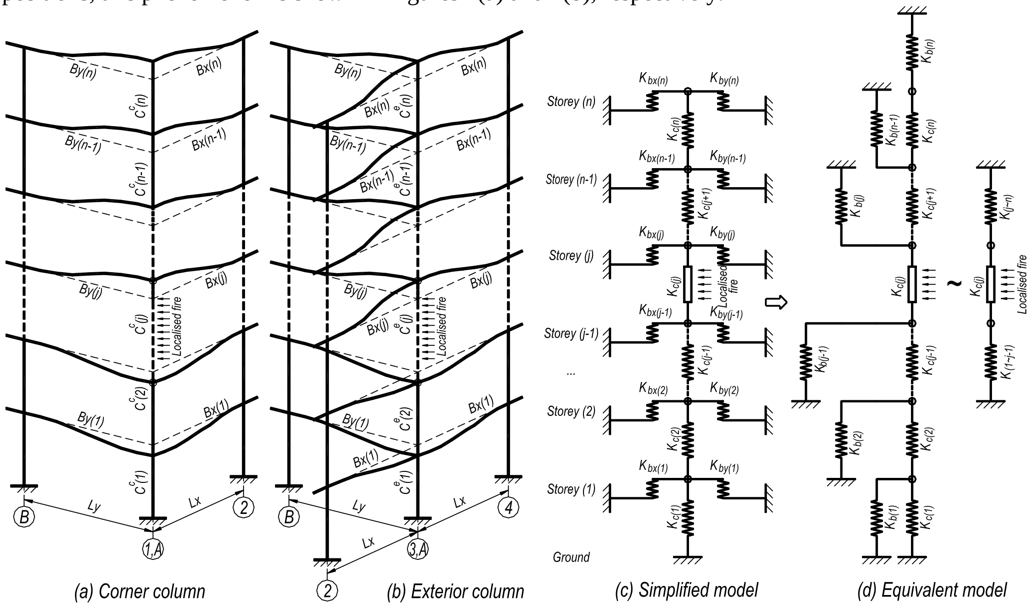

Figure 2. Localized heating on a column supporting storey (*j*).

Since the other columns at the far ends of adjacent beams are still either unheated or at lower temperatures, the beams will undergo differential vertical movements of their ends and exert a vertical restraint force through their own flexural stiffness back onto the heated column, which is $K_b=12E_bI_b/L^3$, where E_b is material elastic modulus, I_b is the second moment of area of the beam cross section, and *L* is the beam span. Hence, the heated column experiences a restraint stiffness, K_b, to its thermal elongation that comes from the congregate sum of flexural stiffness of all adjacent beams framing to that column end. The total restraint that the beams on storey (j) exerted onto the heated column is shown in Equation (1).

$$K_{b(j)} = K_{bx(j)} + K_{by(j)} = n_x \times \frac{12E_b I_{bx(j)}}{L_x^3} + n_y \times \frac{12E_b I_{by(j)}}{L_y^3} \tag{1}$$

where $K_{b(j)}$ is the total flexural stiffness of adjacent beams at storey (j); $K_{bx(j)}$ and $K_{by(j)}$ are the flexural stiffness values of adjacent beams in x- and y-directions, respectively; n_x and n_y are the number of beams in x- and y-directions framing into the heated column, respectively. For interior columns, n_x=n_y=2. For exterior columns on axes A and D (Figure 1(a)), n_x=2 and n_y=1. For exterior columns on axes 1 and 5, n_x=1 and n_y=2. For columns at four corners, n_x=n_y=1.

Together with the aforementioned beams, the columns below and above also contribute on the heated column axial restraints through their own axial stiffness values, namely, $K_c(i)$.

It can be seen from the simplified and the equivalent models respectively shown in Figures 2(c) and 2(d) that the total axial restraint that the heated column is subjected to, K_{tot}, can be determined as follows:

$$\frac{1}{K_{tot}} = \frac{1}{K_{1\sim(j-1)}} + \frac{1}{K_{j\sim n}} \tag{2}$$

where the terms $K_{1\sim(j-1)}$ and $K_{j\sim n}$ are respectively the combinations of axial restraint stiffness of all the related beams and columns below the heated column (i.e. from storey 1 to storey (j-1)) and above the heated column (i.e. from storey (j) to storey (n)), and can be calculated as follows:

$$K_{1\sim(j-1)} = K_{b(j-1)} + \cfrac{1}{\cfrac{1}{K_{c(j-1)}} + \cfrac{1}{K_{b(j-2)} + \cfrac{1}{\cfrac{1}{K_{c(j-2)}} + \cfrac{1}{K_{b(j-2)} + \cfrac{1}{\cfrac{\dots}{\dots K_{b(2)} + \cfrac{1}{\cfrac{1}{K_{c(2)}} + \cfrac{1}{K_{b(1)} + K_{c(1)}}}}}}}}} \tag{3}$$

$$K_{j\sim n} = K_{b(j)} + \cfrac{1}{\cfrac{1}{K_{c(j)}} + \cfrac{1}{K_{b(j+1)} + \cfrac{1}{\cfrac{1}{K_{c(j+1)}} + \cfrac{1}{K_{b(j+2)} + \cfrac{1}{\cfrac{\dots}{\dots K_{b(n-1)} + \cfrac{1}{\cfrac{1}{K_{c(n)}} + \cfrac{1}{K_{b(n)}}}}}}}}} \tag{4}$$

In fact fire incidents frequently occur at ground floor with parking areas. In this case, K_{tot} is also $K_{1\sim n}$, and can be determined by using j=1 in Equation (4).

If it is assumed that: (i) the number of storeys are infinity (n=∞); (ii) the adjacent beams in every floor are identical with a total flexural stiffness $K_{b(i)}$=K_b; and (iii) the columns in upper storeys have the same cross-section with an axial stiffness $K_{c(i)}$=K_c, Equation (4) can be simplified and the total axial restraint stiffness, $K_{r(\infty)}$, can be determined as shown in Equation (5). It is noted that the term $K_{r(\infty)}$ can also be considered as the upper bound of the axial restraint stiffness.

$$K_{r(\infty)} = K_b + \frac{1}{\frac{1}{K_c} + \frac{1}{K_{r(\infty)}}} \Rightarrow K_{r(\infty)} = \frac{K_b + \sqrt{K_b^2 + 4K_bK_c}}{2} \tag{5}$$

If in the building layout shown in Figure 1, the beams along both x- and y-directions are also identical in length (L_x=L_y=L) as well as in cross-section (E_bI_b), based on the terms n_x and n_y introduced in Equation (1), the upper bounds of the ratio between axial restraint stiffness with the heated column axial stiffness, namely, restraint ratio α_r, of interior, exterior, and corner columns can be simply determined in Equations (6), (7), and (8), respectively.

$$\alpha^i_{r(\infty)} = \frac{K^i_{r(\infty)}}{K_c} = \frac{4\overline{K}_b + \sqrt{16\overline{K}_b^2 + 16\overline{K}_bK_c}}{2K_c} = 2.0\times\left(n_{bc} + \sqrt{n_{bc}^2 + n_{bc}}\right) \tag{6}$$

$$\alpha^e_{r(\infty)} = \frac{K^e_{r(\infty)}}{K_c} = \frac{3\overline{K}_b + \sqrt{9\overline{K}_b^2 + 12\overline{K}_bK_c}}{2K_c} = 1.5\times\left(n_{bc} + \sqrt{n_{bc}^2 + \frac{4}{3}n_{bc}}\right) \tag{7}$$

$$\alpha^c_{r(\infty)} = \frac{K^c_{r(\infty)}}{K_c} = \frac{2\overline{K}_b + \sqrt{4\overline{K}_b^2 + 8\overline{K}_bK_c}}{2K_c} = 1.0\times\left(n_{bc} + \sqrt{n_{bc}^2 + 2n_{bc}}\right) \tag{8}$$

where n_{bc} is the ratio between the flexural stiffness $\overline{K}_b$ of a typical beam to the axial stiffness K_c of a typical column as shown in Equation (9).

$$n_{bc} = \frac{\overline{K}_b}{K_c} = \left(\frac{12E_bI_b}{L^3}\right)/\left(\frac{E_cA_c}{H}\right) \tag{9}$$

For concrete buildings, the term n_{bc} can be further derived for typical beams of ($b_b\times h_b$) and columns of ($b_c\times h_c$) in cross-section. The flexural stiffness of a typical beam is:

$$\overline{K}_b = \frac{12E_bI_b}{L^3} = \frac{12\times\frac{0.4E_c}{1+\beta_d}\times\frac{b_bh_b^3}{12}}{L^3} = \frac{0.4E_cb_bh_b^3}{(1+\beta_d)L^3} \tag{10}$$

where the ratio of 0.4 is to account for the effect of cracking, the term (1+β_d) reflects the effect of creep on the beam deflection, and E_c is concrete elastic modulus [5].

For internal columns under pure compression, the effect of cracking can be eliminated. Hence, only creep effect is considered in the column axial stiffness as:

$$K_c = \frac{E_cb_ch_c}{(1+\beta_d)H} \tag{11}$$

Then n_{bc} can be calculated as: $n^i_{bc} = \frac{\overline{K}_b}{K_c} = 0.4\left(\frac{b_b}{b_c}\right)\left(\frac{H}{h_c}\right)\left(\frac{h_b}{L}\right)^3$ (12)

If the cracking effect is considered for columns subjected to uniaxial and biaxial bending, the column axial stiffness K_c in Equation (11) should be multiplied by a ratio of 0.4. As a result, n_{bc} is:

$$n^e_{bc} = n^c_{bc} = \frac{\overline{K}_b}{K_c} = \left(\frac{b_b}{b_c}\right)\left(\frac{H}{h_c}\right)\left(\frac{h_b}{L}\right)^3 \tag{13}$$

It is noteworthy that both Equations (12) and (13) are applicable for the prototype building shown in Figure 1 since the columns located at interior, exterior and corner positions are likely to be subjected to pure compression, uniaxial bending, and biaxial bending, respectively.

It can be deduced from the derivations presented in this section that the practical range of restraint ratio on locally-heated columns in concrete framed buildings are basically dependent on their positions (interior, exterior, or corner), the span/depth ratio of adjacent beams (L/h_b), the length/depth ratio of columns (H/h_c), and the ratio between the beam and column widths (b_b/b_c).

A number of worked examples will be conducted in the next section to provide numerical values of the practical range of restraint ratio α_r.

3 WORKED EXAMPLES

3.1 Worked example No.1

A multi-storey building with a typical layout shown in Figure 1 is studied in this example. The beam spans in both directions are equal $L_x=L_y=L$=6.0m. The typical storey height is taken as H=3.3m. Typical cross-sections of beams and columns are 300×500 and 300mm×300mm, respectively.

The beam-to-column stiffness ratio, n_{bc}, is different for columns at various positions on the building layout. For interior columns that are only subjected to pure compression, n_{bc} is determined based on Equation (12) to be 2.546×10^{-3}. For exterior and corner columns that are respectively subjected to uniaxial and biaxial bending, n_{bc} is 6.366×10^{-3} based on Equation (13). Hence, the upper bounds of axial ratio can be calculated based on Section 2 and the results are listed in Table 1.

Table 1. Worked example No.1 – Cracking effect is considered for exterior and corner columns.

	Interior columns	Exterior columns	Corner columns
Loading	Pure compression	Uniaxial bending	Biaxial bending
n_{bc}	$n_{bc}^{i}=2.546\times10^{-3}$	$n_{bc}^{e}=6.366\times10^{-3}$	$n_{bc}^{c}=6.366\times10^{-3}$
Upper bounds Equations	$\alpha_{r(\infty)}^{i}=0.106$ (6)	$\alpha_{r(\infty)}^{e}=0.148$ (7)	$\alpha_{r(\infty)}^{c}=0.119$ (8)

Equation (4) is used to determine the restraint ratios for ground floor columns in different buildings with overall height varying from 1 to 40 storeys. The results obtained are shown in Figure 3(a).

It can be shown in Figure 3(a) that for buildings up to 10 storeys, restraint ratio α_r rapidly increases from the lower bound with the number of building storeys. For buildings with 10 to 20 storeys, the increase rate of α_r reduces. Above 20 storeys, all the interior, exterior, and corner columns at ground floor of buildings approach their corresponding upper bounds of α_r listed in Table 1.

If cracking effect is not considered for exterior and corner columns that are respectively subjected to uniaxial and biaxial bending, the term n_{bc} in Equation (12) can be applied for all columns, and the results obtained are listed in Table 2. The corresponding curves are plotted in hidden lines in Figure 3(b).

Table 2. Worked example No.1 – Cracking effect is not considered for exterior and corner columns.

	Interior columns	Exterior columns	Corner columns
Loading	Pure compression	Uniaxial bending	Biaxial bending
n_{bc}	2.546×10^{-3}	2.546×10^{-3}	2.546×10^{-3}
Upper bounds Equations	$\alpha_{r(\infty)}^{i}=0.106$ (6)	$\alpha_{r(\infty)}^{e}=0.091$ (7)	$\alpha_{r(\infty)}^{c}=0.074$ (8)

It is shown in Table 2 and Figure 3(b) that when cracking effect is not considered, corner columns attain the lowest restraint ratio whereas interior columns attain the highest. This is due to the difference in the number of adjacent beams framing into the upper ends of the columns, as illustrated in Figure 3. It can also be explained that when cracking effect is not considered for columns, the column axial stiffness increases, resulting in a decrease in restraint ratios of columns at exterior and corner positions. However, the restraint ratios of cracked columns subjected to uniaxial/biaxial bending are both greater than those of uncracked columns under pure compression (Figure 3).

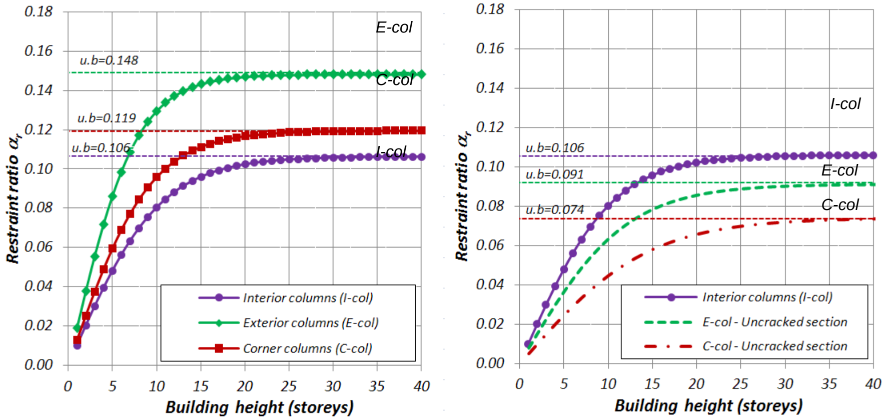

(a) Cracking effect is considered for E and C columns (b) Cracking effect is not considered

Figure 3. Worked example No.1.

3.2 Worked example No.2

In this example, the column and beam cross-sections, the beam spans, and the storey height are varied from those investigated in Worked example No.1. The parameters studied are listed in Table 3.

Table 3. Worked example No.2 – Parameters studied (in m).

Case	H	$b_c \times h_c$	H/h_c	L	$b_b \times h_b$	L/h_b	b_b/b_c
1	3.3	0.3×0.3	11	6.0	0.3×0.5	12	1.0
2	3.6	0.3×0.3	12	6.0	0.3×0.5	12	1.0
3	3.3	0.3×0.3	11	6.0	0.3×0.4	15	1.0
4	3.3	0.3×0.3	11	6.0	0.4×0.5	12	1.3

It is shown in Table 3 that Case 1 is considered in Worked example No.1, Case 2 is only different from Case 1 in (H/h_c) ratio, and Case 3 and Case 4 are different from Case 1 in the ratios of (L/h_b) and (b_b/b_c), respectively. Uniaxially-loaded columns with cracking effect considered are chosen for investigation. Results of the four investigated cases obtained from Equation (4) are shown in Figure 4. It can be observed from the figure that when (H/h_c) ratio increases, restraint ratio α_r also increases (Case 2 vs. Case 1). An increase in (b_b/b_c) ratio also leads to an increase in α_r (Case 4 vs. Case 1). Alternatively, the comparison between Case 3 and Case 1 shows that α_r significantly reduces when (L/h_b) ratio increases. Hence, it can be concluded that the benefit effects of (H/h_c) and (b_b/b_c) ratios as well as the adverse effect of (L/h_b) ratio are not only valid for the upper bounds of α_r shown in Equations (6) to (8) but also for α_r itself.

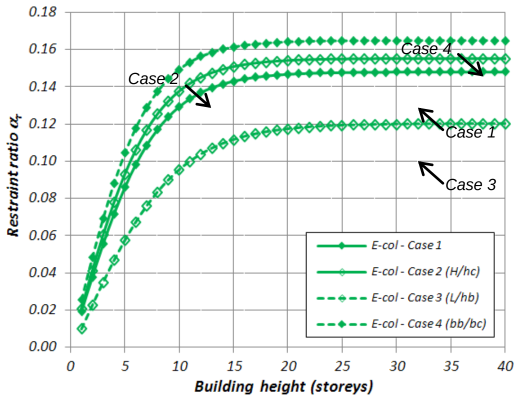

Figure 4. Worked example No.2.

Besides, it is shown in Figure 4 that the maximum value for α_r is 0.165.

3.3 Worked example No.3

In this example, practical design parameters such as the number of storeys (n), the beam spans, the column and beam cross-sections, are varied whereas the storey height is kept unchanged compared to that of Case 2 of Worked example No.2 (H=3.6m). The parameters studied are listed in Table 4.

Table 4. Worked example No.3 – Parameters studied (in m)

Case	n	$b_c \times h_c$	H/h_c	L	$b_b \times h_b$	L/h_b	b_b/b_c
1	1÷5	0.3×0.3	12.0	6.0	0.3×0.5	12.0	1.00
2	5÷10	0.4×04	9.0	6.0	0.3×0.5	12.0	0.75
3	10÷15	0.5×0.5	7.2	7.5	0.4×0.6	12.5	0.80
4	15÷20	0.6×0.6	6.0	7.5	0.4×0.6	12.5	0.67
5	20÷25	0.7×0.7	5.1	9.0	0.5×0.75	12.0	0.71
6	25÷30	0.8×0.8	4.5	9.0	0.5×0.75	12.0	0.63
7	30÷35	0.9×0.9	4.0	12.0	0.6×1.0	12.0	0.67
8	35÷40	1.0×1.0	3.6	12.0	0.6×1.0	12.0	0.60

It is noted in Table 4 that Case 1 of Worked example No.3 is also Case 2 of Worked example No.2. In order to simulate concrete buildings in reality, from Case 2 to Case 8, the column cross-section is gradually increased corresponding to the number of storeys and the increasing beam span that the column supports. Since the storey height is still 3.6m, (H/h_c) ratio is gradually decreased. On the other hand, the ratio of (L/h_b) is around 12 whereas (b_b/b_c) ratio varies from 0.6 to 1.0. Not only interior but also exterior and corner columns without cracking effects are investigated. The results obtained from Equation (4) are shown in Figure 5.

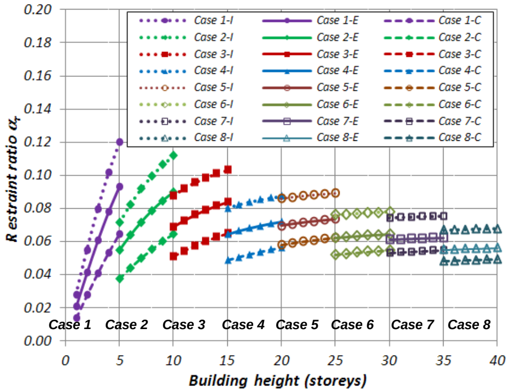

Figure 5. Worked example No.3.

It can be observed from Figure 5 that when the number of storeys (n) increases, the upper bound of restraint ratio α_r decreases. For columns designed to support 1 to 5 storeys, α_r varies from 0.01 to 0.12. For columns supporting 10 to 15 storeys, this practical range of α_r is reduced (0.05 to 0.10). Besides, for interior columns under pure compression plotted in dotted lines, the practical range of α_r is from 0.03 to 0.12. For exterior and corner columns subjected to uinaxial and biaxial bending, which are plotted in continuous and hidden lines, the practical ranges of α_r are (0.02 to 0.09) and (0.015 to 0.07), respectively.

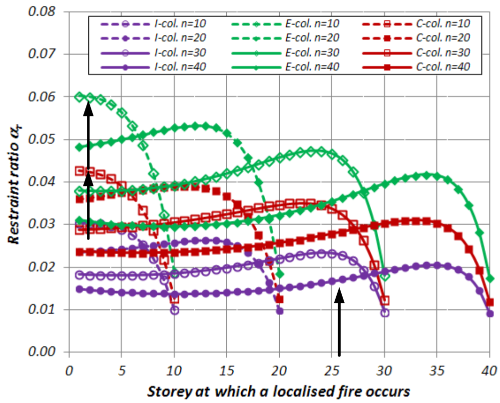

Figure 6. Worked example No.4.

3.4 Worked example No.4

It can be noted that all the above worked examples are only conducted with buildings having columns of constant cross-section along the building height. In reality, column cross-section is purposely reduced for upper floors of multi-storey buildings.

In this example, four buildings with 10, 20, 30, and 40 storeys are investigated. The column cross-sections at ground floors of these buildings are 400×400, 600×600, 800×800, and 1000×1000(mm^2), respectively. The column cross-section dimensions are gradually decreased by 100mm for every upper 5 storeys. All the buildings have identical beam spans of L_x=L_y=6m, beam cross-sections of 300×500(mm^2), and column height of H=3.3m.

Results in Figure 6 provide the values of α_r in various fire scenarios. For example, if a localized fire occurs at the 25th storey of a 30-storey building, the restraint ratios of interior, exterior, and corner columns (with cracking effects) can be determined to be 0.017, 0.035, and 0.028, respectively.

In another case, if a localised fire occurs at ground floor of a 10-storey building, α_r of interior, exterior, and corner columns are 0.003, 0.06, and 0.043, respectively (Figure 6).

It can also be observed from the figure that: (i) restraint ratio α_r increases with an increasing number of building storeys (n); and (ii) the highest restraint ratios α_r occurs at ground, 13, 24, and 35th floors of 10-, 20-, 30-, and 40-storey buildings, respectively.

Figure 6 also shows that for columns with changing cross-sections, the upper bounds of α_r, which are determined for columns with constant cross-sections as presented in Section 2, are no longer valid.

4 DISCUSSIONS

This paper discusses about the axial restraint exerted from surrounding structural members onto a column in concrete framed structures when it is subjected to a localised heating. Theoretical derivations are presented to obtain a better understanding of the nature of the phenomenon. A number of worked examples are conducted to make the issue more practical for structural fire engineers. The following discussions can be made.

Firstly, thermal-induced restraint depends on the position of a column in a building layout. Columns at interior positions are likely to be subjected to pure compression and have higher restraint ratios (α_r) compared to those located along the exterior boundaries and at the corners of the building, which tend to be loaded by uniaxial and biaxial bending, respectively. However, when cracking effect is considered for the exterior and corner columns, restraint ratios of these columns are significantly increased.

Secondly, the parameters having beneficial effects on α_r are: (i) the length/height ratio of column (H/h_c); (ii) the ratio between the adjacent beam and column widths (b_b/b_c); and (iii) the number of building storey (n). Meanwhile, the span/height ratio of beam (L/h_b) exerts a significant adverse effect onto α_r.

Thirdly, for concrete columns with unchanged cross-sections through-out the building height, the limits of α_r can be analytically determined based on Equation (6) to (8). These upper bounds are numerically investigated in Worked examples No.1 to No.3 and the maximum value is 0.165.

Lastly, for reinforced concrete columns with changing cross-sections that are conventionally designed for multi-storey buildings in reality, values of α_r can be analytically determined based on Equations (2) to (4). The practical range of α_r numerically investigated in worked example No.4 is from 0.01 to 0.06.

REFERENCES

[1] Dwaikat M.B., Kodur V.K.R., "A Numerical Approach for Modeling the Fire Induced Restraint Effects in Reinforced Concrete Beams", *Fire Safety Journal*, 43(4), 291-307, 2007.

[2] Lin T.D., Gustaferoo A.H., and Abrams M.S., "Fire Endurance of Continuous Reinforced Concrete Beams", *PCA R&D Bulletin RD072/01B*, 1981.

[3] Steel Construction Institute, "Structural Fire Engineering Investigation of Broadgate Phase 8 Fire", *Steel Construction Industry Forum*, Fire Engineering Group, 1991.

[4] Shepherd P.G and Burgess I.W., "On the Buckling of Axially Restrained Columns in Fire", *Engineering Structures*, 33, 2832-2838, 2011.

[5] MacGregor J.G., Wight J.K., "Reinforced Concrete. Mechanics and Design", Prentice-Hall, Fourth Edition in SI units (Volume 1), 2005.

8th International Conference on Structures in Fire
Guo-Qiang LI, Venkatesh K. R. KODUR, Shou-Chao JIANG, Jian JIANG, Su-Wen CHEN, Guo-Biao LOU (Eds.)
Shanghai, China, June 11-13, 2014

VALIDATION OF A METHOD TO DETERMINE THE STRENGTH OF EPOXY-BONDED REBARS IN CONCRETE WITH A FULL-SCALE ISO 834-1 FIRE TEST

N. Pinoteau*, S. Rémond, P. Pimienta*, Ph. Rivillon*, T. Guillet***

* Centre Scientifique et Technique du Bâtiment, 77447 Marne la Vallée Cedex, France
e-mails: nicolas.pinoteau@cstb.fr, pierre.pimienta@cstb.fr, philippe.rivillon@cstb.fr, thierry.guillet@cstb.fr

** LGCgE, Mines-Douai, GCE, F-59508 Douai, France
e-mail: sebastien.remond@mines-douai.fr

Keywords: post-installed rebar; chemical bond; pull-out; cantilever-wall connection; fire; high temperature

Abstract. *New technics allow bonding rebars into hardened concrete by using polymer structural adhesives. The polymer adhesive is used to bond the rebar inside a hole drilled into an existing concrete element. This post-installation technic can be used to connect new structural elements to already existing structures. At ambient temperature these post-installed rebars have bond strength that is similar to the one of 'classic' cast-in rebars. However, at higher temperatures, the mechanical resistance of the adhesives drops rapidly [1] which causes a substantial decrease of the bond strength. For this reason, there is a need to assess the bond capacity of post-installed rebars in fire conditions in order to ensure structural safety. This paper presents part of a study on the behavior of adhesive-bonded rebars in fire conditions. The goal of this study is to predict the time at which failure of the bond occurs during a standardized ISO 834-1 [2] fire in order to propose a design method.*

1 INTRODUCTION

New adhesive products for bonding rebars inside concrete with chemical adhesives are being increasingly used. These types of fastenings allow a post-installation of the rebar in cured concrete on a building site and may show higher failure loads than regular cast-in rebars at service temperature [3]. However, previous pull-out tests at high temperature have shown that bond capacity decreases rapidly with temperature [4][5][6]. The main difficulty for determination of the bond strength under high temperature is that, in some configurations (such as slab to wall connection), the temperature may not be uniform along the anchorage length. Thus, there is a need to define a design method to predict a bond's capacity under a given thermal distribution along the bonded rebar.

This paper presents a case study of rebar connection in a wall-cantilever structure under a fire situation. The test and thermal analysis is detailed more in depth in [7]. The goal is to predict the failure time determined by the collapse of the cantilever under a thermal loading according to the ISO 834-1 time-temperature curve [2], and to compare predicted values with experimental observations. Thermal calculations have been carried out in accordance with the Eurocode 2, part 1-2 [8] method. Temperatures obtained with this method can be different from the ones measured experimentally. However, this calculation allows to assess the effect this difference could have on the determination of bond capacity. The paper is divided into three main parts: 1) presentation of the theoretical method to predict failure; 2) description of the experimental test member and procedure; 3) analysis of the test data and comparison with calculated predictions.

2 DESCRIPTION OF THE THEORETICAL METHOD

2.1 Design method by bond strength integration

In the entire description, the term 'bond strength' represents the maximal local shear stress at the rebar/mortar interface (along the rebar length and diameter). The bearing load of a bonded rebar is calculated from the bond strength profile along the length of the bond. To determine the bond strength profile, two sets of entry data are necessary. First, the temperature profiles along the bond length are determined at different times during the heating by a numerical method. Secondly, a relationship between bond strength and temperature is determined through pull-out tests.

Knowing the temperature distribution along the bond length at each time, it is possible to associate a bond strength to each temperature by using the bond strength-temperature relationship. Figure 1 illustrates how the bond strength at a given depth (xi) is determined at the time t_2 from the temperature profile.

$$F_t = 2.\pi.r.\int_0^L \tau(\Theta(x,t)).dx \qquad (1)$$

With τ: the bond strength, θ: the temperature (depending on the position and time), r: the rebar radius, L: the embedment depth, F_t: the load capacity of the bond at the time t.

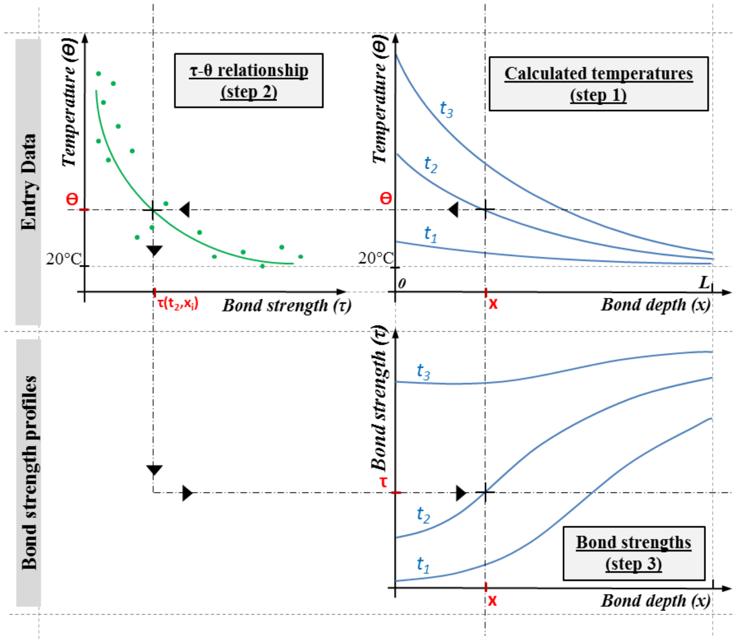

Figure 1: Three step method to determine the bond load capacity under thermal loading

This method allows determining the evolution of the load capacity of a bonded rebar during heating. In the case where the tensile load applied on the rebar remains constant, it is possible to determine the time at which the bond capacity becomes lower than the applied load, which allows predicting the time of collapse.

2.2 Thermal distribution

Evolutions of temperatures with time in the concrete are obtained numerically by the finite element method using specifications given by the Eurocode 2, part 1-2 [8]. For this study, the temperatures were calculated using the finite element method on a 3D mesh. The convective exchange coefficient and emissivity given by the Eurocode 2, part 1-2 [8] for the ISO 834-1 time-temperature heating [2] are presented in Table 1.

Table 1 : Exchange coefficients for concrete surfaces exposed and non-exposed to fire.

	convective exchange h	**emissivity of concrete ε**
Exposed surface	25 W/m²/K	0.7
Non exposed surface	4 W/m²/K	0.7

The variation of thermo-physical characteristics of concrete with temperature (thermal conductivity, mass density and specific heat) are given in Eurocode 2, part 1-2 [8][9]. The peak of the specific heat corresponds to a concrete having a water percentage of 1,5%. The thermal conduction of the steel bars or the polymer mortar was not taken into account for temperature calculation. A more detailed description on the thermal calculation is provided in [7].

2.3 Temperature-bond strength relationship

A testing campaign was performed with 20 tests on rebar diameters ranging from 8 to 16 mm to obtain the relationship between failure temperature and bond strength. Figure 2 presents the variations of failure temperature with bond strength. A study of the effect of the heating rate is developed in another paper which also gives a more detailed description of the testing devices and procedure [4]. The average bond strength at 20°C was determined by three pullout tests performed on the same type of samples (by loading the rebar with a 0,05 mm/s displacement speed).

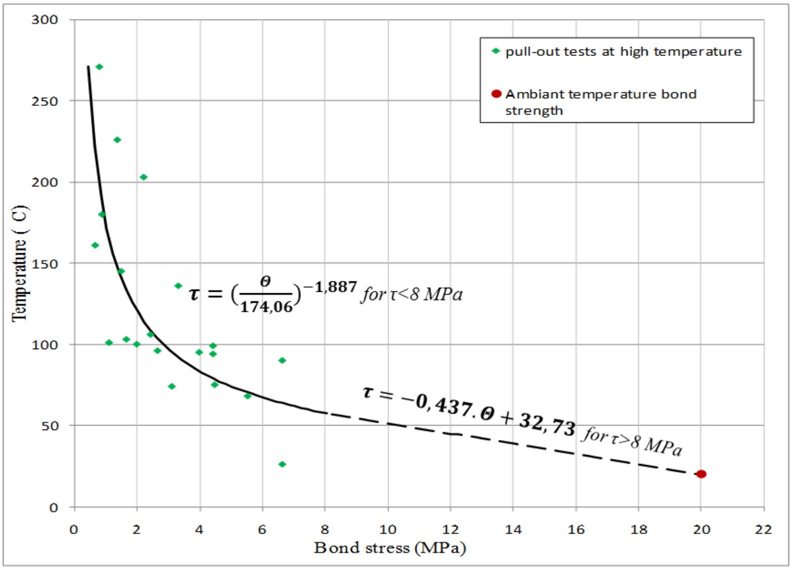

Figure 2: Failure temperature–applied bond stress relationship determined experimentally by pull-out tests

As the applied stress increases, the temperature at failure decreases. The relationship between failure temperature and applied bond stress was established using two analytical expressions. For low bond stress (below 8 MPa), a power trend function was chosen to describe the variation of temperature with bond stress. For high bond stress (above 8 MPa), a linear trend function was chosen. The connection between the power and linear functions was determined in order to obtain continuity of the derivative at the connection point (in this case, at 8 MPa). No extrapolation of bond stresses was performed outside of the range of temperatures that was tested. The highest temperature of a pull-out test was 271°C. Above this temperature, bond stresses were considered equal to zero. In addition, since only the effect of heating is studied here, no temperature occurs below 20°C.

3. TEST SET-UP

3.1 Test structure

An ISO 834-1 [2] fire test was carried out on two full scale wall-cantilever connections (named 'a' and 'b') in order to identify the time of collapse. Heating was applied on the lower and lateral surfaces of the cantilevers and on one surface of the wall (figure 3). The dimensions and technical description of the test is provided in [7]. The connections were ensured by two bonded rebars inside the concrete wall on a length of 250 mm. The two cantilevers had a length of 3 m and a height of 350 mm. the thickness of the wall was 320 mm. A reference bar was positioned 80 mm below one of the rebars in order to measure temperatures close to the ones along the bond. The choice to not equip the HA bonded rebars with thermocouples was made to avoid disturbing the bond geometry because of the presence of the thermocouples. The reference bar was debonded with grease (in the cantilever) in order to avoid participating to the bearing of the cantilever. The thermocouples were displayed symmetrically in the wall and the cantilever at 5, 25, 55, 85, 135, 185 mm from the wall/cantilever interface on both sides.

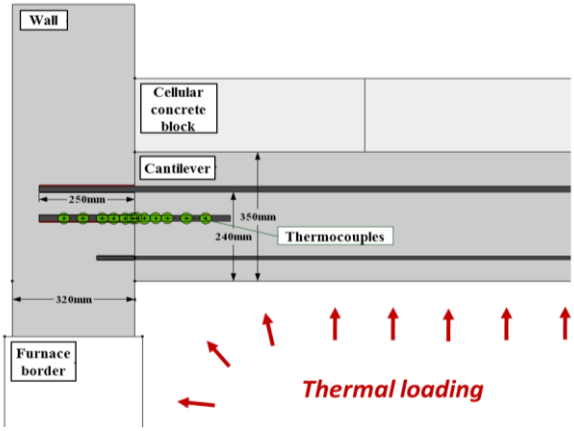

Figure 3: Wall-cantilever test member

4. RESULTS AND DISCUSSION

4.1 Failure observations

The cantilever (b) collapsed after 178 minutes of heating when the temperature inside the gas furnace was of 1110°C, after which the gas burners were turned off in order to start cooling. The second cantilever collapsed 16 minutes later which suggests a satisfactory repeatability between the behavior of the bonded rebar connections on each cantilever. For each cantilever, the collapse was caused by the slip of the bonded rebars. The slip of the rebars occurred along the bonded part (inside the wall) due to the loss of resistance of the polymer mortar. No concrete cone failure was noticed.

4.2 Temperature distribution

Figure 4 presents the measured temperatures (in full lines) and the calculated temperatures (in dotted lines) along the rebar every 30 minutes during the heating for cantilever (b). The positive X-axis represents the depth of the rebar inside the wall (where the rebar was chemically bonded). The negative X-axis represents the depths of the rebar inside the cantilever (where the concrete was casted around the rebar).

Inside the cantilever and at the beginning of the bond, calculated temperatures using the Eurocode 2 [8] method are higher than the measured temperatures. After 180 minutes of heating, the difference between the calculated and the measured temperatures reaches 175% at the wall/cantilever interface. This could be explained by the fact that the thermal convective and radiative exchange coefficients provided by Eurocode 2 lead to overestimating the temperature inside the concrete near the exposed surface for this test. At the end of the bond, calculated temperatures are lower than the measured temperatures. The influence of temperature error will be developed at the end of this paper in part 3.5.

Figure 4 also shows the increase of thermal gradient along the bonded part of the rebar. At 180 minutes, the bond temperature at the wall/cantilever interface is 200°C while at a depth of 185 mm the temperature is 70°C. The evolution of thermal distribution is used in order to determine bond strength profiles with the method described in part 2.1.

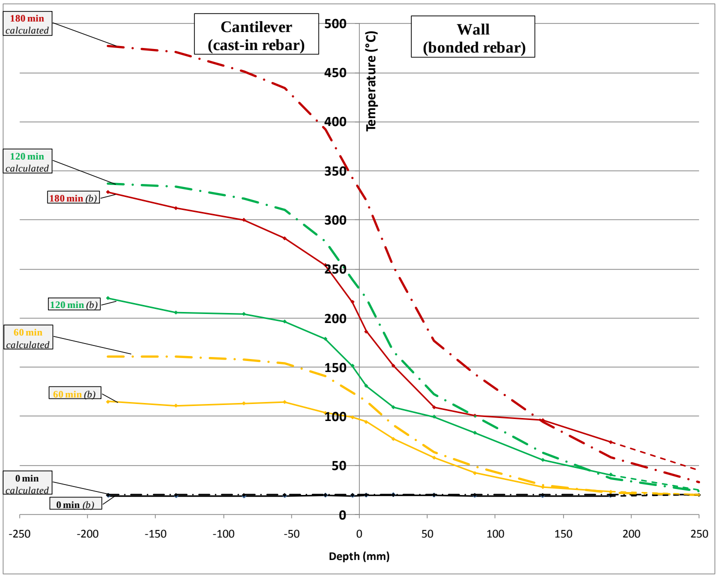

Figure 4: Calculated and measured temperature distributions near the wall/cantilever interface at different times

4.3 Bond strength distribution

Figure 5 presents the strength profiles along the bonded part of the rebar for the cantilever (b) every hour determined using the temperature-bond strength relationship (figure 2).

At the beginning of the fire test, when the entire bond is at 20°C, the strength profile is uniform with a value around 24 MPa. As the temperature increases in the bonded rebar during heating, bond strength progressively decreases. At 120 minutes, the calculated temperatures are 230°C and the measured temperatures are close to 140°C at the wall/cantilever interface. At this time, the bond strength is lower than 4 MPa along the 50 first millimeters.

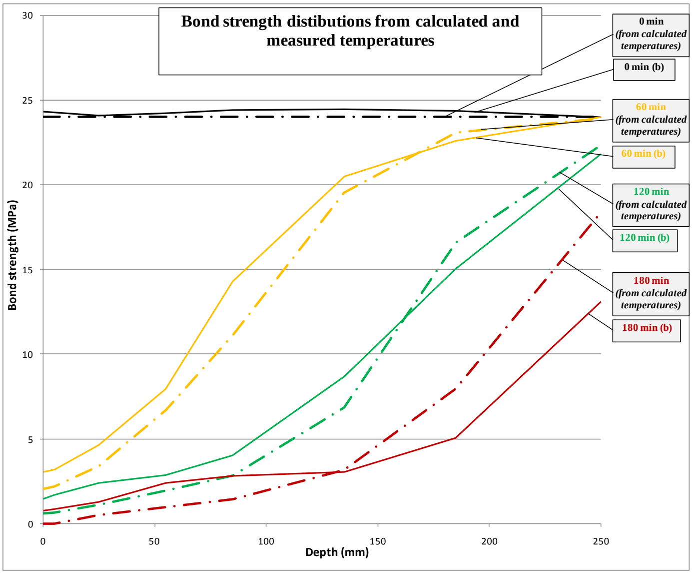

Figure 5: Bond strength profiles every hour determined from calculated and measured temperatures in cantilever (b)

4.4 Bond capacity and prediction of failure

By integrating bond strength along the length of the bonded rebar using equation (1), bond load capacities were determined at different times for calculated and measured temperatures. Table 2 presents the values of bond load capacities in addition to the applied load at different times. The applied load on the rebar was determined from the bending moment in the section of the cantilever at the wall/cantilever interface which varies with temperature, using a thermo mechanical calculation and an experimental method described in [7].

Table 2: Values of applied load and bond load capacities every 30 minutes

Time (min)	Applied load (kN)	Bond Capacity (kN)		
		Determined from calculated bond temperatures	Determined from measured bond temperatures of cantilever (a)	Determined from measured bond temperatures of cantilever (b)
0	42,9	251,2	253,1	253,9
30	82,3	220,8	238,0	239,4
60	82,8	168,0	183,5	177,6
90	75,7	129,6	135,5	140,5
120	Between 55,3 and 69,3*	100,6	92,1	107,9
150	Between 55,3 and 65,6*	79,4	63,5	72,9
180	Between 55,3 and 62,5*	62,0	49,2	53,6

** Applied load determined with a thermo mechanical calculation and with an experimental method [7]*

The bond load capacity decreases as the bonded rebar is heated up. Failure occurs when the bond load capacity becomes lower to the load applied on the rebar. The evolution of bond capacity suggests that the failure should take place between 150 and 180 minutes using measured temperatures and after 180 minutes using calculated temperatures. This prediction is close to the experimental observation of collapse (at 178 minutes for cantilever (b)).

Although there is a large difference between calculated and measured temperatures at the beginning of the bond (Figure 4), bond load capacities are relatively close (Table 2). This is explained by the fact that at the deepest part of the bond, calculated and measured temperatures after 60 minutes are similar in a range of temperatures between 20°C and 100°C and this area of the bond has the highest influence in determining the bond load capacity due to high bond strengths. At temperatures above 100°C, bond strengths are low in comparison to the coolest parts of the bond. This leads to the conclusion that the range of temperatures between 20 to 100°C is mainly of interest for bond characterization to determine bearing loads in a fire situation. At the end of the test, the measured temperatures towards the end of the bond were higher in cantilever (b) than in cantilever (a). This is in good accordance with the order of collapse.

4.5 Limitations of the method

For this test, the theoretical prediction and experimental observation of failure time are close. However, the main weakness of this method is that the value of bond capacity can be very sensitive to temperature calculations due to the fast variation of bond strength with temperature (Figure 2). Due to the slow decrease of bond strength at low temperatures, slight deviations in temperature estimations between 20°C and 100°C lead to high uncertainties on bond strengths. In addition, in these cold areas, the high bond strengths are critical for the determination of the load capacity (as presented at the end of part 3.4).

In the hot area of the bond at 180 minutes, the Eurocode 2 method leads to overestimating temperatures by 175% (from 200°C to 330°C, figure 4). However, this high difference in temperature generates a low uncertainty on the determination of bond strength (less than 0,5 MPa) because of the fast power decrease of bond strength between 200°C and 330°C.

In the cold area of the bond at 180 minutes, the Eurocode 2 method leads to underestimating temperatures by 140% (from 48°C to 34°C, figure 4). This difference in temperature generates a high uncertainty on the determination of bond strength (higher than 6 MPa).

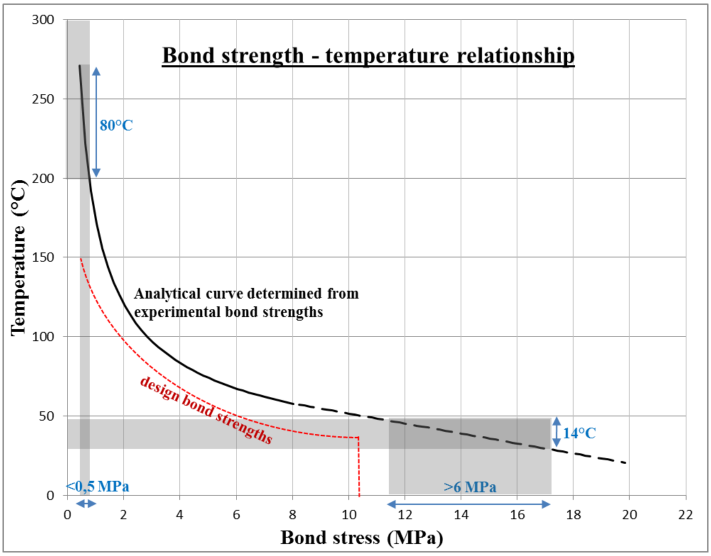

Figure 6: Sensitivity of bond strength with temperature determination

In order to use this method for design, the sensitivity with temperatures should be reduced so that the dimensions of the bond ensure safe load bearing. One solution could be to use a design bond strength-temperature relationship limiting the design bond strength at a maximal value for the low temperatures (such as represented by the dotted line on figure 6). This would have the effect, of decreasing sensitivity of bond design values with temperature deviations while being conservative.

5 CONCLUSION

For this full scale test, the prediction of the failure time is close to the experimental observations at ±30 minutes (for a failure at 3h). Temperature measurements inside the structure show that there is a thermal gradient with temperatures ranging from 200°C to 70°C over 185 mm along the bond after 180 minutes for the wall/cantilever connection. The analysis of bond strength profiles shows that bond capacity is mainly determined by the part in a temperature range between 20 and 100°C since bond strengths are lower than 4 MPa above 100°C.

For this test, large differences appear between calculated and the measured temperatures (reaching 175% between 200°C and 330°C). A high source of uncertainty is induced by the sensitivity of bond strength with temperature at low temperatures (between 20°C and 100°C). Slight deviations in temperatures generate large uncertainties on bond strengths. Work is currently being carried out in order to establish a conservative design bond-strength-temperature relationship from the experimental relationship (figure 2). Limiting this relationship to a maximal design bond strength at low temperatures would reduce the sensitivity of this model to temperature deviations and therefore allow a conservative determination of the load capacity and failure time.

REFERENCES

[1] Chin, J., Forster, A., Ocel, J., Hartmann, J., Fuchs, P., and Hunston, D. (2010). “Thermoviscoelastic Analysis and Creep Testing of Ambient Temperature Cure Epoxies Used in Adhesive Anchor Applications.” J. Mater. Civ. Eng., 22(10), 1039–1046.

[2] CEN. EN 1991-1-2 (2002) Eurocode 1, Part 1-2: Actions on structures: general actions - actions on the structures exposed to fire, CEN, Bruxelles, Belgique.

[3] Bouazaoui L., Li A. April 2008. Analysis of steel/concrete interfacial shear stress by means of pull out test, International Journal of Adhesion and Adhesives, Volume 28, Issue 3, Pages 101-108.

[4] Pinoteau Nicolas, Pimienta Pierre, Guillet Thierry, Rivillon Philippe, Rémond Sébastien. December 2011a. Effect of heating rate on bond failure of rebars into concrete using polymer adhesives to simulate exposure to fire, International Journal of Adhesion and Adhesives, Volume 31, Issue 8, Pages 851-861.

[5] Bingöl Ferhat, Gül Rüstem. August 2009. Residual bond strength between steel bars and concrete after elevated temperatures, Fire Safety Journal, Volume 44, Issue 6, Pages 854-859.

[6] Chiang Chih-Hung, Tsai Cho-Liang. October 2003. Time–temperature analysis of bond strength of a rebar after fire exposure, Cement and Concrete Research, Volume 33, Issue 10, Pages 1651-1654.

[7] N. Pinoteau, J.V. Heck, Ph. Rivillon, R. Avenel, P. Pimienta, T. Guillet, S. Rémond, Prediction of failure of a cantilever–wall connection using post-installed rebars under thermal loading, Engineering Structures 56 (2013) 1607–1619.

[8] CEN. EN 1992-1-2 (2005), Eurocode 2, Part 1-2: Design of concrete structures - General rules - Structural fire design, CEN, Bruxelles, Belgique.

[9] NF EN 1992-1-2/NA (2007), Eurocode 2, Part 1-2: Design of concrete structures - General rules - Structural fire design.

COLLAPSE MECHANISMS OF EDGE AND CORNER SLAB PANELS IN FIRE CONDITIONS

Malte Duchow* **and Anthony K. Abu****
*Institut für Stahlbau & Werkstoffmechanik, TU Darmstadt, Germany
e-mail: malte-duchow@t-online.de

**Department of Civil & Natural Resources Engineering, University of Canterbury, New Zealand
e-mail: tony.abu@canterbury.ac.nz

Keywords: Composite floors, Slab panels, Collapse mechanisms, Corner panels, Fire, Tensile membrane action

Abstract. *The usage of tensile membrane action for the design of composite floors in steel framed buildings in fire conditions has led to a number of simplified design solutions, like the Bailey-BRE method. This method predicts an enhancement of the slab's yield-line load capacity by membrane stresses, on the assumption of continuous vertical support at all edges. However the vertical support is provided by protected edge beams, which deflect under a combination of heat and loading. The loss of vertical edge support results in an eventual collapse of the entire structure. In recent years four collapse mechanisms of composite slab panels have been proposed. The current research improves upon the predicted failure time for edge slab panels and develops a failure mechanism for slab panels located at the corner of a building. The results are checked against finite element simulations.*

1 INTRODUCTION

Research has shown that traditional methods for the design of steel-framed buildings in fire conditions are excessive. Both accidental fires and tests on full-scale buildings have shown that the practice of protecting all exposed steelwork for fire resistance is not necessary to ensure structural stability of a steel-framed building. By taking advantage of tensile membrane action (TMA) structural stability can be ensured with significant reductions in costs [1]. TMA is a high-capacity load-bearing mechanism of thin composite floors under large deflections. The deflection generates radial tension in the centre of the slab balanced by a peripheral ring of compression. Due to its self-sustaining nature, horizontal edge restraint is not required to activate this load-bearing capacity, so that only two-way bending of the slab and vertical support at all edges are necessary. To incorporate this mechanism in design, a building floor is divided into several rectangular zones of low aspect ratio, called slab panels. These slab panels comprise unprotected composite beams in the interior and four edges which primarily resist vertical deflection [2]. The vertical support is usually provided by protected composite beams, which would normally be located on column gridlines, as shown Figure 1.

In fire the unprotected intermediate beams heat up and lose their strength rapidly so that their loads are borne by the slab which undergoes two-way bending and large deflections. With increasing temperature, the deflection of the slab and its resistance increases until the tensile strength of the reinforcement is reached. The advantage of using tensile membrane action is that a large number of floor beams can be left unprotected, which significantly reduces building costs while providing quantifiable structural stability in fire conditions. TMA and whole-structural behaviour of buildings can be modelled in a three-dimensional framework with sophisticated finite element software such as *Vulcan* [3], ABAQUS [4] and SAFIR [5] which incorporate geometrical and material non-linear behaviour. Due to the unsuitability of finite element simulations for day-to-day analyses, as they can be time-consuming costly processes, simpler performance-based methods are often preferred for routine design.

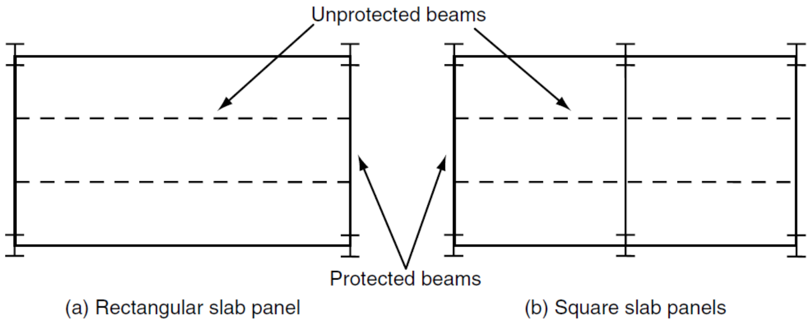

Figure 1. Rectangular and square slab panels [6].

Prominent amongst existing simplified methods incorporating tensile membrane action is the Bailey-BRE method [2] which predicts composite slab capacity by calculating a membrane enhancement to the traditional yield-line load of the slab, by the assumption of continuous vertical support at all edges. However this support is provided by protected edge beams, which heat up and lose strength during fires. The loss of vertical support at the edges results in loss of tensile membrane action in the slab and an eventual failure of the whole slab panel. To encourage the use of simplified design approaches, four different collapse mechanisms have been proposed for composite slab panels in fire conditions [6]. These mechanisms describe different potential collapse scenarios and provide equations to calculate the time of structural failure in fire.

2 COLLAPSE MECHANISMS

The structural failure of a slab panel can be calculated by work-balance equations under consideration of plastic folding, which allows collapse without generating membrane forces in the slab. Following the principle of virtual work the constant external work done by the applied fire limit state load is equated to the internal work done (by the components of the slab panel) which decreases over time with increasing temperature. The time step at which the external work exceeds the internal work defines the failure time of the slab panel for the postulated failure mode. The choice of which collapse mechanism occurs in fire depends on the aspect ratio of the slab, relative beam sizes, location of the slab panel within the building and the extent of the fire. Figure 2 presents the four collapse mechanisms that have been proposed.

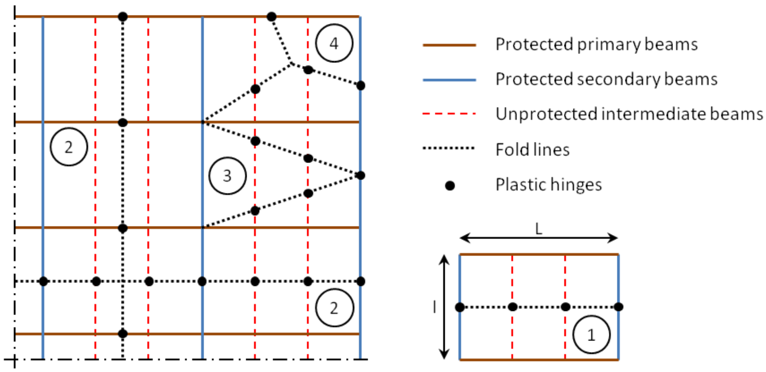

Figure 2. Proposed collapse mechanisms.

As the Bailey-BRE design approach is based on an isolated slab panel, Collapse Mechanism 1 examines the failure of this type of slab panels. Collapse Mechanism 2 addresses large compartments, such as open-plan offices where a large number of slab panels could be involved. It follows the general principles of Collapse Mechanism 1, but considers reinforcement continuity across two opposite edges. Both mechanisms have been checked against finite element simulations and are found to be quite accurate [6]. Edge and corner panels have to be treated differently, due to their different boundary conditions. Collapse Mechanism 3, for slab panels located at the edge of a building, has also been developed. However, the prediction was found to be grossly conservative in comparison with finite element simulations [6]. The current paper improves upon this prediction, and also presents a new mechanism (Collapse Mechanism 4) for slab panels located at the corner of a building.

All collapse mechanisms have been verified with *Vulcan* [3] and checked against the Bailey-BRE limit and the conventional span/20 deflection limit for fire limit state. For comparison with the previous research, the design data for the previous example cases have been maintained. They are based on typical office type loading: dead load (including concrete slab, reinforcement and beam self-weights) = 4.33 kN/m²; live load (maximum office load) = 5.0 kN/m²; trapezoidal decking profile with a trough depth of 60 mm; overall slab thickness of 130 mm and concrete cube strength of 40 N/mm² [6]. The composite floor beams were designed in accordance with EN1994-1-1 [7] and EN1994-1-2 [8], and the edge beams were protected to reach a maximum temperature of 550 ℃ at 60 min of exposure to the Standard Fire.

Two slab panel sizes (12 m × 9 m and 12 m × 12 m, with properties listed in Table 1) were used for the verifications. In both slab panels intermediate beams were spaced at 3 m. The 12 m × 9 m slab panel and its beam sections were chosen for Collapse Mechanism 3, while the 12 m × 12 m slab panel was used to evaluate Collapse Mechanism 4.

Table 1. Slab panel design data.

Slab Panel Size	Beam Type	Beam Section	Load Ratio	Temperature at 60 min	Span (m)
12 m × 9 m	Primary	610 × 305 × 179 UB	0.380	550 ℃	9
	Left Secondary	533 × 210 × 101 UB	0.413	548 ℃	12
	Right Secondary	406 × 178 × 67 UB	0.419	548 ℃	12
	Intermediate	457 × 152 × 67 UB	0.469	941 ℃	12
12 m × 12 m	Top Primary	610 × 305 × 149 UB	0.422	550 ℃	12
	Bottom Primary	838 × 292 × 194 UB	0.463	550 ℃	12
	Left Secondary	533 × 210 × 101 UB	0.446	548 ℃	12
	Right Secondary	475 × 191 × 67 UB	0.437	547 ℃	12
	Intermediate	406 × 178 × 74 UB	0.454	940 ℃	12

2.1 Collapse Mechanism 3

The predicted failure time of the previous research for Collapse Mechanism 3 was conservative and about 30% shy of the equivalent prediction of the *Vulcan* simulation. Likewise the related deflection-time plot of the simulation did not show a clear sign of failure. To enhance the prediction, the present study reviewed the proposed equations for slab panel failure and the *Vulcan* simulations. An artificial horizontal restraint was found in the simulations. As such, the simulation predicted a much higher capacity than would actually be available if the edges could move inwards. The moment capacity of the concrete slab at elevated temperatures was overestimated in the analytical prediction. The equation that considered the collapse of the panel involving the failure of the primary edge beam did not include the capacity of the unprotected intermediate beams. Both assumptions have now been incorporated in the new predictions. The new prediction of the analytical model now occurs 22 minutes earlier than the results of the new *Vulcan* simulations. Significant improvement of the failure prediction was obtained with the selection of an appropriate centre of compression for hogging moments along the continuous edges, as represented in Figure 3.

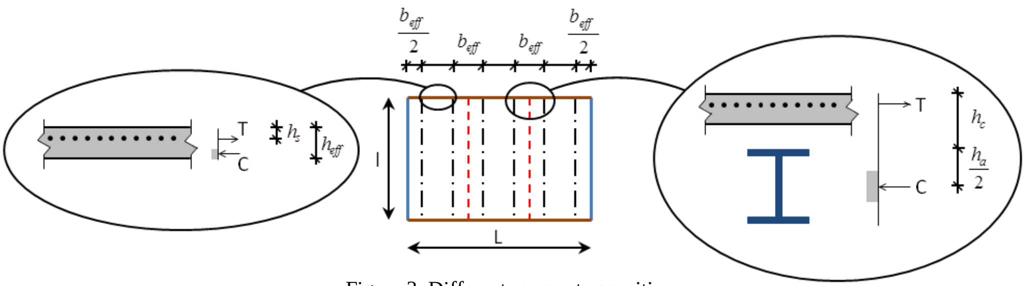

Figure 3. Different moment capacities.

For the moment capacity along the edges of continuity, the total length of the edge was divided into areas for the effective width of each composite beam and areas that only contributed to the slab bending capacity. The areas that only contributed to the slab capacity were treated as having compression in the bottom regions of the concrete slab, while those areas that were part of the effective with of the composite beams had their centres of compression at the middle of the steel beams, on the assumption of simple connections. The larger leaver arm led to significant increase of moment capacity. These improvements were incorporated into the equations and checked against the new simulations, as shown in Figure 4. The figure shows a 24-minute improvement in the failure prediction. These improvements have also been incorporated in Collapse Mechanism 2, to improve its failure prediction as well. This paper focuses on edge and corner slab panels. Thus Collapse Mechanism 2 is not discussed further. Figure 2 and Figure 4 reveal that the intermediate beams fail at an angle which leads to twisting in the beam. Including the twisting capacity into the calculation enhances the prediction by 1 min. The collapse of an edge slab panels can be calculated by Equation (1) and Equation (2).

The following notation is used for the mechanisms presented in this paper (refer to Figures 4 and 6):

L	length of primary beam
$M_{\mathrm{T,pp}}$	plastic sagging moment capacity of top protected primary beam at time t
$M_{\mathrm{B,pp}}$	plastic sagging moment capacity of bottom protected primary beam at time t
$M_{\mathrm{L,ps}}$	plastic sagging moment capacity of left protected secondary beam at time t
$M_{\mathrm{R,ps}}$	plastic sagging moment capacity of right protected secondary beam at time t
M_{int}	plastic sagging moment capacity of unprotected intermediate beam at time t
M_i^-	plastic hogging moment capacity of each beam at connection at time t
$b_{\mathrm{eff,i}}$	effective width of each composite beam
l	length of secondary beam
m^+	sagging moment capacity of slab
m^-	hogging moment capacity of slab
n	number of unprotected intermediate beams
r	aspect ratio
w	applied floor load at fire limit state

Folding across right secondary beam:

$$\frac{wLl}{3}-4\left[\begin{array}{c} M_{R,ps}\frac{1}{l}+nM_{\mathrm{int}}\frac{1}{l}+M_{L,ps}^{-}\frac{1}{l}+M_{R,ps}^{-}\frac{1}{l}+nM_{\mathrm{int}}^{-}\frac{1}{l} \\ +\left(m^{+}+m^{-}\right)\left(L-b_{eff,L,ps}-b_{eff,R,ps}-nb_{eff,\mathrm{int}}\right)\frac{1}{l} \\ +\left(m^{+}+m^{-}\right)\frac{l}{4L} \end{array}\right]\geq 0 \tag{1}$$

Folding across bottom primary:

$$\frac{wLl}{3}-4\begin{bmatrix} M_{B,pp}\dfrac{1}{L}+nM_{\text{int}}\dfrac{1}{4l}+M_{T,pp}^{-}\dfrac{1}{L}+M_{B,pp}^{-}\dfrac{1}{L}+nM_{\text{int}}^{-}\dfrac{1}{4l} \\ +\left(m^{+}+m^{-}\right)\left(l-b_{eff,T,pp}-b_{eff,B,pp}\right)\dfrac{1}{L} \\ +\left(m^{+}+m^{-}\right)\left(L-nb_{eff,\text{int}}\right)\dfrac{1}{4l} \end{bmatrix}\geq 0 \tag{2}$$

It has to be mentioned that Equation (1) is for a slab panel with the right secondary beam located at the edge of a building, and Equation (2) for a slab panel with the bottom primary beam at the edge.

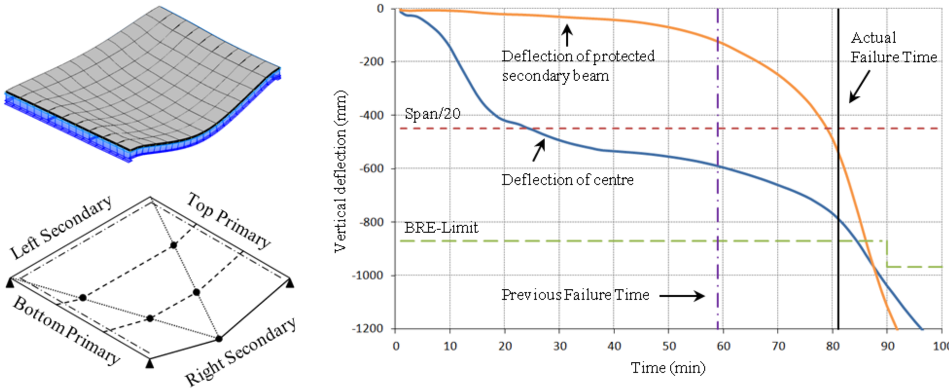

Figure 4. Collapse Mechanism 3 – Comparison.

2.2 Collapse Mechanism 4

To find a new expression for a collapse mechanism of slab panels located at the edge of a building, large-scale simulations were performed. The simulations consisted of four or six slab panels, each panel with a size of 9 m × 9 m or 12 m × 9 m. Two main fire scenarios were explored: a large fire involving all slabs in one large compartment and a fire located beneath the corner slab panel. The results show that fire exposure to the whole compartment leads to structural failure across the secondary beams, which is well described by Collapse Mechanism 2. Of more interest is the simulation with only one slab panel under fire, as highlighted in Figure 5, where the cold adjacent slab panels contribute rotation and deflection support at the internal edges of the corner slab panel. The deflection of these simulations also indicates simultaneous failure of the external beams. Therefore, in developing the mechanism, it was assumed that the internal edge beams maintain their vertical support throughout the fire. With this simplification the predicted collapse from the large simulation of both edge beams could be reproduced with the slab panel properties listed in Table 1.

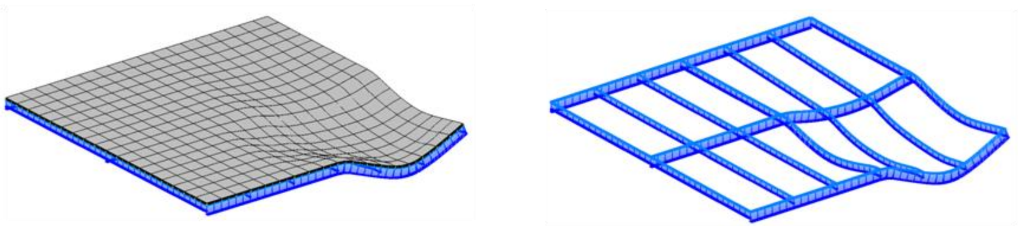

Figure 5. Fire at corner panel – Large-scale simulation.

A similar collapse mechanism had been published [9] for reinforced concrete slabs with simple supports at two adjacent edges, without rotation capacity, and a column at the external corner. For simple concrete slabs the collapse load can be calculated by including the unknowns, which describe the position of maximum deflection, in virtual-work equations and solving their derivatives simultaneously. The present research is extending this approach to the corner slab panel. Initial investigations have yielded no logical solutions. The aim is to employ an energy minimization approach. An alternative solution has been obtained by postulating the location of the maximum deflection of the slab panel, depending on the size of the slab panel, its aspect ratio and beam section properties. This was found after an extensive investigation of Vulcan simulations of corner slab panel failure modes. Consequently Equation (3) has been proposed for Collapse Mechanism 4. The failure mechanism depends on the aspect ratio and the length of the primary beam.

Slab panel failure occurs when:

$$\frac{r\left(375r^2+364\right)}{864\left(r^2+1\right)}wL^2-\frac{8L}{5r}\left[\begin{array}{c}\frac{12r}{5}M_{T,pp}+2M_{R,ps}+M_{\mathrm{int}}\left(n-\frac{15n-17}{15n+5}\right)\\ +rM_{T,pp}{}^{-}+M_{R,ps}{}^{-}+nM_{\mathrm{int}}{}^{-}+L\left(\frac{5r^2}{6}+\frac{25}{36}\right)m^{+}\\ +\left(m^{+}+m^{-}\right)\left[L\left(r^2+1\right)-rb_{eff,T,pp}-b_{eff,R,ps}-nb_{eff,\mathrm{int}}\right]\end{array}\right]\geq 0 \qquad (3)$$

with the aspect ratio: $r = {}^{l}\!/_{L}$

As shown in Figure 6 this type of collapse leads to more interaction between the deflections of the primary and secondary beams. The deflection of the secondary beam is larger than the primary beam until 79 min. Thereafter the primary beam deflection exceeds that of the secondary beam. At 92 min the primary beam temporarily stops deflecting, while more load is transferred to the secondary beam, which consequently deflects rapidly. The deflection of both beams never exceeds the maximum deflection of the slab. From the simulations slab panel failure is predicted at 98 min when the deflection of the slab is about 1500 mm.

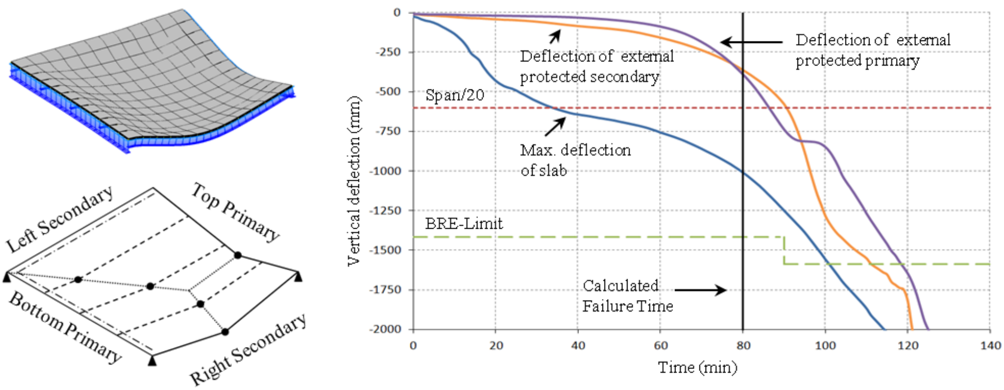

Figure 6. Collapse Mechanism 4 – Comparison.

2.3 Test Comparison

In recent years two full scale tests have been performed in order to investigate various aspects of tensile membrane action in composite slab panels. Both tests: CROSSFIRE (2006) and FRACOF (2008)

[10] were performed by CTICM in France. A comparison was intended for the FRACOF-test, as it was designed to simulate the behaviour of a corner slab panel, with continuity on two adjacent edges. The slab panel size was 8.74 m × 6.6 m with two IPE400 primary beams and four IPE300 secondary beams supported by four short HEB260 columns. The slab itself was constructed with a COFRAPLUS 60 trapezoidal decking profile with a trough depth of 97 mm; overall slab thickness of 155 mm and a C30/37 normal weight concrete. During the test the load was applied by fifteen sand bags uniformly distributed over the floor to generate a uniform live load of 3.87 kN/m². Continuity was obtained by welding the reinforcement on two external steel beams. The two secondary beams in the interior and the composite slab were left unprotected whereas all boundary beams were fire protected to ensure global structure stability for a fire rating of 120 min. The floor was exposed to the standard temperature-time fire for 120 min, and then stopped due to integrity failure of the floor by a large crack in the middle of the slab.

For comparisons between the developed collapse mechanism and the FRACOF test the experimental setup was also modelled in *Vulcan*. However a reasonable comparison of the test behaviour and Collapse Mechanism 4 could not be made because no structural failure occurred in the protected edge beams, due to the very heavy protection regime. The FRACOF-test was performed primarily to demonstrate the advantages of tensile membrane action, and not to investigate potential failure mechanisms. The differences between the FRACOF slab panel and the design slab panels with which Collapse Mechanism 4 has been developed are listed in Table 2.

Table 2. Slab panel comparison.

FRACOF				Design slab	
Beam Type	Load Ratio	Temperature at 60min	Temperature at 120min	Load Ratio	Temperature at 60min
Top Primary	0.22	110 ℃	218 ℃	0.42	550 ℃
Left Secondary	0.27	121 ℃	289 ℃	0.44	547 ℃
Intermediate	0.39	933 ℃	1050 ℃	0.45	940 ℃

The load ratios of the FRACOF-beams are less than would be expected in normal beams, and the temperatures of the protected beams even after 120 min of exposure to the standard fire are below 300 ℃. The steel sections therefore still had 100% strength, whereas the design slab panels were designed to be as realistic as possible, with standard protection regime. It has to be mentioned again that the FRACOF-test was not made to achieve a structural failure of the whole slab panel and therefore it is difficult to compare the test results with the developed collapse mechanism.

3 CONCLUSIONS

Two collapse mechanisms have been proposed to incorporate into the Bailey-BRE method to enhance its use. They include moment capacity at continuous edges and loss of vertical support at slab panel boundaries. One of the proposals, for edge panels, has been developed in recent years but was found to be deficient, so it has been improved to give better predictions of structural failure. The second proposal considers slab panels located at the corner of a building and provides a prediction of the failure time. Comparisons between this collapse mechanism and the FRACOF-test could not be made because the test concentrated on promoting tensile membrane action. Due to this the edge beams had a low load ratio and were heavily protected.

The present study concentrated on collapse mechanisms of particular slab panels. Large-scale simulations have shown that the supporting effect of adjacent slab panels, depending on their orientations, affect the resistance of the panel. These effects have been included with simplifications which may need further development. It has also been observed that the consideration of fire under one slab panel or in a large compartment influences the type of structural failure. In the study, the effects of columns were not considered. Including them into the models will provide some axial restraint to the beams and the slab panels as a whole. The supporting effect of adjacent slab panels and horizontal restraint from columns are subjects for future research.

REFERENCES

[1] Newman G.M., Robinson J.T., Bailey C.G., *Fire Safe Design: A New Approach to Multi-Storey Steel-Framed Building*, Second edition. Steel Construction Institute, Publication P288, Sheffield University, United Kingdom, 2006.

[2] Bailey C.G., *Steel structures supporting composite floor slabs: design for fire*, BRE (Building Research Establishment), Digest 462, Watford, United Kingdom, 2001.

[3] Huang Z., Burgess I.W. and Plank R.J., "Modelling membrane action of concrete slabs in composite slabs in fire. I: Theoretical Development", *ASCE Journal of Structural Engineering*, 129 (8), pp. 1093-1102, 2003.

[4] ABAQUS version 6, Dassault Systemes Simulia Corporation, Providence, RI, USA, 2010

[5] SAFIR 2011, University of Liege, Liege, Belgium, 2011

[6] Abu A.K., Ramanitrarivo V., Burgess I.W., "Collapse Mechanisms of Composite Slab Panels in Fire", *Journal of Structural Fire Engineering*, Volume 2, Number 3, pp. 205-215, Multi-Science Publishing, 2011.

[7] CEN, *Eurocode 4: Design of composite steel and concrete structures – Part 1-1: General rules and rules for buildings Structural fire design, EN 1994-1-1*. European Committee for Standardization, Brussels, Belgium, 2004

[8] CEN, *Eurocode 4: Design of composite steel and concrete structures – Part 1-2: General rules – Structural fire design, EN 1994-1-2*. European Committee for Standardization, Brussels, Belgium, 2005

[9] Park R., Gamble W.L., *Reinforced Concrete Slabs*, Second edition, John Wiley & Sons Inc., New York, United States of America, 2000.

[10] Zhao B., Roosefid M., Vassart O., *Full Scale Test of a Steel and Concrete Composite Floor Exposed to ISO Fire*. Proc. Of the 5th Structure in Fire Workshop SiF'08, pp. 539-550, Singapore City, Singapore, 2008.

EXPERIMENTAL STUDY ON FIRE BEHAVIORS OF SIMPLY-SUPPORTED T-BEAMS AND RESTRAINED T-BEAMS

Bo Wu* and Gui-He Tang*

* State Key Laboratory of Subtropical Building Science, Department of Civil Engineering, South China University of Technology, Guangzhou 510640, P. R. of China
e-mails: bowu@scut.edu.cn, tguihe@scau.edu.cn

Keywords: Reinforced concrete, T-Beam, Fire behaviors, Axial and rotational restraints

Abstract: *Eight simply-supported T-beams and nine axially-and-rotationally restrained T-beams were experimentally investigated in fire. The parameters considered in the fire tests included the width of slab, load ratio, axial restraint stiffness ratio, and rotational restraint stiffness ratio. The experimental results show that: (a) after the fire tests, large deflections were observed for the simply-supported T-beams, while the restrained T-beams remained almost non-deformed; (b) when the load ratio is relatively large, the fire endurance of the simply-supported T-beam increases with the increasing of the width of slab; (c) the influences of the slab's width on both the axial force in the restrained T-beam and the bending moment at the ends of the restrained T-beam can be generally neglected; and (d) residual axial force still exists in the restrained T-beam after fire.*

1 INTRODUCTION

A reinforced concrete (RC) frame structure is composed of beams, columns, slabs, and some other structural components. In the past two decades, a great deal of new knowledge has been generated to understand the fire behaviors of RC structural elements and frame structures [1]. Fire tests and numerical simulations of RC beams were carried out by Guo and Shi [2], and Lu et al. [3]. Empirical formulas were presented by Wu and Hong to determine the fire endurance of normal- and high-strength concrete simply supported beams [4]. Fire performances of axially-and-rotationally restrained RC beams have been experimentally and numerically studied, and the effects of axial and rotational restraints on the beam's internal forces have been investigated [5-7].

Although fire behaviors of isolated or restrained RC beams have been studied by some researchers, the interaction effect between a beam and its adjacent floor slab has not been taken into account in the past studies. To make a better understanding on this interaction effect, a series of fire tests have been being conducted at South China University of Technology. In this paper, the experimental results about fire performances of simply-supported T-beams and restrained T-beams are reported.

2 EXPERIMENTAL PROGRAMME

2.1 Test specimens

Eight simply-supported T-beams and nine axially-and-rotationally restrained T-beams were tested in fire in this study. All of these specimens were designed in accordance with the Chinese Code for Design of Concrete Structures. All beams were reinforced using six longitudinal steel bars with a diameter of 20 mm, and the tensional steel ratio was 0.94%. Steel stirrups with a diameter of 8 mm and a spacing of 150 (80) mm were employed. All the RC slabs were 100 mm thick, and the longitudinal and transverse reinforcements in the slabs were steel bars of 8 mm diameter at 200 mm interval. The measured yield strength and ultimate strength of the steel bars with a diameter of 20 mm were, respectively, 365 MPa and 613 MPa, and those of the steel bars with a diameter of 8 mm were 348 MPa and 497 MPa, respectively. The 28-day and test-day 150 mm cubic compressive strengths of the concrete were 29.5 MPa and 31.4 MPa, respectively. The 25 mm-thick end plates were manufactured from Grade Q345B steel, and were weld to the beam's longitudinal steel bars by virtue of six angle steels. Dimensions and reinforcement details of the specimens are shown in Figure 1 and Figure 2.

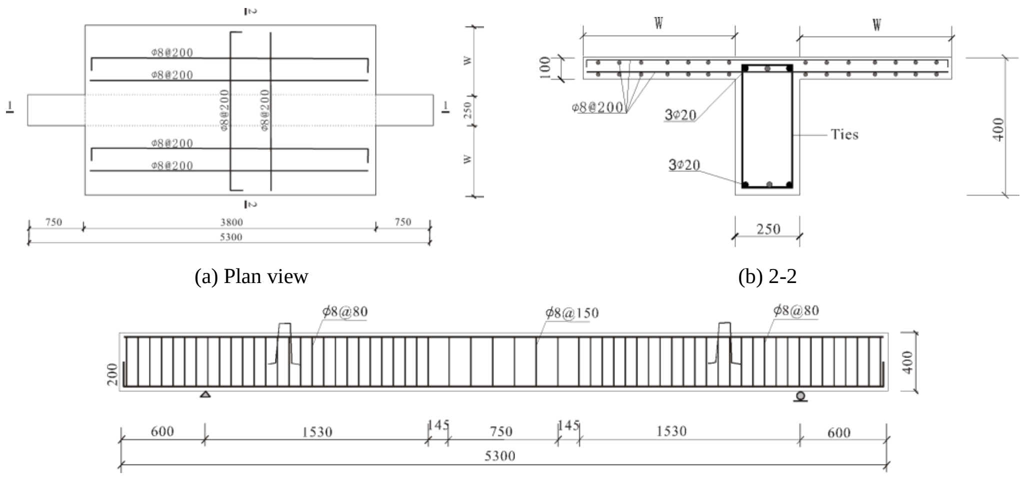

(c) 1-1

Figure 1. Schematic diagrams of simply-supported T-beam (unit: mm).

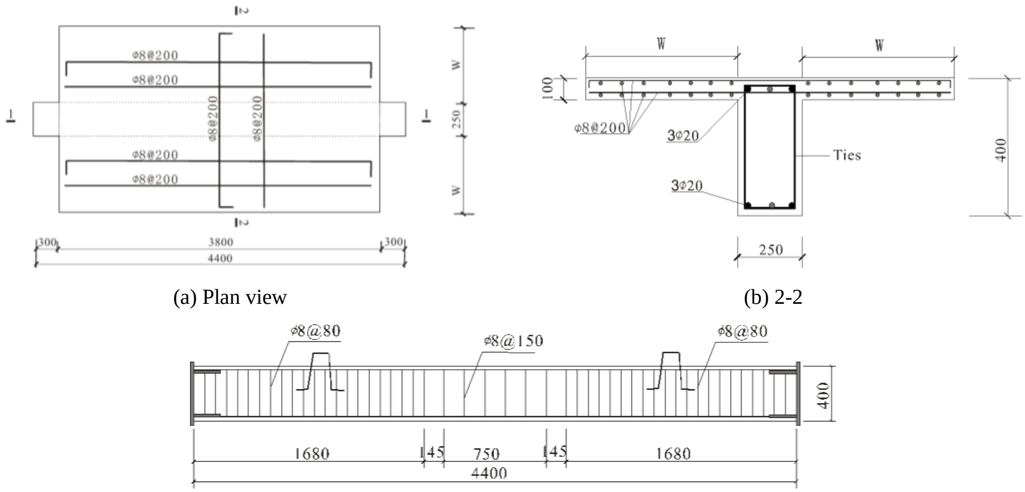

(c) 1-1

Figure 2. Schematic diagrams of axially-and-rotationally restrained T-beam (unit: mm).

Four parameters were considered in the tests, including load ratio μ (i.e., a ratio of the applied moment at the beam's mid-span to the flexural bearing capacity of the simply-supported rectangular beam at room temperature), width of slab W, rotational restraint stiffness ratio β_r, and axial restraint stiffness ratio β_l. It should be noted that in this paper the axial and rotational restraints were only applied to both ends of the rectangular beams and not to the edges of the slabs (i.e., the slab's three edges remained free during the fire test). Details of the specimens are listed in Table 1.

Table 1. Details of specimens.

Simply-supported specimens				Axially-and-rotationally restrained specimens					
Specimen	μ	W (mm)	Fire endurance (min)	Specimen	β_l	β_r	μ	W (mm)	Heating time (min)
SL1	0.3	0	103	RL1	0.066	0.896	0.3	900	120
SL2	0.5	0	85	RL2	0.066	0.896	0.5	900	120
SL3	0.3	500	102	RL3	0.066	0.896	0.3	1350	120
SL4	0.3	900	98	RL4	0.066	0.896	0.5	1350	120
SL5	0.3	1350	118	RL5	0.034	0.634	0.3	900	120
SL6	0.5	500	86	RL6	0.034	0.634	0.5	900	120
SL7	0.5	900	95	RL7	0.034	0.634	0.3	1350	120
SL8	0.5	1350	103	RL8	0.034	0.634	0.5	1350	120
-	-	-	-	RL9	0.034	0.634	0.5	500	120

2.2 Test setups and procedures

All the specimens were tested in a furnace chamber at South China University of Technology. The simply-supported T-beams were simply supported on two walls of the furnace, and the axially-and-rotationally restrained T-beams were connected to the restraint system by using the end plates. The specimens were vertically loaded using a hydraulic jack and three distributive beams. Schematic diagrams of the test setups are shown in Figure 3. Two side surfaces and the soffit of the beam, and the bottom of the slab are subjected to a fire following the ISO834 standard temperature-time curve. Each specimen was heated over a length of 3800 mm. Fig.4 shows a comparison between the measured average temperature–time curve in the furnace and the ISO834 standard curve for Specimen RL8.

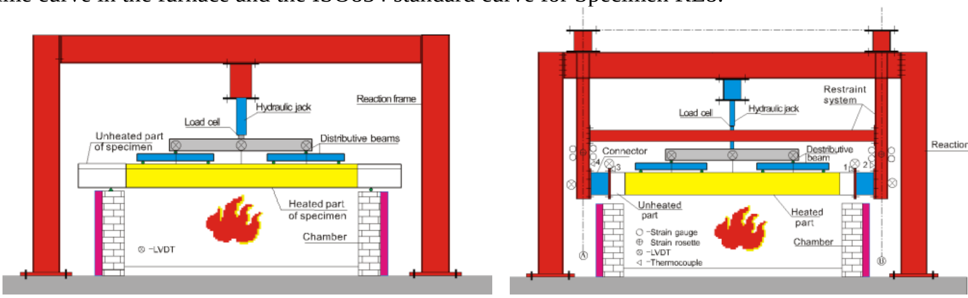

(a) Test setup for simply-supported T-beam (b) Test setup for axially-and-rotationally restrained T-beam

Figure 3. Schematic diagrams of test setups.

After preloading to eliminate possible equipment malfunction, the vertical load was applied to the specimen and maintained constant during the fire test. It should be noted that in this study the vertical load was only applied to the rectangular beam, and no load was applied to the slab.

The fire test of a simply-supported T-beam was terminated when one of the following conditions was attained: (a) the vertical load provided by the hydraulic jack could not be maintained any longer; and (b) the deflection at the beam's mid-span reached $L/20$, where L is the beam span. The heating time is regarded as the fire endurance of the simply-supported specimen. All the axially-and-rotationally restrained T-beams were heated for 120 min, and then the specimens were cooled in the furnace chamber to room temperature. The applied load was maintained constant during the heating and cooling phases.

2.3 Instrumentations

Both the specimen's thermal and structural responses were measured in the fire test and collected automatically by the data loggers. Type WRNK-101 thermocouples with a diameter of 3 mm were installed on the mid-span cross section of each specimen, and the locations of the thermocouples are shown in Figure 5. To measure the specimen's deflections during the fire test, three linear variable differential transducers (LVDTs) were employed as shown in Figure 3. Four thermocouples, eight strain gauges, two strain rosettes, and four LVDTs were placed on the restraint system as shown in Fig.3 to monitor the temperature of this system and to record the deformations of this system from which the restraining forces at the beam ends can be analyzed.

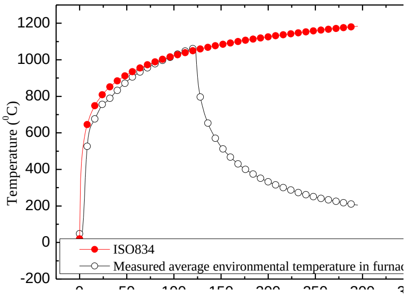

Figure 4. Comparison of average temperature-time curve in furnace with ISO834 standard curve for Specimen RL8.

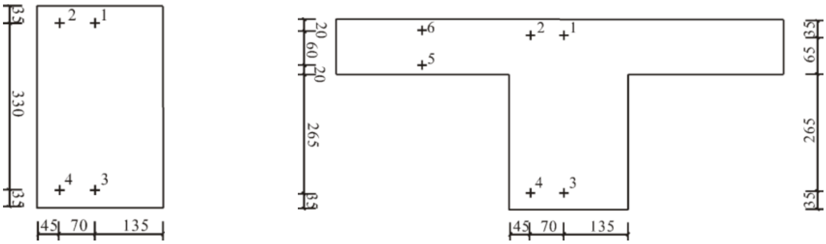

(a) SL1 and SL2 (b) SL3～SL8, RL1～RL9

Figure 5. Locations of thermocouples in specimens (unit: mm).

3 TEST RESULTS AND DISCUSSIONS

Views of typical specimens after fire are shown in Figure 6. It can be seen that large vertical deflections occurred for the simply-supported specimens (SL4 and SL7), while the restrained specimens (RL1 and RL3) remained almost non-deformed. Seldom spalling occurred for all the specimens.

(a) SL4 (b) SL7

(c) RL1 (d) RL3

Figure 6. Views of typical specimens after fire.

3.1 Thermal responses

Figure 7 shows the measured temperature-time curves for Specimens SL5 and RL5 and the restraint system. It can be seen from this figure that: (a) the temperature in the heating phase is inversely proportional to the distance between the thermocouple and the nearest specimen surface exposed to fire;

and (b) the temperatures of the restraint system are all below 50 ^{o}C, so the strain gauges and strain rosettes placed on this system are in good condition during the fire test.

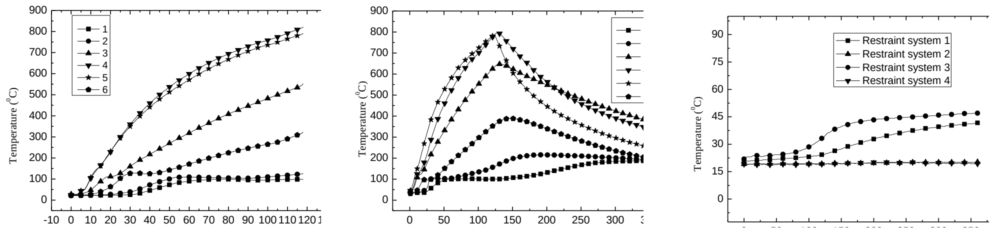

(a) SL5 (b) RL5 (c) Restraint system related to RL5

Figure .7. Measured temperatures-time curves.

3.2 Fire resistance of simply-supported T-beams

The mid-span deflections and fire endurances of the simply-supported T-beams are shown in Fig.8 and Table 1. It can be seen that: (a) when the load ratio is 0.5, the fire endurances of SL6, SL7 and SL8 are, respectively, 1.2%, 11.8% and 21.2% longer than the fire endurance of SL2, implying that the fire resistance of simply-supported T-beams increases with the increasing of the width of slab when the load ratio is relatively large; and (b) the fire endurances of SL6, SL7 and SL8 are, respectively, 84.3%, 96.9% and 87.3% of the fire endurances of SL3, SL4 and SL5, implying that the fire resistance of simply-supported T-beams generally decreases with the increasing of the load ratio.

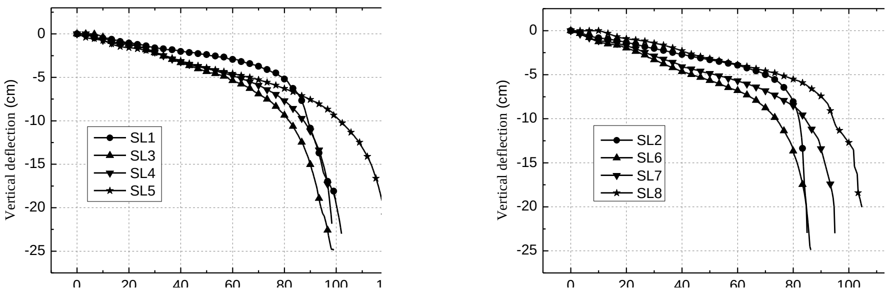

(a) μ=0.3 (b) μ=0.5

Figure 8. Measured mid-span deflection-time curves of simply-supported specimens.

3.3 Structural responses of axially-and-rotationally restrained T-beams

Utilizing the strain gauges and strain rosettes placed on the restraint system, the strains of the restraint system were measured, and then the bending moment at the beam ends and the axial force in the beam could be analyzed. Figure 9 shows the analyzed bending moment-time curves at the beam ends. It can be seen that: (a) the influence of the slab's width on the bending moment-time curves is limited; and (b) the maximum bending moment at the beam ends increases with the increasing of the rotational restraint stiffness ratio.

The analyzed axial force-time curves are shown in Figure 10. It can be seen that: (a) the axial force in the restrained T-beam increases in the heating phase and then drops gradually in the cooling phase, but residual axial force still exists after the fire test; (b) the maximum axial force in the restrained T-beam increases significantly with the increasing of the axial restraint stiffness ratio, but is little affected by the load ratio; and (c) the influence of the width of slab on the axial force in the restrained T-beam can be generally neglected.

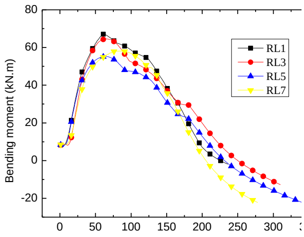

Figure 9. Analyzed bending moment-time curves of restrained T-beams.

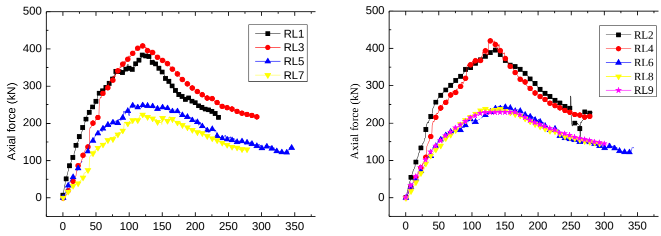

(a) μ=0.3 (b) μ=0.5

Figure 10. Analyzed axial force-time curves of restrained T-beams.

4 CONCLUSIONS

Based on the results of this study, the following conclusions can be drawn:

(1) After the fire test, large deflection was observed for the simply-supported T-beam, while the restrained T-beam remained almost non-deformed.

(2) When the load ratio is relatively large, the fire resistance of the simply-supported T-beam increases with the increasing of the width of slab.

(3) The influence of the slab's width on the bending moment at the ends of the axially-and-rotationally restrained T-beam is limited.

(4) The residual axial force still exists in the axially-and-rotationally restrained T-beam after fire.

(5) The influence of the width of slab on the axial force in the axially-and-rotationally restrained T-beam can be generally neglected.

ACKNOWLEDGEMENTS

The research reported was financially supported by the National Natural Science Foundation of China (51025829, 51378225), the Funds of State Key Laboratory of Subtropical Building Science of China (2011ZB07, 2013ZB24), and the Fundamental Research Funds for the Central Universities (2012ZP0011). The financial supports are highly appreciated.

REFERENCES

[1] Wu B., and Tang G. H., "State-of-the-art of fire-resistance of concrete structures in recent years", *Journal of Building Structures*, 2010, 31(6), 110-121 (in Chinese)

[2] Guo Z. H., and Shi X. D., "Behaviour of reinforced concrete at elevated temperature and it's calculation", *Tsinghua University Press*, 2003 (in Chinese)

[3] Lu Z. D., Zhu B. L., and Zhou Y. H., "Experimental study on fire response of simply supported reinforced concrete beams", *China Civil Engineering Journal*, 1993, 26(3), 47-54 (in Chinese)

[4] Wu B., and Hong Z., "Fire resistance of simply-supported reinforced concrete beam", *Journal of South China University of Technology*, 2006, 34(7), 82-87 (in Chinese)

[5] Wu B., and Lu J. Z., "Numerical study of the behaviour of restrained RC beams at elevated temperatures", *Fire Safety Journal*, 2009, 44(4), 522-531

[6] Wu B., and Qiao C. J., "Axial force analysis of reinforce concrete beams during heating and cooling phases", *Journal of Architecture and Civil Engineering*, 2010, 27(1), 12-20 (in Chinese)

[7] Daikat M. B., and Kodur V. K. R., "A numerical approach for modeling the fire induced restraint effects in reinforced concrete beams", *Fire Safety Journal*, 2008, 43(4), 291-307

8th International Conference on Structures in Fire
Guo-Qiang LI, Venkatesh K. R. KODUR, Shou-Chao JIANG, Jian JIANG, Su-Wen CHEN, Guo-Biao LOU (Eds.)
Shanghai, China, June 11-13, 2014

MEMBRANE ACTION OF TIMBER FIBRE REINFORCED CONCRETE COMPOSITE FLOOR IN FIRE

Eva Caldova*, Petr Vymlatil, Lukas Blesak*, Frantisek Wald* and Anna Kuklikova***

* Czech Technical University in Prague
e-mails: eva.caldova@fsv.cvut.cz, lukas.blesak@fsv.cvut.cz
wald@fsv.cvut.cz, kuklikova@fsv.cvut.cz

** Designtec s.r.o., Brno
e-mail: vymlatil.p@designtec.cz

Keywords: Fibre reinforced concrete, Timber, Slab, Membrane action, Fire exposure

Abstract. *In the two last years, the furnace tests were performed on two full-size floor specimens at the Czech Technical University in Prague. Both floor specimens were 4.5 m long and 3 m wide, consisting of 60 mm fibre concrete topping on plywood formwork, connected to GL floor joists and were subjected the standard fire for over 150 min. / 60 min. The floors were partially protected. The membrane effect of the floor was activated to maintain the global resistance of the floor. Based on the performed tests is prepared a numerical model of the timber fibre reinforced concrete floor slabs in fire. The experimental research results that deal with the effect of membrane action of composite steel fibre reinforced floor slabs exposed to fire offers a new timber-concrete floor with subtle cross-section of timber beam.*

1 INTRODUCTION

The use of timber-concrete structures has considerably increased especially in case of reconstructions and constructions of prefabricated residential houses. In the concrete slab of the timber-concrete composite floor is design reinforcement for restrain caused by shrinkage of concrete and to obtain a sufficient resistance against tensile forces around the shear connectors. Considering the amount and the position of the reinforcement in the slab the thickness of the slab results in a minimum of about 60 mm which leads to an unnecessary high dead-load of the composite floor, see [1]. For this reasons several research studies have been conducted during the last decades, with focus on new timber-concrete composite floor. One of the new kinds of such floor is that the usual reinforced concrete is replaced by steel fibre reinforced concrete (SFRC). This innovative concrete with specific hardened concrete properties and fresh was developed to reduce the slab thickness and to help the construction procedure. One of the most important requirements of a floor structure is its fire resistance. Fire resistance of timber-fibre concrete composite elements is mainly influenced by timber, the connectors and mixture of fibre concrete. The temperature inside the timber member depends particularly on the cross-sectional dimensions, on the density and moisture content of wood and on the fire load and temperature development during the fire. As listed in [5], where spruce timber was tested up to temperature 150 ℃, up to temperature 150 ℃ bending resistance of timber with the initial moisture content 12% decreases 42% and modulus of elasticity decreased linear with increasing temperature, whilst its value decreased 12% when temperature being equal to 150 ℃. This proves the fact, that timber even being not heated to temperatures such as the concrete part of the slab; it loses its properties rapidly with rising temperature. This needs to be prevented either by over sizing the timber elements or by fire protecting them in a proper way. The temperature development in the place of the shear connection can be governed by the cross-sectional dimensions, particularly by the width, and by the sort of the fire scenario. Fire resistance of connectors is influenced both by the material surrounding them and also by changing the self material properties, which in case of steel are quite well known. In case of steel fibre reinforced concrete, this becomes a complex problem, as far as being a combination of several materials. In the case of the presented experiment, properties of SFRC were being examined by material tests.

Experimental and theoretical studies show that the presence of steel fibres increases the ultimate strain and improves the ductility of fibre-reinforced concrete elements, see [2] and [3].

It is possible to use nominal, parametric or natural fire scenarios. Membrane forces are activated by the large deflections of floors caused by fire. Fire has a positive effect on floor constructions membrane behaviour, because the slab with increased temperature deforms according to the temperature gradient and under membrane action the increased deflection has significant influence on bearing capacity. When the slab transcends from slab to membrane behaviour the bearing capacity increases. One simple design method includes the development of membrane influence which may be utilized if the slab is two-way spanned, simply supported along the whole perimeter and its side ratio is 1: 2. In case of fire, the simple design method enables the utilization of the entire construction behaviour and enables to leave out some elements without fire protection.

In the frame of the research work performed at Czech Technical University in Prague, there are currently being developed parallel numerical and analytical models in order to simulate the real behaviour of the described type of structure exposed to fire. Both numerical and analytical models are being developed by various independent methods and computational software. This enables our team to analyze various boundary conditions, material input data and its self behaviour etc., in order to find the proper balance between simplifications and exact solutions of various effects influencing the real slab behaviour whilst having comparable results with the real experiments. The experimental part of the research work is essential, and so right the experiments performed by our team are the major subject this paper focuses on.

For the experiments, material properties tests were carried out at ambient and elevated temperatures. Tensile strength and ductility of fibre reinforced concrete were measured. One of the goals is to estimate the possible utilization of concrete slabs supported with timber beams with the aid of models in ANSYS 14 software [3] to determine its behaviour in loaded floor construction with the utilization of membrane effect for floor constructions with dispersed reinforcement.

2 EXPERIMENTS

The experimental program was divided into two main groups. The first group consists of material properties tests and the second group of tests with structural elements. Tests of concrete material properties consist of the standard cube compressive test, standard cube tensile test and three four- points bending test at ambient and elevated temperature. The aim of these tests was to assess the material properties of SFRC for analysis of mechanical behaviour of a timber-concrete composite floor structure. Testing of structural elements consists of the push-out test of connectors, the composite beam tests at ambient and elevated temperatures, two floor tests at ambient and elevated temperatures. As being well known, there may be not acceptable differences in material properties of timber comparing the real and standard behaviour. Therefore even timber material was tested performing a four-point bending test of specimens taken from not damaged parts of beams after the previous slab test at ambient temperature was over.

2.1 Floor slab test at elevated temperature

Two floor slabs were tested in a furnace at elevated temperature in the PAVUS fire laboratory in Veselí nad Lužnicí during 2012 and 2013. Both full scale floor specimens were designed to span 3.0 m by 4,5 m according to the furnace interior dimensions, loaded in the same way (see the test set in Fig.[1]).

The basic data of the performed tests in 2012 (slab ELE-1-120/160) and 2013 (slab ELE-2-100/160):

- cross section of the secondary beams: 120/160 mm (slab ELE-1-120/160)
  100/160 mm (slab ELE-2-100/160)

- timber class: GL24h (slab ELE-1-120/160)
  GL36c (slab ELE-2-100/160)

- fibre content 70 kg/m^3, HE 75/50 Arcelor steel fibres in both slabs
- in both cases connectors were used TCC 7.3 x 150 mm with screws inclined 45 degrees to the beam axis in two rows; the distance of the screws in one row was 100 mm
- both tests having the SFRC slab 60 mm thick

In both cases, the timber frame was fire protected by timber desks and the secondary beams in the centre of the floor slab were left unprotected. The design fire applied on the lower surface of the floor was the standard fire. The mechanical load during fire was created by concrete blocks uniformly distributed over the floor. All the mechanical action was applied before the self fire started to act. The applied load 4 × 6 kN represents the uniform load 1.8 kN/m^2, which is consistent with loads in a typical office building designed for fire conditions, $q_k = q_{k,fi} / \eta_{fi,t} = 1.8/0.6 = 3$ kN/m^2. The test specimens were designed for fire resistance R60.

As far as the mechanical loading was applied before the self heating, the loading and deformation phases were carefully taken into account when evaluating displacements and deflections.

Figure 1. Floor slab experiment set - in furnace (left), mechanical loading (right).

2 EXPERIMENTAL RESULTS

During the heating phase, the standard fire curve was followed which lasted for 150 min. in the first test and 60 min. in the second test. After that, burners were turned off and the furnace was cooled down naturally. The unprotected timber beams located in the middle of the floor were heated up to 250 °C in case of both slabs. The maximum recorded temperature occurred after 45 min. (first slab) and 39 min. (second slab) at the centre span of beam. Then the secondary beams failed. The full collapse of the first test was reached at 154 min. due to damage of the fire protection of edge beams. In case of the second slab, the heaters were turned off in 60 min. and the slab was left to cool down naturally whilst the data were still recorded till 120 min. The second experiment was, comparing to the first one, prepared not considering the complete failure of the slab, and so after opening the major longitudinal crack the experiment was stopped in order to prevent the slab to collapse into the furnace.

The temperature in the concrete slab continued in rising after the maximum atmosphere temperature, which occurred at 150 min.. The maximum temperature 845 °C reached in the middle of the first slab 20 mm from the bottom surface of the slab and 562 °C in the left corner of the second slab 20 mm from the bottom surface of the slab. Temperature rise at the unexposed face of the composite slab after 150 min. of fire was slightly above 350 ℃. This caused also by the fact the cracks were widely open and the uniformity of the slab was damaged. Some of the analyzed results are listed in Table 1.

Isolation criterion - temperature of the unexposed edge of the slab equal to max. 140℃ was exceeded in 52 min. for the first slab and in 54 min. for the second slab.

Table 1. List of temperature, deflection and beams failure time appertaining to the tested slabs.

Temperature of the upper surface of the particular slabs in various time [℃]			**Deflection in the middle of the span of the particular slabs in various time [mm]**		
Time [min]	1st slab (ELE-1-120/160)	2nd slab (ELE-2-100/160)	Time [min]	1st slab (ELE-1-120/160)	2nd slab (ELE-2-100/160)
0	20	22	0	-	-
20	68	70	20	14	18
40	123	120	40	37	39
60	177	165	60	90	90
80	233	230 (fire off)	80	125	89 (fire off)
100	272	240 (fire off)	100	155	91 (fire off)
Timber beams failure of the particular slabs in time [min]					
1st slab (ELE-1-120/160)			2nd slab (ELE-2-100/160)		
45			40		

At 150 min. of fire, the total deflection of the first floor reached 220 mm. Their flexural load bearing capacity with this level of heating would no longer allow them to bear the applied load alone. The supported concrete slab was not horizontally restrained around its perimeter and the supporting protected perimeter beams maintained their load carrying capacity. They were subjected to small vertical displacements and allowed membrane action to develop with the in-plane forces in the central region of the slab going into tension and in-plane equilibrium compressive forces forming in the slab around its perimeter. Comparing to a steel frame supported slab, the rotation and bending capacity of the timber frame elements represent a big advantage for the slab behaviour, mainly vertical deflection.

The behaviour of the timber-concrete composite floor in fire may be divided into three stages as for the steel-concrete composite floor. In order to define the partial phases, it is very convenient to follow the cracks occurrence. As water evaporates by these cracks, they can be seen very clearly and show the way a fire tested slab behaves (see Figure 2).

Figure 2. Cracks occurrence during the fire loading.

When evaluating the cracks location, there were separated major (local) and so call spread cracks. Right the spread cracking is expected to be prevented by using SFRC material. There may be several reasons for a major crack occurrence in a particular location, such as material, geometry or loading imperfections, however, most of them can be predicted in advance. As the particular “slab behaviour phases” became active, the spread cracks changed their position and dimension. For the major crack after fire test of the second slab see Figure 3.

Figure 3. Major crack location after the experiment (2013).

In the initial stage of fire, when the floor has low temperature, the slab carried applied load mostly in a bending mechanism with small deflections (Stage 1).

In addition to the thermally induced downward deflection, the unprotected beam is losing strength and stiffness due to the increasing temperatures from fire. For the first test, with increasing temperature, between 30-45 min., the strengths of timber and concrete of the slab were reduced, and the floor behaviour is affected more the slab behaviour (Stage 2). After 46 min., the bending capacity of the slab was not enough, and the deflection of the slab had to be further developed, which created major load-bearing capacity under membrane mechanism to maintain the resistance of the slab (Stage 3). How the deflection of the slab is larger, the tensile membrane action is higher. Finally, most of the vertical load on the slab is carried by the membrane action.

Each stage is represented by an action of dominant features of the particular structural elements behaviour. When the slab being bended, timber beams carry most of the loading, however, when vertical

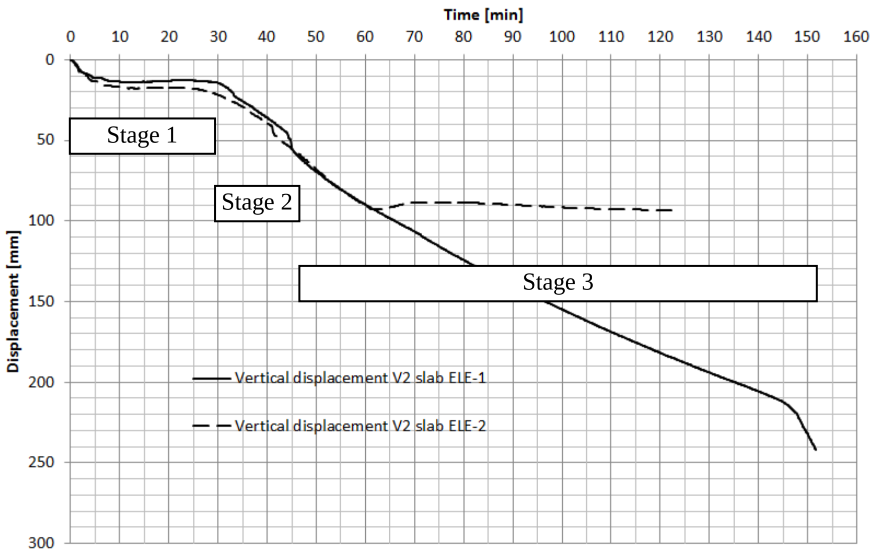

Figure 4. Partial slab behaviour stages for both tested slabs – full line (slab ELE-1-120/160 – marked stages), dashed line (slab ELE-2-100/160).

deflection decreases and timber beams lose their load-bearing capacity due to fire exposure, tension property of SFRC becomes active. Therefore the combination of the structural elements and the used materials is considered to be very convenient for the introduced type of structure and loading. The introduced stages are figured in Figure 4.

3 NUMERICAL AND ANALYTICAL MODELING

As mentioned above, a major part of this research is numerical and analytical modeling of the subjected structure. The main objective of the numerical FE analysis elaborated in the frame of this project is to simulate the behaviour of the first tested slab used for fire test and predict the fire resistance. The temperatures in the furnace are known from the test therefore were not considered neither CFD analysis nor coupling between mechanical analysis and solution of the problem was carried out as one-way coupled thermo-mechanical analysis. Even assuming one-way coupled thermo-mechanical analysis, is the problem very complex due to modelling transient effect in heat transfer analysis, strong geometrical and material nonlinearity and difficult estimation of material data for both room and elevated temperatures and their uncertainties. The main objective of the analytical modeling, currently being in progress, is to develop the most proper calculation method for defining the fire resistance of the described type of slab structure and consequently apply all the gained data into the civil engineering practice. Numerical and analytical modeling is not the subject matter of this paper; therefore it is not described in details.

4 CONCLUSIONS

The timber-concrete slabs performed well supporting the applied load for the duration of the tests and pointed out the strength in the system due to membrane action. Due to membrane action, the existence of secondary timber beams to support the slab is not necessary in the fire condition and these beams can be left unprotected, see [4]. The tested ceiling slabs confirmed the combination of the used structural elements made of the used materials to be convenient for this type of loading. Both tested slabs were analyzed in details and all the gained data were compared to each other. Several predicted facts were confirmed, even some new facts become evident. All these data are currently being applied in numerical and analytical models, which will be presented in the near future.

ACKNOWLEDGEMENT

This work has been supported by the European Union, OP RDI project No. CZ.1.05/2.1.00/03.0091 University Centre for Energy Efficient Buildings.

REFERENCES

[1] K. Holschmacher, S. Klotz and D. Weise, "Application of steel fibre reinforced concrete for timber-concrete composite constructions", *Lacer 7*, 161-170, 2002.

[2] V.K. Kodur and T.T. Lie, "Thermal and mechanical properties of steel-fibre-reinforced concrete at elevated temperatures", Canadian *Journal of Civil Engineering*, 23, 511-517, 1996.

[3] J. Bednář, F. Wald, J. Vodička and A. Kohoutková, "Membrane Action of Composite Steel Fibre Concrete Slab in Fire", *Procedia Engineering,* 40, 498-503, 2012.

[4] C. G. Bailey and D. B. Moore, "The structural behaviour of steel frames with composite floors slabs subject to fire - Part 1 theory", *Structural Engineering*, 78-11 (2000) 19–27.

[5] Glos, P., Henrici, D., "Biegefestigkeit und Biege -E-Modul von Fichtenbauholz im Temperaturbereich bis 150℃. *Holz Roh-Werkstoff*, 49, 471-422, 1991.

8th International Conference on Structures in Fire
Guo-Qiang LI, Venkatesh K. R. KODUR, Shou-Chao JIANG, Jian JIANG, Su-Wen CHEN, Guo-Biao LOU (Eds.)
Shanghai, China, June 11-13, 2014

POST-FIRE PERFORMANCE EVALUATION METHOD OF HIGH-RISE BUILDINGS AND ITS APPLICATION IN THE TELEVISION CULTURAL CENTER, CCTV

Guang-Yong Wang*,Yin-Qing Li*, Cang-Hu Qiu*,Lin-Hai Han, Hong-Xia Yu** and Fu-Di Xie*****

*Institute of Building Fire Research, China Academy of Building Research, Beijing, 100013, China
e-mails: wanggy0609@163.com, cabr2582@126.com, qiuch@vip.sina.com

** Civil Engineering Department, Tsinghua University, Beijing, 100084, China
e-mail: lhhan@tsinghua.edu.cn, inbiscus@163.com

*** Civil Engineering Department, Beijing University of Civil Engineering and Architecture, Beijing, 100044, China
e-mail: 260085927@qq.com

Keywords: Post-fire, Mechanical performance, Evaluation method, High-rise building, Fire model

Abstract. *A fire simulation method of a global high-rise building was proposed in this paper. Then, an evaluation method for the post-fire mechanical performance of a high-rise building was proposed, and the coupling of fire and load can be considered. In the end, the post-fire performance of the Television Cultural Center (TVCC) was evaluated by using the method, and the evaluation conclusion was used to the retrofit of TVCC.*

1 INTRODUCTION

The Television Cultural Center (TVCC) is a high-rise building which has 40 structure floors, and its total height is 159 meters. The building structure is a frame-shear structure. The column is steel reinforced concrete structure, and the beam and the shear wall are reinforced concrete structure, so the building is a mixed structure. On February 9, 2009, a large-scale fire which continued for about 6 hours took place in this building, and the fire caused a direct economic loss of 160 million Yuan and a large area of structural damage. The building in and after fire is shown in Figure 1.

After fire, the mechanical performance of the building structure and its members must be evaluated in order to ascertain the damage degree of the building, based on which a scheme for repairing and retrofitting the fire damaged building can be established. At present, there are very little developments on the research on mechanical performance of a global high-rise building in and after fire. A numerical simulation of the global structure collapse of WTC in fire caused by aircraft impact was performed, but the evaluation on the post-fire mechanical performance of a global high-rise building has never been carried out hitherto. At the same time, an evaluation method for the post-fire mechanical performance of a high-rise building is necessary.

Entrusted by the China Central Television station (CCTV), Institute of Building Fire Research (IBFR), China Academy of Building Research undertook the task of evaluating the post-fire mechanical performance of TVCC after fire. A large number of investigations on the fire site and many experiments on the post-fire mechanical performance of the members of TVCC were carried out by IBFR. With the information obtained, a theoretical research on the post-fire performance of high-rise buildings was carried out, and an evaluation method for post-fire mechanical performance of high-rise buildings was proposed. With the proposed method, IBFR finished the task of evaluating the post-fire performance of TVCC, and gave many valuable conclusions which formed the bases of the reparations and retrofit of TVCC.

(a) Building in fire (b) Building after fire

Figure 1. TVCC fire.

2 FIRE TEMPERATURE INVESTIGATION AND NUMERICAL SIMULATION

It is the most basic and important work to determine actual fire temperature field when evaluating post-fire performance of the structure. There are about three methods to determine the actual fire temperature [1], and sometimes it's necessary to use more than one method comprehensively at the same time. In the first method, fire temperature can be determined based on fire models, and the quantity of the combustible substance, the size of the fire room and the openings are generally the most important parameters for fire models. Fire model includes empirical model, regional model and computational fluid dynamics (CFD) model. CFD model is the method which uses computational fluid dynamics to determine fire temperature, and CFD model is the most time consuming but more accurate model. The second method is based on many kinds of typical physical and chemical phenomena after fire to determine the highest fire temperature. For example, glass sheet begins to flow when temperature arrives at 850℃. Therefore, it can be concluded that the temperature has experienced a temperature higher than 850℃ if glass sheet melt is found after fire. In the third method, the post-fire status of structural members can be used to determine the highest fire temperature, e.g. concrete or steel surface color, spalling degree of concrete, etc. By using the third method, fire temperature of the structural members can be directly determined, so it is often used in fire temperature field determination.

After the fire, IBFR immediately organized professionals to carry out the fire site investigation. The investigated content includes the surface shape and color of the metal members, the color of steel and concrete members, concrete spalling degree and the amount and location of the combustible substance, and so on. On the bases of the site investigation, a large number of photos, video information were obtained. The information was reorganized according to the floor number, so the fire damage distribution of the structure members and the burned fire loads distribution in the global building were obtained though detailed classification.

The next step is to determine the fire temperature distribution in the building with the data obtained above. The highest temperature and the relationship between the air temperature and the fire time are two important factors to determine the fire temperature in a room. The aim of the evaluation work is to assess the post-fire mechanical performance of the structure and the member, so the ambient air temperature around the member is necessary. First, the highest temperature of the member surface was determined by concrete color and concrete spalling degree, and the air temperature around the member can be deduced. Then, the relationship between the temperature and fire time was obtained by empirical model or CFD model. When the temperature distribution was obtained, it was compared with the investigated temperature from the fire site. If the difference between the investigated highest temperature and the calculated exceeded the allowed error, the parameters were modified and was then input into the fire models and calculated again. The temperature determination was a try and error work sometimes. It's appropriate to determine the temperature field using empirical model or regional model if the area of the room doesn't exceed 100m^2, otherwise the CFD model must be used. In the evaluation of the TVCC building temperature, empirical model and CFD model were both used according the situations.

During the fire, the fire firstly occurred on the top of the outer surface of TVCC, and it immediately spread out on the outer surface. The fire soon spread into the inner of TVCC through openings and spread in many floors and rooms. When the fire occurred, the decoration was constructing, and many combustible materials were placed in the aisles and rooms, so the fire continued for about 6 hours and became a large-scale fire. The fire simulation of the global building was necessary in order to find the fire spread sequence and extension when the fire spread in the outer and inner of the building. IBFR established a CFD fire simulation model of the global building by using the professional fire simulation software FDS, and the mesh number was 10 million. The mesh can be refined in the fire region in which attention should be specially paid in order to increase the accuracy. In the evaluation of building fire temperature, the CFD fire model was used to simulate the fire in one floor and the fire on the outer surface because the computation ability of the computer was limited. The global CFD building fire model which was established by FDS is shown in Figure 2. The simulated fire spread on the outer surface of TVCC is shown in Figure 3, in which *t* is fire time. The simulated fire temperature contours in the fourth floor of TVCC is shown in Figure 4.

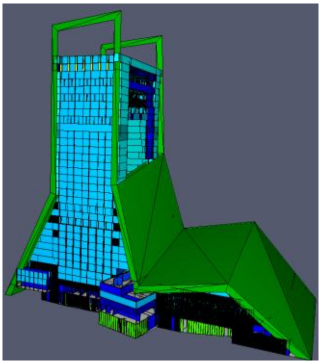

Figure 2. Global building fire CFD model.

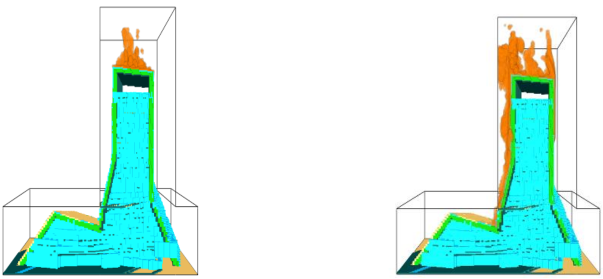

(a) t=300s (b) t=600

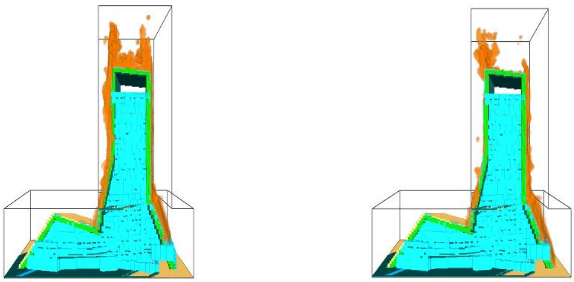

(c) t=800s (d) t=1200

Figure 3. The simulated fire spread on the outer surface of TVCC.

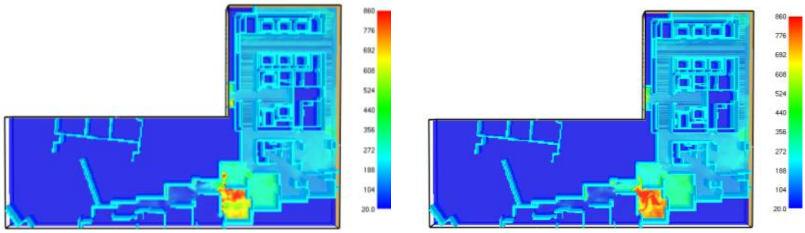

(a) t=300s (b) t=600

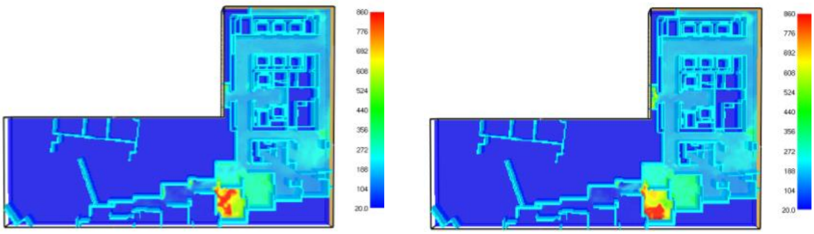

(c) t=900s (d) t=1200

Figure 4. The simulated temperature contours in the fourth floor of TVCC (Unit: ℃).

3 COUPLING BETWEEN LOADS AND FIRE

In fact, a building structure is generally bearing some loads when a fire occurs, such as vertical loads (*N*). With the increase of temperature (*T*), structural deformation will increase gradually due to the thermal expansion action and the degradation of the mechanics performance of structure members [2]. When the fuel is worn out in the fire, the environment temperature will drop down, and the temperature of structure members will drop down soon. After fire, the mechanical performance of steel will recovery in some extent compared with at high temperature, while the mechanical performance of concrete will degenerate compared with at high temperature. At the same time, the structure deformation will recovery in some extent compared with in fire because the thermal expansion will vanish after fire, and the load-carrying capacity of the fire damaged structure will decrease. In order to exactly evaluate the post-fire performance of fire damaged structures, it's beneficial to propose a method that can take into account the coupling of loads (*N*), temperature (*T*) and fire time (*t*) according the principles mentioned above. The logical sequence of loads (*N*), temperature (*T*) and fire time (*t*) during a fire including temperature increase, temperature decrease and loading after fire is shown in Figure 5. In Figure 5, T_o and N_o are ambient temperature and loads before fire, respectively; t_h and t_h' are critical temperature between the temperature increase stage and decrease stage. The structure behaviors actually through A′ →B′ →C′ →D′ →E′ which corresponds to the coupling path among time, loads, and temperature, and the D′ → E′ path is the loading stage after fire.

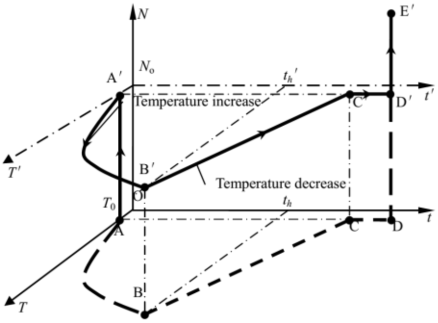

Figure 5. Coupling path of load, temperature and time.

The post-fire performance evaluation method of TVCC was based on the method mentioned above, meanwhile the temperature increase and decrease and the coupling between fire and load were also considered. This method takes into account the coupling between fire and load to the maximum extent, so this method conforms to the actual structure behavior and guarantees the evaluation results are right.

4 GLOBAL STRUCTURE RESPONSE ANALYSES DURING AND AFTER FIRE

Fire will produce two kinds of effect in structures [3]. The first effect is to reduce the load-carrying capacity; the second effect is to produce residual internal force and residual deformation. On the one hand, the load-carrying capacity of structure is decreased because the material strength is deteriorated in and after fire. On the other hand, if plastic deformation produces in the structure, residual internal force and residual deformation will produce in the structure after fire because the structure is usually redundant. Residual internal force and residual deformation will always exist in the structure which has been suffered fire, so its load effect coefficient is the same as dead load. The key point of mechanical performance evaluation of structures suffered fire is to ascertain the residual load-carrying capacity of the members and the residual internal force and residual deformation of the structure after fire.

The residual strength at one point of the member cross-section can be determined according to the highest temperature that the point experiences. The strength in the points of the member cross-section is not same because the highest temperature doesn't distribute uniformly, so the cross-section of the members suffered fire is a composite cross-section comprised of materials without the same strength. The residual internal force and deformation of the structure suffered fire can be obtained through analyzing the response of the global building under the condition that the coupling between the fire and the load is considered. A finite model of the global building is necessary, and a nonlinear response analysis on the mechanical performance of the global building during and after the fire should be carried out. As we know, it is very difficult to set up a finite model of a global building such as TVCC. Even if the model can be set up, it is very difficult to finish such a large amount computation. In fact, there were only more than ten floors suffered fire in TVCC, and the majority floors didn't suffer fire. The structure of the floor that didn't suffer fire can be regarded as the boundary of the fire damaged floors, so the finite model can only include the fire damaged floor and some appropriate parts extending from the fire damaged floor. By using this method, the scale of the finite model of the global building can be reduced, and the computation can be reduced too. At the same time, by using this method, the influence of the global structure on the fire and post-fire performance of a structure member is considered. In the evaluation of

TVCC, some finite models of substructures which were damaged by fire were established, and the post-fire performance of the fire damaged substructures was analyzed while the global structure action was considered.

The analysis procedure can be divided into three stages which include the stage of temperature increase, the stage of temperature decrease and the stage of loading after fire. The first two stages are used to obtain the response of the structure in a fire including temperature increase and temperature decrease, and its aim is to obtain the residual internal force and deformation induced by the fire, which are also called fire induced effect. The third stage continues to analyze the load-carry capacity of the whole substructure on the condition that the fire induced effect is obtained. In the third stage, the load continues to increase until the substructure begins to fail while the temperature of the structure remains at ambient temperature. The post-fire performance is evaluated by studying the results including the load-carrying capacity and deformation of the structure after fire. It's should emphasize that although the temperature remains at ambient temperature after fire, the high temperature that the structure has ever experienced will make the material strength worse and produces residual internal force and deformation in the structure. These effects detailed above should be considered in the third stage. In the evaluation of TVCC, the procedure listed above was used. The finite model of the suspended steel structure on the top of the building is shown in Figure 5. The vertical displacement contour of the suspended steel structure when fire time (t) was 60min is shown in Figure 6. The finite model of the top steel structure is shown in Figure 7, and the vertical displacement contour of the top steel structure is shown in Figure 8.

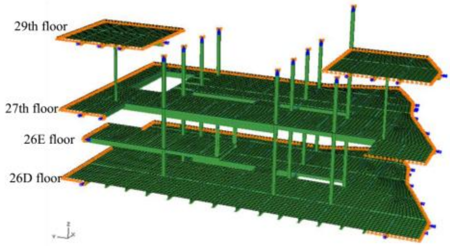

Figure 5. Finite model of suspended steel structure.

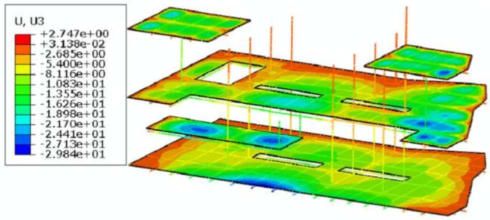

Figure 6. Vertical displacement when t=60min (Unit: mm).

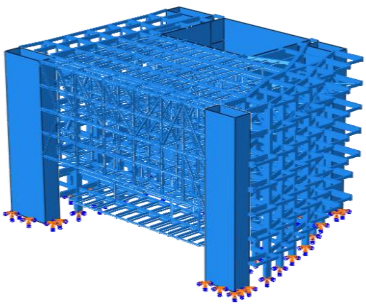

Figure 7. Finite model of the top steel structure.

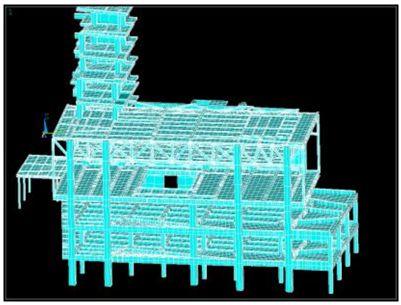

Figure 8. Finite model of the exhibit hall (TVCC annex).

5 EXPERIMENTAL STUDIES

At present, the research on the evaluation method for fire performance of building structures have achieved many developments [4,5], but the research on the evaluation method for post-fire performance of building structures are relatively few both domestically and internationally. In order to ensure the evaluation method is accurate, a large amount experiments on the fire resistance, post-fire performance of materials, structural members and substructures were carried out. There are two purposes for the experiment study. The first purpose is to verify the validity of the theoretical method accuracy, and the second purpose is to obtain material parameters for the finite model.

The material property experiment includes the post-fire bond-slip between rebar and concrete, the post-fire bond-slip between steel and concrete, the post-fire strength of steel and concrete. The structural member property experiment includes the post-fire performance of simply supported reinforced concrete beams and restrained reinforced concrete beams, the post-fire performance of steel reinforced concrete column. The substructure experiment includes the post-fire performance of steel reinforced concrete frames. The fire resistance and post-fire performance experiment frame specimens are shown in Figure 9.

Figure 9. Steel reinforced concrete frame specimens.

In addition, an experiment on the post-fire hysteretic performance was carried out, and eight steel reinforced concrete column specimens were tested. ISO834 temperature-time curve were adopted in the experiment. Some specimens, test set-ups and one typical horizontal load (F)-horizontal displacement (d) hysteretic curve and some F-d skeleton curves of the experiment are shown in Figure 10. In figure 10, t_h is the heating time of the specimens.

Such a large amount of experiments guarantee the validity of evaluation method and the evaluation conclusions of TVCC.

(a) specimens after fire

(b) test set-ups

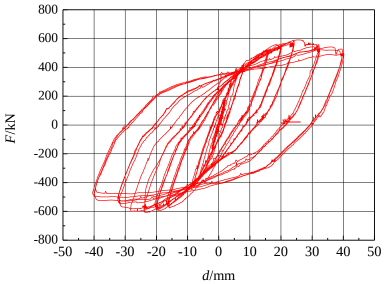

(c) *F*-*d* hysteretic curve

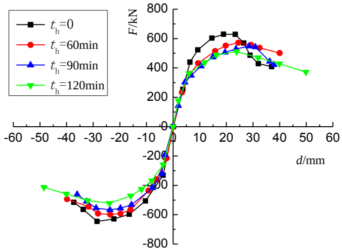

(d) *F*-*d* skeleton curve

Figure 10. Hysteretic experiment of steel reinforced concrete column after fire.

6 CONCLUSIONS

Firstly, a fire simulation method of a global high-rise building was proposed in this paper, and a global building fire can be simulated by using this model. Then, an evaluation method for the post-fire performance of a high-rise building was proposed, and the coupling of fire and loads can be considered in the method. The response of a global building during and after fire can be analyzed by using this method. At the same time, a large amount of experiments on the fire and post-fire performance of material, member and substructure were carried out to verify the validity of the proposed method. In the end, the post-fire performance of TVCC was evaluated by using the method, and the evaluation conclusion was used to the retrofit of TVCC.

ACKNOWLEDGEMENTS

This work was supported by National Nature Science Foundation of China (51278477), the country "12th Five-Year Plan" to support science and technology project (2012BAJ07B01) and China Academy of Building Research Fund (20120106330730073).

REFERENCES

[1] B. Wu, *Post-fire Mechanical Behaviour of Reinforced Concrete Structures*, Science Press, Beijing, 2003. (in Chinese)

[2] L.H. Han, *Concrete filled steel tube structures-theory and practice*. Science Press, Beijing, 2003. (in Chinese)

[3] G.Y. Wang, G.L. Liu, Y.M. Li, "*Failure mechanism of steel reinforced concrete plane frames subjected to fire*", Engineering Mechanics, 29(12), 156-162, 2012. (in Chinese)

[4] G.Y. Wang, L.H. Han, "*Fire performance of reinforced concrete plane frame exposed to local fire*", Engineering Mechanics, 27(10), 81-89, 2010. (in Chinese)

[5] G.Y. Wang, Y.M. Li, "*Performance of plane frames with concrete filled steel tube columns and steel beams subjected to local fire*", Engineering Mechanics, 30(10), 236-243, 2013. (in Chinese)

8th International Conference on Structures in Fire
Guo-Qiang LI, Venkatesh K. R. KODUR, Shou-Chao JIANG, Jian JIANG, Su-Wen CHEN, Guo-Biao LOU (Eds.)
Shanghai, China, June 11-13, 2014

STUDY ON THE FIRE RESISTANCE OF RECTANGULAR CONCRETE COLUMNS EXPOSED TO NATURAL FIRES

L. J. Wang*, R. Caspeele* and L. Taerwe*

* Ghent University, Department of Structural Engineering, Magnel Laboratory for Concrete Research, Ghent, Belgium
e-mail: Lijie.Wang@UGent.be

Keywords: Concrete column, Second order effects, Interaction curves, Slenderness ratios, Natural fires

Abstract. *Natural fires, known as compartment fires, account for the fire load present in the compartment and decrease in intensity once the fuel has been burned. They widely exist and have important effects on concrete columns. In order to explain the mechanism of the combination of external loads and fire effects on concrete columns, an effective and easy-to-use method is required. As a first step in this paper, a numerical cross-section method is introduced to obtain interaction curves of columns exposed to fire. Then, this method is applied to analyze several cases with different slenderness ratios. Furthermore, also different reinforcement ratios, concrete cover thickness as well as eccentric loads are considered. Finally, occupancy-specific fires are adopted to study the fire resistance of columns subjected to different natural fires and tabulated data of columns exposed to natural fires are developed.*

1 INTRODUCTION

In order to know the performance of concrete structures in case of fire, the behaviour of structural concrete members exposed to fire has to be analyzed first. In the past twenty years, Lie [1] carried out several experimental tests to study the influences of concentric loads, cross-section areas, moisture contents and aggregate type. Based on this experimental data, a mathematical approach to predict the fire resistance of circular reinforced concrete columns was developed in [2]. This method was further elaborated in order to include columns with rectangular cross sections in [3]. Moreover, Meda et al. [4] made comparisons between the M-N interaction curves for normal-strength concrete and high-performance concrete. Van Coile et al. [5] developed a cross-sectional calculation model in order to calculate the bending moment capacity for a concrete beam exposed to fire. Using the same calculation model, an improved method was validated and used for calculating columns exposed to fire for different slenderness ratios in [6]. In the current paper, this approach is adopted for analyzing the fire resistance of rectangular columns exposed to different natural fires.

2 CALCULATION MODEL

A numerical calculation model is proposed to calculate the combined effect of an axial force (N) and bending moment (M) on columns, taking into account material strength reduction and thermal strains in case of fire. This model is based on a cross-sectional calculation and was further extended to predict second-order effects of columns exposed to fire.

2.1 Material model and basic assumptions

The stress-strain relationships of concrete and reinforcement bars provided in EN 1992-1-2 [7] are adopted to calculate interaction curves. The following assumptions are made: 1) plane sections remain plane; 2) the tensile strength of concrete is not considered. 3）There is no bond-slip between steel reinforcement and concrete.

2.2 Thermal analysis and structural calculation

The basic calculation includes two parts: a transient thermal analysis and a structural analysis. As the first step in the calculation process, the cross-section is discretized into small calculation elements. In the calculation model for the examples described in this contribution, a 1 mm × 1 mm square is chosen as the basic element size (Figure 1).

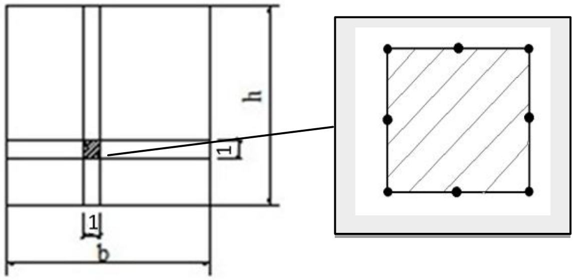

Figure 1. Nodes calculation model.

The heat transfer and temperature calculation is based on Fourier's law for conduction, Newton's law for convection and Stefan-Boltzmann's law for radiation. Consequently, the heat flow between nodes of a cross-section can be calculated by defining a matrix. In the current work, a commercial program has been applied to calculate the heat flow and temperatures of all the nodes automatically.

The same cross-sectional discretization is used for the structural analysis, which is however executed by an own developed calculation tool. The mechanical strain is expressed as follows [8]:

$$\varepsilon_{\mathrm{mech}\ (\xi,\eta)} = \varepsilon_{\mathrm{tot}} - \varepsilon_{\mathrm{th}} = \varepsilon_0 + k_0\eta - \varepsilon_{\mathrm{th}} \tag{1}$$

where $\varepsilon_{\mathrm{tot}}$ is the total strain, $\varepsilon_{\mathrm{th}}$ is the thermal strain, ε_0 is the strain at the centroid point and k_0 is the curvature about the neutral axis, η is a variable related to the distance from calculated point to centroid point.

It is seen in Formula (1) that a curvature-based function is adopted to determine the total strain. As a result, a bending moment-curvature relationship can be obtained using the cross-sectional integration. Further, the maximum allowable bending moment at any normal force is obtained which enables to construct interaction diagrams. This established analytical method has been compared with EN 1992-1-2 [7] in [6].

However, as EN 1992-1-1 [9] declares that second-order effects cannot be neglected, it is not safe to design especially slender columns using only the just mentioned interaction curves. Additionally, second order effects taking into account the deformed shape of the structural element could be more determining in case of fire. Hence, this paper focuses on the cross-sectional calculation tool for interaction curves of columns exposed to fire, taking into account second-order effects.

The virtual work principle is used to calculate the deflection considering first order effects. Next, additional bending moments caused by the defection are calculated with an iterative calculation method adopting the bending moment-curvature curves based on the cross-sectional calculation. Consequently, these are taken into account to calculate the adjusted interaction diagrams when considering the reduced capacity due to second order effects.

3 SECOND-ORDER EFFECTS OF COLUMNS EXPOSED TO NATURAL FIRES

Natural fires, known as compartment fires, decrease in intensity once the fuel has been burned. As they are more representative for fires that can occur, they are widely used for the analysis of concrete structures subjected to fire.

In this paper, a square column is analyzed: the cross-section is 300 mm × 300 mm, with one diameter 32 mm reinforcement bar in each corner and concrete cover 25 mm; concrete compressive strength f_{ck} = 55 MPa, reinforcement yield strength f_y = 500 MPa and young modulus of steel $E_s = 2 \times 10^5$ N/mm^2. A natural fire is considered in a dwelling with the fire load density q_a = 780 MJ/m^2. The temperature-time diagram of the reinforcement bar is illustrated in Fig. 2, where the temperature of the reinforcement bar reaches its peak at 75 min.

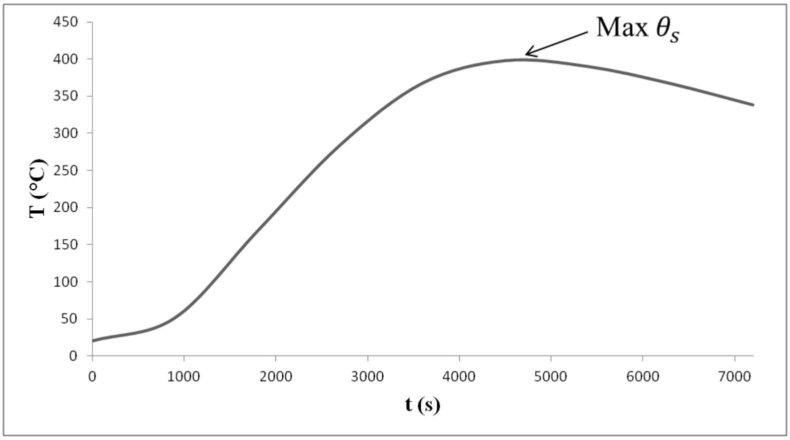

Figure 2. Temperature-time diagram of the reinforcement bar.

Figure 3 shows the maximum allowable bending moment curve at the representative value of normal force n = 0.2. The curve is decreasing during the first 75 minutes. After that, it slightly increases.

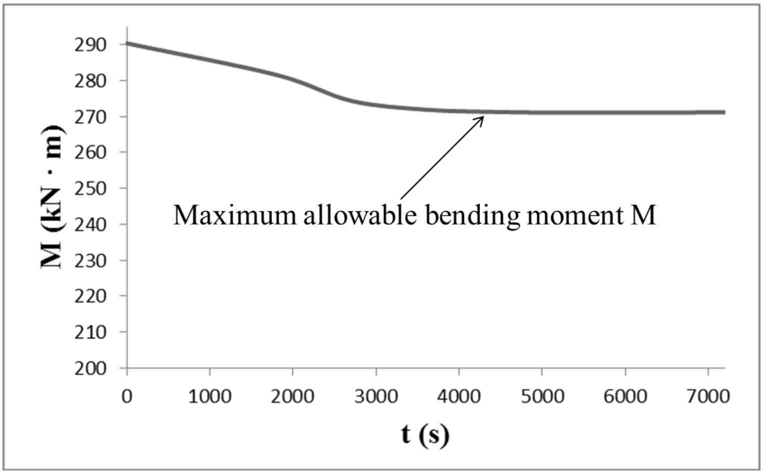

Figure 3. Maximum allowable bending moment at n = 0.2 during a fire with load density q_a = 780 MJ/m^2.

Based on the analytical method, the maximum allowable bending moments for different n are listed in Table 1, where $n = \frac{N_c + N_s}{0{,}7(A_c f_{cd} + A_s f_{yd})}$, A_c is the cross sectional area of concrete, A_s is the cross sectional area of the reinforcement bars, f_{cd} is the design value of the concrete compressive strength, f_{yd} is the design yield stress of the reinforcement, N_C and N_S are the design value of the applied axial force in the concrete and the reinforcement bars, respectively.

Table 1. Maximum allowable bending moment of the column (kN m).

t (min) \ n	0	0.1	0.2	0.3	0.4	0.5	0.6	0.7	0.8	0.9	1
0	188	241	290	326	345	332	301	271	238	199	154
30	185	238	282	304	306	283	249	211	172	130	87
45	183	236	274	285	279	251	205	172	133	93	55
60		235	272	279	266	236	197	152	120	82	43
75		234	271	276	262	230	194	149	117	79	39
90							193	149	115	77	37
105									114	76	35
120										75	34
135										74	33

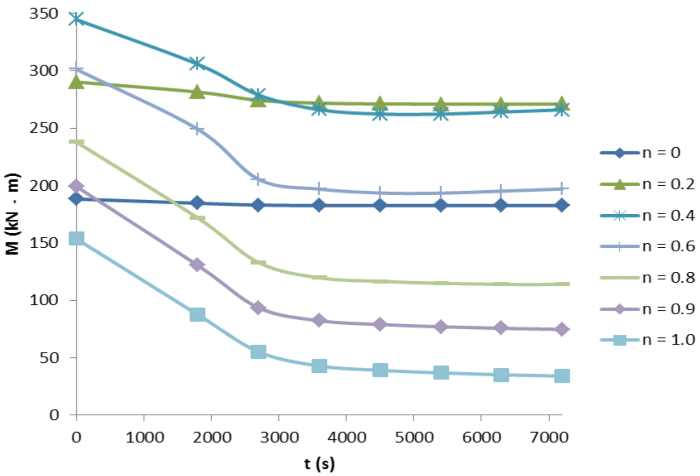

Figure 4. Maximum allowable bending moment under different eccentric loads during the fire.

Figure 4 shows design values of bending moments in case of increasing axial forces. The design value for the bending moment first increases when n increases, then suddenly decreases as soon as n is more than 0.3. Further, the curves indicate that the maximum bending moment does not decrease significantly in function of the fire duration when the axial load is small, because second-order effects are not significant under small eccentric loads. However, the curves perform differently when n is more than 0.3. The maximum allowable bending moment for different n values first decreases until a certain fire duration. After that, it slightly increases. Nevertheless, the most critical bending moments should be taken as design values to make sure the fire resistance of the column during the natural fire is concerned.

Further, natural fires with a load density which ranges from 200 MJ/m^2 to 1000 MJ/m^2 are investigated. Minimum required dimensions of columns for different slenderness ratios and different n values are provided in Table 2 for the case of reinforcement ratio $\omega = 0.5$ and eccentricity $e = 0.025b$ with $e \geqslant 10$ mm, in Table 3 for the case of $\omega = 0.5$ and $e = 0.25b$ with $e \leqslant 100$ mm, in Table 4 for the case of $\omega =$ 0.5and $e = 0.5b$ with $e \leqslant 200$ mm.

Table 2. Minimum dimensions and concrete covers for reinforced concrete columns; rectangular section. Mechanical reinforcement ratio ω = 0.5. Low first order moment: e = 0.025b with e ⩾ 10 mm (natural fires).

Fire load densities [MJ/m²]	λ	Minimum dimensions (mm) / Column width b_{min} [mm]/axis distance a [mm]			
		Columns exposed on more than one side			
		n = 0.15	n = 0.3	n = 0.5	n = 0.7
200	30	150/25	150/25	150/25	150/25
	40	150/25	150/25	150/25	150/25
	50	150/25	150/25	150/25	150/25
	60	150/25	150/25	150/25	150/25
	70	150/25	150/25	150/25	200/25
	80	150/25	150/25	200/25	300/25
400	30	150/25	150/25	150/25	150/25
	40	150/25	150/25	150/25	150/25
	50	150/25	150/25	150/25	200/25
	60	150/25	150/25	150/25	250/25
	70	150/25	150/25	200/25	300/25
	80	150/25	150/25	300/25	350/25
600	30	150/25	150/25	150/25	150/25
	40	150/25	150/25	150/25	150/25
	50	150/25	150/25	150/25	200/25
	60	150/25	150/25	200/25	300/25
	70	150/25	150/25	250/25	350/25
	80	150/25	150/25	300/25	550/25
800	30	150/25	150/25	150/25	150/25
	40	150/25	150/25	150/25	200/25
	50	150/25	150/25	150/25	250/25
	60	150/25	150/25	200/25	300/25
	70	150/25	150/25	300/25	400/25
	80	150/25	200/25	350/25	①
1000	30	150/25	150/25	150/25	150/25
	40	150/25	150/25	150/25	200/25
	50	150/25	150/25	200/25	250/25
	60	150/25	150/25	250/25	350/25
	70	150/25	200/25	300/25	500/25
	80	150/25	250/25	400/25	①

① Requires a width larger than 600 mm.

Table 3. Minimum dimensions and concrete covers for reinforced concrete columns; rectangular section. Mechanical reinforcement ratio ω = 0.5. Moderate first order moment: e = 0.25b with e ≤ 100 mm (natural fires).

Fire load densities [MJ/m^2]	λ	Minimum dimensions (mm) / Column width b_{min} [mm]/axis distance a [mm]			
		Columns exposed on more than one side			
		n = 0.15	n = 0.3	n = 0.5	n = 0.7
200	30	150/25	150/25	150/25	150/25
	40	150/25	150/25	150/25	200/25
	50	150/25	150/25	150/25	300/25
	60	150/25	150/25	200/25	400/25
	70	150/25	150/25	300/25	500/25
	80	150/25	150/25	450/25	600/25
400	30	150/25	150/25	150/25	200/25
	40	150/25	150/25	150/25	250/25
	50	150/25	150/25	200/25	400/25
	60	150/25	150/25	250/25	500/25
	70	150/25	150/25	450/25	①
	80	150/25	250/25	500/25	①
600	30	150/25	150/25	150/25	250/25
	40	150/25	150/25	200/25	300/25
	50	150/25	150/25	250/25	450/25
	60	150/25	150/25	400/25	600/25
	70	150/25	200/25	500/25	①
	80	150/25	300/25	①	①
800	30	150/25	150/25	150/25	250/25
	40	150/25	150/25	200/25	400/25
	50	150/25	150/25	300/25	500/25
	60	150/25	200/25	450/25	①
	70	150/25	250/25	550/25	①
	80	150/25	300/25	①	①
1000	30	150/25	150/25	200/25	300/25
	40	150/25	150/25	250/25	450/25
	50	150/25	200/25	300/25	550/25
	60	150/25	250/25	450/25	①
	70	150/25	300/25	①	①
	80	150/25	400/25	①	①

① Requires a width larger than 600 mm.

Table 4. Minimum dimensions and concrete covers for reinforced concrete columns; rectangular section. Mechanical reinforcement ratio $\omega = 0.5$. High first order moment: e = 0.5b with e ≤ 200 mm (natural fires).

Fire load densities [MJ/m^2]	λ	Minimum dimensions (mm) / Column width b_{min} [mm]/axis distance a [mm]			
		Columns exposed on more than one side			
		n = 0.15	n = 0.3	n = 0.5	n = 0.7
200	30	150/25	150/25	200/25	450/25
	40	150/25	150/25	300/25	500/25
	50	150/25	150/25	400/25	550/25
	60	150/25	200/25	450/25	600/25
	70	150/25	250/25	550/25	①
	80	150/25	300/25	①	①
400	30	150/25	150/25	300/25	500/25
	40	150/25	150/25	400/25	550/25
	50	150/25	200/25	450/25	①
	60	150/25	250/25	550/25	①
	70	150/25	350/25	①	①
	80	150/25	400/25	①	①
600	30	150/25	150/25	350/25	500/25
	40	150/25	200/25	500/25	600/25
	50	150/25	250/25	500/25	①
	60	150/25	350/25	600/25	①
	70	150/25	450/25	①	①
	80	150/25	500/25	①	①
800	30	150/25	150/25	350/25	550/25
	40	150/25	200/25	450/25	①
	50	150/25	300/25	550/25	①
	60	150/25	350/25	①	①
	70	150/25	450/25	①	①
	80	200/25	550/25	①	①
1000	30	150/25	200/25	350/25	550/25
	40	150/25	250/25	500/25	①
	50	150/25	300/25	600/25	①
	60	150/25	450/25	①	①
	70	200/25	500/25	①	①
	80	250/25	600/25	①	①

① Requires a width larger than 600 mm.

Tables 2 to 4 illustrate the minimum required dimensions of columns exposed to natural fires. It can be noticed that a conservative minimum required dimension 250 mm×250 mm corresponding to a maximum slenderness ratios of 80 and fire load density of 1000 MJ/m^2 can be suggested for all fire densities above in case of n=0.3 when the first order moment is low. However, minimum required dimension is increasing quickly with increasing design force due to the high first order moment. As it shows in Table 4, a width higher than 600 mm is required when the slenderness ratio is more than 50 and the fire load density is 400 MJ/m^2 in case of $n = 0.7$.

4 CONCLUSIONS

Based on this approach, natural fires are investigated. Firstly, the results suggest that the design value for bending moment first increases with increasing axial load, then decreases when a certain axial load is exceeded. Secondly, the maximum allowable bending moment has no apparent reduction due to the natural fire when the axial load is low. Thirdly, the bending moment capacity has a slight increase when the column is cooling down. However, the bending moment for design is determined by the minimum value during the natural fire. Finally, tabulated tables are listed for the determination of minimum required dimensions of columns exposed to natural fires for different fire load densities. The developed analytical tool can further be applied to predict interaction curves of columns in case of any tempered distributions and provide a useful tool for designing columns exposed to fire.

ACKNOWLEDGEMENTS

The author would like to thank the China Scholarship Council (CSC) for the financial support.

REFERENCES

[1] Lie T.T., Lin T.D., Allen D.E and Abrams M.S. “Fire resistance of reinforced concrete columns”, Division of Building Research, DBR Paper No. 1167, National Research Council of Canada, Ottawa, Canada, February, 1984.

[2] Lie T.T. and Celikkol B. “Method to calculate the fire resistance of circular reinforced concrete columns”, *ACI Materials Journal*, 1991, 88(1), 84-91.

[3] Lie T.T. and Irwin R.J. “Method to calculate the fire resistance of reinforced concrete columns with rectangular cross section”, *ACI Structural Journal*, 1993, 90(1), 52-60.

[4] Meda A., Gambarova P.G. and Bonomi M. “High-performance concrete in fire-exposed reinforced concrete sections”, *ACI Structural Journal*, 2002, 99(3), 277-287.

[5] Van Coile R., Annerel E., Caspeele R. and Taerwe L. “Full-probabilistic analysis of concrete beams during fire”, *Journal of Structural Fire Engineering*. 2013, 4(3),165-174.

[6] Wang L.J., Caspeele R. and Taerwe L., “Development of an Excel-based calculation tool for interaction curves of rectangular concrete columns subjected to fire.” *IRF'2013. 4th International Conference on. Integrity, reliability & failure.* 2013, 49-50.

[7] CEN. “EN 1992-1-2: Design of concrete structures - Part 1-2: General rules - Structural fire design”, *European Committee for Standardization, Brussels, Belgium*, 2004.

[8] Caldas R.B., Sousa J.B.M and Fakury R.H. “Interaction diagrams for reinforced concrete sections subjected to fire.”, *Eng Struct*, 2010, 32(9), 2832-2838.

[9] CEN. “EN 1992-1-1: Design of concrete structures - Part 1-1: General rules and rules for buildings.”, *European Committee for Standardization, Brussels, Belgium*, 2004.

THE EFFECT OF AXIAL RESTRAINT AND ROTATIONAL RESTRAINT ON THE FIRE RESISTANCE OF STEEL REINFORCED CONCRETE COLUMNS

Chan-Chan Zheng*, Yin-Qing Li* and Guang-Yong Wang*

*Institute of Building Fire Research, China Academy of Building Research, Beijing,100013,China
e-mails: 327473622@qq.com, cabr2582@126.com, wanggy0609@163.com

Keywords: Steel reinforced concrete column, Axial restraint, Rotational restraint, Finite element analysis

Abstract. *Subjected to the restraints of the surrounding components, the actual boundary conditions of steel reinforced concrete frame columns are restrained on both ends in the field of steel reinforced concrete structure. The actual boundary conditions of frame columns could be divided into axial and rotational restraints according to the action of the restraints. A theoretical calculation model under the coupling effects between temperature and load was proposed, and the results of finite element analysis models were in good agreement with the experimental results. The fire performance of steel reinforced concrete columns was researched through detailed parametric analysis; different axial restraints and different rotational restraints were considered for column models. The results show:1) axial restraints have adverse influence on columns with low load eccentricity ratio in fire.2) axial restraints are beneficial to the columns with high load eccentricity ratio in fire.3) rotational restraints could improve the fire performance of columns.*

1 INTRODUCTION

Steel reinforced concrete structure has been widely used in the field of high-rise building structure. Steel reinforced concrete columns, chiefly in the form of concrete-filled steel tubes and embedded steel sections, are used to ensure the main structure safe in the fire. Due to the surrounding restraints, the actual mechanical conditions of frame columns can be divided into axial and rotational restraints which are according to the nature of the restraints. However, the study of steel reinforced concrete columns on fire performance is not so much, which cannot satisfy the need of fire resistance design of structure. Therefore, the intensive study in the mechanical properties and practical fire resistance design methods of steel reinforced concrete columns has important theoretical significance and practical value.

There are some published works presenting experimental results and theoretical research on fire resistance of both steel reinforced concrete and steel columns. Zheng [1] used ABAQUS to analyze the impacts of the bond slip on concrete and steel section. He found out that the bond slip had less influence on column fire resistance. Huang et al. [2] presented an experimental study of the axial restraint effect on fire resistance of four reinforced concrete columns. Both test results and numerical analyses showed that axial restraint could increase internal axial force and then reduced column fire resistance.

Meanwhile, the fire resistance of steel columns has been studied by scholars at home and abroad. Valente [3] and Huang et al. [4-7] carried out a numerical analysis of restrained steel columns under fire. Wang and Danies [8-9], Ali and O'Connor [10], Rodrigues et al. [11] carried out experimental study of restrained steel column in fire. The study showed when the axial restraint was high, the real critical temperature of restrained steel columns could decrease; meanwhile, when the rotational restraint was high, the real critical temperature of rotational restraint could increase. Wu and Qiao [12] used the computer program of SAFIR to research the influence of some parameters (i.e., axial/rotational restraint ratio, sectional dimension, etc.) on axial forces in restrained concrete columns. However, research on fire resistance of end constrained steel reinforced concrete columns is basically a blank.

2 VALIDATION PROCEDURES

In this paper, the program ABAQUS will be used to perform heat transfer analysis and structural analysis, respectively. Before the calculation models of steel reinforced concrete columns are established, the experiment of steel reinforced concrete columns is selected in literature [2] to do numerical comparison. In literature [2], four columns are subjected to axial restraint effect and four-face uniform heating. Because the structure of 4 columns are similar, only column RCC03 would be discussed. In this section, three points which respectively represent mid-web of steel (point 3), rebar (point 7) and concrete (point 9) will be select in Figure 1. The temperature field comparison results of experiment and numerical simulation are showed in Figure 2. Figures 2 (a)-(c) show the three points' temperature within the mid-height section of the column. Experimental data and numerical simulation results of RCC03 are shown in figures, respectively. Generally, the results of experimental data and numerical simulations are in good agreement. The numerical prediction is higher than the experiment data. That is because the thermal properties of concrete model from T.T.Lie are slightly different from actual values. Figures 3 (a)-(d) show the comparison of axial deformation at the top of four restrained columns. The results of experimental data and numerical simulations are substantially the same. The results of comparisons could explain that the numerical simulations of ABAQUS are more conservative and more useful for engineering.

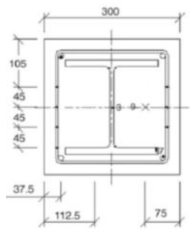

Figure 1. Location of three points within a cross section.

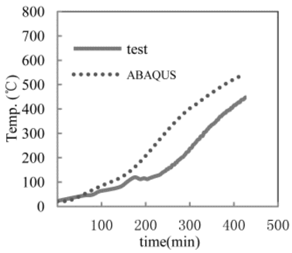

(a) Point 3: encased steel

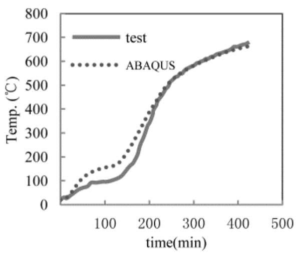

(b) Point 7: rebar

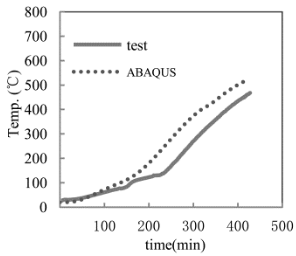

(c) Point 9: concrete

Figure 2. Comparison of cross-sectional temperature of RCC03.

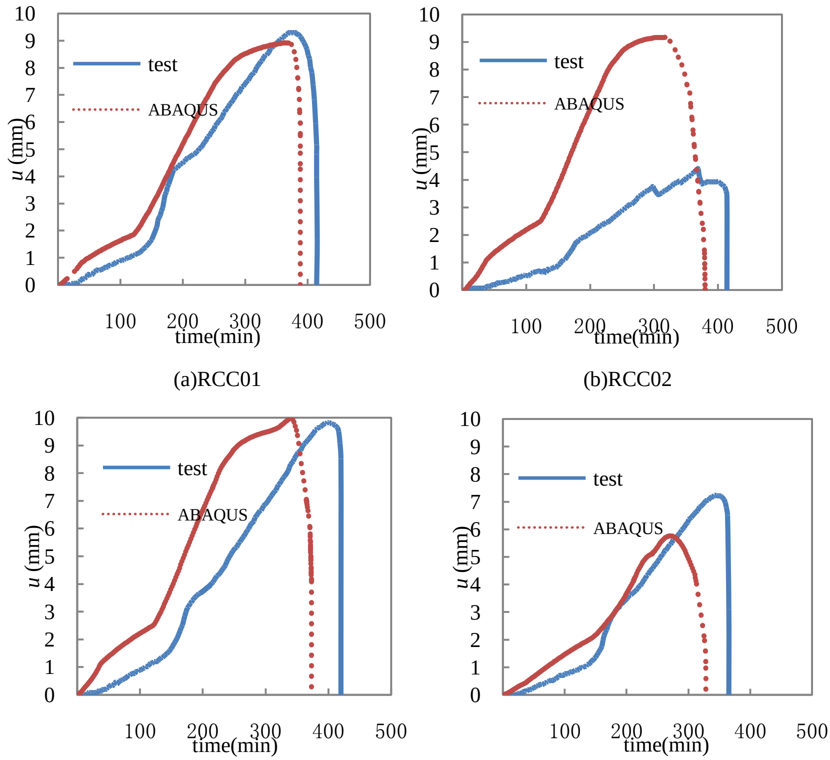

(a)RCC01 (b)RCC02

(c)RCC03 (d)RCC04

Figure 3. Comparison of axial deformation at the top of columns.

3 CALCULATION MODEL

To simplify the finite element model, we take the model of steel reinforced concrete column shown in Figure 4.

The column is hinged at both ends. The axial restraint stiffness at the top of the column is k_l, and the rotational restraint stiffness at both ends of the column is k_r. Heating curve uses international standard temperature curve ISO834. The main variables in the process of calculation include: axial restraint stiffness ratio ($\beta_l=k_l/((E_C^{20}A_C+ E_S^{20}As)/H)$), rotational restraint stiffness ratio ($\beta_r=k_r/(4(E_C^{20}I_C+E_S^{20}I_S)/H)$), loading ratio ($u=N_0/N_u$), eccentricity ratio($\varepsilon=e/0.5h$). The terms E_C^{20}, E_S^{20} respectively represent the elastic modulus of concrete and steel at room temperature. The terms A_C, A_S respectively represent net areas of concrete and steel. The parameter e denotes load eccentricity ratio. In the paper, superscript '20' denotes 20℃ , subscript 'C' and 'S' denote concrete and steel, respectively. The specific parameters of steel reinforced concrete column are shown in Table 1.

In the finite element model, the influence of the above variables is mainly considered. Reference [12] states the axial restraint stiffness ratio is mainly concentrated between 0.005~0.15, and the rotational restraint stiffness ratio is near to 2 in a practical structure. In the finite element model β_l selects 0, 0.025, 0.05, 0.1, 0.2; β_r selects 0.1, 0.5, 1.0, 2.0, 4.0; u selects 0.2, 0.4; e_0 selects 0, 0.2, 0.5, respectively.

During the calculation the following assumptions are made: (1) In the whole process of calculation axial restraint, rotational restraint and axial load remain constant. (2) Assuming that the ends of steel reinforced concrete columns without x direction displacement. (3) The bounding among concrete and steel surfaces is assumed to be perfect with no slipping and no cracking.

Table 1. Material properties of steel reinforced concrete column.

Column	Concrete		Steel		Rebar	
	fc(MPa)	E_C^{20}(MPa)	$fs_{,y}^{20}$(MPa)	ρ_s(%)	$f_{R,y}^{20}$(MPa)	ρ_R(%)
	28	3×10^4	380	4.188	375	0.985

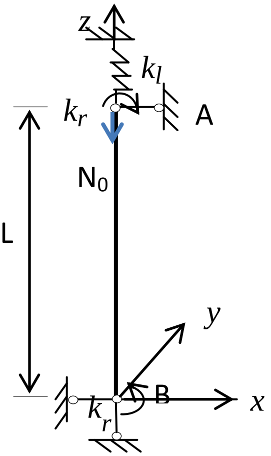

Figure 4. Restrained steel reinforced concrete column model.

4. IMPACT ON THE FIRE RESISTANCE OF STEEL REINFORCED CONCRETE COLUMNS WITH END RESTRAINED

4.1 Impact on the fire resistance of steel reinforced concrete columns with axial restraints

Figure 5 shows column axial force under different loads and different axial restraints. Figure 6 shows the column axial deformation under different loads and different axial restraints in fire. If the column is still carrying capacity at 500min, the axial deformation within 500min will be given. The following rules can be seen from Figure 5 and Figure 6. (1)When the axial load is low (e.g., n = 0.2) without rotational restraint and eccentricity ratio, the column axial force decreases with the increase of axial restraint at the beginning of the fire time. The results of Figure 5 predict the axial restraint share a part of the axial load. In the middle of the affected by the fire, the axial restraint prevents expansion deformation of the column due to the temperature increase, so axial restraint plays an adverse role during this time. In the end, transient thermal strain occurs in concrete internal which could lead to compressive deformation of column. (2) When the axial load is high (e.g., n = 0.4) without rotational restraint and eccentricity ratio, the column is compressed because of the high axial load at the beginning of the fire time. In the middle of the affected by the fire, the column axial force decreases with the increase of axial restraint; and the axial compression decrease with the increase of temperature. Axial restraint is good for the axial force of column during this time. When the column is heated up to a certain degree, transient thermal strain occurs in concrete internal which could lead to compressive deformation. The column is compressed in the whole time.

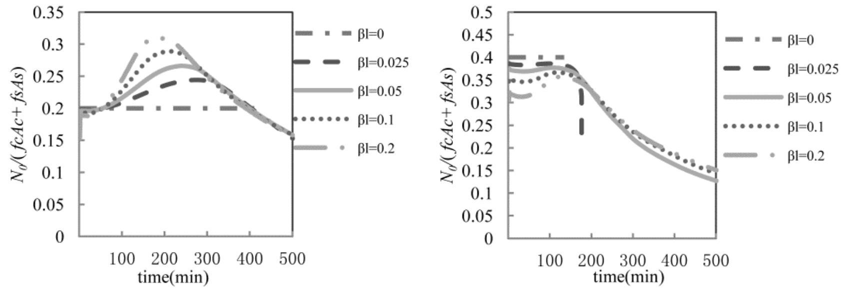

（a）n=0.2,e=0 (b) n=0.4,e=0

Figure 5. Development of column axial force.

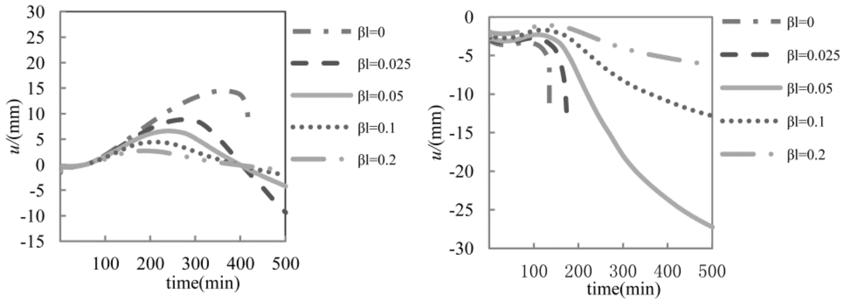

（a）n=0.2,e=0 (b) n=0.4,e=0

Figure 6. Axial deformation at the top of column.

4.2 Impact on the fire resistance of steel reinforced concrete columns with axial restraints

In order to study the effect of rotational restraint on the fire-resistant of steel reinforced concrete column, this paper specially selected different rotational restraints to study the effect on the lateral deformation at the middle of the column. Figure 7 shows column lateral deformation rules under different rotational restraints and different eccentricity ratios when the axial restraint ratio β_l=0.1, loading ratio n=0.4. From Figure 7 we can see that the greater the rotational restraint, the smaller lateral deformation of column half height. Eccentricity ratio can increase the lateral deformation of the column. The existence of the rotational restraint could prevent the axial deformation at the middle of the column. In general, rotational restraint can improve the fire performance of column.

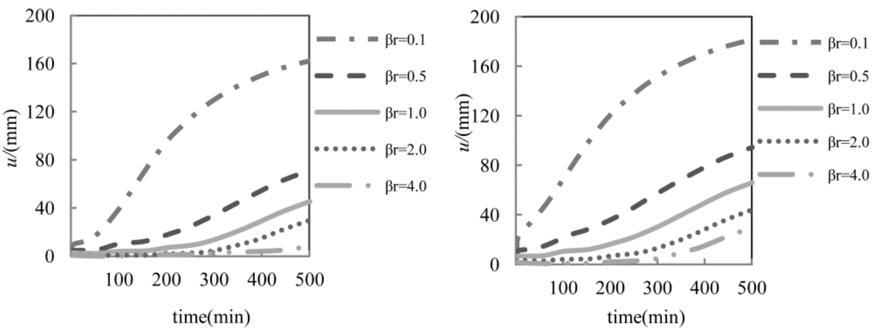

(a) n=0.4,e=0.2 (b) n=0.4,e=0.5

Figure 7. Horizontal deformation at the middle of column.

5 CONCLUSIONS

This paper presents fire resistance simulations conducted on four unprotected real-sized encased I-section composite columns. The effects of axial restraint and rotational restraint are investigated. It is observed that when the load eccentricity ratio is low, axial restraints could increase the axial force of columns. Axial restraints have adverse effect on the fire performance of steel reinforced concrete column. On the contrary, when the load eccentricity ratio is high, axial restraints could decrease the axial force of columns. The axial restraints have good effect on the fire performance of steel reinforced concrete column at this time. The existence of rotational restraints could prevent lateral deformation of the column at the middle height. So, rotational restraints have beneficial effect on fire resistance of steel reinforced concrete column.

ACKNOWLEDGEMENTS

This work was supported by National Nature Science Foundation of China (51278477), the country “12th Five-Year Plan” to support science and technology project (2012BAJ07B01) and China Academy of Building Research Fund (20120106330730073).

REFERENCES

[1] Zheng YQ., “Behavior of Steel Reinforced Concrete Members and Beam-to-Column Connections Subjected to Fire”, *Fuzhou University*， Fuzhou, 2007. (in Chinese)

[2] Huang ZF, Tan KH. and Phng GH., “Axial Restraint Effects on the Fire Resistance of Composite Columns Encasing I-section Steel” , *Journal of Constructional Steel Research*, 63(4): 437-447, 2007.

[3] Valente J C, Neves I C, “Fire Resistance of Steel Columns with Elastically Restrained Axial Elongation and Bending”, *Journal of Constructional Steel Research*, 52(3):319—331. 1999.

[4] Huang Z F, Tan K H, Ting S K, “Heating Rate and Boundary Restraint Effects on Fire Resistance of Steel Columns with Creep”, *Engineering Structures*, 28(6): 805—817. 2006.

[5] Huang Z F, Tan K H, “Rankine Approach for Fire Resistance of Axially-and-flexurally Restrained Steel Columns”, *Journal of Constructional Steel Research*, 59(12): 1553—1571. 2003.

[6] Huang Z F, Tan K H. “Analytical Fire Resistance of Axially Restrained Steel Columns”, *Journal of Structural Engineering*, 129(11): 1531—1537. 2003.

[7] Huang Z F, Tan K H. “Effects of External Bending Moments and Heating Schemes on the Response of Thermally Restrained Steel Columns”, *Engineering Structures*, 26(6): 769—780. 2004.

[8] Wang Y C, Davies J M, “An Experimental Study of Non-sway Loaded and Rotationally Restrained Steel Column Assemblies Under Fire Conditions: Analysis of Test Results and Design Calculations”, *Journal of Constructional Steel Research*, 59(3): 291—313. 2003.

[9] Wang Y C, Davies J M, “Fire Tests of Non-sway Loaded and Rotationally Restrained Steel Column Assemblies”, *Journal of Constructional Steel Research*, 59(3):359—383, 2003.

[10] Ali F, O’Connor D. “Structural Performance of Rotationally Restrained Steel Columns in Fire”, *Fire Safety Journal*, 36(7): 679—691, 2001.

[11] Rodrigues J P C, Neves I C, Valente J C, “Experimental Research on the Critical Temperature of Compressed Steel Elements with Restrained Thermal Elongation”, *Fire Safety Journal*, 35(2): 77—98. 2000.

[12] Wu B., Qiao CJ., “Axial Force in Restrained RC Columns during Heating and Cooling Phases”, *Journal of Civil, Architectural & Environmental Engineering*, 32(2):53-59. 2010. (in Chinese)

EXPERIMENTAL RESEARCH ON FIRE RESISTANCE PERFORMANCE FOR RC COLUMNS WITH DAMAGE CAUSED BY MARINE ENVIRONMENT

Ji-Jun Miao*,Hao Zhang* and Wei Gong**

*School of Civil Engineering Qingdao Technological University ,Qingdao, China
*School of Civil Engineering Qingdao Technological University ,Qingdao, China
e-mails:msyu_990421@sina.com,zhanghao19891026@163.com

**School of Civil Engineering Qingdao Technological University ,Qingdao,China
e-mail:894326207@qq.com

Key words: RC columns, Accelerated chloride migration test, Fire test, Temperature distribution of sections, Formula of bearing capacity

Abstract: *In order to study the mechanical properties of reinforced concrete structures under fire after attack by chloride ion, the fire resistance of reinforced concrete column under axial compression after damaged by marine environment has been researched by means of theoretical analysis and experimental research. Five RC columns under axial compression were designed to simulate the cracks caused by accelerated chloride migration test which was initial damage index for fire test; Fire test of RC columns under axial compression with initial damage was done and the destruction state and the temperature and axial deformation were recorded during the test, the affect of initial damage on the RC column section temperature distribution was also obtained; The high-temperature bearing capacity degradation of RC columns according to the measured section temperature distribution was analyzed, to refine the disaster prevention and mitigation theory and provide a theoretical basis for the reinforcement and repair of RC columns after fire.*

1 INTRODUCTION

The performance of reinforced concrete structures under marine environment or high temperature has been researched by many scholars. Some conclusions obtained during these research as followed: Steel corrosion caused by chloride ion erosion is generally considered the most direct, serious and widespread. The source of the chloride ion can be divided into concrete itself(As to the chloride ion in concrete components) and the external environment. Chloride ion erosion from the external environment is more common in reality. In addition to causing steel corrosion, chloride ions under certain conditions also cause corrosion, destruction or deterioration of concrete. The mechanical properties of concrete decreased obviously under high temperature.

Despite achievements obtained during research, some conclusions are still in dispute. Some scholars have suggested the slope of the heating curve should be reduced in the beginning stage because the heat transfer rate in air is slower than in concrete. The actual tend of the temperature curve in this test is different from the theoretical analysis above, further studies are needed.

Most of the research is about the single factor that effect the performance of Reinforced concrete structures,but these factors work together in reality. The properties of marine reinforced concrete structures in chloride ion erosion coupling with other accidental action (such as fire, explosion and others) has the same research significance. In this paper, the properties of reinforced concrete under marine environment coupled with fire were studied. The conclusions obtained during the test can be used for further research.

2 REINFORCED CONCRETE COLUMNS UNDER AXIAL COMPRESSION CHLORIDE ION PENETRATION TEST

For the purpose of researching the fire resistance of reinforced concrete after injury by marine environment, establishing chloride ion erosion damage (crack width ω) impact on the column cross-section temperature distribution and the bearing capacity degradation law, four RC columns under axial compression were designed to simulate the cracks caused by accelerated chloride migration test, provide initial damage for the subsequent fire tests.

2.1 Design of experiment

In this experiment, take initial crack width(ω) as the damage index produced five reinforced concrete columns(NO. C1,C2,C3,C4,C5) under axial compression. In order to eliminate the size effect of the specimen, take the size of columns as 250mm × 250mm × 1600mm, a protective layer of 40mm, C40 concrete. Through rapid chloride ion penetration, generate ω as 0.05mm, 0.10mm, 0.15mm and 0.20mm on C1-C4 respectively , C5 as control specimens without chloride ion penetration tests.

Immersed specimens into the 5% NaCl solution for 72h, let the electrolytic solution invade into concrete as far as possible then electrify. The current density of the test set at 15 A/m^2 , according to the surface area of reinforcement in concrete, the actual current control in 2A. The steel of the specimen will rust by the erosion of chloride ions, corrosive cracks which perpendicular to the longitudinal reinforcement will occur on the surface of the specimens. Using this crack as the damage index for the fire experiment. Schematic diagram of the experimental apparatus is indicated in Figure 1.

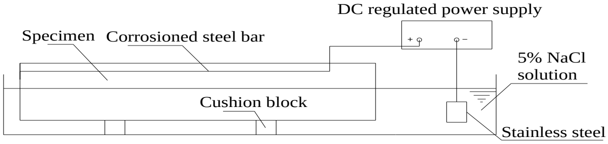

Figure 1. Schematic diagram of the test.

2.2 Experimental phenomena and analysis

Using crack observation instrument(DJCK-2) to observe and record the maximum crack width of specimen until it reaches the damage index ω, stop electricity, move the specimens out of the skin, fire test can be achieved after specimen dried. With a marker pen to draw the shape of the cracks and numbered, put three surface of the specimen into a plane, the eventual cracks of each column as shown in Figure 2.

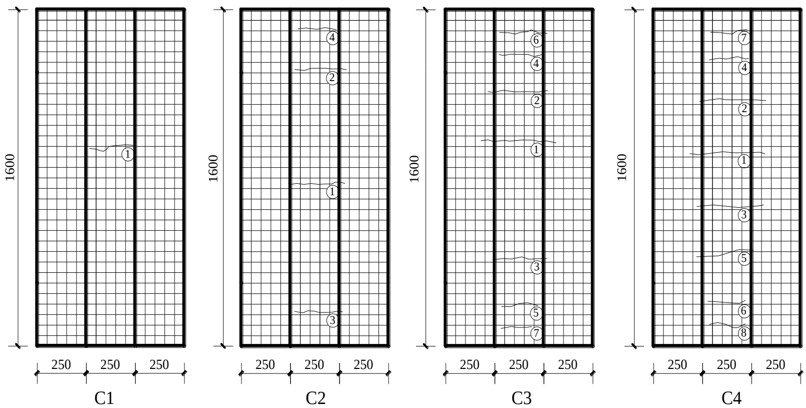

Figure 2. Crack performance of the specimen.

When energized 10 hours or so, micro-cracks along the stirrup located in central of the column can be find through Crack observation instrument, reddish-brown and black rust will precipitate from the part where voids and pits happened. After energized about 15 hours cracks continue to develop into tiny cracks visible to the naked eye, the depth, width and length will increase, new cracks gradually appear from the central of column to both ends, its spacing is roughly the same as the stirrup. Rapid chloride ion penetration test is a good way to simulate the marine environment damage of reinforced concrete structures and produce damage criterion expected, provides the basis for the following fire test.

3 FIRE TEST OF CONCRETE COLUMN UNDER AXIAL COMPRESSION PENETRATED BY CHLORIDE IONS

For the purpose of establishing the relationship between the damage index and fire resistance performance and duration of fire resistance, the temperature distribution, axial deformation and destruction features of five RC columns under axial compression, the influence of marine environment damage on section temperature field distribution under high temperature and ultimate bearing capacity are studied during the experiment.

3.1 Design of experiment

Using ISO standard temperature curves for heating under a constant load of 240kN.Using horizontal fire test system(shown in Figure 3). In order to get the section temperature distribution of each specimen thermoelectric pair were placed into the columns. Thermocouple layout as shown in Figure 4.

Figure 3. Horizontal fire test system.

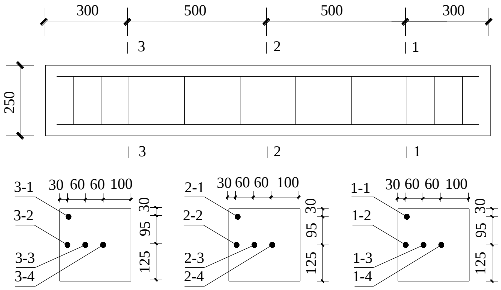

Figure 4. Layout plan of thermocouple.

3.2 Test phenomena and data analysis

All the temperature curves (shown in Figure 5) are similar to the ISO curve, can be considered meet international standards heating curve.

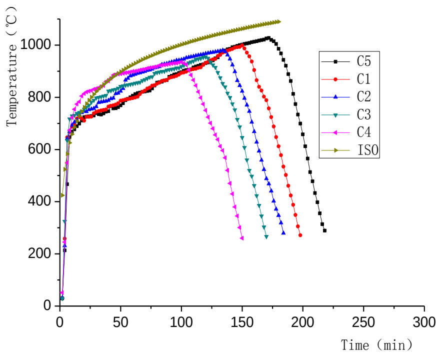

Figure 5. Heating curve.

Figure 6. State of columns after fire.

Conclusions obtained by the Figure 4 can drawn as below:

(1) Different degrees of protective layer peeled off each specimen.

(2) Cracks produced by Rapid chloride ion test have different levels of development,about 5 times the width of the original. The parts undamaged by chloride ion create new horizontal and vertical cracks, its distribution is basically the same as stirrups. This is due to the expansion of steel is faster than concrete under high temperature.

(3) Both ends of the column occur diagonal cracks whose width is about 3mm. Part of the internal reinforcement yield which is consistent with the destruction state of reinforced concrete subjected to axial compression.

3.3 Section temperature distribution of RC column under axial compression

The heating curve of columns (C5,C2,C4) as shown in Figures 7-9. Some of the thermocouple is damaged during the test, the data has not been adopted due to large fluctuations.

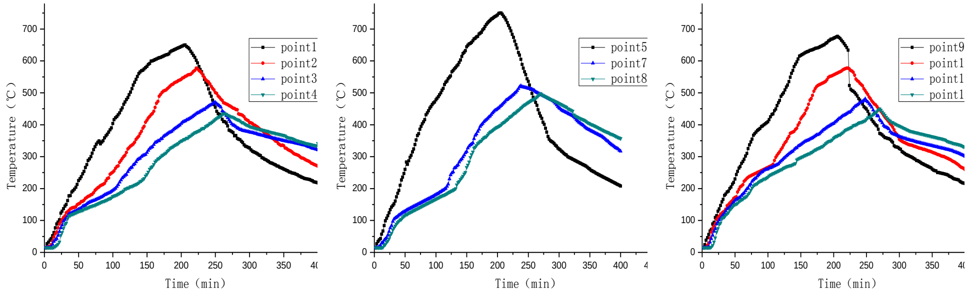

Figure 7. Measuring point temperature of C5.

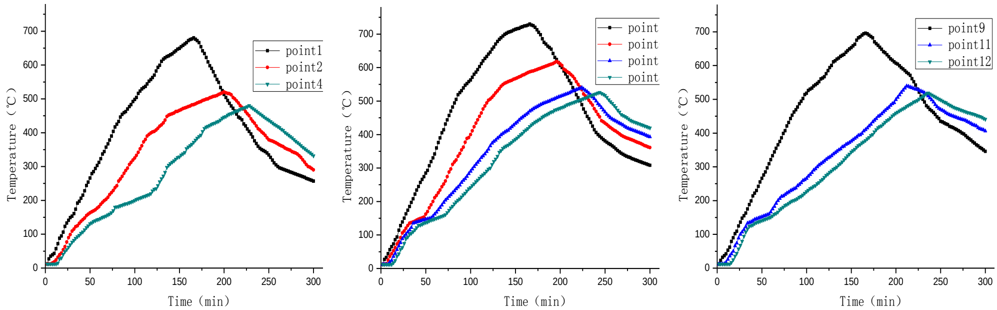

Figure 8. Measuring point temperature of C2.

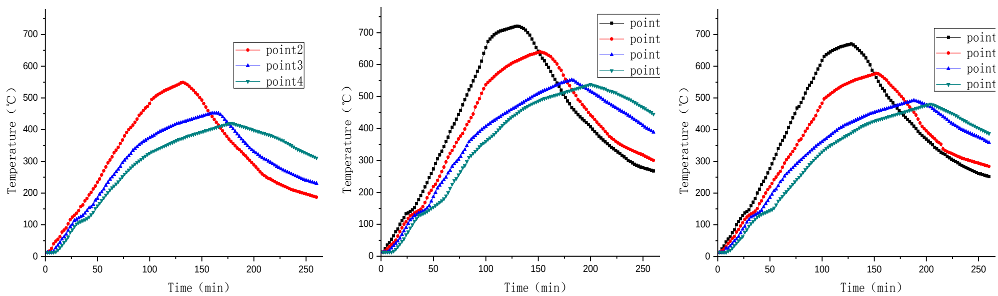

Figure 9. Measuring point temperature of C4.

Temperature field distribution of the different cross sections under similar boundary conditions has the following characteristics:

(1) The more closer the measuring point to the center of the section the later maximum temperature happen. Because the lateral temperature of the column drop after flameout, internal temperature continues to rise. It shows that a short period of time after fire the heat still transfer from from external to internal until reach the balance.

(2) The temperature curve rise smooth at about 130℃, due to thermal loss by water evaporation and water vapor migration.

(3) The measuring point temperature of internal are basically the same when the specimen destroyed, due to the same load applied.

3.4 Measuring point temperature at the same depth of each section along the column

In order to explore the rapid chloride ion erosion damage effect on the temperature field distribution of each section along the column, select temperature curve in the same depth of each section of C4(Figure 10) for further study.

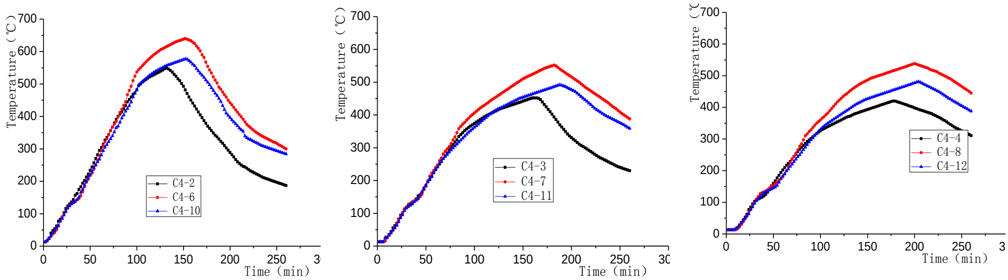

Figure 10. Temperature curve in the same depth of each section of C4.

The middle section temperature was higher than that of the end section, because the initial cracks are mostly located in the middle of the column. Meanwhile, the fire test furnace crater is located in the middle of the column will cause the temperature of the central section more higher.

The bottom of the column temperature is higher than the top during the second half of the heating curve, due to the top of the column extended from the oven for loading and measuring the vertical deflection, which matches the test boundary conditions.

3.5 Relationship between initial damage and the limit of fire resistance

According to the data listed in the Table 1 the relation between the initial crack width and the ultimate of fire resistance can be fitted as formula (1-1).

$$t=167-320\times\omega \qquad (1\text{-}1)$$

Note: ω－initial crack width (mm), t－ultimate fire-resistant time (min).

Table 1. Limit of fire resistance.

Specimen	ω (mm)	Load(kN)	Time(min)	Final state
C1	0.05	240	150	damaged
C2	0.10	240	136	damaged
C3	0.15	240	120	damaged
C4	0.20	240	102	damaged
C5	0	240	175	damaged

3.6Vertical deflection measurement of RC column

By using differential displacement sensor to measure the vertical deflection of the specimens during the test. Test measurement error controlled within 0.5%. Vertical deflection of each column as shown in Figure 11.

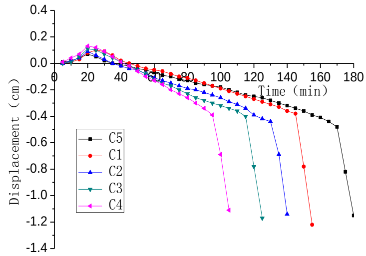

Figure 11. Vertical deflection of columns.

Axial deflection curve of the specimen is divided into two stages rise and fall. The rising stage is due to the expansion of the specimen at high temperatures, falling stage is due to internal temperature gradually increases, bearing capacity gradually decreases. The vertical deformation are basically the same about 1% of the column height which is consistent with the actual situation.

4 BEARING CAPACITY CALCULATION OF COLUMN DAMAGED BY CHLORIDE ION AFTER FIRE TEST

In this paper, the the following assumptions were used in calculating the bearing capacity of reinforced concrete columns:

(1) Specimen cross section temperature field distribution is known, obtained accurate temperature field distribution through temperature acquisition and analysis ;

(2) No relative slip between the concrete and steel;

(3) Ignore the temperature stress of cross section ,assuming the strain of each section is linear, meet the plane-section assumption;

(4) Regardless of the tensile strength of concrete under high temperature;

(5) Regardless of the shear effect on deformation of the specimen;

(6) Assuming the deflection curve of the specimens is in the shape of the sine wave allows specimen with initial deflection.

Calculation of high-temperature strength of reinforcing bars in calculation model suggested by Bolong Zhu as shown in formula (1-2)

$$f_y^T = \begin{cases} f_y & (0℃ < T \leqslant 200℃) \\ (1.33 - 1.64 \times 10^{-3} T) f_y & (200℃ < T \leqslant 700℃) \end{cases} \tag{1-2}$$

Note: f_y^T -- Steel yield strength at high temperature.

Calculation of high-temperature strength of concrete in calculation model suggested by U.Schneider as shown in formula (1-3)

$$f_c^T = \begin{cases} f_c & (T \leqslant 250℃) \\ 0.7 f_c & (250℃ < T \leqslant 500℃) \\ 0.3 f_c & (T > 500℃) \end{cases} \tag{1-3}$$

Note: f_c^T -- Compressive strength of concrete at high temperature.

According to the temperature measured during the test,assuming the same temperature at the same depth of concrete. The temperature field distribution of middle cross-section of the column section is shown in Figure 12 and Table 2. (① isotherm 100mm from the surface of the specimen, ②isotherm 90mm from the surface of the specimen, ③isotherm 30mm from the surface of the specimen).

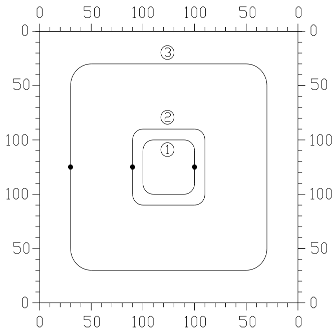

Figure 12. Temperature field distribution.

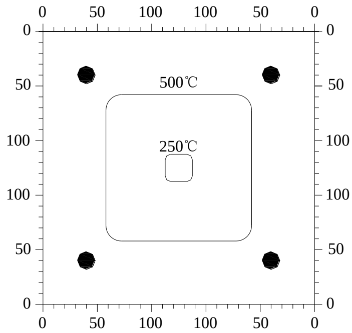

Figure 13. Simplified temperature field of C4.

Table 2. Measured temperature values at isotherm of each column.

Isotherm	C1	C2	C3	C4	C5
①	536	549	542	544	540
②	398	403	408	411	402
③	349	359	362	366	352

Assuming the temperature field distribution between the isotherms is directly proportional. Take C4 for an example, the middle section can be simplified according to isotherm of 250℃ and 500℃ when it destroyed. The simplified temperature field as shown in Figure 13.

The ultimate bearing capacity of column under high temperature was calculated by following formula: Ultimate load of column under high temperature as shown in Table 3.

$$N^{\mathrm{T}} = 0.9\varphi(f_c^{\mathrm{T}} A_c + f_y^{\mathrm{T}} A_s) \tag{1-4}$$

$$f_c^{\mathrm{T}} = \frac{f_c A_1 + 0.7 f_c A_2 + 0.3 f_c A_3}{bh} \tag{1-5}$$

Note: N^{T} --ultimate bearing capacity of column under high temperature

Table 3. Ultimate load of column under high temperature.

Specimen	ω (mm）	Calculated bearing Capacity (kN)	Actual bearing capacity（kN）	Error（%）
C1	0.05	236.5	240	1.46
C2	0.10	233.2	240	2.83
C3	0.15	232.7	240	3.04
C4	0.20	230.8	240	3.83
C5	0	234.4	240	2.33

Note: ωis Initial crack width.

According to the data in the Table 3 conclusion can be get as followed:

(1) The theoretical value of high temperature bearing capacity of the column is closer to its measured value and the errors are within 5 percent. It shows that the calculation method can be used for approximate calculation of bearing capacity of reinforced concrete members under high temperature.

(2) The theoretical value of high temperature bearing capacity is slightly less than the actual value,proved the algorithm is safer.

5 CONCLUSIONS

In this paper, rapid chloride ion erosion experiment was used to creates an initial damage (crack width is the damage index) to simulate marine environment damage, then fire experiment was carried out. Through the analysis of the experimental phenomena and theories of column under the action of the thermal-mechanical coupling, obtained the influence of crack width on the column section temperature distribution and ultimate bearing capacity of high-temperature. Through experimental research and data analysis, mainly draw the following conclusions:

(1) Rapid chloride ion erosion test can be well simulated Marine environmental damage to reinforced concrete member.

(2) The initial damage of the specimen has a great impact on its cross-sectional temperature fild distribution, the greater the damage index (crack width), the faster the heating rate of the section, the shorter the period of fire resistance.

(3) The relationship between the initial crack width and ultimate fire-resistant period can be calculated approximately by formula t=167-320×ω.

(4) Put forward a simplified bearing capacity calculation model of reinforced concrete columns at high temperature under axial compression and the actual results prove that the method is true and reliable.

REFERENCES

[1] Jijun, M.,Wei, G.and Na, C., "Experimental research and numerical simulation analysis on fire resistance performance of RC columns with damages caused by service loading"34(8),56-64,2013 (In Chinese)

[2] Jijun, M.,Na,C.and Xiaoyan H., "Experimental research and numerical simulation analysis on fire resistance performance of RC beams with damages caused by service loading"34(3),1-11,2013 (In Chinese)

[3] Jijun, M.and Junfu, W., "Experimental research on RC frame structure with damages due to elevated temperature" Journal of Building Structures, 33(2), 1-9, 2012 (In Chinese)

[4] Jijun,M.and Caiwei,L., "Fire test on RC columns under axial load" Journal of Building Structures, 33(2), 102-108,2012 (In Chinese)

[5] Caiwei, Land Junfu W., "Experimental Analysis of Fire Resistant Performance of Concrete Frame With Damage Caused by Weak Earthquake" Journal of Civil, Architectural & Environment Engineering,33(6),64-69,2011(In Chinese)

[6] Bolong, Z. and Zhou,D., "Research on fire resistance of structures" Tongji university, institute of engineering structure,1990.

[7] Kodur, V. and Raut, N., "Fire resistance of reinforced concrete columns–State-of-the-art and research needs" *ACI SP-255-5: Designing concrete structures for fire safety*, American Concrete Institute, Farmington Hills, Mich., 1-24.2007

[8] National Fire Protection Association (NFPA). (2011). <http://www.nfpa. org/index.asp>

8th International Conference on Structures in Fire
Guo-Qiang LI, Venkatesh K. R. KODUR, Shou-Chao JIANG, Jian JIANG, Su-Wen CHEN, Guo-Biao LOU (Eds.)
Shanghai, China, June 11-13, 2014

EXPERIMENTAL RESEARCH ON FIRE RESISTANCE PERFORMANCE FOR RC BEAMS WITH DAMAGE CAUSED BY MARINE ENVIRONMENT

Ji-Jun Miao*, Li-Na Ji and Yan-Chun Liu*****

*Professor, School of Civil Engineering, Qingdao Technological University, China;
E-mail:msyu_990421@sina.com
**Graduate student, School of Civil Engineering, Qingdao Technological University, China;
E-mail:568633162@qq.com
***Lecturer, School of Civil Engineering, Qingdao Technological University, China;
E-mail: 65230768@qq.com

Keywords: Fire, Reinforced concrete beam, Bearing capacity degeneration, Temperature field, Chloride ion erosion

Abstract. *Deformation, bearing capacity and seismic resistance of members were damaged after fire, which affected durability and safety of structures especially along the seaside. Concrete reinforcement was eroded by chloride ion in the sea water. In order to avoid the collapse or the damage of the coastal concrete structure in fire, it is particularly important to research the loss of the bearing capacity of the structure or components under the high temperature. In this paper, in the method of impressed current to accelerate corrosion, the corroded reinforced concrete beams were obtained and crack width is the indicator of damage. Under the coupled action of high temperature and marine environmental damage, the flexural performance of reinforced concrete beam is studied. The research contents include:(1) Four RC beams were designed to develop different crack widths caused by chloride ion erosion test. The five members were set on fire and then obtain the data on the temperature field of the beam section.(2)All the members were loaded after fire test in order to obtain the residual bearing capacity. Compared with the load data, bearing capacity degeneration of the damaged beams after fire was discussed in the paper.*

1 INTRODUCTION

Coastal engineering construction is subjected to the chloride ion erosion, The resulting concrete protective layer cracking or spalling will Seriously affect the durability of the concrete structure[1]. Especially when there is a fire, the structure of the mechanical properties will be severely degraded, the consequences will not be able to forecast[2]. For marine environmental damage and fire research, mainly concentrated in ocean environmental durability, fire single factor effect, as well as fire and other factors coupling, etc., and meaningful research results were obtained[3]. Deformation, bearing capacity and seismic resistance of members were damaged after fire, which affected durability and safety of structures especially along the seaside. Concrete reinforcement was eroded by chloride ion in the sea water. In order to avoid the collapse or the damage of the coastal concrete structure in fire, it is particularly important to research the loss of the bearing capacity of the structure or components under the high temperature.

2 EXPERIMENTAL DESIGN ABOUT THE DAMAGE OF CHLORIDE IONS EROSION[4]

2.1 Component design

Five reinforced concrete beams were designed in the experiment and were numbered from L1 to L5.

The strength grade of concrete was C40 and the thickness of the protective layer of concrete beams was 40 mm. The situation of reinforcement was the same for each beam and the specific information on the dimensions and reinforcements was shown in Figure 1. Three groups of concrete blocks (150mm × 150mm × 150mm) were reserved and there were three blocks in each group. The concrete blocks and the beams were cured in the same environment for 28 days. The standard value of the compressive strength was 40.8Mpa. Three specimens were intercepted from all types of steel. Test the specimens and the results were shown in Table 1.

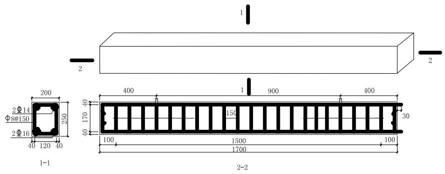

Figure 1. Dimensions and reinforcements for beams.

Table 1. Mechanical properties of steel bar.

Reinforced type	f_y	f_u	E_s	Elongation
Longitudinal bar Φ 16	427MPa	577MPa	2.0×105MPa	22.3%
Longitudinal bar Φ 14	411MPa	523MPa	2.1×105MPa	19.2%
Stirrup Φ 8	324MPa	415MPa	2.0×105MPa	17.6%

2.2 The test of speeding up chloride ion erosion

Electrified accelerated chloride ion erosion test was carried on L1—L4 and the maximum crack are respectively 0.05mm, 0.10mm, 0.15mm and 0.20mm. As the control group, the test was not carried on L5.

The test of speeding up chloride ion erosion simulated Marine environment in Laboratory and the concrete specimens soaked in 5% NaCl solution with dc power supply. The positive pole was connected to the steel bar in concrete which made it act as the anode of the battery. The negative pole was connected with stainless steel tube in the solution which made it act as the cathode of the battery. The circuits were formed by NaCl solution and then the cathode and the anode would produce electrochemical reaction.

2.3 Test results and analyses

In the process of erosion, take out the beams every 12 hours and then using DJCK-2 observed the crack width of each specimen in the process of electricity. When any one of crack width achieved maximum corrosive crack width, we took out the beam and stopped the test. At the same time, we recorded the location and width of cracks. The cracks were shown in Figure 2.

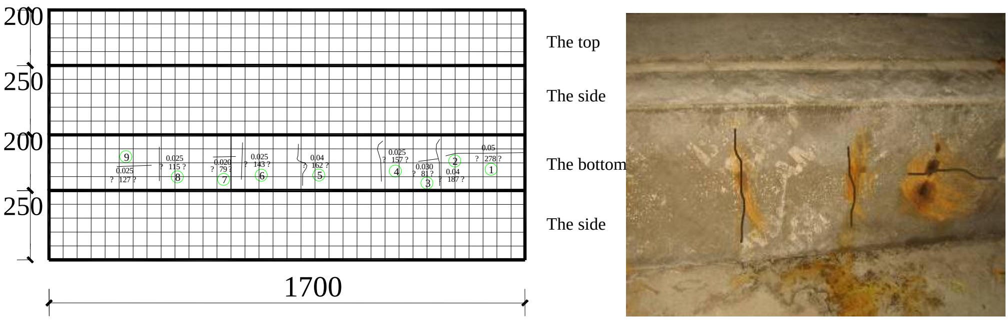

Specimen L1

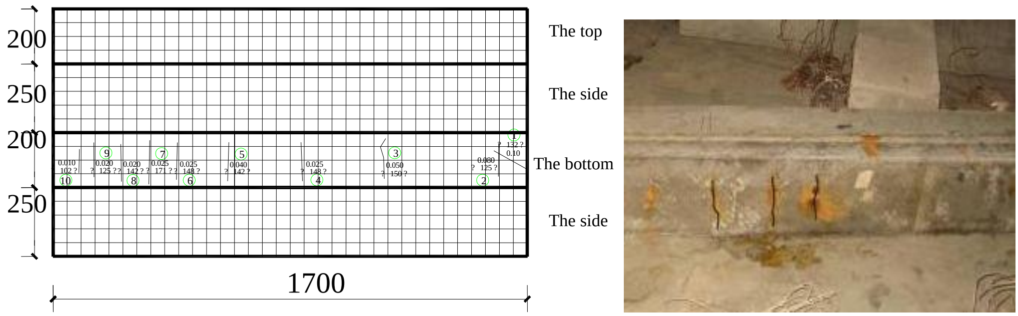

Specimen L2

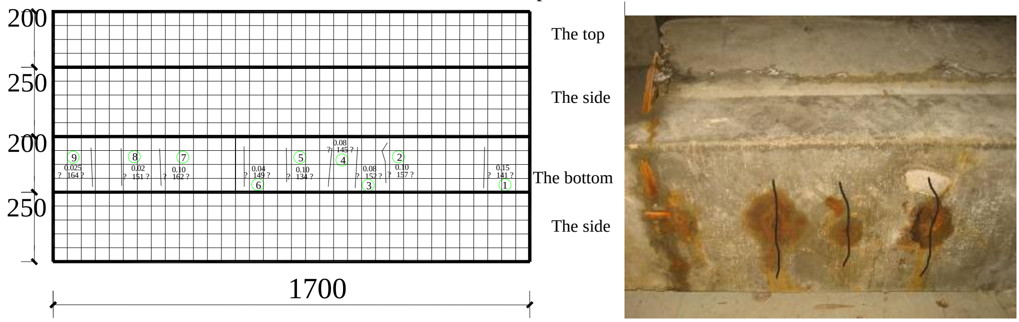

Specimen L3

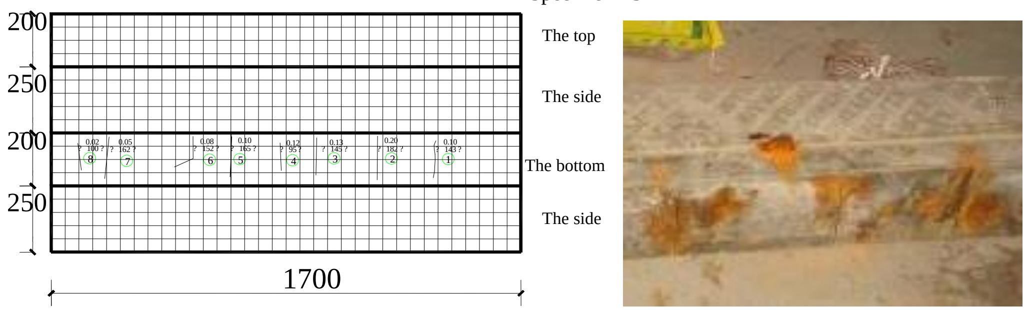

Specimen L4

Figure 2. The schematic diagram of cracks.

Through analysis we could draw the following main conclusions:

The cracks were transverse cracks and the spacing of corrosive crack is roughly near stirrup spacing which showed that the stirrup corrosion is more serious than the longitudinal reinforcement. The stirrup generated large tensile stress which made concrete cracks in stirrup position.

3 THE FIRE TEST

3.1 The experimental device and measurement

The measurement of the test included temperature and displacement. The deformation of the concrete beam used the electromechanical dial indicator to measure. The real-time temperature of the fire furnace and the temperature field of component were measured by the embedded thermocouple and the

Agilent34970A every 2 min. The measuring points of the beam were shown in Figure 3. Because this test was simulated under the stress of the normal service condition, one end set as fixed hinge bearing and the other end set as movable hinge support and the use of the applied load was 20kN. The test used the ISO standard temperature rise test curve.

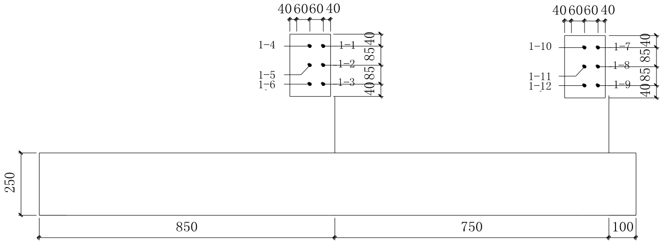

Figure 3. Arrangement of measuring points.

3.2 The test results

The schematic diagrams of cracks were shown in Figure 4.

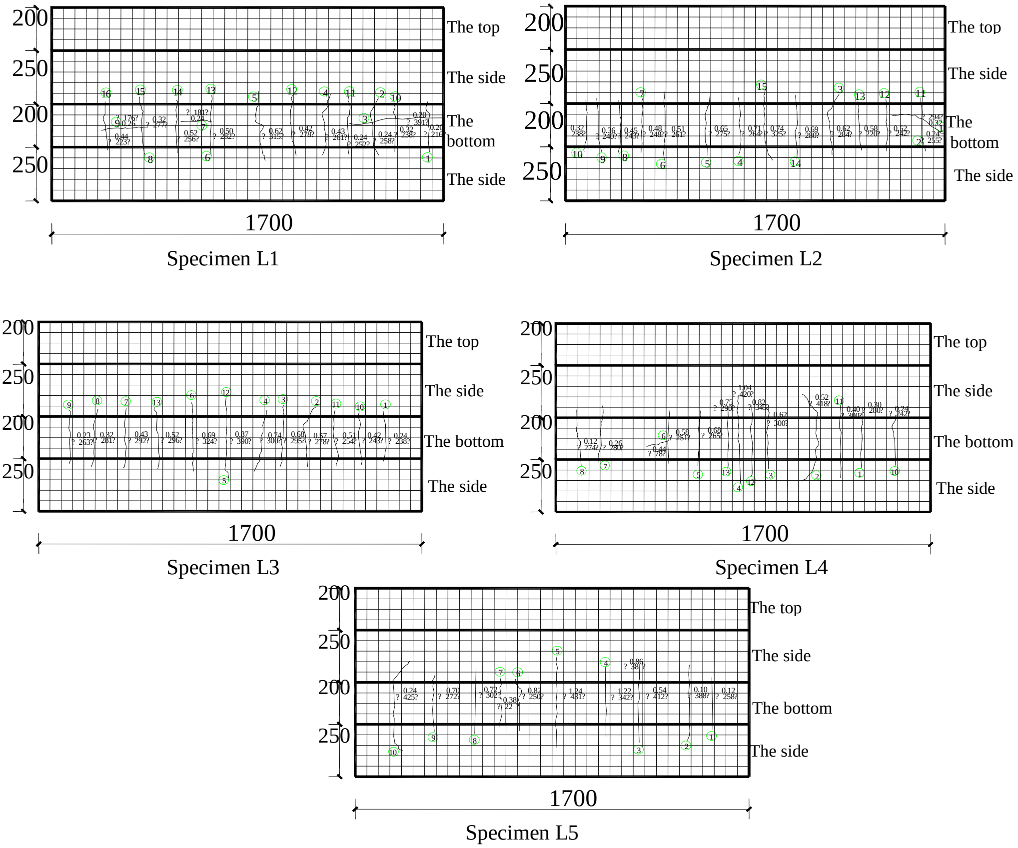

Figure 4. The schematic diagram of cracks.

Through the schematic diagram of cracks (As shown in Figure 4), the following can be concluded:

In the same load and along with the same combustion conditions, the more serious the initial damage, the faster the crack developed and the more obvious the shearing cracks were. This was because the erosion damage was caused mainly by stirrup corrosion, therefore, which reduced the shear bearing capacity of the specimen.

4 TEST ANALYSES

4.1 Thermal response

The temperature curves of the different measuring points from the same component were shown in Figure 5 and the temperature curves of the different components from the same measuring points were shown in Figure 6.

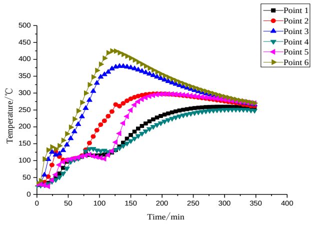

（a）Specimen L1

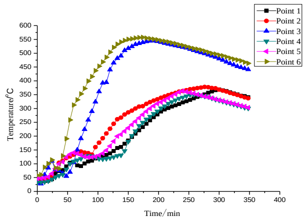

（b）Specimen L2

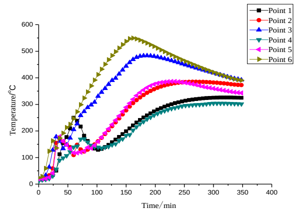

（c）Specimen L3

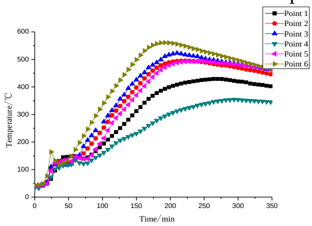

（d）Specimen L4

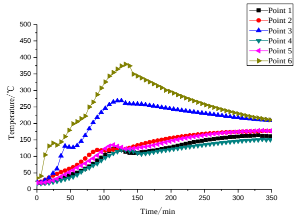

（e）Specimen L5

Figure 5. Temperature curve of beam section.

Through the temperature curves of the different measuring points from the same component (As shown in Figure 5), the following can be concluded:

(1) The temperature difference of the same specimens, both inside and outside, is bigger and up to 100 ℃. But the warming trend of the overall point was roughly the same and the temperature of the each measuring point in the same specimen eventually converged.

(2) The specimen L5 as comparative specimens was without erosion test and the maximum temperature of its measuring points was below the specimens L1 — L4. This suggested that the damage of reinforced concrete beam caused by chloride ion erosion had a significant influence on the fire resistance.

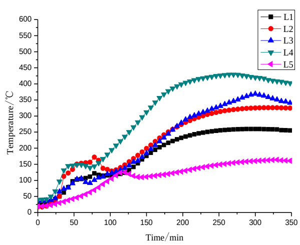

(a) Point 1

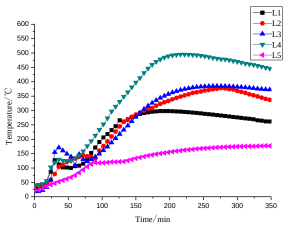

(b) Point 2

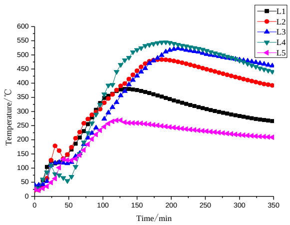

(c) Point 3

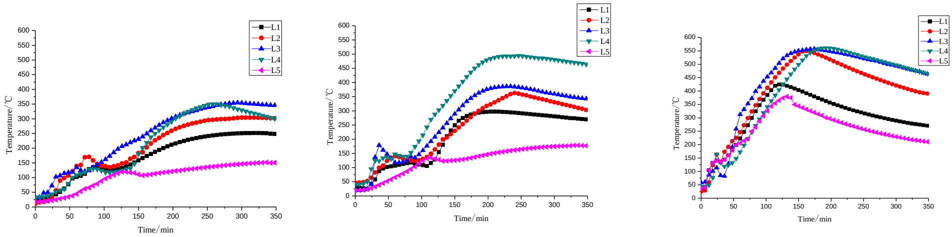

(d) Point 4 (e) Point 5 (f) Point 6

Figure 6. The temperature rise curves of the points.

Through the temperature contrast of the different components in the same station (As shown in Figure 6), the following can be concluded:

(1) The temperature difference of different specimens in the same measuring point was large, but the shape of temperature curves was roughly the same.

(2) The peaks of different measuring points of the specimen L1 — L4 moved to the right and the greater the damage degree, the more obvious curve peak moved to the right.

(3) The greater the damage degree, the greater curve peak was. Time is lengthened reaching the peak.

4.2 The deformation response

The reinforced concrete beam deflection in the process of high temperature was shown in Figure 7.

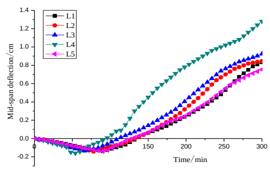

Figure 7. Deflection - time curve.

5 CALCULATIONS

5.1 The simplified calculation of the temperature field on cross section

When the ultimate bearing capacity for the specimen in the high temperature was calculated, the cross section was divided into the following three layers: (1) It was assumed that the concrete compressive strength of the part of the section temperature higher than 800 ℃ is zero. (2) It was assumed that the concrete compressive strength of the part of the section temperature between 300 ℃ and 800 ℃ multiplied by the reduction factor according to the literature[7]. (3) It was assumed that the concrete compressive strength of the part of the section temperature less than 300 ℃ took its value under normal temperature. The temperature field of the component section was shown in Figure 8.

5.2 The bearing capacity calculation under the action of high temperature and erosion damage

About the theoretical calculation for the bearing capacity of reinforced concrete beam after high temperature, this paper adopted the following assumptions[6]:

(1) $f_c(T)=k_cf_c$; $f_y(T)=k_sf_y$; k_c was the result of (15) [7] and k_s was the result of (16) [7].

(2)Temperature field in the depth direction of the cross section conformed to the linear rule.

(3) Beam cross section deformation obeyed the plain section assumption.

(4) The relative slip between steel and concrete was not considered.

Note: f_c（T）—— the cubic compressive strength of concrete under high temperature；

f_c—— the cubic compressive strength of concrete at room temperature；

f_y（T）—— the yield strength of steel under high temperature;

f_y ——the yield strength of steel at room temperature;

When the bearing capacity of the section was calculated, the section was simplified. According to the position of the 300 ℃ isotherm in Figure 8 and the principle of the equivalent ultimate bearing capacity of the cross section, the equivalent width was acquired through multiplying the width of the cross section of the two temperature segment by the corresponding reduction factor (As shown in Figure 8).As a result, when the ultimate bearing capacity of equivalent cross section was calculated, concrete compressive strength used the value at room temperature. The position of the longitudinal reinforcements was not changed and the yield strength of steel used the value according to the literature[5] .

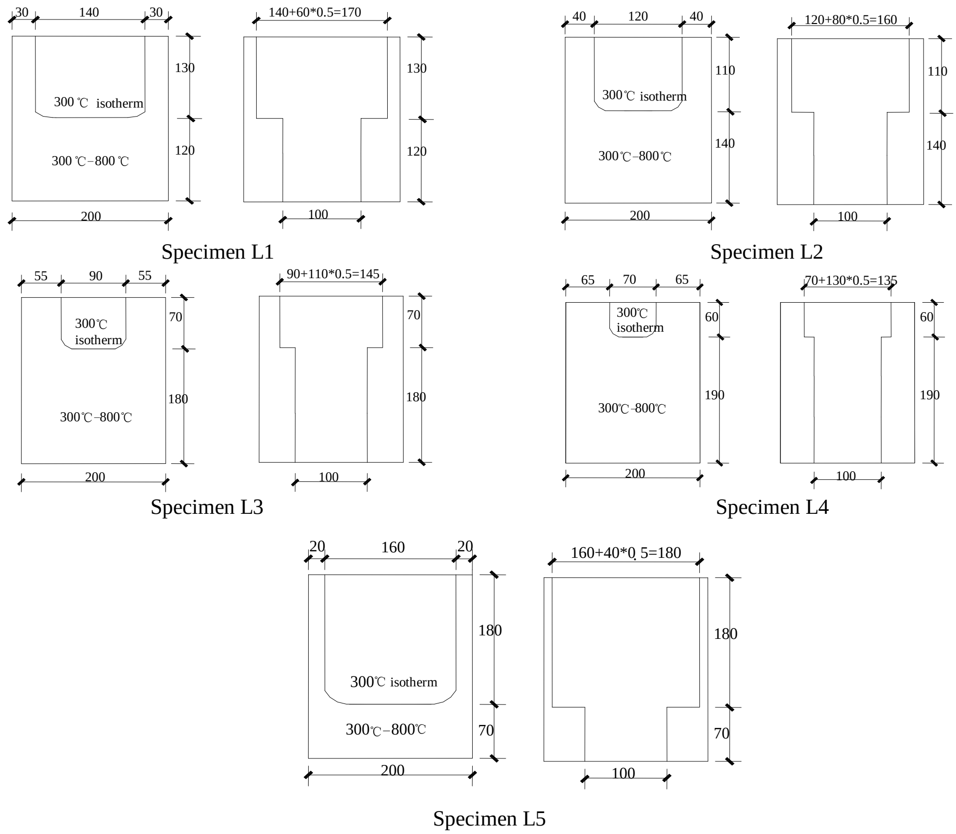

Figure 8. Equivalent cross-section.

Through the reduction of the steel stress and the equivalence of the concrete section, the bearing capacity of the reinforced concrete beam can be simplified into homogeneous concrete equivalent cross section to calculate. The computational formulas were the following formulas (4-1)[7] and (4-2)[7]. The theoretical value and the measured values of the ultimate bearing capacity of the beam cross section after the fire were shown in Table 2.

When $A_s f_y(T) \leqslant f_c b_f h_f$, the depth of compression satisfied that $x \leqslant h_f$:

$$f_c\, b_f\, x = f_y(T)\, A_s \tag{4-1}$$

$$M_{ut,1}(T) = f_c\, b_f\, x\,(h_0 - x/2)$$

When $A_s f_y(T) > f_c b_f h_f$, the depth of compression satisfied that $x > h_f$:

$$f_c\, b_f\, h_f + f_c\, b\,(x - h_f) = f_y(T)\, A_s \tag{4-2}$$

$$M_{ut,1}(T) = f_c\, b\,(x - h_f)\,[h_0 - h_f - (x - h_f)/2] + f_c\, b_f\, h_f\,(h_0 - h_f/2)$$

Note: f_y（T）—— the yield strength of steel under high temperature;

f_c —— the cubic compressive strength of concrete at room temperature；
h_f——the height of the compression flange of the equivalent T- section;
b_f——the calculated width of the compression flange of the equivalent T- section;
b——the width of the web of the equivalent T- section;
h_0——the effective height of section;

Table 2. The theoretical value and the measured values of the ultimate bearing capacity of the beam cross section after the fire.

Member number	Component damage （mm）	$M_{ut,1}$ (kN・m)	M_{ut} (kN・m)	The steel temperature (℃)	Error rate（%）
L1	0.05	24.1	26.0	250	7.30
L2	0.10	23.3	24.2	300	3.72
L3	0.15	22.0	22.5	400	2.22
L4	0.20	20.5	21.2	500	3.30
L5	——	27.5	28.5	200	3.50

Note: $M_{ut,1}$——the theoretical values of the ultimate bending moment of the middle section under high temperature; M_{ut}——the measured values of the ultimate bending moment of the middle section under high temperature;

From Table 2, the following can be concluded:

(1) By loading test, the error for the theoretical value of the ultimate bearing capacity of the beam cross section after the fire by using this model[7] was within 10% which showed the simplified calculation model was feasible.

(2) The ultimate flexural bearing capacity at high temperatures of the maximum damage specimen comparing with the ultimate flexural bearing capacity at high temperatures of the minimum damage specimen dropped 18.5% which showed that the greater the erosion damage of specimens, the lower the flexural bearing at high temperatures was and the ultimate flexural bearing capacity at high temperatures of the specimens was associated with its damage degree.

(3) The ultimate flexural bearing capacity at high temperatures of the maximum damage specimen comparing with the ultimate flexural bearing capacity at high temperatures of the specimen without the damage dropped 25.6% which showed that the damage had a great influence on the ultimate flexural bearing capacity at high temperatures.

REFERENCES

[1] Jin, W. L., and Zhao, Y. C. “The durability of concrete structure” [M]. Science press, Beijing, China, 2003.

[2] Liu, C. W. “Experimental analysis of fire resistant performance of concrete frame with damage caused by weak earthquake.” [D]. Qingdao Technological University, Qingdao, China, 2010.

[3] Chen, N. “Experimental research and numerical simulation on fire resistance performance of RC beams with damage caused by service loading” [D]. Qingdao Technological University, Qingdao, China, 2011.

[4] “Engineering structure experiment” [M]. Tongji University Press, Shanghai, China, 1996.

[5] Zhu, B. L., and Lu, Z. D. (1990). “Research report about the fire resistance of the engineering struct ure.” [J]. Institute for engineering structure of Tongji University.

[6] Zhao, J. C., and Shen, Z. Y. (1996). “Material model of the fire resistance of steel structure.” [J]. In dustrial building, 32(3): 26-28.

[7] Yang, J. P., and Shi, X. D., and Guo, Z. H. (2002). “Simplified calculation of ultimate load bearing capacity of reinforced concrete beams under high temperature.” [J]. Industrial building, 32(3):26-28.

8th International Conference on Structures in Fire
Guo-Qiang LI, Venkatesh K. R. KODUR, Shou-Chao JIANG, Jian JIANG, Su-Wen CHEN, Guo-Biao LOU (Eds.)
Shanghai, China, June 11-13, 2014

EXPERIMENTAL AND NUMERICAL ANALYSIS OF CONCRETE COLUMNS UNDER FIRE

Maria Alzira B. Ramalho* and Miguel C. Gonçalves*

* Faculty of Engineering of University of Oporto, Portugal
e-mails: alzirabeatobarros@gmail.com, miguelcg@fe.up.pt

Keywords: Fire resistance, Columns, Concrete, Eurocode, Experimental tests, Numerical model

Abstract. *The behaviour under fire conditions of three reinforced concrete columns with the same geometry is evaluated by varying the mechanical reinforcement ratio, the stirrups diameter and load level. Results from experimental tests are compared with the ones analytically determined by the application of 500 ℃ Isotherm Method and Zone Method, pointed out in EN 1992-1-2 [1]. Interaction diagrams of design axial load in fire situations are defined considering the effects of geometric imperfections and second order effects, determined using the method based on nominal stiffness indicated in EN 1992-1-1 [2], and diagrams of design resistance in fire situation for the different domains of deployable extensions in the columns' section. The analytical values are conservative when compared with the tests results. This is an important fact, as it was observed the explosive spalling of concrete after 50 minutes, in the column tested with higher load level.*

1 INTRODUCTION

The work presented in this paper basically consists of comparing the results obtained in experimental fire tests on three reinforced concrete columns with the numerically calculated by applying the traditional calculating processes, using the simplified methods specified in EN 1992-1-2 [1] for fire resistance calculation. We intend to further study the factors that led to the discrepancy in the values of these columns fire resistance due to the use of these methods, in relation to the experimental evaluations. The columns features are shown in Table 1.

Table 1. Characteristics of the studied columns.

Column	Cross section		Length	Reinforcement	stirrups	Concrete covering	Concrete	Steel
	b [mm]	*h* [mm]	*l* [m]			[mm]	(Calcareous aggregates)	(NR)
C1	250	250	3,0	4Φ16	Φ6	30	C20/25	S500
C2	250	250	3,0	4Φ16	Φ8	30	C20/25	S500
C3	250	250	3,0	4Φ25	Φ8	30	C20/25	S500

2 EXPERIMENTAL EVALUATION

2.1 Test set-up

The columns used in this study were tested in Laboratory of Testing Materials and Structures of the University of Coimbra, in Portugal, with the same restraint level to thermal elongation (13 kN/mm) due to its heating and considering centric load applied to the columns, thus not having initial eccentricity. The column C2 was tested by the authors and columns C1 and C3 were tested by Rodrigues, J.P.C. *et al*. [3].

The restraint thermal elongation is achieved using two steel frames. One of the frames serves of 2D support where is fixed a hydraulic jack and the other is the immobilization frame 3D. The compression load is applied using the hydraulic jack and the restraining forces are measured by a load cell inserted into a steel cylinder. The thermal action is transmitted to the columns by heating the vertical electric furnace, capable of simulating different fire curves. The temperatures within the column are measured by thermocouples located in five different points in each of the three cross-sections over the columns height, as shown in Figure 1.

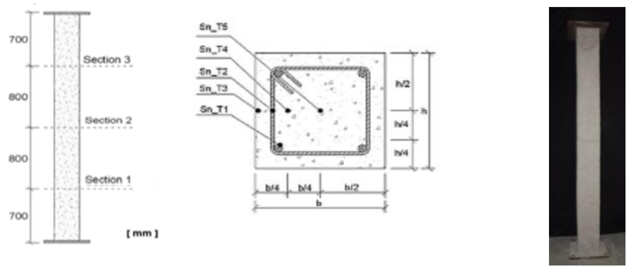

Figure 1. Test specimens and thermocouples position.

The furnace heating followed the standard fire curve ISO 834 [4] about seventeen minutes after the heating start, as seen in the graph of Figure 2. In those early minutes it was observed a slight delay between the two curves, with the furnace heating rate being inferior to the ISO 834 [4] curve.

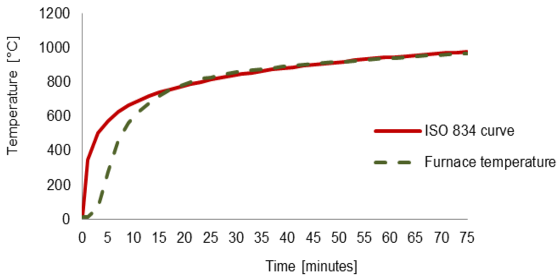

Figure 2. Furnace temperature and ISO 834 [4] curve.

2.2 Results analysis

The axial load initially applied to each of the columns, calculated by considering the effects of geometrical imperfections and second order effects, evolved during the test due to the development of restraining forces, as seen in the graph of Figure 3. In column C2, the increase of restraining forces occurred until the 25th minute, being the maximum value, in that instant, of 715 kN. The restraining force resumed its initial value after 70.5 minutes, followed by the loss of the bearing capacity of the column.

Thus, the variation of the ratio between the restraining forces, P, and the initial load value, P_0, shown in the Figure 3 graph, reaches its maximum value (1,104) at 25 minutes, substantially faster than those achieved in the columns C1 and C3 tests. This difference is mainly due to the fact that the load level at normal temperature, n, and the degree of utilization in the fire situation, μ_{fi}, are substantially higher in column C2 than those of the columns C1 and C3 (Table 2).

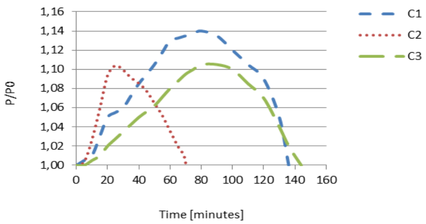

Figure 3. Variation of the ratio between the restraining forces, P, and the initial load, P_0.

For column C2, the temperature variations on the main reinforcement bars along time, for each of the three cross-sections identified in the Figure 1, are represented in the graph of Figure 4.

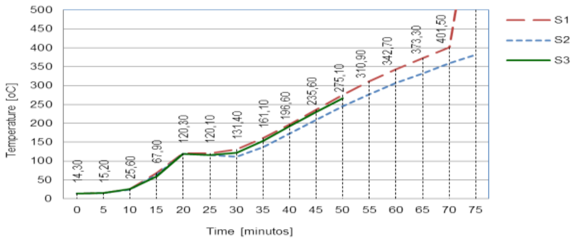

Figure 4. Temperature in the reinforcement bar in each cross section of column P2, function of time.

The explosive spalling of the concrete was observed in this column at minute 50 which led, in that instant, to the destruction of the thermocouple which measured the reinforcement bar’s temperature, in section 2. At this moment in that section, the bar’s temperature was 267ºC and 480ºC at the surface.

Table 2 presents the temperatures measured in the tests of columns C1 and C2 (for column C3, values aren’t available in the literature), at minutes 30, 60, 90 and 120. It is also pointed out the corresponding values defined on the temperature profiles listed in Annex A of EN 1992-1-2 [1]. As it can be seen, the observed temperatures of the tests are always lower than those obtained in the corresponding temperature profiles. This temperature difference is mainly due to the discrepancy, in the first 17 minutes, between the furnace’s heating curve and the theoretical curve adopted.

Table 2. Initial load, P_0, degree of utilization in the fire situation, μ_{fi} and temperature in reinforcement bar.

Column	P_0 [kN]	n	μ_{fi}	Temperature in reinforcement bar (S3) [℃]							
				30 min.		60 min.		90 min.		120 min.	
				Test	Temp. profiles	Test	Temp. profiles	Test	Temp. profiles	Test	Temp. profiles
P1	495	0,60	0,52	170	280	435	440	500	590	590	680
P2	648	0,78	0,69	131	220	343	420	-	-	-	-
P3	656	0,56	0,46	-	180	-	380	-	510	-	610

Figure 5 represents, for column P2, the temperature variation along the height, on the column’s surface and on reinforcement bar, for different exposure times. The largest temperature gradients at face happens between section 3 (2.25 m from base), subject to higher temperatures, and the top, at lower temperatures, because the ends of the columns are not directly exposed to the furnace radiation due to their outside attachment. It’s notorious the occurrence of concrete explosive spalling in Section 2, at the column’s half-height.

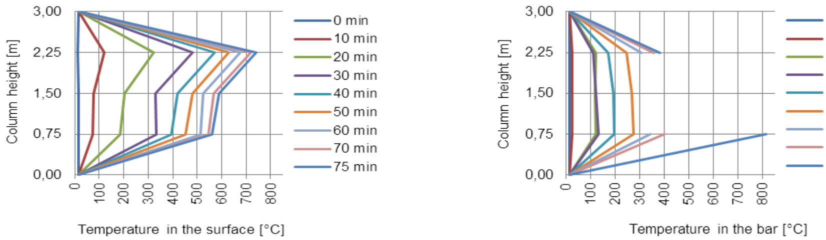

Figure 5. Thermal gradient along the height, in the surface and in the main bar.

3 NUMERICAL EVALUATION

3.1 Interaction diagrams *N*/*M*

3.1.1 Introduction

The force resulting from the load applied to the columns rarely passes through the gravity center of its cross section. Indeed, apart from deviations caused by geometric imperfections (first order effects) which occur during the construction phase, it's necessary to consider the lateral deformations that cause an increase of bending moment, called second order moment (second order effects).

To evaluate the column's resistance capacity and the maximum design load in a fire situation, it must be taken into account two different aspects:

- The column's resistance, which can be defined by tracing a line which limits the cross section's resistance, at uniaxial bending or biaxial bending, obtaining the interaction diagram $N_{Rd,fi}/M_{Rd,fi}$, with a development which depends on different parameters and factors.

- The design values of axial load and bending moment, determined by taking into account the geometric imperfections and second order effects, defining the interaction diagram $N_{Ed,fi}/M_{Ed,fi}$.

For each fire resistance class, the maximum value of design load and bending moment, in a column, are defined by the intersection between the curve corresponding to the interaction diagram $N_{Rd,fi}/M_{Rd,fi}$ and the interaction diagram, $N_{Ed,fi}/M_{Ed,fi}$.

3.1.2 Interaction diagrams $N_{Rd,fi}/M_{Rd,fi}$

To define the interaction diagram $N_{Rd,fi}/M_{Rd,fi}$ corresponding to a column cross-section, for a fire resistance class, it was adopted the following calculation procedure:

- Calculation of the reduced concrete cross-section, using the 500 ºC Isotherm Method or Zone Method, simplified methods indicated in EN 1992-1-2 [1];
- Definition of the temperature in reinforcing bars by consulting the representative graphs of the temperatures profiles for each fire resistance class, presented in Annex A of EN 1992-1-2 [1];
- Determination of the reinforcing bars reduced strength due to elevate temperature. Calculation of $E_{s,\theta}$, $f_{sp,\theta}$ e $f_{sy,\theta}$, by applying the reduction coefficients specified on that European Standard;
- Drawing of interaction diagram $N_{Rd,fi}/M_{Rd,fi}$, according to different possible configurations for concrete and steel reinforcement strains. To quantify $N_{Rd,fi}$ and $M_{Rd,fi}$ it was used the equivalent rectangular stress block method [5], the simplified classic method alternative to the rectangular-parabolic distribution. It was considered the reduction of mechanical properties of the steel due to the elevated temperatures.

The tested columns are inserted in Domain 5, defined by the strains in the steel reinforcement bars A_s between $\varepsilon_{sp,\theta}$ (steel strain corresponding to the stress-strain proportional limit at temperature θ) and zero, to a depth of neutral axis (x) varying between x_5 e x_6, as shown in Figure 6. The Domain 5 boundaries and the interaction diagrams $N_{Rd,fi}/M_{Rd,fi}$ corresponding to each of the columns are represented in Figure 8. The fire resistance classes were selected so that the stress values corresponding to the tested columns remained in the diagram zone between the drawn curves for two consecutive classes. The 500 ℃ Isotherm Method was applied.

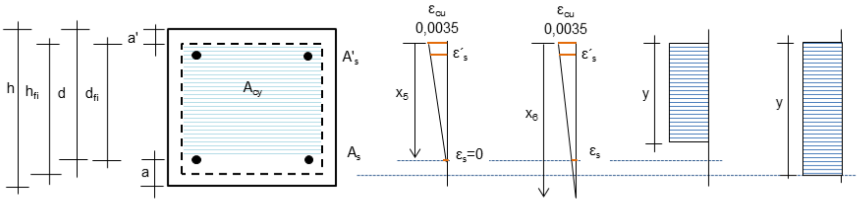

Figure 6. Domain 5, defined for steel reinforcement strain limits $0 \leqslant \varepsilon_s \leqslant \varepsilon_{sp,\theta}$.

Tables 3 and 4 present the expressions for determining the necessary parameters for the drawing of interaction diagrams $N_{Rd,fi}/M_{Rd,fi}$ in this domain.

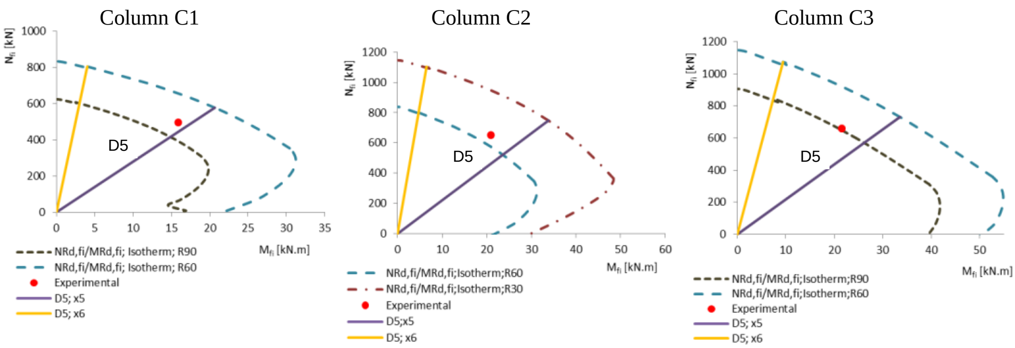

Figure 7. Interaction diagrams $N_{Rd,fi}/M_{Rd,fi}$, Domain 5 limits and tested columns representation.

Table 3. Expressions to calculate x, y, ε_s and σ_s, in Domain 5.

Depth of neutral axis		y	A_{cy}	Reinforcement A_s		Reinforcement A'_s		
				Compression		Strain		Stress
						Tension	Compression	$\varepsilon_{sp,\theta} < \varepsilon'_s < \varepsilon_{sy,\theta}$
x_5	x_6			ε_s	$\sigma_s(\theta)$	ε'_s	ε'_s	$\sigma'_s(\theta)$
d_{fi}	$1{,}25h_{fi}$	$0{,}8.x$	$b_{fi}.y$	$0{,}0035(x-d_{fi})/x$	$\varepsilon_s.E_{s,\theta}$	-	$0{,}0035[x-(a-a')]/x$	$f_{sp,\theta}-c+(b/a).[a^2-(\varepsilon_{sy,\theta}-\varepsilon'_s)^2]^{0,5}$

Table 4. Expressions to calculate de $N_{Rd,fi}$, S_y, e and $M_{Rd,fi}$, in Domain 5.

Depth of neutral axis		Load bearing capacity	Static moment	Bending moment	Eccentricity	Bending moment
		$N_{Rd,fi}$		$N_{Rd,fi}.e_1$	e	
x_5	x_6	$A'_s \rightarrow$ Compression	S_y	$A'_s \rightarrow$ Compression	$e_1>(h/2)-a$	$M_{Rd,fi}$
d_{fi}	$1{,}25h_{fi}$	$0{,}85f_{ck}.A_{cy}+A'_s.\sigma'_s(\theta)+A_s.\sigma_s(\theta)$	$A_{cy}.(d_{fi}-y/2)$	$0{,}85f_{ck}.S_y+A'_s.\sigma'_s.(d-a)$	$e_1-(h/2)+a$	$N_{Rd,fi}.e$

The application of Zone Method leads to less conservative results than the 500 ℃ Isotherm Method, as can be seen in the graphs of Figure 8. For columns C1 and C2, using the first method leads to design load and moment, corresponding to these columns in a fire situation, very close to the fire resistance class R90 in the first column, and R60 in the second.

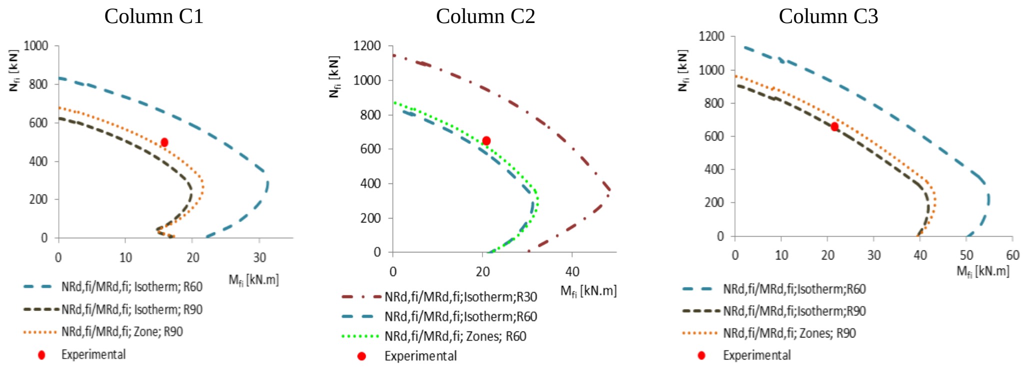

Figure 8. Interaction diagrams $N_{Rd,fi}/M_{Rd,fi}$, considering the application of 500 ℃ Isotherm Method and Zone Method.

3.1.2. Interaction diagrams $N_{Ed,fi}/M_{Ed,fi}$

For drawing the design interaction diagram, $N_{Ed,fi}/M_{Ed,fi}$, it was used the method based on nominal stiffness, pointed in EN 1992-1-1 [2]. By applying this method the total bending moment calculation, including the second order moment, is expressed as a magnification of the bending moment resulting from a linear analysis, which includes the geometric imperfection effects, and is calculated by applying the expression (1).

$$M_{Ed,fi} = M_{0Ed,fi}\left[1+\frac{\beta}{\left(N_B / N_{Ed,fi}\right)-1}\right] \tag{1}$$

where:

$M_{0Ed,}$fi	first order moment in a fire situation, including the geometric imperfection effect;
Β	factor which depends on the first and second order moments;
$N_{Ed,fi}$	design value of axial load, in a fire situation;
N_B	buckling load based on nominal stiffness.

In this study the design value of axial load is calculated in fire situation, considering the reduced cross-section already determined in the previous paragraph for the development of diagrams $N_{Rd,fi}/M_{Rd,fi}$. Figure 10 shows the $N_{Ed,fi}/M_{Ed,fi}$ interaction diagrams, for fire resistance classes R60, R90 and R120. The columns were considered not braced, so that results could be compared to the ones of the experimental tests.

As it can be seen, there is no significant difference in the design N/M values in a fire situation, determined considering the reduced cross-section area of the columns calculated by applying the 500 ℃ Isotherm Method or the Zone Method.

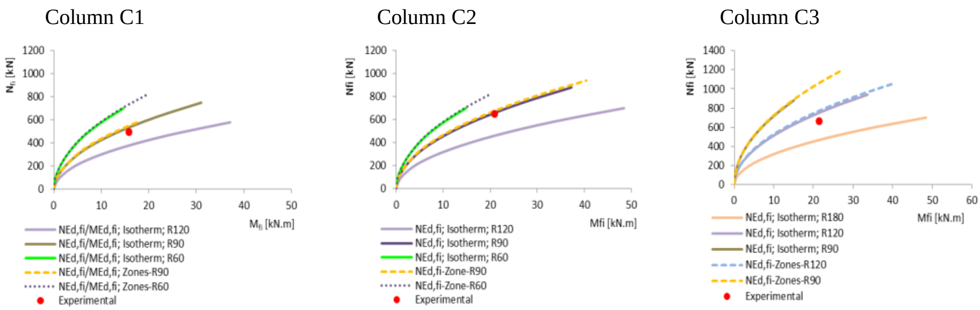

Figure 9. Interaction diagrams $N_{Ed,fi}/M_{Ed,fi}$, considering the 500 ℃ Isotherm Method and the Zone Method.

3.2 Results analysis

The outcomes of the performed analysis are represented in the graphs of Figure 10. The pair of a column's resistance efforts (N_{fi}, M_{fi}) must be contained in the plane delimited by the curves corresponding to diagrams $N_{Ed,fi}/M_{Ed,fi}$ and $N_{Rd,fi}/M_{Rd,fi}$. Thus, considering the analytical calculation, column C1 is classified in the fire resistance class R60, column C2 in class R30 and column C3 in class R90. In the experimental tests, the fire resistance classes corresponding to the fire resistance times of those columns are R120, R60 and R120, respectively. It should be noted however, and by analysing the graphs in Figure 10, that the column's C1 and C2 fire resistance are very close to R90 and R60, respectively.

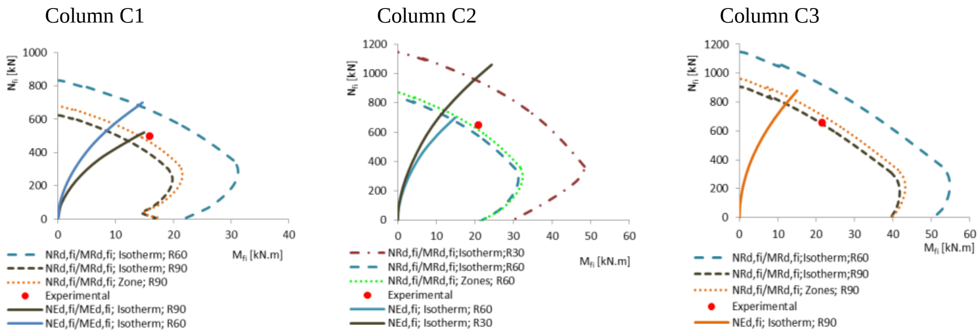

Figure 10. Interaction diagrams $N_{Ed,fi}/M_{Ed,fi}$, $N_{Rd,fi}/M_{Rd,fi}$ and test load and bearing moment.

4 CONCLUSIONS

This study compared the results obtained in experimental fire tests of three columns with the same dimensions by varying the stirrups diameter, longitudinal steel reinforcement diameter, degree of utilization in the fire situation, μ_{fi} and load level at normal temperature, n. It also compared the fire resistance resulting from these tests to the analytically determined by applying the simplified methods indicated in EN 1992-1-2 [1]. It was concluded, essentially, that:

(1) In the experimental tests results, the column's fire resistance was substantially affected by the degree of utilization in the fire situation, μ_{fi} and by the load level, n, as observed in Table 5.

Table 5. Degree of utilization in the fire situation, load level at normal temperature and fire resistance time and classes.

Column	μ_{fi}	n	R_{tests} [minutes]	Class (tests)	$R_{analytical}$
C1	0,52	0,60	136	R120	R60
C2	0,69	0,78	70	R60	R30
C3	0,46	0,56	144	R120	R90

(2) In the longitudinal steel reinforcement bars, the temperatures read on the temperature profiles listed in Annex A of EN 1992-1-2 [1] are superior to those that occurred during the tests, as verified in Table 2, for different exposure times. This may be a factor which most influences the achievement of conservative results, when the simplified methods indicated in that standard are used.

(3) The observed difference of temperatures can be due to the initial gap between the heating furnace curve and the ISO 834 [4] curve, as illustrated in Figure 2. The fact that the test temperature is measured on the face of the bar, and the one defined by the consultation of temperature profiles refer to the bar’s axis does not cause significant differences, as shown by Gonçalves [6].

(4) For the analyzed columns, when calculating the N_{Rd}/M_{Rd} values in a fire situation, the Zone Method leads to less conservative results than the 500 ºC Isotherm Method, as seen in the graphs of Figure 9 and Figure 11. The difference is more significant in the columns with lower load level.

(5) The N_{Ed}/M_{Ed} values, in case of fire, are not significantly affected by the simplified method that served as basis in the reduced cross-section calculation, as verified in the graphs of Figure 10.

(6) The simplified methods used in this study (Zone Method and 500 ºC Isotherm Method) leads to substantially conservative results. This is quite relevant, since the 500 ºC Isotherm Method is used by structure engineers in the verification of fire resistance in current columns.

(7) The graphics development as represented in Figure 11 is of great interest as they allow an efficient realization of the maximum axial load level and bending moment values to which the columns can be submitted in a fire situation.

REFERENCES

[1] CEN, EN 1992-1-2: *Eurocode 2: Design of concrete structures: Parte 1-2: General rules - Structural fire design. European Standard*, December 2004.

[2] CEN, EN 1992-1-1: *Eurocode 2: Design of concrete structures: Parte 1-1: General rules and rules for buildings. European Standard*, December 2004.

[3] Rodrigues, J.P.C.; Laim, L. M., Gonçalves, M.C., “Fire resistance of square and circular cross-section concrete columns”. *Proceedings of the 7th International Conference on Structures in Fire,* Zurich, 823-832, 2012.

[4] ISO 834. “Essais de Résistance au Feu”. Organisation Internationale de Normalisation, Norme Internationale, Genève, Switzerland, 1975.

[5] Jiménez M., Álvaro M., Francisco C. *Hormigón Armado*. 14. ªedicion, ISBN:84-252-1825-x, 2000.

[6] Gonçalves, Miguel J.C.R. *Comportamento ao fogo de elementos estruturais de betão. Análise numérica e metodologia.* Dissertação de Doutoramento, Faculdade de Engenharia da Universidade do Porto, 2007.

8th International Conference on Structures in Fire
Guo-Qiang LI, Venkatesh K. R. KODUR, Shou-Chao JIANG, Jian JIANG, Su-Wen CHEN, Guo-Biao LOU (Eds.)
Shanghai, China, June 11-13, 2014

SIMPLIFIED METHOD FOR FIRE RESISTANCE OF CONCRETE COLUMNS

Miguel Chichorro Gonçalves* and Maria Alzira B. Ramalho*

* Faculty of Engineering of University of Porto, Portugal
e-mails: miguelcg@fe.up.pt, alzirabeatobarros@gmail.com

Keywords: Fire resistance, Columns, Concrete, Eurocode, Experimental test, Numerical model

Abstract. *A column is a structural element with the main function to support axial forces. When these forces are high, a lateral deformation will occur, inducing an increment on the bending moment, known as second order effects. These second order effects have a great effect on the behaviour of the column in fire and must have to be taken into account in the fire analysis methods. Two issues are important in the assessment of the fire resistance of concrete columns: on the side of the resistance, the definition of the interaction N-M diagram of the column and on the side of the actions, the consideration of the geometrical and material non-linearity aspects are both highly temperature dependent. Here is presented the methodology used to develop a numerical model to be a simplified method named SimFIRc, developed for the analysis of concrete columns in fire. The results of the method are compared with the ones obtained with an advanced calculation method, the finite element program SAFIR for the validation of the developed method. SAFIR was developed by Jean-Marc Franssen [1], in the University of Liege, in Belgium, and can perform the material and geometric non-linear analysis of buildings elements in fire. The method implemented in SimFIRc (second-order analysis based on nominal stiffness described in EN 1992-1-1, [2]) is applied to a column.*

1 INTRODUCTION

The SimFIRc model was developed for reinforced concrete structural elements subjected to second order effect with axial load subject to fire. It is necessary to consider in the assessing of the fire resistance of a column, [3]:

- In terms of strength, it is plotted as resistance to bending a section of reinforced concrete column (*N-M* interaction diagram), which depends on numerous factors, including considerations of non-linear materials, function of temperature. This diagram defines the field of possible combinations of *NRd,fi* and *MRd,fi* efforts for a section of reinforced concrete subjected to fire for a particular moment;
- On the side of actions there is the request to input the aspects of the geometric nonlinearity in addition to materials of non-linearity (thermal effect). This assessment will be done using the nominal stiffness method.

For a column subjected to an axial load *N*, with eccentricity *e*, occurs the moment ($N \cdot e$) that causes bending. The deflection then causes an additional eccentricity Δ, and the total bending moment is increased to $N \cdot (e+\Delta)$. The relationship between the force and the additional bending moment is highly nonlinear, dependent on several factors, the main importance of the increase in the value of Δ and the reduction of the mechanical characteristics of the materials constituting the section. For short columns the additional bending moment is negligible, but for slender columns, its load capacity is directly dependent on it. In the method of the nominal stiffness, according to EN 1992-1-1 [2], the section of the column should be reduced according to the zone method. Next, we calculate the second order moment and compared with the interaction diagram of the critical section calculated taking into account the variations of material characteristics with temperature for a given instant.

In this model SimFIRc perform three tasks: a) Calculation of mechanical properties of steel and concrete, defined by EN 1992-1-2 [4], b) Calculation of bearing capacity of the section (the material nonlinearity), and c) Calculation of the corresponding *M-N* relation for the nonlinear material and geometric effects. The numerical model requires various types of data: dimensions of the section, the mechanical properties of concrete and steel reinforcement, loading and eccentricities, structural data such as topology, conditions, mechanical and thermal boundaries and time increments and data for incremental-iterative process.

2 DEVELOPMENT OF METHOD SIMFIRC

2.1 Introduction

According to EN 1992-1-1, [2] and in a situation of structural elements subject to second order effect with axial load, i.e. calculation at room temperature, several aspects should be considered:

- Possibility to use one of two methods of analysis;
  - (a) *A method based on the estimated curvature* - This method applies mainly to isolated elements. This method provides a second order bending moment based in the deformation, which is dependent on the effective length and the estimated maximum curvature;
  - (b) *A method of second order analysis based on nominal stiffness* - This method can be used for isolated structures or structural elements if the values of nominal stiffness are properly calculated. Values of bending stiffness should take into account the effects of cracking, material non-linearity and creep;
- These methods often lead to values of higher order bending moments of 2^{nd} order to those that correspond to the instability of the structural element. This ensures that the bending moment is compatible with the resistance of the section;
- Nonlinear analyses promoted here include geometric nonlinearities through the second order effects but also non-material nonlinearities;
- Should be used stress-strain relations to high temperature of the concrete and steel;
- Must be included the effect of creep by multiplying all strains in the concrete by the factor $(1+\varphi_{ef})$ wherein φ_{ef} is the effective creep ratio.

According to EN 1992-1-1 [2], the section of the column to be reduced in accordance with the Zone method or other. Next, we calculate the second order bending moment and compared with the interaction diagram of the critical section calculated taking into account the variations of material characteristics with temperature for a given instant.

Despite the above in EN 1992-1-2, [4] in section (3) of Annex B in B.3.1 consideration based on the estimated curvature method resulted in a poor strategy for evaluating the fire resistance of columns. Thus, it is redirected the SimFIRc development considering the analysis method based on second order nominal stiffness, adapted to high temperatures. These methods are designated respectively by Article C.1 and C.2 Methods.

Then decided to implement the calculation model based on the method of nominal stiffness. This indeed allowed results generally conservative and in line with the results obtained through an advanced method of calculation.

2.2 Estimated curvature method

This method is primarily used for individual members or normal forces and constants and a defined effective length, l_c. The method provides the nominal second order bending moment based on the deformation which is calculated as a function of the effective length and the maximum curvature calculated by estimated:

$$M_{Ed} = M_{0Ed} + M_2 \tag{1}$$

Wherein:

M_{0Ed} - 1st order bending moment including the effect of imperfections [kN·m]

$M_2 = N_{Ed} \cdot e_2$ - 2nd order bending moment (2)

N_{Ed} - Design value of the axial load [kN]

$e_2 = \frac{1}{r} \cdot \frac{l_0^2}{c}$ - Deformation (3)

2.3 Method of nominal stiffness

The second order effect is calculated with Equation (4), which is a function of the first order moment, the critical load and the load that the columns are subject to:

$$M_{Ed,fi} = M_{0Ed,fi}\left[1+\frac{\beta}{\left(N_B / N_{Ed,fi}\right)-1}\right] \tag{4}$$

Wherein:

β - Worth π^2 / c_0 with $c_0 = 9{,}8$ for 1st order bending moment with parabolic distribution [-]

N_B - Buckling load based on bending load reducing stiffness, also known as N_{cr} [kN]

The buckling load, N_{cr} is calculated using Equation (5) and the stiffness EI calculated with Equation (6).

$$l_c = \pi\sqrt{\frac{EI}{N_{cr}}} \tag{5}$$

$$EI = K_c \cdot E_{cd} \cdot I_c + K_s \cdot E_s \cdot I_s \tag{6}$$

Wherein:

E_{cd} - Design value of the modulus of elasticity of concrete [MPa]

I_c - Moment of inertia of the concrete section [m^4]

E_s - Design value of the modulus of elasticity of reinforcement [MPa]

I_s - Moment of inertia of the armature relative to the CG of concrete section [m^4]

K_c - Correction factor of the effects of cracking [-]

K_s - Correction factor for the contribution of the armour [-]

In Equation (6) were considered six zones of concrete. However the development of the SimFIRc method was calculated $E_{cd}I_c$ through three different procedures to determine the best approach in the final result:

(1) Was used the synergy for calculating considering the average value of $K_{c\theta,m}$ of equivalent wall for all of concrete inside the line defined by a_z (Figure 1). And we calculated the *EI* for the inner zone of concrete through the procedure referred to in EN 1992-1-2, [4] in paragraph B.3.1: $(EI)_z = [K_c(\theta_i)]^2 \cdot E_c \cdot I_z$

(2) Calculated the *EI* for each of the six zones through the procedure referred to in EN 1992-1-2, [4] in paragraph B.3.1: knowing the average temperature of each zone and the respective $K_c(\theta_i)$

(3) The value of *EI* was calculated from the stress-strain diagram of concrete for each temperature in each zone using the procedure described in paragraph 3.1.5 of EN 1992-1-1, [2].

In Equation (6) the value of the Young Modulus of steel, E_s, is evaluated, whether they are for the tensile armour or for those that are to compression, irrespective of whether they are equal with temperatures due to the symmetry of the normal section columns.

3 SIMFIRC – CALCULATION PROCESS

Described in this paragraph, the calculation procedure for determining the load capacity of columns subjected to fire through the numerical model SimFIRc through execution of three tasks:

(1) Calculation of mechanical properties of steel and concrete, defined by EN 1992-1-2, [4];
(2) Calculation of load capacity of the section (non-material linearity) through a classic but here discretized procedure and its own methodology;
(3) Calculation of the *M-N* ratio corresponding to C_1 and C_2 methods respectively for the materials and geometric nonlinear effects.

The main calculation procedure for both methods is briefly described:

(1) Determination of temperature field in the section of the part for a given time through SAFIR model;
(2) Determination of temperature on armour;
(3) Resistance reduction of armour f_{sy}, E_s and f_{sp}, due to temperature - Ratings for $\varepsilon_s > 0.02$ e $\varepsilon_s \leqslant 0.02$;
(4) Determination of temperature in concrete zones;
(5) Reducing the resistance of each zone of the concrete due to temperature, as well as ε_c, ε_{c1} e ε_{cu};
(6) Calculating the reduction of the concrete section;
(7) Use of a calculation method for performing the calculation of the effort axial/bending moment, according to the different strain configurations possible to the section considering the reduced mechanical properties of materials;
(8) Use of a calculation method for performing the calculation of bending moments, depending on the axial loads acting respectively, considering the reduced mechanical properties of materials and the effect of second-order moments;
(9) Comparison of the resistance values with the value of the bending moment acting.

The interaction diagram for axial forces and bending moments is set for ultimate limit state of resistance in which are considered limit strains.

For the determination of the resistance effort is necessary to quantify the limit state for which these efforts are defined, what an analysis of fire resistance is done in terms of maximum strains in concrete (0,0035) and the reinforcement (0,20). These extensions give limit state when at least one of them occurs.

Is shown in Figure 1 a schematic of the boundary conditions mentioned followed by a description of the various situations in which state limits are reached.

It has been found, when one carries out the calculation and definition diagrams *N-M* of exceptional importance that the temperature in the concrete takes. Thus, we present in Figure 1 the layout of the final methodology used to evaluate diagrams *N-M*. The methodology allows to approach each time step: *30*, *60*, *90* and *120* minutes.

Through the elements of Figure 1 settle all the necessary equations to draw those diagrams *N-M*. Those data allows us to define all the extreme situations of calculation in which the variables take discrete values and explain the particular cases.

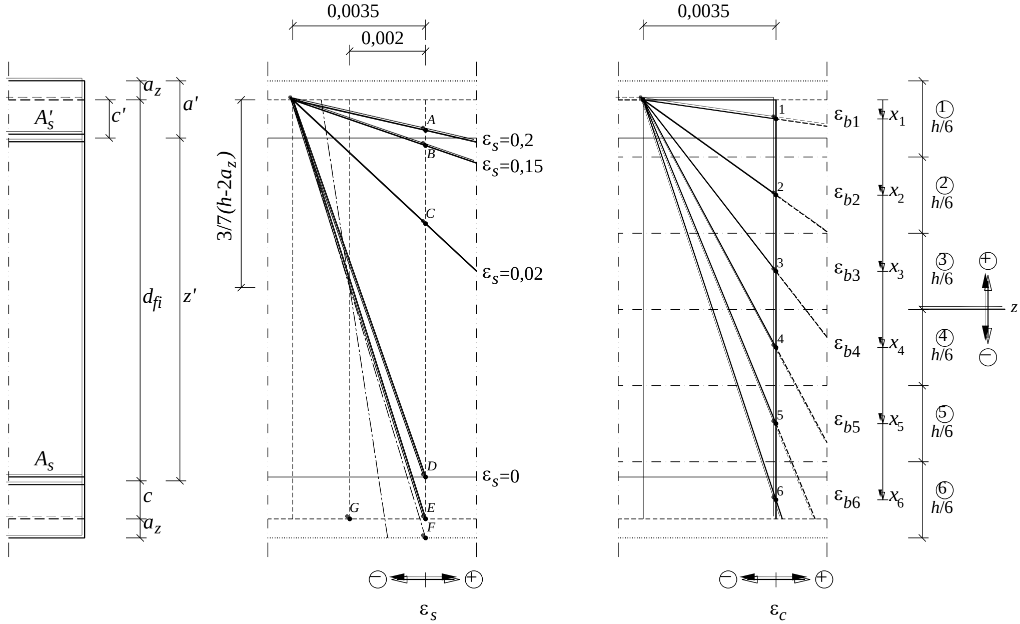

Figure 1. Limit strains in armours and in six zones of concrete (SimFIRc).

It may be noted that the division of section took advantage of the method of calculating the area degraded a_z thickness to the minimum value of $n = 3$. Figure 1 only includes the bending moment and axial effort.

The interaction diagram can be created with the equilibrium Equations (7) and (8) established for a particular moment to which correspond definite temperatures either in armour or in each of the six areas of concrete.

$$N_{Rd,fi} = \sum_{i=1}^{6} b_{fi} \cdot a_i \cdot f_{cd,fi}\left(\theta_i, \varepsilon_{c,i}\right) + \sum_{j=1}^{m} A_{sj} \cdot f_{sy,fi}\left(\theta_j, \varepsilon_{s,j}\right) \tag{7}$$

$$\begin{aligned} M_{Rd,fi} = & \sum_{i=1}^{3} b_{fi}\left[a_i \cdot f_{cd,fi}\left(\theta_i, \varepsilon_{c,i}\right)\right] \cdot \left[\frac{h}{2} - a_z - \frac{a_i}{2} - a_n\right] \quad n < i \\ & - \sum_{k=4}^{6} b_{fi}\left[a_k \cdot f_{cd,fi}\left(\theta_k, \varepsilon_{c,k}\right)\right] \cdot \left[-\frac{a_k}{2} - a_l\right] \quad , l < k \\ & + \sum_{j=1}^{m(armad)} A_{sj} \cdot f_{sy,fi}\left(\theta_j, \varepsilon_{s,j}\right) \cdot z_j \end{aligned} \tag{8}$$

Where m is the number of armours, and l and k are respectively the number of zones above and below the concrete centre of gravity and the remaining variables shown in Figure 1.

Implicitly is shown in Figure 1 the calculation model developed applied to a specific section. The calculation procedure is outlined in Table 1 herein by complementing the information of Figure 1 showing the expressions for calculating the variables involved.

Presented in Table 1 are the necessary equations for the calculation of the variables referred to situations of limit strain or transition in the lower armour expressions. Only the calculation of ε_b (i=1,6) in the six areas of concrete will be taken through the expressions of Table 2, depending on the domain of validity of each case.

Table 1. Basis equations for the calculation of x, ε_s and ε'_s that divides each of the 6 areas.

Situation defined by ε_s – Limit Strains and transition							
	A	**B**	**C**	**D**	**E**	**F**	**G**
x	$x=\dfrac{0{,}0035\cdot d_{fi}}{\varepsilon_s+0{,}0035}$					$x=2{,}75/1{,}75\cdot(h-2a_z)$	$x=\infty$
	$x=3{,}5/203{,}5\cdot d_{fi}$	$x=3{,}5/153{,}5\cdot d_{fi}$	$x=3{,}5/23{,}5\cdot d_{fi}$	$x=d_{fi}$	$x=h-2\cdot a_z$		
ε_s	$\varepsilon_s=0{,}2$	$\varepsilon_s=0{,}15$	$\varepsilon_s=0{,}02$	$\varepsilon_s=0{,}0$	$\varepsilon_s=-\dfrac{0{,}0035\cdot[(h-2\cdot a_z)-d_{fi}]}{(h-2\cdot a_z)}$	$\varepsilon_s=-\dfrac{0{,}00175\cdot[(h-2\cdot a_z)-d_{fi}]}{(h-2\cdot a_z)}-0{,}001$	$\varepsilon_s=-0{,}02$
	$\varepsilon_s=-\dfrac{0{,}0035\cdot[x-d_{fi}]}{x}$						
ε'_s	$\varepsilon'_s=-\dfrac{0{,}0035\cdot[x-\lvert c'\rvert]}{x}$					$\varepsilon'_s=-\dfrac{0{,}00175\cdot[(h-2\cdot a_z)-\lvert c'\rvert]}{(h-2\cdot a_z)}-0{,}001$	$\varepsilon'_s=-0{,}02$

For situations considered basic to diagrams for strains of which intersect each zone concrete at its midpoint equations for ε_b (i=1,6) as shown in Table 2.

Table 2. Basis equations for the calculation of ε_b (i=1,6) in the 6 areas of concrete.

Situation defined by x so taking the average values of each zone concrete		
$\varepsilon_{bi(i=1,6)}$	$\varepsilon_{bi(i=1,6)}=\dfrac{0{,}0035(x+a_z-(i-1)\cdot h/6)}{x}$	$\varepsilon_{bi(i=1,6)}>0{,}0$ $\varepsilon_{bi(i=1,6)}\leq 0{,}0035$

4 APPLICATION AND VALIDATION OF NUMERICAL MODEL

4.1 Evaluation of curvature estimation and nominal stiffness methods

For the method implemented in SimFIRc (second-order analysis based on nominal stiffness) makes up their application to various types of columns studying the effect of the influence of the Young modulus and creep. Complements the validation of the method with a parametric study that changed the height of the column.

The sensitivity analysis performed here involves, on the one hand the numerical aspects considered (usually evaluates the degree of importance of the simplifications introduced) and the aspects defined in the Eurocodes (field of validity of expressions considered), but especially the structural aspects that enable these yes, evaluate the structural behaviour of the columns to fire.

Different types of columns for a square section (0,30 m × 0,30 m) were analysed. The results in Figure 1 correspond to the features of the columns shown in Table 3.

Table 3. Characteristics of the columns analysed.

Section b [mm]	Section h [mm]	Length l [m]	Armour	Stirrups	Covering [mm]	Concrete (Siliceous)	Steel (NR)
300	300	8,0 4,0 e 12,0)	4Φ16 (4Φ16)	Φ8	30	C30/35	S400

It was necessary to assess the intermediate results, said development SimFIRc model, for the parameters that were considered more or less influence on the results obtained. This validation was performed through the analysis performed with the SAFIR model. So calculations were made to detect situations and/or parameters that were not considered in the model and took advantage of those results to weave considerations of consistency in the effort of keeping calculating a qualitative and quantitative balance model to obtain good results.

The results are presented here in graphs representing interaction diagrams $N_{R,fi}$-$M_{R,fi}$, resistance field delimiters of columns subject to bending moments and axial efforts $N_{S,fi}$-$M_{S,fi}$ curves corresponding to the simplified methods (and the evolution of development thereof), reproducing the effects of second order , the geometric nonlinearity in addition to the non-material linearity, setting the domain resistance of column and in particular the characterization point of maximum load capacity of the columns for a given specific situation (time).

The terminology given to the calculation, and is referenced in the following figures is synthetically represented by $C_{Ri,j\text{-}\varphi ef\text{-}t}$ whose indices have the following meaning:

- *i* - Takes the value *1* or *2* depending on the calculation methodology is respectively the method of estimation of curvature or nominal stiffness;
- *j* - Takes the value *1*, *2* or *3* depending on the methodology used to calculate the deformability of the concrete module (only for the C_2 method as described by Gonçalves [3]);
- φ_{ef} - The creep coefficient can take one of three values: *0*, *0,7* and *1,4*;
- *T* - Corresponds to the analysis time, typically *30*, *60*, *90* and *120* min.

Is shown in Figure 2 the curves resulting from the application of Equation (4), [3] for the method of nominal stiffness, considering the 3rd approach for calculating *EI* and a value of creep coefficient of *0* for all ages fire resistance: *30*, *60*, *90* and *120*min.

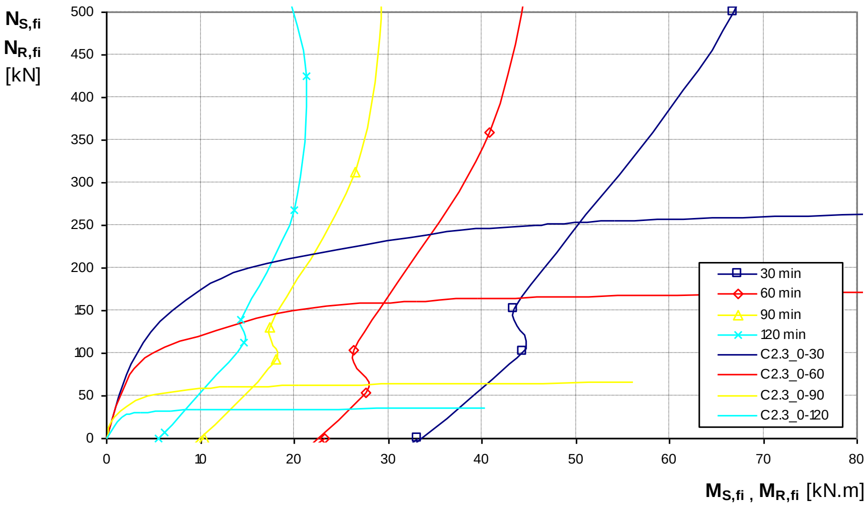

Figure 2. Load capacity of a reinforced concrete column 8m tall, 4ϕ16, a = 4cm - interaction graph $N_{R,fi}$-$M_{R,fi}$ and $N_{S,fi}$-$M_{S,fi}$ for the nominal stiffness method with 3rd methodology of calculation of *EI*.

In Figure 2, each intersection of each set of two curves for each instant of time, represents the maximum capacity of the column composite bending moment. Then joined the pairs of values for the two methods and the method of nominal stiffness with the 3rd method of calculating the designated *EI* SimFIRc (and compares those results with those obtained with SAFIR (Figure 3).

The combined results of the axial load capacity of the column in bending moment are represented in Figure 3.

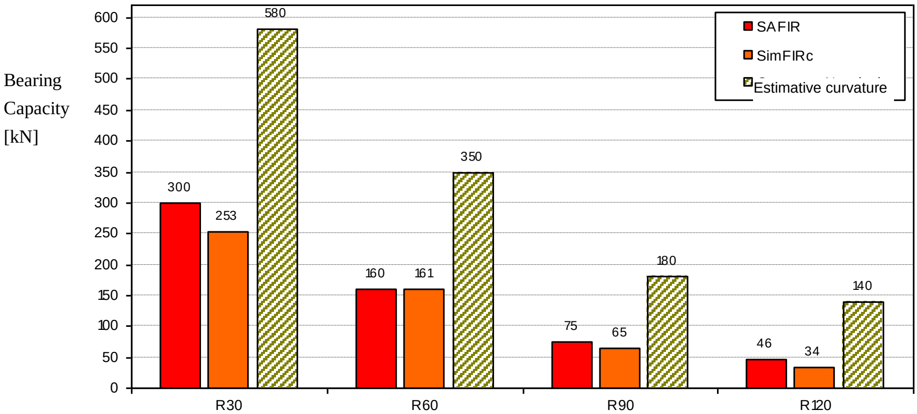

Figure 3. Load capacity of a reinforced concrete column of 8m tall, 4 ϕ16, a=4cm.

We compared the approach with the method of nominal curvature also set in EN 1992-1-1, [2] concluding clearly the good results of the nominal stiffness method with conservative values when compared with the results of SAFIR (Figure 3).

4.2 Evaluation of the Young Modulus and creep of concrete in SimFIRc method.

Comparing the results corresponding to the intersections of the curves for each instant, comparing with the results obtained with SAFIR, it is seen that the 3rd methodology of the calculation of *EI* is one that provides better results (Figure 4), without incurring any additional effort in the final calculation.

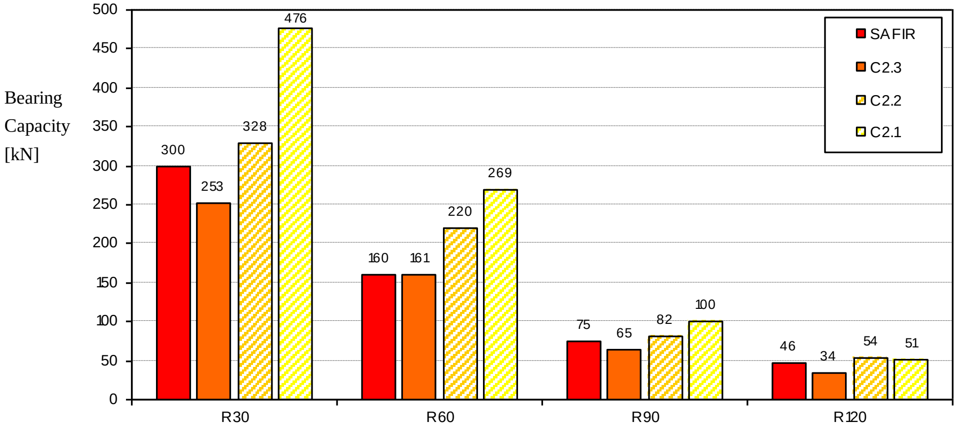

Figure 4. Load capacity of a reinforced concrete column of 8m tall, 4 ϕ16, a=4cm (SAFIR, SimFIRc considering the 3th calculation methodologies *EI*).

4.3 Evaluation of the effect of the height of the columns on the results of SimFIRc method

It is used here the SimFIRc method now in its final implementation in order to evaluate the quality of results, i.e. the effect of applying this method before the variation of some structural considerations, performing a parametric study. The objective is to evaluate as much as possible, the possible limits of application of the simplified method for the characterization of the fire resistance of columns.

The height of the columns was the main parameter considered in this sensitivity analysis insofar as the effect of the second order due to the slenderness is for these structures, a key aspect in the fire resistance. However, many other authors performed sensitivity analyses considering several parameters of evaluation that gave confidence to the current use of the method developed.

The consideration of the height of the column is arguably the greatest obstacle to global behaviour of the column and particularly when subjected to fire parameter, however being imposed generally by architectural issues. Thus, adopting the mechanical boundary conditions considered (enhancing one of the lowest buckling lengths by considering their integration into structures of fixed nodes), then compares the results of the analysed situations.

Is summarized in Figure 5 the results of the loading capacity of concrete columns with 4, 8 and 12 meters and 4ϕ25 obtained with the two SAFIR and SimFIRc models.

It appears that, before a significant change in the importance of the second-order effect, the SimFIRc method provides values close to SAFIR model.

Figure 5 is clearly demonstrative that, in absolute terms in quite disparate resistance capacity values for the three columns. The relative similarity of the heights of the columns represented in the same colour (different shades) shows the quality of the results SimFIRc method. The quantification of this quality is taken for a maximum rise of 24% in the results of the non-conservative side to the column with 4m high and 60min. However there is an absolute variation of the resistances for 60minutes of 650% (940 kN·m to 145kN·m columns to 4m and 12m respectively (Figure 5).

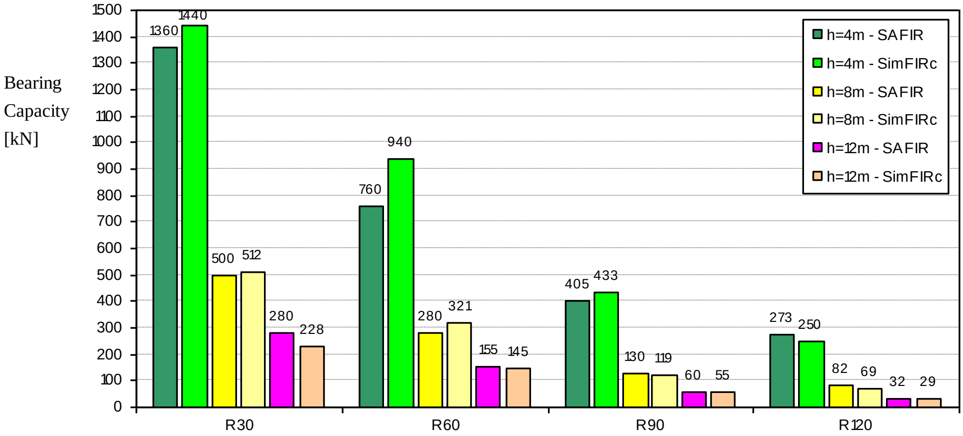

Figure 5. Load capacity of a reinforced concrete columns with 4, 8 and 12m tall, 4 ϕ25 (SAFIR, SimFIRc).

5 CONCLUSIONS

The verification of the numerical model SimFIRc was accomplished through numerous calculations presented by Gonçalves, [3]. The formulation that EN 1992-1-1 own, [2] indicates to calculate the bearing capacity at room temperature, and after suitably adapted by the author, with the specific thermal stress (SimFIRc), potentiated results showed that are similar to the results obtained in advanced calculation models (SAFIR), [1]. The simplified calculation is performed with a methodology whose main advantage is to approach different situations of those who consider themselves tabulated methods. Several methods were indicated in conjunction with Eurocodes while maintaining a reasonable balance of effort calculation on all phases. A relatively simple and powerful tool that provided results on the safety side was created.

REFERENCES

[1] Jean-Marc Franssen, "*SAFIR: A thermal/structural Program for Modelling Structures under Fire*", Engineering Journal /Third Quarter/2005.

[2] EN 1992-1-1, (April 2002), "*Design of Concrete Structures – Part1: General Rules and Rules for Buildings*", European Committee for Standardization, Brussels.

[3] Gonçalves, Miguel Chichorro, "*Fire Behavior of Structural Concrete Elements – Numerical Analysis and Methodology*", Ph. D. Thesis, Faculty of Engineering of the University of Porto, 2007.

[4] EN 1992-1-2, (December 2004), "*Eurocode 2: Design of Concrete Structures – Part1-2: General Rules - Structural Fire Design*", European Committee for Standardization, Brussels, Belgium.

DEVELOPMENT AND EVALUATION OF A MODEL FOR FIRE-RELATED HSC SPALLING FAILURE

Toru Tanibe*, Mitsuo Ozawa, Ryota Kamata***, Yuichi Uchida**** and**

Keitetsu Rokugo *****

* Taiheiyo Materials Corporation and **Gunma University
e-mail: toru-tanibe@taiheiyo-m.co.jp, ozawa@gunma-u.ac.jp

*** Taiheiyo Materials Corporation and ****Gifu University
e-mail: ryouta-kamata@taiheiyo-m.co.jp, uchida@gifu-u.ac.jp
*****Gifu University
e-mail: rk@gifu-u.ac.jp

Keywords: Explosive spalling, Thermal stress, Ring test, Strain failure model, Fire, HSC

Abstract. *This paper reports on an experimental study regarding the behavior of restrained high-strength concrete in response to the type of extreme heating associated with fire. The study was intended to support estimation of thermal stress from the strain in a restraining steel ring and vapor pressure in restrained concrete under the conditions of a RABT 30 rapid heating curve. Thermal stress calculation was based on the thin-walled cylinder model theory. A spalling failure model based on a strain failure model was also proposed. The results indicated that such modeling enables estimation of the point at which spalling starts during heating and the consequent spalling depth.*

1 INTRODUCTION

Fire poses one of the most serious risks to concrete buildings and structures because it often results in explosive spalling of concrete. There are two mechanisms by which concrete can be damaged by fire. The first is restrained thermal dilation resulting in biaxial compressive stress states parallel to the heated surface, which leads to tensile stress in the perpendicular direction (Figure 1) [1]. The second is the build-up of concrete pore pressure due to vaporization of physically/chemically bound water resulting in tensile loading on the microstructure of the heated concrete (Figure 2) [2]. Polypropylene fibers are often added to high-strength concrete (HSC) as an effective measure to prevent explosive spalling [3, 4]. However, few reports to date have outlined actual experimental studies on the exact influence of thermal stress [5]. The authors previously reported that a method involving the restraint of concrete with steel rings in heat testing can be used to clarify characteristics of thermal stress and explosive spalling behavior [6]. The study was intended to support estimation of thermal stress from the strain in a restraining steel ring and vapor pressure in restrained concrete under the conditions of a RABT 30 rapid heating curve. Thermal stress calculation was based on the thin-walled cylinder model theory [7]. A spalling failure model based on a strain failure model was also proposed. The results indicated that such modeling enables estimation of the point at which spalling starts during heating and the consequent spalling depth.

2 MODEL FOR ESTIMATION OF THERMAL STRESS AND STRAIN FAILURE

Figure 3 shows the method used to estimate thermal stress. First, specimens created using concrete with restrained steel rings were subjected to heat testing with the target measurements of internal concrete temperature, steel ring temperature, steel ring strain, vapor pressure inside the concrete, spalling time and spalling depth. Internal concrete deformation due to thermal expansion and vapor pressure caused by heating was restrained by the steel rings, and compressive stress was induced. Although such test setups have previously enabled qualitative evaluation, no simple procedure to routinely quantify the characteristics of materials under restrained expansion has been established. In this study, an instrumented ring setup was used to quantify the behavior of concrete under restrained expansion during heating. Thermal stress calculation was based on the thin-walled cylinder model theory [7] as shown by Equations (1) and (2). Vapor pressure was measured at 10 and 20 mm from the heated surface.

$$\sigma_{re} = \sigma_{th} + \sigma_{vap} \tag{1}$$

$$\sigma_{re} = \varepsilon_{\theta} \cdot E_s \cdot \frac{t}{R} \tag{2}$$

Figure 4 shows a strain failure model of explosive spalling under thermal stress. Strain at a certain depth from the heated surface was calculated using Equations (3) and (4), and the index of the strain failure model was given by Equation (5). Tensile strain failure occurred when the index of the strain failure model exceeded 1.0 ($I_u > 1.0$).

$$\sigma_{re} = \sigma_{x,y} = \varepsilon_{x,y} \cdot E_c \tag{3}$$

$$\varepsilon_z = 2\varepsilon_{x,y} \cdot v_c \tag{4}$$

$$I_u = \varepsilon_z / \varepsilon_{t-f} \tag{5}$$

σ_{re}	:Restrained stress	σ_{th}	:Thermal stress
σ_{vap}	:Vapor pressure	t	:Steel ring thickness
ε_{θ}	:Steel ring circumferential-direction strain	E_s	:Steel ring elastic modulus
R	:Steel ring radius	v_c	:Apparent Poisson's ratio of concrete
E_c	:Elastic modulus of concrete	ε_z	:Strain at a certain depth from the heated surface
$\sigma_{x,y}$	:Stress in the x or y direction	$\varepsilon_{x,y}$	:Strain in the x or y direction
ε_{t-f}	:Ultimate strain upon tensile failure	I_u	:Index of the strain failure model I_u > 1 Tensile strain upon failure

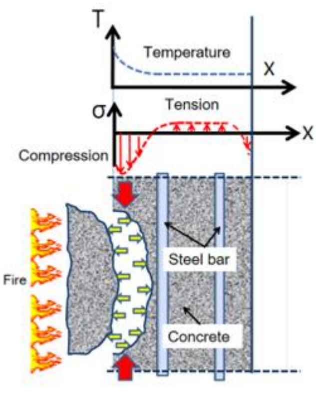

Figure 1. Thermal stress.

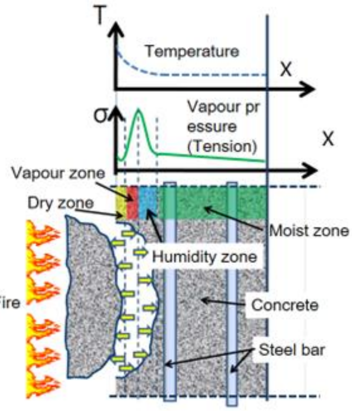

Figure 2. Vapor pressure.

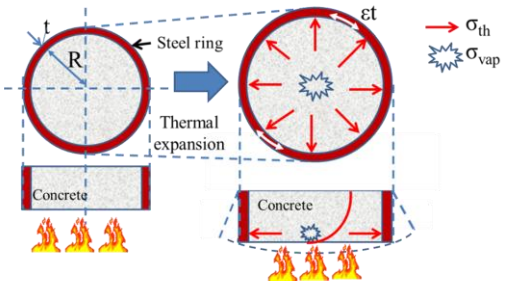

Figure 3. Estimation of thermal stress.

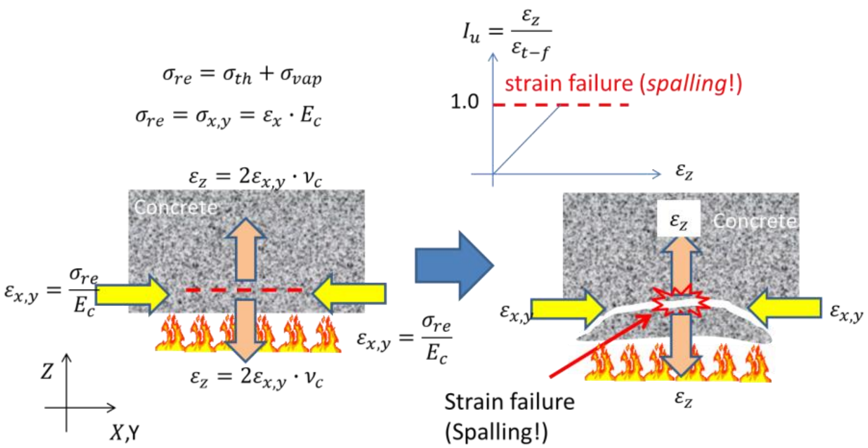

Figure 4. Strain failure model of explosive spalling.

3 OUTLINE OF EXPERIMENT

3.1 Concrete

Table 1 shows the mix proportions of high-strength concrete (HSC). A water-cement ratio of 0.3 and high-early-strength Portland cement (density: 3.13 g/cm^3) were used in this study, and crushed stone with a maximum grain size of 25 mm was used as coarse aggregate. The main component of the super-plasticizer (SP) was polymeric acid. After being cast, the concrete specimens were left in the formwork for one day, and were then wet cured at 20 ± 2 ℃ for 28 days. Heating tests for all specimens were performed after this time. Table 2 shows the values obtained for compressive strength, tensile strength, elastic modulus and water content ratio.

Table 1. Mix.

W/C	Water	Cement	Fine agg.	Coarse agg.1 (less 15 mm)	Coarse agg.2 (less 25 mm)	SP.
0.3	132	440	814	524	524	8.8

Table 2. Mechanical properties.

Compressive strength (MPa)	Elastic modulus (GPa)	Tensile strength (MPa)	Water content ratio (%)
90	42	5.5	3.1

3.2 Specimen dimensions and heating tests

Figure 5 shows the configuration and dimensions of the two specimens used with two pairs of steel rings (diameter: 300 mm; thickness: 8 mm; length: 50 mm; Ec (elastic modulus): 210 GPa; Fy (yield strength): 295 MPa). Two strain gauges and two thermocouples were attached at 25 and 75 mm from the heated surface and outer surface of the steel rings. Stainless steel pipes (inner diameter: 2 mm; length: 200 mm) were placed in the concrete at distances of 10 and 20 mm from the heated surface and parallel to it. Six type-K thermocouples were placed in the central zone of the specimens at 5, 10, 20, 30, 40 and 50 mm from the heated surface. Before testing was performed, a stainless steel pipe extending from the specimen was connected to a miniature pressure transducer (pressure range: 0 – 10 MPa) located outside the furnace. The entire pore pressure assembly (i.e., the stainless steel pipe and the transducer) was filled with hydraulic jack oil, and the pressure transducer and thermocouples were connected to a data acquisition system to enable recording of pressure and temperature values. The heating tests were based on a RABT 30 heating curve (Figure 6). Strain gauges and thermocouples were attached at 25 and 75 mm from the heated surface and the outer surface of the steel ring. The authors previously reported on the effects of steel ring thickness, behavior without steel rings, and spalling depth [8].

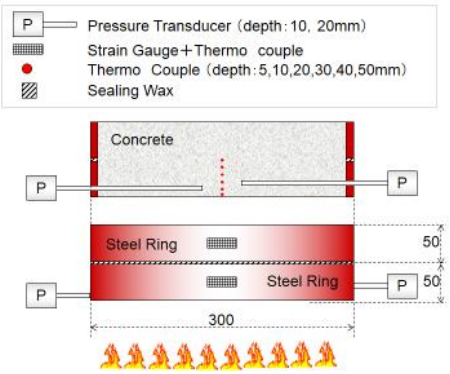

Figure 5. Specimen.

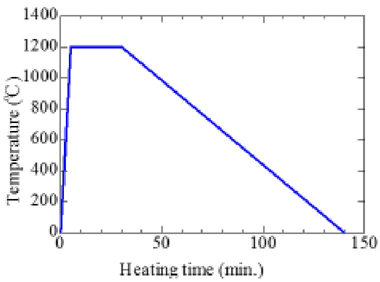

Figure 6. RABT 30 heating curve.

4 RESULTS AND DISCUSSION

4.1 Heating test

Figure 7 shows specimen internal temperatures. Explosive spalling was seen between four and ten minutes of heating time. The values measured at points 5 and 10 mm from the heated surface were 350 and 150 ℃, respectively, at five minutes, and the depth of spalling was up to 10 mm from the heated surface at this time.

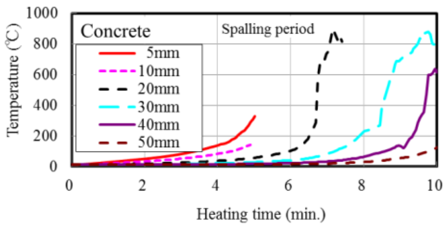

Figure 7. Internal temperatures.

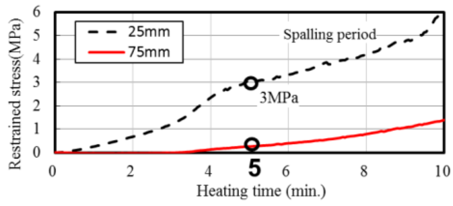

Figure 8. Restrained stress.

4.2 Restrained stress

Figure 8 shows the results of restrained stress calculation based on ring strain at a point 25 mm from the heated surface. After five minutes of heating, the value reached 3 MPa at this point. Distribution of restrained stress was estimated using Equation (6). Restrained stress itself was calculated using an experimental value at a point 25 mm from the heated surface, and was assumed to be in proportion to the temperature increment. Figure 9 shows the results for distribution of restrained stress at three and five minutes. After five minutes of heating, restrained stress 5 mm from the heated surface was about 30 MPa.

$$\sigma_{x,y}(z) = \sigma_{x,y-25} \cdot \frac{\Delta T_c(z)}{\Delta T_{c-25}} \tag{6}$$

$\sigma_{x,y}(z)$	:Restrained stress in the z direction	$\sigma_{x,y-25}$	:Restrained stress 25 mm from the heated surface
$\Delta T_c(z)$	:Temperature increment	ΔT_{c-25}	:Temperature increment 25 mm from the heated surface

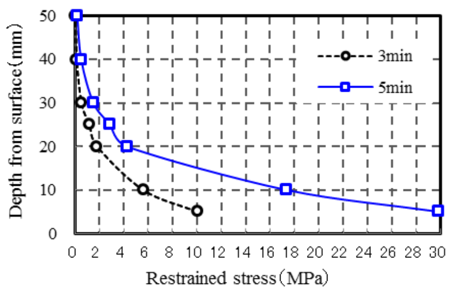

Figure 9. Distribution of restrained stresss.

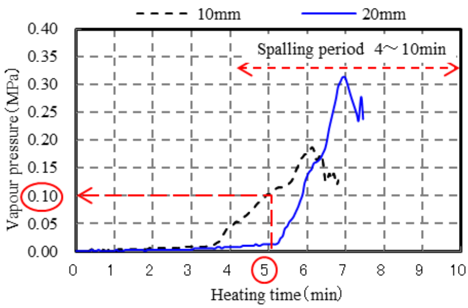

Figure 10. Vapor pressure.

4.3 Vapor pressure

Figure 10 shows a time history of vapor pressure at points 10 and 20 mm from the heated surface at ten minutes. The value started to increase at 100 ℃ and reached 0.1 MPa at a point 10 mm from the heated surface at five minutes, then reached 0.3 MPa at a point 20 mm from the heated surface at seven minutes. When explosive spalling occurred, vapor pressure had built to 0.1 and 0.3 MPa at points 10 and 20 mm from the heated surface, respectively.

4.4 Spalling depth and heating time

Figure 11 shows results for the depth of spalling after the heating test. The maximum value was about 70 mm, and the depth at the center part was greater than that at the outer part. The specimens were severely damaged. Figure 12 shows the relationship between spalling depth and time during the heating test. Spalling began approximately four minutes after heating was started, and the spalling rate was about 10 mm/min. Spalling ended at seven minutes at a depth of 70 mm.

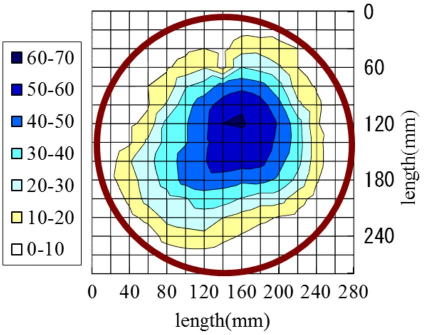

Figure 11. Spalling depth.

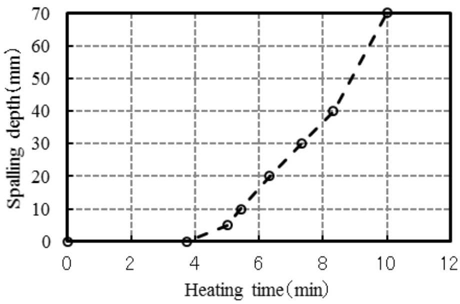

Figure 12. Spalling depth and time.

4.5 Strain failure model verification

In this work, a strain failure model of explosive spalling was verified. The relationship between the ratio of residual elastic modulus and temperature was used in the AIJ model [8] as shown in Figure 13. The residual Poisson's ratio of concrete upon heating was 0.2 [9], and the ultimate strain upon tensile failure ranged from 200 to 500 μ [10]. The spalling depth was estimated using eqs. (3) to (6). It was assumed that spalling occurred if the index of the strain failure model in Eq. (6) exceeded 1.0. Figure 14 shows spalling depth comparison with experimental and estimation values. It can be seen that the maximum spalling depth was estimated to be about 40 mm at nine minutes. These outcomes clearly indicate that the proposed model can be used to estimate spalling depth up to nine minutes from the start of heating. In this study, the range from 200 to 500 μ for the ultimate strain upon tensile failure had no influence on spalling depth estimation.

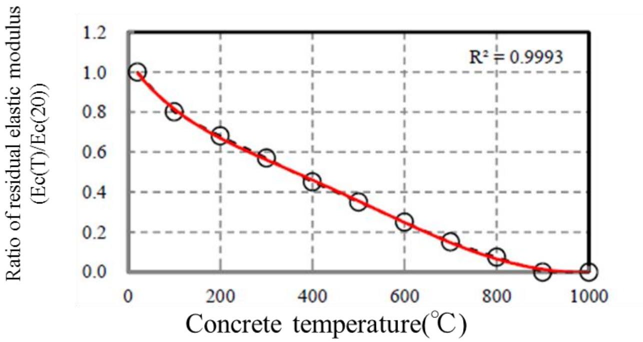

Figure 13. Ratio of residual elastic modulus and temperature.

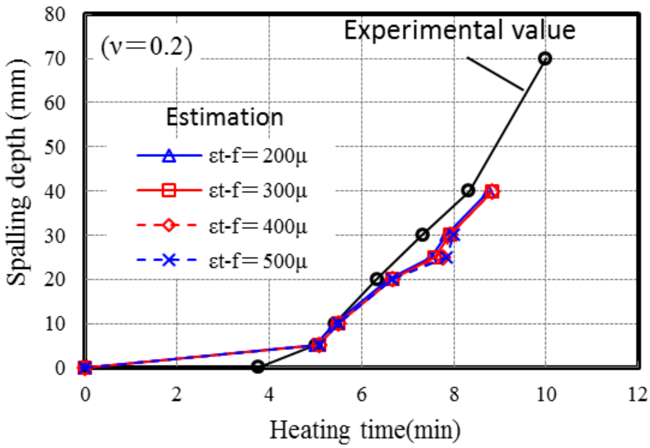

Figure 14. Spalling depth (Experiment. vs. Estimation).

5 CONCLUSIONS

The results obtained from the study can be summarized as follows:

(1) The proposed method involving the restraint of concrete with steel rings in heat testing can be used to clarify characteristics of thermal stress and explosive spalling behavior.

(2) The proposed spalling failure model based on a strain failure model was found to support estimation of spalling depth up to nine minutes from the start of heating.

ACKNOWLEDGEMENTS

This study was supported by a Grant-in-Aid for Scientific Research C (General) from the Japan Society for the Promotion of Science 2013 No. 25420459 (Head: Dr. M. Ozawa) and Japan's Kajima Foundation 2013. The authors would like to express their gratitude to the organization for its financial support.

REFERENCES

[1] Ulm F.J., Coussy O., Bazant Z.P., "The Chunnel Fire. II Analysis of concrete damage", *Journal of Engineering Mechanics*. 125, 283-289,1999.

[2] Anderberg Y., "Spalling phenomena in HPC and OC", *Proceedings of the International Workshop on Fire Performance of High-Strength Concret*e, Phan, L. T., Carino, N.J., Duthinh, D., Garboczi, E. (eds.), Gaithersburg, MD: NIST, 69-73,1997.

[3] Kalifa P., Menneteau F.D., Quenard D., "Spalling and pore pressure in HPC at high temperatures", *Cement and Concrete Research*, 30,1915-1927,2000.

[4] Phan L.T., "Pore pressure and explosive spalling in concrete", *Materials and Structures*, 41, 1623-1632, 2000.

[5] Connolly R.J., "The Spalling of Concrete in Fires", *PhD thesis submitted to Aston University*, 1995.

[6] Tanibe T. et al., "Explosive spalling behavior of restrained concrete in the event of fire", *Proceedings of the 2nd International Rilem Workshop on Concrete Spalling due to Fire Exposure*, Koender, E. A., Dehn, F. (eds.) Netherlands, Delft, 319-326,2011.

[7] Kogouchi Y., “Engineering of Ductwork”, *Mechanical Design*, Kougaku-tosho 1964.(in Japanese).

[8] Architectural Institute of Japan, “Guidebook for fire-resistive performance of structural materials”, 2009.(In Japanese).

[9] Michikoshi S., Kobayashi, H., Kuroiwa S., “Strain Behavior of Compression Concrete at High Temperature”, *AIJ Journal*, 621, 169-174, 2007. (In Japanese).

[10] Michikoshi S., Kobayashi H., Kuroiwa S., ”Compressive Strength of Confined Concrete at High Temperature”, *AIJ Journal*, 632, 143-147, 2008. (In Japanese).

8th International Conference on Structures in Fire
Guo-Qiang LI, Venkatesh K. R. KODUR, Shou-Chao JIANG, Jian JIANG, Su-Wen CHEN, Guo-Biao LOU (Eds.)
Shanghai, China, June 11-13, 2014

SHEAR CAPACITY OF CONCRETE SLABS CONTAINING VOID FORMERS

Tom Molkens*

* M.S.E. & M. Eng, StuBeCo engineering office, Hoevenstraat 155 – 3900 Overpelt, Belgium
e-mails: tom@stubeco.be

Keywords: Shear capacity, Void formers, Lattice girder, Design rule

Abstract. *Concrete slabs with void formers are widely used in Europe, and through the application in a flat slab concept (biaxial bearing capacity) the shear and torsion resistance becomes important. With the knowledge of some critical tests for hollow core slabs there is a real need for a good understanding of the phenomena which can determine the shear capacity of such slabs. At the Warrington fire test laboratory of Ghent (Belgium) a test of such a system called Airdeck was executed several years ago. By the aid of comparison between EC2-1-2 design rules, thermo-plastic calculations and the reported phenomena we propose a design rule based on the test results.*

1 INTRODUCTION

Due to life time design, durability and the demand for constructions which are easy to equip with technical installations, flat slabs have seen a real revival the last years. In Northern Europe they are often constructed by the means of a precast lattice girder slab (with integrated lower reinforcement) and an on-site compression layer with additional reinforcement. Mostly a classic passive reinforcement is used. Post tensioned reinforcement has the disadvantage that in combination with post drilled holes there is a real risk that one or more rods becomes inactive, which leads to a global effect of a local hole.

Comments in EC2-1-1 pointed out that even a less severe limitation of the deflection (mid span relative to the columns) will be sufficient, the thickness remains therefore still reasonable. However there is a penalty arising when spans become large, this in the meaning of the dead load of the slab itself. Several systems are available at that moment. One of these is the Airdeck floor slab concept, just as there also exists Bubble deck, U-boot or several similar variations with PolyStyrene (PS) blocks. Only from the Airdeck floor slab are the test results freely available, and on the other hand, a lot of studies with doubtful results are published about PS void formers [1].

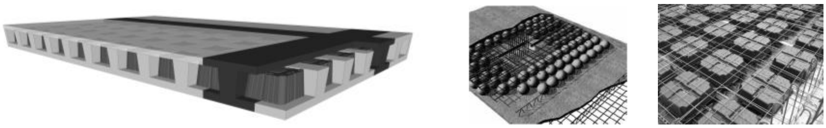

Figure 1. Floor slab with void formers (Airdeck/Bubble deck/U-boot formwork).

A more recent publication [2] showed that concrete crushing with PS void formers can occur in the lower part of the slab due to the difference in heating temperature of the concrete just below an insulation block and the concrete at the same level in the ribs in between the void formers. It seems logical to us, that there is not only an influence of the concrete cover below the void former but also from the dimension of this, relative to that of the ribs. To illustrate this wehave calculated the temperature profiles for a 300 mm×280 mm section with symmetrical boundaries and once with a central cavity of 200 mm×

180 mm containing only air or and once with a insulation material. In Figure 2 the results are shown after 120 minutes of ISO 834 fire. This simulation is made without melting of the insulation, just to show the extreme situation, reality will somewhere in between.

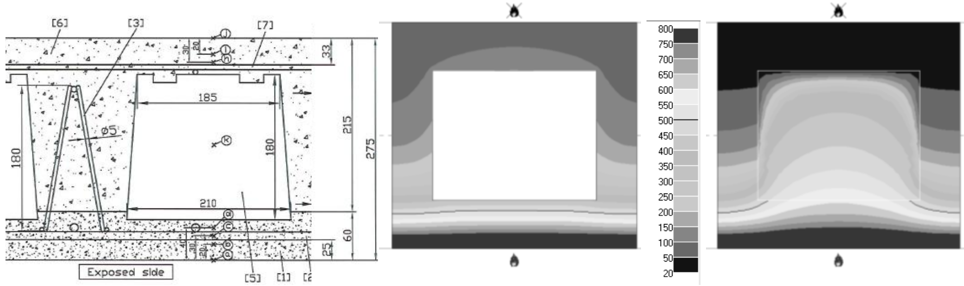

Figure 2. Temperatures after 120' Airdeck versus PS-inclusion, temperatures above 800 ℃ are not shown.

Because of the need for vents following the Italian standard UNI 9502 when polystyrene foam is used, the possibility of toxic gas (styrene), the fragility (crumbling) and the influence on the temperature profile showed above meant that we exclude this kind of void former for the article.

2 SHEAR CAPACITY AT AMBIENT TEMPERATURE

The shear capacity as described in the EC2-1-1 is mentioned for massive floor slabs or for one linear beams. From structural mechanics it is clear that the contribution of the flanges to the total shear capacity becomes important for rather "low" or compact beams where the ratio total height/flange height is limited. The concrete thickness of top and bottom layer relative to the rib dimension determine shear, torsion and punching capacity. For the Airdeck system this slenderness is about 4,2 (= 210/50).

To illustrate the differences in shear behaviour a finite element model was made of an I-beam with and without transverse ribs. A span of 7,2 m, top and bottom flange 50 mm x 300 mm wide, a web of 100mm×230mm height (+ 2 times half flange = 280 mmm total height) and a spring constant of 667 MN/m as support. With an imposed load of 10 kN/m we get the results of Figure 3.

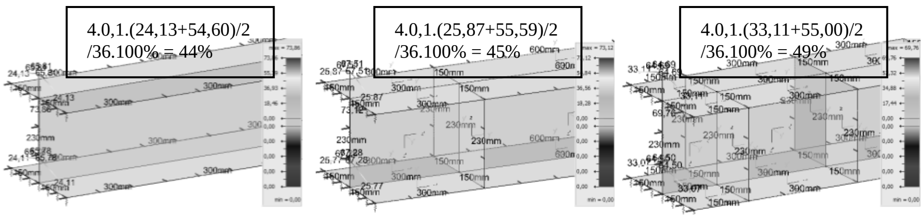

Figure 3. Reaction forces for an I-shape beam and several void lay-outs.

It is seen that for the configuration shown at the right with square voids (top view) "only" 51% of the shear will be transferred to the supports by the web. On the same way we obtain a value of 62% for a floor from 450 mm thickness. Compared with the EC2-1-1 approach, where only the capacity of the web would be taken into account, we are really underestimating the total resistance of this kind of slab. If we use for flange and web the values v_{min} from EC 2-1-1 you will arrive at almost the FEM results.

For this reason, it seems to be more appropriate to discuss the shear capacity of a slab with concrete enclosed void formers, by the aid of a reduction factor ζ applied on a unity width and not by the width of ribs b_w. By referring the shear fraction of the rib alone until the total, and multiplying this by the number of rib per unit width we obtain 0,65. On basis of geometrical parameters an approached value of 0,64 can be calculated, for the 450 mm slab this becomes 0,54 and 0,56 with the geometrical based parameter.

Here be is the horizontal dimension of the circumscribing volume with square base and h his height, the width of the rib t_{rib} in between elements and the flange thickness t_f on top and bottom (minimum value) are also involved parameters. If we regard to EC 2-1-1, shear stress due to torsion will be defined by the minimal wall thickness of an effective channel section. In that way the major influence of the flange thickness seems logic, because for this application the flange thickness is lower as the rib width.

$$\varsigma_{280} = \frac{1}{0{,}51} \cdot \frac{0{,}10}{0{,}30} = 0{,}65 \approx \varsigma_{void} = 1 - \frac{(h - 2.t_f).(b - \frac{t_{rib} + t_f}{2})^2}{h.b^2} = 0{,}64 \tag{1}$$

3 SHEAR CAPACITY IN FIRE CONDITIONS

3.1 Model following EC2-1-2

Regulations from EC2-1-2 for the shear- and torsion capacity are rather limited. Reference is made to the informative annex D and on this way to EC2-1-1 with reduced material parameters. In that way a paradox can be found; at ambient temperature the shear capacity without reinforcement is related to the compression strength to the power of 1/3rd. The loss in compression strength will be smoothed until 1200 °C and will not become zero at 600 °C like the tensile strength.

3.2 Modified proposal

It makes sense at that moment to rewrite the shear resistance under fire of an element with the tensile stress instead of the compression strength. This can be done by the aid of the relations given in Table 3.1. of EC2-1-1 so we get the following modified formula, the normal stress component is erased.

$$v_{Rd,c,void,\theta} = \left[\frac{0{,}18}{\gamma_c} . \min(1 + \sqrt{\frac{200}{d}}; 2).(\frac{A_{sl}}{b.d}.100.(\frac{f_{ctk,0,05,\theta}}{0{,}21})^{3/2})^{1/3} \right] \tag{2}$$

$$V_{Rd,c,void,fi} = \int_i v_{Rd,c,void,\theta,i} . \varsigma_{void,fi,i} . b_i . d_i \tag{3}$$

Due to the variation of the shear resistance with the temperature an integration over the height of the section must be made to arrive at the shear capacity of a section. To simplify the calculation $\zeta_{void,fi,i}$ can be presumed constant with in formula (1), the factor (h-2t_f) replaced by (h-t_f) = bottom part neglected. The temperature of the bottom shell exceeds almost completely the 500 °C isotherm.

2.0,1.(43,62+76,04)/2
/36.100% = 33%

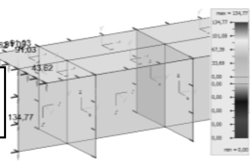

$$0{,}5 \approx \varsigma_{void,fi} = 1 - \frac{(h - t_f).(b - \frac{t_{rib} + t_f}{2})^2}{h.b^2} = 0{,}54 \tag{4}$$

Figure 4. Reaction forces for an T-shape (I without lower flange).

3.3 Interface

With the use of precast lattice girder plates, the shear resistance at the interface between precast concrete and the compression layer on site must be verified, this depends on f_{ctd} and the reinforcement crossing the interface. It will be shown that this is not the weak link for the tested constellation, as is confirmed by the results. To define the contribution of the reinforcement in fire condition we presume a reduction factor k_s = 1 valid at 400 °C, this temperature is coming out of Figure 2 above.

4 TEST RESULTS

4.1 Test set up

In 2006 the fire resistance of an Airdeck system with 275 mm total height is tested in an unidirectional way with a span of 5500 mm at the Warrington fire laboratory in Ghent [3] according to EN 1365-2 with a REI120 result (test report 12743A). The exposed length to fire was 5400 mm, the complete test specimen dimensions are 5700mm×2950mm×275mm. The top flange was limited to 45 mm thickness due to the limitations of the hoisting equipment of the laboratory. Material densities (23,15 kN/m^3 bottom shell & 22,37 kN/m^3 for the on-site concrete) and mechanical characteristics (mean strength of 84,2 N/mm^2 bottom shell and 35,5 N/mm^2 on site) are measured at the time of the test. The quantity of the second phase concrete is equal to 0,137 m^3/m^2. An equivalent superimposed load of 3,60 kN/m^2 was applied, added with two line loads at $1/4^{th}$ of the supports (4 point bending test). The shear load caused by gravity loads pro unity becomes $V_{Sd,FC}$ = 5,5/2.(0,06.23,15+0,137.22,37+3,6) = 22,15 kN/m. The bending moment is 30,45 kNm with a bending stress of about 3,29 N/mm^2 (reduced section) or regarding $f_{ctm,bottom\ shell}$ (= 4,8 N/mm^2) the concrete stays un-cracked in ambient conditions.

4.2 Measured values

The slab was fully equipped with thermo couples under + above, even in the void element and in the rib. Between 75 mm from the bottom shell to 55 mm from the top there were no measurements. Deformations are measured and in addition, visual and noise observations are also reported.

4.2.1 Temperature profile

Before the test was executed the temperature profile was simulated by the aid of Vostra software by the university of KU Leuven [4]. On basis of this information together with the profiles mentioned in the EC2-1-2 annex A, we did the stability to check the furnace for brittle fracture. In Figure 5 the calculated, EC2-1-2, EN 1168 (proposal for hollow core slabs) and measured temperature profiles are pointed out. A very good agreement can be found, except for the middle part of EN 1168 [5]. In Figure 6, left part, the mean values of 7 sections are presented at different levels.

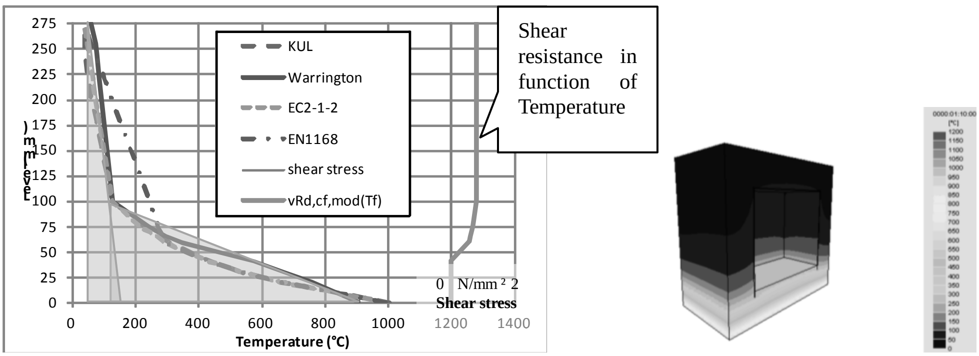

Figure 5. Temperature profile after 107', at the right image out of Vostra [4].

4.2.2 Deformation

During the test, the deflection in the middle of the floor slab was registered, positive values are towards the furnace and are showed at the right side in Figure 6. The shape of the deformation figure can be divided in 3 stages as described in [6], but we disagree about the first stage where the formation of web cracking was described. In a first stage it is bending action which dominates until about a deflection equal to one third of the slab thickness (30'). Thereafter also the membrane action become active and the growth of the deformation slows down (60’). Finally the growth rate rises again which cannot be explained at this moment.

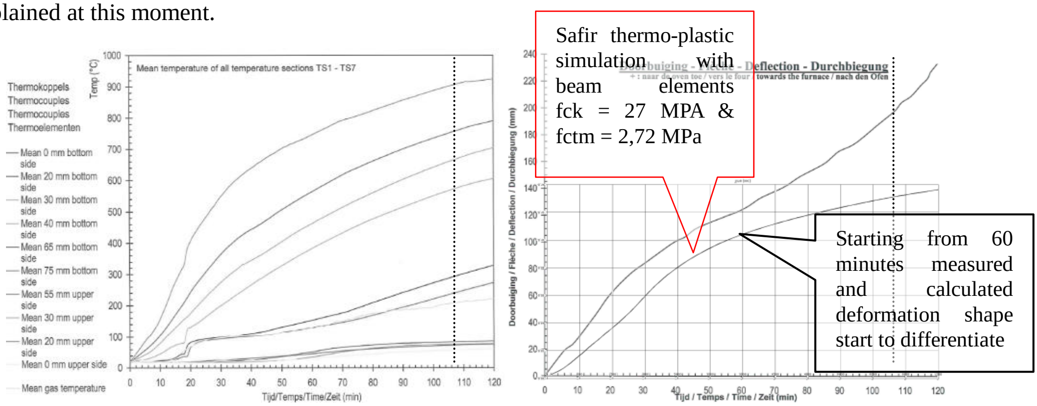

Figure 6. Measured values; at the left temperature profiles and at the right deflection in the middle.

4.2.3 Observations during the test

Besides figures, observations during the test are of a big importance to understand what happens in the different stages of the heating process. After 14 minutes slight spalling was observed, after 99 minutes the deflection amounts 183 mm or L/30, at 107 minutes a light cracking noise is heard and finally the test is stopped after 120 minutes. None of the classic tests failed like ΔT_m, ΔT_M, cotton pad, sustained flaming, deflection D=L ²/400.d, rate of deformation dD/dt=L ²/9000.d, failing with gap gauche of 6 or 25 mm. With figure 5 the 107’ noise cannot be explained. Therefore it was asked to cut the exposed slab in two parts at 900 mm of the end (800 mm from support), at that moment web cracking became visible at 100 mm from the bottom. It was believed that this phenomena was only typical for hollow core slabs.

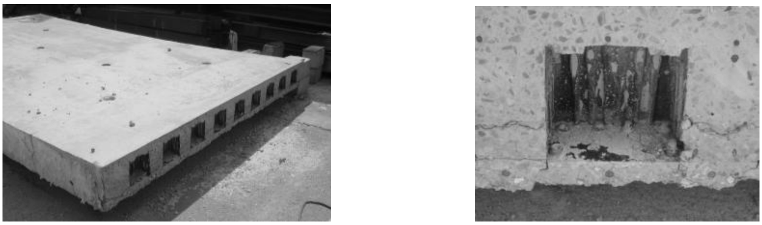

Figure 7. Cut slab after exposure and detail of web cracking.

Unfortunately it is not known if the cracks appear also in the traverse webs, at the edges of the slab we did not see those cracks. Because free thermal expansion in the middle is the most avoided it seems to us that this disconnection will be the reason for the final stage in Figure 6, right hand side.

5 VERIFICATION OF THEORETICAL MODELS BY TEST RESULTS

5.1 Ideal gas law

The temperature in the void reaches after 120’ about 215°C or 488 °K, the ideal gas law predicts at that moment a pressure of 101,3 kPa to 168,72 kPa. From figure 6 it is clear that polypropylene does not contribute to the fire, without vents an pressure of 67,42 kPA is acting on the bottom shell. Compared with tests but with insulation material [2] it can be seen that the temperature stays under 100 ℃ until 35’ and rises much more slowly as with melting insulation material. With a tensile stress of 4,8 N/mm ²only a

13 mm thick bottom part can already withstand the pressure coming from the ideal gas law without vents. Due to water vaporization the pressure could rise temporarily with even 500 kPa, we need then a 35 mm bottom part which is still no problem. For both cases, the tensile stress in the ribs is limited to 0,036 N/mm^2 or 0,26 N/mm^2; this cannot be the reason for the web cracks.

5.2 Thermal expansion

It is already explained that web cracking by hollow core sections occurs due to the difference in heating of the hot bottom shell and the cold top part. With this test result, of a slab with voids, it seems that even with a much greater shear surface and without pre-stressing, web cracking still occurs. Simply by comparing the location of the crack from Figure 6 with the temperature profile of figure 4 it seems that the crack appear where the “slope” in the temperature profile abruptly changes.

Because of the good agreement between the temperature profiles in 3D (Vostra simulation of Figure 4) and a 2-dimensional approach (Figure 2 and 8) we build up a finite element model by the aid of SAFIR [7]. This contains a slice composed of a chain for 1/3rd massive and 2/3^{rds} boxed sections. According to the literature [8] this is acceptable for this kind of slabs. However some limitations are valid; a perfect bond is assumed between concrete and steel, spalling cannot be predicted, and because the finite element deems to satisfy the Bernoulli hypothesis; shear failure cannot be detected.

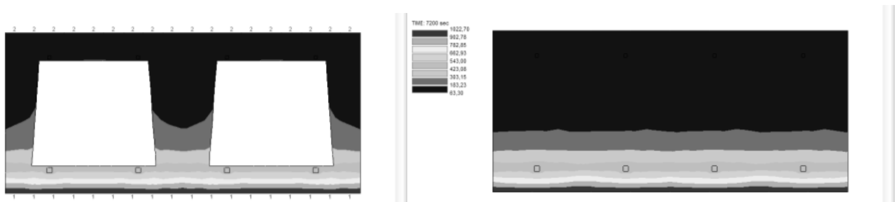

Figure 8. Safir temperature profiles of a “boxed” and massive section.

In figure 5 we have added the time-history curve of the deflections obtained by the SAFIR simulation, until about 60 minutes the difference in thermal elongation at the bottom side of the slab does not affect the slab behaviour. Up to that time the Bernoulli hypothesis seems to be adequate enough, hereafter shear failure occurs in the webs. There is no reason to believe that in the so called “stage 1” there are already web cracks appearing [6]. Thanks to the lattice girders which are spanning the crack, the sections stays more or less intact, nevertheless the stiffness is quickly decreasing. In un-cracked situation it would go from $\approx 275^3$ to 175^3+100^3 without links which is an increase with factor 3,27.

5.2 Shear capacity

From the observations during (noise) and after (saw cut) the test it seems that the shear capacity of the concrete without reinforcement is exceeded. The shear failure after 107’ pass at about 100 mm of the bottom in the web and not at the interface between precast bottom shell and the on-site concrete. Several theoretical simulations can be done to determine the shear capacity with the formulas of EC2-1-1 or the modified version as proposed with formula (2) and a reduction factor (4).

Four types of shear strength $v_{Rd,f}$ (N/mm^2) are summarized in the following table at ambient temperature and after 107’ for several levels (from the bottom). The first column gives the one obtained by EC2-1-1 with application of the appropriate ζ_{275} reduction factor on the unit width. The second one gives the shear strength at the interface without lattice girders, with these we obtained the third value. Thess values are only important at 60 mm from the bottom shell, the reason why the other values are represented between brackets. The last column was obtained by the application of formula (2) in combination with (4). Characteristic instead of design values are used to meet the experimental data. Due to almost the same shear surface in the vertical (540000 mm^2/m) and horizontal plane (533000 mm^2/m) shear resistances can be directly compared.

Table 1. Shear resistance at different temperatures and levels with uniform section temperature.

Condition (temperatures after 107' testing)	$V_{Rd,cf}$ (N/mm^2) EC2 6.2.2	$V_{Rd,if}$ (N/mm^2) EC2 6.2.5	$V_{Rd,if+LG}$ (N/mm^2) EC2 6.2.5	$V_{Rd,cf,mod}$ (N/mm^2) fck->$(fctm/0,21)^{1,5}$
Ambient & after @ ≥ 100 mm	0,633	(0,863)	(0,978)	0,663
@ 75 mm – 241 °C	0,614	(0,620)	(0,735)	0,537
@ 65 mm – 294 °C	0,600	(0,529)	(0,644)	0,496
@ 60 mm – 350 °C	0,587	0,433	0,547	0,448
@ 37 mm – 600 °C	0,485	(0,002)	(0,033)	0
@ 0 mm – 909 °C	0,269	(0,002)	(0,002)	0

Looking at the level of the interface (60 mm) in Table 1 the $v_{Rd,cf}$ according to EC 2 chapter 6.2.2. seems to be larger than the allowable shear capacity at the interface $v_{Rd,i(+LG)}$ (with or without lattice girder). Failure at the interface would be expected, which was clearly not the case during the test. On the other hand with the proposed modification of formula (1) in the last column it is shown that the shear resistance is always less than the one of the interface, which explains the crack in the web and not at the interface. This crack does not mean that there is failure for the shear mode.

By integrating the shear resistance of the last column as described in formula (3), we arrive at a shear capacity of 61,17 kN/m, which is 14 % less than with the compression strength based EC2 rule. The difference with the 22,15 kN/m from gravity laws or a factor 2,76 can be treated as a kind of a missing shear force $V_{thermal}$ = 39,02 kN/m which must be added to $V_{Sd,FC}$ to fit with experiments.

It must be well understood that due to the presence of a mechanical link in the ribs (lattice girder) the effect of passing the shear capacity of the un-cracked concrete stays limited. Starting from this point it is clear that a Bernoulli based thermo plastic deformation simulation underestimates the deformation but that the resistance, which is still the main issue, is still guaranteed.

6 PROPOSAL FOR A DESIGN RULE

Based on the left part of the Figure 5 we are wondering if the underestimation of the shear force cannot be calculated in an easier way. The main question will be if this $V_{thermal}$ will be a magnitude from the gravity shear or if it is an independent factor which is always present. A test can be imagined where an unloaded voided floor element or even hollow core slab would be tested.

A good approach, but at this moment without physical basis, can be obtained as follows, see Figure 5; extend the temperature profile of the upper part to the bottom line and integrate this surface starting from 20 °C = $M_{ambient}$. This is in proportion to the shear stress without thermal expansion factor. Secondly integrate the right part of the curve starting from the previous extended line, this sum will be in proportion due to the thermal effect = $M_{thermal}$. The magnitude factor which must be applied on the shear force at ambient temperature becomes now equal to $[M_{ambient} + M_{thermal}]/ M_{ambient}$. For our test this will become [(275.(186-20)/2)+100.(909-186)/2]/(275.(186-20)/2) = 2,58 or $V_{thermal}$ = (2,58-1).22,15 = 35,00 kN, a scatter of factor 1,11. An extra safety factor of for example 1,15 will be needed.

It would be probably more accurate to start from the force derived from the shear deformation. With reference to Figure 5 we have got a bilinear thermal profile, that which goes over the whole section will lead to a free expansion without stresses. The extra gradient in the lower part is the cause of the previously mentioned $V_{thermal}$. The value with material properties at 500 °C can be, based on theory of elasticity, estimated as = $\Delta T.\alpha_{fi,500}.E_{fi,500}/(1-\upsilon).100/2 = (909-186).5.10^{-3}.1480/(1-0,2).100/2$ = 334388 kN. This is definitely too much, so we recommend the previous approach.

Design rule for slabs with void formers:

- Magnify gravity shear force with a factor $1,15.[M_{ambient} + M_{thermal}]/ M_{ambient}$ to check if web cracking occurs, located where the slope difference in the temperature profile can be found.

- With lattice girders; if the lattice girders diagonals can withstand the tensile force between the two parts there is no risk for shear failure of the section. However deformations obtained by Bernoulli based FEM will be strongly underestimated above the 60 minutes.
- Without lattice girders (for example hollow core slab applications) it is strongly recommended to limit the shear force bellow the value of web cracking. From our test and those one on hollow cores this will be a real risk after 60' of ISO834 testing.

7 CONCLUSIONS

To avoid internal cracks in the webs a magnification of the shear force must be applied in the verification, above R60 requirements (Bernoulli no longer applies). In addition the formula for shear stress in fire condition must be related to the reduced tension stress and not the compression stress.

Thanks to the lattice girder, the upper and lower shell of the concrete slabs stay together and the shear capacity stays intact without influence on deformation or causing brittle fracture as already noticed during tests with hollow core slabs. The mechanical interlock stays secured because the crack width and the temperature at the crack level are limited.

From this investigation it seems to us a very useful recommendation to foresee a lattice girder type of reinforcement for any kind of voided slabs in fire conditions up of REI 60. A first design rule is presented to avoid this kind of brittle failure mechanism.

In particular, if slabs are pre- or post-tensioned, the compression force on the lower part leads towards a buckling phenomenon which acts together with gravity forces if disconnection of upper and lower layer occurs. Verification with tests from [5] can extend this conclusion to hollow core slabs.

REFERENCES

[1] Franchi A., "Test Results on the Fire Resistance of Precast Plates and Panels Provided with Polystyrene Void Formers", *Fire Design of Concrete Structures: What now? What next? – Proceedings of the workshop*, P.G. Gambarova, R. Felicetti, A. Meda, P. Riva (eds.), Starylink Editrice, Brescia, 281-283, 2005.

[2] Scholten P.G.R., Breunese A.J. and Both C., *Oriënterend onderzoek brandgedrag van betonnen vloersystemen met EPS gewichtsbesparende elementen*, Efectis Nederland BV, Rijswijk, 2010.

[3] Tack P. and Vandevelde R., Testreport No 12743A, Waringtonfiregent, Gent, 2007.

[4] Hens H. and De Meulenaar V., *Analyse van de temperatuurindringing in een Airdeck-vloer bij brand*, KU Leuven, Leuven, 2004.

[5] Jansze W., Van Acker A., Della Bella B., Klein-Holte R., Lindström G., Nitsch A., Py J.-P., Robert F. and Scalliet M., "Fire Resistance of Hollow Core Floors Regarding Shear and Anchoring Capacity", *Structures on Fire – Proceedings of the Seventh International Conference*, M. Fontana, A. Frangi, M. Knobloch (eds.), ETH Zurich, Zurich, 709-718, 2012.

[6] Aguado J., Espinos E., Hospitaler A., Ortega J. and Romero M. L., "Fire Resistance of Hollow Core Slabs, Influence of Reinforcement Arrangement", *Structures on Fire – Proceedings of the Seventh International Conference*, M. Fontana, A. Frangi, M. Knobloch (eds.), ETH Zurich, Zurich, 699-708, 2012.

[7] Franssen J.-M., SAFIR. A Thermal/Structural Program Modelling Structures under Fire, Engineering Journal, A.I.S.C., Vol 42, No. 3 (2005), 143-158.

[8] Min. J.-K., Somaini D., Pauli J. and Fontana M., "Numerical Analysis of the Cross-Sectional Capacity of Structural Steel Members in Fire", *Structures on Fire – Proceedings of the Sixth International Conference*, V. Kodur, J.-M. Franssen (eds.), DEStech Publications, Lancaster, 216-223, 2010.

OUT-OF-PLANE FAILURE OF RC BEARING WALLS SUBJECTED TO ONE-SIDED FIRE EXPOSURE: AN EXPERIMENTAL INVESTIGATION

Kevin A. Mueller* and Yahya C. Kurama**

*Department of Civil and Environmental Engineering and Earth Sciences
e-mail: kmuelle4@nd.edu
**University of Notre Dame, Notre Dame, Indiana, 46556, USA
e-mail: ykurama@nd.edu

Keywords: ASTM E119, Bearing walls, Buckling failure, Compartment fire, Reinforced concrete

Abstract. *This paper describes a full-scale experimental investigation on the out-of-plane thermo-mechanical behavior of two planar reinforced concrete (RC) bearing wall specimens under fire. The wall specimens were heated on one surface over half of the wall height through the ASTM E119 standard fire time-temperature curve, while simultaneously being subjected to a constant axial load at the top. The walls were fixed at the base and free to displace vertically and rotate at the top. In the out-of-plane lateral direction, the top of each wall was restrained, representing a rigid floor slab. The test results show that the out-of-plane lateral strength and stability of RC bearing walls under service-level gravity loads can be severely compromised by the unsymmetrical deterioration of concrete and reinforcing steel over the wall thickness, as well as the development of significant out-of-plane moments and shear forces from restrained thermal bowing. For the walls described in this paper, critical out-of-plane shear cracking and ultimate buckling failures were observed at fire durations significantly shorter than the durations from current prescriptive codes.*

1 INTRODUCTION

The need to develop rational performance-based design guidelines for structures under fire has been recently recognized by the engineering community in the United States[1] (U.S.). In accordance with this need, the research project described in this paper considers the importance of RC bearing walls on the service-level gravity load capacity of tall buildings and the unique challenges from compartment (one-sided) fires. Despite their large size, strength, stiffness, and thermal mass, the gravity load resistance of RC bearing walls can be severely compromised during a significant fire as follows:

(1) Fire-induced explosive spalling of concrete and degradation of steel and concrete strength and stiffness can induce out-of-plane instability under service-level tributary gravity loads.

(2) The most probable fire exposure for RC wall structures is from one side of the wall only (i.e., compartment-type fire). This leads to steep thermal gradients, and unsymmetrical fire damage and degradation of concrete (e.g., spalling) and steel across the thickness of the wall, further increasing out-of-plane eccentricity effects and compromising stability.

(3) The main design direction for RC walls in current U.S. practice is for in-plane loads only. Except for certain conditions (e.g., boundary regions in seismic regions), ACI 318[2] does not require transverse steel in the out-of-plane (i.e., thickness) direction of walls. As such, RC walls can be susceptible to out-of-plane shear failure under the shear forces that develop from restrained thermal bowing.

(4) For walls less than or equal to 254 mm thick, Section 14.3.4 of ACI 318 allows the use of a single mat of reinforcement at mid-thickness. The lack of vertical bars near the extreme unheated (i.e., back)

surface of a wall can result in critical conditions with no tension reinforcement against out-of-plane buckling during a fire (buckling occurs with the heated surface in compression as shown in this paper).

Considering these issues, the overall objective of this paper is the development of experimental evidence demonstrating the structural performance of two planar full-scale RC bearing wall specimens under fire. As allowed by Section 14.3.4 of ACI 318, a single mat of vertical and horizontal reinforcement was used at the mid-thickness of each wall. A unique aspect of the project was the development of a special skid-mounted movable gas fire furnace that allowed for one-sided, localized heating through a user-defined fire time-temperature curve (e.g., the ASTM E119[3] standard fire). During testing, the wall specimen formed one face of the furnace (i.e., the wall was not enclosed within the furnace chamber), thus allowing easier visual inspections, monitoring of behavior, and application of large gravity loads and lateral loads/restraint on the unheated surfaces of the structure.

2 EXPERIMENTAL PROGRAM

The two wall specimens discussed in this paper (Specimens 6 and 7) were tested as part of a research program that included five other full-scale walls (Specimens 1-5).[4,5] As shown in Figure 1(a), each wall had a height of 3.05 m, representing full-scale dimensions from a single story of a high-rise building. The specimen length of 1.02 m represented a planar "slice" cut out from a full-length wall. Figure 1(b) shows the cross section, reinforcement detailing, and through-thickness thermocouple measurement locations within the heated region of Specimens 6 and 7, which were 203 mm thick.

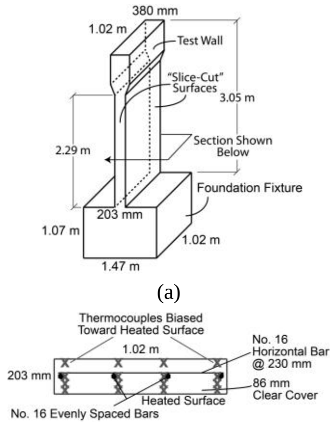

(a)
(b)
Figure 1. Specimens 6 and 7.

The reinforcement was standard ASTM A615M[6] 414 MPa steel with measured yield and ultimate strengths of approximately f_{sy}=560 and f_{su}=680 MPa, respectively, for the No. 16 bars. The concrete was calcareous with a measured compressive strength of approximately f_c'=49 MPa for Specimen 6, and 123 MPa (high-strength concrete) for Specimen 7, on the day that each wall was tested. It was not possible to measure the temperature-dependent properties of the concrete or reinforcing steel; and thus, the material properties given are for ambient conditions. Both specimens were kept indoors in a dry condition from casting until the test day at an age of 147 days for Specimen 6 and 103 days for Specimen 7. Using a moisture probe at 6 mm deep increments through the wall thickness at the mid-length, the relative humidity reached 100% within the first 6 mm of depth for both specimens.

The test setup, shown in Figure 2, included a gravity load application system, an out-of-plane lateral load/restraint application system, and a custom moveable gas fire furnace for one-sided heating.[7] The gravity system, representing tributary loading, applied a total axial force of 2400 kN at the middle of the 380 mm thick region at the top of each wall. As discussed in Mueller et al.,[4,5] the gravity application system was designed to significantly reduce second-order P-Δ effects associated with any lateral displacements of the wall at the top; however, P-δ effects associated with the local out-of-plane displacements of the wall with respect to the chord were still present. The out-of-plane lateral load/restraint system consisted of a servo-controlled hydraulic actuator connected 230 mm below the top at the mid-length of each wall. Both ends of the actuator were free to rotate, resulting in essentially no rotational or axial restraint to the wall at the top. The base of each test specimen was

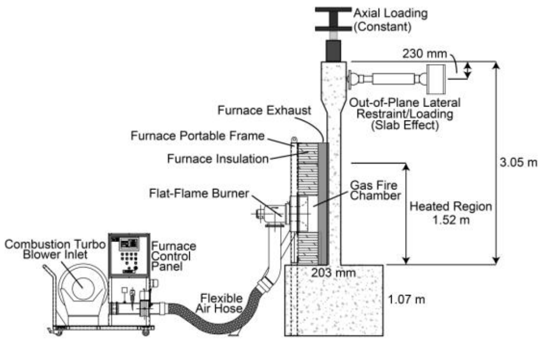

Figure 2. Laboratory test setup.

monolithically supported by a 1.07 m tall and 1.47 m wide foundation fixture that was tied to the strong floor of the laboratory. The gas fire furnace was designed to allow the application of the ASTM E119 standard fire time-temperature (t-T) curve inside a heating chamber that was 1.02 m long, 1.52 m high, and 460 mm deep. The fire load was applied from the top of the foundation fixture over a wall height of 1.52 m. The remaining 1.52 m height of each specimen was outside the furnace but was subjected to elevated exhaust temperatures from an opening at the top of the furnace.

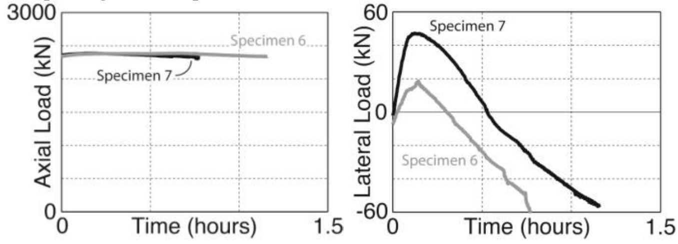

(a) (b)

Figure 3. Applied forces: (a) axial forces; (b) lateral forces.

The axial load was applied to the structure at room temperature, followed by the application of out-of-plane lateral load or restraint. The fire was then started and followed the ASTM E119 standard time-temperature curve until the specimen failed or the test was deemed complete. In Specimens 6 and 7, the out-of-plane lateral displacement of the wall at the actuator location was restrained throughout the fire loading (i.e., the lateral actuator was operated under displacement control to result in no or negligible out-of-plane displacement of the wall top with respect to the base). Figures 3(a) and 3(b) show the total axial load (positive load indicates compression in the wall) and out-of-plane lateral restraint force (positive force indicates compression in the actuator, pushing the wall towards the furnace), respectively, applied on the two walls up to failure, where time was measured from the start of fire. The total fire duration at failure was 46 and 70 minutes for Specimens 6 and 7, respectively. It can be seen that the axial load remained close to the target 2400 kN during each test. The nominal applied axial stress normalized with respect to the concrete strength, $f_c^{'}$ was 0.24 and 0.09 for Specimens 6 and 7, respectively (despite the large axial stress, the normalized stress for Specimen 7 was small because of the use of high-strength concrete).

3 THERMAL RESPONSE AND CONCRETE SPALLING

Figures 4 and 5 show the measured temperatures during the fire loading of Specimens 6 and 7, respectively. Figures 4(a) and 5(a) depict the average furnace control temperatures in each test (from six ASTM E119 thermocouples placed inside capped Inconel tubes within the furnace chamber), together with the target ASTM E119 time-temperature curve and the average temperatures from bare thermocouples placed inside the furnace chamber (these thermocouples were not inside Inconel tubes). The furnace control temperatures generally followed the ASTM E119 target reasonably well, but with some deviations because of the inability of the furnace to exactly match the steep rise in temperatures during the short fire duration in these tests. The bare thermocouples generally showed much greater fluctuations because they were directly exposed to the air temperatures inside the furnace chamber.

Figures 4(b)-(f) and 5(b)-(f) show the through-thickness internal temperatures for Specimens 6 and 7, respectively, at various fire durations. Each line in these figures depicts the temperatures measured by a discrete series of thermocouples embedded within the middle-half of the wall length over the heated height. Note that the temperatures shown on each line are not averages, but rather measurements from individual thermocouples embedded along a straight path over the wall thickness as shown in Figure 1(b) (the extreme thermocouples in each wall were embedded at about 20 mm from the heated and unheated surfaces). The reason for showing discrete temperature measurements rather than averages was because Specimens 6 and 7 experienced extensive explosive spalling starting at about 5 and 8 minutes, respectively, and continuing through the end of the fire exposure. This spalling caused the embedded thermocouples near the heated surface to become directly exposed to the furnace temperatures, but the time and extent of this exposure was different for the different thermocouple locations, thus making average measurements from multiple locations not meaningful (i.e., the temperature trends at different locations in the heated region were significantly different because of the different amounts of spalling).

It can be seen from Figures 4(b)-(f) and 5(b)-(f) that the extensive explosive spalling caused significantly higher temperatures to be measured by the exposed thermocouples as well as higher temperatures through the thickness of each wall at later fire durations. As compared with the other wall specimens tested in this project,[4,5] the greater depth of spalling in Specimens 6 and 7 was likely because of several reasons, including the lack of reinforcement near the heated surface of these walls, the increased axial compression stresses, the large amount of internal moisture (i.e., relatively young age of the walls), and the use of high-strength concrete in Specimen 7. The extent of the increased temperatures over the wall thickness in Figures 4(b-f) and 5(b-f) may give some insight into the depth of concrete spalling in each wall.

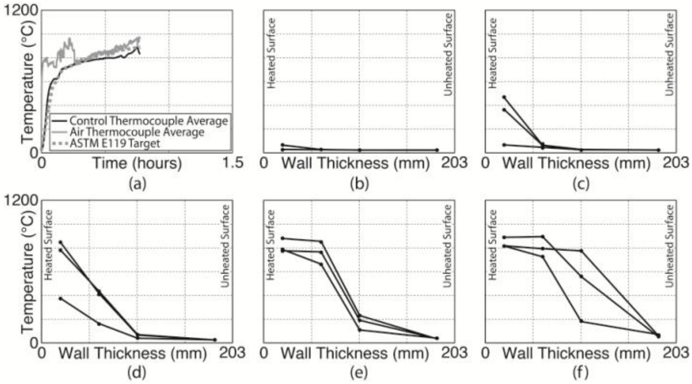

Figure 4. Measured temperatures for Specimen 6: (a) average furnace temperatures; (b-f) wall through-thickness temperatures at 10, 20, 30, 40, and 46 min, respectively.

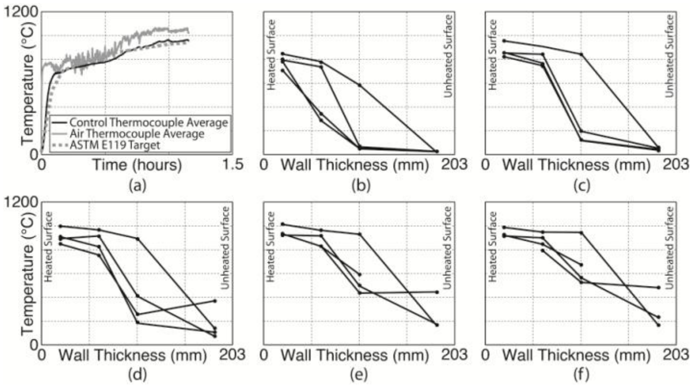

Figure 5. Measured temperatures for Specimen 7: (a) average furnace temperatures; (b-f) wall through-thickness temperatures at 30, 40, 46, 60, and 70 min, respectively.

4 STRUCTURAL RESPONSE

4.1 Out-of-Plane Lateral Displacements

Figure 6 shows the out-of-plane lateral deflected shapes of both specimens relative to the foundation block (positive displacement plotted to the left of origin indicates movement towards the furnace). The circular markers in each plot represent the displacement measurement heights at the mid-length of the wall. Note that the horizontal axes depicting the response of the two walls have been plotted to different scales to show detail in the data, and the displacements and rotations of the foundation block, albeit small, have been removed from the wall displacements. The corresponding lateral displacement time histories at various locations over the height of the walls are provided in Figure 7. It can be seen that the initial out-of-plane deflection due to the applied axial load at the top of each wall was very small, indicating that the axial load was applied essentially concentrically as intended (as stated previously, the lateral restraint at the top was applied after the axial load).

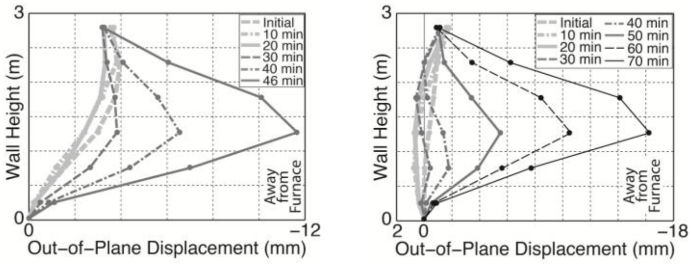

Figure 6. Out-of-plane deflected shapes: (a) Specimen 6; (b) Specimen 7.

Upon fire loading, the restrained boundary condition at the top caused Specimen 6 to undergo curvature reversals over its height. An important observation from Figures 6(a) and 7(a) is the increased away-from-furnace lateral deflection near the mid-height of the wall under increased temperatures, which occurred as the fire-induced concrete damage/spalling caused the concentric axial load at the top to become eccentric with respect to the remaining (i.e., unspalled/undamaged) "reduced" wall section. Since there was no reinforcing steel to carry the tensile stresses developing near the unheated (back) surface of the wall from the eccentric loading condition, the out-of-plane displacement at the mid-height reached its stability limit and caused catastrophic buckling failure of the wall (with the heated surface in compression) after only 46 minutes of fire exposure. The rate of the out-of-plane displacement increase was very large during the last 6 minutes of fire exposure; however, the magnitudes of the displacements were still very small for the imminent buckling failure to be visually observable. A post-test photograph of the buckled wall can be seen in Figure 8.

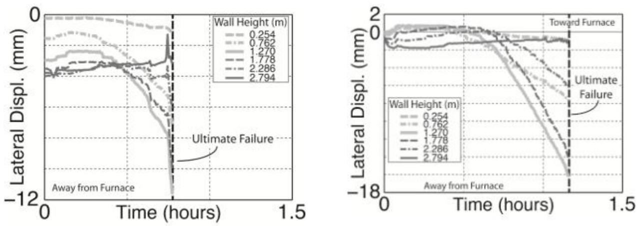

Figure 7. Out-of-plane lateral displacements: (a) Specimen 6; (b) Specimen 7.

Specimen 7 experienced a similar type of out-of-plane buckling failure. The use of high-strength concrete in this wall changed the progression and duration of spalling, resulting in smaller pieces of spalled concrete but at a greater frequency and duration than the normal-strength concrete of Specimen 6. This is possibly due to the increased density (reduced porosity) of high-strength concrete, which resulted in decreased moisture/steam transfer through the concrete. The higher concrete compressive strength of Specimen 7 allowed the wall to resist the fire for 70 minutes, about 50% longer than Specimen 6, but still far shorter than the fire resistance rating according to Table 2.1 of ACI 216.[8] Similar to Specimen 6, large out-of-plane lateral displacements developed at the mid-height of Specimen 7, which accelerated during the last 10 minutes of fire exposure [Figures 6(b) and 7(b)]. Videos of the buckling failures for Specimens 6 and 7, including the propagation of spalling in Specimen 7, can be found on the internet.[9]

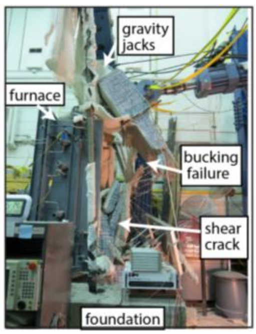

Figure 8. Out-of-plane buckling failure of Specimen 6.

A prominent through-thickness shear crack developed at the base of both Specimens 6 and 7 at early fire times due to the large out-of-plane shear force [Figure 3(b)] caused by the restrained lateral displacement boundary condition at the top of the walls. This shear crack may have accentuated the ultimate buckling failure of the walls. As an important implication for current building codes, RC walls in practice are typically not designed for out-of-plane shear forces, and according to Section 14.3.4 of ACI 318, a single mat of reinforcement can be used at the mid-thickness of walls less than or equal to 254 mm thick. These walls could fail catastrophically due to out-of-plane shear and buckling, as demonstrated in this research. While a 203 mm thick wall with double-mat reinforcement placed near the heated and unheated surfaces was not tested to directly compare with the 203 mm thick Specimens 6 and 7, the considerably better performance of the other five wall specimens[4,5] with double-mat reinforcement supports the validity of this important conclusion.

4.2 Axial Displacements

Figure 9 shows the relative axial displacements (positive displacement indicates elongation) with respect to the foundation of both specimens. The axial displacements were measured at the centerline of the wall thickness at about 1.52 m (i.e., right above the heated region) and 2.54 m (i.e., near the wall top) from the top of the foundation, and were taken as averages from sensors placed on both slice-cut surfaces (Figure 1(a)). As expected, the initial elastic shortening of the walls from the compressive axial load was greater at the top (2.54 m) than at the mid-height (1.52 m) of each specimen. The axial displacements were affected by concrete spalling. As shown in Figure 9(a), Specimen 6 essentially remained at its initial shortened position from the application of axial load for almost the entire fire duration. Immediately before the buckling failure, the wall started shortening at a rapid pace. Specimen 7 (Figure 9(b)) elongated for roughly the first 5 to 40 minutes of fire exposure, after which the wall began to shorten, especially at the mid-height measurement location. At the very end of the test, the axial shortening at both the mid-height and top of the wall increased rapidly, indicating the imminent buckling failure. The axial displacements in both tests were generally very small up until the buckling failure.

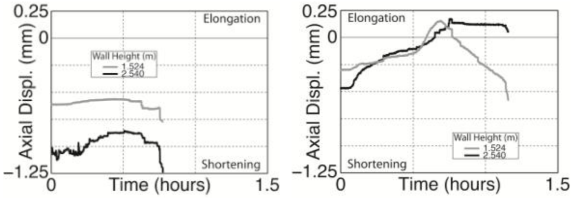

(a) (b)

Figure 9. Axial displacements: (a) Specimen 6; (b) Specimen 7.

4.3 Out-of-Plane Rotations

Figure 10 shows the out-of-plane rotations of both specimens relative to the foundation block (positive rotation plotted to the left of the origin indicates rotation towards the furnace). The circular markers in each plot represent the rotation measurement heights with sensors placed at the mid-thickness of the wall on one of the slice-cut surfaces (Figure 1(a)). Note that the rotation measurements were not taken at regular intervals over the wall height, with no intermediate sensors between the mid-height and the top of the wall. While the available data in Fig. 10 have been connected using straight lines to help with visual comparisons, these results are not necessarily representative of the true wall rotations between the measurement locations.

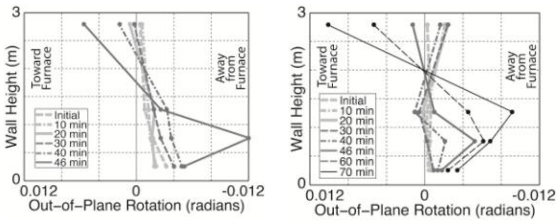

(a) (b)

Figure 10. Out-of-plane rotations: (a) Specimen 6; (b) Specimen 7.

The initial application of axial load produced small rotations in both wall specimens, indicating that the axial load was applied essentially concentrically as intended. During the first 20 minutes of fire, Specimen 6 (Figure 10(a)) remained largely at its initial position. In the subsequent duration of fire until buckling failure, the general trend was for the bottom half of the wall to rotate away from the furnace while the top rotated towards the furnace, which is consistent with the out-of-plane deflected shapes shown in Fig. 6. This trend was especially significant during the final 6 minutes of fire. For Specimen 7

(Figure 10(b)), the rotations during the initial application of fire were more consistent with restrained thermal expansion, with the bottom half of the wall rotating towards the furnace while the top rotated away from the furnace. In the later stages of the fire, the bottom of the wall started to rotate away from the furnace and the top started to rotate towards the furnace, indicating imminent buckling failure due to the eccentric axial loading condition from extensive one-sided spalling and material deterioration.

5 CURRENT CODE DEFICIENCIES

Current building design codes in the U.S. are based on prescriptive relative fire resistance ratings for the individual components of a structure. For example, the International Building Code[10] requires a standard fire resistance rating of 2 to 3 hours (depending on the structure height) for exterior and interior RC bearing walls. ASTM E119 defines the fire resistance rating as the time it takes for the temperature of the unheated surface of a wall to increase by 139 °C relative to its initial temperature prior to fire exposure, rather than by the structural strength or stability of the wall. Based on this criterion and according to Table 2.1 of ACI 216.1, Specimens 6 and 7 would have an estimated fire resistance rating of over 4 hours. While Eurocode 2[11] considers the applied axial load for bearing walls and distinguishes between one-sided and two-sided fires, the estimated fire resistance rating of the specimens based on Table 5.4 of Eurocode 2 would be between 3 and 4 hours, depending on the axial load level. Both of these standard documents grossly overestimate the measured strength/stability-based fire resistance of Specimens 6 and 7 (0.77 and 1.2 hours, respectively), which were designed in compliance with current ACI 318 building code requirements. This unconservative representation of the fire resistance of RC bearing walls can have detrimental effects on the egress time and overall life safety of building structures subjected to extreme fires. The experimental results described in this paper can ultimately be used for the development of rational load-based design methods for fire-exposed walls.

6 SUMMARY AND CONCLUSIONS

The measured behaviors of two full-scale load bearing RC wall test specimens exposed to one-sided fire were documented in this paper. RC bearing walls can be very robust structures with the potential to withstand long periods of time under elevated temperatures. However, consideration must be given to the wall thickness and reinforcement design, which govern the structural behavior under fire. The following conclusions can be drawn from the research:

(1) Restrained thermal bowing of RC walls exposed to one-sided fire results in the development of substantial out-of-plane lateral forces and prominent through-thickness shear cracking in the early stages of the fire. Walls with out-of-plane transverse reinforcement may be able to better control the size of these shear cracks.

(2) Unsymmetrical effects of one-sided fire also cause the concrete and steel strength and stiffness near the heated surface to quickly deteriorate (including concrete spalling), leading to an eccentric axial loading condition on the wall. This coupled effect can ultimately result in the out-of-plane buckling of bearing walls under service-level gravity loads, with the heated surface of the wall in compression and the unheated surface in tension.

(3) Walls that do not include an adequate amount of vertical reinforcement near each surface [as allowed by Section 14.3.4 of ACI 318 for walls less than or equal to 254 mm thick] are especially susceptible to out-of-plane buckling failure under one-sided fire exposure, because there is no steel to carry the tensile stresses that develop near the unheated surface. This catastrophic failure can occur at fire durations far shorter than the fire resistance rating according to Table 2.1 of ACI 216. Thus, an update to the ACI 318 design requirements for bearing walls is recommended to specify the use of two mats of reinforcement (one near each surface), regardless of the wall thickness.

ACKNOWLEDGEMENTS

This project at the University of Notre Dame was funded by the National Science Foundation (NSF) under Grant No. CMMI 0800356. The support of the NSF Program Directors Dr. K.I. Mehta and Dr. M.P. Singh is gratefully acknowledged. In addition, the authors recognize the technical support provided by Dr. T.D. Lin, President of Lintek International, Inc. The following engineers contributed RC building wall design details to the research and their help is gratefully acknowledged: Thomas A. Sabol – Englekirk and Sabol; Paul J. Brienen – PCS Structural Solutions; Brian G. Morgen – Magnusson Klemencic Associates; Michael G. Allen and James O. Malley – Degenkolb Engineers; and Rashid Ahmad – Walker Parking Consultants. The authors are also grateful to StresCore Inc., South Bend, Indiana, for allowing the casting of select wall specimens and other test components at their facility. The furnace used in this project was designed and constructed by Fives North American Combustion, Inc. under the supervision of James Jaworski and Timothy A. Adler. The opinions, findings, and conclusions expressed in the paper are those of the authors and do not necessarily reflect the views of the NSF or the individuals/organizations acknowledged.

REFERENCES

[1] NIST, "Final Report on the Collapse of the World Trade Center Towers," National Institute of Standards and Technology, Gaithersburg, MD, 2005, 298 pp.

[2] ACI Committee 318, "Building Code Requirements for Structural Concrete (ACI 318-11) and Commentary," *American Concrete Institute*, Farmington Hills, MI, 2011.

[3] ASTM E119-12, "Standard Test Methods for Fire Tests of Building Construction and Materials," ASTM International, West Conshohocken, PA, 2012, 36 pp.

[4] Mueller, K., Kurama, Y., McGinnis, M., "Out-of-Plane Behavior of Two RC Bearing Walls under Fire: A Full-Scale Experimental Investigation," *ACI Structural J.*, 2014. (in print)

[5] Mueller, K., Kurama, Y., "Out-of-Plane Behavior and Stability of Five Planar RC Bearing Wall Specimens under Fire," *ACI Structural J.*, 2014. (in review)

[6] ASTM A615/A615M-12, "Standard Specification for Deformed and Plain Carbon-Steel Bars for Concrete Reinforcement," ASTM International, West Conshohocken, PA, 2012, 6 pp.

[7] Mueller, K., Kurama, Y., McGinnis, M., Lisk, M., "Design and Performance of a Skid-Mounted Portable Compartment Fire Gas Furnace and Monitoring System," *Proceedings of the Third International Workshop on Concrete Spalling due to Fire Exposure*, Paris, September 2013.

[8] Joint ACI/TMS Committee 216, "Code Requirements for Determining Fire Resistance of Concrete and Masonry Construction Assemblies (ACI 216.1-07/TMS-216-07)," American Concrete Institute, Farmington Hills, MI, 2007, 28 pp.

[9] Mueller, K., Kurama, Y., McGinnis, M., "Buckling of a Concentrically Loaded RC Bearing Wall under Fire Exposure," Videos, http://www3.nd.edu/~concrete/Fire/RC-BearingWalls/, 2013.

[10] ICC, "International Building Code," International Code Council, Falls Church, VA, 2012, 722 pp.

[11] Eurocode 2, "Design of Concrete Structures. Part 1.2: General Rules-Structural Fire Design (EN1992-1-2)," *Commission of European Communities*, Brussels, 2004.

8th International Conference on Structures in Fire
Guo-Qiang LI, Venkatesh K. R. KODUR, Shou-Chao JIANG, Jian JIANG, Su-Wen CHEN, Guo-Biao LOU (Eds.)
Shanghai, China, June 11-13, 2014

POST-FIRE RESIDUAL CAPACITY OF PROTECTED AND UNPROTECTED CONCRETE FILLED STEEL HOLLOW COLUMNS

David I. Rush*, Luke A. Bisby* and Allan Jowsey**

* BRE Centre for Fire Safety Engineering, School of Engineering, University of Edinburgh, UK
e-mails: d.rush@ed.ac.uk, luke.bisby@ed.ac.uk

** International Paint Ltd., Gateshead, UK
e-mail: allan.jowsey@akzonobel.com

Keywords: Concrete filled steel hollow sections, CFS, Post-fire residual strength, Intumescent coatings

Abstract. *Concrete filled steel hollow structural (CFS) sections are an increasingly popular means to support large compressive loads in buildings. Whilst the response of unprotected CFS sections during a fire is reasonably well researched, their post-fire residual structural performance is less well established. The results of 19 post-fire residual eccentric axial compression tests on unprotected and protected CFS columns is presented, along with six unheated control tests. The tests confirm that as the maximum exposed temperature within the cross-section increases, the residual strength capacity, ductility and axial-flexural stiffness decrease. The data presented herein can be used to assess the ability to predict the residual capacity of CFS columns after fires using available post-fire structural and material models.*

1 INTRODUCTION

Concrete filled steel hollow structural sections (CFS) are hollow steel sections in-filled with plain or reinforced concrete to provide superior load carrying capacity and structural fire resistance as compared with unfilled steel tubes. CFS sections are an attractive, efficient, and sustainable means by which to carry large compressive loads in multi-storey buildings. The concrete infill and the steel tube work together at ambient temperatures, during a fire, and after a fire; the steel tube acts as stay-in-place formwork during casting of the concrete, thus reducing forming and stripping costs, and provides a smooth, rugged, architectural surface finish. The concrete infill enhances the tube's resistance to local buckling, and is further confined by the steel tube, thus slightly increasing the load bearing capacity of the concrete.

Whilst structural fire resistance design guidance is available [1] for CFS columns, after a fire when a building may have not experienced a major structural failure, a question arises as to the level of damage that may have been sustained and whether (and also how) the building can be safely repaired. Relatively little work is available on the post-fire residual strength of fire-exposed CFS columns.

This paper presents tests on the post-fire residual compressive load bearing and lateral deformation capacity of 19 CFS columns after being exposed to fire (notably, in an unloaded condition) and cooled to ambient temperature prior to structural testing to failure; six unheated control columns are also tested.

2 BACKGROUND

Han and colleagues have previously presented tests and analysis of CFS columns after fire exposure, including post-fire material models for prediction CFS columns' capacity [2] and more than 20 post-fire residual tests [2, 3] on both protected and unprotected CFS columns. Han's work considers only the ISO 834 fire curve, with tests on square and circular columns ranging in length between 380 and 1200 mm and cross-section size between 80 and 133 mm. Wall thicknesses between 2.9 and 4.8 mm were considered. Han et al.'s steel tubes were filled with plain concrete ranging in strength from 35 to 72 MPa. Unprotected specimens were heated for 90 minutes whilst protected specimens were heated for 180 minutes, with two thirds of the columns loaded concentrically. Eccentrically loaded columns had initial load eccentricities of 15 to 18 mm and unsurprisingly failed at lower loads than identical concentrically loaded columns.

Han et al.'s work demonstrated that the residual mechanical behaviour of the fire exposed columns under axial load was 'ductile,' and it was also shown that composite enhancement (i.e. confinement) of the concrete core remained present after heating [3]. The post-heated columns failed in either global buckling or local buckling, with accompanying crushing of the concrete core. The fire duration, column section size, and slenderness ratio were observed to have significant effects on the residual strength of the columns, whereas other parameters (steel ratio, concrete strength, and steel strength) had only minor effects. Unsurprisingly, loss of strength was considerably less for protected sections [4]. Interestingly, it was noted that load eccentricity appeared to be important for the *residual strength index* of the columns.

Table 1. Testing matrix and maximum temperatures recorded in steel tube and concrete core during fire testing.

Test specimen[a]	Size (mm)	Wall thick. (mm)	Infill type[b]	Heating regime[c]	F.R.[d]	Temperatures (^{o}C)[e]			
						Steel	Conc. face	35 mm	Conc. cent.
S13FNN	120	**10**	**FIB**	**N**	**N/A**	**20**	**20**	**20**	**20**
S11FNN		**5**	**FIB**	**N**	**N/A**	**20**	**20**	**20**	**20**
S13FIN		10	FIB	I	N/A	991	969	893	886
S11FIN		5	FIB	I	N/A	979	930	856	841
S11FSN		*5*	*FIB*	*S*	*N/A*	*988*	*956*	*833*	*826*
S11FIC		5	FIB	I	90	314	290	281	281
S11FSC		*5*	*FIB*	*S*	*90*	*434*	*383*	*319*	*322*
C11HNN	139.7	**5**	**HSC**	**N**	**N/A**	**20**	**20**	**20**	**20**
C11FNN		**5**	**FIB**	**N**	**N/A**	**20**	**20**	**20**	**20**
C12FNN		**8**	**FIB**	**N**	**N/A**	**20**	**20**	**20**	**20**
C13FNN		**10**	**FIB**	**N**	**N/A**	**20**	**20**	**20**	**20**
C13FIN		10	FIB	I	N	1005	995	924	871
C12FIN		8	FIB	I	N	992	977	913	888
C11HIN		5	HSC	I	N	996	952	835	822
C11FIN		5	FIB	I	N	997	954	834	820
C11FSN		*5*	*FIB*	*S*	*N*	*980*	*935*	*787*	*773*
C13FIC		10	FIB	I	90	375	358	350	349
C12FIC		8	FIB	I	90	389	387	373	361
C11HIC		5	HSC	I	90	348	337	319	317
C11FIC		5	FIB	I	90	403	397	380	340
C11FSC1		*5*	*FIB*	*S*	*90*	*380*	*375*	*368*	*366*
C11FIC.14d	139.7	5	FIB	I	90	404	371	365	365
C11FIC.28d		5	FIB	I	90	470	452	435	432
C11FIC.75		5	FIB	I	75	608	542	509	514
C11FIC.120		5	FIB	I	120	620	579	568	514

[a]*Shape (where S = square and C = circular sections) – size – wall thickness – fill type – fire exposure – protection type (- special test),* [b]FIB = fibre reinforced concrete, HSC = high strength concrete, [c]I = ISO 834, S = smouldering fire, N = unheated, [d]F.R. = fire resistance design rating, [e]ave. max. temp. at TCs.

3 EXPERIMENTAL PROGRAMME

The current testing program involved eccentric axial compressive loading, to failure, of 25 CFS columns; details of the full testing program are given by Rush [5], and an overview is provided in Table 1. Nineteen of the specimens were heated for two hours (or more) prior to structural testing to assess their residual response, whilst the remaining six were used as unheated control specimens. Five parameters were assessed: (1) cross-section shape, (2) steel tube wall thickness, (3) type of infill concrete, (4) applied fire curve, and (5) presence of applied protection. Four additional tests were also performed to evaluate the impacts of (6) concrete age at the time of testing, and (7) intumescent coating thickness. Seven square (S1) and 18 circular (C1) sections were tested with various steel wall thicknesses (5, 8 or 10 mm). The steel tubes were 1400 mm in length and were made from Grade S355 steel. The tubes were filled with ready-mix high strength (70 MPa compressive strength) concrete (HSC) or fibre reinforced concrete (FIB). The FIB mix differed from the HSC mix only in that it incorporated hybrid steel and polypropylene fibre reinforcement at of 45 kg/m^3 and 2 kg/m^3, respectively. Fifteen of the columns were exposed to an ISO 834 (*I*) fire [6] and four were exposed to the Eurocode smouldering (slow-growth) fire (*S*) [7]. Eight columns were unprotected and 11 were protected with a thin film intumescent coating sold under the trade name Interchar 1120 (trade name stated only for factual accuracy).

Temperatures within the cross sections during fire exposure were recorded at two vertical sections (at approximately *L/3* and *2L/3*) using K-Type thermocouples (TCs), as shown in Figure 1. All heated columns were exposed to the fire for 120 minutes as outlined in Table 1 (except in one case where the protection was designed to give 120 minutes fire resistance and the test was continued for 180 minutes), after which point the specimens were allowed to cool within the furnace for a further two hours before the furnace doors were opened. The intumescent coating thicknesses for the protected CFS sections were prescribed using current UK guidance, with a presumed steel tube limiting temperature of 520^{o}C and required fire resistance of 90 minutes (apart from two specimens where the fire resistance was designed for 75 minutes or 120 minutes, respectively).

The details, dimensions, and material properties of the specimens outlined in Table 1 were selected to ensure that the ambient capacity of the CFS columns was less than the 2000 kN maximum load capacity of the available structural testing equipment. Full details of the fire tests are given, along with full and detailed descriptions of the effectiveness of the intumescent fire protection coating, by Rush [5]. For the current paper the key issue is the maximum temperature experienced at various locations within the column cross-sections; these are also given in Table 1.

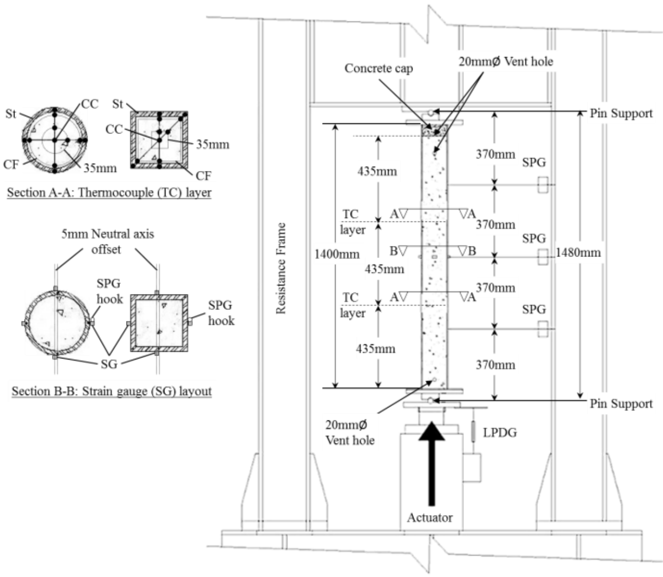

Figure 1. Schematic of tests set up and specimen details for residual capacity tests.

3.1 Test procedure

During structural testing the columns were attached to pin supported plates at either end, through which a small axial eccentricity of 5 mm was introduced to the compressive load; this also controlled the direction of lateral deflection and aided with lateral deflection measurements. The 5 mm eccentricity also agrees with design guidance for structural imperfections (effective length/300). The columns were inserted into a self-reacting structural frame, as shown in Figure 1, with an effective buckling length of 1480 mm. Bonded foil stain gauges (SGs) were installed on the steel tube evenly around the columns' perimeters at their mid-height (Section B-B in Figure 1); two in line with the pin supports and two perpendicular to the pin supports. Three string pot displacement gauges (SPGs) were attached at the columns at their quarter heights to measure lateral deformations. A linear potentiometer displacement gauge (LPDG) measured axial displacement (stroke) of the hydraulic jack used load the columns, and a pressure gauge was attached in-line with an electric hydraulic power pack to record load. Tests were manually controlled using an approximate actuator stroke rate of 2.5 to 3.5 mm/min, and were terminated when the rotation of the top or bottom plate was impeded by the plates attached to the actuator or frame.

4 RESIDUAL CAPACITY TEST RESULTS

Selected results are given in Table 2, including the: observed failure load (N_{test}); axial deflection at failure (δ_y); mid-span lateral deflection at failure (δ_{x2}); and average axial strain at mid-height at failure. Table 2 also gives the observed failure mode and the pre-failure axial stiffness of the columns, measured between applied loads of 200 and 400 kN and based on the average axial strain at mid-height.

Table 2. Observed loads, deflections, and strains at failure, failure type, and pre-failure axial stiffness for residual tests.

	Test data[a]						RSI[b]	
	N_{test}[1]	δ_y[2]	δ_{x2}[3]	ε_{ave}[4]	Failure[5]	k_{cfs} (kN/mm)[6]	N_{FNN}[7]	N_{test}/N_{FNN}
S13FNN	**1949**	**15.7**	**-8.2**	**-2393.7**	**G**	**127.1**	**1949**	**1.00**
S11FNN	**1467**	**14.4**	**-4.7**	**-2687.5**	**LB**	**103.5**	**1467**	**1.00**
S13FIN	1082	10.3	-3.7	-625.2[c]	G	113.6	1949	0.56
S11FIN	617	8.0	-3.7	-4343.9	G	90.2	1467	0.42
S11FSN	*576*	*7.7*	*-3.8*	*-1960.2*	*G*	85.3	*1467*	*0.39*
S11FIC	1243	12.9	-4.2	-1513.8	LB	107.9	1467	0.85
S11FSC	*1215*	*13.3*	*-4.9*	*-1587.3*	*LB*	97.4	*1467*	*0.83*
C13FNN	**1772**	**15.7**	**-10.0**	**-2700.4**	**G**	**137.1**	**1772**	**1.00**
C12FNN	**1664**	**14.8**	**-10.0**	**-2869.9**	**G**	**112.3**	**1664**	**1.00**
C11FNN	**1372**	**13.4**	**-8.3**	**-1760.9**	**G - LB**	**121.6**	**1372**	**1.00**
C11HNN	**1346**	**14.6**	**-10.2**	**-3051.2**	**G**	**90.8**	**1346**	**1.00**
C13FIN	1061	9.7	-3.7	-991.7	G	121.4	1772	0.60
C12FIN	813	8.6	-3.4	-1010.7	G	108.4	1664	0.49
C11FIN	583	10.3	-4.2	-3988.2	G	65.9	1372	0.42
C11HIN	591	7.4	-4.0	-1115.6	G	91.4	1346	0.44
C11FSN	*601*	*7.6*	*-5.2*	*-1566.1*	*G*	96.4	*1346*	*0.45*
C13FIC	1241	11.0	-4.8	-1213.6	G	122.6	1772	0.70
C12FIC	1285	12.8	-5.8	-2105.7	G - LB	113.6	1664	0.77
C11HIC	1192	13.4	-12.5	-3378.8	G - LB	109.1	1346	0.89
C11FIC	714	9.6	-5.8	-1536.5	LB - G	94.5	1372	0.52
C11FSC	*795*	*9.6*	*-3.9*	*-2081.2*	*LB - G*	100.4	*1372*	*0.58*
C11FIC.14d	764	8.9	-5.3	-1359.7	LB - G	104.3	1346	0.57
C11FIC.28d	741	9.2	-4.3	-1630.5	LB - G	92.0	1346	0.55
C11FIC.75	833	12.5	-13.9	-3120.9	G	96.7	1346	0.62
C11FIC.120	835	11.2	-8.9	-2498.7	G	95.2	1346	0.62

[a]Results at failure for; [1]load, [2]axial deflection, [3]mid-height lateral deflection, [4]average strain, and [5]failure mode (G = global buckling, LB = local buckling), and [6]pre-failure axial stiffness; [b]RSI = residual strength index, with[7] $N_{FNN} = N_{test}$; [c]strain gauge failure.

4.1 Overall response

As expected, elevated temperature exposure affected the observed axial failure load (N_{test}), the axial stiffness (k_{cfs}), and both axial deflections (δ_y) and lateral deflections (δ_{x2}). For instance, the axial failure loads for unheated, fire-exposed but protected, and fire-exposed and unprotected columns decreased with exposure to increasingly severe maximum temperatures. Similarly, the reduction of k_{cfs} and axial deflections at failure as exposure temperatures increased is clear. Columns failed in either global buckling (GB) or local buckling (LB). In most cases a global buckling mode occurred first and resulted in the formation of a local buckle close to column mid height, however in some cases the local buckle formed away from the column mid height (typically near the top of the column) before global buckling initiated. Comparatively lower failure loads were observed in the columns that failed due to local buckling as compared with those that initially displayed a global buckling deformed shape. Specific reasons for the different failure modes are not clear, and no obvious trends were apparent in the failure mode test data.

The *residual strength index* (defined as the ratio of the tested strength to the strength of an identical unheated column; RSI = N_{test}/N_{FNN}) shows that the fire protection reduced the loss of strength to between 10% and 40%, this being an improvement of about 30% as compared to unprotected sections. The RSI was also dependent on the size of the steel tube wall, with thicker walls retaining more strength.

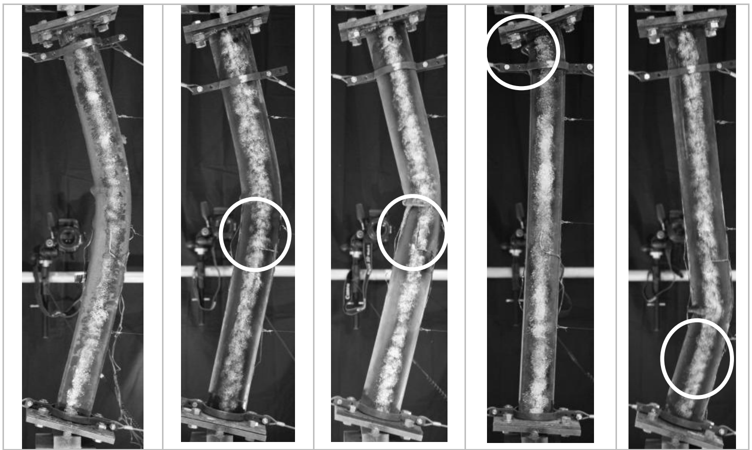

(a)	(b)	(c)	(d)	(e)
S11FIN	C11FNN	C11FIC.28d	S11FNN	C11FIC

Figure 2. Typical deflected shapes and observed failure modes: (a) global buckle; (b) global buckle with local buckling; (c) mid-height local buckle; (d) local buckle at top; and (e) local buckle at quarter height.

4.2 Failure modes

A representative selection of the various failure modes and post failure deflected shapes that were observed are shown in Figure 2. Circular sections failed either by: (1) global buckling as in Figure 2(a); (2) local buckling as in Figure 2(c); or (3) global buckling leading to local buckling of the steel tube as in Figure 2(b). Global buckling failure modes (1) and (3) were observed in all tests of circular sections apart from C11FIC, C11FSC, C11FIC.14d, and C11FIC.28d, all of which were protected, 5 mm wall thickness columns in which failure was by local buckling at approximately the third-height of the column as shown in Figure 2(e). The reason for the local buckling failures could be due to small voids being present within the concrete core as a result of the problems during the initial casting of the concrete (this is strongly suspected by the authors), or may simply be coincidental.

Local buckling was observed in square section tests S11FIC, S11FSC, and S11FNN, all with 5 mm wall thickness, in the region of required moisture venting holes near the tops of the steel tubes, as shown in Figure 2(d). This may be due to the reduced cross-sectional area of steel at this location leading to stress concentrations, initiating failure. Unprotected fire-exposed columns S11FI(/S)N and S13FIN failed in global buckling as the concrete core in these columns had a much lower residual strength. Thus, the residual axial/flexural stiffness of these columns was insufficient to prevent global buckling before the steel yielded around the vent holes. Test S13FNN could not be failed in the testing rig (limited to 2000 kN); however, a global buckling failure mode was observed to be initiating at the maximum load.

5 EFFECTS OF COLUMN PARAMETERS

5.1 Steel tube thickness

Figures 3(a), (b), and (c) show observed load versus axial and load versus lateral deflection responses for C11FI(/N)x (5 mm steel thickness), C12FI(/N)x (8 mm thick), C13FI(/N)x (10 mm wall thickness) CFS sections. As the wall thickness increased the observed failure load and pre-failure axial stiffness also increased, as expected. All sections failed in global buckling apart from C11FIC, which failed in local buckling at the third height of the column. This local buckling failure mode resulted in different load-deflection and load-strain response as compared to those observed during global buckling failure. Figures 3(e) and (f) showed a similar comparison for square cross-section columns. For both shapes, columns with larger steel wall thickness generally experienced greater retention of mechanical properties after fire (other factors being equal).

5.2 Concrete infill type

Figures 3(a) and (d), show load-deflection and load-strain relationships for C11xxx columns filled with either FIB or HSC infill, respectively. The effect of the type of concrete infill had no obvious effect on the load deflection relationships for CFS columns. The only significant change in response is seen by comparing C11FIC and C11HIC, where load versus deflection was markedly different; however this is thought to be due to the different failure modes experienced by C11FIC and C11HIC; these being local buckling failure and global buckling failure, respectively (the reasons for which remain unknown).

5.3 Concrete age and protection thickness

Figure 3(g) shows the load-deflection response for the two specimens that were exposed to fire after 14 days (C11FIC.14d) and 28 days (C11FIC.28d) after concrete casting, to evaluate the impact of the age of the infill concrete (primarily on the thermal response and the effectiveness of the intumescent fire protection during furnace testing). The load-deflection for these two columns were similar to those observed for C11FIC (see Figure 3(a)) since all three columns experienced local buckling failure modes at their third height. Due to the presence of local buckling of the column, other generalizations are difficult to make.

Figure 3(g) also shows the load-deflection response for the two specimens that had dry film thicknesses (DFTs) designed and applied on the basis of required fire resistance times of 75 minutes (C11FIC.75) and 120 minutes (C11FIC.120), respectively. Both of these columns failed in global buckling and achieved similar maximum temperatures throughout their cross-sections. Thus, similar load-deflection and load-strain relationships were observed. A similar response was seen for C11HIC (see Figure 3(d)), which had a DFT designed for 90 minutes fire resistance and also failed by global buckling, however lower temperatures were experienced in C11HIC, and it was stiffer and retained more strength.

5.4 Thermal insult

Figures 3(a) and (e) show the load-deflection response for the C11FSx and S11FSx sections exposed to the smouldering fire [7]. Similar responses were seen as compared to the identical sections exposed to the ISO 834 fire [6], with similar local buckling failure modes for the protected (xxxxxC1) sections and global buckling failure modes for the unprotected (xxxxxN) sections. No obvious differences in response were evident based on the heating curve; this is because similar maximum temperatures were experienced for both types of thermal insult, indicating that the intumescent fire protection performed similarly under both the standard [6] and slow-growth [7] heating curves.

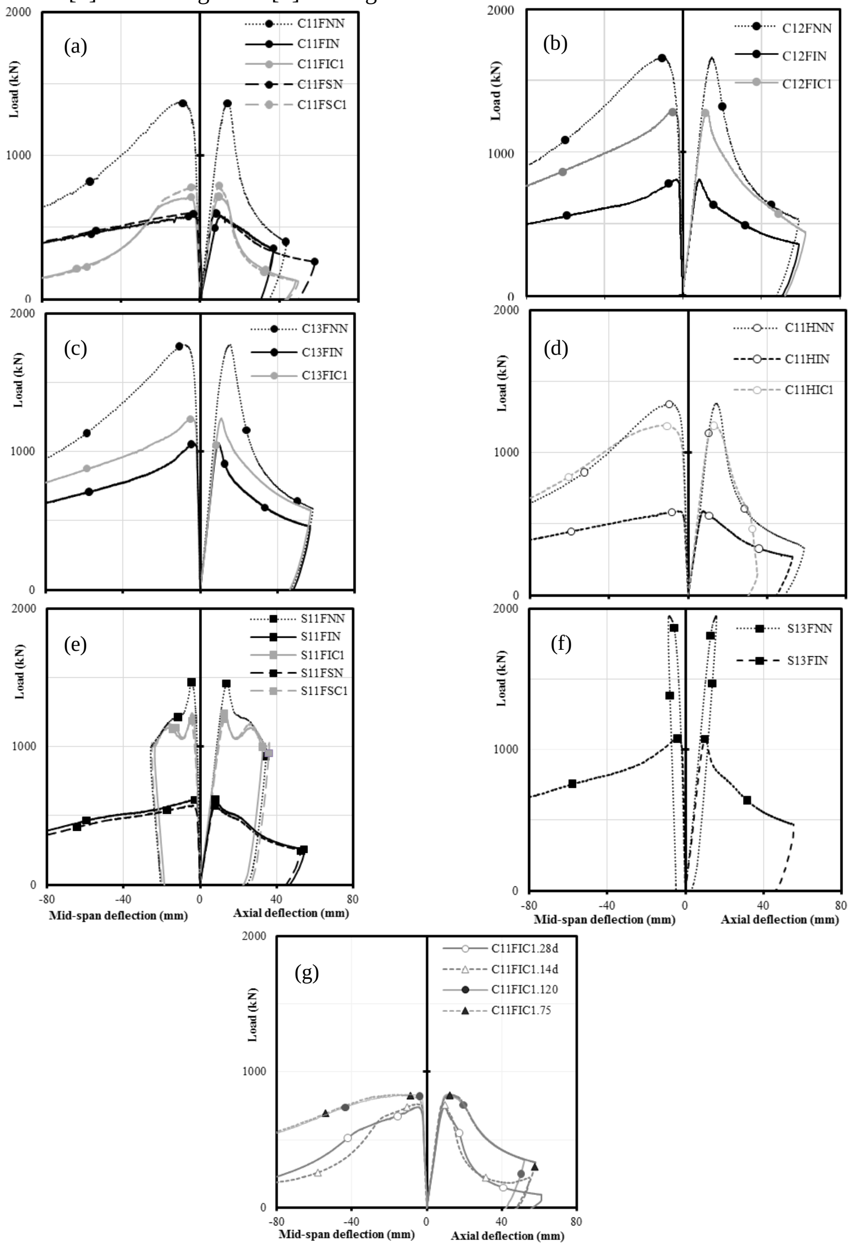

Figure 3. Load versus lateral deflections at mid-height (left), or axial deflections (right), for; (a) C11Fxx; (b) C12Fxx; (c) C13Fxx, (d) C11Hxx, (e) S11Fxx, (f) S13Fxx, and (g) C11FIC.xx columns.

5.5 Cross-section shape

Comparison of Figures 3(a) and (e) or Figures 3(c) and (f) shows the influence of cross-section shape on the load-deflection response for S1xxxx square sections as opposed to C1xxxx columns. The response of the unprotected S1xFIN sections is similar to that seen for the unprotected C1xFIN circles, with global buckling failure modes being observed in these cases. The response of the S11FNN and S11FIC sections was markedly different to any of the other columns; these square sections failed locally at the top of the columns where the cross-sectional area was reduced due to the presence of vent holes in the steel hollow sections, as already noted. Thus, cross-sectional shape appears to influence performance due to the formation of alternative failure modes and this issue should be considered in generating design guidance.

6 CONCLUSIONS

A series of 25 residual strength tests were conducted on CFS columns that had undergone different severities of heating in furnace tests due to the type of thermal insult applied or thr use of intumescent fire protection. The residual tests showed that as the temperatures within the CFS sections increased, the residual axial failure load and axial stiffness of the CFS columns decreased. This is clearly due to the reduction in strength and stiffness of both the steel and concrete due to elevated temperature exposure. It was also observed that protected columns, in which much lower maximum temperatures were experienced due to the protection from the intumescent coatings, retained up to 30% more of their ambient structural capacity compared to the unprotected columns, where the residual strength of the column was as low as 40% of the ambient capacity after 120 minutes of fire exposure. The columns failed either by global or local buckling. For the circular sections local buckling was only observed in the sections with 5 mm wall thicknesses and where the severity of the temperatures experienced in the cross-section were reduced by the presence of intumescent coatings. For the square sections local buckling was observed when the section had not been exposed to fire. The load-deflection and load-strain relationships of different CFS columns were found to be similar, depending on the failure mode experienced. The data presented herein are being used by the authors to assess the ability to predict the residual capacity of CFS columns after fires, using available post-fire structural and material models.

ACKNOWLEDGEMENTS

We gratefully acknowledge support from Arup (Fire), The Ove Arup Foundation, The Royal Academy of Engineering, the Engineering and Physical Sciences Research Council, and the School of Engineering at the University of Edinburgh, part of the Edinburgh Research Partnership in Engineering.

REFERENCES

[1] CEN, *BS EN 1994-1-1*, European Committee for Standardization, Brussels, Belgium, 2004.

[2] Han, L.H. and Huo, J.S., “Concrete filled hollow structural steel columns after exposure to ISO-834 standard fire”, *Journal of Structural Engineering*, 129(1), 68, 2003.

[3] Han, L.H., Huo, J.S. and Wang, Y.C., “Compressive and flexural behaviour of concrete filled steel tubes after exposure to standard fire”, *Journal of Constructional Steel Research*, 61(7), 882–901, 2005.

[4] Han, L.H., Yang, Y.F., Yang, H. and Huo, J.S., Residual strength of concrete-filled RHS columns after exposure to the ISO-834 standard fire. *Thin-Walled Structures*, 40(12), 991–1012, 2002.

[5] Rush, D., *Fire performance of unprotected and protected concrete filled structural hollow sections*, PhD Thesis, University of Edinburgh, 2013.

[6] ISO, *ISO 834*, International Organization for Standardization, Geneva, Switzerland, 1999.

[7] CEN. *BS EN 13381-8*, European Committee for Standardization, Brussels, Belgium, 2010.

PUNCHING SHEAR OF RESTRAINED REINFORCED CONCRETE SLABS UNDER FIRE CONDITIONS

Holly K.M. Smith, Tim J. Stratford and Luke A. Bisby

School of Engineering, The University of Edinburgh, Edinburgh, EH9 3JL, United Kingdom
e-mails: H.Smith@ed.ac.uk, Tim.Stratford@ed.ac.uk, Luke.Bisby@ed.ac.uk

Keywords: Punching Shear, Fire, Reinforced-concrete, Slabs, Experiments.

Abstract. *The punching shear resistance of reinforced concrete slabs involves material property degradation and the effects of restrained thermal expansion in both the slabs and columns, in addition to the complexities of shear mechanisms in concrete. This paper examines how the restraint of thermal expansion in the slab affects its punching shear capacity in fire. It presents a series of tests on fifteen slabs under a combination of applied load and fire, using a purpose-built restraint frame that allowed the boundary restraint actions to be controlled and monitored. The test results demonstrate that unrestrained slabs can fail very soon after the start of heating, whereas the equivalent restrained slabs survive up to two hours of heating. One of the restrained slabs failed in cooling, possibly due to tensile actions that developed due to the restraint conditions.*

1 INTRODUCTION

The shear behaviour of concrete in fire is poorly understood compared to its flexural response, and the Gretzenbach car park failure in Switzerland in 2004 prompted concerns over our lack of understanding of the punching shear response of concrete in fire. Shear in concrete at elevated temperature is dependent upon the effects of temperature on the steel and concrete properties with temperature and differential thermal expansion effects, combined with the complexities of shear behaviour of concrete at ambient temperature which in itself remains the subject of research in its own right.

There have been relatively few investigations of punching shear in fire. Tests have been conducted by Kordina [1], Annerel *et al.* [2], Salem *et al.* [3] and Ghoreishi *et al.* [4], and these have been accompanied by thermo-mechanical models by Annerel *et al.* [5] and Bamonte *et al.* [6]. A summary of prior work can be found in Ghoreishi *et al.* [4].

The shear capacity of concrete at ambient temperature is known to be affected by the presence of in-plane membrane forces [e.g.7]; punching shear capacity is improved by in-plane compression. During fire, membrane forces result from restrained thermal actions, and the above prior work has identified that premature punching shear failure could consequently result from restrained thermal action. There has not, however, been an experimental investigation into the effect of restraint conditions upon the punching shear response of a concrete slab in fire, and these effects are not included in current code provisions. This paper presents an experimental study in which the effects of restrained thermal action upon punching shear in fire were investigated.

2 Experimental programme

2.1 Test Configuration

This paper reports an experimental investigation of the punching shear performance of 1400mm×1400mm flat concrete slabs during fire. The tests were conducted in a purpose-built reaction frame that allowed investigation of the in-plane restraint upon the heated punching shear behaviour. The boundary support conditions are shown schematically in Figure 1: the concrete slabs were either restrained (fixed against in-plane expansion and edge moment), or unrestrained (allowed to expand, and free to rotate).

The test arrangement is shown in Figure 2, although much of the detail is hidden within the restraint frame that supported the four sides of the test slabs. The slabs were heated from above using a 960×990 mm array of propane gas radiant panels (enclosed within ceramic board used to insulate the test frame). Heating from above avoids possible damage to the radiant panels during failure of the concrete slab, but means that the tests were inverted, and consequently this must be borne in mind when interpreting the test results that follow.

Load was applied to a column stub cast into the centre of each slab specimens by means of a thermally-insulated pull rod and actuator placed beneath the slab.

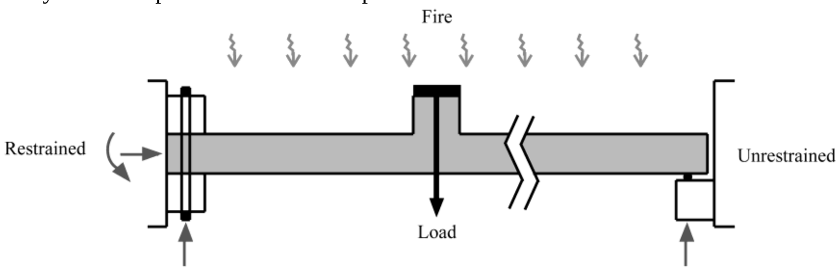

Figure 1. Schematic of test setup (showing fully restrained support arrangement on left; unrestrained support on right).

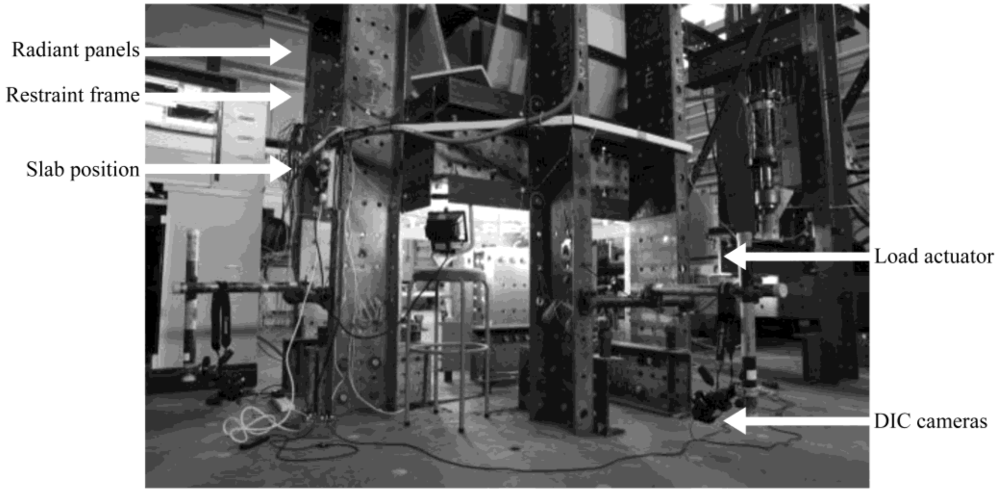

Figure 2. Heated test setup overview.

2.2 Instrumentation

Temperatures were recorded using fifteen thermocouples within each heated slab, with five thermocouples distributed through the depth of the slab at each of three positions, each placed 150 mm outside the expected punching shear perimeter of the slab.

The vertical deflection at the centre of the slab was measured using displacement transducers. In addition, digital image correlation (DIC) was used to record the slab deflection across the whole of the unheated (lower) surface. Three cameras were positioned beneath the slab (Figure 2), and a bespoke 3D algorithm (based upon the GeoPIV image correlation code [8]) was used to determine deflections from the recorded images. It has previously been demonstrated that this is an effective method of recording displacement at high temperatures without the inherent difficulties of traditional contact measurement methods [9].

As well as recording the vertical load applied to centre of the slab, the in-plane reaction force and moment (shown in Figure 1) were recorded on each of the four sides of the slab by means of strain gauges bonded to the reaction frame.

2.3 Test Specimens

The test specimens were 1400×1400mm square reinforced-concrete slabs, with a 120×120×100mm column stub cast into the centre (Figure 1). Readymix concrete was used with a maximum aggregate size of 10mm, and mean ambient compressive cylinder strength of 51 MPa at the time of testing. All the slabs were cured for at least 16 months in a dehumified environment to reduce their moisture content ; spalling of the concrete did not occur during the tests.

Table 1 lists the test specimens and the manner in which they were tested. Three types of tests were performed: ambient tests without edge restraint (AU), heated tests without edge restraint (HU), and restrained heated tests (HR). Five specimens were tested for each of these conditions. Three thicknesses of slab (50,75,100mm) with a 0.8% flexural reinforcement ratio were tested, and a further two 100mm thick slabs were tested with either no flexural reinforcement or a 1.5% flexural reinforcement ratio.

The slab reinforcement was analysed using the ambient design methods of Guandalini *et al.* [10]. Orthogonal flexural reinforcement was placed on the lower, tension face, using the bar diameters and spacing shown in Table 1. For the restrained slabs, the bars were bent back to the upper surface to ensure adequate anchorage at the edge of the slab. Ribbed reinforcing bars were used, with ambient yield strengths for the 6 mm and 8 mm steel bars of 550 MPa and 571 MPa, respectively. Two additional bars were placed in each direction on the upper surface to tie the column stub to the slab in accordance with Eurocode 2 [7]. A nominal concrete cover of 16 mm was used. Shear reinforcement was not provided.

Table 1. Test programme and geometric characteristics of the specimens.

Specimen ID	Fire Scenario	Support Type	Slab Thickness (mm)	Flexural Reinforcement Ratio (%)	Reinforcement diameter ∅ and spacing (mm)
AU50-0.8	Ambient	Unrestrained	50	0.8	6∅ at 114
*AU75-0.*8	Ambient	Unrestrained	75	0.8	6∅ at 65
AU100-0	Ambient	Unrestrained	100	0	-
AU100-0.8	Ambient	Unrestrained	100	0.8	6∅ at 42
AU100-1.5	Ambient	Unrestrained	100	1.5	8∅ at 42
HU50-0.8	Heated	Unrestrained	50	0.8	6∅ at 114
HU75-0.8	Heated	Unrestrained	75	0.8	6∅ at 65
HU100-0	Heated	Unrestrained	100	0	-
HU100-0.8	Heated	Unrestrained	100	0.8	6∅ at 42
HU100-1.5	Heated	Unrestrained	100	1.5	8∅ at 42
HR50-0.8	Heated	Restrained	50	0.8	6∅ at 114
HR75-0.8	Heated	Restrained	75	0.8	6∅ at 65
HR100-0	Heated	Restrained	100	0	-
HR100-0.8	Heated	Restrained	100	0.8	6∅ at 42
HR100-1.5	Heated	Restrained	100	1.5	8∅ at 42

2.4 Test Sequence

The ambient tests were conducted using a displacement rate of 2 mm/min to determine their ultimate capacity. These ambient tests results were first used to calibrate a capacity model using Guandalini *et al.*'s method [10] (recognising the inherent variability of the small number of ambient test results). This model was used to calculate the sustained load to be applied during the heated tests, which was taken to be 70% of the ambient capacity (in accordance with Eurocode 1-2 [11] and similar to other tests [1]). Note that the same load was applied to both the restrained and unrestrained slabs, because the punching shear capacity is not influenced by the edge restraint according to ambient design methods.

The heated slabs were loaded at a displacement rate of 2 mm/min until the required load had been reached. This load was then held constant, whilst the slabs were heated using the gas radiant panels. Heating ended either after two hours or when slab failure occurred. (Note that these tests did not attempt to follow a standard fire curve. The radiant panels applied a nominal heat flux at slab level of approximately 50 kW/m^2, and the thermocouple data will be used to calculate the thermal load during future analysis of the tests).

For the slabs that did not fail after two hours of heating, the applied load was maintained whilst the slabs cooled until temperatures dropped below 150℃ throughout their depth, and then the load was removed at a displacement rate of 2 mm/min. Residual strength tests were conducted the following day on these specimens.

3 Experimental RESULTS AND DISCUSSION

This paper presents key results from the test series in terms of load capacities, slab temperatures, and vertical deflections. Other results (such as the boundary restraint forces and further interpretation of the slab behaviour) will follow after additional analysis.

3.1 Overview of the Test Results

Table 2 summarises the key test results. For the ambient tests, it records the failure load and corresponding central displacement. For the heated tests, the table gives the sustained load that was applied during heating.

(1) The three unrestrained 100mm thick slabs (HU100-0, HU100-0.8, HU100-1.5) failed very soon after heating commenced; the recorded failure loads for these slabs are a little higher than the intended applied loads due to friction in the load application system.

(2) The most heavily reinforced of the restrained 100mm thick slabs (HR100-1.5) failed during cooling.

(3) The remaining heated slabs had not failed after 2 hours of heating. Table 2 gives the residual strengths for these slabs.

Note that gas supply limitations resulted in test HR100-0 being halted after 99 minutes of heating. Furthermore (and as shown below) the gas supply and hence applied heat flux reduced for specimen HR100-1.5, and hence this specimen was heated for 105 minutes.

3.2 Failure Mechanisms and Crack Patterns

Figure 3 shows cross-sections through four representative slabs after failure. HU50-0.8 and HU75-0.8 failed in flexure-shear mechanisms, whereas HR100-0.8 and HR100-1.5 failed in pure shear with the larger punching shear cone that is to be expected for the larger slab thickness. The combination of flexure-shear failure and lack of edge restraint means that the residual deflection of the 50 and 75mm thick slabs is far greater than the 100mm slabs, which failed in pure shear, and had rotational restraint at their edges.

A key result from these tests is that whilst all three of the 100 mm thick unrestrained specimens failed very soon after heating started (after 6, 11, or 14 mins of heating, see Table 2), none of the corresponding restrained specimens failed during heating. Restrained slab HR100-1.5, however, failed during cooling, and is likely to have been affected by the reduction in in-plane compression during cooling, which will be investigated further when the restraining force data is examined.

Table 2. Ambient and residual test results.

Specimen ID	Load Applied During Heating (kN)	Failure Load (kN)	Residual Capacity (kN)	Displacement at Failure Load (mm)	Burn Time (min)
AU50-0.8	-	**54.2**	-	**69.6**	-
AU75-0.8	-	*101.4*	-	*31.8*	-
AU100-0	-	43.8	-	18.3	-
AU100-0.8	-	226.3	-	62.4	-
AU100-1.5	-	279.7	-	38.7	-
HU50-0.8	**25.5**	-	**55.7**	**40.3**	**120**
HU75-0.8	*82.8*	-	*90.7*	*17.7*	*121*
HU100-0	30.0	38.9	-	2.2	6
HU100-0.8	174.6	174.8	-	30.8	11
HU100-1.5	234.0	237.0	-	28.5	14
HR50-0.8	**26.4**	-	**64.4**	**29.4**	**121**
HR75-0.8	*82.0*	-	*115.5*	*20.0*	*120*
HR100-0	33.1	-	82.2	28.2	99 *
HR100-0.8	166.5	-	245.1	20.7	120
HR100-1.5	232.7	233.2	-	21.2	105 **

* Test terminated prematurely (gas supply failure). ** Specimen failed during cooling phase.

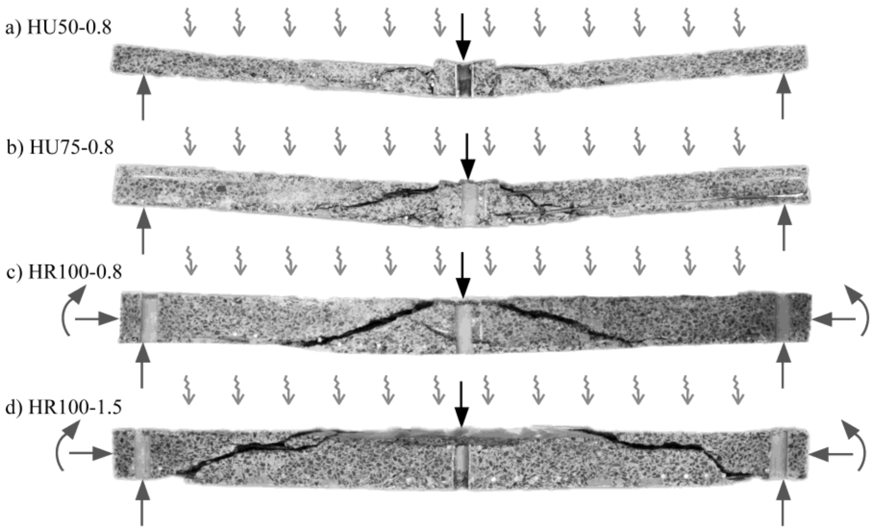

Figure 3. Cross-sections of selected slabs showing the post-failure crack patterns.

3.3 Temperature Evolution

Figure 4 shows an example of the temperature profiles recording during the tests. Temperature profiles are presented through the depth of slab HR100-1.5 at 10 minute intervals after ignition. Note that the heated surface is at the top of the plot due to the inverted test arrangement.

The maximum surface temperature reaches 484 ℃ after 75 minutes of heating. As mentioned above, it was not possible to sustain the heat flux into the slab, and consequently the heated surface of the slab started to cool after 75 minutes, even though the radiant panels were still burning. The radiant panels were turned off after 105 minutes, and the slab was left to cool (shown by the dashed profiles). The temperatures on the unheated surface of the slab reached a maximum during the cooling phase (as the heat front penetrated the slab); for example the maximum temperature in the flexural steel (77mm from the heated surface) was 148 ℃, which occurred 145 mins after ignition, or 40 mins after cooling started.

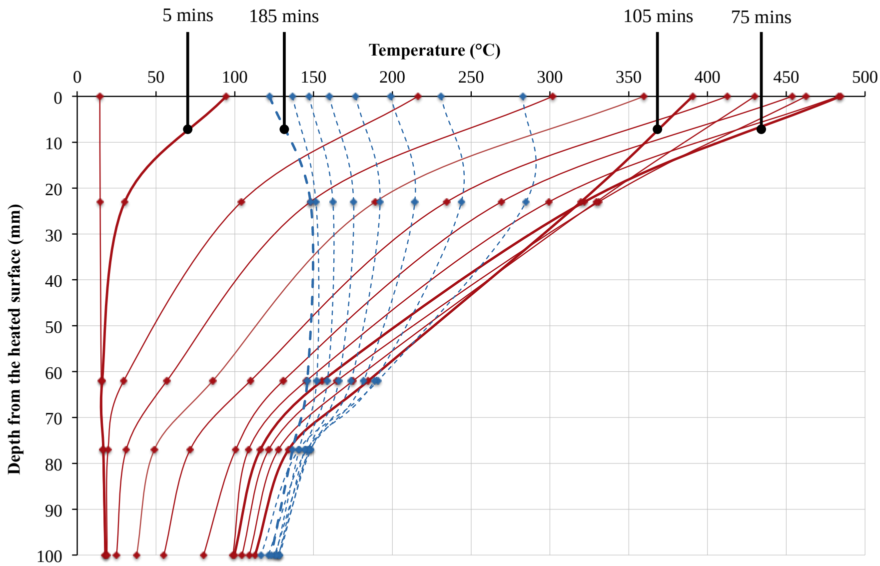

Figure 4. Temperature profiles at 10 minute intervals for specimen HR100-1.5, recorded using five thermocouples through the depth of the slab.

3.4 Vertical Displacements

Figures 5 and 6 plot the vertical displacement versus time for all of the heated tests. Figure 5 shows all of the slabs with 0.8% reinforcement ratio; Figure 6 shows all of the 100 mm thick slabs.

Zero time corresponds to the start of heating, with the negative time region corresponding to loading of the slabs prior to ignition. Positive deflection is downwards (i.e. in the direction of loading, away from the heat source, see Figure 1). The temperature of the flexural steel is also plotted for each test as a dashed line. In both plots, it can be seen that providing edge restraint significantly increases the stiffness of the slabs (as is to be expected).

Figure 6 demonstrates the influence of edge restraint condition upon punching shear capacity during a fire; the 100mm thick unrestrained slabs failed soon after the start of heating; whereas the restrained slabs withstood sustained heating without failure.

During heating it might be expected that the thermal gradient through the slabs (Figure 4) would cause thermal bowing in the opposite direction (towards the heat source), but this was not the case. In all cases, the deflection of the slabs increased in the direction of loading (away from the heat source), indicating that the degradation in concrete properties and non-linear material behaviour dominates as it is heated.

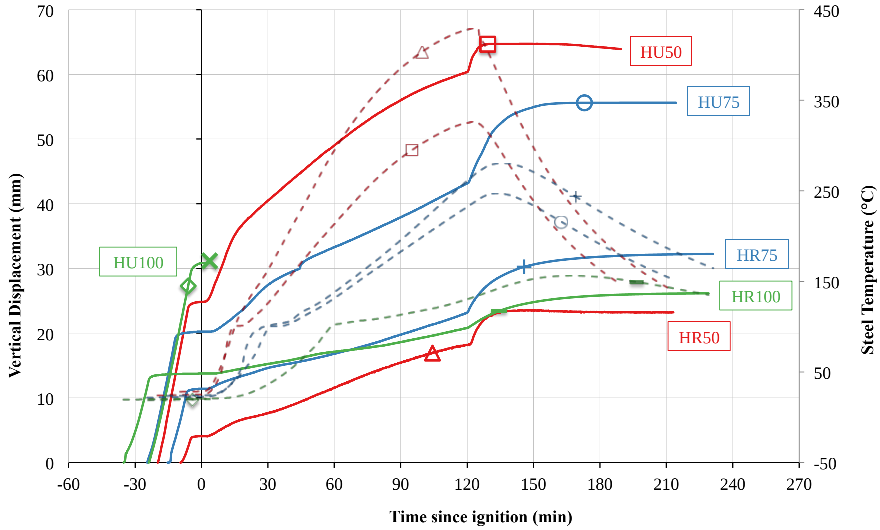

Figure 5. Vertical displacement (solid lines) and steel temperatures (dashed lines) during tests on slabs with 0.8% reinforcement ratio.

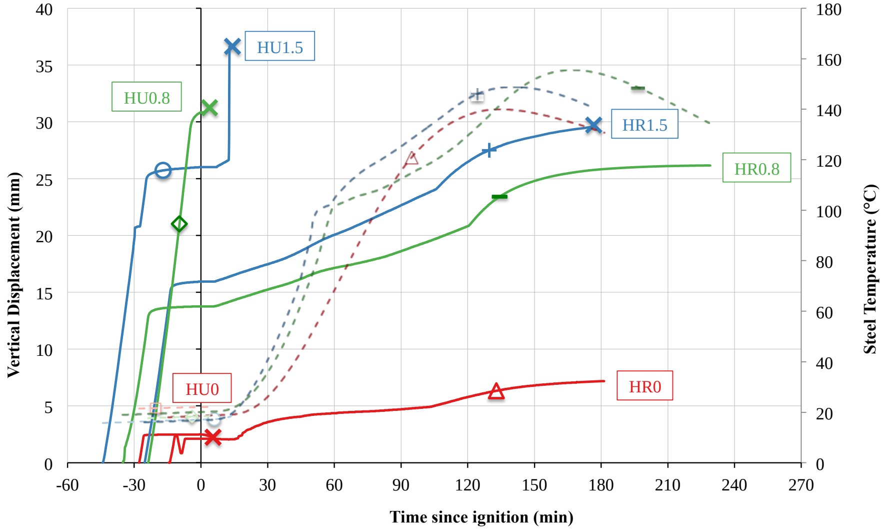

Figure 6. Vertical displacement (solid lines) and steel temperatures (dashed lines) during tests on 100mm thick slabs.

The sharp increase in deflection rate at the start of the cooling phase seen for each of the slabs is consistent with the heated surface cooling down, whilst the heat front propagates deeper into the slab (as observed during the cooling phase in Figure 4). As noted above, it was not possible to sustain the required heat flux during all of the tests, and consequently the surface temperature started to drop before the panels were turned off; this may explain why there is a less distinct change in the deflection rate for the 100mm restrained slabs in Figure 6 (such as HR100-1.5). The authors are in the process of examining the deflected shape of the slabs obtained using DIC, together with the restraint forces recorded on the reaction frame. These are expected to give additional information on the vertical deflection response of the slabs.

5 CONCLUSIONS

This paper has presented a series of tests on model reinforced concrete slabs examining the effect of boundary restraint conditions upon punching shear capacity in fire. The slabs were restrained against in-plane expansion and edge rotation using a bespoke restraint frame that allowed tests to be conducted under either fully restrained or unrestrained conditions. A comprehensive set of temperature, deflection, and restraining actions were recorded during the tests.

The results demonstrate that the restraint conditions have a dramatic effect upon the punching shear capacity of flat slabs. The 100mm thick unrestrained slabs failed very soon after the start of heating, whereas the identical restrained slabs remained intact for up to 2 hours of heating, due to the development of in-plane compression due to restrained thermal expansion. The most heavily reinforced of the 100mm thick restrained slabs failed during cooling, potentially due to tension developing within the slab due to the edge restraint; however, interpretation of the test data has yet to be completed.

REFERENCES

[1] Kordina, K., "Über das Brandverhalten punktgestützter Stahlbetonplatten" (On the Fire Behaviour of Reinforced Concrete Flat Slabs), *Deutscher Ausschuss für Stahlbeton (DAfStb)*, Berlin (Germany), Heft 479, 106 pp, 1997.

[2] Annerel, E., Lu, L., Taerwe, L. "Punching Shear Tests on Flat Concrete Slabs Exposed to Fire". *Fire Safety Journal*, 57, 83-95., 2013.

[3] Salem H., Issa H., Gheith H., Farahet A. "Punching shear strength of reinforced concrete flat slabs subjected to fire on their tension sides". *HBRC Journal*, 8(1), 36-46, 2012.

[4] Ghoreishi, M., Bagchi, A., & Sultan, M. A. "Review of the Punching Shear Behavior of Concrete Flat Slabs in Ambient and Elevated Temperature". *Journal of Structural Fire Engineering*, 4, 259–279, 2013.

[5] Annerel, E., Taerwe, L., Merci, B., Jansen, D., Bamonte, P., Felicetti, R. "Thermo-Mechanical Analysis of an Underground Car Park Structure Exposed to Fire". *Fire Safety Journal*, 57, 96-106, 2013.

[6] Bamonte, P., Fernández, M. R., Muttoni, A. "Punching Shear Strength of R/C Slabs Subjected to Fire". *7th International Conference on Structures in Fire*, Fontana, M., Frangi, A., Knobloch, M. (eds.) Zurich, Switzerland, June 6-8, 2012.

[7] Eurocode 2, *Design of concrete structures, Part 1-1: General rules and rules for buildings*, EN 1992-1-1, 2004.

[8] White D.J., Take W.A., Bolton M.D. "Soil deformation measurement using particle image velocimetry (PIV) and photogrammetry". *Geotechnique*, 53(7): 619–631, 2003.

[9] Gales, J.A., Bisby, L., & Stratford, T. "New parameters to describe high-temperature deformation of prestressing steel determined using digital image correlation". *Structural Engineering International*, 22(4), 476–486, 2012.

[10] Guandalini, S., Burdet, O., & Muttoni, A. "Punching tests of slabs with low reinforcement ratios". *ACI Structural Journal*, *106*(10), 87–95, 2009.

[11] Eurocode 2, *Design of concrete structures, Part 1-2: General rules - Structural fire design*, EN 1992-1-2, 2004.

EFFECT OF TEMPERATURE ON BOND STRENGTH BETWEEN STEEL REBAR AND GEOPOLYMER CONCRETE

Hai-Yan Zhang* and Jia Yan**

*State Key laboratory of Subtropical Architecture Science, South China University of Technology, Guangzhou, 510640, P.R. China
e-mail:583904780@qq.com
**Department of Civil Engineering, South China University of Technology, Guangzhou, 510640, P.R. China
e-mail:1161391385@qq.com

Keywords: Bond stre ngth, rRibbed bar, Geopolymer concrete, Pull-out test

Abstract. *This paper presents experimental tests on bond strength between geopolymer concrete and rebars at ambient temperature and after exposure to high temperatures. Geopolymer concrete was prepared by blending metakaolin, fly ash, potassium silicate solution, coarse and fine aggregates. Bond strength between geopolymer concrete and rebars were evaluated through pull-out tests on 21 composite specimens manufactured using geopolymer concrete and steel bar, similar to the testing methods of pull-out tests on normal concrete structure specimens. The test results showed that bond strength between geopolymer concrete and rebar increases in 25-100^{o}C range, and than decreases with the increase in temperature. Geopolymer concrete exhibits higher bond strength with smaller diameter bar than that with larger diameter bar.The addition of silicon ash can not enhance significantly the bond strength between geopolymer concrete and steel bar.*

1 INTRODUCTION

Concrete is widely used in infrastructure construction. Normal concrete is traditionally made from Portland cement, water, coarse and fine aggregates. Worldwide annual production of cement is estimated to be two billion tons and is expected to increase to 4 billion tons in 30 years [1]. The mass production of Portland cement results in the vast amount of carbon dioxide emission and energy consumption. From the view of environment protection, there is a mounting pursue for a substitution for Portland cement, with less pollution emission and lower energy consumption.

Geopolymer is a new kind of green material, which was first studied by Davidovits [2-4]. Geopolymer is manufactured through blending alkali solution and alumina-silicate source material, such as fly ash and metakaolin. Compared to Ordinary Portland Cement (OPC), the manufacture of geopolymer has the potential to reduce emissions of carbon dioxide by 80% [5]. It also exhibits ceramic-like properties with superior resistance to elevated temperatures. The properties of geopolymer concrete have been intensively studied in recent research [6–11]. These studies have indicated that geopolymer concrete has properties favourable for its potential use as a construction material. It has high compressive strength, little drying shrinkage, low creep and good resistance to acid and sulfate attacks. The bond behaviour between concrete and reinforcing steel is the key for the joint work of concrete and bars. Though research on geopolymer as a binder has been intensively conducted, the data on the bond strength between geopolymer concrete and rebars at elevated temperatures is still lacking.

This paper presents the experimental results on bond strength between geopolymer concrete with ribbed bars at ambient temperature and after exposure to elevated temperatures. Pull-out tests were conducted on 21 composite specimens prepared by geopolymer concrete with different formulation and steel bars with varied diameter. The effect of the thickness of concrete cover, diameter of reinforcing bar and exposure temperatures is quantified based on the test results.

2 EXPERIMENTAL WORKS

2.1 Materials

The primary alumino-silicate source material used in preparing specimens for property tests is metakaolin (MK) and fly ash (FA) mixture. Commercially produced metakaolin with an average particle size of 0.017 mm, was supplied by Shanxi Jinkunhengye Ltd., China, through calcified kaolin under 900℃. Low calcium fly ash, with an average particle size of 0.032 mm, was supplied by Guangzhou Huangpu Power Plant. The chemical compositions of the metakaolin and fly ash are given in Table 1.

Table 1. Chemical composition of metakaolin and fly ash (mass%).

Oxide	SiO_2	Al_2O_3	CaO	Fe_2O_3	TiO_2	K_2O	MgO	SO_3	P_2O_5	Na_2O	SrO	ZrO_2	CuO
MK	52.31	45.37	0.37	0.41	0.53	0.10	0.08	0.05	0.47	0.20		0.04	0.02
FA	50.13	38.9	3.89	2.87	1.36	0.95	0.79	0.36	0.25	0.19	0.11	0.11	0.03

Potassium silicate solution with SiO_2/K_2O molar ratios of 1.0 was used as alkaline-silicate activator. Chopped carbon fibers (CF) were added to MK-FA blend precursor as reinforcement agent. The length, diameter and density of chopped carbon fibers are 6 mm, 7 μm and 1.76-1.80 g/cm^3 respectively.

The reinforcing steel was HRB335 hot-rolled ribbed rebar, which diameter is 14 or 20 mm. Samples of steel bars were tested in the laboratory to obtain the actual ultimate strength.

2.2 Specimen preparation

A total of 21 composite specimens were manufactured for pull-out tests, using geopolymer concrete and ribbed steel bar. For each specimen, a steel bar was embedded in the middle of cubic geopolymer concrete with size of 150mm×150mm×150 mm. The embedded bar was divided into two part. One part with length of 70 mm, is bonded with geopolymer concrete directly. The other part is isolated with geopolymer concrete through a plastic sleeve. For all specimens, the length of bars bonded directly with geopolymer concrete was short enough to prevent yielding of the bar occurring before failure of bond between the bar and geopolymer concrete. The detailed geometry of the specimens is shown in Figure 1.

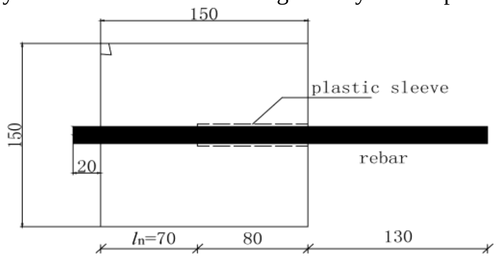

Figure 1. Diagram of specimen size.

Two types of formulations, with different proportion of metakaolin, fly ash and silicon ash, were used for preparing geopolymer concrete. The mix proportions of the two types of geopolymer concrete (Mixture 1 and Mixture 2) are listed in Table 2. The formulation for Mixture 1 of geopolymer concrete was from previous studies [7-10]. The formulation for Mixture 2 is modified on that of Mixture 1, to investigate the effect of silicon ash.

Table 2. Mixture proportions of concrete (kg/m^3).

Ingredients	Mixture 1 (YJ1-5 YJ7-11)	Mixture 2 (YJ6)
Potassium silicate solution	257	257
Potassium hydroxide	71	71
Water	74	74
Metakaolin	219	350
Fly ash	219	22
Silicon ash	0	66
Carbon fiber	0.1	0.1
Fine sand	616	616
Coarse aggregates	1434	1434

The MK-FA precursor (metakaolin, fly ash and silicon ash), chopped carbon fibers and alkaline silicate solution were first mixed for 2 min by hand and another 2 min in a batch mixer. Then the coarse aggregates and river sand were added into the blend and mixed for a further 12 min. After that, Geopolymer concrete mixture was cast into a steel mould, with size of 150mm×150mm×150mm and a steel bar passing through horizontally. Subsequently, geopolymer concrete was vibrated through a poker vibrator. Then the composite specimens were naturally cured in the labratory for 7 days .

The geopolymer concrete mixtures prepared were grouped into three sets, denoted by G1, G2 and G3 respectively, to study the effect of concrete cover (c), bar diameter (d_b) , content of silicon ash and temperature on bond strength. between geopolymer concrete and steel bar. Table 3 presents the details of these specimens.

Table 3. Details of geopolymer concrete specimens.

Group No.	Specimen No.	Bar diameter, d_b (mm)	Cover, c (mm)	c/ d_b	Number of specimens	Temperatures (^oC)	Formulation of geopolymer concrete
G1	YJ1	14	68	4.86	2	25	Mixture 1
G1	YJ2	14	68	4.86	2	100	Mixture 1
G1	YJ3	14	68	4.86	2	300	Mixture 1
G1	YJ4	14	68	4.86	2	500	Mixture 1
G1	YJ5	14	68	4.86	2	700	Mixture 1
G2	YJ6	14	68	4.86	2	25	Mixture 2
G3	YJ7	20	65	3.25	2	25	Mixture 1
G3	YJ8	20	65	3.25	2	100	Mixture 1
G3	YJ9	20	65	3.25	2	300	Mixture 1
G3	YJ10	20	65	3.25	2	500	Mixture 1
G3	YJ11	20	65	3.25	1	700	Mixture 1

2.3 Test procedure and apparatus

Specimens in group YJ2-YJ5 and YJ8-YJ11 were used for the test after exposure to elevated temperatures. After 7-day curing, these specimens were heated at a heating rate of approximately 5℃/min from room temperature to the target temperature. Once the target temperature was attained, the temperature in furnace was maintained for 60 min before the furnace was shut down. And then the specimens were allowed to cool down in the furnace to room temperature. The specimens in Group YJ1, YJ6 and YJ7 were left undisturbed at room temperature for test at ambient temperature.

A steel rig was set up to conduct the pull-out tests. The specimen was placed in the rig. The one end of the steel bar extended from the specimen was clamped by a grip device. Two high-precision displacement sensors are installed at free end of rebar and concrete surface. The top end of the steel rig was subjected to a tensile load. The specimens were tested by a universal material machine UTM5205 in accordance with the Standard for test method of concrete structures (GB/T 50152-2012). The whole loading process is controlled by displacement, loading speed is 1.2mm/min. A schematic diagram and a picture of the set- up of the tests are shown in Figure 2 and Figure 3 respectively.

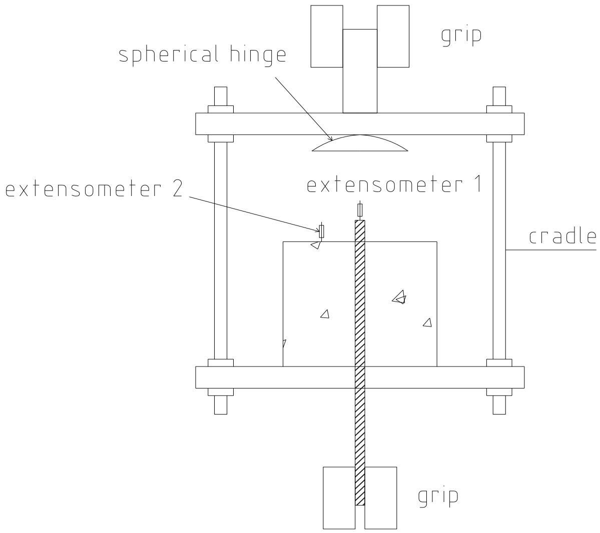

Figure 2. Test equipment sketch.

Figure 3. Picture of test set up.

3. EXPERIMENTAL RESULTS AND DISCUSSIONS

The observed failure of the specimens and the effects of test parameters, including geopolymer concrete cover, bar diamefer, and elevated temperature on bond strength between geopolymer concrete and steel bar were studied using the test results.

3.1 Failure modes of test specimens

With the exposure temperature increasing, cracks occur on the surface of geopolymer concrete. Figure 4 presents a typical photographs of a specimen after exposure to 700oC. It can be observed that several microcracks occur on the surface of geopolymer concrete, which is mainly induced by the difference in thermal expansion between geopolymer matrix and aggregates at high temperatures. It is reported that aggregates undergo expansion, but geopolymer matrix experience contraction at elevated temperatures [12].

Figure 4. Cracks in the geopolymer concrete specimens due to heating700℃.

If the steel rig is lifted up by the material machine, the steel bar in the concrete will be subjected to tensile force. When the tensile load exceeds the bond force between geopolymer concrete and steel bar, the steel bar will be pulled out from the geopolymer concrete and slip occur. All specimens failed by the pulling out of the steel bar from geopolymer, namely bond failure, as shown in Figure 5.

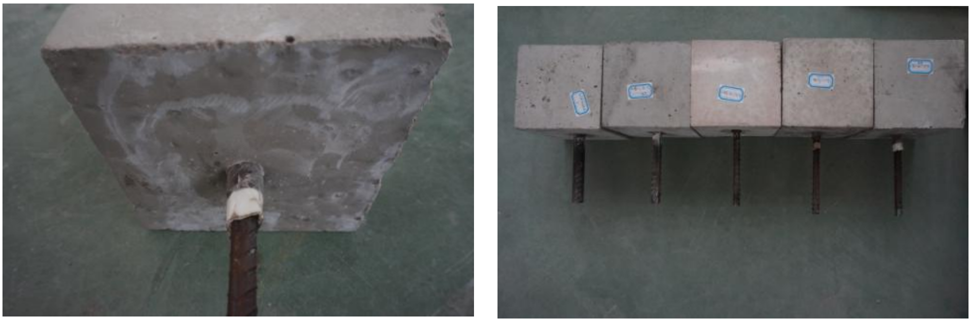

Figure 5. Failure modes of specimens after pull-out tests.

In addition, some cracks was initialized at the interface between geopolymer concrete and steel bar, and then extended to the side of geopolymer concrete during the loading process. This kind of cracks can be found in the top and lateral faces of YJ3-5 and YJ9-11(specimens due to heating 300-700℃). Because splitting tensile strength of geopolymer concrete degraded with the increase in temperatures. Figure 6 presents two typical photographs of the crack propagation in the top and lateral faces of the geopolymer concrete specimens after pull-out tests.

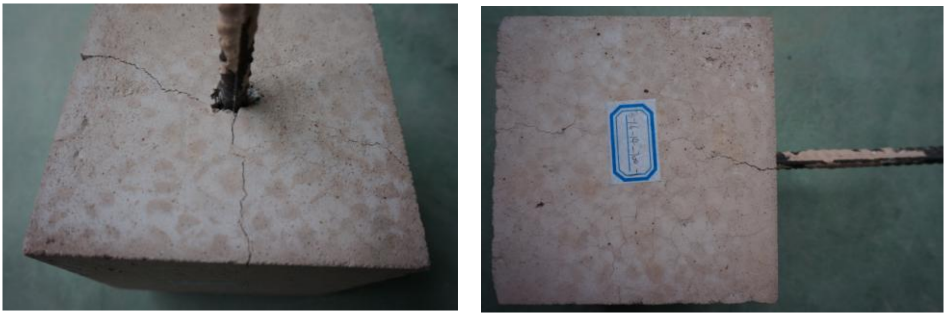

(a) Top face (b) Lateral face

Figure 6. Cracks on geopolymer concrete after pull-out test.

3.2 Bond strength

The bond strength between geopolymer concrete and steel bar is evaluated through the average ultimate pull-out load of specimens in the same group dividing the surface area along the bonded length of the bar. The effect of bar diameter and thickness of geopolymer concrete cover, content of silicon ash and temperature on bond strength is investigated based on these results.

3.2.1 Effect of thinkness of geopolymer cover and bar diameter on bond strength

The variation of bond strength with the ratio of thickness of geopolymer concrete cover to bar diameter (c/ d_b) was plotted in Figure 7. It can be seen that the specimen with higher c/ d_b (4.85) exhibits higher bond strength between geopolymer concrete and steel bar than that with lower c/ d_b (3.25), both at ambient temperature and after exposure to elevated temperatures. This is caused by the fact that the shear-lag effect in the pull-out test gets greater with the increase in bar diameter, which in turn results in the decrease in bond strength between geopolymer concrete and steel bar [13].

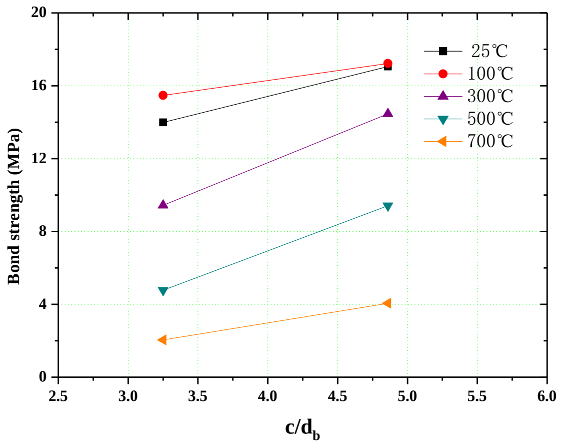

Figure 7. Effect of c/ d_b on bending strength of geopolymer.

3.2.2 Effect of silicon ash content on bond strength

The specimens in group YJ1 and YJ 6 were used to investigate the effect of silicon ash content on bond strength between geopolymer concrete and steel bar. The test results were plotted in Figure 8. It is observed from Fig 8 that YJ6 specimen exhibit lower bond strength than YJ1.Therefore, it can be inferred that the addition of silicon ash can not enhance bond strength between geopolymer concrete and steel bar, which is not in line with the results of reference [10].

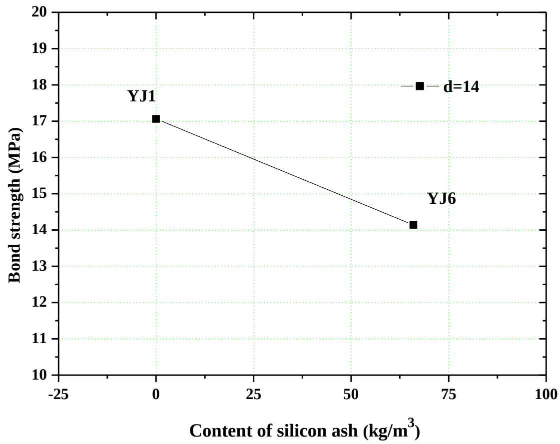

Figure 8. Effect of the content of silicon ash on bending strength of geopolymer.

3.2.3 Effect of temperature on bond strength

The specimens in groups G1 and G2 were used to study the effect of temperature on bond strength between geopolymer concrete and steel bar. The relationship between bond strength and exposure temperature is depicted in Figure 9. It can be seen from this figure that bond strength of the two groups of specimens both increases (1%-11%) at 100°C, and then decreased with the further increase in exposure temperature.

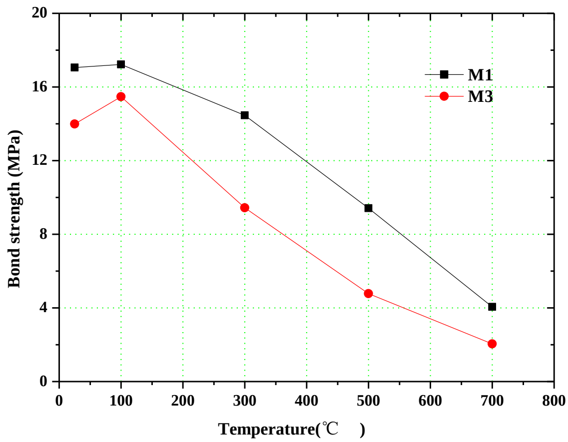

Figure 9. Effect of temperature on bending strength of geopolymer.

4. CONCLUSIONS

In this study, the bond strength between geopolymer concrete and steel rebar was tested at ambient temperature and after exposure to elevated temperatures. From the test results, the following conclusions can be drawn:

(1) Bond strength between geopolymer concrete and steel rebar increases (1%-11%) with the temperature up to 100^oC, and then decreased with the further increase in exposure temperature.

(2) The specimen with smaller bar diameter exhibits higher bond strength than that with larger bar diameter, both at ambient temperature and after exposure to elevated temperatures.

(3) The addition of silicon ash can not enhance bond strength between geopolymer concrete and steel bar.

REFERENCES

[1] Sakai K.,"Environmental management of concrete and concrete structures—toward sustainable development in construction industry",*Analytical models and new concepts in concrete and masonry structures-Proceedings of the 6th international conference*,Lodz,Poland,139–155,2008.

[2] Davidovis J.,"Mineral polymers and methods of making them", *US Patent*, 386,1982.

[3] Davidovits J.,"Geopolymers: inorganic polymeric new materials.",*J Therm Anal*,37,1633–56,1991.

[4] Davidovits J.,"Geopolymers cement to minimize carbon-dioxide green housewarming",*J Ceram Trans*,37,165–89,1993.

[5] Davidovits J.,"Global warming impact on the cement and aggregates industries", *World Resour Rev*,6(2),263–78,1993.

[6] Hardjito D., Wallah SE., Sumajouw DMJ.,"On the development of fly ash-based geopolymer concrete",*ACI Mater J* ,101(6),467–472,2004.

[7] Hardjito D., Wallah SE, Sumajouw DMJ.,"Fly ash-based geopolymer concrete",*Aust J Struct Eng*, 6(1),77–86,2005.

[8] Rangan BV.," Studies on low-calcium fly ash-based geopolymer concrete",*Indian Concrete Institute Journal*, 9–17,2006.

[9] Sumajouw DMJ., Hardjito D., Wallah SE.,"Fly ash-based geopolymer concrete: study of slender columns",*Journal of Materials Science*,42(9),3124–3130,2007.

[10] Dong, O., "Effect of rice husk ash on bond strength between steel bar and hsc/uhsc",*Industrial Construction*,012 ,2003.

[11] Sarker PK., "Analysis of geopolymer concrete columns",*Mater Struct*,,715–724,2009.

[12] Kong, D.L.Y. and J.G. Sanjayan, "Damage behavior of geopolymer composites exposed to elevated temperatures",*Cement and Concrete Composites*, 30(10),986-991,2008.

[13] HAO Qing-duo.,WANG Yan-lei.,HOU Ji-lin.,"Experimental study on bond bahavior of GFRP ribbed rebars",*Engineering mechanics*,158-179,2008.

8th International Conference on Structures in Fire
Guo-Qiang LI, Venkatesh K. R. KODUR, Shou-Chao JIANG, Jian JIANG, Su-Wen CHEN, Guo-Biao LOU (Eds.)
Shanghai, China, June 11-13, 2014

NUMERICAL INVESTIGATION OF PRESTRESSED I-BEAM IN CASE OF FIRE

Huan-Ting Zhou*, Jian Zhang* and He-Bin Nie*

*School of Civil Engineering and Architecture, WuHan University of Technology, Wuhan 430070, China.
Emails:001hawk@163.com, modian0131@163.com, Nie_hebin2510@whut.edu.cn

Keywords: Fire resistance time, Prestressed steel beam, Ratio of prestress, ratio of load, Relax of stress, High temperature

Abstract. *This paper focuses on the effects of prestress and loads on structural fire response up to failure of bare prestressed steel beams (PSB). Simply supported PSB with external tendons were analyzed. The thermal and structural analysis of PSB were accomplished by the commercial program package ANSYS. The thermal response was carried out under three-side fire exposure of standard fire of ISO834. Two key parameters, ratio of prestress and ratio of load, were taken into account. The results showed that the load ratio played an important role in the fire resistance of PSB. The PSB can obtain the maximum fire resistance when LR is 0.35 and PR is more than 0.45. The general trend is that the fire resistance decreases with the load ratio increasing. The stress in the cable strand finally approaches to zero when PSB fail at high temperature. And the ratio of prestress showed very limited influence on the fire resistance defined according to the limited bearing capacity. The high prestress could delay failure of the cable tendons due to being loose and decreases the deflection of the steel beam at the beginning of the standard fire.*

1 INTRODUCTION

Prestressed steel beams (PSB) systems are quite frequently used in large-span buildings and other built infrastructure due to a number of advantages they provide over other materials. The performance of prestressed beam is different from the usual structural system due to the existing of prestress in the members. Once prestress in the cable strand of the beam relaxs, the mechanical performance, such as structural stiffness, changes considerably. Under high temperature, what will happen to the prestressed structures resulting from the effect of thermal expansion and creep of cable strands?

Within the author's knowledge, existing studies of this kind of structure at high temperature appear rare. Lorenc [1]carried out an experimental tests on beams with straight and draped tendons as well as on a non-prestressed beam. The test demonstrated that at the same eccentricity of tendons the tendon shape has no significant effect on the behavior and ultimate resistance of composite steel-concrete beams. Chen[2] tested four groups of prestressed steel-concrete composite beams with external tendons in negative moment regions. The study focused on the cracking behaviors and the ultimate negative moment resistances of the composite beams. The results show that the cracking resistance of the beams can be effectively increased. In order to evaluate the prestressing efficiency and load-carrying capacity of the proposed method, Kim[3] conducted prestressing application tests and static loading tests on three H-shaped beams. The static loading tests showed that the installation of the brackets increased the stiffness, the yield load, and ultimate load of the structure, compared with an unreinforced girder, which meant higher load-carrying capacity than a conventional thermal prestressed structure without brackets. Kim et al.[4, 5] investigated the behavior of the prestressed composite beam with corrugated web. And they proposed a simple approach for the estimation of the accordion effect based on the analysis result. They experimentally studied the flexural behavior of three full-scaled non-prestressed and prestressed composite beams with corrugated web. The test result showed that the flexural strength and stiffness of the prestressed specimens were superior to those of the non-prestressed specimen. Most of these studies above did not related to the fire resistance performance of the prestressed steel structures. A review of literature indicates that limited fire resistance studies have been conducted on the prestressed steel beams. Most of these studies were conducted on composite plate prestressed with external tendons and continuous steel-concrete composite beams prestressed with external tendons at elevating temperature. Xu et al[6] recommended the cover thicknesses of the concrete for fire resistance by analyzing the nonlinear properties of prestressed concrete beams and slabs subjected to fires by ANSYS software. Hou[7] simulated loading process of prestressed concrete(PC) continuous beams and slabs at elevated temperature. The studies showed that support and span restraint effect has significant influence on the fire resistance of PC continuous beams and slabs. When used in buildings, the provision of appropriate fire safety measures for structural members is an important aspect of design since fire represents one of the most severe environmental conditions to which structures may be subjected in their life time. Although many studies have been done on the mechanical performance of the prestressed steel-concrete structures, little information is available on the fire resistance of the prestressed steel beam. The objective of this paper is to demonstrate some particular contribution of these key factors, such as ratio of prestress and ratio of load, on the fire resistance of the prestressed steel beams.

2 MATERIAL PROPERTIES AND FIRE MODEL USED

As the temperature of structural steel increases, its material properties change. This change influences greatly the behavior of the steel elements at high temperature. In the sequentially coupled thermo-mechanical analysis of the study, the material model of steel at elevated temperature in Eurocode 3,part 1.2 was used. The effective yield strength, the elastic modulus and the proportional limit of steel decrease as the temperature increases.

The mechanical properties of cable strand at high temperature in [8] was adopted. As a primary investigation, the creep effect of cable strand at high temperature was not taken into account, but the focus was on the prestress effect on the fire resistance of prestressed steel beams in this study.

The fire load in this paper is assumed to follow the standard temperature-time curve since it is the representative fire model used in design practice.

3 VALIDATION OF MECHANICAL MODELING

In order to validate the numerical modeling of this study, the test conducted by author of this paper was used. This test was performed to investigate the behavior of prestressed steel beam. The beam was simply supported under fire conditions.

The schematic arrangement by the author is shown in Figure 1. In the test, the span of the prestressed steel beam was 6-m long and one concentrated load was applied to the point at midspan. The steel grade of the beam was Q235 (Fy=235MPa). This experimental study considerated two different loads of 20t and 40t. And the beam was partly subjected to the standard fire with three-side exposure.

In the experiencing investigation, the evolution of stress in cable strand was recorded by load cells. The load applied to the beam was kept constant during the experiment.The mechanical modeling of the test is validated by comparison of experimental and simulation results for the beam with the same method applied in this paper.

As shown in Figure 2, the prediction of stress-temperature curve from the mechanical analysis of the cable strand correlates with the experimental results. The stress in cable strand reached zero after the beam was fired about 1000 s. The time when the cable strand becomes loose is almost identical to that observed in the test.

Figure 1. Bending deformation of the prestressed steel bema after the fire test.

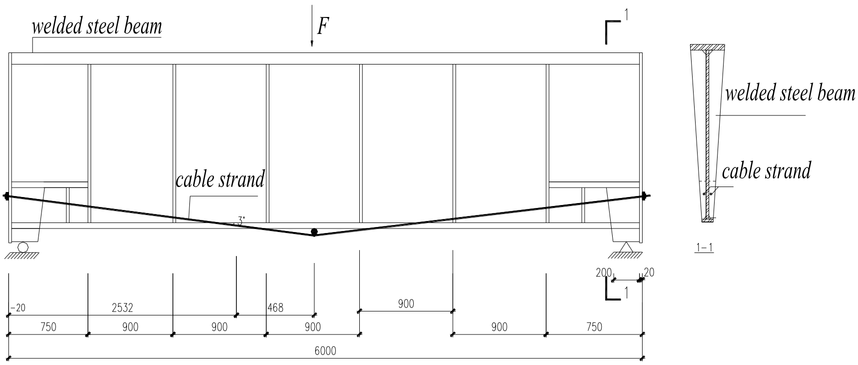

Figure 2. schematic setup of the tested steel beam with prestress.

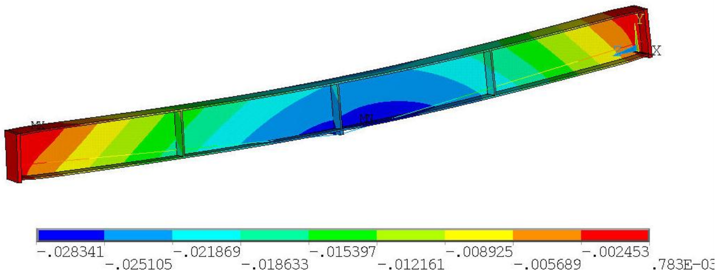

Figure 3. The deflection of the PSB subjected to high temperature.

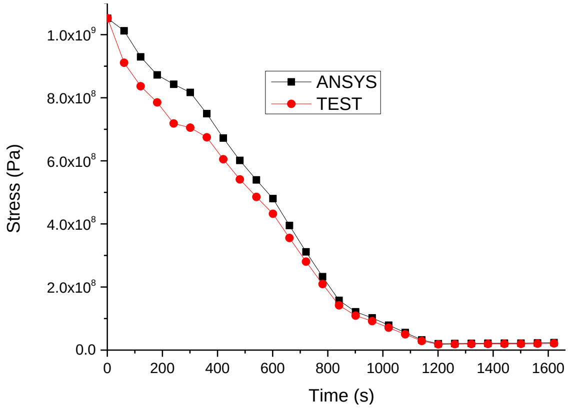

Figure 4. Time-Stress evolution of the tested steel beam with prestress.

4 PARAMETRIC NUMERICAL ANALYSIS

4.1 Parameters considered

The steel section chosen for parametric study is a wide flange shape of nominal H588×300×12×20(depth =588，width=300,web thickness=12，flange thickness=20，in mm). The yield strength and the modulus of elasticity of the steel beam at ambient temperature are 235MPa and 206GPa respectively.

To be general use and simplify the primary study, the influence of the load and prestress of prestressed steel beam was focus of the investigation. The load is defined in a relative manner, load ratio (LR) and prestress ratio (PR). The load ratio is defined as the ratio of the applied load to the ultimate concentrated load at midspan at ambient temperature. The prestress ratio is defined as the ratio of prestress in the cable strand to the ultimate strenght of the cable strand at ambient temperature.

4.2 Results of the parametric analysis

Time–deflection curves obtained by the mechanical analysis reflect the evolution of the stiffness of the prestressed beam under fire. The deflection increases with decreasing of the stiffness of the steel beam under high temperature.

The fire resistant time of prestressed steel beam of this study was determined according to the deflection rates and the convergence of the numerical analysis. When the fired prestressed steel beam approaches limit state, the deflection of the steel beam increases abruptly and numerical analysis can not be converged. All the fire resistant times of prestressed steel beam of this study were determined according to the limit state at this moment.

4.2.1 Influence of the key structural parameters

With keeping the other parameters fixed, analyses reflecting different load ratios and prestress ratio were carried out.

Figure 5(a) demonstrates the following regular pattern: As shown, in Figure 5(a) ,the deflection of the steel beam increases slightly with time in the initial stage of time. With the temperature elevating, the deflection curves become abrupt at some point. We will observer later that the “point” of the deflection curve may be caused by the stress relaxation of the prestress cable strand. This phenomenon can be interpreted as indicating that the cable strand can’t contribute to the global stiffness of the prestressed steel beam when the tensioned cable strand becomes relaxed. So, the deflection of the steel beam becomes greater than the displacement with the cable strand being tensile.

As expected, Figure 5 (b)-(e) shows when the prestress ratio is fixed and the load ratio is increased, the fire resistance time of the steel beam is decreased and the maximum difference of deflections of the steel beam under varied PR is little.

The significant influence of the LR can clearly be observed in Figure 6. When the LR is 0.25 and the PR is 0.55， the steel beam deflection along the opposite direction of the applied load and the fire resistance time is very short. This may be that the beam deflection due to the load is too small relative to the effect of thermal expansion.

Figure 6.(b)-(e) shows, with the LR increasing from 0.35 to 0.55, the deflection-time curves approach to converge. When LR is 0.25, the steel beam fails quickly at about 750s. The curves with different PR showed the PR had a considerable influence on the deflection of the steel beam under high temperature. At the same time, the combination of PR and LR makes the mechanical response of the steel beam complicate. The influence of the varied prestress in the steel beam are summarized in Figure 6.(b)-(e). The results show that the excessive prestress can not increase the fire resistance time of the prestressed steel beams.

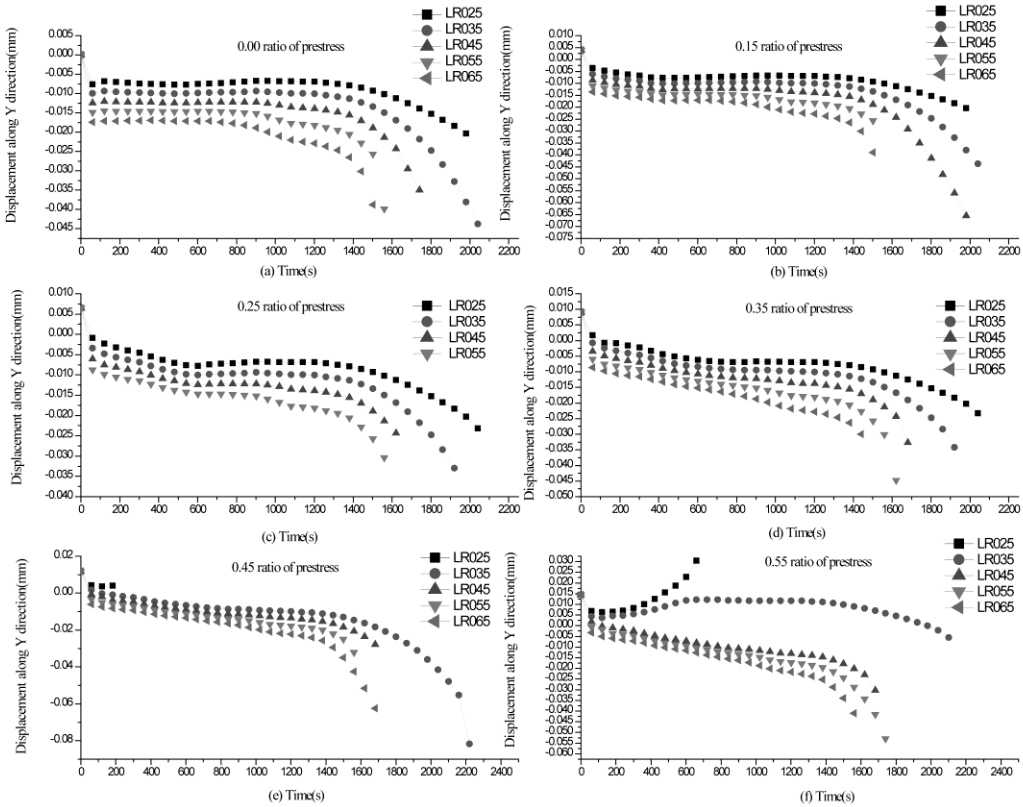

Figure 5. Time–Deflection curves of the steel beams under different PRs.

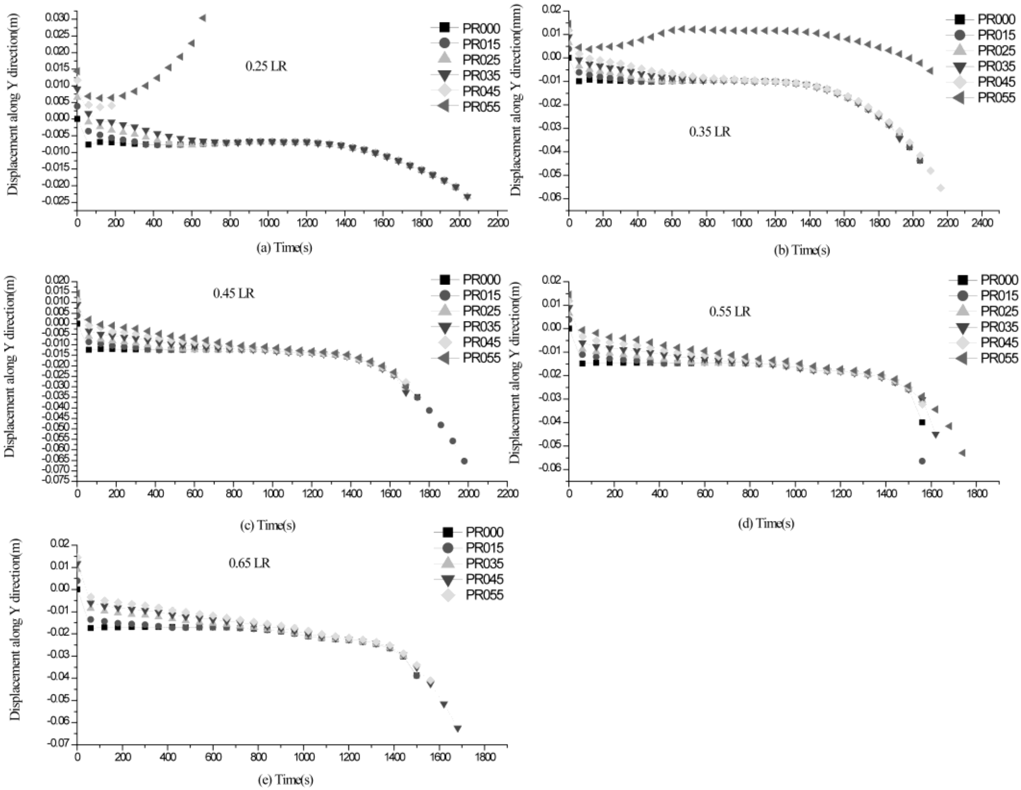

Figure 6. Time–Deflection curves of steel beams under different load ratios (H-600×200×11×17, ratio is …, L/D=15, three-side exposure).

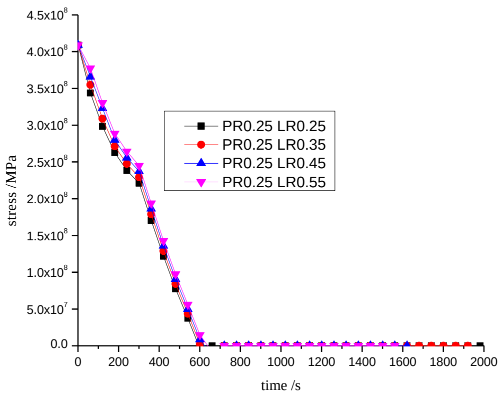

Figure 7. Time–Stress curves in the cable strand of steel beams with the fixed PR and different LR.

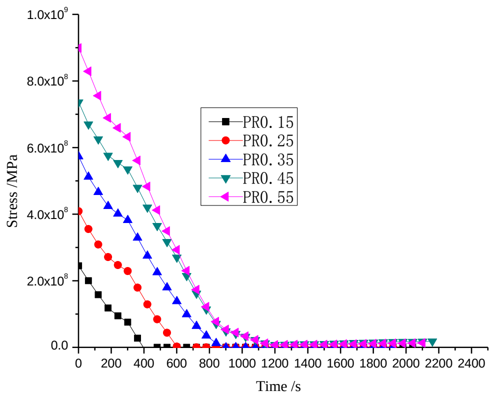

Figure 8. Time–Stress in the cable strand curves of steel beams with the different PR.

The influence of the prestress ratio and load ratio are showed in Figure 7 and Figure 8. The evolution of the stress in cable strand varies little under the fixed PR and different LR. This indicates that the cable stress undergo "the same amount time "with the fixed PR and different LR to converge to zero nearly at the same velocity. So, the variation of stress in cable strand with the fixed PR has little to do with LR under high temperature. Based on the regulation above, Figure 8 shows the evolutions of stress in cable strand in different PR. The cable strand with larger initial prestress will work longer time than that of the cable strand with lower prestress. When the stress in cable strand is nearly relax, the cable strand will not contribute to the global stiffness of the prestressed steel beam. Without the contribution of the cable strand, the deflection of the steel beam will increase abruptly. This is the reason that there is a "abrupt point" on the time–deflection curve of the steel beam in Figure 5.

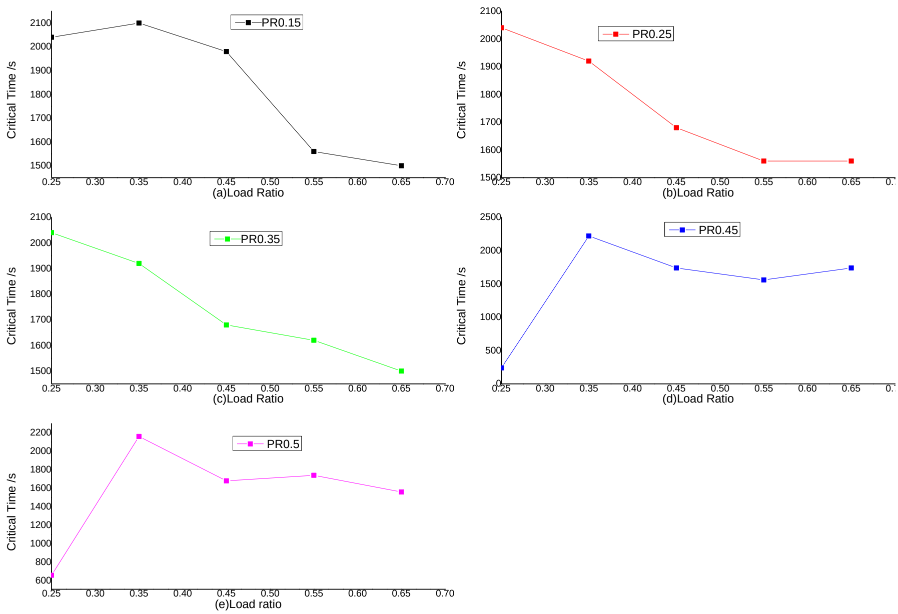

Figure 9. Influence of PR on the critical time of the prestressed steel beam.

Fire resistance time of the PSB is a focus of the fire resistance design. Figure 9 shows the influence of the PR on the critical time of the prestressed steel beam at high temperature. When the PR is 0.15 or more than 0.45, the critical time is increased with the LR and reaches its peak value when LR at 0.35. Afterwards, the critical time is decreased with increasing of LR. While PR is 0.25 and 0.35, the fire resistance time is alwalys decreased with LR increasing.

5 CONCLUSIONS

The influence of the prestress ratio and load ratio under the standard fire was investigated based on the numerical analysis. The results are summarize as follows.

(1) The load ratio showed the most significant influence on the fire resistance of the prestressed steel beams. The prestressed steel beam can obtain the maximum fire resistance when LR is 0.35 and PR is more than 0.45. The general trend is that the fire resistance decreases with the load ratio increasing.

(2) The prestress ratio showed very limited influence on the fire resistance defined according to the limited bearing capacity in this paper. The high prestress could delay failure of the cable strand due to being loose of the cable strand and decreases the deflection of the steel beam at the beginning of the standard fire temperature.

(3) The stress in the cable strand finally approaches to zero when the steel beam fails at high temperature.

REFERENCES

[1] W. Lorenc and E. Kubica, "Behavior of composite beams prestressed with external tendons: Experimental study," Journal of Constructional Steel Research, vol. 62, pp. 1353-1366, 2006-12-01 2006.

[2] S. Chen, "Experimental study of prestressed steel–concrete composite beams with external tendons for negative moments," Journal of Constructional Steel Research, vol. 61, pp. 1613-1630, 2005-12-01 2005.

[3] S. Kim, J. Joung, K. Choi, and C. Jung, "Experimental load-carrying capacity evaluation of thermal prestressed H beam with steel brackets," Journal of Constructional Steel Research, vol. 88, pp. 309-320, 2013-09-01 2013.

[4] K. S. Kim, D. H. Lee, S. M. Choi, Y. H. Choi, and S. H. Jung, "Flexural behavior of prestressed composite beams with corrugated web: Part I. Development and analysis," Composites Part B: Engineering, vol. 42, pp. 1603-1616, 2011-09-01 2011.

[5] K. S. Kim and D. H. Lee, "Flexural behavior of prestressed composite beams with corrugated web: Part II. Experiment and verification," Composites Part B: Engineering, vol. 42, pp. 1617-1629, 2011-09-01 2011.

[6] XU Ming-xin and ZHENG Wen-zhong, "Nonlinear analysis of prestressed concrete beams and slabs subjected to fires," Journal of Harbin Institute of Technology, pp. 558-562, 2006.

[7] HOU Xiao-meng and ZHENG Wen-zhong, "Nonlinear finite element analysis of fire resistance performance for prestressed concrete continuous beams and slabs," Journal of Harbin Institute of Technology, pp. 36-41, 2011.

[8] ZHOU Huan-ting,LI Guo-qiang and JIANG Shou-chao, "Experimental Studies on the Properties of Steel Strand at Elevated Temperatures," Journal of Sichuan University(Enginering Science Edition), pp. 106-110, 2008-09-20 2008.

TOWARDS FRAGILITY ANALYSIS FOR CONCRETE BUILDINGS IN FIRE: RESIDUAL CAPACITY OF CONCRETE COLUMNS

David Rush*, Luke Bisby*, Ioanna Ioannou and Tiziana Rossetto ****

* BRE centre for Fire Safety Engineering, School of Engineering, University of Edinburgh, UK
e-mails: d.rush@ed.ac.uk, l.bisby@ed.ac.uk

** EPICentre, University College London, UK
e-mails: ioanna.ioannou@ucl.ac.uk, t.rossetto@ucl.ac.uk

Keywords: Fragility analysis, Reinforced concrete, Residual strength, Probabilistic design

Abstract. *Fire engineering a building, in general, has one central performance objective – life safety – and property protection is rarely explicitly considered. The engineering is typically based on only one possible fire, which may not represent the most onerous scenario (or may be much too onerous to be considered realistic). Taking inspiration from fragility analyses used in seismic engineering, this paper explores the relationship between post-fire structural response and the 'intensity' of the fire. The influence of 27 different parametric fires on the residual capacity of a reinforced concrete column is theoretically assessed and it is shown that the ventilation factor used to define the fire curves has a clear influence on the calculated residual response of the column, both in terms of peak fire temperature but also total duration of fire exposure. This paper represents a first step towards developing quantified fragility analyses for probabilistic structural fire design of concrete buildings.*

1 INTRODUCTION

The 2011 earthquake in Christchurch, NZ, caused a great deal of damage to the city, which is expensive to repair or replace. The high level of damage and the cost of reinstatement was shocking to the public and insurers alike, however from an engineering perspective the vast majority of buildings performed "very well" on the basis of the explicit design objectives used to engineer them [1]. This suggests that society is largely unaware of the true "performance" objectives that are used by structural engineers in design, whether for earthquake or fire engineering; it may be that a higher 'level' of property protection is actually expected by society (however this is rarely noticed due to the infrequency of severe earthquakes – or fires). In current fire engineering design there is, in general, no accept means of quantifying property protection goals (or of rationally accounting for these goals in design), and design is instead based almost entirely on life safety and property protection is rarely explicitly considered – there is typically little or no consideration of 'damage,' rather simply a pass/fail assessment usually consisting of prescribed fire resistance criteria and times. Furthermore this assessment is usually based on a standard fire (e.g. ISO-834 [2]) that represents only one, physically impossible, fire, and may not represent the most onerous (or more realistic) fire insult that a structure might experience [3]. Real fires are more akin to earthquakes from a risk perspective, no two are the same, and a single fire in any given building will affect different elements within the structure differently. How to assess and quantify the damage caused by a real fire in a real building, so that reuse/repair/replace plans can be developed, is an open question.

The seismic community have, for many years, applied concepts of 'fragility analysis,' where the probability of a structural system reaching a given *damage state* is assessed as a function of some measure of *intensity* (e.g. peak ground acceleration used in earthquake engineering). From this assessment, designers and insurers can calculate the *expected costs* of repair or replacement of the building. Therefore a *fragility analysis* allows designers to rationally and quantifiably account for the *risks* and *costs* associated with the *range* of possible earthquakes, and explicitly accounts for property protection as a desirable design goal. This paper is a step towards quantifying fragility analyses and the critical parameters for probabilistic performance-based fire design of concrete structures..

2 FRAGILITY ANALYSES

Fragility analysis thinking has started to appear in the structural fire engineering literature (e.g. [4]), largely for steel-frames structures, however fragility concepts have specific relevance for concrete structures since concrete structures may perform better: (a) in real rather than standard fires; and (b) than other types of construction in terms of property protection considerations (provided that heat-induced concrete cover spalling is avoided).

Equation 1 represents the probabilistic risk assessment of a building affected by a hazard for a given period of time; for example fires/year. The risk is defined as consequence × hazard, where the consequence is estimated by three stochastic relationships; intensity measure (*IM*) to response measure (*RM*); RM to damage measure (*DM*); and DM to loss or some other decision variable (*DV*). In other words, given the likelihood of an event occurring in a building, the *IM* forces the building to have a response, *RM*, which leads to a measure of damage, *DM*, and subsequent level of loss, *DV*. The fundamental aim of the reasoning represented by Eq. 1 is to provide quantified annual expected loss metrics for a given structure based on the magnitude and risk of a hazard occurring. A fragility analysis is a component of the risk assessment, and consists of two analyses: (1) structural and (2) damage analysis, thus linking the probability of different damage (*DM*) occurring for a given fire intensity (*IM*).

$$gDV = \iiint \overbrace{P\,[DV|DM]}^{\textit{Loss analysis}}\, d\underbrace{P\,[DM|RM]}_{\textit{Damage analysis}}\, d\overbrace{P\,[RM|IM]}^{\textit{Structural analysis}}\, \underbrace{dg_{IM}}_{\textit{Hazard analysis}} \tag{1}$$

The advantage of Equation (1) is that it implicitly assumes that that each of the four analyses can be conducted independently, and that the final products of the conditional distributions presented in Equation (1) can be coupled to estimate the risk to the building over a specified period of time.

The determination of suitable intensity measures is not straightforward since *IM*s also depend on the effect that a hazard has on the structure and the *RM* being assessed (i.e. if deflections were the *RM* then peak rebar temperatures might be the *IM*, however if structural capacity is the *RM* then the area under the fire curve might be a more appropriate *IM*). Ideally a large database of experimental and real fire structural response data would inform decisions on which *IM*s and *RM*s are most suitable for use in designing concrete buildings; however, there is a paucity of data, and thus computational analysis and expert opinion must be relied upon. Once the *IMs* and *RMs* have been decided, *DM*s can be determined (as has previously been attempted in [5]), along with the costs associated with the *DM*s, through expert opinion. The risk assessment framework of Equation (1) estimates the risk to buildings affected by all possible fires likely to occur in a given interval and allows designers to design specifically for property protection.

3 EXAMPLE: AXIALLY LOADED REINFORCED CONCRETE COLUMN

In this paper the relationship between *IM* and *RM* for an example reinforced concrete column is assessed through computational analysis, rather than experimentally, given that there are a range of possible design fires that could affect a concrete column (see Table 1). The *RM* being assessed in the current analysis is the residual axial load capacity (strength) of the concrete column. This depends on the maximum temperature experienced within the cross-section, since temperature adversely influences the residual stress-strain relationships of both reinforcing steel and concrete. The maximum temperatures within the cross-section were calculated (by finite elements) at several depths and under several different time-temperature histories that each represents one possible *IM*.

Table 1. Details of concrete column used in the current study.

L (m)	Size (mm)	K	$l_{e,re}$ (KL - m)	Bars no. × size	A_s/A_c	Cover (mm)	f'_c/f_{cu} (MPa)	f_y (MPa)	E_s (MPa)
3	300 × 300	0.7	2.1	8 × 20 mm Ø	2.8%	30	35/45	500	205000

3.1 Parametric fire calculations

The initial stage of the analysis was to parameterise the design space in terms of *IM*, so a family of 27 design fires have been created based on the Eurocode parametric fires [2]. The fires are initially defined by varying three parameters (A: compartment size, B: fuel load, and C: ventilation), each with three values (1, 2, and 3) to give the broad range of 27 fire intensities outlined in Table 2. Each design fire has two parts; a growth phase and a cooling phase. The growth phase of the temperature (Θ_g) is defined by:

$$\Theta_g = 20 + 1325 \cdot \left(1 - 0.324 e^{-0.2t^*} - 0.204 e^{-1.7t^*} - 0.472 e^{-19t^*}\right) \tag{1}$$

where $t^* = t \cdot \Gamma$, where t is the time in hours, and the dimensionless ratio $\Gamma = (O/b)^2/(0.04/1160)^2$, O is the opening factor (limited to a maximum of 0.2 and minimum of 0.02).

The growth rate of the fire determines the maximum temperature that Equation (2) can reach and is limited by the greater of t_{lim} (Table 2) or $t_{\mathrm{max}} = (0.2\mathrm{x}10^{-3} \cdot q_{\mathrm{t,d}})/O$. If $t_{\mathrm{lim}} > t_{\mathrm{max}}$ the fire is deemed fuel controlled; if $t_{\mathrm{lim}} < t_{\mathrm{max}}$ the fire is deemed ventilation controlled. The design fire load density, $q_{t,d}$, is a function of the fuel load, $q_{f,k}$, which takes into account the risk of fire activation and firefighting measures in relation to the floor and total surface areas of the compartment (Annex E of [2]). The cooling phase of the design fire is linear and is dependent on the size of t_{max} with larger values having shallower gradients.

Table 2. Parametric curve calculation input parameters [2].

	Variables				Constants	
	Room size[a] A_{f} (m^2)		Fuel load[b] $q_{\mathrm{f,k}}$ (kg/m^2)	Opening factor O (m$^{1/2}$)	Boundary Enclosure $b = \sqrt{(\rho.\lambda.c)}$	Enclosure height: *3*m
	A		B	C		
1	9	3 × 3	612[c]	0.02	ρ = 2300 kg/m^3	Growth rate*:*
2	250	15.8 × 15.8	780[d]	0.066149[f]	λ = 1.6 W/mK,	*Medium*
3	500	22.4 × 22.4	948[e]	0.2	c = 1000 J/kgK	t_{lim} = 20 mins

[a] Maximum of 500m^2, [b] Dwelling fuel loads, [c] value B1 = B2 - (B3 - B2), [d] average, [e] 80%ile, [f] opening factor required for Γ = 1; approximation of standard time temperature curves.

Table 3 presents the maximum temperatures obtained from Equation (2) for the 27 parametric fires, whilst Figure 1 shows the 27 design fire time-temperature curves based on the Eurocode's parametric fires [2]. The black marker curves are all ventilation controlled fires; white marker curves are approximations of the standard time-temperature curves and are ventilation controlled; and the grey marker curves are in general fuel load controlled, thus many have the same profile.

3.2 Thermal modelling of cross-section and structural analysis of RC column

A three stage process is required to calculate the residual capacity of the RC column under the 27 different fires shown in Figure 1: Stage (1) is to conduct a heat transfer analysis within the cross section for the entire length of fire duration; Stage (2) is to discretize the cross-section into elements in which the temperature is assumed to be uniform; and Stage (3) is to calculate the structural capacity of the column using maximum temperature dependent residual constitutive material relationships.

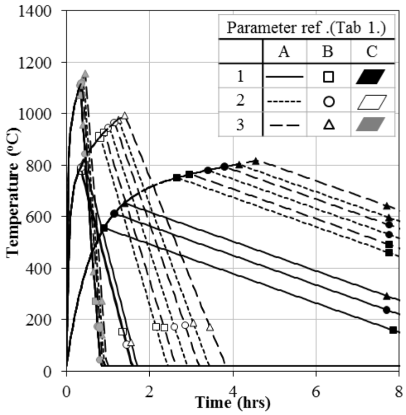

Figure 1. Twenty-seven parametric fire curves.

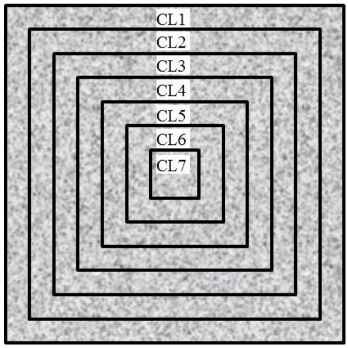

Figure 2. Square segmentation (CL*i* = concrete layer *i*).

Table 3. Maximum fire temperatures and averaged maximum layer temperatures.

Fire A-B-C (Table 2)	Fire (Θ_g)	Maximum temperatures - θmax (°C) CL1	CL2	CL3	CL4	CL5	CL6	CL7	Capacity $N_{re,fi}$ (kN)	RSI^a
000	N/A	20 – Ambient							4255	1.00
1-1-1	556	405	363	344	335	332	331	331	3447	0.81
1-1-2	789	489	337	258	218	206	204	203	3518	0.83
1-1-3, 1-2-3, 1-3-3, 2-1-3, 3-1-3	1110	779	460	313	247	230	227	226	2962	0.70
1-2-1	613	473	425	403	394	390	389	389	3158	0.74
1-2-2	793	497	344	263	222	210	207	207	3493	0.82
1-3-1	653	523	472	448	439	435	434	433	2873	0.68
1-3-2	818	543	379	292	247	232	229	229	3350	0.79
2-1-1	751	667	610	584	573	569	567	567	1943	0.46
2-1-2	911	716	534	428	370	347	342	341	2629	0.62
2-2-1	780	715	661	635	624	619	618	618	1701	0.40
2-2-2	948	781	604	495	435	411	404	403	2276	0.53
2-2-3	1113	784	465	316	249	232	229	228	2947	0.69
2-3-1	804	752	704	679	667	663	662	661	1513	0.36
2-3-2	978	833	664	556	497	472	466	464	1965	0.46
2-3-3	1143	838	519	356	280	258	255	254	2760	0.65
3-1-1	765	690	634	608	597	593	591	591	1838	0.43
3-1-2	928	748	568	459	400	376	370	369	2464	0.58
3-2-1	794	737	687	661	650	645	644	644	1654	0.39
3-2-2	965	813	640	531	471	447	440	439	2264	0.53
3-2-3	1130	814	496	339	267	247	244	243	3157	0.74
3-3-1	818	775	731	706	695	691	689	689	1461	0.34
3-3-2	995	863	701	596	538	514	507	506	1889	0.44
3-3-3	1160	874	554	384	301	277	273	272	2921	0.69

[a] RSI = residual strength index = $N_{re,fi}/N_{re,fi(000)}$

3.2.1 Thermal analysis

The 27 design fires were applied to a theoretical 300mm × 300mm RC column cross-sections and a finite element method (FEM) heat transfer analysis conducted (using ABAQUS). The density, thermal conductivity, and specific heat capacity of concrete were assumed to be constant with values of ρ = 2300 kg/m^3, λ = 1.6 W/mK, and c = 1000 J/kgK (no water), respectively. The model also employed the net heat flux method of heat transfer as suggested by Eurocode 1 [2] with the resultant emissivity of concrete and fire is 0.7 and the convective heat flux coefficient of 25 W/m^{2}K.

3.2.2 Cross-section discretization and layer temperatures

Once the FEM analysis had been completed, the cross-section was discretized into ringed segments of equal thickness in which the temperature is assumed to be uniform. Square sections experience higher temperatures at the corners than at the middle of the flat faces which suggests that a fully discretized 2D analysis is required, however precedence exists [6] to assume an equivalent uniform temperature in each concrete layer in the square section, provided that the uniform temperature chosen for the layer leads to the same (or smaller) contribution to either the plastic resistance in compression or the cross-section's flexural stiffness as would a more complete summation of a 2D grid of concrete elements. This means that a full 2D discretization was not required in this analysis and each of the concrete rings is assumed to have a uniform maximum temperature, averaged from the elemental temperatures in that layer.

The square section was discretized into seven concrete layers,as shown schematically in Figure 2. Clearly, the more layers that are taken the more refined the prediction, however seven layers were used in a previous study conducted [6] by the authors on concrete filled steel hollow sections and was found to predict temperatures and response adequately. The maximum temperatures experienced in each layer are presented in Table 3. It was assumed that the temperature in the rebar was the same temperature as the concrete layer in which is resides (i.e. CL2).

3.2.3 Structural analysis

The calculation of residual capacity of the RC column follows the similar method to Eurocode 4 Annex H [7]. Using a simple spreadsheet analysis the residual capacity of the column, $N_{re,fi}$, is determined from the design axial buckling load of the column during fire. This is found by assuming that all materials experience the same strain at a given time and temperature and then calculating the strain at which the elastic critical or Euler buckling load, $N_{re,cr}$, is equal to the plastic (crushing) resistance to compression of the cross section, $N_{re,pl,Rd}$:

$$N_{re,fi} = N_{re,cr} = N_{re,pl,Rd} \tag{2}$$

$N_{re,cr}$ (Equation (4)) is the summation of the elastic flexural rigidities of the concrete layers (subscript c), and internal steel reinforcement (subscript s), whilst $N_{re,pl,Rd}$ (Equation (5)) is the summation of the crushing strength contributions of the respective materials and layers:

$$N_{re,cr} = \pi^2 \left[\sum E_{c,\theta\max,\sigma} I_c + E_{s,\theta\max,\sigma} I_s \right] / l_{e,re}^2 \tag{3}$$

$$N_{re,pl,rd} = \sum A_c \sigma_{c,\theta\max} + A_s \sigma_{s,\theta\max} \tag{4}$$

In the above equations, $E_{i,\theta\max,\sigma}$ is the tangent modulus of the stress-strain relationship for the material i at maximum temperature θmax and for a stress $\sigma_{i,\theta\max}$, I_i is the second moment of area the material i, A_i is the cross-sectional area of material i, and $l_{e,re}$ is the residual buckling length of the column, which in this analysis is assumed to be the same as in the fire situation.

A bi-linear residual stress-strain materials model is assumed for steel [8], as shown in Figure 3(a), and given by:

$$\sigma_a = \begin{cases} E_a\left(\theta_{a,\max}\right)\cdot \varepsilon_a & \varepsilon_a \le \varepsilon_{sy}(T) \\ f_{sy}\left(\theta_{a,\max}\right) + E_1\left(\theta_{a,\max}\right)\cdot\left[\varepsilon - \varepsilon_{sy}\left(\theta_{a,\max}\right)\right] & \varepsilon_a > \varepsilon_{sy}(T) \end{cases} \tag{5}$$

where $E_a(\theta_{a,max})$ is the Young's modulus of steel; $\varepsilon_{sy}(\theta_{a,max}) = f_{sy}(\theta_{a,max})/E_a(\theta_{a,max})$; $E_1(\theta_{a,max}) = 0.01{\cdot}E_a(\theta_{a,max})$; and $f_{sy}(\theta_{a,max})$ is the yield strength of the steel after exposure to high temperature ($\theta_{a,max}$). This last term can be expressed as [8]:

$$f_{sy}\left(\theta_{a,\max}\right) = \begin{cases} f_{sy} & \theta_{a,\max} \le 400^0 C \\ f_{sy}\cdot\left[1 + 2.33\times10^{-4}\cdot\left(\theta_{a,\max} - 20\right) - 5.88\times10^{-7}\cdot\left(\theta_{a,\max} - 20\right)^2\right] & \theta_{a,\max} > 400^0 C \end{cases} \tag{6}$$

Residual stress-strain materials models for confined concrete are also proposed in [8] and [9], and are used in this analysis but with the confinement factor set to zero. The resulting stress-strain relationship is given in Equation (8) of Table 4 and shown graphically in Figure 3 (b).

Table 4: Residual strength design equations from [8], [9] with confinement factor set to zero.

$$y = \begin{cases} x & x \le 1 \\ \dfrac{x}{\left(0.75\cdot f_{ck}^{0.1}\right)\cdot(x-1)^{\eta} + x} & x > 1 \end{cases} \tag{7}$$

where:	$y = \sigma/\sigma_{0p}\left(\theta_{c,\max}\right) \quad x = \varepsilon/\varepsilon_{0p}\left(\theta_{c,\max}\right)$	$\sigma_{0p}\left(\theta_{c,\max}\right) = f_{cp}\left(\theta_{c,\max}\right)$
	$\varepsilon_{0p}\left(\theta_{c,\max}\right) = \varepsilon_{ccp}\left(\theta_{c,\max}\right) + \left[1330 + 760\cdot\left(\dfrac{f_c^{'}}{24} - 1\right)\right]$	$\eta = 1.6 + 1.5\cdot\left(\dfrac{\varepsilon_{0p}\left(\theta_{c,\max}\right)}{\varepsilon}\right)$
	$\varepsilon_{ccp}\left(\theta_{c,\max}\right) = \left[1 + \left(1500\cdot\theta_{c,\max} + 5\cdot\theta_{c,\max}{}^2\right)\times10^{-6}\right]\cdot\left(1300 + 12.5\cdot f_c^{'}\right)$	$f_{cp}\left(\theta_{c,\max}\right) = \dfrac{f_c^{'}}{1 + 2.4\cdot\left(\theta_{c,\max} - 20\right)^6\times10^{-17}}$

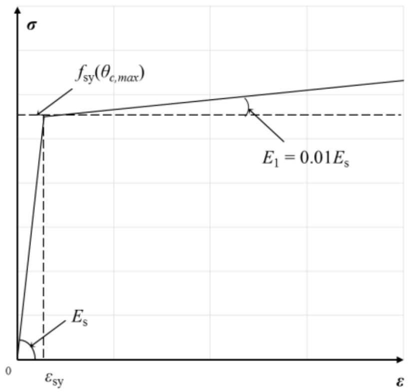

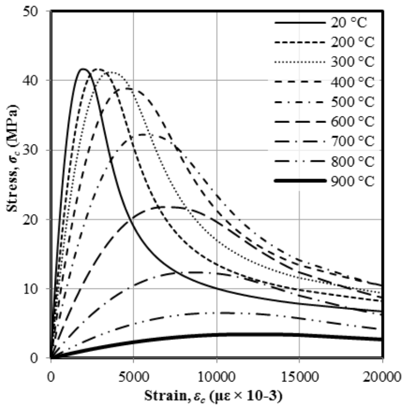

Figure 3. Residual mechanical stress-strain relationships for (a) steel (assumed bi-linear) and (b) unconfined concrete at different maximum temperatures.

4 RESULTS AND ANALYSIS OF CALCULATIONS

Table 3 shows the residual capacities of the column, calculated using Equation 3, after exposure to each of the 27 different time-temperature fire curves, and also shows the relative residual strength (RSI = $N_{re,fi}/N_{re,fi(000)}$) due to each thermal exposure.

4.1 General response

The residual strength index's range from 0.34 to 0.83 depending on the fires involved. It should be noted that in the calculation of the structural capacity, the strain level that produced the maximum capacity was equal to yield strain of the steel, ε_{sy}. This is because, in the material models used, strain levels greater than this value the flexural stiffness of the rebar reduces to 1% of E_a, thus reducing the columns buckling capacity below the crushing capacity of the column. The stress-strain relationship for steel is obviously a simplified model and does not necessarily reflect what would occur in real life.

Table 3 also shows the RSI in general reduces as either floor size and/or fuel load increases, for instance fire 2-1-1 and 3-1-1 produce RSIs of 0.46 and 0.43, respectively. This trend cannot be said for the influence of the opening factor, where the "standard" fire approximation produces the largest RSI when all other factors are equal, for instance fires 1-1-1, 1-1-2, 1-1-3 produce RSIs of 0.81, 0.83, 0.70 respectively. The authors believe that this is again due to the unrealistic and simplified bi-linear steel stress strain relationship. The columns maximum capacity in this analysis is dependent on ε_{sy}, which in turn is dependent on the temperature experienced in the steel. The higher the temperatures are the larger the yield strain, ε_{sy}, and thus, in these models, larger strains are able to develop in the cross-section and in particular the concrete. When the temperatures in the concrete are relatively low (<400°C), but the temperature experienced in the rebar (CL2) are comparatively high (>400°C), then the concrete benefits from the increase in ε_{sy} and the column can take more load. Therefore, in this modelling analysis, columns exposed to a slightly more intense fire, can actually have more residual strength.

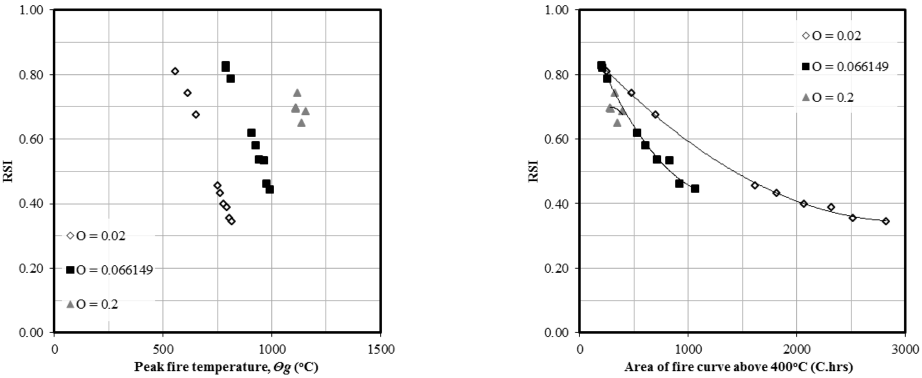

Figure 4. Residual strength index (RSI) relationships to (a) peak fire temperature and (b) area of the fire curve above 400°C; data in both figures separated by opening factor, *O*.

4.2 Relationship of response measure (*RM*) to intensity measure (*IM*)

As mentioned previously, fragility analyses require the appropriate selection of intensity measure (*IM*). For unprotected steel this is relatively easy as steel has high thermal conductivity so the response is highly dependent on the temperature of the fire. Concrete, however, has comparatively low thermal conductivity so peak fire temperature as an intensity measure (*IM*) cannot necessarily capture the full response of the concrete column. This is shown in Figure 4(a) that compares the peak fire temperature to the RSI where, for approximately the same peak fire temperature, the RSI can differ by over 100%. Figure 4(a) shows that the response is influenced by the opening factor, *O*. The opening factor influences both the peak fire temperature and the length of time the fire burns for. Small opening factors will produce longer cooler fires, compared to larger opening factors that will produce shorter hotter fires (see Figure 1). Figure 4(a) shows that the longer, lower temperature fires (small *O*), have a greater effect on the residual strength of the concrete column, thus the time of fire exposure to the concrete is important.

Figure 4(b) compares the RSI to the area under the fire curve for gas temperatures above 400^{o}C, where the "area of the fire curve above 400^{o}C" represents a measure of the amount of energy that the concrete column is exposed to above the threshold of 400^{o}C (the threshold of 400^{o}C was chosen due to the noticeable change in response of the concrete column occurs at temperatures in excess of 400^{o}C as a result of the stress-strain models used in this analysis). Figure 4(b) again shows obvious trends in relation to the influence of the opening factor on the RSI, but also shows that the response is not solely due to the amount of energy absorbed by the concrete column. Figure 4 shows that there is an interaction between the ventilation, "area" of the fire, and temperature that needs further investigation to fully understand.

5 CONCLUSIONS AND RECCOMENDATIONS

The aim of this paper was to initiate the theoretical analysis and critical thinking required to promote the use of probabilistic design methodologies within structural fire engineering of concrete structures. Therefore this paper presented a brief summary of a popular framework that is being employed within the probabilistic design in earthquake engineering and is being developed for use in structural fire engineering. The paper then presented an initial analysis of the residual strength capacity of a reinforced concrete column exposed to twenty-seven different possible fires. The analysis showed that the residual strength capacity response measure of the column is dependent on more complex measures of fire intensity than just peak fire temperature, but is also influenced by the length of time the column is exposed to the thermal insult; short hot fires produce less damage compared to longer shallower fires.

More work is required not only to understand the appropriate intensity measures to use for the post-fire residual strength of concrete columns, but also for developing appropriately verified residual strength material models for both steel and concrete. This paper has presented a first step towards understanding fragility analyses and intensity measures for probabilistic design of concrete structures in fire.

REFERENCES

[1] W. Kam, S. Pampanin, and K. Elwood, "Seismic performance of reinforced concrete buildings in the 22 Feburary Christchurch (Lyttelton) eathquake," *Bull. NZ Soc. Earthq. Eng.*, vol. 44, 2011.

[2] CEN, "BS EN 1991-1-2: Eurocode 1: Actions on structures; Part 1-2: General Actions - Actions on structures exposed to fire," Brussels, Belgium, 2009.

[3] J. Gales, C. Maluk, and L. Bisby, "Large-scale structural fire testing - how did weget here, where are we, and where are we going?," in *ICEM 15 - Porto*, 2012, pp. 1–22.

[4] S. Devaney, D. Lange, A. Usmani, and C. Manohar, "Adapting the peer methodology to account for the fire hazard," in *PLSE*, 2012.

[5] The Concrete Society, *Assessment, design and repair of fire-damaged concrete structures - Technical report no. 68*. Camberley UK: The Concrete Society, 2008.

[6] D. Rush, L. Bisby, B. Lane, and A. Melandinos, "Structural performance of unprotected concrete-filled steel hollow sections in fire: A review and meta-analysis of available test data," *Steel Compos. Struct.*, vol. 12, no. 4, pp. 325–352, 2012.

[7] CEN, "BS EN 1994-1-2: Eurocode 4: Design of composite steel and concrete structures; Part 1-2: Structural Fire Design," Brussels, Belgium, 2005.

[8] L. H. Han and J. S. Huo, "Concrete filled hollow structural steel columns after exposure to ISO-834 standard fire," *J. Struct. Eng.*, vol. 129, no. 1, p. 68, 2003.

[9] H. Yang, L. H. Han, and Y. C. Wang, "Effects of heating and loading histories on post-fire cooling behaviour of concrete-filled steel tubular columns," *J. Constr. Steel Res.*, vol. 64, May 2008.

8th International Conference on Structures in Fire
Guo-Qiang LI, Venkatesh K. R. KODUR, Shou-Chao JIANG, Jian JIANG, Su-Wen CHEN, Guo-Biao LOU (Eds.)
Shanghai, China, June 11-13, 2014

DESIGN OF PARTIALLY RESTRAINED COLUMNS EXPOSED TO LOCALISED FIRES

David Lange* and Johan Sjöström*

*SP Technical research institute of Sweden, department of Fire Research
e-mails: david.lange@sp.se, johan.sjostrom@sp.se

Keywords: Analytical method, Partially restrained column, Localised fires, Non-uniform heating of column

Abstract. *This paper presents an analysis of the response of steel columns to non-uniform heating both through the section and along the length. The method is based on an extension of Euler beam theory to evaluate the response of a steel column which is exposed to a localised fire. The solution also accounts for partial restraint of the columns ends, and allows for rotational restraints of different stiffness to be prescribed to the ends of the column, accounting for both variations in stiffness in the surrounding structure as a result of the member sizes chosen and variations in stiffness arising from heating of the structure providing the restraint at the top of the column.*

1 INTRODUCTION

The design approach for steel columns in fire is typically to prevent an increase in temperature such that the column is able to maintain its strength and stiffness for a specified period of time to stability of the structure for a period. Design procedures are typically based on the assumption that the temperature distribution in columns is uniform. Current trends in structural fire engineering are moving towards understanding the response of structures to localised or travelling fires such as may be expected in modern office buildings [1].

This paper briefly discusses the impact of localised fires on steel columns before using analytical techniques to study the response of steel columns to thermal gradients which are varying along the columns height.

2 NON-UNIFORM TEMPERATURE EXPOSURE

In order to facilitate the discussion of the temperature exposure of unprotected steel columns subjected to localised fires, reference is made to a series of tests reported in [2]. These tests illustrate the potential for a localised fire to lead to a non-uniform temperature distribution both through the section of a steel column and along the height of the column. A column of 200mm diameter was suspended directly over pans of fuel of varying diameter. The flames from the pool fires were affected by natural ventilation in the hall which meant that the flames tilted across the column from one side to the other. Key results from the recorded steel temperatures in a tests with a pan of diesel 1.9m in diameter are:

- The hottest region is close to the fire where the steel is ca. 800 °C at 1 m after ca. 15 minutes
- At 2 m height there is a difference in temperature between opposing sides of the column of ca. 250 °C suggesting a thermal gradient of the order of 1.2 °C/mm.
- At 4m, although the difference is less there is still a thermal gradient through the section.
- Large horizontal displacements were seen along the columns height, induced by the thermal gradient.

This test clearly demonstrates the potential for non-uniform temperature exposure to result in a thermal gradient and thermal bowing in a steel column.

3 CALCULATION OF TEMPERATURE GRADIENT THROUGH THE COLUMN SECTION

In structural fire engineering it is common to idealise the temperature distribution in a steel section as uniform. This assumption is not made in this paper and the ‘real’ temperature distribution in the steel section must be evaluated in order to determine the equivalent temperature increase and the equivalent thermal gradient. This is done using a method detailed in [3]. This thermal gradient will be used to determine the thermal deflection of the column later in this paper. Because the thermal gradient varies with the height of the column when we have a localised fire and because of temperature dependency of the stiffness, the equivalent thermal gradient and equivalent temperature increase can be estimated based on a single reference value of the stiffness. This will allow any calculations of the thermal deflection to take advantage of this reference value while varying only the equivalent thermal gradient.

When determining the distribution of thermal gradient along a columns height it is necessary to take at least two sections of the column for analysis. The same reference stiffness must be used for both sectional analyses. This allows any thermal deflection to be approximated without having to account for a temperature dependent stiffness of the column. More complex however is the consideration of differences in thermal expansion in the sectional analyses. In order to account for this, it is proposed to use the average value of thermal expansion from the sectional analyses when determining the thermal deflections.

4 PRINCIPAL OF COLUMN BEHAVIOUR UNDER NON-UNIFORM THERMAL GRADIENT

4 1 Case 1 – simply supported

4 1 1 Thermal deflections

Consider the behaviour of the simply supported column of height L shown in figure 1a. The column is exposed to a thermal gradient through the section which varies along the height of the column, $T_x'(y)$, and an average temperature increase which also varies along the height of the column, $\Delta T(y)$. It is assumed that the net thermal expansion may be ignored and only the geometric effect of the thermal gradient is considered. In this analysis, the geometric change associated with the temperature increase is considered first, denoted v_{th}. Throughout this paper, derivatives are taken with respect to the height of the column, along the y-axis, except the thermal gradient through the section, explicitly indicated by an x-subscript.

For simply supported elements subject to a thermal gradient, the thermal curvature (v_{th}'', 2nd derivative of the thermally deflected shape) is determined from the thermal gradient and expansion coefficient, α:

$$v_{\mathrm{th}}'' = -\alpha T_{\mathrm{x}}'(\mathrm{y}) \tag{1}$$

Assuming that the thermal gradient varies linearly along the column height, i.e. $T_x'(y)=T_{xa}'+fy$ (where T_{xa}' is the thermal gradient at position a on the column (y=0), f is the slope of the thermal gradient with height between position a and position b where the thermal gradient is denoted T_{xb}'), and assuming that any displacement of the top of the column is small and may be neglected, eqn. 1 can be integrated twice (accounting for the boundary conditions $v_{th}(0) = v_{th}(L) = 0$).

$$v_{\mathrm{th}}(\mathrm{y}) = -\frac{\alpha}{6} f y^3 - \frac{1}{2}\alpha T_{\mathrm{xa}}' y^2 + \frac{\alpha L}{6}(3T_{\mathrm{xa}}' + fL)y \tag{2}$$

The same procedure may be followed for other continuous variations in thermal gradient with height. The deflected shape for a range of different thermal gradient variations is shown in Figure 1(b)-(d) along with mechanical deflections which will be described later. The column chosen is as follows: L=6m; I=5.4e7mm^4; E_∞=E_{ref}=200 000 MPa; α=1.4e-5. This column will be used throughout this paper to illustrate the different stages in the analysis. Figure 2(b), c and d illustrate three possible variations in thermal gradient, including an example where thermal gradient is constant along the height of the column and a case where the thermal gradient changes sign along the columns height (representing e.g. an adjacent fire tilted towards the column). All of these examples have the same average value of thermal gradient along the height of the column. The constant thermal gradient results in a symmetrical column displacement. With same value at mid-height but increasing variation in the gradient; the maximum deflection is larger and its location moves towards the end of the column with higher absolute value of thermal gradient.

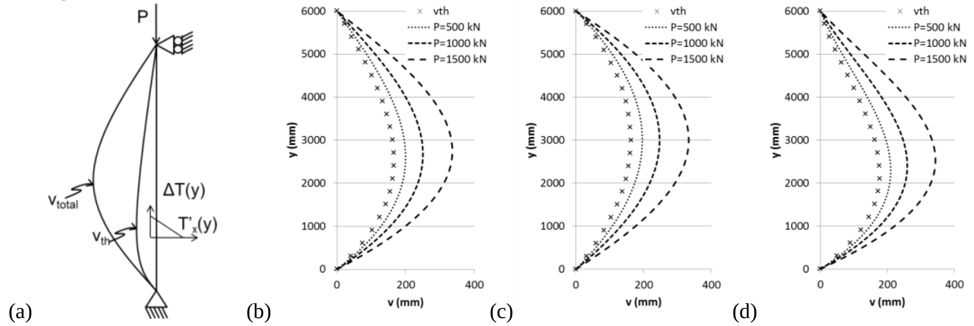

Figure 1. deflections of a pinned column, (a) under different loads with different thermal gradients; (b) $T'_{xa} = T'_{xb} = 3°C/mm$, (c) $T'_{xa} = 6$ °C/mm $T'_{xb} = 0°C/mm$, and d) $T'_{xa} = 9$ °C/mm $T'_{xb} = -3°C/mm$.

4 1 2 Mechanical deflections

Introducing the load, P, as shown in Figure 1a on the column with an initial thermal deflection induces a P-δ moment and an increase in the deflection, v_p. From beam theory, the moment over the height of a column with load P and initial deflection v_{th} is given by:

$$M = -P(v_p + v_{th}) = E_\theta I v_p'' \tag{3}$$

Writing $k = \sqrt{P/E_\theta I}$ yields the following differential eqn, subject to $v_p(0) = v_p(L) = 0$:

$$v_p'' + k^2 v_p = -k^2 v_{th} \tag{4}$$

The solution to Equation (4) is given by:

$$v_p(y) = C_1 \sin ky + C_2 \cos ky - v_{th} + v_{th}''/k^2 \tag{5}$$

$$C_1 = \frac{1}{k^2 \sin kL}\left[v''_{th(0)} \cos kL - v''_{th(L)}\right] = \frac{\alpha}{k^2 \sin kL}[T'_{xb} - T'_{xa} \cos kL], \qquad C_2 = -\frac{1}{k^2} v''_{th(0)} = \frac{\alpha}{k^2} T'_{xa}$$

Thus, the total deflection, v, of the column is given by

$$v(y) = C_1 \sin ky + C_2 \cos ky + \frac{v_{th}''}{k^2} \tag{6}$$

For the linearly varying case described here eqn. 6 is written

$$v(y) = C_1 \sin ky + C_2 \cos ky - \alpha T'_x(y)/k^2 \tag{7}$$

The total deflection for the column in Figure 1a subject to different loads is shown in Figure 1b-d.

4 1 3 Failure criteria

The largest stress occurs in an extreme fibre (with radial distance r), and will vary with y.

$$\sigma_{max}(y) = -\frac{M(y)r}{I} + \frac{P}{A} \tag{8}$$

where A is the sectional area. Recalling Equation (3) this can be written for the linearly varying case as:

$$\sigma_{max}(y) = \frac{P}{A} + rE_{\theta}\alpha\left[(T'_{xb} - T'_{xa}\cos kL)\frac{\sin ky}{\sin kL} + T'_{xa}\cos ky - T'_{x}(y)\right] \tag{9}$$

Figure 2 shows the stresses along the height of the column discussed above subject to different loads and different thermal gradients. Increasing thermal deflections result in larger P-δ moments and mechanical deflections as well as correspondingly larger stresses in the extreme fibre.

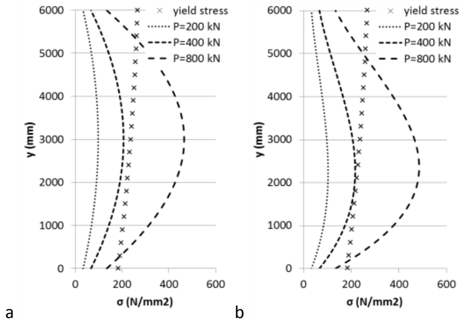

Figure 2. stress in the extreme fibre of the column with varying levels of load, (a) $T'_{xa} = T'_{xb} = 3℃/\mathrm{mm}$, (b) $T'_{xa} = 9\ ℃/\mathrm{mm}\ T'_{xb} = -3℃/\mathrm{mm}$.

For a thermal gradient which varies along the length of the column the maximum stress in an extreme fibre will not occur at mid-height. In order to determine the failure load of a column under these conditions the stress in the extreme fibre along the columns length must be compared with the yield stress in the same fibre. For a given thermal exposure the yield stress will vary with the temperature in the fibre along the y-axis, $\sigma_{Y\theta}(y)$. Values for the temperature dependent yield stress of steel are taken from EN 1993-1-2 [1]. This should be based on the real temperature distribution in the column.

Also plotted in Figure 3 is the temperature dependent yield stress in the column, assuming a linear temperature distribution in the extreme fibre from 550 ℃ at y=0 to 150 ℃ at y=L. Failure occurs when the stress exceeds the yield stress, $\sigma_{max}(y) > \sigma_{Y\theta}(y)$. Increased deflection increases the stress in the extreme fibre. Increasing the thermal gradient at one end of the column while maintaining the same gradient at the mid height will result in higher stresses forming towards the end with the larger gradient.

4 2 Case 2 – Partial rotation restraint

4 2 1 Thermal deflection

Including the effects of partial rotational restraint, Figure 3(a), requires the inclusion of the resisting moment from the springs and the corresponding reduction in the rotations at the supports. The rotational restraints are given as two different stiffnesses, k_{RA} and k_{RB}, as a result of, e.g. construction details or their increased temperature. All other parameters are the same as the previous, simply supported, case.

The partial restraints reduce thermally induced rotations at the a and b through restraining moments. Assuming again a linear variation of T'_x along the column, the free rotations at a and b due to the thermal gradient are given by the first derivative of v_{th} at y=a and y=b, denoted $v'_{th\,(a)}$ and $v'_{th\,(b)}$, respectively.

$$v'_{th\,(a)} = \frac{\alpha L}{6}(3T'_{xa} + fL) \tag{10}$$

$$v'_{th\,(b)} = -\frac{\alpha}{2}fL^2 - \alpha T'_{xa}L + \frac{\alpha L}{6}(3T'_{xa} + fL) \tag{11}$$

The total rotation at a and b also has a component resulting from the restraining moment at a and b. Denoting the restraining moments at a and b from the partial restraint to thermal expansion as $M^r_{th\,(a)}$ and $M^r_{th\,(b)}$ respectively. Also denoting the deflection of a partially restrained column under thermal effects as

v^{r}_{th}, and therefore the rotation at a from the restraining moment at a as $v^{r'}_{aa}$, and the rotation at a from the restraining moment at b as $v^{r'}_{ab}$, The restraining moments at a and b may be related to the rotations at a as:

$$v^{r'}_{aa} = -M^{r}_{th\,(a)}L/3E_{ref}I \tag{12}$$

$$v^{r'}_{ab} = -M^{r}_{th\,(b)}L/6E_{ref}I \tag{13}$$

Similar eqn.s may be written for the components of rotations at b accounting for the restraining moments at a and b, $v^{r'}_{bb}$ and $v^{r'}_{ba}$. Summing the rotations at a and b gives the total rotation at the ends:

$$v^{r'}_{th\,(a)} = v'_{th\,(a)} + v^{r'}_{aa} + v^{r'}_{ab} \tag{14}$$

$$v^{r'}_{th\,(b)} = v'_{th\,(b)} + v^{r'}_{bb} + v^{r'}_{ba} \tag{15}$$

Multiplying by the rotational stiffnesses gives the restraining moments to thermal curvature:

$$M^{r}_{th\,(a)} = k_{RA}\left(v'_{th\,(a)} + v^{r'}_{aa} + v^{r'}_{ab}\right) \tag{16}$$

$$M^{r}_{th\,(b)} = k_{RB}\left(v'_{th\,(b)} + v^{r'}_{bb} + v^{r'}_{ba}\right) \tag{17}$$

Equations (16) and (17) may be solved simultaneously to obtain the moments arising from the partial restraint to thermal bowing at both ends. These moments effectively reduce the rotations due to the thermal gradient, countering part of the thermal curvature strain by an elastic thermo-mechanical strain. Equating the unrestrained thermal curvature to a notional moment, the remaining curvature at a and b in the partially restrained column can then be determined from:

$$v^{r''}_{th\,(a)} = \frac{E_{ref}\,I\alpha T'_{xa} - M^{r}_{th\,(a)}}{E_{ref}\,I} \tag{18}$$

$$v^{r''}_{th\,(b)} = \frac{E_{ref}\,I\alpha\left(T'_{xb}\right) - M^{r}_{th\,(b)}}{E_{ref}\,I} \tag{19}$$

Since the thermal gradient varies linearly with height, the residual thermal curvature also has a linear variation. Denoting the slope of the variation in residual curvature (following application of the restraining moment from the springs to reduce the thermal effect) with height f_r:

$$f_r = \left(v^{r''}_{th\,(b)} - v^{r''}_{th\,(a)}\right)/L \tag{20}$$

The deflected shape can now be calculated in the same way as for a simply supported column, by taking the second integral of the curvature, and applying the boundary conditions $v^{r}_{th}(0) = v^{r}_{th}(L) = 0$.

$$v^{r''}_{th}(y) = v^{r''}_{th\,(a)} + f_r y = -\frac{1}{6}f_r y^3 - \frac{1}{2}v^{r''}_{th\,(a)}y^2 + \frac{L}{6}\left(3v^{r''}_{th\,(a)} + f_r L\right)y \tag{21}$$

Figures 3 (b) – (e) show examples of the thermal deflections of partially restrained columns with the same thermal gradients as in Figure 1. Increased the rotational stiffness results in significantly smaller deflections. Figure 3(e) shows the effect of different rotational restraint stiffness on the column, e.g. a much smaller top rotational stiffness yields much larger gradient of the deflected shape at the upper end.

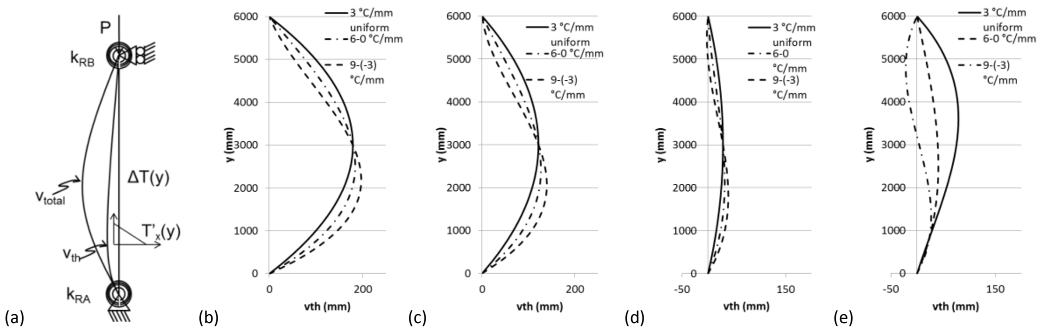

Figure 3. thermal deflections of a partially restrained column, (a) under partial restraint (b) $k_{RA} = k_{RB} = 1x10^8$ N/mm; (c) $k_{RA} = k_{RB} = 1x10^9$ N/mm; (d) $k_{RA} = k_{RB} = 1x10^{10}$ N/mm; and (e) $k_{RA} = 1x10^{10}$ N/mm and $k_{RB} = 1x10^8$ N/mm.

4 2 2 Mechanical deflection

In order to determine the effect of the vertical load under partial restraint, the following steps are taken: starting with the an initial shape which corresponds to the deflection of the column from thermal effects including the partial end restraint, release the end restraints and calculate the deflection of the now pinned, deformed, column under a compressive load P. Then, using the same procedure as in §4 2 1 determine the restraining moments to the mechanical load which are imposed by the rotational restraints. At this stage the moment which is distributed through the column as a result of the partial end restraint to thermal effects is not included, and will be added in later.

Returning to Equation 4, we now write the moment in the column with an initial shape equal to v_{th}^{r} as:

$$v_p'' + k^2 v_p = -k^2 v_{th}^{r} \tag{22}$$

The solution to which is, similar to Equation (5), and referring to Equations (6) and (7):

$$v_p(y) = C_1 \sin ky + C_2 \cos ky - v_{th}^{r} + v_{th}^{r''}/k^2 \tag{23}$$

$$C_1 = -C_2 \cos kL - \frac{v_{th}^{r''}}{k^2}, \qquad C_2 = \frac{M_{th\,(a)}^{r}}{P}$$

Equation (23) gives the deflected shape of a pinned column under axial load P. We now apply partial end restraints and calculate the restraining moment applied by the springs of stiffness k_{ra} and k_{rb}. As above, we denote the restraining moments at a and b from the partial restraint to the applied load P as $M_{P(a)}^{r}$ and $M_{P(b)}^{r}$ respectively, and the rotation at a from the restraining moment at a as $v_{aa}^{rP'}$, and the rotation at a from the restraining moment at b as $v_{ab}^{rP'}$, The restraining moments at a and b may be related to the rotations at a as (similar expressions may be written to describe the moments as a result of rotation at b):

$$v_{aa}^{rP'} = -M_{P(a)}^{r} L/3E_\theta I \tag{24}$$

$$v_{ab}^{rP'} = -M_{P(b)}^{r} L/6E_\theta I \tag{25}$$

Summing the rotations at both ends, we can write similar Equations to (14) and (15), before multiplying by the stiffness of the partial restraint to obtain the moments resulting from the partial restraint for the case in hand which may again be solved simultaneously:

$$M_{P(a)}^{r} = k_{RA}\left(v_{P(a)}' + v_{aa}^{rP'} + v_{ab}^{rP'}\right) \tag{26}$$

$$M_{P(b)}^{r} = k_{RB}\left(v_{P(b)}' + v_{bb}^{rP'} + v_{ba}^{rP'}\right) \tag{27}$$

Finally, by superposition, we can combine the effects of thermal expansion, partial restraint to thermal expansion, and the partially restrained increase in curvature under an applied load P (which must be opposite in sign to curvature arising from the moment which restrains thermal expansion):

$$v_{P(a)}^{r''} = \frac{E_\theta I \alpha T_{xa}' - M_{th\,(a)}^{r} - M_{P(a)}^{r}}{E_\theta I} \tag{28}$$

$$v_{P(b)}^{r''} = \frac{E_\theta I \alpha (T_{xa}' + fL) - M_{th\,(b)}^{r} - M_{P(b)}^{r}}{E_\theta I} \tag{29}$$

Denoting slope of the variation in residual curvature (following application of the restraining moment from the springs to reduce the thermal effect and the curvature from the applied load) with height f_P:

$$f_P = \left(v_{P(b)}^{r''} - v_{P(a)}^{r''}\right)/L \tag{30}$$

The deflected shape is once more calculated by taking the second integral of the curvature, Equation (31). Applying the boundary conditions $v_P^{r}(0) = v_P^{r}(L) = 0$ we obtain Equation (32).

$$v_P^{r''}(y) = v_{P(a)}^{r''} + f_P y \tag{31}$$

$$v_P^r(y) = -\frac{1}{6} f_P y^3 - \frac{1}{2} v_P^{r''} y^2 + \frac{L}{6}\left(3v_{P(a)}^{r''} + f_P L\right) y \tag{32}$$

Figure 4 shows examples of the resulting deflected shapes. On each panel is plotted the thermal deflection based on the mechanical boundary conditions and the non-uniform thermal gradient, as well as the final deflected shape based on the calculation method proposed under 3 different applied loads.

4 2 3 Failure criteria

Referring again to Equation (9), the maximum stress varying along the height in the column is determined by substitution of the appropriate eqn's of deflection from the partially restrained case. However, a moment arising from the partial restraint at both ends must be added to the total moment in this instance.

$$M_{P(a)}^{tot} = E_{ref}\, I\alpha T'_{x(0)} - M_{th\,(a)}^{r} - M_{P(a)}^{r} \tag{33}$$

$$M_{P(b)}^{tot} = E_{ref}\, I\alpha\left(T'_{x(0)} + fL\right) - M_{th\,(b)}^{r} - M_{P(b)}^{r} \tag{34}$$

The distribution of moment along the length of the beam is still linear and therefore the moment as a function of y is given by:

$$M(y) = -P\left(v_{th}^{r}(y) + v_P^{r}(y)\right) + \frac{\left(M_{P(b)}^{tot} - M_{P(a)}^{tot}\right)}{L} y + M_{P(a)}^{tot} \tag{35}$$

Substitution of this into eqn. 16 yields the following for the maximum stress in an extreme fibre:

$$\sigma_{max}(y) = -\frac{\left[-P\left(v_{th}^{r}(y) + v_P^{r}(y)\right) + \frac{\left(M_{P(b)}^{tot} - M_{P(a)}^{tot}\right)}{L} y + M_{P(a)}^{tot}\right] r}{I} + \frac{P}{A} \tag{36}$$

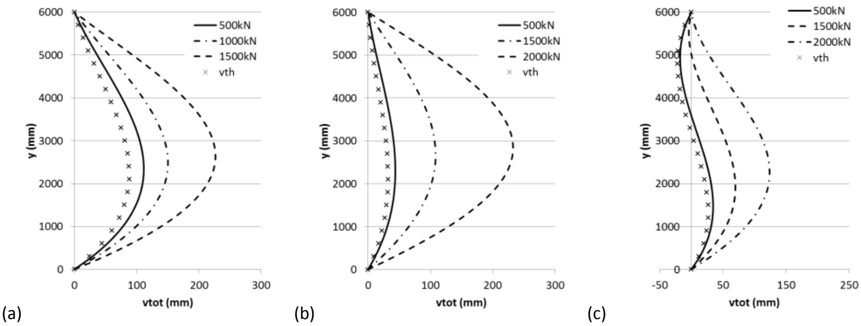

Figure 4. total deflections of a column subject to different non-uniform thermal gradient and different loads (a) $k_{RA} = k_{RB} = 2\text{x}10^9$N/mm, $T'_{xa} = 5$ °C/mm, $T'_{xb} = -1$°C/mm; (b) $k_{RA} = k_{RB} = 2\text{x}10^{10}$, $T'_{xa} = 6$ °C/mm, $T'_{xb} = 0$°C/mm; (c) $k_{RA} = 1\text{x}10^{10}$ N/mm and $k_{RB} = 1\text{x}10^8$ N/mm, $T'_{xa} = 9$ °C/mm, $T'_{xb} = -3$°C/mm.

Figure 5 shows examples of the stress in a partially restrained column. Details of the variation in stiffness and gradient are provided in the figure caption. Where the stress in the column under a load P crosses the dashed line which represents the yield stress as a function of temperature then the column may be assumed to fail. A higher rigidity of the rotational restraint results in a smaller thermal deflection and a lower stress in the extreme fibre compared to a column with lower rotational stiffness. The importance of the non-uniform thermal gradient is clear since the highest stresses in all of the columns, except for the case where the gradient is uniform, clearly occur in the half of the column which is subject to the higher magnitude of thermal gradient. The y-ordinate at which the stress in the column crosses the yield stress is important since it gives an indication of the failure mode. Where the stress crosses the yield stress at the bottom of the column, then failure is a result of squashing – in such instances the thermal deflection makes little difference. Whereas if the stress crosses the yield stress closer to mid height of the column then it is a result of bending failure, and in such instances the increased P-δ moment as a result of thermal deflection may contribute substantially to the failure mechanism.

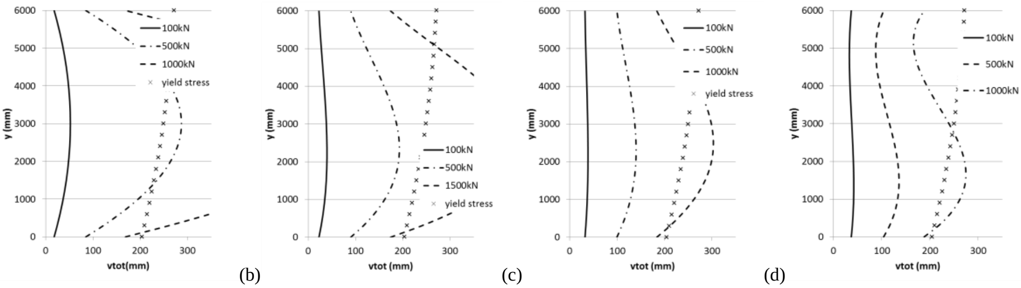

(a) (b) (c) (d)

Figure 5. stress in an extreme fibre of a column subject to different non-uniform thermal gradient along its length and different loads (a) $k_{RA} = k_{RB} = 2x10^8$ N/mm, $T'_{xa} = 3$ °C/mm, $T'_{xb} = 3$°C/mm; (b) $k_{RA} = k_{RB} = 2x10^9$N/mm, $T'_{xa} = 5$ °C/mm, $T'_{xb} = -1$°C/mm; (c) $k_{RA} = k_{RB} = 2x10^{10}$, $T'_{xa} = 6$ °C/mm, $T'_{xb} = 0$°C/mm; (d) $k_{RA} = 1x10^{10}$ N/mm and $k_{RB} = 1x10^8$ N/mm, th$T'_{xa} = 9$ °C/mm, $T'_{xb} = -3$°C/mm.

4 CONCLUSIONS

In this paper we have presented a study of the effects of non-uniform heating along the height of a column on its behaviour. From fundamental principles of structural behaviour we have included the effects of a temperature gradient through a columns section which varies along the columns length. Accounting for varying levels of partial rotational restraint we have derived the thermally deflected shape as well as the deflected shape following application of a mechanical load and as a result of P-δ moments. Assessing the impact of the assumptions made in the analysis presented is the subject of on-going work by the authors.

It has been shown through example that the failure mechanism of a column exposed to localised fire is strongly dependent upon the relative level of restraint provided as well as the thermal deflection arising from the thermal gradient, an aspect which would not be captured if lumped capacitance was assumed.

The method discussed here could be easily adapted to represent composite beams and 1-way spanning slabs. With bending added as a load case the effects of travelling fires on horizontal construction could easily be determined from the analytical expressions developed here. It therefore represents not only an analytical solution for a column under non-uniform temperature effects, it is also a first step towards developing an analytical model which describes structural behaviour under travelling fire conditions.

In the context of modern building design, the tall slender column which was the subject of the fire tests which are referred to in this paper and which the analytical method is exemplified with is an unusual feature, although it might feature as part of, e.g. a façade system or a light weight structure such as might be found in an airport. Nevertheless, the effects of differential heating on columns with larger section size are likely to be limited and the research presented herein is targeted specifically at slender columns.

REFERENCES

[1] J. Stern-Gottfried; Travelling fires for structural design; PhD thesis, the University of Edinburgh, 2011; https://www.era.lib.ed.ac.uk/handle/1842/5244

[2] J. Sjöström; A. Byström; D. Lange; and U. Wickström; Thermal exposure to a steel column exposed to localized fires; SP Report 2012: 43 (2012)

[3] A. S. Usmani and S. Lamont; Key events in the structural response of a composite steel frame structure in fire; Fire and Materials 2004; 28:281–297 (DOI: 10.1002/fam.856)

8th International Conference on Structures in Fire
Guo-Qiang LI, Venkatesh K. R. KODUR, Shou-Chao JIANG, Jian JIANG, Su-Wen CHEN, Guo-Biao LOU (Eds.)
Shanghai, China, June 11-13, 2014

MODELLING THE BOND CHARACTERISTIC BETWEEN CONCRETE AND STEEL BAR IN FIRE

Jamal Khalaf*, Zhao-Hui Huang* and Mi-Zi Fan*

*School of Engineering and Design, Brunel University, Uxbridge, Middlesex UB8 3PH, UK
e-mails: jamal.khalaf@brunel.ac.uk; zhaohui.huang@brunel.ac.uk; mizi.fan@brunel.ac.uk

Keywords: Bond-Slip, Concrete Structures, Fire, Splitting Failure

Abstract. *In this paper a new analytical model for modelling bond-slip between the concrete and steel ribbed bar at elevated temperatures is proposed. This model is established based on a partly cracked thick-wall cylinder theory, with the aid of a smeared cracking approach to take into account the softening behaviour of concrete and average stress-strain of concrete in tension. Also the model considers the splitting failure of concrete cover. The developed model is able to consider a number of parameters, such as different concrete properties and concrete covers, different steel bar diameters. The degradation of bond characteristic between concrete and steel bar at elevated temperatures is also considered in the model. The proposed model is validated against previous tested results.*

1 INTRODUCTION

Exposure of concrete structure to high temperatures leads to significant losses in mechanical and physical properties of concrete and steel reinforcement as well as the bond characteristics between them. Degradation of bond properties in fire may extremely influence the load capacity or flexibility of the concrete structures. Therefore it should be considered for the structural fire design of reinforced concrete structures. Information about the material degradations of concrete and steel under fire exposer are generally available. However, the response of the bond characteristic between concrete and reinforcing steel bar at elevated temperatures is still less understood [1, 2].

Previous research indicates that when the reinforced concrete element is loaded, the stresses in the interface between concrete and steel bar are increased. The capacity of the interface to transmit stress starts to deteriorate at the certain load level, and this deterioration becomes worse at elevated temperatures. The damage at the interface of bond gradually spreads to the surrounding concretes. The development of this process results a slip between the steel and concrete. The mechanism to transfer stresses between concrete and rebar can be represented by adhesion, mechanical interlock, and friction. Adhesion can be defined as the chemical bonds which are developed during the curing process of concrete. This bond is very small and can be lost in the early stages of load or during exposed to fire, therefor it can be ignored in the modelling of bond characteristic in fire. In the case of deformed bars used, stresses are transferred mainly by mechanical interaction between the rebar ribs and the adjacent concretes. Also the friction does not occur until there is a slip between steel bar and concrete [3-6].

For the mechanical interaction of bond, two types of bond failure can take place. The first one is pull out failure (shear off), when the cover of concrete is very large and under high confinement. In this case concretes are split by the wedging action of ribs, and then concretes between the ribs are crushed gradually resulting in a pull-out failure. The second type of failure is splitting failure, when the cracks of concrete cover surrounding the steel bar start to propagate radially. This type of failure is more common for pull-out tests of ribbed steel bars in the real structures [2-4].

At present, a number of analytical models have been developed to calculate bond stress at ambient temperature [3-6, 15]. The most models developed for predicting bond strength are empirical and based on statistics methodology. Thus, these models are highly dependent on the test data, which may limit their validity in different situations [3]. There are a limited number of numerical models available for modelling bond characteristics at elevated temperatures. Pothisiri and Panedpojaman [2] have proposed a mechanical bond-slip model at elevated temperatures based on the theory of thick-wall cylinder and smeared crack of concrete in tension. The model has taken into account the variation of concrete properties with temperature and the differential thermal expansion of rebar and the concrete. However, the model was established to calculate the bond stress only and then improved to calculate the slip based on the correlation between the experimental slip obtained from previous research works [2].

At present, due to a lack of robust model for considering the influence of the bond characteristic between the concrete and steel bar at elevated temperatures, the majority of the numerical models used for predicting the behaviour of reinforced concrete structures in fire is based on the full bond interaction. Hence, the main objective of this paper is to develop a robust numerical model for simulating the local bond-slip between concrete and steel bar under fire conditions. The model presented in this paper is mainly based on the partly cracked thick-wall cylinder theory with the aid of a smeared cracking approach for concrete in tension to simulate the splitting failure of concrete cover. In this numerical model the calculation of the bond slip is based on the constitutive equations of concrete and geometric properties of the rebar. The model can be used to calculate the bond radial pressure, bond stress and slip. Also this numerical model can be easily incorporated into other software, such as VULCAN, for structural analysis of reinforced concrete structures under fire conditions.

2 ANALYTICAL MODEL

The mechanical action between the rebar ribs and the surrounding concretes is explained in Figure 1. The pull out load is decomposed into two directions, parallel and perpendicular to the reinforced steel bar. The transfer of load between a ribbed bar and concrete is achieved by the bearing of the ribs on the concrete. The resultant is compressive forces which are exerted by the ribs. Those forces spread into the surrounding concretes at certain angle. These inclined forces create circumferential tension stresses in the concretes surrounding the steel bar. If these tensile stresses exceed the tensile strength of concrete, splitting failure occurs [5]. Wang and Liu [5] have established a model based on the theory of thick wall cylinder [4] by taking into account the strain-softening of concrete in tension to calculate the maximum radial stress and maximum bond stress.

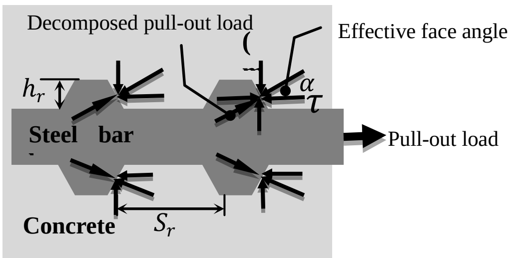

Figure 1. Pull-out load transfer between the steel bar and concrete.

The bond-slip model developed in this paper is mainly based on the partly cracked thick-wall cylinder theory with the aid of a smeared cracking approach and average stress-strain of concrete in tension. As shown in Figure 2, the magnitude of the pressure *P* increases when pull out force acting on the rebar increases. When *P* reaches to the maximum value, which is the capacity of the bond, then the bond will fail and *P* starts to reduce with increasing bond slips. The calculation procedure proposed in this model is:

(1) to assume a R_i ($R_s \leq R_i \leq R_c$); (2) to determine P_i; (3) to calculate the pressure P, the bond stress τ and related bond slip S; (4) to define a point (S, τ) on the bond stress and slip curve.

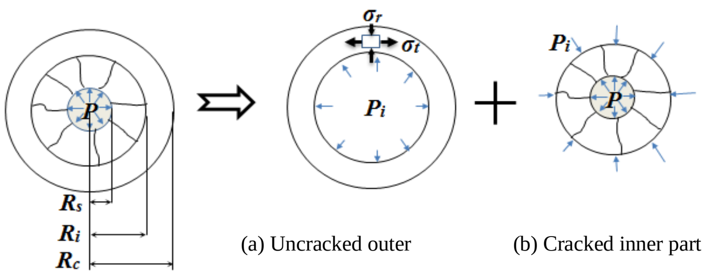

Figure 2. Partly cracked concrete cylinder.

The response of thick wall cylinder method to the internal pressure consists of three stages: the first stage is uncracked stage; the second stage is partly cracked stage; and the third stage is entirely cracked stage [4, 6].

Uncracked stage:

As shown in Figure 3, in this stage linear elastic behaviour of the concrete cylinder is assumed based on the theory of elasticity to calculate the radial stress σ_r as a compressive stress and the tangential stress σ_t as a tensile stress [7]:

$$\sigma_r = \frac{R_i^2 P_i}{R_c^2 - R_i^2}\left[1 - \frac{R_c^2}{r^2}\right] \tag{1}$$

$$\sigma_t = \frac{R_i^2 P_i}{R_c^2 - R_i^2}\left[1 + \frac{R_c^2}{r^2}\right] \tag{2}$$

where:

P_i is the pressure resistance of the elastic zone;
r is a radius from the centre of the rebar;
R_s is the radius of the steel bar;
R_c is the radius of concrete cylinder = R_s+ the least thickness of concrete cover;
R_i is radius of the uncracked inner face.

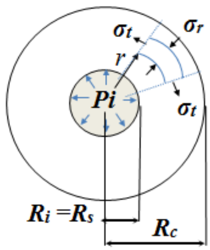

Figure 3. Uncracked elastic stage.

When $R_i = R_s$ at uncracked elastic stage, the tensile stress σ_t can be replaced by the maximum tensile strength of concrete f_{ct} , hence, P_i is calculated as:

$$P_i = f_{ct} \frac{R_c^2 - R_i^2}{R_c^2 + R_i^2} \tag{3}$$

Partly cracked stage:

In this stage the concrete cylinder is subdivided into uncracked outer part and cracked inner part as shown in Figure 2. The contribution of uncracked outer part to the radial stress at the interface with temperature T , $P_{0,T}$ is:

$$P_{0,T} = \frac{R_i}{R_s} P_{i,T} = \frac{R_i}{R_s} \left[f_{ct,T} \frac{R_c^2 - R_i^2}{R_c^2 + R_i^2} \right] \tag{4}$$

In this study smeared cracks are assumed to form in radial direction as tangential stresses exceed the tensile strength of concrete f_{ct} . For the cracked inner part, softening behaviour of concrete in tension, as shown in Figure 4 [5, 8, 9], has to be considered to calculate the tensile stress of concrete σ_t. In the current model average stresses and strains are used. Hence, the tensile stress of concrete σ_t can be determined as:

$$\sigma_t = E_{0,T} \varepsilon_t \qquad (\varepsilon_t \le \varepsilon_{ct,T}) \tag{5}$$

$$\sigma_t = f_{ct,T} \left[1 - \frac{0.85(\varepsilon_t - \varepsilon_{ct,T})}{\varepsilon_{1,T} - \varepsilon_{ct,T}} \right] \qquad (\varepsilon_{ct,T} < \varepsilon_t \le \varepsilon_{1,T}) \tag{6}$$

$$\sigma_t = 0.15 f_{ct,T} \frac{\varepsilon_{u,T} - \varepsilon_t}{\varepsilon_{u,T} - \varepsilon_{1,T}} \qquad (\varepsilon_{1,T} < \varepsilon_t \le \varepsilon_{u,T}) \tag{7}$$

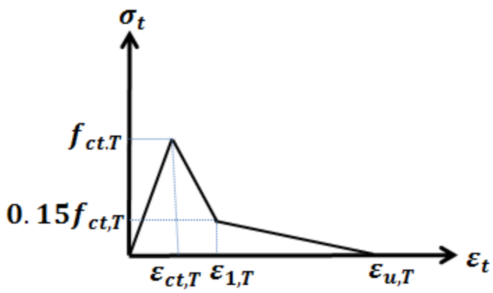

Figure 4. Stress-strain curve of concrete in tension.

where, ε_t is the average of tangential strain at a radial distance r, which can be expressed in terms of tangential elongation, δ_t as:

$$\delta_t = 2\pi r \varepsilon_t \tag{8}$$

When the tensile strength of concrete, f_{ct} , is reached just before the cracks form at a radial distance $r = R_i$ (see Figure 1), by neglecting the effect of Poisson's ratio, the total elongation can be represented as [5].

$$\delta_t = 2\pi r \varepsilon_t \approx 2\pi R_i \varepsilon_{ct,T} \tag{9}$$

Then:

$$\varepsilon_t = \frac{R_i}{r} \varepsilon_{ct,T} \tag{10}$$

At $r = R_s$

$$\varepsilon_{t0} = \frac{R_i}{R_s} \varepsilon_{ct,T} \tag{11}$$

where ε_{t0} is the smeared tangential strain at rebar interface; $\varepsilon_{ct,T}$ is the strain of concrete at tensile strength $f_{ct,T}$. Whereas, $\varepsilon_{ct,T} = f_{ct,T}/E_{0,T}$ and $E_{0,T}$ is the initial elasticity modulus of concrete at elevated temperatures. In Equation (7) $\varepsilon_{u,T}$ is the smeared strain of concrete at tensile stress equal to zero, and $\varepsilon_{u,T} = \beta * \varepsilon_{ct,T}$, $\beta = 10 \sim 25$ [10]. In the current model $\beta = 15$ is adopted. In Equation (6) $\varepsilon_{1,T} = 2/9\ \varepsilon_{u,T}$ is used [10] in which the effect of elevated temperatures is considered.

Now, the total radial stress at the steel bar P_T is equalled to the strength of concrete surrounding the steel bar in which the softening behaviour of concrete is taken into account. Hence, P_T can be calculated as:

$$P_T = \frac{R_i}{R_s} P_{i,T} + \frac{1}{R_s}\int_{R_s}^{R_i} \sigma_t(r)\, dr \tag{12}$$

The integration in Equation (12) can be solved by using Equations (5-7) as [5]:

$$I = \int_{R_s}^{R_i} \sigma_t(r) dr = \frac{f_{ct,T}}{\varepsilon_{1,T} - \varepsilon_{ct,T}} \left[(\varepsilon_{1,T} - 0.15\varepsilon_{ct,T})(R_i - R_s) - 0.85 R_i \varepsilon_{ct,T} \ln\left(\frac{R_i}{R_s}\right) \right] \quad (\varepsilon_{ct,T} < \varepsilon_t \le \varepsilon_{1,T}) \tag{13}$$

$$I = \int_{R_s}^{R_i} \sigma_t dr = \left[\frac{0.15 f_{ct,T}}{\varepsilon_{u,T} - \varepsilon_{1,T}} \left(\varepsilon_{u,T} \frac{R_i \varepsilon_{ct,T} - R_s \varepsilon_{1,T}}{\varepsilon_{1,T}} - R_i \varepsilon_{ct,T} \ln\left(\frac{R_i \varepsilon_{ct,T}}{R_s \varepsilon_{1,T}}\right) \right) \right] + \left[\frac{f_{ct,T}}{\varepsilon_{1,T} - \varepsilon_{ct,T}} \left\{ (\varepsilon_{1,T} - 0.15\varepsilon_{ct,T}) \frac{R_i(\varepsilon_{1,T} - \varepsilon_{ct,T})}{\varepsilon_{1,T}} - 0.85 R_i \varepsilon_{ct,T} \ln\left(\frac{\varepsilon_{1,T}}{\varepsilon_{ct,T}}\right) \right\} \right] \quad (\varepsilon_{1,T} < \varepsilon_t \le \varepsilon_{u,T}) \tag{14}$$

Entirely cracked stage:

In this stage, concrete cover is cracked completely and the confining action of concrete is diminished. This stage is not considered in this paper.

After calculation of radial pressure at elevated temperatures P_T from Equation (12), the bond stress, τ can be determined as [2, 4, 6].

$$\tau = P_T \cot(\alpha) \tag{15}$$

where, α is the effective face angle (see Figure 1) and assumed to be 40^o in the current model.

The effect of high temperature on the bond characteristic is considered by taking into account the degradation of concrete properties at elevated temperatures.

Concrete properties at ambient temperatures specified in Eurocode 2 [12] are adopted in the current model. However, the degradation of concrete tensile strength at elevated temperatures $f_{ct,T}$ proposed by Bazent and Chern [13] is used, that is:

$$f_{ct,T} = f_{ct} \begin{bmatrix} -0.000526\,T + 1.01052 & 20^oC \le T < 400^oC \\ -0.00252\,T + 1.8 & 400^oC \le T < 600^oC \\ -0.0005\,T + 0.6 & 600^oC \le T \le 1000^oC \end{bmatrix} \tag{16}$$

where f_{ct} is the concrete tensile strength at ambient temperature and T is the temperature of concrete. The modulus of concrete elasticity at elevated temperatures $E_{0,T}$ is calculated based on the model proposed by Aslani and Bastami [14]:

$$E_{0,T} = E_0 \begin{bmatrix} 1.0 & 20^oC \le T < 100^oC \\ 1.015 - 0.00154T + 2 * 10^{-7}T^2 + 3 * 10^{-10}T^3 & 100^oC < T \le 1000^oC \\ 0 & T > 1000^oC \end{bmatrix} \tag{17}$$

One of the main contributions of this paper is to develop a procedure to calculate the slippage of the rebar and find the relationship between the bond stress and bond slip based on the constitutive equations of concrete and steel bar's geometries. In this model the bond slip of the rebar can be calculated from three components of displacements. The first component S_h is assumed to act horizontally along the axes of the steel bar (see Figure 1), and equal to the concrete strain in compression between two ribs, that is:

$$S_h = \frac{P_T \mathrm{Cot}(\alpha)\, h_r}{E_{0,T}} S_r \tag{18}$$

where, S_r is the spacing between two ribs of the steel bar and h_r is the height of the ribs.

The second component U_{r1} starts at the beginning of the second stage (partially cracked cylinder). This displacement acts radially when the circumferential elongation is formed due to the propagation of radial cracks and the cracks surrounding the rebar to expand. U_{r1} can be calculated as [15]:

$$U_{r1} = \frac{f_{ct,T}}{E_{0,T}} R_s \frac{\left(\frac{R_c}{R_s}\right)^2 + 1}{\left(\frac{R_c}{R_i}\right)^2 + 1} \tag{19}$$

The third component of the slip U_{r2} is radial displacement resulted from the radial pressure which has a compressive stress affects radially from the steel bar ribs toward the concrete cover $(R_c - R_s)$. U_{r2} is calculated as.

$$U_{r2} = P_T(R_c - R_s)/E_{0,T} \tag{20}$$

Finally the bond slip can be determined as:

$$S = S_h + (U_{r1} + U_{r2})\, cot(\alpha) \tag{21}$$

3 VALIDATIONS

As mentioned above the tested data on the bond characteristics between the concrete and steel bars at elevated temperatures are limited. Hence, the proposed model was validated using two available previous experimental results of pull-out testes at elevated temperature. The first test was carried out by Morley and Royles [16]. In this test the cylindrical specimens were used in order to obtain a uniform heat flow from the outside surface to the bond interface. The length of these samples was 300 mm with bond length of 32 mm. The cubic compressive strength of concrete made with siliceous aggregate was 35.0 N/mm^2 at the time of the test. Cover of the concrete specimens was 55 mm and deformed steel bar was used with diameter of 16 mm. R_c was 63 mm (R_c=*cover+D/2*). All tested material properties and geometries of the specimens were used for the model's predictions. Figure 5 shows the comparison between the tested results and current model's predictions for different tested temperatures at the interface of the bond. It is evident that the current model's predictions agreed reasonable well with the tested data.

The second test was conducted by Diederichs and Schneider [1]. In this study deformed steel bar of 16 mm was used and concrete with range of cubic compressive strengths of 48.0-60.9 N/mm^2. Specimens were made with bond length of 80 mm and concrete cover of 78 mm to give R_c=*78+16/2=86* mm. Figure 6 illustrates the comparison between the tested results and the predictions of the current model for different testes temperatures. Again a good agreement with the tested results was achieved by current model.

4 CONCLUSIONS

In this paper an analytical model has been developed to model the bond-slip relationship between the steel rebar and concrete at elevated temperatures in which the splitting failure of concrete cover is considered. The model is based on the thick-wall cylinder theory with the considering of the partially cracked of concrete cover, and the smeared crack of concrete in tension. The model was validated against the previous tested data and reasonable agreements were achieved. It is evident that this new model is able to take into account the variation of the concrete properties, different concrete covers and steel bars' geometries as well as wide range of temperatures.

The proposed model addresses one of the key problems for modelling structural behaviour of reinforced concrete members under fire conditions. The model presented in this paper can be easily incorporated into other software, such as VULCAN, for structural fire design of reinforced concrete structures.

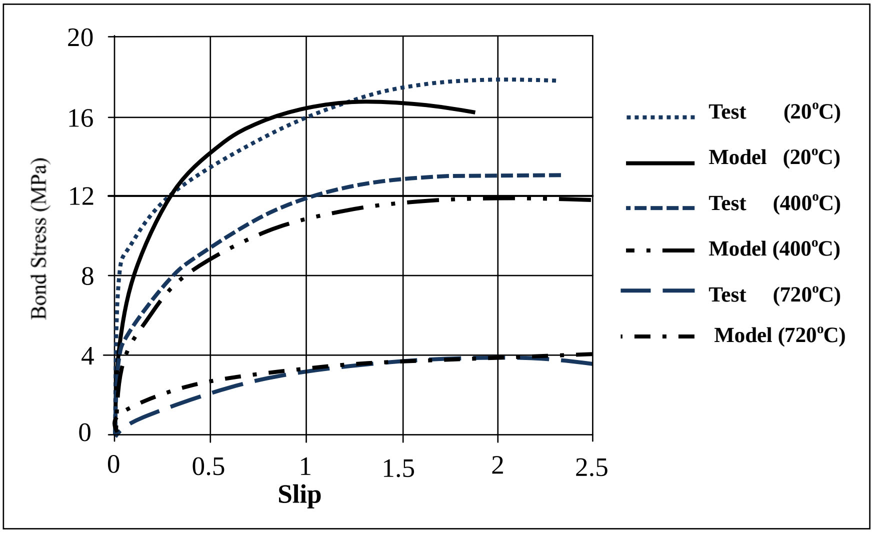

Figure 5. Comparison between the current model's predictions against the tests results [16].

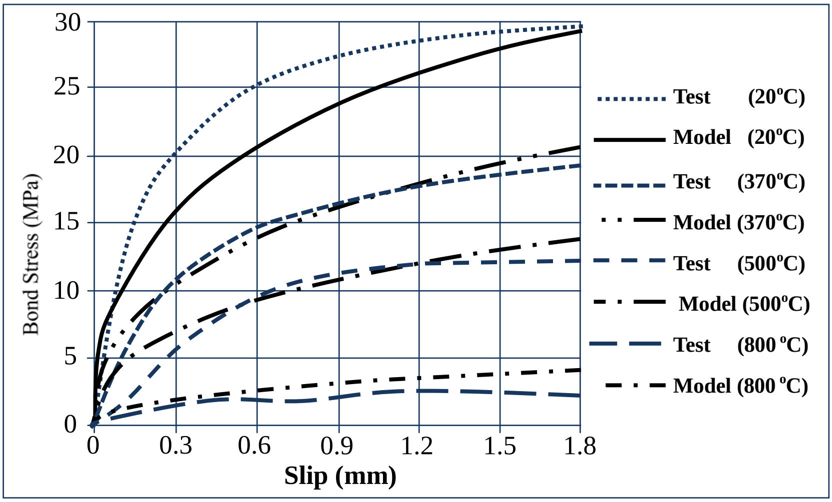

Figure 6. Comparison between the current model's predictions against the tests results [1].

ACKNOWLEDGMENTS

The authors gratefully acknowledge the financial support of the Ministry of Higher Education and Scientific Research of Iraqi government for this PhD project.

REFERENCES

[1] Diederichs U. and Schneider U., “Bond strength at high temperatures,” Magazine of concrete research , 33(115), 75-84, 1981.

[2] Pothisiri T. and Panedpojaman P., “Modeling of mechanical bond–slip for steel-reinforced concrete under thermal loads,” Engineering Structures, 48, 497-507, 2013.

[3] Huanzi W., “An analytical study of bond strength associated with splitting of concrete cover,” Engineering Structures, 31, 968-975, 2009.

[4] Tepfers R., “Cracking of concrete cover along anchored deformed reinforcing bars,” Magazine of concrete research, 31(106), 3-12, 1979.

[5] Wang X. and Liu X., “A strain-softening model for steel-concrete bond,” Cement and Concrete Research, 33,1669-1673, 2003.

[6] BIGAJ A. J., “Structural Dependence of Rotation Capacity of Plastic Hinges in RC Beams and Slabs,” PhD thesis Technische University Delft,1999.

[7] Timoshenko S. and Goodier J. N., Theory of Elasticity, McGraw-Hill Book Company, 1951.

[8] CEB-FIP Model code 1990, final draft ,committe euro-international du beton,Bulletin d'information No.203-205, 1991.

[9] Pantazopoulou S. J. and K. D. Papoulia K. D.,“Modeling Cover-Cracking Due To Reinforcement Corrosion In Rc Structures,” Journal of Engineering Mechanics, ASCE, 127(4), 342 - 351, 2001.

[10] Zhaohui Huang, “The Analysis Of Thermal And Fire Performance Of Cementitious Building Components,” PhD Thesis,University of Central Lancashire,UK, October 1995.

[11] John Robert Prince M. and Bhupinder S., “Bond behaviour of deformed steel bars embedded in recycled aggregate concrete,” Construction and Building Materials, 49, 852–862, 2013.

[12] CEN EUROPEAN STANDARD, Eurocode 2: Design of concrete structures - Part 1-1 : General rules and rules for buildings, London: British Standards Institution, 2004.

[13] Bazant Z.P. and Chern J.C., “Stress-Induced Thermal and Shrinkage Strains in Concrete,” Jornal of Engineering Mechanics, ASCE, 113(10), 1493-1511, 1987.

[14] Aslani F. and Bastami M., “Constitutive Relationships for Normal-and High-Strength Concrete at Elevated Temperatures,” ACI MATERIAL JOURNAL, 108(4), 355-364, 2011.

[15] Nielsen C. V. and Bicanic N., “Radial fictitious cracking of thick-walled cylinder due to bar pull-out,” Magazine of Concrete Research, 54(3), 215-221, 2002.

[16] Morley P.D., Effects of Elevated Temperature on Bond in Reinforced Concrete, PhD Thesis, University of Edinburgh , 1982.

8th International Conference on Structures in Fire
Guo-Qiang LI, Venkatesh K. R. KODUR, Shou-Chao JIANG, Jian JIANG, Su-Wen CHEN, Guo-Biao LOU (Eds.)
Shanghai, China, June 11-13, 2014

STUDY ON BEHAVIOR OF REINFORCED CONCRETE COMPONENT SUBJECTED TO DIFFERENT FIRE CONDITIONS

Zhen-Liang Li*, Jin-Cheng Zhao* and Yong-Feng Zhao*

*Department of Civil Engineering, Shanghai Jiaotong University, Shanghai 200240, China
e-mails: lizhenjiang@sjtu.edu.cn, jczhao@sjtu.edu.cn, zhaoyf@sjtu.edu.cn

Keywords: Reinforced concrete component, ISO834 Fire, FDS fire, Structure fire response analysis

Abstract. *This paper presents numerical studies on behavior of reinforced concrete components subjected to different fire conditions. The ISO834 fire and uniform heating condition have been commonly used for fire tests and simulations. However, the ISO834 fire does not contain the temperature decline part, which may result in structural failure in reinforced concrete structure. Fire in FDS scenario simulation contains 3-stage of fire, i.e. heating part, full development part and decline part. Coupled thermo-mechanical simulations were conducted to obtain the temperature distribution inside the components, and the deformation mode. When subjected to the FDS fire, beam gets an earlier and higher peak temperature, which causes the middle span deflection 45% more than that under ISO834 fire and so does the deformation along beam's width direction. However, by segmented input, both top horizontal displacement and axial displacement of column subjected to FDS fire are less than that of ISO834 fire.*

1 INTRODUCTION

Structural fire-resistant time is determined based on the standard fire condition according to traditional design discipline. Standard fire condition, such as ISO834 fire, is a unified drab heating process, which never attenuates and extinguishes. However, research shows that temperature field distribution in a real fire is closely related to factors such as architectural form, fire load density, and ventilation. Therefore, it may generate large deviation, if standard fire condition is used to represent a real fire. Some scholars believe that if temperature - time curve of a real fire can be got, fire resistant design should be based on it[1].

Along with the deepening of the research on mechanical properties of the structure in fire, more and more researchers have paid attention to the influence of the fire decline part. Due to the thermal inertia of concrete, when fire attenuates, surface temperature of the structure starts to drop, while its internal temperature is still on the heating part, which will form uneven temperature stress and cause a new structure injury. Thus, when mechanical properties of reinforced concrete components in fire were studied, fire decline part should be taken into consideration.

In this paper, the ISO834 fire and average heating curves calculated in FDS will be used to carry out fire response analysis of reinforced concrete components.

2 TWO DIFFERENT FIRE CONDITIONS

2.1 The ISO834 fire

In the research on the structure fire response, the fire temperature of the scene is generally estimated according to ISO834 fire. The formula is as follows[2]:

$$T = 345\log_{10}(8t+1) + T_o \tag{1}$$

where T is the fire temperature, and T_0 is the room temperature, and t is the fire combustion duration. The ISO834 temperature curve is shown in Figure 1.

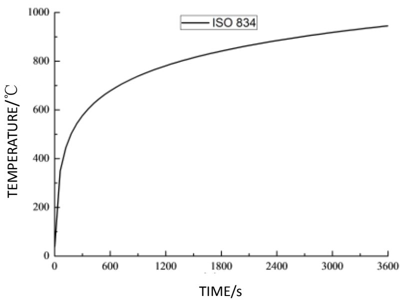

Figure 1. ISO834 temperature curve.

2.2 The FDS fire

FDS is short-hand for Fire Dynamics Simulator, which is an effective and reliable fire smoke movement analysis software[3,4]. In this paper, a "L" type high-rise residential model is established according to the actual structure size, as shown in Figure 2.

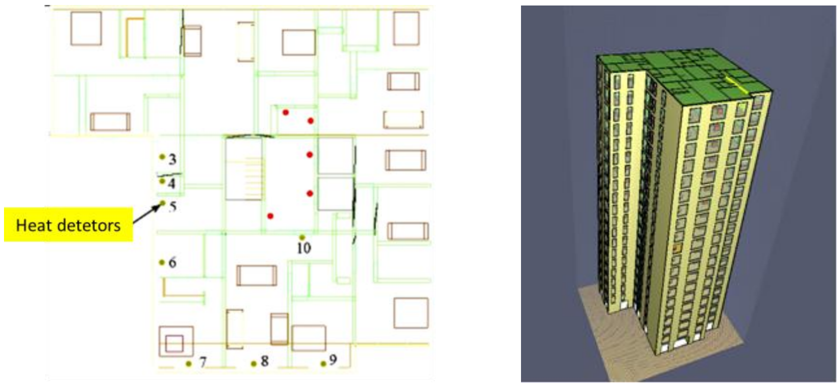

Figure 2. "L" type high-rise residential model.

Fire is set on the mattress of bedroom on the 10th floor. Heat detectors are set beside windows and doors. Once heat detectors reach corresponding temperature, windows and doors will automatically open, which is used to simulate the fire damage to doors and windows.

In the bedroom, 84 heat detectors are set along the surface of beams and columns, and the average temperature-time curve is taken as the FDS fire, as shown in Figure 3.

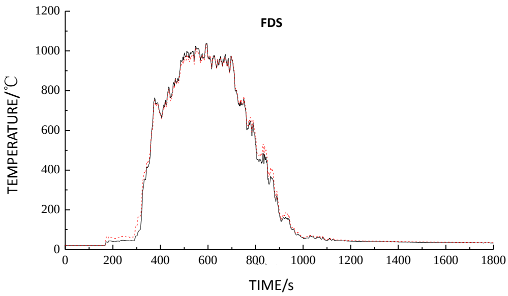

Figure 3. Average temperature curves calculated by FDS.

3 THE FIRE TEMPERATURE FIELD ANALYSIS OF REINFORCED CONCRETE BEAM AND COLUMN

Generally, building indoor fire burns between 15 to 60 min, this article selects t = 30 min(1800 s) as the analysis time, and finite element software ANSYS was used to analyze temperature field distribution of reinforced concrete components under different fire conditions. Table 1 lists the parameters used in the finite element simulation.

Table 1. Parameters of beam and column.

Parameters	Beam	Column
Concrete grade	C40	C40
Steel grade	HRB335	HRB335
Longitudinal steel ratio	0.43%（2 ϕ16）	0.78%（4 ϕ20）
Protective layer thickness	35mm	35mm
Loading ratio	0.4	
Axial compression ratio		0.6
Number of sides subjected to fire	3	4

3.1 Temperature field analysis of beam

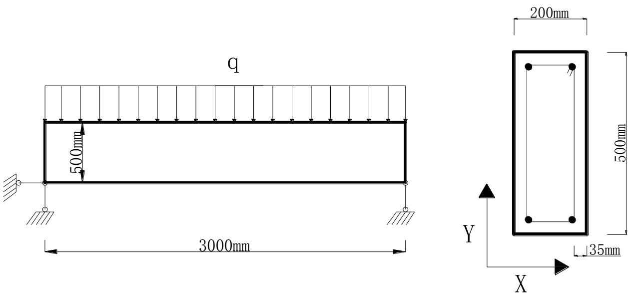

Figure 4. Simple supported beam.

As shown in Figure 4, the beam is simply supported with three sides subjected to fire. In Figure 5, it shows that under ISO834 fire, temperature variation trend on each measuring point is similar, however, with the depth increasing, the amount of temperature increment is gradually reduced. At the time of 1800s, temperature at 25 mm depth is around 400 ℃, temperature at 50 mm depth is around 250 ℃.

Temperature variation trend on each measuring point is obvious different when beam is exposed to FDS fire, along with the depth increasing, it changes to flatten out. There are three stages of temperature changes of beam subjected to FDS fire, heating part, full development part and decline part, and its highest temperature appears inside the cross section at 1800s.

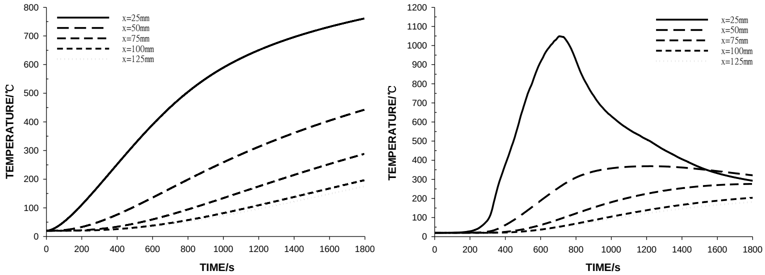

(a) Under ISO834 fire, y=35mm (b) Under FDS fire, y=35mm

Figure 5. Variation of temperature with different depth along the beam’s width direction.

In order to intuitively observe the temperature field distribution inside the beam, temperature nephogram of the cross section at 1800s is shown in Figure 6. The internal temperature of the beams is stratified. Among all, the temperature in the bottom and two flanks is higher than any other place, which is slightly below the fire temperature. Temperature field distribution is not uniform along the vertical and horizontal direction. Within 10-40 mm from surface, temperature gradient is large, while in the internal section, temperature gradient is indistinctive. As with the time grows, the affected area has been increased. FDS fire has a wider influence range than ISO834 fire, as the former has an earlier and higher peak temperature. Because of decline part, the highest temperature at 1800s appears inside the cross section, which means when FDS fire goes into the decline part, the internal temperature of component continues on the rise, and may cause new uneven temperature stress field. Therefore, it tends to be unsafe to only consider fire heating part when structure fire resistance analysis is conducted.

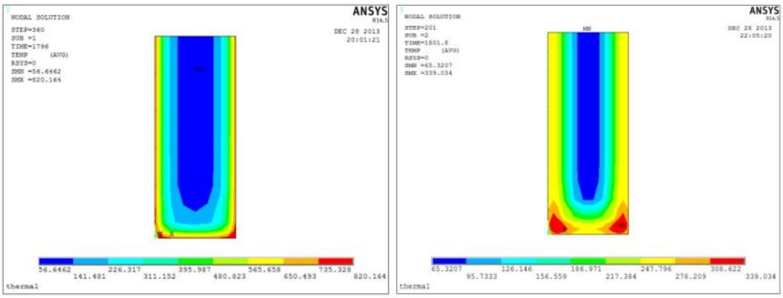

(a) Under ISO834 fire (b) Under FDS fire

Figure 6. Temperature nephogram on the beam cross section

3.2 Temperature field analysis of column

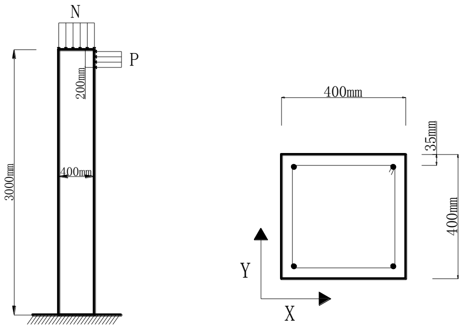

Figure 7. Column with one fixed end.

Generally, when temperature field of the components is studied, the variation of temperature along the component length direction is ignored, and take it as a two dimensional variable. In real fire, it generates amount of high temperature plume, which first gathered to the ceiling, and then spreads around. Thus, there are large differences between temperatures distributed along the vertical direction. Temperature-time curves recorded by heat detectors are set every 30 cm in column's height direction, as shown in Figure 8.

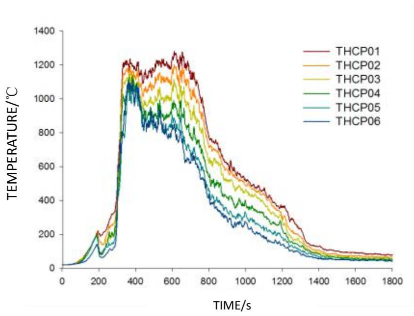

Figure 8. Temperature curves along the column's height direction.

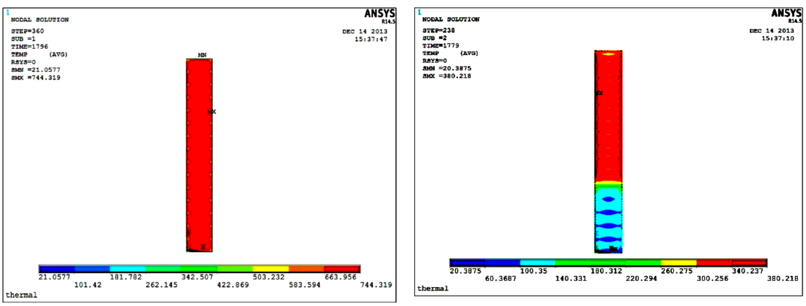

(a) Under ISO834 fire

(b) Under FDS fire

Figure 9. Temperature nephogram along the column's height direction.

As shown in Figure 9, FDS fire is segmented input to reflect the difference of temperature distribution along the column's height direction, which is similar to the real fire scenario. Temperature is hierarchically distributed along the column's height direction, while ISO834 fire is stick to the assumption of two-dimensional temperature field as a compare.

4 THE STRUCTURE FIRE RESPONSE ANALYSIS OF REINFORCED CONCRETE BEAM AND COLUMN

4.1 Structure fire response analysis of beam

The temperature files calculated in the previous section are used to conduct structure fire response analysis for both beam and column.

As shown in Figure 10, middle span deflection of beam at t=0s is corresponding to the room temperature condition, after 1800s exposed to fire, it increases significantly, which fully proves that high temperature has a great influence on the mechanical properties of reinforced concrete material. When temperature exceeds 300 ℃, the expansion of the material is accelerated development, while the elastic modulus falls sharply, and together with the emergence of the short-term high temperature creep, the deflection is growing rapidly. Middle span deflection under FDS fire goes beyond that under ISO834 fire at around 400s. This is because FDS fire simulates the flashover in real fire, in this stage, fire suddenly increases to a peak temperature higher than in ISO834 fire, so that the temperature in the beam rises sharply, and material elastic modulus is greatly reduced, leading to larger middle span deflection. In decline part, although beam's surface temperature decreases, its internal temperature is still on the rise, deflection continues to increase.

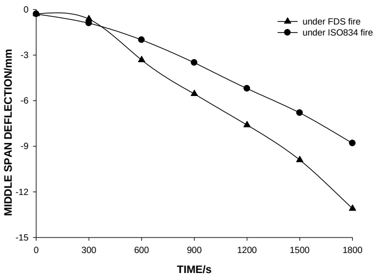

Figure 10. Middle span deflection in different fire conditions.

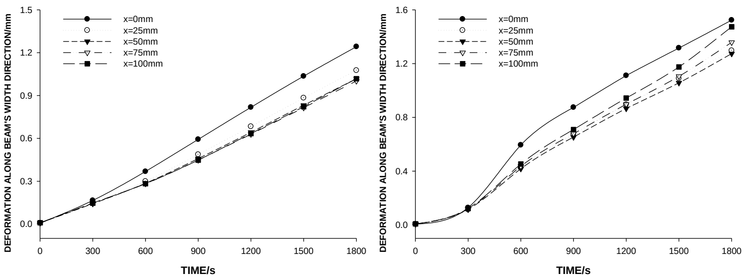

(a) Under ISO834 fire, y=35mm (b) Under FDS fire, y=35mm

Figure 11. Deformation along beam's width direction.

In fire condition, thermal expansion of concrete is far more than the peak compressive strain (about 2×10^{-3}) at room temperature. Due to the thermal inertia of concrete, surface temperature of beam rises faster, and expansion deformation is greater than that in interior. It can be seen clearly from Figure 11 that in fire decline part, thermal expansion rate in surface layer becomes slow and even stall, however, it continues to increase in interior. Deformation along beam's width direction in different fire conditions shows the similar rule. The final deformation in FDS fire is 20% beyond that in ISO834 fire.

4.2 Structure fire response analysis of column

Figure 12 shows top horizontal displacement of axial compression column with a horizontal load and four sides exposed to fire. At the time of 1800s, maximum top horizontal displacement is 11.6 mm under FDS fire, which is less than that under ISO fire. This is on account of segmented input was used to consider the temperature difference along column's height direction. Temperature in the bottom of column is much lower than in the upper part, so that the column has a better horizontal stiffness.

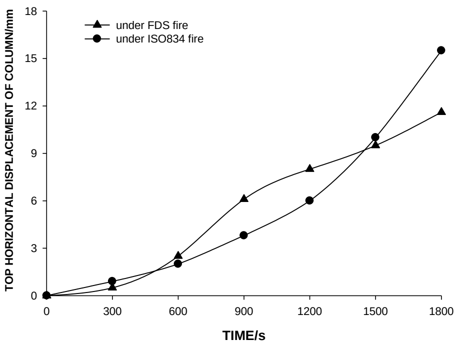

Figure 12. Top horizontal displacement of column.

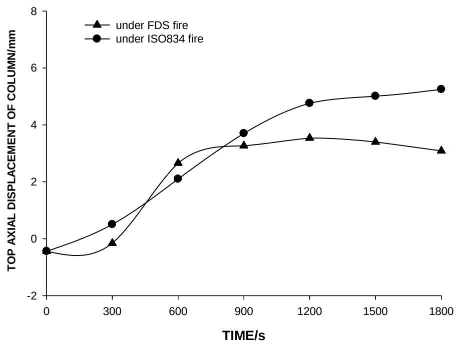

Figure 13. Axial displacement on the top of column.

As shown in Figure 13, initial axial displacement of column is negative (constringent). When the column is subjected to fire, elongation is generated due to thermal expansion. With the temperature rising, the thermal expansion increases, however, elongation of column is under a certain inhibition because of the vertical load. As time goes on, column's stiffness has fallen sharply, while the concrete compressive strain and high temperature transient strain are developed greatly. Column heats up quickly under FDS fire, so it's surface stiffness decreases significantly. During the full development part, the thermal expansion is greater than strain produced by stress, showing as rapid elongation. When FDS fire falls into the decline part, concrete compressive strain increases, and axial elongation begin to decrease.

5 CONCLUSIONS

In this paper, by means of numerical simulation method, high-rise residential indoor fire is simulated, and the fire response analysis of reinforced concrete components has been carried out. The main conclusions are as follows.

(1) When subjected to FDS fire, middle span deflection in beams and deformation along width are both greater than that under ISO834 fire, due to an earlier and higher peak temperature and influence of fire decline part.

(2) The results of column' fire response is on the contrary. By segmented input, both top horizontal displacement and axial displacement of column subjected to FDS fire are less than that of ISO834 fire.

(3) The real fire is a random process. There is large deviation between a real fire and the standard fire. Using FDS fire as temperature input based on the real fire simulation has great significance in improving the precision of structural fire response analysis.

REFERENCES

[1] Guo Z H., Shi X D., *High Temperature Performance of Reinforced Concrete and Its Calculation*, Tsinghua university press, Beijing, 2002.

[2] International Organization for Standardization ISO/TR., "Fire Safety Engineering - Part 2: Design Fire Scenarios and Design Fires", 1999.

[3] Moghaddam A. Z., Moinuddin K. and Thomas I. R., "Fire Behaviour Studies of Combustible Wall Linings Applying Fire Dynamics Simulator", *15th Australasian Fluid Mechanics Conference*, The University of Sydney, Sydney, Australia, 2004.

[4] Mouilleau Y., Champassith A., "CFD Simulations of Atmospheric Gas Dispersion Using the Fire Dynamics Simulator (FDS)", *Journal of Loss Prevention in the Process Industries*, (22/03), 316–323, 2009.

[5] Lange D., Röben C., and Usmani A., "Tall Building Collapse Mechanisms Initiated by Fire: Mechanismsand Design Methodology", *Engineering Structures*, (36), 90-103, 2012.

[6] Tan K H., Nguyen T T., "Experimental Behaviour of Restrained Reinforced Concrete Columns Subjected to Equal Biaxial Bending at Elevated Temperatures", *Engineering Structures*, (56), 823-836, 2013.

[7] Lie T T., Irwin R J., "Method to Calculate the Fire Resistance of Reinforced Concrete Columns with Rectangular Cross Section", *ACI Structural Journal*, (1), 52-60, 1993.

[8] Capua D D., Mari A R., "Nonlinear Analysis of Reinforced Concrete Cross-sections Exposed to Fire", *Fire Safety Journal*, (42), 139-149, 2007.

[9] Gao W Y., Dai J G., Teng J G., and Chen G M., "Finite Element Modeling of Reinforced Concrete Beams Exposed to Fire", *Engineering Structures*, (52), 488-501, 2013.

[10] Kodur V K R., Yu B L., and Dwaikat M M S., "A Simplified Approach for Predicting Temperature in Reinforced Concrete Members Exposed to Standard Fire", *Fire Safety Journal*, (56), 39-51, 2013.

[11] Bratina S., Cas B., Saje M., and Planinc I., "Numerical Modelling of Behaviour of Reinforced Concrete Columns in Fire and Comparison with Eurocode 2", *International Journal of Solids and Structures*, (42), 5715-5733, 2005.

[12] Hou L F, Li M., Cui W Y., and Liu Y C., "Numerical Simulation and Analysis of On-building High-rise Building Fires", *The 5th Conference on Performance-based Fire and Fire Protection Engineering*, Procedia Engineering (11), 127-134, 2011.

8th International Conference on Structures in Fire
Guo-Qiang LI, Venkatesh K. R. KODUR, Shou-Chao JIANG, Jian JIANG, Su-Wen CHEN, Guo-Biao LOU (Eds.)
Shanghai, China, June 11-13, 2014

PERFORMANCE-BASED APPROACH FOR FIRE RESISTANCE DESIGN OF FRP-STRENGTHENED RC BEAMS

Wan-Yang Gao*, Jian-Guo Dai* and J.G. Teng*

*Department of Civil and Environmental Engineering, The Hong Kong Polytechnic University
Email: wangao@polyu.edu.hk, cejgdai@polyu.edu.hk, cejgteng@polyu.edu.hk

Keywords: Fiber-reinforced polymer (FRP), Strengthening, Reinforced concrete (RC) beams, Fire, Performance based design, Finite element analysis

Abstract. *A three-level performance-based approach for the fire resistance design of FRP-strengthened reinforced concrete (RC) beams is presented in this paper. For un-protected FRP-strengthened RC beams (i.e., Level I), an extensive finite element (FE) parametric study was carried out to investigate their fire resistance. The numerical results were then used to develop a set of explicit design formulae with due consideration of the significant design parameters. For RC beams with the FRP strengthening system fully protected to remain effective during a fire (i.e., Level-III), the fire resistance design task degenerates to a thermal analysis problem and can be realized by a simple method previously developed by the authors. For the intermediate level (i.e., Level-II) of design, a simple design-oriented method is presented based on the "500℃ isotherm method" for sectional moment capacity prediction. The validity of the design-oriented method is demonstrated through comparisons with FE predictions.*

1 INTRODUCTION

Externally bonded (EB) fiber-reinforced polymer (FRP) reinforcements have been increasingly used in the strengthening and retrofitting of reinforced concrete (RC) structures. However, the FRP strengthening technique also suffers from one serious limitation, particularly for indoor applications: the mechanical and bond properties of FRP laminates reduce quickly under fire exposure. While standard fire tests can be used to evaluate the fire resistance of RC members strengthened with FRP laminates, not enough tests have been undertake so far to allow the formulation of a comprehensive design approach for the fire resistance design of FRP-strengthened RC members. This lack of research has imposed a significant restriction on the use of the FRP strengthening technique, particularly in fire-critical applications (e.g. indoor applications). This paper aims at bridging the above knowledge gap for FRP-strengthened RC beams in flexure. A three-level performance-based approach for predicting the fire resistance of FRP-strengthened RC beams is presented in this paper based on extensive parametric studies using validated FE models proposed by the authors.

2 THREE-LEVEL PERFORMANCE-BASED DESIGN

The performance-based approach presented in this paper is based on a three-level (i.e., I, II and III) design framework that aims to strike a good balance between the expected strength contribution of the FRP strengthening system and the fire resistance rating to be achieved [1]. Figure 1 provides a description of this three-level design framework, in which the horizontal axis represents the strength contribution provided by the FRP strengthening system and the vertical axis represents the required fire-resistance period. It is clear that, the least demanding level of fire resistance design in terms of fire protection, referred to as Level I, covers situations where fire insulation is not needed and the original RC beam can satisfy the required fire resistance rating under the new service load, regardless of the extent of FRP strengthening. As a result, the fire resistance evaluation of the un-protected FRP-strengthened RC beam can be equated to that of a conventional RC beam; the FRP strengthening system is assumed to become completely ineffective during the very early stage of a fire. The most demanding level (i.e., Level III in Figure1) covers situations where the FRP strengthening system needs to remain fully or partially effective during a fire. In these situations, a thick fire insulation layer is required to protect the FRP strengthening system below a “critical” temperature. This critical temperature depends on the glass transition temperature of the FRP material, leading to an almost full contribution of the FRP strengthening system during the fire [2]. Between these two levels (i.e., the intermediate level or Level II in Figure 1), the fire insulation layer needs to ensure that a sufficiently large portion of the pre-fire strength of the protected RC beam can be retained during a fire even though the FRP strengthening system is allowed to become completely ineffective. In other words, the purpose of fire insulation is to control the temperatures of the concrete and the steel reinforcement so that they can safely resist the service load during a fire while the temperature control for the FRP strengthening system is no longer a concern. This three-level design framework has previously been discussed by other researchers [1], but its implementation needs much more research.

For Level-I fire resistance design, the tabulated methods adopted by existing design codes [3-6] or a simple design equation [7] may be used in the fire resistance evaluation of RC beams. However, the use of the tabulated method for the fire resistance evaluation of RC beams is still a matter of controversy as it does not always lead to conservative fire resistance predictions for RC beams [7]. The equation proposed by Kodur and Dwaikat [7] is for conventional RC beams for which the service load under fire is around 50% of the load-carrying capacity at room temperature. Therefore, the proposed equation is likely to be inapplicable to the Level-I design of un-protected FRP-strengthened RC beams for which higher load ratios (ratios of the service load under fire to the load-carrying capacity at room temperature) are expected as the FRP strengthening system needs to be ignored in the calculation of the load ratio. Therefore, a more refined design method is required for the fire resistance evaluation of FRP-strengthened RC beams with a higher load ratio for the realization of the Level-I approach.

For Level-III design, the fire resistance design task degenerates to a temperature analysis problem. A simple method previously developed by the authors [8] for predicting temperatures in insulated beam sections can be used to determine the thickness of the fire insulation layer needed to ensure that the temperatures in the FRP strengthening system stay below its critical temperature throughout the specified fire duration. Therefore, this paper is focused on developing methodologies for the Level-I and Level-II fire resistance design of FRP-strengthened RC beams. Indeed, most strengthening applications in buildings are likely to require design of these two lower levels of fire protection.

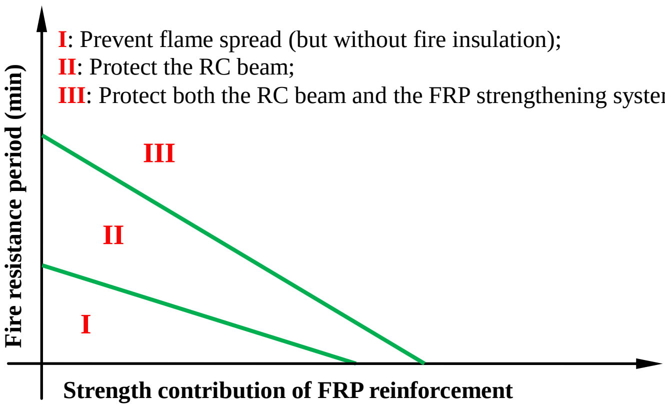

Figure 1. Schematic of three-level performance-based fire resistance design (adapted from Ref. [1]).

This paper consists of two major parts. The first part examines the fire resistance of RC beams (as a close approximation of un-protected FRP-strengthened RC beams) by presenting the results from a finite element (FE) parametric study and a set of explicit design formulae based on these results. The accuracy of the proposed formulae is demonstrated through comparison with both the FE results and standard fire test results available in the literature. The second part presents a simple design-oriented method to assess the moment capacity of insulated FRP-strengthened RC beams under fire in which the contribution of the FRP strengthening system is ignored (i.e., the FRP strengthening system is assumed to be completely ineffective due to the high temperatures it has been subjected to). In this simple design-oriented method, the "500 ^{o}C isotherm method" is used in combination with the temperature field predictions of insulated beam sections as described elsewhere [8,9]. The proposed design-oriented method is validated through comparisons with fire resistance data obtained using an accurate FE model [10]. FE results instead of fire test data of insulated FRP-strengthened RC beams are used in validation because the latter are very scarce.

3 EXPLICIT DESIGN FORMULAE FOR BARE RC BEAMS

3.1 FE parametric study

A large parametric study using an FE model developed by the authors [11] was carried out to examine the fire resistance of bare RC beams exposed to a standard fire. Previous studies [7,12] have revealed that the span-to-depth ratio (l/d), load ratio (γ), concrete cover depth (c), reinforcement ratio of tension steel rebars (ratio of the total area of tension steel rebars to that of the section gross section) (ρ_s), aggregate type of concrete (μ_{ag}), distribution ratio of tension steel rebars (ratio of the total area of corner tension rebars to the total area of tension rebars, $A_{\mathrm{sc}}/A_{\mathrm{st}}$), and beam width ($b$) have significant influences on the fire resistance of RC beams. Some other factors, such as concrete spalling and the axial and rotational restraint conditions of beams, have also been found to affect the fire resistance of RC beams [7,13,14,17]. Concrete spalling is not considered in the present study since most RC beams requiring strengthening are made of normal strength concrete for which concrete spalling is a minor concern. In a real RC building in fire, the restraint conditions of an RC beam are very complicated and may change during the fire as a result of deformations of the adjacent columns. Therefore, only simply supported RC beams were analyzed in the present FE parametric study to provide a simple and conservative approximation [7].

The cases covered by the extensive FE parametric study include three reference concrete cross-sections (250mm×250mm, 250mm×450mm and 250mm×600mm), four different concrete cover depths (20mm, 30mm, 40mm and 50mm), five different ratios of tension steel reinforcement (0.3%, 0.9%, 1.2%, 1.5% and 2.4%), five different load ratios (0.1, 0.3, 0.5, 0.7 and 0.9), two aggregate types (calcareous and siliceous aggregate), six different distribution ratios of tension rebars ($A_{\mathrm{sc}}/A_{\mathrm{st}}$ = 1, 3/4, 2/3, 1/2, 1/3 and 1/4), and seven different beam widths. As the simulated specimens have the same span (i.e., 4 m), the three different cross-sections lead to three different span-to-depth ratios. Besides, the concrete cover depth specified in the parametric study represents the clear distance from the side and the bottom surfaces to the exterior surface of tension steel reinforcement. For all simulated RC beams, the compressive strength of concrete and the yield strength of steel rebars at ambient temperature were assumed to be 30 MPa and 375 MPa respectively; the latter approximates closely the measured yield strengths of the HRB 335 steel bars commonly used in China. The ISO 834 standard fire curve was adopted as the fire scenario. For the purpose of reducing the computational effort, when investigating the effects of aggregate type and distribution ratio of tension rebars, only a single section type (i.e., 250 mm × 250 mm) was considered. Different beam widths lead to different thermal diffusions in the section. In the FE parametric study, fourteen RC beams with seven different beam widths (200mm, 250mm, 300mm, 350mm, 400mm, 450mm, 600mm) but a fixed beam depth of 450 mm were analyzed under two different load ratios (i.e., 0.5 and 0.7). In total, the FE parametric study included 512 simply supported RC beams. For these RC beams, the fire resistance period is deemed to have been reached when [15]:

(a) the maximum mid-span deflection of the beam exceeds $l/20$ at any fire exposure time; or

(b) the rate of mid-span deflection exceeds $l^2/9000d$.

where l is the clear span of the beam specimen and d is the beam depth, both in millimeters.

3.2 FE results versus an existing design method

The FE predictions of the fire resistance periods of 512 beams are herein compared with the results obtained using the tabulated methods (Figures. 2a to 2c) and the simple design equation proposed by Kodur and Dwaikat [7] (Figure 2d). The relevant design tables provided in existing design codes (i.e., the tabulated design methods), such as BS 8110-2 [3], ACI 216.1 [4], EN 1992-1-2 [5] and AS 3600 [6] specify a minimum concrete cover depth and a minimum beam width for a required fire-resistance rating. It is noteworthy that the concrete cover depth defined in BS 8110-2 [3] and ACI 216.1 [4] is the clear distance from the beam surface to the exterior of the tension rebars, whereas it is the distance between the beam surface and the centroid of tension reinforcement in EN 1992-1-2 [5] and AS 3600 [6].

Figures 2a to 2c clearly indicate that the fire resistance predictions by the tabulated methods deviate substantially from the FE results. The tabulated methods underestimate the fire resistance of RC beams at lower load ratios, while provide unsafe designs at higher load ratios. The poor performance of the tabulated methods is mainly due to the omission of some important parameters. The fire resistance periods predicted by Kodur and Dwaikat's equation [7] agree reasonably well with the FE predictions when the load ratios are around 0.5, but not so well when the load ratios are lower (Figure 2d). The major drawback of Kodur and Dwaikat's equation lies in its overestimation of the fire resistance period under higher load ratios (e.g., $\gamma \geq 0.7$). As explained earlier, for un-protected FRP-strengthened RC beams, the fire resistance design becomes the design of bare RC beams under a higher load ratio. Therefore, new design formulae should be developed especially for un-protected RC beams under high load ratios.

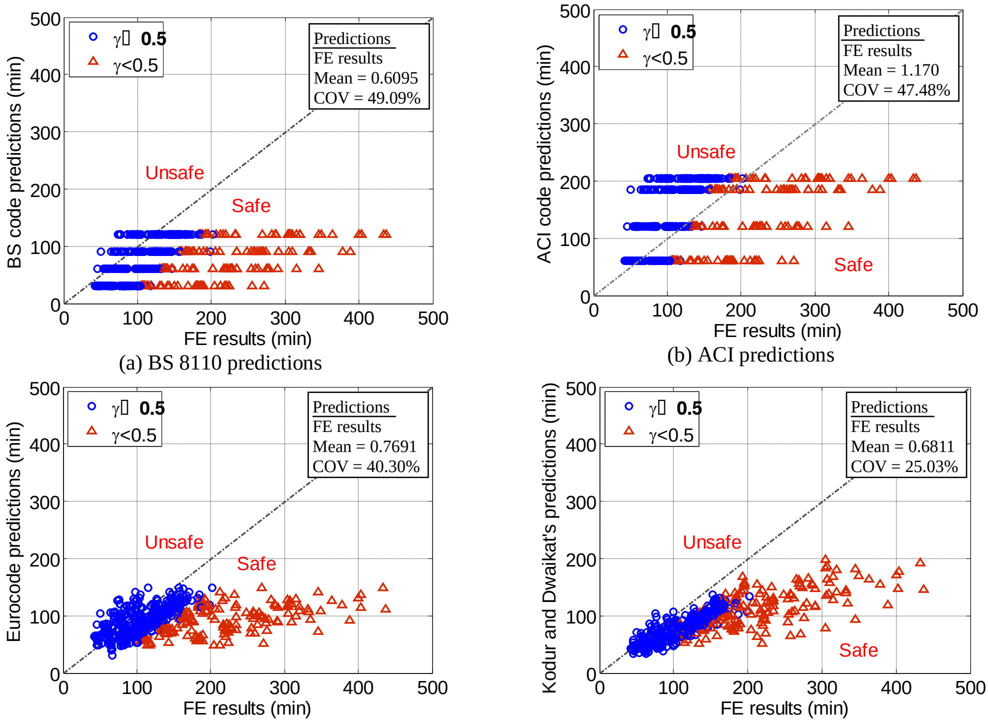

(a) BS 8110 predictions

(b) ACI predictions

(c) Eurocode and AS 3600 predictions

(d) Kodur and Dwaikat's (2011) predictions

Figure 2. Comparison between predictions from existing methods and FE results.

3.3 Explicit design formulae

A generic equation as given below is proposed for the fire resistance periods of bare RC beams:

$$R\left(\gamma, c, \rho, \frac{l}{d}, \frac{A_{sc}}{A_{st}}, \mu_{ag}, b\right) = \varphi(\gamma) \times \omega(c, \rho_s) \times \psi\left(\frac{l}{d}, \rho_s\right) \times \xi\left(\frac{A_{sc}}{A_{st}}\right) \times \mu_{ag} \times \phi(b) \tag{1}$$

where R is the fire resistance period (in min); $\varphi(\gamma)$ accounts for the effect of load ratio; $\omega(c, \rho_s)$ accounts for the combined effect of concrete cover depth and tension reinforcement ratio; $\psi\left(\frac{l}{d}, \rho_s\right)$ accounts for the effect of span-to-depth ratio for a given tension reinforcement ratio; $\xi\left(\frac{A_{sc}}{A_{st}}\right)$, $\phi(b)$, μ_{ag} account for the effects of distribution ratio of tension rebars, beam width and the type of concrete aggregate, respectively.

Based on nonlinear regression analyses of FE results, the following formulae are proposed to describe the effects of various factors (the detailed regression process is explained in Ref. [16]):

$$\varphi(\gamma) = a_1 + a_2 \cdot \gamma + a_3 \cdot \gamma^2 + a_4 \cdot \gamma^3 \tag{2a}$$

$$\omega(c, \rho_s) = \omega_0 + \omega_1 \cdot c \tag{2b}$$

$$\psi\left(\frac{l}{d}, \rho\right) = \psi_0 + \psi_1 \cdot \rho + \psi_2 \cdot \rho^2 \tag{2c}$$

$$\mu_{ag} = 1.04 \tag{2d}$$

$$\xi\left(\frac{A_{sc}}{A_{st}}\right) = \xi_1 + \xi_2 \cdot \left(\frac{A_{sc}}{A_{st}}\right) \tag{2e}$$

$$\phi(b) = d_0 + d_1\left(\frac{b}{250}\right) \tag{2f}$$

where a_1, a_2, a_3, and a_4 are constants, and least-squares regressions suggest that: $a_1 = 2.92\times10^{2}$; $a_2 = -8.15\times10^{2}$; $a_3 = 1.17\times10^{3}$; $a_4 = -6.13\times10^{2}$; the constants d_0 and d_1 are 3.80×10^{-1} and 6.20×10^{-1} respectively. ω_0 and ω_1 are functions of tension steel reinforcement ratio and are given by:

$$\omega_0 = b_0 + b_1 \cdot \rho_s + b_2 \cdot {\rho_s}^2 \tag{3a}$$

$$\omega_1 = c_0 + c_1 \cdot \rho_s + c_2 \cdot {\rho_s}^2 \tag{3b}$$

where $b_0 = 4.06\times10^{-1}$; $b_1 = -4.37\times10^{-2}$; $b_2 = 1.84\times10^{-2}$; $c_0 = 2.11$; $c_1 = -2.83\times10^{-3}$; $c_2 = -4.69\times10^{-2}$. ψ_0, ψ_1 and ψ_2 in Equation (2c) are functions of span-to-depth ratio and are as follows:

$$\psi_0 = 1.78 - 1.03 \times 10^{-1} \cdot \left(\frac{l}{d}\right) + 3.39 \times 10^{-3} \cdot \left(\frac{l}{d}\right)^2 \tag{4a}$$

$$\psi_1 = 6.80 - 1.64 \times 10^{-1} \cdot \left(\frac{l}{d}\right) + 7.61 \times 10^{-3} \cdot \left(\frac{l}{d}\right)^2 \tag{4b}$$

$$\psi_2 = -1.15 \times 10^{-1} + 4.36 \times 10^{-2} \cdot \left(\frac{l}{d}\right) - 2.27 \times 10^{-3} \cdot \left(\frac{l}{d}\right)^2 \tag{4c}$$

ξ_1 and ξ_2 in Equation (2e) are functions of concrete cover depth as follows:

$$\xi_1 = 1.54 - 6.81 \times 10^{-3} \cdot c \tag{5a}$$

$$\xi_2 = -7.91 \times 10^{-1} + 9.73 \times 10^{-3} \cdot c \tag{5b}$$

Using Equations (1) to (5), the fire resistance period of an RC beam exposed to a standard fire can be easily obtained.

3.4 Validation of proposed design formulae

For the 512 beam specimens analyzed in the FE parametric study, Figure 3 shows that the average ratio between the analytical predictions by the proposed formulae and the FE results is 1.0, and the coefficient of variation (COV) is 4.36%. This excellent agreement is expected as the proposed design formulae resulted from regression of the FE results. The proposed formulae are also used to predict the fire resistance of twelve RC beams which were subjected to standard fire tests as reported in the existing literature for further verification. Fire tests on RC beams during early years (i.e., before 1970s) are excluded from the comparison since most of the early fire tests were conducted on small specimens and some of them were concerned with post-fire residual strength evaluation. Due to space limitation, the geometrical details as well as the load ratios of these beams during fire are not provided here, but these details can be found in Reference [16]. Figure 4 shows the comparison between the analytical predictions and the test fire resistance data. Very close agreement is seen in this figure with a coefficient of variation being less than 10% although the prediction for beam N5 tested by Choi and Shin [17] is rather conservative. This conservativeness has probably arisen because this beam had a very thick concrete cover (i.e., 60 mm), which exceeds the maximum cover depth (i.e., 50mm) covered by the present FE parametric study. Owing to this thick concrete cover, the two corner rebars may have been well protected under fire exposure; the effect of distribution ratio of tension steel rebars [i.e., $\xi\ \left(\frac{A_{sc}}{A_{st}}\right)$] considered in the proposed design formulae may overestimate the strength degradation of these two corner rebars and thus underestimate the actual fire resistance performance. Overall, the proposed formulae provide an efficient and reliable tool for the fire resistance evaluation of RC beams exposed to a standard fire.

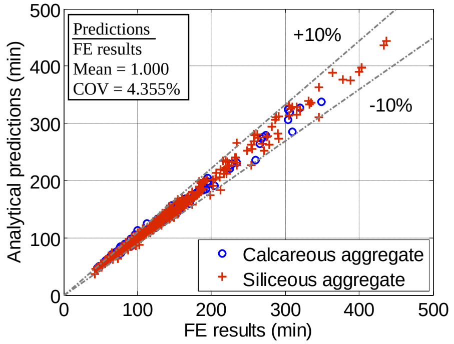

Figure 3. Analytical predictions versus FE results.

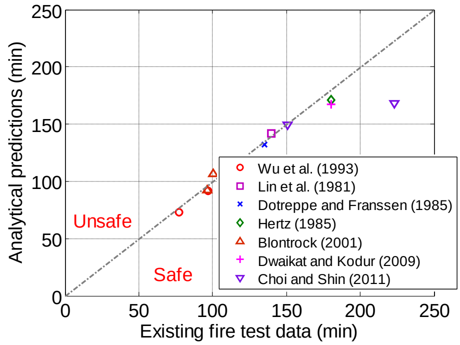

Figure 4. Analytical predictions versus test data.

4 SIMPLE METHOD FOR INSULATED FRP-STRENGTHENED RC BEAMS

The authors [10] have developed a reliable FE approach that provides accurate predictions for both the thermal and the mechanical responses of insulated FRP-strengthened RC beams. In the FE approach, both the mechanical properties of FRP laminates and their bond performance with concrete at elevated temperatures are carefully considered. However, as each commercially available insulation material may have a different set of temperature-dependent thermal properties, it is impossible to develop an explicit formula for the fire resistance of insulated FRP-strengthened RC members that can be applied to different insulation products. Therefore, the simple “500 ^{o}C isotherm method” [5,18], in combination with the explicit method previously developed by the authors for predicting temperatures in insulated concrete beam sections [8,9], is adopted to form a design-oriented method for the fire resistance evaluation of insulated FRP-strengthened RC beams.

4.1 The 500 ^{o}C isotherm method

As a simple hand calculation method recommended by EN 1992-1-2 (2004), the “500 ^{o}C isotherm method” [18] has been widely applied in the evaluation of load-carrying capacity of RC beams under fire exposure. In this method, the compressive zone of concrete in the beam section is reduced by eliminating the parts where the temperatures are greater than 500 ^{o}C while the concrete in the parts of compressive zone where the temperatures are below 500 ^{o}C are assumed to retain its full strength at locations where the temperatures are less than 500 ^{o}C. If the fire exposure duration is denoted by t (in min), the 500 ^{o}C isotherm in a fire-exposed beam section can be properly determined using the explicit method proposed by the authors [8,9]. As illustrated in Figure 5, if the distance between the 500 °C isotherm and the nearest beam side is $x_{500}(t)$, the reduced width of the concrete compression zone can be expressed as:

$$b^{'}(t) = b - 2x_{500}(t) \tag{6}$$

Assuming that this fire-exposed section is loaded to failure, the stresses in the concrete and the steel reinforcement are illustrated in Figure 5. By taking moments about the compression steel reinforcement, the force and moment equilibrium equations can be written as:

$$\begin{cases} b^{'}(t) \cdot \beta y_c(t) \cdot \alpha f_c + \sum_{j=1}^{n} A_{c,j} \cdot f_{yc,j}\left(\theta_{c,j}\right) - \sum_{i=1}^{m} A_{t,i} \cdot f_{yt,i}\left(\theta_{t,i}\right) = 0 \\ M_R(t) = b^{'}(t) \cdot \beta y_c(t) \cdot \alpha f_c \cdot \left[\beta y_c(t) - d^{'}\right] + \sum_{i=1}^{m} A_{t,i} \cdot f_{yt,i}\left(\theta_{t,i}\right) \cdot \left(d - d^{'}\right) \end{cases} \tag{7}$$

where $y_c(t)$ is the depth of neutral axis; $\beta y_c(t)$ is the depth of equivalent compressive stress block in which β = 0.8 [19]; $A_{t,i}$ and $f_{yt,i}\left(\theta_{t,i}\right)$ are respectively the area of the i^{th} tension steel rebar and its tensile stress at temperature $\theta_{t,i}$; $A_{c,j}$ and $f_{yc,j}\left(\theta_{c,j}\right)$ are respectively the area of the j^{th} compression steel rebar and its compressive stress at temperature $\theta_{c,j}$; d and $d^{'}$ are respectively the depths of the centroids of the tension and compression steel reinforcement; m and n are respectively the total numbers of tension and compression steel rebars; and $M_R(t)$ is the moment capacity of the fire-exposed RC section at time *t*. The factor α, a coefficient defining the effective strength, is recommended to have a value of 1.0 according to EN 1992-1-1 [19]. The stress degradations of tension and compression steel rebars at elevated temperatures [i.e., $f_{yc,j}\left(\theta_{c,j}\right)$ and $f_{yt,i}\left(\theta_{t,i}\right)$] are determined based on EN 1992-1-2 [5].

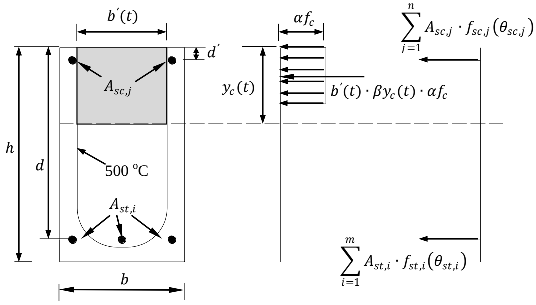

Figure 5. Schematic of the 500 °C isotherm method.

4.2. Validation of the proposed simple design-oriented method

There have been few fire tests on insulated FRP-strengthened RC beams, and most of these existing fire tests were terminated before the fire limit states were reached. Therefore, the existing tests cannot be used to validate the proposed design-oriented method. In the present study, the advanced FE model developed by the authors [10] was used instead to produce the fire resistance data needed for the validation of the proposed method. The input data employed in the FE analyses are summarized in Table 1. In total, 60 insulated CFRP-strengthened RC beams were simulated. All the beams are protected by a U-shaped insulation system and exposed to the ISO 834 standard fire. The mechanical properties of CFRP laminates and the thermal properties of the insulation material were determined according to Blontrock et al.'s tests [20], while the cylinder compressive strength of concrete and the yield strength of steel reinforcement were assumed to be 30 MPa and 375 MPa, respectively.

Table 1. Insulated FRP-strengthened RC beams considered in the FE study.

Aggregate type	Cross-section (mm)	l/d	c (mm)	ρ_s (%)	A_{sc}/A_{st}	CFRP thickness (t_{CFRP}:mm)	γ	Insulation thickness (t_{in}:mm)
Siliceous aggregate	250 × 250	16	25	0.8, 1.2	2/3	0.3, 1.2	0.3, 0.5, 0.7	5, 10, 15, 20, 30

Figure 6 shows how the moment capacity reduces with the fire exposure time for insulated FRP-strengthened RC beams of two different steel reinforcement ratios and five different fire insulation thicknesses. It can be seen that this reduction becomes more gentle as the fire insulation thickness increases. In order to determine the fire resistance period of a simulated RC beam, the predicted moment capacity (M_R)-fire exposure time curve needs to be compared with the moment induced by the service load during a fire. Figure 7 illustrates how the fire resistance period of an insulated FRP-strengthened RC beam with a given load ratio can be found. The fire resistance periods so predicted are compared with the FE predictions in Figure 8. It is seen that both approaches lead to similar predictions despite that the former is based on a strength criterion while the latter is based on a deflection criterion. Therefore, the simple design-oriented method can be used for practical fire-resistance design of insulated FRP-strengthened RC beams as an alternative to the advanced FE approach.

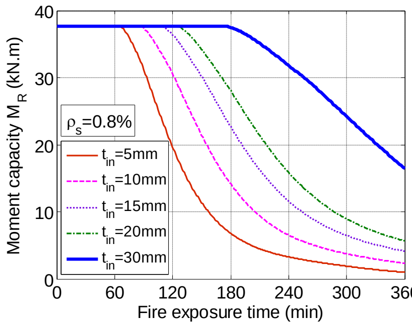

Figure 6. Reductions in moment capacity.

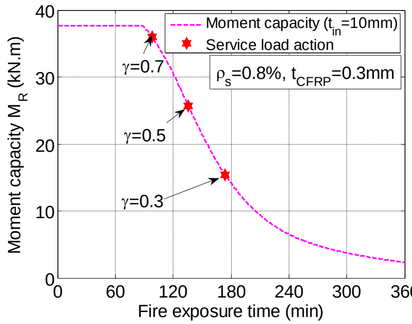

Figure 7. Determination of fire resistance period.

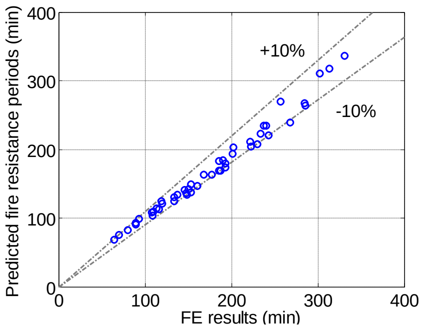

Figure 8. Predictions by the design-oriented method versus FE results.

5. LIMITATIONS OF THE PROPOSED APPROACH

Although the proposed performance-based design approach is applicable to a large range of beams strengthened in flexure with FRP, the following limitations must be noted:

(1) The proposed design formulae offer a practical approach for evaluating the fire resistance of RC beams exposed to a standard fire, which is normally much more severe than a real (natural) fire. The main difference between a standard fire curve and a real fire curve is that the former is characterized by a continuous temperature increase while the latter has both a heating phase and a subsequent decay phase. Therefore, for any real compartment fire, the fire resistance design based upon the proposed formulae is conservative. Where necessary, the design formulae can be modified with due consideration of different fire-exposure intensities experienced in a standard fire and a real fire, for example, following the energy based time equivalent approach proposed by Kodur et al. [21].

(2) The design-oriented method proposed for insulated FRP-strengthened RC beams is based on the assumption that the beam fails in flexure; the method is therefore not applicable to those beams failing in shear. The shear failure mode has indeed been observed in some existing fire tests of FRP-strengthened RC beams, in which a flat insulation layer on the beam soffit was used to protect the FRP (i.e., only the bottom surface of the beam was protected) [22]. Therefore, for insulated FRP-strengthened RC beams with a flat insulation system on the soffit, the FE approach instead of the design-orientated approach is recommended for use in evaluating their fire performance.

6. CONCLUSIONS

This paper has presented a performance-based approach for the fire resistance design of FRP-strengthened RC beams. A three-level design framework has been presented based a compromise between the strength contribution of the FRP strengthening system and the required fire resistance rating. The fire resistance of un-protected FRP-strengthened RC beams (i.e., with Level-I protection) can be approximated by that of bare RC beams; an extensive FE parametric study was thus carried out on bare RC beams to generate results for the derivation of explicit design formulae for their fire resistance. Insulated FRP-strengthened RC beams (i.e., equivalent to insulated RC beams) exposed to the standard fire, a design-oriented method has been established based on the simple “500 ^{o}C isotherm method” to enable the prediction of their time-dependent moment capacity. The fire resistance results obtained from the design-oriented method are in good agreement with the FE predictions, making it more attractive for use in practical design due to its simplicity yet good accuracy. The holistic approach presented in this paper can be adopted in design codes to achieve the required fire resistance rating for FRP-strengthened RC beams.

ACKNOWLEDGEMENTS

The authors are grateful for the financial support received from the Hong Kong Construction Industry Institute/PolyU Innovation Fund (Project No.: 5-ZJE8), the National Basic Research Program of China (i.e. the 973 Program) (Project No.: 2012CB026201) and the Faculty of Construction and Environment of The Hong Kong Polytechnic University provided through a Postdoctoral Fellowship to the first author.

REFERENCES

[1] Green, M.F., Hollingshead, K. and Benichou, N., “Performance in fire of fiber reinforced polymer strengthened concrete beams and columns: Recent research and implications for design”, *Proceedings of the 7th International Conference on Structures in Fire*, M. Fontana, A. Frangi, M. Knobloch (eds.), ETH Zurich, Switzerland, 619-628. 2012.

[2] Kodur, V.K.R., Bisby, L.A. and Green, M.F., “Preliminary guidance for the design of FRP-strengthened concrete members exposed to fire”, *Journal of Fire Protection Engineering*, 17(5), 5-26, 2007.

[3] BS 8110-2, *Structural Use of Concrete--- Part 2: Code of Practice for Special Circumstance*, British Standards Institution, Milton Keynes, 1985.

[4] ACI 216.1, *Code Requirements for Determining Fire Resistance of Concrete and Masonry Construction Assemblies,* American Concrete Institute, Michigan, 2007.

[5] EN 1992-1-2, *Eurocode 2: Design of Concrete Structures --- Part 1-2: General Rules --- Structural Fire Design,* British Standards Institution, Milton Keynes, 2004.

[6] AS 3600, *Concrete Structures*, Standards Association of Australia, Sydney, 2009.

[7] Kodur, V.K.R. and Dwaikat, M.B., "Design equation for predicting fire resistance of reinforced concrete beams", *Engineering Structures,* 33(2), 602-614, 2011.

[8] Gao, W.Y., Dai, J.G. and Teng, J.G., "An explicit approach for predicting temperatures in insulated FRP-strengthened RC members exposed to a standard fire", in preparation, 2014.

[9] Gao, W.Y., Dai, J.G. and Teng, J.G., "Simple method for predicting temperatures in reinforced concrete beams exposed to a standard fire", Accepted by *Advances in Structural Engineering*, 2014.

[10] Dai, J.G., Gao, W.Y. and Teng, J.G., "Finite element modeling of insulated FRP-strengthened reinforced concrete beams exposed to fire", Submitted to *Journal of Composites for Construction*, 2014.

[11] Gao, W.Y., Dai, J.G. and Teng, J.G., "Finite element modeling of reinforced concrete beams exposed to fire", *Engineering Structures,* 52, 488-501, 2013.

[12] Kodur, V.K.R. and Dwaikat, M.B., "Performance-based fire safety design of reinforced concrete beams", *Journal of Fire Protection Engineering*, 17(4), 293-320, 2007.

[13] Wu, B. and Lu, J.Z., "A numerical study of the behaviour of restrained RC beams at elevated temperatures", *Fire Safety Journal*, 44(4), 522-531, 2009.

[14] Kodur, V.K.R. and Dwaikat, M.B., "Effect of fire induced restraint on fire resistance of reinforced concrete beams", *Journal of Structural Fire Engineering,* 1(2), 73-88, 2010.

[15] BS 476-20., *Fire Tests on Building Materials and Structures --- Part 20: Methods for Determination of the Fire Resistance of Elements of Construction (General Principles),* British Standards Institution, Milton Keynes, 1987.

[16] Gao, W.Y., "Fire resistance of FRP-strengthened RC beams: numerical simulation and performance-based design", Ph.D. thesis, The Hong Kong Polytechnic University, Hong Kong, 2013.

[17] Choi, E.G. and Shin, Y.S., "The structural behavior and simplified thermal analysis of normal-strength and high-strength concrete beams under fire", *Engineering Structures*, 33(4), 1123-1132, 2011.

[18] Anderberg, Y., "Analytical fire engineering design of reinforced concrete structures based on real fire characteristics", *Proceedings of the Eighth Congress of the Federation Internationale de la Precontraint*e, Cement and Concrete Association, London, 112-123, 1978.

[19] EN 1992-1-1, *Eurocode 2: Design of Concrete Structures --- Part 1-1: General Rules and Riles for Buildings,* British Standards Institution, London, 2004.

[20] Blontrock, H., Taerwe, L. and Vandevelde, P., "Fire tests on concrete beams strengthened with fiber composite laminates", *Proceeding of the Third International Ph.D. Symposium in Civil Engineering*, K. Bergmeister (ed.), Institute of Structural Engineering, University of Agricultural Sciences, Vienna, Austria, 151-161, 2000.

[21] Kodur, V.K.R. Pakala, P. and Dwaikat, M.B., "Energy based time equivalent approach for evaluating fire resistance of reinforced concrete beams", *Fire Safety Journal,* 45(4), 211-220, 2010.

[22] Liu, F.T., Wu, B. and Wei, D.M., "Failure modes of reinforced concrete beams strengthened with carbon fiber sheet in fire", *Fire Safety Journal*, 44(7), 941-950, 2009.

TIMBER STRUCTURES

FIRE PERFORMANCE OF HYBRID TIMBER CONNECTIONS WITH FULL-SCALE TESTS AND FINITE ELEMENT MODELLING

Sabah G. Ali*, Aaron O. Akotuah*, Jeffrey Erochko* and George V Hadjisophocleous*

*Department of Civil and Environmental Engineering, Carleton University, 1125 Colonel by Drive, Ottawa, ON K1S 5B6, Canada

Keywords: Timber connections, Hybrid connections, Fire resistance, Full-scale fire tests, Ffinite element, ABAQUS

Abstract. *Since wood is generally classified to be a 'combustible'material, its use as a construction material has traditionally been restricted to smaller and shorter buildings by the National Building Code of Canada (NBC)[1] and other building codes around the world; however, with the increased adoption of performance/objective-based design codes and because of the fact that wood is regarded by building designers and architects as a sustainable material, wood use in larger and more complex structures is on the rise. To support this recent drive for larger wood structures, this study investigates the fire performance of hybrid (wood beam to steel columns) connections.*

The effect of different parameters on the fire performance of these connections is investigated by full-scale testing. These tests exposed the test specimens to the standard time-temperature curve defined by CAN/ULC-S101[2]. Test results showed that the fire resistance of these connections depends on the load ratio, the type of connection and the size of the bolts used. Finite element models of the connections under fire were constructed using ABAQUS/CAE and these were validated using the test results. These numerical model results correlate well with test results within a ±10% variation.

1 INTRODUCTION

In Asia and many other parts of the world there are many wood buildings that have survived for hundreds of years, which is a testament to the durability and longevity of wood as a building material; however, because wood is considered to be combustible, its use has been restricted to small and short buildings by the National Building Code of Canada (NBC)[1] and also by other building codes around the world. With the recent adoption of performance/objective-based design codes, this situation has started to change. The perception of wood as a renewable and sustainable material has resulted in a drive to increase its use and expand its range of applicability. This has, in turnresulted in an increased need for the analysis and testing of heavy timber structures and of hybrid timber-steel structures.

In building construction, wood is used in one of two ways:as light-frame construction or as heavy-timber construction. The use of wood in bigger and taller buildings necessitates a heavy-timber construction approach where wood is used in combination with other building materials, such as concrete and steel. This type of construction system is called hybrid building system and is currently being considered for the construction of mid-rise wood buildings.

In timber structures, metal fasteners are typically used to transfer loads between members. Nails, screws and light-gauge steel plates are used for light-frame systems while dowels, bolts and steel plates are often used in heavy timber connections. Due to the susceptibility of these metal components to fire, timber connections have been identified as a weak link in heavy timber construction under fire conditions. In building code design, if fire resistance is required, then codes typically require that connections must have the same fire resistance rating as the connected members.For the fire resistance design of typical heavy timber connections, the NBC provides design guidance including the minimum thickness of the connected timber, spacing between fasteners and spacing between rows and columns of fasteners;however, detailed information or calculation of the fire resistance for hybrid timber-steel connections is not provided. There is no guidance related to the design or selection of hybrid connections provided in the NBC or any other Canadian document.

In recent years, a number of research efforts have been devoted to investigating the fire performance of timber connections to develop calculation methods for estimating their fire resistance[4-13];however, the performance of hybrid timber-steel connections under firehas received little attention from researchers. The analysis of such hybrid connections is complex because the behaviour and properties of steel, and wood are different at high temperatures.

This study investigates the effect of various design parameters on the fire performance of hybrid connections using full-scale tests. A series of fire-resistance tests was conducted to investigate the behaviour of the connections between steel columns and a glulam beam. The tests exposed the specimens to the standard time-temperature curve defined by CAN/ULC-S101[2]. The test assembly consisted of two pin-pin steel columns and a glulam beam loaded using two point loads at 1/3 points along the beam span. The steel columns were fully protected while only the top surface of the wood beam was protected to simulate the presence of the supported floor.

Finite element models were built using ABAQUS/CAE which simulate both heat transfer from the fire and structural behaviour. Temperature-dependent thermal, strength and elastic properties of the test assembly are modelled and brittle cracking failure in the wood is simulated as observed in the test.

2 DESCRIPTION OF TEST FACILITY

The furnace that was used for the tests is located at the Full-scale Fire Research Facility of Carleton University in Almonte, Ontario. This furnace was specifically designed to test the fire performance of connection assemblies. Figure 1 shows an exterior view of the furnace and one of the two propane burners within. The furnace is equipped with a loading frame which is used to support the test assembly and to apply the load. The furnace temperature can be controlled to follow the standard fire curve or other fire curve. Figure 2 shows an interior view of the furnace with the location of the shielded thermocouples and plate thermometers. Plate thermometer measurements are used as input boundary conditions in the numerical finite element modelling.

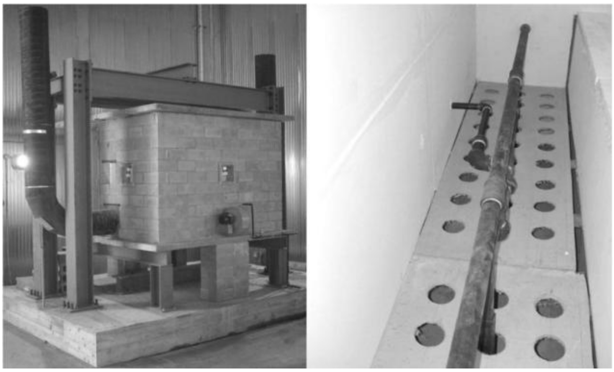
Figure 1. Furnace and propane line burner.

Figure 2. Shielded thermocouples and plate thermometers in the furnace.

2.1 Furnace Calibration

It was necessary to calibrate the furnace temperatures before the fire-resistance tests to make sure that the time-temperature curve could follow the standard. Figure 3 shows the standard time-temperature curve, as defined by CAN/ULC-S101. The area under the time-temperature curve, obtained by averaging the results from the furnace thermocouple readings, was within ±10% of the corresponding area under the standard time-temperature curve for fire tests of 1 hour or less duration.

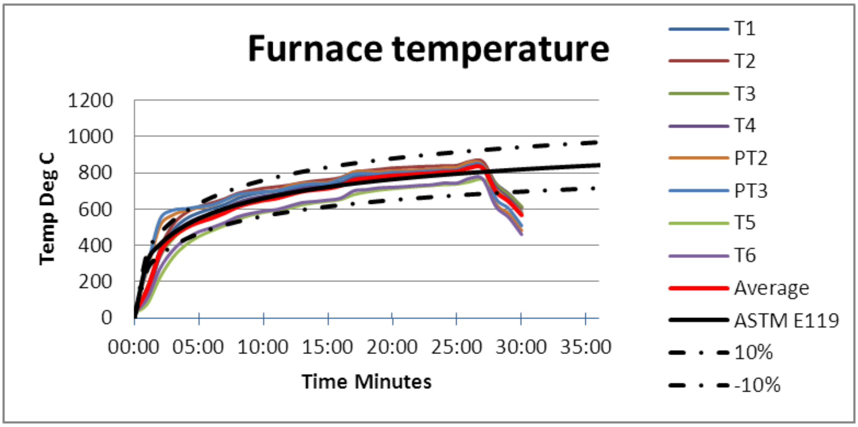

Figure 3. Correlation between standard fire and furnace temperature.

3 DESCRIPTION OF EXPERIMENTS AND TEST SPECIMENS

A series of eleven fire-resistance tests was conducted in the furnace to study the influence of various parameters governing the fire performance of hybrid connections. The test assembly consisted of two pin-pin steel columns (W150×37) which were 3200 mm long and a glulam beam 140×191 mm that was 1900 mm long. The beam was loaded using two point loads at 1/3 points along its span. The steel columns were fully protected while only the top surface of the wood beam was protected to simulate the presence of the floor. A 3/8" shear tab plate with 4-A307 bolts was used to connect the beam to the steel frame. Figures 4 and 5 show the specimen in the furnace before and after testing.

Figure 4. Specimen placed in furnace.

Figure 5. Specimen in furnace after the test.

The parameters considered for the tests include the type of connection,the load ratio and the bolt diameter. The load ratio is the applied constant vertical load on the beam during thetest divided by the ultimate load-carrying capacity of the beam at ambient conditions. The load ratio applied on a structural member during a fire test can have a significant effect on its fire resistance. CAN/ULC-S101[2] recommends that the specimen be subjected to a load that is as close as possible to its factored resistance which is determined in accordance with the design standard published by the Canadian Standards Association, (CAN/CSA O86-09[23] for timber connections). The fire standard also allows lower loads to be used in fire-resistance tests provided that the load conditions are identified and reported. In this study, the load ratio ranged from 30% to 100%. In addition, two different bolt diameters were used: 12.7 mm (1/2”) and 19.1 mm (3/4”).

Three different types of connections were tested: a concealed shear tab connection (CN) (5 tests), an exposed shear tab connection (EX) (4 tests) and a seated beam shear connection (SE) (2 tests). Figure 6 shows the steel plate assembly corresponding to each of the three connection types.

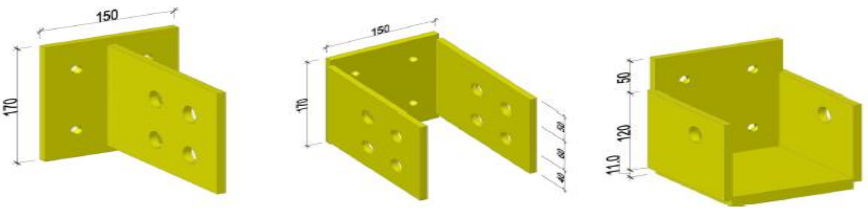

(a) (b) (c)

Figure 6. Types of connections considered: (a) CN;(b) EX;(c) SE.

3.1 Test procedure

The steel columns were connected to the external steel loading structure that surrounds the furnace. Each column was restrained at its top and bottom against the in-plane and out-of-plane lateral movements. The top and bottom ends of the columns were rotationally unrestrained to avoid the development of unnecessary moments in the steel loading structure. After installing the steel-frame test assembly inside the furnace, the test beam was subjected to a constant vertical loading before and during the fire-resistance test. This load was applied as two point loads 700 mm apart. This load was maintained for a minimum of 20 minutes and then the test assembly was subjected to gradually increasing temperatures that followed the CAN/ULC-S101-07[2] standard time-temperature curve until failure.

4 FINITE ELEMENT MODELLING

To simulate the fire resistance test, the system was modelled and analysed using a sequentially coupled thermal-stress procedure. This approach adopts a pure transient heat transfer model to determine the temperature distribution and history on the assembly followed by a static structural analysis at each time step of the heat transfer to determine the mechanical response of the structure.

Three-dimensional diffusive solid elements (DC3D8) in ABAQUS[24] were used to define all components of the assembly for the heat transfer model. Temperature-dependent thermal properties of thermal conductivity, density and specific heat capacity were assigned to each element to calculate heat conduction within the model assembly. Heat transfer between discontinuous contacting surfaces of the assembly was modelled using the gap conductance feature. Heat transfer to the boundary surfaces of the assembly was modelled by supplying an appropriate heat flux to the exposed sides using a DFLUX[17] user subroutine in ABAQUS[24]. The heat flux to the boundary incorporates both the convective and radiation components of the heat from the furnace. The average time-temperature data that was recorded during the test (T_f) was used to estimate the heat flux to the boundary using Equation (1).

$$\dot{q}'' = h_c(T_f - T_s) + \varphi\,\varepsilon_{ff}\,\sigma(T_f^4 - T_s^4) \qquad \text{…………Equation (1)}$$

where:

h_c = convection coefficient $\qquad T_f$ = furnace temperature

T_s = surface temperature of assembly $\qquad \varphi$ = configuration factor

ε_{ff} = effective emissivity σ = Stefan − Boltzman constant, $5.67 \times \frac{10^8\,\mathrm{W}}{\mathrm{m^2\,K^4}}$

The full-Newton method in ABAQUS/Standard was used to solve the temperature at all points within the model. The temperature-time distribution within the assembly was then applied as a predefined time-varying field in the subsequent structural model.

To simulate the structural response of the model, a nonlinear static analysis of the structure was conducted in two stages. First, the full load ratio was applied in increments. Then, the heat from the fire to the assembly was applied while the first stage load remained constant. Three-dimensional continuum elements (C3D8R) in ABAQUS was used to define all components of the assembly. Temperature-dependent Isotropic and Orthotropic elastic properties were assigned to the steel and wood parts respectively. Only half of the full assembly was modelled in ABAQUS due to symmetry (see Figure 7).

4.1 Damage and Failure

Failure in the assembly was predominantly due to brittle crack (splitting) propagation in the glulam beam which eventually leads to the loss of the load-carrying capacity. The extended Finite Element Method (XFEM) in Linear Elastic Fracture Mechanics (LEFM)[24] was used to model the formation and propagation of shear cracks in the continuum elements. Damage is initiated when the maximum shear stress criteria within any element is exceeded. Subsequent propagation of cracks is governed by fracture energies according to Griffith[24].

The initial application of the full vertical load ratio on the structural model does not lead to failure because the load applied is only a fraction of the ultimate failure load. In the second part, the heat added to the assembly degrades the stiffness and strength of the elements. This leads to an increase in internal stresses, damage and eventual failure of the model assembly.

ABAQUS/Standard tracks the progressive damage in the form of energy dissipated by damage (ALLDMD). Figure 8 below is an example of a typical ALLDMD curve which displays three distinct phases. The first phase is marked by a value of almost zero which indicates no inter-laminar damage (no cracks in the glulam). This is followed by a sudden rise which represents energy released in the formation of cracks and their propagation. The third phase which has almost a constant peak value means no further energy can be accommodated through damage, indicating that ultimate failure has occurred.

Ultimate time to failure of the model is observed at the point of sudden rise in the ALLDMD value as shown in the Figure 8. This gives an indication of the time to failure.

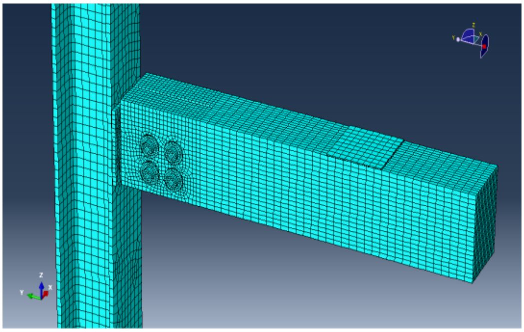

Figure 7. Meshed model in ABAQUS.

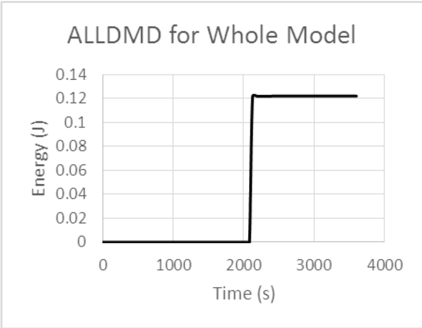

Figure 8. Damage Dissipated Energy (ALLDMD) of whole model.

5 RESULTS AND DISCUSSION

5.1 Fire Resistance (Failure Time)

In this paper the results of two tests will be discussed; a CN connection with 19.1 mm bolts and EX connection with 19.1 mm bolts under 30% and 60% load ratio respectively (see Figure 6).

The predominant failure mode in both tests was the splitting of wood parallel to grain and this was noticed in both the test and the numerical model. These splits originated at the bolt-hole edges, which are regions of high stress concentration. Under loading, the bolt shank transfers compressive stresses to the wood below, which acts as a wedge imposing lateral stresses parallel to grain to form cracks. Once the localized crack at the connection level is formed, it propagates along the beam and eventually leads to splitting failure. This failure mode is shown for the test and model in Figure 9.

Table 1 summarizes the test and model results including the actual failure time and the predicted failure time based on the model. The model predicted the failure time for the CN connection within -0.86% and for the EX connection within +10.8%.

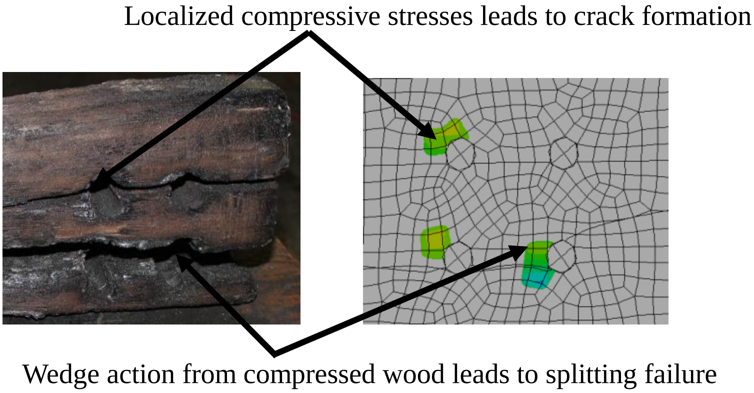

Figure 9. Failure around bolt connection.

Table 1. Test description and failure times.

Test No	Plate	No of Bolts	Bolt Dia. mm	Load ratio %	Load kN	Failure Time min	Model predicted time	Variation %
1	**CN**	4	19.1	30	21.5	35	34.7	-0.86
2	**EX**	4	19.1	60	37.5	25	27.7	+10.8

5.2 Heat Transfer and Charring Rate

Figure 10 shows that the predicted temperature from the model for different locations within the wood section generally complies well with the test results. T21 shows a good correlation of the temperature with time at a depth of 40 mm from the face of the beam while T16 on the other hand gives a good prediction from the model up to about 20 minutes beyond which the temperature rises rapidly and the model results are slightly higher than the test results. This variation after 20 minutes indicates that the radiation component of the heat flux results in an overestimate of the actual flux received underside of the beam. Plate thermometer temperatures at the wood sides were used as the overall average boundary condition in the model whereas the underside of the beam actually receives less radiation temperatures.

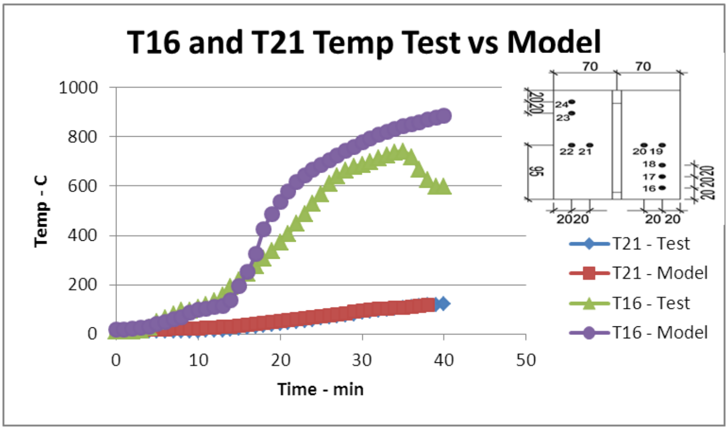

Figure 10. Wood temperature with time at two different points.

Moreover, T16, which is located close to the bottom corner of the beam cross-section, develops a much higher temperature over time than T21, which is located in the middle of one surface. This is shown in both the test and the numerical results, indicating severity of heat flux from two boundary surfaces to T16 as compared to just one surface contribution to T21.

A typical graph of the temperature-depth against time is superimposed with the temperature contour from the ABAQUS model in Figure 11. A 20-mm depth from the sides lie within the range of 650 - 750℃ after 35 minutes of fire exposure and this is also well represented by the yellow to orange temperature contour from the model (631 - 784℃). Temperature distribution within a 40 – 100 mm range of cross-section depth increases gradually from ambient temperature (20℃) at the centre to about 100℃ towards the edges. The distribution of temperature within the cross-section well-defines the corner rounding of the residual section as expected from both the real test and the numerical simulation.

Wood chars at a temperature of approximately 280℃ and above[3]. Figure 12 shows a temperature contour on a cross-section at the beam midspan from ABAQUS alongside a photo of a charred section from the test. An average surrounding thickness of 28 mm lies within the charring temperature region as obtained from the model. This leaves a residual section of about 84 mm from the model as opposed to 85 mm from the test. Table 2 below is a summary of the average charring rate obtained from both the test and the numerical model which is within ±14% from the common standard charring rate of wood[3].

The table also shows that the charring rate at the connection was reduced to 0.56 mm/min for the EX test which can be attributed to the partial protection that the steel plates provide to the wood behind them, therefore delaying its charring.

Table 2. Charring rate.

	Beam Center (CN and EX)	**CN at connection**	**EX at connection**	**Model**	**Average charring rate of Glulam**
Charred layer (mm)	27.5	33	14	28	-
Charring rate (mm/min)	0.78	0.94	0.56	0.8	0.7

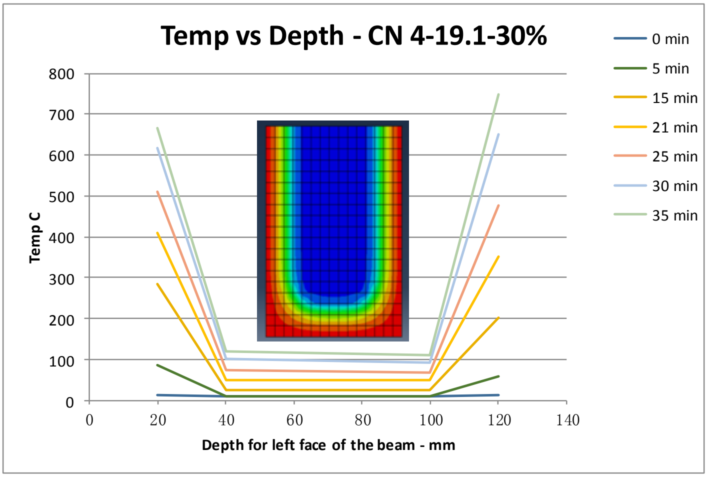

Figure 11. Temperature-depth distribution against time from test and model.

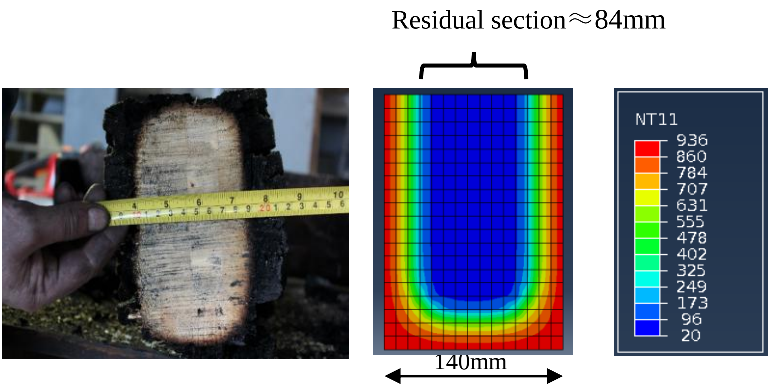

Figure 12. Typical middle charred section after 35 minutes.

The charring at the connection locations is strongly influenced by the bolts and steel plates. For a typical concealed plate connection, the bottom of the plate is subjected to heat flux which transfers heat directly to the center of the beam cross-section, hence increasing the charring rate there. In Figure 13, the influence of the bolt on the charring rate is seen as a further reduction of the residual cross section. This results in an average charred layer of 33 mm and a corresponding charring rate of 0.94 mm/min

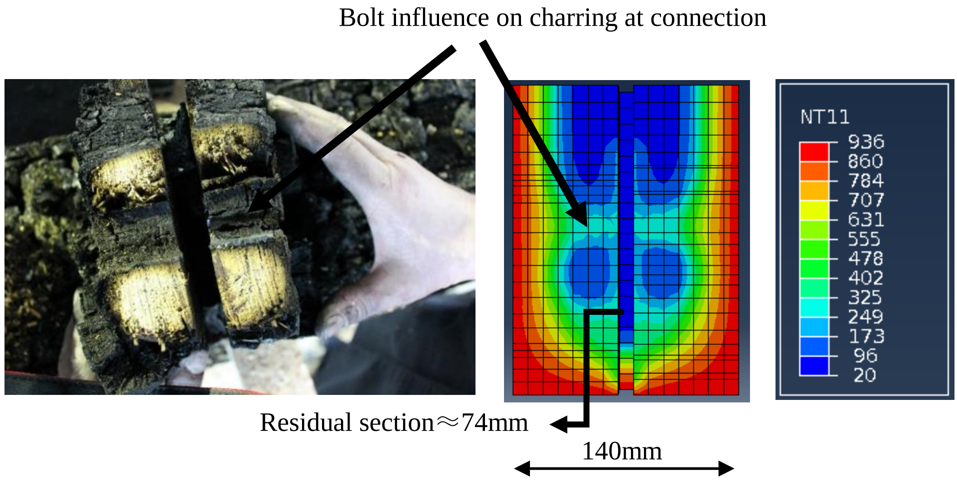

Figure 13. Typical charred section at the connection after 35minutes.

6 CONCLUSIONS

A number of fire resistance tests have been conducted using hybrid connections consisting of steel columns and heavy timber beams. This study investigated the impact of various parameters on the performance of the connection when subjected to the standard time-temperature curve. Two different types of connections have been discussed: a concealed shear tab connection (CN) and an exposed shear tab connection (EX). The finite element analysis program ABAQUS was used to model the test assembly using heat transfer and structural analysis models.

The model results compare well with the tests results; the charring rates measured from the tests for the EX and CN connections at midspan of the beam is 0.78 mm/min as opposed to 0.8 mm/min from the model. The charring rates at the connection were lower in the EX test than in the CN test due to the partial protection provided by the exposed plates to the wood behind. On the other hand, the charring rate at the CN connection was about 0.94 mm/min due to further heat transfer to the core of the wood from the concealed plate and the bolts. The numerical model also predicted the temperature gradients with time within the wood section with only a slight variation.

The recorded failure mode was brittle failure (splitting) which was also represented in the model. The failure time predicted by the model was within ±10% of the test results.

REFERENCES

[1] NBC. National Building Code of Canada in Canadian Commission on Building and Fire Code. 2005. National Research Council of Canada, Ottawa, ON, Canada.

[2] CAN/ULC-S101. Standard methods of fire endurance tests of building construction and materials. 2007. Underwriter's Laboratories of Canada, Scarborough, Canada.

[3] Buchanan, A.H. Structural Design for Fire Safety, John Wiley & Sons Ltd, Chichester, West Sussex, England, 2001.

[4] Noren, J. Load-bearing capacity of nailed joints exposed to fire. Fire and Materials. 1996, 20: p. 133-143.
[5] Dhima, D. Vérification expérimentale de la résistance au feu des assemblages d'éléments en bois. in CTICM Ref. INC-99/399-DD/NB. 1999. CTICM, Paris, France.
[6] Kruppa, J., Lamadon, T. and Rachet, P. Fire Resistance Test of Timber Connections. in CTICM Ref. INC-00/187-JK/NB. 2000. CTICM, Paris, France.
[7] Ayme, N. Assemblages bois-métal en double cisaillement. in Rapport Du Comportement Au Feu D'Assemblages Bois, CTICM Ref. SR21-03/121-NA/PB. 2003. CTICM, Paris, France.
[8] Laplanche, K. Fire performance of timber connections: experimental and modelling approach. Ph.D. Thesis. Clermont-Ferrand: Blaise Pascal University (in French), 2006.
[9] Lau, P.H. Fire resistance of connections in laminated veneer lumber. in Fire Engineering Research Report 06/3. 2006. Dept. of Civil Engineering, University of Canterbury, New Zealand.
[10] Chuo, T.C.B. Fire performance of connections in LVL structures. in Fire Engineering Research Report 07/4. 2007. Dept. of Civil Engineering, University of Canterbury, New Zealand.
[11] Frangi, A., Erchinger, C. and Fontana, M. Experimental fire analysis of steel-to-timber connections using dowels and nails. Fire and Materials. 2009, 34(1): p. 1-19.
[12] Konig, J. and Fontana, M. The performance of timber connections in fire test results and rules of Eurocode 5. in Proceedings of International Rilem Symposium 'Joints in Timber Structures'. University of Stuttgart, Rilem Publications s.a.r.l., Cachan, France, 2001.
[13] Erchinger, C., Frangi, A. and Fontana, M. Fire design of steel-to-timber dowelled connections. Engineering Structures. 2010, 32(2): p. 580-589.
[14] Peng, L. Performance of heavy timber connections in fire. Ph.D. Thesis. Carleton University, Ottawa, Canada, 2010.
[15] Lei Peng, George Hadjisophocleous, Jim Mehaffey and Mohammad Mohammad, Fire Performance of Timber Connections, Part 1: Fire Resistance Tests of Bolted Wood-Steel-Wood and Steel-Wood-Steel Connections, Journal of Structural Fire Engineering, Vol 3, Number 2 pp. 107 -132 (2012)
[16] Lei Peng, George Hadjisophocleous, Jim Mehaffey and Mohammad Mohammad, Fire Performance of Timber Connections, Part 2: Thermal and Structural Modelling, Journal of Structural Fire Engineering, Vol 3, Number 2 pp. 133 -154 (2012)
[17] Lei Peng, George Hadjisophocleous, Jim Mehaffey and Mohammad Mohammad, Predicting the Fire Resistance of Wood-Steel-Wood Timber Connections, Fire Technology, 47, 1101-1119, 2011
[18] Lei Peng, George Hadjisophocleous, Jim Mehaffey and Mohammad Mohammad, Performance of Unprotected Wood-Wood-Wood and Wood-Steel-Wood Connections: A Literature Review and New Data Correlations, Fire Safety Journal, Volume 45, Issue 6-8, 2010, Pages 392-399.
[19] Lei Peng, George Hadjisophocleous, Jim Mehaffey and Mohammad Mohammad, On the Fire Performance of Double-Shear Timber Connections, 10th International IAFSS Symposium, 2011, Maryland, USA, pp 1207-1218
[20] Lei Peng, George Hadjisophocleous, Jim Mehaffey and Mohammad Mohammad, Calculating Fire Resistance of Timber Connections, Fire and Materials – 12th International Conference, 2011, San Francisco, USA. (Best Poster Award)
[21] Lei Peng, George Hadjisophocleous, Jim Mehaffey and Mohammad Mohammad, On the Fire Performance of Wood-Wood-Wood and Wood-Steel-Wood Connections Using Bolts and Dowels, Proceedings of the Twelfth International Conference INTERFLAM, 2010, Nottingham UK, pp. 83 - 94.
[22] Lei Peng, George Hadjisophocleous, Jim Mehaffey and Mohammad Mohammad, Fire Resistance of Wood-Steel-Wood Bolted Timber Connections, Structures in Fire – Proceedings of the Sixth International Conference, 2010, Pages 552-559.
[23] CAN/CSA-O86-09. Engineering Design in Wood CAN/CSA-O86-1. 2009. Canadian Standards Association, Rexdale, ON, Canada.
[24] ABAQUS/CAE Version 6.11 Standard Manual, 2011, Dassault Systemes, Rhode Island, US.

8th International Conference on Structures in Fire
Guo-Qiang LI, Venkatesh K. R. KODUR, Shou-Chao JIANG, Jian JIANG, Su-Wen CHEN, Guo-Biao LOU (Eds.)
Shanghai, China, June 11-13, 2014

CHARRING RATE OF TIMBER IN NATURAL FIRES

David Lange*, Lars Boström*, Joachim Schmid and Joakim Albrektsson***

* SP Fire Research, Sweden
e-mails: david.lange@sp.se, lars.bostrom@sp.se, joakim.albrektsson@sp.se

** SP Wood Technology
e-mail: joachim.schmid@sp.se

Keywords: Timber, Natural fire, Charring rate

Abstract. *A total of 32 glulam beams have been fire tested using three different fire curves and with different load levels. The aim of the project was to study the load bearing capacity and the charring rate under different fire curves and to gather data as to the variation of the response of timber beams in fire.*

Prior to the fire tests, the 32 beams were selected out of a total sample set of 45 glulam beams which was subject to reference testing and then grouping into 5 approximately equal groups in terms of mean and standard deviation of stiffness. One of these groups was subject to static bending tests until failure and was deemed to be representative of the strength of all of the other groups. During the fire tests the charring rate was determined from temperature measurements made at different depths and locations in the tested beams, as well as by inspection of the residual cross section after the fire test.

This paper reports on the test programme as well as the measured charring rates during the fire tests. The results show that the fire intensity has a major influence on the charring rate as well the variance in charring rate over the course of the fire. The charring rate also varies with time during the fire exposure. Other measurements and analysis have been conducted although they are not the scope of this paper.

1 INTRODUCTION

In the design of load bearing timber structures the charring rate is one of the key parameters. Generally the charring rate is assumed to be independent of the exposure time in a standard fire exposure in accordance with EN 1363-1 [1], ISO 834-1 [2] or ASTM E119 [3]. EN 1995-1-2 provides charring rates which can be used for the design of timber structures in fire based on the parametric fire [4]. However both the mechanical and the thermal properties for calculation are based on the response to the standard fire and material properties which are given are effective (i.e. they are dependent upon the moisture transport and heating rate of the specimen during fire exposure; this is implicit in the material properties which are given in EN 1995-1-2). Calculation of timber response to anything other than the standard fire would therefore rely on the use of models for which the material properties are as yet unknown. The reasons for this include the facts that [5]:

- most simple models do not take account of fissures forming in the timber surface. These fissures ncrease the convective and radiative heat transfer to the wood below the char layer or mass transport within the material and out of the material.
- mass transport, (moisture and pyrolysis gases), is not included in the majority of models.

The impact of the use of these effective material properties on the overall level of safety is not known during either the heating phase or the cooling phase. Furthermore the fact that the cooling phase is not considered in the Standard Fire is of concern since tests show that following natural fires, burning of the test specimen may continue well into the cooling phase until failure of the element [6]. This significantly limits the potential for timber to be used in performance based design applications.

This article reports on the methodology and some results of a project which has been designed and executed in order to determine some of the material properties of timber in parametric fires. The methodology comprised a series of 4 tests on glulam timber elements on a horizontal furnace under different fire conditions, including loading, temperature measurement within the specimens during the fire and inspection of the residual cross section following the fire. The scope of this article is limited to a description of the test series and a discussion of the char rate estimated based on the through depth temperature measurements.

2 TEST SPECIMENS

A total of 45 glulam beams with dimensions 140 × 270 × 5400 mm^3 were used during the test series. Due to the large natural variability of the material properties of timber, prior to any fire testing being carried out, the beams were subject to reference testing and grouped into 5 groups of approximately equal distribution of dynamic modulus of elasticity (measured using a hammer and an accelerometer at three points in the beams depths while the beams were suspended over the floor); one group of 10 beams, 4 groups of 8 beams plus 3 spare beams. One of these groups, the group of 10, was used for further reference testing and was assumed to be representative of the other 4 groups which were retained for the fire tests. The mean and standard deviation of the dynamic modulus of elasticity of each of the groups is shown in Table 1.

Table 1. Summary of grouping of the beams.

Group	Dynamic MOE		
	Mean (MPa)	Std dev (MPa)	CoV (%)
1	13 235	394	3.0
2	13 223	401	3.0
3	13 229	349	2.6
4	13 229	386	2.9
5	13 229	356	2.7
spare	13 900	207	1.5
Group 1 - 5	13 229		

In order to verify the static modulus of elasticity and to determine the bending strength all beams in group 1 were loaded to failure under 4-point bending in accordance with EN 408[7]. The distance between the supports was 4860 mm, and the distance between the points of application of the load was 1620 mm. In all cases, the failure type was in tension of the lower lamella. The mean bending strength of the samples were 37.8 MPa with a standard deviation of 6.2 MPa. The mean modulus of elasticity measured under the applied load (static modulus of elasticity) was determined to be 13200 MPa with a standard deviation of 400 MPa. This agrees very well with the mean modulus of elasticity measured using the dynamic testing and the standard deviation of those measurements.

Density and moisture content (as a percentage of weight) were also measured on parts of the beams used in the fire tests on the day of the test or the day following the test. Density was estimated from the weight of the individual specimens cut to 3.3m in length, as required for the fire testing program. Moisture content was determined by measuring the dimensions and weight of a small sample (ca. 50mm × 270mm × 140mm) from the offcut of each beam once it was cut to the required length for the fire test prior to drying at 105 ℃ for 24 hours and then reweighing after drying. Density varied between 420 and 493 kg/m^3 and moisture content varied between 11 and 12.6%. In depth results are not reported here for brevity.

3 FIRE TESTS

3.1 Experimental set-up

In total, four fire tests were carried out, each test comprising eight beams. The fire tests were made in general in accordance with EN 1363-1[8] and EN 1365-3 [9], but with some deviations.

- The fire exposure used deviated from the Standard Fire test in two of the tests made. A description of the applied fire exposure is given below.
- The standard prescribes a minimum fire exposed length of 4000 mm. In these tests the fire exposed length was shorter in order to maximize the number of beams which could be placed on the furnace (in order to gather more statistical information). The fire exposed length of the tested beams was 3300 mm. Figure 1 shows the planned test layout with the positions of the beams on the furnace.
- Temperatures were measured at many different locations within the test specimens, see § 3.2.
- 4 point loading was applied at the 1/3rd points on each of the beams.

The beams were fire exposed on three sides. The top surface of the beams was covered with aerated concrete blocks with dimensions 150 × 200 × 580 mm^3 except at the location of the loading points where an additional timber block was used to transfer the load from the hydraulic actuator to the beam. The aerated concrete blocks were insulated with mineral wool on the fire exposed side. Interaction between the blocks on the individual beams was reduced by placing a 5mm thick light weight insulation material between the blocks. Interaction between the blocks on different beams was reduced by adding a layer of hard and a layer of soft insulation material between the blocks. The beams were simply supported on rollers at each end. The rollers comprised a steel plate 140 mm × 140mm and a 25mm external radius steel pipe section of length 140mm. On one end the pipe was welded to the plate and on the other the two were held under friction only between the beam and the furnace perimeter frame.

The rollers as well as the supporting steel beam which comprised the perimeter frame of the furnace were insulated with ceramic fibre blanket during the fire tests. The ends of the furnace were covered by massive concrete blocks. Figure 2 shows all of the test specimens from test 1 placed on the furnace with the loading system in position prior to the test.

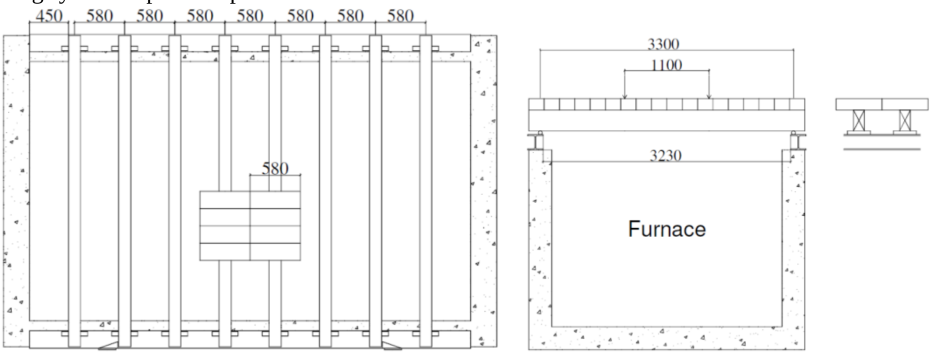

Figure 1. Experimental set-up (measurements in mm).

In all tests, prior to cutting of the beams to fit the furnace, the location of any finger joints was determined and the beams were cut such that no finger joints were located in the bottom two lamellae of the specimens, between the loading points.

In the first two tests, there was some torsional rotation of the beams which meant that adjacent beams were pushed slightly out of position. Therefore in later tests in order to prevent any transfer of rotation between the beams, the ends of the beams were cross-braced against one another. It was considered that this arrangement would not significantly impact upon the behaviour of the individual beams in flexure while allowing the timber elements to brace against one another to prevent rotation about the longitudinal axis.

3.2 Measurement of furnace temperature

The furnace temperature was measured by plate thermometers. A total of 20 plate thermometers were used in each test, evenly distributed around the test specimens. 8 of the plate thermometers were located between the beams facing an adjacent beam, 8 were located below the beams facing the nearest of the short sides of the furnace and 4 were located below the level of the beams facing the floor of the furnace. The furnace temperature was initially controlled using the output from the plate thermometers which were facing the walls and the floor. During the fire tests some of the plate thermometers failed when the individual beams broke. As this continued over the course of the tests the plate thermometers which were facing the adjacent beams were used to control the temperature in the furnace. It was observed following test 1 however that there was little to no difference between the temperature of the plate thermometers which were below the level of the beams and those which were facing the adjacent beams.

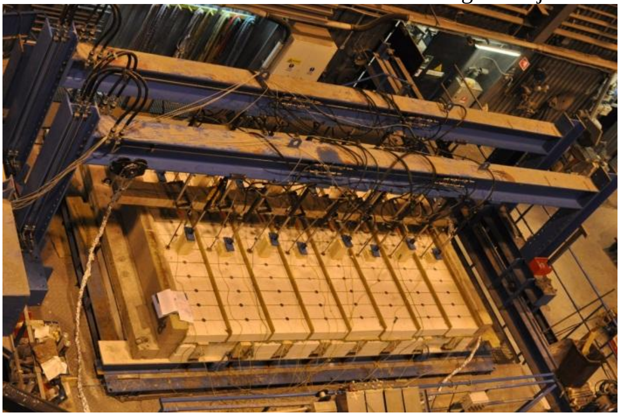

Figure 2. Experimental set-up seen from above.

3.2 Temperature measurements in the test specimens

Thermocouples were mounted within the cross section of the beams in order to determine the temperature rise during the fire exposure. These measurements are used to give an indication of the charring rate during the fire tests. In each beam in the first three tests, 10 thermocouples were mounted, see figure 3, 5 at each end.

Thermocouple number 1 (TC1) was located 10mm from the heated surface, and all other thermocouples were located at 10mm intervals from the heated surface so that TC5 was located 50mm from the heated surface. At the east, or ‘high’, end of the beam TC6, TC7 and TC8 were located at depths coinciding with TC1, TC3 and TC5 at the low end of the beam. TC9 and TC10 were positioned 90mm from the heated surface and 50 and 30mm respectively from the vertical surface of the beams.

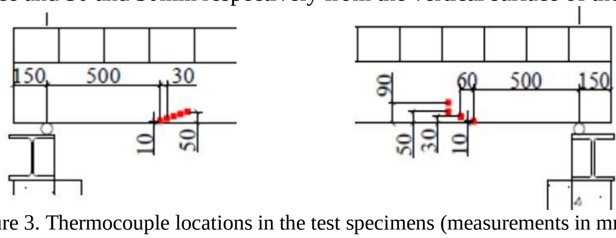

Figure 3. Thermocouple locations in the test specimens (measurements in mm).

3.3 Test procedure

The test procedure was designed in such a way that the following criteria could be satisfied:

(1) The beams should be allowed to fail independently of one another without losing furnace integrity;

(2) There should be no interaction between the test specimens during the test;

(3) Immediately following completion of the test it should be possible to remove the specimens from the furnace with a minimum of delay to extinguish any residual burning.

The test setup was designed in such a way that criteria 1 and 2 could be fulfilled. Any potential shear interaction between the beams was reduced by the use of mineral wool boards between the light weight cement blocks which were placed on top of the furnace. The concrete blocks were deeper than the anticipated displacement at failure. Nevertheless upon failure of the beams some loss of integrity did occur on top of the furnace. When this happened the actuators were retracted and mineral wool board was used to cover the openings in the furnace.

The third criterion was achieved by placing all of the test specimens directly onto a steel frame which was installed at the top of the furnace. Immediately following failure of the final beam in each test any remaining actuators were retracted, the furnace hood was retracted and the loading frame was pushed to one side. Concurrently, all thermocouple cables were cut from the data loggers and all other measurement devices were disconnected. Once the loading frame was fully removed from the test setup a 20 ton crane was used to lift the entire test assembly from the furnace and move it over to rest on 4 support frames so that the timber could be extinguished from underneath. This whole procedure took approximately 6 minutes in every case. In some of the tests, during removal of the test setup the remains of one of the beams fell into the furnace.

4 FIRE CURVES

The objective of running 4 tests was to conduct one test of the timber elements exposed to a standard fire curve and three where the timber elements were exposed to a parametric fire curve. However the loading system failed during the first standard fire test it was decided to carry out two standard fire tests, one loaded and one unloaded, and two parametric fire tests.

The parametric fires chosen were intended to represent a long-cool fire and a short-hot fire, i.e. reasonable extremes above and below the standard fire curve. Therefore the timber elements would be exposed to a slow heating rate for a long period in one of the fires and to a fast heating rate for a short period in the other. As far as was possible during the tests where a parametric fire was used, the cooling regime of the parametric fire was followed, until the last of the beams failed.

The first two of the fire tests were carried out under standard fire exposure. This represents a parametric fire with an opening factor of 0.04 and a thermal inertia of the linings of 1.35×10^6 J^2/m^4sK^2. The parameters required to define the parametric fire in all three instances are summarized in Table 2. The resulting temperature time curves are shown in Figure 4.

Table 2. parameters used in the definition of the fire curves in the tests.

Fire test	Opening factor, O ($m^{1/2}$)	$\sqrt{\rho c \lambda}$ ($J/m^2s^{1/2}K$)	fire growth rate	*qf* (qtd) (MJ/m^2)
1 and 2	0.04	1160		
3	0.2	1160	medium	250 (92)
4	0.02	1160	medium	250 (92)

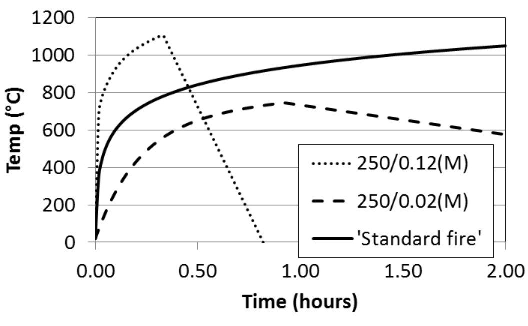

Figure 4. fire curves used in the fire tests (the parametric fires are designated as “qf/O(fire growth rate)”).

5 RESULTS

In this section we report only on the measured temperatures during the fire tests and the variations in those. From the measured temperatures, an estimate of the 1-dimensional charring rate can be made and this is also reported. Discussion of the mechanical response and the failure of the beams in the tests is outside of the scope of this paper and is the subject of other articles under preparation by the authors. In addition, for brevity, measured temperatures in only one of the standard fire tests are reported below.

5 .1 Specimen temperatures

For the second standard fire test, the mean distribution of temperature with depth at different times is shown in figure 5a. These correspond with the temperature penetration measured from the bottom of the beam at the east end of the beam. Figure 5b shows the coefficient of variation of these measurements. This is typically between 10 and 30%, although it is higher further away from the heated surface at later times. This is attributed in this instance to fissuring and cracking of the char layer at later times exposing some of the thermocouples further from the heated surface. Any thermocouples that failed during the test have been removed from the dataset which was used to create these figures.

Average temperature distributions and their coefficient of variation for the same measuring points in the beams in the short-hot fire test are shown in Figures 5c and 5d. Of note is that the cooling phase is clear in the temperature distributions, where a maximum temperature close to the heated surface occurs after about 20 minutes. The position of maximum temperature continues to move through the specimens, away from the heated surface, as would be expected after this time. As with the standard fire test, the coefficient of variation in the temperatures is typically between 10 and 30% for the temperatures measured from the bottom of the beams, although the variation does increase over the course of the test and with distance from the heated surface. The effect of fissuring and cracking, even averaged over all of the beams in this test is evident further from the heated surface in figure 5c.

Specimen through depth temperatures measured from the bottom surface at different times in the long-cool fire are shown in figure 5e. Because of the slower rate of temperature decrease with time during the cooling phase in this test, the temperature continues to increase close to the heated surface of the specimens, as opposed to the 3rd fire test where it was seen to drop during the cooling phase which was part of the test. The coefficient of variation of the through depth temperature measurements is shown in Figure 5f and is typically between 10% and 20%, although no increase is seen during the later stages of the fire. The lower and more constant variance may be attributed to the less aggressive heating regime in this fire test in comparison to the other two tests.

5.2 1-dimensional charring rate

The average 1-dimensional charring rate may be estimated based on the time taken for the isotherm corresponding to the charring temperature to reach the thermocouples which are embedded in the timber specimen. Assuming that charring occurs at a fixed temperature, charring rate is given by the expression:

$$\beta_{\mathrm{1d}} = \frac{d_{\mathrm{tc}}}{t_{\mathrm{Tchar}}} \tag{1}$$

where β_{1d} is the 1-dimensional charring rate in mm/min, d_{tc} is the depth of the thermocouple measured from the nearest surface, and t_{Tchar} is the time in minutes taken for the thermocouple to reach the charring temperature from the start of the test. It should be noted that this expression gives an average charring rate over the distance in question as opposed to the 'real' charring rate.

The charring rate estimated using this method at different depths for each of the different fires, including both 'standard' fire tests, is shown in Figure 6. The error bars represent the coefficient of variation. It can be seen that charring rate in the first standard fire appears to increase from approximately 0.4mm/min at the start of the test to around 0.7mm/min at the end of the test (although it decreases slightly between 0 and 40mm, which is perhaps more in line with the results of fire test 2). Conversely, the charring rate in the second standard fire test plateaus at around 0.5mm/min.

All of these reported charring rates are based on the average times to reach a charring temperature of the thermocouples at different depths within all of the beams in this test. That is to say that for each of the average values reported these are based on at least 8, and at most 16 thermocouples, depending upon reliability of the measurements. A charring temperature of 270 ℃ has been assumed, although this has been seen to have no impact on the resulting charring rate calculated in this way.

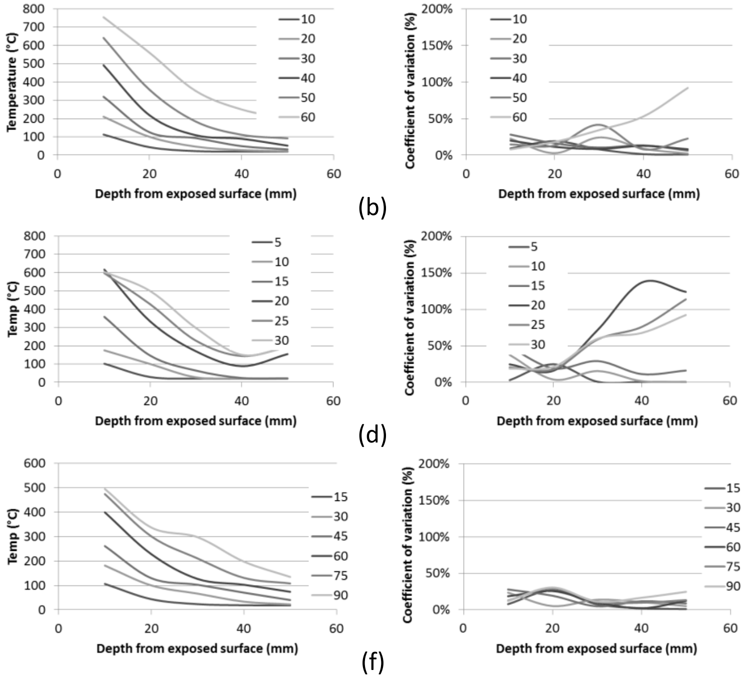

Figure 5. specimen temperatures and coefficient of variation of the measurements and predictions – each series represents a different time during the fire test.

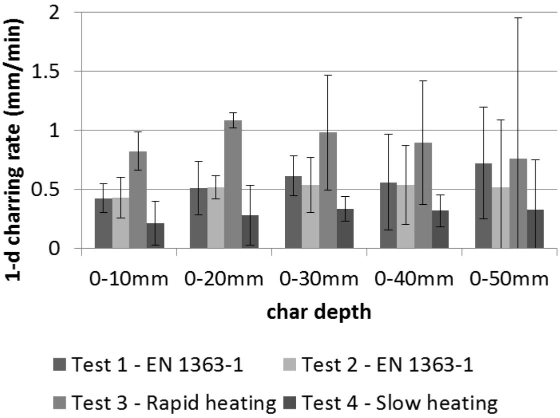

Figure 6. summary of charring rates from the bottom of the test specimens estimated from thermocouple measurements in all fire tests.

During the short hot fire, the charring rate is seen to increase rapidly during the early stages of the fire, to approximately 1.1mm/min over the first 20mm, and then reduces to approximately 0.7mm/min over

50mm. Comparison between the temperature plots in this fire test in figure 5c and the charring rate indicate that the highest charring rate occurs between 15 and 20 minutes into the fire test at the end of the heating phase. The onset of reduction in charring rate therefore corresponds to the cooling phase of the fire test. The average charring rate during the long-cool fire test grows from approximately 0.2mm/min over 10mm and remains constant at around 0.3mm/min from 0 - 20 to 0 - 50mm depth. The temperature of the furnace was relatively constant in the long-cool fire compared with the short-hot fire or the standard fire temperature time curves.

In general, the coefficient of variation can be seen to increase with increasing duration of fire exposure and this is more marked for more aggressive fires.

6 CONCLUSIONS

This article has given a short overview of a series of fire tests which have been carried out at SP in Sweden to investigate the behaviour of timber elements exposed to different fires. The article then reports on the variation in temperature distribution which was found in the fire tests and the resulting charring rate estimated based on measured temperatures in the test series.

The measured temperatures are seen to have a generally large coefficient of variation, between 10 and 30%. In fires with higher temperatures or more severe heating rates this is seen to increase with increased exposure time and depth, and is attributed in this case to a greater degree of cracking of the char layer in the more aggressive fire. The char rates which are estimated based on the temperature measurements are seen to increase in the early stages of standard fire exposure, prior to ‘plateauing’ at later times of fire exposure. This is contrary to what is stated in the Eurocode, where charring rate is constant, and may have positive implications for timber exposed to localized or travelling fires as well as timber which is required to have a short fire resistance. Variation in charring rate also increases with increasing fire exposure. In the test with a parametric fire exposure the charring rate is seen to be dependent upon the heating rate as well as the rate of cooling. In the short hot fire the charring rate reduces significantly during the cooling phase, whereas during the long-cool fire where the cooling rate is low the charring rate remains relatively constant for the measurements which were made.

The test series yielded a large quantity of data, which is the subject of additional articles and reports by the authors of this paper and will be published in due course.

REFERENCES

[1] EN 1363-1:2012; Fire resistance tests – Part 1: General Requirements.

[2] ISO 834-1 Fire-resistance tests - Elements of building construction - Part 1: General requirements

[3] ASTM E119 Standard Test Methods for Fire Tests of Building Construction and Materials

[4] EN 1995-1-2: 2004 Eurocode 5: Design of timber structures – Part 1-2: General – Structural fire design.

[5] J. König, “Effective thermal actions and thermal properties of timber members in natural fires,” Fire and Materials, vol. 30, no. 1, pp. 51–63, Jan. 2006.

[6] J. König, J. Noren, F. B. Olesen, and F. T. Hansen, “Timber Frame Assemblies Exposed to Standard and Parametric Fires Part 1 - Fire Tests,” Stockholm, 1997.EN 1363-1.

[7] EN 408: 2003 Timber structures – Structural timber and glued laminated timber – Determination of some physical and mechanical properties.

[8] EN 1363-1 Fire resistance tests – Part 1: General requirements.

[9] EN 1365-3 Fire resistance test for loadbearing elements – Part 3: Beams.

FIRE RESISTANCE OF PRIMARY BEAM – SECONDARY BEAM CONNECTIONS IN TIMBER STRUCTURES

Veronika Hofmann*, Martin Gräfe*, Norman Werther* and Stefan Winter*

* Ingenieurfakultät Bau Geo Umwelt
Technische Universität München, Arcisstrasse 21, 80333 München, Germany
e-mails: veronika.hofmann@tum.de, m.graefe@tum.de, n.werther@tum.de, winter@tum.de

Keywords: Fire resistance, Timber buildings, Joist hangers, Self-tapping screws, Full thread screws

Abstract. *This research project deals with the fire resistance of primary beam - secondary beam connections in timber structures. The main objective concerns the fire safety design of joist hangers, full thread screws and dovetail connectors. This paper describes a series of small scale furnace fire tests in different configurations of these types of connectors. In conclusion design recommendations are given.*

1 INTRODUCTION

The demand for timber as a construction material is notably increasing all over the world. This is particularly true for residential, office and administration buildings as well as special constructions. The benefits of building in timber are visual and haptic attractiveness, high energy efficiency, quick erection time and a low carbon footprint. Despite these advantages there are large concerns and limitations by authorities and design codes linked to fire safety.

To consider this aspect in a sufficient way European and international design codes have been developed over the past years to assess the fire safety in buildings. The design rules for fire exposed timber structures such as the ones listed in EN 1995-1-2 [1], NZS 3606 [2] or in the U.S. AWC-DCA2 [3] are mostly focused on determining the charring and residual cross section of linear timber members, such as beams and columns. General regulations and design methods for assessing the fire safety of engineered joist to beam and joist to column connections do not exist [4]. Approved and reliable systems are rare.

To overcome this gap of knowledge a German research project has been started early in 2013 which seeks to investigate the thermal and structural performance of typical engineered connections for timber structures in the event of fire, such as joist hangers, screwed connections and dovetail connections (see Figure 1).

Figure 1. Typical joist connections for timber structures. From the left: joist hanger, dovetail connector, full thread screw.

2 CONCEPTION OF INVESTIGATIONS

2.1 Methodical approach

Since experimental investigations allow only a limited number of tests in general, it is projected to extend the results by numerical modelling for further parametrical studies and optimization process.

The investigations conducted in this research project are based on a three pillar strategy:

(1) unloaded small scale fire tests to assess the influence of geometry and material interaction,

(2) mechanical testing of the connections at ambient conditions under consideration of the results and residual cross sections gained in step (1),

(3) loaded full scale fire tests of selected and optimized connection systems, based on the results gained in the previous steps (1) and (2) and the associated FE modelling.

3 EXPERIMENTAL TESTING

3.1 General configurations and setup of small scale tests

3.1.1 Testing Facilities

The unloaded U-shaped specimens were assembled each of one CLT floor and two CLT wall panels with a thickness of 100 mm. The 3-layered CLT panels were used as support structure representing the primary beams. At the inside of the CLT wall panels 300 mm long glulam- as well as sawn timber beam sections were attached with joist hangers, fully threaded screws and aluminum dovetail connectors, respectively, as illustrated in Figure 2. All beams were orientated in such a way that each bottom side was facing to the burner and no thermal shading effects occurred among the beam sections. Each free beam end grain side was covered with 18 mm gypsum boards to ensure an even four-sided fire exposure of the beam sections and to exclude an additional thermal influence for the examined connections.

All timber members were of spruce with a moisture content of approximately 12 %. The resulting U-shaped specimens were placed in a diesel fuel fired furnace, as shown in Figure 2 and exposed to ISO 834 fire for 30 and 60 minutes, respectively. The tests were carried out under variation of beam dimension, type of connectors and fasteners as well as joint dimension to cover a wide spectrum of configurations.

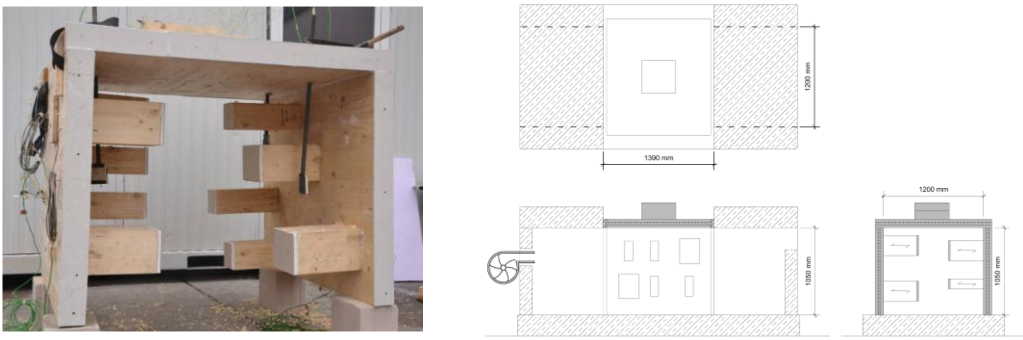

Figure 2. Left: assembled specimen with measurement equipment, right: drawing of furnace and specimen.

3.1.2 Instrumentation

Temperature measurements during the fire tests were realized by Type K thermocouples inside the timber members at the connectors and fasteners. For selected nails and screws thermocouples were welded to head and tip to ensure precise measurements alongside the fasteners. The thermocouples of fastener tips were fed through predrilled holes in the timber members and sealed at the fire unexposed side with mastic.

3.2 Individual setup

3.2.1 Joist Hangers

In the conducted fire tests two sizes of joist hangers for beam dimensions of W × H = 100 mm × 240 mm and 200 mm × 300 mm have been investigated, each for internal and external wings. The joist hangers were made of galvanized zinc coated steel sheets of 2 mm thickness. To fix the joist hangers to the beam sections and CLT wall elements, rink shank nails with a diameter of 4 mm and screws with nominal diameter of 5 mm (core diameter 3.3 mm) have been used as fasteners. Both types were 50 mm and 70 mm in length respectively. For all setups the 50 mm long fasteners were applied to the right side and the 70 mm long fasteners to the left side of the symmetrical joist hangers. An exception was made for the 100 mm wide beams and only 50 mm long fasteners were applied to fasten the beams to the joist hangers. Either screws or nail were used per joist hanger. Therefore eight different combinations were assessed in total. To measure the increase in temperature, thermocouples were installed at fastener heads and tips, in the joint between connector wings and timber members and in the gap between beam sections and wall elements for each configuration as illustrated in Figure 3. In order to ensure practical conditions the beam sections were fastened with a gap of 7 mm to the CLT elements (thickness of steel sheet + fastener head) in all setups. No further protection measure was applied to these gaps. The fire tests with joist hangers were conducted for 30 minutes.

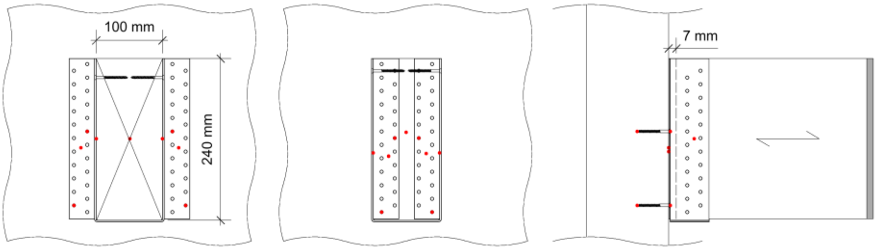

Figure 3. Exemplary fire test setup for joist hangers.

3.2.2 Full Thread Screws

In order to investigate the effect of screw length, diameter, shape of screw head and steel type to the temperature development and charring rate of timber, nine screws have been installed into each CLT ceiling element, as presented in Figure 4 and examined in 30 and 60 minutes fire tests. To enable the assessment of up to 300 mm long screws, the CLT ceiling elements were backed by two additional CLT panels with 100 mm thickness each (see Figure 4).

To all heads and tips of the screws thermocouples were attached. In addition the temperatures for the 200 mm long screws were measured at half-length and for the 300 mm long screws at 1/3 and 2/3 of the total length, as illustrated in Figure 4.

The interaction of edge distance $a_{4,c}$ and the thermal influence of the unprotected screw heads were of special interest. The beam sections were attached to the CLT panels by crosswise installed pairs of screws. Six beam sections were tested for 30 minutes tests and ten for 60 minutes. The screws used in the fire tests had dimensions ($d_{nominal}$ x length) of 6 mm x 160 mm and 12 mm x 300 mm respectively and screwed in under 45°. Following edge distances were examined as protecting wood covering:

a) $a_{4,c} = 3*d_{nominal}$ (in accordance with EN 1995-1-1)
b) $a_{4,c} = 3*d_{nominal} + \beta_n*t + d_0$ (according to EN 1995-1-2)
c) $a_{4,c} = 3*d_{nominal} +(\beta_n*t + d_0)/2$ (half between a) and b))

The position of thermocouples attached to each setup can be taken from Figure 5.

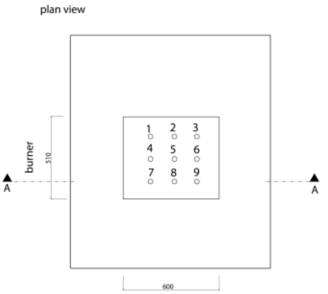

number	nominal screw diameter - $Ø_n$ [mm]	screw length [mm]	steel type	shape of head
1	10	200	stainless	counter sunk
2	10	200	carbon	counter sunk
3	12	200	carbon	cylinder
4	8	300	carbon	counter sunk
5	8	100	carbon	counter sunk
6	8	200	carbon	cylinder
7	8	300	carbon	cylinder
8	8	100	carbon	cylinder
9	6	200	carbon	cylinder

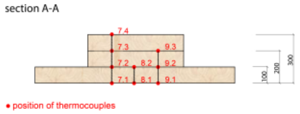

Figure 4. Position of full thread screws in the CLT ceiling element with corresponding measurement points.

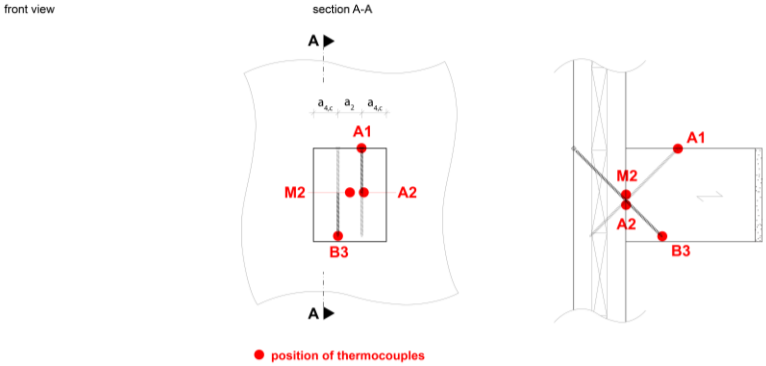

Figure 5. Crossed screws and position of thermocouples in the connection (schematic illustration).

3.2.3 Dovetail Connectors

In a third series of tests concealed aluminum dovetail connectors were assessed under variation of edge distance (protective side cover, a_{fi}) for 30 and 60 minutes fire exposure. Here three different sizes of side covering were examined, each for the smallest (type G: W × H = 45 mm × 60 mm) and the largest (type F: W × H = 75 mm × 200 mm) size of dovetail connector used in this test series. A summary of the assessed setups is given in Table 1. The connectors were installed without a gap between beam sections and wall panels by inserting the connectors into milled notches in the timber members. The influence of gap sizes and further protection methods were examined in additional fire tests [7].

In all setups thermocouples were attached to both aluminum plates of each connector at various positions. The temperatures of screws connecting the aluminum plate to the timber members were not measured.

The tests were conducted to determine the appropriate dimension of side cover by timber, which protects the connectors from direct fire exposure and avoids a critical temperature level of the aluminum (according to EN 1999-1-2 [5]).

Table 1. setup for fire tests with dovetail connectors.

configuration	1		2		3	
type G: 45 mm × 60 mm F: 75 mm × 200 mm	G	F	G	F	G	F
duration of fire exposure	30 minutes		30 minutes		90 minutes	60 minutes
protective side cover a_{fi}	according to technical approval $a_{fi\ (above,\ below)} \geqslant 15$ mm $a_{fi\ (left,\ right)} \geqslant 12{,}5$ mm		at all sides $a_{fi} \geqslant 31$ mm		at all sides $a_{fi} \geqslant 55$ mm	
selected beams W/H [mm]	70/90	100/230	120 /120	140 /260	160 /180	180 /300

4 EXPERIMENTAL RESULTS

4.1 Joist hangers

4.1.1 Influence of Fasteners

The conducted series of fire tests with joist hangers showed, that the type of fastener mainly influences the charring of wood in contact with the fasteners. The unprotected fasteners conducted the heat from the surface into the interior of the timber members resulting in larger charring depth than for the free undisturbed area of the beams. The examined screws with nominal diameter of 5 mm performed better than the 4 mm nails with same length. This is evident from the more slowly heating curve of the screw tips and can be also visualized by less charring of wood in contact with the screws and by the magnitude of discoloration alongside the removed fasteners. The 70 mm long screws were still bright up to a length of 35 mm from the tip while the nails were colored black along their entire length. By dismantling the specimens it turned out that the gripping capacity of screws was much higher than for the corresponding rink shank nails, due to their threads and less charring. A comparison of the temperatures at the fastener tips showed that the 50 mm long fasteners heated up more quickly than the 70 mm long fasteners if the same fastener type and diameter was used. For example the tip temperatures of the 4 × 50 mm rink shank nails reached 450 °C whereas only 230 °C arose for the 4 × 70 mm nails after 30 minutes fire exposure.

4.1.2 Influence of Joist Hanger Geometry

The 100 mm wide secondary beams showed either no or only little residual cross sections in the area of the joist hangers and must therefore be classified as too narrow for further examination. Some of these 100 mm wide beam sections already fell down after the fire test, as a result of the extra time it took to remove the complete specimen from the furnace.

Connections with internal wings showed significant lower temperatures (up to 200 °C) than those with external wings on the surface of the CLT wall element (primary beam) between the wings. This difference was not recorded in the measured temperatures between connector and secondary beams. The influence of the direct fire exposure governed the surface temperatures and charring.

The gaps between the wall elements (primary beam) and the beam section (secondary beam) had a great influence to the charring behaviour of the connection. Larger gaps sizes led to an additional exposure at the end grain side of the attached beam sections and increased the charring due to “the almost five-sided fire exposure”. To reduce charring in this area and consequently maintain the load bearing capacity of the connection the gap size should be as small as possible or supplemented with sealing or top side covering.

4.2 Full thread screws

4.2.1 Influence of Screw Dimension

The length of the full thread screws shows a great influence on the measured temperatures if exposed from the unprotected head side. This effect is confirmed by the previously discussed results of rink shank nails. The comparison of the temperatures in the same depth of a 100 mm and a 300 mm long full thread screw shows lower temperatures at the longer screw. This difference ΔT rises with increasing distance from the exposed surface. In a depth of 100 mm the measured difference was about 100 °C after 60 minutes fire exposure as depicted in Figure 6.

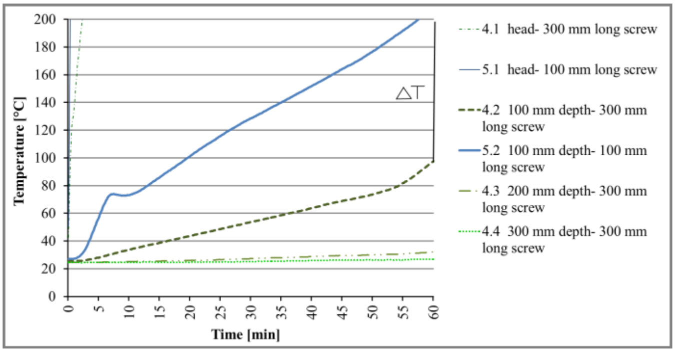

Figure 6. Temperature development for two counter sunk head full thread screws $Ø_n$ 8 mm.

This difference was caused by the larger skin surface and the ability of the longer screw to penetrate with their tip in more distant and cooler timber. Further on the larger thermal capacity of the longer screw has some influence. It is obvious from the results that the screw diameter is influencing the temperature at the screws as well. In the early stages of fire exposure the $Ø_n$ 6 mm screws showed higher temperatures at the screw heads than those with $Ø_n$ 12 mm. After about 20 minutes these head temperatures were comparable to each other again. Contrary to this all temperatures along the $Ø_n$ 6 mm screws lay below the corresponding temperatures of $Ø_n$ 12 mm screws as shown exemplarily in Table 2.

Table 2. temperature distribution along 200 mm long full thread screws after 60 minutes fire exposure.

	head (0 mm)	mid length (100 mm)	tip (200 mm)
$Ø_n$ 6 mm	900 °C	60 °C	35 °C
$Ø_n$ 12 mm	900 °C	110 °C	60 °C

This temperature distribution can be explained by the fact that the peripheral surface increases linear while the cross section area increases quadratic with the diameter of the screw. The shape of screw head did not have any significant influence to the temperature distribution in the screws.

4.2.2 Influence of steel types to temperature distribution

The assessed screws made from stainless steel performed better than the carbon steel screws. The better performance was shown by lower temperatures along the screws and less charring of wood in contact with screws.

Temperature measurements in the middle of the carbon steel screws have been about 80 °C higher than at stainless steel screws. The screw tips only showed a temperature difference of about 30 °C after 60 minutes. This behavior is caused by the different thermal conductivity of the screws. Carbon steel has a significant higher conductivity as stainless steel at ambient temperature. Therefore, the heat is better conducted in greater depth, resulting in higher temperatures within the screw and at the timber. With increasing temperature both thermal conductivities are approaching and behave in the same way from 800 °C onwards, whereby the resulting temperatures equalize again.

4.2.3 Edge Distance

The temperature profile of full thread screws and the surrounding timber in primary – secondary beam connections is substantially influenced by the edge distance $a_{4,c}$. The screw is protected from heat by the wooden side coverage, which is steadily converted into charcoal and therefore reduced during the fire exposure. If there is a sufficient edge distance, the temperature in the screw is mainly influenced by the fire exposed head. The temperatures of the screw heads in the secondary beams showed a linear increase in the beginning, until after 20 minutes a maximum temperature of about 800 °C was reached and held to the end of the test (Measuring point A1, see. Figure 5). Screws exposed for 30 minutes to the fire with an edge distance of $a_{4,c} = 3*d_{nominal} +(\beta_n*t + d_0)/2$ [mm] showed at the measuring point in the middle (A2) temperatures below 160 °C. Screws with a 60 minutes exposure required an edge distance of $a_{4,c} = 3*d_{nominal} +(\beta_n*t + d_0)$ [mm] (according to EN 1995-1-2) to keep the temperatures below 220 °C. The comparison between the A2 temperatures with the temperatures, which have to be expected in the same depth at one-dimensional heat flux shows a significant difference. The differences can be explained with the additional influence caused by the head exposure.

4.3 Dovetail connectors

4.3.1 Influence of Dimension

Timber beams with dovetail connectors exposed 30 minutes to the fire and mounted with a wood coverage of 15 mm at all sides showed remaining sections which were partially smaller than the connector, which led to directly exposed fasteners. A further test with the smallest and biggest connector and a larger wood coverage of 31 mm at all sides showed temperatures which gives reason to expect a sufficient strength for a practical use. At the test specimen “4” with 60 minutes fire exposure and wood coverage of 55 mm the remaining thickness of uncharred timber seemed big enough for a sufficient load bearing capacity for practical application. At test specimen “3” with a wood coverage of 55 mm the temperature measurements after 60 minutes reached temperatures between 170 and 215 °C. Aluminum has remaining strength of about 42 % at 215 °C (according to [5]) compared to the strength in cold condition, which is not sufficient for the load bearing capacity in the case of fire. After 75 minutes a significant increase in the temperature measurements was registered, this can be explained by the end of the steam generation due to the moisture content in the timber. The chosen coverage of 55 mm for an exposure of 60 minutes may be reduced due to the results of the tests “3” and “4”. As the temperature didn’t significantly increase until 75th minute in the 90 minutes test, the charring which took place between 60 and 75 minutes may be subtracted from 55 mm. A subtraction of 0.8 mm/min * 15 minutes = 12 mm leads to a minimum coverage of 43 mm.

4.3.2 Gaps

The connectors may be mounted with gaps or completely covered by the timber. If the connector is mounted with a gap, a gap in the thickness of the connector remains between the timber beams. From the standpoint of fire safety the gap is unfavourable, as the aluminum parts are directly subjected to the flames and therefore heat up rapidly. Result will be a faster softening of the aluminum and an increased charring rate alongside the fasteners. In the production process this option is faster and easier to fabricate, as milling in notches in the main beam. Optimization for the fire safety can be realized by intumescent fire protection materials placed in the remaining gap (cf. [7]).

For the option without gap the connector is placed in a corresponding notch in the main beam. Therefore it is surrounded at all sides by timber, which acts as an insulation material. The direct exposure to the fire at the top may be excluded by a fitting in piece of timber, which leads to a complete coverage. A protection of such kind leads to a significant lower heating rate and accordingly an increased timespan of sufficient strength.

5 CONCLUSIONS

Based on the results the connection of joist hanger to the secondary beam appears as critical area in fire tests and will govern the failure. The results showed that unprotected 50 mm long fasteners are not long enough to embed in the residual timber cross section after 30 minutes and not recommendable for further fire tests with joist hangers. In contrast fasteners with 70 mm length seem appropriate. For that reason the position of the wings has no essential influence, although internal wings are affecting the strength of the connection at the main beam positively. In the interest of a maximum in strength at fire exposure, the gap between the timber beams should be as small as possible. For practical reasons a compromise is necessary, appropriate seems a gap size of 7 mm like in the tests conducted. A width of secondary beams of at least 140 mm, i. e. the double of the minimum length of the fasteners of 70 mm seems to be advisable. Thereby a sufficient remaining cross section in the area of the connection can be reached. For reasonable cross sections heights of about 180 mm can be recommended.

Favourable for the charring depth and the temperature of full thread screws is the use of long screws with small diameters. Screws made of stainless steel performed better than carbon steel screws. The type of head is irrelevant for the temperature alongside the screws. The bigger the edge distance $a_{c,4}$ the smaller is the influence on the temperature of the screw by the fire exposed sides of the cross section. Temperatures lower than 220 °C in the middle of the screws are resulted by side distances of $a_{4,c} = 3 * d_{nominal} + (\beta_n * t + d_0)/2$ for a 30 minute exposure and $a_{4,c} = 3 * d_{nominal} + (\beta_n * t + d_0)$ (according to EN 1995-1-2) for a 60 minute exposure respectively.

Dovetail connectors made of aluminium and mounted without a gap (≤ 1 mm) should be covered by timber at all sides with minimum thickness of 31 mm for 30 min fire exposure and 43 mm for 60 min fire exposure. Connectors mounted with gap should be protected be means of intumescent materials alongside the sides of the connector.

ACKNOWLEDGEMENTS

The authors would like to acknowledge both the students and technicians at TU München for their help assembling the specimens, thank GH-Baubeschläge GmbH, SPAX International GmbH and Merk Timber GmbH for the fasteners and beam specimens, and thank the Federal Institute for Research on Building, Urban Affairs and Spatial Development (BBSR) and the Federal Office for Building and Regional Planning (BBR) for funding this research project in the German research program “Zukunft Bau”.

REFERENCES

[1] European Committee for Standardisation (CEN). Eurocode 5. *Design of timber structures. Part 1-2: General – Structural fire design, EN 1995-1-2*. Brussels, Belgium, 2004.

[2] Standards Council New Zealand. NZ 3603. *Timber Structures Standards*, 1993

[3] American Wood Council: Design for Code Acceptance, *Design of Fire - Resistive Exposed Wood Members*, 2010

[4] Deutsche Gesellschaft für Holzforschung, *Holz Brandschutz Handbuch, 3*. Auflage Ernst & Sohn Verlag, 2009

[5] DIN EN 1999-1-2: 2007 Bemessung und Konstruktion von Aluminiumtragwerken – Teil 1-2: Tragwerksbemessung für den Brandfall

[6] Bauaufsichtliche Zulassung, Z-9.1-550, „ET-Passverbinder als Holzverbindungsmittel“

[7] Stöckl, U.: Verhalten von standardisierten Systemverbindern im Brandfall, Institut für Brandschutztechnik und Sicherheitsforschung GmbH AT-Linz, 2013

8th International Conference on Structures in Fire
Guo-Qiang LI, Venkatesh K. R. KODUR, Shou-Chao JIANG, Jian JIANG, Su-Wen CHEN, Guo-Biao LOU (Eds.)
Shanghai, China, June 11-13, 2014

NUMERICAL INVESTIGATIONS ON THE FIRE BEHAVIOUR OF GLUED-LAMINATED TIMBER BEAMS TAKING INTO ACCOUNT THE INFLUENCE OF ADHESIVES

Michael Klippel and Andrea Frangi

ETH Zürich, Institute of Structural Engineering, 8093 Zurich, Switzerland
e-mails: klippel@ibk.baug.ethz.ch, frangi@ibk.baug.ethz.ch

Keywords: Glued-laminated timber, Adhesive, Fire resistance, Finger joints, Probabilistic investigations

Abstract. *Fire design methods usually assume that the adhesive does not influence the fire resistance of glued-laminated timber beams significantly. However, some concern was raised recently [1]. Thus, a comprehensive research project was conducted to investigate the influence of adhesives on the fire resistance of bonded timber elements. Within this project, fire tests on finger-jointed timber lamellas loaded in tension and exposed to ISO-fire were performed. These fire tests formed the basis to develop effective temperature-dependent tensile strength relationships of finger joints glued with various adhesives similar to those for timber given in EN 1995-1-2. Further, a finite element model was developed considering the natural variability of timber. On the basis of this probabilistic investigation on glued-laminated timber beams the influence of the adhesive used in the finger joint on the fire resistance of such members was quantified for different strength grades and distances between the finger joint.*

1 INTRODUCTION

Traditionally, for bonded connections in timber structures, such as finger joints, phenolic-resorcinol-formaldehyde (PRF) adhesives have been used. To prevent some of the disadvantages of PRF, new adhesives have been developed and introduced into the market. These new adhesives are cheaper, permit shorter hardening times (in the case of melamine-urea-formaldehyde adhesives, MUF) and, in the case of polyurethane adhesives (PUR), are also free from formaldehyde. The thermal stability of some new adhesives in glued engineered wood products has been one of their key criteria, since their mechanical performance declines with increasing temperature. Hence, bonded wood joints using such adhesives might lead to a lower fire resistance of engineered wood products.

To assess the fire performance of finger-jointed lamellas glued with various adhesives, an extensive fire testing series of 49 fire tests under standard ISO-fire exposure was performed [2, 3, 4]. In this campaign, 12 different structural- and non-structural-adhesives of common types (1C PUR, PRF, MUF, EPI, UF, PVAc) were tested in fire tests on finger-jointed connections loaded in tension. The results from these fire tests were used to numerically assess the fire performance of glued-laminated timber beams. This paper first presents numerical simulations on single finger-jointed timber lamellas to develop the temperature-dependent strength reduction of finger joints glued with various adhesives. Next, a probabilistic investigation is presented to evaluate the fire resistance of glued-laminated timber beams considering both the variable strength and stiffness of timber and finger joint.

2 MATERIALS AND METHODS

2.1 Numerical simulations on finger-jointed timber lamellas

The load-bearing behaviour of finger-jointed timber lamellas was studied with the help of non-linear three-dimensional Finite Element (FE) simulations. The simulations use the test data obtained in the fire tests described in [2, 3]. Thermal-mechanical analyses were performed using a three-dimensional FE model implemented in Abaqus. The analyses were performed in order to determine the reduction of strength with increasing temperature of finger-jointed specimens. In accordance to the temperature-dependent reduction of the timber strength given in EN 1995-1-2 [5], also a bi-linear approach was assumed with a breakpoint at 100 ℃. Figure 1 shows the assembly of the finite element model. Three-dimensional solid brick elements were used. The “Concrete Damaged Plasticity” (CDP)-model provided by the Abaqus material library was used to describe the linear elastic brittle behaviour under tensile loading. The same constitutive material property was later used for the FE simulations of glued-laminated timber beams. The CDP-model is able to model both the linear elastic brittle behaviour of timber in tension and the linear elastic-plastic behaviour under compression taking into account the reduction of temperature-dependent strength (see Figure 5 (left)).

First, a thermal analysis was performed in order to simulate the temperature development in the cross-section. Thereby, only the part in the middle of the lamella in lengthwise direction was modelled with a fine mesh (3 mm edge length of the elements) and exposed to fire on two sides. In order to take into account a possible interference of heating from two sides in the middle of the specimens’ cross-section, the cross-section was fully modelled and no symmetry was used. As an example, Figure 1 shows the temperature field of the cross-section after about ten minutes of standard ISO-fire exposure. The elements with temperatures above 300 ℃ represent the char layer with zero stress and thus do not carry any load, as shown in Figure 1 (right).

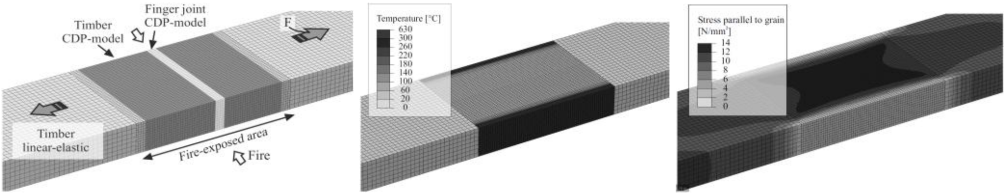

Figure 1. Model to determine the temperature-dependent strength reduction of finger-jointed specimens (40 mm × 140 mm). The middle part of the model is exposed to ISO-fire from the sides. As in the fire tests, a constant tensile load (10 N/mm^2) parallel to the grain is applied, until the fire resistance is reached. The temperature field and the stress parallel to the grain after about ten minutes of fire exposure are also shown.

The one-dimensional charring rate β_0 as a function of time of fire exposure, determined from the thermal analysis of a 140 mm wide specimen, is illustrated in Figure 2 (left). As already found in simulations using two-dimensional models [6], the charring rate increases until 20 minutes of fire exposure to a value of about 0.7 mm/min and slightly decreases with progressing time of fire exposure towards the value of the one-dimensional charring rate β_0 = 0.67 mm/min measured in [7]. This value was, for simplicity, rounded down to 0.65 mm/min and assumed in EN 1995-1-2. In case of the 80 mm wide specimen, between 30 and 40 minutes of fire exposure a superposition of the heat from the two sides is observed, leading to an increase of the charring rate. The model is thus able to describe the temperature development in the cross-section accurately.

In the next step, a thermal-mechanical analysis was performed using the results (i.e. the nodal temperatures) from the thermal analysis as an input. The input parameters for the thermal analysis can be taken from [8]. The same mesh size was used in the thermal and the thermal-mechanical analysis. Since the global behaviour of the finger joints and especially the fire resistance of the connection is of interest, the finger joint was modelled by allocating the finger joints’ material properties to four element-rows in the middle in lengthwise direction of the fire exposed finer mesh part (Figure 1 (left)). The rest of the

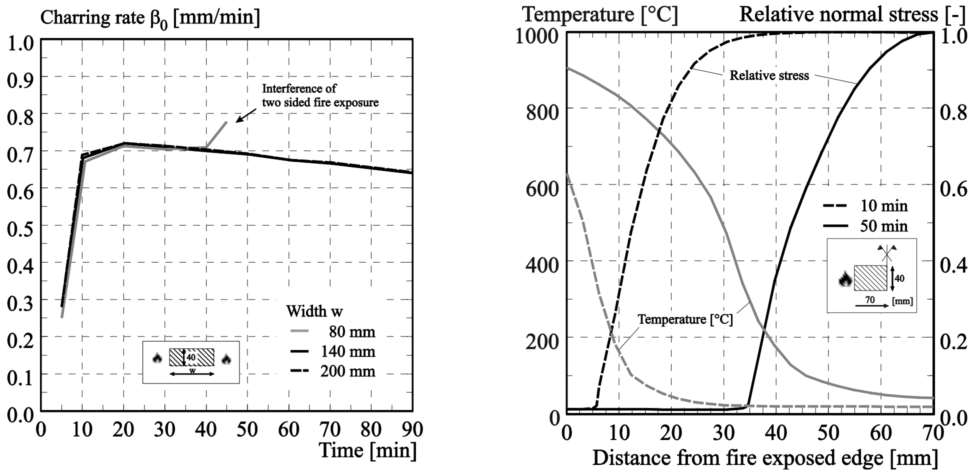

Figure 2. One-dimensional charring rate β_0 with fire exposure time obtained from the thermal analysis (left). Relative strength - related to maximum tensile strength in the middle of the cross-section - depending on the distance from the fire exposed edge after 10 and 50 minutes of fire exposure of a 140 mm wide specimen (right).

finer mesh part was modelled using the CDP-material model allocating the temperature-dependent material properties of timber under tension according to EN 1995-1-2, i.e. by a bi-linear function with a breakpoint at 100 °C and 65% of the timber tensile strength at normal temperature.

Figure 2 (right) shows a temperature profile as well as the corresponding relative tensile strength along the specimens width exposed to fire from two sides for a fire exposure time of 10 and 50 minutes. With increasing temperature, the strength decreases. At 300 °C, timber has completely charred and thus the residual strength is zero. In the middle of the cross-section, with comparatively lower temperatures, the relative strength is the highest. With progressing fire exposure, the load is redistributed to the colder inner part of the cross-section. Figure 2 shows that the model accurately reflects the behaviour inside a fire exposed timber cross-section.

2.2 Numerical simulations on glued-laminated timber beams

After studying the load-bearing resistance of single finger-jointed timber boards, a FE-model of a full beam was developed in Abaqus. This FE-model is capable of taking into account timber's variable material properties and finger joint properties depending on the adhesive. Glued-laminated timber (glulam) beams were modelled using the probabilistic material model developed by Fink et al. [9, 10], see example of a beam in Figure 4. The modelled glulam beams consisted of several boards or finger-jointed lamellas glued on top of each other.

The load-bearing behaviour of simply supported glulam beams was investigated first at normal temperature. As in the study on finger-jointed lamellas, the general purpose 8-node continuum element of type C3D8R with reduced integration was used. The load was applied by a concentrated force on each node along the beams' width. The model "Concrete Damaged Plasticity" (CDP) was used to describe the material behaviour of timber, see Figure 5 (left), whereas the stiffness in compression was assumed to be the same as the stiffness in tension. Further, it was neglected that the temperature-dependent reduction of the stiffness in compression would be higher than in tension. To avoid failure at the support and at the load application points, a linear elastic material behaviour without a failure criterion was assigned to the elements in these areas. Figure 3 shows the model set-up of a common glulam beam used in this study. Both material and geometric non-linearity's were considered in the model.

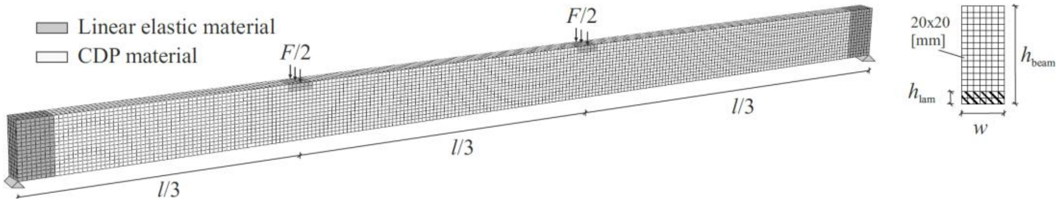

Figure 3. Finite element model set-up.

A mesh convergence study was performed in order to find an optimal mesh size without compromising the accuracy of the results and computational costs. It was found that the mechanical analysis should be performed with elements which were 25 mm in the longitudinal direction and 20 mm × 20 mm in the transversal directions. Each lamella was described with two elements in the height. This size was fine enough to provide accurate results with respect to both the determination of the bending strength at normal temperature and the determination of the fire resistance. Glulam beams with a height h_{beam} = 320 mm and a span l = 5760 mm were modelled following the span to height relationship according to EN 408 [11] of $l = 8 \cdot h$. The bending strength of the beam is either limited by the tensile strength parallel to the grain of the lamellas in tension or of the finger joint connection. Failure occurs when the tensile strength is reached and the load cannot further be increased. The maximum applied load is then used to determine the bending strength of the beam. The FE model was first verified using tests performed by Fink et al. [12]. Figure 5 shows both the estimated bending stiffness and strength obtained from the simulations and the measured values from the experiments for all 24 glulam beams tested in [12]. The model is able to predict the overall behaviour of glulam at normal temperature. The bending stiffness in the simulations had a very good agreement with the experiments. The bending strength was modeled on average on an acceptable level considering the large coefficient of variation typical for timber members.

On the basis of the bending tests on glulam beams with well-known material properties, Fink et al. [9] developed a model to probabilistically describe the material properties of timber (see example of Figure 4). In the present investigation, the model by Fink et al. was implemented in a Matlab script to generate the input files for the subsequent Abaqus simulations allocating each element of the beam its individual material property. In the final step, the output data from the FE simulations were automatically evaluated by another Matlab script. Thereby, the stress in lengthwise direction of the beam for each element located in the tension zone was compared with the ultimate strength allocated to this element. When the ultimate strength of one element was reached, the location of this element was detected by the Matlab script. At this stage, the load could not be increased, the ultimate bending strength was reached.

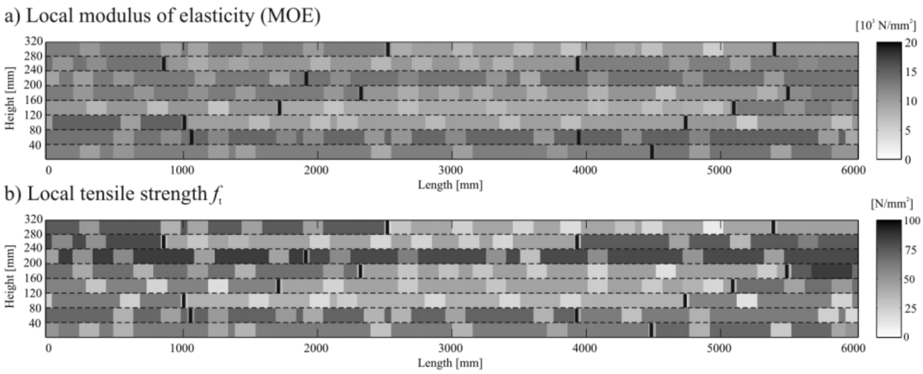

Figure 4. Example of local material properties (stiffness and strength) allocated to the elements of the FE model; the vertical black lines indicate the position of finger joints.

The influence on the fire resistance of glulam beams of the following parameters was studied:

- Timber strength grade (GL24h and GL36h).
- Distance between the finger joints: short(ened) boards: L~N(2.15, 0.50) and long boards L~N(4.30, 0.71) according to [13, 14].
- Temperature-dependent strength of finger joints, representing different adhesives in the finger joint.

The tensile strength of a finger joint was assumed to be equivalent to the tensile strength of a knot cluster section with a tKAR-value of 0.2 [9]. For each type of glulam beam, one hundred simulations were performed with different material properties. Figure 5 (right) shows that the cumulative distribution of the bending strength of 100 simulations follows approximately the lognormal distribution proposed by the Joint Committee on Structural Safety (JCSS) [15]. This diagram shows the cumulative bending strength distribution of beam type "GL24h, short" and "GL36h, short"; whereas the name of the beam type is composed of the strength grade and the distance between the finger joint, which is equivalent to the board length (long and short(ened) boards).

3. RESULTS AND CONCLUSION

3.1 Numerical simulations on finger-jointed timber lamellas

At normal temperature, about 170 tensile tests on finger-jointed timber boards of structural size were performed and documented in [3, 16]. For all these tests, a mean tensile strength of 35.5 N/mm^2 was calculated. Mainly the timber tensile strength determined the load-bearing capacity of the specimens. The finger-jointed specimens reached about 85% of the tensile strength obtained for unjointed solid wood specimens (f_t = 42.9 N/mm^2). For the FE study on finger-jointed specimens, the mean tensile strength $f_{t,j}$ = 35.5 N/mm^2 at normal temperature was used. The reduction of strength with increasing temperature was modeled with a bi-linear approach using the reduction factor $k_{\Theta=100°C}$ to characterize the behaviour. The reduction factor $k_{\Theta=100°C}$ is the relative strength of the finger joint at 100 °C. In the simulations, the relative strength at 100 °C was varied in a range between $k_{\Theta=100°C}$ = 0.1 (representing an adhesive more sensitive to the influence of temperature) and $k_{\Theta=100°C}$ = 0.8 (representing an adhesive less sensitive to the influence of temperature). Figure 6 (left) shows the influence of the temperature-dependent strength depending on the reduction factor at 100 °C.

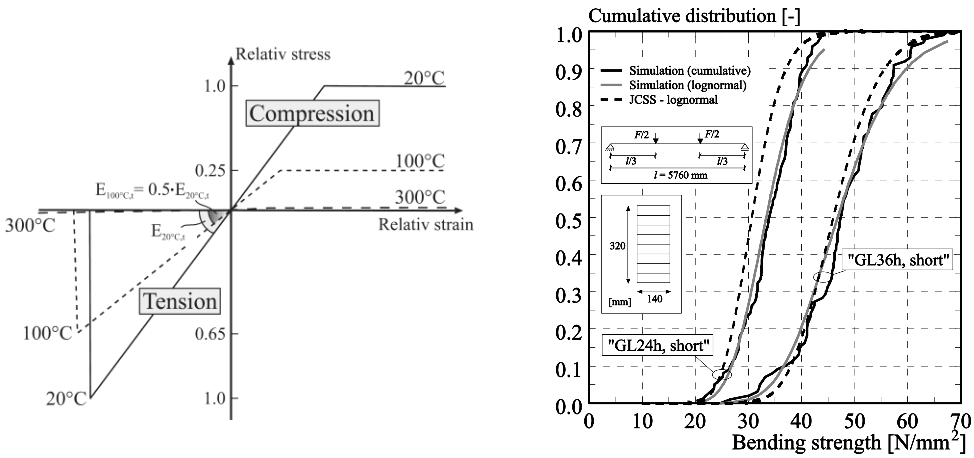

Figure 5. Modeling the mechanical properties of timber at elevated temperatures with Abaqus (left); Simulated cumulative distribution (n=100) of bending strength for strength grades GL24h and GL36h using short boards (right).

The following remarks can be drawn from Figure 6 (left):

- With increasing width of the cross-section, the time of fire resistance increases using the same adhesive – with the same reduction factor $k_{\Theta=100\,℃}$ – in the finger joint. Assuming a finger joint following a bi-linear tensile strength approach with $k_{\Theta=100\,℃} = 0.5$, the fire resistance of 140 mm wide specimens was calculated to 53.8 minutes. The same type of adhesive ($k_{\Theta=100\,℃} = 0.5$) in a finger-jointed 200 mm wide timber lamella results in a fire resistance of 87.5 minutes.
- The difference, with respect to the fire resistance, of using an adhesive with higher thermal stability (coincides with an increase of $k_{\Theta=100\,℃}$) is greater for wide specimens than for thin specimens. This means that if the adhesives' thermal stability is improved, the increase of fire resistance for small specimens, such as I-joists, is very limited (compare the slope of each curve).
- The stiffness of the finger-jointed timber specimen has an influence on the stress distribution inside the cross-section. However, only a small influence of the stiffness on the fire resistance was found.

In the fire tests documented in detail in [3], twelve different adhesives were studied in finger-jointed specimens with cross-sections of 80, 140 and 200 mm width and a depth of 40 mm. On the basis of the fire tests on 140 mm wide specimens, the reduction factor k_{Θ} for finger-jointed specimens was determined, assuming the previously described bi-linear temperature-dependent strength approach. Therefore, the mean fire resistance of the tests with the same adhesive in the finger joint was used. Fire tests, in which an early failure occurred because of a knot or due to any other obvious problem, were neglected. Further, the fire tests in which failure occurred in the finger joint due to exceeding the timber tensile strength were neglected in this evaluation, since the adhesive had still sufficient strength. In such a case, a value of $k_{\Theta=100\,℃} = 0.2$ was calculated, which corresponds to a fire resistance of about 40 minutes. Such low strength of the finger joint could occur independent on the adhesive in the finger joint. Thus, in the evaluation of the fire resistance tests on finger-jointed timber lamellas the failure reason occurring in the finger joint is classified into two groups:

1. Failure along the fingers, which shows most likely an influence of the adhesive and,
2. Failure of the fingers due to exceeding the timber tensile strength.

The latter one usually leads to an earlier failure and the adhesives' fire resistance is higher than the reached value. The temperature-dependent strength approach for finger jointed members loaded in

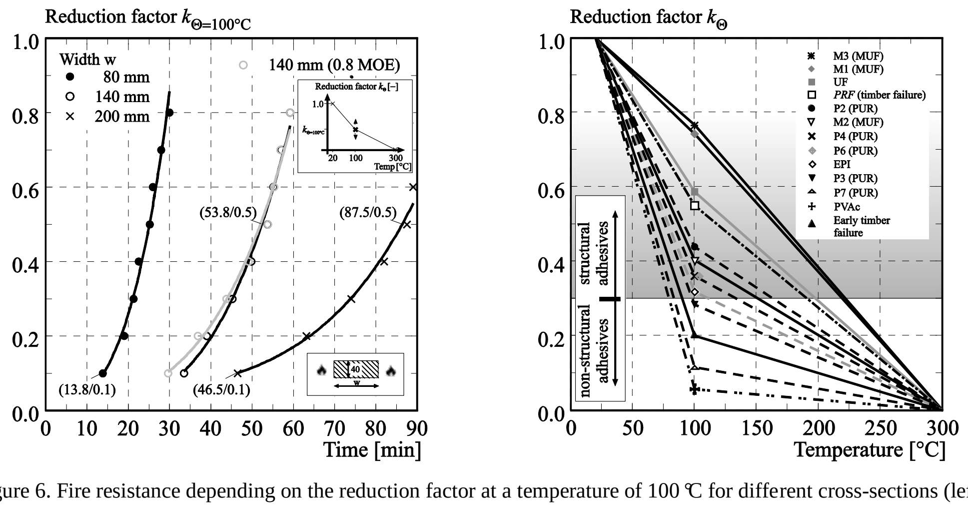

Figure 6. Fire resistance depending on the reduction factor at a temperature of 100 ℃ for different cross-sections (left), Bi-linear approach describing the residual tensile strength for finger-jointed lamellas depending on the adhesive (right).

tension is an "effective" approach similar to the work by König and Walleij [15], who determined the temperature-dependent relationships for timber given in EN 1995-1-2, and does not reflect the "real" material properties. The values can directly be used as material input properties for a FE thermal-mechanical analysis of structural members. Further, it should be noticed that the PRF adhesive did not govern the fire resistance, because in both tests failure occurred due to exceedance of the timber's tensile strength. The approach in Figure 6 (right) represents, therefore, only a lower boundary of the strength reduction for PRF. The actual temperature-dependent strength approach lies above the given curve.

3.2 Numerical simulations on glued-laminated timber beams

About 1600 simulations were performed to investigate the influence of the adhesive used in a finger joint of a glulam beam on the fire resistance. The evaluation of the simulations contains the fire resistance and failure location of each beam as well as the type of failure (finger joint, clear wood, weak section). Among others, some important conclusions from the numerical simulations can be summarized as follows:

- On average, the fire resistance of glulam beams decreases with increasing sensitivity to elevated temperature of the finger joints, as illustrated in Figure 7 (left).
- The fire resistance of higher strength glulam beams is more sensitive to the temperature-dependent strength performance of finger joints than lower graded timber.
- For the finger joints glued with structural adhesives, the effective temperature-dependent strength at 100 °C was determined to be in the range of 30% up to 60% of the initial strength at normal temperature, see Figure 7 (left). If the adhesive limits the fire resistance of the finger joint the following statement can be given: The fire resistance for those adhesives varied between 73% and 96% (for GL36h) in relation to the reference finger joint strength approach, which was defined to exhibit 80% of the initial strength at normal temperature. For GL24h beams, the relative fire resistance was between 86% and 98%. This is in line to fire tests performed in the past [1].

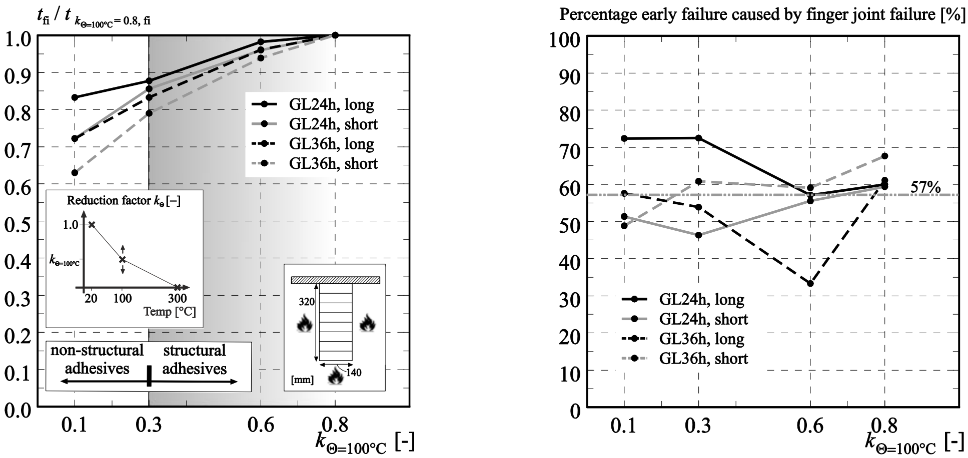

Figure 7. Relative fire resistance for glulam beams depending on the finger joint strength reduction (left); Percentage of finger joint failure (related to the observed number of finger joint failure) for the beams that reached a fire resistance below the mean fire resistance for each beam type (right).

Figure 7 (right) shows that a finger joint failure leads in about 57% of the cases to an early failure of the beam. Early failure occurs when the simulated beam reached a fire resistance below the mean fire resistance of each beam type. As a consequence, there is no clear tendency that a failure in a finger joint leads to early failure of the glulam beam. Moreover, such early failure of glulam beams exposed to fire is attributed to failure of both finger joints and weak section failure and is independent of the finger joint strength and the strength grade. It can be concluded that taking into account the different failure types no significant difference of the fire resistance depending on the adhesive can be found. Some adhesives in the finger joint led to a higher fire resistance of the connection than other adhesives, if the adhesive governed the fire resistance. However, if the adhesive does not govern the fire resistance, early failure occurs independent on the type of adhesive attributed to the timber.

REFERENCES

[1] König, J., Norén, J., Sterley, M.: "Effect of adhesives on finger joint performance in fire"; *Proceedings of 41th CIB-W18 Meeting*; St. Andrews, Canada; 2008.

[2] Klippel, M., Frangi, A., Hugi, E.: "Experimental Analysis on the Fire Behavior of Finger-Jointed Timber Members"; *ASCE Journal of Structural Engineering*; 140 (3); 2014.

[3] Klippel, M., Frangi, A.: "Fire tests on finger-jointed timber boards - Test report"; IBK Bericht vdf Hochschul-Verlag an der ETH Zürich; Zürich; 2014.

[4] Klippel, M.: Fire safety of bonded structural timber elements; PhD thesis, ETH No. 21843; ETH Zurich, Switzerland, 2014.

[5] EN 1995-1-2:2004, Eurocode 5: Design of timber structures – Part 1-2: General – Structural fire design. European Standard. European Committee for Standardization. Brussels. 2004.

[6] Klippel, M., Schmid, J., Frangi, A.: "The Reduced Cross-section Method for timber members subjected to compression, tension and bending in fire"; International Council for Research and Innovation in Building and Construction, Working Commission W18 – Timber Structures, Meeting 45 (CIB-W18 Meeting 2012); CIB-W18 Meeting 2012; Växjö, Sweden; 45; CIB-W18/45-16-1; 2012.

[7] König, J., Walleij, L.: "One-Dimensional Charring of Timber Exposed to Standard and Parametric Fires in Initially Unprotected and Postprotection Situations"; Trätek, Report I 9908029; SP Technical Research Institute of Sweden, Wood Technology; Stockholm, Sweden; 1999.

[8] Klippel, M., Frangi, A., Fontana, M.: "Influence of the Adhesive on the Load-Carrying Capacity of Glued Laminated Timber Members in Fire"; *10th International Symposium on Fire Safety Science (IAFSS 2011)*; Fire Safety Science : Proceedings of the tenth international symposium 1219-1232; 2011.

[9] Fink, G., Frangi, A., Köhler, J.: "Modelling the bending strength of glued-laminated timber - Considering the natural growth characteristics of timber"; International Council for Research and Innovation in Building and Construction, Working Commission W18 – Timber Structures, Meeting 46 (CIB-W18 Meeting 2013); CIB-W18 Meeting 2013; Vancouver, Canada; 46; CIB-W18/46-12-6; 2013.

[10] Fink, G.: Influence of varying material properties on the load-bearing capacity of glued laminated timber; PhD thesis, ETH No. 21746; ETH Zurich, Switzerland, 2014.

[11] EN 408: "Timber structures – Structural timber and glued laminated timber – Determination of some physical and mechanical properties"; Brussels, Belgium 2010.

[12] Fink, G., Köhler, J., Frangi, A.: "Bending tests on glued laminated timber beams with well-known material properties: Test report"; IBK Bericht Nr. 350; vdf Hochschul-Verlag an der ETH Zürich; Zürich; 156; 2013.

[13] Larsen, H.J.: "Strength of Finger Joints"; Otaniemi; Proceedings of 13th CIB-W18 Meeting; 1980.

[14] Ehlbeck, J., Heimeshoff, B.: Biegefestigkeit von Brettschichtholz in Abhängigkeit von Rohdichte, Elastizitätsmodul, Ästigkeit und Keilzinkung der Lamellen, der Lage der Keilzinkung sowie von der Trägerhöhe: Teil A: Karlsruher Untersuchungen, Teil B: Münchner Untersuchungen; Fraunhofer IRB Verlag, 1987.

[15] JCSS, J.C.o.S.S.: "Probabilistic Model Code"; www.jcss.byg.dtu.dk; 2007.

[16] Frangi, A., Bertocchi, M., Clauss, S., et al.: "Mechanical behaviour of finger joints at elevated temperatures"; *Wood Science and Technology*; 46 (5); 793-812; 2012.

8th International Conference on Structures in Fire
Guo-Qiang LI, Venkatesh K. R. KODUR, Shou-Chao JIANG, Jian JIANG, Su-Wen CHEN, Guo-Biao LOU (Eds.)
Shanghai, China, June 11-13, 2014

FIRE RESISTANCE TESTS ON BEAM-TO-COLUMN SHEAR CONNECTIONS

Pedro Palma[*,**], Andrea Frangi[*], Erich Hugi[**], Paulo Cachim[**] and Helena Cruz[****]**

[*] ETH Zurich, Switzerland
palma@ibk.baug.ethz.ch, frangi@ibk.baug.ethz.ch

[**] Empa, Switzerland
erich.hugi@empa.ch

[***] University of Aveiro, Portugal
pcachim@ua.pt

[****] National Laboratory for Civil Engineering, Portugal
helenacruz@lnec.pt

Keywords: Timber, Connections, Fire resistance, Tests, Beam-to-column

Abstract. *This paper presents the results of an extensive experimental campaign on the fire behaviour of beam-to-column timber connections loaded perpendicular-to-the-grain. The experimental campaign addressed the fire behaviour of beam-to-column timber shear connections in a systematic way, testing a wide range of common connection typologies, significantly enlarging their experimental background.*

1 INTRODUCTION

1.1 Background

The fire performance of timber structures is largely influenced by the behaviour of the connections. Current structural fire design methods for timber connections according to EN 1995-1-2:2004 [1] are based on empirical rules [2] derived from a limited number of fire resistance tests on timber members loaded in tension parallel to the grain [3–5]. Given timber's inherent anisotropy, the mechanical properties and failure modes along the direction parallel to the grain, which is usually the longitudinal direction of structural members, are noticeably different from the equivalent properties in the directions perpendicular to the grain. Therefore, connections loaded in the directions parallel and perpendicular to the grain exhibit different behaviours, the latter being prone to brittle splitting failures. Regarding fire resistance, there was a question whether these different failure modes observed at normal temperature would significantly influence the fire behaviour. In addition, and as a consequence of timber's anisotropy, detailing requirements, set by the design at normal temperature, regarding fasteners' spacing, end and edge distances are quite different for connections loaded parallel and perpendicular to the grain. Being metal fasteners responsible for conducting heat into the core of the cross-section and increasing charring, fastener spacing and edge and end distances are bound to play a role on the fire resistance. Given the brittle behaviour observed at normal temperature, the use of perpendicular to the grain reinforcements is a common technique to overcome unwanted brittle failure modes [6]. However, the most common steel reinforcements, self-drilling screws inserted perpendicular to the grain, can contribute to an increased charring and thus to a lower fire resistance [7].

End-grain to side-grain connections, such as beam-to-beam and beam-to-column shear connections (Figure 1), are prevalent situations where members are loaded perpendicular to the grain by connections.

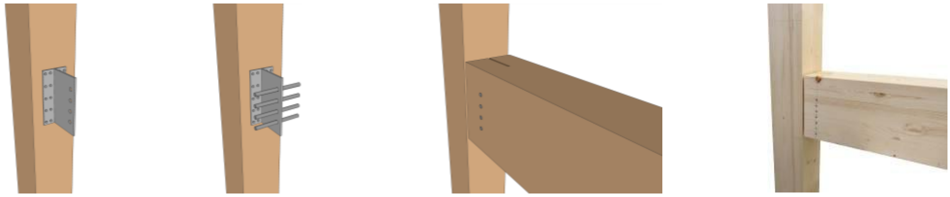

Figure 1. Typical beam-to-column connection loaded in shear (beam end-loaded in tension perpendicular to the grain).

The array of connection typologies used in these situations is quite extensive and comprises exposed and concealed metallic beam hangers (with a nailed header plate and a bearing plate or a dowelled steel-to-timber connection, respectively), dovetail carpenter connections, metallic dovetail connection devices, and diagonally-screwed connections, among others. The problem is that the fire performance of these connections has not been studied; manufacturers and designers addressed this problem by, e.g., adopting larger cross-sections and prescribing smaller tolerances for the gaps between the members.

1.2 Objectives and scope

This paper presents the results of an extensive experimental campaign on the fire behaviour of beam-to-column timber connections loaded perpendicular-to-the-grain. The experimental campaign addressed the fire behaviour of beam-to-column timber shear connections in a systematic way, testing a wide range of common connection typologies, significantly enlarging their experimental background.

2 EXPERIMENTAL CAMPAIGN

2.1 Test programme

The experimental campaign comprised tests at normal temperature and loaded fire resistance tests on beam-to-column connections in shear. Tests at normal temperature were also performed on the *beam-side* of the connection only, which was assumed to be the most exposed to fire and therefore critical for fire resistance. Over 30 full-scale tests at normal temperature were performed, covering 10 different connection typologies, and over 20 loaded fire resistance tests were conducted, including 12 connections typologies. An overview of the experimental campaign is presented in Table 1 and the geometry of the different connection typologies is presented in Figure 2 and Table 2.

2.2 Test specimens – typologies, geometries and materials

Connection typologies A.1 to C.2 are steel-to-timber dowelled connections, on the beam-side (Figure 2.1). In connection A.5, a common commercially available concealed beam-hanger was used, with a geometry that is very similar to the A.1 custom made connection. Typologies A.6 and C.2 are similar to connections A.1 and C.1, respectively, but the beams' cross-section was increased by 40 mm all around. Therefore, connections A.6 and C.2 are rated as R60 (thickness greater than 240 mm) and all the other connections (except D.1) are rated as R30 (thickness greater than 160 mm) [8]. Finally, typology D.1 is a commercially available aluminum dovetail connection, composed by two interlocking parts that are separately screwed to the column and to the end surface of the beam (Figure 3).

The various typologies were selected to test different failures modes, such as ductile dowel or embedment failures (B.1), brittle timber splitting or shear failures (A.1-3, A-6, B.2, and C.1-2), and connections reinforced against splitting (A.4). Construction tolerances, such as wider or smaller gaps between the beam and the column, were also considered (A.1-3).

The connections were produced with glued laminated timber made from spruce wood, strength class GL 24h (EN 1194 [9]). The custom made steel connections were manufactured with 5 mm thick steel plates grade S 355 (EN 10025-2 [10]), steel dowels grade 4.6 (EN 1993-1-8 [11]), and threaded nails grade 4.6 [11] with a diameter of 6 mm and a length of 80 mm. In the connections A.4, the full threaded

Table 1. Overview of the experimental campaign.

Connection typology	Type of test		Load	Number of tests
A.1	20 °C	beam-side	Until failure	3
	20 °C	full-connection	Until failure	1
	Fire	full-connection	0.3 $R_{A.1,mean,20°C}$	2
A.2	Fire	full-connection	0.3 $R_{A.1,mean,20°C}$	2
A.3	Fire	full-connection	0.3 $R_{A.1,mean,20°C}$	2
A.4	20 °C	beam-side	Until failure	1
	Fire	full-connection	0.3 $R_{A.4,mean,20°C}$	1
A.5	20 °C	full-connection	Until failure	1
	Fire	full-connection	0.3 $R_{A.1,mean,20°C}$	1
A.6	20 °C	beam-side	Until failure	1
	Fire	full-connection	0.3 $R_{A.1,mean,20°C}$	2
B.1	20 °C	beam-side	Until failure	5
	Fire	full-connection	0.3 $R_{B.1,mean,20°C}$	2
B.2	20 °C	beam-side	Until failure	5
	Fire	full-connection	0.3 $R_{B.2,mean,20°C}$	2
C.1	20 °C	beam-side	Until failure	3
	Fire	full-connection	0.3 $R_{C.1,mean,20°C}$	2
C.2	20 °C	beam-side	Until failure	3
	Fire	full-connection	0.3 $R_{C.2,mean,20°C}$	2
D.1	20 °C	full-connection	Until failure	1
	Fire	full-connection	0.3 $R_{D.1,mean,20°C}$	1

self-drilling screws used for reinforcement had a diameter of 9 mm, and were made from carbon steel with a characteristic tensile resistance of 25.4 kN. In the connections A.5, the commercial concealed beam hanger was cold formed from a 3 mm thick steel plate grade S 250 GD (EN 10346 [12]) and fixed to the column with threaded nails grade 4.6 [11] with a diameter of 4 mm and a length of 60 mm. The metal dovetail connections D.1 were made from aluminum grade EN AW-6082 (EN 755-2). One part was fixed to the end-grain of timber member, using 13 screws with a diameter of 8 mm and a length of 100 mm, and the other part was screwed to the side of the column member, using 8 similar screws.

3 TESTS AT NORMAL TEMPERATURE

3.1 Test set-up and procedure

A special test set-up was developed to load the beam-to-column connections in the same way during the tests at normal temperature and during the fire resistance tests. This set-up comprises a horizontal steel frame, inside which the connections are placed and loaded, and to which all load and displacement gauges and load actuators are attached. For the tests at normal temperature the steel frame was placed slightly above the floor (Figure 4(a)); and during the fire tests the frame was placed on top of a horizontal furnace, centring the connection with the furnace opening (Figure 4(b)). The load was applied in the beam through a loading plate connected by two rods to the hydraulic cylinders. As no equipment could be inside the furnace during the fire tests, the loading apparatus was placed outside the furnace opening, but as close as possible to the connection. In both the tests at normal temperature and the fire tests, the load was applied at the same distance from the connection, to assure the same distribution of internal forces.

At normal temperature, two types of tests were performed: tests on the beam-side of the connection (replacing the timber column by a steel profile, as presented in Figure (a); and tests of the whole beam-to-column connection (with the same arrangement used in the fire tests, presented in Figure (b). The

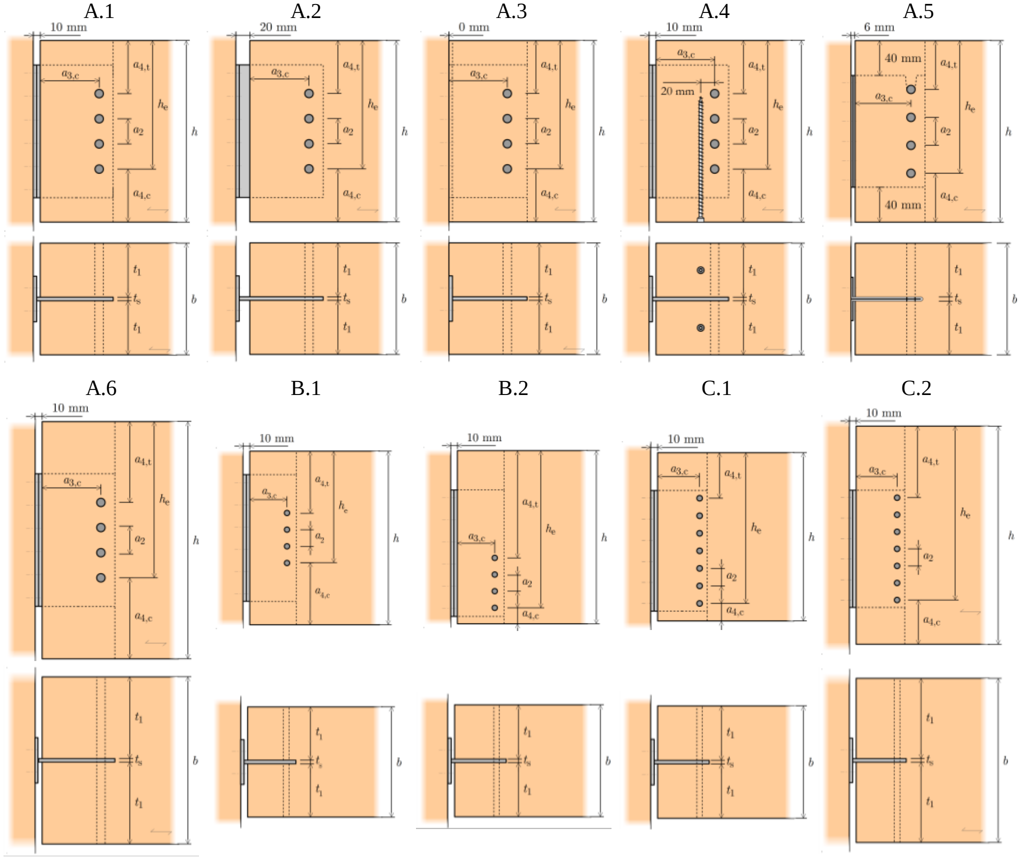

Figure 2. Geometries of the tested dowelled connections.

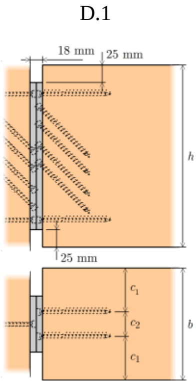

Figure 3. Aluminum dovetail connection

Table 2. Geometries of the tested dowelled connections.

Connection typology	$b \times h$ [mm^2]	d [mm]	n_d	h_e/h [ ]	a_2 [mm]	$a_{3,c}$ [mm]	$a_{4,t}$ [mm]	$a_{4,c}$ [mm]	s [mm]
A.1, A.4	160×260	12	4	0.71	36	84	76	76	10
A.2	160×260	12	4	0.71	36	84	76	76	20
A.3	160×260	12	4	0.71	36	84	76	76	0
A.5	160×260	12	4	0.73	40	80	70	70	6
A.6	240×340	12	4	0.66	36	84	116	116	10
B.1	160×260	8	4	0.64	24	56	94	94	10
B.2	160×260	8	4	0.91	24	56	164	24	10
C.1	160×260	8	7	0.91	24	56	92	24	10
C.2	240×340	8	7	0.81	24	56	132	64	10
D.1	160×260	-	-	-	-	-	-	-	18

b and h are the width and the height of the cross section; d is the dowel diameter and n_d is the number of dowels; h_e is the distance from the most distant fastener to the loaded edge; a_2 , $a_{3,c}$, $a_{4,t}$, and $a_{4,c}$ are the dowel spacing, unloaded end distance, loaded edge distance, and unloaded edge distance, respectively; and s is the gap between the beam and the column.

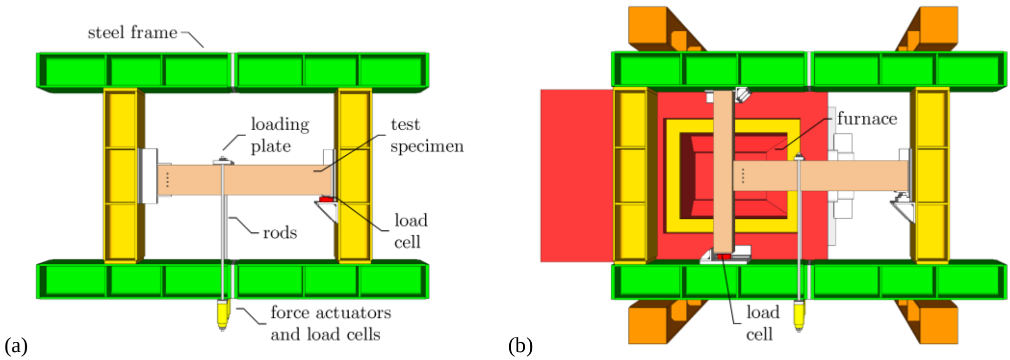

Figure 4. Top view of the test set-up: (a) tests at normal temperature; (b) fire resistance tests.

beam-side only tests were performed because most connections were estimated to fail on the beam-side (Table 3 and Figure 5(a)) and because it was assumed that this part of the connection would be most exposed to fire and therefore critical to fire resistance. The load applied by the loading plate, through the rods and hydraulic cylinders, was monitored using rod-end compression load cells. In the beam-side tests, another load cell was placed in the beam support opposite to the tested connection and the shear load in the connection was calculated by simple equilibrium ($F_{connection} = F_{rod} - F_{support}$). In the tests with the full beam-to-column connection, a load cell was positioned beneath the column and, therefore, the shear force going through the connection was directly measured. In addition to the load cells, displacement transducers were placed in the loading plate and in the connection area to assess the relative displacement between the timber member and the steel plate. The tests at normal temperature were performed at the laboratories of ETH Zurich, Switzerland. They were conducted in accordance with EN 26891:1991 [13], which prescribes a loading procedure based on the estimated load-carrying capacity F_{est} of the connection: the load is increased up to $0.4 \cdot F_{est}$, then reduced to $0.1 \cdot F_{est}$, and thereafter increased until failure.

3.2 Results

The estimated and experimental load-carrying capacities of the tested connections are presented in Table 3 and Figure 5. Most connections were expected to exhibit splitting failures (A.1-3,5-6, B.1, and C.1-2); only connections B.2 and, possibly, A.4, were expected to display ductile dowel failures. Regarding the estimated splitting capacities of the beam-side of the connections, it has to be mentioned that EN 1995-1-1 does not have specific rules for end-loaded members loaded perpendicularly to the grain, but only to mid-span loaded members. However, both the former German code for timber structures DIN 1052:2004 [6] and A. Leijten [14] (who developed the calculation model for mid-span loaded members in EN 1995-1-1) state that for connections at the end of a cantilever the splitting strength is half of the strength of mid-span loaded members.

The results show that the beam-side load-carrying capacity is substantially underestimated by current design methods, even taking into account that $R_{k,estimated}$ are characteristic 5% percentile values and $R_{mean,experimental}$ are mean values. Also worth noticing is that the column-side load-carrying capacity seems to be significantly underestimated, as no failure in the column-side was observed in the full connection tests performed on typology A.5.

Table 3. Estimated and experimental load-carrying capacities of the connections tested at normal temperature.

Connection typology	Type of test	Number of tests	$R_{k,estimated}$ [kN] Beam-side	Column-side	$R_{mean,experimental,20℃}$ [kN]		
A.1	Beam-side	3	27.0	-	51.5	(7%)	-
	Full connection	1	27.0	30.7	51.2	-	(beam-side failure)
A.2	-	-	27.0	28.3	-	-	-
A.3	-	-	27.0	33.6	-	-	-
A.4	Beam-side	3	>27.0	30.7	64.0	(3%)	-
A.5	Full connection	1	28.6	14.3	39.3	-	(beam-side failure)
A.6	Beam-side	3	42.0	30.7	58.5	(11%)	-
B.1	Beam-side	5	23.1	39.9	31.8	(10%)	-
B.2	Beam-side	5	37.6	39.9	46.7	(7%)	-
C.1	Beam-side	3	54.5	39.9	68.6	(8%)	-
C.2	Beam-side	3	62.7	39.9	89.3	(4%)	-
D.1	Full connection	1	52.0 (acc. to the manufacturer)		60.3	-	(column-side failure)

Coefficient of variation between parentheses.

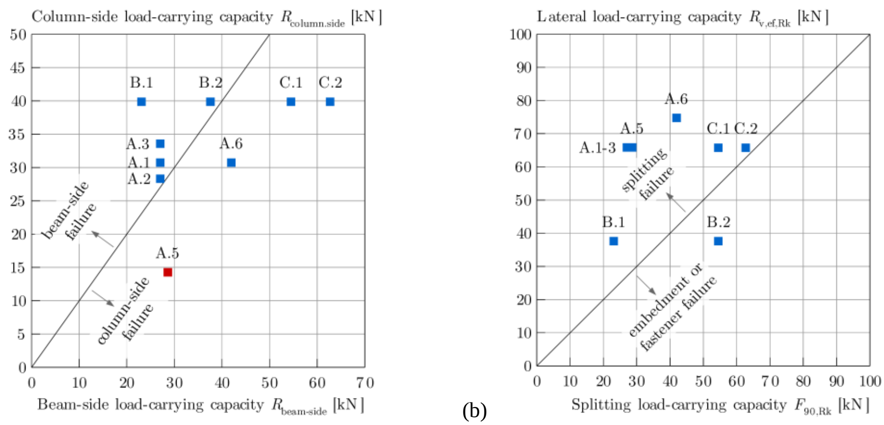

(a) (b)

Figure 5. Estimated load-carrying capacities of the tested dowelled connections: (a) beam-side and column-side capacities; (b) beam-side failure modes.

4 FIRE RESISTANCE TESTS

The fire resistance tests were conducted in the small horizontal furnace of the Laboratory for Fire Testing at the Swiss Federal Laboratories for Materials Science and Technology (Empa), in Dübendorf, Switzerland.

4.1 Test set-up and procedure

As previously described (Figure 4(b)), the test set-up used in the fire tests is very similar to one used in the tests at normal temperature. The same horizontal steel frame was positioned over the furnace, in such a way that the connection area was centred above the furnace's opening. In its plane, the connection was supported on a load-cell, placed at the bottom of the column-member (to measure directly the shear load in the connection, transferred as a compression force in the lower half of the column), and on a roller, located at the opposite end of the beam-member. The load was applied through a loading plate positioned on the top-side of the beam (which during the test it's on its side), connected by two steel rods to the

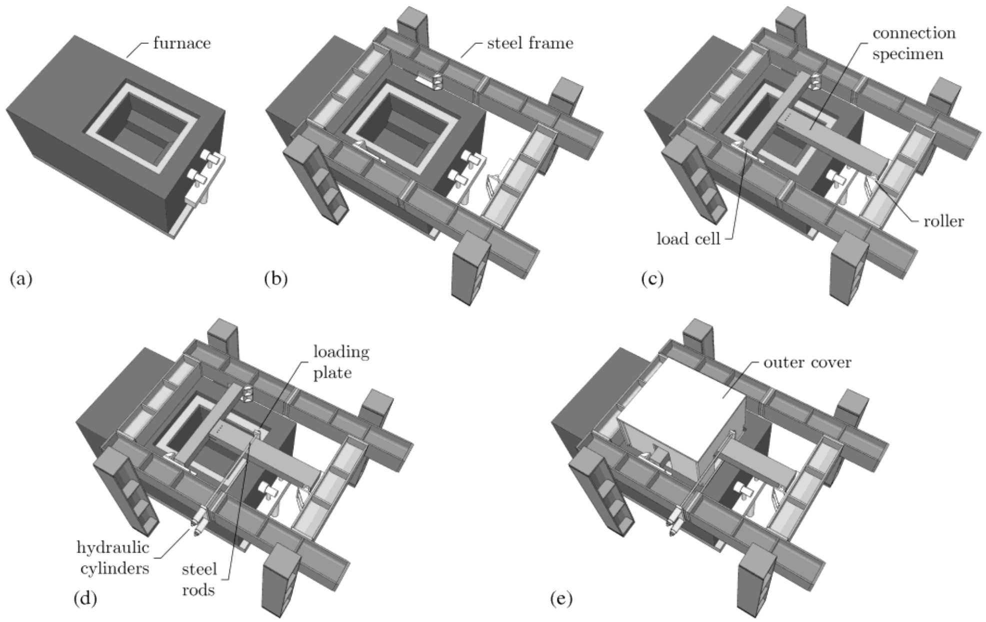

Figure 6. Schematic overview of the fire resistance tests set-up: a) horizontal furnace; b) steel frame over the furnace; c) connection specimen inside the frame; d) loading apparatus; e) outer cover.

hydraulic cylinders. Since no equipment could be exposed to fire, only the displacements of the loading plates were measured, not the relative displacements between the members in the connection. The connection specimen was then partially enclosed by an insulated outer cover that allows the timber members to deform. The test set-up is presented in Figure 66.

After the whole test set-up was ready, the connections were loaded up to the target load level (Table 1), which was approximately 30% of the load-carrying capacity at normal temperature, and that load was maintained throughout the fire test. Once the displacements stabilized, the burners were started and the connection area exposed to the standard ISO 834 [15] time-temperature curve. After failure, reached when the displacements in the beam increased ever rapidly and it no longer could sustain the applied load, the specimens were promptly removed from the furnace and cooled with water (Figure 7).

Since the full connections tested at normal temperature failed on the beam-side (Table 3) and the column-side of the connections (header plate nailed to the column-member) was the same for every connection, except A.5 and D.1 (which were commercially available parts), to assure a beam side failure in the fire tests, the column-member was partially protected with insulation. This was mainly to focus the tests on the beam-side of the connections and to avoid that burning from the sides and the back of the column could promote a premature failure.

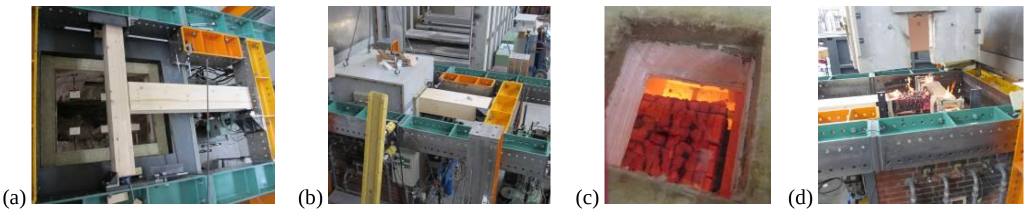

Figure 7. Fire test: (a) connection specimen in the steel frame over the furnace; (b) outer cover enclosing a connection during a test; (c) view of a connection inside the furnace; (d) removal of the outer cover after a test.

4.2 Results and discussion

The main results of the fire resistance tests are presented in Table 4. Two replicas of most connection typologies were tested and the corresponding results were consistent. All the dowelled connections (A, B, and C) exhibited fire resistances higher than 30 minutes and connections A.6 and C.2 reached 60 minutes, which is accordance with Lignum's documentation on the fire resistance of timber connections [8].

Regarding the influence of the gap between the beam and the column, it can be seen that an increase from 10 mm (A.1) to 20 mm (A.2) lead to an average reduction from 44 to 33-34 minutes of fire resistance. On the other hand, a reduction of the gap from 10 mm (A.1) to 0 mm (A.3) led to an increase of the fire resistance of only 3-4 minutes. The larger 20 mm gap between the beam and the column induced failures in the column-side of the connection, unlike the 10 mm and 0 mm gaps for which failure occurred in the beam-side (embedment of the dowels followed by splitting of the beam). As charring from the sides was mostly prevented in the column-members, the heat damage to the column side came mostly from above and below the header plate, directly affecting the outermost nails in withdrawal and compression zone of the header plate, allowing it to rotate.

The connection reinforced with self-drilling screws (A.4) exhibited a fire resistance 5 minutes lower than the corresponding unreinforced connection (A.1). The reinforcement with self-drilling screws is an effective and widespread way to deal with the brittle splitting failures of the unreinforced connections loaded perpendicularly to the grain. However, as observed in a previous experimental campaign performed by the authors on the fire resistance of tension connections reinforced with self-drilling screws [7], the reinforcement screws also conduct heat into the cross-section (Figure 9), which in some cases compromises the fire resistance.

Table 4. Results of the fire resistance tests.

Connection Typology	Specimen	Load E_{fire} [kN]	Fire resistance t_{fi} [min.]
A.1	A.1.F-1 [a]	15.2	40
	A.1.F-2	15.4	44
A.2	A.2.F-1	15.4	33
	A.2.F-2	15.4	34
A.3	A.3.F-1	15.5	48
	A.3.F-2	15.5	47
A.4	A.4.F-1	19.4	39
A.5	A.5.F-1	15.4	39
A.6	A.6.F-1	15.5	76
	A.6.F-2	15.5	83
B.1	B.1.F-1	9.4	49
	B.1.F-2	9.5	43
B.2	B.2.F-1	14.0	43
	B.2.F-2	13.9	45
C.1	C.1.F-1	20.5	44
	C.1.F-2	20.5	42
C.2	C.2.F-1	20.6	78
	C.2.F-2	20.6	73
D.1	D.1.F-1	17.8	36

A.1 (10 mm gap) A.2 (20 mm gap) A.3 (0 mm gap)

Figure 8. Influence of the gap between the beam and the column: connections A.1, A.2, and A.3 after the fire tests.

The common commercially available concealed beam-hanger (A.5) had gap of only 6 mm between the beam and the column (Figure 2 and Table 2), but a much lower estimated load-carrying capacity of the column-side of the connection (Table 3 and Figure 5(a)), although it failed on the beam-side at normal temperature. This commercial connection exhibit a fire resistance 5 minutes lower than the custom A.1 connection and failed in the column-side, with a failure mode similar to that of the connections A.2. However, the load in connection A.5 during the fire test was about 40% of the load-carrying capacity of the beam-side at normal temperature, instead of the 30% in connections A.1-3.

A.4 (reinforced) A.5 (commercial beam-hanger)

Figure 9. Connections A.4 and A.5 after the fire tests.

The influence of the failure mode can be analysed in the connections B.1 and B.2. These connections had smaller sized dowels (diameter of 8 mm) and showed brittle splitting (B.1) and ductile embedment/dowel failures (B.2) at normal temperature. In the fire tests, however, both typologies exhibited similar extensive embedment failures, followed by splitting. In fire, the smaller minimum dowel spacing perpendicular to the grain prescribed by EN 1995-1-1 (only $3{\cdot}d$, compared to $5{\cdot}d$ parallel to the grain) leads to a premature failure when all the wood between the dowels is charred (Figure 10). Also the smaller minimum unloaded edge distances (connection B.2) perpendicular to the grain (only $3{\cdot}d$, compared to $7{\cdot}d$ parallel to the grain) result in the complete charring of the wood surrounding the outermost dowels. Regardless of the failure mode at normal temperature, both connection typologies exhibited approximately the same fire resistance.

B.1 B.2

Figure 10. Connections B.1 and B.2 after the fire tests.

Connections C.1 exhibited shear/splitting failures at normal temperature and the highest load-carrying capacities of the R30 connections (Table 3). In the fire tests, they reached approximately the same fire resistance as connections A.1. In fire, the dowels remained mostly straight and the wood surrounding the dowels closer to the unloaded edge charred completely. After failure, splitting cracks could be observed in the beam side.

C.1

Figure11. Connections C.1 after the fire tests.

Connections A.6 and C.2 reached more than the estimated minimum 60 minutes of fire resistance [8]. Regarding connections A.6 (with 12 mm dowels), the long fire exposure charred the wood below and above the header steel plate nailed to the column, affecting the tension (nail withdrawal) and compression zones and allowing the steel plates to rotate (Figure12, left). The dowels' end distance in connections C.1 (8 mm dowels) was smaller than in connections A.6 and, consequently, so was the moment in the header plate. Therefore, the rotation of the header plate was negligible. On the other hand, the charred depth in the zone between the dowels and the end of the beam was significantly higher than elsewhere in the beam, due to additional heat coming from the burning column-member and transferred by the dowels into the cross-section. After the wood between the dowels charred, the load was mostly transferred through the last dowel and it ultimately bent (Figure12, right).

A.6 C.2

Figure 12. Connections A.6 and C.2 after the fire tests.

Finally, the commercial aluminum dovetail connection D.1 also reached more than 30 minutes of fire resistance, failing in the connector itself after 36 minutes. This connection had a gap of 18 mm between the beam and the column (thickness of the connector), which is larger than the 10 mm of most of the other connections.

D.1

Figure13. Connection D.1 after the fire test.

5 CONCLUSIONS

This paper presents the results of an extensive experimental campaign on the fire behaviour of beam-to-column timber connections loaded perpendicular-to-the-grain. A special test set-up was developed and it was successfully used in both the tests at normal temperature and the fire tests. The results of the fire resistance tests show that the tested typologies of steel-to-timber dowelled connections reached more than 30 and even 60 minutes of fire resistance. However, aspects such as a wider gap between the beam and the column, reduced dowel spacing, and the presence of reinforcement with self-drilling screws all have a negative influence on the fire resistance. Even though the beam-side of these connections is apparently more exposed to fire, failures in column-side also occurred and, therefore, the fire resistance of these connections has to take into account these two parts.

REFERENCES

[1] EN 1995-1-2:2004 Eurocode 5: Design of timber structures – Part 1-1: General – Structural fire design, European Committee for Standardization (CEN), Brussels, 2004.

[2] J. König, M. Fontana, The performance of timber connections in fire – Test results and rules of Eurocode 5, in: Proceedings of International RILEM Symposium "Joints in Timber Structures," RILEM Publications, Stuttgart, Germany, 2001: pp. 639–648.

[3] J. Norén, Load-bearing capacity of nailed joints exposed to fire, Fire and Materials. 20 (1996) 133–143.

[4] D. Dhima, Vérification expérimentale de la résistance au feu des assemblages d'éléments en bois, Centre Technique Industriel de la Construction Métallique (CTICM), Saint-Rémy-lès-Chevreuse, France, 1999.

[5] J. Kruppa, T. Lamadon, P. Racher, Fire resistance tests of timber connections, CTICM - Departement Incendie et Essais, Saint-Remy-Les-Chevreuse, France, 2000.

[6] DIN 1052:2004-08. Entwurf, Berechnung und Bemessung von Holzbauwerken. Allgemeine Bemessungsregeln und Bemessungsregeln für den Hochbau, Deutsches Institut für Normung (DIN), 2004.

[7] P. Palma, A. Frangi, E. Hugi, P. Cachim, H. Cruz, Fire resistance tests on steel-to-timber dowelled connections reinforced with self-drilling screws, in: Proceedings of the 2nd Ibero-Latin-American Congress on Fire Safety – 2nd CILASCI, Coimbra, Portugal, 2013.

[8] A. Frangi, I. Brühwiler, J. Studhalter, R. Wiederkehr, Lignum-Dokumentation Brandschutz. 3.1 Feuerwiderstandsbemessung – Bauteile und Verbindungen, Lignum Holzwirtschaft Schweiz, Zurich, 2011.

[9] EN 1194:1999. Timber structures – Glued laminated timber – Strength classes and determination of characteristic values, European Committee for Standardization (CEN), Brussels, 1999.

[10] EN 10025-2:2004. Hot rolled products of structural steels - Technical delivery conditions for non-alloy structural steels, European Committee for Standardization (CEN), Brussels, 2004.

[11] EN 1993-1-8:2005. Eurocode 3: Design of steel structures – Part 1-8: Design of joints, European Committee for Standardization (CEN), Brussels, 2005.

[12] EN 10346:2009. Continuously hot-dip coated steel flat products. Technical delivery conditions, European Committee for Standardization (CEN), Brussels, 2009.

[13] EN 26891:1991. Joints made with mechanical fasteners – General principles for the determination of strength and deformation characteristics, European Committee for Standardization (CEN),

Brussels, 1991.

[14] A. Leijten, Splitting strength of beams loaded by connections - Model comparison, in: Proceedings of the CIB-W18 Meeting 35, CIB, Kyoto, Japan, 2002.

[15] ISO 834-1:1999. Fire-resistance tests. Elements of building construction. Part 1: General requirements, International Organization for Standardization (ISO), 1999.

8th International Conference on Structures in Fire
Guo-Qiang LI, Venkatesh K. R. KODUR, Shou-Chao JIANG, Jian JIANG, Su-Wen CHEN, Guo-Biao LOU (Eds.)
Shanghai, China, June 11-13, 2014

FIRE BEHAVIOUR OF BLIND DOVETAIL TIMBER CONNECTIONS

P. Racher*, D. Dhima, M. Audebert***, A. Bouchaïr* and C. Florence****

* Clermont Université, Université Blaise Pascal, LaMI, BP 206, F-63000 Clermont-Ferrand, France.
e-mails: (patrick.racher, abdelhamid.bouchaïr)@polytech.univ-bpclermont.fr

** CSTB, 84 avenue Jean Jaurès, 77447 Marne-la-Vallée Cedex 2, France
e-mail: (dhionis.dhima, celine.florence)@cstb.fr

*** Université de Lyon, Ecole Nationale d'Ingénieurs de Saint-Etienne (ENISE), Laboratoire de Tribologie et de Dynamique des Systèmes (LTDS), UMR 5513, 58 rue Jean Parot, 42023 Saint-Etienne Cedex 2, France, e-mail: maxime.audebert@enise.fr

Keywords: Dovetail timber connections, Mechanical behaviour, Fire tests

***Abstract**. The paper presents a summary of results from a series of experimental studies on the mechanical behaviour of blind dovetail timber connections. These tests are conducted in cold and under ISO-fire exposure. Two types of dovetail connections are studied considering the brittle failure criteria induced by the tenon or the mortise in function of the geometry of the tenon. For tests in normal conditions of temperature, the influence of the clearance between the tenon and the mortice is studied. The results for tests in normal conditions are analysed and the failure modes are commented. The failure loads obtained are compared to the ones determined analytically. These failure loads are then used to determine the loads to apply for fire tests. The thermo-mechanical behaviour of the connections is analysed and the fire resistance durations of the tested connections are given and compared to those of other timber connection types.*

1 INTRODUCTION

Among the various structural components of timber structures, the connections are characterized by a complex mechanical and thermo-mechanical behaviour, due mainly to their geometrical configuration. They govern the load-carrying capacity of the structure and its safety, as well in normal conditions as in fire situation. Thus, in the field of timber constructions, the connections represent the key element: an insufficiently controlled conceptual approach can cause significant structural damages. Moreover, as timber is a combustible material, fire safety is of main importance for the development of timber structures complied with the requirements of security. Thus, the thermo-mechanical behaviour of timber connections constitutes a major topic of investigation.

In timber structures, current timber connections are of two types: the carpentry joints and the mechanical connections realized with various types of fastener. Complying with current architectural trends and high strength requirements, timber connections using dowel-type fasteners are mainly used. Otherwise, reconciling aesthetics and mechanical efficiency, the traditional connections mode is now experiencing significant development made possible by the use of CNC (Computer numerical control) woodworking machine. This development must be followed by design rules to remove all obstacles to the use of these traditional techniques that have largely demonstrated their reliability. Considering that the steel fasteners used for mechanical connections, due to their high thermal conductivity, have a negative role on the fire resistance [1], the traditional connections only composed with wood material could present an interesting behaviour in fire situations.

These last years, several researches were carried out to study the mechanical behaviour of timber connections with steel fasteners. For these types of connections, Eurocode 5 [2] proposes design rules relatively simple to use for normal conditions. Recent researches carried out in different countries [3 to 10], on the fire behaviour of doweled and bolted timber connections, made it possible to propose simplified formulas for the design of these connections [11, 12]. On the other hand, there are no standardized design rules applicable to traditional connections with dovetails. In normal conditions, studies conducted in Germany [13, 14] show that the design rules proposed by Eurocode 5 for the connections with tenon are applicable for dovetails. But no study has been conducted yet on the fire resistance of these connections.

Consequently, it appears necessary to establish a simplified design models for the design of these connections under cold and fire conditions. These models need to be validated by experimental results. In this context, this paper presents the first research carried out in France concerning the behaviour of blind dovetail connections under normal conditions [15] and under a conventional fire - ISO R 834 [16]. In a first part, a reminder on the dovetail connections, with their geometrical characteristics and the rules for their justification is made. Then the testing program in normal condition is presented and the main results are analysed. In a last part, are presented the tests realized under fire exposure. The fire resistance of the connections is commented.

2 DOVETAILS TIMBER CONNECTIONS

The strength transmission by contact is a traditional way of assembling the wood frame. The machines with numerical control allow a renewal of these connecting techniques. Their use is made possible by the fact that wood does not fail in oblique or transverse compression. However, they generate shear effects that require compliance with the codes of practice and constructive provisions advocated.

The dovetails timber connections provide the transfer of the reactions between primary beams and secondary beams. The Figure 1 shows the configurations commonly used in Europe. The design of these connections is based on the calculation of the oblique compression and shear stresses in timber. As Eurocode 5 gives no explicit rules for these joints, it's necessary to define a calculation model within the limit states approach [17, 18]. However, it is of main importance to specify the geometrical limits recommended for these connections. The geometry of the dovetail (angle α, depth t_2) depends on the used reamers (Figure 2). The calculation model has to take into account the shear effects for the supported beam and the effects of notch and tension perpendicular to the grain for the supporting beam.

Figure 1. Commonly used dovetails connections.

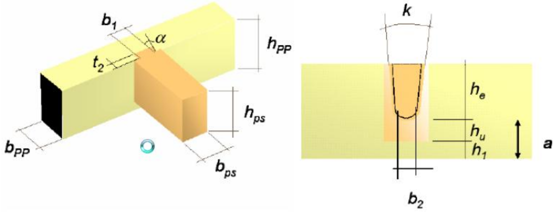

Figure 2. Geometry of current dovetails.

Recent studies conducted in Germany [13, 14] show that the design rules proposed by Eurocode 5 for the connections with tenon are applicable for dovetails. The design of connections with tenon is based on the calculation of the shear and the transverse tensile stresses of the tenon (Figure 3).

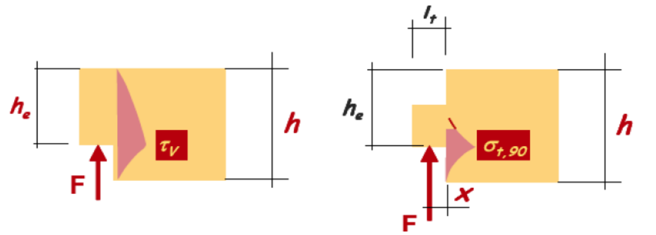

Figure 3. Stresses within timber connection by tenon.

The different calculation rules refer to the following geometric conditions for the tenon:

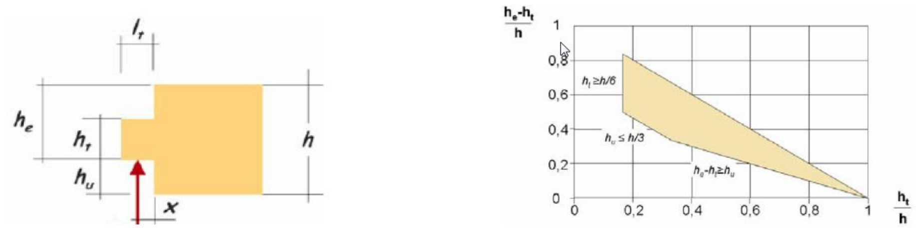

Figure 4. Geometrical limits of tenon.

The load bearing capacity of these connections is then calculated with the following relations:

$$R_k = \min \begin{bmatrix} \frac{2}{3} b h_t k_z k_v f_{v,k} \\ 1,7 b l_{t,ef} f_{c,90,k} \end{bmatrix} \tag{1}$$

with: $$l_{t,ef} = \min\left[l_t + 3cm; 2l_t\right]$$

$$k_z = \beta\left[1+2(1-\beta)^2\right](2-\alpha), \text{ where } \alpha = {h_e}/{h} \text{ and } \beta = {h_t}/{h_e}$$

$$k_v = \min\left[1; \frac{k_n}{\sqrt{h}\left[\sqrt{\alpha(1-\alpha)} + 0,8\frac{c}{h}\sqrt{\frac{1}{\alpha} - \alpha^2}\right]}\right]$$

$k_n = 5$ for hardwood and $k_n = 6,5$ for glued laminated timber

Furthermore, this connection mode may also allow the transmission of tensile forces induced by the overall bracing of the structure. Some studies have analysed the transfer of tensile forces by this connection method considering the contact between mortise and tenon, but this kind of loading is not considered in this study.

3 TESTS IN NORMAL CONDITIONS

3.1 Experimental protocol

In normal conditions of temperature, 14 tests were performed. The study is based on two types of dovetails: connections with fragile tenon (type 1) and those with fragile mortise (type 2). This differentiation is made according to the probable location of the rupture. Furthermore, this work examines the presence of a clearance (*j*) in the case of a rupture of the tenon. This extreme case is considering to quantify the design rules when the transmission of the strengths is performed only on the contact sides of the notch. Figure 5 and Table 1 give the geometrical dimensions and the experimental configurations of the tested connections. Figure 6 shows the experimental configuration. For the connections with angle of 45 and 60 °, similar dimensions are retained.

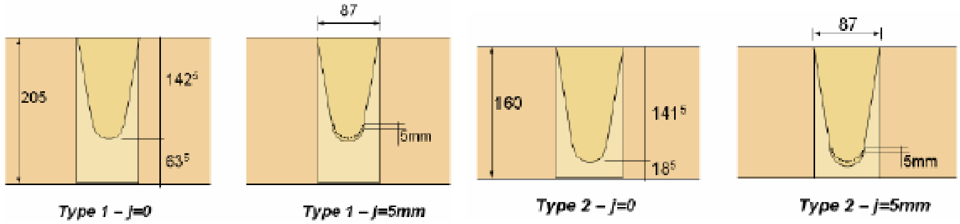

Figure 5. Geometrical configurations of the tested connections.

Table 1. Experimental program.

Connection type	N °test	Clearance	Experimental configuration
Type 1	1-2 3-4	j = 0 j ≠ 0	Connection 90 ° Connection 90 °
Type 2	9-10 11-12	j = 0 j ≠ 0	Connection 90 ° Connection 90 °
Type 2	13-14	j = 0	Connection 90 ° - Straight edges
Type 1	5-6 7-8	j = 0 j = 0	Connection 45 ° Connection 60 °

Figure 6. Experimental device for connections at 90 and 45 °.

In addition to the measurement of the applied load, 5 displacement measurements are performed in order to decompose the various components of deformation: the measurement of the displacement right of the applied force, the measurement of the displacement at mid-span of the supporting beam, the measurement of the relative vertical displacement of the connection, the measurement of the relative horizontal displacement between beams at the level of the upper and lower fibres. The tests are performed with controlled displacement (2mm/mn). From the estimated value of the ultimate force *Fu*, pre-loading cycles are performed (15% of *Fu* then 40% *Fu*) and finally the specimens are reloaded until failure.

3.2 Experimental results

3.2.1 Connections type 1 at 90° (tests 1 to 8)

The connections with fragile tenon lead to a failure in shear at the right of the dovetail and then in bending of the remaining section of the supported beam (Figure 7). This failure mode remains unchanged with the presence of a clearance or for connections with angle of 45 and 60°.

Figure 7. Failure mode of connections type 1.

The mean values of the load bearing capacities of these tested connections are summarized in Table 2. The presence of a clearance at the bottom of the mortise reduces the ultimate resistance of the connections. In fact, it induces the mobilization of the transfer contact in the upper part of the mortise and tenon, which amplifies the phenomenon of "notch" in the supported beam.

3.2.2 Connections type 2 (tests 9 to 14)

For this configuration, the stress states in transversal tension induce a first crack in the supporting beam. It follows a new equilibrium resulting from the transfer of contact loads on the tenon and mortise edges. The ultimate load is reached by yielding of the tenon at the third of its height (Figure 8). The mean values of the load bearing capacities are presented in Table 2.

Figure 8. Failure mode of connections type 2.

To observe the impact of the cutting angle of the tenon on the mechanical behaviour of the connections, a series of tests with straight edges of the tenon was performed (tests 13 and 14). The final failure mechanism is modified with this configuration: the failure of the tenon is reached, while a failure in shear of the supported beam was obtained in previous tests (Figure 9).

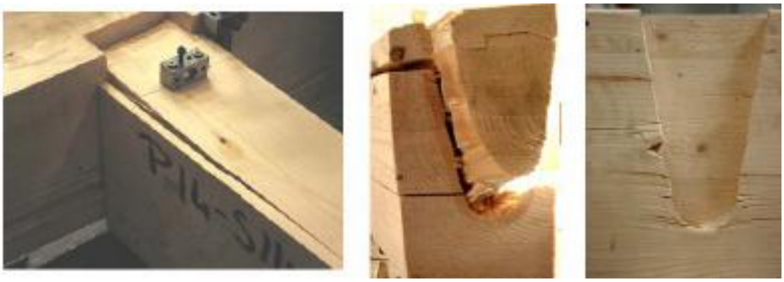

Figure 9. Failure mode of connections type 2 with straight edges of the tenon.

3.2.3 Load bearing capacities of the connections

The results of the load bearing capacities of the tested connections are presented in Table 2. A good homogeneity of the results is obtained. No significant differences of resistance are observed between the two types of tested connections. The mean values of the experimental load-carrying capacities of the connections $F_{u,mean}$ are compared to the design capacity defined by Equation (1) (F_d). From these results, it can be concluded that the design rules used in Germany can be used with safety to calculated dovetails timber connections.

Table 2. Experimental results of load bearing capacities of the connections.

Connection type	N °test	Clearance	$F_{u,mean}$ (daN)	$F_{u,mean}/F_d$
Type 1	1-2	j = 0	2507	3,03
	3-4	j ≠ 0	2060	2,49
Type 2	9-10	j = 0	2392	2,88
	11-12	j ≠ 0	2807	3,38
Type 2	13-14	j = 0	2880	3,47
Type 1	5-6	j = 0	2057	2,46
	7-8	j = 0	2367	2,85

4 TESTS UNDER FIRE EXPOSURE

4.1 Experimental protocol

For fire tests, the specimens consisted of two lateral supporting beams and one joist (Figure 10). The joist was connected at the the middle span of the supporting beams by rounded dovetail joint. The specimens were loaded in bending. The load was applied to the middle span of the joist.

For the two configurations of connections (without clearance), six fire tests were carried out (three for each type). The load ratios of the tested connections were 10%, 20% and 30% of the mean ultimate failure load $F_{u,mean}$ defined by experimental tests under cold conditions. The fire tests realized were conducted in ovens by following the evolution of the temperatures of a conventional fire ISO 834. For each specimen, the temperature is measured by thermocouples in some locations right to the connected zone and at different depths inside timber beams (example Figure 11). The evolution of the temperature in the oven was measured by thermocouples and plate pyrometers. The displacement (slip between the connected members) and the time to failure of the connections were measured. The displacements between the connected members were measured using displacement sensors. These sensors were located outside the oven to measure the total displacement of the tested specimen.

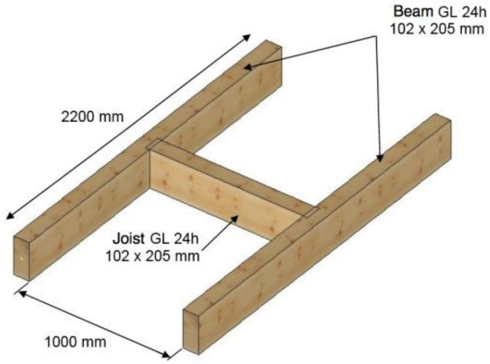

Figure 10. Specimens for tests under fire exposure.

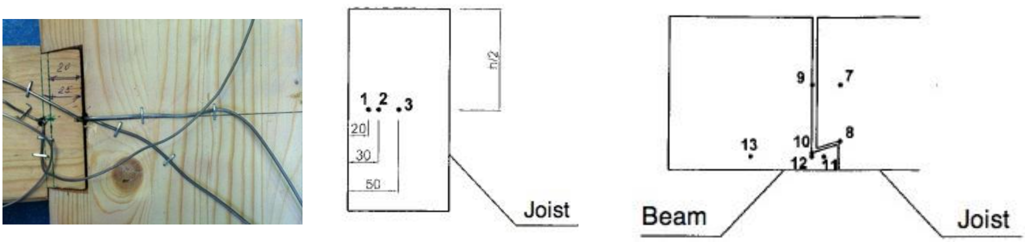

Figure 11. Location of the thermocouples.

The protocol for mechanical loading under fire exposure was defined by the standard NF-EN 26891 [19]. After preloading up to 40% and unloading to 10% $F_{u,mean}$, the specimen was reloaded to the value of $F/F_{u,mean}$, retained as the loads in fire situation (0,1, 0,2 and 0,3). Then, the fire exposure according to the curve ISO 834 was started. The load ratio was kept constant throughout the exposure to fire until the failure of the connection. The supports of the experimental setup were located outside the oven, and the fire action was considered to be homogeneous on all sides of the connection.

The end of the fire tests was defined by a significant acceleration of the measured displacement, with the impossibility to maintain the applied load. The connection specimen was then quickly removed out of the oven and watered to stop the timber combustion.

4.2 Experimental results

4.2.1 Measured temperatures

Figure 12 shows the evolution of the temperature inside timber for dovetail connection type 1 loaded at 30%. Thermocouples 9 to 13 are located on Figure 11. The temperature does not reach more than 100 ℃. As there are no steel elements inside the connection, the heating in the connection area is smaller and the material keeps longer its mechanical properties.

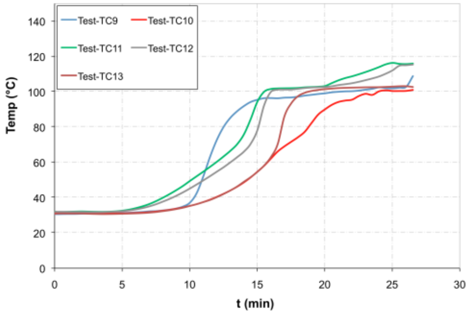

Figure 12. Temperatures within the dovetail connection.

4.2.2 Failure mode

The fire behaviour of the two types of connections is nearly the same.

4.2.3 Fire resistances

During fire tests, the evolution of the deflection at the middle span of the joist is measured to obtain the curves representing the global connection displacement versus the time of exposure to fire (example on Figure 11). Figure 13 shows a quasi-linear evolution of the slip g (mm) in function of time t until about 44 minutes. During this phase, deformations seem to be due to the embedding of wood while its section decreases with the temperature. After this phase, there is an acceleration of the displacement under the constant loads, which represents the failure of the connections. The fire resistance time is then defined as the time from the start of the fire to the time when the specimens cannot withstand the constant load applied. The values of fire resistance $t_{fi,test}$ obtained for all the considered loading ratios are given in Table 3.

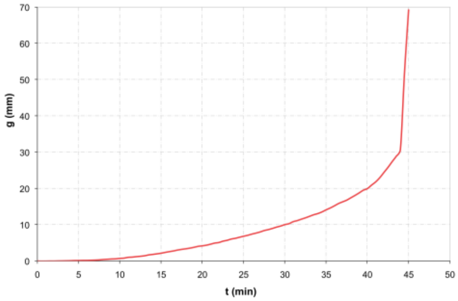

Figure 13. Experimental load-slip curve for connection type 1 (10% of $F_{u,test}$).

Table 3. Experimental results of load bearing capacities of the connections.

Connection type	Load ratio (% $F_{u,test}$)	Load applied (kN)	$t_{fi,exp}$ (min)
Type 1	9,3	4,67	48,5
	9,4	4,69	44
	27,2	13,64	26
Type 2	9,9	4,72	38
	19,7	9,41	54
	28,5	13,64	10,5

Except for connection type 2 loaded at 30% of $F_{u,test}$, all the fire resistance times measured exceed 15 minutes. It can be noticed that for the lowest loading ratio (10% $F_{u,test}$), the fire resistance time is higher than 30 minutes. The experimental value obtained for connection type 2 with load ratio 20% of $F_{u,test}$ is surprisingly high and a new test will be required. Connections of type 1 seems to have a better fire resistance than the ones with fragile mortise.

Comparing these fire resistances with the ones obtained in a previous experimental program conducted on three-dimensional nailing plates connections assembling beam and joist with equivalent geometrical dimensions [20], the tested traditional connections with dovetails present a better fire resistance. Besides their aesthetic and mechanical properties, these traditional connection mode is very relevant in fire.

5 CONCLUSIONS

In conclusion, the test on dovetail connections realized under normal conditions of temperature give values of load bearing capacities which allow to conclude that the design rules used in Germany are reliable and safe. All of the fire tests performed on connections show that a fire resistance time that is higher than 15 minutes or 30 minutes, can be reached. This can be obtained with a reduced loading ratio from 30% to 10% (of the ultimate resistance (Fu) defined at room temperature). These results illustrate the interesting behaviour of this connection mode in fire situations.

This experimental study, based on a reduced number of fire test, should be extended. Moreover, a numerical finite element is currently under development to simulate the mechanical and thermo-mechanical behaviour of blind dovetail connections. This model will be validated on the basis of the experimental results in normal and fire situations. It will make it possible to simulate the behaviour of other configurations of blind dovetail connections. On the basis of the generated results, the simplified models will be proposed for the design of dovetail connections in fire situation.

REFERENCES

[1] M. Audebert, D. Dhima, M. Taazount, A. Bouchaïr, Behavior of dowelled and bolted steel-to-timber connections exposed to fire, Eng. Struct. 39 (2012) 116–125

[2] EN 1995-1-1: Design of timber structures. Part 1-1: General – Common rules and rules for buildings, November 2005, Brussels.

[3] Laplanche K.: "Etude du comportement au feu des assemblages de structures bois – Approche expérimentale et modélisation", Thèses de doctorat de l'Université Blaise Pascal, Clermont-Ferrand, juillet 2006.

[4] Chuo T. C. B.: "Fire performance of connections in laminated veneer lumber", Fire Engineering Research Report 07/04/2007, Canterbury – New Zealand.

[5] Frangi A., Erchinger C., Fontana M.: “Experimental fire analysis of steel-to-timber connections using dowels and nails”, Fire and Materials, John Wiley and Sons, 2009, 19 p.

[6] Racher P., Laplanche K., Dhima D., Bouchaïr A.: "Thermo-mechanical analysis of fire performance of dowelled timber connection", Engineering Structures, Vol. 32, Issue 4, p. 1148-1157, April 2010,.

[7] Peng L., Hadjisophocleous G., Mehaffey J., Mohammad M.: "On the Fire Performance of Double-Shear Timber Connections", 10th International IAFSS Symposium, 2011, Maryland, USA.

[8] Audebert M., Dhima D., Taazount M., Bouchaïr A., “Numerical investigations on the thermo-mechanical behaviour of steel-to-timber connections exposed to fire”, Engineering Structures, Vol. 33, Issue 1, p. 3257–3268, January 2011.

[9] Audebert M., Dhima D., Taazount M Bouchaïr A.: "Thermo-mechanical behaviour of timber-to-timber connections exposed to fire ", Fire Safety Journal, Vol. 56, p. 52-64, February 2013.

[10] Audebert M., Dhima D., Taazount M., Bouchaïr A.: "Behaviour of dowelled and bolted steel-to-timber connections exposed to fire", Engineering Structures, Vol. 39, p. 116-125, 2012.

[11] Fire safety in timber buildings, Technical guideline for Europe, p. 211, published SP Report 2010:19, ISBN 978-91-86319-60-1.

[12] Audebert M.: “Approche expérimentale et modélisation du comportement au feu d’assemblages bois sous différents types de sollicitations”, PhD Thesis, Université Blaise Pascal Clermont-Ferrand et CSTB, France, 233p, 2010.

[13] Werner H. (2001). Queranschlüsse mit Schwalbenschwanz-Zapfenverbindungen Vorschlag für die Bemessung. Verband-High-Tech-Abbund Stand im Zimmerhandwerk.

[14] Hochstrate M. (2000). Untersuchungen zum tragverhalten von CNC-gefertigten Schwalbenschwanz-Zapfenverbindungen. Diplomarbeit, Fachhochschule Hildesheim.

[15] Racher P., Bressolette P., Barrerra A.: "Assemblages traditionnels - Comportement des assemblages par queue d'aronde", Décembre 2007, Laboratoire Génie Civile, CST, Complexe Universitaire des Cézeaux, BP2006 – 63174 Aubière Cédex, France.

[16] Rapport d'essai de résistance au feu d'assemblages bois à queue d'aronde, octobre 2013, CSTB, 84 avenue Jean Jaurès, 77447 Marne-La-Vallée Cedex 2, France.

[17] DIN 1052 (2005). Entwurf, Berechnung und Bemessung von Holzbauwerk.

[18] Ehlbeck J. (1995). Carpenry Joints. Timber Engineering STEP 1, Centrum Hout.

[19] NF-EN 26891, Timber Structures – Joints Made With Mechanical Fasteners – General Principles for the Determination of Strength and Deformation Characteristics. ISO 6891, 1983.

[20] Racher P., Laplanche K., Dhima D., Joyeux D. Fire resistance of joist hangers – International Symposium on Advanced Timber and Timber-composite Elements for Buildings, 233-242, 2004, Italy.

8th International Conference on Structures in Fire
Guo-Qiang LI, Venkatesh K. R. KODUR, Shou-Chao JIANG, Jian JIANG, Su-Wen CHEN, Guo-Biao LOU (Eds.)
Shanghai, China, June 11-13, 2014

FIRE PROTECTION OF TIMBER MEMBERS – DETERMINATION OF THE FIRE PROTECTION SYSTEM CHARACTERISTICS FOR THE VERIFICATION OF THE LOAD-BEARING RESISTANCE BY MEANS OF CALCULATION MODELS

Alar Just*, Joachim Schmid, Norman Werther*** and Andrea Frangi******

* Estonian Academy of Security Sciences
e-mail: alar.just@gmail.com

** SP Wood Technology
e-mail: joachim.schmid@sp.se

*** TUM Technische Universität München
e-mail: werther@bv.tu-muenchen.de

**** ETH Zurich
e-mail: frangi@ibk.baug.ethz.ch

Keywords: Timber, Charring rate, Start of charring, Protection, Testing, Calculation models, Eurocode

Abstract. *Timber members appear in structural assemblies unprotected or protected by a fire protection system. Mostly passive fire protection systems are used which have the ability to delay the start of charring and decrease the charring rate as long the fire protection is attached to the structural element. Together with the failure time of a fire protection system the start of charring and the charring rate are crucial parameters for the residual cross-section which is the dominating parameter for the load-bearing capacity assessed in fire tests or calculation models as given in Eurocode. Calculation models are requested since they allow the variation of building components and are cost effective compared to fire tests. However, the accuracy of the load-bearing prediction under standard fire exposure is highly depending on the input factors (start of charring, failure of the protection system and charring rate) for the calculation of the residual cross-sections. Today no practical system is available to determine these input factors for fire protection system.*

1 INTRODUCTION

According to Eurocode 5 (EN 1995-1-2) [1] the load bearing capacity of any structural member has to be determined in two steps:

(1) Determination of the residual cross-section.

(2) Determination of the load-bearing capacity of the residual cross-section.

The reduction of the original cross-section by char has the largest influence on the load-bearing capacity in the fire situation (Figure 1). The large variety of claddings available on the market may be a challenge for designers since the diverse onset of charring as well as the specific charring rate has to be taken into account calculating the residual cross-section (step 1). A summary of failure times of claddings (gypsum plaster boards) applied to fire exposed timber frame assemblies was published previously [3, 4] and shows a wide range of results.

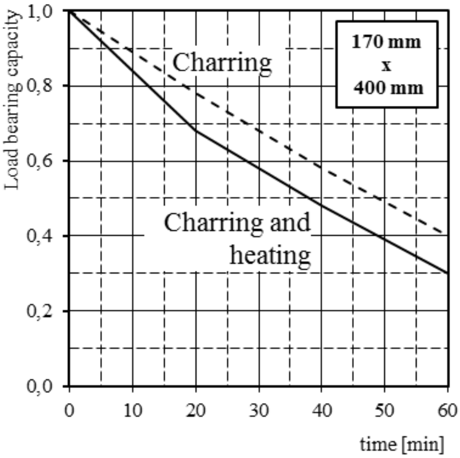

Figure 1. Load-bearing capacity according to Eurocode 5 of an initially unprotected beam 170 mm × 400 mm exposed to fire on three sides using the Reduced Cross-section Method.

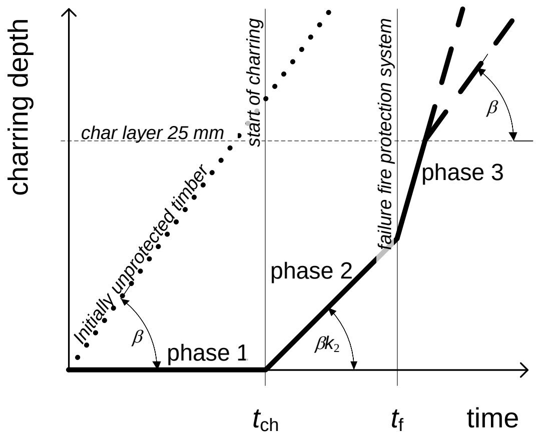

Figure 2. Charring of an unprotected timber member (dotted curve) and an initially protected member (continuous curve).

Generally speaking fire protection claddings are fire protection systems which cover single and multiple layers of one building material (e.g. gypsum plasterboards) or combination of fire protection materials (e.g. gypsum plasterboards and mineral wool). Typically fire protection systems for timber members are passive fire protection systems, however reactive materials such as reactive, intumescent coatings exist.

The reduction of the charring rate can be divided in different phases (Figure 2). The phases differ significantly and are divided by the start of charring (t_{ch}) and the failure time (fall-off) of the protection system (t_{f}). To determine the charring rates of protected members by means of calculation models in Eurocode 5 (EN 1995-1-2), input data are required with respect to the break-points at the start of charring and the failure time of the protection system. The actual testing standard in Europe to determine these data is ENV 13381-7 [5] which is referenced in EN 1995-1-2. ENV 13381-7 [5] is a pre-standard. This standard is rarely known by producers or test labs. Among others, since the standard requires testing of specimens with laminated members that are difficult to produce. The standard is also partly in conflict to EN 1995-1-2.

The claddings used for timber assemblies are typically gypsum plasterboards. However, the product standards EN 520 [6] and EN 15283-2 [7] do not define the data required for the verification of the load-bearing resistance by means of calculation models. Reasons are of many kinds, among others, that the failure time of the gypsum plasterboards is dependent on many variables, e.g. orientation, fixation, backing material.

This paper describes the principles of the new EN 13381-7 which shall replace the existing ENV standard.

Complementary to full-scale testing of protection systems attached to walls, floors or beams, testing in less than full-scale is intended for reactive fire protection materials which may not be activated in fires with slow grow.

2 STANDARD PROCEDURE FOR PROTECTION ABILITIES

Based on the need of input data to increase the use of calculation models CEN/TC 127/WG 1/TG 12 rewrote the EN 13381-7 standard to make it consistent with EN 1995-1-2 and make the test procedure more easy to understand and performable.

Aim of the standard is to allow testing of products for the fire protection systems and determine all needed input data in one single loaded test. Since observations of the behaviour and failure time of the cladding in longer fire tests may lead to difficulties only temperature measurements will be used.

The focus of the standard was

- to make testing less costly;
- to simulate the behaviour of timber members in an appropriate way;
- to formulate criteria in accordance to the other parts of the standard series.

The standardized procedure for determining fire protection system characteristics for the verification of the load-bearing resistance by means of Eurocode 5 is based on testing in standard fire according to EN 1991-1-2[8].

The actual draft of EN 13381-7 knows two types of tests. Tests of

- large-scale, using large scale test specimens and;
- model scale, using model scale test specimens.

2.1 Large scale tests

It is intended to collect all data relevant to assess the contribution of a fire protection system in a large scale test. Three different structures are specified for large scale tests – beams, walls and floors. Regarding the start of charring and the failure of the fire protection system, test results of beam tests are assumed to be corresponding to column tests.

The large scale beam test specimen consists of a load-bearing timber beam with attached fire protection system (Figure 3). The specimen is subjected to fire from three sides. The timber beam may be a solid timber member or a glued laminated member. The adhesive used for the production of the glued laminated beam shall be a certified adhesive according to EN 301 or EN 15425.

The test setup shall ensure that the entire construction deflects uniformly during the fire test taking into account the reduced heat impact to the outer joists. I.e. all load-bearing joists shall exhibit the same stiffness from the beginning of the test to its termination although joists may get charred.

The large scale wall or floor test specimen consists of load-bearing joists, stone wool insulated cavities, a decking on the non-exposed upper side and a fire protection system on the fire exposed lower side (Figure 4).

Fire protection systems comprising boards, slabs or batts, for the fire protection of flat, two dimensional, timber structures shall be arranged such that boards, slabs or batts of the largest practical size are used and that at least one longitudinal joint and one transverse joint, where applicable, are tested within the furnace.

The load of large scale tests is chosen to be 60% of the design load given in EN 1995-1-1 due to several reasons. On one hand due to the analogy with the standard series; On the other hand calculations for ambient design (EN 1995-1-1) show that the maximum utilization of beams/floors is normally lower than 50%. In some cases even lower due to the limitations of vibration behaviour in serviceability limit state (SLS). By using the 5% fractile value (characteristic value) for timber and disregarding the normal design procedure in fire using $k_{mod,fi}$ ($\geqslant$ 1,0) an appropriate load can be computed for the large scale test.

The aim of the large scale test is to deliver values for the start of charring, t_{ch} and the failure time of the protection system, t_f (failure of the protection system, end of stick ability) as well as the charring rate between t_{ch} and t_f.

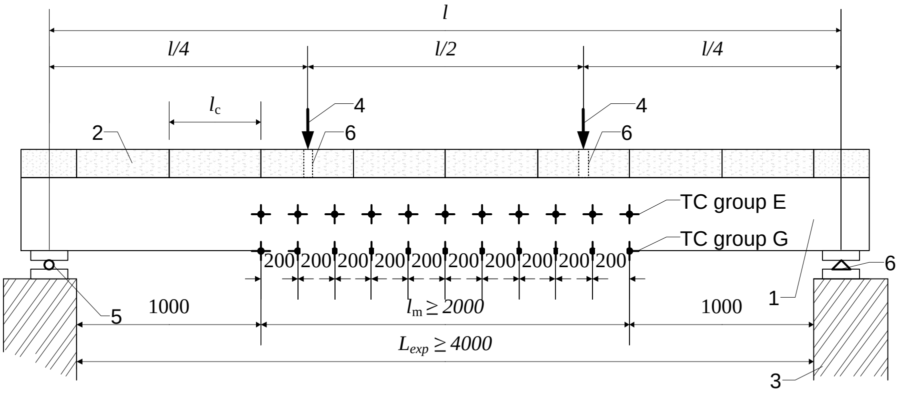

Side elevation

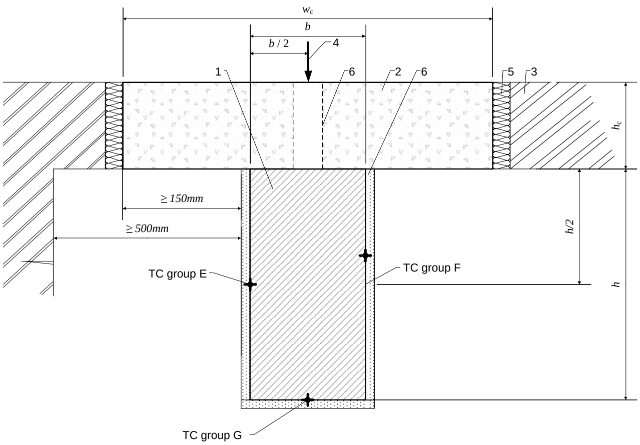

End elevation

Key

1	Instrumented timber beam	b	test specimen width
2	Aerated concrete member	h	depth of the test specimen
3	Test furnace	h_c	depth of the aerated concrete member
4	Load	w_c	width of the aerated concrete member
5	Insulation fitting part	l	span
6	Load spacer	L_{exp}	Fire exposed length
		l_m	Measurement length

Figure 3. Large scale beam test specimen with single layer fire protection system.

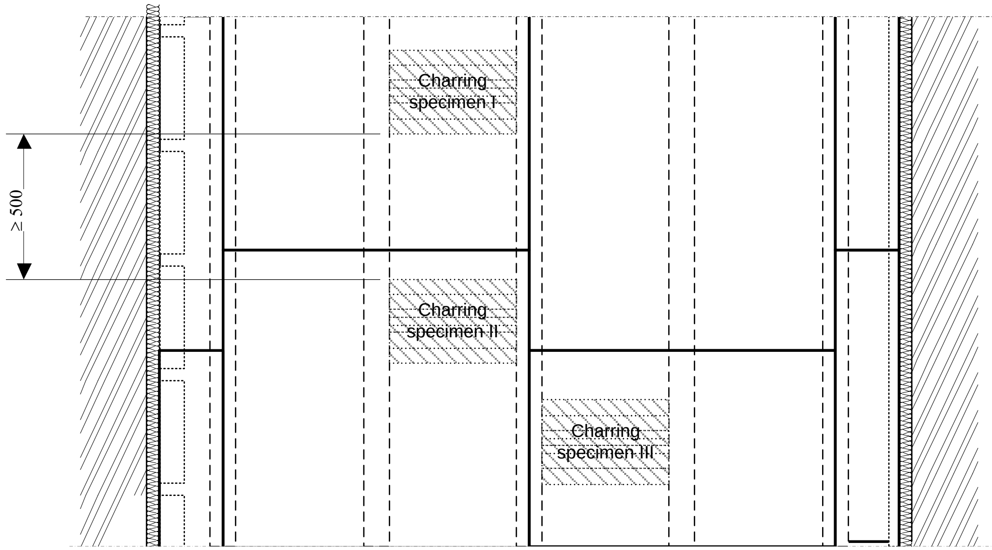

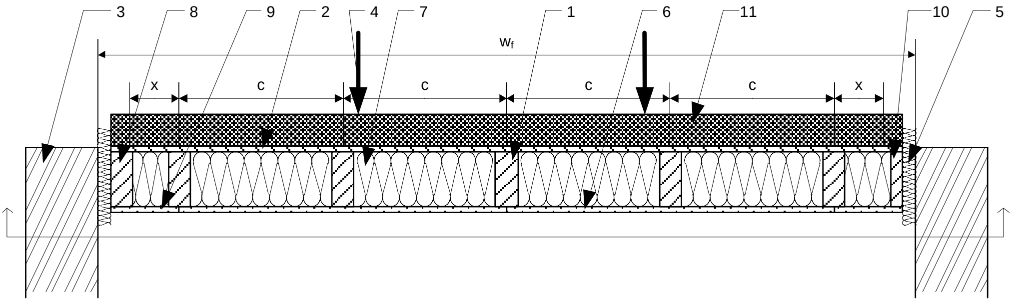

Key

1	Timber joist	7	Cavity insulation
2	Decking	8	Outer joist (example: cut)
3	Furnace	9	Fire protection board (fitting part)
4	Load	10	outer joist (example: half width)
5	Insulation fitting part	d	Board displacement
6	Fire protection board		

Figure 4. Large scale floor specimen.

In the large-scale test specimens and the model scale test specimens charring specimens are incorporated (Figure 5).

The charring test specimen is intended to measure the charring rate behind a fire protection system. It consists of an instrumented timber beam with surface and internal thermocouples. The charring test specimen is based on comprehensive tests performed [2]. These test results have been also confirmed in a numerical finite element (FE) computer simulation. In addition, (FE) parametrical studies were conducted to examine the influence of dimension and number of non-instrumented beams and the thickness of exposed lining to the temperature development in the instrumented beam and exclude any two-dimensional heat flux for the measurement points in the uncharred beam section during fire exposure. Temperature dependent material properties of timber, gypsum plasterboard and thermal insulation were taken from EN 1995-1-2 [1] and the literature [9] and implemented in the transient simulation together with the boundary thermal conditions of EN 1991-1-2 [8].

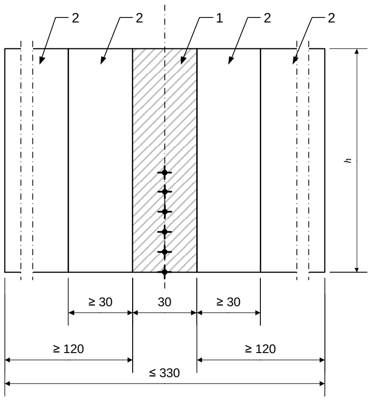

Key
1 Instrumented timber beam
2 Non-instrumented beam

Figure 5. Charring specimen with instrumented beam protected by outer beams.

2.2 Model scale tests

The model scale test is performed with a model scale test specimen and was mainly created to provide an alternative to large scale specimens to proof the protection ability of reactive fire protection materials when exposed to the smouldering fire curve (EN 1991-1-2). The model scale test specimen consists of three charring specimens and is tested unloaded (Figure 6).

Model scale tests are performed unloaded.

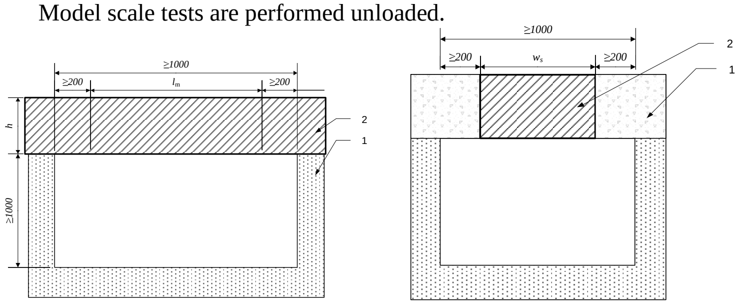

Key
1 Test furnace
2 Test specimen
l_m Measurement length

Figure 6. Model scale specimen.

The model scale test specimen(s) shall be installed horizontally on the furnace in an appropriate test frame. The furnace/test assembly interface shall be sealed with a non-combustible seal.

2.3 Temperature measurements

Plate thermometers of the type specified in EN 1363-1 shall be provided to measure the temperature in the furnace. They shall be uniformly distributed and positioned as specified in the appropriate tests.

The surface temperature of the timber members shall be measured with welded thermocouples (TCs) to have as small temperature measurement devices as possible.

Internal thermocouples are to be applied in charring specimens as well as the model scale test specimen.

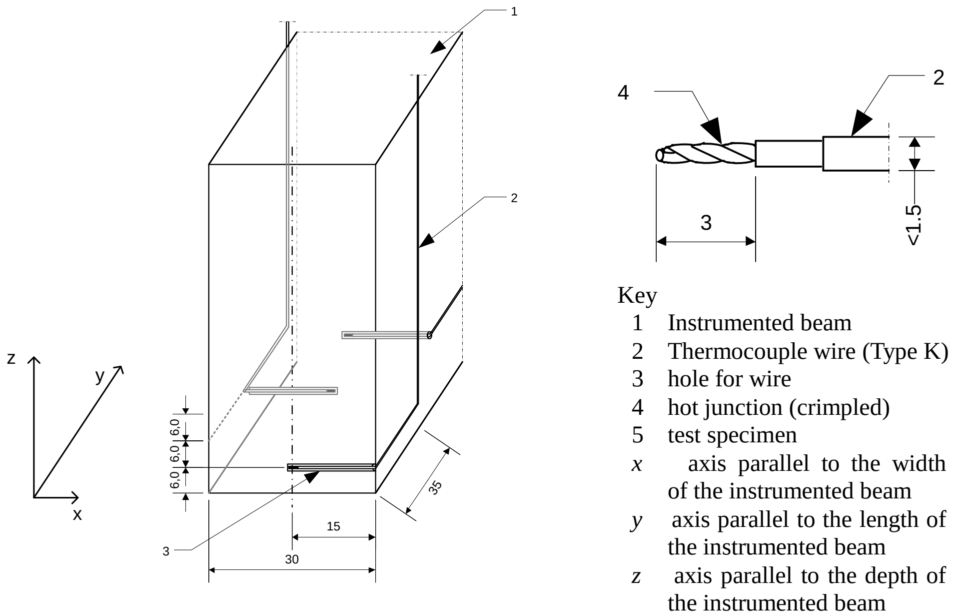

Figure 7. Arrangement of three adjacent internal thermocouples (left) and crimpled thermocouple junction (right).

Thermocouples within the instrumented beam in the centre of the specimen shall have a diameter smaller than 1,5 mm to ensure that the cable can be inserted into a drilled hole of maximum ∅ 1,5 mm. The open end should be placed in the centre of the centre beam. The open end shall be 3 mm long and shall have crimped or welded junctions. The first 50 mm cable from the crimped or welded junction shall be arranged parallel to the isotherms within the specimens (parallel to the lower surface of the test specimen).

2.4 Fixation

The fire protection system shall be attached to the model scale test specimen in such a way that the fixations have no impact on the temperature measurements.

The fixations shall ensure that the fire protection system stays in place longer than during the full scale test performed. Fixations for the model scale test specimen may differ from the fixations used in the large scale test and/or in practice.

EN 1995-1-2 specifies the minimum anchorage length of fixations. Considering the charring depth behind a fire protection system a minimum length of the fixations has to be verified. In the direct applications, the verification is explicitly mentioned; this has to be done for the required time of fire exposure which is at least the failure time t_f assessed by means of EN 13381-7. Although it is assumed that staples can be exchanged with screws this is not given in the direct applications due to little information available.

3 ASSESSMENT OF CHARACTERISTICS

The assessment of the time of start of charring behind the fire protection system (t_{ch}) and the time of loss of stick ability (t_f) shall be done after a large scale test.

The assessment of the rate of charring behind the fire protection system (β_2) shall be done after a large scale test with incorporated charring test specimen (for multi-layer protection systems or single layer protection systems) or a model scale test (for single layer protection systems).

The start of charring shall be determined according to following equation:

$$t_{ch,charring-test-specimen} = \sum_{i=1}^{n} \frac{t_{300,TC1,i}}{n} \tag{1}$$

where

$t_{300,TC1,i}$ is the time when thermocouple reading achieves 300°C

n is the number of test specimens

For the assessment of the charring rate behind the fire protection system, the temperature recordings of all valid thermocouples (TC) of minimum 3 charring specimens exposed in the same fire test shall be used.

The charring rate shall be determined according to following procedure:

The time $t_{300,i,j}$ is the time when the charring of timber is reached i.e. when at the TCi,j for every temperature measurement station j, at the specific depth i, the temperature recording reaches 300°C. Linear interpolation between 2 time records of a TC is permitted.

Calculate the charring rates $\beta_{i,j}$ between 2 consecutive depths for each temperature measurement station j according to the following equation.

$$\beta_{i,j} = \frac{d_{i+1} - d_i}{t_{300,i+1} - t_{300,i}} \tag{2}$$

The standard procedure gives the charring rate for the protection phase only. The protection coefficient k_2 according to Eurocode 5 (EN 1995-1-2) [1] can be found as

$$k_2 = \frac{\beta_{i,j}}{\beta_0} \tag{3}$$

The failure of a protection system is assessed in a large scale test. Failure of the fire protection system is detected if the measurement of any TC located at the timber surface (for timber frame assemblies additionally in the field) when one TC rises steep towards the furnace temperature and the deviation between the TC measurement and the mean value of the furnace measured by plate thermometers is equal or less than 50K or when observation detect the loss of stickability of in total more than 0,25 m^2.

Overview of the possible routes for necessary tests is shown in Table 1.

Table 1. Fire tests depending on the intended use of the fire protection system.

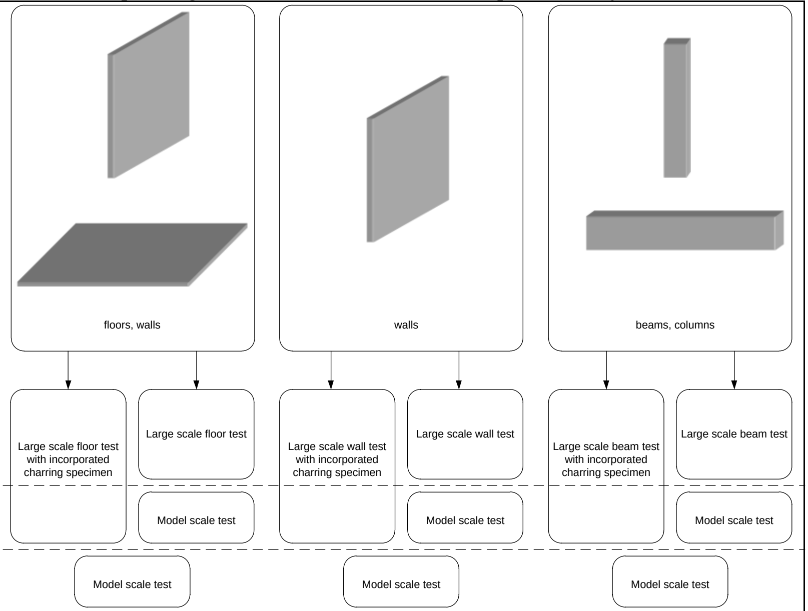

The fire protection system will be attached to	
Determination of the stickability	
Determination of the charring rate	
Determination of the protection ability of fire protection systems comprising reactive fire protection materials	
NOTE: If the model scale test is used for the determination of the charring rate behind the fire protection system, the determined charring rate β_2 is only valid until the failure of the first layer of the fire protection system.	

4 DISCUSSION

The characteristics determined according to the procedure described here are valid only for tested construction configurations.

The charring test specimen is built up with 120 mm side members to ensure the one-dimensional charring rate at the protected phase. The effect of corner roundings is avoided. Two dimensional charring rate is not determined by these tests.

Failure time of claddings is measured by the thermocouples. Sudden rise of temperature is the criteria. Thermocouples measurements avoid the subjective results by visual observations.

Failure time of protection could also be influenced by spacing of fasteners including edge distances. This effect is not taken into account by the procedure described on this paper. There is an approach needed for the influence of fastener types and fastener spacings as well.

The failure time of protection is also influencing charring rate of timber element at the post-protection phase. The methods described in this article do not consider the post-protection phase. Conservatively the charring rate at post-protection phase should be taken as double value compared to the charring rate for initially unprotected member.

5 CONCLUSIONS

This article gives a possible route for a determination process of fire protection system characteristics for the verification of the load-bearing resistance by means of Eurocode 5.

The new standard allows assessing the time when charring starts, the failure time of the cladding and the charring rate for various types of claddings in a practical way.

REFERENCES

[1] EN 1995-1-2 Design of timber structures – Part 1-2: General – Structural fire design. European Standard (2004). CEN, European Committee for Standardization, Brussels.

[2] König J, Rydholm D (2003) Small-scale fire tests of heavy timber components, Trätek Report P 0310036, Swedish Institute for Wood Technology Research, Stockholm, Sweden.

[3] Just A (2010) Structural Fire Design of Timber Frame Assemblies Insulated by Glass Wool and Covered by Gypsum Plasterboards. Doctoral Thesis, Tallinn University of Technology, Tallinn, Estonia.

[4] Just A, Schmid J, König J (2010) Failure times of gypsum boards. Paper presented at the SiF'10, Structures in Fire 2010, East Lansing, Michigan State University, USA.

[5] ENV 13381-7: Test methods for determining the contribution to the fire resistance of structural members - Part 7: Applied protection to timber members (2003). CEN, Brussels.

[6] EN 520: Gypsum plasterboards – Definitions, requirements and test methods (2004). CEN, Brussels.

[7] EN 15283-2. Gypsum boards with fibrous reinforcement – Definitions, requirements and test methods - Part 2: Gypsum fibre boards (2008). CEN, Brussels

[8] EN 1991-1-2 Actions on structures – Part 1-2: General actions – Actions on structures exposed to fire. European Standard (2002). CEN, European Committee for Standardization, Brussels

[9] Schleifer V, (2009) Zum Verhalten von raumabschließenden mehrschichtigen Holzbauteilen im Brandvall, PhD Thesis ETH Zürich

8th International Conference on Structures in Fire
Guo-Qiang LI, Venkatesh K. R. KODUR, Shou-Chao JIANG, Jian JIANG, Su-Wen CHEN, Guo-Biao LOU (Eds.)
Shanghai, China, June 11-13, 2014

VERIFICATION OF THE LOAD-BEARING RESISTANCE OF TIMBER MEMBERS BY MEANS OF THE REDUCED CROSS-SECTION METHOD – BACKGROUND TO THE EUROCODE MODEL AND COMPARISON TO FIRE TESTS IN BENDING

Joachim Schmid*, Alar Just, Michael Klippel***, Massimo Fragiacomo**** and David Lange***

* SP Technical Research Institute of Sweden
e-mails: joachim.schmid@sp.se, david.lange@sp.se

** Estonian Academy of Security Sciences
e-mail: alar.just@gmail.com

*** ETH Zurich, Switzerland
e-mail: klippel@ibk.baug.ethz.ch

**** University of Sassari, Italy
e-mail: fragiacomo@uniss.it

Keywords: Timber, Fire design, Reduced Cross-Section Method, Zero-strength layer

Abstract. *The Reduced Cross-Section Method is included in handbooks and Eurocode to design timber members in fire conditions. This method considers the strength and stiffness reduction beyond the charred layer by adding an additional depth, the so-called 'zero-strength' layer, to the charring depth. Beside the reduction of the original cross-section by the char layer, the zero-strength layer is one of the key parameters for the fire design of timber members. This paper presents the background of the Reduced Cross-Section Method and briefly discusses the mechanical assumptions, simplifications and possible limitations of this design method. Further, the zero-strength layer thickness is determined for members tested in bending, and basic principles for the use of standard experimental tests to determine this quantity are provided. The test results show that the today's design procedure may lead to very unconservative design.*

1 INTRODUCTION

While the compulsory verification of the fire resistance by means of large scale fire tests is costly and time consuming, calculation models may provide an interesting design alternative due to their flexibility and minor cost. For timber members exposed to fire, some guidance for advanced calculations based on the use of FEM is available (e.g. in EN 1995-1-2 [1], Annex B), however this procedure is seldom used due to its complexity. Further, simplified analytical models are available, which allow structural designers to calculate the resistance of timber members by hand. According to Eurocode 5 (EN 1995-1-2) the load-bearing capacity of any structural member has to be determined following an easy-to-use two-step approach:

Step 1 Determination of the residual cross-section.
Step 2 Determination of the load-bearing capacity of the residual cross-section.

The reduction of the original cross-section by char has the largest influence on the load-bearing capacity in the fire situation, but also the reduction of strength and stiffness of the residual cross-section contributes to the load-bearing capacity in the fire condition. The determination of the load-bearing capacity (step 2) can be performed following the reduced properties method (RPM) or the reduced cross-section method (RCSM). The RCSM assumes an effective cross-section which is slightly smaller than the residual cross-section, and has the same material properties at normal temperature all over the section. The effective cross-section can be calculated by reducing the residual cross-section at a specific time of fire exposure by the so-called zero-strength layer, which is assumed to have neither strength nor stiffness. In the RPM, the strength and stiffness properties of the residual cross-section are varied to account for the effect of fire. The RPM exhibits a number of drawbacks [2] and, although included in EN 1995-1-2, is less popular than the RCSM. In contrast to the RPM where every specific member cross-section geometry leads to different modification factors in the fire situation and subsequently to different material properties, the RCSM allows the use of the original material properties, which is an advantage using commercial software packages to solve complex systems. Due to these reasons, the RCSM is recommended to be used but in its present form the correct use is limited and therefore discussed in the following sections.

2 BACKGROUND OF THE REDUCED CROSS-SECTION METHOD

The RCSM was published in the '80s [3] for simply supported glue-laminated (glulam) beams exposed for 30 and 60 minutes to standard fire conditions on three sides and loaded in bending. The method was derived by means of numerical simulations to estimate the influence of different lamellae qualities and the measured natural variation of the timber quality within a strength class. To consider the change of the load-bearing capacity in the fire situation, available results of tests with small-scale specimens at different temperatures were used; the approach described by Schaffer [3] is displayed for beams in Figure 1 and Figure 2.

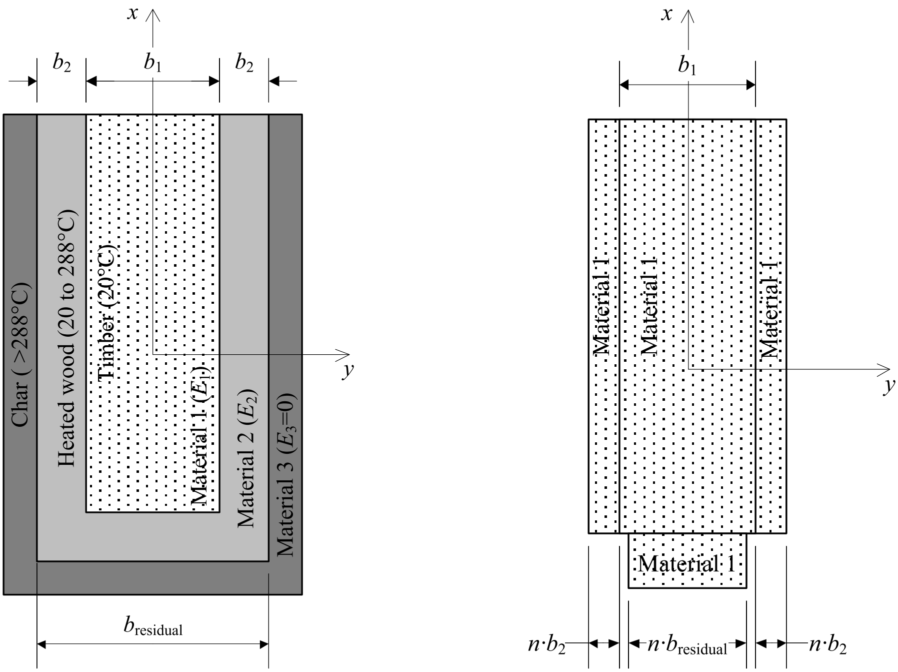

(a) (b)

Figure 1. Principle of the transformed section method described in [3]. (a) shows the simplified cross-section divided into three parts, (b) shows the transformed section made of only one material.

The cross-section of the fire exposed beam is assumed to be divided into three parts (Figure 1a):

(1) a char layer with zero-strength and zero-stiffness (Material 3);

(2) a layer of heated wood with strengths and stiffness lower than that of timber at normal temperature (Material 2); and

(3) an inner part, which exhibits unchanged material properties (Material 1).

Using test results of small-scale samples exposed to different temperatures, reduction factors for tensile and compression strength, and for the modulus of elasticity (MOE), were used to determine material properties depending on the temperature, see Figure 2. For the depth of about 40 mm within the char layer where temperatures higher than 20°C are expected in the fire condition, the mean values of strength and MOE were used to define material properties of “Material 2” in Figure 1(a), see continuous and dashed curves in Figure 2. The transformed section method was used to analyse the section made of “Material 1” and “Material 2” (Figure 1(b) considering

$$n = \frac{E_1}{E_2} \tag{1}$$

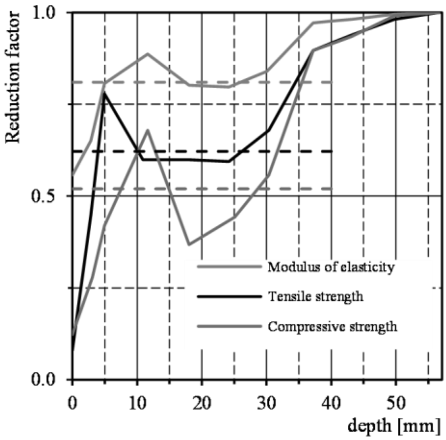

Figure 2. Basics of the Reduced Cross-Section Method presented in [3]: the strength and stiffness distribution within the 40 mm depth was integrated and the so derived mean value used for further calculations.

The full loss of strength was ascribed to a zero-strength layer, which was estimated as about 0.3 inch (7.6 mm) and converted to 7 mm in Eurocode 5.

3 DISCUSSION

3.1 Limitations of the RCSM implemented in Eurocode 5

When proposing the RCSM in [3], the authors mentioned a successful comparison of the proposed method with full-scale test results. However, it remains unknown which tests were analysed and which details (support conditions, material properties, charring rates, fire loads, and failure mode) were considered. The author’s recommendation of further testing in [3] was not followed up by the scientific community before implementing the RCSM in Eurocode 5, as a systematic testing with the evaluation of the zero-strength layer has never been reported.

The field of application of the zero-strength layer originally computed for glulam beams in bending was extended in the Eurocode 5 to other members, for which the failure mechanism is completely different, e.g. timber columns which normally fail in flexural buckling. Although in the same code different reduction curves for tension and compression are provided for the material properties in fire conditions (see Eurocode 5, Annex B), members subjected to pure tension and compression are not excluded from the application of the general 7 mm zero-strength value.

In Eurocode 5, it is assumed that the zero-strength layer will remain unchanged when the time of fire exposure is greater than 60 minutes. However, hardly any experimental tests of beams and columns exposed for 90 minutes and longer are available. Furthermore, no references can be found where the zero-strength layer was determined for times of exposure of more than 90 minutes [4].

The limits of application of the zero-strength layer for members which are significantly different from those specified in [3] is totally missing in the Eurocode 5. The lack of precise limits may lead to a wide range of interpretations by designers and certification bodies: two-dimensional members with charring of one side only (slabs), heterogeneous elements where parts with lower strength and stiffness may overlay with the zero-strength layer (e.g. cross-laminated timber panels), and engineered wood products where different materials are combined together (e.g. wood I-joists) are examples, where the application of the zero-strength layer defined in Eurocode 5 may lead to different and erroneous results.

Eurocode 5 allows the use of advanced calculation methods to design timber members in fire conditions. This possibility is intended for a more accurate design and for more general applications. The idea is that the use of more accurate formulations will lead in general to less conservative designs. However, while the use of the thermal properties provided in Eurocode 5 generally agrees well with the more conservative simplified design methods [5][6], the use of the mechanical properties given in Eurocode 5 leads in many cases to more conservative solutions, i.e. a zero-strength layer of greater depth [6]. Since the advanced method and the RCSM are inconsistent, due to the lack of benefits, designers usually avoid the use of advanced methods. Thus, very few advanced design tools, e.g. finite element models, have been developed to date since no benefits are to be expected and thus the motivation for engagement in this field is not justifiable. As a result, fire safety engineering of timber structures has not made significant progress, the analysis of the global structural behaviour in fire as opposed to simple member is not attractive, and complex issues such as natural, localized and travelling fires are not investigated like for e.g. steel structures.

3.2 Limitations of the original RCSM approach

The RCSM proposed in [3] is an approach to determine the effective cross-section for fire exposed timber beams, which is typical of composite materials. However, unlike steel, wood exposed to fire will still show brittle material properties in tension while plastic behaviour can be observed in compression, see Figure 3. Further, the change in the MOE with temperature is different for the wood in compression and tension, see Figure 4.

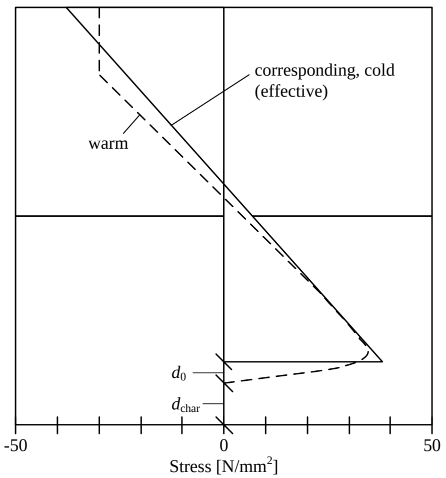

Figure 3. Stress distribution along the centreline of a beam exposed to fire on three sides and subjected to bending (dashed curve), and the corresponding linear stress distribution with normal material properties and the same bending resistance (solid line).

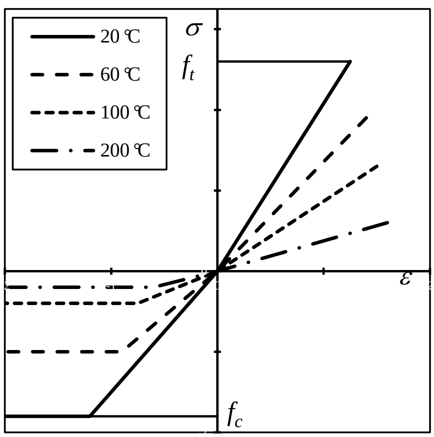

Figure 4. Temperature-dependent stress-strain relationships parallel to the grain for wood at different temperatures with plasticity in compression only.

Other limitations of the approach described in [3] can be mentioned: when transforming the residual cross-section with the heated zone ("Material 2" in Figure 1 with strength from 0 to 100% of the normal temperature value) into an effective cross-section with normal temperature strengths over the whole cross-section, the depth of the zero-strength layer depends upon the time of fire exposure of the section [7]. The influence of a zero-strength depth on the modulus of resistance, in fact, changes when the charring proceeds. For a greater time of fire exposure, the neutral axis moves upwards, see Figure 3. Further, the brittle material behaviour in tension of timber limits the gradient of the stress distribution in the heated zone and thus will influence the position of the neutral axis, compared to the stress distribution depicted in Figure 3. This stress distribution (dashed line) was determined by taking into account the actual reduction in strength and stiffness of wood with temperature due to fire exposure on three sides. Last but not least, elasto-brittle behaviour in tension and elasto-plastic behaviour in compression as displayed in Figure 4 were considered for wood parallel to grain: the reduction in tensile strength with temperature of the lower exposed wood fibres leads to a lower maximum stress in tension; however, the losses are partly compensated by the plastic flow in compression at the unexposed upper side of the beam.

3.3 Correct approach for a RCSM

A correct way to determine a zero-strength layer would be to compare: (i) the load-bearing capacity of the heated cross-section and (ii) the simplified linear-elastic approach assuming material properties as at normal temperature (Figure 4). A comparison could be made between the results of either fire resistance tests or advanced numerical simulations considering the actual mechanical properties of wood exposed to fire, and the results of calculation models given for normal temperature, e.g. in EN 1995-1-1 [8]. The zero-strength layer of a given beam cross-section exposed to standard fire for a certain time is described by the difference d_0 between the depth of the actual (warm) and effective (cold) cross-section as displayed in Figure 3. Analysing a given cross-section over the time of fire exposure, e.g. from 0 to 90 minutes, a curve for the zero-strength value d_0 could be determined. It is expected that in general non-linear curves will be the result of this analysis.

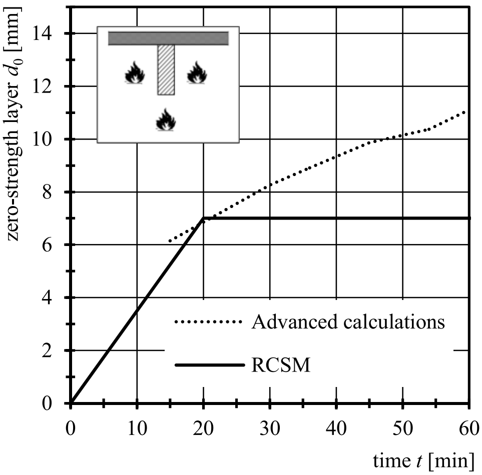

Figure 5. Zero-strength layer beam (134 mm × 420 mm) according to the RCSM and advanced calculations specified in Eurocode 5; the exposed side is in tension [7].

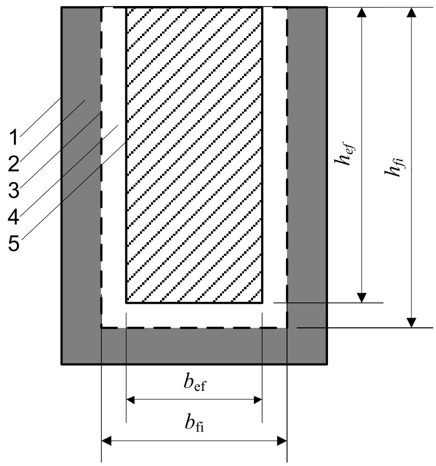

Key:
1 original cross-section
2 char layer
3 residual cross-section
4 zero-strength layer
5 effective cross-section

Figure 6. Simplified (without corner roundings) cross-sections before and during fire exposure.

An easy-to-use and conservative model describing the losses of the heated cross-section would be the use of the linear or other simple envelope curves for a specific cross-section geometry providing sufficient safety; if needed simplified relationships for different cross-section geometries could be determined. An example of a zero-strength layer evaluation is given in Figure 5 for a glulam beam with dimensions of 134 mm $\times$ 420 mm (width $\times$ depth).

4 DETERMINATION OF THE ZERO-STRENGTH LAYER OF MEMBERS IN BENDING

4.1 General

Assuming a known bending strength f_m of a timber beam at normal conditions, the basic condition given by Equation (2) has to be fulfilled: the bending resistance in fire conditions M_{fi} of the actual residual cross-section is equal to the bending resistance M_{ef} of an effective cross-section with an effective depth h_{ef}, an effective width b_{ef} (see Figure 6) and the assumed bending strength at normal conditions f_m. Thus, the thickness of zero-strength layer d_0 of the beam can be derived based on linear elastic theory. For a beam exposed to fire on three sides, the Equation (5a) is to be solved, while for a beam exposed to fire on four sides reference to Equation (5b) is to be made.

$$M_{fi} = M_{ef} \tag{2}$$

$$M_{fi} = W_{ef} \cdot f_m \tag{3}$$

$$M_{fi} = \frac{b_{ef} \cdot h_{ef}^2}{6} f_m \tag{4}$$

$$M_{fi} = \frac{\left(b_{fi} - 2 \cdot d_0\right) \cdot \left(h_{fi} - d_0\right)^2}{6} f_m \tag{5a}$$

$$M_{fi} = \frac{\left(b_{fi} - 2 \cdot d_0\right) \cdot \left(h_{fi} - 2 \cdot d_0\right)^2}{6} f_m \tag{5b}$$

with

b_{fi} cross-section width after fire exposure
h_{fi} cross-section depth after fire exposure
f_m bending strength of the beam at normal conditions
d_0 thickness of the zero-strength layer
M_{fi} moment capacity of the beam in fire conditions
M_{ef} moment capacity in normal conditions of the beam with an effective cross-section
W_{ef} section modulus of the beam with an effective cross-section

For members loaded in tension and compression, a corresponding approach could be developed as described in Equations (2) to (5a) and (5b).

4.2 Possibilities to determine the zero-strength layer for beams

The procedure to determine the zero-strength layer for a bending member is a two-step procedure. In a first step the load-bearing capacity in the fire condition (M_{fi}) has to be determined for a specific point in time; results shall comprise the moment capacity in the fire condition and the corresponding heated residual cross-section. Within this step the behaviour of timber exposed to an unsteady thermal exposure has to be addressed in an appropriate way. To determine the required variables, fire resistance tests or advanced calculation methods can be used. When using advanced calculations, the thermal and mechanical response have to be considered in an appropriate way; Eurocode 5 gives some guidance in Annex B. When using fire resistance tests important details shall be followed in extensions to the requirements of any testing standard:

- the failure time (collapse) of the member tested has to be determined in the test,
- the material properties of the material tested have to be known,

- the residual cross-section at failure time has to be documented.

In a second step the load-bearing capacity of the cold, residual cross section are compared with M_{fi}. In this calculation the characterisation of the residual cross-section and the assumed material properties (f_m) are of significant importance. Using an iteration process, the zero-strength layer d_0 can be computed.

5.3 Example of the determination of the zero-strength layer by means of testing

Standard fire resistance tests were performed on 140 mm × 269 mm glulam beams, the same grade (CE L40c) and the same batch [9]. Prior to the fire tests, reference tests in normal conditions were conducted comprising a characterization of to their eigenfrequency and destructive bending tests. Ten destructive reference tests in bending were performed according to EN 408 [10] at normal temperature to determine the mean ultimate bending resistance. The mean value of f_m = 37.8 N/mm^2 (COV 15,6%) was obtained, which was used for the prediction of the failure load of all beams tested in the fire situation, (Figure 7). In the fire tests the beams were loaded individually which was kept constant until failure. The test results are displayed in Figure 8, where the time to failure of the beams exposed to fire is plotted versus the percentage of the load-carrying capacity in normal conditions based on the predicted bending strength.

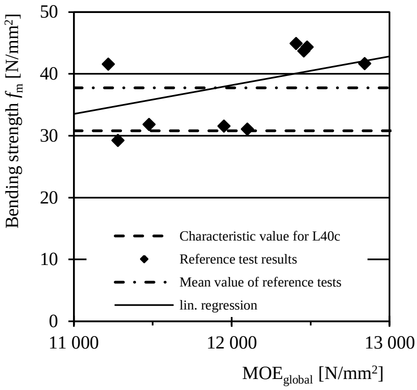

Figure 7. Bending strength vs. Modulus of Elasticity of the beam specimens tested in bending to failure.

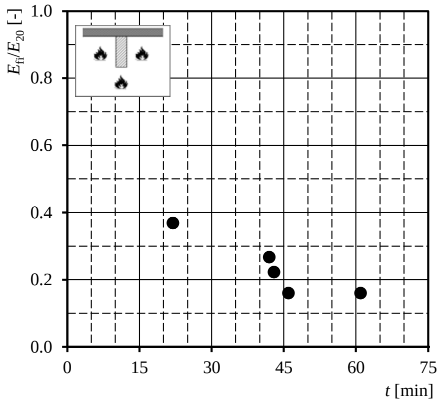

Figure 8. Failure times of the beams exposed to fire in bending and loaded with a certain percentage of the load-carrying capacity in normal conditions.

Due to the testing procedure, the observed residual cross-sections are corresponding to the time of fire exposure which is appropriate for the last beam that failed in the fire test at 61 min.

Table 1. Test characteristics and determined calculation results.

	Test 1	Test 2	Test 3	Test 4	Test 5
Load M_{fi} [kNm]	14.2	23.5	17.1	10.2	10.2
Load ratio E_{fi}/E_{20} [-]	0.22	0.37	0.27	0.16	0.16
Predicted mean strength f_m [N/mm^2]	37.8				
Section modulus of the measured residual cross-section area W_{res} [mm^3 × 10^6]	1.039	1.332	1.052	0.823	1.001
Determined charring depth d_{char} [mm]	30.5	15.5	29.5	43	32.5
Fire resistance [min]	43	22	42	61	46
Determined zero-strength layer d_0 [mm]	16.7	20.1	13.7	9.5	20.1

To determine the residual cross-sections of the other beams, the so-determined charring rate was used, linearity was assumed. Test characteristics and zero-strength layer results for this example are shown in Table 1. Using Equation (5a) for three-sided fire exposure, the zero-strength layer can be calculated for members in bending. The zero-strength layer d_0 of these five tests of glulam beams is in the range of about 9 to 20 mm using the predicted bending strength based on the reference tests; these values deviate considerably from today's design rules in Eurocode following the simplified design approach of the RCSM.

6 CONCLUSIONS

Today's RCSM is a simplified procedure for the verification of the fire resistance of timber members that was developed using simple assumptions which are inaccurate for timber. In this paper, detailed guidance is given on the determination of the zero-strength layer in bending, the analysis of performed full-scale tests show the considerable deviation. This procedure can be used for the determination of the zero-strength layer for specific members for the correct application of the RCSM or the development of a correct design model providing a simplified but conservative tool for the design of timber members in the fire condition.

A systematic review of the actual design approach is recommended since the actual design approach may lead to unconservative design. An improved RCSM taking into account the actual material behaviour of timber in the fire condition can be derived using fire resistance tests in combination of advanced calculation.

REFERENCES

[1] EN 1995-1-2 Design of timber structures – Part 1-2: General – Structural fire design. CEN, European Committee for Standardization, Brussels, 2004.

[2] König J, Structural fire design according to Eurocode 5—design rules and their background, Fire and Materials, 2005;29: 147-63.

[3] Schaffer EL, Structural fire design, U.S. Dept. of Agriculture, Forest Service, Forest Products Laboratory, Madison, Wis., 1984.

[4] Schmid, J., Klippel, M., Just, A., Frangi, A., Review and analysis of fire resistance tests of timber members in bending, tension and compression with respect to the Reduced Cross-Section Method, Fire Safety Journal, accepted for publication 2014/03.

[5] Fragiacomo M, Menis A, Moss P, Buchanan A, Clemente I, Numerical and experimental evaluation of the temperature distribution within laminated veneer lumber (LVL) members exposed to fire, Journal of Structural Fire Engineering, 2010;1: 145-59.

[6] Klippel M, Schmid J, Frangi A. The Reduced Cross-section Method for timber members subjected to compression, tension and bending in fire Conference The Reduced Cross-section Method for timber members subjected to compression, tension and bending in fire 2012. p. CIB-W18/45-16-1.

[7] Schmid J, König J, Just A, The Reduced Cross-Section Method for the Design of Timber Structures Exposed to Fire-Background, Limitations and New Developments, Structural Engineering International, 2012;22: 514-22.

[8] EN 1995-1-1: Design of timber structures - Part 1-1: General - Common rules and rules for buildings. CEN, European Committee for Standardization, Brussels, 2004.

[9] Lange D, et al., Assessment of the impact of different fire scenarios on structural timber performance and reliability – Part 1: Fire tests, Borås, Sweden, SP Swedish Technical Research Institute, 2014.

[10] EN 408: Timber structures – Structural timber and glued laminated timber – Determination of some physical and mechanical properties. CEN, European Committee for Standardization, Brussels, 2010

8th International Conference on Structures in Fire
Guo-Qiang LI, Venkatesh K. R. KODUR, Shou-Chao JIANG, Jian JIANG, Su-Wen CHEN, Guo-Biao LOU (Eds.)
Shanghai, China, June 11-13, 2014

PREDICTING THE FIRE PERFORMANCE OF STRUCTURAL TIMBER FLOORS

James W. O'Neill*, Anthony K. Abu, David M. Carradine***, Peter J. Moss**and Andrew H. Buchanan****

* Holmes Fire LP, Sydney, New South Wales 2000, Australia
e-mail: james.oneill@holmesfire.com

** Department of Civil and Natural Resources Engineering, University of Canterbury, Private Bag 4800, Christchurch 8140, New Zealand
e-mails: tony.abu@canterbury.ac.nz, peter.moss@canterbury.ac.nz, andy.buchanan@canterbury.ac.nz

*** Building Research Association of New Zealand (BRANZ), Private Bag 50908, Porirua 5240, New Zealand
e-mail: david.carradine@branz.co.nz

Keywords: Timber floors, Furnace testing, Structural modelling

Abstract. *This paper describes part of a larger research initiative to predict the fire resistance of engineered timber floor systems. The floor systems described in this paper are prefabricated modular joist and box beam floors, designed for multi-storey building use with spans of five to seven metres. The paper describes 3D numerical modelling of the floor systems using finite element software, carried out as a sequential thermo-mechanical analysis. Experimental furnace testing of these floors is also described, with the aim of validating the numerical modelling. General guidance is provided for users of advanced numerical methods to highlight the possible pitfalls and drawbacks of these methods, focusing on the nuances of modelling structural timber behaviour in fire conditions.*

1 INTRODUCTION

Fire safety is increasingly seen as an important aspect in both the design and construction of new structures in the modern building environment. With an increased awareness of the importance of fire safety comes a greater understanding and drive for research into how structures and their respective elements perform in fires. In recent years engineered timber products have been used in many types of constructions across many different countries. New and innovative methods are being developed to make use of this natural and abundant resource, and numerous tall buildings are now being constructed in large city centres for a huge number of different uses. These buildings range from showcase buildings, which generally have a lot of the timber exposed for aesthetic appeal, to generic office and apartment buildings which may have no timber members left exposed. Each type of building has its own unique challenges with regards to fire safety. The most significant factors which determine these challenges are the intended use of the structure and the possible sources of fire, in addition to the primary choice of material for the loadbearing structure.

The widespread use of structural timber in tall buildings is often restricted because timber is a combustible material, and is commonly perceived to behave poorly in fires. As part of a large research effort to develop timber technologies for use in high-rise and long-span building applications, the present study uses current general purpose structural modelling techniques to estimate the fire performance of prefabricated timber floors in multi-storey buildings.

1.1 Fire Resistance

Generally the fire resistance rating of building elements are assessed under three criteria:

- Stability – to prevent the structural collapse of the element,
- Integrity – to prevent the transmission of fire and smoke through the element,
- Insulation – to prevent an unacceptable level of heat being transmitted through the element.

Floor systems provide the means for directly supporting primary loads of a building, and also provide separation between floor levels to help confine fires to compartments. They are critical to designing for structural fire resistance of a building as they are generally the least protected elements, in comparison with the rest of the supporting structure (e.g. primary beams, columns and walls). The nature of a floor system providing the horizontal separation between levels means that a fire in a building compartment will have the most significant impact on the floor directly above it, hence the greatest heat impact is most likely to be experienced by a floor assembly as opposed to other parts of the structure.

2 TIMBER FLOORS UNDER STUDY

Two major types of floors are investigated in this research; one-way composite joist and box beam floors. The reasoning for this is due to the requirement of developing optimal systems for long-span applications in a multi-storey environment, and also due to the Australasian construction industry's familiarity with these types of floors. In 2008 the Structural Timber Innovation Company Ltd was established as a research consortium to implement structural timber solutions into the commercial sector of the construction industry, with a focus on large multi-storey timber buildings in the Australasian construction environment, and was a major driver for this research. A comprehensive guide on the other major types of timber floor systems available are detailed by Kolb [1].

2.1 Composite Joist Floors

The composite joist floor under study consists of LVL beams 200 mm to 600 mm deep, fixed to a continuous LVL slab system (top flange), as shown on the left of Figure 1 with a fully rigid connection between the joists and slab components. Typically these floors range from 5 metres to 12 metres in length and are designed for normal service loads in office buildings and similar multi-storey applications.

2.2 Composite Box Beam Floors

The composite box beam floor is similar to the composite joist floor, with moderate changes to the construction configuration. The bottom flanges of the joists are made continuous between each second pair and the spacing is modified, resulting in a box type system with every second panel missing a bottom chord, allowing for services to be installed in the gaps. The advantage of a system such as this over the previous composite floor is that the surface area of timber exposed to the fire is greatly decreased; hence the expected fire performance is greater by a simple change in configuration (for the same amount of timber per unit length of floor). A schematic of this type of floor is shown on the right of Figure 1.

Figure 1. Composite joist floor (left) and box beam floor (right) tested.

2.3 Material Properties

The engineered wood product used for these floors was New Zealand laminated veneer lumber (LVL), manufactured from softwood. This consists of 3-4 mm thick rotary peeled veneers of Radiata Pine glued with resorcinol adhesive. These layers have grain orientation running in the same direction (as opposed to plywood, with alternating orthogonal grain orientation) which gives the highest strength properties for bending and tension in one direction. Such beams can resist much greater loads and hence span longer distances compared with traditional sawn timber, and the manufacturing process of LVL also allows for greater dimensional accuracy.

The fire behaviour of LVL has been investigated in recent years. Research by Lane [2] examined the ignition, charring and structural performance of LVL. In terms of the glue lines in LVL affecting the charring rates, Lane found in a number of un-instrumented char tests that there was relatively no difference between charring parallel or perpendicular to the grain. These results suggest that the presence of glue lines does not influence the burning behaviour of the material. Lane conducted cone calorimeter tests on LVL samples, and furnace tests on LVL members. The furnace test consisted of subjecting LVL beams to the standard ISO 834 fire [3] in a pilot furnace, and also in a full-scale furnace under loaded conditions. From this research a charring rate for New Zealand manufactured Radiata Pine LVL of 0.72 mm/min under standard fire exposure was suggested. This is similar to the charring rate of 0.70 mm/min for LVL in Eurocode 5 [4]. Further investigations conducted by Tsai et al [5] at the BRANZ facilities have drawn similar conclusions for one-dimensional charring rates of LVL.

3 EXPERIMENTAL FURNACE TESTING

Experimental furnace testing was conducted on four unprotected timber floor systems in the full-scale fire resistance furnace at the Building Research Association of New Zealand (BRANZ) facilities in 2012. The floors were one-way strip floors with pinned support conditions exposed to the ISO 834 [3] standard fire for varying durations of 30 – 105 minutes. They were loaded under standard office loading conditions of 3.0 kPa live and 1.0 kPa superimposed dead loading. Due to their combustibility, timber assemblies cannot be scaled down in size as their fire behaviour is dependent on the actual cross-section present. This required that the loads on the floor units are scaled up in such a way that similar stresses were induced in the load bearing members of the floor and the same bending moment at the mid-span of the floors was obtained. Although this disproportionately increases the shear load through the floors, care was taken in the design phase to ensure this would not cause failure.

The primary objective of the full-scale testing was to investigate the failure behaviour of the floors when exposed to fire. Vertical midspan displacements and slab temperatures were measured, along with post-furnace measurements of charring damage. Although four furnace tests were conducted, in the essence of keeping the results concise only two floors will be discussed in this paper; the intermediate sized floors for 5 – 7 m span applications. Full details of the testing regime and results of this research are presented in the available literature [6].

3.1 Floor Description

The joist floor tested was made up of two 400 mm deep $\times$ 45 mm wide LVL joists glued in a pair under a 36 mm thick $\times$ 1200 mm wide cross-banded LVL slab. The joists were fixed together in pairs to reduce the area of timber exposed to fire, thus increasing the expected fire resistance of the assembly. Figure 2 shows the underside of the joist floor immediately after a 30-minute exposure to the standard fire.

Figure 2. Furnace test of joist floor at 30 minutes.

Due to failings in the test setup, the furnace test was prematurely terminated at 30 minutes. Despite this, good measurements of displacement and charring were recorded. The box beam floor was similar in comparison to the joist floor, with a box section formed from 360 mm deep $\times$ 45 mm wide LVL joists and a 45 mm thick $\times$ 300 mm wide LVL bottom flange. This box section was fully fixed to a 36 mm thick $\times$ 1200 mm wide cross-banded LVL slab. Figure 3 shows the test of the box beam, until failure at 41 minutes.

Figure 3. Furnace test of the box beam floor at failure (41 minutes).

3.2 Charring

An average charring rate for the joist floor was measured to be 0.70 mm/min at the sides of the joist and on the bottom edge, with a slightly increased rate of charring near the bottom corners of the floor beams where two-dimensional charring was prevalent (approximately 0.80 mm/min). As the box beam floor suffered a catastrophic collapse, no charring measurements could be taken.

4 NUMERICAL MODELLING

A sequentially coupled thermo-stress analysis was conducted on each floor to determine the effects of fire on floor assemblies under load. Firstly a thermal analysis was performed to determine the temperature profile of the floor assemblies for the duration of the fire, and then a stress analysis was performed using the temperature profile as an input into the structural model. This procedure was used as the stress profile of a timber member is influenced by its temperature profile, but the converse is not true. In other words the temperature is not affected by mechanical stresses and can be computed as a separate initial step.

The software ABAQUS [7] was used for the numerical simulations. The approach taken in this research was stepwise, gradually introducing increased levels of detail into both the thermal and structural analyses. The models were constantly compared with test results where applicable to ensure reasonable output was being achieved at each step of the analysis, and also compared to the previous models used to ensure the accuracy and validity of the results and assumptions made in the modelling process.

4.1 Thermal Modelling

An integral part of the numerical modelling process is to determine the thermal profile of the timber assembly being studied under the fire exposure in question (in this case standard fire exposure). The modelling of heat transfer through timber members is complex due to the many internal processes which take place through the section and the thermal and physical changes that occur. This includes mass transfer and the movement of moisture, as well as the physical degradation of the timber member and the property changes through the heated sections of timber. In order to model the heat transfer of timber in fires, assumptions must be made to simplify these processes as long as they are made within the appropriate context and applied in an appropriate fashion from a modelling sense.

In this research the thermal profile objective was achieved by the development of a set of effective material properties based on the values prescribed in Eurocode [4], and validated against the testing conducted forming the baseline for this data [8]. As the combined effort which forms part of this research has been previously described in the literature [9], it will not be discussed further here. The full results of the thermal analysis for these floors can also be found in the Reference [6].

4.2 Structural Modelling

In order to fully account for complex thermal profiles in timber sections, three-dimensional modelling is crucial in evaluating the fire resistance of unprotected timber floor assemblies. The second step in the modelling was to conduct a stress analysis using the thermal model results as an input. Three-dimensional solid continuum brick elements were used, simulating the test conditions and making appropriate use of symmetry on the boundary conditions to reduce computational run times. In the bulk of the analyses, a cross sectional mesh size of 5 mm $\times$ 5 mm was used, with a longitudinal mesh size (along the span of the floors) of 250 mm. These were chosen as the result of detailed sensitivity studies analyzing the impact of the mesh refinement along each axis of the model [6].

After conducting a parametric study on the viability of the pre-set material models in the ABAQUS material library, the concrete damaged plasticity model was used for the analysis. It was found to have the most suitable flexibility in defining strength reduction behaviour, and was the most stable for a sequentially coupled thermo-stress analysis. An in-depth investigation into the major material properties defined in the model was conducted, including the moduli of elasticity and rigidity, Poisson’s ratio, and compression and tension strength at elevated temperatures.

5 RESULTS AND DISCUSSION

The measured vertical displacement of the floors, up to the point of runaway structural failure, was less than span/20 (200 mm) and the rate of increase of displacement was also low (until runaway failure occurred). Some common structural requirements specify deflections of less than span/20 or a limiting rate of deflection when deflection is span/30 [10]. The displacement recordings for both floors are presented in the results and discussion section of the paper.

5.1 Joist Floor Displacement and Modelling

The results of the structural simulation of the joist floor are shown in Figure 4, with the solid line representing the experimental results and the dashed line representing the numerical modelling.

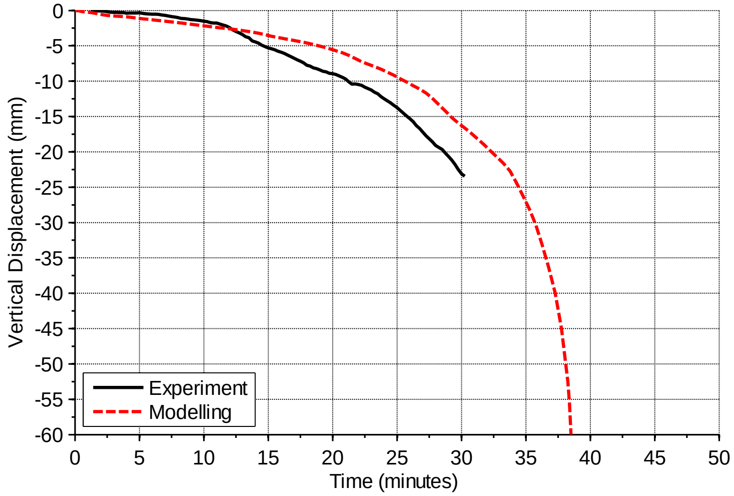

Figure 4. Experimental and modelling results of the joist floor displacement.

As the experiment terminated at 30 minutes the experimental dataset is slightly incomplete, hence the failure time of the floor can be speculated on by considering the displacement response of the floor up to 30 minutes and with comparisons to the box beam test. With this in mind, the modelling effort predicts the displacement response of the experimental results to within a margin of 20% for the entirety of the test. Failure is predicted by the model at 38 minutes.

5.2 Box Beam Floor Displacement and Modelling

A comparison of the structural model and experimental data for the box beam is shown in Figure 5, with the solid line representing the experimental results and the dashed line representing the structural modelling.

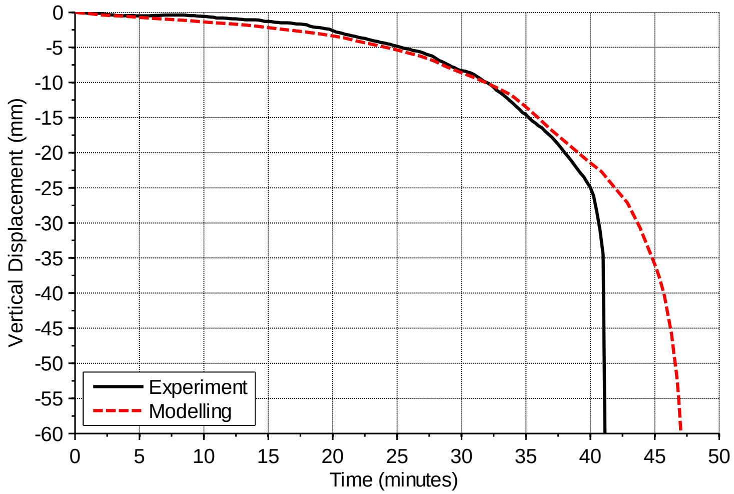

Figure 5. Experimental and modelling results of the box beam floor displacement.

Similar to the modelling results of the joist floor, the model predicts the displacement response of the experimental results for the box beam floor accurately for most of the test duration. Failure is predicted at 47 minutes. It can be seen from the latter stages of the test that the displacement response tends to be over predicted by the numerical model, while the floor displacement throughout the duration of the test (until approximately 38 minutes) is well predicted by the model. This reinforces the choices made with regards to the material properties and boundary conditions; however as seen in the figures, the strength properties of the model in these conditions do not conservatively predict the failure time of the floor.

5.3 Structural Material Model Modification

As a modification to the original material model described above, the strength reduction factor for timber in tension was changed from the value prescribed by the literature [4] of 65% at 100 ℃ to 25%. The large scatter of experimental data available on the influence of elevated temperatures on the tension strength of timber [10] emphasized the importance of varying this value from the one prescribed in the modelling. These test values are commonly derived from small scale tests considering clear specimens in pure tension. A major issue with regards to timber floors in fire is that throughout the floor section a combination of compression, shear, tension, and bending stresses act, and this is further complicated by the redistribution effects and a constantly changing stress profile due to mass loss. It is likely that the combination of stresses have a greater impact on the floor section integrity, and this tension strength reduction factor is a method for accounting for the extra unknown stresses which are not present in the small scale testing from which the data is derived from.

The modified structural modelling effort for the box beam floor is shown in Figure 6, showing both experimental and original modelling results, and the modified modelling represented by a dash-dot line.

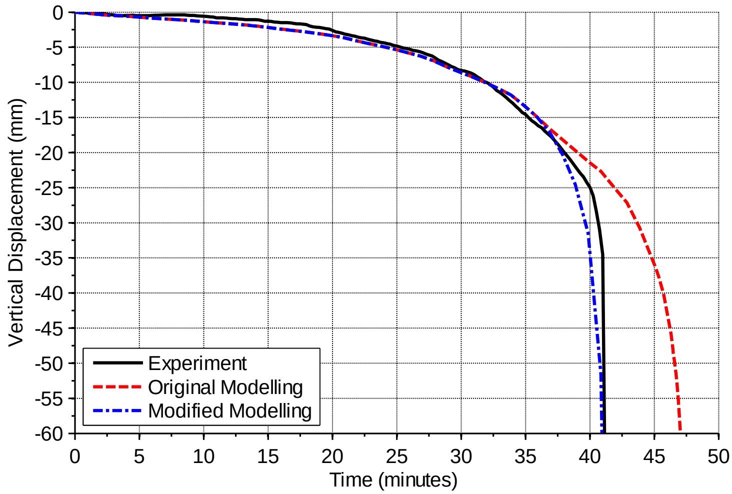

Figure 6. Experimental, modelling and modified modelling results of the box beam floor displacement.

The modified model improves on predicting the displacement of the test, resulting in a close approximation for the entire duration of the test until failure at 41 minutes. The stiffness of the experimental results is very well predicted for the duration of the simulation.

The major physical process approximated by the numerical model is mass loss primarily from the bottom of the section as the floor burns away in the fire. As the top of the slab is protected from the fire this results in the neutral axis of the section rising over the duration of the fire exposure. As the bottom elements of the floor become more slender (due to charring), the tension zone becomes the critical region for failure, and tensile and bending stresses are redistributed throughout the heated bottom portion of the floor. Failure occurs when the bottom elements can no longer redistribute these stresses and the floor begins to displace at an accelerated rate, simulating runaway failure where the ultimate capacity of the timber has been reached in the remaining bottom chord. The critical region is the tension zone as it is most highly impacted by the fire under three-sided exposure. This emphasizes the influence of strength reduction factors on the modelling output and their importance in determining failure in the simulations.

Care must be taken when deviating from prescribed values as a measure of improving modelling results. Due to the lack of available data of LVL at elevated temperatures, and the scatter of the existing values available in the literature from various testing, populating a material model with appropriate properties can be a difficult exercise. An in-depth investigation of material properties and strength reduction factors for better characterizing timber as a material in numerical software is paramount to the future of modelling timber assemblies in fire. In particular, an investigation into the plastic behaviour of timber at elevated temperatures is vital in order to populate numerical models with more adequate stress-strain data, thus enabling more appropriate estimates of strength values at elevated temperatures.

6 CONCLUSIONS

This paper describes the research efforts being conducted to sequentially model timber composite floors under fire exposure. Appropriate thermal properties were defined for the timber, verified against experimental results, allowing 3D thermal modelling to be conducted and temperature profiles of timber cross sections to be determined, as described in previous work. Sequential thermo-stress analyses have been conducted for timber composite floors in two major configurations; joist and box beam floors. These were compared to the experimental data obtained from furnace tests.

It was found that the structural model developed predicted the displacement response of the experimental floors well, but was unconservative when predicting failure times. Modifications to the material model within the structural inputs such as the maximum reduction in mechanical tension strength at elevated temperatures were found to have a significant influence on the modelling response.

REFERENCES

[1] Kolb, J., “Loadbearing Structures and Component Layers”, *Systems in Timber Engineering*, Birkhäuser Verlag AG, Basel, Switzerland, 2008.

[2] Lane W.P., “Ignition, Charring and Structural Performance of Laminated Veneer Lumber”, *Fire Engineering Research Report*, University of Canterbury, Christchurch, New Zealand, 2005.

[3] ISO, Fire Resistance Tests - Elements of Building Construction, *ISO834-1:1999*, International Organisation for Standardisation, 1999.

[4] CEN, Eurocode 5: Design of Timber Structures, Part 1-2: General - Structural Fire Design, *EN1995-1-2: 2004*, European Committee for Standardisation, Brussels, Belgium, 2004.

[5] Tsai, K., Carradine, D.M., Moss, P.J., and Buchanan, A.H., “Charring Rates for Double Beams made from Laminated Veneer Lumber (LVL)”, *Fire and Materials*, Volume 37, Issue 1, pp. 58-74.

[6] O’Neill, J.W., “The Fire Performance of Timber Floors in Multi-Storey Buildings”, *Doctoral Thesis in Fire Engineering*, University of Canterbury, Christchurch, New Zealand, 2013.

[7] ABAQUS, Version 6.10, Dassault Systèmes Simulia Corporation, Providence, RI, USA, 2010.

[8] König, J., and Walleij, L., “One-Dimensional Charring of Timber Exposed to Standard and Parametric Fires in Initially Unprotected and Postprotection Situations”, *Report I 9908029*, Swedish Institute for Wood Technology Research, Stockholm, Sweden, 1999.

[9] Werther, N., O’Neill, J.W., Spellman, P.M., Abu, A.K., Moss, P.J., Buchanan, A.H., and Winter, S., “Parametric Study of Modelling Structural Timber in Fire with Different Software Packages”, *Structures in Fire – Proceedings of the Seventh International Conference*, M. Fontana, A. Frangi, M. Knobloch, (eds.), Zurich, Switzerland, June 6-8, 2012.

[10] Buchanan A.H., *Structural Design for Fire Safety*, John Wiley & Sons Ltd, Chichester, 2001.

8th International Conference on Structures in Fire
Guo-Qiang LI, Venkatesh K. R. KODUR, Shou-Chao JIANG, Jian JIANG, Su-Wen CHEN, Guo-Biao LOU (Eds.)
Shanghai, China, June 11-13, 2014

FIRE PERFORMANCE, INCLUDING THE COOLING PHASE, OF STRUCTURAL GLUED LAMINATED TIMBER BEAMS

H. Kinjo*, S. Yusa*, T. Horio*, T. Hirashima, T. Matsumoto** and K. Saito*****

*Centre for Better Living, Tsukuba Building Research & Testing Laboratory, Japan
2 Tachihara, Tsukuba-shi, Ibaraki Pref., 305-0802, Japan
e-mail: kinjo@tbtl.org

**Chiba University, Dept. of Architecture and Urban Science, Japan

***Saito Wood Industry CO., LTD, Japan

Keywords: Glued laminated timber, Standard Fire, Load bearing capacity, Charring rate, Cooling phase

Abstract. *Timber elements, which are different from other structural elements, have a characteristic problem in that the load bearing capacity decreases due to self-burning in the case of a fire, and this self-burning may continue after other fuel in the room has been exhausted. Therefore, the structural fire performance of timber elements should be clarified during not only the heating phase, but also the cooling phase. However, in examining the load bearing capacity of timber elements in a fire, few studies have considered the cooling phase. In the present paper, the fire performance of glued, laminated timber beams is discussed based on load-bearing fire tests that take the cooling phase into consideration.*

1 INTRODUCTION

Interest in timber structures has increased from the viewpoint of a realizing a sustainable society through carbon offsets. In Japan, large timber buildings required for fire resistance have also appeared in urban areas over the past few years.

In case of fire safety engineering design of timber structures, the effective cross section method is generally used, and the charring rate of the timber exposed to fire heating is a significant factor [1]. Timber elements, which are different from other structural elements, have a characteristic problem in that the load-bearing capacity decreases due to self-burning in the case of a fire, and self-burning may continue even after other fuel in the room has been exhausted. Therefore, the structural fire performance of timber elements should be clarified not only during the heating phase but also during the cooling phase. In Japan, the criterion for fire resistance evaluation of timber elements requires the fire performance during the heating phase and the cooling phase until self-charring stops to be considered. However, there are few reports on the load-bearing capacity of timber elements that take the cooling phase after a fire into consideration.

Based on heating tests and load-bearing fire tests, the present paper discusses the charring rate, the temperature distribution in the section, and the load-bearing capacity of structural glued laminated timber beams not only during the heating phase during a 1-hour standard fire in accordance with ISO 834-1, but also during the cooling phase. Then, the fire resistance obtained as a result of the load-bearing fire tests is discussed based on the effective section method, while taking into account the heating test results for the depth of charring.

2 SPECIMENS AND TEST PROGRAM

The tree species investigated herein was the Japanese larch. The cross sections of all specimens were

210 mm (width) × 420 mm (height), and the length of specimens used in the loading tests were 6,000 mm. The thickness of each lamina was 30 mm, and 14 laminas were bonded using resorcinol-phenol resin. The strength class of all the structural glued laminated timber samples was of the same grade (composition glulam E95-F315).

Table 1 shows the test program. First, a loading test (Test 1) was carried out at ambient temperature in order to obtain the maximum load and stiffness of the structural glued laminated timber beams. Heating tests (Tests 2 and 3) were carried out in order to confirm the charring rate and the temperature distribution in the cross section of the beams. Loading tests under fire conditions were carried out in order to obtain the load-deformation behavior (i.e., the stiffness, maximum load, and ductility) of the beam. Specimen 4 was loaded just after exposure to a 1-hour standard fire. Specimen 5 was loaded after exposure to a 1-hour standard fire and 3 hours of natural cooling in the furnace (i.e., after a total of 4 hours) and was compared to Specimen 4 with respect to fire resistance. A load-bearing fire test (Test 6), which was similar to a standard fire test, was carried out in order to obtain the fire resistance duration under a constant load, which was the maximum load for Specimen 4. A load-bearing fire test (Test 7) was carried out in order to obtain the fire resistance time during the cooling phase under a constant load, which was the maximum load for Specimen 5, and the heating method of Test 7 was same as that of Test 5. All tests were carried out using the furnace for horizontal elements at the Tsukuba Building Research & Testing Laboratory Centre for Better Living.

Table 1. Test program.

Test No.	Test terms
Test 1	Loading test at ambient temperature
Test 2	Heating test (1-hour standard fire and 7 hours of natural cooling under the normal air-content)
Test 3	Heating test (1-hour standard fire and 7 hours of natural cooling under the increased air-content)
Test 4	Loading test at 1 hour (Just after exposure to 1-hour standard fire)
Test 5	Loading test at 4 hours (1-hour standard fire and 3 hours of natural cooling)
Test 6	Load-bearing fire test (constant load = the maximum load of Test 4) (Standard fire heating until the failure)
Test 7	Load-bearing fire test (constant load = the maximum load of Test 5) (1-hour standard fire heating and then natural cooling until the failure)

3 HEATING TESTS

3.1 Test setup

The temperature in the furnace was controlled to follow the ISO834 standard fire for 1 hour. The purpose of the heating tests was to investigate the charring rate and the temperature distribution in the cross section of the beams during the heating phase and the cooling phase. The charring depth of the beam was measured after 1 hour (just after exposure to the 1-hour standard fire) as well as after 2, 3, 4, and 8 hours (under natural cooling). The change in the charring rate with time was obtained based on the results for the charring depth. Figure 1 shows the heating test specimen, which was separated to into five short specimens for measurement of the charring depth at 1, 2, 3, 4, and 8 hours after ignition. The separated short specimens were thermally insulated on both sides by a ceramic fiber blanket and on the top by a fiber mixture of calcium silicate board. The length of the short specimen was 680 mm, and the charring depth was measured at two sections of the short specimen. The specimen density was approximately 0.53 g/cm^3, and the water content was approximately 11% by mass. The divided short specimens were extinguished in the water tank just after being removed from the furnace.

Figure 2 shows the cross section of the specimen, into which 18 thermocouples were installed in the three cross sections of the short specimen for the 8-hour test. In the case of a real fire, the time-temperature relationship depends on the opening factor of the fire compartment, for example, and the self-burning behavior of the timber element during the cooling phase (i.e., the decay term of the fire) may be influenced by various factors. It may be very difficult to predict the self-burning behavior of the timber element. Therefore, the influence of air conditions in the furnace on the self-burning behavior was investigated by comparing the results of Tests 2 and 3. The air-content for Test 3 during the cooling phase was increased to be approximately 130% of the air-content for Test 2 under the normal air-content condition. Figure 3 shows the time-temperature curves in the furnace for Tests 2 and 3.

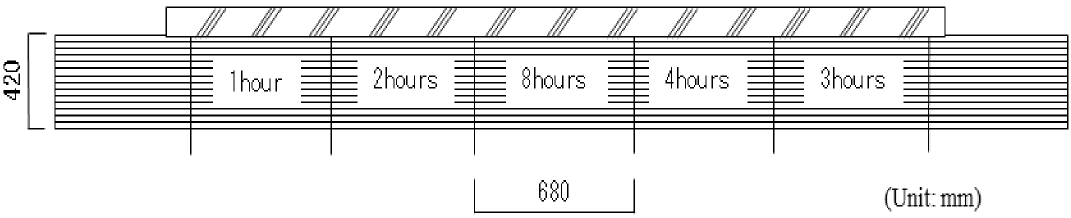

Figure 1. Global aspect of the heating test specimen which was separated to 5 short specimens.

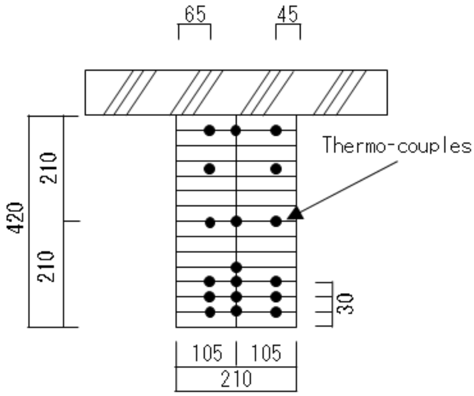

Figure 2. Cross section of the specimen. (Unit: mm).

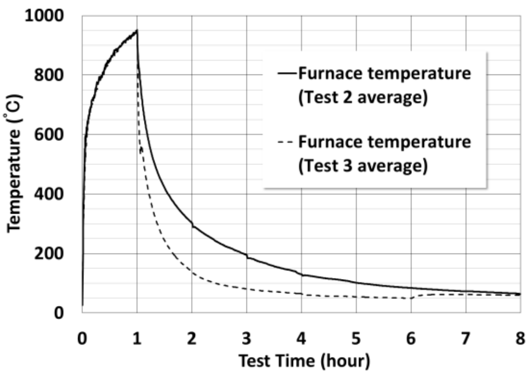

Figure 3. Time-Temperature curve (Tests 2 and 3).

3.2 Results of the charring rate and the temperature distribution

The charring rate during the heating phase, which was obtained from the charring depth of the separated specimens after heating for 1 hour, was 0.61 to 0.68 mm/min. During the cooling phase, the charring rate was near zero, except at the corners, but the dark area was spread around the heating boundary, as shown in Figure 4. This was due to gradual heat transfer in the section of the timber beam, which has low thermal conductivity, during the cooling phase. Tables 2 and 3 show the results for the charring rate. During the cooling phase, the charring rate in the height direction of the section was larger for Specimen 3 than for Specimen 2. In particular, the charring at the bottom corners was developed from observations after the tests. In the case of Test 3, partial self-burning continued for up to 112 min and almost disappeared after 240 min.

Figure 5 shows the temperatures in the section of the beam. The temperatures 30 mm from the bottom surface and at the corner reached 200 ℃ after approximately 40 min and then increased rapidly. The temperature at the centroid reached approximately 30 ℃ after 1 hour and then increased gradually, eventually reaching 100 ℃ after cooling for 4 hours. The temperature 45 mm from the surface was approximately 200 ℃, except at the corner. The temperature distributions in the sections of Specimens 2 and 3 were similar. The cross sectional temperatures began to decrease after 4 hours. All measured temperatures were within 50 to 130 ℃ after 8 hours. The temperature stagnated at around 100 ℃ due to the evaporation of the water contained in the timber specimen at the centroid and 65 mm from the surface of the side.

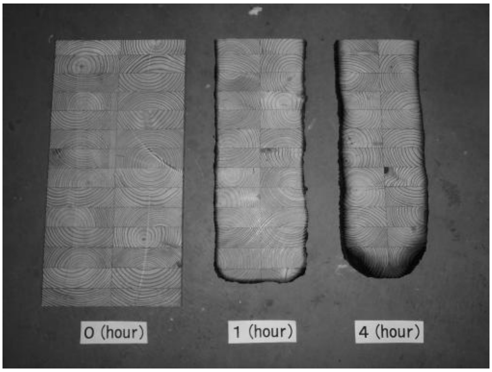

Figure 4. Change of the residual cross-section (Test 2).

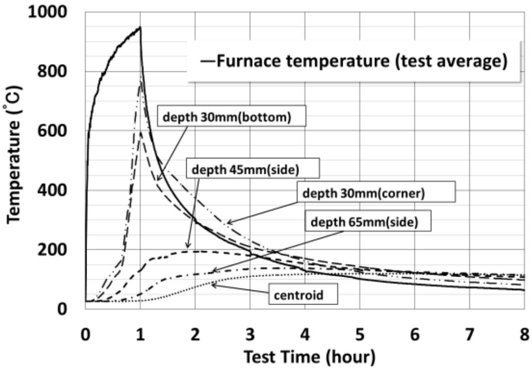

Figure 5. Temperature distribution (Test 2).

Table 2. Charring rate (Test 2).

Mean Charring rate [mm/min]		
Time	width	height
0h-1h (heating phase)	0.61	0.68
1h-2h (cooling phase)	0.05	0.06
2h-3h (cooling phase)	-0.01	0.04
3h-4h (cooling phase)	0.03	-0.01
4h-8h (cooling phase)	0.00	0.00

Table 3. Charring rate (Test 3).

Mean Charring rate [mm/min]		
Time	width	height
0h-1h (heating phase)	0.63	0.61
1h-2h (cooling phase)	0.00	0.08
2h-3h (cooling phase)	0.02	0.10
3h-4h (cooling phase)	0.02	-0.05
4h-8h (cooling phase)	-0.01	0.00

4 LOADING TEST AND LOAD- BEARING FIRE TESTS

4.1 Specimens and test setup

Figure 6 shows the test setup for the loading tests and load-bearing fire tests. The specimens are described in detail in Section 2. The distance between supports was 5,400 mm, and the heated length was 4,000 mm. The distance between two loading points was 1,800 mm. The vertical displacements through the length of the beam were measured by wire-type transducers. The finger-joints of all laminas were located to the outside of the constant-bending-moment zone (i.e., the maximum bending moment zone). The temperature of the furnace was controlled to follow the ISO834 standard fire for 1 hour. The objects of loading tests (Tests 1, 4, and 5) and load-bearing fire tests (Tests 6 and 7) are described in Section 2.

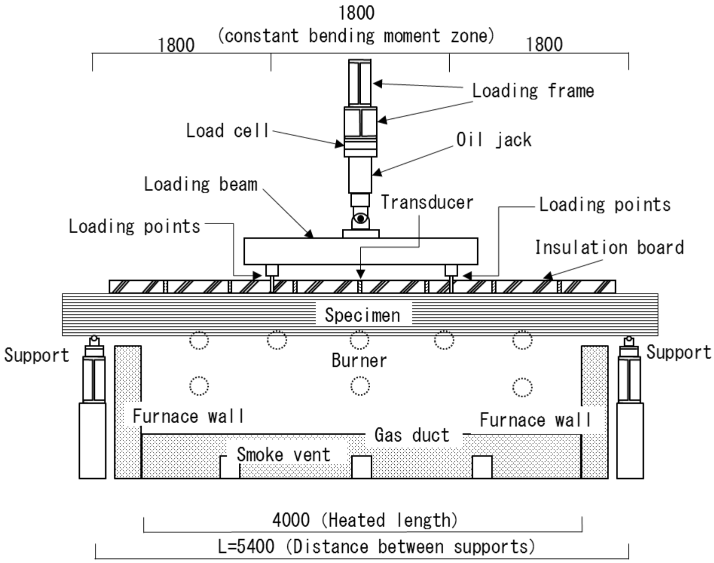

Figure 6. The specimen and test setup. (Unit: mm).

4.2 Load-deflection behavior

Figure 7 shows the load-deflection behavior. The maximum bending moment at the mid-span of Specimen 1 (at ambient temperature) was 262.8 kNm, which is 1.35 times the design bending resistance. The failure occurred from the bottom laminas in the constant-bending-moment zone for tension (i.e., bending failure). The extreme fiber strains at the top and bottom at the mid-span of the beam was approximately $\pm 4{,}000 \times 10^{-6}$. The maximum load of Specimen 4, which was exposed to a 1-hour standard fire, was reduced to approximately 30% of the maximum load of Specimen 1. The maximum load of Specimen 5, which was exposed to a 1-hour standard fire and 3 hours of natural cooling in the furnace, was reduced to approximately 14% of the maximum load at ambient temperature of Specimen 1. The deflections at the mid-span of the beams (Specimens 1, 4, and 5) at their maximum loads were within 50 to 65 mm. The stiffness of the timber beams decreased considerably, but their ductility did not increase. Figure 8 shows the aspect of Specimen 5 after the test. Specimens 4 and 5 failed from the bottom lamina, as was the case for Specimen 1 (i.e., bending failure). However, the influence of shear force was also considered because Specimen 5 failed outside the constant-bending-moment zone.

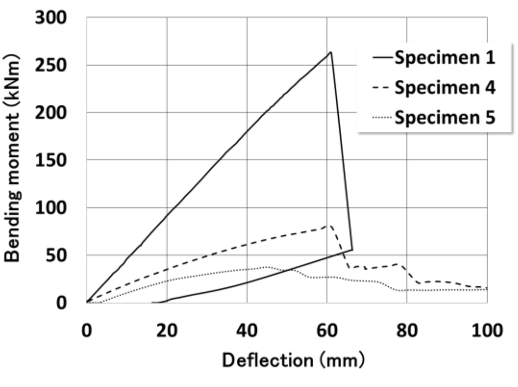

Figure 7. Bending moment-deflection behaviour.

Figure 8. Aspect of Specimen 5 after the test.

4.3 Deflection behavior under constant load in fire

Figures 9(a) and 9(b) show the deflection behavior under constant load in fire. In Figure 9, the deflection of both specimens increases due to heating. The fire resistance time was 79 min, based on the load-bearing fire test (Test 6). Specimen 6 maintained maximum loading strength for 1 hour after heating. In Test 7, the failure time was 121.5 minutes, which was approximately 1 hour after heating was stopped. In Specimen 7, the deflection rate did not decrease after end of heating. Specimen 7 carried out maximum loading strength for 1 hour of heating and 3 hours of cooling; however fire resistance time was reduced to half that of Specimen 5. Figures 10(a) and 10(b) show the failures of Specimens 6 and 7, respectively. Specimen 6 failed in bending. Specimen 7 may have failed due to excessive shear because the bottom lamina did not fail and an axial gap between the laminas at the centroid axis was observed. The adhesive (i.e., resorcinol-phenol resin) used for the specimens has excellent fire resistance characteristics [2], although the test results did reveal some degradation in the performance of the adhesive.

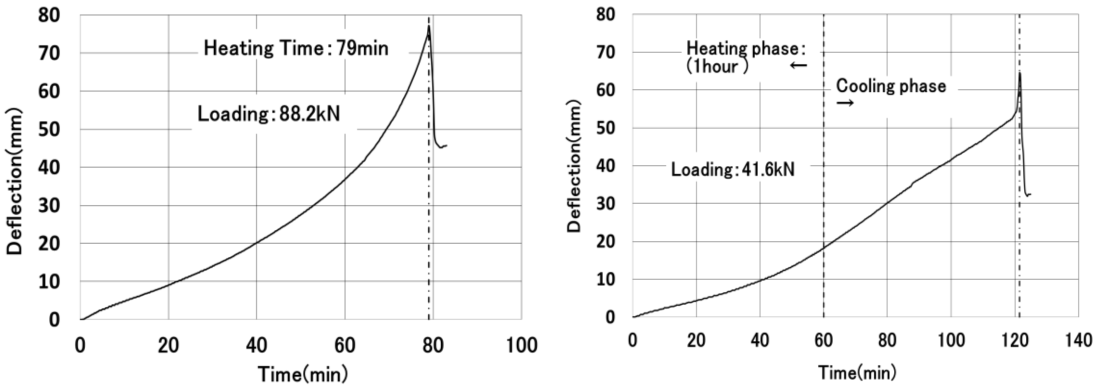

(a) Test 6 (b) Test 7

Figure 9. Deflection behaviour under constant load in fire.

(a) Global aspect of Specimen 6 (b) Failure cross section of Specimen 7

Figure 10. The failure of the specimens for the load-bearing fire test.

4.4 Approximation of fire resistance based on the effective cross section method

Figure 11 shows the reduction ratios of the bending resistance obtained experimentally and through calculations based on the effective cross section method with the charring depth obtained from the heating test results (Specimen 2) and an ineffective dark area depth of 7 mm [3]. The calculation results for the reduction in strength for 1 hour of heating were in fair agreement with the results for Specimens 4 and 6. However, in case of the cooling phase, the experimental values were lower than the calculated values. In particular, the experimental value (Specimen 5) including the cooling phase, was less than half that of the calculated value. The temperature over the entire effective cross-sectional area increased after heating, and the temperature exceeded 100 ℃ after 4 hours. The load-bearing capacity of the timber beam in the fire, including the cooling phase, might be influenced by the reduction in strength of the effective cross section. Therefore, material tests were carried out in order to determine the reduction in strength of the timber at approximately 100 ℃. Compression and tension tests were carried out at temperatures of up to 150 ℃. Figures 12 and 13 show the reduction factors from the results of the compression and tension tests. At ambient temperature, the compression strength was 48.8 N/mm^2 and the tensile strength was 42.9 N/mm^2. These values were the averages of two material tests at ambient temperature. The reduction factor in compression was 92% at 150 ℃, and the reduction factor in tension was 57% at 150 ℃. If the strength reduction factor of the effective cross section at 4 hours was assumed to be 57%, the calculated bending resistance of the timber beam was 57.1 kNm. However, this value exceeds the resistance results obtained in Test 5 (see Figure 7). An approximation method of the fire resistance of timber elements including the cooling phase should be investigated in the future.

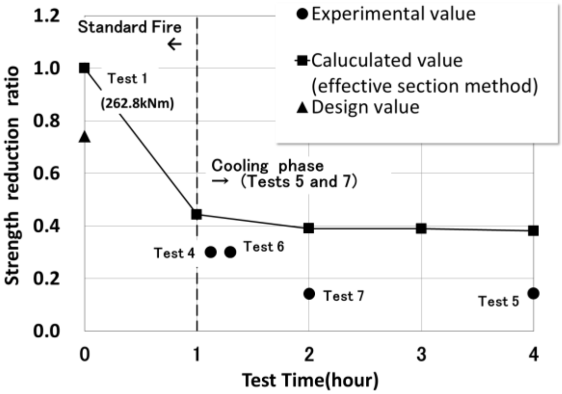

Figure 11. Comparison with the strength reduction ratio.

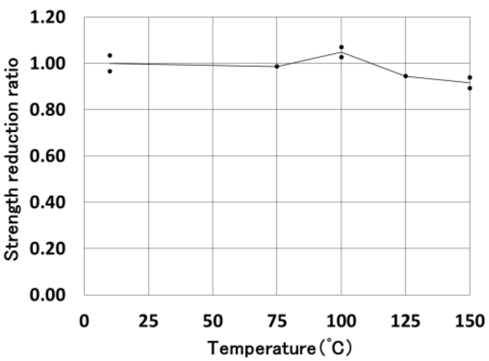

Figure 12. Reduction factor in compression.

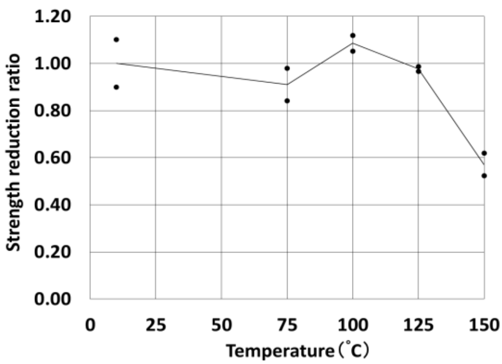

Figure 13. Reduction factor in tension.

5 CONCLUSIONS

The present paper described the fire performance, including the cooling phase, of structural glued laminated timber beams. The main conclusions were:

(1) Charring rate and the temperature distribution:
The charring rate during the heating phase, which was obtained from the charring depth of the separated specimens after heating for 1 hour, was 0.61 to 0.68 mm/min. During the cooling phase, specifically after 2 hours, the charring rate was approximately zero, except at the corners, although a dark area had spread around the heating boundary. The temperature at the centroid reached approximately 30 ℃ after 1 hour and then increased gradually until reaching 100 ℃ after 4 hours, during the cooling phase.

(2) Load-deflection behavior and deflection behavior under constant load in fire:
The maximum load and stiffness of the timber beams decreased considerably in fire, but their ductility did not increase. The maximum load of the specimen exposed to a 1-hour standard fire was reduced to approximately 30% of that of the specimen at ambient temperature. And the maximum load of the specimen exposed to a 1-hour standard fire and 3 hours of natural cooling in the furnace was reduced to approximately 14%. In case of the specimen for the load-bearing fire test including the cooling phase, the deflection rate did not decrease after end of heating and shear failure occurred at approximately 1 hour after heating was stopped.

(3) Approximation of the fire resistance based on the effective cross section method:
The calculation results for the strength reduction during heating for 1 hour were in fair agreement with the test results. However, in the case of the cooling phase, the experimental values were lower than the calculated values. In particular, the experimental value including the cooling phase was less than half that of the calculated value. The load-bearing capacity of the timber beam in fire, including the cooling phase, might be influenced by the reduction in the strength of the effective cross section. An approximation method of the fire resistance of timber elements including the cooling phase should be investigated in the future.

ACKNOWLEDGEMENT

The authors would like to acknowledge Sansei-Giken Co., Ltd. for producing the specimens.

REFERENCES

[1] Architectural Institute of Japan, “Guide book for fire-resistive performance of structural materials”, 1st edition 2004, 2nd edition 2009. (in Japanese)

[2] Harada T., Miyatake A., Kamikawa D., Hiramatsu Y., Shindo K., Inoue A., Miyamoto K., Tohmura S., Hatano Y., Miyabayashi M., “Temperature Dependence of Adhesive Strength and Fire Resistance of Structural Glued Laminated Timber Beams” Japan Wood Research Society. Vol.59, No.4, 219-226, 2013. (in Japanese)

[3] BS EN1995-1-2: 2004, Eurocode 5 Design of timber structures, Part 1-2: General-Structural fire design.

8th International Conference on Structures in Fire
Guo-Qiang LI, Venkatesh K. R. KODUR, Shou-Chao JIANG, Jian JIANG, Su-Wen CHEN, Guo-Biao LOU (Eds.)
Shanghai, China, June 11-13, 2014

FULL SCALE TESTS OF TIMBER BOX BEAMS IN FIRE CONDITIONS

Reuben S. Costello*, Anthony K. Abu*, Peter J. Moss* and Andrew H. Buchanan*

* Department of Civil and Natural Resources Engineering, University of Canterbury, New Zealand
e-mails: reuben.costello@pg.canterbury.ac.nz, tony.aby@canterbury.ac.nz, peter.moss@canterbury.ac.nz, andy.buchanan@canterbury.ac.nz

Keywords: Post-tensioned timber, Full-scale furnace test, LVL, ISO834

Abstract. *Post-tensioned timber is a construction technique that has been developed in recent years and, when utilised in new buildings, can lead to significant advantages, including improved lateral load resistance. However the thin webs used in post-tensioned timber box beams can result in high shear stresses in the webs. No reported test results have identified shear strength as a particular problem except in severe fire exposure, hence the need for this study.*

1 INTRODUCTION

Timber is a combustible material and as such is restricted for use as a building material by many standards and building regulations throughout the world. However, timber structures can perform well in fires and provide very good fire-resistance [1]. Recent research into post-tensioned timber structures has shown that these members also perform well in fires [2, 3]. However, shear failures are possible, because the post-tensioning increases the flexural capacity but not the shear capacity of the beams. As a result of this observation, this research specifically investigates shear performance of post-tensioned timber box beams in fire conditions.

2 POST-TENSIONED TIMBER CONSTRUCTION

Post-tensioning uses high-strength steel tendons that are stressed during construction to apply a compressive stress to the member in order to increase the strength of the member, reduce deflections and to tie adjacent members together [4, 5, 6]. Box beams, as shown in Figure 1, made from Laminated Veneer Lumber (LVL) allow a very efficient use of engineered timber materials. Similar beams can be made from glue laminated timber (glulam), cross-laminated timber (CLT) or other engineered wood. The major benefit of post-tensioned timber construction is a significantly improved seismic performance with little or no residual damage to the structure following a large earthquake. This is achieved through the use of a post-tensioning system which allows "controlled rocking" [7].

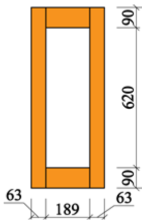

Figure 1. LVL box beam cross section.

Highly-optimised box beams are susceptible to shear failure because the box members utilise relatively thin webs so there is relatively little shear capacity at the centroid of the beam, i.e. in the web, at the location of maximum shear stress. This is further amplified in fire conditions as the beam chars, further reducing the thickness of the webs, and therefore reducing the shear capacity of the beam [8]. Failure in box beams had previously been demonstrated in full scale furnace tests conducted by Spellman [2, 3], as shown in Figure 2.

Figure 2. Box beam following failure during a full scale furnace test. [2]

Post-tensioning tendons can be either straight or draped. Draped tendons, where the eccentricity of the tendon varies along the length of the beam, allows for a more efficient design, as shown in Figure 3 for a two-bay frame. Draped tendons provide an additional benefit in that the shear demand on the member is resisted along the length of the inclined tendon, as a vertical component of the tendon force. This does not apply for straight tendons however, as the tendon force does not act vertically anywhere along the length of the beam. This paper considers box beams with straight tendons only as this is the worst case for shear failure.

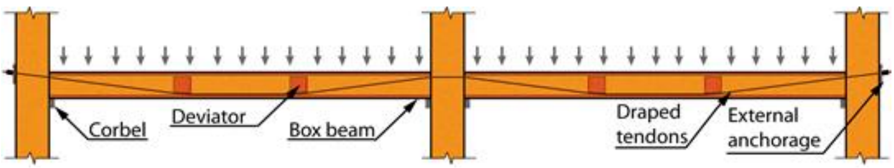

Figure 3. Moment resisting frame in post-tensioned timber building using draped tendons. [8]

4 SIMPLIFIED CALCULATION METHOD

Costello et al. [9] previously proposed a simplified calculation method to determine the fire resistance of post-tensioned box beams. The proposed method aimed to provide a simple and clear process that enables designers to calculate the fire resistance of post-tensioned timber members. Furthermore, the method presents a process that can be used to incorporate the benefits of the post-tensioning system during a fire, which may lead to more efficient structures being designed.

The simplified calculation method is based on completing a series of design calculations to ensure that the design capacity of the member is greater or equal to the design action effect on the member being considered. Equation (1), taken from AS/NZS 1170.0:2002 [10], is the general form of the inequality that must be satisfied for each design action.

$$E_{\mathrm{d}} \leq R_{\mathrm{d}} \tag{1}$$

The design actions considered in the simplified calculation method are bending, shear force, axial force, compressive stress, tensile stress, compressive bending stress, tensile bending stress and combined axial and bending capacity.

Two design strategies can be used in the fire safety design for stability of post-tensioned timber buildings. The first strategy relies on the residual timber only to resist the applied loads during a fire, so the steel post-tensioning components do not need to be protected. The second strategy involves protecting all of the steel components used in the post-tensioning system, i.e. tendons, anchorages etc., so that the effect of the post-tensioning system can be considered when assessing the structural performance of the building in fire conditions. Further detail of the strategies, including design considerations and advantages and disadvantage is presented by Costello [8] and Costello et al. [9].

5 FURNACE TEST

As discussed in Section 3, Spellman [2, 3] concluded that shear failure in post-tensioned timber box beams needed to be investigated in detail. Spellman's conclusion was the catalyst that directly led to this test being conducted. Consequently, this test was designed so that a shear failure mode occurred.

The two objectives of the full scale furnace test of a post-tensioned LVL box beam were:

(1) To investigate the behaviour of post-tensioned LVL box beams, specifically the shear performance.

(2) To obtain data to validate the proposed simplified calculation method discussed in Section 4.

5.1 Test set-up

The test was conducted in accordance with ISO 834 [11] at the Building Research Association of New Zealand (BRANZ) fire lab, as shown in Figure 4(a). A masonry block surround, precast concrete lids and a light timber frame were used to enclose the furnace above the test specimen. A loading frame consisting of a strong beam, 500 kN jack and spreader beam, was used to create a four-point loading arrangement, as represented in Figure 4(b).

Figure 4 (a). Full-scale furnace at BRANZ.

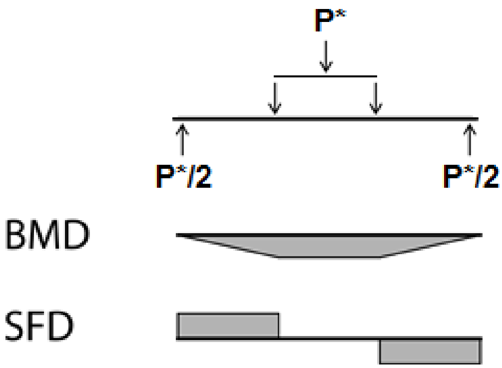

Figure 4(b). Loading arrangement for furnace test.

A 5.0 m long LVL box beam was tested. The span of the beam in the test frame was 4.2 m. The cross section of the beam is shown in Figure 5. This cross section, in conjunction with the loading arrangement, was designed so that shear failure would occur prior to any other failure mode.

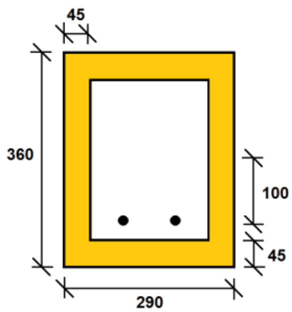

Figure 5. Cross section of box beam used in the furnace test.

Two 12.7 mm tendons were used as post-tensioning in the test specimen, placed 100 mm below the centroid of the section, i.e. the initial tendon eccentricity was 100 mm. The total tendon force was 107 kN. The loading jack applied a 100 kN vertical load to the spreader beam system which transferred the load to the LVL beam. Three thermocouples were attached to each tendon to record the tendon temperatures, located at mid-span and 1.5 m from the each end of the beam, 700 mm inside the furnace. Thermocouples were also attached to the inside surface of the beam 1.2 m from each end of the beam, i.e. 400 mm inside the furnace, to record the temperature of the inner surface layer of the timber. Mid-span deflection was measured using a potentiometer.

5.2 Results

5.2.1 Predicted behaviour

The performance of the LVL beam was predicted using the simplified calculation method described in Section 4. An expected failure time of 29 minutes was calculated. The normalised demand on the beam, i.e. the demand divided by the respective residual capacity for each of the loading actions, was calculated for the duration of the fire. This is graphically represented in Figure 6, which shows that this beam is much more critical in shear than in bending or axial load and so shear failure was predicted to govern.

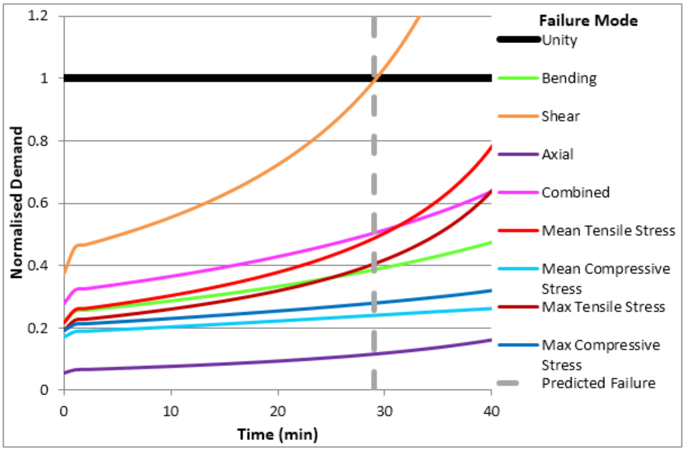

Figure 6. Normalised demand of LVL beam during furnace test.

5.2.2 Experimental results

A shear failure occurred 29 minutes after the start of the test. The deflected shape of the failed beam, seen in Figure 7, illustrates that shear failure occurred in the region between the loading point and the beam support. Six major horizontal cracks occurred across the entire depth of the beam at regular intervals of approximately 40 mm. The cracks were largest under the loading point, which also corresponded with the maximum localised deflection. The shear cracks were approximately 1000 mm in length. The shear cracks did not extend into the timber at the support, i.e. the timber that had been protected from fire exposure by the test frame was not charred. This timber was also not charred in the region of timber that had been milled so was 45 mm thick. It is this thicker timber that provided additional shear reinforcement that prevented the shear cracks from propagating to the end of the beam.

Figure 7. Tested beam after shear failure.

5.3 Discussion

The failure time predicted using the simplified calculation method was within one minute of the test failure time. The simplified calculation method also predicted the failure mode of the beam. This result demonstrates the validity of the proposed simplified calculation method.

It should be noted that only one full-scale fire test was conducted and the reproducibility of testing may result in variations to the accuracy of the predictions. However, it is expected that any differences between the calculation method and additional test results will be small.

6 AMBIENT TEMPERATURE TESTS

Four ambient temperature tests were also conducted on the basis of Spellman's conclusion that shear failure in post-tensioned timber box beams needed to be investigated in detail. The ambient temperature tests were conducted instead of multiple full scale furnace tests, for reasons of cost and time. Each of the ambient temperature tests were designed so that a shear failure occurred.

The two objectives of the full scale ambient temperature tests of LVL box beams were:

(1) To investigate the behaviour of LVL box beams, specifically the shear performance.

(2) To obtain data to validate the simplified calculation method discussed in Section 4.

6.1 Test set-up

The tests were conducted in an Avery Universal Testing machine which has a 1000 kN capacity. As per the furnace test, a four-point loading arrangement was used. The applied loads and mid-span deflections were recorded for each test.

The dimensions of the each of the four LVL beams tested are shown in Figure 9. The beam used in Test 2 incorporated post-tensioning while the remaining tests did not. The webs and bottom flanges of the LVL beams used in Tests 2 and 4 were milled along the length of the beams. Milling the webs and bottom flange simulated three sided charring that would occur in a fire if the top surface of the beam is not exposed to fire, e.g. protected by the floor above. The depth of the milling was 28 mm, which corresponds to the char layer depth for a 30 minute fire using an assumed char rate of 0.7 mm/min plus a zero strength layer of 7.0 mm. The dimensions shown in Figure 9 are those after the milling had been carried out.

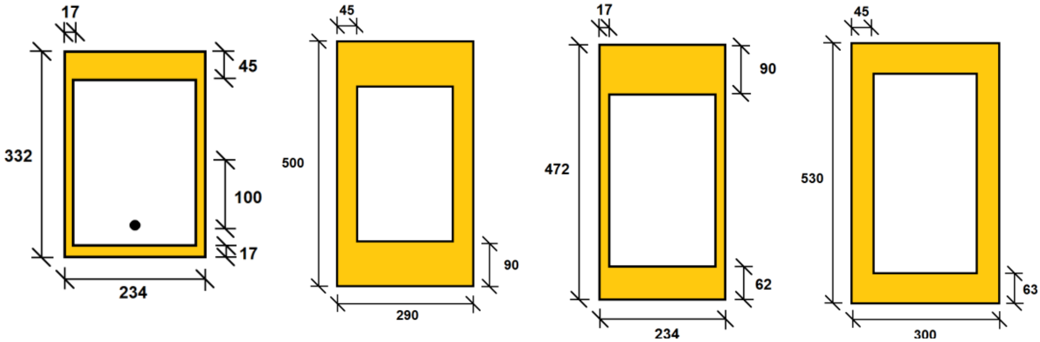

(a) Test 2 (b) Test 3 (c) Test 4 (d) Test 5

Figure 9. Cross section of LVL beams used in ambient temperature tests.

6.2 Results

Shear failure occurred in each test. For example see the location of the cracks in Test 5, in Figure 10. The largest cracks in each test propagated from one end of the beam, which corresponds with a shear failure. The width and length of the cracks were proportional to the failure load of the beam, i.e. larger and longer cracks were observed in beams with higher failure loads.

Figure 10. Major cracks observed in Test 5.

The force–deflection behaviour of a representative test, Test 2, is shown in Figure 11. Table 1 summarises the predicted elastic and actual mid-span deflection at failure and failure loads for each of the tests. Except for Test 4, the actual failure load was approximately 30% greater than predicted in the ambient temperature tests. This corresponded to a shear stress of approximately 7.0 MPa for these three tests, which is significantly higher than the characteristic shear stress of 5.3 MPa given by the manufacturer of the LVL. Similarly, the actual mid-span deflection at failure was significantly under-predicted in all four tests, by as much as 170%.

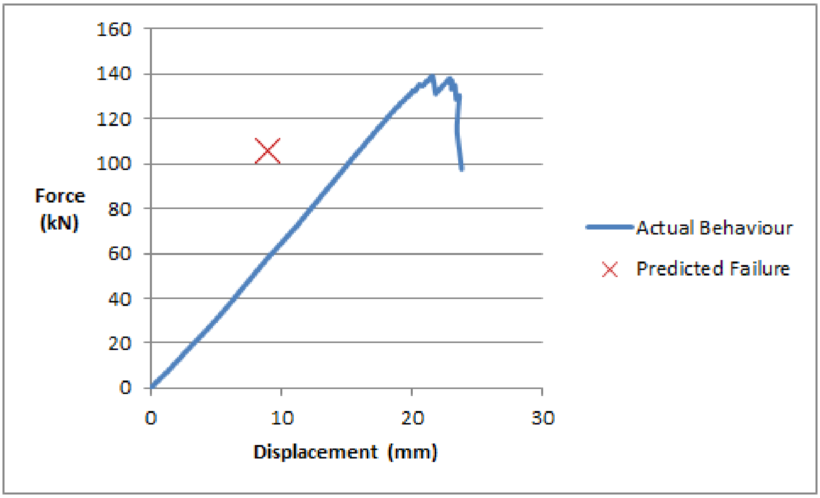

Figure 11. Force-deflection behaviour of Test 2.

Table 1. Predicted and actual behaviour of ambient temperature tests.

Test	Predicted mid-span deflection	Predicted mid-span deflection	Predicted failure load	Actual failure load	Shear stress at failure
2	9 mm	22 mm	106 kN	138 kN	7.0 MPa
3	13 mm	24 mm	364 kN	473 kN	6.9 MPa
4	9 mm	16 mm	146 kN	147 kN	5.3 MPa
5	8 mm	21 mm	392 kN	515 kN	7.0 MPa

6.3 Discussion

The four ambient temperature tests were specifically designed using the proposed simplified calculation method so that the beams failed in shear. All failures were shear failures, which demonstrates that the simplified calculation method is an accurate method of predicting the behaviour of LVL box beams, with and without post-tensioning.

The technique of milling that was used to "char" the specimens used in the ambient temperature testing is an effective method to accurately simulate furnace tests. The tolerance of the milling process was within 1 mm, which allowed the shear strength of the member to be accurately calculated. However, this technique is labour and time intensive and requires a skilled operator with an appropriate machine to complete the work. The cost savings achieved by simulating a charred section using a milling machine, compared to the relatively high cost of conducting a full scale furnace test, must be considered when choosing a testing methodology.

There were significant variations in the shear strengths of the beams used in the tests. The shear strength of the beams used in three tests was approximately 7.0 MPa, which is significantly higher than the characteristic shear strength published by the LVL manufacturer (5.3 MPa). The fact that the actual shear strength was greater than the characteristic shear strength was expected as the published strength is a 5% characteristic value, derived with 75% confidence, so the mean strength of the member is expected to be higher. However, the magnitude of the increased shear strength was unexpected. van Beerschoten [12] found that the characteristic shear strength of 45 mm LVL samples is 6.0 MPa, which is also lower than the shear strength of the beams used in the ambient temperature tests. Further investigation of the shear strength of LVL should be conducted. The use of cross-banded LVL should be considered because this will have higher shear strength. Another option is to use CLT panels as webs of timber box beams.

7 CONCLUSIONS

Five full-scale tests of LVL box beams, including two post-tensioned LVL box beams were conducted. A shear failure mode occurred in each of the five test specimens, specifically in the webs of the beams. These are the first known occurrences of shear failure in LVL box beams. The failure loads predicted using the simplified calculation method were reasonably close to the actual failure loads. However, the mid-span deflections were under-predicted by the simplified calculation method.

The milling technique that was used to simulate charring of the LVL beams is an effective method to accurately simulate furnace tests, although it is labour intensive. This technique should be considered when conducting future full-scale tests.

Further research is needed to investigate the shear strength of timber box beams. The results are expected to apply to other engineered wood materials such as glulam and CLT, but full scale furnace testing are recommended to provide more insight into the behaviour of these members. A detailed numerical model of the behaviour of post-tensioned timber structures in fire conditions should be the main tool for future research on this subject, after calibration with full-scale fire tests.

REFERENCES

[1] Buchanan A.H., *Structural Design for Fire Safety*, John Wiley & Sons Ltd, Chichester, 2001.

[2] Spellman P.M., *The Fire Performance of Post-Tensioned Timber Beams*, MEFE Thesis, University of Canterbury, Christchurch, New Zealand, 2012.

[3] Spellman P.M., Abu A.K., Carradine D.M., Moss P.J. and Buchanan A.H., "Design of Post-Tensioned Timber Beams for Fire Resistance", *Structures on Fire – Proceedings of the Sixth International Conference*, Fontana M., Frangi A. and Knobloch M. (eds.), ETH Zurich, Switzerland, 427-436, 2012.

[4] Palermo A., Pampanin S., Buchanan A.H. and Newcombe M., "Seismic Design of Multi-Storey Buildings using Laminated Veneer Lumber" *New Zealand Society of Earthquake Engineering Conference*, Wairaki, New Zealand, 11-13, 2005.

[5] Newcombe M., *Seismic Design of Multistory Post-Tensioned Timber Buildings*. ME Thesis, University of Pavia, Pavia, Italy, 2007.

[6] Buchanan A.H., Palermo A., Carradine D.M. and Pampanin, S., "Post-tensioned timber frame buildings", *The Structural Engineer*, 89, 24-30, 2011.

[7] Pampanin S., "Emerging Solutions for High Seismic Performance of Precast/Prestressed Concrete Buildings", *Journal of Advanced Concrete Technology*, 3, 207-223, 2005.

[8] Costello R.S., *The Fire Performance of Post-Tensioned Timber Buildings*, MEFE Thesis, University of Canterbury, Christchurch, New Zealand, 2013.

[9] Costello R.S., Abu A.K., Moss P.J. and Buchanan A.H., "Simplified Calculation for Fire Performance of Post-Tensioned Timber Box Beams", *Fire Safety Science - Proceedings of the Eleventh International Symposium*, van Hees P., Jansson, R. and Nilsson, D. (eds.), IAFSS, 2014.

[10] Standards New Zealand, *AS/NZS 1170.0:2002 Structural Design Actions Part 0: General principles*, Standards New Zealand, Wellington, New Zealand, 2002.

[11] ISO, *ISO 834-1975 Fire resistance tests - elements of building construction,* International Organization for Standardization, 1975.

[12] Van Beerschoten W., *Structural Performance of Post-tensioned Timber Frames under Gravity Loading,* PhD Thesis, University of Canterbury, Christchurch, New Zealand, 2013.

FULL SCALE FIRE TESTS OF TIMBER- FRAMED BUILDINGS

Magdaléna Dufková* and Petr Kuklík*

*Czech Technical University in Prague
e-mail: kuklik@fsv.cvut.cz, magdalena.dufkova@fsv.cvut.cz

Keywords: Light timber frame assembly, Real fire, Charring rate, Claddings

Abstract. *The paper is focused on an experimental fire test of timber-framed buildings. The experimental fire test was carried out in the premises of the PAVUS, a. s. company in Veselí nad Lužnicí in July 2013. The main reason of this experimental fire test were research purposes and also to show the behaviour of a timber construction as a whole (including joints, openings) exposed to a real fire to the general public. An increasing interest in timber structures leads to the necessity of a more thorough examination of their behaviour under fire. Eurocode 5 (EN 1995-1-2) allows calculating the fire resistance of timber structures, this code, however, resolves this issue in a simplified way and may only be applied to a limited scope of claddings. Such experiments are indispensable for scientific research and associated development of new analytical and numerical models.*

1 INTRODUCTION

The testing of fire resistance is governed by European test standards for fire tests in laboratories, where the temperature rise in most cases follows the nominal temperature-time curve. Unlike the simulation of a real fire, the calculation of the fire load is followed by parametric temperature-time curves. The computational procedures specified in Eurocode 5 [4] relate to a nominal fire. For a parametric fire, there is Annex A to this standard, but the procedures are applicable only for unprotected timber structures. The goal of this paper is to describe the behavior of timber structures under a real fire.

2 FIRE TEST OF TWO TIMBER-FRAMED BUILDINGS

The simulation of a real fire on a light timber frame construction was prepared for load bearing structures under live load and a temperature rise in accordance with a parametric fire. The object of this experiment were two single-storey buildings. The dimensions of two test objects were 3 × 3 m with a uniform height of 3 m. The compositions of individual walls, including fillings, were varied. In Figure 1, the picture of the timber buildings can be seen. In Figure 2, there is ground plan and cross section of the experimental objects.

Figure 1. Experimental single-storey buildings in Veselí nad Lužnicí.

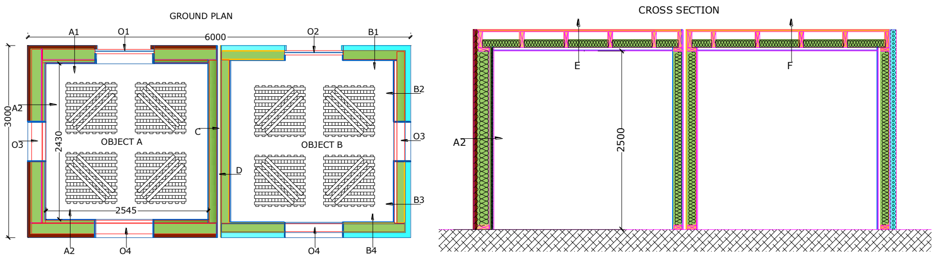

Figure 2. Ground plans and cross sections of experimental objects.

2.1 Object A

Object A was built using diffusion-open assemblies with an insulation system of Inthermo fiberboard (reaction to fire class of E according to [1]). The constructions were made of light timber frame wall and floor assemblies, where timber studs are covered from both sides by some type of claddings (plasterboard, gypsum fibre, chipboard and OSB). Rock wool was used as insulation between the timber studs. The timber studs in wall assemblies had dimensions of 60/160 mm, while the timber studs in the floor assembly had dimensions of 60/220 mm. There were 3 openings in the object, two of them were unfilled (O3 – 600/1 350 mm, O4 – 900/2 100 mm) and one of them was filled (O1 - aluminium fire window 900/1 350 mm), the openings are marked in Figure 2.

2.2 Object B

Object B was made using diffusion-closed assemblies with an insulation system of EPS 70F polystyrene (reaction to fire class of E according to [1]). The constructions were made of light timber frame wall and floor assemblies with the same type of claddings as in object A. Rock wool (in the floor assembly and wall assemblies B1, B2, D) and glass wool (in the wall assemblies B3, B4) were used as insulation between the timber studs. The dimensions of timber studs were the same as in object A. There were 3 openings in the object, two of them were unfilled (O3 – 600/1 350 mm, O4 – 900/2 100 mm) and one of them was filled (O2 - normal plastic window 900/1 350 mm), the openings are marked in Figure 2.

3 FIRE AND MECHANICAL LOAD

The simulation of a real fire was made for load-bearing constructions under imposed loads and a rise in temperature according to a parametrical fire [3].

Mechanical load was designed as for a normal family house, where the variable (imposed) load equals 1.5 kN/m^2. In a fire situation, it is statistically verified that mechanical load is less than the maximum value. On the grounds of this, the quasi-permanent value of variable load ($\psi_{2,1} = 0.3$) for accidental design situations under a fire was used in the calculation. The variable load was imposed using gravel bags, which were placed uniformly on the roof (Figure 3), the load being 0.45 N/m^2. Dead load was formed by the roof construction.

Figure 3. Mechanical loads.

Figure 4. Fire loads.

Fire load was created using timber laths with average moisture of 12 %, Figure 4. The fire load of a common house is defined by the average value $q_{f,k}$ = 780 MJ/m^2. Under the piles of timber laths, there were thin-walled steel C profiles. These profiles were filled by mineral wool and kerosene for an easier initiation of a fire.

4 MEASUREMENT OF TEMPERATURES

Object A:

- 8 pieces of the thermocouples placed in the walls (2/3 of the height);
- 4 pieces of the thermocouples placed in the floor;
- 2 pieces of the thermocouples for measuring temperature in the object (0.5 m below the ceiling);

Object B:

- 14 pieces of the thermocouples placed in the walls (2/3 of the height);
- 4 pieces of the thermocouples placed in the floor;
- 2 pieces of the thermocouples for measuring temperature in the object (0.5 m below the ceiling);

The measurement of temperature patterns by thermocouples was provided by the PAVUS, a. s. accredited fire testing laboratory. Furthermore, the temperature was measured in detail using a thermo camera.

Both objects were set on fire at the same time. In both objects, there were two openings which provide an adequate air supply and one opening with a window (Object A: aluminium fire window, Object B: normal plastic window).

4.1 Comparison of real temperatures with temperature-time curves

The fire was extinguished after 30 minutes. In Figure 6, the development of a real temperature in the object in comparison with the nominal and parametrical temperature-time curve and the zone model are displayed. Maximum temperatures for each curve are highlighted in the graph (Figure 6) for 30 minutes.

The nominal temperature-time curve (fire testing according to standard [2]) is usually on the safe side compared with the natural progress of fire. This assumption was disproved by the experiment. It was demonstrated that at a higher initial temperature with sufficient air supply (it was a summer day, about 35 °C) and other factors positively influencing the combustion, the temperature may reach substantially higher values. To get more accurate information about the fire compartment, it is appropriate to use a parametrical temperature-time curve, a zone model or FDS simulation (Figure 5).

Object A: The real fire showed higher temperatures than the nominal temperature-time curve. For this reason, it can be assumed that the function of individual fire claddings will be lower. The temperature until the 4th min. was lower than the nominal curve. The temperature measured is by about 270 °C higher than the temperature according to the nominal curve in the 4th min.

Object B: The real fire temperature was a little lower than the nominal curve. In the 3rd min. (after the cracking and gradual falling out of the window), the measured temperature was by about 230 °C higher than the temperature according to the nominal curve.

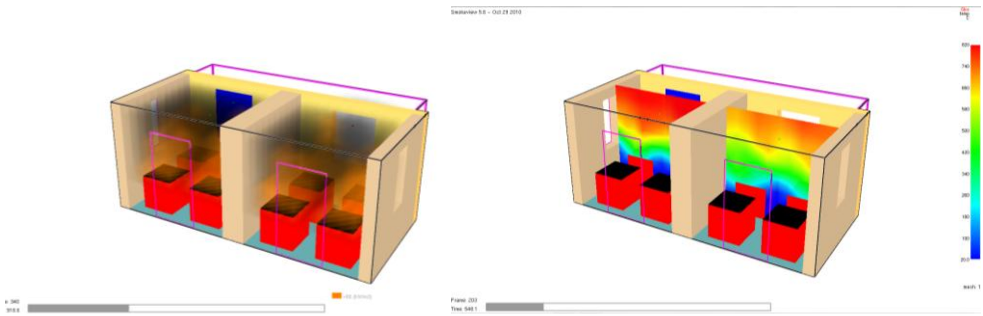

Figure 5. Visualization of the fire using Fire Dynamics Simulator (FDS).

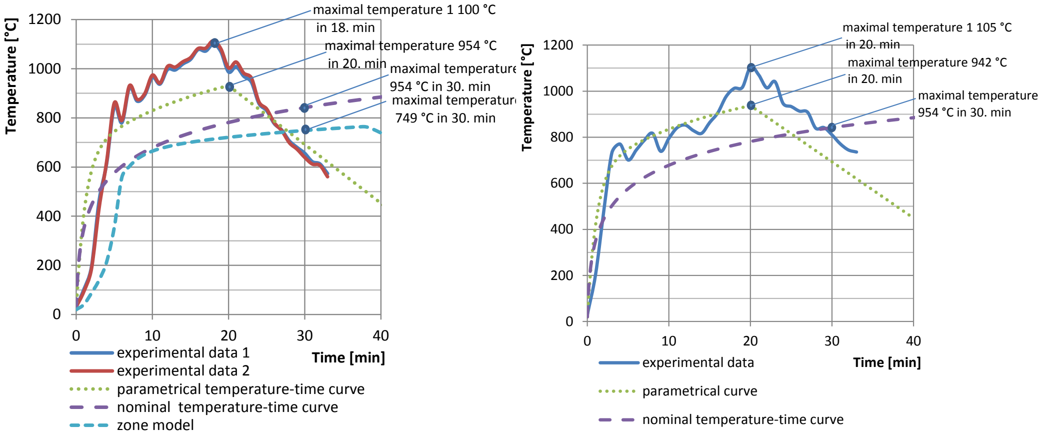

(a) (b)

Figure 6. Comparison of real temperatures with temperature-time curves for object A (left) and object B (right) during the fire experiment.

4.2 The course of fire

The expansion of the fire throughout the room followed immediately after the ignition of timber piles. In object A, there are two openings for the air supply, and one fire window. In object B, there are two openings too, and one normal plastic window. The fire development starting immediately after the ignition nearly suppressed the heating phrase. The cracking of the normal window (object B) started in the 3rd min., while in the 5th min. the temperature reached about 850 °C. The fire expanded very quickly. The first layer of plasterboard started to crack and gradually fall off in the 15th min.

Object B was significantly damaged by fire due to different design solutions and a greater number of openings, which ensured the supply of air. The fire window fulfilled its function in object A. The façade system with plaster fell off in the last 10 minutes of the fire in object B (Figure 7). The fire was extinguished in the 32nd min.

The analysis of the condition of all structures took place after the end of the experiment. The supporting structures were checked, including the degree of charring.

Figure 7. Experimental objects before the intervention of firefighters.

5 EVALUATION

All structures were taken to pieces after the end of the experiment, and the charring depth of individual timber studs was investigated. In Figure 8, there is the development of temperatures in each layer of floor assemblies for both objects. The failure time of protection t_f and the time of the start of charring of timber members t_{ch} were studied. The composition of the floor assembly was: gypsum plasterboard (RF) 15 mm, air gap 40 mm, timber stud 60/220 mm + stone wool 100 mm (37 kg/m^3) and oriented strand boards (OSB) 22 mm.

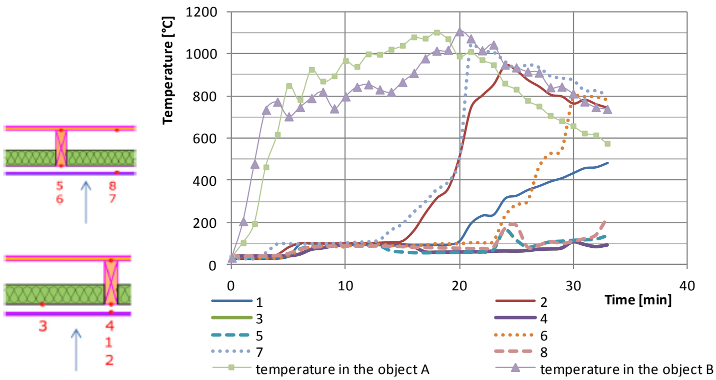

Figure 8. Development of the temperature in the floor assemblies (left higher picture – object B, left lower picture – object A).

In Figure 9, there are pictures of selected studs. Object A (wall C) had the following composition from the exterior side: Rigidur gypsum fibre 12.5 mm, timber stud 60/120 mm + 120 mm stone wool (50 kg/m^3) and Rigistabil gypsum plasterboard 12.5 mm. Object B (wall D) had the following composition from the exterior side: RB gypsum plasterboard 12.5 mm,, OSB 12 mm, timber stud 60/120 mm + 120 mm stone wall (37 kg/m^3), OSB 12 mm. The charring depth where the original profile was 60/120 mm can be seen there. The dot-and-dash line is the dimension of the original stud, while the dotted line is an effective cross-section calculated by Eurocode (nominal fire), and the solid line is the measured reality. The charring depth depends on the type of cladding, the material of insulation and a lot of other parameters.

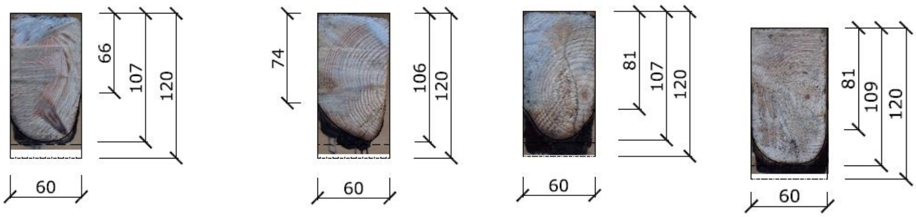

(a) object A (wall C) (b) object B (wall D)

Figure 9. Studs after the fire, original profile: 60/120 mm; (a) object A (wall 3), (b) object B (wall D).

On the basis of the experiment, the following failure times of protection t_f and the time of the start of charring of timber members t_{ch} for the following claddings were determined. Table 1 and 2 present the results from the fire experiment.

Table 1. Determined t_{ch} and t_f for different claddings, object A.

	Composition	t_{ch} [min]	t_f [min]
1st Layer			
Rigidur gypsum fibreboard 12.5 mm	C/A1	20	20
Ristabil gypsum fibreboard 12.5 mm	A2	13	13
2nd Layer			
air gap + mineral wool 40 mm	A1/A2	16	not reached
3rd Layer			
Rigidur gypsum fibreboard 12.5 mm	A1/A2	not reached	not reached

Table 2. Determined t_{ch} and t_f for different claddings object B.

	Composition	t_{ch} [min]	t_f [min]
1st Layer			
gypsum plasterboard (RB) 12.5 mm	B1/B4/D	15.5-16	18-20
gypsum plasterboard (RF) 12.5 mm	B2/B3	14.7	not reached
	F	17	21
2nd Layer			
OSB 12 mm	B1/B4/D	23	23

6 CONCLUSIONS

The claddings which significantly contribute to the fire resistance of the whole structure are very important for the fire protection of light timber frame wall and floor assemblies. These are different plasterboard, gypsum fibre boards, or possibly wood-based panels. Besides, there are other things we must keep in mind in timber buildings, such as compliance with the technological process at work, the right solution of details.

On the basis of this experimental fire test, the time of the start of charring of protected members (delayed start of charring due to protection) t_{ch} and the failure time of protection t_f for some types of cladding were determined.

ACKNOWLEDGMENT

This work has been supported by CTU in Prague, the SGS research project SGS14/177/OHK1/3T/11 “Behavior of light timber-framed buildings exposed to fire” and by the European Union, the OP RDI project No. CZ.1.05/2.1.00/03.0091 – University Centre for Energy Efficient Buildings.

REFERENCES

[1] EN 13501-1+A1 Fire classification of construction products and building elements - Part 1: Classification using test data from reaction to fire tests.

[2] EN 1363-1 Fire resistance tests - Part 1: General requirements.

[3] EN 1991-1-2 Eurocode 1: Actions on structures - Part 1-2: General actions - Actions on structures exposed to fire.

[4] EN 1995–1-2 Eurocode 5: Design of timber structures – Part 1–2: General – Structural fire design.

AUTHORS LIST

AUTHORS LIST

Progress on Safety of

Structures in Fire

结构火灾安全进展

Proceedings of the 8th International Conference on Structures in Fire

第八届结构火灾安全国际会议论文集

June 11-13, 2014, Shanghai, China

Volume Ⅱ

Edited by

Guo-Qiang LI	Venkatesh K. R. KODUR
Shou-Chao JIANG	Jian JIANG
Su-Wen CHEN	Guo-Biao LOU

同济大学出版社
TONGJI UNIVERSITY PRESS

图书在版编目(CIP)数据

结构火灾安全进展：第八届结构火灾安全国际会议论文集 = Structures in fire:proceedings of the eighth international conference: 英文 / 李国强等主编. -- 上海：同济大学出版社, 2014.6
ISBN 978-7-5608-5494-6

Ⅰ. ①结… Ⅱ. ①李… Ⅲ. ①防火－建筑结构－结构设计－国际学术会议－文集－英文 Ⅳ. ①TU352.5-53

中国版本图书馆 CIP 数据核字(2014)第 088466 号

结构火灾安全进展——第八届结构火灾安全国际会议论文集

Structures in Fire—Proceedings of the 8th International Conference on Structures in Fire

李国强 Venkatesh K. R. KODUR **蒋首超 等 主编**

责任编辑 季 慧 特约编辑 何亚楣 责任校对 徐春莲 封面设计 陈益平

出版发行 同济大学出版社 www.tongjipress.com.cn
(地址：上海市四平路 1239 号 邮编: 200092 电话:021-65985622)
经　　销 全国各地新华书店
印　　刷 同济大学印刷厂
开　　本 787mm×1 092mm 1/16
印　　张 84.5 (上、下册)
字　　数 1 690 000 (上、下册)
版　　次 2014 年 6 月第 1 版 2014 年 6 月第 1 次印刷
书　　号 ISBN-978-7-5608-5494-6

定　　价 1 000.00 元 (上、下册)

ACKNOWLEDGEMENT

The conference organizers would like to thank the following sponsors for their much appreciated support to the Conference.

State Key Laboratory of Disaster Reduction in Civil Engineering

Department of Building Engineering, Tongji University

AkzoNobel Protective Coatings China

Tongji Architectural Design (TJAD) (Group) Co., Ltd

SCIENTIFIC COMMITTEE

Chairman

Venkatesh Kodur, Michigan State University, USA

Track 1: Applications of Structural Fire Safety Engineering

Bin Zhao (Leader)	**CTICM, France**
Daniel Joyeux	Efectis France, France
Florian Block	Buro Happold, UK
Olivier Vassart	Arcelor Mittal, Luxembourg
Susan Lamont	Arup, UAE
Ralph Hamerlinck	BOUWEN MET STAAL, Netherlands
Zhaopeng Ni	Tianjin Fire Research Institute, China
Jiann Yang	NIST, USA

Track 2: Concrete structures and any other topics

Kang Hai Tan (Leader)	**Nanyang Technological University, Singapore**
Pietro Gambarova	Politech. Milan , Italy
Faris Ali	University of Ulster , UK
Bo Wu	South China University of Technology, China
Mark Green	Queen's University, Canada
Luke Bisby	University of Edinburgh, UK
Pradeep Bhargava	IIT Roorkee, India
Tony Abu	UC Canterbury, New Zealand
Zhaohui Huang	Brunel University, UK
Luc Taerwe	University of Gent, Belgium
Colin Bailey	University of Manchester, UK

Track 3: Timber structures and fire protection materials

Mario Fontana (Leader)	**ETHZ, Switzerland**
Massimo Fragiacomo	University of Sassari, Italy
Joachim Schmid	SP, Sweden
Steve Craft	Forintek, Canada
Marc Janssens	SW Research Inst, USA

Andrea Frangi	ETHZ, Switzerland
Andy Buchanan	University of Canterbury, New Zealand

Track 4: Numerical Modeling

Asif Usmani (Leader)	**University of Edinburgh, UK**
Martin Gillie	University of Edinburgh, UK
Basam Izzuddin	Imperial College, UK
Zhaohui Huang	University of Sheffield, UK
Jean-Marc Franssen	University de Liège, Belgium
Angus Law	Arup, UK
Suwen Chen	Tongji University, China
Ann Jeffers	University of Michigan, USA

Track 5: Composite structures

Guo Qiang Li (Leader)	**Tongji University, China**
Markus Knobloch	ETHZ, Switzerland
Peter Schaumann	University of Hannover, Germany
Linhai Han	Tsinghua University, China
Ali Nadjai	University of Ulster, UK
Dhionis Dhima	CSTB, France
João Paulo Rodrigues	Universidade de Coimbra, Portugal

Track 6: Steel Structures

Paulo Vila Real (Leader)	**University of Aveiro, Portugal**
Yong C. Wang	University of Manchester, UK
Frantisek Wald	Czech Technical University in Prague, Czech Republic
Didier Talamona	University of Newcastle, Australia
Jyri Outinen	Ruukki Construction Oy, Finland
Ian Burgess	University of Sheffield, UK
Maria Garlok	Princeton University, USA
Michael D. Engelhardt	University of Texas at Austin, USA
Raul Zaharia	University of Timisoara, Romania
Leroy Gardner	Imperial College, UK

ORGANISING COMMITTEE

G.Q. Li, Chair	(李国强)	Tongji University, China
H.H. Zhu	(朱合华)	Tongji University, China
Y. Yuan	(袁　勇)	Tongji University, China
J.Z. Xiao	(肖建庄)	Tongji University, China
K.X. Hu	(胡克旭)	Tongji University, China
S.W. Chen	(陈素文)	Tongji University, China
S.C. Jiang	(蒋首超)	Tongji University, China
J.T. Yu	(余江滔)	Tongji University, China
G.B. Lou	(楼国彪)	Tongji University, China
J. Jiang	(姜　健)	Tongji University, China
L.H. Han	(韩林海)	Tsinghua University, China
B. Wu	(吴　波)	South China University of Technology, China
Y.L. Dong	(董毓利)	HuaQiao Universigy, China
J.C. Zhao	(赵金城)	ShangHai Jiao Tong University, China
W.Z. Zheng	(郑文忠)	Harbin Institute of Technology, Harbin, China
X.H. Qiang	(强旭红)	Harbin Institute of Technology, Harbin, China
G.P. Shu	(舒赣平)	Southeast University, China
L.J. Qu	(屈立军)	Chinese People's Institute Of Armed Police Force, Langfang, China
C.G. Fu	(傅传国)	Shandong Jianzhu University, Jinan, China
Y. Du	(杜　咏)	Nanjing University of Technology, Nanjing, China
P.J. Wang	(王培军)	Shandong University, Jinan, China
W.Y. Wang	(王卫永)	Chongqing University, Chongqing, China
J.F. Wang	(王静峰)	Hefei University of Technology, Hefei, China
H.T. Zhou	(周焕廷)	Wuhan University of Technology, Wuhan, China
J. Zeng	(曾　杰)	Shanghai Fire Bureau, Shanghai, China
Z.P. Ni	(倪照鹏)	Tianjin Fire Research Institute, Tianjin, China

STEERING COMMITTEE

Jean-Marc Franssen	University of Liege, Belgium
Andy Buchanan	University of Canterbury, New Zealand
Venkatesh Kodur	Michigan State University, USA
Paulo Vila Real	University of Aveiro, Portugal

PREFACE

Structural fire safety has raised growing concerns in the design of infrastructures. The "Structures in Fire" (SiF) specialized workshop series was conceived in the late 1990's and the "First International SiF workshop" was held in Denmark in 2000. The workshop was then held every two years until 2008 with the title changed from workshop to conference. Under this new framework the 5th-7th International Conference on SiF were held in Singapore (2008), USA (2010) and Switzerland (2012), respectively. The main mission of SiF conferences is to provide an opportunity for researchers and engineers to share their research, technology and expertise with their peers at an international forum.

Following the great success of previous workshops and conferences, Tongji University was selected to host the 8th International Conference on Structures in Fire SiF'14 in Shanghai on June 11-13, 2014.

The response to call for papers for SiF’14 was overwhelming and the Organizing Committee received more than 280 abstracts for this year’s conference. As a first attempt for parallel sessions, a total of 155 papers from 29 countries were selected for publication in the conference proceedings. The papers are subdivided into 8 chapters with themes including *Applications of Structural Fire Safety Engineering, Steel Structures, Concrete Structures, Composite Structures, Timber Structures, Fire Protection Materials, Numerical Modeling, and any other topics*. It is hoped that the high quality of the technical papers presented in this proceedings will enable researchers and practioners to develop greater insight of structural fire engineering, so that safer structures will be designed for fire-resistance.

We would like to thank all the members of the Scientific Committee for reviewing the abstracts within an incredibly short period of time, in particular the support of Professors Bin Zhao, Kang Hai Tan, Mario Fontana, Asif Usmani, Guo Qiang Li and Paulo Vila Real, taking the burden of the track leaders for the Scientific Committee. Our sincere appreciation must be presented to the SiF Steering Committee for guiding the review process and for providing direction to the successful organization of this conference. Our sincere thanks also go to all authors—the quality of the book is just the corollary of the high standard of their contributions and research activity. Finally, we would like to appreciate the effort and extraordinary support provided by all the members of the Organizing Committee, especially the staff at Tongji University.

Guo-Qiang LI
Chairman of Organizing Committee
Venkatesh K.R. KODUR
Chairman of Scientific Committee

Shanghai, June 2014

CONTENTS

Volume Ⅰ

Steel Structures

Concrete Structures

Timber Structures

Volume Ⅱ

Composite Structures

Connections

Numerical Modeling

Applications of Structural Fire Safety Engineering

Materials Behavior

COMPOSITE STRUCTURES

8th International Conference on Structures in Fire
Guo-Qiang LI, Venkatesh K. R. KODUR, Shou-Chao JIANG, Jian JIANG, Su-Wen CHEN, Guo-Biao LOU (Eds.)
Shanghai, China, June 11-13, 2014

ANALYSIS ON THE FIRE PERFORMANCE OF CFST-COLUMN TO SRC-BEAM PLANE FRAMES

J. Q. Liu*, K. Zhou*, L. H. Han* and X. L. Zhao**

* Department of Civil Engineering, Tsinghua University, Beijing China
e-mails: liujiaqi13@mails.tsinghua.edu.cn,
zhouk12@mails.tsinghua.edu.cn
lhhan@tsinghua.edu.cn

** Department of Civil Engineering, Monash University, Australia
e-mail: ZXL@monash.edu

Keywords: Concrete Filled Steel Tubes (CFST), Steel reinforced concrete (SRC), Temperature, Composite frame, Fire safety engineering

Abstract. *A finite element analysis model is presented in this paper for CFST-column to SRC-beam unbraced composite plane frame with RC slab exposed to fire. The single span, single story composite frame consists of two CFST columns and one SRC beam with reinforced concrete slab. The predictions of the FEA model were validated against experimental data. Based on this model, a fire behaviour analysis was carried out on the composite frames. A parametric analysis was conducted to study the influence of the major factors on the fire performance of the composite frames.*

1 INTRODUCTION

Concrete filled steel tube (CFST) and steel reinforced concrete (SRC) structures have an increasing utilization in high-rise and super high-rise buildings in China. Current studies mainly focus on the fire performance of isolated elements or joints under fire load. For example, Yang et al. (2008) analysed the residual strength of the CFST column after a full-range fire exposure, and Huo et al. (2010) completed the experimental and theoretical analysis of 8 post-fire CFST column to steel beam joints. However there are limited studies on the fire performance of composite frames with CFST-columns and SRC-beam. Usmani et al. (2004) highlighted a number of key events that define the response of a composite steel frame structure in fire. Alderighi et al. (2009) tested the performance of CFST column to steel beam under the combined effect of earthquake and fire.

This paper presents a finite element analysis on CFST-column to SRC-beam composite frames using ABAQUS. The results of the FEA model were validated against the experimental data. Based on this FEA model, further studies were carried out on the composite frames under both loading and fire, including the failure pattern, the displacement (deflection)-time relationship and the re-distribution of the stress in the frame structure. Finally, a parametric analysis on the fire load ratio of both the column and beam, as well as material and geometric parameters were conducted to study the influence of these major factors on the behaviour of the frame at elevated temperatures.

2 FEA MODEL

The commercial finite element analysis software ABAQUS was employed to complete the simulation. A sequential coupled heat transfer-structural analysis was carried out. In the analysis, concentrated loads, axial force N_c and simplified uniform force N_b were first applied to the column and beam respectively at ambient temperature to simulate the service load in real structures. Then the bottom of the slab and the beam, the other two sides of the beam, as well as the external surfaces of the columns were exposed to fire, during which the loads were kept constant. The schematic of the frame and loads are illustrated in Figure 1, where H is the height of the column, L is the length of the beam, measured between the centre of the columns.

2.1 Temperature field analysis

In this paper, the thermodynamic properties of steel and concrete such as the thermal conductivity coefficient, specific heat and density of Lie (1994) were used in temperature filed analysis. According to Eurocode 4, the heat convection coefficient and thermal radiation emissivity of the fire-exposed surfaces were 25 ($Wm^{-2}K^{-1}$) and 0.7 respectively, while the corresponding parameters at ambient temperature were 4 ($Wm^{-2}K^{-1}$) and 0.7 respectively. In heat transfer analysis, 8-node brick elements were employed for modelling concrete and end plates, and 4-node quadrilateral shell elements for shaped steel, 2-node heat transfer link elements for reinforcement bars. Heat resistance between concrete and steel was ignored. Figure 2 shows the FEA mesh for heat transfer analysis and the thermal boundary condition.

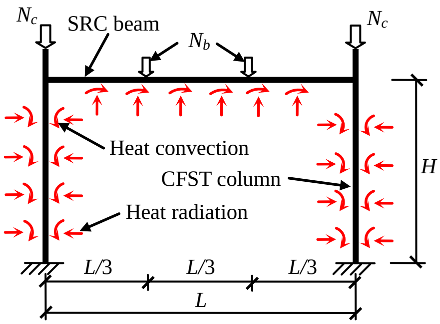

Figure 1. Schematic of the frame and loads.

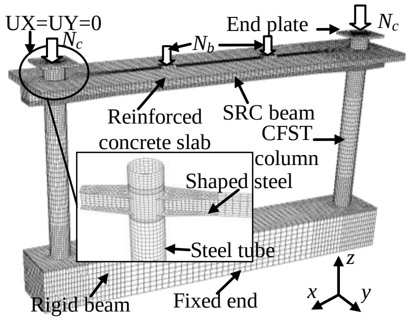

Figure 2. Meshing of the FEA model.

2.2 Structural behaviour analysis

When the temperature distribution of the composite frame was calculated, the same finite element model with identical element number and other characteristics was built for structural analysis. Only plane displacement was allowed in the model, which means UX=UY=0 for the upper surface of end plates and the bottom of the grade beam was a fixed end.

The constitutive models for steel, confined and unconfined concrete in this model adopted those proposed by Tan (2012). Confined concrete refers to the part inside the outer steel tube, and the unconfined concrete refers to the part in the beam and the slab. Both the elastic and perfectly plastic behaviors of steel were considered, as for concrete, the elastic and plastic damaged behaviors were considered.

At elevated temperatures, the strain of steel consisted of mechanical strain, thermal strain and creep strain. In this paper, the stress-strain relation and thermal strain model for steel proposed by Lie (1994) were adopted, while the steel creep strain was ignored to get a better efficiency in calculation. The strain of concrete was made up of four parts. Among them three are similar to those of steel while the additional one was transient strain.

2.3 Verification of the FEA model

This FEA model was validated by the test data of two CFST-column to SRC-beam frames exposed to fire presented in Han and Song (2012). The basic information of the specimens is listed in Table 1. The standard fire described by the ISO-834 curve was adopted as the fire load in this model.

Table 1. Basic information of the test specimens.

Parameter	Symbol	Unit	Specimen CFSRC-1	Specimen CFSRC-2
Column, external diameter×tube thickness×column height	$D\times t\times H$	mm	140×3.85×1456	140×3.85×1456
Beam, height×width ×length	$h\times b\times L$	mm	160×110×2400	160×110×2400
Shaped steel, height×width×web thickness×flange thickness	$h_s\times b_{fs}\times t_w\times t_{bf}$	mm	80×30×4×4	80×30×4×4
Linear stiffness ratio of beam to column, beam /column stiffness	i_b/i_c	/	0.68	0.68
Column load ratio	n	/	0.29	0.29
Axial force of the column	N_c	kN	380	380
Beam load ratio	m	/	0.6	0.3
Axial force of the beam	N_b	kN	36	18
Fire protective layer thickness	a	mm	3	6
Experimental fire resistance time	t_R^E	min	45	85

Test results indicated that the FEA model showed good validity. Due to page limitation, only parts of the results are shown below. Figure 3 shows the comparison of failure modes of the frame. The predicted failure mode is very close to that of the observed one.

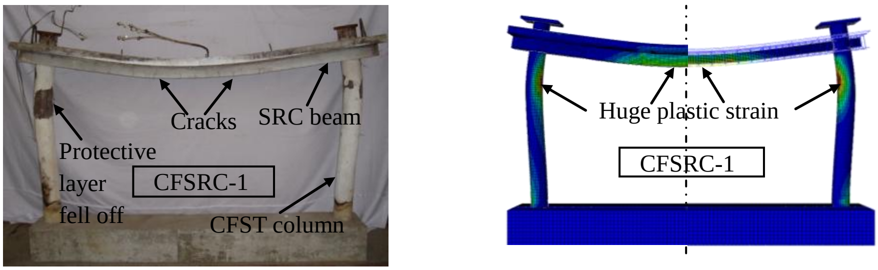

(a) Observed (b) Predicted

Figure 3. Comparison between observed and predicted failure mode of the frame.

The maximum horizontal displacement of the CFST column was near the top end. As for the SRC beam, cracks appeared along the lower surface, and the maximum displacement was near the midspan. In the predicted failure mode, these features can be judged by the major plastic deformation in corresponding areas. The comparisons of the displacement-time relations are illustrated in Figure 4.

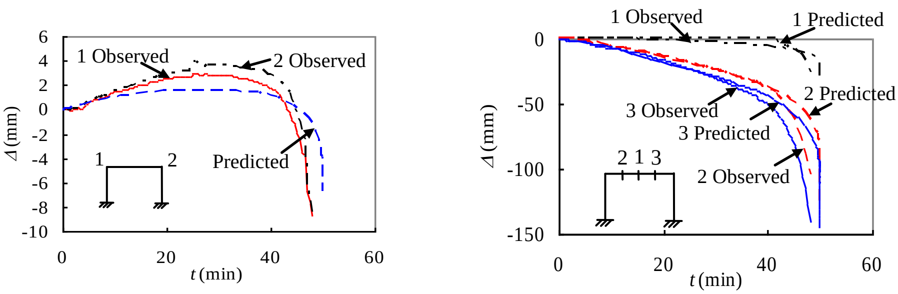

(a) CFST Column (b) SRC Beam

Figure 4. Comparison of displacement-time relation.

It can be found from Figure 4 that the predicted and observed curves also agree well. The vertical displacement of the CFST column went up at the beginning because of thermal expansion. After 30 minutes' exposure to fire, the displacement began to grow sharply in the opposite direction because of the decrease in strength and stiffness of the column as well as the spalling of the protective layer. However, for SRC beams, the displacement underwent a monotonic decrease for all the three observation points.

3 ANALYTICAL BEHAVIOURS

Based on the above FEA model, further investigation was conducted on the fire behaviour and fire resistance of the composite frame.

3.1 Calculation conditions

For design and calculation convenience, a full scale CFST-column to SRC-beam plane frame was separated and put into fire performance analysis from a real project introduced by Han and Song (2012). The main parameters of this typical frame are shown in Table 2.

Table 2. Main material and geometry features of the composite frames.

Parameter	Symbol	Unit	Value
Geometry of the column, external diameter×tube thickness×column height	$D\times t\times H$	mm	600×12×5400
Geometry of the beam, height×width ×length	$h\times b\times L$	mm	650×400×9000
Geometry of the shaped steel	$h\times t_h\times t_w\times b$	mm	315×10×10×250
Yield strength of steel in tube and hidden corbe, and the shaped steel	f_y	MPa	345
Yield strength of longitudinal reinforcing bars	f_{yb}	MPa	335
Compression cube strength of core concrete	f_{cuc}	MPa	60
Compression cube strength of concrete in the beam and slab	f_{cus}	MPa	30

Additionally, to consider the influence of reinforced concrete slab on temperature distribution, a 120 mm-thick and 3000 mm-long reinforced concrete slab was included. The reinforcement in the beam was two Φ20 in the top of the cross-section and eight Φ28 in the bottom. There was also longitudinal and traverse distributed reinforcement in the slab. The thickness of the fire protective layer outside the column was 6 mm. The density (ρ) of fireproof coating was 400 ± 20kg/m^3, thermal conductivity (λ) was 0.097W/(m•K) and specific heat (c) was 1.047×103J/(kg•K).

A typical frame with the load ratio in beam (m) 0.5 and the load ratio in column (n) 0.5 was taken as the basic simulation example. ISO-834 standard fire curve was adopted. The load bearing capacity for beam and column were both determined by FEA analysis.

The ISO-834 also suggested failure criterion for both single column and beam, however, there is no failure criterion for frame structures so far. This paper assumes that the fire resistance t_R of the frame is reached either the column or the beam comes to its limit state.

In the parametric analysis, loading, geometric and physical parameters of the composite frame that may influence the behaviour of the frame structure under fire were selected to investigate their relation with heating time.

3.2 Fire behaviour of the composite frame

The analysis of the fire behaviour of the composite frame mainly includes the deformation of the column and beam, the fire resistance of the composite frame and the internal force redistribution.

Figure 5 shows the deflection-time curves of the CFST column and SRC beam. Load ratio represents the load applied on the structure to the ultimate bearing capacity. The load ratio of the beam m is kept constant 0.5 while with the increase of the load ratio of the column n from 0.3 to 0.7, the expansion caused by elevated temperature of the column was suppressed, meanwhile, the fire resistance of both the column and the beam, expressed by displacement rate, underwent a down trend.

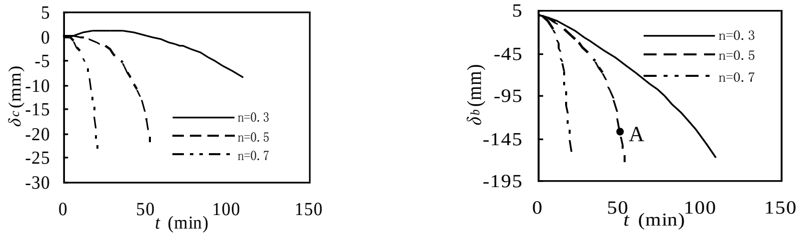

(a) Displacement of upper end of CFST column (b) Displacement of midspan of the SRC beam

Figure 5. Displacement of typical part in the composite frame with different column load ratio *n*.

At point A in Figure 5 (b), the deflection rate was 13.94 mm/min, higher than the limit value 13.85 mm/min regulated in ISO-834, thus the fire resistance time of the beam was 50 min. While for the CFST column, at this particular time, neither the limit of maximum axial contraction nor the rate of axial contraction was reached, which means this typical composite frame was a beam-controlled one, it was deemed to be failed as soon as the SRC beam first reached its fire limit.

Figure 6 and Figure 7 reveal the changes of the internal forces in the top of the column and the midspan of the beam against the heating time *t* respectively. Apart from the total internal force, the forces of each component of the member are also given. Anticlockwise moment, tension force and clockwise shear force are deemed to be positive.

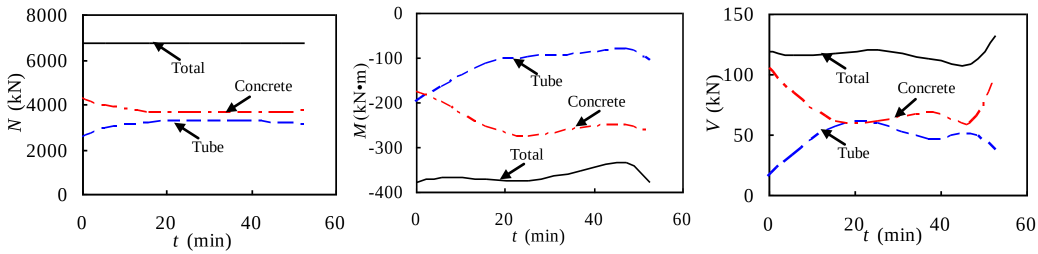

(a) Axial force (b) Bending moment (c) Shear force

Figure 6. Internal force distribution in the CFST column.

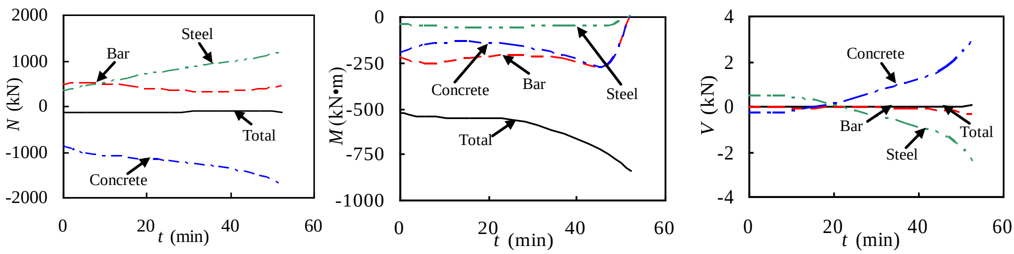

(a) Axial force (b) Bending moment (c) Shear force

Figure 7. Internal force distribution in the SRC beam.

Dramatic redistribution of the internal forces in the frame can be observed. In early stage, the positive bending moment in the midspan of the beam decreased a little, this mainly resulted from thermal expansion in the surface exposed to fire. With further rise of the temperature, due to the deterioration of the material and the sharp increase in deflection, the midspan moment thus rose at a very high speed until it reached the limit state, when a plastic hinge appeared at the joint, and brought about failure to the column as well. Same mechanism applies to the internal force redistribution of the column.

3.3 Parametric analysis

To evaluate the influence of different parameters on the fire resistance of the composite frame, a parametric analysis was carried out. Table 3 shows the ten parameters determined, which were among the main factors that may affect the fire performance of CFST members concluded by Han (2007). When considering the thickness of the steel tube and the web of the shaped steel, the concept of section steel ratio was introduced. The section steel ratio is defined as the ratio of the area of steel to that of the whole cross section.

Table 3. Parameters for parametric analysis.

Type	Parameter	Symbol	Unit	Values of the parameter		
Loading Parameter	Load ratio in column	n	/	0.3	0.5	0.7
	Load ratio in beam	m	/	0.3	0.5	0.7
Physical Parameter	Strength of steel tube	f_y	MPa	235	345	420
	Strength of shaped steel	f_{ys}	MPa	235	345	420
	Strength of longitudinal bar	f_{yb}	MPa	235	335	400
	Strength of core concrete	f_{cuc}	MPa	40	60	80
	Strength of concrete in slab and beam	f_{cus}	MPa	30	40	50
Geometric Parameter	Fire protective layer thickness	a	mm	0	3	6
	Thickness of steel tube	t_b	mm	8	12	16
	Section steel ratio of column	α_c	/	5.55%	8.51%	11.60%
	Thickness of shaped steel	t_s	mm	5	10	15
	Section steel ratio of beam	α_b	/	1.57%	3.13%	4.70%

The influences of each parameter on the fire resistance time t_R of the composite frame are illustrated in Figure 8.

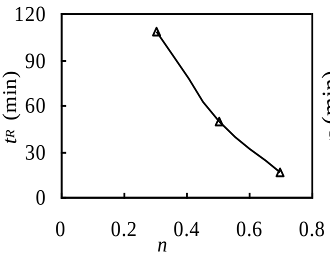

(a) Column load ratio (n)

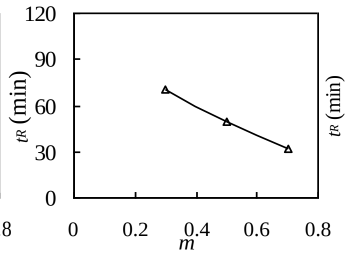

(b) Beam load ratio (m)

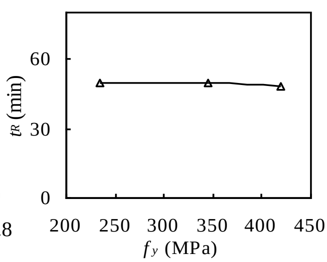

(c) Strength of steel tube (f_y)

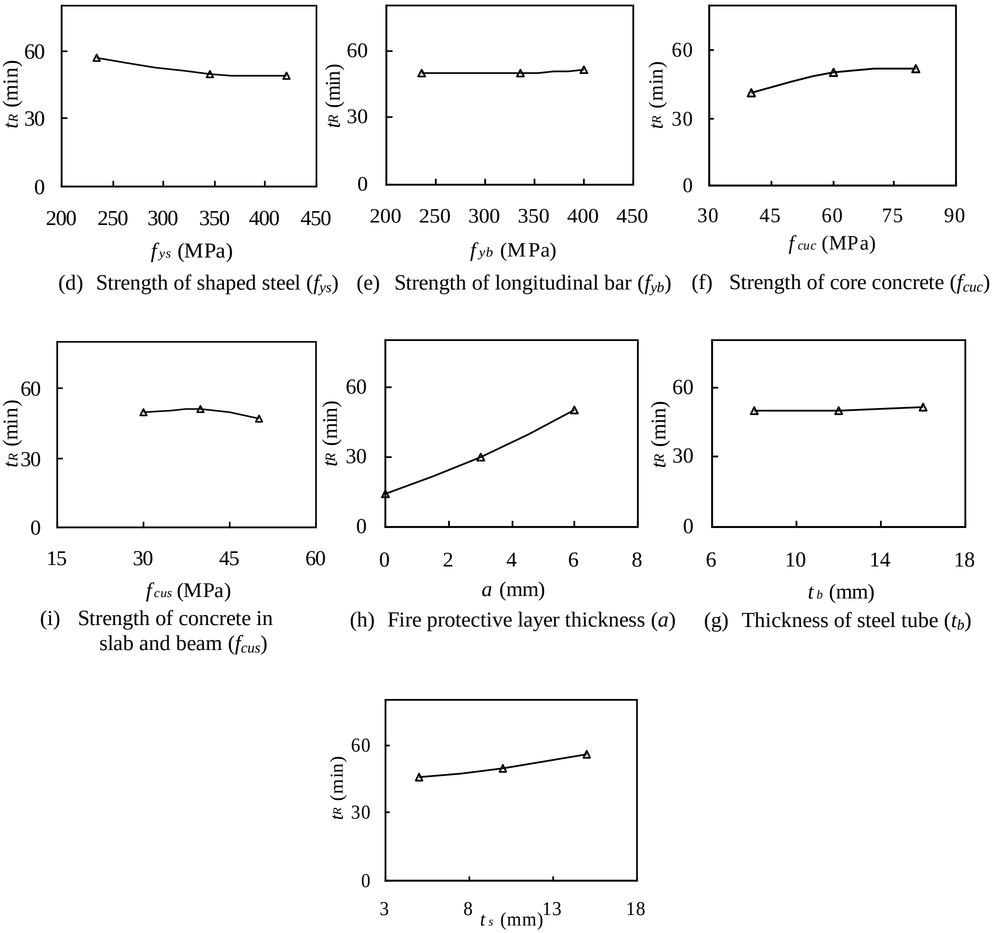

(d) Strength of shaped steel (f_{ys}) (e) Strength of longitudinal bar (f_{yb}) (f) Strength of core concrete (f_{cuc})

(i) Strength of concrete in slab and beam (f_{cus}) (h) Fire protective layer thickness (a) (g) Thickness of steel tube (t_b)

(j) Thickness of shaped steel (t_s)

Figure 8. Influence of different parameters on the fire resistance time of the frame.

As can be seen from Figure 8, some parameters have great influence on the fire resistance of the frame, while others are not so relative. The load ratio and the thickness of the fire protective layer exert a tremendous influence on the frame's fire resistance time and the deformation of the structure. When the column load ratio n was raised to 0.7, the fire resistance time of the frame reduced to 16 min, compared with 108 min for n=0.3. The beam load ratio affected not only the fire resistance, but also the internal force in the beam and the column. No wonder the increase in the thickness of the fire protective layer provided good insulation which slowed down the temperature rise of the outer tube, so the expansion of the column was delayed, as well as the axial contraction, this phenomena was passed on to the beam through the joints and resulted in a deceleration of the deformation in turn. Therefore, although the beam first came to a failure during fire and only the CFST column was covered with fire protective layer, the fire resistance time of the frame was still increased by the thickening of the fire protective layer.

The strength and web thickness of the shaped steel, the strength of the core concrete and the concrete in the beam and slab have certain effect, although not as great as the above few ones, on the fire resistance time of the frame. The relations between the fire resistance of the composite frame and other parameters such as strength and thickness of the steel tube, and the strength of the longitudinal bars are not so obvious. Therefore in real applications, less importance can be laid on these parameters in order to get the best fire resistance at the least cost.

4 CONCLUSIONS

Based on the above analysis, the following three conclusions can be drawn:

(1) The FEA model proposed in this paper is within the acceptable range of accuracy to predict the temperature distribution and structural behaviour of the CFST-column to SRC-beam composite frame under fire.

(2) Under standard fire, observable deformation and huge redistribution of internal forces can be seen in the composite frame, for the frames analyzed in this paper, the SRC beam first came to its limit state followed by a plastic hinge appeared in the joints, which resulted in the total failure of the structure.

(3) The load ratio and the thickness of the fire protective layer exert a tremendous influence on the frame’s fire resistance time and the deformation of the structure, while the relations between the fire resistance and other parameters are not so obvious.

ACKNOWLEDGEMENT

The research reported in this paper is supported by the National Key Project of Scientific and Technical Supporting Programs Funded by Ministry of Science & Technology of China (No. 2012BAJ07B01), and their financial support is highly appreciated.

REFERENCES

[1] Yang H., Han L.H., Wang Y.C., Effects of heating and loading histories on post-fire cooling behaviour of concrete-filled steel tubular columns. *Journal of Constructional Steel Research*, 64(5), 556-570, 2008.

[2] Huo J.S., Han L.H., Wang Y.C., Behaviour of repaired concrete filled steel tubular column to steel beam joints after exposure to fire. *Advances in Structural Engineering*, 1(13), 52-67, 2010.

[3] Usmani A.S., Lamont S., Key events in the structural response of a composite steel frame structure in fire. *Fire and Materials*, 28(2-4), 281–297, 2004.

[4] Alderighi E., Salvatore W., Structural fire performance of earthquake-resistant composite steel-concrete frames. *Engineering Structure*s, 31(4), 894-909, 2009.

[5] Lie T.T., Fire resistance of circular steel columns filled with bar-reinforced concrete. *Journal of Structural Engineering*, 120(5), 1489-1509, 1994.

[6] Tan Q.H., *Performance of steel reinforced concrete (SRC) column and portal frame after exposure to Fire*. Beijing, Tsinghua University, 2012. (in Chinese)

[7] Han L.H., Song T.Y., *Fire safety design theory of steel-concrete composite structures.* Beijing, Science Press, China, 2012. (in Chinese)

[8] ISO-834. Fire-resistance tests-elements of building construction. International Standard ISO 834, 1975.

[9] Han L.H., *Concrete filled steel tube structures: theory and experience*. Science Press, Beijing, 2007. (in Chinese)

8th International Conference on Structures in Fire
Guo-Qiang LI, Venkatesh K. R. KODUR, Shou-Chao JIANG, Jian JIANG, Su-Wen CHEN, Guo-Biao LOU (Eds.)
Shanghai, China, June 11-13, 2014

BEHAVIOR OF HYBRID RC BEAM-CFST COLUMN PLANE FRAME AFTER EXPOSURE TO FULL-RANGE FIRE

K. Zhou*, L. H. Han * and Y. C. Wang**

*Department of Civil Engineering, Tsinghua University, Beijing China
e-mails: zhouk12@mails.tsinghua.edu.cn, lhhan@tsinghua.edu.cn

**School of Mechanical, Aerospace and Civil Engineering, University of Manchester, United Kingdom
e-mails: yong.wang@manchester.ac.uk

Keywords: Concrete Filled Steel Tubular (CFST) column, Reinforced Concrete (RC) beam, Plane composite frame, Full-range fire, Post-fire performance, Residual load bearing capacity.

Abstract. *This paper reports the results of a numerical investigation on plane frames consisting of CFST columns and RC beams. The established finite element analysis model was validated against existing experimental data of isolated CFST columns, RC beams and hybrid RC beam-CFST column plane frames. The validated FEA model was then used to analyze the behaviour of the hybrid plane frame after exposure to full-range fire. Residual load bearing capacity index was defined and calculated. Several parameters were selected and their influence was investigated.*

1 INTRODUCTION

Hybrid composite frame, made of concrete filled steel tubular (CFST) columns and reinforced concrete (RC) beams, is widely used in high-rise buildings and underground structures in China. There have been some published research studies on fire performance of this type of construction and similar composite frames. For example, Ding et al. (2007) experimentally investigated fire performance of steel beam to CFST column composite frames using different types of beam-column joints, and observed development of catenary action. Han et al. (2010) tested six RC beam to CFST column plane frames, and the results indicated that frame behaviour was different from isolated structural members. Han et al. (2012) conducted a theoretical investigation on hybrid RC beam to CFST column plane frames and identified two failure modes, initiated by column and beam failure respectively. Alderighi et al. (2009) experimentally studied performance of steel beam to CFST column assembly under the combined effect of earthquake and fire hazard. Elsawaf et al. (2012) presented a numerical model to investigate the influence of joints on fire performance of steel beam to CFST column frames.

However, these research studies focused on fire resistance of the structures and there is a lack of research on their post-fire performance. Thorough understanding of their post-fire performance is important so that appropriate assessment, repair and strengthening technologies can be deployed to enable such fire damaged structure to be safely reused.

This paper develops a FEA model using the commercial ABAQUS software. The FEA model were validated against existing test data. The validated FEA model was then employed to analyze the thermal and mechanical response of RC beam-CFST column hybrid frames subject to full-range fires that contain not only a heating phase but also a cooling phase. The post-fire performance of the hybrid frames was also investigated, and the ultimate load bearing capacity was defined and calculated. Several parameters that influence the post-fire load bearing capacity were identified, and parametric analysis was conducted to obtain regression equations.

2 FEA MODEL

The sequential coupled heat transfer-structural analysis in ABAQUS was employed.

2.1 Fire exposure

The whole process of real post-flashover fire can be divided into two stages: a heating phase and a cooling phase. For composite construction, it is possible for the structure to fail during the cooling period due to the time lag between the fire and different parts of the composite structure reaching their peak temperatures. Therefore, the ISO-834 full-range fire curve was selected. In the cooling phase, the fire temperature reduced in a straight line slope, whose descending rate depended on the peak temperature, as shown in Figure 1 (Han (2012)). Thus, the analysis had four phases: (1) ambient phase (AA') where the mechanical loads were applied, (2) heating phase (A'B'), (3) cooling phase (B'D') and (4) post-fire phase (D'E'). During phases (2) and (3), the mechanical loads were kept constant. In the post-fire phase, the mechanical loads were increased until the structure came to failure.

2.2 Temperature field (heat transfer) analysis

Figure 2 shows the FE mesh for heat transfer analysis and the thermal boundary condition, where N_b is the concentrated load on beam, and N_c is the concentrated load on column. The thermal conductivity coefficient, specific heat and density of both steel and concrete of Lie (1994) were used. According to Eurocode 4 (European Committee for Standardization 2004b), the convective heat transfer coefficients are 25 (Wm^{-2}K^{-1}) and 4 (Wm^{-2}K^{-1}) on the fire exposed and unexposed surfaces respectively. The resultant emissivity was assumed to be 0.7 for all surfaces. The steel and concrete were assumed to be in contact without any gap.

8-node brick elements were employed for modelling concrete, end plate and fireproof layer, 4-node quadrilateral shell elements were used for steel, and 2-node heat transfer link elements were used for reinforcement bars.

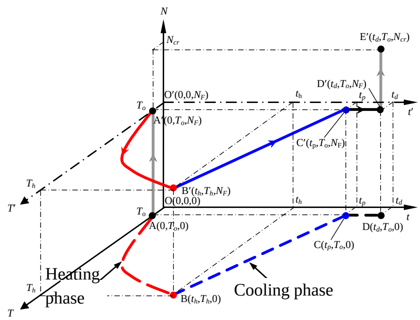

Figure 1. Complete load, temperature- time path.

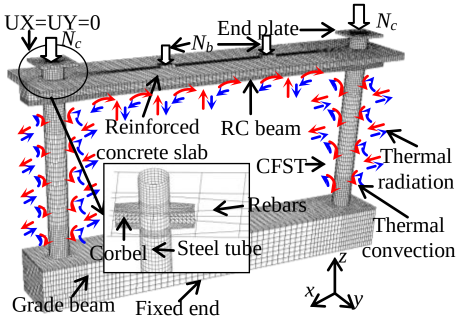

Figure 2. FE mesh modelling and thermal boundary conditions.

2.3 Structural analysis

For mechanical analysis, the steel stress-strain relationship was elastic and perfectly plastic. The damage plasticity model was used for concrete. The concrete in the beam and slab was unrestrained and its stress-strain relations was determined according to Song (2010). The concrete inside the steel tube was restrained by the outer tube and its stress-strain relationship was based on Tan (2012), where the constitutive models of restrained concrete were developed and validated the model by existing test data. The stress-strain relationship of steel at elevated temperatures was according to Lie (1994).

Because the analysis was coupled, the same finite element mesh was used for both thermal and mechanical analyses. Figure 2 also shows the mechanical boundary conditions.

2.4 Validation of FEA model

Results of the FE model were compared against single RC beam tests conducted by Dotreppe and Franssen (1985), single CFST column tests conducted by Han (2007) and hybrid RC beam-CFST column plane frame tests conducted by Han (2010). For brevity, only comparison results against Han (2010) are presented. Table 1 presents basic information of the plane frame tests conducted by Han (2010) and corresponding predictions of fire resistance time. Figure 3 shows comparison between simulation results and test results of Han (2010) for failure modes of the hybrid frame. Fireproof materials were applied on the steel tube external surface. Their thermal properties are: 400±20kg/m^3 and it has thermal conductivity (λ) of 0.097W/(m • K) and specific heat (c) of 1.047×103J/(kg • K). In mechanical analysis, the fireproof materials were not included.

Table 1. Basic information of the tests and predicted results.

Parameter	CFRC-1	CFRC-2	CFRC-3	CFRC-4
Column cross-section (external diameter×tube thickness)	140×3.85	140×3.85	140×3.85	140×3.85
Beam cross-section (height×width)	160×110	160×110	160×110	120×110
Reinforcement (top and bottom)	2Φ16, 2Φ12	2Φ16, 2Φ12	2Φ16, 2Φ12	2Φ12, 2Φ10
Stiffness ratio of beam to column	0.95	0.95	0.95	0.45
Column load ratio n	0.58	0.29	0.29	0.29
Axial force of the column N_c (kN)	760	380	380	380
Beam load ratio m	0.3	0.3	0.6	0.3
Axial force of the beam N_b (kN)	19.5	19.5	39	11.5
Fire protective layer thickness (mm)	7	6	3	6
Experimental fire resistance (min)	40	79	40	83
Predicted fire resistance (min)	43	89	44	101

Figure 3 compares the simulation and measured temperature-time curves for test CFRC-1 of Han (2010). The agreement is reasonable. Some of the predicted results are lower than the measured values. That is because the fireproof layer peeled off in some areas during the fire test, and this was not included in the numerical model.

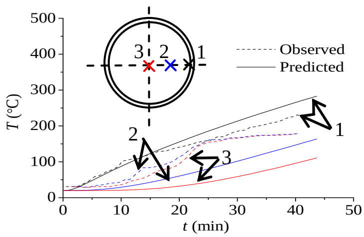

(a) Temperature in CFST column

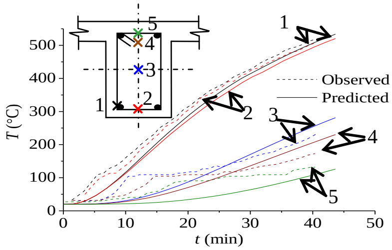

(b) Temperature in RC beam

Figure 3. Comparison of temperature-time relations for test CFRC-1 of Han (2010).

Figure 4 compares the predicted and measured displacement-time relations. The agreement is also reasonable. The final failure time (43 minutes) of the structure was also accurately calculated by the numerical model.

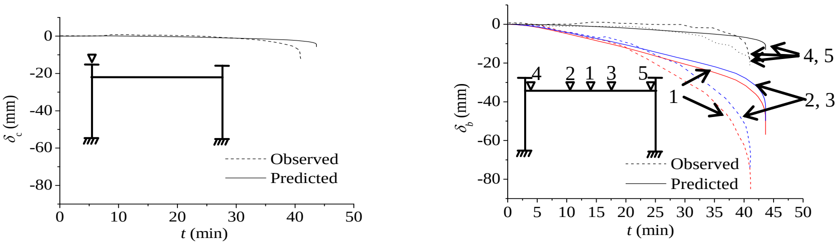

(a) Column

(b) Beam

Figure 4. Comparison of displacement-time relations for test CFRC-1 of Han (2010).

For this structure, the maximum displacement in columns appeared near the top end of the columns. The RC beam cracked at the bottom surface, and the maximum displacement appeared near the midspan. The simulation model revealed the same pattern of behaviour as shown by the major plastic deformation in the corresponding areas, as shown in Figure 5.

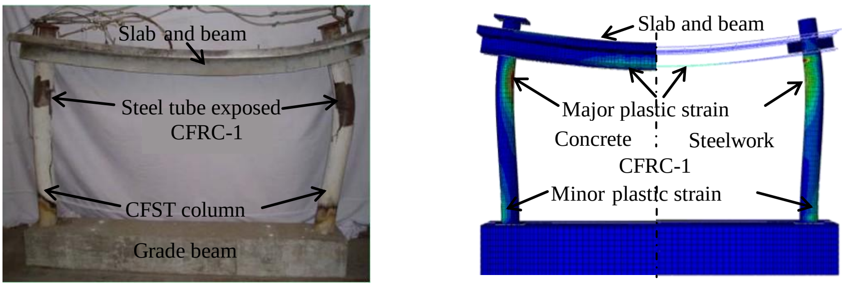

(a) Experiment observation

(b) Simulation

Figure 5. Comparison for failure modes between simulation and test [Han (2010)].

In summary, the FEA simulation model can be considered to be acceptable for further parametric analysis.

3 POST-FIRE PERFORMANCE OF THE HYBRID FRAME

Using the validated FEA model, a parametric investigation was conducted to investigate behaviour of hybrid plane frames after exposure to ISO-834 full-range fire.

3.1 Calculation conditions

The basic information of structure for parametric analysis was determined according to a real project mentioned in Han (2012). It was a full scale hybrid RC beam-CFST column plane frame separated from a spatial frame structure, containing one RC beam and two CFST columns, which was similar to the test model shown in Figure 2. The CFST column is 5400mm high (height H), has an external diameter (D) of 600 mm and a tubular thickness (t) of 12 mm. The RC beam is 9000mm long (measured from the centre of the columns), has a sectional size of 650 mm in height (h) and 400 mm in width (b). The reinforced concrete slab on top of the RC beam has a thickness of 120 mm and a width of 3000 mm. The reinforcement in the beam was two Φ20mm in the top of the cross-section and eight Φ28mm in the bottom. Longitudinal and traverse distributed reinforcement meshes are used in the slab. The yield strength (f_y) of steel for the tube and the hidden corbel is 345MPa, and the yield strength of the longitudinal reinforcing bars (f_{yb}) and the distributed reinforcement meshes are 335MPa and 235MPa, respectively. The compression cube strength of the core concrete (f_{cuc}) inside the steel tube is 60MPa, while that of the concrete in the beam and slab (f_{cus}) is 30MPa. The sprayed fireproof layer is 6 mm in thickness. Its density (ρ) is 400±20kg/m^3 and it has thermal conductivity (λ) of 0.097W/(m•K) and specific heat (c) of 1.047×103J/(kg•K).

The same thermal and mechanical boundary conditions as shown in Figure 2 were adopted in the parametric study. The reference load ratio in the RC beam (m) is 0.5 and the reference load ratio in CFST column (n) is 0.4. The load bearing capacities of the RC beam and the CFST column were both determined by FEA model.

Table 2 gives details of the parametric studies conducted.

Table 2. Parameters used in parametric analysis.

Type	Parameter	Symbol	Unit	Values of the parameter				
Loading Parameter	Column load ratio	n	/	0.17		0.33		0.50
	Beam load ratio	m	/	0.4		0.6		0.8
	Heating time ratio	t_h	/	0.2	0.4	0.6	0.8	0.9
Physical Parameter	Steel tube strength	f_y	MPa	235		345		420
	Core concrete strength	f_{cuc}	MPa	40		60		80
	Strength of concrete in slab and beam	f_{cus}	MPa	30		40		50
Geometric Parameter	Fire protective layer thickness	a	mm	0		3		6

3.2 Full-range behaviour

Figure 6 shows typical axial displacement-time relations of the column and deflection-time relation of the midspan of the beam. Figure 7 shows the corresponding displacement-temperature relations where the temperature was measured at the steel tube. In this simulation example, the fire resistance limit was 126 min with a heating time of 50 minutes (t_h equals 0.4). The important observation is that although the fire entered the cooling stage, the structure was still undergoing further deformation. Failure of the structure was reached with large deflection during the post-fire stage when the load in beam was increased, according to the failure criterion in ISO-834(1999). The beam failed ahead of the column, causing rotation in the joint zone and resulting in the column bending inside in the top end. However, the axial displacement of the columns was relatively small and failure was not reached.

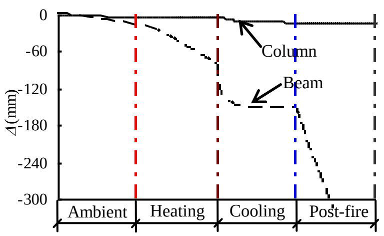

Figure 6. Displacement-time relations.

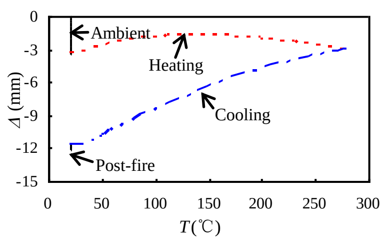

Figure 7. Displacement-temperature relations.

3.3 Residual load bearing capacity

To help evaluate the residual load bearing capacity of hybrid frame, a residual strength index is used. This index is defined as the ratio of the residual load bearing capacity (N_u) of the RC beam to its load bearing capacity at ambient temperature $N_{u,o}$ as follows:

$$k_r = \frac{N_u}{N_{u,o}} \tag{1}$$

The residual load bearing capacity index is zero if the structure fails during the cooling phase.

Tables 3, 4 and 5 summarize failure modes from the parametric study models under different combinations of parameters. In all tables, "post-fire phase" means the structure does not fail during the heating and cooling phases. For this structure, the corresponded residual load bearing capacity index (k_r) is calculated.

Table 3. Influence of beam load ratio (m) and heating time ratio (t_h) on failure mode.

Beam load ratio (m)	Heating time ratio (t_h)				
	0.2	0.4	0.6	0.8	0.9
0.17	Post-fire phase	Post-fire phase	Post-fire phase	Cooling phase	Cooling phase
0.33	Post-fire phase	Post-fire phase	Post-fire phase	Cooling phase	Cooling phase
0.50	Post-fire phase	Post-fire phase	Post-fire phase	Cooling phase	Cooling phase

Table 4. Influence of steel yield strength (f_y) and heating time ratio (t_h) on failure mode.

Yield strength （f_y, MPa）	Heating time ratio (t_h)				
	0.2	0.4	0.6	0.8	0.9
235	Post-fire phase	Post-fire phase	Post-fire phase	Cooling phase	Cooling phase
345	Post-fire phase	Post-fire phase	Post-fire phase	Cooling phase	Cooling phase
420	Post-fire phase	Post-fire phase	Post-fire phase	Cooling phase	Cooling phase

Table 5. Influence of fire protective layer thickness (a) and heating time ratio (t_h) on failure mode.

Thickness (a, mm）	Heating time ratio (t_h)				
	0.2	0.4	0.6	0.8	0.9
0	Post-fire phase	Post-fire phase	Cooling phase	Cooling phase	Cooling phase
3	Post-fire phase	Post-fire phase	Post-fire phase	Cooling phase	Cooling phase
6	Post-fire phase	Post-fire phase	Post-fire phase	Cooling phase	Cooling phase

As can be seen from these tables, the structure tends to survive the full-range fire when the heating time ratio (t_h) does not exceed 0.6.

For the structures that survived the fire and failed in the "Post-fire phase", the residual load bearing capacity indexes were calculated. Figure 8 shows the relations between the selected parameters and residual load bearing capacity coefficient (k_r) against heating time ratio (t_h).

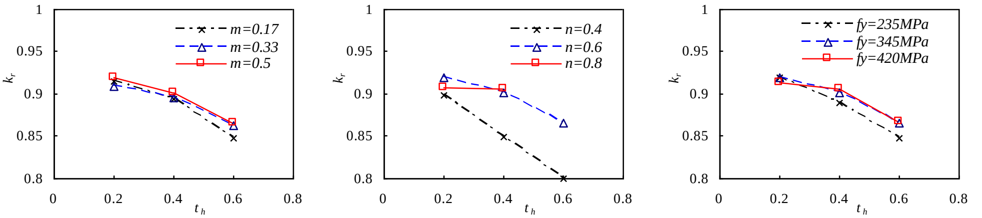

(a) Beam load ratio (m) (b) Column load ratio (n) (c) Steel tube yield strength (f_y)

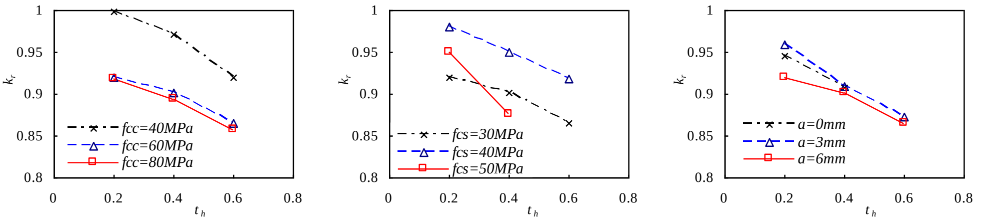

(d) Restrained concrete strength (f_{cuc}) (e) Unrestrained concrete strength (f_{cus}) (f) fire protective layer thickness (a)

Figure 8. Influence of different parameters on k_r.

It can be seen from Figure 8 that k_r decreases with increasing t_h. On the other hand, the parameters m, f_y and a have very minor effects on k_r, while the parameters n, f_{cuc} and f_{cus} had a moderate effects on k_r. In all cases, k_r was within the range of 0.85-0.95, indicating near full load bearing capacity if the structure could survive the heating and cooling phases of the fire attack. This attributes to the fact that the peak temperatures of the steel tube and the reinforcement bars were low as a result of fire protection to the steel tube. However, t_h exceeds a certain critical value, k_r drops suddenly to zero. The critical value is between 0.6 and 0.8.

4 CONCLUSIONS

Based on current research in this paper, the following conclusions can be drawn.

(1) The established FEA model for the hybrid RC beam-CFST column plane frame structure was compared against test data and was shown to be reasonably accurate.

(2) If a structure can survive the heating and cooling phase of the fire without collapse, the residual load bearing capacity can be very high (80-95% of the original value). This means that the hybrid frame can be restored to the original load bearing capacity with relative ease.

(3) The most influential parameter on residual load bearing capacity is the length of heating time. With the heating time was kept constant, the influence of load ratio in beam, yield strength of steel and thickness of fire protective layer was minor.

ACKNOWLEDGEMENT

The research reported in this paper is supported by China National Key Basic Research Special Funds project under Grant No. 2012CB719703, and their financial support is highly appreciated.

REFERENCES

[1] Ding J. and Wang Y.C., "Experimental study of structural fire behaviour of steel beam to concrete filled tubular column assemblies with different types of joints", *Engineering Structures*, 29(12), 3485-3502, 2007.

[2] Han L.H., Wang W.H. and Yu H.X., "Experimental behaviour of reinforced concrete (RC) beam to concrete-filled steel tubular (CFST) column frames subjected to ISO-834 standard fire", *Engineering Structures*, 32(10), 3130-3144, 2010.

[3] Han L.H., Wang W.H. and Yu H.X., "Analytical behaviour of RC beam to CFST column frames subjected to fire", *Engineering Structures*, 36, 394-410, 2012.

[4] Alderighi E. and Salvatore W., "Structural fire performance of earthquake-resistant composite steel-concrete frames", *Engineering Structures*, 31(4), 894-909, 2009.

[5] Elsawaf S. and Wang Y.C., "Methods of improving the survival temperature in fire of steel beam connected to CFT column using reverse channel connection", *Engineering Structures*, 34, 132-146, 2012.

[6] International standard ISO-834. Fire-Resistance Tests Elements of Building Construction, Amendment1, Amendment 2, 1980.

[7] Han L.H., *Fire safety design theory of steel-concrete composite structures*, Science Press, Beijing, 2012. (in Chinese)

[8] Lie T.T., "Fire resistance of circular steel columns filled with bar-reinforced concrete". *Journal of Structural Engineering*, 120(5), 1489-1509, 1994.

[9] European Committee for Standardization. (2004b). *Design of composite steel and concrete structures-Part1-2: General rules - Structural fire design*. Brussels, Belgium.

[10] Tan Q.H., *Performance of steel reinforced concrete (SRC) column and portal frame after exposure to Fire*, Tsinghua University, Beijing, 2012. (in Chinese)

[11] Song T.Y., *Research on post-fire performance of steel-concrete composite beam-column joints*, Tsinghua University, Beijing, 2010. (in Chinese)

[12] Dotreppe J.C. and Franssen J.M., "The use of numerical models for the fire analysis of reinforced concrete and composite structures", *Engineering Analysis*, 2 (2), 61-74, 1985.

[13] Han L.H., *Concrete filled steel tube structures: theory and experience*. Science Press, Beijing, 2007. (in Chinese)

[14] International standard ISO-834-1. Fire-Resistance Tests-Elements of Building Construction, Part1: General requirements, Geneva, 1999.

8th International Conference on Structures in Fire
Guo-Qiang LI, Venkatesh K. R. KODUR, Shou-Chao JIANG, Jian JIANG, Su-Wen CHEN, Guo-Biao LOU (Eds.)
Shanghai, China, June 11-13, 2014

THE PERFORMANCE OF COMPOSITE BEAMS WITH STEEL BAR TRUSS FLOOR SLABS EXPOSED TO FIRE

Ling-Zhu Chen*,*, Shou-Chao Jiang**, Guo-Qiang Li** and Gianluca Ranzi*****

* Department of Building Engineering, Tongji University, Shanghai, China
e-mail: 2lingzhuchen@tongji.edu.cn

** National Key Lab for Disaster Reduction in Civil Engineering, Tongji University, Shanghai, China
e-mails:gqli@ tongji.edu.cn, scjiang@ tongji.edu.cn,

*** School of Civil Engineering, The University of Sydney, Sydney, Australia
email: gianluca.ranzi@sydney.edu.au

Keywords: Steel bar truss floor slab, Shear studs, Elevated Temperatures

***Abstract**. The steel bar truss floor decks are widely used in practice and consist of concrete slabs cast on flat steel sheeting with reinforcement trusses attached to it. This form of construction leads to significant savings in time devoted to the installation of the reinforcement, which in this case is completed off-site, and has been shown to be more cost-effective than other composite floor systems, such as composite slabs with open trapezoidal decks. Despite their similarities, the behaviour of shear connectors embedded in steel bar truss floors is different from the one observed with conventional composite floors and, because of this, this study aims to investigate the performance of shear studs embedded in this kind of slab. This was carried out by performing push-out tests under both ambient and elevated temperatures and, based on these results, a load-slip relationship model for shear studs at high temperatures was proposed. A numerical model was developed to predict the structural performance of composite beams with steel bar truss floor slab under both room and elevated temperatures using the proposed load-slip relationship. Based on the results of a parametric study, it was found that for the beams subjected to same levels of load, variations in the degree of shear connection have negligible influence on the beams' limiting temperatures when the ambient temperature degree of shear connection is greater than 75%, while, for lower values, the limiting temperatures decrease for lower degrees of shear connection. For beams subjected to loads calculated with same load ratios (defined as the applied load during fire divided by the factored design strength at ambient temperature), the beams' limiting temperatures were observed to increase for higher degrees of shear connection at ambient temperature.*

1. INTRODUCTION

The steel bar truss floor slab decks consist of concrete slabs cast on flat steel sheeting with reinforcement trusses attached to it. This form of construction is widely used in practice because of the advantages it can provide when compared to the use of both solid slabs and composite slabs cast on profiled steel sheeting, which include: material savings, shorter construction time, enhanced quality and increased net height available between floors. The steel bar truss deck is comprised of an upper reinforcing rebar, two lower reinforcing bars, and an arrangement of steel braces interconnecting the longitudinal reinforcement. The braces are spot welded to a thin steel deck with thickness of 0.5 mm, which connects several steel bar trusses together as shown in Figure 1.

The steel bar truss decks are fabricated off-site and the concrete is cast on-site, therefore significantly decreasing the amount of time required for the installation of the reinforcement on site. The performance of the steel bar truss floor slab at the ultimate limit state and serviceability limit state was experimentally studied by Tong et al[1]. It was observed that the deflection and the strain of the steel reinforcement during construction could be calculated based on the truss model, while the ultimate moment capacity was taken as the capacity of the reinforced solid slab. The economic benefits of this kind of slab were highlighted when compared to the use of other composite slabs, such as open trapezoidal decks.

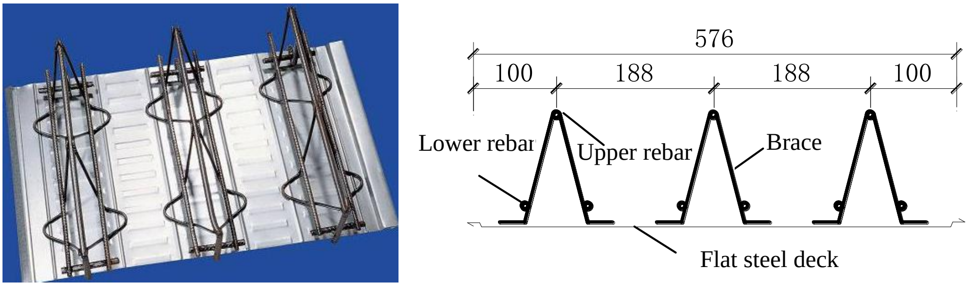

Figure 1. Overview of steel bar truss deck.

The construction technology and design proposal for the steel bar truss floor slab were presented by Li et al. [2]. The shear connectors installed with this arrangement exhibited different behaviours when compared to identical shear connectors embedded in solid slabs and composite slabs with open-trapezoidal steel sheeting. These differences were also observed in the composite beam behaviour. Limited research is available on the performance of the shear connectors and composite beams with steel bar truss floor slabs at both ambient and elevated temperatures. A flat sheet metal was included at the steel beam and concrete interface by Rambo-Roddenberry [3] to study the influence of flat sheet metal on the shear capacity of shear studs at room temperature. In reference [3], it was found that the stud strength was significantly reduced due to the consequent decrease in the friction capacity of the composite system. To further investigate the shear strength of shear connectors embedded in steel bar truss floor slab at both ambient and elevated temperatures, push-out test samples were designed and prepared in accordance with European guidelines to be tested under both ambient and high temperatures. Numerical models were developed to predict the structural performance of composite beams with steel bar truss floor slab under both room and elevated temperatures by using the measured load-slip relationship from the push-out tests.

2. PUSH-OUT TEST

2.1 Test preparation

Eight levels of temperatures (including the ambient one) were selected and used for the ultimate tests as outlined in Table 1. The specimens were prepared following the push-out test requirements specified in Eurocode 4 [4], while some modifications were introduced because dictated by the geometry of the furnace used in the experiment as detailed in Figure 2. In particular, the samples were prepared with a slab thickness of 150 mm, a welded H-shaped section (with flange 150 mm × 12 mm and web 351 mm × 8 mm), 19 mm diameter headed studs with a height of 100 mm after installation, and TD3-120 type steel bar truss (Figure 2).

Table 1. Summary of the specimens and temperature specified in the tests.

Specimen ID	Temperature at 10 mm from stud's base (°C)	Specimen ID	Temperature at 10 mm from stud's base (°C)
S-T1-A	20	S-T5-B	450
S-T2-A	300	S-T6-A	500
S-T2-B	300	S-T6-B	500
S-T3-A	350	S-T7-A	550
S-T3-B	350	S-T7-B	550
S-T4-A	400	S-T8-A	600
S-T4-B	400	S-T8-B	600
S-T5-A	450		

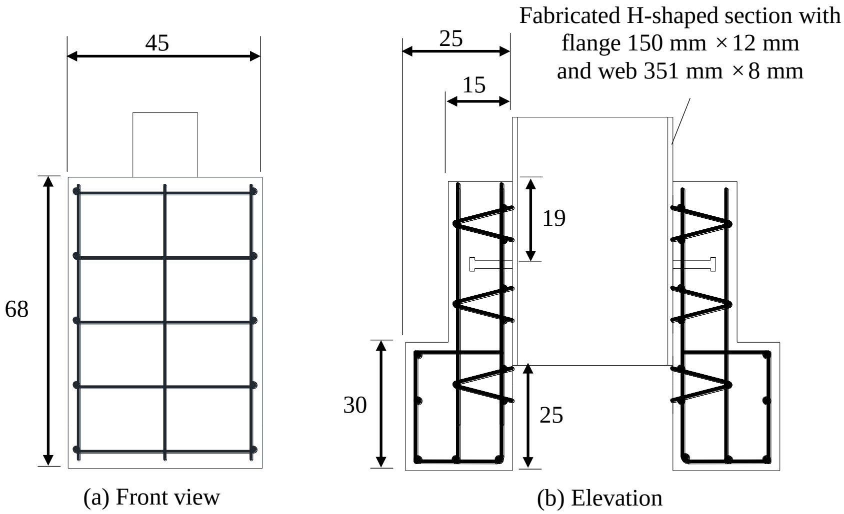

Figure 2. Geometry and detailing of the push−out specimens (dimensions in mm).

The relative displacement between the steel beam and concrete slab was recorded using LVDTs. Thermocouples were used to monitor temperature variations in the shear connectors, steel beam and concrete slab. In particular, the latter were placed on the shear connectors at a distance of 10 mm and 25 mm from their base.

2.2 Test process

The layout of the push-out test setup used for the experiments carried out at both ambient and elevated temperatures is outlined in Figure 3. The furnace was obtained by placing two electric heating plates on the sides of the push-out sample and closing the upper and lower sides of the heated area by means of insulation lids (Figure 3).

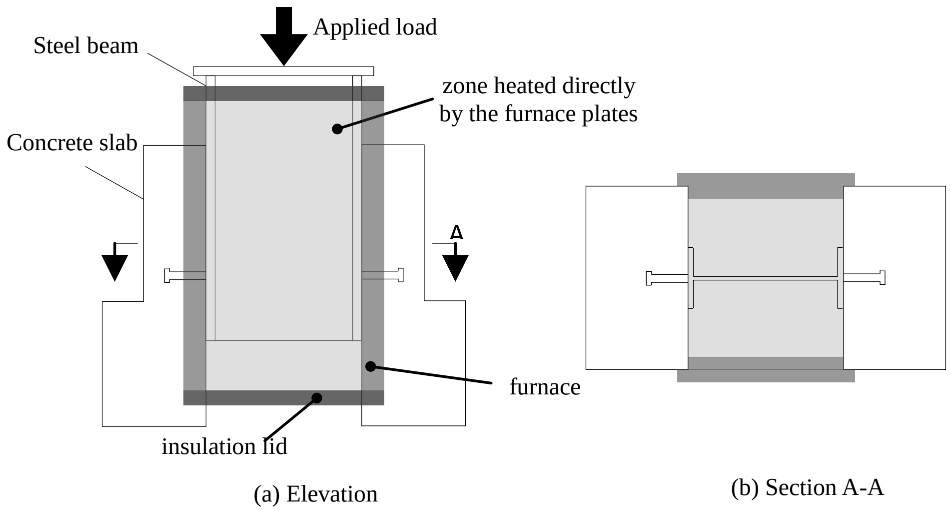

Figure 3. Test setup and loading arrangement.

At the completion of the preload, the sample was unloaded and the heating process started. Once the specified temperature was achieved, as measured from the thermocouples located at 10 mm from the base of the studs, the push-out sample was loaded to failure.

2.3 Test results

The failure mode observed during all experiments consisted of the fracture of the stud at the weld collar, as illustrated in Figure 4. Concrete crushing was also noted to have occurred in the vicinity of the stud base (Figure 4b).

(a) surface of steel section

(b) surface of concrete section

Figure 4. Typical fracture of the shear connector observed in push−out tests.

The load-slip relationship measured for the shear connectors during the ultimate push-out tests are plotted in Figure 5. The stud temperatures included in the first row of Tables 2 and in Figures 6 were taken on the shear connectors at 5 mm from their base. For the tests reported in this paper, the temperature at this height was estimated from the numerical simulations because the stud temperatures were experimentally measured at 10 mm and 25 mm from the connectors' base. In general and as expected, it was observed that the ultimate loads and initial stiffness decreased with increasing stud temperatures.

2.4 Load-slip model

Based on the test result, the load-slip relationship of shear connectors at high temperature for the beam modelling could be calculated according to Equation(1), and the curves are illustrated in Figure 6.

$$\frac{Q_{\mathrm{u}}(T)}{Q_u(20^oC)} = a\left(1-e^{-bx}\right) \qquad (1)$$

where a and b are provided in Table 2.

In the beam modelling, the slip capacity is an important factor to evaluate the possibility of the failure of the shear connectors, which was usually defined as the value of the slip when the load drops to 90% of the ultimate slip. Due to the limitation in the adopted load arrangement, the test was carried out under load-control and the descending curve after the ultimate load was not recorded in the tests by authors. Therefore, only the slip at the maximum load was listed in the third row in Table 2.

Table 2. The value of parameters a and b, and measured slip at peak loads.

Stud temperature	20	100	200	300	400	500	600	700	800
a	1	1	1	0.9264	0.8424	0.6537	0.4591	0.2842	0.1547
b	2.207	2.207	1.700	1.250	1.407	1.770	1.966	1.250	1.080
s_u(mm)	8.5	8.5	8.5	8.5	9.0	9.5	10.0	10.0	10.0

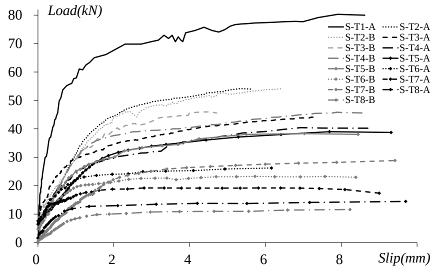

Figure 5. Measured load-slip relationship of shear studs embedded in steel bar truss floor slabs.

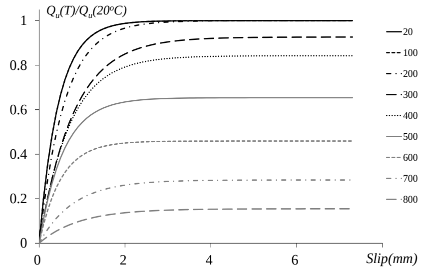

Figure 6. Proposed load-slip relationship for shear studs embedded in steel bar truss floor slabs.

3. NUMERICAL MODEL FOR COMPOSITE BEAMS

An accurate three-dimensional finite element model was developed using the commercial software Abaqus to predict the thermo-mechanical behaviour of the composite beams at elevated temperatures [5-7]. The overall analysis was subdivided in two steps. In particular, a first step included the heat transfer analysis to evaluate the temperature distributions within the sample when subjected to variations in temperatures, such as those produced in a fire scenario. A mechanical analysis was implemented with Abaqus/Standard in the second step to simulate the structural response of the composite beams, in which case the composite beams were subjected to a combination of fire (here defined in terms of a temperature history obtained from the previous heat transfer analysis) and applied loads.

3.1 Thermal analysis

3.1.1 Element type and mesh

A typical finite element model used for the composite beam is illustrated in Figure 7. The 8-node linear heat transfer brick element (DC3D8) was adopted to simulate the steel joist and concrete slab, the 4-node linear heat transfer plane element (DS4) was used to represent steel sheeting, while the reinforcement was modelled with a 2-node linear heat transfer line element (DC1D2).

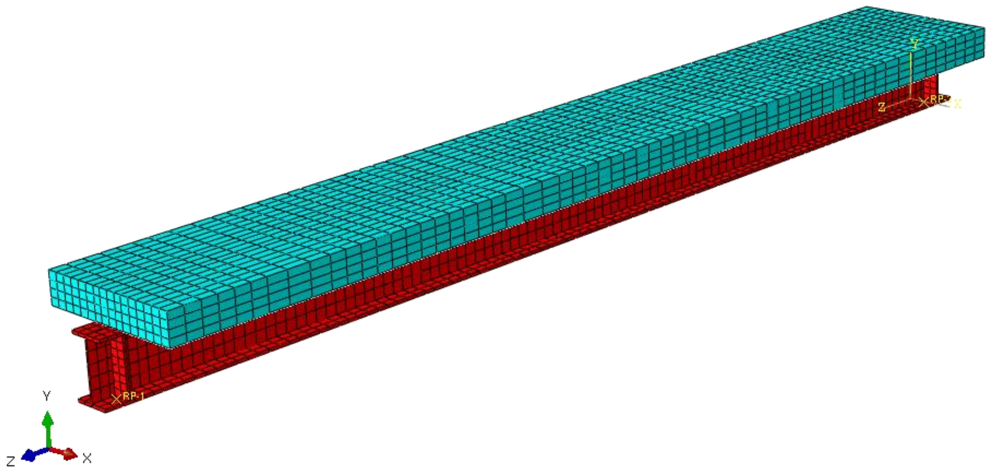

Figure 7. Typical finite element model and coordinate system used for the composite beams.

3.1.2 Modelling of contact regions

The contact between the concrete slab and steel deck, as well as between the steel deck and steel joist, was implemented making use of the surface to surface interaction available in Abaqus. With the consideration that, there would be voids between the concrete and steel deck surfaces, the thermal conductance between the concrete slab and steel deck was taken as 800 W/m^2K, as suggested in reference [8], while large value of thermal conductance was assign for the interface between steel deck and steel joist neglecting the temperature difference between each other.

The boundary conditions in the heat transfer analysis were defined relying on the contact module in Abaqus. On the surface of the parts exposed to the fire, the library options SFILM and SRADIATE were used to specify the convection and radiation heat fluxes, respectively. A convection coefficient value of 25 W/m^2K and an emissivity of 0.7 were used for the concrete and steel surfaces exposed to the natural fire, as recommended in EC1 [9]. The shadow effects developed by the presence of the steel flanges were considered applying a reduction factor to the total heat flux as suggested in EC4 [10]. The sink temperature option in SFILM and the ambient temperature option in SRADIATE were taken as the temperature from the standard fire curve. A convection coefficient of 9 W/m^2K [9] was assigned to the top and lateral surfaces of the slabs (i.e. those not exposed to the higher temperatures) with the Abaqus command SFILM, with the sink temperature taken as room temperature.

3.1.3 Material nonlinear constitutive relationships

The temperature-dependent thermal properties of both concrete and steel materials recommended in EC4 [10] were used in the analysis. The moisture evaporation in concrete was modelled specifying a peak value of specific heat at 115 ^{o}C with a moisture content of 4% of the concrete weight, as suggested in EC4 [10], while a value of 2531.4 J/kgK was used for the thermal conductivity.

3.2 Mechanical analysis

3.2.1 Element type and mesh

The components of the composite beams steel joist and concrete slab were described in the numerical model with the C3D8R element, the reinforcement was simulated with the T3D2 element, and the shear connectors was represented with the Spring2 element. The steel sheeting was not included in the mechanical analysis considering that the temperature of the sheeting is very high and the contribution is negligible. Based on this, the overall arrangement of the mechanical model was equivalent to the one already illustrated in Figure 7 for the thermal analyses.

3.2.2 Boundary conditions and load arrangements

The boundary conditions were applied on reference points. The roller support is enforced restraining displacements of the reference point along the global *x*- and *y*-axes as well as rotations with respect to the *y*- and *z*-axes (where the coordinate system is outlined in Figure 7). The pinned support requires an additional restraint in the longitudinal direction (in the z-direction). The load was applied enforcing pressure on the concrete slab.

3.2.3 Modelling of contact regions

The surface to surface interaction properties available in Abaqus were used to describe the interaction between steel beam and the concrete slab. In these interactions, the HARD contact was specified in the direction normal to the interface plane, while for the tangential behaviour the frictionless option was adopted therefore only including the influence of the shear connectors on the interface. The embedment technique was used to describe for the bond between the reinforcement and the concrete slab.

3.2.4 Material nonlinear constitutive relationships

A bi-linear stress-strain curve is adopted for the steel of the beam and reinforcement, with strain hardening included for temperatures below 400 ^{o}C. The failure of the steel beam relied in the Von-Mises failure criteria. An initial linear-elastic range up to 40% of the compressive strength is applied after which the Concrete Damage Plasticity model available in Abaqus was adopted. The non-linear stress-strain curve suggested in EC4 is adopted for the material model of concrete under uni-axial loading condition. The thermal expansion coefficients of the concrete and steel materials were taken as 1.8×10^{-5} and 1.4×10^{-5}, respectively. Reductions in the material properties of the concrete and the steel materials at elevated temperatures were based on EC4 recommendations [11].

3.3 Model validation against experimental results

To validate the accuracy of the proposed model, the experiments T15 and T16 conducted by Wainman and Kirby [12]were simulated. The layout of the samples are indicated in Figure 8. Both beams have the length of 4530 mm. The steel section consists of a UB 254×146×43, while the concrete slab is 130 mm thick and 642 mm wide. The load-slip relationship of shear connectors at high temperatures presented by Zhao and Kruppa [13] was applied to represent the shear connectors. Comparisons between the calculated temperature values and those measured experimentally are provided in Figure 9(a) and 9(b) for T15 and T16 respectively, and highlight the good predictions of the numerical model in both concrete and steel components, although the predicted temperature of steel top flange in T16 is slightly lower than the measured temperature. It is worth pointing out that the temperature distribution for T15 and T16 should be theoretically the same because the geometry and fire exposure of T15 and T16 were the same; however, the measured steel top flange temperature in T16 was about 80 ^{o}C higher than that in T15. The predicted deflection was also compared with the experimental results in Figure 10 (a) and (b) for T15 and T16 respectively. As expected, the predicted deflection for T16 is slightly higher than the measured deflection due to the larger thermal bowing caused by larger thermal gradient. However, good agreement between the simulation and experiment result can be seen for T15. The measured limiting temperature for T15 and T16 was 737 ^{o}C and 654 ^{o}C respectively，while the simulated limiting temperature was 742.5 ^{o}C and 646.7 ^{o}C respectively，the error of which is within 1%. Therefore, the proposed can be used to conduct further research on the performance of composite beams with steel bar truss slab.

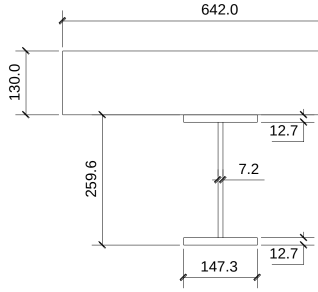

(a) Geometry of the cross-section

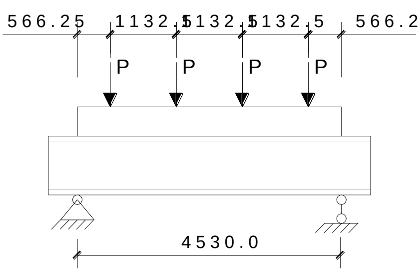

(b) Geometry of the beam span

Figure 8. Geometry of the beam (dimensions in mm).

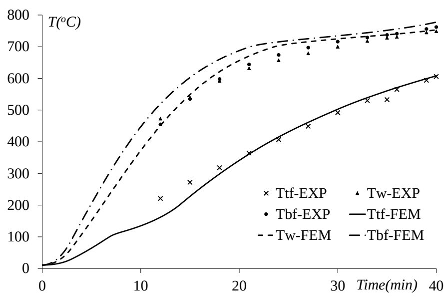

(a) T15

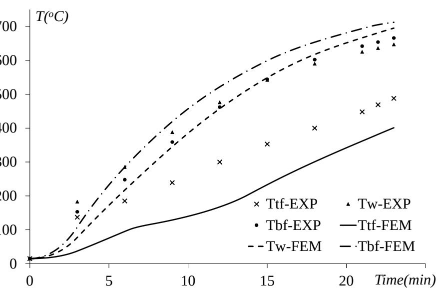

(b) T16

Figure 9. Comparison between the simulated and measured temperature development.

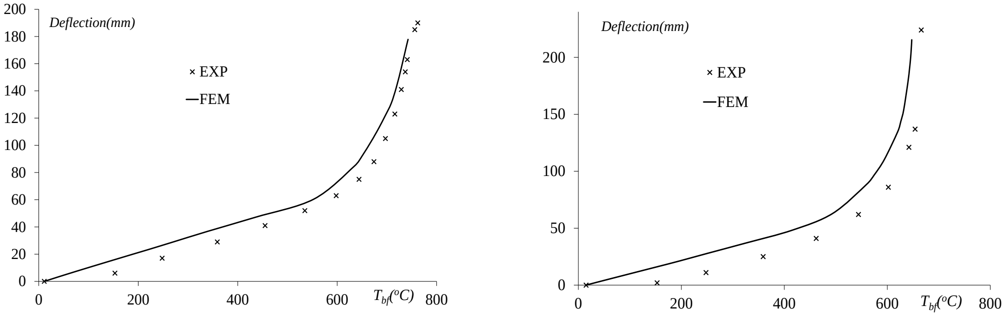

(a) T15

(b) T16

Figure 10. Comparison between the simulated and measured mid-span deflection versus steel bottom temperature.

4. PARAMETRIC STUDY ON COMPOSITE BEAMS

To predict the performance of composite beams with steel bar truss slab at elevated temperatures, the proposed model was used to conduct a series of parametric study. The main variable parameters investigated comprised different degree of shear connection at room temperature, different load ratios (defined as the applied load during fire divided by the factored design strength at ambient temperature) and different design fire rate. A total of 16 beams were analyzed, and the details were summarized in Tables 3 through 6. All the samples were designed with a slab thickness of 100 mm, a welded H-shaped section (with flange 140 mm × 10 mm and web 300 mm × 8 mm), 19 mm diameter headed studs with a height of 80 mm after installation, and TD3-70 type steel bar truss (Figure 1). The span of these samples were taken as 5.26 m. The typical model used for the beam simulation is illustrated in Figure 7. The beams were divided into 4 groups (G1 to G4). The beams within each group of G1, G2 and G3 were designed to support the same load, determined from the specified load ratio (Tables 3-5) and moment capacity at ambient temperature of the beam with full shear connection. The samples with lower degrees of shear connection were still subjected to this load, even if in these cases the load ratios varied when calculating the moment capacity for the partial shear connection cases. In group G4, all the beams were subjected to the same load ratios, with the actual applied load calculated from the specified load ratio and the corresponding moment capacity at ambient temperature. The load ratio in group G2 was designed to be higher than the one in other groups, and the designed fire rate in Group G3 was specified to be higher than the other groups to investigate the influence of the load ratio and fire rate on the performance of composite beams, respectively.

Table 3 shows the simulated limiting temperature of the beams in G1 group, and the calculated limiting temperature from EC4. Figure 11 illustrates the development of mid-span deflection with the steel bottom temperature. Consistent with the prediction from EC 4, the degree of shear connection at room temperature was observed to have slight influence on the limiting temperature of the composite beams with degrees of shear connection higher than 75%. This is a consequence of the fact that the degradation of shear connectors' capacity is much lower than the degradation of the tensile strength of steel beams, since the temperature of shear connectors is lower than steel beam temperature due to the protection from the concrete when the composite beam exposed to fire. However, when the degree of shear connection at room temperature is lower than 75%, the limiting temperature of the composite beam decreases with the decreasing degree of shear connection at room temperature.

Table 3. The limiting temperature from the simulation for beams in G1 group.

Specimen ID	Degree of shear connection at room temperature	Fire rate（h）	Load ratio	$T_{cr\text{-}FE}$（°C）	$T_{cr\text{-}EC4}$（°C）
1	100%	1	0.46	645.6	657.0
2	75%	1	0.49	639.2	657.0
3	50%	1	0.53	627.1	640.5
4	25%	1	0.62	608.8	600.5

Table 4 shows the limiting temperature of the beams in G2 group from the simulation and EC4. Figure 12 illustrates the development of mid-span deflection with the steel bottom temperature. Same trend was observed when compare to the beams in G1 group for which a lower load ratio was specified. The limiting temperatures of beams in G2 group are much lower than the limiting temperatures of beams in G1 group. It is also worth pointing out that the maximum slip experienced by shear studs reached about 10.7 mm at the fire limit state, which exceeded the slip capacity of shear studs; therefore, the failure of shear studs may have occurred before concrete crushing.

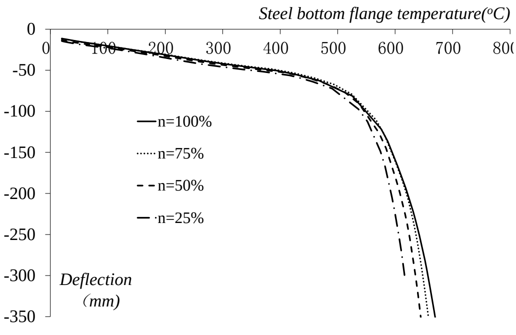

Figure 11. The influence of the deformation of shear studs（G1 group）.

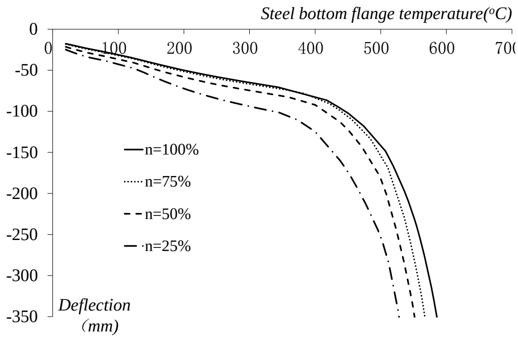

Figure 12. The influence of the deformation of shear studs（G2 group）.

Table 4. The limiting temperature from the simulation for beams in G2 group.

Specimen ID	Degree of shear connection at room temperature	Fire rate（h）	Load ratio	$T_{cr\text{-}FE}$（°C）	$T_{cr\text{-}EC4}$（°C）
5	100%	1	0.70	562.1	572.5
6	75%	1	0.74	545.9	565.9
7	50%	1	0.80	529.0	531.6
8	25%	1	0.94	503.6	490.6

Table 5 shows the limiting temperature of the beams in G3 group from the simulation and EC4. Figure 13 illustrates the development of mid-span deflection with the steel bottom temperature. Same trend was observed when compare to the beams in G1 group which was exposed to a lower fire duration of 1 hour. The limiting temperatures of beams in G3 group is similar to the limiting temperature of beams in G1 group.

Table 5. The limiting temperature from the simulation for beams in G3 group.

Specimen ID	Degree of shear connection at room temperature	Fire rate（h）	Load ratio	$T_{cr\text{-}FE}$（^oC）	$T_{cr\text{-}EC4}$（^oC）
9	100%	2	0.46	646.6	654.9
10	75%	2	0.49	641.7	654.9
11	50%	2	0.53	622.5	639.3
12	25%	2	0.62	607.3	599.5

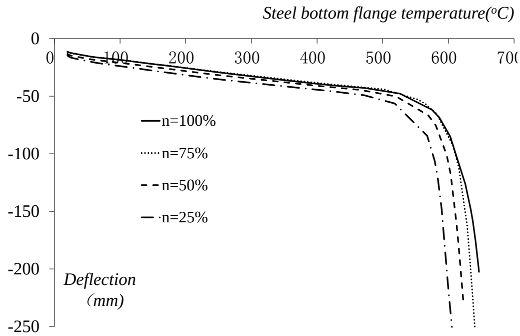

Figure 13. The influence of the deformation of shear studs（G3 group）.

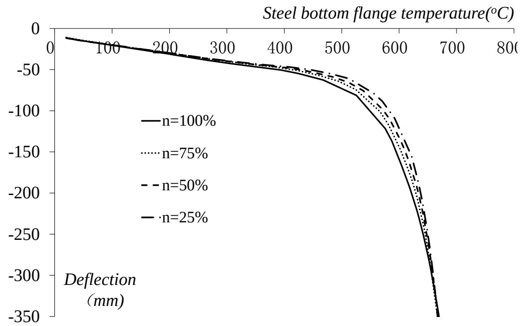

Figure 14. The influence of the deformation of shear studs（G4 group）.

Table 6 lists the limiting temperature of the beams in G4 group from the simulation and EC4. Figure 14 plots the development of mid-span deflection with the steel bottom temperature. Differently from the other three groups, the limiting temperatures of beams in this group were observed to increase with the decreasing degree of shear connection at room temperature. This could be attributed to the different load values applied to these beams. Since the load value applied to each beam was calculated according to the same load ratio and from the moment capacity at ambient temperature (which decrease with the degree of shear connection at room temperature), the beams in this group were exposed to different load levels. As the degradation of shear connectors' capacity is much lower than the degradation of the tensile strength of steel beams, the degree of shear connection at high temperatures is marginally improved, to which it corresponds a slight increase in the composite beam capacity.

Table 6. The limiting temperature from the simulation for beams in G4 group.

Specimen ID	Degree of shear connection at room temperature	Fire rate（h）	Load ratio	$T_{cr\text{-}FE}$（^oC）	$T_{cr\text{-}EC4}$（^oC）
13	100%	1	0.46	645.6	655.5
14	75%	1	0.46	648.3	664.6
15	50%	1	0.46	650.8	669.1
16	25%	1	0.46	652.4	651.4

5. CONCLUSIONS

This paper presented experimental results of push-out tests carried out on shear studs embedded in steel bar truss floor slab. All samples exhibited stud shearing failure followed by concrete crushing in the vicinity of stud base. The shear capacity and stiffness were observed to degrade with increasing levels of temperature. A load-slip model was proposed based on the test results to be used as input data in numerical beam simulations (to define the material behaviour of shear connectors) . A numerical model was developed to predict the structural performance of composite beams with steel bar truss floor slab under both room and elevated temperatures using the proposed load-slip relationship. It was found that for the beams subjected to same levels of loads, the degree of shear connection has negligible influence on beams' limiting temperatures when the degree of shear connection at ambient temperature is greater than 75%, while the limiting temperatures decrease for lower degree of shear connection for the beams with the degree of shear connection at ambient temperature less than 75%. For beams subjected to loads calculated from same load ratios (defined as the applied load during fire divided by the unfactored design strength at ambient temperature), the beams' limiting temperatures were observed to increase for higher degrees of shear connection at ambient temperature.

REFERENCES

[1] G.S. Tong, S.J. Liu, W.B. Liu, Experimental Research on A Self-supported Floor System(In Chinese), Progress in Steel Building Structures, 7 (2005) 16-22.

[2] W.B. Li, Q.Y. Yang, L. Qian, Application of Steel Bar truss Deck in Steel Structure (In Chinese), Construction Technology, 35 (2006) 105-107.

[3] M.D. Rambo-Roddenberry, Behaviour and Strength of Welded Stud Shear Connectors, in, Virginia Polytechnic Institute and State University, Blacksburg, USA, 2002.

[4] EC4, Eurocode 4: Design of composite steel and concrete structures -- Part 1-1: General rules and rules for buildings, in: British Standards Institution, 2004.

[5] F. Tahmasebinia, G. Ranzi, A. Zona, A probabilistic three-dimensional finite element study on simply-supported composite floor beams, Australian Journal of Structural Engineering, 12 (2012) 251-262.

[6] F. Tahmasebinia, G. Ranzi, A. Zona, Probabilistic three-dimensional finite element study on composite beams with steel trapezoidal decking, Journal of Constructional Steel Research, 80 (2013) 394-411.

[7] F. Tahmasebinia, G. Ranzi, A. Zona, Beam tests of composite steel-concrete members: A three-dimensional finite element model, International Journal of Steel Structures, 12 (2012) 37-45.

[8] S. Guo, Experimental and numerical study on restrained composite slab during heating and cooling, Journal of Constructional Steel Research, 69 (2012) 95-105.

[9] EC1, Eurocode 1: Actions on structures —Part 1-2: General actions — Actions on structures exposed to fire, in: British Standard Institution, 2002.

[10] EC4, Eurocode 4: Design of composite steel and concrete structures -- Part 1-2: General rules — Structural fire design, in: British Standards Institution, 2005.

[11] EC2, Eurocode 2: Design of concrete structures —Part 1-2: General rules — Structural fire design, in: British Standard Institution, 2004.

[12] D.E. Wainman, B.R. Kirby, Compendium of UK Standard Fire Test Data, Unprotected Structural Steel-1, in, 1987.
[13] B. Zhao, J. Kruppa, Experimental and numerical investigation of fire behavior of steel and concrete composite beams, in: B.M.S. C. Dale Buckner (Ed.) Proceedings of an Engineering Foundation Conference, The Structural Engineering Institute, Irsee, Germany, 1996, 129-142.

8th International Conference on Structures in Fire
Guo-Qiang LI, Venkatesh K. R. KODUR, Shou-Chao JIANG, Jian JIANG, Su-Wen CHEN, Guo-Biao LOU (Eds.)
Shanghai, China, June 11-13, 2014

FIRE RESISTANCE OF REINFORCED CONCRETE-FILLED STEEL TUBE WITH SQUARE SECTION UNDER THREE-SIDE FIRE

Xue-Tao Lv*, Yu-Zhuo Zhang* and Wei-Wei Wang*

*College of Engineering and Architecture, Liaoning Technical University, Fuxin 123000, P. R. China
e-mails: lxtwww30@sina.com, lntuzyz@126.com, wwwlxt30@sina.com

Keywords: Three-side fire, Bar-reinforced concrete-filled steel tube columns, Fire resistance, Temperature distribution

Abstract. *A numerical program aimed to predict the fire resistance of reinforced concrete-filled steel tube(RCFST) columns subjected to three-side fire was developed. Parametric analysis on the basis of the program for the fire resistance of RCFST columns was conducted, and 194 hypothetical cases were verified with various parameters, including axial load ratio, sectional width, slenderness ratio, loading eccentricity, steel and concrete strength, and the steel bar ratio. Key parameters and their effects were revealed from the simulation results, and a simplified calculation formula for predicting the fire resistance was deduced. The analysis results indicated that the load ratio, sectional width and slenderness ratio are the main parameters that influence the fire resistance of RCFST columns, and the fire resistance increases with the increase of the sectional width and the decrease of the load ratio and the slenderness ratio. The influence of the loading eccentricity is also obvious when load location lean to the unexposed side.*

1 INTRODUCTION

Concrete-filled steel tube (CFST) columns have been widely used in many constructions due to their outstanding performance, such as higher strength and larger stiffness and ductility. In recently years, Japan and other country have been performed experiments that reinforced bars were added into the plain concrete-filled steel tube columns to further improve the bearing capacity and ductility of the columns. Experiments and theoretical analysis have been carried out by Chinese scholars in this area.

In the past, a large number of researches had been developed on the fire resistance behavior of CFST columns, such as Lie and Chabot (1992)[1], Kim (2000)[2], Han (2007)[3], Yang (2008)[4]. In order to further improve the load bearing capacity of the column, at the same time to delay cracking of core concrete under fire, Xu (2006)[5],Zheng (2010)[6],Dong (2009)[7].etc. began to study the fire resistance of RCFST columns, putting forward the calculation methods of fire resistance of columns. However, these studies mainly focused on the behavior of RCFST columns under four-side fire as the current codes and standard fire tests assume that the columns are always attacked by fire uniformly on their four sides. Actually in a real fire exposure situation, most columns except those in a hall are heated non-uniformly i.e. heated on three sides, two sides, or just one side (Figure 1). It is necessary to investigate the fire resistance of RCFST columns heated non-uniformly.

In recent years, the team of the authors [8-12] has been engaged in research to determine the fire resistance of CFST or RCFST columns under non-uniformly fires, both theoretical and experimental studies have been carried out. The research results reported in this paper are part of a wider study on reinforced concrete-filled steel tube columns under non-uniform fire.

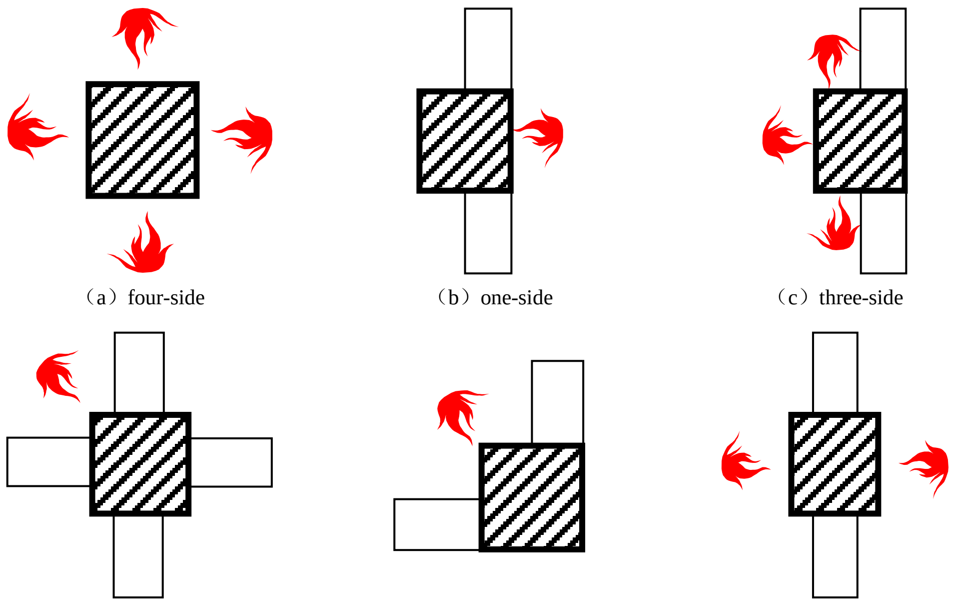

Figure 1. Different fire conditions.

2 VERIFICATION ON THE FIRE RESISTANCE ANALYSIS MODEL

2.1 Temperature field analysis model

Generally, the influence of reinforced bar on the cross section of the temperature field is not considered, because the volume fraction of reinforced bar is small in square section concrete-filled steel tube columns. However, the impact of that is considered in the paper in order to connect the fire resistance calculation model subsequently. On the basis of temperature field analysis model of the plain concrete-filled steel tube column with square section, the temperature field analysis model of the RCFST column with square section was built up in ANSYS software. In thermal analysis, the unit division method is shown in Figure 2. A uniform room temperature of 20℃ was assumed as the initial temperature of the RCFSTs. The ISO 834 standard fire curve was used as the fire action on the RCFST columns in most cases. The coefficients for heat transferring on the boundaries were taken as the following according to the recommendations in BS EN 1994-1-2[13]: the resultant emissivity coefficient ε=0.5, and the convention factor λ=25 W/(m^2 ·℃). The thermal conductivity coefficient (k_W/m℃), thermal capacity (c, J/m^3℃) of concrete and steel adopt the expressions for the thermal properties of concrete and steel provided by Lie and Irwin [6].

2.2 fire resistance analysis model

In the calculation of column strength, the following assumptions were made:

1.Plane sections remain plane.

2. There is no slip between steel and concrete.

3. There is no composite action between the steel and concrete.

4. Concrete has no tensile strength.

5. The reduction in column length before exposure to fire (consisting of free shrinkage of the concrete,

creep, and shortening of the column due to load) is negligible. This reduction can be eliminated by selecting the length of the shortened column as initial length from which the changes during exposure to fire are determined.

The strength of the column reduces gradually with exposure time, when it is below the external load, the strength column becomes unstable and is assumed to have failed. The time to reach this failure point is the fire resistance of the column. Based on these assumptions above, theoretical analysis were conducted using Fortran 90, considering the path of constant loading under elevating temperatures, to investigate the fire resistance of Bar-reinforced concrete-filled SHS columns under three-side, and the second-order effect of axial forces is considered in the program.

The stress-strain relationships of steel at ambient and heating conditions are used according to [1]. The stress-strain relationships of concrete at ambient, heating conditions are used according to [13]. The influences of thermal expansion of concrete and steel are considered according to that recommended by Reference [13].

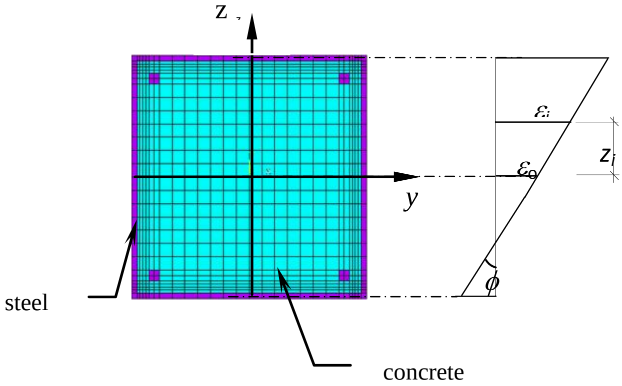

Figure 2. Basic variables of section distortion.

2.3 Validation of the FEA model

So far, there is no test on RCFST columns heated non-uniformly. Therefore, the finite element analysis model including temperature field analysis model and fire resistance analysis model will be validated by the tests results of RCFST column under fire uniformly on their four sides in Chabot et al [14]. exposed to the CAN/ULC-S101(1989) elevated fire. Table 1 lists a summary of the specimens, where B is the outside dimension of square steel tube, t_s is the thickness of square steel tube, L is the length of square steel tube, f_y and f_{yb} is the yield strength of steel and concrete, f_c is the cylinder compressive strength, N_d is the loads under the fire, $t_{R,e}$ is the experimental fire resistance of columns that have been heated to elevated temperature, t_c is the calculated fire resistance under the same situation. A comparison between them is listed in Table 1.

Table 1. Parameters of test specimens and results of fire resistance testing by T.T. Lie [14].

No.	$B\times t_s\times L$ (mm)	reinforce	f_y (MPa)	f_{yb} (MPa)	f_c (MPa)		N_d (kN)	t_{Re} (min)	t_c (min)
					28d	test			
SQ-18	304.8×6.35×3810	4Φ19.5	350	400	42.3	48.1	1440	112	106
SQ-19	304.8×6.35×3810	4Φ19.5	350	400	42.3	48.1	2200	70	76

Figure 3 compares the temperature field and axial deformation-time curve between experimental and calculated results for all tests. FEA model successfully simulated the trend and fire resistance of the rested specimens.

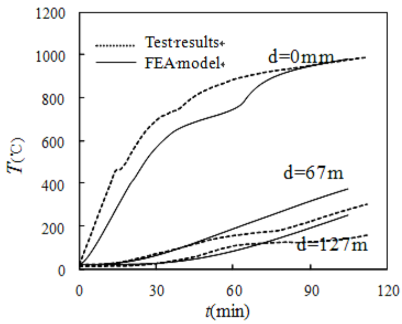

(a) temperature field of SQ-18

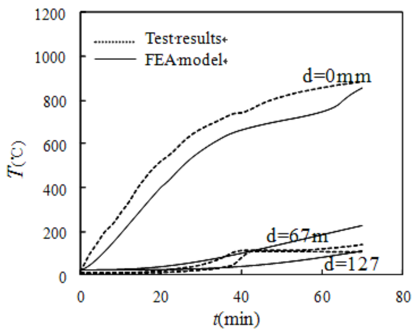

(b) temperature field of SQ-19

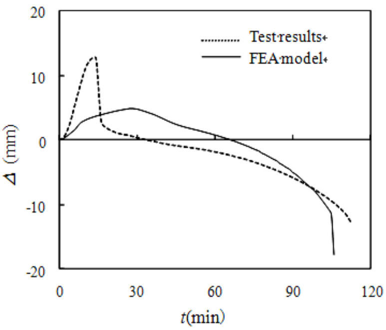

(c) The axial deformation-time curve of SQ-18

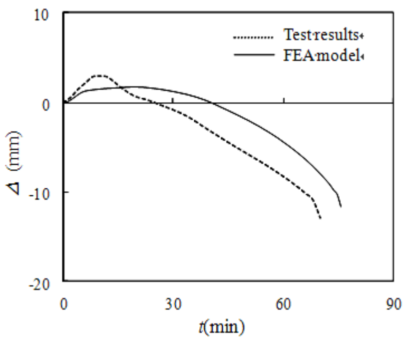

(d) The axial deformation-time curve of SQ-19

Figure 3. Comparison between calculated and tested results of SQ-18,19 [14].

3 PARAMETRIC ANALYSIS

A parametric analysis of the fire resistance has been performed to study the effects of parameters such as axial load ratio (n, $n=N_o/N_u$), cross-sectional width (B), slenderness ratio(λ), load eccentricity(e/r_0), material strength (f_{cu} is concrete cube strength, f_y is yield strength of steel, f_{yb} is yield strength of reinforced bar) and ratio of reinforcement (ρ, $\rho=A_{sb}/A_{core}$: A_{sb} is cross-section area of composite section, A_{core} is cross-secton area of concrete core). The values of those parameters are listed in Table 2.

3.1 Influence of axial load ratio

The influences of axial load ratio parameters on fire resistance of columns are shown in Figure 4. From the figure it can be seen that axial load ratio has a high significant influence on the fire resistance, fire resistance decline with the increase of axial load ratio. Fire resistance of RCFST with square section under three-side fire cannot reach a required level 1 fire resistance. Columns need to conduct fire protection measures when structural fire resistance rating require for level 1.

Table 2. Values of studied parameters.

Parameter	Values	Fixed value
t_h (min)	0, 30, 60, 90, 120, 150, 180	-
n	0.4, 0.5, 0.6, 0.7, 0.8	0.7
B (mm)	200, 300, 400, 500	400
□ λ	20, 40, 60, 80	20
e/r_0	0, ±0.2, ±0.4, ±0.6, ±0.8, ±1	0
f_{cu} (MPa)	30, 40, 50, 60	40
f_y (MPa)	235, 345, 390, 420	235
f_{yb} (MPa)	235, 335, 390, 420	335
ρ (%)	1.0, 3.0, 5.0	1.0

3.2 Influence of cross-sectional width

The influences of cross-sectional width parameters on fire resistance of columns are shown in Figure 5. From the figure it can be seen that cross-sectional width has a high significant influence on the fire resistance, fire resistance increase with the increase of cross-sectional width. The curve approximate linear. With the increase of cross-sectional width, the volume of concrete are greater, and the component heat absorption ability are stronger. At the same exposure time, component temperature reduces with the length of cross-sectional width.

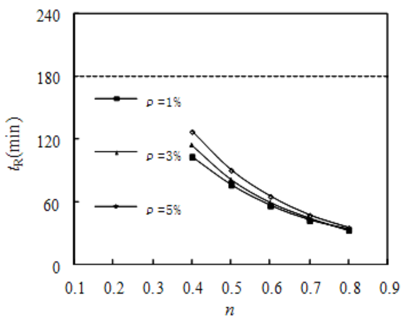

Figure 4. Influence of load ratio.

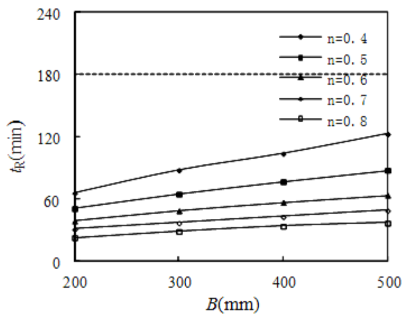

Figure 5. Influence of sectional width.

3.3 Influence of slenderness ratio

The influences of slenderness ratio parameters on fire resistance of columns are shown in Figure 6. From the figure it can be seen that fire resistance decrease with the increase of slenderness ratio. When $\lambda \geqslant 60$, the influence is bigger, because deflection of the component generated by non-uniform high temperature field is the same as that caused by load, which are both convex toward the surface exposed to fire, thus the columns destroyed rapidly with the obvious second-order effects.

3.4 Influence of load eccentricity

The influences of load eccentricity parameters on fire resistance of columns are shown in Figure 7. From the figure it can be seen that, to the curve (λ=40), when $e/r_0 \leqslant 0$, the influence is small, when $e/r_0 > 0$, fire resistance increase quickly with the increase of load eccentricity, the temperature field of columns is uniaxial symmetry and exist a large temperature gradient exposed to three-side fire. To the curve (λ=80), fire resistance of components does not appear to the maximum, because of the obvious second-order effect with the big slenderness ratio.

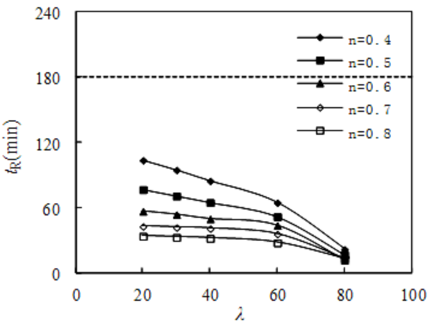

Figure 6. Influence of slenderness ratio.

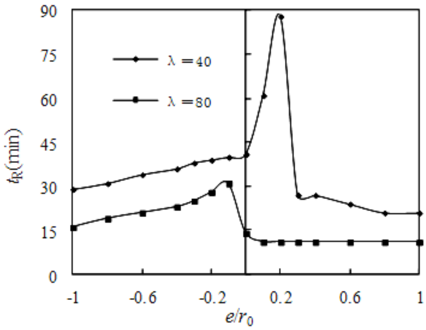

Figure 7. Influence of load eccentricity.

3.5 Influence of material strength and ratio of reinforcement

The influences of yield strength of steel tube, concrete strength and yield strength of steel bar on fire resistance of columns are shown in Figures 8 to 10. From the figure it can be seen that the improvement of fire resistance are with the slightly lower of yield strength of steel tube and the higher of concrete strength. The yield strength of steel bar has little effect on fire resistance of the components. The influences of steel ratio on fire resistance of columns are shown in Figure 11. From the figure it can be seen that ratio of reinforcement has a little significant influence on the fire resistance.

4 A SIMPLIFIED CALCULATION FORMULAR FOR PREDICTING THE FIRE RESISTANCE

The analytical results show that axial load ratio, sectional width and slenderness ratio are the main parameters that influence the fire resistance of RCFST columns. Within the range of parameters used in the project, n=0.4~0.8, B=200~500mm,α=0.05~0.2,ρ=1%~5%,e/r_0=-1.0~1.0,λ=20~80, f_y=235~420MPa,

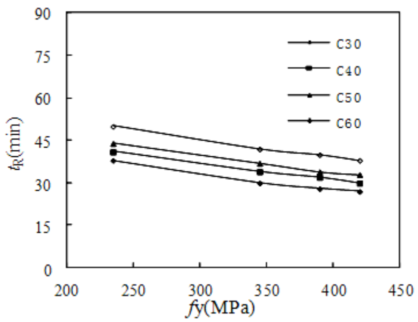

Figure 8. Influence of yield strength of steel tube.

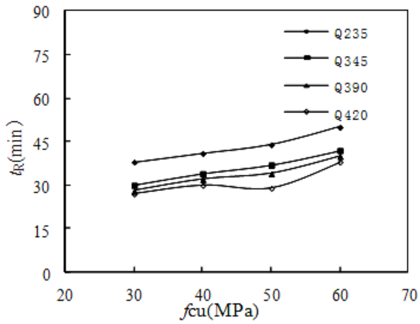

Figure 9. Influence of cube compressive strength of concrete.

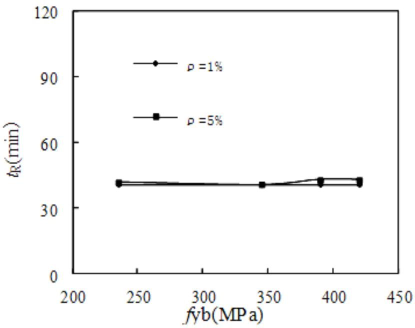

Figure 10. Influence of yield strength of steel bar.

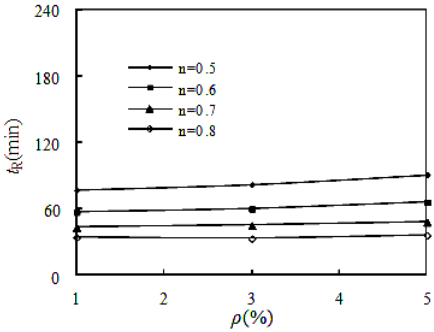

Figure 11. Influence of ratio of reinforcement.

f_{yb}=235~420MPa, f_{cu}=30~60MPa, a simplified calculation formula for predicting the fire resistance was deduced:

$$t_R = 33.34(B/1000)^{0.65}(\lambda/40)^{-0.52}n^{-1.64} \quad (1)$$

Where t_R is the fire resistance, B is the cross-section width, λ is the slenderness ratio, n is the axial load ratio. The formula is intended to predict the fire resistance of RCFST columns with square section under three-side ISO-834 fire. Figure 12 compares the curves between numerical and predicted results. The agreement between test results and predicted results is acceptable.

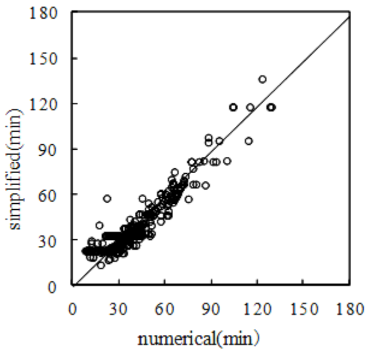

Figure 12. Comparison of t_R between simplified and numerical results.

5 CONCLUSIONS

Numerical models for predicting the temperature distribution and fire resistance of RCFST columns exposed to three-side fire by the general finite element package ANSYS and Fortran separately were set up. Key parameters and their effects were revealed from the simulation results, and a simplified calculation formula for predicting the fire resistance was built up. The following conclusions can be drawn:

（1）The procedures for the fire resistance analysis can be set forth from the comparison between the test results and the computational results, and a good agreement was gotten to validate the accuracy of this model.

（2）The analysis results indicated that axial load ratio, sectional width and slenderness ratio are the main parameters that influence the fire resistance of RCFST columns, and the fire resistance increases with the increase of the sectional width, the decrease of the load ratio and the slenderness ratio. The influence of the loading eccentricity is also obvious when load location lean to the unexposed side.

（3）Key parameters and their effects were revealed from the simulation results, and a simplified calculation formula for predicting the fire resistance was deduced.

ACKNOWLEDGEMENT

The research reported in this paper was sponsored by the National Natural Science Foundation(No. 51208246), a Special Fund of Liaoning Technology University(No.20130309;SCDY2013009). The financial support is highly appreciated.

REFERENCES

[1] Lie T T., Chabot M., “Experimental Studies on the Fire Resistance of Hollow Steel Columns Filled with Plain Concrete”, *NRC-CNRC Internal Report*, 1992.

[2] Kim Dong-kyu., Chot Sung-mo., Chung Kuyung-soo., “Structural Characteristics of CFT Columns Subjected Fire Loading and Axial Force” *Proceedings of the 6th ASCCS Conference*, Los Angeles, USA, 271-278, 2000.

[3] Han Linhai, “Structures of Concrete Filled Steel Tube-Theories and Practices 2nd ed ”,Beijing, *Science Press*, 2007 (in Chinese).

[4] Yang Hua, Han Linhai, Wang Yongchang, “Effects of Heating and Loading Histories on Post-fire Cooling Behaviour of Concrete-filled Steel Tubular Columns”, *Journal of Constructional Steel Research* (5/64), 556-570, 2008.

[5] Xu Lei, Liu Yubin, “Fire Resistance of Bar-reinforced Concrete Filled Square Steel Columns”, *Building Science* (3/22), 21-25, 2006 (in Chinese).

[6] Zheng Yongqian. Calculation of Fire Resistance for Bar-reinforced Concrete-filled Square Steel Tubular Columns[J]. Building Science,201026(9):44-48.(in Chinese)

[7] Han Jinsheng, Dong Yuli, Xu Zhaodong, “Study on Fire-resistance Performance of Reinforced Concrete-filled Steel Tubular Columns”, *Journal of Building Structures* (S2/30). 265-270, 2009 (in Chinese).

[8] Lü Xuetao, YANG Hua, ZHANG Sumei, “Fire Resistance Behavior and Mechanism of Concrete-filled Square Hollow Columns in Non-uniform Fires”, *Journal of Building Structures* (3/34), 35-44, 2013 (in Chinese).

[9] Yang Hua, Lv Xuetao, Zhang Sumei, “Temperature Distributions of Concrete-filled Steel Tubes with Rectangular Sections While Exposure to One-side Fire”, *Journal of Tianjin University, Natural Science Edition* (5/43), 392-399, 2010(in Chinese).

[10] Lv Xuetao, Yang Hua, Zhang Sume, “Fire Resistance Limit of Concrete-filled Square Steel Tube Columns Exposed to Three-faced Fire” *Journal of Natural Disasters* (3/21), 198-203, 2012(in Chinese).

[11] Lv Xuetao, Yang Hua, Zhang Sumei, “Fire Resistance of Concrete-filled Square Hollow Sections Being Exposure to Two-opposite-side Fire” *Industial Construction* (6/42), 148-152, 2012(in Chinese).

[12] Lv Xuetao, Yang Hua, Zhang Sumei, “Effect of Contact Thermal Resistance on Temperature Distribution of Concrete-filled Steel Tubes in Fire” *Journal of Harbin Institute of Technology(New Series)* (1/18), 99-106, 2011.

[13] Guo Zhenhai, Shi Xudong, “Behaiour of Reinforced Concrete at Elevated Temperature and Its Calculation Third Edition”, *Tsinghua University Press*, Beijing, 2003(in Chinese).

[14] Chabot M.，Lie T T., “Experimental Studies on the Fire Resistance of Hollow Steel Columns Filled with Bar-reinforced Concrete”, *NRC-CNRC Internal Report*, No. 628, Ottawa, Canada, 1992.

FAILURE LOADS OF ISOLATED COMPOSITE SLAB-BEAM SUB-ASSEMBLAGES AT ELEVATED TEMPERATURE PREDICTED BY BAILEY-BRE METHOD

Jun-Xian Liu* and Kang-Hai Tan*
*School of Civil and Environmental Engineering, Nanyang Technological University, Singapore 639798, Singapore
E-mails: liuj0055@e.ntu.edu.sg ckhtan@ntu.edu.sg

Keywords: Isolated composite slab, Fire, Bailey-BRE

Abstract. *This paper presents the experimental programme of composite slab-beam sub-assemblages at elevated temperature conducted in Nanyang Technological University. In addition, the test results have been compared with Bailey-BRE method and it shows that the deflection limits defined in Bailey-BRE method is conservative.*

1. INTRODUCTION

The Bailey-BRE method[1] provides a revolutionary design to reduce the fire protection cost for interior beams by taking into account the enhancement from tensile membrane action. However, this model is mainly based on some idealized conditions assuming no effects from boundary continuity and deformation. In reality, the composite slab boundary beam deflection will inevitably take place under fire condition. Moreover, the behaviour will also be affected by the in-plane restraint from the surrounding composite panels.

2. DESIGN OF THE TEST

In this paper, three isolated composite slabs at one-quarter scale were designed to study the effect of boundary beam deformation on the development of tensile membrane action as shown in Figure 1. The interior beams for ISOCS1 and ISOCS1.5 were not fire protected while the rest of the beams and columns were painted with intumescent coating for one hour fire rating.

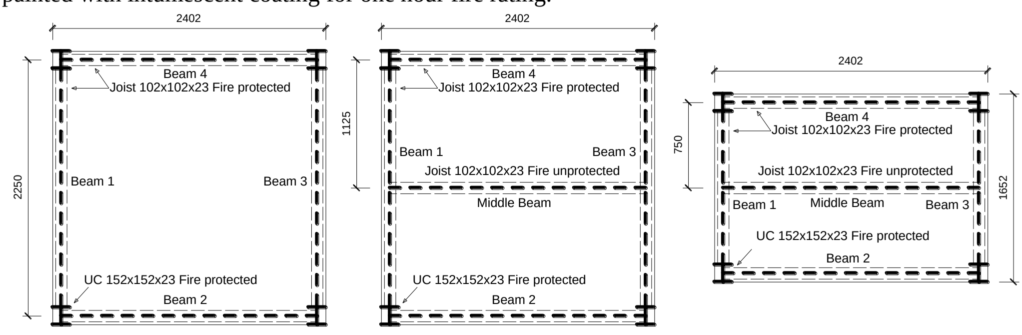

ISOCS1NI (no interior beam) ISOCS1 ISOCS1.5

Figure 1. Specimens for isolated composite slab-beam sub-assemblage. (unit in mm)

2.1 Material properties for test specimens

For comparison purposes, all tested composite slabs were made from concrete grade C25/30, S460 for rebar, S355 for both supporting beams/columns and S500 for profile decks as indicated in Table 1. Detailed material properties are provided in Table 2. All these three specimens are designed with the same thickness h of 60mm and the rebar of depths d_x & d_y are in the middle layer of the concrete slab.

Table 1. General dimensions for tested specimens.

	Properties	*Size*
Concrete slab	C30	60 mm thick
Supporting beams	Grade S355	102x102x23 kg/m
Columns	Grade S355	152x152x23 kg/m
Rebar mesh	Grade S460	Φ6mm/120mm spacing
Profile decks	Grade S500	1 mm thick

Table 2. Material properties for tested specimens.

	Geometry			*Concrete slab*			*Reinforcement*			*Steel beam & column*		
	h mm	d_x mm	d_y mm	f_{cm} MPa	f_{ctm} MPa	E_{cm} GPa	f_y / f_u MPa	Elongation, %	Modulus E_s, GPa	f_y / f_u MPa	Elongation, %	Modulus E_s, GPa
ISOCS1NI	61	31	28	33.2	2.7	30.2	573 /636	20.2	201.4	394 /485	23.1	211.3
ISOCS1	60	30	33	32.5	2.9	32.4	589 /658	22.0	210.1	410 /507	27.0	215.1
ISOCS1.5	62	32	29	34.1	2.6	31.6	559 /647	21.5	206.3	424 /498	22.3	208.7

2.2 Profile decking

Previous researchers [2] ignored the profile decking during the fire test because debonding occurred around 100℃ due to evaporation of water in the concrete. However, from the previous test conducted by the author for one-way composite slab, it has been observed that the profile decking debonded at the beginning when it was heating up to 100℃. However, it has been found out that when temperature increased, the gap between the concrete slab and the profile decking closed up until they were bonded together at around 500℃. Therefore, the profile decking played a very important role in maintaining the integrity of the composite slab as shown in Figure 2 and Figure 3. Hence, in this composite slab-beam system, 1mm thick decking is provided.

100℃ 300℃ 500℃ and above

Figure 2. The behaviour of the profile decking with the concrete slab when temperature increases.

Figure 3. Overall view of the composite slab after the fire test.

2.3 Test setup

Following Trung ‘s work[3], the author used a similar test setup for isolated composite slab-beam system as shown in Figure 4. Since the isolated slabs were smaller than the furnace, some insulation panels were used to cover the gaps between the slab and the electrical furnace as shown in Figure 5.

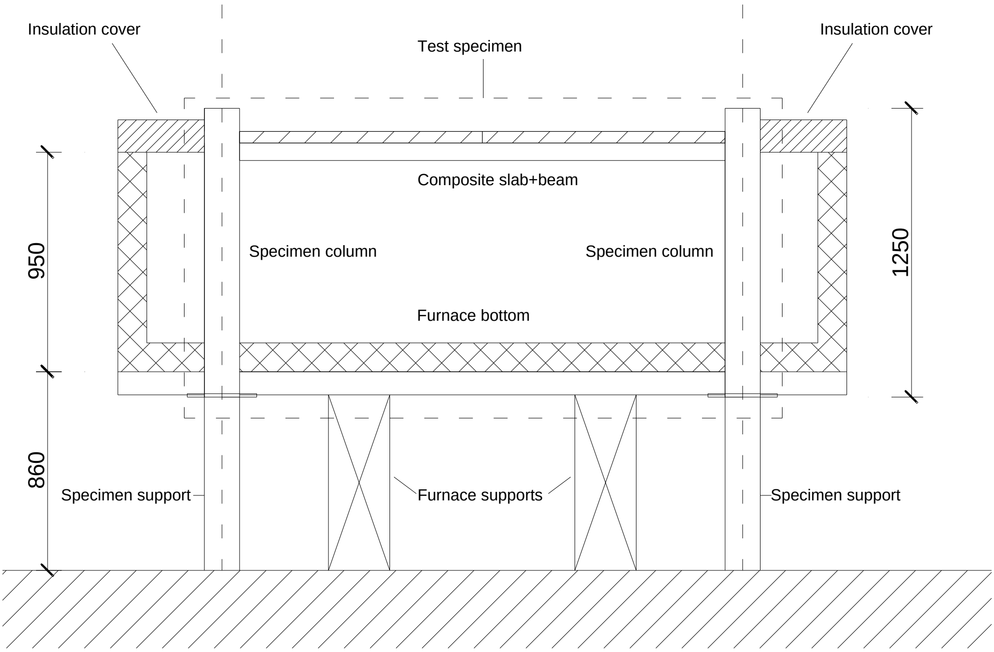

Figure 4. Test setup for isolated composite slab-beam system.

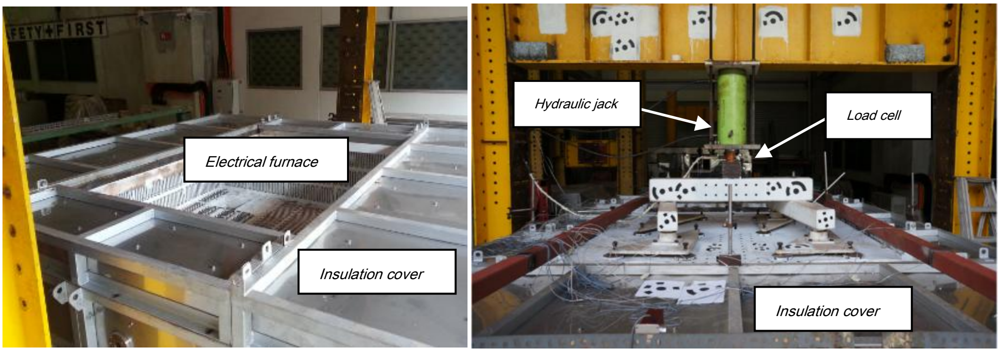

(a) Electrical furnace with insulation cover (b) The typical test setup for isolated composite slab

Figure 5. Typical test setup for isolated composite slab-beam system with insulation covers.

2.4 Applied loading

There are three types of test specimen as shown in Figure 6, viz. (a) composite slabs with an aspect ratio of one without any interior beam, (b) aspect ratio of one with an interior beam and (c) aspect ratio of 1.5 with an interior beam. The yield line mechanism for each type of the composite slab is calculated and summarized in Table 3.

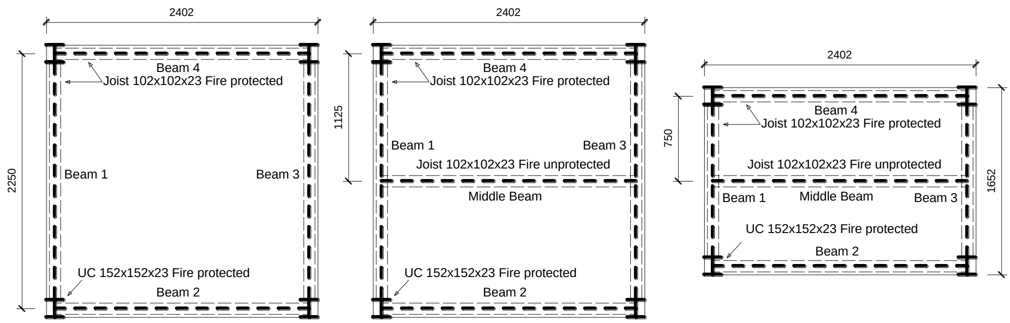

(a) No interior beam (b) With interior beam (c) Aspect ratio 1.5

Figure 6. Three types of test specimens.

Table 3. Summary of the yield-line load for three types of specimens.

	Yield Line Load
Aspect ratio = 1 without interior beam	11 kN/m^2
Aspect ratio = 1 with interior beam	26 kN/m^2
Aspect ratio =1.5 with interior beam	48 kN/m^2

The normal practice for composite slab design load is to have applied load at about 0.4 to 0.6 of the yield line load at ambient temperature. Therefore, the applied load was fixed at 20 kN/m^2 on the 2400× 2400 mm composite slab surface (aspect ratio of to 1) and 30 kN/m^2 on the 2400x1600 mm composite slab surface (aspect ratio of 1.5).

In order to simulate uniformly distributed load on the top surface of the composite slab, following Foster's setup [4], a twelve-point loading system was designed as shown in Figure 7(a) and (b). Triangular plates with three point loads are very stable even at very large displacement, because when one of these three points deflects downwards, the other two points will not be affected by this movement, which means that the three loading points act independently.

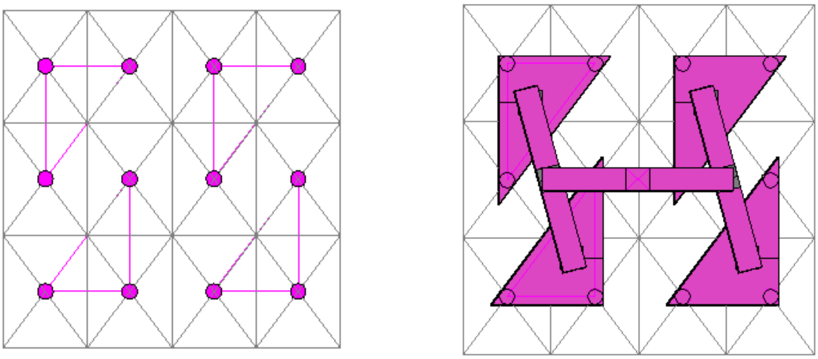

(a) (b)

Figure 7. Illustration of loading system for uniform distributed load.

In addition, strain gages were attached on four supporting circular hollow section (CHS) columns, and reaction forces were monitored and calculated to ensure the load system was in equilibrium. Figure 8 shows the measured reaction forces in these four columns were in good agreement with the total measured external load.

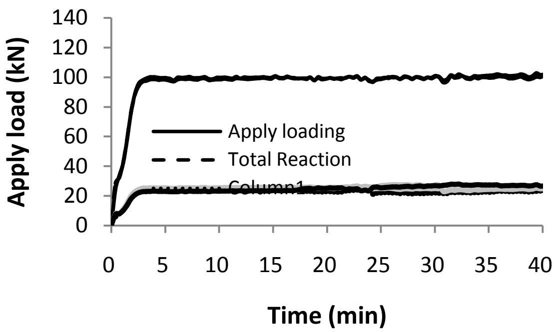

Figure 8. Apply loading versus reaction forces.

2.5 Failure criterion

The failure is governed by the load-bearing capacity as shown in Figure 9. In each test, a hydraulic pump was maintained constant 100 kN on the slab surface and the furnace started to heat up from the bottom surface of the composite slabs. However, the applied load started to drop from 86 min, 100 min and 84 min for ISOCS1NI, ISOCS1 and ISOCS1.5, respectively. Although the author tried his best to pump the jack back to 100 kN, the load cell could not reach 100 kN. The time corresponding to this was defined the failure time for each specimen. In addition, the cross-sectional temperature at bottom of the slab, mesh layer and top surface were recorded.

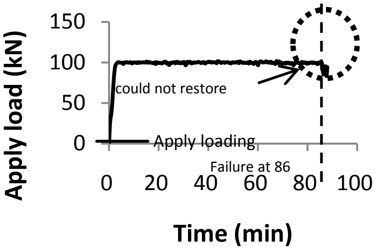

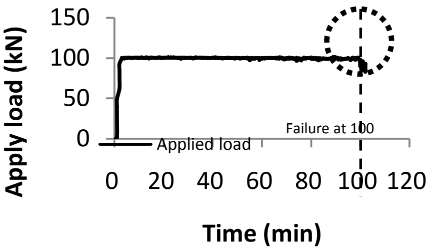

(a) The applying load versus time for ISOCS1NI (b) The applying load versus time for ISOCS1

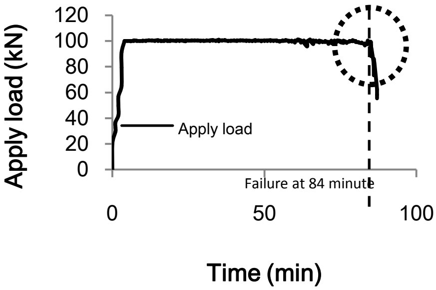

(c) The applying load versus time for ISOCS1.5

Figure 9. Governing failure criterion for load bearing capacity.

3. SUMMARY OF TEST RESULTS AND DISCUSSIONS

3.1 Temperature profile

Due to the constraint of power supply in NTU, the maximum temperature of the electrical furnace is 1000℃ after one hour heating. Therefore, the temperature of the electrical heating furnace started from ambient temperature, attaining 1000℃ after one hour. The furnace was maintained at 1000℃ until failure occurred for the specimen. The temperature profiles of specimens ISOCS1NI, ISOCS1 and ISOCS1.5 are shown in Figure 10.

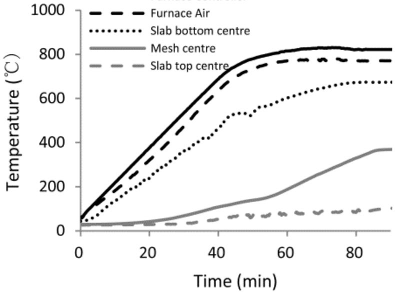

ISOCS1NI

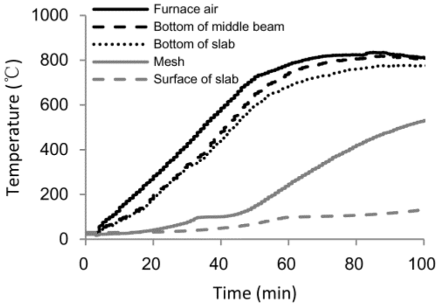

ISOCS1

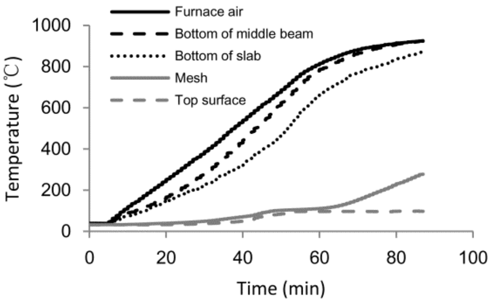

ISOCS1.5

Figure 10. Temperature profiles for ISOCS1NI, ISOCS1 and ISOCS1.5.

3.2 Development of cracks

A demonstration of the development of cracks for specimen ISOCS1NI is shown in this section. Cracks started around the corner of the slab when the gas temperature reached 200℃. After that, cracks parallel to the previous corner began to propagate towards the centre and some minor cracks occurred along the edges of the supporting beams at 300℃ as shown in Figure 11.

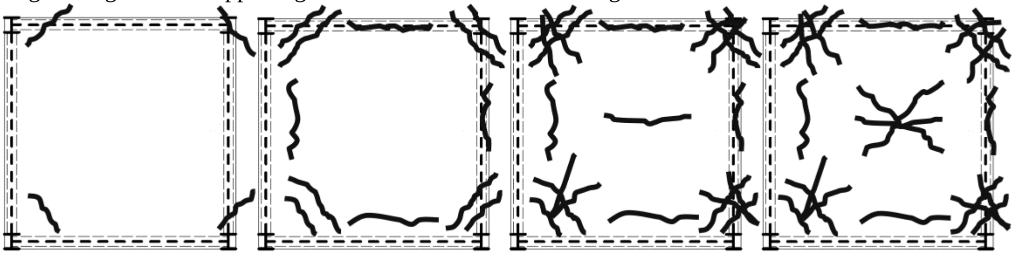

200℃ 300℃ 500℃ 700℃

Figure 11. The development of cracks for ISOCS1NI.

Once the gas temperature breached 500℃, cracks emanated from four columns to the centre of the slab. Meanwhile, middle cracks had been observed. When the gas temperature achieved 700℃, cracks from the corners propagated to the centre of the slab. Finally, the crack width grew bigger and bigger around the corners until the specimen reached the failure point.

All three specimens showed a similar trend of the crack formation as shown in Figure 12. The red colour in the photos indicated the occurrence of cracks. The cracks around the corners and above the supporting steel beams were the dominant factors affecting the failure mode. It was worthy to note that the corner cracks formed at about 45 degrees with respect to their connecting edges and propagated towards the centre of the slabs.

ISOCSNI(no interior beam) ISOCS1(aspect ratio 1) ISOCS1.5(aspect ratio 1.5)

Figure 12. Typical failure modes for isolated composite slab-beam system.

3.3 Displacement

Vertical displacement was measured through a line transducer as indicated in Figure 13(a). A roller was installed to maintain verticality of the line transducer. To prevent the heat from damaging the equipment, the line transducer was located outside the furnace.

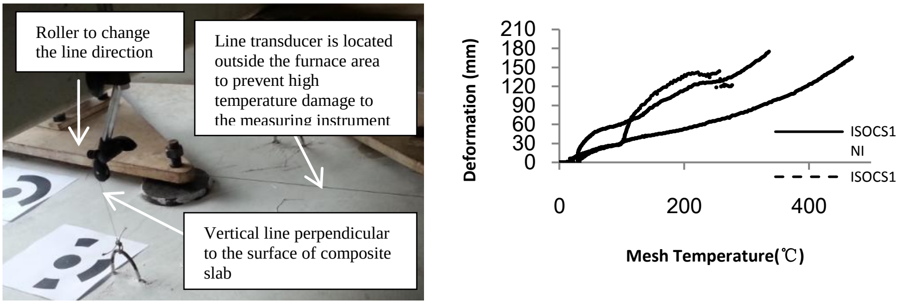

(a) (b)

Figure 13. (a) Illustration of measuring vertical displacement on the top surface of composite slab by using the line transducer; (b) Centre deformation versus mesh temperature relationship.

The major factor governing the deformation of composite slabs under fire condition is the mesh temperature. Therefore, a comparison of the slab centre deflection for the three specimens was conducted with respect to the mesh temperature as shown in Figure 13(b). For the slab with an aspect ratio of one, specimen ISOCS1NI (without internal beam) deformed larger than ISOCS1 (with internal beam) at the beginning stage. However, after 250℃, the deformation rates (deformation/temperature) of these two specimens were similar, probably due to strength reduction of the interior beam from ISOCS1. When the mesh temperature reached 250℃, the average temperature of the unprotected internal beam was about 800℃. According to EC4 part 1-2, for bare structural steel at 800℃, the reduction factor is more than 90%. Therefore, ISOCS1 behaved like ISOCS1NI after the internal beam temperature reached 800℃.

For ISOCS1.5 with a larger aspect ratio of 1.5, the centre deformation was similar to ISOCS1 before 100℃. After that, ISOCS2 deflected much more than ISOCS1NI and ISOCS1 for the same mesh temperature, because ISOCS1.5 with an aspect ratio of 1.5 is like a one-way slab unlike ISOCS1NI and ISOCS1 with an aspect ratio of one. The failure mechanism for ISOCS1.5 had been changed from two-directional tensile membrane action into one-way catenary action. Therefore, the load-carrying capacity for ISOCS1.5 was much lower than ISOCS1NI and ISOCS1.

3.4 Comparison with Bailey-BRE method at the deflection limit

The deflection limit was calculated from Equation (1) from Bailey-BRE method. However, SCI P288 assumes that ($T_2 - T_1$) is equal to 770℃ for fire exposure below 90 minutes and 900℃ thereafter, while SCI P390 assumes that T_2 and T_1 are based on the temperatures at the bottom and the top surface of the slab from the test. A simple numerical analysis of one-dimensional heat transfer has been conducted and shown in Table 4.

$$w = \frac{\alpha\left(T_2 - T_1\right)l^2}{19.2h} + \sqrt{\left(\frac{0.5 f_y}{E_s}\right)_{\text{Reinf't}_{20^{o}\text{C}}} \frac{3L^2}{8}} < w_{\max} = \frac{\alpha\left(T_2 - T_1\right)l^2}{19.2h} + \frac{l}{30} \tag{1}$$

Table 4. Numerical comparison of top and bottom surfaces temperature in SAFIR.

Thickness	T_2-T_1 (℃)			
	60 minute	90 minute	120 minute	480 minute
60mm (test specimen)	604	578	561	563
120mm	852	855	846	826
180mm	918	955	966	975

It can be seen that for the thicker composite slab the temperature differences are larger than 770℃ and 900℃ for below 90 minute and thereafter, respectively. Therefore, SCI P288 is not conservative, which is the reason why SCI P390 suggests using the actual bottom and top surface temperatures to calculate the deflection limit.

Table 5 shows the results of unprotected interior beams (USB) in which the bending resistance of USB ($M_{Rd,\theta}$) is calculated based on bare steel section. Temperatures of the interior beams and the slab were taken at the time when the deflection limit (calculated by Equation. (1)) was reached.

Table 5. Verification of the bending resistance of unprotected interior beam based on steel section (at the deflection limit).

Series	Specimen	Time	USB	Mesh	Slab top	Slab bottom	$M_{Ed,\theta}$	$M_{Rd,\theta}$	Check USB	$p_{b,\theta}$
		min	°C	°C	°C	°C	kN/m^2	kN/m^2		kN/m^2
Isolated	ISOCS1NI	55	N.A.	330	84	672	N.A.	N.A.	N.A.	N.A.
	ISOCS1	60	807	295	97.6	680	6.25	2.96	*failed*	0
	ISOCS1.5	59	812	200	98.5	621	6.25	3.4	*failed*	0

Since the bending resistance $M_{Rd,\theta}$ of USB in all specimens was smaller than the design bending moment $M_{Ed,\theta}$ the unprotected interior beams have failed. Therefore, the increase in the slab load-bearing capacity due to flexural strength of USB, $p_{b,\theta}$, is equal to zero. In other words, the slab alone could resist the entire applied load.

Temperatures at the reinforcement mesh, the slab top and bottom surfaces were used to calculate the slab yield line capacity at the deflection limit ($p_{y,\theta}$). The enhancement factor *e* was calculated based on the deflection limit by considering the tensile membrane effect in SCI P390.

Table 6**.** Calibration of the Bailey-BRE method for isolated series using the deflection limit.

Series	Specimen	p_{test}	$p_{y,\theta}$	Slab deflection w_m	Enhancement factor *e*	Total capacity $ep_{y,\theta}$	Prediction / Test
		kN/m^2	kN/m^2	mm		kN/m^2	
Isolated	ISOCS1NI	20	10.68	67	1.56	16.67	0.83
	ISOCS1	20	10.69	69	1.58	16.9	0.85
	ISOCS1.5	30	19.24	52.7	1.35	26	0.87

It can be seen in Table 6 that the prediction/test load ratios for all specimens are smaller than 1.0. Therefore, it can be concluded that the Bailey-BRE prediction is conservative if the deflection limit (Equation (1)) is from SCI P390.

4. CONCLUSIONS AND FUTURE WORKS

Based on these three isolated composite slab tests, it can be concluded that the profile decking plays a very important role for keeping the integrity of the composite slab under fire condition. For the Bailey-BRE method, it is better to use the actual bottom and top surfaces' temperatures to calculate the deflection limit, which is more conservative for thicker composite slabs. After checking with the three specimens, it has been shown that the deflection limits are all conservative. In future, the boundary conditions, which is considering the internal (four edges continuous), edge (three edges continuous) and corner (adjacent two edges continuous) composite slab panels will be considered in the test, because lateral restraint will affect the development of both compressive membrane action and tensile membrane action.

ACKNOWLEDGEMENTS

The research presented was funded by Agency for Science, Technology and Research (A*Star Singapore) and cooperated with Singapore Civil Defence Force (SCDF). The financial support of A*STAR is gratefully acknowledged.

REFERENCES

[1] G.M. Newman, J.T. Robinson, C.G. Bailey, Fire safe design : a new approach to multi-storey steel-framed buildings, 2nd ed. ed., Steel Construction Institute, Ascot, 2006.
[2] C.G. Bailey, Membrane action of unrestrained lightly reinforced concrete slabs at large displacements, Eng Struct, 23 (2001) 470-483.
[3] N.T. Trung, K.H. Tan, Testing of composite slab-beam systems at elevated temperatures, Proceedings of the 7th International conference on Structural In Fire, Zurich, Switzerland, (2012) 247-256.
[4] S.J. Foster, C.G. Bailey, I.W. Burgess, R.J. Plank, Experimental behaviour of concrete floor slabs at large displacements, Eng Struct, 26 (2004) 1231-1247.

8th International Conference on Structures in Fire
Guo-Qiang LI, Venkatesh K. R. KODUR, Shou-Chao JIANG, Jian JIANG, Su-Wen CHEN, Guo-Biao LOU (Eds.)
Shanghai, China, June 11-13, 2014

EXPERIMENTAL STUDIES ON THE BEHAVIOR OF HEADED SHEAR STUDS AT ELEVATED TEMPERATURES

Sepehr Dara* and Michael D. Engelhardt*

* The University of Texas at Austin
e-mails: sepehrdara@utexas.edu, mde@utexas.edu

Keywords: Shear stud, Load-slip behavior, Elevated temperatures

Abstract. *This paper presents the results of a study on the behavior of headed shear studs in solid slab composite beams at elevated temperatures. In this study, experimental tests as well as analytical studies, including thermal and stress-displacement analysis, are performed on the behavior of shear studs in composite slabs at room and elevated temperatures. As a typical case in practice, 19 mm diameter shear studs are used in the experiments. A total of 10 specimens are tested to generate the load-slip behavior of the shear stud in solid concrete slabs exposed to different furnace temperatures and heating scenarios. In addition to the load-slip behavior, temperatures at different locations inside and outside the specimens are recorded by thermocouples. Utilizing two different heating scenarios resulted in different temperature gradients within the specimen. The ultimate goal of this research is to develop data to support modeling the nonlinear load-deformation response of shear connectors for use in advanced analysis of composite beam subjected to fire. Highlights of the experimental studies are presented in this paper.*

1 INTRODUCTION

Over the last fifty years several researchers have investigated the behavior of shear studs at the room temperature. Shear studs in composite beams are subject to axial, shear, and bending forces simultaneously, and have a complex behavior as the steel stud interacts with the surrounding concrete. At elevated temperatures, this behavior becomes even more complex as material properties of the steel stud and surrounding concrete are affected by temperature and temperature gradients.

Several researchers have focused on this subject, performing experimental and numerical analysis on the behavior of shear studs at elevated temperatures. Zhao and Kruppa [1] have investigated the behavior of shear connectors including headed studs and angles in solid slabs and slabs with corrugated metal deck. They performed 47 push-out tests including 12 tests at room temperature, 4 tests under only thermal loads, and 31 tests at elevated temperatures. It was observed that in all the tests with solid slabs, shear studs sheared off and the recorded strength of the studs were lower than predicted by Eurocode 4 [2] estimates. The authors proposed equations for the shear stud load slip behavior at different temperatures. Choi et al. [3] also investigated the behavior of studs in solid slabs at elevated temperatures. Their specimens were similar to the typical push-out specimens, except that they used one concrete slab instead of two. Their specimens were exposed to the ISO834 fire on one side and were tested at room temperature and temperatures after 30 and 60 minutes of fire. They observed that all the specimens failed at the weld-collar interface and they proposed a modification to the Eurocode equation to predict the stud strength. They also observed a temperature gradient over the thickness of the specimen and have provided the temperatures of different locations on the stud and the steel beam. Mirza et al. [4] performed experimental tests on the headed shear studs in solid slabs and slabs with corrugated metal deck at elevated temperatures. Their push-out tests were performed at ambient, 200 ℃, 400 ℃, and 600 ℃. The authors observed stud strength reduction as the temperature increased and proposed equations to estimate the stud strength based on the temperature value. Chen et al. [5] performed 24 push-out tests at normal and elevated temperatures. They investigated the load-slip behavior and the stud strength reduction, the temperature distribution over the composite specimen, and the specimen failure mechanism. Despite other researchers' conclusion, Chen et al. found Eurocode 4 estimates to be in a good agreement with their experimental results.

Currently there is insufficient data available on the behavior of studs at elevated temperatures and there are some disagreements on the available data. This ongoing research study is aimed to provide experimental data on the load slip-behavior of the studs at different temperatures and heating scenarios, and provide analytical models to perform parametric studies on different contributing variables. A thorough understanding of the stud behavior at room and elevated temperatures is required to perform system level analysis which takes into account the effect of surrounding structure on the behavior of composite beams. The results of experimental part of this research study are provided in this paper and preliminary conclusions are stated.

2 TEST SET-UP

Components of each test specimen consist of one shear stud, a concrete block, and 19 mm steel plates used for the concrete block frame and steel plate attached to the shear stud. A specimen configuration and dimensions are shown in Figure 1. As the typical case in U.S. practice, 19 mm diameter shear studs are used in the experiments and the height of the studs is 10 cm. The manufacturer specified yield strength and ultimate strength of the studs are 351 N/mm^2 and 448 N/mm^2 respectively.

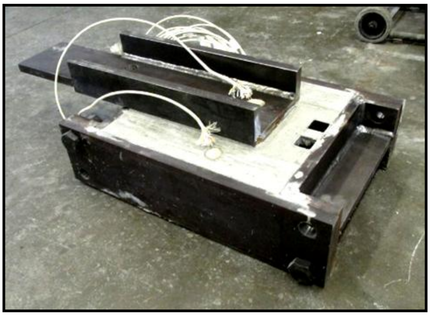

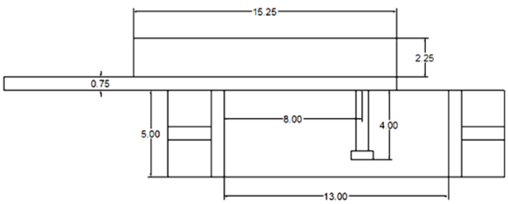

Figure 1. Specimen overview (left) and dimensions (right).

The width and length of the concrete block are 30 cm by 33 cm and the thickness is 12.7 cm. The distance between the shear stud center and the steel frame in the direction of loading is 20.3 cm. This value satisfies the requirement of AISC specification [6] for the minimum distance of the stud to the edge of the concrete slab. Normal strength concrete was used for the concrete material and was cured for 24 hours and then left at the room condition for minimum 28 days before the testing. The concrete compressive strength was approximately 38 N/mm2 when tested, which can be considered representative of the concrete compressive strength commonly used in building construction practice.

Each specimen is set up in an MTS testing machine shown in Figure 2. Extra steel plates shown in Figure 2(a) are used to transfer the loads to the specimen. Unlike the typical push-out tests, only one shear stud and one concrete block are used in the test set-up. Therefore, to minimize the load eccentricity, using the steel plates the line of force is aligned to be close to the shear stud bottom. Two string potentiometers are used to measure the displacement of the shear stud relative to the concrete block. All the tests were displacement controlled with the displacement rate of 2.5 mm per minute.

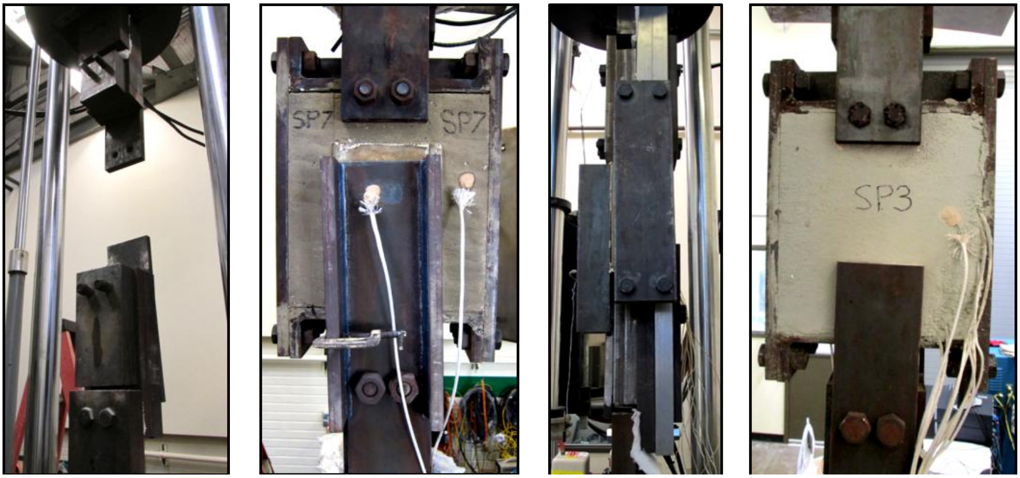

(a) Additional steel plates (b) Front view (c) Side view (d) Rear view

Figure 2. Test set-up.

To measure the temperature, K-type thermocouples were used. Locations of the 12 thermocouples used for each specimen are shown in Figure 3(a). One thermocouple is attached to the steel plate (S_{plate}), three thermocouples were used over the height of the shear stud (S_b, S_m, S_t), three thermocouples were placed inside the concrete and close to the shear stud (C_b, C_m, C_t), three thermocouples were placed inside the concrete and far from the shear stud (C'_b, C'_m, C'_t), and two thermocouples were attached to two sides of the concrete block (C_1, C_2). The furnace temperature was also recorded while heating. The three thermocouples on the surface of the specimen were attached using high temperature cement paste.

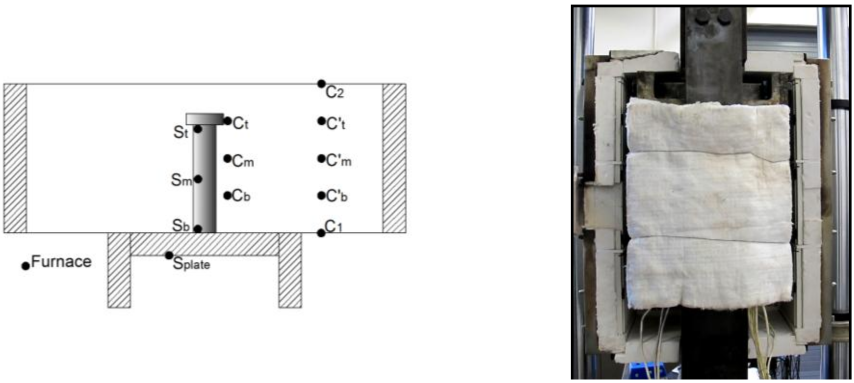

Figure 3. (a) Thermocouple locations; (b) insulation on the rear side of the specimen in second heating scenario.

Two heating scenarios were used to heat up the specimen. In the scenario one, the furnace temperature was increased to a target temperature and as soon as the target temperature was obtained, the loading started. This scenario was meant to represent the heating condition in a fire event; therefore, insulation was placed on the rear side of the specimen as shown in Figure 3(b) so that heat is mostly conducted to the specimen from the front side. In the scenario two, after the target furnace temperature was obtained, the temperature was maintained for around 90 minutes so that relatively uniform temperature was achieved throughout the specimen before loading. These scenarios were selected to evaluate the effect of temperature gradient on the behavior of the shear studs.

In total, ten tests were performed which included one test at room temperature, four elevated temperature tests using heating scenario one, and five elevated temperature tests using heating scenario two. Performed tests are presented in Table 1.

Table 1. Performed tests.

Test Specimen	Scenario	Temperature (℃)
SP0	-	room
SP8	1	500
SP4	1	600
SP1	1	700
SP5	1	760
SP9	2	300
SP7	2	400
SP2	2	500
SP3	2	600
SP6	2	700

3 TEST RESULTS

All ten specimens failed due to shear stud shearing off at the bottom, above the weld-collar location. Three specimens after failure are shown in Figure 4. As can be seen in this figure, the remaining part of the shear stud on the steel plate shows that the failure location moved more toward the shear stud bottom in the tests at elevated temperatures comparing to the failure at the room temperature. Also, less cracking was observed in the concrete in the tests at elevated temperatures.

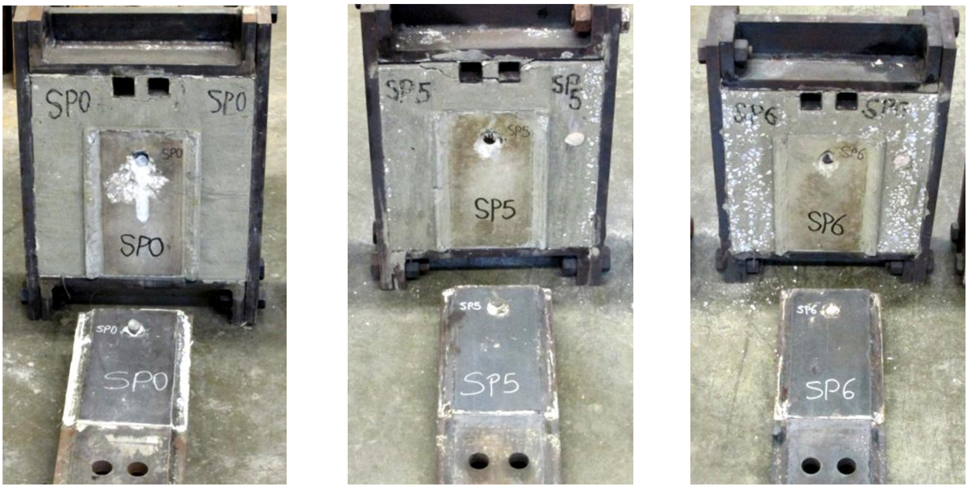

Figure 4. Specimens after failure, tested at (left) the room temperature (middle) 760 ℃ heating scenario one (right) 700 ℃ heating scenario two.

The temperatures over the time at four selected locations for each specimen are shown in Figure 5. The furnace temperature is also shown on the graphs with a solid line. Temperature gradient over the specimen can be observed for the tests with heating scenario one. Shear studs have around 200 ℃ temperature difference between the top and bottom. Since the heating rate in actual fire events may be much higher than the heating rate developed by the electrical furnace used in this experimental program, even higher temperature gradients can be expected in the shear studs and the concrete slab in fire events. It can be observed that for the cases of heating scenario two, temperatures are all in the range of 50 ℃ difference when loading starts.

The load slip curves of selected specimens are shown in Figure 6. The room temperature test result is shown by the solid line and tests with highest and lowest target temperatures for each heating scenario are also shown. It can be observed that for the specimens of each heating scenario, as the temperature increases, strength of the shear studs decreases which is accompanied by less stiffness and more ductility of the specimen.

From the experimental results, it was observed that for the same or even lower temperatures of heating scenario two, in comparison with heating scenario one, shear stud strength decreases more in the cases of heating scenario two. This is the result of temperature gradient inside the specimens when they are heated with heating scenario one in comparison to the relatively uniform temperature inside the specimen heated with heating scenario two. For example, as seen in Table 2, when loading begins, the bottom of stud temperature in the test with 760 ℃ temperature heated in scenario one has a lower value (640 ℃) comparing to the value in the test with 700 ℃ temperature heated in scenario two (720 ℃). Similarly, the bottom of stud temperature in the test with 500 ℃ temperature heated in scenario one has a lower value (280 ℃) comparing to the value in the test with 300 ℃ temperature heated in scenario two (300 ℃).

Table 2. Test results.

Furnace Target Temperature (℃)	Heating Scenario	Shear Stud Bottom Temperature (℃)	Shear Stud Strength (kN)	Normalized Strength
20	-	20	136.25	1.00
760	1	640	43.55	0.32
700	1	580	55.01	0.40
600	1	390	113.90	0.84
500	1	280	116.98	0.86
700	2	720	25.01	0.18
600	2	620	51.12	0.38
500	2	500	76.09	0.56
400	2	420	91.32	0.67
300	2	300	119.98	0.88

In fact, the data shows that the temperature of the shear stud bottom is the most important factor affecting the strength of the shear studs. Figure 7 shows the strength of the shear studs versus the temperature of the bottom of the shear studs at the time of loading. It can be observed that regardless of the heating scenario, there is a correlation between the strength of the studs and the temperature of the bottom of the shear studs. The test results are also compared to the ultimate strength reduction factor provided by Eurocode 4 [2]. As Figure 7 shows, there is a good agreement between the Eurocode and the experiments when shear stud bottom temperatures is higher than 400 ℃, however, for temperatures between 200 ℃ and 400 ℃, Eurocode 4 predicts less strength reduction.

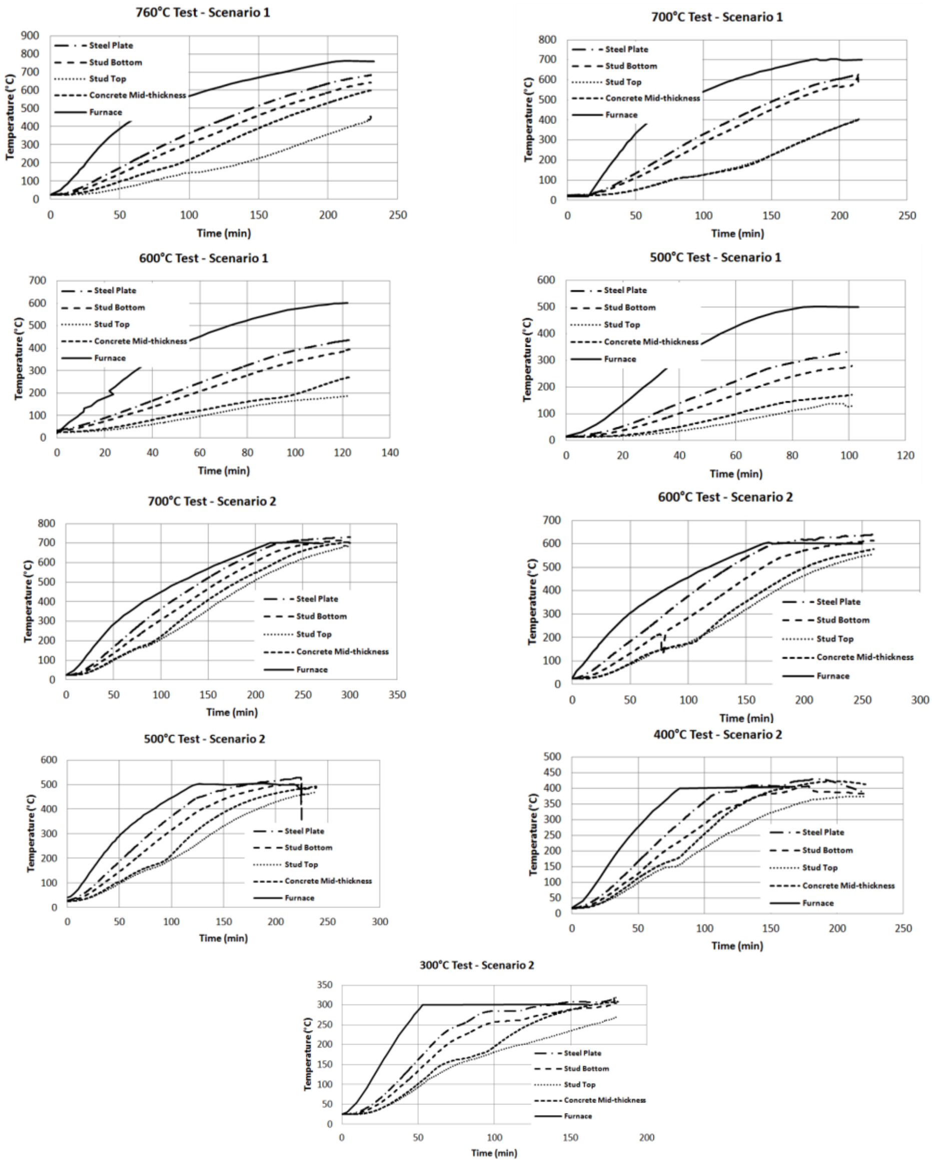

Figure 5. Time vs. temperature curves at selected locations for each tested specimen.

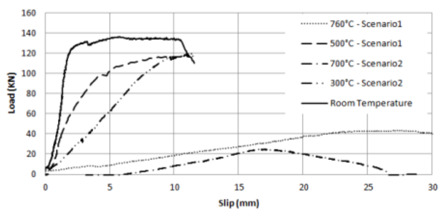

Figure 6. Load-slip behavior of selected specimens.

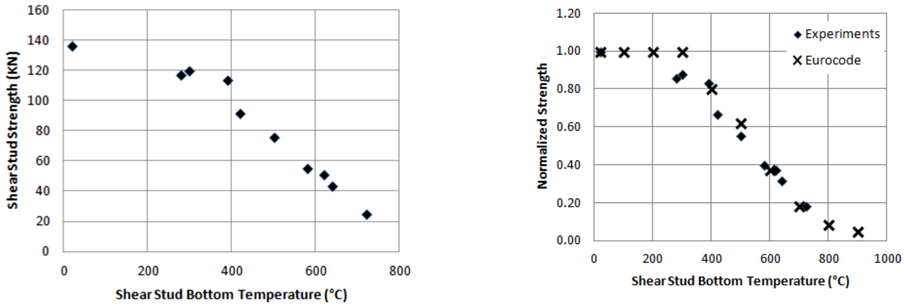

Figure 7. Correlation between the bottom of the stud temperature and the stud strength, and comparison with the Eurocode estimates.

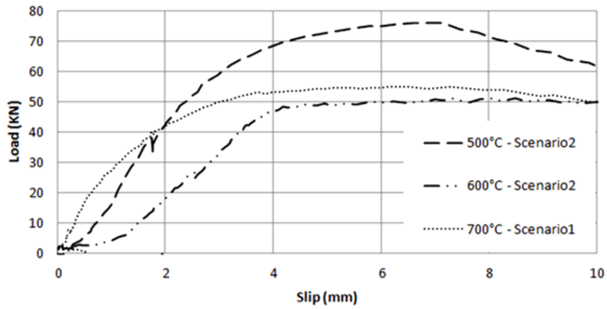

Figure 8. Initial part of the load-slip curve of three selected tests.

The initial part of the load-slip curves of two tests heated with heating scenario two and one test heated with heating scenario one are shown in Figure 8. According to Figure 5, the temperature of the bottom of the stud at the time of loading for the 700 ℃ test is around 580 ℃. According to the figure 8, even though the strength of the shear stud at 700 ℃ test would be the same as a hypothetical 580 ℃ test heated with heating scenario two, the stiffness of the specimen at 700 ℃ is different from the hypothetical test. It can be observed that the heating scenario significantly affects the stiffness of the specimen and for the same bottom of stud temperature, the specimen heated with heating scenario one is stiffer than the specimen heated with heating scenario two. This is the result of temperature reduction over the thickness of the specimen in the tests heated with the heating scenario one.

4 FINITE ELEMENT ANALYSIS

The results of this experimental study will be used to validate the computational analysis of the shear studs. Abaqus finite element software is being used for the computational part of this research study. Figure 9 presents a sample of heat-transfer and stress-displacement analysis on a specimen. The investigation on the contributing factors to the behavior of studs at elevated temperatures will be done by a parametric study. The effect of different material properties, different geometries, and different heating scenarios on the behavior of shear studs will be investigated. This work is still underway by the authors, and results will be presented in future papers.

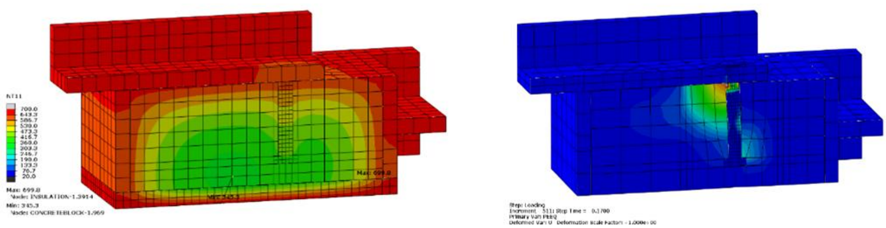

Figure 9. Heat transfer (left) and stress displacement (right) sample analysis.

5 CONCLUSIONS

The following preliminary conclusions can be made from the experimental part of this research study:

(1) When an assembly of a steel stud and a solid concrete slab are exposed to elevated temperature, the peak strength of the stud will often be controlled by fracture of the steel stud, as compared to crushing and failure of the surrounding concrete. This can likely be attributed to the higher thermal conductivity of steel, and the resulting higher temperatures in the steel stud in comparison with the cooler surrounding concrete.

(2) A very high temperature gradient may be expected in the concrete slab and the shear stud in a typical fire event with a high heating rate. It was observed that even with the lower heating rate of the electrical furnace used in these tests, around 200 ℃ temperature difference was measured between the top and the bottom of the shear stud. The concrete has an even higher temperature gradient due to the lower thermal conductivity of concrete.

(3) Degradation of material properties at elevated temperatures results in a reduction of both stiffness and strength of a shear stud. However, the stud exhibits higher ductility at elevated temperatures, as evidenced by higher slip values at failure

(4) The most important contributing factor to the shear stud strength was found to be the temperature at the bottom of the stud. This means that regardless of the heating condition, if the temperature of the bottom of the stud is known, the ultimate strength of the shear studs can be predicted.

(5) While temperature gradients in the stud and surrounding concrete did not have a large effect on the ultimate strength of the studs, temperature gradient had a very large effect on the initial stiffness of the shear stud.

ACKNOWLEDGEMENT

The research reported herein is being conducted as part of a research project on Elevated Temperature Performance of Shear Connectors for Composite Beams supported by the National Science Foundation (NSF Award 1031099). Elevated temperature material tests were conducted using equipment procured through an NSF Major Research Instrumentation Grant (NSF Award No. CMS-0521086 – Acquisition of a High-Temperature Testing Facility for Structural Components and Materials). The support of the National Science Foundation and of NSF Program Director M.P. Singh is gratefully acknowledged.

REFERENCES

[1] Zhao B., Kruppa J., "Experimental and numerical investigation of fire behaviour of steel and concrete composite", *Composite Construction in Steel and Concrete*, 129-142, 1996.

[2] EN 1994-1-2, "Eurocode4, Design of composite steel and concrete structures, General rules-Structural fire design", 2005.

[3] Choi S.K., Han S.H., Kim S.B., Nadjai A., Faris A. and Choi J.Y., 'Performance of Shear Studs in fire", *Application of Structural fire Engineering - Proceeding of International conference,* Prague, 490-495, 2009.

[4] Mirza O., Uy B. and Krezo S., "Experimental Studies on the Behaviour of Headed Stud Shear Connectors for Composite Steel Concrete Beams under Elevated Temperatures". *Advances in Steel and Aluminium Structures-7th International Conference on Steel and Aluminium Structures,* Lau H.H (ed.), Research Publishing Service, Malaysia, 467-473, 2011.

[5] Chen L.Z., Li G.Q. and Jiang S.C., "Experimental Studies on the Behaviour of Headed Stud Shear Connectors at Elevated Temperatures", Structures in Fire - *Proceedings of the Seventh International Conference,* M. Montana, A Frangi, M. Knobloch (eds.), Zurich, Switzerland, 257-266, 2012.

[6] ANSI/AISC 360-10, "Specification for structural steel buildings", 2010

8th International Conference on Structures in Fire
Guo-Qiang LI, Venkatesh K. R. KODUR, Shou-Chao JIANG, Jian JIANG, Su-Wen CHEN, Guo-Biao LOU (Eds.)
Shanghai, China, June 11-13, 2014

PROGRESSIVE COLLAPSE ANALYSIS OF COMPOSITE FRAME WITH CONCRETE-FILLED STEEL TUBULAR COLUMNS SUBJECTED TO MIDDLE COLUMN FIRES

J. X. Wang* and W. D. Wang*

* Key Laboratory of Disaster Prevention and Mitigation in Civil Engineering of Gansu Province, School of Civil Engineering, Lanzhou University of Technology, Lanzhou, P.R. China
e-mails: cewangjx@gmail.com, wangwd@lut.cn

Keywords: Concrete Filled Steel Tube (CFST), Finite element model, Progressive collapse, Static-dynamic analytic procedure, Fire response, Restart and predefined-field function

Abstract. *This paper presents a finite element(FE) model of planar frame with concrete-filled steel tubular (CFST) columns to investigate the mechanism of progressive collapse under loading and middle column fires. A static-dynamic analytic conversion procedure has been developed based on the restart and predefined-field function in the FE model using ABAQUS. The analytic procedure switch between static and dynamic analysis is effective to investigate the progressive collapse of composite frame subjected to fire which shorten the calculation time and show the dynamic characteristics of progressive collapse. The failure modes, displacement and internal force of composite frame were calculated caused by the damage of column subjected to fire. The results shown that the displacement of top column including four stages when exposure to fire, such as inflation deformation in early heating stage, localized failure of heated column, transient equilibrium phase and the progressive collapse phase.*

1 INTRODUCTION

For many types of infrastructure, such as buildings and bridges, ensuring the fire safety is one of the most fundamental requirements of design, construction and operation. Concrete-filled steel tubular structures have been widely used in practical structure due to the favorable composite characteristics of steel and concrete materials and better fire performance. The collapse of World Trade Center Building 7 and Windsor Tower left a deep lesson for the progressive collapse. At present, the design guidelines such as General Services Administration (GSA) [1] and the Unified Facilities Criteria (UFC) [2] addressed progressive collapse due to sudden loss of a main vertical support, called alternative path method, included removal of a key column and did not consider the cause of initial damage. This method can assess the residual capacity for the instantaneous collapse destroyed building, such as explosion and impact failure. Kai *et al*. [3-4] investigated the reinforced concrete beam-column substructure under loss of a corner column and the slab effects. Helmy *et al*. (2012) [5] studied the progressive collapse assessment of framed reinforced concrete structures according to UFC guidelines for alternative path method. Guo *et al*. [6] reported experimental study and numerical analysis of progressive collapse resistance of composite frames under loss of a middle column. Progressive collapse caused by fire was different with instantaneous collapse destroyed under gravity loading, because the structure had a long quasi-static balance stage before collapse. Currently, the progressive collapse analysis of steel structure have been reported when exposure to local fire. Fang *et al* .(2011) [7] investigated the robustness of steel-composite building structures subject to localized fire. Sun *et al.* (2012) [8-10] reported the progressive collapse analysis of steel structures under fire conditions, and developed a simplified numerical procedure based on VULCAN software. Agarwal and Varma(2013) [11] presented a qualitative assessment of the importance of gravity columns on the stability behaviour of a typical mid-rise (10 stories) steel building subjected to corner compartment fires. However, there were few researches on the fire induced progressive collapse of composite frame with concrete filled steel tubular columns and steel beams. This paper will introduce a numerical procedure of static-dynamic conversion method to investigate the mechanical performance of progressive collapse of composite planar frame subjected to middle column fires based on the restart and predefined-field function using ABAQUS. The method can be utilized to allow a structural analysis to continue beyond the temporary instabilities due to any localized members failure when the finite element simulation would be terminated in the full static analysis, which cannot show the dynamic characteristic effect of progressive collapse. However, the full dynamic analysis is also difficult to study the behaviour of fire-induced progressive collapse because the huge unnecessary computing time was needed in long time fire action(from 0.5 to 3h). The analytic procedure switch between static and dynamic analysis is effective to investigate the progressive collapse of composite frame exposure to fire which shorten the calculation time and show the dynamic characteristics of progressive collapse. A 9 story planar frame was developed to study the displacement and internal force when exposure to fire used the numerical procedure of static-dynamic conversion method.

2 STATIC-DYNAMIC CONVERSION METHOD

In order to analysis structure up to complete collapse when exposure to fire, it is important to make sure that simulation can be conducted until final global structure failure happens. However, when using a conventional static procedure will often encounter a fatal numerical singularity in its stiffness matrix when one or more structure members fail or buckle locally. The strain increment is so large that the program will not attempt the plasticity calculation at several points, so the procedure will automatically terminate and cannot show the dynamic characteristic effect of progressive collapse. In order to overcome this shortcoming, a static-dynamic procedure has been developed in this paper using the restart and predefined-field function. ABAQUS Analysis User's Manual [12] introduces the information that restart requests are always associated with a particular step, and you cannot define a restart request for the entire analysis. Restart requests are created by default for every step for ABAQUS/Standard and ABAQUS/CFD steps have a default frequency of 0, while restart requests for ABAQUS/Explicit steps have a default number of intervals of 1. Then, the predefined field function was used to relay the up steps. Figure 1 was given the analysis process using the static-dynamic conversion method to calculate the progressive collapse performance of structure under fire conditions.

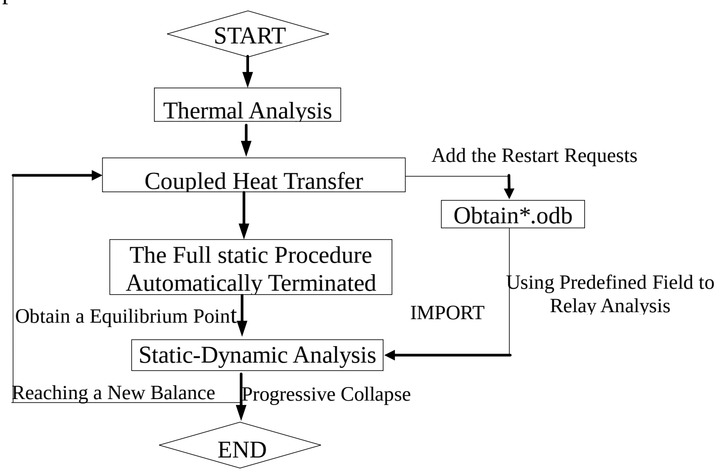

Figure 1. Analysis process using the static-dynamic conversion method.

3 ANALYTICAL MODEL

3.1 Structure details

This paper designed a 9 story composite frame with CFST columns using Midas Building software. Detailed information of frame is: The building has a longitudinal 7 spans with a interval of 6.6 m and transverse 4 spans with a grid space of 7.2m, respectively. The height of each story is 3.6 m. The H shaped steel beam section is 495mm×465mm×15mm×20mm. The columns are circular section with the dimension $D \times t$=500mm×12mm. where D and t are the diameter and thickness of the hollow steel tubes, respectively. The yielding strength of steel is 345MPa for the steel tubes and beams. The cube compression strength of core concrete of CFST columns is 40MPa. DL=5.0kN/m^2, LL=2.0kN/m^2. Figure 2 is the plan and elevation view of the prototype frame.

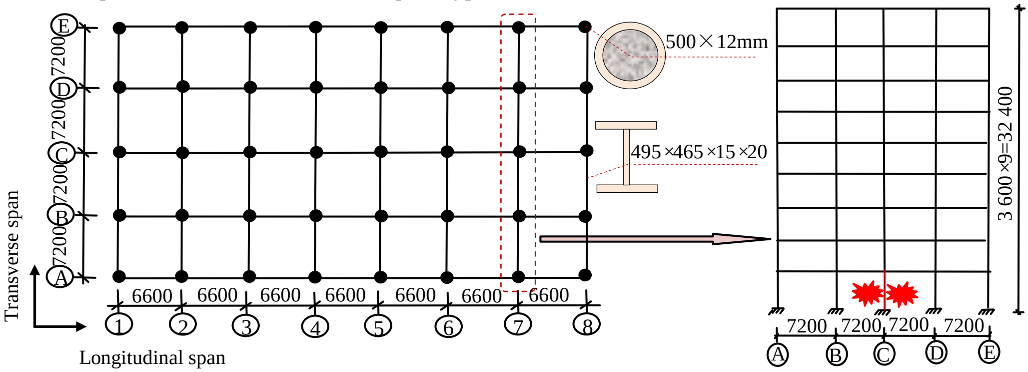

Figure 2. Plan and elevation view of the prototype frame and fire condition.

3.2 Material properties

3.2.1 Concrete constitutive model without fires

Concrete damaged plasticity in ABAUQS element library cannot be used to the Timoshenko B31 element, and concrete smeared cracking model is available for small deformation analysis. Our research group has been developed the user-defined confined concrete and steel uniaxial hysteretic material constitutive model in subroutine UMAT provided by ABAQUS, which can be used to analyse the quasi-static and elasto-plastic performance of the CFST structures. Concrete skeleton curves and loading-unloading criteria curves were shown in Figure 3. Wang *et al.* (2013) [13] has been used the user-defined confined concrete and steel material constitutive model to calculate the progressive collapse of composite frame with CFST columns based on the removal of key columns.

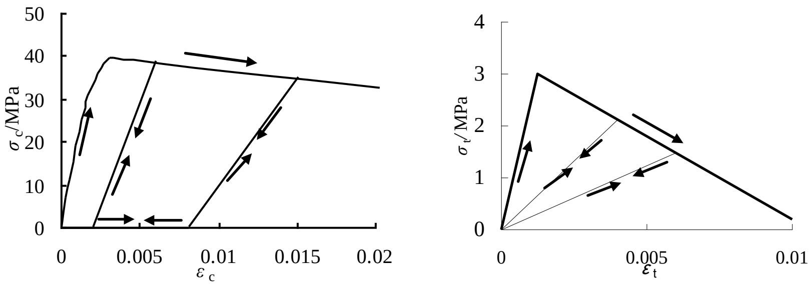

(a) Compression (b) Tension

Figure 3. Concrete skeleton curves and loading-unloading criteria curves.

3.2.2 Concrete and steel constitutive model under fires

The CFST column of FE model used the solid element and shell element in the fire region, respectively. Lie (1994) [14] given the steel constitutive model at ambient and heating phase. Han (2007) [15] given the core concrete constitutive model at ambient and heating phase. The results showed good agreement with the experimental curves. The formula of steel and core concrete are shown as follows:

(a) steel constitutive model

$$\sigma_{\mathrm{s}} = \begin{cases} \dfrac{f(T,0.001)}{0.001}\varepsilon_{\mathrm{s}} & \varepsilon_{\mathrm{s}} \le \varepsilon_{\mathrm{p}} \\ \dfrac{f(T,0.001)}{0.001}\varepsilon_{\mathrm{p}} + f\left[T,(\varepsilon_{\mathrm{s}} - \varepsilon_{\mathrm{p}} + 0.001)\right] - f(T,0.001) & \varepsilon_{\mathrm{s}} > \varepsilon_{\mathrm{p}} \end{cases} \tag{1}$$

in which, ε_{p} is the plastic strain, $\varepsilon_{\mathrm{p}}=4\times10^{-6}f_{\mathrm{y}}$.

$$f(T,0.001) = (50 - 0.04T)\times\left(1 - e^{\left[(-30+0.03T)\sqrt{0.001}\right]}\right)\times 6.9 \tag{2}$$

$$f\left[T,(\varepsilon_{\mathrm{s}} - \varepsilon_{\mathrm{p}} + 0.001)\right] = (50 - 0.04T)\times\left(1 - e^{\left[(-30+0.03T)\sqrt{\varepsilon_{\mathrm{s}}-\varepsilon_{\mathrm{p}}+0.001}\right]}\right)\times 6.9 \tag{3}$$

$$\begin{aligned} f_{\mathrm{yh}}(T) &= \frac{f(T,0.001)}{0.001}\varepsilon_{\mathrm{yh}} = 4\times10^{-3} f(T,0.001) f_{\mathrm{y}} \\ E_{\mathrm{sh}}(T) &= \frac{f(T,0.001)}{0.001} = (50000 - 40T)\times\left\{1 - \exp\left[(-30 + 0.03T)\sqrt{0.001}\right]\right\}\times 6.9 \\ \varepsilon_{\mathrm{yh}}(T) &= \varepsilon_{\mathrm{p}} = 4\times10^{-6} f_{\mathrm{y}} \end{aligned} \tag{4}$$

where $f_{\mathrm{yh}}(T)$ is the yield strength in heating stage, $E_{\mathrm{sh}}(T)$ is the elasticity modulus and $\varepsilon_{\mathrm{yh}}(T)$ is steel strain.

(b) core concrete constitutive model

$$y = \begin{cases} 2x - x^2 & x \le 1 \\ \dfrac{x}{\beta(x-1)^{\eta} + x} & x > 1 \end{cases} \tag{5}$$

where $x = \dfrac{\varepsilon}{\varepsilon_0^{\mathrm{T}}}$, $y = \dfrac{\sigma}{\sigma_0^{\mathrm{T}}}$, $\sigma_0^{\mathrm{T}} = f_{\mathrm{c}}' / [1 + a(\dfrac{T-20}{1000})^{b}]$, $\varepsilon_0^{\mathrm{T}} = \varepsilon_{\mathrm{c}}(T) + 800\cdot\xi^{0.2}\cdot10^{-6}\cdot[1 + 0.18\times(\dfrac{T-20}{100})^{2.2}]$,

$\varepsilon_{\mathrm{c}}(T) = (1300 + 12.5 f_{\mathrm{c}}')\cdot10^{-6}\cdot[1 + 0.18\times(\dfrac{T-20}{100})^{2.2}]$.

4 MATERIAL MODEL VERIFICATION

In order to verify the rationality of the uniaxial material constitutive model of core concrete and steel based on fiber beam-column element model in ABAQUS, this paper developed a large number of examples of CFST columns [15] and composite frames with CFST columns and steel beam[16] under monotonic loading and reciprocal loading. Part specimen information of examples was shown in Table 1. The comparison results of CFST members and composite frame with CFST columns under lateral cyclic load were shown in Figure 4. The calculation results show good agreement between the test and finite element simulation, which enables the used-defined material constitutive model of concrete and steel to be applied in the further research studies of progressive collapse caused by fire of CFST structures.

Table 1. Summary of specimen information.

Specimen Number	Column $B\times t$ /(mm)	f_y/MPa (steel tube)	f_{cu}/MPa (concrete)	Load Ratio n
C108-3	108×4.00	356.0	20.1	0.50
S120-2	120×2.65	*340.0*	20.1	0.33
R60-1	120×60×2.65	340.0	20.1	0.05
CF-22	140×3.34	352.0	42.7	0.30
SF-11	120×3.46	404.0	42.7	0.05

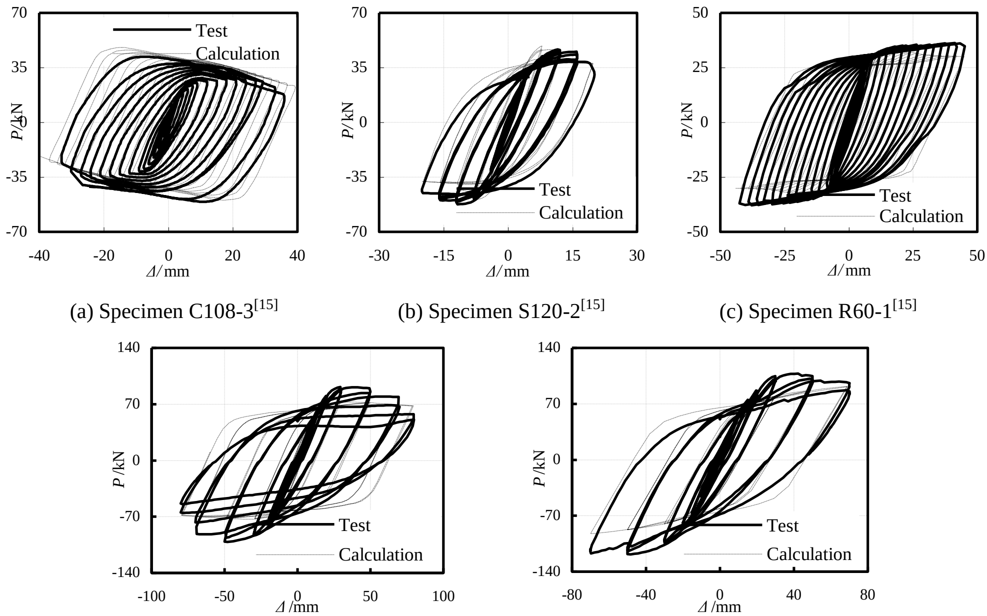

(a) Specimen C108-3[15] (b) Specimen S120-2[15] (c) Specimen R60-1[15]

(d) Specimen CF-22[16] (e) Specimen SF-11[16]

Figure 4. Comparison of results of concrete filled steel tube structures under horizontal cyclic load.

5 PROGRESSIVE COLLAPSE ANALYSIS

5.1 The failure modes

Figure 5 shows the failure modes of planar frame at different stages when exposure to fire. It is shown that the whole fire process including four stages, such as inflation deformation in early heating stage, localized failure of fired column, transient balance phase and the progressive collapse phase. Figure 5(a) is the inflation deformation stage of heated column. The maximum inflation deformation of column is 1.7mm. With the temperature increased, the axial deformation of heated column is turned from inflation deformation to compression deformation. Figure 5(b) shows the failure mode when T is 670℃. Steel tube happened local buckling due to the high temperature. The equivalent plastic strain value (PEEQ) of steel tube foot is 0.002＞0. However, the middle column still has a certain capacity for the heat-absorbing action of core concrete. When the temperature is 740℃, the middle column is unloading for the high temperature. The internal force of steel beam is increased for the internal force redistribution in the Figure

5(c). Finally, the whole frame happened progressive collapse at the temperature is 905℃. The maximum axial deformation of column is 120mm in Figure 5(d).

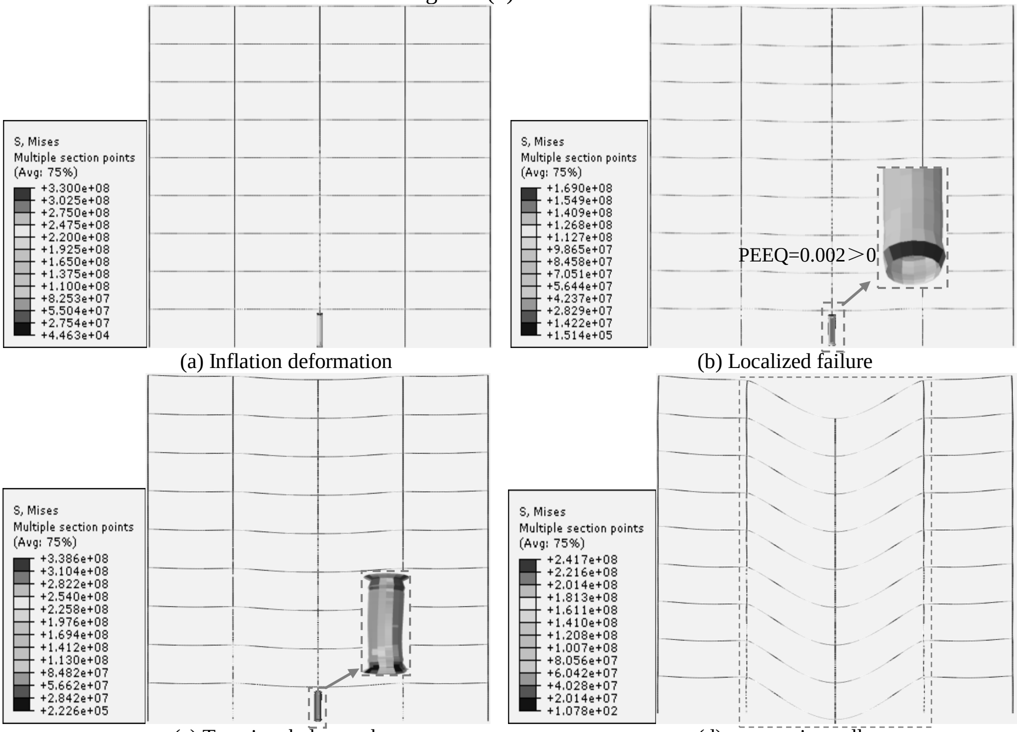

(a) Inflation deformation (b) Localized failure

(c) Transient balance phase (d) progressive collapse

Figure 5. Failure modes of planar frame at different stages.

5.2 Fire failure mechanism analysis

This paper predicted the analysis on the mechanism of progressive collapse of planar frame with CFST columns subjected to local fire based on the static-dynamic conversion method. The results were compared with the completed static analysis until the procedure was automatic termination, in which a equilibrium point was obtained. The temperature, stress, strain and displacement as the initial states were import to the dynamic analysis used the predefined field function. The axial displacement versus temperature curves of failure column are shown in Figure 6. It is found that the planar frame from heating to collapse included four stages, o-a-b-c(c′)-d(d′). o-a is the inflation deformation stage of heated column. The maximum inflation deformation of column is 1.7mm and the temperature is 200℃. a-b stage is localized failure of middle column, the axial displacement is 19.5mm and the temperature is 694℃ at b point. b-c(c′) is transient balance phase due to the constraint of around the unfired members. c(c′)-d(d′) is progressive collapse stage. c-d stage is used the full static analysis method. When up to d point, the procedure is automatic termination and the maximum axial deformation is 30mm and the critical temperature is 870℃. However, the critical temperature is 905℃ and the axial deformation has a sharp increasing at d′ point when using the static-dynamic conversion method. The difference of critical temperature between two methods is 3.8％. Figure 7 gives the axial force versus temperature curves using two different methods and the changing law is similar to Figure 6. Figure 8 is the axial displacement versus time dynamic curves. When the middle column was destroyed, the maximum oscillation displacement is 120mm. Then the amplitude of oscillation displacement decreases gradually and the stable displacement is 90mm.

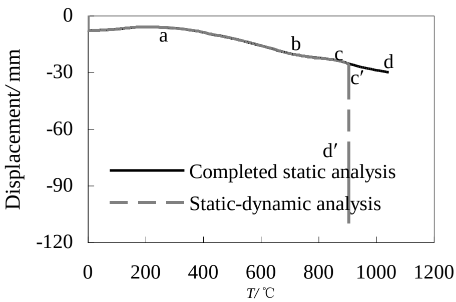

Figure 6. Displacement-temperature curves.

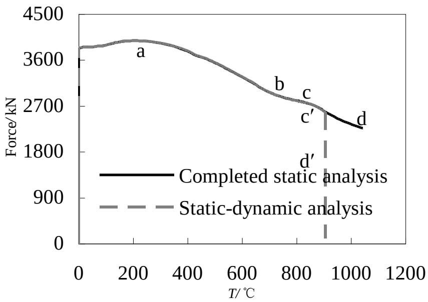

Figure 7. Axial force-temperature curves.

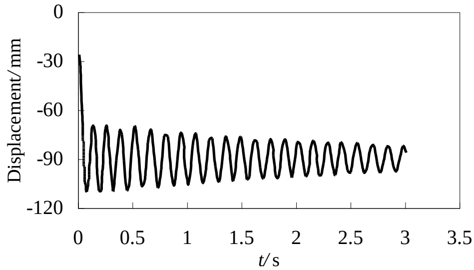

Figure 8. Oscillation displacement -temperature curve.

5.3 Effect of fire load ratios

In order to research the progressive collapse of frame subjected to fire under different fire load ratios, this paper calculated the displacement and force versus temperature curves when the fire load ratios n is 0.2, 0.3, 0.4, 0.5, respectively. $n=N_F/N_u$($n=N_F/N_u$, N_F is the fire load and N_u is the ultimate capacity at ambient). From Figure 9, it is shown that the displacement is increased and the critical temperature is decreased with the fire load ratios increased, the axial force of heated column is also decreased.

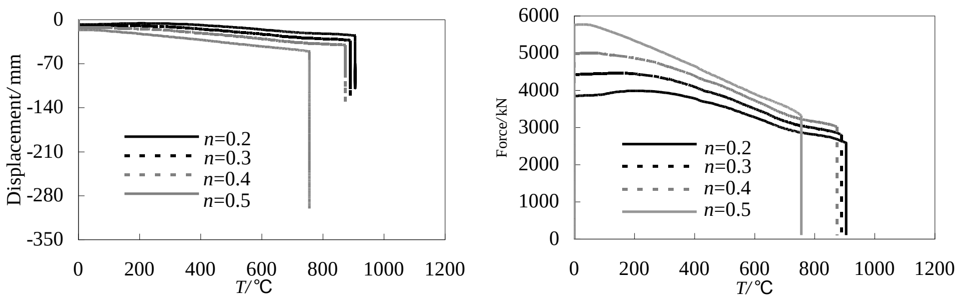

(a) Displacement versus temperature curves (b) Axial force versus temperature curves

Figure 9. Effect of different fire load ratios.

6 CONCLUSIONS

The following conclusions may be drawn with the limitation of the research in this paper:

(1) A static-dynamic conversion analysis method has been developed based on the restart and predefined-field function using ABAQUS. The analytic procedure switch between static and dynamic

analysis was effective to investigate the progressive collapse of composite frame exposure to fire which shorten the calculation time and show the dynamic characteristics of progressive collapse.

(2) From top displacement versus temperature curves, we can found that the planar frame from heating to collapse included four stages, such as inflation deformation in early heating stage, localized failure of heated column, transient balance phase and the progressive collapse phase. The results of critical temperature of progressive collapse did not reveal much difference between completed static analysis method and static-dynamic conversion method.

REFERENCES

[1] General Service Administration. GSA. “Progressive collapse analysis and design guidelines for new federal office buildings and major modernization projects”, USA, 2003.

[2] Department of Defense. DoD. “Design of buildings to resist progressive collapse, unified facilities criteria (UFC, 4-023-03)”. USA; 2009.

[3] Kai Q., ASCE A.M. and Li B., “Performance of three-dimensional reinforced concrete beam-column substructures under loss of a corner column scenario”, *Journal of Structural Engineering*, 139(4), 584-594, 2013.

[4] Kai Q., and Li B., “Slab effects on the response of reinforced concrete substructures after the loss of a corner column”, *ACI Struct. J*, 109(6), 845-855, 2012.

[5] Helmy H., Salem H. and Mourad S., “Progressive collapse assessment of framed reinforced concrete structures according to UFC guidelines for alternative path method”, *Engineering Structure*, 41, 127-141, 2012.

[6] Guo L H., Gao S, and Fu F., “Experimental study and numerical analysis of progressive collapse resistance of composite frames”. *Journal of Constructional Steel Research* , 89, 236-251, 2013.

[7] Fang C., Izzuddin B A. and Elghazouli D A., “Robustness of steel-composite building structures subject to localized fire”. *Fire Safety Journal*, 46(6), 348-363, 2011.

[8] Sun R R., Huang Z H. and Burgess L., “The collapse behaviour of braced steel frames exposed to fire”. *Journal of Constructional Steel Research*, 72, 130-142, 2012.

[9] Sun R R., Huang Z H. and Burgess L., “Progressive collapse analysis of steel structures under fire conditions”. *Engineering Structures*, 34, 400-413, 2012.

[10] Sun R R., Burgess L. and Huang Z H., “Behavior of frame columns in localized fire”. *Journal of Structural Fire Engineering*, 4(3), 175-185, 2013.

[11] Agarwal A., Varma A H., “Fire induced progressive collapse of steel building structures: The role of interior gravity columns”, *Engineering Structures,* 58, 129-140, 2014.

[12] ABAQUS. ABAQUS Analysis User’s Manual. Version 6.10. USA, Rhode Island: ABAQUS, Inc., 2010.

[13] Wang J X., Wang W D. and Zhou X Y., “Progressive collapse analysis on composite frame with concrete-filled steel tubular columns based on initial damage modes”, *Journal of Building Structures,* 34(s1), 15-21, 2013.

[14] Lie T T., “Fire resistance of circular steel columns filled with bar-reinforced concrete”. *Journal of Structural Engineering*, 120(5), 1489-1509, 1994.

[15] Han L H., “Concrete filled steel tubular structure-theory and practice”. 2nd ed. Beijing: *Science Press*, 470-474, 2007.

[16] Wang W D., Han L H. and Tao Z., “Experimental research on seismic behavior of concrete filled CHS and SHS columns and steel beam planar frames”. *Journal of Building Structures*, 27(3), 48-58, 2006.

8th International Conference on Structures in Fire
Guo-Qiang LI, Venkatesh K. R. KODUR, Shou-Chao JIANG, Jian JIANG, Su-Wen CHEN, Guo-Biao LOU (Eds.)
Shanghai, China, June 11-13, 2014

EFFECT OF STIFFNESS OF PROTECTED SECONDARY EDGE BEAMS ON THE MEMBRANE BEHAVIOUR OF COMPOSITE BEAM-SLAB SYSTEMS IN FIRE

Tuan-Trung Nguyen* and Kang-Hai Tan*

* Nanyang Technological Univ., School of Civil and Environmental Engineering, Singapore
e-mails: nguyentt@ntu.edu.sg, CKHTAN@ntu.edu.sg

Keywords: Tensile membrane action, Beam-slab systems, Composite slabs, Fire

Abstract. *This paper presents the experimental behaviour on two one-quarter scale composite beam-slab systems in fire. The aim was to study the effect of bending stiffness of protected secondary edge beams on the fire behaviour of floor assemblies. Two specimens were denoted as P215-M1099 and P486-M1099. To investigate the effect of second moment of area about the major axis of the protected secondary beam (I_{yPSB}), I_{yPSB} of P486-M1099 was increased 2.26 times compared to that of P215-M1099. The main and unprotected secondary beams of two specimens were kept the same. The test results showed that as the stiffness of the protected secondary edge beam increased, the slab deflection decreased and failure of the slab occurred later. However, composite action between the edge beams and the concrete slab played a key role in mobilizing this beneficial effect. Once the composite action had been weakened by parallel cracks in the slab over the main or secondary edge beams, the slab would lose the benefit associated with the greater stiffness of the protected secondary edge beams.*

1 INTRODUCTION

From 2008 till recently, there has been a surge of interest on the membrane behaviour of integrated composite slab-beam floor systems in fire [1-5]. These studies offer valuable insight into the fire behaviour of composite slab-beam systems. However, there is no experimental work investigating the influence of stiffness of protected edge beams on the fire behaviour of the floor assemblies. When the protected edge beams deform under fire conditions, the boundary condition of the composite slab changes and this has significant effect on the development of tensile membrane action (TMA). In literature, there was only a numerical study to address this problem. Lim [6] conducted a parametric study to investigate the slab behaviour with different edge beam sizes. He concluded that as the beam size decreases, failure of the slab occurs earlier with a much greater slab deflection. Although the positive effect of the beam size on the slab behaviour was confirmed by the numerical study, important effects such as concrete cracking and local damages were not taken into account.

To bridge this technical gap, a series of tests including six one-quarter composite beam-slab floor systems in total have been conducted at Nanyang Technological University, Singapore in 2012. A gamut of stiffness ratios for the protected edge beams has been investigated ranging from 1.0 to 2.26 for the protected secondary edge beams and 1.00 to 1.92 for the protected main edge beams. This is so far the only experimental programme studying the effect of stiffness of protected edge beams on the development of TMA. The series to study the effect of the protected secondary edge beams included three specimens, namely, P215-M1099, P368-M1099 and P486-M1099, in which their corresponding stiffness ratios were 1.00, 1.71 and 2.26, respectively. This paper presents only the experimental behaviour of two specimens, P215-M1099 and P486-M1099. The aim was to study the effect of bending stiffness of protected secondary edge beams on the fire behaviour of floor assemblies.

2 TEST SPECIMENS AND SETUP

2.1 Test specimens

Numerical studies [7] showed that in terms of the four geometric properties of the protected edge beams (steel grade, torsional rigidity GI_t, bending stiffness about the major axis EI_y, bending stiffness about the minor axis EI_z), only the bending stiffness about the major axis EI_y has significant effect on the membrane behaviour of floor assemblies. Therefore, the bending stiffness about the major axis EI_y was chosen as the main parameter.

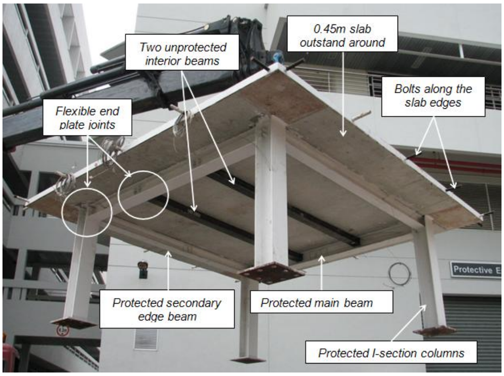

Figure 1. Typical specimen.

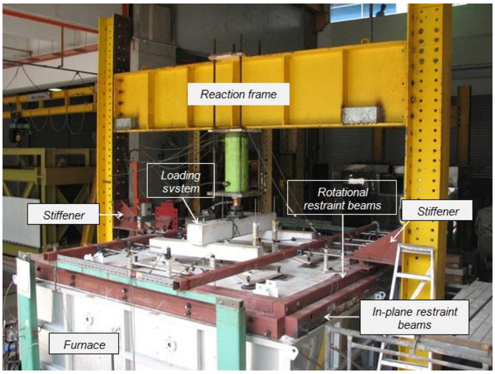

Figure 2. Test setup.

Two specimens were denoted as P215-M1099 and P486-M1099. In this nomenclature, P215-M1099 indicates a specimen which has $215cm^4$ as the second moment of area about the major axis of protected secondary edge beam (I_{yPSB}), and $1099cm^4$ as that of main edge beam (I_{yMB}). Specimen P215-M1099 was chosen as the control specimen. I_{yPSB} of P486-M1099 was increased 2.26 times compared to that of P215-M1099. The protected main and unprotected interior secondary beams for these specimens were kept the same. The effect of two unprotected interior beams on tensile membrane behaviour of beam-slab systems has been investigated separately [8].

Figure 1 shows a typical specimen with the slab 2.25m long by 2.25m wide and an outstand of 0.45m around the four edges. The dimensions of the specimens were limited by those of the electric furnace. Therefore, the slab dimensions were scaled down by ¼ from a prototype floor which was designed for gravity loading in accordance with BS EN 1994-1-1. Along each edge were five M24 bolts with half of these bolt lengths cast into the slab, while the other half were attached to the in-plane restraint system as described in Section 2.2. The locations of these bolts were fixed by using 8mm thick steel plates along the four slab edges. The purpose of these bolts was to simulate accurately the boundary conditions of interior slab panels. The interior slab panels should be rotationally restrained and could only have horizontal straight movement along the four edges.

It is of interest to find out if the slab edges would translate straight if the slab is considered as an interior slab. Considering a composite steel-framed building, the common fire scenario is the situation where the fire heats up the whole soffit of the floor. In this situation, the displacement along the slab edges can be outward caused by thermal expansion, or inward resulted from tensile membrane action mobilized at a later stage. However, the common edges between two interior slab panels must translate straight to ensure displacement compatibility. Therefore, in this case the slab edges can only displace outwards and inwards maintaining a straight edge. This experiment focused on this fire scenario.

The concrete slab thickness was 57mm and 55mm for P215-M1099 and P486-M1099, respectively. Shrinkage reinforcement mesh with a grid size of 80mm × 80mm and a diameter of 3mm (giving a reinforcement ratio of 0.16%) was placed within the slab, 25mm from the top. The mesh was continuous across the whole slab with a yield strength of 689MPa. The specimens were cast using ready-mixed concrete with aggregate size ranging from 5 to 10mm. Six concrete cylinders were tested at 28 days giving a characteristic cylinder strength f_{ck} of 31.3MPa and 28.9MPa for P215-M1099 and P486-M1099, respectively.

Material and geometrical properties of the I-section steel beams are given in Table 1. The beams were designed for full-shear composite action using 40 mm long, 13 mm diameter headed shear studs with a spacing of 80mm so that no unexpected failure occurred due to shear. A common type of steel joints, i.e. flexible end plates, was used for beam-to-beam and beam-to-column connections.

Table 1. Details of steel beams.

Specimen	*Denote*	*Depth*	*Width*	*Web thick.* (mm)	*Flangethick.* (mm)	*Yield strength* (MPa)	*Ultimate strength* (MPa)	*Elastic modulus* (GPa)
P215-M1099	MB1	131	128	7.0	11.0	307	462	211.4
	PSB1	**80**	**80**	10.3	10.0	467	588	210.6
	USB	80	80	10.3	10.0	467	588	210.6
P486-M1099	MB1	131	128	7.0	11.0	307	462	211.4
	PSB3	**102**	**101**	7.2	8.7	356	510	205.4
	USB	80	80	10.3	10.0	467	588	210.6

This experiment applied the fire protection strategy for members recommended in the SCI Publication P288 [9]. All the edge beams and columns were protected to a prescriptive fire-protection rating of 60min. No fire-proofing material was applied to the interior beams and the slabs.

2.2 Test setup

An electric furnace of dimensions 3m long by 3m wide by 0.75m high was setup at Nanyang Technological University. The dimensions of the furnace were dictated by the space constraint of the fire laboratory. Although the furnace could not simulate the ISO 834 fire curve, from the trial tests the furnace air temperature could attain 1000^{o}C within 50 minutes (min), i.e. at a heating rate of about 20^{o}C/min, which was within the practical heating rate for steel sections as prescribed in BS 5950-8.

The specimens were setup together with two restraint beam systems as shown in Figure 2. *The first system* was the rotational restraint system which consisted of four 160x100x6 rectangular hollow section (RHS) beams placed on top of these specimens and fixed to the reaction frame via two triangular stiffeners. It is assumed that reinforcement continuity over the supporting protected edge beams and the 0.45m slab outstand provided very little rotational restraint, since there was only one layer of shrinkage reinforcement inside the slabs.

The second system was the ‘so-called’ in-plane restraint system, which also consisted of four 160×100×6 RHS beams. This system was fixed to four slab edges via five M24 bolts along each edge at a spacing of 750mm (Figure 1). The in-plane restraint system was also connected to the rotational restraint system by a different line of bolts. These two systems aimed to simulate accurately the boundary conditions of interior slab panels. The in-plane restraint system allowed the slab edges to translate inwards or outwards in straight edges, while the rotational restraint system applied flexural restraint on the slab edges. Test results presented in Section 3 indicate that this research purpose has been achieved. It is worth noting that there was a 20mm gap between the in-plane restraint system and the furnace walls to avoid any load taken up by the furnace walls. The gap was filled by insulation material to avoid heat loss.

2.3 Instrumentation

K-type thermocouples and linear variable differential transducers (LVDT) were used to measure temperatures and displacements of the beams and the slab. A similar set of instrumentation was used for the two specimens. Temperature of the slab was measured at Sections 1, 2 and 3 (Figure 3). At each section, temperature was monitored at the top and bottom surfaces, and at the level containing the reinforcing mesh. Temperatures of the beams were measured at Sections A to F at the top and bottom flanges, and at the middle of the beam web. The furnace air temperature was also monitored.

A total of 20 LVDTs were used to measure displacements of the floor assemblies (Figure 4), in which L1 to L3 were 300mm LVDTs to monitor vertical deflection of the slab. L4 to L11 comprised 200mm LVDTs to measure vertical deflections of the beams. Three 50mm LVDTs (L12, L13 and L14) were used to measure horizontal and vertical displacements of a column, while L15 to L20 for horizontal displacements along the slab edges.

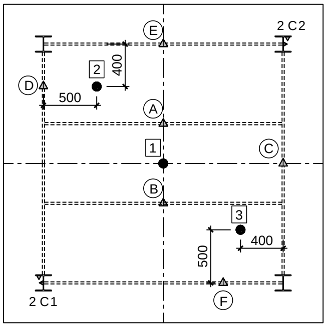

Figure 3. Arrangement of thermocouples.

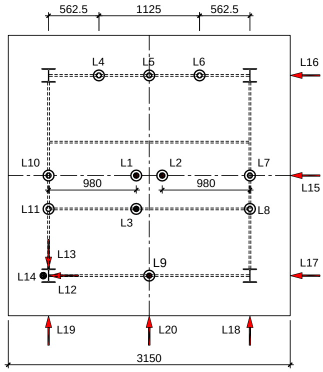

Figure 4. Arrangement of LVDTs.

2.4 Test load

The slabs were initially loaded up to 15.8kN/m^2 by a twelve-point loading system designed to simulate uniformly distributed loads (Figure 2) and then heated up to failure from the soffit of the slab. This value was equal to 0.35 times of the conventional yield-line load at ambient temperature, which was 45.1kN/m^2 based on the slab configuration with two interior beams. The moment capacity of supporting beams does not affect the conventional yield-line load since it was assumed that the slab was “simply-supported” all round. The selection of load ratio is within the practical range of 0.3 to 0.7.

3 EXPERIMENTAL RESULTS AND DISCUSSIONS

3.1 Temperature distributions in the slabs

A comparison of distribution of slab temperatures of P215-M1099 and P486-M1099 is shown in Figure 5. It can be observed that the air temperature developed consistently in both tests. A small discrepancy of 5.8% was found when comparing the temperature at 94min of heating, viz. 966^{o}C in P215-M1099 against 910^{o}C in P486-M1099. On the other hand, temperature at the slab bottom surface increased at the same rate up to 60min of heating. After that, as the temperature increased gradually concrete cracks developed resulting in significant heat loss. Therefore, towards the end of the tests, the temperature at the bottom surface and at the reinforcing mesh showed some discrepancies. Temperature at the top surface was very consistent with the maximum value of 164^{o}C in P486-M1099.

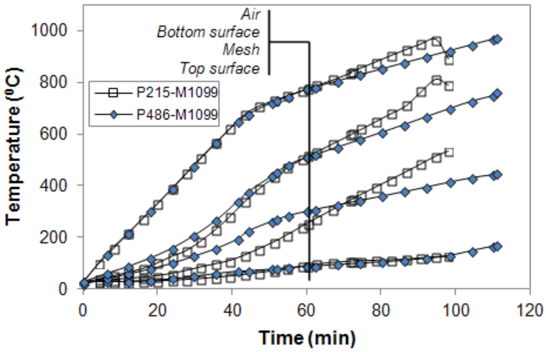

Figure 5. Distribution of slab temperatures.

3.2 Slab displacements

3.2.1 Deflection at the slab centre

Deflection at the centre of P215-M1099 and P486-M1099 against the mesh temperature is plotted in Figure 6. It should be noted that the bending stiffness about the major axis of PSB (EI_{yPSB}) of P486-M1099 had increased 2.26 times compared to that of control specimen P215-M1099.

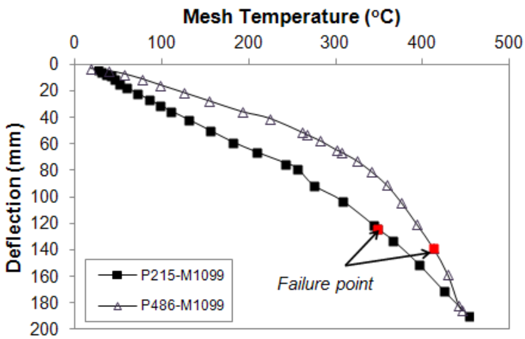

Figure 6. Comparison of deflection at the slab centre

P215-M1099 failed at a deflection of 124mm when the mesh temperature had reached 348°C. The corresponding values were 139mm at 412°C for P486-M1099. It can be observed that as the stiffness of PSB increased, the slab deflection decreased.

Table 2. Summary of test results.

Specimen	h_s	Failure time after fire	Failure temperature* (°C)			p_{test}	$p_{y,\theta m}$	w_{max}	w_{max} / h_s	p_{test} / $p_{y,\theta m}$
	mm	min	θ_t	θ_m	θ_b	kN/m^2	kN/m^2	mm		
P215-M1099	57	72.2	108	348	602	15.6	8.4	124	2.17	1.86
P486-M1099	55	98.2	127	412	697	15.5	8.2	139	2.53	1.89

*θ_t: temperature at slab top surface; θ_m: temperature at reinforcing mesh; θ_b: temperature at slab bottom surface; h_s: slab thickness; $p_{y,\theta m}$: yield line load at failure mesh temperature.

With regard to the maximum deflection at failure, as can be seen in Table 2, P486-M1099 (EI_{yPSB} of P486-M1099 increased 2.26 times compared to that of P215-M0119) experienced a larger deflection, i.e. $2.53h_s$ compared to $2.17h_s$ for P215-M1099 (h_s is the slab thickness), which was an increase of 17%. However, the enhancement factor of P486-M1099 was only slightly greater than that of P215-M1099, 1.89 for P486-M1099 compared to 1.86 for P215-M1099. The enhancement factor is defined here as the ratio between the test load p_{test} and the yield line load at failure mesh temperature $p_{y,\theta m}$. This means that stiffness of the edge beams had little effect on tensile membrane stage of the slab. This was because at tensile membrane stage, the composite action between the edge beams and the concrete slab was weakened by parallel cracks appearing along the protected edge beams as shown in Section 3.4.

Therefore, it can be concluded that an increase of the stiffness of protected secondary edge beams had a positive effect on minimising the slab deflection. However, the composite action between the edge beams and the concrete slab plays a key role in mobilising this beneficial effect. Once the composite action was weakened by parallel cracks along the protected secondary beams, the floor system would lose the benefit associated with a greater stiffness of secondary edge beams.

3.2.1 Horizontal displacement

Figures 7 and 8 show the horizontal displacements of P215-M1099 and P486-M1099 respectively, including the loading phase. In these figures, a positive value indicates inward horizontal displacement, and a negative value outward displacement. The positions of the LVDTs are shown in Figure 4. L15, L16, L17 were placed along the edge parallel to the main beam, while L18, L19, L20 were placed parallel to the secondary edge beam. Three important observations can be drawn from these test results.

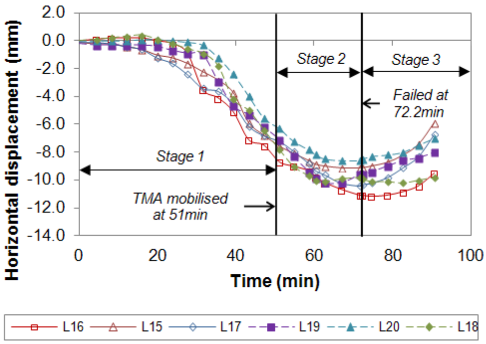

Figure 7. Horizontal displacement of the slab edges vs. time – P215-M1099.

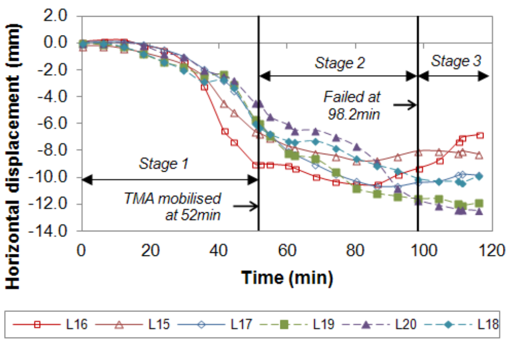

Figure 8. Horizontal displacement of the slab edges vs. time – P486-M1099.

Firstly, the horizontal displacement-time relationship of the slabs can be divided into three stages. *In the first stage*, the slab edges moved outwards due to thermal expansion as the slab temperature increased. Up to 20min of heating, the temperature was low because the moisture in the slab had gradually released. Therefore, displacements of the edges in two horizontal directions were small, only about 2mm. From 20min to about 50min of heating, the displacements increased at a greater rate with the maximum values of 8mm and 9mm for P215-M1099 and P486-M1099, respectively. *In the second stage*, after 50min, when the slab deflection reached about $1h_s$, TMA was mobilised. Therefore, the sum of outward displacements due to thermal expansion and inward displacement due to TMA resulted in an almost constant displacement. *In the third stage*, when the slab experienced large vertical deflections, the slab edges moved inwards significantly. However, intense tensile stresses in the reinforcement above the protected edge beams led to failure in these regions. When the failure had been identified, the furnace was turned off.

Secondly, the onset of TMA can be marked based on the horizontal displacement-time relationship of the slabs. This was the time when the displacement rate reduced and was almost constant. As explained above, this resulted from the sum of outward displacement due to thermal expansion and inward displacement due to TMA. Therefore, TMA was mobilised at 51min and 52min for P215-M1099 and P486-M1099, respectively. These times are confirmed once again by the development of crack patterns in the slabs (Section 3.3).

Thirdly, it can be observed that the recorded horizontal displacements from L15, L16 and L17 along one slab edge and those from L18, L19 and L20 along the transverse slab edge were only slightly different. This indicates that the slab edges initially moved outwards and then inwards in straight lines. Therefore, it can be concluded that the tested slab panels could accurately simulate the continuity conditions of interior panels as initially planned.

3.3 Development of crack patterns

The development of crack patterns of P215-M1099 and P486-M1099 was observed carefully during the tests and is re-plotted in Figures 9 and 10, respectively. The heating times when cracks occurred are indicated, together with the corresponding temperatures in the reinforcing mesh and the corresponding mid-span slab deflections. The crack sequences shown by the numbers were quite consistent in all the tests.

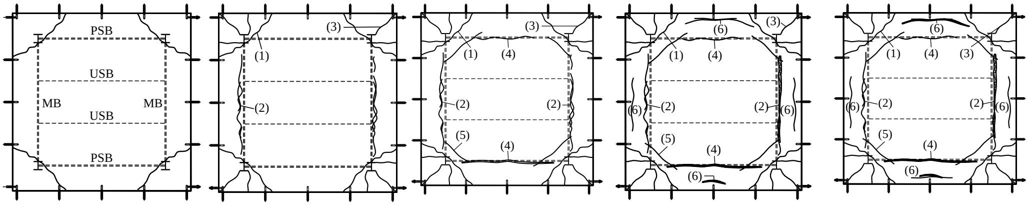

13min – 41^{o}C 9mm | 33min – 91^{o}C 28mm | 51min – 181^{o}C* 59mm ≈ $1.03h_s$ | 72min – 348^{o}C** 124mm | 87min – 458^{o}C 178mm

Figure 9. Development of crack pattern – P215-M1099.

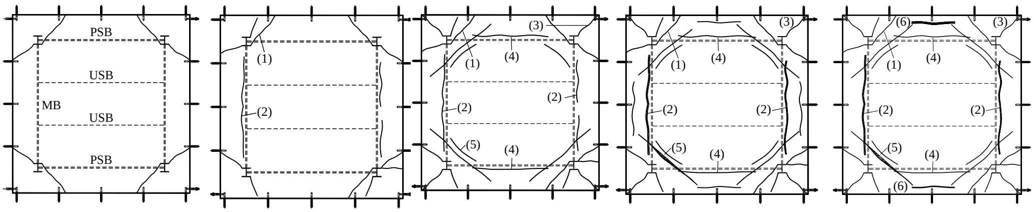

12min – 41^{o}C 7mm | 31min – 79^{o}C 15mm | 52min – 185^{o}C * 54mm ≈ $0.98h_s$ | 98min – 412^{o}C** 139mm | 110min – 496^{o}C 182mm

Figure 10. Development of crack pattern – P486-M1099.

Firstly, diagonal cracks near the beam-to-column joints (crack 1) appeared consecutively at the four slab corners. These cracks were due to biaxial bending of the slab outstand. At these corners, parts of the outstand were in biaxial bending but restrained by the columns.

Secondly, cracks appeared in the vicinity of the main beams (crack 2). The diagonal cracks emanating from the slab corners to the columns (crack 3) were then observed. These diagonal cracks (3) were caused by the bolts which restrained the slab. As the temperature increased, cracks along the protected secondary edge beams (crack 4) appeared.

In P215-M1099 test, after 51min of heating, a compression ring began to form when the mesh temperature had reached 181 ℃ at a deflection of 59mm, 1.03h_s (h_s is the slab thickness). In P486-M1099, a compression ring began to form at the respective mesh temperature of 185^{o}C, after 52min of heating at a mid-centre deflection of 54mm, equal to 0.98h_s. Based on this observation, it can be concluded that TMA mobilized at a slab deflection approximately equal to 0.9 to 1.0 of the slab thickness, irrespective of the stiffness of the protected edge beams. Tensile membrane mechanism in these tests consisted of radial tension in the central area of the slab, surrounded by a peripheral compression ring. Due to its self-equilibrating nature, horizontal edge restraint was not required for the mobilization of TMA.

The onset of TMA can be recognized by appearances of diagonal cracks inside the slab panel at the four corners (crack 5). The more obvious indication was the transition between outward and inward displacements of the slab edges (Section 3.2.1). These indications coincided very well in terms of time.

Severe cracks also appeared at the slab outstand (crack 6). These cracks were due to the bolts along the slab edges. As the slab deflected, these bolts were too stiff to deflect together with the slab causing the cracks near the ends of the bolts. When the slab experienced very large deflections, the cracks opened through the slab thickness and reinforcement was fractured. However, this did not affect the test results because it happened after the failure had been identified.

3.4 Failure modes

The failure mode observed in P215-M1099 and P486-M1099 was fracture of reinforcement close to the protected edge beams (at crack 2 or 4). No run-away failure was observed. Shear studs and connections were shown to be designed adequately. No premature failure at the shear studs or at the connections was observed. Figures 11 and 12 show the final failure mode of P215-M1099 and P486-M1099 after cooling, respectively, in which the crack positions were indicated.

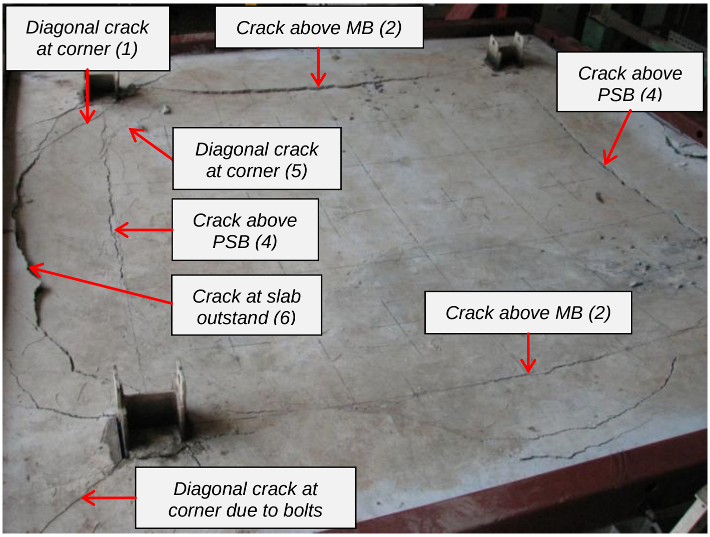

Figure 11. Failure mode of P215-M1099.

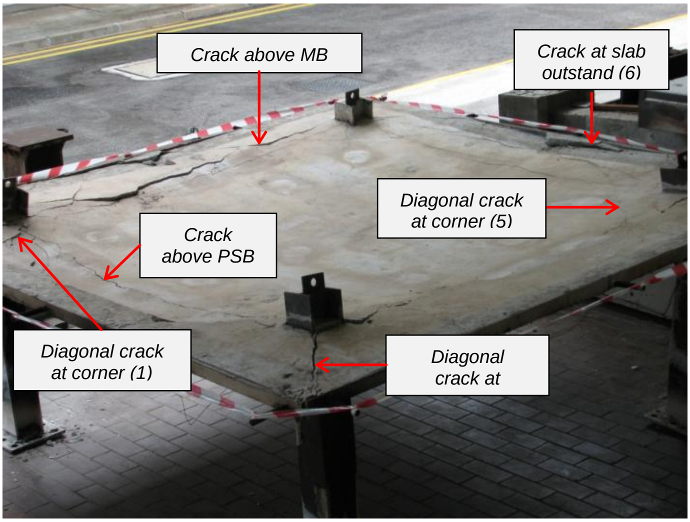

Figure 12. Failure mode of P486-M1099.

4 CONCLUSIONS

This paper presents the experimental results and observation from two composite beam-slab floor systems tested under fire conditions. The aim is to study the effect of *bending stiffness of protected secondary edge beams* on the tensile membrane behaviour of floor assemblies in fire.

The results showed that as the stiffness of the protected secondary edge beams increased, the slab deflection initially decreased. However, composite action between the edge beams and the concrete slab plays a key role in mobilizing this beneficial effect. Once the composite action had bean weakened by parallel cracks in the slab over the main or secondary protected edge beams, the benefit associated with a greater stiffness of the edge beams was lost.

Tensile membrane action was mobilized at a deflection equal to 0.9 to 1.0 of the slab thickness, irrespective of the bending stiffness of the edge beams. The occurrence of tensile membrane stage was marked by one of two indications: (a) concrete cracks which formed a peripheral compressive ring on top of the slabs, and (b) horizontal displacements along the slab edges. In both the tests, these indications were very consistent in terms of occurrence time.

ACKNOWLEDGMENT

The research presented in this paper was funded by Agency for Science, Technology and Research (A*Star Singapore) under Grant No. M4070013. The financial support of A*Star is gratefully acknowledged.

REFERENCES

[1] Zhao B., Roosefid M., and Vassart O. "Full scale test of a steel and concrete composite floor exposed to ISO fire", *Proceedings of the Fifth International Conference on Structures in Fire (SiF'08)*. Singapore, Nanyang Technological University, 539-550, 2008.

[2] Zhang N.-S., Li G.-Q., Lou G.-B., Jiang S.-C., and Hao K.-C. "Experimental study on full scale composite floor slabs under fire condition", *Application of Structural Fire Engineering*. Prague, Czech Republic502-511, 2009.

[3] Stadler M., Mensinger M., Schaumann P., and Sothmann J. "Munich Fire Tests on Membrane Action of Composite Slabs in Fire - Test Results and Recent Findings", *Application of Structural Fire Engineering*. Prague, Czech Republic2011.

[4] Ward F. and Kallerová P. "Fire Test on Administrative Building", *7th International Conference on Steel & Aluminium Structures*. Kuching, Sarawak, Malaysia2011.

[5] Wellman E., Varma A., Fike R., and Kodur V., "Experimental Evaluation of Thin Composite Floor Assemblies under Fire Loading", *J Struct Eng - ASCE*, (Vol 137, N0. 9), 1002-1012, 2011.

[6] Lim L.C.S. *Membrane action in fire exposed concrete floor systems*. Ph.D. Thesis. Department of Civil Engineering. University of Canterbury. 2003.

[7] Nguyen T.-T. *Behaviour of Composite Beam-Slab Floor Systems at Elevated Temperatures*. Ph.D. Thesis. School of Civil and Environmental Engineering. Nanyang Technological University. 2014.

[8] Nguyen T.T. and Tan K.H. "Testing of Composite Slab-beam Systems at Elevated Temperatures", *7th International Conference on Structures in Fire (SiF)*. 6-8 June 2012 Zurich, Switzerland, Swiss Federal Institute of Technology Zurich, 247-256, 2012.

[9] Newman G.M., Robinson J.T., and Bailey C.G., *Fire Safe Design: A new Approach to Multi-Story Steel-Framed Buildings*, in *SCI Publication P288* 2006, The Steel Construction Institute.

8th International Conference on Structures in Fire
Guo-Qiang LI, Venkatesh K. R. KODUR, Shou-Chao JIANG, Jian JIANG, Su-Wen CHEN, Guo-Biao LOU (Eds.)
Shanghai, China, June 11-13, 2014

COMPONENT-BASED MODELLING OF COMPOSITE BEAM-COLUMN JOINTS AFTER COLUMN FAILURE

Bo Yang[*, **] and Kang Hai Tan[***]

[*]School of Civil Engineering, Chongqing University, Chongqing, 400045, P. R. China
e-mail: yang0206@cqu.edu.cn

[**]Key Laboratory of New Technology for Construction of Cities in Mountain Area (Chongqing University), Ministry of Education, Chongqing, 400045, P. R. China

[***]School of Civil & Environmental Engineering, Nanyang Technological University, 50 Nanyang Avenue, Singapore
e-mail: ckhtan@ntu.edu.sg

Keywords: Beam-column joints, Progressive collapse, Web cleat, Composite slab, Column failure, Component-based model

Abstract. *In this paper, component-based models of composite beam-column joints after column failure due to fire, blast or impact have been proposed. Two types of connections, namely, composite web cleat and flush end plate connections, are analyzed. Middle joints under sagging moment and side joints under hogging moment are both considered. Failure criteria are introduced for most connection components, which enable the component-based models to predict the failure of these two types of composite joints. In general, these component-based models give acceptable predictions of the composite beam-column joint behaviour after column failure. In addition, frame analyses were conducted incorporating the developed component-based models for the composite joints. The main objective of the frame analyses is to identify the differences in structural performance between an isolated joint and a frame model after a middle column failure. Finally, parametric studies are carried out to investigate the effects of reinforcement ratios, profile decking and composite slabs on structural behaviour incorporating the composite joint model. It is also found from a parametric study that the beam span-to-depth ratio has a great influence on the frame behaviour after a middle column failure.*

1 INTRODUCTION

In order to develop a better understanding of the behaviour of building structures after column failure due to fire, blast or impact, the structures group at Nanyang Technological University has conducted a series of research projects to investigate the behaviour of steel, composite and concrete structures after column failure. Yang and Tan[1] conducted five experimental tests to investigate the behaviour of composite beam-column joints after a middle column failure. Composite web cleat and flush end plate connections were studied. Two types of joints including middle and side joints were both tested to failure.

EC3-1-8[2] and EC4-1-1[3] recommend component-based method for the analysis and design of steel and composite joints. In this method, the joint is divided into several individual components. The joint behaviour can be predicted by the assembly of various connection components. In the past, numerical and analytical models have also been developed to simulate the behaviour of composite beam-column joints. However, these studies only included moderate joint deformations and were limited to moment-rotation relationships. In this study, component-based models are developed to predict the behaviour of composite beam-column joints up to total failure after a middle column failure. The experimental results obtained from the tests of Yang and Tan[1] are used to validate the proposed component models. Finally, frame analyses are conducted incorporating the developed component-based models.

2 COMPONENT-BASED MODELLING OF COMPOSITE BEAM-COLUMN JOINTS

In this section, component-based modelling of composite beam-column joints will be presented. The behaviour of composite beam-column joints after a middle column failure can be predicted by these models. The experimental results presented by Yang and Tan [1] provide essential test data for the development and validation of the proposed component-based joint models.

2.1 General

The component-based models of composite beam-column joints are shown in Figure 1. The components include bolted-angles in tension, T-stubs in tension, profile decking in tension, beam flange and web in compression, concrete in compression, and reinforcing bars in tension and in compression. It should be mentioned that since in the experimental tests [1] full shear connection was used, the slip of the shear connectors was minimal. Thus, in the proposed joint model, the component of shear connector is not considered. Nevertheless, in the case when partial shear connection is used, this component should be included.

In this set of five experimental tests on composite beam-column joints, no shear failure was observed. Thus, in the component-based models, a rigid shear spring to transfer vertical shear forces is used. In order to predict total failure of composite connections, the respective deformation capacity of individual connection component should be identified and introduced into the component-based models.

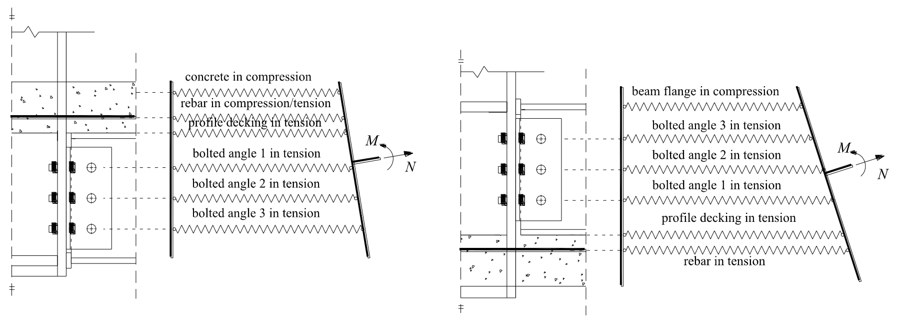

(a) (b)

Figure 1. Component-based models of composite beam-column joints: (a) Web cleat connection at middle joint; (b) Web cleat connection at side joint.

2.2 Simulation of the tests using the component-based models

Based on the proposed mechanical models of the connection components, the force-displacement of each component can be obtained. These force-displacement relationships are then introduced into the general FEM program ABAQUS[4] as properties of connector elements. The beam-column joints are simulated by the assembly of the connector elements. The steel beam is simulated by using beam elements and the composite slab is modelled using shell elements. The composite slab is simulated by using four-node shell elements with a mesh size of 120 mm.

Figure 2 shows the simulated responses of Specimen M-W-9 with the experimental results in terms of (a) vertical forces and (b) beam axial forces versus middle column displacement. The component-based model is based on the predicted load-displacement relationship. From the comparisons it can be found that the proposed component-based models can capture the essential structural behaviour with satisfactory accuracy.

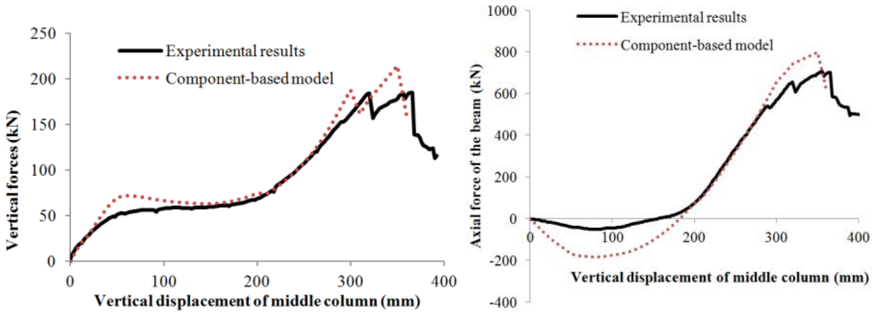

(a) (b)

Figure 2. Comparison of the analytical predictions against the test data of Specimen M-W-9: (a) Vertical force vs. middle column displacement curves; (b) Beam axial force vs. middle column displacement curves.

Due to the paper length limitation, the simulations of other test specimens are not presented in this paper.

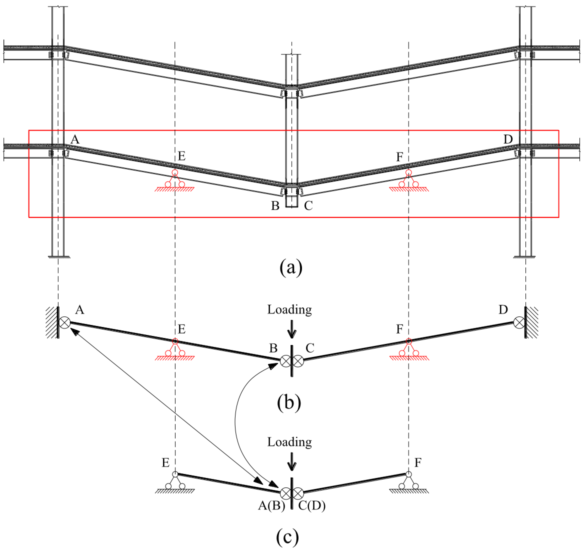

Figure 3. (a) Prototype composite frame with (b) Frame model and (c) Joint model in the analytical works.

3 FRAME ANALYSES

Having gained confidence in the reliability of the component-based models, frame analyses are carried out by incorporating the proposed joint models into the frame analyses. The frame analyses are also conducted based on ABAQUS [4]. The steel beam is simulated by using beam elements and the composite slab by shell elements, which is the same arrangement with the validation studies of the joint models. One of the main objectives of the frame analyses is to identify the difference in structural performance between isolated joints and frame models after a middle column failure. In addition, parametric studies have been carried out to investigate the effects of reinforcement ratios, profile decking and composite slabs. Finally, a parametric study is conducted in order to investigate the effect of beam span-to-depth ratio onto the frame behaviour after a middle column failure.

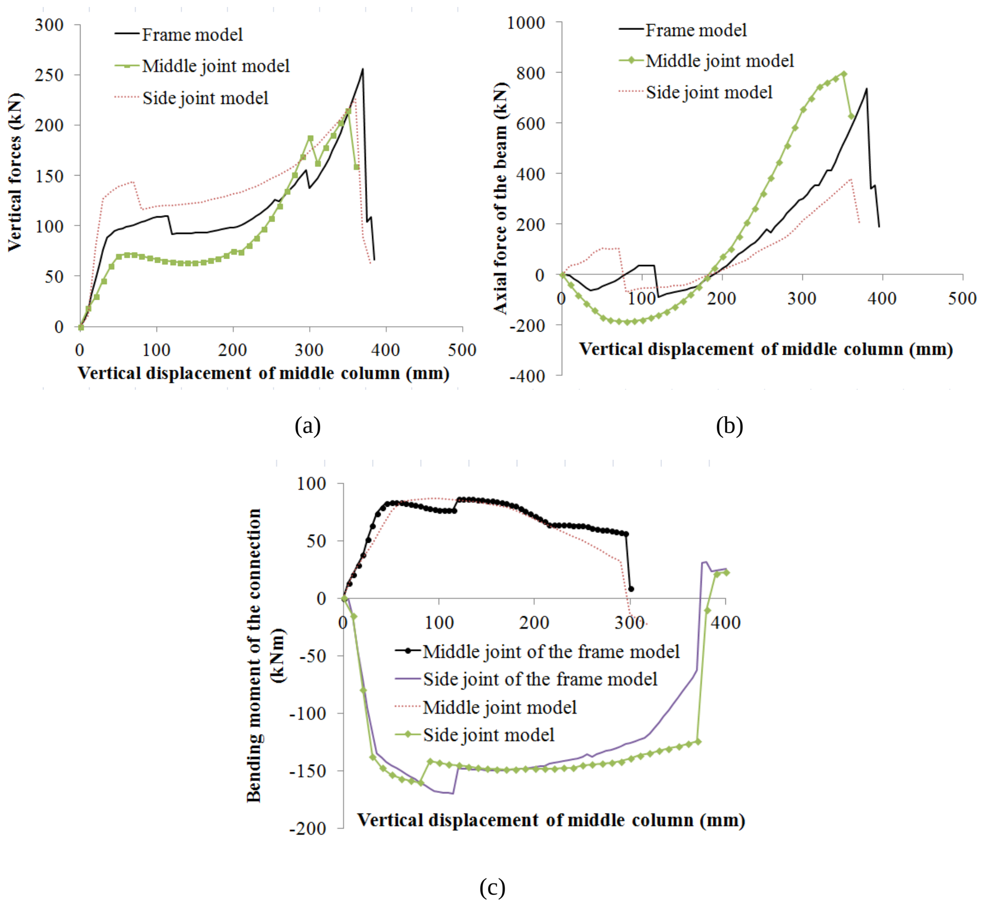

Figure 4. Comparison of the composite fame models against the test results and joint models: (a) Vertical force vs. middle column displacement curves; (b) Beam axial force vs. middle column displacement curves; and (c) Connection moment vs. middle column displacement curves.

3.1 Discussion about frame and joint models

The prototype composite frame is shown in Figure 3 (a). In the frame model shown in Figure 3 (b), the entire two beam spans and four connections at these two spans are modelled. The two columns at the two sides are restrained by surrounding structures. The connections are simulated by the component-based models, presented in the previous sections. In the experimental tests and the joint models, an inflection point was assumed to be located at the middle of the beam span and only one-half of the beam span at both sides of the beam-column joint was used, as shown in Figure 3 (c). However, due to the presence of composite slabs, the inflection point may not be located at the beam mid-span. The developed frame model will be used to study the interaction between the middle and the side joints and the load redistribution after the failure of the middle column. In the analyses of this section, one type of connection has been chosen as an example to demonstrate these effects. The chosen connection type has the same configuration with the web cleat connection (Specimen M-W-9) in Figure 5 (b) of Yang and Tan[1]. For this type of connection, analytical results of the joint model have been presented in the previous sections, and these results will be used to compare with the frame model.

The numerical results of the frame model are compared with the joint models in Figure 4. It can be found from Figure 4 (a) that at flexural action stage, the frame model has different predictions with the middle and side joint models. This is because at this stage, the inflection point is not located at the beam mid-span, which has been explicitly assumed in the joint models. The flexural resistance of the frame model is smaller than the side joint model but larger than the middle joint model. However, it can be found from Figure 4 (c) that in the frame model, the magnitudes of bending moments of the middle and side joints are similar to the joint models. This indicates that the flexural resistances of middle and side joints will not affect each other in the frame model and the inflection point assumption does not affect the flexural resistances of the isolated joints. At catenary action stage, the load-carrying capacity of the frame model is slightly greater than the middle and side joint models. As shown in Figure 4 (b), higher beam axial forces are formed in the frame model than the side joint model. With the additional contribution of flexural resistance of the middle and side joints, a higher load-carrying capacity is achieved in the frame model than the isolated joint models.

3.2 Effects of reinforcement ratios, profile decking and composite slabs

Based on the frame model presented in the last section, further parametric studies have been conducted to investigate the effects of reinforcement ratio, profile decking and composite slab. The beneficial effect of additional reinforcement to increasing the frame load-carrying capacities is illustrated in Figure 5. It should be noted that the 1.3% reinforcement ratio corresponds to the composite specimens presented by Yang and Tan [1]. Figure 5 shows that the increase of the reinforcement ratio causes higher load resistances at flexural action stage as well as catenary action stage.

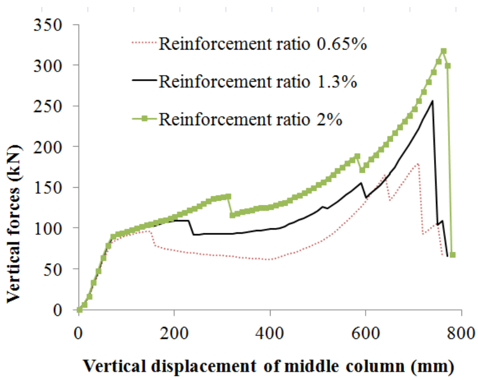

Figure 5. Effect of reinforcement ratio in the frame model.

In order to study the effect of profile decking on the behaviour of composite frames, a frame analysis without profile decking has been conducted and the results are shown in Figure 6. It can be found that the presence of profile decking can increase the load-carrying capacity at flexural action stage. However, at large deformation stage, no difference is observed between the two frame models with or without the profile decking. This is because the profile decking has limited deformation capacity and fractured at small deformation stage. As shown in Figure 6, at a displacement of 220 mm, the profile decking fractured at the side joints. In addition, the effect of composite slabs has been studied by conducting a bare steel frame simulation. As shown in Figure 6, the steel frame can develop catenary action fully. However, without reinforcing bars in the composite slab, the ultimate load resistance of the steel frame is much lower than the composite frame. Also, at flexural action stage, the composite frame could form much higher load-carrying capacity than the steel frame. This is due to beneficial effect of the composite slab. It should be noticed that the development of 3-D tensile membrane action is not studied. If this effect was also included, the composite steel structures would have even higher load resistances than bare steel structures.

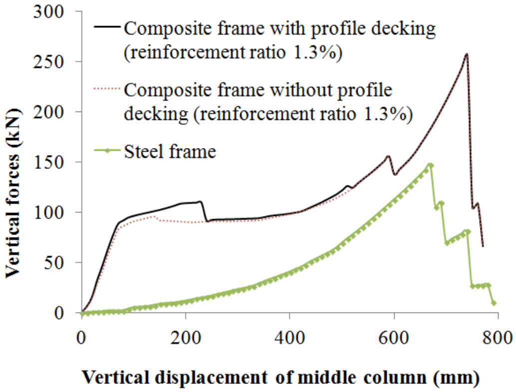

Figure 6. Effects of profile decking and composite slab in the frame model.

3.3 Effect of beam span-to-depth ratio

In practice, the composite beam span-to-depth ratio may vary from 13 to 30. Different beam span-to-depth ratios may affect the frame resistance and the development of catenary action after a middle column failure. Based on the developed frame model, a further parametric study has been conducted in order to study the effect of beam span-to-depth ratio. The beam-column joint models have been validated by the experimental tests. Thus, based on the developed beam-column joint modelling, a series of frames are modelled by varying the length of composite beam span, i.e. composite beam depth and beam-column joint details remain the same but only the beam span varies. In this way, the effect of beam span-to-depth ratio is investigated.

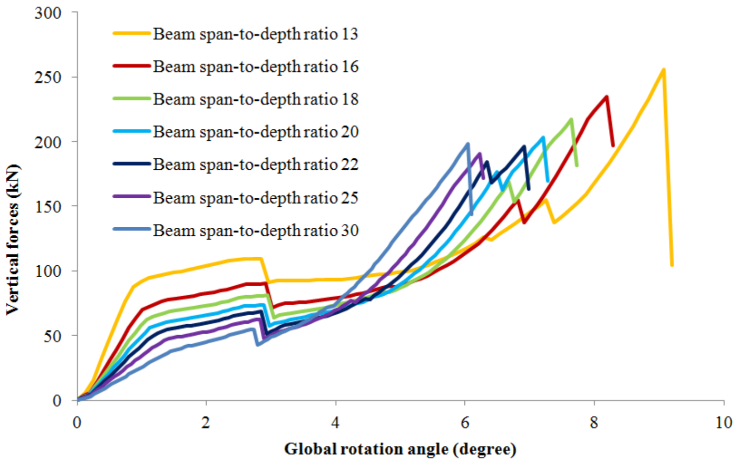

(a) Vertical force-global rotation angle curves

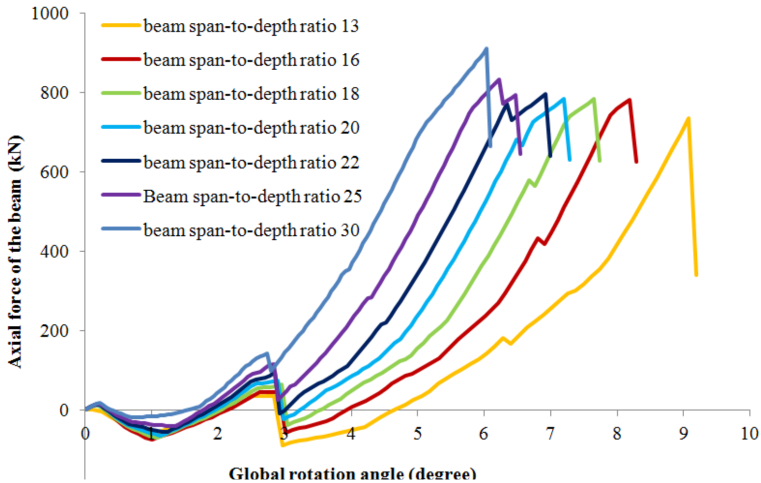

(b) Beam axial force -global rotation angle curves

Figure 7. Effect of beam span-to-depth ratio in the composite frame models.

The effect of beam span-to-depth ratio in the composite frame models is shown in Figure 7. Since these frame models have different spans, they cannot be compared based on the vertical displacement of the middle column. As shown in Figure 7, the vertical forces and beam axial forces of these frame models are compared based on the global slope. The global slope is defined as the ratio between the vertical displacement of the middle column and one composite beam net span. It implies that the entire single-bay beam rotates like a rigid body, which has been observed from the experimental tests [1]. Figure 7 (a) shows that the increase of the beam span-to-depth ratio decreases the load resistance of the composite frames at flexural action stage. This is because the beam-column joint modelling is identical for all the frame models, which means the bending moment resistance of the beam-column joints is not increased.

Figure 7 (a) also indicates that with the increase of beam span-to-depth ratio from 13 to 25, the frame ultimate resistance decreases gradually although when the beam span-to-depth ratio increases from 25 to 30, the frame resistance increases slightly. As shown in Figure 7 (b), the increase of the beam span-to-depth ratio increases the beam axial force slightly. However, it also causes a significant decrease of the frame global rotation angle at the maximum load point, which greatly limits the contribution of catenary action. This is the reason why the frame ultimate resistance decreases with an increase of beam span-to-depth ratio. It can be concluded from Figure 7 that the beam span-to-depth ratio has a great influence on the frame behaviour after a middle column failure.

4 CONCLUSIONS

Component-based models are developed to simulate five experimental tests of composite beam-column joints after a middle column failure, which have been presented by Yang and Tan[1]. The focus of this paper is the frame analyses after the validation of the joint models. Some new knowledge has been obtained by the frame analyses. The following conclusions can be drawn:

(1) By using the developed component-based beam-column joint models, frame analyses indicate that the frame model has different predictions with the middle and side joint models. It is also found that the flexural resistances of middle and side joints will not affect each other in the frame model and the inflection point assumption does not affect the flexural resistances of the isolated joints.

(2) Parametric studies indicate that the increase of the reinforcement ratio causes higher load resistances at flexural action stage as well as catenary action stage. However, presence of profile decking

can only increase the load-carrying capacity at flexural action stage, and at large deformation stage, no difference is observed between the two frame models with and without profile decking.

(3) It is found from a parametric study that beam span-to-depth ratio has a great influence on the frame behaviour after a middle column failure. The increase of the beam span-to-depth ratio increases the beam axial force slightly. However, it also causes a significant decrease of the frame global rotation angle at the maximum load point, which greatly limits the contribution of catenary action.

REFERENCES

[1] Yang B. and Tan K.H., "Behaviour of composite beam-column joints under a middle-column-removal scenario: experimental tests", *Journal of Structural Engineering-ASCE*, 140(2), 04013045, 2013.

[2] Eurocode 3 Part 1-8 (EC3-1-8), *Eurocode 3: Design of steel structures—Part 1-8: Design of joints, BS EN 1993-1-8: 2005*, British Standards Institution, UK, 2005.

[3] Eurocode 4 Part 1-1 (EC4-1-1), *Eurocode 4: Design of composite steel and concrete structures—Part 1-1: General rules and rules for buildings, BS EN 1994-1-1: 2004*, British Standards Institution, UK, 2004.

[4] ABAQUS, *Analysis user's manual version 6.9*, ABAQUS Inc., 2009.

8th International Conference on Structures in Fire
Guo-Qiang LI, Venkatesh K. R. KODUR, Shou-Chao JIANG, Jian JIANG, Su-Wen CHEN, Guo-Biao LOU (Eds.)
Shanghai, China, June 11-13, 2014

RESULTS AND ANALYSIS OF A LARGE-SCALE FIRE TEST ON A MULTI-BAY COMPOSITE STEEL-FRAME FLOOR SYSTEM

David J Proe*

* Professorial Research Fellow, CESARE, Victoria University, Melbourne, Australia
e-mail: david.proe@live.vu.edu.au

Keywords: Fire test, Steel structure, Cardington, Three-dimensional frame

Abstract. *This paper describes a fire test conducted on a large-scale structurerepresenting four corner bays of a typical multi-storey steel-frame office building.Its purpose was to facilitate verification of computer modelling techniques for complex structures exposed to fire and to test the effect of some steel beams being left unprotected. A new and unexpected mode of damage occurred, indicating that an alternate reinforcement detail should be used in combination with unprotected beams.*

1 INTRODUCTION

This paper describes the results and analysis of a fire test conducted as part of an ongoing test program on a large-scale structure. The purpose of the test program is to investigate the holistic fire behaviour of four corner bays of a typical multi-storey steel-frame office building when some steel beams are left unprotected, and to facilitate verification of computer modelling techniques for complex structures exposed to fire. Planning for this test was described in an earlier paper [1].

2 PREVIOUS LARGE-SCALE FIRE TESTS BY OTHERS

This work contributes to the genre of large-scale fire tests on three-dimensional framed structures which have been conducted globally following the Cardington fire test series in the UK in 1995 and 1996 [2]. A detailed summary and review of these types of test has been published by Bisby et al. [3].

The Cardington tests indicated the possibility that the performance in fire of a complete steel-frame structure with interconnected structural elements such as beams, columns and floor slabs may be superior to that of the same elements tested in isolation. An eight-storey building with plan dimensions of 45 m by 21 m was subjected to seven fire tests conducted in various parts of the structure. The largest area of floor exposed to fire at any one time was 21 m by 18 m (Test 5, Large Compartment Test), although the temperatures achieved in this test were too low to convincingly demonstrate structural robustness. A more severe test was conducted over a floor area of approximately 18 m by 9 m (Test 6, Simulated Office Test). This test produced substantial deformation and a maximum floor deflection of 640 mm but no collapse.Various fuel types were used in these tests, including wood cribs, gas burners and office furniture. The tests did not follow the ISO834 standard time-temperature curve (STTC).

Other large-scale fire tests conducted since that time have included two tests by CTICM and ArcelorMittal, known as the FRACOF test and the COSSFIRE test [4]. The FRACOF test structure measured 6.7 m by 8.7 m and incorporated four columns surrounding one bay. The COSSFIRE test measured 6.7 m by 9.0 m and incorporated six columns and two bays. These tests were both conducted on furnaces and followed the STTC.Anothertest was conducted atMokrsko in the Czech Republic by Wald [5]. In this test the floor slab was a single bay measuring 18 m by 12 m. A further test was conducted by

Nadjai et al at the University of Ulster [6]. In this case, the floor consisted of a single bay measuring 15 m by 9 m.

As described in the previous paper [1], the purpose of the current test series is to focus upon various structural performance aspects not adequately explored in the previous tests described above, especially load transfer from unprotected beams to adjacent parallel protected beams. In addition, the four-bay layout enables slab continuity over the internal edges of each bay to be realistically tested.

3 TEST SETUP FOR CURRENT TEST

A four-bay structure has been constructed. Each bay measures 8 m by 10 m, and the overall structure measures 16 m by 20 m (see Figures 1-3). Of the twenty beams supporting the floor slab, the twelve "main grid" beams bounding the bays are protected against fire and the eight internal beams within each bay are unprotected. All nine columns supporting the beams are protected.

The underside of the structure has been enclosed on all four sides, with an adjustable air inlet along the full length of the western edge and a chimney at the eastern edge (see Figure 2). The enclosure walls and vents have been constructed using 0.55 mm galvanised flat steel sheeting lined on the outside with fire-resistant insulation blanket. This system was designed to ensure that the walls would provide no support to the deforming test structure. The walls were held at an angle of 60 °to the horizontal using steel wires at about 1 m intervals. Fuel trays of 1.2 m width and almost 16 m length have been placed near the western edge adjacent to the inlet opening.

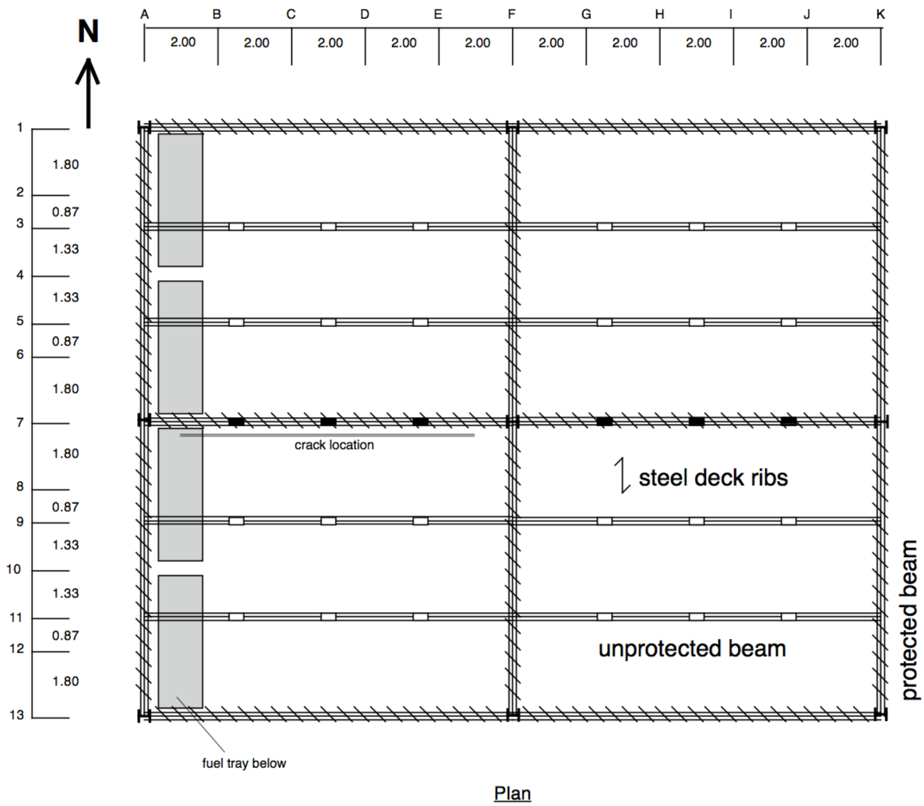

Figure 1. Test structure, plan view showing gridlines and crack location.

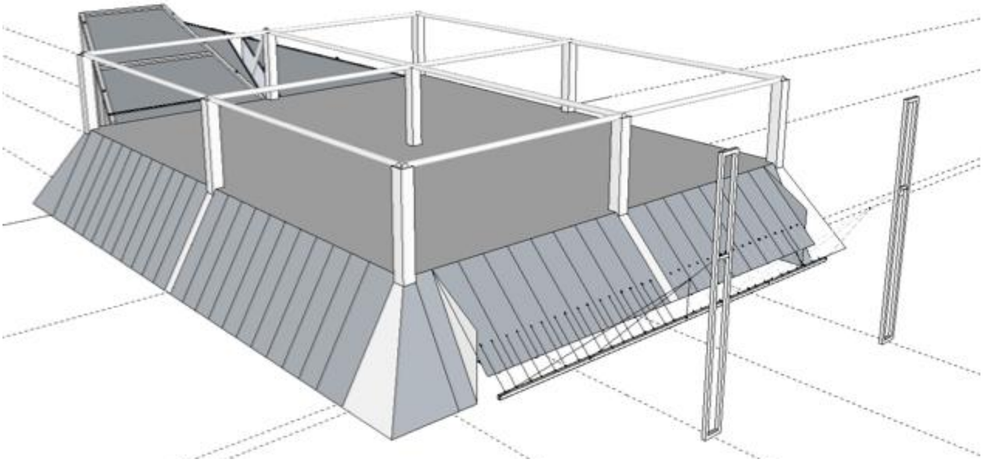

Figure 2. Test structure, isometric view showing fire enclosure, inlet vent and chimney.

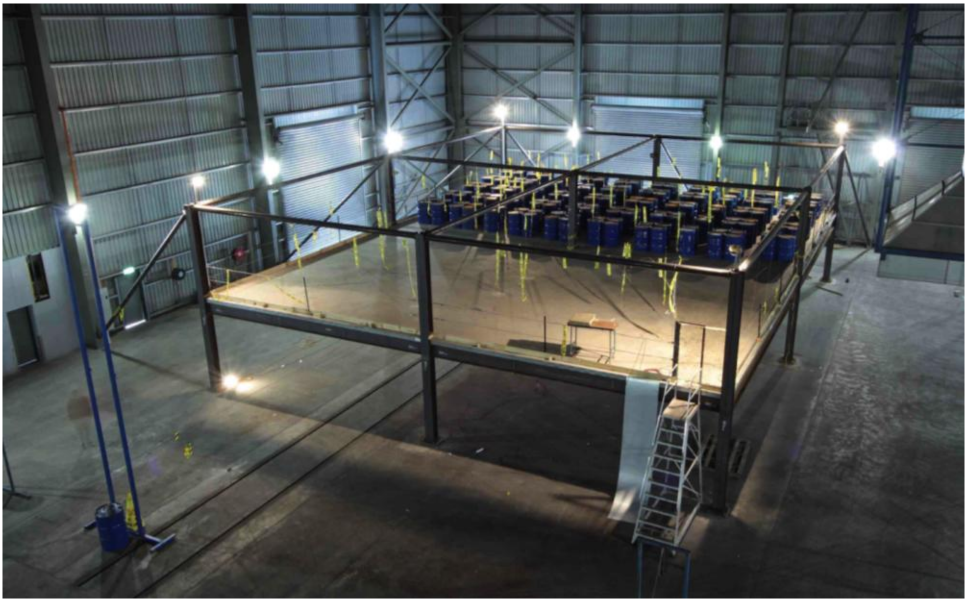

Figure 3. Test structure, some water drums in place, before installation of fire enclosure walls.

4 TEST RESULTS

For the test conducted, 1000 litres of E85 fuel (85% ethanol,15% unleaded petrol) was placed in the fuel trays beneath the structure and ignited. The inlet opening was set to a height of about 300 mm and the fire was allowed to burn freely until the fuel was exhausted, which took approximately 20 minutes.

Loading was applied via 380 steel drums placed on the slab, each able to contain 200 litres of water.Due to time constraints, not all drums had been filled at the time of the test, however. Average loads (including structure self-weight) within each of the four bays were: north-west: 4.8 kPa (72 drums filled), south-west: 5.2 kPa (90 drums), north-east: 3.4 kPa (16 drums), south-east: 4.0 kPa (42 drums).

Temperatures were measured at numerous points beneath and within the structure. Peak air temperatures were about 1000 ℃ and 500 ℃ for thermocouples located in the western and eastern halves of the structure respectively. The temperatures of the unprotected steel beams (western half of structure) reached 900 ℃ in the bottom flange and 650 ℃ in the top flange at about 13 minutes. Protected beam temperatures rose only slightly above ambient during the test. See Figure 4.

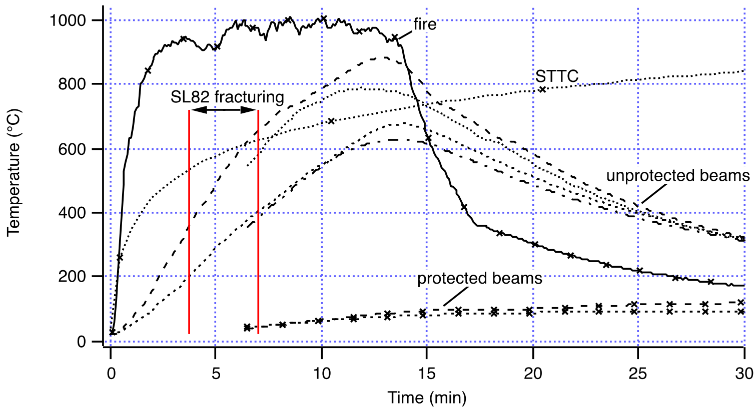

Figure 4. Selected air and beam temperatures.

The increase in air temperature in the vicinity of the fuel trays was much more rapid than the STTC (see Figure 4). Measured air temperatures reached 900 ℃ in 3 minutes, whereas the standard fire takes 44 minutes to reach this temperature. For real firesin offices, a long period of incipient fire growth typically occurs as the fire becomes established. This did not occur in the current test.

It was observed during the test and recorded via video that a series of 52 loud sharp bangs occurred between 3 minutes 45 seconds and 7 minutes into the test. These noises were accompanied by a substantial increase in steam release from the slab and noticeable deflection of the slab.Inspection of the top surface after the test indicated the existence of a long and wide crack running parallel to the protected beamat grid A7-F7, located 300 mm from the centreline of the beam (200 mm from its southern edge), as shown in Figure 1. It was up to 20 mm in widthat the slab surface and about 8 m in length. The slab had dropped approximately 16 mm between the two sides of the crack at some points. Excavation of the concrete at three distinct positions along the crack indicated that a north-south bar of theSL82 shrinkage-and-temperature (S&T) mesh was completely fractured in each case.

The reinforcement layout at the crack location was checked using photographs taken before pouring of the concrete. This check indicated that the S&T mesh was continuous at this location and there were no problems with lapping. It was observed, however, that the crack location coincided closely with the termination point of the shear transfer bars above the steel beam. It was concluded that each of the 52 loud bangs mentioned above corresponded to the fracture of one north-south bar of the S&T reinforcement and that this continuous reinforcement in the top of the slab must have fractured over the whole 8 m length of the crack.

No deflection measurements were taken during the test, but a contour survey of the slab surface was conducted 13 days later (with slab still fully loaded). This indicated a maximum residual deflection of approximately 200 mm in the slab.Inspection of the structure below the slab indicated little damage. In particular, the steel sheeting at the slab soffit below the major crack remained fully intact, with a slight crease being the only evidence of the damage above. Each of the unprotected steel beams in the western half had a deflection of about 180 mm and had also undergone a vertical (shear) displacement of approximately 50 mm acrossthe web penetration at gridline E, but they were otherwise almost undamaged.

The protected beam at grid A7-F7 had deflected 80 mm. The insulation material on the protected beams and columns remained almost fully intact.

5 DISCUSSION OF RESULTS

5.1 General

The most significant outcome of this test was the unexpected cracking in the slab. This cracking possibly represents a new mode of damage not previously observed in fire testing of structures of this type. Because the test was of short duration, it provided the opportunity to study the causes of this damage before they were disguised by further fire exposure. This mode would only occur in a test where multiple continuous bays were simultaneously exposed to fire. As such, any previous slab tests where only one bay was exposed to fire would not reveal this mode.

It appeared likely from observations following the test that the fracture of the S&T mesh was related to the termination of the shear transfer reinforcement at this location. The cross-section detail is illustrated in Figure 5. The Bondek sheeting was not continuous over the beam but the adjacent sheets were butted together and joined to the steel beam via the welding of the shear studs through all sheeting pans, thus providing continuity of the sheeting across the supporting beam. Bending moment calculations have been performed below to estimate the likely cause of this cracking, and whether the ductility of the S&T mesh was a significant factor.

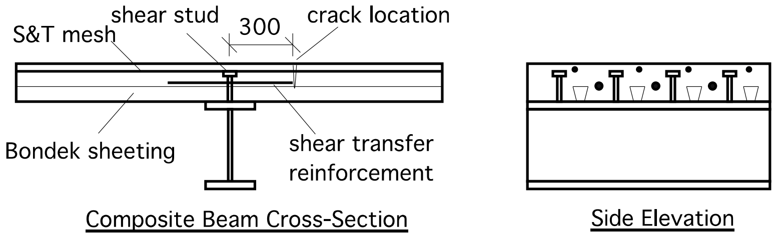

Figure 5. Composite beam and slab detail.

A widely-recognized method of analysis has been proposed by Bailey [7]. This proposal is based on the assumption that the reinforcement crossing any continuous edge of a bay may fracture directly above the main grid beam and so any continuity should conservatively be ignored. For geometries where the observed mode of damage can occur, there is a possibility that this assumption may not be conservative enough, as the reinforcement may fracture to the side of a main grid beam rather than directly above the beam, resulting in loss of vertical support to the slab. On the other hand, the steel sheeting crossing the crack did not fracture, and it is possible that there is sufficient shear interlock remaining that this edge retains adequate vertical support. To investigate this possibility, the theory of shear transfer across cracked cross-sections will be applied, assuming that the steel sheeting acts as effective reinforcement.

5.2 Bending Moments in Slab Caused by Differential Beam Deflection

The crack which occurredis assumed to have commenced near the midspan location of the internal protected beam (between grid positions C7 and D7 in Figure 1). At this location, bending moments would essentially have been one-way. The formation of the crack may therefore be considered in terms of a strip of slab at the midspan of this beam spanning in a north-south direction, as shown in Figure 6.

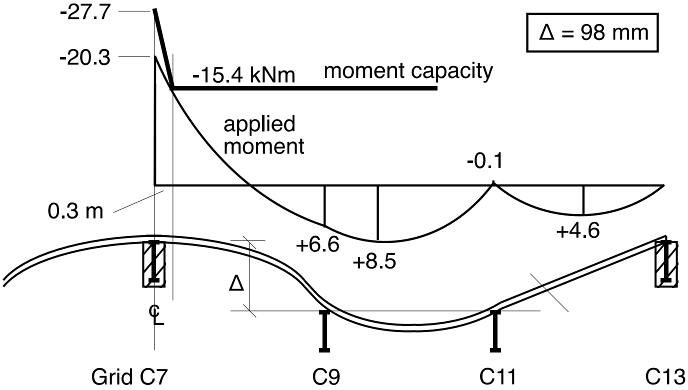

Figure 6. Deflected shape of slab and resultant bending moment diagram.

Treating the structural configuration shown in Figure 6 as a relative support settlement problem (ignoring membrane action), bending moments have been calculatedat about 3 minutes into the fire test, assuming all elements to be at ambient temperature apart from the unprotected beams. Slope-deflection equations have been used. This method of analysis assumes uniform bending stiffness along the full length of the member, which is anapproximate approachas there will be different stiffness magnitudes in negative and positive bending regions and in cracked and uncracked sections. It is further assumed that the applied load is uniformly distributed (5.2 kPa including self-weight), that there is no deflection in the protected beams and that all unprotected beams deflect by the same amount. Although not measured, it has been estimated using available test data that differential deflections exceeding 400 mm may have occurred during the test.

The elastic second moment of area (I) of the cracked cross-section reinforced with SL82 in negative bending has been calculated to be 9.65×10^6 mm^4/m.This value has been used throughout the length. A Young's modulus (E) for concrete of 31 GPa has been assumed, corresponding to a compressive strength of 40 MPa. To calculate negative bending capacities, the pan and vertical parts of the Bondek ribs have been ignored. Considering only the horizontal steel at the top of each Bondek rib gives 160 mm^2/m with a yield stress of 550 MPa. The S&T mesh is SL82 whichgives 247 mm^2/m at 500 MPa. The shear transfer reinforcement is N12 bars at 200 mm centres, giving 565 mm^2/m at 500 MPa. Applying rectangular stress block theory gives a moment capacity of Bondek and SL82 mesh of 15.4 kNm/m and a moment capacity of Bondek, SL82 mesh and N12 bars of 27.7 kNm/m.The calculated cracking moment is 9.1 kNm/m.

The above inputs have been used to calculate the deflection at which the bending moment in the slab at 300 mm from the protected beam equals 15.4 kNm/m. This gives 98 mm differential deflection and a bending moment distribution as shown in Figure 6.Also shown in this figure is the negative moment capacity of the slab, based on a development length of the N12 bars calculated to be 300 mm. As shown, the plastic hinge is predicted to form at the end of the N12 bars rather than at the centre of the support. This explains the reason for the observed crack location, and indicates that it is based on reinforcement detailing rather than on reinforcement ductility.In addition, more advanced calculations have been performed using the software, ‘Response 2000’, from University of Toronto, which performs nonlinear analysis accounting for cracking. These calculations have confirmed the observed fracture location. Repeating the analysis using normal ductility reinforcement has indicated that the additional ductility provides little benefit.The advanced analysis produced smaller deflections at fracture, being 45 mm and 48 mm for low ductility and normal ductility reinforcement respectively.

Further evidence that the observed cracking was the result of reinforcement detailing rather than ductilitycan be obtained from a review of a previous fire test result as described in Addendum A. Low ductility reinforcement similar to SL82 was used at a similar reinforcement ratioin that test, but the slab was continuously reinforced throughout its length. That slab showed particularly ductile behaviour, and an optimal pattern of numerous closely-spaced cracks formed in the slab over the continuous supports.

5.3 Effect of Loss of Vertical Support on Capacity of Slab Bay

The long crack which has occurred in the test is a concern, as it not only removes moment and axial force (membrane) continuity over one edge of both the south-west bay and the north-west bay, but it also potentially removes the vertical support from one edge of the south-west bay.

The design method proposed by Bailey [7] assumes no moment continuity over internal edges of a slab bay, as it is assumed that fracture of reinforcement is likely to occur at this location. The method does require, however, that full vertical support is available at all edges. It appears unlikely that a compression ring will be able to remain stable along a side which does not have full vertical support.

For the current slab, it is estimated that the yield line load capacity for the slab supported on only three sides is about 60% of the capacity with support along all four edges. In addition, the enhancement in capacity due to tensile membrane action is unlikely to occur.

5.4 Shear Transfer Across Cracked Section

As noted above, the Bondek sheeting did not appear to have fractured at the crack location. This raises the possibility that the tensile capacity of the sheeting may be adequate to provide sufficient shear transfer across the cracked section to support this edge of the slab bay.

Tensile testing of Bondek II sheeting at elevated temperature has been performed at Victoria University [8]. This testing indicated that its tensile capacity varied between 66 kN/m width at 60 minutes of standard fire exposure to 36 kN/m at 120 minutes. For reinforcement located at the height of the top of the ribs, these capacities correspond approximately to Grade 500 reinforcing mesh of size SL62 (141 mm^2/m). Alternatively, using the horizontal part at the top of each of the four ribs per 600 mm width of sheeting, the reinforcement area is 160 mm^2/m.

Assuming an effective reinforcement area of 160 mm^2/m, the shear stress capacity due to aggregate interlock has been calculated using the relevant equation from Park and Paulay[9] to be 2.13 MPa. Applying this capacity over an area of 10 m in length by the rib height of 54 mm gives a total vertical shear force capacity of 1150 kN. This may be compared with a support requirement for an area loading of 5.2 kPa and a tributary area of 24 m^2, giving a required shear force of 125 kN.Hence, the available shear force may be capable of providing the necessary support along the edge of the slab bay.

6 CONCLUSIONS

It was concluded that the cracked slab is likely to be able to carry the applied shear forces across the crack and that vertical support along this edge of the bay will be adequate. It is therefore expected that further fire exposure will result in the development of tensile membrane action in the slab and hence result in reasonably robust performance. Further fire testing will be required to determine whether this is the case.

It is recommended that in future, where the arrangement of unprotected beams as tested is to be used, the detailing of the shear transfer reinforcement should be amended to avoid termination in a negative moment region. To achieve this end, the S&T reinforcement could be placed directly on the Bondek ribs and be used as both S&T reinforcement and shear transfer reinforcement.

The author acknowledges grant funding for this project from the AusIndustry ICIP program and industry partners including OneSteel (particularly Mr Anthony Ng), Bluescope Steel, Boral, ASI, NDY, Umow Lai and Page Steel, along with support and guidance from PhD supervisor, Prof Ian Thomas.

7 ADDENDUM A: FIRE TEST WITH LOW DUCTILITY REINFORCEMENT

Two tests have previously been conducted on a structural configuration that would be expected to demand high ductility. Test BFT743 incorporated low ductility reinforcement similar to SL82, while test

BFT742 used a normal ductility reinforcement. The test specimen in both tests was a reinforced concrete slab as illustrated in Figure 7, with continuous top and bottom reinforcement of 314 mm^2/m and 367 mm^2/m respectively. It was placed on top of the furnace and heated from below along its full length (including cantilevers) to follow the STTC. Loading was applied to the central span via steel blocks. Hydraulic jacks were adjusted continuously during the test such that there was zero rotation of the slab over each of the support beams. This loading arrangement simulated a fully built-in span of length 4.7 m.

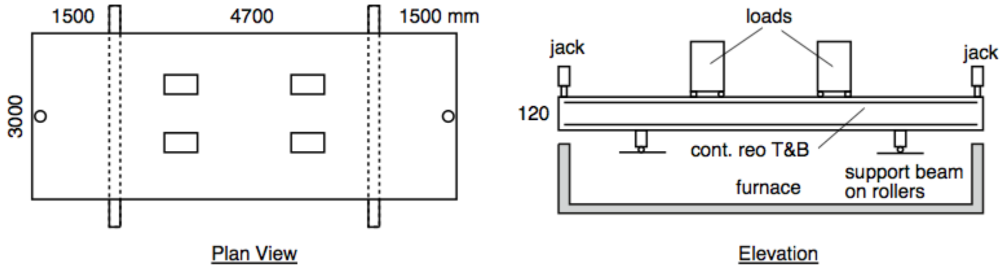

Figure 7. Configuration for previous fire tests on continuous cantilever specimens.

Ductile overall performance was achieved in both tests. The slab thickness of 120 minutes fails the insulation criterion at approximately 120 minutes. Moment-curvature calculations had been performed and it was expected that structural failure would occur at about 120 minutes also. This was based on the assumption that the hinge length over the support would be approximately one to two times the slab depth. Both tests were continued well past 120 minutes, with BFT743 stopped at almost 240 minutes, and no collapse occurred. Numerous narrow cracks occurred over the supports, and it was estimated that the hinge length was approximately 8 times the slab depth. Thus, for a given rotation demand, the curvature would have been much smaller than expected, thus requiring less ductility in the reinforcement. There was no significant difference in the fire endurance of these two specimens, despite the large difference in the ductility of the reinforcement types used.

REFERENCES

[1] Proe DJ, ThomasIR, “Planning for a Large-Scale Fire Test on a Composite Steel-Frame Floor System”, *Proc.6th Int. Conf on Structures in Fire*, pp390-397, 2010.

[2] Kirby B et al, “The Behaviour of Multi-storey Steel Framed Buildings in Fire”, European Joint Research Programme, British Steel Swinden Technology Centre, 1999.

[3] Bisby L, Gales J, Maluk C, “A Contemporary Review of Large-Scale Non-Standard Fire Testing”, Fire Science Reviews, Vol 2, No. 1, 1-27, 2013.

[4] Zhao B, Roosebid M, “Experimental &Numerical Investigations of Steel and Concrete Composite Floors Subjected to ISO Fire Condition”, *Proc. 6th Int. Conf on Structures in Fire*, 407-416, 2010.

[5] Wald F, Silva L, Moore D, Lennon T, Chladna M, Santiago A, Benes M, Borges L, “Experimental Behaviour of Steel Structure Under Natural Fire”, *Fire Safety Journal*, 41(7), 509-522, 2006.

[6] Nadjai A, Bailey CG, Vassart O, Han S, Zhao B, Franssen JM, Simms I,“Full-scale fire test on composite floor slab incorporating long span cellular steel beams”,*StructEngr* 89(21):18–25, 2011.

[7] Bailey CG, Toh WS, “Behaviourof Concrete Floor Slabs at Ambient and Elevated Temperatures”*Fire Safety Journal*, 42(6), 425-436, 2007.

[8] Bennetts ID, Culton M, “Testing and Behaviour of Slabs Incorporating Bondek II Sheeting in Fire”, Report No. VUT/CESARE/2003/001, CESARE, Victoria University, Melbourne, 2003.

[9] Park R, Paulay T, “Reinforced Concrete Structures”, Wiley, 1975.

8th International Conference on Structures in Fire
Guo-Qiang LI, Venkatesh K. R. KODUR, Shou-Chao JIANG, Jian JIANG, Su-Wen CHEN, Guo-Biao LOU (Eds.)
Shanghai, China, June 11-13, 2014

PROS/CONS OF TRANSVERSE REBAR IN STRUCTURAL FIRE RESPONSE OF A COMPOSITE STRUCTURE

Iris Chang*, Graeme Flint* and Neal Butterworth*

* Ove Arup & Partners, United Kingdom
Corresponding Author e-mail: Iris.Chang@arup.com

Keywords: Tall buildings, Composite frame, Transverse reinforcement, Fire

Abstract. *Composite slabs supported by steel frame structures are a common structural system used in the construction industry, especially for office buildings. Such designs include a variety of reinforcing bars acting as tensile reinforcement, anti-crack mesh and as "transverse rebar" to assist in developing composite connection between slabs and beams vie shear studs. Although most structural designs make use of transverse rebar for ambient design, this added reinforcement is generally omitted from structural fire assessments. During a recent commercial modelling project, the effects of transverse reinforcement were included in some of the structural fire models. The observations made when reviewing the finite element outputs are presented. The paper concludes with a discussion regarding the need to include transverse reinforcement in structural fire assessments.*

1 INTRODUCTION

Composite slabs supported by steel frame structures are a common structural system used in the construction industry, especially for office buildings. The Cardington tests [1] demonstrated that unprotected composite steel frame construction inherently performs well when subject to the Fire Limit State. The tests have permitted a wide spread of study into the physics behind the response of composite structural systems in the field of structural fire engineering [2]. Analytical and computational techniques have been developed to determine the load bearing capacity of these composite structures and to characterize their fire performance. The objective in the development of these methodologies is to help define the point of failure of a structural system when exposed to severe compartment fires.

The commonly used assessment methods typically include the effects of reinforcing mesh in the concrete slab as these have been explicitly studied and proven to have beneficial effects. However this is not necessarily the only source of reinforcing steel in a composite slab. Additional loose bars are commonly included, especially over primary beams, to assist in shear transfer in the composite system, i.e. to assist in the transfer of forces from the steel beam into the concrete slab and vice versa via the shear studs. The effects of this additional "transverse" rebar is typically discounted and simply assumed to provide an undefined benefit to robustness.

The authors were recently involved in assessing the structural fire response of a commercial building in London. During this exercise, a number of different assessment methods and areas of analysis were used. This included finite element modelling of the structure at the Fire Limit State and some of these structural models explicitly included the transverse reinforcement within the slab structure. A selection of model output relevant to the behaviour of transverse reinforcement within the slab is discussed in this paper.

1.1 Transverse reinforcement

In ambient structural design, transverse reinforcing bars (shown indicatively in Figure 1) within the slab provide added support to the integrity of the concrete to resist the force that is transmitted from the shear connectors into the slab [3]. It performs the dual role of providing direct shear capacity to the concrete slab as well as providing confinement to the concrete to increase its shear and bearing load carrying efficiency. The transverse rebar is therefore included in the system to assist in the composite action of the system and not to provide direct load bearing capacity for the slab. Studies have been undertaken to investigate the role of transverse rebar in providing extra strength into the structural system at ambient state. It is generally concluded that transverse rebar do not significantly impact on the ultimate flexural strength of the composite structure [4], other than supporting shear force transfer from the studs. Transverse reinforcement is therefore generally disregarded from structural fire analysis because it is not designed to carry load in the ambient state.

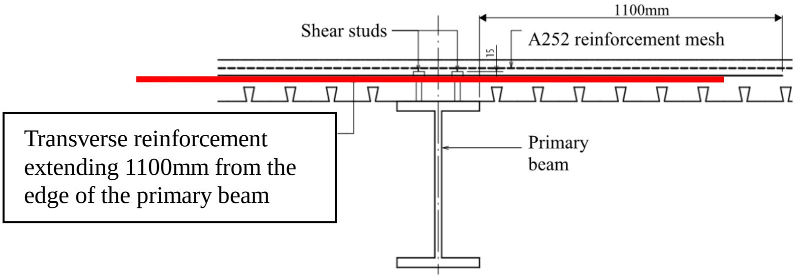

Figure 1. 2D cross section of a typical composite floor structure.

Even though transverse rebar within the slab is generally omitted from computational analysis, there have been instances where the potential benefit of the transverse rebar has not been overlooked. Finite element assessments were undertaken to assess the structural fire response of the building in two different projects; The Kings Place [5] and Ropemaker Place [6], both of which are office buildings in London. The results for the two separate projects illustrated that the modelled structure met their performance criteria in the applied fire scenarios. Despite this, transverse rebar were proposed to be added into the slab structure, over protected secondary spans which form the perimeter beams to the areas of the floor structure undergoing tensile membrane action. This is shown indicatively in Figure 2. This inclusion provides additional steel over key areas of relatively large strain, reducing the probability that the slab would crack significantly and rupture its rebar as it deforms under fire loading, qualitatively

The advantages that Transverse reinforcement can add to the structure in terms of fire have been considered. It will be beneficial to gain a better understanding of the effects of transverse rebar on the structural fire performance. The findings can then be implemented to increase the robustness of the structural fire design for other high rise buildings.

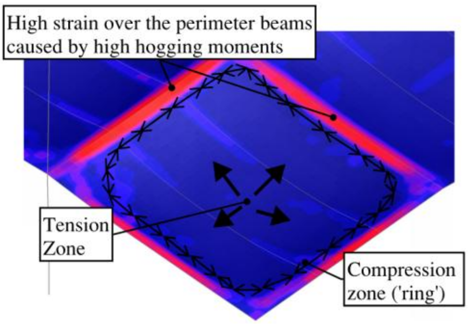

Figure 2. Indicative example of floor structure undergoing tensile membrane action.

1.2 The project

This paper discusses the observations made on the finite element assessment Arup has undertaken for a commercial structural fire modelling project. It concerned a new 18 storey (above ground) office building of composite steel frame construction. The building will have a central concrete core. The composite slab is made up of 150mm deep composite slabs with re-entrant profiled steel decking attached by shear studs to cellular steel beams. The steel beams contain a mix of circular and rectangular holes within the web. The columns are of universal steel column section and the sections become smaller with the rise of the building.

2 THE STRUCTURAL FIRE ENGINEERING ANALYSIS

Structural fire assessment was carried out for a project and the relevant results are presented in this paper. The aim of the analysis was to determine an optimized structural fire protection layout demonstrating an appropriate level of safety for the building structure given its height, anticipated maximum population and use. Finite element analysis was used to explicitly assess the robustness of a partially fire protected structure, i.e. 90-minute-rated structural fire protection to columns and beams connected to columns, and no fire protection to intermediate secondary beams.

A range of partial- and full-floor models were analyzed using the LS Dyna finite element modelling software. Only the observations made on the relevant models will be presented; an idealized model of a six bays floor structure, connected into the building core ,illustrated in Figure 3. The proposed protection layout is also indicated in this figure.

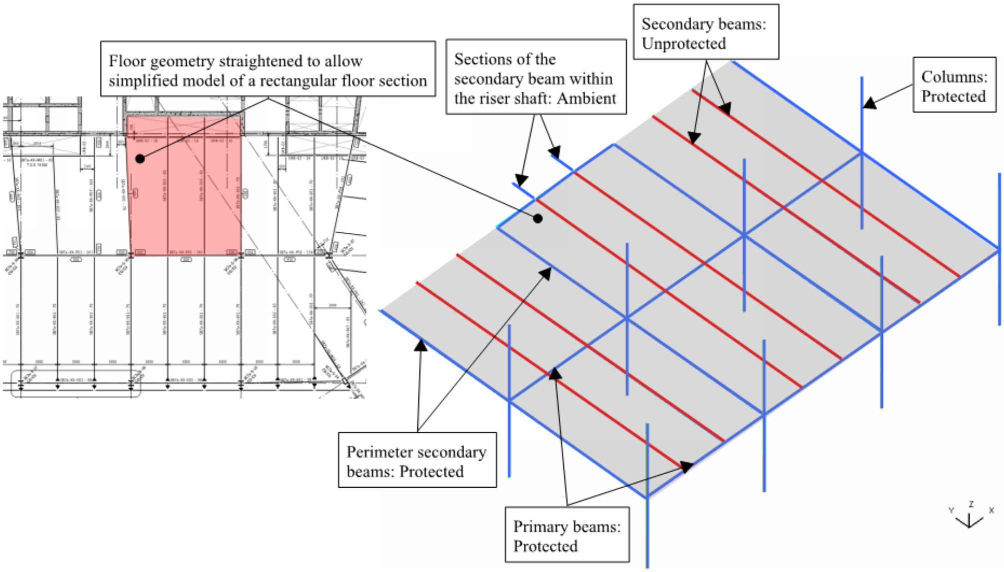

Figure 3. Floor structure modelled.

2.1 Design fires

The building structure was modelled to a range of possible fire scenarios as well as the standard fire scenario: localized compartment fires, full floorplate travelling fires, quick burning, short duration fires and slow burning, long duration fires.

In knowing the physical characteristics of the building, a Monte Carlo analysis [8] was used to determine likely design fires for the building. Figure 4 is a plot of the temperature time curves extracted from the Monte-Carlo simulation for use as model input.

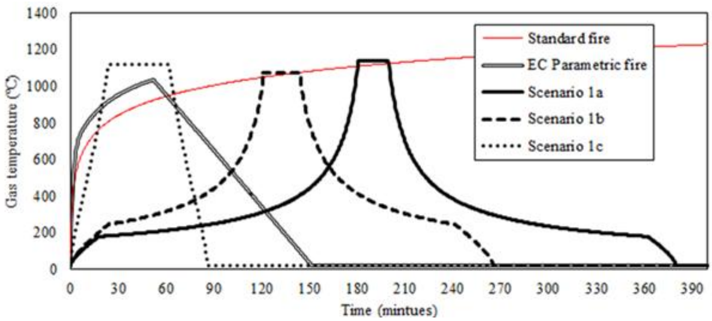

Figure 4. Temperature time curves of the design fires.

2.2 Heat transfer

To assess structural response in fire, heat transfer from the fire into the individual structural elements was determined.

The temperature distributions within the structural members were derived using the lumped mass approach provided in Eurocode 3 [9] and Buchanan [10]. The temperature within the protected and unprotected steel members have been calculated based on the section factor of the member and the assumed limiting temperature. It has been assumed that the top 10% of depth of the beam cross section is cooler than the bottom flange and lower web accounting for shielding effects and the heat sink effect of the slab above.

The temperature gradient, within the assumed effective thickness of the slab, with respect to the time during fire was calculated using a 1D finite difference model.

2.3 Modelling assumptions

This section describes the modelling assumptions necessary to build the structural models and carry out the finite element analysis of the structure during the assigned design fires.

A single storey fire was modelled in line with UK design requirements for accidental fire events. The area in the model includes the longest available spans in the building combined with the most heavily loaded and slender columns This combination of long spans and relatively low restraint from the columns is known to lead to the worst case in terms of vertical deflections and possible column failure modes [11].

The continuity between the modelled structure and its adjacent structure (not modelled) is represented by symmetry boundary conditions. This includes the loading imposed on this boundary from its adjacencies.

The material behaviour for concrete and steel, based on the properties listed in Table 1, has been modelled in accordance with Eurocodes 2 [12] and 3 [13], respectively.

Table 1. Material properties.

Material	Model
Steel members	S355
Light weight concrete	Grade C28/35
Reinforcing mesh	A252 mesh
Transverse reinforcement	H16 bars at 150mm centres, centred over the relevant beams. Spanned 1.1m length from either sides of the beam cross section.

All cellular beams have been modelled as solid section members with a redistributed web thickness to account for the reduced shear capacity of cellular beams. Connections have been modelled as perfectly pinned connections, except where moment resisting connections will be fitted in the structure, which will be modelled as fully fixed.

Mechanical loading on the structure modelled consisted of the self-weight of the structure, the typical office design load applied over the floor structure and the point loads being applied to the column at the modelled levels due to the overlying structure.

2.4 Finite element software

Commercially available general purpose finite element software, LS-DYNA, was adopted. It has been used previously by Arup and others for the investigation of structures subject to fire. Arup has conducted validation and verification on the software to ensure that it can capture the behaviour of composite steel structures in fire adequately. This has been done in accordance with the benchmarks described by Gillie [14].

2-noded linear beam elements are used for all beams and columns, while the slab is represented by a multi-purpose 4-noded reduced integration shell element. The shell element is a composite form with a succession of layers representing the concrete and steel reinforcement as shown in the schematic in Figure 5. The concrete material properties use a smeared cracking formulation to determine material damage and strain based degradation.

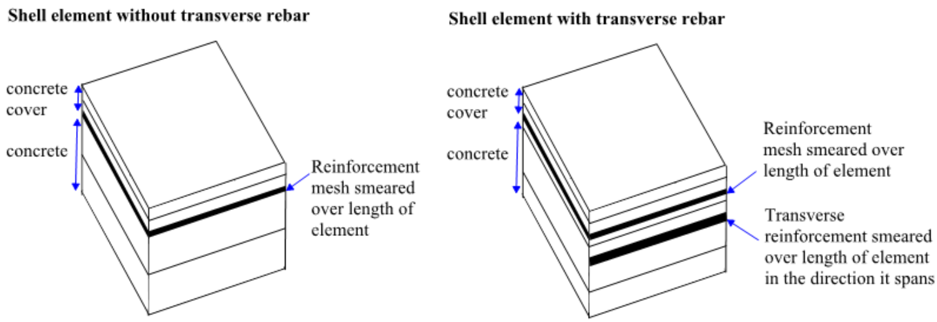

Figure 5. Schematic of shell element representing the floor slab structure.

3 OBSERVATION OF RESULTS

This section of the paper will present the observations made in relation to the results obtained from the model described in Figure 1 and above, where consideration was made on the transverse rebar in the floor structure.

The results obtained from the models relevant to this paper are discussed individually in this section of the paper. The results obtained for each of the presented models are not discussed in detail in this paper, only the observations made relevant to the behaviour of the transverse reinforcement are presented.

Note that this paper does not discuss the acceptability of the results gained in the models, but instead focusses on a comparative study of the effect on response of including additional transverse rebar.

3.1 Fundamental response

The structure was initially modelled to a 90 minutes standard fire with no transverse reinforcement in the slab. 50 minutes into the fire, the reinforcement mesh within the composite structure began to undergo large plastic straining. The large deflections (capable of reaching the magnitude of a span to deflection ratio of 11) common to slabs acting in tensile membrane action means that the slab must bend significantly as it passes over the protected perimeter beams. The plot in Figure 6 shows that after 60 minutes into the fire, the strain in the reinforcement mesh over the primary beams was approximately

26%. Before the end of the planned 90 minutes fire exposure, the floor structure in this model experienced runaway deflection in the slab due to failure of the rebar mesh layer.

A second model was assessed that included transverse reinforcement over the primary beam. The addition of the rebar reduced the strain experienced in the reinforcement mesh as shown in Figure 7 with maximum strains being limited to approximately 16%. The most telling change in response is that the additional stiffness provided by the additional layer of rebar in the slab leads to a change in slab curvature over the relevant beams. Deflection in the zone with the transverse rebar is reduced, while the overall slab deflection is not significantly affected. This leads to a sudden point of curvature at the edge of the transverse rebar zone which attracts high strains in the rebar mesh. Figure 8 shows the difference in deflection across a strip of the composite structure. The difference in deflection within the slab over a protected primary beam with and without transverse rebar is illustrated schematically in Figure 9.

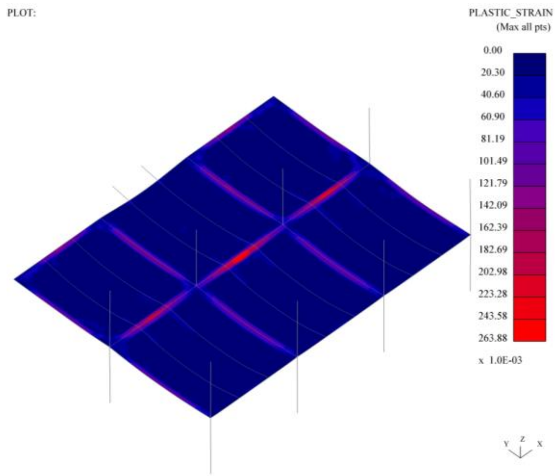

Figure 6. Model with no transverse reinforcement - Plastic strain in the reinforcement mesh after 60 minutes in the standard fire.

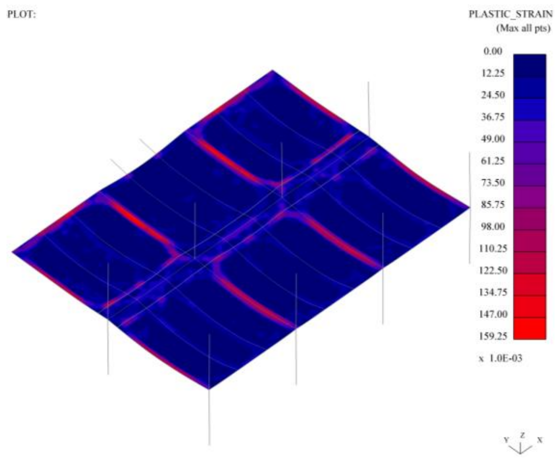

Figure 7. Model with transverse reinforcement - Plastic strain in the reinforcement mesh after 90 minutes in the standard fire.

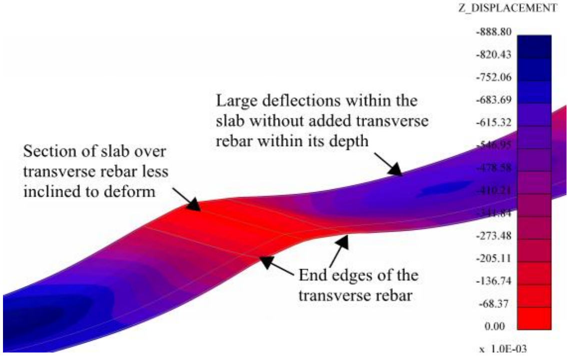

Figure 8. Deflection with a strip of the slab with transverse rebar over the primary beam.

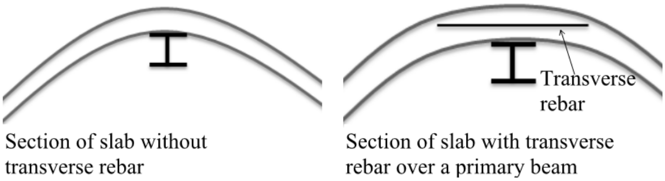

Figure 9. Schematic of slab deflection over a protected primary beam with and without transverse rebar within the slab.

While the model with transverse rebar also experiences high strains at the edge of the transverse rebar zone, the lack of runaway deflections observed in the model indicates that the discontinuity over the protected beam is softened sufficiently to prevent significant damage occurring to the rebar mesh. It is therefore apparent that although the reinforcing bars have not been added into the structure for the purpose of carrying the applied loading, it does contribute to the load bearing capacity of the structure at the fire limit state.

The structure with transverse rebar over the central primary beams was subjected to a number of different heating regimes with a severity equivalent to the 90 minutes standard fire. This was done to determine the effects of different heating rates and of cooling of the structure on its loadbearing capability. For this particular structural arrangement, the worst case fire scenario was determined to be a fast burning fire with a cooling phase.

4 CONCLUSIONS

This paper presents the discussion from an analysis undertaken on a partially fire protected composite floor with steel frame construction. The analysis was to study the response of the structure in fire with respect to the structural stability and the integrity of floor compartmentation. In particular for this paper, the influence made by including, into the analysis, the transverse rebar within the floor slab.

The inclusion of transverse rebar within the floor structure in some of the finite element models undertaken illustrated that they can have an impact on the structure’s response in fire. Although transverse rebar has not been designed to support the applied load in the structural design, it does contribute to the load carrying capacity of the structure in fire. However the added stiffness within the concrete floor structure, due to the transverse rebar, can transfer the high strains from the perimeter beams to the edge of the transverse bars leading to rupture within the reinforcement mesh at these locations.

As the modelling conducted for this project indicates pros and cons to the inclusion of transverse rebar in the slab it is recommended that this addition should no longer be ignored in finite element modelling but should rather be explicitly included. The addition of loose bars within the floor structure gives added strength and stiffness to the areas where the rebars are located, however they can also push high strains to the edge of transverse rebar zones in a fire leading to potentially detrimental geometrical compatibility effects and rebar rupture.

The study conducted for this project was not exhaustive and is based on comparative modelling only. Therefore there is scope for further study in this area. In particular, physical testing of the relationship between the quantity and location of the transverse rebar against the stability of the structure and the integrity of floor compartment. Further investigations must be made to determine if transverse reinforcement can be considered as a universal means to increase the robustness of a composite floor structure in fire, or if its use can introduce unconservative behaviour in a structure at the Fire Limit State

REFERENCES

[1] F. Giroldo, C.G. Bailey, Experimental bond behaviour of welded mesh reinforcement at elevated temperatures, Mag. Concr. Res. 60 (2008) 23–31.

[2] C.G. Bailey, D.B. Moore, The structural behaviour of steel frames with composite floorslabs subject to fire : Part 2 : Design, Struct. Eng. 78 (2006) 28–33.

[3] J.W. Rackham, G.H. Couchman, S.J. Hicks, Composite Slabs and Beams using Steel Decking: Best Practice for Design and Construction, SCI Publ. No. P300 (2009) 70.

[4] E.Y.L. Chien, J.K. Ritchie, Design and Construction of Composite Floor Systems, CISC (Canadian Institute of Steel Construction), 1984.

[5] C. Pozzi, B. Lane, S. Lamont, A. Heise, The role of large strains and consequent mitigation measures for buildings in fire, in: SiF06 (Structures in Fire), Aveiro, Portungal, 2006: pp. 487–498.

[6] D. Rini, A. Fire, O. Arup, S. Francisco, S. Lamont, Performance Based Structural Fire Engineering for Modern Building Design, (n.d.).

[7] C.G. Bailey, D.B. Moore, The structural behaviour of steel frames with composite floorslabs subject to fire : Part 1 : Theory, Struct. Eng. 78 (2000) 19–27.

[8] A. Law, J. Stern-Gottfried, N. Butterworth, Solving design challenges: revisiting time equivalence, in: 13th Int. Conf. Exhib. Fire Sci. Eng., 2013.

[9] EN 1993-1-2, Eurocode 3 - Design of steel structures - General rules -Structural fire design, BSI (British Standard Institution), Brussels, Belgium, 2005.

[10] A.H. Buchanan, Structural Design for Fire Safety, John Wiley & Sons Ltd, Chichester, 2001.

[11] G. Flint, Fire Induced Collapse of Tall Buildings, The University of Edinburgh, 2005.

[12] EN 1994-1-2, Eurocode 4 - design of composite steel and concrete structures - general rules - structural fire design, BSI (British Standard Institution), Brussels, Belgium, 2005.

[13] EN 1993-1-2, Eurocode – Design of steel structures – Part 1-2: General rules, Structural fire design, BSI (British Standard Institution), Brussels, Belgium, 2004.

[14] M. Gillie, Analysis of heated structures: Nature and modeling Benchmarks, Fire Saf. J. 44 (2009) 673–680.

8th International Conference on Structures in Fire
Guo-Qiang LI, Venkatesh K. R. KODUR, Shou-Chao JIANG, Jian JIANG, Su-Wen CHEN, Guo-Biao LOU (Eds.)
Shanghai, China, June 11-13, 2014

CALIBRATION OF A SIMPLIFIED METHOD FOR FIRE RESISTANCE ASSESSMENT OF PARTIALLY ENCASED COMPOSITE BEAMS

Emidio Nigro*, Iolanda Del Prete*, Domenico Sannino* and Giuseppe Cefarelli*

* Department of Structures for Engineering and Architecture, University of Naples Federico II
Via Claudio n. 21, 80125 Napoli (ITALY)
e-mails: emidio.nigro@unina.it, iolanda.delprete@unina.it, domenico.sannino@unina.it,
giuseppe.cefarelli@unina.it,

Keywords: Partially encased composite beams, Sagging and hogging moment resistance, Fire, Simplified and advanced methods, EN1994-1-2

Abstract.*This paper is devoted to evaluate the fire resistance of partially encased composite beam subjected to fire from beneath by using different analysis methods. In particular, for the evaluation of the sagging and hogging moment resistance,Eurocode 4 (EN1994-1-2) suggests two different simplified methods:*

- the "general simplified method": a specific thermal analysis provides the temperature field and the subsequent mechanical analysis is performed according to the plasticity theory;

- the "simplified method" proposed in the Annex F (F.1 and F.2): the mechanical analysis is carried out applying the plasticity theory and the effect of temperature is taken into account by reducing the size of the parts that make up the cross section and/or by reducing the mechanical properties of materials by means of reduction factors (both provided as function of fire exposure time).

The reliability check of the simplified method proposed in the Annex Fand the proposal of further alternative simplified methods are discussed within the activities of Evolution Group of EN1994-1-2, of which some of the authors of this paper are members.

Therefore, in order to evaluate the reliability of the simplified method proposed in the Annex F, the moment resistance, for a fixed fire exposure time, has been calculated by an advanced calculation method (incremental–iterative) based on the construction of the Moment-Curvature diagram, with reference to several case studies, within a parametric analysis. A comparison between simplified and advanced method has been carried out and, based on the noticed criticism, an alternative simplified method, easy to implement and more reliable, has been processed.

1 INTRODUCTION

The performance of steel structures in case of fire are adversely affected by several factors, such as the high thermal conductivity of the steel, the reduction of its mechanical characteristics due to high temperature, the limited thickness of the profile, which can determine critical reduction of both stiffness and resistance during the fire event. These aspects require a careful design and, often, the use of adequate protective coatings to ensure the safety in case of fire. Unlike steel structures, composite steel and concrete structures take significant advantages by both involved materials, both in terms of resistance and protection in case of fire naturally offered by concrete to steel profile [1].

In the field of composite steel and concrete structures, this paper is focused on the evaluation of the sagging and hogging moment resistance under fire conditions of composite beam comprising steel beam with partial concrete encasement.

The European code for fire safety of composite steel-concrete structures is the "Fire Part" of the Eurocode 4 (EN1994-1-2, 2005 [2]) while the Italian reference is the Technical Code for Constructions (D.MIN. II.TT. 14th ofJanuary 2008 [3]).

2 FIRE RESISTANCE ASSESSMENT OF PARTIALLY ENCASED BEAM

For the evaluation of the sagging and hogging moment resistance of composite beams with partial concrete encasement exposed to standard fire beneath the concrete slab, EN1994-1-2 suggests two different simplified methods:

(1) the "general simplified method": a specific thermal analysis provides the temperature field and the subsequent mechanical analysis is performed according to the plasticity theory ([9]);

(2) the "simplified method" proposed in the Annex F (Figure 1 and Figure 2): the mechanical analysis is carried out applying the plasticity theory and the effect of temperature is taken into account by reducing the size of the parts that make up the cross section and/or by reducing the mechanical properties of materials by means of reduction factors (both provided as function of fire exposure time). More details on this method will be in the paragraph 2.1.

The reliability check of the simplified method proposed in the Annex F and the proposal of further alternative simplified methods are discussed within the activities of Evolution Group of EN1994-1-2, of which some of the authors of this paper are members.

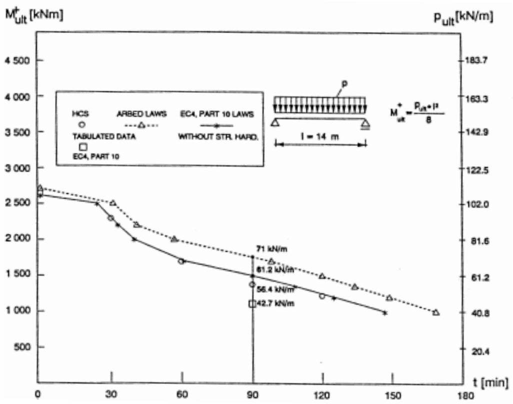

Figure 1. Numerical-numerical comparison in terms of sagging moment resistance ([1][4]).

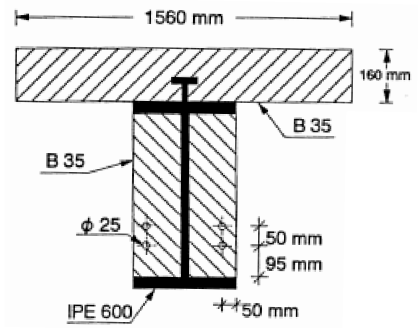

Figure 2. Analyzed beam in sagging moment ([4]).

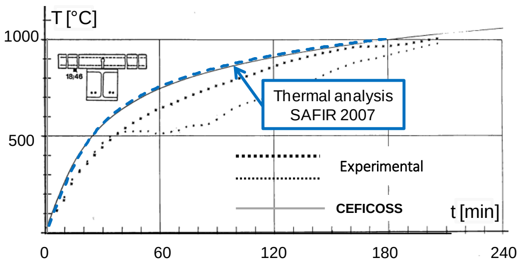

Figure 3. Numerical-experimental comparison in terms of temperature.

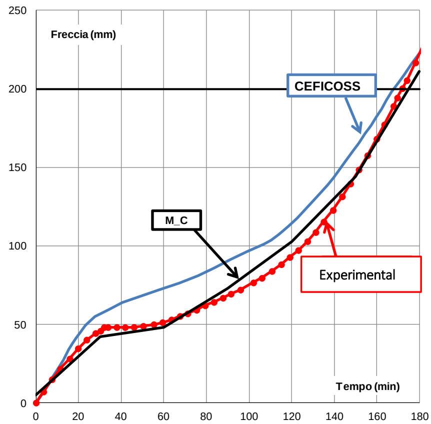

Figure 4. Numerical-experimental comparison in terms of displacement.

In order to evaluate the reliability of the simplified method proposed in the Annex F, the sagging and hogging moment resistance, for a fixed fire exposure time, has been calculated by an advanced calculation method (incremental–iterative procedure, namely M-C method) based on the construction of the Moment-Curvature diagram of the cross-section; the ultimate strength of the section corresponds to the maximum value of bending moment in the moment-curvature diagram. The thermal field at the fixed fire exposure time, useful for the construction of the moment-curvature diagram, was obtained by using the non-linear software SAFIR, developed at the University of Liege (Belgium). More details on the incremental–iterative procedure can be found in Nigro et Al. ([1]).

The reliability of this advanced calculation method was evaluated by comparing its results with some experimental tests data published in [4], shown in Figure 3 e Figure 4, both in terms of temperatures and deflection/stresses: the comparison shows a very good agreement between numerical and experimental results, both in terms of temperature ("Thermal analysis SAFIR 2007" - Figure 3) and displacement (M-C curve - Figure 4). It is important to note that the numerical results obtained through the M-C method (see M-C curve) are generally better than that obtained through the numerical procedure CEFICOSS (see CEFICOSS curve).

2.1 Simplified method proposed in EN1994-1-2 (Annex F)

In EN1994-1-2 (Annex F) a simplified method is proposed for the assessment of both the sagging and hogging moment resistance of partially encased beam, involved in a standard fire ISO834 beneath the concrete slab. This method has some application rules regarding the slab thickness and the dimensional ratio between the steel profile and the concrete cover.

As previously said, this method is based on the mechanical analysis is conducted applying the plasticity theory in which the effect of temperature is taken into account by reducing the size of the parts that make up the cross section and/or by reducing the mechanical properties of materials by means of reduction factors (both provided as function of fire exposure time).

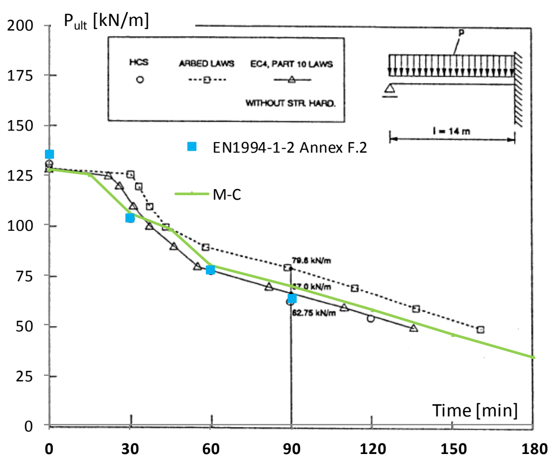

Figure 5. Numerical-numericalcomparison in terms of sagging and hogging moment resistance ([4]).

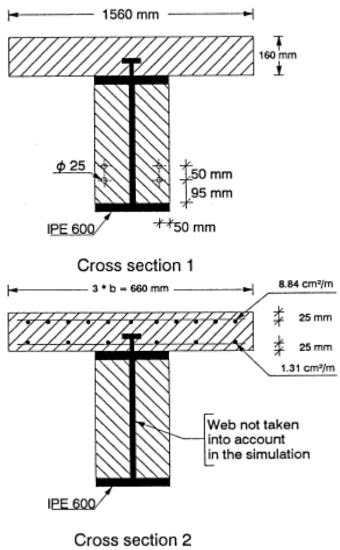

Figure 6. Analyzedbeam in sagging and hogging moment ([4]).

In order to improve the knowledge on the simplified method proposed in Annex F of EN1994-1-2, first of all, a bibliographic overview has been carried out and the background documents of the simplified method proposed in Annex F have been analysed. This study has enabled the authors to find some critical issues about this method. The Annex F methodology, in fact, integrally transposed the simplified method proposed within the European ARBED Recherches[4]. This method, so called HCS, was calibrated on the basis of both "numerical-numerical" and "numerical-experimental" comparisons. The numerical-numerical comparison was carried out between the results of the application of the simplified method on a set of partially encased beams and the analyses results obtained through the software CEFICOSS [5]. As it is shown in Figure 1 (sagging moment resistance) and in Figure5 (sagging and hogging moment resistance) , the HCS method provides, with reference to the beams analysed (Figure 2, Figure6), a moment resistance less than the one obtained through CEFICOSS ("EC4, Part10 Laws" curve); therefore the simplified method is conservative in that case. The numerical-experimental comparison was carried out between the numerical thermo-mechanical results (CEFICOSS) and experimental data. As it is shown in Figure 3 and Figure 4, the numerical results has a good agreement with experimental one.

It is important to note that the constitutive laws and the material's thermo-mechanical characteristics implemented in CEFICOSS are defined according to EC4 – Part10. These parameters have been upgraded during time, until the publication of EN1994-1-2 (2004), which is the current European reference for composite steel-concrete structure's design. Therefore, the simplified method suggested in EN1994-1-2 (Annex F) has been calibrated on the basis of numerical analyses with reference to obsolete material's characteristics.

2.2 Proposed simplified method

The main objective of the proposed simplified method is the assessment of the moment resistance of composite beams with partial concrete encasement exposed to standard fire ISO834 beneath the concrete slab. It is based on the mechanical analysis led according to plastic theory and on a simplified temperature field, characterized by split of the cross-section in uniform temperature parts. Therefore the proposed method is quite similar to the one suggested in EN1994-1-2 (Annex E), but the designer does not need to carry out thermal analyses, because the thermal field can be evaluated through the use interpolation curves, calibrated by authors.

It's firstly assumed for concrete the simplification suggested within the so-called "500°C isotherm method" (see EN1992-1-2 [6]): concrete with temperatures in excess of 500°C is assumed not to contribute to the load bearing capacity of the member, whilst the residual concrete cross-section retains its initial values of strength. In these case of fire which involves the beam beneath the slab and for usual slab thickness, the temperature in compressed concrete slab is usually less than 500°C (see Figure 7). Therefore, the concrete's mechanical characteristics can be assumed equal to the one at ambient temperature (20°C).

The cross section is divided in different parts, as shown in Figure 8. In each part and for each fire exposure time, the temperature is assumed uniform and equal to the mean temperature of the same part. The steel profile's web is divided in order to take into account the important thermal gradient in that area (see Figure 7).

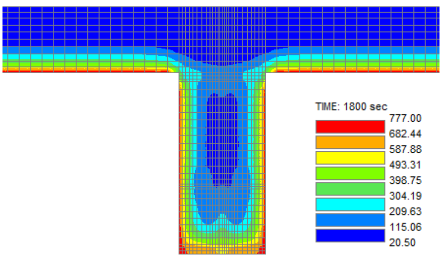

Figure 7. Thermal field of partially encased beam at time *t*=30min.

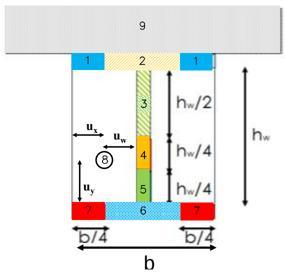

Figure 8. Splitting of the cross-section in uniform temperature parts.

The mean temperature of each part, during the fire exposure, can be evaluated through simplified formulas, calibrated on the basis of thermal analyses carried out through SAFIR2007, on different partially encased composite steel-concrete beams.

In particular, the parametric analysis has been carried out with reference to: IPE and HEB profiles (240-300-360-400-500), composite with concrete slab (thickness 13cm and width 150cm); partial concrete encasement with width b_c equal to the width b of steel profile; steel reinforcement ratio A_s/A_f equal to 0, 0.5 and 1, where A_s is the steel reinforcement's area and A_f is the flange's area.

The thermal field of this section, exposed to the standard fire curve, has been evaluated according to the suggestion of EN1991-1-2 [7], for the definition of thermal flux on the exposed and un-exposed surface of thecross section, and according to EN1994-1-2, for the definition of thermo-mechanical characteristics of steel and concrete, by assuming the "superior limit" curve like thermal conductivity in concrete.

The thermal analyses carried out through SAFIR2007 have enabled to find the mean temperature in each part, in which the section is divided. That temperature, for each instant of time, is the algebraic average of the temperatures in each element, of the cross-section discretization, that belongs to that part.

Based on the mean temperature calculated during fire exposure time, for each part has been calibrated interpolation function that allows to evaluate the part temperature for each fire exposure time. That functions can be expressed through the generic Equation (1), where A_1 and A_2 are coefficients depending on some geometrical characteristics of the cross section and t is the time of fire exposure.

$$T(t) = A_1 \cdot \ln(t) - A_2 \tag{1}$$

Given that the temperature curves will be just used to evaluate the resistance (neglecting the buckling effect) the calibration of that coefficients has been carried out with reference to the values of temperature T > 400 ℃, in fact $k_y(\theta > 400 ℃) < 1$(see EN1994-1-2).

In Table 1 the interpolation curves of different parts are summarized. As it is shown, each equation depends on some geometric factors which influence the temperature in that part.

For example, the temperature in the Top flange - External area (area 1, Table 1 and Figure 8), mainly depends on *b*, flange's width; in particular the temperature decreases when *b* increases. This concept is strictly consistent with the dependence between the flange's section factor and the width's flange (see ((2)): when b increases, the section factor and the temperature decrease.

$$\frac{b+2t_f}{b \cdot t_f} = \frac{1}{t_f} + \frac{2}{b} \tag{2}$$

Similarly, the main parameter for Top flange – Internal area (area 2, Table 1 and Figure 8) is *b*.

In the Web - Top area (area 3, Table 1 and Figure 8) the temperature mainly depends on the concrete cover's width $(b-t_w)/2$: when the concrete cover increases the temperature decreases thanks to the protection naturally offered by concrete to steel. In the area 4, the two components of the heat flux become important, therefore the two important factors are *b* and *b/h* ratio. In particular, when *b* increases, the concrete cover increases and the horizontal heat flux decreases; when the *b/h* ratio is high, the vertical heat flux increases. Similarly in the Web – Bottom area (area 5), the most important geometric parameters are *h/b* e t_f/h: when the flange's thickness decreases the heat flux from below increases. Regarding the areas 6 and 7 the temperature is strictly dependent on *b* and *h* too, and different formulations are provided for different ranges of *h/b* ratios. Finally, the temperature in the steel reinforcement mainly depends on the concrete cover and the distance between the steel bar and the steel flange.

Table 1. Interpolation curves.

1	**Top flange – External area (1)** $T_i(t) = 370 \cdot \ln(t) - (0.4711 \cdot b + 856.19) \geq 400°C$
2	**Top flange – Internal area (2)** $T_i(t) = 370 \cdot \ln(t) - (2.768 \cdot b + 513.5) \geq 400°C$
3	**Web – Top area (3)** $T_i(t) = 415 \cdot \ln(t) - (3.8165 \cdot (b - t_w)/2 + 1067.2) \geq 400°C$
4	**Web – Intermediate area (4)** $T_i(t) = (-0.5736 \cdot b + 568.94) \cdot \ln(t) - (-558.44 \cdot b/h + 1942.3) \geq 400°C$

5	**Web – bottom area (5)** $T_i(t) = (-58.553 \cdot h/b + 525.23) \cdot \ln(t) - (14913 \cdot t_f / h + 369.35) \geq 400°C$
6	**Bottom flange – Internal area (6)** $h/b_c \leq 1$ $T_i(t) = 500 \cdot \ln\left(-2.2407 \frac{h}{b} + 11.611\right)(t) - \left(\frac{-5b + 3200}{t}\right) \geq 400°C$ $h/b_c \geq 1.5$ $T_i(t) = (-101.27 \cdot \frac{h}{b} + 653.47) \cdot \ln\left(-2.2407 \frac{h}{b} + 11.611\right)(t) - \left(\frac{8.8776 \cdot b + 1550}{t}\right) \geq 400°C$ $1 < h/b_c < 1.5$ $T_i(t) = 485 \cdot \ln\left(-2.2407 \frac{h}{b} + 11.611\right)(t) - \left(\frac{3000 \cdot h/b - 400}{t}\right) \geq 400°C$
7	**Bottom flange – External area (7)** $h/b_c \leq 1$ $T_i(t) = (-101.27 \cdot \frac{h}{b} + 633.47) \cdot \ln(-0.005 * b + 12.2)(t) - 3000/t \geq 400°C$ $h/b_c \geq 1.5$ $T_i(t) = (-101.27 \cdot \frac{h}{b} + 633.47) \cdot \ln\left(-5.1471 \frac{h}{b} + 18.044\right)(t) - \left(\frac{16.5 \cdot b + 11.785}{t}\right) \geq 400°C$ $1 < h/b_c < 1.5$ $T_i(t) = (-101.27 \cdot \frac{h}{b} + 633.47) \cdot \ln\left(-4.5 \frac{h}{b} + 16.1\right)(t) - \left(\frac{-3150 \cdot h/b + 5700}{t}\right) \geq 400°C$
8	**Steel reinforcement (8)** $T_i(t) = (0.3777 \cdot u_d + 353.41) \cdot \ln(t) - \left(49.736 \cdot \frac{1}{1/u_x + 1/u_y + 1/(b - t_w - u_x)}\right) \geq 400°C$
9	**Concrete with** *T<500 °C*

3 PARAMETRIC ANALYSIS AND COMPARISON BETWEEN SIMPLIFIED AND ACCURATE METHODS

The proposed simplified method and the other above-mentioned simplified and accurate methods have been applied in order to carry out a comparative parametric analysis, regarding the assessment of the sagging and hogging moment resistance of composite beams with partial concrete encasement in case of standard fire. In the following the results of the comparison about the sagging moment resistance are shown, given that more criticism than hogging moment have been found.

The main aim of the comparative parametric analysis, carried out with reference to the partially encased beams described in the previous section, is the evaluation of the reliability of simplified methods.

In Figure 9, like example, the results of the application of the accurate and simplified methods are plotted with reference the IPE500 partially encased beam. As it is shown, the simplified method proposed in Annex F, compared with the accurate method (M-C method) and the plastic theory is not conservative in its application field, too. Conversely, the simplified method proposed in this paper shows either a good agreement or it is conservative, if compared with the accurate method.

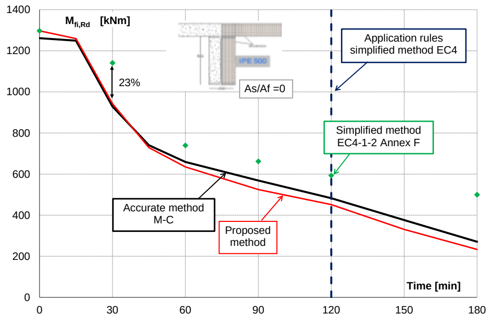

Figure 9. Comparison between simplified and accurate methods (IPE500 partially encased).

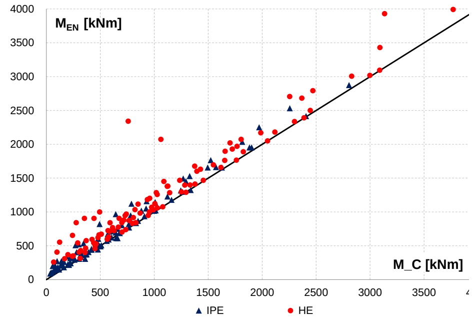

Figure 10. Comparison between simplified method (EN1994-1-2 Annex F) and accurate methods (complete set of analyzed beams).

The same result can be observed with reference to the complete set of analysed partially encased beams (see Figure 10 and Figure 11).

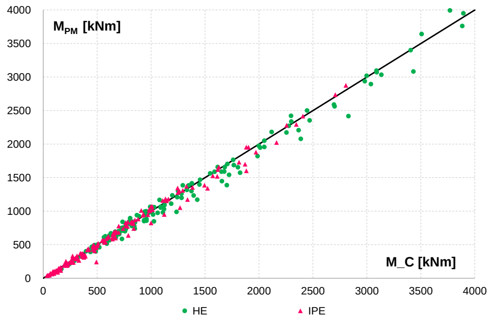

Figure 11. Comparison between proposed simplified and accurate methods (complete set of analysed beams).

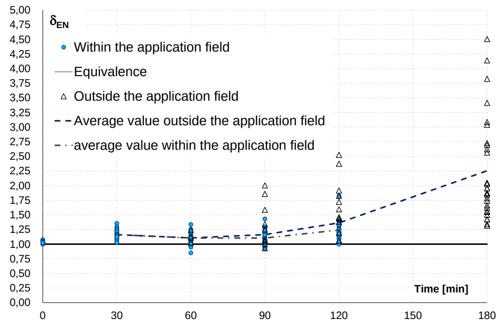

Figure 12. Ratio between the resistance obtained through EN1994-1-2 and accurate methods.

In Figure 12, the coefficient δ_{EN},the ratio between the resistance obtained through the simplified method proposed in EN and the one obtained through the accurate procedure (M-C method), is plotted in order to emphasize the disagreement between the obtained results. Similarly in Figure 13, the□ $_s$coefficient, ratio between the resistance obtained through the proposed simplified method and the one obtained through the accurate procedure (M-C method), is plotted, and as it is shown that coefficient is always less than 1, except for few cases. The average value of δ_s, in fact, is 0.97, while the average value of $\delta_{EN}$is 1.1 in its application field and very high (equal to 1.31) when the method is applied outside the application field. In terms of coefficient of variation (cov), the cov of the proposed method is 0.10, while the cov of the simplified method is 0.13 in its application field and equal to 0.4 when the method is applied outside the application field.

Anyway, in order to increase the reliability of the proposed simplified method, a corrective coefficient could be introduced. By considering, for example, a corrective coefficient equal to 0.9, which corresponds to the fractile 10% of the standard Gaussian distribution of the reciprocal δ_s, the results are always conservatives (Figure 14).

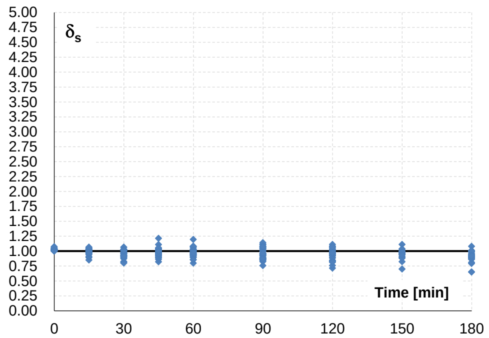

Figure 13. Ratio between the resistance obtained through the proposed simplified method and accurate method.

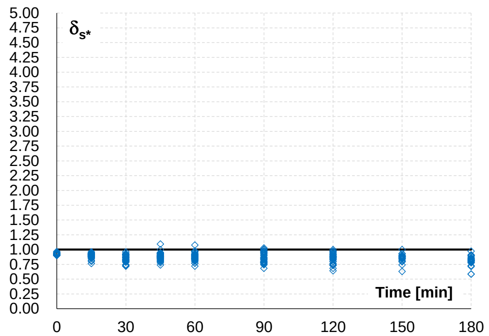

Figure 14. Ratio between the resistance obtained through the corrected proposed simplified method and accurate method.

5 CONCLUSIONS

The performed analyses proves that the simplified method proposed in EN1994-1-2 (Annex F), aimed to the assessment of the sagging moment resistance of composite beams with partial concrete encasement in case of standard fire beneath the slab, is not conservative, if compared with the results of the application of the incremental-iterative procedure and plastic theory.

Therefore, in this work a new simplified method has been proposed. This method is based on the mechanical analysis led according to plastic theory and on a simplified temperature field, characterized by split of the cross-section in uniform temperature parts. In particular, in each part the temperature is assumed equal to the mean temperature of the same part, evaluated through suitably calibrated formulas. This method is very easy to implement and has high reliability, in fact it provides results in good agreement with that obtained through accurate methods. Moreover the advantage of the proposed method is the absence of application rules. Therefore, the new simplified method, presented in this paper, will be proposed within the activities of the Evolution Group of EN1994-1-2, like alternative simplified method.

REFERENCES

[1] Nigro E., Pustorino S., Cefarelli G., Princi P., “Progettazione di strutture in acciaio e composte acciaio-calcestruzzo in caso di incendio secondo gli Eurocodici e le Norme Tecniche per le costruzioni”, Hoepli Milano, 2009

[2] EN 1994-1-2, “Design of composite steel and concrete structures- Part 1-2: General rules - Structural fire design”, October 2005

[3] D.M.Int 14/01/2008, “NormeTecniche per le Costruzioni”, G.U. n. 29 del 4/02/2008

[4] Cajot L.-G.; Schleich J.-B, “The Fire Design of Composite Beams according to the Eurocode 4, Part 10, Structural Fire Design”, RPS N°14/91, 1991

[5] Franssen J.M., “User’s manual for CEFICOSS (Computer Engineering of the Fire resistance of Composite and Steel Structures)”, 1987

[6] EN1992-1-2, “Design of concrete structure – Part 1-2: General rules – Structural fire design”, April 2005

[7] EN 1991-1-2, “Actions on structures - Part 1-2: General actions -Actions on structures exposed to fire”, November 2002

[8] Franssen J.M., “User’s manual for SAFIR2007”, University of Liege, Belgium,2008.

[9] E. Nigro, I. Del Prete, D Sannino, G. Cefarelli, “Calibration of a simplified method for fire resistance assessment of partially encased composite beams”, Eurosteel 2014, 10-12 September 2014, Naples, Italy

8th International Conference on Structures in Fire
Guo-Qiang LI, Venkatesh K. R. KODUR, Shou-Chao JIANG, Jian JIANG, Su-Wen CHEN, Guo-Biao LOU (Eds.)
Shanghai, China, June 11-13, 2014

REINFORCEMENT RUPTURE IN THE STRUCTURAL FIRE DESIGN OF COMPOSITE SLABS

Angus Law* and Neal Butterworth*

* Ove Arup and Partners International Ltd.
e-mails: angus.law@arup.com, neal.butterworth@arup.com

Keywords: Composite slabs, Reinforcement rupture, Finite-element method, Crack width, Slab capacity

Abstract. *Composite floor slabs are one of the most widely used systems in modern construction. Understanding their performance in fire is fundamental to the application of many structural fire engineering techniques. Their performance is also key to both the structural stability of a floorplate, and the life safety strategy within many high and ultra-high rise buildings and is therefore worthy of continued analysis. This paper provides a discussion of the various approaches to the fire design of concrete composite floors and how they protect against reinforcement rupture and integrity failure. Fracture in the reinforcement is identified as an effective metric for checking for failure in finite element models of fully and partially protected structures. The sensitivity of this metric to element length is discussed and the necessity to factor the recorded cracking strain to calculate crack width is outlined. Three methods that can be used to calculate the permissible crack width and, therefore, used to check for reinforcement failure in a finite element models are discussed. This paper concludes that each technique is viable and that additional experimental research is required to support their application.*

1 INTRODUCTION

Steel and concrete composite slabs are one of the most widespread flooring systems used in the construction industry. Design techniques have been developed to assess the loadbearing capacity of composite slabs where protection of secondary elements has been omitted, and finite-element software has been created that can characterise the performance of these system. As with many challenges in fire engineering the key to applying these techniques in design is creation of an appropriate definition of failure.

One of the most common failure modes is a tensile failure within the concrete slab (either in hogging over beams or within the tension zone in the central zone of a slab panel). However the rupture mechanics of reinforcement are rarely explicitly incorporated into the design tools that are applied by practitioners. Instead, proxy failure indicators are applied that are assumed to provide an adequately conservative definition of failure. This is a practical and expedient approach to allow design tools to be readily implemented without recourse to temperature dependent rupture mechanics.

Where reinforcement rupture (or, rather strain in the rebar) is considered in design, additional reinforcement is frequently provided as a measure to mitigate the high levels of strain recorded. This paper documents the key factors that should be considered when using strain as an acceptance criteria, and outlines the approaches available for considering rupture mechanics in more detail.

2 FIRE DESIGN OF COMPOSITE SLABS

Slab capacity design methods and finite-element models can both be used in structural fire design. However, they have fundamentally different approaches to dealing with reinforcement failure. Slab capacity calculations do not account for continuity of reinforcement over protected beams; instead they develop centrally located yield lines whose ultimate capacity is controlled by the rupture of the central reinforcement. Finite element methods typically assume continuity of reinforcement over protected sections; the capacity of the slab is, therefore, provided by maintaining this continuity.

The fire safety strategy for a building defines the fire resistance that each element of the structure is expected to deliver. In the case of the composite slabs compartment floor performance (loadbearing capacity, integrity and insulation) may be required. Alternatively, a composite slab may be required to deliver only loadbearing capacity.

Once the required performance is defined, the engineer will typically propose a fire protection arrangement. If this solution includes the omission of protection from the some of the steel elements, the engineer may use a structural fire engineering modelling technique to demonstrate that the approach meets the performance objectives of the fire strategy.

2.1 Slab Capacity Design Methods

Several authors have created slab capacity calculation methods to permit this analysis. Bailey's approach is frequently applied by design engineers. In relation to the current study, the relevant aspects of this approach are the limits that it places on the maximum capacity of the slab. The work specifically acknowledges the difficulties associated with defining rupture and, instead, defines a maximum deflection which is based on an average maximum strain in the reinforcement and limited to span/30 (not including thermal deformations) [1]. The paper documents that the approach is conservative when combined in conjunction with the other assumptions inherent within the method.

The approach described by Omer [2], [3] is also based around the yield line principles. The key innovation presented in this approach is the explicit inclusion of a reinforcement rupture model based on the bond between the steel and the surrounding concrete. This approach does not, therefore, rely on a proxy method for failure definition. The paper notes that the results compares favourably with the experimental data without the need to undergo a calibration exercise.

Burgess's method, also based around yield line principles, incorporates the rupture of reinforcement into the calculation of enhancement factors [4]. Rather than incorporating a bond stress model into the approach (as described by Omer), Burgess assumes that the strain in the reinforcement develops over the length of inter bar spacing (i.e. between welds in a reinforcing mesh). This approach allows the calculation of a non-linear enhancement factor. Burgess also demonstrates the sensitivity of the result to the maximum ductility of the reinforcement.

Each of these approaches is recognised as being conservative when applied within the limits defined in the method. However, each approach places limits on the geometry that can be analyzed and do not (yet) allow the engineer to design against the rupture of reinforcement over the protected primary beams.

2.2 Finite Element Design Methods

As an alternative to slab capacity methods, and often to overcome the inherent limitations of these methods, practitioners frequently use finite element analyses to demonstrate that partially (or even fully) protected steel composite structures meet the objectives of the fire strategy. In these cases, the acceptance criteria are selected by the design engineer (often in conjunction with the authority having jurisdiction). This is appropriate, as the failure criteria must be informed by the goals of the building's fire strategy and cannot therefore be defined in isolation. Table 1 presents a review of structural fire engineering designs that have been documented in the public domain and the failure criteria that were adopted for each analysis. It should be noted that each paper is not a complete documentation of the structural fire engineering design analysis, and therefore does not present all of the detailed justifications that were conducted as part of the analysis or presented to the approval authorities.

Nevertheless, from this review it is evident that there are two approaches which are frequently adopted when demonstrating that a structure is able to meet the requirements of the fire strategy: the use of deflection limits the defining performance criteria to avoid failure; and the use of cracking strain in the concrete (and resultant strain in reinforcement) to detect and mitigate against failure of the reinforcement. These two approaches are discussed in more detail below.

Table 1. Review of acceptance criteria in previous literature.

Source	Year	Acceptance criteria
[5]	2006	S = 20%
[6]	2007	S = 15%
		D_{prot} = span/23; D_{unprot} = span/8
[7]	2008	D = span/15
[8]	2008	D = span/10
[9]	2008	S = 20%
[10]	2010	D_{prot} = span/20; D_{unprot} = span/10

2.2.1 Deflection as a Failure Criterion

On the basis of the above papers, and the authors' knowledge and experience, there are two levels of deflection that are accepted for composite steel structures in design.

Firstly, a deflection of span/20 is the acceptance criteria that is specified in furnace testing [11] and is adopted for the protected sections on the assumption that passive fire protection will remain effective while deflections (and associated curvatures) are less than this value. For unprotected sections (and the slab), a higher deflection is accepted. This is typically justified by reference to the Cardington experiments where a deflection of span/10 was observed [12]. It is also noteworthy that some authors have conducted a further check on the relative deflections between the unprotected and protected sections [10]. The intent of the latter approach is to minimise the cracking strain that may develop over the protected sections by ensuring that the differential deflection between the protected sections and slab does not exceed span/20. It is assumed that since this level of deflection accords with the furnace testing, that it will not result in cracking and loss of integrity.

These approaches use deflection as a proxy measure of performance to demonstrate that the assembly performs adequately. They are justified on the basis of a comparison against furnace and/or draw validity from the comparison against the testing that was conducted at Cardington.

However it should be noted that any proxy method must be constantly re-evaluated to ensure it remains valid for the proposed design situation. The acceptability of continuing to draw conclusions about the performance of modern construction from the Cardington tests is questionable due to the change in the type of reinforcement that is used in construction. The reinforcing mesh used at Cardington was smooth; current construction (and all construction in the UK) uses ribbed reinforcement. Consequently in modern construction, the degree of cracking that may occur without inducing rupture is likely to be less than that observed during Cardington [13]. Furthermore, it should also be noted that large cracks and reinforcement rupture *were* observed in some locations following the Cardington tests. To cite a test with smooth reinforcement that was observed to rupture does not create a robust case for demonstrating that rupture does not occur given equivalent deflections and ribbed reinforcement. Also, it does not necessarily follow from the test observation that cracking occurred and reinforcing was improperly lapped, that cracking would not have occurred if reinforcement was appropriately lapped.

2.2.2 Strain as a Failure Criterion

Instead of using a deflection limit, designers have attempted to address the mechanics more directly by applying a limit on strain in the reinforcement. This approach relies on the calculation of cracking strain as part of the finite element analysis, and the selection of an appropriate acceptable strain limit in the reinforcement. The maximum strain typically occurs over the protected sections on the unheated surface of the slab (i.e. the location where rupture was observed at Cardington). Some authors have accounted for the reduced strain at the reinforcement location by recalculating the value based on the assumption of minimal mechanical strain at the slab soffit and plain sections remaining plain. The literature shows that the strain limit for steel reinforcement adopted in design has been between 15% and 20% to accord with the rupture values provided in the Eurocode.

The use of strain as a failure criterion has resulted in provision of additional reinforcement over the primary sections to ensure that both stability and integrity is maintained [6]. In some cases, this has been provided such that the additional reinforcement is able to accommodate the ultimate tensile force of the cracking mesh [5]. It is notable that Flint also identifies the introduction of additional reinforcement as a mitigation measure for excessive strains around column locations [14].

These approaches directly consider the failure mechanism of a partially protected structure and specifically identify the mitigation measures that may be appropriate. The methods are reliant on the appropriate implementation of the finite element model, and the consistent interpretation of the results. Furthermore, within these strain analysis approaches there are implicit assumptions regarding the behaviour of the reinforcement and concrete bond; for example, that the length over which the crack strain is smeared is appropriate and commensurate with the length over which de-bonding would occur.

3 BOND STRESS AND RUPTURE

In the context of structural fire engineering of composite slabs, reinforcement rupture can be distilled to an analysis of the maximum permissible crack width that can occur prior to rupture of the reinforcement. This is governed by the total slip of the reinforcement (including mechanical strain) relative to the concrete. There are two approaches for assessing the maximum permissible crack width for given concrete and reinforcement: the direct use of testing results; or the calculation of the total slip by applying knowledge of the properties and behaviour of the materials.

3.1 Results from Testing

The literature for pull-out testing and bond strength at high temperature has recently been reviewed by Giroldo [15]. For the purposes of directly applying results from testing, the key parameter is the maximum slip that occurs in a reinforcing mesh prior to rupture of the reinforcement. The test results of Giroldo provide these for a series of different meshes. These indicate that in smooth bar initial failure occurs due to fracture of the weld; while in ribbed reinforcement failure occurs due to fracture of the longitudinal reinforcement (to which the strain was applied). This demonstrates the tendency for smooth reinforcement to transfer strain back along the length of the rebar, while in ribbed reinforcement the strain becomes more localized. The results from these tests suggest that, for a 100mm length of ribbed reinforcement, the maximum slip that can occur is in the region of 10-20mm for a range of bar diameters and temperatures.

3.2 Calculation Approaches

Two calculation approaches have been identified by the authors. The first is an implementation of the approach described by Omer [2]. The second is a more complex formulation based on the non-linear behaviour of both the steel and bond stress.

3.2.1 Hardening Modulus Approach

The hardening modulus approach is described by Omer and allows the calculation of reinforcement slip based on the hardening modulus between the proportionality limit or yield point and the ultimate tensile stress [2]. This approach permits the derivation of slip by distributing the applied force equally along the length (and surface) of bar that is undergoing yield. When incorporated into Omer's wider methodology, it was found to give a good estimate of maximum slab capacity in comparison to other methods. However, this approach is highly dependent on the value assumed for bond strength. The hardening modulus approach was implemented as part of this study to allow the prediction of the permissible crack width that can develop prior to reinforcement rupture.

Bond strength is known to vary as a function of slip [16] so either an averaged value, or a conservative (maximum) bond stress must be adopted for this analysis. For the purposes of this study, two values have been used – 1.66N/mm^2 for *low bond* reinforcement (for smooth reinforcement in accordance with BS 8110) and 3.47N/mm^2 for *high bond* reinforcement (for ribbed reinforcement in accordance with EN 1992-1-1 assuming f_{ck} = 35MPa). Note – these values are quoted per unit area of bar surface. The permissible crack width, or slip, for a range of temperatures and rebar diameters for the high bond reinforcement is provided in Figure 1. Steel temperature dependent properties were assumed to be in accordance with EN 1992-1-2; maximum bond stress at ambient was assumed in accordance with BS EN 1992-1-1; the proportionality limit was used to calculate the hardening modulus; and the degradation of bond stress was as described by Huang [17]. This shows a significant increase in the crack width that may occur as temperature increases.

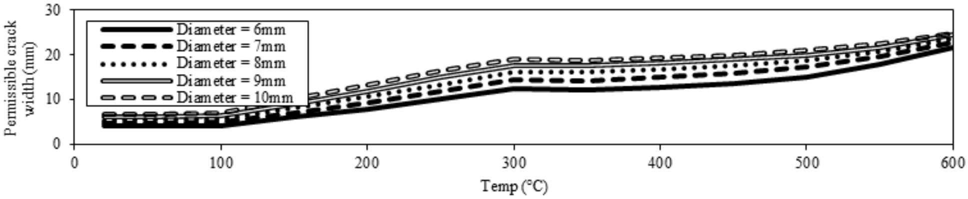

Figure 1. Permissible crack width for ribbed reinforcement.

3.2.2 Variable Bond Stress

The variable bond stress model allows a more detailed assessment of the stress strain behaviour of the steel and bond. Other authors have previously created finite element models which explicitly include these considerations [17]. However, to the authors' knowledge, they have not been used to determine permissible crack widths for a finite element analysis of a composite steel structure. This approach is further complicated by the fact that the literature suggest that the bond stress is a function of both the slip, and also the strain history of the steel (i.e. the constitutive stress/slip curve is different after the yield of the steel) [18]. Although this approach is theoretically viable, it has not been implemented as part of this study.

4 APPLICATION TO A FINITE ELEMENT MODEL

The implementation of these approaches in design allows the designer to define the allowable slip/ permissible crack width, and therefore check a finite element model for reinforcement rupture. This requires the results of the finite element model to be correctly interpreted to account for the concrete model and element size.

Sensitivity to element size is inherent within many finite element models, and the optimum element size selected should provide an adequately accurate result without an excessive computation time. However, the smeared crack models that are typically used in this application [19] are sensitive to element size. Where a crack develops, it is smeared over the whole element, and this is reported as the cracking strain. For a crack of uniform width, a small element will record a greater cracking strain than a large element. Consequently, if cracking strain is measured as part of a finite element design, this value must be factored to correct for element size. Otherwise, the modeller may over- or under-predict the strain in the reinforcement. Larger elements may not detect a failure in the reinforcement, while smaller elements may cause rupture in the reinforcement to occur prematurely due to excessive strain localization. In design, the former of these is potentially unconservative unless the strain in the reinforcement is explicitly checked.

The formula for factoring cracking strain (where $\Delta_{s,model}$ is the crack width, ε_{crack} is the cracking strain as provided by the model, and $L_{element}$ is the effective element length) is:

$$\Delta_{s,model} = \varepsilon_{crack} \times L_{element} \quad (1)$$

4.1 Example

A relatively simple four bay geometry (each bay 6m×6m) was created and analyzed using the finite element software LS-DYNA. Four different models were created each with different element lengths and, for demonstrative purposes, the geometry was subjected to a 60 minute standard fire curve. An A393 reinforcing mesh was assumed to be mid-height within the slab and material properties were in accordance with the relevant Eurocodes. The smeared crack model for the concrete was in accordance with the approach defined by Rots [20].

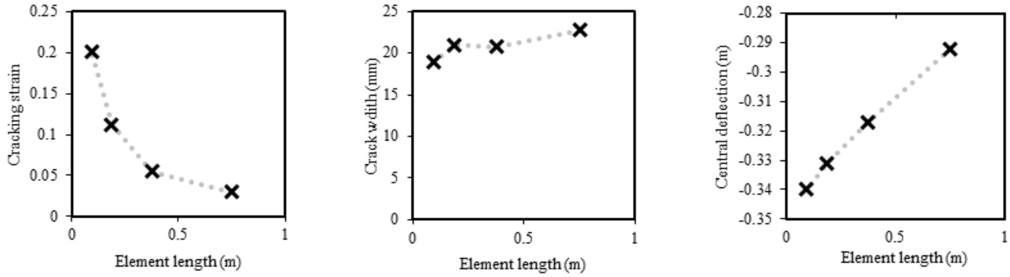

(a) Cracking strain direct from model (b) Factored crack width (c) Central deflection

Figure 2. Sensitivity study of finite element model for a partially protected structure.

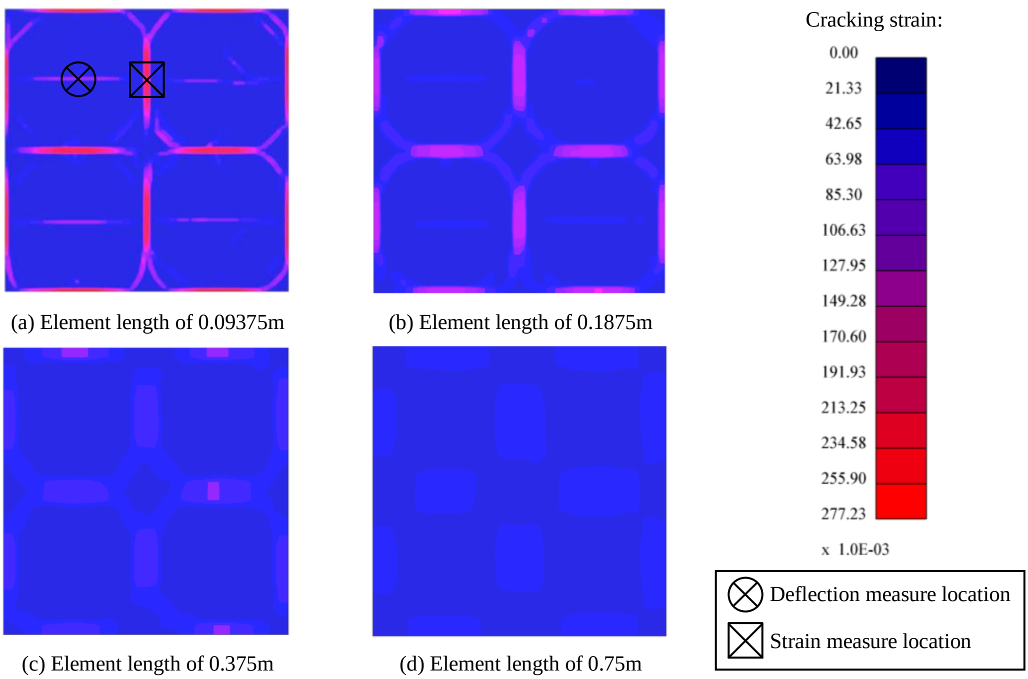

(a) Element length of 0.09375m (b) Element length of 0.1875m

(c) Element length of 0.375m (d) Element length of 0.75m

Figure 3. Cracking strain over protected sections for a four bay finite element model.

The results for cracking strain and crack width over the central primary, and central slab deflection are illustrated in Figure 1. These show the sensitivity of cracking strain to element length and how, by factoring for element length as described in Equation (1), a relatively element length independent crack width can be obtained. The deflection results illustrate how the wider sensitivity of the model to element length follows a pattern that would be typically expected for a finite element model. Figure 2 shows the contour pattern for the cracking strain observed for each of the models. Note, that the scale remains uniform for each of the different analyses. This further illustrates the need (when using strain as a performance metric) to adjust the results of the finite element model to account for element length. Otherwise, if large elements were used, it is possible that the designer may not identify reinforcement rupture, and loss of loadbearing capacity/integrity.

The time dependent permissible crack width calculated at rebar level for the hardening modulus approach (and for the testing results) is shown in Figure 4 relative to the changing crack width derived from the finite element model. It should be noted that the test results were not adjusted to incorporate the 200mm length along which slip may occur – it is likely that this would increase the permissible crack width obtained by this approach (up to a theoretical limit of 30mm). For the purposes of this calculation, it was assumed that the crack width at mid-height within the slab was half of that at the top surface. This analysis demonstrates the viability of this approach for checking the crack width and the potential difference between the allowable slip for smooth and ribbed meshes. However, it also illustrates the hardening modulus is potentially conservative in comparison to the testing results and would prematurely predict failure.

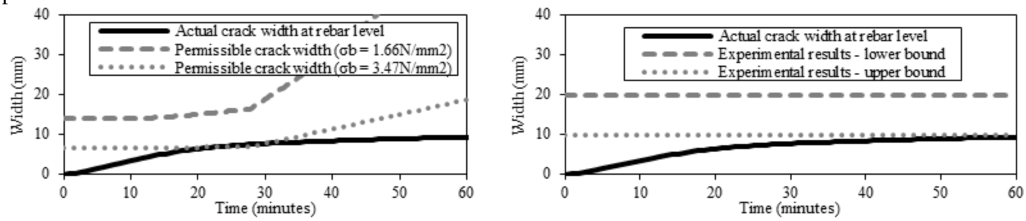

Figure 4. Comparison of crack width from finite element model with permissible crack width.

5 CONCLUSIONS

This paper has presented an overview of the methods available for the design of composite steel structures. It has been found when finite element modelling is used, and continuity is required in negative bending, strain in the reinforcement is the most satisfactory failure metric currently available. Several methods have been described which allow finite element models of steel structures to be checked to ensure that rupture of the reinforcement does not occur. The highly variable permissible crack width predicted by the different methods (and input values) indicates that there is significant scope for further research to improve this design method and provide a more accurate solution.

Fundamental to implementing this approach is that the observed cracking strain must be normalised to account for element length and to obtain a crack width. The observed crack width may then be compared against a permissible crack width obtained from either experimental testing, or calculated based on knowledge of the bond/slip behaviour of the concrete and reinforcement.

It is recommended that further experimental and modelling work should be conducted to allow the permissible crack width for different reinforcement meshes, temperatures, and concrete strengths to be defined. Ultimately, this could lead to the development of lookup tables for use in design.

6 ACKNOWLEDGEMENT

The authors would like to acknowledge Professor Colin Bailey, Professor Ian Burgess, Professor Luke Bisby, Dr Susan Deeny, Dr Martin Gillie, Dr Shan Shan Huang and Professor Bassam Izzuddin, for providing feedback on this work and answering the authors' queries about their own work.

REFERENCES

[1] C. Bailey and D. Moore, "The Structural Behaviour of Steel Frames with Composite Floorslabs Subject to Fire: Part 1: Theory," *Struct. Eng.*, vol. 78, no. 11, pp. 19–27, 2000.

[2] E. Omer, B. a. Izzuddin, and a. Y. Elghazouli, “Failure of unrestrained lightly reinforced concrete slabs under fire, Part I: Analytical models,” *Eng. Struct.*, vol. 32, no. 9, pp. 2631–2646, Sep. 2010.

[3] E. Omer, B. a. Izzuddin, and a. Y. Elghazouli, “Failure of unrestrained lightly reinforced concrete slabs under fire, Part II: Verification and application,” *Eng. Struct.*, vol. 32, no. 9, pp. 2647–2657, Sep. 2010.

[4] I. W. Burgess, X. Dai, and S. S. Huang, “An alternative simplified model of tensile membrane action of slabs in fire,” in *Application of Structural Fire Engineering*, 2013, vol. 7, pp. 361–367.

[5] C. Pozzi, B. Lane, S. Lamont, and A. Heise, “The role of large strains and consequent mitigation measures for buildings in fire,” in *Fourth International Workshop on Structures in Fire*, 2006, pp. 487–498.

[6] A. Heise, G. Flint, and B. Lane, “Effect of Fire on Tall Buildings: Case Study,” in *3rd International conference on steel and composite structures*, 2007.

[7] M. Feeny, C. Clifton, and N. Mago, “Dependable Performance of Steel Structures in Fire - The Britomart East Office Building,” in *Fifth International Conference on Structures in Fire*, 2008, pp. 290–301.

[8] W. S. Toh and N. Bernabe, “Tensile membrane action of composite slab panels in fire - simple vs. advanced models,” in *Sixth International Conference on Structures in Fire*, 2008, pp. 508–517.

[9] D. Rini and S. Lamont, “Performance Based Structural Fire Engineering for Modern Building Design,” in *ASCE Structures Congress*, 2008, pp. 1–12.

[10] F. M. Block, C. Yu, and N. A. Butterworth, “The Practical Application of Structural Fire Engineering on a Retail Development in the UK,” *J. Struct. Fire Eng.*, vol. 1, no. 4, pp. 205–218, 2010.

[11] BS476-20:1987, *Fire Tests on Buildings Materials and Structures - Part 20: Method for Determination of the Fire Resistance of Elements of Construction*. BSI, 1987.

[12] G. M. Newman, J. T. Robinson, and C. G. Bailey, *Fire Safe Design: A New Approach to Multi-Storey Steel Framed Buildings*. Ascot, Berkshire: Steel Construction Institute, 2000.

[13] F. Giroldo and C. G. Bailey, “Experimental bond behaviour of welded mesh reinforcement at elevated temperatures,” *Mag. Concr. Res.*, vol. 60, no. 1, pp. 23–31, Jan. 2008.

[14] G. Flint, S. Lamont, B. Lane, H. Sarrazin, L. Lim, D. Rini, and C. Roben, “Recent Lessons Learned in Structural Fire Engineering for Composite Steel Structures,” *Fire Technol.*, Aug. 2012.

[15] F. Giroldo, “Bond Strength Between Mesh Reinforcement and Concrete at Elevated Temperatures,” University of Manchester, 2010.

[16] Z. P. Bazant and M. F. Kaplan, *Concrete at high temperatures*. Longman Group Limited, 1996.

[17] Z. Huang, “Modelling the bond between concrete and reinforcing steel in a fire,” *Eng. Struct.*, vol. 32, no. 11, pp. 3660–3669, 2010.

[18] CEB-FIP, *Model Code 1990*. Thomas Telford, 1993.

[19] Z. Huang, I. W. Burgess, and R. J. Plank, “Non-linear structural modelling of a fire test subject to high restraint,” *Fire Saf. J.*, vol. 36, pp. 795–814, 2001.

[20] J. G. Rots, G. M. A. Kusters, and J. Blaauwendraad, “The need for fracture mechanics options in finite elements models for concrete strucutres,” in *The International Conference on Computer Aided Analysis and Design of Concrete Sturctures*, 1984, pp. 19–32.

FIRE RESISTANCE OF STAINLESS STEEL STRUCTURAL ELEMENTS WITH CLASS 4 SQUARE HOLLOW SECTIONS SUBJECT TO COMBINED BENDING AND AXIAL COMPRESSION

Nuno Lopes* and Paulo Vila Real*

* LABEST – Civil Engineering Department, University of Aveiro
e-mails: nuno.lopes@ua.pt, pvreal@ua.pt

Keywords: Stainless steel, Beam-columns, Buckling, Numerical study

Abstract. *This paper presents a numerical study on the behaviour of stainless steel thin-walled (Class 4) hollow members subjected to bending plus compression in fire situation. These thin-walled compressed members have, in addition to the flexural buckling failure mode, more susceptibility to the occurrence of local buckling. As these instability phenomena are intensified at elevated temperatures and the material behaviour of stainless steel in case of fire is different from the one of conventional carbon steel, it is important to understand the degree of accuracy and safety of design recommendations that normally propose the use of expressions that were developed for carbon steel stocky I sections (as in Eurocode 3). Hence in this work, the performances of different existing design expressions for steel and stainless steel beam-columns interaction curves are analyzed against numerical results obtained for Class 4 square hollow profiles of different stainless steel grades at elevated temperature.*

1 INTRODUCTION

Stainless steel has various desirable characteristics for a structural material [1]. But, even if its use in construction is increasing, it is nevertheless still necessary to develop the knowledge on its structural behaviour, especially at elevated temperatures.

Structural elements composed of Class 4 [2,3] sections are common in stainless steel buildings structures. Being these thin walled profiles susceptible to the occurrence of both local and flexural buckling failure modes. In addition, cold formed hollow sections are also often chosen for stainless steel columns. These sections typically exhibit specific characteristics that directly affect the final resistance of the corresponded members, such as the corners strength enhancement due to the fabrication process in rectangular section shapes [4]. It is thus important to completely understand the behaviour of these structural elements in fire situation for accurate and safe design purposes.

Part 1-4 of Eurocode 3 (EC3) EN 1993-1-4 [3] provides design rules for stainless steel structural elements at normal temperature, and for their fire resistance it refers to the fire part of the same Eurocode, EN 1993-1-2 [5]. In this Part 1-2 of EC3 it is stated that structural elements made of stainless steel must be checked for its fire resistance using the same design formulae developed for carbon steel I sections. However, as it is also presented in the Annex C of EN 1993-1-2, these two materials have different constitutive laws in case of fire (they have also at normal temperature different stress-strain relationships). Additionally, the fire resistance of members with Class 4 sections is still not completely understood, Annex E of the same Part 1-2 of EC3 proposes de use of the conventional limit of elasticity at 0.2% for members with this section class, which has been shown to be insufficient to obtain a precise approximation to the real behaviour [6].

In fact, the behaviour of stainless steel columns in case of fire has recently been given more attention.

Several studies have been performed in stainless steel columns resulting in different new design proposals. Some of them were based on columns with Class 1 and 2 (stocky) I cross-sections [7] (as the EC3 [5] design rules for carbon steel) and others on columns with hollow sections [8,9].

Because of the different above mentioned reasons (such as the stainless steel stress-strain relationship or the instability phenomena), the accuracy and safety of EC3 interactions curves for structural elements subjected to compression plus bending, with class 4 sections at elevated temperatures, is here analyzed.

The main objective of this work is to present a numerical analysis on stainless steel structural elements, with Class 4 square hollow cross-sections subjected to axial compression plus bending under fire conditions, applying geometrically and materially non-linear imperfect analysis with the program SAFIR [10].

In this study different stainless steel grades were considered, representing different stainless steel groups, according to their metallurgical structures, austenitic, ferritic and austenitic-ferritic grade. Comparisons, between the numerical results and the EC3 rules and other existing interaction curves, such as a previous proposal developed for stainless steel I-sections [11] and the interaction curves recommended in Part 1-1 of EC3 [12], are made.

2 NUMERICAL MODEL

2.1 Case study

In this section it is described the adopted numerical model on the parametric study performed with the finite element software SAFIR. Numerical analyses applying this software were recently validated against experimental fire tests in stainless steel columns [12]. In this work doubled hinged columns subjected to compression plus bending diagrams were analyzed. Three types of bending diagrams were considered: uniform bending (ψ=1), triangular diagram (ψ=0) and bi-triangular diagram (ψ=-1). The stainless steel grades considered in this study were the austenitic 1.4301 (also known as 304), the ferritic 1.4003 and the austenitic-ferritic 1.4462 (also known as duplex) [5].

The cold formed square hollow section (SHS) 200×200×4 was chosen in this study. The internal elements of the section are of Class 4 when subjected to compression and Class 3 in bending according to EN 1993-1-2 and EN 1993-1-4. As local buckling phenomena were likely to occur, shell finite elements were used. The mesh size was chosen in order to capture all the possible failure modes.

Due to the thin walls of these profiles and to the stainless steel high thermal conductivity, the numerical tests were made with uniform temperatures in the cross section. The temperature chosen was 500 ℃ for being a typical critical temperature in steel structural elements subjected to instability phenomena. For each stainless steel grade and bending diagram type, 5 columns lengths were chosen, corresponding to slenderness values at high temperatures (as defined in EC3 [5]) between 0.3 and 2.0.

2.2 Material law

Stainless steels are known for their non-linear stress-strain relationships with a low conventional limit of proportional stress and an extensive hardening phase [3,5] (see Figure 1). There is not a well defined yield strength, being usually considered for design at normal temperature the 0.2% proof strength, $f_y = f_{0.2p}$. In a fire situation higher strains than at room temperature are acceptable, and Part 1-2 of EC3 suggests the use of the stress at 2% total strain as the yield stress at elevated temperature θ, $f_{y,\theta} = f_{2\%,\theta}$, for Class 1, 2 and 3 cross-sections and $f_{y,\theta} = f_{0.2p,\theta}$, for Class 4 which is the proof strength at 0.2% plastic strain, at temperature θ. Comparison of the reduction of strength of structural carbon steel and several grades of stainless steels at elevated temperature (as defined in EC3 [5]), is shown in Figure 1 where $k_{0.2p,\theta} = f_{0.2p,\theta}/f_y$. The numerical modelling of stainless steel in SAFIR was made by a non-elastic plane stress condition, based on the von Mises surface and isotropic hardening [13].

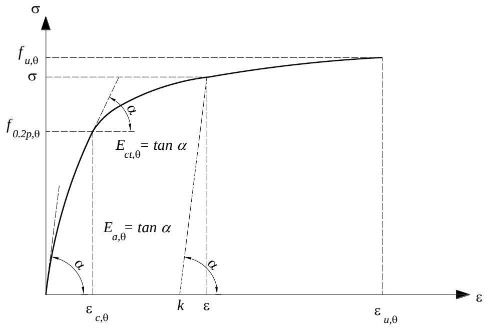

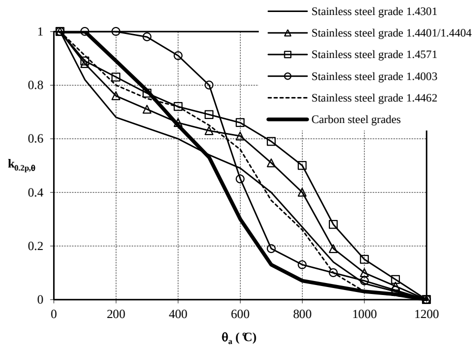

Figure 1. Stress-strain relationship of the stainless steel and strength reduction factor at high temperatures.

2.3 Initial imperfections

2.3.1 Geometric imperfections

The adopted initial imperfections follow the recommendations of Annex C of Part 1-5 of EC3[14], which proposes the use of the shape of the buckling modes with the amplitude equal to 80% of the manufacturing geometry tolerances that can be found in EN 1090-2:2008+A1 [15] and EN10219-2 [16]. The imperfection corresponded to the global buckling mode was obtained by the following expression.

$$y = 0.8L/750\sin(\pi x/L) \tag{1}$$

The geometric imperfections corresponded to the local buckling mode have a maximum amplitude of 0.8*b*/100 (being b the width of the section) and half wave length of *b*. Figure 2 shows on an amplified scale the used imperfections. According to Part 1-5 of EC3 a combination of the previous described imperfections should be introduced in the model. This combination should have a main imperfection which is added to the remaining imperfection reduced to 70%. The consideration of this combination produced very small differences when compared to simply adding the two imperfections. Therefore, this last procedure was adopted.

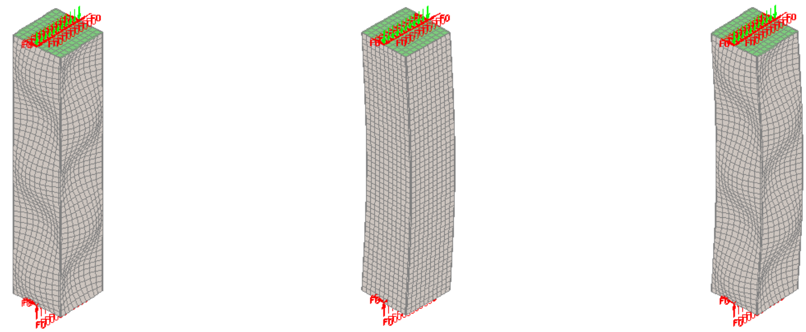

(a) (b) (c)

Figure 2. Initial geometric imperfections:(a) only local;(b) only global;(c) global plus local imperfections.

2.3.2 Residual stresses

Based on the model proposed by Gardner and Cruise [17], for cold formed sections the residual stresses follow the distribution presented on Table 1. Only the membrane residual stresses were considered as it was concluded that the residual stresses influence on the studied cases is small.

Table 1. Residual stresses distribution [17].

	Bending residual stresses	Membrane residual stresses
Central part of the plate	$\pm 0.63\sigma_{0.2}$	$+0.37\sigma_{0.2}$
External part of the plate	$\pm 0.63\sigma_{0.2}$	$-0.24\sigma_{0.2}$
Corners	$\pm 0.37\sigma_{0.2}$	$-0.24\sigma_{0.2}$

2.4 Corner strength enhancement

The cold formed manufacturing process as a positive influence on corners strength of rectangular hollow sections, which improves the cross-section resistance.

On these numerical models the corners regions were considered with strength enhancement following Ashraf et al. [18] studies. The corners regions were considered to spread from the corner for a distance of twice the plate thickness. The proportional limit strength on these corners is given by.

$$\sigma_{0.2,c} = \frac{1.881\sigma_{0.2,v}}{\left(r_i/t\right)^{0.194}} \tag{2}$$

where $\sigma_{0.2,v}$ is the proportional limit strength in the flat region of the plate.

Figure 3 presents the influence of the corners strength enhancement on axially compressed columns of the stainless steel grade 1.4301 at 500 ºC. From this comparison it can be observed that the influence on the member resistance is high.

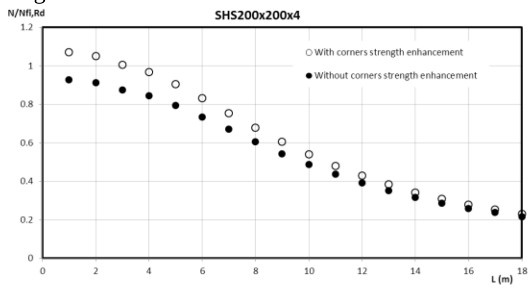

Figure 3. Influence of the corner strength enhancement on the columns ultimate bearing load.

3 DESIGN FORMULAE

The EC3 design formulae for beam columns in case of fire were developed based on carbon steel columns with I sections of Classes 1 and 2 [19]. Previous research works [11] have proposed changes on the interaction curves of those EC3 design expressions based on parametric studies on stainless steel I sections also of Classes 1 and 2. Additionally, Part 1-1 of EC3 [2] proposes two methods for evaluating the resistance of carbon steel columns, which can be applied for Class 4 square hollow sections. On these thin-walled profiles, EC3 [3,14] proposes the use of effective cross-sections which have the width of the internal elements reduced in function of their local buckling susceptibility (A_{eff} and W_{eff}).

In this section the expressions for the determination of those different interaction curves are presented. On the study presented in this paper, for better comparisons purposes, the adopted flexural buckling reduction factor was obtained numerically from the resistance of axially compressed columns. The same main design expression (3) is used in all cases, changing only the interaction factor *k*. As the analyzed section is square, the proposed formulae for the strong axis on the design recommendations were used (k_y *or* k_{yy} on the case of Part 1-1 of EC3).

$$\frac{N_{fi,Ed}}{\chi_{fi} A_{eff} k_{0.2p,\theta} \dfrac{f_y}{\gamma_{M,fi}}} + k \frac{M_{fi,Ed}}{W_{eff} k_{0.2p,\theta} \dfrac{f_y}{\gamma_{M,fi}}} \leq 1 \tag{3}$$

3.1 Part 1-2 of Eurocode 3 interaction factor

Part 1-2 of EC3 states that the safety evaluation of stainless steel members should be made following the same expressions developed for carbon steel members. The recommended interaction factor is

$$k = 1 - \frac{\mu N_{fi,Ed}}{\chi_{fi} A_{eff} k_{0.2p,\theta} \dfrac{f_y}{\gamma_{M,fi}}} \leq 3 \tag{4}$$

where,

$$\mu = (2\beta_M - 5)\bar{\lambda}_\theta + 0.44\beta_M + 0.29 \leq 0.8 \text{ with } \bar{\lambda}_{20°C} \leq 1.1 \tag{5}$$

β_M , which is in function of the bending diagram shape, is given by

$$\beta_M = 1.8 - 0.7\psi \tag{6}$$

3.2 Proposed interaction factor for stainless steel I sections of the Classes 1 and 2

Based on recent studies [11] new interaction factors for stainless steel beam-columns with I sections of the Classes 1 and 2 were proposed. For the strong axis this new interaction factor is

$$k = 1 - \frac{\mu N_{fi,Ed}}{\chi_{fi} A_{eff} k_{0.2p,\theta} \dfrac{f_y}{\gamma_{M,fi}}} \quad \text{com} \quad k \leq 0.8\bar{\lambda}_\theta + 0.9 \text{ e } k \geq \mu - 0.5 \tag{7}$$

For the stainless steel grades 1.4301 e 1.4003:

$$\mu = (4.33\beta_M - 8.56)\bar{\lambda}_\theta + 0.33\beta_M + 0.11 \quad \text{if } \bar{\lambda}_\theta \leq 0.4 \text{ then } \mu \leq 1.0 \text{ else } \mu \leq 0.7 \tag{8}$$

And for the stainless steel grade 1.4462:

$$\mu = (1.27\beta_M - 2.63)\bar{\lambda}_\theta + 0.66\beta_M - 0.49 \quad \text{if } \bar{\lambda}_\theta \leq 0.4 \text{ then } \mu \leq 1.0 \text{ else } \mu \leq 0.8 \tag{9}$$

3.3 Part 1-1 of Eurocode 3 interaction factors

The Part 1-1 of EC3 [2] presents two methods for the determination of the interaction factors on carbon steel beam-columns. Although it is not proposed by EC3, in this work it is evaluated the possibility of using these expressions on stainless steel members with Class 4 square hollow sections submitted to fire.

According to Method 1 for Class 4 sections (Annex A of EN1993-1-1)

$$k = c_m \frac{\mu}{1 - \dfrac{N_{Ed}}{N_{cr}}} \tag{10}$$

$$\mu = \frac{1 - \dfrac{N_{Ed}}{N_{cr}}}{1 - \chi \dfrac{N_{Ed}}{N_{cr}}} \quad \text{and} \quad c_m = 0.79 + 0.21\psi + 0.36(\psi - 0.33)\frac{N_{Ed}}{N_{cr}} \tag{11}$$

Method 2 (Annex A of EN1993-1-1) states that for Class4 tubular square sections

$$k = c_m\left(1 + 0.6\bar{\lambda}\frac{N_{Ed}}{\chi N_{Rd}}\right) \le c_m\left(1 + 0.6\frac{N_{Ed}}{\chi N_{Rd}}\right) \tag{12}$$

$$c_m = 0.6 + 0.4\psi \ge 0.4 \tag{13}$$

4 NUMERICAL RESULTS AND INTERACTION CURVES COMPARISONS

The behavior of the above described interaction curves N-M when compared to the numerical results in stainless steel beam-columns with Class4 square hollow sections (section SHS200×200×4) is here presented. As mentioned in section 3, in these comparisons the influence of the flexural buckling curve on the interaction curves was eliminated considering the numerical results of resistance to axial compression on those interaction curves. As it was acknowledge in other research works [8,9] and can be observed in this paper, for the results obtained with bending moment equal to 0 (pure compression), these buckling curves need to be improved for being too conservative.

The interaction curves chosen for these studied were obtained from:

- Part 1-2 of EC3 “EN 1993-1-2” [5] with the flexural buckling obtained by the formulae of this part of EC3, which corresponds to the actual European prescriptions;
- Part 1-2 of EC3 “EN 1993-1-2 mod” with the flexural buckling obtained numerically;
- Proposed interaction factor for stainless steel I sections of the Classes 1 and 2 “Proposal for I profiles” [11]
- Method 1 and Method 2 from Part 1-1 of EC3 “Method 1” and “Method 2” [2].

Figure 4 shows the obtained results for the stainless steel grade 1.4301 and ψ=1, considering different flexural buckling slenderness corresponded to columns with 3, 9 and 15 meters length.

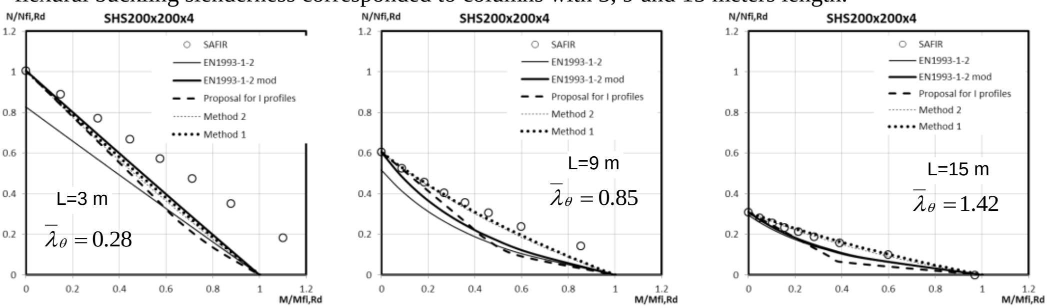

Figure 4. Beam-columns numerical results for the stainless steel grade 1.4301 and ψ=1.

In Figure 5 it is presented the obtained results for the three stainless steel grades 1.4301, 1.4003, 1.4462 and the different bending diagrams, for columns with 6 meters length.

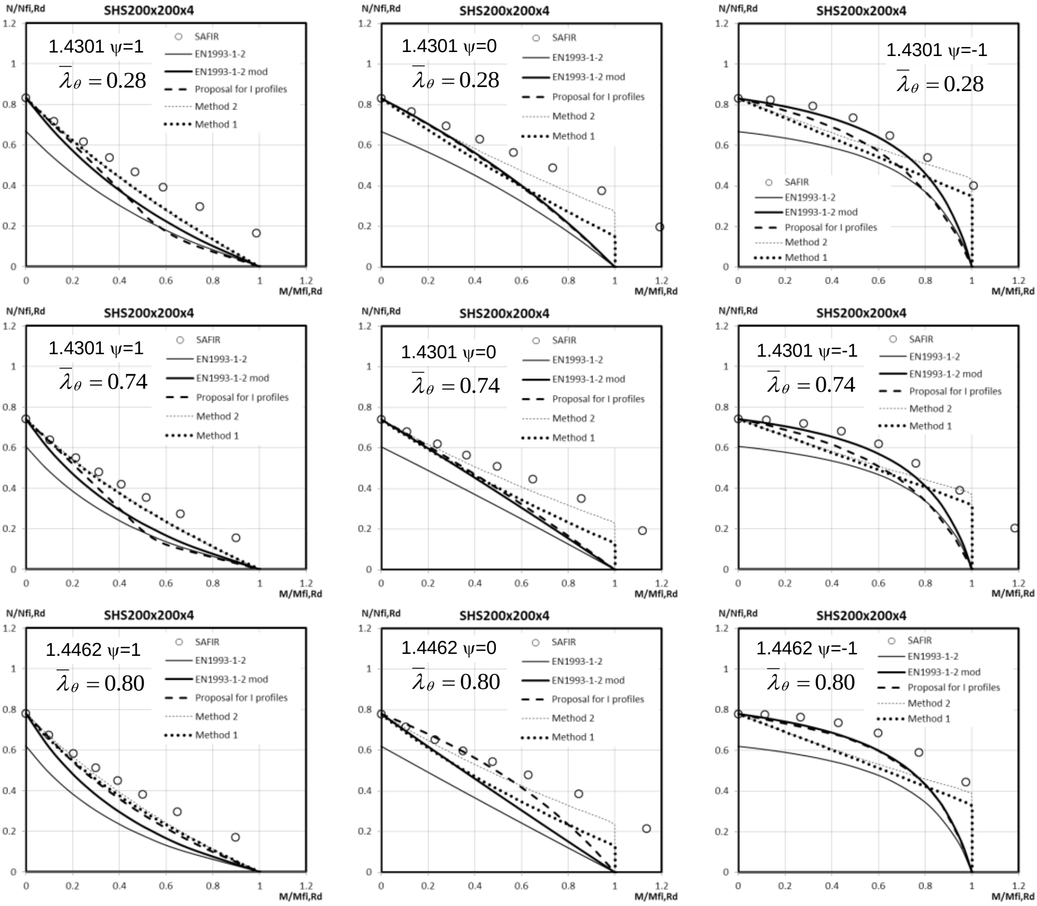

Figure 5. Beam-columns numerical results beam-columns with length of 6 m.

5 CONCLUSIONS

In this paper a numerical study on the behavior of stainless steel members with Class 4 square hollow sections in fire subjected to compression plus bending was presented. Comparisons between the obtained ultimate bearing loads, with the finite element program SAFIR, and different methods for the determination of the interaction curves N-M were performed. It was concluded that:

(1) EC3 presents a safe approximation, but too conservative mainly for small ratios of axial efforts. The differences are higher for uniform and triangular bending moment diagrams;

(2) The proposal developed for stainless steel I profiles with Class 1 and 2 cross-sections is also always on the safe side, having generally a slightly more conservative behavior than EC3;

(3) Method 1 and Method 2 present generally safe comparisons but too conservative for higher ratios of axial efforts and bi-triangular bending moment diagrams. From these two methods, the one that approximates better the numerical results is Method 2.

More studies, with other cross-sections (for considering different local instability susceptibility) and other temperatures, are needed to better assess the behavior of the interaction between axial compression and bending moments in these Class 4 stainless steel tubular profiles.

REFERENCES

[1] Euro Inox and Steel Construction Institute, *Design Manual for Structural Stainless Steel*, 3rd edition, 2006.

[2] CEN, European Committee for Standardisation, *EN 1993-1-1, Eurocode 3, Design of Steel Structures - Part 1-1: General rules and rules for buildings*, Brussels, Belgium. 2005.

[3] CEN, *EN 1993-1-4, Eurocode 3: Design of steel Structures – Part 1-4: General rules – Supplementary Rules for Stainless Steels*, Brussels, Belgium, 2006.

[4] Ashraf M., Gardner L. and Nethercot D., "Finite element modelling of structural stainless steel cross-sections", *Thin-Walled Structures*, Elsevier, 44, 1048-1062, 2006.

[5] CEN, *EN 1993-1-2 Eurocode 3: Design of Steel Structures - Part 1.2: General rules - Structural fire design, Brussels*, Belgium, 2005.

[6] Couto C., Vila Real P., Lopes N., Zhao B., "Lateral torsional buckling of steel beams with class 4 cross-sections in case of fire", *proceedings of the 2 ºCilasci*, pp. 137-146, Coimbra, Portugal, 2013.

[7] Lopes N., Vila Real P., Simões da Silva L., Franssen J.M., "Axially loaded stainless steel columns in case of fire", *Journal of Structural Fire Engineering*, Multi-Science Ltd, vol 1/1, 43-59, 2010.

[8] CTICM/CSM. *Stainless steel column buckling behaviour at elevated temperatures - comparison of euro inox and cticm methods*, 2005.

[9] Ng K.T., Gardner L., "Buckling of stainless steel columns and beams in fire", *Engineering Structures*, vol 29(5), 2007.

[10] Franssen J.M., "SAFIR A Thermal/Structural Program Modelling Structures under Fire", *Engineering Journal* vol 42/3, 143-158, 2005.

[11] Lopes N., Vila Real P., Simões da Silva L., Franssen J.M., "Numerical analysis of stainless steel beam-columns in case of fire", *Fire Safety Journal*, Elsevier, vol 50/(35-50), pp 35-50, 2012.

[12] Scifo A., *Fire resistance of stainless steel hollow section columns*, Université de Liège, Faculté des Sciences Appliquées, 2013.

[13] Lopes N., Vila Real P., Simões da Silva L., Franssen J.M., "Numerical modelling of thin-walled stainless steel structural elements in case of fire", *Fire Technology*, 46/1 91-108. 2010.

[14] CEN, *EN 1993-1-5, Eurocode 3: Design of Steel Structures - Part 1-5: Plated structural elements*, Brussels, Belgium. 2006.

[15] CEN, *EN 1090-2:2008+A1: Execution of steel structures and aluminium structures - part 2: Technical requirements for steel structures*, Brussels, Belgium. 2011.

[16] CEN, *EN 10219-2, Cold formed welded structural hollow sections of non-alloy and fine grain steels - Part 2: Tolerances, dimensions and sectional properties*, Brussels, Belgium. 2006.

[17] Gardner L., Cruise R., "Modeling of residual stresses in structural stainless steel sections", *Journal of structural engineering*, vol 135(1), 42 53, 2009.

[18] Ashraf M., Gardner L., Nethercot D., "Strength enhancement of the corner regions of stainless steel cross-sections", *Journal of Constructional Steel Research*, Elsevier, 61 pp. 37–52. 2005.

[19] Talamona D., *Flambement de Poteaux Métalliques sous Charge Excentrée, à Haute Température* (in French), PhD Thesis University Blaise Pascal, Clermont–Ferrand, France 1995.

THE EFFECT OF FIRE SPREAD ON STEEL-CONCRETE FLOOR

Kamila Horová*, Tomáš Jána* and František Wald*

* Czech Technical University in Prague, Thakurova 7, 166 29 Prague, Czech Republic
e-mails: kamila.horova@fsv.cvut.cz, tomas.jana@fsv.cvut.cz, wald@fsv.cvut.cz

Keywords: Steel-concrete floor, Mechanical behaviour, Fire spread, FDS simulation, FEM model

Abstract. *The paper describes the impact of fire spread on the behaviour of the steel and concrete composite floor. The spatial and temporal evolution of the gas temperature calculated in NIST code FDS, which was validated to experimental measurements, is applied to the composite floor of dimensions 9.0 m by 9.0 m. Mechanical behaviour of the composite slab highly affected by regions of high temperatures and areas with only elevated temperatures is solved in code Vulcan. To highlight the severity of spreading fire causing non-uniform temperature conditions, which after-effects differ from traditional methods, a comparison of both methods is introduced. The calculation of mechanical behaviour of the composite floor is repeated in a serious of three different thermal loading cases. Results of all cases are then compared in terms of vertical displacement and axial force in several positions of the composite floor.*

1 INTRODUCTION

In recent years, traditional design fire methods and their features of realistic description of fire have been criticised. Mainly in buildings with loss of compartmentalization the fire behaviour has been described in different manners. The consequences of larger compartments, evident in several tragic fires as in the World Trade Center or the Windsor Tower in Madrid, show that fires tend to travel. As flames spread within the floor to consume fuel, regions with high temperatures and regions with elevated temperatures are created. In literature numerous studies presenting the experimental evidence of non-uniform temperature across the floor area of a compartment can be found. In relationship of the non-uniform temperature resolution the spatial and temporal evolution of the temperature of the structural elements allowing to determine stresses and deformations within the structure need to be resolved.

An initial study of the structural effects of horizontal fire spread from a single ignition point into adjacent bays of a two-dimensional steel frame was introduced by Bailey [1] in 1996. The structural analysis was carried out by the help of a 2D finite element model. The conclusion of the analysis was summed that the effect of fire spread on the structural behaviour of a two-dimensional steel frame produced higher beam displacements in the source bays compared to simultaneous heating. The effect of fire spread was significant on the magnitude of displacements as well as on the residual forces. However, according to Bailey (1996) this fact cannot be generalized.

To demonstrate the influence of horizontal fire spread on the mechanical behaviour of more realistic three-dimensional structure, a model of the steel and concrete composite floor of geometrical and temperature data taken from full-scale fire test [2], performed by authors in 2011, is used.

2 SPREADING FIRE SCENARIO

2.1 Experimental background

For the purpose of investigation of spreading fire which is arguably a more typical condition than the assumption of uniform temperature throughout the whole floor area of an enclosure, a full-scale fire test was carried out in Czech Republic [2]. A two-storey composite steel-concrete experimental structure of dimensions 10.4 × 13.4 × 9 m was designed. In the upper floor a natural fire spread was simulated by burning of wooden cribs placed closely together on area of 24 m^2. Total volume of ligneous mass used was 2.52 m^3. A thin-walled channel filled by mineral wool and penetrated by paraffin placed on the south side of fire compartment served as a linear outbreak of burning. The sufficient supply of air needed for burning was ensured by an opening of 10 m^2. The gas temperature in the fire compartment was measured by jacketed thermocouples located mainly in the direction of horizontal fire spread. Since the scale of experimental enclosure was not large in comparison to the scale of real buildings, high degree of temperature non-uniformity appeared.

2.2 Numerical results of gas temperature

The spatial and temporal development of gas temperature bellow the steel-concrete floor needed as an input of thermal loading of mechanical behaviour calculation was numerically solved in NIST code FDS 5 [3]. Gas temperature calculated in positions of thermocouples was validated by measurements carried out during the fire test. The simulation confirmed spreading phenomena from the initial outbreak of the fire to the opposite side of fire compartment. However, calculated values were slightly delayed in comparison to the measured values. The numerical model represents the tendency of the measured temperatures mainly in the growing phase, where the highest temperature differences appear. Despite the fore-mentioned, results of the numerical simulation are sufficiently applicable to investigate an impact of non-uniform temperature resolution on a structural behaviour. Detailed description of the numerical simulation can be found in [4].

The range of gas temperature calculated at 18 sensors bellow the composite floor limited by two curves illustrating the maximum and minimum values is shown in Figure 1(a). Maximum degree of gas temperature heterogeneity was reached between 20 and 30 min on sensors below the internal beam 2 and sensors located in the corner of the compartment. Development of gas temperature calculated at sensors TG1, TG2 and TG3, placed in the direction of fire spread bellow the beam 2 is also shown in Figure 1(a). Despite the distance between thermocouples being only 4 m, a significant temperature difference of 355 °C was observed in 20 min.

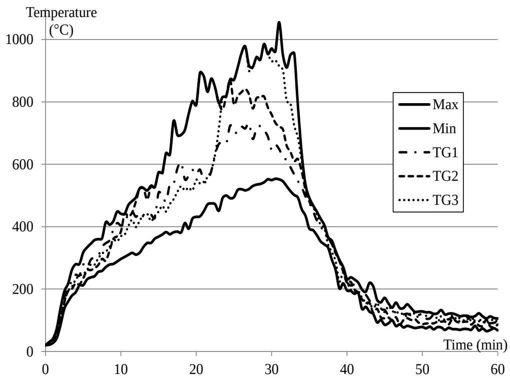

(a)

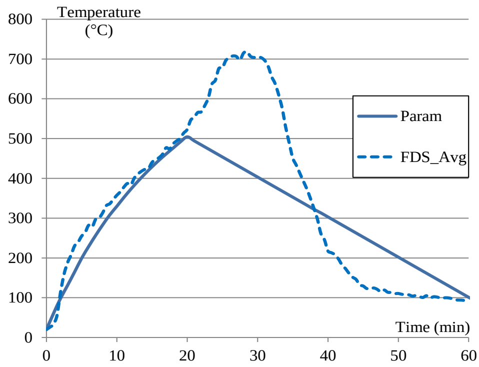

(b)

Figure 1. (a) Calculated gas temperature during travelling fire; (b) Average gas temperature from FDS calculation and parametric temperature curve.

3 MECHANICAL ANALYSIS OF COMPOSITE STEEL-CONCRETE FLOOR

3.1 FEM model of composite steel-concrete floor

The spatial-temporal evolution of gas temperature coming from FDS simulation is applied to a FEM model of the composite floor of dimensions 9.0 m by 9.0 m which represent a part of the experimental floor. The concrete slab composed of trapezoidal sheet and concrete C 30/37 is supported by 3 protected steel beams of profile IPE 240 and 2 unprotected steel beams of profile IPE 270 and IPE 220 forming its perimeter, 2 secondary unprotected steel beams of profile IPE 270 and 6 protected steel columns of profile HE200B. Steel elements are of grade S355. The concrete slab of continuous depth of 70 mm is reinforced by 2 layers of steel bars of area 196 mm^2/m placed 30 mm from the top of the cross-section. Partial interaction between concrete slab and supporting steel beams is ensured by shear connectors of diameter 19 mm of ultimate shear strength 450 N/mm^2 placed in total of 2.11 pieces/m. Data of the floor including geometry, beam cross-sections and mechanical loading employed in the calculation of structural response are illustrated at Figure 2. All structural elements being loaded by respective temperature curves are divided into mesh elements of 1.0×1.0 m. Mechanics equations to determine stresses, internal forces and deformations are then solved by code Vulcan [5, 6].

To compare the impact of fire spread with uniform temperature resolution across the floor area of the fire enclosure the model of the steel and concrete composite floor is subjected to serious of three different thermal loading. Thermal load in terms of uniform temperature distributed bellow the composite floor is simulated firstly by parametric temperature curve (case Param) calculated according to EC1 [7]. Geometry of the fire compartment, fire load density, ventilation and thermal characteristic of surrounding walls are considered the same as it was present during the fire experiment [2]. Secondly, the uniform temperature distribution bellow the floor is applied by the help of average temperate at all sensors calculated in FDS numerical simulation (case FDS_Avg). Comparison of both temperature curves of thermal loading Param and FDS_Avg is shown in Fig. 1b. However the growing phase of both curves corresponds well, the peak temperature of parametric temperature curve is about 200 ℃ lower comparing to average FDS temperature curve. With the view to investigate the influence of spreading fire scenario on the behaviour of composite steel-concrete floor 18 gas temperature developments coming from FDS calculation are applied to certain parts of the floor similarly to location of sensors in FDS model. In most cases temperature curves are applied to area of 3×2 mesh cells. In areas with high temperature heterogeneity - the centre of the floor and bellow the beam 2, temperature resolution is higher.

In the analysis material models of steel, concrete and reinforcement steel at elevated temperatures are referred to EC2 [8] and EC3 [9]. The temperature in the cross-section of the main elements forms a non-uniform pattern in which each major element of the section's temperature is a proportion of the heating temperature curve. These proportions vary with time and with the particular heating curve being applied. Figure 3 indicates the temperature distribution in cross-sections of protected beams, unprotected beams and floor slab. All columns have temperature factor of 0.7 which is uniform across the entire cross section. Temperature patterns used in the analysis follows recommendation in benchmark study of the software [10,11].

3.2 Description of software

The computer program Vulcan is a three-dimensional frame analysis program, which has been developed at the University of Sheffield to model the behaviour of structures under fire conditions. In this program steel-framed and composite buildings are modelled as assemblies of finite beam-column, connection and layered floor slab elements. For composite floor systems it is assumed that the nodes of these different types of element are defined in a common fixed reference plane, which is assumed to coincide with the mid-surface of the concrete slab element. The beam-columns are represented by 3-noded line elements with two Gaussian integration points along their length. The nonlinear beam column element matrices are derived from the general continuum mechanics equations for large-displacement/rotation nonlinear analysis. Each of the three nodes of the beam-column element has six degrees of freedom. The main assumptions of the elements can be summarized as follows: Cross sections remain plane and undistorted under deformation and there is no slip between segments. They do not necessarily remain normal to their reference axis, as they are originally located, as displacement develops. The “small strain and large deformation” theory is adopted. This means the displacements and rotations can be arbitrarily large but strains remain small enough to obey the normal engineers’ definition. The cross section of a beam-column element is divided into a matrix of segments, each segment can then have its own material, thermal and mechanical properties, and its own temperature, at any stage of an analysis. This allows modelling of different temperature distributions across member’s cross-section and, therefore, the different the thermal strains and changes of material properties that accompany different temperatures across the section can also be tracked. For verification and validation studies of the software see References 10 and 11.

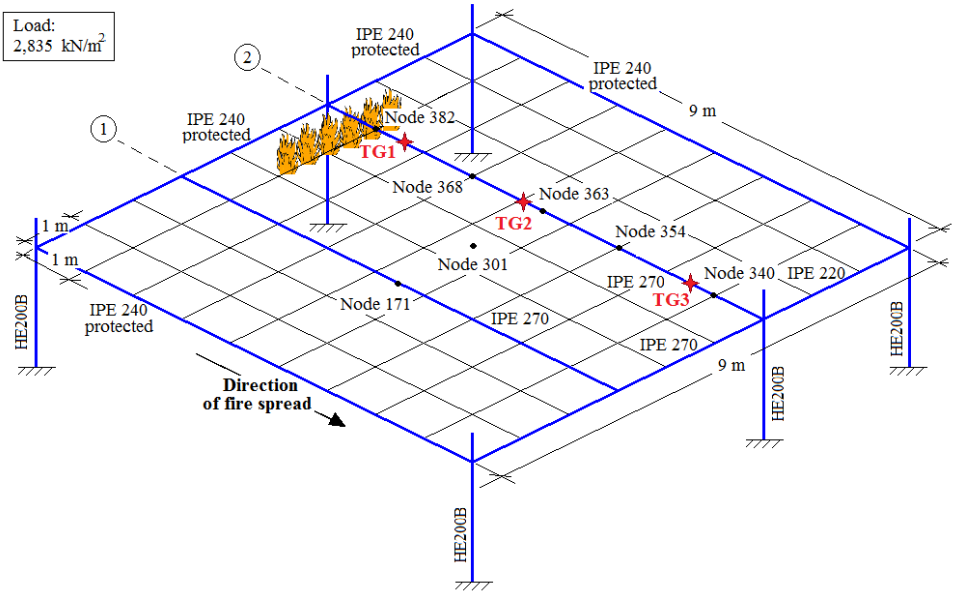

Figure 2. Model of composite steel-concrete floor.

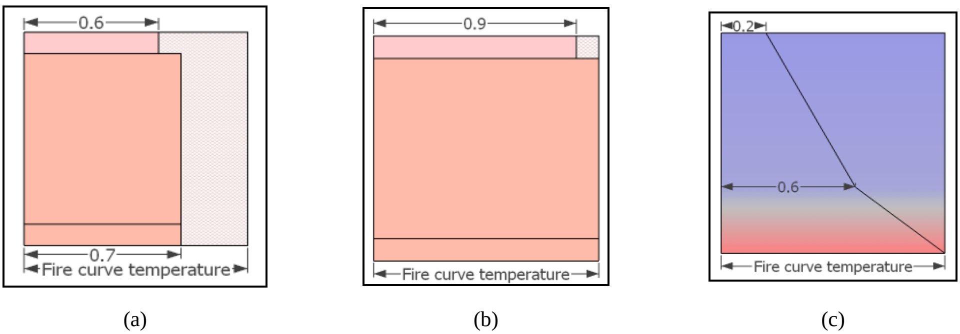

Figure 3. Temperature distribution at cross-section of: (a) protected beam; b) unprotected beam; (c) floor slab.

3.3 Comparison of mechanical behaviour

Mechanical behaviour of steel-concrete composite floor is investigated in terms of displacement in the central point of the floor (Node 301), vertical displacement and axial force along internal beams. The essential results are summarized in Figures 4-7. Figure 4(a) shows the increase of deflection in central point of the floor (Node 301, for location see scheme of the model in Figure 2) for all thermal loading cases: parametric temperature and average temperature calculated from FDS results which are uniformly distributed bellow the entire area of the floor, and travelling fire temperatures coming from FDS calculation which represents natural spreading of the fire. As it can be observed from the figure deflection caused by parametric temperature increases slowly from the beginning to reach its maximum value about 150 mm in 20 min. However, both deflection curves caused by travelling fire and average FDS temperature track the previous one during first 20 min of heating, both starts to increase rapidly after 20 min to reach their peaks in 30 min. The peak value induced by travelling fire is 360 mm, about 35 mm more than the maximum deflection caused by uniformly distributed average FDS temperature. Comparing to deflection incurred by parametric temperature curve the difference is 250 mm. The results demonstrate that the severity of fire spread when temperature of flames and only elevated temperatures act simultaneously in different locations of the floor slab causes more significant mechanical behaviour comparing to uniformly distributed temperature heating. Looking at temperatures and effects of parametric temperature curve it is recommended to modify the parameters of EC1 curve by applying b_{ref} equal to 1900 $J/m^2s^{1/2}K$ according to [12].

As the fire load was placed asymmetrically in the view of location of both internal beams, vertical displacement of middle point of these beams differs. In Figure 4(b) a mid-span displacement of beam 2 is described by Node 363, Node 171 illustrates a mid-span displacement of the beam 1 (for location see scheme of the model in Figure 2). The figure demonstrates the difference caused by uniformly distributed heating by FDS_Avg curve and fire spread (load case FDS). Influence of parametrical curve is no longer introduced. It can be observed that maximal displacement is reached during load case FDS at beam 2. In the same node (Node 363) the displacement caused by FDS_Avg is about 90 mm lower. Looking at beam 1, maximal displacement caused by both loading cases are about the same level, with slightly higher values induced by FDS_Avg loading. The variance of results is mainly caused by acting of flames bellow the beam 2 which high temperature is not suppressed within the use of 18 temperature curves coming from FDS, whereas the average FDS temperature is decreased involving corners elevated temperatures. It can be seen that the location of an element considered is an important factor when choosing a type of thermal loading.

Considering a recovery of displacement which occurs when the temperature is reduced, the spreading fire scenario causes the highest final residual displacements. In Figure 4(a) it can be observed that displacement of the middle point of the slab caused by loading case FDS remains at 200 mm which is about four times higher comparing to uniform heating by parametric temperature curve. Final residual displacement of uniformly distributed FDS_Avg curve stops at 130 mm, which is about 70 mm lower comparing to FDS case. The significant difference in the final residual displacements shows the importance of covering the fire spread scenario into design fire models considered.

To investigate the mechanical behaviour of supporting steel beam 2, where the maximal effects of thermal loading are reached, vertical displacements and axial forces along its length are introduced in Figures 5 and 6. Curves of vertical displacements in time shown in Figure 5 are described by the aid of nodes 382, 368 and 354. These nodes are located at beam 2 according to illustration in Figure 2. As it can be expected according to application of temperature curves simulating the fire spread, the maximal deflection of 350 mm is reached in node 354 where the highest temperatures (TG3) appeared. Vertical displacement of node 368 is about 100 mm lower and displacement of node 382 about 300 mm lower comparing to node 354. The significant difference of displacement along the beam length is caused by high degree of temperature non-uniformity bellow the beam. In contrast, during uniform temperature distribution covering both, parametric temperature and average FDS temperature curve, the maximal deformation occurs in the middle of the beam span. The propagation of deformed shape of the beam caused by all thermal load cases is shown in Figure 7.

In accordance to vertical displacement illustrated in Figure 5 axial forces in corresponding beam elements are introduced in Figure 6. Beam elements used for description in Figure 6 are located subsequently: beam 37 lies between nodes 382 and 368, beam 35 between nodes 368 and 354 and beam 33 lies between node 354 and 340. As the loading temperature is increased compression forces start to decrease by both loading cases. Forces start to turn into tension when the maximal temperature and also deformation is reached. The final residual axial forces remains the highest by loading case of spreading fire, similarly to description of final residual displacements in previous paragraph.

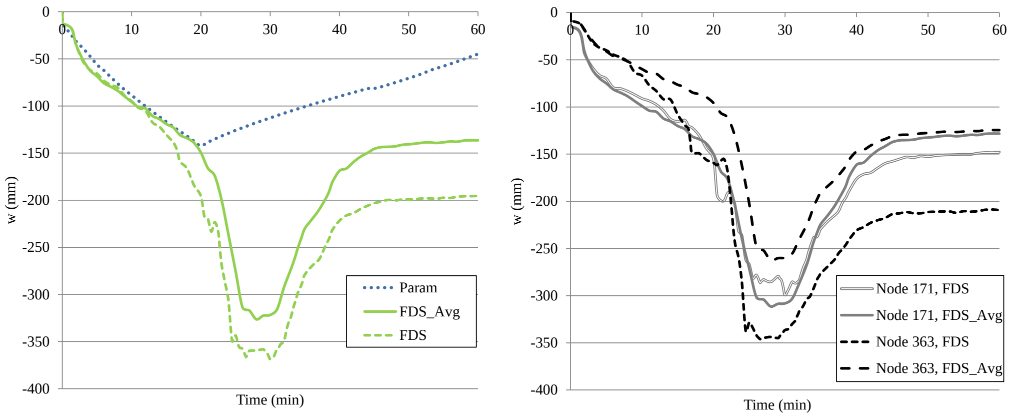

(a) (b)

Figure 4. Comparison of displacement cause by different thermal loading cases in time: (a) in the central point of the floor (Node 301); (b) in mid-span of beam 1 (Node 171) and beam 2 (Node 363).

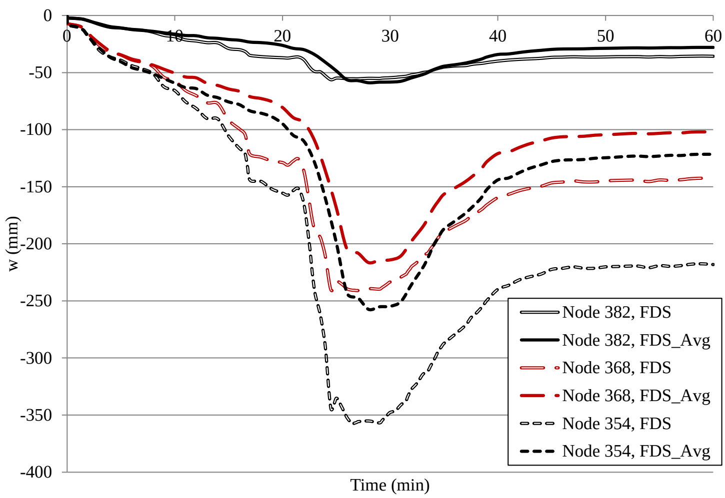

Figure 5. Vertical displacement in several locations of beam 2.

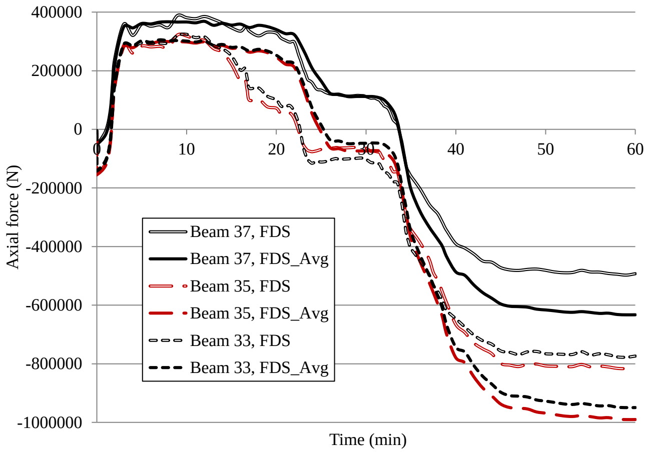

Figure 6. Axial force along the length of beam 2.

4 CONCLUSIONS

The structural analysis described by Bailey [1] was the first study recognizing the need to consider the structural impact of a spreading fire. However, its simulation of fire environment and 2D structure were not realistic enough. To demonstrate the influence of horizontal fire spread on the mechanical behaviour of three-dimensional structure subjected to more realistic temperature loading, a model of the steel and concrete composite floor of temperature data validated to full-scale fire test [2] is investigated in this paper.

By limited results in terms of vertical displacement and axial forces demonstrated in this paper it has been shown that the fire spread when high temperature of flames and only elevated temperature fields act simultaneously in different locations of the floor slab causes more severe mechanical behaviour comparing to uniformly distributed temperature heating. In larger fire enclosures where the temperature heterogeneity can be higher, effects can be even more significant. The influence of average FDS temperature uniformly applied bellow the area of the floor on the structural behaviour depends on the location of an element being considered. As acting of flames inducing higher temperatures is suppressed in this load case an important change in mechanical behaviour at certain places can be missed. Looking at temperatures and effects of parametric temperature curve which gives very low values comparing to spreading fire scenario, it is recommended at least to modify the parameters of EC1 curve by applying b_{ref} equal to 1900 $J/m^2s^{1/2}K$ according to [12]. All introduced results demonstrate the significant impact of the fire spread scenario on final residual forces and displacement which are important in phase of reparation of steel structures after fire conditions.

By the results described in the paper authors would like to show that a methodology allowing to describe the temperature environment in an enclosure more realistic is crucial for examination of structural response to fire.

5 ACKNOWLEDGEMENT

Work on the research presented in this paper is supported by project LD11039 and SGS14/OHK1-090/14. The first author also gratefully thanks to prof. Ian W. Burgess for his guidance during this research.

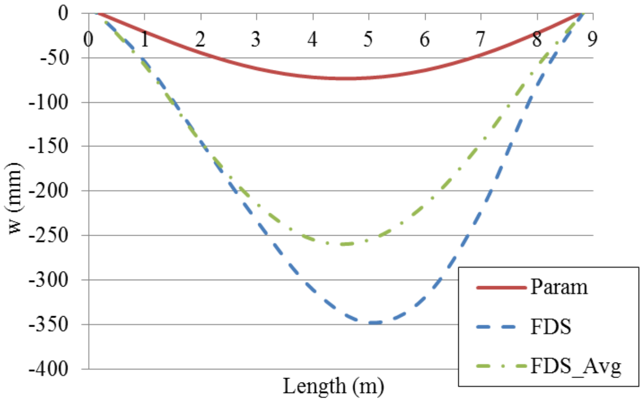

Figure 7. Comparison of deformed shape in 30 min caused by two cases of uniform temperature distribution and spreading fire along the length of beam 2.

REFERENCES

[1] Bailey, CG, Burgess, IW, Plank, RJ, “Analyses of the Effect of Cooling and Fire Spread on Steel-Framed Buildings”, *Fire Safety Journal*, Vol. 26, 1996.

[2] Wald F., Jána T., Horová K., *To demonstration fire test, Design of joints to composite columns for improved fire robustness*, CTU in Prague, 2011.

[3] McGrattan K., Hostikka S., Floyd J., Fire Dynamics Simulator, V5, Users Guide, NIST Special Publication 1019-5, Baltimore, 2010.

[4] Horová, K, Jána, T, Wald, F, “Temperature heterogeneity during travelling fire on experimental building”, *Advances in Engineering Software*, Vol. 62-63, pp. 119-130, 2013.

[5] Vulcan – A software for Structural Fire Engineering, Vulcan Solutions Ltd – A company of Sheffield University Enterprises Limited, Sheffield, UK. Available from http://www.vulcan-solutions.com/index.html.

[6] “Vulcan User’s Manual”, Vulcan Solutions Ltd, Sheffield, UK.

[7] Eurocode 1. Actions on structures, Part 1.2: General actions – Action on structures exposed to fire. Europena Committee for Standardization, 2002.

[8] Eurocode 2. Design of concrete structures, Part 1.2: Structural fire design. Europena Committee for Standardization, 2004.

[9] Eurocode 3. Design of steel structures, Part 1.2: Structural fire design. Europena Committee for Standardization, 2004.

[10] Wald, F., Burgess, I., Kwasniewski, L., Horová, K., Caldová, E., *Benchmark Studies, Verification of numerical models in fire engineering*, CTU Publishing House, 2014.

[11] Wald, F., Burgess, I., Kwasniewski, L., Horová, K., Caldová, E., *Benchmark Studies, Experimental validation of numerical models in fire engineering*, CTU Publishing House, 2014.

[12] Buchanan A.H., *Structural Design for Fire Safety*, John Wiley & Sons Ltd, Chichester, 2001.

FIRE RESISTANCE OF COMPOSITE COLUMNS MADE OF CONCRETE FILLED CIRCULAR HOLLOW SECTIONS AND WITH RESTRAINED THERMAL ELONGATION

Tiago A. C. Pires*, João Paulo C. Rodrigues and José Jéferson Rêgo Silva***

* Federal University of Pernambuco, Recife, Brazil
e-mails: tacpires@yahoo.com.br, jjrs@ufpe.br

**ISISE – Institute for Sustainability and Innovation on Structural Engineering, University of Coimbra, Portugal
email: jpaulocr@dec.uc.pt

Keywords: Fire, CFCH, Column, Restraining, Experimental, Numerical

Abstract. *Despite several research studies (numerical and experimental) on fire resistance of CFCH column, its behaviour in fire is not completely understood. Most of these studies did not consider the restraining to column thermal elongation, important parameter for behavior of the column on fire when that one is inserted in a structure. This paper presents a three-dimensional nonlinear finite element model developed in ABAQUS to predict the behavior in fire of CFCH columns with restrained thermal elongation. The model was validated in comparison with a series of fire resistance tests on CFCH columns with axial and rotational restraining to thermal elongation. The numerical model presents results in close agreement with the experimental data.*

1 INTRODUCTION

Advantages such as the load bearing capacity both at room and high temperatures, reduced costs associated to fast construction times, slenderness and aesthetic appearance are usually mentioned to justify the use of Concrete Filled Circular Hollow (CFCH) columns in construction industry. On the other hand, in order to predict the fire performance of CFCH columns some aspects necessary to the numerical analyses still demand further research, despite the number of models presented in the literature.

Lie [1] presented a mathematical model to predict the behaviour of CFCH columns, filled with steel bar reinforced concrete, subjected to fire. The column temperature was obtained using finite difference method and the strength of the column by an analytical method based on a load-deflection or stability analysis. The authors adopted mechanical properties at elevated temperatures for concrete and steel proposed in [2] and the model considered the moisture effect with the retardation in temperature increase due to evaporation but did not consider a migration toward the column. According to the author, this and others simplifications are the reasons of deviations in the calculated temperatures.

Ding and Wang [3] developed a finite element model employing ANSYS software to access the fire behaviour of CFCH columns. Relevant parameters were study such as external diameter, length of the column, boundary and load conditions. The thermal analysis was developed in a 2D model and the fire resistance in a 3D model. Important features often neglected by others researchers were addressed in this study such as the influence of an air gap and slip at the steel tube – concrete core interface, the concrete tensile behaviour and the column initial imperfection on fire behaviour of the CFCH columns.

Schaumann et al. [4] presented a 2D numerical model to study CFCH columns in fire. The North American and the European recommendations for material properties of high strength concrete at high temperatures were compared and important differences in the numerical results for the CFCH columns filled with this material were addressed. The numerical results were compared with tested columns already present in the literature varying parameters such as external diameter, tube filling, cross-section shape and concrete strength. According to the authors the differences arise from the numerical model that did not consider the local effects like gaping cracks and local plastic buckling.

Hong and Varma [5] proposed a 3D finite element model to predict the behaviour of concrete filled rectangular hollow columns under fire conditions. A three step sequentially coupled analysis was suggested in this research. Initially, fire growth and development was determined with the Fire Dynamics Simulator (FDS), followed by heat transfer and stress analyses, both with ABAQUS finite element program. Relevant parameters that influence the model were pointed out, such as better steel and concrete thermal-mechanical models, geometric initial imperfections and composite interaction steel tube - concrete core.

Espinos et al. [6] presented important improvements on modelling with ABAQUS the behaviour of CFCH columns in fire, such as thermal conductance and friction model for the steel-concrete interface; thermal expansion coefficients; thermo-mechanical models of steel and concrete; and type of finite element employed for the reinforcement bars. The model presented better agreement for the leaner columns than the massive columns. The authors justify the fact due the major contribution of the concrete core in failure mechanism. Also the numerical results presented some divergence with high strength concrete filled columns. Optimal values to represent the thermal-mechanical interface between the steel tube and concrete core are suggested.

These numerical approaches present some differences in relevant parameters when modelling of CFCH columns such as: the initial steel tube imperfections, steel and concrete mechanical properties in fire models, thermal expansion coefficients for steel and concrete, thermal and structural behaviour at interface steel tube - concrete core and mesh elements. These differences reflect the need for further studies because to represent a real fire situation of a building structure by experiments and numerical modelling is a difficult and challenging task. This paper presents a three-dimensional nonlinear finite element model to predict the behaviour of CFCH columns in fire, considering the restraints of columns to their thermal elongation that adds a rather difficult step to the problem analysis and yet not fully investigated. Validation of the proposed model is investigated comparing numeric with experimental data obtained from fire tests conducted on CFCH columns with restrained thermal elongation [7].

2. EXPERIMENTAL TESTS

The results obtained in a set of 40 fire resistance tests on CFCH columns with restrained thermal elongation were taken as reference to compare the numerical results. These tests, carried out in the Laboratory of Testing Materials and Structures of the University of Coimbra – Portugal, studied the influence of parameters in the fire resistance of the columns such as the slenderness, cross-sectional diameter, loading level, stiffness of surrounding structure, steel reinforcement ratio and degree of concrete filling inside the steel tube (completely filled or with a ring around the internal surface of the steel tube wall). The details of the experimental procedure and the results obtained are well described in the literature [7, 8].

3. NUMERICAL MODELLING

This work takes into account the main suggestions proposed in the literature, to present an improved three-dimensional nonlinear finite element model, developed in ABAQUS [9], to model the behaviour of CFCH columns in fire.

3.1 Geometry and Mesh

As commonly adopted in numerical analysis of columns, an initial geometric imperfection is imposed on the columns (due to the manufacturing process, for instance). A large range of different values for the maximum imperfection along the length of the columns can be found in the literature (L/7500 is suggested by Hong and Varma, 2009 while L/1000 up to L/2000 is proposed by Espinos et al. [6]. The value of L/1000 is adopted, as this seems to be the value recommended by most authors.

Three-dimensional twenty node solid elements were used: DC3D20 element for the thermal model and C3D20R element for the structural model. One-dimensional three node truss elements (T3D3 element) were used to mesh the bars for the structural model and three node heat transfer link (DC1D3 element) for the thermal model. An approximate global size of 20 mm for the element was defined and was sufficient for the accuracy of the numerical results to be good. Despite the increase in computing time (computer time was not a variable to be studied in this paper), quadratic elements were preferred to reduce approximation error due to discretization.

Table 1. Mesh details for the numerical models.

Model	Columns	Diameter (mm)	Element type thermal	Element type mechanical	N º of elements	N º of nodes
1	CHS columns	168.3	DC3D20	C3D20R	1728	9538
2	(i.e. without filling)	219.1			2062	11898
3	CHS columns total	168.3	DC3D20	C3D20R	10542	50609
4	filled with PC	219.1			16174	76017
5	CHS columns total	168.3	DC3D20/	C3D20R/	8484	38787
6	filled with RC	219.1	DC1D3*	T3D3*	26464	115611

* for reinforcement steel bars

3.2 Thermal and mechanical properties

The steel model considered the temperature dependent formulation for thermal and mechanical properties presented in EN1993-1-2:2005 [10], as suggested by EN1994-1-2:2005 [11], and the isotropic classical metal plasticity model. A reduction of 10% in the thermal expansion coefficient of steel led to a reduction of the maximum axial deformations (u_{max}), as also observed by Lie [1], and a better agreement with the measured values of this parameter. However, problems with convergence and divergences in critical times were noted for results with this reduced coefficient. Therefore, the thermal elongation of steel recommended by EN1993-1-2:2005 [10] was adopted and this still led to acceptable results.

A wide variety of concrete models, for ambient and elevated temperatures, has been presented in the literature. The numerical model presented in this research used the mechanical and thermal properties presented in EN1992-1-2:2004 [12]. The concrete damaged plasticity model was adopted. A thermal dependent formulation was used to simulate the effects of heating due to fire, except for the thermal expansion coefficient and the density of concrete. The EN1992-1-2:2004 [12] mechanical model for concrete presented very similar results when compared to the model proposed by Lie [1]. Thus, the EN1992-1-2:2004 [12] mechanical model was adopted in this work. Hong and Varma [5] and Espinos et al. [6] followed Lie's model. A constant value of 6x10-6 $℃^{-1}$ for the thermal expansion coefficient of concrete, as suggested by Hong and Varma [5], is adopted as well as a constant value of 2300 kg/m^3 for concrete density, as suggested by most researches instead of the temperature dependent formulation proposed in EN1992-1-2:2004 [12]. The EN1994-1-2:2005 [11] takes into account the effect of moisture in concrete by using a peak value in the specific heat. Values of 2020 and 5600J/kg.K for a moisture content of 3 and 10% of concrete weight are recommended. The numerical model adopts a peak value of 2659J/kg K corresponding to a moisture content of 4.25% determined experimentally.

3.3 Analysis procedure

A sequentially coupled thermal-stress analysis was carried out instead of fully coupled thermal-stress analysis, because the former is less time-consuming and leads to fewer problems of convergence than the latter, as suggested by Espinos et al. [6]. In fact, the first approach simplifies the problem because the stress/strain solution is dependent on the temperature, but the inverse relation is not. In a fully coupled thermal-stress analysis, the conductance thermal gap decreases when the steel tube and concrete core surfaces are detached, due to the different thermal expansion of these materials. Therefore, the thermal and structural solutions affect each other and this approach seems to better represent a real situation than a sequentially coupled thermal-stress analysis.

However, results obtained with sequentially coupled thermal-stress analysis showed good agreement with experimental tests and thus it can be concluded that a more complex analysis does not seem to be necessary. Given this, the numerical analysis runs as follows: the nodal temperatures (output), obtained from thermal analysis of CFCH columns, are the input data for the stress analysis.

The thermal model corresponds to a pure heat transfer analysis. The surfaces of the CFCH columns were submitted to the furnace temperature curve registered in the experimental tests and two mechanisms of heat transfer were considered: convection and radiation. In the inner part of the CFCH columns the conduction was the major heat transfer mechanism. The thermal values suggested in EN1991-1-2:2002 [13] were used and the main parameters are presented in Table 2.

Table 2. Parameters for the thermal model.

Parameter	Value	Unit
Convective heat transfer coefficient (h_c)	25	W/m2 K
Radiation configuration factor (ϕ_r)	1	--
Stephan-Boltzmann constant (σ)	5.67 x 10-8	W/m2 K4
Absolute zero temperature	-273	ºC
Emissivity of the material (ε_m)	0.7	--
Emissivity of fire (ε_f)	1	--
Initial temperature (θ_0)	20	ºC

The structural model corresponds to a non-linear thermal-mechanical stress analysis. The nodal temperatures at the inner and outer surfaces of the CFCH column, obtained from heat transfer analysis, are the input data for the structural model. The meshes were similar for all numerical simulations.

The structural analysis was divided in two steps. In the first step all the load was applied on the top plate of the CFCH column. The plate distributes the load to the steel tube and to the concrete core. In the second step, the restraint to thermal elongation was activated and heating starts. This procedure represented faithfully the methodology followed in experimental tests.

3.4 Interaction - Interfaces

Espinos et al. [6] commented that the thermal interface between the steel tube wall and the surface of the concrete core had been traditionally ignored and recommended a constant gap conductance of 200 W/m^2 K, as suggested by Ding and Wang [3], and a radiation heat transfer for this interface. The recommended emissivity (ε_m) for both materials (steel and concrete) is 0.7 and the radiation configuration factor (ε_r) is 1.0.

In ABAQUS software [9] the mechanical interface may be modelled with normal and tangential behaviour. The normal behaviour considers the “hard” contact formulation that uses the classical Lagrange multiplier method and allows any pressure value when the surfaces are in contact while no pressure is allowed when the surfaces are not in contact. The tangential behaviour considers the penalty method of the friction model which permits some relative motion between surfaces (an “elastic slip”) when they should be sticking to each other. The hard contact option and the friction coefficient equal to 0.3 were adopted in this work, following Espinos et al. [6]. These authors, however, commented that no difference was observed when employing different values of friction coefficient due to the separation of the steel tube from the concrete core in a fire situation. The same behaviour was also observed in this research study.

To define the interface between the reinforcement steel bars and the concrete core, a tie constraint was used, namely each node of the steel bar element was tied to the corresponding node of the concrete core element. This constraint ties two separate surfaces together so that there is no relative motion between them.

A basic axial flexural wire feature connector was applied on the top plate of the CFCH columns to simulate the restraint of the surrounding structure to thermal elongation. An axial-rotational spring was set-up at the top plate with the respective value for the stiffness of the surrounding structure.

3.5 Load and boundary conditions

The load was considered as uniformly distributed over a central square area on the top plate of the CFCH columns to avoid a high concentrated load at a specific point. The gravity load was also considered in the entire column. The bottom plate was fixed, simulating the action of the floor where the columns were supported. The initial load is applied and afterwards, the top plate is submitted to an axial-rotational spring that imposes stiffness to axial deformation and rotation on the top of the columns. These load conditions are coherent for the load conditions used in the experiments presented in section 2. The initial temperature in the columns for the numerical thermal model was 20°C. The final temperatures obtained with this modelling were then applied as the thermal load (input data) for the structural numerical modelling.

4. VALIDATION

The numerical results show a good agreement with the experimental ones. Figures 1 and 2 show the development of the relative restraining forces and axial deformation over time by a comparison between the numerical and experimental results for some CFCH columns.

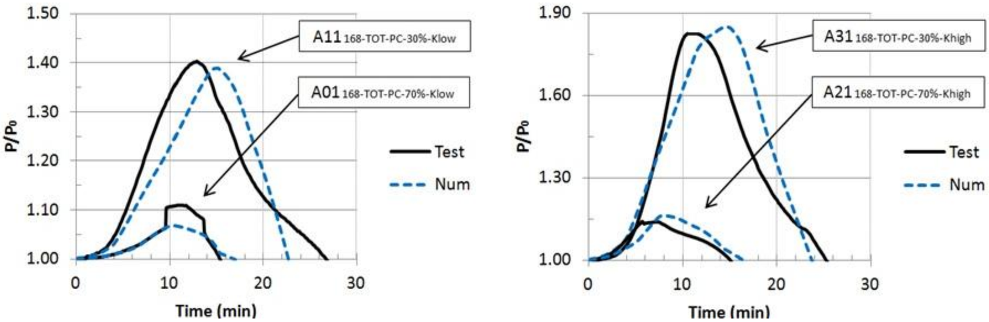

Figure 1. Experimental vs. numerical restraining forces for a load level of 30 and 70%, a column diameter of 168.3mm.

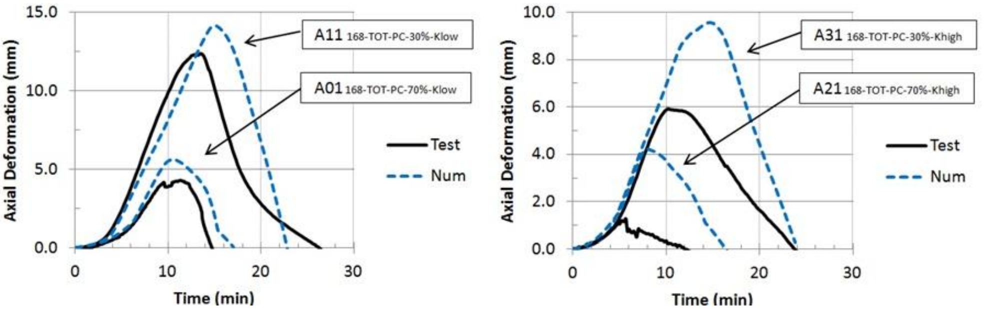

and axial stiffness of the surrounding structure of 13 and 128kN/mm.

Figure 2 . Experimental vs. numerical axial deformations for a load level of 30 and 70%, a column diameter of 168.3mm and axial stiffness of the surrounding structure of 13 and 128kN/mm.

The axial deformations present greater differences between the experimental and numerical results than the relative restraining forces. However this difference (around 3mm) is small if compared with the total length of the columns (3000mm) – see Figure 4. In this way this difference between the numerical and experimental results of axial deformation is insignificant.

4.1 Critical times

The critical time defined in this research is the instant when the restraining forces return to the initial value (*i.e.* the value of the initial applied load). The choice of this definition for a "failure time" rather than the traditional fire resistance is because these tests are not standard fire resistance tests (EN 1994-1-2: 2005 [11]).

In general, the numerical critical times are slightly higher than the experimental ones. In 75% of the cases, the difference between the numerical and experimental critical time was less than 5 minutes. One of the reasons that may explain the critical times in the numerical results being higher than in the experimental tests is that the temperatures calculated with the numerical model were slightly lower than those measured in the experimental. Consequently the critical time of the column will be greater.

Ding and Wang [3], and Hong and Varma [5] pointed out similar differences in temperature values numerically calculated and measured in their tests, especially in the concrete core. Hong and Varma [5] justify the divergence due to variations in the thermal properties of the material and the approach used to model the moisture content of the concrete infill.

In fact, as the numerical model considers the effect of the moisture in the concrete core simply as an increase in the specific heat peak, this may justify the deviation in temperatures principally at the earlier stages (between 100 and 200 ºC), as also suggested by Lie [1]. A better mathematical modelling of the behaviour of the moisture migration along the concrete core leads to an improvement in the results.

After the first few minutes of fire exposure, the temperatures calculated with the model and measured in tests present a tendency of convergence, principally in the steel tube.

For larger columns, those with the largest concrete cores (*i.e.* an external diameter of 219.1mm), the model has presented a reasonable agreement with tests. Espinos et al. [6] report some problems with simulations of massive columns. According to these authors, the errors observed in massive columns are due to the higher contribution of the concrete core and its more complex failure mechanisms. Other authors also presented similar comments (Lie [1], Ding and Wang [3], Schaumann et al. [4], Hong and Varma [5]).

This numerical validation addressed CFCH columns with a maximum diameter of 219.1mm. There are columns with larger diameters in practical situations. Therefore and in agreement with the above comments, further studies should be conducted so as to better represent the behaviour of concrete at elevated temperatures in numerical models.

Finally the average error between the numerical and experimental critical times was 4.2min with a standard deviation of 4.6min.

4.2 Maximum relative restraining forces

Figure 3 indicates the numerical and experimental results of the maximum relative restraining forces. A difference with an order of magnitude of around 10%, between calculated and measured internal forces, is acceptable for practical design purposes. Thus, a 10% error line is also plotted on the graph. The numerical model shows a very good agreement with the test results measured for the maximum restraining forces. The error between the numerical and experimental results was less than 10% for 83.3% of the tests.

4.3 Maximum axial deformation

Figure 4 compares the numerical and experimental results for the maximum axial deformation and note that in general the numerical results are higher than the experimental ones. Error lines of 5mm (1.7‰ of columns length) were plotted. In most cases (87.5%), the difference between the numerical and experimental maximum axial deformation was up to 5mm. This difference was greater than 5mm in only three columns. The average error between the numerical and experimental maximum axial deformation was 2.9mm with a standard deviation of 6.7mm.

The axial deformation (less than 20mm) is too small if compared with the column length (3000mm). Moreover, as suggested by Lie [1], several factors influence axial deformation such as load, the thermal expansion coefficient, bending, creep and these cannot be completely taken into account in software simulations. Due to these factors, the differences between calculated and measured axial deformations obtained here are irrelevant.

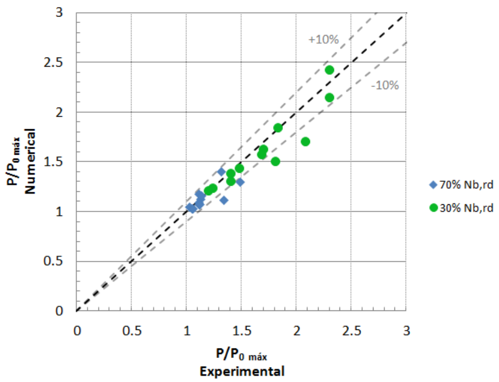

Figure 3. Numerical vs. Experimental maximum relative restraining forces.

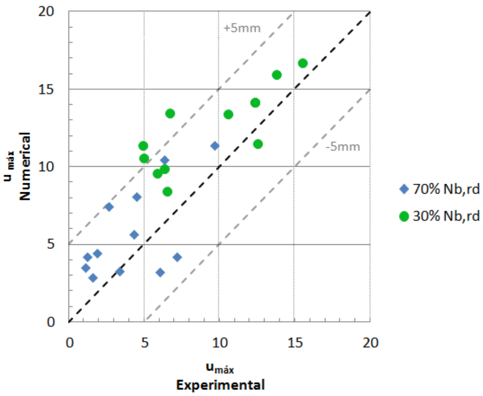

Figure 4. Numerical vs. Experimental maximum axial deformation.

7 CONCLUSIONS

This paper presented a study of a three-dimensional non-linear finite element model developed with ABAQUS [9] to predict the behaviour of CFCH columns and verify the influence of several parameters in fire. The restraining to thermal elongation of the column is an important parameter analyzed in this paper that added a rather difficult step to the numerical modelling. The numerical model was validated with experimental results of fire resistance tests on CFCH columns with restrained thermal elongation, carried out by the authors. The main conclusions from this research are commented on in what follows.

(1) The critical times of the CFCH columns tested in this research were smaller than those registered by the NRCC researchers [1-2] for similar experimental tests – however without restraining to their thermal elongation.

(2) The load level and slenderness of the columns had a great influence on the critical time of the columns. If one of them is reduced, the column critical time increases.

(3) The proposed numerical model presented results in close agreement with those obtained in fire experiments conducted on CFCH columns with restrained thermal elongation. Therefore, the numerical modelling can be considered as an option to assess the fire performance of CFCH columns.

(4) The numerical critical times obtained were slightly higher than the experimental ones. However, in most cases, this difference was not large, less than 5 minutes.

(5) The temperatures calculated with the numerical model were slightly lower than those measured in experimental tests (around 100 °C).

(6) The numerical relative restraining forces obtained were in close agreement with those measured in the experiments. In general, the error was less than 10%.

(7) In general, the numerical axial deformations were higher than the experimental results. However, in most cases this difference was less than 5mm, which is negligible given the length of the columns.

ACKNOWLEDGMENT

The authors would like to thank the PhD scholarship of the first author given by Erasmus Mundus in the framework of the "Improving Skills Across Continents (ISAC)" programme, the Portuguese Foundation for Science and Technology (FCT) due to financial for the research under the framework of PTDC 65696 / 2006 project and A. Costa Cabral S. A. and Metalocardoso S. A. for their support with steel tubes for the specimens.

REFERENCES

[1] Lie TT. "Fire resistance of circular steel columns filled with bar-reinforced concrete", Journal of Structural Engineering, vol. 120, n º05, pp. 1489-1509, 1994.

[2] Lie TT., ed. "Structural fire protection", Manuals and Reports on Engineering Practice, nº 78, ASCE, 1992.

[3] Ding J, Wang YC. "Realistic modeling of thermal and structural behavior of unprotected concrete filled tubular columns in fire", Journal of Constructional Steel Research, vol. 64, pp. 1086-1102, 2008.

[4] Schaumann P, Kodur V, Bahr O. "Fire behavior of hollow structural section steel columns filled with high strength concrete", Journal of Constructional Steel Research, vol. 65, pp. 1794-1802, 2009.

[5] Hong S, Varma AH. "Analytical modeling of the standard fire behavior of loaded CFT columns", Journal of Constructional Steel Research, vol. 65, pp. 54-69, 2009.

[6] Espinos A, Romero ML, Hospitaler A. "Advanced model for predicting the fire response of concrete filled tubular columns", Journal of Constructional Steel Research, vol. 66, pp.1030-1046, 2010.

[7] Pires TAC, Rodrigues JPC, Rêgo Silva JJ. "Fire resistance of concrete filled circular hollow columns with restrained thermal elongation", Journal of Structural Steel Research, 77, pp. 82-94, 2012.

[8] Pires TAC. "Fire resistance of composite columns made of concrete filled circular hollow sections and with restrained thermal elongation", University of Coimbra. PhD Thesis, 2013.

[9] Abaqus User´s manual: volumes I-III, version 6.7. Pawtucket, Rhode Island: Hibbit, Carlsson and Sorensson Inc., 2005.

[10] EN 1993-1-2, "Design of steel structures. Part 1-2: general rules – structural fire design", CEN - European Committee for Standardization, 2005.

[11] EN 1994-1-2, "Design of composite steel and concrete structures. Part 1-2: general rules – structural fire design", CEN - European Committee for Standardization, 2005.

[12] EN 1992-1-2 "Design of concrete structures. Part 1-2: general rules – structural fire design", CEN - European Committee for Standardization, 2004.

[13] EN 1991-1-2, "Actions on structures. Part 1-2: general actions – actions on structures exposed to fire", CEN - European Committee for Standardization, 2002.

[14] EN 1994-1-1, "Design of composite steel and concrete structures. Part 1-1: general rules and rules for buildings", CEN - European Committee for Standardization, 2005.

8th International Conference on Structures in Fire
Guo-Qiang LI, Venkatesh K. R. KODUR, Shou-Chao JIANG, Jian JIANG, Su-Wen CHEN, Guo-Biao LOU (Eds.)
Shanghai, China, June 11-13, 2014

FIRE RESISTANCE OF CIRCULAR AND SQUARE SLENDER CONCRETE FILLED TUBULAR COLUMNS SUBJECTED TO LARGE ECCENTRICITIES

A. Espinós*, M. L. Romero*, E. Serra* and A. Hospitaler*

*Instituto de Ciencia y Tecnología del Hormigón, Universitat Politècnica de València, Valencia, Spain
e-mails: aespinos@mes.upv.es, mromero@mes.upv.es, ensermer@upvnet.upv.es, ahospitaler@cst.upv.es

Keywords: Concrete filled steel tubular column, Fire resistance, Eccentricity

Abstract. *This paper presents the results of a series of fire tests carried out in the framework of the European Project FRISCC (Fire resistance of innovative and slender concrete filled tubular composite columns), where the fire resistance of concrete filled steel tubular (CFST) columns of different section shape is investigated. Within this European Project, results have been obtained on circular and square slender CFST columns subjected to fire, which are discussed in this paper. The influence of the cross-section shape, load eccentricity and percentage of reinforcement on the fire performance of these columns is studied in this paper, with special attention on the effect of large eccentricities combined with high slenderness.*

1 INTRODUCTION

Concrete filled steel tubular columns make use of the combined action of steel and concrete, showing an ideal structural performance. While the steel tube confines the concrete core enhancing its compressive strength, the concrete core prevents the steel tube wall from local buckling.

The fire resistance of CFST columns subjected to concentric axial loads has been widely studied through experimental testing in the framework of the research projects from CIDECT [1–3] and National Research Council of Canada [4–6], or those carried out at Fuzhou University (China) by Han and co-workers [7], researchers from the University of Seoul (Korea) [8] and the authors of this paper [9]. Nevertheless, the effect of eccentricity needs further evaluation, being a situation which can be commonly found in practice.

Some of the main fire testing programs carried out worldwide have taken the load eccentricity into account (Grandjean et al. [2], Kordina and Klingsch [3], Lie and Chabot [4] or Han et al. [7]), but using only a limited number of column specimens. Also in previous tests from the authors of this paper [10], eccentric loads were used, although the load eccentricity ratio applied was reduced ($e/D = 0.13$ and 0.31).

Only one fire testing program focusing on slender CFST columns subjected to large eccentricities has been found in the literature, carried out at CTICM [11], where four CFST columns were tested under large eccentricities ($e/D = 0.75$ and 1.5), being two of them of circular section and another two of square shape. However, the results of this fire testing program are limited and need to be extended. Therefore, the reduced number of cases found considering large eccentricities motivates the need for carrying out new experimental programs, in order to increase the existing experimental database.

After a full review of the results of previous tests, an extensive experimental program has been designed in the framework of the European Project FRISCC (Fire resistance of innovative and slender concrete filled tubular composite columns). One of the aims of this project is to provide a full range of experimental evidence on the fire behaviour of CFST columns, a necessary basis for the development of numerical models and simple calculation rules. Four different section shapes are studied in this project:

circular, elliptical, square and rectangular hollow section columns filled with concrete, although only the results of the circular and square columns are available at the moment.

The experimental investigation presented in this paper, which is part of the fire testing program being carried out in the mentioned project, focuses on slender CFST columns with circular and square cross-section subjected to large eccentricities. This experimental study will allow understanding the influence of the cross-section shape on the fire performance of CFST columns, as well as the effect of the load eccentricity and percentage of reinforcement.

2 EXPERIMENTAL PROGRAM

The experimental program consisted of a total of 12 columns, six of them having circular section and the other six with square section. Two different cross-sectional dimensions were used for each shape, and large eccentricities were applied in most of the tests, with load eccentricity ratios (e/D or e/B) of 0.5 and 0.75. Two of the columns on each group were tested under concentric load, so as to have a reference for evaluating the effect of the load eccentricity. All the columns were bar-reinforced, using reinforcement ratios ranging between 2.4% and 5.15%. The columns were hinged at both ends, having a length of 3180 mm. The steel tubes had a nominal strength of 355 MPa, while the concrete used for filling the columns had a compressive strength of 30 MPa. The load level applied to the columns was a 20% of their load bearing capacity at room temperature.

The square columns were designed to have approximately the same steel area than their circular counterparts (i.e. same quantity of steel), in order to be able to compare their effectiveness in the fire situation for the same steel usage.

The tested specimens, with their particular characteristics and resulting fire resistance measured in minutes, are listed in Table 1 (circular columns) and Table 2 (square columns).

Table 1. Test properties and results, circular columns.

No.	***D* (mm)**	***t* (mm)**	**Reinf.**	ρ **(%)**	***e/D***	f_c **(MPa)**	f_y **(MPa)**	f_s **(MPa)**	$\bar{\lambda}_z$	**Load (kN)**	**Time (min)**
C1	193.7	8	6ϕ12	2.74	0.5	36.37	359.06	512.40	0.73	186.65	26
C2	273	10	6ϕ16	2.40	0.5	37.62	369.73	553.50	0.52	387.46	30
C3	193.7	8	6ϕ12	2.74	0	43.23	359.06	512.40	0.75	535.57	29
C4	273	10	6ϕ16	2.40	0	35.96	369.73	553.50	0.52	882.90	113*
C5	193.7	8	6ϕ16	4.86	0.75	35.76	359.06	553.50	0.75	152.41	29
C6	273	10	8ϕ20	5.00	0.5	36.89	369.73	566.50	0.53	391.53	57*

*Anomalous behaviour during test

Table 2. Test properties and results, square columns.

No.	***B* (mm)**	***t* (mm)**	**Reinf.**	ρ **(%)**	***e/B***	f_c **(MPa)**	f_y **(MPa)**	f_s **(MPa)**	$\bar{\lambda}_z$	**Load (kN)**	**Time (min)**
S1	150	8	4ϕ12	2.52	0.5	45.03	452.74	548	0.91	161.13	26
S2	220	10	4ϕ16+ 4ϕ10	2.80	0.5	39.72	560.25	527 (ϕ16) 575.25 (ϕ10)	0.65	446.53	23
S3	150	8	4ϕ12	2.52	0	43.15	452.74	548	0.90	404.29	32
S4	220	10	4ϕ16+ 4ϕ10	2.80	0	42.39	560.25	527 (ϕ16) 575.25 (ϕ10)	0.66	882.90	54
S5	150	8	8ϕ12	5.04	0.75	48.67	452.74	548	0.94	133.18	29
S6	220	10	4ϕ20+ 4ϕ16	5.15	0.5	38.84	560.25	576 (ϕ20) 527 (ϕ16)	0.66	452.63	29

2.1 Test setup

The tests were performed in the facilities of AIDICO (Instituto Tecnológico de la Construcción) in Valencia (Spain), using a 5m×3 m furnace equipped with a hydraulic jack with a maximum capacity of 1000 kN and a total of 16 gas burners, located at mid-height of the furnace chamber. Figure 1 presents a schematic view of the experimental setup.

In the fire tests, the load was applied to the top end of the columns through a knife-edge bearing (Figure 2), which permitted to apply the desired eccentricity at both column ends. Once the load was applied, it was kept constant while the standard ISO-834 fire curve was prescribed, with unrestrained column elongation.

A 300mm×300mm×15mm steel plate was welded to the bottom end of the columns. The columns were then put in an upright position and filled with concrete, and afterwards shaken by means of an external vibrator in order to consolidate the concrete inside the steel tube. The columns were sealed with plastic at their top ends in order to avoid moisture leaks and left upright for 28 days. After concrete was cured, the top surface of the columns was polished and a second end plate of the same dimensions was then welded to the top end of the columns. For each column specimen, two vent holes of 15 mm diameter were drilled in the steel hollow section wall at 100 mm from each column end. These vent holes were provided for relieving the water vapour pressure produced during the experiment. An additional hole, located near the bottom end of the columns, was used for connecting the thermocouple wires.

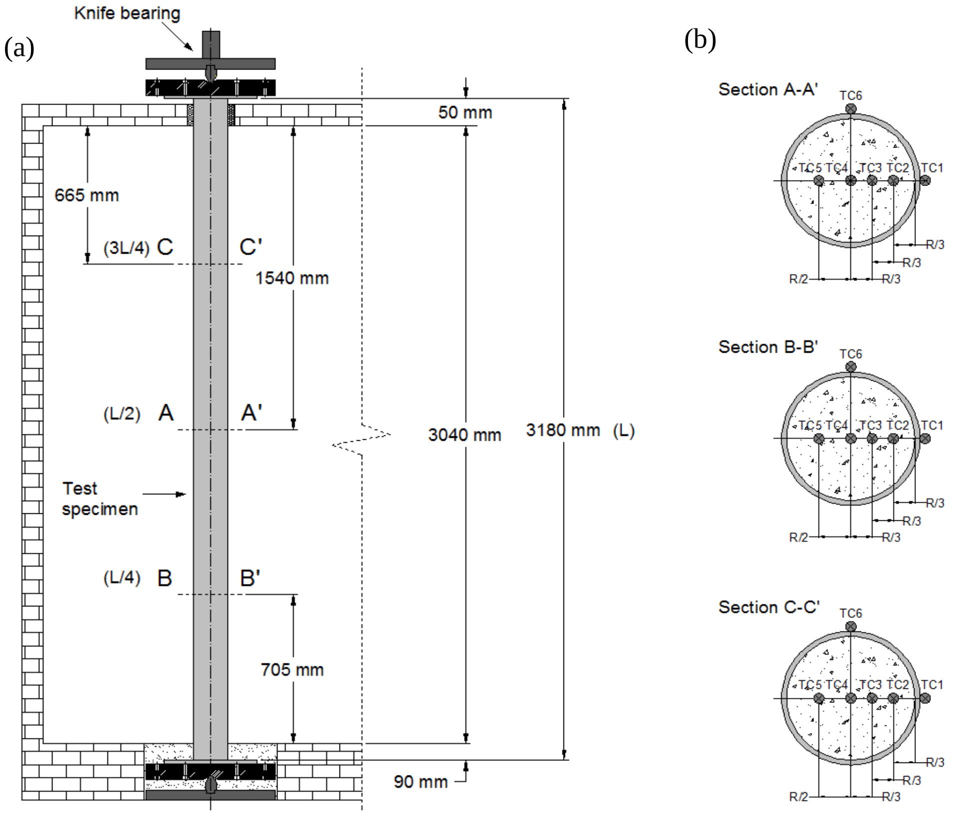

Figure 1. (a) Schematic view of the test setup; (b) Thermocouple locations (circular columns).

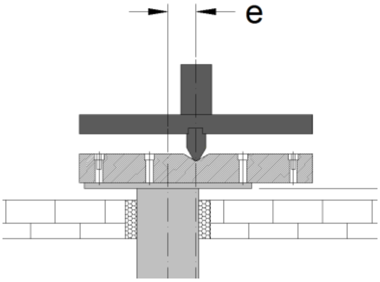

Figure 2. Detail of the knife-edge bearing.

Figure 3 shows one of the square columns inside the furnace, before and after the fire test, while a detail of the eccentricity applied at the bottom end of the column can be seen in Figure 4.

Figure 3. Square column before and after the fire test.

Figure 4. Detail of the eccentricity at the bottom end of the column.

2.2 Instrumentation

In order to register the temperature evolution inside the columns during the fire tests, three layers of six thermocouples each were placed at different heights, as it can be seen in Figure 1. The temperature inside the furnace chamber was automatically registered and controlled during the tests by means of 6 plate thermocouples and a pressure sensor. The axial elongation of the columns was measured by means of a LVDT located outside the furnace.

2.3 Material properties

The hollow tubes used in the experimental program had a S355 steel grade, nevertheless the real strength (f_y) of steel was obtained by performing the corresponding coupon tests, and is summarized in Tables 1 and 2. Normal strength concrete (30 MPa) was used for the column infill. In order to determine the compressive strength of concrete, sets of concrete cylinders were prepared and cured in standard conditions during 28 days. All cylinder samples were tested on the same day as the column fire test. The cylinder compressive strength of all the tested specimens (f_c) can be found in Tables 1 and 2. The bar-reinforced specimens had the arrangements shown in Figure 5 using 6 mm stirrups with 30 cm spacing. The corresponding geometrical reinforcement ratios (ρ) are given in Tables 1 and 2.

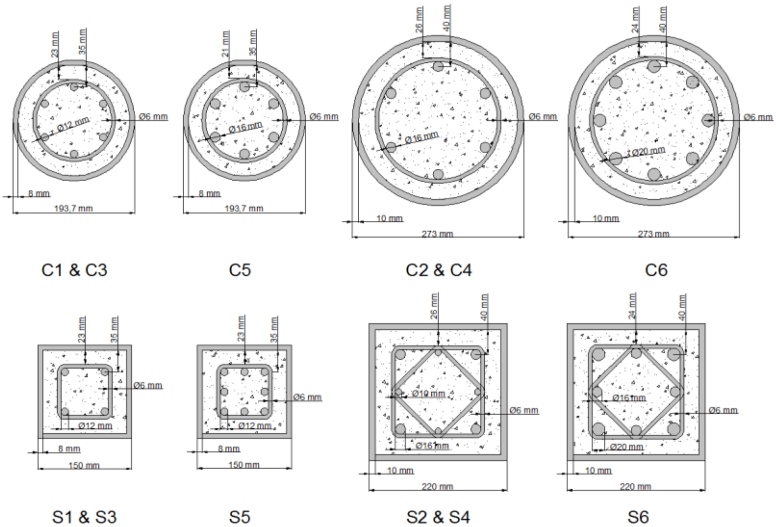

Figure 5. Reinforcement arrangement.

3 ANALYSIS OF RESULTS

The typical failure observed in all the columns was overall buckling. Figures 6 and 7 show the evolution of the axial displacement measured at the top end of the columns versus the fire exposure time for all the tested specimens, grouped according to their section shape (circular or square) and dimensions.

In those tests performed under concentric load, the axial displacement versus time curve presented four stages, with a contribution of the concrete core after the steel tube yielding, which is reflected as a plateau in this curve. Nevertheless, for the columns subjected to eccentric load, only two stages were observed in the axial displacement versus time curve: axial elongation of the column and sudden failure after the yielding of the steel tube occurred, thus not taking advantage of the contribution of the concrete core, due to the high slenderness of these specimens combined with the application of large eccentricities. See reference [11] for a more detailed description on the different failure modes.

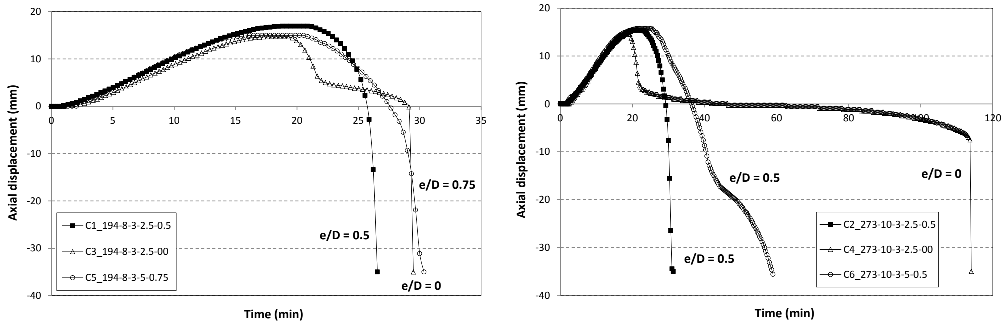

(a) CHS 193.7×8 mm (b) CHS 273×10 mm

Figure 6. Results of the fire tests on circular columns.

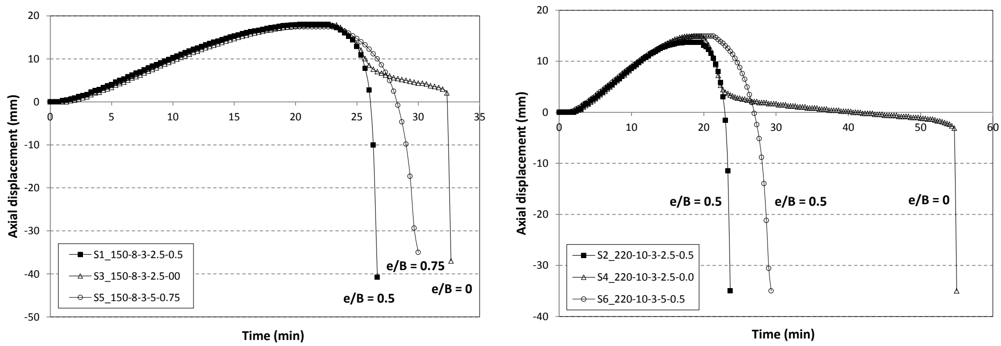

(a) SHS 150×8 mm (b) SHS 220×10 mm

Figure 7. Results of the fire tests on square columns.

Comparing the circular columns with their square counterparts, which made use of the same quantity of steel, the fire response of the circular columns resulted more efficient. This can be seen more clearly in Figure 8 by comparing cases C1-S1 and C5-S5, where for the same fire resistance time, the circular columns sustained higher loads (with increments of 15.8% and 14.4%, respectively), or comparing cases C2-S2 (30.4% time increment with a 13.2% reduction of applied load) and C3-S3 (32.5% load increment with a 9.4% reduction in time). Note that cases C4 and C6 had an anomalous behaviour during the test and cannot be used for comparison. Therefore, it can be concluded that, for the same steel usage, the circular columns present a better fire behaviour than the square columns. It is worth noting that the slenderness values of the square columns were higher in all cases (see Figure 8(d)). It is also important to note that the A/V-ratio of the circular columns was lower than that of the square columns, which made them perform better in the fire situation, as they exposed a lower surface to the fire for the same volume.

The effect of the load eccentricity can be also seen in Figures 6 and 7. If cases S2 and S4 are compared, it can be seen that for the same column dimensions and percentage of reinforcement, the fire resistance time was significantly reduced when applying the eccentricity (23 min), in comparison to the concentrically loaded test (54 min), having the second case twice the load applied to the first case (see Figure 8(c)). If the percentage of reinforcement is increased from 2.5% to 5%, with the same load eccentricity applied (S6 versus S2), the fire resistance time increases (29 min vs 23 min), even when the applied load is also higher. Therefore, this result confirms that the reinforcement contributes slightly to improve the fire resistance of these columns.

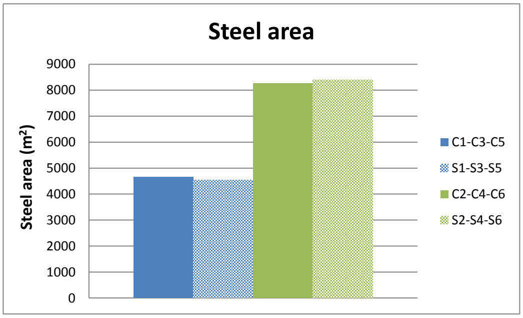

(a) Steel area

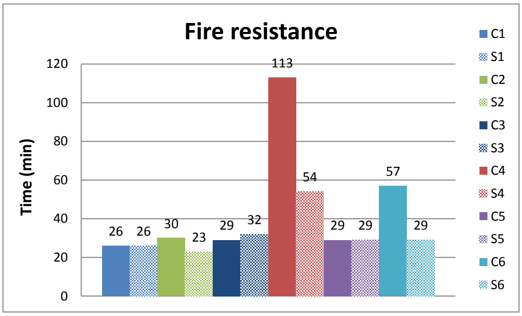

(b) Fire resistance

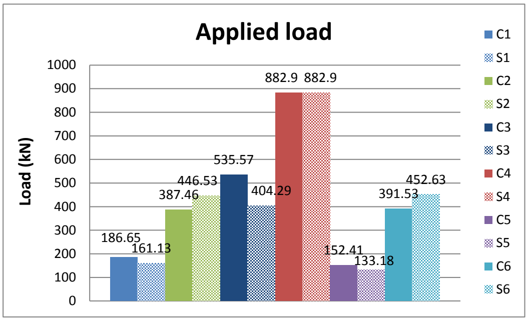

(c) Applied load

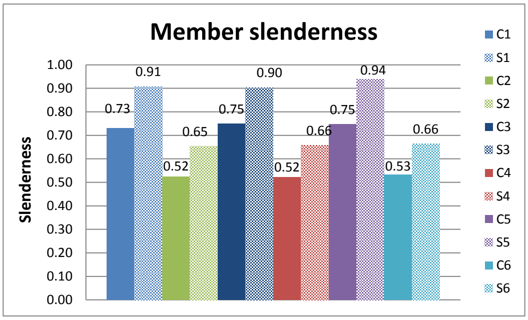

(d) Member slenderness

Figure 8. Comparison between the different circular and square columns tested.

4 CONCLUSIONS

The results of a fire testing program on slender CFST columns of different cross-section shapes subjected to large eccentricities have been presented in this paper. The test parameters covered in this experimental program were the cross-section shape, sectional dimensions, member slenderness, load eccentricity and reinforcement ratio. It was found that, for the same steel usage, the circular columns presented a better fire performance than the square columns. Additionally, for the same column dimensions and percentage of reinforcement, the fire resistance time was significantly reduced when applying the load eccentrically. Furthermore, it was found that for the same load eccentricity, when the percentage of reinforcement was increased, the fire resistance time also increased.

AKNOWLEDGEMENT

The authors would like to express their sincere gratitude to the European Union for the help provided through the Project RFSR-CT-2012-00025, carried out with a financial grant of the Research Programme of the Research Fund for Coal and Steel.

REFERENCES

[1] COMETUBE. 1976. "Fire resistance of structural hollow sections". Cometube research. *CIDECT programme 15A. Final report*.

[2] Grandjean G, Grimault JP, Petit L. 1980. "Determination de la duree au feu des profils creux remplis de beton". *CIDECT Research Project 15B–80/10*. Cologne, Germany: Comité International pour le Développement et l'Etude de la Construction Tubulaire.

[3] Kordina K, Klingsch W. 1983. "Fire resistance of composite columns of concrete filled hollow sections". *CIDECT Research Project 15C1/C2–83/27*. Cologne, Germany: Comité International pour le Développement et l'Etude de la Construction Tubulaire.

[4] Lie TT, Chabot M. 1992. "Experimental studies on the fire resistance of hollow steel columns filled with plain concrete". *Internal report No. 611*. Ottawa, Canada: Institute for Research in Construction, National Research Council of Canada (NRCC).

[5] Chabot M, Lie TT. 1992. "Experimental studies on the fire resistance of hollow steel columns filled with bar-reinforced concrete". *Internal report No. 628*. Ottawa, Canada: Institute for Research in Construction, National Research Council of Canada (NRCC).

[6] Kodur VKR, Lie TT. 1995. "Experimental studies on the fire resistance of circular hollow steel columns filled with steel-fibre-reinforced concrete". *Internal report No. 691*. Ottawa, Canada: Institute for Research in Construction, National Research Council of Canada.

[7] Han LH, Zhao XL, Yang YF, Feng JB. 2003. "Experimental study and calculation of fire resistance of concrete-filled hollow steel columns". *Journal of Structural Engineering* (ASCE) 129(3):346-356.

[8] Kim DK, Choi SM, Kim JH, Chung KS, Park SH. 2005. "Experimental study on fire resistance of concrete-filled steel tube column under constant axial loads". *International Journal of Steel Structures* 5(4):305-313.

[9] Romero ML, Moliner V, Espinos A, Ibañez C, Hospitaler A. 2011. "Fire behavior of axially loaded slender high strength concrete-filled tubular columns". *Journal of Constructional Steel Research* 67(12):1953-1965.

[10] Moliner V, Espinos A, Romero ML, Hospitaler A. 2013. "Fire behavior of eccentrically loaded slender high strength concrete-filled tubular columns". *Journal of Constructional Steel Research* 2013; 83:137-146.

[11] Renaud C, Kruppa J. *Unprotected concrete filled columns fire tests – Verification of 15Q. CIDECT Research Project 15R*. Saint-Rémy-lès-Chevreuse, France: Centre Technique Industriel de la Construction Métallique (CTICM); 2004.

[12] Espinos A, Romero M, Hospitaler A. 2010. "Advanced model for predicting the fire response of concrete filled tubular columns". *Journal of Constructional Steel Research* 66(8-9), 1030-1046.

8th International Conference on Structures in Fire
Guo-Qiang LI, Venkatesh K. R. KODUR, Shou-Chao JIANG, Jian JIANG, Su-Wen CHEN, Guo-Biao LOU (Eds.)
Shanghai, China, June 11-13, 2014

FIBER BEAM MODEL FOR AXIALLY LOADED CONCRETE FILLED TUBULAR COLUMNS FIRE SIMULATION

C. Ibañez*, M. L. Romero, A. Hospitaler** and A. Pascual****

* Departamento de Ingeniería Mecánica y Construcción, Universitat Jaume I, Castellón, Spain
e-mail: ibanezc@uji.es

** Instituto de Ciencia y Tecnología del Hormigón, Universitat Politècnica de València, Valencia, Spain
e-mails: mromero@mes.upv.es, ahospitaler@cst.upv.es, anpaspa1@upvnet.upv.es

Keywords: Concrete filled steel tubular column, Fire resistance, Fiber model, Finite element analysis, Fire simulation

Abstract. *A fiber beam model for the fire response of concrete filled tubular columns is presented in this work. The developed model consists of two components: a circular tubular steel section and a solid circular concrete section placed in parallel and connected by longitudinal and transverse links located at their end nodes. The model accounts for large displacement geometry through the co-rotational formulation of the element employed which is formulated on a system without rigid body mode. Different types of concrete infill are studied: plain, reinforced and steel fiber reinforced concrete of normal or high strength. It is validated against fire tests data from the authors and from other researches. Predictions are also compared against a 3D finite element model with proven accuracy on fire response simulation. The model is capable of simulating the fire response of axially loaded circular concrete filled tubular columns with a reduced computational time in comparison with the 3D model.*

1 INTRODUCTION

In concrete filled tubular columns (CFT), the combined action of the steel tube and the concrete core leads to excellent fire resistance response without external protection. This feature jointly with their positive attributes at ambient temperature has encouraged the use of CFT columns, especially in high-rise buildings. In the last years, the number of research studies about fire resistance simulation of concrete filled tubular columns has increased as a consequence of the growing interest of designers to achieve proper fire behaviour when this kind of columns are employed.

Due to these studies, several model proposals have been developed. In the literature, three-dimensional numerical models which reproduce the exceptionally nonlinear behavior of CFT columns at high temperatures can be found, such as the advanced model presented by Espinós et al. [1] which took into account several realistic considerations neglected by other researchers and gave an accurate estimation of the fire resistance time and captured with precision the whole response of the columns along the fire exposure time.

Despite the fact that the trend of most authors is developing three-dimensional numerical models, the fact is that these models are computationally time consuming and non-efficient when a whole structure is analyzed.

Numerical models based on fiber beam-column elements are an effective alternative for simulating the fire behavior of CFT columns since their simplicity is higher because the material constitutive models are one-dimensional even though the element itself is three-dimensional and has nonlinearity distributed along its length.

In this field, Renaud et al. [1] modelled a composite column by combining beam-column elements representing the different section components. Thermal analysis was carried out by a finite differences method, although gap conductance at the interface was neglected. This model proved to give a good estimation of the fire resistance time but the whole response was not precisely reproduced, even when slip between steel and concrete was considered.

Also, Jeffers and Sotelino [3] presented a three-node fiber heat transfer element which can be implemented in commercial software to run sequentially coupled thermal-mechanical analysis using elements available in the software but they did not focus on developing a model for the fire behavior of CFT columns.

Even though several fiber beam-column models have been developed trying to analyze the fire behavior of CFT columns, it cannot be found in the literature any fiber finite element model that gives accurate fire resistance times and also reproduces with precision the overall response of a CFT column under a fire.

In previous works [1], the authors presented the fire response of CFT columns expressed as the evolution of the column axial displacement along time by means of a three-dimensional model. Four stages can be clearly identified, Figure 1.

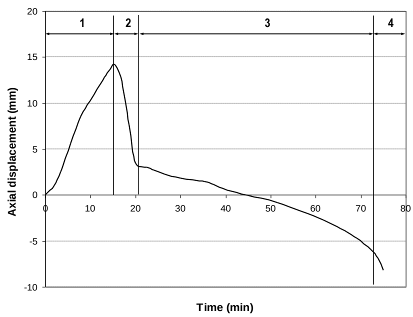

Figure 1. Axial displacement versus time by Espinós et al. [1].

Stage 1. At first stages of a fire, the steel tube expands faster than the concrete core due to its higher thermal conductivity and its direct exposure to fire. The axial displacement rate of both components is uncoupled which, combined with the gap at the steel-concrete interface, causes the concrete core-loading plate separation and the steel tube starts supporting the whole applied load.

Stage 2. The steel tube reaches its critical temperature, local yielding occurs and it starts to shorten, allowing the loading plate to contact back the concrete core.

Stage 3. At this point, the concrete core is the element showing more resistance. The loading plate has contacted back the concrete core and the load sustained by the steel tube has been gradually transferred to the concrete core as the column has shortened.

Stage 4. Finally, the ultimate failure occurs when the concrete core completely loses its strength and stiffness after a significant period of time during which its mechanical properties are completely degraded.

Therefore, the proper simulation of the existing relative sliding and separation between the two components is crucial to reproduce accurately the overall response of CFT columns in fire since this phenomenon is the main responsible of the bearing capacity and response of this type of composite columns under fire

In this work, a fiber element to study the real fire behavior of axially loaded circular CFT columns is presented and the model developed is used to obtain with accuracy both the fire resistance time and the overall fire response. Some realistic considerations that other researchers have not considered such as the influence of the steel-concrete gap or the complete slip between the steel tube and the concrete core are considered. The range of concrete infill types covered is wide: plain, bar reinforced and steel fiber reinforced concrete of both normal and high strength. For the validation of the fiber finite element model presented in this paper simulation results were compared with experimental fire tests data[4,5] and also with results of a three-dimensional model of proven accuracy on fire response simulation [1].

2 NUMERICAL MODEL

2.1 Description

In this work, the model developed took as a basis the FedeasLab [6] platform, a Matlab toolbox for the nonlinear analysis of structures. A thermal analysis model for CFT circular sections was implemented along with a mechanical model considering the temperature. The main parameters of the model were the column length (L), the external diameter (D), the steel tube thickness (t), the end conditions, the axial load level (μ) and the thermal and mechanical material properties. It consisted of three parts: the concrete core, the steel tube and the link elements, which connect the former two.

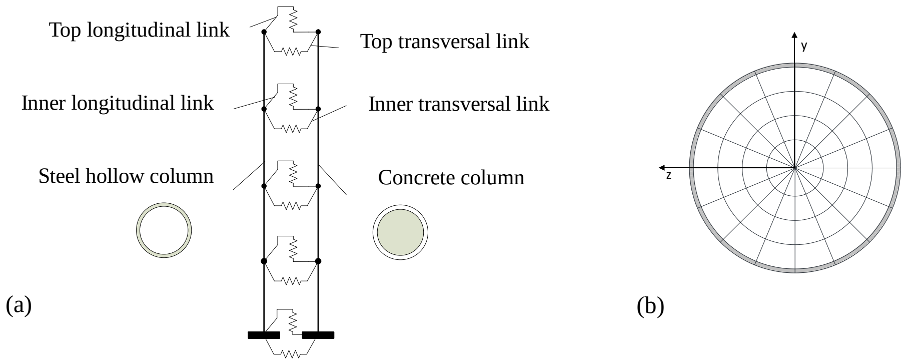

Figure 2. (a) Parallel model scheme; (b) Discretization of the section

The model here developed has the origin in the clear differentiation of phases discussed above and thus, a complete circular CFT column is formed by assembling in parallel two simple columns: a steel hollow section column and a concrete column. These columns are modeled with fiber finite elements connected at their nodes by link elements both longitudinally and transversely as shown in Figure 2(a). Links are point single degree of freedom elements located just at the nodes, knotting the steel tube and the concrete core columns. Transversal link elements have a high stiffness in order to assure that the two simple columns have the same deformed shape.

However, the longitudinal link elements work in a differently way. The inner longitudinal links reproduce the very low friction between the steel tube and the concrete core. The top longitudinal link is designed to show an elevated rigidity under compression. In contrast, when the longitudinal link is in tension its stiffness is practically zero, thus trying to imitate the behavior of the whole composite column. When the load is applied and the link is compressed, the steel tube transfers the load to the concrete core. Once loaded and under fire, the steel tube expands longitudinally faster than the concrete core, so that the link acting in this direction is in tension and is not able to transmit any load to the concrete column.

After a sensitivity analysis, it was observed that using four elements per column was enough to obtain high accuracy in the results with reduced computational time. The fiber beam-column element employed to model the two simple columns has a co-rotational formulation with a mixed interpolation iterative scheme. Mixed formulation for beam finite elements is principally convenient since the numerical solution procedure is more robust.

The scheme shown in Figure 2(b) was used to discretize the cross-section. The mesh calibration was carried out to guarantee sufficient accuracy with the minimum number of fibers for each case. In the circumferential direction, 16 fibers were adopted. In the radial direction, one fiber was assumed for the hollow steel section. For the concrete core the number of fibers was varied to obtain a size of the cell close to 20 mm which is the typical size used in other models [1] and the minimum size recommended for thermal analysis.

With regard to the lack of accuracy affecting the columns due to their own manufacturing process, it is considered by simulating the first buckling mode shape of a pinned-pinned column which exhibits a sinusoidal shape. For the out-of-straightness, the value of L/1000 was adopted since it is the one normally employed by researchers and has proved to give accurate results in other models existing in literature [1].

2.2 Material properties at high temperatures

For normal strength concrete, the Lie's model [7] was used since it proved to give the most realistic response when modeling the infill of CFT columns [1] and thermal properties from EN 1992-1-2 [8] were adopted. For specimens filled with steel fiber reinforced normal strength concrete, mechanical and thermal properties developed by Lie and Kodur [9] were used. In case of high strength concrete and steel fiber reinforced high strength concrete, the model by Kodur et al. [10] and thermal properties proposed by Kodur and Sultan [11] were implemented, since they proved to fit closely the test data. Since during most of the time of analysis the column is subjected mainly to compression, the tensile strength is ignored. This statement was proved by Portolés et al. [12] showing accurate results. With regard to the thermal expansion coefficient, the value recommended by Hong-Varma [13] was employed: α_c = 6x10^{-6} ºC^{-1} for all types of concrete.

For structural steel, the temperature dependent thermal and mechanical properties recommended in EN 1993-1-2 [14] were implemented. For reinforcing steel, according to EN 1994-1-2 [15], thermal properties from EN 1993-1-2 [14] were adopted. The mechanical model employed was the same as that of the structural steel, but with the reduction factors recommended in EN 1992-1-2 [8].

2.3 Analysis procedure

After performing this research, it was observed that running a fully coupled thermal-stress analysis was not worthy since sequentially coupled thermal-stress analysis gave accurate results in these cases.

Therefore, in this work, a simple sequentially coupled thermal-stress analysis was performed. Two analysis steps are differenced: a thermal analysis and a mechanical analysis. First, a thermal analysis is carried out to compute the temperature field of the columns and subsequently, a mechanical problem is solved to obtain the structural response.

For conducting the thermal analysis, a finite difference approach is used. The method was first applied by Lie [7]. To be as realistic as possible, the existence of the gap conductance at steel-concrete interface (200 W/m^2) is considered in the model and equations are derived. For the governing parameters of the heat transfer problem, the values recommended in EN 1991-1-2 [16] were adopted.

3 EXPERIMENTAL TESTS FOR VALIDATION

3.1 Tests carried out by the authors

Results from 14 fire tests of CFT column specimens from an experimental program carried out by the researchers [4] were used for the model validation. The total length of the columns was 3180 mm, although only 3000 mm were exposed to direct heating. All of them were tested fixed at the bottom end and pinned at the top end and subjected to concentric load. The infilling of the columns was of three different types: plain, reinforced and steel fiber reinforced concrete and the values of concrete nominal strength varied from 30 MPa to 80 MPa. The fire curve followed for the heating of the specimens was the standard ISO-834 curve. The tested column data are shown in Table 1.

3.2 Tests carried out by other researches

In addition, experimental results from tests carried out by other authors listed in Table 2 were used in validation. A total of 23 column specimens tested at the National Research Council of Canada (NRCC) [1][4] were simulated. All the columns were 3810 mm long, but only the central 3048 mm were directly exposed to fire. All of them were subjected to concentric load and tested fixed at both ends, except for two of them, tested as pinned-pinned (C-06 and C-15). The values of concrete nominal strength varied from 30 MPa to 50 MPa. In these tests, the standard fire curve followed was the ASTM-E119.

4 NUMERICAL MODEL VALIDATION

4.1 Comparison with experimental data

For each specimen analyzed, the simulated results were compared with the corresponding experimental data. Figure 2(a) shows an example of the comparison made for temperature curves. The calculated temperature evolution along the fire exposure time followed accurately the tests results.

With regard to the mechanical response, it was recorded in terms of axial displacement-time as shown schematically in Figure 1. For one of the specimens analyzed, Figure 2(b) shows the comparison made. The overall response predicted by the model reproduced with high precision the actual fire behavior of these columns. In the case of bar reinforced columns, at the last stages, where the response is controlled by the concrete core, it was observed that experimental and numerical curves deviate slightly.

Table 1. Tests by the authors [4].

Column Name	D (mm)	t (mm)	f_y (N/mm^2)	f_c (N/mm^2)	N (kN)	FRR (min) Test	FRR (min) Sim.	δ_{max} (mm) Test	δ_{max} (mm) Sim.
C159-6-3-30-0-20	159	6	337.8	35.75	198	42	37	19.89	22.8
C159-6-3-30-0-40	159	6	337.8	28.55	396	25	21	14.06	16.87
C159-6-3-30-0-60	159	6	337.8	34.05	594	14	17	9.37	8.2
C159-6-3-80-0-20	159	6	341.4	71.14	335	37	29	15.95	18.52
C159-6-3-80-0-40	159	6	341.4	69	670	11	18	5.33	4.2
RC159-6-3-30-0-20	159	6	337.8	23.9	229	43	34	18.99	21.94
RC159-6-3-30-0-40	159	6	337.8	30	458	30	22	12.47	14.12
RC159-6-3-30-0-60	159	6	337.8	33.7	687	13	16	5.58	3.79
RC159-6-3-80-0-20	159	6	337.8	69.03	343	64	34	15.48	18.2
RC159-6-3-80-0-40	159	6	337.8	77	720	18	18	4.21	3.27
FC159-6-3-30-0-20	159	6	337.8	28.3	198	36	34	20.45	22.9
FC159-6-3-30-0-40	159	6	334.4	26.7	396	22	21	15.45	16.84
FC159-6-3-80-0-20	159	6	337.8	93.62	335	35	34	14.30	18.43
FC159-6-3-80-0-40	159	6	334.4	90.16	670	15	20	7.25	3.39

The fire resistance time and the maximum axial displacement at the top of the column recorded during the tests are also contrasted to values from fiber model (Table 1 and Table 2). Comparisons between measured and calculated values are made in Figure 3(a) y Figure 3(b). As shown, most of the numerical values lie in the region of the 15% error in both FRR and maximum axial displacement analysis. In the case of FRR, it is necessary to mention that those specimens which lie in the unsafe side correspond to columns that having high diameters, present higher D/t ratio and lower slenderness (λ= 0.3-0.34).

Table 2. Tests by other authors [5].

Column	D	t	f_y	f_c	N	μ	FRR (min)		δ_{max} (mm)	
Name	(mm)	(mm)	(N/mm^2)	(N/mm^2)	(kN)		Test	Sim.	Test	Sim.
C-02	141.3	6.55	350	33.1 (sil)	110	0.12	55	54	24.57	25.63
C-04	141.3	6.55	350	31.0 (sil)	131	0.14	57	56	24.09	24.58
C-05	168.3	4.78	350	32.7 (sil)	150	0.16	76	78	22.77	22.56
C-06	168.3	4.78	350	32.7 (sil)	150	0.19	60	56	21.66	22.54
C-08	168.3	4.78	350	35.5 (sil)	218	0.23	56	60	20.48	20.2
C-09	168.3	6.35	350	35.4 (sil)	150	0.13	81	79	25.77	24.61
C-11	219.1	4.78	350	31.0 (sil)	492	0.35	80	80	18.13	14.21
C-13	219.1	4.78	350	32.3 (sil)	384	0.27	102	99	18.77	17.39
C-15	219.1	8.18	350	31.9 (sil)	525	0.28	73	49	19.52	19.48
C-17	219.1	8.18	350	31.7 (sil)	525	0.26	82	76	20.36	19.52
C-20	273.1	5.56	350	28.6 (sil)	574	0.26	112	141	19.44	17.11
C-21	273.1	5.56	350	29.0 (sil)	525	0.23	133	155	20.25	17.97
C-22	273.1	5.56	350	27.2 (sil)	1000	0.45	70	83	5.51	6.93
C-23	273.1	12.70	350	27.4 (sil)	525	0.13	143	136	26.09	23.99
C-31	141.3	6.55	300	30.2 (cal)	80	0.09	82	69	30.53	26.63
C-32	141.3	6.55	300	34.8 (cal)	143	0.17	64	53	28.50	22.94
C-34	219.1	4.78	300	35.4 (cal)	500	0.36	111	96	20.09	13.73
C-35	219.1	4.78	300	42.7 (cal)	560	0.36	108	100	15.59	11.22
C-37	219.1	8.18	350	28.7 (cal)	560	0.25	102	69	20.20	18.7
C-40	273.1	6.35	350	46.5 (cal)	1050	0.37	106	131	15.22	8.19
C-41	273.1	6.35	350	50.7 (cal)	1050	0.37	76	102	16.05	8.08
C-42	273.1	6.35	350	55.4 (cal)	1050	0.35	90	107	14.16	8.05
C-44	273.1	6.35	350	38.7 (cal)	715	0.27	178	151	20.36	15.79

4.2 Comparison with a three-dimensional model results

Similarly, the fiber model results were contrasted with simulations from the three-dimensional model presented by Espinós et al. [1]. In general, temperature prediction of both models matches precisely.

In the case of maximum axial displacement (Figure 3(d)), the agreement between predictions is excellent. However, when comparing FRR results (Figure 3(c)), some values lie out of the 15% area and the fiber model predictions resulted to be more accurate than the 3D model which gave higher values of

FRR. This can be due to the fact that Espinós et al. [1] focused on specimens filled with normal strength concrete and high strength concrete specimens were out of the range of application of the model.

In addition, the analysis computational time of the fiber model is much shorter than that needed by the 3D model, which is an improvement compared to the existing models and is an advantage when a whole structure or a part of it is analyzed.

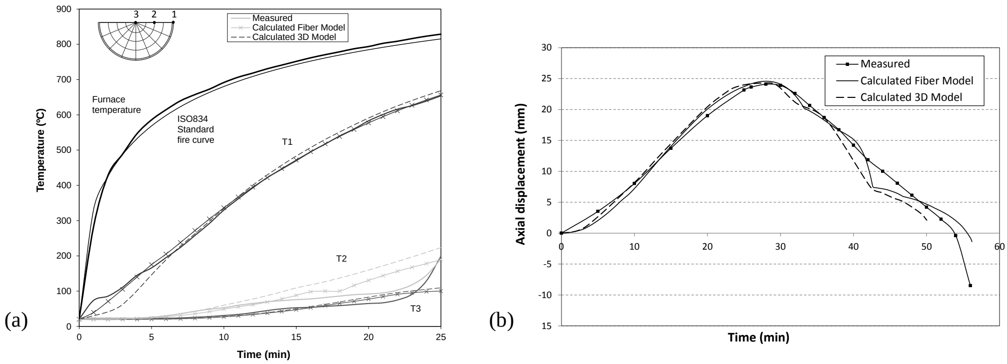

Figure 2. (a) Temperature comparison (C-159-6-3-30-0-40); (b) Axial displacement comparison (C-04).

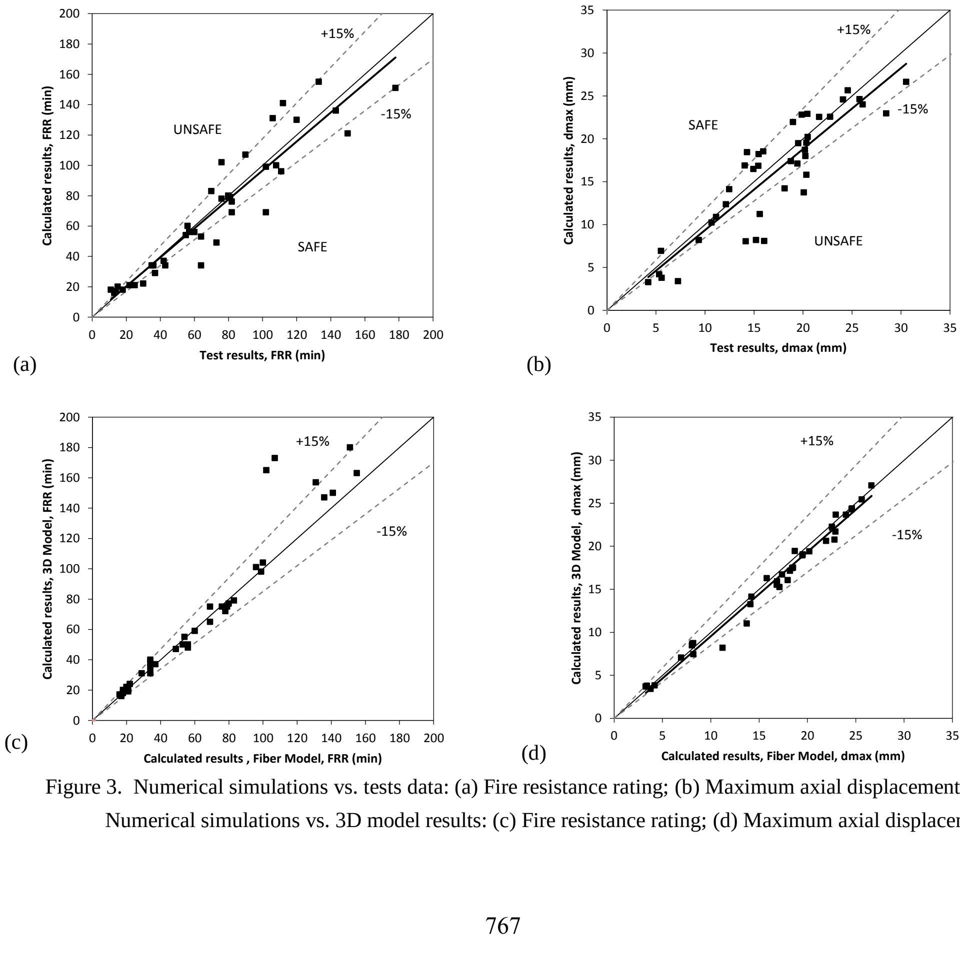

Figure 3. Numerical simulations vs. tests data: (a) Fire resistance rating; (b) Maximum axial displacement
Numerical simulations vs. 3D model results: (c) Fire resistance rating; (d) Maximum axial displacement.

5 SUMMARY AND CONCLUSIONS

By means of the fiber model presented, the behavior under fire of 37 CFT column specimens previously tested was modeled and analyzed. The model showed more error in those columns with lower slenderness and higher D/t ratio, where the role of the concrete was more important. For bar reinforced columns, although the initial stages of the response were well captured, the prediction at the last stages, governed by the concrete core, was less precise. Despite these two aspects, the model was able to produce accurate predictions with a reduced computational time compared to the 3D model.

REFERENCES

[1] Espinos A, Romero M, Hospitaler A. Advanced model for predicting the fire response of concrete filled tubular columns. Journal of constructional steel research 2010; 66(8-9):1030-1046.

[2] Renaud C, Aribert JM, Zhao B. Advanced numerical model for the fire behavior of composite columns with hollow steel section. Steel and Composite Structures 2003; 3(2):75-95.

[3] Jeffers A.E., Sotelino E.D. Fiber heat transfer element for modelling the thermal response of structures in fire. Journal of Structural Engineering 2009; 135(10): 1191-2000.

[4] Romero M.L., Moliner V., Espinos A., Ibañez C., Hospitaler A. Fire behavior of axially loaded slender high strength concrete-filled tubular columns. Journal of Constructional Steel Research 2011; 67: 1953-1965.

[5] Lie TT, Chabot M. Experimental studies on the fire resistance of hollow steel columns filled with plain concrete. Internal report No. 611. Ottawa, Canada: Institute for Research in Construction, National Research Council of Canada (NRCC); 1992.

[6] Filippou F. and Constantinides. FEDEASLab. Getting Started Guide and Simulation Examples. Technical Report NEESgrid-2004-22, Berkeley, CA: Civil and Environmental Eng. Dept. University of California at Berkeley, 2004.

[7] Lie TT. Fire resistance of circular steel columns filled with bar-reinforced concrete. Journal of Structural Engineering-ASCE 1994; 120(5):1489-1509.

[8] CEN. EN 1992-1-2, Eurocode 2: Design of concrete structures, Part 1.2: General rules – Structural fire design. Brussels, Belgium: Comité Européen de Normalisation; 2004.

[9] Kodur V.K.R, Lie TT. Fire resistance of circular steel columns filled with fiber-reinforced concrete. Journal of Structural Engineering-ASCE 1996; 122(7):776-782.

[10] Kodur V.K.R., Wang T.C., Cheng F.R. Predicting the fire resistance behavior of high strength concrete columns. Cement and Concrete Composites 2004; 26:141-153.

[11] Kodur V.K.R, Sultan M.A. Effect of temperature on thermal properties of high-strength concrete. Journal of Materials in Civil Engineering 2003; 15(2):101-107.

[12] Portolés J.M., Romero M.L., Filippou F.C., Bonet J.L. Simulation and design recommendations of eccentrically loaded slender concrete-filled tubular columns. Engineering Structures 2012; 42: 231-244;

[13] Hong S, Varma AH. Analytical modeling of the standard fire behavior of loaded CFT columns. Journal of Constructional Steel Research 2009; 65:54-69.

[14] CEN. EN 1993-1-2, Eurocode 3: Design of steel structures, Part 1.2: General rules – Structural fire design. Brussels, Belgium: Comité Européen de Normalisation; 2005.

[15] CEN. EN 1994-1-2, Eurocode 4: Design of composite steel and concrete structures, Part 1.2: General rules - Structural fire design. Brussels, Belgium: Comité Européen de Normalisation; 2005.

[16] CEN. EN 1991-1-2, Eurocode 1: Actions on structures, Part 1.2: General actions - Actions on structures exposed to fire. Brussels, Belgium: Comité Européen de Normalisation; 2002

8th International Conference on Structures in Fire
Guo-Qiang LI, Venkatesh K. R. KODUR, Shou-Chao JIANG, Jian JIANG, Su-Wen CHEN, Guo-Biao LOU (Eds.)
Shanghai, China, June 11-13, 2014

CONCRETE FILLED CIRCULAR DOUBLE-TUBE STEEL COLUMNS SUBJECTED TO FIRE

M.L.Romero*, A. Espinós*, J.M. Portolés, A. Hospitaler * and C. Ibañez****

* Universitat Politècnica de València, ICITECH, Spain
e-mails: mromero@mes.upv.es, aespinos@mes.upv.es, ahospitaler@cst.upv.es

** Universitat Jaume I, Department of Mechanical Engineering and Construction
e-mail: jportole@uji.es, ibanezc@uji.es

Keywords: Concrete filled steel tubular column, Fire resistance, Double-tube, Ultra-high strength concrete

Abstract. *This paper presents the results of an experimental campaign where the fire resistance of five double-tube concrete filled steel tubular (CFST) columns with different combinations of concrete strength is studied. Firstly, the ultimate axial load of the specimens at room temperature was experimentally obtained and afterwards the fire resistance of such columns subjected to a 20% of their load bearing capacity was measured. The influence of the strength of concrete in the inner ring on the fire performance of these columns is studied in this paper, with special attention on the presence of concrete in the main core of the column and also the variation of thicknesses of the outer and inner steel tubes.*

1 INTRODUCTION

Concrete-filled steel tubular (CFST) members are being increasingly used worldwide as composite columns in new building developments. However, the current European guidelines for member design in fire (EN1994-1-2) have been proved to be unsafe for columns with relative slenderness values higher than 0.5. At the same time, the use of high strength concrete (HSC) is becoming popular thanks to the reduction of its technological costs, in such a way that even ultra-high strength concrete (UHSC) has been introduced recently. The use of this material presents great advantages, mainly in members subjected to considerably high compressive axial forces, as it occurs in columns of high-rise buildings and bridge piers. Nevertheless, it has some disadvantages, such as its brittle behaviour at room temperature, the possibility of experiencing spalling at elevated temperatures and the fact that the Eurocode 4 is still limited to concrete grades up to 50 MPa.

The usage of high strength materials in columns reduces their cross-section while increasing the member slenderness, with the consequent buckling problems and detrimental effect to the fire resistance. For this reason, new innovative solutions are needed in order to guarantee that this type of columns produce the appropriate structural response. In this paper, the initial results to characterize a novel type of cross-section (double-tube) are presented, which solves some of the previously referred problems and shortcomings, being possible to employ different concrete grades in the inner core and outer concrete ring. This would help to prevent spalling problems associated to UHSC by being subjected to lower temperatures in those parts of the column where it is found more useful. The presence of an internal steel tube with a lower temperature would help to resist the second order effects in slender columns.

In this paper, the characterization of a novel type of cross-section (double-tube) with two circular hollow sections (CHS) is initially studied. Some researchers (Han et al. [1] and Espinos et al. [2]) think that the main source of the lack of coherence in the Eurocode 4 in the slender concrete-filled CHS columns is originated by a special local behaviour produced in the head of the column between the concrete core and the steel tube during the fire scenario. However, other researchers (Baley [3]) are not sure if this local behaviour only appears in isolated columns and not in columns as part of a portal-frame.

In Europe, a large amount of experimental work was conducted some time ago by CIDECT (International Committee for the Study and Development of Tubular Construction) on fire resistance of normal strength CFST columns. Worldwide it has been also intensly investigated for years and numerous test programs have been carried out mainly for non-slender columns (Lie and Chabot [4] , Chabot and Lie [5], Kordina and Klingsch [6] , Park et al. [7], Han et al. [1] and Romero et al. [8].

If the steel industry wants to maintain the profitability of concrete-filled hollow steel sections, they should incorporate fire resistance assessment methods for the innovative types of columns that provide higher fire resistance. Regarding them, steel cores inside the columns may increase significantly the fire resistance (FR) and lead to higher load bearing capacity both at room temperature and in the fire situation. This is caused by the slower temperature increase in the steel core due to protection by the concrete filling.

There are several authors who have proposed the so-called “double-skin” CFT column as Zhao, Han and co-workers [9-11] where the inner CHS is empty. Other authors have proposed the solution to embed massive steel sections inside the core (Schaumann, Fontana, etc). In turn, Liew et al. [12] have recently tested a new typology of cross sections called “double-tube” where the inner tube is filled also with concrete.

This paper presents the results of an experimental program carried out comparing double-skin and double-tube concrete-filled slender steel tubular columns. Given the reduced number of experimental results found in the literature, the main objective of this paper is to compare the behaviour of such innovative cross-sections under ambient and high temperatures subjected to axial compression.

2 EXPERIMENTAL STUDY UNDER ROOM TEMPERATURE

2.1 General

The authors have performed several experimental campaigns to study the buckling resistance at room temperature of slender CFST columns with circular, square and rectangular cross-sections [13,14,15]. However, not many results can be found in the literature with tests using concrete in the inner core. The work presented by Liew at al. [12] investigated concentrically loaded stub columns of such typology but not slender columns and neither under high temperatures.

The tests presented in this paper are the initial results of an extensive experimental campaign (30 tests) where the effects of two parameters are analysed: strength of concrete (normal strength and ultra-high strength concrete) and the ratio between the thicknesses of the steel tubes. However, up to date only 5 experiments have been tested at room temperature and 5 under fire.

The sections were selected so as to maintain the total steel area in all the tests (±4%), being equal to that of a CFT column previously tested under fire by the authors [16]. Three of the column specimens were filled with concrete in the inner core (normal or ultra-high strength concrete, i.e. double-tube), while the other two columns were not filled (double-skin). The dimensions of the typical cross-sections can be seen in Figure 1 and Table 1. Nominal plain C30 and C150 grade concretes and steel S355 were used, although the real strengths are summarized in Table 1.

2.2 Column specimen and set up

All the specimens were manufactured at Universitat Politècnica de València (Spain) and tested later at Universitat Jaume I in Castellón (Spain). The buckling length of the columns was 3315 mm in all tests where a 300×300×15 mm steel plate was welded to both ends of the columns. All the specimens were tested in a 5000 kN testing frame in a horizontal position, Figure 1（b）. More details of the test setup can be found in [13-15]. Linear variable displacement transducers (LVDTs) were used to measure the deflection at five points along the column (0.25L, 0.375L, 0.5L, 0.625L and 0.75L). Once the specimen was put in place, displacement control tests were carried out in order to measure post-peak behaviour.

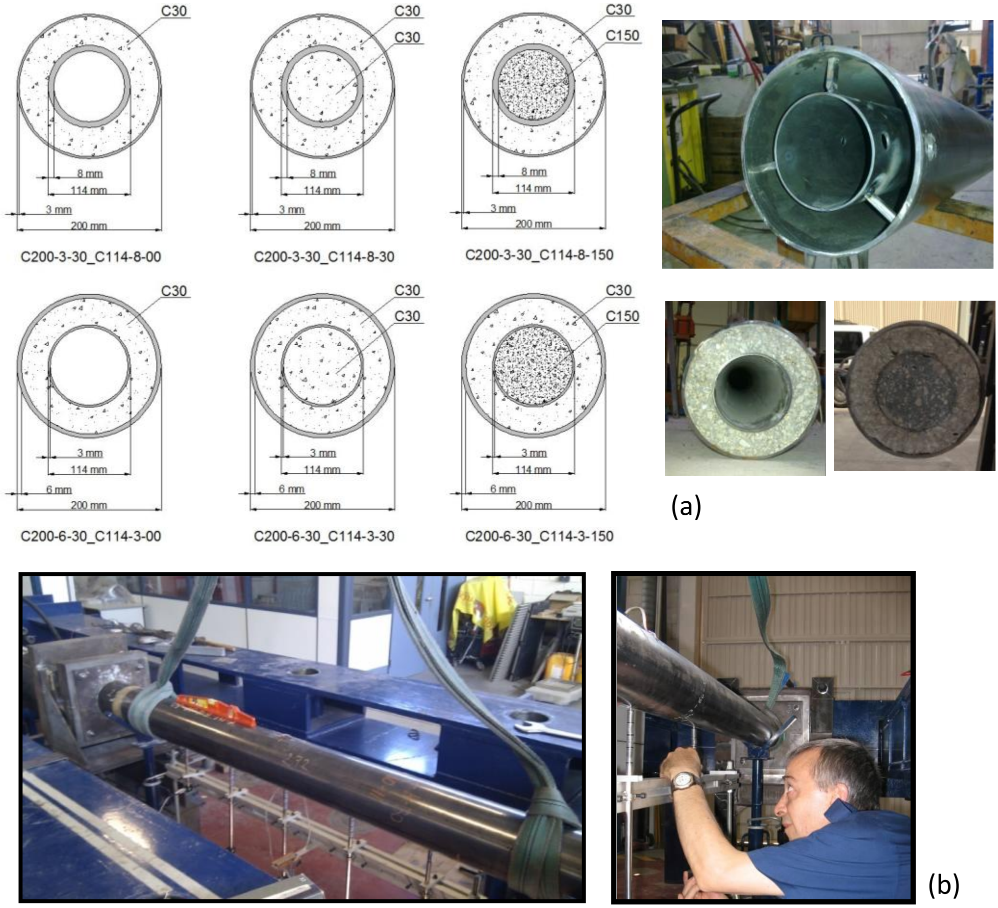

Figure 1. (a) Cross-sections; (b) Ambient Temperature test.

2.3 Materials properties

2.3.1 Steel tubes

Circular steel hollow sections were used in the experimental program, Table 1. The real yield strength of the hollow steel tubes (fy) was obtained for each column specimen by performing the corresponding coupon test.

2.3.2 Concrete

In this initial experimental program, two types of concrete were used, with nominal compressive strength of 30 MPa and 150 MPa. The concrete batches were prepared in a planetary mixer. In order to obtain the real compressive strength of concrete (fc), sets of concrete cylinders were prepared and cured in standard conditions during 28 days. All samples were tested on the same day as the column was tested, as shown in Table 1.

Table 1. Properties of tests.

	Outer Tube				Inner Tube				Ambient Temp	Fire tests	
Column specimen	D_{ext} mm	t_{ext} mm	$f_{y,ext}$ MPa	$f_{c,ext}$ MPa	D_{int} mm	t_{int} mm	$f_{y,int}$ MPa	$f_{c,int}$ MPa	N_u kN	N_{fire} kN	FRR min
C200-3-30-C114-8-00	200	3	300	46	114.3	8	377	00	1418	283	76
C200-3-30-C114-8-30	200	3	332	45	114.3	8	403	45	1627	325	104
C200-3-30-C114-8-150	200	3	342	43	114.3	8	414	135	1774	355	98
C200-6-30-C114-3-00	200	6	386	46	114.3	3	414	00	1644	329	48
C200-6-30-C114-3-30	200	6	406	43	114.3	3	414	43	1964	392	45
C200-6-30-C114-3-150	200	6			114.3	3			*		*

* tested in April 2014   t=thickness   D=diameter   B.C= pinned-pinned

2.4 Experimental results

The maximum axial load of all specimens (Nu) is listed in Table 1 and the axial force versus mid-span displacement response for all tests is presented in Figure 2.

The general trend of the curves results as expected: when the thicker tube is located in the outer part of the section, the maximum load increases although the load is concentric and the total steel area is approximately constant. This is due to the increase in the moment of the inertia of the total section reducing the influence of the second order effects. Besides, if the inner CHS is filled also with concrete the maximum load also increases. However, it must be highlighted that similar maximum loads are obtained for the tests C200-3-30_C114-8-30 and C200-6-30_C114-3-00, where only small differences are found due to the diverse values of the steel yield strength.

Consequently, it can be stated that a double-tube column with the thicker tube in the inner position can reach the same buckling load than a double-skin CFT column with the thicker steel tube in the outer position and without inner concrete.

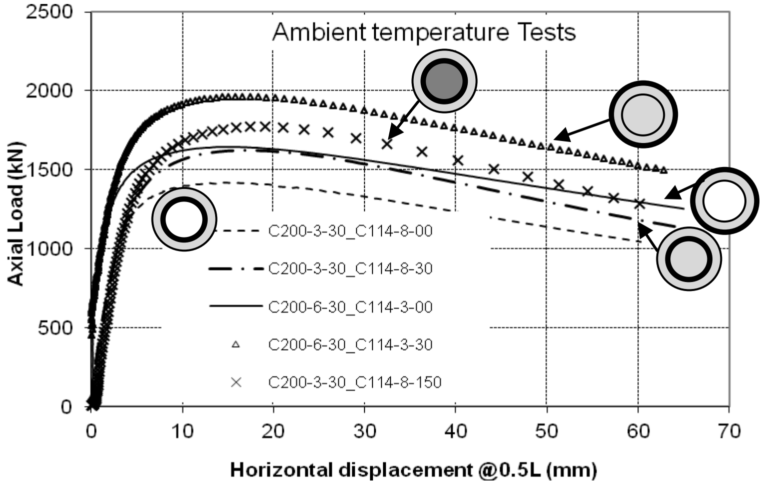

Figure 2. Ambient temperature tests.

Moreover, it is worth noting the reduced effect that presents the UHSC in the inner core in comparison with NSC (tests C200-3-30-C114-8-150 and C200-3-30-C114-8-30). It increases only a 9 % the buckling capacity of the column despite the elevated cost that the UHSC has.

3 EXPERIMENTAL STUDY UNDER ELEVATED TEMPERATURE

3.1 General

Even though a great number of fire tests can be found in the literature on CFT columns of circular and square section, the fire resistance of double-tube CFT slender columns where the inner steel tube is filled with concrete has not yet been investigated through experimental testing.

In this experimental program, five CFST columns equivalent to those previously tested at room temperature were subjected to a fire test.

Both the height of the column specimens and the boundary conditions was maintained equal to the ambient temperature tests. The axial load applied to the columns was a 20% of their real buckling capacity at room temperature. Table 1 lists the main characteristics of the tested specimens.

3.2 Test Setup

The experiments were performed in the testing facilities of AIDICO (Instituto Tecnológico de la Construcción) in Valencia, Spain. The tests were carried out in a 5×3 m horizontal furnace equipped with a hydraulic jack of 1000 kN maximum capacity and a total of 16 gas burners, located at mid-height of the furnace chamber. The test setup was similar to that used in previous experimental programs performed by the authors [8]. The columns were placed vertically inside the furnace, pinned (P) at their bottom end and pinned (P) at their top end. The load was on a first instance applied to the columns at room temperature, and afterwards and maintaining the load constant, the gas burners were activated, following the standard ISO 834 fire curve. A schematic view of the test setup can be seen in Figure 3 and reference [8].

3.3 Material properties

The same steel tubes and concrete infill as those used for the room temperature tests were employed in the fire tests, Table 1, where calcareous aggregates were used in the concrete mix.

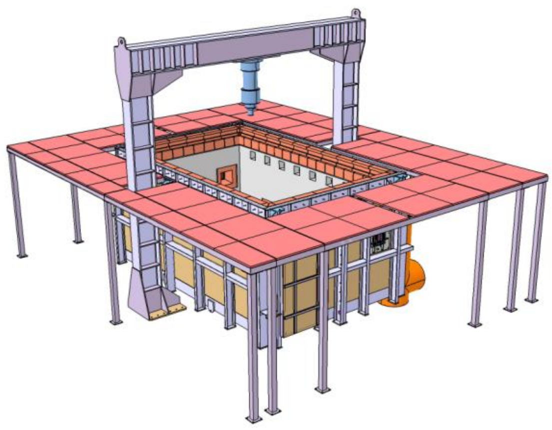

Figure 3. Fire tests.

3.3 Experimental results

The typical failure observed in all the columns was overall buckling, while no local buckling was observed at mid-height of the column or near the column ends.

The evolution of the axial displacement measured at the top end of the column along the fire exposure time is plotted in Figure 4. The resulting fire resistance time (FRR) expressed in minutes is listed in Table 1.

Additionally, a CFT column tested in a previous campaign by the authors (C3 from [16]) is included in this Figure. This column has the same total steel area using a single CHS tube with a diameter of 193.7 mm and a thickness of 8 mm.

The axial displacement versus time curve obtained for the four column specimens tested presents the typical four-part curve described in Reference 2. The first two stages can be clearly identified in the curves plotted in Figure 4, the first stage of these curves corresponding to the elongation of the steel tube and the second stage corresponding to the axial shortening of the column which occurs when the steel tube starts to yield. Subsequently, the load is transferred to the outer ring of concrete which plays an important role in the mechanical behavior of the specimens.

If the inner steel tube is very thin, the increment of the fire resistance is minor in comparison with the single CFT column.

Also it is worth noting that although the load level applied to all the columns was the same (20% of their maximum capacity at room temperature), the value of the load applied to the columns was different, and therefore the resulting fire resistance are slightly influenced.

What is really important from Figure 4 is the behaviour of the three tests where the inner steel tube is thicker (C200-3-30-C114-8-XX), as a new “stage 5” appears. In these tests, the inner steel tube starts to elongate again after the column shortening because it has a lower temperature than the outer tube (which becomes useless in the fire situation).

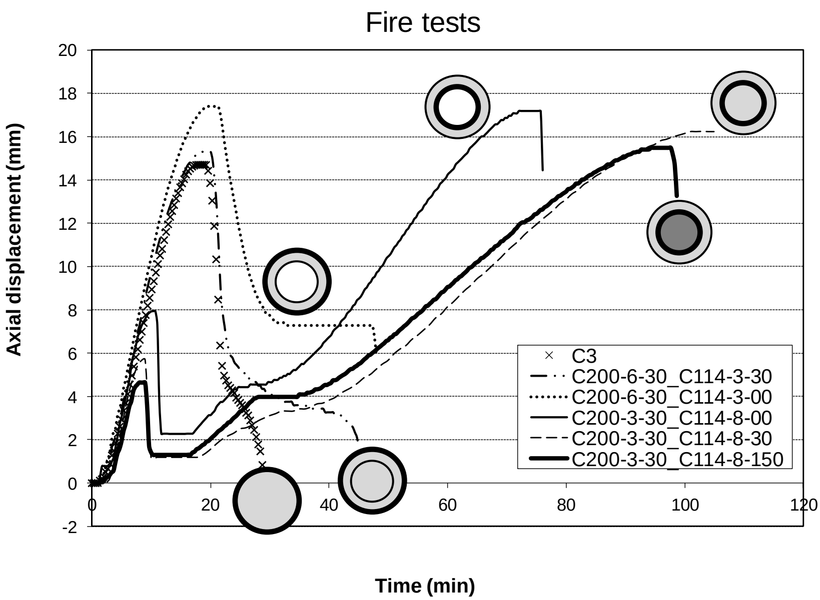

Figure 4. Fire tests.

This effect can be seen in the three tests, where the resulting fire resistance time increases between 1.6 and 2.3 times while the load applied to columns with thicker inner tubes was approximately an 85% of that of the columns with a thicker outer tube.

Surprisingly, the effect of the UHSC (138 MPa) in the inner core produces lower fire resistance. The main reason is because the axial load applied in this test is higher than the case where the inner core is filled with normal strength concrete (44 MPa). As a result, it can be inferred that the inner concrete core is not working properly in these slender columns and only it has the effect of reducing the temperatures in the inner steel tube.

4 CONCLUSIONS

The results of an experimental program on double tube hollow section columns filled with concrete under room and elevated temperatures have been presented in this paper. Given the reduced number of experiments found in the literature, this work provides novel results to the research community.

The main conclusion that can be obtained from them is that a good design strategy for CFT columns could be to split thick steel tubes in two different CHS tube with the same total steel area (and thus similar cost), but placing the thinner CHS in the outer part of the section and the thicker CHS in the inner part. Both rings should be filled up with concrete.

However a reduced number of tests have been performed up to date, and more experiments and extensive numerical models should be accomplished to achieve reliable results.

5 ACKNOWLEDGEMENT

The authors would like to express their sincere gratitude to the Spanish Ministry of Economy and Competitiveness through the project BIA2012-33144 and European Community for FEDER funds.

REFERENCES

[1] Han L, Yang Y, Xu L. 2003, "An experimental study and calculation on the fire resistance of concrete-filled SHS and RHS columns". Journal of constructional steel research; 59(4):427-452.

[2] Espinos A, Romero M, Hospitaler A. 2010, "Advanced model for predicting the fire response of concrete filled tubular columns". Journal of constructional steel research; 66(8-9):1030-1046.

[3] Bailey C, 2000, "Effective lengths of concrete-filled steel square hollow sections in fire", Proc. Instn Civ. Engrs Structs & Bldgs, , 140, May, 169-178.

[4] Lie TT, Chabot M. 1992, "Experimental studies on the fire resistance of hollow steel columns filled with plain concrete". Internal report No. 611. Ottawa, Canada: Institute for Research in Construction, National Research Council of Canada (NRCC).

[5] Chabot M, Lie TT. 1992, "Experimental studies on the fire resistance of hollow steel columns filled with bar-reinforced concrete". Internal report No. 628. Ottawa, Canada: Institute for Research in Construction, National Research Council of Canada (NRCC).

[6] Kordina K, Klingsch W. 1983, "Fire resistance of composite columns of concrete filled hollow sections". CIDECT Research Project 15C1/C2–83/27. Cologne, Germany: Comité International pour le Développement et l'Etude de la Construction Tubulaire.

[7] Park S, Chung K, Choi S. 2007. A study on failure prediction and design equation of concrete filled square steel tube columns under fire condition. International Journal of Steel Structures 7(3):183-191.

[8] Romero, M.L., Moliner, V., Espinos, A., Ibañez, C., Hospitaler, A. 2011, "Fire behavior of axially loaded slender high strength concrete-filled tubular columns", Journal of Constructional Steel Research 67: 1953-1965.

[9] Zhao X, Han L. 2006 "Double skin composite construction". Progress in structural engineering and materials;8(3):93-102

[10] Elchalakani M, Zhao XL, Grzebieta R. 2002, "Tests on concrete filled double-skin (CHS outer and SHS inner) composite short columns under axial compression". Thin-walled structures;40(5):415-441.

[11] Lu H, Han L, Zhao X. 2010, "Fire performance of self-consolidating concrete filled double skin steel tubular columns: Experiments". Fire safety journal;45(2):106-115.

[12] Liew, Xiong D X. 2011, "Experimental investigation on tubular columns infilled with ultra-high strength concrete". In: Tubular Structures XIII. Boca Raton: Crc Press-Taylor & Francis Group; 637-645.

[13] Portoles J M, Romero M L, Bonet J L, Filippou F C. 2011, "Experimental study of high strength concrete-filled circular tubular columns under eccentric loading". Journal of constructional steel research;67(4):623-633.

[14] Portoles JM, Serra E, Romero ML. 2013 "Influence of ultra-high strength infill in slender concrete-filled steel tubular columns". Journal of constructional steel research; 86:107-114.

[15] Hernandez Figueirido D, Romero M L, Bonet J L, Montalva J M. 2012, "Ultimate capacity of rectangular concrete-filled steel tubular columns under unequal load eccentricities". Journal of constructional steel research; 68(1):107-117.

[16] Espinós A, Romero M, Serra E, Albero V. 2014, "Experimental investigation on the fire resistance of slender concrete filled tubular columns of different cross-section shape", Eurosteel 2014, (in press).Buchanan A.H., *Structural Design for Fire Safety*, John Wiley & Sons Ltd, Chichester, 2001.

CONNECTIONS

8th International Conference on Structures in Fire
Guo-Qiang LI, Venkatesh K. R. KODUR, Shou-Chao JIANG, Jian JIANG, Su-Wen CHEN, Guo-Biao LOU (Eds.)
Shanghai, China, June 11-13, 2014

TEMPERATURE FIELD ANALYSIS OF SEMI-RIGID JOINTS FOR CFST COMPOSITE FRAMES

Jing-Feng Wang[*,], Hai-Tao Wang[*], Wei-Wei Shi [*] and Hong-Yu Shen[*]**

* Hefei University of Technology, Hefei 230009, China; ** Anhui Civil Engineering Structures and Materials Laboratory, Hefei 230009, China

Keywords: Concrete-Filled Steel Tubular (CFST), Composite joint, Semi-rigid connection, Temperature filed, Finite Element (FE)

Abstract. *The bearing capacity and stiffness of concrete-filled steel tubular (CFST) structures after long-time high temperature or emergency fire accident were decreased or even serious collapse. To obtain fire resistance of semi-rigid joints for CFST composite frames, temperature filed distribution of composite joints in fire was studied. Thermal properties and boundary conditions of steel and concrete were determined. The temperature filed model of semi-rigid joints to CFST columns with slabs was made by using ABAQUS finite element software, in considering temperature rise stage of fire modeling. The effect of composite slab, fire type and construction location were discussed and the model was verified by the test results. The temperature distribution of composite joint under three or four-side fire condition was studied by the sequentially coupled thermal analysis method. The temperature versus time curves and temperature distribution of various construction and location were analyzed. The research results will become the scientific foundation of mechanical behavior and design method of semi-rigid CFST composite frames in fire.*

1 INTRODUCTION

High temperature in fire has significant effects on the structural material properties. It maybe causes structural damage or even collapse [1]. The bearing capacity and stiffness of concrete-filled steel tubular (CFST) structures decrease after long-term high temperature or emergency fire accident, and even serious structural collapses. The beam-to-column joint is an important part in the steel structures, so its mechanical properties in fire directly affect the structural safety [2].

Following the 1994 Northridge and the 1995 Kobe earthquakes, considerable attention was paid to semi-rigid connections in terms of their energy dissipation capability and ductility. However, a practical difficulty arises for engineers seeking to employ on-site bolting in beam-to-column connections to have the high degree of fixity necessary for moment-resisting frames. The recent development of blind fasteners allows for bolt installation on only one side of the connection without the need for access within hollow steel section (HSS) column.

To overcome the inconvenience of extensive welding and the required high tolerance, there has been a growing research interest in the blind bolted connections. Some studies have been conducted on the static and seismic behavior of HSS or CFST column connections with various blind fasteners [3-7]. Scant effort has been devoted to studying fire performance of the CFST column connections using the blind bolts.

This paper studied the temperature filed distribution of composite joints in fire in order to obtain fire resistance of semi-rigid joints for CFST composite frames. Thermal properties and boundary conditions of steel and concrete were determined. The 3D temperature filed model of semi-rigid joints to CFST columns with slabs was made by using ABAQUS finite element software, in considering temperature rise stage of fire modeling. The effect of composite slab, fire type and construction location were discussed and the analytical model was verified by the test results. The temperature distribution of composite joint under three or four-side fire condition was studied by the sequentially coupled thermal analysis method. The temperature versus time curves and temperature distribution of various construction and location were analyzed.

2 THERMAL PROPERTIES OF STRUCTURAL MATERIAL AT HIGH TEMPERATURE

2.1 Thermal properties of steel

2.1.1 Thermal expansion coefficient

Thermal expansion of steel has the effect on the structural deformation and stress. The thermal expansion coefficient $\alpha_s=\Delta l/(l\times\Delta T)$ and the unit is m/(m · ℃). The thermal expansion coefficient of the structural steel is suggested [8]:

$$\alpha_s=\begin{cases}(0.004T+12)\times10^{-6} & T\le100℃\\ 1.6\times10^{-5} & T>1000℃\end{cases} \tag{1}$$

2.1.2 Specific heat

Specific heat of steel C_S means that the unit quality of steel absorbs or releases heat with temperature increasing or reducing 1℃. The unit is J/(kg ·℃) or J/(kg ·℃). The specific heat of the structural steel was expressed [8]:

$$\rho_s C_s=\begin{cases}(0.004T+3.3)\times10^{6} & 0℃\le T\le650℃\\ (0.068T-38.3)\times10^{6} & 650℃<T\le725℃\\ (73.35-0.086T)\times10^{6} & 725℃<T\le800℃\\ 4.55\times10^{6} & 800℃<T\end{cases} \tag{2}$$

2.1.3 Heat conduction coefficient

Heat conduction coefficient k_s is refer to the heat transferred at unit area and time. The unit is W/(m ·K) or W/(m ·℃). The heat conduction coefficient was suggested [8]:

$$k_s=\begin{cases}-0.022T+48 & 0℃\le T\le900℃\\ 28. & T>900℃\end{cases} \tag{3}$$

2.1.4 Density

The variation of density with temperature is very small, so that ρ_s=7850kg/m^3.

2.2 Thermal properties of concrete

2.2.1 Thermal expansion coefficient

Thermal expansion coefficient of concrete is related to the aggregate type, specimen size, heating rate and sealing of specimen ect The unit is m/(m · ℃). The thermal expansion coefficient of concrete was suggested [8]:

$$\alpha_c = (6 + 0.008T) \times 10^{-6} \tag{4}$$

2.2.2 Specific heat

The main influencing factors of concrete specific heat are temperature, aggregate types, moisture content, and concrete mixture ratio. The concrete specific heat was suggested [8]:

$$\rho_c C_c = \begin{cases} 2.566 \times 10^6 & 0℃ \le T \le 400℃ \\ (0.1765T - 68.034) \times 10^6 & 400℃ < T \le 410℃ \\ (25.0067 - 0.0504T) \times 10^6 & 410℃ < T \le 445℃ \\ 2.566 \times 10^6 & 445℃ < T \le 500℃ \\ (0.016T - 5.4488) \times 10^6 & 500℃ < T \le 635℃ \\ (0.1664T - 100.902) \times 10^6 & 635℃ < T \le 715℃ \\ (176.0734 - 0.221T) \times 10^6 & 715℃ < T \le 785℃ \\ 2.566 \times 10^6 & 785℃ < T \end{cases} \tag{5}$$

2.2.3 Heat conduction coefficient

The main influencing factors of the concrete heat conduction coefficient are the aggregate types, moisture content, and mixture ratio. The concrete heat conduction coefficient was expressed[8]:

$$\alpha_s = \begin{cases} 1.355 & 0℃ < T \le 800℃ \\ 1.7162 - 0.00124T & 800℃ < T \end{cases} \tag{6}$$

2.2.4 Density

The concrete density can be regarded as constant. ρ_s=2300kg/m^3.

3 TEMPERATURE FIELD MODEL OF CFST COMPOSITE JOINTS

There are two methods of thermal coupling analysis in ABAQUS software, such as fully coupled thermo-mechanical method and order coupled thermo-mechanical method. In this paper the order coupled thermo-mechanical method was used to analyze temperature field of CFST composite joints.

3.1 Basic assumption

（1）Steel and concrete are assumed for isotropic materials;

（2）The stress level has no effect on the construction temperature distribution. The influence of construction deformation, stress and strain on the thermal parameters and thermal conduction of material are not considered in temperature analysis.

（3）The influence of thermal contact resistance is ignored;

（4）The indoor air temperature is uniform. The ISO-834 standard temperature curve is used in fire model and $T_g(0)$=20℃;

（5）Local thermal boundary conditions caused by structural deformation is not considered.

3.2 Temperature field model

3.2.1 Element type

The temperature field models of blind bolted endplate connections for CFST composite frame were made by using FE software ABAQUS, showed in Figure 1. Structural material thermal parameters were determined. Linear heat transfer eight node hexahedron element DC3D8 was used in CFST column, endplate, steel beam, slab and blind bolts. The element type is 'Heat transfer'.

3.2.2 Thermal boundary condition

Thermal boundary condition of the analysis model includes three or four-side fire conditions for column cross-section and three-side fire condition for beam cross-section. In this paper, the heat radiative transfer and the convective heat transfer separate calculation method was used. The boundary condition and heat transfer coefficient are listed in Table 1.

Table 1. Boundary conditions and heat transfer coefficient.

Parameter	Convection transfer rate α_c	Integrated radiation Coefficient ε_r	Shape factor φ
steel beam web/ protective layer of steel beam web	25	0.496	0.5
steel beam flange/ protective layer of steel beam flange	25	0.496	1
object fire surface concrete slab	25	0.56	1
back fire surface concrete slab	9	0	1

Note: the radiation heat transfer in back fire surface is not considered and the ambient temperature is 20℃.

3.2.3 Contact and sliding

The heat transfer analysis interface model of single member was used regardless of the temperature change along the member length. Only temperature transfer was assumed along the interface. The binding surface was used between CFST column and endplate, endplate and steel beam, steel beam web and flange, concrete and steel beam top flange. To ensure the integrity of steel and concrete members, the embedded contact model was adopted among blind bolts, endplate, steel tube and concrete. Steel tube and core concrete was bound by 'tie', regardless of the relative slippage effect.

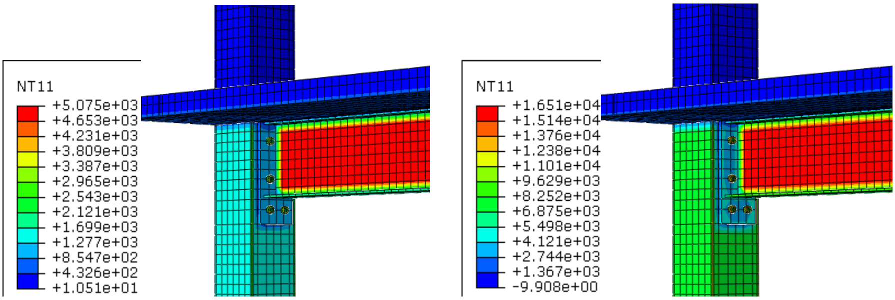

(a) 30min (b) 72min

Figure 1. Temperature field distribution of composite joint.

4 EXPERIMENTAL VERIFICATION

Based on literature [9] provided the test data of CFST column in fire and literature [10] provided the test data of CFST column joints to verify the calculation FE models, as shown in Figure 2-4. It is showed that the analytical result has good agreement with the test results.

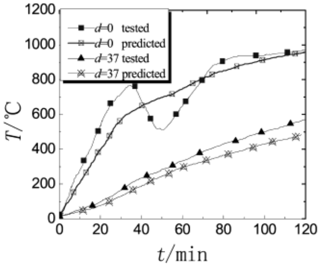

(a) B×t=305×6.35mm

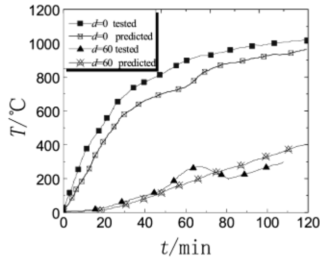

(b) B×t=254×6.35mm

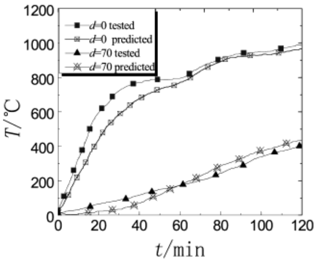

(c) B×t=203×6.35mm

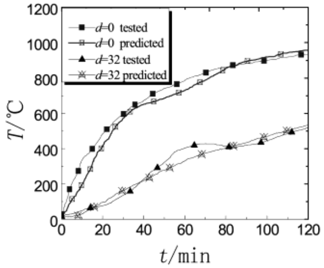

(d) B×t=300×6.35mm

Figure 2. Temperature comparison between calculated and test results of CFST columns.

Note: d is the distance from the column section radial to the column surface.

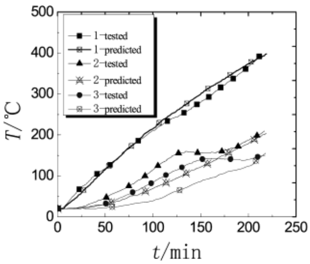

(a) non-joint region

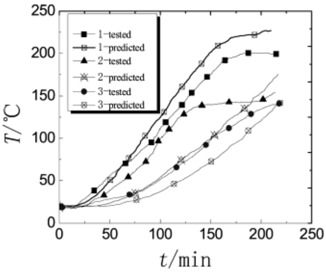

(b) joint region

Figure 3. Temperature comparison between calculated and test results of CFST joint JS1.

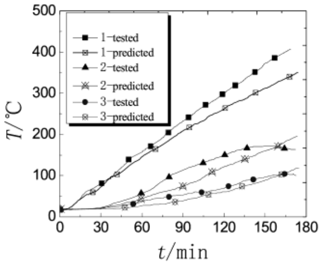

(a) non-joint region

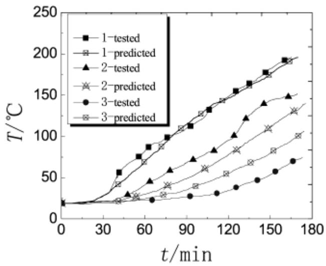

(b) joint region

Figure 4. Temperature comparison between calculated and test results of CFST joint JS2.

5 TEMPERATURE FIELD ANALYSIS OF CFST COMPOSITE JOINTS

5.1 Parametric studies

The temperature field analysis model of CFST and composite beam joints in fire was made. The extended end plate type connections were adopted by using blind bolts to connect the steel beams to CFST columns.

The basic calculating conditions of the examples are determined as follows:

• Joint type and connection details: exterior joint with blind bolts; extended end plate: 630×220×22mm; high strength blind bolt: 10.9M20; bolt extension: 50 mm length and 20 mm diameter.

• Steel beam: HN350×175×11×7mm; span length: 6 m; steel strength: f_y=345N/mm^2.

• CFST column: steel tube□300×300×10 mm; column height: 3m; f_y=345N/mm^2; f_{cu}=60 N/mm^2.

• Concrete slab: slab thickness: 100mm; f_{cu}=30 N/mm^2.

5.2 Temperature field analysis of joints in three-side fire conditions

Figure 5 gives reference point position of each member cross-section. *d* is the distance from the column section radial to the column surface. The cross-section temperature field analysis results of CFST column, steel beam and bolts in three-side fire conditions were described in Figure 6. The analytical results showed that the temperature of the steel tube heated up to 170℃ quickly at 70min. Due to the thermal inertia, the temperature of concrete rose more slowly. The concrete outmost temperature rose to about 80℃ at 70min. The concrete center temperature kept normal and changed little.

It is observed in Figure 6(b) that the steel beam temperature rose quickly, but due to the different surface heated side and the top flange of steel beam with the influence of concrete slab. The increasing temperature of each feature point was not same. The temperature of the steel beam web rose fast at 70 min. The surface temperature was beyond 1500℃, then it followed by the steel beam flange, the bottom flange warmed faster than the upper flange, and the temperature of the outside of the bottom flange increased faster than the inner surface. At 70 min, the outer surface temperature of the bottom flange was over 650℃, the outer surface flange temperature has reached to 250℃ and the inner surface temperature has reached to 700℃.

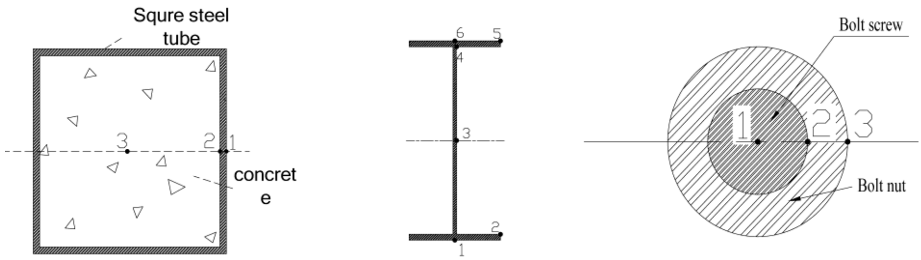

(a)column (b)beam (c)bolt

Figure 5. Feature point position of typical cross-section of construction.

Figure 6(c) gives characteristics of each blind bolt with cross-section each feature points during the heating process. It showed that the temperature of the nut external surface was faster than that of the screw. At 70min, the temperature of the nut external surface was up to 1500℃, while the temperature of the screw was close to 650℃. The heating speed of the screw was only 43% of the nut.

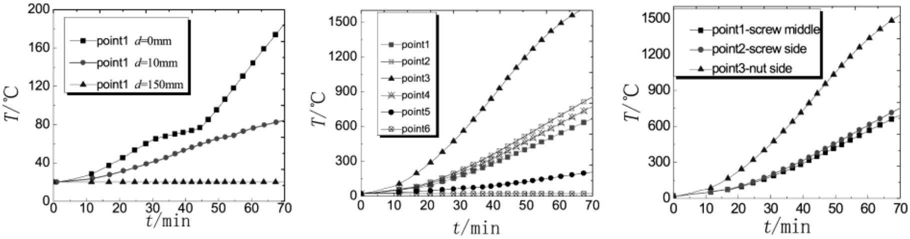

(a) CFST column section (b) steel beam section (c) blind bolt section

Figure 6. T-t curves of member cross-section in three-side fire.

5.3 Temperature field analysis of joints in four-side fire conditions

Figure 7 showed the temperature field analysis results of each member cross-section in four-side fire condition. The analytical results showed that it was observed in Figure 7(a) that the steel tube temperature rose quickly and the concrete temperature rose slower relatively. At 70 min, the steel tube temperature reached 120℃ and the concrete temperature increased linearly; the concrete outermost temperature reached only about 75℃. Figure 7(b) showed that the change of temperature of the steel beam section at different positions, the temperature of the steel tube web surface rose quickly at 75 min, it has reached the limited temperature 1500℃; the heating temperature speed of the flange was slower than that of the web, the inner and outer surface of the bottom flange and the inner surface of the top flange of temperature difference was small. The temperature rising trend were basically identical at 72 min, the highest temperature has reached 700℃~800℃. Due to the influence of the concrete slab, the outer surface temperature of steel beam flange obviously lagged behind the web and the bottom flange. At 72 min, the highest temperature on the external surface of the flange corner point has reached 200℃, and the temperature of intermediate point unchanged and was still for normal temperature 20℃. Figure 7(c) showed that before the bolt reached the highest temperature point, the side point temperature bolt nut rose up faster than the bolt screw side point and midpoint, and it reached the highest temperature 1500℃ firstly, the highest temperature of the bolt screw side points and midpoint only up to 650℃.

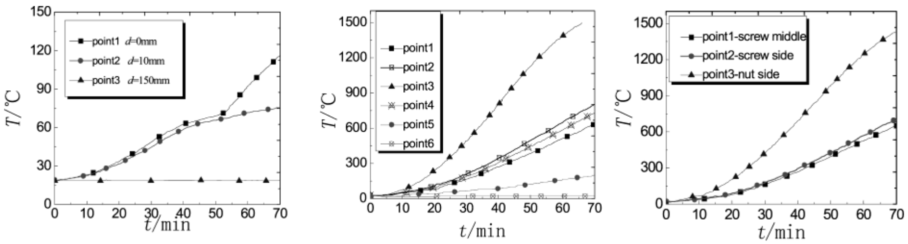

(a) CFST column section (b) steel beam section (c) blind bolt section

Figure 7. T-t curves of construction cross-section in four-side fire.

6 CONCLUSIONS

In this paper, the FE analysis and numerical simulation on temperature field of semi-rigid joints for CFST composite frames in fire have carried out. The thermal properties and boundary conditions of steel and concrete were determined in this paper. The 3D temperature filed model of semi-rigid joints to CFST columns with slabs was made by using ABAQUS software, in considering temperature rise stage of fire modeling. The effect of composite slab, fire type and construction location were discussed and the model was verified by the test results. The temperature distribution of composite joint in three or four-side fire condition was studied by the sequentially coupled thermal analysis method. The temperature versus time curves and temperature distribution of various construction and location were analyzed.

ACKNOWLEDGEMENT

The research reported in this paper is part of Project 51178156 and Project 50808062 supported by the National Natural Science Foundation of China. The authors would also like to acknowledge the Project NCET-12-0838 supported by Program for New Century Excellent Talents in University.

REFERENCES

[1] Li G Q, Han L H, Lou G B, Jiang S C. *Fire resistance design of steel structures and composite structures*. Beijing: China Architecture & Building Press, 2006.

[2] Wang J F, Han L H. *Simplified calculation methods of connections to CFST columns at elevated temperatures*, Progress in Steel Building Structures, 2009,11(2):28-34.

[3] Wang J F, Han L H, Uy B. *Behaviour of flush end plate joints to concrete-filled steel tubular columns*. Journal of Constructional Steel Research, 2009; 65(4):925-939.

[4] Wang J F, Chen L P. *Experimental investigation of extended end plate joints to concrete-filled steel tubular columns*, Journal of Constructional Steel Research, 2012, 79:56-70.

[5] Wang J F, Zhang L, Spencer B F. *Seismic response of extended end plate joints to concrete-filled steel tubular columns*. Engineering Structures, 2013, 49:876-892.

[6] Wang J F, Han L H, Uy B. *Hysteretic behaviour of flush end plate joints to concrete-filled steel tubular columns*. Journal of Constructional Steel Research, 2009, 65(8-9):1644-1663.

[7] Wang J F, Spencer B F. *Experimental and analytical behavior of blind bolted moment connections*, Journal of Constructional Steel Research, 2013, 82:33-47.

[8] Lie T T, Irwin R J. *Fire resistance of rectangular steel columns filled with bar-reinforced concrete*. Journal of Structural Engineering, 1995,121 (5):797-805.

[9] Lie T T, Chabot M. *Experimental studies on the fire resistance of hollow steel columns filled with plain concrete*. NRC-CNRC Internal Report, No.611, Ottawa, Canada, 1992.

[10] Zhen Y Q. *Fire resistance behavior of SRC constructions and beam-to-column joints(2nd edition)*. Fuzhou: Fuzhou University, 2007.

EXPERIMENTAL AND NUMERICAL STUDY ON HIGH STRENGTH STEEL ENDPLATE CONNECTIONS IN FIRE

Xu-Hong Qiang*,, Frans S.K. Bijlaard** and Henk Kolstein****

* Faculty of Civil Engineering, Shenzhen Graduate School, Harbin Institute of Technology, 518055, Shenzhen, China
e-mail: X.Qiang@tudelft.nl

** Department of Structural Engineering, Faculty of Civil Engineering, Delft University of Technology, P.O.BOX 5048, 2600GA Delft, the Netherlands.
e-mails: X.Qiang@tudelft.nl, F.S.K.Bijlaard@tudelft.nl, M.H.Kolstein@tudelft.nl.

Keywords: High strength steel, Endplate connections, Beam-to-column connections, Structural fire performance, Fire

Abstract. *In this paper, a perspective of combining high strength steel endplate with mild steel beam and column in endplate connections is proposed and investigated. Firstly, tests on high strength steel endplate connections were conducted at fire temperature 550 ℃ and at ambient temperature as reference. The moment-rotation characteristic, rotation capacity and failure mode of high strength steel endplate connections in fire and at ambient temperature were obtained through tests and compared with those of mild steel endplate connections. Further, the provisions of Eurocode 3 were validated with test results. Moreover, the numerical study was carried out via ABAQUS and verified against the experimental results. It is found that a thinner high strength steel endplate can enhance the connection's rotation capacity both at ambient temperature and in fire (which guarantees the safety of an entire structure), and simultaneously achieve almost the same moment resistance with a mild steel endplate connection.*

1 INTRODUCTION

Fires in buildings often have enormous consequences on safety and economy. Structural fire safety is therefore a key consideration in the design of buildings and is attracting worldwide attention. Beam-to-column connections are important components of steel framed structures, as they are supposed to resist resultant forces at the end of the beam and transfer them into the columns and surrounding structural components. The fracture of a connection can cause the collapse of the connected beam, which may lead to a progressive collapse of the entire building structure. Therefore the behaviour of connections in a building is of extreme significance, not only at ambient temperature but also in fire.

In Europe, endplate connections are typical beam-to-column connections for steel structures produced by welding at workshops and erected by bolting in situ. The simplicity and economy associated with its fabrication make this type of connection popular in steel structures. Rules for prediction of strength, stiffness and deformation capacity of endplate connections at ambient temperature have been included in current leading design standards, such as Eurocode 3 Part1-8 [1]. According to Eurocode 3, for structural steels up to S460, plastic design of connections may be used. However, for steel grades higher than S460 up to S700 only elastic design of connections can be employed [2], which is very uneconomical for steel structures. This is due to the lack of experimental and theoretical evidence that these high strength steel connections have sufficient deformation capacities. Girao Coelho and Bijlaard [3] have found that the high strength steel S690 endplate connections satisfy the design provisions for resistance and achieve reasonable rotation demands at ambient temperature. However, research results on fire performance of high strength steel endplate connections are not available in literature.

In this paper, a perspective of combining high strength steel endplate with mild steel beam and column in beam-to-column endplate connections is proposed and investigated. The aim of this research is to reveal more information and understanding on behaviour of high strength steel flush endplate connections in fire.

Firstly, 7 full-scale tests on beam-to-column high strength steel endplate connections were conducted at elevated temperature 550 ℃ under steady state fire condition and at ambient temperature as reference. The high strength steel endplates in test connections were made of S690 and S960. The parameters investigated herein are the endplate thickness and the endplate material. All specimens are designed to confine failure to the connections rather than the beam or column. The moment-rotation characteristic, rotation capacity and failure mode of high strength steel endplate connections in fire and at ambient temperature were obtained through tests and compared with those of mild steel endplate connections. Further, the provisions of Eurocode 3 were validated with test results of high strength steel endplate connections. Moreover, the numerical study on high strength steel endplate connections under fire conditions was carried out via the commercial package ABAQUS. The accuracy of this numerical modelling was validated against the experimental results on moment-rotation relationship, failure mode and yield line pattern of endplate connections.

This research opens a perspective of using high strength steels to take place of mild steels in structural optimizing design. The experimental and numerical study on high strength steel endplate connections in fire is expected to be used by structural engineers or researchers as a basis for an effective application of high strength structural steels in civil engineering as well as enhancing the fire safety of steel structures.

2 EXPERIMENTAL STUDY

2.1 Test specimen

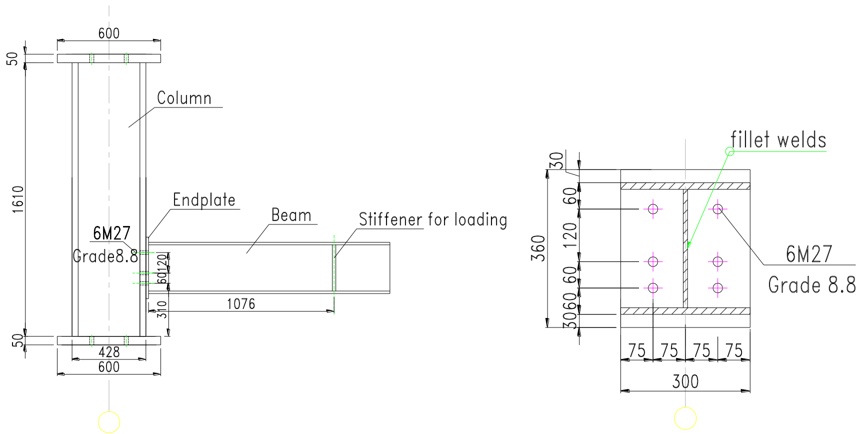

(a) Endplate connection (b) Endplate

Figure 1. Dimension of endplate connection specimen.

In the endplate connections, the endplates are made of high strength steels (S690 and S960) while the beam and column are made of Q345 (mild structural steel, the nominal yield stress of which is 345MPa, similar to S355). The beam sections used in this study are HW300×300 (comparable to European Section HE320A) while the column sections are HW400×400 (comparable to European Section HE300M). For comparison, the connections with endplates made of mild steels Q235 (mild structural steel, the nominal yield stress of which is 235MPa, similar to S235) and Q345 are also included herein. In this experimental study, there are two series of endplate connections, see Table 1. In each of them, the load bearing capacities of the connections are designed to be similar, while the endplate materials and thicknesses vary. In order to compare the behaviour of endplate connections under fire conditions with that at ambient temperature, the tests at ambient temperature on each concerned endplate connection were conducted as well. The overall dimension of the endplate connection test specimen is shown in Figure 1, while the endplate materials and thicknesses of the specimens are shown in Table 1.

Table 1. Test specimens and fire test conditions.

Connection ID	Endplate material	Endplate thickness (mm)	Weld type	Weld Size (mm)	Temperature (℃) of specimens
1-1 A	Q235	20	overmatched	8	20
1-2 A	S690	12	matched	10	20
1-3 A	S960	10	under matched	10	20
2-1 A	Q235	25	overmatched	8	20
2-2 A	Q345	20	overmatched	8	20
2-3 A	S690	15	matched	10	20
2-4 A	S960	12	under matched	10	20
1-1 E	Q235	20	overmatched	8	550
1-2 E	S690	12	matched	10	550
1-3 E	S960	10	under matched	10	550
2-1 E	Q235	25	overmatched	8	550
2-2 E	Q345	20	overmatched	8	550
2-3 E	S690	15	matched	10	550
2-4 E	S960	12	under matched	10	550

2.2 Test set-up

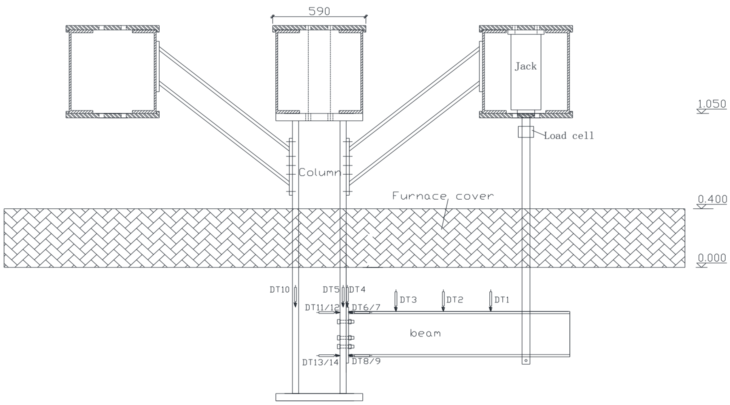

Figure 2. Fire test set-up.

All fire tests were conducted in a gas furnace (4.5m×3.0m×1.7m). Since applying a tensile load under fire conditions is more stable than applying a compressive load, the connection specimens were designed to be located upside down in order to easily apply the tensile load from the outside of the furnace, as shown in Figure 2. The members below the furnace cover are in fire during fire tests, while those above the furnace cover are out of the fire field at ambient temperature, see Figure 2.

2.3 Displacement measurement

In the fire tests, 3 vertical displacement sensors (DT1-DT3) were used to obtain the vertical displacement of the beam, as shown in Figure 2. According to the vertical displacements of beam, the rotation of beam can be calculated. In order to record the displacement of column, 2 vertical displacement sensors (DT5 and DT10) were arranged. According to the displacement of column, the rotation of column can be calculated. In order to measure the displacement of endplate, one vertical displacement sensor (DT4) and 4 horizontal displacement sensors (DT6-DT9) were placed, as shown in Figure 2. According to the displacement of endplate, the rotation of endplate can be calculated. Based on the displacements of the aforementioned components, the rotation of endplate connection in tests can be obtained.

2.4 Test procedure

The full-scale fire tests on endplate connections were conducted under steady state fire condition. The specimens were firstly heated to a pre-selected elevated temperature (550 ℃) at a constant heating rate 10 ℃/min, which corresponds to a natural fire to buildings. When the temperature of the concerned components reached the pre-selected elevated temperature, the mechanical load (moment for the connection) was applied to the specimen at this constant elevated temperature (550 ℃) until failure occurred. During loading, displacement control was employed by controlling the displacement of piston of the hydraulic actuator at a constant rate 10mm/min.

2.5 Test results

2.5.1 Deformation at the end of tests

An overall description on components of all connections at the end of the fire tests is listed in Table 2.

Table 2. Description of components at the end of fire tests.

Test ID	Endplate material	Endplate thickness (mm)	Endplate yielding	Fracture of bolts in top tensile row	Nuts in top tensile row stripped off	Weld failure in heat affected zone
1-1 E	Q235	20	Yes	Yes	No	No
1-2 E	S690	12	Yes	Yes	No	No
1-3 E	S960	10	Yes	Yes	No	No
2-1 E	Q235	25	Yes	Yes	No	No
2-2 E	Q345	20	Yes	Yes	No	No
2-3 E	S690	15	Yes	Yes	No	No
2-4 E	S960	12	Yes	Yes	No	No

2.5.2 Moment- rotation relationship of endplate connections

The Characteristics of moment-rotation relationship for all endplate connections at elevated temperature 550 ℃ obtained from tests are presented in Table 3.

Table 3. Characteristics of connections at elevated temperature 550 ℃.

Series	Connection ID	Endplate		Peak load		Connection rotation
		Material	Thickness (mm)	Moment (kN m)	Force (kN)	ϕ_C (mrad)
1	1-1 E	Q235	20	83.91	77.98	314
	1-2 E	S690	12	105.92	98.44	304
	1-3 E	S960	10	100.05	92.98	313
2	2-1 E	Q235	25	120.40	111.90	191
	2-2 E	Q345	20	111.16	103.31	313
	2-3 E	S690	15	120.78	112.25	330
	2-4 E	S960	12	113.18	105.19	320

3 NUMERICAL STUDY

The finite element software package ABAQUS 6.8 [4] was employed to numerically simulate the behaviour of high strength steel endplate connections in fire and at ambient temperature as well.

3.1 Finite element model

The geometric details of all connections' components modelled in FEM are the same as those of the test specimens. Because the geometric details, load, temperature distribution and boundary conditions of the beam-to-column endplate connection are symmetric, half of the endplate connection was modelled, to reduce computer costs. There were 7 surface-to-surface contact interactions and 7 tie interactions in this FE model, and the materials were endowed with non-linear properties. The whole connection was modelled using C3D8I elements.

3.2 Contact interaction and analysis process

The contact pairs in the endplate connection comprised the bolts-to-column flange, column flange-to-endplate, endplate-to-nuts and bolt shanks-to-bolt holes. The nuts were tied to the corresponding bolt shanks. Surface-to-surface contact, with a small sliding option, was used for all contact surfaces to fully transfer load. The penalty friction with friction coefficient 0.44 was employed in the contact interaction property. To handle contact interaction problem, the whole analysis process comprised five steps. In the first step, the bolts and endplate were restrained of all degrees of freedom temporarily, and then a very small pretension was applied to every bolt for temporarily restraining the bolt assembly. The temperature field for all components was 20 ℃. In the second step, the bolts and the endplate were freed from any temporary restraint. In the third step, the length of every bolt was fixed. In the fourth step, the temperature field for all components was modified to 550 ℃. (For the numerical analysis at ambient temperature, the temperature field was kept constant.) In the fifth step, an equivalent vertical surface traction converted from the vertical load was applied to the beam flange at the stiffener for loading. The first three steps helped contact interactions to be established smoothly, which is effective to decrease calculation time and eliminate errors.

3.3 Material Properties

In this study, the material properties of mild steels (including Q235 and Q345) at ambient temperature were obtained according to tensile tests on the mild steel materials used in full-scale tests; their material properties at elevated temperatures were obtained according to the recommended reduction factors of structural steels in fire from Eurocode 3 part 1-2 [5]. The material properties of Grade 8.8 bolts at ambient and elevated temperatures used herein were those reported by the University of Sheffield [6-7]. The material properties of HSS S690 and S960 at ambient and elevated temperatures input herein were obtained from material tests presented in reference [8-9]. The input mechanical properties of various materials in this FE modelling are true plastic strain and true stress.

4 DISCUSSIONS

4.1 Validation of numerical modelling against experimental results

4.1.1 Deformation at the end of test

The comparisons on final deformation states of all beam-to-column endplate connections at the end of the tests between numerical simulations and experimental results were conducted at elevated temperature 550 ℃ as well at ambient temperature. For instance, Figure 3 shows the comparisons on experimental final deformation state of connection 2-3E (S690 15mm) after failure at elevated temperature 550 ℃ with corresponding contour plots of Mises stress obtained from numerical modelling. It can be found that good agreements exist on the final deformation state of connection 2-3 E (S690 15mm) at elevated temperature 550 ℃. Although the current numerical model cannot simulate the fracture of the bolts, it is able to reveal the location where the fracture initiates and evolves, as shown in Figure 3 (c). The current FE model stops when the first failure of components occurs, i.e. the bolts in the top tensile row for this connection under fire condition. In the experimental study, after the failure of the bolts in the top tensile row, the bolts in the second tensile row experienced significant bending deformation until failure occurred. But the present numerical model is not able to simulate the failure of bolts in the second tensile row and the corresponding deformations of other components after the failure of bolts in the top tensile row. Similar conclusions can be drawn for all 7 connection specimens at elevated temperature 550 ℃ as well as at ambient temperature.

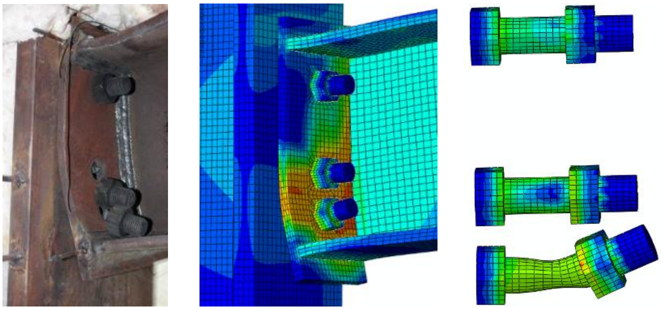

(a) Connection in test (b) Connection in FEM (c) Bolts in FEM

Figure 3. Comparison on final deformation state of connection 2-3 E (S690 15mm) at elevated temperature 550 ℃.

4.1.2 Moment-rotation characteristic

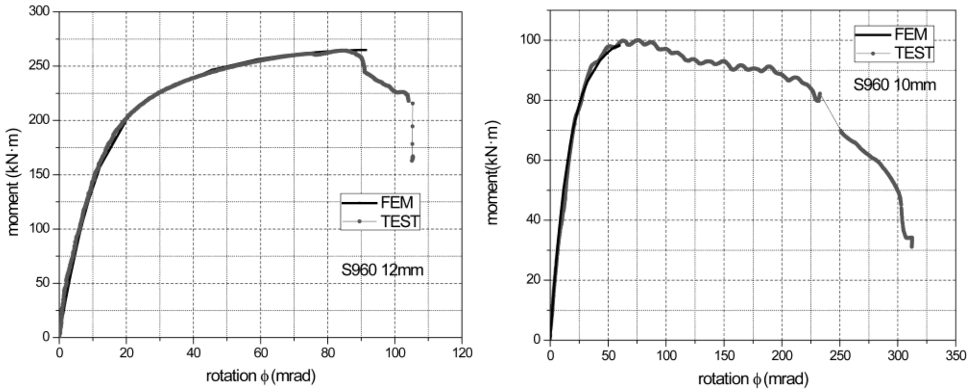

(a) 2-4 A (S960 12mm) at ambient temperature. (b) 1-3 E (S960 10mm) at elevated temperature 550 ℃

Figure 4. Moment-rotation comparison of endplate connections.

The comparisons of numerical modelling and experimental study on the moment-rotation relationship of various endplate connections (both high strength steel endplate connections and mild steel endplate connections) at elevated temperature 550 ℃ as well as at ambient temperature were carried out, where good agreements exist in general on initial stiffness, load bearing capacity and the connection rotation at the maximum load level $\phi_{M\max}$. For example, Figure 4 illustrates the moment-rotation comparison of two connections 2-4 A and 1-3 E.

4.2 Verification of Eurocode 3

4.2.1 Failure modes

According to Eurocode 3 Part:1-8 [1], there are 3 failure modes for endplate connections. Mode 1 is complete yielding of endplate or column flange, Mode 2 is bolt failure with yielding of endplate or column flange, while Mode 3 is bolt failure. Mode 3 is considered to be brittle and should be avoided in practical design. The failure modes of all endplate connections obtained via theoretical analysis based on the rules of Eurocode 3 Part:1-8 [1] were validated against those from tests, as shown in Tables 4. It can be observed that the predictions of Eurocode 3 agree very well with the test results.

Table 4. Failure modes of connections at elevated temperature 550 ℃.

Connection ID	Endplate		Failure mode	
	Material	Thickness (mm)	EC3	Test
1-1 E	Q235	20	Mode 2	Mode 2
1-2 E	S690	12	Mode 2	Mode 2
1-3 E	S960	10	Mode 2	Mode 2
2-1 E	Q235	25	Mode 2	Mode 2
2-2 E	Q345	20	Mode 2	Mode 2
2-3 E	S690	15	Mode 2	Mode 2
2-4 E	S960	12	Mode 2	Mode 2

4.2.2 Plastic flexural resistance

The plastic flexural resistances of all endplate connections at elevated temperature 550 ℃ are compared with the theoretical predictions of Eurocode 3 [1], as listed in Table 5. It can be seen that reasonable agreements exist between the theoretical predictions and the experimental results. By comparing Ratio_3, it can be found that $M_{j,Rd,test,1}$ obtained based on Zanon and Zandonini's definition [10] is generally smaller than $M_{j,Rd,test,2}$, which is defined according to Weynand's proposal [11] as well as the simplified method recommended by Eurocode 3 [1]. By comparing $M_{j,Rd,test,1}$ with the predicted plastic flexural resistance by Eurocode 3, see Ratio_1, it can be seen that the predictions of Eurocode 3 are generally non-conservative when the test result is obtained based on Zanon and Zandonini's definition. However, the comparison of $M_{j,Rd,test,2}$ with the predicted plastic flexural resistance by Eurocode 3 shows that the predictions of Eurocode 3 are generally on the conservative side, when the definition of the test result is based on Weynand's proposal and the simplified method recommended by Eurocode 3.

Table 5. Evaluation of plastic flexural resistance of connections at elevated temperature 550 ℃.

Test ID	Connections	$M_{j,Rd,EC3}$ (kN m)	$M_{j,Rd,test,1}$ (kN m)	$M_{j,Rd,test,2}$ (kN m)	$\text{Ratio}_1 = \frac{M_{j,Rd,EC3}}{M_{j,Rd,test,1}}$	$\text{Ratio}_2 = \frac{M_{j,Rd,EC3}}{M_{j,Rd,test,2}}$	$\text{Ratio}_3 = \frac{M_{j,Rd,test,1}}{M_{j,Rd,test,2}}$
1-1 E	Q235 20mm	76.77	68.13	72.94	1.127	1.053	0.934
1-2 E	S690 12mm	89.90	89.99	105.38	0.999	0.853	0.854
1-3 E	S960 10mm	95.26	84.68	93.74	1.125	1.016	0.903
2-1 E	Q235 25mm	109.29	106.50	108.79	1.026	1.005	0.979
2-2 E	Q345 20mm	107.37	104.68	105.86	1.026	1.014	0.989
2-3 E	S690 15mm	105.94	101.25	120.02	1.046	0.883	0.844
2-4 E	S960 12mm	105.41	104.83	111.90	1.006	0.942	0.937

Note: $M_{j,Rd,EC3}$ is the predicted plastic flexural resistance according to Eurocode 3 [1];

$M_{j,Rd,test,1}$ is the test obtained plastic flexural resistance according to Zanon and Zandonini's method [10];

$M_{j,Rd,test,2}$ is the test obtained plastic flexural resistance according to Weynand's evaluation method [11].

5 CONCLUSIONS

The following conclusions can be drawn from this experimental and numerical study:

(1) The load bearing capacity as well as rotation capacity of endplate connections is dependent on the combination of endplate material and endplate thickness.

(2) The accuracy of Eurocode 3 for plastic flexural resistance of endplate connections both at ambient temperature and in fire is acceptable, no matter the endplate is made of mild steels or high strength structural steels.

(3) The plastic flexural resistance of connections based on the definition of Zanon and Zandonini is generally smaller than that according to Weynand's proposal as well as the simplified method recommend by Eurocode 3. This conclusion is valid for all endplate connections in this study (both mild steel endplate connections and high strength steel endplate connections).

(4) In endplate connections, a proper design using a relatively thin high strength steel endplate can achieve the same failure mode, similar load bearing capacity and comparable or even higher rotation capacity, both at ambient temperature and in fire, in comparison to a connection with relatively thick mild steel endplate.

(5) The challenge of numerical modelling contact interactions considering material and geometric non-linear effects has been solved successfully.

(6) This finite element analysis gives reasonable accuracy compared with the experimental results, providing an efficient, economical, and accurate tool to study the fire performance of high strength steel endplate connections.

(7) This study opens a perspective of using high strength steels to take place of mild steels in structural optimizing design.

REFERENCES

[1] CEN, *Eurocode 3: Design of steel structures, Part 1-8: Design of joints*. Brussels, 2005.

[2] CEN, *Eurocode 3 - Design of steel structures - Part 1-12: Additional rules for the extension of EN 1993 up to steel grades S700*. Brussels, 2004.

[3] Coelho A.M.G., Bijlaard F.S.K., "Experimental behaviour of high strength steel end-plate connections". J Constr Steel Res, 63, 1228-40, 2007.

[4] Abaqus Analysis User's Manual, 6.8 version.

[5] CEN, *Eurocode 3: Design of steel structures, Part 1-2: General rules - Structural fire design*. Brussels, 2005.

[6] Hu Y., *Robustness of flexible endplate connections under Fire Conditions*, PhD thesis. Sheffield, UK: University of Sheffield, 2009.

[7] Theodorou Y., *Mechanical properties of grade 8.8 bolts at elevated temperatures*, Master's dissertation. Sheffield, UK: University of Sheffield, 2003.

[8] Qiang X., Bijlaard F.S.K., Kolstein H., "Dependence of mechanical properties of high strength steel S690 on elevated temperatures". Constr Build Mater, 30, 73-9, 2012.

[9] Qiang X., *Behaviour of high strength steel endplate connections in fire and after fire,* PhD thesis. Delft, the Netherlands: Delft University of Technology, 2013.

[10] Zanon P., Zandonini R., "Experimental analysis of end plate connections". Proceedings of the state of the art workshop on connections and the behaviour of strength and design of steel structures. Cachan, 41-51, 1988.

[11] Weynand K., *Sicherheits- und Wirtschaftlichkeitsuntersuchungen zur Anwendung nachgiebiger Anschlüsse im Stahlbau*. Heft 35, Shaker Verlag. Aachen, 1997.

8th International Conference on Structures in Fire
Guo-Qiang LI, Venkatesh K. R. KODUR, Shou-Chao JIANG, Jian JIANG, Su-Wen CHEN, Guo-Biao LOU (Eds.)
Shanghai, China, June 11-13, 2014

EFFECT OF AXIAL RESTRAINTS TO BEAMS ON THE BEHAVIOUR OF A BOLTED COMPOSITE STEEL-CONCRETE JOINT UNDER A LOCALISED FIRE

C. Haremza*, A. Santiago* and L. Simões da Silva*

* ISISE, Department of Civil Engineering, University of Coimbra, Portugal
e-mails: haremza@dec.uc.pt, aldina@dec.uc.pt, luisss@dec.uc.pt

Keywords: Numerical analysis, Experimental tests, Steel-concrete joint, Bending moment-axial force interaction, Localised fire, Axial restraints

Abstract. *This paper focuses on the joint behaviour study from a composite steel-concrete open car park building subject to fire. Experimental tests to simulate the loss of a column due to a localised fire were undertaken at the University of Coimbra, Portugal [1], and the composite steel-concrete beam-to-column joint was studied in detail. This paper corresponds to the ongoing work within the IMPACTFIRE project. FEM models of the beam-to-column joint subject to the loss of the column due to a localised fire are developed in Abaqus and calibrated against the tests. Following, these FEM models are uzed to evaluate the influence of the beam axial restraint coming from the unaffected part of the building.The results are compared with the M-N interaction curves provided by the analytical methodologydeveloped at the University of Liège [2].*

1 INTRODUCTION

Open car park buildings are characterized by high ventilation that keeps the fire limited on the ignition zone (localized fire), not leading to a flash-over. In this situation, only local damage of structural elements is observed. However, the local damage could be the origin of progressive collapse of the whole building, so that it is essential to design the structure with sufficient inherent robustness in order to avoid such disproportional progressive collapse. The exceptional event considered in this work is the loss of a column under localised fire. Under such an event, the axial restraints to the beams influence the loading of the sub-frame by increasing axial forces in the joint/beam, mainly due to: i) the thermal expansion effects during the heating, and ii) the column collapse. So the heated joint is no longer under predominant bending action, but it is subject to a variable combination of axial forces and bending moments. Therefore, the influence of the joints and their ductile behaviour is particularly important for the structural robustness, especially when the plastic hinge is located in the joint and all global deformations have to be realized mainly by joint rotation/deformation.

The work presented in this paper is part of the European RFCS ROBUSTFIRE project and the National IMPACTFIRE project. The ROBUSTFIRE project developed a design philosophy aiming at the economical design of car parks exhibiting a sufficient robustness under localised fire and derived practical design guidelines for the application of this design philosophy throughout Europe. Experimental tests to simulate the loss of a column due to a localised fire were undertaken at the University of Coimbra, Portugal [1], and the composite steel-concrete beam-to-column joint was studied in detail. A methodology to predict the mechanical response of bolted composite beam-to-column joints at elevated temperatures under M-N was also applied [2].

FEM models of the beam-to-column joint subject to the loss of the column due to a localised fire are developed in Abaqus [3] and calibrated against the previous tests. Following, these FEM models are used to evaluate the influence of the beam axial restraint coming from the unaffected part of the building, and the results are compared with the M-N interaction curves calculated by the analytical methodology mentioned before.

2 REVIEW OF THE EXPERIMENTAL TESTS

A sub-frame extracted from an actual composite open car park building, with real cross-section dimensions: beams IPE 550, columns HEB 300, and bolts M30, cl. 10.9, was tested at the University of Coimbra [1]. The steel beam was fully connected to the composite slab (Figure 1(a)). The main objective of the tests was to observe the combined bending moment (M) and axial loads (N) in the composite joint throughout the entire M-N resistance curve. In order to reach this goal, the effect of the axial restraint to the beam provided by the cold part of the building was simulated: three tests were performed without any restraint to the beam, two tests with total axial restraint to the beam and two tests with a realistic axial restraint to the beam (spring restraint). In order to simulate the effect of the localised fire that led to the column loss, the composite joint (Figure 1(b)) was subject to elevated temperatures: five tests at 500 ℃ or 700 ℃, one test at ambient temperature, and a demonstration test.

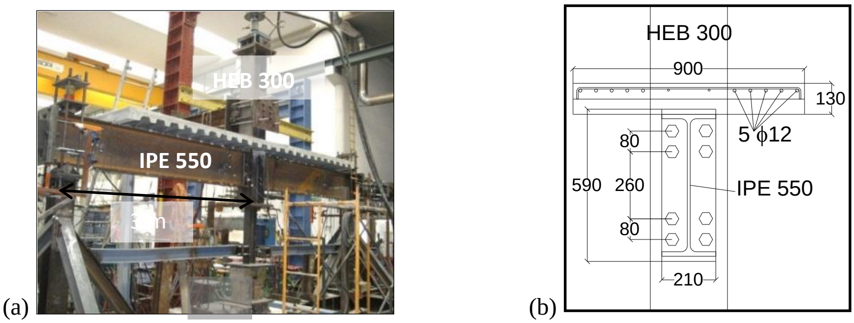

Figure 1. (a) Experimental test outline; (b) Composite beam-to-column joint.

Testing procedure included three main loadings (Figure 2): 1st - an initial hogging bending moment was applied to the joint before the localised fire, simulating the internal loads as in the real car park, 2nd - the joint zone was heated in order to reproduce the effect of the localised fire (except for ambient temperature test), and 3rd - the loss of the column was simulated (without any residual bearing capacity) and the sagging bending moment was increased up to the failure of the joint. Bending moments were applied to the joint by increasing the vertical load at the column top in the upward or downward direction, whereas the vertical displacements of the beams ends were locked. During the 2nd phase, temperatures increased with a linear rate of 300 ℃/hour, up to the target temperature in the beam bottom flanges (500 ℃ or 700 ℃); these temperatures were kept constant during the increase of sagging bending moment (3rd phase). Flexible Ceramic Pad heating elements were used, and the heated zone was defined by a length of 0.6 m of beam to each side of the joint, the bolts and 1 m of column (concrete was not heated) [1].

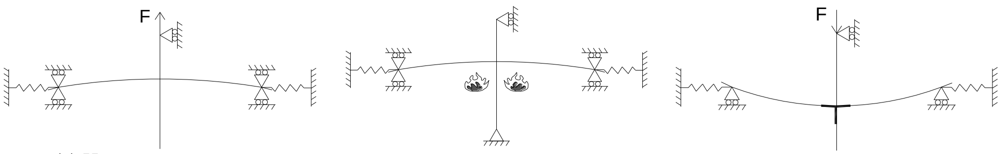

(a) Hogging moment (b) Localised fire (c) Sagging moment

Figure 2. Loading sequence.

2 NUMERICAL MODEL

In the following sections, the procedures for the implementation of a FEM model are described. The commercial FEM package Abaqus, v6.12 [3], is used to perform the simulations.

2.1 General modelling assumptions

The geometry of the specimen and the testing procedure used during the experimental tests are reproduced in the FEM model. In order to save computational time, the symmetry of the joint is taken into account in the model. The displacements out of the plane (x-direction in Figure 3) in the column flange and the beam flanges are restrained, but the local buckling of the webs is accepted. The y-direction at the beam support is restrained, leaving free the z-direction; the top of the column is free in the y-direction, and the z-direction is restrained all along the column web and the slab width. The beam axial restraint is modelled by a spring with a linear elastic behaviour (50 kN/mm in the experimental test).

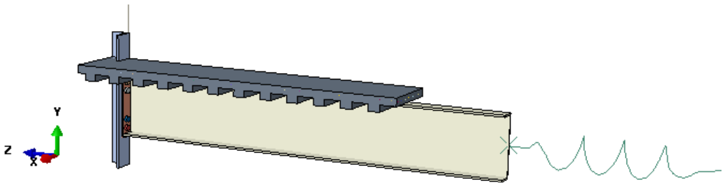

Figure 3. 3D FEM model of the composite steel-concrete frame in Abaqus.

The main steel joint members are modelled with 3D 8-node linear brick reduced integration solid elements (C3D8R). Bolts M30 are modelled with a reduced diameter size d_s equal to 26.73 mm, equivalent to the resistant section A_s (561 mm^2); the hole around the bolt shank is 3 mm higher than the bolt diameter, as in the real connection. Bolt head and nut are modelled circular and include the two washers that were used during the tests; the bolt threads are not modelled. In order to simplify the model and save computational time, the upper part of the steel column, away from the joint zone, is modelled using general B31 beam elements. The steel sheeting of the composite slab is not considered, and the shape of the ribs is simplified by an equivalent rectangular section of width 84 mm. The longitudinal and transversal steel rebars are modelled with two-node three-dimensional truss elements (T3D2). Steel rebars are embedded in the concrete slab by means of an embedded constraint which neglects any relative slip and debonding of the mesh with respect to the concrete. In order to have full integration and avoid any problem of hourglass modesin the slab, incompatible mode solid elements (C3D8I) are used. The shear studs are modelled with solid C3D8R elements.

Because the purpose of this study is the joint behaviour, only the geometrical imperfections in the end plate are considered: the measured initial deformation of the end-plate (gap of 0.6 mm between the end-plate centre and the column flange) is reproduced using a sinusoidal shape between bolt rows 2 and 3.

Welds are not modelled; steel beam is fully connected to the end-plate using the TIE option; shear studs are also tied to the steel beam. Contacts are defined as surface-to-surface contact with a small sliding option[5]. Normal contact is defined as “hard contact” with default constraint enforcement method, and separation is allowed after contact. A friction coefficient of 0.25 is used in the tangential behaviour of steel to steel contact, with penalty friction formulation, and no friction is assumed between concrete and steel surfaces. The bolts and the end-plate are meshed similarly (element size 3-5 mm), whereas the column has a coarser mesh (element size 6-10 mm). In order to correctly model the local deformations out of their plane, three elements are defined on the thicknesses of the end-plate and on the web and flanges of the beam.

2.2 Mechanical and thermal loadings

The general static analysis is used. Several numerical steps are defined: step 1 - pre-loading of bolts; step 2 - hogging bending moment; step 3 - heating; step 4 - loss of the column (the column bottom support is inactivated); step 5 - sagging bending moment. Hogging and sagging bending moments in the joint are simulated by displacement control at the top of the column. Temperatures are defined into specific points as predefined fields, and one amplitude curve defining the evolution of the temperature measured during the test is introduced for each section (Figure 4).

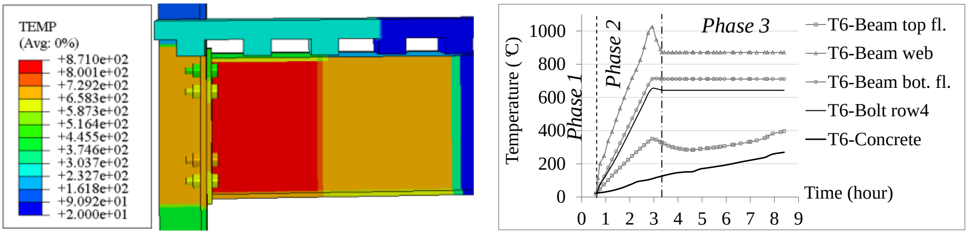

Figure 4. Temperatures distribution in the joint (test 6).

2.3 Mechanical properties

For good correlation with experimental results, the full actual stress-strain relationship of the materials must be adopted in the numerical simulation. The constitutive laws of structural steels S355J0+M and S460M, and of bolts M30, cl. 10.9 (at ambient and elevated temperatures) were determined based on coupon tests [1]. For Abaqus simulation, the nominal stress-strain measures obtained from the standardized curves are converted to the true stress-logarithmic strain values (see Figure 5). The C25/30 concrete properties measured by compression tests at 28 days are considered in Abaqus (f_{ck} = 28.8 MPa and E_{cm} = 32 514 MPa). The stress-strain behaviour and the maximum tensile stress (2.8 MPa) are defined according to Eurocode 2 part 1.1 [4]. The coefficients of expansion for steel and concrete materials are assumed constant and equal to $\alpha_{steel} = 1.4\ 10^{-5}$/°C and $\alpha_{concrete} = 1.8\ 10^{-5}$/°C respectively. Steel rebars are assumed as elastic-perfectly plastic material: $f_{y,sr}$= 500MPa and E_{sr} = 200 GPa, while for the shear studs of 22 mm diameter, the material is modelled by a tri-linear stress strain curve$f_{y,ss}$= 500MPa($\varepsilon_{y,ss}$= 0.2%),$f_{u,ss}$= 480MPa($\varepsilon_{u,sr}$= 0.6%) and E_{ss} = 208 GPa[5].

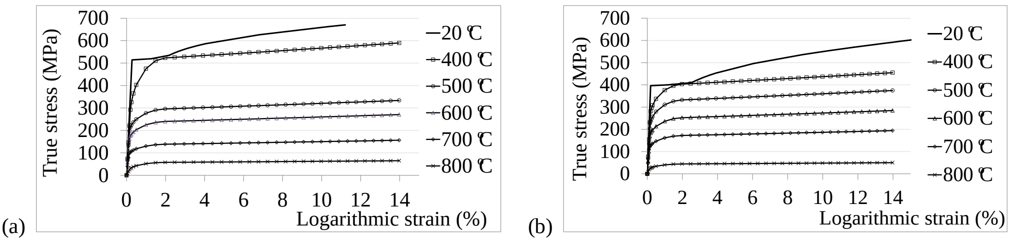

Figure 5.True stress-logarithmic strain steel curves at elevated temperatures for: (a) the flange of columns HEB 300 (S460) and (b) the flange of beams IPE 550 (S355).

2.4 Calibration of the FEM models

The FEM models are calibrated against three experimental tests: two tests without axial restraint to the beam (test 1 at 20 °C and test 3 at 700 °C), and test 6 at 700 °C, with axial restraint to the beam simulated by a spring (50 kN/mm) [5]. It was concluded that the global behaviour of the frame in Abaqus is good modelled. The composite joint failure (concrete crushing in compression followed by the bottom bolt row failure in tension) is also easily approximated. The evolution of the total load applied at the column *versus* the vertical displacement of the joint for the test 1 at ambient temperature is depicted in Figure 6(a). In the FEM model, the bolt failure is assumed once the equivalent bolt strain average on the section reaches the strain to fracture measured during the tensile tests: 11.3% in test 1 (ambient temperature), 28% in test 3 (bolt at 626 °C) and 30% in test 6 (bolt at 643 °C).

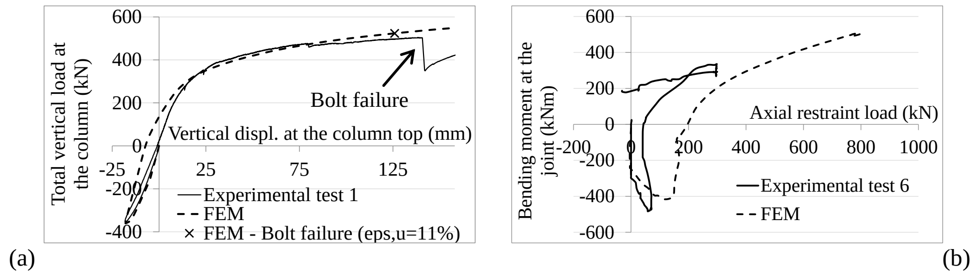

Figure 6.(a) Applied load - vertical displacement for test 1 (20 ℃); (b) Bending moment – axial load for test 6 (700 ℃).

In test 6, during the heating phase, due to the thermal expansions of beams, the beams ends moved in the outward direction, and compression loads were applied by the axial restraint. After the column loss, under sagging bending moment, the axial restraint increased the compression load because the beam end continued to move outwards [1]; the bending moment *versus* the beam axial load is depicted in Figure 6b. In this test, some discrepancies appear for the loads measured at the column top and at the beam axial restraint, and the initial stiffness of the FEM model is slightly higher than observed in the test. In the FEM model, a higher axial compression load is observed in the beam restraint, which increases the sagging bending moment within the joint[5].

3 M-N CURVE OF THE COMPOSITE STEEL-CONCRETE JOINT

3.1Numerical M-N curve of the composite steel-concrete joint

Once the column fails, the joint suffers a vertical displacement downwards, and the joint bending moment changes from hogging to sagging bending moment. The joint is also subject to axial loads created by the axial restraint to the beam coming from the unaffected part of the building. In this section, additional simulations are performed at ambient and elevated temperature (from test 6) in an attempt to draw the M-N curve of the joint. The previously presented FEM models are used to perform the study under ambient and elevated temperature. One FEM simulation provides one point of the M-N curve; this point corresponds to the failure of the joint that could be due to a bolt row in tension or column web buckling in compression. In the tensile zone, the failure of the end-plate in bending or beam web in tension happens before the bolt failure in tension, but this is a ductile failure and it is not easy to be captured; so bolt failure in tension (fragile failure) is assumed as the failure of the joint.

3.2Analytical M-N curve of the composite steel-concrete joint

The numerical M-N curve of the joint is compared to the M-N curve predicted by the analytical method developed at the University of Liège.This analytical method was first developed for steel joints in Cerfontaine[6], then adapted for composite joints in Demonceau [7] and finally enlarged for steel and composite joints subject to elevated temperatures in the ROBUSTFIRE project [2]. This method is in full agreement with the Eurocode component model [8,9], and it is based on the assumption that all components activated at failure are fully ductile, meaning a plastic redistribution of the forces is considered within the joint without any displacement limitations. The joint is divided into different rows that can be activated in tension or in compression. The resistance of each row can be calculated using the component method; the resistance of the row is given by the weakest component involved in it. For given bending moment and axial force, a row will be activated or not depending on the position of the neutral axis and whether the upper rows are in tension or in compression. For any chosen position of the neutral axis (at the very top of the joint, between two successive rows or at the very bottom), the activated rows can easily be determined and they are supposed to sustain a force equal to their resistance (plastic distribution) while the other ones sustain a force equal zero. The corresponding loading (M,N) can be computed using the equilibrium equations [2]: $N = \sum_{activated\ \ rows\ i} F_i$ and $M = \sum_{activated\ \ rows\ i} F_i\, h_i$;

where F_i is the force sustained by row i, and h_i is the distance from row i to the reference axis.The same procedure can be applied at elevated temperature provided the temperature distribution in the joint is known. Each component resistance is then simply evaluated based on the material resistance at its given temperature [2].

The analytical M-N curves presented in this paper consider that:i) the ultimate resistance of the components is used in order to predict the real behaviour of the joint like in the experimental tests and the FEM models, ii) the nominal properties of the material (section 2.3), iii) the safety factors are equal to 1.0, iv) the mid-height of the steel beam section is considered for the reference axis; and v) the component's temperatures for the FEM model of test 6 (section 2.2) are used for the analytical calculation.Some differences are observed between the analytical M-N curves developed within the ROBUSTFIRE project [2]and this updated version; these differences provide from the update of material resistances from available coupon tests and simplifications of components' temperatures based on the FEM models.

3.3Numerical and analytical results

At ambient temperature, a very good correlation is shown between the numerical and analytical M-N curves of the composite joint (Figure 7(a)). In the FEM models, the joint failure mode corresponds to: i) bottom bolt row failure in tension (BT), for axial loads between -1500 kN and +1524 kN; and ii) column web buckling under compression (CWC), for axial loads higher than +1524 kN. This last ductile failure is defined as the end of the FEM models, when it becomes impossible to establish the equilibrium of the structure. The part of the M-N curve drawn by the numerical models provides the required (M, N) points to make the comparison with the analytical results.

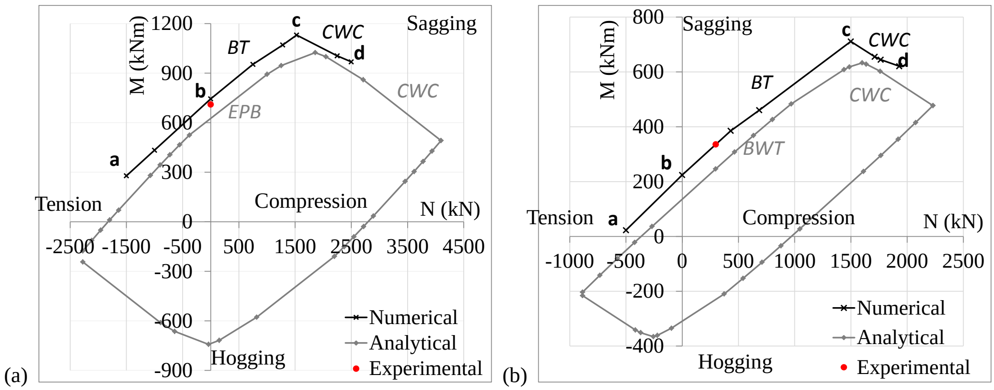

Figure 7. M-N curve at (a) ambient temperature (test 1), (b) elevated temperature (test 6 – 700 °C).

In the analytical model, the resistance of the composite joint under sagging bending moment is governed by: i) the end-plate in bending (EPB); and ii) the column web buckling under compression (CWC). Additionally, the experimental result is represented by the maximum bending moment measured before the 1st bolt failure (710 kNm), which represent 4% of difference with FEM model.

The deformation of the joint and the out of plane displacement at failure at each four points *a, b, c, d* of the FEM M-N curve are depicted in Figure 8. Under tension axial load (point *a*), the neutral axis is situated in the concrete slab and only a small part of the concrete is in compression; in point *b* (only bending), the neutral axis is located between the top bolt row and the beam top flange; this neutral axis drops above the second bolt row under compression axial load (point *c*). It can be observed that lower position of the neutral axis allow for the joint to reach higher vertical displacements before the bolt failure in the bottom bolt row; the ductility of the joint is increased. However, under high axial compression load (point *d*), only the bottom bolt row is in tension, and the column web instability is observed with high deformation out of the plane; this failure mode limits the vertical displacement and deformation capacity of the joint.

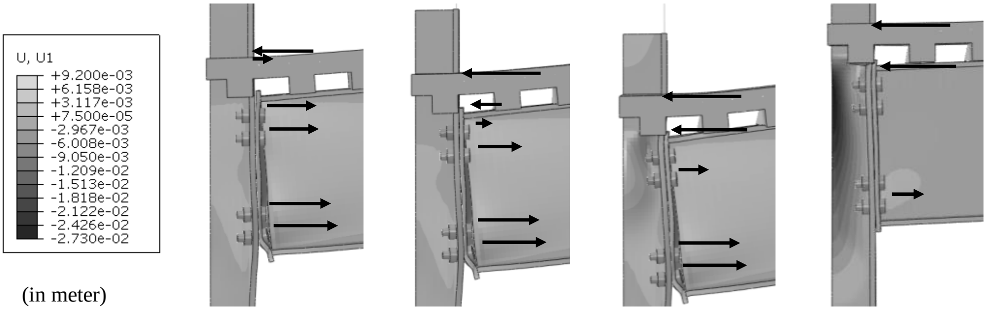

(a) N = -1500 kN (EPB/BT) (b) N = 0 (EPB/BT) (c) N = 1524 kN (EPB/BT) (d) N = 2500 kN (CWC)

Figure 8.Deformation of the joint and out of plane displacement U1 at failure, for various axial loads (scale 2) – ambient temperature.

The numerical and analytical M-N curves of the composite joint at elevated temperature are presented in Figure 7(b); a very good correlation is shown. In the FEM models, the joint failure mode corresponds to: i) bottom bolt row failure in tension (BT), for axial loads between-500 kN and +1499kN; and ii) column web buckling under compression (CWC), for axial loads higher than +1499kN.In the analytical model, the resistance of the composite joint under sagging bending moment is governed by: i) the beam web in tension (BWT); and ii) the column web buckling under compression (CWC). The experimental result of test 6 is also represented inFigure 7(b)(M = 336 kNm).

The deformation of the joint and the out of plane displacement at failure at each four points *a*, *b*, *c*, *d* of the FEM M-N curve are depicted in Figure 9. The failure modes are similar to those observed at ambient temperature; the vertical displacement and deformation capacity of the joint are limited when the column web instability is observed (point *d*).

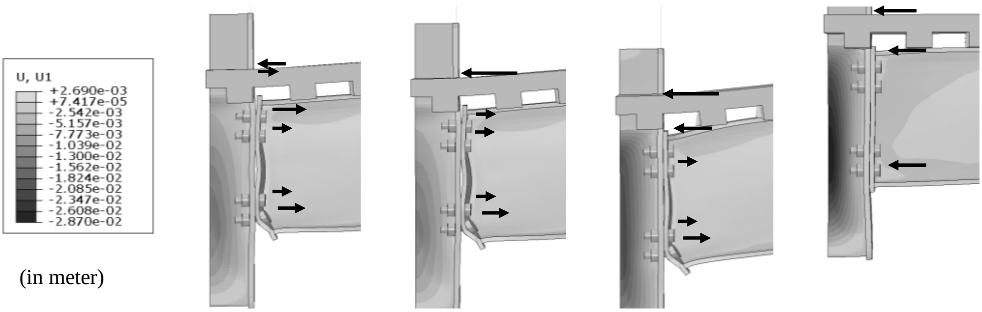

(a) N = -500 kN (BWT/BT) (b) N = 0 (BWT/BT) (c) N = 1499 kN(BWT/BT) (d) N = 1930 kN (CWC)

Figure 9. Deformation of the joint and out of the plane displacement U1 at bolt failure, for various axial loads (scale 2) – elevated temperature (from test 6 - 700 ℃ in the beam bottom flange).

4 CONCLUSIONS

This paper presents a study of the composite steel-concrete joint behaviour from an open car park building subject to fire. FEM models of the beam-to-column joint subject to the loss of the column due to a localised fire are developed in Abaqus and calibrated against experimental tests[1]. These FEM models are used to evaluate the influence of the beam axial restraint coming from the unaffected part of the building.The results are compared with the M-N interaction curves calculated by the analytical methodology developed within the ROBUSTFIRE project [2].

From the results, it can be observed that the sagging bending moment resistance: i) reduces with the increase of tensile axial loads; ii) reaches a maximum value under compression axial loads. The failure of the joint under sagging bending moment is associated to the end-plate in bending at ambient temperature, and to the beam web in tension under elevated temperatures. Under high compression loads, at ambient and elevated temperatures, the column web instability governs the joint resistance.

To avoid any progressive collapse throughout this type of fire event, the joint needs ductility. From the results, it can be observed that the failure mode of the joint is of great importance: failure mode related to the instability of the column web in compression need to be avoided because it limits a lot the deformation capacity of the joint. The joint reaches its maximum resistance and maximum capacity of deformation under the (M, N) loading corresponding to a position of the neutral axis located near the top bolt row: the concrete slab and the beam top flange are under compression and all the bolt rows work in tension.

ACKNOWLEDGMENT

The authors acknowledge financial supports from Ministério da Educação e da Ciência (Fundação para a Ciência e a Tecnologia) for the research project PTDC/ECM/110807/2009,and from the European Union (Research Fund for Coal and Steel) under contract grant RFSR-CT-2008-00036.

REFERENCES

[1] Cécile Haremza, Aldina Santiago, Luís S. da Silva, “Experimental behaviour of heated composite steel-concrete joints subject to variable bending moments and axial forces”, Engineering Structures 51, p150-165, 2013.

[2] Demonceau J.F., Huvelle C., Comeliau L., Hoang L. V., Jaspart J.P., Fang C., et al. “Robustness of car parks against localised fire (Robustfire)”, European Commission, Grant Agreement Number RFSR-CT-2008-00036, Final report, EUR 25864, 2013.

[3] Abaqus 6.12, Theory Manual and Users Manuals, DassaultSystemesSimulia Corp., 2012.

[4] EN 1992-1-1:2004 – “Eurocode 2: Design of concrete structures - Part 1-1: General rules and rules for buildings”, European committee for standardization, December 2004.

[5] Haremza C., Santiago A., Simões da Silva L., "Effect of axial restraint in a composite steel-concrete frame subject to localised fire”, IX CMM, Porto, Portugal, 2013.

[6] Cerfontaine F. “Etude de l’interaction entre moment de flexion et effort normal dans les assemblages boulonnés”. PhDthesispresented at the University of Liège. Belgium, 2004.

[7] Demonceau J.F. “Steel and composite building frames: sway response under conventional loading and development of membrane effects in beams further to an exceptional action”. PhD thesis presented at the University of Liège. Belgium, 2008.

[8] EN 1993-1-8:2005 – “Eurocode 3: Design of steel structures - Part 1-8: Design of joints”, European committee for standardization, May 2005.

[9] EN 1994-1-1:2004 – “Eurocode 4: Design of composite steel and concrete structures - Part 1-1: General rules and rules for buildings”, European committee for standardization, Dec. 2004.

8th International Conference on Structures in Fire
Guo-Qiang LI, Venkatesh K. R. KODUR, Shou-Chao JIANG, Jian JIANG, Su-Wen CHEN, Guo-Biao LOU (Eds.)
Shanghai, China, June 11-13, 2014

THE EXPERIMENTAL BEHAVIOR OF RC AND HFRC TUNNEL SEGMENTAL JOINTS SUBJECTED TO ELEVATED TEMPERATURE

He-Hua Zhu* , Yi Shen* and Zhi-Guo Yan*

* [a] State Key Laboratory of Disaster Reduction in Civil Engineering, Tongji University, 1239 Siping Road, Shanghai 200092, China
[b] Department of Geotechnical Engineering, Tongji University, 1239 Siping Road, Shanghai 200092, China
[c] Key Laboratory of Geotechnical and Underground Engineering of the Ministry of Education, Tongji University, 1239 Siping Road, Shanghai 200092, China
e-mails: zhuhehua@tongji.edu.cn, shenyige@gmail.com, yanzguo@126.com

Keywords: Hybrid fiber reinforced concrete; Shield TBM tunnel; Lining segmental joints; Fire test

Abstract. *The work presented in this paper is focused on the experimental behaviour of TBM tunnel joints in different mechanical boundary condition. The test provides evidences of the thermo-mechanical behavior of joints on their real work conditions under tunnel fire and, therefore, considering several parameters involved in its structural response. Additionally, the test performance over a lining constructed using hybrid fibers as unique concrete reinforcement supplies relevant information about the structural contribution of such material to this structural typology. Thirteen tunnel joint specimens at a scale of 1:3 were tested: six tests for RC (reinforced concrete) specimens and seven tests for HFRC (hybrid fiber reinforced concrete) specimens. Joints in the post-fire group experienced three different initial loading conditions during heating. The effects of the axial force to joint stiffness were also studied: three different axial force levels were applied in loading condition.*

1 INTRODUCTION

Considering that the shield TBM tunnel lining is a special concrete-steel composite structure assembled by several member segments that are connected to one another by lining joints, its behavior and failure mechanism under high temperature are complicated. As a weak link of the tunnel lining due to its low stiffness and high risk of water leakage, the lining joint may significantly affect the behavior of the shield TBM tunnel lining exposed to high temperature. For instance, for metro shield TBM tunnel linings in soft ground with high water pressure, fire may trigger the failure of the joint seal causing tunnel linings leakage or even water gushing into the tunnel.

As for TBM tunnel joints in fire condition, Yan et al. [1] conducted the full-scale experimental test results of actual RC (reinforced concrete) metro shield TBM tunnel linings that were exposed to a standard ISO834 curve with 45 minutes and 90 minutes heating durations. It is beneficial to note that the opening angles and gaps of the tunnel lining joints considerably increase under high temperatures. Yan et al. [2] also carried out comprehensive experimental test results on the behavior of the RC and the steel fiber reinforced concrete (SFRC) shield TBM tunnel lining segments and the lining rings exposed to a HC (Hydrocarbon) curve. The deterioration of properties and the interaction between adjacent member segments result in significant deformations and dynamic internal force redistribution of the RC and the SFRC lining rings, which implies the behavior and configuration of the lining joints significantly affects the mechanical performance and the failure pattern of the lining rings exposed to high temperature. The mechanical behaviour of shield TBM tunnel joints under fire is very complicated. They bear diverse stress states in a tunnel ring. And when fire occurs, comprehensive factors can induce joint deterioration, e.g. concrete spalling, material degradation etc. However, limited holistic research was documented on this topic. On the other hand, the superiority of HFRC (hybrid fibre reinforced concrete) in fire has been proved [3,4,5]. The use of polypropylene fibers can eliminate the spalling of concrete while the steel fibers provide high ductility and reduce cracks propagation for the concrete [6].

The work presented in this paper is focused on the experimental behaviour of TBM tunnel joints in different mechanical boundary condition. Thirteen tunnel joint specimens at a scale of 1:3 were tested: six tests for RC specimens and seven tests for HFRC specimens. Eleven specimens were exposed to a HC (Hydrocarbon) curve and two benchmark tests for each kind of specimen in ambient temperature. Six specimens were loaded to failure under fire and five specimens were loaded post fire. Joints in the post-fire group experienced three different initial loading conditions during heating. The effects of the axial force to joint stiffness were also studied: three different axial force levels were applied in loading condition..

2 EXPERIMENTAL PROGRAM

2.1 Materials and specimens

The laboratory experimental tests were conducted at the isolated segment level. It is notable that there will be the longitudinal restraint to the thermal expansion and displacement of the tunnel lining in the lateral direction in reality. Small scale specimens were employed in our tests here. The lining segments here were 300 mm in width and 120 mm in thickness; their average radius was 990 mm, cf. Figure 1.

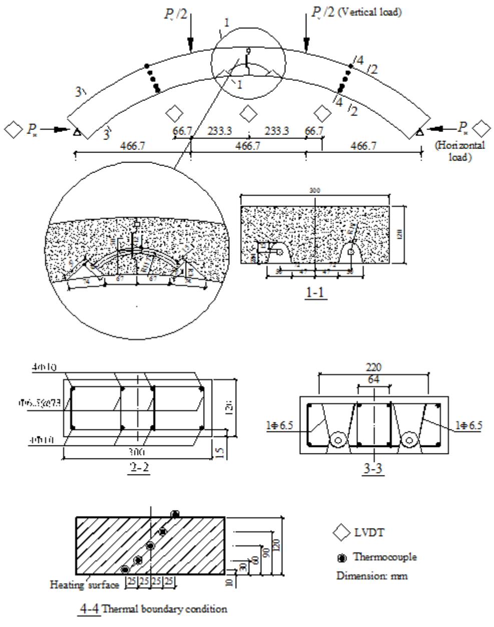

Figure 1. The configuration of the lining segments and the layout of the reinforcements for the RC lining segments.

According to the realistic metro shield TBM tunnel lining segment, the hand hole, the longitudinal tongue and groove of the lining segment were designed and fabricated. Every two member segments were connected by two curved bolts M10, grade 5.8. According to the realistic metro shield TBM tunnel lining, the hand hole, the longitudinal and the circumferential tongue and groove of the lining segment were also designed and fabricated. Rubber waterstop and flexible gasket of the lining joints were ignored.

Properties of the Polypropylene (PP) and steel fibers which provided by the manufacturer are presented in Table 1 and Table 2, respectively. The volume fraction of steel fiber and PP fiber was 78 kg/m^3 and 2 kg/m^3, respectively. The measured standard cube strengths of the plain concrete and the hybrid fiber reinforced concrete at the ambient temperature were 69.8 MPa and 61.1 MPa, respectively, at 28 days. Furthermore, for the RC lining segments, the reinforcements (hot-rolled rebars) were installed with 15 mm concrete cover thickness (cf. Figure1).

Table 1. Properties of polypropylene fiber.

Item	Value
Specific gravity	0.91
Length (mm)	12
Diameter (μm)	18
Tensile strength (MPa)	365
Elastic modulus (MPa)	3300
Melting point (˚C)	160
Ignition Point (˚C)	590
Alkali, acid and salt resistance	High

Table 2. Properties of steel fiber.

Item	Value
Specific gravity	7.8
Length (mm)	50
Diameter (mm)	0.9
Tensile strength (MPa)	1000
Elastic modulus (MPa)	200000
Melting point (˚C)	160
Item	Value
Specific gravity	7.8

2.2 Test procedure and procedure

An international standard HC curve is employed in the experimental tests to simulate the heating phase [7].The peak temperature inside the furnace was 1,100 ˚C, and the heating duration was 60 minutes. A newly-developed thermo-mechanical test system for tunnel lining segments under elevated temperatures was used in this test. This system contains two combustors in industrial grade and controls heating up procedure by programming. The peak temperature in the furnace can reach 1200 ˚C and the maximum heating rate was approximately 250 ˚C/min. This system can simulate the fire scenario with characterizing high speed heating rate and peak temperature and diverse loads and temperatures case combinations can be achieved. Subsequently, taking into account the cooling phase of an actual fire [8], the furnace is turned off, and the specimens are gradually cooled to the ambient temperature.

As exhibited in Figure 1, both ends of the lining segments were constrained by sliding rotations. Based on the load equivalent principle and the mechanical characteristics of the tunnel lining, the point loading strategy was employed in the tests to facilitate the loading control and to highlight the thermal-mechanical effects on the tunnel linings under high temperatures. For the lining segments, the vertical load (P_v) was applied by a hydraulic jack at the two points and the horizontal load (P_u) was applied by two hydraulic jacks from two directions (cf. Figure 1). A load cell was placed under each hydraulic jack to ensure that the applied load remained constant. In addition, the load cells were placed under horizontal jack to precisely measure the horizontal displacement of the support at ends during the test (cf. Figure 1). Three different fire/mechanical loading conditions (LC) were considered, a summary of the test conditions for all the specimens can be found in Table 3, namely:

(i) Loading Case 0 (LC0): ambient temperature test. Two specimens, one for RC (designated as RC1) and one for HFRC (HFRC1), were tested under constant axial force to provide benchmark responses for comparison.

(ii) Loading Case 1 (LC1): residual strength after exposure to fire. In the first step, the test segments were first loaded mechanically to a prescribed initial (service) load level, and then subjected to a complete heating (following HC curve) and cooling process. After complete cooling and unloading, in the second step, the specimens were loaded to failure, by maintaining the horizontal load (40kN) and increasing the vertical load, to investigate the ultimate strength and bending stiffness after exposure to high temperature. Five specimens were tested with LC1, including RC5/HFRC5 (initially loaded by 2kN.m positive moment in the first step); RC6/HFRC6 (initially loaded by 2kN.m hogging moment in the first step); and HFRC7 (initially loaded by 4kN.m in the first step).

(iii) Loading Case 2 (LC2): ultimate strength under fire. The test segments were heated following the standard HC curve, without however any initial loads. After approximately 40 minutes of heating, the specimens were mechanically loaded to failure to investigate the ultimate strength under high temperature. Three pairs of specimens were subjected to LC2 tests, including RC2/HFRC2 (under 20kN horizontal load), RC3/HFRC3 (under 40kN horizontal load) and RC4/HFRC4 (under 40kN horizontal load).

Table 3. Details of the test arrangement and test results.

No.	Initial boundary conditions	Designed loading case	Fire load	Mmax(kN.m)
RCJ1	M_c=0, P_u=40 kN	LC0	-	M_c=11.38
RCJ2	M_c =0, P_u =20 kN	LC2	HC	M_c=6.14
RCJ3	M_c =0, P_u =40 kN	LC2	HC	M_c=9.04
RCJ4	M_c =0, P_u =60 kN	LC2	HC	M_c=15.26
RCJ5	M_c =2kN.m, P_u =40 kN	LC1	HC	M_c=6
RCJ6	M_c =-2kN, P_u =40 kN	LC1	HC	M_c=13
HFRCJ1	M_c =0, P_u =40 kN	LC0	-	M_c=8.68
HFRCJ2	M_c =0, P_u =20 kN	LC2	HC	M_c=8.33
HFRCJ3	M_c =0, P_u =40 kN	LC2	HC	M_c=3.45
HFRCJ4	M_c =0, P_u =60 kN	LC2	HC	M_c=12.7
HFRCJ5	M_c =2kN.m, P_u =40 kN	LC1	HC	M_c=5.4648
HFRCJ6	M_c =-2kN, P_u =40 kN	LC1	HC	M_c=13
HFRCJ7	M_c =-4kN, P_u =40 kN	LC1	HC	-

The temperature distribution, midspan deflection, vertical load and horizontal reaction force at the support were measured in the lining segment tests (cf. Figure 1). Two measuring sections were arranged to measure the temperature within each of the lining segments. For each of the temperature measuring sections, five K type thermocouples had been installed at the positions of 10 mm, 30 mm, 60 mm, 90 mm and 120 mm from the heating surface of the linings, respectively (cf. Figure 1). To avoid the negative effect of heat radiation, concrete spalling and cracks on the accuracy of the temperature measurement, the thermocouples closest to the heating surface were installed at the position of 10 mm. The thermocouples were arranged with 20 mm spacing at least along the width of the linings to avoid interactions between them. In addition, a K type thermocouple was installed at the interface between the linings (120 mm from the heating surface). To install the thermocouples, small holes (5 mm in diameter) were drilled first in the unexposed surfaces. After cleaning these holes, a small amount of fine aluminum powder was injected into the bottom of the holes to ensure good heat conduction between the concrete and the thermocouples. In addition, LVDTs were employed to measure the midspan deflections, the auxiliary vertical deflections and horizontal displacements of the lining segments; the LVDTs were carefully protected from high temperature. As for other measurement instruments, the Pundit Lab is an ultrasonic pulse velocity (UPV) test instrument which is used to examine the quality of concrete. Non-Destructive concrete moisture meter was used in the concrete moisture measurement of the segments. The MikroScan 7600PRO, which is a non-contact, high sensitivity infrared radiometer, was used in this test for checking up the accuracy of temperature measurement. It measures the infrared radiation emitted by the target surface and converts this radiation into a two-dimensional image related to the temperature distribution at the target surface.

Based on the plane section assumption, a method was employed to synchronously monitor the opening gap as well as the opening angle of the lining joints in the tests, as exhibited in Figure 2. The opening angle and opening gaps at the heating surface (inside) and the unexposed surface (outside) of the lining joints can be determined by Equation (1):

$$\begin{cases} \theta = 2\arctan\dfrac{\Delta L_1 - \Delta L_2}{2d_1} \\ \Delta_{inside} = (d_2 + H)\,\dfrac{\Delta L_1 - \Delta L_2}{d_1} - \Delta L_2 \\ \Delta_{inside} = d_2\,\dfrac{\Delta L_1 - \Delta L_2}{d_1} - \Delta L_2 \end{cases} \tag{1}$$

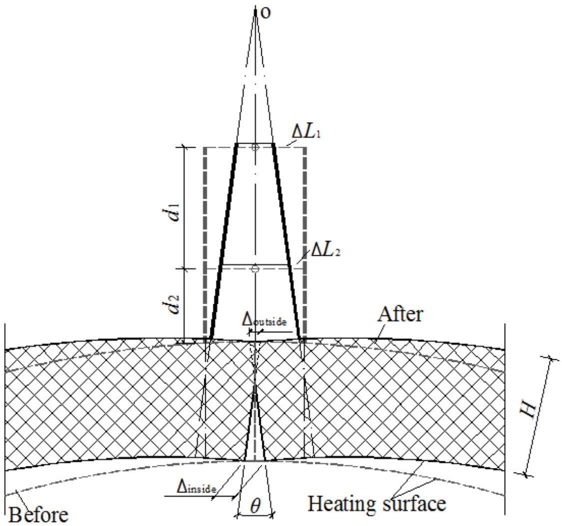

Figure 2. The measuring mechanism of the opening angle of the lining joints.

where θ is the opening angle of the lining joints (in degrees); Δ_{inside} is the opening gap of the lining joints at the heating surface (in mm); $\Delta_{outside}$ is the opening gap of the lining joints at the unexposed surface (in mm); d_1 is the distance between two LVDTs (in mm); d_2 is the distance between the second LVDT and the unexposed surface (in mm); ΔL_1 and ΔL_2 are the displacement increments of the first and the second LVDT, respectively (in mm); H is the thickness of the tunnel linings (in mm).

3 TEST RESULTS AND DISCUSSIONS.

3.1 Temperature fields

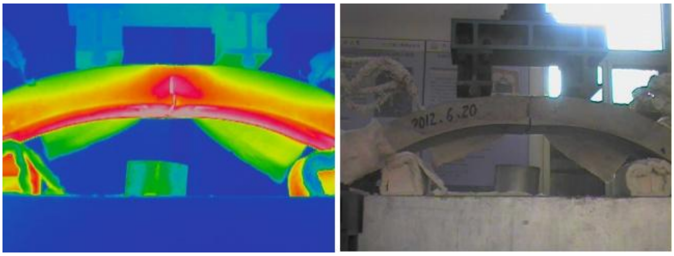

Figure 3. The thermal infrared images of heating lining segment.

It is noteworthy that as the inner side of the joint stretched the heat flux flowed in and propagated outward. That induced the temperature of neighboring concrete of joint section was higher than those of the same depth in lining. During the heating, insulation board blocked the observation on joints. Hence, we used thermal infrared imager to capture the profile of specimen right after shut off the combustor. As can be seen in Figure 3, the joint section was obviously warmer than the surrounding part of the specimen. Based on exporting data, it is found that the average temperature of the joint section is approximately 20% higher than the lining section.

3.2 Spalling and failure mode of joints

(a) RC2 (b) HFRC2

Figure 4. The spalling severity around the handhole of RC and HFRC.

Pervious fire tests and cases indicate that elevated temperature will induce explosive spalling of concrete. The consequences of spalling are much affected by the application for which concrete is being used in tunnel. Alternatively, it can have a serious effect on the fire resistance of the joint because of extensive removal of concrete which destroying the integrity of it. The spalling severity around the handhole of RC and HFRC was observed after the joint bolts failure as shown in Figure 4. For RC2, the spalling zone expanded to the anchoring end of the bolt and removed a piece of the concrete. That spalling zone even exposed a part of the construction reinforcement around the handhole, which is a strong evidence to prove that the spalling can seriously affect the integrity of the joint. Nevertheless, for HFRC2, no spalling was found in the joint and the handhole even maintained integrally after the bolt yielded. That can be attributed to the PP fibre mixed in HFRC eliminated the spalling of concrete. Figure 5 shows two basic failure modes of joints, i.e. the joint bolts yielding and the joint concrete failure. The failure mode of every specimen can be found in Table 3.

(a) Joint bolts yielding(HFRCJ2) (b) Joint concrete failure (RCJ4)

Figure 5. The failure modes of the lining joints.

3.3 Influence of material and axial force on the structural behavior and fire effects

Under fire loading, at 20 kN axial force level, HFRCJ2 (Figure 4 (a)) failed due to joint failure, whilst with the axial force adding up to 40kN and 60kN (corresponding to HFRCJ3 and HFRCJ4), the weakness section at loading point cracking induced the specimen failure. This can be attributed to degradation of HFRC in elevated temperature and the enhancement of flexure stiffness of joints under superior axial force level. Hence, unlike the RC specimens in LC2, the capacity of HFRC specimens didn't improve as the axial force increased. According to the benchmark group, the capacity of the HFRC joint was lower than that of the RC joint. Obviously, in ambient temperature, at the 20kN axial force level, the capacity of the HFRC joint will be still lower than that of the RC joint. However, for RCJ2 and HFRCJ2 that both failed due to joint failure, it can be found that the capacity of HFRCJ2 was 35.7% higher than that of RCJ2. This is due to the RC joint lost its integrity during spalling while the HFRC eliminated the spalling of concrete. As can be seen in Figure 6, the first stage of M-θ curve of HFRC2 stretched more sufficiently than that of RC2, resulting in increased ductility and capacity.

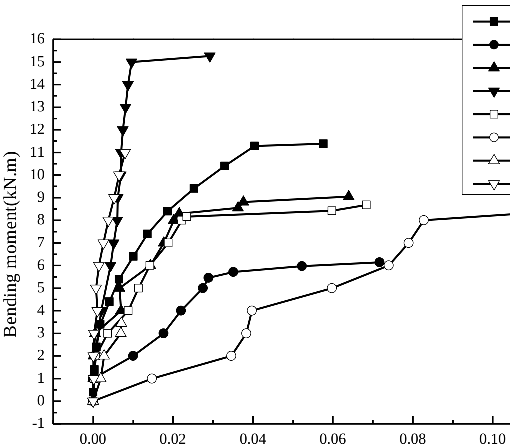

Figure 6. Experimental bending moments versus the rotation of joints for the ambient cases and under-fire cases.

Due to the serious degradation of bolts and surrounding concrete induced by elevated temperature, the failure modes of joints were different from those under ambient temperature. As expected, due to degradation of concrete and bolts, the capacities of the specimens RCJ3 under fire were lower than the match groups (RCJ1) in ambient temperature. At 40 kN axial force level, under ambient temperature, both RCJ1 and HFRCJ1 lost capacity due to the tensile yielding of bolts. Under elevated temperature, the same failure mode occurred in RCJ2 and RCJ3, which were at 20kN and 40kN axial force level, respectively. When the axial force level increased to 60kN, the joint of RCJ4 was failed due to crushing of compressive zone of concrete (Figure 4(b)). According to Table 4, at 40kN axial force level, the capacity of RCJ3 was 47% more than that of RCJ2. At 60kN axial force level, the capacity of the RCJ4 increased to 15.26 kN.m, more than twice that at 20kN axial force level. According to the comparison between specimens under fire composed by same materials, the axial force contributes to improving the capacity. As presented in Figure 6, according to the double broken lines for corresponding cases, as the axial force increases, the inflection point of double broken line also rises up. The opening gap and rotation of joints under fire are also bound up to the axial force level.

4 CONCLUSIONS

In this paper, under-fire and post-fire experimental tests to investigate the behavior of the RC and HFRC shield TBM tunnel lining joint specimens exposed to the standard HC curve have been conducted and carefully analyzed. Based on the presented experimental test results, the following conclusions can be drawn:

(1) It was observed that when the inner side of joint stretched the heat flux flowed and propagated outward, which induced the temperature of neighboring concrete of joint section was 20% higher than those of the same depth in lining.

(2) HFRC can eliminate the spalling of concrete and maintain the integrity of the segment joint. It can not only prevent the sudden structure loss of the segment joint when the fire occurs, but also preserve sufficient structure provision after fire.

(3) The failure modes of specimens under fire are closely related to the axial force level. The more the axial force was, the minor the opening gap and rotation were under the same bending moment condition. The shape of the curve of the bending moment versus the rotation of the joint (M-θ) is in line with double broken line type. As the axial force increases, the inflection point of broken line also rises up.

REFERENCES

[1] Yan Z.G., Zhu H.H., Ju J.W., Ding W.Q. "Full-scale fire tests of RC metro shield TBM tunnel linings", *Construction and Building Materials*, 36, 484-494, 2012.

[2] Yan Z.G., Zhu H.H., Ju J.W. "Behavior of reinforced concrete and steel fiber reinforced concrete shield TBM tunnel linings exposed to high temperatures", *Construction and Building Materials*, 38: 610-618, 2013.

[3] Pliya P., Beaucour A.L., Noumowé A. "Contribution of cocktail of polypropylene and steel fibres in improving the behaviour of high strength concrete subjected to high temperature", *Construction and Building Materials*. 25(4): 1926-1934, 2011.

[4] Suhaendi S.L., Horiguchi T. "Effect of short fibers on residual permeability and mechanical properties of hybrid fibre reinforced high strength concrete after heat exposition", *Cement and Concrete Research*, 36(9), 1672-1678, 2006.

[5] Chen B., Liu J. "Residual strength of hybrid-fiber reinforced high strength concrete after exposure to high temperature", *Cement Concrete Research*, 34(6), 1065-1069, 2004.

[6] Rodrigues J.P.C, Laím L., Correia A.M. "Behaviour of fiber reinforced concrete columns in fire", *Composite Structures*, 92(5), 1263-1268, 2010.

[7] European Committee for Standardization (CEN). Eurocode 1: Actions on structures, EN 1991-1-2, 2002.

[8] Wald F., Simões da Silva L., Moore D.B., Lennon T., Chladná M., Santiago A.. "Experimental behaviour of a steel structure under natural fire", *Fire Safety Journal*, 41(7), 509-522, 2006.

8th International Conference on Structures in Fire
Guo-Qiang LI, Venkatesh K. R. KODUR, Shou-Chao JIANG, Jian JIANG, Su-Wen CHEN, Guo-Biao LOU (Eds.)
Shanghai, China, June 11-13, 2014

STRUCTURAL BEHAVIOUR OF WELDED FLANGE BOLTED WEB BEAM-TO-COLUMN COMPOSITE JOINTS IN FIRE CONDITIONS

Minh-Phuong Nguyen *, Kang-Hai Tan*, Tat-Ching Fung* and Thu-Mai Le **

* School of Civil & Environmental Engineering, Nanyang Technological University, Singapore,
e-mails: CKHTan@ntu.edu.sg, CTCFung@ntu.edu.sg, MPNguyen@ntu.edu.sg,

** Lecturer, Water Resources University, Vietnam,
e-mail: LeMai@wru.edu.vn

Keywords: Beam-to-column joints, Hollow section, Welded flange bolted web (WFBW), Experiment, Fire

Abstract. *Beam-to-column joints are among the most critical structural components in buildings. In a fire, the joints are susceptible to damages. The damage of joints may result in the collapse of the sub structure. This study focuses on the behaviour of welded flange bolted web (WFBW) composite beam-to-column joint subjected to in-plane bending moment under fire conditions. Up till now, a number of studies have investigated the behaviour of composite joints at ambient temperature. However, no research has been conducted on WFBW composite beam-to-column joints at elevated temperatures. Hence, this is among the first study in the world. The novelty of this paper is to analyze the effects of some individual components to its overall behaviour. These new components have not been taken into account by previous research works, namely, the components representing diaphragm in compression, diaphragm in tension, and column loaded face in bending. The paper presents two tests of WFBW joints at elevated temperatures. The focus is on the behaviour of each component between top & bottom beam flange to the column diagram. The paper also introduces finite element (FE) models of the joints and their calibration with established test results.*

1 INTRODUCTION

From the beginning of humanity, fire plays a vital part of human life due to its capacity to serve the needs of human beings. However, fire is also one of the greatest hazards to human lives and properties. Increasing fire resistance of buildings is one way to protect human lives and properties.

In recent years, there has been a great interest in studying the behaviour of composite elements under fire conditions [1-5]. However, there are only a few research works on composite joints at elevated temperatures [6-8] although composite joints are key structural elements in structures as they connect structural members together. They are also the weakest part of a structure due to their discontinuity and geometry. Observations on actual structures and model testing have shown that composite joints are critical structural elements from which failures can initiate. Therefore, it is necessary to study the behaviour of composite joints under fire conditions to avoid catastrophic consequences.

There are many connection types to connect steel I-beam to concrete filled steel rectangular hollow section (RHS) columns, viz. extended end plate connection, T-stub connection, fin plate connection, reverse channel connection, and welded flange bolted web (WFBW) connection. Among these connections, it is found that the WFBW connection has more advantages than the others due to its high ductility, capability of resisting biaxial bending moment, high strength and stiffness, and relative ease to fabricate and install [9,10], this connection type is widely used in USA, Japan and many other countries.

There are many research works [11-16] conducted to study their behaviour at ambient temperature. However, there are hardly any investigations of their behaviour at elevated temperatures. Moreover, external beam-to-column joints between concrete-filled steel tube columns and I steel beams which use WFBW connections - so-called WFBW composite beam-to column joints are complicated due to their geometry and combination of two different materials (Figure 1). Hence, more research works for WFBW composite beam-to-column joints are required in order to provide valuable test data as well as to further study the joint behaviour at elevated temperatures.

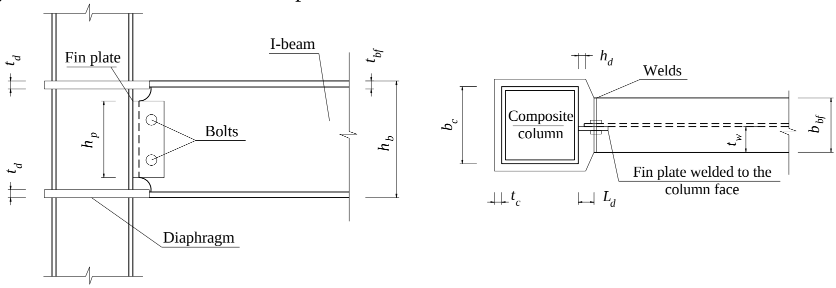

(a) Side view (b) top view

Figure 1. Geometry profile of WFBW joint.

The behaviour of WFBW composite beam-to-column joints subjected to in-plane bending moment at ambient temperature have been studied by many researchers such as Matsui [11], Kawano & Matsui [13], Shin et al. [10], and Park et al. [16]. Most of the research studies focus on joints that fail due to damage at the top or bottom flange of the beam, or at the diaphragm, or at the column web panel. The reason is that diaphragms mainly resist internal forces transferred from the beam to the column due to their high stiffness. Thus, the bolts resist much less internal force. Therefore, it is unlikely that the joint fails due to damage at the bolt region. Besides, one can use high strength bolts. For other failure mechanisms, according to Matsui [11], the failure modes of such joints at ambient temperature could appear at column web panels, diaphragms, and welds. On the other hand, Park et al. [16] observed that failure modes of the joints could occur at the beam flange or the diaphragms. Nonetheless, limited works have been done to study the behaviour of WFBW joints at elevated temperatures. At elevated temperatures, although concrete-filled steel tube column is very stiff, the elastic modulus, the yield strength and the ultimate strength of steel decrease significantly. As a result, it is likely that the WFBW composite beam-to-column joints subject to in-plane bending moment may fail due to local buckling at the compression flange. Hence, this study focuses on the behaviour of the WFBW composite beam-to-column joints subjected to in-plane bending moment at elevated temperatures where failure is due to local buckling at the compression flange adjacent to the joint.

In this paper, two tests on WFBW joints at elevated temperatures are presented. The focus is on the behaviour of each component between top & bottom beam flange to the column diagram. The paper also introduces finite element (FE) models of the joints and their calibration with established test results. The objectives of this experimental programme are twofold. The first objective is to investigate the behaviour of the joints at both ambient and elevated temperatures in terms of moment-rotation curves. The aims are to understand the fire effect on the joint behaviour and to provide test results for validations of the FE models. The second objective is to obtain the ultimate strength and critical failure mechanisms of the joints. The purpose is to appraise the loss of joint capacity at elevated temperatures and to obtain the failure mechanisms of the joints under fire conditions.

2 EXPERIMENT STUDIES

2.1. Test programme and instrumentation

Recently, the behaviour and the ultimate strength of composite joints at both ambient and elevated temperatures have been experimentally investigated [12, 17-20]. However, the authors cannot find any test results for WFBW composite beam-to-column joints subjected to in-plane bending moment at elevated temperatures. Hence, the experimental tests on WFBW composite beam-to-column joints at elevated temperatures were proposed with the aim (1) to investigate the behaviour at both ambient and elevated temperatures in terms of moment-rotation curves. (2) To observe the ultimate strength and critical failure mechanisms of the joints. These two objectives can be obtained by conducting isothermal tests.

Due to space and instrumentation constraints in the laboratory, half-scale fire tests were carried out in this study to gain better understanding of the ultimate strength and behaviour of the joints. For each test, a WFBW composite beam-to-column joint was subjected to a concentrated load at the free end of the beam for targeted temperatures. The displacements and the temperature on specimen in the test were measured by using linear variable differential transducers (LVTDs) and thermal couples, respectively. A load cell was used to measure the applied force. Based on this information, the moment-rotation curves representing the joint behaviour and the joint failure mechanisms could be defined. Any changes on the deflection profile and the joint failure mechanisms due to modification of any parameters indicated the fire effect on the joint behaviour. This, in turn, was useful to understand the effects of each joint component.

The configuration of a WFBW composite beam-to-column joint is illustrated in Figure 2. Due to the availability of structural hollow steel columns and I-beams, the steel column is SHS 160×160×8, and the steel beam is UB254×102×25. Isothermal tests are adopted to investigate the ultimate strength of the joints for a specific temperature. The two temperature levels are 20 and 400^{o}C because material properties of steel change remarkably at these levels.

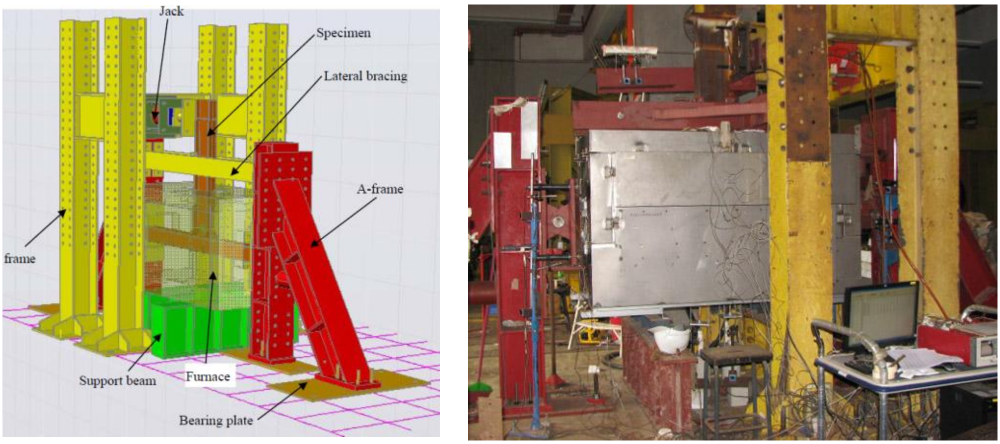

Figure 2. Test setup of the WFBW joints.

The instrumentation consists of thermocouple wires and LVDTs. For each specimen, twenty three K mineral insulated thermocouple wires were used to measure the temperature in the specimen. Eight LVDTs with a maximum stroke of 100mm were used to measure the displacement of columns and the movement of the end supports. An LVDT with a maximum stroke of 300mm was used to measure the displacement of the loaded point at the beam. The LVDTs could be used to directly measure displacement of the specimens at ambient temperature. At elevated temperatures, direct measurement by LVDTs were impossible. Therefore, indirect measurements were conducted for elevated temperature tests. The indirect measurement utilizes ceramic rods to connect points of interest on the specimen inside the furnace to LVDTs outside the furnace. Due to its low thermal conductivity and its low coefficient of thermal expansion ($7.8\times10^{-6}/^{o}C$), ceramic rod does not induce considerable errors in indirect measurements. In high temperature tests, the actual displacement of the measured points was calculated by subtracting thermal expansions of ceramic rods from recorded displacements. The test set up for the instrumentation was presented in this section. Thermocouples were used for elevated temperature tests in order to obtain the temperature distribution for different cross-sections of the joints. From the temperature profile, it could be checked whether or not the temperature distribution inside the furnace was quite uniform. In each elevated temperature test, there were 25 thermocouples (T1-T25) as shown in Figure 3.

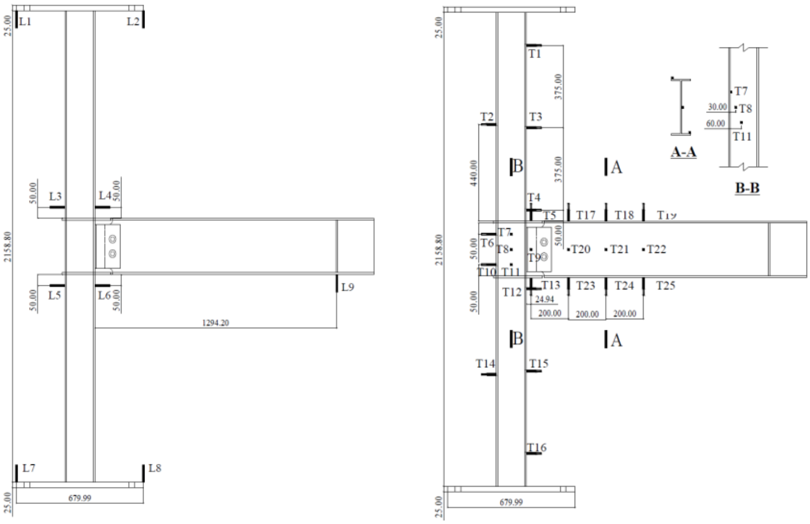

(a) LVDTs locations (b) Thermocouples locations

Figure 3. Instrumentation of the fire test.

Two tests were conducted for one type of joint, one at ambient condition and the another at isothermal temperature of 400^{o}C. The isothermal test consisted of two phases: (1) heating phase and (2) loading phase. In the first phase, the furnace was heated up at a heating rate of 100-110^{o}C/min up to the specified temperature. The heating rate was similar to that of a natural fire (ISO 834 fire curve) in its first five minutes. After the furnace air had reached the test temperature, it was maintained to the end of the test. During the first phase, thermal expansion was observed on the chord. However, the expansion did not cause any stress in the joint since the chord ends were rested on a roller. When the center of the joint reached the 400^{o}C, the joint entered into second phase. Small load was applied to check the adequacy of the test setup, instrumentation and loading system. In this phase, load was applied until the maximum stroke of the hydraulic jack was reached. In the fire test, there were cracking sounds when the joint reached a certain load. After the cracking sounds, the applied load started to decrease.

2.2 Test results

Failure modes of the joint at ambient and 400^{o}C are shown in Figure 4. On the compression side of all connections, a similar failure mechanism was observed. Large plastic deformations were formed on both tensile and compressive flange of the beam where there were welded to the diaphragm. This area called heat-affected-zone (HAZ) since the material was hardened due to welding process. However, at 400^{o}C, in the tension flange of connections, a crack formed on the tension flange while no cracks were found in the ambient test. This was a single crack penetrated through the beam flange thickness as illustrated in Figure 4(b). The cracks caused that significant difference between high temperature and ambient temperature case. At 400^{o}C, the joint strength did not increase after the cracks were formed. The reason is that the HAZ became more brittle at high temperature. Hence, fracture occurred earlier compared to the ambient case at the same load.

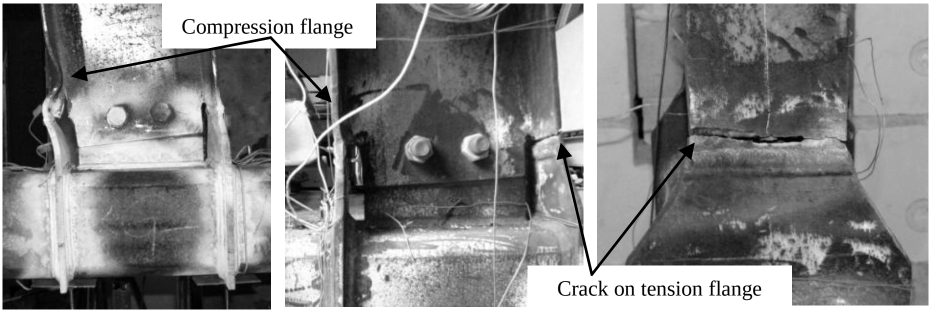

(a) at 20°C (b) at 400°C

Figure 4. Failure mode of the joint TD1 at two temperatures.

The load-displacement curves of the joint at 20°C and 400°C are shown in Figure 5. As the load increased, the joint deformed linearly up to the yield value (80.88 kN), and the strength reached the peak value at 119.8 kN when buckling occured on the compression flange. However, when the temperature was increased to 400°C, the joint started to yield earlier, that is, 60.17 kN. When deformations reached 87.2 mm, there was loud cracking sound and the joints could not take any more loads. Hence the highest load was considered as the ultimate strength of the joints at a high temperature. It can be seen that the capacity of the joint is governed by strength at elevated temperatures instead of deformation control at ambient temperature.

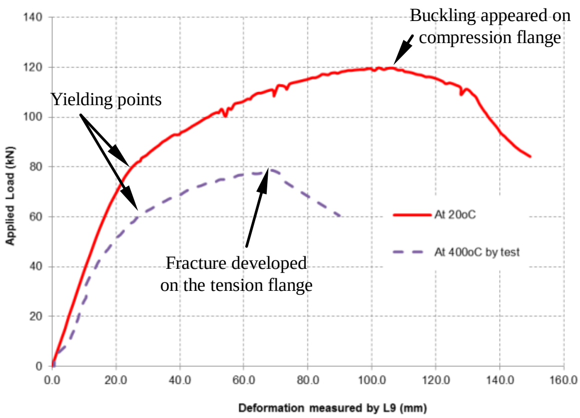

Figure 5. Load-deformation curve of the joint at 20°C and 400°C.

Compared to the strength at ambient temperature, the strength of the joint at 400°C was reduced to 66.2%. Due to deterioration of steel mechanical properties, the initial flexural stiffness changed as well. However, at 400°C, the initial stiffness of the joint was reduced by 38.2%.

3 FE MODELLING

In general, experimental tests offer reliable results of the joint behaviour at both ambient and elevated temperatures. However, in many cases, experimental tests are limited in terms of geometric and mechanical properties. Hence, it may not provide comprehensive understanding of the joint behaviour through testing alone. In addition, the cost of testing is expensive, especially for elevated temperature tests. In this study, WFBW composite beam-to-column joints subjected to in-plane bending moment at elevated temperatures are simulated by using commercial software ABAQUS v6.10-1(2009).

Large deformation, material and geometry nonlinear analysis are used to investigate the behaviour of the joints, especially for determination of the failure mechanisms and ultimate strength of the joints. Solid element type C3D8R is used to simulate the joints due to its ability to simulate large deformation, material and geometric nonlinearities the material. It is noted that the failure of the joints at high temperature is indicating by cracks along the tension flange. Hence, particular emphasis is placed on accurate modelling of ductile fracture initiation within this joint area. Without failure criteria in FE analysis, ultimate strength of the joints at high temperature cannot be simulated. In this study, a damage evolution model for ductile material was adopted. Changes of material models at different temperatures are also taken into account to consider the elevated temperature effects on the joints.

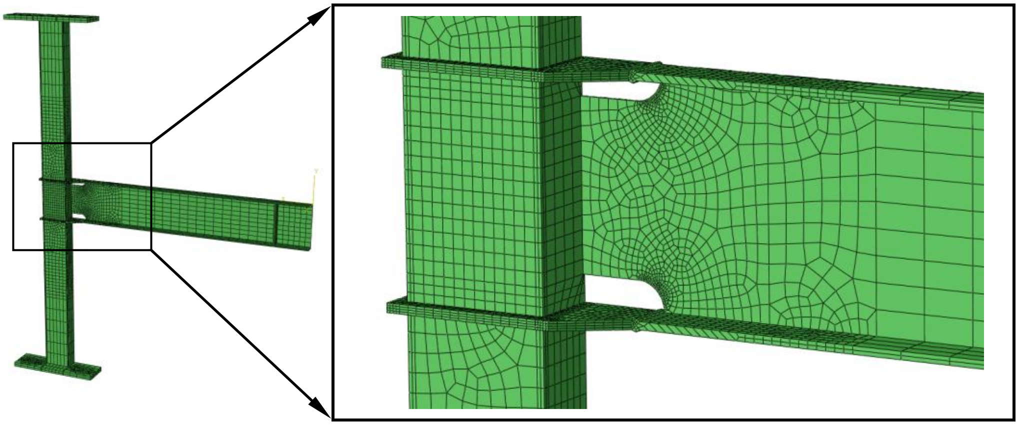

Figure 6. Finite element model of the joint in ABAQUS v6.10-1.

In this study, the model only simulates haft section of the joint due to symmetry (Figure 6). The boundary conditions are fixed at two column ends because they can simulate close-to real behaviour of the joints subjected to in-plane bending moment at elevated temperatures. Each end of the column is strengthened by a welded plate with a thickness of 30mm. The welded plate is fixed by 8φ 30 bolts to a solid support. In the models, each fixed boundary condition is represented by eight holes restrained from displacement.

Figure 7 shows a comparison of finite element predictions with experimental results. It can be seen that reasonable agreement between the trend of experimental load-deformation behaviour and numerical prediction has been achieved. The FE model over predicted the strength by 12.4% and yielding point of the test by 25.6%. The reason is the material properties at heat affected zone play an important role in the FE model. Current model is using standard materials in accordance with EC3.P-1.2 where the materials have higher ductility and strength compared to HAZ material. Material tests will be carried out in the near future to determine stress-strain curve and ultimate strain of the HAZ material. With that information, a better FE model to predict the behaviour of joints at elevated temperature will be established.

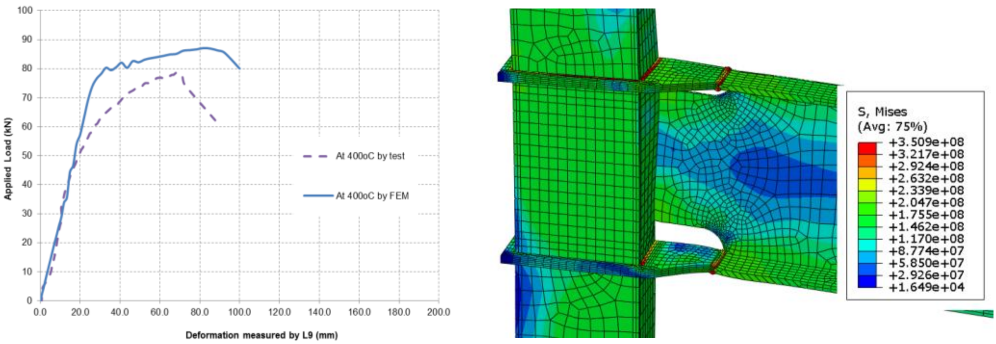

Figure 7. Validation of the FE model to test results at 400°C.

5 CONCLUSIONS

In this paper, the aim of the experimental programme was to investigate the behaviour of WFBW joints subject to in-plane bending under fire condition. It was observed that at high temperature, the joint failure mode has changed from buckling at compression flange to cracks occurring on the tension flange at high temperatures. It was also found that temperature has a great effect on joint strength reduction. In addition to the two tested specimens, numerical model of WFBW-joint under elevated temperature was analyzed based on ABAQUS/Standard v6.10-1 commercial package. The FE model has reasonable agreement with the experimental behaviour of the WFBW joint at elevated temperatures.

ACKNOWLEDGEMENT

The authors want to express their gratitude to the financial support and test specimens funded by ARC 2/07 project entitled “Failures modes and ultimate strength of tubular joints under elevated temperatures” from the Ministry of Education, Singapore.

REFERENCES

[1] Lie, T. T. and Chabot, M. (1990). “A method to predict the fire resistance of circular concrete filled hollow steel columns” *Journal of Fire Protection Engineering*, 2(4), 111-126.

[2] Kodur, V. K. R. (1999). “Performance-based fire resistance design of concrete-filled steel columns” *Journal of Constructional Steel Research*, 51, 21-36.

[3] Han, L.H., Yang, Y.F., and Xu, L. (2003). ”An experimental study and calculation on the fire resistance of concrete-filled SHS and RHS columns” *Journal of Constructional Steel Research*, 59, 427 – 452.

[4] Han, L.H., Huo, J.S., and Wang, Y.C. (2005). “Compressive and flexural behavior of concrete filled steel tubes after exposure to standard fire” *Journal of Constructional Steel Research*, 61, 882-901.

[5] Wong, M. B. (2007). “Adaptation factor for moment capacity calculation of steel beams subject to temperature gradient” *Journal of Constructional Steel Research*, 63, 1009–1015.

[6] Silva, L. A. P., Neves, L. F. N., and Gomes, F. C. T. (2003). “Rotational Stiffness of Rectangular Hollow Sections Composite Joints” *ASCE Journal of Structural Engineering*, 129(4), 487-494.

[7] Wang, Y.C. and Ding, J. (2007). “Experimental Behaviour of Steel Connections to Concrete Filled Steel Tubular Columns in Fire” *Steel structures*, 7, 201-208.

[8] Wang, J. F., Han, L.H., and Uy, B. (2009). "Behaviour of flush end plate joints to concrete-filled steel tubular columns" *Journal of Constructional Steel Research*, 65, 925-939.

[9] Morino, S. and Tsuda, K. (2002). "Design and Construction of Concrete-Filled Steel Tube Column System in Japan." *Earthquake Engineering and Engineering Seismology*, 4(1), 51-73.

[10] Shin, K. J., Kim, Y. J., Oh, Y. S, and Moon, T. S. (2004). "Behavior of welded CFT column to H-beam connections with external stiffener" *Engineering Structures*, 26, 1877-1887.

[11] Matsui, C. (1981). "Design formulas for stiffeners of concrete-filled RHS column connections" *Research Report, Chugoku-Kyushu Branch of Architectural Institute of Japan*, 5, 317-320. (in Japanese)

[12] Kawaguchi, M., Kawano, A. and Matsui, C. (1997). "Strength and deformation capacity of connections with different details between concrete-filled RHS columns and H-section beams" *Research Report, Kyushu Branch of Architectural Institute of Japan*, 36, 553-556. (in Japanese)

[13] Kawano, A., Matsui, C., and Murai, N. (1998). "Load-deformation relation models for local deformations in diaphragm-stiffened connections of H-shaped beams to rectangular CFT columns" *Journal of Constructional Steel, Japanese Society of Steel Construction*, 5 (17), 93-104. (in Japanese)

[14] Fukumoto, T., Yamaya, H. and Morita, K., (2000). "Connections between concrete filled

[15] circular tubular steel column and steel beam reinforced with external diaphragm" *Journal of Structural and Construction Engineering, Architectural Institute of Japan*, 535, 163-170. (in Japanese)

[16] Park, J. W., Kang, S. M., and Yang, S. C. (2005). "Experimental Studies of Wide Flange Beam to Square Concrete-Filled Tube Column Joints with Stiffening Plates Around the Column", *ASCE Journal of Structural Engineering*, 131(12), 1866-1876

[17] Kato, B. (2001). "Structural design of CFT column to H-beam connection" *Int. Journal of Steel Structures, Korean Society of Steel Construction*, 1 (1), 9-14.

[18] Han, L. H., Huo, J. S., and Wang, Y. C. (2007). "Behavior of Steel Beam to Concrete-Filled Steel Tubular Column Connections after Exposure to Fire" *ASCE Journal of Structural Engineering*, 133 (6), 800-814.

[19] Liew, J. Y. R., Teo, T. H., Shanmugam, N. E., and Yu, C. H. (2000). "Testing of steel–concrete composite connections and appraisal of results" *Journal of constructional steel research*, 56, 117-150.

[20] Yao, H., Goldsworthy, H., and Gad, E. (2008). "Experimental and Numerical Investigation of the Tensile Behavior of Blind-Bolted T-Stub Connections to Concrete-Filled Circular Columns" *ASCE Journal of Structural Engineering*, 134(2), 198-208.

8th International Conference on Structures in Fire
Guo-Qiang LI, Venkatesh K. R. KODUR, Shou-Chao JIANG, Jian JIANG, Su-Wen CHEN, Guo-Biao LOU (Eds.)
Shanghai, China, June 11-13, 2014

LOAD-DEFORMATION BEHAVIOUR OF BOLTED DOUBLE-SPLICE FRICTION JOINTS AT ELEVATED TEMPERATURE

T. Hirashima*, Y. Esaki* and S. Ando*

* Chiba University, Dept. of Architecture and Urban Science, Japan
e-mail: hirashima@faculty.chiba-u.jp

Keywords: Bolted friction joints, Fire resistance, Load-deformation behaviour, Component-based model

Abstract. *The fundamental component of the moment-rotation behaviour of the steel beam-splice connection is the load-deformation behaviour of the bolted double-splice friction joints with high-strength bolts. Elevated-temperature tensile tests of bolted double-splice friction joints were performed to investigate the influence of the plate thickness, end distance, fastening, and temperature on their load-deformation behaviour. This paper discusses the load-deformation behaviour, ductility and modelling of bolted double-splice friction joints at elevated temperatures.*

1 INTRODUCTION

In a fire, the connections of structural frames exposed to flame and heat are subjected to severe loading and deformation and need to have sufficient ductility. In particular, the robustness of steel frames in a fire depends on the ductility of the bolted connections. In Japan, steel beam-splice connections have become common for the field connection of beams in rigid steel frames that have beam-to-column connections with full-penetration welds. Also, the fundamental component of the moment-rotation behaviour of the steel beam-splice connection is the load-deformation behaviour of the bolted double-splice friction joints with high-strength bolts. Commonly used beam-splice connections consist of splice plates, which are lapped across the two connected beams and bolted tightly to either side of the web and flanges. In the case of a fire, the critical load-carrying mechanism of the joint may change from the bolt friction mode to bolt bearing, and the strength loss at elevated temperature is larger for the high-strength bolts than for the steel plates or the connected beams. It is important to prevent the failure of such connections for the fire safety design of steel structures.

A component-based model is one useful model for analysing the behaviour of bolted connections, and some experimental and numerical studies have been conducted on the model [1-3]. Meanwhile, there is little fundamental tensile test data on the load-deformation behaviour (including the failure behaviour) of bolted double-splice friction joints at elevated temperatures [4-6]. Therefore, elevated-temperature tensile tests of bolted double-splice friction joints were performed to investigate the influence of the plate thickness, end distance, fastening, and temperature on their load-deformation behaviour. This paper discusses the load-deformation behaviour, ductility and modelling of bolted double-splice friction joints at elevated temperatures on the basis of the tests and finite element analysis (FEA).

2 MECHANICAL PROPERTIES AT ELEVATED TEMPERATURES

The bolted double-splice friction joints consisted of main plates, splice plates, and HSFG (high-strength friction grip) bolts. The steel grade of the main plate and splice plate was SN490B (in accordance with JIS G 3136), whose design strength and design bearing strength are 325 and 490 N/mm^2, respectively. The grade of the HSFG bolt was F10T (in accordance with JIS B 1186), whose design bearing strength is 1000 N/mm^2. The shank diameter of the bolts was 20 mm, and the bolt is designated as F10T-M20.

The stress-strain relationships of the steels were obtained using elevated-temperature tensile tests in accordance with JIS G 0567. The velocity of deformation was controlled using a loading machine, and the specimen deformation was measured by transducers and amplifiers. The rate of strain was 0.3%/min up to 5% strain and then increased to about 4.3%/min. Figures 1 and 2 show the stress-strain curves of the main plate and bolt. The behaviour of both the SN490B plate and the F10T bolt differed in that the strain hardening of the F10T bolt was very low at ambient temperature. The stress increased instantly at 5% strain due to the change in strain rate, and this was remarkable above 500 ℃. As show in these figures, the tensile strength loss at elevated temperature was considerably larger for the F10T bolt than for the SN490B plate. This affected the change of the failure mode for the bolted joints at elevated temperature.

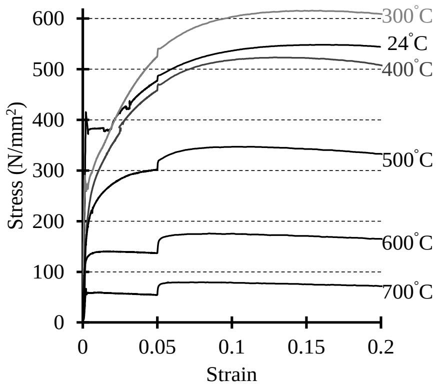

Figure 1. Stress-strain curve of the SN490B plate (9 mm).

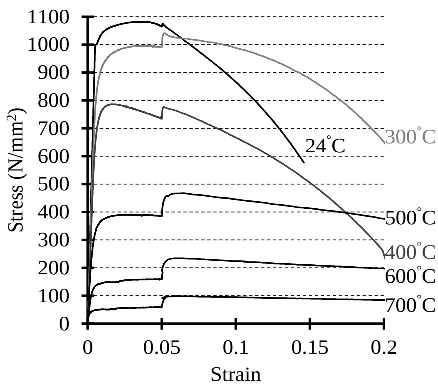

Figure 2. Stress-strain curve of the F10T-M20 bolt.

3 TEST SETUP

The parameters that were varied between the tensile tests for the bolted double-splice friction joints included the main plate thickness, end distance, fastening, and temperature, as shown in Table 1. The design tensile resistance of the thin-plate specimens (in which the main plate thickness was 9 mm) was determined for tear-out failure at the end distance under ambient temperature. Meanwhile, most of the thick-plate specimens (in which the main plate thickness was 19 mm) were assumed to have shear failure in the bolt at ambient temperature.

Table 1. Test program.

Bolt shank diameter *d* [mm]	Main plate thickness *t* [mm] (Splice plate)	End distance *e* [mm]	Fastening	Temperature [℃]	Specimen name
20	9 (6)	30 (1.5*d*)	fastening	AT, 500	t09e30
		50 (2.5*d*)	fastening	AT, 400, 500, 700	t09e50
			unfastening	AT, 500	t09e50uf
		70 (3.5*d*)	fastening	AT, 500	t09e70
	19 (12)	30 (1.5*d*)	fastening	AT, 500	t19e30
		50 (2.5*d*)	fastening	AT, 400, 500, 700	t19e50
			unfastening	AT, 500	t19e50uf
		70 (3.5*d*)	fastening	AT, 500	t19e70

Note: "AT" denotes ambient temperature.

The length of the specimen was 1640 mm, and the gage length (including the bolted joint) was 600 mm, as shown in Figure 3. The fastening specimen was fastened based on the torque-controlled method in accordance with JASS 6 [7]. The standard tensile force of F10T-M20 for fastening was 182 kN.

Elevated-temperature tensile tests for bolted double-splice friction joints were performed with an electric furnace and a 3MN loading frame, as shown in Figure 4. The heating length was about 1100 mm, and the temperature in the gage length could be controlled to be almost uniform. The post maximum load behaviour of the specimen could be obtained because the loading frame has a large stiffness relative to the specimen. The axial deformation of the joint was measured outside of the furnace by means of stainless transmitting bars bolted to the specimen.

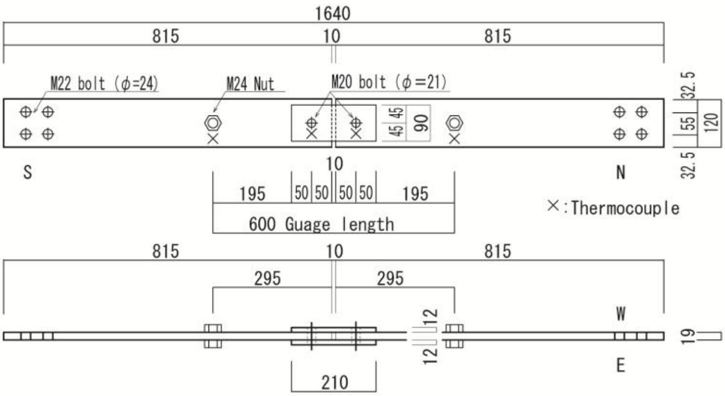

Figure 3. An example of specimen (t19e50).

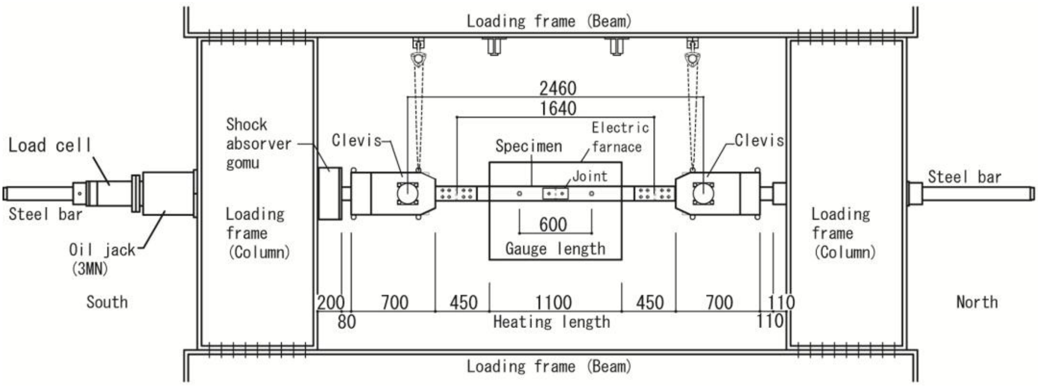

Figure 4. Test setup.

4 LOAD-DEFORMATION BEHAVIOUR OF THE BOLTED JOINTS

4.1 Effect of the plate thickness, end distance, fastening and temperature

Figures 5(a)-(c) and 6(a)-(c) show the load deformation behaviour. The legend for the specimens in these figures is shown in Table 1, and the temperature is added after the specimen name. Moreover, (B) indicates the shear failure of the bolt, and (P) indicates tear-out failure of the main plate in the figures. The degradation of the maximum load (i.e., the tensile resistance of the joint) due to the temperature increase was larger for the bolt shear failure than for the tear-out failure type. In the case of the thin-plate specimen, the failure mode of the joint changed from tear-out failure of the plate to shear failure of the bolt between 400 ℃ and 500 ℃. Figures 5(a) and 6(a) also indicated that the ductility, which is defined as the deformation at the failure of the joint in this paper, was lower for the thick-plate specimen than for the thin-plate specimen. The plate thickness influenced the ductility of the double-splice friction joint, which had bolts on both sides. In the case of the thin-plate specimens, the deformation due to plate bearing could develop on both sides, and the ductility increased.

Figures 5(b) and 6(b) show the effect of the end distance of the joint on the load deformation behaviour. In the case of the thin-plate specimen, the end distance influenced the tensile resistance and ductility at ambient temperature; meanwhile, the effect of the end distance on the tensile resistance decreased at 500 ℃ because the failure mode changed from tear-out failure to bolt shear failure. In the case of t09e50-500, the calculated tensile resistances of both the tear-out and bolt failures were close, and therefore, the deformation due to plate bearing was developed despite the bolt failure. In the case of the thick-plate specimens, the end distance did not influence the tensile resistance or ductility at 500 ℃.

Figures 5(c) and 6(c) show the effect of the fastening of the joint. In the case of the fastening joint under ambient temperature, the joint behaved like an elastic body before the slip, and then, secondary slope of the load-deformation relationship was somewhat steep because the bearing deformation of the plate (including the expansion of the plate thickness around the bolt hole) might be restrained by the fastening bolt in tension. Meanwhile, the effect of the fastening decreased at 500 ℃ because the tensile force in the bolt might decrease due to the relaxation of the bolts under elevated temperature. The fastening did not influence the resistance of the joints.

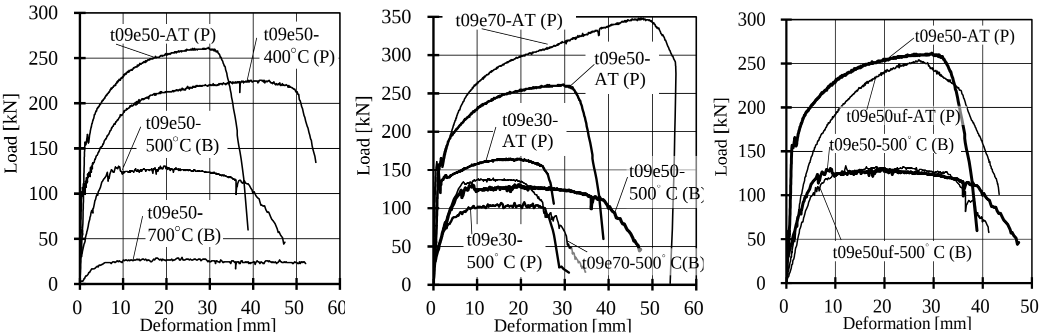

(a) Effect of the temperature (b) Effect of the end distance (c) Effect of the fastening

Figure 5. Load-deformation behaviour (thin-plate specimen t=9 mm).

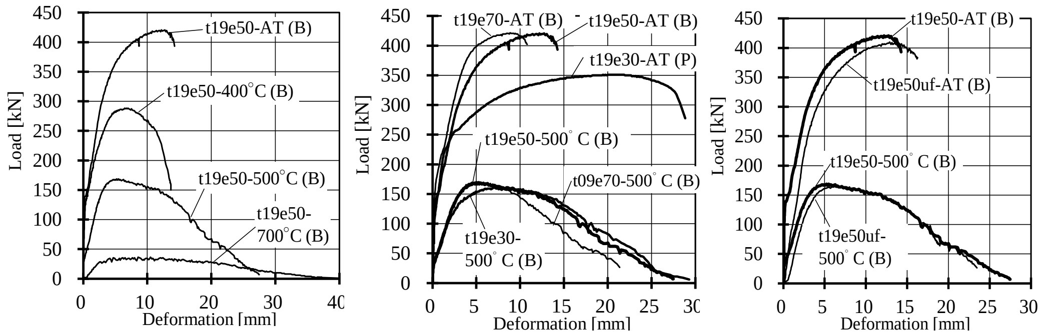

(a) Effect of the temperature (b) Effect of the end distance (c) Effect of the fastening

Figure 6. Load-deformation behaviour (thick-plate specimen t=19 mm).

4.2 Aspect of the deformation and failure after the test

Figures 7 (a) and (b) show the bearing deformation of the main plate and the tear-out failure of the thin-plate specimens. The deformation of the bolt in shear was low. Figure 7(c) shows the bolt shear failure at the screw section and the bearing deformation of the main plate. In the case where the resistance of the bolt in shear was close to that of the plate bearing, the ductility increased because both components (the bolt and plate) could be deformed simultaneously. Figure 7(d) shows the bolt shear failure at both the shank and screw sections. Figure 7(e) shows the brittle failure of the bolt in shear at the shank section for the thick-plate specimen test at ambient temperature. Meanwhile, Figure 7(f) shows the ductile failure of the bolt in shear at the two shank sections at elevated temperature. Above 500 ℃, the bolt was clearly cut by the thick plates, and the thick-plate bearing deformation was low.

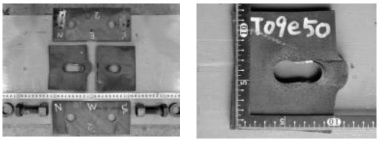

(a) Tear-out failure, Specimen: t09e50-AT

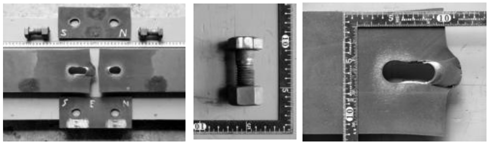

(b) Tear-out failure, Specimen: t09e50-400 ℃

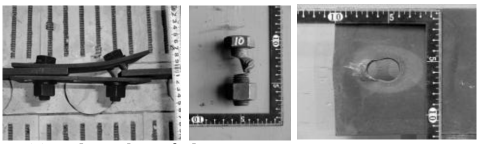

(c) Bolt in shear failure, Specimen: t09e50-500 ℃

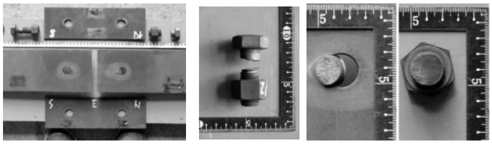

(d) Bolt in shear failure, Specimen: t09e70-500 ℃

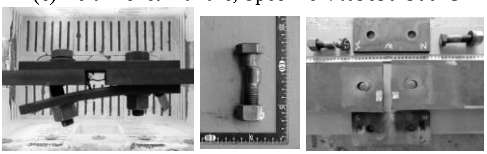

(e) Bolt in shear failure, Specimen: t19e50-AT

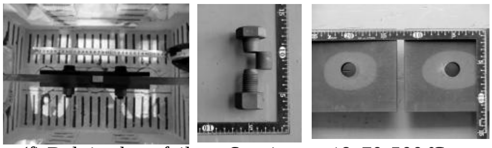

(f) Bolt in shear failure, Specimen: t19e70-500 ℃

Figure 7. Deformation and failure of bolted double-splice friction joints after the tests.

4.3 Maximum load of the bolted joint at elevated temperature

In table 2, the maximum load was compared with the calculation result using the following Equations (1a)-(3). These values were calculated using the results of the elevated-temperature tensile tests.

$$P_{u1} = 0.6 \times (A_{bs} + A_{be}) \cdot \sigma_{bu} \quad \text{For the bolt in shear failure for the thin-plate specimen} \tag{1a}$$

$$P_{u1} = 0.6 \times 2A_{bs} \cdot \sigma_{bu} \quad \text{For the bolt in shear failure for the thick-plate specimen} \tag{1b}$$

$$P_{u2} = e \cdot t \cdot \sigma_u \quad \text{For the tear-out failure of the main plate} \tag{2}$$

$$P_u = \min\left(P_{u1}, P_{u2}\right) \tag{3}$$

where A_{bs}, A_{be} : Cross-section aria at the bolt shank and the bolt screw.

σ_{bu}, σ_u : Tensile strength of the bolt and the plate from the elevated-temperature tensile test

e: End distance, *t*: Main plate thickness.

In the case of the AT (ambient temperature) test, all of the tensile resistances from the test results were slightly larger than the calculated values. The mean resistance of the eight AT tests was 105% of the calculated result. Meanwhile, in the case of the elevated temperature test, most of the resistances from the test were lower than the calculated values. The mean resistance of the 12 elevated-temperature tests was 93% of the calculated result. In the case of the elevated-temperature test, the load rate (or the rate of strain) considerably influenced the resistance of the bolted splice joint and the tensile strength of the bolt and the plate. In this study, the load rate might be lower for the joint tests than for the material test. The validity of the load rate may be clarified by the elevated-temperature transient test.

Table 2. Maximum load of the bolted joint (unit: kN).

Specimen name	AT		400 ℃		500 ℃		700 ℃	
	Test	Cal.	Test	Cal.	Test	Cal.	Test	Cal.
t09e30	165	148			108	94		
t09e50	262	247	226	235	130	156	29	33
t09e50uf	254				133			
t09e70	348	345			139	157		
t19e30	351	306			161	176		
t19e50	421	407	288	297	169	176	36	37
t19e50uf	410				165			
t19e70	422	407			171	176		

5 COMPONENT-BASED MODEL AND FINITE ELEMENT ANALYSIS

5.1 Component-based model for bolted double-splice friction joints

In this paper, the component-based models, which are based on the research of Rex and Easterling [1], Sarraji [2], and Yu *et al.* [3] and the modified model, were compared with the test results. The global stiffness of the bolted double-splice friction joint was given by Equation (4).

$$k = \frac{1}{1/k_{MP} + 1/k_{SP} + 1/k_{bolt}} \times \frac{1}{2} \qquad \text{(up to near the maximum load)} \tag{4}$$

where k : Global stiffness of the joint

k_{MP} , k_{SP} : Bearing stiffness of the main plate and splice plate [1, 2]

k_{bolt} : Stiffness of the bolt in shear [3]

For Equation (4), if the stiffness of one component was zero (this occurred near the maximum load), thereafter, the equation was changed such that the deformation increase was concentrated on the component on one side. Table 3 shows the parameter for the bearing model at elevated temperature. The modified values Ω were determined to agree with the test results.

Table 3. Parameter for the bearing model.

Temp. (℃)	*e*=30 mm (*e*=1.5*d*)				*e*=50 mm (*e*=2.5*d*)			
	Previous [2]			Modified	Previous [2]			Modified
	ϕ	Φ	Ω	Ω	ϕ	Φ	Ω	Ω
AT	2.1	0.012	145	260	1.90	0.010	198	280
400	2.0	0.008	170	No test data	1.85	0.008	185	270
500	2.0	0.008	130	250	1.85	0.008	150	260

5.2 FE analysis

Geometrically nonlinear FEA simulations were performed using ABAQUS [8] with nonlinear material properties. The main plate, splice plates, and bolts were created using solid elements. An explicit dynamic analysis was performed for the analysis of members with discontinuous parts. Interaction between the plate surfaces at the bolted connections were defined as “hard contact” using the kinematic contact method. The frictional slip resistance between the splice plates and the main plate due to the tension in the HSFG bolts is not taken into consideration in this simulation.

5.3 Comparison with the bolted double-splice friction joint tests

Figures 8(a)-(c) shows a comparison between the test, CB (component-based) model, and FEA results. The CB model of the bolt in shear [3] could approximate the load-deformation behaviour of the thick-plate specimen tests well, as shown in Figure 8(a). Meanwhile, the FEA results did not agree well with the test result for the bolt failure. As shown in Figure 8(b), the stiffness was slightly lower for the previous CB model “CB (P)” than for the test results, and the modified parameter for the bearing model “CB (M)” was determined to agree with the test results. The previous CB model was given based on the FEA, which may not sufficiently account for the fastening effect (i.e., the effect of the restraint from the bolt in tension on the expansion of the plate thickness around the bolt hole increases the stiffness of the bolted double-splice friction joints). The FEA result was also lower than the test result for the tear-out failure. Meanwhile, as shown in Figure 8(c), the modified model “CB (M) did not agree with the test results. In case the resistance of the bolt in shear was close to that of plate bearing, it was difficult to predict the load-deformation behaviour well.

Table 4 shows the ratios of the deformations of the components at the failure. The test result was based on the measurement for the bearing deformation of the main plate (MP) and the splice plate (SP) bearing. The deformation of the bolt in shear is the total deformation at the failure minus the bearing deformations. As shown in Table 4, the CB model and FEA results roughly approximated the ratio of the test results. CB model and FEA may be useful for the prediction of the damage of the components in the case of a fire. As shown in Figures 9 (a) and (b), the FEA results could describe the local aspect for the deformation of the specimen after the test.

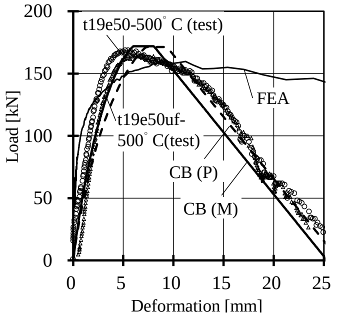

(a) t=19 mm, e=50 mm, 500 ℃

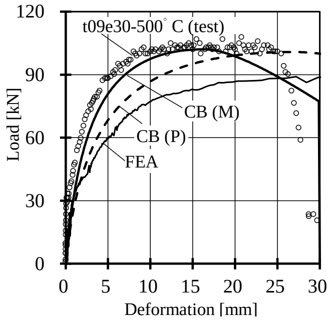

(b) t=9 mm, e=30 mm, 500 ℃

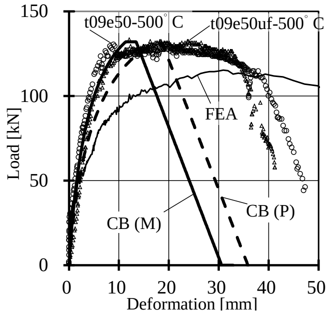

(c) t=9 mm, e=50 mm, 500 ℃

Figure 8. Comparison of the test, FEA results and component-based model.

Table 4. Ratio of the deformation of components at the failure (MP: Main plate, SP: Splice Plate).

Specimen	Test result [%]			Modified CB model [%]			FEA result [%]		
	MP	SP	Bolt	MP	SP	Bolt	MP	SP	Bolt
t09e50-AT	83	2	15	91	4	5	64	24	12
t09e50-400 ℃	78	14	8	92	3	5	50	23	27
t09e30-500 ℃	47	32	21	89	4	8	72	15	13
t09e50-500 ℃	36	9	54	17	4	79	45	13	41
t19e50-500 ℃	10	2	88	5	2	94	4	3	93

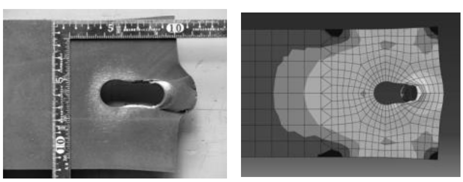
(a) t09e50-400 ℃

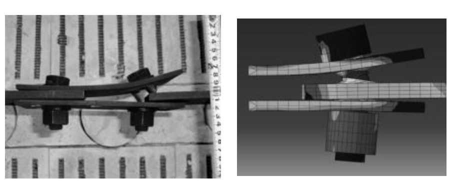
(b) t09e50-500 ℃

Figure 9. Example of FEA results (Left: test. Right: FEA).

6 CONCLUSIONS

This paper has presented the load-deformation behaviour of bolted double-splice friction joints under elevated temperature and has discussed the effects of the plate thickness, end distance, and temperature on the behaviour. The main conclusions were as follows:

(1) The ductility of the joints was larger for the thin-plate specimen than for the thick-plate specimen because bearing deformation of the plate developed in the case of the thin-plate specimen. However, in the case of the thin-plate specimen with a large end distance, the failure mode was changed from plate bearing to bolt shear by the temperature increase and the ductility decreased.

(2) The end distance influenced the resistance and ductility of the joint for not the bolt failure type but the tear-out failure type. The effect of the fastening on the stiffness of the joint was larger at ambient temperature than at elevated temperature.

(3) The mean resistance of the 12 elevated-temperature test results was 93% of the calculated result based on the material test results. The load rate for the test considerably influenced the resistance of the joint and might be lower for the joint tests than for the material test.

(4) The component-based model of the bolt in shear agreed with the test results for the bolt failure type. However, the stiffness from the load-deformation behaviour of the joint was slightly lower for the previous component-based model of plate bearing than for the test results of the bolted double-splice friction joints with tight fastening. Therefore, the modified parameters of the bearing model were determined to agree with the test results.

(5) FEA could not accurately trace the load-deformation behaviour of the bolted double-splice friction joints but described the local aspect for the deformation of the specimen after the test.

Plans for future work include performing additional elevated-temperature tests and the elevated-temperature transient tests for the tear-out failure type and re-examining the component-based model for plate bearing.

AGNOWLEDGEMENT

This work was supported by JSPS KAKENHI Grant Number 24560677.

REFERENCES

[1] Clinton O. Rex and W. Samuel Easterling, "Behavior and Modeling of a Bolt Bearing on a Single Plate", *J. Struct .Eng.*, ASCE, Vol. 129, No. 6. pp. 792-800, 2003.

[2] Marwan Sarraj, "The Behaviour of Steel Fin Plate Connections in Fire", Ph.D. Thesis, University of Sheffield, 2007.

[3] Hongxia Yu, I. W. Burgess, J. B. Davison, R. J. Plank, "Tying capacity of web cleat connections in fire, Part 2: Development of component-based model", *Engineering Structures* 31, pp. 697-708, 2009.

[4] Y. Sakumoto, K. Keira, F. Furumura, and T. Ave, "Tests of Fire-Resistant Bolts and Joints", *J. Struct .Eng.*, ASCE, Vol. 119, No. 11. pp. 3131-3150, 1993.

[5] B. R. Kirby, "The Behaviour of High-strength Grade 8.8 Bolts in Fire", *Journal of Constructional Steel Research*, 33, 3-38, 1995.

[6] Hirashima T., Hamada N., Ozaki F., Ave T. and Uesugi H., "Experimental Study on Shear Deformation behavior of High Strength Bolts at Elevated Temperature", *J. Struct. Constr. Eng.*, AIJ, No.621, 175-180, 2007. (in Japanese)

[7] Architectural Institute of Japan, "Japanese Architectural Standard Specification, JASS 6 Steel Work", 2007. (in Japanese)

[8] ABAQUS Analysis User's Manual Version 6.12, ABAQUS INC., 2012

8th International Conference on Structures in Fire
Guo-Qiang LI, Venkatesh K. R. KODUR, Shou-Chao JIANG, Jian JIANG, Su-Wen CHEN, Guo-Biao LOU (Eds.)
Shanghai, China, June 11-13, 2014

SHEAR PANEL COMPONENT IN THE VICINITY OF BEAM-COLUMN CONNECTIONS IN FIRE

Guan Quan*, Shan-Shan Huang* and Ian Burgess*

* University of Sheffield, Dept. of Civil & Structural Engineering, UK
e-mails: g.quan@sheffield.ac.uk, s.huang@sheffield.ac.uk, ian.burgess@sheffield.ac.uk

Keywords: Shear buckling, Connections, Component-based model, Fire

Abstract. *This research is intended to predict the shear buckling of beam webs in the vicinity of beam-to-column connections in fire. A component-based analytical model, which simulates the behaviour of beam-web shear panels from the elastic stage to failure, has been created for elevated-temperature analysis. ABAQUS models have also been created to validate the component model over a range of geometries. Comparisons between the theoretical and FE models have shown that the proposed component model provides sufficient accuracy to be embodied in due course in global modelling of composite structures in fire.After sufficient validations have been carried out, the new component-based model will be implemented into the software Vulcanas a shear panel element adjacent to the existing connection element.*

1 INTRODUCTION

In fire scenarios, joints are among the key elements which can determine the potential for survival of a steel or composite framed building. The investigation of the “7 World Trade” [1] in the New York City indicated that the total collapse of the whole building was triggered by the fracture of beam-to-column joints, as a result of large thermal expansions of beams. The Cardington Fire Tests [2] indicated that the shear buckling of beams in the vicinity of beam-column joints is very prevalent under fire conditions,as indicated in Figure 1. This phenomenon could have significant effects on adjacent column-face joints. It could increase the transverse drift of a beam, as well as change the force distribution in the joints, leading to changes in their failure patterns. However, no practical research has been carried out to study the shear-buckling behaviour of Class 1 beams at elevated temperatures.

Figure 1. Shear buckling observed after one of the Cardington fire tests [2].

2 DEVELOPMENT OF THE THEORETICAL MODEL

In the proposed theoretical model, for Class 1 or 2 beams, shear response consists of three stages: the elastic, plastic and post-buckling stages. In the elastic stage, it is assumed that no buckling appears in the panel and the principal tensile and compressive stresses are identical. Plate buckling occurs during the plastic stage. After the buckling point, the shear panel enters the post-buckling stage. An example output is shown schematically in Figure 2. In this figure, Point 1 illustratesthe end of the pre-buckling elastic stage. Point 2 refers to initial buckling point, and Point 3 represents failure (equivalent plastic strain reaches 0.15). The aim of this model is to produce a tri-linear force-displacement relationship for any shear panel, from initial loading to failure.

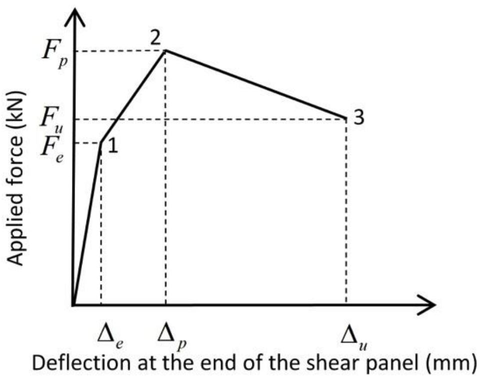

Figure 2. Tri-linear force-deflection relationshipof shear panels.

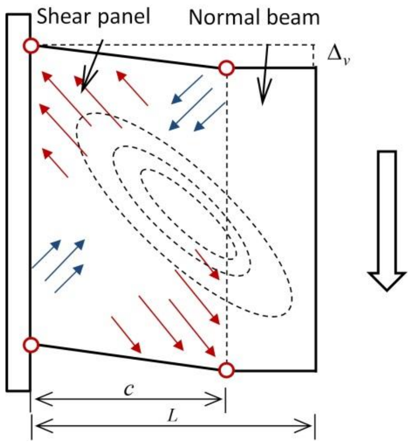

Figure 3. Theoretical model.

The calculation is based on the equality of the internal and external plastic work. The total internal work consists of the energy absorbed by the beam web and the four plastic hinges (indicated by the red circles in Figure 3 formed on the top and bottom flanges. The external work is that done by the movement of the external forces.

$$W_w + W_f = W_e \tag{1}$$

Where W_w is the internal work of the beam web,
W_f is the internal work of the flanges,
W_e is the external work.

It can be seen from Figure 3 that thevertical deflection Δ_v of the shear panel in the post-buckling stage is related to the distance*c* between the two plastic hinges on the same flange, but not to the total length of the buckle wave on the beam web L. Based on the assumption that failure occurs when equivalent plastic strain within the beam web reaches 0.15, the relationship between Δ_v and c can be found.The calculation procedure is firstly to find the value of*c*which corresponds to the smallest uniformly distributed load q, based on the principle of conservation of energy. The next step is to find the vertical deflection Δ_v of the shear panelin terms of c.

2.1 Internal work of beam flanges

In the theoretical model, the four edges of the shear panel are assumed to be rigid. The formation of plastic hingeson the flanges happens soon after the beam enters its plastic stage. Therefore, in the elastic stage, the internal work of the beam flanges has not been taken into consideration. In both the plastic and post-buckling stages, the internal work of the flanges is the work done byrotation of the four plastic hinges on the top and bottom flanges of the beam, as shown in Figure 3.The bending moment capacity of the flange plates, which is the basis of the plastic moment resistance of the four hinges, is

$$M_0 = \frac{1}{4} f_y b_f t_f^2 \tag{2}$$

A reduction factor α is introduced toaccount for the effect of overall cross-section bending, which induces netaxial stressin flanges. The axial stress in turn reduces the bending moment capacity of the flanges. Thereduction factor can be expressed as

$$\alpha = 1 - (\frac{\sigma_{t(c)}}{f_y})^2 \tag{3}$$

2.2 Internal work of beam web

It is initially assumed that the four edges of the shear panel are rigid. The panel is composed oftensile strips in the direction at 45° to the horizontal line, and compressive strips perpendicular to the tensile strips, as shown in Figure 3. The stresses within all the tensile strips are the same, as are the stresses within all the compressive strips. From the elastic stage to the initial buckling point, the compressive stresses are assumed to be identical to the tensile stresses. In the post-buckling stage, the compressive strips are considered as strutswith three plastic hinges, as shown in Figure 4. It has been assumed that the middle plastic hinge always forms at the mid-length of each strut, although this assumption may lead to an out-of-plane deflection shape, which is slightly differentfromreality.Based on force equilibrium, as the out-of-plane deflection δ increases, compressive stresses decrease. Both force equilibrium and the geometric relationship determine that the reduced compressive stress σ_c is only related to the deflection levelin the compressive strips. The tensile stresses within the shear panel are calculated based on the Huber-von Mises plasticity criterion [3]. The internal work of beam web is the sum of the work done by both the tensile and compressive strips.

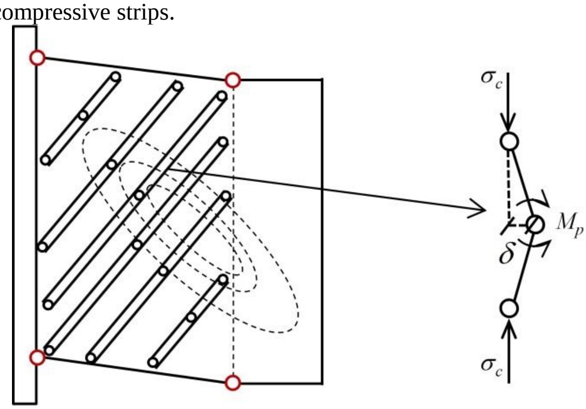

Figure 4. Strutsrepresenting compressive strips.

2.3External work

Assuming that a beam is subject to a uniformly distributed load, the loading condition of the shear panel is as shown in Figure 5. The external work is, therefore, given as

$$W_e = q(l - \frac{1}{2}c)\Delta_v \tag{4}$$

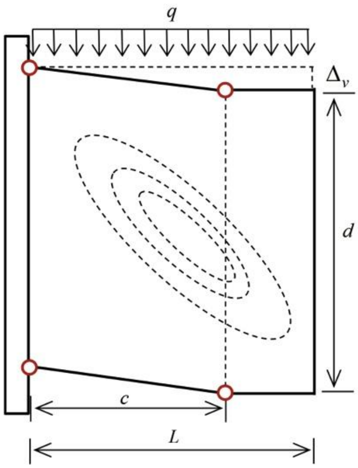

Figure 5. Displacement of the external load.

3 FINITE ELEMENT ANALYSIS USING ABAQUS

The proposed theoretical model has been verified against finite element (FE) modelling. Three-dimensional FE models of Class 1 beams were developed to analyse the shear panel behaviour at elevated temperatures. Temperature was uniformly distributed across the whole beam. The 3D shell element S4R of ABAQUS was adopted. This elementis capable of simulating buckling. Riks analysis wasused to track the descending load path of the shear panel in the post-buckling stage. A mesh sensitivity analysis was initially conducted, and an element size of 20mm × 20mm was found to provide optimum accuracy and efficiency. Aninitial imperfection of amplitude*d*/200 (according to Eurocode 3Part 1-5 [4]) was adopted. The shape of the initial imperfection was based on the first buckling mode analysis.

3.1 Material properties

The EC3 [5] stress-strain relationship has been used in the ABAQUS models, as shown in Figure 6. The reduction factors forthe proportional limit $f_{p,\theta}$, yield strength $f_{y,\theta}$, and the slope of the linear elastic range $E_{a,\theta}$ were adopted. For all temperatures, the limiting strain$\varepsilon_{t,\theta}$ and the ultimate strain $\varepsilon_{u,\theta}$ are 0.15 and 0.2 respectively. Point 3 (which indicates failure) of the force-deflection relationship (as shown in Figure 2) of the web panel, was identified from ABAQUS at a maximum equivalent plastic strain of 0.15.

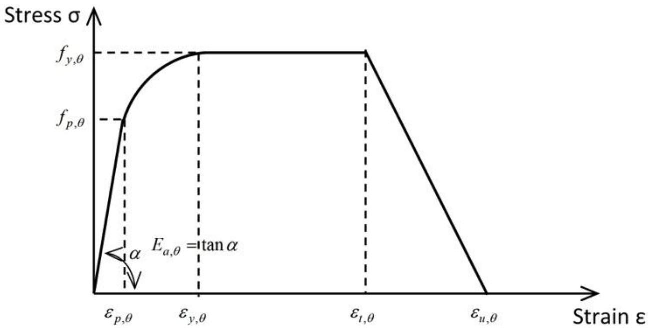

Figure 6. Stress-strain relationship of structural steel at hightemperature [5].

3.2 Geometry of the beam

Figure 7 shows the finite element model of an isolated Class 1 beam. The beam length is 3m. The cross section dimension is as shown in Figure 8.

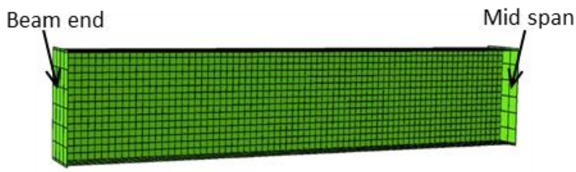

Figure 7. Image of finite element model.

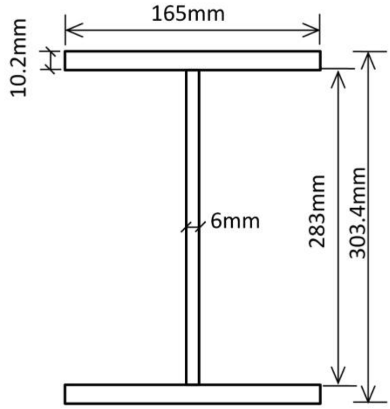

Figure 8. Cross section dimension.

3.3Boundary conditions

Because of itssymmetry, onlyhalf of the beam was modelled. The beam was assumed to be fixed at both ends. Symmetric boundary conditions should be applied to the mid-span of the beam, so that the mid-span can only move vertically without any rotation. However, at high temperatures, axial force caused by restraint to thermal expansion cannot be neglected. As the influence of axial force has not been included in the proposed theoretical model so far, horizontal movement was allowed at the mid-span. Therefore, one end of the ABAQUS model, which simulates the mid-span of the beam, was allowed to move horizontally and vertically without rotation. Rigid bodies were attached to both ends of the model in order to avoid generating stress concentrations. The boundary conditions were then achieved by applying constraints to the mid-point of each rigid body. The boundary conditions are shown in Figure 9 and Table 1.

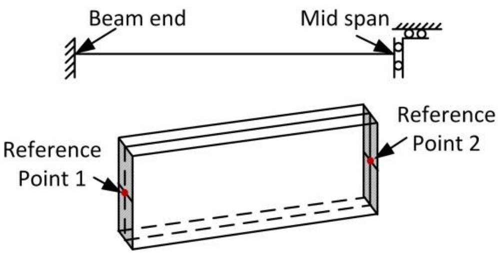

Figure 9. Boundary conditions.

Table 1. Boundary conditions.

	Reference point 1	Reference point 2
U1	1	1
U2	1	0
U3	1	0
UR1	1	1
UR2	1	1
UR3	1	1

Note: U1, U2 and U3 are the translational degrees of freedom (DoF) in the *x*, *y* and *z* directions respectively.UR1, UR2 and UR3 are the rotational DoF in the *x*, *y* and *z* directions respectively. ‘0’ indicates that a DoF is free; ‘1’ means a DoF is restrained.

4 VALIDATION AGAINST FINITE ELEMENT MODELLING

The proposed theoretical model has been validated against the ABAQUS models, focusing on the beam-end reaction forces and the mid-span vertical deflections.

In the theoretical model, the beam-end reaction forceis calculated on the basis of the design plastic shear resistance according to Eurocode 3 Part 1-1 [6] for Point 1 in Figure 2. In the design formula, the ambient-temperatureyield stress has been replaced by the stresses at the proportional limitsat elevated temperatures. Up to this point, the mid-span vertical deflection of a beamis assumed to besolely induced by bending moment. Point 2 represents the initiation of web buckling. The internal work done by both the beam web and flanges has been taken into consideration when calculating the beam-end reaction force for Point 2. It is also assumed that plastic hinges have been formed on the flanges at this stage, and the compressive stresses in the beam web have not been decreased due to the effect of buckling. The mid-span deflection for Point 2 is again assumed only to be caused by bending moment. For Point 3, the post-buckling strength reduction is accounted for by reducing the compressive stresses in the compressive strips. At this stage, the mid-span deflection is the summation of the transverse drift of the shear panel and that caused by curvatures due to bending moment.

Figures 10-12 show comparisons of the beam-end reaction forces and the mid-span vertical deflections from the theoretical and ABAQUS models. The length of the example models is 3m, and they were analyzed at five different temperatures.

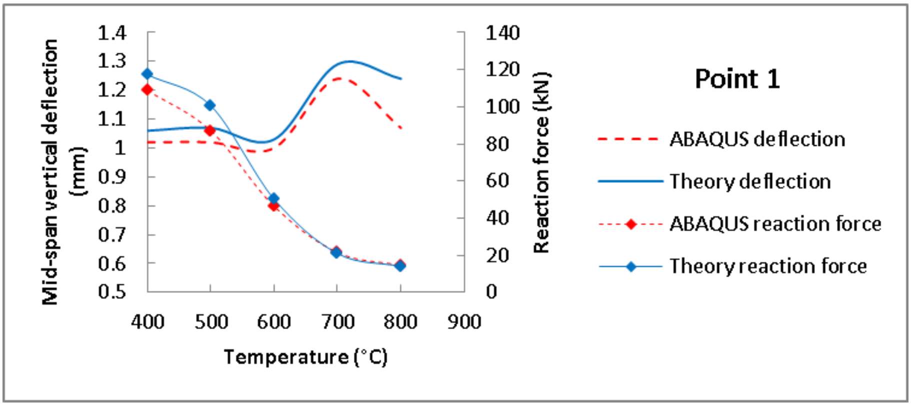

Figure 10. Comparison of mid-span deflections for Point 1 of Figure 2.

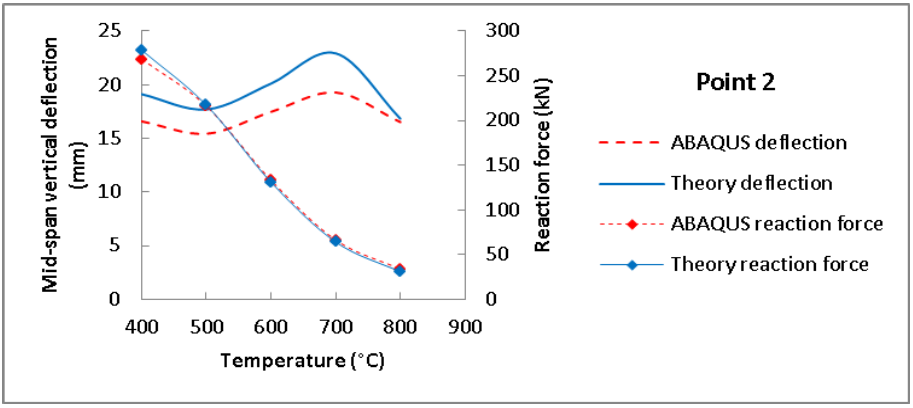

Figure 11. Comparison of mid-span deflections forPoint 2 of Figure 2.

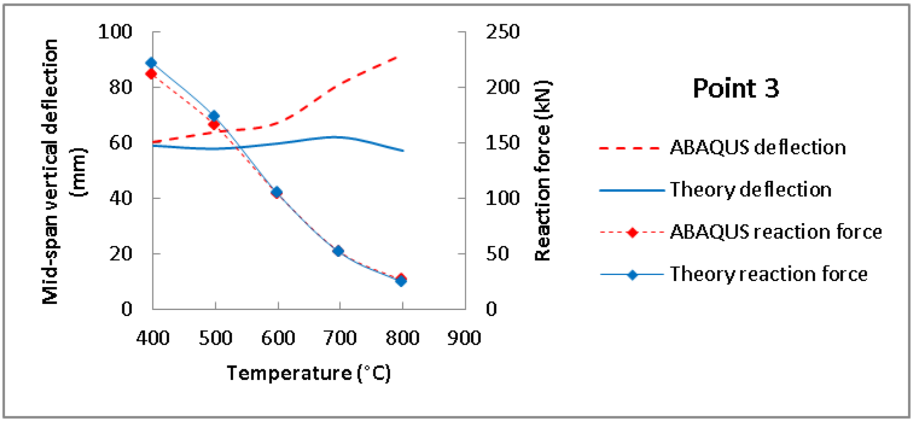

Figure 12. Comparison of mid-span deflections forPoint 3 of Figure 2.

As shown in Figures 10-12, the beam-end reaction forces given by the theoretical model compare well with those of theABAQUS modelat all three stages. The comparison of mid-span deflectionsis acceptable for Points 1 and 2. The results from the theoretical model are always on the safe side. For Point 3, the deflections compare reasonably well for temperatures below 600°C. However, as temperature increases, the proposed theoretical model tends to underestimate the deflections at the post-buckling stage . There may be two reasons for this phenomenon. The first reason is that the structural system at high temperatures may have changed. Taking the mid-span vertical deflection due to bending moment as an example, the theoretical model assumes that a plastic hinge hasformed at each end of the beam, as shown in Figure 13(a). However, as temperature increases, a larger portion of the beam end would become plastic, as captured by the FE modelling (Figure 13(b)). Therefore, the theoretical model may underestimate the vertical deflection caused by beam bending. As the theoretical component-based model will be implemented into the software *Vulcan*, this miscalculation of deflection will automatically be overcome, because *Vulcan* considers non-linear beam bending behaviour instead of the simple hand-calculation used in the proposed theoretical model. In addition, some of the assumptions of the theoretical model, such as the directions of strips and the positions of the plastic hinges on the compression strips, may influence the results. This will be investigated after implementing the model into *Vulcan*.

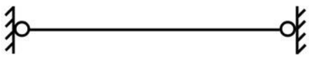

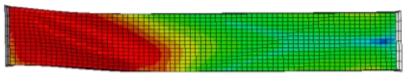

Figure 13. Beam model considering deflection caused by bending moment (a) theoretical model (b) Contours of Von mises stress in ABAQUS model.

5 COMPONENT-BASED MODEL IN *VULCAN*

Vulcan is a three-dimensional non-linear analysis program, which is capable of modelling the global 3-dimensional behaviour of composite steel-framed buildings under fire conditions. Based on the proposed theoretical model, a shear panel element will be created in *Vulcan*, adjacent to the existing component-based connection element [7], as shown in Figure 14.

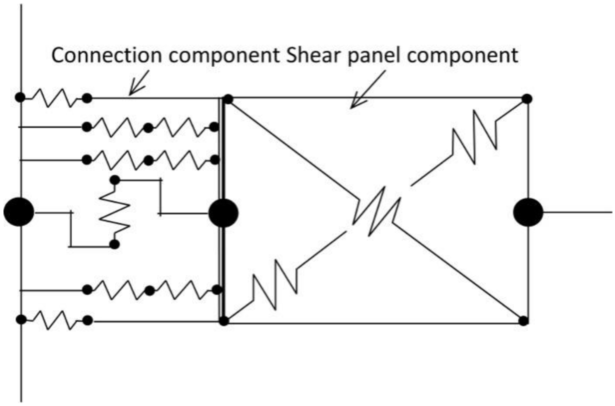

Figure 14. Component-based model including connection and shear panel.

6 CONCLUSIONS

A component-based theoretical model has been created to predict the shear capacity and vertical deflection of shear panels for Class 1 beams, up to failure at high temperatures. This theoretical model has been validated against FE models. Comparing the two models, the simplified theoretical one generally performs well. However, there is some discrepancy in mid-span deflection at the failure stage for temperatures higher than 600°C, which requires some further investigation. The theoretical component-based model will be implemented in the software *Vulcan*, and in due course to be embodied in global modelling of composite structures in fire.

REFERENCES

[1] Gann RG, *Final Report on the Collapse of World Trade Center Building 7, Federal Building and Fire Safety Investigation of the World Trade Center Disaster*,The National Institute of Standards and Technology (NIST), US, 2008.

[2] Newman G, Robinson JT and Bailey CG, *Fire safe design: A new approach to multi-storey steel-framed buildings*, The Steel Construction Institute, Berkshire, 2006.

[3] Von Mises, R., *Mechanik der Festen Korper im Plastisch Deformablen Zustand*, Nachr. Ges. Wiss. Gottingen, 1913.

[4] CEN. BS EN 1993-1-5, *Design of steel structures. Part 1-5: Plated structural elements,* British Standards Institution, 2006.

[5] CEN. BS EN 1993-1-2, *Design of steel structures. Part 1-2: General rules-Structural fire design,* British Standards Institution, 2005.

[6] CEN. BS EN 1993-1-1, *Design of steel structures. Part 1-1: General rules and rules for buildings,* British Standards Institution, 2005.

[7] Burgess IW, Davison JB, Dong G and Huang S-S., "The role of connections in the response of steel frames to fire", *Structural Engineering* International, 449-461, 2012.

8th International Conference on Structures in Fire
Guo-Qiang LI, Venkatesh K. R. KODUR, Shou-Chao JIANG, Jian JIANG, Su-Wen CHEN, Guo-Biao LOU (Eds.)
Shanghai, China, June 11-13, 2014

FIRE PERFORMANCE OF STEEL SHEAR CONNECTIONS IN A COMPOSITE FLOOR

Serdar Selamet*, Tugba Ozdemir* and Caner Bolukbaş**

* Assistant Professor, Department of Civil Engineering, Bogazici University, Istanbul 34342 Turkey
Graduate Student, Department of Civil Engineering, Bogazici University, Istanbul 34342 Turkey
e-mails: serdar.selamet@boun.edu.tr, tugba.ozdemir2@boun.edu.tr

** Graduate Student, Department of Civil Engineering, Bogazici University, Istanbul 34342 Turkey
e-mail: caner.bolukbas@boun.edu.tr

Keywords: Fire, Structural fire, Shear connections, Concrete slab, Fire performance, Connections in fire, Finite element method

Abstract. *The objective of this paper is to investigate the fire performance of a concrete slab with reinforcing steel mesh, the effect of the edge (perimeter) beams and secondary beams to the slab's performance and the resilience of the steel shear connections, which connect the secondary beams to the edge beams. In this study, a 28-story tall steel building is modeled in Abaqus finite element software that allows the analysis of thermo-mechanical problems. The finite element models show that the load carrying mechanism of the reinforced concrete slab significantly differs at ambient and fire temperatures. As long as the edge supports are fire protected, the reinforced concrete slab survives the fire but the single plate connection does not provide sufficient resistance to the excessive rotations. Further, the secondary beams have limited contribution to the reinforced concrete slab fire performance.*

1 INTRODUCTION

Recent fire experiments in steel buildings with composite floor compartment have shown that the compartments resisted collapse because the concrete slab acted like a tensile membrane supported by the fire-protected perimeter beams and columns [1-4]. The most frequently encountered problem in composite floor systems is to accurately simulate the force and moment equilibrium between the concrete slab and the steel member [5]. Another difficulty based on the fire performance of the steel connections is the effect of the concrete slab to the rotation capacity of connections and the internal forces and moment equilibrium of the steel beam section [6-8].

Although the concrete slab has proved to be resilient against the fire exposure and sustain large deflections through tensile membrane forces, it is questionable if the steel shear connections, which connect the secondary beams to the perimeter beams, can sustain large rotation and tensile force [9]. Inadequate connection strength or ductility against the fire-induced forces could trigger a collapse. Another question arises as to whether or not the secondary beams affect the fire performance of compartments at such large deflections during fire [10].

This paper investigates the fire performance of a composite floor compartment by utilizing a full-scale finite element model in Abaqus [11]. The model considers the interaction between the reinforced concrete slab, the steel member and the shear connection components at ambient and fire conditions. The aim is to quantify the effect of the secondary beams to the reinforced concrete slab and the resilience of the shear connection at large deflections.

2 PROBLEM DESCRIPTION

2.1 Case study: Floor compartment of tall steel building

As a case study, a compartment by 9.5 m and 6 m from a steel tall building in Istanbul, Turkey is modeled using the finite element (FE) software Abaqus (see Figure 1(a)). The steel building is 28 stories tall and currently used as a hotel. The compartment consists of the concrete slab with steel mesh reinforcement, four HE400A edge beams and two IPE330 secondary beams, which are connected to HE400A with single plate bolted shear connections as shown in Figure 1(b).

The performance of the reinforced concrete (RC) slab is investigated both at ambient and elevated temperatures. Three FE models with increasing complexity are created in Abaqus and a total of six analyses are run as described in Table 1. The behavior of the single plate connection in M3 and M3f models are also investigated. For the fire condition, ISO-curve for 2 hours is subjected to the structure.

The RC slab is divided by 200 mm×200 mm finite elements of 4-node doubly curved thick shells with reduced integration and large strain formulation (S4R). For simplicity, the ribbed section is modeled as a flat slab with an effective thickness of 95 mm as illustrated in Figure 1(c). For the reinforcement, A142 steel mesh is modeled using *Rebar Layer command in both x- and y- directions at 40 mm below the concrete top surface.

For HE400A and IPE330 beams, and the components of single plate connection, the reduced integration continuum elements (C3D8R) are employed. The beams are tied to the concrete shells using *Surface Tie command and the single plate connection components are assigned with contact configurations using penalty enforcement algorithm to the rest of the structural system. The boundary conditions along the RC slab edges are horizontally free but vertically restrained (roller) for M1 and M1f models whereas the RC slab edges are tied to the HE400A beams in M2, M2f, M3 and M3f models.

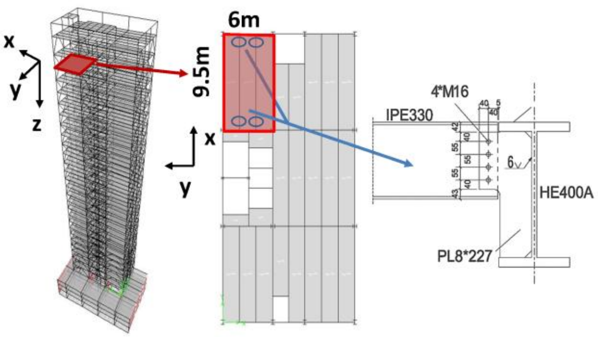

(a) (b)

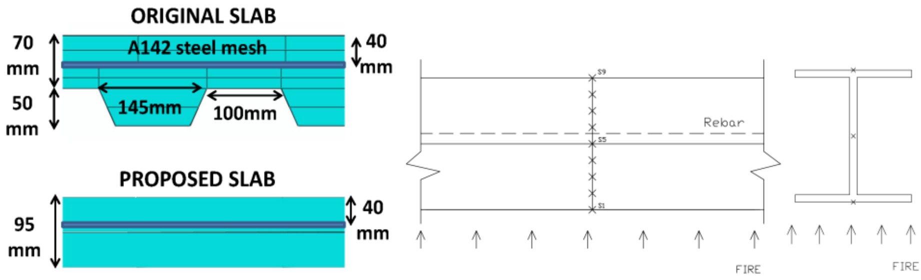

(c) (d)

Figure 1. (a) Case study: The geometry of the compartment from 28- storey tall steel building; (b) the bolted single plate shear connection detail; (c) the RC slab geometry and temperature points and (d) IPE330 temperature points.

Table 1. FE model descriptions.

FE Models	Description
M1	RC slab only at ambient temperature
M1f	RC slab at fire
M2	RC slab + HE400A at ambient temperature
M2f	RC slab + HE400A at fire
M3	RC slab + HE400A + IPE330 + single plate connection at ambient temperature
M3f	RC slab + HE400A + IPE330 + single plate connection at fire

2.2 Material Properties

The mechanical and thermal properties for the reinforcing steel mesh and the siliceous concrete material are shown in Table 2 and Table 3, respectively. For elevated temperatures, Eurocode provisions are used [12,13]. The stress-strain relationship of concrete is adopted from Youssef and Moftah [14]. For the concrete material, both compression softening and tension stiffening ratios are also taken from Youssef and Moftah [14]. The tensile and compressive concrete ultimate strength are taken as 35 MPa and 3.5 MPa, respectively. The concrete damaged plasticity in Abaqus is employed to model the plastic behaviour of the concrete material [11]. The yield strength of the steel reinforcement is 500 MPa without strain hardening. The yield strength of the IPE330 beams and the single plate is 345 MPa with strain hardening. Grade 8.8 bolts with the yield strength of 640 MPa with strain hardening.

Table 2. Mechanical and thermal properties of steel.

Steel Reinforcement	Type	Size of mesh (mm)	Longitudinal wires area (mm^2/m)	Transverse wires area (mm^2/m)	Smeared layer thickness (mm)
	A142	200x200	142	142	0.1414
Steel Properties					
Mechanical (20 °C)	*E* (GPa)	Yield stress steel reinforcement (MPa)	Yield stress IPE 330 and the single plate (MPa)	Yield stress Grade 8.8 bolts (MPa)	
	210	500	345	640	
Thermal (20 °C)	Density (kg/m^3)	Conductivity (W/m K)	Specific Heat (J/kg K)	Expansion (1/ ℃)	
	7850	53.3	440	1.23e-5	

Table 3. Mechanical and thermal properties of C35 siliceous concrete.

Concrete Properties					
Mechanical (20 °C)	*E* (GPa)	Yield stress in compression (MPa)		Cracking stress in tension (MPa)	Dilation angle in yielding (°)
	21	35		3.5	12
Thermal (20 °C)	Density (kg/m^3)	Conductivity (W/m K)	Specific Heat (J/kg K)	Expansion (1/ ℃)	
	2300	1.95	900	0.91e-5	

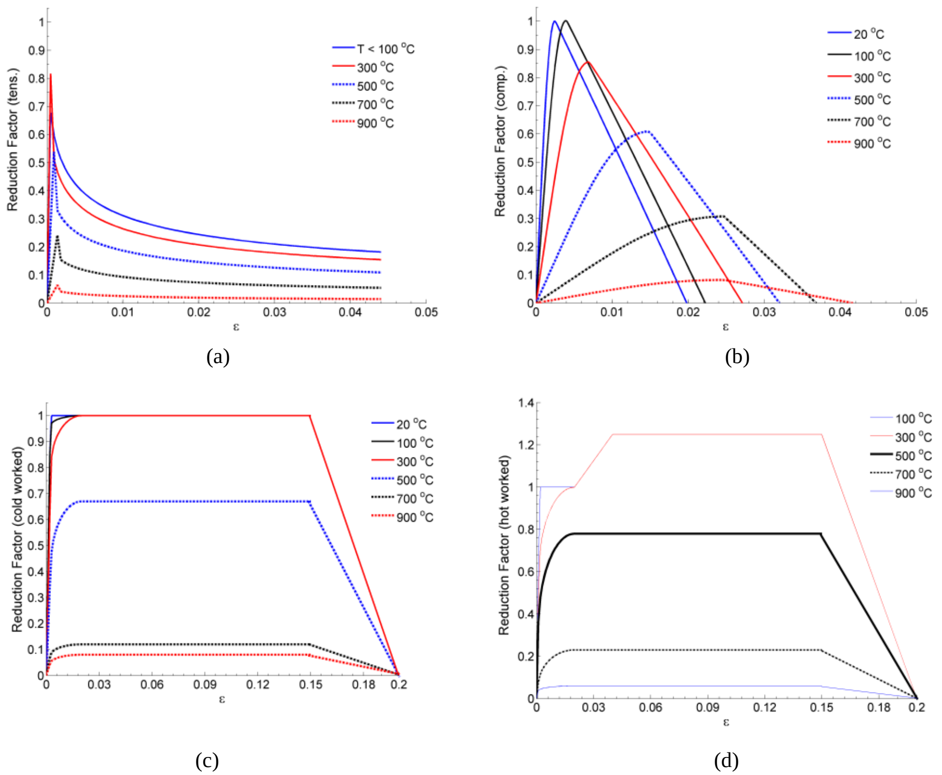

Figure 2. The reduction factors of (a) concrete material in tension; (b) concrete material in compression; (c) the steel reinforcement (cold-worked) and (d) other steel members (hot-worked) in both compression and tension.

3 ANALYSIS AND RESULTS

The solution method is an uncoupled thermal-stress analysis, where the nodal temperatures calculated from the heat transfer analysis are transferred to the structural analysis. The analysis method is dynamic-explicit with Abaqus/Explicit package [11]. A dynamic analysis is favorable because of the concrete material model complexity and the slab collapse behavior. By utilizing mass scaling by a factor of 10 and scaling up the time scale to 1 second for each step, the kinetic energy levels due to inertial forces were within 10% throughout the analysis.

For all the FE models, the compartment is initially (quasi-statically) loaded with 5 kN/m^2 distributed (gravity) load. In the first step, the RC slab is loaded approximately 40% of the ultimate load capacity of the M1 and M1f models. In the second step, two separate analyses are conducted by: (a) increasing the (gravity) loading until 20 kN/m^2 at ambient temperature and (b) subjecting the structure to the ISO-834 fire curve for two hours. M1, M2 and M3 models are at ambient temperature whereas M1f, M2f and M3f models are heated with ISO fire curve for 2 hours.

3.1 Thermal analysis

In M1f, M2f and M3f models, the RC slab, the secondary beams (IPE330) and the connection components are not fire-protected. The temperature distribution within RC slab cross-section (9 section points and steel reinforcement) and IPE330 cross-section (3 section points) are shown in Figures 3(a) and

3(b), respectively. The temperature section points used in Figure 3 are shown in Figure 1. In the RC slab, a significant thermal gradient was observed whereas the steel temperatures were close in the beam cross-section IPE330.

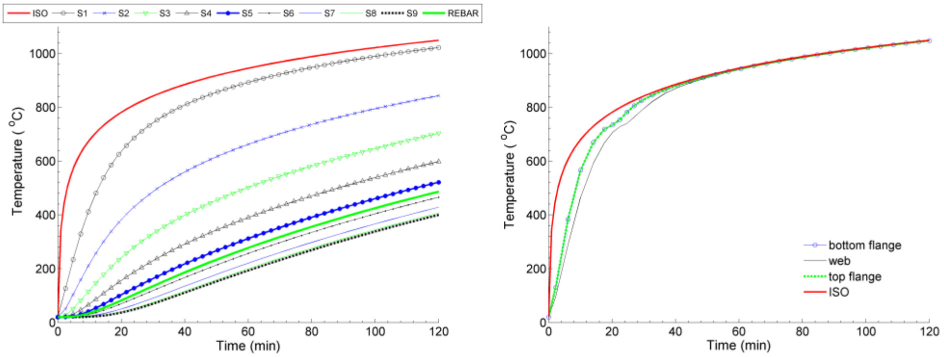

(a) (b)

Figure 3. FE heat transfer results: The temperature distribution of (a) 10 section integration (temperature) points of RC slab and (b) 3 section integration (temperature) points of IPE330.

3.2 Structural analysis

The FE models M1, M2 and M3 were quasi-statically loaded at ambient temperature until 20kN/m^2 distributed load. The FE models M1f, M2f and M3f were quasi-statically loaded until 5kN/m^2 and then subjected to ISO-fire curve for 120 minutes.

3.2.1 RC slab

Figure 4 shows the principal membrane tractions in the RC slab for all the models. At ambient temperature, it is clearly observed that the RC slab behaved significantly different if it was isolated (Figure 4(a)), supported by HE400A beams around the edges (Figure 4(b)) or IPE330 beams in the center (Figure 4(c)). A small tension zone with a compression ring is formed in the RC slab for M1 and M2 models as seen in Figures 4(a) and 4(b). A compression zone is formed in M3 model as seen in Figure 4c. The slab deformations were relatively small at ambient temperature. IPE 330 beams provided significant flexural stiffness to the RC slab. At fire, the fire performance of the RC slab is similar. A large tension zone is developed in the middle section with a compression ring in the outer section as seen in Figures 4(d) — 4(f). The addition of the edge beams around the perimeter (Figure 4(e)) or the secondary beam (Figure 4(f)) does not affect the load carrying mechanism of the RC slab.

Figures 5(a) and 5(b) shows the vertical deflection at RC slab midpoint. At ambient temperature, the deflection significantly differs for each model. M1 model has larger deflection and goes into tensile zone action as seen in Figure 5(a). By adding HE400A (edge) beams, the RC slab in M2 model behaves like having a rotationally fixed 5(a) boundary, and hence the total deflection decreases. As the loading increases, M2 model starts with compressive zone action but later goes into the tensile zone action. M3 model exhibits much smaller deflection since IPE330 beams provide additional flexural stiffness to the structure. Therefore, the RC slab develops only the compression zone action as the distributed loading increases. At fire, the RC slab starts in compression due to the axial restraint on the edges. However, as the stiffness of the slab decreases at elevated temperatures, the vertical deflection increases and the RC slab gets into the tension zone with a compression ring around the perimeter. The secondary beams in M3f contribute to the vertical resistance of the RC slab, although the contribution is much limited compared to the contribution at ambient temperature as seen in Figure 5(b).

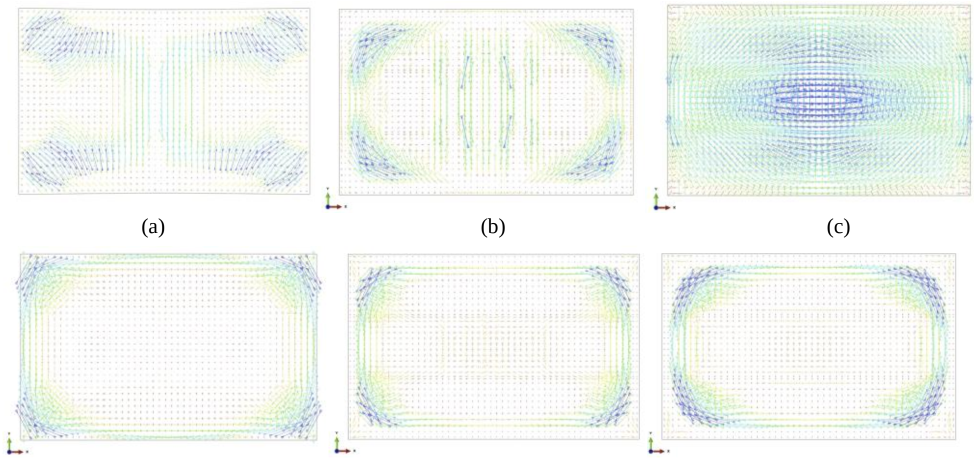

(a) (b) (c)

(d) (e) (f)

Figure 4. Principal membrane tractions (top shell surface) of the reinforced concrete slab in models (a) M1; (b) M1f, (c) M2; (d) M2f; (e) M3 and (f) M3f at the end of the analysis. The blue (darker) lines represent compression and red (lighter) lines represent tension.

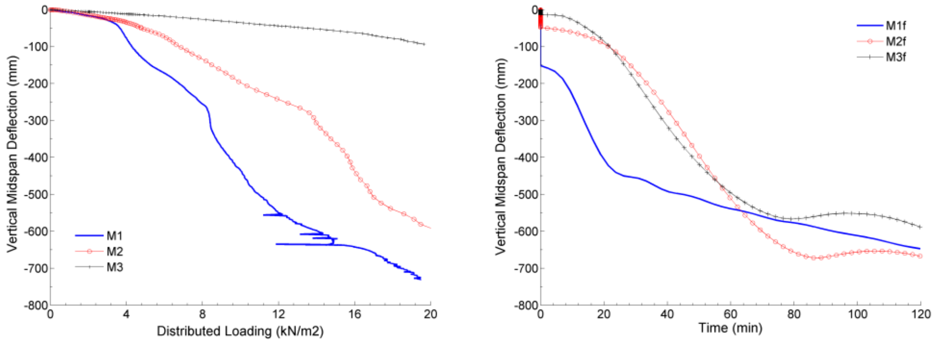

(a) (b)

Figure 5. Vertical deflection at the RC slab midpoint for (a) ambient condition of M1, M2, M3 models and (b) fire condition of M1f, M2f, M3f models.

3.2.2 Single plate connection

The deformation of the M3f model and the single plate connection are shown in Figures 6(a) and 6(b), respectively. Although the RC slab carries the gravity loading at elevated temperatures by the ‘tensile inner zone-compressive outer ring’ mechanism, the slab deflections become very large and the single plate shear connection deforms significantly around the bolt-hole regions in the beam web. Further, due the large connection rotation, the IPE330 flange contacts the plate and causes excessive deformations as observed in Figure 6(b). The von Mises stresses confirm that the bolt shear is the governing limit state failure of this type of connection.

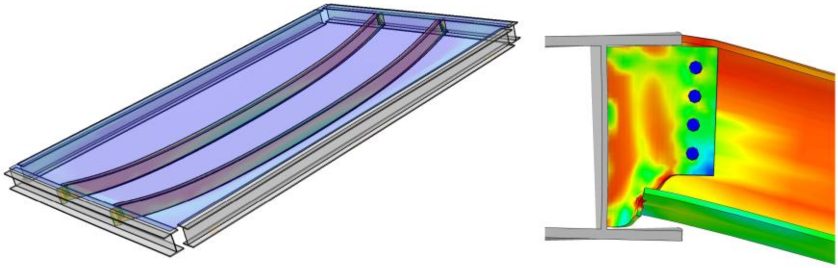

(a) (b)

Figure 6. The von Mises stress contours and deformations of (a) the entire structure and (b) the single plate shear connection of the M3f model.

4 CONCLUSIONS

In this paper, the fire performance of a large compartment with single plate shear connections is studied at ambient and fire temperatures. The finite element models show that the load carrying mechanism of the RC slab differs significantly at ambient and fire temperatures. At ambient temperature, the main mechanism is the compression zone action with relatively small vertical slab deflections. The addition of the edge beam around the perimeter and the secondary beams in the center greater increases the load carrying capacity of the slab at ambient temperature. At fire, the RC slab forms tension in the middle zone and compression in the outer ring. Therefore, the design of the steel reinforcement for tensile membrane action is necessary for a robust fire performance of the RC slabs. As long as the edge supports are fire protected, the RC slab survives the fire. However, the single plate connection does not provide sufficient resistance to excessive rotations. Further, the secondary beams have limited contribution to the RC slab fire performance.

ACKNOWLEDGEMENT

The authors would like to acknowledge the Marie Curie International Incoming Fellowship (IIF) CONFIRE: 58000158, Bogazici University Scientific Research Projects BAP: 7122P, which provided the funding for this study.

REFERENCES

[1] Santiago A., da Silva L.S. and Real P.V., “Numerical modelling of the influence of joint typologies on the 3D behavior of a steel sub-frame under a natural fire”, *Fire Technology,* 46: 49-65, 2010.

[2] Wald F., da Silva L.S., Moore D., Lennon T., Chladna M., Santiago A., Benes M. and Borges L., “Experimental behaviour of a steel structure under natural fire”, *Fire Safety Journal,* 41(7): 509–522, 2006.

[3] Lamont S., “The behaviour of multi-storey composite steel framed structures in response to compartment fires”, *Ph.D. Dissertation,* University of Edinburgh, UK, 2001.

[4] Moss P., Buchanan A.H., Seputro J., Wastney C. and Welsh R., “Effect of support conditions on the fire behavior of steel and composite beams”, *Fire and Materials,* 28: 159-75, 2004.

[5] Lim L., Buchanan A., Moss P. and Franssen J.M., “Numerical modelling of two-way reinforced concrete slabs in fire”, *Engineering Structures,* 26(8): 1081-91, 2004.

[6] Dong Y. and Prasaad K., “Thermal and structural response of a two-story, two bay composite steel frame under fire loading”, *Proceedings of Combustion Institute,* 32: 2543-50, 2009.

[7] Bailey C.G. and Moore D.B., "The structural behavior of steel frames with composite floor slabs subject to fire: Part 1: Theory", *The Structural Engineer*, 78(11) pp. 19-27, 2000a.

[8] Selamet S. and Garlock M.E., "Robust fire design of single plate shear connections", *Engineering Structures*, 32(8) pp. 2367- 2378, 2010.

[9] Beitel J. and Iwankiw N., "Analysis of needs and existing capabilities for full-scale fire resistance testing", *National Institute of Standards and Technology,* NIST GCR 02-843, 2002.

[10] O. Vassart, B. Zhao, "Fracof: Fire Resistance Assessment of Partially Protected Composite Floors, Engineering Background", *Lifelong Learning Programme Leonardo Da Vinci*, Cardington, UK, 1995.

[11] DS-Simulia, "ABAQUS version 6.13 documentation", *Dassault Systèmes*, Providence RI, 2013.

[12] CEN, "Eurocode 2: Design of concrete structures - Part 1-2: General rules - Structural Fire Design, EN 1992:1-2:2004", Brussels, Belgium, 2004.

[13] CEN, "Eurocode 3: Design of steel structures - Part 1-2: General rules - Structural Fire Design, EN 1993:1-2:2005", Brussels, Belgium, 2005.

[14] Youssef M.A. and Moftah M., "General stress-strain relationship for concrete at elevated temperatures", *Engineering Structures,* 29 pp. 2918- 2634, 2007.

8th International Conference on Structures in Fire
Guo-Qiang LI, Venkatesh K. R. KODUR, Shou-Chao JIANG, Jian JIANG, Su-Wen CHEN, Guo-Biao LOU (Eds.)
Shanghai, China, June 11-13, 2014

EXPERIMENTAL RESEARCH ON FIRE RESISTANCE PERFORMANCE FOR RC JOINTS WITH DAMAGE CAUSED BY MARINE ENVIRONMENT

Ji-Jun Miao*, Fang-Zhen Wu and Yan-Chun Liu*****

*School of Civil Engineering, Qingdao Technological University, China
**School of Civil Engineering, Qingdao Technological University, China
e-mails: msyu_990421@sina.Com, 751218443@qq.com

***School of Civil Engineering, Qingdao Technological University, China
e-mails: 65230768@qq.com

Keywords: R.C. joints, Chloride erosion, Fire test, Temperature field, Bearing capacity degradation in fire

Abstract. *Five non full R.C. joints with the same reinforcement , D1~JD5,were designed.JD1~JD4 was designed to simulate chloride ion erosion damaged under marine environment, to provide the damage index of the initial conditions for subsequent fire text. Fixed axial compression ratio of fire test was carried out on the concrete frame joint with different crack index. The test use standard temperature curve. The deformation characteristics and damage form of the high temperature is obtained by experimental observation. The temperature distribution of frame beam and column section was obtained. According to simplified calculation method of section temperature field of concrete, a simplified calculation formula taking into account the damage caused by marine environment for R. C. Joints' bearing capacity under fire was put forward in order to refine the calculation accuracy significantly.*

1 INTRODUCTION

Coastal engineering construction is subjected to the chloride ion erosion, the protective layer cracking of concrete resulted from it will seriously affect the durability of the concrete structure.(Jin and Zhao 2003). Especially when there is a fire, the structure of the mechanical properties will be severely degraded, the consequences will not be able to forecast. For marine environmental damage and fire research, mainly concentrated in ocean environmental durability, fire single factor effect, as well as fire and other factors coupling, etc, and meaningful research results were obtained. (Fan et al. 2011; Liu 2010; Chen 2011). The tests and analysis of fire on reinforced concrete frame structure with the earthquake damage was described in literature [7]. The results show that the influence of earthquake damage to temperature changes of the framework section is bigger. Displacement restoring capacity under high temperature became worse. The bearing capacity reduced. The relationship between the bearing capacity degradation and crack width is linear. Crack affect temperature field of concrete frame under high temperature. The influence of crack width to fire resistance of concrete specimen was studied in some literature (Bian.2012). But how to carry out the response analysis of the structure under fire after marine environmental damage, very few people involved in the study area now. So it is necessary to carry out the research. It can provide a theoretical basis for improving the structure durability and structure fire resistance. It is of great theoretical and practical significance to structure corrosion resistance and fire resistance.

2 EXPERIMENT WAS DESIGNED TO SIMULATE CHLORIDE EROSION ION DAMAGED UNDER MARINE ENVIRONMENT

2.1 concrete node design

Five R.C. Joints with the same reinforcement, D1~JD5, were designed. The strength grade of concrete:C40. The thickness of the protective layer of concrete node is 40 mm. The specific size and reinforcement information is shown in Figure 1.

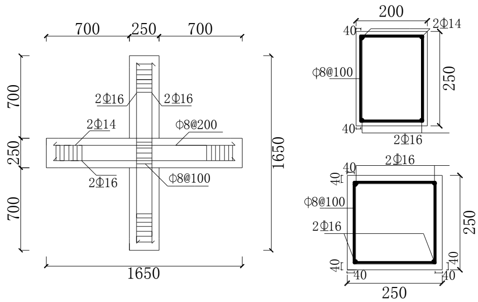

Figure 1. Dimensions and reinforcements for Joints.

1.2 The test of speeding up chloride ion erosion

Electrified accelerated chloride ion erosion test was carried on JD1~JD4 to provide Initial damage index for fire test. Initial damage index refers to maximum corrosive crack width. Maximum corrosive crack width were 0.05mm, 0.10mm, 0.15mm an 0.20mm separately. Chloride ion erosion test was not carried on JD5 as control group.

The test of speeding up chloride ion erosion simulated Marine environment in Laboratory mainly based on the chloride ion erosion system. This system mainly consists of three parts, respectively is insulated tank, current transformer voltage regulator, lead cathode and anode. Concrete specimens soaked in 5% NaCl solution with dc power supply. Positive is connected to the steel bar in concrete to make it act as anode of the battery. Negative pole connected with stainless steel tube in the solution. Make it act as a corrosion cell cathode. Form a loop through NaCl solution. It will produce electrochemical reaction between the cathode and anode. Thus it can accelerate the steel corrosion in the process of the electricity.

1.3 Test results and analysis

In the process of erosion take out the R.C. Joints from insulated tank once every 12 hours. We used PTS-E40 Crack comprehensive tester to measure the crack width. At the same time, recorded the time of occurrence of crack and the quantity of crack, marked crack with the marker pen. When any one of crack width achieved maximum corrosive crack width, we took out the R.C. Joints and stopped the test.

Through analysis we can draw the following main conclusions.

(1) For the first six hours, crack is not carried out. That shown that rust did not led to appear of concrete protective layer cracking. After 6 hours the first crack began to appear. They are mostly the corrosive cracks produced by the transverse stirrups. Width is about 0.03 mm or so.

(2) Joint section finally cracks in general. Time needed is about 48h, most of them are diagonal cracks. Joint section crack growth rate is relatively slow. The reason was the multiple "protection" of concrete.

(3) In the late cracks were mostly transverse stirrups cracks. When the crack reaches a certain width, crack growth slows down and increases slowly. The main reason is that concrete exist space inside. When crack reached to certain width, a large number of black rust flowed from the gaps and cracks and did not get to accumulate. So the expanding force is small to peripheral layer.

2 FIRE TEST

2.1 The experimental device and measurement.

The device of the test includes loading equipment, measuring instruments, etc. This test was done in structure laboratory of Qingdao Technology University. Horizontal fire test furnace was used. Test included the measurement of temperature and displacement. The axial displacement of the specimens was measured by the mechanical dial indicator. The temperature of furnace was measured by N-type thermocouple. Beam-column section of node was measured by Nickel chrome - nickel silicon K type thermocouple. The measuring-point arrangement of nodes was shown in Figure 2. All temperature data was collected in the experiment by the HP Agilent 34970 a type of data acquisition instrument. The time intervals of data acquisition were 2 minutes.

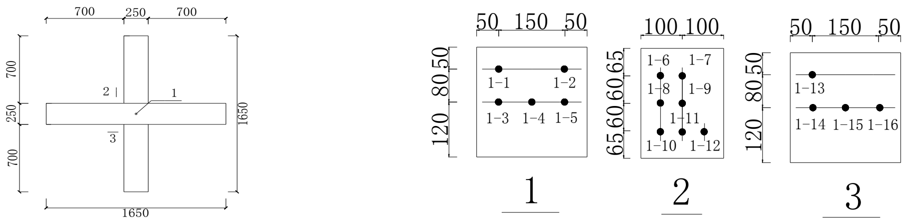

Figure 2. Temperature measurement arrangement.

Table 1. fire resistance limit of every node.

specimen number	Load on column kN	Load on beam kN	Damage index (mm)	fire resistance time (min)
JD1	240	10	0.05	125
JD2	240	10	0.1	105
JD3	240	10	0.15	85
JD4	240	10	0.2	70
JD5	240	10	0	150

2.2 The test results

The fire resistance limit of every node shown in Table 1.

Through comparison and analysis we can draw the following conclusions:

(1) Every 200-250 millimeter, there is a transverse crack through the whole beam height. Spacing is close to the stirrup spacing. The first transverse cracks were not appeared in the section of maximum moment but in the section which has a certain distance with the edge area of node. Because of good conductors of heat, stirrup temperature rises faster than concrete. Uncoordinated deformation is produced between steel and concrete. Then the temperature crack appeared.

(2) It appeared obviously vertical splitting cracks at the end of column. The more obvious the initial damage was, the more serious the splitting phenomenon was. Under the high temperature the end of column constantly expanded and produced the larger expansion forces. But the load at the end of the column limited the expansion. Eventually vertical cracks were produced.

(3) The node was destroyed because of the beam deflection achieved the maximum deflection what literature [6] said. Node area relatively intact and there is no obvious damage. That may be rooted in the multiple "protection" of concrete.

3 TEST ANALYSIS

3.1 The temperature response

The variation in temperature of fire furnace was measured by thermocouple. The results are shown in Figure 3. Because the fire furnace JD1 is not used for a long time, the temperature of the first specimen rose relatively slowly.

Heating curves of measuring point at different cross-section to same specimen shown in Figure 4. Heating curves of same measuring point at the same cross-section to different specimen shown in Figure 5.

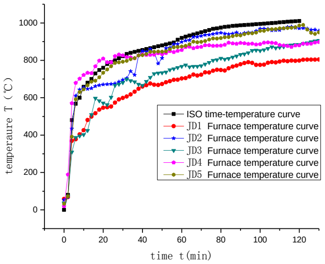

Figure 3. Specimen fire heating curves and ISO curve.

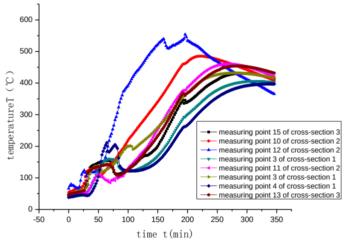

(a) Heating curves at different cross-section to JD1

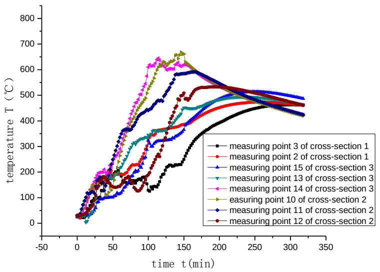

(b) to JD2

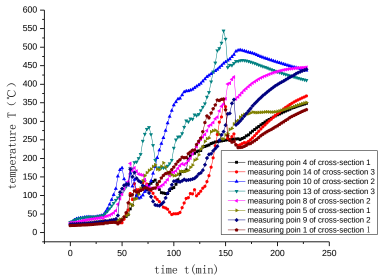

(c) to JD3

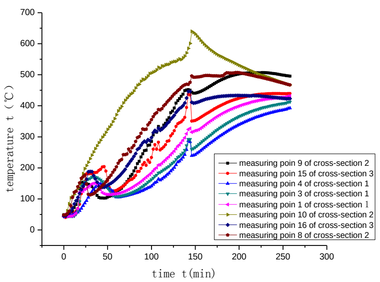

(d) to JD4

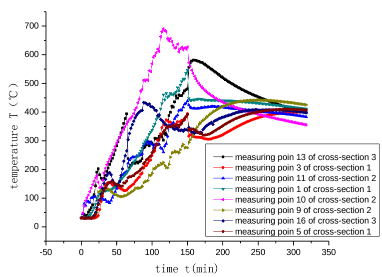

(e) to JD5

Figure 4. Curves of temperature rising at joints.

As you can see from the figure, under the similar combustion environment and heating curves temperature changes within the beam and column section has the following rule:

(1) As we can see from the heating curves, there is a big difference between these measuring points at the same cross-section. The temperature of the measuring point at the outer edge of cross section rose relatively quickly. But it peaked at a slower speed in the inner side of the cross section, and there is still a long rise space in a period of time after the fire, that has an obvious temperature hysteresis. This suggests that the temperature transfer from the heated side to the reverse side for a period of time after the fire, until reaching equilibrium. But the overall heating trend of different points was roughly the same;

(2) The temperature curve has obvious turning point at about 100 ℃-200 ℃, and the slope of curve suddenly got to be small. Temperature changed a little after a period of time, and a temperature platform was formed. This is due mainly to great quantities of water was evaporated under the effect of high temperature.

(3) The temperature of measuring point at node area was lower than the beam and column section. The main reason is the protective effect of concrete.

(4) Some of temperature curves appeared jump phenomena, in other words the temperature changes is not stable. It may be that heat transfer way changed when cracks attained a degree.

As you can see from the figure 6, the temperatures of the same measuring point vary widely between different components. But the overall heating trend of different points were roughly the same; The wider the crack is ,the faster the temperature of the same measuring point rise. The wider the crack is R.C. Joint is easier to achieve duration of fire resistance and to be destroyed. In other words time is shorter by fire. So the final temperature of components with the wider crack is not high.

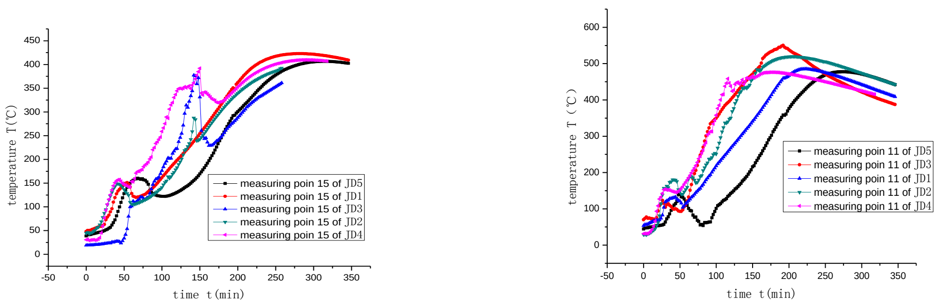

(a) Heating curves of measuring point 15 to column section (b) to beam cross section 11

Figure 5. Curves of temperature rising at the same section.

3.2 The deformation response

In the process of the test, under the effect of load and temperature beam deflection changes greatly. As a result of the test conditions we used mechanical dial gauges to measure deformation of beam and column. We manually recorded the data. According to the data from the test we can draw the deflection change shown in Figure 6.

According to the deflection - time curve we can see that at the beginning of the test the the impact on mechanical behavior of concrete and steel is small and the deformation of the component increased slowly. With the increase of temperature, the growth rate of the deflection was significantly speed up. In addition, The initial crack resulted of the chloride ion erosion had a greater influence on the deflection change of component, especially under the condition of higher temperature. The wider the initial crack width was, the greater the growth rate of the deflection was. RC joint was eventually destroyed due to that the beam deflection of one side had achieved the duration of fire resistance.

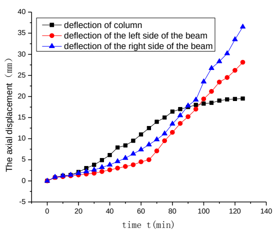

(**a**) The deflection curve 0f JD1

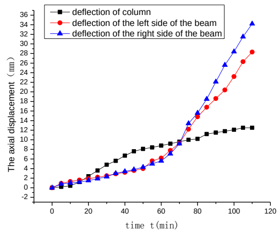

(b) The deflection curve 0f JD2

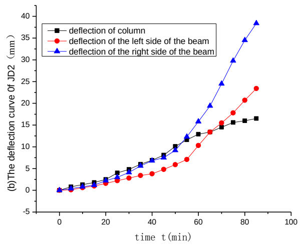

(c) The deflection curve 0f JD3

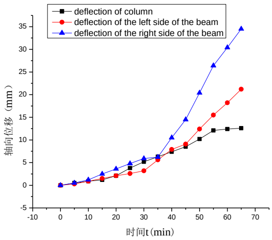

(**d**) The deflection curve 0f JD

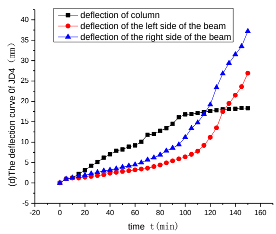

(e) The deflection curve 0f JD5

Figure 6. The deflection curve 0f R.C. Joints.

4 BEARING CAPACITY CALCULATION OF JOINTS UNDER HIGH TEMPERATURE

4.1 The basic assumptions of the assumption of calculation.

The effective area of concrete was divided by 250℃, 500℃temperature line mentioned in the Reference [9]. The strength of concrete at about 250℃-500℃was 80% of the compressive strength at room temperature. The strength of concrete at about 500℃-900℃ was 30% of the compressive strength at room temperature. To simplify the analysis process we made the following assumptions:

(1) Concrete is assumed to be an isotropic material, temperature field in depth along section conform to the law of linear. The temperature was same at the same section depth.

(2) Beam and column section conformed to the horizontal section assumption

(3) The conversion between heat energy and mechanical energy was ignored, in other words, a small number of calories was ignored. These calories came from the transformation of mechanical action such as material deformation and Temperature stress and so on.

4.2 The simplified calculation method of section temperature field.

The concrete sections were equivalent to homogeneous cross section when the section bearing capacity was calculated. The cross sections was divided by 250℃, 500℃ isotherm. According to the principle of cross section ultimate bearing capacity equivalent and the high temperature strength proportion of concrete, the cross section actual width of two different temperature ranges was reduced to get the equivalent width. So we can use the compressive strength of concrete under normal temperature when we calculated the ultimate bearing capacity of equivalent cross section.

The location of all of the longitudinal reinforcement remains unchanged, its yield strength can value according to the method recommended in the Reference [9].

Based on the Standards of Concrete Structure Design (GB50010-2010), Axial compression bearing capacity calculation formula (1) of ordinary stirrups column was used to calculate the compressive bearing capacity of column section. The formula (2), (3) were used to calculate the flexural bearing capacity of beam normal section.

$$N = 0.9\varphi(f_c A + f_y^{'} A_S^{'}) \tag{1}$$

$$\partial_1 f_c bx + f_y^{'} A_S^{'} = f_Y A_S \tag{2}$$

$$M = \partial_1 f_c bx(h_0 - \frac{x}{2}) + f_y^{'} A_S^{'} (h_0 - \partial_s^{'}) \tag{3}$$

φ was defined as the stability coefficient of concrete compression member. The value for the stability coefficient was 0.98. The calculation results was shown in Table 2 and 3.

Table 2. Ultimate bearing capacity of beam in fire.

Name of the frame work	Component damage （mm）	Before the fire (kN m)	After the fire (kN m)	Refractory limit *t*（min）	The steel temperature	Bearing capacity decline ratio （%）
JD1	0.05	33.01	20.04	125	570	39.3
JD2	0.1		20.96	105	540	36.5
JD3	0.15		18.88	85	560	42.8
JD4	0.2		21.49	70	530	34.9
JD5	0	——	——	——	——	——

Table 3. Ultimate bearing capacity of columns in fire.

Name of the frame work	Component damage (mm)	Before the fire(kN)	After the fire(kN)	Refractory limit *t*（min）	The steel temperature	Bearing capacity decline ratio(%)
JD1	0.05	2651.9	1665.7	125	600	37.2
JD2	0.1		1712.6	105	570	35.4
JD3	0.15		1700.9	85	540	35.9
JD4	0.2		1812.4	70	500	31.7
JD5	0	——	——	——	——	——

From the calculation results of Tables 2 and 3, we may draw the conclusion as follows:

(1) Due to the different of chloride ion initial damage, the heating speed and fire endurance time of specimen is not the same. The smaller the crack damage index was, the longer the corresponding refractory time would be. It can be seen from the table, the degradation of bearing capacity of the beams and columns were all serious. The degradation has exceeded 30%. The degradation of beams was the most serious and the maximum value reached 42.8%.

(2) I can be seen through the analysis that ultimate bearing capacity of structure under high temperature depends largely on the strength of the reinforcement. With the increase of temperature, steel strength fell sharply, which leads the ultimate bearing capacity of the component to drop rapidly.

5 CONCLUSIONS

(1) For the first six hours, crack is not carried out. That shown that rust did not led to appear of concrete protective layer cracking. After 6 hours the first crack began to appear. They are mostly the corrosive cracks produced by the transverse stirrups. Width is about 0.03 mm or so. Joint section finally cracks in general. Time needed is about 48h; most of them are diagonal cracks. Joint section crack growth rate is relatively slow. The reason was the multiple "protection" of concrete.

(2) In the late cracks were mostly transverse stirrups cracks. When the crack reaches a certain width, crack growth slows down and increases slowly. The main reason is that concrete exist space inside, when crack reached to certain width; a large number of black rust flowed from the gaps and cracks and did not get to accumulate. So the expanding force is small to peripheral layer.

(3) Trend of cross section temperature field of each component was same. From external to internal the peak of the measuring point temperature curve moved to the right. The temperature of the measuring point at the outer edge of cross section rose relatively quickly. But it peaked at a slower speed in the inner side of the cross section. A temperature platform was formed at about 150℃and the slope of curve suddenly got to be small. Temperature remained unchanged within a short period of time.

(4) The deformation under high temperature and room temperature had very big difference. In the process of high temperature test the beam deflection was nonlinear change over time. At the beginning of the test the deformation of the component increased slowly. With the increase of temperature, the growth rate of the deflection was significantly speeding up. In addition, the initial crack resulted of the chloride ion erosion had a greater influence on the deflection change of component, especially under the condition of higher temperature. The wider the initial crack width was, the greater the growth rate of the deflection was. At the same time the fire resistance of the component was worse.

(5) Under the condition of fire, the bearing capacity of the structure degraded seriously. The degradation of beam was more serious than column. At the time we found that ultimate bearing capacity of structure under high temperature depends largely on the strength of the reinforcement.

So we should consider mainly the protection of steel during the fire resistance design of the structure. There are some ways such as increasing protective layer thickness or spraying fire proofing coatings.

REFERENCES

[1] Jin, W. L., and Zhao, Y. C. *The durability of concrete structure,* Science press, Beijing, China, 2003.

[2] Fan, H., and Wang, P. G. “Research on chloride penetration for RC structures after long-term exposure, ” *J.* Journal of Architecture and Civil Engineering, 32(1):75-83, 2011.

[3] Liu, C. W. “Experimental Analysis of Fire Resistant Performance of Concrete Frame With Damage Caused by Weak Earthquake.” D. Qingdao technology university, Qingdao, China， 2010.

[4] Chen, N. “Experimental research and numerical simulation on fire resistance performance of RC beams with damages caused by service loading” D. Qingdao technology university, Qingdao, China, 2011.

[5] Lu, C, S., and Qu, L, J. *Fire resistance design of building structure*. China building industry press. China, 1995.

[6] Xiao, J, Z., and Xie, M., and Pan, Q, J. “Experimental study on the fire-response and fire-resistance of high-performance concrete frame.” *J.* Journal of Architecture and Civil Engineering, 25(4):1-7, 2004.

[7] Miao, J, J., and Wang, J, F,. Liu, C, W,. “Experimental research on R C frame structure with damages due to elevated temperature” *J.* Journal of Building Structures, 33(2):1-9, 2012.

[8] Bian, Z, L. “Experimental research and numerical simulation on fire resistance performance of RC columns with stress damages” D. Qingdao Technology University, Qingdao, China， 2012.

[9] Zhu Bolong, Lu Zhoudao. Report on fire-resistance of engineering structure [R]. Shanghai: Tongji University. Institute of Structure Engineering and Disaster Reduction, 1990.

EFFECTS OF PLASTERBOARD JOINTS ON THE FIRE PERFORMANCE OF COLD-FORMED STEEL WALLS

Anthony D. Ariyanayagam*, Sivakumar Kesawan* and Mahen Mahendran**

* Science and Engineering Faculty, Queensland University of Technology, Brisbane, Australia
e-mails: a.ariyanayagam@qut.edu.au and k.sivakumar@qut.edu.au

** Professor, Science and Engineering Faculty, Queensland University of Technology, Australia
e-mail: m.mahendran@qut.edu.au

Keywords: Light gauge steel frame walls, Cold-formed steel studs, Plasterboard joints, Back-blocking, Gypsum plasterboards

Abstract. *This paper presents the effect of plasterboard joints on the fire performance of cold-formed steel walls. Plasterboard joints are unavoidable. However, they can be arranged in a way that they do not significantly influence the fire performance of cold-formed steel walls. Hence a research study into the effects of plasterboard joints on the fire performance of plasterboard lined cold-formed steel walls was undertaken using both full-scale fire tests and numerical studies. In this study a back-blocking technique was used to eliminate the plasterboard joints being located over the studs. Instead plasterboard joints were used between studs with 150 mm wide plasterboards as back-blocks. Both experimental and numerical results from this study show that the fire resistance rating of single plasterboard lined cold-formed steel walls can be increased by 25% through the use of a back-blocking joint arrangement in comparison to the traditional plasterboard joint arrangement over the studs.*

1 INTRODUCTION

Light gauge steel frame (LSF) walls have been extensively used in residential, industrial and commercial buildings as primary load-bearing structural members. These walls also act as separating elements between adjacent fire compartments and resist the spread of fire, heat and toxic gases into the compartment. LSF walls are commonly made of cold-formed steel frames and are lined with gypsum plasterboards and insulation. Gypsum plasterboard is used to provide an aesthetic appearance and to delay the stud temperature rise and obtain the required Fire Resistance Rating (FRR), while insulation is primarily used for acoustic purposes. Gypsum plasterboard also provides lateral restraint to wall studs and resists minor-axis buckling and twisting. The type and thickness of plasterboards used will significantly influence the FRR of LSF wall panels. The plasterboard type includes specially manufactured fire resistant gypsum plasterboards or the general purpose plasterboards.

In general, the plasterboard joints in single plasterboard lined LSF walls are located (vertically) over the studs. Recent experimental studies [1-3] conducted on the fire performance of LSF walls have shown that plasterboard joints over the studs significantly influenced the stud temperature rise. In these fire tests, studs which had the vertical plasterboard joints over them showed higher temperatures than those without them. This is due to the opening up of plasterboard joints, as the plasterboard shrinks due to the loss of moisture and thus causing the studs to fail by flexural-torsional buckling much earlier than when lateral plasterboard restraints were present. Plasterboard joints are unavoidable, but can be arranged in a way to not significantly influence the fire performance of LSF walls. Hence a research study into the effects of plasterboard joints on the fire performance of single plasterboard lined LSF walls was undertaken using both full scale fire tests and numerical studies. This paper presents the results of this study and proposes new plasterboard joint arrangements to enhance the fire performance of LSF walls. It also describes the structural and fire performance of LSF walls with back-blocking plasterboard joints in comparison to the fire tests conducted with plasterboard joints along the studs.

2 FACTORS INFLUENCING FIRE RESISTANCE OF LSF WALLS

Many experimental and numerical studies have been conducted on the fire performance of LSF walls. These studies have shown that many factors influence the fire resistance of LSF walls. The experimental studies conducted by [4] have shown that gauge size and thickness of studs, spacing of studs, insulation types and thicknesses, resilient channel installation and load intensity influenced the fire resistance of load-bearing LSF walls. Their studies also highlighted that insulation type and number of gypsum plasterboard layers significantly affected the fire performance of LSF walls. Furthermore, LSF walls without insulation provided higher fire resistance compared to cavity insulated walls. Also the use of rock fibre insulation outperformed glass fibre and cellulose fibre insulations. The number of plasterboard layers had a significant effect on fire resistance rating, where double plasterboard lined walls provided higher fire resistance than a single layer plasterboard lined walls. The studies conducted by [1] demonstrated the superior performance of externally insulated LSF walls over the cavity insulated walls, i.e. nearly 20% increase in FRR when compared with the conventional cavity insulated walls. Their study also confirmed that rock fibre insulation provided higher fire resistance than glass fibre and cellulose insulations in cavity insulated and externally insulated LSF walls. There are also other factors that influence the fire performance of LSF walls such as the type of screw fasteners, plasterboard joint arrangements and plasterboard fall-off. Of these the location of the plasterboard joints is expected to significantly influence the failure of the studs. In normal construction practice the plasterboard joints are placed over the studs. During a fire, plasterboard joints will open up as the plasterboard shrinks due to moisture loss. Hence it will expose the stud to higher temperatures and fail much earlier than the studs without plasterboard joints. Previous experimental studies [1-3] conducted on the fire performance of LSF walls have also confirmed that the studs that had the vertical plasterboard joints over them showed higher temperatures than those without them.

3 EFFECTS OF PLASTERBOARD JOINTS

Plasterboard joints are usually located along the studs in LSF walls (Figure 1). The recessed edges along the edge of the plasterboards are filled with two nearly equal thickness joint filler coats and finished to the top level of the plasterboard. Although it is sealed, it is the weakest section of the LSF wall panel in terms of protecting the stud from the temperature rise. During a fire, gypsum plasterboard becomes weaker as the free and chemically bound water particles evaporate at about 100^{o}C and 150^{o}C, respectively. Hence as the plasterboard shrinks, cracks develop and plasterboard joints open up. Thus it will expose the studs directly to furnace temperatures, especially in single plasterboard lined walls.

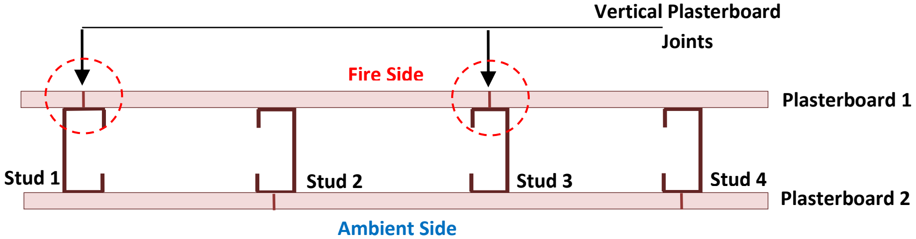

Figure 1. Plasterboard joints along the studs.

Previous tests of single plasterboard lined load-bearing LSF walls confirmed that the studs which had the vertical plasterboard joint showed higher stud hot flange temperatures (Figure 2). Fire test of single plasterboard lined wall specimen [1] under standard fire exposure [5] failed at 53 minutes due to the plasterboard fall-off near the failure. It is clear that if the plasterboard fall-off has not occurred the stud could have survived until 65 minutes (Figure 2(a)). Similarly, in another test (Test LSF3a) conducted for the Eurocode parametric fire exposure [6], Studs 2 and 4 with the vertical plasterboard joints showed higher temperatures throughout the fire test (Figure 2(b)) [2]. This wall panel failed at 39 minutes, and if the plasterboard joints have been avoided along the studs the failure could have been about 47 minutes. Similar temperature increase was also visible in the fire tests conducted for the LSF walls made of a hollow flange stud section (Figure 2(c)) [3]. Hence it is clear that having plasterboard joints along the studs will significantly influence the temperature rise of those studs. As mentioned, this is due to the opening up of plasterboard joints at high temperatures. The gypsum plasterboard when exposed to fire will undergo different processes and reactions. At about 100 to 150°C dehydration reactions occur, where the free and chemically bound water will evaporate from the gypsum plasterboard. At 400°C exothermic reaction occurs, in which the soluble crystal is restructured to lower soluble energy state. Also at 670°C, decomposition of Calcium Carbonate will occur [7-9]. Due to these reactions and processes at elevated temperatures, plasterboard shrinks and joints open up. Hence studs with the plasterboard joint show higher temperatures than those without the plasterboard joints.

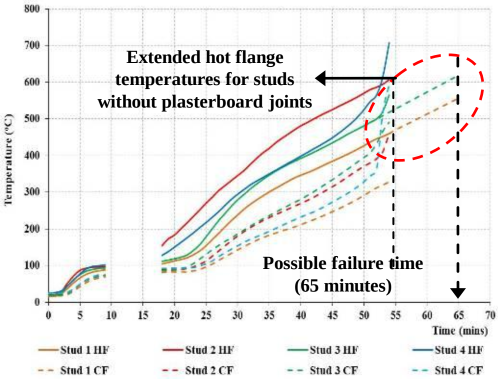

(a) Test 1 failed at 53 mins [1].

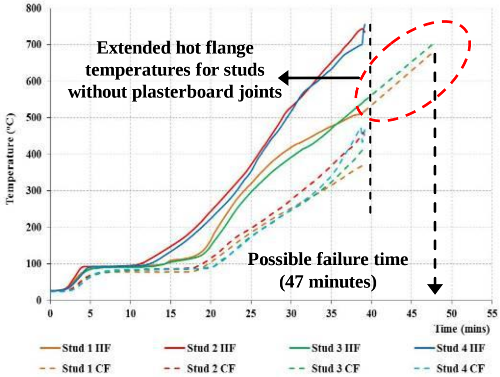

(b) Test LSF3a failed at 39 mins [2].

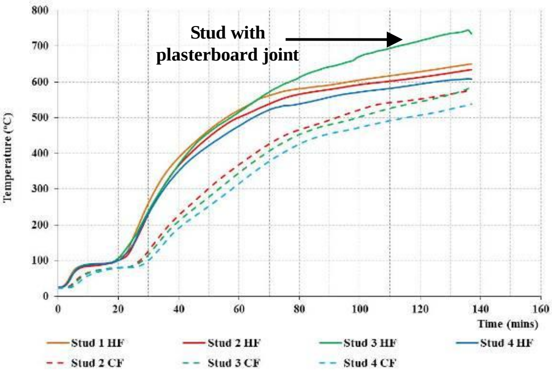

(c) Test 1 failed at 137 minutes [3].

Figure 2. Stud time-temperature curves from fire tests [1-3].

In this study to eliminate the plasterboard joints over the studs, the so-called back-blocking technique used in the standard ceiling design was applied to LSF walls. The back-blocks are used in the construction of plasterboard lined floor and ceilings to prevent cracking of plasterboard joints, where the plasterboard joints were not along the rafters/joists. Hence this method was used in LSF walls, where vertical plasterboard joints over the studs are now located between the studs with 150 mm wide plasterboards as back-blocks (Figure 3). This back-blocking gypsum plasterboard is centrally placed along the full length of the sheet's edge and the plasterboards are screwed together.

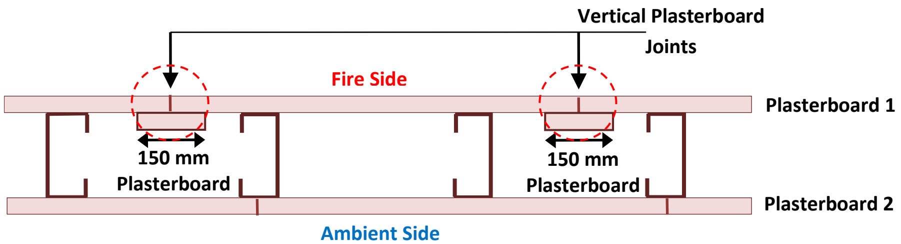

Figure 3. Plasterboard joints with back-blocks.

4 EXPERIMENTAL STUDIES

Two full scale fire tests were conducted on load bearing LSF walls (Table 1). Test walls were made of conventional lipped channel section studs (90 × 40 × 1.15) of 2.4 m in height, which were connected to 2.1 m wide channel section tracks at both ends at spacings of 600 mm [1-3]. This cold-formed steel frame was lined with single layer of 16 mm thick plasterboards on both sides at a screw spacing of 300 mm. However, at the joints the screw spacing was staggered at 200 mm. The plasterboard joint location was the only variable parameter in these two test specimens. In Test 1, conventionally used vertical plasterboard joint was used, where the plasterboard joints were located along Studs 2 and 4. In Test 2, the new plasterboard joint arrangement (Figure 3) was used. The plasterboard joint above the stud surface was eliminated and the joint was exactly placed in the middle of two studs and stabilised by 150 mm wide back-blocks (Figure 4). Thermocouples were attached to the steel stud and plasterboard surfaces. The plasterboard joints were filled with joint sealant (BaseCote90™) manufactured by Boral Plasterboard to the width of the recessed edge and then cellulose based joint tape of 50 mm wide was placed between the two coats of joint filler. The fabricated wall specimen was then placed on the loading frame and each of the studs was loaded up to 15.5 kN, which is 20% of their ultimate capacity at ambient temperature. The load was maintained for nearly 10 minutes and then one side of the wall was exposed to the standard fire time-temperature curve [5]. Load, axial deformation, lateral deflection and temperatures were recorded.

Table 1. Test wall panel configurations.

	Test 1	Test 2
Test wall panel	2.1 m × 2.4 m	
Stud Spacing	600 mm	
Studs Sizes	90 × 40 × 15 × 1.15 mm	
Load Ratio	0.20 (15.5 kN per stud)	
Plasterboard Layers (nos)	One layer	
Plasterboard Type	Firestop Gypsum plasterboard	
Fire Curve	Standard ISO Fire Curve [5]	
Plasterboard Joint Location	Along the Studs (along Studs 2 and 4)	In between the Studs (with 150 mm Back-blocks)

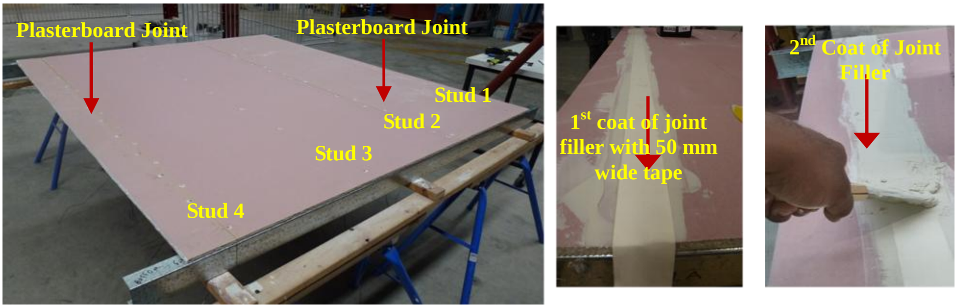

(b) Plasterboard joint along the studs – Test 1 (a) Plasterboard joint protection

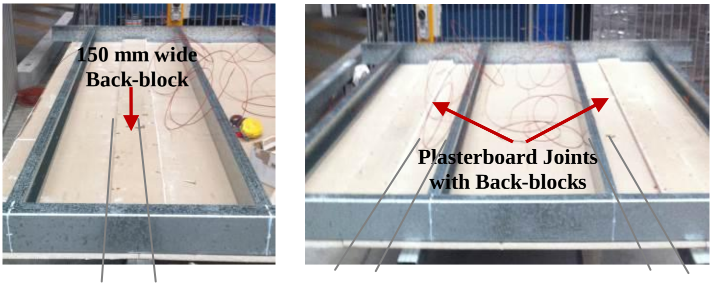

(c) Plasterboard joints with back-blocks – Test 2

Figure 4. Construction of test wall panels.

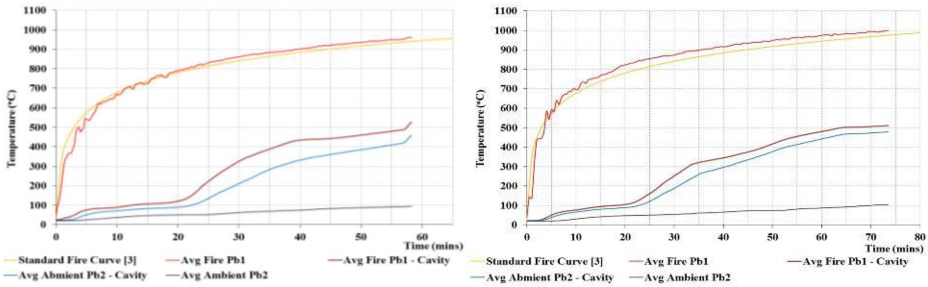

(a) Average plasterboard temperatures – Test 1 (b) Average plasterboard temperatures – Test 2

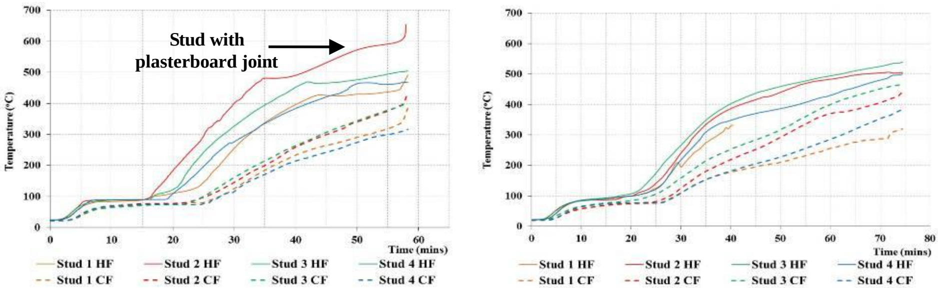

(c) Stud HF & CF temperatures – Test 1 (d) Stud HF & CF temperatures – Test 2

Figure 5. Experimental time-temperature curves – Tests 1 and 2.

In both test specimens exposed to the ISO standard fire curve [5], the target fire curve was achieved reasonably well (within 30^{o}C) as shown in Figures 5 (a) and (b). Also in both tests, the structural failure of studs occurred instead of insulation or integrity failure. Test 1 failed after 58 minutes of fire exposure. As expected in Test 1, Studs 2 and 4 which had the fire side vertical plasterboard joints showed higher temperature than the other two studs. The opening up of fire side vertical plasterboard joint over Stud 2 initiated the failure and a local compressive failure occurred at nearly 1/4th height of Stud 2. Also Stud 2 displayed torsional buckling, which could have occurred near the failure as the cracked fire side plasterboards and dehydrated ambient side plasterboards were unable to resist it (Figure 6(a)).

Test specimen 2 did not have any plasterboard joints along the studs. Instead it had a back-blocking arrangement between the studs for the fire side vertical plasterboards. Test 2 was able to sustain the applied compressive load for a longer duration than Test 1 and failed after 74 minutes of fire exposure. Similar to Test 1, fire side plasterboard joints also opened up in Test 2 (Figure 6), but it did not significantly influence the stud temperatures (Figures 5 (c) and (d)). The stud hot flange temperatures in all four studs merged well and the difference was less than that of Test 1 stud hot flange temperatures. Thermocouple attached to the hot flange of Stud 1 in Test 2 only recorded until 41 minutes, hence it was ignored. Studs 3 and 4 failed locally, and many local buckling waves were visible along the studs. Also neither torsional buckling nor flexural-torsional buckling was observed in Test 2 studs. Thus it indicates that the failure was due to a gradual temperature rise and plasterboards were intact with the studs and protected the stud temperature rise. Hence this test results show that LSF wall with a back-blocking joint arrangement increased the stud failure time by 25% (58 to 74 minutes) compared to the conventional plasterboard joint arrangement over the studs. This is a significant increase in FRR for single plasterboard lined LSF walls. Further, the local compressive failure of studs confirms that gypsum plasterboards were present until the failure of studs and provided the required lateral restrains. In Test 1, plasterboards were fixed to studs with screws within 10 mm from the plasterboard edges along the joints. This could also have influenced the opening up of plasterboard joints (Figure 6(a)). However, having back-blocks and joints between the studs eliminated this issue and protected the studs being exposed to high furnace temperatures.

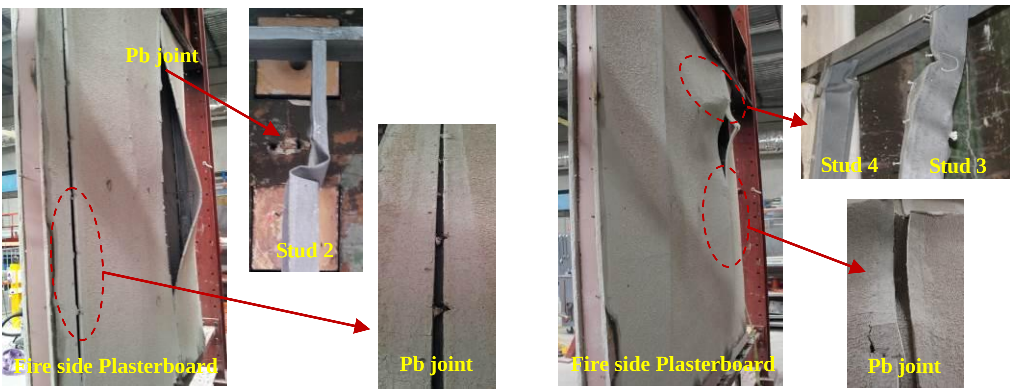

(a) Test 1 (b) Test 2

Figure 6. Test specimens after fire tests – Tests 1 and 2.

5 NUMERICAL STUDIES

The structural behaviour of LSF wall stud under fire conditions was then simulated using FEM (Finite Element Modelling) using ABAQUS. The element type and mesh size were selected based on the studies conducted by [10-13]. The mechanical properties of the steel at elevated temperatures were based on the reduction factors proposed by [14] for Australian cold-formed steels. The local geometric imperfection of 0.6 mm (b/150) was used with the critical eigen buckling mode shape. Steady state analysis was conducted using the measured stud time-temperature curves obtained from the fire tests for the failed studs (Stud 2 in Test 1 and Stud 3 in Test 2). In the steady state analysis, the studs were raised to the experimental temperatures for different time periods and then the load was increased until the failure to obtain the FRR/failure stud temperatures versus ultimate compression load relationships.

Figure 7 shows the load ratio versus stud failure time (FRR) obtained from FEA using the time-temperature curves of the failed studs in Tests 1 and 2 at different time intervals. Here the load ratio is defined as the ultimate compression load of stud exposed to fire to that at ambient temperature. Figure 7 highlights that there is a significant difference between the FRR for load ratios at different intervals. For instance, FRR of Test specimens 1 and 2 are 25 and 33 minutes, respectively, for a load ratio of 0.6. Thus FRR of Test specimen 2 is 32% higher than that of Test specimen 1. However, at lower load ratios, this improvement is further increasing as seen in Figure 7(a). Hence it can be concluded that if the stud temperature rise due to the effect of plasterboard joint along the studs can be eliminated the FRR of LSF wall systems lined with single layer of gypsum plasterboards will increase by more than 25%. This also suggests the importance of adapting improvised plasterboard joint arrangement for the fire design of LSF wall systems. The construction of Test specimen 2, i.e. having plasterboard joints between the studs and back-blocking the plasterboard joint could be costly in terms of workmanship. But considering the increase in FRR of single plasterboard lined LSF walls, it is less expensive than adding layers of plasterboard to achieve the required FRR. Another solution is to manufacture plasterboards with modified plasterboard edges and use them as shown in Figures 7 (b) and (c) [15] instead of using back-blocking.

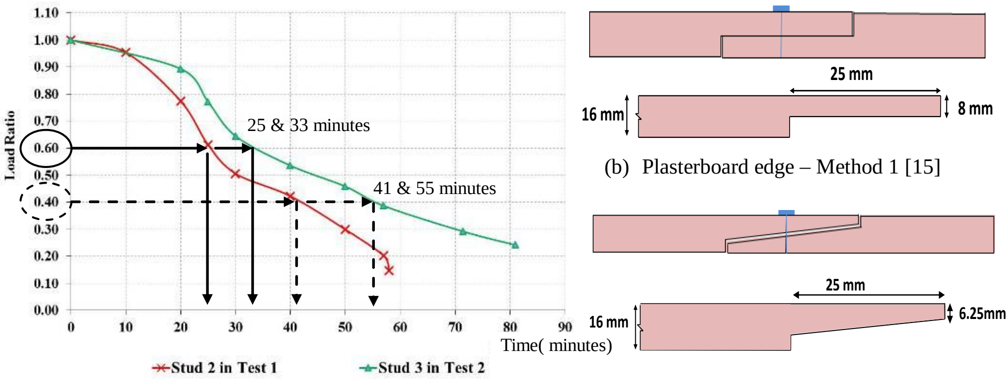

(a) Steady state FEA results for Tests 1 and 2

(b) Plasterboard edge – Method 1 [15]

(c) Plasterboard edge – Method 2 [15]

Figure 7. Steady state FEA results proposed plasterboard edge layouts.

6 CONCLUSIONS

This paper has summarized the main parameters that influence the fire resistance rating (FRR) of LSF walls from previous studies and highlighted the significant influence of plasterboard joint arrangements in the fire design of single plasterboard lined LSF walls. It has quantified the effect of plasterboard joints on the FRR of LSF walls based on both experimental and numerical studies conducted for the conventional and the new plasterboard joint arrangements. Two full-scale fire tests of single plasterboard lined LSF walls were conducted in this study and their structural and thermal performances are described in this paper. The measured stud time-temperature distributions were used in the numerical studies and the load ratio versus stud failure time (FRR) relationships were obtained. Both experimental and numerical results show that the fire resistance rating of LSF wall with back-blocking plasterboard joint arrangement increased by 25% compared to the traditional plasterboard joint arrangement used over the studs. This is a significant increase in FRR for single plasterboard lined LSF walls, as they are not a preferred wall configuration due to its susceptibility to plasterboard fall off compared to other LSF wall configurations.

ACKNOWLEDGEMENT

The authors wish to thank Australian Research Council for the financial support to this project, QUT for providing testing facilities and Boral Plasterboard for providing the required plasterboards.

REFERENCES

[1] Gunalan, S., Kolarkar, P.N. and Mahendran, M., "Experimental study of load bearing cold-formed steel wall systems under fire conditions", *Thin Walled Structures*, 65, 72–92, 2013.

[2] Ariyanayagam, A.D. and Mahendran, M., "Experimental Study of Load Bearing Light Gauge Steel Frame Walls Exposed to Realistic Design Fires", *Journal of Structural Fire Engineering*, 2014. (Accepted)

[3] Kesawan, S. and Mahendran, M., "Experimental Study on the Fire Performance of Superior LSF Wall Systems", *Proceedings of the Pacific Structural Steel Conference*, Singapore, 540–547, 2013

[4] Kodur, V.K.R. and Sultan, M.A, "Factors influencing fire resistance of load-bearing steel stud walls", *Fire Technology*, 42, 5-26, 2006.

[5] ISO 834-1, *Fire Resistance Tests – Elements of Buildings Construction – Part-1 General Requirement*, International Organization for Standardization, Switzerland , 1999.

[6] ENV 1991-1-2 Eurocode 1, *Actions on Structures, Part 1.2: Actions on Structures Exposed to Fire*, European Committee for Standardization, Brussels, Belgium, 2002.

[7] Wakili, K.G., Hugi, E., Wullschleger, L. and Frank, T.H., "Gypsum board in Fire - Modelling and Experimental Validation", *Journal of Fire Sciences*, 25(3), 267-282, 2007.

[8] Keerthan, P. and Mahendran, M., "Numerical Studies of Gypsum Plasterboard Panels under Fire Conditions", *Fire Safety Journal*, 53, 105-119, 2012.

[9] Keerthan, P. and Mahendran, M., "Numerical Modelling of Non-Load Bearing Light Gauge Cold-formed Steel Frame Walls under Fire Conditions", *Journal of Fire Science*, 30(5), 375-403, 2012.

[10] Gunalan, S. and Mahendran, M., "Finite element modelling of load bearing cold-formed steel wall systems under fire conditions", *Engineering Structures*, 56, 1007-1027, 2013.

[11] Ariyanayagam, A.D. and Mahendran, M., "Numerical Modelling of Load Bearing Light Gauge Steel Frame Walls Systems Exposed to Realistic Design Fires", *Thin-Walled Structures*, 78, 148-170, 2014.

[12] Gunalan, S. and Mahendran, M., "Fire Performance of Cold-formed Steel Wall Panels and Prediction of their Fire Resistance Rating", *Fire Safety Journal*, DOI. 10.1016/j.firesaf.2013.12.003, 2014.

[13] Gunalan, S. and Mahendran, M., "Development of Improved Fire Design Rules for Cold-formed Steel Wall Systems", *Journal of Constructional Steel Research*, 88, 339-362, 2013.

[14] Dolamune Kankanamge, N. and Mahendran, M., "Mechanical Properties of Cold-formed Steels at Elevated Temperatures", *Thin-Walled Structures*, 49, 26-44, 2010.

[15] Kesawan, S. and Mahendran, M., "Review of the Fire Performance of LSF Walls", *Proceedings of the Pacific Structural Steel Conference*, Singapore, 554–561, 2013.

NUMERICAL MODELING

8th International Conference on Structures in Fire
Guo-Qiang LI, Venkatesh K. R. KODUR, Shou-Chao JIANG, Jian JIANG, Su-Wen CHEN, Guo-Biao LOU (Eds.)
Shanghai, China, June 11-13, 2014

MODELLING LOCALIZED FRACTURE OF REINFORCED CONCRETE BEAMS UNDER FIRE CONDITIONS

Fei-Yu Liao and Zhao-Hui Huang

School of Engineering and Design, Brunel University, Uxbridge, Middlesex UB8 3PH, UK
e-mails: feiyu.liao@brunel.ac.uk, zhaohui.huang@brunel.ac.uk

Keywords: Localized crack, Reinforced concrete beams, Fire, XFEM, Crack opening

Abstract. *For performance-based fire safety design, it is important to assess the integrity of reinforced concrete members subjected to localized cracks. At present very little research has been done on the modelling of localized failures of reinforced concrete structural members in fire. To address this, a robust finite element procedure for modelling the localized fracture of reinforced concrete beams at elevated temperatures is developed in this paper. In this model a reinforced concrete beam is represented as an assembly of 4-noded quadrilateral plain concrete, 3-noded main reinforcing steel bar, and 2-noded bond-link elements. The plain concrete element is subdivided into layers for considering the temperature distribution over the cross-section of a beam. An extended finite element method (XFEM) has been incorporated into the plain concrete elements to capture the localized cracks within the plain concrete. The new model has been validated against previous fire test results on the reinforced concrete beams.*

1 INTRODUCTION

Under fire conditions, reinforced concrete structural members (such as beams or slabs) are often forced into high deformation. This results in the formation of large individual cracks within the members, which has been observed in previous experimental tests [1]. These large individual cracks influence the exposure condition of the reinforcing steel bar to the fire. In some cases the steel reinforcements are directly exposed to fire, significantly reducing the fire resistance of the structures. In some extreme cases, localized large cracks could even result in integrity failure of the structures [1]. A key factor in assessing the fire resistance of the structures is through predicting the localized fracture of their structural members. In the past two decades, plenty of numerical simulations and analyses have been done for modelling concrete structures at elevated temperatures. Those studies were all based on the continuum approach, in which smeared cracking was adopted to simulate the cracks within concrete members. Existing research indicates that models based on smeared cracking can predict global responses, such as deflection and structural stability, with reasonable accuracy. But the smeared cracking model cannot capture the localized fracture within structural members, and quantitatively predict crack openings. Little research has yet been done on modelling localized fractures for reinforced concrete structural members under fire conditions.

The main objective of this paper is to develop a robust finite element procedure for modelling the localized fracture of reinforced concrete members under fire conditions. The extended finite element method (XFEM) [2] is incorporated into plain concrete elements in order to capture the localized cracks of concrete within the member. The new model has been validated against some previous fire tests of reinforced concrete beams. The model presented in this paper provides a very useful tool for researchers and designers to assess the integrity of reinforced concrete structural members under fire conditions.

2. DEVELOPMENT OF THE NONLINEAR PROCEDURE

As shown in Figure 1, a reinforced concrete beam is modelled as an assembly of plain concrete, main reinforcing steel bar, and bond-link elements. The plain concrete elements are subdivided into layers to take into account the temperature distribution over the cross-section of a beam. The bond-link elements are used to represent the interaction between the plain concrete, and reinforcing steel bar elements.

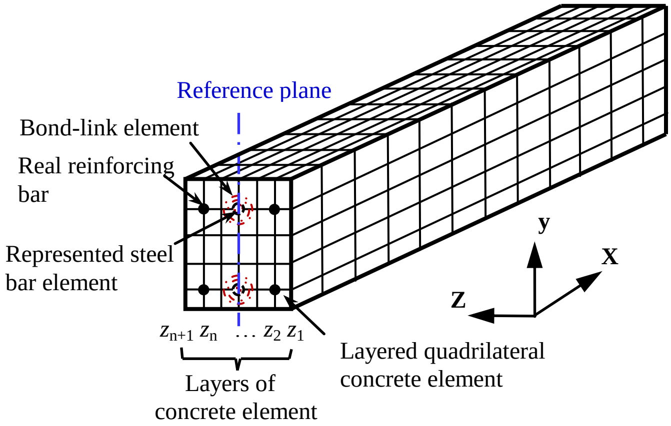

Figure 1. Nonlinear layered finite element procedure for modelling a reinforced concrete beam.

2.1 Layered quadrilateral concrete elements with extended finite element formulations

2.1.1 Element stiffness matrix and internal force vector

A 4-noded layered quadrilateral element is used to simulate the plain concrete for a reinforced concrete beam under fire conditions. Each node of the element contains two translational degrees of freedom. In order to consider the temperature distribution over the beam cross-section, the plain concrete elements are divided into layers in the z direction, and each layer can have a different but uniform temperature. Within the element the stress-strain relationships may change independently for each layer.

In order to model the localized fracture of plain concrete, the extended finite element method (XFEM) is used for the development of plain concrete elements. Considering a four-noded quadrilateral element crossed by a discontinuity (Γ_d) (see Figure 2) the domain is divided into two distinct domains referenced to an element, which are represented as Ω^+ and Ω^- on the different sides of the discontinuity in an element. Then, the total displacement field $\mathbf{u}$ consists of a continuous regular displacement field $\mathbf{u}_{cont}$ and a discontinuous displacement field $\mathbf{u}_{dis}$, that is:

$$\mathbf{u} = \mathbf{u}_{cont} + \mathbf{u}_{dis} = \sum_1^4 N_i \mathbf{u}_i + \sum_1^4 N_i \Psi_i(\mathbf{x})\mathbf{a}_i \tag{1}$$

where N_i is the shape function, $\mathbf{u}_i$ is the regular node displacement, $\mathbf{a}_i$ is the additional node displacement to describe the discontinuity, and $\boldsymbol{\Psi}_i(\mathbf{x})$ is the enhancement function:

$$\Psi_i(\mathbf{x}) = sign(x) - sign(x_i) \quad (i=1\sim4) \tag{2}$$

in which *sign* is the sign function and defined as: *sign*(x)=+1 if $x \in \Omega^+$, and *sign*(x)=-1 if $x \in \Omega^-$.

Compared with the conventional XFEM models, the *sign* function given in Equation (2) is shifted by *sign*(x_i). Using the shifted *sign* function can make the enrichment displacement field vanish outside the enhanced element. One significant advantage for using *sign* function is that only the elements cut by the crack need to be enhanced, as the resulting enhancement vanishes in all elements not crossed by the crack. The utilizing of a shifted *sign* function may greatly simplify the implementation of the extended finite element model, without altering the approximating basis. Especially for modelling reinforced concrete structures this advantage is more significant, as normally multiple cracks distributed within a reinforced concrete member (due to the bond action between steel bars and concrete). Other than the simplification in term of implementing the procedure, the key reason of using the shifted enhancement function is to obtain the total nodal displacement directly from the procedure rather than only the regular part of XFEM nodal displacement can be outputted from the procedure. This makes the compatibility of total nodal displacements of plain concrete element and bond-link element feasible. Hence, the bond-link element can be used to link plain concrete elements and steel bar elements in a conventional way.

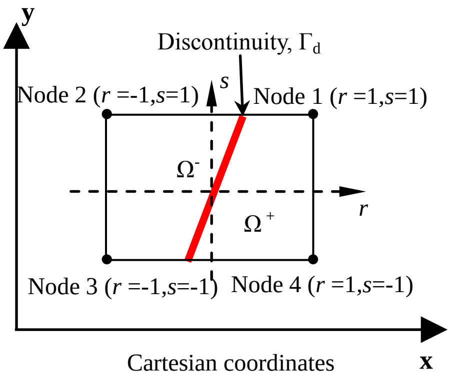

Figure 2. A quadrilateral element cut by a discontinuity.

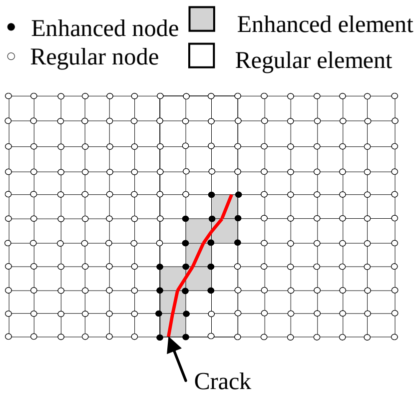

Figure 3. Concrete structure with a crossed crack.

The strains ($\boldsymbol{\varepsilon}$) within an enhanced element also consists of the regular and enhancement parts, which are related to the regular nodal and enhanced nodal displacements, respectively. The strain vector $\boldsymbol{\varepsilon}$ can be expressed as:

$$\boldsymbol{\varepsilon} = \boldsymbol{\varepsilon}_{cont} + \boldsymbol{\varepsilon}_{dis} = \begin{Bmatrix} \varepsilon_x \\ \varepsilon_y \\ \gamma_{xy} \end{Bmatrix} = \mathbf{B}\hat{\mathbf{u}} = \begin{bmatrix} \mathbf{B}^u_{sta} & \mathbf{B}^a_{enr} \end{bmatrix} \begin{Bmatrix} \mathbf{u}_i \\ \mathbf{a}_i \end{Bmatrix} \tag{3}$$

where $\boldsymbol{\varepsilon}_{cont}$ is the continuous strain, $\boldsymbol{\varepsilon}_{dis}$ is the discontinuous strain, $\mathbf{B}^u{}_{sta}$ is the standard strain-displacement transformation matrix corresponding to the regular degrees of freedom $\mathbf{u}_i$, and $\mathbf{B}^a{}_{enr}$ is the enrichment strain-displacement transformation matrix corresponding to the additional degrees of freedom $\mathbf{a}_i$. Hence, the strain-displacement transformation matrix $\mathbf{B}$ can be written as $\mathbf{B}$=[$\mathbf{B}^u{}_{sta}$ $\mathbf{B}^a{}_{enr}$], in which:

$$\mathbf{B}^u_{sta} = \mathbf{LN} \tag{4}$$

$$\mathbf{B}^a_{enr} = \Psi_i(\mathbf{x})\mathbf{LN} = \Psi_i(\mathbf{x})\mathbf{B}^u_{sta} \tag{5}$$

where $\mathbf{N}$ is the shape function of a general quadrilateral element, and the matrix $\mathbf{L}$ contains differential operators. The detail calculations of $\mathbf{B}^u{}_{sta}$ and $\mathbf{B}^a{}_{enr}$ can be found in Reference [3].

Since the effect of thermal expansion is included in the model, the total strains ($\boldsymbol{\varepsilon}$) include both thermal and stress-related strains at elevated temperatures. The stress-related strains can be obtained by deducing the thermal strains ($\boldsymbol{\varepsilon}_T$) from the total strains ($\boldsymbol{\varepsilon}$). If strains are reasonably small the stress vector $\boldsymbol{\sigma}$ can be obtained from the stress-related strain vector as:

$$\boldsymbol{\sigma} = \begin{Bmatrix} \sigma_x \\ \sigma_y \\ \tau_{xy} \end{Bmatrix} = \mathbf{D}(\boldsymbol{\varepsilon} - \boldsymbol{\varepsilon}_T) = \mathbf{D}\left(\mathbf{B}^u_{sta}\mathbf{u}_i + \Psi_i(\mathbf{x})\mathbf{B}^u_{sta}\mathbf{a}_i - \boldsymbol{\varepsilon}_T\right) \tag{6}$$

in which **D** is the constitutive matrix of concrete related to plane stress.

In a finite element model, the equilibrium conditions between internal and external ‘forces’ have to be satisfied. In this study the cracked concrete is treated as a quasi-brittle heterogeneous material, and the cohesive crack concept is used for simulating quasi-brittle fracture. The internal force vector $\mathbf{f}^{\mathrm{int}}$ contains the regular part ($\mathbf{f}_u^{\mathrm{int}}$), the enhancement part ($\mathbf{f}_a^{\mathrm{int}}$), and the traction part ($\mathbf{f}_\Gamma^{\mathrm{int}}$). The regular internal force ($\mathbf{f}_u^{\mathrm{int}}$) balances the external force ($\mathbf{f}^{\mathrm{ext}}$), and the enhancement part ($\mathbf{f}_a^{\mathrm{int}}$) is related to the traction of the crack ($\mathbf{f}_\Gamma^{\mathrm{int}}$) only [3]. Using the Principle of Virtual Work on the equilibrium equation, the element stiffness matrix can be obtained as:

$$\mathbf{K}\,\mathbf{d}\hat{\mathbf{u}} = \begin{bmatrix} \mathbf{K}_{uu} & \mathbf{K}_{ua} \\ \mathbf{K}_{au} & (\mathbf{K}_{aa} + \mathbf{K}_\Gamma) \end{bmatrix} \begin{Bmatrix} \mathbf{du}_i \\ \mathbf{da}_i \end{Bmatrix} = \begin{Bmatrix} \mathbf{f}^{\mathrm{ext}} \\ 0 \end{Bmatrix} - \begin{Bmatrix} \mathbf{f}_u^{\mathrm{int}} \\ \mathbf{f}_a^{\mathrm{int}} + \mathbf{f}_\Gamma^{\mathrm{int}} \end{Bmatrix} \tag{7}$$

where $\mathbf{K}_{uu}$ is the element stiffness matrix with reference to the regular degrees of freedom, $\mathbf{K}_{aa}$ is the element stiffness matrix with reference to the enhancement degrees of freedom, $\mathbf{K}_{ua}$ and $\mathbf{K}_{au}$ are related to both, and $\mathbf{K}_\Gamma$ is the element stiffness matrix of the traction. In this study, Gauss quadrature is employed to calculate the stiffness matrix of quadrilateral elements. Therefore, all stresses, strains, and the constitutive matrix of material discussed above correspond to Gauss integration points. Since the elements are divided into layers along *z*-axis (see Figure 1), and the material properties are assumed to be constant within each layer at each time or temperature step, the integration of constitutive matrix and stress vector along the *z*-axis can be performed separately and replaced by summation over the layers.

For the regular four-noded element without a crack, four Gauss integration points are used. But for those enhanced elements containing a crack, the scheme that partitioned the element into sub-triangles is adopted for its flexibility because it might be desirable to add other enhancement functions into the procedure in the future research. More detailed information related to the integration schemes can be found in Reference [3]. Due to the high non-linearity of the current model, a full Newton-Raphson solution procedure is adopted.

2.1.2 Constitutive modelling of concrete at elevated temperatures

At present, there is still very little data and few theoretical models available, regarding the constitutive modelling of concrete - under biaxial states of stress at elevated temperatures. Huang et al. [4] developed a biaxial concrete failure envelope at elevated temperatures by considering all the relevant material properties as temperature-dependent. The model was validated against the test results. Hence, this model is adopted to determine the cracking and crushing of concrete in this paper. Within this model the initiation of a cracking or crushing process at any location occurs when the concrete stresses reach one of the failure surfaces. It is also assumed that after concrete crushing all strength and stiffness are lost. The models specified in Eurocode 2 are used to determinate the uniaxial properties and thermal elongation of concrete at elevated temperatures. For concrete in the biaxial stresses case, it is assumed that free thermal expansion produces zero shear strain.

2.1.3 The determination of enhancement elements and nodes

Under fire conditions, each concrete layer within an element has different temperatures and material properties. The magnitude and orientation of principle stresses at a Gauss point may also not be the same for each layer. Therefore, the failure envelope of concrete at a Gauss point, which is temperature-dependent, may change over the different concrete layers. So a criterion is needed for determining whether or not an element should be enhanced. In this study, the weighted average values of maximum principal stresses and concrete material properties over the element are proposed to examine the initiation of crack in an element. For an element, the weighted average stress in the x direction ($\sigma_{x,ave}$), and the weighted average tensile strength of concrete $f_{t,ave}(T)$ can be expressed as (see Figure 1):

$$\sigma_{x,ave} = \frac{\sum_{l=1}^{n}\sum_{g=1}^{m}\sigma_{x,g}^{l}\left(z_{l+1}-z_{l}\right)}{m(z_{n+1}-z_{1})} \tag{8}$$

$$f_{t,ave}(T) = \frac{\sum_{l=1}^{n} f_t^{\,l}(T)\left(z_{l+1}-z_{l}\right)}{z_{n+1}-z_{1}} \tag{9}$$

where $\sigma_{x,g}$ is the stress in x direction at g-th Gauss point of l-th layer, $f_t^l(T)$ is the tensile strength of l-th layer concrete, m is the total number of the Gauss points in each layer, n is the total layer number of an element, and (Z_{n+1}-Z_1) is the total thickness of an element. Using the same procedure, the weighted average stress in the y direction ($\sigma_{y,ave}$), and the weighted average shear stress ($\sigma_{xy,ave}$) can also be calculated. The weighted average principle stresses $\sigma_{p1,ave}$ and $\sigma_{p2,ave}$ can be obtained from $\sigma_{x,ave}$, $\sigma_{y,ave}$ and $\sigma_{xy,ave}$. Again, the same method is used to calculate the weighted average compressive strength $f_{c,ave}(T)$ and weighted average modulus of elasticity $E_{c,ave}(T)$ for the concrete element. Based on those parameters the biaxial concrete failure envelope can be constructed for each concrete element at each time or temperature step.

At each time or temperature increment, all concrete elements are examined one by one. Once the average principal tensile stresses of a concrete element reaches one of the 'average failure surfaces', either in the biaxial tension region or in the combined tension-compression region, a straight crack is inserted through the entire element, and the orientation of the crack is normal to the average maximum tensile principal stress. The initial crack is assumed to go through the centroid point of a quadrilateral element. Then when the average principal stresses of the next element reach one of the tension failure surfaces, the crack will propagate from the tip of the existing crack into the next element, following the orientation normal to the corresponding average maximum tensile principal stress of the element.

Since the enhancement function (*sign* function) related to enhancement nodes is shifted by $sign(x_i)$, the enhanced displacement field vanishes outside the element enclosing the crack. Hence, only the elements crossed by the crack need to be enhanced, rather than all the elements that contain enhanced nodes. This procedure is illustrated in Figure 3, where the enhanced elements are filled with grey colour, and the enhanced nodes are indicated by the solid circles and regular nodes by the hollow circles. To model multiple cracks within a reinforced concrete member, the model developed in this paper allows two or more cracks to initiate and propagate at the same time. For simplicity, it is assumed that only one crack may exist within a particular element.

After concrete cracking, the constitutive model based on the cohesive crack concept is adopted for the cracked element. The crack opening is related to the traction forces acting on the crack. A concrete bi-linear softening curve is used herein to describe the decrease of traction with the increase of crack opening [3]. At elevated temperatures, the temperature-dependent fracture energy is determined according to CEB-FIP Model Code.

2.2 Reinforcing steel bar and bond-link elements

As shown in Figure 1, a reinforced concrete beam is modelled as an assembly of plain concrete, reinforcing steel bar, and bond-link elements. Previously a general 3D three-noded beam-column element was developed by the second author. This three-noded beam element is employed in this paper to model the reinforcing steel bar. The steel mechanical properties and thermal elongation are calculated based on the models specified in Eurocode 2. In order to model the bond characteristic between the concrete and reinforcing steel bar in fire, a two-noded bond-link element developed by the second author is employed in this research, to link the nodes between a plain concrete element, and reinforcing steel bar element. The bond-link element is capable to model full, partial, and zero interactions between the concrete and reinforcing steel within the reinforced concrete structures. The details of three-noded beam-column element and bond-link element can be found in Reference [3].

3 NUMERICAL EXAMPLE AND VALIDATIONS

For modelling reinforced concrete beam in fire, the first step of the analysis is to perform the thermal analyses on the beams modelled. Huang et al. [5] developed a two-dimensional nonlinear finite-element procedure FPRCBC-T, to predict the temperature distributions within the cross sections of reinforced concrete members subjected to a given fire time-temperature curve. In this study, the program FPRCBC-T is used to obtain the temperature history across the section of reinforced concrete beams. The predicted temperature histories are then used to perform structural analysis for the reinforced concrete beams.

As a numerical example, a simply supported reinforced concrete beam (subjected to ISO834 standard fire, three-face heating from its bottom and two sides) was modelled, to demonstrate the capability of the current model developed for capturing the localized fracture of reinforced concrete beams in fire. The beam was reinforced by two ribbed 16 mm diameter tensile steel bars and two ribbed 10 mm diameter compressive steel bars. The compressive strength of concrete was 23.8 MPa. The yield strengths of the 16 mm diameter bar, and 10 mm diameter bar were 406 MPa and 365 MPa respectively. The transverse point load at mid-span was 40 kN, and kept constant during the fire. The beam was modelled with considering different bond characteristics.

The predicted cracking pattern of the beam, with perfect bond condition at failure is shown in Figure 4. The predicted deformed meshes of the beams with perfect bond and partial bond-smooth bar are shown in Figure 5 (a) and (b), respectively. It can be seen that the XFEM finite element model developed in this paper can reasonably predict the formation and propagation of individual cracks. For the perfect bond case at failure, the openings of two major cracks at mid-span were 23.0 mm and 17.4 mm respectively. However, the cracks near the supports were only 0.14 mm and 0.16 mm, respectively. As shown in Figure 5 (b), for the smooth bar case, the maximum opening of the major crack at mid-span reached to 94.6 mm. In both cases, the mid-span elements appear obviously distorted, because the mesh held a very big localized crack. It is evident that the model proposed is able to capture the localized fracture of reinforced concrete beams under fire conditions very well.

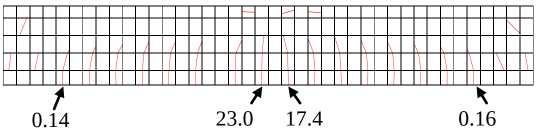

Figure 4. Predicted cracking pattern of the beam with perfect bond (unit: mm).

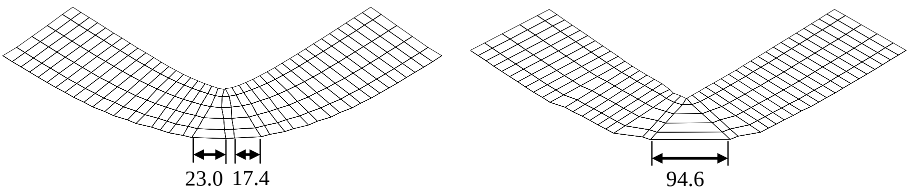

(a) Perfect bond (b) Partial bond-smooth bar

Figure 5. Predicted deformed mesh (unit: mm).

In order to validate the model proposed in this paper, two fire tested reinforced concrete beams (designated Beams 1 and 3) conducted by Lin et al. [6] were modelled herein, where the ASTM fire heating curves was used. The tested beams were subjected to three-face heating from its bottom and two sides. Those tested material properties were used for the validations. The detailed configurations and material properties of the beams can be found in Reference [6].

In the analysis, each beam was modelled as an assembly of 1652 (14 × 118) layered quadrilateral plain concrete elements, 146 steel bar beam elements, and 296 bond-link elements. The mesh sensitivity test was conducted before the analysis, where the doubly finer mesh was used for the comparison. The results of the current mesh and the finer mesh were almost identical to each other. It is evident that the predicted results are not sensitive to the element size under the current mesh used. The predicted maximum vertical deflections are presented in Figure 6. It is evident that the predictions of the developed model agree reasonably well with the test results for the two beams in terms of deflections. From Figure 6 it can be seen that there is no obvious difference between the ribbed bar case and perfect bond case, in terms of deflections until the later stage of fire. Two predicted deflection curves diverted: after 180 min for Beam 1, and 225 min for Beam 3. It is evident that the bond characteristics have considerable influence on these two beams, in terms of the deflections at the later stages of a fire. Therefore, if a perfect bond condition is assumed, for modelling the interaction between reinforcing steel bars and concrete, the predicted results may be on the unconservative side.

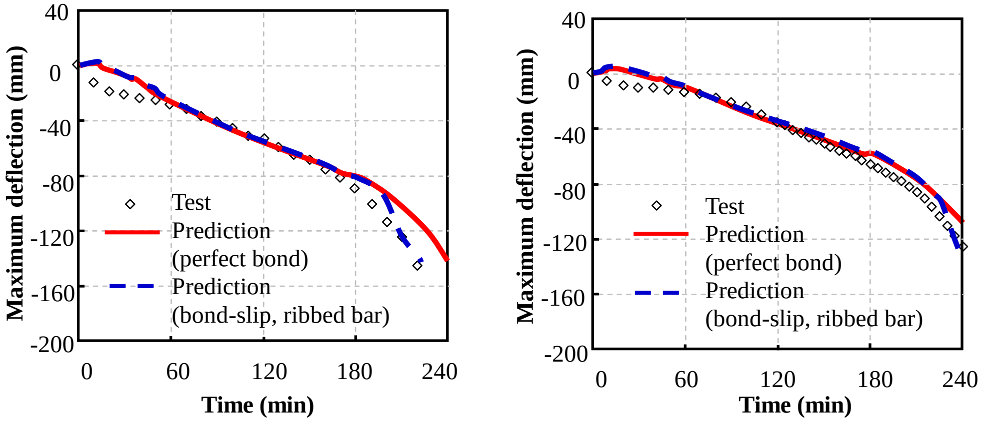

(a) Beam 1

(b) Beam 3

Figure 6. Comparison of predicted and measured maximum deflections [6].

Figure 7 presents the predicted cracking patterns of Beam 1. It is evident that the current model can predict the formation and propagation of individual cracks quite well. The predicted crack patterns are reasonable, where the flexural cracks caused by sagging moment distribute at the lower part of mid-span areas, whilst the flexural cracks caused by hogging moment distribute at the upper part over the

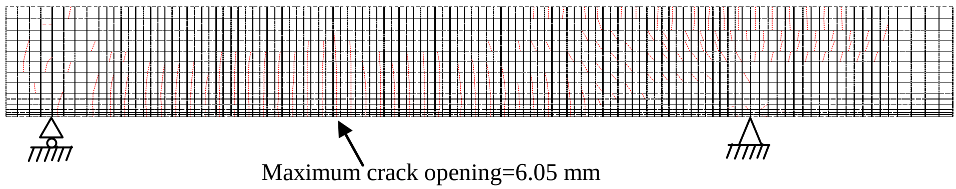

Figure 7. Predicted cracking pattern of Beam 1.

continuous support. Besides that, diagonal cracks were also found within the reinforced concrete beam. The maximum crack opening of Beam 1 attained 6.05 mm near the mid-span.

4 CONCLUSIONS

In this paper a robust layered finite element procedure is proposed for modelling the localized fracture of reinforced concrete beams at elevated temperatures. In this new model, the plain concrete is modelled by 4-noded layered quadrilateral elements, incorporated with the extended finite element method (XFEM). The element is divided into layers, to take into account the temperature distribution over the cross-section of the beam. A criterion based on a weighted average stress approach is proposed to determine initiation of individual cracks within the plain concrete elements. The complications of structural behaviour under fire conditions, such as thermal expansion, bond characteristic between reinforcing steel bars and concrete at elevated temperatures, and change of material properties with temperature, are all considered in the model.

The new model has been validated against previous fire test results on reinforced concrete beams. A numerical example of modelling a simply supported reinforced concrete beam (subjected to ISO834 fire) has been analyzed to demonstrate the capability of the current model for capturing the localized fracture of reinforced concrete beams under fire conditions. It has been shown that the XFEM nonlinear procedure proposed can predict the global response of reinforced concrete beams with good accuracy. The formation and propagation of individual cracks within the beams are also modelled, capturing the localized fracture, and predicting crack openings. The model developed in this paper provides an excellent numerical approach for assessing both structural stability (global behaviour) and integrity (localized fracture) of reinforced concrete members in fire. The model proposed here can be further developed for modelling of localized fracture of reinforced concrete slabs under fire conditions, for assessing the integrity failure of concrete floor slabs.

ACKNOWLEDGEMENT

The authors gratefully acknowledge the support of the Engineering and Physical Sciences Research Council of Great Britain under Grant No. EP/I031553/1.

REFERENCES

[1] Foster, S., “Tensile membrane action of reinforced concrete slabs at ambient and elevated temperatures”, *Ph.D. thesis,* Department of Civil and Structural Engineering, University of Sheffield, 2006.

[2] Möes, N., Dolbow, J., and Belytschko, T., “A finite element method for crack growth without remeshing*”, Internal Journal for Numerical Methods in Engineering*, 46(1), 131-150, 1999.

[3] Liao, F.Y., and Huang, Z., “A nonlinear procedure for modelling localized fracture of reinforced concrete structures”, *Report No. SED-DCE-2003-1*, Brunel University, UK, 2013.

[4] Huang, Z., Burgess, I.W., and Plank, R.J., “Nonlinear analysis of reinforced concrete slabs subjected to fires”, *ACI Structural Journal*, 96(1), 127-135, 1999.

[5] Huang, Z. et al., “Non-linear finite element model to predict temperature histories within reinforced concrete in fires”, *Build and Environment*, 31(2), 109-118, 1996.

[6] Lin, T.D et al., “Flexural and shear behaviour of reinforced concrete beams during fire tests”, *Report No. NBS-GCR-87-536,* Center for Fire Research, National Bureau of Standards, 1987.

8th International Conference on Structures in Fire
Guo-Qiang LI, Venkatesh K. R. KODUR, Shou-Chao JIANG, Jian JIANG, Su-Wen CHEN, Guo-Biao LOU (Eds.)
Shanghai, China, June 11-13, 2014

3D FINITE ELEMENT MODELLING OF BEAM–COLUMN FLEXIBLE END-PLATE COMPOSITE CONNECTIONS AT ELEVATED-TEMPERATURES

Khalifa S. Al-Jabri*, Prashob Pillay*, Muhammad B. Waris* and Tasneem Pervez**

* Department of Civil and Architectural Engineering, Sultan Qaboos University, Sultanate of Oman
e-mails: aljabri@squ.edu.om, m091846@squ.edu.om, waris@squ.edu.om

** Department of Mechanical and Industrial Engineering, Sultan Qaboos University, Sultanate of Oman
e-mail: tasneem@squ.edu.om

Keywords: FEM, Composites, Joints, Fire

Abstract. *The paper presents a 3D finite element model developed to represent behaviour of flexible end-plate beam-column composite connection in fire. The numerical results are verified with previous experiment data. The connection components for bare steel were modelled using a four noded tetrahedral element coupled with temperature and displacement. Modelling of concrete was done using the damaged plasticity model. EC3 recommendations for degradation in steel strength and stiffness were used in the study. Three fire test regimes were considered to compare the finite element analysis and experiment, using temperature-rotation results and mode of failure of the connection. The developed FE-model produced good agreement with the experimental results.*

1 INTRODUCTION

Composite beams are always subjected to combined actions of bending and shear. The flexural rigidity, deformation characteristics, and moment capacity of composite beam-column joints have significant effects on the structural behaviour of isolated and semi continuous beams. Results on composite connections from accidental fire and experimental tests revealed that joints fail in the tension zone i.e. through bolts or end plates due to high cooling strains induced by distortional deformation of connected members [1].

In general, laboratory experiments provide acceptable results that can describe the behaviour of the beam-to-column connections. However, in many cases experiments are either not feasible or too expensive. Though of high importance, they are always limited in number on the virtue of geometrical and mechanical parameters. Therefore these tests cannot provide thorough understanding of connection performance.

With advancements in computational capability and availability of reliable commercial software for numerical modelling, complex boundary value problems can be handled. Also considering the costs, time and effort in conducting experimental investigations, finite element method is extremely powerful in simulating possible real world cases where a wide range of parameters could be modelled that would be both time and cost effective. Therefore in order to set general recommendations or guidelines for the connection behaviour in fire, it is essential to develop a reliable model that could extend the database of test results to different structural forms and configurations together with a consideration of various fire scenarios.

Use of FEM for modelling connection behaviour at elevated temperature has attracted interest in recent years due to scarcity of experimental data and difficulty in the setup where the connection is subjected to fire. Factors affecting the accuracy of FE modelling include meshing of the configuration (optimum mesh size), simulation of bolts, choice of elements, modelling of concrete slab and shear studs, material behaviour and most importantly modelling of contact and gap elements.

Early modelling of connections at elevated temperature was performed by Liu [2] who developed a finite element program FEAST, to simulate various types of connection in the event of fire. The beam, column, end-plate and stiffeners were modelled using 8-noded shell elements including the consideration of material plasticity and degradation with temperature. A close comparison was found with experimental results.

Sarraj et al. [3] performed finite element modelling of steel fin plate connection at elevated temperature using 8-noded hexahedral incompatible brick element (C3D8I) using ABAQUS. Three layers of elements were used to simulate the thickness of endplate, beam web and beam flange. Surface to surface with finite sliding option was used to define all contact surfaces. The results were validated with the experimental data available and results were found to be closely agreeing with the experimental results.

Later Al-Jabri and Al-Jawhari [4] used an advanced finite element model in ABAQUS to study the flexible end-plate between steel beams and column at elevated temperature and generated temperature-rotation diagrams that described the behaviour of the connection. A linear temperature gradient was assigned at the connection vicinity at an approximate coverage of 100mm to accurately simulate the experimental conditions. The model was meshed using 29,582 numbers of 8-noded coupled brick, tri-linear, displacement and temperature elements. Results reflected that the predicted behaviour of joints was in good agreement with their actual behaviour. Modelling of composite joints is scarce in the literature due to the difficulty associated with the modelling of the composite stab and the interaction behaviour between the concrete slab and the bare-steel components

The objective of this research was to develop a simple yet reliable model capable of representing the behaviour of the composite connection in fire. FE-models were prepared to verify the experimental investigation carried out by Al-Jabri [1]. Four sets of numerical simulation were carried out, one for the ambient temperature to find the moment capacity of the joint and three under reduced loading (32%, 46% and 78% of moment capacity) under fire.

2 GEOMETRY AND FINITE ELEMENT MODEL

2.1 Geometric configuration of the joint.

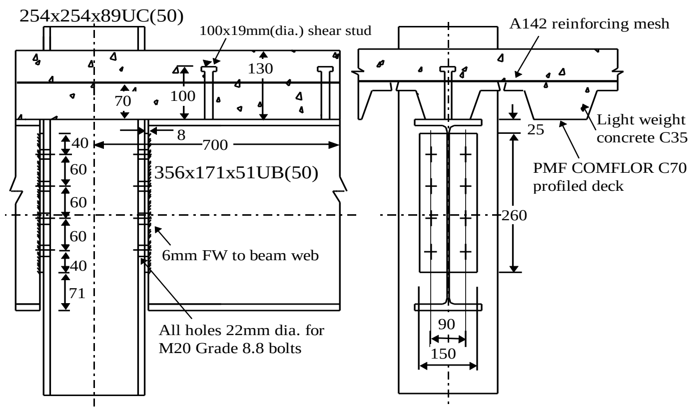

Figure 1. Details of Group 4 Fire Test Connection [1].

Figure 1 shows the cruciform, bolted flexible end-plate beam-column connection tested experimentally by Al-Jabri [1]. The composite connection comprised of a pair of 356 × 171 UB51 beams connected to a 254 × 254 UC89 column by an 8mm thick flexible steel end-plate with eight M20 grade

8.8 bolts. Composite slab with 130mm overall slab depth using lightweight concrete of grade C35 with a nominal anti crack mesh was cast on the steel beam. The length of the continuous slab across the connection was 1400mm with a width of 1200mm. Composite action was provided by shear studs. The elevated temperature tests were performed under isothermal conditions. The maximum applied bending moment based on calculated moment capacity of the connection at ambient temperature was used as reference. Based on experimental results, the moment capacity of the connection was 104.5 kN • m. Three fire tests with applied bending moment of 34 kN • m, 46 kN • m and 82 kN • m accounting to 32%, 46% and 78% of the estimated moment capacity were carried out. Load was applied at a distance of 1369 mm from the face of the column flange to produce the desired moment.

2.2 Finite element modelling considerations.

Bilateral symmetry allows the subdivision of the connection into four similar parts and therefore in order to reduce the size of the model and the analysis time, only one fourth of the configuration was modelled. Figure 2 shows a quarter of the three-dimensional geometric model configuration used to measure the lateral deflection of the beam subjected to an initial constant concentrated force applied along the negative y-axis at the free end of the beam section. The connection between the beam flanges and the column consists of placing a flat flexible end-plate between them and connected together using steel bolts.

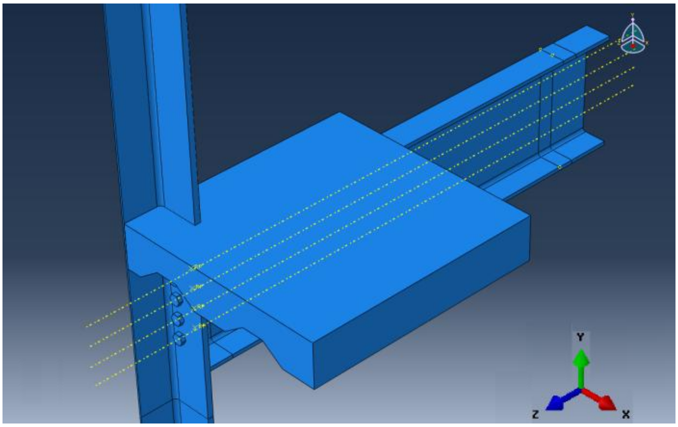

Figure 2. Geometric model of the Connection.

3D homogeneous solid elements were used to model the column flange, beam web, end-plate, bolts, concrete slab and shear studs, while truss element was used to model the anti-crack mesh. The studs were modelled as a part of the beam component assuming the weld to be strong enough to withstand the temperature and load. Also it was anticipated that the temperature of the shear studs would be much lower than the other steel elements due to their shielded position within the concrete slab. It is also worth mentioning that the steel deck was assumed to have negligible contribution to the connection's behaviour and hence not considered in the developed model.

Due to the geometric non uniformity of the components, 4-noded thermally coupled tetrahedral elements with 3 degrees of freedom at each node were used. Coupled temperature truss elements having 2 degrees of freedom were selected for the anti-crack mesh steel bar. The beam was meshed using 78,589 C3D4T elements, column was meshed using 53,183 C3D4T elements, each bolt was meshed using 1496 C3D4T elements, concrete slab was discretized using 309,617 C3D4T elements and the anti-crack mesh was discretized using 565 T3D2T elements.

For accurate results a finer mesh was used in the vicinity of the connection where a high stress and strain gradient was expected. This model leads to fairly accurate results around the connection, which is the region of prime interest. The method used in this paper is the standard coupled temperature-displacement with transient state response using the Newton's iterative technique.

3 MATERIAL PROPERTIES

At elevated temperatures, the connection undergoes large plastic deformation, thereby; an elasto-plastic material model was incorporated in the finite element analysis. The stress-strain characteristics of structural steel at elevated temperatures as recommended by EC3: Part 1.2 [5] were used in this study.

3.1 Steel

The following properties for steel were incorporated into the developed model.

Steel for Structural Components -Grade 355 and grade 8.8 (for bolts).

Yield Stress – 412 MPa and 480 MPa(For Bolts)

Density – 7800 Kg/m^3.

Modulus of Elasticity – 195 GPa

Poisson's Ratio – 0.3

Conductivity – 0.605 E-5 W/mm ℃

Coefficient of Thermal expansion – 1.20 E-5 / ℃

Specific Heat – 434 J/Kg ℃

Von Mises yield criterion with isotropic hardening rule was used to represent the failure mode of the beam, flexible end plate, column flange and the bolt components.

3.2 Concrete

The nonlinear material behaviour of concrete was described by the "Concrete Damaged Plasticity" model. The model is a 3D continuum-plasticity damage model for concrete, capable of predicting both the compressive and tensile behaviour of concrete under cyclic and dynamic loading. The concrete damaged plasticity model does not contain a failure criterion and thus does not allow the removal of elements during analysis [6]. Concrete slab was modelled as a solid homogenous element with initial elastic behaviour. The main parameter of damage was the cracking of the concrete slab before the failure of the connection. For the elasticity parameters the following values were used.

Density – 3500kg/m^3.

Conductivity – 1.45 E-5 W/mm ℃

Coefficient of Thermal Expansion – 1×10^{-5} / ℃

Specific Heat – 0.96 J/Kg ℃

Modulus of Elasticity – 20.5 GPa

Poisson's Ratio – 0.175.

4 NUMERICAL MODELLING

4.1 Boundary conditions and loading

The connection was subjected to a pre-defined concentrated force at a distance of 1369mm from the face of the column flange which would develop the required moment about the connection. The temperature in the vicinity of the connection was then gradually increased to the desired level to study the effect of temperature on the structural behaviour of the beam-column configuration.

As shown in Figure 2, only one quarter of the geometry was considered, therefore symmetric conditions were applied along x-axis for the beam. Column flange and the concrete slab were modelled with symmetric boundary conditions along the x- and z- axis.

Elevated temperature condition was applied to the portion of the beam, concrete slab and a portion of the column to reflect the real fire scenario. The temperature was increased linearly with time, such that the final desired temperature was achieved at the end of the simulation. The column was assumed to be fixed at the bottom since no displacements were expected to take place at the nodes far away from the connections and free to expand vertically at the top to take care of the expansion of the column when temperature is increased. In order to reflect the experimental setup, the beam was allowed to deflect downward only. The transverse movement was restrained to prevent any possibility of premature failure due to lateral torsional buckling. The beam was also allowed to expand freely along the longitudinal axis, thus ensuring that no thermal stresses are generated. Only the area around the connection including the composite slab was subjected to full temperature regime. The heating regime of the connection was assumed to vary linearly with time to reach 900 ℃ in 90 minutes.

4.2 Connections and contact surfaces.

The connection between the column flange and beam connected with a flexible end-plate was facilitated through bolts. Bolts were modelled as a 3D rigid member and were allowed to slip inside the end-plate and column within the hole clearance of 1mm. In the vertical interface, the bolts were tied to the column and end plate, restraining the uncontrolled motion of the bolt in 2- directions. The bolt face was tied to the end-plate face and column face.

The interconnection between the concrete slab and anti-crack mesh was defined using the embedded region option available in ABAQUS 6.10. Embedment was defined using the embedded constraint and was achieved by suppressing the host solid while constraining the rebar element within the entire model.

Contact between components was modelled using penalty friction formulation with a coulomb friction coefficient of 0.10. Since the rotational degrees of freedom are not active for solid elements in ABAQUS 6.10 the vertical deflection was determined at a certain point along the beam as illustrated in Figure. 3 and the connection rotation, θ, is determined from the following expression:

$$\theta = \tan^{-1}\left(\frac{u}{L}\right) \tag{1}$$

where,
u: deflection of the point along the beam;
L: distance from the connection centreline to the point where deflection is determined.

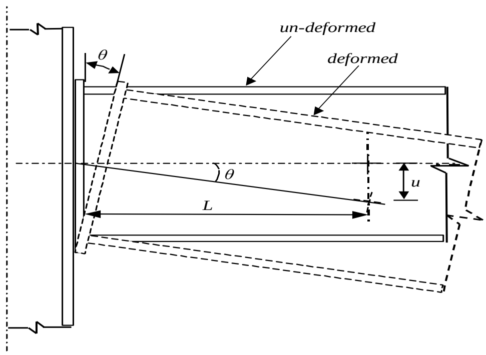

Figure 3. Connection Rotation.

5 RESULTS AND DISCUSSIONS

Results from the simulations were compared with results of experiments conducted by Al-Jabri [1] in terms of failure mode and temperature-rotation characteristics of the connection.

It was observed that there was local deformation at the top of the end plate around the top bolt i.e. the portion subjected to the highest tensile stresses. In line with the assumption of the damaged plasticity model, the concrete slab was assumed to have fully yielded before the deformation of the end-plate. This was followed by the deformation of the end-plate until the lower flange of the beam comes in contact with the column flange. This however was not incorporated, as the model was not able to model the collapse mode of the flexible end plate bottom touching the column thereby producing the aforementioned effect. This was particularly attributed to the modelling of concrete properties which played a vital role in modelling the connection response in presence of the concrete slab. Figure 4 shows the failure mode comparison between the FEM model and the experiment. As shown, there is no considerable distortion of the bolts. The top bolts were subjected to the highest tensile stress.

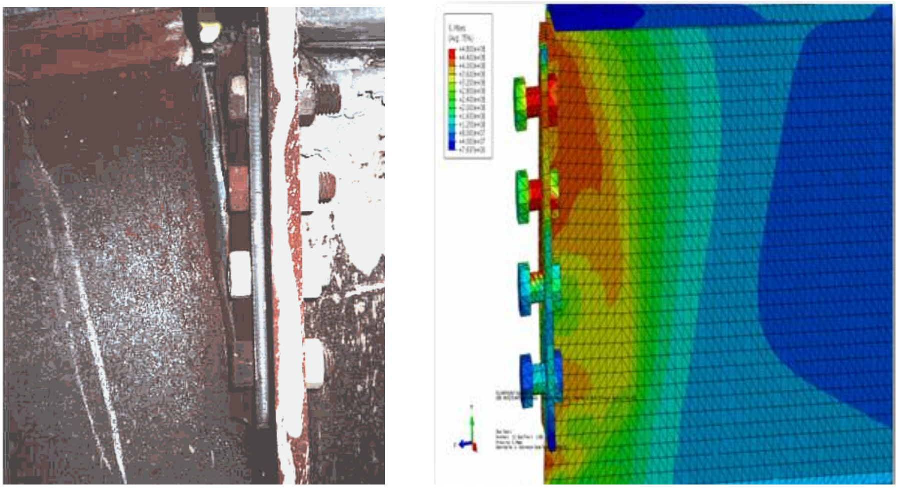

(a) Experiment [1]

(b) FEM Simulation

Figure 4. Connection Rotation.

For the ambient temperature the load was applied to get an equivalent moment of 105 kN • m. As shown in Figure 5, similar to the experiment, a linear response was observed in the simulation at the beginning up to 50 kN • m. However the increased rotation stiffness, which is indicated by as sudden steep slope at approximately 69 kN • m is attributed to the contact of the beam lower flange with the column due to the end plate deformation. Since this collapse was not incorporated by the finite-element model, this could not possibly be observed during simulation. The possible reason for this could be the presence of the concrete slab that prevented the beam to rotate freely.

For the moment of 34 kN • m applied to the connection under fire, the response is summarized in Figure 6 as temperature-rotation relationship. The predicted results showed good agreement with the experimental results in the elastic zone. The response of the connection in the plastic zone was slightly underestimated by the model which predicted a slight higher temperature than the experimental results for similar levels of rotation.

For the case of 47 kN • m, the temperature-rotation relationship is presented in Figure 7. There was a gradual increase in rotation for temperature up to 480 ℃ after which the connection behaviour becomes plastic with increase in rotation. Simulation results showed good agreement with experimental findings except that rotations were slightly underestimated at higher temperature.

The load on the connection was increased to obtain an equivalent moment of 84 kN • m. Results of the connection response are shown in Figure 8. Results show good agreement with the experimental results with a slight under-estimation of rotation in the elastic range. FEM results show good agreement in the plastic zone of the connection response.

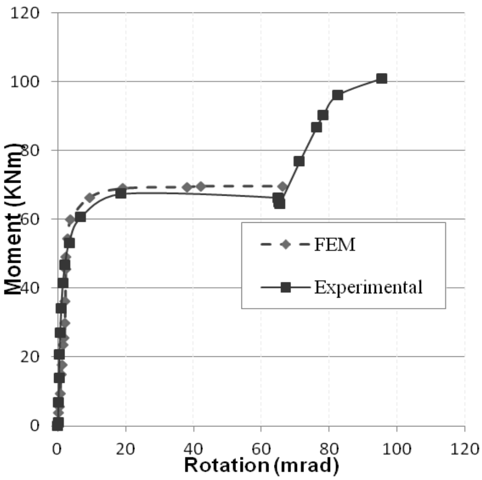

Figure 5. Comparison of FEM and Experiment [1] at Ambient Temperature.

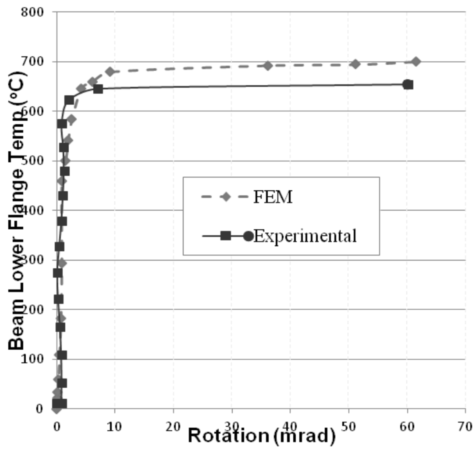

Figure 6. Comparison of FEM and Experiment [1] for Moment of 34kNm.

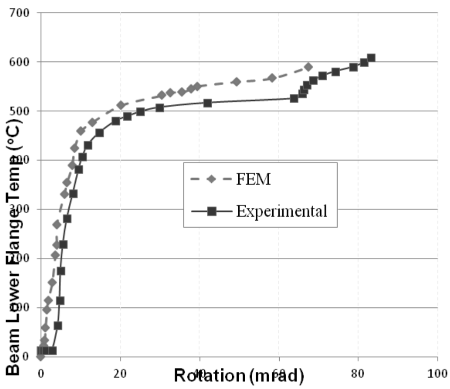

Figure 7. Comparison of FEM and Experiment [1] for Moment of 47kNm.

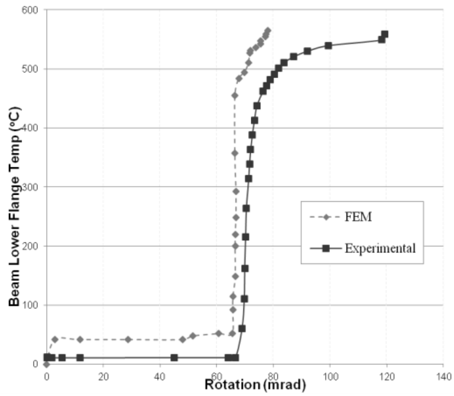

Figure 8. Comparison of FEM and Experiment [1] for Moment of 84kNm.

6 CONCLUSIONS

This work presented finite element simulations carried out to study the behaviour of composite flexible steel-concrete end-plate joint under fire using linear temperature gradient. A validation exercise was carried out by comparing the results of the simulation with experimental investigation carried out by Al-Jabri. Comparison was made in terms of moment-rotation characteristics of the joints at ambient temperature and beam lower flange temperature-rotation response of the joint. The modelling was carried out using ABAQUS 6.10. The geometric non-linearity and material inelastic behaviour of all joints components were considered. Connection components were modelled using three dimensional linear tetrahedral elements. The entire stress-strain-temperature curves were incorporated in the model to simulate the degradation of the components. Concrete was modelled using the concrete damaged plasticity model. One ambient temperature and three elevated temperature test were validated.

Predicted results showed good agreement with measured responses both in the elastic and plastic regions. Also the failure mode of the joints was well predicted by the developed model. This gives a confidence that the finite-element technique is capable of predicting the composite joint response with an acceptable degree of accuracy from the engineering practice point of view. Properly calibrated FE model could be used to further investigate the joint behaviour without the necessity of conducting expensive and time consuming experimental investigations.

REFERENCES

[1] Al-Jabri, K.S., (2000). "The Behaviour of Steel and Composite Beam-to-Column Connections In Fire. PhD thesis", *University of Sheffield*.

[2] Liu, T.C.H. (1998). "Finite-Element Modeling of Behavior of Steel Beams and Connections In Fire" - *Journal of Construction Steel Research,* Vol. 35 (3), P. 181-199.

[3] Sarraj, M., Burgess, I.W., Davison, J., and Plank, R.J. (2007). "*Finite-Element Modeling of Steel Fin Plate Connections In fire"*- Fire safety Journal, Vol. 42, P.408-415.

[4] Al-Jabri, K.S., and Al-Jahwari, F. (2012). *"Advanced Finite-Element Modeling of Flexible End - Plate Beam-Column Joints in Fire"*- Journal of Structural Fire Engineering, Vol. 3(1), P. 71-80.

[5] ENV 1993-1-2, Eurocode 3, (2005). "Design of Steel Structures, Part 1.2: *General Rules-Structural Fire Design",* London, British Standard Institution.

[6] Tomasz Jankowiak and Tomasz Odygowski. (2005). *"Identification of Parameters of Concrete Damage Plasticity Constitutive Model"*- Foundation of Civil and Environmental Engineering Institute of Structural Engineering Poland, Vol. 6, P. 53-69.

RELIABILITY-BASED APPROACH FOR EVALUATION OF BUILDINGS UNDER POST-EARTHQUAKE FIRES

Negar Elhami Khorasani*, Maria E. Garlock* and Paolo Gardoni**

* Graduate Student – Princeton University, Associate Professor – Princeton University
e-mails: nelhami@princeton.edu, mgarlock@princeton.edu

** Associate Professor - University of Illinois at Urbana-Champaign
e-mail: gardoni@illinois.edu

Keywords: Post-earthquake fire, OpenSees, Reliability, Steel frame

Abstract. *This paper demonstrates a framework to perform reliability analysis of buildings under fire following earthquake scenarios. The paper starts with modifications to the new thermal module in OpenSees. The modifications are aimed to make a seamless transition from seismic to thermal analysis in OpenSees. The constitutive material model for one of the material classes is changed, and a strain-based formulation is used to capture strain reversals. The program is then used to study performance of a 9-story steel building under a fire following earthquake scenario. The uncertainties in fire load density, steel yield strength and modulus of elasticity are included.*

1 INTRODUCTION

Resilient cities are the future of our communities, where the cities have the capacity to cope with extreme hazards. The infrastructures in such cities should be designed to perform adequately after extreme hazards and ensure human safety. As part of the design procedure for resilient cities, an evaluation of the response of structures to multi-hazard events should be performed, and an assessment of their performance under primary (e.g., earthquake or blast) and secondary (e.g., fire) hazards should be completed. The evaluation procedure involves many uncertainties, such as the intensity and characteristics of primary and secondary hazards, structural properties, and response of elements in the building. Therefore, system-level reliability analysis is recommended for quantification of building performance under multi-hazard scenarios.

The objective of this paper is a step towards a methodology to quantify the probability of failure of steel buildings under Fire Following Earthquake (FFE) scenarios. Previous research, implemented on structural performance of post-earthquake fires, studied the problem in two different programming environments for seismic and thermal analyses and within a deterministic approach [1, 2]. Recent studies in fire safety engineering are heading towards probabilistic frameworks for fire risk assessment [3, 4]. This paper discusses the approach to perform nonlinear seismic and thermal analyses in one programming environment and within a system-level probabilistic framework. In order to efficiently perform reliability analysis under post-earthquake fires, there is a need for a tool that is capable of (1) nonlinear dynamic analysis, (2) nonlinear thermal analysis, (3) seamlessly transferring from seismic to thermal analysis, and (4) incorporating randomness in material properties during the analysis.

Finite element packages, such as ABAQUS, SAFIR, or OpenSees, are available to perform nonlinear structural analysis. Among the available tools, ABAQUS and OpenSees are capable of performing both seismic and thermal analysis. The goal is to perform reliability analysis that involves Monte-Carlo Simulations (MCS), therefore this work intends to model the structure and run the analyses efficiently such that hundreds of simulations are completed in a reasonable time frame. Given the constraints, OpenSees with the newly added thermal module [5], is the only available finite element package that has the capacity to seamlessly transfer from dynamic to thermal analysis in one environment, and perform a parametric study through MCS with a reasonable computational time.

The new thermal module in OpenSees requires certain modifications in order to be adopted for FFE studies. The current constitutive material model for steel at elevated temperatures does not properly capture the behavior in a FFE scenario. The constitutive model is modified to capture the effect of plastic strains and strain reversals during heating or cooling. The calculation of the moment resultant is changed to be consistent with the conventions in the field. The thermal module is also modified in accordance with the reliability modules of OpenSees to incorporate uncertainties in temperature dependent yield strength F_y and modulus of elasticity E during the analysis. This paper provides an overview of the modifications to the thermal module and uses the new code to perform a case study. The performance of a 9-story steel office building is studied under FFE scenarios, considering uncertainty in fire load density, F_y and E.

2 OPENSEES MODIFICATIONS

2.1 Constitutive Material Model

The new material class that is capable of handling both seismic and thermal loads for steel structures in the new thermal module is *Steel01Thermal*. This thermal class includes the Eurocode (EC) temperature-dependent material properties. The constitutive material model in *Steel01Thermal* is currently programmed with a bilinear elastic perfectly plastic model at elevated temperatures, and a stress-based formulation (as opposed to strain-based) that ignores strain reversals.

The bilinear material model could be taken as a simplification, but stress-strain relationship of steel at elevated temperatures should ideally include the nonlinearity between the points of proportional limit, σ_p, and yield, σ_y (Figure 1(a)). The implication of the stress-based formulation is that the program is only able to start thermal analysis from a state of zero strain (which would not be the case in a FFE scenario). In addition, performance of the structure during cooling may not be correctly captured since strain reversals are not considered. Previous studies by Franssen [6] and El-Rimawi et al. [7] show that the plastic strain, rather than the maximum stress level, should be used to describe the complete stress-strain history as the steel temperature changes during heating or cooling. The fundamental assumption of the applied formulation is that, at any point during heating or cooling, the full stress-strain curve can be constructed by knowing the plastic strain (point O' in Figure 1(b)) and the elastic modulus for the given temperature [6, 7]. In Fig. 1b, OAB is the path that the material would take starting from a zero strain. However, plastic strain develops in the steel material when it is loaded beyond its proportional limit. If the plastic strain is calculated to be at point O', a new full stress-strain path should be constructed starting at O'. Point A is the intersection of path OAB and the line extending from O' with slope E (initial slope at O). During strain reversals, point C can be found knowing that the length of the linear portions is always the same (i.e., $2\sigma_p$ and $2\varepsilon_p$ are the two projections). Finally point A' is the mirror of point A with respect to O. The material would therefore travel on path A'CO'AB.

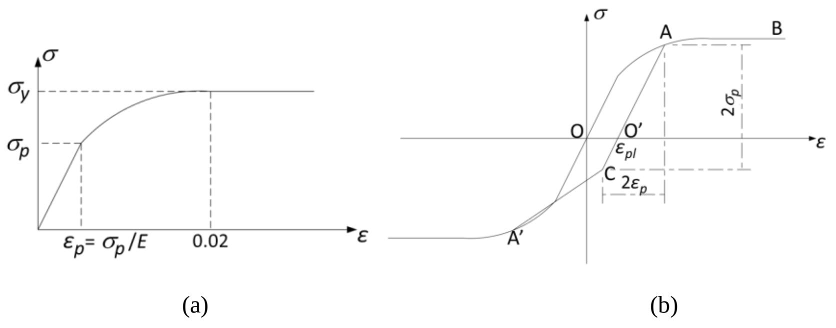

Figure 1. (a) Stress-strain plot for steel at high temperature, (b) Material model with plastic strain.

The *Steel01Thermal* class is modified to include nonlinearity between the points of proportional limit and yield at elevated temperatures according to the EC formulation. Also, the constitutive model is modified such that, at the start of every step in the analysis, the two parameters of plastic strain and reduced modulus of elasticity are calculated. Then, the full stress-strain history of the material, including the effect of proportional limit, is constructed. This way the effect of strain-reversals is incorporated in the constitutive model.

2.2 Resultant Moment

Axial load and moment values are calculated by stress integration along the fibers in the cross section in the Fiber Section 2d Thermal class in OpenSees. In the seismic module of OpenSees, the reference axis for calculating the moment is taken as the geometric centroid of the cross section. However, in the thermal module, the reference axis for calculating the moment is the effective centroid (the center of stiffness). When thermal gradient is present, the effective centroid is not necessarily equal to the geometric centroid. This has been modified by the authors so that moment is always calculated in the thermal module with respect to the geometric centroid.

2.3 Reliability Setup

The main uncertainties to consider during the thermal analysis are fire load density (demand variable), as well as yield strength F_y and modulus of elasticity E of steel at elevated temperatures (capacity variables). Variation in fire load density can be considered by generating a number of temperature-time curves and running the thermal analysis for a set of fire curves. The approach is similar to the consideration of the uncertainty in ground motions in seismic analysis, in which the model is analyzed for a set of selected ground motions.

In order to consider uncertainties in the material properties during the thermal analysis, the user should (1) set up the random variables in the OpenSees “tcl” interface, (2) calculate temperature-dependent material properties, and (3) update the variables at every time-step. The set up requires the use of *randomVariable*, *parameter* and *updateParameter* commands in OpenSees. After the model is built, the random variables and related parameters should be defined. At every time step during the thermal analysis, random values for F_y and E should be generated, and all the parameters should be updated using the *updateParameter* command. In order for the setup to work, the temperature dependent equations for F_y and E had to be removed from the *Steel01Thermal* material class, and the user controls and updates the variables from the Opensees tcl interface.

The advantage of this set up is that if no randomness is included in the generation of F_y and E, the analysis is equivalent to a deterministic model. The user also has the flexibility of choosing the model that calculates the material properties (such as NIST, and ASCE) and is not limited to the default EC equations in *Steel01Thermal*.

3 METHODOLOGY

The methodology to quantify probability of failure for a building subject to FFE includes the following steps: (1) Selecting an earthquake scenario; (2) Selecting fire location on the frame; (3) Defining a fire scenario with the full temperature-time curve; (4) Performing heat transfer analysis to develop temperature-time curves of the columns and the beam in the compartment; (5) Performing seismic structural analysis; and (6) Performing a fire-structural analysis. In order to quantify the probability of failure, a routine Monte Carlo Simulation can be incorporated, where every iteration should include randomness in demand (Steps 1 and 3), location of ignition (Step 2), and capacity (temperature dependent material properties in Step 6). This paper shows a sample study including uncertainties in fire load density (Step 3) and material properties (Step 6). Available procedures in the literature can be used to model uncertainties in the ground motion. Also, location of fire should be randomly selected as fire may ignite in lower or upper stories, and interior or perimeter compartments.

4 CASE STUDY

The modified thermal module in OpenSees is used in a case study to analyze a FFE scenario. The purpose of this paper is to perform a case study to demonstrate a robust methodology for FFE analysis in OpenSees. Therefore, as a sample study, performance of one compartment in a 9-story frame is studied under ten fire scenarios and one earthquake. The analysis is performed for the cases of only fire as the hazard (Fire-only), and fire that follows an earthquake. In these analyses, randomness in fire load density and steel material properties are included.

4.1 Design Description

The geometry and building description of the prototype Moment Resisting Frame (MRF) is based on the SAC steel project [8]. The MRF in the present study is a 9-story frame that is located in downtown Los Angeles and has been designed based on ASCE7-10 [9] specifications for stiff soil. The design checks applied in the design of the MRF are based on the guidelines in the AISC Steel Construction Manual (2010), and AISC Seismic Provisions for Structural Steel Buildings (2010). The frame has a period of 2.0 seconds. The floor plan and elevation of the 9-story structure is presented in Figure 2, and design of the 9-story MRF is summarized in Table 1.

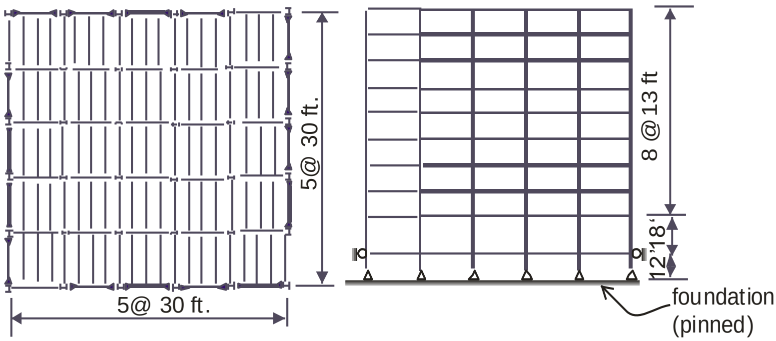

Figure 2. Plan and elevation of the 9-story frame.

Table 1. Design of the 9-story frame based on ASCE 7-10.

Level	Beam	Interior Column	Interior tdoubler*	Exterior Column	Exterior tdoubler*
9-roof	W24X76	W14X342	0.00	W14X257	0.00
8-9	W30X108	W14X342	0.47	W14X257	0.00
7-8	W33X169	W14X455	0.92	W14X370	0.00
6-7	W33X169	W14X455	0.92	W14X370	0.00
5-6	W36X194	W14X550	0.70	W14X500	0.00
4-5	W36X194	W14X550	0.70	W14X500	0.00
3-4	W36X194	W14X605	0.38	W14X550	0.00
2-3	W36X210	W14X605	0.63	W14X550	0.00
1-2	W36X210	W14X665	0.45	W14X605	0.00
Basement-1	W36X210	W14X665	0.45	W14X605	0.00

* Thickness of column web doubler plate in the panel zone area.

4.2 Analytical Model in OpenSees

Figure 3 shows the developed analytical model for the 9-story frame in OpenSees. The nonlinear behavior of the 9-story building under dynamic loading is modelled by the concentrated plasticity concept and using rotational springs. The frame is modelled with elastic beam-column elements that are connected with zero-length elements. The zero-length elements serve as the rotational springs that follow a bilinear hysteretic response based on Modified Ibarra Krawinkler Deterioration Model [10, 11, 12]. Panel zones are also modelled to capture the shear distortion in beam-column joints [13]. A leaning-column that carries gravity load is linked to the frame to simulate P-Delta effects. The leaning-column is modelled with elastic beam-column elements with large cross section area and moment of inertia to capture the effect of gravity columns on response of the frame.

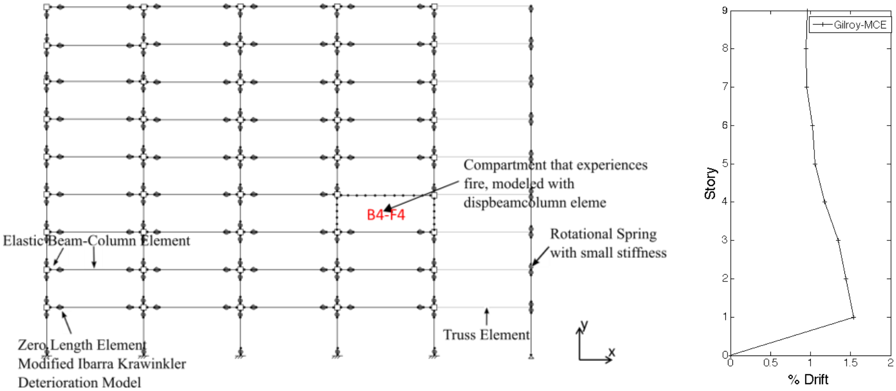

Figure 3. (Left): Analytical model in OpenSees for seismic and thermal analysis, (Right): % drift at the end of EQ.

The objective of this study is to efficiently perform a post-earthquake fire analysis, and to seamlessly transition from seismic to thermal analysis in OpenSees environment. However, thermal modelling in OpenSees is only possible with *dispBeamColumnThermal* type element [14], while the seismic model discussed above uses various other element types, including zero-length deterioration spring elements to capture nonlinear behavior. The approach in this study is to model the 9-story frame using the seismic modelling with the springs, except for the beams and columns that are assumed to be heated in a fire (which will be modelled with *dispBeamColumnThermal* elements) as shown in Figure 3. The *dispBeamColumnThermal* element is defined using fibers and considers plasticity along its length. The thermal element is modelled using 8 fibers in the web, and 4 fibers in each flange. The element requires temperature inputs through the depth of the cross section. The temperature is defined using 9 temperature points (8 layers) through the depth and steel time-temperature curves.

Modification of the model is necessary when transferring from the seismic to the thermal analysis. During the seismic analysis, a constraint is placed on the nodes of every floor to ensure that they move together horizontally, representing the effect of concrete slab in the composite structure. However, a previous study by Quiel and Garlock [15] shows that, during the thermal analysis, steel in the composite girder heats up faster and thus experiences a faster increase in temperature than the slab, which eventually results in cracking of concrete, thus rendering the slab negligible for axial restraint [15]. Therefore, after the seismic analysis is completed, the constraint on the nodes of the compartment that would experience fire is removed. It should be noted that Quiel and Garlock’s study [15] shows that the slab has a considerable effect on the thermal analysis of the composite girder and the temperature of the top flange, which will be discussed later.

4.3 Ground Motion Selection

The ground motion used in this study will be referred to as “Gilroy” ground motion, which is the Loma Prieta earthquake, occurred in the U.S.A. in 1989 and was recorded at station 47381 Gilroy (Array #3). Only one component of the ground motion (the G03090 component) is applied since two-dimensional models are being used. The location was on stiff soil, and the earthquake had a magnitude of

6.9 with the closest distance from a fault rupture zone of 8.95 miles. The one hazard level chosen for this study is the Maximum Considered Earthquake (MCE). The scaling procedure is based on the work of Somerville [16]. The scale factor for the Gilroy ground motion is calculated to be 2.78 for the MCE level.

4.4 Fire Load and Heat Transfer

As stated previously, the purpose of this paper is to perform a case study to demonstrate a robust methodology for FFE analysis in OpenSees. Therefore ten random fire scenarios are considered. The heat transfer analysis is performed to obtain steel temperatures for the beams, perimeter columns and interior columns of the fire location shown in Figure 3. Equation (1) is a probabilistic model for fire load density, q, in office buildings [17], where A_f is the area of the compartment and ε is a random variable that follows the standard normal distribution. The equation is derived using a Bayesian methodology and survey data [17]. The full fire temperature-time history is constructed using q values from Equation (1), and based on the work of Quiel and Garlock [18] to resemble an actual fire event. This study assumes a single compartment (20 ft wide by 30 ft deep) in every floor that is subject to fire. Given that the fire occurs after an earthquake, it is assumed that the compartment has *no* functional active fire-fighting measures and the passive fire protection has been damaged enough to render it ineffective. Figure (4) shows the Probability Density Function (PDF) and the Cumulative Distribution Function (CDF) for the maximum fire temperature reached in the compartment based on random q values. The CDF for the maximum fire temperature shows that the probability of exceeding temperature of 1000°C is less than 0.1. For the purpose of this study, ten events with the maximum fire temperatures higher than 1000°C are selected randomly. The range of the maximum fire temperatures in the selected cases are from 1009°C to 1173°C.

$$q = \exp[6.951 - 0.0047(A_f \times 10.76) + 0.5712\varepsilon] \tag{1}$$

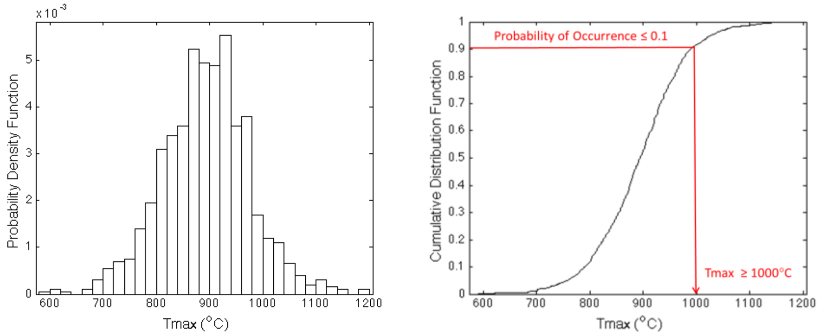

Figure 4. PDF and CDF for the maximum fire temperature.

Heat transfer for the two columns and a beam in the fire compartment is mainly based on the closed-form solution developed by Quiel and Garlock [18] based on a lumped-mass method. The solution is slightly modified for the beam to include the effect of concrete slab (which acts as a heat-sink) on the top flange temperature. An empirical equation developed by Ghojel et al. [19] is used to calculate the heat flux between the top flange and the slab.

4.5 Material Properties

In order to properly perform a reliability analysis of a structure and quantify its probability of failure, the uncertainties in the material properties should also be incorporated. Yield strength and modulus of elasticity of steel are the two major parameters in the structural analysis of a building. Experimental data shows that determination of such parameters at elevated temperatures involves uncertainty. In this paper, the two probabilistic models shown in Figure 5 and Equations (2) and (3) are used to randomly generate F_y and E values [20]. The models are developed using a logistic function, T is the temperature in Celsius, and ε is a random variable that follows the standard normal distribution. The data used to develop the models, shown in Figure 5, are collected by NIST.

$$F_{y,T} = F_y \times 1.2 \times \frac{e^{(1.65-2.3\times10^{-3}\times T-2.6\times10^{-6}\times T^2+0.338\varepsilon)}}{1+e^{(1.65-2.3\times10^{-3}\times T-2.6\times10^{-6}\times T^2+0.338\varepsilon)}} \tag{2}$$

$$E_T = E \times 1.08 \times \frac{e^{(2.93-3.2\times10^{-3}\times T-3.2\times10^{-6}\times T^2+0.317\varepsilon)}}{1+e^{(2.93-3.2\times10^{-3}\times T-3.2\times10^{-6}\times T^2+0.317\varepsilon)}} \tag{3}$$

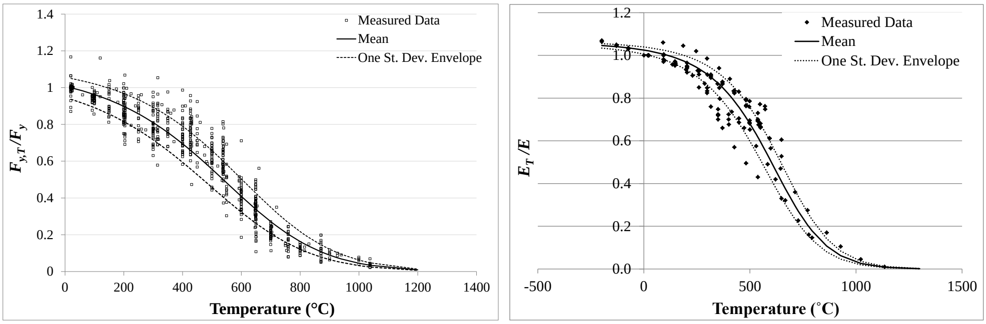

Figure 5. Probabilistic models for F_y and E using logistic function.

5 RESULTS

This section presents the results for the behavior of the 9-story frame under two scenarios: fire-only, and fire that follows an earthquake. The location of fire in the frame is shown in Figure 3, labelled as B4-F4 (the 4th bay and 4th floor). The frame is subjected to the Gilroy ground motion and the ten fire scenarios, explained in sections 4.3 and 4.4, respectively.

Tables 2 and 3 summarize the results for the two cases of fire-only and FFE respectively, and Figure 6 provides schematics of the compartment deformations during and after the fire. The tables include the maximum fire temperature for each case, the maximum vertical deflection at mid-span of the beam in the compartment, the maximum drift during fire, and the residual drift after the fire ends. The tables also include two types of limit states that the beam in the compartment may reach. The first limit state is when three plastic hinges form in the beam, initiating an instability. Generally, two plastic hinges first form at the two beam-ends. After a few minutes, a third plastic hinge forms at the beam mid-span. The second limit state that is considered is excessive deflections, which is reached if the mid-span deflection exceeds the limit of 18 inches (span/20 based on [21]). Finally, the maximum tension at beam-ends is provided in the table. The tension force developed during the cooling phase will likely cause a connection failure.

The results in Table 2 show that four of the 10 cases in the fire-only scenario reach the three-hinge limit state, one of which exceeds the limiting deflection. Three of the four cases reach temperatures above 1080 °C, while one case (Case 3) has a maximum temperature of 1023°C. The fact that Case 3 fails, while Cases 4-7 with higher temperatures do not fail, shows the effect of randomness in material properties. In comparison with Cases 4-7, Case 3 had a lower ε value (in Equation (2)), implying that the yield strength at elevated temperatures was below and far from the mean. The maximum and residual drifts in the fire-only scenario remain smaller than 2%. In the majority of cases, the maximum drift is the same as the residual drift at the end of fire (i.e. the right column in Figure 6(b)) since "maximum" refers to the largest positive or negative value. Table 2 thus shows that in most cases, the maximum drift occurs when the structure has cooled down.

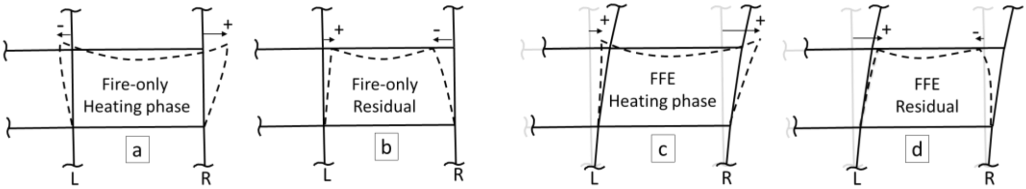

Figure 6. Schematics of the compartment deformation for (a) Fire-only scenario, heating phase; (b) Fire-only scenario, residual; (c) FFE scenario, heating phase; (d) FFE scenarios, residual.

Table 2. Results for fire-only scenario.

Case	Max Temp (°C)	Displacement *			Limit State Time (min)		Max Tension (kips)
		Max vertical at mid-span (in)	Max Drift (%)	Residual Drift (%)	3-hinge form	Δ=L/20	
1	1009	-3.9	R: -1.53	R: -1.53	-	-	1802
2	1014	-2.0	R: +1.21	R: -0.578	-	-	1402
3	1023	-11.2	R: -1.97	R: -1.97	34	-	1494
4	1025	-3.8	R: -1.25	R:-1.25	-	-	1454
5	1027	-2.5	R: +1.24	R: -0.619	-	-	1378
6	1031	-4.4	R: -1.60	R: -1.60	-	-	1523
7	1074	-4.9	R: +1.21	R: -0.775	-	-	1308
8	1082	-17.0	R: -1.57	R: -1.57	24	-	1400
9	1099	-16.7	R: -1.55	R: -1.55	24	-	1705
10	1173	-42.5	R: -1.25	R: -1.25	20	24	1509

* Conventions for drift values are shown in Figs. 6a and 6b.

Table 3. Results for FFE scenario.

Case	Max Temp (°C)	Displacement *			Limit State Time (min)		Max Tension (kips)
		Max vertical at mid-span (in)	Max Drift (%)	Residual Drift (%)	3-hinge form	Δ=L/20	
1	1009	-3.5	R: +1.95	L: +1.55	-	-	1441
2	1014	-1.9	R: +2.57	L: +1.46	-	-	1347
3	1023	-5.5	R: +1.75	L: +1.53	36	-	1481
4	1025	-3.4	R: +2.19	L: +1.49	-	-	1437
5	1027	-2.3	R: +2.61	L: +1.45	-	-	1302
6	1031	-3.9	R: +2.05	L: +1.48	-	-	1473
7	1074	-4.4	R: +2.62	L: +1.47	-	-	1277
8	1082	-17.1	R: +1.65	L: +1.51	25	-	1544
9	1099	-17.0	R: +1.66	L: +1.53	24	-	1903
10	1173	-42.5	R: +2.25	L: +1.53	20	24	1465

* Conventions for drift values are shown in Figs. 6c and 6d.

Based on the FFE results in Table 3, four of the cases, similar to fire-only scenario, form three hinges in the beam, with only one case exceeding the limiting deflection of 18 inches. Six of the cases exceed drift of 2% during fire. Following the scaled Gilroy EQ, the building with residual drift of 1.2% at the fourth floor, leans towards the positive x-axis (shown in Fig. 6). During the heating phase of fire, the beam in the compartment under study tends to expand, and the perimeter column leans further out of the frame. Therefore, the earthquake and fire drifts act in the same direction and the perimeter column experiences larger drifts compared to the fire-only case. The interior column also experiences a positive drift after the earthquake. However, during the heating phase of fire, as the beam expands, the interior column moves back towards its original position, implying that the drifts from the earthquake and fire are in opposite directions. The maximum residual drift after fire remains below 2%. The maximum tension force in the beam connections can approach 1900 kips.

Fig. 7 shows the CDF of the maximum drift in the B4-F4 compartment for the fire-only and FFE scenarios. The plot shows that a fire that follows an earthquake may lead to an increase in the drift with respect to the case of fire only. In the case of this sample study, the maximum drift in FFE case exceeds 2% in 60% of the times.

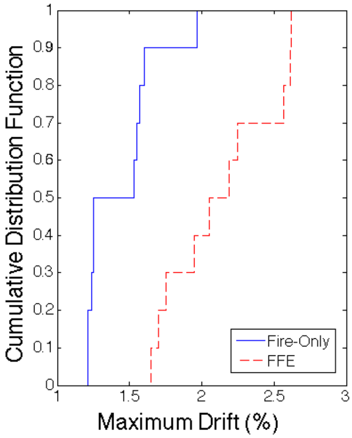

Figure 7. CDF for the maximum drift of Fire-only or FFE events.

11 CONCLUSIONS

This paper proposes a set of modifications to the new thermal module of OpenSees to make probabilistic analyses of fire following earthquake scenarios possible. The changes include a strain-based formulation for the constitutive material model that considers strain reversals. The new formulation takes the effect of proportional limit into account. The new code is also adopted to be used along with the reliability module of OpenSees, so that the thermal module can be used within a probabilistic study.

The thermal module, including the proposed modifications, is used in a case study to evaluate performance of a 9-story steel building under fire and FFE scenarios. Uncertainties in fire load density, steel yield strength, and modulus of elasticity are included in the analysis. The behavior of one compartment in the frame is studied under one earthquake and ten fire scenarios. The results show that, in comparison with the fire-only case, the earthquake does not increase the probability of an element reaching a limit state during a FFE scenario. However, the combination of earthquake and fire typically results in larger drifts.

REFERENCES

[1] Della Corte G., Landolfo R., and Mazzolani F.M., "Post-earthquake fire resistance of moment resisting steel frames", *Fire Safety Journal*, 38, 593-612, 2003.

[2] Yassin H., Iqbal F., Bagchi A., and Kodur V.K.R., "Assessment of Post-Earthquake Fire Performance of Steel Frame Building", *Proceedings of the 14th World Conference on Earthquake Engineering*, Being, China, 2008.

[3] De Sanctis G., Fischer K., Kohler J., Fontana M., Faber M.H., "A probabilistic framework for generic fire risk assessment and risk-based decision making in buildings", *Proceedings of the 11th International Conference on Application of Statistics and Probability in Civil Engineering*, ICASP11, August 1-4, Zurich, Switzerland, 2011.

[4] Lange D., Usmani A., Torero J., "A Risk Based Framework for Performance Based Fire Safety Design of Steel and Composite Structures", *Proceedings of the 5th Int. Conference on Advances in Steel Structures*, ICASS, December 5-7, Singapore, 2007.

[5] UoE OpenSees wiki. Edinburgh University – OpenSees Developers, 2014. [https://www.wiki.ed.ac.uk/display/opensees/UoE+OpenSees]

[6] Franssen J.M., "The Unloading of Building Materials Submitted to Fire", *Fire Safety Journal*, 16, 213-227, 1990.

[7] El-Rimawi J.A., Burgess I.W., Plank R.J., "The Treatment of Strain Reversal in Structural Members During the Cooling Phase of Fire", *Jnl of Constructional Steel Research*, 37(2), 115-135, 1996.

[8] SAC Joint Venture. *FEMA 355C: State of the Art Report on System Performance of Steel Moment Frames Subject to Earthquake Ground Shaking*. Federal Emergency Management Agency. September, 2000.

[9] ASCE, *Minimum Design Loads for Buildings and Other Structures* (ASCE/SEI 7-10), American Society of Civil Engineers, Reston, VA, 2010.

[10] Lignos D.G., and Krawinkler H., "Deterioration Modeling of Steel Components in Support of Collapse Prediction of Steel Moment Frames under Earthquake Loading", *ASCE Jnl of Structural Eng*, 137 (11), 1291-1302, 2011.

[11] Ibarra L., and Krawinkler H., *Global collapse of frame structures under seismic excitations*. Tech. Rep. 152, the John A. Blume EQ. Eng. Rsch Center, Dept of Civil Eng, Stanford University, 2005.

[12] Rahnama M., and Krawinkler H., *Effect of soft soils and hysteresis models on seismic design spectra*. Rep. No. TB 108, the John A. Blume Earthquake Engineering Center, Stanford University, Stanford, CA. 1993.

[13] Gupta A., and Krawinkler H., *Seismic Demands for Performance Evaluation of Steel Moment Resisting Frame Structures*. Technical Report 132, the John A. Blume Earthquake Eng Rsch Center, Dept of Civil Eng, Stanford University, Stanford, CA, 1999.

[14] Jiang J., and Usmani A., "Modeling of steel frame structures in Fire using OpenSees", *Journal of Computers and Structures*, 118, 90-99, 2013.

[15] Quiel S.E., and Garlock M.E.M., "Parameters for Modeling a High-Rise Steel Building Frame Subject to Fire", *Journal of Structural Fire Engineering*, 1(2), 115-134, 2010.

[16] Somerville P., Smith N., Punyamurthula S., Sun J., and Woodward-Clyde Federal Services, *Development of Ground Motion Time Histories for Phase 2 of the FEMA/SAC Steel Project*, BD-97/04 SAC joint venture, 1997.

[17] Elhami Khorasani N., Garlock M.E.M., Gardoni P., "Fire Load: Survey Data, Recent Standards, and Probabilistic Models for Office Buildings", *Jnl of Engineering Structures*, 58, 152-165, 2014.

[18] Quiel S.E., Garlock M., "Closed-Form Prediction of the Thermal and Structural Response of a Perimeter Column in a Fire", *The Open Construction and Building Technology Jnl*, 4, 64-78, 2010.

[19] Ghojel J.I., and Wong M.B., "Three-sided heating of I-beams in composite construction exposed to fire", *Journal of Constructional Steel Research*, 61, 834-844, 2005.

[20] Elhami Khorasani N., Garlock M.E.M., Gardoni P., "Probabilistic Evaluation of Steel Structural Members under Thermal Loading", Submitted to *Jnl of Engineering Structures*.

[21] BRE: Building Research Establishment Ltd, *The Integrity of Compartmentation in Buildings During Fire*, Project report No. 213140(1), 2005.

FIRE-INDUCED PROGRESSIVE COLLAPSE OF BRACED STEEL STRUCTURES

Jian Jiang[*], Guo-Qiang Li[*,] and Asif Usmani[***]**

[*] College of Civil Engineering, Tongji University, Shanghai 200092, China
email: jiangjian_0131@163.com

[**] State Key Laboratory for Disaster Reduction in Civil Engineering, Tongji University, Shanghai 200092, China
email:gqli@tongji.edu.cn

[***] School of Engineering, the University of Edinburgh, Edinburgh EH9 3JF, United Kingdom
email: asif.usmani@ed.ac.uk

Keywords: OpenSees, Progressive collapse, Steel frame, Bracing system, Fire scenario, Collapse mechanism

Abstract. *This paper investigates progressive collapse mechanisms of braced steel frames subjected to ground floor fire scenarios using OpenSees, an open-source object-oriented software developed at UC Berkeley. The OpenSees framework has been recently extended to deal with structural behavior under fire conditions by authors. The study considers two types of bracing systems (vertical and hat bracing) The thermal expansion of heated beams at early heating stage and their catenary action at high temperature have great influences on the collapse mechanisms. The vertical bracing systems has positive effects on increasing the lateral restraint of the frame against local or global drift, while when arranged at Edge Bays of frames they negatively contributes to the spreading of a local damage to a global collapse in the form of sequential buckling of adjacent columns through load-transfer mechanisms. Instead, using hat bracing can effectively optimize the load-transfer path through a more uniform redistribution of loads in columns and enhance the resistance of structures against progressive collapse. The application of vertical bracing systems alone on the steel frames to resist progressive collapse is proved to be unsafe and a combined vertical and hat bracing system is recommended in the practical design.*

1 INTRODUCTION

The progressive collapse of structures is defined as "the spread of an initial local failure from element to element, eventually resulting in the collapse of an entire structure or a disproportionately large part of it"[1]. The assessment of collapse performance of structures and measures for the mitigation of disproportionate collapse can be found in various design codes [1-3]. Recent large building frame tests (Cardington fire tests) in real fire conditions as well as investigations on the collapse of WTC under terrorist attack have shown that detailing of connections and structural redundancy are key to enhance robustness of structures against fire-induced progressive collapse. The redundancy allows a structure to transfer loads retained previously by damaged components to its surrounding parts through a variety of load paths to prevent a local or global failure. Bracing systems, as one of the effective measures to enhance the redundancy of structures, are most commonly used to resist seismic and wind loading. Several researchers have studied the potential of braced frames to mitigate progressive collapse of structures [4-7].

In a fire situation, the concept of bracing system can also be applied to the design against progressive collapse of steel framed structures. However, relevant researches are lacking. Usmani [8] proposed a possible progressive collapse mechanism for tall frames such as the WTC twin towers in fire. Lange et al.[9] proposed two collapse mechanisms of tall buildings subjected to fire on multiple floors, namely, a weak floor failure mechanism and a strong floor failure mechanism. Sun et al. [10] carried out static-dynamic analyses of progressive collapse of steel structures under fire conditions using Vulcan. The influences of load ratios, beam size and horizontal restraint on the collapse mechanisms were discussed. The same procedure was then used to study the collapse mechanisms of bracing steel frames exposed to fire [11].

OpenSees is an open-source object-oriented software framework developed at UC Berkeley [12]. OpenSees has so far been focused on providing an advanced computational tool for analyzing the non-linear response of structural frames subjected to seismic excitations. Given that OpenSees is open source and has been available for best part of this decade it has spawned a rapidly growing community of users as well as developers who have added considerably to its capabilities over this period, to the extent that for the analysis of structural frames it has greater capabilities than that of many commercial codes.

The static analyses of structures in fire using developed OpenSees have been extensively verified and validated by authors [13-15]. The main objective of this paper has been to study the influence of bracing systems on the progressive collapse resistance of steel moment resisting frames (MRF) in fire using the developed OpenSees framework.

2 DETAILS OF STEEL FRAMES STUDIED

A 2D steel frame of seven bays with 6m span and eight storey with 4m storey height was modeled in this study, as shown in Figure 1. Two types of bracing systems were taken in this study. These are a "hat truss" and a vertical bracing system. The configuration of bracing systems is supposed to have great influence on its effectiveness against progressive collapse of frames. To filter the effect of configuration of bracings as well as make simplicity but without losing generality, in this paper, the hat bracing was reduced to a series of rigid beams cross the top storey of the frame model, whilst the vertical bracing was represented by a series of lateral restraints on each storey to restrain the horizontal movement of the frame. Both the beams and columns in the compartment exposed to fire were heated and the adjacent compartments were left at ambient temperature. In this way, the catenary action of the heated beam due to large deflections was considered. Uniform temperature distributions based on the temperature-time curve defined in the standard fire ISO834 were assumed in the heated members, not only along their length but across the depth of the cross-section. Two ground-floor fire scenarios was used in this study. Fire 1 is a fire occurring in the Central Bay and Fire 2 represents a fire in the Edge Bay. The Newmark dynamic analysis was carried out in OpenSees to study the behavior of the steel frame under fire conditions. The Newmark parameters β and γ were taken as 0.8 and 0.45, respectively [16]. The corotational geometrical transformation in OpenSees was used to consider the geometric nonlinearity [17].

The reason for selecting implicit over explicit analysis solution scheme is because an implicit analysis solves the system of equations for each increment and performs Newton-Raphson iterations until it reaches convergence while explicit analysis does not attempt to reach a converged solution for each time step. For that reason an explicit analysis typically uses many more time steps than an implicit one. Franssen and Gens [16] have suggested that the numerical damping is accurate enough for most "structures in fire" applications since there are no highly dynamic effects present despite fire's transient nature. They proposed increasing the Newmark parameters β and γ when using the Newmark integrator. A similar procedure is followed in this paper by adding numerical damping when conducting dynamic analyses of structures in fire. This has been achieved in OpenSees by using the Newmark integrator with the values suggested (0.8 and 0.45) by Franssen and Gens [16].

In this case, all the beams and columns are taken as UB 305x165x40 and UC 254×254×89, respectively. A mesh of 8 and 12 elements were employed for each beam and column, respectively. The temperature dependent bilinear plastic material (Steel01Thernal) was used for steel members. The strain hardening was adopted with a slope of 1% of the initial modulus of elasticity to facilitate the convergence of the analysis. The modulus of elasticity and yield strength of steel at ambient temperature were taken as 200GPa and 280MPa, respectively. The properties of the steel material at elevated temperature referred to Eurocode 3.

In this study rigid connections between beams and columns are assumed, in which their failure and fracture were not considered in the analyses. The hat truss bracing systems and vertical bracing systems are reduced to rigid beams on the roof and lateral restraints against horizontal displacements, respectively. Hence, the buckling and failure of the bracing members were ignored in this paper. Although several idealizing assumptions have been made the study gives an insight into the performance of bracing systems in redistributing forces within the frame and preventing progressive collapse after the buckling of the heated columns.

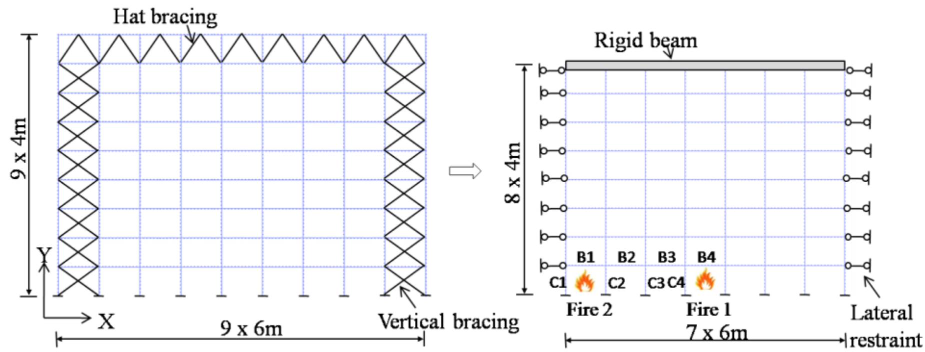

Figure 1. Schematic of the steel frame in fire modelled in OpenSees.

3 PROGRESSIVE COLLAPSE ANALYSIS OF STEEL FRAMES

4.1 Case 1: Behavior of frames without bracing

4.1.1 Central Bay fire (Fire 1)

Figure 2 shows the collapse procedure of the steel frame under Central Bay fire (Fire 1), plotted together with the formation of plastic hinges in beams and columns against temperature. Due to the symmetry, the plastic hinges are plotted on half the model. It can be seen that the collapse is triggered by the buckling of the heated column and aggravated by the pull-in of the upper remainder of the frame above the heated floor. At the early heating stage the heated compartment expands outwards through the thermal expansion of the heated beam and columns. Additional compression forces are generated in the heated members due to the restrained thermal expansion by the surrounding cool structure. The compression forces in the heated column C4 increases first as the yield strength of steel material keeps constant before 400^{o}C. Once the compression forces in C4 exceeds its buckling load, the column buckles at around 540^{o}C as shown in Figure 2a. Beyond this point the floor above the heated column C4, losing vertical supporting and having to sustain the vertical loads previously carried by the heated column, experiences large deflection which leading to the formation of plastic hinges at the ends of beams at the adjacent bay at 650^{o}C, as show in Figure 2b. On the other hand, due to the large deflection, tension force can be generated in the heated beams, i.e. catenary action, after 600^{o}C. The tension force in the beam starts to gradually pull in the upper frame, leading to the formation of plastic hinges at the two ends of ground floor columns when the temperature reaches 750^{o}C as shown in Figure 2c. In this way a local mechanism forms among the ground columns where the P-Δ effect will aggravate the their drift inwards and complete collapse of the whole frame occurs.

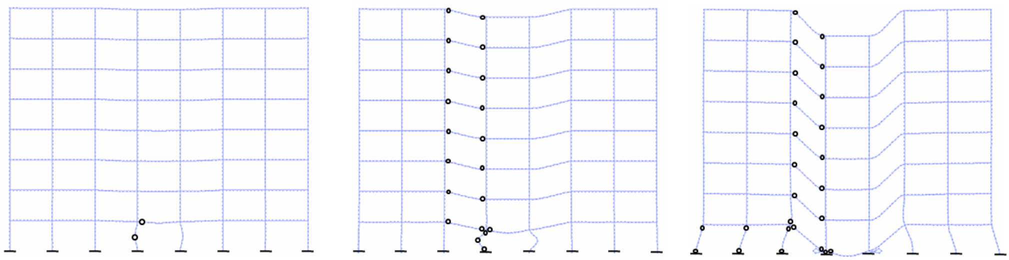

(a) 540°C (b) 650 °C (c) 750 °C

Figure 2. Failure process of the steel frame without bracing under Fire 1.

4.1.2 Edge Bay fire (Fire 2)

The collapse procedure of the steel frame subjected to Fire 2 is depicted in Figure 3. Similar to Fire 1, the collapse of the frame is triggered by the buckling of the heated columns. The inside heated column C2, sustaining twice as much as load of the edge column C1, buckles first at about 550°C. The buckling of the two heated columns leads to large deflection of the heated bay, causing plastic hinges form in beams at adjacent bay, as shown in Figure 3(b). Without the support of the column, the deflection of the beams above the column on the first floor accelerates under large compression forces caused by their restrained thermal expansion. The material degradation at elevated temperature aggravates the deformation of the beams. As the deflection increases, the load-bearing capability of the beams changes from bending to catenary action where tension forces are generated in the beams, pulling the edge column inward after 800°C as shown in Figure 3(c). The lateral drift of the heated column generates great P-Δ effects in it which leads to its large vertical displacements and finally results in the collapse of the frame. Similar to Fire 1, the forces sustained by the heated columns are transferred to the adjacent columns C3 alone with the other columns drift away in a rash.

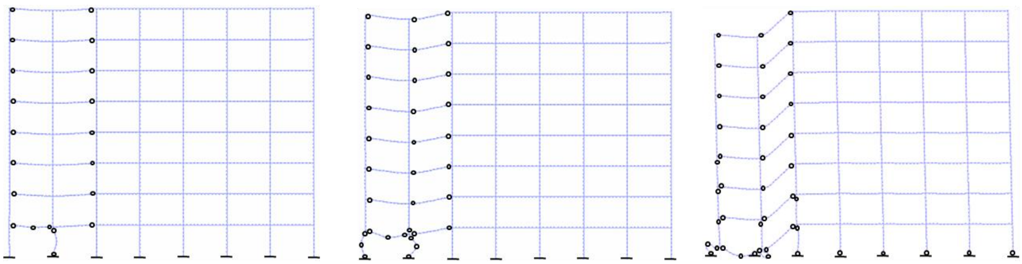

(a) 550°C (b) 670 °C (c) 800 °C

Figure 3. Failure process of the steel frame without bracing under Fire 2.

Three stages can be identified for the collapse of steel frames exposed to fire: (1) the buckling of the heated column as the trigger of the collapse; (2) Catenary action, generating in the heated beam under large deflection, pull in the surrounding parts of the frame; (3) the pull-in of columns, leading to the formation of plastic hinges at their ends, cause the global collapse of structures. It can be concluded that the load-redistribution capacity and lateral restraints are two significant factors affecting the robustness of structures against progressive collapse in fire. In the following sections, vertical bracing and hat bracing are to be applied to enhance the structural resistance against progressive collapse.

4.2 Case 2: Frames with vertical bracing alone

The failure modes of frames subjected to ground floor fires show obvious drift phenomenon caused by the catenary action in beams above the buckled columns. The horizontal drift of frames can be restrained using vertical bracing. The collapse pattern of laterally braced frames after buckling of the heated columns under Fire 1 and Fire 2 are illustrated in Figure 4 and 5, respectively. Similar to the unbraced case, the buckling of heated columns occurs first during the initial heating stage. Instead of horizontal drift, the frame experiences sequential buckling of columns, spreading from the heated bay to the neighboring bays.

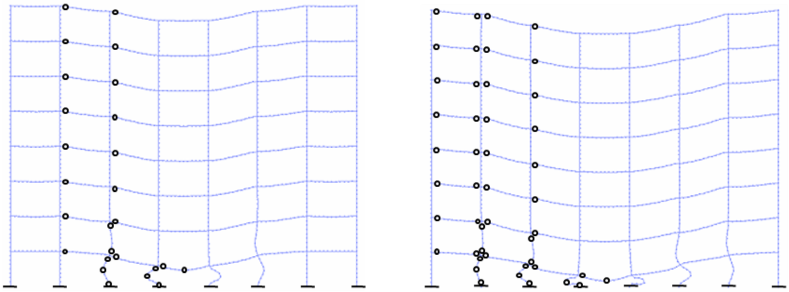

(a) 660 °C (b) 750 °C

Figure 4. Failure process of the steel frame with vertical bracing under Fire 1.

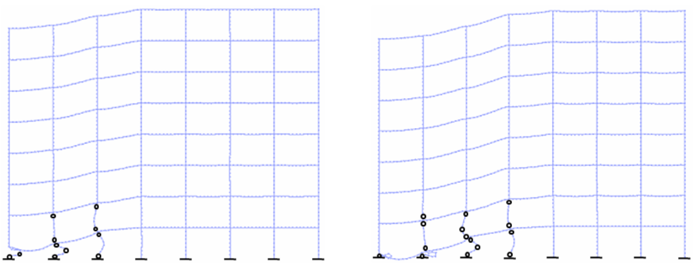

(a) 700 °C (b) 800 °C

Figure 5. Failure process of the steel frame with vertical bracing under Fire 2.

4.3 Case 3: Frames with hat bracing alone

The application of the vertical bracing can resist the sway of the frame but at the expense of sequential buckling of columns in which way the local damage is transferred to the surrounding components, leading to a global collapse. If the columns are strong enough to resist the redistribution load, the frame is safe. Otherwise, the local damage will spread to the adjacent bays and trigger the domino effect, leading to a global failure which is considered to be a more dangerous situation. It is believed that a locally heated frame may progressively fail, eventually generating an overall instability, unless it has sufficient force redistribution capability to continue carrying its vertical loads. If the force redistribution capacity of the frame is sufficient, it may only collapse locally rather than lose overall stability. A hat bracing is an effective mean of distributing vertical loads to columns and its effect is studied for the two fire scenarios in this section.

By applying the hat bracing to the frame in the form of a rigid roof, the steel frame under central bat fire (Fire 1) survives in collapse, accompanied by large deformation in the heated members, with final deformation mode as shown in Figure 6(a). The loads previously sustained by the buckled column are shared by all the other ground floor columns simultaneously, avoiding the reloading on the individual adjacent column alone as observed in Case 2.

It is not the case for frames under Edge Bay fire (Fire 2). Figure 6(b) shows its failure process after the buckling of the heated columns. The reduction in the compression forces in the buckled heated columns are compared to sharp redistribution of loads in the adjacent columns sequentially, leading to their buckling with a short interval, as shown in Figure 6(b). Beyond this point plastic hinges start to form at the ends of all the columns on the ground floor as shown in Figure 6b. This may be attributed to the fact that the thermal expansion of the heated beam push the two heated columns outward asymmetrically and the P-Δ effects resulting from the large UDL generate great additional moment at the bottom of the frame which leads to the premature formation of plastic hinges in them. The development of plastic hinges in the ground floor columns makes the frame a mechanism and drift laterally, eventually leading to the downward collapse of the whole frame.

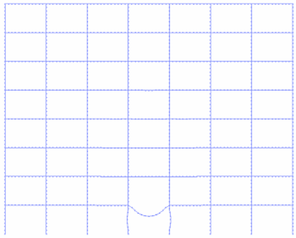

(a) Fire 1(stand)

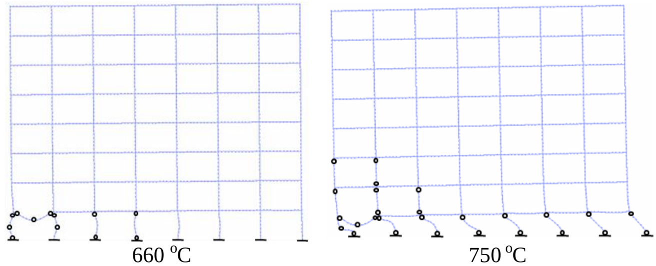

(b) Fire 2

Figure 6. Failure process of the steel frame with hat bracing.

4.4 Case 4: Frames with combined vertical and hat bracing

From the results presented, it can be seen that a bracing system can enhance capability of a steel frame to resist progressive collapse under fire conditions. A vertical bracing can effectively prevent a localized or global drift of frames but has high potential of sequential buckling of columns, spreading the local damage to the whole frame. In contrast, the application of a hat bracing can increase the load-transfer capacity after local failure, but obvious drift of frames can still induce progressive collapse of steel frames under Edge Bay fire as shown in Figure 6(b). Therefore, it is proposed that a combination of these two bracing systems might provide a greater variety of load-transfer paths and sufficient lateral restraint. Figure 7 shows the final mode of the frame under ground floor Edge Bay fire where it stand the progressive collapse, although several the ground columns buckle.

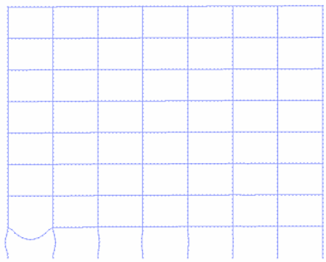

Figure 7. Deformation mode of the steel frame with combined bracing under Fire 2.

Based on the four cases studied, it is concluded that the pull-in of columns is one of the main factors contributing to progressive collapse of the frame. The pull-in of columns is initiated by catenary action in the heated beam above the buckled heated columns and aggravated by P-Δ effect. The application of bracing systems increase the redundancy of the structure, and provides alternative load-redistribution paths.

5. CONCLUSIONS

The effectiveness of bracing systems in preventing progressive collapse of steel frames under various fire scenarios have been investigated in this study using the developed OpenSees framework. The conclusions may be drawn as follows:

(1) In general, the collapse of steel frames in fire is triggered by the buckling of the heated columns followed by the buckling of adjacent columns at the same storey of the heated column or below. The collapse mode is characterized through collapse of heated bay followed by lateral drift of upper storey of the frame above the heated floor. The thermal expansion of the heated beams at low temperature and catenary action at high temperature have great effects on the collapse mechanisms of steel frames exposed to fire.

(2) Using vertical bracing can increase the lateral restraint against local or global drift in the frame through the sequential force-redistribution on adjacent columns. When the bracings are arranged at Edge Bays of frames, the load-transfer mechanism may spread the local damage to the neighboring bays which will lead to a global downward collapse of steel frames through sequentially buckling the columns on the ground floor. The vertical bracing system can slow down the collapse by sequentially buckling the columns through load-redistribution in them one by one. However, its application alone in the steel frame under fire conditions is unsafe.

(3) Alternatively, the hat bracing can effectively enhance the resistance of steel frames against progressive collapse. This is done through uniform force-redistribution in columns. However, local lateral drift of the heated floor occurs in the hat braced frame under multi-compartment fire on the ground floor, which leads to a global collapse of the frame.

(4) The fire-induced progressive collapse of steel frames can be prevented using a combined vertical and hat bracing system which is recommended in the practical design of structures in fire.

ACKNOWLEDGEMENTS

The work presented in this paper was supported by the National Natural Science Foundation of China with grant 51120185001 and Chinese Post-doctoral Foundation with grant 2013M531216.

REFERENCES

[1] ASCE 7. American Society of Civil Engineers Standard 7 Minimum Design Loads for Buildings and Other Structures, American Society of Civil Engineers, 2005.

[2] DoD. Design of Buildings to Resist Progressive Collapse. Unified Facilities Criteria (UFC) 4-023-03, US Department of Defense (DoD), 2013.

[3] GSA. Progressive Collapse Analysis and Design Guidelines for New Federal Office Buildings and Major Modernization Projects, US General Services Administration (GSA), 2003.

[4] Khandelwal K, El-Tawil S, Sadek F. Progressive collapse analysis of seismically designed steel braced frames. Journal of Constructional Steel Research, 65: 699 – 708, 2009.

[5] Kim J, Youngho Lee Y, Choi H. Progressive collapse resisting capacity of braced frames. Structural Design of Tall and Special Buildings, 20(2): 257 – 70, 2011.

[6] Asgarian B. and Rezvani F.H. Progressive collapse analysis of concentrically braced frames through EPCA algorithm. Journal of Constructional Steel Research, 70: 127-136, 2012.

[7] Lotfollahi M. and Alinia M.M. Effect of tension bracing on the collapse mechanism of steel moment frames. Journal of Constructional Steel Research, 65: 2027-39, 2009.

[8] Usmani, A.S. Stability of the Word Trade Center Twin Towers Structural Frame in Multiple Floor Fires, Journal of Engineering Mechanics 131(6) : 654-65, 2005.

[9] Lange D., Roben, C. and Usmani, A.S. Tall Building Collapse Mechanisms Initiated by Fire: Mechanisms and Design Methodology, Engineering Structures 36: 90-103, 2012.

[10] Sun R.R., Huang Z.H. and Burgess I. Progressive Collapse Analysis of Steel Structures under Fire Conditions, Engineering Structures 34: 400-413, 2012.

[11] Sun R.R., Huang Z.H. and Burgess I. The Collapse behavior of Braced Steel Frames Exposed to Fire, Journal of Constructional Steel Research 72: 130-142, 2012.

[12] McKenna, F. T. Object-Oriented Finite Element Programming: Frameworks for Analysis, Algorithms and Parallel Computing. PhD thesis, University of California, Berkeley, 1997

[13] Jiang J. (2012) Nonlinear Thermomechanical Analysis of Structures using OpenSees. PhD Dissertation, University of Edinburgh, Edinburgh, UK, 2012.

[14] Jiang, J., Jiang L.M., Kotsovinos P., Zhang, Jian., Usmani A.S., McKenna, F. and Li G.Q. OpenSees Software Architecture for the Analysis of Structures in Fire. Journal of Computing in Civil Engineering. (accepted)

[15] Jiang J. and Usmani A.S. Modeling of Steel Frame Structures in Fire using OpenSees. Computers & Structures 118: 90-99, 2013.

[16] Franssen J. M., Gens F. Dynamic analysis used to cope with partial and temporary failures, Proceedings of SiF'04: Third International Structures in Fire workshop, IRC, 297-310, 2004.

[17] Taucer F. F. and Filippou F. C. A Fiber Beam-column element for seismic response analysis of reinforced concrete structures. Report of University of California, Berkeley, 1991.

8th International Conference on Structures in Fire
Guo-Qiang LI, Venkatesh K. R. KODUR, Shou-Chao JIANG, Jian JIANG, Su-Wen CHEN, Guo-Biao LOU (Eds.)
Shanghai, China, June 11-13, 2014

TESTING THE ACCEPTABILITY OF DIFFERENT CREEP STRAIN CALCULATION MODELS IN STRUCTURAL FIRE ANALYSIS

Neno Torić*, Rui Rui Sun and Ian W. Burgess*****

* University of Split, Faculty of Civil Engineering, Architecture and Geodesy, Matice Hrvatske 15, 21000 Split, Croatia
e-mail: neno.toric@gradst.hr

** MMI Engineering, AVC Business Centre, Wellington Circle, Aberdeen, AB12 3JG, UK

e-mail: rsun@mmiengineering.com

*** University of Sheffield, Department of Civil and Structural Engineering, Sir Frederick Mappin Building, Mappin Street, Sheffield, S1 3JD, UK

e-mail: ian.burgess@shef.ac.uk

Keywords: Steel, Fire, Creep strain, Numerical model

Abstract. *This paper investigates the accuracy of a selection of creep models in predicting the structural behaviour of steel under various heat rates and load ratios. Most of the commonly-used stress strain laws of steel for structural fire engineering have already implicitly considered the creep strain, however, these considerations cannot adequately capture the effects of the stress level, heat rate and strain rate on the creep strain of the steel. In this paper, several available creep models were implemented into the finite element code-Vulcan and the acceptability of these creep models was tested by the comparisons with published experimental results. In order to introduce an explicit creep model into the structural fire analysis, the substantial implicit creep should be removed from the initial material laws. A practical way to obtain the creep-free material curves from established material laws is proposed and it has been demonstrated that the combination of an creep-free stress strain curve with an explicit creep model can improve the accuracy of the prediction of the creep strain of steel in fire.*

1 INTRODUCTION

Creep strain is a temperature-, time- and stress-dependent variable in common structural fire analysis procedures, which is rarely included explicitly. Prediction of creep strains is rather complicated, compared to calculation of the other strain components in steel, because of the different physical phases of creep that occur in stressed steel during a fire. The influence of creep on structural behaviour is usually experienced through a reduction in fire resistance, and strong dependence of the behaviour on the temperature-time history. Generally, passive fire protection causes slow growth and decay of the structure temperatures in fire, and "natural" fire curves including a cooling phase may further slow heating rates in the protected steel members. In such cases the creep strains are likely to influence structural response of these members significantly. There are two ways of introducing the realistic creep strain into the structural fire analysis. One is to use the effective temperature-stress-strain curves extracted from the standard tests and the other is to use specific and proper creep model in the structural analysis. The first approach requests amount of data bases from the standard tests and may not be handy for the engineers' use, whereas the second approach is better for general engineering use but does request cautions when selecting the proper creep models. Recently the effects of creep strain of steel on the performance of buildings in fire, considered explicitly within the thermo-structural analysis rather than implicitly in equivalent stress-strain curves, has been attracting growing research interest. However, creep strain models suitable for adoption in performance-based structural fire engineering design and assessment practice still need to be explored and developed.

Although a steel temperature of 400 ℃ is generally assumed to be the temperature above which creep strains can become significant within the time-scale of some building fires, the ranges within which creep strains should be taken into account in thermo-structural analysis are still vague. Further investigation of the influence of heating rates and stress levels on creep strain development is necessary to identify where creep strains need to be explicitly included.

As an initial investigation of the ways in which creep influences the behaviour of steel structures in fire, and the issues to be covered when embedding creep strain calculation into global modelling used in performance-based structural fire engineering design, this study attempts to combine different creep models with commonly used constitutive laws for steel, and to test the reliability of these combinations in structural fire analysis.

This paper presents the results of some recent enhancements of the *Vulcan* research code in conducting creep analysis, including verification against experimental data. Several types of explicit creep development models [1-3] are implemented for this purpose. Comparisons are made with results from published experimental studies [4-6]. The experimental studies were conducted on common contemporary structural steel, of grades S275 and S355. In order to investigate the influence of the basic stress-strain material model on the creep analysis, two such models (Eurocode 3 and Ramberg-Osgood) were used in the simulations.

Furthermore, the paper investigates practical ways of expressing constitutive laws for steel, to be used in fire engineering analysis, as a combination of a basic (creep-free) ambient-temperature stress-strain curve, temperature-dependent reduction factors on these, and a temperature-dependent creep law.

2 NUMERICAL MODELLING

2.1 Implemented creep models

Generally, there are two types of formulations to predict the creep in steel, i.e. time hardening formulation and strain hardening formulation. Time hardening rule is based on the assumption that the stress level during fire exposure is constant and that the creep strain rate is a function of stress and time. Strain hardening rule is based on the assumption that stress level changes during fire exposure and that the creep strain rate is function of previously accumulated creep strain and stress. Three widely-used creep strain models were implemented in *Vulcan* research code for this study. The details of these models are described as follow.

First implemented creep model (*Creep_model 1*) follows Harmathy's strain hardening rule [2], which can be expressed as:

$$\varepsilon_{cr} = Z \cdot exp\left(-\frac{\Delta H}{R \cdot T_R}\right) \cdot coth^2\left(\frac{\varepsilon_{cr,c}}{\varepsilon_{cr,0}}\right)\Delta t \tag{1}$$

where T_R is the temperature (K), R is the universal gas constant (J/molK), ΔH is the creep activation energy (J/mol), Z is the Zener-Hollomon parameter (h^{-1}), $\varepsilon_{cr,0}$ is a dimensionless creep parameter, $\varepsilon_{cr,c}$ is previously accumulated creep strain and Δt is the time increment.

Second implemented creep model (*Creep_model 2*) follows Harmathy's a time hardening rule [1], which can be expressed as:

$$\varepsilon_{cr} = \frac{\varepsilon_{cr,0}}{\ln 2} \cdot cosh^{-1}\left(2^{\frac{Z\theta}{\varepsilon_{cr,0}}}\right) \qquad \left(\theta < \theta_0\right) \tag{2}$$

$$\varepsilon_{cr} = \varepsilon_{cr,0} + Z\theta \qquad (\theta \geq \theta_0) \tag{3}$$

$$\theta_0 = \varepsilon_{cr,0} / Z \tag{4}$$

where θ is temperature compensated time θ [1].
Third implemented creep model (*Creep_model 3*) is Plem's strain hardening rule [3], which can be expressed as:

$$\varepsilon_{cr} = \varepsilon_{cr,0}(2\sqrt{Z\theta / \varepsilon_{cr,0}}) \qquad (0 \leq \theta < \theta_0) \tag{5}$$

$$\varepsilon_{cr} = \varepsilon_{cr,0} + Z\theta \qquad (\theta \geq \theta_0) \tag{6}$$

where θ_0 is determined from Equation (4). Temperature compensated time θ for Plem's model is calculated as:

$$\theta = \theta^0 + exp^{\frac{\Delta H}{RT_R}} \Delta t \tag{7}$$

where θ^0 represents shifted temperature-compensated time, which is a function of previously accumulated creep strain. Material parameters Z, ΔH, R and $\varepsilon_{cr,0}$ are taken from study [7] for steel A36, which is equivalent to Eurocode steel grade S275:

$$\varepsilon_{cr,0} = 1.03 \cdot 10^{-6} \sigma^{1.75} \tag{8}$$

$$Z = 3.75 \cdot 10^8 \sigma^{4.7} \quad (\sigma \leq 103\,\text{MPa}) \tag{9}$$

$$Z = 1.23 \times 10^{16} exp^{0.0435\sigma} \quad (103 < \sigma \leq 310\,\text{MPa}) \tag{10}$$

$$\frac{\Delta H}{R} = 38900\,\text{K} \tag{11}$$

2.2 Experimental studies

The results of two different experimental studies were chosen to test the reliability of selected creep models.

A series of transient coupon tests at various heating rates and stress level were conducted by Wainman and Kirby [4]. The heat rates varied between 2.5 ℃/min to 20 ℃/min and the stress level ranged from 25 MPa to 350MPa. British standard steel grades 43A and 50B were tested in the study, which correspond to Eurocode 3 steel grades S275 and S355, respectively.

Boko *et al* [5] conducted a small series of transient coupon tests on a more recent alloy of steel grade S355 at various stress levels between 50-400 MPa. A single heating rate of 10 ℃/min was used in the transient tests.

Above experimental tests were selected since they focused on commonly used steel grades in engineering practice. The heat rate in the tests conducted by Wainman and Kirby [4] and Boko *et al* [5] are of interest for the development of creep-free material law, which will be described in detail in section 2.3.

The coupon tests mentioned above were modelled by three-noded beam elements with segmental cross section in *Vulcan*. The same boundary conditions and load levels as in the experimental tests were applied on the finite element models. The coupons were pre-loaded before the temperatures start to increase according to the heat rates in the experimental tests.

2.3 Creep-free material law

Eurocode 3 material stress-strain law [8] is very commonly used in structural fire design and analysis by scientists and structural engineers and it has implicit consideration of the creep strain. These

considerations were on the basis of Kirby's tests [4] with heating rate of 10 ℃/min and only included the "likely" deformations due to creep during the time of exposure to the fire. Recent research [9-10] have shown that implicit creep contained in the Eurocode 3 curves cannot account for the effects of creep strains on structural response if prolonged temperature exposure over 400 ℃ is present.
With the purpose to introduce proper creep models into the structural fire analysis, it is necessary to omit the implicit creep consideration in the mechanical stress-strain curve in order to avoid the over- or under-estimation of the creep strain. A practical procedure of excluding implicit creep from Eurocode stress-strain curves will be presented briefly in the paper.

A series of transient coupon tests at different stress levels are modelled in *Vulcan* in order to obtain corresponding temperature-creep strain curves. These curves can be used to construct a series of stress-creep strain curves, which are then used to subtract the initial material stress-strain curves. This procedure is basically a reverse of the methodology by which a stress-strain curve is constructed from a series of transient tests. The proposed methodology was applied to the Eurocode 3 and Ramberg-Osgood material curves to generate corresponding creep-free stress-strain laws.

3 COMPARISON OF RESULTS

In this section a selection of study results is presented. Figure 1 presents the comparison of the results from Kirby's experimental tests [4] with stress level of 150MPa with the predictions from *Vulcan* using *Creep_model 3* .

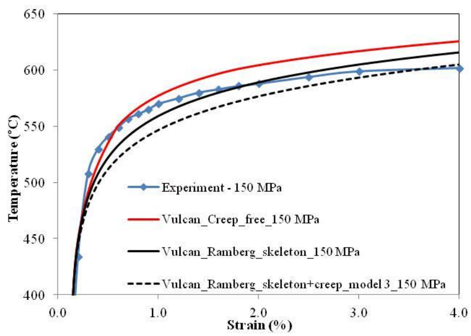

(a) S275 10 ℃/min – Ramberg-Osgood curves

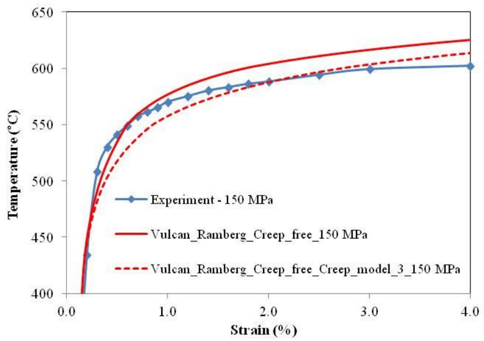

(b) S275 10 ℃/min – Ramberg-Osgood creep free curves

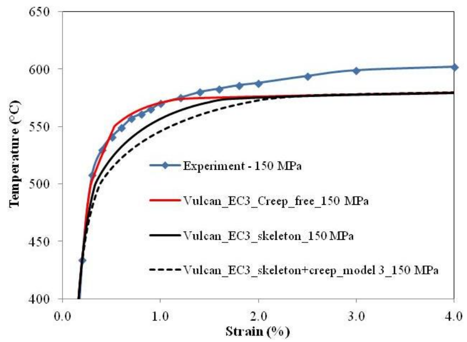

(c) S275 10 ℃/min – EC3 curves

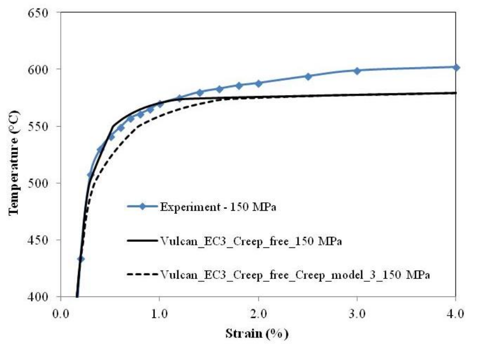

(d) S275 10 ℃/min – EC3 creep free curves

Figure 1. Comparison of results between *Vulcan* predictions and tests from study [4].

Figure 2 presents the comparison between Boko's experimental study [5] with stress level of 250 MPa and the *Vulcan* predictions using *Creep_model 2* and *Creep_model 3*.

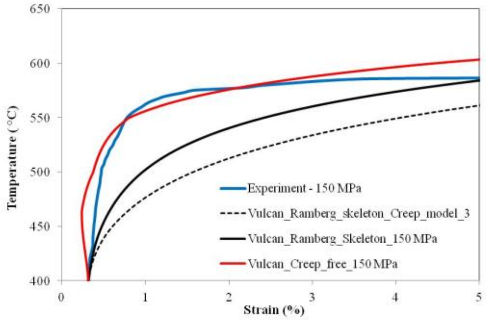

(a) S355 10 ℃/min – Ramberg-Osgood curves

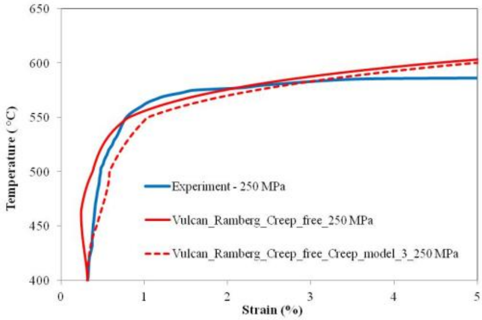

(b) S355 10 ℃/min – Ramberg-Osgood creep free curves

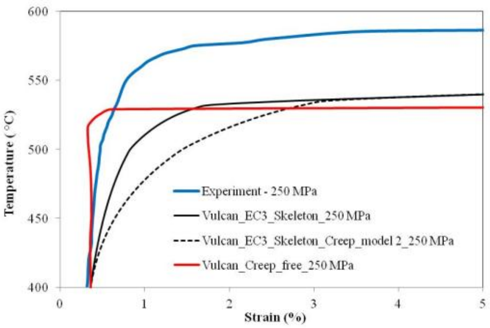

(c) S355 10 ℃/min – EC3 curves

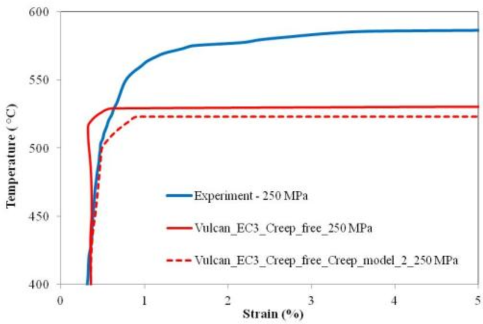

(d) S355 10 ℃/min – EC3 creep free curves

Figure 2. Comparison of results between *Vulcan* predictions and tests from study [5].

Table 1 presents a comparison of results between simulations from Figure 1 conducted with creep-free curves in predicting creep strains and implicit creep.

Table 1. Accuracy of creep-free curves in predicting total strain from study [4] for steel grade S275 at 150 MPa.

Strain (%) / Temperature (℃)	Exp [4]	Ramberg_skeleton+Creep_model 3	EC3_skeleton+Creep_model 3	Ramberg_creep_free+Creep_model 3	EC3_creep_free+Creep_model 3
1.0	570	547	545.5	559	559
1.2	575	555	554	566.5	565
1.4	580	561.5	560.5	573.5	569.5
1.6	583	568	565	580	573
2.0	588	577	572.5	589	575.5

4 DISCUSSION

Comparisons of the results in Figure 1 indicate that both Eurocode 3 and Ramberg-Osgood implicit curves (marked as “skeleton“) provide unrealistic predictions of total strain (creep+mechanical) of the experimental tests. The predictions become even more inaccurate if combining commonly-used stress-strain curves with explicit creep models. This is evident by the comparisons of the results of the numerical modelling and the experimental tests [4-5] for steel grades S275 and S355. However, better correlation with the experimental results can be achieved if combining creep-free stress-strain curves with the explicit creep model. This is particularly evident for Ramberg-Osgood material law which has excellent correlation with the experimental results. Simulations conducted with Eurocode 3 creep-free curves yield a better correlation only for steel grades from study [4]. Figures 1 and 2 provide a good illustration of the level of implicit creep strain which is present in Eurocode 3 and Ramberg-Osgood curves. These results indicate, firstly, that the conventional material laws in elevated temperature consist certain level of inaccuracy, and secondly, that the combination of the creep-free material laws and proper creep models can provide better prediction of the behaviour of steel in fire.

4.1 Creep free material laws

In light of the presented results, an optimal set of creep-free stress-strain curves is necessary in order to utilize the creep strain models in structural fire analysis. One of the approaches is to use the proposed “reverse-engineering” methodology to optimize the existing engineering curves, such as EC curves.

4.2 Effects of strain rate

Limited numbers of tests and research have been carried out to study the effects of the strain rate on the steel material in fire. The presented creep strain models cover the strain from a certain load but they do not reflect the stress due to the changing strain rate. Tests conducted by Renner [6] studied the influence of different strain rates on the stress-strain material law of steel grade S275 between 400-700 ℃. A total of 25 coupons were tested under three different displacement speeds (0.7-6.0 mm/min) per temperature level. It has revealed that the strain rate has significant impact on the stress-strain material law of steel under elevated temperature and should not be neglected.

The presented strain hardening creep model (*Creep_model 1*) was used to model these tests because the stress levels in the coupons changed during the displacement control tests. A displacement control solver was utilized to simulate the experiment process. Three displacement speeds (0.7 mm/min, 3.1 mm/min and 6.0 mm/min) were model on the Material B coupons with yield strength of 308 MPa. Figure 3 plots a typical comparison between the results from the numerical model and the test result. Table 2 shows the creep strains in the coupon for different displacement speeds.

Table 2. Creep strain predict by present creep model for different displacement speeds in Renner’s tests [6] at 500 ℃.

Strain (%)	0.7 mm/min	3.1 mm/min	6.0 mm/min
0.5	0.0112	0.0068	0.0053
1.0	0.0156	0.0092	0.0072
1.5	0.0185	0.0108	0.0084
2	0.0206	0.0121	0.0095

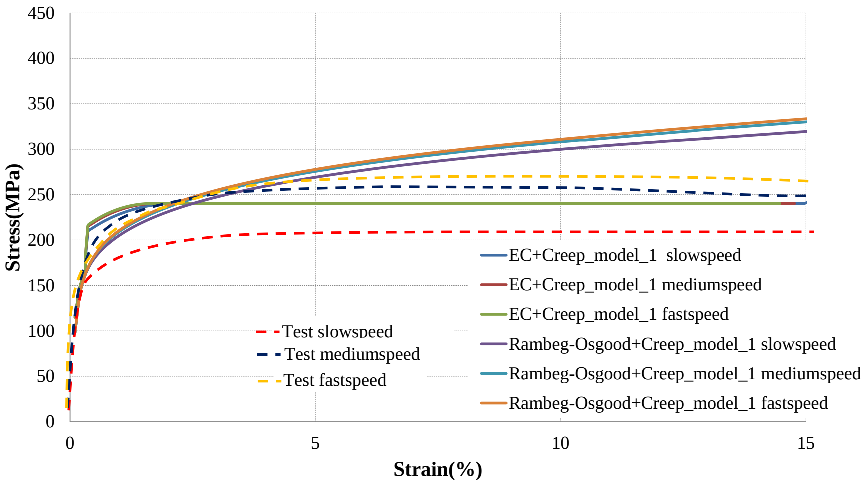

Figure 3. Comparison of results between *Vulcan* predictions and tests from Renner's tests [6].

It can be observed that the creep strains do contribute to the reduction of the strength of the steel as the displacement speeds decrease, however, the creep models is not adequately capable of tracking the strain rate effect on the material behaviour of steel under elevated temperature. This indicates that during the selection of the optimal creep-free stress strain curves, the strain rate effect should be taken into account. Ideally, there will be a group of creep-free stress strain curves for each strain rate.

5 CONCLUSIONS

Comparing the results of the simulations conducted using different creep and constitutive models with the coupon experiments have illustrated:

(1) Explicit creep analysis combined with implicit material curves yields imprecise predictions of creep strain in structural fire analysis.

(2) It is possible to exclude the influence of implicit creep from existing material stress-strain curves by creating creep-free curves.

(3) Accurate numerical prediction of transient coupon tests using explicit creep models cannot be achieved if the material's basic stress-strain law is determined from transient coupon tests conducted with heating rates of 10 ℃/min. This indicates that a suitable basic stress-strain constitutive model given by rapid (although not dynamic) testing at constant temperatures is as important as the nature of the creep model itself.

(4) As the displacement speed raises, the creep strain decrease as well as the ultimate strength of the steel under elevated temperature.

(5) The presented creep models have limited capacity of modelling the strain rate effect on the material properties of steel in fire. During the selection of the optimal creep-free basic stress-strain curves, the strain rate effect should be taken into account.

REFERENCES

[1] Harmathy, T.Z., "A Comprehensive Creep Model", *Journal of Basic Engineering*, 89(3), 496-502, 1967.

[2] Harmathy, T.Z., "Creep Deflections of Metal Beams in Transient Heating Processes, with Particular Reference to Fire", *Canadian Journal of Civil Engineering*, 3(2), 219-228, 1976.

[3] Plem, E., Theoretical and experimental investigations of point set structures, Swedish Council for Building Research, Document, D9, 1975.

[4] Wainman, D.E. and Kirby, B.R., Compendium of UK Standard Fire Test Data: Unprotected Structural Steel – 1 & 2, British Steel Corporation, 1988.

[5] Boko, I., Torić, N., Peroš, B., "Structural fire design parameters and procedures – analysis of the potential of Eurocode 3", *Materialwissenschaft und Werkstofftechnik*, 43(12), 1036-1052, 2012.

[6] Renner, A., The Effect of Strain-Rate on the Elevated-Temperature Behaviour of Structural Steel, Research dissertation, University of Sheffield, Department of Civil and Structural Engineering, 2005.

[7] Harmathy T. Z. and Stanzak W. W., Elevated-Temperature Tensile and Creep Properties of Some Structural and Prestressing Steel, National Research Council of Canada, Division of Building Research, Otawa, ON, 1970.

[8] EN1993-1-2:2005, Eurocode 3 – Design of Steel Structures - Part 1-2: General Rules - Structural Fire Design, European Committee for Standardization, Brussels, 2005.

[9] Kodur V., Dwaikat M., Fike R., "High-Temperature Properties of Steel for Fire Resistance Modeling of Structures", *ASCE Journal of Materials in Civil Engineering*, 22(5), 423-434, 2010.

[10] Torić N., Harapin A., Boko I., "Experimental Verification of a Newly Developed Implicit Creep Model for Steel Structures Exposed to Fire", *Engineering Structures*, 57, 116-124, 2013.

8th International Conference on Structures in Fire
Guo-Qiang LI, Venkatesh K. R. KODUR, Shou-Chao JIANG, Jian JIANG, Su-Wen CHEN, Guo-Biao LOU (Eds.)
Shanghai, China, June 11-13, 2014

3D SPATIAL HOMOGENIZATION ALGORITHM FOR COUPLING CFD FIRE SIMULATIONS WITH FINITE ELEMENT HEAT TRANSFER ANALYSES OF STRUCTURES

Paul A. Beata* and Ann E. Jeffers*

* University of Michigan, 2350 Hayward St., 2340 GG Brown, Ann Arbor, MI, USA 48109
e-mails: pbeata@umich.edu, jffrs@umich.edu

Keywords: Computational fluid dynamics, Finite element analysis, Fire simulation, Heat transfer

Abstract. *Coupling computational fluid dynamics (CFD) fire simulations with finite element (FE) heat transfer models is a promising approach for analyzing structures exposed to natural fire conditions. While computationally demanding, CFD fire simulations are well-developed for accurately modelling the dynamics of a natural fire scenario. The fine mesh size of 3D FE models consisting of solid elements also provides another source of computing demand. A spatial homogenization algorithm is presented for coupling the fire and solid domains and using efficient heat transfer shell elements to arrive at an accurate and efficient solution. As an example, the homogenization algorithm and heat transfer shell element were used to analyse a flat plate exposed to a local fire. The results demonstrate that the spatial homogenization algorithm is able to capture non-uniform thermal boundary conditions accurately and that the method is a suitable approach for use with macro heat transfer elements.*

1 INTRODUCTION

The assumption of a uniform gas temperature for analyzing structures exposed to local fires simplifies the physics of the problem. Uniform gas temperature methods, including the parametric fire curve [1], fail to capture the non-uniform thermal boundary conditions associated with natural or traveling fires. Structural components are not uniformly heated during exposure to traveling fires in larger, open floor plans where compartment model assumptions are not valid [2]. Natural fires can be modelled using computational fluid dynamics (CFD) programs for simulating the fire scenario. However, due to the disparity in scale between the fire and solid domains (as shown in Figure 1), transferring data from the fire to the structure is a challenging analysis task.

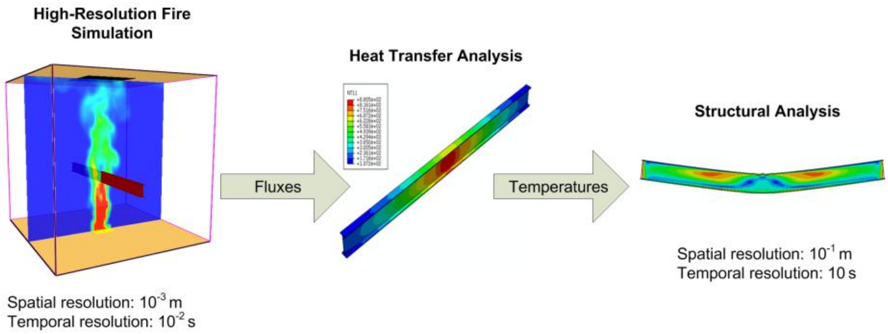

Figure 1. Sequentially coupled analysis of a beam illustrating the differences in scale.

The main issues in coupling CFD fire simulations with finite element (FE) structural models is the differences in scale for the both the temporal and spatial data. A typical process for sequential coupling is provided in Figure 1 where a beam exposed to a local fire in the CFD environment was then analyzed in the FE environment. Coupling between the CFD fire simulation and the FE heat transfer model was accomplished through the use of incident surface fluxes, as shown in the figure.

The temporal resolution was addressed by Yu and Jeffers in a previous study [3] in which temporal data from the CFD fire were passed to the FE heat transfer model through temporal sub-cycling. The current issue of spatial scale is presented here and a solution involving spatial homogenization is employed. The spatial homogenization algorithm was developed for use with macro heat transfer elements [4-6]. A preliminary study by Beata and Jeffers [7] demonstrated the need for this algorithm and its usefulness in handling non-uniform thermal boundary conditions which may change rapidly across a single element surface. The methodology is extended here by considering its implementation with a macro heat transfer element and providing a fire exposure calculated by CFD.

2 METHODS

A spatial homogenization algorithm is presented for capturing non-uniform boundary conditions in the analysis of structures exposed to localized fires. The methods used for accomplishing this task are based on the sequential coupling of a CFD fire simulation with a FE heat transfer model.

The matrix-vector form of the governing differential equation for heat transfer using FE theory is stated as follows:

$$[C]\{\dot{T}\}+[K]\{T\}=\{R\} \tag{1}$$

where $[C]$ is the specific heat matrix, $[K]$ is the thermal conductivity matrix, $\{R\}$ is the flux vector, and $\{T\}$ is the temperature vector representing the field variable [8]. The capital letters are used to indicate that the equation is written for the global system. In general, the right-hand side of Equation (1) is composed of the various components of thermal boundary conditions:

$$\{R\}=\{R_c\}+\{R_r\}+\{R_q\}+\cdots \tag{2}$$

where the subscripts refer to various boundary conditions in the system such as convection (c), radiation (r), and applied surface fluxes (q). Equation (2) is left open to acknowledge other potential contributions to the total heat flux vector $\{R\}$.

The methods developed for the spatial homogenization algorithm were based on using the applied flux vector $\{R_q\}$ to pass incident surface flux data from the fire simulation to the heat transfer model through the calculation of equivalent nodal fluxes. However, the methodology can be extended to other types of boundary conditions such as convection and radiation. The applied flux vector $\{R_q\}$ from the global form of Equation (2) can be written at the element level as follows:

$$\{r_q\}=\int_S \{N\}\, q''\, dS \tag{3}$$

where $\{N\}$ is the vector of element shape functions, q'' is the applied surface flux, and the integral is carried out over the element surface S where the applied flux is a specified boundary condition. In two dimensions (i.e., for planar applications), S is simply the edge of an element. For extension to 3D structures, the spatial variation in fire exposure may occur in two dimensions across the surface of an element.

In a previous study [7], several methods were considered for calculating equivalent nodal fluxes from incident surface fluxes measured in the fire simulation. These methods were considered for planar problems (2D) whereby structural components were exposed to local fires at a single edge. The main goal in the initial study was to evaluate a group of methods for capturing a thermal boundary condition varying in only one spatial dimension. In all, four types of methods were used to compute in the integral in Equation (3): averaging, sampling, least squares, and the trapezoid rule method. The trapezoid rule method provided the highest level of accuracy and consistent convergence.

Instead of characterizing the local flux data and representing it at the quadrature points, the trapezoid rule was used to evaluate the integral using the entire set of flux data available at the element boundary. Of the many approaches analyzed for providing an accurate representation of the non-uniform boundary condition, the trapezoid rule for computing the integral in Equation (3) was the most successful in calculating nodal fluxes. The trapezoid rule method makes use of each flux data point associated with a particular element boundary; as a result, it is regarded as an "energy-equivalent" method in this context (as opposed to the other methods which only approximate the boundary condition).

Using the trapezoid rule to compute the applied flux vector proved to be a successful approach in the 2D application to planar problems. Guided by the results of the 2D analyses in the previous study [7], the concept of energy equivalence was extended to a second spatial dimension in order to integrate over the surfaces of 3D elements in the heat transfer model. The purpose of the spatial homogenization algorithm is to represent the spatially varying boundary condition shown in Figure 2 (a) as equivalent nodal fluxes in Figure 2 (b).

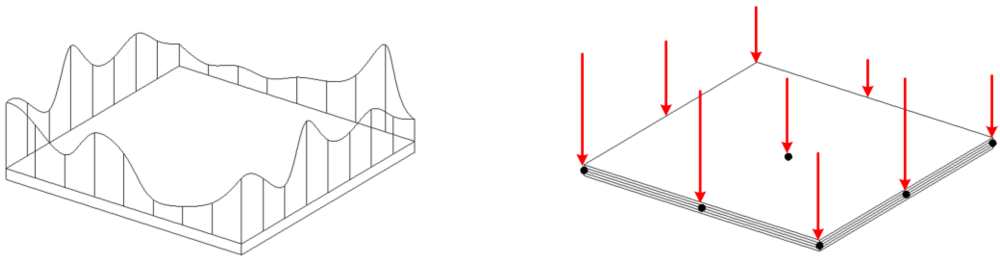

(a) (b)

Figure 2. (a) Single element exposed to a spatially varying thermal boundary condition; (b) Energy equivalent nodal fluxes representing the variable boundary.

3 IMPLEMENTATION

As mentioned earlier, the proposed homogenization algorithm is intended for use with macro heat transfer elements (e.g., shell elements) rather than solid elements (e.g., brick elements). The macro element used in the current study is a 9-node quadratic shell with a layered formulation [6]. The use of macro elements allows the model to employ a relatively coarse element mesh without losing the spatial variability in boundary condition (as handled by the spatial homogenization algorithm) and in a manner that is much more efficient than a solid element model. As a result of using the macro heat transfer elements, the mesh size of flux data points will most certainly be smaller than the coarser FE model mesh, which justifies integration by the trapezoid rule.

The use of 3D shell elements allows spatial variation in the thermal boundary conditions to exist in two dimensions of the element surface. As a result, flux data measurements in the fire simulation are recorded in a grid pattern over the surface of the structure. The definition of q'' is clarified to indicate the distribution in two dimensions as $q''(x,y)$ in the physical space. Equation (3) can be expressed as:

$$\{r_q\} = \int_y \int_x \{N\}\, q''(x,y)\, dx\, dy \qquad (4)$$

Using an isoparametric formulation in the development of the shell heat transfer element, a mapping from the parent domain of the bi-unit element is required for carrying out the integration in Equation (4) on intervals of [-1,1] in each spatial dimension across the element surface. The mapping from natural coordinate space ξ-η to the physical space x-y (Figure 3) is accomplished through the Jacobian matrix [*J*]. To evaluate the integral of Equation (4) for an isoparametric element, the equation becomes:

$$\{r_q\} = \int_{-1}^{+1}\int_{-1}^{+1} \{N\}\, q''\, \det[J]\, d\xi\, d\eta \tag{5}$$

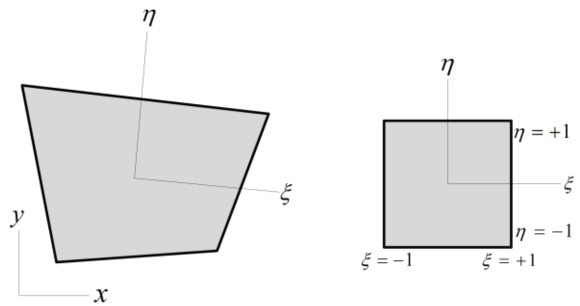

Figure 3. Isoparametic mapping from the parent domain to the physical space.

An important distinction to note when using the heat transfer shell element instead of a brick element is that the shape functions are in the ξ-η plane only and thus the ζ-direction is not mapped; thus, [*J*] is the 2D Jacobian matrix. Another important note from Equation (5) is that *q"* is written in its contracted form again, however, it is implied that this spatially varying flux term is mapped to the parent domain as well. The term *q"* does not represent a continuous function but rather a set of discrete flux data points as measured in the CFD fire simulation in a grid pattern.

Numerical integration is performed using the trapezoid rule with surface flux data measured in an (*m*+1) by (*n*+1) grid. First, in a quite straightforward manner, the trapezoid rule is used to compute the first integral in Equation (5) along slices in the ξ-dimension:

$$\{I\}^{(j)} = [\{N\}\, q''\, J]\big|_{(\xi_0,\eta_j)} + 2\sum_{i=1}^{n-1}[\{N\}\, q''\, J]\big|_{(\xi_i,\eta_j)} + [\{N\}\, q''\, J]\big|_{(\xi_n,\eta_j)} \tag{6}$$

where the determinant of the Jacobian matrix has been abbreviated as *J* and the vertical bar notation $|_{(\xi,\eta)}$ is meant to indicate "evaluated at". A dummy variable {*I*} is introduced to define the *j*-th integral along the element surface in a single dimension for *j* = 0, 1, …, *m*. The full integration in Equation (5) is completed by applying the trapezoid rule in the η-dimension to the vectors $\{I\}^{(j)}$ computed in the first round:

$$\{r_q\} = \frac{(\eta_m - \eta_0)}{2m}\left[\{I\}^{(0)} + 2\sum_{j=1}^{m-1}\{I\}^{(j)} + \{I\}^{(m)}\right] \tag{7}$$

An illustration of the integration process in slices is provided in Figure 4. It shows a general (*m*+1) x (*n*+1) grid in Figue 4 (a) represented by the intersecting lines on a single element surface. In the figure, the lines intersect at the smaller circles on the element surface which represent locations where the incident surface flux is measured. Integral slices are shown in Figure 4 (b). It is the resulting vectors $\{I\}^{(j)}$ from these slices that used to perform the trapezoid rule again in the second dimension in Equation (7).

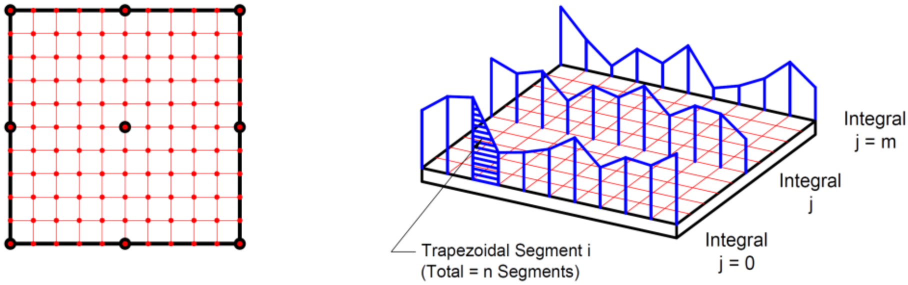

(a) (b)

Figure 4. (a) General flux data grid from a CFD fire simulation projected onto a single element; (b) Calculation of the applied flux vector using the trapezoid rule in two spatial dimensions.

4 APPLICATION

The spatial homogenization algorithm was used in the analysis of a steel plate exposed to a local fire. The purpose of the application was to perform a CFD fire simulation and couple it with a FE heat transfer model to observe how the trapezoid rule (when used with shell elements) compared with a model using solid elements with the incident surface fluxes applied on a one-to-one grid. In particular, a horizontal plate structure was exposed to a local fire for 12 minutes and temperatures at the mid-depth of the plate were compared between a converged solid element model (serving as the reference solution) and a series of shell element models.

Figure 5 shows the plate structure in the CFD fire simulation. Fire Dynamics Simulator (FDS) was used for the fire analysis. As mentioned previously, coupling between the fire simulation and heat transfer models was accomplished using incident surface fluxes measured on a fine grid in the CFD model and transferred to the FE model using the spatial homogenization algorithm presented in Equations (6)-(7) for integration over the surface in two spatial dimensions.

The fuel source was a small pool of heptane with a peak heat release rate of 110 kW and it was designed to extinguish just before the 12-minute mark. The fire was located 100 cm below the centre of the plate and a grid size of 2.5 cm was chosen. Dimensions of the plate were 200 cm x 100 cm x 4 cm and the properties were selected to match those of steel at ambient temperature: specific heat = 465 J/kg K, density = 7,833 kg/mg/m^3, and thermal conductivity = 54 W/m K. Temperature-dependent material properties were not used as the results showed maximum temperature elevations of about 140 ℃ in this particular fire scenario.

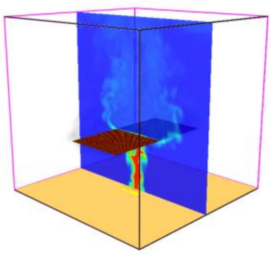

Figure 5. Plate structure exposed to a local fire in FDS.

As a result of the CFD grid size and the dimensions of the plate, incident surface flux data was recorded on an 80 x 40 grid for a total of 3,321 measurements on both the top and bottom surfaces. The heat transfer analysis was performed using Abaqus. Two heat transfer models were used for comparison: one serving as the reference model composed of built-in solid elements and the other employing the user-defined shell elements [5]. The solid element model had a one-to-one match between the flux data measured in FDS and the element size used in Abaqus and thus fluxes were applied uniformly at the element surfaces. The shell element model employed the spatial homogenization algorithm which made use of the coarser FE grid size with a large number of flux data points. Each model accounted for losses by convection and radiation to ambient (T_∞ = 20 ℃) at the top and bottom of the plate using a heat transfer coefficient of 25 W/m^2 K and an emissivity of 0.8.

A convergence study was conducted by systematically refining the mesh size in the FE model employing the shell heat transfer elements with the spatial homogenization algorithm. In the thickness direction of the plate, only one shell element was used (taking advantage of the layered formulation to model the temperature distribution through the plate depth). In the plan dimensions (the x-y plane), meshes used in the analyses included 2×1, 4×2, 8×4, and 16x8, which produced square elements in this plane for each mesh. The solid element model required a mesh that was finer than the CFD grid in order to capture the temperature distribution through the plate thickness. As a result, the mesh used four elements through the thickness and 80×40 in plan providing a typical element size of 1.25 cm x 1.25 cm x 1 cm. The solid elements used in the reference model were built-in, 8-node, linear brick elements. A comparison of the density of elements used in the shell element model and the solid element model is shown in Figure 6.

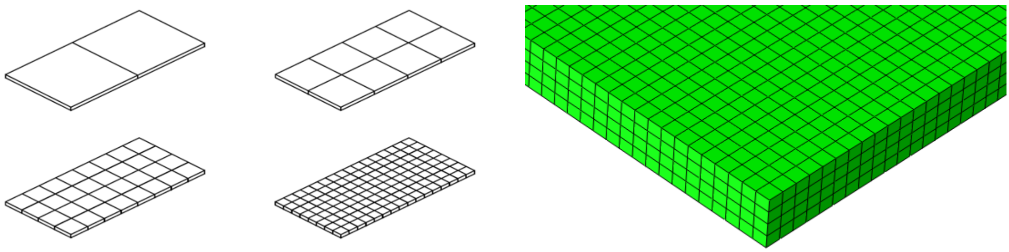

(a) (b)

Figure 6. (a) Mesh configurations used in the convergence study using shell elements; (b) Refined mesh of the solid element model requiring four elements through the plate thickness (only one corner shown for comparison purposes).

5 RESULTS

The analysis of a steel plate exposed a local fire provided favourable results when comparing between the shell element and solid element models. The temperature field in the shell element models was obtained by interpolating between nodal temperatures and errors were calculated by comparison to the solid element model using the L_2 norm measure. Contour plots of the temperature fields at 12 minutes (the end of the fire simulation) are shown in Figure 7 for the mid-depth of the plate structure; only two shell element meshes are shown. It can be seen that the shell element model converges to the solid element model solution as the number of elements increases. A plot of the temperature distribution through the plate thickness after 6 minutes of fire exposure is shown in Figure 8 where convergence of the temperature distribution is seen. The L_2 norm errors are presented in Table 1. The shell element model with the spatial homogenization algorithm converged rapidly to the reference solution. Simulation times are also shown in Table 1. The time required for the fire simulation in FDS is not included in this table as it was the same for each model. Errors were within 5% for the 4x2 mesh and within 1% for the 8×4 mesh.

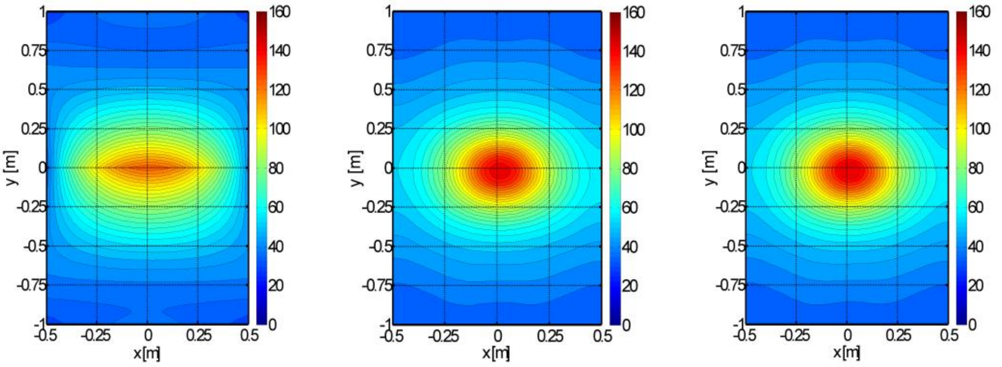

(a) (b) (c)

Figure 7. Contour plots of the mid-depth temperature field for (a) the 2×1 shell element model; (b) the 16×8 shell element model; (c) the converged solid element model.

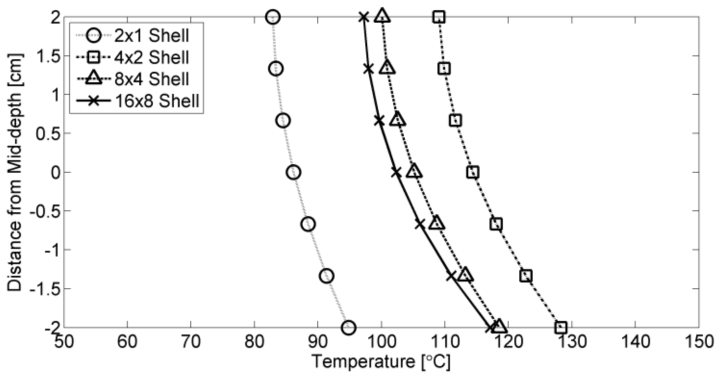

Figure 8. Temperature distribution through the plate thickness after 6 minutes of fire exposure.

Table 1. L_2 norms as relative percentage errors (columns 3-6) and simulation times.

Element Type	Mesh	3 min	6 min	9 min	12 min	Simulation Time
Plate	2×1×1	7.34	9.31	9.71	9.09	26.3s
Plate	4×2×1	1.92	3.05	3.33	3.43	35.0s
Plate	8×4×1	0.92	1.04	1.08	1.10	68.4s
Plate	16×8×1	0.49	0.35	0.32	0.40	213s
Solid	160×80×4	--	--	--	--	5.4d

6 CONCLUSIONS

The spatial homogenization algorithm was presented for representing spatially varying boundary conditions as equivalent nodal fluxes. Incident surface fluxes measured in a regular grid in the CFD fire simulation were used as the boundary conditions in the FE heat transfer model. The algorithm was based on the trapezoid rule for numerical integration over two spatial dimensions to calculate equivalent nodal fluxes based on the thermal boundary at an element surface in the FE model. It proved to be an accurate method for representing the thermal boundary conditions measured in CFD fire simulations when compared with a converged solid element model.

Implementation using the heat transfer shell element is essential for taking advantage of the accuracy in using all the flux data points by employing the trapezoid rule. The heat transfer analysis of a plate structure like the one presented here can still be done simply using the flux data directly from the CFD model and using solid elements. However the combination of the spatial homogenization algorithm with the heat transfer shell elements provided a much more efficient analysis tool without sacrificing accuracy of the solution (i.e., the 16×8 shell element model employing the spatial homogenization algorithm required only 3.5 minutes compared to the solid element model which took five days).

As mentioned earlier, this approach was designed for macro heat transfer elements. The spatial homogenization algorithm is used to represent spatially varying thermal boundary conditions by an energy equivalent technique for capturing the distribution over larger surface areas. This ability was not previously available when using coarser meshes of macro element models and thus the solid element model was the only practical way to represent the variability of the boundary. The current research has not addressed the high computational cost of using CFD fire simulations to represent the natural fire and additional work is in preparation regarding more complicated structural geometries such as tilted plates and curved surfaces.

The research presented is part of an ongoing study aimed at providing a fully coupled analysis environment for combined CFD fire simulations and FE structural models. The structural analysis phase of the sequentially coupled analysis shown in Figure 1 is the focus of future work. In the effort to provide the fully coupled analysis, the macro heat transfer element will be superimposed on to a mechanical plate element. The element will employ temporal sub-cycling and spatial homogenization algorithm techniques in order to complete a unified analysis of the structure exposed to a local fire in real time.

REFERENCES

[1] Eurocode 1: Actions: General actions – Actions on structures exposed to fire, BS EN 1991-1-2, British Standards Institution, London, 2009.

[2] Stern-Gottfried J. and Rein G., "Travelling fires for structural design - Part I: Literature review", *Fire Safety Journal*, 54, 74-85, 2012.

[3] Yu X. and Jeffers A., "A comparison of subcycling algorithms for bridging disparities in temporal scale between the fire and solid domains", *Fire Safety Journal*, 59, 55-61, 2013.

[4] Jeffers A. and Sotelino E., "An efficient fiber element approach for the thermo-structural simulation of non-uniformly heated frames", *Fire Safety Journal*, 51, 18-26, 2012.

[5] Jeffers A., "Heat transfer element for modeling the thermal response of non-uniformly heated plates", *Finite Elements in Analysis and Design*, 63, 62-68, 2013.

[6] Jeffers A. and Beata P., "Generalized shell heat transfer element for modeling the thermal responses of non-uniformly heated structures", *Finite Element in Analysis and Design*, 83, 58-67, 2014.

[7] Beata P. and Jeffers A., "Capturing Spatial Variations of Applied Heat Fluxes in Finite Element Analyses of Structural Members", *Interflam 2013 – Proceedings of the Thirteenth International Conference,* S. Grayson (ed.), Interscience Communications Ltd., Nr Windsor, UK, 6-25-2013.

[8] Cook R., Malkus D., Plesha M. and Witt R., *Concepts and Applications of Finite Element Analysis,* John Wiley & Sons, 2002.

8th International Conference on Structures in Fire
Guo-Qiang LI, Venkatesh K. R. KODUR, Shou-Chao JIANG, Jian JIANG, Su-Wen CHEN, Guo-Biao LOU (Eds.)
Shanghai, China, June 11-13, 2014

EXPERIMENTAL BEHAVIOUR OF FLAT DECKING PROFILE COMPOSITE SLABS IN STANDARD FIRE CONDITIONS

Minh-Phuong Nguyen* and Kang Hai Tan*

* School of Civil & Environmental Engineering, Nanyang Technological University, Singapore,
e-mails: MPNguyen@ntu.edu.sg, CKHTan@ntu.edu.sg

Keywords: Fire resistance, Composite slab, Flat decking profile, Experiment

Abstract. *Structural fire response of composite slabs has been the subject of extensive research in recent years. Due to its effect on heat transfer across the slab thickness, the configuration of steel decking profile plays an important role in fire resistance of composite slabs. While the design code of trapezoidal and re-entrant decking profiles are available, there is rather limited literature on fire resistance of flat decking profile. When exposed to fire, the totally embedded vertical webs and top ribs of the decking have much lower temperature compared to the bottom. Hence, the fire reinforcement required at the bottom of the slab can be reduced or even eliminated. The present paper investigates heat transfer of a series of composite slabs under the standard fire condition where a new type of flat profile steel decking is used. The study aims to provide actual temperature profile across the slab thickness for different durations (up to four hours). The temperature measurements were initially used for calibration of FE models. The FE models were also developed for trapezoidal and re-entrant profile in accordance with Eurocode 4.Part 1-2 (2005). Comparison among the three models was carried out to show the effectiveness of using flat decking in fire conditions. The test and FE results were then used to establish the temperature distribution of flat decking profile for practical design purpose.*

1 INTRODUCTION

In the last twenty years, structural fire response of composite slabs has been the subject of extensive research [1-5]. They provided the background for many design codes for fire safety in building structures either using prescriptive approach or performance-based approach. The essential assessment in both approaches is to determine the fire resistance of structural elements under specific fire exposure. Currently, Singapore uses Eurocode 4: Part 1-2 (EC4.P1-2) (2005) for designing composite slabs in fire conditions. The slab fire resistance is determined through a semi-empirical design method. It is worthy to note that, in this code, only the design for trapezoidal and re-entrant steel decking profiles are available. Practically, these steel deckings are not considered in calculating the fire resistance of the slab due to debonding from concrete and fast deterioration at an early stage when directly exposure to fire.

This research investigates a new type of decking profile where part of its web and the top flange of this decking are embedded in the concrete slab. The profile decking is manufactured by a LCP Building Products Private Limited company [6]. This configuration of steel decking profile plays an important role in the fire resistance of composite slabs. When exposed to fire, the embedded areas of the decking have much lower temperatures compared to the bottom exposed face. In addition, due to the embedment of its web and flange, the steel decking remains intact with concrete through fire for duration up to four hours. By considering these advantages, the steel decking can be taken into account when calculating the fire resistance of composite slabs. It is expected that the fire reinforcement [7] at the bottom of the slab can be reduced or even eliminated.

In this present paper, heat transfer of a series of composite slabs under standard fire condition Eurocode 1. Part 1.2 (EC1.P1-2) (2002) is investigated both experimentally and numerically where a new type of flat profile steel decking is used. The study aims to provide the actual temperature profile across the slab thickness for different durations (up to four hours). The temperature measurements were first used for calibration of FE models, which were also developed for trapezoidal and re-entrant profile in accordance with EC4.P1-2 (2005). Comparison among the three models was carried out to show the effectiveness of using flat decking for fire conditions. The test and FE results were then used to establish the temperature distribution of flat decking profile for practical design purpose.

2 EXPERIMENT STUDIES

2.1. Test programme and instrumentation

A total of four composite slabs having identical steel decking, normal-weight concrete and steel mesh were tested. Each slab was 0.9m by 2.2m and simply supported at its two ends. However, the thickness of the slab was designed to satisfy the requirements for structural adequacy and integrity (Table 4.8, EC4.P1-2 (2005)). For all the slabs, there was no fire reinforcement except an anti-crack mesh (A6) placed 20mm beneath the top surface in accordance with ambient temperature design. The noclamentures of specimens are given in Table 1 and design of slab is illustrated in Figure 1.

Table 1. Summary of tests.

Specimens	Decking thickness (mm)	Slab thickness (mm)	Fire scenarios (minutes)	Age of specimen at test date (days)
S.105.1H	0.75	105	60	71
S.120.2H	0.75	120	120	91
S.150.3H	0.75	150	180	96
S.170.4H	1.00	170	240	106

The slabs were cast by laying the metal deck on the factory floors and building formwork around the perimeter. Therefore, there was no deflection of the deck during the concreting. It should be noted that only the end of the slab were supported while their longitudinal edges were laid onto flexible heating insulation material. Thus, they were one-way spanning slabs.

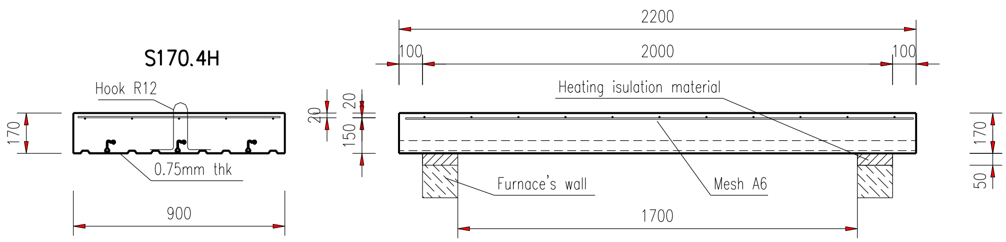

Figure 1. Profile of composite slab S174.4H.

To understand the heat transfer process across the thickness of the composite slabs in fire condition, different fire durations denoted as 1H, 2H, 3H and 4H were simulated. All fire scenarios strictly followed the standard ISO-834 (EC1.P1-2) fire curve, given by

$$T_{furnace} = 20 + 845 \times \log(8t + 1) \tag{1}$$

where $T_{furnace}$ is the furnace temperature (^{o}C), and t is the elapsed time (in minutes). The heating for each fire scenarios were controlled automatically using the electrical furnace as shown in Figure 2.

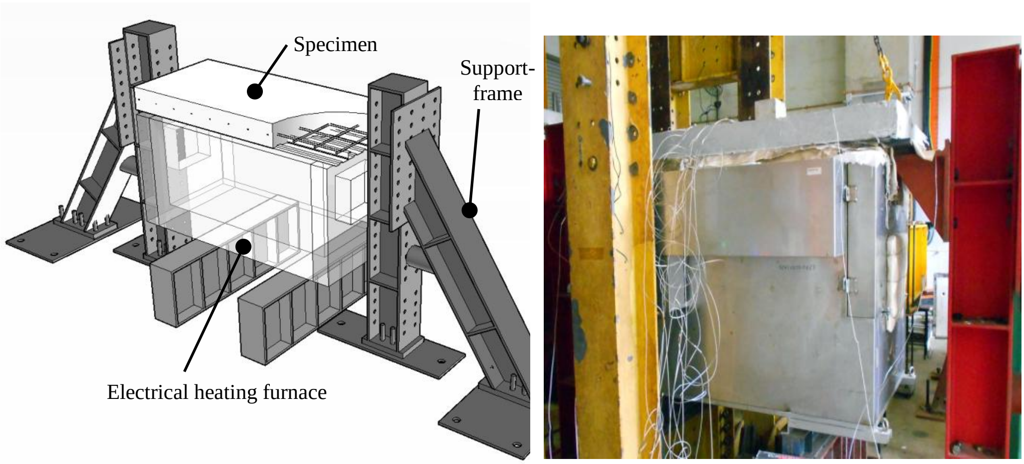

Figure 2. Test setup of the composite slabs.

Since the objective of the tests was to determine the temperature profiles, there was no loading applied onto the specimen throughout the test. The instrumentation for each test only consisted of thermocouples. Locations of the thermocouples are illustrated in Figure 3 including the bottom, middle of the web, top of the decking, anti-crack mesh and top concrete surface. Besides, three temperature profile gauges (T1, T2 and T3) were embedded in the slabs. The gauges provided temperature developments at incremental distance of 25mm from the soffit of the slab.

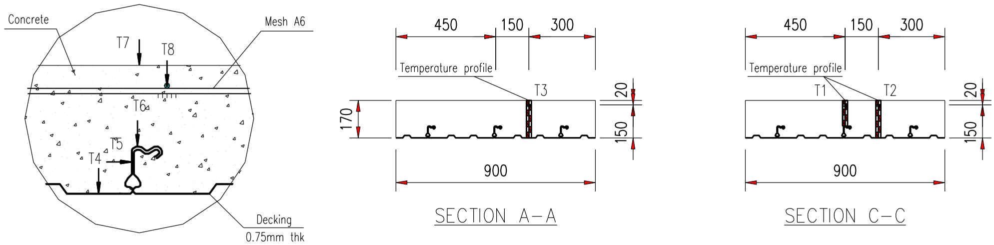

Figure 3. Distribution of embedded thermocouples.

2.2 Test results

In the fire test, the specimens were heated at the bottom by an electrical furnace. Therefore, it was difficult to observe the soffit of the slab during testing. However, after the test, the specimens lifted up and the bottom could be observed. As shown in Figures 4, the steel decking was debonded from the side of specimens. However, it should be noted that at the two sides of each specimen only one half of the decking was used. Hence, only one of its side rib was embedded to the concrete (as shown in Figure 1). At the middle location where the deck ribs were fully embedded into the concrete, the composite slab remained intact even when it was subjected to 3-hour rating. For 4-hour rating, the decking melted as shown in Figure 4(b). Notably, there was no crack penetrating through the top of the surface. Therefore, it can be concluded that in practice where the decking ribs are fully embedded to the concrete, slab integrity can be satisfied.

Although the specimen was used with 1mm thick flat decking profile, the large part of the melted decking was not able to prevent spalling of concrete at the slab soffit. At the end stage of 4-hour fire testing, the temperature of decking was about 1100^{o}C which was the melting point of steel.

(a) Bottom surface of specimens S150.3H

(b) Bottom surface of specimens S170.4H

Figure 4. Integrity of specimens after the fire test.

Temperature profiles of all specimens were captured and analyzed, including (i) the bottom steel decking, (ii) top flange and middle rib of steel decking, (iii) anti-crack steel mesh, (iv) top surface of specimens (for insulation checking), (v) temperature profile between the deck ribs at an interval distance of 25mm across the thickness and (vi) temperature profile above the deck ribs at an interval distance of 25mm across the thickness. Due to the limited space, it was not possible to present all the test data in the paper. For specimen S170.4H, the maximum temperature of bottom decking, anti-crack mesh, top concrete surface and concrete temperature development across the slab thickness are presented in Figure 5.

Location	Maximum temperature (^{o}C)
Bottom decking	1118.4
Top flange	832.1
Middle rib	951.2
Anti-crack mesh	145.3
Top slab surface	74.2

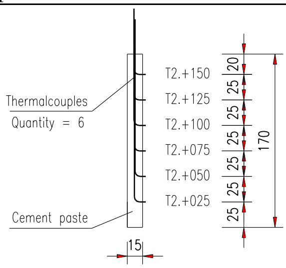

Temperature profile gauge T2

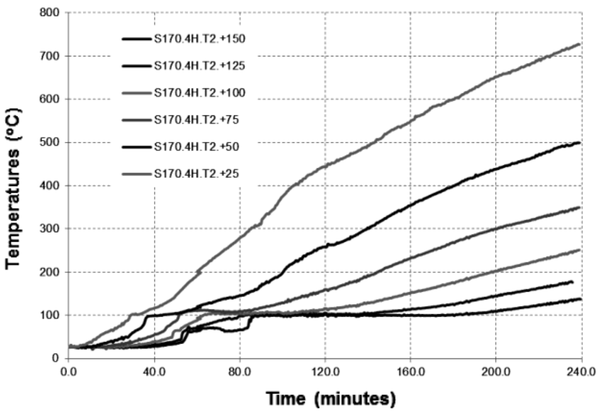

Figure 5. Temperature development of specimen S170.4H subjected to four-hours standard fire.

As shown in Figure 5, for concrete, the temperatures developed reasonably well across the slab thickness. There was a temperature increase to 100^{o}C followed by a plateau and then an increase again in all specimens. This was probably because the moisture in the concrete migrated upward and become saturated, hence, preventing the increase of temperature in a certain time. It should be noted that the concrete was grade C30 and therefore the matrix was more porous. For the steel decking, after four hours subjected to fire, the bottom deck started to melt. The rib temperature reached 950^{o}C and there was almost no strength left; however, the top flange had the lowest temperature of 832^{o}C. Although fire reinforcement is recommended for four-hour rating, the top flange of the rib can be taken into consideration for the slab fire resistance.

3 FE MODELLING

There are many numerical models to simulate the thermal and mechanical behaviour of composite slab exposed to fire [8-13]. In these numerical models, the heat transfer analysis was conducted mostly using the FE method. In this study, the focus is to demonstrate the effectiveness of using the new profile decking compared to common profile type i.e. trapezoidal and re-entrant. Hence, the FE models by Chung [10] are employed using ABAQUS v.6.10 FE software package.

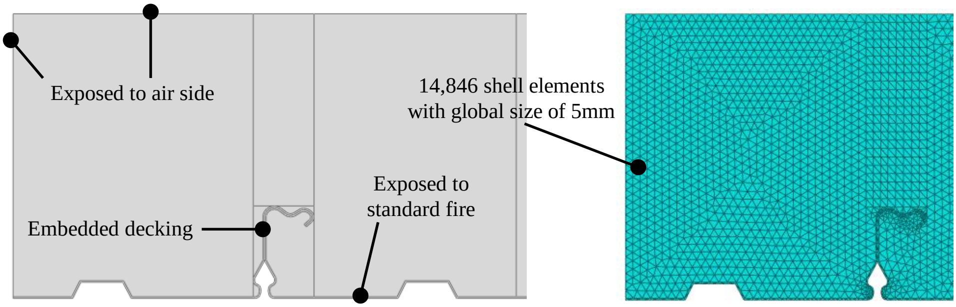

Figure 6. General FE model of profiled decking.

The general FE model of slabs is illustrated in Figure 6. The thermal fluxes due to both convection and radiation of the standard fire are given in EC1.P1-2(2002). The coefficient of heat transfer by convection for the fire-exposed surface is 24 W/m^{2}K and 10W/m^{2}K on the surface exposed to air. The resultant emissivity of the fire exposed surface is 0.4, similar to the value recommended by Both [2]. The effect of moisture in concrete is considered by introducing latent heat for energy loss into the specific heat capacity of concrete. The value of this latent heat is denoted by $C_{c,peak}$, as in EC2.P1-2(2003). When the temperature is between 100^{o}C and 115^{o}C, $C_{c,peak}$ is equal to 1470 J/kg.^{o}C and 2020 J/kg.^{o}C for the 1.5% or 3.0% moisture by weight, respectively. Since, there is no established, numerical method to consider concrete spalling [14], this phenomenon is, it is not modelled.

As shown in Figure 7, the development temperature of bottom decking and concrete across the slab thickness converge generally. For the temperature development of concrete, Figure 7(b), in the early stage, numerical models somewhat underestimated the actual temperature results, which may be attributed to the development of moisture in the gap between the decking and concrete. However, upon increase in the temperature, the predictions get closer to the test results. It also should be noted that at this stage, the material properties remain almost unchanged as the temperature is still relatively low (less than 100^{o}C). Hence, this underestimation of temperature has negligible effect on the performance of the slab. Although there are some limitations of the model such as modelling of debonding behaviour and air gap between decking and concrete at bottom slabs, it can be concluded that the FE model is able to predict the development of temperature in composite slabs with reasonable accuracy.

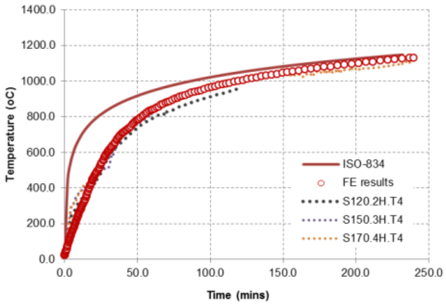

(a) Bottom decking temperature of all specimens subjected to ISO-834 standard fire

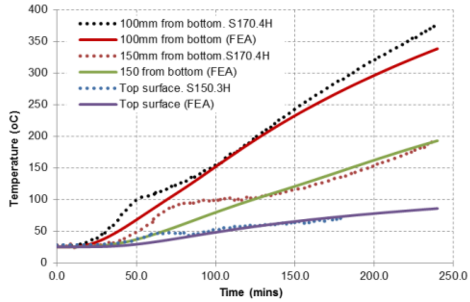

(b) Comparisons of concrete temperatures at 100, 150 from bottom and top covers

Figure 7. Validation of FE models with test results.

The model was then be used to demonstrate the effectiveness of the flat decking profile compared to two typical decking profiles i.e. trapezoidal and re-entrant profile. The results are shown in Figure 8. It can be seen that the temperature at the bottom of three types of decking are almost identical. This is a reasonable result since the bottom surface was directly exposed to the fire. However, there is a significant difference when comparing the temperature of the top decking flange among the three cases. While the top flange temperature of trapezoidal and re-entrant decking are close to those of the bottom decking, the top flange temperature of flat decking is much lower. After two hours of fire, the flange temperature is less than 600^{o}C. This explains why the typical profile deckings are normally neglected in fire resistance calculation. It should be noted that there is significant area of the top flange (with low temperature) for the flat decking profile, i.e. 112mm^2 for 300mm wide slab based on 1mm thick decking. This steel area can be considered as fire reinforcement

Furthermore, at the level of anti-crack mesh, the temperature development of the flat decking is the lowest among the three profiles. Note that when the elastic modulus of steel starts to deteriorate after 200^{o}C, the flat decking is not only stronger but also has lower rotation near columns and main beams where hogging moment is a dominant force. Therefore, the deformation of flat profile decking slab would be lesser to that of commonly used types.

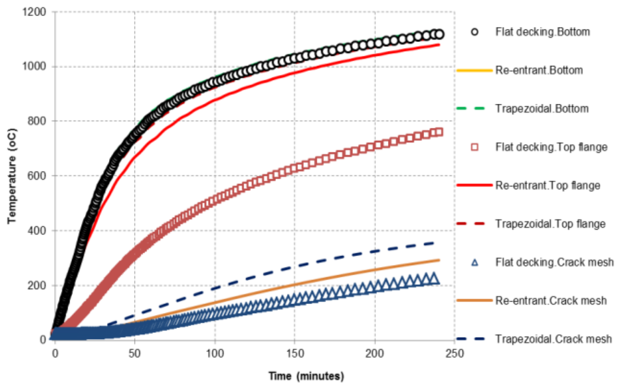

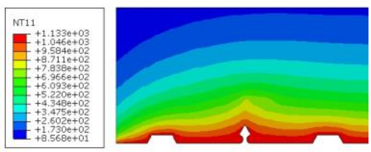

Temperature distribution of flat decking

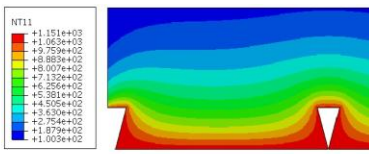

Temperature distribution of Re-entrant decking

Figure 8. Bottom of a specimen subjected to three hours ISO-834 standard fire.

4 EMPIRICAL FOMULATION FOR TEMPERATURE PROFILE

Using the current design procedure proposed in EC4.P1-2 (2005), the study proposed a set of empirical formulation of temperature profile across the slab for design purpose. The empirical formulation for concrete temperature development is

$$T_{c,below\_rib\_height} = a \times x^2 + b \times x + c$$
$$T_{c,above\_rib\_height} = a \times (x-55)^2 + b \times (x-55) + c \qquad (2)$$

where T_c is the temperature of concrete in ^oC; x is the distance of the reference point to the bottom of slab in millimetre; *a, b* and *c* is the empirical factor determined based on a curve-fitting. The concrete temperature database of 328 data points is generated using both the experimental and test results. The result is presented in Table 2.

Table 2. Empirical parameter to determine the development of concrete.

For bellow rib height				For above rib height			
Rating (minutes)	a	b	c	Rating (minutes)	a	b	c
30	0.009	-1.9	127	30	0.08	-13	600
60	0.007	-1.6	170.75	60	0.23	-25	850
90	0.006	-2.05	243.25	90	0.23	-25.5	950
120	0.005	-2.25	290.25	120	0.21	-25	1030
150	0.003	-2.65	355	150	0.2	-24	1070
180	0.001	-2.85	434.5	180	0.18	-22	1100
210	0.001	-2.95	451.75	210	0.17	-21.5	1120
240	0.001	-3.15	494.125	240	0.165	-21	1150

The temperature development of top decking flange can be predicted using the following fomulae:

$$T_{s,topflange} = -0.0086 \times t^2 + 6.177 \times t + 49.08 \qquad (3)$$

where $T_{s,top\ flange}$ is the temperature of top flange in ^oC, and t is the fire duration time in minutes.

5 CONCLUSIONS

This paper presents a study on the temperature development of a flat decking slab in standard fire condition. The temperature profiles across the slab thickness were quantified experimentally and numerically for four different fire durations (1-, 2- 3- and 4-hours). The test showed that the slabs satisfy the integrity and insulation criteria according to EC4.P1-2. The experimental temperature measurements were used for calibration of FE models. The validated numerical model models were used to show the effectiveness of the flat decking compared to trapezoidal and re-entrant profiles. And finally, the test and FE results were to establish the temperature profile for design purpose.

ACKNOWLEDGEMENT

The authors want to express their gratitude to the financial support and test specimens from LCP Building Products Pte. Ltd for this study. The authors are also grateful to Mr. Johnny Lim for his discussion in the early stage of the experimental program.

REFERENCES

[1] Bailey, C.G. and D.B. Moore, *Structural behaviour of steel frames with composite floorslabs subject to fire: Part 1: Theory.* Structural engineer London, 2000. 78(11): p. 19-27.

[2] Both, C. and J.W.B. Stark. *Fire exposed composite steel-concrete slabs*. in *Proceedings of the Conference: Composite Construction in Steel and Concrete IV, May 28, 2000 - June 2, 2000*. 2000. Banff, Alta., Canada: American Society of Civil Engineers.

[3] Abu, A., V. Ramanitrarivo, and I. Burgess. *Collapse mechanisms of composite slab panels in fire*. in *6th International Conference on Structures in Fire, SiF'10, June 2, 2010 - June 4, 2010*. 2010. East Lansing, MI, United states: DEStech Publications Inc.

[4] Wald, F., et al. *To the composite slab on beams with corrugated web exposed to fire*. in *Final Conference on COST Action C26: Urban Habitat Constructions under Catastrophic Events, September 16, 2010 - September 18, 2010*. 2010. Naples, Italy: CRC Press/Balkema.

[5] Abu, A.K., I.W. Burgess, and R.J. Plank, *Tensile Membrane Action of Thin Slabs Exposed to Thermal Gradients.* Journal of Engineering Mechanics, 2013. 139(11): p. 99-109.

[6] LCP. L.PTE., *Structural steel deck - Design manual,* 2014, p. 20.

[7] Abu, A.K., I.W. Burgess, and R.J. Plank, *The effect of reinforcement ratios on composite slabs in fire.* Proceedings of the Institution of Civil Engineers: Structures and Buildings, 2012. 165(7): p. 385-398.

[8] Bailey, C.G., D.S. White, and D.B. Moore, *Tensile membrane action of unrestrained composite slabs simulated under fire conditions.* Engineering Structures, 2000. 22(12): p. 1583-1595.

[9] Cashell, K.A., A.Y. Elghazouli, and B.A. Izzuddin. *Failure criteria for composite slabs subject to extreme loading conditions*. in *6th International Conference on Advances in Steel Structures and Progress in Structural Stability and Dynamics, ICASS 2009, December 16, 2009 - December 18, 2009*. 2009. Hong Kong, China: The Hong Kong Institute of Steel Construction.

[10] Chung, K.F. and A.J. Wang. *Numerical modelling of composite slabs in fire - Thermal analyses*. in *5th International Conference on Advances in Steel Structures, ICASS 2007, December 5, 2007 - December 7, 2007*. 2007. Singapore, Singapore: Research Publishing Services.

[11] Guo, S., *Experimental and numerical study on restrained composite slab during heating and cooling.* Journal of Constructional Steel Research, 2012. 69(1): p. 95-105.

[12] Schaumann, P., et al., *Membrane action of composite slabs in fire - Numerical investigation Membranwirkung von Verbunddecken bei Brand - Numerische Untersuchungen.* Stahlbau, 2011. 80(12): p. 911-915.

[13] Zaharia, R., et al., *Numerical analysis of partially fire protected composite slabs.* Steel and Composite Structures, 2013. 14(1): p. 21-39.

[14] Huang, Z.-F., et al., *Fire resistance of composite columns with embedded I-section steel - Effects of section size and load level.* Journal of Constructional Steel Research, 2008. 64(3): p. 312-325.

8th International Conference on Structures in Fire
Guo-Qiang LI, Venkatesh K. R. KODUR, Shou-Chao JIANG, Jian JIANG, Su-Wen CHEN, Guo-Biao LOU (Eds.)
Shanghai, China, June 11-13, 2014

SOFTWARE FIRELAB FOR PROBABILISTIC ANALYSIS OF STEEL-FRAMED STRUCTURES IN FIRE

Shaun Devaney* and Asif Usmani*

* School of Engineering, The University of Edinburgh, The King's Buildings, Edinburgh EH9 3JL, UK
e-mails: s.devaney@ed.ac.uk, asif.usmani@ed.ac.uk

** Indian Institute of Science, Bangalore 560 012, India
email: manohar@civil.iisc.ernet.in

Keywords: FireLab, Software, Performance based design, Probabilistic design, Structural fire design

Abstract. *The analysis and design of structures in fire is a complex task which requires knowledge of a range of topics. In order for structural fire design to be applied in practice, engineers need access to educational material and design tools. This paper presents a software tool (FireLab) which has been developed with the aim of encouraging the use of structural fire engineering. FireLab allows engineers to design structural members under fire loading. FireLab features a range of fire models, heat transfer models and structural models. The tool also features a range of deterministic and probabilistic analysis options. Probabilistic analysis allows the designer to examine the effects of a wide range of loads and to calculate the probability of failure of the structure. This is a distinct advantage over prescriptive design where the level of safety is unquantifiable. Examples of the application of FireLab are given for simple structural members.*

1 INTRODUCTION

A software tool (*FireLab*) is presented that allows engineers to systematically use performance based engineering methods for fire resistance design of regular steel framed composite buildings while also accounting for uncertainties in key design parameters. FireLab may be used to check if a structural element can withstand specific load combinations or it may be used to quantify the probability of failure of an element. It features a range of fire models, heat transfer models and structural models (Figure 1). The temperature-time data from the chosen fire model is fed into heat transfer models in order to calculate the temperature distributions within the structural members. Finally a suitable structural analysis model is used to calculate the response of the structure. The output of the software tool varies depending on the type of analysis chosen. Deterministic analyses output deformations or stresses and strains. Probabilistic analyses output information on the mean deformations or stresses and strains, as well as the probability of failure.

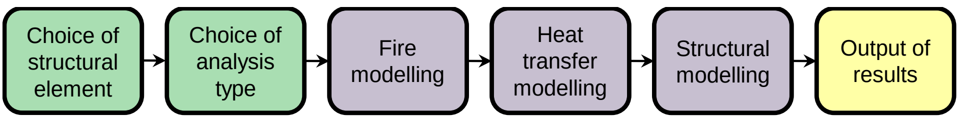

Figure 1. Outline of the program procedure.

FireLab includes probabilistic analysis methods for evaluating the reliability of structures subject to fire. In-built methods include Monte Carlo simulation, First Order reliability method and a performance based engineering methodology based on the PEER-PBEE framework [1,2]. An example application of the program for the analysis of two typical structural members is presented.

2 FIRE MODELS

FireLab features the standard temperature-time curve, the hydrocarbon temperature-time curve and the parametric temperature-time curve (all taken from the Eurocodes) [3]. Also included is the temperature-time curve specified in the JCSS model code [4]. The parametric temperature-time curve is most suited to stochastic analysis as it allows the inputs to be varied and is capable of producing a wide range of outputs. Important inputs such as the fuel load and area of ventilation may be specified as stochastic variables in order to produce a library of possible fires. The range of different fire curves are shown below in Figure 2.

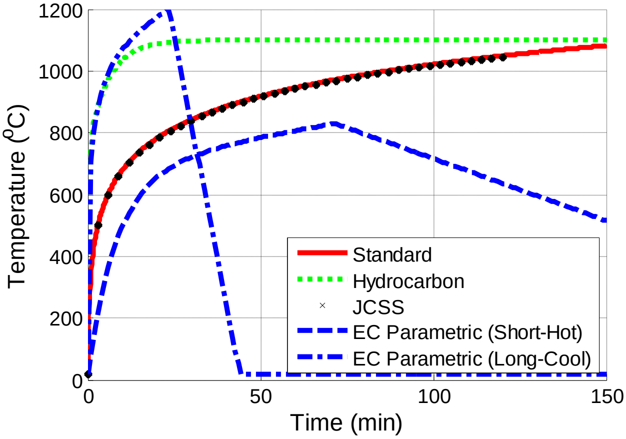

Figure 2. Comparison of the various in-built fire curves.

3 HEAT TRANSFER MODELS

Heat transfer methods have been incorporated into the program for calculating the temperature of typical structural elements. Lumped capacitance methods have been incorporated for calculating the temperature of steel sections [5]. A one dimensional finite difference approach has been implemented for calculating the temperature distribution through the depth of a concrete slab [6]. Steel reinforcement temperatures are assumed to be equal to the temperature of the surrounding concrete.

4 STRUCTURAL MODELS

The software tool is aimed at analyzing steel framed composite buildings. Three different types of structural analyses are possible using solvers programmed into FireLab: a steel-concrete composite beam, a composite slab and tall building frame stability under multiple floor fires. The built-in structural analysis is analytically based in order to reduce both the complexity and the run-time of the analysis so that it remains practical to run a large number of analyses to adequately resolve the uncertain parameters chosen.

Two analytical solution methods have been implemented that allow the composite beam to be modeled either with or without fire protection. The first method is based on an approximate "engineering approach" using finite slices of the composite section and a "plane sections remain plane" assumption to determine forces and displacements in the beam [7]. The second method is based on a method by Cameron and Usmani [8] developed from the solution of the differential equations of a beam under thermo-mechanical loading under large displacement assumptions.. Three methods have been implemented for the analysis of composite slabs. The first is a method developed by Cameron and Usmani, similar to the beam method mentioned above [9]. The second is a method developed by Bailey at the BRE and the third is a method developed by Omer, Izzuddin and Elghazouli [10,11]. The third analysis option uses a nonlinear direct stiffness method solution to analyse a multi-storey column under vertical loading from floors above the fire floors and horizontal loading from adjacent fire affected floors.

To make the software of greater general interest, interfaces have been developed for finite element analysis using either OpenSees [12] or Abaqus [13], which can be used to carry out similar analyses for more complex and more general structural configurations. Three structural materials are defined: concrete, structural steel and reinforcing steel. All three materials are temperature dependent and are based on the Eurocode material definitions [14,15]. The concrete may be defined as calcareous, siliceous or lightweight. In addition to specifying a nominal value for any of the material parameters the user may opt to treat the parameter as a stochastic variable and may also specify a distribution type and a coefficient of variation.

5 PROBABILISTIC METHODS

FireLab offers a variety of probabilistic analysis methods. The simplest type of probabilistic analysis calculates the probability of failure of an element. The probability of failure may be calculated using either Monte Carlo (MC) simulation or the first-order reliability method (FORM) [16]. Monte Carlo simulation is a process based on the repeated random sampling of the inputs in order to calculate the likelihood of occurrence of the outputs. FireLab uses Latin hypercube sampling when producing the inputs in order to ensure that the chosen input values are representative of the true variability of the input parameters [17]. This sampling process improves the rate of convergence of the MC simulation. FORM may be used as an alternative to MC simulation. FORM is based on the repeated evaluation of the performance function, in order to find the point on the limit state surface that is most likely to occur [18]. The software tool also features a framework for the evaluation of the expected annual cost (related to accidental fire events) associated with a design [2]. This framework is based on the PEER framework from earthquake engineering [1]. The costs may be considered as monetary losses and/or downtime due to repair.

6 EXAMPLE

An 8-storey steel framed composite building, which represents a typical UK office building, has been chosen as an example case in order to illustrate the use of the software for probabilistic analysis. Full details on the design assumptions, layout and construction details are given in the SCI report "Comparative Structure Cost of Modern Commercial Buildings". The use of these methods is based on a set of requirements:

- The loads are assumed to be transferred from the slab to the beams and onto the columns. The capacity of each part of this load path must be checked.
- The floor slab must be divided into rectilinear panels which are supported on all sides by protected beams.
- All edge beams and beams connecting to columns are assumed to be protected, to prevent disproportionate collapse.
- The slab panels are assumed to be restrained against lateral translation along the boundaries, but free to rotate.
- The structure should meet the reliability requirements set out in the Eurocodes. The maximum failure probability of an office type building with a 55 year design life is 7.23×10^{-5} [19,20].

The building features a regular column grid laid out on 7.5m by 7.5m spacings, as shown in Figure 3. The maximum size of each of the individual slab panels is illustrated with red broken lines and further possible sub divisions of the slab are shown with a yellow broken line. The size of the panel defines the area considered in the slab analysis and is defined by the presence of supporting beams. Shown in Figure 3 are the slab area to be analysed and the beam area to be analysed.

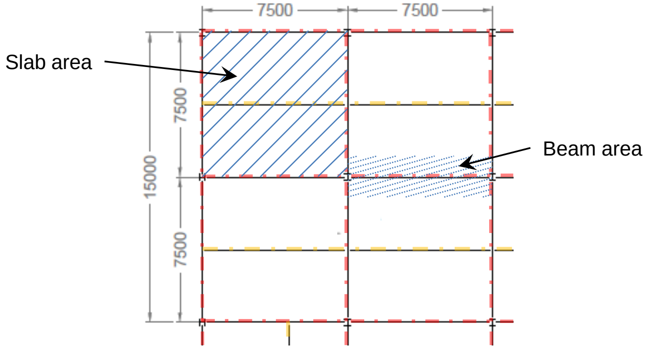

Figure 3. Partial floor plan showing the required slab boundaries marked by broken red lines and possible additional boundaries marked by broken yellow lines.

6.1 Slab analysis

The slab is analyzed for two different design options; in the first the secondary beam is left unprotected and the slab is assumed to span 7.5 × 7.5 metres and in the second option the secondary beam is assumed to be protected and the slab dimensions are taken as 7.5 × 3.75 metres. An initial Monte Carlo analysis was undertaken for both design cases, each consisting of 10000 runs. The important input variables were identified through a one-way sensitivity analysis prior to running the Monte Carlo simulation and these variables were treated as stochastic inputs, as described in Table 1 below.

The parametric temperature-time curve from Eurocode 1 was used as the fire model, with the area of ventilation and the fuel load modelled as stochastic variables [3]. This provided a wide range of variation in the applied fire load. Heat transfer to the structure was carried out using a 1-D finite difference formulation for heat transfer through the depth of the slab. Temperature dependent material models were used for all of the materials and important material parameters such as the Young's modulus of concrete were treated as stochastic variables. The inputs defining the geometry of the beam, such as the length, breadth, depth and depth to the rebar were also treated as stochastic variables.

The performance of the slab was judged based on the maximum mechanical strain occurring in the steel reinforcement. This analysis is concerned with evaluating the likelihood of collapse; therefore the performance limit is taken as the ultimate strain capacity of the reinforcement bars. Eurocode 2 states that reinforcement with a diameter of less than 12mm should have an ultimate strain capacity of 2.5% [21]. The results of the initial Monte Carlo analysis are shown below in Figure 4. The 7.5m × 7.5m slab with no support from the secondary beam clearly does not meet the performance limit, whereas the results of the 7.5m × 3.75m slab simulation are less than the limiting strain.

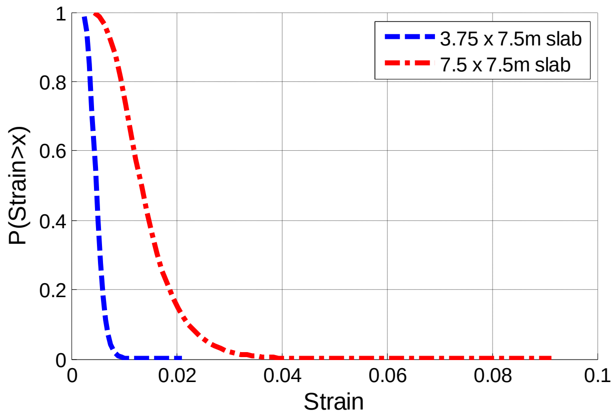

Figure 4. Comparison of strain exceedence curves for both slab cases.

A second Monte Carlo simulation of 500000 runs was then carried out to find an accurate estimate of the probability of failure of the rectangular slab. The probability of failure from this simulation was found to be 7×10^{-5}, which meets the Eurocode reliability requirements.

6.2 Composite beam analysis

The stochastic analysis of a composite beam exposed to fire, with various levels of protection, is presented as an example application of the program. The beam is a typical steel-concrete composite beam (Figure 5). An initial Monte Carlo analysis of the beam was conducted with three different thicknesses of fire protection applied to the beam; no protection, 12.5mm of protection and 25mm of protection. The Monte Carlo simulation of each beam consisted of 10000 runs. Several of the input variables were treated as stochastic variables, based on the results of a one-way sensitivity analysis.

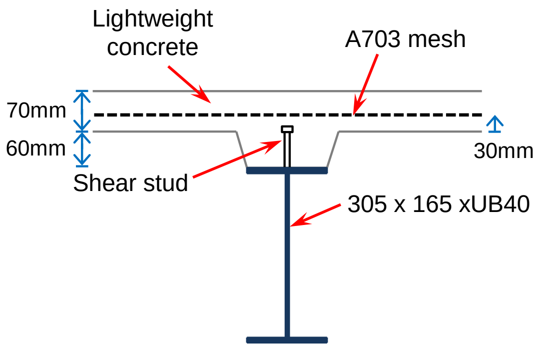

Figure 5. Cross section of the composite beam.

The parametric temperature-time curve was used, with the same inputs as those used for the slab analysis above. Heat transfer to the structure was carried out using lumped capacitance methods for the steel beam and a 1-D finite difference formulation for heat transfer through the depth of the slab.

Table 1. Stochastic inputs.

Model	Variable	Units	Distribution type	Distribution parameter 1	Distribution parameter 2
Fire	Fuel load	MJ/m^2	Gumbel	363.29 (mode)	98.24 (scale)
Fire	Area of ventilation	m^2	Truncated log-normal	60 (upper limit)	0.25 (standard deviation)
Beam	U.D.L.	N/m	Gumbel	5054.9 (mode)	1637.4 (scale)
Beam	Length of beam	m	Log-normal	7.500 (mean)	0.005 (C.o.V.)
Beam	Depth to the rebar	m	Gaussian	0.04 (mean)	0.02 (C.o.V.)
Beam	Young's modulus of steel	kN/mm^2	Log-normal	210 (mean)	0.03 (C.o.V.)
Beam	Young's modulus of concrete	kN/mm^2	Log-normal	35 (mean)	0.15 (C.o.V.)
Beam	Yield stress of the rebar	N/mm^2	Log-normal	562.3 (mean)	0.07 (C.o.V.)
Slab	U.D.L.	kN/m^2	Gumbel	3.7912 (mode)	1.2280 (scale)
Slab	Length of slab	m	Log-normal	7.50 (mean)	0.005 (C.o.V.)
Slab	Width of slab	m	Log-normal	3.75 (mean)	0.005 (C.o.V.)
Slab	Depth of slab	m	Log-normal	0.07 (mean)	0.005 (C.o.V.)
Slab	Depth to the rebar	m	Gaussian	0.04 (mean)	0.02 (C.o.V.)
Slab	Young's modulus of concrete	kN/mm^2	Log-normal	35 (mean)	0.15 (C.o.V.)

Two different models were used to carry out the structural analysis; a model based finite slices of the section was used for the protected sections and a model based on the catenary capacity was used for the unprotected section [7, 22]. The results of the Monte Carlo simulations may be used to calculate the mean performance of the beam, to calculate the nominal probability of failure of the beam or to examine the full range of behaviour of the beam. Figure 6 shows the complementary cumulative distribution functions for the maximum midspan deflection of each beam. These curves were derived from the results of the Monte Carlo simulations. They show that, given the occurrence of a well-developed fire, an unprotected beam will suffer from large deflections. It also shows that applying a basic level of fire protection to the steel beam will lead to much lower levels of deflection but doubling the basic level of fire protection yields a negligible increase in the deflection performance of the beam.

The performance of the composite beam is evaluated against a limiting deflection, which is taken as the deflection at which the steel reinforcement reaches its ultimate strain capacity. The method for calculating the limiting deflection is given in Equation (1).

$$w_{\lim} = \frac{L}{\pi}\sqrt{4\varepsilon_{\lim}} \tag{1}$$

where w_{lim} is the limiting deflection, L is the length of the beam and ε_{lim} is the limiting strain. A second Monte Carlo simulation was undertaken in order to obtain an accurate estimate of the probability of failure of the composite beam with 12.5mm of protection. This simulation consisted of 500000 runs. The final probability of failure of the beam with 12.5mm of fire protection applied was found to be 1.6×10^{-5}, which is within the limits of the Eurocodes.

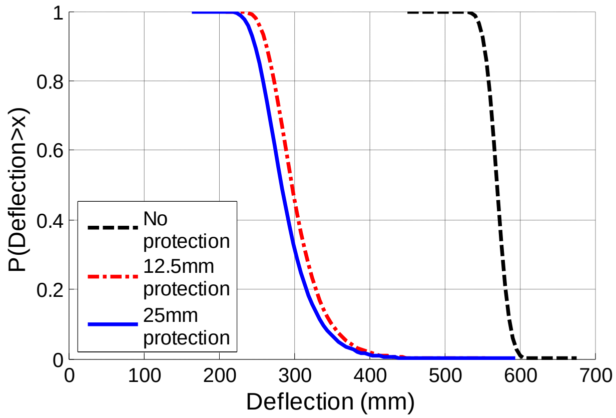

Figure 6. Deflection exceedence curves for each composite beam design option.

The analyses discussed above considered the structural performance of the composite beam and slab within the office structure. A full analysis of the structure would also require the analysis of the columns to ensure that they are capable of carrying the loads from the weakened beams. It is important to note that the connections between steel elements can suffer large forces and deformations during a fire and these should be also considered during the design process.

7 CONCLUSIONS

A software tool (FireLab) has been presented for the performance based design of steel-framed structures in fire. The tool features a variety of fire models, heat transfer models and structural analysis models. Interfaces to external finite element software have been created to allow for the analysis of a broader range of problems involving heat transfer and structural analysis. The tool may be used to carry out deterministic or probabilistic analysis of composite beams, slabs or tall building stability based on analytical solutions built-in to the software, it may also be used to carry out probabilistic analyses for more general steel frame structures through the interfaces provided for OpenSees and Abaqus. Available probabilistic methods include Monte Carlo simulation, FORM and the PEER framework. An example application of using FireLab for the stochastic analysis of a composite beam and slab within a typical office building has been presented. Initial analyses were used to evaluate the performance of various design options. A preferred design option for both the beam and slab was then chosen and comprehensive analyses were conducted in order to establish an accurate estimate of the reliability of these components.

ACKNOWLEDGEMENTS

This work was supported by Tata Steel Europe and the EPSRC in the form of an Industrial CASE award for Mr Shaun Devaney and their support is gratefully acknowledged.

REFERENCES

[1] K. A. Porter, “An Overview of PEER’s Performance-Based Earthquake Engineering Methodology,” in *Ninth International Conference on Applications of Statistics and Probability in Civil Engineering (ICASP9)*, 2003, no. 1995.
[2] D. Lange, S. Devaney, and A. Usmani, “An application of the PEER performance based earthquake engineering framework to structures in fire,” *Eng. Struct.*, vol. 66, pp. 100–115, 2014.
[3] “BS EN 1991-1-2:2002. Eurocode 1: Actions on structures - Part 1-2: General actions-Actions on structures exposed to fire.” BSI, 2002.
[4] “JCSS Probabilistic Model Code - Part 2: Load Models.” The Joint Committee on Structural Safety, p. 73, 2001.
[5] A. Buchanan, *Structural Design for Fire Safety*. Wiley-Blackwell, 2001, p. 444.
[6] D. Drysdale, *An Introduction to Fire Dynamics*, Third Ed. John Wiley & Sons, Ltd., 2011.
[7] A. S. Usmani, “Understanding the Response of Composite Structures to Fire,” *Eng. J.*, vol. Second Qua, pp. 83–98, 2005.
[8] N. J. K. Cameron, “The Behaviour and Design of Composite Floor Systems in Fire,” The University of Edinburgh, 2003.
[9] N. J. K. Cameron and A. S. Usmani, “Ultimate Capacity of Composite Floor Slabs at the Fire Limit State,” in *Proceedings of Designing Structures for Fire*, pp. 217–226.
[10] C. G. Bailey, “Membrane action of unrestrained lightly reinforced concrete slabs at large displacements,” *Eng. Struct.*, vol. 23, no. 5, pp. 470–483, May 2001.
[11] E. Omer, B. A. Izzuddin, and A. Y. Elghazouli, “Failure of Lightly Reinforced Concrete Floor Slabs with Planar Edge Restraints under Fire,” *J. Struct. Eng.*, vol. 135, no. 9, pp. 1068–1080, 2009.
[12] “OpenSees.” University of California, Berkeley.
[13] Abaqus, “Abaqus analysis user’s manual.” Dassault Systemes, Simulia Corp., Providence, 2008.
[14] “BS EN 1993-1-2:2005. Eurocode 3: Design of steel structures - Part 1-2: General rules - Structural fire design.” BSI, Sep-2005.
[15] “BS EN 1992-1-2:2004. Eurocode 2: Design of concrete structures — Part 1-2: General rules - Structural fire design.” BSI, 2004.
[16] R. E. Melchers, *Structural Reliability Analysis and Prediction*, Second. John Wiley & Sons, 1999.
[17] M. D. McKay, R. J. Beckman, and W. J. Conover, “A Comparison of Three Methods for Selecting Values of Input Variables in the Analysis of Output from a Computer Code,” *Technometrics*, vol. 21, no. 2, pp. 239–245, 1979.
[18] O. Ditlevsen and H. O. Madsen, *Structural Reliability Methods*, 2nd ed., no. July. John Wiley & Sons, Ltd., 2005, p. 363.
[19] “IMPLEMENTATION OF EUROCODES - Handbook 2: Reliability Backgrounds.” Leonardo Da Vinci Pilot Project, p. 254, 2005.
[20] “BS EN 1990: 2002. Eurocode - Basis of structural design.” BSI, 2002.
[21] “BS EN 1992-1-1:2004. Eurocode 2: Design of concrete structures - Part 1-1: General rules and rules for buildings.” BSI, 2004.
[22] A. S. Usmani and N. J. K. Cameron, “Limit Capacity of Laterally Restrained Reinforced Concrete Floor Slabs in Fire,” *Cem. Concr. Compos.*, vol. 26, no. 2, pp. 127–140, Feb. 2004.

8th International Conference on Structures in Fire
Guo-Qiang LI, Venkatesh K. R. KODUR, Shou-Chao JIANG, Jian JIANG, Su-Wen CHEN, Guo-Biao LOU (Eds.)
Shanghai, China, June 11-13, 2014

AN INTEGRATED MODELLING STRATEGY BETWEEN FDS AND SAFIR: THE ANALYSIS OF THE FIRE PERFORMANCE OF A COMPOSITE STEEL-CONCRETE OPEN CAR PARK

Nicola Tondini*, Andrea Morbioli*, Olivier Vassart, Sullivan Lechêne*** and Jean-Marc Franssen******

* Department of Civil, Environmental and Mechanical Engineering, University of Trento, Italy
e-mails: nicola.tondini@unitn.it, andrea.morbioli@unitn.it

** R & D Long Product, Arcelormittal, Luxembourg
e-mail: olivier.vassart@arcelormittal.com

*** Centre Scientifique et Technique du Bâtiment (CSTB), France
e-mail: sullivan.lechene@cstb.fr

**** Structural Engineering Department, University of Liege, Belgium
e-mail: jm.franssen@ulg.ac.be

Keywords: CFD-FE coupling, Open car parks, Steel structures, Fire behaviour

Abstract. *This paper analyses the fire performance of a composite steel-concrete open car park performed by exploiting an integrated modelling strategy developed between the Computational Fluid Dynamics (CFD) code Fire Dynamics Simulator (FDS) and the Finite Element (FE) software SAFIR. First, it concisely presents the assumptions and the issues that arise when developing an integrated modelling methodology between a CFD software applied to fires in compartment and a Finite Element (FE) software applied to structural systems with particular emphasis on the FDS-SAFIR weak coupling approach. Then, in order to show the potential benefits of such a methodology, a multi-storey composite steel-concrete open car park was designed according to the Eurocodes for which simplified localised fire models are in their range of applicability. Thus, a typical design approach employing the Hasemi model is compared with a more advanced analysis that relies on the proposed FDS-SAFIR coupling. Results are thoroughly presented in the paper.*

1 INTRODUCTION

The possibility to apply a performance-based approach for fire design of structures as foreseen by the EN1991-1-2 provisions [1] allows employing natural fire curves that are established on physically based thermal actions. For instance, the simplified Hasemi localised fire model [2] and incorporated in [1] is suitable for analysing the fire performance of open car parks. It provides the heat flux at the ceiling level; thus, being appropriate for beams and slab. However, simplified models that provide information about the thermal action along the height of a column owing to localised fires are not yet available and cautionary assumptions are usually taken. As a result, this may lead to a conservative fire design. In order to overcome this issue, Computational Fluid Dynamics (CFD) advanced fire models that are capable of an accurate modelling, both in time and in space, of the fire development represent a tempting alternative.

2 PROPOSED WEAK COUPLING METHODOLOGY

In this section, a concise description of the proposed methodology is presented. For an exhaustive presentation, the interested reader may refer to Tondini et al. [3]. In the developed weak coupling (or one-way) approach the mutual interactions are discarded, as illustrated in Figure 1. The CFD software models the fire development, while the FE program performs the thermal and the mechanical analyses. The fire development is calculated independently of the thermal response in the linear elements of the structure such as, for example, steel columns, beams or truss girder. If part of the structure is made of planar elements that also constitute boundaries of the compartment such as, for example, concrete walls or slabs, they must be modelled, perhaps with some degrees of approximation, in the fire development analysis. The detailed temperature field in these structural elements will nevertheless be computed subsequently by the FE software.

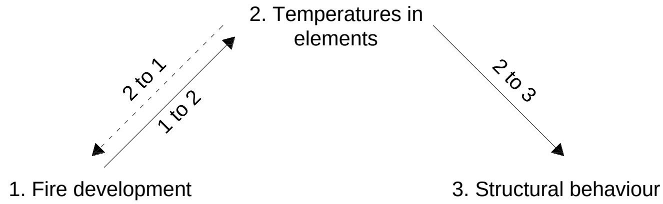

Figure 1. Weak coupling strategy between the main phenomena involved in a compartment fire.

Nonetheless, these simplifications imply some limitations:

(1) the dimensions of the structural elements and their displacements perpendicular to their longitudinal axis must be small compared to the dimensions of the compartment in order not to significantly influence the temperatures and the air flow around the elements.

(2) It is possible, for each 2D thermal analysis, to consider the boundary conditions at the surface of the section at the same point, namely the point of the section located on the node line of the beam element, for example at the centre of gravity of the section. This is consistent with the fact that the structure is not present in the CFD analysis.

(3) Generally, in the CFD model the dimensions of a parallelipedic compartment correspond to the clear distances between opposite walls. However, in the FE model a slab is generally modelled in correspondence to its centreline. Thus, the slab would fall outside the CFD domain and assumptions have to be made in order to determine thermal information at the slab centreline. In this methodology, if any structural points fall outside the CFD domain for the reason described above, they are moved to the closest boundary of the CFD domain where the Cartesian interpolation can be made, namely the boundary corresponding to the centre of the outermost cells because FDS provides the information at the centre of cells.

(4) Since the structure is not included in the CFD model, the effect of shielding from any structural elements on others cannot be detected.

(5) Irrigated structures in which water is circulating in order to keep the temperature of the structure within acceptable limits cannot be neglected because they may contribute in evacuating important amount of energy from the compartment.

This procedure is thus particularly well adapted for metallic structures made of relatively thin members (frame, truss girders) and located in very large compartments (railway or airport entrance halls, exhibition halls) where a localised fire is developing and simplified thermal models, such as those proposed in EN1991-1-2 [1], cannot be employed because the geometry of the compartment is too complex or the position of the structure in the compartment or with respect to the position of the fire is not within the field of application of simplified model. In this case, the application of the Hasemi model poses the issue about the definition of the thermal action along the height of the column. Thus, the application of a CFD-FE coupling represents an appealing alternative. All assumptions were scrutinised and discussed in the paper.

3 DESCRIPTION OF THE OPEN CAR PARK

The structure is a four-storey steel-concrete composite open car park. The elevation and plan layouts are illustrated in Figure 2. The steel-framed structure was designed according to the Eurocodes and was made of steel grade S275, of a composite slab of concrete class C25/30 and profiled steel sheets, of secondary beams IPE 400 and IPE 450, of primary beams IPE 500 and IPE 400 and of steel columns HEB 200, HEB 220 and HEB 240. Moreover, it was assumed the structure as braced. An adequate degree of openings along the perimeter was allowed for the car park to be classified as open. Both primary and secondary beams were considered as simply supported whilst columns were continuous along their entire height. No fire protection was applied to the structure.

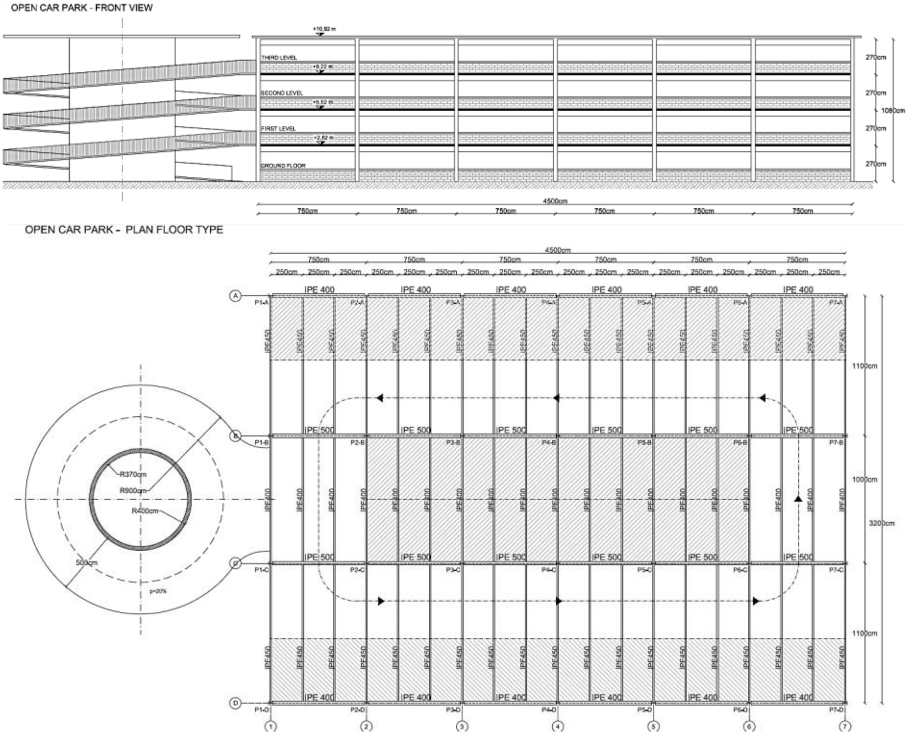

Figure 2. Elevation and plan views of the car park.

4 DEFINITION OF FIRE SCENARIOS

Different fire scenarios with a variable number of vehicles assuming Rate of Heat Release (RHR) curves representative of burning cars of Class 3 were considered [4]. Taking into account the car park layout, the most critical scenarios were analysed, three of them are shown in Figure 3. When multiple cars were involved into a fire, a time shift ignition between nearby cars was envisaged as observed in real car fires. As a result, the ignition of cars just next to the first that ignites the fire was delayed of 12 min. Moreover, it is worth pointing out that worst fire scenario for the column, i.e. four cars burning cars around it, was not considered because of the car park layout. In fact, the likelihood of occurrence of this scenario is very low owing to the absence of face-to-face parking spots around the column, see Figure

2(b). Then, based on the definition of the significant fire scenarios the two approaches, i.e. Hasemi model and FDS-SAFIR coupling, were employed.

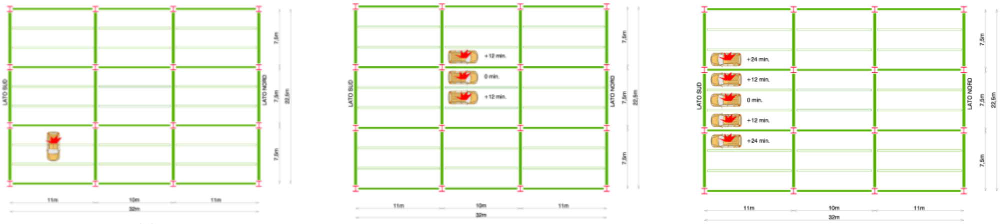

(a) (b) (c)

Figure 3. Significant fire scenarios for half car park: (a) one car in the driveway under a secondary beam FS1; (b) three cars parked close to the column with central car ignites first FS2; (c) five cars with central car ignites first FS3.

5 3D FINITE ELEMENT MODEL

In order to evaluate the fire performance of the open car park, a 3D FE model was developed in SAFIR [5]. Since the deterministic fire scenarios for car parks, as provided in [4], are localised fires, only a small part of the car park could be significantly influenced by each fire scenario. Thus, half of it was actually modelled and boundary conditions that guaranteed slab continuity were applied. Moreover, it is very unlikely that a fire could spread to all floors; consequently, only the 2nd one was modelled, also relying on the fact that the slab was capable of preventing any fire spread.

The slab was modelled by means of shell elements, whereas beams were modelled with Bernoulli beam elements. In order to take into account the column continuity, the columns of the floor above were also included into the model, as illustrated in Figure 4, and they were kept at ambient temperature. In the Figure 4 two critical sections are highlighted: i) the top section of the nearest column to the fire (point HEB220); and the section of the secondary beam that under the critical fire scenario experiences the largest vertical displacement (point IPE400). In the remainder of the article, comparisons were made at such points.

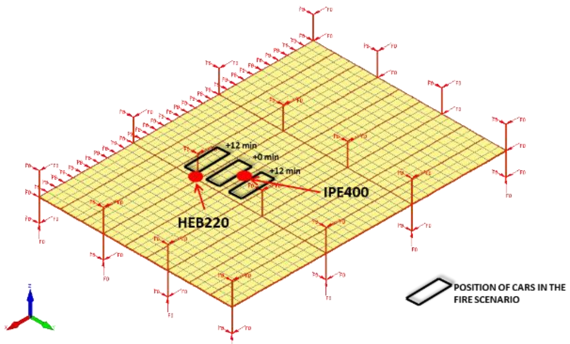

Figure 4. 3D finite element model of half car park and positions of the cars in FS2.

6 FIRE ANALYSIS OF THE CAR PARK WITH THE HASEMI MODEL

The study of the fire performance of the car park was initially carried out by analysing it under all significant fire scenarios by means of the Hasemi model. This allowed the identification of the most critical one that was then analyzed through the application of the FDS-SAFIR integrated strategy. This way of proceeding was pursued because the FDS-SAFIR coupling is more computationally demanding and time consuming. Furthermore, SAFIR already implements the Hasemi model; thus it results quite handy to perform such an analysis.

6.1 Thermal analysis

Thermal analyses were conducted on each structural element: slab, columns and beams. Primary beams were considered exposed on 3 sides with the slab on top of them whilst secondary beams were exposed on 4 sides since more than 15% of the top flange was not covered by the steel sheet of the slab. The slab on the top of the primary beams was used in thermal analyses for reproducing the non-uniform temperature distribution in the section. However, in the mechanical analyses it was not effective because the slab was already modelled by means of shell elements. In the absence of a simplified model, a cautious thermal action was applied along the entire height of the column and equal to the heat flux determined at its summit with the Hasemi model. This is certainly a conservative approach but widely used in the design practice. As an a result, the temperature distribution at failure in the HEB220 column top section and in the critical section of the IPE400 secondary beam owing to FS2, as depicted in Figure 3, is shown in Figure 5.

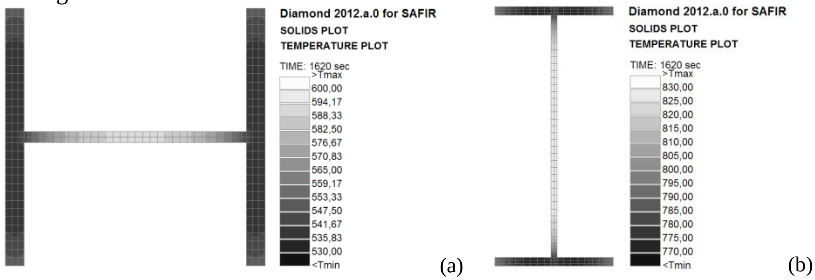

Figure 5. Hasemi model – FS2: temperature distribution in significant sections at failure (t = 27 min): (a) at the top of the HEB220 column; (b) in the IPE400 secondary beam.

6.2 Mechanical analysis

From the results of the mechanical analyses performed for each fire scenario, it was found out that FS2 was the most critical one as it entailed the collapse of the HEB220 column directly located next to the burning cars. FS3 also caused structural failure but later on in the analysis because of a larger time shift in the ignition of cars next to the column. The deformed shape of the structure at collapse (t = 27 min) is illustrated in Figure 6(a). Fig. 6b shows the evolution of the vertical displacements at the sections of the column and of the secondary beam highlighted in Figure 4.

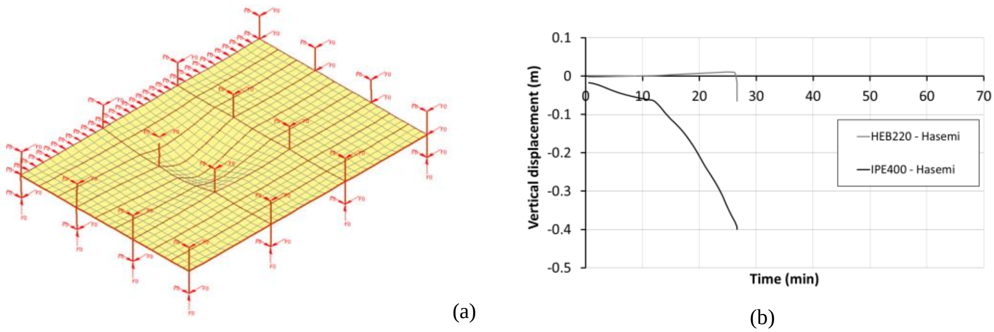

Figure 6. Hasemi model – FS2: (a) deformed shape at failure amplified by 5; (b) vertical displacements at the critical sections of the HEB220 column and of the IPE400 secondary beam.

7 FIRE ANALYSIS OF THE CAR PARK WITH THE FDS-SAFIR COUPLING

7.1 Modelling of the fire development

The same portion of the car park was modelled in FDS and the fire development under the most significant scenario (FS2) was analyzed. According to the proposed strategy no structural elements across the compartment were included in the CFD model, see Figure 7(a). Thus, the influence of columns and beams on the smoke flow was initially neglected. The boundary conditions were consistently modelled with physical parameters that described the thermal properties of the concrete slab, floor and parapets. The burning cars were simulated by assigning to obstructions located at 30 cm from the floor, i.e. the wheel mean height, the relevant Class 3 car RHR curve according to the INERIS document [4]. The mesh of the compartment was selected by means of a sensitivity analysis to provide an adequate grid capable of accurately modelling the characteristics of the localised fire. Figure 7(b) shows the temperature evolution with different cell grid dimensions at the ceiling level above the 3-car fire with slightly time modified RHR in order to reach the peak in a shorter time. The difference in temperature is very small between the two grids; thus, a $15\times15\times15$ cm^3 mesh grid seemed to be adequate to model such a localized fire. Furthermore, the capability of this mesh to accurately represent the localized fire was also verified according to Ma and Quintiere [6] and to the guidelines included in the FDS user manual [7] that confirmed its adequacy.

At the end of the analysis, the transfer file with the relevant information about the fire development was created in order to be exploited by SAFIR for the thermal and mechanical analyses.

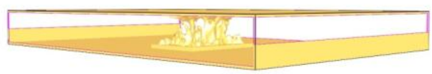

(a)

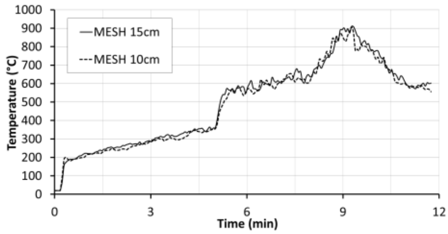

(b)

Figure 7. FDS-SAFIR – FS2: (a) fire development modelling; (b) temperature development at the ceiling level with different mesh grids owing to a Class 3 3-car time shifted fire.

For this structure, the ratio between the beam and the ceiling heights suggested an additional analysis that included the beams in the CFD model as they likely act as a barrier that traps the hot gases to some extent influencing the smoke flow. Hence, the effect of modelling the beams in the CFD model was analysed. They were approximately and conservatively included into the CFD model by means of adiabatic surfaces of the same height of the actual beams. Then, the fire development analysis was re-run and the results of the two analyses are compared in Figure 8. In particular, the qualitative temperature distribution at the ceiling level in the compartment after 30 min and the gas temperature evolution around the top of the nearest column to the fire, i.e. HEB220 in Figure 4, are shown. As expected, the influence of the beams on the smoke flow is present and locally the increase in gas temperature is not negligible. Therefore, for this structural typology the influence of the CFD modelling of beams has always to be carefully checked. Nonetheless, it will be shown that this local effect on the global mechanical behaviour is small.

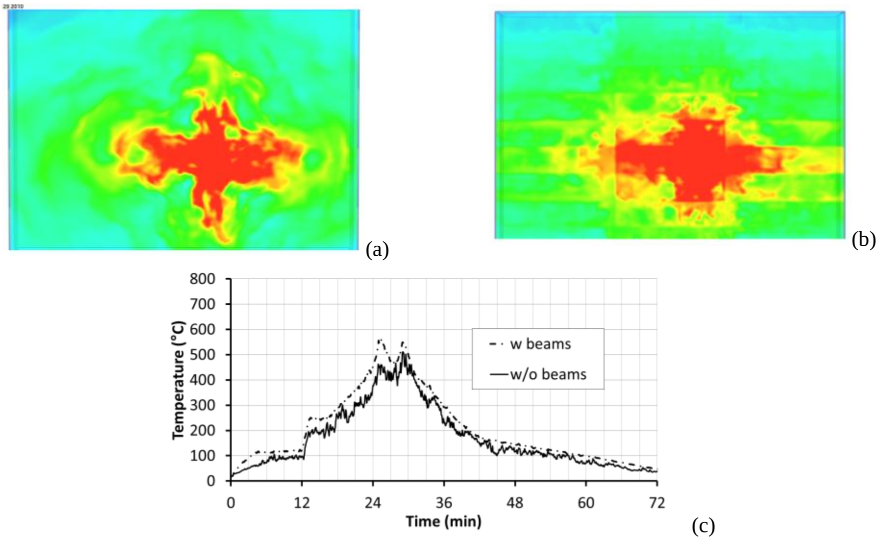

Figure 8. FS2 fire development: (a) qualitative gas temperature distribution at ceiling level at 30 min without including beams; (b) qualitative gas temperature distribution at the ceiling level (2.5 m) at 30 min including beams; (c) gas temperature evolution around the top of the HEB220 column (2.5 m) without (w/o) and with (w) beams included in the CFD model.

7.2 Thermal analysis

The data obtained from the CFD analyses were then exploited by SAFIR in order to perform the thermal analyses in each section. The results in the significant sections of the most critical elements are shown in Figure 9 and 10(a). From Figure 10(a), it is possible to note that the temperatures produced by the Hasemi model are much higher than those obtained from CFD data. The main reasons of this marked difference are the following: (1) the Hasemi model has been derived by means of experimental tests performed with a ceiling made of perlite boards, i.e. an insulating material, so that heat absorption through the ceiling was negligible whereas the concrete slab behaves as a heat sink that causes a decrease in gas temperature at the ceiling level; (2) the Hasemi model implicitly assumes that the flame impacts the ceiling but as observed in the CFD analysis and as estimated by the Heskestad model [1], it only occurs for about one sixth of the fire duration; (3) the flux computed by means of the Hasemi model was applied to structural sections without considering any shadow effects and flux orientation with respect to the position of the structural elements. The ability of the proposed methodology of taking into account flux orientation and shadow effects is clearly visible in Figure 9.

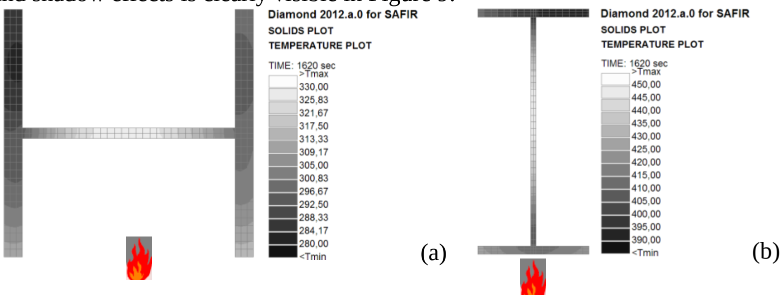

Figure 9. Temperature distribution at 27 min in the critical section: (a) of the column (HEB220) and (b) of the secondary beam (IPE400).

7.3 Mechanical analysis

The comparison of the mechanical analyses (Figure 10(b)) highlights that no failure occurred when the integrated strategy FDS-SAFIR was applied owing to a more realistic analysis of the fire development that resulted in lower thermal actions on structural elements, above all along the columns. The presence of the beams in the CFD model influences the smoke flow; however, they did not affect the global behaviour to a large extent, as illustrated in Figure 10(b).

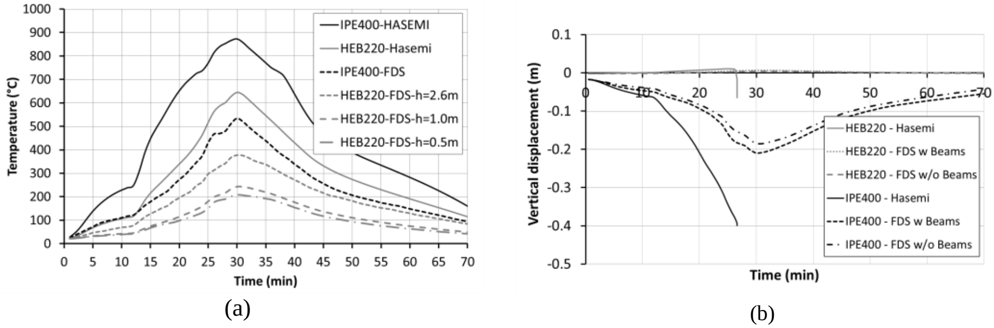

Figure 10. (a) Comparison of the temperature evolution in the web of critical sections of the column (HEB220) and of the secondary beam (IPE400); (b) comparison of the mechanical response of IPE400 and of HEB220 in their critical sections.

8 CONCLUSIONS

This study has shown the benefit of employing the proposed FDS-SAFIR integrated strategy. In fact, such a methodology allows overcoming shortcomings of simplified models by performing the thermal analysis in the structural elements based on a more realistic modelling of the fire development. Conversely, the Hasemi model revealed to be more conservative in terms of thermal action. In particular, its application entailed the collapse of the structure under study after 27 minutes, whereas by means of the proposed FDS-SAFIR integrated modelling the structure survived for the whole duration of the most critical fire scenario.

REFERENCES

[1] EN 1991-1-2: 2004, "Actions on structures – Part 1-2: General actions – Actions on structures exposed to fire".

[2] Pchelintsev A., Hasemi Y., Wakamatsu T., Yokobayashi Y., "Experimental and Numerical Study on the Behaviour of a Steel Beam under Ceiling Exposed to a Localized Fire", *Fire Safety Science – Proceedings of the fifth International Symposium*, 1153-1164, Melbourne, 1997.

[3] Tondini N., Vassart O. and Franssen J.-M, "Development of an interface between CFD and FE software", *7th International Conference on Structures in Fire*, ETH, Zurich, 459-468, 2012.

[4] INERIS, "Parcs de stationnement en superstructure largement ventiles. Avis d'expert sur les scénarios d'incendie", 2001.

[5] Franssen J.-M., SAFIR. A Thermal/Structural Program Modelling Structures under Fire, *Engineering Journal*, A.I.S.C., Vol 42, No. 3 , 143-158, 2005.

[6] Ma T.G. and Quintiere J.G., "Numerical simulation of axi-symmetric fire plumes: Accuracy and limitations", *Fire Safety Journal*, 38(5), 467-492, 2003.

[7] McGrattan K., Klein B., Hostikka S. and Floyd J., "Fire Dynamics Simulator (Version 5). User's guide", NIST, 2007.

FIRE-RESISTANCE OF REDULAR PYRAMIDIA GRID STRUCTURES EXPOSED TO LOCALIZED FIRE WITH NEW TEMPERATURE-TIME CURVE

Yong Du*, Xi Li* and Jing Gu**

* School of civil engineering, Nanjing Tech University, China
e-mails: yongdu_mail@njtech.edu.cn, lixi@njtech.edu.cn
** Shanghai Xian Dai Architecture, Engineering & Consulting Co., Ltd
e-mail: jin_gu@xd-ad.com.cn

Keywords:Localized fire, Grid structure, Structural fire-resistance, Non-uniform temperature distribution

Abstract. *The regular pyramidia grid (RPG) structure is classified as the long span spatial steel structure and has been employed to cover the complex buildings, e.g. airports, train stations, conference & exhibition halls, sport studios, warehouses, storages and so on. Usually, this kind of buildings is with high ceiling and large area, which encloses a large volume space. The steel ceiling always exposes to localized fire. Firstly, a new transient temperature-time curve described localized fires has been introduced for analysis of spatial steel structural fire-resistance. Then, the studies reveal some ideas as following. The degree of stiffness for supports with elastic rubber pads, which originally were set to release thermal expansion due to weather variation, influences the RPG structural fire-resistance heavily, and the location of full fixed supports too. With the increasing degree of non-uniform temperature distribution in RPG structures caused by localized fire, the restraints between cooler chords and hotter chords increase significantly, and decreased the structural fire-resistance. According to the histories of stress and thermal expansion, the restrained chords, i.e. key chords, are distinguished from global structure based on the numerical analysis. A simple mechanical model for restrained chords was established to capture the buckling resistance capacity different from steel columns at axial force due to initial lateral deformation exposed to fires. Finally, some strategies have been presented for design of RPG structures fire safety.*

1 INTRODUCTION

The wider use of electronic computers and the development of software to enable space grid structures to be analysed more accurately increased confidence in their use for larger span and greater height structures. Since the late 1980s, a large number of regular pyramidia grid (RPG) structures have been erected and covered 2,000,000m^2 per year in China. It has been wildly and successfully used for stations, airport boarding halls, aircraft hangars, exhibition halls, storage buildings, factories and so on. Architects always prefer to exhibit a clear and uncluttered grid structure for the most aesthetic appeal. Then, increasing the cross-section of elements is better than providing high insulation level to get the superior fire-resistance capacity for RPG structures. Although the software enables the larger and longer space RPG structures to be analysed more accurately in fire-resistance. It is necessary that proposed design strategies for RPG structures to obtain or improve the initial fire-resistance capacity focused on key factors. A study of the behaviour of the RPG structure exposed to localized fires can let us capture the key factor and understand how to improve its fire-resistance capacity.

A general review of the fire-resistance analysis of double-layer grids has been presented by reference [1]. Firstly, it is emphasised that a localized fire concept should be introduced for large compartments.

Then, the loss of member load-bearing capacity due to both, decaying steel properties and possible plastic buckling, will result in a redistribution of internal forces within the structure. So the failure of a member due to the effects of a fire does not necessarily produce the overall failure of the complete structure. The complex nature of both fire behaviour and structural response leads to the study of the RPG structure fire safety step by step as follows.

2 TEMPERATURE-TIMR RELATIONSHIP FOR LOCALIZED FIRES

Based on the zone model, there are a few temperature-time relationships to describing localized fire given in NFPA 92B and PReN1991-1-2. Based on the field model, a new temperature-time curve has been introduced in reference [2] to describe the non-uniform temperature distribution transiently. A wide range of result from a series of large space fire scenarios simulated by FDS (Fire Dynamics Simulator), revealed three important facts.

Firstly, temperature distributions throughout the large space fire are non-uniform and pole asymmetric from the fire source. Then, a basic equation has been established to describe the transient non-uniform temperature distribution, $T(x,z,t)$ for localized fires as follows

$$T(x,z,t)=T_g(0)+T_g^{max}\cdot f(t)\cdot k_{sm} \tag{1}$$

where, x is from the vertical axis to the point in the horizontal plane and z is the height of the horizontal plane shown in Figure 1, t is the fire time, $T_g(0)$ is the ambient temperature; T_g^{max} is the maximum temperature given by Equation (2), $f(t)$ is the function of time for temperature history given by Equation (3), k_{sm} is the regressing function of distance given by Equation (4).

Secondly, the key factors, i.e. fire growth type, heat release rate, dimension of internal space and fire area, influence on the temperature distribution significantly.

Finally, the maximum temperature, T_g^{max} is higher with the increasing heat release rate, and lower with the increasing the floor area or the internal space height. With the decreasing of coefficient 'η', the maximum temperature decays more heavily from the vertical axis of fire plume.

$$T_g^{max}=(20Q+80)-(0.4Q+3)H+(52Q+598)\times10^2/A_{sp} \tag{2}$$

$$f(t)=1-0.8e^{(-\beta t)}-0.2e^{(-0.1\beta t)} \tag{3}$$

$$k_{sm}=\eta+(1-\eta)e^{(D/2-x)/7}\text{, if } x<D/2\text{, then } x=D/2\text{, where } D=2\sqrt{A_q/\pi} \tag{4}$$

where, Q is the heat release rate; $A_{sp}$is the larger floor area; H is the height of ceiling, β is regression parameter dependent on the fire growth type listed in Table 1(dimensionless), t is the time from fire ignition (s). D is the effective diameter of fire bed, A_q is the area of fire bed, η is the non-uniform factor dependent on the floor area and ceiling height, listed in Table 2.

Table 1. Factor β with fire growth types.

	Fire growth type			
	Slow	Medium	Fast	Ulter fast
β	0.001	0.002	0.003	0.004

Table 2. Factor η with dimension of buildings.

A_{sp}/ m^2	H/m				
	6	9	12	15	20
500	0.60	0.65	0.70	0.80	0.85
1000	0.50	0.55	0.60	0.70	0.75
3000	0.40	0.45	0.50	0.55	0.60
6000	0.25	0.30	0.40	0.45	0.50

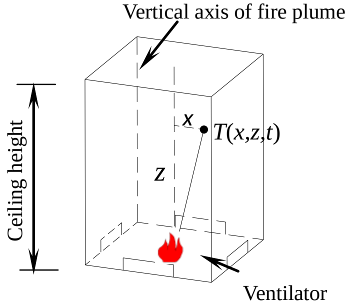

Figure 1. Virtual space for locazedfire scenario.

However, the functions mentioned above take no account of the flame radiation and fire moving, which would induce higher temperature in localized part of structures and more non-uniform temperature distribution detailed by reference [3].

3 STRUCTURAL MODEL AND NUMERICAL ANALYTICAL METHOD

Fire-resistance of RPG structures is based on structural model created and analyzed using the ANSYS software. Non-linear material models dependent on elevated temperature are given by CECS200:2006 in china.[4] In order to ignore secondary bending, the point loads upload at each node and axial forces are assumed to pass through the centre of the joint, and chords are pinned at each node with tapered cone section, shown as Figure 2. Equation (5) and Equation (6) are employed to describe the initial load ratio for compression and tension chords respectively. It is interesting to note that there are two ways to choice the section of each chord at ambient temperature. If each chord is with the full initial load ratio, all chords would be in ultimate limit state and with different section. This is the ideal case for structural design but difficult to establish the numerical analysis model. On the other hand, it is convenience to get the structural model with the same section, which will induce the same stability coefficient and slender for each chord within the similar unit. However, the reality RPG structure is with neither style mention above. As the products of civil engineers, chords in RPG structure are always with a several of section size which will induce the close initial load ratio instead of the same one. Then, there are both random and definite characters for initial load ratio of each chord, which will influence on the failure route. At each temperature step, compression chords should be checked by Equation (7) and tension chords by Equation (8). It should be noted that the initial tension chords will be inversed to compression due to restraints.

$$\left(N/\varphi A\right)/f_y = \text{ Initial load ratio for compression chords} \tag{5}$$

$$\left(N/A\right)/f_y = \text{ Initial load ratio for tension chords} \tag{6}$$

where, N is the axial internal force of chords at ambient temperature, φ is the stability coefficient, A is the size of the cross-section, f_y is the nominal value of yield strength, γ_R is the partial safety factor for the resistance.

$$\frac{N_T}{\varphi_T A} = \eta_T f_y \tag{7}$$

$$\frac{N_T}{A} = \eta_T f_y \tag{8}$$

where, N_T is the axial force of chords in fire case, A is the section size, Ψ_T is the stability coefficient at elevated temperature given by CECS200:2006, η_T is the reduction factor for the nominal value of yield strength at elevated temperature given by CECS200:2006 in china.

Figure 2. Tapered cone nodes.

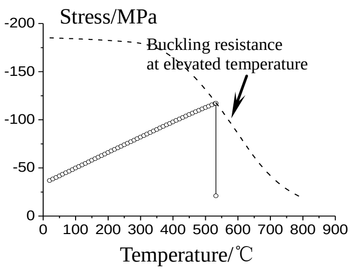

Figure 3. Stress history for compression chord pre-buckling.

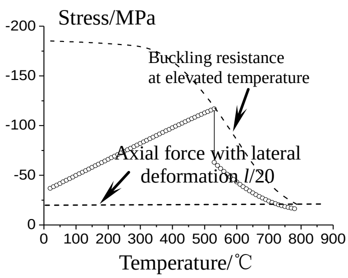

Figure 4. Stress history for compression chords post-buckling.

It is supposed that the external load is maintained constant while the temperature increasing. Shown as Figure 3, compression chords at pre-buckling are checked by Equation (7), and tension chords by Equation (8) at elevated temperature. Compression chords at post-buckling should be checked by lateral deformation *l*/20, shown as Figure 4.

4 SUPPORTS ACTION ON STRUCTURAL FIRE RESPONSE

4.1 Support locations

Usually the RPG structure should be provided with full, intermittent edge or corner supports. Shown in Figure 5, all of the perimeter upper nodes are supported, and restrained in different direction. There are three types of support location for RPG structures.

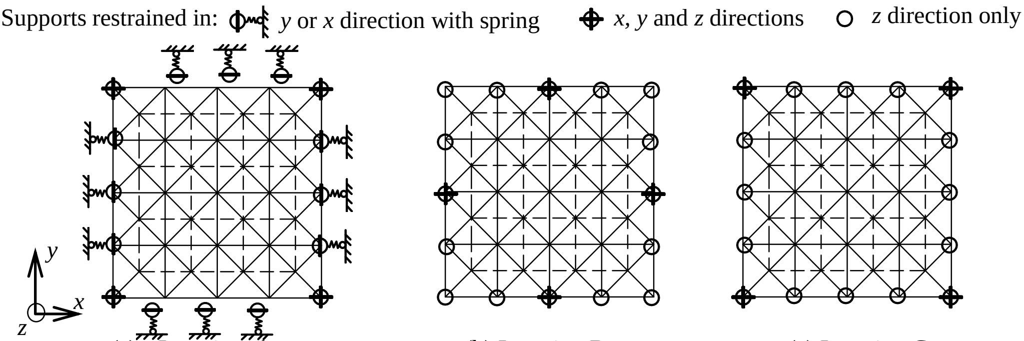

(a) Location A (b) Location B (c) Location C

Figure 5. Types of support location for RPG structures.

4.2 Structural response with different support locations

The support location in Figure 5(a) is employed by two different RPG structural models created and analyzed using ANSYS software. Structural model A is with 24m×24m square and 1.4m depth. Structural model B is with 36m×36m square and 1.6m depth. Model A is with higher load ratio than model B. Both models are subjected to uniform temperature distribution and with the same grid module 3m. The spring stiffness, k_s , is from 0.1×10^5 N/m to 40×10^5 N/m. Shown as Figure 6, the critical temperature decreases nonlinearly with increasing stiffness of spring supports and load ratio.

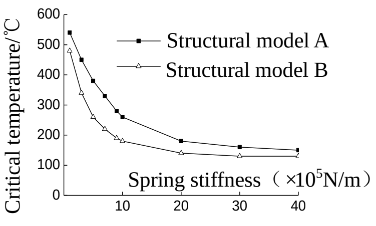

Figure 6. Critical temperature by supports with different spring stiffness.

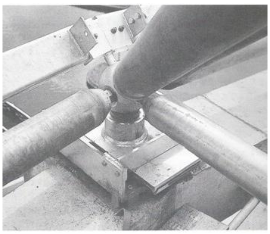

Figure 7. Slipping support.

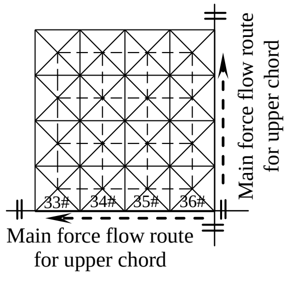

Figure 8. A quarter of structural model.

In order to release the thermal expansion, sliding supports shown in Figure 7 has been employed and located as Figure 5(b) and Figure 5(c). Which type of support location is better? It is demonstrated that location C can provide expansion movement much better than location B as followings.

A quarter of a RPG structure model is shown as Figure 8. The stress history of upper chord $36^{\#}$ with the highest compression force in the main force flow route increased more sharply under the support location B than location C, shown in Figure 9. Along the main force flow route, the supports in the middle of the edge restrained the thermal expansion strongly. With the main force flow route breaking at very low temperature, the global RPG structure collapsed immediately. Shown in Figure10, a series of critical temperatures have been resulted from numerical simulations based on structure models with different load ratio exposed to uniform temperature. Then, released the restraints in the main force flow route direction can improve the fire-resistance capacity of the RPG structure.

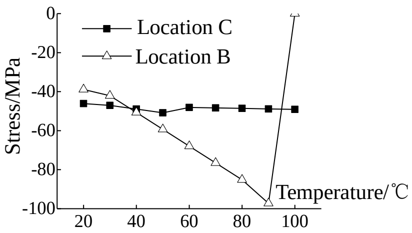

Figure 9. The typical stress history for the RPG structure for different support location.

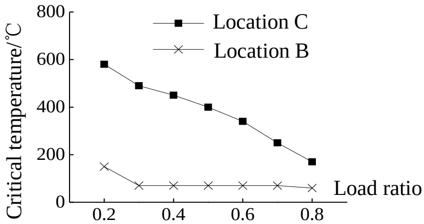

Figure 10. Critical temperatures for a RPG structure with different support location.

5 EFFECTS OF NON-UNIFORM TEMPERATURE DISTRIBUTION

5.1 Structure exposed to localized fire with non-uniform temperature distribution

In order to focus the localized fire actions on RPG structures, a series of cases for RPG structure with lower load ratio of diagonal web chords has been established with supports location C, and fire bed in the middle of the floor. Subjected to fire with uniform temperature distribution, the stress histories of upper chords, shown in Figure 8, remain the constant as Figure 11. Exposed to the localized fire with non-uniform temperature distribution, the stresses in these upper chords increase significantly, shown in Figure 12. It is demonstrated that localized fire induced non-uniform elevated temperature in the RPG structure, and the thermal expansion in hotter chords was restrained by cooler chords. Not only the weaker material properties but also the thermal force decays the fire load-bearing capacity of RPG structures subjected to localized fire. The chords 36# fell to buckling primarily, and other upper chords succeed to buckling. Upper chords are key members for RPG structure fire-resistance.

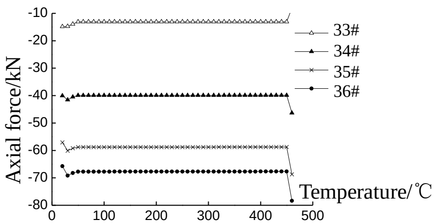

Figure 11. Stress history of chords for a RPG structure subjected to uniform temperature.

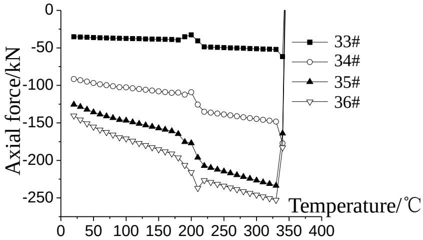

Figure 12. Stress history of chords for a RPG structure subjected to localized fire.

5.2 Effects of the degree of non-uniform temperature distribution

Non-uniform temperature distribution is the typical property for localized fire. Equation (4) describes the degree of non-uniform and Table 2 lists the values of non-uniform coefficient, η, which is dependent on the floor area and ceiling height. A RPG structure with 4m grid module and 24m×24m square has been exposed to localized fire with different degree of non-uniform temperature distribution, the stress of a compression diagonal chord with loading ratio R=0.5 and slender λ=200 increased more sharply with the degree of non-uniform temperature distribution increasing, shown as Figure 13. It indicates that chords are subjected to stronger restraint under more non-uniform temperature distribution.

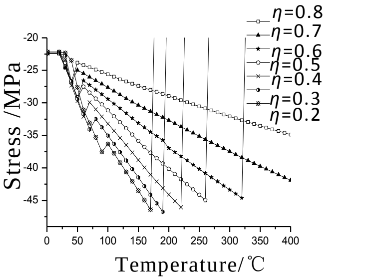

Figure 13. The degree of non-uniform temperature influences on stress histories.

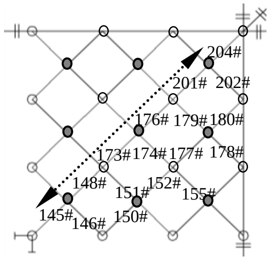

Figure 14. The number of diagonal web chords for a RPG structure with 4m grid module and 24m×24m square.

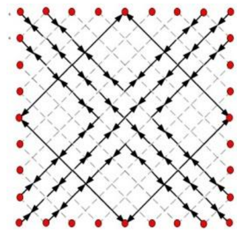

Figure 15. Shear mechanism of diagonal web chords for RPG structures.

5.3 Behaviour of diagonal web chords at elevated temperature

According to the load ratio given by Equation (5) and Equation (6), each chord of this ideal RPG structure model is with the same loading ratio R=0.2. This ideal global structure is exposed to localized fire with non-uniform temperature distribution coefficient η=0.7. Supports locate as Figure 5(c). The number of diagonal web chords is shown as Figure 14. The shear mechanism of diagonal web chords is shown as Figure 15 at elevated temperature. In the dot line direction, whether initial compression or tension diagonal web chords keep the compression stress increasing. In the mean time, perpendicular to dot line, the web chords keep the tension stress increasing. All of upper chords keep the compression stress increasing, and all of lower chords keep tension stress increasing. This is the membrane action for RPG structures, which is very different from the behaviour at ambient temperature.

Shown in Figure 16, the tension chord, 173#, failed primarily and the 201# failed secondly, then, the compression chord 176#. The 204# is with the highest temperature, but with the constant stress during the temperature history. It indicates that both tension web chords and compression web chords are restrained along the dot line direction. Based on the same loading ratio, if the initial tension chords alter to compression due to restraint, they would be with the lower fire loading capacity than the initial compression chords. Then, in the direction of the dot line, both initial tension chords and compression chords should be check by Equation (7).

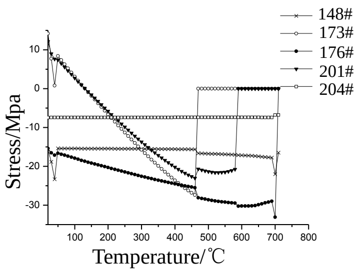

Figure 16. The stress history of diagonal chords in the dot line direction.

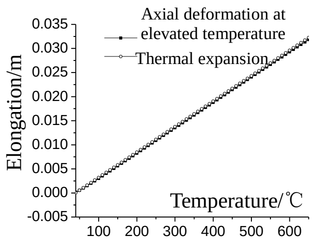

Figure 17. The elongation history for the diagonal web chord 204#.

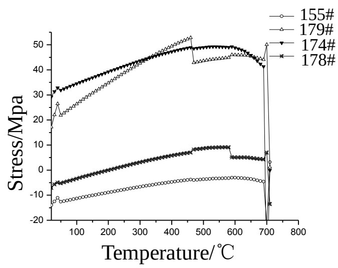

Figure 18. The stress history of diagonal chords perpendicular to the dot line.

The diagonal chord 204# is with the highest temperature and the elastic module decreased heavily. Shown in figure 17, the axial deformation of the chord 204# due to elastic module decreasing equals to the thermal expansion $\Delta L_T = \alpha l \Delta T$ due to temperature increment, the stress of chord 204# keeps in the constant. Figure 18 shows that tension chords and compression chords perpendicular to the dot line keep tension stress increasing at elevated temperature. It is implied that the deformation of chords perpendicular to the dot line always larger than their thermal expansion. Thus, the web chords along the dot line are key chords if the load ratios all over the global structure are similar.

5.4 Axially restrained chord behaviours at elevated temperature

The colder chords restrain the thermal expansion and enhance thermal stress in hotter chords before buckling. After buckling, the restraint limited the large deformation progress and the gradual deformation released the thermal expansion with the axial inter force decreasing. It is worth noting that most chords of spatial structures are with larger slenderness ratio than frame columns with the same length. However, there is different buckling resistance capacity between case1, which is taken no account of later-deformation and case 2 with later- deformation, shown as Figure 19. Chords with large slenderness and restraint stiffness ratio, β_l, get higher buckling temperature due to initial later-deformation, l/1000. Because the initial lateral deformation is beneficial to release the effect of initial crookedness is relatively larger.

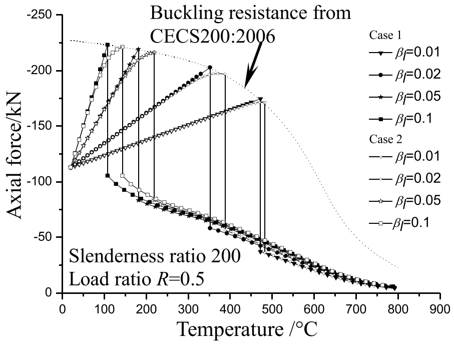

Figure 19. Histories of axial force for the restraint chord with large slenderness ratio.

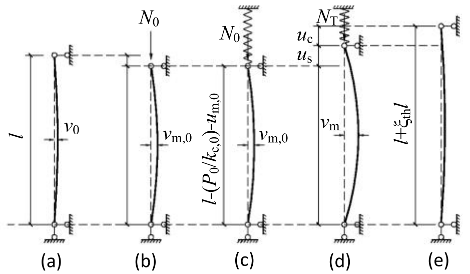

Figure 20. Mechanical model of the chord in RPG structure exposed to localized fire before buckling.

Figure 20 graphically shows that the deformation history of the restrained chord during the fire. Figure 20(a) is the initial state with initial lateral-deformation, v, and axial stiffness, $k_{c,0}$, before fire. Figure 19(b) is loading axial force and with lateral-deformation, $v_{m,0}$, before fire. Based on the Figure 20(b), the chord will be restrained by a spring with stiffness, k_s, at the beginning of the fire, shown in Figure 20(c). During the fire history, thermal expansion in the restrained chord lets to the deformation, u_s, shown in Figure 20(d). Figure 20(e) shows the thermal deformation without axial restraint. Compared Figure 20(d) and Figure 20(e), there is deformation, u_c, is restrained. Based on the mechanical mention above, an Equation (9) has been developed to calculate the history of the axial internal force, N_T, for restrained chords at elevated temperature before buckling step by step. [5]

$$N_0 + \frac{k_s k_c}{k_s + k_c}\{\varepsilon_{th} l - u_{mec} + \frac{\pi^6 I^2 v_0^2}{4l}[(\frac{E_0}{N_0 l^2 - E_0 I \pi^2})^2 - (\frac{E_T}{N_T l^2 - \pi^2 E_T I})^2]\} - N_T = 0 \tag{9}$$

where, u_{mec} is given by Equation (10), k_c is the axial stiffness of the restrained chord at elevated temperature, E_T is the elastic module at elevated temperature, ε_{th} is the thermal strain, I is second moment of area, $u_{m,0}$, is vertical displacement caused by chord bending at ambient temperature.

$$u_{mec} = \frac{N_0}{k_c} - \frac{N_0}{k_{c,0}} \tag{10}$$

N_T should be checked for resistance in fire ultimate limit state at each temperature step and get buckling temperature. The increase rate of axial stress and buckling temperature depend on the slenderness, load ratio and the restraint stiffness ratio.

6 DESIGN CRITERIA

The stability of RPG structures exposed to localized fire depends basically on the loading ratio level, fire severity, non-uniform temperature distribution, location of the fire bed and support conditions. Then, not only upper chords but also diagonal web chords would fall buckling primarily or lower chords lose strength probably at elevated temperature. In general, the primary failure is important for the global structural fire-resistance capacity. Based on the RPG structure behaviours mention above, there are some measures for improving or capturing the RPG structure fire-resistance capacity.

Initial loading ratio of chords represents of the residual space before buckling. It is obvious that the global structure or chords with lower initial loading ratio would get higher loading capacity complying with fire ultimate limit states, and the size of the chords could be enhanced to obtain the superior load-bearing capacity at elevated temperature. But over size of the chords is uneconomical.

The thermal stress in chords due to restraints depends very much on the supports with horizontal restraints. Supports bolted to the supporting structure with rubber cushion or slipping plate can provide relative movements for the RPG structure at elevated temperature history. In order to prevent rigid movement due to horizontal loading, besides spring supports along perimeter, full fixed supports located at each corner of the global structure is better than in the middle of the perimeter. The fire load-bearing capacity of RPG structures with corner-supported only is dependent on the diagonal web chords adjacent to each corner support heavily because the full fixed support restrains thermal expansion strongly and let to buckling at very low temperature.

If the maximum load ratio of web chords is similar to the minimum load ratio of upper chord, the upper chords would be focused and checked by fire ultimate limit state. Otherwise, web chords along the dot line and upper chords should be checked altogether. Only enhancing size of key members should be priority to improve fire-resistance capacity for RPG structure.

7 CONCLUSIONS

The fire analysis of RPG structures has been presented. It is emphasised that the steel ceiling always exposes to localized fire. Then, a new transient temperature-time curve described localized fires has been introduced for analysis of spatial steel structural fire-resistance. The degree of stiffness for supports with elastic rubber pads or slipping plate influences the RPG structural fire-resistance heavily, and the location of full fixed supports too. With the increasing degree of non-uniform temperature distribution in RPG structures caused by localized fire, the restraints between cooler chords and hotter chords increase significantly, and decreased the structural fire-resistance. According to the histories of thermal stress and elongations of chords, the key chords are distinguished from global structure. A simple mechanical model for restrained chords was established to capture the buckling resistance capacity which is different from steel columns due to initial lateral deformation exposed to fires. Finally, some strategies have been presented for fire safety design of RPG structures.

REFERENCES

[1] Yarza A., Pavia P. and Parke G.A.R.. “An introduction to the fire analysis of double-layer grids”. *Proceedings of the Fourth International Conference on Space Structures*. Thomas Telford. 1993: pp683～693.

[2] Du Yong, Li Guo-qiang. (2012). “A New Temperature Curve for Analysis of Structural Fire-resistance”. *Fire Safety Journal*, Vol.54:11, pp113-120.

[3] Du Yong, Li Guo-qiang. (2009).Effects of Flame Radiation on Temperature Elevation of Steel Members in Large Space Buildings Fire. *Applications of Structural Fire Engineering, Proceedings of International Conference,* Prague.

[4] China Association of Engineering Construction Standardization. *Technical Code for Fire Safety of Steel Structures in Buildings (CECS200-2006)*. China Plan Press, 2006.

[5] Jie Zou, Yong Du. “Calculation Method of Post-Buckling Load-Bearing Capacity for Axially Restrained Tubular Members in Grid Structures Exposed to Localized Fire”. *Proceedings of the 7th European Conference on Steel and Composite Structures*, Italy, 2014.

8th International Conference on Structures in Fire
Guo-Qiang LI, Venkatesh K. R. KODUR, Shou-Chao JIANG, Jian JIANG, Su-Wen CHEN, Guo-Biao LOU (Eds.)
Shanghai, China, June 11-13, 2014

RELIABILITY EVALUATION OF RESIDENTIAL BUILDINGS IN FIRE

Qianru Guo*, Enrique M. Palacios*, Jason Martinez* and Ann E. Jeffers*

* Department of Civil and Environmental Engineering, University of Michigan, Ann Arbor, MI USA
e-mails: qianru@umich.edu, jffrs@umich.edu

Keywords: Structural reliability, Monte carlo simulation, Probabilistic model

Abstract. *Performance-based design is becoming more widespread in structural fire engineering, but it is still inconsistent with the design of other types of hazards. This study works on extending the reliability evaluation framework to consider the system level structural reliability under fire by using Latin Hypercube sampling. A computational zone model was used to simulate the realistic fire scenario with the help of a fire spread model based on the NFPA's latest fire incident report system. The temperatures of structural members were obtained by a heat transfer simulation, and a 3D frame model was created in Abaqus to predict the structural responses. This study demonstrates that the structure in a realistic multi-compartment fire could have different failure modes in comparison to the single compartment fire, and the more realistic fires may cause more severe structural damages.*

1 INTRODUCTION

The structural fire engineering community is working on moving from the current prescriptive design to the performance-based design. This evolution aims to provide the structural engineers freedom to pursue safer and more economic fire resistant designs. However, the structural reliability evaluation, which is important for evaluating how well the target performances are achieved, is still inconsistent with the design of other types of hazards [1]. This is partially caused by the fact that the fire behaviour cannot be determined for a given building as it depends on a number of uncertain conditions (e.g. fire ignition location, ventilation conditions, fire load and the type of fuel) and there are too many uncertainties during the simulation of each physical domain that affect the final structural response.

Some progress has been made in recent years, such as to derive the probability-based load and resistance factors on design [2]; to account for the uncertainties in the fire resistance tests [3-4]; and to conduct risk based structural fire design [5]. The authors have previously proposed a framework to evaluate component level reliability using Latin Hypercube sampling and the First/Second Order Reliability methods for a multitude of random parameters in the fire, thermal, and structural models [6]. However, the reliability-based fire resistant design of structures has still not achieved a system level probabilistic simulation that is commonly used in other engineering disciplines.

This study seeks to improve the reliability framework to include a more comprehensive probabilistic fire model and to consider the structural system behaviour. The computational zone fire model is able to provide an efficient and more realistic simulation of the fire growth and spread in a building with multiple rooms, and it allows a more realistic treatment of the random parameters, including the ignition time, properties of the thermal boundaries, and fire growth rates. A 3D frame model was created using Abaqus to simulate the structural system response under different fire exposures. Due to the system level analysis, multiple failure criteria can be considered.

2 PROBABILISTIC STRUCTURE-FIRE SIMULATION MODEL

The probabilistic approach to structural fire simulation involves a sequentially coupled CFAST fire model, heat transfer model, and structural model. A common two bedroom apartment shown in Fig.1 has been chosen for the multi-compartment fire simulation. The apartment is superimposed on the structural model, which is the 8-floor composite steel-framed building in the Cardington fire tests [7].

2.1 Fire simulation: CFAST model

In most structural reliability evaluations, the fire model was simplified to the ASTM E119/ISO 834 standard fire curve, or the parametric fire curve defined by Eurocode. Although the parametric fire curve provides a way to include several realistic parameters to obtain the fire scenario, it is only a regressive model and cannot realistically capture the uncertainty that exists in the fire behaviour. Additionally the parametric fire model is limited to a single compartment fire scenario and cannot consider the possibility of fire spread among rooms in residential buildings. This study uses the two zone model, CFAST, to simulate the possible fire scenario in a multi-compartment area.

The floor plan of the two bedroom apartment is shown in Figure 1. There are 5 major rooms in it: a living room, a kitchen, two bedrooms, and a bathroom. As the compartment type is similar to the Dalmarnock fire test [8], a preliminary model was built based on the Dalmarnock fire test, and the CFAST result was compared with the test result as shown in Figure 2. This comparison illustrates that CFAST is able to predict the fire temperature in the compartment. It should be noted that this verification used the estimated heat release rate according to the oxygen consumption measured outside of the living room window as the input of the fire object [9].

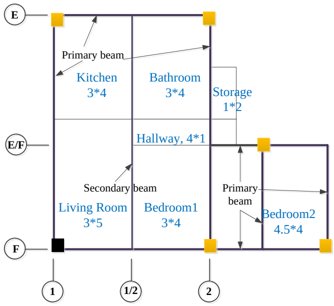

Figure 1. Floor plan of the apartment.

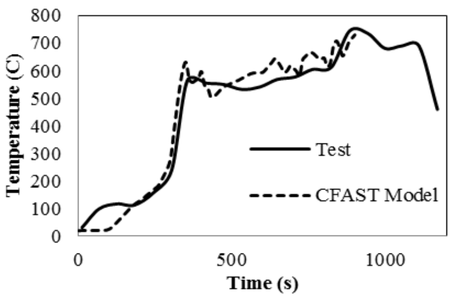

Figure 2. Verification of Dalmarnock test.

The challenges to conducting the realistic fire simulation in CFAST are how to define the first ignited room, the first ignited object, the fire spread from one object to other objects, and fire spread beyond the original ignited room. There are several stochastic fire spread models [10-11]; however, they cannot easily be adopted into this probabilistic study, and they are not able to combine the latest survey data. Therefore, we created a concise fire growth and spread model that includes that latest data on ignition, fuel load density, and fire spread to conduct the probabilistic fire simulation in an apartment.

Table 1. Fire model in residential buildings.

Room functions	Fire load (MJ/m^2)		First ignited	Spread beyond the room
	Mean	STD		
Living Room	427.6	86.9	6.7%	45%
Bedroom	495.7	170.1	11.7%	42%
Kitchen	673.0	206.9	69.9%	6%
Bathroom	382.5	124.1	-	-

For the fire growth inside of a room, a single burning item was used to represent the entire fire load in each room. Koo et al. [9] used both single burning item and two burning items to approach the fire growth in the Dalmarnock fire test, and the differences between them were not significant. In our study, we used a single burning object as it is able to capture the general fire behaviour and could significantly simplify the fire growth model. The fire load of each room followed Kumar and Rao's [11] survey result as shown in Table 1. The t-square fire curve was used to approach the actual heat release rate of the burning object. The peak heat release rate in the t-squared fire curve was according to the predication equation of the heat release rate for wood fuel. The t-squared fire curve also includes different fire growth rates, and we assumed that each of the slow, medium, fast, and ultrafast growth rates had equal occurrence rate.

The fire spread beyond a room was based on the U.S. home structure report of 07-11 by the National Fire Protection Association (NFPA) database [13]. NFPA developed a national fire incident reporting system (NFIR 5.0) to collect information of fire incident information that summarizes the ratio of the first ignited object in different rooms and the subsequent possibility of spread beyond the first ignited room, as listed in Table 1. If the fire spread happens, the fire will spread to the room closest to the first ignited room, and the beginning time of spread is assumed to be any time point before the fire becomes extinct in the first ignited room. The fire spread beyond the apartment was not considered in this study.

The source of uncertainty considered in the fire simulation includes the peak heat release rate in each room, the total combustion energy in each room, the fire growth rate in each room, the spread index, the fire spread time, and thermal inertia of the surroundings.

2.2 Heat transfer: Eurocode and Abaqus 2D heat transfer model

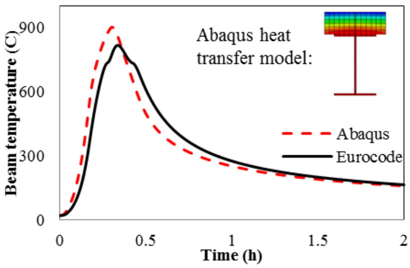

Figure 3. Beam temperature.

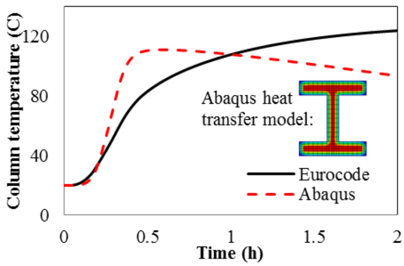

Figure 4. Column temperature.

The heat transfer analysis by Eurocode and Abaqus were applied to determine the temperature development of each structural member during the fire. Eurocode provides a simple design approach of calculating the thermal response of unprotected/protected steel members, in which the temperature is uniformly distributed over the entire member. Two 2D heat transfer models were built in Abaqus and compared with the Eurocode approaches for the unprotected beam and the protected column, as shown in Figure 3 and Figure 4. There was very good agreement between Abaqus and Eurocode for the unprotected beam. The Eurocode and Abaqus had some differences in the column model, but the two models arrived at the same peak temperature. Therefore, this study used the simple approach from the Eurocode to calculate the beam and column temperatures. The Eurocode does not have a similar simplified approach for the concrete slab under arbitrary fire exposure, which is because that the temperature gradient cannot be ignored in a concrete slab. A 2D Abaqus heat transfer model was built to calculate the temperature of the concrete slab in different layers. The temperature dependent thermal properties (i.e. thermal conductivity, density, and specific heat) of the steel and the concrete are based on Eurocode.

The uncertainty considered in the heat transfer model included the thickness of ceramic fibre blanket for columns and the thermal conductivity of the concrete.

2.3 Structural model: Abaqus 3D frame model

The apartment was assumed to be located in a corner of the first floor, which has the same location with the Cardington corner test, so its accuracy could be conveniently verified by the actual test results. As shown in Figure 5, a 3D finite element model was built using Abaqus. The model only considered the slab systems and beam-column system of the second floor, and only one quarter of the whole floor system was modelled here to increase the computing efficient of the structural analysis. The beams and columns were simulated by the beam element. The general shell element in Abaqus was used to model the slab with a uniform thickness of 70mm without considering the steel deck and concrete ribbed portion. The behaviour of the shear studs between beam and slab were modelled by the temperature independent linear Cartesian connector with stiffness was based on the study by Huang et al. [14]. The vertical deformation and relative rotation between the slab and beams were connected rigidly. The temperature dependent nonlinear mechanical property of steel and concrete followed the definition given in Eurocode. In the verification, the temperature data measured in the Cardington corner test was directly used to define the structural member temperature. The comparison between the test result and the simulation result at the middle span of the secondary beam is shown in Figure 6. It was also the location with the largest deflection among the whole area during the test. The finite element model was capable of predicting the maximum deflection of the structure at elevated temperature by this comparison.

The uncertainty considered in the structural model included the dead load, live load, load factors, and yield stress of two different strengths of steel.

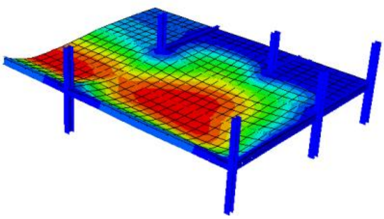

Figure 5. Cardington corner test.

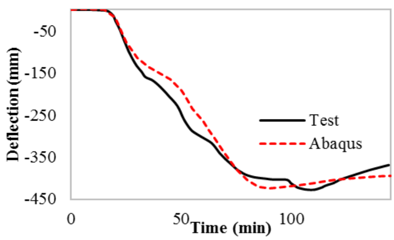

Figure 6. Mid-span deflection of beam 1/2.

One thousand Latin hypercube samples were generated by considering the statistical properties of each random parameter. The three parts of the simulation were controlled and connected by a Matlab code, so the fire temperature data and structural member temperature could be seamlessly transferred to the structural model. Due to the large computational demand, analyses were conducted in parallel on the flux system housed at the University of Michigan's Center of Advanced Computing. The total number of simulations was distributed to ten nodes to run the jobs. The total simulation time required is around 4 hours in the parallel computing system.

3 RESULT

Based on the statistical characteristics of all uncertain parameters considered in the fire simulation model, a series of fire scenarios with different ignited rooms, ignition times, fire growth rates, and fire loads were obtained. The mean fire temperatures in different rooms are shown in Figure 7 along with the 0.05 and 0.95 fractiles. As illustrated, the fire temperature in each room followed a wide range. The maximum fire temperature was close to 1000C while in some cases the temperature remained at ambient temperature. Because some rooms did not ignite in all fire scenarios, the mean temperature appears to be considerably lower than the maximum temperature in Figure 7.

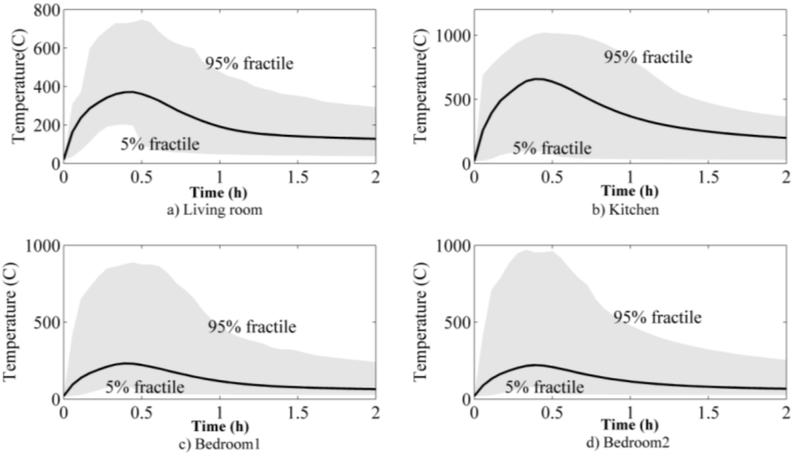

Figure 7. Room temperatures.

These fire scenarios were transferred to the heat transfer analyses to obtain the temperatures of the beams, columns, and slabs. As the kitchen has the highest possibility of first ignition, it has the highest fire temperature among all of the fire scenarios. In Figure 8., the mean and 0.05 and 0.95 fractiles for the structural members around the kitchen are plotted. The unprotected beams had temperatures that were very close to the fire temperatures. The columns were protected by the insulation, and the highest temperature of the column in the kitchen was under 250 ℃ in all fire scenarios. This illustrates that there was almost no material degradation in the column, so the failure would not happen in the column unless the fire protection had prior damage. The lower layer temperature of the slab reached as high as 1000 ℃, and the highest temperature at the middle layer of the slab was around 500 ℃. The temperature at the unexposed surface of the slab is not shown in Figure 8(d) because the temperatures were lower than 200 ℃. According to the heat transfer analysis, the structural members in some fire scenarios have a possibility of failure as their temperatures exceeded 800 ℃.

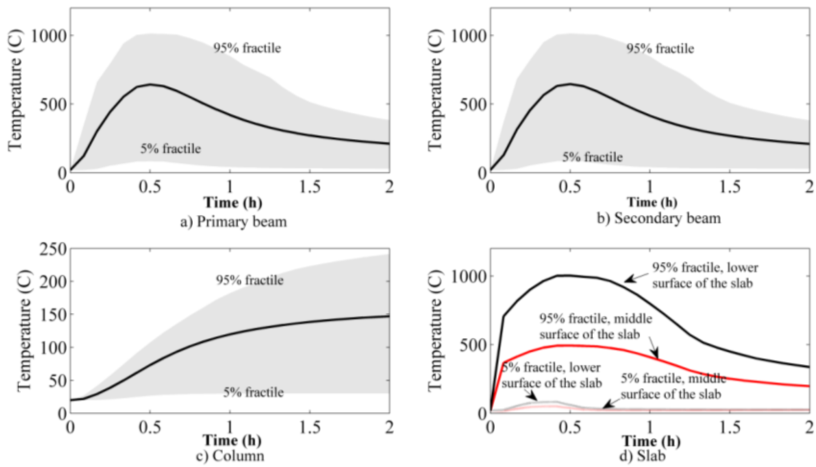

Figure 8. Structural members’ temperature.

The temperature of each structural member was transferred to the structural model along with the random values related to the mechanical properties of the structural materials and the load related parameters. The mean and 0.05 and 0.95 fractiles of mid-span deformations of the structural members around kitchen are shown in Figure 9. The maximum deflection of these structural members mostly occurred at the secondary beam and in the slab between secondary beams and the primary beams. The mean deformation increased in the first 30 minutes to one hour, and then kept increasing slowly in most cases.

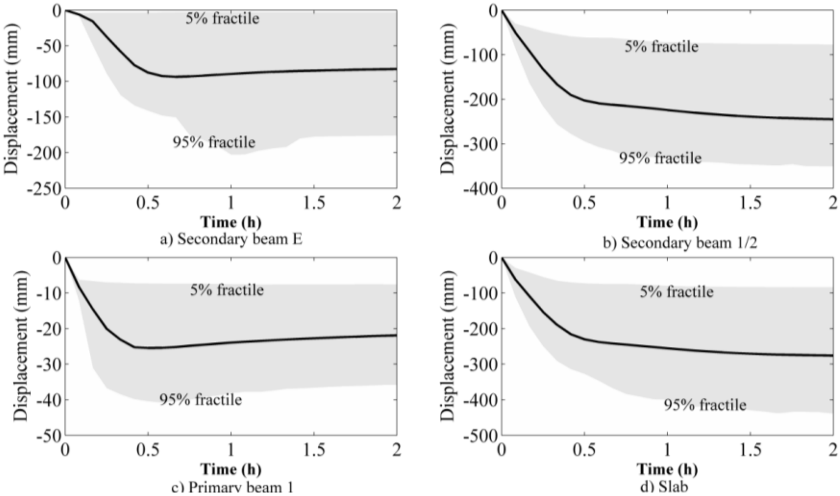

Figure 9. Structural response.

In the cases in which a fire spread occurred, there was more than one peak in the deformation curve, with the last peak points tending to cause the largest displacement. In order to see how the multiple-compartment fire spread affected the structural response, one single case of the 1000 simulations was chosen to plot in Figure 10. In this case, the fire was first ignited in the kitchen with a medium fire growth rate, and after 40 minutes the fire spread to the living room as shown in Figure 10(a). The maximum slab deformation in the kitchen increased to 0.4m after the fire first ignited in the kitchen, and kept increasing another 10% after the fire spread to the living room, even though the following maximum temperature in the living room was lower than the initial peak temperature. This result illustrates that the building with smaller compartments could have different failure pattern than a single large compartment, and the fire spread between rooms could cause more severe situations than just considering the single compartment fire.

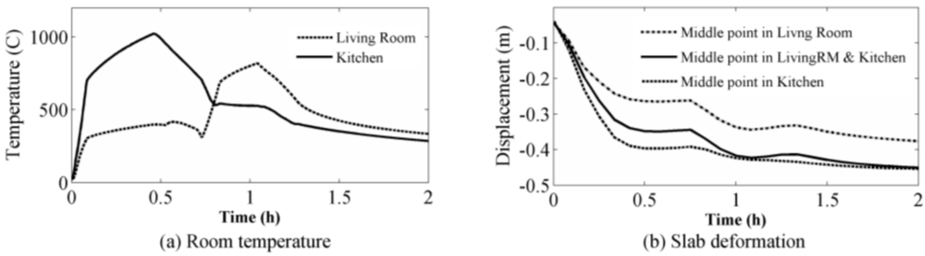

Figure 10. Single case analysis (case 61).

To evaluate the reliability of the system, failure was defined by the limiting displacement of L/20 for each beam and slab. The probability of failure P_f was calculated by evaluating the ratio of the total failure cases in all sampling cases. There were 56 simulations that failed out of a total of 1000 simulations, resulting in a failure probability of 5.6%. Among the 56 failed cases, only 8 of them related to the failure of the beam, and 47 of them included the failure of the slab between the primary and secondary beam, which has the largest span and largest possibility of failure.

4 CONCLUSIONS

This paper presents a preliminary study into the system level reliability evaluation of structures in fire. The Latin hypercube sampling method was used in conjunction with a sequentially coupled fire simulation, heat transfer analysis, and the structural model. A fire spread model based on the latest NFPA survey result was combined with the zone fire model software, CFAST, to conduct a realistic fire simulation in a multi-compartment area. The thermal and mechanical responses of the structure were simulated by a heat transfer model and a 3D structural model, respectively. A Matlab program was built to generate random parameters and to couple the three phases of the simulation.

This study successfully extended the Latin hypercube sampling method to evaluate a system level structural reliability under fire, allowing the analyst to conduct a system design based on an acceptable level of risk. The quantification of structural reliability in fire is essential to realize a holistic performance-based framework in which structural fire resistance in appropriately accounted for. This study also illustrates that the fire spread between multiple rooms could create more severe situation for the structure, which challenged the current design procedure of just considering single compartment fire and will promote the future study about travelling fire.

REFERENCES

[1] Ellingwood, B.R., "Load Combination Requirements for Fire-Resistant Structural Design", *Journal of Fire Protection Engineering*, 15, 43-61, 2005.

[2] Iqbal, S., and Harichandran, R.S., "Capacity Reduction and Fire Load Factors for Design of Steel Members Exposed to Fire", *Journal of Structural Engineering*, 136, 1554-1562, 2010.

[3] Jensen, E., Van Horn, J., and Eamon, C.D., "Variability of Fire and Concrete Temperatures and the Associated Uncertainty in Structural Behavior", *Proceedings of 6th International Conference on Structures in Fire*, Kodur, V., and Franssen, J.M., Eds., DEStech Publications, USA, 959-966, 2010.

[4] Van Coile, R., Annerel, E., Caspeele, R., and Taerwe, L. (2011), "Probabilistic Analysis of Concrete Beams during Fire", *Proceedings of the International Conference on Application in Structural Fire Engineering*, Wald, F., Horova, K., and Jirku, J., Eds., Prazska Technika, Prague, 127-132.

[5] Lange, D., Devaney, S., and Usmani, A., "An application of the PEER performance based earthquake engineering framework to structures in fire", *Engineering Structures*, 66, 100-115, 2014.

[6] Guo, Q., Shi, K., Jia, Z., and Jeffers, A. E., "Probabilistic evaluation of structural fire resistance", *Fire technology*, 49(3), 793-811, 2013.

[7] Gillie, M., Usmani, A. S., and Rotter, J.M., "A structural analysis of the Cardington British steel corner test", *Journal of Constructional Steel Research*, 58(4), 427-442, 2008.

[8] Rein, G., and Carvel, R. (Eds.), The Dalmarnock fire tests: experiments and modelling. School of Engineering and Electronics, University of Edinburgh, 2007.

[9] Koo, S.H., Fraser-Mitchell, J., Upadhyay, R., and Welch, S, "Sensor-linked fire simulation using a Monte-Carlo approach", *Proceedings of 9th International Symposium about Fire Safety Science*. Karlsruhe, Germany, 2008.

[10] Elms, D.G., and Buchanan, A.H., Fire spread analysis of buildings, Research Repart R35, Building Research Association of New Zealand.

[11] Ramachandran, G, "Probability-based fire safety code", *Journal of Fire Protection Enginering*, 3(2), 37-48, 1990.

[12] Kumar, S., and Rao, C.V.S., "Fire load in residential buildings", *Building and Environment*, 30(2), 299-305, 1995.

[13] Ahrens, M., Home structure fires, Quincy: National Fire Protection Association, 2013.

[14] Huang, Z., Burgess, I. W., & Plank, R. J., "The influence of shear connectors on the behaviour of composite steel-framed buildings in fire", *Journal of Constructional Steel Research*, 51(3), 219-237, 1999.

8th International Conference on Structures in Fire
Guo-Qiang LI, Venkatesh K. R. KODUR, Shou-Chao JIANG, Jian JIANG, Su-Wen CHEN, Guo-Biao LOU (Eds.)
Shanghai, China, June 11-13, 2014

OPTIMIZATION OF THE TALL BUILDINGS STRUCTURAL SYSTEM FOR RELIABILITY AGAINST PROGRESSIVE COLLAPSE

F. Gentili* and F. Bontempi**

* ISISE, Civil Engineering Department, University of Coimbra, Coimbra, Portugal
e-mail: filippo.gentili@uc.pt

** Department of Structural and Geotechnical Engineering, Sapienza University of Rome, Rome, Italy
e-mail: franco.bontempi@uniroma1.it

Keywords: Optimization, Outrigger system, Structural organization, Tall buildings, Nonlinearities, Fire-induced collapse

Abstract. *Structures should be designed exploiting all their resources in order to counter accidental actions. For complex structures, the consequences of such actions can be very serious and therefore they should be limited. In particular, actions, such as fire, can determine local or global collapse. This paper is focused on the progressive collapse susceptibility that depends on the structural system organization. The attention is focused especially on the role of vertical bracing systems and the outrigger. The location of these systems could be optimized in order to ensure the best possible performance to the structural system. In relation to a steel high-rise building, the investigations take into account a full nonlinear response of the structure. A spatial model has been implemented, capable of highlighting possible out of plane displacements of the elements in a commercial finite element code. Investigations carried out on substructures have highlighted the effectiveness of different structural solutions.*

1 INTRODUCTION

For tall buildings, fire is a very serious threat [1]. The objectives of the fire safety strategies are to limit to acceptable levels the probability of death, injury and property loss. The balance between life safety and property protection varies in different countries, depending on the type of building and its occupancy. Three different aspects can affect fire design of both non-structural and structural measures in tall building: (i) building evacuation, (ii) fire spread, (iii) the susceptibility of tall buildings to disproportionate collapse.

This paper focuses on the third aspect. The susceptibility to disproportionate collapse is one of the most significant topic in tall buildings because the consequences of a fire-induced collapse are enormous in term of safety of people and integrity of the structure and the risk associated to the event can be significant, even if the occurrence of a structural fire is very low. In addition, tall buildings generally are considered iconic because they are unusual in height and design. Also for this reason, the loss of these structures is not acceptable by the society.

The organization of the structural system is one of the most relevant aspect in order to evaluate the progressive collapse susceptibility. Structural development of tall buildings has been a continuously evolving process. These stages range from rigid frame, tube, core-outrigger to diagram systems with several classification for efficiency [2, 3].

The ratio of strength and stiffness of adjacent elements can influence the progressive collapse susceptibility of the system [4]. Another consideration concerning the propagation of failures is that a particularly dangerous situation is represented by a possible spread of failures to elements not directly involved in the fire, i.e. element that due to their location or because of greater insulation have still a relatively low temperature at the time of failure [5].

Starossek [6] examines five general approaches for achieving this goal: non-structural protective measures, specific local resistance, alternative paths, isolation of collapsing sections through structural segmentation, and prescriptive design rules.

The analysis of cases of WTC and Windsor Tower allows assessing the role of the structural organization in countering extreme events such as fire.

In WTC case, there were four major structural subsystems in the towers, referred to as the exterior wall, the core, the floor system and the hat truss [7]. The latter, formed by a set of steel braces, was located from 107th floor to the roof of each tower. The initial buckling of the heated floor slabs induced by hindered thermal expansion would have subsequently caused the buckling of the columns, because of the loss of horizontal restrains of the floors.

The Windsor Tower was a 32-storey concrete office building with a reinforced concrete core and a height of 106 m. The structure had two technical floors without windows in the middle. It was believed that the multiple floor fire, along with the simultaneous buckling of the unprotected steel perimeter columns at several floors, triggered the collapse of the floor slabs above the 17th floor [8]. It seems that collapse of first horizontal slab, impacting on the slab below, causes its failure in turn. The portion of the building that collapsed consisted of the outer portions of floor slabs and perimeter walls throughout the upper third of the building (the 21st through 32nd floors). After the fire, the building was demolished.

In both structures, the outrigger has played a central role in the development of collapse. In general, outriggers serve to reduce the overturning moment in the core that would otherwise act as pure cantilever, and to transfer the reduced moment to the outer columns through the outriggers connecting the core to these columns [3, 9]. In WTC with the impact damage, the core subsystem leaned to the southeast and was supported by the south and east perimeter walls via hat truss and floors. As the core weakened, it redistributed loads to the perimeter walls through the hat truss and floors. In Windsor Tower, the pancake-type progressive collapse [10] seems to have come to a halt in correspondence of two technical floors, which represented a localized stiffening of the system.

2 CASE STUDY

In this paper, a steel tall building is taken as case study, whose premises are devoted to offices and residential use and the response of the building is investigated up to the crisis of the structure with respect to a standard fire. This case has been selected following the geometry of a building recently built up in Latina, Italy. The building is composed of 40 storeys and has a framed structural system (Figure 1). A vertical bracing system (in bold in the left plant floor of Figure 1) provides stiffness against horizontal actions, while no horizontal bracing system is present within the floor planes, since a bidirectional concrete floor slabs should provide the necessary in-plane stiffness. The inclusion of hollow spheres in the concrete floor slab, together with the biaxial symmetry of the slabs, allowed for the presence of beams with relatively small profiles spanning long distances. On the other hand, the sections of the columns are quite big, as the resistance against horizontal loads is totally entrusted to the columns. As a result, the difference in the section dimensions of the horizontal and vertical elements is quite high in this type of structural system and becomes particularly significant in the bottom floors, where the column sections are the biggest. This characteristic may influence the structural response in case of fire, as highlighted in [4].

Aim of the investigations

The main goal of the paper is to highlight the role played by vertical braced systems and by outriggers in the fire induced collapse mechanisms and in the possible propagation of the initial failures to zones of the structure not directly involved in the fire. To this purpose, simplified fire design and verification methods on isolated elements are not sufficient and the response of the structural system as a whole [11] has to be investigated. This is a quite difficult task, which in case of complex structures such as a tall building [12], necessarily requires some simplifying assumptions in the modelling of the action and of the structure. In case of tall building subject to fire action, the Performance-Based Approach is a useful method [13, 14, 15].

In general three aspects have to consider: (i) a measurable quantity (performance); (ii) a method of measure (performance criteria); (iii) an acceptable limits (performance limits).

The investigations presented here have three main different goals: i) to identify the time and type of failures; ii) to understand the main resistance mechanism; iii) to outline a possible propagation of the collapse.

In consideration of the aim of these analyses, two different level of collapse can be identified: (i) a local collapse of a single element occurs for the runaway of a significant point [5] or for achieving of critical conditions of stress (buckling or yielding); (ii) a global collapse of the structure. In case of complex structural systems, the conventional definition of the collapse may prove to be important and not trivial [16]. Since the objective is a global behaviour evaluation, a good performance could be the overall deformation of the structure; this can be assessed by the displacement of the last floor of the frame (performance criterion); the imposed limit as collapse indicator is equal to one meter of horizontal or vertical displacement.

Two fire scenarios have been considered (see the floor plan on the right of Figure 1). In both cases, fire involves only one floor (sixth).

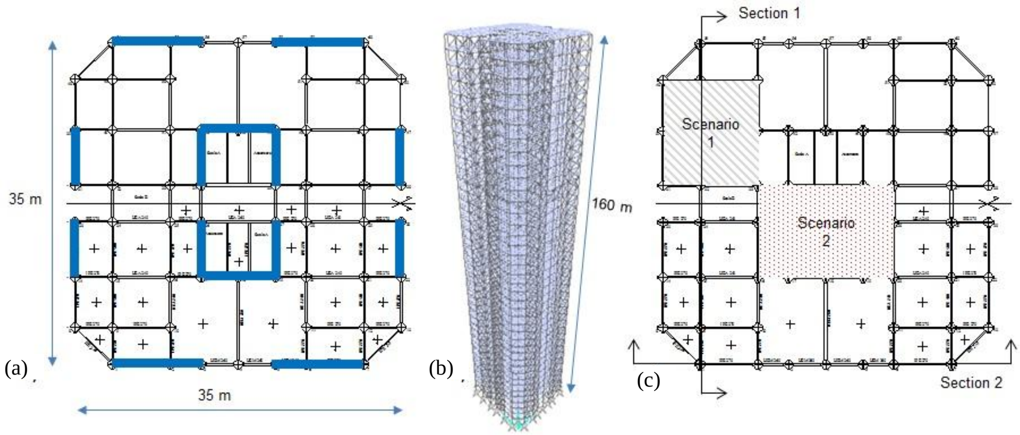

Figure 1. Case Study: (a) Floor plan; (b) Three-dimensional view; (c) fire scenarios.

Characteristic of the Finite Element Models

It has to be pointed out that the interest of this study is focused on the behaviour of the steel framed structures. The investigations take into account a full nonlinear response of the structure, influenced by material degradation at high temperatures, possibility of buckling, large displacements and deformations and exploitation of plastic reserve of the elements. Other important issues that have a strong influence on fire behaviour of a structure, as slab properties and passive protection measures, have been neglected. Finite element models have been implemented by using beam elements, which has been properly meshed.

A three-dimensional spatial model (126132 D.O.F.), capable of highlighting possible out of plane displacements of the elements, vertical progression of the collapse and spatial resisting mechanisms, has been used for the assessment of the overall performance of the building under two significant fire scenarios.

Several sectional models (about 22000 D.O.F.) have allowed developing an optimization procedure in a simplified and rational way. In order to simulate the presence of beams perpendicular to the frame, transversal restraints have been applied to the sectional model in the 3rd dimension.

Dead and live loads have been applied as line loads along the axis of the beams and considered together with the self-weight in a first load step. In a second load step the heating curves calculated for the steel profiles have been applied to the nodes of the elements pertinent to the area of the fire scenario considered, while other elements have been assumed to remain cold throughout the investigation.

An explicit dynamic solver has been used in order to overcome convergence problems due to the formation of local mechanisms, thus enabling to trace down the propagation of failures. The analyses carried out allow studying the evolution of the collapse, but they do not provide any information on the effect of the impact of the elements failed elements on the remaining part of the structure.

3 ORIGINAL CONFIGURATION

3.1 Fire Scenario 1

Scenario 1 that concerns a lateral zone covers an area of 117 m^2 (10.1% of the total floor area). Scenario 1 involves 9 columns and 12 beams. The first collapse occurs after about 57 min and regards the part of structure near columns 9 and 10. Figure 2 shows the evolution of collapse through the displacement of the top floor. The gray part represents area that has more of 1m of displacement. After 60 min the involved area is 130m^2 (11.21%), after 75min is 208m^2 (17.98%), after 90min is 325 m^2 (28.01%) and 350m^2 (30%) after 120min.

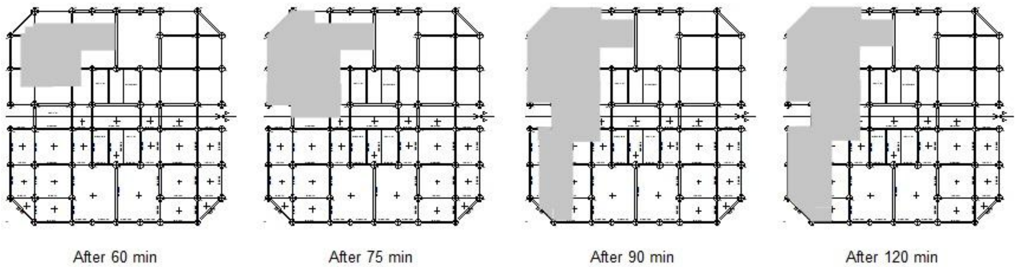

Figure 2. Evolution of the area of the top floor with a displacement major than 1m for Fire Scenario 1.

3.2 Fire Scenario 2

Scenario 2 that concerns the core of the floor covers an area of 146 m2 (12.5% of the total floor area) Scenario 2 involves 13 columns and 16 beams The first collapse occurs after about 80 min and regards the part of structure near columns 20, 25, 28, 33 and 36. Figure 2 shows the evolution of collapse through the displacement of the top floor. After 90 min the involved area is 149m^2 (12.88%), after 120min is 326m^2 (28.08%) and 779m^2 (67.11%) after 150min.

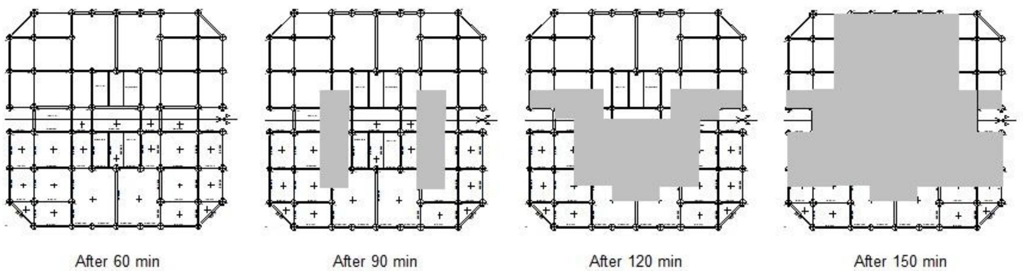

Figure 3. Evolution of the area of the top floor with a displacement major than 1m for Fire Scenario 2.

4 OPTIMIZATION OF THE STRUCTURAL SYSTEM

To improve the performance of the building a rigorous procedure on the 3D model could represent a notable limitation due computational effort. In addition, also the interpretation of results could be not easy and lead to wrong interpretation of the structural behaviour. For these reasons two sectional frame have been considered (see Frame A and Frame B of Figure 4). In a first step several configurations have been assessed under fire scenario of Figure 1 in order to identify the pattern which best could represent a compromise between the increase of the material and the performance improvement. The spatial extension of fire represents a crucial factor in order to highlight possible deficiencies and weaknesses of the structural system. In two selected configurations, an analysis on the extension of fire length has been carried out in order to evaluate the progressive collapse susceptibility of the structural system.

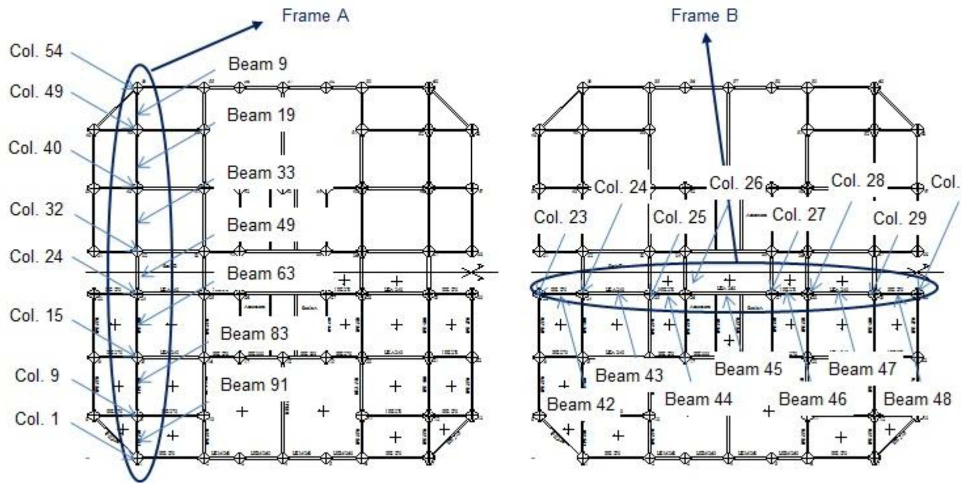

Figure 4. Substructures: Frame A (on the left) and Frame B (on the right).

For Frame A the possibility of inclusion of an outrigger system has been taken into account (Figure 5). In particular, a comparison between fire performances of a moment resistant frame (A1), a frame with a vertical bracing system (A2), a frame with an outrigger placed at 40th floor (A3), at 36th floor (A4) or 29th floor (A5) is proposed.

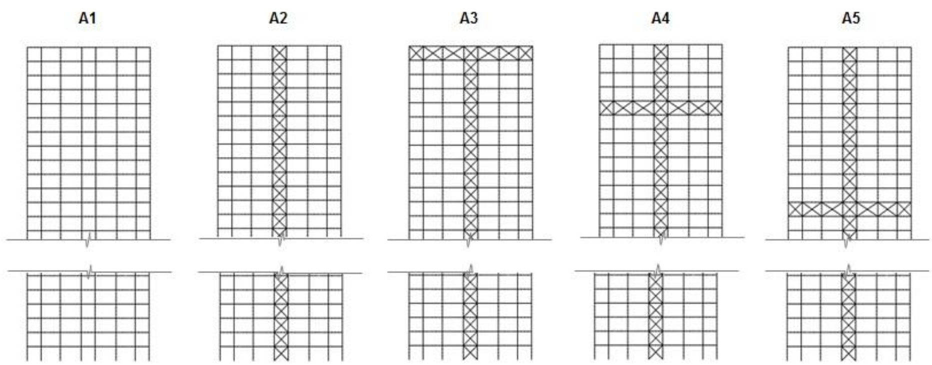

Figure 5. Analysed configurations for Frame A.

In Frame B the effectiveness of vertical bracing systems has been assessed (Figure 6), through investigations on a moment resistant frame (B1), a frame with a vertical bracing system placed in the central area (B2), a frame with two (B3) or three (B4) vertical bracing systems.

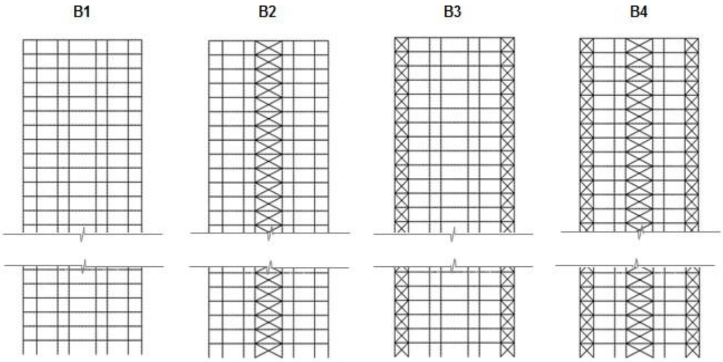

Figure 6. Analysed configurations for Frame B.

For Frame A, the collapse can be avoided only with the presence of the outrigger (configuration A3, A4 and A5 in Table 1). Nevertheless, the best position for that system is at 29th floor (A5) because when the system is placed in an upper floor the global response to horizontal forces worsens, despite the steel mass does not change. Actually, after 180 min fire exposure the maximum lateral displacement of the top floor is 55cm that represents a lower value than that found for Configuration A4 (64cm) and Configuration A3 (68cm).

For Frame B different systems did not lead to a significant improvement (Table 1) due to fire extension on the frame. Fire scenario represents a too severe condition that does not allow the development of alternative resistant mechanisms.

Table 1. Fire Resistance.

Frame A			Frame B		
Configuration	Steel Mass [ton]	Fire Resistance ¨min	Configuration	Steel Mass [ton]	Fire Resistance ¨min
A1	799	75	B1	758	59
A2	857	75	B2	855	61
A3	877	180	B3	881	59
A4	877	180	B4	978	62
A5	877	180			

4.1 Progressive collapse susceptibility

4.1.1 Frame B

The thermal action involves Frame B (Configuration B3) at sixth floor. At this height, design includes as profiles for columns HEM1000star (Col.25 and Col.28) and HEM900star (Col.23, Col.24, Col.26, Col.27, Col.29 and Col.30). These section profiles have a low and quite similar ratio Am/V (about 71 1/m). Beams provided are IPE270 (Beam 42, Beam 44, Beam 46 and Beam 48), HEA240 (Beam 43 and Beam 47) and HEA260 (Beam 45): for these profiles the ratio Am/V is higher (respectively 232, 182 and 175 1/m).

In the first analysis, the thermal load is applied only on a column of the floor and on adjacent beams. The crisis occurs when axial force reaches the plastic limit of the column (calculated taking into account the degradation of the yield stress with temperature). It occurs in correspondence of about 696 ℃ after 30 minutes. The axial force has a value quite low at the beginning of the thermal load application. This quite low load-resistance ratio is due to load combination considered. In addition, the stress does not grow significantly with temperature because the thermal expansion is not completely avoided. This extension of the thermal load causes only a local crisis: before the column crisis, the heated beams are subjected to instability and they reached enormous displacement that led to their failure.

This operation was repeated for each column of the sixth floor. In each of eight cases studied, a local crisis of the column occurs for approximately the same temperature and the same time.

The collapse becomes more significant for a fire applied on a greater extension of the floor. For example, in order to consider the case of thermal load on two subsequent columns the worst combination is the one that provides Col.25 and Col.26 (and adjacent beams) under fire conditions. In this case, after 65 minutes there is the global collapse condition with the overcoming of a meter of the vertical displacement in the top of the structure. After almost 110 minutes, the area surrounding the heated columns collapses, whilst vertical bracing systems still stand. On the other hand, not all cases with two heated columns determine a global collapse: if the thermal load is applied on Col.24 and Col.25 with adjacent beams, it does not occur.

When fire is applied on three subsequent columns, a global collapse occurs for each combination. These collapses take place within a narrow time interval (between 63 and 70 minutes). The worst-case scenario is constituted by the thermal action on Col.25, Col.26 and Col.27.

Differences among the various combinations of load are reduced: for a fire on four columns, the global collapse occurs between 59 and 63 minutes, for a fire on five columns it occurs between 59 and 62 minutes.

Table 2 synthetizes results found for the Frame B in terms of time of resistance to fire: average, minimum and maximum values are reported for 5 fire extensions. The graph on the left underlines that:

- the thermal load acting on a column and the resulting local failure do not affect the global behaviour of the frame; which column is involved by the fire does not matter;
- for a thermal load applied on two columns, two different collapse mechanisms (and time of resistance to fire) can be develop, in function of the columns involved;
- a global collapse occurs in every case after about 60-70 minutes for a major fire extension, whatever columns are involved.

Table 2. Fire Resistance of Frame B.

Heated	Columns	Fire		Resistance
No.	Cases	Avg	Min	Max
1	8	180	180	180
2	7	108.4	65	180
3	6	65.7	63	70
4	5	62.2	59	63
5	4	60.5	59	62

4.1.2 Frame A

The thermal action involves Frame A (Configuration A5) at sixth floor (Figure 8). At this height, design includes as profiles for columns HEM1000star (Col.9, Col.15, Col.40 and Col.49) and HEM900star (Col.1, Col.24, Col.32 and Col.54). Beams provided are IPE270 (Beam 9 and Beam 91), IPE 300 (Beam 19, Beam 33, Beam 63 and Beam 81) and HEA260 (Beam 49): also Frame A, as Frame B, is characterized by a stiffness ratio between column and beam very high.

Table 3 synthesizes results found for Frame A following the above described procedure with the application of an increasing thermal load:

- the load acting on a column or on two subsequent columns do not affect the global behaviour of the frame. Which column the fire involves does not matter;
- for a thermal load applied on three columns, two different situations can be occur, in function of the columns involved: if fire is applied also on the external column a global collapse occurs after about 80 minutes; on the other hand, if fire is near the vertical braced system;
- the thermal action upon four columns determines a global collapse in each case: if fire affects the central zone of the frame, the resistance time is greater than that caused by a lateral fire;
- all combinations characterized by the involvement of five subsequent columns lead to a global collapse for similar times (almost 70 minutes).

Table 3. Fire Resistance of Frame A.

Heated Columns		Fire Resistance		
No.	Cases	Avg	Min	Max
1	8	180	180	180
2	7	180	180	180
3	6	143.6	80	180
4	5	88.4	78	103
5	4	67.5	66	69

The plasticity spread allows highlighting the role of individual elements within the global behaviour: the outrigger system at 29th floor is able to stress redistribute due a local failure of elements until a certain fire extension; when it becomes ineffective, there is a total failure of the structure.

For the first extension, the worst case is when the fire is considered to directly affect Col.15 at sixth floor: after the beam failures, axial force of column (red curve of Figure 12) reaches the plastic limit for 640 °C after 26 minutes. The crisis of the column is absorbed by the structure through several load paths. The redistribution of the stresses caused to the plasticity of a beam in the outrigger. Despite the exposure to 180 min of fire, no other damage occurred in the frame.

When fire affects Col.15 and Col.9, the failure of the first column occurs after 28 minutes for a temperature of 680 °C. The exposure to fire leads to a greater spread of plasticity than in previous case in the beams around the outrigger system.

When fire involves Col.15, Col.9 and Col.1, the first collapse happens after 29 minutes for a temperature of 690 °C. In this case, the outrigger is not able to withstand the increase in stress due to local failures: the vertical braced system allows isolating the collapse in one side of the structure.

For a major fire extension, the collapse propagates also on the rest of the frame.

4.1.3 Comparison

The comparison between the behaviour of the two frames allows the following considerations:

- In frame B, the two vertical systems represent the most rigid part of the frame and remain on for the various cases of analysis but are unable to effectively support the rest of the structure. For a fire applied on two columns there is a considerable loss of fire resistance; a further abrupt loss occurs if fire involves three consecutive columns. Every major extension does not cause a significant deterioration in the weather resistance, which is around a quite low value.
- In frame B, the central system of bracing and outrigger represent the rigid part. The coupling of the two systems makes it more ductile the frame and allows a more gradual loss of performance with respect to the previous frame.

4.2 Conclusion

Starting from above considerations, the following improvements are proposed for the structure:

- an outrigger system placed at 29th floor placed along sections 1 and 2 of Figure 1c;
- vertical braced systems according to Configuration A5 and Configuration B3.

5 OPTIMIZED CONFIGURATION

The optimized structure, found taking into account improvements of previous sections, has been analysed in fire conditions of Figure 1c. In addition, in this case, a good parameter for following the global behaviour of the building is the displacement on the top floor. Figure 7 shows the evolution of the collapse. Structural changes determine a good improvement in case of Fire Scenario 1 (top of Figure 1) delaying the collapse that began about xx minutes later and covers a reduced area. During the exposure to fire, the lower percentage of involved area is still evident (Table 4). In the case of Fire Scenario 2, collapse starts for the same fire exposure, but it is clear the reduction of the propagation of the crisis.

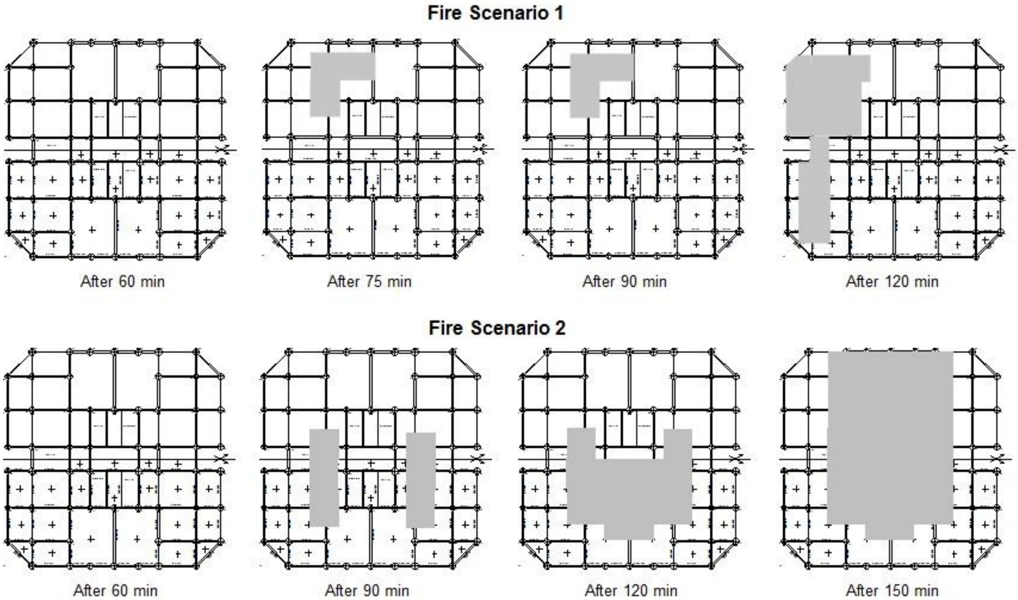

Figure 7. Evolution of the area of the top floor with a displacement major than 1m for Fire Scenario 1 (top) and for Fire Scenario 2 (bottom).

Table 4. Fire Resistance of Frame B.

	Scenario 1				Scenario 2			
	Collapsed Floor Area [m2]		Collapsed Floor Area Percentage [%]		Collapsed Floor Area [m2]		Collapsed Floor Area Percentage [%]	
Time	Original	Optimized	Original	Optimized	Original	Optimized	Original	Optimized
60min	130.26	0.00	11.21	0.00	0.00	0.00	0.00	0.00
75min	208.71	76.71	17.97	6.60	0.00	0.00	0.00	0.00
90min	325.21	76.71	28.01	6.60	149.62	149.62	12.89	12.89
120min	350.21	230.31	30.16	19.83	326.1	271.1	28.09	23.35
150min	No Con.	397.22	No Con.	34.21	779.25	587.6	67.12	50.61

6 CONCLUSIONS

The paper focuses on the susceptibility to progressive collapse that characterizes tall buildings. This is strongly influenced by the structural organization of the system. This aspect can be investigated only considering the structural system as a whole. In order to highlight the role of braced systems, a thermal load due to fire was applied on a three-dimensional model and fire performances were showed for two fire scenarios. A possible and rational approach to optimize the structural system is the individuation of resistant mechanisms, possible deficiencies and weaknesses. With this purpose, two substructures have been considered and analyzed in several possible configurations and under the action of different fire extension. These investigations have allowed proposing some structural improvements. In particular, the presence of an outrigger delays the collapse and reduces the part of the building involved.

REFERENCES

[1] Hall J., *High-rise buildings fire*, NFPA, 2011

[2] Khan F.R., "Recent structural systems in steel for high-rise buildings", *Proceedings of the British Constructional Steelwork Association Conference on Steel in Architecture*. London: British Constructional Steelwork Association, 1969.

[3] Ali M.M and Moon K.S., "Structural Developments in Tall Buildings: Current Trends and Future Prospects", *Architectural Science Review*, 50:3, 205-223, 2007

[4] Gentili F., Giuliani L., Bontempi F., "Structural response of high-rise buildings to fire: system characteristics and failure mechanisms", *Journal of Structural Fire Engineering*, p. 9-26, Volume 4, Number 1, 2013.

[5] Usmani A., Chung Y. and Torero J. "How did the WTC collapse: a new theory", *Fire Safety Journal*, 38(6), 2003.

[6] Starossek U., *Progressive Collapse of Structures*, Thomas Telford Publishing, London, 2009

[7] NIST NCSTAR 1. *Final Report on the Collapse of the World Trade Center Towers*, National Institute of Standards and Technology, Gaithersburg, MD, 2005.

[8] Craighead G. *High-rise security and fire life safety*. 3rd ed. U.S.A, Elsevier, 2009.

[9] Taranath B., *Steel, Concrete, & Composite Design of Tall Buildings*, McGraw-Hill, NewYork.

[10] NILIM. Report on the Windsor Building Fire in Madrid, Spain (in Japanese), Japan: National Institute for Land and Infrastructure Management, 2005.

[11] Usmani AS O'Connor MA, Rotter JM, Elghazouli AY, Drysdale DD, Sanad AM. Gillie M & Lamont S. Behaviour of Steel Framed Structures under Fire Conditions, s.l.: DETR-PIT Project, 2000.

[12] Research Fund for Coal and Steel of the European Community. Multi-storey steel buildings - Part 6: Fire Engineering, Steel Building in Europe design manual, 2008

[13] Petrini F. (2013). "Performance-based fire design of complex structures", *International Journal Life-Cycle Performance Engineering*.

[14] Arangio S. and Bontempi F. (2012). Basis of the analysis and design for fire-induced collapses in structures. *International Journal Lifecycle Performance Engineering*.

[15] Haremza C., Santiago A., Simões da Silva L., "Design of steel and composite open car parks under fire", International journal of advanced steel construction, 2013, Vol.9, No. 4, pp. 350 – 368.

[16] Giuliani L., Budny I., "Different design approaches to structural fire safety", *International Journal of Life-Cycle and Performance Engineering,* Special Issue on Fire Safety Design and Robustness Considerations in Structural Engineering, 2013 Vol.1, No.2, pp.135 – 158.

8th International Conference on Structures in Fire
Guo-Qiang LI, Venkatesh K. R. KODUR, Shou-Chao JIANG, Jian JIANG, Su-Wen CHEN, Guo-Biao LOU (Eds.)
Shanghai, China, June 11-13, 2014

AN INVESTIGATION OF THE LUMPED CAPACITANCE ASSUMPTION FOR UNPROTECTED STEEL MEMBERS

JohanSjöström* and David Lange*

*SP Technical research institute of Sweden, department of Fire Research
e-mails: johan.sjostrom@sp.se, david.lange@sp.se

Keywords: Steel, Fire, Lumped capacitance, Diffusion, Eurocode

Abstract. *Anybody exposed to fire will experience diffusive heating as a result of conductive heat flux through the member. It is common however in structural fire engineering to assume that the energy which is absorbed by a steel element exposed to fire is distributed evenly through the cross section and that the section therefore exhibits a uniform temperature increase; this assumption is commonly called lumped capacitance. However, for steel sections exposed to fire it may be shown that the web experiences higher temperatures faster than the two flanges, and for sections which are not heated at the top of the upper flange the difference in temperature between the upper flange and the web can be significant.*

This may have two effects on the behaviour of heated steel sections; firstly, the hotter regions may experience a higher degradation in material properties, resulting in larger deflections, local deformations in the elements, or earlier shear failure where the element is subject to large shear loads; additionally, the resulting thermal gradient may cause thermal bowing to occur in the beam resulting in larger deflections occurring earlier than may be predicted when lumped capacitance is assumed. This paper illustrates through example these effects and demonstrates a methodology which is being used to study the potential impact of diffusive heating on unprotected steel beams.

1 INTRODUCTION

Materials exposed to fires are generally heated non-uniformly and surfaces are cooled by conduction of heat into the interior of a body. However, for materials with a small dimension parallel to the direction of heating and a high conductivity, the heating can often be accurately described by a lumped capacitance assumption. For such instances any net heat flux at a surface is assumed to heat the body uniformly such that no temperature gradients exist within the volume. This is typically done when assessing the behaviour of either protected or unprotected steel members in fire according to Eurocode EN 1993-1-2, [1], which explicitlyemploys the lumped capacitance method for calculating steel temperature development.

$$\Delta T(\Delta t) = \frac{A_m/_V}{\rho c}\dot{q}_{net}\,\Delta t \tag{1}$$

where A_m and V are the exposed surface area and volume of the member per unit length, respectively (and the ratio of A_m and $V$is termed the section factor*)*, ρ is the density of the steel, *c*is the specific heat,$\dot{q}_{net}$ the net heat flux per unit area to the member and Δt the time step in the calculations.Note that $\dot{q}_{net}$ is labelled $\dot{h}_{net}$ in EN 1993-1-2.

One way of evaluating whether lumped capacitance is a reasonable assumption is to evaluate the heat penetration time for the body. Consider a semi-infinite homogeneous body of uniform temperature exposed to a step increase in its surface temperature. After time *t* the temperature at depth *x* has reached just over 50 % of the step increase when $x/\sqrt{\alpha t} = 1$, in which$\alpha = \lambda/(\rho c_p)$ is the thermal diffusivity, λ

thermal conductivity. The diffusivity of steel isbetween 15 and 5.7 mm^2/s for temperatures from 20 to 600 ℃. For a steel section, with a typical flange or web thickness of 10 mm the heat penetration time is therefore $t = x^2/\alpha$ =6 to 18 seconds. Clearly this is suitable for considering lumped behaviour across the thickness, something often utilized in fire sciences [2,3].

However, bodies with different thicknesses heat up at different rates, due to the different thermal mass,as do bodies being heated from one side only. Therefore, in order to consider the lumped capacity behaviour of the entire section, as proposed in the EN 1993-1-2[1], we need to consider the penetration time for the entire height or width of the section. For an HEB300 beam the corresponding penetration time from flange to flange is between 1.6 and 4.4 hours. Thus, the lumped capacity assumption may not always be representative of the temperature distribution in the section, and significant differences in temperature across the section may manifest during fire for unprotected steel members. From the perspective of the mechanical behaviour of unprotected beams exposed to fire, we do not know whether or not this assumption has any impact.

To address this, we investigate the behaviour of 5 HEB sections using finite element (FE) modelling. The modelling is carried out in two stages.

Firstly, all 5 sections are studied using a variety approaches to the heat transfer analysis based on varying assumptions with increasing levels of simplification. The heat transfer is thus dealt with using one of the following approaches; (1) the lumped capacity assumption, (2) a simplified version which treats the two flanges and web as isolated elements with individual lumped heat capacities and (3) a heat transfer simulation accounting for diffusion within the member.

Secondly, the mechanical behaviour of 3 of the sections is studied using finite element analysis and assuming temperatures associated with the first two approaches described above.

The results are analyzed in terms of both differences in temperatures observed in the models and differences in the resulting mechanical behaviour of the models.

2 MODELLING

The physical dimensions of the sections are given in table 1. They are assumed to support a light weight roof deck which does not contribute to their capacity and are heated on all surfaces but the top of the upper flange. All beams span 5 metres and are loaded at 1 and 2 thirds of their length. The applied load in each case corresponds to 45 % of theplastic bending moment at ambient temperature of the beams.

$$F = 0.45 \times 3\left(bt_f(d - t_f) + 0.25 \times\ t_w(d - 2t_f)^2\right)\sigma_y/L \tag{2}$$

where F is the load at one of the loading points, b is the breadth of the section, t_f is the thickness of the flange of the section, $d$is the depth of the section, σ_y is the yield strength of the material and L is the length of the beam.

Table 1.Dimensions of the HEB sections in the study.b is flange width, h total height of web (incl. flange thickness), s and t are thickness of web and flange, respectively.

Name	b (mm)	d (mm)	t_w (mm)	t_f (mm)	t/s (-)
HEB120	120	120	6.5	11	1.69
HEB240	240	240	10	17	1.70
HEB360	300	360	12.5	22.5	1.80
HEB500	300	500	14.5	28	1.93
HEB700	300	700	17	32	1.88

The fire exposure to the surface is assumed to be homogeneous such that we only study the assumptions related to the lumped capacitance. However because of the non-uniform temperature distribution within the section the net heat flux is inhomogeneous. Therefore, at all surfaces, except the upper surface of the upper flange, the net heat transfer through the surface is given by a convective heat transfer using a heat transfer coefficient of $h_c = 25$ W/mK and a gas temperature following the ISO 834 standard time temperature curve, T_{ISO}. A radiant heat transfer is also considered given a surface emissivity of $\varepsilon = 0.8$ and a radiation temperature also following ISO 834.

$$\dot{q}''_{net} = \varepsilon\sigma(T_{ISO}^4 - T_s^4) + h_c(T_{ISO} - T_s) \quad (3)$$

where T_s is the surface temperature and σ Stefan-Boltzmann's constant. The upper surface of the upper flange is assumed to be perfectly insulated.

As discussed, three different approaches are considered for the distribution of heat inside the beams.

(1) A lumped capacitance model which considers a uniform temperature increase in all the beam according to the design method given by Equation (1).

(2) A simple model treating the lower flange, the web and the upper flange as three isolated lumped capacity bodies with no heat transfer between them.

(3) A diffusive model which solves the heat diffusion equation within the section.

For the thermal part of the study, comsolmultiphysicswas used to create and study the temperature distribution within the steel section when diffusion within the member is taken into account.

For the mechanical analysis.The mechanical behaviour of the beams using the different thermal approaches is modelled using the finite element method in Abaqus 6.11-1 (using the standard solver). The model comprised 4-noded shell elements with 5 section points. For the first and second approaches described the temperature was calculated externally and was applied as a boundary condition to the nodes during the analysis. Future work includes repeating the mechanical analysis using the temperatures calculated during the diffusive heating analysis to determine the difference in mechanical behaviour between the three thermal assumptions.For the mechanical analyses, the modulus of elasticity of the steel at ambient was assumed to be 210 000 MPa, yield stress at ambient was assumed to be 275MPa. All other material properties and material property distributions such as density, thermal conductivity and specific heat capacity are taken from EN 1993-1-2, as was the surface emissivity.

The mechanical model took advantage of symmetry at the mid-span. Mechanical boundary conditions comprised a rigid body constraint at the support end with restraint in only the y-direction, i.e. vertical support with no horizontal restraint, applied at the reference point for the rigid body. This reference point was located at mid-height of the web. At the symmetry line, restraint comprised a symmetry restraint about the x-axis (the model spanned along the z-axis). In all analyses the length was kept constant, total length was 5000mm. The load was applied via a 100mm long plate with the same width as the upper flange, 50mm thick. The intention with this thickness was to have the plate reasonably rigid, although the actual thickness was chosen arbitrarily. Load was applied to the plate as a pressure, and the plate was not subject to any thermal loading. The nodes of the plate were tied to the upper flange surface. The mechanical loading was applied prior to any thermal loading.

Loading was applied in two steps, firstly the mechanical loading was applied and then the thermal loading was applied in an additional step in one of the manners described above depending upon the individual model.

3 RESULTS AND DISCUSSION

3.1 Thermal modelling

FE simulations verify, as expected, that the lumped capacitance assumption is valid through the thickness of the web and flanges of the membersince minimum variation in the temperature was seen in any of the analyses from one side of either the web or the flanges to the other, or the midpoint. For example, in the model of the HEB360 beam the difference between the inner parts and the surface of the web after five minutes of exposure is less than two degrees.

The temperature distributions along the flanges and web of the models of the HEB120, 360, 500 and 700 sections are given at various times in figure 1 based on the three different approaches outlined above.Results are plotted along an arc spanning from the edge of one of the upper flanges down through the web and to the corner of one of the lower flanges. For all the beams the qualitative behaviour is the same. The 2nd heat transfer methodology described, termed the simple model, with lumped capacitance assumed for the web and the flanges individually,exhibits a similar temperature in the lower flange in comparison with the lumped capacitance model. On the other hand, the web is, as expected, much hotter in the simple model compared to lumped capacitance due to the fact that: the web is much thinner than the flanges and therefore requires less energy to heat up; and the fact that the insulated surface of the upper flange is not affecting the web of the simple model. In the upper flange the temperature is markedly colder in the simple model compared to the lumped capacitance.

The diffusive model behaves very similarly to the simple model with smooth transitions between the different regions and generally with lower maximum temperatures in the individual regions. Naturally, there is more resemblance between the diffusive and the simple model for the larger beams as the diffusive distance grows. Figure 2 shows the temperature distribution of the HEB240 beam at different times. Towards higher temperatures the temperature in the lower flange and web approach one another as the convective contribution to the net heat flux decreases and the heat transfer becomes dominated by the radiation temperature. This has the effect of decreasing the heat transfer to high temperature regions. It is also evident from Figure 2 that the web temperature of the diffusive and simple models are more similar after longer times.

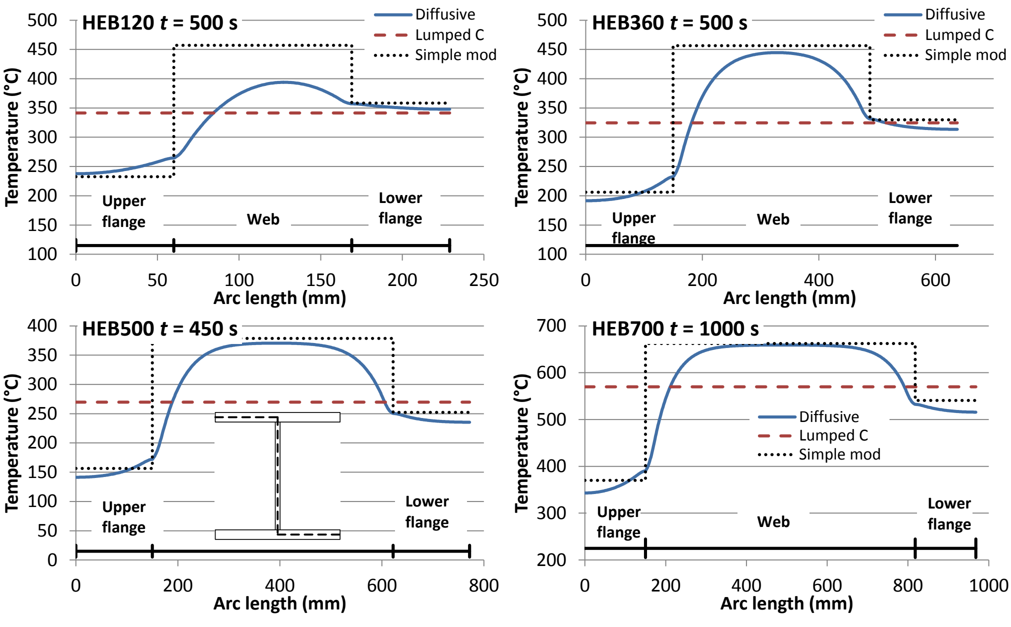

Figure 1.Temperature distributions of different beams at different time stamps. The temperature is from mid-thickness of the section from upper flange, through the web to the lower flange as depicted in the inset in the lower left panel.

It is worth noting that the higher web temperatures of the diffusive or simple model exceed the lumped capacitance temperatures by well over 100 ℃ for many of the cases shown here. This will naturally have a large impact on the material properties in the different regions such as elastic modulus or yield stress. However, the impact on the whole structure needs still to be investigated.

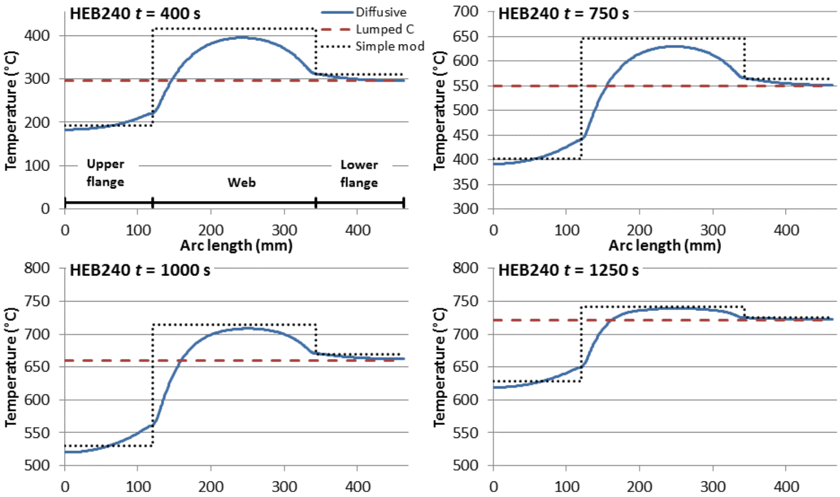

Figure 2. Temperature distributions of the HEB240 beam at different times.

3.2 Mechanical modelling

The thermal behaviour of the diffusive model is similar to the simple model. Therefore, results of the mechanical modelling are presented in this section for the simple model and the lumped capacitance model. As mentioned earlier the application of the temperatures from the diffusive heating analysis is the subject of on-going work by the authors.

The deflected shape of the HEB 240 beam is shown in Figure 3. On the left of the figure is the model with lumped capacitance assumed and on the right of the figure is the model with the simple heat transfer model applied. The contour plots show the equivalent plastic strain in the model, with the maximum set to 3‰. The line of symmetry is at the bottom left corner of each of the illustrations. In the lumped capacitance model the region where the load is applied is visible as a region of plastic strain in the upper flange. Note in the figure the greater portion of the upper and lower flange in the simple model which are subject to plastic strains. Also note in the mechanical model with the simple heat transfer model results applied that the web is subject to plastic strains all the way along its length, whereas in the model with lumped capacitance assumed there is only minimal plastic strains in the web, and these are localized to the areas around the upper and lower flange between the point with load application and the line of symmetry. The temperature of the web in this instance is 650 ℃, as opposed to 550 ℃ if lumped capacitance is assumed. At these two temperatures, the yield strength of steel is 35% and 62% the strength at ambient, respectively, which is quite a considerable difference.

To illustrate this, the time-deflection histories for 3 different section sizes are shown in Figure 4, the HEB 120, HEB 240 and HEB 360 beams. Again, results are limited to the mechanical model with temperatures arising from the lumped capacitance calculation and the simple heat transfer calculation applied. In all three cases the displacement history is plotted for the first 1000 seconds of a standard fire exposure. The general shape of the deflection histories agrees fairly well with that shown in, e.g. [6] for a simply supported steel beam, although there is some recovery of deflections following sudden increases, e.g. in the HEB 360 lumped capacitance displacement history at 600 seconds. Also shown in figure 4 is the displacement resulting from thermal curvature, calculated for each beam based on the method presented in [5]. The horizontal dashed line indicates an estimate of the magnitude of the displacement induced by thermal curvature and the vertical line indicates the time at which this was calculated. The initial mechanical deflection has been removed from the displacement in all of these cases, so the displacement shown is only that which occurs during the thermal analysis step. The displacement as a result of thermal bowing at the times it is shown in Figure 4 is also reported in Table 2.

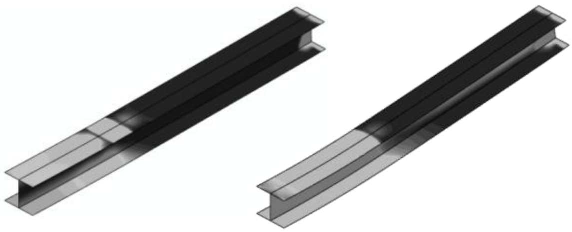

Figure 3. Plastic strain distribution in the HEB 240 beam at 740 seconds (left: lumped capacitance, right: simple heat transfer model).

In the case of both the HEB 240 and the HEB 360 beams, the two modelling approaches result in a gradual increase in deflection, up to about 500 seconds in the case of the HEB 240 and up to about 500 seconds in the case of the HEB 360 with the simple model and 600 seconds in the case of the HEB 360 assuming lumped capacitance. Following this there is some plateau in the response up until a continued increase in the deflection. Generally, it can be seen that the simple model has a higher rate of deflection during the early stages of heating than the model assuming lumped capacitance. This is mostly attributed to the thermal curvature in the section. For example, in the case of both the HEB 240 and the HEB 360 beams the thermal curvature accounts almost entirely for the difference in the deflection between the simple model and the model assuming lumped capacitance. In both of these cases, the plateau in the time deflection history in the simple model is also less distinct, possibly as a result of a larger reduction in the web strength and stiffness in these models.

In the HEB 120 model, the mechanical response under the simple heat transfer assumption is seen to experience a very rapid increase in deflection. This section is the smallest of the three which are discussed here and is more susceptible to the increase in curvature induced by the thermal gradient – not only is the temperature difference similar to the other section, but the section is smaller. In addition, the deflection history assuming lumped capacitance shows a sudden increase in deflection. This was accompanied by the sudden formation of a plastic hinge in the cross section adjacent to the loading point. In the other examples shown, the development of plastic strains indicating a hinge forming in the flanges was not immediately accompanied by plastic straining through most of the depth of the web.

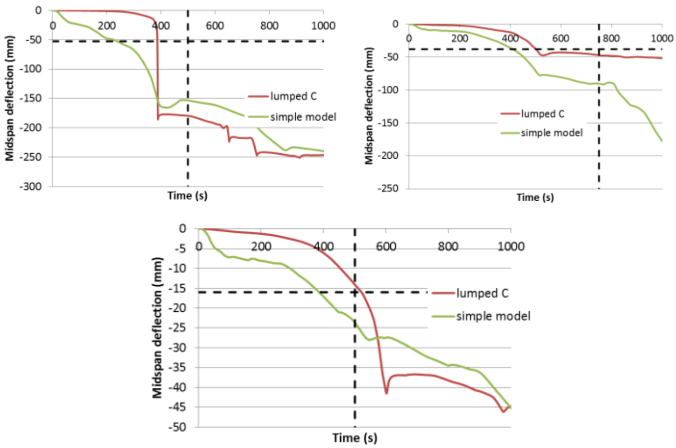

Figure 4. Midspan deflections of the HEB 120, HEB 240 and HEB 360 models (dashed lines indicate the thermal curvature at the shown times).

Table 2. Displacement in the beams resulting from thermal curvature*.

Beam	Time (s)	Displacement (mm)
HEB 120	500	-53
HEB 240	750	-38
HEB 360	500	-16

* note that the thermal curvature shown is taken arbitrarily at a time to correspond with one of the temperature plots in figure 1 or figure 2 and is not indicative of any final thermal curvature.

4 CONCLUSIONS AND FURTHER WORK

We have shown in this paper the impact of lumped capacitance on the temperature response and the deflection history of a small number of steel beams of a fixed length and load ratio. The temperature response was compared with the temperature response of the same section assuming a simple non-diffusive model which accounted for the capacitances of the flanges and the web individually as well as a model which accounted for diffusion throughout the section. A reasonable approximation to the diffusive model was seen for the simple model of the beam section split into the flanges and the web, whereas the lumped capacitance model underestimated the temperature in the web by over 100 °C in some cases, and overestimated the temperature in the upper flange by over 150 °C in some cases. Clearly this may have an impact on the mechanical response of beams exposed to fire with different combinations of shear and bending load. The impact on the level of safety has however not been evaluated in this paper.

The deflection history was also shown to be dependent upon the assumption of lumped capacitance, and it was postulated that thermal curvature, even given the relatively small thermal gradients seen in this study, may account largely for the total displacement where non-uniform heating was accounted for.

The impact of this difference in behaviour on the actual capacity of unprotected steel beams in fire has not been evaluated.

Results presented here did not include a discussion of the difference in the mechanical response of steel beams exposed to fire when the diffusive heating heat transfer mode was used. This will be addressed in future work by modelling of the response of beams to diffusive heating.

The results presented here are limited to only one length of beam and only a few sections subject to the same load ratio. This paper reports on a method which has been developed and which will be applied in the future to a greater number of sections and lengths of beams to evaluate the impact of the assumption of lumped capacitance on the resistance of unprotected steel sections. As such it is the intention of the authors to continue their research into this area and to consider different combinations of length and load ratio on a variety of unprotected steel sections. We will also consider alternative fire scenarios and localised heating of steel beams.

5 REFERENCES

[1] European Committee for standardisation (CEN). EN 1993-1-2: 2004 Eurocode 3: "*Design of Steel Structures. Part 1.2 General Rules - Structural Fire Design*", CEN, Brussels, Belgium, 2004.

[2] Malhotra H.L., *Design of Fire-Resisting Structures*, Surrey University Press, London, 1982.

[3] Iqbal S. and Harichandran R.S., "Capacity Reduction and Fire Load Factors for Design of Steel Members Exposed to Fire", *Journal of Structural Engineering*, 126(12), 1554-1562, 2010.

[4] Usmani AS, Rotter JM, Lamont S, Sanad AM, Gillie M. Fundamental principles of structural behaviour under thermal effects. Fire Safety J 2001;36:721–44.

[5] A. S. Usmani and S. Lamont; Key events in the structural response of a composite steel frame structure in fire; Fire and Materials 2004; 28:281–297 (DOI: 10.1002/fam.856).

[6] Usmani AS, Röben C, Al-Remal A. A very simple method for assessing tall building safety in major fires. Int J Steel Struct 2009;9:17–28.

8th International Conference on Structures in Fire
Guo-Qiang LI, Venkatesh K. R. KODUR, Shou-Chao JIANG, Jian JIANG, Su-Wen CHEN, Guo-Biao LOU (Eds.)
Shanghai, China, June 11-13, 2014

ANALYTICAL SOLUTIONS FOR NONLINEAR RESPONSE OF PLATES UNDER THERMAL LOADING

Payam Khazaeinejad* and Asif S. Usmani*

*School of Engineering, The University of Edinburgh, The King's Buildings, Edinburgh EH9 3JL, UK
e-mails: p.khazaeinejad@ed.ac.uk, asif.usmani@ed.ac.uk

Keywords: Plate, Large deflections, Thermal gradient, Fire, Tensile membrane action

Abstract. *An analytical method is presented to quantify the development of tensile membrane action in thermally-loaded rectangular plates. Both geometrical and material nonlinearities are considered in the proposed method. The geometric nonlinearity is based on the von Karman large deformation theory. The material nonlinearity arises from degradable nonlinear material behaviour of the plate at elevated temperatures. The temperature distribution in the plate is assumed to vary nonlinearly across the thickness. The analysis is carried out based on quasi-static conditions ignoring any dynamic effects. The accuracy of the proposed method is assessed through a number of numerical examples.*

1 INTRODUCTION

Membrane action in plates (for example reinforced concrete slabs) generally develops either in the form of compressive membrane action (CMA) and/or tensile membrane action (TMA). The former develops at small vertical displacements of the plate under conditions of restraint to lateral translation while the latter develops at large vertical displacements, also anchored by restraint to lateral translation at the boundaries. These phenomena are therefore naturally very sensitive to the boundary restraint conditions of the plate. It is well known that the development of both CMA and TMA can enhance the ultimate load-carrying capacity of floor slabs. In simply supported slabs (where translation across boundaries is unrestrained) undergoing large displacements, a degree of TMA can still occur. A feature of this mechanism is the appearance of a "compressive ring" in the slab as a manifestation of CMA in the outer regions of the slab which provides restraint to TMA occurring in the central region of the slab, not dissimilar to the relatively rigid ring surrounding a trampoline as illustrated in Figure 1. This was recognised as an important load-carrying mechanism of "last resort" in the full-scale fire tests at Cardington [1]. This "compressive ring" mechanism has however not been fully investigated and therefore has never been properly quantified.

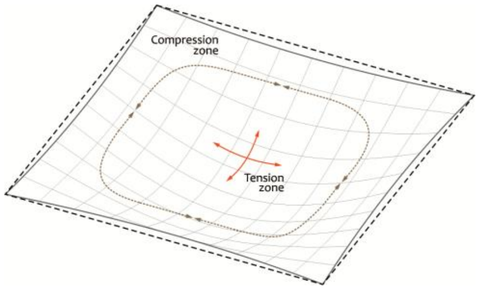

Figure 1. Mechanism of TMA in laterally unrestrained slabs.

A simple model for determining TMA of composite slabs in fire was presented by Bailey [2] which predicts the load-bearing capacity of slabs by calculating the enhancement of their traditional yield line load capacity due to TMA. As the work of Bailey does not account for the correct shape of the floor system under the influence of heating, Cameron and Usmani [3] proposed a three-step method to analyse the deflected shape and limit capacity of laterally restrained reinforced concrete slabs in fire. Abu et al. [4] developed it using the variational Rayleigh-Ritz method so that incorporates both thermal and mechanical effects into the prediction of slab behaviours at both ambient and elevated temperatures.

A key objective of our research is to develop an analytical procedure for understanding the mathematical underpinnings of the compressive ring supporting TMA in slabs under fire conditions in order to produce a simple graphical visualisation of the ring under a range of thermal and gravity load combinations and properly quantify its contribution to the load carrying capacity of thermally deformed plates. The following observations provide the inspiration for this work:

（1）Full-scale tests have clearly demonstrated that slabs may be able to support loads much higher than those predicted by the well-established yield line analysis method (YLA) (up to 4 times for CMA [5]).

（2）The rich theory of classical numerical methods such as weighted residual and Rayliegh-Ritz (which are the foundations of the powerful finite element methods) suggests that a good approximation method for estimating structural forces and deformations depends upon using trial functions that are able represent the deformed geometry of the structure as closely as possible. In this context the use of YLA by some researchers for slabs subjected to thermal gradients may have some practical engineering justification for purposes of expediency but it has little or no mathematical justification as YLA is only applicable to very small displacements (which is almost never the case with floor slabs subjected to flashed over fires).

（3）The change of shape of the slab because of significant thermal bowing in fire allows TMA to occur more naturally resulting in enhanced load carrying capacity, even if there is loss of strength [1, 6].

An analytical method is presented for geometrically and materially nonlinear analysis of rectangular plates. The plate experiences large displacements which required using appropriate strain definitions. Rotations parallel to the boundary are assumed to be free while translations across the boundary may be free or restrained. Temperature-dependency of the material properties is also considered in the analysis.

2 FORMULATION

A four-step analysis process is proposed which includes: (1) generating a non-uniform temperature distribution on the plate (2) considering the temperature dependency of the material properties and consequently the material nonlinearity (3) determining the large displacements and the stress distribution caused by the thermal loading and uniform distributed load (UDL) and (4) quantifying the evolution of the compressive ring in TMA. The formulation of the problem is briefly described here.

2.1 Temperature-dependency of material properties

For this paper it is assumed that the constituent materials behave in a linear elastic manner in both compression and tension, however the reduction in material stiffness at elevated temperature is included in the model. The degradation of material properties at elevated temperatures are provided in tabular forms in the Eurocode [7]. Likewise, the following empirical expressions are provided by the Australian Standard [8] for the elastic modulus of structural steel

$$\frac{E_s(\theta)}{E_{s0}(20)} = \begin{cases} 1+\theta/[2000\ \ln(\theta/1100)] & \text{when} \quad 0°\text{C}<\theta \le 600°\text{C} \\ 690\ [1-(\theta/1000)]/(\theta-53.5) & \text{when} \quad 600°\text{C}<\theta \le 1000°\text{C} \end{cases} \tag{1}$$

and for the elastic modulus of concrete [9]

$$\frac{E_c(\theta)}{E_{c0}(20)}=\begin{cases}1 & \text{when} \quad 0°\mathrm{C}\le\theta\le 60° \\ (720-\theta)/660 & \text{when} \quad 60°\mathrm{C}<\theta\le 720°\mathrm{C}\end{cases} \tag{2}$$

where θ is the three-dimensional temperature field, E_{s0} and E_{c0} are the elastic moduli of steel and concrete at ambient temperature (20 ℃), respectively, and E_s and E_c are the counterpart elastic moduli at elevated temperatures. No equation is provided in both standards for the coefficient of thermal expansion α. However, it can be obtained as the first derivative of the thermal elongation provided in the Eurocode [7] as presented here for steel

$$\frac{\alpha_s(\theta)}{\alpha_{s0}(20)}=\begin{cases}1.2\times10^{-5}+0.8\times10^{-8}\theta & \text{when} \quad 20°\mathrm{C}<\theta\le 750°\mathrm{C} \\ 0 & \text{when} \quad 750°\mathrm{C}<\theta\le 860°\mathrm{C} \\ 2\times10^{-5} & \text{when} \quad 860°\mathrm{C}<\theta\le 1200°\mathrm{C}\end{cases} \tag{3}$$

and normal weight concrete

$$\frac{\alpha_s(\theta)}{\alpha_{s0}(20)}=\begin{cases}9\times10^{-6}+6.9\times10^{-11}\theta^2 & \text{when} \quad 20°\mathrm{C}\le\theta\le 700°\mathrm{C} \\ 0 & \text{when} \quad 700°\mathrm{C}<\theta\le 1200°\mathrm{C}\end{cases} \tag{4}$$

where α_{s0} and α_{c0} are the coefficient of thermal expansion of steel and normal weight concrete at ambient temperature, respectively, and α_s and α_c are the counterpart coefficient of thermal expansion at elevated temperatures. The coefficient of thermal expansion for lightweight concrete is constant and equal to 8×10^{-6} (℃$^{-1}$). Figure 2 shows the temperature-dependency of the structural steel and concrete based on acquired data from the Eurocode [7] and the Australian Standard [8, 9].

2.2 Fundamental relations

The expressions for the mechanical strains in the large displacements are

$$\begin{Bmatrix}\varepsilon_{xx(\mathrm{mech})} \\ \varepsilon_{yy(\mathrm{mech})} \\ \gamma_{xy(\mathrm{mech})}\end{Bmatrix}=\begin{Bmatrix}u_{,x}+0.5w_{,x}^2 \\ v_{,y}+0.5w_{,y}^2 \\ u_{,y}+v_{,x}+w_{,x}w_{,y}\end{Bmatrix}-z\begin{Bmatrix}w_{,xx} \\ w_{,yy} \\ 2w_{,xy}\end{Bmatrix}-\begin{Bmatrix}\alpha\Delta\theta \\ \alpha\Delta\theta \\ 0\end{Bmatrix} \tag{5}$$

where u, v, and w are the middle surface displacements in the x, y, and z directions, respectively, and $\Delta\theta$ ($=\theta-\theta_R$) is the change in temperature field relative to reference temperature θ_R. The membrane tractions can then be found as follows:

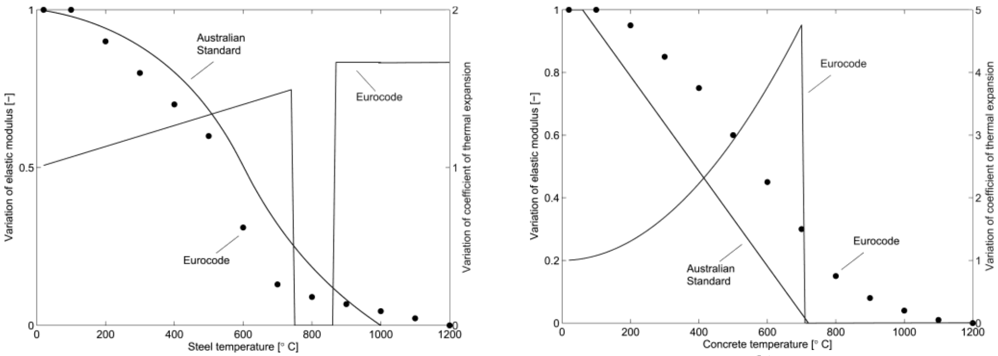

(a) (b)

Figure 2. Degradation of material properties at elevated temperatures for (a) steel and (b) concrete.

$$\begin{Bmatrix} N_{xx} \\ N_{yy} \\ N_{xy} \end{Bmatrix} = \begin{bmatrix} A_{11} & A_{12} & A_{13} \\ A_{21} & A_{22} & A_{23} \\ A_{31} & A_{32} & A_{33} \end{bmatrix} \begin{Bmatrix} u_{,x} + 0.5w_{,x}^2 \\ v_{,y} + 0.5w_{,y}^2 \\ u_{,y} + v_{,x} + w_{,x}w_{,y} \end{Bmatrix} - \begin{bmatrix} B_{11} & B_{12} & B_{13} \\ B_{21} & B_{22} & B_{23} \\ B_{31} & B_{32} & B_{33} \end{bmatrix} \begin{Bmatrix} w_{,xx} \\ w_{,yy} \\ 2w_{,xy} \end{Bmatrix} - \begin{Bmatrix} N^{\theta} \\ N^{\theta} \\ 0 \end{Bmatrix} \tag{6a}$$

$$\begin{Bmatrix} M_{xx} \\ M_{yy} \\ M_{xy} \end{Bmatrix} = \begin{bmatrix} B_{11} & B_{12} & B_{13} \\ B_{21} & B_{22} & B_{23} \\ B_{31} & B_{32} & B_{33} \end{bmatrix} \begin{Bmatrix} u_{,x} + 0.5w_{,x}^2 \\ v_{,y} + 0.5w_{,y}^2 \\ u_{,y} + v_{,x} + w_{,x}w_{,y} \end{Bmatrix} - \begin{bmatrix} D_{11} & D_{12} & D_{13} \\ D_{21} & D_{22} & D_{23} \\ D_{31} & D_{32} & D_{33} \end{bmatrix} \begin{Bmatrix} w_{,xx} \\ w_{,yy} \\ 2w_{,xy} \end{Bmatrix} - \begin{Bmatrix} M^{\theta} \\ M^{\theta} \\ 0 \end{Bmatrix} \tag{6b}$$

where the coefficient are defined in the Appendix. The thermal force and thermal moment resultants (N^{θ} and M^{θ}, respectively) are defined by

$$(N^{\theta},\, M^{\theta}) = \int_{-h/2}^{h/2} \frac{E\alpha\theta}{1-\nu}\,(1, z)\, dz \tag{7}$$

By introducing the stress function F such that

$$N_{xx} = \frac{\partial^2 F}{\partial y^2}, \qquad N_{yy} = \frac{\partial^2 F}{\partial x^2}, \qquad N_{xy} = -\frac{\partial^2 F}{\partial x \partial y} \tag{8}$$

the following governing equations for the large deformations of rectangular plates subjected to UDL and thermal gradient, as shown in Figure 3, are derived:

The compatibility equation:

$$\begin{aligned} a_{22}F_{,xxxx} + (2a_{12} + a_{33})F_{,xxyy} + a_{11}F_{,yyyy} = {} & w_{,xy}^2 - w_{,xx}w_{,yy} \\ & - b_{12}w_{,xxxx} - (b_{11} + b_{22} - 2b_{33})w_{,xxyy} - b_{12}w_{,yyyy} \\ & - a_{12}N^{\theta}_{,xx} - a_{11}N^{\theta}_{,yy} - a_{22}N^{\theta}_{,xx} - a_{12}N^{\theta}_{,yy} \end{aligned} \tag{9a}$$

The equilibrium equation:

$$\begin{aligned} d_{11}w_{,xxxx} + (2d_{12} + 4d_{33})w_{,xxyy} + d_{22}w_{,xxyy} = {} & q + F_{,yy}w_{,xx} + F_{,xx}w_{,yy} - 2F_{,xy}w_{,xy} \\ & + c_{12}F_{,xxxx} + (c_{11} + c_{22} - 2c_{33})F_{,xxyy} + c_{12}F_{,yyyy} \\ & - (c_{11} + c_{12})N^{\theta}_{,xx} - (c_{12} + c_{22})N^{\theta}_{,yy} - M^{\theta}_{,xx} - M^{\theta}_{,yy} \end{aligned} \tag{9b}$$

where $q(x, y)$ is the UDL. The effect of temperature-dependency of the material properties is also included in the formulation. The corresponding coefficients a_{ij}, b_{ij}, c_{ij} and d_{ij} are defined in the Appendix.

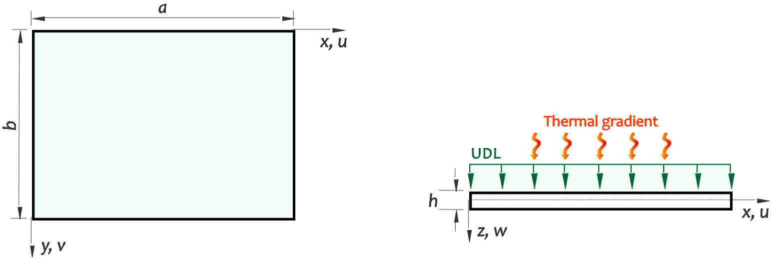

Figure 3. Configuration of the problem studied.

Two types of in-plane boundary conditions are considered, displacements 1) restrained and 2) unrestrained against lateral translation. For both cases the transverse deflection is set to zero along the boundary. The following double Fourier series satisfy these conditions:

$$w = \sum_{m=1}^{\infty}\sum_{n=1}^{\infty} W_{mn} \sin\frac{m\pi x}{a} \sin\frac{n\pi y}{b} \tag{10a}$$

$$F = \frac{P_x y^2}{2bh} + \frac{P_y x^2}{2ah} + \sum_{m=1}^{\infty}\sum_{n=1}^{\infty} F_{mn} \sin\frac{m\pi x}{a} \sin\frac{n\pi y}{b} \tag{10b}$$

$$(N^{\theta},\ M^{\theta},\ q) = \sum_{m=1}^{\infty}\sum_{n=1}^{\infty} (N^{\theta}_{mn},\ M^{\theta}_{mn},\ q_{mn})\ \sin\frac{m\pi x}{a} \sin\frac{n\pi y}{b} \tag{10c}$$

where P_x and P_y are equivalent reaction loads at the plate boundaries. For the restrained case the reaction loads can be obtained using the elongation of the plate in the x and y directions. However, for the unrestrained case, where translation across the plate boundaries is allowed, the following equations are obtained for the in-plane displacements

$$u = \sum_{m=1}^{\infty}\sum_{n=1}^{\infty}\left[-\frac{m^2\pi^2}{4a^2}\left(x + \frac{a}{2m\pi}\sin\frac{2m\pi x}{a}\right) w_{mn}^2 \sin^2\frac{n\pi y}{b} + \eta_1 W_{mn} + \eta_2 F_{mn} + \eta_3 \right] \tag{11a}$$

$$v = \sum_{m=1}^{\infty}\sum_{n=1}^{\infty}\left[-\frac{n^2\pi^2}{4b^2}\sin^2\frac{m\pi x}{a}\left(y + \frac{b}{2n\pi}\sin\frac{2n\pi y}{b}\right) w_{mn}^2 + \eta_4 W_{mn} + \eta_5 F_{mn} + \eta_6 \right] \tag{11b}$$

The coefficients η_i are also introduced in the Appendix. To minimise the possible error raised from the introduction of the finite series in Equations (10), upon substitution of Equations. (10) into the governing Equations (9), the left parts of the Equations (9) (denoted by L_1 and L_2, respectively) are integrated over the plate area such that

$$\int_0^a\int_0^b L_1\ \sin\frac{m\pi x}{a}\sin\frac{n\pi y}{b}\ dy\ dx = 0 \qquad \text{and} \qquad \int_0^a\int_0^b L_2\ \sin\frac{m\pi x}{a}\sin\frac{n\pi y}{b}\ dy\ dx = 0 \tag{12}$$

where it leads to the following algebraic system for the rectangular plate problem

$$\sum_{m=1}^{\infty}\sum_{n=1}^{\infty}\left[\chi_1 F_{mn} - \chi_2 W_{mn}^2 - \chi_3 W_{mn} - \chi_4 N^{\theta}_{mn} \right] = 0 \tag{13a}$$

$$\sum_{m=1}^{\infty}\sum_{n=1}^{\infty}\left[\chi_5 W_{mn} - \chi_6 q_{mn} - \chi_7 F_{mn} W_{mn} - \chi_8 F_{mn} - \chi_9 M^{\theta}_{mn} \right] = 0 \tag{13b}$$

The coefficients χ_i are not listed to economise on space (they must be calculated for any assumed temperature function).

3 NUMERICAL EXAMPLES

The large deflection for the horizontally unrestrained case is computed using one term in the series (m=n=1) whereas for the restrained case it is computed using three terms (m, n=1, 2, 3). This resulted in a considerable saving in computation time without losing accuracy. To investigate the accuracy of the proposed method, two numerical examples of plate behaviour subjected to linear thermal gradient and UDL.

Example 1: First, results from comparison studies are presented for the large deflections of a square slab at uniform ambient temperature. Table 1 shows the deflections of a square plate under UDL having horizontally unrestrained and restrained boundary conditions. The results obtained using the method presented are compared with results derived by an analytical method [10] using the von Karman plate theory. They agree very well with those listed in the table with almost zero error for the horizontally unrestrained case and 3.15% error for the restrained case.

Table 1. Non-dimensional centre deflection (w/h) for a square plate under UDL (qa^4/Eh^4).

Boundary condition	Analytical method [10]	FEM [11]	Present study	
Horizontally unrestrained	1.88 (6)*	1.8827 (3)	1.88 (1)	1.78 (6)
Horizontally restrained	1.27 (6)	—	1.31 (3)	1.32 (6)

* The digits in parentheses are the number of terms in the series taken for convergence.

Example 2: In this example the results from the method presented are validated for elevated temperatures. A horizontally restrained square plate with a side length of 5 m, thickness of 0.1 m, modulus of elasticity of 40 GPa, coefficient of thermal expansion of 8×10^{-6} 1/℃ and Poisson's ratio of 0.3 is considered. A temperature distribution causing an equivalent thermal gradient of 5000 ℃/m and an equivalent thermal expansion of 200 ℃ is chosen. The calculated non-dimensional central deflection (w/h) using the method presented is compared with the solutions of ABAQUS finite element (FE) package [3] and an analytical method in Table 2. Comparing the results obtained by these three methods reveals that the result predicted by the present method is in very good agreement with the one predicted by the FE analysis [3], indicating this is the more accurate solution for determining the deflection in a plate subjected to elevated temperatures.

Table 2. Non-dimensional centre deflection (w/h) for a horizontally restrained square slab under linear thermal gradient.

Solution method	Centre deflection (w/h)
Analytical method [3]	1.48 (1)*
FE [3]	1.36
Present	1.37 (3)

* The digits in parentheses are the number of terms in the series taken for convergence.

To understand the formation of the compressive ring in the slabs, the influence of two limiting cases (rigid restraint or zero restraint) on TMA is investigated. Figures 4 and 5 clearly show TMA in the slab with tensile and compressive membrane stresses in the central zone and around perimeter of the slab respectively. The slab has the same material properties and geometry as those mentioned in example 2 and is subjected to a linear thermal gradient (=200+5000z) and UDL of 100 kPa. The existence of both tension zone (in the middle) and compression zone (around premier) in membrane tractions (N_y) leads to the formation of a compressive ring as illustrated in the Figures 6 and 7 for both types of boundary restraint. It should be noted that there is a stress-free edge condition for the unrestrained boundary case.

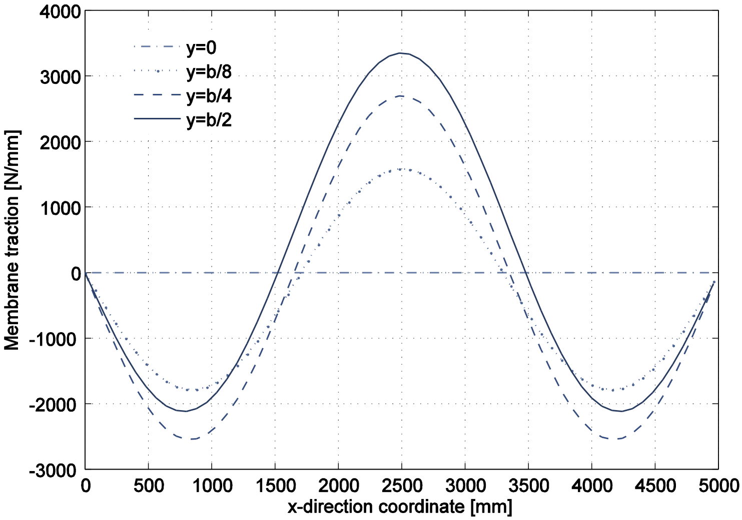

Figure 4. Membrane tractions (N_y) for the horizontally unrestrained slab across the span.

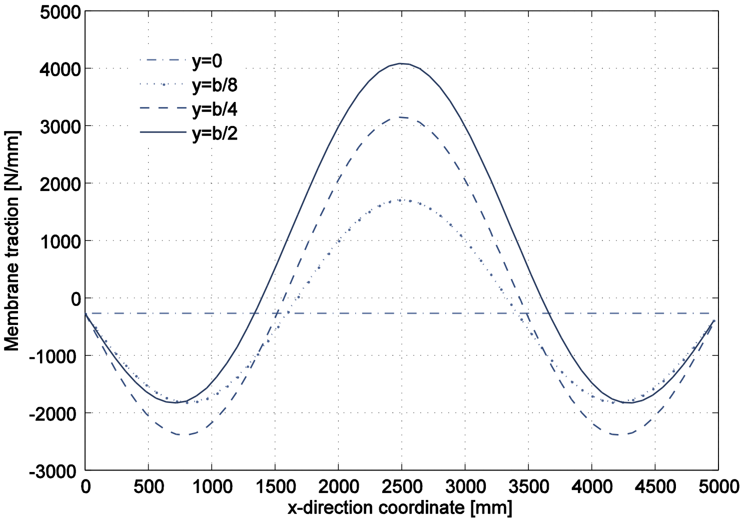

Figure 5. Membrane tractions (N_y) for the restrained slab across the span.

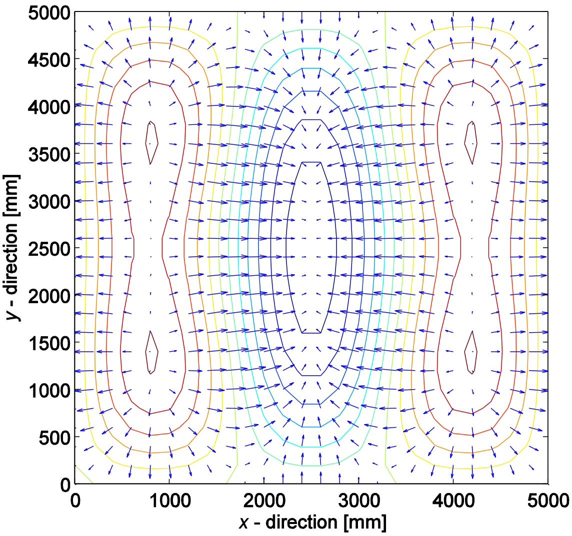

Figure 6. Formation of the compressive ring in TMA for the horizontally unrestrained slab.

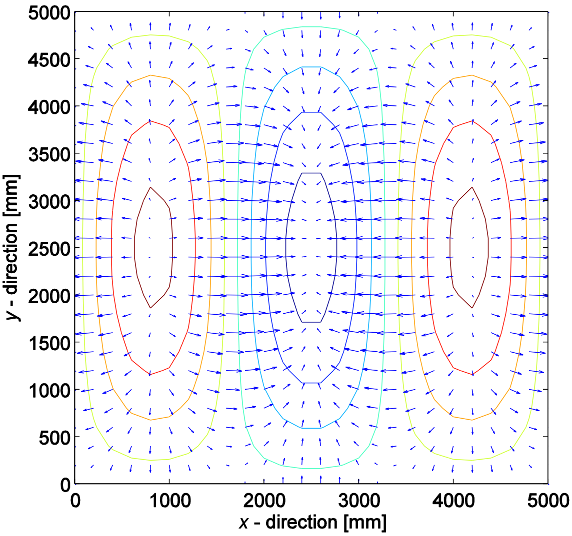

Figure 7. Formation of the compressive ring in TMA for the restrained slab.

4 CONCLUSIONS

In order to investigate the effect of the TMA in improving the fire performance of slabs, a geometrically nonlinear analysis was carried out using an analytical solution of the equilibrium and compatibility equations. The accuracy of the proposed method was assessed through a number of numerical examples in order to validate the proposed method against reliable previously published results.

The method was developed to understand the mathematical underpinnings of the compressive ring supporting TMA in slabs under fire conditions. Since the choice of the type of series depends on the boundary conditions of the problem, expanding the deflection and stress function in appropriate series are very important to quantify the evolution of the compression zone (ring). The sinusoidal double Fourier series for stress function satisfied the stress-free boundary condition, however, three series terms were needed to consider in the calculations for the horizontally unrestrained case. The analysis method may also be adopted as the basis of a simple and efficient design calculation method that does not rely upon expensive and time consuming finite element analysis, for situations where this can be justified.

ACKNOLEDGEMENTS

The authors acknowledge financial support for this research through the Edinburgh Research Partnership in Engineering (ERPe) funding.

APPENDIX

The coefficient of the governing Equations (9) are defined as

$$\begin{bmatrix} a_{11} & a_{12} & a_{13} \\ a_{21} & a_{22} & a_{23} \\ a_{31} & a_{32} & a_{33} \end{bmatrix} = \begin{bmatrix} A_{11} & A_{12} & A_{13} \\ A_{21} & A_{22} & A_{23} \\ A_{31} & A_{32} & A_{33} \end{bmatrix}^{-1} \tag{A.1}$$

$$\begin{bmatrix} b_{11} & b_{12} & b_{13} \\ b_{21} & b_{22} & b_{23} \\ b_{31} & b_{32} & b_{33} \end{bmatrix} = \begin{bmatrix} A_{11} & A_{12} & A_{13} \\ A_{21} & A_{22} & A_{23} \\ A_{31} & A_{32} & A_{33} \end{bmatrix}^{-1} \begin{bmatrix} B_{11} & B_{12} & B_{13} \\ B_{21} & B_{22} & B_{23} \\ B_{31} & B_{32} & B_{33} \end{bmatrix} \tag{A.2}$$

$$\begin{bmatrix} c_{11} & c_{12} & c_{13} \\ c_{21} & c_{22} & c_{23} \\ c_{31} & c_{32} & c_{33} \end{bmatrix} = \begin{bmatrix} B_{11} & B_{12} & B_{13} \\ B_{21} & B_{22} & B_{23} \\ B_{31} & B_{32} & B_{33} \end{bmatrix} \begin{bmatrix} A_{11} & A_{12} & A_{13} \\ A_{21} & A_{22} & A_{23} \\ A_{31} & A_{32} & A_{33} \end{bmatrix}^{-1} \tag{A.3}$$

$$\begin{bmatrix} d_{11} & d_{12} & d_{13} \\ d_{21} & d_{22} & d_{23} \\ d_{31} & d_{32} & d_{33} \end{bmatrix} = \begin{bmatrix} D_{11} & D_{12} & D_{13} \\ D_{21} & D_{22} & D_{23} \\ D_{31} & D_{32} & D_{33} \end{bmatrix} - \begin{bmatrix} B_{11} & B_{12} & B_{13} \\ B_{21} & B_{22} & B_{23} \\ B_{31} & B_{32} & B_{33} \end{bmatrix} \begin{bmatrix} A_{11} & A_{12} & A_{13} \\ A_{21} & A_{22} & A_{23} \\ A_{31} & A_{32} & A_{33} \end{bmatrix}^{-1} \begin{bmatrix} B_{11} & B_{12} & B_{13} \\ B_{21} & B_{22} & B_{23} \\ B_{31} & B_{32} & B_{33} \end{bmatrix} \tag{A.4}$$

where

$$\left(\begin{bmatrix} A_{11} & A_{12} & A_{13} \\ A_{21} & A_{22} & A_{23} \\ A_{31} & A_{32} & A_{33} \end{bmatrix}, \begin{bmatrix} B_{11} & B_{12} & B_{13} \\ B_{21} & B_{22} & B_{23} \\ B_{31} & B_{32} & B_{33} \end{bmatrix}, \begin{bmatrix} D_{11} & D_{12} & D_{13} \\ D_{21} & D_{22} & D_{23} \\ D_{31} & D_{32} & D_{33} \end{bmatrix} \right) = \int_{-h/2}^{h/2} \frac{E}{1-\nu^2} \begin{bmatrix} 1 & \nu & 0 \\ \nu & 1 & 0 \\ 0 & 0 & \dfrac{1-\nu}{2} \end{bmatrix} (1, z, z^2)\, dz \tag{A.5}$$

The coefficients of the in-plane displacements (11) are found to be

$$\eta_1 = \int_0^a \left\{ -\left(b_{11} \frac{m^2\pi^2}{a^2} + b_{12} \frac{n^2\pi^2}{b^2} \right) \sin\frac{m\pi x}{a} \sin\frac{n\pi y}{b} + 2b_{13} \frac{mn\pi^2}{ab} \cos\frac{m\pi x}{a} \cos\frac{n\pi y}{b} \right\} dx \tag{A.6}$$

$$\eta_2 = \int_0^a \left\{ -\left(a_{11} \frac{n^2\pi^2}{b^2} + a_{12} \frac{m^2\pi^2}{a^2} \right) \sin\frac{m\pi x}{a} \sin\frac{n\pi y}{b} - a_{13} \frac{mn\pi^2}{ab} \cos\frac{m\pi x}{a} \cos\frac{n\pi y}{b} \right\} dx \tag{A.7}$$

$$\eta_3 = \int_0^a (a_{11} + a_{12})\, N^\theta dx \tag{A.8}$$

$$\eta_4 = \int_0^b \left\{ -\left(b_{21} \frac{m^2\pi^2}{a^2} + b_{22} \frac{n^2\pi^2}{b^2} \right) \sin\frac{m\pi x}{a} \sin\frac{n\pi y}{b} + 2b_{23} \frac{mn\pi^2}{ab} \cos\frac{m\pi x}{a} \cos\frac{n\pi y}{b} \right\} dy \tag{A.9}$$

$$\eta_5 = \int_0^b \left\{ -\left(a_{21} \frac{n^2\pi^2}{b^2} + a_{22} \frac{m^2\pi^2}{a^2} \right) \sin\frac{m\pi x}{a} \sin\frac{n\pi y}{b} - a_{23} \frac{mn\pi^2}{ab} \cos\frac{m\pi x}{a} \cos\frac{n\pi y}{b} \right\} dy \tag{A.10}$$

$$\eta_6 = \int_0^b (a_{21} + a_{22})\, N^\theta dy \tag{A.11}$$

REFERENCES

[1] The University of Edinburgh, "Behaviour of Steel Framed Structures Under Fire Conditions", *Technical Report Main Report*, *DETR-PIT Project*, School of Civil and Environmental Engineering, King's Buildings, Edinburgh, UK, 2000. Available from: http://www. civ.ed. ac. uk/ research/ fire/public_html/ Cardington/main.pdf.

[2] Bailey C.G., *Steel Structures Supporting Composite Floor Slabs: Design for Fire*, BRE Digest 462, 2001.

[3] Cameron N.J.K. and Usmani A.S., "New design method to determine the membrane capacity of laterally restrained composite floor slabs in fire. Part 1: Theory and method", *The Structural Engineer* 83(19), 28–33, 2005.

[4] Abu A.K., Burgess I.W. and Plank R.J., "Tensile membrane action of thin slabs exposed to thermal gradient", Journal of Engineering Mechanics, 139, 1497–1507, 2013.

[5] Johansen K.W., *Yield Line Theory*, translated by Cement and Concrete Association, London, UK, 1962.

[6] Gillie M., Usmani A.S. and Rotter J.M., "A structural analysis of the Cardington British Steel Corner Test", *Journal of Constructional Steel Research*, 58, 427–442, 2002.

[7] EN1993-1-2, *Eurocode 3: Design of steel structures, Part 1–2: General rules – Structural fire design*, 2005.

[8] Standards Australia, *Steel Structures*, AS4100, Sydney, Australia, 1998.

[9] Standards Australia, *Concrete Structures*, AS3600, Sydney, Australia, 2001.

[10] Wang D., El-Sheikh A.L., "Large-deflection mathematical analysis of rectangular plates", *ASCE Journal of Engineering Mechanics*, 131, 809–821, 2005.

[11] Reddy J.N., *Mechanics of Laminated Composite Plates and Shells: Theory and Analysis*, CRC Press, Baca Raton, 2nd ed., 2004.

8th International Conference on Structures in Fire
Guo-Qiang LI, Venkatesh K. R. KODUR, Shou-Chao JIANG, Jian JIANG, Su-Wen CHEN, Guo-Biao LOU (Eds.)
Shanghai, China, June 11-13, 2014

COMPUTATIONAL SIMULATION OF STEEL MOMENT FRAME TO RESIST PROGRESSIVE COLLAPSE IN FIRE SCENARIOS

Ha Nguyen*, Ann E. Jeffers* and Venkatesh Kodur**

* Civil and Environmental Engineering, University of Michigan, USA
e-mails: hanguyen@umich.edu, jffrs@umich.edu

** Civil and Environmental Engineering, Michigan State University, USA
e-mail: kodur@egr.msu.edu

Keywords: Fire, Structures, Simulation, Moment frame, Connection, Progressive collapse

Abstract. *The study addresses a need for improving the structural resilience in the multi-hazard threats including fire and progressive collapse caused by column loss (in fire or in blast). The focus is on a steel moment frame using moment connections between the beams and columns. A 3D finite element (FE) model was created in ABAQUS and the material properties at elevated temperature were based on Eurocode. The model matched well with experimental data at ambient and elevated temperature. Two scenarios were considered with validated material: fixed load with increasing temperature and fixed temperature with increasing load. A macro element (or component-based) model was also introduced and validated against FE model and experimental test.*

1 INTRODUCTION

Investigations into recent building collapses (e.g., the World Trade Centre buildings 1, 2, and 7, [1] and the Faculty of Architecture Building at Delft University in the Netherlands [2]) have demonstrated the damage caused by a structurally significant fire is real and can be catastrophic despite its low probability of occurrence. The rising interests and demands on sustainable buildings also indicate a need for enhancing the performance of building systems in fire and multi-hazard conditions. The improvement in structural resilience cannot only protect life safety but also reduce cost and impacts due to destruction and reconstruction after those extreme threats. This is especially crucial in important buildings, where human safety is the most priority and the cost for property loss and operation disruption is unparalleled.

During catastrophic fire, the heated floor system undergoes significant thermal expansion followed by sudden contraction due to catenary action. Recent research done by Lange et al. [3] has shown that in the case where fire occurs in three consecutive floors, the thermal expansion and subsequent sag of floor systems produces lateral forces on columns that can lead to buckling instability, particularly in perimeter columns. In a similar investigation on steel high-rise building exposed to vertically developing fire, Garlock and Quiel [4] concluded that the heated beams expand and create large lateral deformation in perimeter columns, which may result in structural collapse if the beams are not fire protected. Agarwal and Varma [5] studied two ten-story office buildings (one-hour fire protection for beams and columns) where corner compartment fire occurs in the fifth story. In both cases (interior rigid core and perimeter MRFs), the interior column experienced yielding and inelastic buckling failure after approximately 85 min in fire. It is indicated that either exterior or interior columns are prone to fail during long fires, putting the structure in a danger of progressive collapse.

Furthermore, there are a number of studies [6,7] investigating the behaviour of steel building frame in fire after it has been damaged by blast or impact (for example earthquake). Whether the column is removed after fire or fire occurs after column removal (through blast or impact), combined fire-and-column-loss scenario should be addressed in both fire safety engineering and progressive collapse design. The study seeks to explore the potential of mitigating fire-induced collapse under column loss through the use of beam-to-column moment connections.

Recent research into structural resistance against progressive collapse in fire has consider the behaviour at the system level [5,6,7], modelling beam-to-column connections as simply pinned or fully fixed. These types of simulation are acceptable at ambient temperature but when temperature increases, the beam-to-column connection will lose a large amount of stiffness as well as capacity due to significant thermal degradation and expansion of steel. In other words, the connections need to be taken into consideration in structural simulation at elevated temperature in order to properly predict the real reaction of steel frame exposed to fire. In the scope of this research, welded unreinforced flange – bolted web (WUF-B) connections were investigated. Both 3D high-resolution finite element and component-based (or macro element) models were adopted in the simulation and verified against experimental data at ambient temperature from NIST [8] and elevated temperature from Mao et al. [9]. The study aimed to explore the possibility of using moment connections to improve the progressive collapse resistance of steel-framed structures in fire.

2 MODEL SETUP

The research builds on the methodology that is adopted in U.S. specifications for designing collapse resistant structures, which presently do not consider collapse resistance under fire or multi-hazard load events involving fire. NIST beam-column subassembly test [8], which were taken from exterior moment resisting frame in real building designed for seismic category D, were used to validate the simulated results at ambient temperature as well as predict the performance in combined fire and column removal condition. For structural response at elevated temperature, two different conditions were modelled: (1) fixed load and increasing temperature, corresponding to fire after column removal (in a blast or impact) scenario; and (2) fixed temperature and increasing load, corresponding to the column removal during exposure to fire. Because NIST's experimental tests did not include the elevated temperature cases, another test carried out in Taiwan (Mao et al.) [9] was used to validate thermal and mechanical property of steel at elevated temperature in simulation model.

2.1 NIST test

The subassembly in the NIST test [8] was taken from an exterior moment resisting frame in a building designed for seismic category D. It consisted of three columns connected with two 6.1-meter-long beams, in which the middle column was removed. Half of the subassembly is shown in Fig. ure 1. The column removal effect was achieved by applying a vertical load on the middle column, which then redistributed to surrounding beams and columns, leading to progressive collapse. Our research focuses on welded unreinforced flange-bolted web (WUF-B) connections, which are widely used in the U.S. in regions of moderate seismicity. The beam web was connected to the shear plate by 25-mm-diameter ASTM A490 bolts, and the shear tabs and the beam flanges were welded to the column flanges, as shown in Fig. ure 2. The subassembly was originally designed for ambient temperature tests and analyses that were performed by NIST.

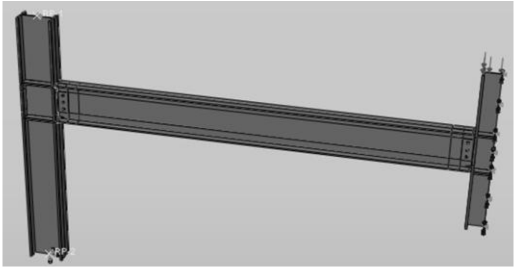

Figure 1. NIST test set-up (half subassembly).

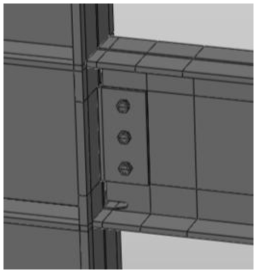

Figure 2. Beam-to-column connection.

2.2 Mao et al. test

Figure 3 shows the setup for Mao et al. test [9], which consisted of a 4.35-meter-high column (H600x600x25x36H600×600×25×36) and a 3.1-meter-long beam (H600x300x12x25H600×300×12×25). Beam flanges were welded to the column flange and the beam web was connected through a bolted fin plate connection, as illustrated in Fig. ure 4. Five M22 F10T bolts were used. The rest of steel was ASTM A572 Gr.50. Three different cases were tested: (1) fixed temperature at 550 ℃, (2) fixed temperature at 650 ℃, and (3) ISO 834 standard fire curve. In test (1) and (2) the beam was loaded until failure while in test (3) a loading of 34 tons was applied and kept constant during the entire experimental test.

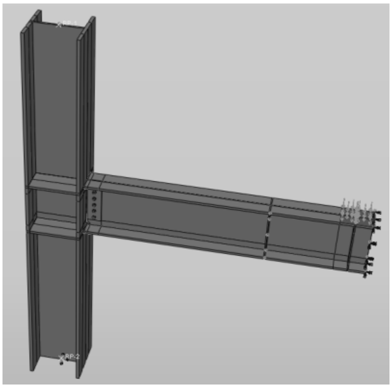

Figure 3. Mao et al. set-up.

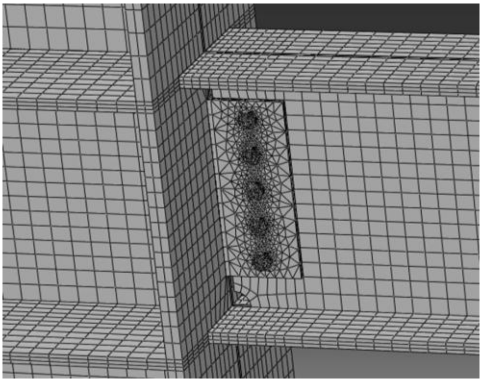

Figure 4. Beam-to-column connection.

3 ANALYSIS AND RESULTS

3D solid finite elements in ABAQUS were adopted to simulate the NIST and Mao et al. tests. The material properties were taken from Eurocode 3 [10] with 0.5%E strain hardening. Interactions ("hard" contact and friction coefficient of 0.3) were used to model contact between the bolts and beam web, bolts and shear tab, and beam web and shear tab, whereas constraints were used to model shear tab – column and beam flange – column welding. The relationship between the applied load and vertical displacement at the end of beam was plotted and validated against the experimental results. Because of symmetry, only half of the subassemblies were simulated in the finite element model in order to reduce the computational cost, as illustrated in Figures. 1 and 3. The perimeter column was restrained at the top and bottom; symmetric boundary conditions were also applied at the centre-line of the sub-assembly.

A macro-element model was introduced to model Mao at al. tests. The concept is to use frame element to model the beam and column components, and a spring system to model the connection between the beam and column (Fig. ure 5) in order to reduce a significant amount of computation cost while providing reasonable prediction of structural response. The spring system accounts for all possible failure mechanisms occurring at the connection, depending on the type of connection. In the WUF-B moment connection, the failure mechanisms consist of shear tab bearing, beam web bearing, bolt shear, friction between shear tab and beam web, and axial force (compression or tension) in the beam flange which also accounts for local buckling around the connection. The component model was developed based on the failure mechanisms observed in experimental tests and simulations [8,9] as well as component-based models for shear connections [11]. The stiffness of each spring is determined by calibration to a finite element model for each component.

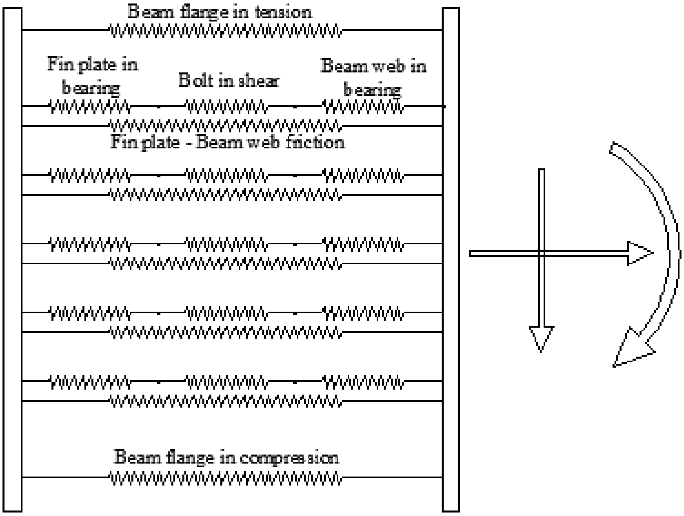

Figure 5. Macro-element model for beam-to-column connection in Mao et al. test.

3.1 Validation against the NIST ambient temperature test

For model validation at ambient temperature, both ABAQUS implicit and explicit dynamic models were adopted and verified against the experimental data. The implicit model required less computational time but artificial damping was needed in order to achieve convergence. The magnitude of artificial damping depends on the structure, the applied load, and the temperature and is determined based on experience and trial-and-error. For preventing spurious structural behaviours due to excessive damping, the artificial damping energy must be checked and ensured that it is less than 10% of internal energy. On the other hand, the explicit model was able to simulate the response beyond structural instability, which usually causes convergence issue in complicated structural models involving contact. However the explicit model requires a significant amount of computational time (which is reliant on the mesh size, the number of elements, and the time period). In the explicit model, kinetic energy should not exceed 10% of internal energy. The total time period in the explicit model needed to be long enough to reduce the dynamic effect of explicit model (kinetic energy should be less than 10% internal energy). However, it should not be too long to avoid an excessive computational time and cost. In this case, time period was chosen between 1.0 - 1.1 s.

Both implicit and explicit models provided results close to NIST test data at ambient temperature, as shown in Figure 6. The implicit model stopped when the deflection reached 170mm while the explicit model could go beyond 400mm deflection. Both models conservatively predicted the ultimate capacity.

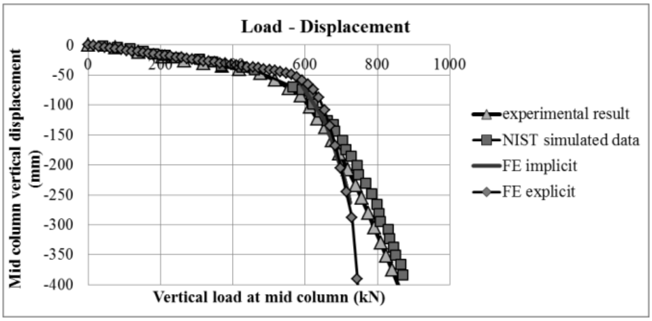

Figure 6. NIST test at ambient temperature.

3.2 Validation against the Mao et al. tests

The relationship between the applied load and vertical displacement at the beam end is shown in Fig. ure 6 for the constant temperature tests. Furthermore, the displacement is plotted against temperature in Fig. ure 7 for the ISO 834 fire experiment. It can be seen the Eurocode model yielded a reasonable result and is conservative (in the FE model). The macro-element model yielded acceptable results compared to finite element and experimental data, as shown in Fig. ure 7 (for 550 ° and 650 ℃) and Fig. ure 8 (for standard fire test).

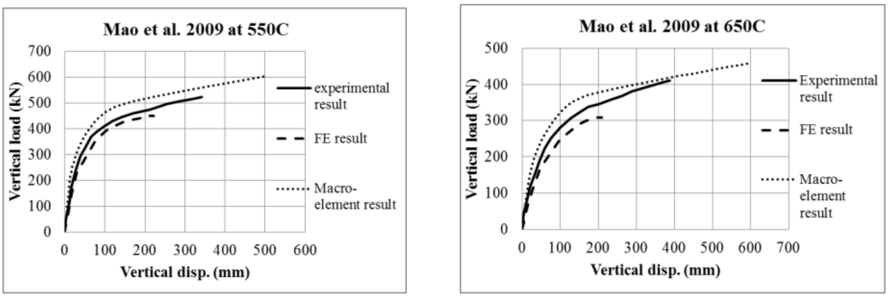

(a) (b)

Figure 7. Mao et al. test at constant temperature (a) at 550 ℃ and (b) at 650 ℃.

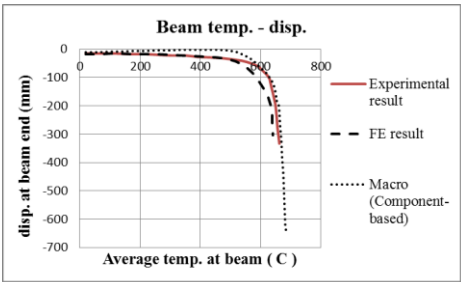

Figure 8. Mao et al. result in ISO 834 standard fire test.

3.3 Simulation of multi-hazard scenarios

The study considered both cases of multi-hazard threats: (1) fixed load and increasing temperature, representing fire after column removal (in a blast or impact) scenario; and (2) fixed temperature and increasing load, representing the column removal during exposure to fire. Following common requirements for fire protection, the beam had one-hour rate fire protection while the column had two-hour rate fire protection; an 8-inch-thick concrete slab was also put on top of the beam to simulate the heat sink effect of the slab in reality. A heat transfer model had been simulated first in order to get elevated temperatures at different elements of the protected structure exposed to standard fire. These temperatures were then inputted into structural model as predefined field at the second phase. Due to long period of fire event, implicit model (with an artificial damping) was used to simulate the fixed load-increasing temperature case. An explicit model was used to simulate the fixed temperature-increasing load case.

Similar to the Mao et al. test, all contact between the bolt-beam web, bolt-shear tab, beam web-shear tab were modelled as “hard” contact in the normal behaviour and with a friction coefficient of 0.3 in the tangential behaviour. The welding between the beam flange and column and between the shear tab and column were assumed to be rigid, thus modelled as constraints in ABAQUS. All thermal and mechanical properties of steel for the elevated temperature cases followed Eurocode 3 [10], which was validated against experimental data at elevated temperatures from Mao et al. [9].

3.3.1 Multi-hazard case 1: fire after column removal (blast or impact scenario)

Three cases were investigated where 0.3-0.6 ultimate load was applied. It is clearly shown that the larger the load is, the less time the structure can stand in fire, as illustrated in Figure 9. When only 0.3P was applied, the frame can withstand the fire for 100 mins while at 0.6P, the frame can withstand the fire for 40 mins. It can be concluded that fire protection is necessary to ensure the resilience in this multi-hazard condition. If adequately protected, the system appears to be capable of transferring the load to the adjacent columns.

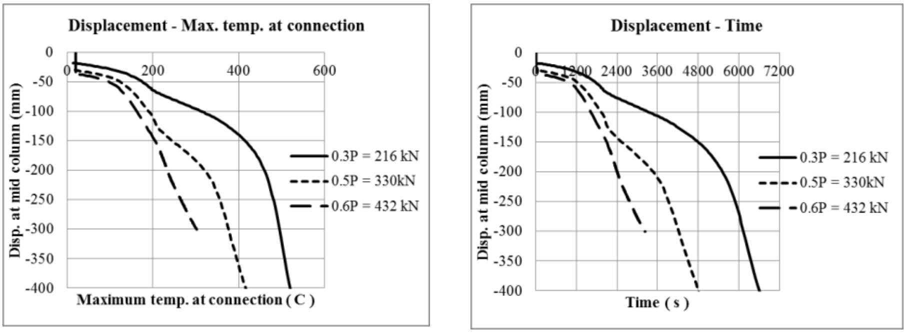

Figure 9. NIST test in fixed load – increasing temperature scenario.

3.3.2 Multi-hazard case 2: column removal during long fire

A fixed temperature and increasing load was applied in this case to evaluate the ultimate capacity of the structure at different levels of temperature ranging from 200 ℃ to 600 ℃. Additionally, a parametric study was carried out to evaluate the integrity and ductility of structure in different floor levels with different sizes of members (see Table 1). The results were then compared to each other to understand the effect of elevated temperature to the capacity and relative strength of structure.

Table 1. Component sizes of different floor levels.

	Beam	Column	Shear tab
Floor 1-3	W21x73W21×73	W18x119W18×119	1/2"x12×12"x6×6"
Floor 5-6	W21x68W21×68	W18x97W18×97	1/2"x12×12"x6×6"
Floor 8-10	W21x44W21×44	W18x55W18×55	3/8"x12×12"x6×6"

Fig. ure 10 shows the decrease in structural strength at elevated temperatures in the floor levels 1-3, 5-6, and 8-10. The failure mechanisms were the buckling at beam flange around the connection (in both sides of the beam) and the shear failure in bolts, shown in Fig. ure 11; that was also observed in experimental test [8].

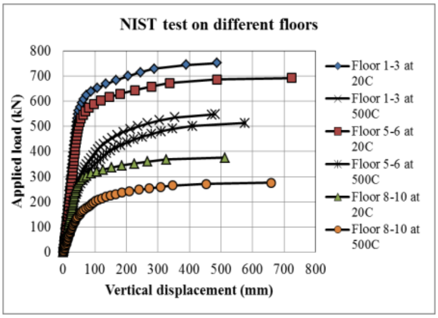

Figure 10. Strength reduction at elevated temperature.

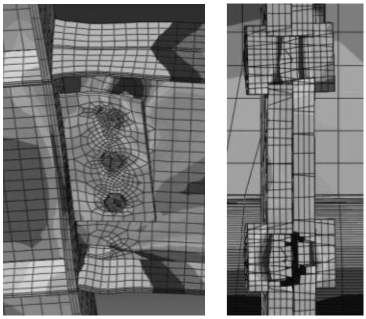

Figure 11. Failure mechanisms of connection.

Relative strength was determined as the ratio between ultimate strength at elevated temperature and ultimate strength at ambient temperature (shown as P/P_u in Fig. ure 12). It was used to determine the effect of elevated temperature on the strength reduction and how temperature influenced differently on different sets of components (or different floor levels). Fig. ure 12 demonstrates that at 500 ℃ the strength decreases to about 70% and at 600 ℃ the structure remains only 50% of its capacity; this reduction is consistent with strength degradation in steel at elevated temperature. Also, there are no significant differences between floor levels in terms of relative stiffness.

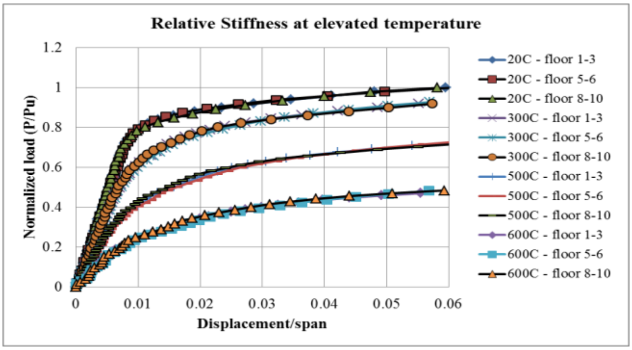

Figure 12. Relative strength of 3 floor levels at elevated temperatures in NIST test.

4 CONCLUSIONS

This research investigated the response of steel frame using moment beam-to-column connection in combined fire-and-progressive-collapse scenarios. It was verified that the finite element model can provide a good prediction at ambient and elevated temperature; and Eurocode material properties are adequate for the simulation. Though both implicit and explicit model can yield reasonable results, each method is suitable for different case of consideration due to its advantages and disadvantages. While explicit model is better for evaluating structural performance in fixed temperature - increasing load (corresponding to column loss after a long time in fire), implicit model is more suitable in fixed load – increasing temperature (corresponding to fire occurring after a blast or an impact). There are two major failure mechanisms: shear failure at bolts and buckling and excessive yielding at beam flange, both of them appear at the beam-to-column connection. Another conclusion is that the structure will lose more capacity at higher temperature but the temperature does not affect much the relative strength (showed in case 2 of NIST test).

A macro-element (or component-based) model can provide an adequate evaluation for structural response and it requires much less computational cost as well as avoids the convergence issue caused by contact simulation in finite element. Though macro-element model was still on development, it promises a possibility of simulating complicated structures under extreme loads and effects.

REFERENCES

[1] NIST NCSTAR 1, "Final Report on the Collapse of the World Trade Center Towers", *National Institute of Standards and Technology*, Gaithersburg, MD, 2005.

[2] Engelhardt M., Meacham B., Kodur V., Kirk A., Park H., Straalen I., Maljaars J., Weeren K., Feijter R., Both K., "Observations from the Fire and Collapse of the Faculty of Architecture Building, Delft University of Technology", *Structures Congress ASCE*, 2013.

[3] Lange D., Roben C., Usmani A., "Tall Building Collapse Mechanisms initiated by Fire: Mechanisms and Design Methodology", *J Engineering Structures 36* (2012) 90-103, 2012.

[4] Garlock M., Quiel S., "the Behavior of Steel Perimeter Columns in a High-Rise Building under Fire", *Engineering Journal*, 359-372, 2007.

[5] Agarwal A., Varma A., "Fire induced Progressive Collapse of Steel Building Structures: the Role of Interior Gravity Columns", *J Engineering Structures 58* (2014) 129-140, 2014.

[6] Quiel S., Marjanishvili S., "Fire Resistance of a Damaged Steel Building Frame Designed to Resist Progressive Collapse", *Journal of Performance of Constructed Facility*, ASCE, 2012.

[7] Neal M., Garlock M., Quiel S., Marjanishvili S., "Effects of Fire on a Tall Steel Building Designed to Resist Progressive Collapse", *Structures Congress ASCE*, 2012.

[8] Sadek F., Main J., Lew H., Robert S., Chiarito V., El-Tawil S., "An Experimental and Computational Study of Steel Moment Connections under a Column Removal Scenario", *NIST Technical Note 1669*, 2010.

[9] Mao C., Chiou Y., Hsiao P., Ho M., "Fire Response of Steel Semi-Rigid Beam-Column Moment Connections", *Journal of Constructional Steel Research 65* (2009) 1290-1303, 2009.

[10] Eurocode 3, "Design of steel structures, part 1.2: General rules structural fire design", *Brussels: Commission of European Communities (EC3)*, 2005.

[11] Sarraj M., "The Bahaviour of Steel Fin Plate Connection in Fire", PhD. Thesis, Department of Civil and Structural Engineering, *University of Sheffield*, UK, 2007.

8th International Conference on Structures in Fire
Guo-Qiang LI, Venkatesh K. R. KODUR, Shou-Chao JIANG, Jian JIANG, Su-Wen CHEN, Guo-Biao LOU (Eds.)
Shanghai, China, June 11-13, 2014

AN OPENSEES-BASED INTEGRATED TOOL FOR MODELLING STRUCTURES IN REALISTIC DESIGN FIRES

Li-Ming Jiang*, Ya-Qiang Jiang, Jian Jiang***, Asif S.Usmani* and Su-Wen Chen*****

* School of Engineering, The University of Edinburgh, The King's Buildings, Edinburgh EH9 3JL, UK
e-mails: liming.jiang@ed.ac.uk, asif.usmani@ed.ac.uk

** Sichuan Fire Research Institute, Chengdu, P. R. China
email: yaqiang.jiang@gmail.com

*** College of Civil Engineering, Tongji University, Shanghai, 200092, P. R. China
emails: jian.jiang@tongji.edu.cn, swchen@tongji.edu.cn

Keywords: Design fires, Finite element, Composite structures, Fire modelling, Heat transfer

Abstract. *This paper describes the development of OpenSees on integrating the heat transfer and thermo-mechanical analyzes for modelling structures in fires. The Heat transfer to a composite beam subjected to localized fire is investigated within OpenSees, and the robustness of adopting two dimensional approximation of heat transfer analysis has been reviewed. Non-uniform thermal action is implemented in OpenSees and its performance having been verified.*

1 INTRODUCTION

Research over the last two decades has increasingly enabled leading international consulting engineers to consider performance based engineering (PBE) approaches for providing passive fire resistance to buildings. This represents a relatively rapid transfer of knowledge from research to industry as much of this development owes to significant synergistic collaboration between industry and academic research, for example the support of BRE and Arup to the research group at the University of Edinburgh. Currently, the use of PBE approaches is relatively ad-hoc and depends very much on decisions made by individual consultants based on what may be acceptable to local building regulators. In terms of knowledge development, there are two key limitations to the more widespread and routine use of PBE methodologies: the lack of a standardized PBE framework that is acceptable to industry, and an easy to use integrated computational tool that is also robust and powerful enough to enable the modelling of more realistic fire scenarios, such as the structural response to localized or moving fires [1, 2]. This paper is concerned with only the second of these issues. An integrated computational tool would allow greater insights into the fire hazard and their effects on structures in order for new simplified methodologies to be devised by researchers to facilitate the wider adoption of PBE. Although there are many commercial and proprietary software packages available that solve part of the problem, currently there is nothing that solves the complete coupled problem in an automated manner. Figure 1 shows the approach that will be taken to develop such an integrated tool initially based upon open source analysis engines FireFoam and OpenSees. The middleware indicated will be implemented on high performance computing platforms to enable whole structures under realistic (e.g. moving) fires to be modelled in reasonable timescales, eventually also accounting for uncertainties by integrating a probabilistic analysis layer in the computational tool. The middleware will be developed to allow other analysis engines, such as FDS, ABAQUS, ANSYS etc. to be substituted in place of FireFOAM and OpenSees based on user preference.

Figure 1. Schematic of the integrated computational tool to be developed

This paper describes the development of the right hand half of the above integrated tool based on the OpenSees platform. The authors' work on the thermomechanical modelling of structures [3] was incorporated in the OpenSees release of October 2012, with routine updates since then. The heat transfer modelling work has been completed and the work on the HT-TM middleware has continued and should become available to be incorporated in OpenSees by the end of 2014. The rest of the paper also discusses the application of this work to a realistic design fire [8], such as Eurocode1 (EC1) localized fire action. A paper by Chao Zhang presents the analyses done with ANSYS on restrained steel beams subject to localized fire [5], which concludes that the localized fire could generate highly non-uniform temperature distributions both along the beam length and through the depth when the fire plume impinges on the ceiling. The work presented in the paper [6] investigated the effects of non-uniform temperature distributions on lateral torsional buckling resistance of steel I-beams, pointing out that the beam behaviour is controlled by the average temperature at low load ratios, and by the temperature of the less heated flange for high load ratios. Those researches suggest the great necessity to review the heat transfer analyses and the structural behaviour of the beams subjected to the localized fires, which are mainly discussed in the third and fourth section in this paper, and being initially conducted with the OpenSees platform.

2 INTEGRATING HEAT TRANSFER AND STRUCTURAL ANALYSIS IN OPENSEES

In addition to many improvements to the original OpenSees thermomechanical modelling capability, a heat transfer module was also implemented within the OpenSees software framework in order to model two and three dimensional (2D and 3D) heat transfer into structural elements resulting from a range of of fire models (also included in the framework). This work was a necessary pre-requisite for establishing the HT-TM type coupling discussed earlier.

Figure 2 shows the current scheme used to integrate the various modelling capabilities. A simple mesh tool is built up for creating heat transfer models, which will be able to work with Tool Command Language (Tcl) soon. Meanwhile, a library of fire models are developed to offer a location-correlated, heat flux based definition of boundary conditions for considering fire exposure. Fire actions can be applied to the structural members through convective, radiative, and prescribed heat flux. Once the model is established and analysed, the requested temperature data will be stored by recorders that are modified from the original OpenSees recorder facilities. The recorded temperature data will be written in the files in a list format (each line reading as “time temp1 temp2 temp3…tempn”), which could be automatically imported by the Thermal Action classes. The PathTimeSeriesThermal class, whose name implies that the class is developed on the basis of original PathTimeSeries in OpenSees, is responsible for handling the time-temperature information for elemental or nodal thermal actions. In addition to these, new thermo-mechanical materials including SteelECThermal and ConreteECThermal are available to use for obtaining the full Eurocode behaviour of steel and concrete materials. The detailed manual and introduction to these new features is posted on the Edinburgh University OpenSees wiki page, which can be found at https://www.wiki.ed.ac.uk /display/OpenSees.

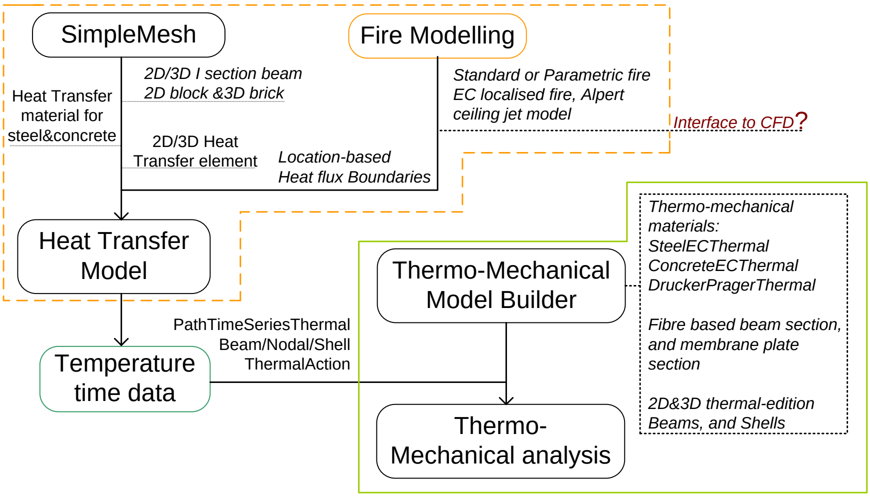

Figure 2. Current scheme of integrating heat transfer and thermo-mechanical analyses in OpenSees.

3 HEAT TRANSFER ANALYSIS FOR LOCALIZED FIRE ACTION

Once the desired fire action is established for the structural members to be analyzed, its potential lack of uniformity may suggest the necessity of conducting a full 3D heat transfer analysis in order to obtain an accurate temperature profile evolution as a result of the fire action. However, running a 3D analysis is expensive in terms of computational cost, time and analyst effort. An alternative to this is to carry out a series of 2D heat transfer analyses at different sections of a beam or column member. This should produce reasonable results under post-flashover compartment fires as the heat fluxes on the structural member surfaces may be quite uniform (at least for beam members) and therefore also the thermal gradients along the member length. However for more variable fire actions, such as for a localized fire, a considerable gradient of heat flux will exist along the length and a cross-sectional 2D heat transfer analysis may not be sufficient to resolve the thermal profile evolution accurately enough. In Figure 3, the variation of the net heat flux is plotted about the horizontal distance to the fire origin, which is according to the localized fire model in Eurocode 1. In this particular example, the heat release rate $\dot{Q}$ of the fire is 3MW, with a pool diameter D as 1m, and a 3m high ceiling. Then the unconfined flame length L_f of the fire can be derived by Heskestad's formula;

$$L_f = -1.02D + 0.235\dot{Q}^{2/5} \tag{1}$$

The calculated virtual fire length is 4.79m, indicating that the fire is impinging on the ceiling. The net heat flux $\dot{h}$ (W/m^2) received by the ceiling is given in EC1 as,

$$\dot{h} = 100000 \qquad \text{if } y \leqslant 0.30 \tag{2a}$$

$$\dot{h} = 136300 - 121000y \qquad \text{if } 0.30 < y \leqslant 1.0 \tag{2b}$$

$$\dot{h} = 15000y^{-3.7} \qquad \text{if } y \geqslant 1.0 \tag{2c}$$

The heat flux varies with the parameter y which depends upon the horizontal distance r from the vertical axis of the fire and the vertical distance H to the fire source.

$$y = \frac{r + H + z'}{L_h + H + z'} \tag{3}$$

Where L_h is the horizontal flame length (horizontal spread of the impinging flame), z' is the vertical distance between the virtual fire origin and the fire source.

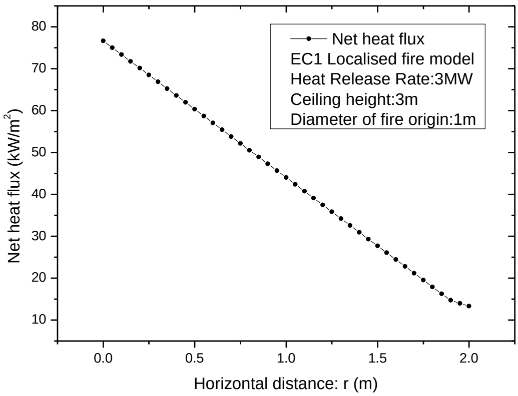

Figure 3. Net heat flux versus horizontal distance given by an EC localized fire.

The correlation between the net heat flux and the horizontal distance *r* is plotted in Figure 3, the heat flux dramatically decrease from 76.6kW/m^2 to13 kW/m^2 as the distance changes from 0m to 2m. Since the beam is heated by the localized fire in such a non-uniform pattern, the conduction through the hotter to the cooler area may not be ignored. The robustness of 2D and 3D approaches for addressing the temperature profile inside the structural members may be necessary to be reviewed, which is demonstrated with a composite beam exposed to localized fire.

The investigated composite beam is 3m long, consisting of a steel beam with a British universal beam section UB 356 × 171 × 51, with a 0.1 m thick concrete slab on top. The heat transfer to the composite beam is simulated under a localized fire action.

Table 1. Heat transfer model for a composite beam.

Model information	Used in simulation
Beam type	Composite beam without ribs
Beam length	3m
Steel Beam section	UB 356 × 171 × 51
Concrete slab thickness	0.1m

The curves plotted in Figure 4(a) show the steel beam bottom flange temperature resulting from a standard fire exposure. The results verify that 2D and 3D analyses for uniform fire actions, such as the standard fire, produce very similar results, as expected. Different time step increments are also used to ensure that the results are reliable. In case of the localized fire, Figures 4(b) and 4(c) show the temperature variation along the beam length in the bottom and the top flanges respectively, while Figure 4(c) shows the temperature variation at mid-depth of the concrete slab. As can be expected, the 3D analysis produces lower temperatures in the cross-sections than the 2D analysis and it also shows a more rapid decline with distance from the fire source. This clearly demonstrates that 2D heat transfer analysis overestimates temperatures by ignoring the heat flow along the member length and therefore is not a suitable approximation when incident heat flux varies along member length.

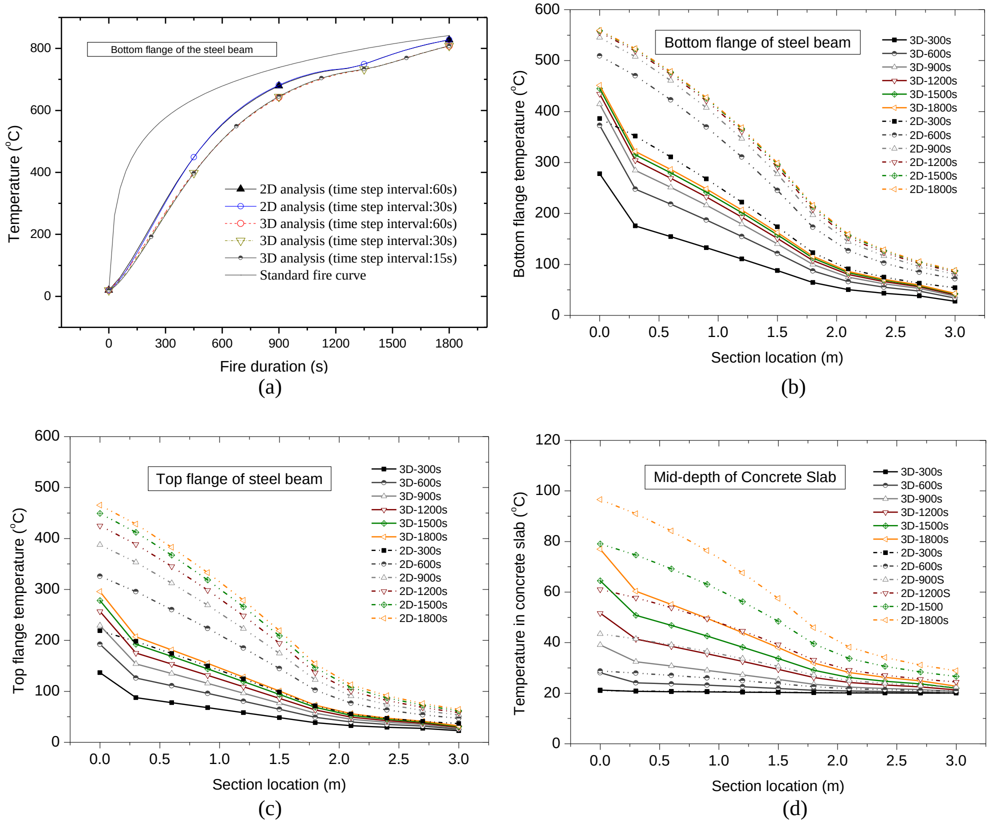

Figure 4. Heat transfer analyses for composite beam subject to standard fire and localized fire respectively: (a) Comparison for standard fire exposure; (b)bottom flange in localized fire; (c) top flange in localized fire; (d) mid-depth of the concrete slab.

4 NON-UNIFORM THERMAL ACTION ALONG THE BEAM USING OPENSEES

The analysis presented in the previous section shows that non-uniform thermal loading would be required over structural elements when the fire action is localized. The implementation of non-uniform thermal action would also enable using fewer elements in thermomechanical analyses.

4.1 Strategy for considering non-uniform thermal action in OpenSees

Displacement based beams are normally used in framed structures. For a 2D beam illustrated in Figure 5, the elemental formulation is based on the trial displacement ΔL and end rotations φ_1 and φ_2. The axial displacement and deflection in terms of local position x can be written as,

$$u(x) = x \cdot \Delta L, w(x) = L(\frac{x^3}{L^3} - 2\frac{x^2}{L^2} + \frac{x}{L})\varphi_1 + L(\frac{x^3}{L^3} - \frac{x^2}{L^2})\varphi_2 \tag{4}$$

Meanwhile, the axial strain and curvature can be derived as,

$$\varepsilon(x) = \frac{\Delta L}{L}, \theta(x) = (\frac{6x}{L} - 4)\varphi_1 + (\frac{6x}{L} - 2)\varphi_2 \tag{5}$$

In OpenSees, the beam cross-section is represented using fibre based sections, which deform as described in Equation 5. The expression for axial strain is modified as,

$$\varepsilon(x)=\frac{\Delta L}{L}+\bar{\varepsilon}_T^{e}-\bar{\varepsilon}_T^{i},\bar{\varepsilon}_T^{e}=\bar{\varepsilon}_T^{i}\bullet wt(i),\bar{\varepsilon}_T^{i}=\frac{\sum\varepsilon_j\bullet A_j}{\sum A_j} \tag{6}$$

Where $\bar{\varepsilon}_T^{e}$, $\bar{\varepsilon}_T^{i}$ are the elemental and sectional average thermal strain (elongation), respectively. $w_t(i)$ is the weight ratio at each section , and A_j is the area of single fibre.

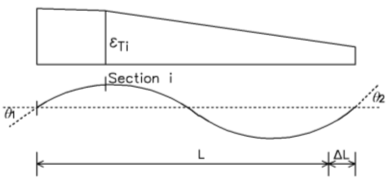

Figure 5. Displacement based beam element.

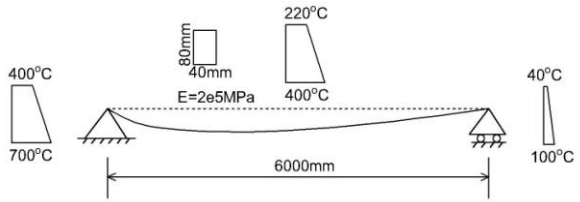

Figure 6. Beam with nodal thermal action applied.

4.2 Comparisons between non-uniform and uniform thermal action

A 40mm×80mm rectangular section beam is assumed to have temperature increases at the both ends but with different gradients as shown in Figure 6. The temperature increase inside the element is idealized to be linearly interpolated along the length, which gives an average elemental beam thermal action as 400°C at the bottom, and 220 °C at the top. Figure 8 shows the deflection of the beam simulated using different number of elements and different materials (ElasticThermal only applies a thermal expansion with a constant coefficient 1.2e-5, while the reduction of stiffness and strength can be included using SteelECThermal). The beam deflection modelled using Elastic Thermal material matches the theoretical calculation, showing lesser displacement than the beam simulated by SteelECThermal.

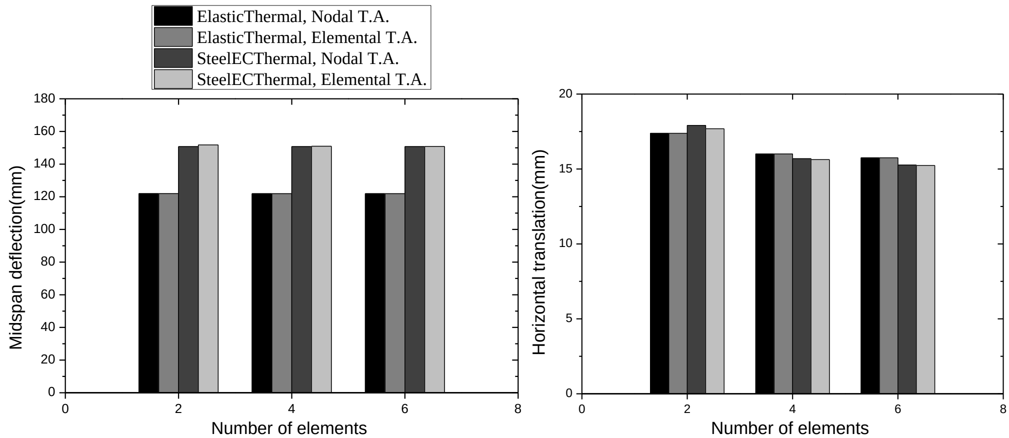

Figure 7. Comparison of the beam displacements using different definitions of thermal action.

As the beam is simply supported, its mid-span deflection and the translational displacement at the unrestrained end are of interest. According to the comparison shown in Figure 7, it appears that non-uniform thermal action will not generate much better results. Nevertheless, the external load effect hasn't been included yet, which is shown by the curves presented in Figure 9. The same beam as shown in Figure 6 is modelled with SteelECThermal material and applied with a constant clock-wise moment 9.6kNm (half of the moment-resisting capacity) at the left end initially, and then followed by the previously described thermal actions. The initial rotation contributed by the constant moment is gradually neutralised while the thermal gradient is applied to the beam. Then as the temperature increases, the section with higher temperatures will enter the plastic state earlier due to the reduction of stiffness and strength, this leads to a sudden reversal of the rotation (because of the action of the applied moment). From Figure 9, it can be seen that a beam element with non-uniform thermal action can model this phenomenon with a similar accuracy by using fewer elements.

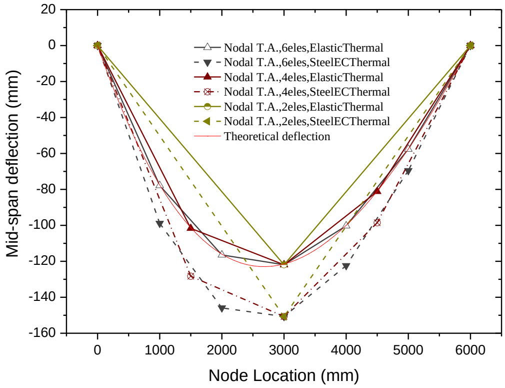

Figure 8. Deflection of the beam subject to thermal gradient.

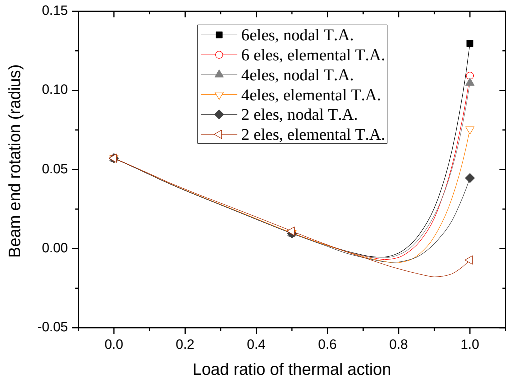

Figure 9. External load effect on the beam behaviour.

5 CONCLUSIONS

The recent OpenSees development on modelling structures in fire has been presented in this paper. The main objective of the work is providing an integrated environment for analysing the structural behaviour in realistic design fires.

The heat transfer to a composite beam from the localized fire is investigated with 2D and 3D approaches respectively, demonstrating that 2D heat transfer analysis overestimates the temperatures by ignoring the heat flow along the length. Therefore it may not be appropriate to apply 2D approximation when incident heat flux varies along member length.

Non-uniform thermal action along the beam is implemented in OpenSees, having shown a better performance compared to the elemental uniform thermal action when the beam entering the plastic state duo to the external loading.

ACKNOWLEDGEMENT

The first author gratefully appreciates the China Scholarship Council and The University of Edinburgh for providing a joint scholarship on his PhD project. The authors also would like to thank Dr Frank Mckena at UC Berkeley for his assistance during the development process.

REFERENCES

[1] Eurocode1: actions on structures:part1-2:general actions-actions on structures exposed to fire.BSI;2002.

[2] J. Stern-Gottfried, G. Rein, “Travelling fires for structural design-Part I:Literature review”, *Fire Safety Journal*, 54 ,74-85, 2012.

[3] Jiang J, Usmani A. “Modeling of steel frame structures in fire using OpenSees”. *Computers & Structures*; 118, 90–99, 2013.

[4] A. Usmani, J. Zhang, J. Jiang, Y. Jiang, I. May. "Using OpenSees for structuresin", *Journal of Structural Fire Engineering*, 3(1), 57-70, 2012.

[5] C. Zhang, G.-Q. Li, and A. Usmani, "Simulating the behavior of restrained steel beams to flame impingement from localized-fires", *Journal of Constructional Steel Research*, 83, 156–165, 2013.

[6] Yin, Y.Z., and Y.C. Wang, "Numerical Simulations of the Effects of Non-Uniform Temperature Distributions on Lateral Torsional Buckling Resistance of Steel I-Beams." *Journal of Constructional Steel Research* , 59(8), 1009-1033, 2003.

[7] Dwaikat, M.M.S., V.K.R. Kodur, S.E. Quiel, and M.E.M. Garlock, "Experimental Behavior of Steel Beam–columns Subjected to Fire-Induced Thermal Gradients." *Journal of Constructional Steel Research*, 67(1), 30–38, 2011.

[8] C. Fang, B. a. Izzuddin, a. Y. Elghazouli, and D. a. Nethercot, "Robustness of steel-composite building structures subject to localised fire," *Fire Safety Journal*, 46(6), 348–363, 2011.

8th International Conference on Structures in Fire
Guo-Qiang LI, Venkatesh K. R. KODUR, Shou-Chao JIANG, Jian JIANG, Su-Wen CHEN, Guo-Biao LOU (Eds.)
Shanghai, China, June 11-13, 2014

EXPERIMENTAL EVALUATION OF COMPOSITE BEAMS SUBJECTED TO FIRE LOADING

Kristi L. Selden*, Erica C. Fischer* and Amit H. Varma*

* Bowen Laboratory, School of Civil Engineering, Purdue University
1040 S. River Road, West Lafayette, IN 47907
e-mails: kselden@purdue.edu, fischere@purdue.edu, ahvarma@purdue.edu

Keywords: Composite beam, Fire, Experimental testing, Finite element modeling

Abstract. *An innovative experimental testing program was developed to evaluate the fundamental behavior and mechanics of composite beams with end shear connections subjected to combined gravity and thermal loading. A series of large-scale composite beams designed according to U.S. codes and standards were tested in which service level gravity loading was applied first, followed by heating with high-temperature ceramic radiant heaters. This paper discusses the results from three of the tests in detail. Additionally, two modeling techniques were developed to further investigate the behavior: (i) a 3D finite element model and (ii) a fiber-based model. Using the experimental test data, these models were benchmarked for further use in parametric studies. This will add in the development of design methods that account for the structural performance of composite beams in the event of a fire.*

1 INTRODUCTION

An experimental testing program was developed to investigate the thermal and structural behavior of composite beam systems at elevated temperatures. While there have been a variety of studies conducted internationally on composite beams in fire [1-4], the focus of this testing program was on composite beams designed according to U.S. codes and standards. Rather than testing isolated composite beams, the specimens were connected to the columns of a load frame using typical simple shear connections. The system was subjected to a combination of gravity loading and elevated temperatures using high-temperature ceramic radiant heaters.

The goals and objectives of this project were to: (i) conduct large-scale experimental testing on composite beams with simple shear connections at elevated temperatures, (ii) develop numerical modeling techniques for predicting the behavior, (iii) use the test results, as well as data from other researchers, to verify the modeling techniques, and (iv) use the benchmarked model to conduct additional parametric studies to aid in the development of a design methodology for composite beams at elevated temperatures.

2 TESTING SETUP

The large-scale experimental tests were conducted on 3.80m long specimens that each consisted of a steel beam that was composite with a flat, lightweight concrete slab through the use of shear studs. The beam was connected to a portal frame using either a shear tab, single-angle all-bolted connection, or double-angle all-bolted connection. The experimental testing setup is shown in Figure 1a. Vertical load was applied using a hydraulic actuator located at the midspan of the portal frame, and the load was distributed evenly to two points along the composite beam using a load spreader, as shown in Figure 1b.

The bottom surfaces of the specimens were heated using high-temperature ceramic radiant heaters to simulate the temperature effects of a fire on a floor system.

2.1 Heating equipment and arrangement

Surfaces of the composite beam were heated using Watlow high-temperature ceramic radiant heating panels. With the heaters positioned close to the surfaces and with independent temperature controls, the concrete and steel surfaces were heated using a specified time-temperature curve. A total of 20 heaters were used for these large-scale composite beam tests. Four sets of heater assemblies were arranged along the length of the beam to heat the cross section, as shown in Figure 1(c). The bottom surfaces of the flat concrete slab, as well as the bottom surface of the bottom flange, and both sides of the web of the steel beam were heated directly with the ceramic fiber heaters. With each heater operating on its own Watlow controller, the steel heaters were programmed to follow the same time-temperature curve, and the concrete heaters were programmed to follow another time-temperature curve. The heating rates varied, depending on the test, and the details are provided in the test matrix shown in Table 1.

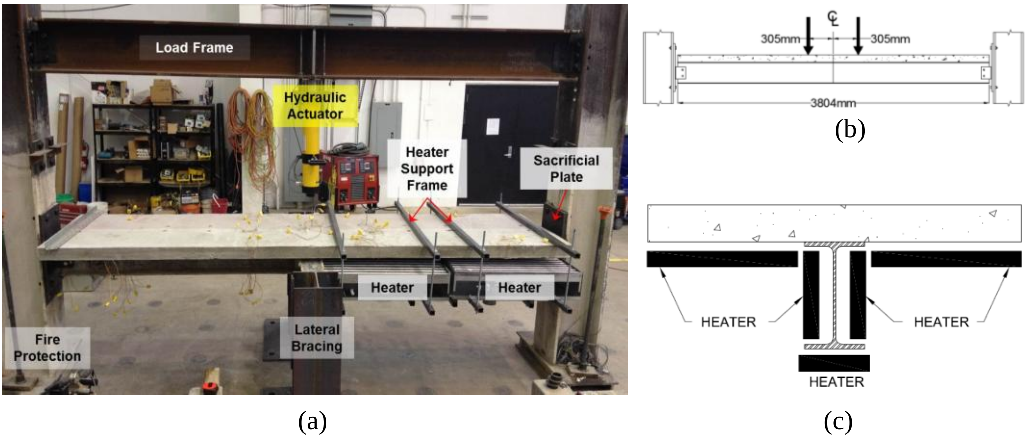

Figure 1. (a) Experimental testing setup for large-scale composite beam tests (with only half of the heaters shown), (b) vertical loading configuration, and (c) high-temperature ceramic heater arrangement.

2.2 Instrumentation

The thermal and structural response of the composite beams was monitored using a series of instrumentation. In addition to traditional voltage-based displacement measurements, high-resolution digital cameras and close-range photogrammetry techniques were used to measure the deformations at elevated temperatures. Tracking the pixel movement of target points located at the ends of the concrete slab allowed for measurement and determination of the horizontal and vertical motion of the slab ends, as well as calculation of the average rotation of the composite beam end. The temperatures through the depth of the cross-section were measured using thermocouples. Type K thermocouples were welded to the steel beam and were also attached to the top and bottom exterior surfaces of the concrete slab. Thermocouples were also embedded in the concrete slab to measure the temperature distribution through the thickness of the slab.

2.3 Test Matrix

The experimental test series included variations in loading level, heating and cooling regime, and connection type. The complete test matrix is provided in Table 1. For the purposes of this paper, only the results from tests CB-3, CB-4, and CB-5 are discussed in detail.

Table 1. Test matrix for large-scale composite beam tests.

Specimen	Connection	Testing Protocol	Max. Steel Temperature	Day of Test f_c' (MPa)
CB-A	Shear Tab	(1) Load to failure at ambient	N/A	47.1
CB-1	Double-angle, all-bolted	(1) Heat to 550 ℃ (2) Cool (3) Load to failure at ambient	550 ℃	42.7
CB-2	Double-angle all-bolted	(1) Heat to 500 ℃ (2) Load to failure	500 ℃	57.2
CB-3	Shear Tab	(1) Load to 156kN (2) Heat to 600 ℃ (3) Cool	600 ℃	54.4
CB-4	Shear Tab	(1) Load to 111kN (2) Heat to 700 ℃ (3) Cool	700 ℃	52.1
CB-5	Single-angle, all-bolted	(1) Load to 111kN (2) Heat to 700 ℃ (3) Cool	700 ℃	52.7

2.4. Loading and Heating Protocol

Each of the composite beam tests featured the combination of vertical loading and heating of the bottom surfaces. The details varied among the tests, but overall, the testing protocol was similar. In all three cases discussed here, the vertical load was applied first, followed by heating and cooling. The load was distributed evenly to two points with the load spreader, each located 305mm from the beam centerline. CB-3 had a total service load of 156kN, while CB-4 and CB-5 had a reduced service load of 111kN. This corresponded to a maximum moment in the beam that was 60% and 43% of the ambient nominal moment capacity, respectively. Following the load application, the steel and concrete surfaces were heated according to the specified heating rates. Regardless of the heating rate and amount of loading, the tests continued with the simultaneous application of load and heat until the average bottom flange surface temperature reached the goal temperature. At this point, heating of the specimen was terminated and the specimen was allowed to cool, following a 12 ℃/min cooling path. Data was still recorded during this process to observe the behavior of both the composite beam and the associated beam-to-column connections.

3 EXPERIMENTAL TESTING OBSERVATIONS AND RESULTS

3.1 Composite Beam 3 (CB-3)

Each of the composite beam tests were conducted with the loading and heating cycles in sequential steps. The CB-3 specimen used a shear-tab connection to attach the composite beam specimen to the loading frame. The beam was loaded to a service level load of 156kN at the midspan load spreader, which corresponded to 60% of the ambient composite beam flexural capacity. After the load was applied, the bottom flange of the steel beam and the webs were heated to 600 ℃ at a rate of 7 ℃/min. The underside of the composite slab was heated to 400 ℃ at a rate of 4 ℃/min. When these goal temperatures were obtained, the composite beam had a midspan deflection of 77mm. A controlled cooling curve then followed, where both the underside of the concrete and the steel beam surfaces were cooled at a rate of 12 ℃/min. The load was maintained at the midspan for the duration of the cooling phase. Figure 2 shows the temperature histories and midspan displacement response of the composite beam.

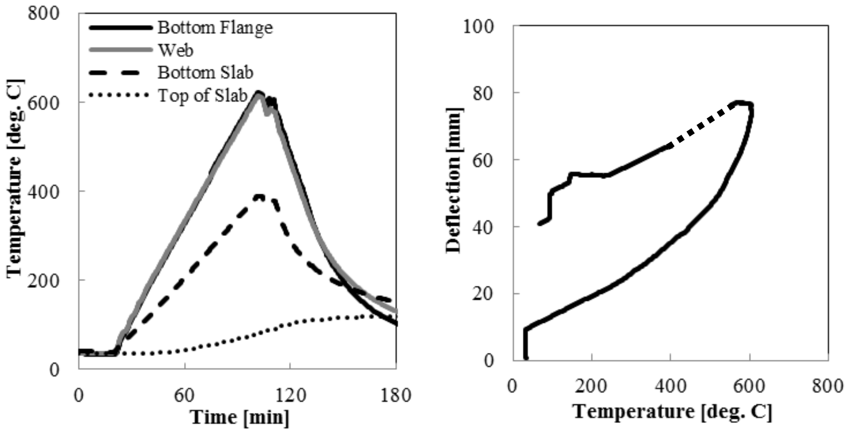

(a) (b)

Figure 2. (a) Surface temperature histories for CB-3 and (b) midspan displacement vs. average bottom flange temperature.

Figure 3(a) illustrates the load-deflection history for the CB-3 test specimen. During the cooling phase, at an approximate steel temperature of 525 ℃, a pop was heard from the south end connection of the test setup. Controlled cooling continued with the full 156kN load applied to the midspan until the specimen reached a steel temperature of 250 ℃. At this time, out-of-plane rotation was observed in the specimen, and to prevent additional out-of-plane rotation, the load was reduced to 111kN while controlled cooling continued. The specimen continued to rotate, and at a steel temperature of 150 ℃ all load was removed from the specimen. After the specimen cooled naturally to room temperature, the ceramic fiber heaters were removed from the specimen. At that time, a fracture in the south shear-tab connection was visible in front of the weld (Figure 3(b)), and the shear tab was distorted in the out-of-plane direction.

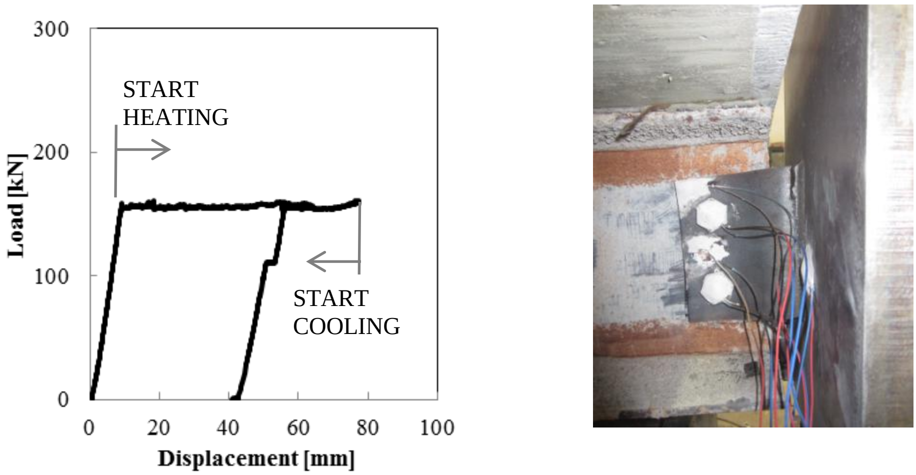

(a) (b)

Figure 3. (a) Load vs. midspan displacement and (b) south shear tab fracture of CB-3.

3.2 Composite Beam (CB-4)

The CB-4 specimen also featured a shear-tab connection. The beam was loaded with a reduced service level load of 111kN using the midspan load spreader. This corresponded to 43% of the ambient flexural capacity of the composite beam specimen. Only the steel bottom flange and the webs were heated. The concrete was not heated to avoid spalling of the concrete slab. The temperature histories for the specimen are shown in Figure 4(a). The steel beam bottom flange and web surfaces were heated to 700 ℃ at a rate of 7 ℃/min while the midspan loading was maintained. When the steel beam reached the maximum desired temperature and there was a vertical deflection of 75mm, controlled cooling at a rate of 12 ℃/min was initiated with the load maintained on the midspan load spreader.

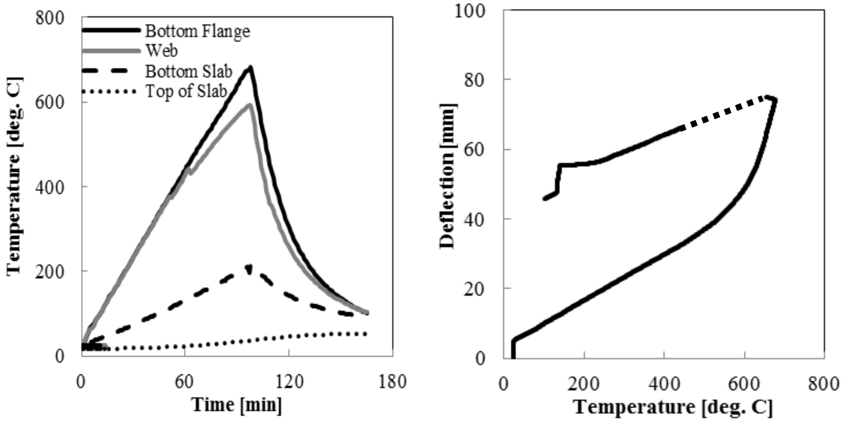

(a) (b)

Figure 4. (a) Surface temperature histories for CB-4 and (b) midspan displacement vs. average bottom flange temperature.

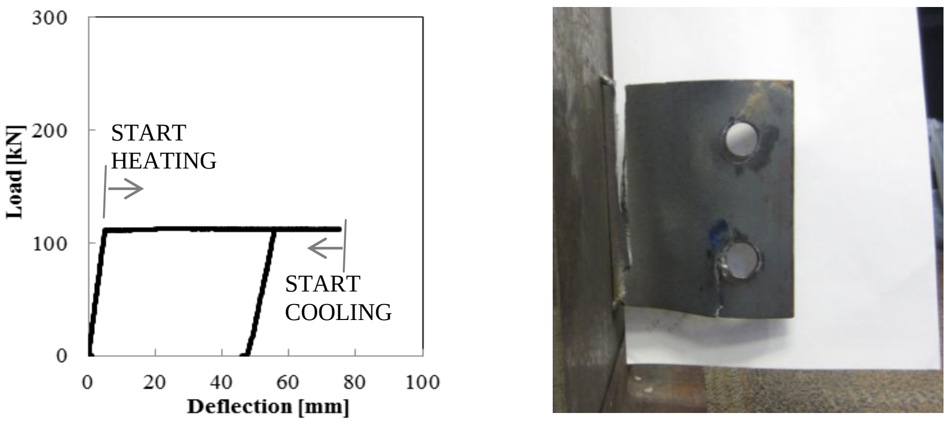

(a) (b)

Figure 5. CB-4 experimental test results: (a) load vs. midspan displacement and (b) north shear tab fracture.

At a temperature of approximately 165 ℃ during the cooling cycle, there was a loud noise from the north connection end of the specimen. This was followed by out-of-plane rotation of the specimen. In order to prevent further out-of-plane rotation, the load was removed entirely from the specimen, and the specimen was allowed to naturally cool to room temperature. When the heaters were removed, a fracture in the shear tab at the location of the weld was observed. This fracture is shown in Figure 5(b).

3.3 Composite Beam 5 (CB-5)

The final specimen (CB-5) featured an all-bolted single-angle connection. It was also loaded with the reduced service load of 111kN, similar to that of CB-4, using the midspan load spreader. Only the steel bottom flange and the webs were heated to avoid spalling of the composite concrete slab during the heating cycle. The steel beam was heated at a rate of 7 ℃/min to a maximum temperature of 700 ℃. At this point, the midspan displacement was 52mm.

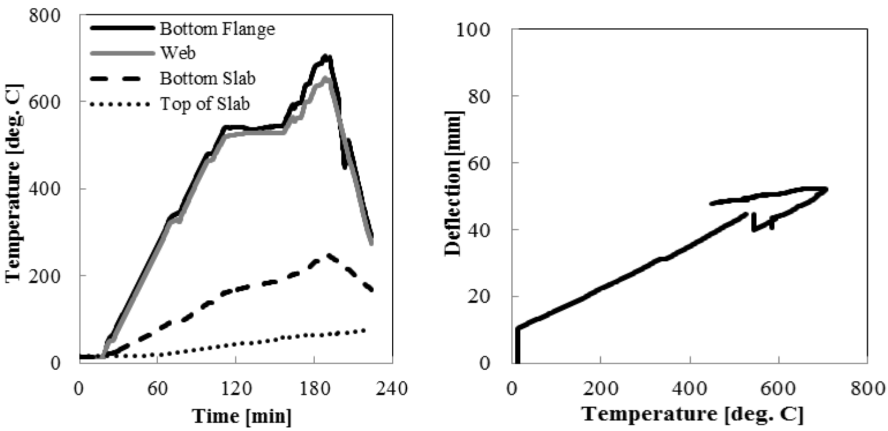

(a) (b)

Figure 6. (a) Heated surface temperature for CB-5 and (b) midspan displacement vs. average bottom flange temperature.

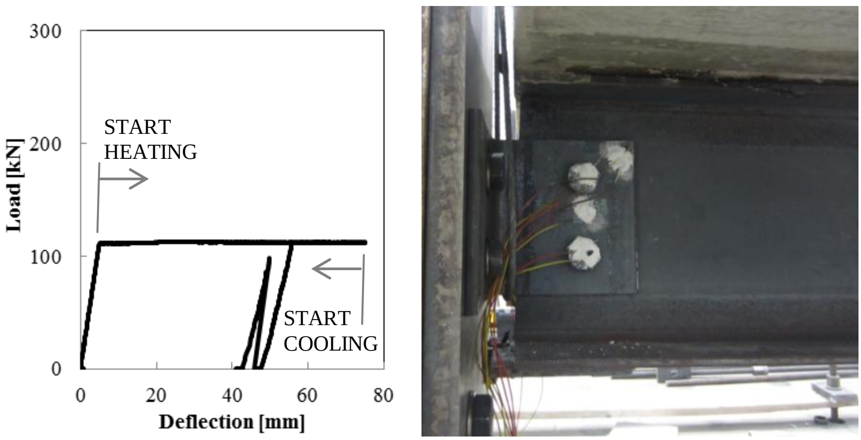

(a) (b)

Figure 7. CB-5 experimental test results: (a) load vs. midspan displacement and (b) south connection post-test.

At a temperature of 600 ℃, a loud pop came from the south connection. At this time, the load was removed from the specimen, and the specimen was allowed to naturally cool to room temperature. Figure 6(a) illustrates the temperature history of the specimen. Figure 7(a) shows the load-displacement relationship for the CB-5 test. After the specimen cooled to room temperature, significant prying was observed at both the north and south connection. Additionally, there was shear deformation of the bolts attaching the single-angle to the web at the south end of the composite beam. Bolt hole elongation was present on the beam web at both ends.

4 MODEL DEVELOPMENT AND RESULTS

4.1 3D Finite Element Modeling

A sequentially coupled, 3D finite element model (FEM) of the composite beam was developed using the commercially available program ABAQUS [5], where the concrete slab was modeled using solid elements and the steel beam was modeled using shell elements. A heat transfer analysis was conducted first to obtain the nodal temperature histories for the cross-section. The resulting nodal temperature histories were used in the nonlinear structural model that accounted for concrete cracking and temperature dependent material properties, including the force-slip behavior of the shear studs [3]. The data from the composite beam tests were later used to verify this modeling technique.

4.2 Fiber-Based Model

Additionally, a fiber-based model was developed to evaluate the section level behavior of a composite beam. Dividing the cross-section into a series of fibers and considering the thermal gradient through the depth, the moment-curvature-temperature (M-Φ-T) relationship could be determined for the given cross-section. In addition, the load-displacement response of the beam can also be estimated using numerical integration. Assuming plane sections remain plane, the fiber model accounts for slip at the steel-concrete interface, stud fracture, and temperature dependent material properties for the concrete, steel, and shear studs. Due to the efficiency of the program, it could also be used as a design tool to determine the moment capacity at elevated temperatures, rather than having to build the full 3D finite element model.

4.3 Comparison of Models to Test Data

Both modeling techniques were verified using the experimental test data. Plots of the predicted and actual midspan displacement with respect to bottom flange temperature for two of the experimental composite beam tests (CB-3 and CB-4) are shown in Figure 8.

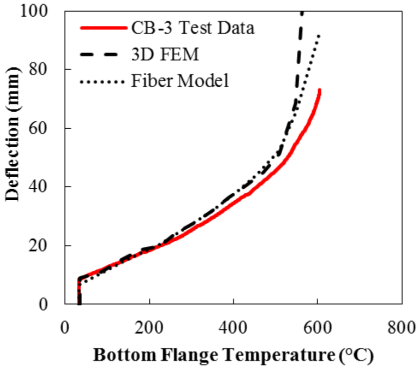

(a)

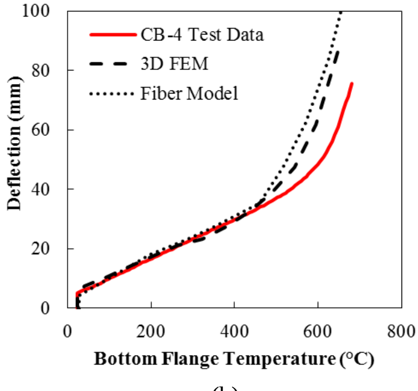

(b)

Figure 8. Experimental test results compared to the 3D finite element model (FEM) and the fiber model.

The thermal and structural behavior of the composite beam can be adequately predicted using both modeling approaches. The modeling techniques provide reasonable and conservative predictions of the deflection response of the composite beams. Any differences between the model and actual test data occurred at the higher temperatures (above 500 °C). This corresponds to the point at which there is significant reduction in steel strength and stiffness. The results here reflect some of the conservatism inherent to the material model at the higher temperatures. The Eurocode [7] material models were used for the concrete and steel, and the temperature dependent force-slip relationships developed by Zhao and Kruppa [3] were used for the shear studs.

5 CONCLUSIONS AND FUTURE WORK

A series of large-scale composite beam specimens were tested to evaluate the response to the combination of service level loading and heating to temperatures that would be common in a structural fire. These tests not only provided insight to the mechanical response of the partially composite beam, but observations could also be made regarding the failure modes of the associated beam-to-column connections. The experimental test results were used to benchmark approaches that can be used to model composite beams. Additional parametric studies can be conducted using these models, in an effort to propose a design equation for calculating the elevated temperature moment capacity of composite beams designed according to US codes and standards. Future work also includes further investigation and quantification of the connection behavior during both heating and cooling.

REFERENCES

[1] Wainman, D.E. and Kirby, B.R. (1987), "Compendium of UK Standard Fire Test Data, Unprotected Structural Steel – 1," Ref. No. RS/RSC/S10328/1/98/B, British Steel Corporation (now Corus), Swinden Laboratories, Rotherham.

[2] Newman, G.M. and Lawson, R.M. (1991), "Fire Resistance of Composite Beams", Technical Report, Publication 109, The Steel Construction Institute.

[3] Zhao, B. and Kruppa, J. (1997), "Fire resistance of composite slabs with profiled steel sheet and of composite steel concrete beams Part 2: Composite Beams." Final Report, ECSC – Contract No. 7210 SA 509, CTICM, France.

[4] Nguyen, T.T. and Tan, H.K. (2012). "Testing of Composite Slab-Beam Systems at Elevated Temperatures." Proceedings of the 7th International Conference on Structures in Fire, Zurich, Switzerland, pp. 247-256.

[5] ABAQUS/Standard Version 6.12 User's Manuals (2012), Providence, RI: Dassault Systemes Simulia Corp.

[6] AISC 360 (2011), Specification for Structural Steel Buildings - 14th Edition, American Institute of Steel Construction, Chicago, IL.

[7] European Committee for Standardization (2005). *Eurocode 4: Design of composite steel and concrete structures, Part 1.2: General Rules - Structural Fire Design.* Brussels, Belgium.

APPLICATIONS OF STRUCTURAL FIRE SAFETY ENGINEERING

8th International Conference on Structures in Fire
Guo-Qiang LI, Venkatesh K. R. KODUR, Shou-Chao JIANG, Jian JIANG, Su-Wen CHEN, Guo-Biao LOU (Eds.)
Shanghai, China, June 11-13, 2014

CLASSIFICATION OF BRIDGES FOR MITIGATING FIRE HAZARD

Mohannad Z. Naser* and Venkatesh K. Kodur**

* PhD Candidate, Civil and Environmental Engineering, Michigan State University
e-mails: nasermoh@msu.edu,

** Professor, Civil and Environmental Engineering, Michigan State University,

email: kodur@egr.msu.edu

Keywords: Fire hazard, Importance factor, Bridge collapse, Probabilistic risk, Structural fire safety

Abstract. *This paper presents an approach for classification of bridges based on risk due to fire hazard. The probable risk of fire occurring on bridges is derived and the possible collapse of structural members of bridge resulting from such fire is estimated. An importance factor for assessing fire risk is derived taking into account the degree of vulnerability of a bridge to fire and also the critical nature of a bridge from traffic functionality point. The proposed importance factor for fire design, which is similar to the one currently used for evaluating wind, and snow loading in buildings, is validated against previous bridge fire incidents. It is shown through this validation that the proposed method for importance factor can be used as a practical tool for identifying critical bridges from the point of fire hazard and also to develop relevant design strategies for mitigating fire hazard in bridges.*

1 INTRODUCTION

There have been numerous fire incidents in bridges in recent years and in some cases these fires lead to significant damage to structural members or full collapse of bridges [1]. The majority of these bridges fires were initiated by the collision of vehicles with other automobiles in the vicinity of bridges or collision of automobiles with bridge structural members [2-4]. Such collisions occur at high speeds and often lead to burning of highly flammable hydrocarbon based fuels. Thus, fires in bridges can be explosive in nature and can reach extremely high temperatures in the range of 1000˚C. These high temperatures can produce rapid degradation of capacity of structural members, due to temperature-induced strength and stiffness deterioration in steel and concrete. Such degradation can lead to partial or full collapse of bridges [3, 4]. Even in the case of minor fire incidents, where no significant damage occurs, proper investigation, inspection and maintenance, in the aftermath of a fire incident, is required before the bridge is opened to traffic. Shutting down a bridge for maintenance would require traffic detouring to nearby routes which can impose significant traffic delays in the affected region.

In recent years, there is an increase in trucks carrying hazardous and spontaneously combustible materials and high intensity fires can break out in the vicinity of a bridge due to collision or over-turn of such trucks or fuel tankers [5-7]. Further, bridges are open to general population and easily accessible to general public; with minimum or no security at all, hence they are susceptible to vandalism which often can lead to occurrence of fires [8].

The magnitude of fire problem in bridge can be illustrated through a fire incident that occurred at I-20/I-59/I-65 interchange in Birmingham, Alabama, USA, where on January 5, 2002 a fuel tanker carrying 37,000 liters of gasoline caught fire. The bridge at this interchange comprised of steel girders spanning 36.6 m. The fire resulted in an intense heat producing temperatures in the range of 1100˚C. This rapid rise in steel temperature degraded strength and stiffness properties of steel girders causing the girders to sag about 3 m, as illustrated in Figure 1 [9]. After this fire incident, the bridge had to be shut down and commuters were detoured to alternative highway routes. The bridge, after necessary repairs, was re-opened for traffic after 54 days [9].

Figure. 1 I-20/I-59/I-65 interchange bridge after fire [9].

In spite of number of fire accidents in bridges, there are no specific requirements in codes and standards for designing bridges to withstand fire hazard. This is on the presumption that fires on bridges is of rare occurrence and that in many cases life safety is not at stake since occupants can escape to safer places and also that the fires tend to burn-out quickly or are extinguished through firefighting. Further, it is not economical or practical to design all bridges for fire hazard. However, as illustrated in recent studies, fire can represents a significant hazard to bridges and in some cases can lead to partial or total collapse of bridges [1, 2, 4, 6-9].

Fire hazard in bridges can be minimized to a certain extent through provision of appropriate fire resistance to structural members, such as girders, piers, etc. Fire resistance can be achieved through proper design, selection of materials and detailing of the structural members. Provision of such fire resistance may increase cost and thus only critical bridges may need to be protected from fire hazard. Thus, bridges are to be classified based on fire risk. For evaluating fire risk, an importance factor similar to that used for evaluating snow or wind loading in the design of buildings, can be quite useful [2]. This paper presents the development of an importance factor for classification of bridges based on fire risk..

2 PROBABILISTIC RISK OF FIRE IN BRIDGES

The magnitude of fire problem in bridges can be gauged by looking at some of the fire statistics available in literature. Further, a comparison of bridge fire statistics with building fire statistics will provide a relative risk of fire hazard in bridges. The occurrence of fire on bridges and buildings is a random event that follow a stochastic approach. This stochastic (probability) approach can be assumed to follow in accordance with Poisson distribution.

In order to determine probability of fire occurrence in the vicinity of a bridge, statistical data on total bridge population and fire incidents is required. However, there is a lack of reliable data on the number of fires that occurred on bridges; usually only major fire incidents are well documented. Still one can arrive at a rough estimate of the probability of fire based on available data on vehicle fires on highways. Using available data, probability of collapse of bridges due to fire can be estimated.

According to National Fire Protection Association (NFPA) [10], there have been 195,600 highway vehicle fires in the USA in 2011. Out of these, a total of 90,000 fires occurred on highways and commercial roads. For the sake of this comparative study, it is assumed that intensity of fire is constant and equal to a certain value (ρ), where (ρ) is the mean of the Poisson distribution, and is computed as: year-1. Using probability principles and utilizing Poisson distribution function, the probability of at least one fire occurring every year on a given highway is: (37%), where (t) is the number of years. Since there is not any available information on the number of fire incidents on bridges, one can assume a reasonable fraction of the total highway fire incidents to occur in the vicinity of a bridge. If 5 and 10% of total fire incidents are assumed to occur in the vicinity of bridges, the probability of a fire breaking out near a bridge is 2.3% and 4.5%, respectively.

Further, according to most recent published statistical data [11-13], the total number of highway bridges in the US was 691,060. In 1989-2000 period, there were 503 bridge failures, out of which 16 bridges collapsed solely due to fire causes. Following the same assumption of constant fire intensity, the Poisson distribution factor for collapse of bridges due to fire is: year-1. Thus, the probability of at least one bridge collapsing due to fire in a yearly period is: (3.1%). Therefore, the probability of a bridge collapsing due to fire in a period of 10 and 50 years (out of the total collapsed bridges due to other reasons) is 27.3% and 79.8%, respectively.

In comparison to bridges, there were 4.5 million residential buildings in the USA in 2003. Approximately 381,200 fire incidents occurred in residential buildings out of a total of 1,584,500 fire incidents reported in the same year [14]. Hence, the probability of a fire occurring in a residential building is 21.4%; (21.4%), year-1. This is almost ten times higher than those assumed to occur in bridges. Further, risk of building collapse due to fire can be estimated knowing the number of recorded building collapses due to fire. In 1970-2002 period, there were 15 fire-induced building collapses [14]. The total number of building failures from various catastrophic incidents, including fire, from 1989-2000 is 225 [14]. Hence, probability of a typical building to collapse due to fire effects is 6.4% in one year. Similarly, the probability of one typical building collapsing due to fire in a period of 10 and 50 years is 48.6% and 96.4, respectively.

The above statistical data clearly indicate that probability of fire occurring in buildings is much higher than that of bridges. Structural members in buildings need to be designed to satisfy fire resistance requirements since occupant safety is of primary interest in the case of buildings. On the other hand, bridges are open structures and thus there is high probability that people can evaluate to safety quickly in the event of fire. But the consequences of a fire on a bridge can produce significant adverse impact from the point of traffic flow, property damage and other considerations. Since it is neither impractical, nor economical to design all bridges for fire safety, only critical bridges are to be designed for fire safety. In order to classify bridges, from fire hazard point of view, a fire-based importance factor can be of great aid. For this purpose an importance factor is derived in the next section.

3 CRITICAL FACTORS INFLUENCING FIRE RISK IN BRIDGES

The importance factor for assessing fire risk is related to performance of structural members to resist fire exposure and adverse impact of that fire incident on traffic flow and economic losses. The performance of structural members of a bridge is influenced by the degree of vulnerability of structural members to a fire. On the other hand, the impact of fire on a bridge is dependent on the critical nature of the bridge from the point of traffic functionality and the extent of fire losses. The key factors that influence the fire performance of bridges are discussed below.

3.1 Vulnerability of bridges to fire

There are several factors that contribute to vulnerability of structural members of a bridge to fire hazard, such as geometrical features, materials used in construction, loading and restraint (support) conditions and probable fire severity. For example, the thermo-physical and mechanical properties of constituent materials significantly affect the response of structural members under fire. In general, all materials experience loss of strength and stiffness properties at high temperatures. However, the rate of loss vary depending on the composition of constituent materials. The type and intensity of loading, as well as restraint conditions, can influence the fire performance of structural members. Typically, high load levels subject the members to additional stresses; hence rapid degradation of load carrying capacity occurs under high temperatures generated in a fire. Restrained support conditions can significantly enhance fire resistance of flexural members due to development of fire induced restraint forces that can counter balance the load induced moments. In the case of concrete structural members, concrete cover thickness to internal steel reinforcement has a direct bearing on the fire response of reinforced concrete structural members in concrete bridges. Further, fire intensity in a bridge and its duration depend on the available fuel type and quantity. Presence of highly flammable hydrocarbon products, unlimited oxygen supply and lack of fire protection (or fighting) measures can accelerate the rate of growth of fires, producing high intensity fires.

3.2 Critical nature of bridges

The second major factor to be accounted for in evaluating the importance of a bridge, from fire hazard point of view, is the critical nature of the bridge. The critical nature of a bridge is mainly influenced by the location of bridge and traffic density on the bridge. For instance, if the bridge is located in a route connecting natural obstacles (such as valleys or rivers) and if there are no alternative routes for traffic detours, then any closure of that bridge due to fire damage will significantly slow down or shut down the traffic in the region. Similarly, traffic density can determine the critical nature of the bridge. If a bridge is located on a condense highway or in the surroundings of urban area that serves large number of vehicles daily, loss of operation of such a bridge due to fire will cause significant traffic disruptions in the region.

4 APPROACH TO EVALUATE FIRE RISK IN BRIDGES

The level of fire risk in bridges can be accounted for through a fire based importance factor. The proposed approach for importance factor is derived by considering vulnerability of bridge structural members to fire, as well as critical nature of the bridge to traffic flow and extent of fire losses. Several steps are associated with the development of fire based importance factor for bridges and these steps are explained below.

4.1 Calculation of importance factor

In order to evaluate the importance factor for a given bridge, several parameters are to be accounted for. In general, these parameters are based on the vulnerability of bridge structural members to fire, as well as the critical nature of the bridge from traffic flow consideration. The vulnerability of a bridge to fire arises from structural members' geometric dimensions and design features and likelihood of a fire occurring near that bridge. Based on previous fire incidents on bridges, such factors were found to have the highest impact on the bridge's vulnerability to a fire hazard [1].

Alternatively, traffic demand, economic consequences after a fire incident, and expected fire losses define the critical nature of a bridge. Accordingly, bridges with high traffic volumes are more likely to experience higher losses and traffic interruption due to fire. Furthermore, after a fire incident, inspection and maintenance work could lead to temporary closure of a fire damaged bridge. Such closure requires detouring traffic to alternate routes, which would amplify traffic intensity in nearby highways and affect the traffic flow in the region.

The key characteristics that shape the fire-based importance factor, namely; vulnerability to fire and critical nature of bridges to traffic flow, are grouped under five classes; namely geometrical properties and design features, hazard (fire) likelihood, traffic demand, economic impact, expected fire losses. Each class covers various influencing parameters that contribute to the importance factor.

Within each parameter, there are various sub-parameters that determine the conditions of a specific bridge. Based on engineering judgment and recommendations of previous studies [1, 2, 14-17] weightage factors ($\varphi_{i,x}$) are assigned to different sub-parameters on a scale of 1 to 5, as shown in Table 1.

Knowing the maximum weightage factor for different parameters within each class (from Table 1), a class factor (ψ_x) is calculated as:

$$\psi_x = \frac{\sum \varphi_{x(\max)}}{\varphi_{total}} \tag{1}$$

where,

$\varphi_{x(\max)}$ is the maximum weightage factor of each parameter in class (x)

φ_{total} is the summation of maximum weightage factors of all parameters in all five classes

Then, a class coefficient (Δ_x) is calculated as the ratio of the summation of the weightage factors of all sub-parameters in class (x) to the summation of the maximum weightage factors of all the parameters in the same class:

$$\Delta_x = \frac{\sum \varphi_{i,x}}{\sum \varphi_{x(\max)}} \tag{2}$$

where,

$\varphi_{i,x}$ is the weightage factor of sub-parameter (i) in class (x)

$\varphi_{x(\max)}$ is the maximum weightage factor of each parameter in class (x)

Finally, an overall class coefficient (λ) is evaluated as the summation of the product of class coefficient (Δ_x) and corresponding class factor (ψ_x).

$$\lambda = \sum \Delta_x \psi_x \tag{3}$$

The overall class coefficient *(λ)* is then utilized to assign a fire risk grade for a bridge. The fire risk grades are grouped under four categories; namely, "critical", "high", "medium" and "low". This task is completed by comparing the value of the overall class coefficient *(λ)* of the bridge with a numerical score provided in Table 2. Based on this comparison, an importance factor (*IF*) can be arrived at. The risk grades and related overall class coefficient *(λ)* scores are given in Table 2.

Table 2. Risk grades and associated importance factors for fire design of bridges.

Risk grade	Overall class coefficient (λ)	Importance factor (*IF*)
Critical	⩾0.95	1.5
High	0.51-0.94	1.2
Medium	0.20-0.50	1.0
Low	<0.20	0.8

Application of the above approach to numerous bridges indicate that parameters in classes 1, 2, 3, 4 and 5 contribute by 44%, 23%, 11%, 13% and 9%, respectively, to the importance factor. Also through analysis of previous fire incidents, it was found that about 5% of total bridges fall under "critical" risk category and about 15% of bridges fall under "high" risk category. Provision of appropriate fire resistance to structural members in "critical" and "high" risk bridges can minimize the adverse effects of fire hazard to a great extent. Further information on the classes, parameters, rationale for assigning weightage factors and risk grades can be found elsewhere [17].

4.2 Validation of the proposed approach

The above developed approach was validated by evaluating importance factor for several bridges that experienced major fire incidents. Two fire incidents on bridges are considered for illustrating the validation of the proposed importance factor approach to classify bridges based on fire risk. The first fire incident relates to a fire that occurred at Bill Williams River Bridge, AZ, and the second fire incidents relates to fire that occurred at I-75 Overpass near Hazel Park, MI. Full details of validation and additional case studies are provided elsewhere [17].

In Parker, AZ, a fuel tanker crossing the Bill Williams River Bridge over-turned initiating a huge fire on July 28, 2006. This bridge, built in 1967, was made of prestressed concrete girders and a composite concrete deck. The fourteen precast AASHTO Type III concrete girders were of 23.3 meter span with a 165 mm cast-in-place concrete deck. Once the fuel tanker over-turned, the diesel fuel of about 29,000 liters in the truck, spilled and lead to a rapid burning. Although the fire burned for two and a half hours and affected three spans (8, 9 and 10) of the bridge, much of diesel fuel reached the underside of the bridge through the deck drains, thus reducing the fire intensity. Post fire inspection has shown significant spalling in top and bottom flanges of girders of span 9. Further, localized spalling was also noticed in girders of spans 8 and 10. During post fire inspection, traffic had to be detoured to nearby routes. After inspection and necessary repairs, the bridge was re-opened to traffic. The total cost of retrofitting the bridge was about $700,000 [18].

The above developed approach is applied to evaluate the importance factor for this bridge against possible fire hazard. Base on the available data for this bridge, the various parameters and sub-parameters needed for assessing the importance factor were collected. Then, different steps discussed above were applied to evaluate importance factor. The overall class coefficient for this bridge was found to be 0.54, and thus the importance factor for this bridge works out to be 1.2, which places the bridge under “high” risk grade. Since the bridge falls under “high” risk category, designing structural members for fire effects would enhance the fire performance of the bridge and lower adverse consequences due to fire hazard.

On July 15, 2009 a major fire broke out under the 9-mile road overpass at the I-75 expressway near Hazel Park, MI., after a fuel tanker carrying highly flammable fuel crashed into another truck. This collision proceeded a high intensity fire on the bridge resulting from the burning of 50,000 liters of fuel being transported in the fuel tanker. The fire temperatures were in the range of 1100˚C. The unprotected 58 m long steel girders were weakened due to high temperatures in steel and finally collapsed in about 22 minutes. The collapse of the overpass caused $12 million in fire losses and lead to major traffic delays [19].

To assess the applicability of the proposed approach, the importance factor was evaluated for this bridge. The various characteristics (sub-parameters) of this bridge were compiled from literature and the corresponding weightage factors are assigned. The overall class coefficient (λ) for this bridge works out to be 0.66, thus this bridge comes under “high” risk category for fire hazard, leading to an importance factor for this bridge to be 1.2. The unprotected steel girders in this bridge reached their strength limit state in 22 minutes. Hypothetically, the bridge could have survived if the steel girders were protected with some level of fire insulation.

5 STRATIGIES FOR OVERCOMING FIRE HAZARD IN BRIDGES

The proposed importance factor can be applied for evaluating fire risk associated with bridges at design stage or prior to rehabilitation of an existing bridge. This rehabilitation process could be due to scheduled maintenance, upgrading, improving the bridge’s state to meet current code provisions, or retrofitting after any adverse incident.

The vulnerability of a bridge to fire can be assessed through the proposed fire based importance factor. If the bridge is found to be in “critical” or “high” risk category, the vulnerability of the bridge to fire hazard can be minimized by providing some level of fire protection to structural members. The required fire protection to bridge structural members can be arrived at based on conventional prescriptive approaches (fire rating) or performance based design methods. The prescriptive approaches generally utilize tabulated fire ratings published in directories and standards. However, most of these fire ratings are based on fire tests conducted under ASTM E119 or ISO834 standard fire scenarios that represent cellulosic-type fuel fires which occur in buildings. In the case of bridge fires, which occur due to burning of hydrocarbon products and in an open environment, thus these fires are much more intense. Bridge fires are generally represented by hydrocarbon fire scenarios; NFPA 502 discusses possible fire scenarios in bridges and tunnels [20]. Hence, the use of fire ratings based on prescriptive approaches and derived from ASTM E119 or ISO834 standard fires may not be appropriate for bridge structural members i.e., 1 hour rating based on ASTM E119 may be equivalent to less than 1 hour exposure under hydrocarbon or RWS fire exposure. On the other hand, implementation of performance based design methods can provide designers with state-of-the-art solutions that are efficient, optimum and economical. Performance based design methods use rationale and engineering principles to arrive at unique solutions for bridges prone to high fire risk [6, 7].

In general, bridges with high vulnerability to fire and of importance to the transportation network can be provided with fire ratings of one to two hours. In the case of concrete bridges, 1 to 2 hour of fire rating to structural members can be achieved through the provision of sufficient concrete cover thickness. Hence, no external fire protection may be needed for conventional concrete members. However, in the case of steel and timber bridges, external fire proofing to structural members may be needed to achieve desired fire ratings. On the other hand, composite bridges can achieve adequate fire resistance through the utilization of composite action and also proper application of concrete cover to members.

In the case of high risk bridges near urban centers, additional strategies such as establishing a fire station closer to the location of these bridges can minimize vulnerability of such bridges from fire hazard risk. Through these fire stations, response time to reach fire incident site can be reduced. Also, flow of fuel tankers on critical bridges can be regulated. For instance, limiting number of fuel tankers that travel across a critical bridge to certain times and weather conditions.

6 CONCLUSIONS

Based on the presented information above, the following conclusions can be drawn.

(1) Fire represents severe hazard in bridges and can induce significant damage or collapse of structural members.

(2) The probability of fire breaking out in bridges is ten times lower than that in buildings, however, impact of such fire on bridges can be much more devastating due to lack of adequate fire protection measures in bridges.

(3) The probability of fire induced collapse of a bridge over 10 and 50 year period is estimated to be 27% and 80%, respectively, which is much less than that in buildings.

(4) A weightage factor methodology is applied for deriving fire based importance factor for classification of bridges based on fire hazard. This weightage factor based approach takes into account the vulnerability of structural members to fire hazard and critical nature of the bridge from the point of traffic functionality.

(5) The proposed importance factor can be used as a benchmark to assess relative fire risk in bridges and also to develop appropriate strategies for mitigating fire hazard in bridges.

ACKNOWLEDGMENTS

This material is based upon the work supported by the National Science Foundation under Grant number CMMI-1068621 to Michigan State University. Any opinions, findings, and conclusions or recommendations expressed in this paper are those of the authors and do not necessarily reflect the views of the sponsors.

REFERENCES

[1] Kodur, V., Gu, L., and Garlock, M., "Review and Assessment of Fire Hazard in Bridges", Transportation Research Record*: Journal of the Transportation Research Board*, 2172, 23-29, 2010.

[2] Garlock, M., Paya-Zaforteza, I., Kodur, V., and Gu, L., "Fire hazard in bridges: Review, assessment and repair strategies", *Engineering Structures* 35, 89-98, 2012.

[3] Bai, Y., Burkett, W., and Nash, P., "Rapid Bridge Replacement under Emergency Situation: Case Study", *J. Bridge Eng.*, 11(3), 266–273, 2006.

[4] Guthrie, D., Goodwill, V., and Hicks, M., "Tanker fire shuts down I-75, collapses Nine Mile bridge", The Detroit News, 2009.

[5] U.S. Department of Transportation, Federal Highway Administration, Highway Statistics, 1995-2010: Ibid., Highway Statistics (Washington, DC: Annual Issues), 2010.

[6] Aziz, E., Kodur, V., “An approach for evaluating the residual strength of fire exposed bridge girders.” *Journal of Constructional Steel Research*, 88, 34-42, 2013.
[7] Kodur, V., Aziz, E., and Dwaikat, M., “Evaluating Fire Resistance of Steel Girders in Bridges.” *J. Bridge Eng.*, 18(7), 633–643, 2013.
[8] Science Applications International Corporation (SAIC), “A Guide to Highway Vulnerability Assessment for Critical Asset Identification and Protection,” Transportation Policy and Analysis Center, Vienna, VA 22182, 2002.
[9] Barkley, T., and Strasburg, G., “Bridge Rebuilt on the Fast Track”, *Public Roads* Sept/Oct 2002, FHWA, 66, 2002.
[10] NFPA, (2008) U.S. vehicle fire trends and patterns. National Fire Protection Association, 1 Batterymarch Park, Quincy, MA 02169-7471.
[11] Federal Highway Administration (FHWA). 2000. ‘‘National bridge inventory record count 1998–2000.’’http://www.fhwa.dot.gov/bridge/ allbridg.htm
[12] Karter, M., “Fire loss in the United States during 2011.” *National Fire Protection Association*, 2012.
[13] Beitel, J., and Nestor, I., “Historical Survey of Multi-Story Building Collapses Due to Fire”, *Fire Protection Engineering*, Retrieved at May 14th, 2013 at: http://magazine.sfpe.org/structural-fire-resistance/historical-survey-multistory-building-collapses-due-fire
[14] Wardhana, K., and Hadipriono, F., “Study of recent building failures in the United States”, *Journal of perf. Of Const. Facilit*. ASCE 17(3), 151-158, 2003.
[15] Wardhana, K., and Hadipriono, F., “Analysis of Recent Bridge Failures in the United States”, *J. Perform. Constr. Facil*. 17(3), 144–150, 2003.
[16] Scheer, J., *Failed Bridges: Case Studies, Causes and Consequences*, John Wiley & Sons, 2010.
[17] Kodur, V., and Naser, M., “Importance Factor for Design of Bridges Against Fire Hazard”, *Engineering Structures*, 54, 207-220, 2013.
[18] Stoddard R. Inspection and Repair of a Fire Damaged Prestressed Girder Bridge, Report IBC-04-17, Washington State Department of Transportation, Olympia, WA 2004.
[19] National Steel Bridge Alliance. Steel bridge news, Chicago, 2010.
[20] National Fire Protection Association (NFPA). NFPA 502 Standard for road tunnels, bridges, and other limited access highways, Quincy (MA), 2008.

APPENDIX

Table 1 Weightage factors based on the different features of a bridge.

Class I: Geometrical properties and design features			
Parameter	***Sub-parameters***	$\varphi_{i,x}$	$\varphi_{i,x(\max)}$
Structural system	Truss/Arch	1	5
	Girder - continuous	2	
	Girder - simply supported	3	
	Cable-stayed	4	
	Suspension	5	
Material type	Reinforced concrete	1	5
	High strength/(pre-stressed) concrete	2	
	Steel-concrete composite	3	
	Concrete members strengthened with FRP	4	
	Steel and timber	5	
Span (m)	<50	1	4
	50-200	2	
	200-500	3	
	>500	4	
No. of lanes	2	1	3
	2-4	2	
	>4	3	
Age (years)	<15	1	4
	15-29	2	
	30-50	3	
	>50	4	
Current rating	100	1	5
	60-80	2	
	40-60	3	
	20-40	4	
	<20	5	
Additional service features	1 deck	1	5
	2 decks + pedestrians	2	
	Accommodates railroad	3	
	Multi-level	4	
	Above water	5	

Class II: Hazard (fire) likelihood			
Parameter	***Sub-parameters***	$\varphi_{i,x}$	$\varphi_{i,x(\max)}$
Response time (min)	<5	1	5
	5-10	2	
	10-20	3	
	20-30	4	
	>30	5	
Hist./arch.significance	Conventional	1	3
	Landmark	2	
	Prestigious	3	
Threat perception	None (low)	1	3
	Not available (medium)	2	
	Frequent (high)	3	
Fire scenario	A small vehicle fire above /under the bridge	1	5
	A large truck collision and fire with other vehicles	2	
	A fuel tanker collision and fire with bridge sub-structure	3	
	Major fuel tanker collision and fire with multiple vehicles and against bridge sub-structure	4	
	Fire due to fuel freight ship collision with a bridge pier	5	

Class III: Traffic demand			
Parameter	***Sub-parameters***	$\varphi_{i,x}$	$\varphi_{i,x(\max)}$
ADT (vehicles/day)	<1,000	1	5
	1,000-5,000	2	
	5,000-15,000	3	
	15,000-50,000	4	
	>50,000	5	
Facility location	Rural	1	3
	Sub-urban	2	
	Urban	3	

Class IV: Economic impact			
Parameter	***Sub-parameters***	$\varphi_{i,x}$	$\varphi_{i,x(\max)}$
Closeness to alt. routes	<10 km	1	3
	10-20 km	2	
	>20 km	3	
Time expected for repair	<3 months	1	3
	3-9 months	2	
	>9 months	3	
Cost expected for repair	< 1 million	1	3
	1-3 million	2	
	>3 million	3	

Class V: Expected fire losses			
Parameter	***Sub-parameters***	$\varphi_{i,x}$	$\varphi_{i,x(\max)}$
Life/property losses	Minimum to no injuries	1	3
	Minimum casualties	2	
	Many casualties	3	
Env. damage	Minor damage	1	3
	Significant damage	2	
	Unacceptable damage	3	

8th International Conference on Structures in Fire
Guo-Qiang LI, Venkatesh K. R. KODUR, Shou-Chao JIANG, Jian JIANG, Su-Wen CHEN, Guo-Biao LOU (Eds.)
Shanghai, China, June 11-13, 2014

A STUDY ON DIFFERENT TECHNIQUES OF RESTORATION OF HEAT DAMAGED R.C. BEAMS

A.B.Danie Roy*, Umesh.K. Sharma and Pradeep Bhargava*****

* Research Scholar Indian Institute of Technology Roorkee

**Associate Professor Indian Institute of Technology Roorkee
e-mails: danieroy2002@yahoo.com, umuksfce@rediffmail.com

*** Professor Indian Institute of Technology Roorkee
e-mail: bhpdfce@iitr.ernet.in

Keywords: Concrete beams, Heat damage, Strengthening, Flexural strength, Stiffness, ductility

Abstract. *The main aim of the present investigation is to examine the capabilities of some commonly used retrofitting techniques in restoring the structural capacity of heat damaged reinforced concrete beams. A series of 27 reinforced concrete T- beams of length 1400 mm were cast using normal strength concrete. After 90 days of ageing, the beams were heated to 600^{o}C and 900^{o}C temperatures in an electric furnace. It was observed that the beams exposed to different temperatures experienced a reduction in ultimate load carrying capacity ranging from 14 % to 61%. The secant stiffness and energy dissipation were reduced in the range of 34% to 56% and 10% to 41% respectively. The study shows that GFRP wraps were quite capable of restoring the flexural strength of heat damaged beams. However, this strengthening scheme was not able to restore the energy absorption capacity of heated beams. On the contrary, the HSFRC and FC techniques though indicated only nominal improvement in the strength capacities, however they were quite capable in restoring the secant stiffness and energy absorption capacity of heat damaged RC beams.*

1 INTRODUCTION

In today's built environment, the various civil engineering structures are liable to be exposed to fire or elevated temperature conditions. It has been observed that the structures, especially concrete structures, are generally not completely destroyed at such high temperatures. There is always a possibility for their restoration and rehabilitation after the heat exposure. Many researches have examined different aspects of concrete when exposed to high temperature [1-2]. The aim of this research is to damage the reinforced concrete beam under various high temperatures and then strengthen the damaged element with different techniques.

Many experimental studies have been under taken in recent years to strengthen RC structures using suitable retrofitting and strengthening techniques. Strengthening pattern involves the use of materials other than that in original structure. Conventional materials for strengthening include Fiber Reinforced Polymer, Ferrocement, High Strength Fiber Reinforced Concrete, Steel plate bonding etc. Apart from low maintenance cost and improvement in the service life of buildings, Fibre Reinforced Polymer (FRP) wrapping has several benefits e.g. high strength, light weight, resistance to corrosion, low cost, and versatility. Also the interaction between concrete and fiber enhances concrete strength and ultimate strain. Significant research have been undertaken on retrofitting the old concrete beams with FRP at room temperature conditions [3 - 8] but limited research has been reported on the repairing of fire damaged concrete elements [9 - 11]. Ferrocement (FC) is a special method, in which the wire mesh are uniformly dispersed in matrix to improve the properties such as tensile strength, flexural strength, toughness, crack control, fatigue resistance and impact resistance. Other advantages of FC include ease of availability of raw materials, which can be easily wrapped around concrete structures of various shapes and does not require skilled manpower. Increased strength and ductility has been observed in FC encased elements. Apparent stiffness and ultimate load carrying capacity has been increased by FC retrofit coatings in new structures and repair and rehabilitation of existing structures [12-15], its application in repairing of fire damaged reinforced concrete beam is unexplored. Recently, a new method has been used for strengthening concrete structures via thin jackets made of high strength fibre reinforced concrete [16 - 18]. The advantages of this method are high compressive strength, high tensile strength and there is no need to have reinforcement bars as rebars and stirrups and no specified concrete cover, and the thickness of the jacket can be as small as 15 – 40 mm. Several studies have previously been undertaken into the feasibility of using HSFRC for the rehabilitation and strengthening of damaged members but limited research has been reported on the repairing of fire damaged concrete elements [19 – 23]. The main aim of this research is to investigate the effectiveness of applying HSFRC, FC and GFRP jackets on heated damaged reinforced concrete beams; and to study the behavior of damaged and strengthened elements in terms of strength gain, ductility and failure modes.

2 EXPERIMENTAL PROGRAM

An experimental programme was designed to examine the efficiency of different above mentioned techniques to restore the structural performance of heat damaged beams. A series of 27 reinforced concrete beams were constructed using normal strength concrete. The details of the specimens are illustrated in Table 1 and Figure 1. Experimental variables included temperature of exposure and type of strengthening. The concrete was prepared with crushed limestone aggregate of maximum size 12.5 mm, ordinary Portland cement, natural river sand (zone 2), and portable water. The tension reinforcement consisted of 2 numbers of 12 mm diameter bars of 622.5 MPa yield strength, compression reinforcement of 4 numbers of 8mm diameter of 650 MPa yield strength, while 580 MPa of reinforcing steel with a diameter of 6 mm were used as stirrup reinforcement. The spacing of stirrup used was 100mm as shown in Figure 1.

Three types of strengthening materials were used namely hooked end steel fiber, bi directional welded wire mesh and uni-directional FRP. The properties of the materials are illustrated in Tables 3 to 5. The slurry mix proportions used for HSFRC and FC jacketing was1:0.6:0.15:0.35:0.01 by weight of cement, sand, silica fume, water and super plasticizer respectively. Prepared slurry mix had a high compressive strength of about 68.06MPa and a high flow as measured by a standard ASTM C939 flow cone (about 32 seconds).

Table 1. Details of specimens.

Beam designation	Beam condition	Strengthening methods
TBA	Control	none
TB6	Heat damaged 600^{o}C	none
TB9	Heat damaged 900^{o}C	none
TB6 HSFRC	Heat damaged 600^{o}C	High strength fiber reinforced concrete
TB6 FC		Ferrocement
TB6 GFRP		Glass fiber reinforced polymer
TB9 HSFRC	Heat damaged 900^{o}C	High strength fiber reinforced concrete
TB9 FC		Ferrocement
TB9 GFRP		Glass fiber reinforced polymer

All the beams were of same cross-section and length. The quantities of all materials were kept ready in required proportion to cast a beam at a time from one batch of concrete with three cubes, prisms and cylinders in order to monitor the strength at the time of testing. A concrete cover of 15 mm was provided in all the T-beams. Six K type thermocouples were placed in each beam during casting in order to monitor the temperature at the time of heating. Three K type thermocouples were placed at the center of the web and the other was attached to flange area. The specimens were cast using steel moulds in the laboratory. Needle vibrator was used during the casting of T- beams. After 24 hrs, the beams were removed from the moulds and covered with gunny bags for curing. The water curing period lasted for 28 days after which the beams were kept in the laboratory at ambient temperature and humidity conditions for another 120 days.

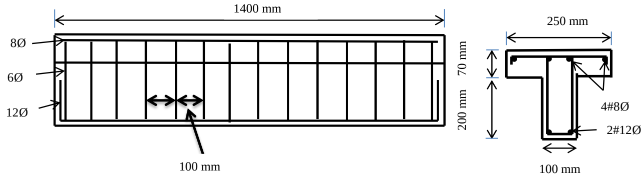

Figure 1. Details of beam.

2.1 Thermal Testing

Beam specimens were subjected to heat treatment using table mounted electrical furnace. The programmable electrical furnace with a maximum heating temperature of 1200 ℃ was used for heating the specimens, Figure 2. The temperature inside the furnace was measured with K-type thermocouples. The beams were exposed to two different target temperatures 600^{o} C and 900^{o}C after 150 days. The beam were placed in the furnace upside down so that heat won't affect the flange directly, which indicate the real condition of beams in the structure.

Figure 2. Table mounted Furnace.

The heating rate was set at 10^{0}C /min, which has been shown to be reasonable for structures exposed to fire. Each target temperature was maintained for three hours to achieve a thermal steady state condition as shown in Figure 3. On completion of the exposure time, the furnace was switched off, and samples were left in the furnace to allow natural cooling till room temperature. The data from the thermocouples was recorded in a computer through a data logger.

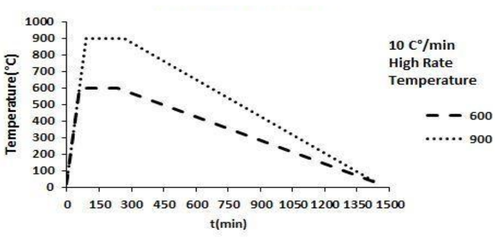

Figure 3. Heating Regimes.

2.2 Strengthening of heat damaged specimen

After heating and cooling the heat damaged specimens were strengthened with various techniques namely HSFRC, FC and GFRP jacketing. The specimens which were heated to 900 ℃ temperature were first repaired and their section was restored before wrapping. The loose concrete was removed using steel wire brush, chisels and hammer as shown in Figure 4. The surfaces of specimen were cleaned thoroughly to ensure no dust. A primer coat of bonding was applied on the spalled surface of the specimen to achieve good bonding between the old concrete and new repair material i.e. micro concrete. In the specimens exposed to 600 ℃, a primer epoxy bonding was applied after the surface was cleaned in order to provide good bonding between the substrata and the new strengthening material.

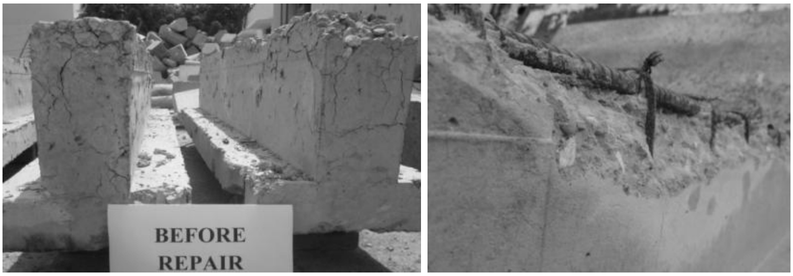

Figure 4. Heat damged T- Beam after 900^{o}C and after removing loose concrete.

The heat damaged specimens meant for strengthening with HSFRC jacketing were placed inside the moulds. HSFRC slurry reinforced with hooked steel fiber at a volume fraction of 2% was poured into the steel mould to form a 20 mm thick jacket on bottom of web, side of web and bottom flange of the specimens. The FC jacketing was reinforced with two layers of welded wire mesh of 13mm × 13mm. At several places, the first and the second layers of the wire mesh were tied together with the same diameter steel wire. Wooden mallets were used to keep the wire mesh close to the surface of beams and in web, the mesh were anchored with small screws. Slurry with high compressive strength of about 68.06 MPa was poured into the mould to form 20mm thick FC jacket (Figure 5). The strengthened specimens were covered with damped gunny bags for 14 days after demoulding. Before GFRP jacketing the surface of heat damaged specimens were scraped lightly to remove surface contaminants. Then the surface of the concrete was coated with a layer of epoxy primer on the external surfaces of the concrete to fill air voids and to provide good bond strength. Thereafter a thin layer of the two part saturant solution consisting of resin and hardener mixed as per the manufacturers specifications was applied over the web bottom and side of web on both sides of shear regions. Then the first layer of GFRP sheets was wrapped on the bottom of the web carefully. A roller was used to remove the entrapped air between the fiber and excess saturant so as to allow better impregnation of the saturant. Special attention was taken to ensure that no air voids were left between the fiber and the concrete surface. After the application of the first wrap, a second layer of saturant solution was applied on the surface of the first layer. The roller was used again to remove any trapped air and to force the resin in the fibers. All the specimens were stored at room temperature for at least 28 days before testing.

Figure 5. Strengthening of T- beam with FC and GFRP.

2.3 Instrumentation and test setup

Mechanical testing of the specimens was carried out after a complete cycle of heating, cooling and then strengthening. The test beams were loaded using a 200 Ton capacity hydraulically hand operated jacks connected to a data acquisition system through load cells. The beams were tested under monotonic increasing load. The deflection of the beam was noted using linear variable differential transducer (LVDT), placed at five locations at the bottom of beams connected to data logger as shown in Figure 6. The strain gauges were mounted on bottom of web and side of web in GFRP jacketing. The recorded data from the LVDTs, strain gauges and load cell were fed into a data acquisition system and stored on a computer.

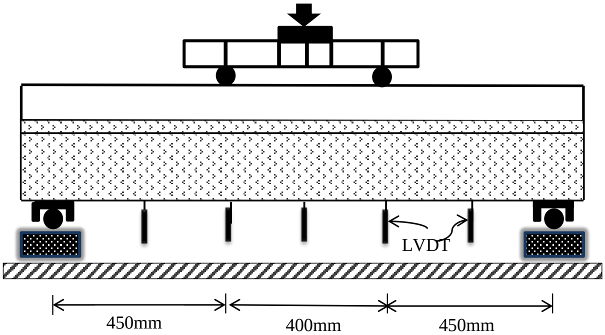

Figure 6. Test Setup.

3 OBSERVATIONS AFTER HEAT DAMAGE

When evaluating the condition of heat damaged beams, visible damage and the results of visual observations are used to identify damage and assess its magnitude. Visible damage can be cracks, spalled areas, colour change etc. In this study the colour of concrete changed to light greyish at 600 ℃. However, the colour of specimens changed to ash white when exposed to 900 ℃. Some hairline cracks were observed at 600 ℃. The number of cracks became relatively pronounced at 900 ℃. The structure of the cement mortar after temperature exposure was observed to have become loose because of the pore expansion owing to the vaporization of the absorbed water. Slight spalling was observed at 900 ℃. During cooling, the ionized CaO decomposed from Ca $(OH)_2$ and absorbs water and then becomes Ca $(OH)_2$ again, which results in the expansion of the concrete volume (24).

4 RESULTS AND DISCUSSION

The performances of beams were assessed through the load deflection curves Figures 7 – 9 and results are summarized in Table 2.The yield load P_y was the applied load at which the beam starts to yield and Pu was the ultimate load measured on each beam. The μ_Δ is the deflection ductility index and Δy and Δu are the mid span deflection at yield load and ultimate load of the beam respectively.

4.1 Failure modes of Control Specimen and Heat Damaged beams

The overall behavior of reinforced concrete undamaged beam and heat damaged beam were assessed by studying the load–deflection diagram. The results of the beam are summarized in Table 2 and Figure 7. The ultimate strength of all heat damaged beams was lesser when compared with undamaged beams. The undamaged beam failed at 195 kN, whereas the heat damaged 600°C and 900°C failed at 166 and 76 kN respectively. The decrease in ultimate load was steeper beyond 600°C.

When the undamaged beams were loaded in the laboratory they developed flexural tensile crack in the hinge region at an average load of 43kN. Around 153kN, the beam started to yield and the beam finally failed in flexure at a load of 195kN. Similarly in 600^{o}C heat damaged beam first crack load was at 26kN and flexural crack develop in the mid- span region and cracks were initiated in shear span region but finally failed in flexure at a load of 166kN. Also 900^{o}C heat damaged beam the first crack load was 21kN shows significant decrease in first crack load as compared to undamaged beam.

Table 2. Summary of beam test results.

Beam Designation	Load(kN)		Deflection		Deflection Ductility Factor	Failure Mode
	Yield Load P_y(kN)	Ultimate Load P_u(kN)	Δy(mm)	Δu(mm)	$\mu_\Delta=\Delta u/\Delta y$	
TBA	153	195.36	6.84	20.01	2.925	Flexural
TB6	141	166.00	9.13	25.77	2.822	Flexural
TB9	60	76.09	9.03	17.86	1.977	Shear failure at support
TB6 HSFRC	142	197.63	7.82	28.81	3.684	Flexural
TB6 FC	153	201.30	7.71	23.7	3.073	Flexural
TB6 GFRP	194	225.90	7.48	10.89	1.455	Flexural failure and debonding of shear fabric
TB9 HSFRC	98	138.88	3.68	12.14	3.298	Flexural
TB9 FC	106	141.43	3.68	15.65	4.252	Flexural
TB9 GFRP	140	195.91	6.99	14.29	2.044	Debonding of fabric in shear region

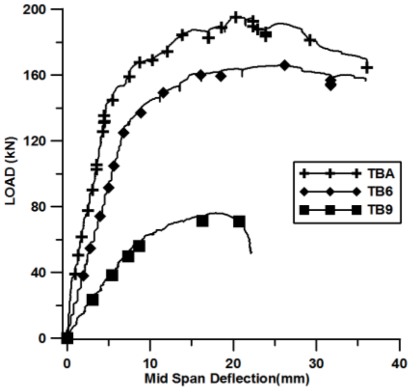

Figure 7. Load–deflection relationship of control and heat-damaged specimens.

4.2 Failure modes of Strengthened Heat Damaged Beams

The load deflection behavior of the strengthen heat damaged beam with different strengthening schemes are shown in Figures 8 to 9. Figure 8 shows the load deflection behavior of 600^{o}C and 900^{o}C heat damaged strengthened beam with 20mm thick HSFRC and FC jacketing. The strengthening technique improves the ultimate load capacity of 600^{o}C heat damaged beams, no strength gain was observed in case of 900^{o}C heat damaged beam when compared to undamaged beams. The 600^{o}C heat damaged beam strengthened with HSFRC and FC took 1%, 3% more ultimate load when compared to undamaged beam respectively, 18%, 21 % respectively when compared with that of heat damaged ones. 900^{o}C heat damaged beams strengthened with HSFRC and FC shows reduction in ultimate load carrying capacity by 27%, 29% respectively of that of undamaged beams. HSFRC and FC beams have higher deflection ductility and energy ductility when compared with GFRP strengthening. The energy dissipation capacity of strengthen beam is reduced considerably when compared with undamaged and damaged beams.

Figure 9 shows the load deflection behavior of 600^{o}C and 900^{o}C heat damaged strengthened beam with GFRP jacketing. The strengthening technique improves the ultimate load by 15%, 1% respectively when compared with undamaged beams, 35%,156% correspondingly when compared with damaged once. GFRP strengthen beam exhibited less displacement and energy ductility than that of control beams. The energy dissipation capacity of strengthened beam is reduced considerably when compared with undamaged and heat damaged beams.

5 CONCLUSIONS

The performance of heat damaged reinforced concrete beams strengthened with HSFRC, FC and GFRP techniques subjected to different strengthening schemes are presented in this paper. Based on the observations and experimental results following conclusion are made:

(1) In reinforced concrete exposed to different temperature ultimate load carrying capacity was affected by about 14 %, 61% respectively when compared with undamaged beams.

(2) An increase in ultimate load is achieved with GFRP laminate in all heat damaged specimens. Subsequently HSFRC and FC techniques improves the ultimate load capacity of 600^{o}C heat damaged

beams, strength achieved in case of 900^{o}C heat damaged beam was lesser when compared to undamaged beams.

(3) The beam heat damaged at 600 ^{o}C and 900 ^{o}C showed less ductility when compared with undamaged beams of about 4% and 32% respectively. The HSFRC and FC strength beam were more ductile when compared with undamaged beams. All GFRP strengthen beam behaved less ductile than that of undamaged beam.

(4) Among the proposed strengthening technique for heat damaged beams, GFRP seems to be more effective in all the cases when compared with HSFRC and FC technique.

(5) The load corresponding to concrete cracking increased considerably when the damaged beam are strengthen with different strengthening techniques.

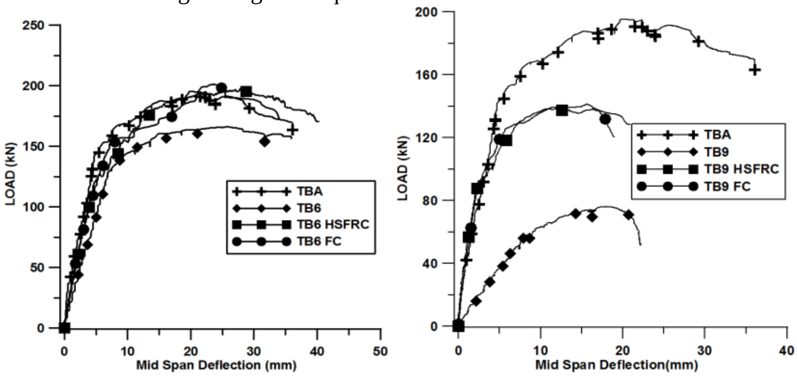

Figure 8. Load–deflection relationship of heat-damaged HSFRC & FC strengthened specimens.

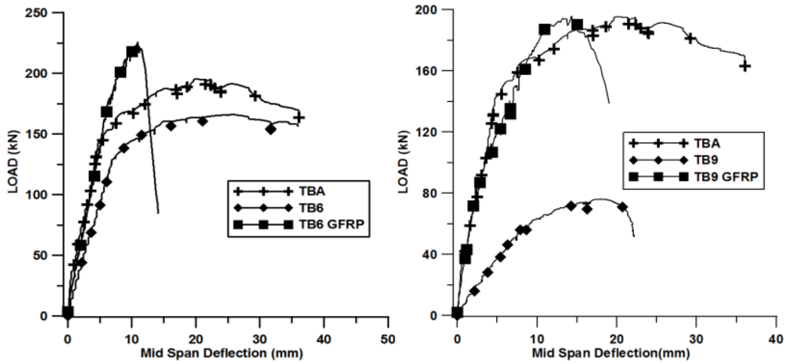

Figure 9. Load–deflection relationship of heat-damaged GFRP strengthened specimens.

ACKNOWLEDGEMENT

Authors thankfully acknowledge funding received from UKIERI for carrying out the work.

REFERENCES

[1] Anderberg,Y., Thelandersso.S.,(1976). Stress and deformation characteristics of concrete at high temperatures, *Lund Institute of Technology*, Lund, Sweden.

[2] Fletcher, I., Carvel, R., Welch, S., Torero, J., (2007). The behaviour of concrete structures in fire. *Thermal Science*, 11(2), 33-57.

[3] Ceroni F (2010).Experimental performances of RC beams strengthened with FRP Material. *Construction and Building Materials*. 24: 1547-1559.
[4] Esfahani MR, Kianoush MR, TajariAR (2007). Flexural behavior of reinforced concrete beams strengthened by CFRP sheets. *Engineering Structures*, 29(10): 2428-2444.
[5] Gangarao HVS, Vijay PV (1998). Bending behavior of concrete beams wrapped with carbon fabric. *Journal of Structural Engineering*-ASCE., 124(1): 03-10.
[6] Saadatmanesh H, Malek AM (1998). Design guidelines for flexural strengthening of RC beams with FRP plates. *Journal of CompositesConstruction*. 2(4): 158-164.
[7] Alagusuundaramoorthy P, Harik I E, & Choo C C. (2003). Flexural behaviour of RC beams strengthened with carbon fibre reinforced polymer sheets or fabric. *Journal of Composites for Construction*, 7(4):292-301.
[8] Chajes M J, Thomson T, Finch W W, & Januszka T. (1994). Flexural strengthening of concrete beams using externally bonded composite materials. Construction and Building Materials,8(3):191-201.
[9] Kai, X., & Guohui, W. (2011). Flexural Strengthening of Fire-damaged Reinforced Concrete Continuous T-Beams with CFRP sheets. *Fire Research*, 372-379.
[10] Yaqub, M., Bailey, C. G., Nedwell, P., Q.U.Z. Khan, Q.U.Z., & Javed, I. (2013). Strength and stiffness of post-heated columns repaired with ferrocement and fibre reinforced polymer jackets. *Composites: Part B* 44, 200–211.
[11] Bisby, L.A., Chen, J.F., Li, S.Q., Stratford, T.J., Cueva, N., Crossling, K. (2011). Strengthening Fire-Damaged Concrete by Confinement with Fibre-Reinforced Polymer Wraps. *Engineering Structures*, 33, 3381–3391.
[12] Al-kubaisy, M. A, & Zamin, M. (2000). Flexural behaviour of reinforced concrete slabs with ferrocement tension zone cover. Construction and Building Materials.14, 245-252.
[13] Bansal, P. P., Kumar, M, Kaushik, S.K. Effect of Wire Mesh Orientation on Strength of Beams Retrofitted Using Ferrocement Jackets. *International Journal*, 2(1), 8-19.
[14] Kondraivendhan, B., &Pradhan, B. (2009). Effect of ferrocement confinement on behavior of concrete. *Construction and Building Materials*, *23*(3), 1218-1222.
[15] Mourad, S. M., &Shannag, M. J. (2012).Repair and strengthening of reinforced concrete square columns using ferrocement jackets. *Cement and concrete composites*, 34(2), 288-294.
[16] Martinola, G., Meda, A., Plizzari, G. A., &Rinaldi, Z. (2010). Strengthening and Repair of RC Beams with Fiber Reinforced Concrete. *Cement and Concrete Composites*, *32*(9), 731-739.
[17] Mostosi, S., Meda, A., Riva, P., and Maringoni, S. (2011). Shear Strengthening of RC Beams With High Performance Jacket. *Symposium Journal in Modern Foreign Literatures*, 955-958.
[18] Skazlic, M. (2009). Utilization of high performance fiber-reinforced micro-concrete as a repair material. *Concrete Repair, Rehabilitation and Retrofitting II* – Alexander et al (eds), 859-862.
[19] Haddad, R H, Shannag, M. J., &Hamad, R. J. (2011). Repair of heat-damaged reinforced concrete T-beams using FRC jackets. *Concrete*, *9831*(3), 223-231.
[20] Haddad, R. H. (2008). Effect of elevated temperature on bond between steel reinforcement and fiber reinforced concrete. *Fire Safety Journal*, *43*, 334-343.
[21] Haddad, R H, Al-mekhlafy, N., &Ashteyat, A. M. (2011). Repair of heat-damaged reinforced concrete slabs using fibrous composite materials. *Construction and Building Materials*, *25*(3), 1213-1221.
[22] Haddad, Rami H, &Shannag,. M. J. (2008). Repair of heat-damaged RC shallow beams using advanced composites. *Materials and Structures*, 287-299.
[23] Leonardi, A., Meda, A., & Rinaldi, Z. (2011). Fire-damaged R / C Members Repair With High-Performance Fibre-Reinforced Jacket. *Stress: The International Journal on the Biology of Stress*, *47*, 28-35. 2013
[24] Mehmet (2013). Effect of cooling regimes on compressive strength of concrete with lightweight aggregate exposed to high temperature. *Construction and Building Materials*, 41, 21–25.

8th International Conference on Structures in Fire
Guo-Qiang LI, Venkatesh K. R. KODUR, Shou-Chao JIANG, Jian JIANG, Su-Wen CHEN, Guo-Biao LOU (Eds.)
Shanghai, China, June 11-13, 2014

NUMERICAL SIMULATION AND PRACTICAL CALCULATION METHOD FOR THE SHEAR STRENGTH OF CONCRETE SHORT COLUMNS AFTER EXPOSURE TO 3-FACE HEATING

Yu-Ye Xu*, Bi-Lan Lin and Dan Li***

* College of Civil Engineering, Huaqiao University, Xiamen, Fujian Province 361021, People's Republic of China
e-mails: yuyexu@hqu.edu.cn, 184748303@qq.com

** College of Materials Science and Engineering, Xiamen University of Technology, Xiamen, Fujian Province 361024, People's Republic of China
e-mail: linbilan@xmut.edu.cn

Keywords: Concrete column, Shear strength, After fire, Numerical Simulation, Practical calculation method

Abstract. *A numerical model is developed for the push-over analysis of concrete short columns after exposed to fire, and it is verified by the experimental results of seven columns. The effects of the horizontal force direction, fire duration, axial load ratio, sectional dimension, shear span ratio and stirrup spacing on shear strength of concrete short columns after exposure to 3-face heating were investigated. The average reduction coefficient of the compression strength in concrete sections was calculated, and a practical calculation method for the shear strength of concrete columns after 3-face heating was proposed. The results indicate that: (1) the shear strength of concrete short column after fire is well predicted by the established model. However, the prediction of the full curve of load-displacement behaviour needs further improvement. (2) The proposed formula provides a certain safety margin and can be used to assess the residual shear strength of concrete columns after 3-face heating.*

1 INTRODUCTION

Residual mechanical behaviour of concrete structure after fire is the foundation of structure identification and strengthening design after fire. Recently, the relative studies have been widely reported [1-6]. Xu et al developed a finite element program for the eccentric compression performance of concrete column after fire, and established the corresponding practical calculation formula for the square columns [1]. Tang et al experimental studied the failure model, deformation characteristics and residual capacity of concrete columns under compression after fire[2]. Wu et al experimental investigated the axial bearing capacity and axial compressive stiffness of concrete columns with axial restraint after fire[3], and also researched the earthquake seismic performance including strength, stiffness, ductility, and hysteretic characteristics of concrete columns after fire[4]. Chen at el tested the mechanical properties of concrete columns with biaxial eccentric compression after fire[5]. Huo et al also experimental researched the axial bearing capacity, stiffness and ductility of concrete short columns with initial compression during fire[6]. It should be pointed out that the current researches mainly focused on the normal section bearing capacity of concrete column members after fire, but the diagonal shear properties have rarely been reported. In the previous studies[7], the shear failure of the concrete short columns was experimental studied; the earthquake seismic performance of seven concrete short columns after exposure to 4-face heating and one concrete short column without fire was experimental investigated; the effects of fire duration, axial load ratio and shear span ratio on the shear capacity was analyzed; and the corresponding practical calculation formula for concrete columns after exposure to 4-face heating was proposed. In addition, the effects of them on hysteretic behaviour and damage process of concrete short columns after fire were also studied[8].

In this paper, the finite element model for the push-over process of concrete short columns after fire is further developed; the effects of horizontal direction force, fire duration, axial load ratio, shear span ratio, section dimension, stirrup spacing on the shear strength of concrete short columns after exposure to 3-face heating are analyzed using numerical simulation and the corresponding practical calculation formula for shear capacity is established.

2 FINITE ELEMENT MODEL AND EXPERIMENTAL VALIDATION

2.1 Element type and mesh generation

The numerical analysis model was established using ABAQUS finite element software. During the thermal analysis at elevated temperature, the 8-node 3D solid element DC3D8 for concrete was employed and the two-node beam element DC1D2 for reinforcement was used. During the push-over analysis after fire, the 3D 8-node reduced integration element C3D8R was adopted; the 3D 2-node bar element T3D2 for reinforcement, of which the transverse shear was neglected, was used; the reinforcement was embedded in the concrete; and the slip of concrete and reinforcement was not considered.

Mesh generation of the push-over analysis after fire and the thermal analysis during fire is similar. To guarantee the co-node of concrete and reinforcement in the meshing process, the concrete was segmented according to the reinforcement location. The established finite element model for concrete short column is shown in Figure 1.

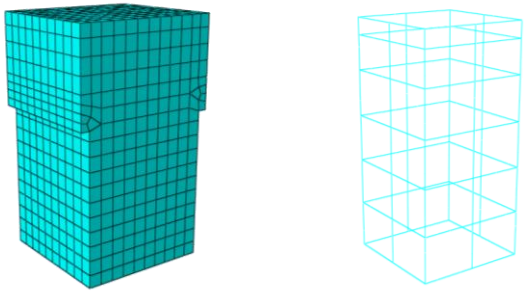

(a) Concrete (b) reinforcement

Figure 1. Finite element model of the specimens.

2.2 Material properties

The thermal performance including thermal conductivity, volumetric heat capacity and thermal expansion coefficient of concrete (siliceous aggregate) and reinforcement was selected according to the formula suggested by Lie et al in Reference [9].

The mechanical performance of reinforcement after fire was totally recovered, assuming that the stress-strain relation of reinforcement after fire was similar to that without fire, and the ideal elastic-plastic model for reinforcement was used.

The plastic damage constitutive model for concrete was employed, and the essential parameters of plastic potential equation and yield surface equation were proposed after repeated calculation. The dilation angle was 45°, the flow eccentricity was 0.1. The ratio of biaxial isobaric yield strength to uni-axial compression strength was 1.16. The second stress invariant ratio on the meridians of tension and compression was 2/3.

The tensile softening property of concrete was described by concrete fracture energy criterion. The fracture energy of C20 concrete was 40 N/m, and that of C40 was 120 N/m. For other grades, the fracture energy could be calculated by interpolation or extrapolation methods [10].

The compression stress - strain relation of concrete after fire was predicted according the model proposed by LU et al [11].

2.3 Boundary condition and analytical procedure

Temperature field analysis at elevated temperature was firstly carried out based on ABAQUS software. Before heating, the temperature inside the specimen was uniform and was the same to the environment temperature. During heating and cooling processes, the environment temperature was changed along the ISO834 standard curve of temperature rising and cooling. However, comparing to the experimental results, the environment temperature was the actual measuring curve of furnace temperature during fire test, and the furnace wall temperature was the furnace temperature multiplied by 0.9. The convective heat transfer coefficient of heating surface was 25 W/(m^2 • K) and that of surface unexposed to fire was 9 W/(m^2 • K), and the heat emissivity of heating surface was 0.5W/(m^2 • K). The point-face Tie restraint of reinforcement and concrete were used, so the temperature of different materials at the element node was similar.

For the constitutive relations of reinforcement and concrete after fire were closely related to the maximum heating temperature of every point. The results of temperature field analysis under high temperature were post-treated using Python programming language. An embedded loop program was developed. The temperature of each node at each analysis step was compared. The serial number and the maximum heating temperature of each node were saved in the form of temp.fil which could be read in the subsequent calculation. The temp.fil document was introduced into step-1 from the predefined field, and this is the initial condition of simulating the push-over process after fire.

Then, the numerical simulation of the push-over process of concrete short column after fire was carried out. The bottom of the specimen was fixed constraints. Two load steps were used. Firstly, a reference point RP1 was found and was coupled with the top surface of the column; and a stable vertical load was imposed on RP1. Secondly, a reference point RP2 was established and was coupled with the horizontal loading surface of the column; and the horizontal displacement control loading according to the displacement curve was applied on RP2. The coupling of the reference point and loading surface could avoid the early cracking and crushing caused by the directly concentrated force, thus the difficulty of the convergence would be resolved.

2.4 Calculation results and analysis

The quasi-static tests of seven reinforced concrete short columns after fire and one contrastive specimen at ambient temperature were carried out by the authors in Reference [7]. All columns have a cross section of 300 mm × 300 mm, and were reinforced with 8 longitudinal bars, each with a diameter of 20 mm. These bars were tied using 8 mm ties with a spacing of 100mm. The thickness of concrete protection layer for the longitudinal bars is 30 mm. The average compressive cubic strengths of the concrete measured at the quasi-static tests is 41.4 MPa. The yield strengths of the main reinforcing bars and the stirrups were 439 and 390 MPa, respectively, and their ultimate strengths were 575 and 525 MPa, respectively.

The temperature-time curves of each measuring point in column Z2 in Reference [7] were calculated using ABAQUS software, and are compared to those of the experimental results, as shown in Figure 2. The results of the temperature field analysis almost agree well with the experimental ones. Part of errors of the simulation and experimental results may be due to the buried position error of thermocouple, the inconsideration of the moisture migration during numerical simulation, a certain discreteness of thermal parameters, and so on.

The shear capacity of the concrete short columns after fire, Z2 to Z8 in Reference [7], was calculated using ABAQUS software and was compared to that of the experimental results, as listed in Table 1. In Table 1, t_{fir} is the fire duration, n is the axial ratio, λ is the shear span ratio, $V_{\mathrm{u}}^{\mathrm{t}}$ is the measured shear capacity, V_u^c is the calculated shear capacity, η is the relative error of the calculated value and the measured value. As shown in Table 1, the simulated values of the shear capacity are in good agreement with the experimental results, and the former is slightly smaller than the latter, maybe due to the inconsideration of the evaporation and migration of the moisture in concrete.

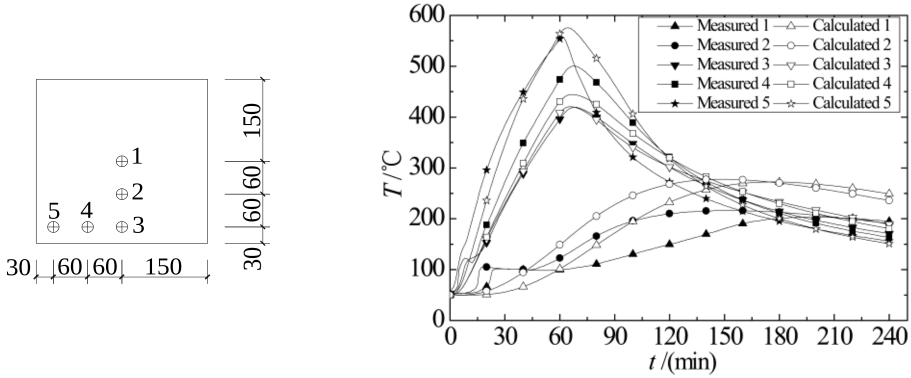

(a) Positions of thermocouples (b) Z2

Figure 2. Comparison between numerical simulation results and experimental results of the temperature-time curves.

Table 1. Comparison between simulation results and experimental results of shear strength.

Column ID	t_{fir} /h	n	λ	V_{ut} /kN	V_{uc} /kN	η
Z2	1	0.2	1.78	297.4	273.6	-8.0%
Z3	1.5	0.2	1.78	269.5	247.6	-8.1%
Z4	2	0.2	1.78	230.8	219.3	-5.0%
Z5	1	0.1	1.78	267.3	238.4	-10.8%
Z6	1	0.3	1.78	288.3	294.0	2.0%
Z7	1.5	0.2	1.58	284.2	281.9	-0.8%
Z8	1.5	0.2	1.98	251.4	224.2	-10.8%

The force-displacement curves (*P-Δ* curves) during mono-directional push-over process of the concrete short columns Z2 to Z8 in Reference [7] were simulated using ABAQUS software and were compared to the experimental results, as shown in Figure 3. In the ascending stage of the *P-Δ* curves, the calculation values roughly accord with the experimental results, and the former is slightly larger than the latter. But in the descending stage of the *P-Δ* curves, the agreement degree of them is decreased. The above calculated error of the maximum heating temperature will lead to the error of the *P-Δ* curves. Moreover, a certain difference of the selected and practical constitutive relation of the materials after fire, and the inconsideration of the slip of reinforcement and concrete and the crushing and cracking of concrete during simulation will also cause the error of the simulated and experimental results. And the latter one will make the slope in the ascending stage increase slightly.

3 FACTOR ANALYSIS

In this paper, the concrete square column after exposure to 3-face heating was investigated, and the environment temperature of the heating face was according to the ISO834 standard temperature curve. An typical example was calculated and the effect laws of the horizontal load direction, fire duration t_{fir}, load ratio n, shear span ratio λ, sectional dimension a and stirrup spacing s on the shear capacity of the concrete short column after fire were analyzed. The calculation conditions of the example are as follows: t_{fir}=1h, n=0.2, λ=1.78, a=300mm, the stirrup is A8@100, the longitudinal reinforcement is 8C20, the thickness of concrete cover c is 30 mm, the yield strength of longitudinal reinforcement f_y is 484 MPa, the yield strength of stirrup f_y is 425 MPa, and the compression strength of concrete cube f_{cu} is 41.1 MPa.

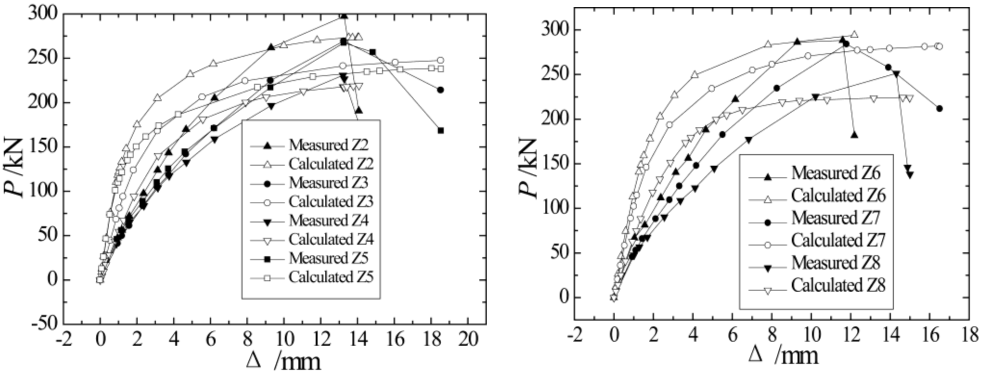

(a) Z2~Z5

(b) Z6~Z8

Figure 3. Comparison between numerical simulation results and experimental results of force-displacement curves.

In the case of 3-face heating, there may be two directions of horizontal force when it was along the symmetry axis, as shown in Figure 4. The first direction is the tension face without heating, and the second direction is the compression side without heating.

Figure 5 shows the P-Δ curves of the push-over process of concrete short column in two different directions of horizontal force. The curves in two directions are almost overlapped, indicating that the direction of the horizontal force has little effect on the push-over process of concrete short column after 3-face heating. The shear capacity of load direction 1 is slightly smaller than that of load direction 2, and the error of them is about 1.4%. The horizontal force usually was cyclically loaded and the shear capacity is the smaller one of two directions. Therefore, load direction 1 of horizontal load was used to calculate the shear capacity subsequently.

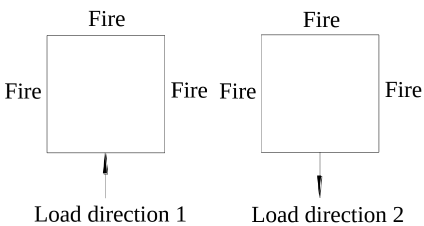

Figure 4. Direction of horizontal force.

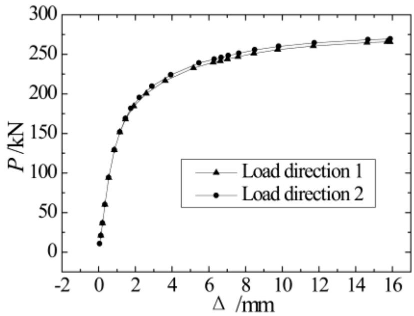

Figure 5. Force-displacement curves for different load directions.

The changes of the shear capacity V_u of concrete column after 3-face heating with the fire duration t, the load ratio n, the shear span ratio λ, the stirrup spacing s and the sectional dimension a are present in Figures 6-10, respectively. As shown in Figure 6, with an increase with fire duration, V_u is approximately linearly decreased.

As shown in Figure 7, for n smaller than 0.3, V_u is increased linearly with n; for n in the range of 0.3 to 0.5, V_u almost is stable; and V_u is decreased for n larger than 0.5. It indicates that the axial load in a suitable range is benefit to the shear capacity of the concrete column after 3-face heating. And this is similar to that without fire.

V_u is decreased approximately linearly with an increase in λ and s (in Figures 8 and 9), but it is increased linearly with an increase in sectional size (in Figure 10).

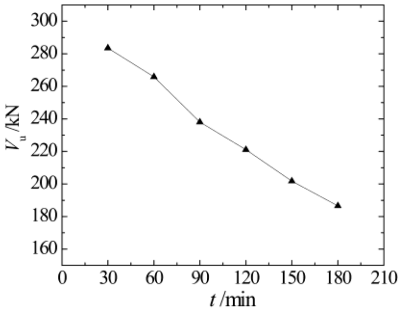

Figure 6. Variation of shear strength with fire exposure time.

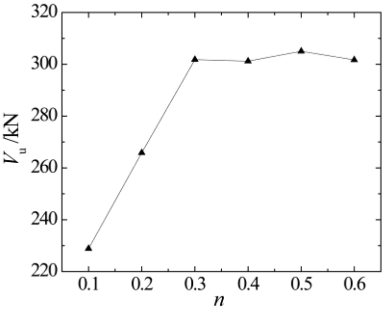

Figure 7. Variation of shear strength with axial load ratio.

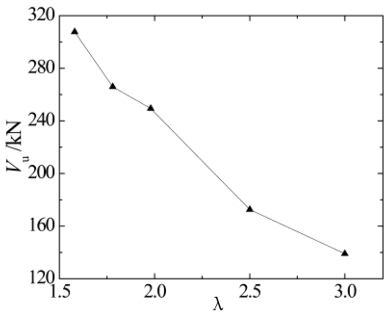

Figure 8. Variation of shear strength with shear span ratio.

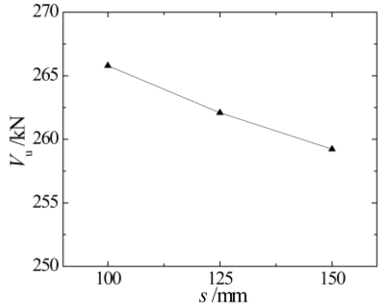

Figure 9. Variation of shear strength with stirrup spacing.

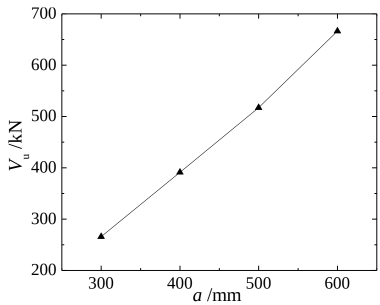

Figure 10. Variation of shear strength with sectional dimension.

4 PRACTICAL CALCULATION FORMULAS

With reference to the calculation formula of the shear capacity of concrete column without fire in Reference [12], the shear capacity V_u of concrete column after exposure to 3-face heating is expressed as

$$V_u = 0.9\frac{1.75}{\lambda+1}k_c f_t b h_0 + 0.9 f_{yv}\frac{A_{sv}}{s}h_0 + 0.07N \tag{1}$$

in which f_t is the design value of axial tensile strength of concrete, f_{yy} is the design value of tensile strength of stirrup, b is the width of column cross-section, h_0 is the effective height of column cross-section, A_{sv} is the section area of stirrup, s is the stirrup spacing, N is the design value of axial pressure corresponding to the shear design value V. When N was larger than $0.3k_cf_cA$, N is $0.3k_cf_cA$. Where A is the section area of specimen, f_c is the design value of axial compression strength of concrete, k_c is the average reduction factor of compression strength of concrete after 3-face heating. k_c and 0.9 (the second one in formula 1) is due to the decrease of shear capacity of concrete and stirrup after fire. The first 0.9 in formula 1 is ascribed to the asymmetric heating loss of concrete short column after 3-face heating. The intensity center of cross section is deviated to the tension face of the column, resulting in the increase of eccentricity of vertical load and the decrease in shear capacity.

k_c of concrete square column with different section dimension after 3-face heating for different time was calculated according to the methods in Reference [7] and is listed in Table 2. For other section dimension and fire duration of concrete square columns, k_c can be calculated using interpolation method.

Table 2. Values of parameter k_c.

a /mm \ t /min	30	60	90	120	150	180
300	0.873	0.746	0.644	0.559	0.482	0.410
400	0.904	0.805	0.726	0.659	0.560	0.547
500	0.923	0.843	0.776	0.721	0.672	0.628
600	0.934	0.869	0.810	0.764	0.722	0.683
700	0.942	0.887	0.835	0.793	0.757	0.724
800	0.949	0.900	0.854	0.815	0.782	0.753

The relation of k_c, a and t is non-linearly regressed using SPSS software and the data in Table 2, and the expression is as

$$k_c = 0.747 + 0.953a - 0.294t + 0.0179t^2 - 0.799a^2 + 0.206at \tag{2}$$

in which the unit of a and t is meter and hour respectively. The calculated results of k_c according to formula (2) are totally in good agreement with the data in Table 2, and the relative coefficient of them is 0.996. The average value and the mean square deviation of the ratio of the latter one to the former one are 1.001 and 0.015 respectively. It indicates that formula (2) has a good precision and can be used to calculate k_c.

The push-over processes of six concrete columns after 3-face heating were analyzed using ABAQUS software according to the methods in the second section and the corresponding shear capacity V_{u1} was obtained. The shear capacity V_{u2} was also calculated using the formula (1). And V_{u1} and V_{u2} are listed in Table 3. In column ID Zxx-yy, xx is the fire duration and its unit is minute, yy is the load ratio. The essential parameters for the samples are defined. The sectional dimension is 400 mm×400 mm; the stirrup is A8@100; the longitudinal reinforcement is 8C20; the shear span ratio λ is 1.78; the fire duration t is 1h and 2h; the axial load N is 250kN, 500kN and 750kN; the yield strength of longitudinal reinforcement f_y is 484 MPa; the yield strength of stirrup f_y is 425 MPa; the compression strength of concrete cube f_{cu} is 41.1 MPa; the axial tensile strength of concrete f_t is 2.43MPa. Because the formula used to calculate the shear capacity usually has a certain safety assurance. As shown in Table 3, the formula (2) can be used to practically calculate the shear capacity of concrete short column after exposure to 3-face heating.

Table 3. Comparison of simulation and simplified calculated shear strength.

Column ID	V_{u1} /kN	V_{u2} /kN	V_{u1}/ V_{u2}	Column No.	V_{u1} /kN	V_{u2} /kN	V_{u1}/ V_{u2}
Z60-0.1	338.6	315.4	1.07	Z120-0.1	316.0	286.5	1.10
Z60-0.2	391.4	332.9	1.18	Z120-0.2	355.6	304.0	1.17
Z60-0.3	438.7	350.4	1.25	Z120-0.3	387.0	321.5	1.20

5 CONCLUSIONS

The numerical model of the push-over process of concrete column after fire was established based on ABAQUS finite software. The effect laws of the corresponding parameters on shear capacity of the concrete short column after 3-face heating were analyzed. And the practical calculation methods of the shear capacity of concrete short column after 3-face heating were proposed with reference to the existing standard formulas. The main conclusions are as follows.

(1) The shear capacity of concrete column after fire can be calculated more accurately using ABAQUS finite element software. However, the prediction of the full curve of load-displacement behaviour needs further improvement.

(2) If the horizontal force was applied in the symmetry plane, the direction of the horizontal force has little influence on shear strength of concrete short column after 3-face fire.

(3) With an increase in axial load ratio, the shear strength of concrete short column firstly increases linearly, then tends to stabilization when it is between 0.3~0.5, and follows by decreasing for larger than 0.5.

(4) The proposed formula to calculate the shear capacity of concrete column after 3-face heating has a certain safety assurance, and it can be used to the damage assessment of the shear capacity of this kind of specimen.

REFERENCES

[1] Xu Yuye, Wang Quanfeng, "Research on residual strength of reinforced concrete columns after exposure to fire", *Engineering Mechanics*, 27(2), 84-89, 2010.

[2] Tang Yuefeng, Liu Mingzhe, Yu Changhai and Li Junhua, "Experimental study on residual load bearing capacity of reinforced concrete columns after exposure to fire", *Journal of Ningbo University*, 24(4): 112-115, 2011.

[3] Wu Bo, Li Yihai, "Experimental study of the residual axial behavior of axially restrained reinforced concrete columns after fire", *China Civil Engineering Journal*, 43(4): 85-91, 2010.

[4] Wu Bo, Ma Zhongcheng, Ou Jinping, "Experimental study on seismic properties of R.C. columns after high temperature", *China Civil Engineering Journal*, 32(2): 53-58, 1999.

[5] Chen Y H, Chang Y F, Yao G C and Sheu M S, "Experimental research on post-fire behaviour of reinforced concrete columns", *Fire Safety Journal*, 44(5): 741-748, 2009.

[6] Huo J S, Zhang J G, Wang Z W and Xiao Y, "Effects of sustained axial load and cooling phase on post-fire behavior of reinforced concrete stub columns", *Fire Safety Journal*, 59: 76-87, 2013.

[7] Xu Yuye, Yang Qingwen, Wu Bo and Xu Ming, "Experimental study on seismic performance of reinforced concrete short columns after fire", *Journal of Building Structures*, 34(8): 12-19, 2013.

[8] Lin Yanqing, Xu Yuye, Yang Qingwen and Luo Yi, "Hysteretic behaviours and damage assessment of concrete short columns after fire", *Journal of Huaqiao University (Natural Science)*, 34(5): 563-569, 2013.

[9] Lie T T, Celikkol B, "Method to calculate the fire resistance of circular reinforced concrete columns", *ACI Materials Journal*, 88(1): 84-91, 1991.

[10] Wang Yuzhuo, Fu Chuanguo, *Analysis and example of ABAQUS in structural engineering*, China Architecture & Building Press, Beijing, 2010.

[11] Lu Zhoudao, Zhu Bolong, Xiong Haibei and Ding Wei, "Research on strengthening of reinforce concrete structures after fire", *Sichuan Building Science*, 21(3): 7-12, 1995.

[12] *GB 50010—2010 Code for design of concrete structures*, China Architecture & Building Press, Beijing, 2011.

8th International Conference on Structures in Fire
Guo-Qiang LI, Venkatesh K. R. KODUR, Shou-Chao JIANG, Jian JIANG, Su-Wen CHEN, Guo-Biao LOU (Eds.)
Shanghai, China, June 11-13, 2014

STRUCTURAL FIRE RESPONSE OF TALL BUILDINGS WITH INCLINED AND BI-LINEARPERIMETER COLUMNS

Panagiotis Kotsovinos*, Angus Law*, Susan Deeny* and Neal Butterworth*

* Ove Arup&Partners, United Kingdom
e-mails: Panagiotis.Kotsovinos@arup.com, Angus.Law@arup.com, Susan.Deeny@arup.com, Neal.Butterworth@arup.com

Keywords: Tall buildings, Inclined and bi-linear perimeter columns, Failure mechanisms

Abstract. *This paper considers the effect of perimeter column angle-of-inclination on the structural response of tall buildings subject to fire.The purpose of the study is to aiddesigners when doing structural fire assessments of tall buildings. The consequences of columnangle-of-inclination and its interaction with the floor-plate are examined. It has been found that inclined and vertical columns have a similar structural fire response.However,bi-linear columns that have two angles-of-inclination have been found to behave differently compared to linear columns when exposed to fire. Bi-linear columns induce increased in-plane axial forces on the floor slab during both ambient and fire conditions. Thisaffects the behaviour of the floor under fire conditions. A parametric study was carried out for a range of bi-linear columns by varying the angle-of-inclination and applied axial load.It was found that bi-linear outwards columns are more vulnerable to the effects of fire than bi-linear inwards columns due to the P-delta effect on the adjoining beams. This may result in bi-linear columns not achieving their specified fire resistance period unless additional mitigation measures are provided and/or an analysis is conducted to verify the performance under fire conditions.*

1 INTRODUCTION

The last decade has seen an increase in the number of tall and super-tall buildings around the globe. The collapse of the World Trade Centre buildings (WTC1, 2 and 7) and other partial collapses (such as the Windsor Tower and theTechnical University of Delft building) posed questions on the stability of tall buildings in fire. Due to their often innovative and complex architecture, tall buildings can have non-typical forms; when exposed to the effects of fire, these structural forms may induce behaviours that prescriptive guidance (and standard fire testing) does not consider. In these cases, structural fire engineering may be used to identify and address structural vulnerability to fire.Flint *et al.*[1] have recently presented a review of structural forms with potentialweaknessesin fire based on the experience of finite element modelling of several proposed buildings.

Columns are an integral component of the stability of buildings. The failure of perimeter steel columns in fire conditions can either be due to (global or local) buckling [2–4] or by combined compression and bending caused by thermally induced pull-in forces (typically associated with multiple floor fires) from the floor system [5–7]. Previous work has mainlyconsidered frames with orthogonality between beams and columns(notably, work by Jowsey identified braces which changed direction and transferred forces to the floor-plate [8]).This paper will present the results of a numerical study that was carried out on inclined and bi-linear columns using the finite element modelling software LS-DYNA[9].The motivation for this analysis was the authors' recent structural fire analysis of a proposed 35 storey officebuilding in the City of London, UK.

2 NUMERICAL MODEL

The layout of the floor-plate examined is based on the structural design of a proposed tall building in the City of London, UK. For the purposes of this paper, a typical (and idealized) baywas been selected for analysis and is illustrated Figure 1(a). Internal boundary conditions were assumed to be symmetric, and the model was free to expand laterally. Columns were fixed in translation one storey above and below slab level and fixed in rotation 1.5 storeys above and below slab level as presented by Flint *et al*. [1]. For the purposes of this paper, all the structural members are protected to keep the members below their limiting temperature (notionally assumed to be 550 ℃ for columns and 620 ℃ for beams) for 90 minutes of the standard fire.

The numerical analyses described in this paper have been carried out using LS-DYNA's [9] explicit time integration. Nonlinear 2-noded beam elements have been used to represent beams and columns and 4-noded shell elements for slabs. A mesh size of 0.25m mesh was adopted. Connections were assumed to be pinned. Material properties were in accordance with BS EN 1994-1-2 [10] and for the purposes of this paper (and to allow comparison between the results), a parametric fire was assumed for all analyses.

A range of column inclinations was studied. The naming convention for these arrangements is illustrated in Figure 1(b), includes linear vertical, linear outwards, linear inwards, bi-linear outwards, and bi-linear inwards. These are illustrated indicatively in Figure 1(b).

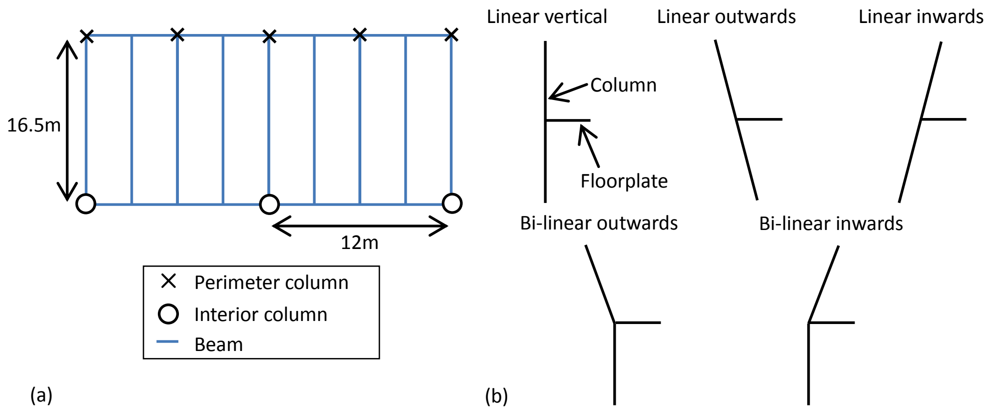

Figure 1. (a) Plan view of floor-plate (b) various possible arrangements for perimeter columns.

3 EFFECT OF ANGLED AND BI-LINEARCOLUMNS

A comparative study was performed which considered several possible inclinations of the perimeter columns. The angle of inclination used (~8 ° from vertical) was the same for all studies (other than the linear vertical analysis). This angle represents the inclination in the proposed building which forms the motivation for this study.For each study, the floor-plate and column immediately below the floor-plate was heated in accordance with a parametric fire heating and cooling curve.

3.1 Comparative Study

Each analysis was compared using several metrics; vertical deflection in the centre of the 16.5m beam, horizontal deflection at the intersection between the beam and the column, and maximum axial force in the beam. These results are illustrated in Figure 2. It was found that:

- The provision of inclined linear columns (either inwards or outwards)did not significantly affect the fire performance of the structural frame compared to vertical columns.
- The provision of bi-linear columns had a significant impact on the performance of the structural frame compared the vertical columns – failure was observed in both analysis with bi-linear columns.

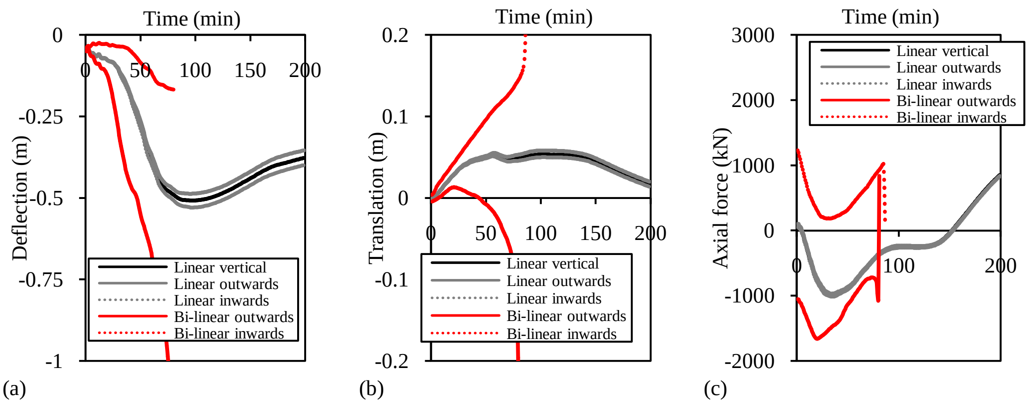

Figure 2. (a) Midbay deflection; (b) column horizontal translation; (c) axial force in the steel beam.

3.2 StructuralBehaviour

The difference between the behaviour of the bi-linear and inclined columns is due to a difference in the load paths at ambient, and the subsequent changes at high temperature.

3.2.1 Ambient Mechanics

In vertical or inclined columns the load from upper stories is transferred directly down the columns. No additional forces are required to maintain equilibrium (other than to provide bracing). In the case of the bi-linear arrangement, an additional force is required at the bifurcation point to maintain equilibrium. This force is provided by the slab and beam which are connected to the column. The force may be tensile or compressive, depending on the angle of the column. This is illustrated indicatively in Figure 3. Where the column is bi-linear outwards, a compressive force develops in the beam; where the column is bi-linear inwards, a tensile force develops in the beam. It should be noted that at ambient, a moment also develops in the column below the bifurcation point which also acts to resist the applied load.These pre-existing forces and moments are fundamental to the performance during a fire.

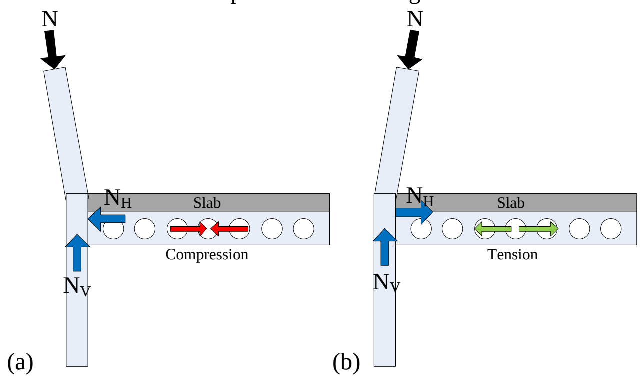

Figure 3. (a) Outwards angled bi-linear column; (b) Inwards angled bi-linear column.

3.2.2 Effect of High Temperature

At high temperature, the expansion of the floor-plate acts to destabilise the equilibrium that is achieved at ambient. Section 3.1 shows that the bi-linear columns are particularly vulnerable to this destabilising effect. The key events that lead to loss of stability for bi-linear columns are outlined below.

For bi-linear outwards columns, the stages are as follows:

(1) The floor-plate begins to expand and pushes the column outwards;

(2) The beams weaken and, consequently, vertical deflection increases;

(3) The pre-existing compressive force in the beam causes increase in moment in beam (i.e. a P-delta effect in the beam);

(4) Due to the increased vertical deflections of the beam, the column begins to be pulled inwards (i.e. the net effect of the thermal expansion and the deflection is to cause the column to move inwards);

(5) The axial force that the beam carries begins to decrease;

(6) The beam continues to weaken and central deflection increases further;

(7) Due to the deflection in the beam, the column beings to be pulled inwards;

(8) The axial force in the beam continues to decrease and equilibrium is maintained by an increase in moment in the column below the floor-plate (i.e. load shedding occurs from axial force in the beam to moment in the column);

(9) Deflections of the beam and inwards translation of the column increase until the moment in the column exceeds its capacity;

(10) Bending failure occurs in the column.

For bi-linear inwards columns, the stages are as follows:

(1) The floor-plate begins to expand and pushes the column outwards;

(2) The beams weaken and vertical deflection increases (note that the high tensile force in the beam results in a relatively low deflection in comparison to the bi-linear outwards case);

(3) The expansion of the floor-plate reduces the axial load in the beam as this is transferred to moment in the column;

(4) The expansion of the floor-plate simultaneously increases the effective angle of inclination of the column (and therefore also increases the force that must be resolved to maintain equilibrium) this is resisted primarily by a moment in the column below the floor-plate;

(5) Horizontal translation at the column continues to increase due to the thermal expansion, and applied column force;

(6) This continues until a bending failure occurs in the column.

The occurrence of failure in bi-linear columns can be observed in Figure 4. This figure shows the recorded moments in the column at the location immediately below the floorslab. In addition the sectional capacity of the columns is plotted (adjusted for applied axial load).

The outwards and inwards inclined bi-linear columns are under combined compression and bending (beam-columns) and failure occurs when a plastic hinge is formed in the column when the applied moments reach the plastic moment capacity of the column. This form of failure resembles that presented by previous researchers [5–7] when considering the stability of tall buildings under multiple floor fires. It can also be observed from figure 4 that no failure occurs in the vertical column. It should be noted that this analysis was also conducted for the inclined columns; the results were similar to the vertical column and, to improve clarity, are not presented below.

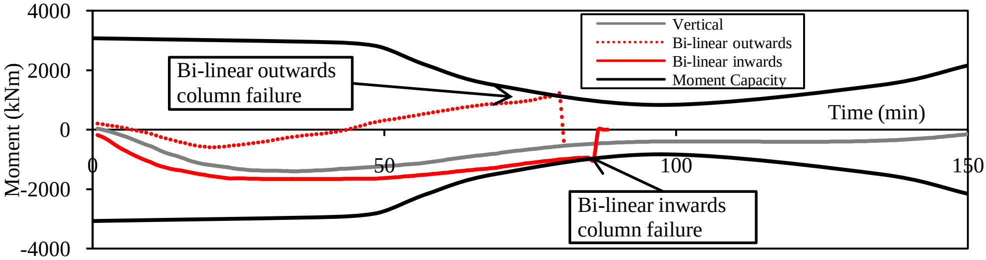

Figure 4. Moment in column and calculated reduction in moment capacity with time.

4 PARAMETRIC STUDYONBI-LINEAR COLUMNS

The example provided above illustrates the failure modes for a particular structural arrangement. Although the phenomena can be described, the exact results are arrangementspecific and there are a number of parameters which may affect the behaviour. This section presents a parametric study on two of the parameters: angle of column inclination, and applied axial load.

There are a range of other parameters that are also likely to have an impact on the results including: span, column bending stiffness, composite beam bending stiffness, composite beam axial stiffness, and heating regime. These are not covered in this paper and remain the subject of on-going study by the authors.

4.1 Angle of inclination

The angle of inclination of the column above the bifurcation point was varied between -10.1 ° (outwards) and +10.1 °(inwards). The results for horizontal translation at the bifurcation point, and axial force in the beam are plotted in Figures 5 and 6.

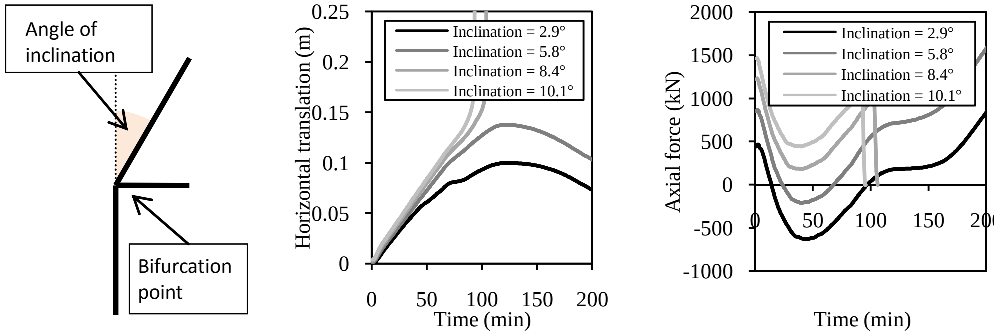

(a) (b) (c)

Figure 5. (a) Bi-linear inwards column; (b) Horizontal translation; (c) Axial forces in beam.

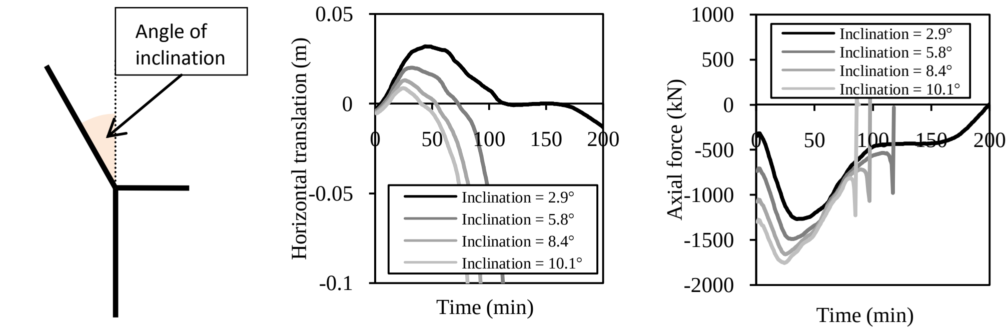

(a) (b) (c)

Figure 6.(a) Bi-linear outwards column; (b) Horizontal translation; (c) Axial forces in beam.

These results show that the columns with a greater angle of inclination fail earlier than the columns with a smaller angle of inclination. The sensitivity of the results to variation in the angle of inclination can further be analysed by assessing the utilisation in the column for each model. Utilisation was calculated based on the moment capacity (adjusted for applied axial load as illustrated in Figure 4). Figure 7 shows the utilisation for each angle and for a range of temperatures over the course of the analysis.

This analysis shows that during the early stages of a fire, the utilisation in the bi-linear outwards is lower than the bi-liner inwards columns. However, as temperatures increase, the utilisations in the bi-linear outwards column begin to increase more rapidly. The results also show that the bi-linear outwards columns are more sensitive to change in angle of inclination than the bi-linear inwards columns.

The sensitivity of the bi-linear outwards to both temperature and angle of inclination is due to the feedback associated with the P-delta effect in the beams. This effect does not occur with the bi-linear inwards columns and consequently, they are less sensitive to both change in angle of inclination and temperature.

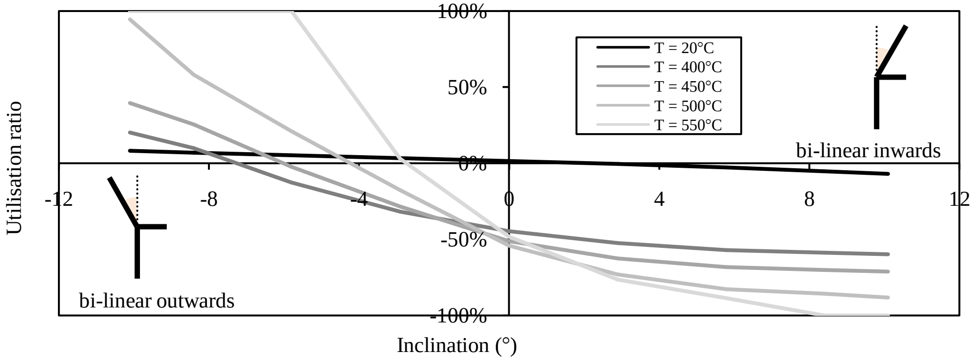

Figure 7. Column section utilisation as a function of angle of inclination.

4.2 Applied axial load

The applied axial load was also varied to examine the effect that preloading may have on the response of the frame. Four cases were considered 50%, 75%, 100% and 125% of the proposed applied fire limit state axial load; the study was repeated for both bi-linear inwards, and bi-linear outwards columns (with an inclination of ~8°). Figures 8 and 9 show the column horizontal translations and axial forces in the beam for both the bi-linear inwards and bi-linear outwards columns.

These results demonstrate that the reduced axial loads allow the bi-linear columns to resist the applied thermal load. Figure 9(a) shows the horizontal translation at the bifurcation point for the bi-linear outwards columns. It is notable that two of the models exhibit run-away failure (due to the P-delta effect discussed above), and two of the models do not. Each of these models exhibit the strain reversal that is associated with the on-set of the P-delta feedback – however, loads in the 50% and 75% models are not sufficient to induce a runaway failure mode.

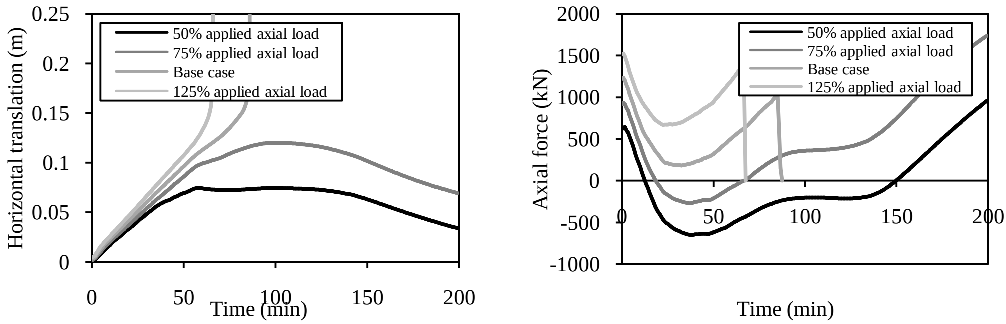

(a) (b)

Figure 8. (a) Horizontal displacement; (b) Axial forces for the inwards bi-linear columns.

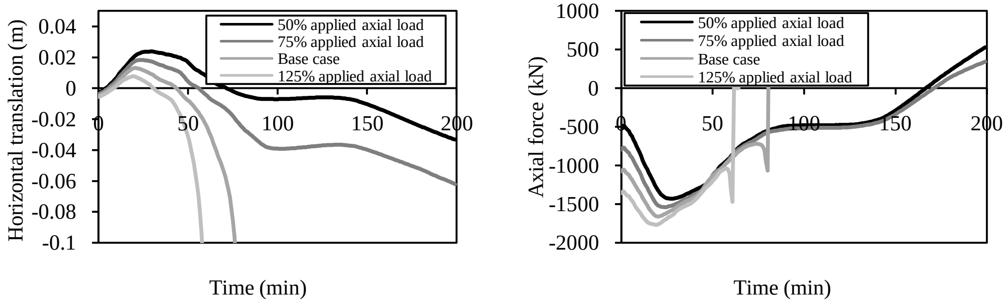

(a) (b)

Figure 9. (a) Horizontal displacement; (b) Axial forces for the outwards bi-linear columns.

Figure 10 shows the utilisations for each of the analyses at various different temperatures. This demonstrates that the bi-linear inwards columns are at a higher utilisation for most of the analysis. However, the bi-linear inwards columns are less sensitive to both change of temperature, and change in applied axial load. The sensitivity of the bi-linear outwards columns is due to the P-delta effect noted above. This relative sensitivity is demonstrated in Figure 10 with fitted curves: the utilisation in the bi-linear inwards columns is approximately a linear function of applied axial load; the utilisation in the bi-linear outwards columns is approximately a quadratic function of applied axial load.

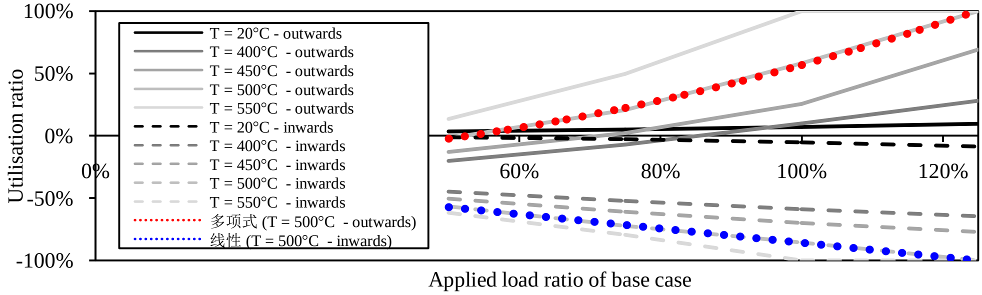

Figure 10. Colum section ultilisation as a fuction of applied axial load.

5 DISCUSSION

The failure of the bi-linear columns due to deflections in the floor is analogous to the failure modes previously identified due to *strong floor* failure modes [7,11]. However, for bi-linear outwards columns the key driver for both the greater deflections in the floor, and subsequent failure, is the pre-existing forces transferred into the floor due to the change in column inclination. There is potential to characterise the failure mechanisms using an algebraic relationship as described by Lange [12].

The parametric study has shown that the outwards bi-linear columns are more sensitive to both axial load and angle of inclination than the bi-linear inwards columns. The results of both parametric studies confirm the P-delta feedback that occurs in the bi-linear outwards columns is the cause of the failure of these assemblies. The results also illustratethe run-away nature of the failure that is caused by the P-delta effect in the beams.The bi-linear inwards columns are also vulnerable to the effects of fire. Their behaviour is more analogous to a linear vertical column where the horizontal translation of the floor-plate is increased by the action of the axial load from above.

The failure modes identified for the bi-linear columns mean any bi-linear column (particularly those which a greater angle of inclination) that is designed to achieve a fire resistance based on the factored ambient design load is unlikely to achieve the specified fire resistant period. It is recommended, therefore, that these assemblies should be analysed to identify any mitigation measures which may be introduced to ensure they can achieve the required fire resistance.The authors propose that further work should be conducted to better characterise each of the parameters that may affect the behaviour of a bi-linear column during the fire limit state – and the available mitigation measures.

6 CONCLUSIONS

This paper has examined the effect of angle-of-inclination of perimeter columns on the response of tall buildings in fire. Several different cases have been examined, and it has been found that:

(1) Buildings with linearlyinclined columns (irrespective of direction of incline) show similar structural fire behaviour to buildings with vertical columns.

(2) Bi-linear columns that undergo a change in inclination over their height (either outwards or inwards) induce compressive or tensile axial forces, respectively,intothe floorplate. This significantly affects the structural behaviour under fire conditions.

(3) Bi-linear outwards columns are more vulnerable to the effects of fire than bi-linear inwards columns due to the P-delta effect on the adjoining beams.

(4) Consequently it is concluded that – unless additional mitigation measures are provided and/or an analysis is conducted to verify the performance – bi-linear columns that are designed to achieve a fire resistance based on the factored ambient designloads are unlikely to achieve the specified fire resistance period.

REFERENCES

[1] Flint G, Lamont S, Lane B, et al. "Recent Lessons Learned in Structural Fire Engineering for Composite Steel Structures." *Fire Technology* 2012.

[2] Franssen J-M. "Failure temperature of a system comprising a restrained column submitted to fire." *Fire Safety Journal* 34, 191–207, 2000.

[3] Ali F, O'Conner DJ. "Structural performance of rotationally restrained steel columns in fire." *Fire Safety Journal* 36, 679–691, 2001.

[4] Shepherd PG, Burgess IW. "On the buckling of axially restrained steel columns in fire." *Engineering Structures* 33, 2832–2838, 2011.

[5] Usmani AS, Chung YC, Torero JL. "How did the WTC towers collapse: a new theory." *Fire Safety Journal* 38, 501–533, 2003.

[6] Flint G, Usmani A, Lamont S, et al. "Structural Response of Tall Buildings to Multiple Floor Fires." *Journal of Structural Engineering* 133, 1719–1732, 2007.

[7] Kotsovinos P. "Analysis of the structural response of tall buildings under multifloor and travelling fires." PhD Thesis, University of Edinburgh, 2013.

[8] Jowsey A, Lim L, Lane B. "Structural Fire Analysis for Perimeter Braced Framed Structure." *Applications of Structural Fire Engineering* 2009.

[9]. "LS-DYNA Keyword User's Manual, Volume II, Material Models (Version 971 R6.1.0)." 2012.

[10]. "BS EN 1994-1-2 Eurocode 4: Design of composite steel and concrete structures. General rules - Structural fire design." 2005.

[11] Usmani A, Röben C, Al-Remal A. "A very simple method for assessing tall building safety in major fires." *International Journal of Steel Structures* 9, 17–28, 2009.

[12] Lange D, Röben C, Usmani A. "Tall building collapse mechanisms initiated by fire: Mechanisms and design methodology." *Engineering Structures* 36, 90–103, 2012.

8th International Conference on Structures in Fire
Guo-Qiang LI, Venkatesh K. R. KODUR, Shou-Chao JIANG, Jian JIANG, Su-Wen CHEN, Guo-Biao LOU (Eds.)
Shanghai, China, June 11-13, 2014

A NEW INSTRUMENTATION TECHNIQUE FOR MEASURING 3-D DISPLACEMENT PROFILES OF COMPOSITE SLABS UNDER FIRE CONDITION

Jun-Xian Liu* and K.H. Tan**

*Research student in School of Civil and Environmental Engineering, Nanyang Technological University, Singapore 639798, Singapore
e-mail: liuj0055@e.ntu.edu.sg
**Professor in School of Civil and Environmental Engineering, Nanyang Technological University, Singapore 639798, Singapore
e-mail: ckhtan@ntu.edu.sg

Keywords: Photogrammetry, Fire, Composite slab

Abstract. *This paper presents the advantages of using the new technology photogrammetryto measure three-dimensional displacements of the composite slab surface under fire condition. The general methodology is presented in this paper and is compared with direct measurements from Linear Variable Differential Transformer (LVDT). It has been shown that the instrumentation is reliable for detecting multiple displacements of different points in x, y and z directions.*

1. INTRODUCTION

Instrumentation at elevatedtemperature is always a challengefor researchers. Traditional methods involving line transducers and ceramic rods connected to external LVDTs (linear variable differential transformer) have been used in the fire teststo minimise damage of instrumentation equipment at high temperature. However, all these methods can only obtain information at discrete points and in a fixed direction. In addition, this fixed direction may be changed due to translation or rotation of the measuring point itself. Conventional approach does not allow measurements of displacements in three dimensions during testing. Besides, researchers are also interested in the displacement profile along a cross section. Conventional method does not have the added flexibility for researchers to study other locations which may be more critical than the measured points.Displacement profiles are crucial in that it allows researchers to study the collapse mechanism of the test specimen and to make comparisons with finite element modelling at the analysis stage.

2. PHOTOGRAMMETRY

Inthis paper, photogrammetry is introduced to monitor displacement profiles of thecomposite slab at elevated temperature, which can not only capture the clearly marked points, but also the overall profile of the deformation shape for the composite slab surface under fire condition. The detailed procedure of the photogrammetrywill be presented in this session.

2.1 Camera calibration

For this new approach, the calibration of camera is the most important step. In Figure 1(a), a 10 by 10 dots pad with four referencepoints was used to calibrate the camera setting configuration, such as the focal length, lens distortion and quality values asshown in Figure 1(b). The information was processed by the software *PhotoModeler*. In addition, the maximum residual values should be controlled toensure good quality of images obtained through photogrammetry.

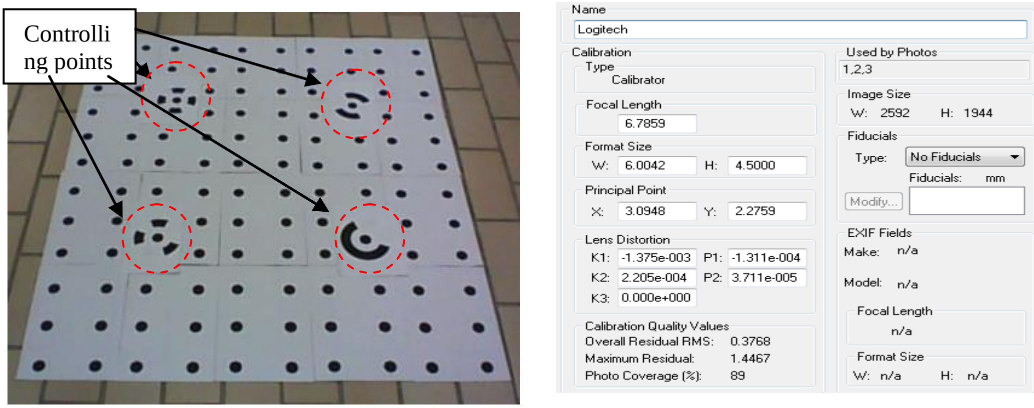

(a) Calibration based on 10 by 10 dots with 4 referencepoints (b) Calibrated configurationfor camera

Figure 1. Calibration procedure to obtain camera information.

2.2 Automatic photo capture system

After configuring the camera, similar black dots were painted onto the top surface of the isolated composite slab panel. The test set up was similar to Trung[1]'s composite slab test. In order to calculate the displacementsof themarked points on the composite slab surface, it is importantto capturephotographs at the same time from different angles. Therefore, a special macro programme is designed to take three photographs from three different angles at the same time as shown in Figure 2. It can be seen that every three photos from the camera are taken atone minute interval. In the next step, these three photos from different angles are used to determine displacements of the 10 by 10 dots pad.

Figure 2. Illustration of auto-control system.

2.3 Coordinates setup

The principle for photogrammetry is to capture the interested locations by two additionalcameras mounted at about the similar height but from different perspectives. The angle of view between the two cameras at the interested point should be larger than 60 degree.

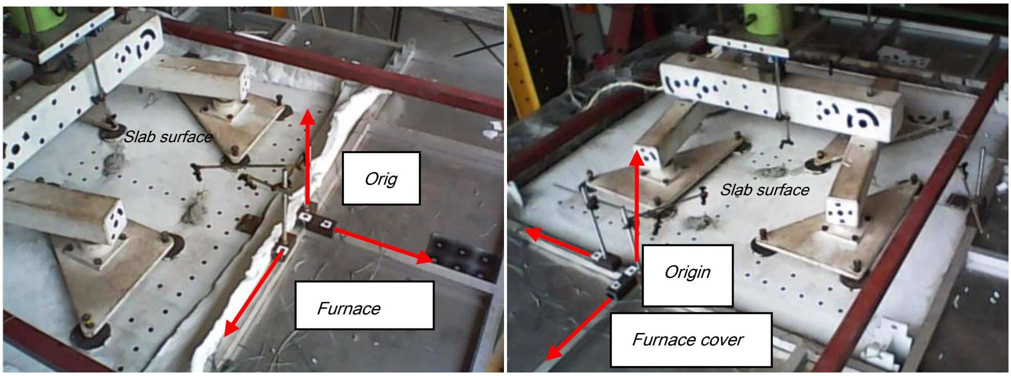

Figure 3. Applyingphotogrammetry to monitor slab surface deformation at elevated temperature.

Figure 3 shows two photographs that have been taken from two different angles at the same time. The origincan be defined by three black dots on top of the furnace cover, which remained fixed during the slab deformation. Based on this fixed origin, coordinates of all measuring points couldbe calculated. As the temperature increased, deformations of the composite slab becamelarger. The two connected cameras wereprogrammed to take photographs at the same time. Hence, the relative displacement could be calculated by simple subtraction from the previous coordinate information in three directions.

3. NUMERICAL ANALYSIS AND VALIDATION

3.1 Numerical model

In this paper, only ISOCS3 and ISOCS1 are discussed and shown in Figure 4. Since there wereonly limited measuring points in the test, the numerical modelswereestablished by SAFIR to validate the deformation shape. The details of these test specimens can be found from Liu[2].

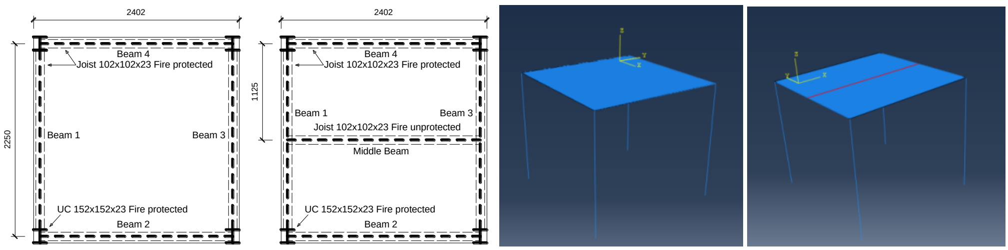

ISOCS3(no interior beam) ISOCS1 ISOCS3 model ISOCS1 model

Figure 4.Specimens for isolated composite slab-beam sub-assemblageswith ABAQUS modelling (unit in mm).

The temperature profiles for both specimens are recorded and input as the temperature gradient through the composite slab thickness as shown in Figure 5. It is also noted that the measured mesh temperatures for both specimens were below the FEM predictions because accumulated water within the composite slab evaporated during the tests, which could not be modelled by the FEM. Due to this phenomenon, the mesh temperatures in both specimens werelower than the FEM results.

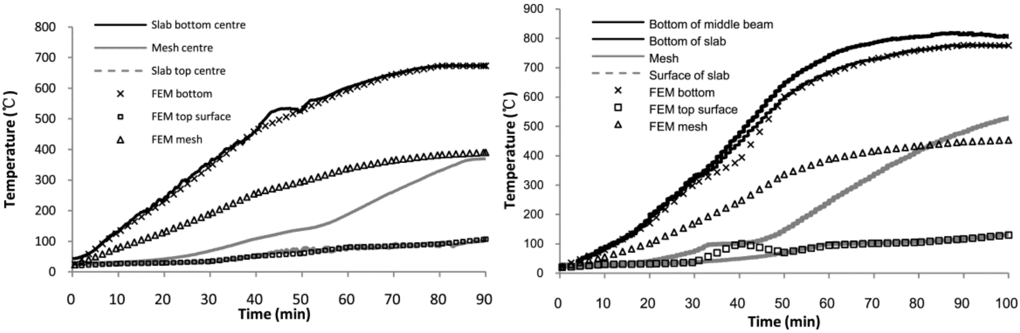

ISOCS3 ISOCS1

Figure 5. Input temperature profiles for ISOCS3 and ISOCS1 composite slabs.

Therefore, the numerical predictionshave been compared with the test results as shown in Figure 6. Because of the higher mesh temperature, both the numerical slab centraldeformation and the centralbeam deformation are slightly larger than the experimental results. Afterwards, this FEM model will be used in the later stage to compare the deformation with the photogrammetry results.

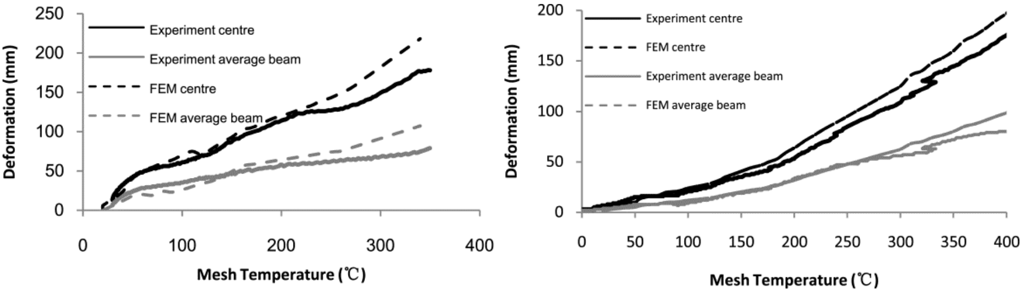

ISOCS3 ISOCS1

Figure 6. Experimental and numerical comparisons for slab centre and average edge beam centre deformation.

3.2 Photogrammetry model

The interestedpoints painted on the surface of the composite slab are automatically detected and marked by the software from three different angles as shown Figure 7. The black paint used for marked points can resist high temperature up to 1300℃. In addition, every three photos from different angles taken at the same time were used to build up the 3D model at that specific time frame. Besides, the mesh temperature was also recorded. Therefore, the deformation versus mesh temperature can be plotted out. In this manner, the final deformation model of the composite slab is shown in Figure 8.

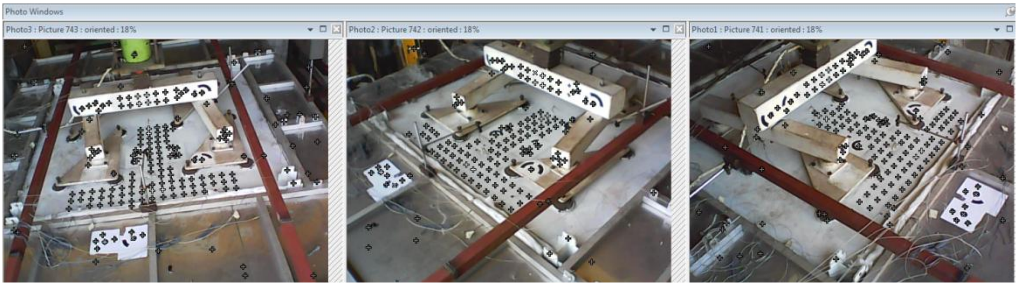

Figure 7. The setup of the photogrammetry model at the beginning stage.

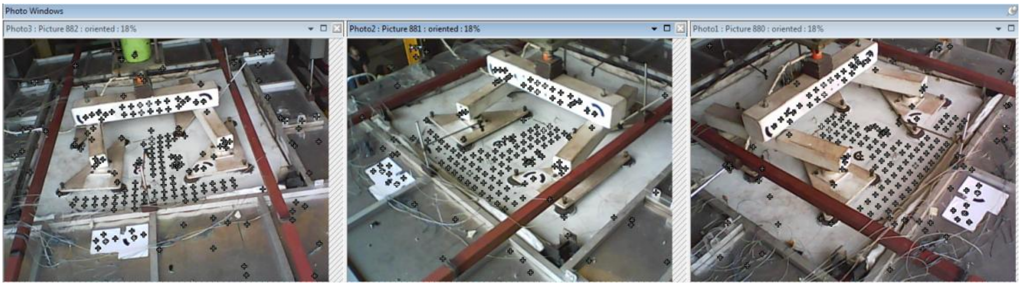

Figure 8. Final deformation of the photogrammetry model.

To verify the accuracy of this approach, measured centre deformation and average beam deformation by a line transducer were compared with the photogrammetry method. Figure 9 shows that there is good agreement between the two methods at large displacement but not for small displacementat the beginning stage. Generally, if small deformation is concerned, it is suggested to use a long focus lens to obtain detail information of the movement; while for large deformation, a wider angle lens should be applied in order to obtain the overall view of the deformation. Therefore, in this research, three cameras with wider angle lens have been installed to capture more broad-ranging of interested points at large deformation. That is reason why at small deformation the error is up to 20% while at large deformation the discrepancy is only about 5%. Hence, this approach is robust and flexible depending on the purpose and the range of lens. Additionally, the final profile is shown in Figure 10 for illustration.

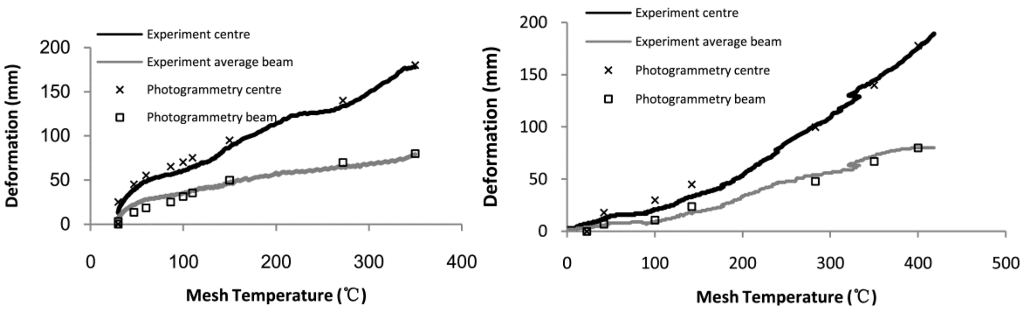

Figure 9. Comparison between the photogrammetry and the direct measurement from line transducer.

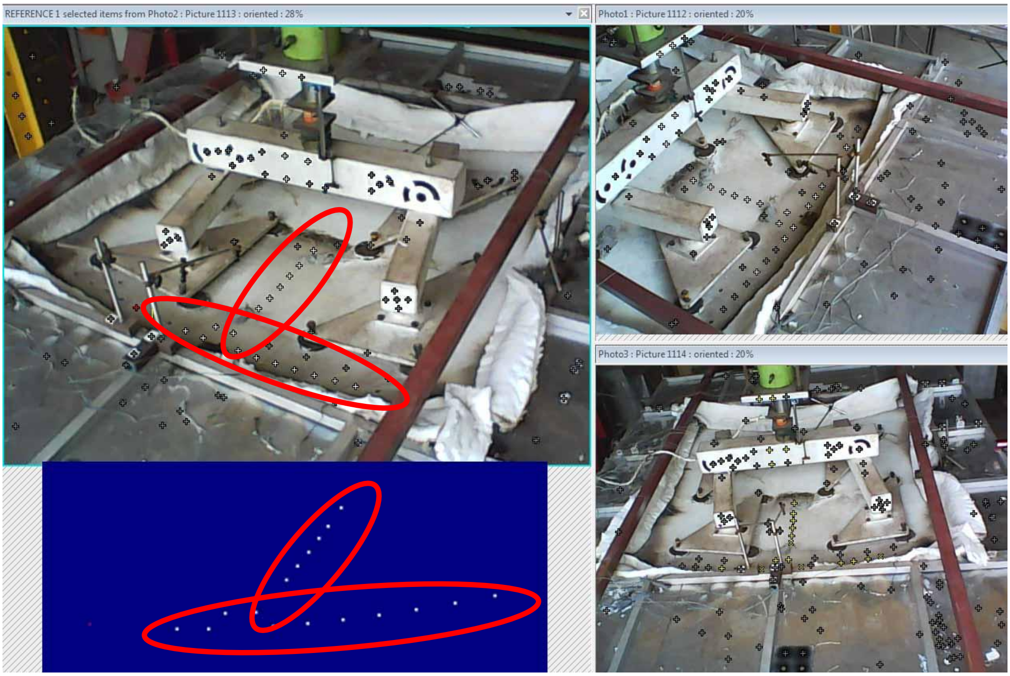

Figure 10. 3D profiles of the composite slab by photogrammetry.

3.3 Deformation profile

Due to obstructed view from the triangular loading plateson the top surface of the composite slab, only half of the centre cross section and one perimeter beam deformation profiles can be obtained from photogrammetry. Based on the numerical analysis from ABAQUS, the mid-span cross section and the perimeter beam deformation profiles are compared as shown in Figure 11. It can be seen that only limited points from the perimeter beam were captured from photogrammetry because some points were blocked by the insulation cover after largedeformation of the composite slab occurred. Meanwhile, some points from mid-span could not be detected due to damage of painted points from concrete cracking. Overall, the FEM and the photogrammetry show similar trends of deflection profiles at the final stage of these two composite slab tests.

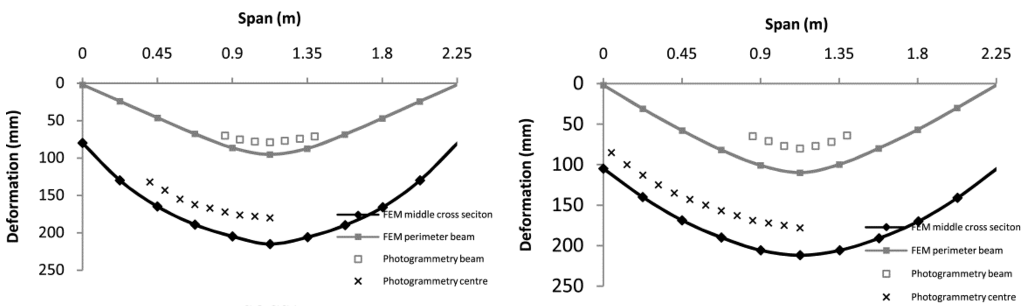

ISOCS1 ISOCS3

Figure 11. Deformation profile comparison of FEM model with Photogrammetry for mid-span and perimeter beam.

4. DISCUSSION AND CONCLUSIONS

The merits of using this photogrammetry method are (1) to obtain the 3D deformation profile of a specific cross section and (2) to measure displacements in all three dimensions. However, there are also some limitations for using this method. Some points may be obscured by rising smoke as shown in Figure 12 angle 2.

(a) Angle 1 (b) Angle 2 (c) Angle 3

Figure 12. Limitation for photogrammetry if the marked points are obscuredby the smoke.

In Figure 13, these obstructed points could still be worked outindicated by two cross linesin the software albeit with lower accuracy. Moreover, photogrammetry also requires sufficient lighting condition for the camera to capture these points from different angles at the same time. Overall, the photogrammetry indirect measurement is quite promising for fire engineering application with high accuracy.

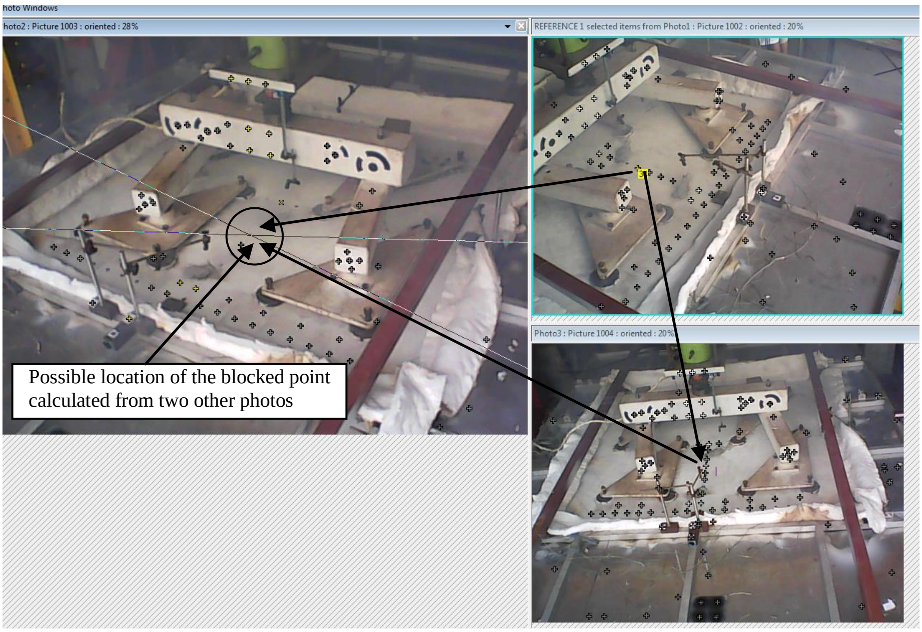

Figure 13. Method of finding the obstructed points through related photos.

REFERENCES

[1] N.T. Trung, K.H. Tan, Testing of composite slab-beam systems at elevated temperatures, Proceedings of the 7th International conference on Structural In Fire, Zurich, Switzerland, (2012) 247-256.
[2] J.X. Liu, K.H. Tan, Study the isolated composite slab-beam sub-assemblage at elevated temperature compared with Bailey-BRE method, in: Proceedings of the 8th International conference on Structural In Fire, Shanghai, China, 2014.

8th International Conference on Structures in Fire
Guo-Qiang LI, Venkatesh K. R. KODUR, Shou-Chao JIANG, Jian JIANG, Su-Wen CHEN, Guo-Biao LOU (Eds.)
Shanghai, China, June 11-13, 2014

APPLICATION OF STRUCTURAL FIRE SAFETY ENGINEERING TO THE CANOPY OF THE FORUM DES HALLES, IN PARIS

Nicolas Henneton*, Mohsen Roosefid* and Bin Zhao*

* CTICM (Centre Technique Industriel de la Construction Métallique)
e-mails: nhenneton@cticm.com, mroosefid@cticm.com, bzhao@cticm.com

Keywords: Fire safety engineering, FDS, ANSYS, One-way coupling

Abstract. *Actually, in the very heart of Paris, Châtelet-Les Halles, an outstanding redevelopment project is being undertaken with the purpose of creating a new landmark building with a vast steel structured roof called as "Canopy", covering the whole ground area of "Forum des Halles" shopping centre and the central subway exchange hub of Paris. According to the prescriptive rules of French fire safety regulation, a heavy standard fire resistance rating is required for this building. However, the extraordinary characters of this structure have led to a specific solution on the basis of the performance-based fire safety engineering (FSE) methodology. The fire model FDS and the FEM code ANSYS were used to analyze in detail the fire performance of the structure for each selected design fire scenario. Obtained results show that even with the most challenging scenario (library fire inside the building with external flames) there was no risk of failure of the structure. Consequently, the fire safety engineering methodology has permitted to demonstrate that the fire protection of the steel structure of the Canopy can be fully avoided.*

1 INTRODUCTION

The "Canopy" covering an area of about 7 000 m² is a sort of large metal marquee, requiring in total 3800 tons of steel, giving the impression of a swaying surface, very closely like a canopy of trees (Figure 1). It is composed of 15 translucent slats made of sheet glass and supported by architectural styled steel trusses called as "ventelles", with a maximum span of 96 m (Figure 2). It rests on two symmetrical three-story buildings with curved facades of which the occupancy corresponds to a range of urban services (library, conservatory, workshops, shops, etc.). Each of the large-span trusses is composed of two primary double directions curved circular tubes welded at each end to a long U-shape box girder located above the three-story buildings. The upper and lower primary double directions curved circular tubes are connected together by a steel link system. Moreover, a secondary steel structure, claw shaped, with smaller spans supporting also the glass panels is attached to the front of U-shape box girder (Figure 7).

Figure 1. View of the "Canopy" covering the Forum des Halles, in Paris.

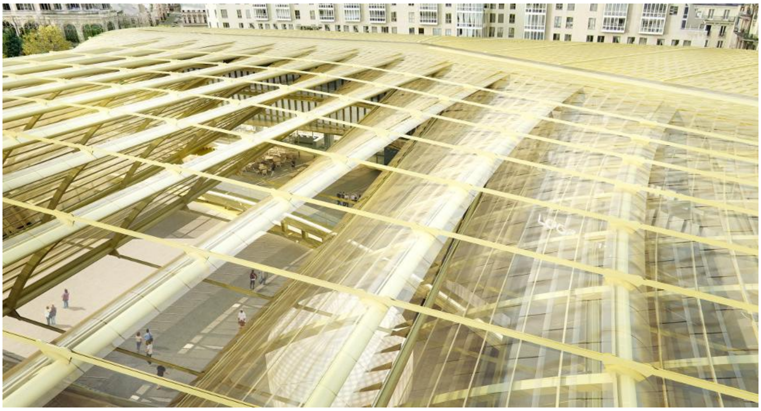

Figure 2. Above view of the large-span trusses supporting the sheet glasses.

As regards to the fire performance of the steel structure of the canopy, it was prescribed by local authorities on the basis of French fire safety regulation to reach the standard fire resistance rating of 90 minutes. However, due to the fact that the large volume space (area of 10 000 m^2 and 10 meters high) under the roof is not closed, and considering that the roof itself is on the one hand partially opened (see Figure 2), thus providing natural smoke extraction in case of fire and on the other hand far from ground level, this prescriptive approach based on a generalized fire is fully inappropriate in comparison with the real fire risks and would increase substantially and in particular unnecessarily the costs for fire protection of the steel structure.

Consequently, with the approval of city hall of Paris (client), it was decided to use the Fire Safety Engineering (FSE) methodology [1] to assess the fire resistance of the Canopy in real fire conditions, in order to determine, if necessary, the adequate fire-protective measures. This engineering approach, authorized in the French fire regulation relative to public buildings [3], consists of following steps in its application:

- Definition of the fire safety objectives and the performance criteria,
- Selection of the design fire scenarios impacting the structure,
- Determination of the thermal actions on the structural members,
- Evaluation of both thermal and mechanical responses of the structure.

2 STRUCTURAL FIRE SAFETY ENGINEERING STUDY

2.1 Fire safety objective and performance criteria

In this study, the fire safety objective clearly defined in French fire safety regulation is no increase of risk to life safety of occupants, fire fighters and others in the Forum des Halles, due to the structural behaviour of the Canopy in case of fire. Above basic fire safety objective needs to be translated into specific functional requirements so that practical performance criteria [2] can be derived for fire safety engineering study. In this case, the associated functional requirement is the lack of any structural collapse during the entire duration of a design fire scenario. Then, two performance criteria have been adopted to evaluate whether this requirement is met:

- The maximum heating of a steel member, for each design fire scenario, is lower than its critical temperature (the temperature at which failure is supposed to occur in a structural steel member with a uniform temperature distribution, for a given load level).
- If above criterion is not met, a detailed thermo-mechanical analysis is performed and the failure would be considered to be avoided if the maximum mechanical strain inside structural members does not exceed 20 %.

2.3 Design fire scenarios and design fires

Fires are considered to occur at almost any place inside the two buildings. Besides, on the pedestrian esplanade under the Canopy, some activities involving combustible materials such as newsstands, food stalls and Christmas market have to be also taken into account. It is therefore impossible to include all possible fires, and the realistic worst case design fire scenarios have to be selected. The different parameters used to select the more challenging design fire scenarios concern the fire itself (quantity of fire load, heat release rate…), factors influencing the fire development (ventilation conditions, fire compartment size, etc.), and finally from structural engineering point of view, the relative position of the fire to the structural members. In agreement with local authorities, it was firstly considered following most challenging fire scenario situations:

- A fire involving 4 stalls of Christmas market occupying an area of 144 m^2 and located on the pedestrian esplanade under the Canopy, with a maximum heat release rate of 72 MW;
- A library fire inside the buildings, of which the façade toward the Canopy will have some openings created by glass break in order to have external flames impacting mainly the box girder supporting the trusses.

The design fires selected for above two situations are indicated in Figure 3.

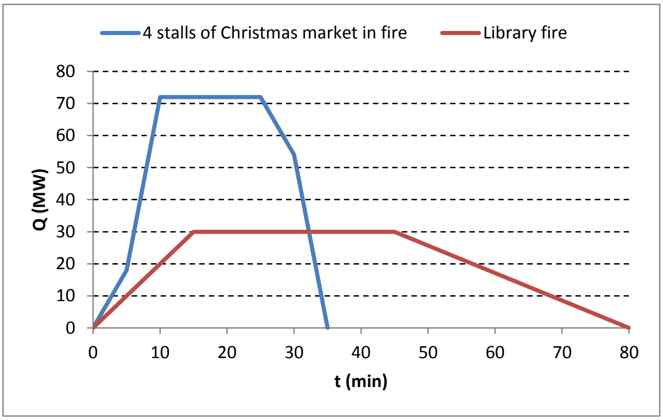

Figure 3. Design fires selected in agreement with local fire authorities.

Then, on the basis of these two situations, structural engineering considerations led to the selection of 9 design fire scenarios (their positions are indicated in Figure 4):

- Scenario 1: fire involving 4 stalls of Christmas market under the box girder overhanging the pedestrian esplanade, at mid-span, in order to have a maximum deflection of the structural elements;
- Scenario 2: fire involving 4 stalls of Christmas market under the large-span trusses with the minimum thickness (12 mm) at mid-span;
- Scenario 3: fire involving 4 stalls of Christmas market under the large-span trusses with the lowest height at mid-span (8 m above the esplanade);
- Scenario 4: fire involving 4 stalls of Christmas market to study specifically the mostly compressed link member between trusses;
- Scenario 5: fire involving 4 stalls of Christmas market to study specifically the structural members called the “claws”;
- Scenarios 6, 7 and 8: library fires inside one of the buildings, with external flames impacting mainly the box girder supporting the trusses;
- Scenario 9: library fire (identical to Scenario 7) to study specifically the effect of the wind, which may send more external flames to the box girder.

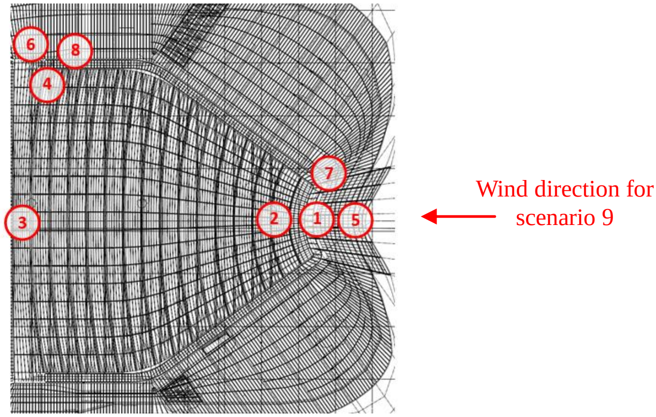

Figure 4. Position of the design fire scenarios.

2.4 Hypothesis in the design fire scenarios

For each design fire scenario involving a library fire inside the buildings, the area of openings created by glass break was determined in preliminary calculations, in order to have maximum realistic external flames which could challenge the box girder. These calculations were achieved with the one-zone model Ozone [6], and the area of openings was tuned in order to have a ventilation controlled fire in the library. It was found opening areas of 12 m ^{2}and 15 m ^{2}, depending of the compartment size used in the scenario.

Besides, the roofing system of the two buildings is made of insulation materials including polyurethane foam. Since the U-shape box girder is located very close to this combustible material, and given the lack of precise data concerning the combustible characteristics of the foam, it was decided to allow the spread of a fire starting in the library to the roofing system. To be on a safe side, an ignition temperature of 300 ℃ and a heat release rate of 500 kW/m ^{2}were used for the polyurethane foam.

2.5 Engineering tools

The FDS code [7] was used to simulate fire development of all fire scenarios and a coupling procedure between FDS and the FEM code ANSYS [8] developed within the scope of the European research project FIRESTRUC ([9, 10]) was used to predict the thermal actions to structural members of the Canopy. The FEM code ANSYS was applied to deal with the thermal and structural analysis of investigated structures. The modelling assumptions are detailed below.

2.5.1 FDS modelling

The whole area is modelled with FDS (Figure 5), but depending on the scenario, the simulated domain is reduced to limit the computational time, considering that it would not affect the results. The grid is uniform and the cells dimensions are 50 cm by 50 cm by 50 cm. A finer mesh size was tested (50 cm × 50 cm × 25 cm) for the design fire scenario 1, but the results remained identical.

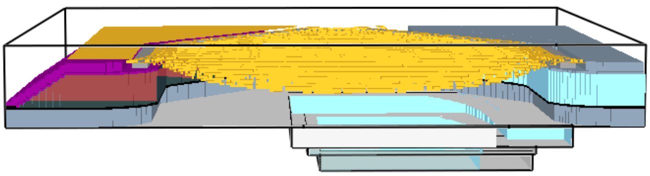

Figure 5. FDS model.

The values of all parameters employed for the simulations are the default ones implemented in FDS. For design fire scenarios involving the 4 stalls of Christmas market, the fire area is intentionally elevated to 3 m high, in order to be on a safe side (Figure 6, scenario 2). For the design fire scenarios involving a library fire, the opening location is specifically chosen in order to have the most severe but realistic external flames challenging the box girder (Figure 6, scenario 7).

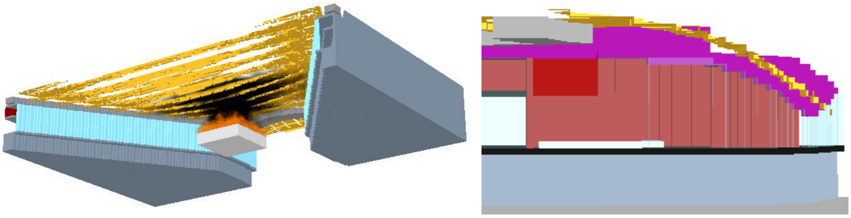

Figure 6. Simulation of fire development with FDS, design fire scenarios 2 (left) and 7 (right).

2.5.2 Assumptions and specific modelling features for structural analysis

The following hypotheses are considered in the FEM (ANSYS) modelling:

- According to room temperature design, the structural members are mainly made of Grade S460 (fy=460 MPa), except certain elements, such as stiffeners which are of Grade S355 (fy=355 MPa). The variation of yield strength with wall thickness is also taken into account. Modulus of elasticity of steel at room temperature is taken as 210000 MPa.
- The load combination in fire situation comprises the permanent fixed action (self-weight of the structural elements) and 20 % wind loads in accordance with EN1990 [4]. As far as design snow loads are concerned, they are much lower than the vertical wind loads. The load is considered to be constant during fire;
- The thermal properties of the steel (nonlinear properties for thermal capacity and conductivity) are those given in EN1993-1-2 [5];
- The mechanical material properties of steel at elevated temperatures used in this modelling are fully in accordance with those recommended by the fire part of Eurocode 3 [5];
- The heat transfer analysis of the structural members subjected to thermal actions is predicted using the automatic coupling procedure with help of 3D thermal solid element SOLID70 and thermal surface effect element SURF152;

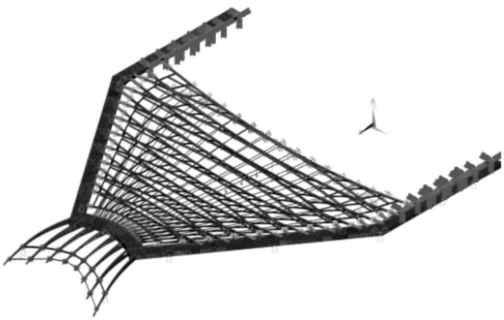

Figure 7. Thermo-mechanical model (ANSYS), part of substructuring model using superelement MATRIX50.

- The global structural analysis approach using substructuring of a finite elements group into one superelement in ANSYS is adopted in order to reduce the required computation time (Figure 7). Thus, BEAM188 elements are used for the exposed trusses (or SHELL181 elements for the box girder) and a superelement MATRIX50 is used for other structural elements after identifying a set of master DOFs at the interface between the super-element and other elements;

- When assessing the fire behaviour of the box girder, due to symmetry in geometry and loading, only one half of structure is analyzed whereby the appropriate boundary conditions have been applied.

2.6 Results

Obtained results are summarized in Table 1. As it can be seen, in case of large part of design fire scenarios, the maximum temperatures of steel members are lower than their critical temperatures. Besides, concerning Scenarios 8 and 9, only fire development has been simulated with FDS, because thermal actions were found to be inferior to those obtained with, respectively, Scenarios 6 and 7.

Table 1. Results.

Scenario	Structural element	Maximum heating (℃)	Critical temperature (℃)
1	Box girder	295	450
2	Trusses	367	700
3	Trusses	533	780
4	Link	237	500
5	Claws	320	670
6	Box girder	407	450
7	Box girder	507	450
8	Box girder	< 407	450
9	Box girder	< 507	450

It needs to be mentioned here that the critical temperature of different steel members are obtained with help of a global structural analysis under ISO fire condition which means that all structural members are subjected to the same fire exposure. In consequence, the critical temperatures obtained in this way are certainly on the safe side.

The maximum heating of the large-span trusses was found to be 533℃, in case of the design fire scenario 3 (Figure 8). Indeed, for this scenario the trusses are only 5 m above the fire. Even if this temperature is less than the critical temperature of the trusses, a thermo-mechanical simulation was conducted and showed that the maximum deflection of the trusses due to the fire is only 0.245 m, with a maximum mechanical strain of 0.3 %.

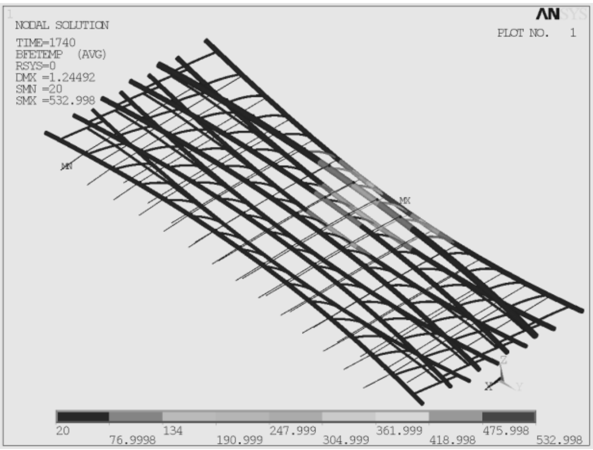

Figure 8. Maximum heating of the large-span trusses in case of scenario 3.

However, with the most challenging scenario (scenario 7, library fire inside the building), a maximum temperature of 507 ℃ was obtained for the lower face of the box girder (Figure 10), superior to its critical temperature under ISO fire condition. Figure 9 shows that the external flames impact the part of the box girder located in front of the opening. Consequently, a detailed thermo-mechanical analysis was performed with ANSYS. The maximum deformation was obtained along the Z axis, as indicated in Figure 11. At this location, the equivalent plastic strain was found to be 13 %, which is inferior to the criteria of 20 %, demonstrating that there is no risk of failure of the box girder.

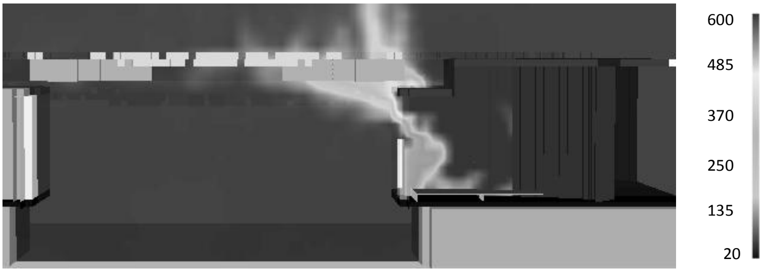

Figure 9. Temperature (℃) slice computed by FDS at 30 minutes, for scenario 7 (library fire).

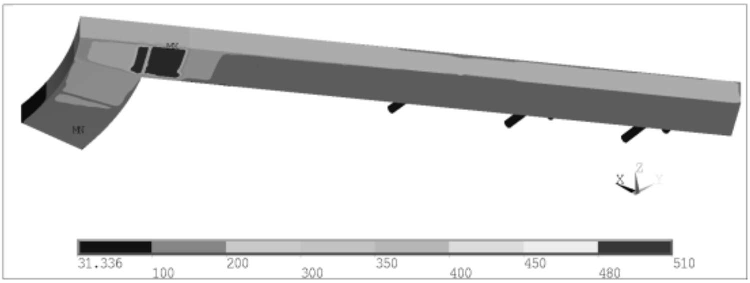

Figure 10. Maximum heating (℃) of the box girder at 50 minutes of fire, for scenario 7 (library fire).

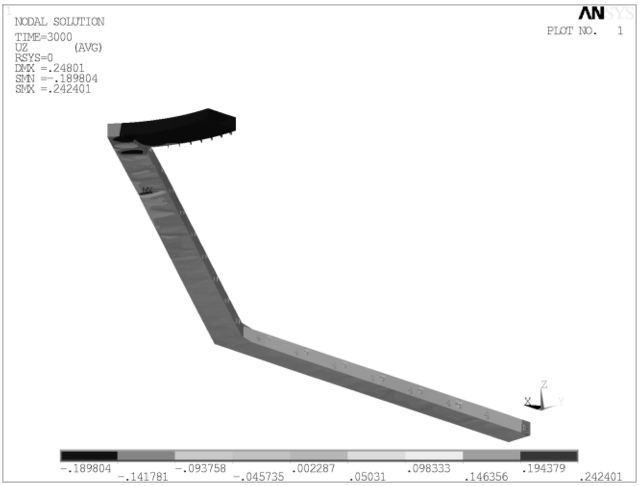

Figure 11. Vertical displacement of the box girder (along Z axis), at 50 minutes of fire, for Scenario 7.

3 CONCLUSIONS

The fire safety engineering methodology has been applied to a vast steel structured roof called as "Canopy", covering the whole ground area of "Forum des Halles" in the heart of Paris. It was initially prescribed by local authorities, on the basis of French fire safety regulation, to reach the standard fire resistance rating of 90 minutes. However, due to the fact that the large volume space under the roof is not closed, and considering that the roof itself is partially opened and far from ground level, it was obvious that such a prescriptive approach based on a generalized ISO fire was fully inappropriate in comparison with the real fire risks and would increase substantially and in particular unnecessarily the costs for fire protection of the steel structure.

In agreement with local authorities, design fire scenarios have been selected, considering either a fire involving 4 stalls of Christmas market located on the pedestrian esplanade under the Canopy, or a library fire inside the buildings, with external flames impacting the box girder supporting the trusses. The obtained results show that in case of majority of design fire scenarios, the reached maximum temperatures of steel members are lower than their critical temperatures. However, with the more challenging scenario (library fire inside the building), it was then necessary to analyse in detail the fire performance of this structure to finally conclude that there was no risk of failure of this structure. Consequently, the fire safety engineering methodology has permitted to demonstrate that the fire protection of the steel structure of the Canopy can be fully avoided.

REFERENCES

[1] ISO/TS 24679:2011, *Fire safety engineering - Performance of structures in fire*, International Organisation of Standardization, Geneva, Switzerland, 2011.

[2] ISO 23932:2009, *Fire safety engineering - General principles*, International Organisation of Standardization, Geneva, Switzerland, 2009.

[3] Ministry of Interior, Decree dated 22 March 2004 related to the fire resistance of construction materials and systems.

[4] EN 1990, *Eurocode 0: Basis of structural design*, European Committee for Standardisation (CEN), Brussels, Belgium, 2002.

[5] EN 1993-1-2, *Eurocode 3: Design of steel structures - Part 1-2: General rules – Structural fire design*, European Committee for Standardisation (CEN), Brussels, Belgium, 2005.

[6] Cadorin J.F. and Franssen J.M., "A tool to design steel elements submitted to compartment fires – OZone V2", *Fire Safety Journal*, 38, 395-451, 2003.

[7] McGrattan K., McDermott K., Hostikka S. and Floyd J., "Fire Dynamics Simulator (Version 5) - User's Guide", NIST Special Publication 1019-5, SVN Repository Revision: 6701, September 3, 2010.

[8] ANSYS, ANSYS User's Manual for Revision 14.0 - Volume IV - Theory. Swanson Analysis SYSTEM, INC., Houston, USA, 1992.

[9] Zhao B., Desanghere S. and Darche J., "CFD and FEM Coupling With Computer Codes FDS and ANSYS For Fire Resistance", *Interflam - Proceedings of the Eleventh International Conference*, University of London, UK, 1461-1466, 2007.

[10] BRE, Arcelor Profil Luxembourg, CTICM, TNO Efectis and Université de Liège, "FIRESTRUC - Integrating advanced three-dimensional modelling methodologies for predicting thermo-mechanical behaviour of steel and composite structures subjected to natural fires", Final Report of RFCS Project, Contract No RFS-CR-030300, 2007.

THERMOMECHANICAL BEHAVIOUR OF CELLULOSE-BASED MATERIALS: APPLICATIONTO A DOOR UNDER FIRE RESISTANCE TEST

Guillaume Cueff*, Jean-Christophe Mindeguia*, Virginie Drean,Gildas Auguin** and Denys Breysse***

*University Bordeaux, UMR CNRS 5295, I2M (Institute of Mechanics and Engineering)
Address: I2M – Dpt GCE, Université Bordeaux, 351 Cours de la Libération, A11 bis, 33405 Talence, France
e-mail: guillaume.cueff@efectis.fr, jean-christophe.mindeguia@u-bordeaux.fr, denis.breysse@u-bordeaux.fr

** Efectis France, Espace Technologique, Bât. Apollo, Route de l'Orme des Merisiers, F-91193 Saint-Aubin, France
e-mail: virginie.drean@efectis.fr, gildas.auguin@efectis.fr

Keywords: Wood, Particleboard, Fire, Pyrolysis, Heat transfer, Temperature

Abstract. *In the context of fire safety, industrial products used in the building construction market have to satisfy a standard fire resistance test. Fire resistance tests are restrictive and costly for manufacturers. In this context, a research program was initiated of which main objective is to develop a numerical thermo-mechanical model for simulating a fire resistance test on a door-set composed of wood and wood-based materials (particles and fibres boards). Based on simulated temperature field and estimation of the global bending of the fire door, the model can be used as a tool for improving the design of the door through parametrical studies in order to improve the fire resistance. In this paper, a numerical model for fire degradation of wood-based products is firstly presented. Then, simulation results of (i) a thermal transfer under standard fire curve ISO-834-1 through a linen fibreboard and (ii) its thermo-mechanical behaviour are detailed.The numerical results are compared with experimental data.*

1 INTRODUCTION

Fire safety is a major concern in the field of civil safety and mainly in the case of building construction. It is based on the combination of active and passive protection, including means preventing or slowing the spread of smoke and flames. New industrial products must satisfy technical approvals, including fire resistance tests, which are experimentally assessed in accredited laboratory furnaces [1]. The validation process of a product regarding a fire resistance test is complex which can slow down the innovation.

In that context, the use of simulation tools can offer an alternative to real fire resistance tests, for instance during preliminary design stages. The concept of "Virtual Furnace" is therefore developed in some laboratories [2] in order to model a fire resistance test. The concept is based on the coupled simulation of on one hand the gas temperature and flux (using computational fluids dynamics software) and on the other hand the thermal or thermo-mechanical behaviour of the structure (most often carried out with finite element solvers). Such a tool virtually recreates the thermo-mechanical behaviour of the tested product when it is exposed to a standard fire in a laboratory furnace. Using a "Virtual Furnace" allows better analysing and evaluating a large number of technical alternatives, before carrying out a conclusive fire resistance test. During the development phase, manufacturers can design their products in collaboration with the fire resistance laboratory, and then achieve more efficient solutions (from both technical and economical point of view). Finally, numerical simulations may improve the testing conditions including heating power (control of the furnace) and metrology.

In the fire research field, there are many studies about the behaviour of solid wood under fire exposure [3] whose reason is the wide use of wood as a structural product in constructions (timber). On the other side, wooden-based products like linen fibreboard are mostly used for claddings, furniture or door manufactures. Since they are not considered as load-bearing elements, their behaviour at high temperature is quite less studied than solid wood. By consequence, very few data are available in the literature about the thermal degradation of wooden-based products and on how it can influence their thermal and mechanical properties. For that reason, an experimental program was established, aiming to overcome the lack of data from the literature. The work presented in this paper uses data from this experimental program.

From the point of view of heat and mass transfer simulations, many numerical models are available in the literature to describe pyrolysis of wood [3]. These complex models generally need a lot of input parameters that are difficult to measure, especially at high temperature.At the opposite, simple calculations are often done by using properties given bythe Eurocode 5 [4], which is based on a security-based approach, and do not take into account the particularity of the material.For these reasons, it has been decided to develop aspecific thermal model aiming to simulate wood degradation at high temperature(drying and pyrolysis) and the impacts it can have on both thermal and mechanical properties.

The work presented in this paper is part of the “VIRGILE” project, aiming to model the fire behaviour of a product and its interaction with the testing furnace [2]. Collaboration between Efectis France, accredited laboratory in fire resistance, and the Institute of Mechanics and Engineering of the University of Bordeaux (I2M) has been established in that way. The main objective of the collaboration is to develop a numerical model able to simulate the thermo-mechanical behaviour of wooden-based doors when tested under standard fire.

In the first part of the paper,thermaland mechanical modelsdeveloped to describe the heat transfer inside a cellulosic material at high temperature and its mechanical induced behaviourare presented. Above all, the model is able to take in account the thermal degradation reactions of wood or wooden-based material, namely the vaporization of water, the pyrolysis of wood particles and glue, the combustion of pyrolysis gases and the thermally-induced variation of the thermal and mechanical properties. The thermal model consists in a first order vaporization and pyrolysis reactions controlled by two independent Arrhenius laws. In one hand, the reactions rates are used to recalculate the thermal and mechanical properties of the cellulosic composite at each time step. In a second hand, the reactions rates are used to calculate sources of energy corresponding to water vaporization (endothermic reaction) and to solid pyrolysis (exothermic reaction). The mechanical model consists inthe calculation of the material stiffness based on the pyrolysis reaction rate.

In the second part of the paper, simulation results of the heat transfer through linen fibreboard and its thermo-mechanical behaviour are presented. Temperatures inside and on the unexposed face of the material are presented, as well as of thehorizontal displacements of the panel. Simulation results are compared with data from a fire resistance test carried out in Efectis France Laboratory on a linen fibreboard.

2 NUMERICAL MODEL

In this part, the numerical model developed to simulate the heat transfer in a cellulosic material and the induced mechanical behaviour is presented. Calculations are performed on the finite element software CAST3M [5] that allow adding specific procedures in order to take into account the thermal degradation and the variation of material properties at high temperature. The thermal model developed to take into account the thermal transformations and degradation of cellulosic material at high temperature is first presented. Then a mechanical model is exposed that takes into account the orthotropic behaviour of the material and the reduction of the mechanical stiffness, depending on the kinetics of the thermal degradation (pyrolysis) of wood.

2.1 Thermal model

2.1.1 Heat transfer equation

The heat transfer by conduction inside the solid is resolved using a modified Fourier law (1) in which energy sources are added aiming to take in account the thermally-induced reactions. Q_w and Q_s are sources of energy for respectively vaporization of water contained in the material (negative term, i.e. energy sink) and the pyrolysis of wood and glue (positive term, i.e. energy input).

$$\rho_s \, Cp_s \frac{dT}{dt} = \nabla(\lambda \nabla T) + Q_w + Q_s \tag{1}$$

Both thermal reactions, vaporization and pyrolysis, are governed by two independent Arrhenius laws that are presented in section 2.1.2.

2.1.2 Source of energy

Since water vaporization and cellulosic material pyrolysis are thermally-activated reactions, two independent Arrhenius laws are used to simulate them. For each of them, the degree of reaction $\alpha_{w,s}$ is linked to the kinetic of reaction $\frac{d\alpha_{w,s}}{dt}$, according to Equation (2).

$$\frac{d\alpha_{w,s}}{dt} = k_{w,s}(1 - \alpha_{w,s}) \tag{2}$$

Equation (2) is based on a first-order Arrhenius law, representative for the thermal reactions schematized in Figure 1.

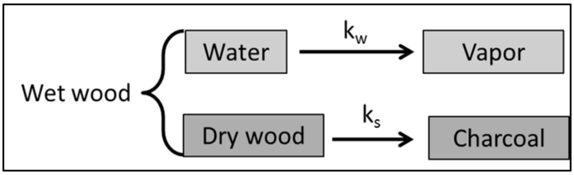

Figure 1. Thermal degradation reaction model used to take in account the vaporization of water (k_w) and the pyrolysis of wood (k_s).

In Equation (2), $k_{w,s}$ is the rate constant, which is dependant of temperature according to equation (3).

$$k_{w,s} = A_{w,s} \exp\left(\frac{-Ei_{w,s}}{RT}\right) \tag{3}$$

At each time step ti, the rate constants are calculated at each node of the meshed geometry, depending of the temperature field calculated at the time ti-1.

Finally, the sources of energy Q_w and Q_s are linked to the kinetic of reactions, respectively vaporization and pyrolysis, according to Equation (4).

$$Q_{w,s} = \frac{d\alpha_{w,s}}{dt} \times \rho_{w,s} * Hr_{w,s} \tag{4}$$

Where $\rho_{w,s}$ is the compound density and $Hr_{w,s}$ the heat of reaction associated with vaporization and pyrolysis.

In addition to the pyrolysis source Q_s, the cellulosic material combustion is taken into account by adding a source of energy Q_c linked with pyrolysis reaction and localized only onto the exposed surface of the sample. It is considered that 80% of pyrolysis gasesare combustible according to the Equation (5) where Hr_c is the heat of reaction for the combustion.

$$Q_c = \alpha_s \times Hr_c * 0.8 \quad (5)$$

2.1.3 Variation of the thermal properties with temperature

Generally, when construction materials are exposed to fire, the thermal properties are affected by the temperature. The variation of thermal properties with temperature has a non-negligible impact for thermal simulations. In order to take into account the temperature impact on the thermal properties of linen, a mixture law was developed. Thermal conductivity and density depend on the mass fraction of the three following phases: dry linen (including glue), water and charcoal, according to Equations (6) and (7). Specific heat depends on the volume fraction of these three phases, according to equation (8). At each calculation time step, the proportion of each phase is calculated thanks to the Arrhenius laws described in section 2.1.2.

Equations (6) to (8) take in account the degrees of reaction α_w and α_s, that respectively refer to the water vaporization and the cellulosic material pyrolysis. The formation of charcoal is represented by the production rate χ (expressed as a mass fraction of dry linen). Initial water content of the material is taken into account thanks to the coefficient β.

$$\lambda_{tot} = (1-\alpha_s).\ \lambda_s + \frac{\rho_s}{\rho_{char}}.\chi.\ \alpha_s.\ \lambda_{char} + \frac{\rho s_w}{\rho_w}.\beta.(1-\alpha_w).\ \lambda_w \quad (6)$$

$$\rho_{tot} = \rho_s.\ [1 + \alpha_s(\chi - 1) + \beta(1-\alpha_w)] \quad (7)$$

$$Cp_{tot} = \frac{(1-\alpha_s).Cp_s + \chi.\ \alpha_s.\ Cp_{char} + \beta(1-\alpha_w).\ Cp_w}{[1+\alpha_s(\chi-1)+\beta(1-\alpha_w)]} \quad (8)$$

3.2 Mechanical model

The evolution of solid wood mechanical properties at high temperature is well documented in the Reference [6]. However, very few data are available for wood-based materials as linen particleboards. This can be explained by the fact that particleboards are not considered as load-bearing elements. By consequence, it has been decided to use a mechanical model which takes into account the orthotropic behaviour of the material and a reduction of the elastic modulus as a function of the degree of reaction of the pyrolysis α_s.

The in-plane modulus of elasticity of the panel ($E_{x,y}$) is calculated at each time step from Equation (9) where E_0 is the elastic modulus measured at 20°C and α_s is the degree of pyrolysis reaction.

$$E_{x,y} = E_0 \cdot \alpha_s \quad (9)$$

As seen in Reference [7], the modulus of elasticity of particleboard is highly dependent onthe orthotropic directions. It appearsthat the out-of-plane modulus is 80 to 90% lower than the in-plane modulus.Due to thelack of data, it is assumed that theout-of-plane modulus of elasticity is equal to 20% of$E_{x,y}$.

Poisson coefficients are considered equal in each orthotropic direction ($\nu_{xy}=\nu_{yz}=\nu_{xz}$).The initial value has been measured at 20℃ and is equal to 0.2. At higher temperatures, the same reduction ratio that the Eurocode 5 reduction of the rigidity is applied on Poisson coefficients [4].

Very few shear modulus data are available for linen particleboards. A simple elastic equation (10) isused for the shear modulus G_{xy}. Shear modulus G_{yz} and $G_{xz}$are assessed according to Najafi work's [7], see equation (11). The temperature dependence of shear modulus is driven by the elastic modulus E_x:

$$G_{xy} = \frac{E_x}{2(1+\nu_{12})} \quad (10)$$

$$G_{yz} = G_{xz} = E_x/8 \quad (11)$$

Thermal dilatation coefficients and their evolution with temperature arepoorly documentedin the literature. Data can be found between -50℃ to 80℃ but not for higher temperatures.However, it is known that the thermal dilatation coefficient is 5 to 10 times greater in the perpendicular direction of wood fibres than in the longitudinal direction of fibres. This was also observed in our experimental measurements. The out-of-plane thermal dilatation coefficient φ_z of the linen fibreboard is then taken 10 times larger than in-plane coefficients φ_x and φ_y.

$$\varphi_z = 10\varphi_x = 10\varphi_y \tag{12}$$

4 HEAT TRANSFER TEST

To calibrate the numerical model, a fire test on small-scale doors was carried out at Efectis France laboratory. Small-scale doors (dimensions 1000 mm x 465 mm x thickness) were exposed to the standard thermal loading EN-1363-1 [1], until ultimate collapse. Simulations will be compared to the experimental results in section 5.

The heat transfer test consisted in measuring temperatures and displacements onto six wood-based panels as shownon Figure 2 (a). The work presented here only focuses on the linen fibreboard fixedby three steel hinges (hinge's dimensions: 60 x 50 mm^2) (Figure 2 b). The panel's dimensions are 1000 x 465 x 33.5 mm^3, witha density of 390 kg/m^3. Around 30% of the panel is composed of linen fibres. The rest of the product is composed by wood fibres, urea formaldehyde glue and water (no product information sheet available). This type of linen panel is often usedas a basic component for fire doors and was provided by a French door manufacturer.

Instrumentation consisted in 17 type K thermocouples located on the unexposed side and inside the material (8, 16.5 and 25 mm from the exposed side). Out-of-plane displacements were recorded by using two draw-wire sensors. Displacements were measured at the centerof the panel and at the upper corner of the panel (at the opposite side of hinges).

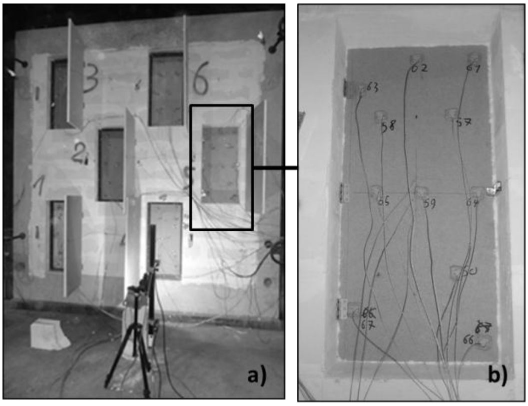

Figure 2. (a) Unexposed face of the furnace with the six wood-based panels; (b) Linen fibreboard fixed on three hinges with a metal angle screwed as a door lock.

5 NUMERICAL SIMULATIONS

Simulationsof the heat transfer testusing the developed thermo-mechanical model (see Section 3) are discussed and compared to experimental data (see Section 4).

5.1 Heat transfer simulation

A validation of the thermal model is presented here. In order to reduce the duration of the simulation, aunidirectional heat transfer through the thickness of the linen fibreboard is considered. A thin 2D mesh (quadratic elements) is used with thermal boundary conditions onto the exposed and unexposed faces as presented on Figure 3. Exchange with the EN-1363-1 standard temperature on the exposed face and with the room temperature on the unexposed face are taken into account with convective heat transfer coefficients H respectively equal to 25 and 4 W/m^2K and radiative transfer coefficients ε equal to 0.9.Water content β before heat transfer test is estimated at 10%.

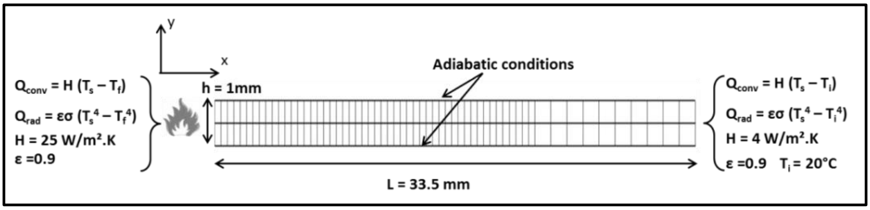

Figure 3. Boundary conditions used for thermal transfer simulations in linen panel.

The thermal properties and the Arrhenius laws parameters used for simulations are presented in table 1. Simulated temperatures on the unexposed surface and inside the material (8, 16.5 and 25 mm from the exposed surface) are compared to heat transfer test measurements.

Table 1.Thermal properties of the linen panel and data used in Arrhenius laws.

Component	ρ (kg/m³)	Cp (J/kg.K)	λ (W/m.K)	Arrhenius parameters	Water vaporization	Pyrolysis	Combustion
Linen	373	1636	0.123	Ei (J/mol)	$1.6 \cdot 10^5$	$3.3 \cdot 10^5$	-
Charcoal	93*	1150	0.125	A (/s)	$1.0 \cdot 10^{19}$	$5.1 \cdot 10^{31}$	-
Water	997	4286	0.658	Hr (J/kg)	$-1.2 \cdot 10^7$	$2.0 \cdot 10^6$	$17 \cdot 10^{6}$**

* 93 kg/m³ is for χ = 0.25 (section 2.1.3)

** 80 % of pyrolysis gases are considered to be combustible

Comparison between simulated and measured temperatures in the linen panel is presented in Figure 4. With the model developed, it can be noted that the kinetics of temperature is mostly governed by the value of conduction coefficient λ and by the two energy values Hr respectively corresponding to water vaporization and pyrolysis. With the data set used here, the temperature elevation below 100 ℃ is somehow slower in the simulation than in the experiment, which results in a slight delay in the simulated temperatures under 100 ℃. Above this temperature the general trend of the thermal transfer is well simulated. Taking into account the sink of energy associated with water vaporization allows obtaining a temperature slowdownaround 100 ℃. Due to thermal damping across the material, the delay is higher for deeper measurement, as for instance on the unexposed side of the panel, like it is observed during experiments.

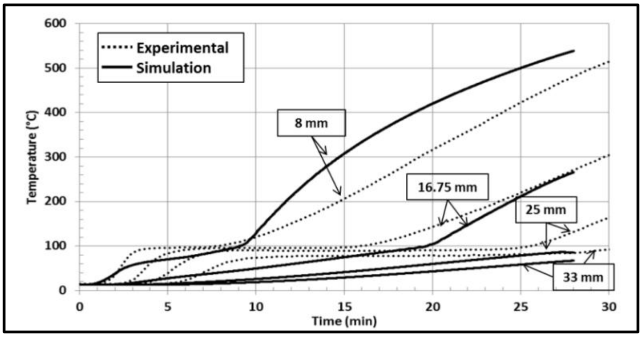

Figure 4.Simulated (solid lines) and measured temperatures (dotted lines) for the thermal transfer in a linen fibreboard.

The comparison between simulated and experimental temperatures shows that correctly simulating the thermal behaviour around the vaporization process is complex. This may be due to the fact that the model does not account for the mass transfer inside the material. On another hand, developing heat and mass transfer models would require to identify a much larger number of material parameters, e.g. permeability and porosity, which are often not measurable at high temperatures.

5.2 Thermo-mechanical simulation

Thermo-mechanical simulation is performed on a full-scale 3D mesh (quadratic elements) of the tested panel. Same thermal boundariesthan the thermal simulation (Section 5.1) are used for this simulation (see Figure 5). Mechanical boundaries consist in blocking the displacements and rotations of hinges and lock. Steel thermal and mechanical properties used for hinges and lock are taken from the European standard EN 1993-1-1.

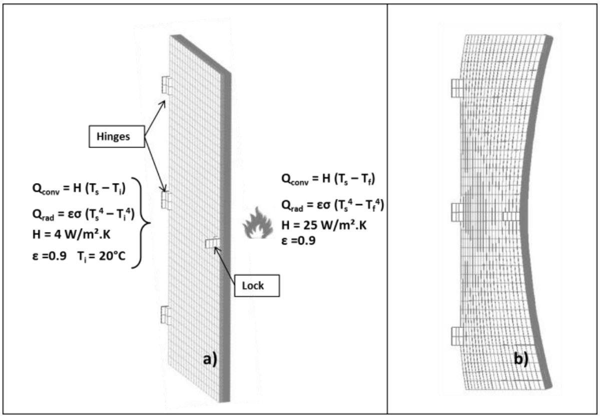

Figure 5.Boundary conditions used for thermal transfer simulations onto linen panel.

Initial mechanical properties used in this simulation are presented in Table 2. Values athigher temperatures are calculated as explained in Section 3.2. Thermal expansion coefficientsare based on Tabaddor'swork [8] and values are given at Figure 6 (a).

Table 2. Initial mechanical properties of the linen panel.

T (℃)	$E_{x,y}$ (MPa)	E_z (MPa)	$\nu_{xy, yz, xz}$	G_{xy}(MPa)	$G_{yz, xz}$(MPa)
20	650	130	0.2	271	81.3

Simulated displacement at the centre of diagonals is provided at Figure 6 (b) (dotted line). Displacement at the center isclose to the measured one. At 28 min, i.e. at the end of the fire test, a displacement of 10.3 mm is simulatedwhilea value of 18 mm wasmeasured. It can also be seen that the evolution with time of these displacements is not identical, with a slower evolution in simulation. The first possible explanation is the difference between experimental and simulated thermal transfers inside the material (see Section 5.1). Secondly, assumptionsabout mechanical properties (especially for the orthotropic properties) were made for this simulation and might be improved.The values of thermal dilatation coefficients are derived fromTabaddor's work on solid woodexposed to fire. An experimental program is currently undertaken, aiming to measure thermal dilatation coefficients of linen fibreboard.

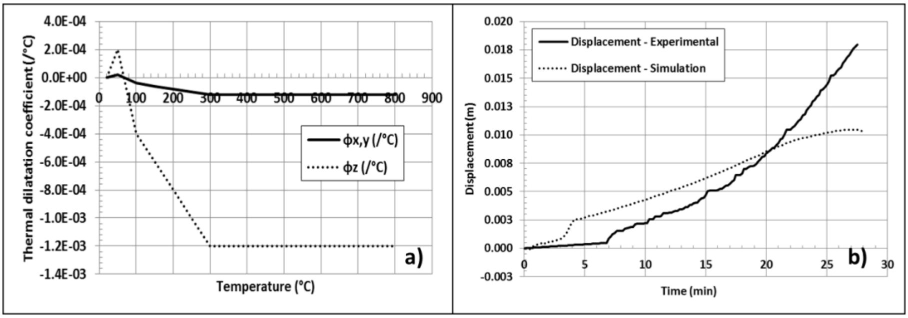

Figure 6. (a) Thermal dilatation coefficients used in thermo-mechanical simulation and (b) Experimental (solid line) and simulated (dotted line) displacements at the leaf center of the linen fibreboard.

6 CONCLUSIONS

In this work, a thermo-mechanical model for the simulation of thermal and mechanical behaviour of cellulosic materials when exposed to a fire resistance test has been developed. Two main difficulties had to be overcome. The first one is the complexity of coupled phenomena that are involved in the thermo-mechanical response of wood components. The second one is the lack of knowledge and data about the value of thermal and mechanical properties of wooden based materials for the whole range of temperatures of the tests. The choice has been done of developing a simplified model capable of describing the main features of materials transformation during pyrolysis, while carrying on an important experimental program in order to identify the range of values of material properties.

Results show that correctly simulating the thermal transfer in wood is complex. The main features of tests are reproduced, and the experimental results have been correctly fitted. Some weaknesses remain, mainly due to the vaporization process near 100 ℃. The quality of results might be improved by adding a mass transfer model but this would increase needed parameters which are not easily measurable at high temperature.To improve the quality of displacement estimation, it will be necessary to replace prior values taken for thermal expansion coefficients by values more representative of the linen fibreboard.Tests are currently carried out to measure these parameters, while accounting for the orthotropic character of the thermal strain.

REFERENCES

[1] AFNOR, "NF-EN-1363-1, Fire resistance tests, Part1: General requirements",*AFNOR*,2000.

[2] Cayla F., Leborgne H., Joyeux D., "Application of a virtual resistance furnace: fire resistance test simulation on a plasterboard membrane", *Application of Structural Fire Engineering*, COST Action TU0604, 2011.

[3] Di Blasi C., "Comparison of semi-global mechanisms for primary pyrolysis of lignocellulosic fuels",*Journal of Analytical and Applied Pyrolysis*, 47, 43 – 64, 1988.

[4] AFNOR, "EN 1995-1-2, Design of timber structurePart 1-2: General structural fire design", *AFNOR*, 2004.

[5] CAST3M-2009, Finite element software, CEA, www-cast3m.cea.fr, 2009.

[6] Knudson R.M, "Performance of structural wood members exposed to fire", *Forest Products Journal*, 25 (2), 1975.

[7] Najafi S.K., Bucur V. and Ebrahimi G., "Elastic constants of particleboard with ultrasonic technique", *Materials Letters*, 59, 2039 – 2042, 2005.

[8] Tabaddor M., "Thermal and mechanical finite element modeling of wood floor assemblies subjected to furnace exposure", *Underwriters Laboratories*, 2008.

8th International Conference on Structures in Fire
Guo-Qiang LI, Venkatesh K. R. KODUR, Shou-Chao JIANG, Jian JIANG, Su-Wen CHEN, Guo-Biao LOU (Eds.)
Shanghai, China, June 11-13, 2014

A NOVEL TEST METHOD FOR MATERIALS AND STRUCTURES IN FIRE

Cristian Maluk* and Luke Bisby*

*BRE Centre for Fire Safety Engineering, School of Engineering, The University *of* Edinburgh
e-mails: c.maluk@ed.ac.uk, luke.bisby@ed.ac.uk

Keywords: H-TRIS, Thermal exposure, Heat flux, Time-temperature curve, Fire resistance test

Abstract. *A novel testing method/apparatus named the Heat-Transfer Rate Inducing System (H-TRIS) has been developed to control the time-history of incident heat flux imposed on test specimens. H-TRIS can be used to simulate a broad range of thermal exposures, from those encountered in a standard fire resistance test in a furnace to those encountered in any real (or design) fire in a real building. This is made possible by implementing a rational understanding of the fundamentals of heat transfer and a paradigm shift (from a structural fire engineering perspective) in how standard thermal exposures are prescribed; i.e. not by a single temperature in a furnace (e.g. gas temperature) but rather by a time-history of incident (or absorbed) heat flux. H-TRIS enables comprehensive experimental thermal studies with high statistical confidence and repeatability relative to furnace testing at comparatively low economic and temporal costs.*

1 INTRODUCTION

Fire safety considerations in the design of buildings' structural systems have traditionally been based on the concept of compliance, wherein the 'design' of individual structural elements is required to comply with prescribed fire safety 'acceptability' criteria defined by the regulatory authority having jurisdiction [1]. More than a century of research and development in structural fire testing has converged into widespread use of standard fire resistance tests (i.e. large scale furnace tests) as the sole means of experimentally fire rating (in the time domain of 'fire resistance') the 'performance' of a structural element exposed to a 'standard' fire (furnace time-temperature curve). The standard fire resistance test replicates only one presumed worst-case fire, despite the infinite potential fires that could occur in reality.

The current compliance testing approach results in a simplified, comparative regulatory system in which the true performance of materials and structural systems in real fires is rarely known or acknowledged. While real structures fail only rarely in fires, when they do fail it is almost always for reasons that would not be expected on the basis of standard fire resistance testing; this compellingly suggests that the complexities of real fires in real buildings are not captured in standard fire tests [2].

> *"Most of the existing tests had to be developed by trial and error, and they are open it is true to the objection that they do not truly indicate how a material will behave in an actual fire. They may tell us which is the better of two materials, but not whether one or both is good enough for the job."* [3]

2 STANDARD FIRE RESISTANCE TEST

At the turn of the 20th Century, efforts were made both by US and European testing organizations, as well as by other stakeholders involved in the building construction community, to define a uniform 'standard' fire resistance test. As indicated in 1917 by Ira Woolson, then Chairman of the National Fire Protection Association's (NFPA) Committee on Fire-Resistive Construction, the overarching goal of these efforts was to *"unify all fire tests under one single standard and remove an immense amount of confusion within the fire testing community"* [4].

2.1 Thermal exposure

Once fire testing organizations had developed standards for 'harmonizing' the thermal exposure (i.e. furnace time-temperature curve) to be imposed during standard fire resistance tests, the fire testing community (industry) experienced considerable growth in the number and cost of standard fire testing facilities around the world; and thus developed considerable industry inertia. Efforts aimed at further standardizing the thermal exposure experienced by tested elements during furnace tests continue to present day; for instance by seeking to regulate the materials used for furnace linings, the instruments used to control furnace temperatures, and/or the limiting gas pressure levels inside furnaces [5]. Nevertheless, current guidelines for the design and operation of fire resistance testing furnaces present relatively few requirements which aim, but which are insufficient, to truly standardize thermal exposures.

Considerable differences remain in the design, construction, and operation of fire resistance testing furnaces globally (e.g. dimensions, lining materials, positions of burner outlets, procedures to control the burner operation, fuel type, etc.) with minimal standardization schemes for both construction and operation [6]. As a result, most considerations taken into account during the design, construction and operation of a fire testing furnace are based on past experience accumulated by furnace manufacturers, rather than on a standard specification for furnace design and construction to ensure that all furnaces are as 'equal' as possible. This inequality between furnaces has consequences for the heat transfer to the test specimen that occurs in standard furnace tests [5]. The thermal exposure to which a structural element is exposed in a standard fire resistance test is defined in terms of a prescribed time-temperature curve. Technical and philosophical discussions on how and where temperatures (gas or otherwise) are measured and controlled in standard fire test furnaces are countless in the available literature [e.g. 7-10].

While a thorough analysis of heat transfer processes in furnaces is avoided in the current paper, two noteworthy issues must be raised that are commonly misunderstood (typically by structural engineers) in regards to the definition of thermal exposure: first, that temperature variation is the result of a thermal energy exchange between a source (e.g. the 'fire') and a receiver (e.g. the structural element); and second, that the amount of thermal energy exchanged is directly dependent on the thermal conditions of both the *source* and the *receiver* [5]. The consequence of these realities is that it is fundamentally incorrect to control the amount of thermal energy imposed on a surface solely by controlling a single temperature (e.g. gas temperature). Two structural elements, made out of different materials but tested in the same furnace controlled to follow the same time-temperature curve are unlikely to yield a fair comparison of their performance during some presumed identical compartment fire.

> *"It is rather disturbing that fire resistance ratings developed for various building elements may depend to quite an extent on the laboratory conducting the tests."* [11]

The fact that that the *size* or *severity of the fire* defined in terms of a furnace time-temperature curve negates the potential for standard fire resistance tests to impose a truly standardised thermal exposure. By prescribing a single temperature (e.g. gas temperature) in the furnace, the incident heat flux imposed on a test specimen – in essence the *size of the fire* – can only be indirectly controlled [5]. Whilst the above might seem obvious to those in the fire science community, within structural fire testing it is generally accepted that controlling the time-history of temperature inside a furnace (time-temperature curve) is equivalent to controlling the thermal exposure to the element being tested. This neglects the complex thermal interactions between the specimen, gases, linings, and potential presence of luminous flames inside the furnace [5].

2.2 Mechanical loading and restraining conditions

The mechanical conditions imposed on elements tested in standard fire resistance tests, which can differ greatly from those in real building, significantly impacts upon their performance during fire.

Mechanical boundary conditions imposed during a fire resistance test may be designed to provide restraint against thermal expansion, contraction, and/or rotation, or to offer freedom of movement. Available furnaces' dimensions limit the size of the structural system (or elements) being tested, resulting in the tests being conducted on isolated elements typically smaller than 4 m in maximum dimension (with a few notable exceptions internationally). Most standard fire resistance tests are executed under 'fully fixed' or 'fully free' mechanical conditions, both being a technical challenge to achieve in practice.

> *"We no longer build by simply supporting beams on walls and yet we all carry out our fire tests in a way appropriate to this form of construction imposing vertical loads only."* [12]

Modern testing facilities make use of highly sophisticated or overly simplified techniques for applying mechanical loading to test specimens. These include hydraulic systems, mechanically automated systems, dead weights, and others. The imposed mechanical load level applied to test specimens is defined on the basis that it should provide a reasonable representation of the mechanical conditions that would be encountered by the tested element during a fire under normal in-service conditions in a real building; this is no easy task given that thermal deformations in real structures are likely to result in time-varying mechanical loads and conditions. In recent years, considerable effort has been devoted to adapting existing testing facilities with mechanical reaction frames capable of simulating, in some cases in real-time using feedback from load and displacement sensors during the test, the mechanical actions and reactions imposed on an isolated furnace-tested element from a computationally modelled full structure [2]. Such attempts have not been particularly successful, however, therefore a gradual shift in testing philosophy to large scale nonstandard fire testing, using 'real' rather than standard fires, is underway and a number of custom made non-standard testing facilities have recently come on line or are nearing completion [2].

3 REACTING TO A NEED

The standard fire resistance test was conceived in the early 1900s mainly to standardise a field that was in need of regulation. Despite more than a century of advances (mostly technical) aimed at standardizing (and rationalizing) furnace testing procedures, numerous fundamental problems remain within structural fire testing; these include high operating costs, poor repeatability, unrealistic and/or inappropriate boundary conditions, and poor statistical confidence. Kruppa and Curtat [13] have suggested that a fundamental change is needed: *"in principle, the change in the control mode implies a change in the overall heat supply to the object tested."* During experimental research studies carried out at The University *of* Edinburgh on spalling of medium scale concrete specimens [5], a novel test method was conceived and developed based on the following characteristics:

- *Impose a rational, quantifiable thermal exposure* – define thermal exposure in terms of a time-history of incident heat flux, rather than a traditional time-history of temperature (e.g. furnace gas temperature) inside a furnace; hence the *"size/severity of the fire"* is directly controlled.
- *Impose a range of thermal exposures* – alongside the development of this unique testing apparatus, an inverse heat conduction model was developed to calculate the time-history of incident heat flux which yields an equivalent thermal exposure to that experienced by structural elements under potentially any heating condition (e.g. a standard fire resistance test, large scale fire test, etc.). Alternatively, a time-history of incident heat flux can be specified using outputs from a fire model (e.g. computational fluid dynamics model, zone model, etc.).
- *Repeatability* – calibration of the test method is repeated periodically (or before each new test) to account for the specific ambient conditions on any given day, allowing a very high level of repeatability between tests, thus a good statistical confidence for research studies carried out.
- *Operate at low economic and temporal cost* – experimental fire resistance research is generally limited by the high economic and temporal costs associated with performing standard fire resistance

tests, thus few (or in most cases single) tests are performed for each test variable during any particular research project. A similar scenario is experienced within compliance-driven testing schemes.

The resulting test method/apparatus, named the Heat-Transfer Rate Inducing System (H-TRIS), is the result of a mental shift associated with controlling the thermal exposure not by a single temperature but rather by the time-history of incident heat flux.

4 HEAT-TRANSFER RATE INDUCING SYSTEM (H-TRIS)

Fire test control by incident heat flux is by no means a revolutionary concept; this approach has been widely implemented by various researchers in a number of studies within the broader fire science community [e.g. 14]. Furthermore, various researchers have suggested replacing the prescribed time-history of temperature used in standard fire resistance tests with a more rational definition of thermal exposure [5].

Commercially available testing apparatuses such as the Cone Calorimeter and the FM Global (Factory Mutual Research Corporation) Fire Propagation Apparatus (FPA) are widely used to test small scale material specimens by controlling the incident heat flux imposed on a tested specimen. Arrays of fixed or mobile gas- or propane-fired radiant panels have formerly been used for testing various construction materials by controlling (or rather, imposing) a chosen incident heat flux [5]. However, in all of these prior cases the imposed time-history of incident heat flux has been calculated either based on a somewhat arbitrarily defined presumed ‘realistic’ condition, or based on a complicated heat transfer model of the conditions within a standard fire resistance testing furnace. The following sections provide a brief description of an inverse heat conduction model used to calculate the time-history of incident heat flux which yields an equivalent thermal exposure to that experienced by structural elements under potentially any heating condition, as well as the technical aspects of H-TRIS (Figure 1).

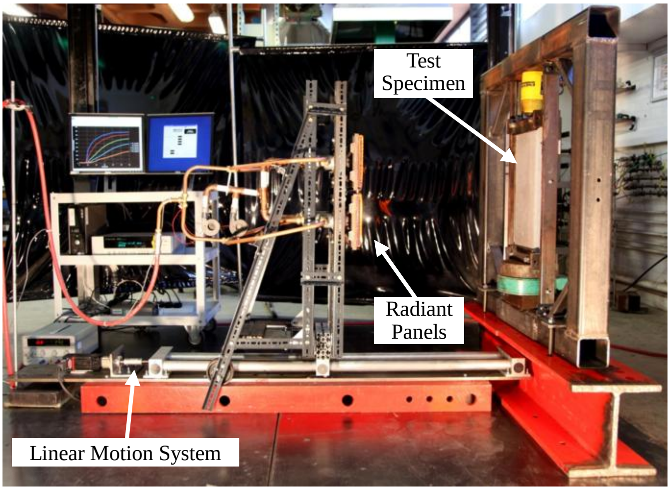

Figure 1. H-TRIS (side elevation) in its current incarnation.

4.1 Inverse heat conduction model

Calculation of transient boundary conditions for a thermodynamic system by inverse modelling is frequently performed for a number of applications in various different fields of study [5]. In its most rudimentary form, an inverse heat conduction model calculates the time-history of a thermal boundary condition based on through-thickness temperature measurements taken within a body during heating. The particular model applied herein calculates the time-history of incident heat flux (imposed with H-TRIS on the target exposed surface of the test specimen) that yields an equivalent time-history of through-thickness temperatures for identical specimens exposed to heating in a standard fire resistance test. The procedure can potentially be used to calculate the time-history of incident heat flux which yields any time-history of through-thickness temperatures for any source of heating on essentially any material with reasonably well characterized thermal properties [5].

Calculations of incident heat flux are made by considering the particular thermal conditions encountered when testing a specimen with H-TRIS at the exposed and unexposed surface of the test specimens. The time-history of incident heat flux at the target exposed surface is calculated as:

$$\varepsilon \cdot \dot{q}''_{inc} = \dot{q}''_{abs} + \dot{q}''_{rad} + \dot{q}''_{conv} \tag{1}$$

Where $\dot{q}''_{abs}$ is the time-history of absorbed heat flux which yields the time-history of through-thickness temperatures for identical specimens exposed to heating in a standard fire resistance test (or other source of heat), and $\dot{q}''_{rad}$ and $\dot{q}''_{conv}$ are the losses due to radiation and convection at the exposed surface, respectively. Convective losses are determined using an empirical correlation for free convection from a heated surface. Figure 2 presents the results (outputs in terms of the calculated absorbed heat flux based on through thickness temperature measurements in the materials) of an inverse model carried out for steel, concrete and Aircrete® test specimens during a furnace test. Aircrete® is a lightweight material made from pulverised fuel ash (80%), which presents similar thermal properties to those of a furnace's linings. Figure 2 demonstrates a potentially important material dependency of thermal exposure in fire testing; i.e. different materials tested under the same time-temperature curve do not experience the same time-history of absorbed (nor incident) heat flux. This confirms that the idea of a prescribed time-temperature curve for fire testing of different materials is fundamentally flawed. A thorough experimental validation of H-TRIS' ability to replicate the through-thickness temperature of various test specimens and various materials during a furnace test has previously been performed and is presented elsewhere [5].

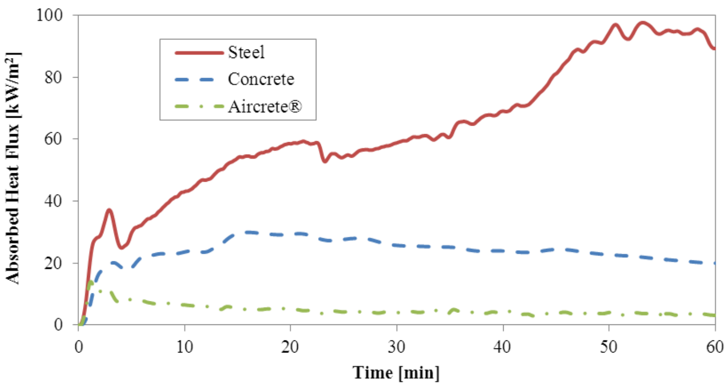

Figure 2. Calculated absorbed heat flux experienced by a range of materials during a standard fire resistance test, calculated using an inverse heat conduction model.

4.2 Technical aspects of H-TRIS

Practically speaking, H-TRIS uses a mobile array of propane-fired radiant panels along with a mechanical linear motion system (see Figure 1). The radiant panels' position is actively controlled to uniformly expose a target exposed surface (200 mm × 400 mm in the tests described herein) on test specimens to a predefined time-history of incident heat flux [5]. This allows for minimum (farthest position to the target exposed surface) and maximum (closest position to the target exposed surface) incident heat fluxes of about 3 and 100 kW/m^2, respectively. Work is currently underway to develop a new version of H-TRIS, which will be capable of achieving multiple and larger exposed surfaces, as well a higher maximum incident heat fluxes sufficient to simulate hydrocarbon and tunnel fire exposures [15]. Additionally, H-TRIS is complemented with a purpose built structural loading frame designed to apply constant or variable axial compressive loads on test specimens during heating. In its current incarnation, specimens can be loaded in axial or bi-axial compression whilst being exposed to heating; up to a maximum capacity in each axis of 150 kN.

5 RESEARCH STUDIES

To date, numerous research-driven as well as product development projects have been executed or are scheduled with H-TRIS; these have tested a broad range of building construction materials (e.g. concrete, intumescent fire protection coatings, plaster and magnesium oxide board, glass wall panels, and cross-laminated timber panels). A brief description of some of these exemplar projects is given in the following sections.

5.1 Concrete

Although compliant with available testing standards, a study performed by the authors [5] showed that non-homogeneity of the temperature distribution inside a furnace (5 to 10% deviation during the first 30 minutes of the test), appeared to have an important influence on the occurrence of heat-induced concrete spalling of large scale prestressed high-performance self-consolidating concrete (HPSCC) slabs tested simultaneously during a single standard fire resistance test. Fair comparison of spalling test results is therefore questionable if thermal exposure variability is not considered. Consequently, neither a rational understanding of heat-induced concrete spalling nor an ability to prevent it during real fires is likely to be achieved only by performing additional standard fire resistance tests in furnaces.

A comprehensive yet practical experimental study of heat-induced concrete spalling was carried out using H-TRIS, with emphasis on studying the use of polypropylene (PP) fibres of various types, sizes, shapes, and dosages to mitigate heat-induced concrete spalling. Eleven different high-performance, high-strength, self-compacting concrete (HPSCC) mixtures were evaluated (Figure 3).

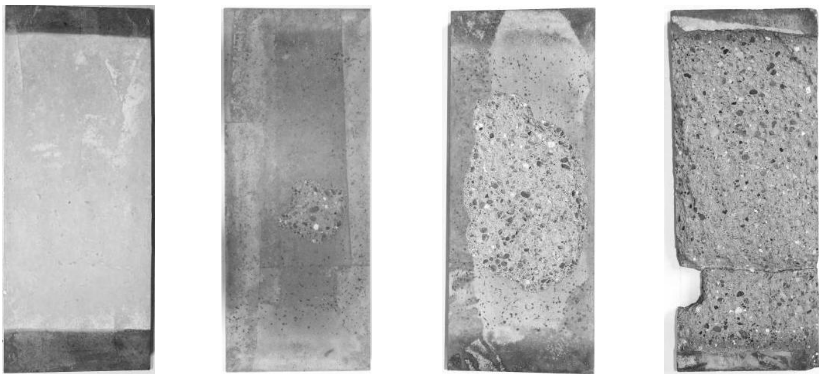

(a) no spalling (b) 100 g spalled (c) 1503 g spalled (d) 3095 g spalled

Figure 3. Post-test photographs of concrete specimens tested with H-TRIS [5]. Various severities of spalling observed for various concrete mixes and PP fibre doses.

H-TRIS allowed parameters and conditions that are known to promote (or avoid) the occurrence of spalling to be repeatable and inexpensively investigated. Unlike traditional furnace tests, tests carried out with H-TRIS enabled precise quantification of the time to first spalling, the mass of concrete spalled (see Figure 3), and the accumulated 'absorbed heat density' (i.e. the area under the time-absorbed heat flux curve) of the tested specimens. This last parameter could potentially allow for rational comparison between specimens tested under various thermal exposures (i.e. tested under different time-histories of incident heat flux). The occurrence of heat-induced concrete spalling for specimens tested with H-TRIS was in good agreement (in terms of time-to-spalling) with identical concrete specimens tested during a set of full scale fire resistance tests previously performed by the authors [16]. All tests in this study (>80 tests in total) were performed during a total period of only 30 days, demonstrating the low temporal costs involved in using H-TRIS for simulating thermal exposures of concrete specimens during furnace tests; this would likely have taken a year or more in a standard fire testing furnace.

5.2 Intumescent coatings

Results from an experimental study on intumescent (reactive) coatings using H-TRIS allowed examination of the effective variable thermal conductivity (the basis for the design of protected structural steel in fire) of a commercially available intumescent coating when subjected to various time-histories of incident heat flux. Test results showed that the heating rate and thickness of the coating do not drastically affect the development of the coating's effective thermal conductivity, leading to a proposal for a simplified method for experimentally characterizing and specifying coating requirements and/or for performing heat transfer design calculations when designing to protected structural steel elements in non-standard heating regimes [17]. Such variable thermal conductivities are essential for rational performance-based structural fire safety design of intumescent protected steel framed buildings.

5.3 Timber

The behaviour of glued, nailed, and dowel laminated timber has been experimentally evaluated by testing medium scale timber panel specimens with H-TRIS; in this case programed to replicate the thermal exposure experienced by equivalent timber specimens during a standard fire resistance test in a fire resistance testing furnace. Three time-temperature curves were evaluated in this study: standard cellulosic, smouldering, and hydrocarbon [15] in addition to a number of ad-hoc time varying incident heat flux scenarios intended to replicate thermal exposure arising from rationally defined t-squared design fires. This study has demonstrated that once established, the Eurocode [18] timber charring rate of 0.65mm/min is broadly correct for the various different heat flux curves, however the initiation of charring may vary and in some cases the charring rate may be unconservative. The charring rate dependency on thermal exposure is indispensable to apply alternative design fire scenarios, particularly travelling fire scenarios [19], in the rational performance-based structural fire safety design of cross laminated timber (CLT) buildings.

6 CONCLUSIONS

The standard fire resistance furnace test has traditionally been used for assuring regulatory compliance of structural elements and assemblies, and in countless cases also for scientific understanding of experimental structural response to fire. As the fire engineering community drives towards the acceptance and implementation of performance based structural fire engineering designs [5], it is fundamentally incorrect to depend entirely on conventional fire testing and rating (or equivalent) of structural and non-structural systems as the sole motivation (and experimental tool) for product manufacturers, designers, regulators and researchers.

H-TRIS is an experimental tool that allows researchers to conduct studies with high repeatability and quantifiable (and rational) thermal boundary conditions, all at low economic and temporal cost. This will potentially allow for the execution of comprehensive experimental studies with high statistical confidence relative to furnace testing. H-TRIS can be used to replicate a broad range of thermal exposures, from those encountered in a standard fire resistance test to those encountered in any 'real' design fire.

It is hoped that forthcoming research projects and developments around H-TRIS will promote an industry-wide move away from the modern pass/fail large scale furnace testing environment, characterized by its high operating costs, poor repeatability, unrealistic and/or inappropriate boundary conditions, and poor statistical confidence.

REFERENCES

[1] Building Regulations (2010). Approved Document B: Volume 2 – Buildings Other than Dwelling Houses. *National Building Specification*, 170 pp.

[2] Bisby L, Gales J., and Maluk C. (2013). A Contemporary Review of Large-scale Non-standard Structural Fire Testing. *Fire Science Reviews*, 2 (1), 27 pp. (Invited)

[3] Clarke S.H. (1957). Twenty Five Million Pounds go up in Smoke. *Fire Research Notes 286 – Joint Fire Research Organization Radio Talk*, 4 pp.

[4] NFPA (1917). Report of the Committee on Fire-Resistive Construction, *Proceedings of the 21st National Fire Protection Association Annual Meeting*, Boston, US, 391-413. Available via http://www.nfpa.org.

[5] Maluk C. (2014). Development and Application of a Novel Test Method for Studying the Fire Behaviour of CFRP Prestressed Concrete Structural Elements. PhD Thesis, *The University of Edinburgh*, UK, 442 pp.

[6] CEN (2000). Eurocode: Fire Resistance Tests – Part 3: Verification of Furnace Performance (EN 1363-3:2000). *European Committee for Standardization*, Brussels, 24 pp.

[7] Harmathy T.Z. and Lie T.T. (1970). Fire Test Standard in the Light of Fire Research. . *Fire Test Performance – ASTM Special Technical Publication 464*, 85-97.

[8] Law M. (1981). Designing Fire Safety for Steel – Recent Work. *Proceedings of the ASCE Spring Convention, American Society of Civil Engineers*, New York, 16pp.

[9] Wickström U. (1986). A Proposal Regarding Temperature Measurements in Fire Test Furnaces. *Technical Report from the Nordtest Project 355-82*, 37 pp.

[10] Torero J.L. (2013). Structures in Fire or Fires in Structures? Assessing the True Performance of Structures in Fire. *Proceedings of the 5th International Conference on Structural Engineering*, Cape Town, South Africa, 1919-1923.

[11] Mehaffey J.R. and Harmathy T.Z. (1981). Assessment of fire resistance requirements. *Fire Technology*, 17 (4), 221-237.

[12] Lawson J.R. (1968). Fire Research and Its Impact on Society. *Fire Research Station (Note No.711)*, UK, 38 pp.

[13] Kruppa J. and Curtat M. (1995). Comments on Wickström's "The Plate Thermometer – A Simple Instrument for Reaching Harmonized Resistance Tests”. *Fire Technology (letter to editor)*, 31 (1), 84-90.

[14] Robertson A.F. and Genensky S.M. (1956). Theoretical Heat Transfer Scaling Relationships for Fire Endurance of Reinforced Concrete. *National Bureau of Standards Report #4854*, US, 32 pp.

[15] CEN (1999). Eurocode: Fire Resistance Tests – Part 2: Alternative and Additional Procedures (EN 1363-2:1999). *European Committee for Standardization*, Brussels, 20 pp.

[16] Terrasi G., Bisby L., Barbezat M., Affolter C., and Hugi, E. (2012). Fire Behavior of Thin CFRP Pretensioned High-Strength Concrete Slabs. *Journal of Composites for Construction*, 16 (4), 381–394.

[17] Elliott A., Temple A., Maluk C., and Bisby L. (2014). Novel Testing to Study the Performance of Intumescent Coatings under Non-Standard Heating Regimes, *Proceedings of the 11th International Symposium on Fire Safety Science (IAFSS)*, Canterbury, New Zealand, 14 pp.

[18] CEN (2004). Eurocode 5: Design of Timber Structures – Parts 1-2: General rules – Structural fire design (EN 1995-1-2:2004). *European Committee for Standardization*, Brussels, 84 pp.

[19] Stern-Gottfried J. (2011). Travelling Fires for Structural Design. PhD Thesis, *The University of Edinburgh*, UK, 166 pp.

8th International Conference on Structures in Fire
Guo-Qiang LI, Venkatesh K. R. KODUR, Shou-Chao JIANG, Jian JIANG, Su-Wen CHEN, Guo-Biao LOU (Eds.)
Shanghai, China, June 11-13, 2014

EVALUATING DESIGN GUIDANCE FOR INTUMESCENT FIRE PROTECTION OF CONCRETE FILLED STEEL HOLLOW SECTIONS

David Rush*, Luke Bisby* and Allan Jowsey**

* BRE Centre for Fire Safety Engineering, University of Edinburgh, Edinburgh, UK
e-mails: d.rush@ed.ac.uk, luke.bisby@ed.ac.uk

** International Paint Ltd, AkzoNobel, Newcastle, UK
e-mail: allan.jowsey@akzonobel.com

Keywords: Composite columns, Intumescent fire protection, Forensic analysis, Section factor, Design

Abstract. *Design of intumescent protection systems for concrete filled structural steel hollow (CFS) sections in the UK typically requires three input parameters: (1) a required fire resistance rating; (2) an 'effective' section factor; and (3) a limiting steel temperature for the hollow section. While the first of these is generally prescribed in building codes, the latter two require engineering judgement. This paper examines results from furnace tests on 21 CFS sections, 12 of which were protected with intumescent coatings by applying current UK design guidance. The protected sections demonstrate highly conservative fire protection under standard fire exposure; this is not typically observed for protected unfilled steel sections. Possible causes of the observed conservatism are discussed. It is demonstrated that the assumptions used in design guidance to calculate the effective section factor for protected CFS columns are physically unrealistic and inaccurate. Interim design guidance is given.*

1 INTRODUCTION

Concrete filled steel hollow structural sections (CFS) are increasingly specified in the design of multi-storey buildings; these often require structural fire resistance (F.R.) ratings of two hours or more. CFS sections may provide adequate fire resistance without the need for applied fire protection due to load sharing between the steel tube and concrete core. However in some cases available design guidance [e.g. 1] may show that adequate fire resistance cannot be achieved without protection; in these cases external fire protection must be applied, and in the UK the preferred method is intumescent coatings. In practice, design of intumescent fire protection systems for CFS sections is difficult for three reasons: (1) there is a paucity of test data on the performance of intumescent coatings when applied on CFS sections; (2) quantifiably observing the comparatively complex thermal response intumescent coatings during fire resistance tests in furnaces is difficult; and (3) fundamental differences exist between the thermal gradients in unfilled and filled hollow sections. This paper assesses current UK fire resistant design guidance for intumescent fire protection systems applied on CFS sections and identifies causes of conservative outcomes observed in a series of furnace tests on protected and unprotected CFS columns.

2 SPECIFICATION OF INTUMESCENT COATINGS FOR CFS SECTIONS

Intumescent protection (i.e. design DFTs) of structural steel is typically performed using three input parameters: (1) the required F.R.; (2) a *section factor*, the ratio of the section's heated perimeter, H_p, to its cross sectional area, A; and (3) the assumed steel *limiting temperature* (usually 520 °C). These are used in conjunction with empirically determined, product specific, design tables to determine the required coating DFT. The product specific design tables are highly optimised, based on many large scale furnace tests on *plain* structural steel sections (i.e. not CFS's) with various H_p/A and DFTs values.

To apply existing DFT tables for protection of CFS sections an 'effective' section factor, H_p/A_{eff}, is needed; this must incorporate the effect(s) of the concrete infill on the heating rates of the steel and on the load bearing capacity of the composite column. Equation (1) gives the current UK approach to determining the effective section factor for CFS sections. Equation (1) treats the problem by using DFT design guidance developed for unfilled steel sections but adds an 'equivalent' steel wall thickness, t_{ce} , which is dependent on the internal breadth of the section, b_i, and fire resistance time, t_{FR}, to the existing steel wall thickness, t_s, to account for the so-called 'thermal sink' effects of the concrete core, decreasing the effective H_p/A:

$$\frac{H_p}{A_{eff}} = \frac{1000}{t_{se}} = \frac{1000}{t_s + t_{ce}} \qquad \text{where} \qquad t_{ce} = \begin{cases} 0.15 b_i, & b_i < 12\sqrt{t_{FR}} \\ 1.8\sqrt{t_{FR}}, & b_i \geq 12\sqrt{t_{FR}} \end{cases} \tag{1}$$

This approach is physically unrealistic and potentially flawed on a number of grounds. Neither the physical rationale nor the theoretical or empirical basis for t_{ce} are reported in the literature. A key objective of the research presented herein was to validate (or otherwise) this approach.

3 FURNACE TESTS ON UNPROTECTED AND PROTECTED CFS SECTIONS

Twenty-one circular CFS columns, 12 protected and 9 unprotected, were exposed to the ISO-834 [2] standard fire in a fire testing furnace for 120 minutes (in most cases), see Table 1. The DFTs for the 12 protected CFS sections were prescribed using effective H_p/A_{eff} values given by Equation 1 with a presumed limiting steel temperature of 520^{o}C and a required F.R. of 90 minutes. One specimen was designed to a F.R. of 75 minutes (but tested for 120 minutes) and one was protected for 120 minutes F.R. (but tested for 180 minutes). A typical test specimen is shown in Figure 1.

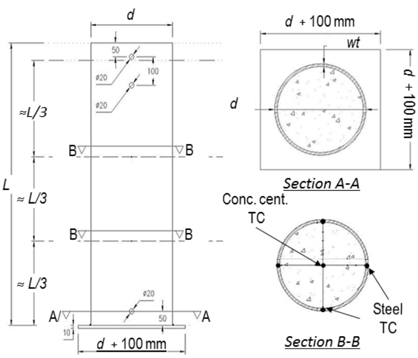

Figure 1. Specimen schematic layout.

Temperatures were recorded at two heights during testing, as shown in Figure 1. Nineteen of the tests were conducted in a full scale floor furnace whereas tests 20 and 21 were conducted in a smaller cube furnace. All specimens were constructed from Grade S355 steel sections and filled with a hybrid steel and polypropylene (PP) fibre reinforced concrete mix incorporating 40 kg/m^3 and 2 kg/m^3 of steel and PP fibres, respectively, with a compressive strength of between 46.1 and 59.4 MPa and a moisture content between 3% and 6% by mass at the time of testing. Full details of the tests are presented in [3].

4 RESULTS AND DISCUSSION

Table 1 shows the average steel tube (θ_s) and concrete core ($\theta_{c.cent}$) temperatures observed at 90 minutes and 120 minutes during testing. Figure 2 shows the average, maximum, and minimum observed steel temperatures, θ_s, for all unprotected and protected tests (excluding tests 20 and 21). The data show that: (a) the observed steel temperatures in the protected sections are well below (often by > 300^{o}C) the target design limiting temperature of 520°C at the required F.R. time; (b) the limiting temperature of 520°C was reached in only tests 20 and 21, and in both cases this occurred more than 30 minutes after the required F.R.; (c) the temperature difference between the steel tube and the concrete core was greater in unprotected sections than in those with protection; and (d) the size of the concrete core affects the temperatures observed within the steel tube; lower steel temperatures are observed with larger cores.

Table 1. Specimen details and average temperatures recorded at 90 and 120 minutes of fire exposure.

	No.	Size (d) (mm)	Wall thickness (mm)	Length (L) (mm)	F.R. (mins)	H_p/A_{eff} (m^{-1})	DFT (mm)	θ_s (°C)		$\theta_{c.cent}$ (°C)	
								90 mins	120 mins	90 mins	120 mins
Unprotected	1	323.9Ø	10	1000				875	949	121	132
	2	323.9Ø	8	1000				862	931	119	134
	3	219.1Ø	10	1400				902	981	193	377
	4	219.1Ø	8	1400				887	971	180	330
	5	219.1Ø	5	1400		N/A		889	973	178	331
	6	139.7Ø	10	1400				944	1005	684	844
	7	139.7Ø	8	1400				925	991	737	882
	8	139.7Ø (a)	5	1400				926	997	564	756
	9	139.7Ø (b)	5	1400				927	996	574	754
Protected	10	323.9Ø (a)	10	1000	90	40	3.5	204	244	60	86
	11	323.9Ø (b)	10	1000	90	40	3.6	206	246	57	80
	12	323.9Ø	8	1000	90	42	3.48	202	238	54	76
	13	219.1Ø	10	1400	90	39	3.55	210	254	107	142
	14	219.1Ø	8	1400	90	41	3.5	204	275	114	136
	15	219.1Ø	5	1400	90	46	3.5	230	283	109	147
	16	139.7Ø	10	1400	90	44	3.53	247	320	140	170
	17	139.7Ø	8	1400	90	46	3.52	259	350	180	254
	18	139.7Ø	5	1400	90	50	3.53	264	366	137	169
	19	139.7Ø	5	1400	90	50	3.51	234	311	141	166
	20	139.7Ø	5	1400	75	52	2	461	603 [a]	179	326
	21	139.7Ø	5	1400	120	47	4.06	270	387 [b]	151	192

(a) 520°C at 106 minutes; (b) 520°C at 155 minutes and 611°C at 180 minutes.

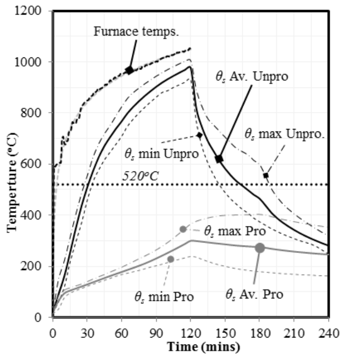

Figure 2. Unprotected and protected steel tube temperatures for CFS sections observed in furnace tests.

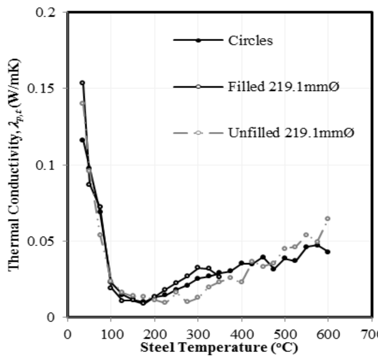

Figure 3. The intumescent variable $\lambda_{p,t}$ on filled (tests herein) and unfilled (data from industry partner) CFSs.

It is clear from Figure 2 and Table 1 that use of current guidance and DFT design data from unfilled sections to prescribe DFTs for CFS sections results in conservative steel temperatures in furnace tests. Thus, if current guidance is used to prescribe DFTs for CFS sections excessive fire protection will be applied; whilst conservative this is non-optimal. The conservatism could be caused by: (1) inherently conservative DFTs in the tabulated data from unfilled section tests; (2) changes in the response, and thus the effective thermal conductivity, of the intumescent coatings when applied to sections with different thermal masses; or (3) incorrect or unrealistic calculation of H_p/A_{eff} for CFS sections.

4.1 Conservative DFT tabulated data

Available product specific tabulated DFTs are highly optimized for protecting plain steel sections. Furnace tests have shown that in most cases the designed limiting temperatures upon which the DFTs for design are based are typically reached at, or shortly after, the required F.R. times for protected unfilled sections. For instance, a 219 × 16 mm Ø circular hollow section designed for fire resistances of 90 minutes reached a limiting temperature of 520^{o}C, at 92 minutes. Inherently conservative design tables for the plain steel sections are not considered likely to be the cause of the conservatism observed in Figure 2.

4.2 Variable thermal conductivity of protection

The variable effective thermal conductivity of the intumescent protection was assessed according to guidance given in BS EN 13381-8 [4] to investigate whether the observed conservatism in Figure 2 is due to changes in the response of the coating, for substrates of significantly different thermal mass:

$$\lambda_{p,t} = d_p \cdot \frac{A_{eff}}{H_p} \cdot c_s \cdot \rho_s \cdot \left(\frac{1}{(\theta_t - \theta_{s,t}) \cdot \Delta t} \right) \cdot \Delta\theta_{s,t} \tag{2}$$

$\lambda_{p,t}$ is the variable effective thermal conductivity; d_p is the protection DFT; A_{eff}/H_p is the inverse of the calculated effective section factor, H_p/A_{eff}; c_s and ρ_s are the specific heat capacity and density of steel, respectively; θ_t is the furnace temperature; $\theta_{s,t}$ is the steel tube temperature; Δt is the analysis time step; and $\Delta\theta_{s,t}$ is the change in steel tube temperature during a time step. Figure 3 shows the calculated variable effective thermal conductivity, $\lambda_{p,t}$ (Equation (2)), for the same intumescent protection coating on all of the protected CFS circular sections (tests 10 to 21); for the protected 219.1 mm Ø *filled* CFS sections (tests 13 to 15); and for *unfilled* 219.1 mm Ø tubes. This shows that increasing the thermal mass of the CFS by filling with concrete has no obvious impact on the variable insulating response of the coating, and therefore that the conservatism seen in Figure 2 is unlikely to be a result of Cause (2) postulated above.

4.3 'Effective' section factors for CFS sections

To assess the hypothesis that calculation of the effective section factor for CFS sections based on Eq. 1 is flawed, and to determine whether improvements can be made, the development of the current H_p/A_{eff} guidance (Equation (1)) must be examined.

4.3.1 Development of current guidance

Edwards [5] developed the existing H_p/A_{eff} guidance (Equation (1) [6]) with three assumptions: (1) CFS sections can be treated as hollow steel tubes in which the concrete core provides an equivalent additional thickness of steel wall, using an empirical equation based on its required fire resistance time; (2) the effective section factor for unprotected CFS sections can be determined in the same manner as protected CFS sections as for protected versus unprotected unfilled sections; and (3) the increase in steel temperature for an unprotected steel hollow section, or CFS section using effective properties, can be calculated using an energy balance equation given in BS EN 1993-1-2 [7]:

$$\Delta\theta_{s,t} = \frac{\dot{h}_{net}}{c_s \cdot \rho_s} \cdot \frac{H_p}{A} \cdot \Delta t \tag{3}$$

The increase in steel temperatures, $\Delta\theta_{s,t}$, during a time interval, Δt, is determined based on the section factor, H_p/A, the net heat flux, $\dot{h}_{net}$, and the thermal capacity of the steel, $c_s \cdot \rho_s$. Edwards [5] used data from six standard furnace tests on unprotected CFS columns to determine an *instantaneous* effective section factor, H_p/A_{eff} (exp), at each instant in time by rearranging Equation (3), giving:

$$\frac{H_p}{A_{eff}}(\exp) = \frac{\Delta\theta_{s,t} \cdot c_s \cdot \rho_s}{\dot{h}_{net} \cdot \Delta t} \tag{4}$$

The density of steel is taken as ρ_s = 7850 kg/m^3, and the specific heat of steel is taken as c_s = 473 + 20.1 $\cdot(\theta_s/100)$ + 3.81 $\cdot(\theta_s/100)$ up to a temperature of 800^{o}C, after which a constant value of 877.6 J/kg K [5]. Edwards [5] uses the BS EN 1991-1-2 [8] method for calculating $\dot{h}_{net}$, where the net heat flux is the sum of the radiative and convective fluxes. Importantly, a resultant emissivity of 0.32 is assumed [5].

From test data it was determined that the instantaneous effective section factor, H_p/A_{eff} (exp), varied with time during a furnace test. This is in contrast with unfilled steel sections in which the section factor remains constant due to the high thermal conductivity of steel which yields a nearly uniform temperature profile throughout the section. Using the calculated H_p/A_{eff} (exp), Edwards [5] calculated the apparent instantaneous thickness of the steel tube, t_{se}, and thus the apparent effective increase in the steel tube thickness resulting from the concrete core, t_{ce}; how this led to Equation (1) is not clear.

4.3.2 H_p/A_{eff} (exp) for unprotected CFS sections

Using Edwards' process [5] it is possible to calculate the instantaneous H_p/A_{eff} (exp) for the 12 unprotected CFS sections of the current study listed in Table 1. To calculate H_p/A_{eff} (exp), an experimental net heat flux is required. A separate finite element heat transfer analysis on the unprotected CFS sections in Table 1 [3] determined that an assumed furnace emissivity of 0.38, along with a temperature dependent emissivity of steel (from [9]) were needed to properly model the temperatures experienced during the tests. The resultant emissivity thus varied with temperature between 0.08 for steel temperatures of 20-350^{o}C, increasing to 0.25 at 565^{o}C, and being constant at 0.25 above 565^{o}C. The temperature dependent specific heat capacity of steel was assumed based on BS EN 1993-1-2 [7].

Figure 4(a) shows a comparison of calculated instantaneous H_p/A_{eff} (exp) using Eq. 5 and Edwards' [5] theoretical H_p/A_{eff} (Th) (Equation (1)) for a typical unprotected CFS section (Test 4). It is noteworthy that: (1) the mild peak highlighted with a data marker in the H_p/A_{eff} (exp) curve coincides with a phase change in the steel at 735^{o}C; and (2) the considerable variability in calculated instantaneous H_p/A_{eff} (exp) during the first 30 minutes of heating is due to the imperfect, variable control of furnace temperatures.

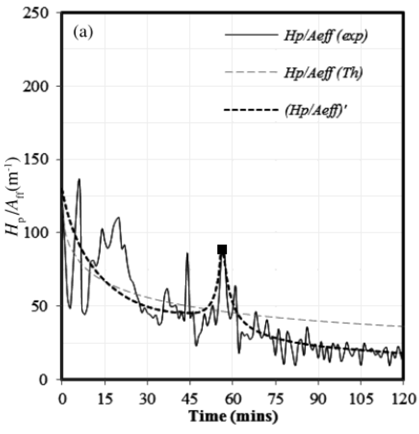

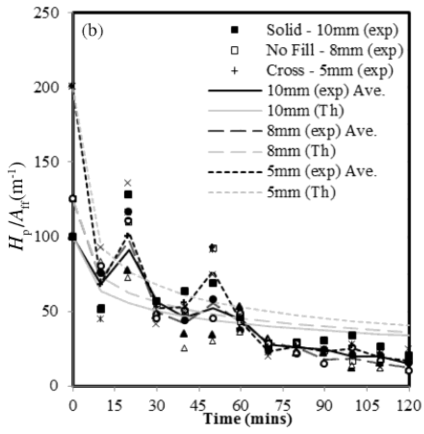

Figure 4. Instantaneous H_p/A_{eff} (exp) and Edwards' [10] effective H_p/A_{eff} (Th) for (a) a representative section (test no. 4) and (b) for all unprotected tests listed in Table 1, with data partitioned by steel wall thickness.

Figure 4(b) shows the instantaneous H_p/A_{eff} (exp) values calculated at 10 minute intervals throughout the tests, and shows that the instantaneous H_p/A_{eff} (exp) values are generally slightly lower at a given fire exposure time than Edwards' H_p/A_{eff} (Th). Figure 4(b) also shows that the 'effective' contribution of the concrete core varies with time, due to the steep thermal gradients in the unprotected CFS sections that would not exist in hollow steel tubes. Larger concrete cores will have more pronounced thermal gradients that persist for longer durations of fire exposure; the contribution of the core thus also depends on its size – a factor that Edwards' guidance fails to account for.

4.3.3 Concrete core size and theoretical effective H_p/A_{eff} values

To calculate the instantaneous H_p/A_{eff} for unprotected CFS sections in a physically realistic manner the effect of the concrete thermal gradients and core size need to be incorporated. Equation 5 proposes a new method to calculate the instantaneous section factor, $(H_p/A_{eff})'$, by converting the concrete core into an equivalent *area* of steel based on the size of the core, A_c, the ratio of the respective heat capacities of concrete and steel, and an empirically determined concrete core efficiency factor, η. Using the instantaneous H_p/A_{eff} (exp) calculated from the tests in Table 1 as inputs for Equation 5 (i.e. H_p/A_{eff} (exp) = $(H_p/A_{eff})'$), values of the core efficiency factor, η, can be calculated during each time interval as follows:

$$\left(\frac{H_p}{A_{eff}}\right)' = \frac{H_p}{A_s + \eta \cdot \dfrac{(c_c \cdot \rho_c)}{(c_s \cdot \rho_s)} \cdot A_c} \tag{5}$$

In the above equation $c_c = 1000$ J/kg^{o}C , $\rho_c = 2300$ kg/m^3, c_s is the temperature dependent relationship described in Section 3.3.1 (4) of EC4 [1] to account for the phase change in steel, and $\rho_s = 7850$ kg/m^3. Figure 5(a) plots η against fire exposure time, t_{furn}, for all unprotected sections in Table 1. The relationship between η and the furnace time, t_{furn}, is approximately linear; however with considerable variability due to the measured steel and furnace temperature change being small and measured with a resolution of 1^{o}C at 60 second intervals. If it is assumed that the relationship between η and fire exposure time, t_{furn}, is linear, then a larger gradient of η/t_{furn} is found for smaller internal breadths of concrete, as expected given that smaller cores have less thermal mass and will heat up more rapidly. The internal breadth, b_i, of a CFS section can therefore be compared to the gradient η/t_{furn}, as shown in Figure 5(b) to give a relationship for η/t_{furn} for circular sections based on the internal breadth of the concrete core.

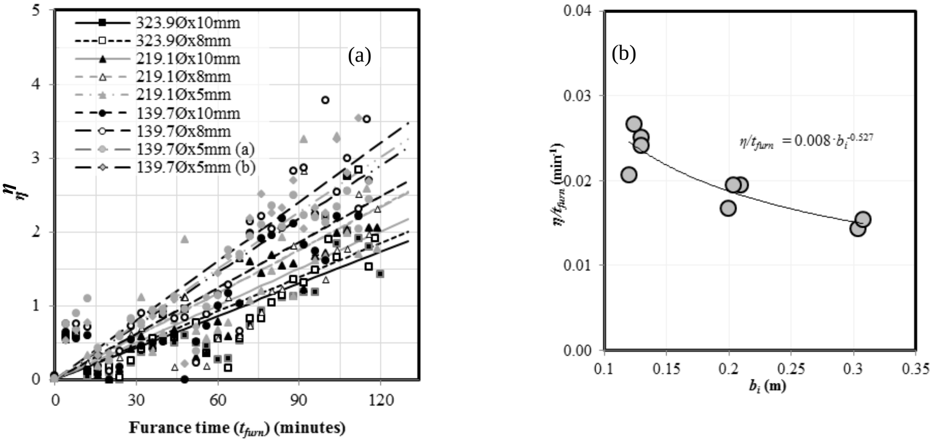

Figure 5. (a) Variation of core efficiency factor, η, with furnace exposure time, t_{furn}, for an assumed linear relationship; and (b) relationship of η/t_{furn} to b_i.

Instantaneous theoretical $(H_p/A_{eff})'$ values can then be calculated with respect to time using η values calculated from Equation 6, with an iterative process involving calculation of the change in steel temperature using Equation 3. Figure 4(a) compares the variation of both the instantaneous (H_p/A_{eff})', H_p/A_{eff} (*Th*) (Equaton 1), to the instantaneous H_p/A_{eff} (exp) calculated from Test 4 data (Equation 4) with time; this shows that the instantaneous (H_p/A_{eff})' is an accurate and more realistic predictor of the instantaneous H_p/A_{eff} (exp). It is noteworthy that the instantaneous (H_p/A_{eff})' at 60 minutes is counter intuitively higher than the value at 45 minutes due to a peak caused by the phase change in steel at about 735°C.

η can be expressed in terms of the internal breadth, b_i, and time of furnace exposure, t_{furn}, as:

$$\eta = 0.0080 \cdot b_i^{-0.527} \cdot t_{furn} \tag{6}$$

4.2.4 Instantaneous (H_p/A_{eff})' and design

The instantaneous (H_p/A_{eff})' calculation (Equation 5) is a superior predictor of the observed instantaneous effective section factor for unprotected CFS sections during furnace exposure. However, (H_p/A_{eff})' only calculates the effective section factor values at one specific instant in time, and does not account for the full time history effect of the concrete on the overall heat transfer. The temperatures experienced by the steel tube of an unprotected CFS result from cumulative heating where the (H_p/A_{eff})' varies with time. Calculating steel temperatures using a single instantaneous (H_p/A_{eff})' over a period of time will result in unconservative steel temperatures and thus under-predict the amount of protection required. It is thus inappropriate to use a single instantaneous value of (H_p/A_{eff})' to calculate either the steel temperature after a given length of time or the required DFT for protection.

However, specifying intumescent coating thicknesses from tabulated DFT data requires a single effective section factor. A single time-averaged effective section factor, $(H_p/A_{eff})'_{t.ave}$, that accounts for the cumulative heating of a CFS section resulting from time dependent instantaneous (H_p/A_{eff})' values (Equation 5) must therefore be found. This must result in the same steel tube temperature when used in Eq. 3 as would be found if using the variable time dependent instantaneous (H_p/A_{eff})' values for a specific fire resistance time. By calculating $(H_p/A_{eff})'_{t.ave}$ for a series of fire resistance times, a trace of the time-averaged effective section factor, $(H_p/A_{eff})'_{t.ave}$, can be created (Figure 6(a)) for a representative unprotected test.

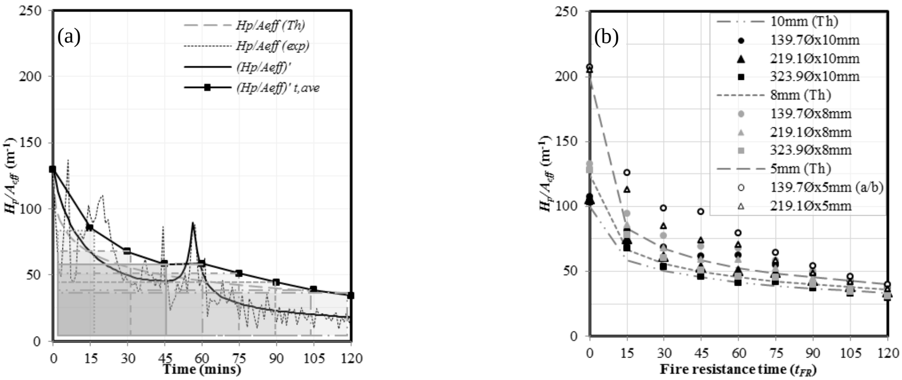

Figure 6. (a) representative comparison of (H_p/A_{eff})', H_p/A_{eff} (exp), H_p/A_{eff} (Th), and $(H_p/A_{eff})'_{t.ave}$, (219.1Øx8mm); and (b) comparison of H_p/A_{eff} (Th) and $(H_p/A_{eff})'_{t.ave}$, for unprotected tests presented herein.

Figure 6(b) compares $(H_p/A_{eff})'_{t.ave}$ to the current effective section factor guidance H_p/A_{eff} (Th) values with time of fire exposure for all unprotected CFS sections in the current study, and shows that the $(H_p/A_{eff})'_{t.ave}$ values are generally greater than the H_p/A_{eff} (Th) values at the same fire resistance time. Therefore, if the time-averaged $(H_p/A_{eff})'_{t.ave}$ values for the unprotected CFS sections are used a thicker DFT would be prescribed. Whilst the new time-averaged $(H_p/A_{eff})'_{t.ave}$ values may be more physically realistic than Edwards' approach, they appear not to address the observed conservatism in furnace tests.

Fundamental changes exist in the thermal gradients within protected CFS sections compared to those in unprotected sections. Protected sections experience a less severe thermal gradient within the core, which effectively increases the effect that the concrete core has on the effective section factor. The thermal gradient within a protected section depends on the heating rate of the steel, which is affected by: (1) the limiting temperature to which the steel is protected – higher limiting temperatures result in more severe thermal gradients in the core and diminish the effect of the concrete; (2) the required F.R. – longer F.R. produces shallower thermal gradients, increasing the effect of the concrete core; and (3) the intumescent coating performance, especially its variable effective thermal conductivity and physical charring characteristics.

Additional analytical and experimental work on protected CFS sections is needed to avoid the inherent conservatisms in the current approach for the specification of intumescent protection CFS sections, so that the effective section factor for protected CFS sections is better understood and a more rational method developed. For the time being, the authors recommend that current guidance from Eq. 1 [6] be used to determine the effective section factor for CFS columns, since the testing and analysis presented herein show this approach to be conservative.

5 CONCLUSIONS

This paper has presented results from standard furnace tests on 12 unprotected and 14 intumescent fire protected CFS sections. The following conclusions can be drawn:

(1) The current method of prescribing intumescent coating DFTs for CFS sections is overly conservative.

(2) This paper has proposed a more physically realistic instantaneous effective section factor model for unprotected CFS sections, incorporating the effects of the size of the section and the required fire resistance time. However, the new method is even more conservative for protected CFS columns.

(3) The observed conservatism in the current UK approach to specifying design DFTs results from the inappropriate application of unprotected CFS effective section factors for prescribing intumescent coatings on protected CFS sections. Until a more rational method for determining the effective section factors for protected CFS sections is developed the current guidance [6] should be used.

REFERENCES

[1] CEN, "BS EN 1994-1-2: Eurocode 4: Design of composite steel and concrete structures; Part 1-2: Structural Fire Design," Brussels, Belgium, 2005.

[2] ISO, "ISO 834: Fire resistance tests-elements of building construction," Geneva, Switzerland, 1999.

[3] D. Rush, "Fire performance of unprotected and protected concrete filled structural hollow sections," University of Edinburgh, 2013.

[4] CEN, "BS EN 13381-8:2010: Test methods for determining the contribution to the fire reistance of structural members; Part 8: Applied reactive protection to steel members," Brussels, Belgium, 2010.

[5] M. Edwards, "Reinstatment of concrete filled structural hollow section columns after short duration fires - Phase 2: Standard fire tests on full size columns.," Corby, Northants, 1998.

[6] S. J. Hicks, G. M. Newman, M. Edwards, and A. Orton, "Design guide for concrete filled columns," Corus Tubes, Corby, Northants, 2002.

[7] CEN, "BS EN 1993-1-2:2005: Eurocode 3: Design of steel stuctures; Part 1-2: General rules - Structural fire design," Brussels, Belgium, 2009.

[8] CEN, "BS EN 1991-1-2: Eurocode 1: Actions on structures; Part 1-2: General Actions - Actions on structures exposed to fire," Brussels, Belgium, 2009.

[9] T. Paloposki and L. Liedquist, *Steel emissivity at high temperatures - Research notes*. Tampere, Finland: Technical Research Centre of Finland, 2005.

8th International Conference on Structures in Fire
Guo-Qiang LI, Venkatesh K. R. KODUR, Shou-Chao JIANG, Jian JIANG, Su-Wen CHEN, Guo-Biao LOU (Eds.)
Shanghai, China, June 11-13, 2014

SELECTION CRITERIA OF FIRE SCENARIOS FOR BUILDINGS

Iolanda Del Prete*, Giuseppe Cefarelli*, Anna Ferraro*,
Emidio Nigro* and Domenico Sannino*

* Department of Structures for Engineering and Architecture, University of Naples Federico II
Via Claudio n. 21, 80125 Napoli (ITALY)
e-mails: iolanda.delprete@unina.it, giuseppe.cefarelli@unina.it, a.ferraro@unina.it,
emidio.nigro@unina.it, domenico.sannino@unina.it

Keywords: Fire scenario, EN1991-1-2, Fire risk assessment, Event tree

Abstract*. This paper is devoted to a crucial aspect of the application of Fire Safety Engineering, which is the definition of fire scenarios. FSE requires, moreover, the choice of performance levels, the choice of fire models and, generally, advanced thermo-mechanical analyses.*
In the paper the choice of the design fire scenarios is explained with reference to two possible procedures: (a) the Fire Risk Assessment (FRA), according to which the Risk, associated to each fire scenario, is considered equal to the probability of occurrence multiplied by the consequence of each fire scenario; (b) the procedure proposed in EN1991-1-2 (Annex E), according to which a single group of design fire scenarios is defined, taking into account the phenomena capable to modify the fire development, by introducing some coefficients in the calculation of fire density load.

In this paper, the main concepts of the two methodologies are illustrated and a synthetic comparison is proposed with reference to a case study.

1 INTRODUCTION

"Fire Safety Engineering" (FSE), defined according to ISO/TR 13387-1 ([1]), was created long ago but is still a new concept in many countries. In Sweden and UK, the countries that have most experience from it, local authorities still have a great influence on which solutions are approved locally especially as concerns fire design [2]. It, applicable either in the lack of prescriptive rules or in the case of "derogation" of prescriptive rules ([9]), allows a more accurate assessment of the safety measures with reference to a specific risk of the building through qualitative and quantitative criteria, which have to be applied in agreement with the competent fire authority and hence provide an acceptable starting point to assess the fire safety of a building.

European countries have started applying Eurocodes to fire design. In the past they used to have separate structural and fire codes, which are now integrated into a single standard system [2]. In particular, the European codes for structural fire safety are the "Fire Parts" of Structural Eurocodes ([3][5]), while the Italian reference is the Technical Code for Constructions [7], published in 2008.

These documents define five safety performance levels of buildings (Table 3.5.IV [7]) according to the safety objectives required by the Directive 89/106/CEE ([6]), recently upgraded as Regulation on construction products n.305/2011. In addition, the new Technical Code for Constructions refers to specific technical codes issued by the Italian Ministry of Interior for all activities under the control of the National Fire Brigades ([8][9]). The safety performance levels, depending on the importance of the building, establish the damage level that can be accepted.

The performance-based fire design unlike the prescriptive approach, is divided in two stages: the first one is a preliminary stage, in which qualitative analyses are carried out (definition of fire safety performance levels; selection of design fire scenarios); in the second stage (quantitative analyses), "advanced calculation models" are implemented both for fire modelling (natural fire curves and thermal flux) and for thermo-mechanical analyses (non-linear analyses, thermal strain prevented, etc.). Between the first and second stage, in Italy, the approval of design fire scenarios by the Fire Brigades is needed.

The principles of Italian Codes have been taken like reference in this work, because the analysed case study concerns the application of Fire Safety Engineering to an Italian existing office building.

2 CRITERIA FOR FIRE SCENARIOS DEFINITION

The last important step of the first "qualitative stage" of performance-based design consists in selection of design fire scenarios, due to the influence of fire scenarios on structural behaviour [10].

The design fire scenario is a qualitative description of the fire development during the time, identifying key events that characterise the fire and differentiate it from other possible fires. It typically defines the ignition and fire growth process, the fully developed stage, decay stage. In general, the number of distinguishable fire scenarios is too large to permit analysis of each one, therefore the design fire scenarios should be defined, in order to analyze the most severe cases for the structure.

The choice of the design fire scenarios should be carried out based on the risk R, associated to each fire scenario, equal to the probability of occurrence multiplied by the consequence of each fire scenario ([11], Equation (1).

$$R = P \cdot C \tag{1}$$

In general, the design fire scenarios may be defined through two possible procedures:

- the Fire Risk Assessment (FRA), characterized by the choice of the design fire scenarios on the basis of direct estimation of the Risk of each fire scenario;
- EN1991-1-2 (Annex E), according to which a single group of design fire scenario is defined, taking into account the phenomena capable to modify the fire development, by introducing some coefficients in the calculation of fire density load.

2.1 Application of Fire Risk Assessment to office buildings

The FRA is aimed to the evaluation of prevention and protection measures to be undertaken in order to mitigate the risk. Actually, the Fire Risk Assessment allows to individuate scenario structures of manageable size and allows to make the case that the estimation of fire risk based on these scenarios is a reasonable estimation of the total fire risk ([11]). In particular, key aspects of the process are: identification of a comprehensive set of possible fire scenarios; estimation of probability of occurrence of each fire scenario; estimation of the consequence of each fire scenario; estimation of the risk of each fire scenario (combination of the probability of a fire and a quantified measure of its consequences, in accordance with Equation (1); ranking of the fire scenarios according to their risk.

The Fire Risk Assessment is performed through the *event tree approach*, according to ISO-16732 Guidelines ([11]). A fire scenario, in an event tree, is given by a sequence path from the initial condition, through a succession of intervening events, to an end-event; therefore, each fire scenario corresponds to a different branch of the event tree (Figure 1); the incidental sequences are characterized by their probability of occurrence.

In the following, an application of Fire Risk Assessment with reference to office building (case study) is shown. The main events considered in this case study, that may affect the development of the fire, are: first aid suppression; alarm activation (smoke detectors); sprinklers activation; sprinklers suppression. Moreover, the secondary events that may be relevant for the assessment of life and structure's safety are: barrier effectiveness; windows and door state (open or closed).

The event tree obtained combining the main events is shown in Figure 1. Probability of occurrence of each event and consequence value of each fire scenario is obtained both by direct estimation from available data ([12][15]) and engineering judgment, summarized in the following:

- Available statistic data show that the probability of detecting fire manually and automatically is 69%. By considering that in 4% of cases, there's no manual or automatic detection system, this probability reaches 72%. By considering a probability of success equal to 87%, p(1st Event)=62% .

- Smoke detectors reliability decreases during time, if maintenance operations aren't provided. In the examined case, by considering that system works for a year, and one maintenance operation is provided for each year, it can be assumed p(2nd Event)=70% .
- Statistical analyses, carried out in USA (with reference to time period 2003-2007), show that, during fire event in building with office use, sprinkler activates in 96% of cases, and the system is effective in 99% of cases .
- Available data show that barrier effectiveness, in building equipped with sprinkler, is equal to 99,6%, while is equal to 92,8% in other cases. So, p(5th Event)=99,6% .

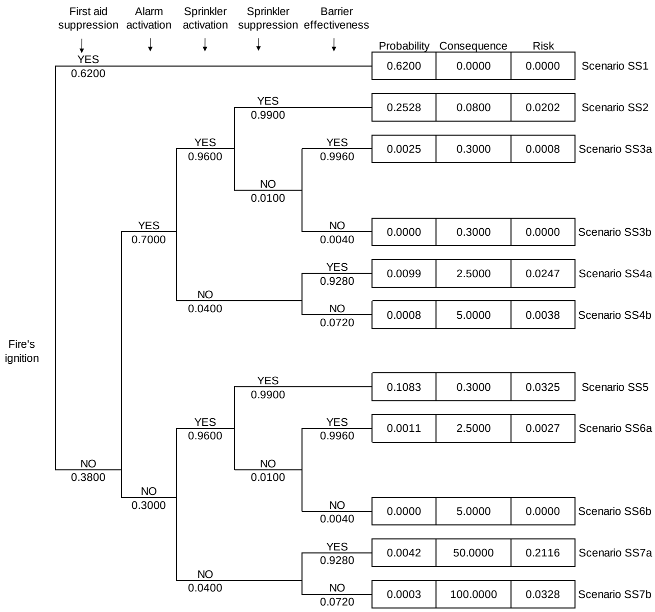

Figure 1. Event tree (case study).

Table 1. Numerical index of consequences.

Scenario	*1st event*	*2nd event*	*3th event*	*4th event*	*5th event*	*Damage (%)*	*Description*
SS1	YES					0%	Damage is limited to thing involved in fire
SS2	NO	YES	YES	YES		0.08%	Damage is limited to ½ room
SS3a	NO	YES	YES	YES	YES	0.3%	Damage is limited to 2 rooms
SS3b	NO	YES	YES	NO	NO	0.3%	Damage is limited to 2 rooms
SS4a	NO	YES	NO	NO	YES	2.5%	Damage is limited to the compartment (15 rooms)
SS4b	NO	YES	NO	NO	NO	5.0%	Damage is limited to the entire floor (30 rooms)
SS5	NO	NO	YES	YES		0.3%	Damage is limited to 2 rooms
SS6a	NO	NO	YES	NO	YES	2.5%	Damage is limited to the compartment (15 rooms)
SS6b	NO	NO	YES	NO	NO	5.0%	Damage is limited to the entire floor (30 rooms)
SS7a	NO	NO	NO	NO	YES	50.0%	Collapse of a part of building
SS7b	NO	NO	NO	NO	NO	100.0%	Collapse of entire building

The probability of occurrence of each fire scenario, represented by a branch of the event tree, is obtained by multiplying the probability of occurrence of each event of the branch. The consequence value is expressed as a fraction of the economic value of the building. Therefore, in the Table 1 the numerical index of consequence associated to each fire scenario is shown.

The combination of the main events determines, in the examined case, 11 fire scenarios (groups of scenarios), for which the secondary events, taken into account directly in fire model, and the localization of fire scenario within the floor and along the height, could determine some design fire sub-scenarios.

Based on these assumption, the Risk Ranking shows that the scenario characterized by the highest risk value and low probability of occurrence is the SS7a scenario. With reference to this fire scenario the performance level chosen is Level III, based on "maintenance of fire resistance requirements which ensure the lack of partial and/or complete structural collapse for a sufficient time with emergency management". Therefore, the criteria for fire scenario definition leads to the fire scenario characterized by the maximum risk value, for which the ultimate limit state (ULS) could be achieved after a sufficient time for evacuation of occupants and public rescue intervention, but allowing for the extended damage of the structure.

Another design scenario to be considered is SS5 scenario, characterized by a risk value lower than SS7a scenario, but higher probability of occurrence. With reference to this fire scenario the performance level chosen is Level IV, based on limited damage of structure after fire exposure. This choice is equivalent to a service limit state (SLS) check.

The thermo-mechanical analyses carried out with reference to design fire scenarios defined through the FRA for the considered case study are shown in section 3.1.

2.2 Application of the procedure suggested in EN1991-1-2 (Annex E)

The performance based design (Engineering Approach), according to EN1991-1-2 (as far as in Decree of the Ministry of the Interior of 09/03/2007,[8]), needs advanced thermo-mechanical calculation models in order to verify the load bearing capacity of the structures with reference to natural fire curves, obtained through: experimental fire models; simplified fire models; advanced fire models.

In the cases in which simplified fire models (parametric curves) and advanced fire models (one-zone and two-zone models) are implemented, the safety check, generally, is carried out with reference to a single event, in which the protection systems capable to modify the fire development are taken into account through a "semi-probabilistic" method, which defines the design fire density load adopted as input for the fire model.

The design value of fire density load $q_{f,d}$ is defined through the Equation (2).

$$q_{f,d} = \delta_{q1} \cdot \delta_{q2} \cdot (\Pi_i \delta_{ni}) \cdot q_f \tag{2}$$

where: q_f is the characteristic value of fire density load; δ_{q1} is the factor taking into account the fire activation risk due to the size of the compartment (see Table E.1in EN1991-1-2); δ_{q2} is a factor taking into account the fire activation risk due to the type of occupancy (see Table E.1); $\delta_n = \Pi_i \delta_{ni}$ is a factor, calibrated in probabilistic way, taking into account the different active fire-fighting measures (sprinkler, detection, automatic alarm transmission, firemen, see Table E.2 in EN1991-1-2). In the examined case, $\delta_{q1} = \delta_{q2} = 1.0$ and fire protection systems considered are:

- Automatic Water Extinguishing System, for which the δ_{n1} coefficient is equal to 0.61;
- Automatic Alarm Transmission to Fire Brigade, for which the δ_{n5} coefficient is equal to 0.87,
- Off-site Fire Brigade, for which the δ_{n7} coefficient is equal to 0.78;
- Safe access route, for which the δ_{n8} coefficient is equal to 0.9;
- Fire-fighting devices, for which the δ_{n9} coefficient is equal to 1.

Therefore $\delta_n = 0.37$, which means that the design fire density load is 37% of its characteristic value.

In the case study, the characteristic fire load densities q_f is assumed equal to 750 MJ/m^2, because the reference value 511 MJ/m^2, defined in EN1991-1-2 according to office use (80% Fractile, see Table E.4 in EN1991-1-2), has been multiplied by the ratio "compartment area/rooms area" in order to take into account the net load density in a room of the building.

The thermo-mechanical analyses carried out with reference to design fire scenario defined through the EN1991-1-2 (Annex E) are shown in section 3.20. Also in this case the secondary events, taken into account directly in fire model, and the localization of fire scenario within the floor and along the height, could determine some design fire sub-scenarios.

3 SAFETY CHECK IN CASE OF FIRE

The safety check of structures in case of fire, generally, requires the thermo-mechanical analyses. For more complex structures the analysis may be carried out through software based on thermo-mechanical modelling of materials and structural elements, by considering mechanical and geometric non-linearity.

In the next sections the structural safety checks of a building case study, performed according to fire scenarios selected through FRA and EN1991-1-2 respectively, are shown and compared. The thermo-mechanical analyses are carried out through the non-linear software SAFIR2011, developed at University of Liegi [16], decoupling thermal and mechanical analysis, according to EN1991-1-2 suggestions.

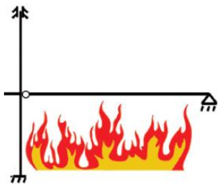

Figure 2. Analysed substructure.

Figure 3. Column's section.

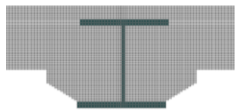

Figure 4. Beam's section.

In the case study, due to the building's large size, in order to reduce the computational time the substructure analysis is adopted, according to Eurocode provisions (see [5]).The analysed substructure representative of the global structural behaviour of a large size building [17] is shown in Figure 2. This substructure is made of unprotected columns (thin square hollow steel section 350mmx350mmx10mm, Figure 3), while a concrete coating protects steel beams HE260B (Figure 4) by fire exposure.

3.1 Structural Safety check in fire scenarios selected through FRA

Thermo-mechanical analyses, described in this section, are carried out on the substructure of Figure 2 with reference to fire scenarios defined through the FRA (see section 2.1).

As previously said, SS7a is a design fire scenario because it is characterized by the highest risk value (due to the associated consequences), while SS5 is an important fire scenario to be analyzed because it is characterised by high probability of occurrence.

The fire curve for fire scenario SS7a (see Figure 6), is obtained by a one-zone model applying Ozone software [18], with reference to the Heat Release Rate (RHR curves, Figure 5) deduced in accordance with EN1991-1-2 for building with office use and characteristic fire load densities equal to 750 MJ/m^2. Thermo-mechanical analyses have been carried out by considering four different column axial loads, that is four different utilisation factor of the column ($\mu=E_{d,fi,0}/R_{d,fi,0}$): μ=0.3; μ=0.45; μ=0.6; μ=0.75. Thermo-mechanical analyses results show that the substructure is subjected to important indirect action: in fact the beam's restrained thermal expansion determines the increase of beam's axial force (Figure 8) and the lateral displacement on the top of exposed column. The latter determines the increase of bending moment on the top of hot column, while after few minutes of exposure the bending moment reduces due to the reduction of column's stiffness (Figure 9). The column, which is the weak element of substructure, fails with a critical temperature dependent on the utilisation factor: θ_{cr}=680 °C when μ=0.3 (t=35min); θ_{cr}=635 °C when μ=0.45 (30min); θ_{cr}=569 °C when μ=0.6 (25min); θ_{cr}=524 °C when μ=0.75 (22.5min). In Figure 9 the safety check of column with μ=0.45 is shown, by comparing the stress and resistance for all fire exposure time. Therefore, in the fire scenario SS7a the Performance Level III is not satisfied, if the range 22.5-35 min, dependent on utilisation factor, is not sufficient to guarantee the emergency management.

In fire scenario SS5, the RHR, according to [14], decreases quickly after the sprinkler activation (see Figure 5), therefore the temperature in structural elements is very low (Figure 10) and no damages are attained, according to Performance Level IV.

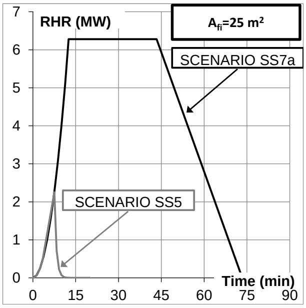

Figure 5. RHR curve for fire scenario SS7a and SS5.

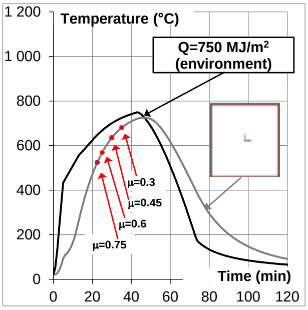

Figure 6. Fire model and temperature curve in column – SS7a scenario.

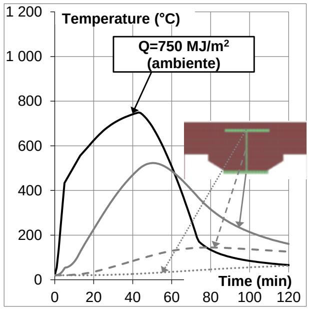

Figure 7. Fire model and temperature curve in beam – SS7a scenario.

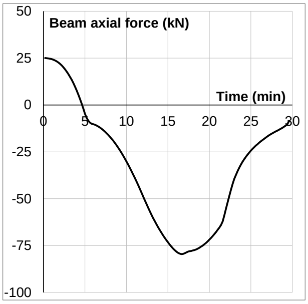

Figure 8. Beam axial force on beam (μ=0.45).

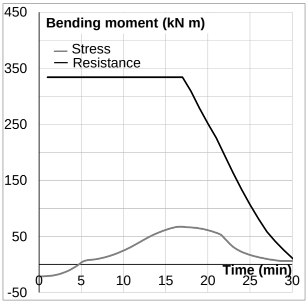

Figure 9. Safety check of hot column (μ=0.45) –SS7a.

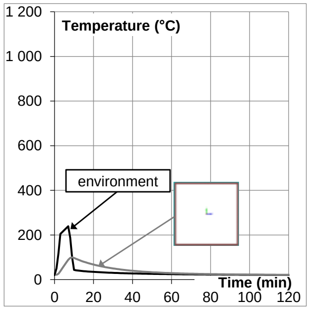

Figure 10. Fire model and temperature curve in column – SS5.

3.2 Structural Safety check in a fire scenario defined through EN1991-1-2 (Annex E)

Thermo-mechanical analyses, described in this section, are carried out on the substructure of Figure 2 with reference to the fire scenario defined according to EN1991-1-2 (see section 2.2).

Fire curve is obtained by a one-zone model applying Ozone software [18], with reference to the Heat Release Rate (RHR curves, Figure 11) deduced in accordance with EN1991-1-2 for building with office use and with reference to a design fire density load equal to the 37% of the characteristic value. As shown in Figure 12 the temperature in the exposed column is less than the critical value when the utilisation factor is equal to 0.3, 0.45, and 0.6, therefore the structure maintains the load bearing capacity for the overall time of fire exposure. Just in the case in which the utilisation factor is μ=0.75, the column fails after about 23 min of fire exposure.

4 CONCLUSIONS

In this work different key aspects of Fire Safety Engineering, as the choice of performance levels, the definition of design fire scenarios, the choice of fire models and advanced thermo-mechanical analyses, are analysed with reference to an office building, assumed as case study.

A crucial aspect of the application of Fire Safety Engineering is the definition of fire scenarios. The choice of the design fire scenarios may be carried out through two possible procedures: a) the Fire Risk Assessment (FRA), according to which the choice of the design fire scenarios is based on the direct estimation of the Risk of each group of fire scenarios; b) the procedure proposed in EN1991-1-2 (Annex E), according to which a single group of design fire scenarios is defined, taking into account the factors capable to modify the fire development, by introducing some coefficients in the calculation of fire density load.

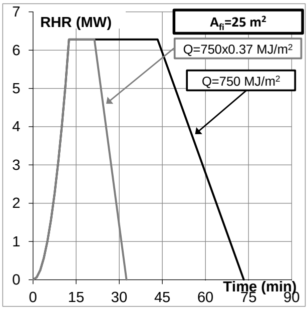

Figure 11. RHR curves: characteristic fire load density (black line), design fire load density (grey line).

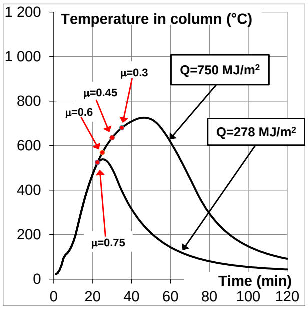

Figure 12. Temperature curve in column – characteristic fire load density and design fire load density.

The Fire Risk Assessment, by applying the event tree approach according to ISO-16732 Guidelines, provides different groups of fire scenarios; therefore different Performance Level could be associated to different fire scenarios. With reference to the risk analysis carried out on a office building, the scenario with the highest risk value and low probability of occurrence (Scenario SS7a) is characterized by: failure of first aid suppression; failure of alarm activation (smoke detectors); failure of sprinklers activation; barrier effectiveness. With reference to this fire scenario the Performance Level III has been chosen, based on “maintenance of fire resistance requirements which ensure the lack of partial and/or complete structural collapse for a sufficient time with emergency management”. Therefore, the criteria for fire scenario definition leads to the fire scenario characterized by the maximum risk value, for which the ultimate limit state (ULS) could be achieved after a sufficient time for evacuation of occupants and public rescue intervention, but allowing for the extended damage of the structure. The other selected group of design scenario is SS5 scenario, characterized by a risk value lower than SS7a scenario, but with high probability of occurrence. The main events that affect this fire scenario are: failure of first aid suppression; failure of alarm activation; sprinkler activation and effectiveness; barrier effectiveness. With reference to this fire scenario the performance level chosen is Level IV, which requires limited damages of structure after fire exposure. This choice is equivalent to a serviceability limit state (SLS) check.

The mentioned design fire scenarios should be considered as a group of fire scenarios: in fact, the secondary events, taken into account directly in fire model, and the localization of fire scenario within the floor and along the height, could determine some design fire sub-scenarios.

In the case study, analyses results of the fire scenario SS7a show that the column, which is the weakest element of substructure, fails with a critical temperature dependent on the utilisation factor (θ_{cr}=680 ℃ when μ=0.3; θ_{cr}=635 ℃ when μ=0.45; θ_{cr}=569 ℃ when μ=0.6; θ_{cr}=524 ℃ when μ=0.75) after, respectively 35min, 30 min, 25 min, 22.5 min of fire exposure. Therefore, in the fire scenario SS7a the Performance Level III is not satisfied, if that available time is not sufficient to guarantee the emergency management. In fire scenario SS5, the RHR curve decreases quickly after the sprinkler activation, therefore the temperature in structural elements is very low and no damages are attained, according to Performance Level IV.

The application of the procedure proposed in EN1991-1-2 (Annex E), provides a design fire density load equal to 37% of its characteristic value, in order to take into account the active protection systems capable to modify the development of fire. In this case study, the considered active protection system are: automatic water extinguishing system; automatic alarm transmission to fire brigade; off-site fire brigade; safe access route; fire-fighting devices. In this case, the temperature in hot column is lower than the critical value when the utilisation factor is equal to 0.3, 0.45, and 0.6, therefore the structure maintains the load bearing capacity for the overall time of exposure. Just in the case in which the utilisation factor is μ=0.75, the column fails after about 23 min of fire exposure.

The comparison carried out between the two procedures used to define the fire scenarios points out that the traditional procedure proposed in EN1991-1-2 (Annex E), for the case study proposed, is not conservative, if it is compared with the results obtained with reference to the highest risk fire scenario, defined trough the FRA. Therefore, the Fire Risk Assessment should be the reference approach for the most accurate selection of the design fire scenarios, also because it has enable to associate different performance levels to different group of fire scenarios.

REFERENCES

[1] ISO/TR 13387 (1999), *Fire safety engineering*.

[2] M. Heinisuo, M. Laasonen, J. Outinen. "Fire design in Europe". In: *Urban habitat construction under catastrophic events*. Napoli, 16-18 settembre 2010, CRC Press, p. 375-402, ISBN/ISSN: 9780415606851.

[3] EN 1991-1-2 (2002), Eurocode 1. Actions on structures - Part 1-2: General actions - actions on structures exposed to fire, November.

[4] EN 1992-1-2 (2004). Eurocode 2. Design of concrete structures – Part 1-2: General Rules – Structural Fire Design. March.

[5] EN 1993-1-2, Eurocode 3. Design of steel structures - Part 1-2: General rules - Structural fire design, April 2005.

[6] Construction Product Directive (1988), 89/106/CEE, Construction of European Community, December, upgraded as Regulation on construction products n.305/2011.

[7] Ministry of Infrastructure and Transport (Italian Government) 2008. Technical Code for the Constructions. G.U. n. 29 of 14/02/2008.

[8] Ministry of Interior (Italian Government) 2007a. Decree 09/03/2007, *Prestazioni di resistenza al fuoco delle costruzioni nelle attività soggette al controllo del Corpo nazionale dei vigili del fuoco*.

[9] Ministry of Interior (Italian Government) 2007b. Decree 09/05/2007, *Direttive per l'attuazione dell'approccio ingegneristico alla sicurezza antincendio*.

[10] E. Nigro, A. Ferraro, G. Cefarelli. "The influence of fire scenarios on the structural behaviour of composite steel-concrete buildings". *Applied mechanics and materials*, Vol. 82 (2011), p. 368-373. ISSN: 1662-7482. ISBN-13 978-3-03785-217-0. doi:10.4028/www.scientific.net/AMM.82.368.

[11] ISO/DS 16732: "Fire safety engineering – Guidance on fire risk assessment", Draft 2010.

[12] NFPA (2003). Operation of fire Protection Systems - a Special Edition of the Fire Protection Handbook. One Batterymarch Park, Quincy, Massachussets 02269 (2003).

[13] Hall, J.R. (2010). U.S. Experience with Sprinklers and other Fire Extinguishing Equipment. Fire Analysis and Research Division National Fire Protection Association, February 2010.

[14] Nystedt F. (2011). Verifying Fire Safety Design in Sprinklered Buildings. Department of Fire Safety Engineering and Systems Safety, Lund University, Sweden, Report 3150, Lund 2011.

[15] Hasofer A. M., Beck V. R., and Bennetts I. D. (2007). "Risk Analysis in Building Fire Safety Engineering". Oxford: Elsevier Ltd., 2007.

[16] Franssen J.-M. (2005). "SAFIR. A Thermal/Structural Program Modelling Structures under Fire". *Engineering Journal*, A.I.S.C., Vol 42, No. 3 (2005), 143-158.

[17] E. Nigro, I. Del Prete, A. Ferraro, D. Sannino, G. Cefarelli, G. Manfredi. "Structural fire engineering approach applied to an existing italian tall office building - part I: safety check of actual state". *Proceedings of Eurosteel 2014*, Naples, 10-12 September 2014.

[18] Cadorin J.F., Franssen J.M., and Pintea D., 2001, "The design Fire Tool Ozone V2.2 – Theoretical Description and Validation on experimental Fire tests", *Rapport interne SPEC/2001_01* University of Liege.

FIRE SAFETY CHECK OF EXISTING TALL OFFICE BUILDINGS APPLYING FIRE ENGINEERING APPROACH: A CASE STUDY

Emidio Nigro*, Iolanda Del Prete*, Giuseppe Cefarelli*, Anna Ferraro*, Domenico Sannino* and Gaetano Manfredi*

* Department of Structures for Engineering and Architecture, University of Naples Federico II
Via Claudio n. 21, 80125 Napoli (ITALY)
e-mails: iolanda.delprete@unina.it, giuseppe.cefarelli@unina.it, a.ferraro@unina.it,
emidio.nigro@unina.it, domenico.sannino@unina.it

Keywords: Fire safety engineering, Sub-structure, Advanced calculation models, Steel structures

Abstract.*The topic of this paper is the application of Structural Fire Engineering to an Italian existing tall office building in order to evaluate the actual fire safety conditions. The building is equipped with different fire protection systems, therefore the additional aim of the thermo-mechanical analyses has been the evaluation of the effectiveness of different fire protection systems as well.*

It has to be noticed that a passive protection system can be used like fire protection system if its characteristics are "certified" through an experimental campaign, which proves the effectiveness of the system in case of fire. The knowledge of thermal characteristics enables to apply advanced calculation models for the assessment of structural fire resistance. Nevertheless, in case of existing building, that characterization is not usually available, even if the certificates of fire resistance are provided. In this case, the proposed approach, shown in the following, is a kind of "back analysis", which enables to find the material's thermal characteristics on the basis of experimental results carried out to provide the REI certification.

In this paper, the back analyses carried out on different fire protection systems as calcium-silicate carter, mineral fibre ceiling and intumescent paints. These systems were applied in Italy during the 90's.

1 INTRODUCTION

Current Italian and European codes ([1-4])allow the use of the performance based approach through the concept of "Fire Safety Engineering" (FSE or Engineering Approach)), which enables a more accurate assessment of the safety measures with reference to a specific risk of the building through qualitative and quantitative criteria, which are agreed with competent authority and hence provide an acceptable starting point to assess the safety of a building design.

The complex procedure based on the performance-based fire designis properly described in [6].

One of the most important step of this procedure is the structural safety check in each defined fire scenario. The concept of "resistance in case of fire" becomes fundamental in order to save life, protect property and preserve the environment and heritage, with the Construction Product Directive (1988), 89/106/CEE [7], recently upgraded as Regulation on construction products n.305/2011. Therefore, in order to improve the safety conditions in case of fire, the following five objectives should be achieved: the structural load bearing capacity has to be granted for a certain time of fire exposure; the spread of flame and smoke has to be controlled in the buildings; the fire spread to the nearest building has to be avoided; the users have to be able to leave the building in safety conditions; the rescuer's safety has to be considered.

Regard the structural load bearing capacity, the passive protection systems sometimes ensure the mentioned requirement, reducing the heating of the structural elements and the following reduction of stiffness and resistance, through the own limited thermal conductivity.

A passive protection system can be used like fire protection system if its characteristics are "certified" through an experimental campaign, which proves the effectiveness of the system in case of fire. The certification process provides a "Certificate of Fire Resistance", which is part of the "Test Report", in which the test's results, like graphs and tables about the temperatures read by appropriate thermocouples, are shown. Moreover, during the last decade, the material's thermal characteristic, are shown as well.

The knowledge of thermal characteristics enables to apply advanced calculation models for the assessment of structural fire resistance. In fact, the thermal analyses can be carried out just if the overall material's thermal properties, including the protective materials, are known.

Nevertheless, in case of existing building, the specific material's characterization of protection systems is not usually available, even if the certificates of fire resistance are provided; sometimes the thermal properties at ambient temperature are available, but these values are not adequate for the application of advanced calculation models. In this case, the proposed approach, shown in the following, is a kind of "back analysis", which enables to find the material's thermal characteristics on the basis of experimental results carried out to provide the REI certification. Moreover some thermal and structural analyses (developed with the non-linear software SAFIR), carried out, as part of the application of the FSE, on a substructure representative of the global structural behaviour of the studied tall building [8], are illustrated.

2 CASE STUDY: TALL BUILDING WITH OFFICE USE

The building analysed, intended for office use, is atower 101.00m high and has 29-storeys above the ground. The floor can be divided into four zones, named (see Figure 1(a)): i) Lamellare, ii) Emicicli , iii) Nucleo, iv) Antinucleo.

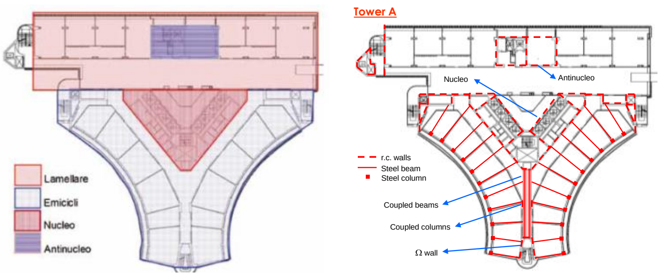

Figure 1. Tower analyzed: (a) Floor Map; (b) Structural elements.

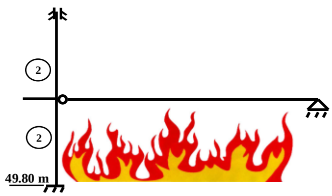

Figure 2. Analysed substructure [8].

In particular the third and fourth zone, made of reinforced concrete, represent the bracing and seism-resistant structures of the Tower at each floor. Other stiffening reinforced concrete structures (Figure 1(b)) are: stairwells, omega wall and coupled columns. Until 30.00m above sea level the bracing structures are connected to a reinforced concrete framed structure, which have large beams and columns, whereas, from 30.00m above sea level, for 25 storeys, the bracing structures are connected to steel frames which have an interstorey height equal to 3.30 m.Referring to "emicicli" zone (see Figure 1 (a)), from 30.00m above sea level, there are primary steel beams arranged in a radial pattern, which join the exterior steel columns to the reinforced concrete wall of the "nucleo" zone or to the coupled beams (which join the "□ wall" to the "nucleo" zone wall, see Figure 1 (a)). All members are connected by pinned joints [9]. The coupled beams with IPE450 steel profile are partially encased with concrete. The primary steel beams, arranged in a radial pattern, are also partially encased with concrete and have several cross-section dimensions as a function of span length. In particular, there are four types of cross-section, with steel profile HEB 240, HEB 260, HEB 300 or HEB 340. The floor deck, with an overall depth equal to 220mm and superior concrete slab equal to 40mm, are reinforced concrete members with lightweight polystyrene blocks. The secondary beams are IPE 180 steel profile. The steel columns are square hollow steel section $350x350mm^2$ with thickness varying between 10mm and 20mm along the height. The tower is equipped with several passive protection system, such as gypsum boards (REI 120) and intumescent paints on beams and columns, applied during the 90's.

3 THERMAL PROPERTIES MODELING OF FIRE PROTECTION SYSTEMS

The passive protection systems are usually applied on different structural elements, in order to reduce the thermal effects on the material due to high temperature. Protective materials can be applied, for example, on steel structures, in order to reduce the temperature achieved in the structural elements, during the fire, increasing the fire resistance time.

The fire protection systems applied on the structural elements of the building analysedare: ceiling in mineral fiber (horizontal diaphragms) or intumescent paint on beams and carter in calcium silicate or intumescent paints (coatings)on columns.

After the approval of the Directive 89/106/CEE, the experimental tests procedures of protected steel elements and the methodologies for the assessment of the results have been defined by the CEE Countries.

The experimental tests, mentioned above, for the assessing of the material thermal properties, are usually carried out with reference to the standard ISO834 curve.It has to be noted that in this case study, the specific material's characterization of protection systems weren't available, therefore, the proposed approach, shown in the following, is a kind of "back analysis", which enables to find the material's thermal characteristics on the basis of experimental results carried out to provide the REI certification.

3.1 Calcium-silicate carter characterization

The analyzed calcium-silicate carter are made of a hydrate calcium-slicate matrix, fiber-reinforced through special cellulose fiber and inorganic additives, formed at high pressure in a steam autoclave. The volumic mass is 500 kg/m^3 and the water content is 15 kg/m^3. The thermal characterization has been carried out on the basis of the available test reports. The certificate of fire resistance has been provided by the manufacturer based on the tests carried out in an authorized laboratory.

Table 1. Thermal properties of calcium-silicate carter.

Temperature T (℃)	Thermal conductivity λ (W/mK)	Specificheat c (J/kgK)	Density ρ (kg/m^3)
≤400	0.2	1000	500
420≤T≤1200	0.18	1000	500

The tested sample (Figure 3) was made of a steel profile HE300A, with steel grade Fe430 (S275 in the current classification), protected by calcium silicate carter, 25mm thick.

The thermal properties influencing the heat transfer are: thermal conductivity, specific heat, density and, for concrete, the water content. Given that the evaluation of all thermal properties is not possible through the back analysis, the specific heat and density have been considered constant and equal to the value at ambient temperature, while the temperature-thermal conductivity curve has been defined in order to obtain the best fit between numerical and experimental temperature in the cross section.

The thermal analysis has been carried out on the 2D model represented in Figure 3, subjected to the ISO834 curve, through the software SAFIR 2007 [10], by considering the thermal properties shown in Table 1 and a water content of 15 kg/m^3. As it is shown in Figure 4, a very good agreement between the numerical and experimental temperature has been obtained.

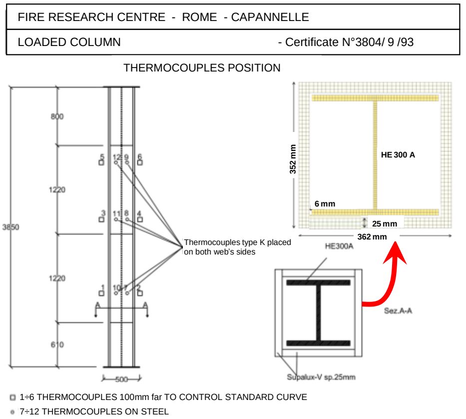

Figure 3. Sample and numerical model.

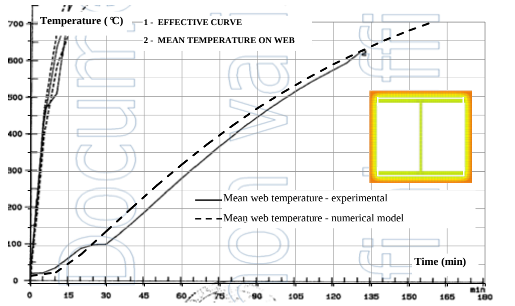

Figure 4. Numerical-experimental comparison.

3.2 Mineral fiber ceilingcharacterization

The ceiling, thermally characterized in the following, is made of inorganic mineral fiber for the 90%, with density equal to 300kg/m^3, supported by a metal frame structure (Figure).

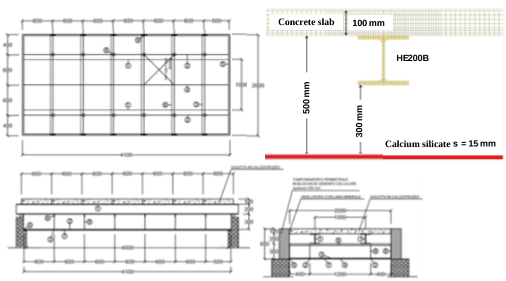

Figure 5. Sample and numerical model.

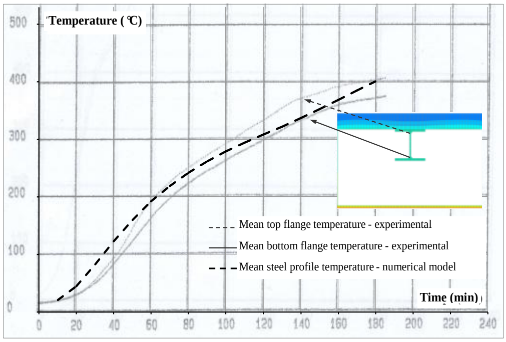

Figure 6. Numerical-experimentalcomparison.

Table 2. Thermal properties of mineral fiber ceiling.

Temperature T (℃)	Thermal conductivity λ (W/mK)	Specificheat c (J/kgK)	Density ρ (kg/m^3)
≤300	0,015	800	300
≤500	0,04	800	300
≤1200	0,2	800	300

The certificate of fire resistance has been provided by the manufacturer based on the tests carried out in an authorized laboratory, as well as in the previous case. The tested sample (Figure) was made of: 2 steel beams HEB200, a concrete slab 100mm thick, a mineral fiber ceiling 15mm thick, in order to protect the steel beams, 300mm far from the bottom flange and 500mm from the slab's soffit.

In the thermal analysis the thermal parameters shown in Table 2 and a water content equal to 0 kg/m^3, have been considered, because no data were available. As it is shown in Figure , a very good agreement between the numerical and experimental temperature has been obtained.

3.3Intumescent paint characterization

The thermal characterization of the intumescent paint has been carried out with reference to the tests performed on the 4 steel profile shown in Table 3.

In general, the intumescent paints at high temperature increase their volume and an insulating foam, 50 times thicker than the value of thickness at ambient temperature, is produced; it ensures low temperature and a delayed achievement of the critical temperature.

Table 3. Geometrical details of the profiles.

Specimen	Profile	Length L (mm)	Theoritical area A (cm^2)	Massivity S/V (m^{-1})	Web thickness t_w (mm)	Flange thickness t_f (mm)
1	Scatolare 350x350	1000	163.4	80	12.5	
2	HEA220	1000	64.3	196	7	11
3	HEA280	1000	97.3	164.4	8	13
4	HEA240	1000	76.8	178.4	7.5	12

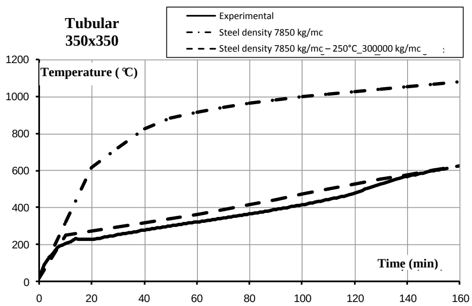

Figure 7. Numerical-experimentalcomparison.: average temperature in 350x350 profile.

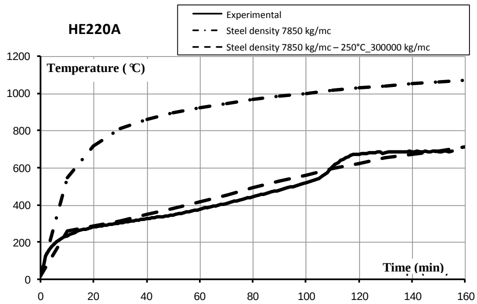

Figure 8. Numerical-experimental comparison.: average temperature in HE220A profile.

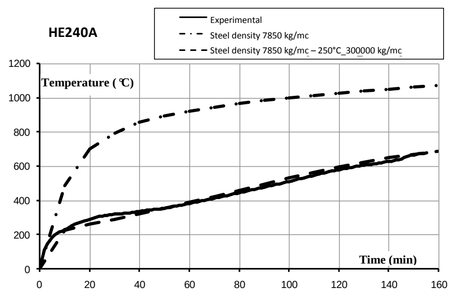

Figure 9. Numerical-experimental comparison: average temperature in HE280A profile.

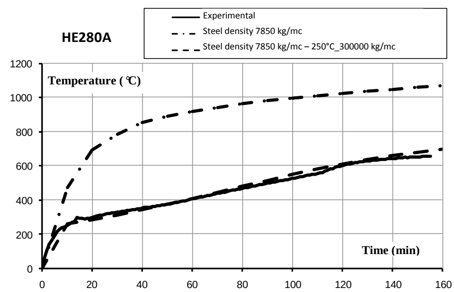

Figure 10. Numerical-experimental comparison.: average temperature in HE240A profile.

Since the particular nature of the intumescent paints, a different procedure has been implemented.

Obviously, the modeling of the temperature dependent thickness is not possible, therefore the protective layer has not been modeled but, in order to insulate the structural element, an equivalent temperature dependent steel's density has been considered. Regarding the other thermal properties (thermal conductivity and specific heat), the values proposed in EN 1993-1-2[4] have been assumed.

The thermal analyses carried out, has enabled to define two different temperature dependent densities: the first one for steel I profiles (ρ=7850kg/m^3 if T$\leqslant$250 ℃, ρ=555000kg/m^{3}if T>250 ℃), the second one for tubular profiles (ρ=7850kg/m^3 if T$\leqslant$250 ℃, ρ=300000kg/m^{3}if T>250 ℃). In Figure -Figure , the comparison between the numerical and experimental temperature proves the effectiveness of the considered steel densities (temperature dependent). Moreover, in these graphs, the temperature obtained in the case in which ρ=7850kg/m^3 is shown.

4 ASSESSMENT OF PROTECTION SYSTEM'S EFFECTIVENESS

The thermal and structural analyses (developed with the non-linear software SAFIR) have been carried out, as part of the application of the FSE, on a substructure representative of the global structural behaviour of the studied tall building [8], protected with several fire protection system. The substructure (Figure 2)has been considered subjected to a natural fire curve (Figure 11), obtained applying Ozone [11]. In particular, the fire model has been obtained with reference to a compartment of 36.4 m^2 (mean dimension of the rooms in the building), based on a RHR curve according to EN1991-1-2 [2] for building with office use (q_{fid} = 750 MJ/m^2=511 MJ/m^2 $\times$ $A_{rooms}/A_{compartment}$).

The analyzed substructures have the following protection systems:partially encased beam protected by mineral fiber ceiling and steel column protected by calcium silicate carter ("Structure 1"); partially encased beam and un-protected steel column ("Structure 2"); partially encased beam protected by mineral fiber ceiling and column protected by calcium-silicate carter ("Structure 3"); partially encased beam protected by mineral fiber ceiling and column protected by intumescent paints ("Structure 4"); steel beam and column protected by intumescent paint ("Structure 5").

Analyses results show that the column is the weakest element in the structure with a critical temperature Θ_{cr}=630 ℃. In Fig. 11 the temperature in the column protected by carter is shown and the maximum value is 250°C. This value doesn't produce reduction in steel strength, but only stiffness reduction, in fact mechanical analysis results show that the structure preserves the load bearing capacity during all fire exposure time. In the same figure, the temperature in un-protected column is shown and the maximum value is 700 ℃, greater than the critical one. Therefore, after 33 min of fire exposure the structure loses the load bearing capacity (Figure 14). In the Figure 13 a comparison between "Structure 1" and "Structure 2"is shown and a very important reduction of stress on structural elements can be observed when the structure is protected. In the same figures the behaviour of the "Structure 3" is shown as well (protected column and un-protected beam).

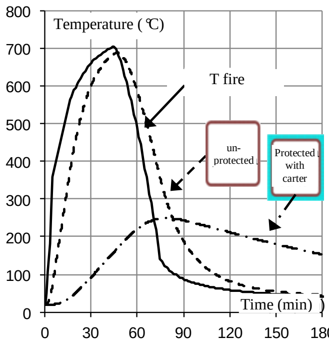

Figure 11. Column's temperature.

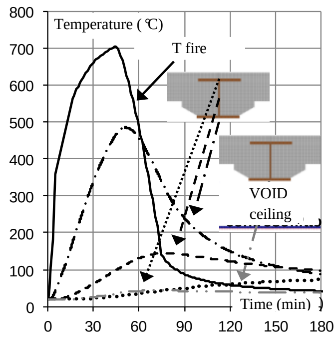

Figure 12. Beam's temperature.

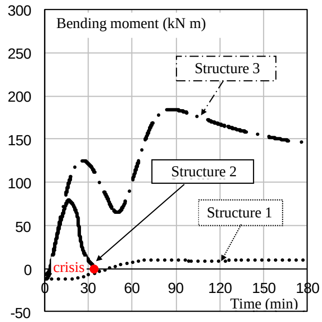

Figure 13. Bending moment on top of hot column.

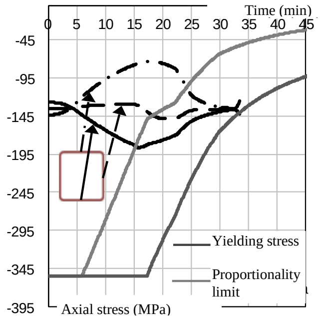

Figute 14.Stress on un-protected column.

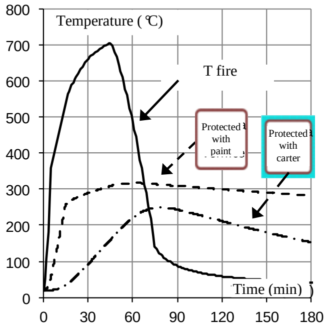

Figure 15. Column's temperature.

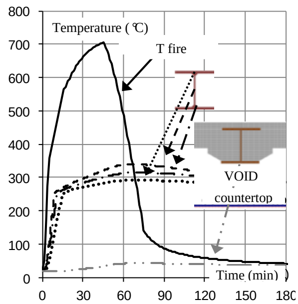

Figure 16. Beam's temperature.

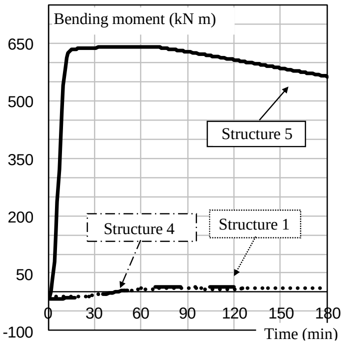

Figure 17. Bending moment (top of hot column).

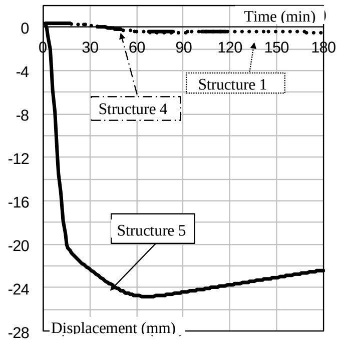

Figure 18. Lateral displacement (top of hot column).

The behaviour of the beam in terms of bending moment (and similarly the axial load) can be observed: after about 55 min of fire exposure the stress on the beam starts to increase again and it can be justified analysing the temperature in column and beam, plotted in Figure 11and Figure 12: after about 55 min of fire exposure the thermal curvature on beam decreases, while the thermal elongation, due to the web's temperature, varies with a low gradient. Few minutes later, the cooling phase of the column starts and, becoming stiffer than in the previous phase, it is able to achieve greater value of bending moment, due to the beam's elongation. Finally the reduction of column's bending moment (and similarly of beam's axial stress) after 90 min of fire exposure is due to the reduction of top column's displacement.The Figure 15 shows the temperature in column protected by either calcium-silicate carter or intumescent paint. The intumescent paint has enabled to keep the temperature in steel column and beam quite low (less than 350 °C).

Obviously in the case in which the beam is partially encased, the temperature in the beam is significantly lower than 350°C. That temperature doesn't produce reduction in steel strength, in fact mechanical analysis results shows that the structure preserves the load bearing capacity during all fire exposure time.

However, as it is shown in Figure 17 important indirect actions can be induced by prevented thermal strain. Moreover in the "Structure 5" the lateral displacement (Figure 18), and so the bending moment (Figure 17) on the top of hot column is greater than that in "Structure 1" and "Structure 4" (structure with partially encased beam), due to the high temperature achieved in un-protected and "nude" beam.

5 CONCLUSIONS

In this paper the application of Structural Fire Engineering (according to Italian and European Technical Codes) to an Italian existing tall office building has been shown. The aim of this study isthe evaluation of the actual fire safety conditionsand the effectiveness of different fire protection systems applied on the structure during the 90's.

The assessment of the effectiveness of different passive fire protection systems analyzed in this paper, has been carried out after the thermal characterization of involved materials ("back analysis"), and based on the thermo-mechanical results referring to protected and un-protected substructures.

The analyses results show that the protection systems have enabled to keep the temperature in structural elements lower than that produces reduction in steel strength, in fact the structures preserve the load bearing capacity during all fire exposure time. On the other hand, the un-protected structure fails after a time exposure dependent on the critical temperature of the weakest element in the structure.

However the comparison between the different protection systems applied on the column (calcium-silicate carter and intumescent paint) shows the greater effectiveness of the carter than the intumescent paint, given the high temperature achieved in column in the latter case.

REFERENCES

[1] Ministry of Infrastructure and Transport (Italian Government) 2008. "Technical Code for the Constructions". G.U. n. 29 of 14/02/2008.

[2] EN 1991-1-2 (2002), "Eurocode 1. Actions on structures - Part 1-2: General actions - actions on structures exposed to fire", November.

[3] EN 1992-1-2 (2004). "Eurocode 2. Design of concrete structures – Part 1-2: General Rules – Structural Fire Design". March.

[4] EN 1993-1-2, "Eurocode 3. Design of steel structures - Part 1-2: General rules - Structural fire design", April 2005.

[5] Ministry of Interior (Italian Government) 2007b. Decree 09/05/2007, "Direttive per l'attuazione dell'approccio ingegneristico alla sicurezza antincendio". GU n. 117 of 22/05/2007.

[6] I. Del Prete, G. Cefarelli, A. Ferraro, E. Nigro, D. Sannino. "Selection criteria of fire scenarios for buildings". Proceedings of SIF conference 2014, 8th International Conference on Structures in Fire, Shanghai, China, June 11-13, 2014

[7] Construction Product Direttive 89/106CEE, Construction of European Community.

[8] E. Nigro, I. Del Prete, A. Ferraro, D. Sannino, G. Cefarelli, G. Manfredi. "Structural fire engineering approach applied to an existing italian tall office building - part I: safety check of actual state". Proceedings of Eurosteel 2014, Naples, 10-12 September 2014

[9] E. Nigro, G. Cefarelli, F.M. Mazzolani, I. Del Prete, A.Anna Ferraro, G. Manfredi, D. Sannino. "Application of structural fire engineering to the towers of the courthouse of Naples", Proceedings of COST Action TU0904 "IFER" (Integrated Fire Engineering and Response), "Case Studies", p. 7-23, Editors: F. Wald, I. Burgess, G. Rein, L. Kwasniewski, P. Vila Real, K. Horova. CTU Publishing Production, Czech Technical University in Prague, March 2012. ISBN: 978-80-01-05004-0, Chania, 14 - 15 October 2011.

[10] Franssen J.-M.: "SAFIR. A Thermal/Structural Program Modelling Structures under Fire". Engineering Journal, A.I.S.C., Vol 42, No. 3 (2005), 143-158.

[11] Cadorin J.F., Franssen J.M., and Pintea D.: "The design Fire Tool Ozone V2.2 Theoretical Description and Validation on experimental Fire tests", University of Liege, 2001

8th International Conference on Structures in Fire
Guo-Qiang LI, Venkatesh K. R. KODUR, Shou-Chao JIANG, Jian JIANG, Su-Wen CHEN, Guo-Biao LOU (Eds.)
Shanghai, China, June 11-13, 2014

PRACTICAL COST-BENEFIT APPLICATIONS USING STRUCTURAL FIRE DESIGN

Allan Jowsey*, Peter Scott* and Yu-Jie Wang*

* Structural Fire Design Department, AkzoNobel, Stoneygate Lane, Felling, NE10 0JY, UK
e-mails: allan.jowsey@akzonobel.com, peter.scott@akzonobel.com, yujie.wang@akzonobel.com

Keywords: Passive, Fire, Protection, Structures, Optimization

Abstract. *This paper considers a frame analysis of a steel structure with attention being given the influence of the design and assessment at the fire limit state in accordance with the Eurocodes. Specifically the paper presents a number of design options to show that a design incorporating structural fire design principles can result in a coordinated cost-effective solution that aligns with regulatory structural codes and standards. It is these solutions which are now commonly being requested on projects across the UK and Europe.*

1 INTRODUCTION

Historically, it has not been typical for structural engineers to undertake an in-depth assessment of their structure at the fire limit state. For too long it has not been considered as part of their remit, with the majority of structural fire protection being associated within the realm of an architect. In some instances, a structural fire engineering exercise may be undertaken by a specialist Fire Engineer, however this is currently only done for a small minority of buildings around the world.

While it is recognized that such an approach can yield significant cost savings yet retain robust and safe designs, it is commonly considered to be a very specialized methodology that in some instances can carry a high risk of approval, require complex calculations and demand cost and time that cannot always be afforded for non-iconic buildings.

The reality is that structural engineers are more than capable of assessing their structure for the effects of high temperature using similar methodologies to those currently employed for the purposes of ambient design. In doing so, they can demonstrate a highly optimised steel structure that ensures a cost-effective design up front rather than delaying such an approach until late in the design, often as part of a value engineering exercise.

This paper is structured in such a way as to bring together a practical application of structural fire engineering from the perspectives of a structural engineer, a steelwork fabricator, a fire protection supplier and an applicator of the fire protection system. Often considered as disciplines with exclusive defined tasks in the design and construction of a building, this paper demonstrates that the four are in fact very closely linked.

This paper considers a frame analysis of a steel structure with attention being given the influence of the design and assessment at the fire limit state in accordance with the Eurocodes. Specifically the paper presents a number of design options to show that a design incorporating structural fire design principles can result in a coordinated cost-effective solution that aligns with regulatory structural codes and standards.

Discussion is provided with respect to designer responsibilities to ensure that a flow of the required information is understood to enable an optimized structural fire assessment, including steelwork specifications, development of fire safety strategies, marking-up of drawings, material take-offs, selection of protection material and other general considerations that the authors believe will provide benefit to the structural engineering community.

2 OVERVIEW

There is an increasing paradigm shift in the way of thinking by passive fire protection suppliers towards recognition of structural fire design approaches. Many structural engineers and fabricators are starting to collaborate closely with manufacturers in terms of product performance knowledge.

Many structural design codes and guidance documents include 'fire resistant' design. In the UK the relevant standard is BS 5950 Part 8:2003 and in Europe the relevant codes are EN 1993-1-2:2005 [1] for steel and EN 1994-1-2:2005 for composite steel and concrete design. In North America, ANSI/AISC 360-05 provides provisions for structural design for fire conditions, while other bodies including ABS, DNV, NORSOK and API all have structural guidance documents which reference elevated temperature design.

In the above standards, methods are given for determining the thermal and mechanical response of the structure and evaluating the fire protection required, if any, to achieve the specified performance. An important feature of these standards is that they use the concept of a variable steel temperature, i.e. the limiting steel temperature before the critical failure temperature is reached.

3 THE IMPORTANCE OF STRUCTURAL ANALYSIS AT FLS

At ambient, structural design uses the concept of ultimate (ULS) and serviceability (SLS) limit states. Associated safety factors to represent these states are applied to the given loads acting on the structure. The resultant loads are used in a structural assessment to generate steel member sizes. At the fire limit state (FLS) however, the safety factors for loads may be different to those for ambient.

The resulting load in the fire limit state is effectively reduced to account for the probability that in the event of a fire the structure is unlikely to be loaded to its capacity and can be justified using statistical evidence of actual loading. The ratio of the effective load applied on the member in the event of a fire to the load at ambient is termed the 'load ratio'.

British Standards, the Eurocodes and ANSI/AISC 360-05 use the concept of load ratio as a measure of the applied load that a member can resist at the time of a fire. In practical designs within the built environment, the load ratio may vary from 0 to 0.7. In oil and gas applications, where the structure may be predominately dead load, the load ratio may be higher.

For a given load ratio, the maximum permitted temperature is termed the limiting temperature. In essence, the steel member will function satisfactorily at the limiting temperature but will fail at higher temperatures.

Industry prescriptive temperatures vary across the world in accordance with relevant legislation. For example, ASTM E-119/NFPA 251/UL 263 uses a maximum limiting steel temperature of 538 °C (1000 °F) for columns and 593 °C (1100 °F) for beams; in parts of Europe, the temperature is commonly 500 °C and in China the concept of limiting steel temperature does not exist – this is in place of a single protection thickness to cover all steelwork. In the off-shore industry, Classification Societies typically set a maximum critical core temperature of 400 °C.

It has been publicised in the past, that the industry default temperatures are acceptable for most circumstances but not always.

4 FLOWS OF INFORMATION

Within the structural design and structural fire protection industry there are many different ways of approaches and communicating the need for and the specification of appropriate protection.

It is the authors' experience that the majority of structures around the world specify fire protection purely in relation to the fire resistance period, e.g. 90 minutes. Little, if any regard or attention is given to the structural performance or member capacity to complement the fire resistance period. Occasionally, iconic structures may be the subject of a fire engineered assessment that considers the fire development and behaviour to justify reducing the period of fire resistance, e.g. from 90 minutes to 60 minutes. While some of these assessments may include a limited structural assessment, they often provide insufficient structural information to complement the steelwork fire protection specification to the extent that it can be used effectively by fire protection estimation teams. The typical process is described in the flowchart in Figure 1. The Structural Engineer's ambient (ULS) design is provided in conjunction with the Main Contactor to a number of Steelwork Fabricators to permit tendering for a specific job. It is not uncommon for the fire protection scope to fall into the remit of the Fabricator. Estimates for fire protection are made and factored into the overall price as part of tendering documentation. In the absence of the appropriate information being made available, conservative estimates are frequently made and since the cost of fire protection can be up to 20% of the cost a structural frame, this pricing approach can make the Steelwork Fabricator's quote seem excessively high. The lack of transparency in information being passed within the contract chain regarding fire protection requirements often results in large variations in fire protection costs from a number of tenders which can result in further confusion. Additionally once all tenders are provided and the (often excessive) cost of fire protection seen, the project may seek cheaper solutions in the form of value engineering – it is at this point that a Fire Engineering consultant may be brought on board to look to rationalize the fire resistance period or to eliminate in part the requirement for fire protection.

While the flowchart and thought processes depicted in Figure 1 are common, it is acknowledged that alternate processes exist to arrive at a fire protection solution.

A more comprehensive structural fire assessment is depicted in Figure 2. This links the Structural Engineer's ULS design directly with a FLS design prior to tendering. This approach ensures that the correct information is passed to the Steelwork Fabricators to enable more accurate assessments of the cost of fire protection.

The FLS design should account for the member specific failure temperatures to complement the fire resistance period. Member steel failure temperatures are a function of the applied load with respect to capacity. Consideration should also be to oversize certain members to lower the structural utilization ratio at fire. This will increase the limiting temperature and therefore reduce the amount of fire protection required. It has been shown that a cost-benefit study that includes the cost of steel, fire protection and application rates can yield cost effective designs when extra steel is used to over design members [2].

In the absence of an FLS design prior to tendering, it is still possible to obtain an economical and more accurate assessment of fire protection costs by ensuring that steelwork specifications are written such they permit greater flexibility rather than just stating a fire resistance period. Statements may include, for example: -

"*Fire protection estimates to be based on 100% utilisation of the structural members at ambient (ULS) in conjunction with imposed load reduction factors relating to occupancy.*"

or

"*Fire protection estimates to be based on actual member utilisation as indicated on drawings or commensurate with the loading strategy documentation.*"

The above statements are sufficient for manufacturers to provide optimised thicknesses of protection that are more representative of the structural design rather than a catch-all conservative assumption of temperature.

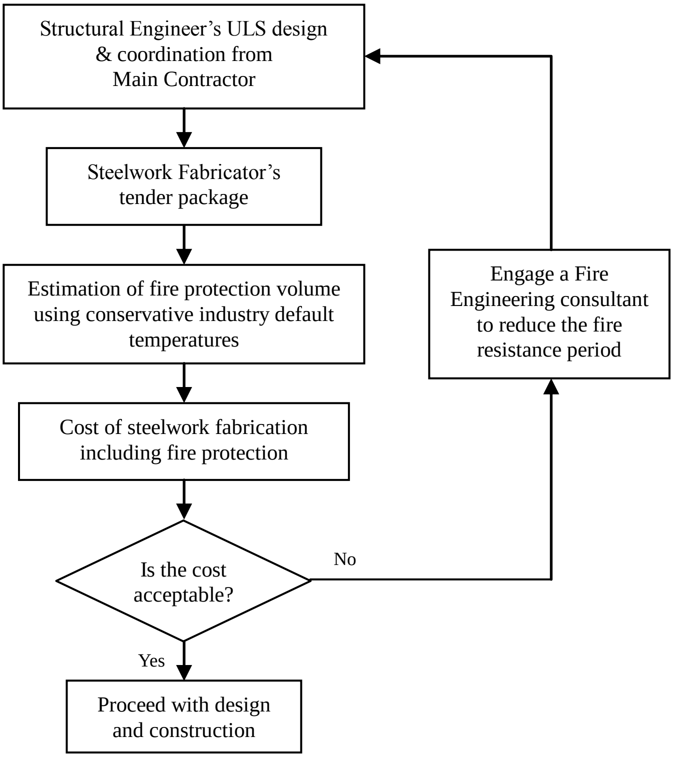

Figure 1. Flowchart to highlight a simplified flow of events and thought processes involved in the specification of fire protection to structural steelwork.

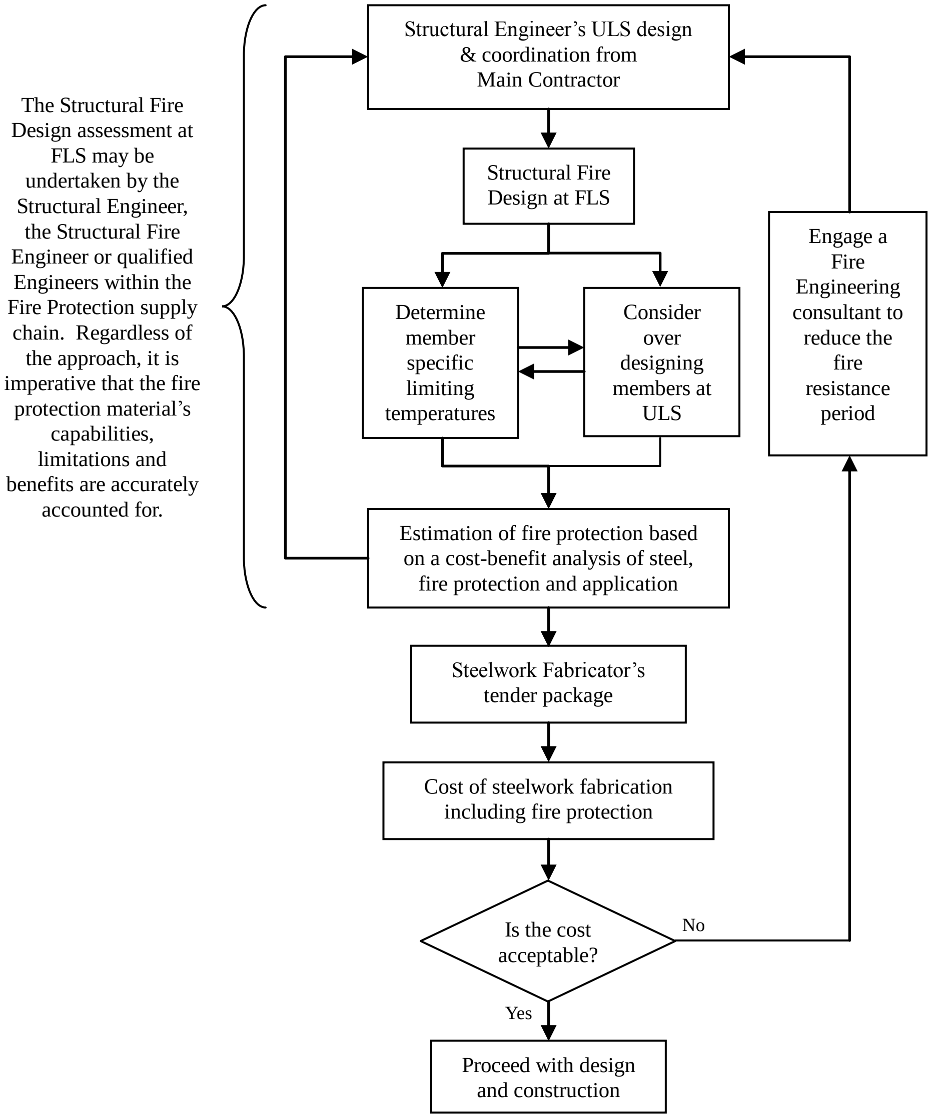

Figure 2. Flowchart to highlight a structured flow of events and thought processes involved in the specification of fire protection to structural steelwork with specific reference to structural fire design.

5 WORKED EXAMPLE

This section provides an example of how a structural design can be used to inform an optimised level of fire protection and the benefits that this can bring.

A single floor-plate of a multi-storey office building is considered acting under dead (permanent) and live (variable) gravity loads. Specific details: -

- Dead load: 3.0 kN/m ^{2}
- Live load: 4.5 kN/m ^{2}
- Design in accordance with the base Eurocode (no National Annex)
- All beams considered as non-composite
- Typical bay spans: approximately 8 m
- Columns fixed at their base
- Combination factor of 0.5 (Category B) for live load reduction in fire
- Fire resistance period: 120 minutes (R120)

Figure 3 shows the representative floor-plate from the structural model incorporating bracing. Figure 4 shows the same model but with beam profiles rendered and an indication of the bending moment distribution acting on the frame.

The highest degree of ULS utilisation in the steel fame was in one of the columns at 79%. Under the applied loads at FLS, this equated to approximately 42%.

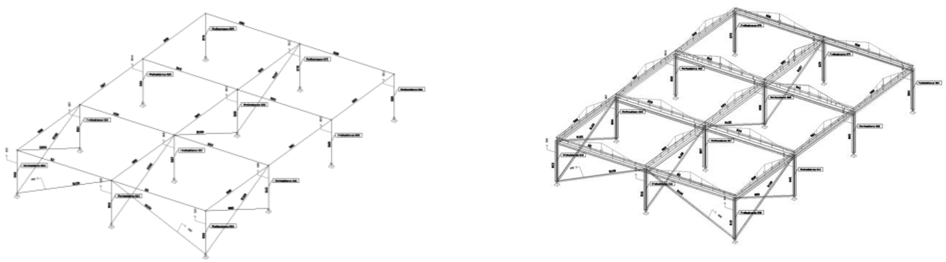

Figure 3. (Left) Stick model with member references representing the structural frame under consideration for the worked example (Right) Model showing simplified bending moment distribution at ultimate limit state.

Table 1. Overview of options to investigate cost-benefit analysis of fire protection options.

Option	Scenario	Comments
1	R120 all members 500 °C	Basic steelwork specification for a multi-storey building with no FLS design.
2	R90 all members 500 °C	Basic steelwork specification following a fire engineered assessment. No FLS design.
3	R120 temperatures assessed on 100% ULS utilisation	Fire resistance period maintained as per original spec. Temperatures assessed using conservative utilisation.
4	R120 temperatures assessed on 80% ULS utilisation	Fire resistance period maintained as per original spec. Temperatures assessed using actual utilisation values.
5	R90 temperatures assessed on 80% ULS utilisation	Fire engineered resistance period Temperatures assessed using actual utilisation values

An assessment of fire protection volume is made for five different scenarios as outlined in the following section. In all cases, the potential saving back to the original specification of R120 is made to quantify the benefits. A conservative default limiting steel temperature of 500 ℃ for all members was taken as per the norm in mainland Europe in the absence of an FLS assessment. The five options for fire protection are given in Table 1.

Table 2 shows the breakdown of fire protection volume (litres of intumescent paint) assuming Interchar 1120 tested and assessed in accordance with EN 13381-8 [3] to align with the recommendations of EN 1993-1-2.

Table 2. Determination of fire protection material volume for (Option 1) 120 minutes fire resistance with a limiting steel temperature of 500 ℃ with no fire engineering or structural fire design.

Ref	Designation	Total Length (m)	Sides Exposed	A_m/V (m^{-1})	Total Area (m^2)	DFT (mm)	Volume (L)
1	UC 254x254x73	7	4	160	10.4	4.07	63
2	UB 457x191x89	80	3	129	117.4	2.16	373
3	UB 610x229x101	56	3	143	103.2	2.37	359
4	UC 203x203x60	35	4	158	42.4	4.04	252
5	SHS 100x100x6.3	79	4	172	31.6	7.50	384
						Total =	**1395**

Table 3 shows the volume of fire protection required for each of the different options.

Table 3. Volume (litres) of fire protection material for the different options considered within this paper.

Ref	Designation	Option 1 R120 θ_a = 500 ℃	Option 2 R90 θ_a = 500 ℃	Option 3 R120 100% ULS utilisation	Option 4 R120 80% ULS utilisation	Option 5 R90 80% ULS utilisation
1	UC 254x254x73	63	40	50	45	24
2	UB 457x191x89	373	225	242	208	144
3	UB 610x229x101	359	213	230	197	135
4	UC 203x203x60	252	161	203	183	97
5	SHS 100x100x6.3	384	229	332	328	158
	Total (L) =	**1395**	**868**	**1057**	**961**	**558**
	Saving on Option 1 =	**0%**	**38%**	**25%**	**31%**	**60%**

The potential saving using the different options is plotted in Figure 3. This plot considers the saving in volume of fire protection material with respect to the degree of complexity, time and cost in achieving the desired outcome together with the risk associated with acceptance by the approving authority. The scale to describe this is based on the authors' experience having worked on similar projects across the world. For this reason it can be considered subjective however the authors believe it reflects real life scenarios.

It is seen that similar savings in volume are achieved between reducing the fire resistance period from 120 to 90 minutes while retaining a temperature of 500 ℃ in comparison to assessing the temperatures based on actual utilisation of the structures yet maintaining the 120 minute fire resistance period. The latter is considered to be a relatively straightforward and quick process in comparison to the former.

A combination of a fire engineered fire resistance period and an FLS assessment using actual member utilisations can result in a considerable saving, albeit with greater effort to achieve the desired solution.

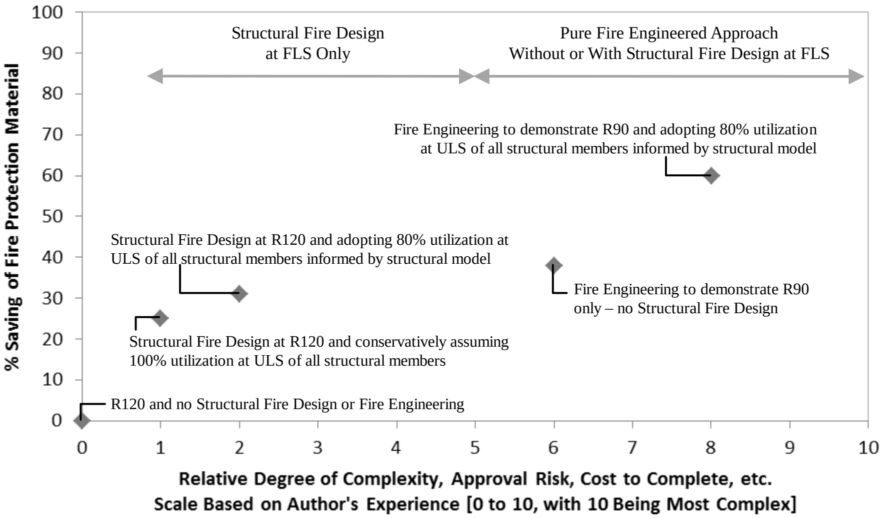

Figure 3. Plot of saving in fire protection material for the different options presented in this section with respect to relative complexity of each approach. Descriptions of each option are provided on the plot to ease understanding.

6 CONCLUSIONS

(1) Few structures currently adopt an FLS assessment and resort to conservative steel temperatures resulting in expensive fire protection designs.

(2) An assessment at FLS is a quick method of bringing up-front added value to a design.

(3) A complex fire engineered solution to reduce fire resistance periods may only provide similar benefit to a relatively straightforward FLS assessment.

(4) A combined fire engineered approach and structural fire design approach will provide the optimum solution for a project, albeit with greater initial cost and time demands.

REFERENCES

[1] BS EN 1993-1-2:2005. "Eurocode 3: Design of Steel Structures – Part 1-2: General Rules – Structural Fire Design" 2005.

[2] Jowsey, A. and Scott, P. "Structural analysis to value-engineer passive fire protection". *Proceedings of the First International Conference on Performance-based and Life-cycle Structural Engineering*, Hong Kong. December 2012, pp.459-468.

[3] EN 13381. "Test Methods for Determining the Contribution to the Fire Resistance of Structural Members." 2010.

8th International Conference on Structures in Fire
Guo-Qiang LI, Venkatesh K. R. KODUR, Shou-Chao JIANG, Jian JIANG, Su-Wen CHEN, Guo-Biao LOU (Eds.)
Shanghai, China, June 11-13, 2014

CALCULATING THE RESPONSE OF BRIDGES TO A VEHICLE-BASED HYDROCARBON FIRE: SIMPLIFIED METHODOLOGY AND CASE STUDY

Spencer Quiel*, Takayuki Yokoyama, Lynne Starek** and Shalva Marjanishvili****

* Department of Civil and Environmental Engineering, Lehigh University, Bethlehem, PA, USA
e-mail: squiel@lehigh.edu

** Hinman Consulting Engineers, Inc., San Francisco, CA, USA
e-mail: tyokoyama@hce.com, lstarek@hce.com, smarjanishvili@hce.com

Keywords: Bridges, Hydrocarbon pool fire, Solid flame model, Radiation heat transfer

Abstract. *A streamlined simplified methodologyis proposed for the efficient calculation of a bridge's response to a vehicle-based hydrocarbon pool fireresulting from a tanker truck crash via a three-step methodology: (1) calculate the fire's characteristics and geometry; (2) calculate the heat transfer from the fire to the structural elements; and (3) calculate the temperature increase and resulting material and mechanical response of the structural elements. The approach, which uses a modified discretized solid flame model, synthesizes numerous existing techniques for calculating pool fire characteristics and radiation heat transfer to quantify the extent of damage caused by a specified fire threat. The methodology is demonstrated via a case studyof the 2007 MacArthur Maze fire near Oakland, CA, USA.*

1 INTRODUCTION

Transportation infrastructure is susceptible to fire due to the constant presence of vehicle traffic, including tanker trucks, and the potential for crashed or overturned vehicles to become fuel sources due to their flammable contents. Because of their confined environment, tunnels have received significantly more consideration than bridges with regard to designing for fire. For example, NCHRP recently commissioned a synthesis report which summarized available methods and design guidance for tunnel fires [1]. Little guidance, however, is provided in either the relevant US [2] or European [3] standards for the design of bridges regarding the approach to calculating applicable fire hazards. Tanker trucks ferrying gasoline and diesel, which are common and necessary to meet our society's current transportation demands, have provided the fuel for most of the recent severe fire events involving bridge structures. Comprehensive lists of recent severe bridge fire events in the US which clearly highlights the threat posedby tanker truck fires, have been compiled by Garlock et al. [4] and as part of a recently concluded National Cooperative Highway Research Program (NCHRP) study of bridge fire hazards [5].

This study focuses on the effects of hydrocarbon pool fires resulting from a tanker truck crash or sabotage since the quantity and flammability of its contents poses one of the worst-case hazards to a nearby bridge. The calculation of a bridge's response to a vehicle-based fire hazard consists of three steps: (1) determine the fire's characteristics (e.g. footprint, flame height, duration, and intensity); (2) calculate the heat transfer from the fire to the structural elements; and (3) calculate the temperature increase and resulting material and mechanical response of the structure. The authors have recently developed a streamlined, simplified approach for efficient calculation of a bridge's response to a vehicle-based hydrocarbon pool fire which synthesizes numerous existing techniques for calculating pool fire characteristics and radiation heat transfer. The geometry and intensity of the hydrocarbon fire are calculated based on the pool fire footprint and the fuel properties. Radiation heat transferis calculated usinga modified discretized solid flame approach which models the fire as having two zones: the luminous band (i.e. unobscured flame region) and the smoke-obscured upper region. The fire scenario considered is that of a large pool fire (approximately 4 meters to 25 meters in size) resulting from an overturned fuel tanker truck. Radiation is the dominant heat transfer mode for open-air pool fires of this size [6] (i.e. convective heating is neglected). Due to its efficiency, this approach can be used to calculate the effects of a wide range of fire types, sizes, and locations. These results can then ultimately be used to develop an envelope of performance for which the risk of damage and the effectiveness of potential fire protection measures can be evaluated. The methodology is demonstrated via a case study of the 2007 fire-induced collapse of an overpass in the MacArthur Maze freeway corridor near Oakland, CA, USA.

2 EXISTINGMETHODOLOGIES

2.1 Standard Fire Curves and Other Simple Models

In order to avoid making a calculation of the fire's characteristics, engineershave often appliedthe temperature-time histories of standard hydrocarbon fire curves such as that in the Eurocode [3]tobridge elements that are assumed to be exposed to a given fire hazard[7]-[9]. Even more simplified is the use of a constant high temperature, usually representing the maximum temperature (~1200 ℃) of the fire[10]. Though efficient, these approaches involve numerous approximations and may, at best, deliver an approximate and conservative prediction of the fire's affects since the applied temperatures are based on empirical data that represents a worst-case for fire growth. The standard curve and constant temperature approaches also have no decay phase and can therefore be used only to determine a time to failure rather than to calculate whether the exposed bridge elements would survive the duration of the fire event. The extent over which the standard fire temperatures are applied must be determined by the user based on the assumed extent of the fire.

2.2 Computational Fluid Dynamic (CFD) Modelling

At the high end of model complexity, structural-fire analysis of bridges performed in a research or forensic setting has commonly used computational fluid dynamics (CFD) software packages, such as NIST's Fire Dynamics Simulator (FDS) [11], to calculate the temperatures imparted to the structural elements from the defined fire hazard[5],[12],[13]. These tools are robust and generate significant levels of numerical resolution; however, they are also computationally expensive and may not be practical in many applications due to budgetary and scheduling constraints. These models require a large amount of input, much of which must be assumed if relevant data, observations, or design guidance is not available. Numerical simulations create large amounts of data which must be transferred between models (e.g. from a fire dynamics simulation to thermal and structural finite element models of the bridge components). Applying the results of one model to another is complicated by varying levels of spatial or temporal discretization required for convergence or precision in each model. This type of high-fidelity analysis is also not conducive to performing sensitivity studies on the parameters of the fire event, for which there is significant uncertainty due to their high degree of required computational effort.

2.3 Intermediate ApproachesUsing Fire Dynamics

Additional methodologies are available in whichthehydrocarbon pool fire is represented usinganalytical calculations of the fire characteristics (e.g. height, heat release rate, duration, and radiative intensity) based on idealized and semi-empirical combustion models. The results of these models can then be used to calculate or estimate radiation heat transfer from the fire to the structural elements, as has been done,for example, in a recent study of cable-stayed bridges [14].These methods are significantly less intensive than CFD solutions and allow for the fire to be rationally represented in the solution. By obtaining the fire's geometry and intensity for its given location, the distribution of fire effects over the bridge structure can be calculated. Although these solutions are significantly less detailed than those offered by CFD, they can provide a conservative model of the fire hazard with greater efficiency. Due to their efficiency, these approaches offer the potential for conducting a parametric study of the effects of fire scenario uncertainty, such as the footprint of the hydrocarbon spill, the exact location of the spill, or the rate at which fuel is potentially dispersed from the area via drainage.

A thorough discussion of analytical methods for calculating radiation heat transfer due to hydrocarbon pool fires is provided in the *SFPE Handbook for Fire Protection Engineering* [15]. Once the heat release rate [16]and fire height [17]of the fire are calculated for the given fuel type, fuel quantity, and pool size, the fire can be represented as a radiation-emitting object which can be used to calculate heat transfer to structural elements. The simplest approach is to represent the pool fire using a point source radiation model,in which the fire geometry is neglected when calculating radiation heat transfer with the exception of using the fire height to determine its vertical position [15]. The point source model is considered accurate at far-field standoff distances but unrealistically represents the spatial distribution of emitted radiation at standoffs less than a few fire diameters since the radiation source is concentrated at a single point[18].A more detailed method is the solid flame model, in which the fire is represented as a solid vertical object (typically a cylinder) that emits radiation from all sides. Fire heights are calculated using semi-empirical expressions [17], and radiation heat transfer from the solid flame cylinder to a target can be calculated using pre-calculated view factors [15].

Gasoline and diesel, which together constitute a large portion of overall truck-transported fuel, produce a large amount of soot and smoke during their combustion and develop a vertical fire structure with two zones: the luminous band (i.e. unobscured flame region) and the smoke-obscured upper region[18]. The two-zone characteristic of pool fires involving high-soot yielding fuels has been well established in several recent experimental studies, including that by Munoz et al. [20]. Variations to the solid flame model to include the two-zone representation have been previously proposed by McGrattan et al. [18] and Ufuah and Bailey [19].

3 PROPOSED METHODOLOGY

The pre-calculated shape factors in the most commonly used solid flame models[15]greatly simplify the calculation of radiation heat transfer from the pool fire. However, two issues arise when using the current models for bridge fire events. First, if the pool fire's footprint is similar in size compared to the standoff to the target (i.e. near-field), the contoured distribution of radiation heat flux delivered to the targets may not be realistic because the radiation source of the fire is located at the fire's centrerather than at its edges. Secondly, currentview factors also limit the model to using a cylinder to represent the fire, which uniformly emits radiation in all radial directions. Ideal fuel spills on a flat surface result in circular pool shapes, and most experimental testing has therefore been performed using circular pools. Realistic pool fires, however, almost always occur on surfaces that have slope - this is particularly true for fuel spills on roadways, which are sloped to induce proper drainage. A solid flame model which captures realistic behaviour should therefore be able to accommodate fire footprints of varying size and shape.

Rather than use view factors that are calculatedfor the entire fire's solid shape, the authors have taken the approach of uniformly discretizing the solid flame's surface into rectangular elements, each of which emits radiation toward potential targets. Calculating the summation of radiation heat flux from all fire surface elements introduces additional computational expense but replaces the need for a single view factor and allows the user to choose varying fire footprint sizes and shapes, as well as assign varying distributions of thermal emissivity from each vertical zone of the fire. This approach is called the modified discretized solid flame (MDSF) model, the details of which are outlined below. Since this approach requires more sophistication than a simple spreadsheet calculation, the authors have developed a computer program in Matlab to perform these calculations.

3.1 Modelling the Hydrocarbon Pool Fire

Before calculating the fire's characteristics, the user must first select the fuel type and volume as well as the footprint (shape and dimensions) of the pool resulting from the fuel spilling from the tanker truck. Variables to consider include the assumed rate of spill, the slope of the roadway, the presence of drainage, etc. For many fuel spills, a rectangular or trapezoidal footprint will account for sloping pavement in either one or two directions, respectively. The footprint shape discussed here will focus on a rectangular shape. Most of the semi-empirical equations for calculating pool fire characteristics are based on the circular pool shape – similar expressions for non-circular pool fires are not widely available. The pool fire diameter, D_f, is a required variable for most semi-empirical calculations, and therefore an equivalent value $D_{f,eff}$ can be calculated using a circle with the same area as the rectangular footprint. For pool fire footprints with an approximate aspect ratio (long edge to short edge) greater than two, the $D_{f,eff}$ is calculated by limiting the pool fire area, A_f, to a rectangle with dimensions of the short edge by two times the short edge. $D_{f,eff}$ for areas with aspect ratios greater than 2.5 may lead to inaccuracy when using the circle-based semi-empirical equations [18].The maximum heat release rate (HRR),$\dot{Q}_{f,max}$, of the pool fire can then be calculated as follows:

$$\dot{Q}_{f,max} = \dot{m}''\Delta H_{c,eff}\, A_f\left(1 - e^{-k\beta \cdot D_{f,eff}}\right) \tag{1}$$

where $\dot{m}''$is the mass loss rate (kg/m^2 • sec), $\Delta H_{c,eff}$ is the effective heat of combustion (kJ/kg), and $k\beta$ is the empirical constant (m^{-1}). These variables are fuel specific and can be obtained from standard references [16]. Assuming a no-wind condition, the resulting height of the pool fire is calculated using Heskestad's correlation [17]:

$$H_f = 0.235\dot{Q}_{f,max}^{0.4} - 1.02D_{f,eff} \tag{2}$$

3.2 Assembling the Heat Release Rate Time History

The duration of the pool fire, t_b (sec), can be calculated as the time needed to consume all available fuel over the pool area based on the fuel's mass loss rate, $\dot{\boldsymbol{m}}''$, and density. A simplified approach to assembling the pool fire's HRR time history would be to assume a constant HRR over the duration t_b. In order to account for a realistic rapid increase of heat release as well as a decay phase, the proposedapproach implements a time history model similar to that used in for tunnel design fires [1]. The time of fire growth, t_g, is taken as the minimum of t_b/5 or 10 minutes, and $\dot{\boldsymbol{Q}}_{f,max}$experiences a quadratic increase. The time of fire decay, t_d, is taken as the minimum of of t_b/2.5 or 20 minutes, and $\dot{\boldsymbol{Q}}_{f,max}$ experiences exponential decay.

3.3 Calculating the Heat Transfer

The solid flame model with the assumed footprint and calculated height $H_f$is discretized into n total rectangular elements that each emitsradiation heat flux. Each surface i is assigned an emissive power, E_i (kW/m^2) based on its location in either the luminous zone or the smoke zone. Results of an experimental study by Munoz et al. [20] indicated that the luminous zone of the fire was located in the lower 0.45H_f for gasoline fires and 0.35H_f for diesel fires. For this approach, the luminous zone is conservatively and simply modelled as the lower half of the solid flame model, as was previously used by Ufuah and Bailey [19]. Though several mathematical relationships are available to quantify the emissive power of pool fire flames and smoke [19], values of E_{flame} = 100 kW/m^{2}and E_{smoke} = 40 kW/m^{2}are used for this study in accordance with the experimental study of Munoz et al. [20].

The radiation heat flux imparted to a target j,$\dot{q}''_j$(kW/m^2), located outside the pool fire (i.e. the target is not enveloped by the solid flame model) can be calculated as the summation of each fire element's emissivity times the view factor from each fire element to that target, $F_{i\rightarrow j}$ (dimensionless):

$$\dot{q}_j'' = \sum_{i=1}^{n} E_i F_{i\rightarrow j} = \sum_{i=1}^{n} E_i \frac{A_i \cos\theta_i \cos\theta_j}{\pi r_{i\rightarrow j}^2} \tag{3}$$

$F_{i\rightarrow j}$ accounts for the area of the fire element, A_i (m^2); the distance between the fire element and the target, $r_{i\rightarrow j}$ (m); the absolute angle between the radius vector and the fire element's normal vector, θ_i; and the absolute angle between the radius vector and the target's normal vector, θ_j.Fire elements that have no "view" of the targets outside the pool fire impart no radiation heat flux. For targets enveloped by the solid flame, $\dot{q}''_j$equals an in-fire value of 120 kW/m^2 in the luminous zone in accordance with [15] and is linearly tapered across the height of the smoke-obscured zone from 120 kW/m^2 to E_{smoke}.

3.4 Calculating the Target's Response

Having obtained the radiation heat flux for each target, the increase in the target's temperature can be calculated using a lumped mass approach. This paper will focus on the calculation of the temperature increase of steel bridge beams since they provide the primary structural support to a large portion of the highway bridge inventory. These elements are represented as line elements that are discretized along their lengths into multiple targets to for which lumped mass heat transfer is calculated. When calculating θ_j for a line element representing a beam, the normal vector for the line is assumed to be perpendicular to the beam line element and lies in the same plane as the beam line and the radius vector between the target *j* and the emitting fire surface *i*. Assuming the case of a single beam that is discretized into *k* total elements along its length, the heat transferred to the lumped mass of beam element j,$\dot{Q}_{j,in}$, accounting for heat loss to the ambient environment, can be calculated as follows:

$$\dot{Q}_{j,in} = F_j \dot{q}''_{j,t} - (F_{j,total} - F_j)\left(h_{amb}\left(T_{j,t-1} - T_{amb}\right) + \sigma\varepsilon\left(T^4_{j,t-1} - T^4_{amb}\right)\right) \quad (4)$$

where F_j is the target's surface area (m^2) that is exposed to the fire's radiation; h_{amb} is the ambient convective heat transfer coefficient (taken as 20 W/m^2-K for natural convection); ε is the relative emissivity (taken as 0.5 for steel); and σ is the Stefan-Boltzmann constant (56.7E-9 W/m^2-K^4).The conduction heat transfer between adjacent targets, for example *j-1* and *j*, can be calculated as follows:

$$\dot{Q}_{j-1\to j} = \frac{(k_{j-1,t-1}+k_{j,t-1})(T_{j-1,t-1}-T_{j,t-1})}{2A_j L_j} \quad (5)$$

Thermal conductivity, *k*, is temperature dependent and is averaged between the adjacent elements. It is assumed that the cross-sectional area, A_j, and length, L_j, between beam elements are uniform along the length of the beam. Note that thermally dependent properties are calculated with a one-time-step lag (at *t-1*) – this approach has been used effectively for time steps of no more than 1 minute by the lead author in previous lumped mass heat transfer studies [21]. The temperature at each time step *t* is therefore calculated by considering the total heat transfer for the target *j*:

$$T_{j,t} = T_{j,t-1} + \left(\frac{\Delta t}{V_j \rho_{j,t-1} c_{j,t-1}}\right)\left(\dot{Q}_{j,in} + \dot{Q}_{j-1\to j} - \dot{Q}_{j\to j+1}\right) \quad (6)$$

where V_j is the target's material volume (m^3), ρ_j is the target's density (kg/m^3), and c_j is the target's specific heat (J/kg-K). The temperature change of each target can be used to calculate the corresponding decrease in material strength and stiffness as well as thermal expansion. Time histories of these responses can then be used to evaluate structural behaviour either via simple demand-to-capacity calculations or by mapping the results to a finite element model.

4 CASE STUDY: THE MACARTHUR MAZE COLLAPSE

On April 29, 2007, a tanker truck carrying 8,600 gallons of gasoline crashed while traveling on a connector ramp from southbound I-80 to I-880 in the MacArthur Maze freeway corridor near Oakland, CA, USA [10]. The crash caused the fuel to spill onto the road surface, covering all lanes of the connector directly under the eastbound overpass for I-580 and I-980 and state Highway 24, and soon thereafter burst into flame. The first span of the eastbound overpass collapsed approximately 17 minutes following the start of the fire, and a second adjacent spanin that overpass also collapsed about 5 minutes following the first collapse[10],[12],[13].

The simplified methodology described in this paper is able to predict the collapse of the two critical spans of the eastbound overpass, predict the timing of the first span collapse, and correctly indicate that othernearby spans would not fail due to the fire. A 30ft. (9.1meters) by 60ft. (18.3meters) rectangular fire is represented with a MDSF model as previously described. The fire is approximately located on the I-80/I-880 connector based on existing images and documents [10],[12],[13], and is shown in Figure 1.The geometry of the MacArthur Maze, including elevations, is modelled based on digitized satellite images from Google Earth. All girders are assumed to be the same section with a uniform dead load of 1.0 k/ft (14.5kN/m), based on typical plate girder dimensions for the relevant spans [13]. The dead load of the bridge induces an initial demand-to-capacity ratio (DCR) of 0.1.

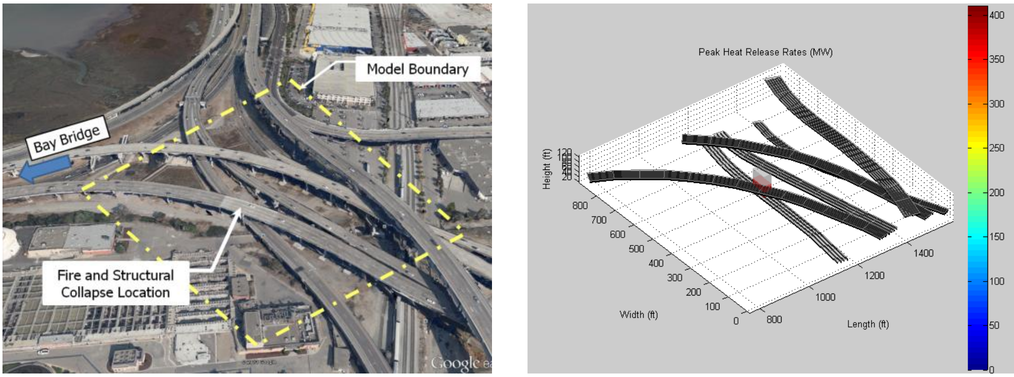

Figure 1. The MacArthur Maze overpass bridges: (left) satellite image and (right) fire model.

Previous case studies of the event have implemented a variety of approaches to model the heat output of the fire, including the use of a constant maximum temperature [10],[12] and an assumed HRR per unit area[13]. To illustrate the proposed methodology,theHRRis based on the 30 ft. by 60 ft. fire footprint with fuel consumption of 75% of total volume, assuming that 25% spills over the side of the bridge. The MDSF model and Equation 3 are used to calculate the heat flux delivered to each target (Figure 2). Temperature time histories are then calculated for each target based on Equation 6 (Figure 3). Each girder is discretized into 1-ft. lengths that are each modelled as lumped masses. For simplification, slabs are assumed to obstruct radiation heat transfer (i.e. the fire has no "view" of elements concealed by slabs).

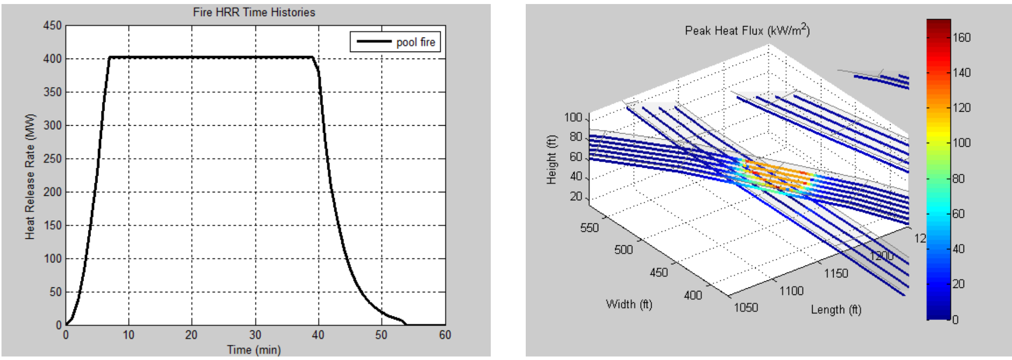

Figure 2. MacArthur Maze case study: (left) HRR of pool fire and (right) resulting maxheat flux to bridge girders

As a result of fire exposure, Figure 3 shows a steady temperature increase that peaks in the closest girders at nearly 1250℃ in 20 minutes, similar to the temperature history models presented in previous studies [10],[13]. Colour maps are created to show the corresponding envelope of temperature-dependent yield strength reduction (Figure 4) according toEurocode 3 [22]. These colour maps show which elements undergo significant strength loss and indicate areas of potential structural collapse.Time histories are also generated for target elements which show the rate of the strength loss. Based the initial dead load DCR of 0.1, "failure"is indicated when the residual yield strength reaches 10% (i.e. zero live load is assumed during the fire event). Figure 4 shows a plot of the yield strength time histories for all girders of the first failure span and indicatesa time to failure between 13 and 17 minutes for these girders. This shows conservative agreement with the published observations and previous studies [10],[12],[13]. The colour map in Figure 4 also indicates that the fire does not significantly affect the structure of adjacent spans in the I-580 overpass beyond the two that collapsed as well as thestructure of the other nearby overpasses. The predicted damage pattern is consistent with the actual overall outcome of the MacArthur Maze event.

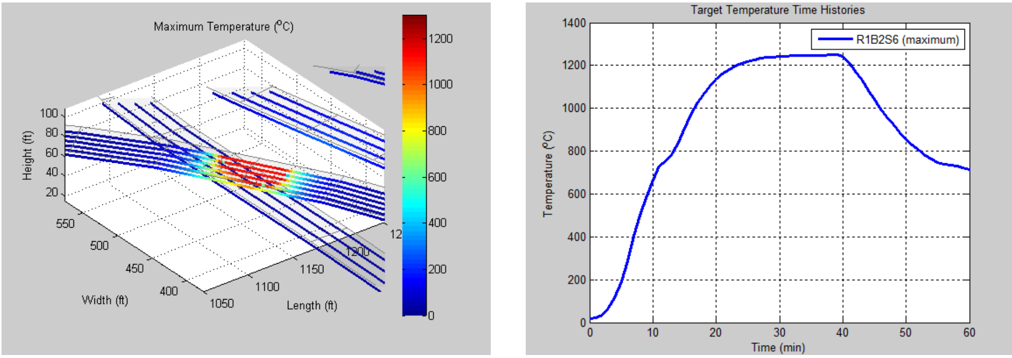

Figure 3. MacArthur Maze case study: (left) max T(℃) colour map and (right) single girder segment T(℃) history.

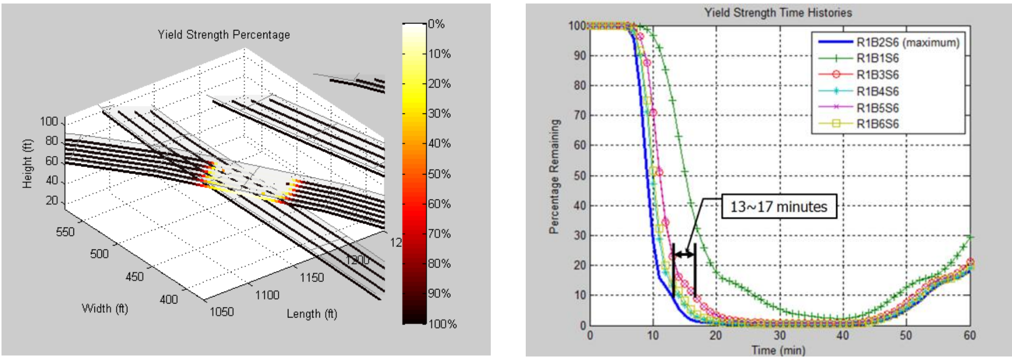

Figure 4. MacArthur Maze case study: (left) min yield strength % and (right) yield strength % history for collapse span.

5 CONCLUSIONS

This paper presents a simplified methodology for calculating the response of bridges to vehicle-based hydrocarbon fires. The approach synthesizes numerous calculation techniques based on both semi-empirical and physics-based models to quantify the extent of damage caused by a specified fire threat. This methodology includes models of the hydrocarbon pool fire, the radiation heat transfer to structural elements, and the degradation of the structural elements' strength and stiffness. The result is a computationally efficient and reasonably accurate tool for understanding the response of bridges to open-air vehicle-based hydrocarbon pool fires. A case study of the 2007 MacArthur Maze fire event shows that the methodology generates results that show good agreement with observed times to collapse during the event and effectively indicates the areas of collapse as well as areas that are unaffected by the fire.

REFERENCES

[1] Maevski, I.Y., *NCHRP Synthesis 415: Design Fires in Road Tunnels*, Transportation Research Board, Washington, DC, 2011.

[2] NFPA, *NFPA 502: Standard for road tunnels, bridges, and other limited access highways*, National Fire Protection Association, Quincy, MA, 2008.

[3] CEN,*Eurocode 1: Actions on structures, part 1-2 –General actions on structures exposed to fire,* European Committee for Standardization, Brussels, Belgium, 2002.

[4] Garlock, M., Paya-Zaforteza, I., Kodur, V., Gu, L., "Fire hazard in bridges: Review, assessment, and repair strategies," *Engineering Structures*, 35, 89-98, 2012.

[5] Wright, W., Lattimer, B., Woodworth, M., Nahid, M., Sotelino, E., *NCHRP Project No. 12-85: Highway Bridge Fire Hazard Assessment*, Transportation Research Board, Washington, DC, 2013.

[6] Babrauskas, V., "Estimating large pool fire burning rates," *Fire Technology*, 19, 251-261, 1983.

[7] Paya-Zaforteza, I., Garlock, M.E.M., "A numerical investigation on the fire response of a steel girder bridge," *Journal of Constructional Steel Research*, 75, 93-103, 2012.

[8] Kodur, V., Aziz, E., Dwaikat, M., "Evaluating fire resistance of steel girders in bridges," *Journal of Bridge Engineering*, 18, 633-643, 2013.

[9] Dotreppe J.C., Majkut S., Franssen J.-M., "Failure of a tied-arch bridge subjected to a severe localized fire," *Proc. 2005 IABSE Sym.*, Lisbon, Portugal, 2005.

[10] Astaneh-Asl, A., Noble, C.R., Son, J., Wemhoff, A.P., Thomas, M.P., McMichael, L.D., "Fire protection of steel bridges and the case of the MacArthur Maze fire collapse," *Proc. 2009 Technical Council on Lifeline Earthquake Eng. (TCLEE) Conf.*, Tang, Werner (Eds.), Oakland, CA, 2009.

[11] McGrattan K, McDermott R, Hostikka S, Floyd J.,*NIST Special Publication 1019-5: Fire Dynamics Simulator (version 5). User's Guide*, NIST, Gaithersburg, MD, 2010.

[12] Bajwa, C.S., Easton, E.P., Adkins, H., Cuta, J., Klymyshyn, N., Suffield, S., "The MacArthur Maze fire and roadway collapse: A 'worst case scenario' for spent nuclear fuel transportation?" *Proc. ASME 2012 Pressure Vessels & Piping Division Conference*, Toronto, Ontario, Canada, 2012.

[13] Choi, J., *Concurrent fire dynamics models and thermomechanical analysis of steel and concrete structures*, Ph.D. dissertation,Georgia Institute of Technology, Atlanta, GA, 2008.

[14] Bennetts, I., Moinuddin, K., "Evaluation of the impact of potential fire scenarios on structural elements of a cable-stayed bridge," *Journal of Fire Protection Engineering*, 19, 85-106, 2009.

[15] Beyler, C.L., "Chapter 3-10: Fire Hazard Calculations for Large, Open Hydrocarbon Fires," *SFPE Handbook on Fire Protection Engineering, 4th Ed.*, NFPA, Quincy, MA,2008.

[16] Babrauskas, V., "Chapter 3-1: Heat Release Rates," *SFPE Handbook on Fire Protection Engineering, 4th Ed.*, NFPA, Quincy, MA,2008.

[17] Heskestad, G., "Chapter 2-2: Fire Plume, Flame Height, and Air Entrainment," *SFPE Handbook on Fire Protection Engineering, 4th Ed.*, NFPA, Quincy, MA,2008.

[18] McGrattan, K.B., Baum, H.R., Hamins, A., *NISTIR 6546: Thermal Radiation from Large Pool Fires*,NIST, Gaithersburg, MD, 2000.

[19] Ufuah, E.,Bailey, C.G., "Flame radiation characteristics of open hydrocarbon pool fires." *Proc. World Congress on Engineering, Vol. III*, London, UK, 2011.

[20] Munoz, M., Planas, E., Ferrero, F., Casal, J., "Predicting the emissive power of hydrocarbon pool fires," *Journal of Hazardous Materials*, 144, 725-729, 2007.

[21] Quiel, S.E., Garlock, M.E.M., "Closed-form prediction of the thermal and structural response of a perimeter column in a fire," *Open Construction and Building Technology Journal*, 4, 64-78, 2010.

[22] CEN, *Eurocode 3: Design of Steel Structures, Part 1.2: General Rules – Structural Fire Design*, European Committee for Standardization, Brussels, Belgium, 2001.

8th International Conference on Structures in Fire
Guo-Qiang LI, Venkatesh K. R. KODUR, Shou-Chao JIANG, Jian JIANG, Su-Wen CHEN, Guo-Biao LOU (Eds.)
Shanghai, China, June 11-13, 2014

ASSESSMENT OF FIRE DAMAGE IN CONCRETE STRUCTURES: NEW INSPECTION TOOLS AND COMBINED INTERPRETATION OF RESULTS

R. Felicetti*

*Dept. of Civil and Environmental Engrg - Politecnico di Milano, Milan (Italy)
email: roberto.felicetti@polimi.it

Keywords: Assessment, Concrete, Damage, Non-Destructive Testing (NDT), Residual properties

Abstract. *The assessment of fire damage in concrete structures involves two complementary major tasks: on-site investigation and interpretation of the observed evidences. Concerning the first point, some innovative and viable inspection techniques are briefly illustrated in the paper. Their common trait is the ability to provide an immediate feedback, with no need for time-consuming laboratory analyses. As for the interpretation of results, the main issue is to harmonize the information provided by the available diagnostic tools, which is limited to specific ranges of temperature and to definite depths in the exposed concrete cover. The proposed approach relies on the parametric analysis of the compartment temperature developed in a set of realistic fire scenarios. The resulting temperature profiles are then checked against the results of the Non-Destructive inspection techniques, in order to select the most likely thermal input undergone by the structural members.*

1 INTRODUCTION

The assessment of the post-fire bearing capacity and durability of concrete structures is a complex and still open issue involving different areas of expertise, from Material Science to Structural Engineering, from Non-Destructive Testing to Fire Engineering. Developing new tools for the material inspection and devising new procedures for the interpretation of the test results are the two key aspects to be addressed in order to allow a substantial progress in this field.

The first step in the evaluation of fire damage implies a thorough inspection of the structure at different scales [1]: global (fire scenario, irreversible deformation of members), intermediate (cracks, spalling and rebar buckling within the cross-sections) and local (material identification in specific points). An overview on the established approach to the problem can be found in a couple of recognized technical publications on the assessment and repair of fire damaged structures [2, 3].

At the smallest scale of observation, the challenging issue is represented by the strong variability of the material condition at different depths from the heated surface. Due to the steep thermal gradients that develop during a fire, the concrete cover has to be regarded as a strongly layered stratum. This applies to the mechanical response (compressive and tensile strength, Young's modulus, hardness, velocity and attenuation of elastic waves) as well as to a number of physicochemical properties that are markedly affected by the exposure to high temperature (density of micro-cracks, porosity, humidity, chemical composition, colour, electric conductivity, etc.) [4, 5].

Many dedicated methodologies have been proposed for tackling the problem of material identification at this local scale [6]. Unfortunately, most of them rely on demanding laboratory analyses to be repeated on small samples taken at different depths within the cover (e.g. thin disks cut from a core). As a first tentative to go beyond this limitation, some innovative and viable inspection techniques were proposed by the author at the 4th SiF workshop (simplified interpretation of Ultrasonic Pulse refraction, discoloration measurement based on a digital camera and monitoring of the drilling resistance) [7]. Their common feature is the ability to provide an immediate feedback on the material condition, allowing to direct any further test on the structure being inspected. In recent years, other methods have been developed in the same perspective: the hammer drill pulse transmission (far more sensitive than the original drilling resistance method) [8], the chemo-physical analysis of the drilling powder (not requiring any sample preparation) [9] and the dynamic hardness of rebars (addressing the residual capacity of the reinforcement) [10]. A brief account on these methods is provided in the first part of this paper.

Despite of the wide range of available inspection tools, it has to be remarked that in most cases the information they provide is limited to specific ranges of temperature (or damage) and to definite depths within the exposed concrete cover. Combining different techniques is then essential to offset these restrictions, improving the reliability of the results. This requires a coordinated comparison of different indications against the possible temperature profile. The latter is the result of the temperature developed in the compartment, whose impact is smoothed by heat conduction in the exposed structural members.

In some regards, concrete elements in fire respond by both filtering the thermal input from the compartment and mapping the maximum experienced temperatures, by way of the physicochemical transformations occurring in the material. Even if not all the parameters governing the fire scenario are accurately known (fire duration, maximum temperature, decay rate, etc.) a parametric analysis can be performed, in order to produce a set of possible temperature profiles within the member, to be validated by checking their consistency with the experimental results. Besides allowing to merge the results pertaining to different temperature ranges and different depths, in the end a fire scenario of realistic severity is validated, extending the significance of results well beyond the inspected members. This kind of approach is discussed in the second part of the paper.

2 NEW INSPECTION TOOLS FOR MATERIAL ASSESSMENT

The assessment of the residual condition of fire damaged concrete can take advantage of a number of available tools [1]. They range from well established and relatively simple techniques (e.g. chiselling, surface hardness) to rather sophisticated test methods (surface waves, pulse refraction) or thorough laboratory analyses (sliced-core examination). However, in-situ viability, quickness and reliability are important requirements they fail to harmonize in most cases. Keeping this in mind, some innovative techniques for the material assessment at the local scale have been proposed by the author in recent years. A brief summary of their pros and possible limitations is given in the following.

2.1 Hammer drill pulse transmission

Monitoring the resistance encountered while drilling the concrete cover (time and work spent for a unit advance of the bit) is an effective method for post-fire in situ investigation [7]. The technique is very quick (about 10s per test) and not influenced by possible cracks or surface roughness due to spalling. On the other hand, the above drilling resistance indicators are not very responsive to mild fire damage, since a decrease is recognized just for a compressive strength decay exceeding 50%. Moreover, the local disturbance due to the hard coarse-aggregate pebbles require to average some tests for recognizing a clear trend in the material response.

To overcome these limitations, a new version of the drilling technique has been developed [8], taking

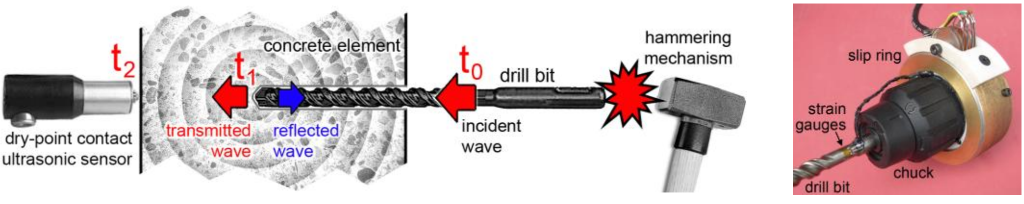

Figure 1. Working principle of the Hammer-Drill Pulse Transmission method and bit-strain measuring system.

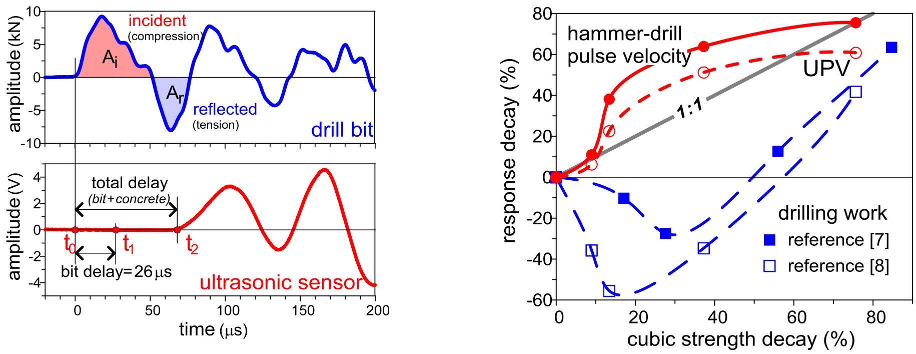

Figure 2. Time of flight of one hammer-drill pulse and sensitivity to thermal damage of the pulse velocity compared to the drilling work (UPV = conventional Ultrasonic Pulse Velocity).

inspiration from the Seismic While Drilling methods that are commonly used in geophysical surveys. In this case, the strong compressive pulses generated by the hammering mechanism of the drill are monitored, with the objective of measuring their time of flight to a fixed receiver positioned opposite to the drilled side of the member (pulse velocity scan, Figure 1). The implementation of this principle implies some technicalities, like strain gauges glued on the bit shank, a slip ring for signal transmission (Figure 1), a wide-band bridge-amplifier and a USB scope.

Thanks to the relatively low frequency of the excited waves (~ 15 kHz, i.e. wavelength ~ 0.3 m), the method is not influenced by the coarse aggregate and can be applied to strongly damaged and rather thick members. A series of calibration tests on uniformly damaged concrete cubes (150 mm side, original strength $f_{c,cube}$ = 52 N/mm^2) showed a very good sensitivity in the whole range of interest (Figure 2), with the same trend as the well established Ultrasonic Pulse Velocity test. Nonetheless, the potential of the method becomes evident when dealing with damage gradients. In the case of a concrete panel made of the same concrete and heated on just one side (thickness = 135 mm, T_{max} = 840-120 ℃), the intensive monitoring of the drilling process (10-20 pulses/mm) allows to produce a detailed profile of the residual pulse velocity (Figure 3). Also the repeatability of results is to be remarked.

Further studies are in progress, aimed at the interpretation of results in case of indirect transmission (drill and sensor on the same side), that is a relevant issue in case of single-sided access to the inspected member (e.g. walls, slabs and tunnel linings).

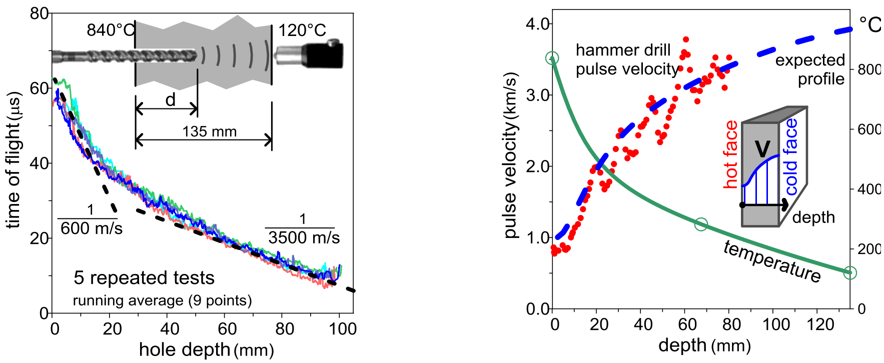

Figure 3. Time of-flight of pulses to the ultrasonic receiver in a thermally damaged concrete panel and profile of the pulse velocity through its thickness.

2.2 Analysis of sorted samples of drilling powder

A number of physico-chemical analyses suitable for the local condition assessment of fire damaged concrete require a preliminary grinding of the material into a fine powder (X-ray diffraction, thermo-luminescence, Differential Thermal Analysis DTA, Thermo-Gravimetric Analysis TGA, etc.). Moreover, some tests that are normally performed on intact samples, may be in principle carried out also on the pulverized material (carbonation depth, colour measurement, etc.). This evidence casts the base for merging the results of the drilling test and the following examination of the ensuing powder.

In the problem at issue, characterized by steep variations of the investigated properties with the drilling depth, an important requirement is to preserve the order of extraction, so to trace the original location of the powder. A special device has been developed to this purpose (Carbontest®, www.carbontest.it), which allows the continuous collection of the ground-concrete streaming through the helical flutes of the drill bit [9]. Basically, it consists of a annular head with a circular brush, to be pierced with the drill bit (Figure 4). The head is fitted with a funnel which directs the powder down into a vertical test-tube. This can be of transparent material, allowing to control the regular flow of the powder during drilling and to perform a first visual inspection. A narrow longitudinal cut, thin enough to prevent the powder to pass, makes possible to infiltrate the sample with the liquid chemicals used in some analyses (e.g. the phenolphthalein solution for the carbonation test).

One application of this device in the field of fire damage assessment concerns the detection of the pink-red discoloration taking place in heated concrete in the range 300-600 ℃ [1, 9]. By properly processing a digital image of the powder filled test-tube, a profile of the colour alteration along the depth of the drilled hole can be obtained. Another implementation is the Differential Thermal Analysis (DTA), a test that involves the heating of a small sample of ground concrete in order to trace the transformations (and then the temperatures) that were not yet developed during the fire. A special nickel-chromium test-tube was devised to this purpose, with a series of small holes to allow monitoring the temperature of the powder sample during its heating to 1000 ℃, performing then several DTA tests in one take. The main limitation observed in these first two examples was the impracticality of controlling whether to include or not the coarse aggregate in the sample, leading to some dispersion in the results.

Going back to the original purpose of the Carbontest® device (namely to check the pH in the concrete cover), it has to be remarked that the main source of alkalinity in concrete pores is portlandite (calcium hydroxide), that decomposes gradually above 450 ℃ and whose absence in the cement mortar is a marker of particular significance in fire safety of concrete structures. Although the de-hydroxylation of portlandite is a reversible process [11], the actual reinstatement of the pH conditions requires a sustained moist curing [12], which can be usually ruled out in elements protected from the rain.

In order to check the effectiveness of this method in post-fire damage assessment, the de-alkalinization depth was measured in the same concrete panel that was the object of the Hammer-Drill Pulse Velocity tests. By considering the scale factor between the length of the powder sample and the actual hole depth (about 2:1 for 10 mm bits), an almost uniform 26 mm depth was found (Figure 4),

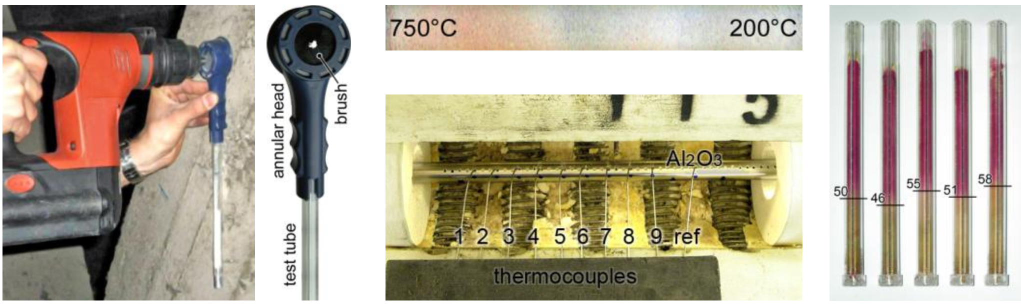

Figure 4. The Carbontest® tool for collecting the drilling powder, discoloration of a powder sample, setup for the multiple Differential Thermal Analysis, de-alkalinization depth in the panel of Figure 3 (scale 2:1, in mm).

corresponding to a maximum temperature of 575 ℃ (see the temperature profile in Figure 3). This is in good agreement with the generally recognized point beyond which all the original portlandite is decomposed.

It is worth to note that this kind of analysis could not be performed on drilled cores, since the water used for cooling the diamond tool would reinstate the alkalinity in the pores before being able to perform the test. Moreover, the original carbonation depth in the structure at issue has to be preliminarily assessed, in order not to confuse the effects of normal ageing and exposure to fire.

2.3 Dynamic hardness of rebars

Contrary to concrete, whose deterioration due to fire is largely irreversible, steel rebars may recover a significant share of their initial strength during cooling. This feature strongly depends on the type of material (carbon vs stainless steel, quenched vs micro-alloyed bars, hot worked vs cold drawn bars) and a specific study is often required to determine the permanent damage undergone by the reinforcement [13].

An interesting alternative is provided by the dynamic hardness test (Leeb test, ASTM A956). Contrary to traditional static hardness tests (Brinell, Rockwell, Vickers), which require a bench-mounted tester and a precise optical measuring system, the Leeb method is well suited to on-site applications. In this test a body fitted with a hard spherical tip (Ø = 3 mm) impacts the sample surface under a spring force. The impact and rebound velocities are measured at approximately 1 mm from the impact point, through the electric potential induced in a coil by a permanent magnet mounted inside the impact body (Fig. 5). The ratio of these velocities, multiplied by 1000, is defined as the Leeb hardness number.

This scheme allows to develop compact handheld devices that can be easily positioned on the tested rebar. The method requires a flat and smooth surface, though with not very stringent limits (average roughness < 2 μm). Moreover, the sample should be firmly restrained, so to prevent any vibration which may reduce the impact object rebound. This may be not the case of rebars embedded in a damaged concrete cover, due to the possible debonding ensuing from different thermal strain or buckling.

In order to ascertain the sensitivity of this method to the decay of the residual yield strength, the following steel rebars have been tested:

- Quenched and Self-Tempered bars (QST - Ø = 10 and 16 mm). It is presently the most extensively used reinforcing steel in Europe.
- Micro-Alloyed bars (MA - Ø = 10 mm), incorporating alloying elements (Niobium and Vanadium).
- Cold-worked Stainless-Steel bars (austenitic AISI 304L steel - SS - Ø = 12 mm). Contrary to hot rolled bars of the same material, this steel is very susceptible to high temperature.
- Square-section, Carbon-Steel bars (CS - side = 12 and 20 mm). Currently produced in Italy in 1950-70, they exhibit a higher strength, but are more fire sensitive than smooth hot-rolled carbon-steel bars.

Normal 0.6 m samples (for tensile testing) and shorter pieces of rebars (for hardness testing) were

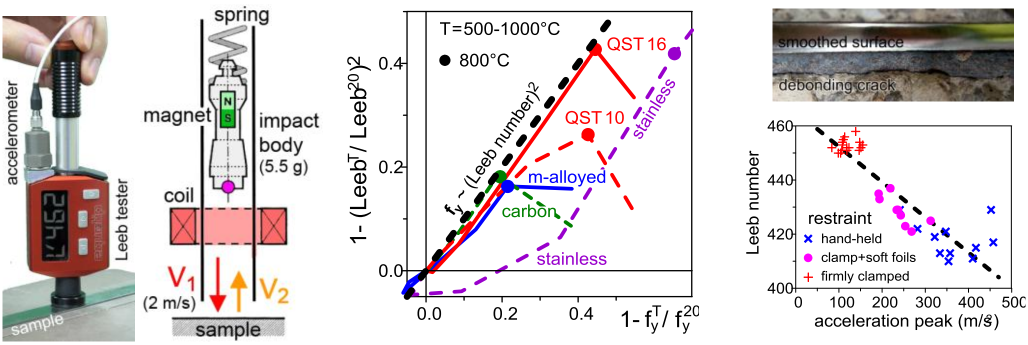

Figure 5. The Leeb tester fitted with the accelerometer for sample vibration compensation, functioning scheme of the instrument, correlation with the residual yielding strength and influence of the lack of restraint due to rebar debonding.

submitted to a series of thermal cycles (T_{max} = 500, 600, 700, 800 and 1000 °C). The hardness tests were performed by clamping the samples in a heavy machine vice. The top side of each sample was milled and then polished with sandpaper. About 30 tests were performed on two samples for each steel-temperature combination, with fairly repeatable results (coefficient of variation < 5%).

The experimental evidence for all carbon steels up to 800 °C (Figure 5) show a very good correspondence between the decay of the residual yield strength and the reduction of the square of the Leeb number (namely the rebound kinetic energy). At higher temperatures an increasing hardness and a larger dispersion are observed, probably because of grain coarsening in the crystalline microstructure. Nonetheless, the cited correlation allows an easy assessment of the residual performance of carbon steel rebars in the temperature range of major interest, without requiring any prior knowledge about the type of steel. A totally different behaviour characterizes cold-drawn stainless-steel, possibly because of the lack of a true yield point and the remarkably increasing strain hardening exhibited by the damaged rebars (strength ratio $f_t / f_y > 2.5$), enhancing the role of tensile strength f_t compared to yield strength f_y.

Concerning on-site applications, it has been found that an ordinary angle grinder fitted with flap-discs is a viable solution to flatten the rebar side, provided that work piece is not overheated. The final smoothing is performed by using a mini-drill and high grit sandpaper discs. Regarding the possible vibration of the tested bar due to debonding, a linear relation has been found between the peak acceleration of the tester body and the reduction of the Leeb number relative to the case of an effective restraint. If neglected, this effect may lead to an underestimate of the residual strength up to 10-15%.

3 COMBINED INTERPRETATION OF RESULTS

Despite of the wide assortment of inspection tools that may be conveniently used for post-fire assessment, a complete characterization of both the maximum damage at the surface and the heat penetration in the core of a concrete member generally requires the combined implementation of several methods. Limiting the discussion to techniques not requiring too demanding on-site operations nor laboratory analyses, the following brief summary can be drawn (Figure 6), based on direct experience of the author [1, 5] and literature review [2, 3, 6]:

- Rebound hammer. It detects the average response of the cover at a notional depth of about 15 mm, provided that the experienced temperature exceeds 500 °C.
- Cut And Pull-Out (CAPO) test. It exhibits an excellent sensitivity to the strength decay in the whole range from pristine to severely damaged. The information pertains to just a few millimeters depth.
- Colorimetry. The pink discoloration occurring at 300 °C -600 °C can be detected at any depth, once a proper sample has been taken from the structure. In the author experience the 450 °C isotherm can be detected with digital image processing without a specific calibration for the concrete at issue.

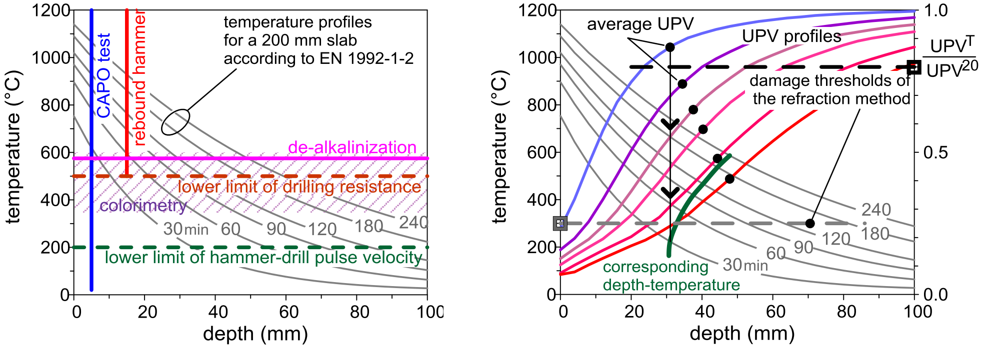

Figure 6. Sensitivity range of some common inspection techniques and connection between the temperature profiles and the expected pulse velocity values sensed by the ultrasonic techniques.

- De-alkalinization depth. A much sharper front than pink discoloration is detected by using a pH indicator on a dry powder sample. It corresponds to a maximum temperature of about 575 °C.
- Drilling resistance. In principle, the drilling work and time can be measured at any depth. The onset of the thermal decay is generally observed at about 500 °C.
- Drilling pulse velocity. This new technique is definitely more sensitive than its predecessor. One limitation of the present version is that a double-sided access to the inspected member is required.
- Average Ultrasonic Pulse Velocity via direct transmission. It provides the total transit time of ultrasonic pulses through the member thickness (integral of the slowness, i.e. 1 / pulse velocity). Due to the remarkable heterogeneity of crossed layers, the interpretation requires some assumptions on the temperature profile and the velocity decay [1]. This is functional to work out a velocity profile (Figure 6) and, finally, to validate the measured value of the average pulse velocity (1 / average slowness).
- Ultrasonic Pulse Refraction via indirect transmission. The pulse velocity profile can be identified by applying both ultrasonic probes on the surface exposed to fire, according to the refraction technique. The migration algorithms commonly used in geophysics may be implemented to reveal the velocity profile. As an alternative, some correlation diagrams have been produced [1, 7] to detect the thickness of the significantly damaged layer (UPV < 80% UPV^{20}, T > 300 °C).

As concerns the temperature profiles which develop in concrete members exposed to fire, they are the final result of heat conduction under the thermal input coming from the burning compartment. In fully developed room-fires this latter depends mainly on the specific fire load (q_t, referred to the total surface area of the compartment), the opening factor (O, governing the rate of heat release in ventilation controlled fires) and the thermal properties of the enclosure surface (which rule the heat absorbed and later released by the lining materials).

By considering the parametric temperature-time curves indicated by Eurocode 1, the envelope profiles of the maximum experienced temperature have been worked out (Figure 7), including the further

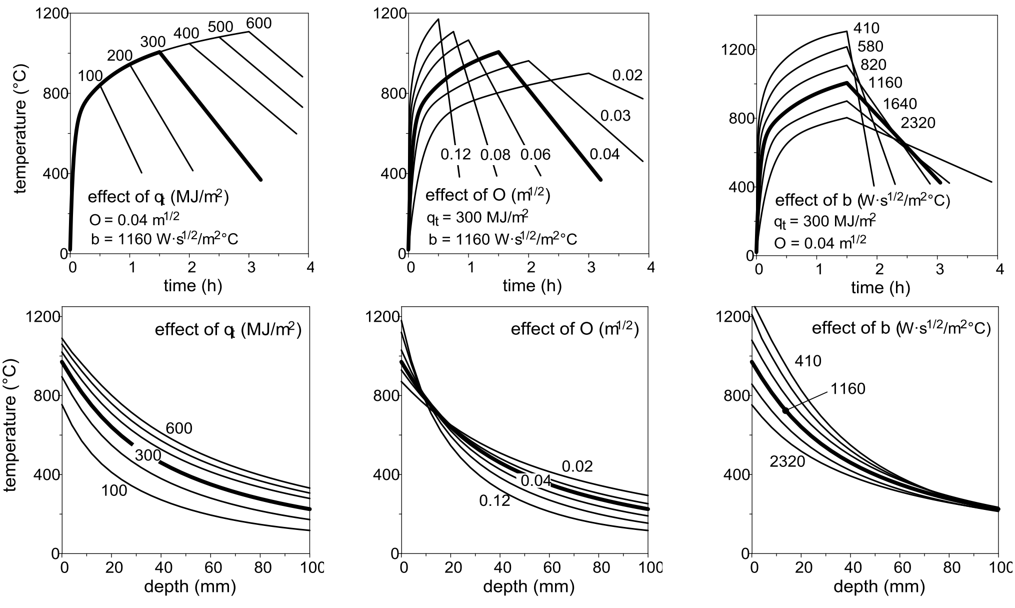

Figure 7. Influence of specific fire load q_t, opening factor O and square root of thermal inertia b on the parametric temperature-time curve and on the corresponding maximum temperature profiles in a 200 mm thick concrete slab.

heat propagation occurring during the decay stage of the fire. It transpires that all the cited techniques are expected to exhibit a good response to a variation of the fire load, thanks to the regular evolution of the temperature profiles. If one considers also the fuel loss due to external flaming, this is often the most uncertain parameter in the identification of a fire scenario. On the other hand, a change of the opening factor may lead to wrong conclusions if one relies on just a surface inspection, since small vents translate into relatively colder but - on the whole - more severe fires. This aspect can be hardly revealed by the techniques detecting a temperature threshold of 450-600 ℃ (e.g. colorimetry and de-alkalinization). Finally, the presence of insulating and lightweight lining materials (low values of b) tends to boost the surface damage compared to the average impact on the cross section, though also in this case a combination of assessment techniques pertaining to different depths should allow to tackle this aspect.

4 IDENTIFICATION OF THE FIRE SCENARIO IN A FURNITURE SHOP

One example of merging the results ensuing from several assessment techniques, through a parametric analysis of the fire scenario, is provided by the case study of the total burnout of a furniture shop. The building has a regular open plan (12.5 × 40 m) and comprises 3 storeys above ground, characterized by different soffit heights (3.8, 3.3, and 3.0 m from ground to roof) and different opening factors (O = 0.18, 0.09 and 0.06 $m^{1/2}$ respectively). The bearing structure is a cast-in-place concrete frame, constructed in many batches of rather variable quality, according to the normal practice in the '60s. Based on the fire brigades report and photographic evidence (Figure 8), the fire started at ground floor and propagated through an open stair directly to the second floor, and later to the first floor. The burning stage at each floor lasted between 30 and 60 minutes.

The complex sequence of the events, the vertical draught through the stair and the lack of data on the distribution of the fire load dissuaded from modelling the fire scenario of the entire building. Nonetheless, the results of the ND tests performed all over the structure indicated that the N-E edge of each storey was the most severely affected part of the building. Then, these portions were considered as separate virtual compartments, to be analysed via a numerical zone model (Ozone 2.2.5), including the realistic description of the opening factor and of the thermal properties of the materials lining the compartments. Conversely, the fire load was kept as a free parameter, allowing to adjust the fire severity until the indications provided by the on-site inspections were met.

Limiting the discussion to the possible fire scenario developed at the first floor, a series of time-temperature curves have been produced (Figure 8), under common assumptions concerning the evolution in time of the Rate of Heat Release (t-squared growth with medium rate, max RHR = 250 kW/m^2, decay starts at 30% residual fire load). Due to the relatively large opening factor, both the numerical analyses and the EN 1991-1-2 parametric fire would indicate a remarkably fast cooling in the decay stage. It is worth to note that the Ozone software doesn't allow for the inverse heat flux returned by the enclosure walls in the end of the fire. This issue has been addressed by Feasey and Buchanan, who proposed some refinements to the reference parameters and the time scaling factors of the parametric fire [14].

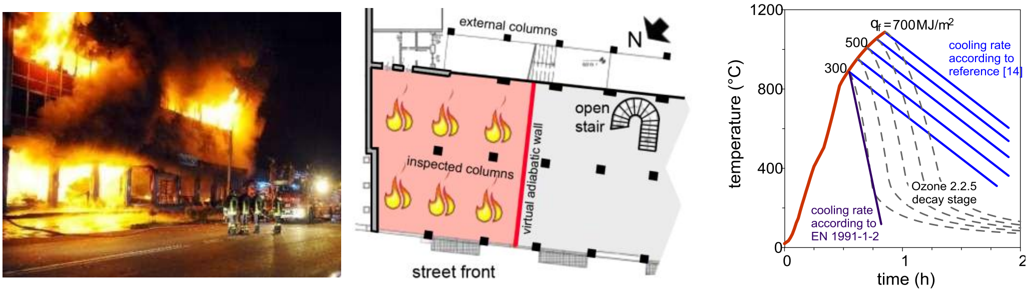

Figure 8. View of the burning stage at the ground and second floor of the furniture shop, sub-compartment considered in the analysis of the fire scenario at the first floor and time-temperature curves obtained via the zone-model.

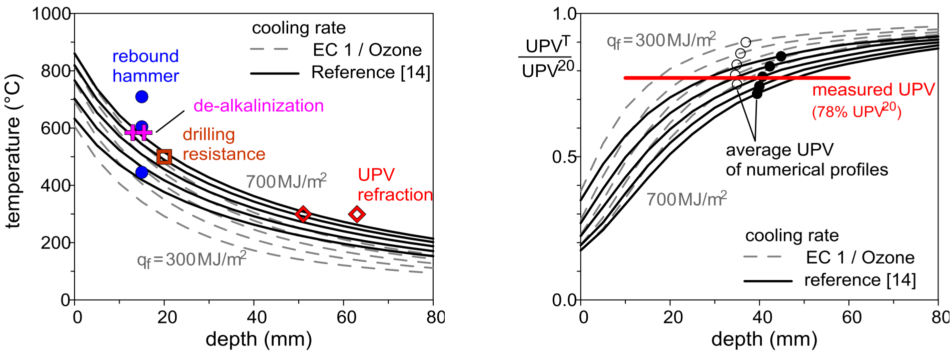

Figure 9. Comparison between the results of the on-site inspection techniques and the temperature profiles produced by the time-temperature curves of Figure 8 along the cross-section axis of a 400 mm×400 mm concrete column; corresponding Ultrasonic Pulse Velocity profiles and comparison with the average through transmission velocity.

As concerns the onsite inspection of the damaged elements, it has been decided to focus the attention on the top part of the central columns, due to their representative location and the minor influence of rebars and cracks compared to the beams. The columns (400 mm×400 mm, loaded at about 10% of their mean capacity) were lined with a 10 mm layer of plaster, which partly fell off during the fire. Being the progress of this occurrence unknown, a permanent plaster layer of half thickness has been considered in the thermal analyses. A summary of the ND results and the potential temperature and Ultrasonic Pulse Velocity profiles are reported in Figure 9 (the latter are based on the decay plot presented in [1, 7]).

It has to be pointed out that the interpretation of many ND results relies on the comparison between the material responses before and after damage. In real situations just the average original quality of concrete can be assessed, by checking like elements not exposed to fire (in this case the columns located outdoor and in the basement). Due to the poor quality control during construction of the structure at issue, the apparent effects of fire in a specific member may be enhanced (or offset) by the initially lower (or higher) grade of concrete compared to the average. This is a further reason for merging the results from several techniques, preferably taken from different members of the same compartment. In principle, the depth of de-hydroxylation (related to a specific chemical transformation) and the drilling resistance (based on a comparison between deep and shallow layers crossed by the same hole) should be less influenced by this source of uncertainty.

The final outcome is that the highest fire load in the considered range (q_f = 600-700 MJ/m^2 per unit floor area) and the slower decay rate [14] seem to fit better the experimental results. A larger dispersion is exhibited by the surface hardness, whereas the drilling result required averaging more tests (5 in this case) for detecting the onset of the drilling work decay. The ultrasonic refraction method entailed a careful examination of the received signals, due to the dramatic attenuation of pulses in the damaged cover. The direct transmission of the ultrasonic pulses proved to be far more viable, although the interpretation would have not been possible without the aid of a fire scenario model and of the corresponding temperature profiles. This latter technique involves the entire thickness of the inspected member and is less influenced by the further weakening which may affect the external layers in the months following the fire (due to moisture absorption from the environment).This is probably the reason why a slightly lower fire load (q_f = 500 MJ/m^2) is more consistent with this latter results.

5 CONCLUSIONS

In this paper new inspection tools and a procedure for the coordinated interpretation of the results have been presented, aimed at devising a practical and sound approach to post-fire damage assessment of concrete structures. The main conclusions that can be drawn from this work are listed in the following.

(1) Monitoring the velocity of the strong pulses generated by a hammer-drill combines the viability of the drilling method with a definitely higher sensitivity to mild damage levels. Some studies are in progress to develop a more affordable tool and a more flexible test configuration.

(2) Tracing the alkalinity of a sorted sample of drilling powder is a very quick method (about 1 minute per test) for detecting the depth of the 600 °C isotherm. Further investigations are needed to check the influence of concrete composition, ageing and ambient moisture.

(3) The standard dynamic hardness test is a practical solution to assess the residual yield strength of rebars. A quite general correlation has been found for ordinary carbon steels up to 800 °C. For other materials (work hardened and stainless steels) the method can be used to extend the results of destructive tests. The possible bar debonding may translate into to a sizeable strength underestimate.

(4) The coordinated comparison of on-site inspection results against the temperature profiles produced by a parametric analysis of the fire scenario is an effective way (i) to merge indications pertaining to different ranges of depth and temperature and (ii) to form a more reliable picture of the residual condition of the structure. Since in the end a fire scenario of reasonable severity is validated, the significance of the results may be extended well beyond the inspected members.

REFERENCES

[1] Felicetti R., "Assessment Methods of Fire Damages in Concrete Tunnel Linings", *Fire Technology,* 49(2), 509-529, 2013.

[2] CIB W14 Report, "Repairability of Fire Damaged Structures", *Fire Safety J.,* 16, 251-336, 1990.

[3] Concrete Society, "Assessment and repair of fire damaged concrete structures", TR 68, 2008.

[4] RILEM, "Properties of Materials at High Temperatures: Concrete", Schneider U. (ed), Dept. Civil Engrg University of Kassel, Germany, 1985.

[5] FIB Task Group 4.3, "Fire design of concrete structures - structural behaviour and assessment", Fib bulletin 46, 63-114, 2008.

[6] Laboratoire Central des Ponts et Chaussées, "Présentation des techniques de diagnostic de l'etat d'un béton soumis à un incendie", Report ME 62 (in French), 2005.

[7] Colombo M. and Felicetti R., "New NDT techniques for the assessment of fire-damaged concrete structures", *Fire Safety Journal*, 42, 461-472, 2007.

[8] Felicetti R., "Assessment of Fire Damaged Concrete via the Hammer-Drill Pulse Transmission Technique", *Int. Symp. on NDT of Materials and Structures (NDTMS 2011)*, 205-212, 2011.

[9] Felicetti R., "Assessment of the deteriorated concrete cover by combined while-drilling techniques", *ASCE Journal of Infrastructure Systems*,18 (1), 25-33, 2012.

[10] Felicetti R. and Gambarova P. G., "Assessment of the Residual Strength of Fire-Damaged Steel-Rebars" , *Int. Symp. on NDT of Materials and Structures (NDTMS 2011)*, 213-218, 2011.

[11] Alarcon-Ruiz L., Platret G., Massieu E. and Ehrlacher A., "The use of thermal analysis in assessing the effect of temperature on a cement paste". *Cement and Concrete Research*, 35, 609-613, 2005.

[12] Poon C.-S., Azhar S., Anson M. and Wong Y.-L., "Strength and durability recovery of fire damaged concrete after post-fire-curing", *Cement and Concrete Research*, 31, 1307-1318, 2001.

[13] Felicetti R., Gambarova P.G. and Meda A., "Residual behaviour of steel rebars and R/C sections after a fire", *Construction and Building Materials*, 23 (12), 3546-3555, 2009.

[14] Feasey R. and Buchanan A. H., "Post-flashover fires for structural design", *Fire Safety Journal*, 37 (1), 85-105, 2002.

8th International Conference on Structures in Fire
Guo-Qiang LI, Venkatesh K. R. KODUR, Shou-Chao JIANG, Jian JIANG, Su-Wen CHEN, Guo-Biao LOU (Eds.)
Shanghai, China, June 11-13, 2014

RESISTANCE OF STEEL SPACE FRAMES SUBJECTED TO LOCALIZED TRAVELLING FIRE

Hong-xia Yu*, Xiao-qian Sun* and Kelvin Wong*

* Arup International Consultants (Shanghai) Co., Ltd
e-mails: vala.yu@arup.com, allen.sun@arup.com, kelvin.wong@arup.com

Keywords: Steel frame, Fire resistance, Travelling fire, Localized fire, Fire model, Heat transfer

Abstract. *Large open spaces such as airport terminals have much lower fire risk because heat cannot accumulate as in a confined space and flashover is unlikely to happen. Therefore, conventional design fires, either standard fire or natural compartment fire, are not applicable. Traditionally, combustion of single item has been considered for the performance-based design of these buildings. However, when combustibles are placed relatively close, such as a restaurant, it is still possible that fire spread to adjacent item by direct flame contact. Fire spread is a more threating fire scenario than one localized fire and should be considered when evaluating the structural safety.*

This paper aims to assess the potential fire damage to a conservatory bridge and determine it is possible to leave the roof structure of the conservatory bridge unprotected. As both post-flashover fire and localized fire seem not-applicable, a travelling fire model, which simulates the procedure of fire spread from one table to another in a restaurant, is developed. Corresponding methods for determination of the fire size, heat transfer procedure and steel member temperatures are introduced. Structural analysis model was built in finite element program LS-DYNA and the temperature load including both heating and cooling phase corresponding to the fire travelling procedure was applied. The results showed that if the size of the heated zone is reasonable compared to the length of the structure, the roof structure can maintain stability by force-redistribution.

1 INTRODUCTION

In a mixed development project, a sky bridge is designed to connect several high-rise towers at high altitude. Over the bridge is a conservatory space to hold functions such as banquet halls, restaurants and gyms. Figure 1 shows the cross-section of the conservatory bridge. Below the main deck is the huge truss to support the structure. Over the main deck is an oval-shaped steel frame as the roof structure. The roof structure is formed by continuously-arranging two-dimensional truss with triangular cross-section. The trusses are pin-supported at both ends with a span of 32m and 12m high. The total length of the bridge is nearly 300m, but the roof structure is divided to segments of roughly 50m long with flexible joints in between to allow for thermal expansion. A typical segment of the structural form is also shown in Figure 1. According to China's fire design code for high rise building [1], roof structure should be provided with 1.5h fire resistance. Considering the size of this project, fire protection of all structural members means huge cost and when the fire painting ages, it will be extremely difficult to replace it at such a high altitude. Therefore, it is proposed that a performance-based approach should be adopted to identify the fire hazard of the conservatory structure and then determine whether the structure needs to be fire protected.

When designing structures for fire safety, two kinds of fire models have been widely used. One is a post-flashover fire model, which is typically used to confined space. It is assumed the whole space is consumed by fiercely burning fire and all members in the space are enclosed by a relatively uniform temperature field. The other is a localized fire model, which is typically used in large empty spaces like airport terminals. As the combustion generally involves only one item, the fire size is limited and its impact to the structure depends on the relative distance between them. For the conservatory bridge, flashover is unlikely to happen on the main deck because the space in the conservatory is large and high, which means the smoke takes a long time to accumulate and its temperature gets cooler during rising. It is unlikely to accumulate sufficient heat to incur flashover. Even if the smoke under the roof becomes sufficiently hot, it is quite possible to break the glazing and lead to an open combustion. Therefore, the post-flashover fire model is not applicable. However, a localized fire model also appears to be un-conservative. Using restaurants as an example, the tables and chairs can be placed very close to each other. If one table catches a fire, it is quite possible to spread to the adjacent item by direct flame impingement. As the fire spread may cause a long-lasting fire that affects an extensive part of the structure, it is a risk that has to be considered during the analysis.

To solve this problem, a localized travelling fire model is developed to simulate the procedure of fire spread from one item to another in a large open space.

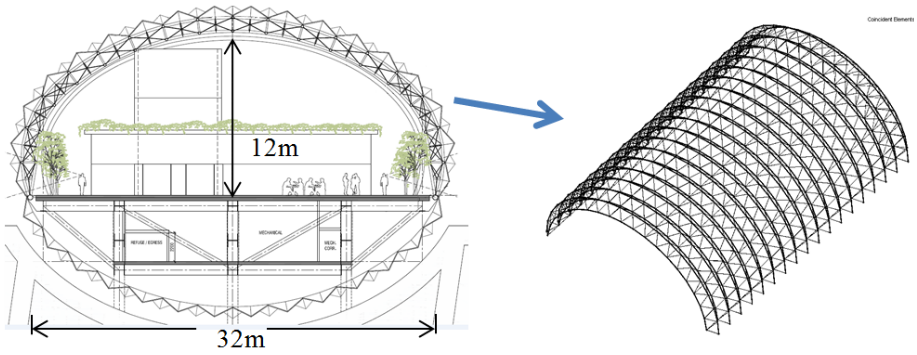

Figure 1. The conservatory bridge and roof structure.

2 FIRE SPREAD MODEL

The fire spread model was established for the banquet hall, which is the largest fire zone on the conservatory bridge. The banquet hall takes the whole width of the bridge and is 18m long with the dining table arrangement as shown in Figure 2. Generally, a fairly wide aisle will be left in the middle to allow for people flow or holding activities. This aisle can work as a natural fire separation band to prevent fire spread

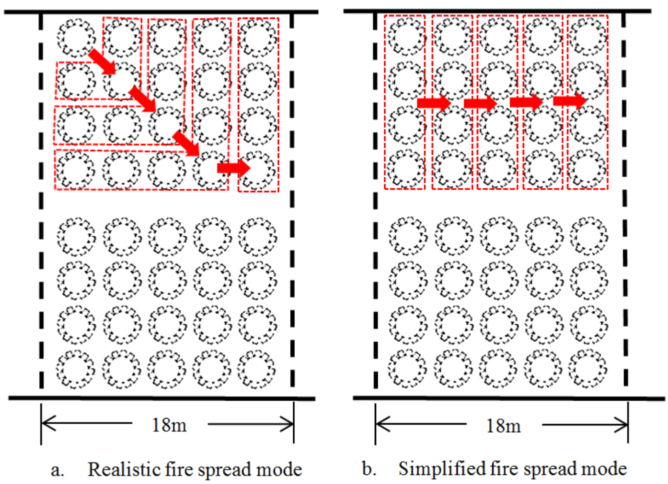

Figure 2. Table layout and fire spread direction.

from one side to the other. Therefore, it is reasonable to assume that the worst fire scenario involves combustion in half of the banquet hall. In the following calculation, it is also assumed that each table (including 12 chairs) is 3.5m×3.5m. A more natural fire travelling mode should be that fire starts from one item and then spreads outside as shown in Figure 2(a). To simplify the calculation procedure, it is more conservatively assumed that fire spread along the longitudinal direction of the bridge as shown in Figure 2(b).

2.1 Heat Release Rate of One Table

Apart from tables and chairs, combustibles in the banquet hall also include carpet, upholstery, cabinet, etc. To avoid limitation to the applicability of the proposed method, it is decided that the heat release rate of one table should not be determined from combustion test. Instead, it is calculated according to the survey data of heat release rate per unit area.

Eurocode 1: Part 1.2 [2] recommends an average heat release rate of 500kW/m^2 for theatre and 250kW/m^2 for office and retail. CIBSE design guide [3] recommends 290kW/m^2 for office and 550kW/m^2 for retail. Based on that, it may be conservative to assume a heat release rate of 500kW/m^2 for the banquet hall. As each table takes an average area of 3.5x3.5, its peak heat release rate is 0.5×3.5×3.5=6.125MW. Using the t^2 fire development model and assuming a fast developing fire, the time to reach the peak heat release rate is $t_0 = \sqrt{Q} \times 150 = \sqrt{6.125} \times 150 = 372.23\text{s} = 6.2\,\text{min}$. The fire duration time is determined by the fire load density. Survey to 15 restaurants [4] suggests the fire load density to be 652MJ/m^2. Combustibles generally do not completely burn out during fire and Eurocode 1: Part 1.2 [2] recommends a combustion rate of 80%. Following the recommendations, the total combustible energy for one table is 652×80%×3.5×3.5=6395MJ and the fire duration of each table is $t = (6395 - 6.125 \times 372.23/3)/6.125 = 920\text{s} = 15.3\,\text{min}$.

The heat release rate for the combustion of one table is shown in Figure 3. The first 6.2min is the fire development phase. From 6.2min to 21.5min is the steady combustion. To further simply the calculation, the fire development procedure is ignored and the fire duration is simply assumed to be a steady combustion of 17.4min as shown by the dashed line.

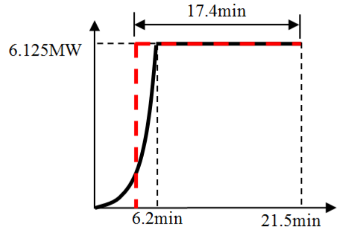

Figure 3. Heat release rate for one table.

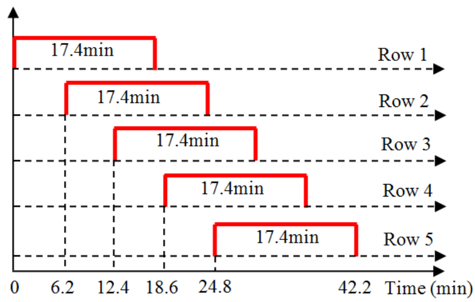

Figure 4. Heat release rate for a spreading fire.

2.2 Heat Release Rate of A Travelling Fire

The fire development phase can be interpreted as the procedure when fire starts from one location of the object and gradually develops to engulf the whole object. For the fire spread from table to table, it is then reasonable to assume that fire start from one side of the table, and when it develops to the other side of the table, i.e., the whole table is engulfed in fire and the heat release rate reaches the peak value, it ignites the adjacent object. Based on this assumption, the heat release rate for the fire spread model in Figure 2b can be shown in Figure 4, where each row is ignited at 6.2 min after the previous row starts to burn. The entire burning procedure lasts for 42.2 min.

3 HEAT TRANSFER TO THE STEEL MEMBERS

3.1 Heat Transfer Calculation Principle

Eurocode 3: Part 1.2 [5] recommends an incremental method to calculate the steel temperature rise when subjected to fire. The basic principle of this method is within a small time increment of Δt, the heat transfer to the steel member h will cause a temperature rise of

$$\Delta T_s = (h \times \Delta t)/(V_s \rho_s C_s) \quad (1)$$

where h is the heat transfer to the steel; V_s, ρ_s,and C_s are the volume, density and specific heat of the steel member.

The calculation for h needs to identify all heat transfers occurring to the steel member. This includes the radiation from the flame, the convection between the member and the surrounding air and the radiation from the steel member to the surrounding air**.** For the radiation from the flame, the SCI report [6] recommends a method to calculate the temperature of steel members outside an external wall opening and subject to spilled flames from the window. Following the same principle, a similar approach is adopted here and the net heat influx to the steel member is

$$h = A_s \varepsilon_c \sigma \Phi \times \left(T_f^{\,4} - T_s^{\,4}\right) - A_s \alpha_c \left(T_s - T_m\right) - A_s \varepsilon_s \sigma \times (T_s^4 - T_m^4) \quad (2)$$

In the equation, T_f, T_s and T_m are the temperatures of the fire, steel, and ambient air respectively; A_s is the surface area of the steel member； ε_c is the flame emissivity; ε_s is the steel emissivity; σ is the Stephan-Boltzmann constant; Φ is the view factor from the flame to the steel member surface.

The flame temperature is actually non-uniform and the average of the core temperature and the surface temperature is used as the fame temperature in the calculation, which is 1113K. To calculate the view factor, the flame is simplified to a block, whose all external surfaces are treated as radiation panels. To calculate the radiation to the steel member, the view factors for all the panels are calculated respectively and added together.

3.2 Flame Size

During the calculation of view factors, the flame is simplified to a block of L×w×h, where L×w is the size of the fire bed, h is the height of the flame. According to SFPE Handbook [7], the height of the flame is calculated as

$$H_f = 0.23 Q^{2/5} - 1.02 D \quad (3)$$

where Q is the total heat release rate of the fire, D is the flame diameter and calculated as

$$D = \sqrt{(4 \cdot Q)/(\pi \cdot q_e)} \quad (4)$$

q_e is the heat release rate per unit area.

3.3 Ambient Air Temperature

For a fire with a steady heat release rate of Q, the convective part of the heat release rate is generally calculated as

$$Q_c = Q/1.5 \quad (5)$$

According to SFPE Handbook [7], the temperature rise at the center of the plume is

$$\Delta T_0 = 9.1[T_\infty /(g c_\rho^2 \rho_\infty^2)]^{1/3} Q_c^{1/3} (z - z_0)^{-5/3} \quad (6)$$

where, $9.1[T_\infty/(gc_\rho^2\rho_\infty^2)]^{1/3} \approx 25$, z is the height along the center of the plume, z_0 is the virtual fire origin.

Away from the plume center, the air temperature reduces gradually. At a horizontal distance R from the plume center, the air temperature rise can be calculated as

$$\Delta T_{\mathrm{m}} = \Delta T_0 \exp\left(-\left(\frac{R}{0.144(z-z_0)\sqrt{T_0/293}} \right)^2 \right) \tag{7}$$

3.4 Heat Transfer Calculation For a Travelling Fire

The principle for calculating the heat transfer from one fire is introduced in Section 3.1. For a spreading fire, the steel member may be subjected to the actions from several fire sources at the same time. In this case, the radiations from all fire sources are calculated respectively and then added together. Using one planar steel frame as an example, the fire exposure sequence is shown in Figure 5.

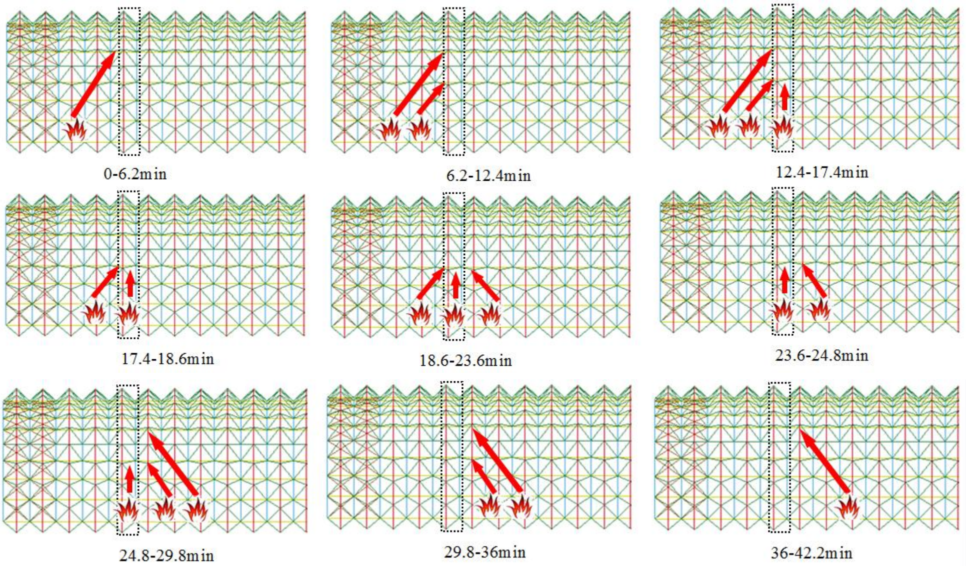

Figure 5. The sequence of fire exposure for one frame.

For each specific row of tables, the radiations from three sides are considered. One top panel represents the top surface of the flames and two side panels represent the two sides of the flames.

3.5 Steel Temperatures

Temperatures were calculated for the frame subjected to the fire as shown in Section 3.4. As the fire travels under the frame, the temperature of the steel member increases first and then reduces gradually until finally cools down to ambient temperature. The peak temperatures for the half of the frame above the fire bed is shown in Figure 7

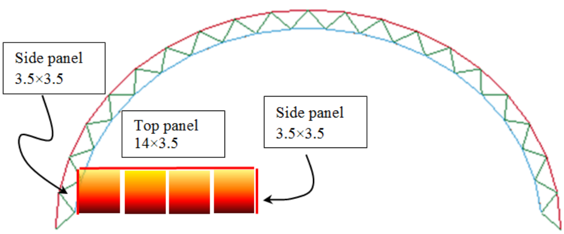

Figure 6. Radiation from the flame panels to the steel frame.

Peak temperature of the heated half of the frame where Node 1 and Node 2 are in direct contact with the flame, so their temperatures are assumed to be equal to the flame temperature. The temperatures of all other nodes are obtained using the incremental method introduced in Section 3.1.

To simplify the temperature distribution, the half frame was divided to four temperature zones. They are shown in Figure 7 in terms of both the temperature range and the applied nodal range. The temperatures of Node 1, Node 3, Node 6 and Node 9 were used to represent a uniform temperature distribution for their zone respectively. The time-temperature relationships for these four nodes are shown in Figure 8.

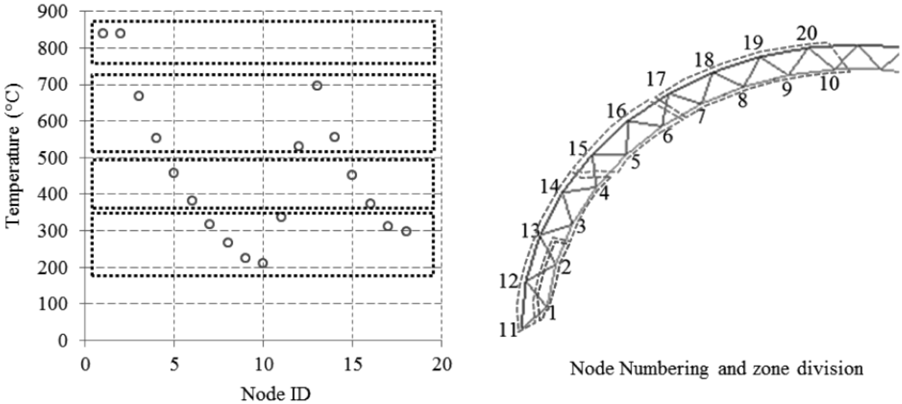

Figure 7. Peak temperature of the heated half of the frame.

Divide the part of the steel frame above the banquet hall into zones of 3.5m wide. Shown in Figure 7 and Figure 8 are the temperatures of the zone sitting right above the third row of table and experience the entire fire travelling procedure. The adjacent zones will experience only some of the phases as shown in 5 depending on their locations. Here, it is again simplified to assume that the fire zone is long enough so each zone will experience the same fire exposure procedure and have the same temperature development, but with 6.2 min delay from one zone to the next. Using N1 as an example to analyse the temperature distribution pattern, the fourth zone started to burn at 18.6min and N1 reaches the peak temperature (Node 1) after another 21min. At this time of 39.6 min, the temperature of the first zone has dropped to 670 ℃. So at one time, there can have a maximum of three zones with the temperature of N1 being over 800 ℃.

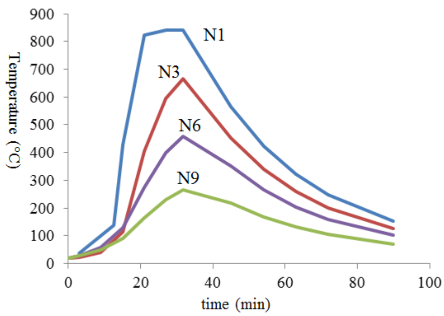

Figure 8. The temperature development of four typical locations.

4 STRUCTURAL RESPONSE IN FIRE

One segment of 50m long roof structure is used for analysis. During the analysis, this segment is assumed to be free standing, which is conservative because the support provided by the adjacent segment is ignored. All steel members are circular tubes with steel grade Q345. In the analysis, their nominal yield strength 345MPa is used at ambient temperature and the material strength reduction at higher temperature follows China’s design specification [8]. It is also assumed that steel could recover its strength during cooling.

Before the start of the fire, a combination of dead load, live load, cladding load and wind load was applied to the roof according to the fire limit state load combination. Due to the effect of wind, the stress state is not symmetrical. The maximum stress of 145MPa is observed to occur to the lower chord members at the medium high locations. At the bottom of the frame, where the highest temperature load is experienced, the stress is on average 70MPa, which means an initial stress state of 0.2.

The wind load is arranged so that the half of the frame with higher stress is heated. The temperature distribution at time=40 min is shown in Figure 9. The first row has entered the cooling phase. The second, third and fourth row are in the peak range of combustion with highest temperature. The fifth row is in the very initial phase of burning with very low temperature.

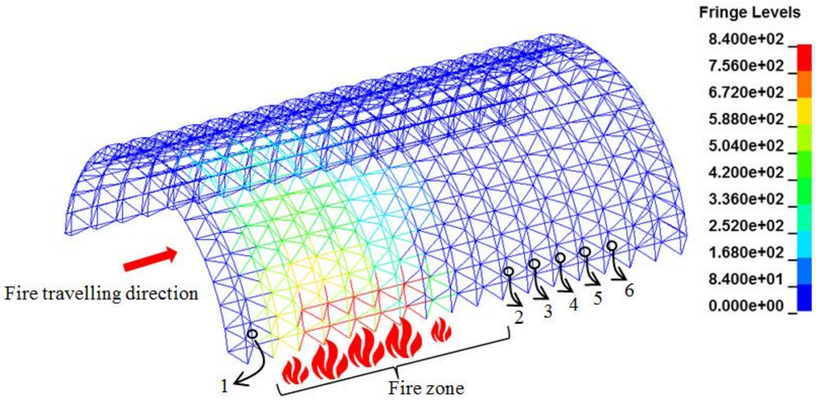

Figure 9. Temperature distribution at 40min.

The analysis was run for 90 min and structure showed no signs of collapse during the fire. At 90 min, all five rows of fire have entered the cooling phase and the peak temperature of the structure is 360 ℃. The fire damaged zone shows clearly residual deformation. The maximum deflection at the roof top has increased from 20 mm to 146 mm. The lower chord members of the fire affected zone shows significant member buckling deformation.

Examination to the member forces show that the structure maintained stability by transferring the loads to adjacent members. A large number of inclined bracing members allows the load to be transferred to members at a certain distance away from the fire. Using the node numbering in Figure 7, as the structure is supported on Node 1, the axial forces of the members connecting Node 1 and Node 3 give clear indication of the transfer of the vertical load to the support. Figure 10 shows the axial forces of these members. All the members in the heated zone are shown with solid lines.

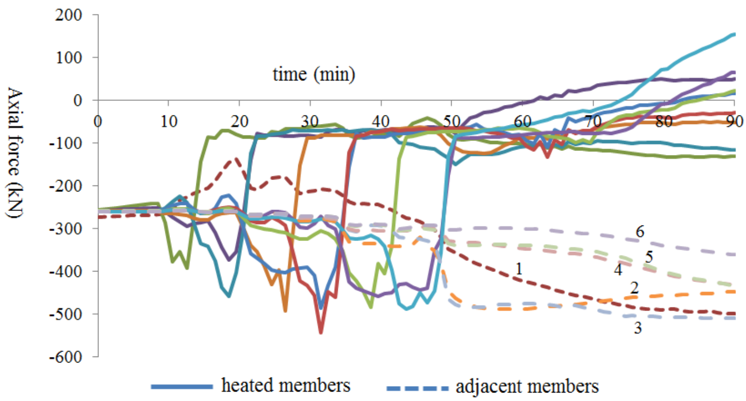

Figure 10. Change of the member forces during the fire.

It can be seen from the figure that all heated members experience an increase of the axial forces due to thermal expansion and also unloading of the members heated before itself. When the peak temperature is arrived, their axial forces drop to less than100kN and never recovered during the cooling phase. The adjacent members are labelled as 1-6 as shown in Figure 9. Among them, member 1 has its axial force reduced slightly during the cooling, but experienced significant increase of the axial force during the cooling. All other five members have their axial forces increased during the cooling.

The axial force of member 6 shows only marginal increase after the fire, which means the effect of the fire has become very small at this location. However, within the range, members 1 to 5 have all made significant contributions to the load resistance. Therefore, the key factor that determines the stability of a space frame when subjected to a travelling fire is the size of the structure in comparison to the fire zone. Outside the fire zone, there should be sufficient cool members to help redistribute the load. For the studied structure, if the fire zone is 20m long, a free-standing assembly should be no less than 50m long.

5 CONCLUSIONS

A travelling fire model is developed to simulate the continuous burning of dining tables in a banquet hall with high ceiling and flashover is judged to be unlikely to happen. The corresponding heat transfer method is also proposed based on the heat transfer principles. With the proposed method, the time-temperature relationship can be calculated for a steel member subjected to a fire that starts from a certain distance, travels through the member and moves away gradually. The time-temperature history is then applied to finite element analysis program to obtain the structural behaviour in fire.

Analysis results show that space framed structures can maintain stability by re-distributing the load to members at a certain distance away from the heated zone. Given that there are sufficient members to undertake the extra load, the space frame can be left unprotected. Members that are subjected to extremely high temperature show obvious local buckling and they cannot recover their load resistances after fire.

Generally for large space, one localized fire is assumed, which is the combustion of one table in the current case and the fire is supposed to damage steel members within approximately 4m wide zone as each table is 3.5 m. In the proposed travelling fire scenario, the fire travels through five tables and damaged steel members within a 18m long zone. Therefore, travelling fire can cause much more extensive fire damage and should be considered for large spaces where fire load can be fairly close to each other.

REFERENCES

[1] GB50045-95 *Code for fire protection design of tall buildings*, China Ministry of Construction, 2005.

[2] CEN, *BS EN 1991-1-2:2002 Eurocode 1: Actions on structures- Part 1-2: General actions-actions on structures exposed to fire*, British Standard Institution, 2002.

[3] CIBSE, *Fire safety engineering, CIBSE Guide E,* Third edition, 2010.

[4] Chow W. K., *Zone model simulation of fires in Chinese Restaurants in Hong Kong*, Journal of Fire Sciences, Vol13, no.3, p.235-253, 1995.

[5] CEN, *BS EN 1993-1-2:2005 Eurocode 3: design of steel structures- part 1-2: general rules-structural fire design*, British Standard Institution, 2005.

[6] Bailey C.G., Newman G.M., Simms W.I., *SCI Report 186 Design of Steel Framed Buildings without Applied Fire Protection*, Steel Construction Institute, the UK, 1999.

[7] SFPE, *Handbook of Fire Protection Engineering*, Third edition. National Fire Protection Association, the US, 2002.

[8] CECS, *CECS 200: 2006 Technical code for fire safety of steel structure in buildings*, China Association for Engineering Construction Standardization, 2006.

8th International Conference on Structures in Fire
Guo-Qiang LI, Venkatesh K. R. KODUR, Shou-Chao JIANG, Jian JIANG, Su-Wen CHEN, Guo-Biao LOU (Eds.)
Shanghai, China, June 11-13, 2014

EVALUATING WEATHERING STEEL PERFORMANCE AT ELEVATED TEMPERATURES: THE I-195 BRIDGE FIRE CASE STUDY

Samy Labbouz*, Jonathan D. Glassman*, Maria E. M. Garlock* and James Ricles**

* Department of Civil & Environmental Engineering, Princeton University
e-mails: labbouz@princeton.edu, jdglassm@princeton.edu, mgarlock@princeton.edu

** Department of Civil & Environmental Engineering, Lehigh University
e-mail: jmr5@lehigh.edu

Keywords: Weathering steel, Fire, bridge, Post-fire, Material properties

Abstract: *Weathering steels, due to their high-corrosion resistance properties, are increasingly being used internationally in bridge construction. However, their mechanical properties at high temperature are unknown, making it difficult to understand or model the structural response of weathering steel bridges affected by fire as well as assess their post-cooling strength. This research investigates the high temperature and residual (post-cooling) properties of A588, a weathering steel commonly used in bridge construction, as part of a case study of a recent bridge fire.*

1 INTRODUCTION

Steel highway bridges face threats of irreparable damage or collapse when subjected to a fire. These fires typically result from tanker trucks or other vehicles crashing beneath or adjacent to a bridge and igniting. Numerous examples of these bridge fires exists; a survey of bridge collapses in the United States (US) from 1876 to 2011 conducted by the New York Department of Transportation and covering 18 states, including California, found that about three times as many bridges collapsed from fire than from earthquakes [1].

Motivating this research is a recent bridge fire that occurred on October 3, 2012. A dump truck traveling south on the NJ Turnpike crashed into the abutment under a bridge that carries I-195 over the Turnpike, catching fire (Figure 1). TheI-195 overpass had been recently widened and had timber shielding beneath it, providing some protection to the steel girdersfrom the fire. The original girders, G3-G8 (Figure 1(b)), were made of A588 weathering steel, and the new girders used in widening, G1 and G2, were made of A709. Although load tests confirmed the bridge still possessed sufficient capacity to carry traffic load, it was decided not to pursue repairs since it was already scheduled to be demolished [2].

Weathering steels are high-strength low-alloy steels with particularly good corrosion resistance. This resistance results from the capacity of their alloying elements, which include Cu, Cr, Ni, P, Si to form a dense and tightly adhering patina, or rust layer, when oxidizing which consequently acts as a protective layer that prevents further corrosion. This high resistance to corrosion and the consequent reduced life-cycle costs from rust-proof painting and maintenance have made weathering steels a popular choice for bridge construction in the US, employed today in 40%-45% of new bridges built in the US, 90% in Canada, and hundreds of bridges throughout Europe and Japan [3,4]. Yet, high temperature properties of weathering steels are essentially unknown, and not covered by Eurocode specifications for high temperature steel properties, making it difficult to accurately predict and model structural behavior of weathering steel bridges in fire and post-fire.

This project examines the 2 types of steel present in the I-195 bridge fire case study, A588 and A709. A588, a weathering steel commonly used in bridge construction is the main focus of this study, and its properties are compared to those of another steel whose mechanical properties and chemical composition allow it to be classified according to ASTM as A709 or A992, two non-weathering steels [5-7].

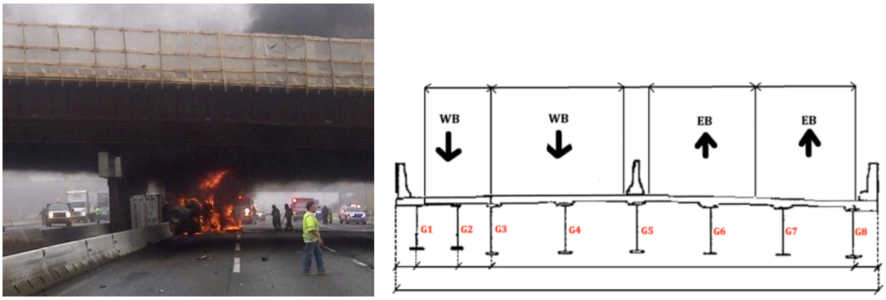

Figure 1. From left to right, (a) dump truck fire beneath I-195 and (b) cross-section of I-195.

2 EXPERIMENTAL SETUP

The test matrix for all of the specimens is presented in Table 1. The parameters that were investigated were: (1) material; (2) heating temperature; and (3) cooling method. Table 1 also indicates the tests performed on each specimen, where E8 refers to tensile tests, E18 to Rockwell surface hardness tests, and E23 to Charpy V-notch (CVN) fracture toughness tests based on ASTM [8-10}, respectively.The nomenclature for each test is as follows:

- **2** represents A588 weathering steel; **1** represents A709 or A992 based on ASTM chemical and mechanical material properties.
- **A** = **A**mbient temperature with no previous heating; this represents the baseline case.
- **H** = test done with the specimen at an elevated temperature steady state (**H**ot)
- **Ca** = specimen was tested after being **c**ooled in **a**ir
- **Cw** = specimen was tested after being **c**ooled in **w**ater
- The last number represents the target maximum temperature (in ^{o}F) of the specimen

Table 1. Test matrix with nomenclature and ASTM test performed for each specimen.

Temp.	**Material**	**Cooling**	**Maximum steady state temperature**				
			70 F (20C)	**800 F (538 C)**	**1000 F (538 C)**	**1200 F (649 C)**	**1500 F (815 C)**
Hot	**A709**	-	*1A (E8, E23, E18)*	*1H-800 (E8)*	*1H-1000 (E8)*	*1H-1200 (E8)*	*1H-1500 (E8)*
	A588		*2A (E8, E23, E18)*	*2H-800 (E8)*	*2H-1000 (E8)*	*2H-1200 (E8)*	*2H-1500 (E8)*
Cooled (Residual)	**A709**	air	-	*1Ca-800 (E8, E23, E18)*	*1Ca-1000 (E8, E23, E18)*	*1Ca-1200 (E8, E23, E18)*	*1Ca-1500 (E8, E23, E18)*
	A588		-	*2Ca-800 (E8, E23, E18)*	*2Ca-1000 (E8, E23, E18)*	*2Ca-1200 (E8, E23, E18)*	*2Ca-1500 (E8, E23, E18)*
	A709	water	-	*1Cw-800 (E8, E23, E18)*	*1Cw-1000 (E8, E23, E18)*	*1Cw-1200 (E8, E23, E18)*	*1Cw-1500 (E8, E23, E18)*
	A588		-	*2Cw-800 (E8, E23, E18)*	*2Cw-1000 (E8, E23, E18)*	*2Cw-1200 (E8, E23, E18)*	*2Cw-1500 (E8, E23, E18)*

A combination of flat and round specimens were used due to physical constraints of different universal testing machines (UTMs) utilized in the test program. For the hot tensile tests conducted at Lehigh University, extra long test specimens were based on the ASTM E8 standard rectangular (flat) tension test coupon with extended regions beyond the gauge length. The A588 specimens had a 36” length, while the A709 specimens were only 30” long. For the ambient tensile tests conducted at Princeton University, the ASTM E8 standard round specimen was used [8]. To confirm that the data from flat and round specimens could be used interchangeably, 2 extra long round specimens (based on ASTM E8) were also fabricated and tested at ambient temperature.

2.1 ‘Hot’ Tension Tests

Figure 2 shows the furnace andUTM setup at Lehigh University used to determine high temperature mechanical properties of the specimens. To ensure that the steel in the grips region never reached high temperatures, copper plates, through which cold water continuously flowed, were clamped to the specimen in those regions. Moreover, temperatures were continuously monitored along the length of the specimen using high temperature-resistant thermocouples.

Figure 2. Furnace and UTM setup atLehigh University.

The first step of the procedure consisted of heating the specimens to the target temperature. During the heating phase, only the bottom grip was fully clamped, allowing the top end of the specimen to freely expand due to thermal expansion. Once the desired temperature was achieved in measurements by both thermocouples within the furnace, a minimum of a 20-minute wait time at constant temperature was allowed to ensure steady state testing conditions. After this wait time the tensile loading began.

A constant strain rate of 0.1 in/min was used for all tensile tests. In addition to head travel, a string potentiometer was used to measure the crosshead displacement during the tensile test.

2.2 Residual Mechanical Properties Tests

Residual mechanical properties of Young’s modulus (E), yield and ultimate stress (σ_y and σ_u), and surface hardness were tested using lab facilities at Princeton University. Charpy V-notch testing for residual fracture toughness was done at Lehigh University. To determine the residual mechanical properties, the standard round and CVN specimens were heated using an electric furnace at Princeton. To ensure that the test specimens reached their target temperatures, a companion specimen was fabricated and tested simultaneously. This companion specimen had a hole drilled longitudinally along its centerline to the middle of the gauge length. A thermocouple was placed inside this hole and the companion and test specimen were heated together. This setupconfirms that the test specimen had reached the target temperature through the thickness, and tracks the cooling rate of each specimen.

Residual tensile strength tests were done in accordance with ASTM E8 using an Instron 600 DX loading frame with a 135 kip (600 kN) load capacity. An extensometer measured strain during the initial portion of the tensile test and was removed after yield strength, but before ultimate tensile strength was reached to avoid damaging the extensometer at fracture. Similar to the hot tensile tests conducted at Lehigh University, a loading rate of 0.1 in/min was specified, again based on ASTM E8 standards [8].

Rockwell hardness testing was done using a Mitutoyo ATK-600 testing machine in accordance with the ASTM E18/AASHTO T80 specification [9]. Rockwell Hardness Scale B (HRB) was used except for

Specimen 2Cw-1500, where the cooled steel was too hard for HRB, thus Scale C(HRC) was employed. Note however that the values reported in Table 5 were converted to HRB scale [10].

Lastly, Charpy V-notch tests were conducted at Lehigh University in accordance with ASTM E23/AASHTO T266 specifications [11]. Figure 3 provides images of all 3 test setups.

Figure 3. Experimental Setup: (a) UTM; (b) Impact test; (c) Rockwell Hardness machines.

3 EXPERIMENTAL RESULTS

3.1 Ambient Test Results (Control Group)

Table 2 summarizes the ambient temperature results for all tests undertaken. These results will be used as ‘control’ values, with respect to which many of the following results will be normalized to indicate more clearly the property changes with temperature. From this table, differences between the two materials testedcan be observed, namely: A709 has larger fracture toughness (from CVN testing) and has a smaller σ_u than A588, while the latter is harder.

Table 2. Ambient test results.

Specimen	Tensile tests			CVN Tests		Rockwell B Tests	
	σ_y (ksi) avg.	σ_u (ksi) avg.	E (ksi) avg.	(ft-lb) avg.	std. dev	Hardness B-Scale avg.	std. dev
A709 (1A)	55.5	71.0	28900	183	20	80.7	0.6
A588 (2A)	56.8	84.8	30037	125	10	86.1	0.4

3.2 ‘Hot’ Tension Test Results

Table 3 presents the maximum stress values (σ_u) obtained when the specimens were tested in the hot condition. Figure 4 plots the ratio of the hotσ_u values to the ambient σ_u value. As expected, σ_u decreases with increasing temperature. Figure 4 also shows that the A588 material experiences a larger reduction in its ultimate strength compared to the non-weathering steelwith a temperature increase. Compared to the Eurocode (EC) reduction values ($k_{y,\theta}$, from [12]), Figure 4 shows that the non-weathering steel matches very well, but the A588 values are smaller. Even though $k_{y,\theta}$ refers to ‘yield’ in the EC, it represents the maximum stress and is therefore equal to σ_u in the analysis herein. Figures 5 and 6 plot the load displacement curves for the hot specimens, where a nonlinear response of the material is observed.

Table 3. Hot tension test results.

	Spec.	σ_u (ksi) avg	σ_u (ksi) ratio*
A709	1A	71.0	-
A709	1H-800	69.0	0.97
A709	1H-1000	44.1	0.62
A709	1H-1200	23.7	0.33
A709	1H-1500	8.7	0.12
A588	2A	84.9	-
A588	2H-800	61.9	0.73
A588	2H-1000	42.4	0.50
A588	2H-1200	21.1	0.25
A588	2H-1500	7.9	0.09

*ratio=the average value of the 1H or 2H specimens divided by the average value of specimen 1A or2A.

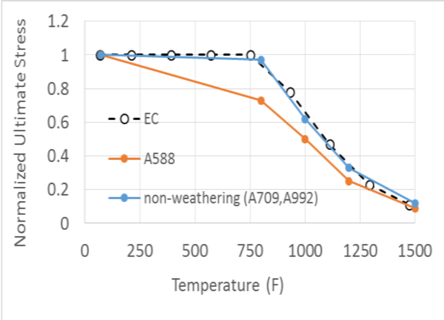

Figure 4. Normalized ultimate stress against temperature for A709 (Material 1) and A588.

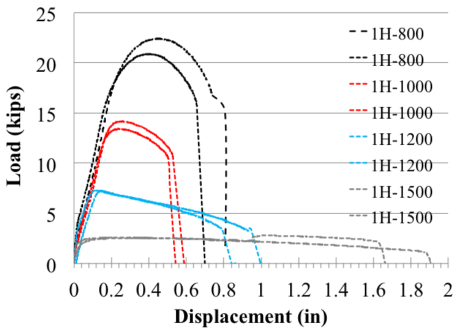

Figure 5. Load displacement plots for A709 steel at elevated temperatures.

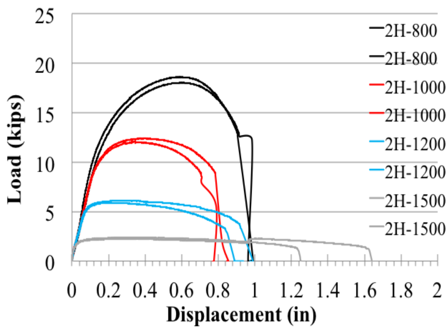

Figure 6. Load displacement plots for A588 steel at elevated temperatures.

3.3 'Residual' Tension Test Results

The residual tension test results for both A709 and A588 are presented in Tables 4 and 5, respectively, normalized by the unheated specimen values (control specimens) given in Table 2. All values presented are the averages from two tests for each specimen type.The σ_y values are all determined using the 0.2% offset method. For both materials, brittle failure was observed for the specimens cooled in water (CIW) that were heated to 1500°F.

For A709, residual σ_y values tended to stay within 10% of the control value, except for CIW specimens heated to 1500°F, where a 16% increase was observed. Similarly, residual σ_u values generally stayed within 10% of the control value except for CIW specimens heated to 1500°F, where a 58% increase was observed. For the residual E value, while the cooled in air (CIA) values generally fluctuate within 10% of the control value, the CIW values tended to be larger. At 1000°F and 1200°F, 13% and 17% increases were observed in the residual E value, respectively.

For the A588 specimens, residual σ_y values were similar to the control values, regardless of cooling method, up to 1200°F. At 1500°F, CIW specimens were observed to have a 69% increase in σ_y. This similar trend is also observed for residual σ_u values. The residual σ_u values remain close to the control values, up to 1200°F, but for CIW specimens heated to 1500°F, an 88% increase in σ_u was observed. Residual E values were generally observed to be within 10% higher than the control value for CIA specimens, with the only exception being the CIA specimens heated to 800°F, where a 19% increase in residual *E* was observed. For the CIW specimens,residual *E* values tended to fluctuate within approximately 5% (above or below) the control value, except for the specimens heated to 1200°F for which we observed a13% decrease in E.

Table 4. Summary of residual test results for **A709.**

	Spec.	σ_y	σ_u	E	CVN (ft-lb)			Hardness (HRB)		
		ratio*	ratio*	ratio*	avg	std. dev.	ratio*	avg	std. dev.	ratio*
CIA	1Ca-800	1.01	0.99	1.11	164	24	0.90	80.8	0.5	1.00
	1Ca -1000	1.07	1.02	0.92	198	35	1.08	80.3	0.8	1.00
	1Ca -1200	1.01	1.00	1.08	193	41	1.05	80.6	0.6	1.00
	1Ca -1500	0.93	1.00	0.98	218	16	1.19	79.1	1.5	0.98
CIW	1Cw-800	1.07	1.03	1.02	177	33	0.97	81.5	1.1	1.01
	1Cw-1000	1.04	1.05	1.13	195	34	1.07	83.5	1.0	1.03
	1Cw-1200	1.1	1.10	1.17	156	10	0.85	86.2	0.9	1.07
	1Cw-1500	1.16	1.58	1.03	54	6	0.30	92.4	1.1	1.14

*ratio= values normalized by the ambient temperature properties presented in Table 2 (using average values).

Table 5. Summary of test results for **A588**.

	Spec.	σ_y	σ_u	E	CVN (ft-lb)			Hardness (HRB)		
		ratio*	ratio*	ratio*	avg	std. dev.	ratio*	avg	std. dev.	ratio*
CIA	2Ca-800	1.01	1.00	1.19	143	37	1.14	87	0.6	1.01
	2Ca -1000	1.04	1.00	0.99	133	36	1.06	87.9	0.8	1.02
	2Ca -1200	1.04	0.99	1.01	156	18	1.25	88	0.8	1.02
	2Ca -1500	0.79	0.94	1.02	127	38	1.02	88.9	1.5	1.03
CIW	2Cw-800	1.00	1.01	1.05	132	21	1.06	88.4	0.6	1.03
	2Cw-1000	1.01	1.02	0.99	127	25	1.02	89.8	0.5	1.04
	2Cw-1200	1.04	1.03	0.87	150	26	1.20	91.3	1.1	1.06
	2Cw-1500	1.69	1.88	0.97	9	1	0.07	104	1.0	1.21

* ratio= values normalized by the ambient temperature properties presented in Table 2 (using average values).

3.4 Residual Fracture Toughness

Results from the impact test (CVN energy) are presented in Tables4 and 5 for both materials. At least 5 tests were conductedfor each specimen to account for anyvariation in the test results.Specimens were heated to the target temperature and then cooled (CIW or CIA) before testing. For A709, residual CVN values remain the same as the control value regardless of the cooling method for specimens heated to 800°F and 1000°F. At 1200°F, CIW specimens have lower CVN energy values compared with their CIA specimens and the control value. At 1500°F, the CIW specimens show a large reduction in residual CVN energy, while the CIA specimens have an approximate 20% increase.

For A588, residual CVN energies tend to be higher than the control value regardless of the cooling method. At 1500°F, however, a dramatic reduction in residual CVN energy is observed for the CIW 1500°F specimens, while the CIA specimens have values close to the control value.

3.5 Residual Rockwell Hardness

Average values for Rockwell hardness tests are included in Tables 4 and 5 for both materials. To obtain these values, 3 CVN specimens associated with each temperature and cooling method were randomly selected and 3 hardness measurements were taken on each. The average values presented, therefore, represent an average over 9 readings. As seen from the normalized hardness values, the residual hardness for the CIA specimens of both A709 and A588 remain close to the ambient control value, indicating that hardness is unaffected. For the CIW specimens, however, as the temperature increases, the residual hardness was also observed to increase.

3.6 Conclusions from Experimental Results

The results from high temperature testing of A709 and A588 showed results consistent with expectations of steel properties with decreasing ultimate strength as temperature increased. The results from the post-cooling tests, which included tensile, toughness and hardness evaluation, highlighted several trends, depending on material, cooling method (cooled in air or water) and temperature reached.

Generally, the specimens heated and cooled slowly in air showed little variation in terms of residual properties with respect to the control (unheated) specimens. For the specimens cooled in water, however, significant changes occurred, particularly for the specimens heated to 1500^{o}F. A709 and A588 showed a 58% and 88% increase inσ_u, respectively. Similarly, A709 and A588 showed a 16% and 69% increase inσ_y,respectively. It is important to note thatfor both materials brittle behaviour was observed for specimens heated to 1500^{o}F and cooled in water. However, no significant change in E was observed irrespective of heating temperature, material or cooling method.

Toughness test results showed insignificant variations in CVN energy for the specimens cooled in air, irrespective of material or heating temperature. For the specimens cooled in water, however, a clear trend of decreasing CVN energy with increasing heating temperature was observed for both A709 and A588, only conserving 30% and 7% of their original CVN value, respectively, when heated to 1500^{o}F. The opposite trend was observed for the Rockwell hardness tests. Both materials showed insignificant variations in surface hardness for the specimens cooled in air, but the specimens cooled in water showed a trend of increasing hardness with increasing temperature, with a 14% and 21% increase for A709 and A588, respectively, when heated to 1500^{o}F and cooled in water.

4 CONCLUSIONS AND FUTURE WORK

This research examined the elevated temperature properties of A588 weathering steel, which is increasingly used internationally in bridge construction butwhose elevated temperatures were unknown. A database of mechanical properties for this steel at elevated temperatures was developed and compared with another type of steel, A709 non-weathering, also experimentally studied in this project.

The studies showed that at temperatures of 1200 ℉ and below, the residual material properties of both materials studied (representing the post-fire condition), were affected no more than on the order of 10% compared to the unheated steel. Examining the residual properties of the cooled in water (CIW) specimens, there is a clear trend of decreasing fracture toughness with increasing temperature. There is also a clear trend of increasing hardness with increasing temperature. It is expected that the CIW method produces different microstructure changes than the cooled in air method, resulting in the trends observed.

By1500 ℉ the steel has gone through a phase change; further, and practically speaking, a bridge that reaches 1500 ℉ will experience significant permanent deformations if this temperature is widespread and in that case it will likely need to be demolished. Therefore, based on the results obtained thus far, it is likely that if significant permanent deformations are not observed, a bridge of A588 weathering steel has the potential to be put back into service following a fire.

This work was undertaken as part of the case study of the I-195 bridge fire, in which A709 and A588 steel girders were exposed to fire from a tanker truck accident. The databases of properties obtained experimentally in this research can be used to model and predict structural performance of weathering steel bridges affected by fire, as well as evaluating their capacity and safety post-fire. A finite element model of the I-195 bridge girders is under development to examine the response of these due to exposure to different fire curves and steel types. These results will be subject of a different publication.

5 ACKNOWLEDGMENTS

Funding for this research was provided by the state of New Jersey Department of Transportation (DOT) and the U.S. DOT Federal Highway Administration through the Center for Advanced Infrastructure and Transportation. The authors also gratefully acknowledge the advice and support of Sougata Roy of the ATLSS Center, Lehigh University. We also thank High Steel Inc. of Lancaster, PA for donating the A588 steel, and Lehigh University's ATLSS labs for donating the A709 steel. Finally, Carl Bowman, Instrumentation Manager of the ATLSS Engineering Research Center, and Joe vocaturo, Senior Lab Manager of CEE at Princeton University provided invaluable support in the labs. All opinions, findings, and conclusions expressed in this paper are the authors' and do not necessarily reflect the policies and views of the sponsors.

REFERENCES

[1] Garlock, M., Paya-Zaforteza, I., Kodur, V., Gu, L., "Fire Hazard in Bridges: Review, Assessment and Repair Strategies", *Engineering Structures*, Elsevier, V. 35, 2012.

[2] CAIT, 'On call, on site, and on the case: New CAIT bridge program supports NJDOT as the care for our state's bridges", *CAIT Newsletter*, Issue 11, January 2013.

[3] McDad, B., Laffrey, D.C., Dammann, M., Medlock, R.D., "Performance of Weathering Steel in TxDOT Bridges", Texas Department of Transportation, 2000.

[4] Wiss, Janney, Elstner Associates, Inc. "Assessment of Weathering Steel Bridge Performance in Iowa and Development of Inspection and Maintenance Techniques", Final Report, Iowa DOT, 2013.

[5] ASTM, Standard Specification for High-Strength Low-Alloy Structural Steel, up to 50 ksi [345MPa] Minimum Yield Point, with Atmospheric Corrosion Resistance, ASTM **A588**, American Society for Testing and Materials, West Conshohocken, PA, 2010.

[6] ASTM, Standard Specification for Standard Specification for Structural Steel Shapes, ASTM **A992**, American Society for Testing and Materials, West Conshohocken, PA, 2011.

[7] ASTM, Standard Specification for Structural Steel for Bridges, ASTM **A709**, American Society for Testing and Materials, West Conshohocken, PA, 2013.

[8] ASTM, Standard Test Methods for Tension Testing of Metallic Materials, ASTM **E8**, American Society for Testing and Materials, West Conshohocken, PA, 2009.

[9] ASTM, Standard Test Methods for Rockwell Hardness of Metallic Materials, ASTM **E18**, American Society for Testing and Materials, West Conshohocken, PA, 2008.

[10] ASTM, Standard Hardness Conversion Tables for Metals, ASTM E140-12b, American Society for Testing and Materials, West Conshohocken, PA, 2013.

[11] ASTM, Standard Test Methods for Notched Bar Impact Testing of Metallic Materials, ASTM **E23**, American Society for Testing and Materials, West Conshohocken, PA, 2000.

[12] BSEN1993-1-2 European Committee for Standardisation, CEN, Eurocode 3: Design of Steel Structures. Part 1-2, General rules. Structural Fire Design, 2005.

8th International Conference on Structures in Fire
Guo-Qiang LI, Venkatesh K. R. KODUR, Shou-Chao JIANG, Jian JIANG, Su-Wen CHEN, Guo-Biao LOU (Eds.)
Shanghai, China, June 11-13, 2014

DETERMINATION OF THE SERIES OF CRUCIAL FIRE SCENARIOS FOR THE SKELETAL STRUCTURES

M. Malendowski*, A. Glema* and W. Szymkuc*

*Poznan University of Technology, ul. Piotrowo 5, 60-965 Poznan
e-mails: michal.malendowski@put.poznan.pl, adam.glema@put.poznan.pl,
wojciech.szymkuc@put.poznan.pl

Keywords: Fire scenarios, Complexity, Coupled problems, Multiphysics problems, Natural fire, Fire engineering, Localised fire

Abstract. *In this work the method for determination of fire scenarios in accordance to load conditions is presented. Proposed method corresponds to nowadays trends in design, where fire safety is no longer related only to environmental aspects and structural safety is provided by simple prescriptive requirements, but more and more engineers are preparing calculations in accordance to performance based methods. Method is implemented and verified in the case of 3D hall subjected to local fires. Because of strong mathematical basis, method is robust and seems to be considerably easy to apply for any structural model of skeletal building created in FEM software. One of the main features of this method is direct association with actual mechanical load combination, what leads to direct determination of series of fire scenarios in large complex structures, where distribution of external loads can significantly affect the utilisation of particular members.*

1 INTRODUCTION

After architectural design, the first step in design process is establishing loads acting on the structure. Here, structural engineer must find the most severe load cases to provide robust and reliable design. That accounts for both standard and accidental actions, like fire. While the standard load cases like self-weight, imposed loads, wind and snow actions are well-established in design codes, there is no exact method for determination of fire load localisation in order to reflect the most dangerous mechanical state of structure. In this contribution, the method for determination of crucial fire scenarios as a consequence of previously settled load schemes and combinations is introduced, verified and tested with respect to coupled CFD-FEM simulation. General idea of this method works is shown in Figure 1.

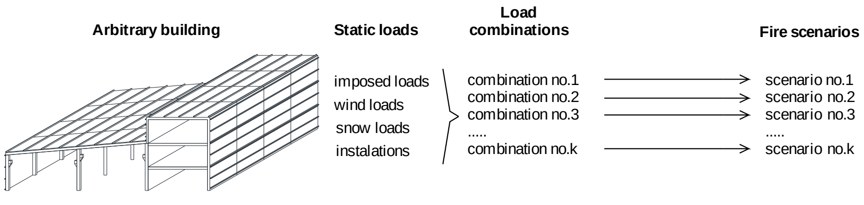

Figure 1. Application of proposed method.

2 METHOD DESCRIPTION

2.1 Theoretical bases

The method is based on work done by De Biagi and Chiaia [1], where they introduced the metric for structural complexity by adopting the quantification of system complexitytaken from graph theory, used for example in computer science. Generally, complexity of a system can be calculated by considering the amount of information carried by this system, what for structures means the geometry, connections types, cross-section stiffness and external loads scheme.

As well as in cited work [1], also in this contribution all the consideration of structural complexity regards the static conditions of the structural scheme. Nonetheless, in this article authors are modifying the approach in order to make feasible analyses of real structural 3D models of skeletal buildings.First of all, proposed method uses justthe basis of the Virtual Work Theorem in the form of Clapeyron’s Theorem, instead of the Meanbrea’s Theorem (The Principle of the Minimum of Complementary Potential), what in principle gives the same results, but virtual work is easier to understand regarding the finite element method used for static calculations and do not requires evaluation of statically determinable structures.

Let us consider the ordinary finite element method problem given by the system of equations described in the matrix form:

$$\boldsymbol{K} \cdot \boldsymbol{d} = \boldsymbol{f} \tag{1}$$

All information about the structure are stored in stiffness matrix $\boldsymbol{K}$ and external loads vector $\boldsymbol{f}$. Note that vector $\boldsymbol{f}$, similar to displacement vector $\boldsymbol{d}$,corresponds to nodal degrees of freedom complement with nodal forces and moments.In accordance to the Clapeyron’s Theorem, the total elastic work of deformation E_{el} can be calculated in accordance to well-known formula:

$$W_{el} = \frac{1}{2}\boldsymbol{f}^{T} \cdot \boldsymbol{d} \tag{2}$$

Note that for different load schemes and combinations, the total elastic work of deformation varies with respect to variety load conditions. Nevertheless, at each time when the system is in equilibrium the value of elastic work reach the minimum.

2.2 Complexity measures

Ordinary mechanical models of skeletal structures consist of the finite number of beam elements connected with themselves in nodes and subjected to boundary conditions and external loads. As far as the structure is statically indeterminable, it is possible to find certain number of substructures with the same number of nodes, but with the less static indeterminably order. To clarify the idea, consider the 2D frame given in Figure 2a, which is 3-times statically indeterminable. We can release 3 bonds, what mean that we can do one cut over the element, thus considering the loads acting just in nodes, it is possible to remove one beam element to obtain fundamental structure with the same loading as initial one, but different load bearing mechanism.In this contribution, the same idea is applied to 3D system, where just the difference is the number of nodal degrees of freedom. The number of elements combinations for fundamental structures can be calculated using binominal coefficient:

$$c = \binom{n}{k} = \frac{n!}{k!\,(n-k)!} \tag{3}$$

where n is the initial number of elements and k is the number of elements removed from the initial system. What is was mentioned, that approach can be used both for 2D and 3D structures, remembering just the appropriate number of nodal degrees of freedom.

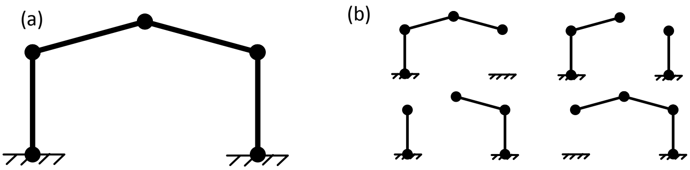

Figure 2. (a) initial structure, (b) possible fundamental structures.

Considering all fundamental structures resulted from the initial one and the same nodal loads schemes,it is possible to calculate the total elastic work of deformation of i-th fundamental structure (W_{Si}). Then comparing it with the initial structure's work of deformation (W_{in}) it is possible to calculate a performance factor ψ_i referred to the i-th fundamental structure:

$$\psi_i = \frac{W_{in}}{W_{Si}} \tag{4}$$

This factor is always less than 1,0 regarding the reduction of system's stiffness caused by removing elements from the initial structure. Comparing values of the preformation factor of all distinguished fundamental structures the one yielding the smaller value is the most utilized (carried the most load).

In accordance to [1], by keeping the all values of preformation factors, we are able to calculate the next measure for complexity, called the structural complexity index SCI:

$$SCI = -\sum_i \frac{\psi_i}{\sum_j \psi_j} \log_2 \left(\frac{\psi_i}{\sum_j \psi_j} \right) \tag{5}$$

For practical application the quantity which is easier to understand is normalized structural complexity index NSCI calculated as following:

$$NSCI = \frac{SCI}{-\log\left(\frac{1}{s}\right)} \tag{6}$$

Where s is the total number of fundamental structures obtained from the initial statically indeterminable structure. In that sense we can say that when $NSCI \approx 0$, just one element of the system carries the majority of load, contrary to $NSCI \approx 1$, when all the elements have the same weight in the overall behaviour of the structure. For more detailed information for the mathematical bases of introduced quantities please refer to [1].

As a result of previous consideration, it is possible to define the element's importance factor, β_i, relative to the i-th element and reflecting the importance of each single element in the skeletal structure. It can be calculated using the following expression:

$$\beta_i = \frac{\sum_j \psi_j \rho_{ij}}{\sum_j \psi_j} \quad , \quad \text{where} \rho_{ij} = \begin{cases} 1 & i \in S_j \\ 0 & \text{otherwise} \end{cases} \tag{7}$$

2.3 Application to the 3D structural system

In case of 3D structural models of the structures, the common approach is to create the overall finite element model consisting of both main and secondary elements. From load carrying capacity point of view, the crucial are main structural members, whereas the secondary elements just transfer loads and provide the 3D stiffness of structure. That redefines the usability of method proposed by De Biagi and Chiaia. Consider now the 3D system consisting of several elements performing different role in load carrying act, like in Figure 3.In such a situation, we can group sets of finite elements from model into the group of main structural members in the real sense.

In such a case the number of variables can be reduced with respect to original method proposed by [1] from initial 126 (number of finite elements in model in Figure 8) to 20, what corresponding to number of main structural members. That is the main benefit from modification of method introduced by De Biagi and Chiaia. This situation can be even more favourable for bigger structures, where the ratio between secondary structural elements and main structural members rises significantly. Without those modifications, number of combinations of fundamental structures makes the complexity analysis incomputable and unreliable. From the other side, keeping secondary elements in computational model makes the computations possible by providing the stiffness matrix positive-definite and non-singular, so it keeps the problem stable.

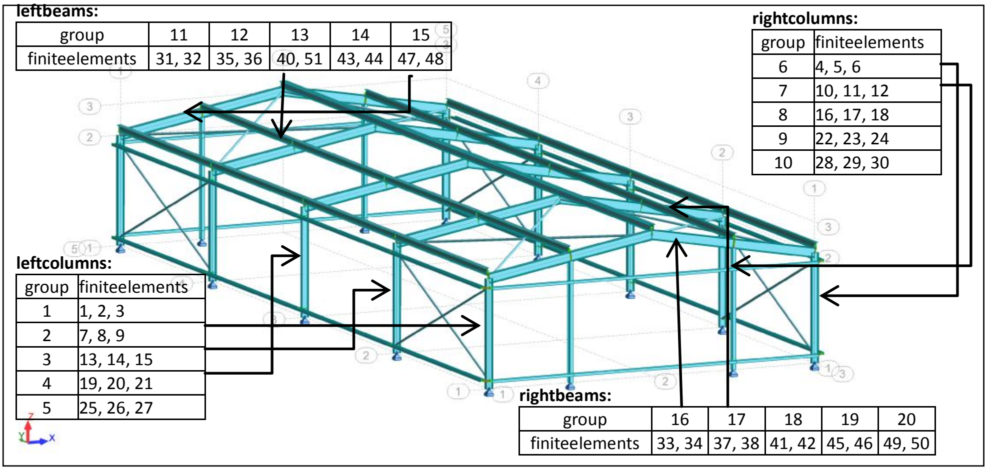

Figure 3. Finite element method model and groups of main structural elements.

3 DETERMINATION OF FIRE SCENARIOS

During design process, structural engineer analysing natural fire scenarios, must decide where to place the fire source inside the structure to get the most dangerous impact on the overall structural safety. Usually the answer came out from his individual intuition and for complex structures might be unreliable. Comparing to problems solved by fire safety engineers, structural engineer have to solve the issue of very different class. In this case fire scenario have to result directly from mechanical justification of structure, whereas previously other factors affecting design decisions seem to be more important. Therefore process of determination of fire scenarios, from mechanical point of view, should be replicable and should result directly form assumptions made on previous stages of design, like static schemes and load conditions. Moreover, this process should be also computable to give possibility to quantify results.

Method proposed by authors allow engineer to find,within the structure, certain elements or sub-structureswhich are crucial from the point of view of the portion of total load they carry on.Thus, assuming the natural fire conditions, localization of fire source can be determined using the information stored in the structural model, so fire scenario can be chosen based on the mathematical operations on stiffness matrix and force vector. In this case, authors propose the following algorithm for determination of crucial elements or assemblies within structural model (Figure 4).

Note that this approach gives a set of results, where each answer, in the sense of fire scenario, corresponds to certain load scheme (or load combination). So the results are strict and directly connected with mechanical considerations about structural system.

4 ANALYSIS SCHEME

Analyses are carried out according to scheme presented in Figure 5. At first, previously derived static loads are applied into the Finite Element Method model. Then, several fundamental structures are separated from the complex structure and the one handling the minimum of elastic work is chosen and interpreted as the most critical sub-structure. That information is used for determination of the most severe localisation of fire with respect to specific combination of static loads. Next, fire scenario determined in this way is applied into CFD model of fire development and the coupled CFD-FEM analysis are carried on by using special external scripts in order to solve multiphysical problem of heat transfer from the ambient environment into the solid phase of structural members [2, 3].

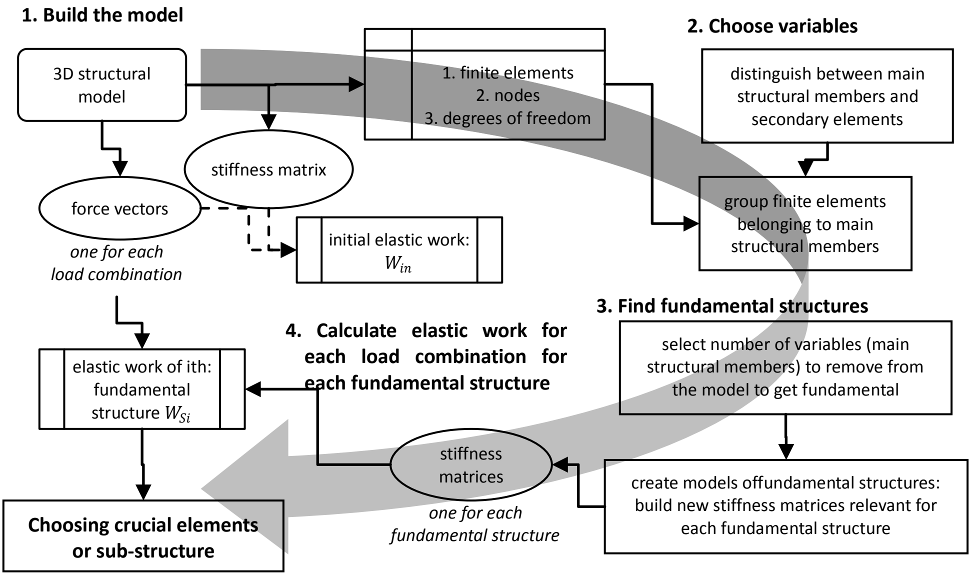

Figure 4. Algorithm for determination of crucial elements/assemblies within structural model.

In order to implement proposed method for determination of fire scenarios, special scripts are created in Matlab software [4] with incorporation of CALFEM function [5]. General finite element model are made in Autodesk Robot Structural Analysis software [6], which is dedicated for structural engineers and allow to calculate and design structures in accordance with Eurocode rules. After that model's informations are spread over other software used in analysis: 1. mentioned earlier Matlab, where determination of fire scenario is made, 2. Abaqus [7], where elasto-plastic analysis of structure in fire is made, 3. Scilab [8], code very similar to Matlab, where coupling between CFD and FEM model is managed, by own scripts [2]. CFD simulation of structure in fire was performed in Fire Dynamics Simulator (FDS) [9].

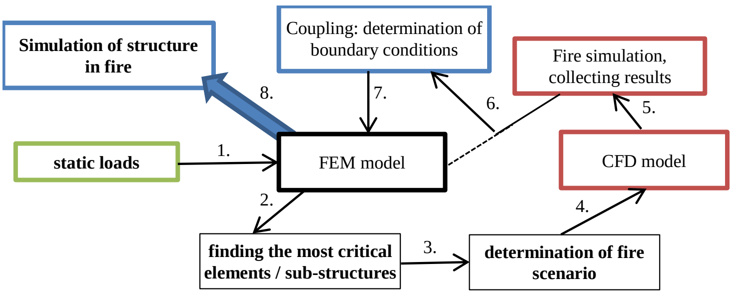

Figure 5. Scheme of analysis.

4.1 Finite element method model

Finite element method computations used in analysis take into account both material and geometrical non-linearity using material parameters as a function of temperature based on Eurocode's material model [10] and using second order analysis in order to reflect redistribution of internal forces in deflected structure. Used finite elements consist of 7 integration points over cross-section so steel temperature along cross-section can vary and cause addition bending resulted by non-uniform heating of elements. Detailed information about the FEM model used in coupled CFD-FEM analysis can be found in [11].

4.2 Computational fluid dynamics model

In case of fire modelling, full 3D computational fluid dynamics model is created. Four fire scenarios have been considered in order to verify that chosen earlier fire scenario is really the one which gives severe situation (Figure 6). Compartment has only four windows with total area of openings equal to 3 m^2, as it was originally fabricated in experiment conducted by [12].

Figure 6. Fire scenarios taken into analysis.

From the material point of view, in CFD model all boundaries of compartment are defined taking into account layered structure of sandwich panels used as external elements both for walls and roof. Computations are carried on in Fire Dynamics Simulator (FDS) software [9], using 20 cm grid size. All structural elements like columns, girders, etc. are omitted in CFD model. Nonetheless, proper devices are placed in corresponding points to measure gas temperature and heat fluxes acting on the structural elements in real situation. More detailed information about the CFD model are described in [11].

5 RESULTS

5.1 Crucial elements and structural complexity

Initial structural model is divided into group of elements as shown previously in Fig.3. Self and imposed loads were collected and 24 load combinations are distinguished, with respect to rules given by Eurocode 1990 [13]. Two main outputs are selected: Normalized Structural Complexity Index (Figure 7), in order to describe the complexity of structure according to load conditions and Element's Importance Factor (Figure 8), what directly gives an information about the place where fire source should be placed. That analysis is conducted only for accidental load combinations used for fire situation.

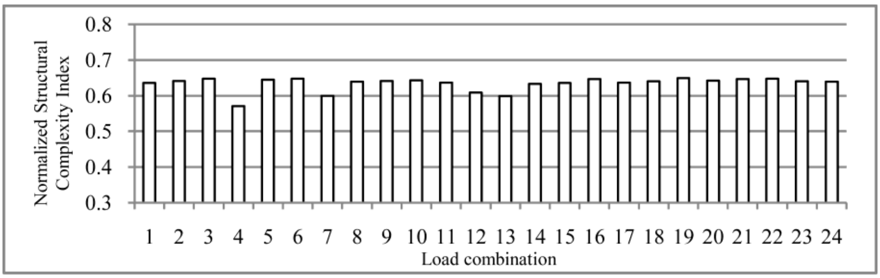

Figure 7. Normalized Structural Complexity Index with respect to load's combination.

Figure 7 shows, that the complexity of the structure do not vary significantly with respect to combinations of loads. In case of analysed frame it is rather predictable because of leading role of self-weight in accidental load combinations. From the same reason also elements which can be recognized as crucial in load bearing process should repeat over the whole load combinations, and it is really so. In Fig.8 it is shown, that Element's Importance Factor do not change significantly over all combinations of loads (standard deviation is nearly negligible).

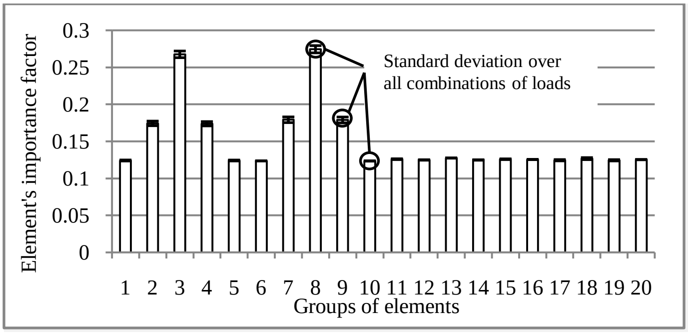

Figure 8. Beam importance factor averaged over all combinations of loads.

From that consideration it can be seen, that the crucial elements are No.3 and No.8 which correspond to middle frame columns and after that elements 2, 4, 7, 9, which are columns in frames one before last.

5.2 Coupled CFD-FEM analyses of structure in fire

From coupled CFD-FEM analyses of structure subjected to local fire, two main outputs are shown in Fig.9: relationship between vertical displacement of meaningful point affected by fire with respect to time and gas temperature in the vicinity of that point. In case of "Local_1", "Local_3" and "Local_4" displacement of top of columns affected by fire was measured, whereas in case of "Local_3" fire vertical displacement of frame ridge was measured.

Apart from pure mechanical analysis of fire resistance of structure against local fire, what is discussed more detail in [11], here it is enough to note, that those results precisely correspond to predictions which were made in accordance to Figure 8. Columns of middle and one before last frames are the ones with the lower fire resistance, what is about 15 minues and 75 minutes. Nonetheless, it is important to mention that in all cases no global failure is observed and overall integrity of structure is not exceeded.

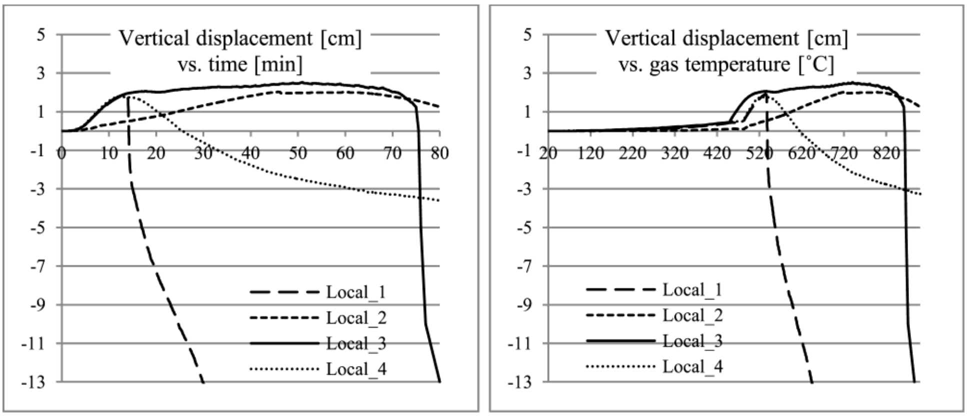

Figure 9. Relationship between vertical displacement and: (a) time, (b) gas temperature.

6 SUMMARY AND CONCLUSIONS

In this work the method for determination of fire scenarios in accordance to load conditions have been presented. Method have been implemented and verified in the case of 3D hall subjected to local fires. Because of strong mathematical basis, method is robust and seems to be considerably easy to apply for any structural model of skeletal building created in FEM software. One of the main features of this method is direct connection with actual mechanical load combination, what leads to direct determination of series of fire scenarios in large complex structures, where distribution of external loads can significantly affect the utilisation of particular members.

The future work on this method may be focused on relation between structural complexity and the real fire resistance of structure against the natural fire. Also the method for finding the most crucial fundamental structures could be improved, in order to speed up the process. Actually, authors are still testing some genetic algorithms to do that and preliminary results are promising.

Altogether, proposed method seems to be a good contribution in the fire structural engineering field, what corresponds to nowadays trends in design, where fire safety is no longer connected only with environmental aspects and structural safety is provided by simple prescriptive requirements, but more and more engineers are preparing calculations in accordance to performance based methods.

ACKNOWLEDGEMENT

The financial support of Ruukki Construction OY within scientific grant 11-962/2011-14 is gratefully acknowledged.

REFERENCES

[1] De Biagi V., Chiaia B., “Complexity and robustness of frame structures”, *International Journal of Solids and Structures*, 50, 3723-3741, 2013.

[2] Malendowski M., Glema A. “Influence of Natural Fire by coupled CFD-FEM Analysis of Steel Construction”, *Fire Safety Journal (submitted 2014)*.

[3] Wickström U., *Personal Correspondence*, 2012.

[4] MathWorks, *MatLab Documentation*, 2011.

[5] AustrelP.E., et al., *CALFEM. A finite element toolbox. Version 3.4*, Structural Mechanics, LTH, Sweden, 2004.

[6] Autodesk, *Robot Structural Analysis Documentation*, 2014.

[7] DassaultSystemes, *Abaqus Documentation*, 2012.

[8] INRIA, *Scilab Documentation*, 2013.

[9] McGrattan K., Hostikka S., Floyd J., *Fire Dynamics Simulator (Version 5) - User’s Guide*, NIST Special Publication 1019-5, 2010.

[10] European Committee for Standardization, *EN 1993: Part 1.1; Part 1.2,* 2013.

[11] Malendowski M., Glema A., Szymkuc W., “Fire resistance of steel frame structure. Comparison between standard Eurocode design procedureand advanced coupled CFD-FEM simulation”, *Eurosteel 2014 – Proceeding of 7th European conference on steel and composite structures*, (accepted), 2014.

[12] Pyl L., Schueremans L., Dierckx W., Georgieva I.,“Fire safety analysis of a 3D frame structure based on a full-scale fire test”, *Thin-Walled Structures*, 61, 204-212., 2012.

[13] European Committee for Standardization, *EN 1990*, 2012.

8th International Conference on Structures in Fire
Guo-Qiang LI, Venkatesh K. R. KODUR, Shou-Chao JIANG, Jian JIANG, Su-Wen CHEN, Guo-Biao LOU (Eds.)
Shanghai, China, June 11-13, 2014

DEVELOPMENT OF A METHODOLOGY TO PREDICT TRANSIENT HEAT FLUX ON EXTERNAL STEEL STRUCTURE BASED ON REALISTIC FIRES

Tad-Song Kho*, Florian M. Block* and Iain Macfarlane*

* Buro Happold Ltd
e-mails: Tad-Song.Kho@BuroHappold.com, Florian.Block@BuroHappold.com,
Iain.Macfarlane@BuroHappold.com

Keywords: External steel structures, OZone, Natural fire scenarios

Abstract. *The expression of structural frame external to the façade of a building is currently an architectural trend. For this purpose the SCI P009 approach has been traditionally used to assess the temperature of external steelwork. While the approach considers distinct flame shapes for steady-state fire and ventilation conditions the proposed approach aims to represent the full burnout of a compartment fire. Comparison between the proposed method and experimental work shows that the method is generally conservative and correlates relatively well with experiment. A qualitative assessment has been carried out to compare the traditional approach with CFD models. It is found that the notional flame shapes do not always agree with the CFD results for compartments with wide windows and long balconies. Despite this, the method generally still gives conservative results in terms of radiative heat flux and the proposed method is considered an improvement to the current method by accounting for the transient state of realistic fires.*

1 INTRODUCTION

In current architecture it is a trend to express the structural frame external to the façade of a building. In some cases this style is used in high-rise steel frame apartment buildings allowing free internal layouts without structural restrictions. These buildings have the challenge that the fire protection to the external steelwork needs to be weather resistant and of a high architectural appeal as the structure is very visible from often luxurious apartments. On the other hand an external steel structure is often subjected to less onerous heating conditions resulting from the radiation of the compartment and the radiation and convection from the flames breaking out of the windows. Therefore, there is scope to use structural fire engineering to optimise the external structure to be sufficiently safe without applied fire protection allowing for a cheaper, more durable and more appealing finish.

In the early 1970s Margaret Law developed an approach to predict the heat-flux on external steel members from different types of compartment fires [1]. This approach was published by the Steel Construction Institute (SCI) under the number P009 [2], which has been widely adopted for the design of real buildings. This early guidance was adopted into Part 1.2 of Eurocode 1 [3] and Eurocode 3 [4]. This approach was also published in the US by the AISI in 1979 under the name of Fire-Safe Structural Steel, A Design Guide [5]. The approach uses constant compartment temperatures and mass burn rates to predict standardised flame shapes for different fire severities and ventilation conditions in order to calculate the heat-flux to the external steel members. Based on this combined heat-flux the average steady-state temperature of a steel member is then calculated and used in design. From here on this method shall be known referred to as the P009 method.

This method has been extensively used in the past but has its limitations if one is interested in a more realistic time-depended heat-flux to the external steelwork in line with the natural fire approach. More specifically, the steady-state fire assumption in combination with the calculations of the steel temperature based on thermal equilibrium often leads to very conservative results for external members with a low

Am/V value. Also the effects of changing opening sizes due to breakage of glazing and or façade burnout cannot be readily incorporated into the assessment. Furthermore, the effects of differential heating in the cross section for external members, which naturally have different heat-flux values on their sides, are ignored despite the well-known fact that non-uniform heating introduces additional thermal curvature into the sections, which could lead to additional moments and increased P-Delta effects potentially critical for slender compression members.

This paper aims to improve on the P009 method by summarising a new approach that has been developed as part of a tall residential tower with exposed 4 story long steel diagonals. The building has balconies projecting up to 3 metres with an all-glass façade on its elevation. The new approach uses the time-depended compartment temperature and mass burn rate results from the well-known zone model OZone [6], developed at the University of Liege, as a time dependent input data for a modified version of the external steelwork approach as defined in Eurocode 1-1.2 and 3-1.2. Currently, the proposed approach only considers no force draught scenarios but extends the original flame shapes by ones that include large balconies above the windows.

Numerous experiments on the external venting of flames from compartment openings have been conducted over the years. While experiments by Yokoi [7] were carried out to characterize the flame profile breaking out of the openings, Oleszkiewicz [8]carried out experiments to investigate the floor-to-floor fire spread in buildings. Their experiments involve placing heat flux measuring devices on the façade of the building along the height of the building. Lin [9] conducted similar experiments but they were mainly interested in investigating the flame spread behaviour to adjacent buildings. The beneficial behaviour of horizontal projections above the compartment opening in preventing fire spread to the floor above has been investigated by Yokoi [7], Oleszkiewicz [8]. Weiner and Poh [10] conducted CFD studies on the same topic but these were again mainly focused on the effect of external flames to the facades of the building.

2 METHODOLOGY

To calculate transient external steel temperatures the proposed approach can be divided into 4 steps as outlined below:

(1) Use OZone to predict the fire behaviour and use the results for the compartment gas temperature and the burn rate as input parameters for the original approach for external steelwork in a time dependent manner;

(2) Calculation of the external flame shape and temperature distribution along the length of the flame including the effects of the balconies;

(3) Calculation of the radiation and convection emitted from the fire and the flame and received by the external steelwork; and

(4) Calculation of the steel temperature using the heat fluxes from the previous step.

Signs and notations consistent to those in SCI P009 are adopted here; therefore readers are referred to the publication for details on the conventional approach for calculating temperature external of external steelwork. In this paper aspects which deviate from the conventional P009 method are described. Note that the method described in Eurocode 1-1.2 [3] and 3-1.2 [4] are based on the same principles to that of SCI P009, and the notations used in this paper are consistent with those used in the Eurocodes.

With information about the geometry and characteristics of the fire compartment, it is possible to run an OZone analysis which would yield a time-dependent rate of burning and fire temperature within the room; these will replace the average rate of burning R and the temperature of the fire within the room T_f respectively in the P009 approach. Since OZone can include changing ventilation conditions based on glass-breakage as well as the thermal properties of the compartment boundaries it can predict the fire temperatures in the compartment and the mass burn rate much more realistically than the equations used in the external steelwork in fire approach currently in SCI P009.

Some of fundamental notations and assumptions used in the conventional P009 method are explained here to provide clarity on the proposed method. The P009 method assumes a steady-state fire in which the flame breaks out of the compartment opening. The external flaming is simplified into a notional flame shape; for no forced draught conditions calculations are done based in the flame shape shown in Figure 1. If a balcony or an awning is present above the opening, the flame trajectory is different to a case which does not have a horizontal projection. However, the length along the flame axis, denoted L_f, for both cases will remain unchanged. L_f is calculated with respect to the line of the façade/window and for a no forced draught case is located at a distance $h_{eq}/3$ below the top of the window, where h_{eq} is the height of the window. It is also worth noting that the width of the flame will be the same as the window opening. When the flame projects outwards and upwards, it is assumed to deflect by 45°.

Generally the incident heat fluxes acting on the steel come from three sources, these being radiative heat flux from the external flame, radiative heat flux from the fire at the window and convective heat flux. For the proposed method, depending on the stage of the fire the heat flux acting on the steel can be a combination of two or all of these sources. Knowing the length of the flame axis L_f and the length of the balcony, denoted here as $L_{B,}$ allow the horizontal projection of the flame axis, denoted here as L_H, to be calculated; this in turn allows the fire stage to be determined. Another parameter – the effective horizontal edge of the fire denoted L_{EH} is calculated in determine whether the steelwork is engulfed in the flame; Table 1 explains this. Basically if L_{EH} is greater than the distance between the column and the window then the column is deemed to be engulfed in the flame. The origin of $L_{H\ \mathrm{and}}\ L_{EH}$ are the same as L_f where flame projecting outwards from the window takes a positive value. A typical flame shape for a fully developed fire with flames spilling over a balcony is shown in Figure 1, assuming a balustrade at the edge of the balcony and $h_{eq} < 1.25w$ with w being the width of the window. The new notations used for the proposed method, $L_{H\ \mathrm{and}}\ L_{EH}$, are illustrated alongside the conventional ones.

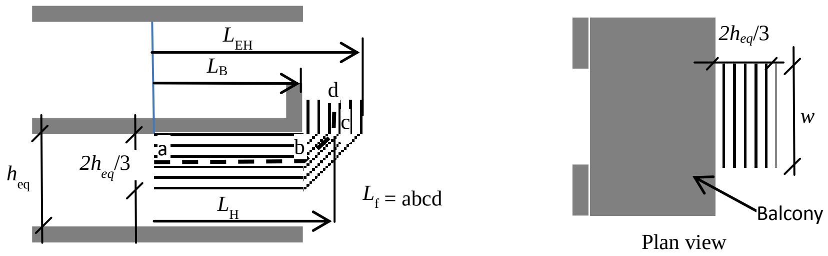

Figure 1. Nominal flame shape.

To account for the development and subsequent burn-out of a fire taking place in a compartment which have a balcony above the opening, the fire is split into four stages. Stage 1 is where a compartment fire is still underdeveloped and still confined within the compartment; Stage 2 occurs when the fire break out of the opening but is not big enough to spill over the balcony; Stage 3 is taken as the intermediate stage between Stage 2 and Stage 4, in which the flame tip projects beyond the edge of the balcony but does not rise above the balcony; Stage 4 is as described in the paragraph above in which the flame spills over and above the balcony. The four fire stages are graphically illustrated by the figures in Table 1 below. The notional flames shapes shown in the figures and their corresponding assumptions stated in the table form the basis of the proposed method in calculating the evolution of the external steel temperature. The approach is quite detailed and has therefore been programmed as an in-house Excel spreadsheet, which has been validated against the design examples given in the SCI P009.

The result from the spreadsheet is the incident heat fluxes to the external steelwork for each side of the member separately as a function of time; this allows a detailed time-dependent calculation of the steel temperature profile, using for example the 2D heat-transfer program TASEF [11], for the full duration of the fire including the decay phase.

Table 1. External flame stages.

Stage	Stage 1	Stage 2	Stage 3*	Stage 4
Illustration	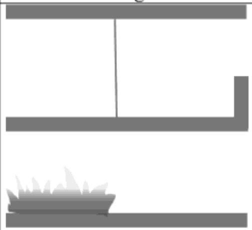	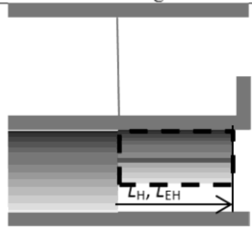	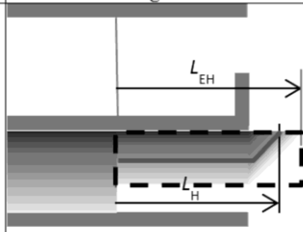	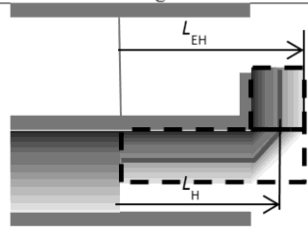
Condition	If L_H <= 0	If L_H > 0 and L_H <= L_B	If L_H > L_B and L_H <= $L_B + h_{eq}/3$	$L_H > L_B + h_{eq}/3$
Description	Occurs when flame length L_f is calculated to negative, meaning the flame has yet to break out of the window.	Occurs when tip of the external flame is still under the balcony and have yet spill over its edge.	Occurs when tip of the external flame is still under the balcony and but have spilled pass the edge of the balcony.	Occurs when the external flame has spilled pass and above the balcony edge.
Source of heat flux	- convective heat flux - radiative heat flux from window	- convective heat flux - radiative heat flux from window - radiative heat flux from flame	- convective heat flux - radiative heat flux from window - radiative heat flux from flame	- convective heat flux - radiative heat flux from window - radiative heat flux from flame
Radiative heat flux panel from flame	Not present.	Present, only 1 radiating panel from the flame under the balcony.	Present, only 1 radiating panel from the flame under the balcony.	Present, 2 radiating panels to represent flame under the balcony and flame above balcony. **

* L_{EH} in Stage 3 can be linearly interpolated between Stage 2 and Stage 4 which works out to be $L_{EH} = L_B + 2\,(L_H - L_B)$. If column is not engulfed an equivalent front rectangle of length L_{EH} is used to calculate the radiation acting on the surface of the column.

** For Stage 4 the radiative heat flux from flame is divided into two panels if the column is not engulfed. One represents the equivalent front rectangle from under the balcony and the other represents the front rectangle above the edge of the balcony. Note that the conventional P009 method does not seem to account for the first panel, but here it is included as the emissivity of the flame below the balcony can be very high due to the length of the balcony and can thus contribute a lot of the incident radiative heat flux to the steel column.

3 EXPERIMENTAL AND CFD COMPARISON

There is unfortunately limited existing study available on this particular subject which involves the assessment of external steel temperatures whilst accounting for the effect of a balcony above the compartment opening. Therefore, a combination of experimental work and CFD study are carried out to gauge the capability of the proposed method from different aspects.

3.1 Transient fires – comparison with experiments

Experimental work by Lin [9] has been chosen to assess the new method's ability to model the transient state of incident heat fluxes acting on an external steel structure. While the original aim of Lin's work is to study the exposure fire spread between buildings by radiation, the experimental set up is suitable for comparison with the proposed method as radiation to an external surface is recorded over time. One of the experiments is replicated, whereby a 25kg/m^2 of fire load was used as fuel in a compartment measuring 2.64m in width, 3.64m in depth and 3.0m in height. The window opening measures 2.64m in width and 1.72 in height with the window sill being placed 1.1m above ground. The window placed along the width of the compartment provides the only means of ventilation. No horizontal projection was placed above the opening. The walls and floors are 12cm thick, with two sides of the wall perpendicular to the opening being built from bricks while the rest of the compartment was constructed using reinforce concrete with the other exception being the wall containing the opening, which is largely made from ALC bricks. From the start of the experiment the window opening is kept fully open.

The heat release rate during the course of the experiment was not measured; therefore the heat release rate per unit area of the design fire in OZone of 400kW/m^2 is selected, which produces temperatures that are similar to what was measured 10cm below the ceiling within the compartment during the experiment, see Figure 2. This would eliminate the uncertainty associated with the prediction of the design fire in OZone to ensure that the design fire used for the proposed method would be similar to what occurred in the experiment as it is of more interest to access the capability of the modified P009 method to predict the incident heat flux over time.

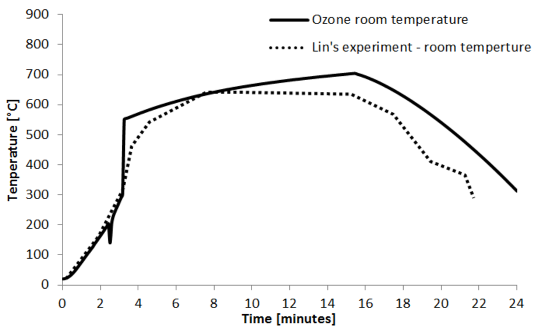

Figure 2. Temperature results in Ozone versus temperature measured 10cm underneath ceiling in Lin's experiment [9].

Radiometer readings placed 0.6m above the top of the opening and at a distance 2m, 3m and 5m away from the façade of the building are plotted with the incident heat fluxes predicted with the proposed method in Figure 3. It can be shown that the proposed method generally gives more conservative values compared to experimental records, and agrees well with the time envelope of the heat flux recorded in the experiment. The convective heat flux was not measured in the experiment; hence the comparison with this parameter was not carried out. The seamless change from one fire stage to another is outlined in the same graph and shows that relatively seamless transition can be achieved. When the height of the flame between the recorded flame height in the experiment and the calculated flame height is compared in Figure 4, it again shows reasonable correlation especially the maximum flame height which is approximately 2.3m.

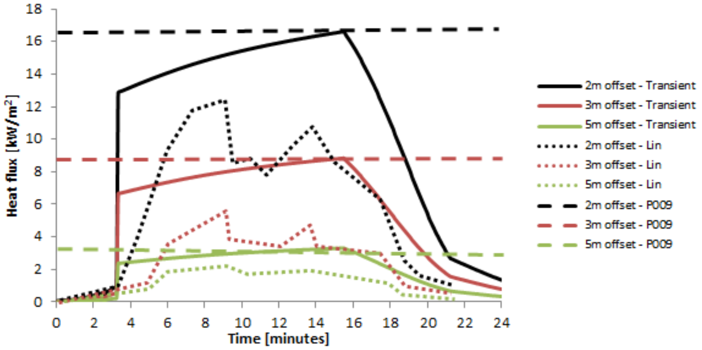

Figure 3. Radiative heat flux comparison between proposed transient method, Lin's experiments [12] and conventional steady-state P009 method.

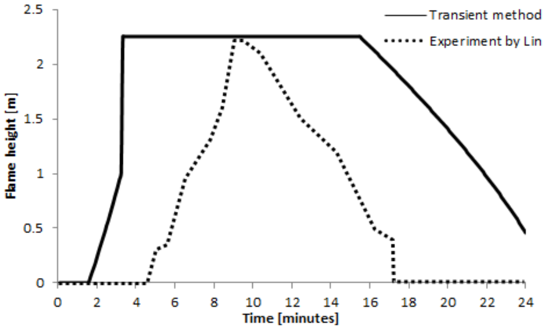

Figure 4. Flame height comparison.

From this study it can be concluded that the new method is capable of predicting transient radiative heat fluxes which give conservative results, provided reasonably realistic design fires can be established, which is not within the scope of this paper.

3.2 Balcony effect above window – CFD comparison

For a CFD comparison a compartment measuring 12.5m in width, 11.75m in depth and 2.75m in height is created in Fire Dynamics Simulator (FDS) [12]. The floor and ceiling of the compartment consists of 0.25m thick concrete whereas the walls are made of block work which is similarly thick. One side if the compartment measuring 12.5 m and 2.75m is kept fully open whilst all other parts of the compartment remain enclosed. In front of this opening a few different balcony and column configurations have been investigated as shown in Table 2.

Table 2. Balcony configurations in CFD study.

Case	Balcony length [m]	Column offset from façade [m]	Balustrade at edge of balcony?
C1	0	1	No, but wall present above opening.
C2	4	4.5	No
C3	2	4.5	No
C4	2	2.5	Yes

The steady state of the CFD model is compared with the proposed method for a comparable scenario. An unlimited fuel load is prescribed in the CFD model; combustion of the fuel is set to burn at a heat release rate of 2.57kg/s throughout the compartment. The fire in the simulation is then allowed to grow to a steady state before readings on the devices are extracted and averaged at every 10-second interval.

A column was not explicitly placed in front of the opening; instead RADIATIVE HEAT FLUX GAS measuring devices are placed on the four sides of a steel column. From experimental observations Law and O'Brien [2] concluded that steel temperature at the top of the window typically experiences the highest temperatures. Thus for this study results from the measuring devices are placed at the same level as the top of the opening. The devices are orientated such that the device points outwards and perpendicular to the column surfaces in which they measure the radiant heat flux acting. This is to mimic the exposure and shielding effects which each side of the column would experience relative to the fire within the compartment and external flame. Side 4 of the column for instance is not exposed to the fire in the compartment nor exposed to the flame unless it is being directly engulfed by the flame.

The resulting incident heat flux predicted by the proposed method gives a safety factor of up to 3 when compared to the results from the CFD study. Several interesting observations were noted as they do not tally with some of the existing assumptions laid out in the SCI P009 guide. Temperature of the flame tip in FDS is taken as 540ºC in line with assumption in SCI P009 and outlined in Figure 5 below. The notional flame shapes suggested in the SCI P009 guidance are superimposed alongside the temperature plot results in the CFD study. As it can be observed the thickness of the flame generated in FDS is generally half of to that of the notional flame shape. In addition the length of the flame in the numerical models is greater than what is suggested in the P009 guidance.

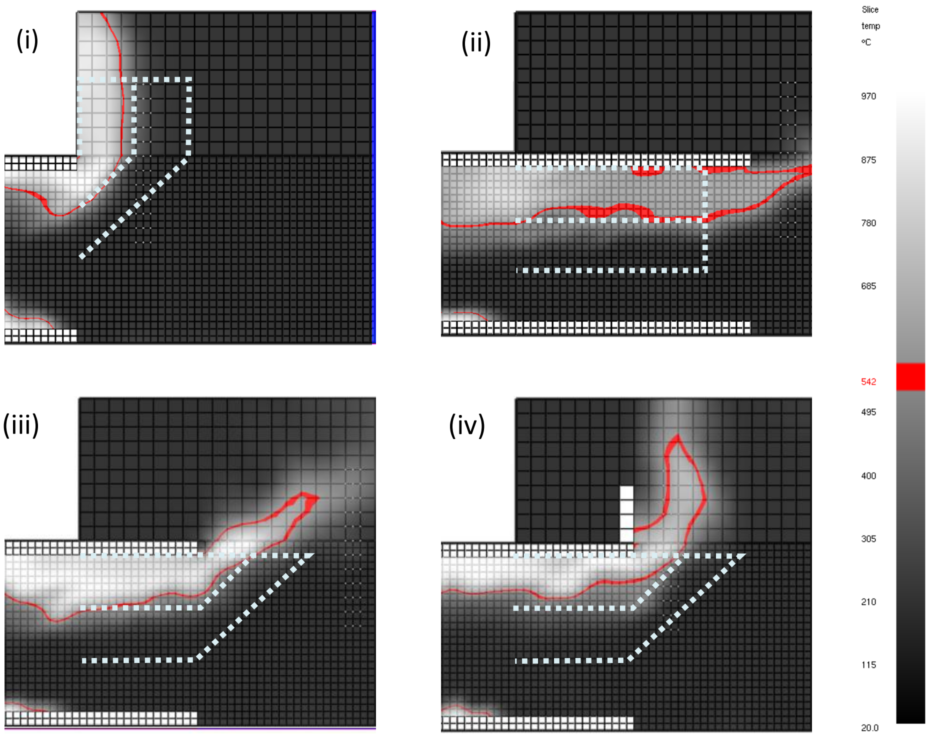

Figure 5. CFD temperature plots with superimposed nominal flame shapes for Case C1(i), C2(ii), C3 (iii) and C4 (iv).

The notional flame shape assumed in the calculations is fundamental towards the heat flux calculation. The discrepancy between the numerical and P009 guidance illustrated in the figure above can make a difference between a column being engulfed or not for the same case; this in turn will affect the calculation of radiative heat flux acting on each side of the steel column. Therefore, there should be a need to re-access the notional flame shape in the guidance accompanied with more experimental and numerical studies on the effects of really wide windows and long balconies – two parameters which are thought to contribute towards the discrepancy observed in this study. The SCI P009 method has been formulated over the based on work done from 1960s onwards where experiments took place in compartments with relatively small window sizes. In addition, most of the experiments with horizontal projections carried out thus far have projections of only up to 1m. Therefore there is still a lack of understanding on how these two factors affect the calculation of heat flux to the external steel.

4 CONCLUSIONS

The results of the new approach have been compared with existing experiments designed to investigate external flaming of compartment fires as well as with purpose built simple CFD models. Reasonable and safe correlations could be found with the experimental work and the proposed model. The CFD study is conducted to qualitatively assess the existing assumptions made on the flame shapes. It is found that the notional flame shape which is the base of the radiative heat flux the calculations is found to be different from the results from the CFD study. With the increasing popularity of all-glass facades and long balconies in residential buildings it is important to recognize that existing methods which were devised from experiments in the 1960s may be over-conservative or no longer valid in today's settings.

The proposed approach summarised in the paper is the first step to a new, more realistic and safer design approach of external steel structures that can be used for structural fire engineering assessments based on realistic fire scenarios. The method is conservative and is deemed to be an improvement to the conventional method which assumes a steady state temperature calculation.

REFERENCES

[1] Law, M., "Fire-Safety of External Building Elements - The Design Approach", *American Iron and Steel Engineering Journal*. Second Quarter, 59-74, 1978.

[2] Law, M. and O'Brien, T., "*Fire safety of bare external structural steel"*, The Steel Construction Institute, SCI Publication 009, U.K, 1989.

[3] European Committee for Standardisation. "*EN1991-1-2: 2002. Eurocode 1: Actions on Structures: Part 1-2: General Actions - Actions on Structures Exposed to Fire*". Brussels, 2002.

[4] European Committee for Standardisation. "*EN1993-1-2: 2005. Eurocode 3: Design of Steel Structures: Part 1-2: General Rule – Structural Fire Design*". Brussels, 2005.

[5] American Iron and Steel Institute (AISI), *Fire-Safe Structural Steel – A Design Guide*, Washington, DC, 1979.

[6] Cadorin, J-F., Pintea, D., and Franssen, J-M. "*Technical reference of OZone V2"*. Rapport interne SPEC/2001_01, Département des Structures University of Liège, 2001.

[7] Yokoi, S., "*Study on the Prevention of Fire-Spread Caused by Hot Upward Current"*, Report of the Building Research Institute, Japan, Report # 34, 1960.

[8] Oleszkiewicz, I., "*Vertical separation of windows using spandrel walls and horizontal projections*", Fire Technology 27(4), 334–340, 1991.

[9] Lin, C.Y., "Study of exposure fire spread between buildings by radiation", *Journal of Chinese Institute of Engineers*, 23(4), 493-504, 2000.

[10] Weinert, D. and Poh, W., "*Performance of horizontal projections in vertical separation of openings in external walls – comparison with BCA solutions*". Proceedings of the International Conference on Fire Safety Engineering, Gold Coast, Australia, 2006.

[11] Wickstrom, U., "*TASEF-2: A computer program for temperature analysis of structure exposed to fire*" Lund Institute of Technology, Sweden, Report No. 79-2, Lund 1979.

[12] McGrattan, K. B., Klein, B., Hostikka, S., and Floyd, J. *Fire Dynamics Simulator (Version 5), User's Guide*. NIST special publication, 1019(5), 1-186, 2008.

RESILIENCE ASSESSMENT OF CRITICAL INFRASTRUCTURE AGAINST EXTREME FIRES

Hossein Mostafaei*, Mohamed Sultan* and Ahmed Kashef*

* National Research Council Canada
e-mails: Hossein.Mostafaei@nrc-cnrc.gc.ca, Mohamed.Sultan@nrc-cnrc.gc.ca,
Ahmed.Kashef@nrc-cnrc.gc.ca

Keywords: Extreme fire, Hydrocarbon fire, Critical infrastructure, Bridges, Tunnels, Fire resistance, Fire protection, Property protection

Abstract. *This paper provides results of a literature review of recent studies on resilience and protection of critical infrastructures against extreme fires, e.g. fuel storage or tanker fires. The main objectives of these studies were to develop a better understanding of the fire severity for critical infrastructures, current extreme fire resistance test methods, and potential fire protection materials and technologies for such extreme fires. The MacArthur Maze Bridge collapse on April 27, 2007, a critical bridge in the San Francisco area, is an example of such extreme fire threats to critical infrastructures.*

This paper also provides the results of current hydrocarbon fire, extreme fire, test methods and their applicability for extreme fire resistance assessment of the critical infrastructures. For demonstration, a calibration test, simulating an extreme fire for bridges/buildings, was performed using the upgraded testing facility at the National Research Council Canada (NRC). A summary of the results is included. As well, it provides a list of fire protection solutions and suggested criteria for selection of fire protection materials for critical infrastructures.

The results indicated that there is a lack of standard for test of critical infrastructure in fire. An extreme fire testing method was suggested for critical infrastructure until further experimental studies become available. Criteria for the selection of fire protection materials are suggested based on the thermal properties, fire severity and exposure conditions.

1 INTRODUCTION

Recent studies on transportation infrastructures to extreme fires [1, 2] indicated that critical infrastructures such as bridges are not designed for extreme fires, hydrocarbon fires, and are vulnerable to such threats. Studies on the recent bridge fires reported more than 500 fatal crash events on bridges in the last 14 years across the U.S. and Canada [1, 3]. These incidents resulted in millions of dollars of loss due to the direct cost of the bridge damage and repair and indirect economic impact on the community as a result of the delay for the bridge recovery after the incidents.

Currently, the only document available in North America that reflects some requirements for protection of transportation infrastructures against extreme fire is NFPA 502 “Standard for Road Tunnels, Bridges, and Other Limited Access Highways” [4]. NFPA 502 provides designers and regulators with guidelines for the construction, operation, maintenance, and fire protection of tunnels and bridges to mitigate hazards, maintain structural integrity, and protect lives. Although the scope of NFPA 502 is tunnels and bridges, most of the developed information is for design and protection of tunnel linings. Currently, there is no guideline for assessment, protection and design of the critical infrastructures such as bridges against extreme fires.

The current available fire protection materials and technologies are mainly evaluated and designed for normal building fires. There are a few types of fire protection materials available that would be suitable for extreme fires. However, these materials are for specific applications such as fire protection of refinery structures or protection of tunnel linings. Fire protection materials need to be selected based on thermal properties of the materials, e.g. thermal conductivity, severity of the fire, e.g. normal fire or extreme fire, and exposure conditions, e.g. high humidity, salt spray, and freeze-thaw.

This paper provides a summary of the results from two research projects that studied extreme fire resistance methods and fire protection solutions for critical infrastructures to extreme fires.

2 CURRENT HYDROCARBON FIRE TESTS

Some of the current fire resistance test standards for buildings are ASTM E119 [5], and CAN/ULC S101 [6]. These standards are not applicable for use to assess the fire resistance of structure members that are subject to extreme fires, e.g. hydrocarbon fires. There are other fire resistance standards or guides that could be more appropriate for extreme fire resistance tests. These standards include ASTM E1529 [7], NFPA 502 [4], UL 1709 [8] and Efectis Nederland BV document [9].

Hydrocarbon pool fires, or extreme fire, are fires with rapid rise of temperatures and massive heat fluxes that can expose structural members to a thermal shock which is much greater than those resulting from burning of solid fuels. This section provides a summary of the current main standards and their applicability for critical infrastructures.

2.1 NFPA 502-11, Standard for road tunnels, bridges and other limited access highways

This standard provides minimum fire protection and fire life safety requirements, for road tunnels, bridges, elevated highways, depressed highways, and roadways that are located beneath air-right structures. This standard requires that critical structural members be protected from collision and high-temperature exposure which result in dangerous weakening or collapse of the bridge or elevated highway. However, it doesn't provide information on fire exposure or test sample size or the duration of fire exposure and failure criteria for bridges. For tunnels, the standard provides information on the use of the Duch Rijkswaterstaat (RWS) time-temperature curve for the fire resistance evaluation of critical structures or any HJA acceptable curve following an engineering analysis. The RWS time-temperature curve requirements are being adopted internationally as a realistic design fire curve that is representative of typical tunnel fires with peak HRR range from 70 to 200 MW. The RWS curve was developed by the Rijkswaterstaat, Ministry of Transport in the Netherlands based on the assumption that in a worst case scenario, a 50 m^3 fuel, oil or petrol tanker fire with a fire load of 300MW could occur, last for up to 120 minutes. The RWS curve was based on results of testing carried out by TNO in the Netherlands in 1979. The NFPA 502 standard states the requirements of 120 min duration of fire exposure and failure criteria of preventing concrete spalling in concrete tunnels and limited temperature rise to 300 ^{o}C for protected steel or cast iron tunnel lining [9].

2.2 ASTM E1529-10, Standard test methods for determining effects of large hydrocarbon pool fires on structural members and assemblies

This standard provides specifications for fire-test of load bearing and non-load bearing columns, girders, beams, walls that are employed in hydrocarbon processing industry facilities under controlled laboratory conditions using a fire resistance test furnace with a specific time-temperature curve that represents fluid-hydrocarbon pool fires. The standard requires exposure of the test specimen to heat flux and temperature conditions representative of total engulfment of free burning fluid hydrocarbon pool fire. Within the first 5 min, the test specimen is exposed to a heat flux of 158 kW/m^2 ± 8 kW/m^2. The furnace temperature should reach 815 ^{o}C at 3 min exposure and be kept between 1010 ^{o}C to 1180 ^{o}C at all times after the first 5 min [5].

2.3 UL 1709, Standard for safety- rapid rise fire tests of protection materials for structural steel

This standard provides a test method for a fire resistance evaluation of protective material applied to steel structural members in a rapid-temperature-rise fire without load bearing conditions. The test requires a heat flux of 204 kW/m^2 ±16 kW/m^2 and a rapid temperature rise of 1093 ^{o}C in 5 min and then remains constant to the end of test. In UL 1709 standard, the performance criteria is set such that the temperature between the steel and protective material during the period of fire exposure would not exceed 538 ^{o}C on the average of thermocouple readings and not exceed 649 ^{o}C on a single thermocouple reading [9].

2.4 2008-Efectis-R0695 Netherland BV, guide for fire testing procedure for concrete tunnel linings

The Efectis Netherland report R069 [9] is a document that provides a guide for a test of tunnel lining to extreme fires. The report described two tests; Test 1, for spalling behaviour of concrete (spalling test) and test 2, for measuring concrete temperature at the exposed and at reinforcement (thermal insulation test). To prevent or mitigate damages resulting from fire, the report states a few measures, such as avoid or limit concrete spalling, concrete temperature at surface and in and around reinforcement, concrete unexposed surface as well as limit propagation of concrete cracking into the unexposed side. The time-temperature curve, test procedure and failure criteria have been incorporated into the NFPA 502, explained in section 2.1.

2.5 Other extreme fire tests

There are other standards or guidelines available for extreme fire tests used by other countries. The main difference among these standards is the fire severity or time-temperature curve.

The Hydrocarbon (HC) Curve presented by Eurocode 1, the Modified Hydrocarbon (MHC) Curve, used by French regulations to test fire resistance of tunnel structures, and the RABT Curve used by German for fire resistance testing of structures and linings of road tunnels are other examples of existing standards [10].

For comparison, Figure 1 shows time-temperature curves for all the reviewed standards.

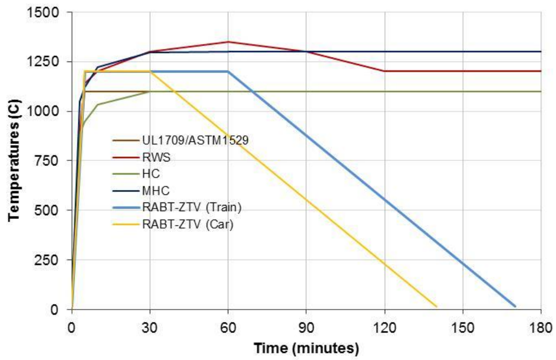

Figure 1. Time-temperatures curves by different extreme fire standards.

3 FIRE SEVERITY IN BRIDGES, TUNNELS AND BUILDINGS SUBJECT TO EXTREME FIRE CONDITIONS

This section provides results of a brief review on fire severity for extreme fire conditions in bridges, tunnels and buildings.

3.1 Extreme Fire Conditions in Bridges

Unlike the tunnels, there is no full-scale tests reported, in literature, for bridges but there are two studies on the San Francisco MacArthur Maze road bridge fire incident. The San Francisco MacArthur Maze Freeway fire Accident occurred in 2007 as a result of a tractor-trailer rig carrying 8600 gallons of fuel overturned on Interstate 880 in Oakland, CA. After the accident, several studies were conducted to investigate the bridge collapse due to fire. In a study by Noble, C.R, et al [11], on the thermal structural analysis of the San Francisco MacArthure bridge collapse, showed that the bridge collapse occurred due to a weakened steel superstructure that failed in 18 min. In this study, the coupled thermal-structural finite element analysis was performed using a mass scaling methodology in thermal analysis to reduce the overall simulation time. The analysis used showed that the structural failure occurred due to thermal softening of steel at approximately 18 min using a fixed fire temperature of 1200 ^{0}C and thermal properties. There is a second study by the US Nuclear Regulatory Commission, of the same fire accident and published by Bajwa, C. S. et al [12], titled “The MacArthur Maze Fire: How hot was it?” This study examined the samples collected from the collapsed bridge using the traditional metallurgical methods. Based on the metallurgical analyses that were carried out, it was reported that, the steel structure was exposed to a temperature that is close to 1000 ^{o}C. Considering the average temperatures obtained from these two studies, and since ASTM E1529 and UL 1709 time temperatures represent a refinery fire severity with petroleum fuel, the time temperature curve required by these two standards are suggested for extreme fire testing of bridge elements until further experimental data is available. Figure 2 shows the suggested time-temperature curve.

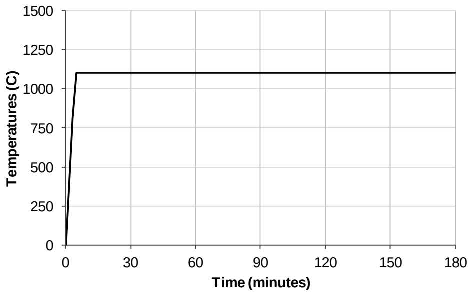

Figure 2. Time-temperature curves proposed for extreme fire tests of bridges and buildings.

3.2 Extreme Fire Conditions in Buildings

The September 11, 2001 airplane attacks on the World Trade Center (WTC) in New York City represent an extreme fire condition in building. A study [13] that was conducted to investigate the fire induced thermal and structural response of the World Trade Center Towers showed that, the hydrocarbon fires generated temperatures up to about 1100 ^{o}C; however, NIST [14] reported that the maximum upper hot layer air temperature was about 1000 ^{o}C in the WTC fire. In a different project, an extreme fire experimental program was carried out to investigate arson in buildings that involved fast fire growth [15]. The main purpose of the study was to investigate the risks posed by such fires to fire fighters, as part of a forensic study. Based on the temperatures reported at the ceiling during the tests, one may observe an average max temperature of 1100 ^{o} C. ASTM E1529 and UL1709 are standards for oil refinery structure facilities require similar fire severity as those of the above building studies. Therefore, these two standards are also suggested for extreme fire tests of building elements until further experimental data is available. Figure 2 shows the suggested time-temperature curve.

3.3 Extreme Fire Conditions in Tunnels

For tunnels, there are some small-scale and 4 full-scale fire tests found in literature that were conducted in 2003 [16, 17]. The small-scale tests were carried out at the SP Swedish National Laboratory while the full-scale tests were carried out at the Runehamar tunnel in Norway. The objectives of small-scale tests were to obtain data for fire behaviour, heat release rate, smoke production and hazardous gases for several combustible commodities that were used in the full-scale tunnel test program. The combustible commodities include cartons with PS cups, mixture of wood pallets and plastic pallets and mixture of wood pallets. The objectives of the four large scale tests (UPTUN project with 41 partners from 17 European countries) was to produce data on fire development and fire spread, using a simulated set-up of a semi-trailer cargo, and heat exposure to tunnel linings in the vicinity of the fire site inside the tunnel. The full-scale tests provided data on smoke spread in the tunnel, upstream and downstream of the fire, conditions under which firefighters with breathing apparatus may have to work with, smoke development from various types of fire loads, gas temperature and heat fluxes close to the fire site inside the tunnel and heat release rate. Test-1, with the highest fire load, produced the highest temperature of 1365 ^{o}C for the longest period of time of 30 min before it reduced down to 300 ^{o}C at 60 min. Tests 2, 3 and 4 produced a lower temperature, 1250 ^{o}C, and lower durations of fire exposure compared to Test 1. In the simulated tests mentioned above, where the fire was located 560 m away from one end of the tunnel, the effect of fire location inside the tunnel i.e. closer to the tunnel entrance was not investigated to determine the fire severity where a large amount of air can be sucked-in. On the other hand, the tests were performed with tunnel linings being protected. For unprotected linings, in which a large amount of heat will be absorbed by the concrete and a lower maximum temperature is expected, no fire test data is available. Until further experimental studies are available the RWS time-temperature curve is suggested for transportation tunnel tests as shown in Figure 3.

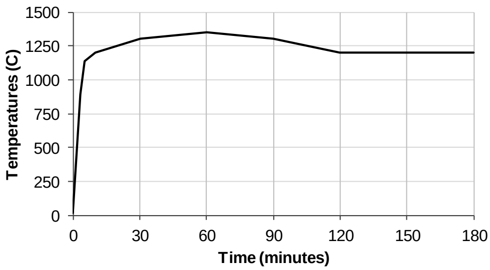

Figure 3. Time-temperature curve for tunnel test.

3.4 Extreme Fire Test Procedure

A test procedure was developed for extreme fire resistance evaluation of critical infrastructures. The detail of the test procedure is provided by Mostafaei et. al. [18]. Critical infrastructures included in the test procedure are bridges, tunnels and buildings. In the test procedure, the main standard referred to for extreme fire tests of bridges and buildings was ASTM E1529 and for tunnels NFPA 502. One of the main differences between testing of critical infrastructures compared to other conventional infrastructures and buildings is their requirement for property protection in addition to life safety. For a critical infrastructure, such as a major bridge, recovery time after an incident is very important to be as short as possible to reduce in the interruption in the traffic. Therefore, the test procedure for critical infrastructures needs to also evaluate the level of damage to the asset or structure in addition to the requirements of insulation, integrity and stability, for typical structures. The main failure criteria for property protection of concrete elements (until further studies are available) were suggested as [9]:

(1) when the spalling is greater than a 10% loss of column, beam, slab, or wall thickness (in the direction of spalling) as measured at the deepest points of spalling;

(2) when the temperatures on the steel reinforcing exceeds 210 ℃ for any single measurement;

(3) when explosive spalling occurs.

For steel structures, temperature of steel would be the main criteria to check. Until further studies are available, a conservative temperature of 210 ^{o}C could be suggested as the failure criteria for property protection of steel structures in fire. Steel needs to be protected for the extreme fire.

4 DEMONSTRATION OF EXTREME FIRE TESTS

A demonstration test was performed to ensure that application of the developed test procedure and simulation of the suggested extreme fire, with the required heat flux and temperature history, are feasible. The test was done to produce an extreme fire based on ASTM E1529 (UL1709) calibration procedure. Both standards almost have the same calibration test procedure. This calibration test was a demonstration for testing of loaded or unloaded bridge and building column elements**.**

4.1 Test specimen and setup

For calibration, sample sizes and specifications are mostly the same in ASTM E1529 and UL1709. Figure 4 shows the test specimen after construction and when it is installed in the column furnace.

Figure 4. Test specimen and test setup in a column furnace.

4.2 Test Results

The test was performed using the NRC column furnace. Average temperature in the furnace was controlled to meet the time-temperature curve in Figure 2. Figure 5 shows both heat flux and temperatures in the furnace during a one hour test. The figure indicates that the test met both the required minimum heat flux and the limits for temperatures for both standards and as indicated by the test procedure. Note that UL 1709 and ASTM E1529 also require checking maximum heat flux. However, this was not found easily feasible due to a minimum generated heat flux in the furnace for the required temperature. Hence, the proposed test procedure only required satisfying the minimum heat flux requirement, which is on the conservative side for the assessment.

5 FIRE PROTECTION MATERIALS AND TECHNOLOGIES FOR CRITICAL INFRASTRUCTURES

Fire protection technologies and materials are categorized in two main types; active and passive fire protections. Active fire protections, e.g. sprinkler systems, foam application system and detectors, require a certain amount of heat or smoke in order to work. However, passive fire protections are integrated within the infrastructures. At present, critical infrastructures such as bridges or critical buildings, e.g. government buildings, embassies, are not typically designed for protection in extreme fire events, e.g. hydrocarbon fire. This paper mainly discussed passive fire protections for critical infrastructures.

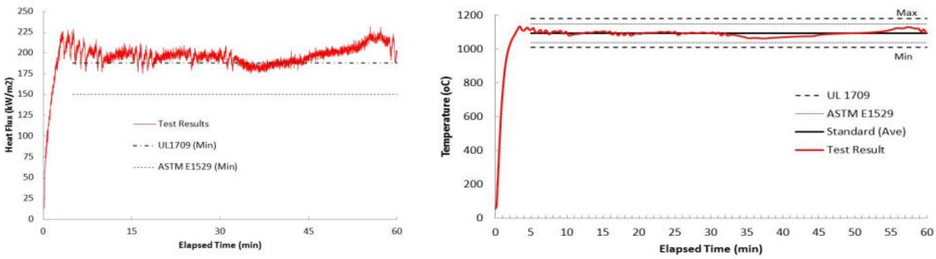

Figure 5. Test results for heat flux on the left and temperatures on the right during the test.

Currently, there are different fire protection technologies and materials for facilities such as oil refineries and offshore structures against extreme fires. There have also been studies on enhancing fire resistance and protection of tunnels, e.g. developing new concrete design mix or fire protection materials. The main passive fire protection materials for critical infrastructure include:

- Exposure and impact resistant cementitious Spray-Applied Fire Resistive Materials (SFRMs): for steel and concrete bridges and tunnels when exposure resistance is required with low cost and when inspection is not required or it could be done using non-destructive assessment methods.
- Exposure and impact resistant intumescent paint: for steel bridges when higher cost is affordable. Inspection would be more feasible in this method than the SFRM method. This method would not change the geometry of the structures as much as the SFRMs do.
- Flexible protection jacket system: this is a relatively expensive approach. However, the protection could be designed for a high exposure resistance, and completely removable for inspection. This might be suitable for critical elements in major bridges, e.g. cable bridges and long span bridges.
- Concrete encasement: this would be a low cost protection method for steel bridges and buildings. However, the concrete may be prone to spalling during fire. This method would increase the size of the elements and the dead load of the structure, substantially.
- Panel systems such as gypsum boards: this method mostly suitable for building applications when exposure conditions are not required.
- Other Spray-Applied Fire Resistive Materials (SFRMs) such as gypsum-based SRFM: this would also be suitable for building applications when exposure conditions are not required.
- Steel and Polypropylene fibres mixed in concrete: this method is suitable for new constructions such as new concrete tunnels, buildings or bridge structures.

The main criteria when selecting fire protection materials/technologies for critical infrastructure include:

- Thermal properties: The higher the thermal conductivity of the protection systems, the better the fire performance of the critical infrastructures.
- Fire Severity: the higher the fire severity is imposed to critical infrastructures the higher fire resistance is required. For buildings and bridges fire severity required by ASTM E1529 would be recommended and for tunnels RWS fire severity would be suggested.
- Exposure conditions: for bridges and tunnels, fire protection materials should have the required exposure resistant, e.g. weathering, salt (as specified by NFPA 502 and UL1709). This may not be required for buildings when the structure is not exposed to such conditions.

6 CONCLUSION

The following conclusions can be made based on the outcome provided in this paper:

(1) The time-temperature curve of ASFTM E1529 (UL1709) was suggested for testing of bridges and critical buildings and the time-temperature curve of RWS was recommended for tunnels.

(2) Property protection is an important requirement for design of critical infrastructure. Hence, the fire resistance tests for critical infrastructure need to include failure criteria to meet this requirement.

(3) There is a lack of experimental data to determine fire severity of the unprotected tunnels.

(4) The main criteria for selection of fire protection materials and technologies include: thermal properties, fire severity, and exposure conditions.

REFERENCES

[1] Mostafaei, H. and McCartney, C. (2012). "Vulnerability of Bridges and other Critical Transportation Infrastructure to Extreme Fire and BLEVEs", NRC Research Report No. 4259, pp. 68.

[2] Mostafaei, H., Cowalchuk, R., Kashef, A., Sultan, M., McCartney, C., and Leroux, P. (2013). "Resilience of Critical Infrastructure to Extreme Fires - Gaps and Challenges", NRC_CSSP Research Report, pp. 74.

[3] Wright, W., Lattimer, B., Woodworth, M., Nahid, M., and Sotelino, E. (2013). "Highway Bridge Fire Hazard Assessment Draft Final Report, Prepared for the NCHRP Program Transportation Research Board of The National Academies, Virginia Polytechnic Institute and State University, pp. 492.

[4] NFPA 502 (2011). "Standard for Road Tunnels, Bridges, and Other Limited Access Highways", National Fire Protection Association, pp. 51.

[5] ASTM E119 (2012). "Standard Test Methods for Fire Tests of Building Construction and Materials, American Society for Testing and Materials.

[6] CAN/ULC-S101 (2007). "Fire Endurance Tests of Building Construction and Materials", Underwriters' Laboratories of Canada, Scarborough, ON.

[7] ASTM E1529 (2010). Standard Test Methods for Determining Effects of Large Hydrocarbon Pool Fires on Structural Members and Assemblies.

[8] UL 1709 (2011). Rapid Rise Fire Tests of Protection Materials for Structural Steel, UL.

[9] Breunese, A.J., Both, C., Wolsink, G.M. (2008). "Fire testing procedure for concrete tunnel linings", Efectis-R0695, pp. 25.

[10] Promat, "Fire curves", Promat website, www.promat-tunnel.com.

[11] Noble, C.R., Wemhhoff, L.D. and McMichael, L.D. "Thermal-Structural Analysis of the MacArthur Maze Freeway Collapse", ASME Summer Heat Transfer Conference, Jacksonville, FL, USA, 2008.

[12] Bajwa, C.S., Easto, E.P. and Dunn, D.S. 'The MacArthur Maze Fire: How Hot was it? Wm2009 Conference, Phoenix AZ, 2009.

[13] Prasad, K, Hammins, A., McAllister and Gross, J. "Fire Induced Thermal and structural Responses of the World Trade Center Towers", Fire Safety Science Proceedings of the Ninth International Symposium, 2008.

[14] National Institute of Standards and Technology (NIST) Federal Building and Fire Safety Investigation of the World Trade Center Disaster, Answers to Frequently asked Questions, Question 7, Http://WTC.nist.gov/pubs/factsheets/faqs_8_2006.htm.

[15] Keltner, N.R., Hasegawa, H.K., White, J., Jr. High Temperature Accelerant Arson," Very Large Scale Fires, ASTM STP 1336, N. R. Keltner, N. J. Alvares and S. J Grayson, Eds, American Society for Testing and Materials, Philadelphia, 1980

[16] Ingason, H. "Project Description and Planning of Large-Scale Tests in Runehamar Tunnel, SP Swedish National Testing and Research Institute 2003.

[17] Brekelmans, J. "Summary of Large Scale Fire tests in the Runehamar", TNO Building and Construction Research, Centre for Fire Research 2003.

[18] Mostafaei, H., Sultan, M.A., Kashef, A. "A Tool for Rating the Resilience of Critical Infrastructures in Extreme Fires", National Research Council Canada, A report for DRDC-CSSP, 2014, pp.63.

MATERIALS BEHAVIOR

8th International Conference on Structures in Fire
Guo-Qiang LI, Venkatesh K. R. KODUR, Shou-Chao JIANG, Jian JIANG, Su-Wen CHEN, Guo-Biao LOU (Eds.)
Shanghai, China, June 11-13, 2014

EXTREME CONCRETES EXPOSED TO HIGH TEMPERATURE: THE EFFECT OF EXPANDED POLYSTYRENE BEADS AND BARITIC AGGREGATES

Francesco Lo Monte* and Pietro G. Gambarova*

*Department of Civil and Environmental Engineering, Politecnico di Milano, Milan (Italy)
e-mails: francesco.lo@polimi.it; pietro.gambarova@polimi.it

Keywords: Light-weight concrete, Baritic concrete, Thermo-mechanical properties, Damage indexes, Expanded polystyrene

Abstract. *The high-temperature characterization of a recently-proposed light-weight concrete (containing polystyrene beads as micro void-formers) and of one heavy concrete (containing baritic aggregate) have been lately performed in Milan in residual conditions, to gather new or fresh information on the extremes of the broad spectrum of cementitious composites.*

Two light-weight mixes, one baritic mix cured in two different environments and a reference mix (f_c = 26-35 MPa) were subjected to thermal cycles up to 700-750°C. Roughly one hundred cylinders were tested in compression and in tension by splitting, to evaluate the compressive and tensile strengths, and the elastic modulus. Damage indexes were worked out as well, on the basis of the elastic modulus and of the ultrasonic velocity, to have information on materials deviation from linear elasticity at various temperatures. Last but not least, the thermal diffusivity was derived by instrumenting five cylinders.

At any temperature both concrete types behave similarly to ordinary concrete, but baritic concrete tends to retain its linear behavior longer than both EPS and ordinary concretes, and EPS concrete is weakened by the macroporosity due to EPS beads, thus requiring much higher cement contents.

1 INTRODUCTION

Concrete mechanical and thermal properties at high temperature have been investigated for a long time and are now well known and codified, but the introduction of innovative concretes and the growing interest for certain unusual mixes require further tests to be performed in order to ascertain whether – and to what extent – their properties are affected by high temperature, compared to ordinary concrete.

Such cementitious composites as light-weight aggregate, high-performance, ultra high-performance and self-compacting concretes have received a lot of attention in the last 10-to-15 years with reference to fire and high temperature, while other concretes – whose applications are either more limited or not well understood – are still waiting for a proper investigation. This is the case of two extremes in terms of mass per unit volume, i.e. light concretes containing Expanded-Polystyrene Syntherized particles – EPS [1-4] and heavy concretes containing baritic aggregates [5-8]. In the former case, three goals are achieved, as the specific mass is reduced by 10%-20%, the insulation properties are markedly increased and constructions sustainability is enhanced, as EPS particles or beads come from grinding the polystyrene waste ensuing from the packaging of myriads of goods; no information, however, can be found in the literature about the high-temperature behavior of EPS concrete. In the latter case, the objective is to increase concrete radiation-shielding capability by using heavy aggregates, that bring in a 20%-50% increase of the specific mass; there are some old data on baritic concrete at high temperature (see refs. in [9]), but fresh information is badly needed, even more since the revamping of numerous rather old nuclear power plants is in full swing, not to mention the X-ray chambers of the medical facilities and the waste repositories for the disposal of radioactive products.

The results of two parallel research projects recently completed at the Politecnico di Milano (Milan, Italy) on EPS concretes and baritic concretes exposed to high temperature are presented in this paper, to make comparisons under the umbrella of ACI and *fib* provisions for ordinary concrete in residual conditions (i.e. past a thermal cycle at high temperature). The tests on two EPS mixes (ρ_c = 1850-1950 kg/m^3) and one reference mix indicate a slightly higher heat sensitivity for EPS concretes, and a definitely lower mechanical performance, but superior insulating properties at any temperature (up to 700 °C).

The tests on one baritic mix cured in two different environments (ρ_c = 3100-3200 kg/m^3) confirm that baritic concrete behaves similarly to ordinary concrete and even slightly better at very high temperature, since the detrimental effect of barite highly micro-fractured structure is counterbalanced by the closeness of the thermal dilatancies of coarse baritic aggregate and baritic mortar. Both concretes are more brittle than ordinary concrete at least up to 500-550 °C, as shown by the stress-strain curves in compression, and EPS concretes are also much more deformable, at any temperature.

Last but not least, the damage indexes based on the elastic modulus and on the ultrasonic pulse velocity show that the loading branches of baritic concrete are closer to linear elasticity than those of EPS concrete, probably because the latter is affected by bead-related notch effect.

2 CONCRETE TYPES AND THEIR AGGREGATES

2.1 EPS Concrete

EPS concrete has been investigated for very different EPS contents, ranging from rather low fractions of the total volume (10% [1]) to more than 50% ([1-3], see also refs. in [10]). However, only by limiting the EPS content by volume to less than 20% a suitable mechanical performance can be guaranteed ($f_c \geq 17.2$ MPa according to ACI 213R-87, 1999). The above-mentioned relatively high values of the compressive strength come at the cost of huge cement contents, that span from 350 kg/m^3 to more than 500 kg/m^3, not including silica fume and fly ash, that are often used to increase the strength and the workability of the mix (see refs. in [10]).

Depending on EPS content (from 2 to 12 kg/m^3 in the studies carried out so far) and density (improved by syntherization, typically from 20 to more than 40 kg/m^3), concrete density may range from 500 to 2000 kg/m^3, but only in the range 1450-1850 kg/m^3 can EPS concrete be considered as a *light* and *structural* material, according to ACI 213R-87 (1999). EPS generally is in the form of small spheres (called also *beads*, whose diameter is comprised between 3 and 8 mm), or particles, all coming from reground EPS waste. In terms of mechanical performance, the compressive strength and the elastic modulus of EPS concretes are linearly decreasing functions of both the EPS content by volume (see refs. in [10]) and of concrete density, while the tensile strength by splitting decreases less than linearly [2]. Silica fume increases the adhesion between EPS particles and concrete [2], while fly ash decreases water absorption and moisture migration [3]. The possible extra heat-sensitivity of EPS concrete may derive from: (a) EPS physical changes (*melting*/*decomposition*/*ignition* at 100/230-270/450-500 °C); (b) bead-related notch effect because of the voids occupied by the beads; and (c) EPS combustion (95% of bead volume is occupied by air).

2.2 Baritic Concrete

Concrete attenuation properties are reached by replacing certain constituents of ordinary mixes and/or by adding new constituents, like replacing the coarse aggregates and adding soluble organic super-plasticizers, in order to increase the compactness and to reduce the water content, without impairing the workability. To increase the attenuation properties, dense concretes are used, with heavy aggregates against X and γ rays, and rather light aggregates against fast neutrons ([5]; see also refs. in [9]). In general, if the radiation level is rather low (like in the X-ray chambers of the medical facilities) the required density is below 3500 kg/m^3, and concrete densities between 2800 and 3500 kg/m^3 are often adopted, similarly to what is usually done in such infrastructures as waste repositories for lightly-irradiated products (see Reference [9]).

Among the aggregates used to make concrete heavier, barite (consisting of barium sulphate) is often used for its chemical stability (melting temperature 1580 ℃), closeness of the thermal-expansion coefficients of coarse baritic aggregate and baritic mortar (*hydrated cement + baritic fines*), and barite greater creep at any temperature (compared to ordinary aggregates). The last two properties are advantageous at high temperature, because they reduce the aggregate-to-mortar thermal incompatibility.

The possible extra heat-sensitivity of baritic concrete may derive from: (a) barite highly microfractured structure (which makes the material rather soft, and whose fractured and intersecting surfaces tend to act as preferential paths in favoring rock splitting); and (b) the various heat-sensitive products (like clay containing chalcedony, quartz and zeolites [9]) filling barite microfractures.

3 MIX DESIGN AND COMPRESSIVE STRENGTH OF THE VIRGIN MATERIALS

The constituents as well as the main physical and mechanical properties of the concrete investigated in this paper are summarized in Table 1, with reference to two EPS mixes (Mixes M1 and M2, differing mostly for the cement content) and one baritic mix cured in two different environments past the usual 28-day curing at T = 22 ℃ and R.H. ⩾ 95% (Mix MM kept for three years in *moist* conditions, i.e. in a controlled room, and Mix MD kept for three years in ordinary *dry* conditions with T = 20 ℃ -25 ℃ and R.H.= 70%-80%). The mix design of a fifth mix (Mix M0) is reported too, as a reference. (The target strength was between 25 and 30 MPa).

Mix M1 was designed to have a compressive strength similar to that of the reference mix (Mix M0), while Mix M2 was intended to explore to what extent adding cement would increase the strength of an EPS mix. (Of course, Mix M2 has a disproportionate content of cement, compared to its rather limited compressive strength). The two heavy mixes were meant to represent: (a) the loss of water because of desiccation in the outer layers in massive members (Mix MD); and (b) the nearly sealed conditions characterizing the aging of the inner layers (Mix MM).

4 SPECIMENS, THERMAL CYCLES AND INSTRUMENTATION

For each mix, a number of *long* cylinders (10 for Mixes M0, M1 and M2, and 12 for Mixes MM and MD) was available for testing in compression (mostly with ∅ = 100 mm and some with ∅ = 150 mm; all with h/∅ = 2), while six or twelve *short* cylinders (all with ∅ = 100 mm; h = 30 mm in Mixes M0, M1 and M2; and h = 80 mm in Mixes MM and MD) were tested in indirect tension by splitting. In this way, from 16 to 24 cylinders were available for each mix (Figure 1).

Table 1. Mix design, mass per unit volume and compressive strength of the five concretes.

Concrete Mix	M0 (REF)	M1 (LWC)	M2 (LWC)	MD (HVC)	MM (HVC)
Cement type (R 42.5)	C-II-A	C-II-A	C-II-A	C-II-B	C-II-B
Cement content (c) [kg/m^3]	286	643	815	340	340
Mixed aggr. = sand+gravel [kg/m^3]	1815*	1066*	930*	204**	204**
Baritic aggregate [kg/m^3] ***	-	-	-	2500	2500
Effective water (w/c) [kg/m^3]	200 (0.70)	220 (0.34)	220 (0.27)	170 (0.50)	170 (0.50)
EPS Beads [kg/m3] ****	-	5.09	5.32	-	-
Superp. Polycarboxylate (sp/c) [kg/m^3]	3.90 (1.4%)	7.05 (1.1%)	9.11 (1.1%)	1.70 (0.5%)	1.70 (0.5%)
Air-entraining agent (ae/c) [kg/m^3]	-	2.12 (0.33%)	2.73 (0.33%)	-	-
Viscosity modifier (vm/c) [kg/m^3]	3.90 (1.4%)	7.05 (1.1%)	9.11 (1.1%)	-	-
Nominal/actual mass [kg/m^3]	2309/2239	1951/1899	1991/1951	3216/3059	3216/3104
Compressive strength f_c [MPa] ^	25.8	26.9	28.4	34.6	27.4

Aggregate size: (*) d = 0-12 mm; (**) d = 0-8 mm; (***) d = 0-25 mm; mass per unit volume = 4000 kg/m^3.

(****) 3-mm beads; mass per unit volume = 38 kg/m^3 after syntherization; EPS volume fraction = 13.5%-14%.

(^) At the beginning of the tests. REF/LWC/HVC = reference/light-weight/heavy concrete.

Beside being tested at 20 ℃ (no heating), Mixes M0, M1 and M2 were investigated in compression after heating to 4 reference temperatures and in tension after heating to 2 reference temperatures (T = 150, 300, 500 and 700 ℃, and T = 300 and 600 ℃, respectively, Figure 2(a)), while Mixes MM and MD were tested in compression or tension after heating to 5 reference temperatures (T = 105, 250, 400, 550 and 750 ℃). For each mix, one of the two cylinders to be heated to the maximum temperature (700 or 750 ℃) was instrumented with two thermocouples placed in the mid-span section, to evaluate the thermal diffusivity from 20 to 700-750 ℃. After cooling down to room temperature, these cylinders were tested as well (T = 700 or 750 ℃). For each mix and reference temperature, the repeatability of the two nominally-identical tests – in compression or tension – was excellent, as shown in Figure 2(b) for Mix MD.

All the tests in compression were displacement controlled. The shortening of the specimens was measured via 3 resistive gauges placed at 120° astride the mid-height section (base length 50 mm); moreover, 3 LVDTs measured the platen-to-platen distance of the press to monitor the post-peak behavior of the specimens. In all the tests in compression, stearic acid was smeared on the end sections of the specimens to reduce platen-to-concrete friction. All the tests in indirect tension were force controlled; all the dimensions (diameter and loading strips) were scaled down by 1/3 compared to the prescriptions of the European Standard EN 12390-6 (∅ = 100 mm in the tests, instead of 150 mm), but the length-to-diameter ratio was by necessity smaller (h/∅ = 0.3 in Mixes M0, M1 and M2, and = 0.8 in Mixes MM and MD, instead of 1.0).

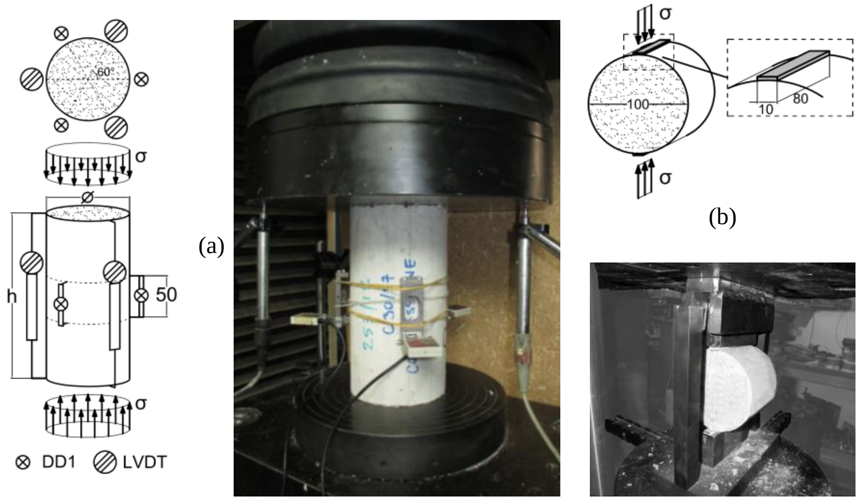

Figure 1. Typical instrumented specimen ready to be tested in compression (a); and test layout in indirect tension (b).

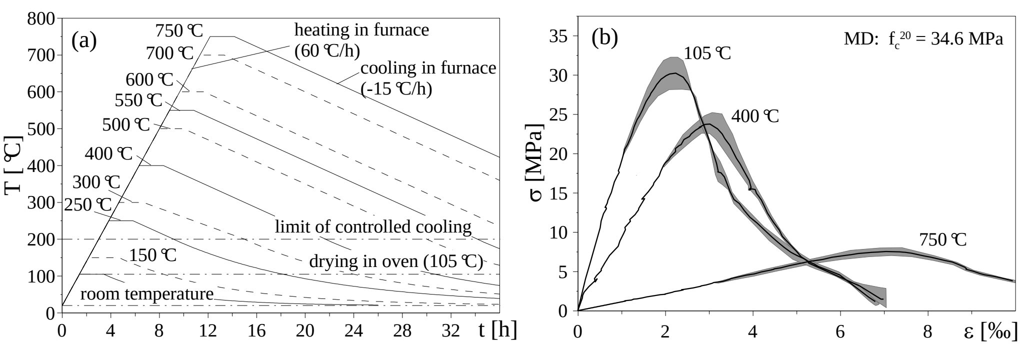

Figure 2. (a) Thermal cycles (full/dashed curves for baritic/EPS concretes); and (b) examples of test repeatability.

5 THERMAL DIFFUSIVITY

The thermal diffusivity (whose physical meaning is the ratio between the heat transmitted and the heat stored by the unit mass of the material) is defined as: $D = \lambda/(c\ \rho)$, where λ is the thermal conductivity, c is the specific heat and ρ is the mass per unit volume. In a long cylinder ($h \geqslant 2\varnothing$) subjected to a constant heating rate (v_h = mean heating rate inside the specimen), the thermal diffusivity can be evaluated by means of the following equation:

$$D = v_h\ R^2/(4\ \Delta T) \tag{1}$$

where $\Delta T = T_2 - T_1$ is the difference between the temperatures measured in two points (at – or close to – the surface and along the axis in the mid-span section), while R is the distance between the two points.

Five cylinders – one for each mix – were instrumented with 2 thermocouples and slowly heated from 20 to 700 °C (Mixes M0, M1 and M2) or to 750 °C (Mixes MM and MD). As shown in Figures 3(a), (b), between 200-250 and 500 °C -550 °C the thermal diffusivity of all mixes is roughly constant, and the reference mix (Mix M0) adheres very well to the curve worked out from the equations of the conductivity, specific heat and mass per unit volume prescribed by EC2. Both Mixes M1 and M2 exhibit a lower diffusivity (from -40 to -20%, Figure 3(a)), something well known for other light-weight concretes. Also Mixes MM and MD exhibit a somewhat smaller thermal diffusivity compared to ordinary concrete (from -20 to -14%, Figure 3(b)), but not comparable with EPS. In EPS concretes, the smaller diffusivity is mainly due to the smaller thermal conductivity, and in baritic concretes to the greater mass per unit volume.

6 RESIDUAL MECHANICAL PROPERTIES

Stress-strain curves in compression (Figures 4(a)-(c)): reference is made only to Mixes M0, M1 and MD, that are the most representative among the five mixes examined in this paper. All mixes are characterized by well-defined linear loading branches, nonlinearities more or less pronounced close to the peak, and descending branches, but Mix M0 is definitely tougher, with rather rounded peaks and a regular softening, at any temperature, while Mixes M1 is definitely more brittle and Mix MD is in between; the same can be said for Mixes M2 [10] and MM [9]. Note that Mix MD exhibits a limited but not negligible strength recovery between 250 and 400 °C, something often found especially in high-performance concrete. The greater brittleness of EPS and baritic mixes has certainly to do with the bead-induced notch effect in the former case, and with the microfractured structure of baritic aggregate in the latter case.

Strength in compression (Figure 5): the normalized plots for Mix M0, as well as for EPS and baritic mixes (Figures 5(a) and (b), respectively) are close to the two curves provided by ACI 216-1.07 (2007); on the whole, EPS concretes tend to be more heat sensitive than ordinary concrete (especially Mix M1, Figure 5(a)), while baritic concretes are aligned with ordinary concrete (Figure 5(b)) with a slightly higher heat resistance above 500 °C.

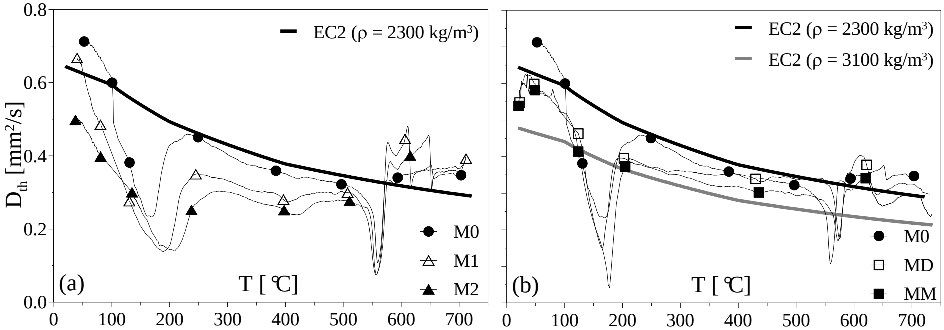

Figure 3. Thermal diffusivity of EPS concretes (a); and baritic concretes (b) versus ordinary concrete.

Tensile strength (Figure 6(a), where only Mixes M0, M1 and MD are considered): as expected, the tensile strength is slightly more temperature-sensitive than the compressive strength, but – on the whole – the normalized decay in tension is pretty much the same in EPS, baritic and ordinary concretes, as indicated also by the bi-linear curve suggested in EC2-EN 1992-1-2 (2004) for direct tension and hot conditions.

Elastic modulus (Figure 6(b), Mixes M0, M1 and MD): the heat sensitivity of EPS concrete is slightly higher than that of ordinary concrete, as shown by the cloud of the test results examined by Phan and Carino (1998, see ref. in [10]), while baritic concrete exhibits a better behavior above 300 ℃, compared to both ordinary and EPS concretes, probably because of the thermal stability of baritic rocks.

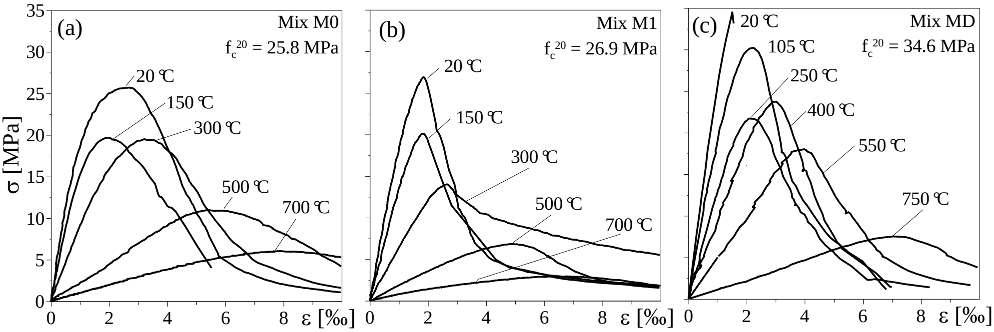

Figure 4. Typical mean stress-strain curves in compression: (a) Mix M0; (b) Mix M1; and (c) Mix MD.

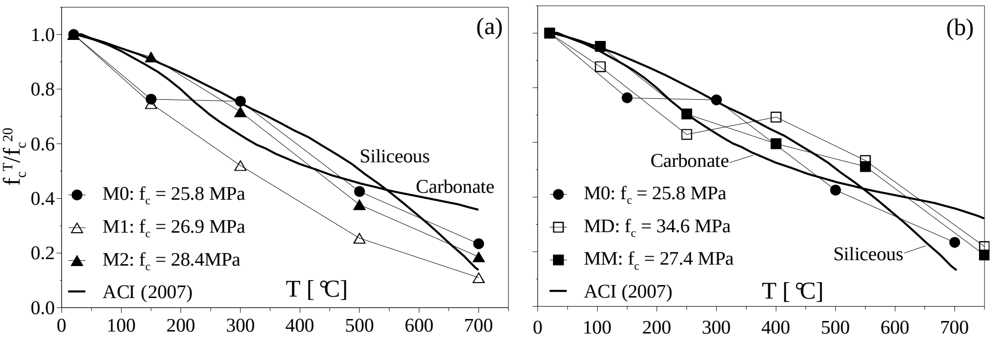

Figure 5. Normalized plots of the compressive strength: (a) EPS mixes; and (b) baritic mixes.

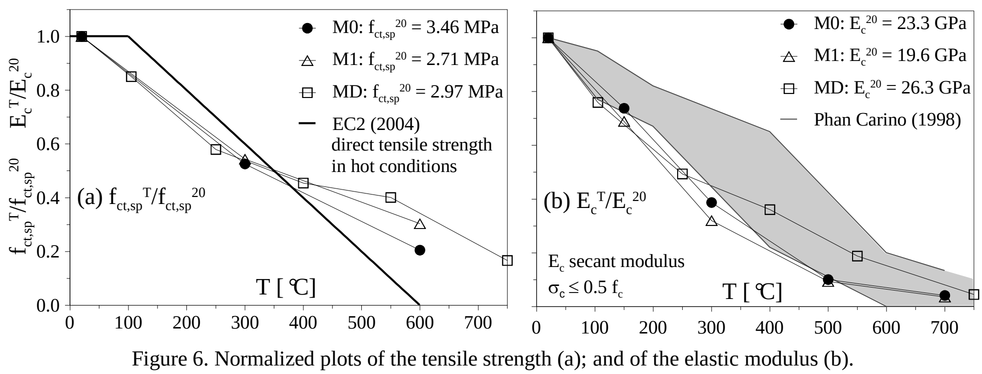

Figure 6. Normalized plots of the tensile strength (a); and of the elastic modulus (b).

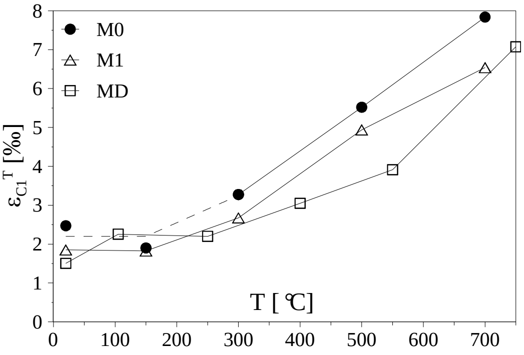

Figure 7. Plots of the strain at the peak stress.

Strain at the stress peak (Figure 7): only Mixes M0, M1 and MD are considered, as the plots for M1 and M2, and for MM and MD are hardly different; in all cases the strain at the stress peak is close to 2‰ up to a *transition temperature* (close to 150 ℃ in ordinary and EPS concretes, and to 250 ℃ in baritic concrete); at higher temperatures, the strain at the stress peak tends to increase almost linearly with the temperature.

Summing up, looking at the normalized curves of EPS concretes, increasing cement content beyond certain limits hardly improves the mechanical performance at any temperature (compare Mixes M1 and M2), while in the case of baritic concretes, aging in ordinary conditions (Mix MD) tends to improve the mechanical properties at any temperature, with respect to aging in moist conditions (Mix MM), something unexpected.

7 DAMAGE INDEXES

Temperature-induced damage in quasi-brittle materials – mainly in the form of microcracking and porosity – can be quantified by means of *damage indexes*. Among the various indexes proposed in the literature (see refs. in [10]), those based on the elastic modulus (D_E^T, Eqation 2) and on the velocity of the ultrasonic waves ($\underline{D}_V^T$, Equation 3) are rather popular (both parameters decrease with the temperature):

$$D_E^T = 1 - (E_0^T/E_0^{20}) \quad ; \quad \underline{D}_V^T = 1 - (v_{us}^T/\, v_{us}^{20})^2 \tag{2,3}$$

where E_0 is the Young's modulus at the origin of the stress-strain curve. Since in an elastic continuum the elastic modulus is proportional to the square of the velocity of the ultrasonic waves times the mass per unit volume ρ, the damage index $\underline{D}_V^T$ can be formulated also as follows:

$$D_v^T = 1 - (\rho^T/\rho^{20}) \bullet (v_{us}^T/\, v_{us}^{20})^2 \tag{4}$$

Note that in a perfectly elastic continuum (E^T/E^{20}) and [$(\rho^T/\rho^{20}) \bullet (v_{us}^T/\, v_{us}^{20})^2$] coincide (if the Poisson ratio is neglected), while in an actual (inelastic) continuum the results are more or less different (Figure 8), depending on the definition of *E* (for instance *secant* or *tangent;* in the following the secant modulus is used, for $\sigma \leqslant 0.1f_c$).

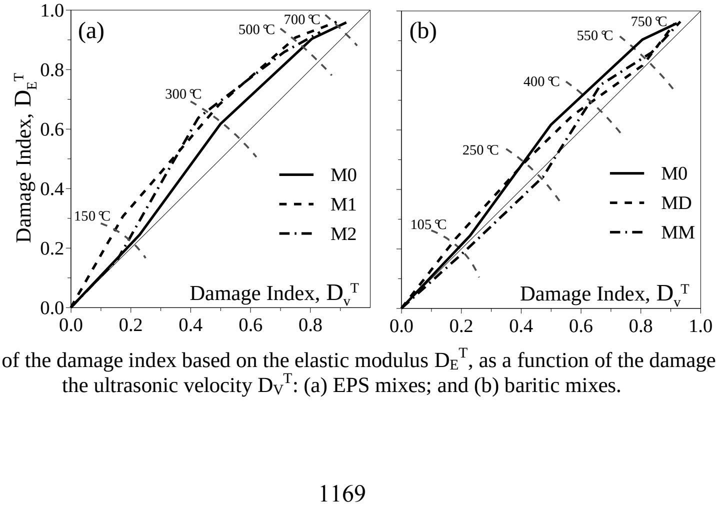

Figure 8. Plots of the damage index based on the elastic modulus D_E^T, as a function of the damage index based on the ultrasonic velocity D_V^T: (a) EPS mixes; and (b) baritic mixes.

Hence, plotting D_E^T as a function of D_V^T allows to quantify the non-linearity of the material at increasing temperature, since perfect linear elasticity would make D_V^T and D_E^T coincident at any temperature. The two indexes are plotted in Figure 8(a) for EPS concretes, and in Figure 8(b) for baritic concretes. On the whole, the two indexes are closer (and closer to the reference concrete) in the case of baritic concretes (Figure 8(b)) compared to EPS concretes (Figure 8(a)), which means that baritic concrete keeps a linear behavior even at high temperature more than either EPS or ordinary concretes.

8 CONCLUSIONS

The EPS and baritic concretes examined in this paper exhibit a normalized mechanical decay that is on the whole rather similar to that of ordinary concrete in terms of tensile strength, elastic modulus and strain at the stress peak. As for the normalized compressive strength, however, EPS concrete is more heat-sensitive than ordinary concrete up to 700 °C, unless disproportionate amounts of cement are used (with no sizable advantage for the strength in compression), while baritic concrete is aligned with ordinary concrete and is even slightly better above 350 °C.

As for the thermal diffusivity – that is an index of the insulation capability of the material – EPS concretes are aligned with expanded-clay concretes, whose thermal diffusivity is markedly lower than that of ordinary concrete, while the diffusivity of the baritic concretes examined in this paper (not particularly *heavy*) is only slightly smaller than that of ordinary concrete.

The damage indexes based on the elastic modulus and on the velocity of the ultrasonic waves show that baritic concretes keep a well defined linear behavior even after a cycle at high temperature, more than both EPS and ordinary concretes.

REFERENCES

[1] Miled K., Sab K. and Le Roy R., "Particle Size Effect on EPS Lightweight Concrete Compressive Strength: Experimental Investigation and Modelling", *Mechanics of Materials*, 39, 222-240, 2007.

[2] Chen B. and Liu L., "Properties of Lightweight Expanded Polystyrene Concrete Reinforced with Steel Fiber", *Cement and Concrete Research*, 34, 1259-1263, 2004.

[3] Babu D.S., Babu K.G. and Tion-Huan W., "Effect of Polystyrene-Aggregate Size on Strength and Moisture Migration Characteristics of Light-Weight Concrete", *Cement and Concrete Composites*, 28, 520-527, 2006.

[4] Trussoni M., Hays C.D. and Zollo R.F., "Comparing Lightweight Polystyrene Concrete Using Engineered or Waste Materials", *ACI Materials Journal*, 109 (1), 101-107, 2012.

[5] Bouniol P., "Bétons Spéciaux de Protection", *Techniques de l'Ingénieur - Génie Nucléaire*, BN 3 740, 29 pp., 2001.

[6] Sakr K. and El-Hakim E., "Effect of High Temperature or Fire on Heavy-Weight Concrete Properties", *Cement and Concrete Research*, 35, 590-596, 2005.

[7] Revuelta D., Alonso M.C., García J.L. and Barona A., "Experimental Study on a Barite Heavy-Weight Self-Consolidating Concrete", *ACI – American Concrete Institute, SP 261-7* "Recent Advances in Concrete Technology and Sustainability Issues", 101-114, 2009.

[8] Topçu I.B., "Properties of Heavyweight Concrete Produced with Barite", *Cement and Concrete Research*, 33, 815-822, 2003.

[9] Lo Monte F., Bamonte P. and Gambarova P.G., "Mechanical and Thermal Properties of a Heavy Radiation-Proof Concrete Exposed to High Temperature", *Proc. 7th Int. Conf. on Concrete under Severe Conditions – CONSEC 13*, Nanjing (China), V.2, 1672-1684, September 23-25, 2013.

[10] Lo Monte F., Bamonte P. and Gambarova P.G., "Physical and Mechanical Properties of Heat-Damaged Structural Concrete Containing Expanded Polystyrene Syntherized Particles", *Fire and Materials*, in press (DOI: 10.1002/fam.2230), 14 pp., 2014.

POST-FIRE REDUCTION OF CONCRETE'S MECHANICAL PROPERTIES AND ITS IMPACT ON RESIDUAL LOAD CAPACITY

Neno Torić*, Ivica Boko*, Sandra Juradin* and Goran Baloević*

* University of Split, Faculty of Civil Engineering, Architecture and Geodesy, Matice Hrvatske 15, 21000 Split, Croatia
e-mails: neno.toric@gradst.hr, ivica.boko@gradst.hr, sandra.juradin@gradst.hr, goran.baloevic@gradst.hr

Keywords: Concrete, Fire, Compressive strength, Residual property

Abstract. *This paper investigates the reduction of mechanical properties of four different light-weight concrete mixes containing expanded clay aggregate in a short time period after exposure to high temperature regime. The research has shown that compressive strength exhibits additional reduction up to 10%-20%, 96 hours after being cooled down to ambient temperature. A numerical example of simply supported concrete column exposed to standard fire from four sides is given, illustrating the effects of post-fire strength reduction on residual load capacity. The results obtained indicate that the effect of short-term reduction of the compressive strength of concrete in real structures damaged by fire could have a significant effect on the post-fire load bearing capacity of structures and should be accounted for in the engineering building codes.*

1 INTRODUCTION

The post-fire reduction phenomenon of the compressive strength of concrete has already been noted by researchers [1-3]. Their results indicate the compressive strength tends to reduce and partially recover over a time period of 1-2.5 years. The reported researches regarding the post-fire behaviour have been conducted mainly for normal-strength (NSC), high-strength (HSC) and self-compacting concrete (SCC). However, the consequences of post-fire reduction of the compressive strength on the load bearing capacity have not yet been understood in entirety, nor has the influence of moisture conditions on the reduction process been investigated enough.

Post-fire reduction of the mechanical properties of concrete is governed by chemical and physical processes occurring in concrete after cooling. The most important ones are formation of calcium hydroxide and rehydration of cement paste [1]. The level of thermal damage (temperature level) and the moisture conditions following the cooling process represent the two most important factors which seem to affect the level of post-fire reduction of mechanical properties. Both processes generally govern the reduction of the compressive strength of concrete, whose strength minimum is usually reached within the time period of 1-6 months. After that, depending on the type of concrete, a partial or full compressive strength recovery is possible.

Regardless of the recovery process, the mechanical properties of concrete tend to reduce over a long time period. This reduction could have a substantial impact on the residual load capacity of concrete if the post-fire reduction level proves to be significant. It is noteworthy that the strength reduction of concrete after fire exposure is not taken into account explicitly in common engineering building codes [4,5] since it is generally considered that no significant strength reduction may occur in concrete after its exposure to fire.

Most of the ongoing research concerned with the reduction of the mechanical properties of concrete has focused on concrete's hot and residual properties, which generally exhibit higher values than the post-fire properties. On the other hand, taking post-fire property values into consideration can be deemed as a more realistic approach in determining the compressive strength of fire exposed concrete. The results of a previously conducted research point out that the short-term strength reduction of HSC's compressive strength can be substantial [6] and that it should be accounted for in the analysis of the assessment of post-fire resistance of concrete structures. The objective of the proposed study is to further investigate the level of strength reduction in short time intervals (48 and 96 hours after exposure to high temperature) of four different LWC mixes in order to obtain further insight into post-fire behaviour of LWC and its level of post-fire reduction.

2 EXPERIMENTAL PROGRAMME

2.1 Equipment and specimen description

Determination of post-fire properties was conducted on cylindrical specimens with a Ø of 75/225 mm. Experimental programme included determination of the following concrete properties: compressive strength, stress-strain curves and dynamic modulus of elasticity.

Specimen dimensions were adopted according to the recommendations of the RILEM committee for compressive strength testing [7]. A 3000 kN FORM TEST testing machine was used to conduct the compressive test. To determine the stress-strain curve of a specimen, an LVDT recording the displacement of platens (Figure 1(b)) was mounted on the testing machine; while the increase of the pressure inside the machine was monitored by a pressure transducer SENSE STK131. Both devices were connected to National Instruments data acquisition card USB 6255. Heating of the specimens was conducted using programmable NABERTHERM L9/11/P330 furnace. A general view of the furnace and the testing machine is presented in Figure 1(a).

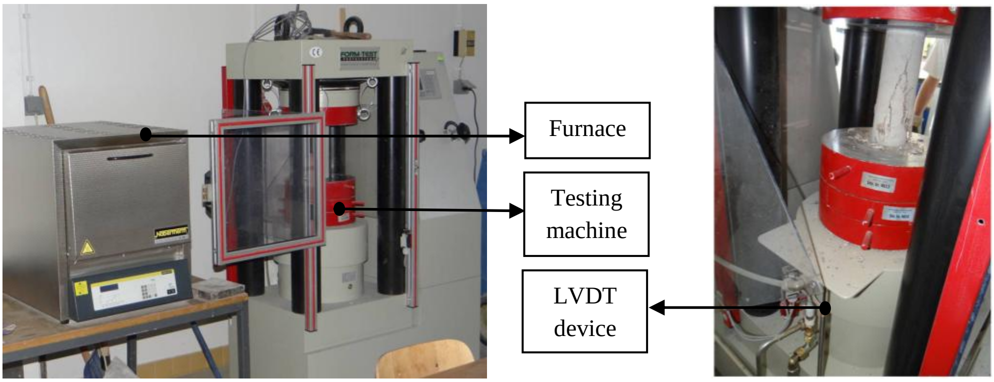

(a) General view of the experimental setup (b) Rear view of the testing machine

Figure 1. Experimental setup – test machine and the furnace.

Temperature increase in the specimens during the heating stage was recorded with one NiCr thermocouple placed in the middle of the specimen during moulding. The thermocouple was connected into NI data acquisition card USB 6255.

2.2 Mix proportions

This paper accounts for a testing of 4 different mix designs of LWC in fresh and hardened states. The intention of the research was to test the amount of binder and type of admixture as variables influencing the reduction of the mechanical properties of light-weight concrete. In all of the mixes same cement, superplasticizer and aggregate were used, whereas admixtures were varied. The cement used was Portland cement of CEM I 42.5 R type that complies with the requirements of EN 197-1, having a specific weight of 3.14 kg/dm^3. The super-plasticizer was the liquid PCE (poly-carboxylic acid-ether) with a specific weight of 1.06 kg/dm^3. A very light granulated product manufactured by expansion of natural clay was used as the light-weight aggregate. Concrete mixes contained two fractions, the fine light-weight aggregate of 0-2 mm and the coarse light-weight aggregate of 4-8 mm. Gradation of aggregate in the mixes was adjusted by using 70 % of coarse and 30 % of fine light-weight aggregate. Mixes LWC1, LWC2 and LWC4 were designed with the same amount of binder of 470 kg/m^3. LWC1 was prepared only with cement, LWC2 with cement and silica fume and LWC4 with cement and metakaolin. Characteristics of admixtures are given in Table 1.

Table 1. Admixtures' characteristics.

Type of admixtures	Specific area according to Blaine (cm^2/g)	Specific weight (g/cm^3)
silica fume	> 15000	2.3
metakaolin	ca 24000	2.6

The LWC3 mix was prepared with the least amount of cement and the highest water-cement ratio. Mix proportions prepared in this study are given in Table 2.

Table 2. Mix proportions of LWC.

Concrete compounds (kg)	LWC1	LWC2	LWC3	LWC4
cement	470	420	350	420
w/c	0.40	0.42	0.50	0.45
water	188	177	175	190
silica fume	-	-	-	50
metakaolin	-	50	-	-
superplasticizer	4.7	4.7	3.5	4.7
FLA 0-2 mm	321	302	341	301
CLA 4-8 mm	750	727	819	723

The test results of fresh concrete mixes are given in Table 3. Slump, air-content and unit weight of fresh concrete mixes were determined in accordance with EN 12350-2, EN 12350-7 and EN 12350-6, respectively.

Table 3. Test results of fresh concrete mixes.

Mix	Slump (mm)	Air (%)	Unit weight (kg/m^3)
LWC1	245	2.7	1915.2
LWC2	250	4.0	1859.0
LWC3	35	4.0	1841.4
LWC4	185	6.0	1810.9

2.3 Curing and storage conditions

Curing and storage conditions prior to heating were adopted from RILEM recommendations [6]. The specimens were kept in a mould for one day and moved afterwards into a curing room with a temperature of 20±3 °C and a relative humidity of 95% for a period of 6 days. Following that, the specimens were taken into a chamber with an air temperature of 20 °C±3 °C and a relative humidity of 50% until testing.

Testing programme was initiated when the specimens were three months of age. Prior to the heating cycle, the specimens were kept at a temperature of 100 ℃±5 ℃ in a drying oven over a period of 24 hours so as to extract evaporable moisture content.

2.4 Testing procedure

Mechanical properties were determined by heating the specimens up to 200 °, 400 ° and 600 ℃. They were calculated as the mean value of the results determined from the three tested specimens. Heating cycle consisted of heating the specimens with heating rates between 1-2.5 ℃/min up to the target temperatures. After reaching a target temperature, the specimens were kept at it for 2.5 hours. Subsequently, the specimens were cooled down slowly to ambient temperature. Some were tested immediately after cooling to ambient temperature (initial cooling).

In order to investigate a further reduction of concrete's strength, specimens were further tested 48 and 96 hours after the initial cooling. The specimens tested 48 and 96 hours after cooling were stored in laboratory conditions (temperature of 20 ℃±3 ℃ and relative humidity 30%). Compressive test was conducted by loading the specimen with a stress rate of 0.5 MPa/s.

3 RESULTS

3.1 Post-fire reduction of compressive strength

In the following section a selection of the results of post-fire reduction are shown. Table 4 presents the results of the compressive strength of the four mixes at ambient temperature.

Table 4. Compressive strength at ambient temperature.

Compressive strength (3 months)	$f_{c,20}$ (MPa) LWC1	$f_{c,20}$ (MPa) LWC2	$f_{c,20}$ (MPa) LWC3	$f_{c,20}$ (MPa) LWC4
Specimen 1	52.9	54.4	53.4	55.7
Specimen 2	48.2	51.5	52.6	55.1
Specimen 3	49.5	53.9	54.3	53.9
Average	50.2	53.2	53.5	54.9
St. dev.	2.4	1.6	0.9	0.9

Table 5 presents the results of the post-fire reduction of compressive strength after exposing the specimens to a temperature of 400 ℃ for all four mixes.

Table 5. Reduction of compressive strength after initial cooling.

Test time after cooling (h)	$f_{c,400}/f_{c,20}$ LWC1	$f_{c,400}/f_{c,20}$ LWC2	$f_{c,400}/f_{c,20}$ LWC3	$f_{c,400}/f_{c,20}$ LWC4
0	0.66	0.58	0.74	0.66
48	0.63	0.46	0.67	0.54
96	0.55	0.41	0.59	0.50

Figure 2 presents a reduction of compressive strength of the mixes immediately after cooling and 48-96 hours after cooling. The results have been compared with the reduction factors taken from Eurocode 2 and Eurocode 4 for high-strength concrete, normal-weight concrete and light-weight concrete. The reduction factors from Eurocodes have been scaled by 10% because the original reduction values from Eurocodes are given for hot strength and are generally higher if compared to the initial residual strength.

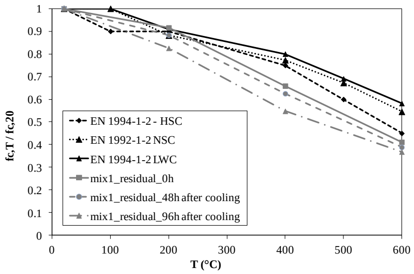

(a) LWC1

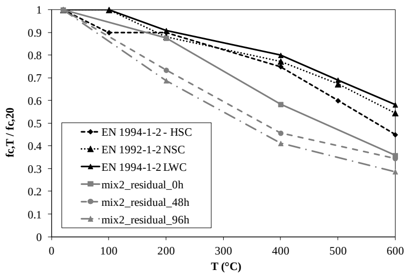

(b) LWC2

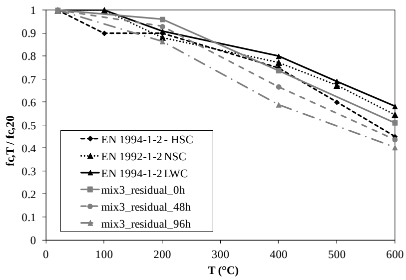

(c) LWC3

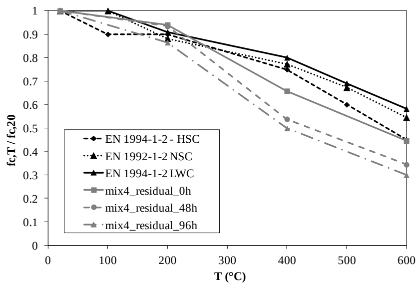

(d) LWC4

Figure 2. Study results – post-fire reduction of compressive strength.

Figure 3 presents the mass change of specimens taken from LWC mix3 proportions in the period up to 96 hours after cooling for three temperature levels.

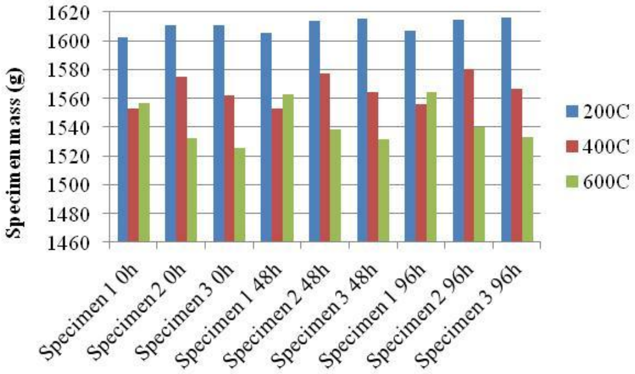

Figure 3. Mass change of specimens from mix3 during 96 hours after cooling.

3.2 An example of assessment of the residual load capacity

To illustrate the influence of post-fire strength reduction of LWC on the residual load capacity, a numerical example of a fire exposed concrete column with a rectangular cross-section of 30/30 cm was chosen. Temperature isochrones from Eurocode 2 [4] for columns exposed to 30 minutes of ISO fire from all four sides were used as a representation of fire exposure; as shown in Figure 4.

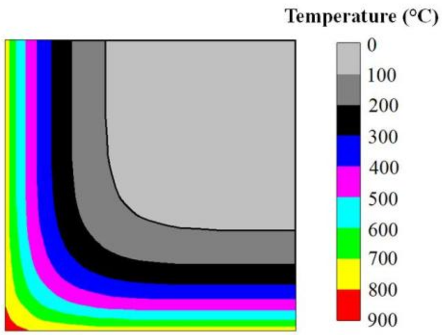

Figure 4. Temperature field in one quarter of a column after 30 minutes of ISO fire [4].

Following the exposure to 30 minutes of ISO fire and cooling of the column to ambient temperature, the axial load resistance of its cross-section was determined in relation to the maximum temperature exposure in the cross-section. The residual load bearing capacity was calculated immediately after cooling by using residual strength reduction factors from the presented experiment. Analogously, post-fire load bearing capacity was estimated by using post-fire reduction factors at a certain time after cooling.

Table 6 presents the results obtained by a numerical analysis of the axial resistance of the column using different levels of post-fire reduction for compressive strength of LWC from Figure 2.

Table 6. Post-fire reduction of residual load capacity of a column exposed to 30 min of ISO fire.

$N_{fi,Rd}$ (kN)	LWC1	LWC2	LWC3	LWC4
Residual	3180.3	3250.0	3551.4	3528.1
48h after cooling	3069.2	3014.4	3419.9	3321.4
96h after cooling	3012.2	2914.3	3266.0	3230.9

4 DISCUSSION OF THE RESULTS

A comparison between Eurocode 2 reduction factors for LWC and the reduction factors obtained by testing the mixes indicates that the reduction factors for mixes 3&4 are close to the proposal of Eurocode 2. Some difference exists but can be attributed to the fact that the reduction factors given in Eurocode 2 were determined for a LWC with different type of aggregate than the one used in the study. However, reduction factor results for the analyzed LWC point out that the concrete mixes containing natural clay aggregate can be considered as a reliable construction product with adequate fire resistance up to 600 ℃.

Results from Figure 2 and Table 2 also indicate a distinctive reduction in the compressive strength of LWC (10-20%) in the short time period of 96 hours after cooling. The level of post-fire reduction of the compressive strength seems to vary depending on the composition of the mix. LWC mix3 has proved to have the highest fire resistance of all the mixes. In addition, mix3 has the lowest post-fire reduction factors for compressive strength as well. Both of these characteristics can be attributed to the proportions of the mix. The results show that a mix with the lowest amount of binder that includes all particles smaller than 0.125 mm has the lowest level of post-fire reduction factor. The three remaining mixes have a higher binder amount.

Levels of post-fire reduction of LWCs' residual capacity has been shown in Table 6 where post-fire load bearing capacity reduction amounts up to 7% for 48 hours and 10% for 96 hours after initial cooling. It can be noted that the calculated level of post-fire reduction is not negligible for concrete members exposed to all four sides. Level of post-fire reduction could be even greater than 10% if a concrete member was exposed to fire temperatures over a period longer than 30 minutes.

This points out to the fact that post-fire reduction of the mechanical properties of concrete should be accounted for in the assessment of residual capacity of concrete structures. It is important to note that storage conditions after cooling used in the study were chosen so as to exclude the influence of moisture absorption, which is known to contribute strength loss after cooling. Since a very small level of moisture absorption occurred during the storage period after initial cooling, mass gain of the specimens was negligible, as it is shown in Figure 3.

5 CONCLUSIONS

The discussion of the results points out that the effect of short-term reduction of light-weight concrete's compressive strength in real structures damaged by fire may have a significant effect on the post-fire load bearing capacity of a structure. This is due to an apparent reduction of the residual load capacity as illustrated on a simple example (Section 3.2) where post-fire reduction of load bearing capacity amounts to approximately 10%.

Further research into these issues will include an analysis of post-fire reduction of mechanical properties over a longer time period after cooling so that the maximum reduction of the load bearing capacity that could occur in concrete structures after cooling may be assessed. Additionally, to capture more realistic moisture boundary conditions that can occur in concrete structures, the influence of storage conditions, i.e. moisture absorption on the strength reduction, is also planned in some future research.

ACKNOWLEDGMENT

The authors would like to thank Liapor GmbH and Cemex Croatia for providing material for this research.

REFERENCES

[1] Felicetti R. and Gambarova P. G., "Expertise and assessment of materials and structures after fire", *FIB Bulletin 46: Fire Design of Concrete Structures-Structural Behaviour and Assessment*, 63–114, 2008.

[2] Felicetti R. and Gambarova P. G., "Effects of High Temperature on the Residual Compressive Strength of High-Strength Siliceous Concretes", *ACI-Materials Journal* 95(4), 395-406, 1998.

[3] Annerel E. and Taerwe L., "Residual and post-cooling stress-strain curves for traditional and self-compacting concrete", *Structures in Fire – Proceedings of the Seventh International Conference*, M. Fontana, A. Frangi and M. Knobloch (eds.), ETH Zurich, Institute of Structural Engineering, Zurich, 561-569, 2012.

[4] EN1992-1-2:2004, Eurocode 2 – Design of Concrete Structures - Part 1-2: General Rules - Structural Fire Design, European Committee for Standardization, Brussels, 2004.

[5] EN1994-1-2:2005, Eurocode 4 – Design of Composite Steel and Concrete Structures – Part 1-2: General Rules – Structural Fire Design, European Committee for Standardization, Brussels, 2005.

[6] Torić, N., Boko, I. and Peroš, B., "Reduction of Postfire Properties of High-Strength Concrete", *Advances in Materials Science and Engineering*, Vol. 2013, 2013.

[7] RILEM TC 129 MHT: Test methods for mechanical properties of concrete at high temperatures, Part 3: Compressive strength for service and accident conditions, *Materials and Structures* 28, 410-414, 1995.

8th International Conference on Structures in Fire
Guo-Qiang LI, Venkatesh K. R. KODUR, Shou-Chao JIANG, Jian JIANG, Su-Wen CHEN, Guo-Biao LOU (Eds.)
Shanghai, China, June 11-13, 2014

EFFECT OF PRE-DAMAGE ON CONFINED CONCRETE AT ELEVATED TEMPERATURES

Praveen Kamath*, Pradeep Bhargava*, N.M. Bhandari* , Umesh K. Sharma* and Asif Usmani**

* Department of Civil Engineering, Indian Institute of Technology Roorkee, Roorkee - 247667
e-mails: praveen.kamath@hotmail.com, bhpdpfce@iitr.ac.in, nmbcefce@iitr.ac.in, umuksfce@iitr.ac.in

**Institute for Infrastructure and Environment, School of Engineering, The University of Edinburgh, Edinburgh EH9 3JL

Keywords: Confined concrete, Elevated temperature, Pre-damage, Mechanical properties

Abstract. *Evaluation of mechanical properties of damaged confined concrete at elevated temperature finds its applications in development of constitutive models essential for carrying out numerical analysis of earthquake damaged structures. In this regard, uniaxial compression tests were conducted on number of pre-damaged circular columns at elevated temperatures. Two levels of confinement, C1 and C2 were considered in the investigation. Damage was induced in the specimens by loading them up to three pre-defined levels, D1, D2 and D3 corresponding to three levels of strain: 0.0033, 0.0056 and 0.008 respectively. Mechanical properties such as stress-strain curves, modulus of elasticity and peak stress are re-established by considering the factor of damage.*

1 INTRODUCTION

Possibility of fire accidents in mass populated urban destinations is a growing matter of concern in most of the developing and developed countries in the world. Existing reinforced concrete structures in these regions needs to be evaluated for their behavior in case of a major fire event. Reinforced concrete structures located in active seismic zones, during their lifetime, experience at least one or many sequential effects. Most of these effects are potential of causing damage to the structures. An event of fire following an earthquake may be taken as one of the many instances causing recurrent damage effects [1]. It is imperative to study the response of structures under such loading effects by carrying out numerical investigation. However, while considering sequential effects of fire after earthquake, the constitutive models proposed for undamaged concrete may under-predict the analysis results. Besides, a unique fire behavior is demonstrated by the concrete structures damaged by external influences other than earthquake such as impact, prolonged vibration and ageing. Theoretical stress-strain relationships for confined concrete at elevated temperatures have been proposed by many researchers based on undamaged temperature dependent material properties [2-4]. Very few or no experimental studies have been carried out to ascertain the actual behaviour [5]. Although no theoretical or experimental studies suggesting constitutive laws of damaged materials exist for consideration in numerical simulations. This elicits a detailed experimental investigation on damaged concrete subject to elevated temperatures.

In the current paper, a detailed experimental investigation has been carried out to reckon the mechanical properties of both undamaged and damaged confined concrete at elevated temperatures subject to three different pre-damage levels: Mild, Moderate and Severe. Over one hundred confined concrete specimens; cylindrical in shape (150mm $\times$ 600mm), with two different confinement spacing C1 and C2 (42mm and 68mm) were tested. The specimens in damage category, D1, D2 and D3 were initially preloaded under uniaxial compression corresponding to three pre-defined levels of strain: 0.0033, 0.0056 and 0.008 respectively. Specimens were exposed to three different levels of target temperatures: 250 ℃ (T1), 500 ℃ (T2) and 750 ℃ (T3), in a split-type furnace coupled with a 500 ton compression testing machine. Upon attainment of the desired steady state, the specimens were loaded to failure. Compressive strength, modulus of elasticity and strain at peak stress were primary among the mechanical properties acquired. Various relationships such as stress vs. strain, normalized modulus of elasticity vs. temperature and normalized peak stress vs. temperature were obtained. Also, the effect of damage levels and influence of confinement were analyzed.

2 EXPERIMENTAL PROGRAMME

A rigorous experimental programme was carried out on confined concrete specimens in the current study. Uniaxial compression tests were planned on undamaged and pre-damaged confined concrete specimens at elevated temperatures. In resemblance to the three existing methods of concrete testing at elevated temperatures: stressed test, unstressed test and residual test, another type of test was proposed, however in conjunction with damage, i.e., damaged unstressed test at elevated temperature. Damaged unstressed tests are the tests conducted on specimens in which a desired level of pre-damage is imparted in terms of strains, worked out by carrying out compression tests on confined concrete specimens at ambient temperature. Table 1 shows different damage levels considered and their nomenclature.

Table 1. Damage levels.

Damage Level	Strain Level	Displacement (mm)	Zone on the Stress-Strain Curve
D0	-	-	Undamaged
D1	0.0033	0.5	Before Yield Point
D2	0.0056	0.85	At Yield Point
D3	0.0080	1.20	Post-Yield

After achieving the desired level of strains, the specimens were exposed to the desired level of elevated temperature and loaded in compression to failure in steady state. Figure 1 shows the schematics of damaged unstressed test at elevated temperature.

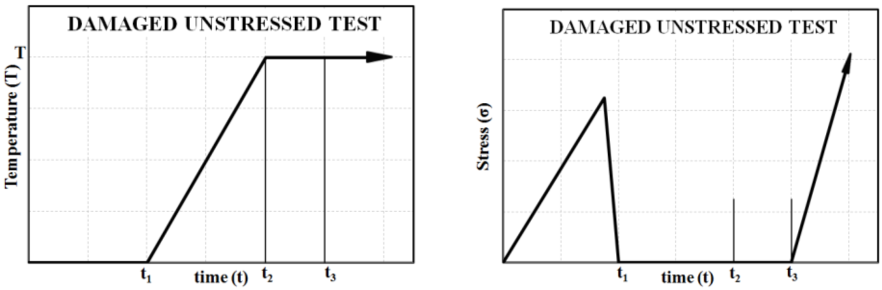

Figure 1. Schematics of the damaged unstressed test: temperature-time curve and stress-time curve.

2.1 Specimens

The specimens, both plain and confined concrete, considered for testing at elevated temperatures had a cylindrical cross-section of 150 mm diameter and a height of 600 mm as mentioned in the prior section. The dimensions of the concrete specimen were so chosen to accommodate a gauge length of 150 mm inside the furnace, representing a zone of uniform exposure. A total height of 450 mm of the specimen was encapsulated in the furnace and exposed to elevated temperature. The specimen was made of normal strength concrete, which registered an average cube compressive strength 52.23 Mpa. The longitudinal reinforcement consisted of 6 number 8 mm TMT ribbed reinforcing bars. Circular hoop rings made out of 6 mm plain reinforcing bars were used as confinement bars. Two different spacing of transverse reinforcement: 42 mm (Confinement C1) and 68 mm (Confinement C2), were considered for the investigation. Two titanium grade 12 rods were embedded inside the concrete during casting. These rods marked the gauge length and facilitated the measurement of displacement with the help of displacement transducers.

2.2 Instrumentation

Confined concrete specimens were well instrumented with embedded sensors to capture strains and temperature. Two K-type thermocouples, one at the core and the other at the cover level at mid-height, were embedded inside the specimen during casting. The split-vertical furnace was equipped with three thermocouples, one each at top, center and bottom, which helped in monitoring the furnace temperatures. Displacements were measured using two Linear Variable Displacement Transformer (LVDT) transducers clamped on the titanium bars protruding outside the furnace. An attempt was made to record the strains in the confining steel during compression at elevated temperatures. Bondable strain gauges with heat treatment and weldable strain gauges (generically modified bondable strain gauges) were used in an attempt to capture the variation in confining strains at the mid-height during loading as well as heating. However, the strain gauges were devoid of their capability to acquire strains at temperatures as low as 320 ℃ in undamaged and 270 ℃ in damaged concrete specimens. All the sensors were connected to a data-logger programmed to acquire the data at a triggering rate of 2 seconds.

2.3 Test Setup

The test setup used in elevated temperature compression test basically consisted of a specially fabricated split-type vertical furnace, capable of attaining a maximum temperature of 1200 ℃, coupled with a 500kN compression testing machine without any structural / functional modifications of the machine. Figure 2 shows the test setup used for conducting the elevated temperature compression tests. The heating sequence was programmed for different temperatures and fed to the control unit of the electric furnace. The specimens in undamaged category were placed in the furnace and the furnace was sealed from top and bottom with layers of glass wool. The furnace is programmed to achieve the target temperature at the rate of 10 ℃/min and maintain it until the steady state is reached. The temperature is maintained for about an hour beyond reaching steady state and then being loaded to failure. In case of specimens under the damaged category, the specimens were initially stressed to three pre-defined damage levels by imparting a load induced damage, after which they were exposed to desired elevated temperatures (250 ℃, 500 ℃ and 750 ℃) and thereafter loaded to failure in compression.

Figure 2. Testing of confined concrete at elevated temperature: Test setup and failure of specimens.

3 RESULTS AND DISCUSSION

This section sheds light on three main mechanical properties of undamaged and damaged concrete: stress-strain relationship, modulus of elasticity and peak stress.

3.1 Stress-Strain Curves

Literatures [2-4] highlight the fact that the mechanical properties like concrete strength, concrete initial modulus of elasticity, concrete strain at maximum stress, thermal strain, transient creep strain, yield strength of reinforcing bars, and bond strength of reinforcing bars affect the stress-strain relationship of confined concrete at elevated temperature. In addition to this, present study introduces another variable that is believed to affect the stress-strain relationship: an induced pre-damage imparted by pre-loading.

The experimental program carried out in the present investigation primarily consists of undamaged and damaged confined concrete members (four damage levels: D0, D1, D2, D3 and two confinement levels: C1 and C2) being tested in compression at ambient and elevated temperatures (three target temperatures: 250 ℃, 500 ℃ and 750 ℃). Figures 3(a-c) and 4(a-c) show various stress-strain plots obtained at elevated temperatures from specimens with confinement C1 and C2 respectively. Overall, degradation in strength and stiffness was observed in terms of degradation in mechanical properties of confined concrete specimens at elevated temperatures. Different mechanical properties like modulus of elasticity, confined peak stress and strain at peak stress were worked out from the stress-strain relationships plotted using the experimental data both for undamaged and damaged specimens and are discussed in the following subsections.

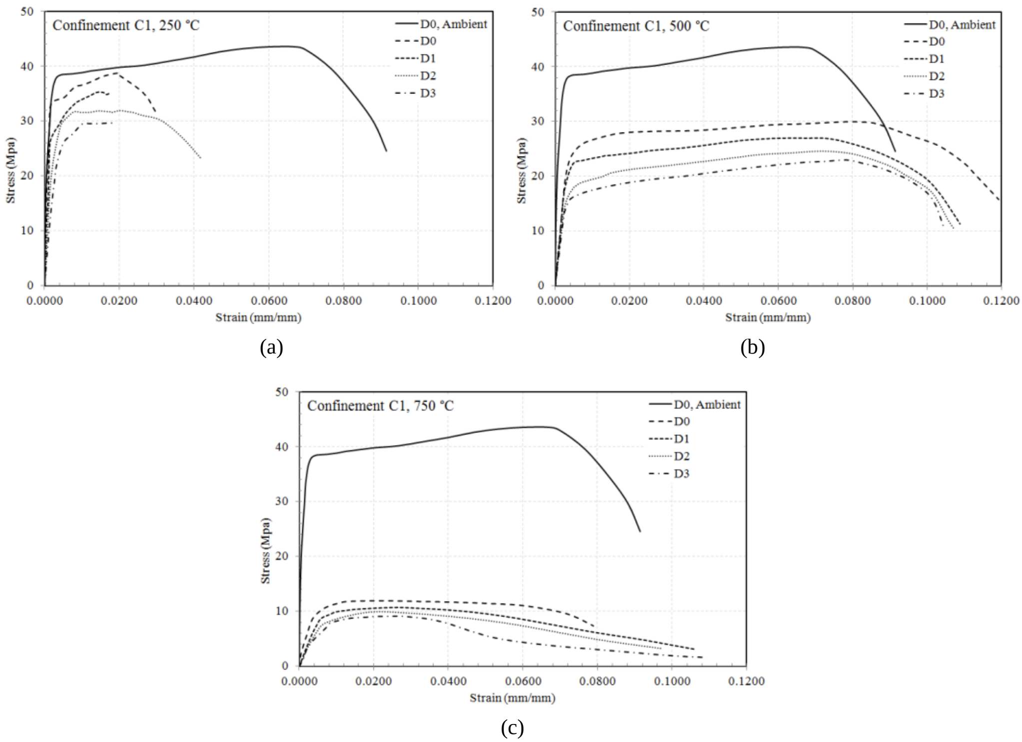

Figure 3. Stress-Strain curves for specimens with confinement C1 at 250 ℃, 500 ℃ and 750 ℃.

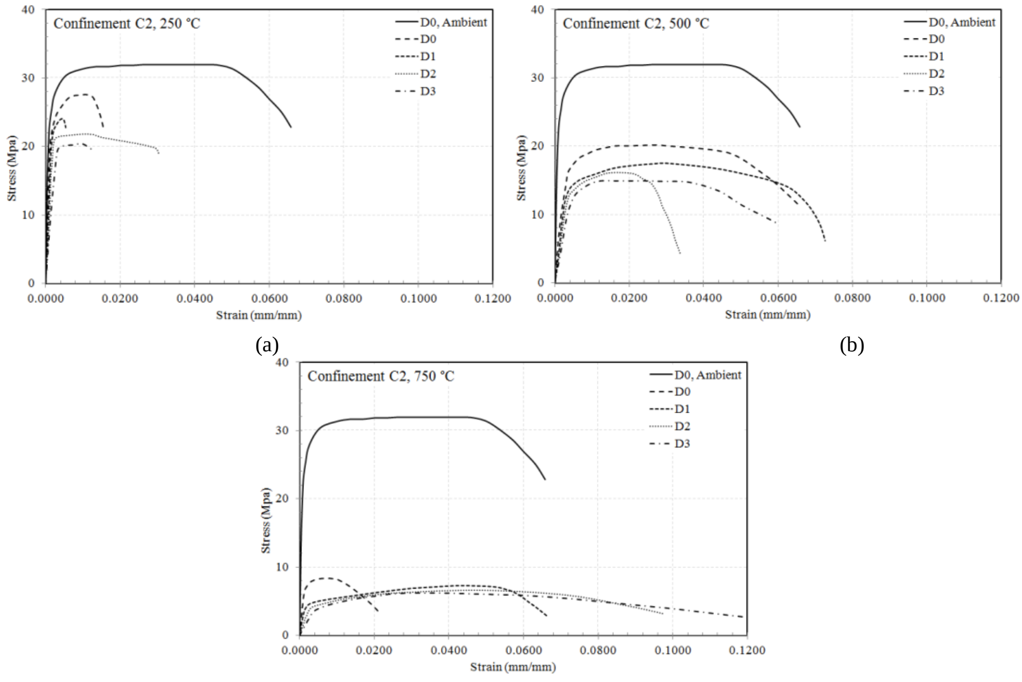

Figure 4. Stress-Strain curves for specimens with confinement C2 at 250 ℃, 500 ℃ and 750 ℃.

3.2 Modulus of Elasticity

An average value of 36000 Mpa of initial elastic modulus has been obtained under ambient conditions irrespective of degree of confinement. This confirms the fact that initial elastic modulus of concrete (unconfined / confined) for any grade at ambient temperatures is unaffected by the confinement [1,6,7]. Figures 5 (a) and (b) depicts the ratio of initial elastic modulus of confined concrete at elevated temperatures, E_{cT}, with respect to ambient temperature, E_{c0}, for different damage levels and temperatures. Moreover, in contrast to the observation at ambient temperature, it may be noted that the confinement ratio does marginally effect the modulus of elasticity at elevated temperature.

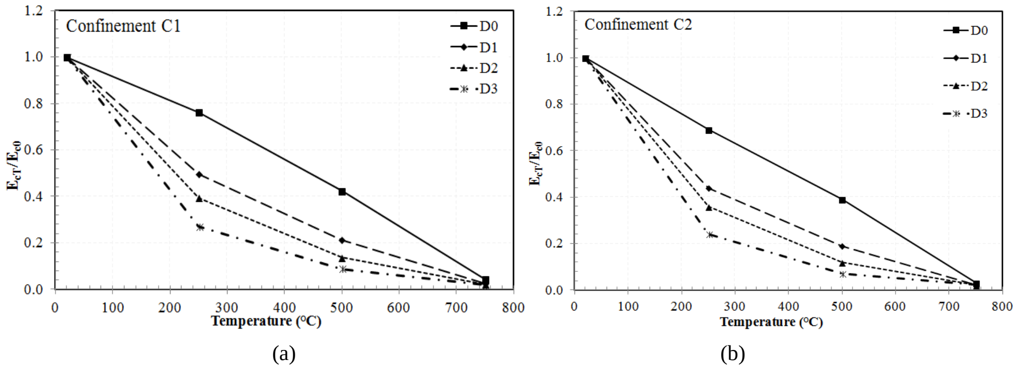

Figure 5. Initial modulus of elasticity at elevated temperatures for confinement: (a) C1; (b) C2.

For confined specimens with no damage, a degradation of about 24%, 58% and 96% for C1 - confinement and 31%, 61% and 97% for C2 - confinement with respect to modulus of elasticity at ambient temperature has been recorded at temperatures 250 ℃, 500 ℃ and 750 ℃ respectively. It is also apparent from the Figures that the degradation effect is more pronounced in the case of damaged confined specimens at temperatures 250 ℃ and 500 ℃, though this trend was unseen at 750 ℃ due to considerable loss of strength and stiffness.

3.3 Peak Stress and Corresponding Strain

Figures 3 and 4 suggest that the temperature, the confinement and the level of damage significantly influence the value of the confined peak stress and the corresponding strain value. It is apparent that the peak stress value reduces with an increase in the temperature and the effect becomes more pronounced in the case of pre-damaged specimens.

For C1 - confinement specimens, an average degradation of 22% in peak stress has been observed at a temperature of 250 ℃, though for the undamaged specimens, degradation was limited to 11% in comparison to the peak stress at ambient temperature. The reduction in the peak stress was found to increase with an increase in the damage levels and was in the order of 19%, 27% and 32% of the peak stress. Specimens with damage registered a higher loss in peak stress in comparison with the specimens with no damage at 250 ℃. Figure 3(a) suggests that at 500 ℃, the degradation in peak stress almost got doubled indicating an average reduction of 40% in peak stress. Percentage reduction calculated in confined concrete specimens with no damage and the three damage levels were in the order of 31%, 38%, 43% and 47% respectively. At 750 ℃, the confined concrete specimens experienced a rapid loss of strength and stiffness due to loss of confinement as shown in Figure 3(c). On an average, about 76% reduction of peak stress was registered and the effect of the imparted damage was negligible.

For C2 - Confinement specimens, as is evident from Figure 4(a), at 250 ℃, an average degradation of 27% in peak stress has been observed (D0: 14%, D1: 25%, D2: 32% and D3: 36%). Figure 4(b) gives the stress-strain relationship for confined concrete specimens with all damage levels exposed to a temperature of 500 ℃. Congruent to the specimens with confinement C1, the degradation in peak stress doubled at 500 ℃. An average degradation of 46% in peak stress was observed at this temperature. Percentage reduction observed for damage levels D0, D1, D2 and D3 were in the order of 37%, 45%, 47% and 53% respectively. At a target temperature of 750 ℃, the confined concrete specimens experienced a greater loss of strength and stiffness due to loss of confinement. An average loss of 78% recorded for specimens with confinement C2, was although 2% less than that of the specimens with confinement C1, was merely significant. The stress-strain plots for all four damage levels at 750 ℃ are shown in Figure 4 (c). The effect of damage diminished to a greater extent at this temperature. About 74%, 77%, 79% and 81% reduction in peak stress was observed at the four damage levels respectively. Irrespective of the amount of confinement steel provided, at high temperatures, confinement effectiveness abates due to softening of steel reinforcement. The reinforcing bars become red-hot and soften. Any dilatation in the circumferential zone within the gauge length will not be restricted by the effect of confinement. The confining hoop reinforcement exhibits a very low or no-stress state. The hoop steel dilates along with the concrete thus leading to the failure of the specimen due to failure of concrete. Also, the difference in degradation of peak-stress in damaged confined concrete is more pronounced at lower temperature levels and reduces with increase in temperature. Figures 6(a) and (b) depict the variation in normalized peak stress (σ'_{ccT} / σ'_{cc0}) with temperature for concrete specimens with confinement C1 and C2 respectively.

4 FAILURE IN CONFINED CONCRETE SPECIMENS *(UNDAMAGED / DAMAGED)*

The confined concrete specimens failed in compression generally in the middle third of the specimen under uniform temperature exposure and high confinement pressure. An estimate of the confinement pressure was unable to be established due to failure of strain gauges before the specimen attaining target temperatures. Failure widely occurred due to buckling of longitudinal reinforcement under direct compression and opening of lateral ties (hoop rings).

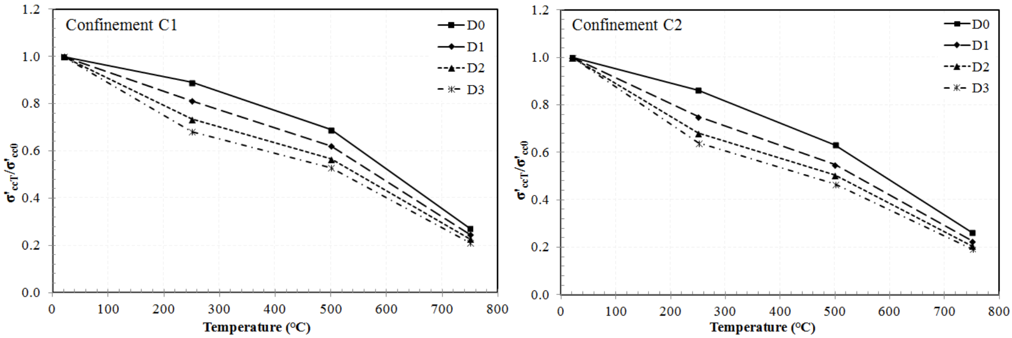

(a) (b)

Figure 6. Normalized peak stress at elevated temperatures for confinement: (a) C1; (b) C2.

At elevated temperatures, it was also observed that the bond between aggregate surface and cement paste separated, which resulted in the loss of integrity in the aggregate-cement paste matrix. The coefficients of thermal expansion of steel and concrete being different, exposure of the specimens to elevated temperature introduces a differential thermal gradient. This results in separation of cover concrete from core concrete due to loss of bond between them. However loss of cover in entire specimen was observed in the entire specimen at 250 ℃ only. At 500 ℃ and 750 ℃, the cover failure was localized in the heating zone only. This is attributed to development of differential thermal gradients along the length of the section as shown in Figure 7(a). Figure 7(b) shows a typical failure pattern that occurred in C1 – confined concrete at different damage levels and temperatures. Another prominent feature observed at 750 ℃ was the loss of confinement pressure. Confining steel rebars lose their strength at high temperatures and when compression force is applied on the specimen, the reinforcement expands along with the concrete till it fails. The temperature growth inside the specimen is dependent on the microcracks that appear during the loading of specimens. Any damage induced prior to temperature exposure accelerates the process due to formation of cracks that act as a passage for heat penetration. The fact was well observed in case of damaged specimens where the failure earlier than in undamaged specimens. Higher the damage, greater was the reduction in strength.

(a) (b)

Figure 7. Failure of concrete specimens (a) Confined concrete failure at 750 ℃; (b) Failure pattern at different temperatures.

5 CONCLUSIONS

This paper summarizes the testing methods and results of undamaged and damaged confined concrete specimens subjected to elevated temperatures. In the present study, two different levels of confinement were considered. Three pre-defined levels of damage were induced to the specimens in the 'damaged' category before exposing them to target temperatures. The study was primarily focussed on reckoning the effect of pre-damage on confined concrete specimens exposed to 250 ℃, 500 ℃ and 750 ℃. It was observed that the mechanical properties such as peak stress and modulus of elasticity showed degradation with an increase in temperature in the specimens under undamaged category. Damage induced prior to heating causes further degradation of these properties. From the current study it may be inferred that damaged concrete is more vulnerable in case of fire accidents in reinforced concrete structures. From the tests, it was also evident that the effect of confinement is greatly reduced at a temperature of 750 ℃.

ACKNOWLEDGEMENTS

The authors gratefully acknowledge the funding from British Council under UK-India Education and Research Initiative (UKIERI) to carry out this research work.

REFERENCES

[1] Sharma, U., Bhargava, P., Singh, B., Singh, Y., Kumar, V., Kamath, P., Usmani, A., Torero, J., Gillie, M., Pankaj, P., May, I., and Zhang, J. "Full-scale testing of a damaged reinforced concrete frame in fire", *Proceedings of the ICE - Structures and Buildings*, 165(7), 335–346, 2012.

[2] Youssef, M. and Moftah, M. "General stress-strain relationship for concrete at elevated temperatures". *Engineering Structures* 29(10), 2618–2634, 2007.

[3] Bastami, M. and Aslani, F. "Preloaded high-temperature constitutive models and relationships for concrete", *Civil Engineering,* 17(1), 11-25, 2010.

[4] Aslani, F. and Bastami, M. "Constitutive relationships for normal- and high-strength concrete at elevated temperatures", *ACI Materials Journal,* 108(4), 355-364, 2011.

[5] Wu, B., Ma, Z. and Ou, J. "Experimental research on deformation and constitutive relationship of concrete under axial loading and high temperature", *Journal of Building Structures* 20(05), 42, 1999.

[6] Mander, J. B., Priestley, M. J. N. and Park, R. "Theoretical stress-strain model for confined concrete", *Journal of Structural Engineering*, 114(8), 1804-1826, 1989.

[7] Paultre, P., and Legeron, F. "Confinement reinforcement design for reinforced concrete columns", *Journal of Structural Engineering*, 134(5), 738-749, 2008.

[8] Naus, D. J. "The effect of elevated temperature on concrete materials and structures - A literature review", *US Nuclear Regulatory Commission,* Washington, DC, 2006.

[9] European Committee for Standardization, "Eurocode 2: Design of concrete structures - Part 1-2: General rules - Structural Fire design. No. EN 1992-1-2" in *Forschung Strassenbau und Strassenverkehrstechnik* CEN, Brussels, 2005.

8th International Conference on Structures in Fire
Guo-Qiang LI, Venkatesh K. R. KODUR, Shou-Chao JIANG, Jian JIANG, Su-Wen CHEN, Guo-Biao LOU (Eds.)
Shanghai, China, June 11-13, 2014

IMPROVED PERMEABILITY MODEL FOR CONCRETE AT HIGH TEMPERATURE

Fang-Xia Lu*, Eike Klingsch*, Mario Fontana* and Dilum Fernando**

* ETH Zurich, Institute of Structural Engineering (IBK), 8093 Zurich, Switzerland
e-Mails: Lu@ibk.baug.ethz.ch, Klingsch@ibk.baug.ethz.ch, Fontana@ibk.baug.ethz.ch

** The University of Queensland, School of Civil Engineering, Queensland 4072, Australia
e-Mail: dilum.fernando@uq.edu.au

Keywords: UHPC, High temperature, Permeability tests, Moisture content, Pore pressure, Permeability model, TH-model

Abstract: *A "dense" concrete with a low permeability shows an increased risk towards explosive spalling. Tests on the permeability of UHPC without PP-fibers added to the concrete showed a decrease of permeability in the temperature range of T = 175 °C - 275 °C compared to the initial value at room temperature. These observations are consistent with results presented by Schneider et al. (1989). Based on these results an improved permeability model for concrete at high temperatures as part of a Thermo-Hygro (TH)-model is developed. This paper presents the main results from tests on temperature dependent permeability of concrete as well as the development of an improved permeability model as part of a TH-model to compute pore pressure inside heated concrete.*

1 INTRODUCTION

Improvements in concrete technology including the use of silica fume lead to new high (HPC) and ultra-high performance concrete (UHPC) mixes with a compressive strength of f_c = 150 MPa or more. However, apart from increasing the strength grade due to a very "dense" matrix, the use of silica fume is known to decrease the permeability of these concrete mixes [1].

Recent tests at ETH Zurich on the spalling behavior of concrete mixes with low permeability showed an increased risk towards explosive spalling in fire [2]. When moisture inside concrete vaporizes at temperatures exceeding T > 100 °C it causes a rising pressure inside the concrete. The permeability of concrete changes at high temperatures. This is essential for the relief of pressure and is markedly influencing the risk of explosive spalling. Migration processes of vapor and the relief of pressure to the outside are more pronounced with a higher permeability.

Usually, the permeability of concrete is assumed to increase with higher temperatures which is implemented in several models [3, 4]. However, tests on the permeability of concrete at high temperature performed by Schneider in 1989 [5] showed a significant decrease in permeability within a temperature range of T = 150 °C - 250 °C.

Improved permeability data is essential as temperature dependent input parameter and should include the decrease in permeability which is usually not covered by existing data. This data is required in favor to analyze the probable pressure development inside concrete at high temperature with a TH-model. A series of tests on the residual permeability of concrete after cooling from high temperature was performed at ETH Zurich. The tested concrete contained a high content of silica fume. In addition, the influence of steel- and PP-fibers added to the concrete on the permeability were studied. As the next step, an improved permeability model is developed. It is based on these tests and covers modifications to the concrete mix.

This paper presents the main results from the tests on permeability of concrete as well as the development of the improved permeability model.

2 TESTS ON PERMEABILITY

Tests on the permeability of concrete at high temperatures are difficult to perform, in particular for very “dense” concrete mixes with a low permeability like found for HPC and UHPC. Schneider et al. performed tests on the permeability of ordinary performance concrete at high temperatures in 1989 [5]. They inserted compressed air to the heated concrete and analyzed the volume of air penetrating through the concrete. As mentioned, they noticed a significant decrease in permeability within a temperature range of $T = 150$ °C - 250 °C which they attributed to the formation of a moisture clog where vapor causes congestion inside the pore system and lowers the permeability. This temperature range varied according to the tested concrete mix. A higher compressive strength of the concrete shifted this decrease in permeability to higher temperatures.

To quantify general changes in permeability of concrete at high temperatures and to provide input data for the improved permeability model, tests on the residual permeability after cooling from high temperatures were performed. These tests are easy to perform and can be made using the Torrent method [6] by simply placing a low pressure cap onto the surface of concrete specimens after cooling from different temperatures. Even though this test set-up provides an easy tool to assess the permeability, possible influences during the cooling phase might remain unknown. The influence of vaporizing and condensing moisture inside heated concrete may have significant influence on the permeability as well as hardening effects due to a pozzolanic reaction or thermal cracks [2, 7]. These effects can only be analyzed with tests on the hot permeability.

Figure 1. Residual permeability according to the Torrent method.

2.1 Tests on the residual permeability after cooling

As first quantifying tests, the residual permeability of concrete was analyzed after cooling from high temperatures according to the Torrent method [2]. A temperature range between $T = 20$ - 500 °C was chosen. Concrete disks ($ø = 150$ mm, $h = 40$ mm) were heated slowly (details are given below) to different target temperatures, conditioned and cooled again to ambient temperature, before the permeability was tested.

Figure 1 shows the test set-up. The permeability is measured simply by placing a low pressure cap onto one concrete disk and outgassing this cap. The pressure difference and flow of air towards the cap leads to the permeability which is than displayed directly on the device.

The test on residual permeability was performed on one UHPC mix (M1, Table 1) with three different sub-mixes. The mix -V1 was fiber free, -V2 contained 2.5 Vol.-% of steel fibers and -V3 contained 2.5 Vol.-% of steel fibers and 2.0 kg/m^3 of PP-fibers added to the mix. As steel fiber a common fiber was chosen ($ø = 0.15$ mm, $l = 6$ mm, $f_t = 2400$ N/mm^2) and thin and short PP-fibers ($ø = 15.4$ μm, $l = 6.0$ mm) which were designed for spalling protection in fire [8].

The M1 UHPC mix contained 832 kg/m^3 cement CEM I, 975 kg/m^3 and 207 kg/m^3 quartzite sand and powder. A total of 135 kg/m^3 of silica fume was added to the mix. The water content was 166 l/m^3 plus additional 3.0% of superplasticizer compared to the cement content. This leads to a water / cement ratio of w/c = 0.22.

Common cylinders (ø = 150 mm, l = 300 mm) were concreted and cut into disks (ø = 150 mm, h = 40 mm) after de-molding. The disks were smoothened at both ends and stored for t = 28 d (T = 20 ℃, 95% rel. humidity) prior testing. Table 1 gives an overview on the main mechanical properties of the concrete.

Table 1. M1 concrete design parameter.

Concrete mix	M1-V1	M1-V2	M1-V3
Steel fibers in Vol.-%	-	2.5	2.5
PP-fibers in kg/m^3	-	-	2.0
Silica fume content	≈5.7% (of concrete weight)		
w/c ratio	0.22		
Initial moisture content[1)]	1.22%	1.03%	1.06%
ρ in kg/m^3	2280	2422	2414
f_c in MPa	108.2	148.7	147.6
Young's Modulus in GPa	52.0	48.2	48.0
Initial permeability in m^2 (T = 20 ℃)[①]	$1.40 \cdot 10^{-18}$	$1.35 \cdot 10^{-18}$	$1.25 \cdot 10^{-18}$

① after drying to constant in mass at T = 105 ℃ (Δm < 0.1% / 24h).

After drying the concrete disks at T = 105 ℃ to constant in mass (Δm < 0.1% / 24h) and determining the initial permeability at T = 20 ℃, the concrete specimens are heated to the different target temperatures of T = 105 ℃, 150 ℃, 175 ℃, 200 ℃, 250 ℃, 300 ℃, 400 ℃ and 500 ℃. A new concrete disk was taken for each temperature level. A heating rate of $\dot{T}$ = 2.5 K/min was chosen to a target temperature of T = 250 ℃. This rate was reduced to $\dot{T}$ = 0.5 K/min for higher temperature levels. After reaching the target temperature, specimens were conditioned for t = 4 h before they were cooled inside the closed furnace to ambient temperature by switching off the electric heating. The average cooling rate was between $\dot{T}$ = 0.2 - 0.5 K/min to avoid thermal shocks. Tests on the permeability were made at a temperature of T = 50 - 60 ℃ to minimize the intake of moisture.

The permeability tests were carried out by placing the low pressure cap on the surface of the concrete and starting to outgas. Depending on the temperature level and permeability, the duration for each test varied from t = 5 – 12 min. The residual permeability of the concrete after cooling is displayed by the testing device and is independent from the level of the low-pressure during testing.

2.2 Initial permeability

Table 1 shows the initial permeability at T = 20 ℃ of the three tested concrete mixes after drying to constant in mass. The initial permeability is not influenced by the presence of fibers added to the concrete mixes. The test showed the same initial permeability within the range of $k_v(T) = 1.3 \times 10^{-18}$ m^2 for all M1 concrete mixes. The slight differences are within the usual spread of results and occur with the used Torrent method. Similar results in terms of presence of PP-fibers are mentioned in literature [9, 10]. Zeiml observed a slightly higher initial permeability for those concrete mixes containing PP-fibers which are considered to be "practically the same" [9]. Bošnjak, Ožbolt et al. [10] noticed no difference in initial permeability between HPC mixes with and without PP-fibers.

2.3 Results from tests on residual permeability

Figure 2 shows the relative residual permeability after cooling from high temperature compared to the initial permeability as given in table 1. The temperature-dependent losses in weight for the M1 concrete after drying to constant mass at T = 105 ℃ are shown in Figure 3.

The M1 concrete sub-mixes without any fibers (-V1) and with steel fibers (-V2) showed a significant decrease in permeability between temperatures of T = 175 °C and T = 275 °C. Within this area an even lower permeability than the initial permeability at T = 20 °C was noticed. With higher temperatures of T = 275 °C, the permeability exceeds the initial permeability. An almost constant increase in permeability is observed for temperatures exceeding T = 300 °C.

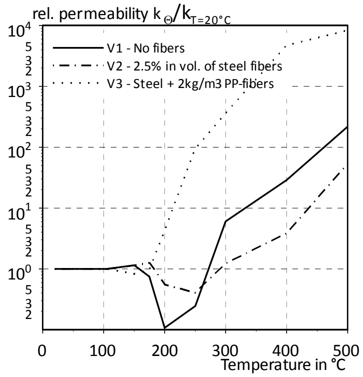

Figure 2. Relative residual permeability after cooling from high temperatures.

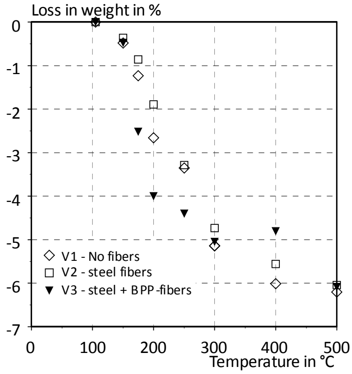

Figure 3. Additional losses in weight during heating.

The -V3 concrete mix shows a significant increase in permeability with temperatures exceeding T = 175 °C. The melting of the PP-fibers leads to a significant higher permeability. The majority increase of permeability is observed after exceeding the melting temperature of the PP fibers. The increase gets less pronounced with higher temperatures.

Figure 3 shows the additional temperature-dependent losses in weight after they were dried to constant mass at T = 105 °C and after heating to the target temperature for measuring the residual permeability. Even though the specimens were dried to constant in mass at T = 105 °C, it should be mentioned that the heating of the concrete to higher temperatures leads to a significant additional release of moisture. It is interesting to notice, that the loss in weight of the -V1 and -V2 mixes up to a temperature of T = 250 °C is less pronounced compared to that of the -V3 mix containing PP-fibers. At a temperature of T = 200 °C, the additional losses in weight for the -V2 mix are about Δm = 2% in mass, while the -V3 mix showed additional losses of Δm = 4% in mass. At higher temperatures, the difference between the three sub-mixes becomes less significant.

When testing the residual permeability of the -V1 and -V2 mix between temperatures of T = 175 °C and T = 275 °C, a significant higher moisture content is still present inside the concrete. This might be one explanation for the decrease in permeability within this temperature range. These effects are discussed within the permeability model for concrete.

It remains unanswered whether the decrease in permeability for the M1-V1 and -V2 concrete mix would also be different if the permeability was tested at high temperatures (hot permeability). Possible temperature-related effects like moisture content, thermal expansion and cracking might have an influence on the test results

2.4 Test set-up for the hot permeability

To assess the hot permeability experimentally, a new testing device is under development at ETH Zurich and first tests are due. It mainly consists of two lids with two sealing rings and a pipe segments as outer sealing. As test specimen, a concrete disk with same dimensions as used for the residual tests ($\o$ = 150 mm, h = 40 mm) is placed between the two lids and sealed with a high temperature adhesive. This test set-up requires a high grade of dimension accuracy of the test specimen. The permeability can be measured by inserting compressed air into the upper lid and measuring the volume of air penetrated via the concrete. Figure 4 shows the main components of this device.

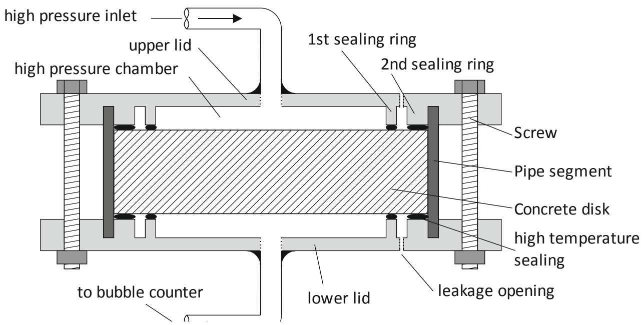

Figure 4. Concept of testing device for hot permeability.

The entire testing device is placed into an electric furnace and heated to the same temperature levels as used for the tests on residual permeability. Compressed air with different pressure levels migrates through the concrete disk according to its permeability. The volume of air penetrating through the concrete is measured with a bubble counter. Compressed air was chosen since the dynamic viscosity of compressed air is known and very similar to an ideal gas.

3 PERMEABILITY MODEL FOR CONCRETE

Permeability of concrete changes with temperature and pore pressure. Gawin, Schrefler et al. [3, 4] provided a common equation to estimate changes in permeability with the increase of temperature and pore pressure:

$$k_T = k_0 \times 10^{C_T(T-T_0)} \left(\frac{P}{P_0} \right)^{0.368} \tag{1}$$

In here k_T is the intrinsic permeability of concrete at temperature T, k_0 the initial intrinsic permeability of concrete at room temperature, P_0 =101.325 Pa, P is the gas pressure, C_t is a material parameter. The influence of pressure P on permeability, i.e. the micro cracks induced by high pressure during heating is taken into account. This formula considers the effect from temperature and the change of pore pressure. However, this model on the permeability of concrete at high temperatures doesn't consider changes in permeability with moisture content as observed in tests. In particular, the decrease in permeability within the temperature range of T = 175 ℃ - 275 ℃ cannot be predicted. Based on the test results, an improved permeability model is developed. The new model considers the pore pressure, temperature and viscosity of water and vapor at high temperature. It takes into account the observations from tests, in particular the decrease in permeability caused by the moisture clog or the increase due to the melting of PP-fibers.

3.1 Permeability model for concrete

The viscosity of fluid is usually treated as constant in concrete which is basically valid for concrete at room temperature. However, it varies significantly at high temperature. The test results have shown that the decrease in permeability from T = 100 ℃ to more than T = 300 ℃ exceeds one order of magnitude. This is similar to the results from Schneider [5]. Elevated temperature initiates the release of physically bounded water. The water filled pores block the movement of vapor and fluid, as the proportion of the saturated pores increases. However, if the concrete is kept for long time at elevated temperature, no such decrease of permeability is observed, since the concrete dries out. Thus, the permeability changes not only with temperature and pore pressure, the moisture content is influential as well. When the penetration is governed by moisture in the range T > 120 ℃, the permeability and viscosity difference between vapor and fluid should be taken into account.

As in the Darcy's expression, flow is determined by both, the intrinsic permeability k_T and the viscosity μ. Hence the jump of permeability due to the block of moisture would depend on the change of viscosity.

$$\mu = \begin{cases} \mu_{gv}, \ T < 120°C \ or \ T > 374°C \\ (1-w)\mu_{gv} + w\mu_{liq}, \ \text{else} \end{cases} \tag{2}$$

Where μ_{gv} is the dynamic viscosity of vapor ($\mu_{gv} = \mu_{gv0} + a_v(T-T_0)$, with $\mu_{gv0} = 8.85\times10^{-6}$ Pa, a_v = 3.53×10^{-8} Pa s K^{-1}), μ_{liq} the dynamic viscosity of water ($\mu_{liq} = 0.6612\times(T-T_0)^{-1.562}$), and w is the relative moisture content. For dried concrete the value of w is small. The permeation is governed by vapor and the viscosity is taken as the viscosity of vapor. The desorption of physically bounded water starts from T = 120 ℃. The influence of moisture is increasing and the viscosity can be expressed as a combination of the viscosity of both: vapor and liquid. No moisture as liquid exists at temperatures exceeding T = 374 ℃, and the flow is governed by the viscosity of vapor. In this way, a permeability decrease in the temperature range from T = 120 ℃ - 374 ℃ can be modeled, which is significant in high performance concrete. It's interesting to notice from the test results that the concrete with steel fibers (-V2) shows moderate change of permeability with temperature. Neither the decrease nor the increase afterwards is significant, which also agrees well with the current permeability model.

3.2 Permeability model for concrete with PP-fibers

A decrease of permeability is not observed with the use of PP-fibers. The positive effect of the PP-fibers preventing spalling has been highlighted in many studies [2], but no valid model to quantify the influence on permeability is available. The behavior of concrete with PP-fibers at high temperature is strongly affected by the melting of polypropylene around T ≈ 160 ℃. It has been shown in this study that PP-fibers increases the permeability significantly. The decrease of permeability due to the moisture clog is not observed. At T = 160 ℃ the permeability increases by one order of magnitude, which is attributed to the melting of PP-fibers. The permeability of concrete with PP-fibers at elevated temperature can be expressed as given in Equation (3) and (4):

$$k_{T,PP} = \begin{cases} k_0 \times 10^{C_T(T-T_0)} \left(\dfrac{P}{P_0}\right)^{0.368}, \ T \le 160°C \\ a_{k,T} \times k_0 \times 10^{C_T(T-T_0)} \left(\dfrac{P}{P_0}\right)^{0.368}, \ T > 160°C \end{cases} \tag{3}$$

$$\mu = \mu_{gv} \tag{4}$$

Where $k_{T,PP}$ is the initial intrinsic permeability of concrete with PP-fibers at temperature T, $\alpha_{k,T}$ is permeability increasing factor, which is assumed constant. According to tests results, $\alpha_{k,T}$ is 10 for the M1 mix. Dynamic viscosity of vapor μ_{liq} is used to model the flow.

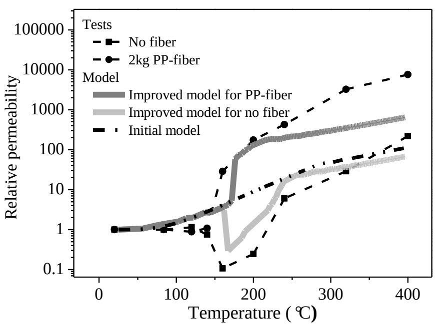

Figure 5. Permeability at different temperature (M1 mix).

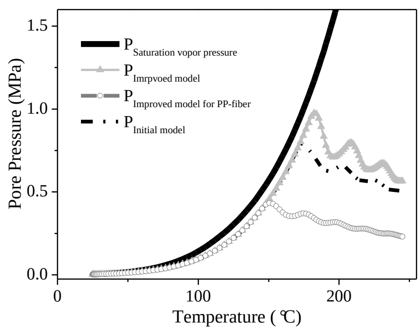

Figure 6. Pore pressure in 3mm depth (M1 mix).

Figure 5 shows the results from the initial [3, 4] and new permeability model compared to test results for the M1 concrete mix and based on an initial permeability of k_0 = 1.8×10^{-18} m^2 at T = 20 ℃. It can be seen that, the initial permeability model cannot predict the decrease of permeability in the temperature range from T = 120 ℃ - 374 ℃. However, the improved model predicts a changing trend of permeability during heating, especially the decrease of permeability is modeled. As for the PP-fibers, this permeability model also meets well with the tests results. The effects on permeability from PP-fibers are considered due to the melting of PP-fibers from T = 160 ℃. The increase of permeability due to the melting is taken into account. But the increase of permeability from T = 200 ℃ is underestimated by the improved model. This could be addressed to the assumption of constant permeability increasing factor. Permeability increasing factor $\alpha_{k,T}$ will be further studied for different concrete mixes in tests on hot permeability.

As next step, the modeled permeability is used in the TH-model for the prediction of the pore pressure (P_{Pore}). The development of the pore pressure inside the heated concrete is based on the assumption that the conservation of mass for water and vapor applies for this TH-model. The equations are based on applications of the ideal gas law similar to the considerations by Dwaikat and Kodur [10].

Figure 6 presents the predicted pore pressure from initial model [3, 4] and modified model with and without PP-fibers. Based on the properties of the M1 mix, when exposed to ISO-fire, the pore pressure developments inside the concrete in 3 mm depth are shown. The pressure is compared to the saturation vapor pressure curve (P_{vs}). It can be seen, the pore pressure follows the P_{vs}-curve with rising temperatures as long as sufficient moisture is available inside the pores (saturated zone). However, pores are getting dry due to evaporation and the pore pressure decreases. This process mainly depends on the temperature dependent permeability of the saturated zone and the corresponding pressure inside this zone. The decrease of permeability reduces the drying process, and the pore pressure increases further following the saturation curve up to P = 1.1 MPa. The initial model predicts no decrease of permeability, accordingly the relief of moisture is faster, which then lowers the peak pressure as well. In the case of concrete with PP-fibers, a higher permeability due to melting of the fibers leads to a more pronounced drying of the concrete and a lower peak pressure ($P_{PP\text{-}fibers}$).

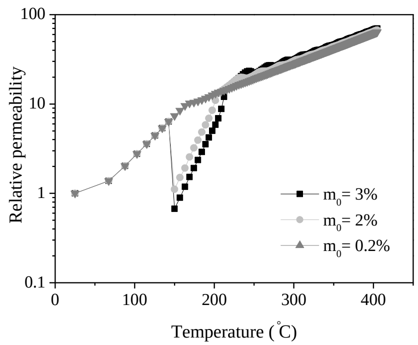

Figure 7. Relative permeability of concrete with different moisture content.

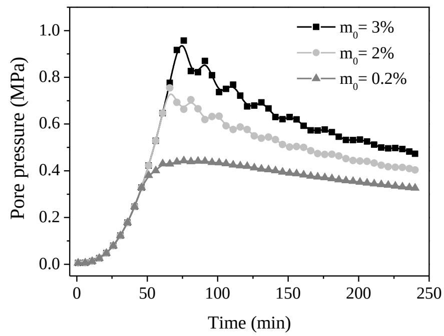

Figure 8. Pore pressure in 5 mm depth with different moisture content.

Figure 7 shows the influence of initial moisture content on permeability, since it influences permeability at high temperature. A typical decrease of permeability during heating, which is induced by the moisture clog starting at temperatures of T = 120 ℃, can be simulated with high moisture content. However, with lower moisture content, no significant decrease in permeability with temperature is predicted in this model, which is similar to Schneider's observations. In this way, the influence of moisture content is taken into account and the decrease of permeability is also simulated. The development of pore pressure in concrete in 5 mm depth with different moisture content is shown in Figure 8. It can be seen that the modeled pore pressure changes with different moisture content. The predicted pore pressure with low moisture content is about 50% of that with high moisture content. This indicates that the dried concrete shows a lower risk of spalling, as seen in tests [2].

This permeability model simulates the development of pore pressure, considering the melting of PP-fibers. The permeability increasing factor $\alpha_{k,T}$ must be verified with further tests. The results indicate that the TH-model is capable of representing observations from tests, using the improved permeability model.

4 CONCLUSIONS

Based on the experimental and numerical results as presented in this paper, the following conclusions can be drawn:

(1) Steel- and PP-fibers have no influence on the initial permeability of concrete.

(2) The use of PP-fibers significantly increases the permeability of concrete for temperatures of $T > 170$ °C as seen with the measurements on residual permeability.

(3) The decrease in permeability within the temperature of $T = 175$ °C - 275 °C as observed in specimens without fibers can be explained with the high moisture content inside the concrete.

(4) A permeability model including the observations from tests in terms of temperature dependent de- and increases in permeability, depending on the concrete mix and fiber content was developed.

(5) Based on this permeability model, the expected pore pressure at high temperatures is calculated with a TH- Model [11], considering the influence of moisture content and PP-fibers.

(6) Tests on the hot permeability are planned. Further studies are required to predict fire spalling due stresses initiated by a high pore pressure and stresses due to thermal gradients.

REFERENCES

[1] Kodur, V.K.R. and L. Phan, *Critical factors governing the fire performance of high strength concrete systems.* Fire Safety Journal, 2007. 42(6-7): p. 482-488

[2] Klingsch, E., A. Frangi, and M. Fontana, *Explosive spalling of concrete - Test report.* IBK Tests report No. 352. 2013: Institute of Structural Engineering (IBK), ETH Zurich

[3] Gawin, D., C.E. Majorana, and B.A. Schrefler, *Numerical analysis of hygro-thermal behaviour and damage of concrete at high temperature.* Mechanics of Cohesive-frictional Materials, 1999.

[4] Gawin, D., F. Pesavento, and B.A. Schrefler, *Simulation of damage-permeability coupling in hygro-thermo-mechanical analysis of concrete at high temperature.* Communications in Numerical Methods in Engineering, 2002. 18(2): p. 113-119.

[5] Schneider, U. and H.-J. Herbst, *Permeabilität und Porosität von Beton bei hohen Temperaturen.* Deutscher Ausschuss für Stahlbeton, 1989. Heft 403 (in German)

[6] Torrent, R., G. Frenzer, *Studie über "Methoden zur Messung und Beurteilung der Kennwerte des Ueberdeckungsbetons auf der Baustelle".* 1995, Bundesamt für Strassenbau. 106 S. (in German)

[7] Klingsch, E. „Explosive spalling of concrete in fire“ PhD Thesis ETH Zurich No.: 21650, 2014

[8] Knack, I., *“New PP-fibre with exceptional melting characterstics for improved fire protection in concrete building”*, in 1st International Workshop on Concrete Spalling due to Fire Exposure, F. Dehn and E.A.B. Koenders, Editors. 2009: Leipzig, September 03.-05.2009.

[9] Zeiml, M., et al., *Identification of residual gas-transport properties of concrete subjected to high temperatures.* Cement and Concrete Research, 2008. 38(5): p. 699-716.

[10] Bošnjak, J., Ožbolz, J., et al., Permeability of concrete at high temperatures and modelling of explosive spalling. 8th International Conference on Fracture Mechanics of Concrete and Concrete Structure, Toledo, Spain, March 10-14, 2013

[11] Dwaikat, M.B. and V.K.R. Kodur, *Hydrothermal model for predicting fire-induced spalling in concrete structural systems.* Fire Safety Journal, 2009. 44(3): p. 425-434.

8th International Conference on Structures in Fire
Guo-Qiang LI, Venkatesh K. R. KODUR, Shou-Chao JIANG, Jian JIANG, Su-Wen CHEN, Guo-Biao LOU (Eds.)
Shanghai, China, June 11-13, 2014

DUCTILE SPRAY-APPLIED FIRE-RESISTIVE MATERIAL FOR ENHANCED FIRE SAFETY

Qian Zhang[*] and Victor Li[*,]**

* Department of Civil and Environmental Engineering, University of Michigan, 48105, USA
e-mails: maplezq@umich.edu, vcli@umich.edu

** School of Transportation, Southeast University, Nanjing 210096, China

Keywords: Spray-applied fire-resistive material, Engineered cementitious composite, Fire, Steel structures, Tensile ductility

Abstract. *Spray-applied fire-resistive material (SFRM) is one of the most widely used passive fire protection material in North America. However, SFRM is inherently brittle and tends to dislodge or delaminate under extreme loading conditions (earthquakes or impacts) and even under normal service conditions such as impacts caused by maintenance work. Such loss of fire protection material puts the steel structure in great danger under fire loading, especially under multi hazards (post-earthquake or post-impact fires). As an alternative to conventional brittle cementitious material, engineered cementitious composites (ECC) is a family of high performance fiber reinforced cementitious composites. ECC typically exhibits strain hardening behavior with very high tensile ductility (3-5%) under loading. In this paper, a new spray-applied fire-resistive material that combines the desirable thermal insulation property, ease of construction (facilitated by sprayability), light-weightness of SFRM and the enhanced ductility of ECC is developed as an alternative material to current SFRM. The newly developed spray-applied fire-resistive ECC (SFR-ECC) exhibits density as low as 550 kg/m^3 yet with tensile strength of 1.1 MPa and tensile strain capacity of 3.0%, significantly higher than those of conventional SFRM with tensile strength of less than 0.1MPa and no inelastic tensile strain. The thermal conductivity and sprayability of SFR-ECC are measured to be comparable to conventional SFRM, which ensures the proper functionality of SFR-ECC. SFR-ECC with enhanced mechanical performance is expected to improve the overall fire safety of steel structure under both service and extreme loads.*

1 INTRODUCTION

Spray-applied fire-resistive material (SFRM) is the most widely-used passive fire protection for steel structures in North America. SFRM offers many advantages, such as low thermal conductivity, cost-effectiveness, ease of construction (facilitated by sprayability) and low self-weight, over other fire protection methods. Apart from the functionality properties (thermal insulating properties and sprayability), the performance of SFRM also naturally depends on its durability characteristics (mainly refers to the ability to stay on the steel). However, due to the brittle nature, very low strength and poor bond (to steel) of SFRM, the durability of SFRM is often called into questions. Studies have shown that SFRM could easily delaminate or get damaged during earthquakes or impacts, [1, 2] as well as vibration caused by regular maintenance work. Loss or damage of insulation significantly reduces the fire resistance of the steel structures. [3, 4] This puts the steel structures in great danger, particularly under multi hazards, such as post-earthquake/post-impact fires.

Adhesion and cohesion are two major durability characteristics of SFRM. While adhesion is interfacial property, and sometimes could be enhanced by applying external bonding agent on the interface, cohesion is an intrinsic material property closely associated with the strength and deformation capacity of the material. SFRM are inherently brittle and has very low tensile strength and ductility (e.g. medium density SFRM have typical tensile strength less than 0.1MPa and tensile strain capacity less than 0.01%). Therefore, poor cohesive property is the major bottleneck of conventional SFRM and leads to limited functional performance of protecting steel structures.

Engineered Cementitious Composites (ECC) is a special family of ultra-ductile high performance fiber reinforced cementitious composites. ECC has been developed based on micromechanics principles [5,6] over the last decade as a ductile construction material alternative to conventional concrete. Its tensile strain capacity under uniaxial tension reaches 3-5%, about 300-500 times that of normal concrete. Under tensile load, ECC develops multiple micro-cracks instead of one large crack, and the load carrying capacity continues to increase after first crack thus achieving pseudo strain-hardening behavior. The high tensile ductility and damage tolerance of ECC lend itself to significantly improved cohesive properties.

Recent study [7] demonstrated the feasibility of using lightweight ECC as a passive fire-resistive material. The fire-resistive ECC (FR-ECC) uses hollow glass microspheres as lightweight aggregates and successfully combines the thermal insulating property and high tensile ductility in one material. It has also been experimentally demonstrated that FR-ECC can be tailored to possess high adhesion to steel by incorporating acrylic latex into the mixture. [8] Therefore, with intrinsic high cohesion and tailored high adhesion, FR-ECC exhibits significantly enhanced durability characteristics over conventional SFRM.

FR-ECC studied in the previous researches, however, consists high cost and energy consumption materials: glass microspheres and PVA fibers, which leads to possible increase of material cost. In addition, the previous version of FR-ECC is not sprayable. Without the sprayability, the construction cost of FR-ECC is also expected to increase. These may impede the broader adoption of such material in the construction industry and lessen the advantage of FR-ECC over some other alternatives, such as intumescent.

In an attempt to address these deficiencies, this study aims at developing a version of sprayable fire-resistive ECC (SFR-ECC) with more accessible and low cost materials including vermiculite and polypropylene (PP) fiber. In this study, SFR-ECC containing vermiculite and high tenacity polypropylene (HTPP) fibers has been successfully designed following a parallel design process. Characterizations of both functionality and durability performance of the newly developed SFR-ECC have been conducted and are reported in this paper.

2 SFR-ECC MIXTURE DESIGN

SFR-ECC material development involves designing the material for multiple performance targets (high tensile ductility, low thermal conductivity, sprayability) simultaneously in one mixture. There are many interrelating design parameters involved in this process. Designing for low thermal conductivity is essentially designing the microstructure of the material to possess high air void content and small air void size. This can be achieved by using porous or hollow lightweight aggregates in the mixture. Designing for tensile ductility requires tailoring the micromechanical parameter of the mixture, including keeping the matrix toughness low and tailoring the interfacial bond property between fiber and matrix. This often requires using small-sized smooth-shaped aggregates that have less resistance to crack propagation, and carefully selecting the fiber type, geometry and content. Designing for the sprayability involves controlling the rheology of the mixture. This is often achieved by controlling the water content, chemical admixtures, aggregate absorption and geometry, using non-abrasive aggregates, and properly selecting the fiber content and geometry. To simultaneously attain the desired properties of SFR-ECC, the design process for one target needs to be conducted in parallel to the design process for other target performance, recognizing all the interdependencies and potential conflicts.

Following the parallel design methodology, super fine grade vermiculite was chosen as the main lightweight aggregates in the SFR-ECC based on several considerations. Vermiculite is one of the most commonly used lightweight aggregates in conventional SFRM due to its low density (64-160 kg/m^3), high water absorption (200%-325% by weight and 20%-50% by volume), low thermal conductivity (0.05-0.071 Wm^{-1}K^{-1}), high thermal stability, abundance in nature and low cost. In addition, SFRM use vermiculite to facilitate the application (typically low pressure spray) due to its water holding and non-abrasive nature. Despite all the advantages of vermiculite, it has never been used as a constituent in ECC material before. Vermiculites are generally accordion-shaped granule. According to the micromechanics underlying ECC design, such irregular-shaped aggregates generally increase the matrix toughness, which is undesirable for achieving strain-hardening behavior. Therefore, in the design of SFR-ECC, super fine grade vermiculite of particle size less than 1.5 mm was used in conjunction with a small volume fraction of 3M K25 glass microspheres (economical alternative to S38 glass microspheres that were used in previous FR-ECC) to counter balance the potential increase of matrix toughness.

Acrylic latex bonding agent was also used in the SFR-ECC mixture aiming at better adhesive property to steel. Recent work demonstrated that adding latex bonding agent in the previous FR-ECC mixture significantly improves the adhesive energy between FR-ECC and steel. In addition, adding latex into the mixture is expected to increase the viscosity of the fresh mix, which is favorable for dispersing the fibers uniformly. It is worth noting that acrylic latex could also increase the matrix toughness and fiber/matrix interfacial bond, which could influence the mechanical property of the hardened material.

Low content of High Tenacity Polypropylene (HTPP) fibers were used in SFR-ECC mixtures. HTPP fibers are more than 50% cheaper than PVA fibers that are typically used in ECC material including the previous FR-ECC. HTPP fibers have lower strength and lower bond to the matrix. However, since SFR-ECC is a nonstructural material and has relatively low strength requirement, the use of HTPP fibers could be justified. The fiber content was kept under 2% by volume fraction to avoid difficulty in pumping and spraying process.

Three mixtures were designed as listed in Table 1. All mixtures are composed of 1.5% (by volume fraction) HTPP fiber.

Table 1. Mix details of SFR-ECC.

Mix ID	Cement	Water	Acrylic Latex Bonding Agent	Vermiculite	Glass Microspheres
1	1	1.08	0.12	0.3	0.125
2	1	1.08	0.12	0.3	0.2
3	1	1.14	0.06	0.3	0.2

3 CHARACTERIZATION OF DURABILITY PROPERTIES

The major durability characteristics of SFR-ECC include cohesion and adhesion. Both properties are critical in keeping SFRM in place on the steel under multiple loading conditions.

The tensile strength and ductility of SFR-ECC were characterized using direct uniaxial tension test recommended by JSCE [9]. The tensile stress strain curves for SFR-ECC Mix 1-3 are plotted in Figure 1. Among all three mixes, Mix 2 exhibits the highest tensile ductility, with tensile strength of 1.1 MPa and an average strain capacity of 3.0%. Mix 3 also shows robust tensile strain hardening behavior, however, with less strain capacity. The decrease in ductility from Mix 2 to Mix 3 is associated with the decrease in the margin between ultimate tensile strength and first crack strength. Micromechanics design theory indicates that a sufficient margin between the ultimate tensile strength and first crack strength is required for robust multiple cracking. The lower acrylic latex dosage in Mix 3 leads to lower first crack strength and lower ultimate tensile strength, however, lower margin between them that is undesirable. Mix 1 behaves similarly to conventional fiber reinforced cementitious composites with localized crack and strain softening behavior. Comparing Mix 1 and Mix 2, the higher glass microsphere content in Mix 2 effectively lowers the matrix toughness that governs the first crack strength and leads to robust strain-hardening behavior. Considering the tensile performance, Mix 2 is the most promising candidate for SFR-ECC and is thus studied for other durability and functionality characteristics. The dry-density of Mix 2 is 550 kg/m^3 at 28 day, which falls into the medium density SFRM range. The compressive strength at 28 day is measured to be 3.5 ± 0.2 MPa. The strength and ductility values are one or two orders of magnitude larger than conventional SFRM of the same density range.

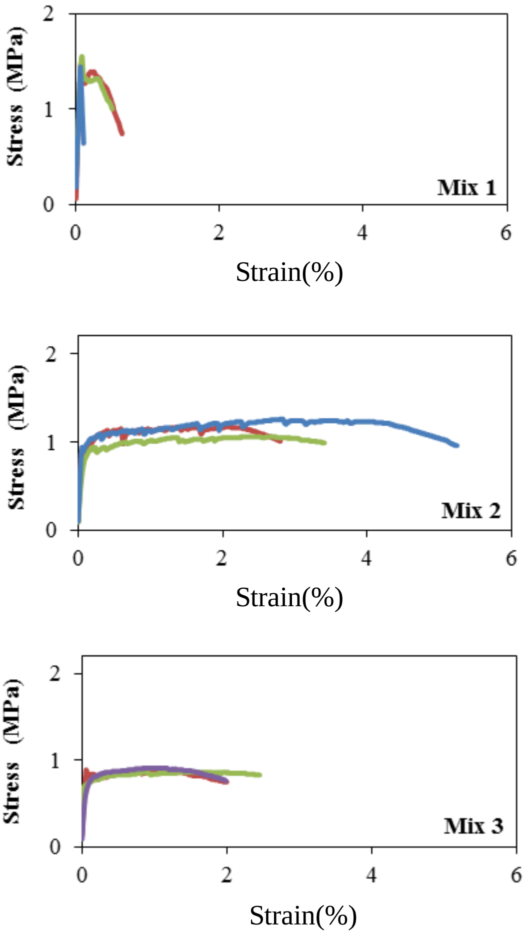

Figure 1. Ductile behavior of SFR-ECC under tension can be attained with appropriate mix design.

The adhesion property of SFR-ECC was characterized using a recently developed fracture energy based test method [10]. A medium density Portland cement based conventional SFRM was used as control in this study. During the experiment, structural steel strips of approximately 13 mm wide, 1.3 mm thick and 250 mm long that were bonded to the SFR-ECC/SFRM were peeled off by lifting one end. The load and corresponding interfacial crack length were recorded. Fracture resistance R-curves were then constructed. The adhesion is characterized by the steady-state critical energy release rate of the interfacial fracture, which is the plateau value of the R-curve.

The measured adhesion fracture energy of SFR-ECC (to structural steel) at 28 day is 104.3 ± 15.4 J/m^2, about an order of magnitude higher than that of conventional medium density SFRM used as control specimen in this study (11.1 ± 1.4 J/m^2). For both SFR-ECC and control SFRM, fracture occurs within the cementitious material adjacent to the interface. For SFR-ECC, the HTPP fibers actually bridge across the interfacial crack (as shown in Figure 2) and SFR-ECC/steel interface exhibits a ductile fracture behavior with a rising R-curve. While SFRM/steel interface exhibits a typical brittle fracture behavior. For SFR-ECC, due to the large process zone and dimension limit of the specimen, the true steady-state critical energy release rate (plateau value of R-curve) were not reached; the adhesion energy was calculated as an average value measured between 150-200 mm crack length instead of the true plateau value for conservative and realistic considerations. The significantly higher adhesion of SFR-ECC compared to conventional SFRM helps to resist delamination of fire insulation under various loading conditions.

The enhanced cohesion and adhesion properties are expected to dramatically improve the durability of SFR-ECC fire protection over conventional SFRM.

Figure 2. Fibers bridge across the delamination crack between steel and SFR-ECC.

4 CHARACTERIZATION OF FUNCTIONALITY PROPERTIES

As spray-applied fire-resistive material, apart from durability requirements, the thermal insulation property and sprayability represent important characteristics to ensure proper functionality of SFR-ECC.

To assess the thermal insulation property of SFR-ECC, the apparent thermal conductivity of SFR-ECC was measured in accordance with ASTM E2584 [11]. A square steel plate of 152 mm × 152 mm × 13 mm was covered by the SFR-ECC specimen (152 mm × 152 mm × 25 mm) on one side and insulation material of super low thermal conductivity on all other sides (to prevent heat transfer in all other directions) and then the assembled specimen was placed in a box furnace and heated up at 5 ℃/min. During the test, the temperature in the steel plate and on the outer surface of the specimen was monitored and recorded. Then the apparent thermal conductivity of SFR-ECC was calculated based on a classic one-dimensional heat transfer model. The fire resistance of SFRM / steel system mainly comes from the very low thermal conductivity of SFRM. Therefore, instead of running large scale fire resistance test, comparing the measured apparent thermal conductivity of SFR-ECC and conventional SFRM could be an alternative way of assessing the fire resistance of SFR-ECC / steel system. The same medium-density conventional SFRM was used for thermal property comparison.

The measured apparent thermal conductivity is shown in Figure 3. The thermal conductivity of SFR-ECC is comparable to the conventional SFRM over the investigated temperature range. The dip in the curve indicates that endothermic reactions occur, such as evaporation of moisture, and delay the temperature rise. This is represented as very low apparent thermal conductivity over the corresponding temperature range. In this small-scale test that simulates large-scale fire resistance test, the time for the steel slug to reach critical point (537 ℃) from room temperature (23 ℃) is 180-182 min for SFR-ECC and 178-181 min for control specimen. This also indicates that SFR-ECC and control SFRM possess similar effectiveness in delaying temperature rise.

Sprayability is another important functionality associated with the construction stage. Sufficient build-up thickness is critical for the construction phase of SFR-ECC. Direct spray test was conducted to evaluate the sprayability of SFR-ECC. SFR-ECC were mixed according to a typical ECC mixing procedure as detailed in the reference [12], and then the fresh mixture were transferred to a peristaltic pump before pumped and sprayed horizontally onto the structural steel panel placed vertically on the ground. The maximum built-up thickness were measured when the fresh mix were about to fall off the steel panel. The direct spray test shows that built-up thickness of 10-15 mm can be achieved in first spray application. And in a consecutive spray application after the first layer has been dried, another 30 mm can be further built up. The final build-up thickness after two sprays adds up to 40-45 mm as shown in Figure 4. Typical thickness of SFRM used for steel structures is 10-50 mm often achieved by multiple sprays. The built up thicknesses of SFR-ECC are therefore acceptable for field application.

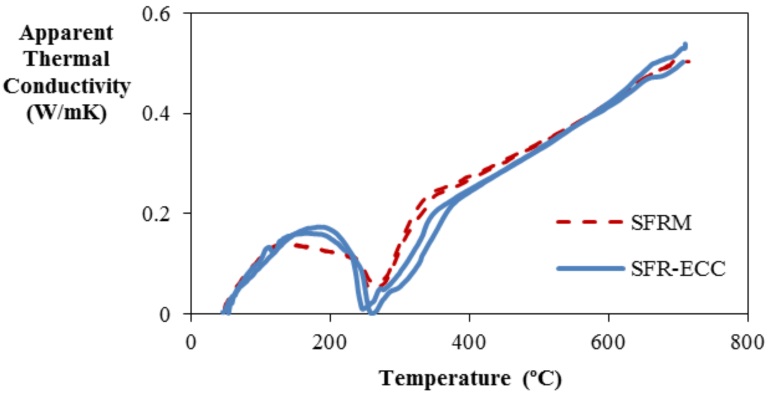

Figure 3. Comparable apparent thermal conductivity of SFR-ECC to SFRM.

(a) (b)

Figure 4. SFR-ECC can build up to 40-45mm in 2 sprays (a) front view, and (b) side view.

5 CONCLUSIONS

Based on above findings, the following conclusions are drawn:

(1) Ductile SFR-ECC with tensile strength of 1.1 MPa, strain capacity of 3.0% and interfacial adhesive energy (with steel) of 104.3J/m^2, which are 1~2 orders of magnitude higher than those of SFRM, has been developed and characterized.

(2) SFR-ECC has apparent thermal conductivity and sprayability comparable to conventional SFRM, which ensures proper functionality of SFR-ECC as fireproofing material.

SFR-ECC with enhanced durability properties and proper functionality is promising as a durable alternative to the current SFRM and contributes to enhanced fire safety of steel structures.

REFERENCES

[1] Braxtan, N. L. and Pessiki, S. P., "Postearthquake fire performance of sprayed fire-resistive material on steel moment frames", *Journal of Structural Engineering*, 137(9), 946-953, 2011.

[2] Carino, N. J., Starnes, M. A., Gross, J. L., Yang, J. C., Kukuck, S., Prasad, K. R., and Bukowski, R. W., *Federal building and fire safety investigation of the World Trade Center disaster: passive fire protection*, NIST NCSTAR, 2005.

[3] Ryder, N. L., Wolin, S. D., and Milke, J. A., "An investigation of the reduction in fire resistance of steel columns caused by loss of spray-applied fire protection," *Journal of Fire Protection Engineering*, 12(1), 31-44, 2002.

[4] Keller, W. J. and Pessiki, S., "Effect of earthquake-induced damage to spray-applied fire-resistive insulation on the response of steel moment-frame beam-column connections during fire exposure," *Journal of Fire Protection Engineering*, 22(4), 271-299, 2012.

[5] Li, V. C. and Leung, C. K., "Steady-state and multiple cracking of short random fiber composites," *Journal of Engineering Mechanics*, 118(11), 2246-2264, 1992.

[6] Li, V. C., Wang, S., and Wu, C., "Tensile strain-hardening behavior of polyvinyl alcohol engineered cementitious composite (PVA-ECC)," *ACI Materials Journal*, 98(6), 483-492, 2001.

[7] Zhang, Q., Ranade, R. and Li, V.C., "Feasibility Study on Fire-Resistive Engineered Cementitious Composites," *ACI Material Journal*, in print, 2013.

[8] Zhang, Q. and Li, V.C., "Adhesive Bonding of Fire-Resistant Engineered Cementitious Composites (ECC) to Steel," *J. Construction and Building Materials*, submitted, 2014.

[9] JSCE, *Recommendations for Design and Construction of High. Performance Fiber Reinforced Cement Composites with Multiple Fine Cracks (HPFRCC)*, 2008.

[10] Tan, K. T., White, C. C., & Hunston, D. L., "An adhesion test method for spray-applied fire-resistive materials," *Fire and Materials*, *35*(4), 245-259, 2011.

[11] ASTM E2584, "Standard Practice for Thermal Conductivity of Materials Using a Thermal Capacitance (Slug) Calorimeter", *ASTM International*, West Conshohocken, PA, 2010, DOI: 10.1520/E2584-10, www.astm.org.

[12] Felekoğlu, B., Tosun-Felekoğlu, K., Ranade, R., Zhang, Q. and Li, V.C., “Influence of Matrix Viscosity, Fiber Mixing Procedure, and Curing Conditions on the Mechanical Performance of HTPP-ECC,” *Composites Part B: Engineering*, *60,* 359-370, 2014.

HIGH TEMPERATURE PERFORMANCE OF SUSTAINABLE CONCRETE WITH RECYCLED CONCRETE AGGREGATES

John Gales*, Thomas Parker, Mark F. Green***, Duncan Cree*** and Luke Bisby****

*Carleton University
e-mail: john.gales@carleton.ca

**University of Edinburgh
e-mails: T.Parker@sms.ed.ac.uk and luke.bisby@ed.ac.uk

***Queen's University
e-mails: greenm@queensu.ca and creed@queensu.ca

Keywords: Sustainable concrete, Recycled concrete aggregate, High temperature material testing, Digital image correlation, Scanning electronic microscopy, Fire

Abstract. *The substitution of conventional aggregates in concrete with recycled concrete aggregates (RCA) can act to lower environmental impact. Applications of concrete with RCA are limited because of a lack of research providing clear design guidance. Specifically, the performance in fire must be considered. To address this need, three different concrete mixes were assessed for performance at high temperature with the only variable being the proportion of coarse aggregate substituted with RCA. For each mix, ambient and high temperature compression tests were performed using novel digital image correlation measurement. Small-scale concrete slabs were heated to evaluate thermal and deformation behaviours of these mixes. Results indicated that strength reductions at high temperature were more pronounced with increasing RCA content. However, even with 100% RCA content, the strength reductions at high temperature were within the range suggested by Eurocode provisions.*

1 INTRODUCTION

The impact of human activity on the natural environment is more important today than it has ever been. The reliance on conventional structural concrete to satisfy society's infrastructure needs is producing considerable greenhouse gas emissions, depleting quarries, and consuming large amounts of energy. Thus, sustainable measures of construction with low environmental impact are urgently needed. One sustainable construction measure gaining interest is substituting conventional coarse aggregate with recycled concrete aggregates (RCA) in concrete. RCA can come from concrete demolition waste that is crushed and graded. Incorporating RCA into structural concrete has been limited by the lack of sufficient research and clear guidelines on use, especially in regard to the fire performance of this material. To date, only the post-heated behaviour has been considered by researchers [1]. The more critical aspect of behaviour at high temperature has been neglected. To protect the public, all structural materials must demonstrate reliability, integrity, and resistance in fire before use in design. With the global importance of climate change, research into the fire performance of such sustainable materials is more essential than ever. Therefore concrete with RCA merits consideration in fire and elevated temperatures before its implementation as a suitable construction material. Prior to performing expensive full-scale standard fire tests or recommending new design guidance, it is first necessary to understand the effect that substituting coarse aggregate with RCA will have on the high temperature performance of concrete. The effect of this substitution is the central theme discussed herein.

2 METHODOLGY

To investigate the effect of adding coarse RCA to concrete at high temperature, three different concrete batches were cast during May 2013 at the University of Edinburgh for comparison. Each concrete batch used the same mix design amounts: ordinary Portland cement content; water; fine aggregate; and 10 mm max graded coarse aggregate (limestone by default). The only difference between each batch was the mass proportion of a coarse aggregate substituted with coarse RCA (at 0, 30 and 100%). The coarse RCA was sourced and graded from a decommissioned flooring system with known and therefore controlled structural properties (Grade 40/50). The coarse RCA was sourced from undamaged locations of these flooring systems. This was exactly the same flooring system as reported by Gales et al. [2,3]. The testing programme described in this paper considers four cubes (100 mm×100 mm×100 mm) and two unreinforced small-scale concrete slabs (500 mm×200 mm×50 mm) for each concrete mix. The limited number of specimens was controlled by the volume of the onsite concrete mixer.

The cubes were tested in compression under ambient and high temperature at Queen’s University, Canada to comparatively characterize mechanical properties of the respective concrete mixes. The cubes were not cast with thermocouples because this would have complicated international shipping.

The small-scale slabs were tested in a steel restraining frame with high radiant heat at the University of Edinburgh to assess thermal properties and deformation behaviour of each concrete mix. All slabs were cast with two K-type thermocouples to measure exposed soffit temperatures (placed to a precision of ±2 mm). The thermocouples were placed at the centre-most location of the soffit.

All testing occurred at a minimum of six months after casting. Selected concrete mix details are tabulated in Table 1. Testing procedures are detailed below.

Table 1. Concrete mix properties.

% of coarse RCA	Slump mix (mm)	Moisture content by mass at slab testing (%)	Density (kg/m^3)
0	50	1.4	2120 (+/-70)
30	55	1.9	2160 (+/-30)
100	65	2.4	2140 (+/-40)

2.1 Compression tests

The concrete cubes were tested in compression using an Instron 600LX servo-hydraulic materials testing frame equipped with a furnace and a viewing window. The furnace was capable of heating samples safely up to a temperature of 585 °C. Therefore, all cubes had to be tested below this temperature. Two specific soak temperatures were considered for comparison; ambient and the 500 °C isotherm temperature [4]. Because concrete is known to be variable, at least two samples were considered at each temperature. Repeatability and testing at two temperatures was considered by the authors to be of more importance than testing one cube at four different temperatures.

The concrete cubes were heated without any applied stress at a furnace control rate of 2 °C/min to the target temperature and held for two hours. During the soak time, considerable thermal expansion of the concrete was observed within the first 15 minutes but then reduced considerably suggesting that the concrete was approaching uniform temperature. After two hours of soaking, the change in extension was negligible with time. After soaking at the target temperature for two hours, the specimens were loaded to failure. All compressive tests (ambient and high temperature) were loaded using stroke control at approximately 0.5 mm/min. Under ambient temperature this loading rate is expected to induce a minimum loading rate in compliance with North American testing standards. The choice of stroke control allowed the authors to stop the tests after peak stress in a safe and controlled manner. Had load rate control been used there was a substantial risk of damaging the furnace's viewing window at specimen failure. The strain was calculated using a novel and non-contact Digital Image Correlation (DIC) technique (detailed below) to allow the approximate relative stiffness loss (by calculating the 40% f'_c secant modulus). Other measurable variables such as thermal expansion and transverse strain (the Poisson effect) are beyond the scope of this current paper. For every test, the ultimate strength of the cube was also recorded for direct comparison.

The accurate derivation of high temperature material properties is challenging using conventional instrumentation (due concrete's brittle failure) and therefore as described above, a non contact DIC technique was employed. DIC is capable of measuring deformation by comparing a sequence of high resolution digital photographs using an image processing (pixel tracking) algorithm. At high temperature, DIC has been shown to accurately describe the deformation behaviour of various structural materials and assemblies ([5, 6]). For this study, DIC was performed using a digital single lens reflex (SLR) Canon EOS 5D mark III camera acquiring images at a predefined rate of 1 Hz. The GeoPIV8 image processing algorithm [7] was used to translate pixel movement into deformation measurement. Figure 1a illustrates the experimental set up and the default strain measurement location for each compressive test. Before using the DIC technique to describe the concrete compressive deformation in ambient and high temperature, a brief confirmation exercise was performed to confirm the technique's applicability. Unlike previous studies that have used DIC for high temperature deformation measurement (i.e. steel) concrete is brittle and has much lower strain at failure. In order for the DIC measurement procedure to be as accurate as possible, a virtual gauge length of 1500Px (75 mm) was used [5]. Figure 1a defines the location of the 'virtual' strain gauge for every test. The expected scatter in measurement with this gauge length would be less than 0.004% strain [5]. The confirmation exercise was a compressive test of a conventional concrete cube at ambient temperature. Measurement from a strain gauge was compared to the measured DIC strain. The maximum deviation between these values was less than 0.05% strain. The strain gauge stopped functioning just prior to failure below 1% strain. The dilation of the concrete towards the camera was assumed to be negligible since the digital image correlation measurement matched satisfactorily to the strain gauge reading. A second confirmation exercise, was performed at both ambient and high temperature by comparing the difference between the theoretical extension rate of the cross head (0.5 mm/min) and the DIC as measured extension rate. The differences in loading rate measured by DIC was found to be at maximum 4% different than the theoretical extension rate of the cross head.

Without thermocouples in the concrete cubes, some uncertainty exists regarding the uniformity of the temperature of the specimens during heating. However, in separate testing by one of this paper's co-authors, using the same experimental set up but using slightly larger concrete specimens with K-type thermocouples installed at the centremost portions of the specimen, it was found that a soak time of two hours was satisfactory to ensure uniform specimen heating at a furnace control near 500 ℃ [8].

2.2 Small-scale slab tests

The small-scale concrete slabs were tested at high temperature in a custom frame and radiant heater assembly without mechanically applied stress. Heating was via four propane fuelled radiant heaters (each of dimensions 200 mm × 143 mm) placed in a 2 × 2 grid. The heaters, as supplied from *FiberTech Company*, would induce higher temperature exposure than was possible in the compression tests. During testing, both temperature and (when possible) deflection were recorded. Figure 1(b) illustrates the experimental configuration for the tests reported herein. Every slab test used a calibrated and constant incident radiant heat flux for one hour. For every concrete mix, at least two slabs were tested for repeatability. Details on the construction, calibration, and control of this heating system and restraining frame are provided by Elliot et al. [9].

Two tests for each concrete mix were conducted with the bespoke loading frame and radiant heaters. Exposed soffit temperatures were calculated based on the average of the two K-type thermocouples. The maximum deviation between thermocouples was within the manufacturer's allowable error (+/- 0.0075*T*, where *T* was the maximum recorded temperature). The unexposed surface of concrete was measured with one attached K-type thermocouple in an assembled pad. This assembled pad was constructed out of 100 mm^2 aluminium tape placed directly on to the concrete surface, a 100 mm^2 ceramic fibre insulating ceramic wool that encompassed the thermocouple, and a covering of 120 mm^2 aluminium tape to adhere to both the concrete surface and the insulating ceramic wool.

Deflection near the centremost point of the unexposed surface was measured using linear potentiometers (LP). In many cases, this measurement was aborted because of a risk of damaging the instrument from the elevated temperature.

The thermal exposure of constant incident radiant heat flux was chosen because: (1) for these slab dimensions it represented an exposure capable of inducing temperatures through the concrete surface similar to what would be observed in a ASTM E119 standard fire for a target time of one hour [10]; (2) future numerical modelling efforts could be simplified with such a straightforward input thermal boundary; and (3) each test would yield a simple yet comparable thermal gradient that would allow the absorbed heat to be rationally compared.

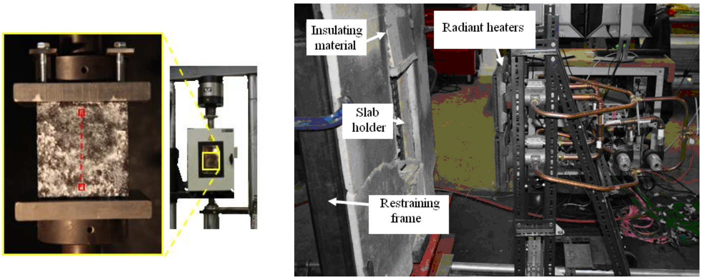

(a) (b)

Figure 1. (a) Compression test experimental set up using DIC with virtual strain patch shown in red; (b) Radiant heaters and loading frame.

3 COMPRESSION TEST RESULTS

At ambient temperature, compressive tests showed a strength increase with increase in proportion of RCA coarse aggregate (Figure 2(a)). This behaviour may have been influenced by the raw RCA coarse aggregate strength being 20% greater than that of the concrete in the new mix design. These tests showed considerable variability between measured ultimate strain and elastic secant modulus (Figure 2(b)). Less variability was observed in ultimate strength (less than 1.5 MPa).

At elevated temperature, compressive tests showed a strength decrease with increasing RCA content (Figure 2(a)). However, at the 500 ℃ critical isotherm, the 100% RCA was shown to meet the strength reduction guidance of the current Eurocode with less than 25% strength reduction [4]. The 100% RCA concrete mix had comparable strain at ultimate load as specified by the Eurocode guidelines (1.4% strain compared to 1.5% strain as reported by the Eurocode [4]). The high temperature specimens had a lower modulus of elasticity (Figure 2(b)) than their ambient counterparts. As the RCA content increased this behaviour was more pronounced. However, like their ambient counterparts, the high temperature tests showed variability between both measured ultimate strain, and elastic secant modulus. Little variability was observed in ultimate strength (less than 1.1 MPa).

The reduced performance of sustainable concrete in high temperature with RCA is hypothesised to be due to: (1) a weak interface between the old cement on the RCA and the new cement, (2) and/or micro-cracking in the RCA possibly induced during sourcing. These hypotheses are considered in greater detail in Section 5.

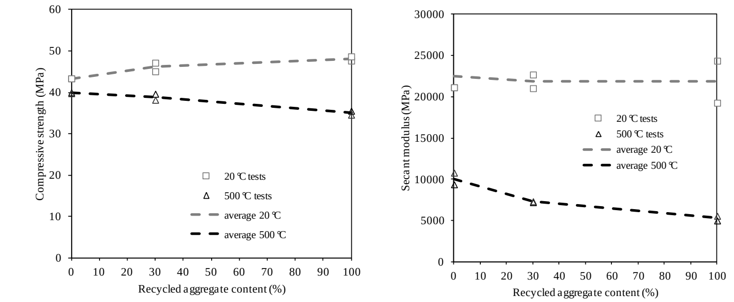

(a) (b)

Figure 2. (a) Compressive strength at ambient and high temperature; (b) Secant modulus at ambient and high temperature.

4 SMALL-SCALE SLAB TEST RESULTS

The measured temperatures of the two tests performed with 30% coarse RCA are illustrated in Figure 3(a). All test series for each concrete mix showed very similar exposed soffit temperature measurements indicating satisfactory repeatability in heating. The maximum deviation between tests of the same series was 30 ℃. Discrete thermal cracking was present in the 30% coarse RCA mix tests. These cracks ran longitudinally along the exposed surface at approximately 1 mm in width to outside the heating zone. An investigation into the tensile properties of RCA concrete may help explain these cracks. Discrete (10 mm in diameter) ‘pop-corn’ spalling was observed in each of the 0% and 30% mix coarse RCA mixes. The 100% RCA concrete slabs did not show any evidence of spalling. Figure 3(b) illustrates the measured thermal gradient (the difference taken directly between the exposed and unexposed surface temperature) for each test. As RCA content increases it can be seen that the thermal gradient becomes larger (and thus also the expected deformation due to slab bowing increases). These small differences in thermal gradient can be due to a multitude of factors such as RCA aggregate type, thermal conductivity (functions of specific heat, density and diffusivity), moisture content, porosity etc. However, the thermal gradient between all tests differed at most by 68 ℃ indicating that a direct substitution of coarse RCA with conventional coarse aggregate, as has been done herein, appears to have minimal impact on the thermal properties of the slab. Figure 3(b) also suggests that, at some point in all tests, the thermal gradient in each slab began to decrease. Throughout the duration of testing, the deflection increased continuously (reaching a maximum of less than 5 mm). This increase in deflection could have been be caused by either increased thermal stresses which cracked the slab, non uniformity in heating, errors in surface temperature measurement, or high temperature exposure to the LPs compromising the readings. Future modelling may help interpret these measurements.

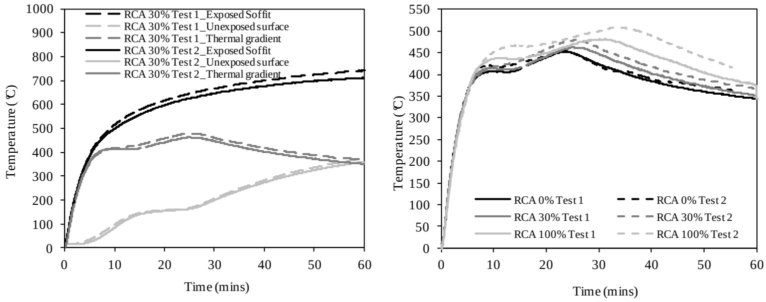

(a) (b)

Figure 3.(a) Thermal behaviour of 30% RCA concrete slab; (b) Temperature gradient in each slab test.

5 POST HEATING EVALUATION

Scanning electronic microscopy (SEM) imaging analysis was conducted on samples from virgin (un-cast) coarse RCA (10 mm), heated and unheated failed concrete cubes (20×20×20 mm) and samples from heated and unstressed small-scale slabs (20 mm×20 mm×20 mm). These samples were used to evaluate the micro-mechanical changes of the concrete containing coarse RCA with high temperatures in an effort to help explain the behaviour observed in Sections 3 and 4. Imaging was done using a MLA 650 FEG Environmental Scanning Electron Microscope (ESEM) housed within the Queen's University Facility for Isotope Research. Images for each sample were taken at regions of interest (aggregate interfaces, spalling, pores, and cracking) at varied resolutions.

Imaging of high temperature exposed failed cubes showed numerous micro-cracks at the interfaces between the old to new cement (see Figure 4(a) for an example) whereas imaging of samples that had been exposed only to ambient temperature showed no identifiable cracking at the same interfaces. Both samples showed dispersed cracking within the RCA. Virgin coarse RCA also showed dispersed micro-cracking (Figure 4(b)) throughout. Therefore, it was difficult to confirm whether the reduced RCA performance at high temperature was dependent on micro-cracking at the interfaces between the old and new cement during heating, or on micro-cracking within the coarse RCA before it was even cast.

Imaging of the 100% RCA concrete small-scale slab specimens showed identifiable micro-cracking at old to new cement interfaces (Figure 5(a)), but no identifiable cracking in the 0% RCA slab counterpart at the aggregate-cement interface. Imaging of 100% RCA samples indicated significant amounts of visible pores (see Figure 5(b)).

The ESEM was also used to perform an elemental chemical analysis to identify exposed aggregates found in the spalling region of the slabs. The aggregate was confirmed to be limestone for both the 0 and 30% RCA concrete slab samples.

The SEM observations support the hypothesis that the sustainable concrete mixes with RCA are weakest at the old to new cement region at high temperature and that porosity could be the contributing factor for thermal heating behaviour for the higher RCA mixes considered in this paper.

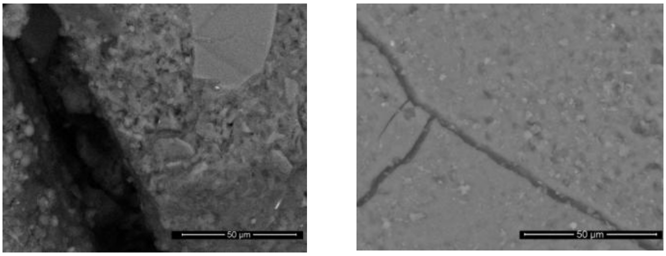

(a) (b)

Figure 4. (a) Old to new cement interface of 100% RCA tested cube after testing with applied stress; (b) micro-cracking in virgin RCA before casting (<3 µm crack).

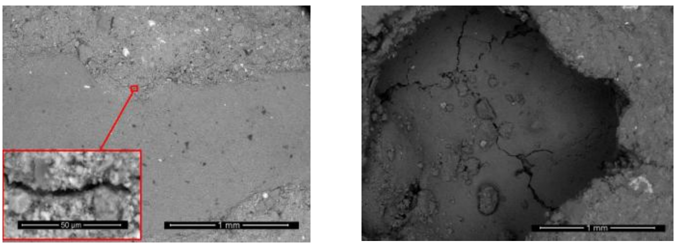

(a) (b)

Figure 5. (a) Old - new cement interface of 100% RCA tested slab after testing under no applied stress (< 4 µm crack); (b) Visible pore of 100% RCA tested slab after testing under no applied stress.

6 FUTURE WORK

The testing herein should not be interpreted as a recommendation for new design guidance. This paper only presents an investigation at ambient and high temperature into the effect of adding coarse RCA to concrete. Initial test observations indicate that, by using coarse RCA in sustainable concretes, a reduction in fire performance should be expected. However, limited testing also indicated that, even with a concrete mix of 100% coarse RCA, the resulting concrete may meet current Eurocode strength reduction design recommendations for performance at high temperature [4]. If sustainable concrete with coarse RCA is to be used as a suitable construction material, the following is a brief list of future research that should be considered to complement the work presented herein:

- **Improvements in testing equipment** – Concrete mechanical behaviour at high temperatures has a time and load dependency factor (creep and load induced thermal straining). The compression tests were controlled using one non-constant loading rate. A more systematic testing procedure capable of minimizing equipment damage will be essential for providing accurate material design recommendations.
- **Investigate effects of substituting commercially available coarse RCA in high temperature –** In reality when commercial RCA is prepared there is uncertainty regarding the quality of the aggregates (strength, impurities, damage from fabrication etc). To an extent, this uncertainty was eliminated in the specimens tested herein; however, this may not be so with commercially available coarse RCA. These uncertainties could have consequence for the high temperature performance of sustainable concretes. Therefore, the behaviour of commercially available coarse RCA in sustainable concretes should be evaluated. In the event that the commercially obtained coarse RCA mixes show poor fire performance, suitable investigation should be undertaken to explore various additives that may improve the performance of sustainable concrete.
- **More compressive testing –** Two compressive tests at each temperature are not representative to recommend new design guidance. Such a limited number of tests will not capture the variability that can be found in concrete. While testing was primarily done at 500 ℃, a temperature widely considered as a critical limiting isotherm [3], the behaviour of the concrete mixes may show increased complexity across the whole temperature spectrum. Additional tests in both quantity and other temperatures should be considered in the future.
- **Tensile testing needed –** No tests were conducted for tensile behaviour in high temperature, but unstressed coarse RCA small-scale slab tests showed significant cracking along their exposed soffits. The tensile behaviour of sustainable concretes containing coarse RCA should be studied at high temperatures.
- **Further analysis of digital image data –** Digital images from the compressive tests allow for additional investigation into the thermal expansion, thermal dilation, and transverse strain behaviour of sustainable concretes with RCA. These properties should be also investigated with the data already obtained.
- **Further slab testing –** Additional small-scale slab tests can be conducted under load to investigate the behaviour of these concrete mixes while concrete is submitted to stresses and high temperatures as would be seen in a fire. These tests should be conducted.
- **Full scale testing –** Once a suitable sustainable concrete mix can be defined, full-scale testing is required to demonstrate reliability, integrity and resistance in fire. This will facilitate applications of sustainable concrete mixes in design.

7 CONCLUSIONS

Despite the large strength reduction of the 100% coarse RCA mix at elevated temperatures, it was shown that the strength reduction guidance of the current Eurocode for the critical isotherm of 500 ℃ could be met by using controlled RCA sources in sustainable concretes. The small-scale slab tests suggested that the addition of adding coarse RCA to a concrete mix had negligible effects on the slab's thermal behaviour. Various future research needs are identified herein which would help improve the understanding of sustainable concrete mixes with coarse RCA and allow its use in structural design.

ACKNOWLEDGEMENTS

The authors acknowledge the financial support of the Natural Sciences and Engineering Research Council of Canada (NSERC) through their Discovery, Fellowship, and Collaborative Research and Training Experience (CREATE) programs, The Ove Arup Foundation, Ove Arup and Partners Limited, the Royal Academy of Engineering, and the Leverhulme Trust. Dr. A Take, C Maluk, JP Hidalgo-Medina, Z Triantafyllidis and A Dobosz are also acknowledged for their considerable technical assistance.

REFERENCES

[1] Cree, D., Green, M., and Noumowé, A. Residual strength of concrete containing recycled materials after exposure to fire: A review. Construction and Building Materials 45,208–223, 2013.

[2] Gales, J, and Bisby, L. "Deformation and Response of Continuous and Restrained Post-Tensioned Concrete Slabs at High Temperatures" *Proceedings of the Eighth Structures in Fire Conference*. Shanghai, China. 8 pp. 2014.

[3] Gales, J., Bisby, L., Stratford, T., and Krajcovic, M. "Tests of continuous post-tensioned concrete slabs under localised fires", *Interflam 2013: 13th International Conference and Exhibition on Fire Science and Engineering.* Royal Holloway College, Windsor, UK. 1131-1142, 2013.

[4] CEN. "Eurocode 2: Design of Concrete Structures, Parts 1-2: General rules- Structural fire design, EN 1992-1-2." European Committee for standardization, 2004.

[5] Gales, J., Bisby, L., and Stratford, T. "New Parameters to Describe High Temperature Deformation of Prestressing Steel Determined using Digital Image Correlation" *Structural Engineering International*. 22(4), 476-486, 2012.

[6] Spyrou, S. and Davison, J. "Displacement Measurement in Studies of Steel T-stub Connections." *Journal of Constructional Steel Research*. 57. 647-659. 2001.

[7] White, DJ., Take, WA., Bolton, MD. "Soil Deformation Measurement Using Particle Image Velocimetry (PIV) and Photogrammetry." *Geotechnique*, 53(7), 619-631, 2003.

[8] Cree, D., Pliya, B and Green M. "Behaviour of Stressed and Unstressed Concrete with and without Polypropylene Fibres at High Temperatures." *Proceedings of the Eighth Structures in Fire Conference*. Shanghai, China. 8 pp. 2014.

[9] Elliott A., Temple A., Maluk C. and Bisby, L. "Novel Testing to Study the Performance of Intumescent Coatings under Non-Standard Heating Regimes". *Proceedings of the eleventh IAFSS.* Christchurch, NZ, 14pp. 2014.

[10] ASTM. "Test Method E119-12: Standard Methods of Fire Test of Building Construction and Materials" Rep. No. E119-12, American Society for Testing and Materials, West Conshohocken, PA. 2012.

THERMAL PROPERTIES OF JUTE FIBER CONCRETE AT HIGH TEMPERATURES

Mitsuo Ozawa *, Choe G. Cheol, Kim G. Yong ***, Ryoichi Sato**** and**

Keitetsu Rokugo*****

* Gunma University and **Chung-nam National University
e-mail: ozawa@gunma-u.ac.jp, choegc@cnu.ac.kr

*** Chung-nam National University and ****Gifu University
e-mail: gyuyongkim@cnu.ac.kr, s3121013@edu.gifu-u.ac.jp

*****Gifu University
email: rk@gifu-u.ac.jp

Keywords: Jute fiber, PP fiber, Residual strength, High-performance concrete, Fire

Abstract. *In this study, the effects of high temperatures on the compressive strength and elastic modulus of HPC with pp and jute fiber (jute fiber addition ratio: 0.075 vol%; length: 12 mm; PP fiber addition ratio: 0.075 vol%; length: 12 mm) were experimentally investigated. The work was intended to clarify the influence of elevated temperatures ranging from 20 to 500 °C on the material mechanical properties of HPC at 80 MPa.*

1 INTRODUCTION

The behavior of high-performance concrete (HPC) at high temperatures is very complex, and also affects the global behavior of heated HPC-based structures. Concrete exposed to fire undergoes spalling owing to two phenomena. The first is restrained thermal dilation of water inside the material's pores, which generates biaxial compressive stress parallel to the heated surface. This leads to the development of tensile stress perpendicular to the heated surface and the second phenomenon – a build-up of pressure in pores caused by the vaporization of physically/chemically bound water in the cement, thereby applying tensile stress to the heated concrete microstructure (Figure 1) [1]. The second phenomenon has recently been investigated by comparing the vapor pressure of water inside concrete pores with the saturated vapor pressure (SVP) of water in specimens (Figure 2) [2]. Several studies have examined the synergistic effects of various fiber combinations on the behavior of HPC exposed to fire, with results showing that some combinations increased the material's fire-resistance properties [3, 4].

Researchers have also reported how various types of fiber affected the mechanical properties of cement-based materials at high temperatures. Adding synthetic fiber (especially the polypropylene (PP) type) to HPC is a widely used and effective method of preventing explosive spalling [5 – 9].

Although researchers have experimentally determined the permeability of heated PP-fiber-reinforced HPC [10], few studies have investigated how adding natural fiber such as jute to this type of concrete might prevent spalling.

Previous studies by the authors [11, 12] examined the spalling behavior of HPC reinforced with natural jute fiber (Figure 3). In this study, the effects of high temperatures on the compressive strength and elastic modulus of HPC containing pp and jute fiber (jute fiber addition ratio: 0.075 vol%; length: 12 mm; PP fiber addition ratio: 0.075 vol%; length: 12 mm) were experimentally investigated.

The work was intended to clarify the effects of elevated temperatures ranging from 20 to 500 ℃ on the material mechanical properties of HPC at 80 MPa.

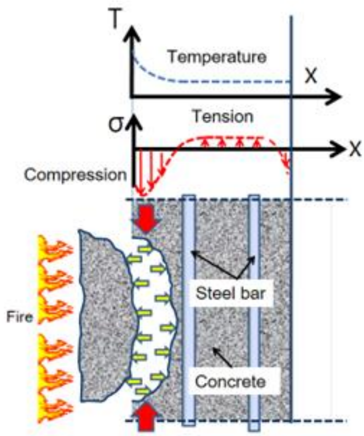

Figure 1. Thermal stress.

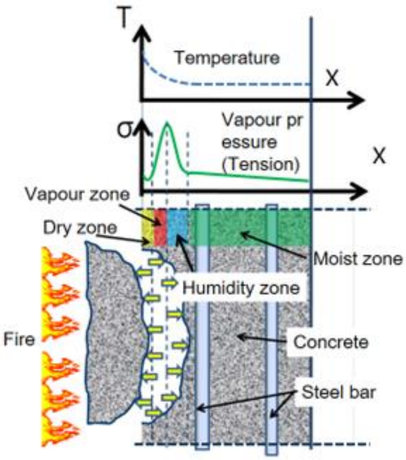

Figure 2. Vapor pressure.

2 EXPERIMENTAL WORK

2.1 Experimental program

The experimental program is summarized in Table 1. To investigate the effects of jute and pp fiber amounts and the residual mechanical properties (compressive strength, elastic modulus, thermal strain) of concrete exposed to high temperatures, the water-to-cement (*w*/*c*) ratio adopted was 0.30, and 0, 0.075% of jute and PP fiber by concrete volume were used.

Table 1. Experimental program.

W/*C*	Fiber	Fiber contents (vol %)	Heat	Test item
0.3	Jute	0	1℃/min	• Strength properties - Compressive strength (MPa) - Elastic modulus (GPa)
				• Residual strength properties
	Polypropylene	0.075		- Compressive strength (MPa) - Elastic modulus (GPa) • Thermal strain

2.2 Materials and mixture

Table 2 lists the compositions of the mixtures used to fabricate the control concrete specimen and the specimens containing jute and pp fiber. The water-to-cement ratio for all three mixtures was 0.3, and ordinary Portland cement (3.15 g/cm^3) was used in all cases. Table 3 details the properties of the constituent materials of the mixtures.

Crushed granite pieces with a maximum size of 20 mm were used as coarse aggregate for the three specimens. The main component of the super-plasticizer used was polymeric acid. After casting, the concrete specimens were left in the formwork for one day before being wet cured at 20 ±2 ℃ for 56 days and then heat-tested.

Table 3 lists the properties of the jute and PP fiber used in the study. The ratio of addition was 0.075% by volume, and the length of both fiber types was 12 mm. Figure 4 shows the jute, whose fiber had a straw-like structure as highlighted by scanning electron microscopy (SEM).

Table 2. Mixture proportion.

W/*C*	Unit weight(kg/m^3)			
	W	*C*	*S*	*G*
0.3	170	440	814	1048

Table 3. Materials.

Material		Physical properties
Cement		OPC (density : 3.15 g/cm^3,specific surface area : 3,200cm^2/g)
Fine aggregate		Sea sand (density : 2.65 g/cm^3, absorption : 1.00%)
Coarse aggregate		crushed granitic aggregate (size : 20mm, density : 2.7 g/cm^3, absorption : 0.9%)
Fiber	Poly propylene	Diameter : 12 μm, length : 12mm, density : 0.91g/cm^3, melting temp. : 165℃
	Jute	Diameter : 10-30 μm, length : 12mm, density : 1.3-1.45g/cm^3

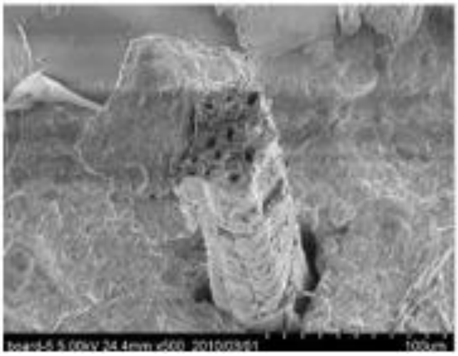

Figure 3 Jute fiber in concrete (SEM)

2.3 Test setup and temperature control [13]

To study the effects of transient high temperatures on the strength and deformation characteristics of high-strength concrete, test specimens at 80 MPa with and without fiber were subjected to temperatures of up to 500 ℃ and loaded to failure under axial compression. For each type of concrete, the specimens were tested under stressed conditions.

The tests were performed in a closed-loop servo-controlled 4,600-kN hydraulic testing machine equipped with an electric furnace as shown in Figure 5. Special cylindrical carbon-based alloy attachments were designed to transmit loading from the frame to the specimen under high-temperature conditions, and a continuous circulation water-cooling system was used to protect the instruments and avoid heating the testing frame. The specimens were encased in a stainless steel heat transmission jig to ensure heating throughout and prevent explosive failure as shown in Figure 6.

During the tests, specimen loading and displacement were measured. Loading was measured using the MTS system, and displacement was determined as the average of two pairs of LVDT values.

For each set of tests at a given temperature, three specimens from the same batch were also tested at room temperature. The target temperatures were varied from 100 to 500 ℃ at 100 ℃ increments. As shown in Figure 7, the rate of heating for all specimens was set at 1.0 ℃/min using a RILEM TC 129-MHT unit [14].

Figure 4. Loading and Heating machine.

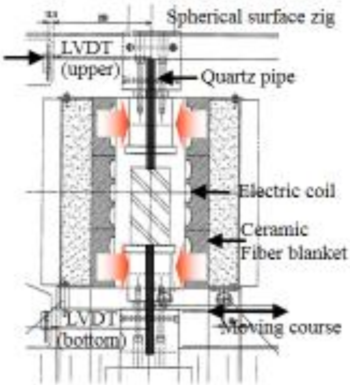

Figure 5. Measurement system.

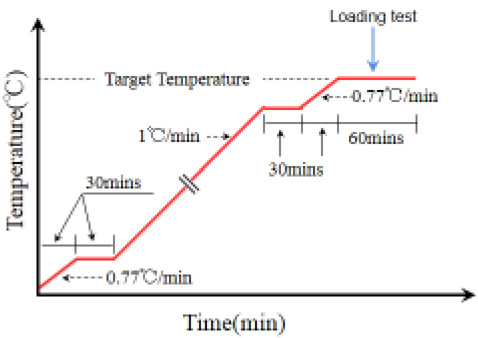

Figure 6. Heating curve.

3 RESULTS AND DISCUSSION

3.1 Stress-strain curves

Figures 7 to 9 shows stress-strain curves for plain, jute-fiber and PP-fiber concrete after exposure to high-temperature conditions. The initial contours of the curves rise almost linearly.

For temperatures of 300 ℃ or below, the curve shape essentially exhibits no change from that of unheated concrete. After exposure to 500 ℃, specimen heat damage increases gradually and the stress-strain curve flattens as the temperature rises.

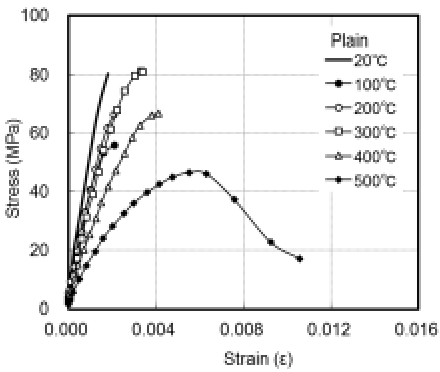

Figure 7. Stress-strain curve (Plain).

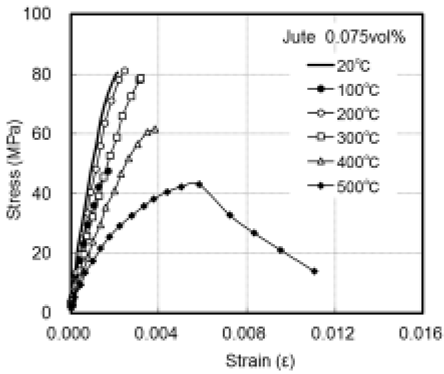

Figure 8. Stress-strain curve (Jute).

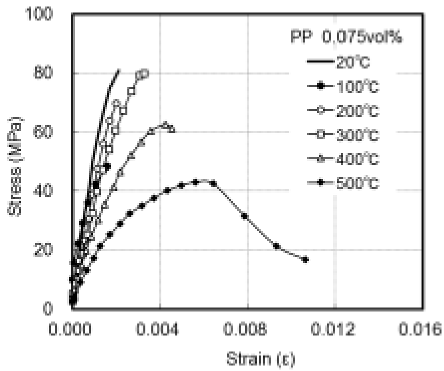

Figure 9. Stress-strain curve (PP).

3.2 Residual compressive strength

Figure 10 shows temperature-related variations in the compressive strength ratio for the three types of high-strength concrete. Each point in the figure represents the average maximum compressive strength of the specimens normalized with respect to the average maximum compressive strength at room temperature. Changes in the strength of the plain and PP-fiber concrete specimens appear to follow a common trend. Initially, as the temperature rose to 100 ℃, strength decreased in relation to that observed at room temperature. Strength at 100 ℃ was 60 to 70% of the room-temperature value. With further increases in temperature at 300 ℃, the specimens recovered strength to 100% of the room-temperature value. In the temperature range from 400 to 500 ℃, strength dropped sharply and bottomed out at 80 and 60% of initial strength at 400 and 500 ℃, respectively.

Changes in the strength of the jute-fiber concrete specimens also appear to follow a common trend. Initially, as the temperature increased to 100 ℃, strength decreased in relation to that observed at room temperature. Strength at 100 ℃ was about 60% of the room-temperature value. With further increases in temperature at 200 ℃, the specimens recovered strength to 100% of the room-temperature value.

3.3 Residual elastic modulus

Figure 11 shows the elastic modulus (defined as the ratio of the elastic modulus (taken as the tangent to the stress-strain curve at the origin) at a specified temperature to that at room temperature) as a function of temperature.

As the temperature increased to 100 ℃, the elastic modulus decreased in relation to that observed at room temperature. The elastic modulus at 100 ℃ was 70 − 90% of the room-temperature value. With further increases in temperature, the specimens recovered elastic modulus to 90% of the room-temperature values for jute-fiber and pp-fiber concrete.

Up to around 300 ℃, the elastic modulus of all three types of high-strength concrete decreased in a similar fashion, reaching about 60% of their respective initial values.

In the temperature range from 100 to 400 ℃, as dehydration progressed and the bonds between materials were gradually lost, the modulus of elasticity decreased to 20 − 35% of the value observed at room temperature [15].

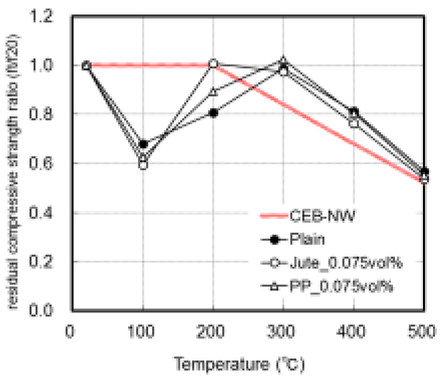

Figure 10. Residual compressive strength ratio.

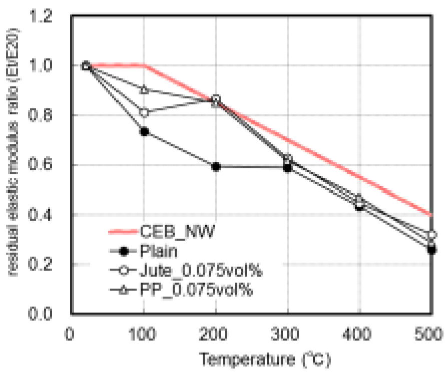

Figure 11. Residual elastic modulus ratio.

3.4 Thermal expansion strain

Figure 12 shows the relationship between thermal expansion strain and the temperature of plain, jute-fiber and pp-fiber concrete. Thermal expansion in all specimens increased between 20 and 500 ℃, and thermal expansion strain in all specimens was 0.006 at 500 ℃. This was considered mainly due to thermal expansion of the concrete’s constituent aggregates.

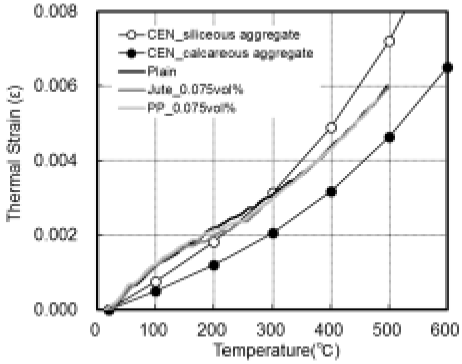

Figure 12. Thermal expansion strain.

4 CONCLUSIONS

The above results can be summarized as follows:

(1) HSC with jute fiber showed a compressive strength loss of about 40% at 100 ℃ before recovering to full strength between 200 and 300 ℃.

(2) The elastic modulus of high-strength concrete decreased by 10%− 40% between 100 and 300 ℃. At 500 ℃, the elastic modulus was only 30% of the room-temperature value.

(3) The thermal expansion strain of all specimens was 0.006 at 500 ℃.

REFERENCES

[1] Bazant ZP., "Analysis of pore pressure, thermal stress and fracture in rapidly heated concrete", *Proceedings of the International Workshop on Fire Performance of High-Strength Concrete*, NIST, Gaithersburg, Maryland,155-164,1997.

[2] Anderberg Y., "Spalling phenomena in HPC and OC" , *Proceedings of the International Workshop on Fire Performance of High-Strength Concrete*, NIST, Gaithersburg, Maryland, 69-73, 1997.

[3] Mugume RB., Horiguchi T., "Effect of fiber type and geometry on maximum pore pressures in fiber-reinforced high strength concrete at elevated temperatures", *Cem Concr Res*, 42,459-466, 2012.

[4] Lee G., Han D., Han MC., Han CG., Son HJ., "Combining polypropylene and nylon fibers to optimize fiber addition for spalling protection of high-strength concrete", *Const Build Mat*, 34, 313-320, 2012.

[5] Çavdar A., "A study on the effects of high temperature on mechanical properties of fiber reinforced cementitious composites", *Compos: Part B* ,43, 2452-2463, 2012.

[6] Pliya P., Beaucour AL., Noumowé A., "Contribution of cocktail of polypropylene and steel fibers in improving the behaviour of high strength concrete subjected to high temperature", *Const Build Mat* ,25, 1926-1934, 2011.

[7] Xiaoa J., Falknerb H., "On residual strength of high-performance concrete with and without polypropylene fibers at elevated temperatures", *Fire Saf J* . ,41,115-121,2006.

[8] Won P., Choi SW., Lee SW., Jang CII., Lee SJ., "Mix proportion and properties of fire-resistant wet-mixed high-strength polypropylene fiber-reinforced sprayed polymer cement composites", *Compos Struct*,92,2166-2172, 2010.

[9] Heo YS., Sanjayan JG., Han CG., Han MC., “Relationship between inter-aggregate spacing and the optimum fiber length for spalling protection of concrete in fire”, *Cem Concr Res*, 42, 549- 557, 2012.

[10] Noumowe AN., Siddique R., Debicki G., “Permeability of high-performance concrete subjected to elevated temperature (600 ℃)”, *Constr Build Mat*,23,1855 – 1861,2009.

[11] Ozawa M., Morimoto H., “High strength concrete reinforced jute fiber and water-soluble PVA fiber under high temperature”, *Structures in fire, Proceedings of the Sixth Int Conference,* Michigan State University, 864-871, 2010.

[12] Ozawa M., Iizuka T., Rokugo K., Morimoto H., “Relationship between spalling behavior and internal vapor pressure of high-strength concrete reinforced with natural fiber under high temperature”, *Proceedings of the First International Workshop on Concrete Spalling due to Fire Exposure*,140-149,2009.

[13] Kim YS., Lee TG., Kim GY., “An experimental study on the residual mechanical properties of fiber reinforced concrete with high temperature and load”, *Materials and Structures,* 46, 607-620, 2013.

[14] RILEM129-MHT., “Methods for mechanical properties of concrete at high temperatures (Part 3. Compressive strength for service and accident conditions)”, *Materials and Structures*, 410 – 414, 1995.

[15] Kim GY., Kim YS., Lee TG., “Mechanical properties of high-strength concrete subjected to high temperature by stressed test”, *Transactions of Nonferrous Metals Society of China*,19,1,128-133, 2009.

EXPERIMENTAL STUDY ON THE EXPLOSIVE SPALLING IN HIGH-PERFORMANCE CONCRETE: ROLE OF AGGREGATE AND FIBER TYPES

Francesco Lo Monte[*], Jihad M. Miah[**], Aktar Shamima, Riccardo Negri, Chiara Rossino[***] and Roberto Felicetti[*]

[*]Department of Civil and Environmental Engineering, Politecnico di Milano, Milan (Italy)
e-mails: francesco.lo@polimi.it, roberto.felicetti@polimi.it

[**]Université Paris Est, CSTB, Centre Scientifique et Technique du Bâtiment, Marne la Vallée (France)
e-mail: Jihad.MIAH@cstb.fr

[***]CTG Italcement Group, Bergamo (Italy)
e-mail: c.rossino@itcgr.net

Keywords: Aggregate, Concrete, Fiber, Pore pressure, Spalling, Tensile behavior

Abstract. *A complete description of the mechanical behavior of High-Performance Concrete in fire still requires further efforts to fully understand the tricky phenomenon of spalling. The complexity comes from the interaction among different phenomena, namely: the microstructural changes occurring in concrete at high temperature, the pressure rising in the pores, and the stress induced by both thermal gradients and external loads. To what extent these different aspects influence each other is still not completely clear. Within this context a comprehensive experimental campaign has been launched at the Politecnico di Milano, focusing on the role played by concrete grade, aggregate type, and fiber type and content. Eleven concrete mixes are investigated considering three grades ($f_c \geqslant 40$, 60 and 90 MPa), three aggregate types (silico-calcareous, basalt and calcareous aggregates) and different fiber types and contents (steel and monofilament or fibrillated polypropylene fibers).*

1 INTRODUCTION

Explosive spalling is the violent or non-violent breaking off of layers or pieces of concrete from the surface of R/C structural members when exposed to rapidly rising temperature, as experienced in fire. Low-porosity High-Performance Concrete is more prone to such phenomenon with respect to Normal-Strength Concrete due to the higher values of pore pressure developed during heating [1], as a consequence of material low permeability [2].

Concrete spalling is generally recognized to ensue from the interaction between thermal and load-related stresses (thermo-mechanical mechanism, figure 1(b)), and pore pressure rise due to water vaporization (thermo-hygral mechanism, Figure 1(c)), both aspects being influenced by heat-induced damage and microstructural changes in concrete.

An effective way to reduce concrete spalling sensitivity is to add polypropylene (pp) fiber. Even though the reason way pp fiber reduces spalling risk is not fully understood, it seems to be related to an increase of concrete permeability induced by three main processes: (a) fiber melting at 160 °C-170 °C, which leaves free channels for vapor release, (b) thermal dilation of melting fiber, that favors cement paste microcracking and the ensuing interconnection among the pores, and (c) further microcracking in the cement matrix due to stress intensification around the edges of the channels left free by the fibers (notch-effect, sizable mainly at $T \geqslant 250$ °C -300 °C [3,4]).

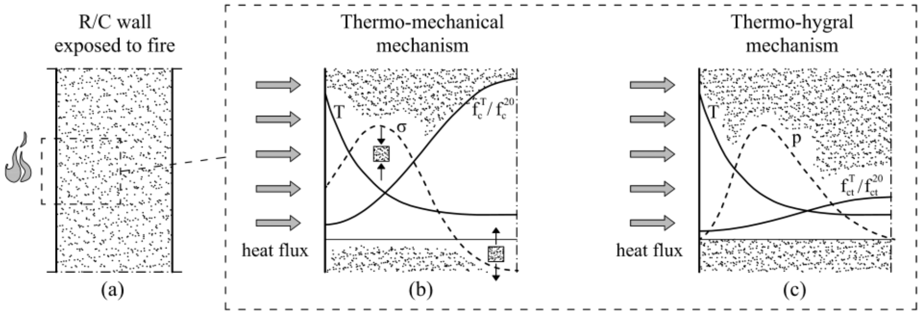

Figure 1. (a) Concrete spalling mechanisms in a heat-exposed wall; qualitative plots of: (b) temperature T, thermal stress σ and normalized compressive strength f_c^T/f_c^{20}; and (c) pore pressure p and normalized tensile strength f_{ct}^T/f_{ct}^{20}.

Even though some studies regarding pore-pressure mechanism have been carried out in the past, how pore pressure affects concrete tensile strength and how mix design influences the interaction between the former two quantities are still open issues. Within this context, a few experimental investigations have been conducted showing that the decay of the "apparent" indirect tensile strength due to pore pressure can be equal to – or even exceed – the value of the pressure itself [5-7]. Furthermore, the role played by the main constituents of the mix design (first of all aggregate and fiber) on the tensile strength versus pore pressure relation have to be tackled, with the aim of giving to designers and contractors useful tools to assess spalling sensitivity of a given concrete and to optimize the mix design [7].

To this end, a comprehensive experimental campaign has been recently launched at the Politecnico di Milano, involving eleven concrete mixes (see [7,8] for more details): three grades have been considered ($f_c \geqslant$ 40, 60 and 90 MPa, silico-calcareous aggregates); for the intermediate class, also calcareous and basalt aggregates were used, and in the case of silico-calcareous aggregates, both plain and fiber-reinforced mixes were cast (with steel and monofilament or fibrillated polypropylene fibers).

2 TEST PROCEDURE

In order to investigate concrete spalling sensitivity and the role played by aggregate and fiber types, compressive tests in residual conditions and splitting tests under different levels of sustained pore pressure have been performed on the eleven mixes.

Compressive behavior has been characterized at room temperature and after heating to 105, 250, 500 and 750 °C. Thermal cycles have been defined in order to induce in each specimen a uniform thermal field and to consider the heat-induced damage uniformly distributed; to this end, reference to the indications given in RILEM TC 129-MHT Committee (1995) was made. Hence, all specimens were slowly heated to the reference temperature (heating rate = 1 °C/minute), at which they rested for two hours to guarantee the uniformity of the thermal field. Afterwards, the specimens were slowly cooled down to 200 °C in controlled conditions (cooling rate = 0.25 °C/minute) and to 20 °C in natural conditions (inside the closed furnace). The thermal cycles are plotted in figure 2a.

For all mixes, fifteen cylinders were cast (∅ = 100 mm, h = 200 mm, figure 2b), so that three specimens were available for each mix and reference temperature. All tests in compression were displacement-controlled and the strain of the specimens was measured via 3 resistive gauges placed at 120° astride the mid-height section (DD1, base length 50 mm); moreover, 3 LVDTs measured the platen-to-platen distance to monitor the post-peak behavior (see figure 2b). In all tests in compression, stearic acid was smeared on the end sections of the specimens to reduce the platen-to-concrete friction.

An electro-mechanical press was used (Schenck, capacity = 1000 kN) and the displacement rate was defined complying the indications by EN 12390-3 (2009) in terms of initial stress rate. The stiffness (elastic modulus, E_c) was evaluated from the stress-strain curves in compression as secant modulus ($\sigma_c \leqslant 0.5\ f_c$).

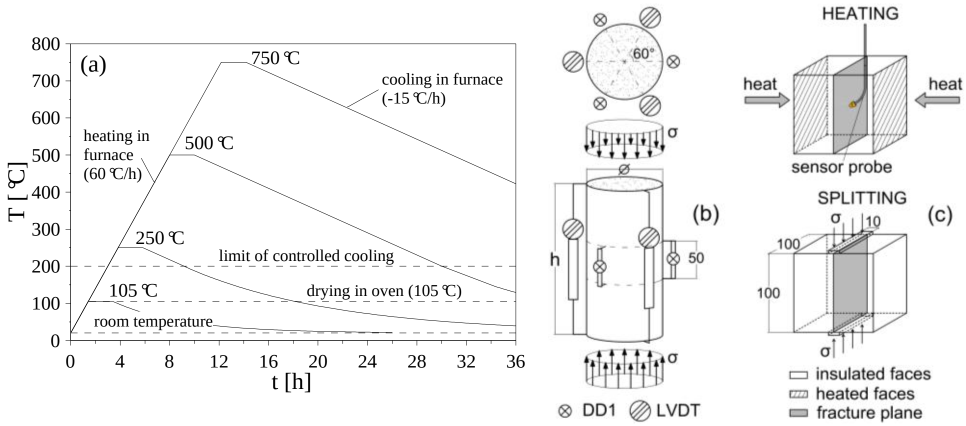

Figure 2. Test in compression: (a) adopted thermal cycles and (b) typical specimen (the top platen is connected to a self-blocking spherical head); (c) Scheme of the splitting test under sustained pore pressure.

Splitting tests under sustained pore pressure have been performed on cubic specimens (L = 100 mm) for all the mixes except steel fiber-reinforced concretes. Heating was applied on two opposite faces, while the other four faces were sealed and insulated in order to instate a transient unidimensional hygro-thermal flux (Figure 2(c)). Pore pressure and temperature were measured in the centroid of the specimens by means of customized probes and when peak pressure was reached, splitting test was performed by aligning the fracture and the symmetry planes, according to the procedure described in [5-7].

3 EXPERIMENTAL RESULTS AND DISCUSSION

3.1 Stress-strain curves in compression

The mean stress-strain curves in uniaxial compression are shown in Figure 3, comparing for each temperature the curves related to all mixes.

As expected, pp fiber does not influence significantly compressive strength in neither virgin nor residual conditions (the differences are mainly related to the scattering that characterizes a heterogeneous material such as concrete). On the contrary, the addition of pp fiber brings in a greater heat-sensitivity with respect to plain concrete in terms of stiffness, mainly after exposure to 250 and 500 ℃, where it seems clear that the higher the fiber content, the lower the stiffness. This can be ascribed to the microcracking favored by fiber melting and expansion (at 160-170 ℃), and by stress intensification at the edges of the channels left free by melt fiber (notch-effect, for $T \geqslant$ 250-300 ℃).

Steel fiber sizably affects compressive strength after heating to 500 ℃, leading to definitely higher values than in plain mix; this is due to the increased dilatancy of damaged concrete and to the effective confinement provided by steel fiber. On the contrary, there is no influence on concrete stiffness. (Note that increasing steel fiber content above 40 kg/m^3 gives no further beneficial effects).

Aggregate type proves to play a major role. In virgin conditions calcareous concrete exhibits a compressive strength comparable to that of silico-calcareous concrete, while the elastic modulus of the former is definitely higher (f_c^{20} = 68.7 and 63.7 MPa, E_c = 40.8 and 31.7 GPa, respectively). In residual conditions, however, calcareous aggregate brings in the highest thermal sensitivity in terms of compressive strength and elastic modulus, this being probably caused by a more pronounced microcracking induced by heating. Basalt concrete shows the highest compressive strength in virgin conditions (f_c^{20} = 78.8 MPa), but also the lowest elastic modulus (E_c = 26.2 GPa). Basalt concrete, however, proves clearly to be the least heat-sensitive in terms of both strength and elastic modulus. Hence, it is possible to state that moving from basalt to silico-calcareous and calcareous aggregates, concrete soundness at high temperature decreases due to increasing microcracking.

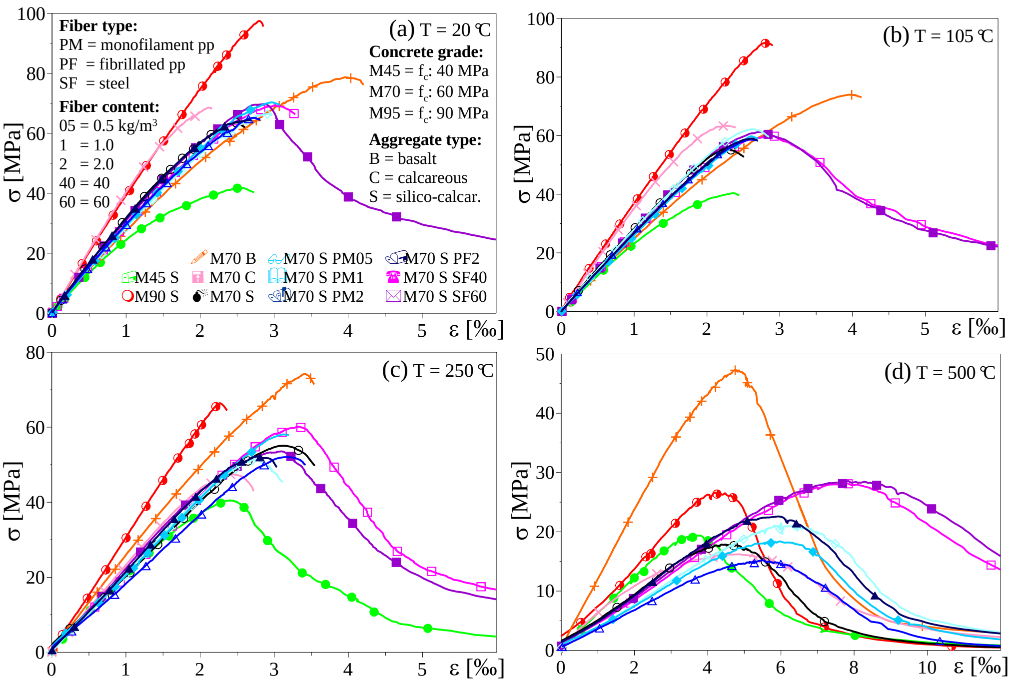

Figure 3. Mean stress-strain curves in uniaxial compression for all the mixes at different temperatures.

3.2 Splitting tests under sustained pore pressure

Splitting tests under sustained pore pressure on 100 mm-side cubes have been performed on all mixes, except steel fiber-reinforced concretes. In Figure 4 the pressure development in the centroid of the specimens is plotted as a function of the temperature together with the vapor saturation pressure curve P_{SV} (Clausius-Clapeyron equation). Generally speaking, the scattering among the tests is rather limited and is higher in fiber concretes due to the random dispersion of the fibers in the cement matrix. The experimental curves, however, are rather close to P_{SV} (as in [5]).

As concern the peak pressure reached by each concrete mix, Figure 5a shows that: (1) the higher the concrete grade, the higher the maximum pore pressure (compare M45 S and M70 S for HR = 2 ℃/min, and M70 S and M95 S for HR = 0.5 ℃/min), due to the decrease of porosity and permeability and the ensuing increase in compactness; (2) basalt and silico-calcareous concretes yield similar results, while calcareous concrete is characterized by a lower value; (3) adding increasing amount of monofilament pp fiber leads to a sizable decrease of pore pressure due to the increase of concrete permeability (and the subsequent decrease in compactness); (4) monofilament pp fiber is definitely more effective than fibrillated pp fiber in reducing the pressure (0.5 kg/m^3 of the former are more efficient than 2 kg/m^3 of the latter).

In Figures 5b-d the values of the apparent indirect tensile strength f_{ct} are plotted for all the tests against the pore pressure measured during the splitting test p_{sp}. For the nine mixes, a linear regression was performed in order to investigate the influence of pore pressure on concrete fracture behavior. In the insert of figure 6, the absolute values of slope k and intercepts f_{ct}^{th} (namely, the tensile strength of concrete at zero pressure) of the linear regressions are shown together with the maximum pore pressure p_{max} reached by each mix and the experimental tensile strength by splitting in virgin conditions f_{ct}^{20}.

Note that for the adopted heating rate (0.5 ℃/min), the thermal stress and the ensuing microcracking are negligible [6,7].

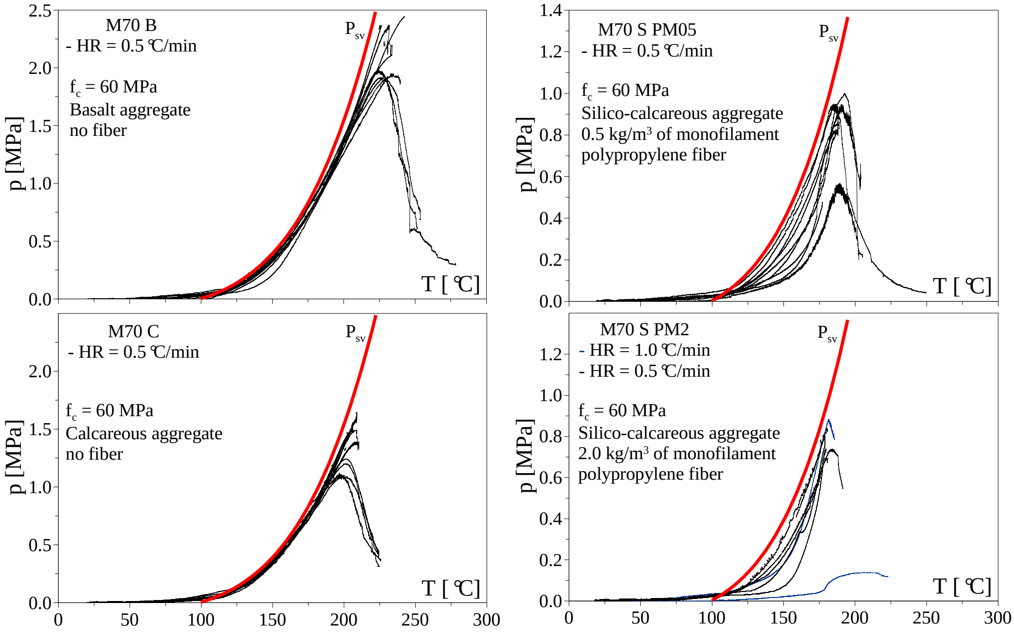

Figure 4. Pressure as a function of the temperature in the centroid of the specimen, together with the vapor saturation pressure curve P_{SV} (Clausius-Clapeyron equation), for two plain and two pp fiber concretes.

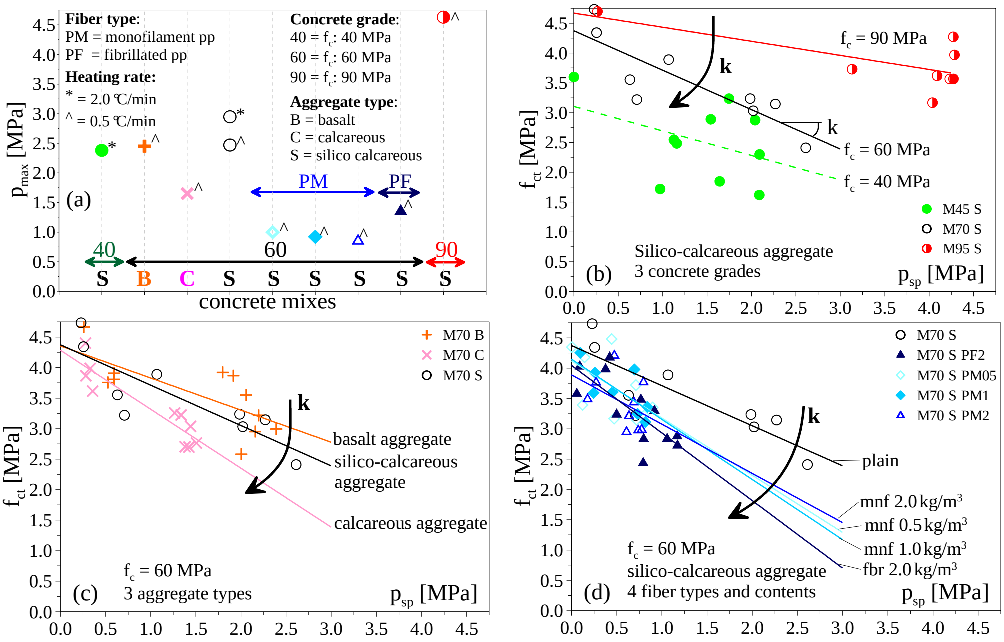

Figure 5. Plots of: maximum pore pressure p_{max} reached by each concrete mix (a); indirect tensile strength by splitting f_{ct} with respect to the pressure in the centroid of the specimen during the splitting test p_{sp} – three concrete grades (b); three aggregate types (c); and concrete with and without monofilament/fibrillated polypropylene fiber (d).

It is worth noting that both the maximum pore pressure p_{max} and the slope k (i.e. the magnitude of the tensile strength loss per unit value of pore pressure) are related to concrete microstructure (porosity, microcracks pattern and permeability); this is reasonable because both mass transport phenomena and fracture mechanics are influenced by concrete microstructure.

In all the cases, the values of k are definitely higher than the value of the porosity and in five cases approach the unit value (for calcareous and pp fiber concretes).

As regards concrete grade, no specific trends appear evident. However, neglecting the results regarding the lowest grade (f_c = 40 MPa), whose sizable scattering makes any comment hardly possible, a trend linking concrete grade and k looks possible: the higher the concrete grade (hence, the higher the compactness), the lower the influence of pore pressure on the tensile strength.

This can be explained by recalling Biot's coefficient for porous media and making an analogy with Soil Mechanics. In fact, for heavily-cemented sedimentary rocks, Biot's coefficient is close to the value of porosity, while for lightly-cemented sedimentary rocks is close to 1. This is also the case of low- and high-porosity concretes, respectively. This evidence is consistent, also, with the value of k for fiber concretes, where k is close to the unit value (fiber concretes are characterized by higher values of porosity compared to plain mix).

The same comment can be made regarding aggregate type: basalt concrete shows the lowest thermal sensitivity (hence, the highest compactness at high temperature) and the lowest value of k, while calcareous aggregate brings in the largest thermal sensitivity and the highest value of k. This suggests, once more, that the higher the compactness, the lower k.

In figure 6 the plots of the fitting curves for slope k and normalized maximum pore pressure p_{max}/f_{ct}^T are drawn together with the experimental data related to silico-calcareous concretes heated at the rate of 0.5 °C/min, as a function of concrete compactness C_c (= 1 - n_{75}, where n_{75} is the porosity related to the pores with radius greater than 75 nm, evaluated after exposure to 250 °C).

The critical pore radius of 75 nm has been chosen assuming that permeability and strength are influenced by large-radius pores rather than by total porosity, as reported in the works by Goto and Roy [9], and Mehta and Manmohan [10], where the values of the threshold pore radius affecting concrete water permeability were found to be 75 and 66 nm, respectively.

Figure 6 shows that, with a good approximation, increasing values of concrete compactness are associated with increasing values of the maximum pore pressure and decreasing values of the slope k.

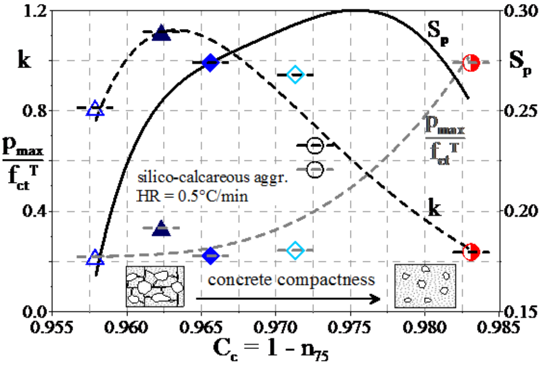

	Mix	k [-]	p_{max} [MPa]	f_{ct}^{th} [MPa]	f_{ct}^{20} [MPa]
	M45 S	0.411	2.38	3.10	3.98
	M70 B	0.526	2.45	4.35	4.97
	M70 C	0.967	1.65	4.28	4.57
○	**M70 S**	0.661	2.47	4.37	4.70
◇	**M70 S PM05**	0.944	1.00	4.12	4.71
◆	**M70 S PM1**	0.992	0.92	4.15	4.63
△	**M70 S PM2**	0.813	0.85	3.89	5.31
▲	**M70 S PF2**	1.115	1.35	4.05	4.89
◐	**M90 S**	0.236	4.63	4.67	5.39

$$S_p = k \cdot \left(\frac{p_{max}}{f_{ct}^T}\right) = \frac{\Delta f_{ct,max}}{f_{ct}^T} \qquad k = \frac{\Delta f_{ct}}{p} \qquad \frac{p_{max}}{f_{ct}^T}$$

Figure 6. Plots of the fitting curves of slope k, normalized maximum pore pressure p_{max}/f_{ct}^T and spalling sensitivity index S_p, together with the experimental data for silico-calcareous mixes heated at 0.5 °C/min, as a function of C_c.

C_c = concrete compactness = 1 - n_{75}.

n_{75} = volume of the pores with radius ≥ 75 nm, per unit volume of concrete (after exposure to T = 250 °C);

$k = \Delta f_{ct}/p$ = slope of the regression lines in figures 5b-d; p_{max} = maximum pore pressure;

$f_{ct}^T = f_{ct}^{th}$ = indirect tensile strength at zero pressure (= intercept of the regression lines in figures 5b-d);

f_{ct}^{20} = indirect tensile strength by splitting in virgin conditions.

The index S_p related to pore-pressure role in triggering concrete spalling can be defined as the product between the normalized maximum pore pressure reached by the given concrete mix and the value of k (S_p = maximum normalized decay of concrete tensile strength due to pore pressure [7]):

$$S_p = k \cdot \frac{p_{max}}{f_{ct}{}^T} = \frac{\Delta f_{ct,max}}{p_{max}} \cdot \frac{p_{max}}{f_{ct}{}^T} = \frac{\Delta f_{ct,max}}{f_{ct}{}^T} \quad (1)$$

where $f_{ct}{}^T$ is the indirect tensile strength at the temperature T at zero pressure, assumed to be equal to the intercept of the regression lines in figures 5b-d (= $f_{ct}{}^{th}$).

A qualitative plot of S_p, obtained by multiplying the fitting curves of slope k and normalized maximum pressure $p_{max}/f_{ct}{}^T$, is reported in figure 6 as a function of concrete compactness. Since k and p_{max} have opposite trends with respect to concrete compactness (the former decreases, while the latter increases), any possible change of S_p related to concrete type cannot be foreseen.

As regards the effect of pp fiber, moving from plain concrete to concretes containing increasing amounts of monofilament pp fiber, the normalized index S_p decreases (from 0.37 in plain concrete to 0.23, 0.22 and 0.18 for 0.5,1 and 2 kg/m^3 of pp fiber, respectively), as a demonstration of the decreasing spalling risk brought in by adding pp fiber. (No reduction can be observed when fibrillated pp fiber is introduced, being S_p = 0.37 for both plain mix and concrete with 2 kg/m^3 of fibrillated pp fiber).

No clear trends appear with concrete grade (S_p = 0.32, 0.37 and 0.23, for f_c = 40, 60 and 90 MPa, respectively). Nevertheless, note that S_p gives information just about the activation of spalling induced by pore pressure, but no indications about fracture propagation when spalling occurs. Concerning this issue, the higher brittleness and the markedly higher pore pressure typical of High-Performance Concrete make this material more prone to explosive spalling compared to Normal-Strength Concrete, with more violent fracturing processes.

As concerns the aggregate type, the index S_p is equal to 0.30 in basalt concrete and 0.37 in calcareous and mixed-aggregate concretes, showing that the pore-pressure related spalling risk is almost the same in these latter two mixes, and lower in the former.

4 CONCLUDING REMARKS

The influence of transient hygro-thermal conditions in concrete fracture response has been investigated with two objectives: firstly, to quantify the influence of pore pressure on the tensile strength decay and, secondly, to understand the role played by concrete grade, aggregate type, fiber type and content in the relation between pore pressure and tensile behavior.

The experimental results show that adding 0.5 kg/m^3 of monofilament polypropylene fiber is sufficient to reduce dramatically the risk of spalling (even more than adding 2 kg/m^3 of fibrillated polypropylene fiber), for the heating rates considered in the present study.

The rate k of the strength loss in tension due to pore pressure, $\Delta f_{ct}{}^T = k \cdot p(T)$, depends on concrete microstructure: the higher the compactness, the lower k, according to Soil Mechanics analogy. In particular k decreases for higher concrete grades, while increases when polypropylene fiber is added and if calcareous or mixed aggregates are preferred to basalt aggregate. Pore pressure exhibits an opposite trend: the higher the compactness, the higher the maximum pore pressure.

The index of spalling sensitivity S_p, related to pore-pressure contribution to spalling activation can be defined as the product between slope k and normalized maximum pore pressure $p_{max}/f_{ct}{}^T$ (S_p = maximum normalized tensile strength loss induced by pore pressure). The experimental results show that:

- the spalling sensitivity index S_p decreases moving from plain mix to concretes containing increasing amounts of monofilament polypropylene fiber;
- adding fibrillated polypropylene fiber is less effective than adding similar or lower amounts of monofilament polypropylene fiber;
- using basalt aggregate instead of calcareous or mixed aggregates decreases spalling sensitivity;
- no particular trends are evident in terms of how concrete grade affects spalling sensitivity.

Note that explosive spalling should occur when the index S_p reaches the critical value of 1, which means that the tensile strength decay is equal to the tensile strength itself. In this work, however, the maximum value of S_p was only 0.37, suggesting that pore pressure as such is unable to trigger concrete spalling and that other factors should come into play (like thermal and load-induced stresses).

Furthermore, the index S_p gives no information on fracture propagation when spalling occurs, this limitation being critical in the case – for instance – of High-Performance Concrete, which is more prone to explosive spalling because of the dramatically higher values of pore pressure (as confirmed by the splitting tests performed by the authors, which demonstrate that even relatively small values of pore pressure make the fracture process increasingly faster). The conclusion is that the interaction among the various actors playing a role in concrete spalling – pore pressure in the front line – is still an open problem in need of further – and hopefully exhaustive – experimental evidence.

ACKNOWLEDGMENTS

The authors would like to thank Professor Pietro G. Gambarova (Politecnico di Milano, Milan, Italy) for all suggestions and helpful discussions during the development of the present work.

The experimental campaign was financed by CTG Italcementi Group (Bergamo, Italy), which cast all the specimens, within the Project "Thermo-Mechanical and Spalling Sensitivity of High-Performance Concrete subjected to High Temperature" (2012-2014).

REFERENCES

[1] Khoury A. G., "Effect of fire on concrete and concrete structures", *Progress in Structural Engineering and Materials*, 2, 429-447, 2000.

[2] Kalifa P., Menneteau F. D. and Quenard D., "Spalling and Pore Pressure in HPC at High Temperatures", *Cement and Concrete Research*, 30, 1915-1927, 2000.

[3] Pistol K., Weise F., Meng B. and Schneider U., "The Mode of Action of Polypropylene Fibres in High Performance Concrete at High Temperatures", *Proc. of the 2nd Int. W. Concrete Spalling due to Fire Exposure*, October 5-7, Delft (the Netherlands), 289-296, 2011.

[4] Tsimbrovska M., Kalifa P., Quenard D. and Daı¨an, J.F., "High performance concrete at elevated temperature: permeability and microstructure", *Transactions of the 14th Int. Conf. on Structural Mechanics in Reactor Technology*, Lyon (France), 475-482, 1997.

[5] Felicetti R., Lo Monte F. and Pimienta P., "The influence of pore pressure on the apparent tensile strength of concrete", *Proceedings of the 7th International Conference on Structures in Fire – SIF'12*, June 6-8, Zurich (Switzerland), 589-598, 2012.

[6] Felicetti R. and Lo Monte F., "Concrete Spalling: Interaction between Tensile Behavior and Pore Pressure during Heating", *Proc. of the 3rd Int. W. on Concrete Spalling due to Fire Exposure*, September 25-27, Paris (France), DOI: 10.1051/matecconf/20130603001, 2013.

[7] Lo Monte F., *Reinforced Concrete in Fire: from Materials Behaviour to Spalling Sensitivity and Structural Modelling*, PhD Thesis, (Supervisors: Gambarova P.G. and Felicetti R.), Politecnico di Milano, Milan (Italy), 2014.

[8] Rossino C., Lo Monte F., Cangiano S., Felicetti R. and Gambarova P.G., "Concrete Spalling Sensitivity versus Microstructure: Preliminary Results on the Effect of Polypropylene Fibers", *Proc. of the 3rd Int. W. on Concrete Spalling due to Fire Exposure*, September 25-27, Paris (France), DOI: 10.1051/matecconf/20130602002, 2013.

[9] Goto S. and Roy D.M., "The Effect of W/C Ratio and Curing Temperature on the Permeability of Hardened Cement Paste", *Cem. and Conc. Research*, 11 (4), 575-580, 1981.

[10] Mehta P.K. and Manmohan D., "Pore Size Distribution and Permeability of Hardened Cement Pastes", *Proc. of the 7th Int. Congress on the Chemistry of Cement*, Paris (France), V.III, pp.VII-1-5, 1980.

8th International Conference on Structures in Fire
Guo-Qiang LI, Venkatesh K. R. KODUR, Shou-Chao JIANG, Jian JIANG, Su-Wen CHEN, Guo-Biao LOU (Eds.)
Shanghai, China, June 11-13, 2014

MECHANICAL PROPERTIES OF FIBRE REINFORCED POLYMER REINFORCEMENT FOR CONCRETE AT HIGH TEMPERATURE

Emma R.E. McIntyre*, Antonio Bilotta, Luke A. Bisby* and Emidio Nigro****

* BRE Centre for Fire Safety Engineering, School of Engineering, The University of Edinburgh, UK
e-mails: emma.mcintyre@ed.ac.uk, luke.bisby@ed.ac.uk

** Department of Structures for Engineering and Architecture, University of Naples Federico II, Italy
e-mails: antonio.bilotta@unina.it, emidio.nigro@unina.it

Keywords: Fire, FRP, Experimental, High temperature, Concrete reinforcement, Glass

Abstract. *Fibre reinforced polymer (FRP) bars are increasingly used as replacement of steel reinforcing bars for design and construction of concrete buildings. However, the deterioration of mechanical properties of FRP materials at elevated temperature has not been well quantified or characterized for FRP bars that are currently available. This hinders application of FRP materials in many cases. To better understand the complexities of FRP bars' response at high temperature, an experimental study is presented into the tensile mechanical response of FRP reinforcing bars at high temperature. Dynamic mechanical analysis (DMA) and thermo-gravimetric analysis (TGA) are used to evaluate the glass transition (T_g) and decomposition temperatures (T_d) of a specific commercially available glass FRP (GFRP) reinforcing bar for concrete. Results are presented from direct tensile tests on the GFRP bar at different steady-state temperatures varying from 20 °C to temperatures at which crystallization of the resin occurs (500 °C). These are compared against results from the small-scale tests and a novel predictive model for the reduction in tensile strength of FRP materials at high temperature is proposed.*

1 INTRODUCTION

Fibre reinforced polymer (FRP) reinforcing bars have considerable advantages as compared against steel reinforcement (in particular their resistance to electrochemical corrosion) and are thus increasingly being used for internal reinforcement of sustainable and durable concrete structures. FRP reinforcement is particularly common as flexural reinforcement for reinforced concrete beams and slabs. A key concern for the behaviour of concrete members reinforced with FRP bars is their response during fire. The mechanical and bond properties of FRP bars in concrete deteriorate at high temperatures, and this has the potential to cause reductions in load carrying capacity and stiffness of FRP reinforced concrete structural elements [1, 2].

While it is well known that FRP bars suffer reductions in mechanical and bond properties at elevated temperature, the wide variety of specific proprietary FRP materials of different composition that are currently available in practice makes it difficult to make broad generalizations regarding quantification of their high temperature mechanical and bond properties. Thus, each candidate FRP material must be separately characterized through numerous tensile and bond pullout tests at elevated temperature before it can be used with confidence by designers. This investment in testing is expensive, inefficient, and time consuming, and as a result the required data are generally not available for most currently available FRP reinforcing materials; this hinders the widespread application of FRP materials in concrete buildings.

2 BACKGROUND

The current paper focuses on a single type of commercially available glass FRP reinforcing bar for concrete. It is very well established that the mechanical properties of FRPs deteriorate (as for all structural materials) with increasing temperature. The limiting temperature for 'adequate' performance of FRP materials is commonly taken to be the glass transition temperature (T_g) of the polymer matrix [1, 2]. This is typically in the range of 90-200^{o}C for the epoxy or vinylester polymer matrix materials that are used for concrete reinforcing applications, when manufactured using a pultrusion process. It should be noted that degradation of mechanical properties is observed even before T_g since in reality the transition occurs over a range of temperatures. The anisotropy of unidirectional FRP materials means that transverse strength, shear strength and stiffness, and bond strength are more severely affected by elevated temperatures, decreasing rapidly in the range of T_g.

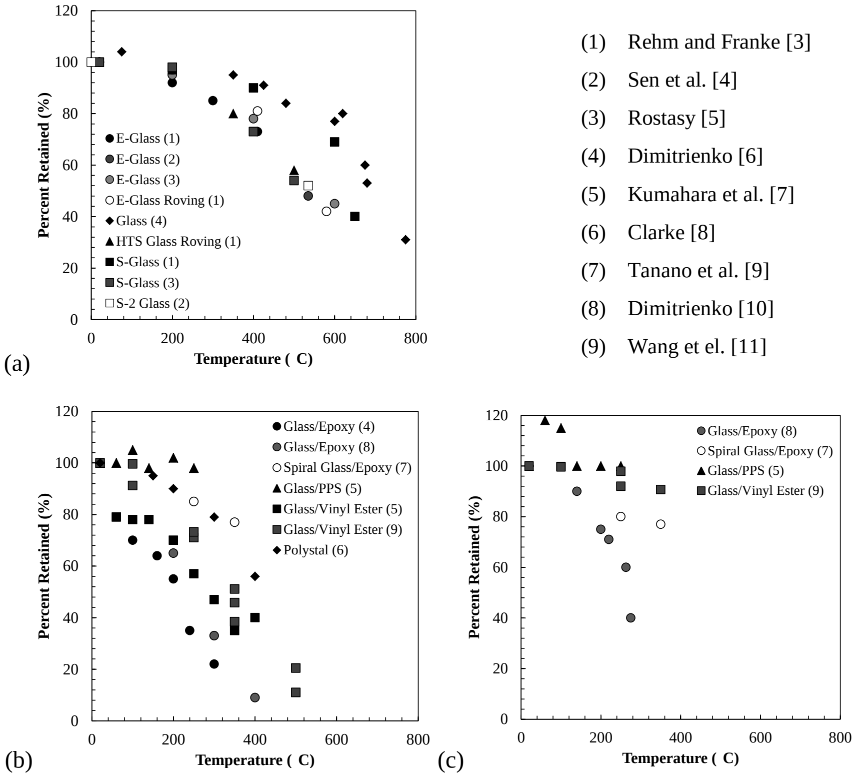

Figure 1. Summary of available data on high temperature performance of glass FRP bars:
(a) Tensile strength of bare glass fibres; (b) FRP bar tensile strength; (c) FRP tensile elastic modulus.

Several studies are reported in the literature studying the high-temperature mechanical properties of FRP materials and their constituent materials; a full review of these has been presented by Bisby et al. [12]. Degradation of mechanical properties is governed by the properties of the polymer matrix, since commonly available fibres are relatively more resistant to thermal effects; however, quantification of the degradation in tensile strength and stiffness of specific FRP products remains a challenge in practice.

Figure 1 shows the temperature-dependent ultimate tensile strength of bare glass fibres, the ultimate tensile strength of various GFRP bars, and the tensile elastic modulus of GFRP bars used as reinforcement for concrete, at elevated temperature, based on data available in the literature and assembled by Bisby et al. [12]. These figures demonstrate that both bare glass fibres and GFRP bars are sensitive to elevated temperature, however the FRPs are considerably more sensitive than the bare fibres themselves. This is because load sharing between the fibres is reduced at temperatures in the range of T_g due to loss of the resin's ability to transfer loads through shear stresses, resulting in reduced bulk strength for the GFRP bars in comparison to individual glass fibres. This is the motivation to understand the contribution of the FRP's matrix resin at high temperature with particular emphasis on defining behaviour within and above the T_g range.

There is considerable scatter in all three plots shown in Figure 1. This is expected given the wide range of possible matrix formulations, fibre orientations (spiral and braided fibres in some cases), and fibre volume fractions represented in the data. It appears that some GFRP materials are more sensitive to elevated temperature than others, and that generalizations are hard to make. A central purpose of the current paper is to attempt to define the minimum suite of tests needed to credibly characterize the expected reductions of mechanical properties of FRP bars at elevated temperature, without the need to perform a wide range of tensile tests over a range of temperatures from ambient, through the T_g range, and increasing above the resin decomposition temperature (T_d) (discussed below).

3 EXPERIMENTAL PROGRAMME AND RESULTS

3.1 Characterzation of FRP Materials

Dynamic mechanical analysis and TGA tests were performed to determine the glass transition temperature (T_g) and the decomposition temperature (T_d) for the GFRP bars studied herein. T_g is a characteristic value for FRP materials, which is used to nominally differentiate between stiff, glassy and soft, rubbery states of the polymer resin matrix. It is often presented by FRP bar manufacturers as a single point value, however in the current study (and in reality) T_g is defined using various currently accepted definitions over a range of temperatures representing different stages of resin transitioning (softening).

Dynamic mechanical analysis (DMA) is one of a variety of test methods that can be used to determine T_g for an FRP material. The test works by applying an oscillatory load to a small sample of FRP and measuring the load versus displacement response of the sample with increasing temperature. As output, DMA testing gives the variation in storage modulus (effectively the flexural elastic modulus of the sample), as well as a parameter known as 'Tan δ', where δ is the phase angle between the elastic and viscous responses of the material under sinusoidal loading. On the basis of these data, T_g can be defined by multiple definitions, three of which are shown in Figure 2(a): $T_{\mathrm{g\_Onset}}$ is defined by the intersection of tangent lines defined by initial slope and the maximum negative slope of the storage modulus reduction curve; $T_{\mathrm{g\_Midpoint}}$ is defined by the temperature at which the maximum negative slope of the modulus reduction curve is observed, and $T_{\mathrm{g\_Tan}\,\delta}$ is defined by the peak value of the tangent of the phase angle, Delta. All of these definitions are essentially arbitrary, but they all relate to a softening of the polymer resin from which the FRP is made. Figure 2(a) shows that for the GFRP material used in the current study the T_g values are: $T_{\mathrm{g\_Onset}} = 59^\circ\mathrm{C}$; $T_{\mathrm{g\_Midpoint}} = 74^\circ\mathrm{C}$, and $T_{\mathrm{g\_Tan}\,\delta} = 100^\circ\mathrm{C}$.

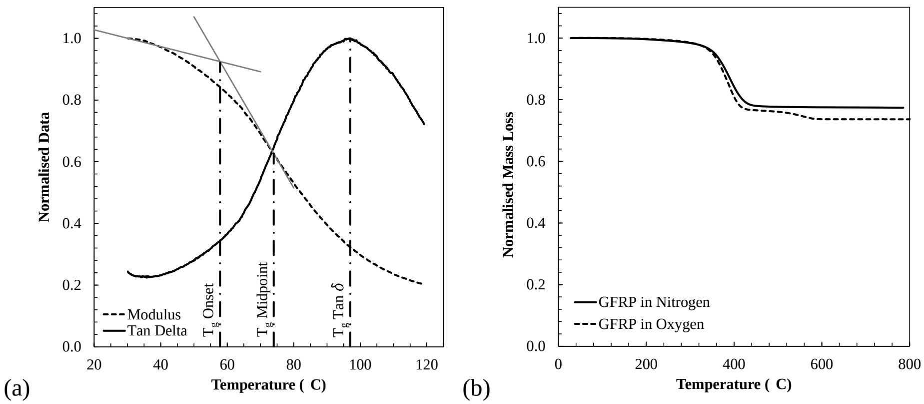

Figure 2. Characterzation of GFRP bar presented in this study: (a) DMA (b) TGA.

Thermo-gravimetric analysis (TGA) measures mass loss with increasing temperature. This test is useful in determining the temperatures at which the organic polymer resin from which an FRP material is manufactured undergoes decomposition by breakdown of chemical bonds and pyrolysis, eventually leaving only the inorganic fibres (in the case of glass FRPs, for which there is no oxidation of the glass fibre themselves). Thermo-gravimetric testing can also give an indication of the approximate fibre volume fraction of an FRP material, since the bulk of the mass remaining after the polymer resin burns off can be attributed to the fibres (with a small amount of residual polymer char). T_d suffers from the same problems in definition as T_g based on its output and the fact that it decomposition occurs over a range of temperatures. For instance, from a mass loss curve such as that given in Figure 2(b) for the GFRP treated herein various T_d values might be defined; in the current study T_d has been taken as 440^{o}C.

3.2 High Temperature Tensile Tests

Direct tensile tests on GFRP bars were performed on glass FRP bars over a range of temperatures. A summary of the test results are shown in Table 1.

Table 1. Tensile Test Results.

Specimen ID	Temperature (°C)	Peak Load (kN)	Tensile Strength (MPa)	Failure Mode
25a	25	86.40	764	Anchor Failure
25b		101.44	897	Coating Failure
25c		119.24	1054	Bar Rupture
59a	59	100.24	886	Bar Rupture
59b		101.23	895	Bar Rupture
74a	74	92.18	815	Bar Rupture
74b		93.52	827	Bar Rupture
100a	100	90.50	800	Bar Rupture
100b		83.88	742	Bar Rupture
111a	111	85.28	754	Bar Rupture
111b		72.45	641	Anchor Failure
111c		86.74	767	Bar Rupture
150a	150	78.10	691	Bar Rupture
200a	200	79.91	707	Bar Rupture
315a	315	79.58	704	Bar Rupture
315b		78.80	697	Bar Rupture
375a	375	36.39	322	Bar Rupture
375b		38.62	341	Bar Rupture
440a	440	55.05	487	Bar Rupture
440b		43.98	389	Bar Rupture
495a	495	16.90	149	Bar Rupture
495b		15.14	134	Bar Rupture

The tests were performed using an Instron 600LX materials testing frame with a built-in environmental chamber. The samples extended through the chamber on both sides as shown in Figure 3. Due to the low transverse strength of the FRP bars, it was necessary to anchor the bar to the test frame. Steel tubes were used to pot the ends of the FRP bars with a microsilica-filled epoxy system. It should be noted that the steel potted anchors were maintained outside of the environmental chamber during testing, thus ensuring cold anchorage and avoiding bond failures. This is extremely important, since the current study is interested in mechanical properties of *well-anchored* FRP materials, and inherently assumes that a cold anchorage zone is provided in order to avoid bond pullout failures. In the absence of cold anchorage the results presented herein are not valid and should not be used.

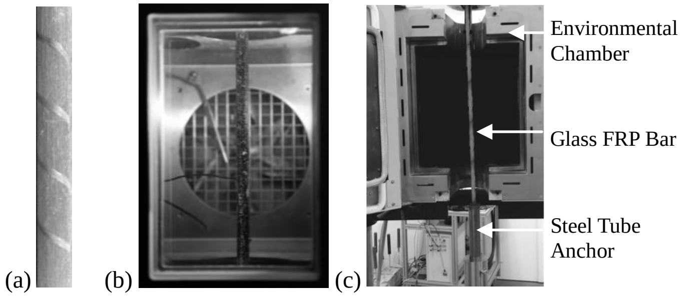

Figure 3. Tensile tests and setup: (a) Glass FRP bar; (b) view through chamber door, and; (c) overview of test setup.

All tension tests were performed under steady-state thermal conditions wherein the bars were heated up to their test temperature at a rate of 5°C per minute until the target test temperature was reached, the sample was held at the target temperature for 15 minutes, and the loading was then applied in displacement control at a crosshead stroke rate of 2 mm per minute until failure. Digital image correlation (DIC) analysis was also used to measure the bars' tensile elastic modulus at a frame rate of 0.2 Hz.

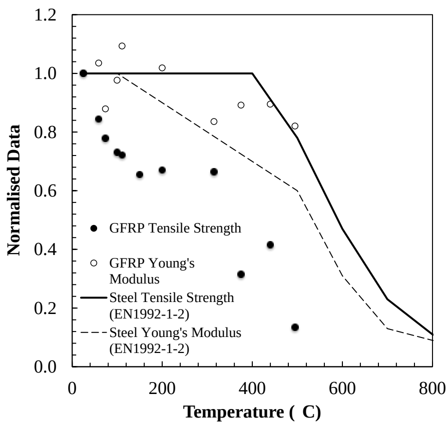

Figure 4. Reduction in ultimate tensile strength and tensile elastic modulus with increasing temperature for the bars tested in the current study (Eurocode 2 [13] reduction curves for mild steel reinforcement included for comparison).

Figure 4 provides a visual summary of the tension test results in terms of ultimate tensile strength and tensile elastic modulus (both normalized to the value at ambient temperature). The tensile strength is considerably reduced at even mildly increased temperatures (for instance >15% reduction at T_{g_Onset}), whereas the tensile elastic modulus appears to be less sensitive to elevated temperature exposure. This agrees in general with the majority of the data available in the literature (refer to Figure 1). Also included in Figure 4 are the Eurocode's [13] recommended strength and modulus reduction curves for mild steel reinforcement at elevated temperature, confirming that GFRP bars are more sensitive in terms of ultimate tensile strength reduction, but possibly less sensitive with respect to stiffness reduction (notwithstanding the scatter in the experimental data).

In general the bars failed by tensile rupture, however there were a few exceptions in which the anchors failed (as noted in Table 1). The rupture mode however changed with temperature; at ambient temperature the failures were sudden and violent; at temperatures above T_g popping noises could be heard indicating failure of the outer fibres of the FRP bar, and failure was gradual, non-violent, an characterized by loss of interaction between the individual fibres due to resin softening and crystallization. The increase in test temperature was matched by decreasingly violent failure modes.

4 SEMI-EMPIRICAL MODELLING

As stated earlier, a central goal of the current study was to define the minimum suite of tests necessary to predict reductions in tensile strength (and ideally also stiffness) for a given FRP reinforcing bar product while avoiding the need to perform a large number of difficult, costly, and time-consuming elevated temperature tension tests.

A number of analytical and semi-empirical models for reduction in mechanical properties of FRP materials with increasing temperature are available in the literature [14-18]. Most previous authors in this area have noted a link between the glass transition response of the FRPs polymer resin (i.e. storage modulus reduction curve from DMA testing) to a reduction in mechanical properties for the FRPs themselves, leading to am S-shaped 'step' reduction in tensile properties with increasing temperature in the region of T_g. A smaller number of prior authors have also linked a second S-shaped step reduction in tensile properties to decomposition of the resin in the region of T_d. However, most of the resulting predictive models have required curve fits to experimental data, so they do not avoid the need to perform a large number of tension tests on FRP bars themselves.

On careful inspection of the tension test data shown in Figure 4, a two-step reduction response is clearly apparent, with the first step appearing to be linked to the T_g response of the resin, and the second appearing to be linked to its T_d response. The level of the plateau between the first and second steps will depend on the specific fibres and resin used in the FRP, as well as its manufacturing process, fibre volume fraction, etc. (as will the level of the second plateau, presumably). On the basis of the ultimate tensile strength data given in Figure 4, the plateau for the glass FRP bars treated herein appears to be in the range of 0.7, when normalized against the average ambient temperature ultimate tensile strength.

Using the rationale presented above, it is possible to propose both the minimum suite of tests needed to predict the tensile strength of a given pultruded FRP bar at elevated temperature, as well as a model to give the necessary predictive information for use by designers. The proposed minimum suite of tests is:

(1) DMA to determine the storage modulus reduction with temperature up to $2T_{g\_Midpoint}$;

(2) TGA to determine the mass loss curve with temperature up to $1.2T_d$ (note that the coefficient 1.2 is essentially arbitrary);

(3) A minimum of 2 to 3 direct tension tests on the FRP bar in question at a temperature in the range of $(T_{g\_Midpoint} + T_d)/2$ to define the first plateau; and

(4) A minimum of 2 to 3 direct tension tests on the FRP bar in question at a temperature in the range of $1.2T_d$ to define the second plateau;

The model is then described by the following equations (with reference to Figure 5, below):

$$k_f = \frac{f_T}{f_{amb}} = \alpha_g + k_1 \cdot \left(1-\alpha_g\right) \cdot \alpha_d + k_2\left(1-\alpha_g\right) \cdot \left(1-\alpha_d\right) \tag{1}$$

Where f_t is the ultimate tensile strength at temperature T and f_{amb} is the ambient temperature ultimate tensile strength. The first step in the reduction of tensile strength with temperature is given by:

$$\alpha_g(T) = \frac{\dfrac{E'_T}{E'_{amb}} - \dfrac{E'_g}{E'_{amb}}}{1 - \dfrac{E'_g}{E'_{amb}}} \; for \;\; 20°C < T < 2T_g \qquad \text{with} \qquad \begin{aligned} E'_T &= E'(T) \\ E'_{amb} &= E'(T_{amb}) \\ E'_g &= E'(2T_g) \end{aligned} \tag{2}$$

$$\alpha_g(T) = \alpha_g(2T_g) = 0 \, for \;\; T > 2T_g$$

Where E'_T, E'_{amb}, and E'_g are the normalized storage modulus values at T, ambient temperature, T_{amb}, and twice T_g (from the 'Midpoint' definition using DMA testing). The second step in the reduction of tensile strength is given by:

$$\alpha_d(T) = 1\,for\;\; 20°C < T < 2T_g$$
$$\alpha_d(T) = \frac{m_T - m_d}{m_g - m_d}\;for\;\; 2T_g < T < T_d \qquad \text{with} \qquad m_T = m(T),\;\; m_g = m(2T_g),\;\; m_d = m(T_d)$$
$$\alpha_d(T) = \alpha_d(T_d) = 0\,for\;\; T > T_d \tag{3}$$

Where m_T, m_g, and m_d are the normalized mass loss values at T, twice T_g, and T_d (from TGA testing). The coefficients k_1 and k_2 represent the plateaus and are given by:

$$k_1 = \frac{f_{T_1}}{f_{amb}} \text{ and } k_2 = \frac{f_{T_2}}{f_{amb}} \quad \text{with} \quad T_1 = \frac{T_g + T_d}{2} \text{ and } T_2 = 1.2 \cdot T_d \tag{4}$$

Where f_{T1} and f_{T2} are the tensile strengths of the bar in the first and second plateaus, delineated by T_1 and T_2 as shown.

The above equations lead to the predicted reduction in tensile strength (for the specific FRP bar treated in the current study) shown in Figure 5. The agreement between the test data and the analytical prediction is reasonable in this case, although additional tensile test data are clearly needed to corroborate the agreement; such tests are underway. Also underway are tests on other glass (and carbon) FRP bars in order to verify that the model can equally be applied to other FRP materials from various manufacturers and with various fibre and resin types.

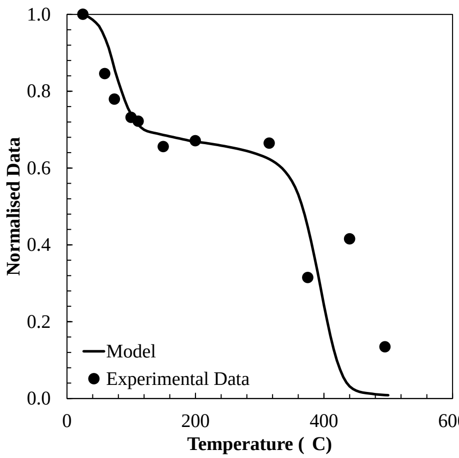

Figure 5. Comparison of model with direct tensile test data presented herein.

5 CONCLUSIONS

The mechanical (tensile) response of FRP bars is assessed as a function of tensile stiffness and ultimate tensile strength. The results demonstrate that the ultimate strength of the specific glass FRP bars in this study reduces more rapidly than the tensile stiffness on heating, and that significant strength reductions become obvious at temperatures above the lowest of the glass transition temperatures (T_{g_Onset}) in the defined range. The initial trend of the tensile strength reduction correlates well with the storage (elastic) modulus reduction curve obtained during DMA testing. Severe deterioration of mechanical properties, both strength and stiffness, are obtained only after reaching the thermal decomposition temperature (T_d) of the FRPs' polymer resin. This indicates that well-anchored FRP materials may be able to retain a considerable proportion of their tensile strength at temperatures well above T_g (by any defensible T_g definition).

It has been demonstrated that DMA and TGA tests may be suitable small-scale tests to use for development of analytical predictive models for reduction of tensile strength of GFRP bars with temperature. A possible predictive mode has been proposed which relies on a comparatively small suite of necessary tests in order to define all relevant parameters. While the model shows promise, additional testing is needed before it should be applied in practice.

REFERENCES

[1] Bisby, L.A. and Kodur, V.K.R., "Evaluating the fire endurance of concrete slabs reinforced with FRP bars: Considerations for a holistic approach", *Composites: Part B*, 38(5-6), 547–558, 2007.

[2] Nigro, E., Cefarelli, G., Bilotta, A., Manfredi, G. and Cosenza, E., "Fire resistance of concrete slabs reinforced with FRP bars. Part I: experimental investigations on the mechanical behavior", *Composites: Part B*, 42, 1739–1750, 2011.

[3] Rehm, G. and Franke, L., *Kunstharzgebundene Glasfaserstabe als Bewehrung im Betonbau Deutscher Ausschuss fur Stahlbeton*, Heft 304, 1979.

[4] Sen, R., Mariscal, D. and Shahawy, M., "Durability of Fiberglass Prestensioned Beams", *ACI Structural Journal*, 90(5), 525-533, 1993.

[5] Rostasy, F., *Fiber Composite Elements and Techniques as Non-Metallic Reinforcement of Concrete*, Brite Project 4142/BREU-CT 91 0515, Evaluation of Potentials and Production Techniques of FRP, Technical Report Task 1, 1992.

[6] Dimitrienko, Y.I., *Thermomechanics of Composites under High Temperatures*, Klewer Academic Publishers, London, UK, 1999.

[7] Kumahara, S., Masuda, Y., Tanano, H. and Shimizu, A., "Tensile Strength of Continuous Fibre Bar Under High Temperature', *FRPRCS-I*, American Concrete Institute, Detroit, USA, 731-742, 1993.

[8] Clarke, J., *Alternative Materials for Reinforcement and Prestressing of Concrete,* Blackie Academic and Professional, Glasgow, UK, 1993.

[9] Tanano, H., Masuda, Y., Kage, T., Fukuyama, H., Nishida, I. and Hashimoto, T. "Fire Resistance of Continuous Fibre Reinforced Concrete", *FRPRCS-II*, E&FN Spon, London, UK, 368-375, 1995.

[10] Dimitrienko, Y.I., "Thermomechanics of Composite Materials and Structures under High Temperatures: 1. Materials", *Composites: Part A*, 28A, 453-461, 1997.

[11] Wang Y.C., Wong P.M.H. and Kodur V. "An experimental study of the mechanical properties of fibre reinforced polymer (FRP) and steel reinforcing bars at elevated temperatures", *Composite Structures*, 80, 131-140, 2007.

[12] Bisby, L.A., Green, M.F. and Kodur, V.K.R., "Response to fire of concrete structures that incorporate FRP", *Progress in Structural Engineering and Materials*, 7(3), 136-149, 2005.

[13] CEN, BS EN 1992-1-2, European Committee for Standardization, Brussels, Belgium, 2004

[14] Gibson A.G., Wu Y-S., Evans J.T., Mouritz A.P., "Laminate theory analysis of composites under load in fire', *Journal of Composite Materials,* 40(7), 639–58, 2006.

[15] Mahieux C.A., Reifsnider K.L., Case S.W., "Property modelling across transition temperatures in PMC's: Part I tensile properties", *Applied Composite Materials,* 8(4), 217–34, 2001.

[16] Wang K., Young B., Smith S.T., "Mechanical properties of pultruded carbon fibre reinforced polymer (CFRP) plates at elevated temperatures", *Engineering Structures,* 33(7), 2154-2161, 2011.

[17] Bai Y., Keller T., "Modeling of strength degradation for fiber-reinforced polymer composites in fire", *Journal of Composite Materials,* 43(21), 2371–2385, 2009.

[18] Correia J. R., Gomes M. M., Pires J. M., Branco F. A., "Mechanical behaviour of pultruded glass fibre reinforced polymer composites at elevated temperature: Experiments and model assessment", *Composite Structures*, 98, 303–313, 2013.

BOND STRENGTH OF GEOPOLYMER MORTAR AFTER EXPOSURE TO HIGH TEMPERATURES

Hai-Yan Zhang[*,] and Liang Cao[**]**

[*] State Key laboratory of Subtropical Architecture Science, South China University of Technology, Guangzhou, P.R. China

[**] Department of Civil Engineering, South China University of Technology, Guangzhou, P.R. China
e-mails: 583904780@qq.com, 1139225221@qq.com

Keywords: Bond strength, Metekaolin, Fly ash, Carbon fiber, Geopolymer mortar, High temperature

Abstract. *This paper presents the experimental results of bond strength of geopolymer mortars prepared by using different proportions of metekaolin, fly ash, potassium silicate solution, sands and carbon fibers. A great amount of tensile tests were conducted at ambient temperature and after exposure to high temperatures to evaluate bond strength of geopolymer mortars. Comparative tests were carried out on ordinary Portland cement mortar specimens. The results from tests show that geopolymer mortar with sand-binder ratio of 3 can achieve the highest bond strength. The addition of a small amount of chopped carbon fibers improves bond strength of geopolymer mortar. Geopolymer mortar with water-binder-sand ratio of 0.45:1:3 exhibits higher bond strength than cement mortar with similar formulation, both at ambient temperature and after exposure to elevated temperatures.*

1 INTRODUCTION

Ordinary Portland cement concrete (OPC) is widely used in various kinds of structures, such as civil buildings, industrial buildings, bridge, tunnel, due to its high compressive strength, excellent durability and abundance of raw materials. While the mass production of cement has resulted in high volume of carbon dioxide (CO_2) emission, which is a main cause of the greenhouse effect. It is reported that the CO_2 emission of OPC production worldwide accounts for about six percent of the total CO_2 emission [1].

Geopolymer, as a new environmentally friendly inorganic binder, has drawn public attention recently, due to its comparable performance with OPC [2]. The typical source materials used for making geopolymers include metekaolin (MK) or industrial waste materials like fly ash (FA), slag and rise husk ash [3, 4]. The carbon dioxide (CO_2) emission and energy consumption during the production of geopolymers is much less than that of OPC. In addition, the utilization of industrial waste precursor like FA in the synthesizing of geopolymer materials will also enhance the environmental and economic credentials of the final product [5].

Geopolymer exhibits many excellent properties, such as high compressive strength, low creep, low shrinkage, good anti-acid and anti-alkali properties [6-8]. thus it is regarded as a promising alternative of OPC and can be used to make geopolymer mortar and concrete [2]. A large number of researches on geopolymer were conducted in literatures [2-8], but the study on geopolymer mortar is not much [9, 10] especially the data on mechanical properties of GM after exposure to high temperatures is lacking.

In the current study, the bond strength of geopolymer mortar with different formulations was evaluated by tensile tests at ambient temperature and after exposure to high temperatures, and the effects of temperature and content of carbon fibers were quantified.

2 EXPERIMENTAL PROCEDURE

2.1 Raw materials

The geopolymer mortar specimens used in this study is composed of MK, FA, alkaline solution, sand and carbon fiber (CF). Commercially produced GM with an average particle size of 0.017 mm, was supplied by Shanxi Jinkunhengye Ltd., China, through calcified kaolin under 900^oC. Low calcium FA, with an average particle size of 0.032 mm, was supplied by Guangzhou Huangpu Power Plant. Potassium silicate solution with SiO_2/K_2O molar ratios of 1.0 was used as alkaline-silicate activator. The fine aggregate is local river sand with a maximum size of 2 mm. Chopped CFs were added to MK-FA blend precursor as reinforcement agent. The length, diameter and density of chopped carbon fibers are 6mm, 7μm and 1.76-1.80g/cm^3 respectively. The chemical compositions of MK and FA are presented in Table 1. For preparing CM specimens, 32.5 ordinary Portland cement was added as binder material except tap water and fine aggregate mentioned above.

Table 1. Chemical compositions of MK and FA.

Oxide (wt.%)	SiO_2	Al_2O_3	CaO	Fe_2O_3	TiO_2	K_2O	MgO	SO_3	P_2O_5	Na_2O	SrO	ZrO_2	CuO
MK	52.31	45.37	0.37	0.41	0.53	0.10	0.08	0.05	0.47	0.20		0.04	0.02
FA	50.13	38.9	3.89	2.87	1.36	0.95	0.79	0.36	0.25	0.19	0.11	0.11	0.03

2.2 Preparation of specimens

A total of 96 specimens grouped into 6 sets, with different water-binder ratio, sand-binder ratio and CF content, were prepared to investigate the bond strength of them at ambient temperature and after exposure to different temperatures. A constant ratio of MK to FA in geopolymer precursor (1:1) was used for these specimens.

Comparative tests were conducted on 24 cement mortar specimens, grouped into 2 sets, which have the same sand-binder ratio (3) but different water-binder ratios (0.4 and 0.45). The mix proportions of geopolymer mortar and cement mortar specimens and test temperatures are tabulated in Table 2. In this table, the designation of Group "GM" denotes geopolymer mortar specimens, and that of "CM" denotes cement mortar specimens. Six specimens are tested for each group at each temperature.

Table 2. Mix proportions of GM/CM and target temperatures for tensile tests.

Group No.	Water-binder ratio	Sand-binder ratio	Binder material	CF/(MK+FA)	Temperature (^oC)
GM1	0.4	2.5	geopolymer	0	25
GM2	0.4	3	geopolymer	0	25
GM3	0.4	3.5	geopolymer	0	25
GM4	0.45	3	geopolymer	0.5%,1%,2%	25
GM5	0.45	3	geopolymer	0	25,100,300, 500,700
GM6	0.45	3	geopolymer	1%	25,100,300, 500,700
CM1	0.4	3	cement	0	25
CM2	0.45	3	cement	0	25,300,700

The MK-FA precursor, chopped CFs and alkaline silicate solution were first mixed for 2 min by hand and another 2 min in a batch mixer. The river sand was then added into the blend and mixed for a further

12 min. After that, the mixture was cast into standard moulds with a shape of “8” and vibrated using a vibrating table for 5 min to release air bubbles. Subsequently, specimens were covered with plastic films and cured in a tank at a constant 21^{o}C temperature and 95% humidity for 6 days, and then taken out to dry naturally in a room for 1 day before testing.

2.3 Heating methods

In order to test bond strength of GM and CM after exposure to target high temperatures (100,300,500 and 700^{o}C), specimens were first heated through an electrical furnace at a fixed heating rate of 5^{o}C/min from room temperature to target high temperature. Before allowed to cool naturally to room temperature inside the furnace, the specimens were kept at the target temperature for 1 hour. The bond strength test for GM and CM specimens exposed to the elevated temperatures was conducted one day after the heating.

2.4 Test procedure

The tensile tests of all specimens were conducted as per Chinese Code DLT5193-2004, using an electronic universal testing machine UTM5205 in displacement control regime (as shown in Figure 1), at a loading rate of 2 mm/min.

Figure 1. Test setup.

3 RESULTS AND DISCUSSION

3.1 Results from testing at room temperature

3.1.1 Qualitative observations

Specimens in Group GM1, GM2, GM3 and GM4, subjected to tensile loads at ambient temperature, were generally broken at the minimum section of the “8” shaped specimens, as presented in Figure 2(a). And the fracture surfaces are relatively even (see Figure 2(b)). Several specimens were not broken at the minimum normal section, but at a diagonal section (Figure. 2(c)), due to the heterogeneity of the mixture and bubble distribution in mortars. The data from these specimens were not adopted. The bond strength of geopolymer mortar was evaluated as the average results of the valid maximum load from six specimens divided by the fracture section area.

(a) Failure of specimens.

(a) Fracture section.

(c) Invalid specimens.

Figure 2. Failures of geopolymer mortar specimens.

3.1.2 Effect of sand-binder ratio on bond strength at ambient temperature

Specimens from Group GM1, GM2 and GM3, with different sand-binder ratios of 2.5, 3 and 3.5 but a constant water-binder ratio of 0.4, were used to investigate the effect of sand-binder ratio on bond strength of GMs. The test results of these specimens are presented in Figure 3. It can be seen that the three groups of GM specimens all exhibit high bond strength (>3.5 MPa). And the bond strength of GMs greatly increases with an increase in sand-binder ratio and then slightly decreases. The highest bond strength (4.1MPa) is achieved at a sand-binder ratio of 3 (Group GM2). The comparative tests on CM specimens (Group CM1), having the same sand-binder ratio and water-binder ratio with GM2, showed that the CM specimens exhibit extremely low strength (0.6Mpa). The main reason is the poor workability of CM mixture with the water-binder ratio of 0.4, which results in high porosity of CM specimens, as shown in Figure 4(a). At the same water-binder ratio (0.4), better workability was observed in GM specimens (as seen in Figure 4(b)), due to FA particles having microstructure of spherical shape, which results in the lower requirement on water quantity[11]. Several trial experiments found that GM and CM specimens both can achieve good workability at a water-binder ratio of 0.45, thus water-binder ratio of 0.45 was adopted in the subsequent tests.

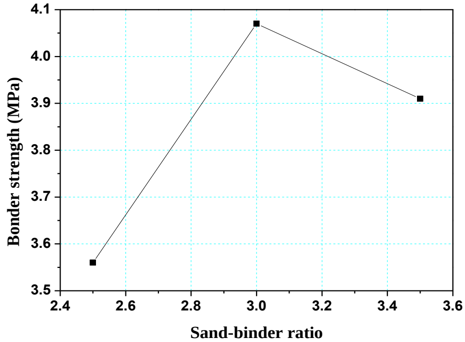

Figure 3. Effect of sand-binder ratio on bond strength.

(a) Specimen in Group CM1 (b) Specimen in Group GM2

Figure 4. Surface features of CM and GM.

3.1.3 Effect of CF content on bond strength of GM at ambient temperature

For exploring effect of CF content on bond strength of GMs, four different mass ratio of chopped CF to MK-FA precursor (0, 0.5%, 1% and 2%) were used for preparing GM specimens. The variation of bond strength of GMs (Group GM4) at ambient temperature with CF content is plotted in Figure. 5. It can be seen that the bond strength of GM specimens with 0.5% CF is close to that of GM specimens without CFs, while bond strength of GM specimens with 1% and 2% CF gets significantly enhanced, compared to that of specimens without CFs.

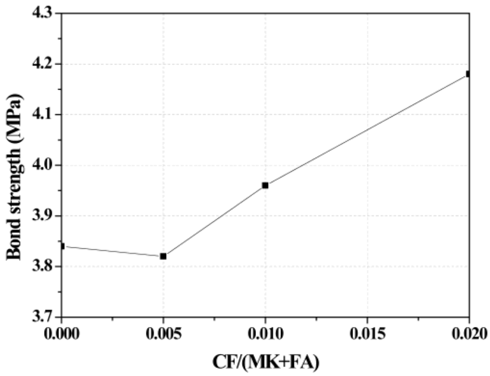

Figure 5. Effect of carbon fiber content on bond strength.

In fiber reinforced mortars, matrix and fibers act as a whole to bear external forces, thus the emergence and development of crack is delayed. Once cracking occurs, stress that had been born by geopolymer matrix is transferred to carbon fibers through interfacial bond [12], which enhance the bond strength of geopolymer mortar.

3.2 Results from testing after exposure to high temperatures

3.2.1 Qualitative observations

The positions and shapes of fracture surface of GM specimens tested after exposure to elevated temperatures (Group GM5 and GM6) are similar to that of specimens tested at ambient temperature. But with increase in exposure temperature, cracks occurred on the surface of GM specimens without CF (GM5). As shown in Figure 6 (a), a few of cracks, with maximum width of 0.2 mm, can be observed on the surface of specimen in Group GM5 after exposure to 500^{o}C. However, there is no noticeable cracks occurred on GM specimens with CF content of 1% (GM6). This clearly infers that chopped CFs can provide effective crack control mechanism in GM under high temperatures.

(a) Specimen without CF (GM5) (b) Specimen with 1% CF (GM6)

Figure 6. GM specimens with and without CF after exposure to high temperatures.

3.2.2 Comparison of bond strength of GM and CM after exposure to elevated temperatures

Specimens from Group GM5 were tested at ambient temperature and after exposure to elevated temperatures, to study the effect of temperature on bond strength. Comparative tests were conducted on cement mortar specimens (CM2). The tested results are plotted in Figure 7. As seen from Figure 7, the bond strength of GMs increases at 100^{o}C, and then decreases from 200 to 700^{o}C. Rapid deterioration in bond strength occurs at 300^{o}C and 500^{o}C and it only retains 25% of ambient temperature strength after exposure to 500^{o}C. In the previous works, investigations on properties of GM showed that free water at 100^{o}C promotes further hydration of cementitious material, which is similar to the effect of steam curing [13, 14]. Therefore, GM exhibits higher bond strength after exposure to 100^{o}C. Strength deterioration of mortars after exposure to 300,500 and 700^{o}C is mainly due to the dehydration of free and chemically-bound water, as well as the differences in the thermal expansion between the aggregate and the geopolymeric paste [15]. As the external temperature increases, moisture within the specimen rapidly migrates towards the surface of the specimen and escapes. This in turn causes surface-cracking and internal damage in the overall structure of GM. Compared to CM, GM exhibits higher bond strength at ambient temperature. Although the deterioration in bond strength of GM in 100-300 ℃ is greater than that of CM, the bond strength of GM after exposure to elevated temperature is higher than that of CM throughout the temperature range from 25 ℃ to 700 ℃. This makes it an excellent building material for structural repair application, when fire resistance is a basic design requirement of buildings.

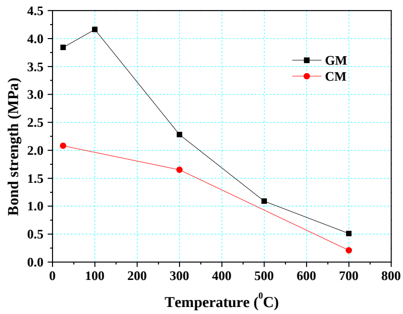

Figure 7. Comparison of bond strength of CM and GM.

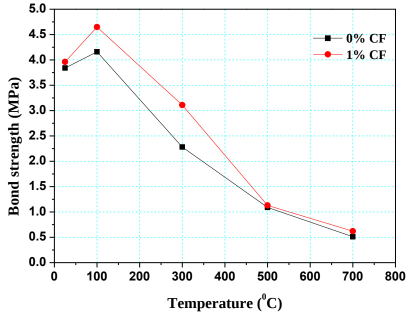

Figure 8. Effect of CF content.

3.2.3 Effect of CF content on bond strength of GM after exposure to elevated temperatures

Test results from specimens in Group GM5 and GM 6 are used to evaluate the effect of carbon fibers on bond strength of GM after exposure to elevated temperatures. Fig 8 presents the comparison of bond strength of these two groups of specimens. It can be seen in Fig 8 that GMs with 1% CF content exhibit relatively higher bond strength than that of GMs without CF throughout the temperature range, but the strength difference between the two groups of specimens decreases with temperature, and approaches almost zero beyond 500^{o}C. This is attributable to the fact that the reinforcing effect of CF on the bond strength of GMs diminishes with increase in temperatures. It is reported that the tensile strength of CFs decreases with increase in temperature, and only retains 25% of ambient temperature strength after exposure to 500^{o}C [16]. Thus, the addition of CF almost has no influence on bond strength of geopolymer mortars after exposure to 500^{o}C.

4 CONCLUSIONS

(1) The sand-binder ratio of 3 in geopolymer mortar is the optimum based on the comparison of bond strength of geopolymer mortar with varied binder-sand ratio.

(2) The bond strength of geopolymer mortar at ambient temperature gets significantly enhanced with an increase in CF content.

(3) The addition of chopped carbon fibers in geopolymer mortars provides effective crack control mechanism on geopolymer mortar at high temperatures.

(4) Geopolymer mortar with water-binder-sand ratio of 0.45:1:3 exhibits higher bond strength than cement mortar with similar formulation, both at ambient temperature and after exposure to elevated temperatures.

REFERENCES

[1] McCaffrey R. "Climate Change and the Cement Industry, Environmental overview," *GCL Magazine，environmental special issue*, 2002.

[2] Davidovits J. "Geopolymers and geopolymeric materials," *Journal of thermal analysis*, vol. 35, pp. 429-441, 1989.

[3] Knobloch, M., Fontana, M. and Frangi A., “Steel beam-columns subjected to fire”, *Steel Construction – Design and Research*, 1(1), 51-58, 2008.

[4] D. P, F.-J. A, P. JL, L. GC, P. A, and v. D. JSJ., "Geopolymer technology: the current state of the art," *J Mater Sc*, vol. 42:2917–33, 2007.

[5] R. WD, T. J, and v. R. A, "Thermal analysis of geopolymer pastes synthesised from five fly ashes of variable composition," *J Non-Cryst Solids,* vol. 358:1830–9, 2012.

[6] C. TW and C. JP, "Fire-resistant geopolymer produced by granulated blast furnace slag," *Mater Eng,* vol. 16:205–10, 2003.

[7] C. TW, "Effect of additional materials on the characterization of glassceramic produced from incinerator fly ashes," *Chemosphere,* vol. 56:127–31, 2004.

[8] T. J, M. A, R. W, L. M, W. I, and R. A, "Preparation of metakaolin based geopolymer coatings on metal substrates as thermal barriers.," *Appl Clay Sci,* vol. 46:1–9, 2009.

[9] Ueng T.-H., S.-J. Lyu, H.-W. Chu, H.-H. Lee, and T.-T. Wang, "Adhesion at interface of geopolymer and cement mortar under compression: An experimental study," *Construction and Building Materials,* vol. 35, pp. 204-210, 2012.

[10] Jumrat S, Chatveera B, and Rattanadecho P, "Dielectric properties and temperature profile of fly ash-based geopolymer mortar," *International Communications in Heat and Mass Transfer,* vol. 38, pp. 242-248, 2011.

[11] Zhang M.R, Sun. Y.F, and Qiao. H.X, "The Study of Water-Reducing Effect and Strength Rule of Various Fly Ashes in Mortars," in *FLY ASH COMPREHENSIVE UTILIZATION*, ed, 2011, pp. 15-17+21.

[12] Li B.X and Chen Y, "The Analysis on Performance of Polypropylene Fiber Mortar," *Technology & Economy in Areas of Communications,* pp. 7-9, 2009.

[13] Li Q.H, Yao Y, Sun. B, and Li Z.J, "Mechanism of Effect of Elevated Temperature on Compressive Strength of Cement Mortar," *JOURNAL OF BUILDING MATERIALS,* pp. 699-703, 2008.

[14] Feng J.J, Fu YF, Chen. Z.H, and Zhang R, "Effect of High Temperatures on Microstructure of Cement-Based Composite Material," *JOURNAL OF BUILDING MATERIALS,* pp. 318-322, 2009.

[15] Arellano-Aguilar R, Burciaga-Diaz O, Gorokhovsky A.and Escalante-Garcia J.I ,"Geopolymer mortars based on a low grade metakaolin: Effects of the chemical composition, temperature and aggregate:binder ratio," *Construction and Building Materials,* vol. 50, pp. 642-648, 2014.

[16] Gao X.N., Zhang H.Y., "Comparison of tensile strength of BFRP sheets and CFRP Sheets after high temperature exposure", *Journal of Disaster Prevention and Mitigation Engineering* 32(1), p. 6, 2012.

8th International Conference on Structures in Fire
Guo-Qiang LI, Venkatesh K. R. KODUR, Shou-Chao JIANG, Jian JIANG, Su-Wen CHEN, Guo-Biao LOU (Eds.)
Shanghai, China, June 11-13, 2014

STRESS-STRAIN MODEL FOR AUSTENITIC STAINLESS STEEL AFTER FIRE EXPOSURE

Zhong Tao*, Xing-Qiang Wang, Tian-Yi Song* and Lin-Hai Han*****

* Institute for Infrastructure Engineering, University of Western Sydney, Penrith, NSW 2751, Australia
e-mails: z.tao@uws.edu.au, t.song@uws.edu.au

** Department of Civil Engineering, Shandong Polytechnic, Jinan 250013, China
e-mail: xingqiangwang03@163.com

*** Department of Civil Engineering, Tsinghua University, Beijing 100084, China
e-mail: lhhan@tsinghua.edu.cn

Keywords: Stress−strain relations, Stainless steel, Post-fire, Damage evaluation, Temperature effects

Abstract. *An experimental research has recently been conducted to investigate the mechanical properties of austenitic stainless steel after heating and cooling down to room temperature. A simplified stress−strain model is proposed accordingly to consider the influence of fire damage. This model is a revised version of Rasmussen's stress−strain model for stainless steel at ambient temperature. The accuracy of the proposed model was validated by comparing with the test results.*

1 INTRODUCTION

Stainless steel is of increasing interest to structural engineers due to its additional benefits, such as corrosion resistance, ease of maintenance and aesthetic appeal. The high amount of chromium present makes stainless steel different from carbon steel. Some stainless steel grades also contain certain amount of nickel, molybdenum and/or titanium.

Due to the high alloy content, the shape of the stress (σ)-strain (ε) curve of stainless steel is a “roundhouse” type, and the pronounced yield plateau widely observed in mild steel stress−strain curves does not exist for stainless alloys. Plenty of research has been done before to capture the σ-ε relationship of stainless steel at ambient and elevated temperatures, and a number of σ-ε models have been proposed accordingly [1-3].

For the evaluation of damage to a structure after exposure to fire, post-fire σ–ε models are required to conduct an accurate structural analysis. For stainless steel material, Felicetti et al. [4] tested stainless steel bars (austenitic grade 1.4307) after being heated up to 850 ℃. Both hot-rolled (ϕ12 mm) and cold-worked (ϕ24 mm) stainless steel bars were tested. For hot-rolled stainless steel bars, it was found that the yield strength (f_y) degraded if the temperature was higher than 500°C. The observed strength loss was only 6.5% for f_y at a given temperature of 850 ℃, and the fire exposure had no apparent influence on the ultimate strength of the hot-rolled bars. On the contrary, cold-worked stainless steel bars had a totally different behaviour with a slight strength increase up to 400°C and a strong decay at higher temperatures. A decrease of 80% in f_y was found for the cold-worked stainless steel bar heated up to 850°C and cooled to room temperature. To the best knowledge of the authors, no research has been done on the mechanical behaviour of structural stainless steel after fire exposure.

Recently, the authors conducted tests to investigate the mechanical properties of austenitic stainless steel of grade 1.4301 after heating and cooling down to room temperature [5]. Full-range σ-ε curves were measured. The test results indicate that the influence of heating time on post-fire mechanical properties of stainless steel is minor. For flat coupons, only the yield strength demonstrates an obvious decrease when the temperature T exceeds 500°C. But the fire exposure has a higher impact on corner material than on flat material. Based on the test results in [5], a simplified σ–ε model is proposed in this paper to consider the influence of fire damage on austenitic stainless steel.

2 FIRE TESTS

Fire tests [5] that were recently conducted at the University of Western Sydney, Australia, will be used to develop the simplified σ–ε model. Steel coupons were cut from structural hollow sections, which were made from hot-rolled steel strips by cold forming. Flat coupons were cut from the middle of the flat surfaces of a square hollow section (SHS, 200 mm×200 mm×6 mm). To investigate the corner effect, corner coupons were cut from the corners of the same SHS tube. Meanwhile, curved coupons were cut from a circular hollow section (CHS, 260×3 mm). All coupons were cut along the longitudinal direction of the steel tubes. The coupons were heated from ambient temperature to the predetermined target temperature (T) at a heating rate of 20 ℃/min, and then the maximum temperature was kept stable until the pre-selected soak time was reached. The target temperatures T ranged from 200 ℃ to 1000 ℃. After a coupon soaked in the furnace for a designated time, the coupon was cooled down to room temperature in the furnace naturally. Then the coupons were taken out from the furnace and tensile tests were conducted afterwards. During the tensile testing, the full-range σ–ε curve was recorded for the coupon.

The measured full-range σ–ε curves for the flat and corner coupons are shown in Figures 1 and 2, respectively. The effect of fire exposure on curved coupons is similar to that on flat coupons. In general, the influence of the fire exposure on the σ–ε curves of flat and curved coupons is not significant, but the influence is very significant on corner coupons. It can also be found that the post-fire σ–ε curves maintain the same basic shape of the “roundhouse” type as observed for stainless steel at ambient temperature.

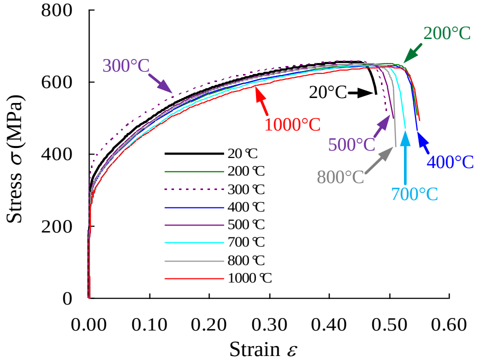

Figure 1. Post-fire σ–ε curves for flat coupons.

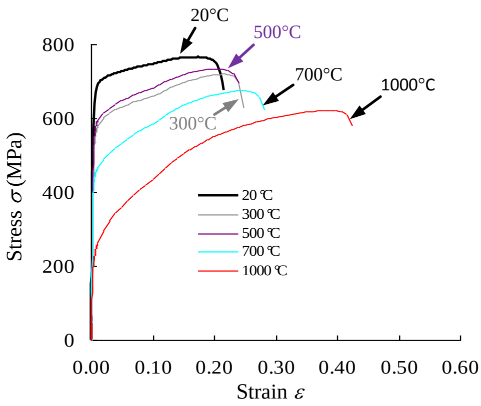

Figure 2. Post-fire σ–ε curves for corner coupons.

3 STRESS–STRAIN MODEL

Since fire exposure does not change the shape of σ-ε curves as shown in Figures 1 and 2, it is possible to use a same stress–strain curve expression for both room temperature stainless steel and fire-damaged stainless steel. A number of σ-ε models are available for flat regions of stainless steel at room temperature. But no specific σ-ε model has been proposed for stainless steel at corner regions to address the cold forming effect.

Three σ-ε models were reviewed and compared by Tao et al. [6], and it was found that there is no significant difference among the three model predictions. In general, Rasmussen's model [1] is the simplest to use and only three parameters are required to determine the full-range curve. In the following, more recent test data collected from the literature are used to further evaluate Rasmussen's model, and then this model is revised to consider the cold forming effect for stainless steel at corner regions. After that, a revised model is proposed to include the influence of fire exposure. Important parameters to define the σ-ε curve of a post-fire flat or curved coupon include the modulus of elasticity (E_{sT}), 0.2% proof yield strength (f_{yT}), ultimate strength (f_{uT}), corresponding ultimate strain (ε_{uT}) and strain hardening exponent (n_T). For comparison purposes, their corresponding parameters of steel without heat-treatment are designated as E_s, f_y, f_u, ε_u and n, respectively. Similarly $E_{sT,c}$, $f_{yT,c}$, $f_{uT,c}$, $\varepsilon_{uT,c}$ and $n_{T,c}$ are further defined as parameters for post-fire corner material; and $E_{s,c}$, $f_{y,c}$, $f_{u,c}$, $\varepsilon_{u,c}$ and n_c are corresponding parameters for corner material without fire exposure.

3.1 Stress-strain model at ambient temperature

3.1.1 σ-ε model for flat regions

For circular hollow sections or flat regions of square or rectangular hollow sections (RHS), the cold forming process leads to only a slight increase in strength compared with the virgin stainless steel sheets. This influence is generally moderate and Rasmussen's σ-ε model can be used for both CHS sections and flat regions of SHS/RHS sections. For this reason, there is no need to differentiate the results of flat coupons for SHS section and curved coupons for CHS section in this paper in terms of predicting σ-ε curves.

To describe the nonlinear σ-ε curves of stainless steel at room temperature, Rasmussen [1] proposed a full-range σ-ε relationship, which was verified by over 200 test data and 28 full-range σ-ε curves collected from the literature. His model has been widely used by other researchers. With the increasing interest in using stainless steel, numerous new test data were reported in recent years for different stainless steel materials. A total of 135 new test data and 33 full-range σ-ε curves from 16 studies were collected by the authors for austenitic and duplex stainless steels, which have not been used to verify Rasmussen's model before. The majority of the test data were reported for flat material cut from cold-formed SHS or RHS sections. The verification indicates that Rasmussen's model agrees with the new test data very well.

3.1.2 σ-ε model for corner regions

Figure 3 shows the influence of cold forming on the σ–ε curve for austenitic stainless steel at ambient temperature based on the tests in [5]. Compared with the flat material, an increase in the yield strength $f_{y,c}$ and ultimate strength $f_{u,c}$ as well as a decrease in the ultimate strain $\varepsilon_{u,c}$ can be found for the corner material. Meanwhile, the corner material shows less strain hardening than the flat material during the tensile deformation.

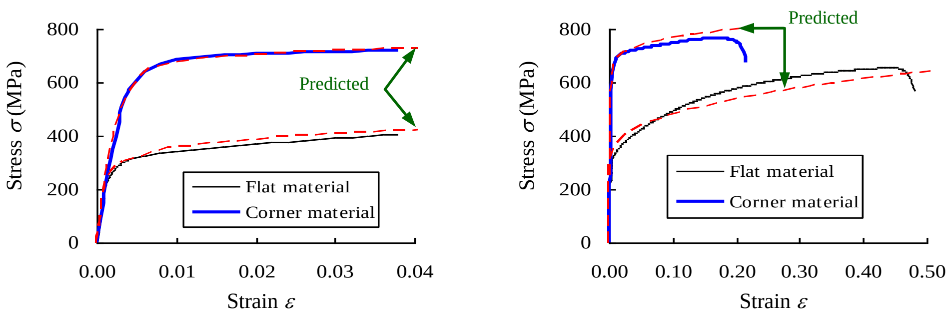

Figure 3. Influence of cold forming on σ–ε curves of stainless steel at room temperature.

To develop a reliable σ-ε model for corner material, a range of tensile test data is collected for corner coupons cut from austenitic or duplex stainless steel hollow sections, including a total of 85 test data and 24 full-range σ-ε curves reported in 15 references. The collected data indicate that the elastic moduli $E_{s,c}$ for corner material are quite close to the elastic moduli E_s of flat material. Therefore, $E_{s,c}$ of the corner material is assumed the same as E_s of the corresponding flat material in this paper.

Since σ-ε curves for corner material are still of the "roundhouse" type as shown in Figure 3, it is proposed to make suitable modifications to Rasmussen's model to include the effect of the corner strength enhancement. The following σ–ε model is proposed for corner material at room temperature:

$$\varepsilon = \begin{cases} \dfrac{\sigma}{E_s} + 0.002\left(\dfrac{\sigma}{f_{y,c}}\right)^{n_c} & \text{for} \quad \sigma \le f_{y,c} \\ 0.002 + \dfrac{f_{y,c}}{E_s} + \dfrac{\sigma - f_{y,c}}{E_{y,c}} + \varepsilon_{u,c}\left(\dfrac{\sigma - f_{y,c}}{f_{u,c} - f_{y,c}}\right)^{m_c} & \text{for} \quad f_{y,c} < \sigma \le f_{u,c} \end{cases} \tag{1}$$

where m_c is a material parameter; and $E_{y,c}$ is the tangent modulus of the σ–ε curve of the corner material at $f_{y,c}$, which is determined by Equation (2).

$$E_{y,c} = \frac{E_s}{1 + 0.002 n_c E_s / f_{y,c}} \tag{2}$$

To determine the full-range σ–ε curve as specified by Equation (1), five parameter of $f_{y,c}$, $f_{u,c}$, $\varepsilon_{u,c}$, n_c and m_c need to be determined for the corner material. These parameters may be related to the three basic parameters of E_s, f_y and n for the flat material, where n is the strain hardening exponent determined by Equation (3) and is related to f_y and 0.01% proof yield strength $f_{0.01}$. A statistic analysis is carried out in the following to find out possible relationships based on the test data collected.

$$n = \frac{\ln(20)}{\ln(f_y / f_{0.01})} \tag{3}$$

(1) Determining $f_{y,c}$

Figure 4 shows the relation between $f_{y,c}/f_y$ and f_y, which shows a trend of decreasing $f_{y,c}/f_y$ with increasing f_y. It indicates that lower strength steel demonstrates higher corner strength enhancement. Based on the regression analysis, Equation (4) is proposed to predict $f_{y,c}$ from f_y.

$$\frac{f_{y,c}}{f_y} = 1 + 0.05 e^{900/f_y} \tag{4}$$

where f_y is in MPa.

(2) Determining $f_{u,c}$ and $\varepsilon_{u,c}$

The experimental values of $(f_{u,c}/f_{y,c})/(f_u/f_y)$ are plotted in Figure 5, which demonstrates a clear correlation between $(f_{u,c}/f_{y,c})/(f_u/f_y)$ and f_y. An expression for the relationship can be taken as:

$$\frac{f_{u,c}}{f_{y,c}} = \left(0.56 f_y^{\,0.226} - 1.4\right)\frac{f_u}{f_y} \tag{5}$$

in which f_u is the ultimate strength of the flat material determined by Equation (6) proposed by Rasmussen [1]; and $f_{y,c}$ is the yield strength of the corner material given by Equation (4). Therefore, $f_{u,c}$ is actually a function of f_y and E_s.

$$\frac{f_y}{f_u} = 0.2 + 185\frac{f_y}{E_s} \tag{6}$$

For the corner material, it is found that a similar equation proposed by Rasmussen [1] can still be used to predict $\varepsilon_{u,c}$. Therefore, $\varepsilon_{u,c}$ is expressed as:

$$\varepsilon_{u,c} = 1 - \frac{f_{y,c}}{f_{u,c}} \tag{7}$$

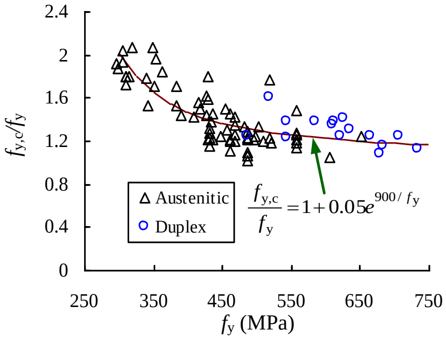

Figure 4. The relation between $f_{y,c}/f_y$ and f_y.

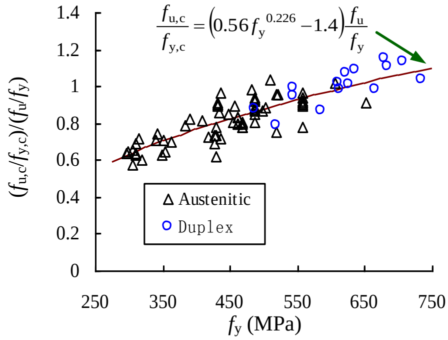

Figure 5. Ratio of $(f_{u,c}/f_{y,c})/(f_u/f_y)$ as a function of f_y.

(3) Determining n_c and m_c

Statistics analysis indicates that there is a relationship between the ratio of n_c/n^2 and n, and n_c/n^2 decreases with an increase in n-value. Equation (8) is proposed to predict n_c from n.

$$n_c = 0.9n^2 e^{-0.3n} \tag{8}$$

The value of m_c greatly affects the shape of the strain-hardening curve. The trial and error method was used to determine m_c from measured stress–strain curves. It is found that a higher value of m_c gives a better prediction of the σ–ε curve of corner material with a higher f_y. The following expression is proposed to determine m_c:

$$m_c = 0.04 f_y - 8 \tag{9}$$

3.2 Post-fire stress-strain model for flat regions

As suggested by the test results in [5], only the post-fire yield strength f_{yT} demonstrates an obvious decrease when T exceeds 500 ℃ for flat material, whereas other material parameters including E_{sT}, f_{uT}, ε_{uT} and n_T remain unchanged in general compared with the corresponding values of E_s, f_u, ε_u and n at ambient temperature. Therefore, Rasmussen's model is revised by replacing f_y with f_{yT} to consider the effect of fire damage.

$$\varepsilon = \begin{cases} \dfrac{\sigma}{E_s} + 0.002\left(\dfrac{\sigma}{f_{yT}}\right)^n & \text{for} \quad \sigma \le f_{yT} \\ 0.002 + \dfrac{f_{yT}}{E_s} + \dfrac{\sigma - f_{yT}}{E_{yT}} + \varepsilon_u\left(\dfrac{\sigma - f_{yT}}{f_u - f_{yT}}\right)^{m_T} & \text{for} \quad f_{yT} < \sigma \le f_u \end{cases} \tag{10}$$

where,

$$E_{\mathrm{yT}}=\frac{E_{\mathrm{s}}}{1+0.002nE_{\mathrm{s}}/f_{\mathrm{yT}}} \tag{11}$$

$$m_{\mathrm{T}}=1+3.5\frac{f_{\mathrm{yT}}}{f_{\mathrm{u}}} \tag{12}$$

$$\varepsilon_{\mathrm{u}}=1-\frac{f_{\mathrm{y}}}{f_{\mathrm{u}}} \tag{13}$$

The subscript T of the post-fire yield strength (f_{yT}) indicates that f_{yT} is a function of the maximum temperature (T). Since E_{yT} and m_{T} are related to f_{yT} as shown in Equations. (11) and (12), respectively, they also have a subscript T indicating they are a function of T.

Regression analysis is used to propose an equation for f_{yT} based on the test data shown in Figure 6. It is found that Equation (14) gives reasonable prediction of f_{yT}.

$$f_{\mathrm{yT}}=\begin{cases} f_{\mathrm{y}} & T\le 500°\mathrm{C} \\ \left[1-1.75\times10^{-4}(T-500)-2.71\times10^{-7}(T-500)^2\right]f_{\mathrm{y}} & T>500°\mathrm{C} \end{cases} \tag{14}$$

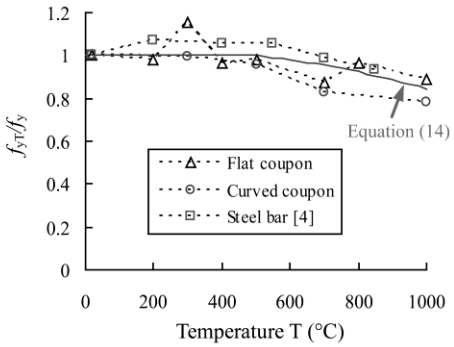

Figure 6. Ratio of $f_{\mathrm{yT}}/f_{\mathrm{y}}$ as a function of temperature.

3.3 Post-fire stress–strain model for corner regions

As mentioned before, corner parts of the stainless steel hollow section show a strength enhancement and a decrease in ductility at room temperature due to the cold forming. Test results in [5] indicate that this influence can be eliminated by fire exposure. After exposure to a temperature of 1000°C, the mechanical properties of the corner material are virtually the same as those of the flat material except that the ultimate strain of the corner material is 89% of that for the flat material without fire exposure.

To propose a reasonable post-fire σ–ε model for corner stainless steel, the following assumptions are made based on the test results presented in [5]:

(1) With suitable modifications, Rasmussen's model can still be used for corner stainless steel after fire exposure based on the observation of the test curves.

(2) The elastic modulus of corner material is not affected by fire exposure, and can be taken as E_{s} of flat material at room temperature.

(3) The corner effects due to cold forming disappear when T is 1000 ℃, but the ultimate strain $\varepsilon_{\mathrm{uT,c}}$ of post-fire corner material can be taken as $0.89\varepsilon_{\mathrm{u}}$, where ε_{u} is the ultimate strain of flat material without fire exposure.

(4) When 20 ℃<T<1000 ℃, the mechanical properties of corner stainless steel with a temperature of T vary linearly between those at ambient temperature and those of the corner stainless steel after exposure to 1000 ℃.

Based on the above assumptions, the post-fire σ–ε model for corner stainless steel after fire exposure is expressed as follows:

$$\varepsilon=\begin{cases}\dfrac{\sigma}{E_{\mathrm{s}}}+0.002\left(\dfrac{\sigma}{f_{\mathrm{yT,c}}}\right)^{n_{\mathrm{T,c}}} & \text{for} \quad \sigma\le f_{\mathrm{yT,c}}\\ 0.002+\dfrac{f_{\mathrm{yT,c}}}{E_{\mathrm{s}}}+\dfrac{\sigma-f_{\mathrm{yT,c}}}{E_{\mathrm{yT,c}}}+\varepsilon_{\mathrm{uT,c}}\left(\dfrac{\sigma-f_{\mathrm{yT,c}}}{f_{\mathrm{uT,c}}-f_{\mathrm{yT,c}}}\right)^{m_{\mathrm{T,c}}} & \text{for} \quad f_{\mathrm{yT,c}}<\sigma\le f_{\mathrm{uT,c}}\end{cases} \tag{15}$$

where $f_{\mathrm{yT,c}}$ and $f_{\mathrm{uT,c}}$ are the residual yield strength and ultimate strength of the corner material heated up to a temperature of T, respectively; $\varepsilon_{\mathrm{uT,c}}$ is the ultimate strain corresponding to $f_{\mathrm{uT,c}}$; $n_{\mathrm{T,c}}$ and $m_{\mathrm{T,c}}$ are the strain hardening exponent and a material parameter for the fire-damaged corner stainless steel; and $E_{\mathrm{yT,c}}$ is the tangent modulus of the σ–ε curve at yield strength $f_{\mathrm{yT,c}}$, which is determined by Equation (16). Based on the fourth assumption, $f_{\mathrm{yT,c}}$, $f_{\mathrm{uT,c}}$, $\varepsilon_{\mathrm{uT,c}}$, $n_{\mathrm{T,c}}$ and $m_{\mathrm{T,c}}$ can be determined by Equations (17)-(21), respectively. According to Equation (14), f_{yT} of flat material equals to $0.845f_{\mathrm{y}}$ when T is 1000 ℃. Therefore, f_{yT} at 1000 ℃ is directly replaced by $0.845f_{\mathrm{y}}$ in Equation (17).

$$E_{\mathrm{yT,c}}=\frac{E_{\mathrm{s}}}{1+0.002n_{\mathrm{T,c}}E_{\mathrm{s}}/f_{\mathrm{yT,c}}} \tag{16}$$

$$f_{\mathrm{yT,c}}=f_{\mathrm{yc}}-(f_{\mathrm{yc}}-0.845f_{\mathrm{y}})\frac{T-20}{980} \tag{17}$$

$$f_{\mathrm{uT,c}}=f_{\mathrm{uc}}-(f_{\mathrm{uc}}-f_{\mathrm{u}})\frac{T-20}{980} \tag{18}$$

$$\varepsilon_{\mathrm{uT,c}}=\varepsilon_{\mathrm{uc}}-(\varepsilon_{\mathrm{uc}}-0.89\varepsilon_{\mathrm{u}})\frac{T-20}{980} \tag{19}$$

$$n_{\mathrm{T,c}}=n_{\mathrm{c}}-(n_{\mathrm{c}}-n)\frac{T-20}{980} \tag{20}$$

$$m_{\mathrm{T,c}}=m_{\mathrm{c}}-(m_{\mathrm{c}}-m_{1000})\frac{T-20}{980} \tag{21}$$

In Equation (21), m_{1000} is m_{T} of flat material with a T of 1000°C, and can be calculated from Equation (12). If f_{yT} is taken as $0.845f_{\mathrm{y}}$, m_{1000} can be expressed as:

$$m_{1000}=1+2.96\frac{f_{\mathrm{y}}}{f_{\mathrm{u}}} \tag{22}$$

In general, the predicted $f_{\mathrm{yT,c}}$ and $f_{\mathrm{uT,c}}$ have good agreement with the test results.

3.4 Comparison between predicted and test curves

According to the discussion in previous subsections, at a given T, only the three basic Ramberg-Osgood parameters at room temperature, i.e., E_{s}, f_{y} and n, are required to determine the full-range σ-ε curve of fire-damaged stainless steel. For the σ-ε model proposed for corner regions, it is valid for austenitic and duplex stainless steel hollow sections with a f_{y} ranged from 300 to 750 MPa. For the post-fire σ-ε model, it is only valid for austenitic stainless steel with a f_{y} of around 300 MPa and a maximum historical temperature of 1000 ℃. More tests need to be done in the future to expand the validity range of the post-fire model and suitable modifications may be made if necessary.

The proposed model is used to predict the measured σ-ε curves. Reasonably good agreement is achieved between the predictions and measured σ–ε curves under different circumstances. Figure 3 shows the comparison for corner material at room temperature. Figure 7 shows typical comparisons for post-fire flat and corner material. It should be noted that in predicting the post-fire corner material, the ultimate strain $\varepsilon_{uT,c}$ is overpredicted for the tests in [5]. This error, however, does not affect the shape of the predicted σ–ε curve owing to the excellent ductility of austenitic stainless steel. Therefore, Equation (15) is valid to be used for post-fire corner material within strains of general structural interest.

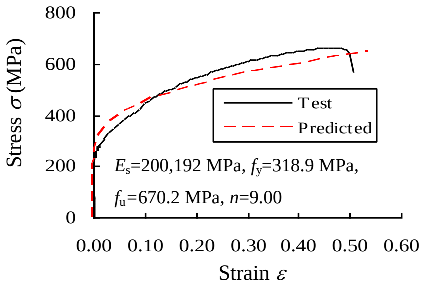

(a) Curved coupon (T=1000°C)

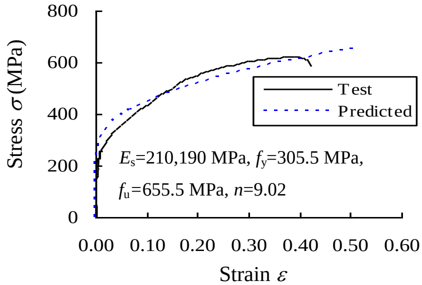

(b) Corner coupon (T=1000 °C)

Figure 7. Comparison between measured and predicted σ–ε curves.

4 CONCLUSIONS

Tests were recently conducted to investigate the mechanical properties of austenitic stainless steel of grade 1.4301 after heating and cooling down to room temperature. These results were used in this paper to develop a post-fire stress–strain model for austenitic stainless steel. To propose such a model, more recent test results were collected to verify Rasmussen's model for flat austenitic stainless steel at room temperature first. The verification indicates that Rasmussen's model agrees with the new collected test results very well. By incorporating into corner effects, Rasmussen's model was revised for corner stainless steel at room temperature. Then a post-fire stress–strain model was proposed to capture the mechanical properties of flat and corner stainless steel after exposed to elevated temperatures. The accuracy of the proposed model was validated by comparing with the test results.

REFERENCES

[1] Rasmussen K.J.R., "Full-range stress–strain curves for stainless steel alloys", *Journal of Constructional Steel Research*, 59(1), 47-61, 2003.

[2] Chen J. and Young B., "Stress-strain curves for stainless steel at elevated temperatures", *Engineering Structures*, 28(2), 229-239, 2006.

[3] Gardner L., Insausti A., Ng K.T. and Ashraf M., "Elevated temperature material properties of stainless steel alloys", *Journal of Constructional Steel Research*, 66(5), 634-647, 2010.

[4] Felicetti R., Gambarova P.G. and Meda A., "Residual behavior of steel rebars and R/C sections after a fire", *Construction and Building Materials*, 23(12), 3546-3555, 2009.

[5] Wang X.Q., Tao Z., Song T.Y. and Han L.H., "Mechanical properties of austenitic stainless steel after exposed to fire", *Proceedings of the Fifth International Conference on Structural Engineering, Mechanics and Computation*, A. Zingoni (ed.), Cape Town, South Africa, 1483-1488, 2013.

[6] Tao Z., Uy B., Liao F.Y. and Han L.H., "Nonlinear analysis of concrete-filled square stainless steel stub columns under axial compression", *Journal of Constructional Steel Research*, 67(11), 1719-1732, 2011.

EXPERIEMENTAL AND NUMERICAL STUDIES ON DAMAGE MECHANISMS IN CEMENTITIOUS COATINGS ON STRUCTURAL STEEL MEMBERS

Su-Wen Chen*, Li-Ming Jiang, Asif Usmani** and Guo-Qiang Li***

* State Key Laboratory for Disaster Reduction in Civil Engineering, Tongji University
e-mails: swchen@tongji.edu.cn,gqli@tongji.edu.cn

**School of Engineering, The University of Edinburgh
e-mail: s1134128@staffmail.ed.ac.uk, asif@staffmail.ed.ac.uk

Keywords: Cementitious coating, Cohesive Zone Finite Element (CZFE), Damage mechanism, Mechanical property, Monotonic loading test, Steel structure

Abstract. *Cementitious coatings are widely used as fire protection in steel structures however they are vulnerable to damage from structural deformations, which may gradually reduce the fire resistance of buildings. Although there are no existing requirements in international building regulations to assess the deterioration in building fire protection over time, the increasing emphasis on life-cycle performance in current structural engineering thinking suggests that this should be a concern. To quantify the damage in fire proof coatings, researcheshave been carried out by the authors over the last few years, comprising: (1) mechanical property tests on the cementitious material; (2) monotonic loading tests on coated structural steel members in tension, in compression and in bending respectively; (3) corresponding numerical simulations using a cohesive zone finite element (CZFE) scheme, capable of modelling interfacial damage between the coating and the steel substrate as well as internal coating damage; and (4) a parametric study on the influence of coating its dimensions on the damage mechanism. The results of the experimental and numerical studies clearly reveal distinct damage mechanisms in cementitious coatings on structural steel members under simple loading. Parametric studies show that increasing the thickness of coating may cause earlier cracking and more severe damage.Findings from this study provide the foundation for developing practical methods to determine the condition of cementitious coatings on steel framed structures after a short duration extreme loading or long duration cumulative damage from routine and moderate levels of repeated non-monotonic loading.*

1 INTRODUCTION

Cementitious fireproof material has been widely used to protect steel structures due to their low density, low thermal conductivity, low cost, and non-toxic emissions when exposed to fire. However, the mechanical properties of cementitious coating and adhesive strength are very weak [1-3] and vulnerable to damage. Previous researchers have shown that partial damage of the coating could significantly reduce the member's fire resistance [4-7].

To evaluate the damage of coating on protected steel members subjected to external load, Wang [8] presented an analytical study using an elastic FE analysis to study the interlaminar stress, indicating that cementitious coating damage is most likely to start from interfacial cracks at an early stage of loading. An elastic model, however, is not able to simulate damage propagation and interfacial behaviour, which should be addressed properly as in numerical approaches adopted in laminated composite structures. Dwaikat and Kodur [9]analyzed the damage of Spray-applied Fire-resistant coating under impact loading.

This paper presents mechanical properties tests of cementitious coatings, comprehensive experimental and numerical studies on damage mechanisms of cementitious coating for steel members under monotonic loading. The results from experimental and numerical studies clearly reveal distinct damage mechanisms in cementitious coatings on structural steel members under simple loading

2 MECHANICAL PROPERTY TESTS ON THE CEMENTITIOUS MATERIAL

Tests are conducted for obtaining the following mechanical properties: (1) Tensile strength; (2) Compressive strength; (3) Normal Bond Strength; and (4) Tangential Bond Strength. The test setup and failure modes are shown in Figure1. Detailed introduction about mechanical property tests can be found in reference [1].

(a) Tensile strength (b) compressive strength (c) normal bond strength (d) tangential bond strength

Figure 1. Tests for mechanical property and bond strengths.

The mechanical properties of cementitious material and bond strengths based on the test results are tabulated in Table 1. The results demonstrate that the normal bond strength at the coating-steel interface is slightly weaker than the tensile strength of cementitious material itself, which explains that that cracks usually initiate along the coating-steel interface. It is necessary to point out that large variations in mechanical properties are observed from the results obtained from different groups of specimens tested.

Table 1. Results of mechanical properties tests.

Density (ρ)	Elastic Modulus (E_c)	Compressive Strength (f_c)	Tensile Strength (f_t)	Normal Bond Strength (f_{nb})	Tangential Bond Strength (f_{tb})
0.55 g/cm^3	40.33 MPa	0.59 MPa	0.05 MPa	0.04 MPa	0.07 MPa

3 MONOTONIC LOADING TESTS ON COATED STEEL MEMBERS

The damage in cementitious coatings can be assumed to only relate to the deformation of steel member. To avoid more complex stress states, cementitious coating is applied away from the edges over the central surface area of the steel members and monotonic loading cases are investigated, which are axial tensile loading, axial compressive loading and flexuralloading.

3.1 Axial tensile loading test

For the case of axial tensile loading (as shown in Figure 2(a)), the coating used for the first set of tests is in a rectangular patch of length, *L* of 200mm, width, *W* of 60mm, and thickness, *T* of 20mm. The steel plate thickness, t for all tensile tests is 8mm. As shown in Figure 2(b), axial tensile load is gradually applied on the partially coated steel plate. As the steel strain increases to 0.08% to 0.12%, the interfacial cracks start from both ends and propagate towards the center (Figure 2(c)). This is followed by transverse cracks in the cementitious coating (Figure 2(d)), which once opened, keep getting larger until the end of the test.

(a) specimen dimension (b) test setup (c) interfacial cracks (d) transverse cracks in coating

Figure 2. Axial tensile loading test on coated steel plates.

3.2 Axial compressive loading test

To avoid local and overall bucking in the steel plates due to initial eccentricity, a mini-column is fabricated from 8mm thick steel plates (Figure 3(a)). When the average strain in the four sides of steel plates reaches approximately 0.2%, coating-steel interfacial cracks appear at both top and bottom ends (Figure 3(c)), and then propagate towards the center with further increase of the load. When the steel strain reaches approximately 0.3%, cracks spreads all over the coating-steel interface but without any internal damage in the coatings. Soon after that, the coatings peel off as shown in Figure 3(d).

(a) specimen dimension (b) test setup (c) interfacial cracks (d) coating peeling off

Figure 3. Axial compressive loading test on cementitious material coated steel members.

3.3 Flexural loading test

To make sure that the tested plate with cementitious coating is in pure bending and avoid more complex stress states, the test setup is designed as shown in Figures 4(a) and (b), where the insulated length L is 500mm, the width b is 60mm and the thickness is 20mm. The steel plates are of size 800 mm ×100 mm×20mm (L×W×T).

The observed failure mode is that the coating on the tension side fractures into several segments, and the coating on the compression side delaminates from the steel and fractures due to large curvature. When the curvature at the neutral surface reaches 0.6×10-4 mm-1, interfacial cracks are observed at both ends on the compression side (No. 1 in Figure 4(e)) and propagate towards the center. When the curvature reaches 0.9×10-4 mm-1, the first transverse crack (No. 2 in Figure 4(c)) occurs on the tension side. When the loading further increases, more transverse cracks on the tension side (Figure 4(c) and 4(e)) and shear fracture (No. 8 shown in Figure 4(d) and 4(e)) on compressive side are observed. The reason for shear fracture on compressive side is due to large curvature, which causes a restraining force on the coating from the steel plate at both ends while the center of the coating remains attached to the plate.

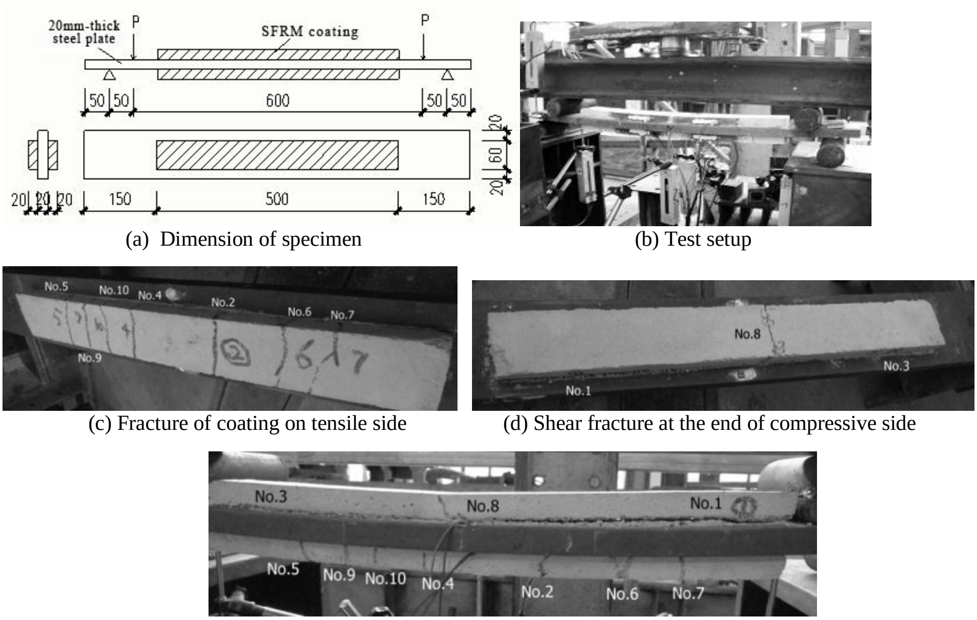

(a) Dimension of specimen

(b) Test setup

(c) Fracture of coating on tensile side

(d) Shear fracture at the end of compressive side

(e) Failure mode

Figure 4. Flexural loading test on coated steel member.

3.4 Results from monotonic loading tests

The monotonic loading tests clearly illustrate the damage modes of cementitious coatings.Under tensile loading, interfacial cracks initiate from the ends when steel strain reaches around 0.08% to 0.12% and propagate towards the center, followed by the occurrence of transverse cracks. The final failure mode is that the coating fractures into several segments but continues to adhere loosely to the steel plate. Under compressive loading, interfacial cracks initiate at the ends when steel strain reaches around 0.2% and then propagates to cover the whole interface. The final failure mode is the peeling off of the coating.Under flexural loading, interfacial cracks initiate from both ends on compressive side when the curvature in neutral surface reaches around 0.6×10^{-4}mm^{-1} and propagate towards the center, followed by the occurrence of transverse cracks on tensile side. The final failure mode is that the coating on the tension side fractures into several segments and the coating on the compression side peels off.

4. NUMERICAL SIMULATION FOR MONOTOLIC LOADING TESTS

4.1 Finite Element Model

From the experiments two types of damage in cementitious coatings are found, which are (1) Mechanical damage within the coating and (2) Interfacial cracking between the coating and steel substrate.

In this paper a cohesive zone finite element (CZFE) scheme is adopted, in which CZM in conjunction with contact pair (Conta173 and Target 171 in ANSYS) is employed for simulating coating-steel interfacial damage. Detailed introduction for CZM can be found in paper [10]. With CZFE approach, the interface is modeled with zero-length (initial state) elements. The constitutive law of the interface is the relationship between interface tractions and relative displacements. For the uncoupled model, two bilinear-one dimensional relationships can be assumed for normal (α=n) and tangential (α=t) direction respectively, as shown in Figure 5[11]. Where, $\delta_{o\alpha}$ and $\delta_{c\alpha}$ are the elastic and critical relative displacements.

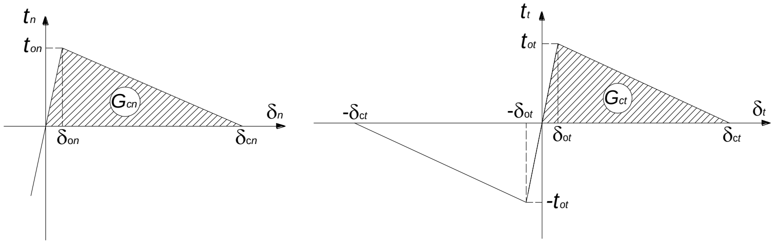

(a) Normal direction (b) Tangential direction

Figure 5. Uncoupled Constitutive relationships [11].

Since a real debonding should consider both the opening mode and the sliding mode, a modified mixed-mode constitutive relationship is shown as Equations (1)-(3) and an energy-based damage formulation is presented as Equation (4)[11].

$$t_\alpha = \varphi_m K_\alpha \delta_\alpha = (1-d_m) K_\alpha \delta_\alpha \tag{1}$$

$$d_m = \max\left(1,\ \frac{1}{\eta}\left(\frac{\Delta_m^* - 1}{\Delta_m^*}\right)\right) \quad \eta = 1 - \frac{\delta_{on}}{\delta_{cn}} = 1 - \frac{\delta_{ot}}{\delta_{ct}} \tag{2}$$

$$\Delta_m^* = \max_{0\le\tau'\le\tau}\left(\sqrt{\Delta_n^2(\tau') + \Delta_t^2(\tau')}\right) = \max_{0\le\tau'\le\tau}\left(\sqrt{\left(\frac{\langle \delta_n(\tau')\rangle}{\delta_{on}}\right)^2 + \left(\frac{\langle \delta_t(\tau')\rangle}{\delta_{ot}}\right)^2}\right) \tag{3}$$

$$\left(\frac{G_n}{G_{cn}}\right) + \left(\frac{G_t}{G_{ct}}\right) = 1,\quad G_n = \int t_n d\delta_n,\quad G_t = \int t_t d\delta_t,\quad G_{cn} = \frac{1}{2} T_{cn}\delta_{cn},\quad G_{ct} = \frac{1}{2} T_{ct}\delta_{ct} \tag{4}$$

Where G_n and G_t are fracture energies calculated by the following equations, G_{cn} and G_{ct} are critical fracture energies calculated in accordance with the single-mode delamination. The maximum traction along normal and tangential direction (T_{cn}, T_{ct}) can be set equal to normal and tangential bond strength (f_{nb}, f_{tb}) respectively, provided in Table 2.

Solid65 with Concrete damage model is employed to address the internal damage of cementitious coating. A crack in Solid65 element is represented through modification of the stress-strain relations by introducing a plane of weakness in a direction normal to the crack face. Hence the shear transfer coefficients (βt and βc) for the open and closed crack should be specified. Element solid45 with Bilinear Kinematic Hardening (BKIN) material model is employed to simulate the steel plate. Material properties adopted for numerical simulation are listed in Table 2.

The proposed CZFE scheme has been previously employed by the authors for investigating interfacial stress distribution between the coating and steel substrate on axially loaded steel members and verified by comparing against analytical interlaminar stress solution, directly constrainednodal displacements and contact analysis using zero-length spring elements [10].

Table 2. Material properties.

CZM and contact elements	K_n	T_{cn}	δ_{cn}	K_t	T_{ct}	δ_{ct}
	16 N mm^{-3}	0.04MPa	0.005	10 N mm^{-3}	0.07MPa	0.014
Cementitious coating	E_c	v	f_t	f_c		
	40.33MPa	0.2	0.05MPa	0.59MPa		
Steel	E	v	E_p	f_y		
	200GPa	0.3	1000 MPa	315MPa		

4.2 Results from the numerical simulations for axial monotonic loading tests

For the axial tensile loading case, the damage propagation in the coating (200mm×60mm ×20mm) is shown in Figure 6, where the cracks in Solid65 elements are plotted in red, and the deformation has been amplified 50 times. From the simulation results, it can be found that the damage appears at both ends of the interface when steel strain reaches ε_s=0.84×10^{-3}, which is represented by a sharp drop of interfacial stresses as shown in Figure 7. As the steel strain increases to 0.89×10^{-3}, it is noticed that delamination doesn't propagate along the interface to the center, instead by a set of short diagonal cracks occuring in the Solid65 elements as shown in Figure 6a. Then the short diagonal cracks propagate toward the center until the steel strain increases to 1.19×10^{-3} (Figure 6(b)), where the first pair of transverse cracks forms in coating(solid65 elements). As the tensile load continues increasing, the short diagonal cracks in the bottom coating elements continue to spread along the interface, which is followed by the second pair of transverse cracks when the steel strain reaches 1.55×10^{-3}(Figure 6(c)). Compared to the damage mode shown in Figure 2, the tensile damage mechanism of cementitious coatings observed from the tests seems to have been adequately simulated.

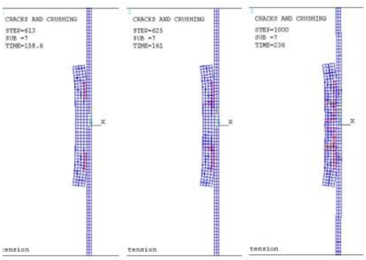

(a) ε_s=0.89×10^{-3}(b)ε_s=1.19×10^{-3}(c)ε_s=1.55×10^{-3}

Figure 6. Damage propagation (ε_s is steel strain).

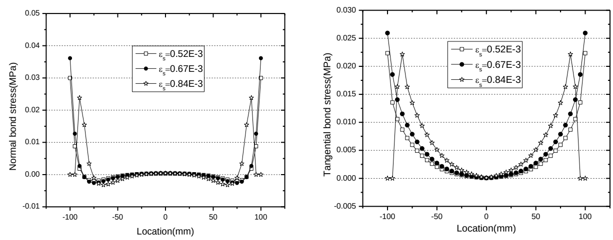

(a) Normal bond stress (b) Tangential bond stress

Figure 7. Interfacial stresses under axial tensile loading.

For the case of compressive loading, the development of coating damage is found only in the vicinity of the coating-Steel interface, which agrees with the test results of the compressive loading cases. The finite element model and development of contact element status on the interface is plotted in Figure 8. As the axial compressive load increases, the interface gradually develops delamination from both ends and moves towards the center with the final failure mode as the peeling off of the coating. This is because the maximum tangential bond stress, forming at the ends of the interface, dominates the damage mechanism since the interface is under compression at the ends along the normal direction.

When the steel plate is in pure bending, the effect of curvature is found to have a significant influence on the damage mechanisms found in coatings on steel members in bending, compared to axially loaded members, resulting in more severe damage. Thus, the steel curvature at the neutral plan is adopted to interpret the coating damage since strain can be represented with curvature and depth. The damage mode and damage propagation observed from the simulation agrees well with the test results as shown in

Figure4. As shown in Figure 9, the final failure mode is that the coating fractures into several segments with delamination at the ends on the tension side and the delamination of the coating with shear fracture at both ends on the compression side.

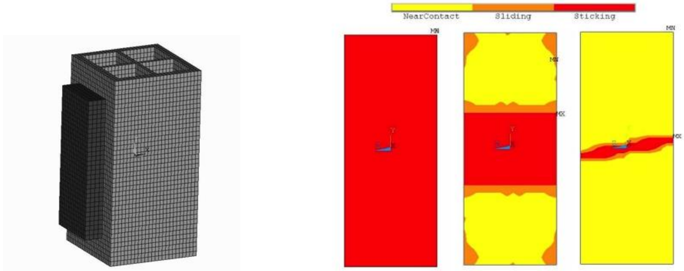

(a) Finite element model (b) $\varepsilon_s=1.82\times10^{-3}$ (b) $\varepsilon_s=2.30\times10^{-3}$(c) $\varepsilon_s=3.62\times10^{-3}$

Figure 8. Finite element model and contact element status under axial compressive loading.

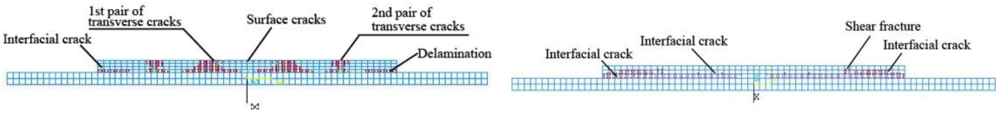

(a) Tension side (b) Compression side

Figure 9. Damage mode of cementitious coating on steel member in bending.

5 PARAMETRIC STUDY ON COATING SIZE

Parametric studies are carried out to investigate the influence of coating thickness andcoating length on the damage mechanisms.It is noted that increasing the coating thickness causes an earlier (at lower strain or curvature) occurrence of interfacial crack (Figure 10(a)) and transverse cracks, and an earlier failure as well as the change of the damage mechanism (Figures 10(b) and 10(c)). For the flexural loading case, no shear fracture is observed on the compressive side when the coating thickness reaches 40mm(Figure 10c). But the length of coating does not have anobvious effect on the damage propagation if it is long enough for shear transfer at interface. Similar phenomena have been observed for the axial tensile and compressive loading cases.

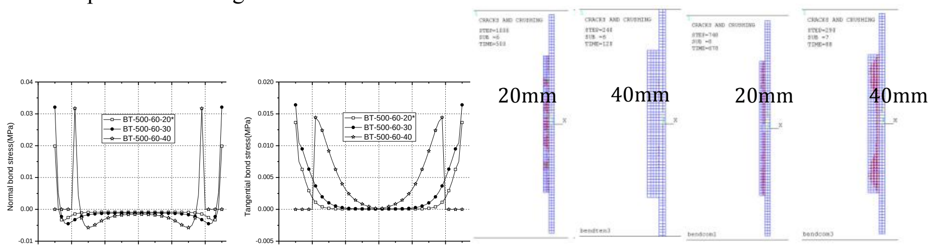

(a) Normal &Tangential bond stresses on tension side (b) On tension side (c) on compression side

Figure 10. Stress distributions and failure modesfordifferent thickness for flexural loading case.

6 CONCLUSIONS

Mechanical properties tests, monotonic loading tests and corresponding numerical simulations are presented in this paper for revealing the damage mechanisms of cementitious coatings for steel members. Main findings are listed as below.

(1) Under tensile loading, the damage begins with interfacial cracks at both ends, followed by transverse cracks within the coating resulting in its ultimate fracturing into segments.

(2) Under compressive loading, the damage also initiates at the ends with interfacial cracks and propagates towards the centre until the coating completely peels off.

(3) Under flexural loading, a similar failure mode is observed except that the effect of curvature causes more severe fracturing on the tension side and shear fractures at both ends on the compression side.

(4) It is also found that the thickness of the coating affects the damage mode. The thicker the coating is, the earlier the interfacial cracks appear. For the compression side in case of flexural loading, no shear fracture occurs for thicker coatings.This finding is useful for proposing solutions to reduce the damage to coating.

ACKNOWLEDGEMENT

Financial support from the Natural Science Foundation of China (Grant No. 50808143) and Key innovative Research Project of Shanghai Municipal Education Commission (Grant No. 09ZZ37) to this study is gratefully acknowledged.

REFERENCES

[1] Chen S.W., Jin C, and LI G.Q. (2010). A study on damage mechanism of thick fireproof coating for steel member subjected to monotonic loading. *Structures in Fire: Proceedings of the Sixth International Conference*.130.

[2] Tan K.T., White C.C., and Hunston D. L.(2011), An adhesion test method for spray-applied fire resistive materials, Fire and Materials, 35, 245-259

[3] Braxtan N.L. and Pessiki S.(2011), Bond Performance of CEMENTITIOUS COATING on Steel Plates Subjected to Tensile Yielding, Journal of Fire Protection Engineering, 21(1), 37-55

[4] Milke JA, Ryder N, and WolinS(2003). Analyses of the impact of loss of spray-applied fire protection on the fire resistance of steel columns. Fire Safety Science--Proceedings of the Seventh International Symposium.

[5] Ryder NL, Wolin SD, and Milke JA (2002). An investigation of the reduction in fire resistance of steel columns caused by loss of spray-applied fire protection. Journal of Fire Protection Engineering.12(1):31-44.

[6] Wang W.Y., and Li G.Q. (2009). Behavior of steel columns in a fire with partial damage to fire protection. Journal of Constructional Steel Research. 65(6):1392-1400.

[7] Keller W.J. and Pessiki S.(2012), Effect of Earthquake-induced damage to spray-applied fire-resistive insulation on the response of steel moment-frame beam-column connection during fire exposure, Journal of Fire Protection Engineering, 22(4), 271-299

[8] Wang, W.Y (2008). Damage mechanism of fire protection on steel columns under earthquake and influence of damage on the fire. PhD Dissertation. College of Civil Engineering Tongji University (in Chinese)

[9] Dwaikat M, and Kodur V (2011). Modeling Fracture and Delamination of Spray-Applied Fire-Resisting Materials under Static and Impact Loads. Journal of Engineering Mechanics. 137(12).901-910.

[10] Chen S.W., Jiang L.M., Usmani A.S. and Li. G.Q. (2012), A Numerical Approach for Damage Simulation of Spray-Spplied Fire-Resisting Materials on the Axially Loaded Steel Members, First International Conference on Performance-based and Life-cycle Structural Engineering (PLSE 2012), Hong Kong, China, Dec. 5-7

[11] Alfano G, and Crisfield MA (2001). Finite element interface models for the delamination analysis of laminated composites: mechanical and computational issues. International Journal for Numerical Methods in Engineering. 50(7):1701-1736.

A COMPARISON OF TWO TEMPERATURE-DEPENDENT STRESS-STRAIN MODELS FOR STRUCTURAL STEEL UNDER TRANSIENT HEATING CONDITION

Lisa Choe*, William Luecke* and John Gross*

* National Institute of Standards and Technology, Gaithersburg, MD 20899, USA
e-mails: lisa.choe@nist.gov, william.luecke@nist.gov, john.gross@nist.gov

Keywords: Conference, Fire, Structures, Steel, Temperatures, Columns

Abstract. *The finite-element method (FEM) requires accurate constitutive models for predicting the behaviour of steel components, structural members, or systems subjected to fire. As part of the World Trade Centre collapse investigation, the National Institute of Standards and Technology (NIST) developed an elevated temperature stress-strain model for structural steel, based on a combination of critically evaluated literature data and high temperature tensile tests conducted on structural steel recovered from the collapse site. The proposed stress-strain model accounts for temperature-dependence of elastic modulus, yield stress, and post-yield strain hardening as well as the strain-rate sensitivity. This paper presents (i) the strain-rate dependent behaviour of steel at elevated temperature using a prescribed heating rate, which can be used for the finite-element modelling of steel members subjected to increasing temperatures and (ii) detailed finite element models to predict the inelastic buckling behaviour and failure temperature of column specimens tested at Purdue University, USA. In this study, two full-scale ASTM A992 W14x53 column specimens, tested under transient heating conditions, are modelled. Each column specimen (with the length of 3.5 m) was subjected to a constant axial load but different heating (uniform or non-uniform temperatures through the cross-sections). The results of the 3D FEM analyses using the NIST proposed high temperature stress-strain models are thoroughly compared with those using Eurocode-3 and with the Purdue experimental results. The influence of thermal gradients and temperature-dependent strain- rate sensitivity on the inelastic column buckling is also discussed.*

1 INTRODUCTION

The finite-element method (FEM) requires accurate temperature-dependent material properties for simulating the behaviour of steel components, structural members, or systems subjected to fire. As part of investigation on the collapse of the World Trade Centre (WTC), the National Institute of Standards and Technology (NIST) presented the mechanical properties of structural steel recovered from the collapse site [1]. With continuing efforts, Luecke et al. [2] later proposed the new constitutive model based upon a combination of high-temperature tensile test results of recovered steels and many other evaluated test data, representing a total of 42 individual structural steels. This model accounts for the temperature dependence of the elastic modulus, yield stress, the change in strain hardening with temperature, and the effect of strain-rate on strength. The proposed model has been recommended for the 2016 edition of the ANSI/AISC-360 to replace the current tabular format based on the Eurocode-3[3] stress-strain curves.

The current AISC compressive member design [4] for fire conditions uses the column curve of I-shaped steel members proposed by Takagi and Deierlein [5]. This curve is developed based upon axial load capacities calculated using the Eurocode-3 stress-strain model and needs to be revised since the NIST proposed stress-strain model is recommended for fire resistance design. Zhang et al. [6] has developed the column design equations calibrated to the recommended model. Both the Eurocode-3 and the recommended stress-strain models are also evaluated by using them in simplified finite-element models that predict the failure temperature of forty seven steel columns from five laboratory tests conducted in the past twenty years. The results indicate that the NIST proposed stress-strain model predicts the failure temperature more accurately than the current AISC model [4] for four of five data sets. Although a simplified finite-element model used in the study is useful to quickly assess the axial load capacity or failure temperature of steel columns, it is limited in evaluating the effect of strain-rates on the buckling behaviour of columns.

Therefore, this paper presents (i) the strain-rate dependent behaviour of steel under transient heating conditions, which can be implemented in the finite-element modelling of steel members subjected to elevated temperatures and (ii) detailed finite-element models to predict the inelastic buckling behaviour and failure temperature of column specimens tested at Purdue University, USA. The detailed finite-element models account for both geometric and material nonlinearity to simulate inelastic buckling behaviour, non-uniformity of temperatures in column specimens, and the temperature-dependent thermal expansion model [3] to calculate the axial elongation of columns with increasing temperatures. In this study, two full-scale ASTM A992 W14x53 column specimens, tested under transient heating conditions, are modelled. The results of the 3D FEM analyses using the NIST proposed high temperature stress-strain models are thoroughly compared, and the effects of thermal gradients and temperature-dependent strain-rate sensitivity on the inelastic column buckling is also discussed.

2 MATERIAL MODEL

The Eurocode-3 stress-strain-temperature (σ-ε-T) model of steel has been widely accepted for structural design under fire conditions. The model was developed based on the British Steel Corporation data [7] of BS 4360 Gr. 43A and 50B steels tested at the heating rate of 10 ^{o}C/min [8]. Kirby and Preston [9] later created the stress-strain curves from these transient heating tests by assembling the collection of strain-temperature data points (up to $\varepsilon = 0.02$) at fixed stresses. The shapes of these derived σ-ε curves are similar to the Eurocode-3, but the temperature-dependent elastic modulus critical for column buckling analyses is 90% of the Eurocode-3 value [2].

The NIST proposed σ-ε-T model was based on the experimental behaviour of the retained high-temperature yield strength of 42 individual structural steels and the post-yield behaviour derived from eight (recovered from WTC site) of those steels. The model was then developed using curve fitting to test data. The model consists of temperature-dependent linear elastic regime in Eq. (1) and power-low strain hardening curve in Equation (2) for plastic strain, which joins at a temperature-dependent yield stress, $F_y(T)$. Elastic modulus, $E(T)$, is represented by an exponential function in Equation (3). Equation (4) calculates the retention factor, R, the ratio of $F_y(T)$ to its room-temperature value (F_{yo}), and Equation (5) is the temperature dependence of strain-rate sensitivity, m. Note that the strain-rate effect on strain-hardening in Equation (2) is negligible when the strain-rate ($d\varepsilon/dt$) is equal to 8.333×10^{-5}/sec (0.005/min), the rate used in most high-temperature tensile testing [2]. In this model, T is steel temperature in ^{o}C. The uncertainties associated with this model is reported in Luecke et al. [2] and not presented here for brevity.

$$\sigma = E(T)\cdot\varepsilon \tag{1}$$

$$\sigma = \left(R\cdot F_{yo} + \left(1006 - 0.759\cdot F_{yo}\right)\exp\left(-\left(\frac{T}{540}\right)^{7.820}\right)\left(\varepsilon - \frac{R\cdot F_{yo}}{E(T)}\right)^{0.503}\right)\left(\frac{d\varepsilon/dt}{8.333\times10^{-5}}\right)^{m} \tag{2}$$

Where,

$$E(T) = E_o\cdot\exp\left(-\frac{1}{2}\left(\frac{T-20}{639}\right)^{3.768} - \frac{1}{2}\left(\frac{T-20}{1650}\right)\right) \tag{3}$$

$$R = \frac{F_y(T)}{F_{yo}} = 0.090 + (1 - 0.090)\exp\left(-\frac{1}{2}\left(\frac{T-20}{588}\right)^{7.514} - \frac{1}{2}\left(\frac{T-20}{676}\right) \right) \tag{4}$$

$$m = 0.0108 + 0.126\left[1 - \exp\left(-\left(\frac{T}{613}\right)^{7.308} \right)\right] \tag{5}$$

Figure 1 plots the strain-rate sensitivity (m) as a function of temperature. Strain-rate sensitivity starts to increase at temperature beyond 400 ^{o}C. The Eurocode-3 model is compared with the NIST model plotted for various strain-rates ($d\varepsilon/dt$) and at elevated temperatures of 400 ^{o}C, 500 ^{o}C and 600 ^{o}C. As shown, the post-yield stresses of the NIST model increase with increasing strain-rates. The change in stresses due to strain-rates becomes significant at the higher temperatures. Figure 1 indicates that at $d\varepsilon/dt$ = 8.3×10^{-5}/sec, the stress at the strain of 2% is very close to that obtained from the Eurocode-3. At $d\varepsilon/dt$ = 1×10^{-4}/sec, the stress at the strain of 0.5% is comparable to that obtained from Eurocode-3 at 400 ^{o}C and 500 ^{o}C, but the NIST model generates post-yield stresses conservatively at 600 ^{o}C or higher.

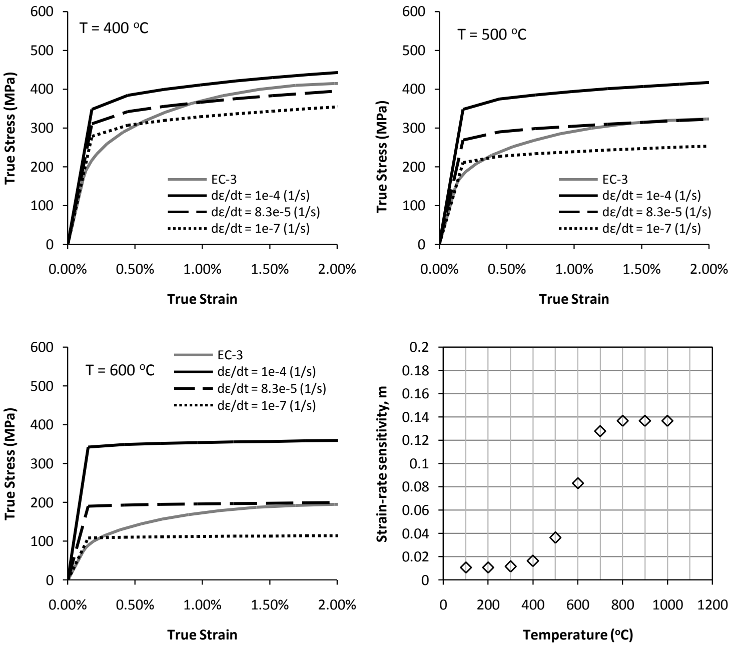

Figure 1. Eurocode-3 model versus NIST models with various strain-rates and temperature-dependence of strain-rate sensitivity of NIST model.

3 STRAIN-RATE EFFECTS IN TRANSIENT HEATING TESTS

Unlike the Eurocode-3 model, the NIST model was developed based on high temperature tensile coupon tests under steady-state heating conditions. Individual coupons exposed to a target temperature and then were loaded with a specified strain-rate. In order to evaluate strain-rate effects of the NIST model in transient heating tests, the finite-element models were developed to compute strain-temperature data points. The 571 mm × 127 mm coupon was modelled using four-node shell elements with reduced integration (S4R) implemented in ABAQUS ver. 6.12-1 [10]. The square-element size was equal to 21.2 mm × 21.2 mm. Using the Modified Newton-Raphson method, each coupon was subjected to some portion of the tensile yield strength at ambient temperature (σ/σ_{y20} = 0.05 to 0.95) and then was subjected to increasing temperature with a heating rate of 10 ^{o}C/min. No explicit thermal creep model was included; instead, different levels of strain-rates were incorporated.

Figure 2 shows the result of simulated transient heating tests for initial stress (σ/σ_{y20}) of 0.5 and five choices of strain-rates using the NIST model. Similarly, the true strain-temperature curve of the Eurocode-3 model is plotted for comparison. True strain-temperature curve is plotted up to strain of 0.5% because the small strain regime is critical for steel column buckling behaviour which is a particular interest in this study. As shown, the critical temperature, which can be defined by the temperature at the true strain of 0.5%, increases with increasing strain-rates in the NIST model. The critical temperature at $d\varepsilon/dt$ = 1×10^{-6}/sec is very close to that simulated using the Eurocode-3 model. While true strains estimated using the Eurocode-3 are developed gradually in the entire temperature ranges, those using the NIST model seldom increased until the critical temperature reached.

Figure 2 also plots the low strain behaviour of the transient-state tests for various initial stresses (σ/σ_{y20} = 0.6 to 0.9), simulated using the NIST model with $d\varepsilon/dt$ = 8.3×10^{-5}/sec (0.005/min). The critical temperatures decrease significantly with increasing the applied stresses. Also, it was observed that, at heating rate of 10 ^{o}C/min, there was no significant variation in strain-temperature behaviour when the applied initial stresses lower than 0.5. The slower strain-rates in the NIST model seem to influence the strain-temperature behaviour insignificantly when compared with the change due to initial stresses. Although there is yielding at the extremely low strain-rates, the accumulated strain is also insignificant.

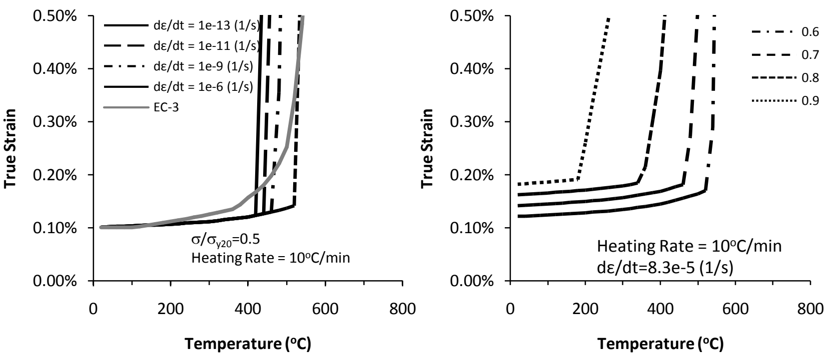

Figure 2. Effects of strain-rates and initial stresses in transient heating tests.

Figure 3 shows more comparisons of the simulated strain-temperature behaviour using the Eurocode-3 and the NIST models with the higher initial stresses (σ/σ_{y20} = 0.6 to 0.9). The applied heating rate is 10 ^{o}C/min. Two different strain-rates ($d\varepsilon/dt$ = 8.3×10^{-5}/sec and 1×10^{-6}/sec) were considered in the NIST model. It is observed that the shape of strain-temperature curves using the Eurocode-3 model varies with different initial stresses. The nonlinear behaviour diminishes with increasing stresses. At lower stresses, the strains are developed gradually until the critical temperature achieved while at very high stresses the post-yield strains increase linearly with temperatures.

However, there is no considerable change in the shape of curve simulated using the NIST model with increasing stresses except the elastic regime gets shorter with increasing stresses. Again, the predicted critical temperature (at strain = 0.5%) using the NIST model with $d\varepsilon/dt$ = 1×10^{-6}/sec compares well with that using the Eurocode-3 model up to σ/σ_{y20} = 0.8. For all stress levels, the predicted critical temperature at dε/dt = 1×10^{-6}/sec is smaller than that at dε/dt = 8.3×10^{-6}/sec. The difference in critical temperatures at two different strain-rates does not indicate any trend with increasing stresses.

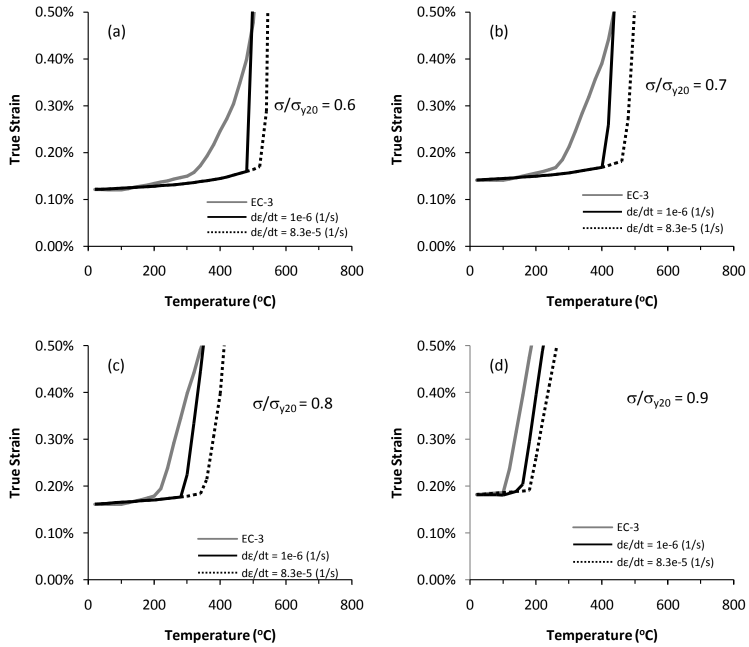

Figure 3. Comparison of strain-temperature behaviour using the Eurocode-3 and the NIST model.

Figure 4 shows the effects of applied heating rates (2 °C/min or 10 °C/min) on the strain-temperature behaviour predicted using the NIST model for varying initial stresses. At lower stress levels, it is expected that the strain-temperature behaviour at the heating rate of 2 °C/min is very similar to the behaviour at 10 °C/min, and the critical temperature (at ε = 0.5%) is identical. At the higher stress, one can imply from this plot that rapidly increasing temperature is beneficial to increase the failure temperatures; however, the time to reach the critical temperature becomes much shorter for a rapid heating rate.

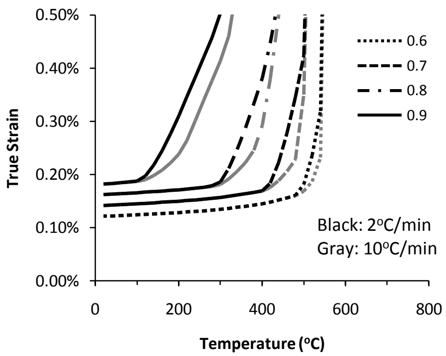

Figure 4. Effects of heating rates in strain-temperature behaviour.

4 INELASTIC BUCKLING OF COLUMNS

4.1 Purdue column tests

Choe [11] tested full-scale steel columns under transient heating conditions in Bowen laboratory, Purdue University, USA. The specimens were simply-supported wide-flanged steel columns with ASTM A992 W14x53 sections. The slenderness ratio was equal to 71. Using the specially designed test setup and hydraulic control, free thermal elongation of the specimens were allowed as temperature increased. Various fire protection schemes were used to develop thermal gradients through the cross-sections.

Two specimens were considered in this study: the specimen SP3-W14x53 was subjected to thermal gradients along the flanges (i.e., about the weak axis of the cross-sections), and the specimen SP4-W14x53 was subjected to uniform temperatures. Figures 5(a) and 5(b) show the experimentally measured temperature-time responses of the specimens SP3 and SP4, respectively. In both column tests, the axial load ratio (σ/σ_{y20}) was equal to 0.35, and the radiant heat was increased at 7 ^{o}C/min until failure. Test results indicated that thermal gradients along the weak axis caused bowing of column specimens toward the hotter side, which introduced second-order moments. Although column specimens failed by inelastic flexural column buckling, the fire resistance of the SP3 specimen was much lower than that of the SP4 specimen in terms of the average section temperature.

4.2 3D FEM models

The experimental behaviour and measured fire resistance of the tested specimens were compared to the results from detailed non-linear finite-element analyses. Each column specimen was modeled using eight-node linear brick elements with reduced integration (C3D8R) implemented in ABAQUS. The column cross-section was discretized into eighty-seven nodes. The simply supported boundary condition was assumed at column ends.

The analysis scheme followed the actual test protocol: (1) applying an axial load at ambient temperature, and then (2) increasing the temperature until failure occurred. In each step, the experimentally measured axial load-temperature-time (*P-T-t*) data was enforced to capture the complete stability failure of the columns. The models also included the assumed residual stress distributions through cross-sections as specified in ANSI/AISC-360 [4] and the assumed global geometric imperfection (i.e., sweep equal to L/1500).

4.3 Comparisons with 3D FEM predictions

Figures 5(c) and 5(d) compare the numerically predicted lateral deformations to those measured in the tests. As shown, the 3D FEM model predicted the overall lateral deformation behavior of column specimens reasonably well, given that the experimentally measured *P-T-t* curves were used. Both the test result and the 3D FEM model of the SP3 indicate continuously increasing lateral deformations due to thermal bowing from non-uniform heating. For the SP4, lateral deformations seldom increase under uniform heating conditions, and buckling occurred when the critical temperature was achieved.

It is interesting to note that thermal gradients in SP3 overwhelm the effects of different steel models, and the numerical results using the Eurocode-3 compare very well with the NIST models. Also, the strain-rate effects appear to be negligible showing that the results of the NIST models with two different strain-rates are top on each other in Figure 5(c). However, the fire resistance of the SP4 predicted by 3D FEM models with the Eurocode-3 and the NIST model was quite different. The strain-rate effects are also evident as well. Overall, the 3D FEM models using the NIST model compare better with the test results. The Eurocode-3 model predicts the fire resistance conservatively due to the nonlinearity developed in small strains ($\varepsilon \leqslant 0.5\%$).

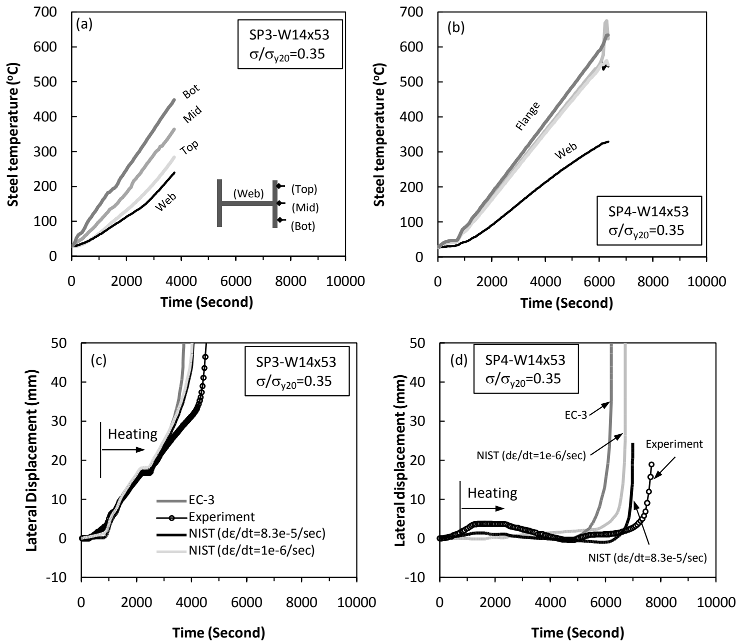

Figure 5. Temperature-time and lateral displacement-time responses of steel columns.

5 CONCLUSIONS

This paper presents the strain-rate dependent behaviour of steel at elevated temperature. Transient heating tests were simulated using the NIST model for different choices of initial stresses and strain-rates at the prescribed heating rate. Their strain-temperature behaviour were compared with those predicted using the Eurocode-3. The strain-rates in the NIST model can affect the transient behaviour but the applied stress level can overwhelm the strain-rate effects. While the NIST model predicts sharp yielding about the time to reach the critical temperature, the Eurocode-3 model indicates the gradual development of strains throughout entire temperature range (or time). In this study, two full-scale ASTM A992 W14× 53 column specimens, tested in Purdue University, are modelled to evaluate the strain-rate effects on the inelastic column buckling. Each column specimen (with the slenderness ratio of 71) is subjected to a constant axial load but varying temperatures along the length and across the sections. The results indicate that thermal gradients in the column specimen can overwhelm the effects of different steel models, showing that lateral deformation behaviour predicted using the Eurocode-3 compare very well with the NIST models. Also, the strain-rate effects appear to be negligible. However, for the column subjected to uniform heating, the fire resistance predicted using the Eurocode-3 model is quite different from that using the NIST model, and the strain-rate effects on the fire resistance are observed. Overall, the 3D FEM models using the NIST model compare better with the test results. The Eurocode-3 model tends to predict the fire resistance conservatively.

REFERENCES

[1] Luecke, W. E., McColskey, J. D., McCowan, C. N., Banovic, S. W., Fields, R. J., Foecke, T., Siewert, T. A., and Gayle, F. W., "Federal building and fire safety investigation of the World Trade

Center disaster: Mechanical properties of structural steel", *Technical Report NCSTAR 1-3D*, National Institute of Standards and Technology, 2005.

[2] Luecke, W. E., Banovic, S. W., and McColskey, J. D., "High-temperature tensile constitutive data and models for structural steels in fire", *Technical Note 1714*, National Institute of Standards and Technology, 2011.

[3] ECS., "Eurocode-3. Design of steel structures. General rules. Structural fire design", *Standard EN 1993-1-2*, European Committee for Standardization, 2005.

[4] AISC, "Specification for structural steel buildings", *Specification ANSI/AISC 360-10*, American Institute of Steel Construction, Chicago, IL., 2005.

[5] Takagi, J. and Deierlein, G. G., "Strength design criteria for steel members at elevated temperatures", *Journal of Constructional Steel Research*, 63(8), 1036–1050, 2007.

[6] Zhang, C., Luecke, W. E., Choe, L., Gross, J. L., "Modeling flexural buckling of steel columns in fire", *Engineering Journal*, American Institute of Steel Construction, *submitted*, 2014.

[7] Kirby, B., Preston, R., "The behaviour of structural steels manufactured by BSC under stress controlled anisothermal creep condition", *Technical Report SH/RS/3664/4/83/B*, British Steel Corporation, Swinden Laboratories, 1983.

[8] Twilt, L., "Stress-strain relationships of structural steel at elevated temperatures: Analysis of various options & European proposal, Part F: mechanical properties", *Report BI-91-015*, Netherlands Organization for Applied Scientific Research, 1991.

[9] Kirby, B., Preston, R., "High temperature properties of hot-rolled, structural steels for use in fire engineering design studies", *Fire Safety Journal*, 13(1), 27-37, 1988.

[10] ABAQUS, *ABAQUS/Standard Version 6.12 User's Manuals: Volume I-III*, Hibbitt, Karlsson, and Sorenson Inc., Pawtucket, RI., 2012.

[11] Choe, L., "Structural mechanics and behaviour of steel members under fire loading", *Ph.D. Thesis*, Purdue University, West Lafayette, IN., 2011.

8th International Conference on Structures in Fire
Guo-Qiang LI, Venkatesh K. R. KODUR, Shou-Chao JIANG, Jian JIANG, Su-Wen CHEN, Guo-Biao LOU (Eds.)
Shanghai, China, June 11-13, 2014

BEHAVIOUR OF STRESSED AND UNSTRESSED CONCRETE WITH AND WITHOUT POLYPROPYLENE FIBRES AT HIGH TEMPERATURES

Duncan E. Cree*, Prosper B. Pliya* and Mark F. Green**

* Queen's University, Department of Civil Engineering, Kingston, Ontario, Canada
*Université de Cergy-Pontoise, L2MGC, F–95000 Cergy-Pontoise, France
e-mails: creed@queensu.ca, prosper.pliya@u-cergy.fr

** Queen's University, Department of Civil Engineering, Kingston, Ontario, Canada
e-mail: greenm@civil.queensu.ca

Keywords: Concrete, Temperature, Thermal gradient, Polypropylene fibres, Strength, Porosity

Abstract. *This paper presents the results of an experimental study to compare the influence of polypropylene fibres (f-PP) on the behaviour of high strength concrete (HSC) subjected to elevated temperatures in stressed or stress-free hot conditions. Very few studies are available in the literature on the behaviour of HSC containing PP fibres subjected to stressed or stress-free state with simultaneous application of elevated temperature (tested hot). One group of concrete specimens was subjected to an initial preload of 40 % of the initial room temperature compressive strength during the heating (stressed hot), while a second group was in a non-loaded condition during heating (stress-free hot). Results show the stressed concrete had a lower thermal gradient, a decrease in relative porosity when PP fibres were added and an improved compressive strength with or without fibres as compared to the stress-free HSC.*

1 INTRODUCTION

Concrete behaviour at high temperature has been the subject of several investigations [1-8]. Concrete thermal instability could be the result of vapour pressure build-up mechanisms and/or restrained thermal dilatation mechanisms [2-3]. Parameters such as water content, porosity, permeability, and aggregate type have an influence on thermal instability. An effective method to reduce the risk and improve thermal instability in concrete mixes is the addition of polypropylene (PP) fibres as demonstrated by many studies [4-8]. Thermal differential analyses conducted by Kalifa et al. [4] and Noumowé [7] have shown PP fibres melt at approximately 160-170 °C and vaporize around 340 °C. Melting of PP fibres produces expansion channels and lowers internal vapour pressure at the interior of the concrete which reduces the likelihood of explosive spalling. Vapour pressures within concrete specimens with and without PP fibres were measured by Kalifa et al. [4] and they found that PP fibres decreased the vapour pressures during heating. In addition, they found that the peak pressure dropped as the fibre content increased until reaching a maximum plateau at 1.75 kg/m^3 of fibres.

Four types of heating and compressive loading conditions exist to evaluate the fire resistance of concrete cylindrical specimens: (i) stressed and tested 'hot', (ii) stress-free and tested 'hot', (iii) stressed at high temperature but tested at ambient temperature after heating, and (iv) stress-free at high temperature and tested at ambient temperature after heating. The majority of studies conducted were to evaluate the latter, post-fire room temperature residual strengths after heating. Hot strength data for concrete containing PP fibres is limited. It is equally important to evaluate concrete for its hot compressive strength since strength should be maintained throughout the duration of a fire. HSC without fibres and under a compressive load at elevated temperatures was found to have an increase in the risk of spalling [9]. The addition of PP fibres is generally added to concrete to prevent explosive spalling, however in some cases, HSC was shown to be susceptible to spalling under a compressive load even with PP fibres [10].

The objective of this research study was to investigate how the PP fibres in various dosages affect the spalling, water content, compression strength, water porosity and evolution of internal temperature gradient of specimens under stressed or stress-free at elevated temperatures. In addition, secondary electron microscope (SEM) images were obtained from fractured samples to understand changes in microstructure before and after heating**.**

2 EXPERIMENTAL SCHEDULE

2.1 Materials

The experimental program consisted of casting 102 mm × 203 mm HSC specimens with or without PP fibres. The mixture was prepared from Portland Limestone Cement, Type GUL. Coarse aggregates were river rounded granite pea stone with a high percentage of calcareous aggregates and fine river sand. To increase the workability of all mixtures, BASF Glenium 7700 superplasticizer (High Range Water Reducing Admixture) was added to the mix. Commercially available polypropylene fibres were Duomix® fire (M6) fine monofilaments with a length of 6 mm, diameter of 18 µm and a melting temperature of 160-165 °C. HSC without fibres (C) and with fibres were studied by adding two volume fractions of PP fibres in the concrete; 0.11% and 0.22% (equivalent to 1 (CP1) and 2 (CP2) kg/m^3). All mixtures had the same water/cement (w/c) ratio of 0.35 and had a slump between 180 and 190 mm. Table 1 provides details of the mixture proportions for HSC with and without fibres. The moisture contents at 28 days are included with their respective standard deviations (±). The samples were de-moulded after 1 day and sealed in plastic bags at ambient temperature to prevent moisture loss. Heating and testing was conducted after 28 days of curing.

Table 1. Mix proportions for HSC with different fibres additions.

Concretes	Components (kg/m^3)						Slump	Moisture	Density
	Water	Cement	Gravel	Sand	Super.	F-PP	(mm)	Content (%)	(kg/m^3)
C	166	475	888	888	0.3	0	180	3.8 ± 0.2	2417
CP1	166	475	888	888	0.4	1	190	4.4 ± 0.2	2418
CP2	166	475	887	887	0.4	2	190	4.5 ± 0.2	2417

2.2 Heating procedure

Specimens were tested at ambient temperature and at elevated temperatures of 150 °C, 300 °C and 450 °C. Elevated temperatures were provided with an electric Instron box furnace, series 3119 chamber that can reach a temperature of 600 °C. The furnace was controlled with a Eurotherm 2408 temperature controller. The specimens were heated at a rate of 15 °C/min from room temperature up to their respective target temperatures and held until the centre temperature was equal to the surface temperature by ~2 °C. All tests were conducted at temperature in a stressed or stress-free condition. Three type-K thermocouples (TC) were used to monitor the temperature of the furnace, cylinder surface temperature and cylinder core temperature as shown in Figure 1. The thermocouple at the centre core of the specimen was positioned in place during casting and was located at mid-height and mid-diameter.

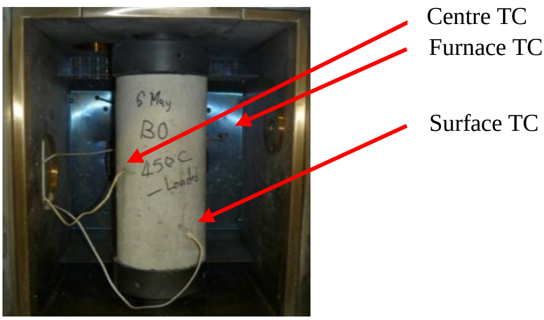

Figure 1. Compression test set-up in box furnace.

2.3 Testing methodology

For each tested condition, five representative samples from the broken cylinder were obtained to conduct the water porosity test. The specimens were oven dried at 80 ℃ for 24 hours until no weight change was observed and further immersed in distilled water to obtain saturated specimens. The total porosity measurements were obtained by first weighing the dry samples in air, weighing immersed saturated specimens in water, and weighing specimens in a saturated but surface dry condition.

Compressive strength measurements were carried out in accordance with ASTM C39 at a loading rate of 0.5 MPa/s. Room temperature strength measurements were made after 28 days of curing on three specimens and averaged. Preloading was done at 40 % of the room temperature strength (24 MPa).

Microstructure analysis was conducted using a high resolution SEM model Quanta 650 FEG with an accelerating voltage of 15 keV. Relatively small, flat broken samples from compression tests were analyzed without any special preparation.

3 RESULTS AND DISCUSSION

3.1 Temperature and SEM

The water content of concrete at 28 days ranged from 3.8 % (C) to 4.4 % (CP1/CP2) and no surface cracks or spalling was observed during the various heating and loading cycles. A slight increase in water content was observed in concrete containing PP fibres.

The results for the temperature evolution as a function of time are given in Figure 2. The surface temperature profiles for concretes C, CP1, and CP2 for both stressed and stress-free situations remained relatively consistent. At the beginning and end of the heating profiles, the surface temperatures were in agreement with the furnace air temperature. After about 5 minutes of heating, the deviation was more pronounced because of the relatively large thermal mass of the concrete compared to air.

Short plateaus occurred for the centre temperature profiles between 179°C -235°C (dependent on loading condition and fibre content) after 50 minutes of heating which were indicative of moisture evaporation within the concrete. These plateaus also occurred at testing temperatures of 300 °C but were not visible at 150 °C. Irrespective of the loading condition, water evaporated at a higher temperature for concrete without PP fibres, which may have been due to lower moisture content. In general, HSC under stress produced an evaporation plateau at a lower temperature than that for the stress-free samples. Loading may have increased the moisture content at the centre of the specimens. As anticipated, the temperature rise at the centre of the concrete cylinder was slower compared to that at the surface because of the low thermal conductivity of the concrete.

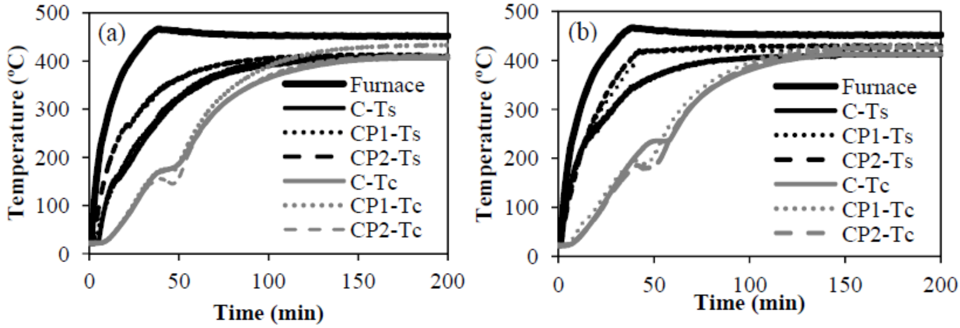

Figure 2. Evolution of surface and centre temperatures as a function of time during heating to 450 ℃ for (a) stressed and (b) stress-free specimens.

Although the furnace was maintained at a constant heating rate, the interior of the concrete between the surface and the centre of the cylinders with and without fibres experienced different heating rates as represented by the thermal gradient (e.g. slope) changes in Figure 3. The thermal gradient profiles for the stressed and stressed-free concrete without fibres are divided into five stages (e.g. stage I, II, III, IV and V) shown by the short vertical dashed lines. A high positive thermal gradient in stage I to II indicated that the surface temperature was increasing faster than the core temperature. A negative or constant thermal gradient in stage II to III indicated a reduced heating rate between the surface and the core temperature. During stage III to IV a final temperature increase was observed at a maximum thermal gradient of 2.9 °C/mm due to heating and moisture evaporation in the core. From stage IV to V a steep negative thermal gradient indicated a sharp temperature change between the core and the surface in which the core temperature was increasing faster than the surface temperature.

Regardless of the loading condition, adding PP fibres increased the thermal gradient after the melting temperature of the PP fibres which can be related to a more open pore structure. In general, stressed concretes with and without PP fibres had lower thermal gradients than the stress-free concrete possibly due to a decrease in the pore structure. Loading concrete may reduce the amount of micro-cracks and micro-voids available for transferring heat from the surface to the core.

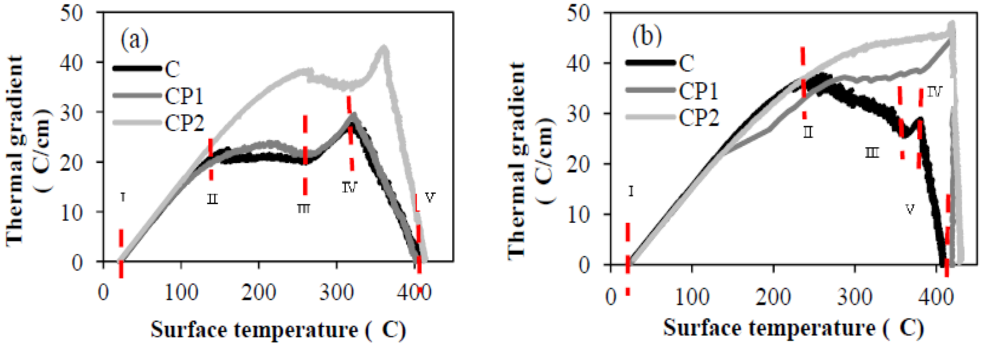

Figure 3. Evolution of thermal gradient as a function of surface temperature during heating to 450 ℃ for (a) stressed and (b) stress-free specimens.

3.2 Porosity and compressive strength

The results for the relative compressive strength and relative porosity are summarized in Table 2. The compressive strengths at room temperature for C, CP1 and CP2 concretes were 60.0 ± 1.0 MPa, 55.9 ± 3.7 MPa and 56.4 ± 0.6 MPa, respectively. The porosities after drying at 80 ℃, for C, CP1 and CP2 concretes were 11.6 ± 0.8%, 12.8 ± 0.8% and 13.6 ± 0.8%, respectively. The relative compressive strengths and porosities were calculated by dividing the compressive strength (or porosity) for each heating cooling cycle by the compressive strength (or porosity) obtained at room temperature (after drying at 80 ℃).

Table 2. Relative compressive strength and porosity.

Concretes	Relative compressive strength [%] (f_{cT}/f_{c20})						Relative porosity [%] (P_T/P_{80})					
	Stress-free [℃]			Stressed [℃]			Stress-free [℃]			Stressed [℃]		
	150	300	450	150	300	450	150	300	450	150	300	450
C	67.2	110.2	93.1	75.4	109.5	92.1	112.3	114.6	135.7	111.0	125.5	137.2
CP1	76.9	102.0	89.8	80.4	102.5	91.1	106.7	118.3	131.8	104.4	115.2	129.5
CP2	69.7	97.5	75.0	81.4	102.0	87.0	101.3	107.6	127.0	102.5	107.8	121.7

The porosity was influenced by an increase of PP fibre content in the unheated concretes. For example, by comparing C and CP2, the porosity of concretes increased by 17 % in their unheated state with the addition of 2 kg/m^3 fibres. This additional porosity created by the presence of PP fibres was related to adsorbed water on the fibre's surface. The moisture accumulated on the surface of the PP fibres and created voids between the fibre/cement interfaces after concrete hydration. The moisture content of concrete was also measured and showed an increase of 18 % as fibre content increased to 2 kg/m^3 as shown in Table 1.

The evolution of relative porosity as a function of heating temperature is given in Figure 4. The porosity of all concrete specimens with or without PP fibres was observed to increase after heating. For example, the relative porosity of stress-free C concretes increased from 112 % at 150 ℃ to 136 % at 450 ℃, while the concretes under stress increased from 111 % at 150 °C to 137 % at 450 °C. This translated to a 21 % and 24 % increase in relative porosity for concretes without fibres, respectively. The results suggested that the effect of stress on porosity was not as significant for concrete without fibres. Since PP fibres were not present, the increase of porosity was due to various physical and chemical concrete transformations during heating as opposed to changes in the fibres.

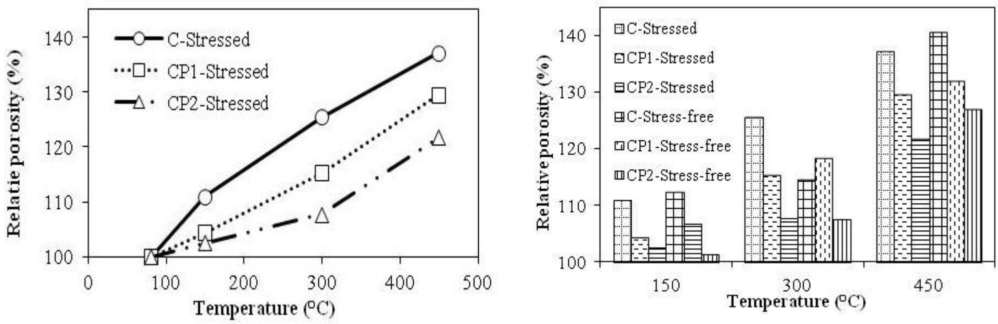

Figure 4. Relative porosity as a function of heating for stressed and stress-free conditions.

The influence of PP fibre additions is also noted for both stressed and stress-free studies. The relative porosity of concretes with fibres increases less rapidly than that of concrete without fibres. Fibres thus consume heat in latent form which could limit the increase of the pore volume. Comparing stressed and stress-free concretes, the relative porosities vary little for each temperature studied. At each test temperature, the relative porosity for stress-free and stressed concretes tends to decrease with PP fibre additions. A stressed condition during heating may reduce the amount of micro-cracks and micro-voids which has an impact on the thermo-hydro transfer as provided during the evolution of the temperature at the centre of the specimens in Figure 2.

Figure 5 shows the evolution of the relative compressive strength as a function of temperature. Compressive strength of concrete with or without fibres decreased with the rise in temperature. The behaviour was the same for all concretes. The PP fibres did not influence the evolution of compressive strength as a function of the temperature and this is consistent with the literature. The compressive strength of unheated C and CP2 concretes were 60 MPa and 56 MPa, respectively which translated to a 7 % decrease in strength due to a volume fibre fraction addition of 0.22 %. Correspondingly, water porosity measurements showed an increase in porosity with an increase in PP fibres. These results confirm the reduction in compressive strength. In general, the compressive strength of concretes with fibres remains less than that of concretes without fibres for all heating cycles studied.

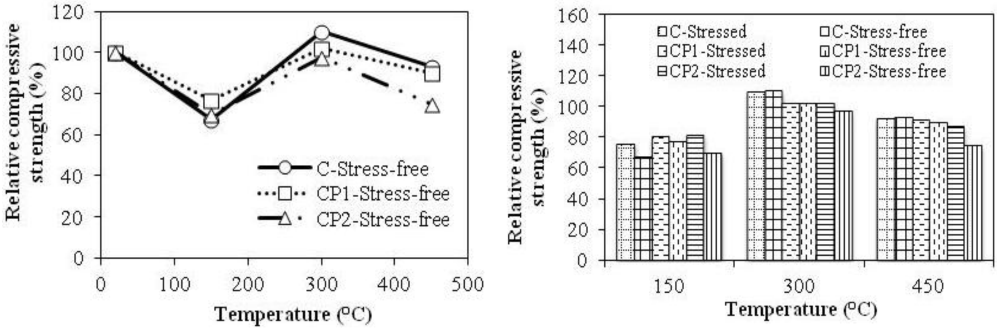

Figure 5. Relative compressive strength as a function of heating temperature for unstressed and stressed conditions.

HSC under a 0 % or 40 % stress improved in hot strength at 300 °C compared to its room temperature properties, but the strength was reduced at 150 °C and 450 °C regardless of fibre additions. The compressive strength of concretes with or without fibres appeared to be better at lower temperatures when the stressed and stress-free conditions were compared. For instance at 150 °C, concretes C, CP1 and CP2 increased in strength by 12 %, 5 % and 17 % when the HSC was under stress compared to the stress-free specimens. However, the HSC at 300 °C and 450 °C was not improved under a preload. Concrete with 2 kg/m^3 of polypropylene fibres lost less compressive strength. The relative strength of concrete with and without stress subjected to 450 °C was 87 % and 75 %, respectively. The results for the relative porosity of stress-free and stressed concretes at the same temperature were 127 % and 122 %, respectively. Fibres not only improved the thermal stability of concrete but also limited damage to the material under certain conditions.

The failure mode of the HSC cylinders produced similar fractured shapes at all temperatures, whether stressed/stress-free and with or without fibre additions as shown in Figure 6. According to ASTM C39-14 [11], the failures were categorized as either Type 1 (formation of a large cone on each end of the cylinder as shown in Figure 6 (a)) or Type 2 (cone and a split type fracture as shown in Figure 6 (b and c)).

(a) (b) (c)

Figure 6. Typical HSC loaded to failure after heating at (a) 150 °C, (b) 300 °C and (c) 450 °C in the stressed and stress-free condition with and without fibres.

The microstructures of the HSC exposed to different elevated temperatures were studied by SEM at 20 °C, 150 °C, 300 °C and 400 °C. Concretes submitted to temperatures below 150 °C had fibres that were intact, well distributed, and bonded to the dense cement matrix. After exposure to temperatures above 160-170 °C, the fibre melted and vaporized leaving open hollow circular channels and longitudinal depressions as shown in Figure 7. These fine networks allowed internal water vapour and gases to escape thus reducing the overall pore pressure build-up generally observed in HSC.

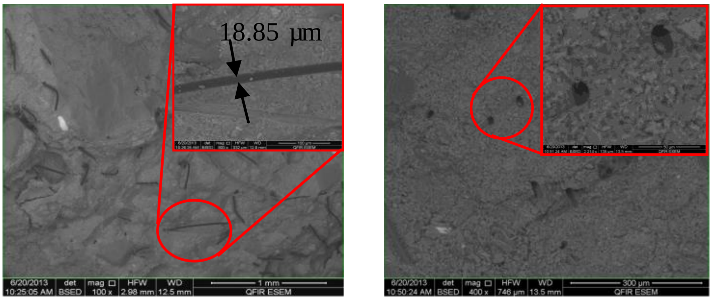

Figure 7. SEM well distributed fibres (left), hollow channels (right).

4 CONCLUSIONS

In this study, HSC with or without PP fibres were evaluated in hot stressed or stress-free conditions at different elevated temperatures.The following conclusions can be made:

- Surface cracks and explosive spalling did not take place on any of the samples. HSC containing PP fibres had higher moisture content than concrete without fibres.
- For both stressed and stress-free HSC, water evaporation plateaus occurred at the centre of the specimens. The plateau occurred at higher temperatures for concrete with lower moisture contents and stress-free conditions. The thermal gradient of HSC was increased after the melting temperature of the PP fibres was reached which was due to a more open pore structure. Stressed HSC with and without PP fibres had lower thermal gradients than the stress-free concrete possibly due to a denser structure.
- SEM has shown the PP fibres to be well dispersed throughout the matrix at low temperatures. At elevated temperatures, the PP fibres were melted and dissolved into the cement paste leaving empty cavities to allow internal water vapor and gases to escape.
- The porosity measurements showed concrete damage due to high temperature. The porosity increased with heating, and the addition of polypropylene fibres limited the increase of the pore volume. Stressed and stress-free conditions showed little influence on the variation of the porosity. A slight decrease in the relative porosity was observed for all stressed concretes of polypropylene fibres.
- The compressive strength of concretes with fibres remained less than that of concretes without fibres for all heating cycles studied. Concrete with 2 kg/m^3 of polypropylene fibres lost the least compressive strength at high temperature.

REFERENCES

[1] Phan, L.T, Lawson, J.R. and Davis F.L. “Effects of elevated temperature exposure on heating characteristics, spalling, and residual properties of high performance concrete”, Materials and Structures, 34, 83-91, 2001.

[2] Anderberg Y. Spalling phenomena of HPC and OC. "International workshop on fire performance of high-strength concrete", NIST, Gaithersburg, M D, 13-14 February 1997. US Department of Commerce, Technology Administration, National Institute of Standards and Technology.

[3] Ulm, F-J., Coussy, O. and Bazant Z.P. "The "Chunnel" fire. I: chemoplastic softening in rapidly heated concrete", Journal of Engineering Mechanics, March, 272-282, 1999.

[4] Kalifa, P., Chene, G. and Galle C. "High-temperature behavior of HPC with polypropylene fibres-from spalling to microstructure", Cement and Concrete Research, 31, 1487-1499, 2001.

[5] Bilodeau, A., Kodur, V.K.R. and Hoff G.C. "Optimization of the type and amount of polypropylene fibres for preventing the spalling of lightweight concrete subjected to hydrocarbon fire", Cement and Concrete Composites, 26, 163-174, 2004.

[6] Zeiml, M., Leithner, D., Lackner, R. and Mang H. "How do polypropylene fibers improve the spalling behavior of in-situ concrete?", Cement and Concrete Research, 36, 929-942, 2006.

[7] Noumowé A. "Mechanical properties and microstruture of high strength concrete containing polypropylene fibres exposed to temperatures up to 200 ℃", Cement and Concrete Research, 35, 2192-2198, 2005.

[8] Pliya, P., Beaucour, A-L. and Noumowé A. "Contribution of cocktail of polypropylene and steel fibres in improving the behaviour of high strength concrete subjected to high temperature", Construction and Building Materials, Vol. 25, 2011, p. 1926-1934.

[9] Long, T. Phan, Carino, N. J., Duthinh, D., & Garboczi, E. J. (1997). "International Workshop on Fire Performance of High-Strength Concrete", NIST, Gaithersburg, MD, February 13-14, 1997. US Department of Commerce, Technology Administration, National Institute of Standards and Technology.

[10] Hertz K. D., "Limits of spalling of fire-exposed concrete", Fire Safety Journal, 38(2), 103-116, 2003.

[11] ASTM. ASTM C39-14, "Standard test method for compressive strength of cylindrical concrete specimens", West Conshohocken, PA, USA: American Society for Testing and Materials, 2014.

8th International Conference on Structures in Fire
Guo-Qiang LI, Venkatesh K. R. KODUR, Shou-Chao JIANG, Jian JIANG, Su-Wen CHEN, Guo-Biao LOU (Eds.)
Shanghai, China, June 11-13, 2014

EFFECT ON STRENGTH DURING STAGES OF HEATING, RETENTION AND COOLING REGIMES FOR CONCRETE

Subhash C. Yaragal*, Jishnu Warrier*, Ramesh Podila* and K S Babu Narayan*

* Department of Civil Engineering
National Institute of Technology Karnataka, Surathkal – 575 025, India
e-mail: subhashyaragal@yahoo.com

Keywords: Heating, Cooling, Regimes, Thermally deteriorated concrete

Abstract. *Concrete suffers strength loss when subjected to elevated temperatures during an accidental event such as fire. The loss in strength of concrete is mainly attributed to decomposition of C-S-H gel and release of chemically bound water, which begins when the temperature exceeds 500˚C. But it is unclear about how much strength loss occurs in different stages of heating, retention and cooling regimes. This work is carried out to separate the total strength loss into losses during different stages of heating, retention and cooling. Tests were carried out on Ordinary Portland Cement (OPC) based concrete for 200˚C, 400˚C, 600˚C and 800˚C with a retention period of 1 hour for each of these temperature levels. Furnace cooling was adopted throughout the experiment. This study reports strength loss contributions during heating, retention and cooling regimes for OPC based concretes.*

1 INTRODUCTION

Concrete is the most widely accepted construction material. Its characteristics such as mouldability and high compressive strength have made it a versatile building material. Concrete offers good resistance to heat because of its low conductivity and incombustible nature and further, no toxic fumes are emitted from concrete surface when it is heated. Because of all these characteristics concrete can be rated as the best building material as far as resistance to elevated temperature is concerned.

Concrete is possibly exposed to elevated temperatures during fire accidents or when it is near to furnaces and reactors. The mechanical properties such as strength, modulus of elasticity and volume stability of concrete are significantly reduced during these exposures. This may result in undesirable structural failures. Therefore, the properties of concrete retained after a fire are of vital importance for determining the load carrying capacity and for reinstating fire-damaged structures. It is observed that there would be decrease of compressive strength, density, thermal conductivity and thermal diffusivity in concrete because of increase of porosity and permeability, due to thermal deterioration.

Fire resistance of concrete is affected by many factors, including constituent materials such as the type of aggregate and cement used in its composition, size of structural members and moisture content of concrete. The other factors include rate of heating, maximum temperature attained, duration of exposure at the maximum temperature, method of cooling after the maximum temperature is reached and the level of applied load. The influence of elevated temperatures on the mechanical properties of concrete is more important for fire resistance studies. Heat-resistant materials are increasingly being used for structural purposes. The need for such building materials is of particular interest in chemical and metallurgical industries and also for the thermal shielding of nuclear plants. In such installations structural members may be subjected to sustained and cyclic thermal exposures at the lower heat levels, at which the use of refractory materials is not essential. Concrete generally resists the effects of high temperatures, but in some cases it is aimed to produce concrete which is more resistant to fire, as a functional requirement.

An assessment of degree of deterioration of the concrete structure after exposure to high temperatures can help engineers decide whether structure could be repaired or to be demolished. There are already several publications that deal with the residual strength of concrete [1,2,3,4,5,6]. But it is unclear regarding how much strength is lost in the heating stage , heat retention stage (soaking) and cooling stage separately. Most of the works have focused attention on total strength loss in concrete at elevated temperatures. The objective here was to work out a method to separate the total loss into three sub-heads, that is in heating, in retention and during cooling stages. Performing this separation for different grades of concrete at several temperatures and at different heating rates, cooling rates and retention periods, can actually give a very useful database to understand the loss in compressive strength at any specified time of thermal exposure without any ambiguity. This clear information enables one to decide the correct type of repair work to be under-taken. The present work is an attempt in this direction.

2 MATERIALS AND METHODS

2.1 Normal Concrete

Cement used was 43 Grade Ordinary Portland Cement. The nominal mix proportion used was 1:2:4. The river sand used had a specific gravity of 2.65 and classified as zone 3. 50% of coarse aggregate of size less than 20mm and remaining 50% of size less than 12.5mm was used which gave well graded aggregates, with specific gravity of 2.69. Water cement ratio of 0.48 was chosen. The concrete was mixed in a concrete mixer and poured into moulds of size 100mm x 100mm x 100mm and were compacted by table vibration. The cubes were demoulded after 24 hours and cured for 28 days in water. Cubes were taken out of the curing tank after 28 days and kept outside for sometime to dry, after which they were used for further experiments.

2.2 Blended Concrete

Concrete blended with GGBFS was made with the same nominal mix proportion of 1:2:4. 30% of cement was replaced with GGBFS. Mixing, placing, demoulding and curing followed are the same as discussed above for normal concrete.

2.3 Methodology

Exposure studies were carried out using electric furnace as shown in Figure 1. Tests were carried out for 200 ℃, 400 ℃, 600 ℃ and 800 ℃. For each temperature, four different tests were carried out. Three specimen were taken for each testing and an average value was taken as the final result. The four tests are:
Test 1: Finding the compressive strength of the cubes without exposing to elevated temperatures, for reference.
Test 2: Finding the residual compressive strength of the cube as soon as it reaches the desired elevated temperature. For this, the furnace is switched off as soon as the cubes reach the desired temperature and the door is opened. The cubes are handled using long forceps and tested under the compression testing machine, immediately.
Test 3: Finding the residual compressive strength of the cubes after a retention period of 1 hour. The procedure adopted is same as explained in Test 2.
Test 4: Finding the residual compressive strength of the cubes after they have undergone a complete cycle of heating , retention and cooling to the room temperature in the specified rates.
The difference in the residual strengths of Test 2 and Test 1, gave the value of the loss in strength during the heating stage. The difference in the residual strength of Test 3 and Test 2 gave the value of the loss in

the strength during the retention period. The difference in the residual strength of Test 4 and Test 3 gave the value of the loss in strength during the cooling stage.

Figure 1. Programmable electric furnace.

3 RESULTS AND DISCUSSION

Standardisation of electric furnace operating conditions

3.1 Furnace performance with no charge

In order to understand the behaviour of the working of the furnace, it was operated for various temperatures (200 ℃, 400 ℃, 600 ℃, 800 ℃). To decide the rate of heating to be chosen, the maximum rate of heating of the furnace was observed. Any rate less than the maximum rate of heating of the furnace is acceptable. Theoretically the solution for this is to set the rate of heating as infinity i.e; time for heating has to be set as zero. Practically the time for heating was set to a minimum value of 1 minute and retention period was arbitrarily set as 1 hour so that the heater does not automatically switch off after 1 minute. The maximum rate of heating experiment was carried out for 800 ℃. The experiment was carried out with no charge. This is presented in Figure 2.

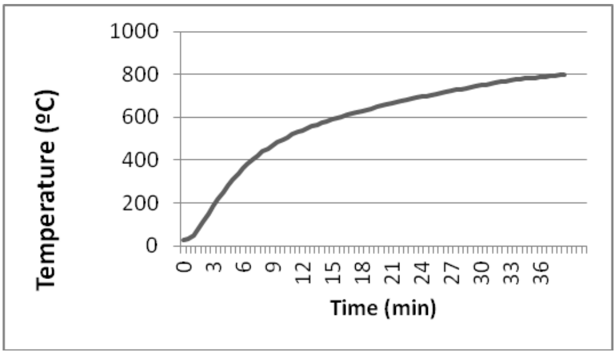

Figure 2. Maximum rate of heating of furnace with no charge.

It was found that rate of heating was more up to 400 ℃ and then at a slower rate up to 800 ℃. A rate slower than the maximum rate of heating was assigned for different temperatures. An arbitrary cooling rate was assigned for different temperatures and furnace performance was checked. A retention period of 1 hour was assigned for each case. The experiments were carried out with no charge.

A total of 8 different heating or cooling rates can be assigned at a time in the furnace. In order to understand this, a complete cycle of heating, retention and cooling was carried out assigning 8 sets of values for 200 ℃, 400 ℃, 600 ℃ and 800 ℃.

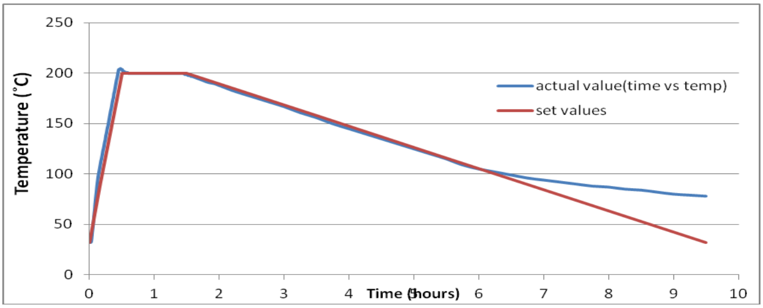

Figure 3. Furnace performance at 200 ℃ and no charge.

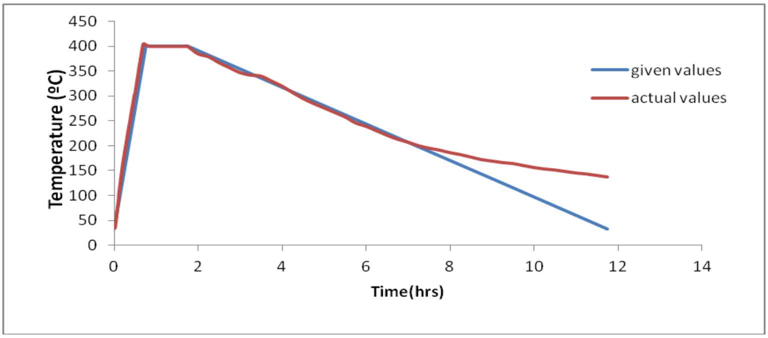

Figure 4. Furnace performance at 400 ℃ and no charge.

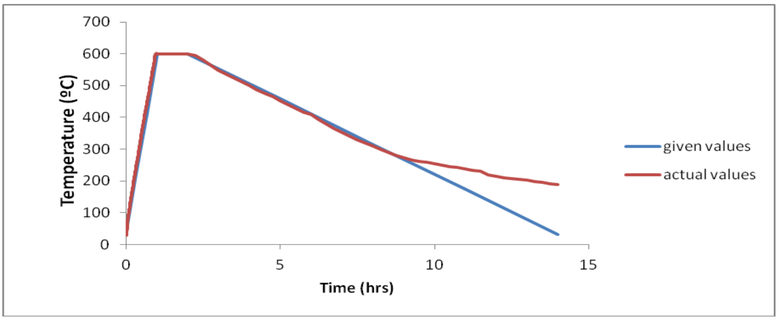

Figure 5. Furnace performance at 600 ℃ and no charge.

From the Figures 3-5, it was found that the furnace was behaving according to the chosen heating and cooling rates almost throughout the cycle. An average value of 9 ℃/min as the common heating rate and 0.8 ℃/min as the common cooling rate were chosen for further experiments.

3.2 Furnace Performance with Variation in Charge

To study the performance of furnace when it is loaded with concrete cubes, experiments were repeated with 20kg, 40kg and 60kg charge for each experiment. The variation for the case of 40kg charge is presented below in Figures 6-8.

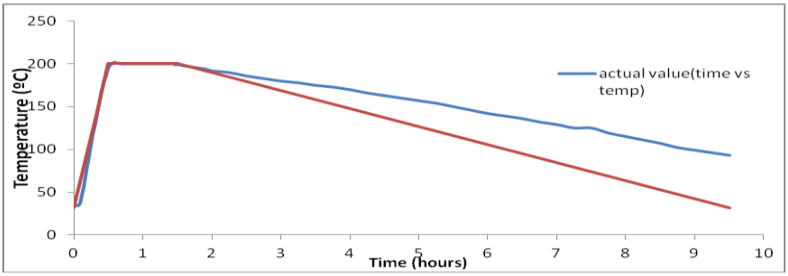

Figure 6. Furnace performance at 200 ℃ with 40kg charge.

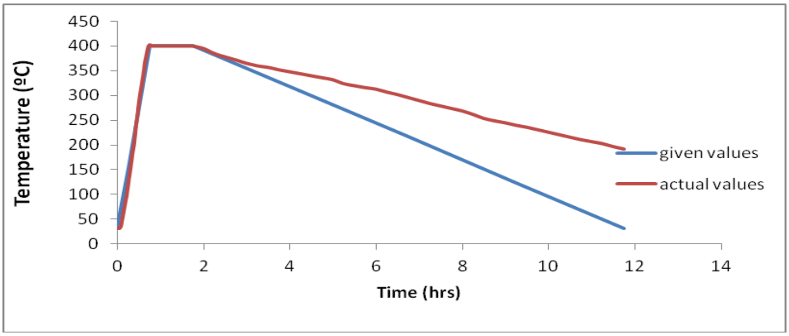

Figure 7. Furnace performance at 400 ℃ with 40kg charge.

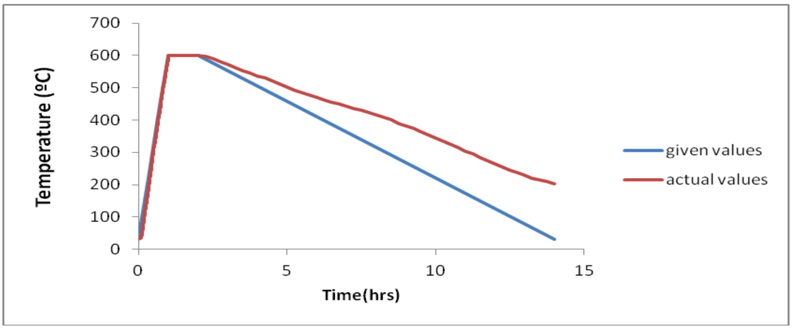

Figure 8. Furnace performance at 600 ℃ with 40kg charge.

From the above experiments , it was found that there is a lag in both rising and the cooling limb of the graphs . The lag in the rising limb in more evident in the graph drawn to a larger scale . Whereas the lag in the cooling is very much evident and the lag increases as the charge increases. For 60kg and 40kg (800 ℃) charge, there is a lag throughout the rising limb whereas for other charges, there is initial lag which gets compensated at the end of the rising limb. That means the furnace has a capacity to heat almost upto 40kg charge without a lag at the end of the rising limb. The rate of heating and cooling tends to slow down as the charge in the furnace increases.

The rate of heating was fixed as 9 ℃/min and the cooling rate was fixed as 0.8 ℃/min. It is also reported that as the charge increases, the rate of heating and cooling also decreases. The furnace was found to heat almost up to 40kg charge without a lag at the end of the rising limb .

3.3 Contributions to strength loss by rising limb, retention period and decay limb

Here the various strength loss contributions have been explained for both OPC based concrete. Table 1 shows the residual compressive strength of the cubes at different stages of heating and cooling processes.

Table 1. Residual compressive strength at different stages (OPC).

Temp (℃)	Normal strength (MPa)	Residual strength at rising limb end (MPa)	Residual strength at rising+ retention limb end (MPa)	Residual strength at rising + retention and cooling end (MPa)
200	47.0	44.8	51.6	44.3
400	44.0	44.0	43.7	34.6
600	47.3	40.1	38.0	28.0
800	45.7	30.5	26.9	08.7

From the above Table 1, it is observed that for 600 ℃ and 800 ℃ a decreasing pattern in their residual compressive strength is evident. Unlike expected, 200 ℃ and 400 ℃ show a variation from this pattern. For 200 ℃, there is an increase in the residual strength after the retention period and in 400 ℃ there is more or less no change in the residual strength even after heating the cubes to 400 ℃. Both these results vary from the expected pattern because of a phenomenon called autoclave effect in concrete.

As we know, concrete is a heterogeneous mixture of cement, fine aggregate, coarse aggregate and most importantly water. It is this water that initiates the chemical reaction in cement to form a C-S-H gel. This chemically bonded water which breaks out from the C-S-H gel gets converted to steam at 100 ℃ and the pores within the concrete gets filled with this steam as the heat rises above 100 ℃ within the concrete. Further as the temperature is increased, the pressure within the pores due to the steam keeps building up like the pressure within pressure cooker. So there is an outward pressure from within the pores which resists the external compressive force that we apply on the cubes while testing. This gives a higher compressive strength than expected. It is more evident after the retention period for 200 ℃ as by that time, heat would penetrate deeper into the cubes and more pores are filled with steam. For 400 ℃ autoclave effect is predominant in the heating stage as by that time itself heat would penetrate into the cube. But there is not much interference of autoclave effect after retention in 400 ℃ because thermal cracks start forming at 400 ℃ and the pore pressure is released through those cracks, giving us the correct value of residual strength.

Table 2. Loss of strength in percentage (OPC).

Temp (℃)	Normal strength (%)	Loss in rising limb (%)	Loss in rising+ retention limb (%)	Loss in full cylcle (%)
200	100	4.5	9.7	5.6
400	100	0.0	0.6	21.4
600	100	15.3	19.7	40.8
800	100	33.2	41.0	81.0

Table 2 shows the loss of strength in each limb or stage of the experiment i.e., rising limb, retention limb, and cooling limb. Loss in the rising limb is obtained by subtracting residual strength after rising limb from normal strength. Loss in retention period is obtained by subtracting the residual strength after the retention period from the residual strength after the rising limb. Loss in the cooling limb is obtained by subtracting the residual strength after the full cycle from the residual strength after the retention period. All these have been expressed in percentage.

Table 3. Total loss split in three stages (OPC).

Temp (℃)	Normal strength (MPa)	Loss in rising limb (MPa)	Loss in retention limb (MPa)	Loss in cooling limb (MPa)	Total loss (MPa)
600	47.3	7.2	2.1	10.0	19.3
800	45.7	15.2	3.6	18.3	37.0

Table 3 presents data for 600 ℃ and 800 ℃. The temperatures of 200 ℃ and 400 ℃ are not considered, as results are affected by autoclave effect.

Table 4. Percentage of total loss in each stage (OPC).

Temp (℃)	Loss in rising limb (%)	Loss in retention limb (%)	Loss in cooling limb (%)	Total loss (%)
600	39	11	50	100
800	40	11	49	100

Table 4 shows the percentage of the total loss lost in each stage of the experiment. Proper pattern is obtained for 600 ℃ and 800 ℃ cases. 200 ℃ and 400 ℃ experiments are affected by autoclave effect . What can be observed is that a major share of the total loss occurs during the cooling stage, followed by the heating stage and least is lost during the retention period. Loss in cooling stage is more than heating stage as cooling stage requires more time. As there are evident results that loss is more during heating and cooling stages, it means cracking due to temperature gradient is playing more role in the loss of strength ie expansion and contraction. There is also an increase in the loss of strength as the temperature increases. The most important conclusion from Table 4 is that around 40% of the total loss is during the heating stage , around 10% is in the retention period and around 50% of it is in the cooling stage. Explosive spalling was noticed in a few specimen. This may be due to high water content.

3 CONCLUSIONS

Elevated temperature tests at 200 ℃, 400 ℃, 600 ℃ and 800 ℃ were conducted for OPC based concrete and GGBFS blended concrete. Heating rate of 9 ℃/min, retention period of 1hour and cooling rate of 0.8 ℃/min were chosen. From the above experiments, the following conclusions have been drawn,

(1) Autoclave effect was present for 200 ℃ and 400 ℃ cases of experiments. This is due to the presence of high water content which gets converted to steam at 100 ℃ and at such low temperatures like 200 ℃ and 400 ℃, there are not enough cracks for the steam to escape out of the specimen. Proper mix design to find the optimum water content should solve this problem.

(2) 600 ℃ and 800 ℃ followed a similar pattern of decreasing compressive strength at each stage showing the absence of autoclave effect. This means there are enough cracks for the steam to come out of the specimen. This shows extensive cracking that starts at around 500 ℃.

(3) In these experiments, major loss of strength occurred during the cooling period. Followed by the heating period. Least strength loss occurred during the retention period.

(4) Loss of strength due to temperature gradient is predominant in these experiments.

(5) In these experiments, around 50% of the strength loss occurred during the cooling period. Around 40% occurred in the heating stage and only 10% of the strength loss occurred in the 1 hour retention period.

REFERENCES

[1] Subhash C. Yaragal et al., “Studies on Normal Strength Concrete Cubes Subjected to Elevated Temperatures”, *Journal of Structural Fire Engineering*, 1(4), 249-262, 2010.

[2] Subhash C. Yaragal et al., “Strength Characteristics of Concrete Exposed to Elevated Temperatures and Cooled Under Different Regimes”, *Journal of Structural Fire Engineering*,3(4),301-310, 2012.

[3] Efe E. Ikponmwosa et al., “Effect of Heat on Laterised Concrete”, *Maejo International Journal of Science and Technology*, 4(01), 33-42, 2010.

[4] Omer Arioz, “Effects of Elevated Temperatures on Properties of Concrete”, *Fire Safety Journal,* 42, 516-522, 2007.

[5] Luigi Biolzi, “Evaluating Residual Properties of Thermally Damaged Concrete”, *Cement and Concrete Composites,* 30, 907-916, 2008.

[6] A. Ferhat et. Al., “Effect of Elevated Temperatures and Cooling Regimes on Normal Strength Concrete”, *Fire and Materials,* 33, 79-88, 2009.

8th International Conference on Structures in Fire
Guo-Qiang LI, Venkatesh K. R. KODUR, Shou-Chao JIANG, Jian JIANG, Su-Wen CHEN, Guo-Biao LOU (Eds.)
Shanghai, China, June 11-13, 2014

EFFECTIVE THERMAL CONDUCTIVITY OF FIRE PROOF MATERIALS AND A SIMPLE METHOD TO PREDICT THE TEMPERATURE OF PROTECTED STEEL MEMBERS

Jun Han*, Guo-Qiang Li ** and Guo-Biao Lou**

* College of Civil Engineering, Tongji University, Shanghai, China
e-mails: jun.han@yahoo.com

** National Key Lab for Disaster Reduction in Civil Engineering, Tongji University, Shanghai, China
e-mail: gqli@ tongji.edu.cn , gblou@tongji.edu.cn

Keywords: Fire, Spray coating, Steel members, Thermal conductivity

Abstract. *Thermal conductivity of the materials is necessary to assess insulation of conventional fire proof materials, or to calculate the temperature response of insulated steel members. Thermal conductivity of fire proof materials are temperature-dependent and varies with temperature elevation, thus applying constant values of thermal conductivity of the materials, which are measured at ambient temperature, to calculate the insulated steel temperature in fire condition might yield great errors. In practice, effective thermal conductivity of fire proof materials has been adopted. This paper introduced a new concept of effective thermal conductivity and proposes a test method to determine the effective thermal conductivity of fire proof materials. Based on temperature of steel specimens protected with fire proof materials obtained by standard fire test, this method can reflect the actual property of fire proof materials in fire. Comparison between theoretical and experimental results shows the method is valid and convenient to determine the temperature of insulated steel members in fire. What's more, ISO 834-11 provided the assessment method to determine the contribution of fire protection system, in which full size beams and columns are required. Fire tests of protected steel sections were also carried out and the calculated effective thermal conductivities were compared with that of steel plates. The comparison results showed great consistency, which indicates that using small size plates to test the effective thermal conductivity of fire proof materials is suitable. Moreover, a simple method to predict the temperature of protected steel sections was presented, and numerical modelling of steel sections was made with calculated thermal conductivity in the method shown in ISO834-11. The difference between the simple method and the numerical modelling was acceptable, which indicates that the simple method to test effective thermal conductivity of fire proof materials with small size steel plates and predict the temperature of protected steel sections is reasonable.*

1 INTRODUCTION

Thermal conductivity of fire proof materials generally has a great change as temperature elevate while steel temperature usually range from room temperature to over 1000℃ in fire. Thus, calculation based on thermal conductivity at room temperature will lead to large errors despite its great convenience in calculation.

Part 11 of Assessment method of fire protection system applied to structural steel members [1] provides a method to calculate thermal conductivity of fire protection materials based on steel components standard fire test and can comprehensively reflect the performance of fire coating in fire. In this method, the thermal conductivity of fire proof materials was calculated directly by iterative formula and non-explicit relationship lies between temperature and thermal conductivity, so manual computation is difficult. In addition, the method proposed the thermal conductivity of fire proof material by every temperature range of 50℃, which apparently lead to more accurate result but more complicated calculation in determining the steel temperature in fire. Moreover, the existing furnaces used for standard fire test of steel components are of large sizes, such as the beam and plate furnace sized 3m×4m×1.5m and the column furnace sized 3m×4m×4m, which are extremely time consuming and expensive for small-scaled tests.

Measuring method of fire insulation parameters of steel structures [2] and equivalent thermal conductivity of non-expansive fire proof coating and its test method [3] have showed some tests of protected steel specimens in fire. However, the design of specimens has some disappointments and there is not enough evidence to certificate the practicability of the simple method.

In view of this, this paper proposed two definitions of effective thermal conductivity and a simple method to predict the temperature of protected steel members, in order to reflect the actual performance of fire insulation in fire. In total, 9 steel plates with 3 different schemes of layer thickness and 18 I shaped steel sections with two different cross dimensions and 3 different schemes of layer thickness were fire tested.

Thermal transaction of protected steel sections were numerical modelled with Abaqus, in which thermal conductivity obtained as ISO 834-11 required by every temperature range of 50℃.

2 THE EFFECTIVE THERMAL CONDUCTIVITY

2.1 Calculation of thermal conductivity

In fire condition, the equilibrium between the heat absorbed by the steel member and the heat transmitted through the insulation can be expressed as [4-6]:

$$T_s\left(t+\Delta t\right)-T_s\left(t\right)=\frac{\alpha}{\rho_s c_s}\cdot\frac{F_i}{V}\cdot\left[T_s\left(t+\Delta t\right)-T_s\left(t\right)\right]\Delta t \tag{1}$$

$$\alpha=\frac{1}{\dfrac{1}{\alpha_c+\alpha_r}+\dfrac{d_i}{\lambda_i}} \tag{2}$$

$$R_i=\frac{d_i}{\lambda_i} \tag{3}$$

where t —— time (s);
Δt —— time intervals (s);
T_s , T_g —— temperature inside the steel members and ambient temperature (℃);
ρ_s —— density of steel (kg/m^3);
c_s —— specific heat of steel (J/kg·K);
F_i —— cross-sectional area of steel member in unit length (m^2/m);
V —— volume of steel member in unit length (m^3/m);
R_i —— thermal resistance of fire insulation (m2/W·K);
d_{i} —— thickness of fire insulation (m);
λ_{i} —— thermal conductivity of fire insulation (W/m·K);

α —— complex heat transfer coefficient (W/m^2·K);
α_c —— convective heat transfer coefficient, fire to insulation, α_c =25 (W/m^2·K);
α_r —— radiative heat transfer coefficient, fire to insulation (W/m^2·K)。

Usually, the d_i / λ_i is much larger than $1/(\alpha_c + \alpha_r)$, so the complex heat transfer coefficient can be expressed approximately as Equation 4.

$$\alpha \approx \frac{1}{R_i} = \frac{\lambda_i}{d_i} \tag{4}$$

As a iterative formula, Equation 1 is inconvenient in practice, so Equation 5 was developed as a simple formula of Equation 1 by mathematical fitting approach to determine the temperature of the steel members protected with fire proof material in ISO834 fire.

$$T_s = \left(\sqrt{5 \times 10^{-5} \times \alpha \cdot \frac{F_i}{V} + 0.044} - 0.2 \right) t + 20 \tag{5}$$

The comparison between Equation 1 and Equation 5 indicated that the simple formula is close to Equation 1 especially in the temperature zone of 400~700℃, which covers the critical temperature of most steel members, as is shown in Figure 1. The explicit formulation greatly simplifies the calculation of the temperature of steel members.

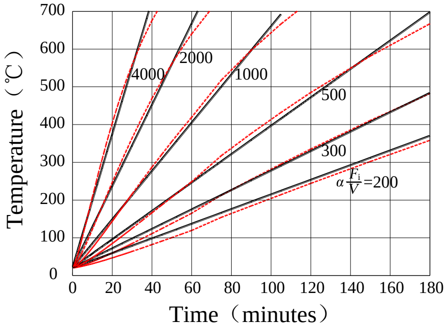

Figure 1. Comparison between the calculating results of Eq.1 and Equation 5.

Thermal resistance of the fire insulation can be easily obtained, if temperature-time curve is known, as Equation 6 shows. Afterwards, the thermal conductivity of fire insulation can be calculated from Equation 7.

$$R_i = \frac{5 \times 10^{-5}}{\left(\dfrac{T_s - 20}{t_0} + 0.2 \right)^2 - 0.044} \cdot \frac{F_i}{V} \tag{6}$$

$$\lambda_i = \frac{d_i}{R_i} \tag{7}$$

2.2 Definition of effective thermal conductivity

The relationship between thermal conductivity and temperature can be derived from Equation 7 according to the specimen temperature-time curve in steel structures standard fire test. The time-dependent thermal conductivity brings much difficulty to determine the temperature of steel members.

Consequently, the concept of effective thermal conductivity is proposed to represent the insulation property of fire proof materials with a constant, and the two definitions of effective thermal conductivity are drawn as follows:

(1) Def.1: the average of the thermal conductivities when the specimen temperature was 400~600℃

The critical temperature of most steel members is in the temperature zone of 400℃~600℃, in which the calculated temperature should be as close as the measured temperature. The average of thermal conductivities in this temperature zone can accomplish this object.

(2) Def.2: the thermal conductivity when the specimen temperature was 540℃ (1000℉)

In Standards Test Methods for Fire Tests of Building Construction and Materials (ASTM E119), the standard fire test will be stopped if the temperature of steel members is higher than 1000℉(538℃) , which is defined as the critical temperature. Defining the thermal conductivity of fire proof material when the specimen temperature was 540℃ (1000℉) as the effective thermal conductivity can greatly simplify calculation.

Comparison of the two definitions has been made and detailed below.

3 TEST SETUP AND SPECIMENS

3.1 Test setup

A mini-sized furnace was developed for small-scaled test of fire coating, whose technical specifications are as follows:

(1) Furnace size: 1.0m×1.0m×1.2m;

(2) Furnace Temperatures: ISO834 fire, Hydrocarbon fire and customized heating curves are available and ISO 834 fire was employed in the experiment;

(3) Data Acquisition and Control: the pressure and the temperature of the furnace, loading and unloading, the data acquisition, the secure alarm are all integrally controlled with a computer, so as to reach the convenient operation.

As is shown in Figure 2, four standard specimens can be placed on channel steel [14b with fire protection in the furnace.

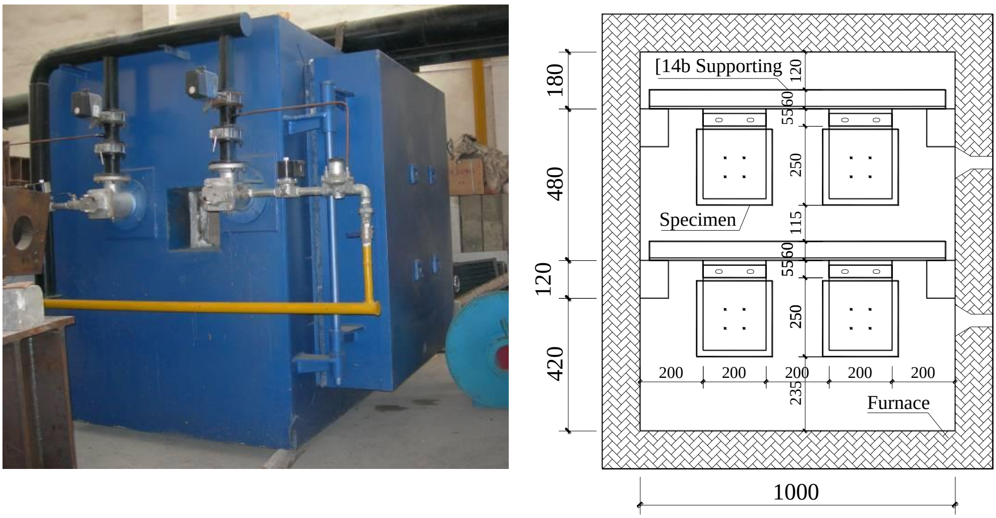

(a) Furnace (b) The cross-section and the arrangement of specimens

Figure 2. The testing furnace and the arrangement of specimens.

3.2 Test specimens

As shown in Fig. 1, steel plate specimens with dimensions of 16mm×200mm×270mm were chosen. Steel sections with dimensions of H200×400×16×12 and H200×400×20×16 were chosen and H200×400×16×12 protected with fire spray materials is shown below.

(1) The shape and configuration of specimens should be as simple as possible, so steel plate was selected;

(2) The size of the steel plate should be as small as possible to reduce cost but not too small to ensure the uniformity of temperature field of steel plate, which is necessary to simulate one-dimensional heat transfer.

(3) The typical thickness of steel plates was chosen as16mm, because steel plates with thickness of 6mm~25mm are usually used in practice. Moreover, shape parameter of the selected steel plate is 142.5m^{-1}, which is similar with the shape parameter of specimens used in Fire resistive coating for steel structure (GB 14907-2002) [7], as is shown in Tab.1. The shape parameters of the steel plates and I shaped sections were listed in Table 2.

(4) Specimens with three different thicknesses (10mm, 20mm, 30mm) were carried out to determine the effect of layer thickness on the thermal conductivity, and then the appropriate thickness will be select as a typical thickness.

(5) Figures 3 and 4 show three measuring points on every specimen and the temperature will be measured with thermal couples. Theoretically, the temperatures at point 1 and point 3 are the same, while the small deviation in practice can confirm the uniformity of the temperature field inside the steel plates.

Table 1. Shape parameter F_i/V of the specimen used in GB 14907-2002.

Specimen Type	Shape Parameter F_i/V （m^{-1}）	
	Four sides in fire	Three sides in fire
I36b	142.1	125.6
I40b	137.0	121.7

Table 2. Shape parameter F_i/V of the specimen tested.

Specimen Type	Shape Parameter F_i/V （m^{-1}）
Steel Plates	142.5
I Shaped Sections-1	145.7
I Shaped Sections-2	102.6

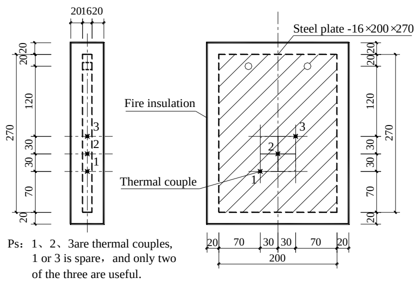

Figure 3. Dimensions of plates specimens and arrangement of thermal couples.

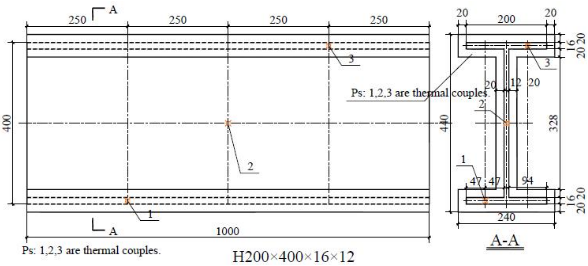

Figure 4. Dimensions of section specimens and arrangement of thermal couples.

4 TESTING RESULTS

The fire insulation showed peace performance with no obvious change and the temperature of the steel member rose steadily in fire. Cracks appeared on the surface of the insulation after fire, as is shown in Figure 5.

The effective thermal conductivities calculated from the tested temperatures of the steel plates and the I shaped sections in the two definitions were showed in Figure 6, which indicate that the effective thermal conductivity calculated from the steel plates match well with that from I shaped sections, especially for the specimens protected with 20mm coating and 30mm coating.

(a) Protected steel plate after fire

(b）Protected sections after fire

Figure 5. Specimens after fire.

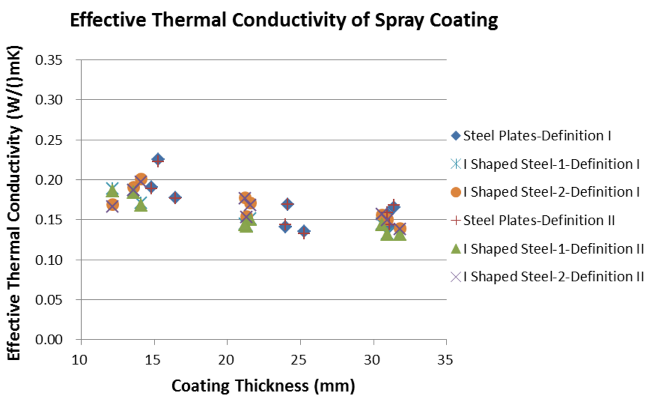

Figure 6. Effective Thermal Conductivity of Spray Coating.

5 NUMERICAL MODELING

Numerical modelling of the temperature of I shaped steel in fire was made based on the effective thermal conductivity calculated with the test results of steel plates. The comparison between the tested temperatures and the modelled temperature of I shaped section shows the small size plates and the effective thermal conductivity calculated can be used to predict the temperature of I shaped sections.

In the numerical model, completed heat insulation for the two ends of the section was assumed and uniform initial temperature field was set. What's more, the ISO834 temperature curve was run during the analysis.

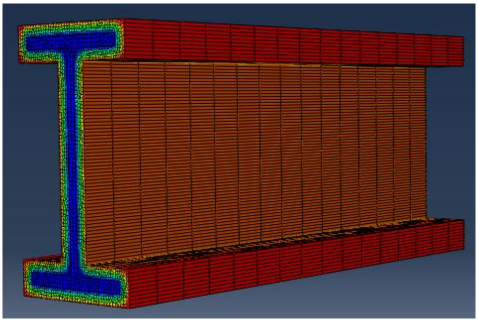

Figure 7. Numerical Model in Abaqus.

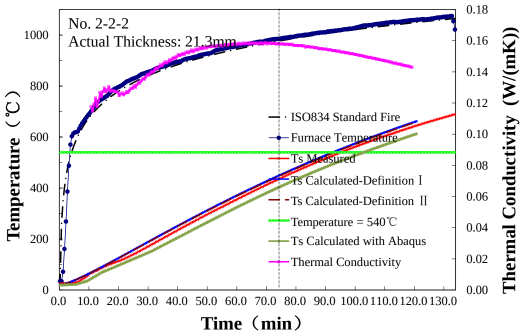

Figure 8. Comparison between test result and numerical result.

6 CONCLUSION

The main work and conclusions may be drawn as follows.

(1) Proposed a measuring method suitable for thermal conductivity of fire proof materials.

(2) Proposed two definitions of effective thermal conductivity.

(3) Verification of the two definitions was proposed. Comparison between the calculated temperature and the measured temperature indicated that the two definitions met the engineering requirements. In practice, the second definition is suggested for its more convenience than the first one.

(4) Comparison between the calculated effective thermal conductivity obtained by selected steel plates and that obtained by steel sections was made and the results showed great consistency, which indicated that method using small size plates to test the effective thermal conductivity of fire proof materials is suitable.

(5) A simple method to predict the temperature of protected steel sections was presented and numerical modelling of steel sections was made with calculated thermal conductivity in the method shown in ISO834-11. The difference between the simple method and the numerical modelling was acceptable, which indicates that the simple method to test effective thermal conductivity of fire proof materials with small size steel plates and predict the temperature of protected steel sections is reasonable.

(6) 20mm can be chosen as typical thickness of the standard test specimens as the steel specimens protected with fire proof coating with that thickness can be representative of the performance of the fire proof coating in fire.

REFERENCES

[1] ISO/CD 834-11: 2003, MOD. "Fire Resistance Tests— Elements of Building Construction, Assessment method of fire protection system applied to structural steel members", International Organization for Standardization, 2003.

[2] Han J., "Measuring Method of Fire Insulation Parameters of Steel Structures", Bachelor Thesis, Tongji University, Shanghai, China, 2009.

[3] Han J., Li G.Q., Lou G.B., "Equivalent Thermal Conductivity of Non-expansive Fireproof Coating and Its Test Method", *Journal of Disaster Prevention and Mitigation Engineering*, 2012, 2012(02) 191-196.

[4] Li G. Q., Han L. H., Lou G. B., Jiang S. C., Fire-resistant Design of Steel and steel - concrete composite structure ,*China Architecture & Building Press*, Beijing, China, 2006.

[5] CECS200:2006, “Technical code for fire safety of steel structure in buildings”, China Association for Engineering Construction Standardization, China Planning Press, Beijing, 2006.

[6] EN 1993-1-2. Eurocode 3, “Design of Steel Structures”, Part 1.2: Structural Fire Design, 2005.

[7] GB 14907-2002, “Fire resistive coating for steel structure”, General Administration of Quality Supervision, Inspection and Quarantine of PRC, 2002.

AUTHORS LIST

AUTHORS LIST